Special Issue No. 75 • Vol.1

Journal of Coastal Research

Proceedings of the 14th International Coastal Symposium
Sydney, 6-11 March 2016

Edited by:
Ana Vila-Concejo, Eleanor Bruce,
David M. Kennedy, and R. Jak McCarroll

THE UNIVERSITY OF SYDNEY
GEOCOASTAL RESEARCH GROUP
COASTAL EDUCATION & RESEARCH FOUNDATION, INC.
JCR

JOURNAL OF COASTAL RESEARCH

An International Forum for the Littoral Sciences

THE *JOURNAL OF COASTAL RESEARCH* (JCR) (ISSN 0749–0208) IS PUBLISHED BIMONTHLY FOR $115.00 FOR INDIVIDUAL US CERF MEMBERS, $125.00 FOR INDIVIDUAL INTERNATIONAL CERF MEMBERS, $519.00 FOR US INSTITUTIONS, AND $541.00 FOR INTERNATIONAL INSTITUTIONS BY THE COASTAL EDUCATION AND RESEARCH FOUNDATION, INC. (CERF), 5130 NW 54TH STREET, COCONUT CREEK, FL 33073–3713. PERIODICALS POSTAGE PAID AT FORT LAUDERDALE, FL AND ADDITIONAL MAILING OFFICES. **POSTMASTER:** SEND ADDRESS CHANGES TO *JOURNAL OF COASTAL RESEARCH*, ALLEN PRESS ASSOCIATION MANAGEMENT, P.O. BOX 1897, LAWRENCE, KS 66044–3018.

JOURNAL OF COASTAL RESEARCH

An International Forum for the Littoral Sciences

Supporting Scientific Institutions

- Consorzio Nazionale Interuniversitario per le Scienze del Mare (Co.N.I.S.Ma.) [Rome, Italy; www.conisma.it/]
- Delft University of Technology [Department of Hydraulic Engineering, Delft, The Netherlands; http://www.citg.tudelft.nl/over-faculteit/afdelingen/hydraulic-engineering/]
- Duke University [Earth and Ocean Sciences Division, Durham, North Carolina, U.S.A.; https://nicholas.duke.edu/marinelab]
- Griffith University [Center for Infrastructure Engineering and Management, Southport, Queensland, Australia; https://www.griffith.edu.au/]
- Ibaraki University [Center for Water Environmental Studies, Mito, Japan; http://www.cwes.ibaraki.ac.jp/]
- International Geographical Union (IGU) [Commission on Coastal System (CCS); http://www.igu-ccs.org/]
- Royal Belgian Institute of Natural Sciences [Management Unit of the North Sea Mathematical Models (MUMM), Brussels, Belgium; http://www.mumm.ac.be/EN/index.php]
- Rutgers University [Institute of Marine and Coastal Sciences (IMCS), New Brunswick, New Jersey, U.S.A.; http://marine.rutgers.edu/main/]
- Universidad de la República [Marine Science Unit, Montevideo, Uruguay; http://www.imber.info/Science/National-Network/URUGUAY]
- Universidade Nova de Lisboa [e-Geo Center for Geographical and Regional Planning Studies, Lisbon, Portugal; http://e-geo.fcsh.unl.pt/]
- University of California, Santa Cruz [Institute of Marine Sciences, Santa Cruz, California, U.S.A.; http://ims.ucsc.edu/]
- University of Delaware [School of Marine Science and Policy, Newark, Delaware, U.S.A.; http://www.ocean.udel.edu]
- University of Maine [Climate Change Institute, Orono, Maine, U.S.A.; http://climatechange.umaine.edu/]
- University of Sydney [Coastal Studies Unit, Sydney, New South Wales, Australia; http://sydney.edu.au/]
- University of Szczecin [Institute of Marine and Coastal Science, Szczecin, Poland; http://www.wnoz.ztikm.szczecin.pl/en/1/inom/structure/]
- University of Ulster [Environmental Sciences Research Institute, Coleraine, Northern Ireland; http://www.ulster.ac.uk/es/research/]
- University of Wales, Trinity Saint David [Swansea Metropolitan University, Mount Pleasant, Swansea, South Wales, U.K.; http://www.uwtsd.ac.uk/]
- U.S. Army Corps of Engineers [Coastal and Hydraulics Laboratory (CHL), Vicksburg, Mississippi, U.S.A.; http://chl.erdc.usace.army.mil/]
- U.S. Geological Survey [National Wetlands Research Center, Lafayette, Louisiana, U.S.A.; http://www.nwrc.usgs.gov/]

Aims and Scope of the Journal

Journal of Coastal Research, an International Forum for the Littoral Sciences, is dedicated to all aspects of coastal research. These include geology, biology, geomorphology (physical geography), climate, littoral oceanography, hydrography, coastal hydraulics, environmental (resource) management, engineering, and remote sensing. Although each field functions effectivelywithin itsownpurview, the cross-disciplinarynature of coastal studies requires familiarity with other fields as well. Hence, the scope of topics is necessarily broad in order to address the complexity of coastal biophysical and socio-economic interactions. Because of the wide range of interrelated topics, the journal invites original contributions and manuscripts dealing with theory, methodology, techniques, and field or applied topic studies on interdisciplinary coastal issues.

The journal encourages the dissemination of knowledge and understanding of the coastal zone by promoting cooperation and communication between specialists in different disciplines. Natural scientists, for example, are encouraged to collaborate with professionals in other fields to prepare contributions relating to the coastal zone that foster increased appreciation of coastal environments and processes. By means of this journal, with its scholarly and professional papers, systematic review articles, book and symposia reviews, communications and news, and special topical issues, an international forum for the development of integrated coastal research is provided.

Advertising, Editorial, and Subscription Information

Advertising and Editorial Office: All advertising and editorial correspondence should be sent to Dr. Charles W. Finkl, Editor-in-Chief, Journal of Coastal Research, 5130 NW 54th Street, Coconut Creek, FL 33073, U.S.A. PHONE: 828-333-2300. E-MAIL: cfinkl@cerf-jcr.com

Subscription Information: The *Journal of Coastal Research* is a bimonthly publication. Calendar-year (2016) print and online subscription prices for the JCR are: $115.00 for US CERF members / $125.00 for International CERF members ($95.00 for online only), and $519.00 for US institutions / $541.00 for International institutions ($437.00 for online only). Additional surface charges may apply to subscribers located outside of the USA. For additional membership and subscription forms and information, please go to www.CERF-JCR.org. To obtain a membership or subscription form by mail, please send request to Journal of Coastal Research, P.O. Box 7065, Lawrence, KS 66044. Back Issues and Special Issues of the JCR, when available, can be directly purchased at www.CERF-JCR.org.

The *Journal of Coastal Research* is currently surveyed in *Applied Science & Technology Abstracts; Applied Science & Technology Index (H.W. Wilson); Aquatic Sciences & Fisheries Abstracts; BIOBASE; Biological Abstracts; BIOSIS Previews (Thomson); CAB International Abstracts (CABI); CSA Civil Engineering Abstracts (ProQuest); Current Awareness in Biological Sciences (Elsevier); Current Contents/Agriculture, Biology, & Environmental Sciences (Thomson); Ecology Abstracts (ProQuest); Environmental Sciences & Pollution Management; GeoAbstracts [Geographical Abstracts: Physical Geography; Ecological Abstracts; Geological Abstracts; GEOBASE] (Elsevier); GeoRef; Meteorological & Geoastrophysical Abstracts (ProQuest); Oceanic Abstracts (ProQuest); Oceanographic Literature Review (Elsevier); Physical Sciences Digest (CSA, Ebsco); Pollution Abstracts (ProQuest); Referativnyi Zhurnal; Science Citation Index; SciSearch (Thomson); SCOPUS; Water Resources Abstracts (Bethesda); Zoological Record (Thomson).*

JCR- SI75

Proceedings of the 14th International Coastal Symposium

ICS2016

Sydney, NSW, Australia

6th-11th March 2016

Volume 1

Edited by:

Ana Vila-Concejo[1], Eleanor Bruce[1], David M. Kennedy[2] and R. Jak McCarroll[1].

Coastal Education Research Foundation (CERF)

[1]Geocoastal Research Group, School of Geosciences, The University of Sydney.

[2] School of Geography, The University of Melbourne.

Acknowledgements

Putting these volumes together has required a lot of effort, dedication and enthusiasm. We would like to thank everyone involved in this process: Lee Devereux, Andrew Broderick, Tommy Fellowes, Jordan Gacutan, Madi Patterson, Steph Duce, Susan Warner. Mandi Thran not only helped with text formatting; she designed the artwork for the cover.

Journal of Coastal Research Special Issue No. 75

14th International Coastal Symposium ICS2016

Sydney, NSW, Australia

6th-11th March 2016

Local Organising Committee

International Advisory Committee

International Scientific Board

ISSN 0749-0208

Front cover photo: Ana Vila-Concejo
Back cover photos: Peter Frith (Top), Bottom (Geocoastal Research Group)

Published by
Geocoastal Research Group,
School of Geosciences F09, The University of Sydney,
http://www.grgusyd.org/
http://sydney.edu.au/science/geosciences/index.shtml

TABLE OF CONTENTS

COASTAL STUDIES UNIT

RIVERS

ESTUARIES

ESTURINE BEACHES

DUNES

OCEAN BEACHES

CONTINENTAL SHELVES AND SLOPES

CORAL REEFS

ROCKY COASTS

MANAGING THE PRESENT

VOLUME 2

To view the links to papers of volume 2, please open the Volume 2 document

PAST CLIMATE AND SEA LEVEL CHANGE

DECADAL COASTLINE AND ESTUARINE EVOLUTION

HYDRODYNAMICS (CONTEMPORARY PROCESSES)

FUTURE FORECASTS

MANAGING THE FUTURE

COASTAL HAZARDS

Journal of Coastal Research	SI	75	1-7	Coconut Creek, Florida	2016

The Coastal Studies Unit and Development of the Australian Beach Models

Andrew D. Short

Geocoastal Research Group
School of Geosciences
University of Sydney
NSW Australia

www.cerf-jcr.org

www.JCRonline.org

ABSTRACT

Short, A D, 2016. The Coastal Studies Unit and development of the Australian beach models. *In:* Vila-Concejo, A.; McCarroll, R.J.; Kennedy, D.M., and Bruce, E. (eds.), *Proceedings of the 14th International Coastal Symposium* (Sydney, Australia). *Journal of Coastal Research*, Special Issue, No. 75, pp. 1-7. Coconut Creek (Florida), ISSN 0749-0208.

The Australian coast provides an ideal laboratory in which to undertake beach research on a continental scale. The 30 000 km of open coast surrounds an entire continent that ranges from tropical to temperate latitudes (9-43°S); with tides ranging from <0.5 to 12 m; average breaker wave height from <0.5 m to ~3 m; beach sediment from fine to medium sand, half of which is carbonate; and many of the ~12 000 beach systems are embayed. Commencing in the mid-1970s this laboratory was utilized by members of the Coastal Studies Unit (CSU) leading to the development of beach models that encompass the full range of beach types and states that incorporate every Australian beach and most global beaches. This paper will review the development of these models, based initially on beach research on the micro-tidal, wave-dominated southeast coast; then expanding into both the higher wave energy environments of southern Australia and the higher tide range environments of northern Australia; culminating with an assessment of every beach system around the coast. The end result was the wave-dominated, tide-modified and tide-dominated beach models.

ADDITIONAL INDEX WORDS: *beach, surf zone, beach models*

INTRODUCTION

Australia has one of the world's great national coastlines as well as that of an entire continent. Its coastline is renown for its sheer size – 30 000 to 60 000 km depending on how it is measured; its latitudinal range (9-43°S); its full range of orientations, exposing it from very low to the world's highest waves; its full range of tides from micro to mega; and its climatic diversity from tropical to temperate and from humid to arid. When you put all these together, combined with a robust coastal flora, extensive climatically-controlled coral-algal reefs, mangroves, seagrasses, beachrock and aeolianites, and a diverse and generally ancient coastal geology you have the making of an interesting coast, half of which consists of sandy beaches.

The coast can be viewed from a range of perspectives. From a geological perspective it is generally an ancient, denuded and flat continent, the oldest, flattest and driest (after Antarctica) on the planet. At the coast it consists of a western-central coast composed of ancient cratons, while successive accretionary fold belts formed the eastern third. Buckling around the coast since the Cretaceous formed a series of more recent sedimentary basins three of which contain Australia's longest beaches. More broadly however, the geology dominates the coast producing thousands of generally short, headland bound-beaches (average length = 1.37 km). The geological stability of the largely passive margin coast has also left a legacy of successive highstand coastal deposits that reach back to the Pliocene and can extend hundreds of kilometers inland. Tropical-arid though humid climates dominate the north, while temperate-arid through humid dominate the south, both having profound effects on coastal sediments, diagenesis and ecology, including the extensive areas of beachrock and dunerock. The surrounding ocean climates deliver the world's largest, longest and most persistent waves to the southern half of the continent, while more benign trade and monsoonal winds produce more moderate waves across the north. These same winds build some of the most extensive and largest coastal dune systems in the world. The coastal vegetation has adapted to the climatic conditions and robust sand stablizing species thrive in even the harshest environment resulting in primarily vegetation-controlled coastal dune systems. Finally, the marine ecology is manifest in coral-algal reefs ringing the northern coast, together with the world's third largest mangrove systems, and the world's most extensive tropical and temperate seagrass meadows, the latter of which has profound impacts on the southern coast and its beaches. The geology, ecology and climates combine to supply the coast with generally mature polycyclic quartz sand along the more humid north and east coasts, while shelf and nearshore marine carbonate sands dominate the south and west coasts.

This paper reviews how this coast was utilized as a natural laboratory to investigate the impact of variable waves, tides and sediment, together with geological control, to influence the type of beaches that formed around the coast. These investigations in

DOI: 10.2112/SI75-001.1 received 15 October 2015; accepted in revision 15 January 2016.
*Corresponding author: andrew.short@sydney.edu.au

turn lead to the development of the wave-dominated (WD) beach model (Wright and Short, 1984), the tide-modified (TM) beach model (Masselink and Short, 1993) and finally the tide-dominated (TD) model (Short, 2006), as well as the impact of geological inheritance and embaymentisation on these beach systems (Short and Masselink, 1999; Short 2010a).

BACKGROUND

The Australian coast, and particularly its beaches, received very little scientific attention until the beginning of the 20th C with reports on a series of damaging storms. In the next few decades there were individuals working on rock platforms (Jutson, Edwards) and sea level (Fairbridge) but it was not until, the 1960-70s, that scientists like Jennings, Davies and Bird began publishing systematic studies of parts of the coast and coastal systems, including the first classification of the coast (see Thom, 1984a and Thom and Short, 2006 for reviews). The first detailed investigation of beach morphodynamics was by McKenzie (1956) who described the various rip current systems on the Sydney coast. The catalyst for the so-called 'Australian' school of beach research can be traced back to the 1960s when at the University of Sydney under the supervision of Professor T Langford-Smith a number of honours and graduate students including B G Thom, L D Wright and A D Short, began more systematic coastal and beach investigations. All three went on to complete Ph.D.s on coastal topics at Louisiana State University (LSU). Here they were introduced to the more holistic approach to studying the world's coastal systems developed at LSU's Coastal Studies Institute (CSI) by people like R J Russell, W McIntire and J Coleman, and transferred to the beach environment by C J Sonu (Sonu, 1973; Short and Jackson, 2010). By the mid-1970s all three were back at the University of Sydney, with Thom, Wright and Langford-Smith establishing the Coastal Studies Unit (CSU) in the Department of Geography, in 1976, in part a second generation to the LSU-CSI. At the same time Wright and Thom (1977) wrote the seminal paper on coastal morphodynamics, providing a blueprint for what was to follow, later updated by Cowell and Thom (1994).

Over the next 30 years the CSU undertook coastal research covering the entire Australian coast. In the process its members developed the wave-dominated beach model (Wright and Short, 1984), followed by the tide-modified model (Masselink and Short, 1993), and finally the full spectrum of beaches also including the tide-dominated and rock/reef-affected states (Short, 2006). In addition its members conducted wide-ranging research into rip currents (Short, 1985; Brander, 1999; Brander and Short, 2000); Quaternary coastal evolution (Thom, 1984b; Roy and Thom, 1981); the relationship between waves-beaches and dunes (Short and Hesp, 1982; Hesp, 1984); foredune morphodynamics (Hesp 1988); estuarine evolution and classification (Roy, 1984; Nichol, 1991; Lessa and Masselink, 1996); beach stratigraphy (Short, 1984b); beach groundwater and swash dynamics (Turner, 1993; Hughes, 1992); beach hazards and safety (Short and Hogan, 1994; Brander 2010); shoreface morphodynamics and sedimentation (Roy, *et al.*, 1997; Cowell, *et al.*, 1995); beach rotation (Short, *et al.*, 1995; Short and Trembanis, 2005); the role of embaymentisation and geological inheritance on beaches (Short and Masselink, 1999); the impact of the 9000 km long temperate coastal carbonate factory on the adjoining coast, beaches and dunes (Short, 2002, 2013); and finally, all 11,761 open coast mainland beaches and 2261 barrier systems were investigated as to their beach type-state and hazards and barrier type, size and stability (Short, 2006, 2010b). This paper will briefly review the development of the three beach models: wave-dominated, tide-modified and tide-dominated.

CSU: 1976-1082

The CSU's first six-years were to be an exciting, humorous, at times adventurous, but very productive phase. It was an era that firmly established the CSU and its reputation in beach research, as well as establishing its field-oriented approach to coastal research and the so-called 'Australian school' of coastal geomorphology and morphodynamics. At the helm was L D Wright. His approach to research was to gather a team of reliable assistants and students, inspire them with his (then) pipe-puffing ideas, and lead them into the field to literally battle with the surf. In the field Wright often came off second best and in hospital, but the data flowed as did the papers. A D Short arrived at CSU in November 1977, when he replaced B G Thom who had taken up a position at the UNSW Faculty of Military Studies (Duntroon). The first field experiments took place during 1976 and 1977 on two of Sydney reflective beaches: Jibbon and Pearl; and in 1977 on the NSW south coast at the reflective Bracken (Mckenzie) beach, followed by work on the nearby rip-dominated Bengello beach (originally called Moruya) (Figure 1) and Sydney's Palm Beach. The aim of these experiments was to document and record the morphodynamic character of each 'type' beach, including its morphology, wave and current transformation across the surf zone and eulerian and lagrangian surf zone circulation, the latter using CSU members as rip-floaters.

In the 1970s off-the-shelf equipment did not exist and the first pressure sensors and ducted-current meters were constructed in-house, using a CSI design. This equipment was attached to home-made concrete 'pods' with legs designed to hold the equipment on the seabed, and hardwired back to shore to a Tektronix 4051 minicomputer with a RAM of 13 kb and to ink chart recorders (to show the instruments were recording). It had to be housed in an air-conditioned camper-van to prevent overheating. This was supplemented in 1978 with a Mr Floppy z80 micro-computer running CPM operating system, it had twin diskette drives and a then massive 48 kb RAM. This pre-dated the IBM PC, considered by many to be first PC, by three years. It had just enough memory to run a FFT on 20 minutes of field data, using home-made software. There was also a 16 channel multiplexing data logger constructed for connecting up to the 4051, which controlled the data logging via the software. This rate was about 0.25 sec for a single instrument and more than a second for all 16 channels.

Many problems were encountered starting in the surf zone (Figure 2) with the pods moving, summersaulting and/or being buried, the current meters clogging, and the wires tangling or breaking; while on the beach the chart recorders would run out of ink and the computer mal-function, run out of memory or overheat.

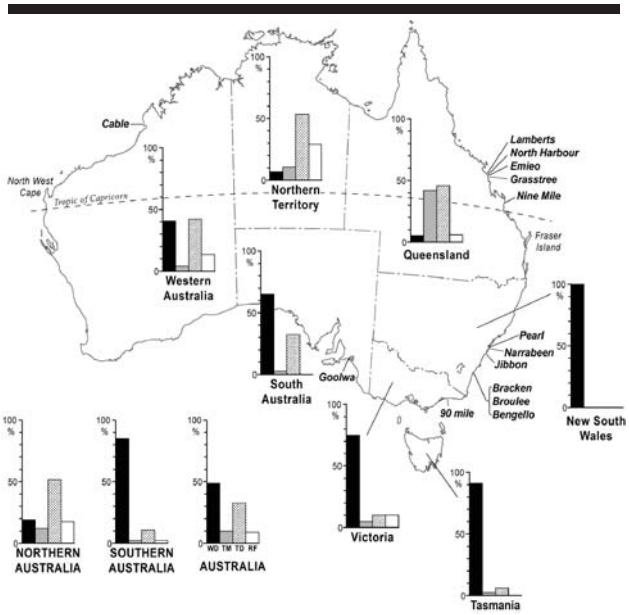

Figure 1. Map of Australia showing the distribution of beach types by state, region and continent, as well as site of the major field studies. WD=wave-dominated, TM=tide-modified, TD=tide-dominated, RF=rock/reef flats.

Figure 2. Deploying field equipment in the dissipative Goolwa surf zone, 1980. The aerial holds pressure sensors and current meters and indicates location in deeper water.

Buoyed with the success of these initial field experiments and boosted by an US Office of Naval Research (ONR) grant in 1980 it was decided to take on the high-energy southern Australian coast, at a site scouted by Short in 1978, Goolwa beach, South Australia (Figure 1). This beach is exposed to the full force of the Southern Ocean with wave averaging 2.5-3 m. It is a 500 m wide, fully dissipative double bar system. The team camped in the sand dunes and ran a successful though very tiring and hazardous field experiment in the very energetic inner surf zone (Wright at al., 1982d; Figure 2) with outer breaker waves averaging 3-4 m thoughout the experiment. It was then decided we needed to look into the impact of high tides on the beaches and after much discussion and pouring over maps and phone calls to local people, Cable Beach in Broome, north Western Australia was chosen, with its 10 m tides. In November the nine-member team left Sydney on the 5500 km, 10-day drive to Broome, camping along the way and at Cable Beach, an adventure in itself. This was to be another successful field experiment (Wright *et al.*, 1982a).

The final ONR funded experiment took place in 1981 at Eastern Beach (Ninety Mile Beach) on Victoria's wild Bass Strait coast. The long storm driven beach is a classic bar-trough system. The CSU team instrumented the swash zone out through the 3 m deep trough to bar and and with the help of a local fishing boat onto the shoreface (Wright at al., 1982b). It was the final major experiment involving Don Wright who left for the Virginia Institute of Marine Science (VIMS) in 1982. However by that time the CSU team had covered all the main wave-dominated beach types (R, TBR, RBB, LBT, D) as well as the tide-modified ultradissipative (UD) Cable beach (Table 1).

Table 1. *List of major CSU field experiments/sites and publications.*

Year	Location	Beach state[1]	Publications
Wave-dominated (WD):			
1976	Narrabeen	R-LBT	Short 1979a, b
1976	Jibbon	R	Wright *et al.* 1979
1976	Pearl	R	Wright *et al.* 1979
1977	Bracken	R	Wright *et al.* 1979, 1982c
1977	N Broulee	LTT-TBR	Wright *et al.* 1979
1977	Bengello-Moruya	TBR	McLean and Thom, 1975 Chappell and Wright, 1978 Wright *et al.*, 1979; Thom and Hall, 1991
1980	Goolwa	D	Wright *et al.*, 1982c,1982d
1980	Palm Beach	TBR	Wright *et al.*,1982c
1981	Eastern	RBB-LBT	Wright *et al.*, 1982b, 1986
Tide-modified (TM):			
1980	Cable	UD	Wright *et al.*, 1982a, 1982e
1992	Nine Mile	R+LTR	Masselink and Short, 1993; Turner 1993
1992	Lamberts Nth Harbour	R+LTT R+LTT	Masselink and Short, 1993; Turner, 1993
1992	central Qld	TM	Masselink and Short, 1993
1997	Muriwai, NZ	R+LTR	Brander and Short, 2000
Tide-dominated (TD):			
1988-2001	Australia-wide	WD-TM-TD	Short, 2006

[1] R=reflective; LTT= low tide terrace; TBR = transverse bar and rip; RBB = rhythmic bar; LBT = longshore bar and trough; D =dissipative; R+LTT = R+low tide terrace; R+LTR = R+low tide rips; UD = ultradissipative

While all these experiments were successful in undertaking the first morphodynamic experiments across a range of representative beach types and states, because of their limited time span, they could not record longer term (days-weeks-months) beach change and in particular transformation between beach states. However three complementary projects already in train were able to provide this information. In the early 1970s I Eliot monitored rip currents and bar behavior at Durras Beach (Eliot, 1973); while in 1972 R McLean and B G Thom commenced monthly cross-shore beach profiles of Bengello beach (McLean and Thom, 1975); then in 1976 Short commenced monthly surveys of Narrabeen beach in addition to 18 months of daily beach monitoring when the wave-surf conditions and the location of all bars, channels, rips, berms, cusps, etc. were recorded. The latter two surveys continue to this day, though the Narrabeen surveys have been complemented by DGPS, video camera, Lidar, and UAV surveys (Harley *et al.*, 2015), and recently contributed to the circum-Pacific wave-beach study (Barnard *et al.*, 2015). Based on the repetitive surveys, beach observations, photographs and sketches, three papers emerged illustrating the sequential changes in wave-dominated beach state. Short (1979a, b) developed the full range of accretionary and erosional sequences, while Wright *et al.* (1979) presented a similar range of accretionary states together with their morphodynamic signatures. These papers laid the foundations for the first wave-dominated (WD) beach model.

CSU: POST 1982

The wave-dominated 'Beach Model'

The two complementary models mentioned above were then merged and incorporated with the results of the wide-ranging field experiments into the beach model presented by Wright and Short (1984). This model was quickly and widely adopted, and now forms the basis of the wave-dominated beach model.

However it was not without some scrutiny. Lippman and Holman (1990) found " *The bar types defined in the classification scheme … are unique and encompass the range of possible morphologies from fully dissipative to fully reflective. The model is similar to the previous classification scheme of Wright and Short [1984], although derived in a different, independent manner*." Their independent " … *scheme is consistent with previous work and, in particular, compares well with the most highly evolved classification model of Wright and Short [1984].*" While more recently Masselink *et al.* (2015) found "*... the most comprehensive and rigorous longitudinal study of beach types so far by Scott et al. (2011), including almost one hundred wave-dominated, tide-affected and geologically-controlled beach settings in the UK, confirmed the general validity of the Wright and Short (1984) model.*"

The robustness of the model and its wide applicability is due to the simplicity of beach systems, a simplicity that was observed across a range of wave-dominated Australian beaches. Beaches require just four variables, which can be reduced to three in micro-tidal environments, that is, wave height (H_b), wave period (T) and sediment size (W_s). By observing how changes in the full range of wave height (H_b<0.5 to 3.5 m), period (<5 to 15+s) and sediment size (fine to coarse sand) affected beach morphodynamics and associated beach state the six WD beach states, their characteristics and morphodynamic signature were identified (D, LBT, RBB, TBR, LTT, R) around the southern Australian coast. Further, they could be quantified using the dimensionless fall velocity (Ω) (Gourlay 1968) where $\Omega = H_b/W_sT$ (Wright and Short, 1984).

However, as each of these variables can change in both time and space, additional work was required to quantify these spatial and temporal changes in beach character. The daily observations and monthly beach surveys at Narrabeen quantified the changes in beach state through time in response to changing wave height, enabling the transition time between states to be identified both in the accretionary and erosional cycles (Wright at al., 1984). Likewise the role of grain size (beach gradient) and wave period on the number of bars was assessed by Short and Aagaard (1993); the impact of changing wave height and period on both beach state and the spacing of rhythmic features, particularly rip currents was reviewed by Short and Brander, (1999); and the impact of changing sediment size on beach state were observed and quantified by (Short, 1984b; Short 1999). This work provided robust models of both the beach character associated with each beach states, as well as the transformations that occur when H_b, T and W_s change.

Tide-modified beaches

It became apparent early on however, that the wave-dominated model did not directly apply to areas of higher tide range, resulting in the field experiments at the mega-tidal Cable beach in 1980. A second surge of beach experiments in high tide range locations took place in the early 1990s when Short's graduate students Turner, Masselink, Lessa and Brander undertook a series of beach and estuarine experiments in the meso- to macro-tidal central Queenland coast. The experiments took place across a range of tide-modified beaches, barriers and estuaries. These experiments investigated both beach morphodynamics during the tidal cycle, as well as its impact on the beach groundwater and barrier stratigraphy (Masselink and Lessa, 1995; Turner 1993), resulting in the tide-modified beach model of Masselink and Short (1993). This model also introduced the role of spring tide range (TR) into the relative tide range (RTR) parameter where $RTR = TR/H_b$

Now with four variables (H_b, T, W_s and TR) beaches from wave-dominated through tide-modified (TM) environments could be classified.

Tide-dominated beaches

In 1986 Short was invited to assist Surf Life Saving New South Wales (SLNSW) in compiling a database on all NSW beaches, including the hazards associated with each beach system (Short, 1993). When this was finished, he was invited in 1990 by Surf Life Saving Australia (SLSA) to expand the program Australia-wide, as the Australian Beach Safety and Management Program (ABSAMP). Over the next 14 years every beach on the Australian mainland and thirty major islands was inspected and incorporated in an Australia-wide database, in total 10,796 mainland beaches and 965 beaches on 30 islands. In investigating and recording these beaches it soon became apparent that not all fitted the WD or TM models, particularly many of the higher tide range and lower energy beaches across northern Australia. In order to accommodate these beaches, a new series of four tide-dominated (TD) beaches (RTR>10) was

developed. These include the Beach + ridged sand flats (B+RSR), B + sand flats, (B+SF) B + tidal sand flats (B+TSF) and B+ tidal mud flats (B+TMF) (Short, 2006), though the latter two may range from sand to mud.

In addition there were a few hundred beaches that did not fit any of the WD, TM and TD models. These were high tide beaches fronted by intertidal rock or coral reef flats. Two more beach states were required to accommodate these beaches: the R + rock flats (R+RF) and R + coral reef flats (R+CF) (Short, 2006). With these additional beach types and states the full range of Australian beaches could be accommodated by four beach types and 15 beach states, six WD, three TM, four TD (Figure 3a) and the two fronted by rocks/reefs (Short and Woodroffe, 2009). But how widely applicable are these models?

As Figure 3 indicates while there are close similarities between the UK and Australian beaches, especially the WD-TM boundary (~3) and the general location of the TM beaches, there are also subtle differences, particularly beyond an RTR of ~10. Whereas the Australia beaches grade into the TD beaches all the way to an RTR of 50, the UK beaches transition into multiple intertidal-barred (MITB), before reaching an RTR of 20 where the transition to tidal flats begins, though these may be what are considered TD beaches in the Australian model. What this indicates is three things: first, the boundaries are porous and not meant to be precise; second, there is room for more field data from other coastal environments to accurately quantify the nature and full range of beach states; and third, one might expect there will be subtle variations between coastal environments, such as the higher energy meso-macro-tidal UK environments, compared to their lower energy Australian meso-macro counterparts. For example, the UK multiple intertidal-barred beach (MITB), is not found on the lower energy TM-TD northern Australian beaches. Clearly more research in other coastal environments is required to achieve the definitive spectrum of beach types and states, as well the processes that control both the bars and ridges on both the MITB and R+RSF beaches.

The foregoing beach models assume long, straight uninterrupted beaches. However, Australian beaches average only 1.37 km in length, and many of the world's beaches are similar, being curtained, bordered and affected by headlands, rock, reefs and structures. McKenzie (1958) recognized this when he described the headland rips that occur on most of Sydney's embayed beaches. The role of these same headlands in producing megarips was also noted by Short (1985), followed by documentation of the beach rotation occurring within the embayed Narrabeen beach (Short *et al.* 1995). The full range of embayment impacts on beaches was presented in more detail by Short and Masselink (1999) who introduced the embaymentization parameter; and discussed the impact of headlands and structures on beach planform, beach rotation and headland sand bypassing, as well as the impacts of beach structures like groynes, training walls, breakwaters, seawalls. Finally, Short (2010a) examined the role of geological inheritance on Australian beach morphodynamics.

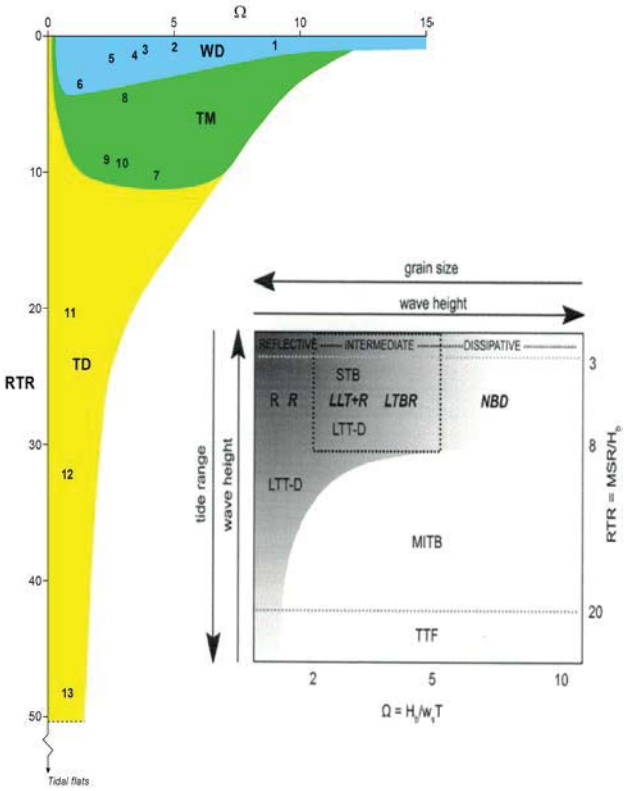

Figure 3. a) Relationship between Ω and RTR in controlling Australian beach type and state (WD=wave-dominated, TM=tide-modified, TD=tide-dominated) (source Short and Jackson, 2013). Numbers refer to the mean location of WD (1-6), TM (7-9) and TD (10-13) beach states; b) similar diagram from Scott *et al.* (2011) based on UK beaches.

SUMMARY AND CONCLUSIONS

The development of the Australian beach models by CSU researchers provided a framework for locating, classifying and understating the morphodynamics of Australian beach systems. Because of the size and variety of beaches around Australia these models have also been widely applied in other coastal locations, including most wave and tidal environments. The excellent work by the Plymouth group (Scott *et al.*, 2011; Masselink, *et al.*, 2015) has added scrutiny and robustness to these models particularly in the energetic and high tide range environments of the United Kingdom, and indicates that more work in other coastal environments is required to verify the full range of beach states.

These beach models and the role of embayments provide a simple framework for identifying and classifying a beach. Using four simple readily obtained variables (H_b, T, W_s and TR) beaches can be fitted into one of the 15 beach states, then by adding the embaymentisation parameter, based on H_b and the beach planform, together with other local inputs, the full morphodynamic character of the beach can be understood. With this knowledge a wide range of generic processes and behavior can be associated to any beach. The models provide a first step

in understanding a particular beach. However, detailed site specific field work and monitoring is still required to understand how any particular beach behaves, particularly over time, where other parameters such as extreme events and sediment supply may play a role.

ACKNOWLEDGMENTS

I would like to acknowledge the CSU pioneers not already mentioned: Peter Cowell, Patrick Hesp, Mark Bradshaw, Mal Green, Felicity Coffy, Peter Nielsen, Graham Lloyd, Julia Short and Graham Holmes; also Ian Eliot; John Chappell from ANU; Karl Shaw from ADFA; and Bob Hales from Macquarie University; all of whom made the CSU a vibrant, exciting and productive place to work. Also many thanks to Chris Hogan and Katherine McLeod for assistance with ABSAMP.

REFERENCES

Barnard, P.L., Short, A.D., Harley, M.D., Splinter, K.D., Vitousek, S., Turner, I.L., Allan, J., Banno, M., Bryan, K.R., Doria, A., Hansen, J.E., Kato, S., Kuriyama, Y., Randall-Goodwin, E., Ruggiero, P., Walker, I.J. and Heathfield, D.K., 2015, Coastal vulnerability across the Pacific dominated by El Niño/Southern Oscillation. *Nature Geoscience*, DOI: 10.1038/NGEO2539

Brander, R.W., 1999. Field observations on the morphodynamics of rip currents. *Marine Geology*, 157, 199-218.

Brander, R.W., 2010, *Dr Rip's Essential Beach Book*. UNSW Press, Sydney, 238 pp.

Brander, R.W. and Short, A.D., 2000, Morphodynamics of a large scale rip current system. *Marine Geology,* 165, 27-39.

Chappell, J and Wright, L D, 1978, Surf zone resonance and coupled morphology. *Proceedings 16th International Conference on Coastal Engineering*, ASCE, 1359-1377.

Cowell, P.J. and Thom, B.G., 1994. *Morphodynamics of coastal evolution.* In Carter, R.W.G. and Woodroffe, C.D. (eds.), *Coastal Evolution: Late Quaternary Shoreline Morphodynamics,* Cambridge University Press, Cambridge, 33-86.

Cowell, P.J., Roy, P.S. and Jones, R.A., 1995. Simulation of large-scale coastal change using a morphologic behaviour model. *Marine Geology,* 126, 45-61.

Eliot, I., 1973, Preservation of rip current patterns on sandy beaches. *1st Australian Conference on Coast and Ocean Engineering, Sydney*. Institute of Engineers Australia, National Publication 73/1, 29–34.

Harley, M.D., Turner, I.L., Short, A.D., Bracs, M.A., Phillips, M.S., Simmons, J.A. and Splinter, K.D., 2015. Four decades of coastal monitoring at Narrabeen-Collaroy Beach: the past, present and future of this unique dataset. *Australasian Coast and Ports Conference*, Auckland, Institute of Engineers, Australia.

Hesp, P.A., 1984. Foredune formation in southeast Australia. In Thom, B G (ed.), *Coastal Geomorphology in Australia*, Academic Press, Sydney, 69-97.

Hesp, P.A., 1988. Surfzone, beach, and foredune interactions on the Australian South East Coast. *Journal of Coastal Research* SI1: 15-25.

Hughes, M.G., 1992. Application of a non-linear shallow water theory to swash following bore collapse on a sandy beach. *Journal Coastal Research,* 8, 562-578.

Lessa, G., and Masselink, G., 1996. Morphodynamic evolution of a macrotidal barrier estuary: *Marine Geology*, 129, 25-46.

Lippmann, T.C. and Holman, R.A., 1990. The spatial and temporal variability of sand bar morphology. *Journal Geophysical Research*, 95, 1575-11590.

Masselink, G., Austin, M., Scott, T., Poate, T. and Russell, P., 2015. Role of wave forcing, storms and NAO in outer bar dynamics on a high-energy, macro-tidal beach. *Geomorphology*, DOI: 10.1016/j.geomorph.2014.07.035

Masselink, G. and Lessa, G., 1995. Barrier stratigraphy on the macrotidal central Queensland coastline, Australia. *Journal Coastal Research*, 11, 454-477.

Masselink, G. and Short, A.D., 1993. The effect of tide range on beach morphodynamics, A conceptual beach model. *Journal Coastal Research*, 9, 785-800.

McKenzie, P., 1958. Rip current systems, *Journal of Geology*, 66, 103-113.

McLean, R.F. and Thom, B.G., 1975. Beach changes at Moruya, 1972-1074. *Second Australian Conferences on Coastal Engineering*. Gold Coast, Institute Engineers Australia, 12-17.

Nichol, S.L., 1991. Zonation and sedimentology of estuarine facies in an incised valley, wave dominated, microtidal setting, New South Wales, Australia, In: Smith, D.G., Zaitlin, B.A. and Rahmani, R.A. (eds), *Clastic Tidal Sediments*. Canadian Society of Petroleum Geologists Memoir, 16, 42-58.

Roy, P.S., 1984. New South Wales estuaries: their origin and evolution In Thom, B G (ed.), *Coastal Geomorphology in Australia*, Academic Press, Sydney, 99-121.

Roy, P.S. and Thom, B.G., 1981. Late Quaternary marine deposition in New South Wales and southern Queensland - an evolutionary model, *Journal Geology Society Australia*. 28, 471-489.

Roy, P.S., Zhuang, W-Y., Birch, G.F., Cowell, P.J. and Li C., 1997. *Quaternary geology of the Forster-Tuncurry shelf, SE Australia.* Geological Survey Rept. GS 1992/201, Dept. of Mineral Resources, NSW, 405 pp

Scott T., Masselink, G. and Russell, P., 2011. Morphodynamic characteristics and classification of beaches in England and Wales. *Marine Geology*, 286, 1-20.

Short, A.D., 1979a. Wave power and beach stages: A global model, *Proc. 17th International Conf. Coastal Engineering*, Hamburg, ASCE, 1145-1162.

Short, A.D., 1979b. Three-dimensional beach stage model, *Journal Geology*, 87, 553-571.

Short, A.D., 1984a. Temporal change in beach type resulting from a change in grain size, Search, 15, 7-8.

Short, A.D., 1984b. Beach and nearshore facies, south east Australia. *Marine Geology*, 60, 261-282.

Short, A.D., 1985. Rip current type, spacing and persistence, Narrabeen beach, Australia. *Marine Geology*, 65, 47-71

Short, A.D., 1993. *Beaches Of The New South Wales Coast.* Australian Beach Safety and Management Project, Sydney, 358 pp.

Short, A.D., 1999. Wave-dominated beaches. In Short, A D, (ed), *Beach and Shoreface Morphodynamics*. John Wiley and Sons, Chichester, 173-203.

Short, A.D., 2002. The distribution and impacts of carbonate sands on southern Australia beach-dune systems. In Magoon, O T, Robbins, L L and Ewing, L (eds), *Carbonate Beaches 2000*, American Society of Civil Engineers, Reston, 236-250.

Short, A.D., 2006. Australian beach systems – nature and distribution. *Journal of Coastal Research*, 22, 11-27.

Short, A.D., 2010a. Role of geological inheritance in Australian beach morphodynamics. *Coastal Engineering,* 57, 92-97. DOI: 10.1016/j.coastaleng.2009.09.005

Short, A.D., 2010b. Sediment transport around Australia – sources, mechanisms, rates and barrier forms. *Journal of Coastal Research,* 26, 395-402.

Short, A.D., 2013. Australia's temperate carbonate coast: sources, depositional environments and implications. In Martini, P and Wanless, H R (eds), SP388 *Sedimentary Coastal Zones from High to Low Latitudes: Similarities and Differences*. Geological Society of London SP388, London. doi: 10.1144/SP388.5

Short, A.D. and Aagaard, T., 1993, Single and multi-bar beach model. *Journal of Coastal Research,* SI 15, 141-157.

Short, A.D. and Brander, R., 1999. Regional variation in rip density. *Journal of Coastal Research*, 15, 813-822.

Short, A.D., Cowell, P.J., Cadee, M., Hall, W. and van Dijck, B., 1995. Beach rotation and possible relation to the Southern Oscillation. *Ocean and Atmosphere Pacific*, Adelaide.

Short, A.D. and Hesp, P.A., 1982. Wave, beach and dune interactions in south eastern Australia. *Marine Geology*, 48, 259-284.

Short, A.D. and Hogan, C.L., 1994. Rips and beach hazards, their impact on public safety and implications for coastal management. *Journal of Coastal Research*., SI 12, 197-209.

Short, A.D. and Jackson, D.J.W., 2013. Beach Morphodynamics. In Shroder, J.F. (ed) *Treatise in Geomorphology*, v. 10, Academic Press, San Diego, 107-129.

Short, A.D. and Masselink, G., 1999. Embayed and structurally controlled beaches. In Short, A D, (ed), *Beach and Shoreface Morphodynamics.* John Wiley and Sons, Chichester, 230-250.

Short, A.D. and Trembanis, A., 2004. Decadal scale patterns in beach oscillation and rotation Narrabeen Beach, Australia- time series, PCA and wavelet analysis. *Journal of Coastal Research*, 20, 523-532.

Short, A.D. and Woodroffe, C.D., 2009. *The Coast of Australia*. Cambridge University Press, Melbourne, 288 pp.

Sonu, C J, 1973, Three dimensional beach changes. Journal Geology, 81, 42-64.

Thom B.G., 1984a. Geomorphic research on the coast of Australia: a preview. In Thom B G (ed) *Coastal Geomorphology in Australia*. Academic Press, Sydney, 1-21.

Thom, B.G., 1984b. Transgressive and regressive stratigraphies of coastal sand barriers in eastern Australia. *Marine Geology*, 56, 137-158.

Thom, B.G., and Hall, W., 1991. Behaviour of beach profiles during accretion and erosion dominated periods. *Earth Surface Processes and Landforms*, 16, 113-27.

Thom, B.G. and Short, A.D., 2006. Australian Coastal geomorphology 1984-2004. *Journal of Coastal Research*., 22, 245 pp.

Turner, I.L., 1993. The total water content of sandy beaches. *Journal Coastal Research*, SI 15, 11-26.

Wright, L.D. and Short, A.D., 1984. Morphodynamic variability of surf zones and beaches: A synthesis. *Marine Geology*, 56, 93-118.

Wright, L.D., Chappell, J., Thom, B.G., Bradshaw, M.P. and Cowell, P.J., 1979. Morphodynamics of reflective and dissipative beach and inshore systems, Southeastern Australia. *Marine Geology*, 32, 105-140.

Wright, L.D., May, S.K., Short, A.D. and Green, M.O., 1984. Beach and surf zone equilibria and response time. Proc. 19th *International. Conf. Coastal Engineering*., Houston, 2150-2164.

Wright, L.D., Nielsen, P., Short, A.D. and Green, M.O., 1982a. *Morphodynamics of a macrotidal beach*. Coastal Studies Unit Tech. Rept. No. 82/1, Coastal Studies Unit, University of Sydney, Sydney, 53 pp.

Wright, L.D., Nielsen, P., Short, A.D., Coffey, F.C. and Green, M.O., 1982b. *Nearshore and surf zone morphodynamics of a storm wave environment: Eastern Bass Strait, Australia*. Coastal Studies Unit Tech. Rept. No. 82/3, Coastal Studies Unit, University of Sydney, 154 pp.

Wright, L.D., Short, A.D. and Nielsen, P., 1982c. *Morphodynamics of high energy beaches and surf zones: a brief synthesis*. Coastal Studies Unit Rept. No. 82/5, Coastal Studies Unit, University of Sydney, 64 pp.

Wright, L.D., Guza, R.T. and Short, A.D., 1982d. Dynamics of a high-energy dissipative surf zone. *Marine Geology*, 45, 41-62.

Wright, L.D., Nielsen, P., Short, A.D. and Green, M.O., 1982e. Morphodynamics of a macrotidal beach. *Marine Geology*, 50, 97-128.

Wright, L.D. and Thom, B.G., 1977. Coastal depositional landforms, a morphodynamic approach, *Progress in Physical Geography,* 1, 412-59.

Journal of Coastal Research	SI	75	8-12	Coconut Creek, Florida	2016

Surfzone-Beach-Dune interactions: Flow and Sediment Transport across the Intertidal Beach and Backshore

Patrick A. Hesp[†] and Thomas A.G. Smyth[†]

[†]Beach and Dune Systems (BEADS) Laboratory,
School of the Environment, Flinders University,
Faculty of Science and Engineering,
Bedford Park, Adelaide, South Australia

www.cerf-jcr.org

www.JCRonline.org

ABSTRACT

Hesp, Patrick A. and Smyth, T.A.G., 2016. Surfzone-Beach-Dune interactions: Review; and flow and sediment transport across the intertidal beach and backshore. *In:* Vila-Concejo, A.; Bruce, E.; Kennedy, D.M., and McCarroll, R.J. (eds.), *Proceedings of the 14th International Coastal Symposium* (Sydney, Australia). *Journal of Coastal Research*, Special Issue, No. 75, pp.8-12. Coconut Creek (Florida), ISSN 0749-0208.

The original wave-beach-dune model (Hesp, 1982) stated that in the medium to long term, modal dissipative beaches display maximum onshore wave driven sediment transport, maximum aeolian transport off beaches, the largest foredune heights and volumes, and the largest Holocene dunefields. Modal reflective beaches display the opposite, while modal intermediate beaches display a trend in these from relatively high to relatively low sediment transport, foredune volumes, and Holocene barrier volumes with a trend from dissipative to reflective. New Computational Fluid Dynamic (CFD) modelling of flow and calculation of sediment transport over three modal beach types presented here shows that the original conceptual ideas and field data regarding aeolian sediment transport are correct. Dissipative beaches show the greatest long term potential for sediment delivery to the backshore whilst reflective beaches display the least, with a trend from relatively high to low in the intermediate beach state range.

ADDITIONAL INDEX WORDS: *Surfzone-beach-dune model and interactions, modal beach types, flow and aeolian transport.*

INTRODUCTION

The original generation of the wave-beach-dune model of beach and dune interactions was formulated by Hesp (1982) for micro-tidal beaches in eastern and southern Australia, although it might be argued that it would work in many cases for meso-tidal beaches (< ~4m range). Most of these micro-tidal beaches were apparently not limited in sediment supply during the latter part of the Holocene transgression and particularly in the last 7000 years (cf. Thom and Roy, 1985). Sea level crossed the present around 6,500 to 7000 years ago, rose +1m and eventually fell to the present following a typical southern hemisphere pattern (Dillenburg and Hesp, 1999).

The model development followed the publication of a robust micro-tidal beach model with reasonably high predictability (Short, 1979; Wright and Short, 1984). The beach model enabled one to classify micro-tidal beaches into six states ranging from dissipative through intermediate to reflective states with characteristic morphologies and mobilities. Subsequent research has extended the original model to meso- and macro-tidal beaches and as Aagaard *et al.* (2013) note, later research has largely confirmed the basic model. An analysis of beach and backshore morphologies and flow characteristics for different surfzone-beach types allowed Hesp (1982) to develop actual and theoretical links between beach backshore morphology, potential aeolian transport, foredune state and morphology, and dunefield type and development (Short and Hesp, 1982; Hesp, 1988). In brief, the model claims that in the medium to long term, modal dissipative beaches display maximum onshore wave driven sediment transport, maximum aeolian transport off beaches, the largest foredune heights and volumes, and the largest Holocene dunefields. Modal reflective beaches display the opposite, while modal intermediate beaches display a trend in these from relatively high to relatively low sediment transport, foredune volumes, and Holocene barrier volumes with a trend from dissipative to reflective.

In the following, the six surfzone-beach types and their morphologies are taken as read (see Sherman and Bauer, 1993). Recent research on wave driven sediment transport to the different beach types is reviewed. Post-1982-1988 research on medium to long term aeolian transport off beaches is largely lacking, and in addition, Houser and Ellis (2013) state that discrepancies between the beach-dune models "largely reflects a poor understanding of the relative importance of sediment supply and aeolian transport potential" (p.281). Thus, in the following, the importance of beach morphology and mobility for long term landwards aeolian sediment transport is re-stated. In concert with this, new research on wind flow and sediment transport over three modal or typical beach types is presented.

DOI: 10.2112/SI75-002.1 received 15 October 2015; accepted in revision 15 January 2016.
*Corresponding author: Patrick.Hesp@flinders.edu.au

METHODS

Three modal beach types were selected for modelling in this study. The dissipative profile is a mean or modal profile from Goolwa Beach, SA, and is taken from 30 years of survey data. The intermediate and reflective modal profiles are from several years of beach surveys in Fens embayment near Hawks Nest and Jimmy's Beach, Port Stephens, NSW respectively (Hesp, 1982).

All computational fluid dynamics (CFD) modelling was performed using OpenFOAM. The SIMPLE (Semi-Implicit Method for Pressure Linked Equations) algorithm was used to solve the Navier-Stokes equations (cf. Smyth and Hesp, 2015). This method produces a steady-state, averaged solution of flow. Turbulence was modelled using the RNG k-epsilon method which accounts for the smaller scales of motion and offers improved predictions for separated flows than the original k-epsilon model. A second-order, linear spatial discretisation scheme was employed and simulations were deemed complete once the initial residuals for Ux and Uz were 4 orders of magnitude smaller than the maximum residual calculated.

The mesh for each beach had a horizontal resolution of 0.1 m and a vertical resolution of 0.02 m at the surface, increasing to 1.05 m at the top of the computational domain, 24 m above the surface of the beach.

In each simulation, wind at the inlet was defined as a logarithmic boundary layer with a wind speed of 10 m s^{-1} at 1 m above the surface. Surface roughness for each simulation was defined as the grain diameter divided by 30 (Bagnold, 1954). Aeolian sediment transport was calculated using White's (1979) corrected derivation of Kawamura's (1951) equation.

SURFZONE TO BEACH SEDIMENT TRANSPORT

Hesp (1982; 1999) and Short and Hesp (1982) argued that dissipative surfzones would have the highest potential wave driven onshore transport while reflective beaches would have the lowest, based on observations of Holocene sediment volumes contained in some Australian barrier systems developed landwards of those beaches. In more recent times, while models such as SBEACH and CROSMOR generally predict offshore rather than onshore transport (e.g. Aagaard et al., 2004; Aagaard and Sorensen, 2012), large-scale modelling (e.g. Cowell *et al.*, 1995) and field observations (e.g. Aagaard *et al.*, 2004, 2013; Miot da Silva, 2011) indicate the opposite. It is also a fact that very many of the largest barrier and coastal dunefields in the world are found on high energy surfzone-beach types, particularly dissipative beaches (Short, 1988, 2010; Aagaard *et al.*, 2004; Hesp, 2013; Hesp and Walker, 2013; Houser and Ellis, 2013). For example, transgressive dunefields are most commonly found on high energy dissipative and high energy intermediate surfzone-beach systems (e.g. Australian east, southern and west coasts, South Africa, Brazil; west coast USA; east and west coast Mexico; NZ North Island west coast; Peru and Chile coasts; France, Spain, Holland and Portugal coasts). Research by Dillenburg and Hesp (2009), Miot da Silva and Hesp (2010), and Miot da Silva *et al.*, 2012) support this contention for southern Brazilian transgressive dunefield barrier systems.

BEACH MOBILITY

Beach mobility refers to the coefficient of variation of mean shoreline position (see Short and Hesp, 1982; Short (1999, his table 7.1), and in reality indicates the amount of volumetric and profile change the beach and backshore experiences over time, and through erosion to accretion phases. Dissipative and reflective beaches have minimal backshore mobility, while intermediate beaches range from relatively low, through moderate–high to relatively low as one progresses from the dissipative to reflective ends of the intermediate range. In a review of surfzone-beach interactions Houser and Mathew (2011) ignored beach mobility as a factor in such interactions, but mobility is important because the greater the beach mobility, the greater the beach morphological variability, and therefore the greater the potential for variations in net aeolian sediment transport. If a beach's mobility is moderate to high, the fetch distance across which the wind can blow towards the backshore can vary significantly both temporally and spatially, and as Bauer and Davidson-Arnott (2003) note, less beach width equals less transport potential. For example, Houser and Mathew (2011, p.66, para 3) show that the largest dunes on South Padre Island are associated with the largest supratidal volumes and widths (although confusingly, they later contradict this (see their p. 70, section 6). In addition, the presence of scarps, and/or curvaceous to stepped topography result in reductions in the near-surface wind flow and aeolian sediment transport (Hesp, 1988; see below).

FLOW AND AEOLIAN SEDIMENT TRANSPORT ACROSS MODAL BEACH TYPES

In 1994 Sherman and Lyons conducted a model test to examine if aeolian sediment transport did actually differ across the three modal beach types, dissipative, intermediate and reflective. Their model utilised three different typical beach slopes but all beaches had the same width and shear stress was constant at 0.5 ms^{-1} across the profiles. They found that sand transport off the dissipative beach was 20% higher than off the reflective beach if just slope and grain size were taken into account. When moisture content was added, transport rates were nearly two orders of magnitude higher off the dissipative beach compared to the reflective beach. We have repeated *exactly* Sherman & Lyons (1994) non-moisture model which utilised White's (1979) *incorrect* transport equation (see corrections in Namikas and Sherman, 1997). The results are similar; there is significantly greater transport across the dissipative profile compared to the reflective profile.

Since it is unlikely that shear stress would remain constant over a beach surface with variable slope and topography, a CFD model was then run over three modal beaches, (a typical dissipative, intermediate and reflective beach) but in this case with the shear stress computed continuously across the three beach topographies. Sediment transport in this case was calculated using White's (1979) derivation of Kawamura's (1951) equation as corrected by Namikas and Sherman (1997). Figure 1 illustrates the velocity bands, Figure 2 the sediment transport across the three topographies, and Figure 3 the velocity profiles sensed at various positions across the beach topographies. The velocity bands depicted in Figure 1 show

there is minimal disturbance of the flow across the dissipative beach, and only when the wind approaches the topographic break where the beach meets the seaward toe of the backshore is there a slight reduction in flow velocity.

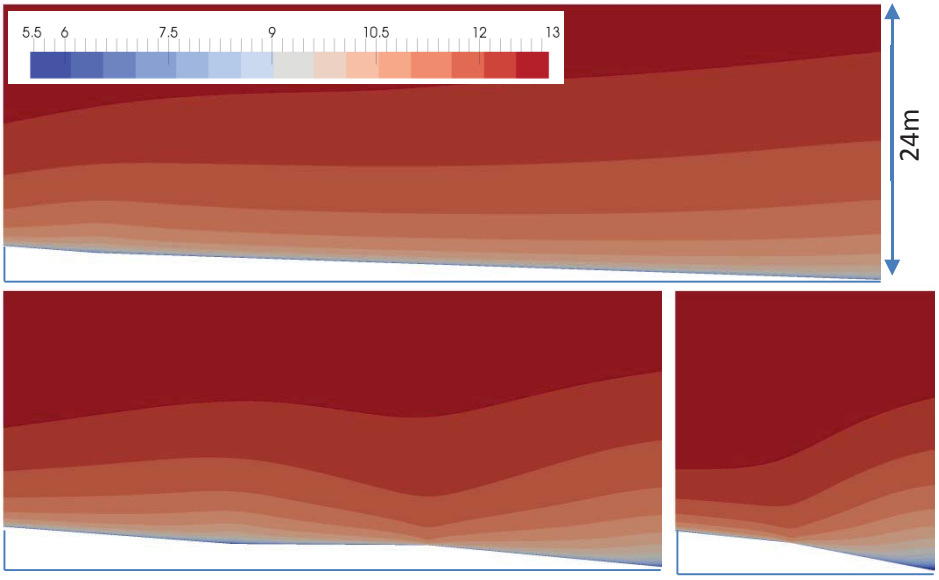

Figure 1. CFD generated velocity bands (scale bar in msec^{-1}) across dissipative (Goolwa, uppermost), intermediate (Hawks Nest, lower left) and reflective beach (Jimmys) profiles illustrating minimal flow disturbance across the majority of the dissipative profile compared to the intermediate and reflective beaches. Horizontal distances are 80m, 60, 23m respectively (see fig 2). Wind flow is from right to left (and in the following diagrams).

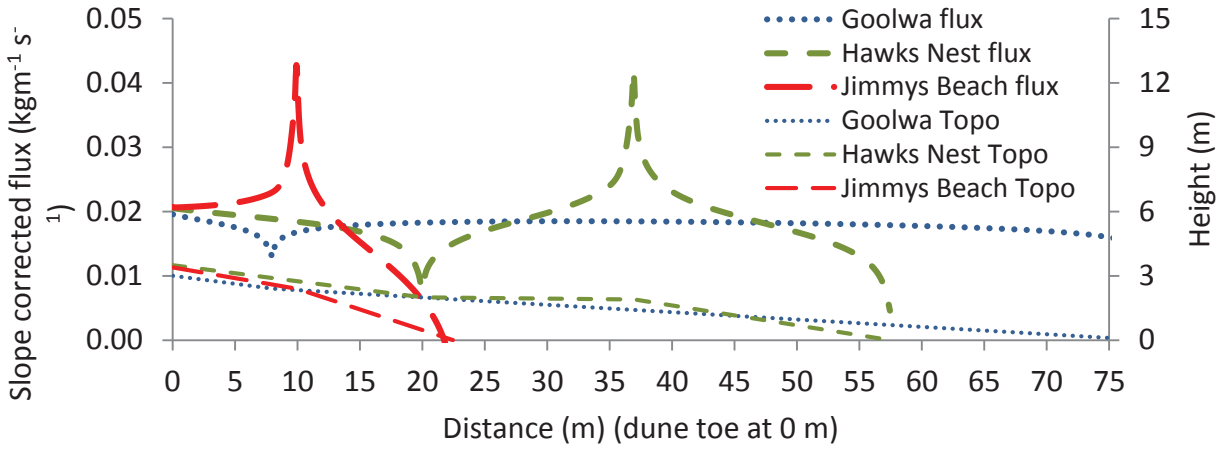

Figure 2. CFD modelling of sediment transport (upper lines) across modal dissipative (Goolwa), intermediate (H. Nest) and reflective (Jimmys) beach profiles (lower less weighted lines) calculated using White's (1979) corrected sediment transport equation derived from Kawamura (1951) and constantly adjusting the shear velocity across the profiles. Transport is initially increasing then constant across the majority of the dissipative beach slope until the topographic break is reached at the lower backshore position (~ 8m distance). Transport peaks at the berm crests of the intermediate and reflective beaches but drops significantly landwards of the berm crests.

Sediment transport slightly increases and then is largely constant across much of the dissipative profile. The sediment transport peaks locally at the berm crests, and is lower landwards of these crests on the intermediate and reflective topographies (Figure 2). The velocity profiles increase up- and across-slope in the case of the dissipative beach. On the intermediate and reflective beaches, the velocity accelerates up the beach face (highest speedup for the reflective beach as shown by Hesp's 1982 velocity profiles), reaching a maximum at the berm crests. It then decelerates in the back berm crest swale (berm tread region) on the intermediate beach, and is somewhat lower on the steeper reflective upper beach (Figure 3).

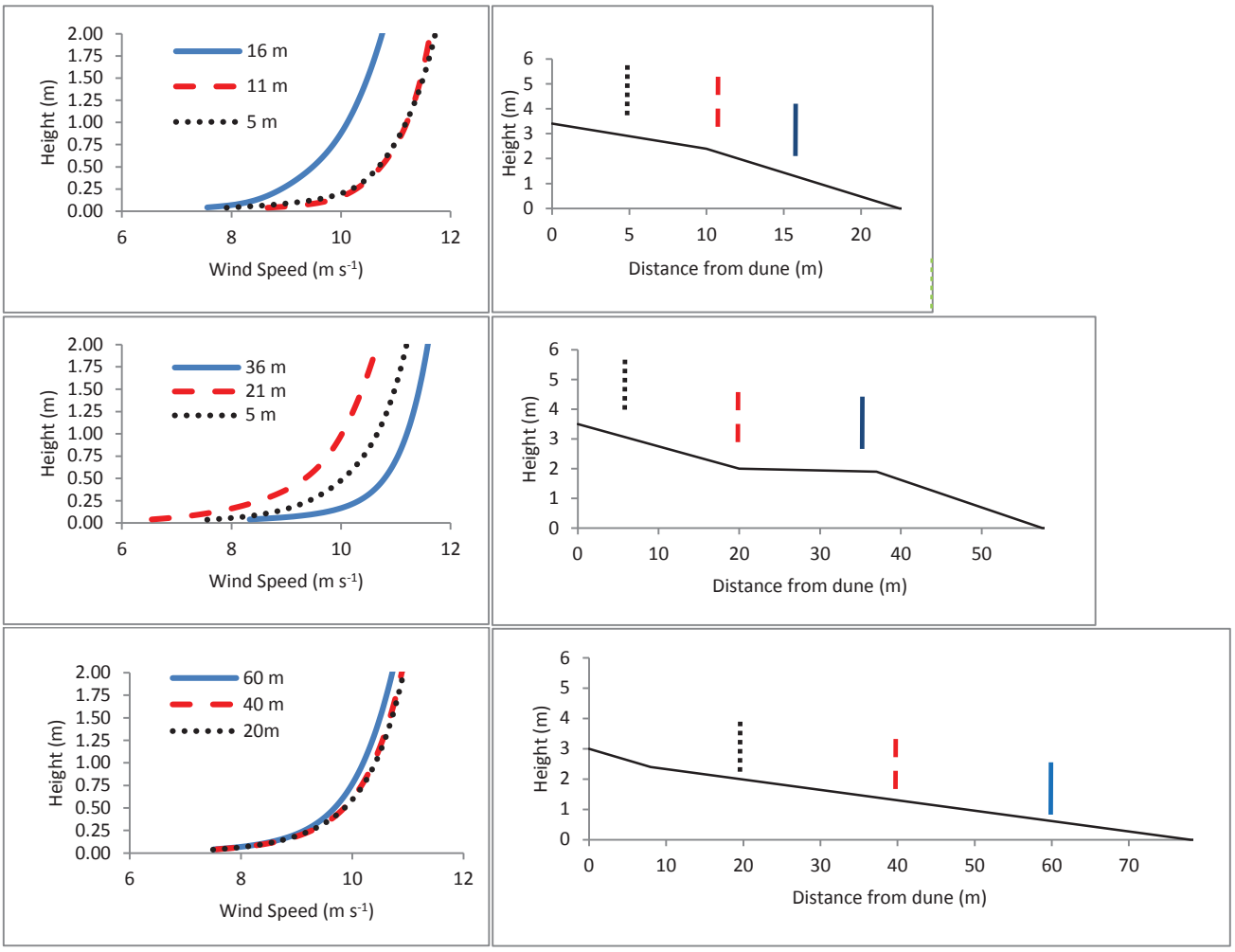

Figure 3. Wind velocity profiles derived from CFD simulations and sensed at every 1cm height (starting at 2cm) above the bed across the three modal beach topographies. Note the consistently high velocity profiles across the dissipative beach, and minimal flow disturbance compared to the other two.

CONCLUSIONS

The sediment transport portions of the wave-beach-dune model published in 1982 (Hesp, 1982; Short and Hesp, 1982) were part conceptual, part field validated (the beach mobility, beach flow fields and foredune volume data in particular) (Hesp, 1988). In this work utilising a CFD model shows that the original conclusions regarding sediment transport off the modal intertidal beach to backshore types were largely accurate. Dissipative beaches (without berms) display minimal topographic variability, maintain máximum fetch widths, and experience mínimum flow disturbance and decelerations across the profiles, thus mazimising aeolian sediment transport across those beaches. While at times, higher wide berm portions (the berm tread) can have high aeolian sediment transport, particularly because they can remain dry for reasonable periods compared to curvilinear to straight dissipative beaches, their greater mobility

means that on average, net medium to long term aeolian transport is greater off dissipative beaches. The surfzone-beach-dune model clearly does include and characterise the relative importance of sediment supply and aeolian transport potential for the range of modal beach types.

ACKNOWLEDGMENTS

Thanks to DEWNR (SA) for the provision of the Goolwa beach profiles, Flinders University for support, and Douglas Sherman and Andrew Short for reviews.

LITERATURE CITED

Aagaard, T., Davidson-Arnott, R., Greenwood, B., and Nielsen, J., 2004. Sediment supply from shoreface to dunes: linking sediment transport measurements and long term morphological evolution. *Geomorphology,* 60, 205-224.

Aagaard, T., Greenwood, B., Hughes, M., 2013. Sediment transport on dissipative, intermediate and reflective beaches. *Earth-Science Reviews,* 124, 32-50.

Aagaard, T., Hughes, M.G. and Greenwood, B., 2011. Sediment transfer from bar to beach? Measurements using a pulse-coherent acoustic Doppler profiler. *J. Coastal Research,* SI 64, 2002-2006.

Aagaard, T. and Sorensen, P., 2012. Coastal profile response to sea level rise: a process-based approach. *Earth Surface Processes and Landforms,* 37, 354-362.

Bagnold, R.A., 1954. *The Physics of Blown Sand and Desert Dunes*. Chapman and Hall, 265pp.

Bauer, B.O. and Davidson-Arnott, R.G.D., 2003. A general framework for modelling sediment supply to coastal dunes including wind angle, beach geometry, and fetch effects. *Geomorphology,* 49, 89-108.

Davidson-Arnott, R.G.D., 1988. Temporal and spatial controls on beach/dune interaction, Long Point, Lake Erie; in: N.P. Psuty (ed), Dune/Beach Interaction. *J. Coastal Research Special* Issue No. 3, 131-136.

Davidson-Arnott, R.G.D., 2010. *Introduction to Coastal Processes and Geomorphology.* Cambridge Univ. Press, 442pp.

Davidson-Arnott, R.G.D. and Law, M.N. 1996. Measurement and prediction of long-term sediment supply to coastal foredunes. *J. Coastal Research,* 12 (3), 654-663.

Davis, R.A. Jr. and Fitzgerald, D.M., 2004. *Beaches and Coasts.* Blackwell Publishing, 419pp.

Dillenburg, S. and Hesp, P.A. (Editors), 2009. *Geology and Geomorphology of Holocene Coastal Barriers of Brazil.* Springer-Verlag Lecture Notes in Earth Sciences 107. Springer.

Hesp, P.A., 1982. *Morphology and Dynamics of Foredunes in S.E. Australia.* Ph.D Thesis, Dept. of Geography, University of Sydney.

Hesp, P.A., 1988. Surfzone, beach and foredune interactions on the Australian south east coast. *J. Coastal Research,* SI 3, 15-25.

Hesp, P.A., 1999. The Beach Backshore and Beyond. In: A.D. Short (Ed), *Handbook of Beach and Shoreface Morphodynamics*, 145-170. John Wiley and Sons, Chichester.

Hesp, P.A., 2013. Conceptual models of the evolution of transgressive dunefield systems. *Geomorphology,* 199, 138–149.

Houser, C., 2009. Synchronization of transport and supply in beach-dune interaction. *Progress in Physical Geography,* 33(6), 733-746.

Houser C., and Ellis J., 2013. Beach and Dune Interaction. In:
John F. Shroder (ed.) *Treatise on Geomorphology*, Vol10, pp. 267-288. San Diego: Academic Press.

Houser, C. and Hamilton, S., 2009. Sensitivity of post-hurricane beach and dune recovery to event frequency. *Earth Surface Processes and Landforms* 34, 613-628.

Kawamura, R., 1951. *Study of Sand Movement by Wind*. Hydraulic Engr. Rept. HEL-2-8.

Miot da Silva, G., 2011. Wave dynamics and beach - dune interactions: Moçambique Beach, Santa Catarina Island, Brazil. In: Wang, P.; Rosati, J.D.; Roberts, T.M., (Eds.) 2011. *Proceedings Coastal Sediments*, Miami, Florida, 1, 725-738.

Miot da Silva, G. and Hesp, P.A., 2010. Coastline orientation, aeolian sediment transport and foredune and dunefield dynamics of Moçambique Beach, southern Brazil. *Geomorphology,* 120, 258-278.

Miot da Silva, G., Siadatmousavi, S.M. and Jose, F. 2012. Wave-driven sediment transport and beach-dune dynamics in a headland bay beach. *Marine Geology,* 323, 29-46.

Namikas, S., Sherman, D.J., 1997. Predicting aeolian sand transport: revisiting the White model. ESPL 22, 601-604.

Sherman, D.J. and Bauer, B.O., 1993. Dynamics of beach-dune interaction. *Progress in Physical Geography,* 17, 413-447.

Sherman, D. J. and Lyons, W., 1994. Beach-state controls on aeolian sand delivery to coastal dunes. *Physical Geography,* 15, 381-395.

Short, A.D., 1979. Three-dimensional beach stage model. *J. Geology,* 87, 553-571.

Short, A.D., 1988. Holocene coastal dune formation in southern Australia—a case study. *Sedimentary Geology*, 55, 121–142.

Short, A.D., 1999. Wave-dominated beaches. In: Short, A.D. (Ed.), *Handbook of Beach and Shoreface Morphodynamics*, 173-203. J. Wiley and Sons Ltd.

Short, A.D., 2010. Sediment transport around Australia – sources, mechanisms, rates and barrier forms. *J. Coastal Research,* 26(3), 395-402.

Short, A.D. and Hesp, P.A., 1982. Wave, beach and dune interactions in South Eastern Australia. *Marine Geology,* 48, 259-284.

Smyth, T.A.G., Hesp, P.A., 2015. Aeolian dynamics of beach scraped dunes. *Coastal Engineering,* 99, 38-45.

Thom, B. G., & Roy, P. S., 1985. Relative sea levels and coastal sedimentation in southeast Australia in the Holocene. *Journal of Sedimentary Research*, 55(2), 257-264.

White, B.R., 1979. Soil transport by wind on Mars. *J. of Geophysical Research*, 84, 4643-4651.

Wright, L.D. and Short, A.D., 1984. Morphodynamic variability of beaches and surfzones: A synthesis. *Marine Geology,* 56, 92- 118.

Journal of Coastal Research	SI	75	13 - 17	Coconut Creek, Florida	2016

Using simplified bathymetry and SAR imagery in the validation of a hydraulic model for the Tagus River floodplain

Maria Amélia V.C. Araújo [†§*], Rita Pestana[‡], Magda Matias[‡], Dora Roque[††], António Trigo-Teixeira[†], and Sandra Heleno[‡]

[†] CEHIDRO, Instituto Superior Técnico, Universidade de Lisboa, Lisbon, Portugal

[‡] CERENA, Instituto Superior Técnico, Universidade de Lisboa, Lisbon, Portugal

[††] LabImagem, Laboratório Nacional de Engenharia Civil Lisbon, Portugal

[§] Centre for Environment, Fisheries and Aquaculture Science (Cefas), Lowestoft, Suffolk, UK

www.cerf-jcr.org

www.JCRonline.org

ABSTRACT

Araújo, M.A.V.C.; Pestana, R.; Matias, M.; Roque, D.; Trigo-Teixeira, A., and Heleno, S., 2016. Using simplified bathymetry and SAR imagery in the validation of a hydraulic model for the Tagus River floodplain. *In:* Vila-Concejo, A.; Bruce, E.; Kennedy, D.M., and McCarroll, R.J. (eds.), *Proceedings of the 14th International Coastal Symposium* (Sydney, Australia). *Journal of Coastal Research*, Special Issue, No. 75, pp. 13 - 17. Coconut Creek (Florida), ISSN 0749-0208.

This work presents several approaches in the validation of the hydrodynamic model Tuflow on the simulation of flood extents and water levels, based on satellite SAR imagery. A methodology that uses a simplified bathymetry in the river main course is employed, which proves to be reliable and accurate for high-flow events. This was made possible as the digital terrain model was acquired in a dry period, accounting for large dry areas in the river bed, avoiding in this way the need of expensive river bathymetry surveys. Also, two methods are applied to the SAR imagery to extract the flood boundaries: visual interpretation followed by manual delimitation and an object-based algorithm approach. The hydraulic model is tested on a reach of the Tagus River, Portugal, where the largest flood inundation areas occur, using a historical flood event to verify its robustness and reliability. The accuracy of model prediction is done through comparisons of water levels at a hydrometric station and the determination of commission and omission errors of flood extent, between the reference SAR image and the predicted inundation. It was concluded that the methodology followed in this work is well suited for the hydraulic model validation.

ADDITIONAL INDEX WORDS: *simplified bathymetry, SAR imagery, commission and omission errors, Tuflow.*

INTRODUCTION

The importance of having accurate representation of floods and robust planning guidelines for floodplains, including land use and flood evacuation planning, has been recognized. However, the development and application of numerical models to support these activities is sometimes complex, as often several man-made features and structures must be included.

Flood extent maps derived from remotely sensed data are often used to validate hydraulic models of river flood flow (*e.g.* Bates *et al.*, 1997; Garcia-Pintado *et al.*, 2013). The use of these maps may overcome current data constraints, due to the lack of suitable calibration and validation datasets. Combining together 2D hydraulic models, terrain data and satellite imagery derived information, such as SAR (Synthetic Aperture Radar), floods can be more easily simulated leading to more reliable flood predictions. Nevertheless, one must bear in mind that this imagery has some inherent uncertainty. The uncertainty may be related to variation in backscatter from the various land cover types neighbouring the flood, effects of meteorological conditions on the water surface, or even the presence of vegetation. Therefore, the application of accurate algorithms for flood delimitation in satellite imagery is fundamental, in order for those images to be considered as the ground-truth in the representation of real features and materials on the ground.

Recent studies have emphasized that although a detailed high-resolution data is valuable for flood inundation modelling, the model accuracy is not necessarily increased by higher precision in these datasets since there are other uncertainty sources (Dottori *et al.*, 2013). The optimum representation of the topographic surfaces, in these models, has also been underlined upon the use of high-resolution topographic datasets derived from airborne laser altimetry.

The lower Tagus River (Santarém region), in Portugal, has been experiencing flooding approximately every 2.5 years (Azevêdo *et al.*, 2004). This work presents various approaches in hydraulic modelling of a historical flood in the Tagus floodplain, which took place in November 7th 1997. A methodology for representing the bathymetry in the river main course is applied. Flood extents are determined using the Tuflow 2D hydraulic model. The model results are compared with measured water levels and with information retrieved from SAR

DOI: 10.2112/SI75-003.1 received 15 October, 2015; accepted in revision 15 January, 2016 .

*Corresponding author: amelia.araujo@cefas.co.uk

imagery, to verify the ability of the model in replicating past flood events with good accuracy.

Description of the study area

The Tagus is the longest river in the Iberian Peninsula and it flows into the Atlantic Ocean at the city of Lisbon. Its basin produces 17,670 hm^3 of water, 5,476 hm^3 in Portugal (Azevêdo *et al.*, 2004), and the flow regime is controlled by several dams. Many of the floods that occur in the Santarém region (see Figure 1), especially in the past, are the result of an inadequate management of the dams between the Spanish and the Portuguese authorities. As represented in Figure 1, Tagus follows a very constricted course up to Almourol, but after that region it enters a large alluvial valley which is prone to flooding.

In Figure 1 the study area is represented, corresponding to a 70 km stretch between the hydrometric stations of Tramagal and Ómnias. The Tagus floodplain and the hydrometric station of Almourol are also shown, as well as the main rivers and dams along the river course. The maximum discharge capacity of the main river channel, in Ómnias, is around 500 m^3/s (Laia Fernandes, personal communication 2013), which is not enough in many situations, leading to flooding in the upstream regions. This figure also shows the Alpiarça region on the left side of the river, which has a 30 km long channel built with the purpose of draining the marshlands after the floods. This channel receives flows from the Ulme River, located around 12 km north of the Alpiarça village, and works as a collector of all hydrographic basins of the hillsides along its length. However, the Alpiarça channel only receives water directly from the Tagus River for flow rates above 5,200 m^3/s (Laia Fernandes, personal communication 2013) measured in Almourol, which is the river flow causing the overtopping of its banks.

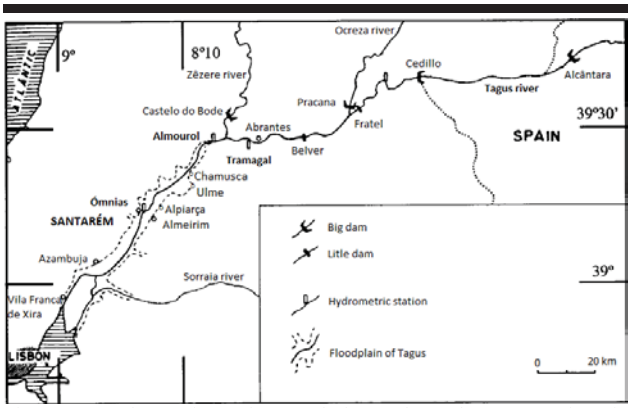

Figure 1. Hydrometric stations and dams along the Tagus River in Portugal (adapted from Azevêdo *et al.*, 2004).

METHODS

Digital terrain model

The digital terrain model (DTM) was provided by the Intermap Technologies Company, which collected the elevation data using an aircraft equipped with Interferometric Synthetic Aperture Radar technology. The DTM resolution was 5 m, with a vertical accuracy of 1 m. Data acquisition was carried out in March/April 2008, during a dry period, enabling data acquisition at a lower level, within the river main course, including the margins, sandbanks and islets. This is an important aspect since the technique cannot measure into the water. For that reason, the bathymetric values used in the main course channel are artificial, *i.e.* they were obtained through an interpolation from the acquired heights for the right and left banks, resulting in a horizontal bottom profile. In order to assess the applicability of this methodology, those interpolated values were compared with several bathymetric cross-sections surveyed during a field campaign, along the river course, in 1998 and 2012. These profiles were measured using a real-time GNSS receiver Leica SR530 and a single beam SONAR (echo-sounder ODOM MKII).

Figure 2 shows a comparison of the bathymetric data for 1998, 2008 and 2012, for 2 cross-sections of the river. Data is referred to mean sea level. It is shown that the 2008 DTM is accurate and the river bed did not suffer large modifications during the last 14 years. In fact, the river configuration and morphology have not changed in time, also because there was not much human intervention. This makes it acceptable to use topographic data acquired in 2008 in the simulation of floods that took place in past years. One can assume that the regions not measured by the remote sensing technique, due to the impossibility to penetrate the water surface, do not play an important role in the river hydrodynamics floods. In fact, and also because a 2D model is used, the cross-section conveyance will be the same in a flood period, whether or not the gap which exists between the artificial and the measured bathymetry is used, as shown in Figure 2. This test shows that the gap is not significant and can be neglected specially when simulating high-flow events. Therefore, those low-flow portions of the river bed may be disregarded and it is valid to consider the mentioned simplified bathymetry in the river main course. In this way, it was decided to not use any of the surveyed cross-section profiles in the DTM, which were spaced of around 3 km. Due to the great bathymetric variability present in the river bed, the distance was considered to be too large to make interpolations. This is a very promising methodology when data acquisition is performed during low water levels, as expensive field campaigns may be avoided.

The DTM provided does not include the existing dykes in the domain of study, which were built as defence structures against floods. Therefore, and given their relevance to the simulations, 5 overtopping-prone dykes were introduced in the hydraulic model as 2D structures (see Figure 5).

Land use data

Land cover data for the study area was retrieved from Corine Land Cover 2006 with spatial resolution of 100 m. Since there are no roughness coefficient values defined for the study area, the initial roughness coefficient map used in the simulations was based on the Corine classes, crossed with roughness coefficient values in the literature for other study areas (*e.g.* Kalyanapu *et al.*, 2009). For classes 511 and 512 (water courses and water bodies, respectively) the value of 0.05 $sm^{-1/3}$ was used for the Manning coefficient. It was verified that the floodplain presents just a few classes: 212, 221 and 242, corresponding to permanently irrigated lands, vineyards and complex cultivation

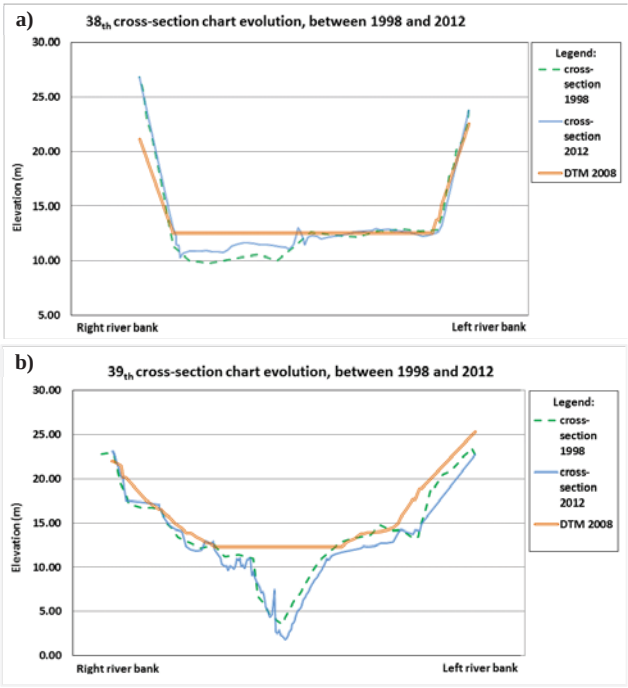

Figure 2. Cross-section profiles on different positions in the river.

patterns, respectively. The Manning coefficient was, for each class, 0.037, 0.037 and 0.020 $sm^{-1/3}$, respectively.

Boundary conditions

The upstream and downstream boundaries in the hydraulic model were chosen at hydrometric stations (upstream in Tramagal and downstream in Ómnias (see Figure 1)), where the water elevation values are known. Figure 3 presents the hydrograph of the river discharge in Tramagal for the period of simulation, with a peak flow of 4,820 m^3/s. The river discharge was obtained through the water levels provided by the Portuguese Environmental Agency (APA), using rating curves from the National Water Resources Information System (SNIRH).

The black vertical line marks the instant of the SAR image acquisition (satellite ERS-2), which corresponds to 19 h after the peak flow in Tramagal. However, the time of imagery acquisition corresponds to the flood peak in Ómnias, which is the most affected area. Almourol is a control station that was used as a calibration/validation point for water levels.

Satellite imagery

SAR imagery was used to validate the numerical model, comparing the flooded area in the imagery and in the simulation, for the same instant in time. SAR imagery was acquired by satellite ERS-2 SAR from ESA (European Space Agency), with a spatial resolution of 25 m. The image was firstly orthorectified and calibrated using the software NEST from ESA and the 5 m resolution DTM, as described in Roque *et al.* (2014).

Figure 4 presents the SAR image for the flood of November 1997, where the darker regions correspond to water. The delimitation of the flooded area was carried out using two different methods: an object-based algorithm (or automatic) approach and a visual interpretation followed by manual delimitation, as detailed by Roque *et al.* (2014).

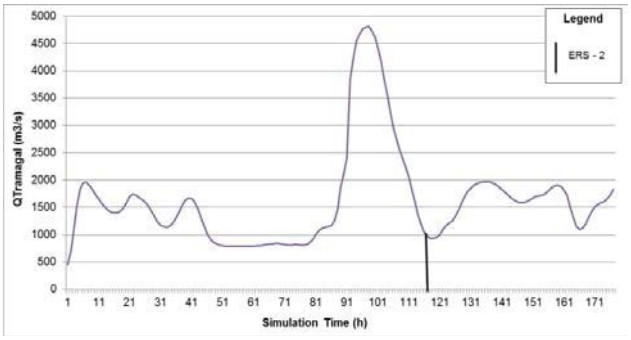

Figure 3. Hydrograph of the river discharge in Tramagal.

The object-based algorithm was applied both to the SAR image and the DTM. The image was first segmented into objects with homogeneous characteristics, using a segmentation algorithm. Since the darkest objects have the highest probability of corresponding to flooded areas (due to the specular reflection of the microwave radiation in smooth water surfaces), these are taken as starting points in an iterative region-growing approach that uses both radiometric and altimetry information. The use of the altimetry information from the DTM is critical for the identification of water surfaces disturbed by wind, rain or emerged vegetation.

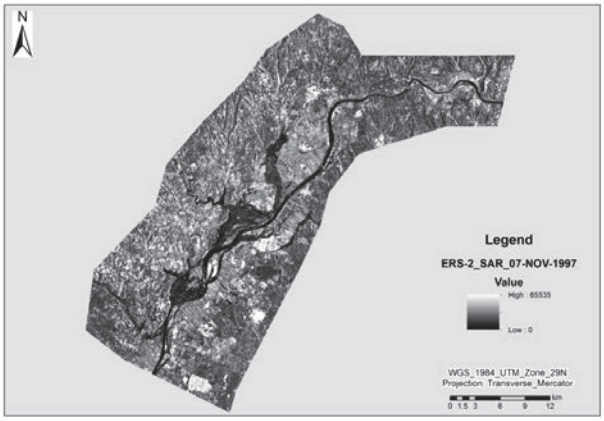

Figure 4. SAR image acquired during the flood of November 1997.

The accuracy of a classified image refers to the extent to which it agrees with a set of reference data. Most quantitative methodologies to assess classification accuracy involve a confusion matrix built from the two data sets. Those data sets

are the remotely-sensed digital data, which are the referenced data in this work, and the data obtained by hydrodynamic simulations. The confusion matrix represents an effective way to present accuracy, including overall accuracy, kappa coefficient of agreement, errors of exclusion (omission errors) and errors of inclusion (commission errors) (Maingi *et al.*, 2002). The overall accuracy is computed by summing the number of pixels correctly classified and dividing by the total number of pixels in the matrix, which corresponds to the percentage of flooded area correctly detected. For values of kappa superior to 0.75, there is a strong agreement between the evaluations of two situations, being the perfect agreement for a value of 1. The errors of omission refer to pixels of a known category that were excluded from that category due to classification error, *i.e.* correspond to the percentage of flooded area not detected by the applied methodology. The errors of commission refer to pixels in the classified image that are included in categories in which they do not belong, *i.e.* correspond to the percentage of detected flooded area, which in fact is not flooded.

Hydrodynamic model and test conditions

Tuflow is a model for simulating depth-averaged, two and one-dimensional unsteady free surface flows, applied to rivers, floodplains, estuaries, coastal waters and urban areas, where the flow behavior is essentially 2D in nature (Syme, 2001). This model is especially applicable to reproduce flood events in rural areas, which are usually characterized by long duration and mixed supercritical and subcritical flow conditions. A structured regular computational grid 30 x 30 m was generated with more than 2 million elements. This grid density proved to be adequate for bathymetry interpolation, so the most important length scales of topographic information were accounted for, what is a concern in flood inundation models. The simulations were carried out from November 2nd 1997 4 p.m. to November 9th 1997 12 a.m., totalling 177 h.

RESULTS

The validation of the hydraulic model was performed comparing the flood extension obtained in the simulations with the identified flooded area in the imagery using both the automatic segmentation algorithm and the manual delimitation methods. Figure 5 presents the flood extents using the automatic algorithm delimitation and the simulation results. It can be observed that there are some regions not flooded by the model (on the left bank), which are actually flooded, and there are some regions flooded that should not be (especially on the right bank). The November 1997 flood is rated as a medium flood in the river, therefore the dykes were not overtopped (Laia Fernandes, personal communication 2013). Though for flow rates above 4,000 m^3/s, the flood discharger dyke of Vinte is operating. The region appearing as not flooded in the simulation but flooded in the image (on the left bank) corresponds to the Alpiarça channel. However, that water is not a result from the overtopping neither of the Tagus banks nor the Junceira dyke since the maximum flow rate is lower than 5,200 m^3/s, but from the Ulme River. Thus, simulation results are qualitatively in agreement with the flood delimitation based on the image.

Figure 6 shows the measured and simulated water levels at the Almourol station. At the peak flow there is an offset between the measured and simulated values of 0.23 m, being the simulated value greater.

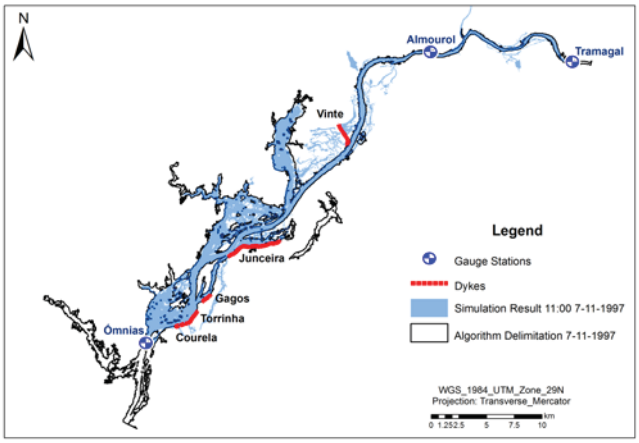

Figure 5. Flood extents resulting from the algorithm delimitation (black contour) and the simulation results (in blue).

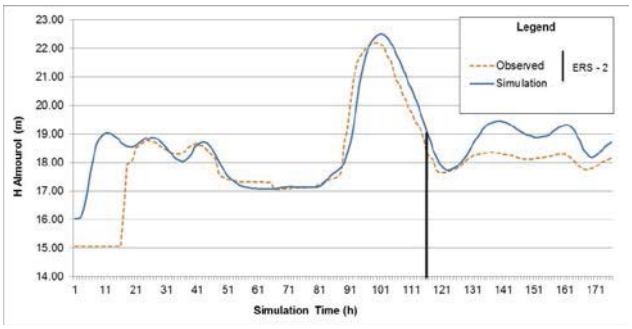

Figure 6. Measured and simulated water levels at the Almourol station.

DISCUSSION

Because the land adjacent to the Vinte dyke (on the right bank) has cultivated crops, it is very permeable, justifying the absence of water in the imagery (Figure 5). That land has been bulldozed for agricultural purposes, leading to a higher infiltration rate. Yet, that infiltration and even evaporation are not accounted for by the model. However, in this region the simulated water depth is quite small, mostly less than 0.2 m, as shown by Figure 7. This is in concordance with the imagery since that layer of water may be easily infiltrated/evaporated.

Table 1 presents the overall accuracy, kappa coefficient and commission and omission errors, for the comparison between the flood extension obtained in the simulations and the manual and automatic (object-based algorithm) delimitation in imagery. The values of these variables are also presented for the cases considering or not the 0.2 m water depth. This table shows that the automatic and manual delimitation methods give similar accuracy assessment parameters, with overall accuracy above 97%. As the simulation results may be used to produce hazard

maps, more importance is given to the omission errors. These errors are lower when considering all the water depth, using any of the methodologies, being made worse when discarding the 0.2 m water depth, as expected. The opposite is found for the commission errors. The high omission errors are mainly due the Alpiarça channel, which appears as a flooded region in imagery. However water does not flow there from the Tagus River, as mentioned before, rather coming from a river which is outside the simulation domain.

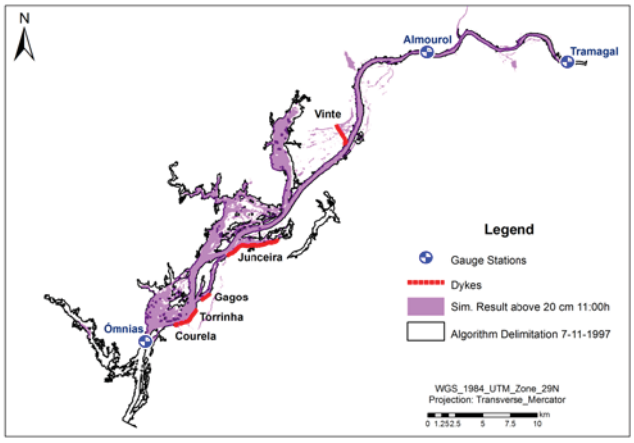

Figure 7. Flood extent for water depth greater than 0.2 m.

Table 1. *Overall accuracy, kappa coefficient and commission and omission errors.*

	Manual delimitation		Algorithm delimitation	
Water level range (m)	0 - 219	0.2 - 219	0 - 219	0.2 - 219
Overall accuracy (%)	97.23	97.41	97.14	97.42
K coefficient	0.75	0.74	0.75	0.75
Commission (%)	24.90	16.41	25.31	15.96
Omission (%)	22.65	31.70	22.56	30.88

Based on the flood extents and water levels, and on the discussion above, one may conclude that the modelling approaches provided acceptable results. Some of the differences in the results might come from uncertainties in the boundary conditions, as the inflow is very often derived from rating curves established with limited measurements. Furthermore, some uncertainties may be linked to the processes used to extract the flood boundaries from the SAR imagery, although the algorithms used have shown a good performance (Roque *et al.*, 2014). In this work, the computational flood extents correspond to the peak of the flood at the region of interest, which coincides with the time of satellite image acquisition. Flooded areas at their peak are often required and, in this case, the time gap between the satellite passage and the flood peak can make a great difference.

CONCLUSIONS

In this study, a SAR derived flood extent map is used to validate the hydraulic model Tuflow of a river flood flow. The study site is a 70 km stretch of the lower Tagus River, in Portugal, and the simulated event is a historical flood that occurred in November 1997. The methodology adopted in using a simplified bathymetry in the river main course proved to be efficient for high-flow events. These findings confirm the conclusions obtained by Dottori *et al.* (2013), arguing that to provide reliable inundation extent predictions, too much detail in the data is often unnecessary. This constitutes an important strategy, which can be used in other flooding studies, as this method will avoid expensive and time consuming field surveys, mainly in the river course. The accuracy of the results is quantified by comparing simulated flood extents with those obtained from the SAR imagery using two methodologies: an automatic (object-based algorithm) approach and a manual delimitation. Besides, the measured water levels at one gauging station located within the modelled area were compared with the predicted values. The results show that the applied methodologies are appropriate for the validation of the hydrodynamic model.

ACKNOWLEDGMENTS

This study was supported by Portuguese Foundation for the Science and Technology (FCT) through the project RIVERSAR (PTDC/CTEGIX/099085/2008). SAR imagery was provided by ESA through category-1 project 9441. SNIRH and APA are acknowledged for making the hydrometric data available. The authors are grateful for the information given by Laia Fernandes.

LITERATURE CITED

Azevêdo, T.M.; Nunes, E., and Ramos, C., 2004. Some morphological aspects and hydrological characterization of the Tagus floods in the Santarém region, Portugal. *Natural Hazards*, 31, 587-601.

Bates, P.D.; Horritt, M.S.; Smith, C.N., and Mason, D., 1997. Integrating remote sensing observations of flood Hydrology and hydraulic modelling. *Hydrological Processes*, 11, 1777-1795.

Dottori, F.; Di Baldassarre, G., and Todini, E., 2013. Detailed data is welcome, but with a pinch of salt: Accuracy, precision, and uncertainty in flood inundation modeling. *Water Resources Research*, 49, 6079-6085.

García-Pintado, J.; Neal, J.C.; Mason, D.C.; Dance, S.L., and Bates, P.D., 2013. Scheduling satellite-based SAR acquisition for sequential assimilation of water level observations into flood modeling. *Journal of Hydrology*, 495, 252-266.

Kalyanapu, A.; Burian, S., and McPherson, T., 2009. Effect of land use-based surface roughness on hydrologic model output. *Journal of Spatial Hydrology*, 9(2), 51-71.

Maingi, J.K.; Marsh, S.E.; Kepner, W.G., and Edmonds, C.M., 2002. *An accuracy assessment of 1992 Landsat-MSS derived land cover for the upper San Pedro watershed (U.S./Mexico)*. Environmental Protection Agency, Washington, DC, US, *EPA/600/R-02/040 (NTIS PB2002-107521) Report*.

Roque, D.; Afonso, N.; Fonseca, A.M., and Heleno, S., 2014. OBIA flood delimitation assisted by threshold determination with PCA. *Photogrammetric Engineering and Remote Sensing*, 80(6), 551-557.

Syme, W.J., 2001. TUFLOW – Two & one-dimensional Unsteady FLOW software for rivers, estuaries and coastal waters. *IEAust 2D Seminar*, Sydney

Journal of Coastal Research	SI	75	18 - 22	Coconut Creek, Florida	2016

Runoff and sediment Transport of Portel-Melgaço Water System in an Amazonian estuarine System

Mauricio S. Costa[†*], Marcelo Rollnic[†], Yuri O. Prestes[†], Renan P. Rosário[‡]andThais A. C. Borba[‡]

[†]Physical Oceanography Laboratory, Oceanography Faculty
Federal University of Pará
Belém, Brazil

[‡]Marine Geophysical Laboratory, Graduate Program in Geophysics (PPGf). Federal University of Pará
Belém, Brazil

www.cerf-jcr.org

www.JCRonline.org

ABSTRACT

Costa, M. S.; Rolnic, M., P.D.,Prestes, Y.O., Rosário, R.P., and Borba, T. A.C., 2016. Runoff and Sediment Transport of Portel-Melgaço Water System in an Amazonian Estuarine System. *In:* Vila-Concejo, A.; Bruce, E.; Kennedy, D.M., and McCarroll, R.J. (eds.), *Proceedings of the 14th International Coastal Symposium* (Sydney, Australia). *Journal of Coastal Research*, Special Issue, No. 75, pp. 18 - 22.CoconutCreek (Florida), ISSN 0749-0208.

The Pará River, located in northern Brazil, receives hydrological and sediment contributions from a complex network of basins, such as the Amazon, Portel/Melgaço, and Tocantins river basins. Portel/Melgaço basin, a fluvial-estuarine system situated between the Amazon and Tocantins river basins, is still poorly known. Therefore, the objective of this study is to identify whether there is any hydrological and sediment contribution from Portel/Melgaço river basin to the Pará River. For that purpose, two campaigns were carried out: 1) June, 2013 (transitional season) and 2) March 2014 (wet season). Samplings were carried out over a tidal cycle (13 h) and consisted of a bathymetric surveys; tide measurements; cross sections of streamflows (Acoustic Doppler Current Profiler); and vertical turbidity profiles (Optical Backscatter Sensor) with water sampling (surface and bottom for Suspended Particulate Matter) at three points of the cross section. Our main conclusion is that the inflow from Pará and Amazon Rivers to Portel/Melgaço river basin is higher than the outflow and appears to be highest in the dry season.Thus, the Amazon and Pará Rivers are the main source of suspended sediments to the system, and this characterizes Portel/Melgaço river basin as a retention basin.

ADDITIONAL INDEX WORDS: *Pará River, Amazon Coastal, Volume Transport.*

INTRODUCTION

The Pará River, located in northern Brazil, is formed by three different basins: Amazon, Portel-Melgaço, and Tocantins. Portel-Melgaço river basin, which is located between the Amazon and Tocantins River basins, might be characterized as a fluvial-estuarine system (Silva, 2009; Costa, 2014), influenced by the Pará and Amazon Rivers. Portel-Melgaço river basin occupies an area of 46,368.43 km^2, 3.71% of the Pará State, and is drained through by the following rivers: Anapú, Pacajá, Caxuanã, Pracuri, Camaparí, and Jacundá; these rivers converge to form Melgaço Bay, through which water and sediment flow towards the Pará or Amazon Rivers (Figure 1). Although this basin is 380 km away from the mouth of the Pará River, it has dynamic tides with semidiurnal characteristics.

Thus, water and sediment exchange might take place between the streamflows of Amazon and Pará Rivers and Melgaço Bay, and the bay might work as water or sediment importer or exporter, which is the hypothesis addressed in this study. Therefore, the objective of this study is to identify whether there is any hydrological and sedimentary contribution fromPortel / Melgaço river basin.

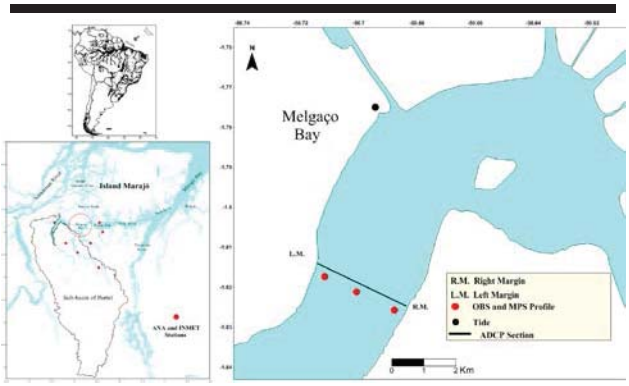

Figure 1. Study area with sampling points.

The climate in this area is equatorial wet, with temperatures ranging from 18ºC to 36ºC and mean of 27ºC. Its maximum humidity is around 90% with high rainfall in the first six months of the year. The rainiest quarter is February, March, and April, reaching 350 mm, while the less rainy season is in August, September, and October, with rainfall of approximately 70 mm in October. Annual rainfall is around 2300 mm (INMET, 2015; ANA, 2015).

According to Bahia *et al.,* (2004), this region is characterized by igneous rocks upstream (Charnockitoids), Alter do Chão formation (Rough Sandstone), and recent fluvial deposits on the

DOI: 10.2112/SI75-004.1 received 15 October, 2015; accepted in revision 15 January, 2016 .
*Corresponding author: mauricio.oceo@gmail.com

drainage margins and in the connection to the Pará River. The rivers drain through these terrains, forming acomplexsystemcarrying sediments towards Melgaço Bay. Volume transport and transport of suspended particulate matter (SPM) over a tidal cycle provide estimates for export and/or import. These estimates allow for detecting variations in flood and ebb tides, as well as potential erosion and sedimentation patterns, with which morphological changes might be inferred.

MATERIALS AND METHOD

Two field samplings were carried out: the first one took place during the climatological transitional season, in June, 2013, and the second one during the wet season, in March, 2014. Samplings consisted of bathymetric surveys with crosscut profiles 500 meters apart and longitudinal profiles. In addition, cross sections of streamflows (intensity and direction with *Acoustic Doppler Current Profiler - ADCP*) were performed to obtain water volume transport over a tidal cycle (13 hours). Samplings were also comprised of: vertical turbidity profiles performed at three points of the river cross section; and water sampling (surface and bottom) to obtain SPM.

A pressure sensor was installed on the river margins during the campaigns to characterize the local tide. Harmonic data from the gauging station in the city of Breves were also obtained via the Sea Research Foundation catalogue (FEMAR, 2014).

Volume transport was calculated based on two methodologies. ADCP volume transport 1 (TV1) was developed by Gordon, (1989); Simpson and Oltmann (1990). Volume transport 2 (TV2) was based on equations for flow and property transport for a known vertical profile (h) of a section, described by Miranda, *et al*. (2002), replacing h (t) by the section area A(t), and thus having the volume transport for a river section (Table 01).Subsequently, the resulting volume transport was calculated, which is the sum of all measurement sections, given in cubic meters per tidal cycle (m³/tidal cycle), indicating whether water was imported or exported in the study field.

Table 1. *Volume transport methods.*

TV 1	TV 2
$\iint_s V_f \,.\, n.\, d_s$; $d_s = \lvert V_b \rvert d_z d_t$;	$\frac{1}{T}\int_0^T \bar{u}\ (t)\ A\ (t) d_t$;
d_s= Differential area;	$\bar{u}$= Longitudinal mean velocity
V_f= Mean water velocity vector;	
n = Normal unit vector;	A(t) = Area of section (m²)
d_z= Differential depth;	
d_t= Differential time;	d_t= Time throughout a tidal cycle
V_b=Mean vessel velocity vector	

Total basin discharge was estimated based on Schreiber empirical method (Miranda *et al*. 2002), using data ranging from 1980 to 2014 from the National Water Agency (ANA) and the National Meteorology Institute (INMET), which have 7 fluviometric stations in the region.

SPM samplings were carried out at the surface (1 meter) and at the bottom using a Van Dorn bottle. SPM was determined by the method of volatilization gravimetry, according to Baumgarten *et al*., 1996. Vertical profiles were performed with an OBS (Optical Backscatter Sensor) turbidity sensor simultaneously to water collection and using FTU (Formazin Turbidity Unit) as unit. SPM transport calculation was based on two methods: Colby's transport method (T1) (1957) and transport (T2) by Miranda *et al*., (2002); the unit is tons per tidal cycle (ton/ tidal cycle) (Table 2).

Table 2. *SPM transport methods.*

T 1	T 2
$t.\ Q.\ C_{SS}\ / 10^6$	$\frac{1}{T}\int_0^T u\,.\,[C_{SS}]\,.\ A\,.10^6 d_t$
10^6= milligram conversion factor by ton	
t = Ebb and flood time (in seconds)	
Q= flood or ebb transport volume	$\bar{u}$ = average flood or ebb velocity
	A(t) = section area (m²)
Css= Average SPM in flood or ebb	

RESULTS

The results are divided into topics in order to give a better explanation. They encompasses morphodynamics and hydrological analyses.

Morphological analysis

Morphological profiles showed a mean width of 2 to 3 km in a quite winding stretch, with high variations in depth. There are narrow tidal plains, with floodplain vegetation opposite the main channel. The main channel is rectilinear, with mean depth of -9.5 m and maximum depth of -26 m. Compact, muddy facies were observed, as well as some sandy banks along the river, with minimum depth of -10 meters, which do not hinder navigation through the main channel even during low tide. A bathymetric chart of the area was elaborated based on interpolated bathymetric profiles (Figure 2).

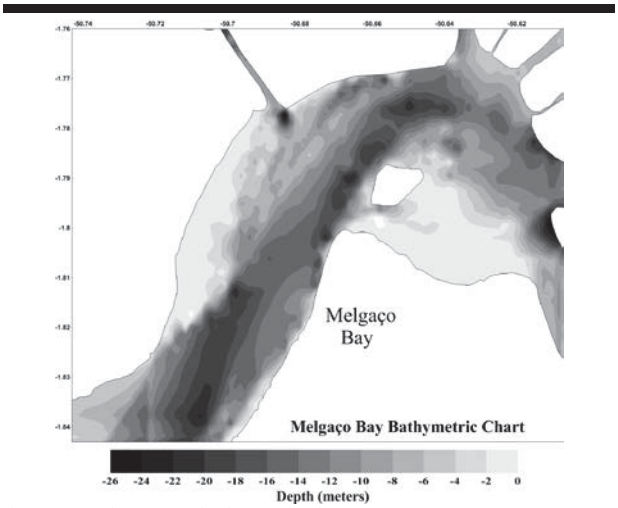

Figure 2: Melgaço Bay bathymetric chart.

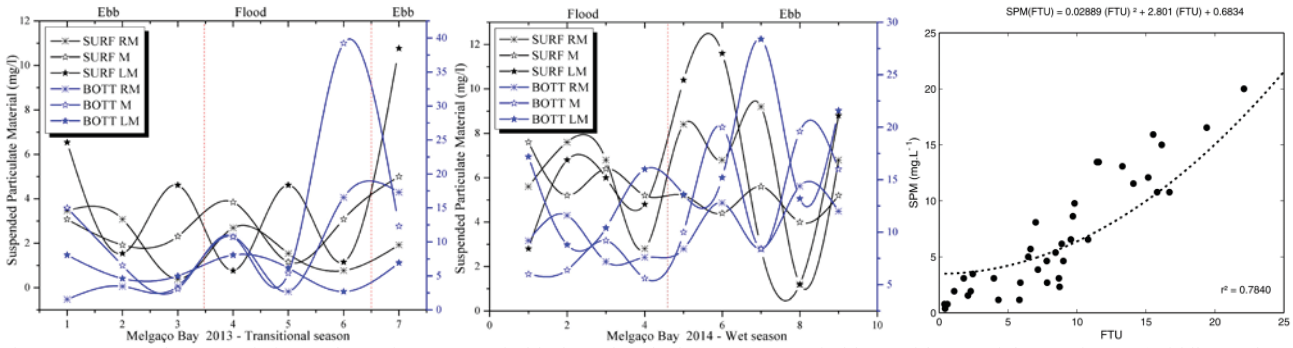

Figure 4. Temporal SPM variation at the surface (SURF, in black) and at the bottom (BOTT, in blue), with RM (right margin), M (Middle), and LM (left margin); and correlation between SPM and Turbidity (FTU).

Current

Negative values represent flood velocities (in dark gray) and positive values represent ebb velocities (in ligth gray). Longitudinal velocities were similar in the transitional season, and mean (0.22 m/s) and maximum (0.36 m/s) values were similar during flood and ebb. In the wet season, the fluvial component was emphasized, with mean of 0.19 m/s during flood and 0.23 m during ebb; and maximum values of -0.3 m/s during flood and 0.4 m/s during ebb. Values close to zero in temporal variation graphs represent the inversion of tides along the entire water column. The highest velocities occurred at the surface and they decreased with depth due to friction. Tide predominance is evident based on the resulting flow, even in the microtidal regime of the area, and the influence of the fluvial component was restricted to the central part of the channel, Figure 3.

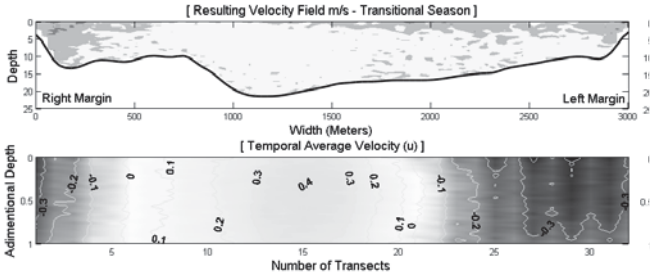

Figure 3: Resulting velocity field (above) and temporal velocity (below) in Melgaço Bay in transitional and wet seasons

SPM and Turbidity

SPM and FTU concentrations are directly related to the influence of tide. Therefore, variations over the tidal period might have a greater influence on SPM concentrations in the water column than seasons; and, consequently, on sediment and volume transport. SPM and turbidity were lower than 40 mg^{-1} and 30 FTU in Melgaço Bay during both seasons (Figure 4) based on a correlation that adjusted their values. This correlation resulted in a high value, evidencing a direct relationship and proving that both SPM and turbidity follow the same trend. Average SPM concentrations in the water column were higher during the wet season, with 5.9 $mg.L^{-1}$ at the surface and 12.5 $mg.L^{-1}$ at the bottom; average SPM concentrations were 3 $mg.L^{-1}$ at the surface and 9 $mg.L^{-1}$ at the bottom in the transitional season. Turbidity followed a similar pattern. The highest SPM and turbidity values occurred in the transitional season during flood; and in the wet season, they were higher during ebb.

Comparing to Costa (2014), SPM and turbidity values in Melgaço Bay are 3 to 6 times as small in dry and wet seasons, respectively, and these parameters are controlled by seasonal variations and daily hydrodynamic processes

Volume and SPM transport

The instantaneous volume transport in Melgaço Bay was higher during the wet season, with an addition of 19% during ebb and a reduction of 6.5% during flood compared to transitional values. In the transitional season, the bay imported 26.3 - 28.5 thousand m^3/tidal cycle upstream, and it exported 29.3 - 8.2 thousand m^3/tidal cycle towards the Pará or Amazon Rivers in the wet season (Figure 5). SPM transport indicated import of 1074 - 1015 tons/tidal cycle during the transitional season, and export of 528.1 - 306.2 tons/tidal cyclein the wet season (Table 03).The difference between Volume transport methods derives from the fact that TV2 uses mean longitudinal current and TV2 uses the sum of measurement cells, which accounts for a. different transport volume in each method at the

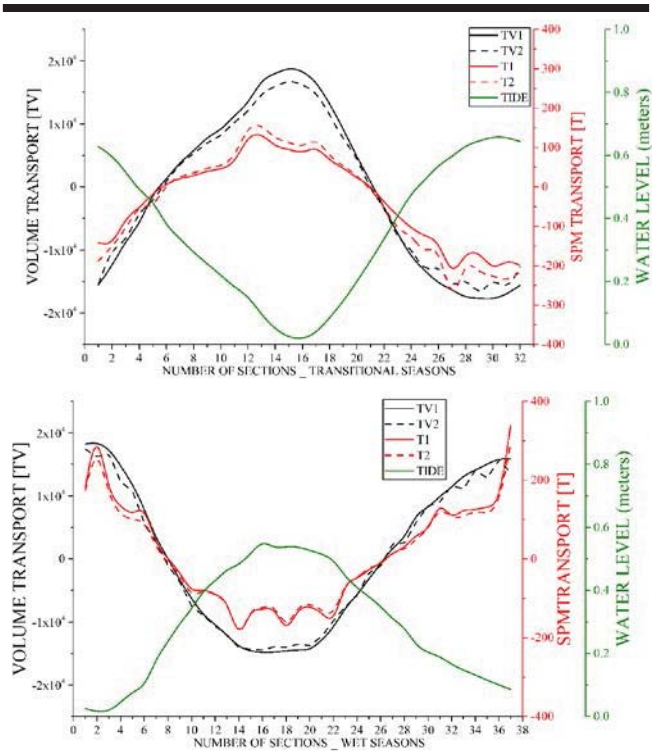

Figure 5. Temporal variation of Instantaneous volume transport (TV, in black) and SPM transport (T, in red) with water level (in green).

Table 3. *Instantaneous volume and SPM transport of Melgaço Bay river*

	TRANSPORT		VOLUME		SPM	
RIVER	SEASON	TIDE	TV1	TV2	T1	T2
MELGAÇO BAY	TRANSITIONAL	EBB	16971 5.9	15061 5.6	999.7	887.4
		FLOOD	-19603 5.0	-17917 1.7	-2074.1	-1902.7
		RESULTANT	**-26319.1**	**-28556.1**	**-1074.4**	**-1015.2**
	WET	EBB	20819 5.5	18909 5.9	2384.8	2135.8
		FLOOD	-18423 6.0	-18081 0.0	-1856.7	-1829.6
		RESULTANT	**23959.5**	**8285.9**	**528.1**	**306.2**

moment of transition of tides (ebb or flood), directly reflecting the discrepancies between transport periods.

Bay discharge and Tide Prism

The total discharge of Melgaço Bay was estimated through gauging stations in Portel-Melgaço Basin for better data consistency. Average annual discharge is 580 m^3/s and discharge distribution follows rainfall. The period ranging from January to June (wet season) accounts for 80% of the annual rainfall, peaking in April (15%), and the period ranging from July to December (dry season) accounts for 20% of the rainfall, with minimum rainfall in October (2%). Daily temperature variations are more important than seasonal variations because variations in rainfall are more significant, directly reflecting evapotranspiration rate. The same method was applied in Northeastern and Southeastern Brazil by Medeiros & Kjerfve (1993) in Itamaracá Island, and Kjerfve *et al.,* (1996) in Araruama Lake, with much lower values, highlighting the differences between equatorial and tropical zones.

Based on volume flow, tide prism and river discharge were calculated for Melgaço Bay, with a volume of 258.7 $x10^6$ m^3 in the transitional season and of 209.4 $x10^6$ m^3 in the wet season, indicating that basin discharge is low for a microtidal regime. This directly influences the renewal capacity of the water mass in each tidal cycle, which must be slowly renewed in the transitional season for a total river discharge of 232 $x10^6$ m^3, withretention of 26.2 milhões m^3 in each tidal cycle; and faster in the wet season for a discharge of 235 x 10^6 m^3, allowing for a renewal of 25.6 million m^3 in each tidal cycle.

DISCUSSION

Melgaço Bay is a region with clear waters and low hydrodynamics; there is no saline water inflow, only dynamic tide inflow, and the microtidal regime is responsible for sediment exchange and flow inversion, enabling sedimentation due to its low water renewal period.

Low Turbidity and SPM values characterize Melgaço Bay as a clearwater environment (Sioli, 1968), meaning its water has low suspended material, as observed in the waters of Xingu and Tapajós Rivers, and different from the surrounding areas, with white waters rich in suspended matter (Costa, 2014).

Volume and SPM transports indicated import during the transitional season, possibly even higher in the dry season, and export in the wet season; however, export is 55% lower than import, characterizing Melgaço Bay as a retention basin.

Once the basin discharge was assessed without considering the effects of tide, i.e., considering a unidirectional flow compared to the resulting volume transport of -579.7 m^3/s in the transitional season and 596.9m^3/s in the wet season, it became evident that the basin discharge is only effective in the wet season; in transitional and dry seasons, it suffers hydrostatic pressures from the Amazon and Pará Rivers, in addition to the daily influence of the tide from the Bay.

Using harmonic tide data, a distortion of the tidal wave was identified in Breves, with M4 amplitudes accounting for over 10% of the M2 amplitude in Melgaço Bay. The difference in phase between the semidiurnal lunar component (M2) and the shallow water component (M4) represented a value < 180°, indicating a positive asymmetry of the tidal wave, with more intense flows and shorter duration in flood than in ebb.

The surrounding area exerts a strong hydrostatic pressure, both in dry and wet seasons. According to Costa (2014), the Amazon River exports to the Pará River during the wet season through Jacaré Grande River, one of the channels that interconnect Pará River to Amazon River; and some of these channels connect to Melgaço Bay. Thus, the Amazon River might also export to Melgaço Bay; moreover, in the dry season, the Pará River

directs its flow towards the Amazon River, and consequently, to Melgaço Bay, but with lower intensity.

CONCLUSIONS

Melgaço Bay is a Clearwater region, with low hydrodynamics and microtides, and the tide is responsible for exchange processes and mostly for short-period processes. Volume and SPM transports have already shown a trend towards import in the transitional season and a trend towards export in the wet season, and the resulting volume transport is very similar to basin discharge in the wet season. This is because the basin discharge is only effective, positive, in the wet season. Our conclusion is that the contribution of the Pará and Amazon Rivers to Melgaço Bay is higher, and not the other way around; and the greatest contribution from the Amazon and Pará Rivers is possibly in the dry season. They are also the main source of suspended sediments to the system, which characterizes the Portel/Melgaço Basin as a retention basin.

ACKNOWLEDGMENTS

This work is the result of cooperation between Physical Oceanography Laboratory (LOF) and Marine Geophysical Laboratory (GEOFMAR).

LITERATURE CITED

AGÊNCIA NACIONAL DE ÁGUAS (ANA). 2011. http://www.ana.gov.br/PortalSuporte/frmSelecaoEstacao.aspx.

Bahia, R. B. C., Faraco, M. T. L., Monteiro, M. A. S., Camozzato, E., Oliveira, M. A. O. *Folha SA. 22-Belém*. In: Schobbenhaus, C., Gonçalves, J. H., Santos, J. O. S., Abram, M. B., Leão Neto, R., Matos, G. M. M., Vidotti, R. M., Ramos, M. A. B., Jesus, J. D. A. de (eds.). C*arta Geológica do Brasil ao Milionésimo, Sistema de Informações Geográficas. Programa Geologia do Brasil*. CPRM, Brasília. 2004.

Baumgarten, M. G. Z.; Rocha, J. M. B; Niencheski, L. F. H. 1996. *Manual de análises em Oceanografia Química*, Editoras FURG/Pallotti, 142 p.

Colby, B. R. 1957. Relationship of unmeasured sediment discharge to mean velocity. *Amer. Geophy. Union, Trans.,* 38(5), 708-717.

Costa, M. S. 2014. Aporte hídrico e do material particulado em suspensão para a Baía do Marajó: contribuições dos rios Jacaré Grande, Pará e Tocantins. Masters Thesis. Programa de Pós-Graduação em Geologia e Geoquímica - Universidade Federal do Pará.

Fundação Estudos Do Mar (FEMAR). 2014. *Catálogo de estações maregráficas brasileira*. http://www.fundacaofemar.org.br/biblioteca/emb/tabelas/037.html.

Gordon, R. L. 1989. Acoustic Measurement of River Discharge. *Journal of Hydraulic Engineering*, 115(7), 925-936.

INSTITUTO NACIONAL DE METEOROLOGIA (INMET). 2015.http://www.inmet.gov.br/portal/index.php?r=home/page&page=rede_estacoes-auto-graf.

Kjerfve, B.; Schettini, C.A.F.; Knoppers, B.; Lessa, G.; Ferreira, H.O. Hydrologyand Salt Balance in a Large, Hypersaline Coastal Lagoon: Lagoa de Araruama, Brazil. *Estuarine, Coastal and Shelf Science***.** 42(6), 701–725.

Medeiros, C. & Kjerfve, B. 1993. "Hidrologyof a Tropical Estuarine System: Itamaracá, Brazil". *Estuar. Coast. Shelf Sci.*, 36, 495-515.

Miranda, L. B.; Castro, B. M.; Kjerfve, B. 2002. *Princípios de Oceanografia Física de Estuários*. São Paulo, EDUSP, 424 p.

Prestes, Y. O.; Rollnic, M; Silva, M. S.; Rosário, R. P. 2014. Volume transport in the tidal limit of the Pará River, Brazil. *Proceedings of the 17th Physics of Estuaries and Coastal Seas conference*, Porto de Galinhas, Pernambuco, Brazil, 19–24.

Silva, I. O. 2009. Distribuição da Vazão Fluvial no Estuário do Rio Amazonas. Dissertação (mestrado). COPPE/Programa de Engenharia Oceânica, Universidade Federal do Rio de Janeiro.

Simpson, M. R. & Oltmann, R. N. 1990. An Acoustic Doppler Discharge Measurement System. *Proceedings of the 1990 National Conference on Hydraulic Engineering*, 2, 903-908.

Sioli, H. 1968. Hidrogeochemistry and geology in thebrazilian Amazon region. *Amazoniana*, 1, 267-277.

Journal of Coastal Research	SI	75	23 - 27	Coconut Creek, Florida	2016

Acoustic attenuation due to bi-modal size distributions of suspended sediment

Daniel M. Hanes

Department of Earth and Atmospheric Sciences
Saint Louis University
Saint Louis, MO, USA

www.cerf-jcr.org

www.JCRonline.org

ABSTRACT

Hanes, D.M., 2016. Acoustic attenuation due to bi-modal size distributions of suspended sediment. *In:* Vila-Concejo, A.; Bruce, E.; Kennedy, D.M., and McCarroll, R.J. (eds.), *Proceedings of the 14th International Coastal Symposium* (Sydney, Australia). *Journal of Coastal Research*, Special Issue, No. 75, pp. 23 - 27. Coconut Creek (Florida), ISSN 0749-0208.

Acoustic backscatter is a technique commonly used to remotely measure the concentration profile of suspended sediment. The technique generally involves an inversion, because the backscattered sound intensity depends upon the range dependent concentration and size distribution of the sound-scattering particles. This work examines the attenuation of sound due to particles, and in particular evaluates the relative contributions of viscous attenuation verses scattering attenuation as a function of the size of the particles. It is found that under some conditions viscous attenuation is dominated by smaller sized sediment and scattering attenuation is dominated by larger size sediment, but this result is not true in general, and depends upon the particular particle size distribution.

ADDITIONAL INDEX WORDS: *hydro-acoustics, suspended sediment*

INTRODUCTION

The profiles of suspended sediment concentration and size are sometimes measured using acoustic backscatter techniques. The principle underlying the measurement technique is to transmit a pulse of sound energy into water and interpret the range-gated sound pressure received back at the same transducer, as described by Hay (1983). For example, acoustic systems with frequencies of 1 to 5 MHz were used by Libicki et al. (1989) in the deep ocean and by Hanes et al. (1988) in the shallow nearshore zone, following the concepts reviewed by Thorne and Hanes (2002). Interest in extracting sediment concentration from the backscatter signal strength has recently increased in a variety of environments with the widespread use of commercial Acoustic Doppler Current Profilers (ADCP's). For example, Gartner (2004), and Hoitink and P. Hoekstra (2005) report using ADCP's to measure suspended sediments, mainly in the clay to silt size ranges, in coastal environments. An interesting topic of scientific discussion that has emerged in recent years involves the impact and importance of enhanced viscous dissipation of sound due to fine sediment [e.g. Sassi et al. (2012), Hanes (2012, 2013), Guerrero et al. (2014)]. The phenomenon of enhanced viscous dissipation due to small particles in water was initially documented by Urick (1948) and Flammer (1962). Until recently the viscous dissipation due to water and sediment had generally been ignored in acoustic interrogations of suspended sediment because the attenuation of sound due to scattering by particles was much larger than viscous attenuation. In many of the environments being investigated, such as the nearshore zone, the sediment was typically well-sorted sand. In other environments, however, bi-modal suspended sediment size distributions are sometimes present. In rivers, for example, Wright et al. (2010), through largely empirical means, measured the concentrations of suspended silt and clay (combined) and suspended sand in the Colorado River using a single frequency backscatter system. Their success is probably due to conditions in which the clay/silt sized fraction dominated the viscous dissipation of sound energy and the sand sized fraction dominated the backscattering of sound. Their success probably also depended on the relatively stable size distribution over time, and the relatively homogeneous suspended sediment concentration along the acoustic beam path, which was directed approximately horizontally from the river bank toward the center of the river. Moore et al. (2013) inverted attenuation measurements from a multi-frequency system with varying degree of success, when compared with particle size measured with a laser diffraction instrument. Similarly, Latosinski et al. (2014) inverted vertical profiles in a river by assuming vertically homogeneous, *known* size sediment. Routine inversion of vertical profiles of sediment backscatter still remains elusive, in part due to the wide range of particle characteristics, and in part due to the common bi-modality or broad range of the sediment size distribution in nature. This context motivates the present work.

METHODS

The theory of sound scattering from an aqueous suspension of particles and the practice of using acoustic backscatter to measure suspended sediments has been previously reviewed by

DOI: 10.2112/SI75-005.1 received received 15 October, 2015; accepted in revision 15 January, 2016 .*Corresponding author: dhanes@slu.edu

Thorne and Hanes (2002) and updated by Thorne and Hurther (2014). A typical goal is to interpret the measured backscattered sound pressure to calculate the range-dependent concentration and size of the suspended particles. The backscattered sound pressure measured at a transducer is due to the integration of sound scattering and attenuation due to the particles and fluid along the two-way acoustic path between the transducer and the ensonified volume. Due to the variations in sediment along the sound path, an inversion is typically required to convert the measured backscattered pressure to the range dependent concentration and size of the suspended particles. When a single frequency acoustic system is employed, there is a fundamental shortcoming in that the backscattered sound depends upon both the concentration and the size of the suspended sediment, even if the size of the grains is uniform. This leads to non-unique inversions for sediment concentration and size. This shortcoming can be overcome in theory through the use of two or more acoustic frequencies, although in practice this has proven quite challenging. More commonly the size of the suspended sediment is measured independently and assumed not to vary significantly in space or time.

Key parameters that describe acoustic-particle interactions are the attenuation due to particles, and the backscatter target strength. The backscattering strength of the target particles is characterized by the backscatter form factor, f, defined so that the acoustic scattering *intensity* is proportional to particle area multiplied by f^2. The total attenuation derives from three sources: the viscous attenuation due the clear fluid, the viscous attenuation due to the interactions between particles and fluid, and the (non-backwards) scattering of sound due to the particles. Typical values for the viscous attenuation due to sediment, the scattering attenuation due to sediment, and the sediment backscatter form factor, all for uniform sized sediment, are shown in Figure 1 (from Hanes, 2012), as a function of sediment size, for three different sound frequencies. Of particular relevance here is the peak in viscous attenuation due to fluid-sediment interactions for the smaller grain sizes, which can for some cases cause greater attenuation than that due to the scattering of sound from particles.

The backscatter form function and the attention depend strongly on grain properties such as size and shape, and weakly upon sediment density and water viscosity for most environments, with any particular acoustic instrumentation system. If there exists a distribution of grain sizes, then the attenuation and backscatter must be appropriately integrated over the grain size distribution such as described, for example, by Thosteson and Hanes (1998) or Moate and Thorne (2009, 2012). The total attenuation from a distribution of particle sizes is additive, weighted by the concentration of each size. In contrast to the attenuation, the total backscatter is calculated as the square-root of the sum of squared backscattered pressure due to individual size classes, and thus depends upon the square root of concentration for each size sediment.

In the next section the theoretical acoustic attenuation will be calculated for various distributions of grain sizes. The grains are all considered to be the same material, and spheres, with only size varying. All of the examples show results for 500 KHz sound and a bi-normal distribution (the sum of two normal distributions) of sediment size by mass, with one peak of the distribution in the clay/silt range, and one in the sand size range. The standard deviation of each normal distribution is equal to 25% of the mean size. For illustrative purposes, the fine and coarse fractions have equal mass concentration in all of the examples to be shown.

Acoustic attenuation is often characterized by the natural logarithm of the sound pressure at two locations separated by a unit of distance, expressed for example, as Nepers/cm, where Nepers= $\ln(P_2/P_1)$. Nepers are similar to Decibels except that Decibels are normally defined using the signal power (pressure squared for acoustics) and the base 10 logarithm, so Decibels=$20\ \log_{10}(P_2/P_1)$. For conversion, 1 Neper = 8.686 Decibels. All the attenuation values in this work are normalized by volume concentration, and are expressed as Nepers/cm/C, where C is volume concentration.

RESULTS

Figure 2 introduces the conceptual implications of a bi-modal sediment size distribution. For comparison with uniform sized grains, the red curve is the total (viscous plus scattering) attenuation for sediment with uniform grain size, as a function of particle radius. The red curve clearly shows the peak in viscous attenuation related to fine grains and the peak in scattering attenuation related to coarse grains, as was demonstrated previously in Figure 1. The red circles indicate the total attenuation if the uniform sediment radius was 1 micron, or if the uniform sediment radius was 200 microns. The green curve (and right axis) shows the cumulative bi-modal sediment size distribution, where sand mean radius is 200 microns and clay mean radius is 1 micron. The blue curve is the total attenuation for the bi-normal sediment size distribution. Note that for this particular example the attenuation increases sharply due to

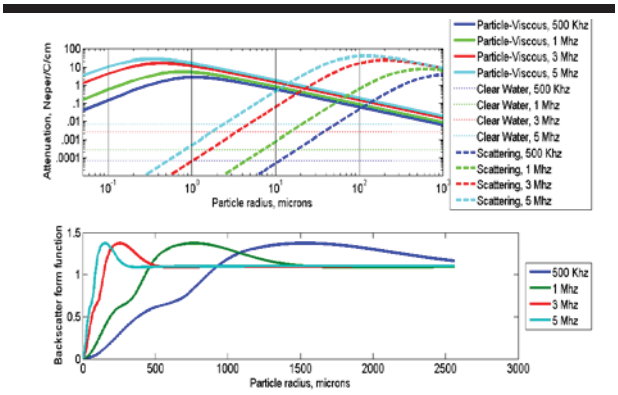

Figure 1: Upper panel: Normalized attenuation coefficients as a function of particle radius. Lower panel: Backscatter form function as a function of particle radius.

viscous dissipation from the fine sediment, and then it increases a bit more due to scattering from the coarse sediment. The blue x at the right side of the blue curve is the attenuation that would be obtained by simply summing the two red circles, as if half the

sediment was 1 micron radius and half was 200 microns radius. For this example the total attenuation is primarily due to the viscous attenuation due to the fine sediment. But this is not a general result; rather the relative importance of viscous attenuation relative to scattering attenuation depends upon the shape of the size distribution of the sediment. In the next section a range of size combinations will be considered.

Figure 3 shows the total attenuation for a range of bi-normal size distributions, where one peak lies in the size range of clay/silt (diameter between 1 micron and 63 microns) and the other peak lies in the size range for sand (diameter 64 microns to 3 mm). The horizontal axis is diameter of the coarse fraction and the vertical axis is diameter of fine sediment. The horizontally aligned bright area is due mainly to the viscous dissipation peak near 1 micron, and the vertically aligned bright area is due mainly to the peak in the scattering around 3 mm. There are combinations of sizes where the attenuation is dominated by either the viscous dissipation due to fine sediment or the scattering attenuation of the coarse sediment. But there are other combinations of sizes where both the fine and the coarse sediment contribute to the attenuation. It should be noted that all the results presented are based on equal concentrations of fine and coarse sediments. If the concentration varied with sediment size in a more general sense then the shape of the size distribution could significantly alter the results.

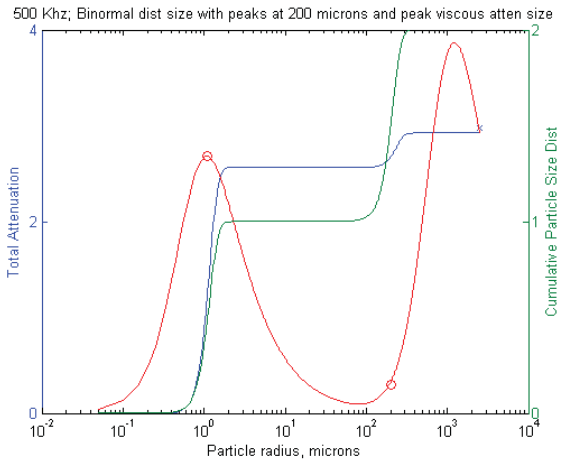

Figure 2: Attenuation due to a bi-modal mixture of 1 micron radius clay and 200 micron radius sand, with 500 KHz sound.

of Figure 3. If all attenuation were due to viscous dissipation the ratio is 0 (dark blue) and if all were due to scattering the ratio is 1 (dark red). The bluer shaded colors indicate where The relative importance of viscous and scattering attenuation is demonstrated by the ratio of the scattering attenuation to the total attenuation, as shown for Figure 4, for the same conditions viscous dissipation dominates, the red shaded colors indicate where scattering attenuation dominates, and the aqua-yellow shades show where both viscous and scattering attenuation are important.

DISCUSSION

Hanes (2012, 2013) considered an idealized uniform suspension with only two widely different particle sizes. He showed that in order for the attenuation and backscatter to be decoupled from each other for this situation, the attenuation needs to be dominated by the fine sediment while the backscatter is dominated by the coarse sediment. The present simulations examine this possibility for bi-normal distributions of sediment size, where one peak is in the size range of clay/silt and the other in the size range of sand.

CONCLUSIONS

These simulations provide support for the idea that under certain conditions a single frequency acoustic backscatter system can, in theory, measure the suspended sediment concentration of both the clay/silt size range and the sand size range. The explanation is essentially similar to that provided previously: the fine sediment can dominate the attenuation while the coarse sediment dominates the backscatter. This work also points to the sensitivity of acoustic attenuation to the size distribution of the suspended sediment, implies that the explanation provided above is not a general result for size distributions different from those simulated. This suggests that independent measurements of the particle size distribution (e.g. using laser diffraction), and multi-frequency measurements of acoustic attenuation could be very valuable to field measurements of acoustic backscatter, in order to measure the concentration and size profiles of suspended sediment.

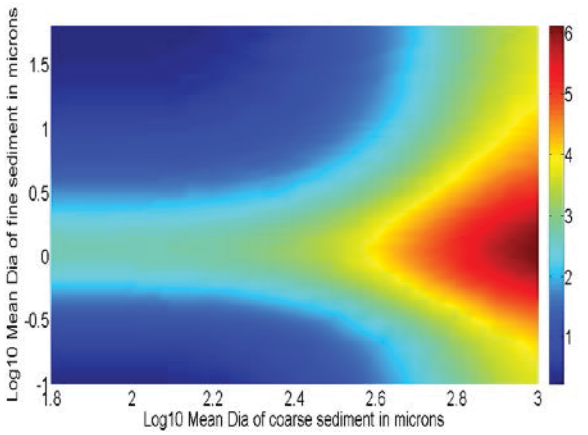

Figure 3: Total attenuation for a bi-normally distributed mixture of clay/silt and sand, for 500 KHz sound.

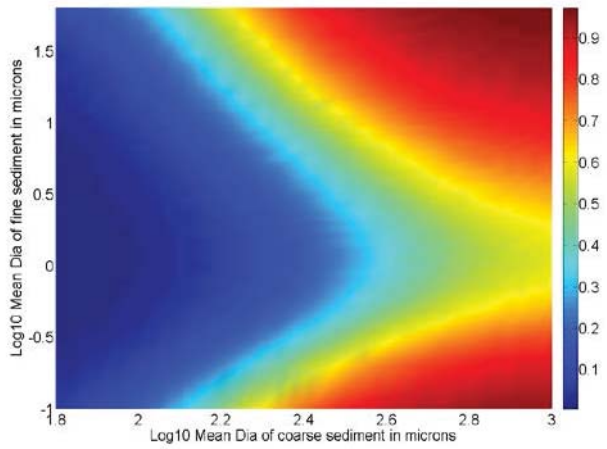

Figure 4: Ratio of the scattering attenuation to the total attenuation for a bi-normally distributed mixture of clay/silt and sand, for 500 KHz sound.

ACKNOWLEDGMENTS

The work of DMH on this paper was supported by Saint Louis University. Discussions on this subject with Yogi Agrawal and Scott Wright are greatly appreciated.

LITERATURE CITED

Flammer, G.H. (1962): Ultrasonic measurement of suspended sediment, U.S. Geological Survey Bulletin, 1141-A, 48 pp.

Gartner, J.W., 2004: Estimating suspended solids concentrations from backscatter intensity measured by acoustic Doppler current profiler in San Francisco Bay, California, *Marine Geology*, 211, 169-187.

Guerrero, M., N. Ruther, and R. Archetti, 2014: Comparison under controlled conditions between multi-frequency ADCP's and LISST-SL for investigating suspended sand in rivers, *Flow Measurement and Instrumentation*, v. 37, 73-82.

Hanes, D. M., C. E. Vincent, D. A. Huntley, and T. E. Clarke, 1988: "Acoustic measurements of suspended sand concentration in the Canadian Coastal Sediment Study experiment at Stanhope Lane, Prince Edward Island", *Marine Geology*, 81(1), 185-196.

Hanes, D., 2012: On the possibility of single frequency acoustic measurement of sand and clay concentrations in uniform suspensions; *Continental Shelf Research*, 46, doi: 10.1016/j.csr.2011.10.008.

Hanes, D.M., 2013: Erratum to ''On the possibility of single-frequency acoustic measurement of sand and clay concentrations in uniform suspensions'', *Continental Shelf Research*, http://dx.doi.org/10.1016/j.csr.2012.10.003.

Hay, A.E., 1983: On the remote acoustic detection of suspended sediments at long wavelengths, *J. Geophysical. Res.*, 88 (C12), 7525-7542.

Hay, A.E. and J. Sheng, 1992: Vertical profiles of suspended sand concentrations and size from multi-frequency acoustic backscatter, *J. geophysical. Res.* 97 (C12), 15,661-15,677

Hoitink, A.J.F. and P. Hoekstra, 2005: Observations of suspended sediment from ADCP and OBS measurements in a mud-dominated environment, *Coastal Engineering*, 52, 103-118.

Latosinski, F.G., Szupiany, R.N. Garcia, C.M., Guerrero, M. and M.L. Amsler; 2014: Estimation of concentration and load of suspended bed sediment in a large river by means of acoustic Doppler technology, *J. Hydraulic Eng*.

Libicki, C., K.W. Bedford, J.F. Lynch; 1989: The interpretation and evaluation of a 3-Mhz acoustic backscatter device for measuring benthic boundary layer sediment dynamics, *Journal Acoustic Society of America*, 85(4), 1501-1511.

Moate, B.D., and P.D. Thorne, 2009: Measurements and inversion of acoustic scattering from suspensions having broad size distributions, *Journal of the Acoustical Society of America*, 126(6), 2905-2917.

Moate, B.D., and P.D. Thorne, 2012: Interpreting acoustic backscatter from suspended sediments of different and mixed mineralogical composition, *Continental Shelf Research*, 46, 67-82.

Moore, S.A., J. Le Coz, D. Hurther and A. Paquier, 2013: Using multi-frequency acoustic attenuation to monitor grain size and concentration of suspended sediment in rivers. *Journal Acoustic Society of America,* 133, 1959-1970.

Sassi, M.G., Hoitink, A.J.F., and B. Vermeulen, 2012: Impact of sound attenuation by suspended sediment on ADCP backscatter calibrations, *Water Resources Research,* v. 48, W09520, doi: 10.1029/2012WRR012008.

Thorne, P. D. and D. Hanes; 2002: A review of acoustic measurement of small scale sediment processes, *Continental Shelf Research,* 22, 603-632.

Thorne, P.D. and D. Hurther, 2014: An overview on the use of backscattered sound for measuring suspended particle size and concentration profiles in non-cohesive inorganic sediment transport studies, *Continental Shelf Research*, 73, 97-118.

Thorne, P.D. and R. Meral, 2012: Formulations for the scattering properties of suspended sandy sediments for use in the application of acoustics to sediment transport processes, *Continental Shelf Research*, 28, 309-317.

Thosteson, E.D. and D.M. Hanes, 1998: A simplified method for determining sediment size and concentration from multiple frequency acoustic backscatter measurements, *Journal Acoustic Society of America*, 104(2), 820-830.

Urick, R.J., 1948: The absorption of sound in suspensions of irregular particles, *Journal Acoustic Society of America*, 20(3), 283-289.

Wright, S.A., Topping, D.T., and Williams, C.A., 2010: Discriminating silt-and-clay from suspended-sand in rivers using side-looking profilers, Proceedings of the 2nd Joint Federal Interagency Sedimentation Conference, June 2010, Las Vegas NV.

Journal of Coastal Research	SI	75	28 -32	Coconut Creek, Florida	2016

Simulation of Tsunami Runup in the Tone River Using Generalized Coordinate System and Influence of River Mouth Bar on Tsunami Water Level

Ryuji Nikaido [†*], Shin-ichi Aoki[‡], Hirotoshi Tamura[††], and Masanobu Jinbo[†]

[†]Coastal & Ocean Engineering Section
CTI Engineering Co., Ltd.,
Saitama, Japan

[‡] Department of Civil Engineering
Osaka University
Osaka, Japan

[††]Water Management & Research Division
CTI Engineering Co., Ltd.,
Tokyo, Japan

www.cerf-jcr.org

www.JCRonline.org

ABSTRACT

Nikaido, R.; Aoki, S.; Tamura, H., and Jinbo, M., 2016. Simulation of tsunami runup in the Tone River using generalized coordinate system and influence of river mouth bar on tsunami water level. *In:* Vila-Concejo, A.; Bruce, E.; Kennedy, D.M., and McCarroll, R.J. (eds.), *Proceedings of the 14th International Coastal Symposium* (Sydney, Australia). *Journal of Coastal Research*, Special Issue, No. 75, pp. 28 - 32. Coconut Creek (Florida), ISSN 0749-0208.

This study simulated the tsunami runup in the Tone River using generalized coordinate system and discussed influence of river mouth bar on tsunami water level. This simulation focused on the 2011 off the Pacific Coast of Tohoku Earthquake Tsunami. Numerical simulation of the 2011 Tsunami runup in the Tone River and comparison of the results with the field data showed that the model using generalized coordinate system gave more accurate results than the model using the Cartesian coordinate system. This may be because the configuration of the curved river was precisely represented by the generalized coordinate system. Comparison of the computed results between the three cases, no removal, half removal and all removal of the river mouth bar, showed that the existence of the river mouth bar decreased water level and reduced inundation depth in the Tone River estuary. Therefore, the river mouth bar has tsunami reduction effects of tsunami disaster in the river.

ADDITIONAL INDEX WORDS: *Numerical analysis, generalized coordinate system, Cartesian coordinate system, tsunami runup in a river, the 2011 off the Pacific Coast of Tohoku Earthquake Tsunami.*

INTRODUCTION

Because the 2011 off the Pacific Coast of Tohoku Earthquake Tsunami (denoted hereafter as the 2011 Tsunami) exceeded tsunami height predicted before the 2011 Tsunami, government and many local governments are making disaster mitigation plan against tsunami. Simulation of tsunami runup is often carried out in the planning, where numerical models with the Cartesian coordinate system are commonly used (e.g., MLIT, 2012).

One of the methods which can reproduce precise configuration of a curved river is using the generalized coordinate system and unstructured grids. Although this method is mainly used for flood simulation, only a few studies are found in tsunami simulation (Goto and Shuto, 1981, Akoh and Ishikawa, 2012). The advantage of the model using the generalized coordinate system and unstructured grids has not been well discussed.

In this study, numerical simulations of tsunami runup in the Tone River (Figure 1) using both the generalized coordinate system and the Cartesian coordinate system were carried out. The results of the water level were compared with the observed data and the difference between the two methods were discussed. Moreover, the influence of river mouth bar on tsunami runup in the Tone River was evaluated by using the simulation model.

DOI: 10.2112/SI75-006.1 received 15 October, 2015; accepted in revision 15 January, 2016 .
*Corresponding author: nikaidou@ctie.co.jp

The reason for targeting the Tone River in this study is that there are many data obtained in the event of the 2011 Tsunami, which allow us to evaluate the reproduction simulation. In addition, the Tone River has curved configuration and a river mouth bar, which is suitable to see these influences.

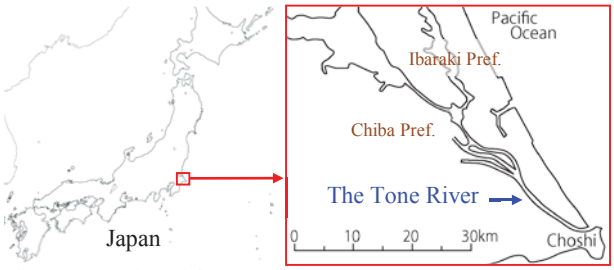

Figure 1. Location of the Tone River

SUMMARY OF THE TONE RIVER

Figure 2 shows the plan view of the Tone River downstream. In the reproduction simulation of the 2011 Tsunami in the Tone River, the followings are considered:

- The Tone River has the training jetty and the sand bar at the river mouth (near KP0.0). Hasaki fishing port (left side of the river) and Choshi fishing port (right side of the river) are also located near the river mouth.

- The section from KP-1.5 to KP 4.0 in the river is curved.
- The width of the low water channel is approximately from 400 to 1,000 m, the narrowest cross section is near KP0.0 where the training jetty and the river mouth bar exist (Figure 2 and 3).
- The estuary barrage is located at KP18.5, the bed slope in the downstream side of the barrage is approximately 1/10,000 (WRDPC: Water Resources Development Public Corporation). Therefore, the water level in normal period is determined by tide. When the 2011 Tsunami occurred, the average outflow discharge from the estuary barrage (KP18.5) was approximately 100 m^3/s (WRDPC), thus the outflow discharge did not affect the water level in the river downstream.
- The 2011 Tsunami overflowed the estuary barrage (KP18.5). The crown height of the barrage is Y.P. +2.0 m (Y.P.(Yedogawa Peil)±0m=T.P.(Tokyo Peil)-0.84m).
- The Tone River has some observation points which provided the data of water level in the 2011 Tsunami (Figure 2).
- The soliton fission could not be clearly confirmed in the water level judging from the images of CCTV obtained at KP10.0 and KP18.5.
- Some sections in the downstream side of the estuary barrage did not have embankment (Figure 2), inundation occurred from part of these sections.
- The amount of crustal deformation by the 2011 Earthquake was -0.15 m at CHOSHI GPS-based Control Station (Geospatial Information Authority of Japan).
- The river mouth bar was not remarkably eroded by the 2011 tsunami (Figure 3). This may be because the overflow height on the river mouth bar was small with influence of the training jetty.

REPRODUCTION SIMULATION

Methods and fundamental equations

This study used two classes of simulation models. The first one used the Cartesian coordinate system, and the second one used the generalized coordinate system. Both of the models are based on the nonlinear long wave theory on two dimensional plane. Advection term is considered using the first-order upwind difference scheme. Fundamental equations on the Cartesian coordinate system are shown in Equations (1), (2) and (3), finite difference method was used for the discretization.

$$\frac{\partial Z}{\partial t}+\frac{\partial M}{\partial x}+\frac{\partial N}{\partial y}=0 \quad (1)$$

$$\frac{\partial M}{\partial t}+\frac{\partial}{\partial x}\left(\frac{M^2}{h}\right)+\frac{\partial}{\partial y}\left(\frac{MN}{h}\right)+gh\frac{\partial Z}{\partial x}+\frac{gn^2}{h^{7/3}}M\sqrt{M^2+N^2}=0 \quad (2)$$

$$\frac{\partial N}{\partial t}+\frac{\partial}{\partial x}\left(\frac{MN}{h}\right)+\frac{\partial}{\partial y}\left(\frac{N^2}{h}\right)+gh\frac{\partial Z}{\partial y}+\frac{gn^2}{h^{7/3}}N\sqrt{M^2+N^2}=0 \quad (3)$$

On the other hand, the fundamental equations on the generalized coordinate system (e.g., Hosoda *et al.*, 2001) are shown in Equations (4), (5) and (6), the finite volume method was used for the discretization.

$$\frac{\partial}{\partial t}\left(\frac{h}{J}\right)+\frac{\partial}{\partial \xi}\left(\frac{Uh}{J}\right)+\frac{\partial}{\partial \eta}\left(\frac{Vh}{J}\right)=0 \quad (4)$$

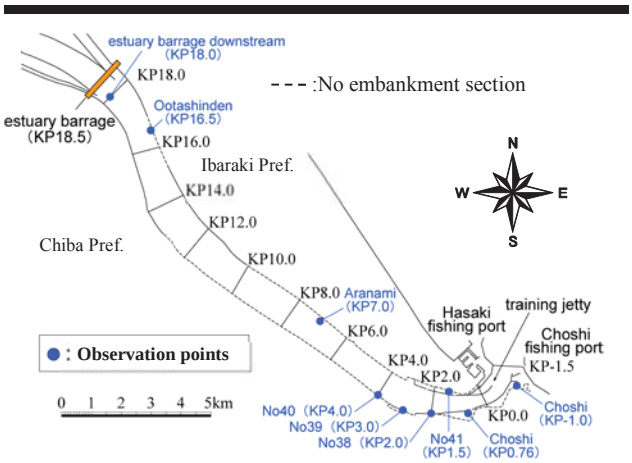

Figure 2.The plane view in the Tone River, downstream of the estuary barrage. Blue points correspond to observation points.

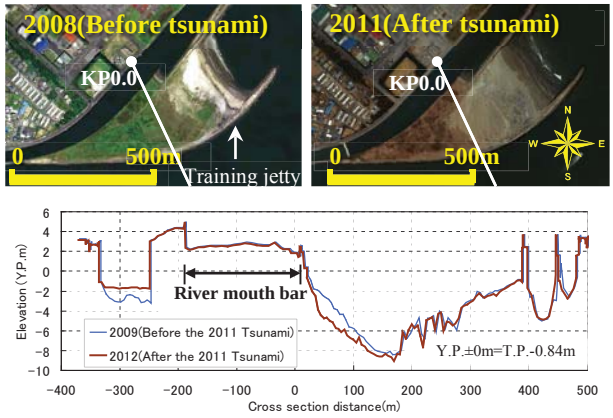

Figure 3.Aerial photography and cross section of the river mouth bar before and after the 2011 Tsunami at KP0.0. The river mouth bar was not remarkably eroded by the 2011 Tsunami.

$$\frac{\partial}{\partial t}\left(\frac{Q^{\xi}}{J}\right)+\frac{\partial}{\partial \xi}\left(\frac{UQ^{\xi}}{J}\right)+\frac{\partial}{\partial \eta}\left(\frac{VQ^{\xi}}{J}\right)-\frac{M}{J}\left(U\frac{\partial \xi_x}{\partial \xi}+V\frac{\partial \xi_x}{\partial \eta}\right)$$
$$-\frac{N}{J}\left(U\frac{\partial \xi_y}{\partial \xi}+V\frac{\partial \xi_y}{\partial \eta}\right)+gh\left(\frac{\xi^2{}_x+\xi^2{}_y}{J}\frac{\partial Z}{\partial \xi}+\frac{\xi_x\eta_x+\xi_y\eta_y}{J}\frac{\partial Z}{\partial \eta}\right)+\frac{\tau_b{}^{\xi}}{\rho J}=0 \quad (5)$$

$$\frac{\partial}{\partial t}\left(\frac{Q^{\eta}}{J}\right)+\frac{\partial}{\partial \xi}\left(\frac{UQ^{\eta}}{J}\right)+\frac{\partial}{\partial \eta}\left(\frac{VQ^{\eta}}{J}\right)-\frac{M}{J}\left(U\frac{\partial \eta_x}{\partial \xi}+V\frac{\partial \eta_x}{\partial \eta}\right)$$
$$-\frac{N}{J}\left(U\frac{\partial \eta_y}{\partial \xi}+V\frac{\partial \eta_y}{\partial \eta}\right)+gh\left(\frac{\xi_x\eta_x+\xi_y\eta_y}{J}\frac{\partial Z}{\partial \xi}+\frac{\eta^2{}_x+\eta^2{}_y}{J}\frac{\partial Z}{\partial \eta}\right)+\frac{\tau_b{}^{\eta}}{\rho J}=0 \quad (6)$$

In the equations above, t is the time, x and y are the axis of the Cartesian coordinate system, ξ, η are the axis of the generalized coordinate system, Z is the water level, h is the depth, g is the gravitational acceleration (= 9.8 m/s^2), ρ is the density of water, n is the manning's roughness coefficient, M and N are the flow flux in the x and y directions, u and v are the flow velocity vector in the x and y directions, Q_ξ and Q_η are the flow flux in the ξ and η directions, U and V are the flow velocity vector in the ξ and η directions, J is the Jacobian of coordinate transformation, ξ_x, η_x, ξ_y and η_y are the metrics of coordinate transformation.

Now, the variables are defined as follows and the subscripts ξ, η, x and y of variables show partial differentiation.

$$\tau_b^{\xi}=\xi_x\frac{\rho gn^2}{h^{7/3}}M\sqrt{M^2+N^2}+\xi_y\frac{\rho gn^2}{h^{7/3}}N\sqrt{M^2+N^2}\quad,\quad U=\xi_x u+\xi_y v\quad,$$

$$\tau_b^{\eta}=\eta_x\frac{\rho gn^2}{h^{7/3}}M\sqrt{M^2+N^2}+\eta_y\frac{\rho gn^2}{h^{7/3}}N\sqrt{M^2+N^2}\quad,\quad V=\eta_x u+\eta_y v\quad,$$

$$Q^{\xi}=\xi_x M+\xi_y N\quad,\quad Q^{\eta}=\eta_x M+\eta_y N\quad,\quad J=1/(x_\xi y_\eta-x_\eta y_\xi)\quad,$$

$$\xi_x=Jy_\eta\quad,\quad \eta_x=-Jy_\xi\quad,\quad \xi_y=-Jx_\eta\quad,\quad \eta_y=Jx_\xi$$

Simulation setting

Table 1 shows details of the numerical simulations of tsunami runup. Figure 4 shows images of mesh generation corresponding to the three cases in Table 1. The generalized coordinate system expresses well the configuration of a curved river, while the Cartesian coordinate system gives a jagged line because of the square grid of the Cartesian coordinate system. The details of the computation conditions are shown in Table 2.

Results of reproduction simulation

In order to select the best model among the three cases (Table 1), the computed results are compared with the observation data. Figure 5 shows time series of water level at several observation points, where five representative observation points were selected.

Waveforms of the time series of the water level are similar in the three cases. However, the water level in case1 shows larger values than case2 and case3, and more accurate results in comparison with observation data. The models on Cartesian coordinate system (case2 and case3) show same tendency, the difference in grid size does not affect much on the results.

Thus, the generalized coordinate system (case1) could reproduce observation data the best among the three cases. This may be because the configuration of the curved river was precisely represented by the generalized coordinate system.

INFLUENCE OF RIVER MOUTH BAR

Situation of river mouth bar

Figure 6 shows the picture of the river mouth of the Tone River. There are a training jetty and a sand bar near KP0.0 on the left. Figure 7 shows cross section of the river mouth bar at KP0.0. Elevation of the river mouth bar is about Y.P.+3 m (Figure 7) and thus the tide level does not reach the crown height of the bar.

Simulation setting

To examine the influence of the river mouth bar on tsunami runup, the model utilized the generalized coordinate system, adopted in the reproduction simulation.

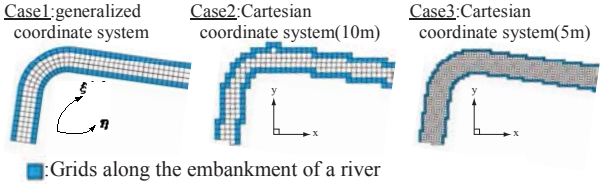

Figure 4. Images for mesh generation of each case

Table 1. *Simulation cases (reproduction simulation)*

Case	Model	Mesh size	Mesh structure
Case1	Generalized coordinate system	About 10m	Along the river
Case2	Cartesian coordinate system	10m	*x* axis: east-west direction
Case3		5m	*y* axis: north-south direction

Table 2. *Computation conditions (reproduction simulation)*

Item	Setting
Simulation area	KP-1.5 ～ KP20.0 (including the estuary barrage (KP18.5) downstream, significant impact area by the 2011 Tsunami)
Grid size	Case1(generalized coordinate system) : approximately 10 m×10 m, grid size is different in each mesh Case2(Cartesian coordinate system) : 10 m×10 m Case3(Cartesian coordinate system) : 5 m×5 m
Topography	Land area : Aerial survey data measured in 2011 (after the 2011 Tsunami) River area : Narrow multibeam survey measured in November 2011 from KP-1.5 to KP5.0 (after the 2011 Tsunami). Cross sectional survey measured in 2009 and 2010 (before the 2011 tsunami) upstream KP5.0, added the amount of crustal deformation by the 2011 earthquake.
Structure	Considered as geographical grid for embankments of river, breakwaters of fishing ports, estuary barrages, training jetties.
Manning's roughness ($m^{-1/3}\cdot s$)	low water channel : 0.027(KP-1.5～KP0.0), 0.015(KP0.0～KP20.0) high water channel : 0.036(KP17.0 on the left) , 0.039(KP18.5 on the right), 0.045(KP18.5 on the left) ,0.057(KP15.5～KP16.0 on the left, KP19.5 on the right),0.060(KP13.0 ～ KP15.0 on the left,KP13.0～KP18.0 ,KP19.0 and KP20.0 on the right)
Boundary condition at downstream end (KP-1.5)	Incident the water level at Choshi observation point (KP-1.0) is Stretched to maximum Y.P.+3.6 m using pictures taken at Choshi fishing port. (The pictures of the water level at Choshi fishing port breakwater (KP-1.5) reached maximum Y.P.+3.6 meter.) Incident the water level for cross section (KP-1.5) was fixed.
Boundary condition at upstream end	Boundary of transmission.
River discharge	It was not considered. Because the estuary barrage downstream side is tidal area, the water level for normal period is determined by tide.
Computation time step Δt	Case1(generalized coordinate system) : 0.05s Case2, 3(Cartesian coordinate system) : 0.10s

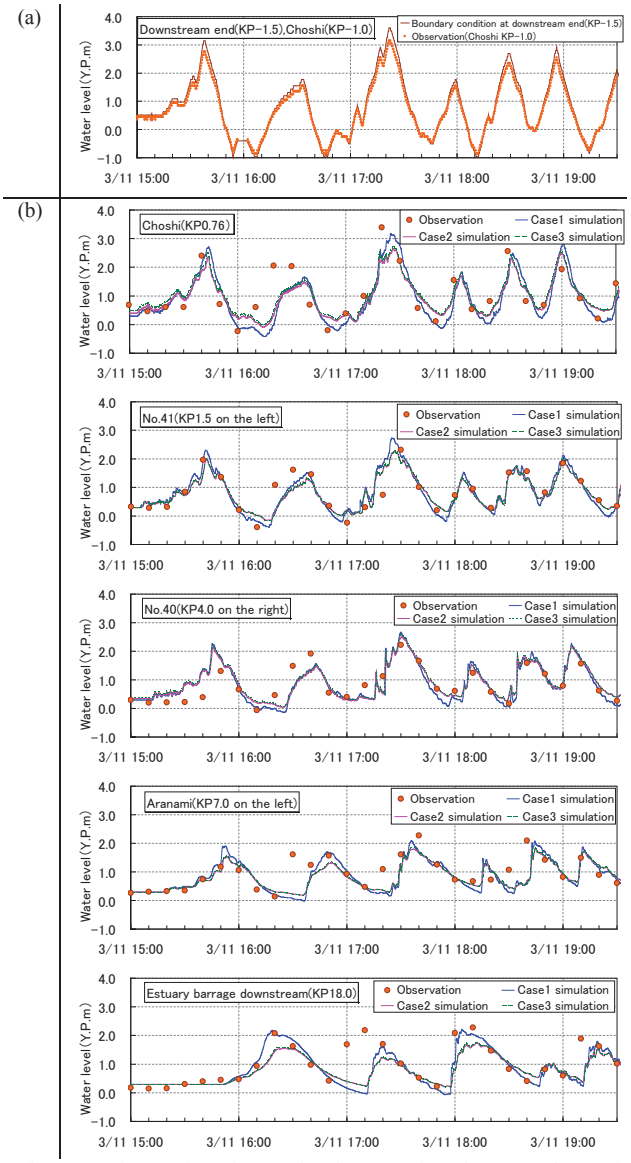

Figure 5. Time series of water level: comparison between observation and simulation for five observation points. (a) the observation (KP-1.0) and boundary water level at downstream end (KP-1.5) for simulation. (b) comparison between the observation data every 10 minutes and computed results of the three cases.

Table 3 shows the details of the simulation cases, in which sand excavation volume is changed. In Case A, no sand is removed, *i.e.* the same configuration as the present river mouth bar. In Case B, half of the sand of the bar is removed. In Case C, whole of the sand bar is removed.

Figure 7 shows the cross sections at KP0.0 in the three cases. Simulation conditions are almost the same as Table 2 except for the topography of the river mouth bar.

Figure 6. River mouth bar of the Tone River (January 19, 2007).

Table 3. *Simulation cases (influence of river mouth bar)*

Case	Model	River mouth bar	Sand excavation volume
Case A (=Case 1 in Table 1)	Generalized coordinate system	No removal (present situation)	0m^3
Case B		Half removal	300,000m^3
Case C		All removal	650,000m^3

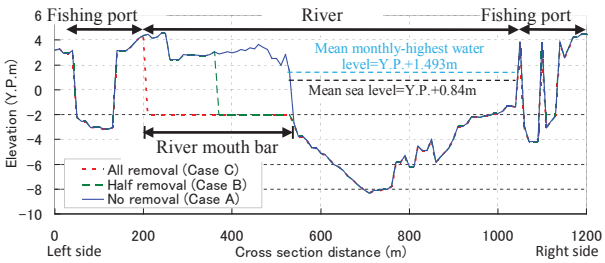

Figure 7.Cross section of the river mouth bar at KP0.0. The river mouth bar was excavated in the three cases.

Influence of river mouth bar against tsunami

Figure 8 shows distribution of the maximum water level for each case. Figure 9 shows longitudinal variation of the maximum water level in low water channel. As the sand excavation volume increased, the water level in the river was raised in the upstream side of the bar. On the other hand, in the downstream side of the river mouth bar, the sand excavation decreased the water level. It may be because of the runup of tsunami over the bar.

Table 4 shows inundation area in each case. In the case of excavating the river mouth bar, inundation area was increased by increasing water level in the Tone River.

Based on the above results, it is confirmed that the river mouth bar has reduction effects of tsunami runup in the river.

Table 4. *Inundation area in figure 8 (including high water channel)*

Case	River mouth bar	Inundation area	Ratio
Case A	No removal	3.19 km^2	-
Case B	Half removal	3.46 km^2	1.08 (B/A)
Case C	All removal	3.65 km^2	1.14 (C/A)

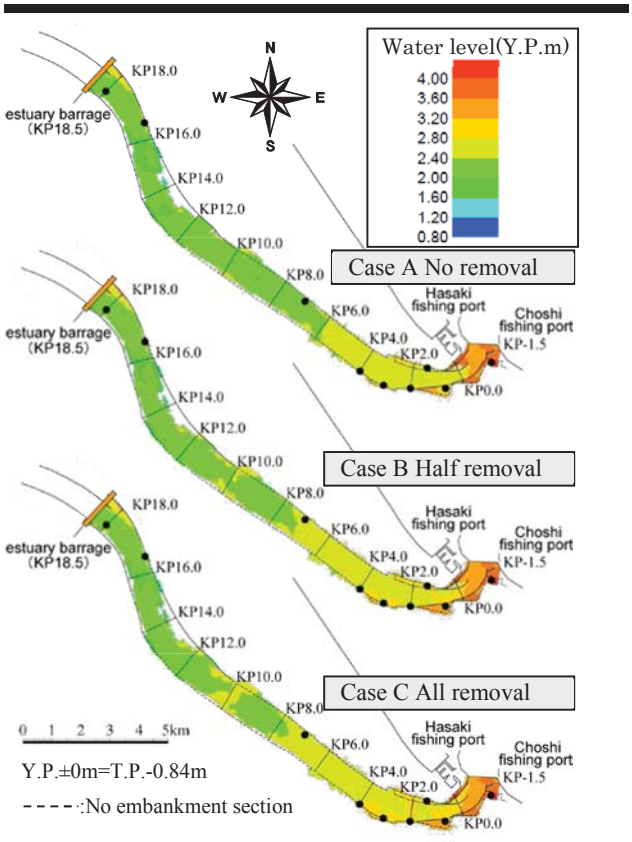

Figure 8. Distribution of the maximum water level

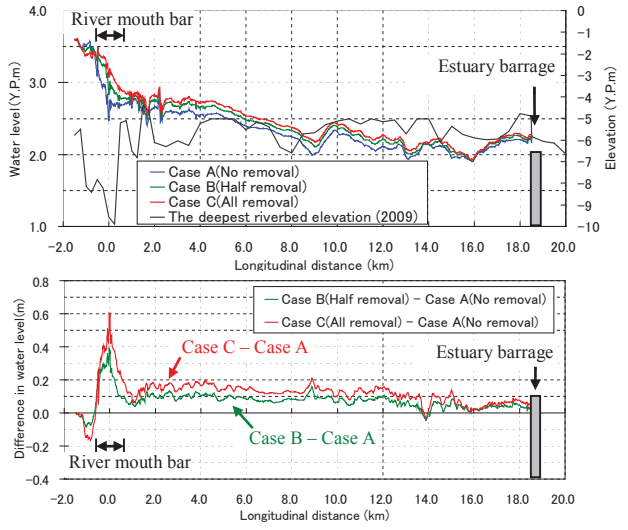

Figure 9. Longitudinal variation of the maximum water level and difference in water level in low water channel

CONCLUSIONS

In this study tsunami runup in the Tone River was computed using the generalized coordinate system and the Cartesian coordinate system. Also the influence of the river mouth bar on tsunami height in the river was discussed.

Main results are as follows:

- Numerical simulation of the runup of the 2011 Tsunami in the Tone River and comparison of the results with the field data showed that the model using the generalized coordinate system gave more accurate results than the model using the Cartesian coordinate system. This may be because the configuration of the curved river was precisely represented by the generalized coordinate system.
- Comparison of the computed results between the three cases with different volume of excavation of the river mouth bar showed that the existence of the river mouth bar decreased tsunami runup and reduced inundation area.

ACKNOWLEDGMENTS

Survey data of the Tone River were provided by Tone River Downstream Work Office, Kanto Regional Construction Bureau, Ministry of Construction. Tsunami observation data at CHOSHI (KP-1.0) were provided by Japan Meteorological Agency. The authors would like to appreciate their cooperation.

LITERATURE CITED

Akoh, R. and Ishikawa, T., 2012. The numerical simulation of runup tsunami in tone river caused by the 2011 off the pacific coast of tohoku earthquake. *Annual Journal of Hydraulic Engineering*, 68(4), 1543-1548. (in Japanese)

Geospatial Information Authority of Japan, *Crustal deformation of the 2011 off the Pacific coast of Tohoku Earthquake*. http://www.gsi.go.jp/common/000059961.pdf. (accessed September 21, 2015)

Goto, T. and Shuto, N., 1981. 2-dimensional numerical analysis of tsunami runup. *Annual Journal of Coastal Engineering*, 28, 64-68. (in Jananease)

Hosoda, T.; Nagata, N.; Kimura, I.; Michibata, K., and Iwata, M., 2001. A depth averaged model of open channel flows with lag between main flows and secondary currents in a generalized curvilinear coordinate system. *In*: Wada, A.; Ninokata, H., and Tanaka, N.(eds.), *Proceedings of the 8th International Symposium on Flow Modeling and Turbulence Measurements* (Tokyo , Japan), pp.63-70.

Ministry of Land, Infrastructure, Transport and Tourism, http://www.mlit.go.jp/river/shishin_guideline/bousai/saigai/tsunami/shinsui_settei.pdf. (accessed December 6, 2015)

Water Resources Development Public Corporation, http://www.water.go.jp/kanto/tonekako/report/pdf/21teiki_hp.pdf. (accessed September 21, 2015)

Water Resources Development Public Corporation, http://www.water.go.jp/kanto/tonekako/index.html.(accessed April 20,2011)

Journal of Coastal Research	SI	75	33-37	Coconut Creek, Florida	2016

GIS-based modelling of vulnerability of coastal wetland ecosystems to environmental changes: Comerong Island, southeastern Australia

Ali K. M. Al-Nasrawi*†, Brian G. Jones*, Sarah M. Hamylton*

*School of Earth and Environmental Sciences (SEES),
University of Wollongong, NSW, Australia.

www.cerf-jcr.org

www.JCRonline.org

ABSTRACT

Al-Nasrawi, A.K.M.; Jones, B.G., and Hamylton, S. M., 2016. GIS-based modelling of vulnerability of coastal wetland ecosystems to environmental changes: Comerong Island, southeastern Australia. *In:* Vila-Concejo, A.; Bruce, E.; Kennedy, D.M., and McCarroll, R.J. (eds.), *Proceedings of the 14th International Coastal Symposium* (Sydney, Australia). *Journal of Coastal Research*, Special Issue, No. 75, pp. 33-37. Coconut Creek (Florida), ISSN 0749-0208.

Sustainable management of coastal zones has become a complicated issue. The majority of the human population lives along the coast, where their activities, together with a range of environmental changes, have altered the natural ecosystem processes and caused changes in coastal wetlands. To ensure sustainable use of coastal resources, a comprehensive set of modelling tools can help managers to make decisions. This study uses Comerong Island (southeastern NSW, Australia) as a case study to demonstrate the importance of modelling modifications to environmental change. Several data-based modelling approaches are employed to explore how human activities have altered this estuarine island setting over the last sixty years (1949 – 2014). Multi-temporal changes in land cover, shorelines and sediment delivery are estimated from remote sensing data, GIS analysis, and laboratory tests on water and sediment samples (grain size, X-ray diffraction and loss on ignition and water analysis). Results show there are significant changes to the areal extents and elevation of mangroves, saltmarshes and shorelines in the wetlands on Comerong Island over the time period of analysis, including northern accretion (0.4 km^2), eastern, middle and southern erosion (0.7 km^2) of the island. The implementation of modelling using GIS tools, water and sediment samples to monitor ecosystem processes, such as sediment transport and erosion/deposition, will allow resource managers to make more informed decisions by evaluating the potential consequences of the existing situation.

ADDITIONAL INDEX WORDS: *eco-geomorphology, sediment transport, erosion, human modifications.*

INTRODUCTION

Coastal wetlands are among the most productive, sensitive and responsive ecosystems affected by climate change and human influences that control most of the eco-geomorphological processes and pressures (DSE, 2007). Human and natural hazards that have influenced coastal wetlands should therefore be monitored, whether for the direct threats of loss to the wetlands itself or indirect loss to its catchment. Particularly within New South Wales, coasts and their hinterlands have been substatially modified after European settlement.

Early civilizations inhabited coastal areas (e.g. Mesopotamia; Postgate, 1992) and nowadays 70% of the human population and 86% of Australians live along the coasts for ecological and economic reasons (Cherfas, 1990; Neumann *et al.*, 2015). Human-induced stressors that resulted in challenges of degradation have increased since last century and caused loss of coastal ecosystems, particularly within coastal wetlands (DSE, 2007). Wetland studies across the globe have indicated the negative effects of human activities on wetlands (Ehrenfeld, 2000).

DOI: 10.2112/SI75-007.1 received 15 October 2015; accepted in revision 15 January 2016.
†Corresponding author: akman685@uowmail.edu.au

In addition, modifying the catchment and its water usage has caused many problems. For example, 60% of fresh water has been diverted from coastal NSW, Australia, since the start of European settlement (Saintilan and Imgraben, 2012). Kingsford (1990) revealed that direct and indirect human influences can change estuarine habitats, which can then affect the conservation of shorebirds.

Background

The NSW coastline is a great natural asset, making an enormous contribution to the economy. Although conservation rules are strictly applied in Australia, many studies have estimated significant indirect destructive impact of human activities in Australian wetlands. Thus, examining the existing situation and modelling the current modifications to natural processes is important for any applicable study site. Comerong Island (Figure 1) represents an ideal example of this context that reflects disturbed regimes.

Comerong Island Nature Reserve is located approximately 170 km south of Sydney and 11 km to the east of Nowra. It is situated between the Shoalhaven River mouth-entrance, Greenwell Point and Orient Point (see Figure 1). The nature reserve consists of coastal sand barrier, tidal flats and islands built up of river silt behind the dune barrier sands within the Shoalhaven River delta.

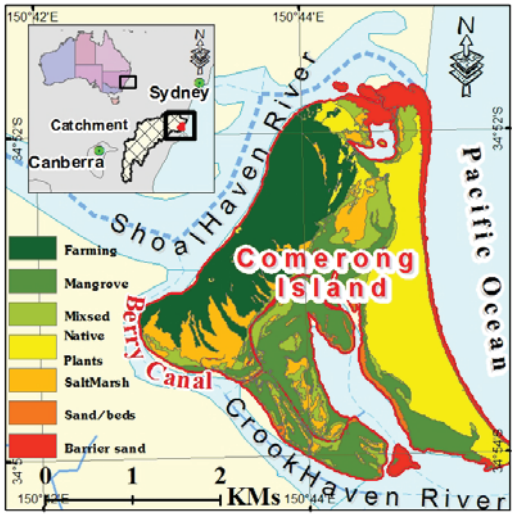

Figure 1. Location of the study site, southeast NSW, Australia.

Comerong Island is part of an infilled coastal deltaic estuary and is mostly made of sediments derived from the Shoalhaven River catchment associated with its ocean sandy barrier built up from marine sand during the Holocene transgression (Woodroffe *et al.*, 2000; Wright, 1970). The Shoalhaven River has a 7177 km^2 of catchment area, which is the sixth largest catchment in NSW (OWA, 2010). This large catchment provide abundant sediment during high flood flows which move down to the delta. This has resulted in the estuary becoming infilled during the past 7000 years (Umitsu *et al.*, 2001; Woodroffe *et al.*, 2000). In 1822 Alexander Berry built a canal that linked the Shoalhaven and Crookhaven Rivers (Figure 1) as an alternative entrance since the Shoalhaven Heads. This entrance had become very shallow causing higher water levels that threated the estuary and all associated human settlements (Thompson, 2012). The area encompassed by the two rivers and the canal became Comerong Island (Umitsu *et al.*, 2001). After the construction of the Berry Canal both the Shoalhaven and Crookhaven (5 km south) entrances act as discharge points to the sea. Berry Canal was originally only 190 m long and 5.5 m wide, but erosion pressure on the banks and bed of the canal has increased its width to 250 meters (Thompson, 2012; Umitsu *et al.*, 2001).

The study site on Comerong Island has faced strong human modifications since European settlement that have caused a series of sediment availability and transport problems and have negatively affected natural processes. Water flow and sediment transport have been further modified since the construction of Tallowa Dam in 1976, Figure 2 (SCA, 2015). The dam has blocked most of the water and its sediment derived from the upper catchment making it effectively inactive (Figure 2). Moreover, 35% of the catchment has been used for agriculture and a further 11% for forestry (OWA, 2010; Figure 2).

Human activities are placing unprecedented pressure on these coastal resources. Studies conducted on the effects of human activities on wetlands indicate the multiple needs of wetlands for different purposes, such as urban development, business, agriculture, tourism, recreational and conservation (Shahbaz *et al.*, 2009). The Shoalhaven River floodplain, which covers approximately 5% of the catchment, has a reputable history of being one of the richest dairy areas in NSW (NPWS, 1998). Other significant industries include commercial fishing, oyster growing and vegetable farming (Shahbaz *et al.*, 2009). Additionally, the tourism industry is one of the main human activities, where recreation fishing, surfing and boating are the order of the day (NPWS, 1998). The floodplain is also experiencing considerable urban and industrial growth, particularly in and around Nowra (OWA, 2010). To protect the marine and coastal wildlife, artificial wetlands have been constructed to provide additional habitat (Murray *et al.*, 2013).

This exploratory study investigates the effects of human activities on the ecosystems and biodiversity around Comerong Island. The study is based on a literature review augmented by sampling and subsequent GIS modelling to provide a qualitative outcome that can be used to offer possible sustainable management solutions.

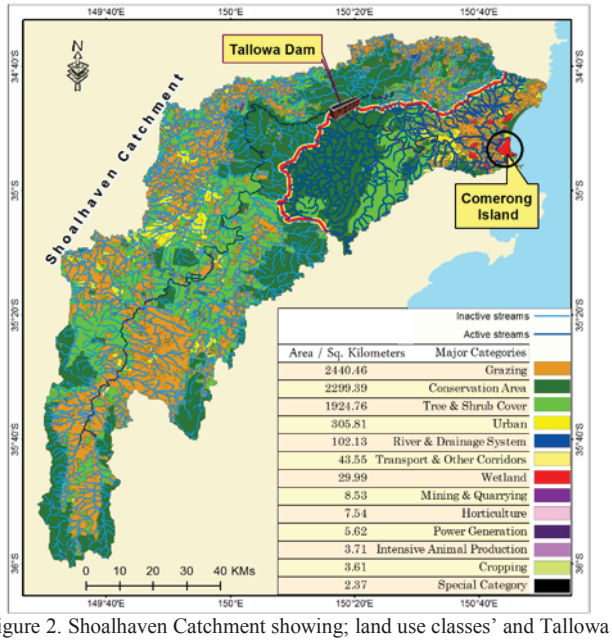

Figure 2. Shoalhaven Catchment showing; land use classes' and Tallowa Dam that separates the upper and lower catchments.

METHODS

This study is based on a continuous assessment of multi-temporal changes in landcover, shorelines, and elevation stability. The reduced or increased areas of wetlands have been assessed by measuring the landcover on aerial photographs and satellite images over time. Analysis of the shoreline has determined the changes in erosion/accretion rates around Comerong Island. Changes of mangrove and saltmarsh areas (as a landcover function) illustrate the shoreline position and elevation stability in the Comerong coastal wetlands. This approach has been achieved through continuous monitoring methods. This project entails the assessment of threats, such as shoreline erosion and sediment delivery problems. In addition,

effects of artificial modification in the catchment are the principle element addressed.

Achieving the project targets was done on several levels. It started with GIS and RS-based analysis to identify and classify the landcover and shoreline changes at this specific study sites depending on recent and historical records of aerial photography, satellite and LiDAR data. This was combined with sampling of the water, soil and sediment. The main objectives of the paper are to monitor and measure the coastal wetland shorelines, land cover and elevation changes/trends in order to model potential modifications for rehabilitation of the wetlands. To achieve these aims, this study divided the methodology into three parts as seen in Figure 3.

Data Collection

Various data have been collected to achieve the study aims. Remote sensing (RS) and GIS data were used to classify land use classes. LiDAR (2004 and 2010) and SRTM (2011) data have been used in ArcGis10.2 to create DEMs.

Field work recovered 113 sediment and soil samples from Comerong Island. Grain size analyses, X-ray diffraction (XRD) and loss on ignition (LOI) tests on these samples yielded the grain size and proportions of minerals and organic matter. A Yeo-Kal 615 multi-parameter water quality analyzer was used in the field to measure water samples in real time to test it for pH, conductivity, dissolved oxygen (DO), salinity and turbidity.

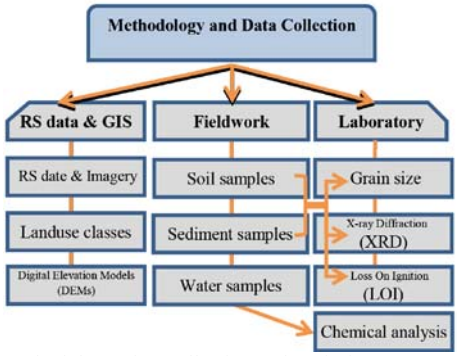

Figure 3. Methodology; data collection and analysis sequences.

RESULTS

Results showed significant coastal wetland challenges of degradation and change, which caused losses that are addressed as follows:

The multi-temporal analysis of remote sensing (RS) and GIS data indicates that Comerong Island and its environment have suffered a significant loss of wetlands (aproxmatly 0.3 km^2). Additionally, it indicated that some of the saltmarsh areas were converted to agricultural usage, and the mangrove cover lost ground as a result of shoreline erosion (Figure 4). This study also determined the effects of human modification within the wetland's catchment and assessed the extent of the human activities impact during sea level rise stresses.

DEMs have shown significant elevation changes over time on Comerong Island (Figure 5). So far, the western, mid and southern sides of the island have eroded as mapped in red on Figure 5. Meanwhile, accretion has expanded the northern region with minor erosion in the middle of that area.

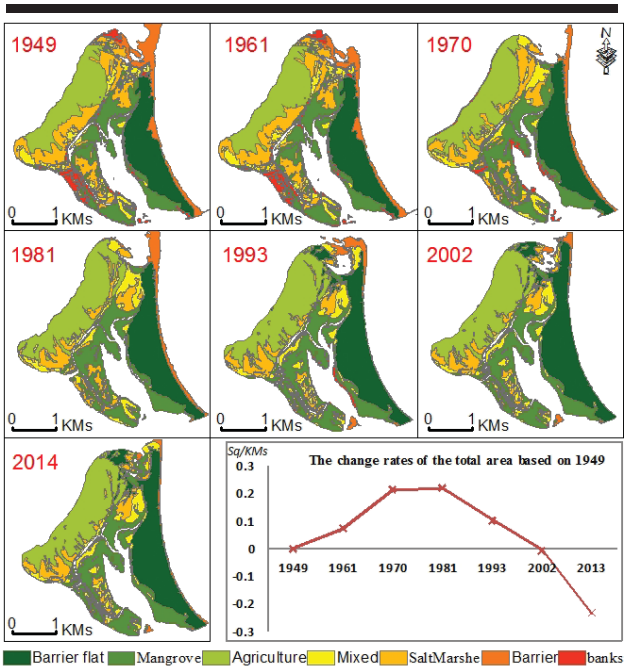

Figure 4. Multi-temporal imagery (1949 – 2014) showing significant changes of land cover, shorelines and total area.

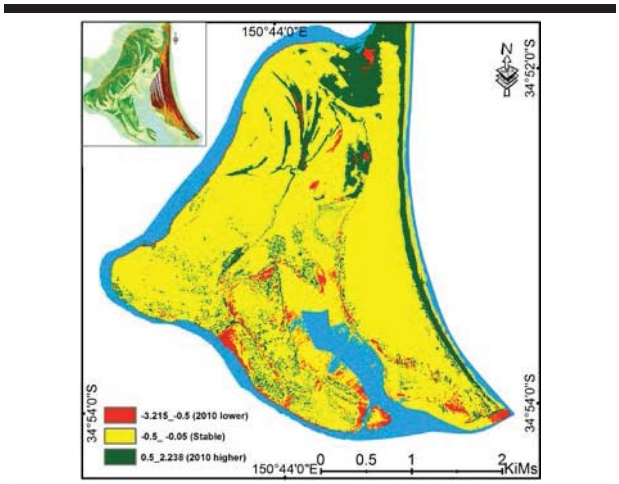

Figure 5. DEMs analysis showing significant loss in red and accretion in green while stable areas are shown in yellow (LPI, 2004 & 2010).

Soil and sediment samples have been checked for their grain size using a Mastersizer 2000 laser diffraction particle size analyzer, which generated results shown in Figure 6.

Most of the island is made of sand, especially along the north, east and south sides, where wave energy has built those parts of the island (Figure 6). The silt and clay present along the western side of Comerong Island have been derived from the Shoalhaven

River catchment. The rates of sedimentation and types of sedimentary sequences could then be related to events such as the flood history records.

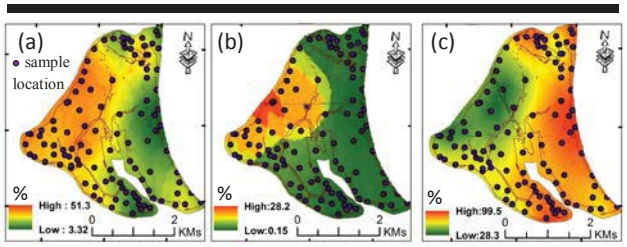

Figure 6. Soil, sediment samples and grain size analysis from Comerong Island; (a) clay proportion, (b) silt proportion and (c) sand proportion.

Twenty four samples tested with X-ray diffraction (XRD) showed that all samples are dominated by quartz, especially along the eastern beach and barrier where wave action has eliminated most of the softer minerals and clays (Figure 7). Along the western and southern sides of Comerong Island and in the active channel areas feldspar and lithic sand grains form a prominent component representing fluvial sands derived from volcanic, volcaniclastic and mudstone rocks in the source area. Clay content in the samples is highest in the low energy environments around the island, but also occurs in the fluvial lithic sands through the diagenetic alteration of feldspar and lithic sand grains.

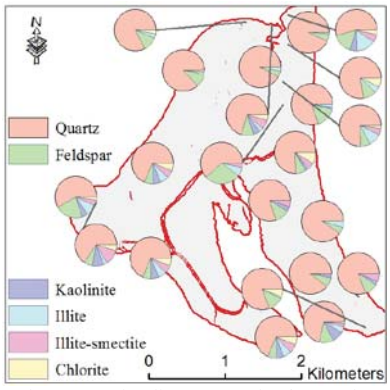

Figure 7. Mineral content of sediment samples / around Comerong.

Twenty samples chosen from an east-west cross-section were analyzed for organic matter using loss on ignition (LOI). this has been applied to check how much the biotic and abiotic components playing roles in changing the elevation. LOI data show two main areas have the highest proportion of organic matter; one positioned in the very muddy section in the middle of the island represented by mangrove area, and the other occurs in the area with the highest density of native plants in the eastern part of the island. LOI data was also used to evaluate changes in elevation with respect to the water table.

The average discharge of the Shoalhaven River has been below five megalitres per day from 1914-2014 with the exception of flood related events. However since these gauging stations are located in the upper reaches of the river system, they do not reflect the situation downstream, thus eight samples from below Tallowa Dam have been collected and tested. Water samples from the Shoalhaven River show very low amounts of suspended sediment downstream from Tallowa Dam (Figure 8).

The water samples show a significant increase in conductivity, dissolved oxygen and turbidity downstream from the dam reflecting an increase in suspended sediment and salinity. These results clearly prove there is less sediment delivery and high rates of bank erosion in these downstream areas, which leads to increasing turbidity and siltation in the adjacent wetlands.

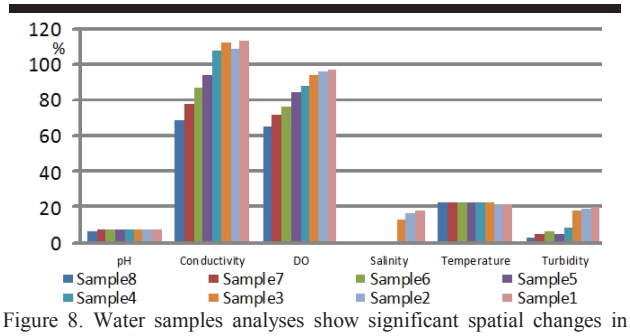

Figure 8. Water samples analyses show significant spatial changes in conductivity, dissolved oxygen and turbidity.

DISCUSSION

This multi-temporal study of the Comerong Island wetland shows a significant loss of coastal wetland in southeastern Australia. The main losses were changes in landcover, shoreline and elevation which resulted from the negative effects of human activities on the wetland's catchment. This comprehensive monitoring, plus other studies conducted by multiple researchers, has revealed the serious negative effects of human activities on the wetlands in and around Comerong Island. A number of spatial and temporal monitoring solutions should be considered for effective coastal wetland management. Significant results include:

1. Modelling aerial photographs and RS data (1949-2014) of the shorelines shows the northern part of the island has expanded by 0.41 km^2, whereas, the western and southern portions have been eroded by 0.73 km^2. This situation has resulted from the sediment delivery and erosion/deposition processes, that are mostly controlled by human infrastructure up stream such as Tallowa Dam, combined with the ocean tidal affected by sea level rise. Together these have caused a reduction in sediment delivery, which cannot balance the erosion/deposition caused by natural processes.

2. Grain size tests show most of the island is composed of sand, with clay in the west and uniform silt contents. Comerong Island is therefore made of soft materials, which are more easily eroded and lost than in other coastal ecosystems that may be more sensitive to rising sea level.

3. XRD tests show the minerals that Comerong Island is made of sediments that originale from both the catchment and the ocean. Northern accretion on the island has been caused by

addition of ocean sediment via the open mouth of Shoalhaven River.

4. Using loss on ignition proves high plant density in the east and mid parts of the island. The high proportion of organic matter included biotic components, such as leaf litter, mangrove debris and roots. This organic matter plays an important role on elevation changes and surface accretion.

5. Construction of the Berry Canal appears to have dropped water levels and reduced the wetland area, especially saltmarshes, on Comerong Island.

This modelling framework could be applied to study coastal wetlands all over the world. This project proved significant, detailed and accurate results of changing coastal wetlands in an eco-geomorphological context for risk assessment, using modern modelling methods. Such information will be essential for government agencies to issue and revise their policies. It will also be important for the general public and scientists who are currently focusing their attention on the best way to preserve wetland ecosystems to achieve conservation targets.

CONCLUSIONS

Both natural and anthropogenic processes control the balance between sediment deposition and erosion rates. The Shoalhaven River has provided high sedimentation rates, historically. These high sedimentation rates and lower erosion rates have controlled the natural accretion processes around Comerong Island. The aerial photographs and RS data (1949, 1961, 1973 and 1982) show that the island has grown constantly. After 1982, however, the island has eroded and its size has declined as shown in the aerial photographs and RS data (1993, 2002 and 2014). The reason behind this change was the building of Tallowa Dam, which blocked most of the sediments collected from the catchment. Thus 80.1% of the catchment (5,750 km^2 of 7177.5 km^2) was converted to inactive catchment geomorphologically. That caused serious sediment transport and availability problems, which changed the positive sedimentation rates to negative values, and favored erosion.

Initially after Tallowa Dam was constructed in 1976, the sediment rates remained high and the island continued to grow. This was due to the new water level within the Shoalhaven River that dropped below the dam (for 58.8 km until it reached Comerong Island) which caused erosion of the river bed and edges providing sediment to the Comerong Island area. This occurred for a few years only, after which the natural processes failed to erode additional sediment resulting in less sediment availability and deposition in the lower reaches. This is reflected in higher erosion rates that now control the site. This study has shown that the shoreline eroded by 0.73 km^2 since 1982 (0.02 km^2 annually). Meanwhile, the northern part of the island has grown significantly (about 20% between 1949 and 2014). This can be related to barrier deposition by natural tidal processes that have affected northern area during periods when the river mouth was open.

To restore the coastal wetland ecosystems fully there is a need to monitor its extent carefully to ensure long-term success. One can choose a natural mechanism that will offer a self-sustaining approach or self-management. By considering the findings from scientific studies, relevant policies need to be implemented to repair the damage from human activities in such wetlands.

LITERATURE CITED

Cherfas, J., 1990. The fringe of the ocean - under siege from land: the ecology of the ocean margins, crucial to human life, is being disrupted by our activities - and perhaps by global change. *Science*, 248(4952), 163.

DSE, 2007. Index of Wetland Condition: Review of Wetland Assessment Methods. Melbourne, Australia: *Department of Sustainability and Environment*, 30p.

Ehrenfeld, J.G., 2000. Evaluating wetlands within an urban context. Ecological Engineering, 15(3), 253-265.

Kingsford, R.T., 1990. The effects of human activities on shorebirds, seabirds and waterbirds of Comerong Island, at the mouth of the Shoalhaven River. *Wetlands (Australia)*, 9(1), 7-12.

Land and Property Information (LPI), 2004 & 2010. *LiDAR data.*

Murray, C.G.; Kasel, S.; Loyn, R.H.; Hepworth, G., and Hamilton, A.J., 2013. Waterbird use of artificial wetlands in an Australian urban landscape. *Hydrobiologia,* 716(1), 131-146.

Neumann, B., Vafeidis, A. T., Zimmermann, J. & Nicholls, R. J. 2015. Future Coastal Population Growth and Exposure to Sea-Level Rise and Coastal Flooding-A Global Assessment. *PloS one*, 10, e0118571.

NPWS, 1998. Seven Mile Beach National Park and Comerong Island Nature Reserve, plan of management. Sydney, Australia: National Parks and Wildlife Service, 33p.

OWA, 2010. The Shoalhaven River Catchment-CS1. Sydney, Australia: OceanWatch Australia. http://www.oceanwatch.org.au/wp-content/uploads/2010/02/CS1-Shoalhaven-Catchement.pdf.

Postgate, N. 1992. Early Mesopotamia: Society and Economy at the Dawn of History (Book Review), London, Oxford University Press, 198p.

Saintilan, N. and Imgraben, S., 2012. Principles for the monitoring and evaluation of wetland extent, condition and function in Australia. *Environmental Monitoring and Assessment*, 184(1), 595-606.

SCA, 2015. Tallowa Dam The Centrepiece of the Shoalhaven System (Facts and History) Sydney, Australia: Sydney Catchment Authority. http://www.sca.nsw.gov.au/water/visit/tallowa-dam.

Shahbaz, K.; Mohsin, H.; Akhtar, A., and Aftab, A., 2009. Spatial assessment of water use in an environmentally sensitive wetland. *AMBIO,* 38(3), 157-165.

Thompson, C.M., 2012. Recent Dynamic Channel Adjustments of Berrys Canal- Shoalhaven Region, NSW. Wollongong, Australia: *University of Wollongong*, Batchelor's thesis.

Umitsu, M.; Buman, M.; Kawase, K., and Woodroffe, C.D., 2001. Holocene palaeoecology and formation of the Shoalhaven River deltaic-estuarine plains, southeast Australia. *The Holocene*, 11(4), 407-418.

Woodroffe, C.D.; Buman, M.; Kawase, K., and Umitsu, M., 2000. Estuarine infill and formation of deltaic plains, Shoalhaven River. *Wetlands (Australia),* 18(1), 72.

Wright, L., 1970. The influence of sediment availability on patterns of beach ridge development in the vicinity of the Shoalhaven River delta, NSW. *The Australian Geographer*, 11(4), 336-348.

Journal of Coastal Research	SI	75	38-42	Coconut Creek, Florida	2016

Modern sedimentary processes and seasonal variations of organic matter in an urban tropical estuary, Jaboatão River (PE), Brazil

Roberto L. Barcellos †, Manuel J. Flores-Montes†, Tatiana M. F. Alves†, Plínio B. Camargo‡

† Oceanography Department
Federal University of Pernambuco
Recife, Brazil

‡ Center of Isotopic Energy in Agriculture
University of São Paulo
Piracicaba, Brazil

www.cerf-jcr.org

www.JCRonline.org

ABSTRACT

Barcellos, R.L., Flores-Montes, M.J., Alves, T.M.F. and Camargo, P.B. 2016. Modern sedimentary processes and seasonal variatios of organic matter in a urban tropical estuary, Jaboatão River (PE) Brazil. *In:* Vila-Concejo, A.; Bruce, E.; Kennedy, D.M., and McCarroll, R.J. (eds.), *Proceedings of the 14th International Coastal Symposium* (Sydney, Australia). *Journal of Coastal Research*, Special Issue, No. 75, pp. 38-42. Coconut Creek (Florida), ISSN 0749-0208.

The aim of this research is to evaluate the environmental conditions in the Jaboatão River estuarine system (8°14'S/34°55'W), by studying sedimentary organic matter, which may provide information about anthropogenic influence in this tropical mesotidal estuary. The catchment area is 442 km² with a population estimated at 500,000 inhabitants, and is characterized as an urban coastal plain estuarine system. Thirty surface sediment samples were collected in November-2010 (dry season) and May-2011 (rainy season). Results indicated that the adjacent sediments from continental shelf are sandy, moderately sorted and bioclastic (74.8%$CaCO_3$), differing from estuarine sediments, which although sandy (silty-sand) are lithoclastic (17.4%$CaCO_3$) and poorly sorted. The predominance of sand observed in both seasons is due to the small length of the river (75km) and to the low supply of mud sediments, since its drainage basin is located mostly on sandy coastal plain. Carbon and nitrogen contents indicates a sensitive seasonal variation with large ranges, varying from 0.03-8.51% and from 0.00-0.54%, respectively, with higher contents prevailing in the inner portions of the estuary and gradually decreasing towards the shelf. The organic matter origin, according to the C/N ratios and $\delta^{13}C$ values reflected the occurrence of marine organic matter in shelf samples (C/N<7.0/$\delta^{13}C$>-20.0‰PDB). However, the estuary terrigenous organic matter proportion increases upward (C/N>15.0). The $\delta^{13}C$ values are typical of C_4 higher plants (-27.0‰PDB) and domestic sewage mix (-26.7‰PDB), ranging from -28.0 to -25.9‰PDB and indicating evidences of urban pollution in Jaboatão estuarine sediments.

ADDITIONAL INDEX WORDS: *Seasonal estuarine sedimentation, organic matter, pollution.*

INTRODUCTION

Estuaries are the marine-influenced portion of a drowned valley (Dalrymple, *et al*., 1992; Nichols, 2009). They can be regarded as a major sinks and stores of sediments, particurarly terrestrial and are also historically important sites for human settlement and industry (Haslett, 2003; French, 2007). When this coastal sedimentary environment is associated with populated areas, it is subjected to anthropogenic inputs such as waste products from urban, industrial and portuary areas, and there is increased sediment input as result of dredging operations and agricultutal products (French, 2007).

One of the sediment compounds that is commonly trapped in estuarine systems is sedimentary organic matter, in general adsorbed by clay minerals. High organic matter contents are related to high mud contents directly linked to low hydrodynamic areas, or a high primary productivity region (Pettijohn, 1975; Tyson, 1995). Sedimentary organic matter in coastal marine areas is a good tool for environmental evaluation and is also used to correlate several oceanographic processes, such as water masses dynamics, sedimentation rates, sedimentary processes associated to local hydrodynamics, oxi-reduction potential and land-derived materials input (Romankevich, 1984; Meyers, 1997; Lamb *et al.*, 2006).

The nature of the organic matter allows analysis about its sources, terrigenous or marine, through the use of C/N ratio (Saito *et al.*, 1989; Stein, 1991). Stable carbon isotope has proven to be an effective indicator of material sources and also to trace organic matter flow in many coastal studies (Emery *et al.*, 1967; Emerson and Hedges, 1988; Ruttenberg and Goñi, 1997; Oliveira *et al*., 2014; Barcellos *et al*., 2014). It is observed, in estuaries, a linear increase in $\delta^{13}C$ values from the inner estuary to its oceanic portion (Thornton and McManus, 1994; Tyson, 1995, Barcellos *et al*., 2005). The $\delta^{15}N$ isotopic signatures are more affected by biogeochemical processes than $\delta^{13}C$ (Ogrinc *et al.*, 2005). Carbonate contents can also be used as a parameter that allows inferences about land-derived material input influences in a depositional site (Paraopkari *et al.*, 1991).

The aim of this research is to evaluate the environmental conditions in the Jaboatão River estuarine system, through studies of sedimentary organic matter that may provide information about anthropogenic influence in this estuary and a

DOI: 10.2112/SI75-008.1 received 15 October 2015; accepted in revision15 January 2016.
*Corresponding author: oceanografofisico@gmail.com

better understanding on its modern sedimentary processes and seasonality.

Study site

The Jaboatão River estuarine system (8°14'S/34°55'W) is a well-mixed coastal plain estuary (Figure 1), sheltered by a 2.2 km long sandy spit in its lower portion adjacent to the inlet at Atlantic Ocean (Figure 2). The river is 75 km long, the whole catchment area is 442 km² with a population estimated at 500,000 inhabitants (IBGE, 2010). This estuary is located 20 km to the south from the city of Recife, the Pernambuco State capital, and is characterized as an urban estuarine system from Recife Metropolitan Region (RMR: 3,700,000 hab)

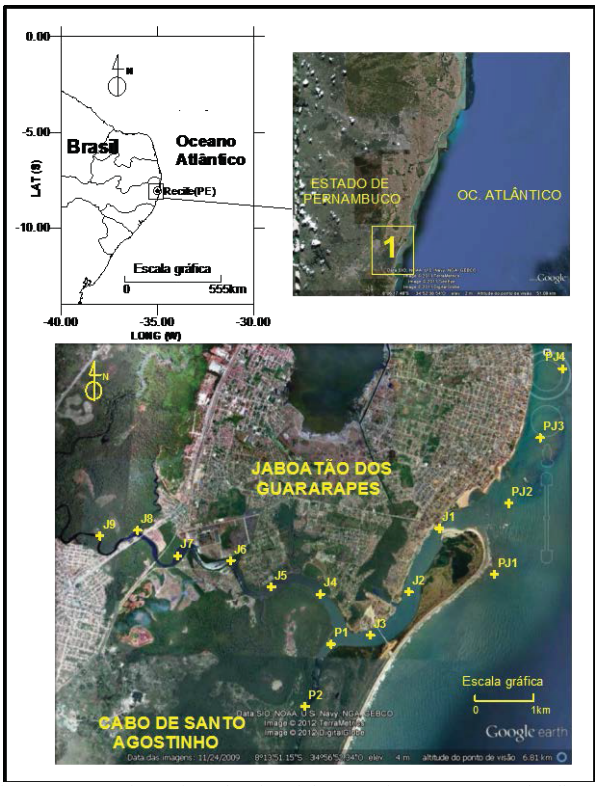

Figure 1: Location of study site: jaboatão river estuary and adjacent inner shelf.

Geologically it is inserted in Pernambuco marginal sedimentary basin and the predominant geomorphological features are marine terraces and the Quaternary costal strandplain, composed mainly by fine and medium quartz sands (Lima Filho, 1998; Pfaltzgraff *et al.*, 2002).

The climate is tropical humid (mean 25.5ºC and 2.8ºC of thermal range), AWs' according to Köppen classification, and the average annual rainfall and evaporation are respectively 2,000 and 1,200 mm (CPRH 1995, 1996). Prevailing winds are SE trade winds with a mean speed of 3.2 $m.s^{-1}$. The region has two well-defined seasons. From February to August, with half of annual rainfall occurring between April and July. During these months, it is not uncommon for precipitation to exceed 400mm/month and hydrological balance is strongly positve. The dry season extends from Sepetember to January, when monthly rainfall is less than 60 mm and the evaporation rate exceeds precipitation (Araújo *et al*., 1999).

Tides at its mouth are semidiurnal with a mean neap range of 1.3m and mean spring range of 2.2m. The specific and decenal flows are 3.40 $L.s.km^2$ and 2034.00 $L.s^{-1}$. Shallow depths, 1 to 6m deep, are observed in whole Jaboatão estuarine area (Aquaplan, 1990; Araújo *et al.*, 1999; Souza and Tundisi, 2003).

The watershed drains a high populated area of 6 municipalities (80 hab/km^2), including areas covered by the original Atlantic forest and sugar cane fields. It receives large loads of domestic and industrial wastes as well as a seasonal input of high levels of organic matter from sugar cane, alcohol, food, paper, textile, boiler, industrial gases, chemical, metallurgical industries at its mid-course, while its lower section is surrounded by relatively well-preserved fringing mangrove forests, but subjected to high untreated domestic sewage inputs. The main sources of pollution to the Jaboatão riverine and estuarine basins are a mill, *Usina Bulhões* that in summer discharges effluents to the river, and *Portela*, a paper and cellulose manufacturer (Araújo *et al.*, 1999; Souza and Tundisi, 2003; Noriega *et al*., 2005; Silva *et al*., 2010; Lima, 2011).

Figure 2. Jaboatão river estuary inlet and the sand spit. Picture taken by Roberto Barcellos in 14/06/2011.

METHODS

Thirty surface sediment samples were collected in November 2010 (dry season) and May 2011 (rainy season). The following parameters were employed: particle size, calcium carbonate ($CaCO_3$) contents and elemental (C, N) and isotopic analysis ($\delta^{13}C$, $\delta^{15}N$) of organic matter.

Grain size was analyzed by a sieving and pipeting method (Müller, 1967) and the calcium carbonate contents were determined by the weight difference prior to and after acidification, with 1 N HCl (Ingram, 1971). The organic contents (C and N elemental and isotopic) were obtained through a Carlo Erba (CHN-1110) elemental analyzer linked to a Finnigan Delta Plus mass spectrometer. About 0.5g of dried and weighed sediment were decarbonated with 1 M solution of HCl, washed 3 times with deionized water, filtered and freeze-

dried again, before being placed in the analyzer (Hedges & Stern, 1984). The data were treated according to Folk and Ward (1957) statistical parameters and Shepard (1954). The maps and figures are products from the software *Surfer for Windows (8.0).*

RESULTS AND DISCUSSION

The results indicate that, independent of the season, the sediments from continental shelf adjacent to the estuary are sandy according to Shepard (1954) classification (Figure 3), moderately sorted (Folk and Ward, 1957) and bioclastic (74.8% $CaCO_3$) (Larssoneur *et al*., 1982), differing from estuarine sediments, which although sandy (silty-sand and clayey-sands) are siliciclastic (17.4% $CaCO_3$) and poorly sorted.

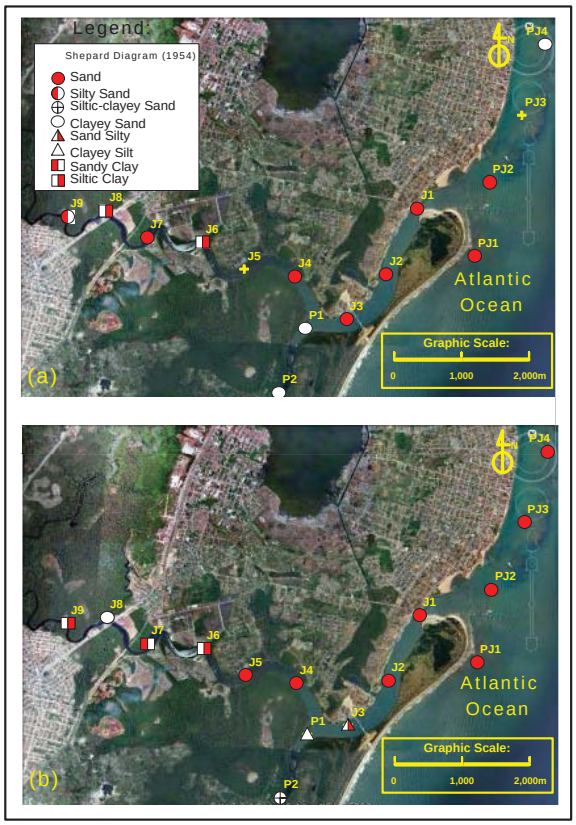

Figure 3: Sediments texture according to diagram classification of Shepard (1954) for Nov/10 (a) and May/11 (b) samples.

The predominance of sand observed in both seasons is due to the small length of the river (75km) and to the low supply of mud sediments, since its drainage basin is located mostly on sandy coastal plain. These conditions promote a low suppy and deposition of mud sediments, distinctly from the ones observed for Capibaribe estuary, located in RMR 20 km to the north, that presents siltic sediments in the whole extension of its estuarine area (Oliveira *et al.*, 2014).

Despite the low amounts of mud, it was observed that the rainy period (May/11) had around 10% higher mud contents (+3% of silt and +7% of clay), when compared to November 2010. This is probably directly associated to heavy rains and a flood that occurred in the beginning of May 2011, just before the winter samples field work. According to INMET (2013), May 2011 recieved 756 mm of precipitation, two times higher than the local average. Oliveira (2014) observed the same seasonal sedimentary trend for Capibaribe estuary. In this study, the winter samples (Aug/14) presented, in average, 25% more mud than the summer samples (Dec/13).

Organic carbon (OC) contents has large ranges, varying from 0.08 to 7.07% (average: 2.48%) and from 0.03-8.51% (average: 2.79%), in November of 2010 and May of 2011 respectively. Total Nitrogen (TN) varies from 0.00 to 0.45% (Nov/10: average of 0.16%) and from 0.00 to 0.54% (May/11: average of 0.21%). The spatial distribution for both elements is directly related to sediment texture ($r^2 > 0.77$), and has a well-defined geographical distribution, with higher contents prevailing in internal portions of the estuary and gradually decreasing towards the shelf, as observed by Thornton and McManus (1994), Barcellos *et al.* (2009) and Barcellos *et al*. (2014). The significant correlation between this two parameters ($r^2 > 0.90$) indicated common sources as in Capibaribe estuary (Oliveira *et al.*, 2014). Similar to the mud contents, slightly higher average percentages of OC and TN were observed in May/11 compared to Nov/10, 2.79 x 2.48% and 0.21 x 0.16%, respectively. Also denoting the seasonal behavior for the elemental sedimentary organic matter (SOM).

For the dry period (Nov/10) the C/N, $\delta^{13}C$, $\delta^{15}N$ values ranges were 6.3 to 25.5, -20.0 to -27.6‰PDB and 4.1 to 6.8‰Air, respectively. In the case of rainy period samples (May/11), the observed ranges for the same parameters were: 6.0 to 26.7, -18.8 to -28.0‰PDB and 4.6 to 7.5‰Air. The organic matter origin, according to the $\delta^{15}N$ obtained values that ranged between 4.1-7.5‰Air, does not seem to be a sensitive indicator to anthropogenic influence for the area. According to Stein (1991) $\delta^{15}N$ ratio contents for a different kind of material presents a superposition, avoiding a more accurate indentification of SOM sources through this parameter.

On the other hand, C/N ratios and $\delta^{13}C$ (Figure 4) values reflected the occurrence of marine organic matter in shelf samples (C/N < 7.0 / $\delta^{13}C$ > -20.0‰PDB), located adjacent to estuary inlet. They also indicates that the estuary's terrigenous organic matter proportion increases upward (C/N>15.0), and the $\delta^{13}C$ ratio contents are typical of C_4 higher plants (-27.0‰PDB) and domestic sewage mix (-26.7‰PDB) (Andrews *et al*., 1998; Ogrinc *et al*., 2005). The natural sources of material came from the well-preserved fringing mangroves and remnants of Atlantic forest that surrounds the Jaboatão river estuary. These contents range from -28.0 to -24.1‰PDB and indicate evidences of urban pollution in Jaboatão estuarine sediments, as well as observed by Oliveira *et al.* (2014) for the Capibaribe estuary. In fact Souza and Tundisi (2003) observed anthropogenic influences in the whole catchment area of Jaboatão river, including its estuarine portion, related to fecal contamination and water discharges from upstream industrial plants. However, Lima (2011) points out that the sediments of Jaboatão estuary could be considered of good quality when related to heavy metal contamination. Lastly, no sensitive seasonal variation were observed in this study for C/N and $\delta^{13}C$ ratios.

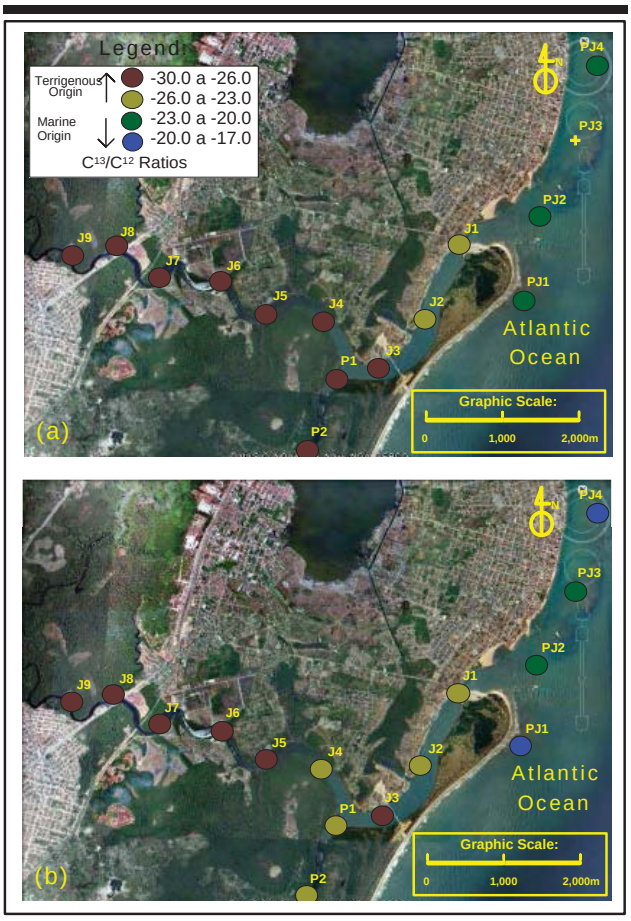

Figure 4: November 2010 (a) and May 2011 (b) $\delta^{13}C$ isotope ratio distribution (‰PDB) of Jaboatão estuarine system surface sediments

CONCLUSIONS

The Jaboatão river estuary has significant differences in sedimentation between the sandy bioclastic adjacent shelf samples and the silty-sand and clayey-sand siliciclastic estuarine samples.

From the shelf and lower estuary to upstream, the muds and elemental organic matter (OC,TN) concentrations increase, where medium to high contents of SOM (> 4.0%) are observed. This pattern occurs mainly due to natural and anthropogenic inputs, associated to a descrease of hydrodynamic energy to upper estuary. It is typical from the coastal plain rivers with low flows, which sediments transport are dominated by the tides.

Seasonal differences in sedimentation processes were observed between November 2010 and May 2011, reflected by the increase of mud contents, OC and TN. It seems to be directly related to oceanographic-climatic regional processes, since it was possible to associate a high rainfall events that occurred before the May/11 field work, and consequently the input of silt/clay and SOM to the system.

On the other hand, the origin of organic matter by $\delta^{13}C$ and C/N ratios do not show differences between rainy and dry periods. In both seasons the sedimentary organic matter seems to be a mix of C_4 higher plants and domestic sewage, and from marine origin in adjacent shelf samples.

Apart from the $\delta^{15}N$, the proxies employed in this research indicated that the estuary is subjected to significant environmental impacts of anthropogenic origin, especially associated to domestic sewage.

ACKNOWLEDGMENTS

The authors wish to express their thanks to the National Research Council (CNPq) by the financial support given for CRECOPE project (nº: 558106/2009-9): "*Transport of Total Organic Carbon and the interaction with marine acidification processes in oceanic and coastal-estuarine áreas in the North and Northeast Brazilian regions*". Thanks are also due to Mr. Gustavo Lima Barcellos, for the revision of the text.

LITERATURE CITED

Acquaplan. 1990, *Estudo de impacto ambiental da barragem do rio Jaboatão*, Recife, ACQUAPLAN.

Andrews, J.E.; Greenaway, A.M., and Dennis, P.F., 1998. Combined Carbon isotope and C/N ratios as indicators of source and fate of organic matter in a poorly flushed, tropical estuary: Hunts bay, Kingston Harbour, Jamaica. *Estuarine, Coastal and Shelf Science*, 46, 743-756.

Araújo, M.; Medeiros, C., and Ribeiro, C. 1999. Energy balance and the time scales of mixing and stratification in Jaboatão estuary, NE-Brazil. *Rev. Bras. de Oceanogr.*, 47 (2), 145-154.

Barcellos, R.L.; Camargo, P.B.; Brizzotti, M.M., and Furtado, V.V. 2005. Seasonal stable carbon isotope ($\delta^{13}C$) variations in sediments of Cananéia-Iguape lagoonal-estuarine system, São Paulo State, South-Eastern Brazil. *Materials and Geoenvironment, Materiali in Geookolje,* 52 (1), 188.

Barcellos, R.L.; Camargo, P.B.; Galvão, A., and Weber, R.R. 2009. Sedimentary organic matter in cores of Cananéia-Iguape lagoonal-estuarine system, São Paulo State, Brazil. *J. Coast Res.*, SI56, 1335-1339.

Barcellos, R.L.; Braga, E.S.; Furtado, V.V., and Berbel, G.B.B., 2014. Sedimentary and Geochemical Aspects of a Refinery Impacted Coastal Area, A Case Study of the Todos os Santos Bay (Bahia, Brazil). *Int. Jour. of Geosciences,* 5, 1451-1467.

CPRH (Companhia Pernambucana de Controle da Poluição Ambiental e de Administração dos Recursos Hídricos)., 1995. Monitoramento das bacias hidrográficas do Estado de Pemambuco, Projeto CPRH-DRN-GMO-URHi. 174 p.

CPRH (Companhia Pernambucana de Controle da Poluição Ambiental e de Admin. Recursos Hídricos)., 1996. Avaliação do impacto da poluição sobre os recursos pesqueiros do R. Jaboatão(PE). Proj CPRH-PJ-UFRPe-FAS. 129 p.

Dalrymple, R.W.; Zaitlin, B.A., and Boyd, R., 1992. Estuarine facies models, conceptual basis and stratigraphic implications. *Jour. of Sedimentary Petrology*, 62, 1130-1146.

Emerson, A., and Hedges. J. I., 1988. Processes Controlling the Carbon Content of Open Ocean Sediments. *Paleoceanography*, 3, 621-634.

Emery, K.O.; Wigley, R.L.; Bartlott, A.S.; Rubin, M., and Barghoom, E.S., 1967. Fresh water peat on the continental shelf. *Science*, 158, 130-137.

Folk, R. L. & Ward, W. C., 1957. Brazos River Bar, Study of the Significance of Grain Size Parameters. *Journal of Sedimentary Petrology*, 27, 3-27.

French, P., 2007. Delataic and estuarine environments. *In*, Perry, C., and Taylor, K. (eds.), *Environmental Sedimentology*. Oxford, Blackwell, pp. 223-262.

Haslett, S.K., 2003. *Coastal Systems*. London, Routledge, 218p.

Hedges, J.I., and Stern. J. H., 1984. Carbon and nitrogen determinations in carbonate-containing solids. *Limnology and Oceanography*, 29 (3) , 657-663. ISSN, 0024-3590.

IBGE. 2010. Censo Demográfico 2010- Resultados do Universo - Características da População e dos Domicílios. 2010. http,//www.sidra.ibge.gov.br/cd/cd2010universo.asp

Ingram, C., 1971. Carbon Determination. *In*, CARVER, R. E. (ed.) *Procedures in Sedimentary Petrology*. New York, Wiley-Interscience. p. 573-596.

INMET (Instituto Nacional de Meteorologia), 2013. Estações Meteorológicas, Estações Recife e Curado. http,//www.inmet.gov.br

Lamb, A L..; Graham, P.W., and Leng, M. J. 2006., A review of coastal palaeoclimate and relative sea-level reconstructions using $\delta^{13}C$ and C/N ratios in organic matter. *Ear-Scienc. Rev*., 75, 29-57.

Larssoneur, C.; Bouysse, P., and Aufret, J. P., 1982. The Superficial Sediments of the English Channel and its Western Approach. *Sedimentology*, 29 (6), 851-864.

Lima, M.M.R.B.F., 2011. Evolução geoquímica ambiental e avaliação da qualidade dos sedimentos estuarinos do Rio Jaboatão, Pernambuco. Recife, Pernambuco, Federal University of Pernambuco, Ph.D. dissertation, 120p.

Lima Filho, M. F., 1998. Análise estratigráfica e estrutural da Bacia de Pernambuco. São Paulo, São Paulo, University of São Paulo, Ph.D. dissertation, 180p.

Meyers, P. A. 1997., Organic Geochemical Proxies of Paleoceanography, Paleolminologic and Paleoclimatic Processes. *Organic Geochemistry,* 27, 213-250.

Nichols, G., 2009. *Sedimentology and Stratigraphy*. Chichester, Wiley-Blackwell, 419p.

Noriega, C.D.; Muniz, K.; Araújo, M. C.; Travassos, R. K., and Neumann-Leitão, S. 2005. Fluxos de nutrientes inorgânicos dissolvidos em um estuário tropical – Barra das Jangadas – PE, Brasil. *Tropical Oceanography*, 33 (2), 133-143.

Ogrinc, N.; Fontolan, G.; Faganeli, J., and Covelli, S. 2005. Carbon and nitrogen isotope compositions of organic matter in coastal marine sediments (Gulf of Trieste, N Adriatic), indicators of sources an preservation. *Mar. Chem.* 95, 163-181

Oliveira, T.S., 2014. Processo sedimentar atual e distribuição da matéria orgânica no sistema estuarino dos rios Capibaribe, Beberibe e Bacia do Pina (Recife-PE). Recife, Pernambuco, Federal University of Pernambuco, Master's thesis, 113p.

Oliveira, T.S.; Barcellos, R.L.; Schettinni, C.A.F., and Camargo, P.B., 2014. Processo sedimentar atual e distribuição da matéria orgânica em um complexo estuarino tropical, Recife-PE, Brasil. *Rev. da Gestão Cost. Int.*, 14(3), 399-411.

Paraopkari, A.L., Iyer, S.D., Chauan, O.S., and Babu, C.P., 1991. Depositional environments inferred from variations of calcium carbonate, organic carbon and sulfide sulfur, a core from southeastern Arabian Sea. *Geo-Mar. Lett.*, 11, 96-102.

Pettijohn, F.J. 1975. *Sedimentary rocks*. New York, Harper and Row Publishers, 628p.

Pfaltzgraff, P.A.S.; Leal, O.; Souza Júnior, L.C.C.; Souza, F. J.C.; Accioly, A. C. A.; Santos, A. S.; Melo, C. P.; Moreira, F. M.; Almeida, I. S.; Araújo, L. M. N.; Rocha, D. E. G. A.; Oliveira, R. G.; Shinzato, E.; Amaral, A. A. & Ferreira, R. V., 2002. Sistemas de informações geoambientais da Região Metropolitana. Recife, CPRM – Serviço Geológico do Brasil.

Romankevich, E.A., 1984. *Geochemistry of organic matter in the ocean*. New York, Springer-Verlag, 334p.

Ruttenberg, K. C., and Goñi, M.A., 1997. Phosphorus Distribuition, C,N,P Ratios, and $\delta^{13}C$ in Arctic, Temperate and Tropical Coastal Sediments, Tolls for Characterizing Bulk Sedimentary Organic Matter. *Mar. Geol.*, 139 (1/4), 123-145.

Saito, Y.; Nishimura, A., and Matsumoto, E., 1989. Transgressive and sheet covering the shelf and upper slope off Sendai, northeastern Japan. *Mar Geol.*, 89(3/4), 245-258.

Silva, J. B.; Galvíncio, J. D.; Moura, M. S. B. & Silva, S. G., 2010. tendências fluviométricas nas áreas estuarinas de goiana-megaó e pirapama/jaboatão e das tabuas de maré no Porto de Suape-PE. *Rev. Bras. de Geog. Física*, 2 (2), 70-82.

Souza, A.D.G & Tundisi, J.G. 2003. Water Quality in watershed of the Jaboatão River (Pernambuco, Brazil), a Case Study. *Brazilian Archives of Biology and Tech.*, 46 (4), 711-721.

Shepard, F. P. 1954. Nomenclature Based on Sand-Silt-Clay Ratios. *Journal of Sedimentary Petrology*, 24 (3), 151-158.

Stein, R., 1991. Accumulation of organic matter in marine sediments. Results from Deep Sea Drilling Project/ocean Drilling Program. In, Bhattacharji, S., Friedman, G.M., Neugebauer, H.J., Seilacher, A., Eds., *Lectures Notes in Earth Sciences*. Springer, Berlin, 34v., 217pp.

Thornton, S.F. and McManus, J. 1994. Application of organic carbon and nitrogen stable isotope and C/N ratio as source indicators of organic matter provenance in esturine systems, evidence from the Tay Estuary, Scotland. *Est, Coas. Shelf. Scie.*, 38, 219-233.

Tyson, R. V. 1995. *Sedimentary Organic Matter*. London, Chapman & Hall. 589p.

Journal of Coastal Research	SI	75	43-47	Coconut Creek, Florida	2016

Runoff quantification on Amazonian Estuary based on hydrodynamic model.

Thais A.C. Borba[†*], and Marcelo Rollnic[†]

[†]Laboratoty of Marine Geophysics, Programa de Pós Graduação em Geofísica – CPGF
Federal University of Para.
Belem, Brazil

www.cerf-jcr.org

www.JCRonline.org

ABSTRACT

Borba, T.A.C., and Rollnic, M., 2016. Runoff quantification on Amazonian Estuary based on hydrodynamic model. *In:* Vila-Concejo, A.; Bruce, E.; Kennedy, D.M., and McCarroll, R.J. (eds.), *Proceedings of the 14th International Coastal Symposium* (Sydney, Australia). *Journal of Coastal Research*, Special Issue, No. 75, pp. 43-47. Coconut Creek (Florida), ISSN 0749-0208.

The Amazonian Estuary encompasses a large number of water bodies and four of the 20 largest rivers of the world. It is composed of two conected branches: the Amazon River Estuary and Para River Estuary. This research aims to quantify the net runoff through these branches during wet and dry season based on 2D numerical model. D-Flow Flexible Mesh was used to simulate the hydrodynamics of Amazonian Estuary. The domain encompasses rivers and channels of Amazonian Estuary and floodplain area. The domain covers ≈700 km along the coastline and 145 km offshore. It reaches 716 km upstream through the Amazon River and 430 km through Para/Tocantins River. Curvilinear meshes combined with triangles and 1D channels networks were used during the mesh definition. The net discharge was calculated for one tidal cycle. Five cross-sections were defined to quantify the estuary runoff: four on the Amazon River Estuary and one Para River Estuary. The lateral cross-sections on Amazon River Estuary present net runoff of magnitude of almost 10^7 m^3 for wet season and 10^6 m^3 for dry season, both in downstream direction. The central cross-sections on Amazon River Estuary present runoff of magnitude of 10^4 and 10^5 m^3 for wet season, both in upstream direction. The cross-section on Para River Estuary presents runoff of magnitude of 10^6 m^3. The Pará River Estuary presents magnitude near to that presented by Amazon River Estuary, making it an important channel of matter transport from continent to ocean.

ADDITIONAL INDEX WORDS: *Amazonian Estuary, hydrodynamic model, Northern Brazil.*

INTRODUCTION

Estuaries are very important for human life since they have biological, economic and social importance. Their dynamics, morphology and location allow the development of several natural and anthropological activities, for instance, ports, fishing, tourism as well as the growing of biological species.

The Amazonian Estuarine System is very important as well; in addition to the mentioned characteristics, it is composed of hundreds water bodies in which the 4 biggest rivers are in the group of the world's largest 20 rivers (Dai and Trenberth, 2002). These rivers are: Amazon River, Tapajos River, Xingu River and Tocantins River.

It is composed of two main branches: Amazon River Estuary and Para River Estuary that are connected by a network channels called Breves Strait. To date, a lot of attention has been given to the Amazon River Estuary. Here the focus is all the Amazonian Estuarine System and this present research aims to quantify the outflow through these two branches during wet and dry season based on 2D numerical model.

Background

The Amazonian Estuarine System is located in the Northern Brazil.

Several water bodies, encompassing tidal channels, downstream section of big rivers, flood plain areas and part of the Amazonian Continental Shelf, compose it (Figure 1).

Its funnel shape allows classifying the Amazon River basin mouth as a coastal plain dominated by tide (Sioli, 1984), where the tidal currents are the main force for morphological changes.

Semidiurnal mesotide and macrotide drive the estuarine system and can penetrates into the estuary distances of about 1,000 km through the Amazon River Estuary branch from the coastline (FEMAR, 2013).

As previously mentioned, it is composed of two main branches: Amazon River Estuary and Para River Estuary. The former flows on the west side of Marajo Island and flows into the Atlantic Ocean with most part of the Amazon, Tapajos and Xingu rivers runoff. The latter receive the Tocantins Rivers and Guajara Bay water runoff but also from the first branch through Breves Strait (Figure 1), from which receives less than 5% of Amazon River discharge (Silva, 2009).

About the circulation patterns, there is some authors disagreement, some of them classify as a mixed estuary (Baltazar *et al*., 2011; Bezerra *et al*., 2011), others as a stratified system with the estuarine plume located on the continental shelf due to the high river discharge (Geyer *et al*., 1996). The difference is where the salinity is measured: if the measurement is lead before the coastline, the salinity is very low with values less than 10; on the other hand, some investigation on the

DOI: 10.2112/SI75-009.1 received 15 October 2015; accepted in revision 15 January 2016.
*Corresponding author: tacborba@gmail.com

adjacent continental shelf show stratification with a well-defined estuarine plume with salinity between 15 and 35.

River discharge and tidal currents drive the salinity gradients at this area. The drainage system of Amazon River basin consist of more than 500 large rivers and uncountable small water bodies (Dai and Trenberth, 2002). However, at downstream area the main rivers are the Amazon River itself, Tapajos River, Xingu River and Tocantins River. About the discharge magnitude, the first have magnitude of 10^5 m^3/s and the others 10^4 m^3/s (Figure 2).

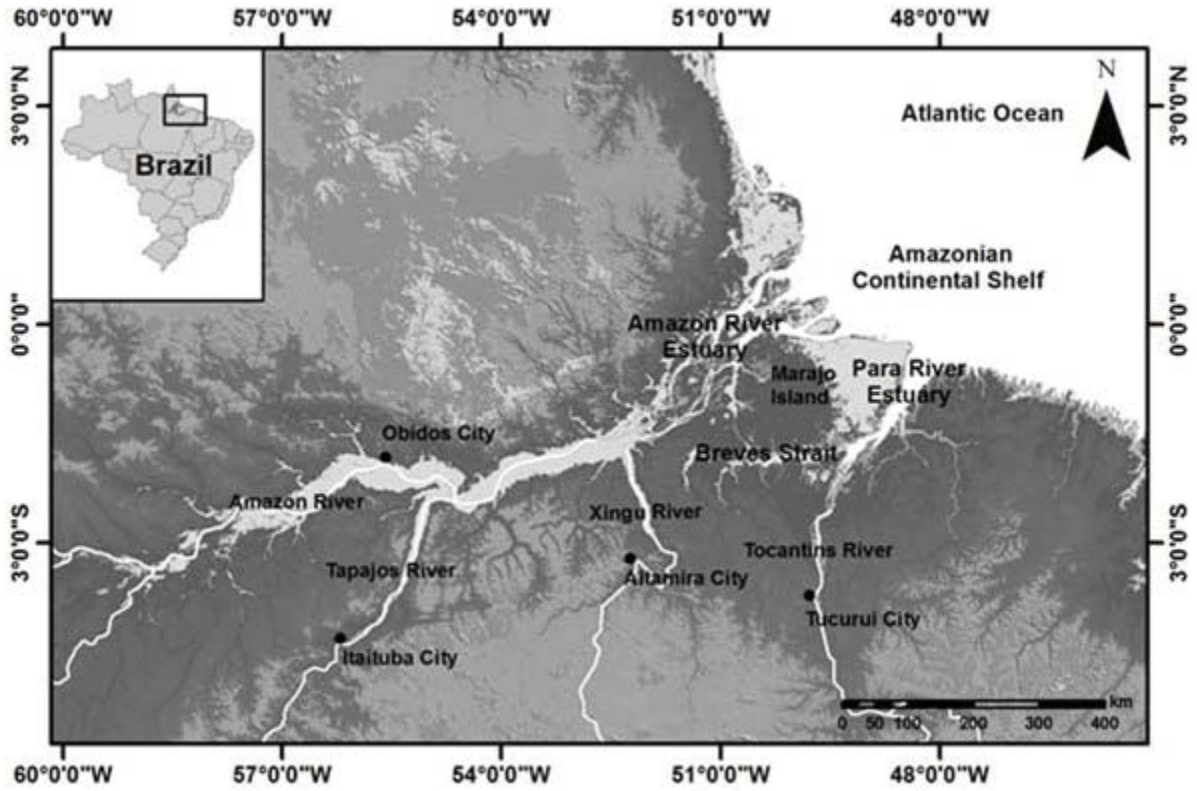

Figure 1. Location of Amazonian Estuary System and main water bodies.

Rain feed these rivers and the climate is the main responsible by them runoff seasonality. The climate is equatorial, hot and humid, with 2 main seasons well defined: wet and dry. The maximum rate of atmospheric precipitation occur between February and August, but, due to the dimension of the study area, there are different periods of maximum rate of atmospheric precipitation for each river. The Amazon river have the biggest river discharge between May and July and the others between March and April (Sioli, 1984; Dai and Trenberth, 2002; Mikhailov, 2010) (Figure 2).

The local bathymetry is irregular with occurrence of longitudinal sand bars and channels both formed and displaced by tidal currents and river flow, however the waves act by ressuspension of sediment and construction of estuarine beaches. Therefore, the morphodynamics is the result of the combination of tidal currents, river currents and wave action (Gregório and Mendes, 2009). The depth can range between less than 20 m and much than 100 m.

Sand and clay compose the bottom sedimentology but sediment with coarse grain size can occur in the internal part of the estuary. The variation can also occurs in transversal direction resulting of ebb and flood currents (Costa *et al*., 2003; Corrêa, 2005; Costa *et al*., 2013).

METHODS

In order to simulate the hydrodynamics of Amazonian Estuary System, the used hydrodynamic simulation package was D-Flow Flexible Mesh. Borba (2014) describes the setup and calibration of the Amazonian Estuary System model. The main rivers and channels of this estuary compose the domain, for instance, the rivers Amazon, Tapajos, Xingu, Tocantins and Para River, Guajara Bay, Marajo Bay and Breves Strait. The floodplain area also compose the domain that covers about 700 km along the coastline and 145 km offshore.

The domain reaches 716 km upstream through the Amazon River and 430 km through Para River Estuary and Tocantins River (Figure 3). The inner limits are the points where the tidal

amplitude is 0 in order to avoid tide wave reflectance the cities in which were placed these limitis are Obidos, Itaituba, Altamira and Tucurui (Figure 1 and Figure 3).

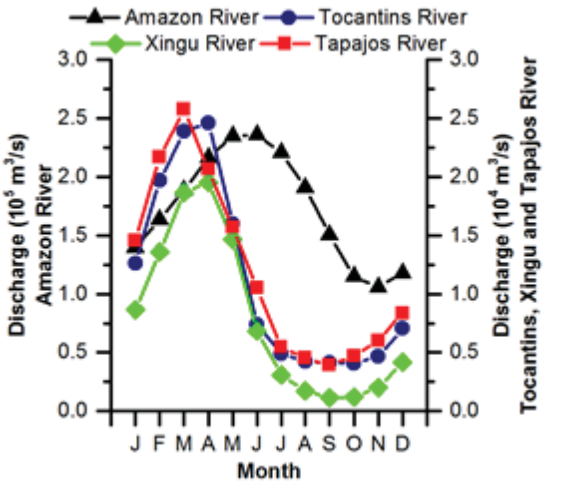

Figure 2. Average monthly discharge to the main rivers on Amazonian Estuary system.

D-Flow Flexible Mesh allows the mesh definition by using curvilinear meshes combined with triangles and 1D channels (Kernkamp *et al*., 2011). In this research, the curvilinear meshes cover the main rivers and continental shelf; triangular cells were applied to the floodplain and to link curvilinear meshes with different number and size of cells, in addition, 1D-channel networks were defined for Breves Strait channels that present width smaller than 5 km.

In order to quantify the runoff through the two branches of Amazonian Estuary, 5 cross-sections were defined: four on the Amazon River Estuary (L1, L2, L3 and L4, from west to east) and one on Para River Estuary (L5) (Figure 4). Two water level observation points were used to identify the tidal cycles that was used to calculate the net discharge.

The model genereted result for eight scenarios: (1) June/spring tide, (2) June/neap tide (3) October/spring tide, (4) October/neap tide, (5) November/spring tide, (6) November/neap tide, (7) April/spring tide, and (8) April neap/tide.

The months were chosen based on the average monthly discharge of Amazon River and Tocantis River. June and November represent the maximum and minimum discharge of Amazon River, respectively, in the same way, April and October for Tocantins River.

Since the study area presents mesotide and macrotide regime, to calculate the diferences between spring and neap tide is also important.

The model was set to give results of discharge for each 10 minutes. The net discharge was calculated by integration of these outputs during a tidal cycle for each scenario.

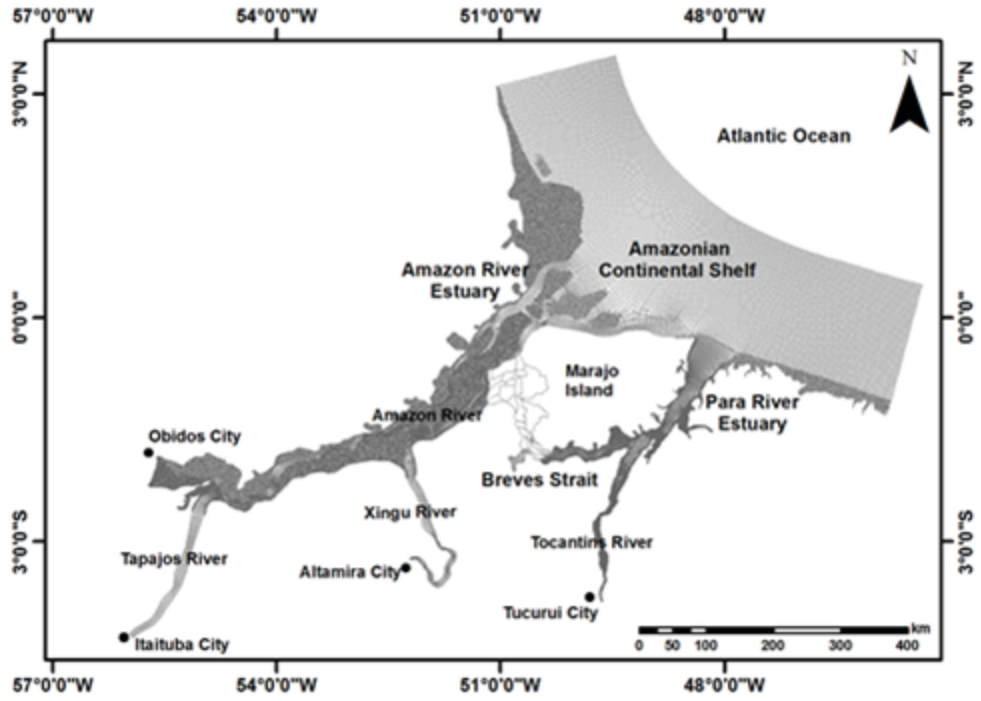

Figure 3. Model domain (modified from Borba, 2014).

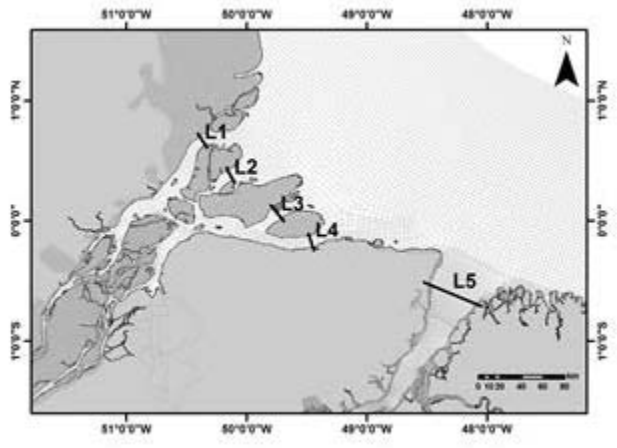

Figure 4. Location of the 5 cross-sections for net to net discharge quantification.

RESULTS

The model results show that the river discharge seazonality and the tidal range variation have the important role in the Amazonian Estuarine System net runoff variation. Figure 5 and Table 1 present these results.

L1 and L4 present the higher values of net runoff when it is compared to L2 and L3. Former sections present magnitude values of 10^6 m^3 for November and October (lower discharge of Amazon River). They also present values of magnitude 10^6 m^3 for June and April (higher discharge of Amazon River), however, for this months the values almost reach magnitude of 10^7 m^3. Furthermore, the variation of net runoff for L1 and L4 values follows mainly the river discharge seasonality than tidal range variation.

L2 and L3 present magnitude of values of net runoff of 10^4 and 10^5 m^3 for the months that were investigated. The variation of net runoff values for L2 is driven by tidal range variation but, in smaller scale, by river discharge seasonality also. For L3, this variation was driven by both processes. Until the submission of this research, no fieldwork was done in order to investigate the runoff of these channels (L2 and L3). We suggest that future researches investigate these runoff with in situ data since these channels present significant values of this property based on modelling data.

By continuing the analysis for the cross-section on the west side of Marajo Island, the lateral cross-sections (L1 and L4) present net runoff in downstream direction (positive values), and the central cross-sections (L2 and L3) in upstream direction (negative values), with one exception: L3 during neap tide of June.

The results shows magnitude of net runoff of 10^5 and 10^6 m^3 for L5, on the east side of Marajo Island. The values of net runoff were drive mainly by river discharge seasonality and present positive values (downstream direction). The higher values occur during April that is the month of maximum discharge in Tocantins River (main tributary of Para River Estuary). This cross-section shows lower influence of Amazon River Estuary seasonality.

DISCUSSION

The results give huge values of net runnof for both branches of Amazonian Estuarine System. The discharge with similar magnitude (about 10^4 and 10^5 m^3/s) were found by Geyer *et al*. (1991), in the same way the Table 2 show that the model gives discharge values in same magnitude.

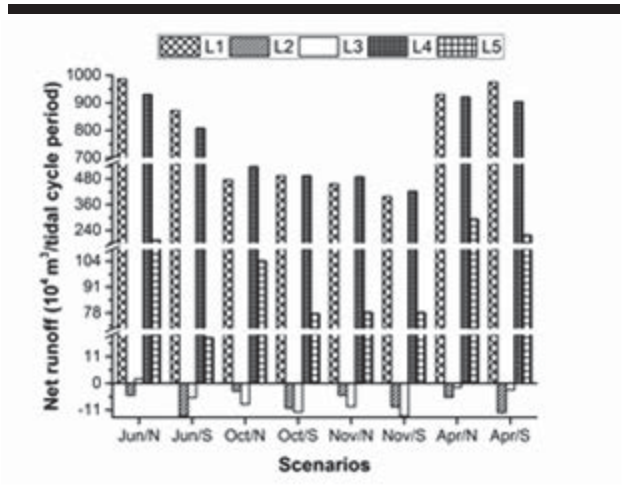

Figure 5. Net runoff for the 8 simulated scenarios (N means neap tide and S means spring tide). Positive values indicate downstream direction and negative values upstream values.

Until now, there are few studies about the hydrodynamic of Para River Estuary. These researches have study areas in small scale, in the other words, they focus a specific water body like a tidal channel, a small bay or a specific point located into this estuary, for instance, Baltazar (2011).

Table 1. *Net runoff for the 8 simulated scenarios in m^3 per tidal cycle.*

Scenario	L1	L2	L3	L4	L5
Jun/neap	9.9×10^6	-5.0×10^4	1.9×10^4	9.3×10^6	1.9×10^6
Jun/spring	8.7×10^6	-1.4×10^5	-5.9×10^4	8.1×10^6	1.9×10^6
Oct/neap	4.8×10^6	-3.2×10^4	-8.6×10^4	5.4×10^6	1.0×10^6
Oct/spring	4.9×10^6	-1.0×10^5	-1.2×10^5	4.9×10^6	7.8×10^6
Nov/neap	4.6×10^6	-4.9×10^4	-9.6×10^4	4.9×10^6	7.8×10^6
Nov/spring	4.0×10^6	-9.6×10^4	-1.4×10^5	4.2×10^6	7.8×10^6
Apr/neap	9.3×10^6	-5.7×10^4	-1.8×10^4	9.2×10^6	2.9×10^6
Apr/spring	9.8×10^6	-1.2×10^5	-2.7×10^4	9.0×10^6	2.2×10^6

Nevertheless, Prestes *et al.* (2014) found instantaneous volume transport values in the Para River Estuary with levels similar to those found in the Amazon River Estuary.

Regarding net runoff, L2 and L3 presented negative value of net discharge. This result can be related with grid definition, since L2 and L3 are in a shallower area and do not have well defined channels into the estuary like L1 and L4 as can be seen

in Borba (2014), thus the outflow flows through these latter preferably.

L1 and L4 presented dowstream direction, thus they are the main channels of outflow on the west side. The larger net discharge for both channels occurs during wet season.

CONCLUSIONS

L5 presents values positives of net discharge, thus it also is an outflow channel to this estuary. Although the biggest discharge source is from Amazon river, L5 present net discharge in same order of L1 and L4 (main channels on west side).

The river discharge seazonality was presented as the main responsable for runnof variation to L1, L4 and L5.

Table 2. *Discharge in m^3/s*

Discharge	L1	L2	L3	L4	L5
Maximum	3.4×10^5	7.7×10^4	1.6×10^4	3.4×10^5	4.9×10^5
Minumum	-2.3×10^5	-9.2×10^4	-3.0×10^4	-1.5×10^5	-6.7×10^5

In summary, the model represented quite well the applied forces to the water into the estuary and its responses when compared with in situ observed hydrodynamic patterns. It also shows that the Pará River Estuary presents magnitude near to that presented by Amazon River Estuary, making it an important channel of matter transport from continent to ocean.

ACKNOWLEDGMENTS

This research is one product from the MSc dissertation of Thais Borba of Program de Pós-Graduação em Geofísica (UFPA/Brazil). We thanks CTHidro/Finep and Office of Naval Research for financial suppot, and Laboratorio de Oceanografia Física (UFPA/Brazil), Laboratoty of Marine Geophysics (UFPA/Brazil) and Office of Coastal Engineering and Port Development (Unesco-IHE/The Netherland) for data survey and data processing.

LITERATURE CITED

Baltazar, L.R.S.; Menezes, M. O. B., and Rollnic, M., 2011. Contributions to the Understanding of Physical Oceanographic Processes of the Marajó Bay - PA, North Brazil. *Proceedings of the 11th International Coastal Symposium. Journal of Coastal Research*, Special Issue No. 64, pp. 1443-1447.

Bezerra, M. O.; Medeiros, C.; Krelling, A. P. M.; Rosário, R. P., and Rollnic, M. Physical oceanographic behavior at the Guama/Acara-Moju and the Paracauari river mouths, Amazon coast (Brazil). *Proceedings of the 11th International Coastal Symposium. Journal of Coastal Research*, SI 64, 1448-1452.

Borba, T. A. C., 2014. Hydrodynamic modelling in Amazonian Estuary: A flexible mesh approach. Belém, Brazil: Universidade Federal do Pará, Master's thesis, 46p.

Corrêa, I. C. S., 2005. Aplicação do diagrama de Pejrup na interpretação da sedimentação e da dinâmica do estuário da Baía de Marajó-PA. *Pesquisas em Geociências*, 32(2), 109–188.

Costa, M. H.; Botta, A., and Cardille, J. A, 2003. Effects of large-scale changes in land cover on the discharge of the Tocantins River, Southeastern Amazonia. *Journal of Hydrology*, 283(1-4), 206–217.

Costa, M. S.; Rollnic, M.; Silveira, O. F. M.; Miranda, A. G. O., and Santos, R. R L., 2013. Morphological and sedimentological processes of an Amazon Estuary, Maguari River (Pará - Northern Brazil). *Proceedings of the 12th International Coastal Symposium. Journal of Coastal Research*, Special Issue No. 65, pp. 1110–1115.

Dai, A. and Trenberth, K. E., 2002. Estimates of Freshwater Discharge from Continents: Latitudinal and Seasonal Variations. *Journal of Hydrometeorology*, 3(6), 660–687.

FEMAR - Fundação de Estudos do Mar, 2013. Catálogo de Estações Maregráficas. http://www.fundacaofemar.org.br/.

Geyer, W. R.; Beardsley, R. C.; Lentz, S. J.; Candela, J.; Limeburner, R.; Johns, W. E.; C.; Belmiro, M., and Dias Soares, I, 1996. Physical oceanography of the Amazon shelf. *Continental Shelf Research*, 16(5–6), 575–616.

Gregório, A. M. S. and Mendes, A. C, 2009. Characterization of sedimentary deposits at the confluence of two tributaries of the Pará River estuary (Guajará Bay, Amazon). *Continental Shelf Research*, 29(3), 609–618.

Kernkamp, H. W. J.; Van Dam, A.; Stelling, G. S., and de Goede, E. D., 2011. Efficient scheme for the shallow water equations on unstructured grids with application to the Continental Shelf. *Ocean Dynamics*, 61(8), 1175–1188.

Mikhailov, V. N, 2010. Water and sediment runoff at the Amazon River mouth. *Water Resources*, 37(2), 145–159.

Prestes, Y. O. ; Rollnic, M. ; Souza, M., and Rosário, R. P., 2014. Volume transport in the tidal limit of the Pará River, Brazil. In: 17th Physics of Estuaries and Coastal Seas (PECS), Porto de Galinhas. http://www.pecs-conferences.org/Xabs/xabs_036_P restes_et al.pdf.

Silva, I. O., 2009. Distribuição da vazão fluvial no estuário do rio Amazonas. Rio de Janeiro, Brazil: Universidade Federal do Rio de Janeiro, Master's thesis, 106p.

SIOLI, H., 1984. The Amazon and its main affluents: hydrography, morphology of the river courses, and river types. *In*: SIOLI, H, *The Amazon*. The Netherlands: Springer, pp. 127-165.

Journal of Coastal Research	SI	75	48-52	Coconut Creek, Florida	2016

Spatiotemporal variation in salinity during drought years in an Amazonian estuary (Taperaçu)

Ádila K. R. da Costa†, Luci C. C. Pereira†, Suzane F.S. Costa†, Natália R. Leite†, Manuel de J. Flores-Montes‡, and Rauquírio M. da Costa†

†Instituto de Estudos Costeiros,
Universidade Federal do Pará,
Bragança, 68600-000, Brazil

‡Departamento de Oceanografia,
Universidade Federal de Pernambuco,
Recife, Brazil.

www.cerf-jcr.org

www.JCRonline.org

ABSTRACT

Costa, A.K.R.; Pereira, L.C.C.; Costa, S.F.S.; Leite, N.R; Flores-Montes, M.J., and Costa, R.M., 2016. Spatiotemporal variation in salinity during drought years in an Amazonian estuary (Taperaçu), *Proceedings of the 14th International Coastal Symposium* (Sydney, Australia). *Journal of Coastal Research*, Special Issue, No. 75, pp. 48-52. Coconut Creek (Florida), ISSN 0749-0208.

This study investigated the spatial and temporal variation in salinity in an Amazonian estuary (Taperaçu). Data were collected in the field every three months between April 2012 and March 2015. During each field campaign, CTDs were used to collect data over a 25-hour period at three fixed stations, in the upper, middle and lower estuary. Precipitation data were obtained from INMET (Brazilian Institute of Meteorology). March to May were the months of highest precipitation (around 1000-1400 mm), although 2012 and 2013 were considered to be drought years in eastern Amazonia (annual precipitation < 1800 mm). While the Taperaçu does not have any direct fluvial input, it is connected to the Caeté Estuary through the Taici creek and is connected to adjacent wetlands. Salinity varied considerably between seasons, peaking in the dry season (in particular, in December) in the lower sector of the estuary (40). During the rainy season, salinity reached values of less than 10 in the upper estuary. The drought years (2012-2013) were characterized by higher salinity in comparison with more typical years (2014-2015). These results indicate that the minor estuaries of the Amazon coast, such as the Taperaçu, may contribute to the understanding of the influence of atypical climatic periods on hydrological variables (such as salinity), and their implications for the local biological communities.

ADDITIONAL INDEX WORDS: *Salinity, drought, Amazonian estuary.*

INTRODUCTION

Major climatic events, such as El Niño, La Niña, and droughts, are becoming progressively frequent, and are responsible for an ever-growing number of natural and socio-economic disasters around the world. Given this, scientists and governments are becoming increasingly preoccupied with the consequences of these natural phenomena.

The Amazon region has experienced three major drought events during the past two decades, in 1997-1998, 2004-2005 and 2009-2010 (Coelho *et al.,* 2012). These events are normally associated with the occurrence of intense El Niño events (high temperatures at the surface of the Pacific Ocean) or the "drought" events that are anomalous warming of the surface temperature of the Atlantic Ocean (Marengo *et al.,* 2011). This increase in the frequency of drought events in the Amazon has attracted the attention of scientists not only because of the impacts on local populations, but also because of the implications for global climate patterns (Gloor *et al.,* 2013; Marengo *et al.,* 2008, 2011).

The Amazon coastal zone is dominated by macrotides (4–11 m), and is characterized by a highly irregular and indented coastline that encompasses 23 estuaries associated with river basins that drain a total area of 330,000 km² (Dominguez, 2009; Souza-Filho, 2005). The region has a humid equatorial climate, characterized by two distinct seasons, a rainy season during the first half of the year (when approximately 85% of the annual precipitation is recorded), and a less rainy season during the second half of the year. Mean annual precipitation is around 2500 mm. The surplus of rainfall during the first half of the year favors the reduction of the salinity of the local coastal waters to close to zero during the period of greatest fluvial discharge, rising to close to 40 by the end of the dry season, when evaporation rates reach their maximum (Pereira *et al.,* 2012, 2013).

An abnormal reduction in precipitation, such as that observed during drought or El Niño periods, is believed to affect the salinity of coastal waters and, as a consequence, the characteristics of the local biological communities. However, few data are available on the effects of climate anomalies on the Amazon coastal zone. In this context, the present study investigated the effects of the recent droughts, recorded in 2012 and 2013, on the coastal waters of the Amazon region. As salinity is the principal factor affecting the structure of planktonic communities (Magalhães *et al.,* 2015; Pereira *et al.,* 2012), this parameter was monitored within the Taperaçu Estuary over a three-year period. The Taperaçu Estuary is not influenced directly by fluvial discharge, but is connected to

DOI: 10.2112/SI75-010.1 received 15 October 2015; accepted in revision 15 January 2016.
*Corresponding author: adila.rc@hotmail.com

adjacent wetlands during the rainy season, and is linked to the neighboring Caeté River through the Taici creek.

STUDY AREA

The present study focused on an Amazonian estuary in the Brazilian state of Pará. The Taperaçu Estuary is located in the municipality of Bragança, approximately 150 km southeast of the mouth of the Amazon River, between longitudes 46°42'W and 46°45'W and latitudes 00°50'S and 00°57'S (Figure 1). The estuary is part of the Caeté-Taperaçu Marine Extractivist Reserve, where the inhabitants survive through the practice of subsistence fishing and small-scale agriculture (Magalhães *et al.,* 2011). The estuary is located within one of the world's largest continuous tracts of mangrove forest (Kjerfve and Lacerda, 1993). The predominant mangrove tree species are *Rhizophora mangle* L., *Avicennia germinans* L. and *Laguncularia racemosa* (L.) C.F. Gaertn (Menezes *et al.,* 2008).

The Taperaçu Estuary has a water surface area of 21 km², and a drainage basin of approximately 40 km², with no discernible fluvial discharge (Asp *et al.,* 2012). In addition to high levels of precipitation, the freshwater found in the estuary is derived from local wetlands that are flooded during the rainy season, while some brackish water is derived from the Caeté River, through the Taici creek. This tidal creek is some 3 km long, and round 15 m wide, and connects the upper Taperaçu Estuary to the mid-sector of the Caeté Estuary (Araújo Jr. and Asp, 2013).

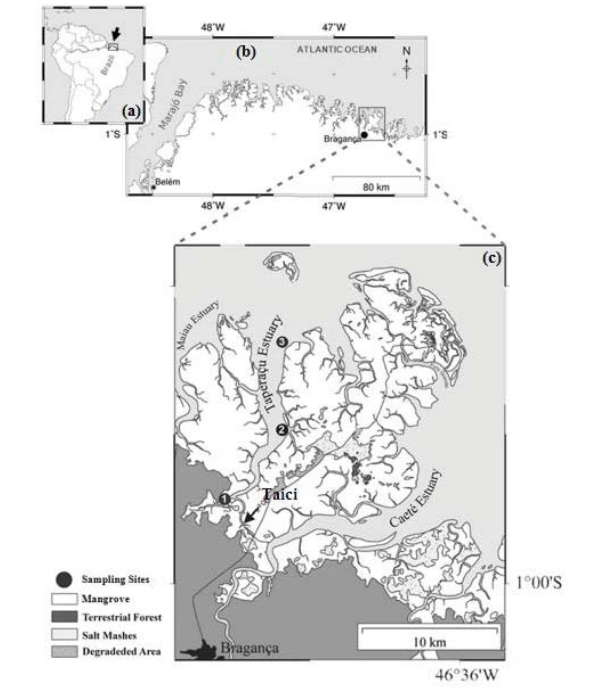

Figure 1. Study Area: (a) South America; (b) Location of the Taperaçu Estuary on the Amazon Macrotidal Mangrove coastal; (c) Positions of the sampling stations in the upper (1), middle (2), and lower (3) sectors of the Taperaçu Estuary, with the arrow indicating the position of Taici creek, which connects the Taperaçu and Caeté estuaries.

This estuary is relatively shallow (mean depth of 4 m) and funnel-shaped, with large sandbanks running along its mid-section. The Taperaçu is dominated by semi-diurnal macrotides, which may range up to 4–6 m during spring tides, and 3–4 m during neap tides, near the mouth of the estuary. The tidal currents are typical of shallow estuaries, and are stronger during the flood period, when they reach speeds of up to 2 m s^{-1}, and salinity is vertically homogeneous (Magalhães *et al.,* 2009).

The local climate is humid equatorial, with a period of relatively high precipitation (rainy season), typically occurring between January and June, when total rainfall may often exceed 2000 mm and mean temperatures are around 26–27°C. The rainiest months are between March and May, when more than 70% of the annual precipitation is normally recorded. During the second half of the year (dry season), mean monthly precipitation is normally no more than 100 mm and mean temperatures are around 28°C (INMET, 2013). The driest months are between September and November, when precipitation is negligible, resulting in an excess of evaporation over precipitation. Annual precipitation levels recorded in the study area over the past 16 years (Figure 2) show that 2012 and 2013 (arrows) were anomalously dry, and thus defined here as drought years.

METHODS

To understand the functioning of this small estuary during an atypical period of climate (drought), spatial and temporal oscillations in hydrological (salinity and turbidity) and hydrodynamic (tides) variables were monitored over a 36–month period, between April 2012 and March 2015. Thirteen field campaigns were conducted during this period, during the (i) rainy season: April 22-23 and June 13-14, 2012; March 19-20 and June 3-4, 2013; April 22-23 and June 5-6, 2014; and March 4-5, 2015, and (ii) dry season: September 22-23 and December 5-6, 2012; September 27-28 and November 25-26, 2013; September 22-23 and December 3-4, 2014.

Rainfall data were obtained for the analysis of the influence of precipitation levels on the salinity of the water. Daily precipitation data were obtained from the Brazilian Meteorological Institute's (INMET) Tracuateua station in Pará, which is located 17 km southwest of the municipality of Bragança, which includes the Taperaçu Estuary.

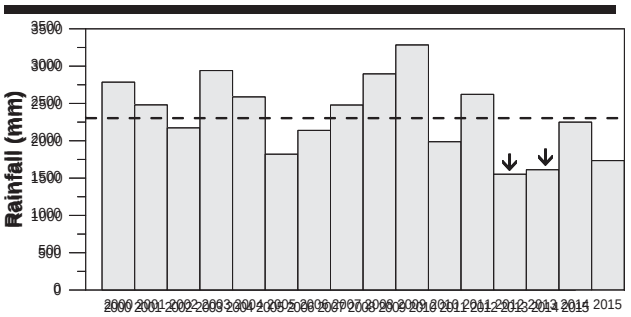

Figure 2. Annual precipitation recorded near the study area 2000 and 2015. The arrows indicate the years considered atypical in the present study. Dash line represents the mean of the historical data.

Field campaigns

During each campaign, data loggers were bottom-mounted simultaneously at three collecting stations representing the upper, middle and lower estuary, over 25-hour period. The CTDs were moored to measure the tidal elevation and salinity, and were programmed to collect data every 10 minutes.

Statistical Analysis

The hydrological data were analyzed spatially (comparing the upper, middle and lower sectors), seasonally (dry *vs.* rainy seasons), and in relation to the month and tidal phase (flood or ebb). The assumptions of normality of the data were evaluated using Lilliefors' test (Conover, 1971), and the homogeneity of variances was tested using Bartlett's Chi-square (Sokal and Rohlf, 1969). When these assumptions were not satisfied, the data were log (x+1) transformed to obtain a homogeneous near-normal distribution. A two-way analysis of variance (ANOVA) was then applied to the hydrological data collected in the different estuary sectors, tides, months, and seasons. When the data were not corrected by the log-transformation, the nonparametric Mann-Whitney and Kruskal-Wallis procedures were used to test the data.

RESULTS

Precipitation

Rainy season precipitation levels (Figure 3) recorded in 2012 (1321 mm) and 2013 (1291.8 mm) were abnormally low when compared with 2015 (1735.6 mm). During the study period, the rainiest months were March, April, and May 2013, with a total of approximately 1000 mm of precipitation accumulating during these three months. Between September and December, by contrast, total rainfall was only 65 mm. The rains of 2012 were 23.7% lower than those of 2014, and those of 2013, 28.4% lower.

Hydrodynamics

The tides were influenced by the connectivity between the Taperaçu Estuary and adjacent systems. During the study period, the oscillations recorded in water levels (Figure 4) were characteristic of meso - (neap) and macro-tidal conditions characteristic of meso- (neap) and macro-tidal conditions (spring tides). The highest tidal ranges (4.7 m) were recorded in the lower sector in December 2014 and March 2015.

Comparing the lower and upper sectors of the estuary, attenuation was of the order of 10% during the dry season (December 2012) and 50% during the rainy season (June 2013). In the upper sector, the tidal range varied from 1.8 m in June 2014 to 2.7 m in December 2014. The semi-diurnal tides were asymmetrical, with a much shorter flood phase.

Salinity

Salinity was influenced primarily by precipitation and the variation in tides (Figure 4). The low precipitation levels recorded in the atypical years were reflected in the high mean salinity in 2012 (31.2±51.7) and 2013 (33±36.2), principally during the flood phase, when the marine intrusion occurs in the lower estuarine sector. The lowest salinity was recorded in 2014, reaching its lowest values in April.

Considerable variation was also recorded between seasons, with lower values being recorded during the rainy season, when precipitation levels increased. Salinity is lower during this period because there is a predominance of less saline water along the whole adjacent coastal zone, which encroaches the estuary during this flood period, together with less saline water

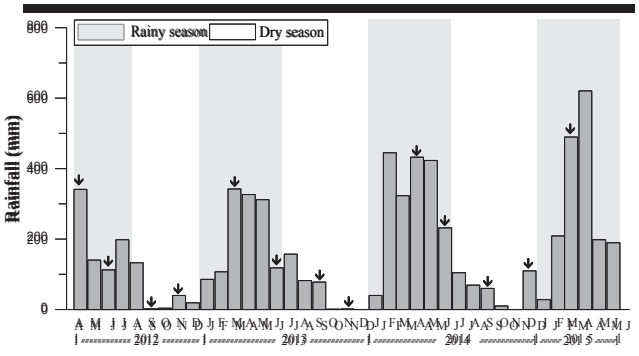

Figure 3. Monthly precipitation recorded near the study area between April 2000 and June 2015.

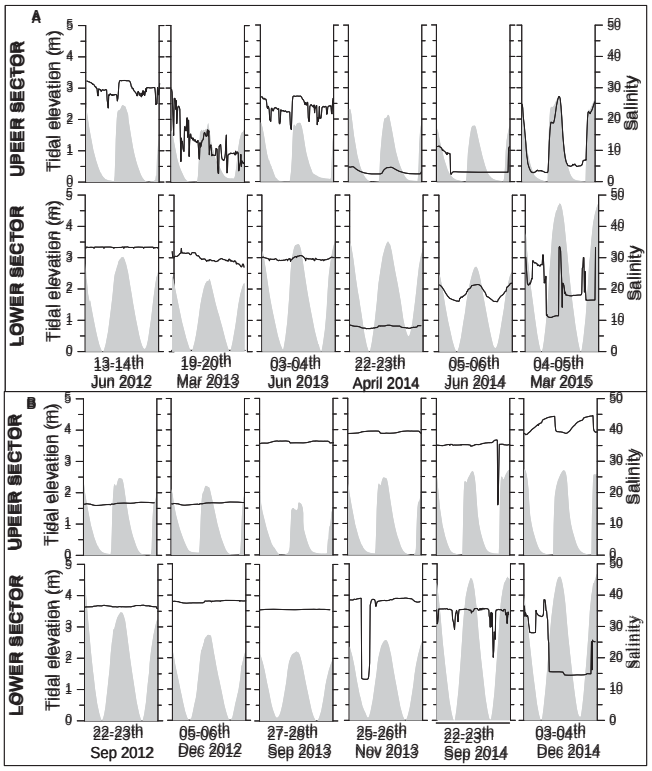

Figure 4. Oscillations in the water level (m) measured in the upper and lower sectors of the Taperaçu Estuary, during (A) the rainy season, and (B) the dry season. Shadowed area represents the oscillation of the water level and black line, the salinity.

from the Caeté Estuary, which passes through the Taici creek, and the input of freshwater from the surrounding wetlands.

However, the values did not fall so low during the rainy seasons of the drought years, especially 2012, when the mean value in the lower sector of the estuary was 30.8±5.0.

Significant differences were found between the rainy and dry seasons ($F = 54.12$; $p = 0.00$), with much higher salinity being recorded during the dry season (34.4±6.2). Significant differences were also found among months ($F = 46.6$; $p = 0.00$), with the highest mean salinity being observed in November 2013 (37.7±4.8).

Salinity also varied considerably among sites, increasing progressively from the upper to the lower sector of the estuary ($F = 36.18$; $p = 0.00$). This variation became more pronounced in 2012 and 2013, reflecting the low precipitation rates along the whole of the Amazon coast. Mean salinity ranged from 4.2±1.0 in the upper sector to 37.9±0.3 in the lower sector.

DISCUSSION

The typical climatic conditions of equatorial coastal regions represent one of the principal physical forces that control the considerable oscillations in hydrological variables recorded in local estuaries. The Intertropical Convergence Zone (ITCZ) is the primary phenomenon determining the seasonal variation in climate found on the Amazon coast.

Precipitation levels have a direct influence on the hydrological and hydrodynamic conditions of coastal areas, as shown by Pereira *et al.* (2013) during a La Niña event in an area adjacent to the Taperaçu Estuary, when abnormally high precipitation rates were reflected in much less saline coastal waters. The present study revealed the opposite pattern in the Taperaçu Estuary during the droughts of 2012 and 2013. Previous studies have shown that, under typical precipitation conditions, the seasonal shift in rainfall patterns controls the salinity of the estuary's waters, and as a consequence, the population dynamics of its planktonic organisms (Costa *et al.,* 2013; Magalhães *et al.,* 2015; Souza-Junior, 2013).

Durante a rainy season, the increase in fluvial discharge is a dominant force in most Amazonian estuaries (Pereira *et al.,* 2010; Pamplona *et al.,* 2013), affecting the salinity of the region's coastal waters, including those of the Taperaçu, even though it is not affected directly by fluvial discharge (Asp *et al.,* 2012). In the present study period, the reduction in precipitation levels during the rainy seasons of 2012 and 2013 were directly responsible for the high salinity recorded in the Taperaçu Estuary.

However, when the rains are excessive, as observed typically during La Niña events, Pereira *et al.* (2013) observed that the coastal waters of this region were low in salinity, richer in nutrients, and had a higher phytoplankton biomass. A similar pattern has been observed in other regions at low latitudes (Gorgues *et al.,* 2010; Valiela *et al.,* 2012; Yamasaki *et al.,* 2008).

On the other hand, when rainfall decreases during drought periods, there is a decline not only in salinity, but also dissolved nutrient and chlorophyll-a concentrations. While the tidal range also plays an important role in the control of the dissolved nutrient profile, through the inundation of adjacent mangroves and wetlands (Pamplona *et al.,* 2013), the decrease in fluvial discharge inevitably contributes to an increase in salinity, a reduction in dissolved nutrients, and consequently, in phytoplankton biomass. These conditions can also affect local fishery resources, and it seems likely that these results can be extrapolated to other macrotidal estuaries in the equatorial region that are influenced by major estuarine systems.

CONCLUSIONS

Rainfall is the principal physical variable controlling oscillations in salinity, and when precipitation decreases, as observed during droughts, salinity increases significantly in comparison with typical years. The tidal cycle also plays an important role in the oscillations in local salinity, through the incursion of more saline waters from adjacent coastal environments during the flood tide, and the transfer of less saline waters from the Caeté, and freshwater from adjacent wetlands, flooded during the rainy season. However, the reduction in precipitation and consequently, in fluvial discharge, result in more saline waters, which appear to be poorer in dissolved nutrients and consequently in phytoplankton biomass. It thus seems likely that there is a decline in biological productivity during these periods. These results indicate that the minor estuaries of the Amazon coast, such the Taperaçu, may contribute to the understanding of the influence of atypical climatic periods on hydrological variables, and their consequences for local biological communities.

ACKNOWLEDGMENTS

This research was supported by CNPq (Universal project - 483913/2012-0), CAPES (Ciências do Mar II, Edital 43/2013 and Pró-Amazonia - 23038.000750/2013-82), and FAPESPA (79/2014). The authors Pereira LCC (310909/2014-7 and 200629/2014–0) and Costa RM (306061/2011–2 and 200622/2014–5) would also like to thank CNPq for research grants. We are grateful to the Coastal Studies Institute at the Federal University of Pará for providing logistic support during this study. We also thank Dr. Stephen Ferrari for his careful revision of the English.

LITERATURE CITED

Araújo JR., W.P. and Asp, N.E., 2013. Hydrodynamic connectivity between two macrotidal Amazonian estuaries. *Journal of Coastal Research*, 65, 1086-1091.

Asp, N.E.; Schettini, C.A.F.; Siegle, E.; Silva, M.S., and Brito, R.N.R., 2012. The Dynamics of a Frictionally-dominated Amazonic Estuary. *Brazilian Journal of Oceanography*, 60(3), 391-403.

Coelho, C.A.S.; Cavalcanti, I.A.F.; Costa, S.M.S.; Freitas, S.R.; Ito, E.R.; Luz, G.; Santos, A.F.; Nobre, C.A.; Marengo, J.A., and Pezza, A.B., 2012. Climate diagnostics of three major drought events in the Amazon and illustrations of their seasonal precipitation predictions. *Meteorological Applications,* 19, 237–255.

Conover, W.O.J., 1971. *Practical nonparametric statistics*. New York: John Wiley, 302p.

Costa, A.K.R.; Pereira, L.C.C.; Costa, R.M.; Monteiro, M.C., and Flores-Montes, M., 2013. Oceanographic processes in an Amazon estuary during an atypical rainy season. *Journal of Coastal Research*, 65, 1104-1109.

Dominguez, J.M.L., 2009. The Coastal Zone of Brazil, p. 1752. In: Dillenburg, S.F., Hesp, P.A. Geology and Geomorphology of Holocene Coastal Barriers of Brazil (eds). New York: SpringerVerlag. *Series: Lecture Notes in Earth Sciences*, 107, 380p.

Gloor, M.; Brienen, R.J.W.; Galbraith, D.; Feldpausch, T. R.; Schöngart, J.; Guyot, J.-L.; Espinoza, J. C.; Lloyd, J., and Phillips, O.L., 2013. Intensification of the Amazon hydrological cycle over the last two decades. *Geophysical Research Letters*, 40, 1–5.

Gorgues, T.; Menkes, C.; Slemons, L.; Aumont, O.; Dandonneau, Y.; Radenac, M.H.; Alvain, S., and Moulin, C., 2010. Revisiting the La Niña 1998 phytoplankton blooms in the equatorial Pacific. *Deep Sea Research Part I: Oceanographic Research Papers*, 57 (4), 567-576.

Inmet, Instituto Nacional de Meteorologia, 2013. Normas climatológicas. Brasília, Distrito Federal.

Kjerfve, B. and Lacerda, L. D., 1993. Mangroves of Brazil. International Society for Mangrove Ecosystems/ITTO. *Okinawa, Japan*: (L. D. Lacerda, Ed.), 245-272.

Magalhães, A.; Bessa, R.S.C.; Pereira, L.C.C., and Costa, R.M., 2009. Variação temporal da composição, ocorrência e distribuição dos Copepoda (Crustacea) do estuário do Taperaçu, Pará, Brasil. *Boletim do Museu Paraense Emílio Goeldi, Série Ciências Naturais*, 4(2), 133-148.

Magalhães, A.; Nobre, D.S.B.; Bessa, R.S.C.; Pereira, L.C.C., and Costa, R.M., 2011. Seasonal and short-term variations in the copepod community of a shallow Amazon estuary (Taperaçu, Northern Brazil). *Journal of Coastal Research*, 64, 1520-1524.

Magalhães, A.; Pereira, L.C.C., and Costa, R.M., 2015. Relationships between copepod community structure, rainfall regimes, and hydrological variables in a tropical mangrove estuary (Amazon coast, Brazil). *Springer*, 69, 123–136.

Marengo, J.A.; Nobre, C.A.; Tomasella, J.; Oyama, M.D.; Oliveira, G.S.; Oliveria, R.; Camargo, H.; Alves, L.M., and Brown, I.F., 2008. The drought of Amazonia in 2005. *Jornal of Climatology,* 21, 495–516.

Marengo, J.A.; Tomasella, J.; Alves, L.M.; Soares, W.R., and Rodriguez, D.A., 2011. The drought of 2010 in the context of historical droughts in the Amazon region. *Geophysical Research Letters,* 38, L12703.

Menezes, M.P.M.; Berger, U., and Mehlig, U., 2008. Mangrove vegetation in Amazonia: a review of studies from the coast of Pará and Maranhão States, north Brazil. *Acta Amazonica,* 38(3), 403-420.

Pamplona, F.C.; Paes, E.T., and Nepomuceno, A., 2013. Nutrient fluctuations in the Quatipururiver: A macrotidal estuarine mangrove system in the Brazilian Amazonian basin. *Estuarine, Coastal and Shelf Science*, 133, 273 - 284.

Pereira, L.C.C.; Monteiro, M.C.; Guimarães, D.O.; Matos, J.B., and Costa, R.M., 2010. Seasonal effects of waste water to water quality of the Caeté River estuary, Brazilian Amazon. *Anais da Academia Brasileira de Ciências*, 82(2), 467-478.

Pereira, L.C.C.; Nayra, I.S.S.; Costa, R.M.; Asp, N.E.; Costa, K.G., and Vila-Concejo, A., 2012. Seasonal changes in oceanographic processes at an equatorial macrotidal beach in northern Brazil. *Continental Shelf Research*, 43, 95-106.

Pereira, L.C.C.; Oliveira, S.M.O.; Costa, R.M.; Costa, K.G., and Vila-Concejo, A., 2013. What happens on an equatorial beach on the Amazon coastal when La Niña occurs during the rainy season? *Estuarine, Coastal and Shelf Science*, 135, 116-127.

Sokal, R.R. and Rohlf, F.J., 1969. *Biometry. The principles and practice of numerical classification in biological research*. San Francisco, California: W. H. Freeman, 776p.

Souza Filho, P.W.M., 2005. Costa de Manguezais de Macromaré da Amazônia: Cenários Morfológicos, Mapeamento e Quantificação de Áreas Usando Dados de Sensores Remotos. *Revista Brasileira de Geofísica,* 23(4), 427-435.

Souza-Junior, A.N.; Magalhães, A.; Pereira, L.C.C., and Costa, R.M., 2013. Zooplankton dynamics in a tropical Amazon estuary. *Journal of Coastal Research,* 65, 1230-1235.

Valiela, I.; Camilli, L.; Stone, T.; Giblin, A.; Crusius, J.; Fox, S.; Barth-Jensen, C.; Monteiro, R.O.; Tucker, J.; Martinetto, P., and Harris, C., 2012. Increased rainfall remarkably freshens estuarine and coastal waters on the Pacific coast of Panama: Magnitude and likely effects on upwelling and nutrient supply. *Global and Planetary Change*, 92-93, 130-137.

Yamasaki, M.; Sasaki, A.; Oda, M., and Domitsu, H., 2008. Western equatorial Pacific planktic foraminiferal fluxes and assemblages during a La Niña year (1999). *Marine Micropaleontology*, 66 (3-4), 304-319.

Journal of Coastal Research	SI	75	53-57	Coconut Creek, Florida	2016

Effective Roughness Height in High-Concentrated Flows

Jiayu Fang[†], Yongping Chen[†*], Peng Yao[‡], and Min Su[‡]

[†]State Key Laboratory of Hydrology-Water Resources and Hydraulic Engineering
Hohai University
Nanjing, China

[‡]Section of Hydraulic Engineering, TU Delft
Delft, The Netherlands

www.cerf-jcr.org

www.JCRonline.org

ABSTRACT

Fang, J.Y.; Chen, Y.P.; Yao, P., and Su, M., 2016. Effective Roughness Height in High-Concentrated Flows. In: Vila-Concejo, A.; Bruce, E.; Kennedy, D.M., and McCarroll, R.J. (eds.), *Proceedings of the 14th International Coastal Symposium* (Sydney, Australia). *Journal of Coastal Research*, Special Issue, No. 75, pp. 33-37. Coconut Creek (Florida), ISSN 0749-0208.

The effective roughness height is an important parameter in coastal sediment transport models. It has been extensively investigated in the past but few research results are related to the high-concentrated flows which often occur in a silty coast. A series of experiments has been carried out in a wave-current flume with silt-sized sediment bed. The mean velocity profiles were measured under different combined wave-current conditions. The effective roughness heights were calculated based on the curve fitting of measured velocity profiles by following the velocity profile model of You (1994). The accuracy of three empirical models, namely, Grant and Madsen (1982), Li and Amos (1998) and You (1996) was examined with the 'measured' effective roughness heights. The results show that all the models are not much accurate for the high-concentrated flows, particularly in the case with a relatively small sediment size. Therefore, cautions should be taken when applying those models in the silty coast, particularly during the extreme events.

ADDITIONAL INDEX WORDS: *bed resistance, silty coast, sediment transport model.*

INTRODUCTION

Silty coast is a type of coast which distributes widely in the north and east of China (Cao *et al*., 2009). In this type of coast, silt-sized sediments could be easily stirred up and transported acutely during extreme weathers and quickly deposit when the weather comes back to normal. This phenomenon may cause a big trouble to the ports which are built in the silty coast since the sudden deposition inside the navigational channel can seriously affect the port operations.

Based on the study carried out by Zhao *et al.* (2002), a high-concentrated layer exists between the bed-load layer and the suspended layer when large waves are presented in the wave-current flume with a silt sediment bed. The existence of this layer may change the physical characteristics of the boundary layer, and then change the effective roughness height, which is an important parameter to quantify the resistance force to the flows from the sea bed in the coastal sediment transport models.

The common method to calculate the effective roughness height is based on the curve fitting of the measured velocity profile (You, 1996). Apart from that, the effective roughness height may also be derived from the energy dissipation (Camenen *et al*., 2009) or the empirical relationship with the sheet-flow layer thickness (Pugh and Wilson, 1999). Among these methods, the first one is the most prevailing method because it is easy to be carried out and is suitable for different kinds of flows.

There are many models for estimation of flow velocity profiles in combined wave-current flows, such as the models of Grant and Madsen (1979), Sleath (1991) and You (1994). Most of these models applied the eddy viscosity concept to build the connection between the shear stress and the velocity gradient, in order to close the fluid motion equations and then derive the theoretical solutions which can be used to predict the distribution of current velocity profiles. Among them, the model of You (1994) is the most efficient one because it does not need any iterations when calculating physical parameters, while its accuracy can be guaranteed at the same time.

There are several models intended to predict the effective roughness height with simple empirical formulas. Grant and Madsen (1982) divided the effective roughness height into three parts, namely, grain roughness height, form roughness height and bed-load roughness height. The grain roughness height is related to the skin friction drag of bed materials, and it can be determined by the grain size; the form roughness height is related to the horizontal pressure gradient which is generated by ripples; and the bed-load roughness height is related to the energy dissipation inside the bed-load layer. Their model was derived based on the experiments carried out under the wave only conditions. Li and Amos (1998) modified the model of Grant and Madsen (1982) and expanded it to a combined wave and current condition based on the field data measured in the Scotian Shelf. You (1996) also proposed a model to estimate the effective roughness height. Unlike aforementioned two models, this model did not consider the mechanism of roughness but derived directly from the model of wave-current velocity profiles (You, 1994). There is an important assumption in this

DOI: 10.2112/SI75-011.1 received 15 October 2015; accepted in revision 15 January 2016.
*Corresponding author: ypchen@hhu.edu.cn

model, which is that the flow should be regarded as "clean water". It should bear in mind that the above models were derived under the conditions of sandy beds. Up to now, few research studies have been conducted on the effective roughness height in silty coasts. When we face the sediment transport problems in this kind of coast, we usually refer the models derived from sandy coasts; however, whether those models are applicable to the silty coasts need to be further investigated.

In this study, a series of flume experiments over silty beds with the presence of high-concentrated flows has been carried out. The effective roughness heights derived from the experimental data and from the empirical models were compared to verify whether those models are suitable in the silty coast, particularly with high-concentrated flows.

Experimental setup

The experiments were carried out in a large wind-wave-current flume in Hohai University, China. The flume is 85 m long, 1.0 m wide and 1.5 m deep. A wave generator is set up at one end of the flume, and a gravel beach is placed to reduce the wave reflection. Two types of sediments, *i.e.*, d_{50}=47 μm and 88 μm, collected from Jiangsu silty coast were put into the flume as the sediment beds, respectively. The length of the sediment bed is 15 m and the height is 0.15 m. Two concrete ramps were placed at the beginning and the end of the sediment bed respectively to support the sediment bed. The horizontal section of ramps are both 50 cm and the slope of them are 1:40. The schematic design of the flume is shown in Figure 1.

Three wave height meters were fixed along the flume to monitor and record the water surface variations (see Figure 1). An Acoustic Doppler Velocimeter (ADV) was used to measure the current velocity. It was set up on a beam which could be moved up and down automatically by the remote control of a computer and the positioning accuracy is 1 mm. The measuring points of combined wave-current velocity were 0.6cm, 0.1h, 0.2h, 0.3h, 0.4h, 0.5h, 0.6h above the bed (h is the water depth). The sampling frequency of ADV was 25 Hz and the total sampling time was 60 s. The instantaneous sediment concentration was measured by an Optical Backscatter Sensors (OBS). A suction system was also used to measure the average sediment concentration.

The water depth was set as 0.3 m in all experimental cases. Regular waves were generated, with a constant wave height of 12 cm and wave period of 1.5 s. The depth-averaged current velocities varied in the range from 0.28 m/s to 0.38 m/s in two directions (*i.e.,* following and opposing waves). Detailed parameters of the experiments are listed in Table 1.

Table1. *Basic experimental parameters and effective roughness height*

NUMBER	Wave Height H(m)	Water Depth h(m)	Wave Period T(s)	$\overline{U}$(m/s)	k_s(m)
S1CWF1	0.12	0.3	1.5	0.34	0.01
S1CWF2	0.12	0.3	1.5	0.36	0.0001
S1CWF3	0.12	0.3	1.5	0.38	0.00001
S1CWO1	0.12	0.3	1.5	0.32	0.01
S1CWO2	0.12	0.3	1.5	0.34	0.05
S1CWO3	0.12	0.3	1.5	0.38	0.08
S2CWF1	0.12	0.3	1.5	0.28	0.40
S2CWF2	0.12	0.3	1.5	0.33	0.20
S2CWF3	0.12	0.3	1.5	0.37	0.10
S2CWO1	0.12	0.3	1.5	0.30	0.50
S2CWO2	0.12	0.3	1.5	0.35	0.25
S2CWO3	0.12	0.3	1.5	0.38	0.20

Note: S1 = the median size of sediment is 47 μm; S2 = the median size of sediment is 88 μm; CWF = currents following waves; CWO = currents opposing waves; $\overline{U}$ = mean current velocity; k_s =effective roughness height.

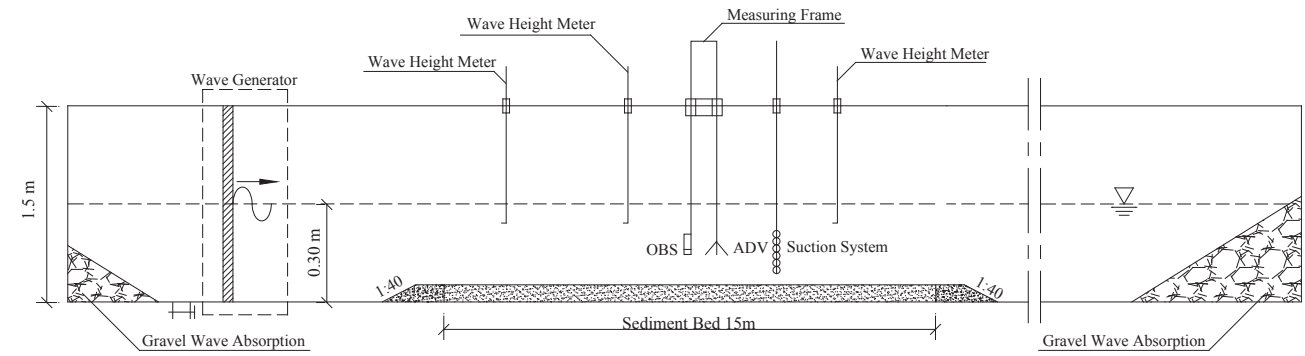

Figure 1.Schematic design of the wind-wave-current flume and the layout of measured instruments.

METHODS

Following the model of You (1994), the wave-current velocity profiles can be divided into three layers, namely wave-dominant layer, wave-current interaction layer and current-dominant layer. The velocity equations in each layer are as follows:

$$\bar{u} = \frac{\overline{u_*}}{\kappa}\left(\frac{\overline{u_*}}{u_w^*}\right)\ln\frac{z}{z_0} \quad z_0 \le z \le \delta_1 \tag{1}$$

$$\bar{u} = \frac{\overline{u_*}}{\kappa}\left(\frac{\overline{u_*}}{u_w^*}\right)\left\{\frac{z}{\delta_1} + \ln\frac{\delta_1}{z_0} - 1\right\} \quad \delta_1 \le z \le 2\delta_1 \tag{2}$$

$$\bar{u} = \frac{\overline{u_*}}{\kappa}\ln\frac{z}{z_1} \quad z \ge 2\delta_1 \tag{3}$$

κ is the von Karman constant, which is approximately equal to 0.4.

δ_1 is the thickness of the wave boundary layer which can be calculated by:

$$\delta_1 = \frac{0.5\kappa u_w^*}{\omega} \tag{4}$$

in which ω is the angular frequency of regular waves and $\omega=2\pi/T$; T is the wave period.

z_0 is the zero-intercept of logarithmic current profile. It can be estimated by:

$$z_0 = \frac{k_s}{30} \tag{5}$$

in which k_s is the effective roughness height.

z_1 is the apparent roughness due to the presence of waves. It can be estimated by:

$$z_1 = 2\delta_1\left\{\frac{e\delta_1}{z_0}\right\}^{-\bar{u}_*/u_w^*} \tag{6}$$

u_w^* is the maximum wave friction velocity associated with the wave motion, which can be calculated by the following equation:

$$u_w^* = \sqrt{0.5 f_w}A\omega \tag{7}$$

in which f_w is the wave friction factor. The explicit formula for this factor was suggested by You *et al.* (1991):

$$f_w = 0.108\left(\frac{A}{K_s}\right)^{-0.343} \tag{8}$$

where A is the semi-excursion just outside the wave boundary layer. It can be calculated by:

$$A = \frac{H}{2\sinh kh} \tag{9}$$

in which H is the wave height, k is the wave number and h is the water depth.

$\bar{u}_*$ is the current friction velocity which can be calculated by:

$$A_1 = \frac{\ln\left(\frac{e\delta_1}{z_0}\right)}{u_w^*} \quad B_1 = \ln\left(\frac{z_r}{2\delta_1}\right) \quad C_1 = -\kappa\bar{u}_r \tag{10}$$

$$\bar{u}_* = \frac{-B_1 + \sqrt{B_1^2 - 4A_1C_1}}{2A_1} \tag{11}$$

in which $\bar{u}_r$ is a reference current velocity at an arbitrary level z_r. The reference current velocity should be given in advance and the reference level is suggested to be a little higher than the wave-current interaction layer.

According to the above equations, we can calculate the effective roughness height k_s by the following procedures. First, an estimated value is assigned to effective roughness height k_s. Then the reference current velocity $\bar{u}_r$ at z_r is given by the measured data. In this study, we select the 0.2h as the level of the reference velocity. After that, all the parameters in Equations (1)-(3) can be calculated by Equations (4)-(11). Finally, the current velocity profile can be derived from Equations (1)-(3). By comparison with the measured data, the value of effective roughness height can be adjusted until the correlation coefficient between the calculated current velocities and measured data from 0.1h to 0.3h is more than 0.95.

RESULTS

The effective roughness heights derived from the curve fitting of the measured data for each case are listed in Table 1. The comparison between the best-fitted flow velocity profiles and the measured experimental data show that the model of You (1994) can be applied to fit the measured data, as shown in Figure 2. Although there are a few deviations near the bottom and the upper part (above 0.4h) in some cases, those deviations might be attributed to the measurement error and the nonlinear effect between the wave and current, which is expected to have less effect on the calculation of effective roughness height.

As we have got the values of effective roughness height for each case, we can use those data to examine the accuracy of the models of Grant and Madsen (1982), Li and Amos (1998) and You (1996) in the prediction of roughness height, under our experimental conditions. The results are shown in Figure 3(a), Figure 3(b) and Figure 3(c), respectively.

It can be seen from Figure 3(a) and Figure 3(b) that the models of Grant and Madsen (1982) and Li and Amos (1998) overestimate the effective roughness height significantly for the cases with the sediment median size of 47 μm. As for the cases with median size of 88 μm, these two models behave much better. In these cases, the predicted values are about 0.51-1.24 times of the measured ones. It is shown that there is only a little difference between these two models, despite that Li and Amos (1998) modified the model of Grant and Madsen (1982) with the consideration of the combined wave-current effect.

Figure 3(c) show that the model of You (1996) over-predicts the effective roughness height in all cases. However, unlike the former two models, the discrepancies between the predicted and measured results in this model are relatively small when the median size of sediment is 47 μm.

Figure 4 displays the overall performance of these three models. In general, all the three models predict the effective roughness height reasonably when the median size of sediments is 88 μm, but there are quite large discrepancies for the case that the median size is 47 μm, although the model of You (1996) behaves slightly better than the other two models.

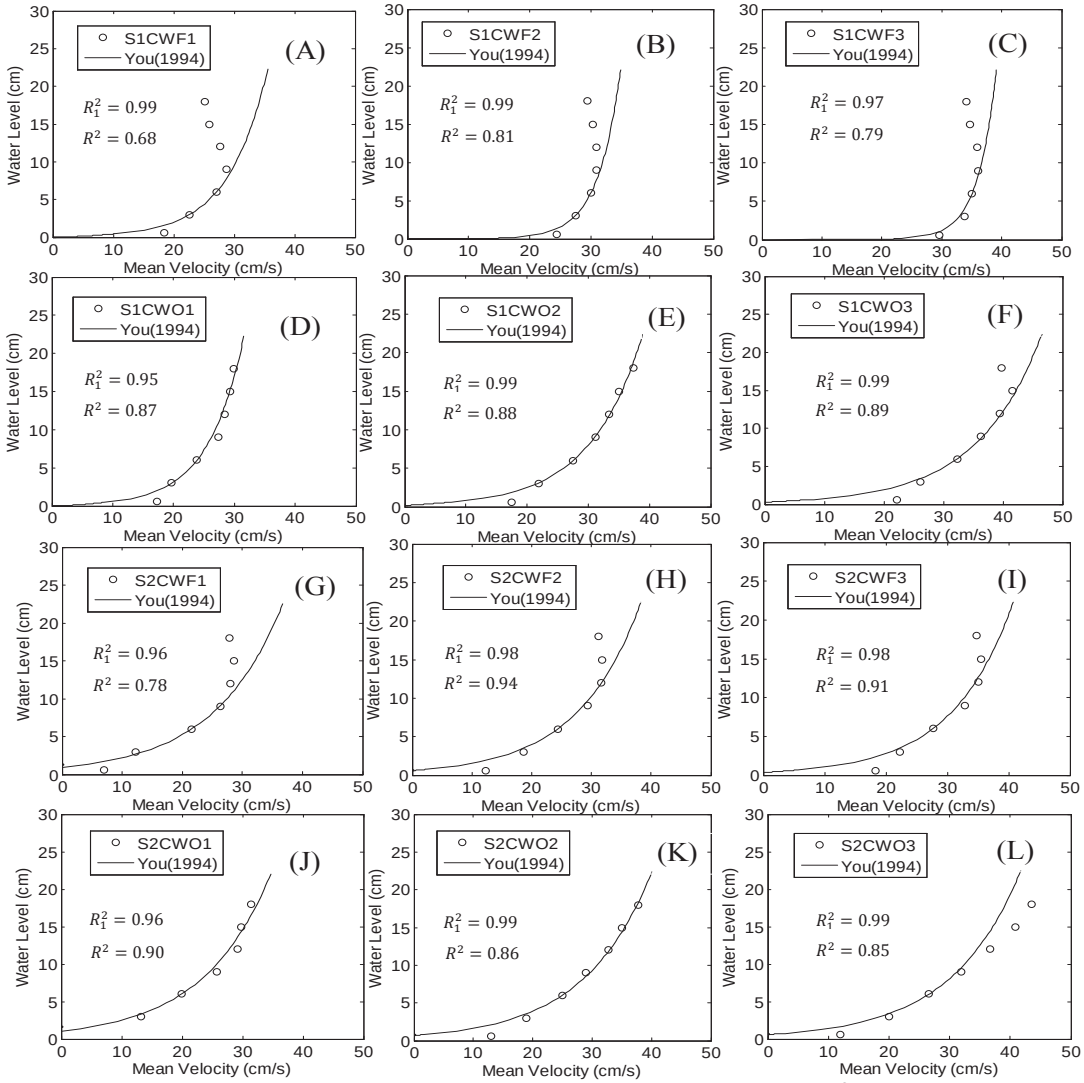

Figure 2.Comparison of wave-current velocity profiles of You's model (1994) and measured data. Note that $R_1^2$is the correlation coefficient between You's model (1994) and measured velocities in the range from 0.1h to 0.3h. R^2 is the correlation coefficient in the entire water depth.

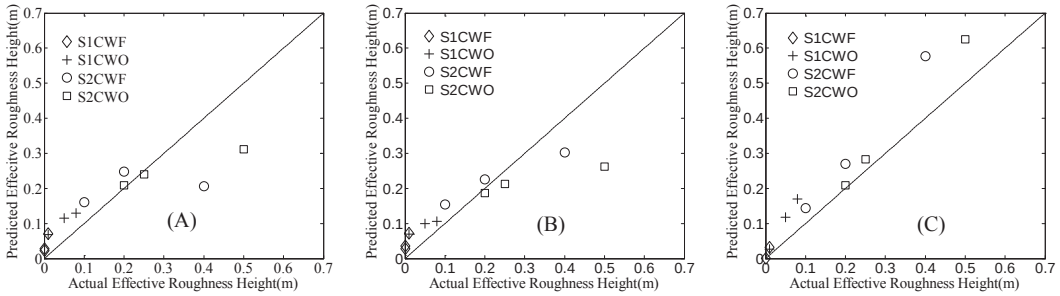

Figure 3.Comparison of 'measured' effective roughness heights with the ones predicted by the models of (A) Grant and Madsen (1982); (B) Li and Amos (1998) and(C) You (1996).

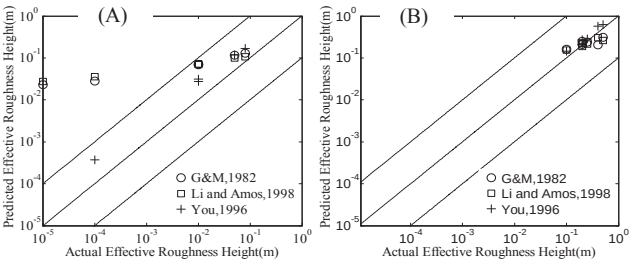

Figure 4.Comparison of 'measured' effective roughness heights with the ones predicted by aforementioned three models when (A) the median size is 47 μm and (B) the median size is 88 μm.

DISCUSSION

According to the above results, the models of Grant and Madsen (1982) and Li and Amos (1998) both over-predict the value of effective roughness height when the median size is 47 μm; and both deviate the 'measured' values slightly when the median size is 88 μm. The main reason leading to the deviations is that these two models are both derived from sandy beds. As the silty sediment is much easy to be initiated under combined wave-current conditions and the sediment concentration near the bottom is quite high based on the measured data (Yao *et al.,* 2015), we can surmise that sediments mainly move as suspended load. If there are many suspended sediments in the water, the viscosity of flow can be changed. It means that the energy dissipation would be decreased and the resistance caused by the bed would be reduced accordingly. Therefore, the formulae which were given by Grant and Madsen (1982) and Li and Amos (1998) shall be modified to account for this issue.

As for the model of You (1996), its predicted results are all larger than the 'measured' ones. Although his model could fit well with the measured data in his study, it is debatable whether it is suitable for the high-concentrated flows. The reason is that the high sediment concentration developed over a silty bed will reduce the rationality of the assumption of "clean water" as that over a sandy bed. But, this assumption is fairly important in his model. Therefore, it is not surprising to find that the predicted results of this model are not very good. If the "clear water" assumption was modified, the prediction accuracy might be improved for the silty coasts. It will be addressed in more detail in our future study..

CONCLUSIONS

Based on a series of experiments, the effective roughness height in high-concentrated flows was studied and the following conclusions can be found:

(1)The wave-current velocity model of You (1994) can generally fit the experimental data well. (2)The model of Grant and Madsen (1982) and Li and Amos (1998) both over-predict the effective roughness height when the median size is 47 μm. It is because these two models are derived from sandy beds and they may not be suitable for silty beds. (3)The model of You (1996) over-predict the effective roughness height in all cases. It is because flows could not be regarded as "clean water" when the sediment concentrations are fairly high. (4) In general, all the three models are demonstrated not suitable for the calculation of effectiveness height of high-concentrated flows at their present forms. Hence, we should be careful if we have to apply those formulae in the sediment transport model of silty coast, particularly during the extreme events.

ACKNOWLEDGMENTS

This work is financially supported by the National Natural Science Foundation of China (Grant No. 51379072) and the 111 Project of the Ministry of Education and the State Administration of Foreign Experts Affairs, China (Grant No. B12032).

LITERATURE CITED

Camenen, B.; Larson, M., and Bayram, A., 2009. Equivalent roughness height for plane bed under oscillatory flow. *Estuarine Coastal & Shelf Science*, 81(3), 409–422.

Cao, Z.D.; Yang, S.S., and Yang, H., 2009. Definition of silt-sandy beach and its characteristics of sediment movement. *Port & Waterway Engineering*, 1(1), 1–5. (in Chinese with English abstract)

Grant, W.D. and Madsen, O.S., 1979. Combined wave and current interaction with a rough bottom. *Journal of Geophysical Research*, 84(4), 1797–1808.

Grant, W.D. and Madsen, O.S., 1982. Moveable bed roughness in unsteady oscillatory flow. *Journal of Geophysical Research*, 87(1), 469–481.

Li, M.Z. and Amos, C.L., 1998. Predicting ripple geometry and bed roughness under combined waves and currents in a continental shelf environment. *Continental Shelf Research*, 18(9), 941–970.

Pugh,F. and Wilson,K., 1999. Velocity and concentration distributions in sheet flow above plane beds. *Journal of Hydraulic Engineering*, 125(2), 117–125.

Sleath, J.D., 1991. Velocities and shear stress in wave-current flows. *Journal of Geophysical Research*, 96(8), 15237–15244.

Yao, P.; Su, M.; Wang, Z.B.; Rijn, L.C.V.; Zhang, C.K.; Chen, Y.P., and Stive, M.J.F., 2015. Experiment inspired numerical modeling of sediment concentration over sand-silt mixtures. *Coastal Engineering*, 105(2015), 75-89.

You,Z.J., 1994. A simple model for current velocity profiles in combined wave-current flows. *Coastal Engineering*, 23(94), 289-304.

You, Z.J., 1996. Moveable bed roughness and current profiles in the presence of irregular waves with an arbitrary angle to currents. *Ocean Engineering*, 23(3), 225–242.

Zhao, C.J.; Liu F.Q., and Cao Z.D., 2002. Laboratory study on moving features of silty sand. *Journal of Waterway and Harbour*, 23(4), 259-287. (in Chinese with English abstract).

Journal of Coastal Research	SI	75	58-62	Coconut Creek, Florida	2016

Mixing and Dispersal of Low Saline Waters in Estuarine Coastal Waters of the Yellow Sea

ChangShik Kim[†*]

[†]Operational Oceanography Research Center,
Korea Institute of Ocean Science and Technolgoy (KIOST) / University of Science and Technology (UST)
Ansan, South Korea

www.cerf-jcr.org

www.JCRonline.org

ABSTRACT

Kim C.S., 2016. Mixing and dispersal of low saline waters in estuarine coastal waters of the Yellow Sea. *In:* Vila-Concejo, A.; Bruce, E.; Kennedy, D.M., and McCarroll, R.J. (eds.), *Proceedings of the 14th International Coastal Symposium* (Sydney, Australia). *Journal of Coastal Research*, Special Issue, No. 75, pp. 58-62. Coconut Creek (Florida), ISSN 0749-0208.

This study investigates the mixing and dispersal processes of low saline waters that is mass discharged into estuarine coastal waters of the Yellow Sea. During the monsoon season, huge amounts of fresh water are discharged naturally into the Changjiang River Basin and they undergo mixing and dispersion in the coastal waters of the Yellow Sea. In 2003, a very valuable phenomenon showing meandering and patches with vertical lenticular shapes of low saline waters was observed in the Yellow Sea. The observed data presumably are unique as they represent the natural state before the construction of the Three Gorges Dam in China. However, many studies on the general circulation of the Yellow Sea that were conducted for the purposes of implementing a climatological approach were shown to be far from realistic with regard to the observed features of the meandering and dispersal of patches. In this study, we have used a similar numerical method, the ROMS ocean model system for fundamental modeling. However, here the study focuses on the combined effect of down-scaled local surface forcing and tides, applied to low saline water masses of water. The results clearly reveal a process of mixing and dispersal of low saline waters due to the vorticity balance between the Ekman transport and the tidal disturbance that yields meandering and patches with a vertical lenicular structure as observed in the natural field.

ADDITIONAL INDEX WORDS: *Low saline water, wind and tidal forcing, meander, patch and lenticular structures, vorticity balance.*

INTRODUCTION

The Changjiang River is the largest river influencing the coastal dynamics in the Yellow Sea in northeastern Asia (Figure 5) with an annual mean discharge rate of 28,400 m^3/s (Shen *et al*., 1998). As part of the Yellow Sea system, the estuary and inner-shelf dynamics around the Changjiang River are very important for supplying the terrigenous nutrients and sediments to the central part of the Yellow Sea. Discharged fresh water plays a very important role in controlling the coastal dynamics in a large part of the Yellow Sea and adjacent waters.

In numerous studies on the characteristics and behavior of low saline waters (LSW), it has been a common feature that the LSW spreads and extends northeastward from the Changjiang estuary in summer, while in winter the LSW flows southwestward hugging the Chinese coastline (Lie *et al*., 1986; Kim *et al*., 1991; Chang and Isobe, 2003; Kim *et al*., 2004). Typical shapes of LSW spreading in the surface layer have been reported as tongue-shaped. Most previous investigations on LSW spreading are either based on synoptic hydrographic analysis or numerical modeling with climatological forcing. Consequently, several possible major causes for the LSW moving behavior have been studied: flow inertia (Beardsley *et al*., 1985), monsoon winds (Na *et al*., 1992), and tidal residual currents (Lee and Beardsley, 1999).

However, recent field observations using a hydrographic survey and satellite-observed drifters show detailed patterns of Changjiang plume spreading. It may not be surprising that the LSW spreading takes the form of patches as observed in Lie *et al*. (2003) and in other field observations. According to recent observations (Lie *et al*., 2003; Lee *et al*., 2004), the Changjiang River plume in summer was observed to move northeastward in patches of LSW with approximately 2 psu drop in 100 km. With climatological forcing (Chang and Isobe, 2003; Kim *et al*., 2004), no such phenomena were revealed. We set our hypothesis to be that as the LSW surface buoyant plume is discharged into the Changjiang estuary it immediately undergoes horizontal and vertical mixing due to the tidal action and then varying local winds develop an instability in the horizontal shear flow. Steady and synoptic forcing on the plume would develop the tongue-shape dispersion, while additional disturbance of tidal action and

DOI: 10.2112/SI75-012.1 received 15 October 2015; accepted in revision 15 January 2016.
*Corresponding author: surfkim@kiost.ac.kr

fast-varying local wind would accelerate the amplification and modification, yielding meander, patch, and lenticular structures, as observed in the field.

Up until now, it has been far from clear as to how such plume behavior as the meanders, patchs, and lenicular structures occurs. The present study focuses on the Changjiang River plume instability influenced by local wind action and tidal stirring. Numerical simulation has been implemented using the ROMS (Regional Ocean Modeling System) that has been applied to the Yellow Sea in Kim *et al*. (2004) and Park *et al*. (2015). This study investigates the behavior of LSW under the influence of local surface forcing and tidal action in the summer monsoon of 2003. This period covers the time of natural discharge of the Changjiang River in the summer before the construction of the Three Gorges Dam upstream.

METHODS

Initial and Boundary Conditions

The main goal of this study is to investigate the subtidal pattern of Changjiang plume movement as driven by fine-scale local winds and local wind and tidal stirring.

The model description and geographic setting are well described in Kim *et al*. (2004) and Park *et al*. (2015). For the detailed information on the model implementation, please refer to those previous works.

Surface Forcing

The basic state of the Yellow Sea is modeled with climatological forcing as described in Kim *et al*. (2004). In this study, we enhance the surface forcing at a fine scale in time and space. The refined local surface forcing data are compiled by blending with hindcasted MM5 (an operational weather forecasting program at Korea meteorological agency) and the NCEP data, yielding 6-hourly 9km-grid surface forcing data over 111˚E – 144˚E and 25˚N – 47˚N (Park *et al*., 2015). It is noticeable that the refined local wind data show significant mesoscale variability in space as well as in time with a wind stress of the order of 0.5 N/m^2. It is noticeable that the climatological monthly-mean wind stress in August is southerly and very weak, at 0.05 N/m^2.

Changjiang River discharge

The Changjiang River (the world's fourth largest) discharges fresh water into the southern part of the Yellow Sea. The annual mean discharge is 28,400 m^3/s. The monthly mean discharge peaks in July at 48,600 m^3/s and levels off in January with 10,400 m^3/s (Shen *et al*., 1998).

The model grid system in this study allows for very shallow water depth and complex river shapes. With it, it is possible to load fresh water of salinity 0.0 psu in the upper most cell of Changjiang River. The estuarine mixing process allows the fresh water to change into brackish water near the river mouth.

Tidal Forcing

In this study, tidal forcing has been combined with surface forcing in simulation of the Changjiang River plume to investigate the tidal stirring effect. Typical tides in the Yellow Sea have been studied extensively, including major constituents (Naimie and Blain, 2001; Lee *et al*., 2001) as well as shallow-water nonlinear tides (Kang *et al*., 1991 and 1998). The tides in the Yellow Sea are mixed diurnal/semi-diurnal, with average M2 and K1 amplitudes of the order of 1.0 and 0.25 m, respectively. The semi-diurnals in particular have a complex spatial structure. There are 4 amphidromic points for the semi-diurnals, while the diurnals have 2 amphidromics.

In this study, 4 major tidal constituents of M2, S2, K1, and O1 have been used as tidal forcing imposed at the open boundary. The harmonic constants for forcing have been verified in Lee *et al*. (2001) and Lee and Kim (2001), and also applied in Kim *et al*. (2004).

RESULTS

Combined local winds and tidal influence on LSW

We have added tidal forcing to the refined local surface forcing for investigating the tidal stirring effect on the Changjiang River plume dispersion. Tidal forcing has been imposed with 4 major constituents that are adapted from Lee *at al.* (2001).

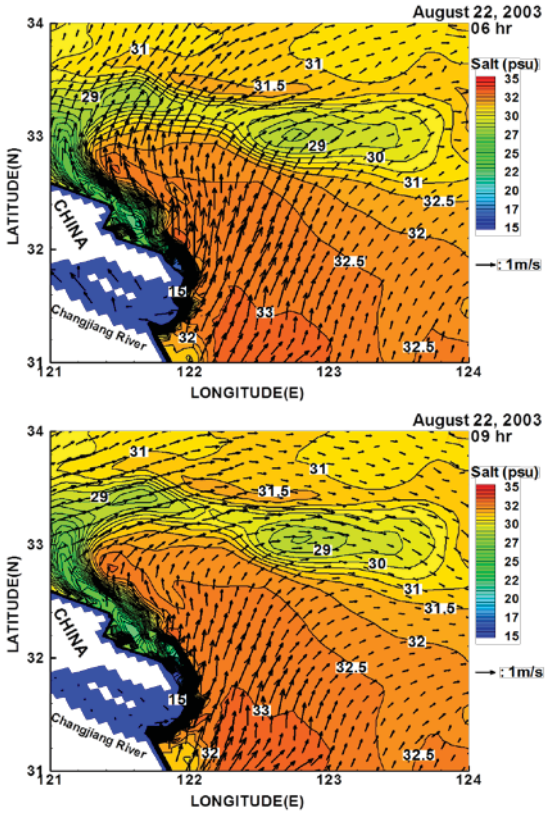

Figure 1. Flow field and salinity distribution at 3-hour intervals on August 22, 2003 based on a simulation that uses refined surface forcing and tidal forcing together.

Figue 1 shows 3-hourly varying local wind-driven and tidal-forced surface currents around the meandering patch on August 22, 2003. The significant contribution of hourly varying tidal currents would enhance the mixing processes. Through scrutiny and examination of the tidal effect on the Changjiang, plume dispersion is found to play a major role in the strong mixing of the less saline waters with adjacent ambient waters, yielding distinct coastal fronts. The lenticular structures of the LSW with sharp salinity fronts imply horizontally wider and vertically deeper mixing than would occur with winds-only forcing.

Figure 2 shows the hourly variation of surface salinity at the point (122.75˚E, 32.95˚N) in the center of the patch, predicted on August 22, 2003. The time series of hourly varying surface salinity shows the time span of patch core trespass at approximately 5 days. The salinity signal suggests the fluctuation at the semidiurnal tidal frequency ranges from less than 0.5 psu in and out of the meandering axis to 1 psu while inside the patch area. If we estimate the patch size surrounded by 31 psu as 200 km along the elongated axis, the moving speed would be on the order of 40 cm/s. The speed of the surface patch is relatively much faster than both the geostrophic or depth-integrated flow that is of the order of 5 cm/s (Yanagi *et al*., 1997) and the satellite-tracking surface drifter speed which is of the order of 20 cm/s (Lie *et al*., 2003). The present study is designed to resolve the surface layer in very high resolution by using a terrain-following vertical coordinate, while the moving speed of the surface buoyant patch driven by local winds and tidal action would reflect realistic surface dynamics.

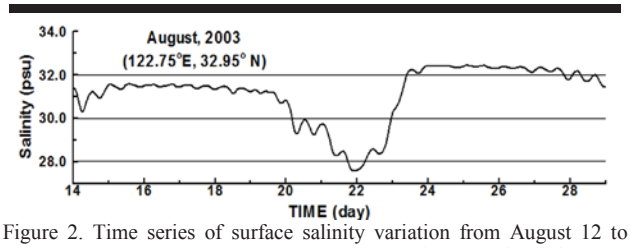

Figure 2. Time series of surface salinity variation from August 12 to August 29, 2003 at a point (122.75ºE, 32.95ºN) that is on the pathway of low saline patch trespass.

Figure 3 illustrates the hourly varying time series of the salinity profile at the same point (122.75 ˚ E, 32.95 ˚ N) as described above, starting from August 14 and ending on August 29, 2003. The depth variation reflects the tidal elevation at the point. At first glance, it is very noticeable that the isohalines from the surface to the bottom layer fluctuate at a major tidal period.

The tidal range is approximately 1 m during this period. Allowing for the sea surface fluctuation at tidal range, the isohaline fluctuation larger than the tidal range would be significant in realm. The 32 psu isohaline is acting as the baseline of the low saline waters patch. The thickness of the patch in this case rarely exceeds 20 m. The trespass time is indicated to be approximately 5 days.

When tidal action is added to local winds, the surface layer clearly shows the enhanced coastal fronts developed by the fresher water plume (Figure 4). However, along the meandering path of LSW the tidal stirring might be efficient enough to mix the surface fresher water with the adjacent waters, to yield a low saline patch or a lenticular shape with salinity lower than would be the case with winds-only forcing.

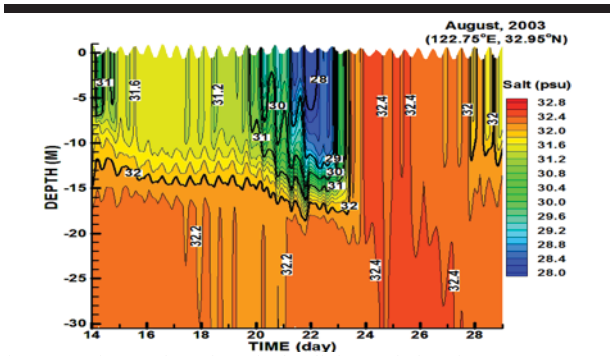

Figure 3. Time series of vertical salinity variation from August 12 to August 29, 2003 at a point (122.75ºE, 32.95ºN) that that is on the pathway of low saline patch trespass.

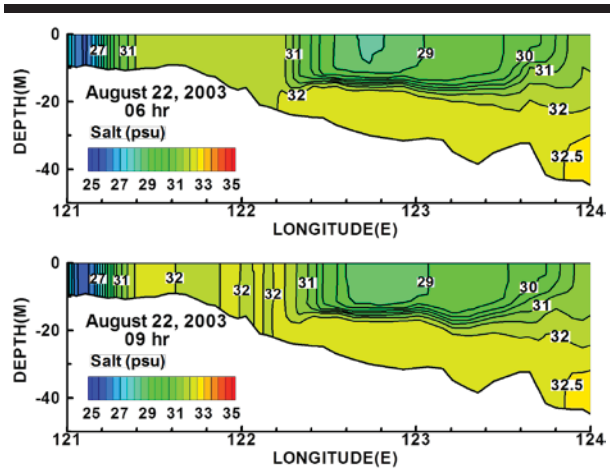

Figure 4. Vertical view of salinity profile at 3-hour intervals on August 22, 2003 along the cross-section at 33˚N that is crossing the low saline patch.

It seems to be interesting to ask how the surface front might change in characteristics during a tidal cycle. Instead, adjacent water outside of the core undergoes faster mixing while the core of the patch flows along the advection axis. It has been analyzed that the lens size of the LSW core is on the order of 50 ~ 200 km horizontally, depending upon the various conditions of momentum balance. It is noticeable that the coastal front line takes onshore and offshore excursions with the tidal cycle, but near the core of the lens the sharp gradient of salinity gets smoother as time passes. In summary, the meandering of the LSW dispersion is driven by the momentum balance between the inertia of the LSW discharge and local winds at the first approximation, and the patch and/or lens patterns observed in field works (Lie *et al*., 2003; Lee *et al*., 2004) are secondary

features created by the balance between Ekman transport and tidal stirring. as shown in Figure 5. The horizontal size of the patches ranges from 50 to 200 km and the vertical thickness rarely exceeds 20 m water depth. The moving speed of the patch core has been estimated as approximately 40 cm/s along the major axis of the meandering path with a life span of 10 to 20 days, dependent upon the local winds and tidal action.

Vorticity Field around Meandering Plume

To examine the rotation of the surface flow around the meanders and patches of the Changjiang River plume, the vorticity field has been estimated for winds with tides. A coastal flow overridden by a river plume is usually shear flow due to complicated momentum balance involving buoyancy, local wind stress, relative vorticity and tidal advection etc. The present study adopts a numerical implementation to solve the fully nonlinear momentum equations. Estimation of the absolute effect of individual contributors on the full momentum balance is not simple in nonlinear processes. However, examining the sensitivity of forcing and flow structure in the study area, the flow fields are composed of three major contributors: upper-most Ekman transport acting on the buoyant plume, baroclinic transport in the column of density change, and barotropic currents due to the tidal advection. Around the boundary of the meanders or patches of the Changjiang plume, vorticity is easily generated due to the wind stress curl and shear flow associated with tidal advection and the salinity discontinuity. The vorticity arising from the horizontal shear would be shed into the wake of the meandering boundary, giving stronger mixing in stronger vorticity zones.

Figure 5 illustrates the vorticity field estimated from flow fields simulated without tides (upper) and with tides (lower) on August 22, 2003. There is a clear indication of clustered negative vorticity (lower part of Figure 5) along the central axis of the Changjiang plume pathway on August 2003 in the flow field driven by local wind forcing combined with tides. Without tidal forcing (upper part of Figure 5), any distinct feature in the vorticity field is not shown, implying less shear around the patch boundary, hence less mixing without tidal advection.

Through the vorticity field experiment, the local wind stress and tidal advection are very important contributors controlling the meander, patch, and lenticular structures of the Changjiang River plume dispersion in summer.

CONCLUSIONS

Numerical simulation using the ROMS model was conducted to examine the influence of local surface forcing and tidal action on the transport pathway of the Changjiang River plume.

The patch and sometimes the so-called ‘lens’ of the LSW were generally observed in the field survey. However, up until now those features and dynamics have not been fully elucidated with synoptic hydrographic surveys or modeling with climatological forcing.

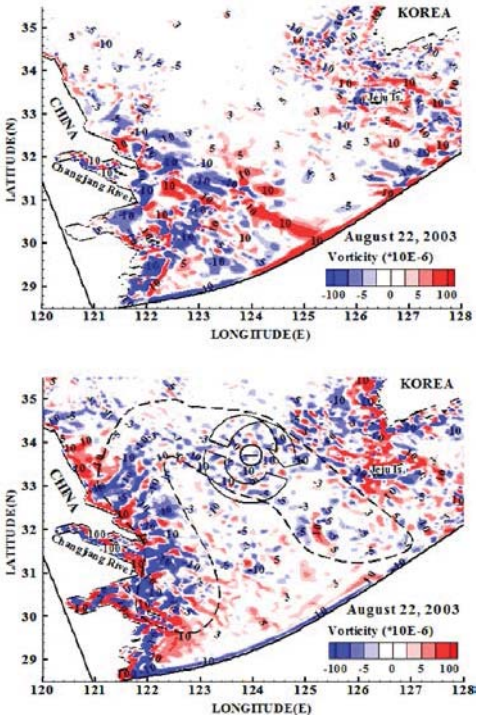

Figure 5. Vorticity field on August 22, 2003 estimated without tide (upper) and with tide (lower) on the wind-driven flow field around the meandering low saline waters body.

The present study elucidates the generation, pathway, and transforming processes of the Changjiang River plume in meander, patch, and lenticular structures, as reported in many field observations (Lie *et al*., 2003; Lee *et al*., 2004). To simulate the pathway of the Changjiang plume dispersion, the terrain-following ROMS model has been applied. The model has been run for three months of the summer of 2003, which covers a period of natural discharge of fresh water from the Changjiang River into the Yellow Sea before the construction of the Three Gorges Dam upstream. Available field data coincide with similar conditions in a summer of typical fresh water discharge and wind conditions.

LSW dispersion into the interior of the Yellow Sea takes various pathways depending upon the forcing imposed in the model implementation. When the refined surface forcing varying in mesoscale time and space has been applied, the plume dispersion shows quite a different pattern from the climatological view. Episodic strong southerly winds advects the plume northward, then Ekman transport pulls its pathway towards the northeast and eastward, developing into the meandering of the LSW belt. Persistent winds eventually break apart the meandering belt, forming patches of LSW core water of less than 29 psu. The patches undergo further mixing with adjacent waters, becoming elongated with the dominant current, until their shapes fade out. The effect of the tidal stirring in the surface layer enhances the coastal front near the estuary while there is strong lateral mixing around the patch boundary. The

simulated distributions and fate of low saline waters in the south Yellow Sea during summer in 2003 are remarkably similar to the claims of Lie *et al*. (2003) and Lee *et al*. (2004). The scale of patches ranges from 50 to 150 km horizontally and 10 to 20 m in vertical thickness. The life spans of the the patches varies with the winds, stratification, and tidal action. During the summer of 2003, the life span has been estimated as approximately 20 days, from generation of meandering to fading out from the lens shape.

ACKNOWLEDGMENTS

This study was partly supported by the research project, "Development of Korea Operational Oceanographic System (KOOS PhaseII)" funded by Ministry of Ocean and Fisheries Korea. The author thanks to HSL and JJY for their help in the early stage of the work, and to JAK for her final touch on the manuscript.

LITERATURE CITED

Beardsley, R. C.; Limeburner, R.; Yu, H., and Cannon, G. A., 1985. Discharge of the Changjiang (Yangtze river) into the East China sea. *Continental Shelf Research*, *4*(1), 57-76.

Chang, P. H., and Isobe, A., 2003. A numerical study on the Changjiang diluted water in the Yellow and East China Seas. *Journal of Geophysical Research: Oceans (1978–2012)*, *108*(C9).

Kang, S. K.; Lee, S. R., and Lie, H. J., 1998. Fine grid tidal modeling of the Yellow and East China Seas. *Continental Shelf Research*, *18*(7), 739-772.

Kang, S. K.; Lee, S. R., and Yum, K. D., 1991. Tidal Computation of the East China Sea. The Yellow Sea and the East Sea. *Elsevier oceanography series*, *54*, 25-48.

Kim, C. S.; Lim, H. S.; Yoon, J. J., and Chu, P. C., 2004. Numerical simulation of Hydrodynamics and water properties in the Yellow Sea. I. Climatological inter-annual variability. *Korean Society Of Oceanography*, *39*(1), 72-95.

Lee, S. H., and Beardsley, R. C., 1999. Influence of stratification on residual tidal currents in the Yellow Sea. *Journal of Geophysical Research: Oceans (1978–2012)*, *104*(C7), 15679-15701.

Lee, J. H.; S. T. Jang; I. C. Pang; T. Matsuno and D. K. Lee, 2004. The CDW lens and its movement. *In Proceedings of 2nd International Symposium on PEACE*, Kyushu Univ. Japan, 1-3.

Lee, J. C. and C. S. Kim, 2001. Tide computation in the Northeast Asian Seas using Topex/Poseidon altimetry data, *Korean Society Of Oceanography* 'Bada', 6, 1-12.

Lee, J. C.; Kim, C. S., and Jung, K. T., 2001. Comparison of bottom friction formulations for single-constituent tidal simulations in Kyunggi Bay. *Estuarine, Coastal and Shelf Science*, *53*(5), 701-715.Lie, H. J., 1989. Tidal fronts in the southeastern Hwanghae (Yellow Sea). *Continental Shelf Research*, *9*(6), 527-546.

Lie, H. J.; Cho, C. H.; Lee, J. H., and Lee, S., 2003. Structure and eastward extension of the Changjiang River plume in the East China Sea. *Journal of Geophysical Research: Oceans (1978–2012)*, *108*(C3).

Na, J. Y.; Seo, J. W., and Han, S. K., 1992. Monthly-mean sea surface winds over the adjacent seas of the Korean Peninsula. *J. Oceanol. Soc. Korea*, *27*(1), 10.

Naimie, C. E.; Blain, C. A., and Lynch, D. R., 2001. Seasonal mean circulation in the Yellow Sea—a model-generated climatology. *Continental Shelf Research*, *21*(6), 667-695.

Park, K. S.; Heo, K. Y.; Jun, K.; Kwon, J. I.; Kim, J.; Choi, J. Y., and Jeong, S. H., 2015. Development of the Operational Oceanographic System of Korea. *Ocean Science Journal*, *50*(2), 353-369.

Yanagi, T.; Morimoto, A., and Ichikawa, K., 1997. Seasonal variation in surface circulation of the East China Sea and the Yellow Sea derived from satellite altimetric data. *Continental Shelf Research*, *17*(6), 655-664.

Journal of Coastal Research	SI	75	63-67	Coconut Creek, Florida	2016

Stratification of tidal influenced navigation channel

Nam-Hoon Kim†, Jin Hwan Hwang†*, and Hyeyun Ku†

†Department of Civil and Environmental Engineering
Seoul National University
Seoul, Republic of Korea

www.cerf-jcr.org

www.JCRonline.org

ABSTRACT

Nam-Hoon Kim; Jin Hwan Hwang, and Hyeyun Ku, 2016. Stratification of tidal influenced navigation channel. *In:* Vila-Concejo, A.; Bruce, E.; Kennedy, D.M., and McCarroll, R.J. (eds.), *Proceedings of the 14th International Coastal Symposium* (Sydney, Australia). *Journal of Coastal Research*, Special Issue, No. 75, pp. 63-67. Coconut Creek (Florida), ISSN 0749-0208.

Field observation was performed to understand the mixing and stratifying processes in an estuarine navigation channel. An artificial gate located at the mouth of Geum River in Korea discharges freshwater to the coastal sea. While the stratification in this channel is artificially controlled by gate operation, the mixing is determined by tide with about 6 m amplitude of semidiurnal constituent. Discharged freshwater mostly flows though the southern navigation channel and leads to the strong stratification, which could be due to the strong advection in the upper layer during the ebb. At the interface between buoyant current and bottom saltier water, the features of internal waves were observed also with the reduced gravity of 15-22 kg/m^3. The gradient Richardson numbers show the seasonal variations of the stratification as expected. Relatively water column was pretty stably stratified in March and partially or well mixed in April and August throughout the regions of navigation channel.

ADDITIONAL INDEX WORDS: *Richardson number, stratification, mixing, ROFI, ADCP, CTD.*

INTRODUCTION

In the Region Of Freshwater Influence (ROFI, Simpson, 1997), freshwater and seawater interact each other very strongly and also oppositely form a front, which can act as a barrier to inhibit not only water bodies but also materials and chemicals from mixing and transporting. Such strong stratification could lead to physical and environmental changes affecting the ecosystem (Hwang *et al*., 2014; Jang *et al*., 2011). ROFI can also be determined by how and how much freshwater was released. For example, the angle of the released path, the shape of the river mouth and the changes of depths and slope could modify the location, area, and strength of the stratification over the whole estuarine area (Hwang *et al*., 2011).

The Geum River Estuary is located at the mouth of one of the rivers in Korea and categorized as a well mixed type, where semidiurnal tide dominates. Before the water gate and dam were constructed in 1994, mixing and stratification were mainly controlled by the tide rather than the river discharge. However, after constructing them, freshwater was released artificially depending on the water level in the reservoir and the tidal influence also decreased since the dam inhibits tidal momentum from propagating toward upstream. Along with the dam and gate, a long sea dyke was built for providing the navigation channel, which changed well-mixed characteristics to other types of this estuary (Figure 1). In the meanwhile, that channel is very important path for transporting freshwater to the coastal area because most freshwater is delivered through this channel. Also, freshwater and seawater mix each other during passing through this channel. After certain amount of mixing between seawater and freshwater through channel, the mixed water is released to the open coastal sea. From this point, freshwater can be spread out the whole ROFI. Therefore, the study of the mixing and transport mechanism in the channel is a key in understand how the ROFI develops in this coastal and estuarine area.

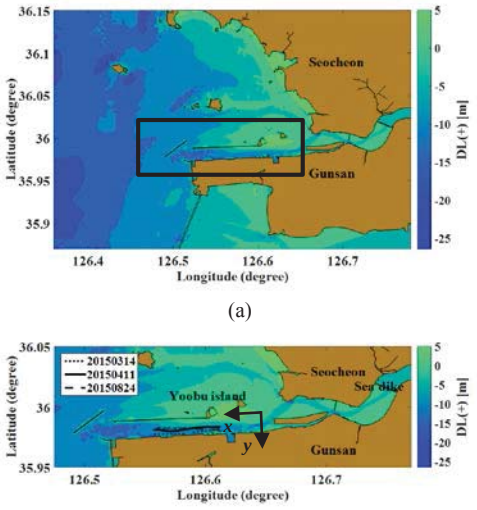

Figure 1. (a) Location of study area. (b) Observation transects. Positive along-channel (x) and cross-channel (y) directions are indicated. Positive along-channel velocity (u) is in the direction of the ebb tide, while positive cross-channel velocity (v) is toward Gunsan.

DOI: 10.2112/SI75-013.1 received 15 October 2015; accepted in revision 15 January 2016.
*Corresponding author: jinhwang@snu.ac.kr

While the stratification is pretty much dependent on the amount of the released freshwater, mixing could be strongly governed by the tidal process here. Therefore, appearances of mixing and stratification vary depending on the discharges of freshwater and the amplitudes of tide in the diverse tidal cycles and phases. Generally in the downstream of the river, during the flood period, strong barotropic flow derives water bodies to mix vertically well and have strong horizontal gradients of density in the river mouth. The ebb flows enhance stratification by increasing surface freshwater advection and tilting the horizontal gradient with less vertical mixing (Simpson *et al*., 1990). Such processes strongly depend on the ratio of horizontal density gradients and bottom shear stresses. If the horizontal gradients are not sharp enough, then when it is tiled during the ebb, bottom shear generated turbulence can overcome stratification. However, the present navigation channel does not have sharp enough horizontal gradient to show such Strain Induced Periodic Stratification (SIPS, Simpson, *et al*., 1990).

The Simpson number could determine whether the SIPS occurs based on the order of unity for the transition between mixed and stratified conditions. This number represents the balance between mixing force of bottom boundary layer and the stabilizing force of the horizontal density gradient, when such gradients are tilted. The Simpson number of this navigation channel is much larger than unity since the channel has almost uniform horizontal gradient in the flow direction and this criterion can be applicable to the rather larger rivers than this channel. Even though SIPS may not occur in the navigation channel, other tidal processes still influence mixing in this channel as like as internal waves with currents.

Features of flows in the channel could be categorized into a surface buoyant current or river plume. Surface advected current in the upper layer will persist and behave as like as density current during the ebb. Instability or internal waves must exist and contribute to the mixing along with the tidally generated barotropic currents. In other words, we suspect that the mixing is governed by the much smaller scale process in this channel rather than the large scale process directly influenced by the tide. Generally in large scale mixing controlled by tide, turbulence generated at the bottom could be a significant process in the strongly stratified estuary (e.g., Geyer, 2008; Griddings *et al*., 2011; MacDonald and Horner-Devine, 2008; Tedford *et al*., 2009) but it must be more significant in partially mixed estuaries (Peters, 1997; Stacey *et al*., 1999). In the present work, the Simpson number is much larger than unity and so the bottom boundary process does not reach to the surface and the other processes at the interface could be more critical.

To explain more detailed interfacial process, the finer scale observation technique must be required. Therefore, the present work employed a moving vessel profiling method to gather the data with the finer resolutions. Based on those observations, the gradient Richardson numbers were compared to examine the small scale mixing processes in shallow, semidiurnal tide, strongly stratified navigation channel.

Background

The Geum River Estuary is located in the eastern part of the Yellow Sea and the west coast of Korea (Hwang *et al*., 2014). This area is shallower than 20 m and the maximum width of the river mouth is 2 km. Just after the river mouth, the river channel diverges into two channels of the south and north by the sand dunes near the Yoobu island. Through the north channel, only a small amount of the freshwater passes to the coastal sea since tidal flat formed the most of this area (Kwon and Lee, 1999; Lee *et al*., 2001) and the most of the freshwater discharges mainly through the south channel (Lee *et al*., 2001). Therefore, we have surveyed through the south channel of navigations after freshwater was released from the dam gate during the ebb. A map of the Geum River Estuary is overlain with the transects and the coordinate system in Figure 1: x, y, and z represent each along-channel, cross-channel, and vertical directions u, v, and w means the velocities in each direction.

METHODS

M9, Acoustic Doppler Current Profiler (ADCP, Sontek) measured velocity fields and Yoing Ocean Data Acquisition Profiler (YODA, JFE-Adventch) measured conductivity and temperature. ADCP and YODA were operated on a vessel, which cruised at a speed of 1-2 m/s. GPS data was logged concurrently with the ADCP data to ensure accurate positioning. The falling velocity of the YODA profiler was adjusted to approximately 0.2 m/s, which corresponds to a vertical resolution of 0.04 m. The data was sampled at 10 Hz and recorded internally (Masunaga and Yamazaki, 2014). All data were averaged by 1 m bins, which equal to the ADCP and interpolated by using triangulation-based cubic spline method with the second order of accuracy. Table 1 shows the summarized measurement description. The reason why the number of measuring points are different is because of fishing nets.

Table 1. *Measurement description.*

Date	Observation condition	Rate of freshwater discharge	Instruments	No. of measuring point
14 March (Spring)	24 hrs after discharge	162.7 t/min	ADCP, CTD	50
11 April (Spring)	24 hrs after discharge	242.1 t/min	ADCP, CTD	138
24 August (Summer)	72 hrs after discharge	159.8 t/min	ADCP, CTD	183

The relative strength of the stratification and mixing was measued by the gradient Richardson number, given by

$$Ri_g = \frac{N^2}{S^2}, \tag{1}$$

where N and S are the buoyancy frequency and the shear, respectively. N and S are;

$$N = \sqrt{-\frac{g}{\rho_0}\frac{\partial \rho}{\partial z}} \approx \sqrt{-\frac{g}{\rho_0}\frac{\Delta \rho}{\Delta z}}, \tag{2}$$

$$S = \sqrt{\left(\frac{\partial u}{\partial z}\right)^2 + \left(\frac{\partial v}{\partial z}\right)^2} \approx \sqrt{\left(\frac{\Delta u}{\Delta z}\right)^2 + \left(\frac{\Delta v}{\Delta z}\right)^2}. \tag{3}$$

where g is gravitational acceleration, ρ density and ρ_0 reference density. The larger Ri_g indicates the stronger stratification and the critical Richardson number, Ri_c is around 0.25 (Miles, 1961). When Ri_g<0.25, the region may have the actively mixed condition and it still remains in the possibly mixed condition when 0.25<Ri_g<1. Whereas, the regions of Ri_g>1 are considered stably stratified (Gridding *et al*., 2011).

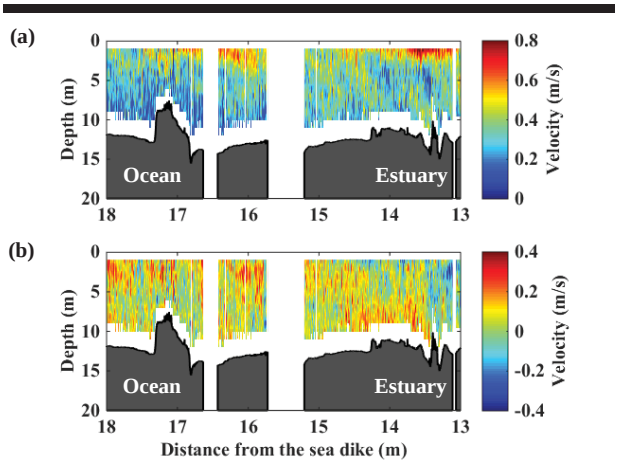

Figure 2. Velocity components of (a) x and (b) y on March 14, 2015.

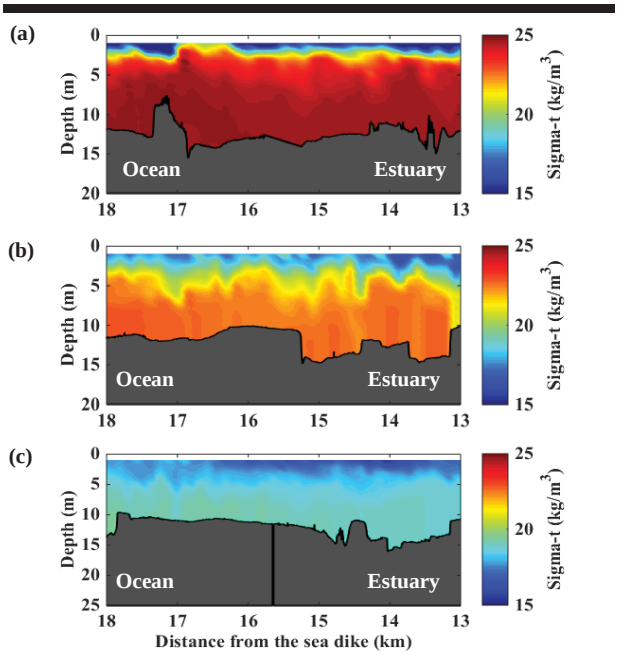

Figure 3. Density anomaly (kg/m^3) (a) 14 March, (b) 11 April, and (c) 24 August in 2015.

RESULTS

The velocity profiles are presented in Figures 2. The along-channel velocities (u) are in the phase with the ebb tide with approximately 0.4-0.8 m/s near the free-surface and less than 0.4 m/s at middle and bottom ranges. The cross-channel velocities (v) are slightly positive (i.e. moving southward) through the transects since the measurement was not done at the center of the channel due to depth and existence of along channel secondary flow. The velocity profiles on April and August also show similar phases.

Figure 3 shows the vertical profiles of the density along the transects. There exist two layers of fresh light upper layer and saltier heavy lower layers. Salinity and temperature contribute almost equivalently to the density change in this region (Figure 4). Between two layers, we could observe strong interface over all cases at near 5 m. At the interface, small wave-like features were observed and those density anomalies distribute in the ranges of 15 and 22 kg/m^3.

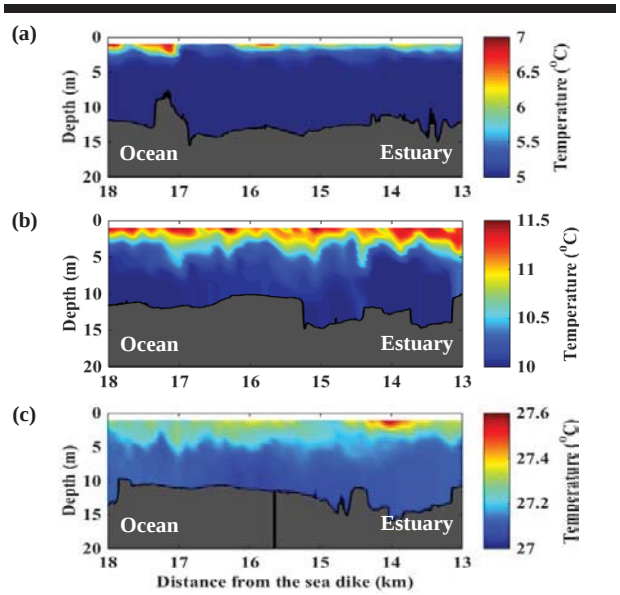

Figure 4. High-resolution observation data of temperature (°C) (a) 14 March, (b) 11 April, and (c) 24 August in 2015.

The difference of temperatures in the upper and lower layers is about 1.5 °C in spring and 0.5 °C in summer, respectively. In other words, in this region, water column was stratified stronger in spring than summer. In order to more clearly determine the stratification, we calculated the gradient Richardson number, Ri_g. Figure 5 shows the gradient Richardson numbers which were normalized by the critical Richardson number, Ri_c.

As mentioned, in the regions of Ri_g/Ri_c<1 there is active mixing, while the regions of Ri_g/Ri_c>4 are considered as stable. As in Gridding *et al*. (2011), another zone was defined in the range of 1<Ri_g/Ri_c<4. In Figure 5, blue markers indicate active mixing, red markers mean possibly mixing and black represents stable. In March, the navigation channel is almost stably stratified and most of measurements present black dots. In April, red markers spread more and water bodies mix possibly. In

August, blue and red dots prevail and mean two layers mix more than in two previous months.

The probability of the occurrence rate of the gradient Richardson numbers are summarized in Table 2. Since the Richardson numbers cannot be easily determined in the small area, the probability of the occurrence should be more reasonable than deterministic values. Based on the occurrence rates, the probability of mixing gradually increases changing from spring to summer. As the weather becomes warmer, the differences of temperatures in the upper and lower layers decrease (Figure 4) and the stratification decreases. Comparing April with March, April has the smaller Richardson numbers (Table 2) and less stratification, which seems to be controlled dominantly by the shear rates. Figure 6 shows a scatter diagram of the shear rates versus the buoyancy frequencies in the logarithmic scales. Dashed line illustrates the Ri_g=1, namely critical condition. The navigation channel has stronger stratification preventing mixing by the strong restoring buoyancy force (high N) in March. On the contrary, weaker stratification leads to stronger mixing in April and August than March.

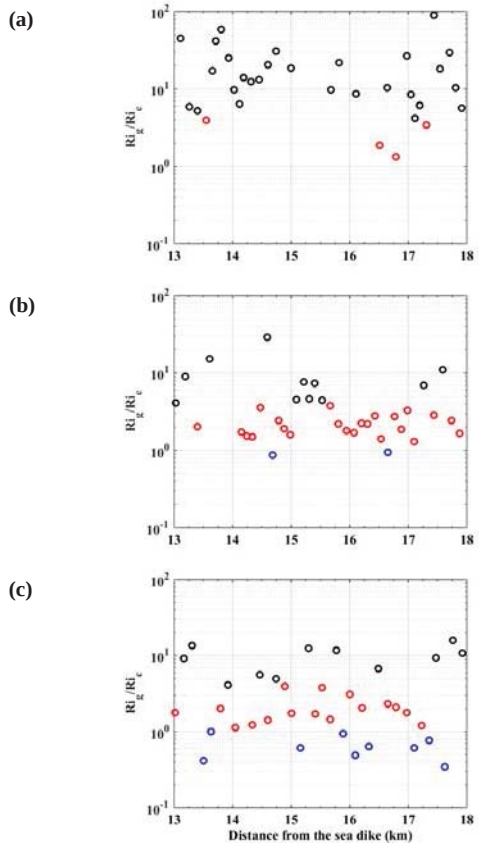

Figure 5. Gradient Richardson number ratios of Ri_g/Ri_c. Ri_g/Ri_c are plotted on a log scale (a) 14 March, (b) 11 April, and (c) 24 August in 2015. Rigions of Ri_g/Ri_c < 1 (blue dot), regions with Ri_g/Ri_c > 4 (back dot) are considered stable. We also call out a third region where $1<Ri_g/Ri_c<4$ (red dot).

While the buoyancy frequency has ranges between -7 to -5 in both months, the shear rate has in the range of -10 to -6 in March, -7 to -3 in April (Figure 6). Therefore, the transition of stratification from March to April depends more on the shear rate rather than temperature or density changes. We could not observe clear transition between April to August. In this case, both shear rate and buoyancy frequency decreases, but the buoyancy frequency decreases slightly more than the shear rate.

Table 2. *Probability of mixing on the basis of gradient Richardson number.*

Date	Probability of potentially mixing ($Ri_g < 0.25$)	Probability of partially mixing ($0.25<Ri_g < 1$)	Probability of strable stratification ($Ri_g > 1$)
14 March	0 %	11 %	89 %
11 April	5 %	61 %	34 %
24 August	24 %	44 %	32 %

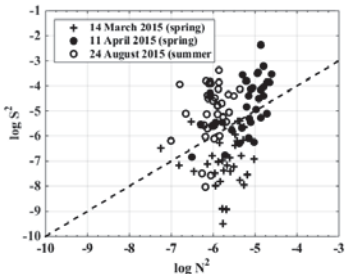

Figure 6. Scatter diagram of log S^2 as a function of log N^2. The dashed line illustrates the Ri_g = 1 condition ($logN^2 = logS^2$).

DISCUSSION

The mixing rate of navigation channel can be determined by the balance between the density gradient and shear rate. The density gradient or difference between upper and lower layer has variations along with the changes of shear rate in the navigation channel. Strong stratification in spring is weakened to the partially mixed condition in summer. Comparing the summer and earlier spring, if temperature difference will be more significant in stratification during summer, the shear rate must become larger in summer to have smaller Richardson number as in Figure 5, 6, and Table 2 than spring. But, the amounts of discharge were almost similar since operation totally depends on the water level in the reservoir, and there was no specific event to change operations during those periods. Nevertheless, the mixing rate in April is larger than in March because of the rate of freshwater discharge.

Comparing April and March, density gradients were not significantly different from each other as in Figure 6. Also, we could find the increase of the shear rates in April, which means the increases of the discharge or the tidal currents. Generally, tidal currents at the very near river mouth are not baroclinic but almost barotropic, and in such a condition shear cannot be generated significantly by tide. So, it can be concluded that the

discharge of freshwater is slightly stronger in April than March and this increases mixing. We could not find similar relationship between April and August. Still, it could not robustly be concluded that which factors can affect more dominantly the mixing rate in the navigation channel since the present observations have limitation in measuring during the ebb period and short tidal cycle which cannot be representative for the whole tidal effects to mixing.

If there are enough data collections, then we can have appropriate calculations for the Simpson number. The Simpson numbers estimated with the present results roughly were almost over two orders. It means that the bottom friction does not affect the surface processes as we discussed. Both Simpson and Richardson numbers guarantee that the present channel is totally strongly stratified. In this condition tide is no more generating turbulence at the bottom, an indirect process generated nonlinearly by the tidal process will produce interfacial mixing in this channel, which will be studied more in future.

CONCLUSIONS

Most of the freshwater discharge flows above the saltier seawater and constructs two layers through the navigation channel and the vertical gradient of density over the depth becomes smaller in summer than in spring. When there is sharp interface between the layers, internal waves and instabilities seem to be generated by the advected currents from the upstream at the surface. To capture such detailed small scale processes, the present work employed a moving vessel profiling with high frequency. To assess quantitatively the mixing process, the gradient Richardson numbers were determined. The Richardson number seems to be larger than the critical value over the measured periods. The navigation channel was almost stably stratified condition in March, showed possibly mixed condition in April, and included some observational locations which showed actively or possibly mixed condition in August.

ACKNOWLEDGMENTS

The authors acknowledges the support from the National Research Foundation of Korea (NRF) Grant (No. 2015R1A5A 7037372) funded by MSIP of Korea. Also, the authors were supported by "Development of integrated estuarine management system", funded by the Ministry of Oceans and Fisheries, the republic of Korea.

LITERATURE CITED

Geyer, W.R.; Scully, M.E., and Ralston, D.K, 2008. Quantifying vertical mixing in estuaries. *Environmental Fluid Mechanics*, 8(5-6), 495-509.

Griddings, S.N.; Fong, D.A., and Monismith, S.G., 2011. Role of straining and advection in the intratidal evolution of stratification, vertical mixing, and longitudinal dispersion of a shallow, macrotidal, salt wedge estuary. *Journal of Geophysical research*, 116, C03003

Hwang, J.H.; Ahn, J.E.; Park, Y.G.; Jang, D.M., and Kim, B.R., 2011. The growth of the bulge near a river mouth. *Journal of Coastal Research*, SI64, 1048-1052.

Hwang, J.H.; Sy, P.V.; Choi, H.J.; Chang, J.S.; and Kim, Y.H., 2014. The physical processes in the Yellow Sea. *Ocean and Coastal Management*, 102, 449-457.

Jang, D.M.; Hwang, J.H.; Park, Y.G.; and Park, S.H., 2011. A study on salt wedge and river plume in the Seom-Jin River and Estuary. *KSCE Journal of Civil Engineering,* 16(4), 676-688.

Kwon, H.K., and Lee, S.H., 1999. Physical environment changes in the Keum River estuary by the dyke gate operation I. Mean sea level and tide. *Journal of Korean Society of Oceanography*, 4(2), 93-100. (in Korean)

Lee, S.H.; Choi, H.Y., and Kwon, H.K., 2001. Physical environment changes in the Keum River Estuary due to dike gate operation: III. Tidal modulation of low-salinity water. *Journal of the Korean Society of Oceanography*, 6(3), 115-125. (in Korean)

Macdonald, D.G., and Horner-Devine, A.R., 2008. Temporal and spatial variability of vertical salt flux in a highly stratified estuary. *Journal of Geophysical Research*, 113, C09022, DOI:10.1029/2007JC004620.

Masunaga, E., and Yamazaki, H., 2014. A new tow-yo instrument to observe high-resolution coastal phenomena. *Journal of Marine Systems*, 129, 425-436.

Miles, J.W., 1961. On the stability of heterogeneous shear flow. *Journal of Fluid Mechanics*, 10, 496-508.

Peters, H., 1997. Observations of stratified turbulent mixing in an estuary: Neap-to-spring variations during high river flow. *Estuarine Coastal Shelf Science*, 45, 69-88.

Simsson, J.H.; Brown, J.; Matthews, J., and Allen, G., 1990. Tidal straining, density currents, and stirring in the control of estuarine stratification. *Estuaries*, 13(2), 125-132.

Simpson, J.H., 1997. Physical processes in the ROFI regime. *Journal of Marine Systems*, 12, 3-15.

Stacey, M.T.; Monismith, S.G., and Burau, J.R., 1999. Observations of turbulence in a partially stratified estuary. *Journal of Physical Oceanography*, 29, 1950-1970.

Tedford, E.W.; Carpenter, J.R.; Pawlowicz, R.; Pieters, R., and Lawrence, G.A., 2009. Observation and analysis of shear instability in the Fraser River estuary. *Journal of Geophysical Research*, 114, C11006, DOI:10.1029/2009JC005313.

Journal of Coastal Research	SI	75	68-72	Coconut Creek, Florida	2016

An Influence of Salinity on Resuspension of Cohesive Sediment

Kyunghoi Kim[†*], Han-sam Yoon[‡], In-Cheol Lee[†] and Tadashi Hibino[††]

[†]Department of Ocean Engineering,
Pukyong National Univeristy
Busan, 608-737, Korea

[‡]Department of Ecological Engineering,
Pukyong National Univeristy
Busan, 608-737, Korea

[††]Graduate School of Engineering, Hiroshima University
Higashi-Hiroshima, 739-0035, Japan

www.cerf-jcr.org

www.JCRonline.org

ABSTRACT

Kim, K.H.; Yoon, H.S., Lee, I.C. and Hibino, T., 2016. An influence of Salinity on Resuspension of Cohesive Sediment. *In:* Vila-Concejo, A.; Bruce, E.; Kennedy, D.M., and McCarroll, R.J. (eds.), *Proceedings of the 14th International Coastal Symposium* (Sydney, Australia). *Journal of Coastal Research*, Special Issue, No. 75, pp. 68-72. Coconut Creek (Florida), ISSN 0749-0208.

Field observations were carried out at Tenma River which passes through Hiroshima City to investigate turbidity variations in various salinity conditions. And resuspension experiments with cohesive sediments were conducted using an unidirectional flow channel with varying salinity. Changes in the sediment strength due to the salinity variation were evaluated by using liquid limit test. It was found that turbidity varied in reverse proportion to the salinity in the Tenma River. Also, increases in salinity reduced the resuspension flux and enhanced the settling velocity of cohesive sediment by enhancing the cohesion between the particles. From the results obtained above, we concluded that salinity is an important factor in the transport of cohesive sediment in addition to shear stress and water content in estuaries and blackish rivers.

ADDITIONAL INDEX WORDS: *Resuspension, cohesive sedimenet, salinity, blackish river.*

INTRODUCTION

The concentration of organic contaminants in cohesive sediment is much higher than in the water column (Chapman, 1986). Therefore, it has been reported that cohesive sediment in marine environments affects the spatial distribution and dynamics of all benthic organisms, from bacteria to macro-benthos, and has the potential to impair water quality through its resuspension (Danovaro *et al*., 1995; Duineveld *et al*., 1997). Several articles have insisted that the resuspension of cohesive sediment plays an important role in the functionality and health of coastal areas (Lee and Hoshika, 2000; Ali and Lemckert, 2009). Therefore, analyzing the mechanism of cohesive sediment resuspension is an important component in the assessment of the health of aquatic environments.

Most papers concerning the resuspension of cohesive sediment have focused on bottom shear stress induced by currents and waves (Black 1998; Houwing, 1999; Kim *et al*., 2010). It is well known that salinity enhances the cohesion of particles (formation of flocs), and this process may also influence the transfer of cohesive strength (Jean and Lee, 1999). Since estuaries and blackish rivers are characterized by the interaction of marine and fluvial systems, changes in salinity affect the resuspension of cohesive sediment by altering the strength of the cohesion.

The work presented in this paper describes data from a study of the transport of turbidity in various salinity conditions at a measuring station located in the Tenma River, Japan. In addition, the paper examined the influence of salinity on the settling and resuspension of cohesive sediment.

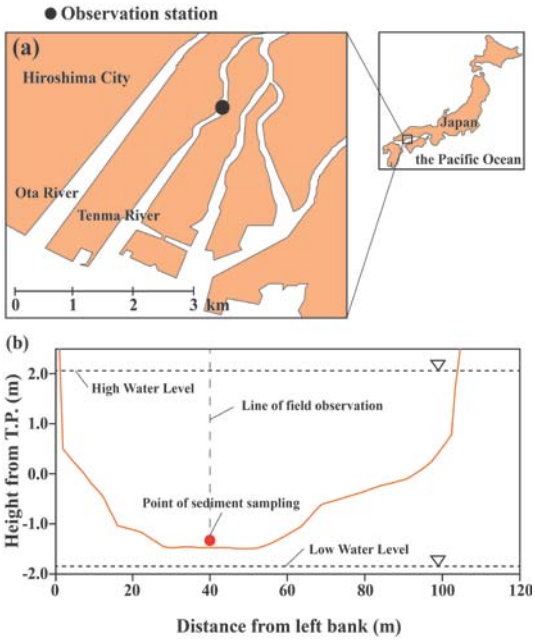

Figure 1. Map showing (a) location of study area and (b) cross-section of Tenma River where the field observation was carried out.

DOI: 10.2112/SI75-014.1 received 15 October 2015; accepted in revision 15 January 2016.
*Corresponding author: hoikim@pknu.ac.kr

METHODS

In order to clarify the effects of salinity on resuspension of cohesive sediment, field observations, liquid limit test and resuspension experiment were carried

Field observation

Field observations were carried out at Tenma River which passes through Hiroshima City, Japan, where the deposition of cohesive sediment on the river tidal flat has become an environmental problem (Figure 1(a)). Observation was carried out 5.4 km upstream from the river mouth on 17 Sep. 2008 (flood tide) and 17 Sep. 2009 (flood and ebb tide). A water quality profiler (AAQ RINKO, JFE Advantech, Japan) was used to collect time-series of water depth, salinity, turbidity and water temperature.

Liquid limit test

Liquid limit test was carried out to investigate change of liquefaction of cohesive sediment depends on the porewater salinity condition. To compare an effect of organic matter, experiments were performed with both bentonite and cohesive sediment. Experimental conditions are shown in Table 1.

Casagrande device was used for determination of liquid limit. Before the experiment, the interstitial water of the cohesive sediment was removed by centrifugation (3000 rpm, 20 min). Thereafter water with different salinity conditions was mixed with the cohesive sediment and the bentonite. After the experiment, the interstitial water of the sediment was collected by centrifugation (3000 rpm, 20 min), and the salinity was determined with a water quality meter AAQ RINKO.

Table 1. *Experimental cases for liquid limit test.*

Case limit (%)	Materials	Porewater salinity (psu)	Liquid
L1	Bentonite	0	367
L2	Bentonite	10	227
L3	Bentonite	47	111
L4	Cohesive Sediment	13	130
L5	Cohesive Sediment	16	126
L6	Cohesive Sediment	27	118

Resuspension experiment

In order to clarify the effect of overlying water salinity on the resuspension of cohesive sediment, indoor experiments were carried out using a unidirectional flow channel (Figure 2). Cohesive sediment sampled from Tenma River was set in the tray, which was located in the center of the unidirectional flow channel. The propeller generates various speeds of unidirectional flow. The experimental conditions are presented in Table 2.

The concentrations of suspended cohesive sediment were measured using a laser-type turbidity meter. The bed shear stress was determined from the measured vertical velocity profile. Ignition loss (IL) was measured using an oven (600 ^{o}C, 4 hours) after the samples were dried at 100^{o}C for 1 day. The salinity of the overlying water was determined with an AAQ RINKO water quality meter.

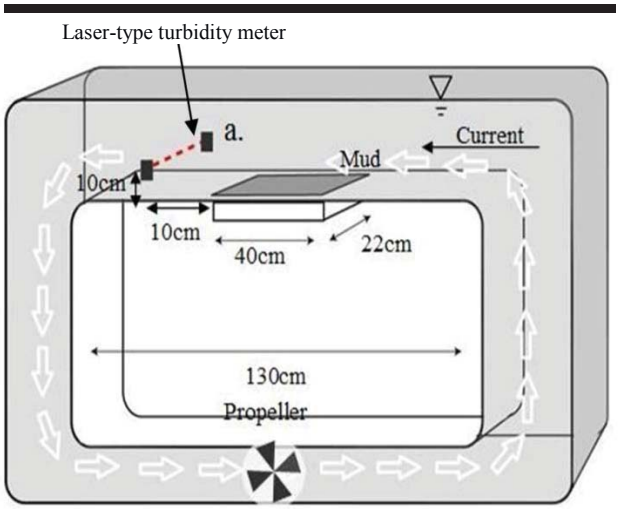

Figure 2. Concept of unidirectional flow channel for the experiment on resuspension of cohesive sediment in various salinity conditions.

Table 2. *Experimental cases for resuspension of cohesive sediment in various salinity conditions.*

Case (%)	Salinity of flowing water(psu)	Water content after Exp.
E1	0	65
E2	1	65
E3	10	65
E4	30	64

Settling experiment

Settling experiments were carried out in a cylindrical tank (Φ=20 cm, h=70 cm) using the sampled sediment. The sediment (100 g) was diluted in saline water (30 PSU) and fresh water, and thereafter the turbidity was monitored for 5 days at a 10 cm depth using the AAQ RINKO.

RESULTS

Variations in turbidity in Tenma River

Figure 3 shows the temporal-vertical profiles of (a) salinity, (b) turbidity and (c) temperature observed in Sep. 2008 and Sep. 2009. The salinity in the river water during both observations ranged from 5 to 25 PSU. Salinity increased with time in flood tide and decreased in ebb tide. Turbidity ranged from 2 to 20 FTU. Halocline was formed with an increase of salinity. An increase in turbidity to over 16 FTU was observed at the bottom layer of The Tenma River at the beginning of flood tide. Thereafter, the turbidity decreased gradually until it reached 4 FTU by the end of the ebb tide. The water temperature ranged from 23-26^{o}C, and no significant change was observed during the observation periods.

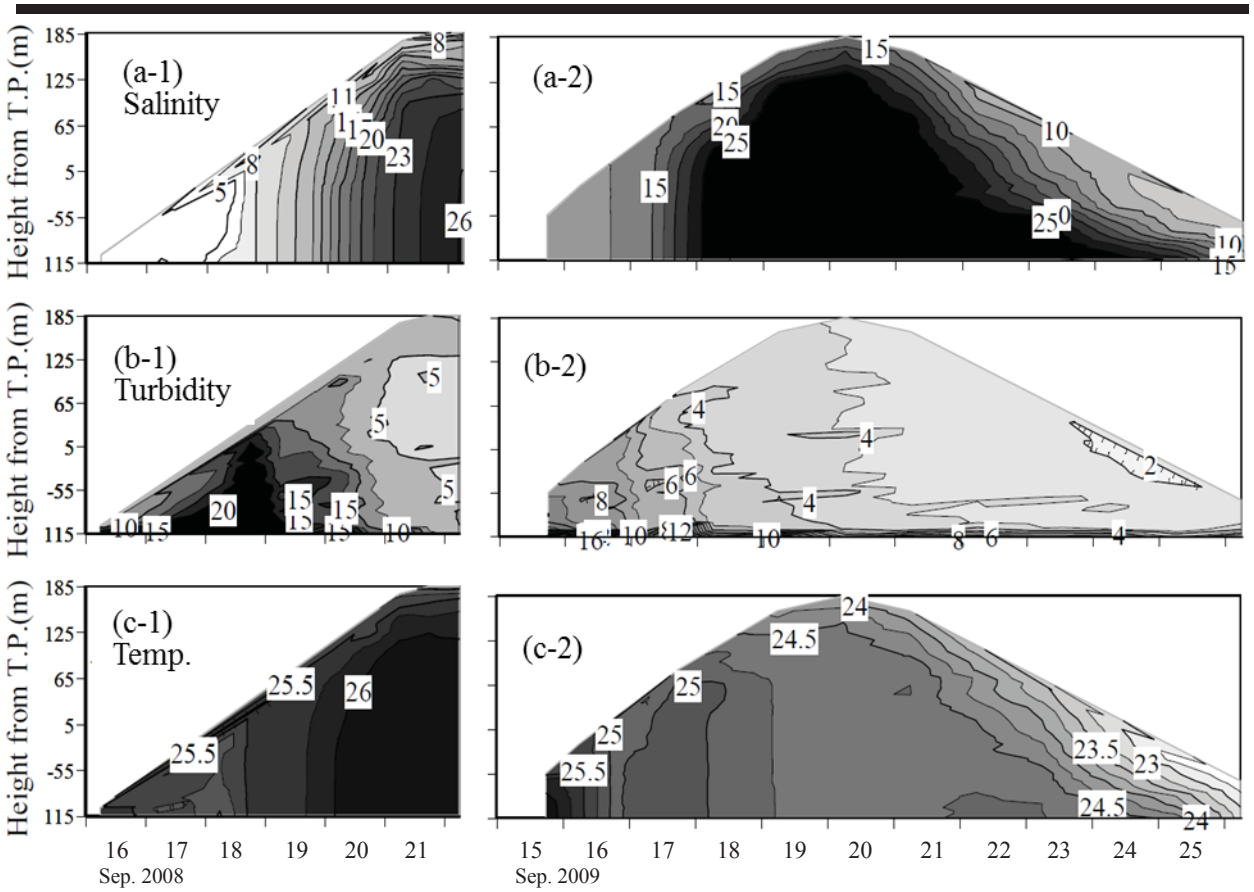

Figure 3. Temporal variations in (a) salinity, (b) turbidity and (c) temperature in the Tenma River.

Effect of salinity on liquid limit

Figure 4 shows the results of the liquid limit test in various salinity conditions using (a) the bentonite and (b) the cohesive sediment. The liquid limit of bentonite decreased by 140% with a 10% increase of salinity. The other experiments using cohesive sediment tended to show a liquid limit of lower magnitude, but the liquid limit decreased as the salinity increased.

Resuspension of cohesive sediment in various salinity conditions

Figure 5 shows the relationship between bottom shear stress and resuspension flux. Similar plots were created for all cases. The resuspension flux exponentially increased with increases of bottom shear stress. The resuspension flux showed large variations between the experimental cases, and was highest in E1 (fresh water) and lowest in E4 (salinity = 30 PSU). The critical erosion threshold regressed as the salinity decreased.

Settling of cohesive sediment in saline and fresh water

Figure 6 shows the experimental results of turbidity variations in fresh water and saline water. Turbidity in saline water decreased rapidly for 1 day and then gradually decreased until reaching ca. 0 FTU. In contrast, turbidity in fresh water decreased to 100 FTU in 1 day, and thereafter it decreased grad-

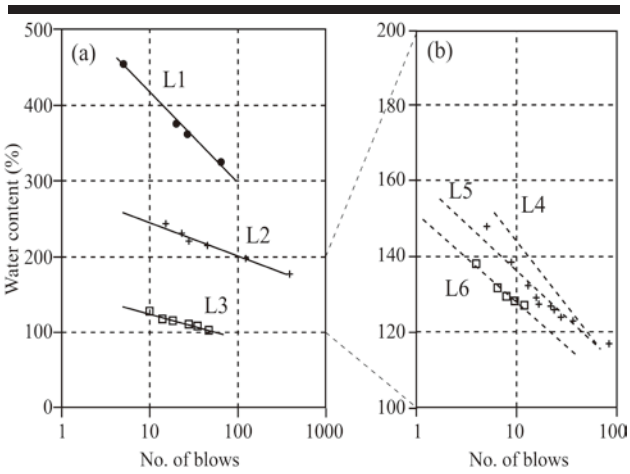

Figure 4. Results of liquid limit test using (a) bentonite and (b) cohesive sediment.

ually to ca. 70 FTU until the end of the experiment. Settling of the diluted sediment was faster in the saline water.

Figure 7 shows the relationship between salinity and turbidity observed at the bottom layer (20 cm height from river bottom) of the Tenma River. Turbidity ranged from 3-29 FTU during flood tide while it decreased to 1-3 FTU during ebb tide. Turbidity and salinity had positive correlations during the flood tide (r^2=0.6) but negative correlations during the ebb tide.

DISCUSSION

At low tide, the surface of the bottom sediment is contact with river water (fresh water) (Figure 3). Thereafter, the surface of the bottom sediment is in contact with saline water during flood tide. Turdibity varies in inverse proportion to salinity. Adachi and Iwata reported that the liquefaction of colloid is enhanced in saline conditions (Adachi and Iwata, 1997). The increase of salinity during flood tide may have increased fluidity by enhancing the cohesion of sediment particles (Figure 4). In other words, the low salinity of the river water on the river bottom may have reduced the critical shear stress of the bottom sediment and, as a result, the resuspension flux was enhanced (Kimiaghalam *et al*., 2015) (Figures 5 and 7). Thus turbidity is higher at the beginning of the flood tide when the salinity is less than 10 PSU (Figure 3). Thereafter, the particles of bottom sediment may have been deposited due to the intrusion of high salinity water after the maximum flood tide.

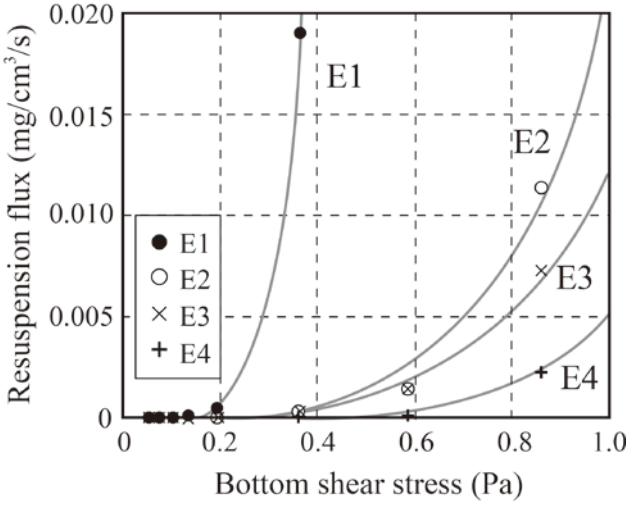

Figure 5. Relationship between bottom shear stress and resuspension flux.

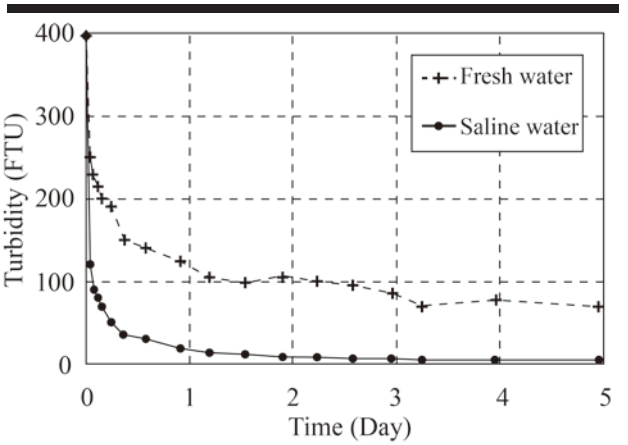

Figure 6. Temporal variations of turbidity in fresh water and saline water.

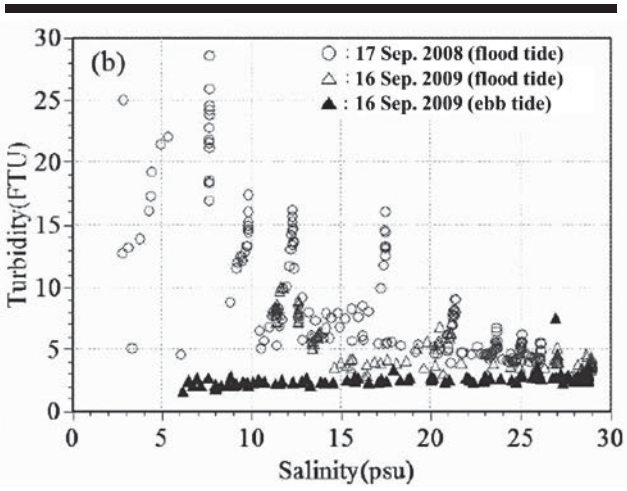

Figure 7. Relationship between salinity and turbidity observed at the bottom layer of the Tenma River.

Cohesive sediment tends to aggregate and form flocs in saline water. These flocs generally have a higher settling velocity than the constituent particles (Willem T.B. and Van der Lee, 2000). Thusm the higher settling velocity in saline water than in fresh water is likely due to the formation of flocs (Figure. 6). An increase of salinity enhances the cohesion of the cohesive sediment and leads to both the reduction of resuspension and enhancement of the settling of cohesive sediment.

The variation in the liquid limit of the cohesive sediment was lower than that of bentonite (Figure 4). This difference in the liquid limit between bentonite and cohesive sediment may have been due to the bonding structures of the particles. The bonding structures of the particles depend not only on the salinity, but also on the organic matter contained in the cohesive sediment. Another possible reason for this difference in the liquid limit could be the electrochemical force of the cohesive sediment. In cohesive soils, electrochemical forces acting on the particle surfaces cause a resistance to motion (Kimiaghalam *et al*., 2015).

CONCLUSIONS

We here analyzed the variations in turbidity under various salinity conditions in the Tenma River using field monitoring and examined the effects of variations in the salinity on the resuspension and settling of cohesive sediment.

It was found that turbidity varied in reverse proportion to the salinity in the Tenma River. Also, increases in salinity reduced the resuspension flux and enhanced the settling velocity of cohesive sediment by enhancing the cohesion between the particles. From the results obtained above, we concluded that salinity is an important factor in the transport of cohesive sediment in addition to shear stress and water content in estuaries and blackish rivers.

ACKNOWLEDGMENTS

This work was supported by the Pukyong National University Research Fund in 2014 (C-D-2014-1264). A part of this research was funded by a grant from the Yaaksu Research Foundation in 2014 (C-D-2014-1318), Korea.

LITERATURE CITED

Ali, A. and Lemckert, C. J., 2009. A traversing system to measure bottom boundary layer hydraulic properties. *Estuarine, Coastal and Shelf Science*, 83, 425-433.

Adachi, Y. and Iwata, S., 2009. *Tsutinokoroidogensyou*, 246-249. (in Japanese)

Black, K.S., 1998. Suspended Sediment Dynamics and Bed Erosion in the High Shore Mudflat Region of the Humber Estuary, UK. *Marine Pollution Bulletin*, 37, 122-133.

Chapman, P.M., 1986. Sediment quality criteria from the sediment quality triad: and example. *Environmental Toxicology and Chemistry*, 5, 957-964.

Danovaro, R.; Fraschetti, S., and Belgrano, A., 1995. The potential impact of meiofauna on the recruitrmemt of macrobenthos in a subtidal coastal benthic community of the Ligurian Sea (northwestern Mediterranean): a field study. *Preceeding of the XXVIII European Marine Biology Symposium* (Fredesborg, Demark), pp. 115-122.

Duineveld, G.C.A.; Lavaleye, M.S.S.; Berghuis, E.E.; Wilde, P.A.W.J.; Weele, J.; Kok, A.; Batten, S.D., and Leeuw, J.W., 1997. Patterns of benthic fauna and benthic respiration on the Celtic continental margin in relation to the distribution of phytodetritus. International Revue der Gesamten Hydrobiologie und Hydrographie, 83, 395-424.

Houwing, E.J., 1999. Determination of the Critical Erosion Threshold of Cohesive Sediments on Intertidal Mudflats Along the Dutch Wadden Sea Coast. *Estuarine, Coastal and Shelf Science*, 49, 545-555.

Jean, D.S. and Lee, D.J., 1999. Effect of salinity on expression dewatering of waste activated sludge. Journal of Colloid and Interface Science, 215(2), pp. 443-445.

Kim, K.H.; Abe, M.P.; Komai, K., and Hibino, T., 2009. The Effect of Pore Water Infiltration on the Re-suspension of Sea Bottom Sediment. *Annual Journal of Coastal Engineering*, 56, pp. 971-975 (in Japanese, with English abstract).

Kimiaghalam, N.; Clark, S.P., and Ahmari, H., 2015. An experimental study on the effects of physical, mechanical and electrochemical properties of natural cohesive soils on critical shear stress and erosion rate. *International Journal of Sediment Research*, in press.

Lee, I.C. and Hoshika, A., 2000. Prediction of oyster culture and water quality change in Hiroshima Bay development of water-sediment ecosystem model. Report of Chugoku National Industrial Research Institute, 54, pp. 33-41 (in Japanese, with English abstract).

Willem T.B. and Van der Lee, 2000. Temporal variation of floc size and settling velocity in the Dollard estuary. *Continental Shelf Research*, 20, pp. 1495-1511.

Journal of Coastal Research	SI	75	73-77	Coconut Creek, Florida	2016

Applicability of 3D Beach Evolution Model with Wave-current Interaction to River-mouth Bar Formation

Masamitsu Kuroiwa[†*], Yoko Shibutani[‡], Yoshiyuki Yasumoto[††] , Hajime Mase[§], and Yuhei Matsubara[†]

[†]Department of Civil Engineering
Tottori University,
Tottori, Japan

[‡] Office for Gender Equality
Tottori University,
Tottori, Japan

[††]Tottori Prefectual Government
Tottori, Japan

[§]Disaster Prevent Research Institute
Kyoto University,
Kyoto, Japna

www.cerf-jcr.org

www.JCRonline.org

ABSTRACT

Kuroiwa, M.; Shibutani, Y.; Yasumoto,; Mase, H, and Matsubara,Y., 2016. Applicability of 3D beach evolution model with wave-current interaction to river-mouth bar formation. *In:* Vila-Concejo, A.; Bruce, E.; Kennedy, D.M., and McCarroll, R.J. (eds.), *Proceedings of the 14th International Coastal Symposium* (Sydney, Australia). *Journal of Coastal Research*, Special Issue, No. 75, pp. 73-77. Coconut Creek (Florida), ISSN 0749-0208.

A coastal area model with wave-current interaction was presented, and then the performance and applicability of the numerical to morphodynamics around river mouths due to waves, wave-induced currents and river flows were investigated. First, model tests were carried out under a variety of wave and river discharge conditions to investigate their capability of predicting the formation of sand spit and terrace topographies. Second, model verification using a field site was conducted and the applicability was investigated. From the computed results, it was confirmed that the prediction of presented model had good qualitative agreement with an actual sand spit formation.

ADDITIONAL INDEX WORDS: *Morphological change, river-mouth, numerical model.*

INTRODUCTION

River-mouth bars, such as sand spits, occur in river mouths connecting to sea areas with low tidal range mainly owing to wave action. If the river discharge is small, then the river mouth closes. The prevention of flooding due to heavy rains and maintenance of the function of the river mouth requires the control of river discharge and prediction of morphodynamics around river mouths. The flow field around a river mouth is extremely complex owing to river discharge, waves, wave-induced currents, and tidal currents of different densities. Therefore, it is difficult to predict the flow field and morphodynamics around river mouths.

Topographic features around river mouths are roughly classified into the three types following the work by Sawaragi (1995). (1) In a river-flow-dominating type, deltas and terraces form in front of the river mouth. (2) In a wave-dominating type, a river-mouth bar and asymmetric bars form under normal wave conditions. A longshore bar forms under an extreme wave condition. (3) In a tidal-current-dominating type, sand bars form in the river under high tide and high wave conditions. Furthermore, topographic patterns are classified into 11 types based on the characteristics of incident waves, discharge flows and tidal currents.

Many 3D morphodynamic coastal area models for predicting medium-term beach evolution have been proposed. The coastal area models are classified into two types. Those of one type are based on a depth-averaged nearshore current model (e.g., Watanabe *et al*., 1986, Sawaragi *et al*., 1985, de Vriend *et al*., 1993). The others are based on a quasi-3D model (de Vriend *et al.*, 1988, Bos *et al.*, 1996, Pechon *et al*., 1996, Ranasinghe *et al*., 1999, Kuroiwa *et al*., 2000). We have proposed a coastal area model that can compute shoreline changes (Kuroiwa *et al*., 2004, 2006). These models have been applied to many practical problems, such as beach evolution due to the construction of coastal structures, coastal erosion and filling-up problem of ports.

Kuroiwa *et al.*(2008) tried to simulate sand bar formation around river-mouth, and investigated to the applicability to a field. However, morphodynamics involving the formation of river-mouth bars and blockage of river mouths due to waves, river flow and nearshore currents have not been fully investigated. And also, the wave-current interaction was not considered in the previous model, despite of strong river currents.

The purpose of this study is to develop a coastal area model that can predict 3D morphodynamics considering wave-current interaction around a river mouth. The coastal area model presented in this study is based on that developed by Kuroiwa *et al.* (2012). In this paper, model tests for the bathymetry involving a river mouth were carried out. Furthermore, the results of the presented model were compared with field data.

METHODS

In this study, Multi-directional random wave model based on the wave action balance equation proposed by Mase *et al*.(2004)

DOI: 10.2112/SI75-‘015.1 received 15 October 2015; accepted in revision 15 January 2016.
*Corresponding author: kuroiwa@cv.tottori-u.ac.jp

was added the 3D model presented by Kuroiwa *et al.*(2008). The presented model in this study consists of 4 modules as shown in Figure 1. Computations of the wave and nearshore current field are iterated in order to obtain a steady state.

The wave module is based on the multi-directional random wave model, which is based on the wave action balance equation associated with energy dissipation terms for the wave breaking and wave diffraction (Mase *et al.*, 2004). The governing wave action balance equation with the wave diffraction effects is

$$\frac{\partial(C_x N)}{\partial x}+\frac{\partial(C_y N)}{\partial y}+\frac{\partial(C_\theta N)}{\partial \theta} = \frac{\kappa}{2\sigma}\left\{\left(CC_g\cos^2\theta N_y\right)_y-\frac{1}{2}CC_g\cos^2\theta N_{yy}\right\}-\varepsilon_b N \quad (1)$$

where N is the wave action density, defined as the wave energy density divided by the angular frequency σ relative to the current (Doppler shift). The horizontal coordinates are x and y, and θ is the wave direction measured counterclockwise from the x-axis. κ is the diffraction intensity parameter, which is set to 2.5. C and C_g are the wave celerity and group velocity, respectively.

In this module, the wave-current interaction was calculated. The nearshore current module is based on the Hybrid model with Q-3D mode and 2DH mode, proposed by Kuroiwa *et al.* (2006). The Q-3D is selected when the undertow filed in the surf zone should be estimated under stormy waves and then the Q-3D mode is based on the model using the fractional step method.

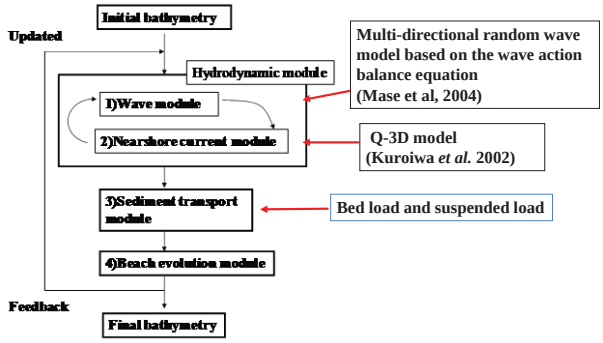

Figure 1. Computational flow of the presented three-dimensional morphodynamic model.

The total sediment transport rates in the cross-shore and longshore directions are defined as the sum of the sediment transport rates due to waves and nearshore currents with river flow. The total sediment transport rate is

$$\vec{q}=\vec{q_w}+\vec{q_c}+\vec{q_s} \quad (2)$$

where $\vec{q_w}$ is the bed load due to the wave component and $\vec{q_c}$ is the bed load due to the steady current component at the sea bottom. The bed loads due to waves and steady currents are based on the Watanabe model:

$$\vec{q_w}=A_w\left(u_*^2-u_{*c}^2\right)\vec{\hat{u}_w}/g \quad (3)$$

$$\vec{q_c}=A_c\left(u_*^2-u_{*c}^2\right)\vec{U_b}/g \quad (4)$$

where A_w and A_c are dimensionless coefficients, u_* is the friction velocity, u_{*c} is the critical friction velocity, and $\vec{U_b}$ is the steady current vector with river flow. The coefficients are given by a function of the median diameter d_{50} (Shimizu *et al*, 1996) as

$$\left.\begin{aligned} B_w &= C_w\left(\sqrt{d_{50}}/w_f\right)^3 \\ A_w/B_w &= w_f\sqrt{0.5f_{cw}}/\left\{(1-\lambda)s\sqrt{sgd_{50}}\right\} \\ A_c &= 10A_w \end{aligned}\right\} \quad (5)$$

where C_w is a dimensionless coefficient, w_f is the fall velocity of sand, f_{cw} is the sea-bottom friction factor, λ is the porosity of the bed, and s is the specific gravity in the water.

In this study, the friction velocity u_* presented by Sawaragi *et al.* (1985) is adopted to consider the river flow:

$$u_*^2=\frac{1}{2}f_w F_b^2 \quad \left(f_w=0.02\right) \quad (6)$$

$$F_b^2=\frac{1}{2}\hat{u}_w^2+\frac{2}{\pi}\hat{u}_w^2\left\{|U\cos\theta|+|V\sin\theta|\right\}+\frac{\left(U^2+V^2\right)}{4} \quad (7)$$

The suspended sediment transport rate $\vec{q_s}$ is determined by multiplying local vertical profiles of current velocities and sediment concentrations and then integrating from the sea bottom to the mean water surface. The sediment transport rate is expressed as

$$\vec{q_s}=\int_{-h}^{\bar{\eta}}C(z)\vec{U}dz \quad (8)$$

where $\vec{U}$ is the local nearshore current velocity, which is determined from the quasi-3D current velocity. The concentration $C(z)$ can be expressed as

$$C(z)=C_b\exp\left(-w_f/\nu_s\cdot z\right) \quad (9)$$

C_b is the concentration at which the sediment starts moving and ν_s is the diffusion coefficient of sand, which is estimated from the sea-bottom friction velocity and the dissipation rate due to wave breaking. C_b is found using the Shields parameter ψ:

$$C_b=C_s\frac{(\psi-0.05)\nu}{b\sqrt{sgd_{50}}} \quad (10)$$

where b is estimated as $b = 100d_{50}$, C_s is a dimensionless coefficient and ν is the kinematic viscosity.

To calculate shoreline changes, the sediment transport rate in the run-up region is determined, by using a simple method proposed by Kuroiwa *et al.* (2004). Changes in water depth are calculated using the equation for the conservation of sediment transport, presented by Watanabe *et al.* (1986).

RESULTS

In this study, a model test associated with sand recycling between two groins with an artificial reef and field verification were conducted.

Model Tests

Model tests for uniform bathymetry and a river mouth were conducted to investigate the performance of the present model. The sea-bottom slope in the sea area was 1/50 and the width of the river was 100m. The computation area extended 900m along the shore and 900m across the shore. The grid sizes of Δx and Δy were set to 10m. The wave and river-flow conditions in the model tests are listed in Table 1. The model tests focused on the four types of morphodynamics.

In Table 1, U_{rf} represents the depth-averaged river flow velocity at the up-stream boundary of the river and *Cw* and *Cs* are dimensionless coefficients for the sediment transport formulas given as Eqs. (5) and (10). For cases 1–4, the topographic changes after 180 days were simulated. The hydrodynamic computations were carried out 90 times to obtain a final topography.

Table 1. *Computational conditions of model tests*

Case	H_s (m)	T_s (s)	θ	Ur(m/s)	Cw	Cs
1	1.5	7.0	0	0.0	0.2	0.01
2	1.5	7.0	20	0.0	0.2	0.01
3	1.5	7.0	0	0.6	0.2	0.01
4	1.5	7.0	20	0.6	0.2	0.01

Figures 2(a) and (b) show computed significant wave height distribution and depth-averaged steady current vectors under oblique incident wave, in the initial bathymetry. Computed results for Case 2 and Case 4 are without and with river flow,respectively. We found that longshore current occurred in both cases. In Case 2, a circulation flow occurred around river-mouth. Therefore, wave height became large owing to the offshore current generated in front of the river-mouth. From the computed results for Case 4, the wave height in front of the river-mouth became more lager than that of Case2, owing to strong river flow of 0.6 m/s. These computed results indicated that it is important to take account for the wave-current interaction for computation of hydrodynamics around river-mouth.

Figure 3 shows the computed bathymetries at 180 days later for Case 1, 2, 3 and 4. In Case 1, sand spits on both sides of the river mouth were reproduced, and in Case 2, an asymmetrical sand spit due to the longshore current was reproduced. The width of the channel in both cases became narrow. Terrace also reproduced in fron of the river-mouth, despite no discharge from river. These computed results indicate that the present model might be able to predict the blockage of a river mouth. From the computed results for river flow of 0.6 m/s as shown in Figs.3 (c) and (d), it can be seen that sediment was not so trapped at the river mouth. Therefore, the magnitudes of sand spits at the river mouth were smaller than those in Case 1 and 2. Furthermore, in both cases, terraces formed in front of the river mouth.

Figure 4 shows an example of temporal variation of sand bar formation in the river-mouth, regarding with Case 2. It was found that the presented model can demonstrate a sand spit gradually was formed due to wave action. The time variation of a sand spit formation was successfully simulated.

Field Verification

To verify the applicability of the presented model to actual sand spit formation in the field, it was applied to morphodynamics of the Ara River, which is located in Niigata Prefecture, facing the Sea of Japan. Figure 5 shows aerial photos taken in 1980, 1985, and 2002. A sand spit formed at the river mouth. In 1985, a jetty on the left bank side and groins on the right bank side were constructed. After the construction of the groins, the width of the sand spit became small.

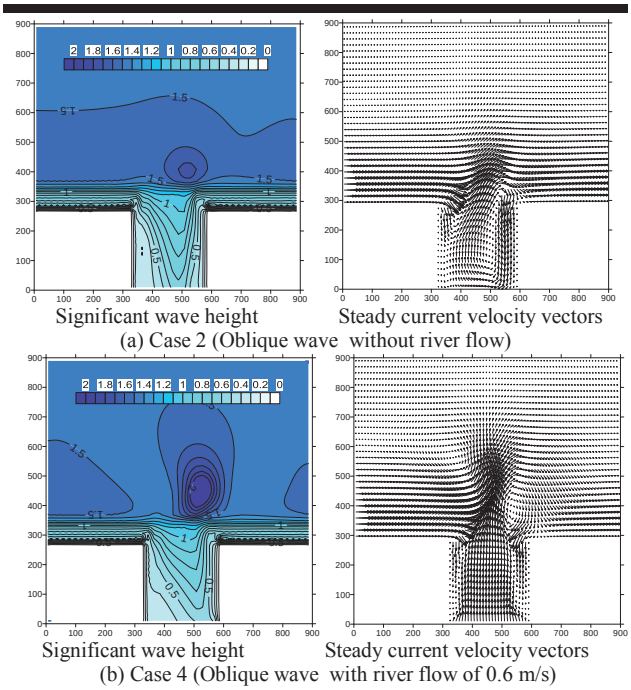

Figure 2. Computed Significant wave height distribution and Steady current velocity vectors for Case 2 and Case 4.

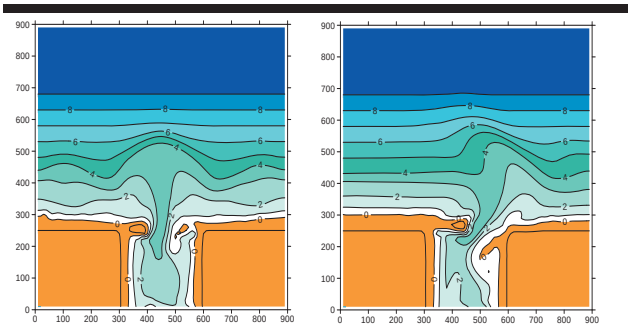

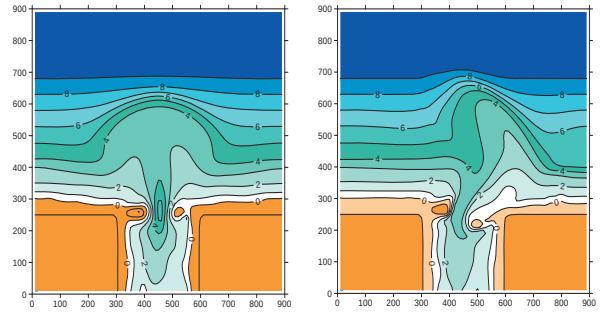

(c)Case 3 (d) Case 4

Figure 3. Computed bathymetries at 180 days later for Case 1 and Case 2, without river flow.

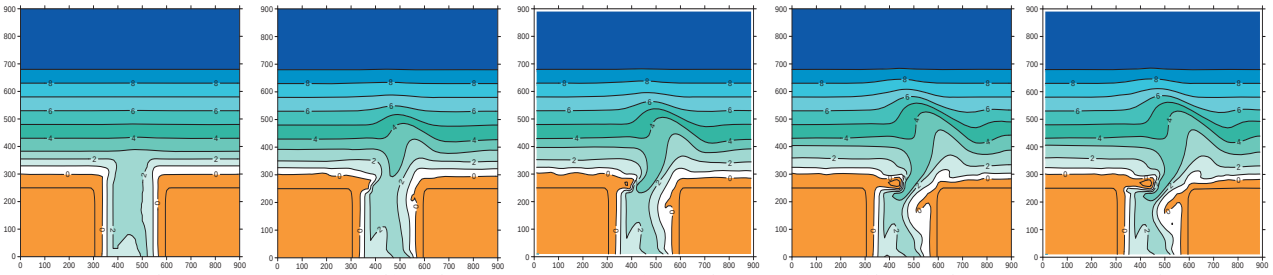

(a)10 days (b) 80 days (c) 120 days (d) 140 days (e) 180 days

Figure 4. Temporal variation of sand bar formation under oblique incident wave condition, without river flow for Case 2.

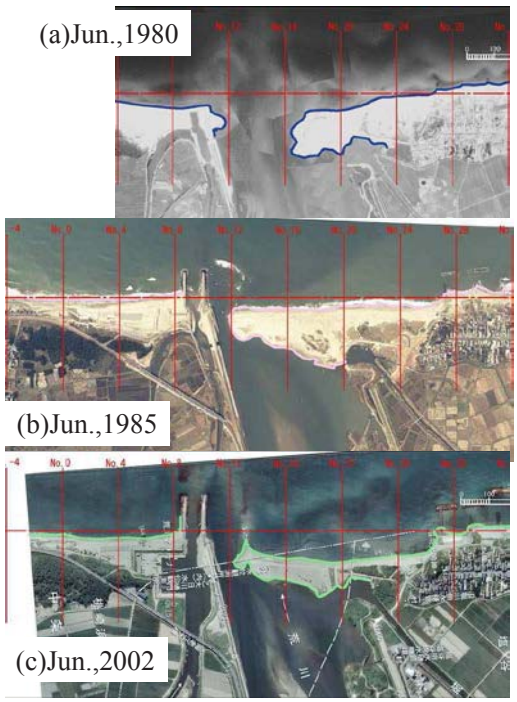

Figure 5. Aerial photos around Ara River mouth, taken in 1980, 1985, and 2002.

We firstly attempted to simulate the sand spit formation without coastal structures such as the situation in 1980, and with the jetty and groins such as the situation in 2002, as shown in Fig.5. Modeled initial bathymetries were prepared to investigate the model applicability, because of the lack of a detailed bathymetry dataset. Therefore, morphological changes in winter were computed. Significant wave height input at offshore boundary and period were set at 1.67 m and 6.79 s, according to the conditions as energy averaged-wave height in winter seasons, according to Kuroiwa *et al.*(2008).

Figure 6 shows the modeled initial bathymetry corresponding to the aerial photos in 1980, and computed steady current vectors for the initial bathymetry.

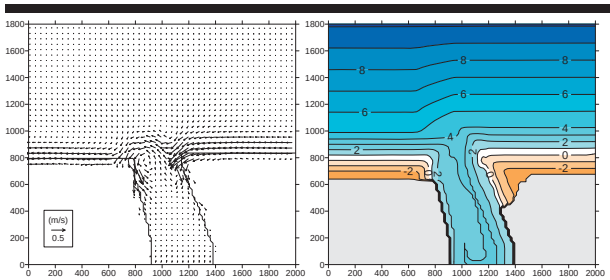

Figure 6. Computed current velocity and initial bathymetry , corresponding to sand bar formation, as shown in areal photo in 1980.

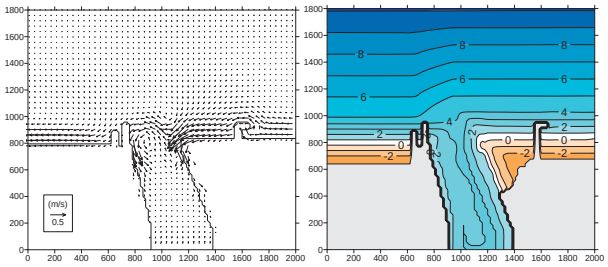

Figure 7. Computed current velocity and initial bathymetry , corresponding to sand bar formation, as shown in areal photo in 2002.

Figure 8 shows the results, corresponding to the aerial photos in 2002. We found that sand bar formed in both cases and the width of the river-mouth became narrow. These sand bar formed by sediments owing to longshore currents. The computed results are qualitatively agreement with field sites. However, the width of sand bar, regarding the case without jetty and groin in 1980, was very small.Whereas, regarding with sand bar formation in 2002, the computed sand bar shows good agreement with field site.

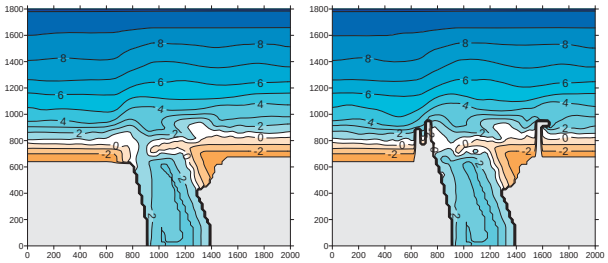

(a) Sand bar in 1985 (b) Sand bar in 2002

Figure 8. Computed bathymetries , corresponding to sand bar in 1985 and 2002.

CONCLUSIONS

In this paper, a 3D morphodynamic model for considering wave-current interaction was presented.

First, model tests for four cases, which are with and without river flow, under normal and oblique incident waves, were carried out to investigate the performance of the present model. In the case where river flows were dominant, a terrace in front of the river mouth was predicted. For the case of oblique incident waves, there were longshore currents and an asymmetric sand spit formed at the river mouth. The time variation of a large sand spit formation was successfully simulated. The computed results have qualitatively good agreement with an actual sand spit.

Second, the model was applied to the morphodynamics of the Ara River to verify the applicability of the present model to a field site. It was confirmed that the sand spit at the Ara River formed owing to wave action during winter seasons. The computed sand spit formation qualitatively agreed with the field formation.

ACKNOWLEDGMENTS

This work was a joint study between Tottori University and Kurayoshi Office, Chugoku Regional Development Bureau, Ministry of Land, Infrastructure, Transport and Tourism. We would like to appreciate the support of research funds from the Kurayoshi Office.

LITERATURE CITED

Bos,J.K.; Roelvink, J. A., and Dingemans, M.W., 1996. Modeling the impact of detached breakwaters on the coast. *Proceedings of 25th International Conference on Coastal Engineering*, ASCE, pp.2022-2035.

De Vriend, H.J. and J.S.Ribberink., 1988. A quasi-3D mathematical model of coastal morphology. *Proceedings of 21th International Conference on Coastal Engineering*, ASCE, pp.1689-1703.

De Vriend, H.J.; Zyserman,J.; Nicholson,J.; Roelvink,J.A.; Pechon,P., and Southgate, H.N., 1993. Medium-term 2DH coastal area modeling, *Coastal Engineering*, 21, 193-224.

Kuroiwa,M.; Noda,H.; Son, C.B.; Kato,K., and Taniguchi,S., 2000. Numerical prediction of bottom topographical change around coastal structures using quasi-3D nearshore current model. *Proceedings of the 27th International Conference on Coastal Engineering*, pp.2914-2927.

Kuroiwa K.; J. W. Kamphuis; Kuchiishi,T.; Matsubara,Y., and Noda,H., 2004. Medium-term Q-3D coastal area model with shoreline change around coastal structures. *Proceedings of 29th International Conference on Coastal Engineering*, ASCE,

Kuroiwa,M.; Kuchiishi,T., and Matsubara,Y., 2006. Prediction System of 3D Beach Evolution with 2DH and Q3D Hydrodynamic Modes. *Proceedings of 16th International Offshore and Polar Engineering Conference*, pp.751-757.

Kuroiwa, M.; Kuchiishi , T.; Kato,K.; Sunagawa,S., and Matsubara, Y., 2008. Applicability of coastal area model to mophodynamics around river mouth. *Proceedings of the 31st International Conference on Coastal Engineering*, pp.2218-2230.

Kuroiwa,M.; Khaled Seif, A.; Matsubara,Y., and Ichimura,Y., 2012. A coastal area model considering wave-current interaction and its application to wide-crested submerged breakwater. *Proceedings of 33rd Conference on Coastal Engineering*, Paper#: sediments. 12.

Mase, H.; Yuhi, M.; Amamori, H., and Takayama, T., 2004. phase averaging wave prediction model with breaking and diffraction effects in wave-current coexisting field. *Annual Journal of Coastal Engineering*, JSCE., 51, No.1, pp.6-10. (In Japanese).

Pechon, P. and Tession,C., 1996. Numerical modelling of bed evolution behind a detached breakwater. *Proceedings of 25th International Conference on Coastal Engineering*, ASCE,pp.2050-2062.

Ranasinghe, R.; Pattiaratchi,C., and Masselink,G., 1999. A Morphodynamic model to simulate the seasonal closure of tidal inlets. *Coastal Engineering.*, Vol. 37, 1-36.

Sawaragi,T.; Lee, J.S., and I. Deguchi. 1985. A new model for prediction of beach deformation around river mouth. *Proceedings of International Symposium on Ocean Space Utilization*'85, 229-236.

Sawaragi,T., 1995. Coastal engineering -waves, weaches, wave-structure interaction. *Development in Geotechnical Engineering*, 78, Elsevier, pp.304-308.

Shimizu,T.; Yamada, A., and Watanabe, A., 1996. Coefficient and cross-shore distribution of alongshore sediment transport rate. *Proceedings of Coastal Engineering*, JSCE, Vo.43, 571-575.(in Japanese)

Watanabe; A.; Maruyama, K.; Shimizu,T., and Sakakiyama,T., 1986. A numerical prediction model of three-dimensional beach deformation around a structure. *Coastal Engineering in Japan*, 29, pp.179-194.

Journal of Coastal Research	SI	75	78-82	Coconut Creek, Florida	2016

Biological response of a coastal plain estuary to torrential episodes: a modelling study

Longo, R.S. [†], Picado, A.[†], Vaz, N.[†], Dias, J.M.[†,*]

[†] CESAM, Departamento de Física, Universidade de Aveiro, 3810-193 Aveiro - Portugal

www.cerf-jcr.org

www.JCRonline.org

ABSTRACT

Longo, R.S., Picado, A., Vaz, N. and Dias, J.M., 2016. Biological response of a coastal plain estuary to torrential episodes: a modelling study. *In:* Vila-Concejo, A.; Bruce, E.; Kennedy, D.M., and McCarroll, R.J. (eds.), *Proceedings of the 14th International Coastal Symposium* (Sydney, Australia). *Journal of Coastal Research*, Special Issue, No. 75, pp. 78-82. Coconut Creek (Florida), ISSN 0749-0208.

Estuaries are highly dynamic systems with an important impact on biogeochemical cycles and primary production, which may be affected and modified in a climate change context, namely due to extreme rainfall events. This study aims to research chlorophyll-a (Chl-a) and nutrients dynamics in the Tagus estuary under extreme freshwater discharge in a climate change context, using a 2D biophysical model. Three scenarios were set changing the inputs from the main tributaries – Tagus and Sorraia rivers. First, a scenario with one day of extreme discharge for both rivers was considered. Next, and in order to understand the importance of each river, two more scenarios were set considering the extreme discharges separately. Results show that Chl-a concentrations follow the same trend as the imposed discharges, however with a delay of one day. The results also reveal that the biogeochemical characteristics of the Tagus estuary are mainly influenced by the Tagus River inflow. Moreover, in the scenario where the extreme discharges are imposed for both rivers, Chl-a levels increase in the entire estuary and consequently a decrease in nitrate concentrations is observed. Otherwise, phosphate concentrations slightly increase. This suggests primary producers inside the estuary preferentially consumes nitrate, at a higher rate than it is being loaded.

ADDITIONAL INDEX WORDS: *Chl-a concentration, nutrients, biogeochemical model, Tagus estuary.*

INTRODUCTION

Estuaries are unique environments where sea water meets freshwater, dictating the interactions between land and sea. Among the most important processes occurring in these systems are biogeochemical cycles and primary production. All these interactions and reactions affect life in a large scale and are becoming progressively threatened over the years due to human and natural stresses. Given the vast influence that biogeochemical cycles have on phytoplankton growth/decay and primary production, and on marine life in general, the study of the threats that they are facing or will face in the next years becomes a matter of great interest. Primary production carried out by phytoplankton is the first level of the trophic chain. All the other levels depend on it and their evolution and follow its trends. Primary production in marine environment is the result of the water masses movement coupled to nutrient and light availability. These elements can also limit production, either by absence or excess, making the study and the attempt to predict these processes highly relevant to become aware of the threats faced by estuaries. One of the main actual threats is climate change, which has a direct impact in the mean sea level and especially in the freshwater discharging into estuaries, which modulates the nutrient cycles and generation of phytoplankton, dictating primary production in these environments. In this setting, this study aims to research the biological response of Tagus estuary to extreme freshwater discharge induced by torrential episodes in a climate change context.

The Tagus Estuary (Figure 2 - D3) is the largest estuarine system in Portugal, being located near Lisbon (38°44' N, 9°08' W). It has a total surface area of 320 km^2, a mean volume of 1900×10^6 m^3 and is a relatively shallow mesotidal estuary dominated by a semi-diurnal tidal regime with a mean tidal amplitude of 2.2 m (Mateus and Neves, 2008; Mateus *et al.* 2012; Valentim *et al*., 2013). About 20 to 40% of the estuarine area is intertidal, composed mainly by mudflats (Mateus and Neves, 2008; Valentim *et al*., 2013). The hydrodynamic conditions are determined by the balance between the inflow of saline water from the Atlantic Ocean and the riverine discharges from the three contributors (Vaz *et al*. 2011): Sorraia, Trancão and Tagus Rivers (Figure 2 - D3). The Tagus River is the most significant in terms of freshwater flow, with an annual average of 400 m^{3}s^{-1} (Neves, 2010), and integrates urban, industrial and agricultural effluent discharges. Sorraia and Trancão rivers are comparatively small, with average annual discharges of 35 and 2.5 m^{3}s^{-1}, respectively.

The interaction between meteorological conditions and riverine inputs induces high seasonality to the hydrodynamic and biogeochemical estuarine conditions (Mateus and Neves, 2008). Primary production limiting nutrients are known to be nitrogen and silica, but they are usually available inside the

DOI: 10.2112/SI75-016.1 received 15 October 2015; accepted in revision 15 January 2016.

*Corresponding author: joao.dias@ua.ptl

estuary (Mateus, 2012). Nutrient limitations may be found significant only in lower estuarine areas and mostly during summer. Consequently, light is believed to be the main factor controlling the primary production on Tagus Estuary (Mateus and Neves, 2008).

METHODS

The numerical model MOHID (Martins *et al*., 2001) was used to study the impact of extreme freshwater events on Chl-a and nutrients distribution along the Tagus estuary.

Initially, a simulation covering the period from April 2003 to December 2004 was performed and the biogeochemical properties, including ammonia, nitrate, Chl-a and oxygen concentration, were qualitatively compared with measured data at four stations distributed along the NE-SW direction of the estuary (S1, S2, S3 and S4: Figure 2 - D3). The data used for this comparison are described in Mateus *et al*. (2012) and Mateus and Neves (2008). Only the results for S2 are presented herein (see Figure 3).

As the main goal of this study consists in researching the biological response of Tagus estuary to extreme freshwater discharge induced by torrential episodes, three scenarios were set defining extreme values to the main tributaries flow: Tagus and Sorraia. Trancão river was not included in these scenarios considering its flow negligible and consequently without impact in the estuary biogeochemistry. Primarily, a scenario considering one day of extreme discharge for the Tagus (6000 m^3s^{-1}) and Sorraia (200 m^3s^{-1}) rivers was considered (Scenario #1). Next, in order to assess the impact on the estuarine biogeochemistry of the freshwater discharge from each river separately, two more scenarios were defined: one considering only high discharge from Tagus (Scenario #2) and other only high discharge from Sorraia (Scenario #3).

Freshwater discharges considered in this study are depicted in Figure 1 and were set based on fluvial regime climatology: between days 6 and 8 discharges from both rivers linearly increase from a base flow (250 m^3s^{-1} for Tagus and 25 m^3s^{-1} for Sorraia) to a peak value (6000 for Tagus and 200 m^3s^{-1} for Sorraia), remaining constant during a day (from day 8 to 9) and then decreasing, during a day, to the base flow again. This pattern was defined to assess the estuarine response to a torrential episode and evaluate its behaviour under the relaxation period. All simulations were performed for 20 days periods, to evaluate Chl-a and nutrients concentration distribution and temporal evolution as well as the relaxation period to extreme discharges. From numerical predictions, Chl-a and nutrients (nitrate and phosphate) maxima concentrations were computed for each cell of the estuarine numerical grid for three different periods: before the flow peak (A), during the peak (B) and after the peak (C) (see Figure 1).

Model description and set up

MOHID (Martins *et al.* 2001) is a three-dimensional baroclinic finite volume model, designed for coastal and estuarine shallow water applications (Valentim *et al*., 2013). The model solves the three-dimensional incompressible primitive equations and assumes the hydrostatic equilibrium as well as Boussinesq and Reynolds approximations (Valentim *et al.* 2013).

Along the Portuguese coast, MOHID has been previously successfully applied to coastal lagoons: Ria de Aveiro (Vaz *et al.*, 2005, Picado *et al*. 2013) and Ria Formosa (Martins *et al*., 2004) and to estuaries: Sado (Martins *et al.*, 2001) and Tagus (Vaz *et al*., 2011, Vaz and Dias 2014), showing a good performance when simulating flows in shallow water systems. Regarding the biogeochemical processes, a few works were carried out with MOHID. For instance, Mateus *et al*. (2012) studied the influence of physical, chemical and environmental parameters on the biogeochemistry of the Tagus estuary.

In this study, a coupled circulation and biogeochemical model was implemented through a downscaling methodology, which consists on simulating hydrodynamics and water quality on a local scale based on information provided by large-scale models, considering three nested domains (Figure 2). In the first domain (D1) is used a 2D barotropic tidal driven model forced by FES2004 global solution, which covers up most of the Atlantic Coast (from 33 to 50ºN and 0 to 13ºW) and has a horizontal resolution of ~6 km. The time step used was 180 s. The second domain (D2) comprises a region from 8º30' to 10º30'W and 36 to 40ºN, with a horizontal resolution of ~1.6 km and a time step of 60 s. Finally, the third domain (D3) includes Tagus estuary area (from 38º30' to 39ºN and 8º42'W to 9º30'W). It has a numerical grid with 335×212 cells with a horizontal resolution of 200 m. The time step was set to 15 s and the horizontal viscosity to 5 $m^2\ s^{-1}$. D3 is forced by the tide from D2. Both D2 and D3 are two-dimensional barotropic models.

Tagus River discharges were provided by Sistema Nacional de Informação de Recursos Hídricos (SNIRH, www.snirh.pt). Due to the lack of data for Sorraia and Trancão rivers, climatological values were imposed. Atmospheric forcing consisting in wind, radiation, air temperature, relative humidity and precipitation data was imposed with hourly temporal resolution. These data were measured at a nearby meteorological station: Estação Meteorológica da Guia (http://www.mohid.com/tejo-op/).

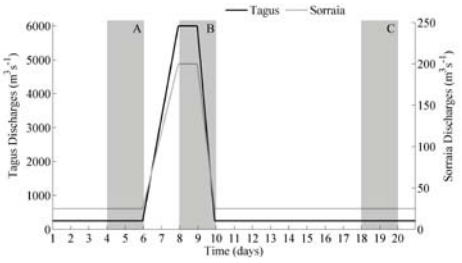

Figure 1. Discharges (m^3s^{-1}) imposed on Tagus and Sorraia rivers. A, B and C represent the periods for which the results are evaluated.

The biogeochemical model was only considered in the D3 domain, through the module Life (Mateus, 2012). Life is a multi-parameter biogeochemical model that is coupled to MOHID and simulates nutrients, primary producers, secondary producers and decomposers. The model has a decoupled carbon-nutrients dynamics with explicit parameterization of carbon, nitrogen, phosphorus, silica and oxygen cycles. It considers two major groups of producers, diatoms and autotrophic flagellates,

and also the microbial loop dynamics and organic matter components (Mateus *et al*., 2008). Chlorophyll synthesis is simulated according to Geider *et al.* (1997) and the threshold for limitation is defined by the Redfield ratio (Mateus *et al*. 2008).

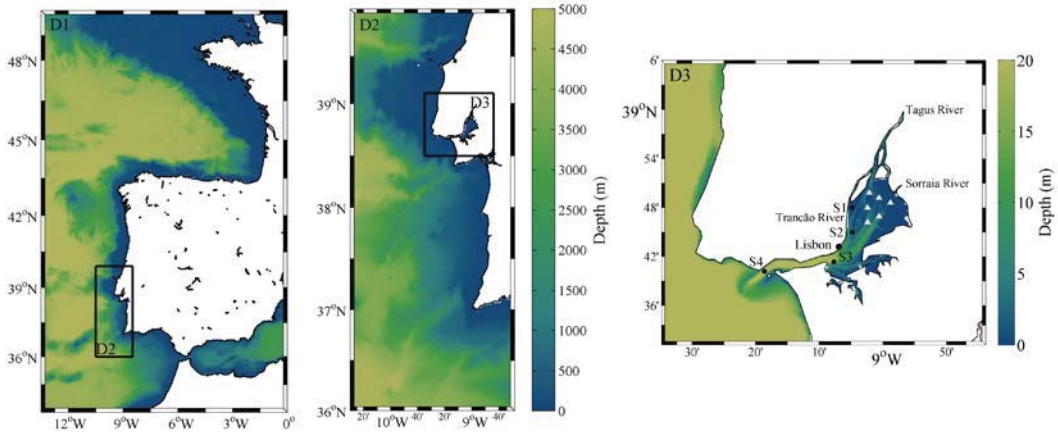

Figure 2. Three nested domains used for the numerical simulations, with bathymetry in meters. Location of the calibration stations (S1, S2, S3 and S4) and location of the local station of time series analysis (white triangles).

Model validation

The implementation of the hydrodynamic model used in this study was already validated in Mateus *et al*. (2012), and therefore it was assumed that physical parameters are being correctly simulated. Thus, only the biogeochemical parameters are qualitatively compared with measurements. Results are presented in Figure 3,
where the grey area comprises the daily maximum and minimum model prediction for each property and the dark grey line the daily mean. Measured data are represented by the dots.

Model predictions show strong seasonality of ammonia concentration, with high values in winter and low in spring and summer (see Figure 3), showing good agreement with observations and demonstrating that observed trends are correctly reproduced by the model. However predictions are slightly lower than the observations, meaning that model captures ammonia dynamics. Model nitrate concentrations also show a marked seasonality, with higher values in winter (>1 mg m^{-3}) than in summer (0.5 mg m^{-3}). According to Figure 3 it can be concluded that model represents well the nitrate dynamics, but slightly overestimating observations. In general, predicted oxygen reproduces well the data, with the exception of the first measurement. Finally, the predicted Chl-a concentration also shows high seasonality, with high values occurring in late spring/early summer, with maximum values of 4 mg m^{-3}.In this case, model results are, in general, lower than observations. The same data set was used by Mateus and Neves (2008) to validate a different implementation of MOHID in the study area and similar results were achieved.

RESULTS

The results are primarily analysed in terms of Chl-a time series, once this variable is assumed as a natural bio-indicator considering its complex and rapid response to changes in environmental conditions (Livingston, 2001).

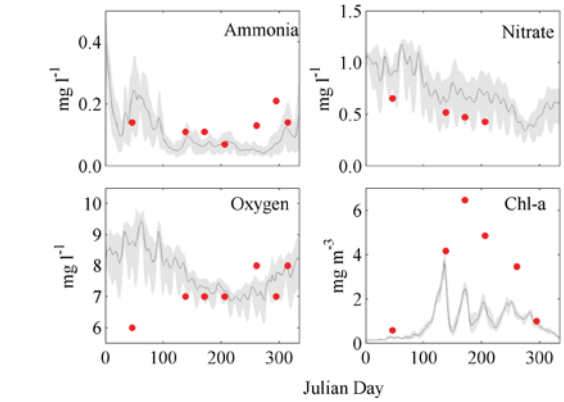

Figure 3. Comparison between ammonia, nitrate, oxygen (mg l^{-1}) and Chl-a (mg m^{-3}) model predictions (grey area and line) with observation (dots), for S2 station. The days are referred to 2004.

Figure 4 depicts the mean Chl-a concentration time series at six stations located in the central estuary (triangles in Figure 2 - D3). Chl-a concentration follows the same trend as the imposed discharges for Scenarios #1 and #2, however a time delay close to one day was found (discharges increase from day 6 and Chl-a from day 7 – Figure4). Two days after the imposed discharge, Chl-a levels remain high, oscillating around 4 mg m^{-3} during approximately 3 days, then it decrease to the base value, with concentrations lower than 0.5 mg m^{-3} after seven days. It is noteworthy that the mean values of Chl-a concentration after the relaxation period are slightly lower than the ones observed before the imposed extreme discharges. For Scenario #3, when an extreme discharge is imposed only in Sorraia River, the pattern is completely different: Chl-a concentration slightly increase from day 7 to the end of simulation.

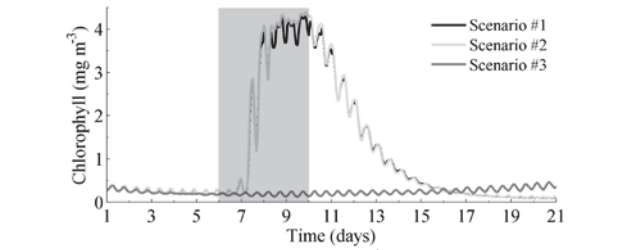

Figure 4. Mean time series of Chl-a (mg m^{-3}) for the Scenario #1, #2 and #3. The shaded area represents the period of extreme discharges.

Based on these results, Chl-a and nutrients (nitrate and phosphate) maxima were assessed only for Scenario #1 and for three periods (see Figure 1): one before the high discharge (A), other during the peak (B) and a third period after the relaxation period (C).

Before the extreme discharge (period A) were found low maxima Chl-a concentrations in the whole estuary (Figure 5 – upper panel A), with values ranging from 0.2 mg m^{-3} on the middle estuary to 1.0 mg m^{-3} on the upper estuary (right next to the Tagus River mouth) and on the estuary mouth. As the Chl-a concentrations are low, nutrients (nitrate and phosphate) are expected to be high. Indeed, high nitrate concentrations are found in the whole estuary, with the highest values (2.0 mg m^{-3}) detected near Sorraia mouth (where Chl-a is lower). Phosphate concentrations are relatively uniform along the estuary, with mean values about 0.8 mg m^{-3}. These results are in accordance with Mateus *et al*. (2012), which found relatively low concentrations during winter in the estuary and concluded that the nutrient concentrations tend to be low with the increased distance from the upper estuary areas.

For period B, a significant rise of the Chl-a maxima was observed (Figure 5, top panel, B), with values ranging from 3.5 to 5.0 mg m^{-3} on the entire estuary, except for the lower areas where minor values are observed (between 1.0 and 1.2 mg m^{-3}). At this period the nitrate concentration (Figure 5 - middle panel, B) decreases significantly on the upper estuary (from values higher than 1.0 to 0.5 mg m^{-3}), next to Tagus River mouth, exactly on the same areas where Chl-a concentration increase. Otherwise, the maxima phosphate concentrations (Figure 5 - bottom panel, B) slightly increase in the middle estuary (approximately 0.15 mg m^{-3}), relative to the maxima found for period A, and at the mouth of the estuarine channel (more than 0.4 mg m^{-3}).

Finally, after the relaxation period Chl-a maxima concentrations (Figure 5 – top panel, C) drop to values lower than the those observed before the extreme discharge, ranging from 0.2 at the Tagus River mouth to 0.5 mg m^{-3} at the estuary mouth. Regarding the nitrate, the maxima concentrations drop along the entire estuary, except next to Tagus River mouth, where an increase of approximately 0.2 mg m^{-3} is observed. Otherwise, no significant changes are observed in phosphate concentrations from period B to C.

DISCUSSION

The transfer of nutrients, organic matter and other materials from terrestrial to estuarine systems is a key feature governing the ultimate source of productivity (Jickells, 1998; Granskog *et al*., 2005). In the Tagus estuary, river discharge can be considered the major input of nutrients into the system, carrying higher concentrations of nitrate than phosphate (Ferreira *et al*. 2003).

According to the previous results achieved for Tagus estuary the freshwater inflow is a key driver of Chl-a and nutrients distribution along the entire estuary.

Moreover, results also suggest that Tagus River discharge has greater influence in nutrients and Chl-a patterns than Sorraia. These results are corroborated by Mateus and Neves (2008), that based on measured data analysis found a clear influence of the Tagus River discharge in the estuary biogeochemistry.

Additionally, when extreme discharges are imposed on Tagus and Sorraia rivers, maxima Chl-a concentration clearly rise in the entire estuary and consequently the nitrate values drop, suggesting that the nitrate is being consumed at an higher rate than it is being loaded. Otherwise, a slightly increase in the phosphate concentrations after the imposed extreme discharge is observed, suggesting that the primary producers inside the estuary preferentially consumes nitrate.

CONCLUSIONS

Three scenarios were designed and their results analysed to study the influence of torrential episodes and consequent extreme fluvial discharges on the biogeochemistry of the Tagus estuary. Results demonstrate that Chl-a concentration evolution depends essentially on extreme discharges from Tagus River, with a time response of approximately one day after the maximum freshwater flow and a relaxation time of seven days. Under extreme discharge from Sorraia River, Chl-a slightly increased along time, but with concentrations much smaller than achieved under Tagus discharge. Therefore, it may be concluded that the biogeochemical characteristics of the estuary are mainly influenced by the Tagus River discharge, while Sorraia River do not induce major changes in the assessed properties.

Under extreme discharges from Tagus River was found that after the relaxation period Chl-a maxima concentration drop to values lower than observed before this event, while nitrate slightly increases. This may be due to the decrease of phytoplankton transported from rivers and/or to its mortality. The phytoplankton mortality increases the dissolved organic and particulate organic materials, which attenuate the light penetration in the water column. Consequently, although there are nutrients available, Chl-a decreases to such low values as light is the main factor limiting primary production in Tagus estuary (Mateus and Neves, 2008).

ACKNOWLEDGMENTS

This study was supported by the National Foundation for Science and Technology (FCT), CESAM (UID/AMB/ 50017/2013). A.P. was supported by the Fundação para a Ciência e Tecnologia doctoral grant (SFRH/BD/79920/2011), Quadro de Referência Estratégico Nacional (QREN) and Programa Operacional de Potencial Humano (POPH), co-founded by Fundo Social Europeu and by Ministério da Educação e Ciência (MEC).

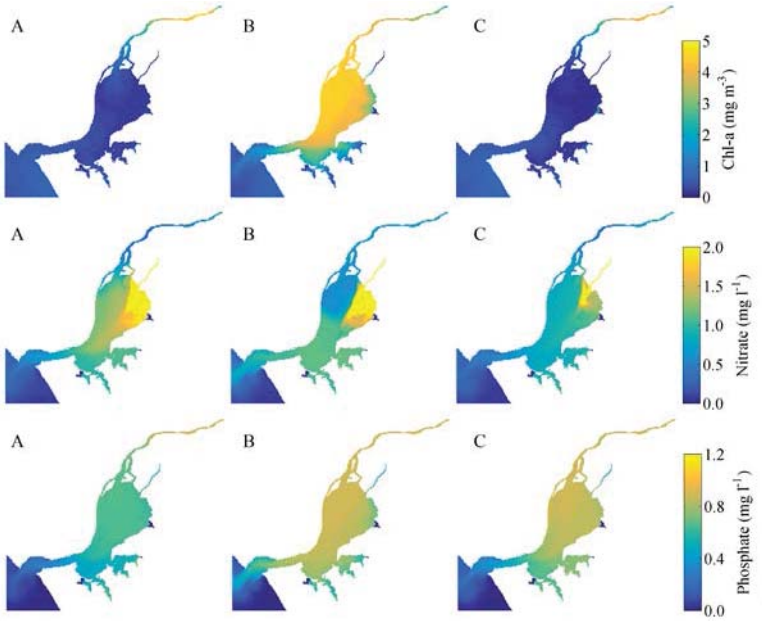

Figure 5. Maxima Chl-a (top panel), nitrate (middle panel) and phosphate (bottom panel) concentration for Scenario #1, for periods A, B and C (Figure 2).

LITERATURE CITED

Ferreira, J.G.; Simas, T.; Nobre, A.; Silva, M.C.; Schifferegger, K., and Lencart-Silva, J., 2003. *Identification of SensitiveAreas and Vulnerable Zones In Transitional and Coastal Portuguese Systems. Application of the United States National Estuarine Eutrophication Assessment to the Minho, Lima, Douro, Ria de Aveiro, Mondego, Tagus, Sado, Mira, Ria Formosa and Guadiana systems.* INAG/IMAR.

Geider, R.J.; MacIntyre, H.L. and Kana, T.M., 1997. Dynamic model of phytoplankton growth and acclimation: Responses of the balanced growth rate and the chlorophyll a: carbon ratio to light, nutrient-limitation and temperature. *Marine Ecology-Progress Series,* 148(1-3), 187-200.

Granskog, M.A.; Kaartokallio, H.; Thomas, D.N., and Kuosa, H., 2005. Influence of freshwater inflow on the inorganic nutrient and dissolved organic matter within coastal sea ice and underlying waters in the Gulf of Finland (Baltic Sea). *Estuarine, Coastal and Shelf Science*, 65, 109-122.

Jickells, T.D., 1998. Nutrient biogeochemistry of the coastal zone. *Science*, 281, 217-222.

Livingston, R.J., 2001. *Eutrophication processes in coastal systems: Origin and succession of plankton blooms and effects on secondary production in Gulf Coast estuaries*. Center for Aquatic Research and Resource Management. Florida State University, CRC Press, 327pp.

Martins, F.; Leitão, P.; Silva, P., and Neves, R., 2001. 3D modelling in the Sado estuary using a new generic vertical discretization approach. *Oceanologica Acta*, 24(1), 1-12.

Mateus, M. and Neves, R., 2008. Evaluating light and nutrient limitation in the Tagus Estuary using a process-oriented ecological model. *Journal of Marine Engineering and Technology*, No. A12.

Mateus, M., 2012. A process-oriented model of pelagic biogeochemistry for marine systems. Part I: Model description. *Journal of Marine Systems* 94, S78-S89.

Mateus, M.; Vaz, N., and Neves, R., 2012. A process-oriented model of pelagic biogeochemistry for marine systems. Part II: Application to a mesotidal estuary. *Journal of Marine Systems,* 94, S90-S101.

Neves, F.J., 2010. Dynamics and Hydrology of the Tagus Estuary: Results from in Situ Observations. Lisbon, Portugal: University of Lisbon, PhD thesis. 210p.

Picado, A.; Lopes, C.; Mendes, R.; Vaz, N., and Dias, J.M., 2013. Storm surge impact in the hydrodynamics of a tidal lagoon: the case of Ria de Aveiro. *Journal of Coastal Research*, SI 65, 796-801.

Valentim, J.M.; Vaz, N.; Silva, H.; Duarte, B.; Caçador, I., and Dias, J.M., 2013. Tagus estuary and Ria de Aveiro salt marsh Dynamics and the impact of sea level rise. *Estuarine, Coastal and Shelf Science*, 130, 138-151.

Vaz, N.; Dias, J.M.; Leitão, P., and Martins, I., 2005. Horizontal patterns of water temperature and salinity in an estuarine Tidal channel: Ria de aveiro. *Ocean Dynamics*, 55, 416-429.

Vaz, N.; Mateus, M., and Dias, J.M., 2011. Semidiurnal and spring-neap variations in the Tagus Estuary: Application of a process-oriented hydro-biogeochemical model. *Journal of Coastal Research*, SI 64, 1619–1623.

Vaz, N. and Dias, J.M., 2014. Residual currents and transport pathways in the Tagus estuary, Portugal: the role of freshwater discharge and wind. *Journal of Coastal Research*, SI 70, 610-615.

Journal of Coastal Research	SI	75	83-87	Coconut Creek, Florida	2016

Depositional evolution in a estuarine lagoonal system under a port influence in Northeastern Brazil

Silvio E. M. Martins[†*], Roberto L. Barcellos[†] Manuel J. Flores-Montes[†] and Elvis J. de França[**]

[†]Geological Oceanography Laboratory (LABOGEO), Oceanography Department Federal University of Pernambuco

[*] Sedimentology Laboratory, Institute of Engineering and Geosciences Federal University of Western Pará Santarém, Brazil

[**] Nuclear Sciences Regional Center, North-East (CRCN-NE), Recife, Brazil

www.cerf-jcr.org

www.JCRonline.org

ABSTRACT

Martins, S. E. M; Barcellos, R. L; Flores-Montes, M. J. and França, E. J. 2016. Depositional evolution in a lagoonal estuarine system under a port influence in Northeastern Brazil. *In:* Vila-Concejo, A.; Bruce, E.; Kennedy, D.M., and McCarroll, R.J. (eds.), *Proceedings of the 14th International Coastal Symposium* (Sydney, Australia). *Journal of Coastal Research*, Special Issue, No. 75, pp. 83-87. Coconut Creek (Florida), ISSN 0749-0208.

The Holocene evolution reconstruction corroborates to understand sediment dynamics and, recent anthropogenic environmental changes; in addition, may subsidize the future prospects of its development. The aim of this work is to elaborate a historical comparative analysis of the total organic matter content (TOM), calcium carbonate ($CaCO_3$) and grain size variation in a estuarine environment and adjacent inner shelf area under influence of Recife Port (8°03'S/34°53"W), Northeastern Brazil. Two sediment cores were collected (Jun/2013), one (1.26m long) in the inlet of the estuarine system (T2E); and another (1.30m long) in a sheltered area of a breakwater adjacent to the estuary mouth (T3E). The sedimentation rate, measured based on breakwater building (1909), was 1.18 cm.year^{-1} in T3E and 0.81 cm.year^{-1} in T2E. The cores presented preservation of structures indicative of waves and currents processes, such as erosive surfaces, linsen bedding, flaser bedding, and wavy bedding, environment features of shallow platform. Both cores presented variations in sediment composition with an essential carbonate sandy base ranging upward to a terrigenous mud on their tops. The change in sediment composition indicates environmental changes such as the increase in the sediment suspension concentrations, directly influenced by changes in coastal engineering in the Recife Port. The results indicate how important local rivers sediments input and estuarine processes are to deposition features in the estuarine lagoonal system, like the mud trapping and preservation in the inner shelf shallow areas adjacent to the Recife Port.

ADDITIONAL INDEX WORDS: *Tropical Estuary, Temporal evolution, Cores, Total organic matter, $CaCO_3$.*

INTRODUCTION

The Holocene evolution reconstruction corroborates to understand sediment dynamics and recent anthropogenic environmental changes; it also may subsidize the future prospects of its development (Delgado *et al*, 2012).

The understanding of sedimentation in port areas is necessary to implement management strategies, develop economic activities, and provide a correct environmental forecast for portuary regions.

Port and estuary relate in a conflicting way. The estuary has complex dynamics, where two water bodies of different natures meet, the sea water and the continental water. Estuary systems are responsible for dissipating organic matter to other coastal enviromenments, relating directly with coral reefs, tidal flats, mangroves, among other coastal and marine environments (Algesten *et al*, 2003; Muñoz, 2004; Lamb *et al.*, 2006).

In contrast, port areas tend to suffer several interventions and coastal engineering works, such as the construction of jetties, groynes, breakwaters (Guerra and Marçal, 2010). These interventions influence the natural dynamics of coastal environments. There may be changes in the physical patterns of hydrodynamics, sedimentation, erosion, and coastal currents.

The estuarine-lagoonal system subject of this study follow the same characteristics. The estuarine system Capibaribe River/Beberibe River/Pina Basin is located in Recife Metropolitan Region (8º03'S/34º53'W) and it is of great importance for Brazilian Northeast economic development. Port activities in the region date back to the Sixteenth Century, with the arrival of the first European vessels.

Conversely, Port of Recife structures, in its current patterns, date from 1909, with the publication of Decree no. 7447, when the company *Societé de Construction du Port from Pernambuco* was allowed to build the new structures. Among them, there was the rise of low walls on top of the natural reef which is parallel to Recife's coast, as well as its extension; also the construction of jetties at the Isthmus of Olinda and the breakwater at the English Bank, located east of the estuarine system exit (Castro, 1976).

According to Barcellos *et al.* (2009), Holocene evolution studies at decadal timescales are used as a comparison parameter with the current sedimentary process and its understanding, supporting information for future perspectives of its evolution. To understand the processes that influence a depositional system as well as the impact on the structures and sedimentary composition, sedimentological tools are used, as well as geochemical proxies (such as total organic matter (TOM) and calcium carbonate contents), mineralogical, palynological, and so forth (Seshan, Natesan and Deepthi, 2010).

DOI: 10.2112/SI75-017.1 received 15 October 2015; accepted in revision 15 January 2016.

*Corresponding author: oceanografofisico@gmail.com

Figure 1. Study area.

The aim of this work is to elaborate a historical comparative analysis of the total organic matter content (TOM), calcium carbonate ($CaCO_3$) (Ingram, 1971), grain size variation in an estuarine environment and adjacent inner shelf area under influence of Recife Port (8°03'S/34°53"W), Northeastern Brazil.

METHODS

The study area comprises the estuarine system of the Capibaribe and Beberibe Rivers and the Pina Basin (Figure 1), located in the central portion of the Recife Metropolitan Region (RMR), Pernambuco State, Northeastern Brazil (8°03'S/34°53'W). It is a densely urbanized site (whole RMR: 3,859,845 hab. in 2013) associated to a tropical (25°C/>2000mm.year^{-1}) mesotidal (2,5m) coastal plain estuarine complex. The Capibaribe is the larger river in the Pernambuco coastal zone; 240km long and with 19m^3.s^{-1} of average flow. The shallow estuarine basin (< 14m depth), classified as partially-mixed, receives inputs from different anthropogenic sources as urban and industrial (chemical, textile, food and drink industries) sewage/runoff and hydrocarbons from Recife Port activities (Oliveira, 2014).

The Capibaribe River estuary extends more than 15 km, mostly within urban areas in the city of Recife. The Capibaribe/Beberibe/Pina estuarine lagoonal system is a coastal plain, sheltered by a 3.7 km length breakwaters in its lower portion adjacent to the inlet at Atlantic Ocean and another 1.3 km length breakwaters (English bank) in inner shelf (Figure 2A and 2B).

Two sediment cores were collected (Jun/2013), one (1.26m long) adjacent to the inlet of the estuarine system (T2E); and another (1.30m long) in a sheltered area of breakwater adjacent to the estuary mouth (T3E). The sections were opened longitudinally, photographed, macroscopically described as textures, structures and sedimentary composition. They were sub-sampled in 2cm deep layers for calcium carbonate analysis (Ingram, 1971), sedimentary organic matter, grain size by sieving and pipetting (Müller, 1967). After obtaining the results, the data were analyzed according to Folk and Ward (1957) statistical parameters. For data analysis, Pearson correlation coefficient (r) was used.

Figure 2. Output of the lagoon estuarine system (A), bordered by the port jetties and the breakwater at the English Bank (B). Pictures taken by Roberto Barcellos in 06/2011.

RESULTS

The sedimentation rate, was 1.18cm.year^{-1} in T3E and 0.81cm.year^{-1} in T2E. Both cores presented variations in sediment composition with an essential carbonate sandy base ranging upward to a terrigenous mud on their tops. This limit is at 126cm depth in T3E, while in T2E (next lower estuary) it is observed at 85cm depth. (Figure 3)

It was observed in the T3E section a higher concentration of carbonate in the gravel fraction (r = 0.75) and a moderate relationship with the sands (r = 0.48), while T2E section presented significant correlations among the carbonates and both gravel (r = 0.77) and sand (r = 0.76) fractions.

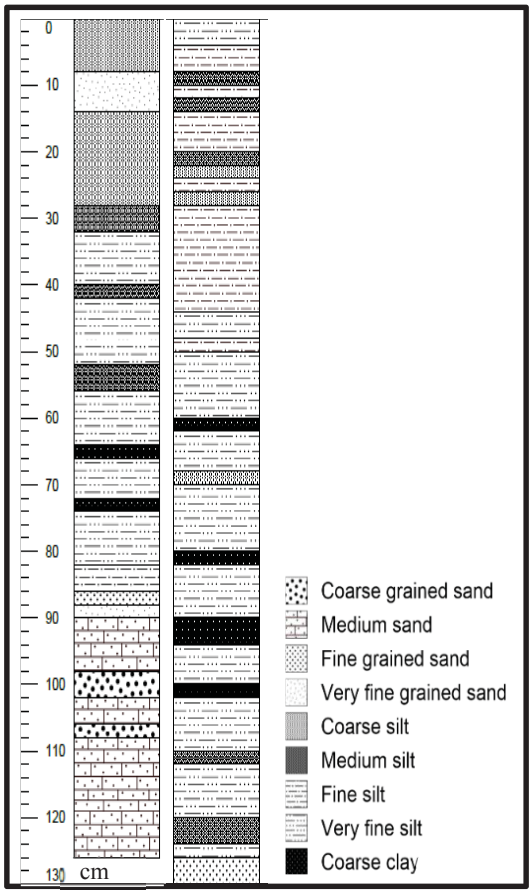

Figure 3. Cores T2E (left) and T3E (right).

The correlations of TOM and both sand (r = -0.44) and mud (r = 0.44) were moderate for T3E. The T2E the mud layers were significantly correlated with TOM levels (r = 0.76). Mud levels in the sedimentary composition are inversely related to $CaCO_3$ levels (r = -0.79). There was a moderate correlation between the sands and the sediments sorting (r = 0.62).

It is observed a decrease in the average grain size until the base of T3E core, while T2E keeps an average of coarse sand to medium sand downward to near 92 cm deep when the average grain size decreases until it becomes very close to the value observed for T3E at 80 cm depth. These average values keep varying from coarse silt to very fine silt until 22 cm deep, when the average grain size differ and T2E values become close to very fine sand while the average size of T3E sediment becomes close to fine silt size

We observed flaser bedding structures at 90 cm depth in T2E core. In addition, we identified linsen between parallel laminations. At 59 and 42 cm depth we noticed wavy bedding structures. Another linsen bedding was present between parallel laminations at 32 cm. Sediments presented reverse graded bedding between 30 and 20 cm deep. We recorded normal graded bedding across 20 cm and the top, with flaser bedding at 12 cm and another linsen bedding at 2 cm depth.

The T3E core presented wavy laminations above an erosive bedding from 126 to 117 cm depth. Some parallel laminations were observed between 113 and 110 cm, and 97 and 93 cm depths. Tubes of organisms were observed at 45, 60 and 70 cm deep. We observed lamination bedding with coarsening-upward between 25 and 14 cm depths.

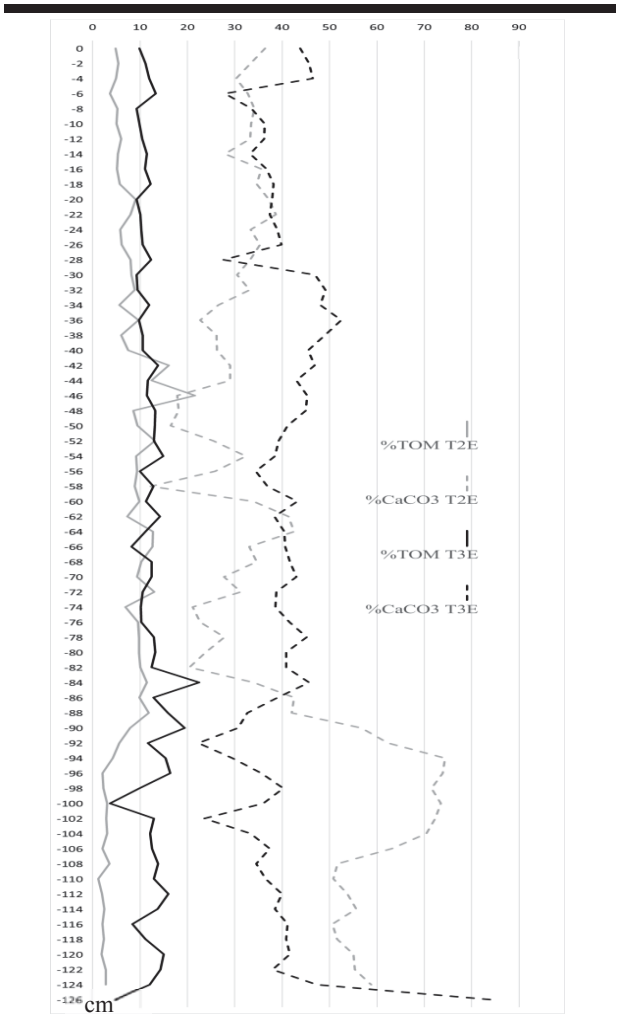

Figure 4. Vertical distribution of TOM and $CaCO_3$ composition at T2E (grey) and T3E (black) cores.

The organic matter presented high rates in the inner shelf deposits (T3E). At the inlet of the estuarine system (T2E), most of the pelitic material was concentrated between 30 and 80 cm levels, being very close to the levels that had the highest TOM concentration, mainly observed between 20 and 90 cm deep (Figure 4).

Carbonates reached the highest concentration at the sedimentary composition of baseline levels, being between 90 and 126 cm at T2E (Figure 4).

Lower TOM levels are associated with basal carbonate facies, and also with T3E at 1 m depth, with silty-mud composition. It was observed at some depth levels inversions of TOM minimum peaks and $CaCO_3$ maximum (1.26m, 1m, 0.86m, 0.82m, 0.66m, 0.56m 0.32m, 0.20m and 0.8m), indicating a greater marine influence on depositional process. In the other way, layers such as 1.2m, 1.12m, 1.02m, 0.96m 0.90m, 0.62m, 0.54m 0.28m e 0.06m, presented evidences of TOM contents increase with decrease of the calcium carbonate percentages.

This indicates less marine influence and the increase of the fluvial contribution in the studied system. Such layers depths may be associated with major flooding events of the Capibaribe River Basin in the years 1914, 1920, 1924, 1950, 1966, 1975, 2000 and 2010 (Diário de PE, 2004). The depths in the cores related to the floods dates of Capibaribe River system presented high correlation between the degree of sediments sorting and the sand ($r = 0.82$), as well as between the sorting and the mud ($r = -0.81$). The correlation between $CaCO_3$ parameter with TOM contents presented a fair correlation: $r = 0.40$ (Figure 4).

DISCUSSION

With regard to coastal processes, the T3E core preserved waves and currents structures, characteristic of shallow platform environment, such as erosive surfaces and wavy bedding; observed at its base. Commonly massive bedding structures indicate fast sedimentation, with insufficient time to develop pattern bed. These features are common in turbid current deposits, grain flows and detritus (Pettijohn, 1975; selley, 2000).

The flaser bedding cross stratification structures in T2E core, the linsen bedding, and the levels of wavy bedding indicate the intensity of alternating influence on coastal dynamic processes in the vicinity of the studied inlet. Variations of reverse graded bedding to normal graded bedding near the top indicate, in the first case, increasing of the flow rate during settling. It may indicate that the lower portion or the sediment mass flow deposits are flow deposits of grains and detritus. Layers normally graded deposited resulting from flows that lose competency, then with flow deceleration coarser particles are deposited, followed by thinner particles; typical layering of storm current deposits (Pettijohn, 1975; selley, 2000).

The parallel lamination observed in both cores is related to suspension deposition of silt, or by low-density currents caused by high input of fine sediments from the estuarine system.

The sedimentation rates obtained are equivalent to other rates observed in Brazilian estuaries, for example: Cananéia (SP): (0.5 – 1 $cm.year^{-1}$, according to Saito *et al*, 2001); São Francisco, (SE/AL): (1.66 $cm.year^{-1}$, according to Santos 2007); Caravelas, (BA): (0.67 $cm.year^{-1}$, according to Neto, 2008); Amazonas, (PA/AP): (1.76 $cm.year^{-1}$, according to Nery, 2009).

Pearson's correlations ($r > 0.75$) indicated marine dominance in sands and gravels depositional processes for both sections of the cores. The significant data correlation for mud and organic matter content of T2E section ($r = 0.76$), near the inlet of the studied system, denote the open relation of these parameters and indicates as its main influence of sedimentary nature, the one coming from the contribution of continental pelitic matter.

The moderate and low correlations between TOM levels and other parameters for T3E section ($-0.44 < r < 0.44$) indicate the high influence of the continental shelf in dynamic processes on marine material sedimentation at this protected area to the west of English Bank breakwater. It is due to S/N coastal current that it tends to lead the plume of suspended terrigenous mud embedded with TOM towards north of the studied system, adjacent to the north groin. Such current also explains well sorted sands concentration for T3E ($r = 0.62$).

At depths related to flood events of the Capibaribe River, it was observed an increase of sediments sorting with the increase of sands percentage ($r = 0.82$), indicating a rise and energy stability in the environment so the grain-size sorting occurs. On the other hand, an inverse correlation with the mud ($r = -0.80$) indicates that the energy increase will also suspend pelitic sediments previously deposited. This increase of the load of suspended sediments and decreasing the sorting of these sediments, given that there will be more mix of different grain-size, as noted by Qiao *et al* (2013) and Colby and Boardman (1989) in port areas.

The direct and positive relation between carbonate and TOM contents corroborate the hypothesis of flood events depths indicators in the studied system as it indicates an increase of TOM and terrigenous mud, regardless of the presence of carbonates from the continental shelf.

The high TOM levels in the lower estuary indicate the strong contribution of the Capibaribe River/Pina Basin and the Beberibe River, as also observed by Oliveira *et al*. (2014). The sudden change in the gravelly carbonate sediments composition to continental pelitic sediments, close to the base of core sections, denotes a period of approximately one century of sedimentation considering that the changes undergone by the depositional environment is directly associated with the breakwater construction and extension in 1909 (Castro, 1976). It shows an artificialized deposition system and with high potential for retention of muddy sediments of predominantly estuarine origin, although the carbonate contents are relatively high (40%) as observed by Smith *et al.* (2009) and Seshan *et al*. (2010). This process denotes also marine influence on local sedimentary processes (Dahm, 2011).

The energy variation due to sediments depositional pattern in some levels of T2E section is directly related to the location of this core. The T2E is under the influence of energy increase due to swell waves that are reflected as they pass by English Bank breakwater, located east of the T3E core.

According to Pedrosa (2007), the coastline north of Olinda Jetty is indicated as an erosion area, as corroborate the data of research conducted by University of Grenoble (Castro, 1976), which state that the erosion processes were intensified from changes in the coastline in the Port of Recife area.

Therefore, the sediments trapping occur within the system, reducing the amount of sediments towards North, for the

beaches and other coastal systems of Olinda city, located adjacent to Recife habour area.

CONCLUSIONS

The results indicate how important local rivers sediments input and estuarine processes are to deposition features in the estuarine lagoonal system, like the mud trapping and preservation in the inner shelf shallow areas adjacent to the Recife Port. The change in sediment composition indicates environmental changes such as the increase in the sediment suspension concentrations, directly influenced by changes in coastal engineering in the Recife Port. These modifications, such as the construction of jetties and breakwaters created areas of lower energy, which facilitated the deposition of terrigenous fine sediments and thus increased the TOM levels and decreased levels of carbonates. The data will be best complemented with isotopic composition information ($\delta^{13}C$ e $\delta^{15}N$) of sedimentary organic matter, which are being processed.

ACKNOWLEDGMENTS

The authors would like to acknowledge the support of National Council for Scientific and Technological Development (CNPq), Nuclear Sciences Regional Center -NE (CRCN-NE), Science and Technology Support Foundation of the Pernambuco State (FACEPE) and the Project: Carbon Transport in coastal region of Pernambuco State (CARECOS). FACEPE / FAPESP (APQ 080-1.08 / 11). The authors would like to thank Betânia Martins for the development of the maps. Luciana Dantas, the technician of geological oceanography laboratory. The colleague Diego Xavier, by the help in describing the cores and the trainees Lucas Alves and Ricardo Torres-Homem. Thanks are also due to Mr. Gustavo Barcellos and Ms. Bia Dias, for the revision of the text.

LITERATURE CITED

Algesten, G.; Sobek S.; Bergström, A.-K.; Ågren, A.; Tranvik, L. J.; and Jansson, M., 2003. Role of lakes for organic carbon cycling in the boreal zone. *Global Change Biology*, 10, 141–147.

Barcellos, R.L.; Camargo, P.B.; Galvão, A., and Weber, R.R., 2009. Sedimentary organic matter in cores of Cananéia-Iguape lagoonal-estuarine system, São Paulo State, Brazil. *In*: Silva, C. P. (ed.), *Proceedings, 10th International Coastal Symposium. Journal of Coastal Research,* SI 56, 1335-1339.

Castro, L. A., 1976. Porto do Recife: Síntese retrospectiva de sua evolução. *Revista Quebra-mar*, 2(4), 16-19.

Colby, N. D. and Boardman, M. R., 1989. Depositional evolution of a windward, high-energy lagoon, Grahams Port, San Salvador, Bahamas: *Journal of Sedimentary Petrology*, 59, 819-834.

Dahm, J., 2011. *Shoreline changes – at river and tidal entrances. Dune restoration trust of New Zealand*. Rotorua: Scion Digital Print Centre. 8p

Delgado, J; Boski, T*;* Nieto, J. M; Pereira, L; Moura, D; Gomes, A; Sousa, C; García-Tenorio, R., 2012. Sea-level rise and anthropogenic activities recorded in the late Pleistocene/Holocene sedimentary infill of the Guadiana estuary (SW Iberia). *Quaternary Science Reviews.* **33***,* 121–141.

Diário de Pernambuco. 2004. Histórico das enchentes em Pernambuco. http://www.pe-az.com.br

Folk, R. L. and W. C. Ward. 1957. Brazos River Bar: Study of the Significance of Grain Size Parameters. *Journal of Sedimentary Petrology*, 27, 3-27.

Guerra, A.J.T and Marçal, M dos S. 2010. *Geomorfologia ambiental*. 3º Ed., Rio de Janeiro: Editora Bertrand Brasil. 190p.

Ingram, C., 1971. Carbon Determination. *In*: Carver, R. E. (ed.) *Procedures in Sedimentary Petrology*. New York, Wiley-Interscience. p. 573-596.

Lamb, A L..; Graham, P.W. and Leng, M.J. 2006. A review of coastal palaeoclimate and relative sea-level reconstructions using $\delta^{13}C$ and C/N ratios in organic matter. *Earth-Science Reviews,* 75, 29-57.

Muñoz. J. M. B., 2004. Superando conflitos entre porto e estuário, *In: Portos no Ambiente Costeiro*. Ícaro Cunha (ed.). Santos: Editora Universitária Leopoldianum. 128p.

Neto A.M. 2008. *Modificações da zona costeira do extremo sul da Bahia nos últimos 150 anos, e sua relação com a sedimentação do banco de Abrolhos*. Ph.D thesis. Bahia: Federal University of Bahia, 176 p.

Oliveira, T. S; Barcellos, R. L.; Schettini, C. A. F; Camargo, P. B. 2014. Processo sedimentar atual e distribuição da matéria orgânica em um complexo estuarino tropical, Recife, PE, Brasil. *Revista da Gestão Costeira Integrada*, 14, 399-411.

Pedrosa, F. J. A. 2007. *Aspectos da evolução de linha de costa e da paisagem litorânea do município de Olinda entre 1915 e 2004: Evidencias do Tecnógeno em Pernambuco*. Ph.D thesis. Recife: Federal University of Pernambuco. 193 p.

Pettijohn, F. J. 1975. *Sedimentary Rocks*, Harper & Row Publ., New York, USA, 718 p.

Qiao, Y., Y. Yang, J. Zhao, R. Tao and R. Xu, 2013. Influence of urbanization and industrialization on metal enrichment of sediment cores from Shantou Bay, South China. *Environ. Pollut*., 182, 28-36.

Saito R.T., Figueira R.C.L., Tessler M.G., Cunha I.I.L. 2001. ^{210}Pb and ^{137}Cs geochronologies in the Cananeia-Iguape estuary and in the southern continental shelf of São Paulo State, Brazil. *J. Radio analytical Nuclear Chemistry*, 250(1) 109-115.

Santos E.S. 2007. *Aplicação de marcadores geoquímicos para a avaliação dos impactos das barragens nos sedimentos do estuário do Rio São Francisco (Al/Se).* Ph.D thesis, Rio de Janeiro: Universidade Federal Fluminense, 139p.

Selley, R. C. 2000. *Applied Sedimentology*. San Diego: Academic Press, 523p.

Seshan, B. R. R.; Natesan, U.; Deepthi, K., 2010. Geochemical and statistical approach for evaluation of heavy metal pollution in core sediments in southeast coast of India. *Int. J. Environ. Sci. Tech*., 7(2), 291-306.

Smith, J.P., Bullen, T.D., Brabander, D.J., Olsen, C.R., 2009. Strontium isotope record of seasonal scale variations in sediment sources and accumulation in low-energy, subtidal areas of the lower Hudson River estuary. *Chem. Geol*. 264(1), 375–384.

Journal of Coastal Research	SI	75	88-92	Coconut Creek, Florida	2016

Changes in the Frequency and Duration of Closures of the Opihi Hapua Following Construction of the Opuha Dam

Sarah L. McSweeney[†*], Deirdre E. Hart[‡], Derek J. Todd[‡] and David M. Kennedy[†]

[†]School of Geography
The University of Melbourne
Victoria Australia

[‡]Department of Geography
The University of Canterbury
Christchurch New Zealand

www.cerf-jcr.org

www.JCRonline.org

ABSTRACT

McSweeney, S.L.; Hart, D.E., Todd, D.J., and Kennedy, D.M. 2016. Changes in the Frequency and Duration of Closures of the Opihi Rivermouth Following Construction of Opuha Dam. *In:* Vila-Concejo, A.; Bruce, E.; Kennedy, D.M., and McCarroll, R.J. (eds.), *Proceedings of the 14th International Coastal Symposium* (Sydney, Australia). *Journal of Coastal Research*, Special Issue, No. 75, pp. 88-92. Coconut Creek (Florida), ISSN 0749-0208.

Hapua are coastal lagoons found at the mouths of braided gravel rivers that experiee a semi-permanent connection with the ocean related to fluvial discharge and marine sediment deposition. Sustained closure is driven by low river flows and is associated with a decrease in water quality, the impedance of fish passage and flooding. On many Hapua, irrigation schemes have modified natural flow regimes, yet there is little field data on how this affects the dynamics of the lagoon. In this study we examine the Opihi rivermouth (New Zealand) which has a naturally seasonal low flow regime and a hydrology extensively modified through irrigation abstraction and dam construction Analysis of the entrance morphodynamics pre and post-dam construction indicates a decrease in the frequency and duration of rivermouth closures. This is due to the more constant flow regime maintained by the dam. Despite this, seasonal patterns of closure still persist over summer which illustrates the importance of marine processes in driving entrance condition. Three scenarios of natural closure are identified: summer low flows, fluvial slug deposition, and coastal storms. Closure duration was also observed to be extended when river flows are low, onshore wave energy is high and when the outlet channel is considerably offset.

ADDITIONAL INDEX WORDS: *Hapua, coastal management, lagoon, coastal morphology.*

INTRODUCTION

Hapua are a form of coastal lagoon which exist at the mouths of braided gravel rivers discharging through mixed sand and gravel beaches where the coastline is in a state of long term retreat (Kennedy, 2011). Hapua are characterised by a shore parallel predominantly fresh waterbody impounded by a gravel-dominated beach barrier (Kirk, 1991). The barrier is formed by onshore sediment movement sourced from longshore drift and wave action when fluvial discharge is insufficient to maintain an open entrance (Hart, 2009). Hapua are almost exclusively found in New Zealand and most commonly on the east coast of the South Island (Kirk, 1991; Kirk and Lauder, 2000).

Waves are a key control of outlet morphology. Storm waves can both close an entrance by intensive sediment transport and induce new outlet breaches through wave overtopping of the barrier (Hart, 2007; Taylor and Frobel, 2003). Unlike the majority of estuaries, hapua do not experience a diurnal exchange of tidal waters due to their irregular connection to the ocean (Shulmeister and Kirk, 1993). Sediment size and characteristics also play a vital role in hapua morphodynamics and affect the ease at which river flows can breach or percolate through the barrier (Carter and Orford, 1984). Hapua closures occur when seaward flows of freshwater are insufficient to maintain a channel through the beach berm (Sewell, 1988). As a mouth closes, longshore drift can shift the entrance laterally, considerably offsetting it from its flood flow position (Todd, 1983; 1992). Conversely, when a river is in flood, the impounding spit is prone to breaching directly opposite the main channel. The contribution of fluvial and marine dominance rarely exists in prolonged equilibrium which contributes to the dynamic nature of hapua (Hart, 2007). Prolonged closures are common when river flows are low and the hapua becomes wave-dominated. Fundamentally, the longer the duration of closure, the greater the adverse effects upon lagoon water quality, due to an increased residence time of waters (Kirk, 1991; Todd, 1983).

Sustained mouth closure during low flow periods is a primary management concern as it is associated with decreased water quality, impedance of fish passage to the ocean, and flooding (Kirk and Lauder, 2000; Zenkovitch, 1967). Nearly all hapua exist on rivers with hydrology that has been modified through irrigation abstraction which has led to changes in entrance morphodynamics, in particular, closure frequency. In recent times at many hapua, flows are maintained above minimum thresholds in an attempt to minimise the adverse effects of closure on water quality. It is however sometimes insufficient when combined with periods of naturally low flow (Lynn *et al.* 2007). This study explores the impact of the Opuha Dam on the frequency and duration of closures of Opihi River mouth.

STUDY AREA

The Opihi River is a braided gravel river that flows across the Canterbury Plains on the East Coast of New Zealand (44.280ºS, 171.351ºE) (Figure 1). The headwaters originate in the foothills

DOI: 10.2112/SI75-018.1 received 15 October 2015; accepted in revision 15 January 2016.
*Corresponding author: slmcs@student.unimelb.edu.au

of the Southern Alps (de Joux, 1982) and the rivermouth has a catchment area of 2372 km^2 and a mean annual sediment yield of 1000 t/km^{-2}/yr^{-1} (Kirk, 1991). The coastline is microtidal, wave-dominated and consists of steep, reflective mixed sand and gravel beaches (Allan *et al.,* 1999). Naturally occurring seasonal low flows occur throughout October to April and have been exacerbated by excessive abstraction from the river for irrigation (Kirk and Lauder, 2000). The mean annual rainfall at Fairlie, the nearest station 55 km from the hapua, is 800 mm but increases closer to the Alps. Peak rainfall occurs in winter and flood events are produced by both long duration (2 - 4 days) rainfall and high intensity storms of a shorter duration (16 - 24 hours). The mean flow is 5.5 m^3/s^{-1}, the mean 7-day mean low flow is 1.3 m^3/s, mean annual flood is 170 m^3/s and the 10-year flood is 330 m^3/s taken from flow recorders 7 km upstream of the rivermouth (ECAN, 2005; 2007). Opuha Dam was constructed in 1998 upon the Opuha tributary of the Opihi River. The Opuha River joins the Opihi 20 km downstream of the dam and is 40 - 50 km upstream of the rivermouth. A major influence of the dam on natural river flows is the reduction in flow variability as flood peaks are effectively captured within the dam. Opuha Dam consists of an upper storage reservoir which feeds a lower, smaller reservoir controlled by a weir. This configuration limits the peak magnitude of controlled releases to approximately 35 m^3/s and operation is governed by a mínimum flow requirement of ~4 m^3/s^{-1} (subject to seasonal variation) (Lessard *et al.,* 2012).

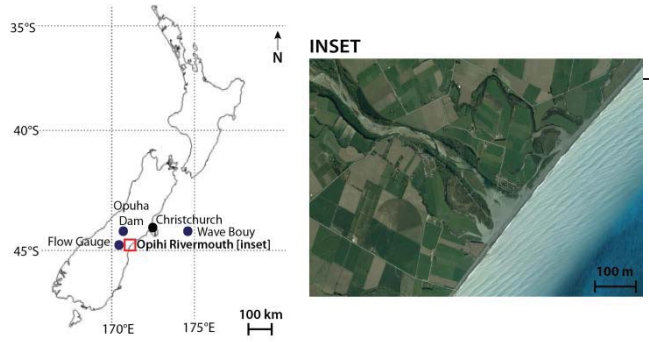

Figure 1. Study area and location of Opuha Dam, Opihi Rivermouth, SH1 Flow Gauge and Wave Rider Bouy. (Inset) Opihi rivermouth and associated Hapua, Milford Lagoon. Image from Google Earth.

METHODS

Daily mean river flow records and rivermouth closure records were compared over a five-year timeframe either side of dam construction. Marine and climatic parameters were also analysed including: wave and tidal data, daily mean temperatures, precipitation and storm frequency. Mean daily river flows were taken from the ECAN SH1 Opihi River site, the closest gauge site to the rivermouth (7 km NW), below which most wáter extractions occur thereby providing a relatively true reflection of flows entering the rivermouth. Daily rivermouth closure records were sourced from Fish and Game New Zealand. Wave data for the Canterbury coast was collected at 30 minute intervals using a Directional Waverider Buoy located offshore of Banks Peninsular in 76 m water depth. The onshore wave energy from this site is unhindered by minimal refraction as it is directly northwest of the Opihi rivermouth. Wava data was unavailable for the pre-dam period so values were calibrated with hindcast data (Gorman *et al.,* 2003). Climate statistics were sourced from the New Zealand Meteorological Service. Rainfall is used as a proxy for river flow when flow data was unavailable. Statistical data analysis was undertaken using Excel and SPSS software.

Table 1. *Rivermouth closure records, rainfall and river flows pre (October – April, 1989 - 1993), and post-construction of the Opuha Dam, (October - April, 2006 – 2011. River flows only available for post-dam period but rainfall values were similar across both periods.*

	Summer period	Mean Annual Flow (m^3/s)	Annual Rain (mm)	No. of closures	Dates of Closure	Annual Closure Duration (days)
Pre Dam Period	Oct-Apr 1989		553.2	9	5/11, 13/11, 25/11, 2/12, 6/12, 13/12, 22/12, 28/12	13
	Oct-Apr 1990		574.3	10	13/11, 22/11, 23/12, 1/3, 23/3, 3/4, 1/11, 13/12, 29/12	39
	Oct-Apr 1991		596.1	7	23/1, 12/2, 6/3, 11/3, 21/3, 10/4, 5/1, 15/1.	36
	Oct-Apr 1992		531	6	28/2, 2/3, 13/3, 2/4, 8/4, 4/1	53
	Oct-Apr 1993		438	4	23/2, 28/2, 1/3, 19/3	34
	Mean		538.5	7.2		35
	St. Dev.		61.2	1.8		12.6
Post Dam Period	Oct-Apr 2007	16.9	610	2	1/10, 15/10	1
	Oct-Apr 2008	8.6	452	6	29/1, 9/2, 25/2, 3/3, 14/3, 26/3	12
	Oct-Apr 2009	13.2	487.1	5	17/1, 28/1, 2/2, 17/3 , 23/3	8
	Oct-Apr 2010	9.6	583.8	8	1/1, 16/1, 9/2, 17/2, 28/2, 16/3, 8/12, 18/12	12
	Oct-Apr 2011	12.4	616	8	18/1, 24/2, 23/3	12
	Mean	12.1	549. 8	5.6		9
	St.Dev.	3.27	75.3	2.8		4.8

RESULTS

Table 1 presents statistics on rainfall and mouth closure for five yearly summer periods (Oct - April) prior (1989 - 1993) and post (2006 - 2011) construction of Opuha Dam. The five yearly period were chosen due to similar summer rainfall being received in each period and the extent of data for closure records being limited to this timeframe. For the period prior to dam construction, there was a mean closure duration of 35 days and a mean closure frequency of 7.4 closures per summer (Table 1). Following construction of the Opuha Dam rivermouth closure duration declined to a mean of 9 days per summer (Table 1). The reduced entrance closures are considered most likely to be a function of the consistency in year round base river flow reaching the rivermouth as maintained by the dam. The mean frequency of rivermouth closures post-dam construction is 5.6 closures per summer. Standard deviations indicate that the

overall range of closure frequency and duration post-dam construction is also reduced. This indicated less variability in the opening regime of Opihi rivermouth. Comparison of the available data for both frequency and duration indicates that although both values have declined following the construction of Opuha Dam, the most profound change is visible in the duration of rivermouth closures, not the frequency at which these occur.

Periods of high river flow are coincident with higher catchment precipitation, and this results in an extended state of hapua openings (Figure 2). For example, the most constant level of flow that is maintained over each annual summer period occurs in 2006 - 2007 (Figure 2A). This period also has the highest mean annual river flow 16.9 m^3/s which results in only two hapua closures. In other more variable or lower flow years (Figure 2B - E; Table 1), closure occurrence is increased. More frequent closures of the rivermouth occur when a constant low flow is present, especially from November to March where the majority of closures take place. Low duration peak flood events are common and following a sharp peak in flow, a series of closures can be observed over the subsequent weeks. Closure appears to be more likely when daily mean flow is broadly reduced to less than 10 m^3/s for a period longer of several weeks. The mean daily flow across the post dam period now ranges from 16.9 - 8.6 m^3/s with an overall mean of 12.1 m^3/s.

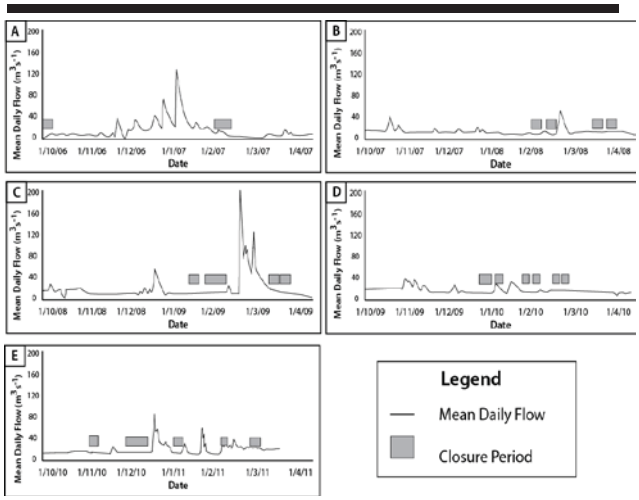

Figure 2: Opihi River flows as taken at SH1 site and rivermouth closures over 5 years post construction of Opuha Dam. October 2006 - April 2011. Data from ECAN and Fish and Game NZ.

Sustained periods of rivermouth closure occurr in conjunction with a wide range of wave directions from 56.5° to 201°. A lower angle of wave approach (dir) appears to result in a reduced closure duration with the majority of closures which lasted for one day having an onshore wave direction of <100 degrees (for example: 17/1/09 – 97.2°; 16/1/09 – 96.7°; 18/1/11 – 84.5°; 24/2/11 – 48.3°). Despite further data over a longer period being required to confirm this relationship, the results support wave processes as a main control on entrance condition. Waves from <100° all propagate from north of the rivermouth, which are not likely to generate high sediment transport rates, hence this suggests the greater ability for lower river flows to breach in these times, thus resulting in shorter duration closures. Wave bouy data for pre dam years were unavailable but hindcast data from 1979 – 1998 shows similar values for all data compared to Table 2 (Gorman *et al.* 2010).

Table 2. *Post-dam period wave statistics at Banks Peninsula. Data range is from 2006 - 2011 showing: maximum and significant wave height (H_{max}, H_s) Period (T_s) and mean wave direction (Dir). Statistics are shown for the corresponding periods of closure.*

Year	Closure Date	Mean H_s (m)	Mean H_{max} (m)	Mean T_s (s)	Mean Dir (°)
2007	15/10	2.64	9.5	9.7	174
2008	29/1-1/2	2.8	7.4	7.9	104.8
	9/2-11/2	3.51	10.2	10.9	97.8
	25/2-26/2	2.82	8.5	8.7	74
	3/3-6/3	3.75	8.4	8.6	162.5
	14/3	2.65	9.8	9.8	174.3
		3.12	9.7	10.9	189.9
2009	17/1	3.36	8.9	9.4	97.2
	28/1-30/1	2.72	9.7	10.2	186.7
	2/2-3/2	3.9	9.5	9.8	201
	17/3	2.88	9.9	9.7	177.4
	23/3	3.9	8.7	8.9	165
2010	1/1-5/1	3.79	8.9	9.2	174.5
	16/1	4.15	8.7	9.6	96.7
	9/2-10/2	3.3	9.8	9.8	183.2
	17/2-18/2	4.13	10.6	10.8	177.2
	28/2	3.03	8.6	8.4	105.8
	16/3-17/3	5.28	10.3	10.7	195.1
	8/12-9/12	5.36	9.3	9.3	193.8
	18/12-21/12	3.58	7.5	7.5	56.5
2011	18/1	4.79	9.4	9.8	84.5
	24/2	2.89	7.6	8	48.3
	23-3/25/3	3.18	10.2	10.9	177.6
Mean		3.54	9.12	9.5	143.4
Std. Dev.		0.80	0.90	0.98	50.2

DISCUSSION

The construction of Opuha Dam has led to both the frequency and duration of rivermouth closures to decrease (Table 1). This is most likely due to the more continuous rate of river flow maintained by Opuha Dam as opposed to a natural flow regime where consistent low summer flows dominate. Results indicate that closure duration was reduced more profoundly than frequency across the whole study period (Table 1). This is most likely due to the influence of marine processes, especially wave energy and associated longshore transport.

In years of high precipitation and mean river flow, there was a lower incidence of rivermouth closure. On the otherhand, low rainfall and corresponding decreased river flows are recognised to directly reduce fluvial energy reaching the hapua. This is illustrated throughout this study when periods of reduced precipitation lead to low river flows, and ultimately induce rivermouth closures (Table 1; Figure 2). In all instances, rivermouth closures occurred in summer (Dec – Mar) (Figure 3). This also coincides with periods of high water demand and irrigation abstraction due to the intensive agricultural land use of the surrounding area (de Joux, 1982; Hearnshaw *et al.*, 2010).

Opuha Dam has therefore not changed the period in which most rivermouth closures occur (Figure 2).

Following the construction of Opuha Dam, the frequency of rivermouth closures has decreased irrespective of rainfall. These findings suggest that the Opuha Dam could, despite low rainfall years, act to offset reduced precipitation to maintain a more constant level of baseflow to maintain an open rivermouth against the processes driving closure from the marine side. Conversely, this could mean that factors independent of climate may have a stronger influence upon rivermouth closure. It is observed that rivermouth breaching from intensive, short duration flood events are often followed by a subsequent string of closures. For example, the openings following flood events of a high magnitude experience closures in the days to weeks, as opposed to months, following cessation of elevated river flows (Figure 2A – E) For example, two rivermouth closures occuring within a week of a peak flood event and within 6 days of each other are observed in March 2009 (Figure 2C). When the hapua is open, fluvial sediment is deposited into the nearshore, and as flooding diminishes it moves landward and is transported by longshore drift to offset and close the hapua entrance channel (Hart, 2009; Todd, 1983). Years which did not display this trend had flood peaks of a lower level in comparison meaning flow is likely to not have sufficient energy to mobilise a more sediment into the marine zone (Figure 2B; D). As this pattern is still evident in post-dam periods, Opuha Dam did not appear to alter this natural deposition pattern. This may not necessarily be a negative effect as coastal sediment inputs are still essential to the system which is otherwise in a long-term net state of erosion (Kelly *et al.*, 2005; Kennedy, 2011; Kirk and Lauder, 2000).

Closures tend to occur relatively rapidly, within days as opposed to weeks, following a decline of fluvial energy. Flood breaching allows the hapua to drain, but it is likely that following the breach, insufficient hydraulic head exists to maintain an open outlet against the high levels of wave energy and longshore driven sediment. As such events are short lived (ie. 1 - 2 days maximum), there is less time to increase the negative effects of closure such as flooding and water quality degradation (Carter and Woodroffe, 1994). Periods of high wave energy appear also to result in more short-term closures as moderate rather than low river flows are still maintained throughout the closure period. This contrasts to closure by seasonal low flows which appear to open the hapua outlet less rapidly but for an increased duration.

An elevated mean offshore wave height appears to be a common factor in all closure periods of the Opihi rivermouth and would be more influential during a summertime low-flow season where the balance of counteracting fluvial energy is reduced (Todd, 1983; Hart, 2009). Similarly, the strength and direction of longshore drift are important as this is drives sediment transport across the mouth which will ultimately close the entrance (Hart 2009; Kirk and Lauder, 2000; Larkin, 2013;). The effect of coastal storms upon rivermouth closure are unpredictable as they can close, by sediment deposition, or open hapua, by extreme wave activity breaching the barrier to raise water levels - especially in moderate to low flows (Todd, 1983).

Identified Closure Scenarios and Schematic Model

Three specific scenarios of rivermouth closure were evident at the Opihi rivermouth. These include closure by: summer low flows, fluvial deposition and coastal storms (Figure 3 A - C).

Firstly, a summer low flow closure (Figure 4A) occurs due to low river flows resulting from both high abstraction rates and reduced precipitation. Rivermouth closure usually occurs for a longer period and is preceeded by a period of low or declining flow (Figure 2B). In the second senario, deposition of a fluvial slug (Figure 3B) was found to occur during a short-term, intensive floods when the river was abl to transport large volumes of sediment into the nearshore. Waves act to return the coast to an equilibrium state and transport sediment into the rivermouth often offsetting the outlet once flood waters recede. The occurrence and duration of this scenario appears to be largely dependent on the volume and entrance morphology of individual hapua. Coastal storms (Figure 3C) are the final mechanism of closure whereby marine sediment is reworked by high wave energy resulting in rapid barrier building. The fluvial energy required to breach the barrier is therefore increased. In this situation wave overtopping is likely to raise lagoon water levels. Storm-induced closures appeared to be of lesser duration compared to those occuring during prolonged summer low flows. Furthermore, storm induced closure could be reduced in likelihood when moderate, not low river flows are present, especially as a result of the more constant flow regime maintained by Opuha dam.

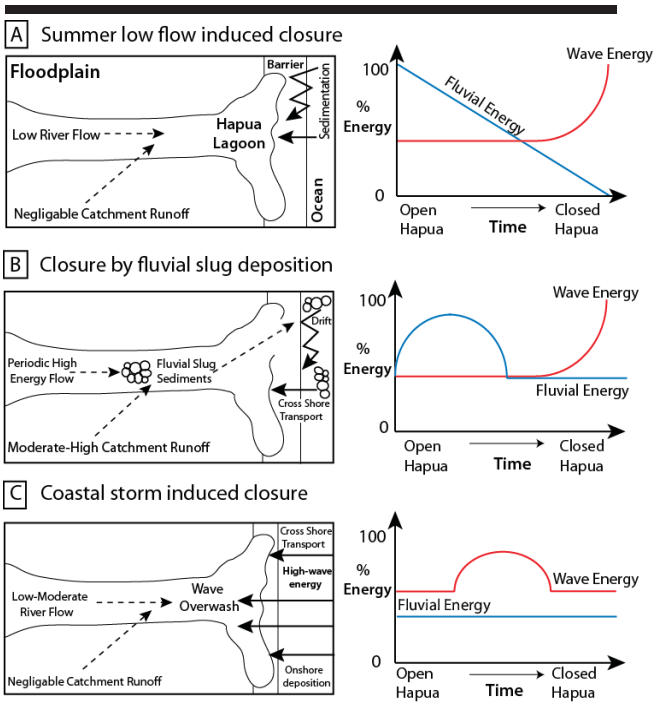

Figure 3: Schematic representation (right) and energy distribution (left) of closure scenarios observed at Opihi rivermouth. A) Closure by summer low flow scenario; b) Closure from deposition of fluvial slug; c) Closure by a coastal storm.

CONCLUSIONS

A distinctive natural cycle of rivermouth migration and closure exists at the Opihi River mouth where fluvial discharge works to maintain an open outlet, while marine processes, particularly longshore drift and onshore wave action, act to force outlet migration and closure. Any changes to this natural balance of energy becomes particularly important throughout the summer where naturally low flows are exacerbated by high levels of water abstraction. The Opuha Dam has acted to regulate flows of Opihi River downstream of the dam and the more constant higher summer flows now maintain an open rivermouth for longer periods of time. This outcome resulted in a reduction in both the frequency and duration of rivermouth closures but was most noticeable in terms of closure duration. This illustrates that marine processes are an equally important driver of entrance condition as fluvial flow. The Opuha Dam has reduced the duration of rivermouth closures and altered the dynamic nature of the rivermouth by prolonging the state in which fluvial discharge and marine energy exist to maintain a choked but open outlet.

ACKNOWLEDGMENTS

This study was undertaken as part of a BSc(Hons) project at The University of Canterbury. Thank you to Fish and Game for closure records, to Environment Canterbury for wave and river flow data, and to NIWA for climate data.

LITERATURE CITED

Allan, J.C., Kirk, R.M.; Hemmingsen, M.; and Hart, D., 1999. *Coastal Processes in Southern Pegasus Bay: A Review - A Report to Woodward-Clyde New Zealand Ltd. and the Christchurch City Council.* Christchurch, New Zealand: Land and Water Studies (International) Limited.

Carter, R.W.G. and Woodroffe C.D. 1994. *Coastal evolution: Late Quaternary shoreline morphodynamics*, Cambridge: Cambridge University Press, 517 pp

Carter, R.W.G. and Orford, J.D., 1984. Coarse clastic barrier beaches: a discussion of the distinctive dynamic and morphosedimentary characteristics. *Marine Geology,* 60(1-4), 377-389. doi:10.1016/0025-3227(84)90158-0

Cooper, J.A.G., 2001. Geomorphological variability among microtidal estuaries from the wave-dominated South African coast. *Geomorphology* 40(1) 99-122.

de Joux, R.T. 1982., *The water resources of the Opihi and Temuka Rivers*. Timaru, New Zealand: South Cantebury Catchment Publication Number 28.

Environment Canterbury, 2000. *Opihi River Regional Plan.* Christchurch, New Zealand: Environment Canterbury. Report R00/16, 73p.

Environment Canterbury, 2005. *Regional Coastal Environment Plan for the Canterbury Region.* Christchurch, New Zealand: Environment Canterbury. Report R04/13/1, Volume 1, 266p.

Environment Canterbury, 2007. *Natural Resources Regional Plan*. Christchurch, New Zealand: Environment Canterbury. Report R04/15.

Gorman, R.M.; Bryan, K.R., and Laing, A.K., 2003. Wave hindcast for the New Zealand region: Nearshore validation and coastal wave climate. *New Zealand Journal of Marine and Freshwater Research*, 37(3), 567-588.

Hart, D.E., 2007. River-mouth lagoon dynamics on mixed sand and gravel barrier coasts, *In:* Lemckert, C. (ed.), *Proceedings of the 9th International Coastal Symposium* (Gold Coast, Australia). *Journal of Coastal Research*, Special Issue No. 50, pp. 927-931.

Hart D.E., 2009. Morphodynamics of non-estuarine rivermouth lagoons on high-energy coasts. *In*: da Silva, C.P. (ed.), Proceedings of the 10 th International Coastal Symposium, *Journal of Coastal Research,* SI, 56(2), 1355-1359.

Hearnshaw, E.J.; Cullen, R.; and Hughey, F.D., 2010. *Ecosystem Services Review of Water Storage Projects in Canterbury: The Opihi River Case.* Lincoln University, 63p.

Kelly, D.; McKerchar, A.; and Hicks, M., 2005. Making concrete: Ecological implications of gravel extraction in New Zealand rivers. *Water and Atmosphere*, 13, 20-21.

Kennedy, D.M. 2011. Tectonic and Geomorphic Evolution of Estuaries and Coasts. *In:* Wolanski, E., and McLusky, D., (eds.), *Treatise on Estuarine and Coastal Science*, Vol. 1: Classification of Estuarine and Nearshore Coastal Ecosystems - 1st Edition, Waltham, pp. 37-59.

Kirk R.M., 1991. River-beach interaction on mixed sand and gravel coasts: a geomorphic model for water resource planning. *Journal of Applied Geography*, 11(4), 267-287.

Kirk R.M., and Lauder, G.A., 2000. Significant coastal lagoon systems in the South Island, New Zealand: coastal processes and lagoon mouth closure. *Science for Conservation,* 146, 1173-2946.

Larkin, G., 2013. *Waituna Lagoon Mechanical Opening Site Assessment*. Southland, New Zealand: Environment Southland Technical Report. 43 pp.

Lessard, J.; Hicks, D.M.; Snelder, T.H.; Arscott, D.B.; Larned, S.T.; Booker, D.; and Suren, A.M., 2013. Dam design can impede adaptive management of environmental flows: a case study from the Opuha Dam, New Zealand. *Environmental Management*, 51(2), 459-473.

Lynn, I.H.; Harrison, J.; Basher, L.R.; and Webb, T.H.; 1997. *A Geomorphologic Interpretation of the Orari, Waihi, Temuka and Opihi River Floodplains.* Christchurch, New Zealand: Landcare Research. Report No. U97/36.

Sewell, R.J., 1988. Late Miocene volcanic stratigraphy of central Banks Peninsula, Canterbury, New Zealand. *NZ Journal of Geology and Geophysics*. 30(1), 41-64.

Shulmeister, J. and Kirk, R.M., 1993. Evolution of a mixed sand and gravel barrier system in North Canterbury, New Zealand, during Holocene sea-level rise and still-stand. *Sedimentary Geology* 87(3), 215–235.

Taylor, R.B. and Frobel, D., 2003. Rapid transformation of upper beach characteristics along breached coastal barriers. *Proceedings of the Canadian Coastal Conference*, 1-17.

Todd D.J., 1983 Effect of Low River Flows on Closure of the Opihi River Mouth. Canterbury, New Zealand: University of Canterbury, MSc thesis, 187 p.

Todd, D.J., 1992. River mouth and coastal processes of the Ashburton River mouth. Christchurch, New Zealand: Natural Resources of the Ashburton River and Catchment Canterbury Regional Council Report, 92(36) 208-234p.

Zenkovitch, V.P., 1967. *Processes of Coastal Development.* London: Oliver and Boyd, 738p.

Journal of Coastal Research	SI	75	93-97	Coconut Creek, Florida	2016

Salinity variation in the macrotidal mixing zone: the Paracauari River estuary, Marajó Island (Northern Brazil)

Sury M. Monteiro †* and Maâmar El-Robrini †

†Instituto de Geociências
Universidade Federal do Pará, Brasil

www.cerf-jcr.org

www.JCRonline.org

ABSTRACT

Monteiro, S.M. and Robrini, M., 2016. Salinity variation in the macrotidal mixing zone: the Paracauari River estuary, Marajó Island (Northern Brazil). *In:* Vila-Concejo, A.; Bruce, E.; Kennedy, D.M., and McCarroll, R.J. (eds.), *Proceedings of the 14th International Coastal Symposium* (Sydney, Australia). *Journal of Coastal Research*, Special Issue, No. 75, pp. 93-97. Coconut Creek (Florida), ISSN 0749-0208.

The objective of this study is to delineate the estuarine zones (Riverine Zone – RZ, under river influence; Mixing Zone – MZ, under marine influence) across different seasonal periods in the macrotidal Paracauari River estuary – Marajó Island (Northern Brazil). We measured salinity (S) and electric conductivity (EC) in the water column using a multi-parameter probe. We also collected data on suspended particulate matter (SPM – gravimetric estimation) along 40 km of the estuary during higher rainfall (660 mm), transitional (260 mm), and lower rainfall (10 mm) periods in 2008. The first sampling station was located at the river mouth (marine domain) and the last sampling station was in riverine domain. Due to La Niña phenomenon, the Paracauari River estuary showed mean EC and S ranging from 256 $\mu S.cm^{-1}$ and 0.1, respectively, in the higher rainfall period, to 11002 $\mu S.cm^{-1}$ and 6.1 in the lower rainfall period. Maximum SPM concentrations (93.72 $mg.L^{-1}$) occurred during the higher rainfall period and minimum values (15.49 $mg.L^{-1}$) occurred during the lower rainfall period. Therefore, RZ (oligohaline, $S < 1.0$) prevails during higher rainfall period; during the transitional period, an eight km-wide MZ (oligohaline, $S = 1.5$) is present and the RZ is upstream; in the lower rainfall period, marine waters penetrate as far as 40 km from the mouth, thus characterizing this stretch as MZ (mesohaline, $2.5 < S < 7.5$). Hence, the zonation of the Paracauari River estuary is influenced by river waters during periods of higher rainfall rates and by marine waters during periods of lower rainfall rates.

ADDITIONAL INDEX WORDS: *Amazon estuary, Maximum Turbidity Zone, Salinity.*

INTRODUCTION

Marajó Island is situated in a river-estuarine interface at the mouth of the Amazon (Northwest) and Pará (Marajó Bay) (Southeast) Rivers and it also borders the Atlantic Ocean to the north. On this island's eastern margin, the Paracauari River estuary (Figure 1) is a highlight compared to other estuarine systems, due to particular characteristics. For instance, this estuary is heavily affected by freshwater discharges from regional drainages and macrotidal regimes, which spatio-temporally change the salinity gradient, the vegetation succession (*e.g.*, mangrove forests), the primary production of ecosystems, and economic activities, mainly subsistence fishery.

The high rainfall rates in Marajó Island (2,500 mm) impacts the regional drainage and, consequently, the contents of substances such as salts and suspended particulate matter in the waters of the Paracauari River estuary. Considering riverine and tidal forces, estuaries may be subdivided in riverine, mixing, and coastal zones. The Riverine Zone (RZ) is susceptible to the rise and fall of sea level despite the absence of salinity. On the other hand, the Mixing Zone (MZ) is influenced by tidal phases and is characterized by the mixing of water masses and strong gradients of physical and chemical properties. This is where a Maximum Turbidity Zone (MTZ) may be observed. The Coastal Zone (CZ) is the section between the MZ and the river plume boundary (Fairbridge, 1980).

The main purpose of this study is to establish the boundaries of the estuarine zones (RZ, within the riverine domain; and MZ, within the marine domain) in different seasonal periods in the Paracauari River estuary – Marajó Island (Brazil), under the influence of La Niña event (2008). We considered that, throughout the high rainfall period, freshwater discharge hinders the penetration of marine waters into the estuary; hence, it raises the concentrations of suspended particulate matter (SPM > 0.45 mm) and negatively affects salt contents.

Background

The watershed of the Paracauari River estuary, which is part of the Amazon River Basin, is located in the eastern section of Marajó Island. It encompasses an area of 706 km^2 and approximately 50 km of a forcefully-meandering main channel, which flows westward in the medium and low river course, controlled by structural elements of neotectonic architecture (França, 2003) and with a high inflection point (*i.e.*, a 90º angle). On the other hand, it runs north-south and southeastward during high river course (Souza, 2010). The waters of this estuary are subject to semidiurnal incursion of meso to macrotides (3 to 6 m) (Diretoria de Hidrografia e Navegação, 2008).

DOI: 10.2112/SI75-019.1 received 15 October 2015; accepted in revision 15 January 2016.
*Corresponding author: surymonteiro@yahoo.com.br

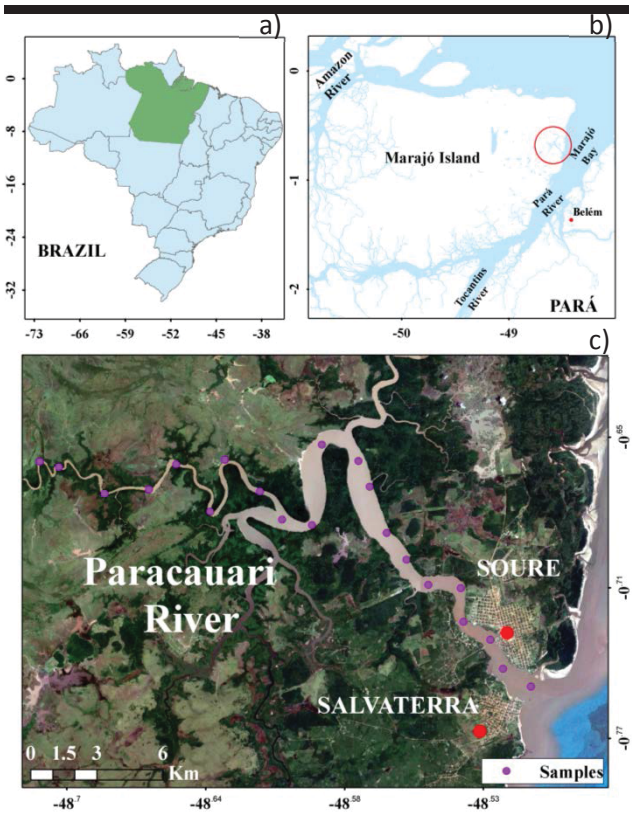

Figure 1. Location of the study area: a) Pará State in northern Brazil; b) Marajó Island (The red circle in the figure corresponds to the Paracauari river); c) The Paracauari river and water sampling.

This estuary separates the cities of Soure and Salvaterra, where there are mostly Quaternary sediments and it is possible to identify two morphostructural units: the coastal plateau which predominates in the city of Salvaterra and the coastal plain in Soure (Rossetti *et al*., 2007).

As it is situated in a tropical region, this estuary is characterized by low sunlight and temperature fluctuations, and a humid tropical climate, with annual average temperature of 27 ºC, and mean rainfall of 3,000 mm/year. It occurs in two distinct seasonal periods, determined by the shift of the Intertropical Convergence Zone (ITCZ): higher rainfall from December to May (with mean precipitation of 2,566 mm) and lower rainfall from July to November (with mean precipitation of 414.3 mm) (Martorano *et al*., 1993). During the La Niña event in 2007/2008, the rainfall volume in March was above climatological standards (1961 to 2009) (Souza *et al*., 2009), which indicates a contribution of a 650 mm increase in rainfall in the Eastern Amazon.

METHODS

Water samplings were carried out along the Paracauari River estuary under the influence of La Niña phenomenon. A total of three (03) samplings were carried out, considering the climatic seasonality of the region and the effects of spring tide: 1) a higher rainfall period (March/2008); 2) a transitional period (June/2008); and 3) a lower rainfall period (September/2008).

Water sampling was performed down the water column, from the mouth upstream, at fifteen sampling stations 1.5 km apart. The 15th sampling station was located upstream, within riverine domain, but still subject to the influence of the tide. The remaining stations were located in the estuarine zone, where the mixing of freshwater from continental drainage with sea water occurs, according to the definition by Kjerfve (1990). Sampling stations were placed using a GPS (Global Position System) sensor. Consequently, the 1st station (P1) was selected to represent the points under greater influence of ocean waters, or brackish waters from the Marajó Bay; and the 15th station (P15) was selected to represent the points under greater influence of continental waters. Nonetheless, six sampling stations were added to the sampling design over the period of lower rainfall, in order to attain the study objective, thus totaling 21 sampling stations (Figure 1c).

At each sampling station, surface and bottom water were sampled with a Van Dorn bottle in order to analyze SPM (by using gravimetric estimation) (Strickland and Parsons, 1972) and also in situ analyses of parameters such as temperature, pH, electric conductivity, total dissolved solids, and salinity, were performed using a HANNA multi-analyzer, model 9828.

Statistically, we found variations between variables (ANOVA) considering: o) point and depth of collection; and ii) study period (March, June, and September, 2008).

Throughout the sampling period, tidal water levels were measured by using a graduated ruler installed onto a pier in the city of Soure, meteorological data (air temperature and relative air humidity) were collected at the meteorological station in the same city.

RESULTS

Electric conductivity and salinity parameters showed significant seasonal variation (sig.<0.05) in the Paracauari River estuary. Their respective means were 256 µS.cm^{-1} and 0.12 ppt in the higher rainfall period, 1962 µS.cm^{-1} and 0.96 ppt in the transitional period, and 11002 µS.cm^{-1} and 6.18 ppt in the lower rainfall period.

Fluctuations within the water column were not significant (sig.>0.05), since surface values were similar to the ones at the bottom: EC values were 262.46 and 256.46 µS.cm^{-1} and S values were 0.12 and 0.11 ppt at surface and bottom, respectively, during the period of higher rainfall; 1787.13 and 1896.06 µS.cm^{-1} and 0.86 and 0.95 ppt during the transitional period; and 10938.00 and 11040.66 µS.cm^{-1} and 5.24 and 5.28 ppt during the lower rainfall period.

Along the estuary, during higher rainfall period, an increasing gradient was observed mouth-upstream for both EC and salinity, with minimum values (127.5 µS.cm^{-1} and 0.06 ppt) obtained at the river mouth and maximum values (300.5 µS.cm^{-1} and 0.2 ppt) obtained upstream from the estuary.

Due to decreased river levels over transitional and lower rainfall periods, decreasing EC and S gradients occurred mouth-upstream. Maximum values were spotted at the mouth and minimum values were observed at the river source, ranging from 3210 to 148 µS.cm^{-1} and 1.63 to 0.06 ppt, respectively, during

transitional period; and from 14080 to 6283 µS.cm^{-1} and 7.56 to 3.63 ppt during lower rainfall period.

The highest SPM concentrations (93.72 mg.L^{-1}) occurred during higher rainfall period and the lowest (38.21 and 15.49 mg.L^{-1}) occurred during transitional and lower rainfall periods, respectively, with no significant variations (sig.>0.05) in the water column (Figure 2).

SPM concentration showed spatial variation during higher rainfall period, with minimum values (87.66 mg.L^{-1}) near the mouth and maximum values (105.00 mg.L^{-1}) upstream from the estuary, near an "igarapé" (tidal channel that drains water from the floodplain). During transitional period, this increasing pattern was also spotted, with a lower concentration (30.50 mg.L^{-1}) at the mouth and a higher concentration (52.16 mg.L^{-1}) upstream. It was not possible to observe significant spatial variations (sig.>0.05) during lower rainfall period, with similar concentrations at the mouth (14.29 mg.L^{-1}) and upstream (15.71 mg.L^{-1}).

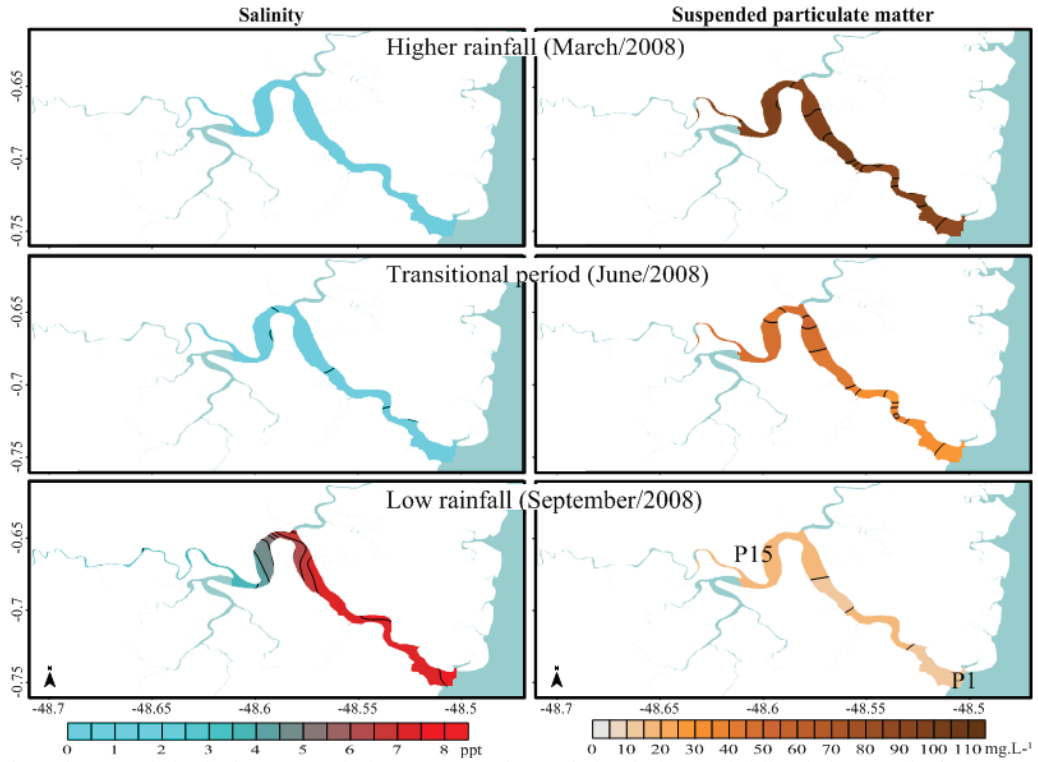

Figure 2. Salinity and MPS variation in the Paracauari River estuary, and MTZ during the lower rainfall period (September/2008).

DISCUSSION

The parameters analyzed varied over a temporal scale according to the seasons of the year combined with the climate of the Amazon region, whereas changes down the estuary are mostly controlled by river discharge, tide, and currents.

In the Paracauari River estuary, the decrease in both EC and S values is caused by the dilution of waters attributable to the increase in rainfall rates that is typical of the period, when river discharge is higher.

During this period, there is a reversal in saline pattern, i.e., higher salinity values upstream from the estuary. This is a consequence of the rise in water levels, which causes flooding of the riverbank along the Paracauari river estuarine region and helps export salts retained in this area into the estuary. Therefore, this floodplain is thought to act as a regulating mechanism of the salt content in these waters.

During the lower rainfall period, the highest EC and S values are associated to the decrease in riverine water input, which allows for further penetration of marine waters into the estuary. In this scenario, brackish waters reached the upstream river (P15 showed S=3.70 ppt), making it necessary to broaden the sampling design so as to check the penetration of marine waters into the Paracauari River estuary as far as approximately 40 km from its mouth.

The waters of the Paracauari River estuary may be classified in oligohaline (salinity value below 5 ppt) during the period of higher precipitation rates and mesohaline (salinity value between 5 and 18 ppt) during the period with lower precipitation rates (Kennish, 1994). Tropical estuaries, including the ones from the Amazon region, show high SPM concentrations over periods of higher rainfall, when the areas bordering the estuary are flooded. During the period of lower rainfall, however, low SPM concentrations reflect the influence of winds, tides, and marine intrusion (Bradley and Philip, 1999).

The estuarine waters of the Paracauari River may be classified as "white waters", resulting from suspended organic-mineral matter that is transferred into the estuary by countless rivers, "holes", and *igarapés*, mainly over the higher rainfall

period. This organic-mineral complex is made up of organic and clayish matter, predominantly kaolinitic (Lima and Kobayashi, 1988).

It was not possible to define the maximum turbidity zone (MTZ) during the period of higher precipitation rates, because high SPM concentrations along the estuary and the absence of salinity hampered the identification of this zone. Under these circumstances, MTZ may undergo an advection process through tens of kilometers towards the continental shelf, which depends on freshwater input, and therefore, there is little sedimentation within the estuarine system (Geyer *et al*., 2004).

MTZ occurred in association with the brackish waters that penetrate the estuary in the period of lower precipitation rates so it was identified upstream from the estuary (P10 to P15). This occurrence is likely due to residual circulation (Cancino and Neves, 1999; Jay and Musiak, 1994), which is ruled by tide asymmetry, due to a non-linear response of shear stress to velocity, and this effect is especially important in macrotidal estuaries (Cancino and Neves, 1999).

Tropical estuaries, including the ones from the Amazon region, have high SPM concentrations over periods of higher rainfall, when the areas bordering the estuary are flooded. During the period of lower rainfall, however, low SPM concentrations reflect the influence of winds, tides, and marine intrusion (Bradley and Philip, 1999).

The estuarine waters of the Paracauari River may be classified as "white waters", resulting from suspended organic-mineral matter that is transferred into the estuary by the various rivers, "holes", and igarapés, mainly over the period of higher rainfall. This organic-mineral complex is made up of organic and clayish matter, predominantly kaolinitic (Lima and Kobayashi, 1988).

It was not possible to define the maximum turbidity zone (MTZ) during the period of higher precipitation rates because high SPM concentrations along the estuary and the absence of salinity hampered the identification of this zone. Under these circumstances, the MTZ may undergo an advection process across tens of kilometers towards the continental shelf, which depends on the freshwater input; therefore, there is little sedimentation within the estuarine system (Geyer *et al*., 2004).

MTZ occurs in association with the brackish waters that enter the estuary in the lower rainfall period, and therefore, it was identified upstream from the estuary (P10 to P15). This occurrence is likely due to residual circulation (Cancino and Neves, 1999; Jay and Musiak, 1994), which is ruled by tide asymmetry, through a non-linear response of shear stress to velocity, and this effect is especially important in macrotidal estuaries (Cancino and Neves, 1999).

Upstream from the Paracauari River estuary, the water column is shallow (5-m depth) compared to the estuarine course (10 to 15 m) and this region has siltic-sandy sediment with high hydrodynamics and a sand content of approximately 55 % (Ferreira, 2013). This favors the resuspension of sediments and their transportation due to the turbulence generated by tidal currents. Thereby, the MTZ moves upstream or towards the estuary mouth according to tidal phases, flood or ebb tides, respectively.

Considering geological criteria, the Paracauari River estuary may be classified as a coastal plain estuary, as per the definition by Pritchard (1967). Nonetheless, this estuary does not discharge directly into the ocean, because it is inserted in a complex estuarine system, characterized by high freshwater discharges, from both the Pará and Amazonas River, which cause sea water dilution.

The circulation in this estuary is regulated by macrotides and it may be classified as tide-dominated according to Davis and Hayes (1984), as well as a Type-1, well-mixed estuary, according to Hansen and Rattray's Stratification-Circulation Diagram (1966) (Ferreira, 2013). Despite the vertical homogeneity, this estuary shows zonation, with spatial variations regarding the studied parameters.

This study proposes an experimental comparison between the Paracauari River estuary and the estuarine model suggested by Kjervfe (1990), comprised of three zones: Riverine Zone (RZ), Mixing Zone (MZ), and Coastal Zone (CZ) (Figure 3).

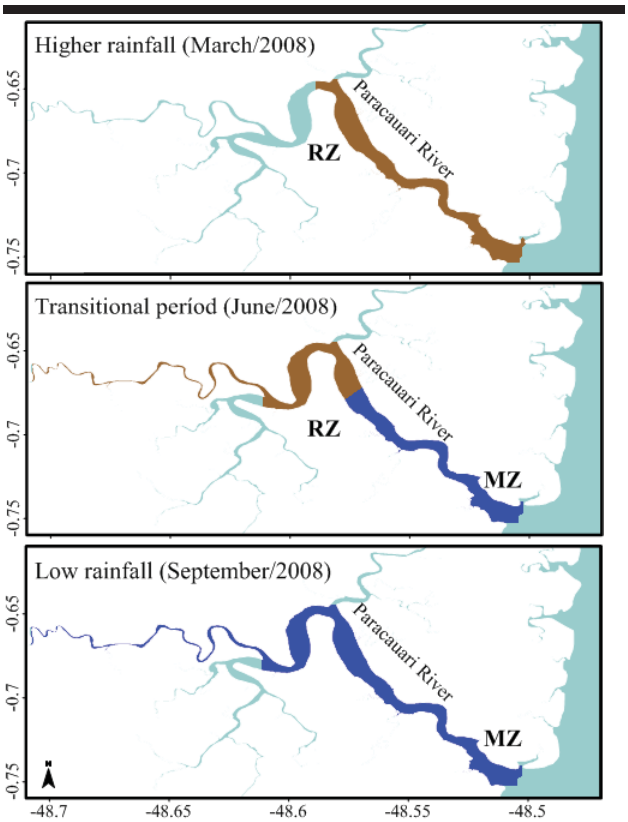

Figure 3. Riverine Zone and Mixing Zone in the Paracauari river.

In the Paracauari River estuary, the higher freshwater discharge during higher rainfall period causes this estuary to become a RZ (S < 1.0), once the MZ may have been undergone an advection process from the semi-closed region to the CZ. Over the transitional period, it was possible to identify an approximately 8 km-long MZ from the mouth, followed by the RZ; and over the lower rainfall period, the brackish waters enter the estuary as far as 40 km, which characterizes this section as MZ, from the mouth to the source, where the waters are not

totally brackish due to the dilution attributed to the high water input from the Pará and Amazonas Rivers. This incursion of brackish waters into the estuary is favored by the decrease in freshwater discharge, the low estuary slope and the force of macrotides, which are capable of inducing vertical homogeneity of the water column and spreading upstream from the estuary to considerable distances (Miranda and Castro, 2002).

CONCLUSIONS

In the Paracauari River estuary, there is a spatio-temporal variation of the analyzed parameters according to tide and climatic seasonality of the Amazon region, which influences freshwater discharge.

The Paracauari River discharge, during higher rainfall period, dilutes the content of dissolved salts, and consequently, estuarine waters become oligohaline. On the other hand, the estuary is mesohaline during lower rainfall period owing to the dilution caused by the waters of the Pará River (Marajó Bay), which acts as a barrier to the invasion of ocean waters.

The zonation pattern indicates that: during higher rainfall period, the Paracauari River estuary is a RZ, whilst during the transitional period, there is a formation of an approximately 8 km MZ followed by the RZ upstream from the river, within river domain. During the lower rainfall period, a MZ of about 40 km extends from the mouth of the estuary to its headwaters, where it is possible to spot a MTZ. This MTZ occurs in the interface between fresh and brackish waters, in an oligohaline environment ($0.5<S<5.0$), located 12 km from the estuarine channel, conditioned by river morphology and transport.

These zones have a direct effect on the local fishery, which is traditionally subsistence-based; the distribution and transportation of compounds (particulate organic matter, salts, sediments, nutrients, pollutants); the settling of fine grains; and the distribution of vegetation on the tidal plain (mangrove forest or floodplain).

ACKNOWLEDGMENTS

The authors would like to thank the support of Coordenação de Aperfeiçoamento de Pessoal de Nível Superior.

LITERATURE CITED

Bradley, E. and Philip, B., 1999. A comparative study of nutrient behavior along the salinity gradient of tropical and temperate estuaries. *Estuaries*, 22(2), 313-326.

Cancino, L. and Neves, R., 1999. Hydrodynamic and sediment suspension modelling in estuarine systems - Part II: Application to the Western Scheldt and Gironde estuaries. *Journal of Marine Systems*, 22(2), 117–131.

Davis, JR.R.A and Hayes, M.O., 1984. What is a wave-dominated coast? *Marine Geology*, 60(1), 313-329.

Diretoria de Hidrografia e Navegação. *Tábua das Marés. Marinha do Brasil*. http://www.mar.mil.br.

Fairbridge, R.W., 1980. The Estuary: its identification and geodynamic cycle. *In*: Olausson, E. and Cato, I. (ed.), *Chemistry and Bioquemistry of Estuaries*. New York: Wiley, pp. 1-36.

Ferreira, G.P., 2013. Caracterização hidrodinâmica e do transporte de sedimentos na região fluvio-estuarina do rio Paracauari, Ilha de Marajó, Pará. Recife, Pernambuco: Universidade Federal de Pernambuco, Ph.D. dissertation, 104p.

França, C.F. de., 2003. Morfologia e mudanças costeiras da margem leste da ilha de Marajó (PA). Belém, Pará: Universidade Federal do Pará, Master's thesis, 144p.

Geyer, W.R.; Hill, P.S. and Kineke, G.C., 2004. The transport, transformation and dispersal of sediment by buoyant coastal flows. *Continental Shelf Research*, 24(7-8), 927–949.

Jay, D.A. and Musiak, J., 1994. Particle trapping in estuarine tidal flows. *Journal of Geophysical Research*, 99(10), 445-461.

Kennish, M.J., 1994. *Practical Handbook of Marine Science*. Boca Raton, Florida: CRC Press, 566p.

Kjerfve, B., 1990. *Manual for investigation of hydrological processes in mangrove ecosystems*. New Delhi, India: UNESCO/UNDP, 79p.

Lima, W.N. and Kobayashi, C.N., 1988. Sobre o quimismo predominante nas águas do sistema fluvio-estuarino de Barcarena, PA. *Geochimica Brasiliensis*, 2(1), 53-71.

Martorano, L.G.; Pereira, L.C.; Cezar, E.G. M.; Pereira, I.C.B., 1993. *Estudos Climatológicos do estado do Pará, classificação climática (Köppen) e deficiência hídrica (Thorntwhite, Mather)*. Belém: SUDAM/EMBRAPA, 53p.

Miranda, L.B. and Castro, B.M.B., 2002. *Princípios de Oceanografia Física de Estuários.* São Paulo: Editora da Universidade de São Paulo, 400p.

Pritchard, D.W., 1967. What is an Estuary: Physical View Point. In: Lauff, G.H. (eds.), *Estuaries*. Washington: American Association for Advance of Science, pp.3-5.

Rossetti, D.F.; Goes, A.M.; Valeriano, M.M. and Miranda, M.C.C., 2007. Quaternary tectonics in a passive margin: Marajo Island, northern Brazil. *Journal of Quaternary Science,* 23(2), 121–135.

Souza, E.B; Lopes, M.N.G.; Rocha, E.J.P.; Souza, R.S.; Cunha, A.C.; Silva, R.R.; Ferreira, D.B.D.; Santos, D.M.; Carmo, A.M.C.; Sousa, R.A.; Guimarães, P.L.; Mota, M.A.S.; Makino, M.; Senna, R.C.; Sousa, A.M.L.; Mora, G.V.; Kuhn, P;A.F., Souza, P.F.S.; Vitorino, M.I., 2009. Precipitação sazonal sobre a Amazônia oriental no período chuvoso: observações e simulações regionais com o RegCM3. *Revista Brasileira de Meteorologia*, 24(2), 111-124.

Souza, L.S.B., 2010. Evidências tectônicas no leste da ilha do Marajó: integração de dados morfoestruturais e geofísicos. São Paulo, São Paulo: Universidade de São Paulo, Master's thesis, 202p.

Strickland, J.D.H. and Parsons, T.R., 1972. *A practical handbook of seawater analysis.* Ottawa: Fisheries Research Board of Canada, 311p .

Journal of Coastal Research	SI	75	98-102	Coconut Creek, Florida	2016

The Trophic Status of an Amazonian Estuary Under Anthropogenic Pressure (Brazil)

Marcela C. Monteiro[‡†*], Luci C. C. Pereira[†], and José A. Jiménez[‡]

[‡]Universitat Politécnica de Catalunya, Barcelona Tech, Spain. Laboratori d'Enginyeria Maritima, C/ Jordi Girona 1-3, Campus Nord, Ed. D1, 08034 Barcelona, Spain.

[†]Instituto de Estudos Costeiros, Universidade Federal do Pará, Bragança, 68600-000, Brazil.

www.cerf-jcr.org

www.JCRonline.org

ABSTRACT

Monteiro, M.C.; Pereira, L.C.C., and Jiménez, J.A., 2016. The trophic status of an Amazon estuary under anthropic pressure (Brazil). *In:* Vila-Concejo, A.; Bruce, E.; Kennedy, D.M., and McCarroll, R.J. (eds.), *Proceedings of the 14th International Coastal Symposium* (Sydney, Australia). *Journal of Coastal Research*, Special Issue, No. 75, pp. XX-XX. Coconut Creek (Florida), ISSN 0749-0208.

The effects of the anthropogenic process on the trophic status of the Caeté estuary (located 150 km southwest of the Amazon delta) were undertaken under different climate conditions. To do this, oceanographic data were carried out, covering the dry season of 2010 (August–December: rainfall 363 mm), and the wet (January–July, rainfall 2483 mm) and dry seasons of 2011 (August–October, rainfall 135 mm). During the dry season (2010 and 2011) the mean discharge of the Caeté River was less than 20.0 m^3 s^{-1}, while, during the wet season, the mean discharge increased to 73.6 m^3 s^{-1}. Tidal ranges oscillated between 2.2 and 3.8 m, and current speeds varied from 0.6 and 0.7 m s^{-1} in both seasons (wet and dry). Salinity (under 3.0) and pH (under 6.0) were typical of fluvial systems. Turbidity (up to 150 NTU), dissolved oxygen (6.7 mg L^{-1}) and dissolved nutrient (nitrite, nitrate, phosphate and silicate, but not ammonium) concentrations reached their maximum levels during the dry season, when the runoff decreased. The high chlorophyll *a* concentrations (values of up to 10.0 mg m^{-3}) were typical of environments with high levels of primary productivity. According to the trophic index (TRIX), the waters of the Caeté estuary were characterized by moderate levels of eutrophication and good water quality during the wet season, shifting to high levels of eutrophication and bad water quality during the dry season. A comparative analysis indicates that eutrophication is less intense during neap tides in comparison with spring tides.

ADITIONAL INDEX WORDS: *Macrotidal regime, Neap tide, Trophic index, Amazon estuary.*

INTRODUCTION

Estuaries represent a complex and dynamic ecosystem which is subject to both marine (influx of saline water and sediments, tides and waves) and fluvial (river water and sediment) processes (Dalrymple, 2006). These environments are considered to be the world's most productive natural areas (Kennish, 2002). In tropical and sub tropical regions, they are associated with extensive mangrove forests, which are responsible for their high primary and secondary productivity (Adame and Lovelock, 2010).

Considered susceptible to anthropogenic perturbations that may disturb their natural conditions, estuaries are among the world's most intensively used and degraded natural ecosystems (Wetz and Yoskowitz, 2013). On the Amazon coast, these impacts are associated primarily with unregulated urban growth and the lack of basic services for local populations. The lack of adequate wastewater treatment systems results in the discharge of untreated domestic and industrial effluents directly into local bodies of water, including estuaries (Pereira *et al*., 2010; Gomes *et al*., 2011). As a consequence, the levels of nitrogen and phosphorous in Amazonian estuaries, which are environments naturally rich in nutrients, have been increasing steadily over the past few decades.

The present study focuses on the estuary of the Caeté River, which is located on the Amazon Macrotidal Mangrove Coast of the northern Brazilian state of Pará. The Caeté estuary is dominated by macrotides, which play an important role in the supply of dissolved nutrients, due to the flooding of the extensive area of mangrove during each tidal cycle

Anthropogenic impacts have resulted in a progressive increase in local nutrient levels, primarily through the discharge

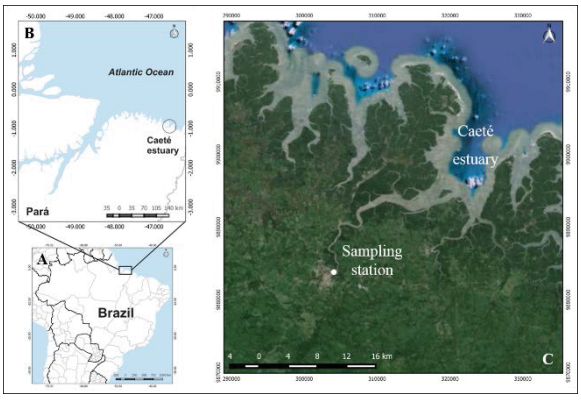

Figure 1. (A) Location of the Caeté estuary in northern Brazil, (B) the northern coast of Pará and (C) the Caeté Estuary.

DOI: 10.2112/SI75-020.1 received 15 October 2015; accepted in revision 15 January 2016.

*Corresponding author: rosigleyse@yahoo.com.br

of untreated sewage into the estuary, mainly from the unregulated growth of urban development in the upper sector of the estuary. To investigate the effects of this process on the trophic status of this Amazonian estuary, the present study monitored the temporal oscillations in physical-chemical, chemical and biological variables in the upper Caeté estuary, and evaluated its trophic status under different climate conditions.

Background

The Caeté Estuary is part of the Amazon coastal in Pará, northern Brazil (Figure 1). The main channel meanders for more than 40 km, and is 150 m wide at its southernmost (upper) limit, and 4600 m wide at the mouth (Guerra and Cunha, 1998).

The climate of the study area is equatorial humid, with a wet season, which normally extends between January and June, when total rainfall may exceed 2000 mm, and mean temperatures of 26ºC–27°C, and a dry season between July and December, when mean monthly rainfall is less than 100 mm, and mean temperatures of 28ºC–30°C (INMET, 2009).

The area has a semi-diurnal tide regime, with a 4-6 m tidal range during spring tides and a 2-4 m range during neap tides (Pereira *et al*., 2010).

The estuary is located in the Caeté hydrographic basin, which covers a total area of 2195 km², and has population of approximately 300,000 (IBGE, 2010). Around 40% of this population (120,000 inhabitants) is concentrated in the town of Bragança, located on the upper estuary.

METHODS

Rainfall data were recorded daily by the Brazilian Meteorology Institute – INMET (-1.06º S -46.9º W), while river discharge data was obtained from the Brazilian Water Agency – ANA (-1.16º S -46.5º W).

Oceanographic data were collected every two months during the flood phase of the neap tide between September 2010 and October 2011 (with the final sample being collected in October, rather than September), near the urban zone of Bragança, in the upper estuary (Figure 1).

Tidal height was measured using tide data loggers (TWR 2050) during 13 hours. Cross-section of current profiles were recorded near the sampling station, during dry and wet seasons. This data was recorded with a Workhorse 1200 kHz Acoustic Doppler Current Profile (ADCP) by Teledyne® RDI™.

Salinity, turbidity, dissolved oxygen (DO) and oxygen saturation (DO%) were recorded during 5 min by CTDO at 1.0 m below the surface of the water and 1.0 m from the bottom of the estuary. A Niskin oceanographic bottle (General OceanicsTM) was used to obtain vertical water samples (surface and bottom). These samples were used to determine the pH, and the dissolved nutrient and chlorophyll *a* concentrations. The pH was measured with a pHmeter and dissolved nutrients (nitrate–NO_3^-, nitrite–NO_2^-, ammonium-NH_4^+, phosphate-$PO^3{}_4^-$ and silicate-$SiOH^+$) were analyzed according to the Strickland and Parsons (1972) and Grasshoff *et al*., (1983) methods. Chlorophyll *a* concentrations were estimated by the Parsons and Strickland (1963) and UNESCO (1966) methods.

The tidal prism was estimated by: P = H x A, where H is the mean tidal range and A is the surface area of the basin (220 km², according to Wolf *et al*., 2000). The trophic state of the estuary was given by: TRIX = ($\log_{10}$[Chl *a* x |DO_2%| x DIN x DIP] + k)/m, following Vollenweider *et al*., (1998), where Chl *a* is the chlorophyll *a* concentration, DO_2% is the oxygen saturation rate, DIN is the dissolved inorganic nitrogen (NO_2^- + NO_3^- + NH_4^+), and DIP is the concentration of dissolved inorganic phosphorus (PO_4), while k and m are constants with values of 1.5 and 1.2, respectively. Water is classified on the following scale: (i) 0–4: low eutrophication and high water quality; (ii) > 4–5: moderate eutrophication and good water quality; (iii) > 5–6: high eutrophication and bad water quality and, (iv) > 6–10: elevated eutrophication and poor water quality.

To verify possible tidal and seasonal (wet *vs.* dry) differences in the parameters monitored, the normality of the data was evaluated using the Lilliefors test (Conover, 1971). When a normal distribution was not found, the data were log-transformed (x+1) in the PRIMER v6 software (Clarke and Warwick, 2001) and once again tested for a normal distribution. The data were then tested for homogeneity of variances using Bartlett's χ^2 (Sokal and Rohlf, 1969). When homogeneous, the data were analyzed using the *t* test (α = 0.05), whenever necessary, Fisher's (LSD) exact test was applied. When the variances were heterogeneous, the nonparametric Mann-Whitney (U test) and Kruskal-Wallis' H (Zar, 1999) were used. Analyses were run in the STATISTICA® v6 software (StatSoft, 2001).

RESULTS

In this section were described the climatological and oceanographic conditions of the study area, as well as data on water quality obtained during oceanographic campaigns.

Climatological and Oceanographic Conditions

Based on the precipitation records, the study period included the dry season of 2010 (August to December, 363 mm), and the wet (January to July, 2483 mm) and dry seasons (August to October, 135 mm) of 2011. There was considerable seasonal variation, with only 18% of the total annual precipitation being recorded during the dry season of 2010, and only 5% in 2011. During the dry season, the mean discharge of the Caeté River was 9.1 $m^3\ s^{-1}$ in 2010, and 17.1 $m^3\ s^{-1}$ in 2011, increasing to 73.6 $m^3\ s^{-1}$ during the wet season. Monthly precipitation and river discharge values are shown in Figure 2.

The tidal range varied between 2.2 m and 3.8 m. In general terms, current speeds were between 0.6 and 0.7 m s^{-1}, in both seasons (wet and dry). The vertical current profile in the Caeté estuary lacked gravitational circulation and was characterized by a predominance of mixing of freshwater and marine water, with

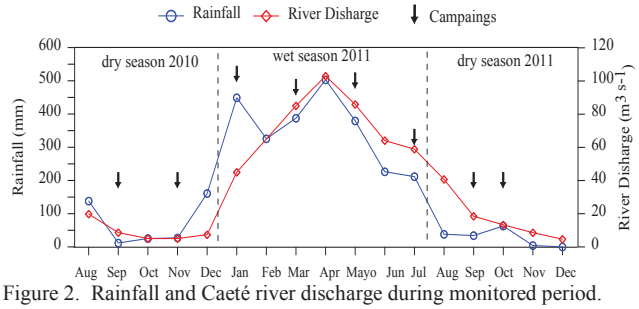

Figure 2. Rainfall and Caeté river discharge during monitored period.

differences in the water column of only 0.1 m s^{-1} (Figure 3). The greatest difference between the subsurface and bottom current speeds was recorded during the wet season (0.5 m s^{-1}) indicating weak mixing and slight stratification. This value was recorded in May 2011, when fluvial discharge was high (monthly mean of 85 $m^3.s^{-1}$). The tidal prism ranged from 50 to 72 m^3 x 10^6 with the highest values in November 2010 and July 2011 (Figure 4).

Water Quality

The analysis of the hydrological data found no significant difference between the surface and bottom layers. Given this, a single, mean value representative of the water column was calculated for this parameter.

The salinity (under 3.0) and pH (under 6.0) of the study area reflect the fluvial characteristics of the upper Caeté estuary during the study period, including the dry season, when the discharge of the river decreased, to lower than 17.1 m^3 s^{-1} (Figure 5).

Turbidity (up to 30 NTU) and dissolved oxygen concentrations (up to 3.7 mg L^{-1}) peaked during the dry season, in the months influenced by the equinoctial tides, that is, September 2010 and October 2011, respectively (Figure 5).

Seasonal fluctuations also influenced the input of nutrients, although significant seasonal differences were only recorded in phosphate ($U = 140$ $p = 0.00$).

During the wet season, when the mean discharge of the Caeté River reached levels of up to 45 m^3 s^{-1} (in January, March and May, 2011) dissolved nutrients (except ammonium) all decreased, with nitrite decreasing to 0.2 µm, nitrate to 4.4 µm, ammonium to 2.8 µm, phosphate to 0.2 µm, and silicate to 30.7 µm. In the dry season, by contrast, the concentrations were higher, nitrite increasing to 0.3 µm, nitrate to 14.4 µm, ammonium to 2.6 µm, phosphate to 0.3 µm, and silicate to 86.6 µm (Figure 5). Nitrate was the dominant nitrogenous component (more than 50% of total DIN). Ammonium – the least oxidized form of nitrogen – was more abundant during the wet season (March, 2011), when it represented 50% of the dissolved inorganic nitrogen (Figure 6).

High chlorophyll *a* concentrations (up to 10.0 mg m^{-3}) were common in both seasons, with peaks of around 20.0 mg m^{-3} being more frequent during the wet season (Figure 6), coinciding with the peaks in the availability of ammonium (March, 2011).

The TRIX analysis showed a moderate level of eutrophication in the Caeté estuary, together with good water quality during the wet season (TRIX values between 4 and 5), shifting to high eutrophication and bad water quality during the dry season (TRIX values of between 5 and 6) (Figure 6). This is consistent with the seasonal pattern in dissolved nutrients described above.

DISCUSSION

In the Amazon region, estuarine dynamics are driven by annual precipitation of over 2000 mm – a phenomenon found on only 7% of the world's surface (Corlett and Primack, 2011) – and the local macrotidal regime, which determines the characteristics of the interaction between the river and the sea. A lower influence of the tides (neap tides) and the increase of the rainfall during the study period resulted in lower salinity and pH levels in comparison with those recorded by Pereira *et al*., (2010) in the same study area during spring tides.

The Caeté is considered to be a well-mixed estuary (Wolf *et al*., 2000), however, the slight stratification of the water column in Mayo 2011 indicates low levels of turbulence. This pattern is typical of periods of high fluvial discharge and reduced tidal intrusion (Dyer, 1996), as observed during the wet season in the neap tide period.

The local macrotidal regime provoke the turbulent mixing of the estuary waters and strong currents, such as those observed in the Caeté estuary (up to 0.5 m s^{-1}) also supported the resuspension of the fine particles from the bottom into the water column, and the oxygenation of the waters. There are also a number of pollution sources located on the Caeté estuary (12 sewage outlets, 5 ice factories, a fish processing plant and a garbage dump), and the discharge of effluents from these installations adds to the turbidity and eutrophication of the estuary waters, due to their input of organic material and dissolved nutrients (Monteiro *et al*., accepted).

In general, the input of dissolved nutrients into estuaries peaks during the period of maximum fluvial discharge, as observed in the Godavari and Patuxent estuaries (Boynton *et al*., 2008) where rainfall rate is higher than 1000 mm. This is because large amounts of terrestrial nutrients and other substances are carried to the water through surface runoff, atmospheric deposition, and groundwater discharge. By contrast, studies of the Caeté estuary conducted during the spring tide have shown that the fluvial discharge contributes to the dilution of the effluents released into the water, and that this effect increases during the wet season, when runoff is at its highest level (Pereira *et al*., 2010; Monteiro *et al*., 2011). In the present study, the good quality of the water and the moderate levels of eutrophication recorded during the wet season reflect this process.

The high concentrations of nitrate and low levels of nitrite and ammonium recorded in the Caeté estuary confirmed an active nitrification process in its waters. This indicates the ammonium is being oxidized by anaerobic bacteria, which is common in well-oxygenated environments, such as those found

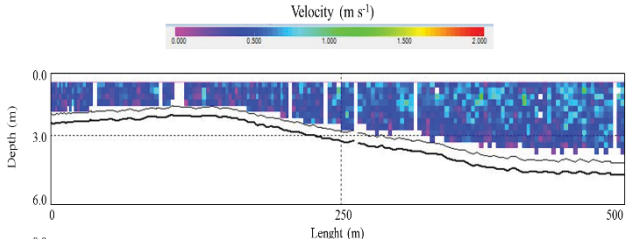

Figure 3. Current velocities in the Caeté estuary during the wet season of the study period.

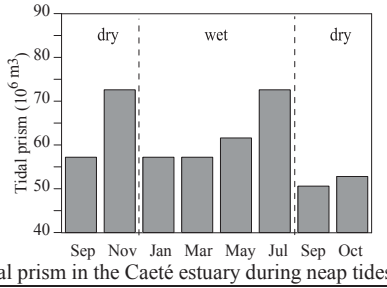

Figure 4. Tidal prism in the Caeté estuary during neap tides.

on the Amazon Coast (Costa *et al*., 2013). Similar results were obtained in the Quatipuru estuary, 40 km from the Caeté, which is also inserted within an area of mangrove forest (Pamplona *et al*., 2013). By contrast, studies in estuaries associated with mangroves in the United States found that NH_4^+ was the dominant type of DIN (Childers *et al*., 2006). Dittmar and Lara (2001) found a similar situation in an earlier study of the Caeté estuary during the dry season.

While the input of wastewater from anthropogenic sources increases over time due to the region's population increases by approximately 20% per decade, the eutrophication observed during the present study (neap tide) was less accentuated than that observed during previous years by Monteiro *et al*., (accepted) on the spring tide. The reduction of the tidal prism during the neap tide probably reduced the flooding of the mangrove, resulting in a reduced outwelling to the estuary. It is also important to note that the relatively high rainfall rates recorded in the present study may have contributed for an improvement in the water quality during this period, due to the dilution and transportation of nutrients to the lower estuary, as observed in the previous studies of Pereira *et al*., (2010) and Monteiro *et al*., (2011).

The reduction in the availability of this nutrient during the wet season, and the high productivity observed (high chlorophyll *a* concentrations) indicate that a reduction in dissolved nutrient concentrations did not affect phytoplankton growth, as observed in the estuaries of northeastern Brazil (Noriega *et al*., 2009).

Given this, it is possible to conclude that the periods during which dissolved nutrient concentrations tend to decline (*i.e*. during the wet season and neap tides), the Caeté estuary sustains high levels of productivity.

CONCLUSIONS

During neap tides, the reduced intrusion of salt water favored a slight stratification of the estuary (*i.e*. during the wet season). The dilution of dissolved nutrient concentrations during the wet season resulted in less eutrophic waters during this period. This did not affect the biological productivity of the estuary. The nutrient levels reflect a reduced input during neap tides, possibly due to a decrease in the outwelling from the mangrove.

ACKNOWLEGDEMENTS

This study is result of a Research Project (558105/2009-9) supported by Brazilian Council for Scientific and Technological Development (CNPq). The first author was supported by Erasmus Mundus (EB09D1449PA) and a CNPq Ph.D scholarship (202546/2011). Pereira is grateful to CNPq for providing a grant (310909/2014-7 and 200629/2014–0). The work of Jiménez was supported by the PaiRisC-M project, funded by the Spanish Ministry of Economy and Competitiveness (CTM2011-29808).

LITERATURE CITED

Adame, M.F., and Lovelock, C.E., 2011. Carbon and nutrient exchange of mangrove forests with the coastal ocean. *Hydrobiologia*, 663, 23–50.

ANA - Agência Nacional de Águas, 2012. Portal do sistema nacional de informações sobre recursos hídricos. http://www.ana.gov.br/portalsnirh/.

Boyton W.R.; Hagy, J.D.; Cornwell, J.C.; Kemp, W.M.; Greene, S.M.; Owens, M.S.; Baker, J.E., and Larsen, R.K., 2008. Nutrient Budget and management actions in the Patuxent River estuary, Maryland. *Estuaries and Coasts,* 31, 623-651.

Childers, D.L.; Boyer, J.N.; Davis, S.E.; Madden, C.J.; Rudnick, D.T., and Sklar, F.H., 2006. Relating precipitation and water management to nutrient concentrations in the oligotrophic ''upside-down'' estuaries of the Florida Everglades. *Limnology Oceanography*, 51(1), 602–616.

Clarke, K.R. and Warwick, R.M., 2001. *Change in marine communities: an approach to statistical analysis and interpretation*. Plymouth: Primer-E Ltd., 172p.

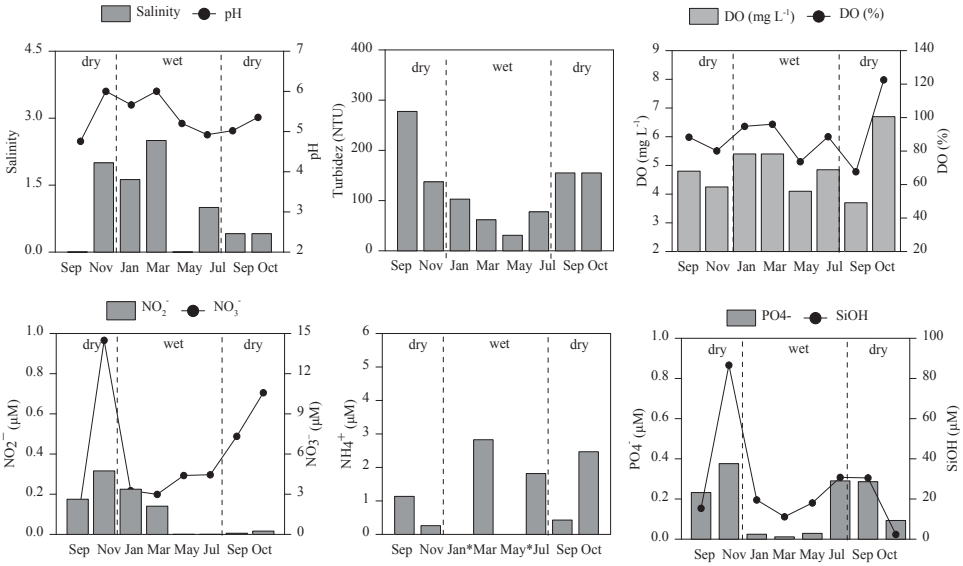

Figure 5. Salinity, pH, turbidity, dissolved and saturated oxygen levels and dissolved nutrients in the Caeté estuary. (*) not collected data.

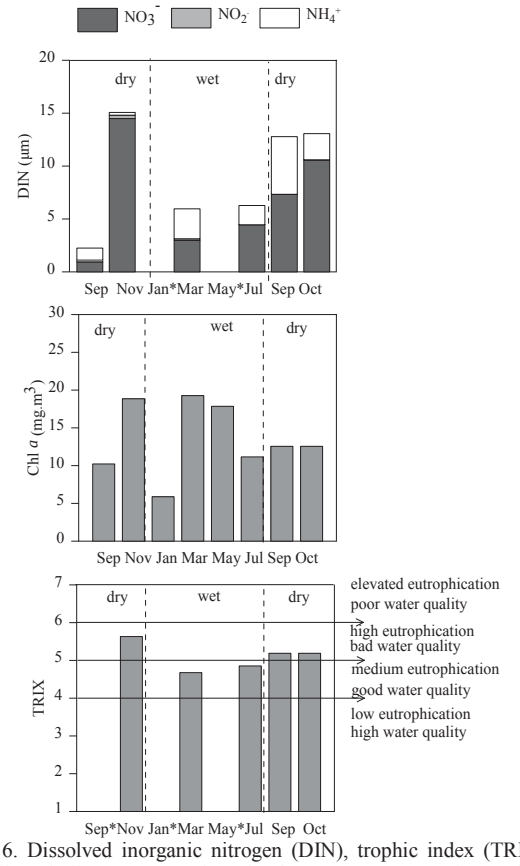

Figure 6. Dissolved inorganic nitrogen (DIN), trophic index (TRIX) and Chlorophyll *a* concentrations in the Caeté estuary. (*) no data collected.

Conover, W. O. J., 1971. *Pratical nonparametric statistics*. New York: Jonh Wiley, 302p.

Corlett, R.T. and R.B. Primack., 2011. *Tropical Rainforests: An Ecological and Biogeographical Comparison*. Oxford: Wiley-Blackwell. 336p.

Costa, A.K.R.; Pereira, L.C.C.; Costa, R.M.; Monteiro, M.C., and Flores-Montes, M.J., 2013. Oceanographic processes in an Amazon estuary during anatypical wet season. *In:* Conley, D.C., Masselink, G., Russell, P.E., and O'Hare, T.J. (eds.), *Proceedings 12th International Coastal Symposium*. *Journal of Coastal Research*, Special Issue No. 65, pp. 1104-1109.

Dalrymple, R.W., 2006. Incised valleys in space and time: an introduction to the volume and an examination of the controls on valley formation and filling. *In*: Dalrymple, R.W., Leckie, D.A., and Tillman R.W. (eds.), *Incised valleys in space and time*. Tulsa: Society for Sedimentary Geology, pp. 5–12.

Dyer, K.R., 1996. *Estuaries – a Physical Introduction*. Chichester: John Wiley & Sons, 195p.

Dittmar, T. and Lara, R.J., 2001. Do mangroves rather than rivers provide nutrients to coastal environments south of the Amazon River? Evidence from long-term flux measurements. *Marine Ecology Progress Series,* 213, 67-77.

Grasshoff, K.; Emrhardt, M., and Kremling, K., 1983. *Methods of seawater analysis*. New York: Verlag Chemie, 419p.

Gomes, R.K.S.; Takiyama, L.R.; Pereira, L.C.C.; Silva, U.R.L., and Ferreira, R.C.M., 2011. Social diagnosis and guidelines for coastal management in environmental protection areas of the Amazon Littoral (Amapá, Brazil). *In*: Furmancyz, K.; Giza, A., and Terefenko, Pawel. *(*eds.*), Procedings, 11th International Coastal Symposium. Journal of Coastal Research*, Special Issue No. 64, pp. 1331-1334.

Guerra, A.J.T. and Cunha, S.B., 1998. *Geomorfologia: uma atualização de bases e conceitos*. Rio de Janeiro: Bertrand Brasil, 388p.

IBGE – Instituto Brasileiro de Geografia e Estatística, 2010. http://www.ibge.gov.br/home/estatistica/populacao/censo2010/default.shtm.

Kennish, M.J., 2002. Environmental threats and environmental future of estuaries. *Environmental Conservation,* 29, 78-107.

INMET - Instituto Nacional de Meteorologia, 2009. http://www.inmet.gov.br/sonabra/maps/automaticas.php.

Monteiro, M.C.; Pereira, L.C.C.; Guimarães, D.O.; Costa, R.M.; Souza-Filho, P.W.M.; Vieira, S.R., and Jiménez, J.A., 2011. Influence of natural and anthropogenic conditions on the water quality of the Caeté River Estuary (NE Brazil). *In*: Furmancyz, K.; Giza, A., and Terefenko, Pawel. *(*eds.*), Procedings, 11th International Coastal Symposium. Journal of Coastal Research*, Special Issue No. 64, pp. 1535-1539.

Monteiro, M.C.; Jiménez, J.A., and Pereira, L.C.C. Natural and human controls of water quality of an Amazon estuary (Caeté-PA, Brazil). Accepted.

Noriega, C. and Araújo, M.C., 2009. Nitrogen and phosphorus loading in coastal watersheds in northeastern Brazil. *Journal of Coastal Research*, Special Issue No. 56, pp. 871-875.

Pamplona, F.C.; Paes, E.T., and Nepomuceno, A., 2013. Nutrient fluctuations in the Quatipuru river: A macrotidal estuarine mangrove system in the Brazilian Amazonian basin. *Estuarine, Coastal and Shelf Science*, 133, 273-284.

Parsons, T.R. and Strickland, J.D.H., 1963. Discusson of spectrophometric determination of marine-plant pigments, with revised equations for ascertaining chlorophyll *a* and carotenois. *J. Mar. Res.*, 21, 105-156.

Pereira, L.C.C.; Monteiro, M.C.; Guimarães, D.O., and Costa, R.M., 2010. Seasonal effects of wastewater on Caeté Estuary water quality in the Brazilian Amazon littoral zone. *Anais da Academia Brasileira de Ciências,* 82(2), 1-12.

Sokal, R. R. and Rohlf, F. J., 1969. *Biometry: The principles and pratice of numerical classification in biological research*. California: W.H. Freeman, 776p.

Strickland, J.D.H. and Parsons, T.R.A., 1972. Manual of seawater analysis. *B. Fish. Res. Board Can.,* 125, 1-185.

UNESCO – United Nations Educational, Scientific and Cultural Organization. 1966. *Determination of photosynthetic pigments in sea water*. Paris: Unesco. 69p.

Vollenweider, R.A.; Giovanardi, F.; Montanari, G., and Rinaldi, A., 1998. Characterization of the trophic conditions of marine coastal waters, with special reference to the NW Adriatic Sea: proposal for a trophic scale, turbidity and generalized water quality index. *Environmetrics*, 9, 329-357.

Wetz, M.S. and Yoskowitz, D.W., 2013. An extreme future for estuaries? Effects of extreme climatic events on estuarine water quality. *Marine Pollution Bulletin*, 69, 7-18.

Journal of Coastal Research	SI	75	103-107	Coconut Creek, Florida	2016

Random Wave-Induced Onshore Scour Characteristics around Submerged Breakwaters on Mild Slopes

Dag Myrhaug[†*] and Muk Chen Ong[‡]

[†]Department of Marine Technology,
Norwegian University of Science and Technology,
Trondheim; Norway

[‡]Department of Mechanical and Structural
Engineering and Materials Science,
University of Stavanger, Stavanger, Norway

www.cerf-jcr.org

www.JCRonline.org

ABSTRACT

Myrhaug, D. and Ong, M.C., 2016. Random Wave-Induced Onshore Scour Characteristics around Submerged Breakwaters on Mild Slopes. *In:* Vila-Concejo, A.; Bruce, E.; Kennedy, D.M., and McCarroll, R.J. (eds.), *Proceedings of the 14th International Coastal Symposium* (Sydney, Australia). *Journal of Coastal Research*, Special Issue, No. 75, pp. 103-107. Coconut Creek (Florida), ISSN 0749-0208.

This paper provides a stochastic method by which the two-dimensional onshore scour characteristics along the base of submerged breakwaters exposed to normally incident random waves on a mildly sloped sandy seabed can be derived. Here the formulas for the regular wave-induced scour characteristics provided by Young and Testik (2009) combined with the Battjes and Groenendijk (2000) wave height distribution for mild slopes are used. These formulas are combined with describing the waves as a stationary random process. An example is included to calculate the significant values of the random wave-induced onshore scour characteristics; the maximum scour depth, the scour length, and the distance of the maximum scour depth location from the onshore breakwater face. The present results can be used to make assessment of the random wave-induced scour characteristics based on available wave statistics.

ADDITIONAL INDEX WORDS: *Submerged breakwater, vertical breakwater, semicircular breakwater, mild slopes, scour, random waves, stochastic method.*

INTRODUCTION

Submerged breakwaters are frequently used to protect exposed coastal areas, i.e. they can be used to reduce the erosion of the shorelines and the wave impact on protection seawalls and breakwaters. However, the occurrence of scour around breakwaters is one of the major failure modes of these structures (see e.g. Sumer and Fredsøe, 2002). During its lifetime a breakwater may experience a range of seabed conditions, i.e. the bed may be flat or rippled and the structure may be surrounded by scour holes. This is due to the complicated flow generated by the interaction between the incoming flow, the structure and the seabed. The results will depend on the incoming flow velocity (e.g. the relative magnitude between waves and current), the geometry of the seabed and the bed material, as well as the ratio between the oscillatory fluid particle excursion amplitude and a characteristic dimension of the structure. Moreover, real waves are stochastic, making the problem more complex. Further details on the background and complexity of the problem including reviews are given in e.g. Whitehouse (1998) and Sumer and Fredsøe (2002). Results on research performed on submerged breakwaters are reported in e.g. Coastal Engineering (2005). More specifically, Sumer *et al.,* (2005) gives a summary of results of an experimental study on scour around submerged breakwaters.

The purpose of the present paper is to provide a tentative practical approach by which the random wave-induced scour characteristics around submerged breakwaters can be derived. The two-dimensional onshore scour along the base of submerged vertical and semicircular breakwaters exposed to normally incident random waves on a mildly sloped sandy bottom is given. The random wave-induced scour characteristics are determined by using regular wave formulas given by Young and Testik (2009) combined with assuming the wave motion to be a stationary random process and adopting the Battjes and Groenendijk (2000) wave height distribution for mild slopes. Examples of calculation are given to demonstrate the application of the method. This work is complementary to that of Myrhaug and Ong (2010) who provided a similar stochastic method on the same issue based on the Young and Testik (2009) formulas and the more restrictive assumptions of a stationary Gaussian narrow-band random wave process.

SCOUR IN REGULAR WAVES

Young and Testik (2009) investigated the two-dimensional onshore scour along the base of submerged vertical and semicircular breakwaters exposed to normally incident regular waves breaking on the breakwaters. The investigations were performed in laboratory tests on both sloping (slope 1/20) and horizontal sandy bottoms. Data were obtained for bedload mode transport of quartz sand with the median grain size diameter d_{50} =0.67mm. It was found that the results are independent of submerged breakwater type, and that the beach slope does not have a noticeable effect on the scour characteristics. Two scour regimes were identified in the experiments. These were attached scour where the scour hole is connected to the onshore face of breakwater, and detached scour where the scour hole is not connected to the breakwater (see Figure 1). Results for three scour characteristics were presented: the maximum scour depth, S_{max} (m); the scour length, L_s (m); and the distance of S_{max} from

DOI: 10.2112/SI75-021.1 received 15 October 2015; accepted in revision 15 January 2016.
*Corresponding author: dag.myrhaug@ntnu.no

the onshore breakwater face, D_s (m). It was found that L_s and D_s depend on the scour regime, while S_{max} is independent of the scour regime. The following empirical formula for S_{max} for regular waves with incident wave height H (m) at the location of thebreakwater (see Figure 1) was obtained

$$\frac{S_{max}}{W_{bw}} = 0.0125\psi^{0.5} KC \tag{1}$$

in terms of the governing non-dimensional parameters Keulegan-Carpenter number

$$KC = \frac{H\pi}{W_{bw}} \tag{2}$$

and the mobility number at the seabed

$$\psi = \frac{\left(\frac{H\pi}{T \sinh kh}\right)^2}{g(s-1)d_{50}} \tag{3}$$

Here W_{bw} (m) is the crest width of the breakwater, h (m) is the water depth, T (s) is the wave period, g (m/s^2) is the acceleration of gravity, $s = 2.65$ is the sediment density to fluid density ratio for quartz sand, and k (rad/m) is the wave number determined from the dispersion relationship $\omega^2 = gk \tanh kh$, where $\omega = 2\pi/T$ is the angular wave frequency. It should be noted that H is the incident wave height at the location where the breakwater would be located, i.e. H was measured without the presence of breakwater and at a location 0.5m offshore of where breakwater face would be located. More details are given in Young and Testik (2009).

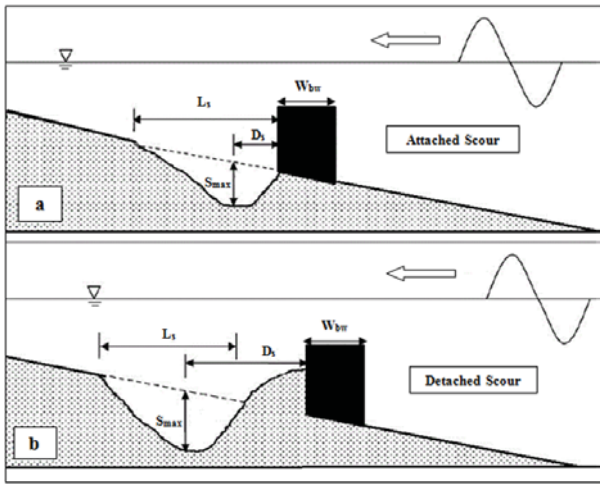

Figure 1. Definition sketch of onshore scour characteristics around breakwaters for the scour regimes: (a) attached scour; (b) detached scour (reproduced from Young and Testik (2009)).

In shallow water ($kh << 1$) Eq. (3) reduces to

$$\psi = \frac{H^2}{4h(s-1)d_{50}} \tag{4}$$

where the dispersion relationship $\omega = k(gh)^{0.5}$ and $\sinh kh \approx kh$ have been used. In this case it should be noted that ψ is independent of ω.

The scour length L_s (see Figure 1) was found to follow the empirical formula

$$\frac{L_s}{W_{bw}} = aKC \tag{5}$$

where the coefficient a is given as

$$a = \begin{cases} 1 \text{ for } & KC \le \pi \text{ ; attached scour} \\ 0.5 \text{ for } & KC > \pi \text{ ; detached scour} \end{cases} \tag{6}$$

The distance of S_{max} location from the onshore breakwater face D_s (see Figure 1) was found to follow the empirical formula

$$\frac{D_s}{W_{bw}} = b\,KC \tag{7}$$

where the coefficient b is given as

$$b = \begin{cases} \frac{1}{\pi} \text{ for } & KC \le \pi \text{ ; attached scour} \\ 1 \text{ for } & KC > \pi \text{ ; detached scour} \end{cases} \tag{8}$$

From Eqs. (2), (6) (and (8)) it appears that attached scour occurs when the incident wave height at the breakwater (H) is less or equal to the crest width of the breakwater (W_{bw}), while detached scour occurs when H exceeds W_{bw}. The two-dimensional scour formation onshore of a submerged breakwater is caused by the turbulent jet formed by the wave breaking due to the presence of the breakwater. The seabed shear stress induced by the resulting turbulence and complex fluid motion causes sediments to be suspended and transported. For attached scour ($H \le W_{bw}$) the turbulent jet formed by the breaking wave hits the crest of the breakwater and thereby causing scour to start at the onshore face of the breakwater. The scoured sediments are transported onshore towards the shoreline of the scour hole rather than being accumulated in form of a hump onshore of the scour hole (see Figure 1a). For detached scour ($H > W_{bw}$) the turbulent jet formed by the breaking wave hits the seabed at a distance away from the onshore face of the breakwater, and thereby causes scour to start away from the breakwater. The vortex associated with the jet hitting the seabed causes sediments to be accumulated at the onshore face of the breakwater, and a deposition hump is formed (see Figure 1b). More details on the mechanisms of onshore scour around submerged breakwaters are given in Young and Testik (2009).

PRESENT ANALYTICAL CALCULATIONS OF RANDOM WAVE-INDUCED SCOUR ON MILD SLOPES

Here a stochastic method will be outlined following the approach presented in Myrhaug and Ong (2010), except for the modification associated with that for mild slopes by adopting the Battjes and Groenendijk (2000) wave height distribution and based on the less restrictive assumption of stationary random waves. As a first approximation, it is assumed that the scour formulas by Young and Testik (2009) described in the previous section can be applied for the case of mild slopes as well. For mild slopes the relative change in water depth should be of the order of 1%, i.e. the slope should be milder than about 1:50. In the following, results for shallow water will be given.

Theoretical background

In shallow water the wave-induced scour are given in Eqs. (1) to (8). By substituting $H = \hat{H} H_{rms}$ in Eqs. (1), (2) and (4), Eq. (1) can be rearranged to

$$S \equiv \frac{S_{max} / W_{bw}}{0.0125 \psi_{rms}^{0.5} KC_{rms}} = \hat{H}^2 \tag{9}$$

where H_{rms} is the *rms* (root-mean- square) value of H, and

$$KC_{rms} = \frac{H_{rms} \pi}{W_{bw}} \tag{10}$$

$$\psi_{rms} = \frac{H_{rms}^2}{4h(s-1)d_{50}} \tag{11}$$

Similarly, by substituting $H = \hat{H} H_{rms}$ in Eqs. (5) and (6), they can be re-arranged to

$$L \equiv \frac{L_s / W_{bw}}{aKC_{rms}} = \hat{H} \tag{12}$$

where

$$a = \begin{cases} 1 & \text{for } \hat{H} \le \pi / KC_{rms} \text{ ; attached scour} \\ 0.5 & \text{for } \hat{H} > \pi / KC_{rms} \text{ ; detached scour} \end{cases} \tag{13}$$

Moreover, Eq. (7) can be re-arranged to

$$D \equiv \frac{D_s / W_{bw}}{bKC_{rms}} = \hat{H} \tag{14}$$

$$b = \begin{cases} 1/\pi & \text{for } \hat{H} \le \pi / KC_{rms} \text{ ; attached scour} \\ 1 & \text{for } \hat{H} > \pi / KC_{rms} \text{ ; detached scour} \end{cases} \tag{15}$$

Now the Battjes and Groenendijk (2000) parametric wave height distribution based on laboratory experiments on shallow foreshores is adopted. This cumulative distribution function (*cdf*) is composed of two two-parameter Weibull distributions of the non-dimensional wave height $\hat{H} = H / H_{rms}$:

$$P(\hat{H}) = \begin{cases} P_1(\hat{H}) = 1 - \exp[-(\frac{\hat{H}}{\hat{H}_1})^{k_1}] \text{ ; } \hat{H} < \hat{H}_{tr} \\ P_2(\hat{H}) = 1 - \exp[-(\frac{\hat{H}}{\hat{H}_2})^{k_2}] \text{ ; } \hat{H} \ge \hat{H}_{tr} \end{cases} \tag{16}$$

where $k_1 = 2$, $k_2 = 3.6$, $\widehat{H_1} = H_1 / H_{rms}$, $\widehat{H_2} = H_2 / H_{rms}$, $\widehat{H_{tr}} = H_{tr} / H_{rms}$. Here H_{tr} is the transitional wave height corresponding to the change of wave height where there is a change of the distribution associated with depth-induced wave breaking, given by

$$H_{tr} = (0.35 + 5.8 \tan\alpha) h \tag{17}$$

where α is the slope angle, and H_{rms} is related to the zeroth spectral moment m_0 by

$$H_{rms} = (2.69 + 3.24 \sqrt{m_0} / h) \sqrt{m_0} \tag{18}$$

It should be noted that the deep water value of Eq. (18) is $H_{rms} = 2.69 \sqrt{m_0}$ corresponding to a 5% reduction of the factor 2.83 obtained from the Rayleigh distribution, accounting for finite bandwidth effects obtained by Goda (1979).

The values of H_1 and H_2 can either be read from Table 2 in Battjes and Groenendijk (2000), or they can be solved by an iteration procedure solving two equations (see their paper for more details). The model is a so-called point model, i.e. depending on local parameters regardless of the history of the waves in deeper water. It should be noted that the effect of the bottom slope is of a secondary nature compared to the effect of water depth (see Battjes and Groenendijk (2000) for more details). Although the *cdf* in Eq. (16) is a continuous function of H, but with an abrupt change of its shape at $H = H_{tr}$ (i.e. the derivative and thus the *pdf* is discontinuous at this point), which is physically unrealistic, this feature is acceptable since all the integral statistical properties of the wave height are well defined. This change in the *cdf* (and *pdf*) is related to depth-induced breaking, and thus H_{tr} is expressed as the limiting wave height for non-breaking waves (i.e. defined as for purely depth-limited breaking, by excluding the steepness effect on wave breaking). Thus the effect of wave breaking is inherent in the *cdf* for H larger than H_{tr} (see Battjes and Groenendijk (2000) for more details). However, on mild slopes the effect of wave breaking is of minor importance, i.e. the main contribution to the statistical quantities will be from the *cdf* for H smaller than H_{tr} . This will be exemplified in the next section.

The zeroth spectral moment is obtained as

$$m_0 = \int_0^\infty S(\omega, h) d\omega \tag{19}$$

where $S(\omega,h)$ is the wave spectrum in finite water depth, which can be obtained by multiplying the deep water wave spectrum $S(\omega)$ with a depth correction factor $\psi(\omega,h)$ as

$$S(\omega, h) = \psi(\omega, h) S(\omega) \tag{20}$$

where, according to Young (1999),

$$\psi(\omega, h) = \frac{[k(\omega,h)]^{-3} \partial k(\omega,h) / \partial \omega}{\{[k(\omega,h)]^{-3} \partial k(\omega,h) / \partial \omega\}_{kh \to \infty}} \tag{21}$$

ensuring that the frequency part of the wave spectrum becomes proportional to k^{-3} irrespectively of the water depth (see Young (1999) for more details). From Eq. (21) it follows that (see Jensen, 2002)

$$\psi(\omega, h) = \frac{\omega^6}{(gk)^3 [\tanh kh + kh(1 - \tanh^2 kh)]} \tag{22}$$

In shallow water ($kh << 1$), the wave spectrum is obtained as

$$S(\omega, h) = \frac{\omega^2 h}{2g} S(\omega) \tag{23}$$

Now m_0 is obtained by combining Eqs. (19) and (23)

$$m_0 = \frac{h}{2g} \int_0^\infty \omega^2 S(\omega) d\omega \tag{24}$$

Then it follows that m_{0h1} and m_{0h2} at two different water depths h_1 and h_2 in shallow water are related by

$$m_{0h2} = \frac{h_2}{h_1} m_{0h1} \tag{25}$$

It should be noted that strictly Eq. (25) is only valid if energy dissipation is neglected, but always existing due to bottom friction and wave breaking, where the latter contributes significantly. However, as discussed previously in this section (and as will be exemplified in the next section), the effect of wave breaking is of minor importance on mild slopes, and thus Eq. (25) is considered as an acceptable approximation.

Outline of stochastic method

Based on the Battjes and Groenendijk (2000) distribution the statistical quantities of interest of the maximum random wave-

induced scour can be calculated; e.g. the expected (mean) value of the maximum random wave-induced scour caused by the (1/n)th highest waves given as

$$E[x(\hat{H}) \mid \hat{H} > \hat{H}_{1/n}] = n \int_{\hat{H}_{1/n}}^{\infty} \hat{H}^2 p(\hat{H}) d\hat{H} \tag{26}$$

Here x represents S (Eq. (9)), L (Eq. (12)) and D (Eq. (14)), i.e. $x = \hat{H}^2$ for $x = S$ and $x = \hat{H}$ for x = L and D, $p(\hat{H}) = dP(\hat{H})/d\hat{H}$ with $P(\hat{H})$ as given in Eq. (16) is the probability density function (*pdf*) of $\hat{H}$, and $\hat{H}_{1/n}$ is the value which is exceeded by the probability 1/n, i.e. determined from $1 - P(\hat{H}_{1/n}) = 1/n$. The integral in Eq. (26) can be evaluated by using the results given in Abramowitz and Stegun (1972, Chs. 6.5 and 26.4) as

1. for $\hat{H}_{1/n} < \hat{H}_{tr}$

$$E[x(\hat{H}) \mid \hat{H} > \hat{H}_{1/n}] = n \int_{\hat{H}_{1/n}}^{\hat{H}_{tr}} \hat{H}^2 p_1(\hat{H}) d\hat{H} + n \int_{\hat{H}_{tr}}^{\infty} \hat{H}^2 p_2(\hat{H}) d\hat{H}$$

$$= n\hat{H}_1^2 \left\{ \Gamma\left[1+\frac{2}{k_1}, \left(\frac{\hat{H}_{1/n}}{\hat{H}_1}\right)^{k_1}\right] - \Gamma\left[1+\frac{2}{k_1}, \left(\frac{\hat{H}_{tr}}{\hat{H}_1}\right)^{k_1}\right] \right\}$$

$$+ n\hat{H}_2^2 \Gamma\left[1+\frac{2}{k_2}, \left(\frac{\hat{H}_{tr}}{\hat{H}_2}\right)^{k_2}\right] \tag{27}$$

$$\hat{H}_{1/n} = \hat{H}_1 (\ln n)^{1/k_1} \tag{28}$$

2. for $\hat{H}_{1/n} > \hat{H}_{tr}$

$$E[x(\hat{H}) \mid \hat{H} > \hat{H}_{1/n}] = n \int_{\hat{H}_{1/n}}^{\infty} \hat{H}^2 p_2(\hat{H}) d\hat{H}$$

$$= n\hat{H}_2^2 \Gamma\left[1+\frac{2}{k_2}, \left(\frac{\hat{H}_{1/n}}{\hat{H}_2}\right)^{k_2}\right] \tag{29}$$

$$\hat{H}_{1/n} = \hat{H}_2 (\ln n)^{1/k_2} \tag{30}$$

Here $\Gamma(\bullet,\bullet)$ is the incomplete gamma function. It should be noted that $E[\hat{H}_{1/n}]$ for n = 3, 10 and $\hat{H}_{1/n}$ for n = 50, 100, 1000 are given in Battjes and Groenendijk (2000, Table 2).

For prediction of the wave-induced scour due to random waves, a commonly used procedure is to use characteristic statistical value of the wave-related quantities in an otherwise deterministic approach, e.g. to substitute $\hat{H} = E[\hat{H}_{1/n}]$ in Eqs. (9) to (15). This will be exemplified in the next section.

EXAMPLES OF RESULTS

To the authors' knowledge no data exist in the open literature for random wave-induced scour on mild slopes. Hence examples of calculating the characteristic wave-induced scour for these conditions based on the results in the previous section are provided. It should be noted that the formulation in the previous section is valid for a finite water depth. However, in this example the shallow water approximation is used to serve the purpose of demonstrating the application of the analytical method for practical purposes using data typical for field conditions.

The given flow conditions are: The water depths h = 5m, 3.5m, 2m on the slope α = 1/100, and the water depths h = 5m, 2m on the slope α = 1/50 (see Figure 2); zeroth spectral moment at h = 5m, m_0 = 0.0625m^2; spectral peak period T_p = 8.2s, corresponding to the spectral peak frequency $\omega_p = 2\pi/T_p$ = 0.766 rad/s; k_p at h = 5 m from the shallow water dispersion relationship corresponding to ω_p, i.e., $k_p = \omega_p/\sqrt{gh} = 0.109$ rad/m (which is 4.4 percent smaller than the finite water depth value; justifying the shallow water approximation used in this example).

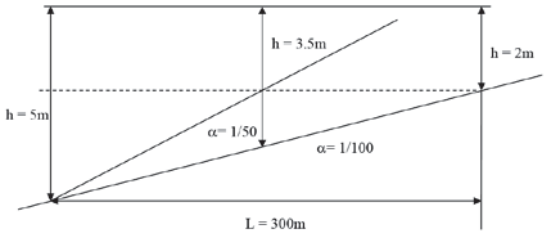

Figure 2. Definition sketch of mild slope conditions with slopes.

The calculated quantities are given in Table 1. The results are exemplified for n = 3. Now m_0 at h =2 m and 3.5 m is obtained from Eq. (25); H_{tr} is obtained from Eq. (17) and $\hat{H}_{1/3}$ from Eq. (27) or Eq. (29) ; $\hat{H}_1$, $\hat{H}_2$ and $E[\hat{H}_{1/3}]$ are read from Battjes and Groenendijk (2000, Table 2). For both slopes and the three water depths it appears that $\hat{H}_{1/3} < \hat{H}_{tr}$, and thus the wave-induced scour is calculated from Eqs. (26) and (27). It should be noted that the values of the scour characteristics given in Table 1 correspond to the expected maximum values caused by the (1/3)rd highest waves, i.e. corresponding to the significant values of the scour characteristics. The deterministic values of the scour characteristics are calculated by substituting $\hat{H} = E[\hat{H}_{1/3}]$ in Eqs. (9) to (15).

The example results given in Table 1 demonstrate that: First, for both slopes the scour characteristics (S_{max}, L_{smax}, D_{smax}) are smaller at h = 2 m than those at h = 5 m. This is due to the shoaling of waves, and is dominated by the decrease in KC_{rms}. Second, the effect on the scour characteristics by increasing the slope α from 1/100 to 1/50 at both h = 2 m and h = 5 m is insignificant. Third, the effect of changing the slope at a given horizontal location, e.g. by changing the water depth from h = 3.5 m on the slope α = 1/100 to h = 2 m on the slope α = 1/50, is to reduce the scour characteristics. Also these changes are dominated by the decrease in KC_{rms}. Fourth, in this example the stochastic method gives values which are about 6% larger than those obtained by the deterministic method for S_{max}. However, it should be noted that other statistical values can give other results, and it is generally recommended to use a stochastic method. For L_{smax} and D_{smax} the stochastic and deterministic methods coincide, and are valid for detached scour. Fifth, as mentioned in the previous section the effects of wave breaking on mild slopes are of minor importance, i.e. that the main contribution to the statistical quantities will be from the *cdf* of H smaller than H_{tr}. This is demonstrated in Table 1 by giving the values of $P(\hat{H}_{tr}) = P_1(\hat{H}_{tr})$ using Eq. (16), showing that the contribution from the *cdf* is larger than 95%.

Moreover, an assessment of breaking waves can be made by using the surf parameter $\xi_p = (H_{s0}/((g/2\pi)T_p^2)^{-1/2} \tan\alpha$ defined in terms of the significant wave height in deep water H_{s0} and the spectral peak period T_p. A Phillips spectrum is chosen as the deep water wave spectrum (see e.g. Tucker and Pitt (2001)), $S(\omega) = ag^2/\omega^5$ for $\omega > \omega_p$ and zero elsewhere, and a = 0.0081 is the Phillips constant. Then, by using Eqs. (23) and (24), it follows that the deep water and shallow spectral moments are related by $m_{00} = gm_0/(h\omega_p^2)$. Thus $H_{s0} = 3.8\sqrt{m_{00}}$ = 1.74 m, giving ξ_p = (0.08, 0.16) for the slopes (1:100, 1:50). For individual waves the surf parameter is defined as $\xi_p = (H/((g/2\pi)T_p^2)^{-1/2} \tan\alpha$, where H is the deep water wave height. Types of breaking waves are defined in terms of this surf parameter (see e.g. Battjes (1974)); spilling if $0 < \xi < 0.5$ and plunging if $0.5 < \xi < 3$. Thus, if breaking occurs in this example there will most likely be spilling breakers, and therefore the effect of these modest breaking waves on the wave-induced current will be of minor importance. This suggests that the method should be limited up to including spilling breakers.

SUMMARY

A simple analytical method which can be used to give estimates of the two-dimensional onshore scour characteristics along the base of a submerged breakwater exposed to normally incident random waves on mild slopes is provided. The formulation is valid for finite water depths, but here examples of application based on the shallow water approximation are given to serve the purpose of demonstrating the application of the analytical method for practical purposes. The statistical values of the maximum wave-induced scour considered here are the significant values of the scour characteristics.

Example calculations demonstrate that: the scour characteristics decrease as the water depth decreases due to shoaling for a given slope; the effect of the slope is negligible for mild slopes; the effect of changing the slope at a given horizontal location is to reduce the scour characteristics.

Generally, it is recommended to use a stochastic approach rather than using e.g. the significant wave height in an otherwise deterministic approach. However, the difference between the two approaches in this example is within 6%. Comparison with data is required before a conclusion regarding the validity of this method can be given. In the meantime the present analytical results can be used to make assessment of the wave-induced current based on available wave statistics.

Table 1. *Example of calculations with h = 2 m, 3.5 m, 5 m, slopes α=1/100 and 1/50, n = 3.*

	h = 5 m		h = 2 m		h = 3.5 m
	α=1/100	1/50	α=1/100	1/50	1/100
$m_0(m^2)$	0.0625		0.025		0.0438
H_{rms}(m), Eq. (18)	0.71		0.47		0.61
$k_p h$	0.547		0.346		0.458
KC_{rms}, Eq. (10)	2.23		1.48		1.92
ψ_{rms}, Eq. (11)	15.28		16.73		16.11
$\hat{H}_{tr} = H_{tr}/H_{rms}$, Eq. (17)	2.87	3.28	1.74	1.98	2.34
$\hat{H}_1 = H_1/H_{rms}$	1.0	1.0	1.011	1.004	1.001
$\hat{H}_2 = H_2/H_{rms}$	1.60	1.63	1.287	1.357	1.459
$E[\hat{H}_{1/3}]$	1.416	1.416	1.413	1.415	1.415
$P_1(\hat{H}_{tr})$	0.9997	0.99998	0.95	0.98	0.996
Stochastic					
S_{max} (m)	0.230	0.230	0.156	0.157	0.202
Deterministic using significant values					
S_{max}(m)	0.218	0.218	0.151	0.152	0.193
Stochastic and deterministic	**Detached scour since** $E[\hat{H}_{1/3}] > \pi/KC_{rms}$				
$L_{s\max}$ (m)	1.58	1.58	1.05	1.05	1.36
$D_{s\max}$ (m)	3.16	3.16	2.09	2.09	2.72

LITERATURE CITED

Abramowitz, M. and Stegun, I.A., 1972. *Handbook of Mathematical Functions.* New York: Dover, 1046p.

Battjes, J.A., 1974. Surf similarity. *Proceedings of the 14th International Conference on Coastal Engineering* (New York, ASCE), pp. 466-479.

Battjes, J.A. and Groenendijk, H.W., 2000. Wave height distributions on shallow foreshores. *Coast. Eng.*, 40, 161-182.

Coastal Engineering, 2005. Special Issue. *Low crested structures and the environment.* 52(10-11), 815-1126.

Goda, Y., 1979. *A review on statistical interpretation of wave data. In: Report of the Port and Harbour Research Institute, Japan,* 18, pp. 5-32.

Jensen, J.J., 2002. Conditional short-crested waves in shallow water and with superimposed current. *Proceedings of the 21st International Conference on Offshore Mechanics and Arctic Engineering* (Oslo, Norway), Paper No. OMAE2002-28399.

Myrhaug, D. and Ong, M.C., 2010. Random wave-induced onshore scour characteristics around submerged breakwater using a stochastic method. *Ocean Engineering*, 37, 1233 – 1238.

Sumer, B.M. and Fredsøe, J., 2002. *The Mechanics of Scour in the Marine Environment.* Singapore: World Scientific, 536p.

Sumer, B.M.; Fredsøe, J.; Lamberti, A.; Zanuttigh, B.; Dixen, M.; Gislason, K., and Di Penta, A.F., 2005. Local scour at roundhead and along the trunk of low crested structures. *Coastal Engineering*, 52 (10-11), 995-1025.

Tucker, M.J. and Pitt, E.G., 2001. *Waves in Ocean Engineering*. Amsterdam: Elsevier, 521p.

Whitehouse, R.J.S., 1998. *Scour at Marine Structures. A Manual for Practical Applications.* London: Thomas Telford, 198p.

Young, I.R., 1999. *Wind Generated Ocean Waves*. Amsterdam: Elsevier, 288p.

Young, D.M. and Testik, F.Y., 2009. Onshore scour characteristics around submerged vertical and semicircular breakwaters. *Coastal Engineering*, 56(8), 868-875.

Journal of Coastal Research	SI	75	108-112	Coconut Creek, Florida	2016

Downscaled Numerical Modelling to Study the Climate Change Effects on the Estuarine Stratification

Dongmin Jang †, Hwan J. Hwang +*, and Thao T.H. Nguyen+

†Korea Institute of Science and Technology Information
Daejeon, Rep. of Korea

+Dept. of Civil & Env. Eng.,
Seoul National University
Seoul, Rep. of Korea

www.cerf-jcr.org

www.JCRonline.org

ABSTRACT

Jang, D.; Hwang, H.J.; and, Nguyen, T.T.H., 2016. Downscaled numerical modelling to study the climate change effects on the estuarine stratification. *In:* Vila-Concejo, A.; Bruce, E.; Kennedy, D.M., and McCarroll, R.J. (eds.), *Proceedings of the 14th International Coastal Symposium* (Sydney, Australia). *Journal of Coastal Research*, Special Issue, No. 75, pp. 108-112. Coconut Creek (Florida), ISSN 0749-0208.

The climate change affects adversely the estuarine systems by acidifying and increasing temperature of the seawater. Also temperature rises faster in the surface layer than the deep water and this strengthens the stratification. Such changes of the stratification could affect circulation, water quality and so ecosystem of an estuary in the various ways. Therefore, the prediction of the changes of the stratification in the estuary is critical in mitigating the damage to the ecosystem of the estuaries. However, the prediction of the stratification in the coastal water bodies requires highly resolved information for the complicate circulations and complex coastal lines of the estuaries. Therefore, we downscaled data from the large-scale operational ocean models to the local regional models to simulate an estuary of Korea for the near present years and 50 years later with the sea level rise. Based on these downscaled results, Potential Energy Anomalies (PEAs) are numerated, which can help to assess quantitatively the stratification. Based on the PEA analysis, the stratification effects are expected to be much more significant in the estuarine river channel than the coastal sea and it means that the sea level rise affects both the coastal sea and upstream fresh water area.

ADDITIONAL INDEX WORDS: *Downscaling, Unstructured grid, Climate change, Estuary, Stratification.*

INTRODUCTION

Dam construction and land reclamation have changed the hydrological and morphological conditions and affected the stratification and water circulations of the Seomjin River estuary since 1970s. The dependence of salinity, temperature and density of the estuarine system on the morphological and hydrological changes were reported in the numerous works (e.g., Howarth *et al*., 2000; Scavia *et al*., 2002). Also, the shoreline changes in the coastal estuary due to dyke construction can affect on tidal circulation and so the distributions of gradient of salinity (Park *et al*., 2014). Such variations of thermo-haline distributions are also expected to occur in future due to the climate change. The amount of the freshwater discharge will be different from the present due to changes of the amount and patterns of the precipitation. The climate change will raise the seawater temperature and the sea surface level. The reduced amount of freshwater lowers flow rate in the upper layers of the river, which reduces mixing and makes lower layer saltier by intrusion. These changes of the estuarine stratification also can alter types of the estuaries (Jang and Hwang, 2013).

To study the stratification and water circulation in an estuary, a series of the numerical simulations was performed in the divers scenarios. For the general purpose, initial and boundary conditions are constructed based on the rough observations or large-scale global ocean models as like as global Hybrid Coordinate Ocean Model (HYCOM). Even though such large-scale models are considered to be reliable (Chassignet *et al*., 2007), the publically provided data are too roughly resolved (e.g., 9 km in HYCOM) and so lead to less accuracy when it is applied directly to the small-scale regions. Therefore, the finer regional ocean models such as Regional Ocean Modeling System (ROMS) or Finite Volume Community Ocean Model (FVCOM) should simulate a regional circulation of the water .In many models, FVCOM has been chosen to nest the data into smaller domain in some previous researches (Alvera-Azcárate *et al*., 2009; Zheng and Weisberg, 2012) since compared to the ROMS with structured grid, the unstructured grids of FVCOM have more advantages in capability of resolving small and complicated topographies.

Therefore, the present work downscaled Environmental Fluid Dynamics Code (EFDC) data to provide the input data to the unstructured grid regional model to study the stratification process in the Seomjin river estuary. The roles of climate change are implied through the scenarios with the different seasonal temperatures and sea water levels and EFDC already run several cases of scenarios near the Korean coastal sea. Finally, the results of temporal and spatial variations of the stratification are quantitatively assessed by the analysis of potential energy anomaly (PEA), which presents the strength of the stratification process (Simpson *et al*., 1981).

METHODS

This section explains how each parameter was downscaled, how scenarios were constructed and how PEA was determined in the dynamic equations.

The initial and open boundary conditions

EFDC produced data near Korea for 2001 and 2050 based on the CMIP5. The data in the structured grid from EFDC were used as the initial and open boundary conditions of the FVCOM by downscaling. The resolution of EFDC is 250 m with uniform

DOI: 10.2112/SI75-022.1 received 15 October 2015; accepted in revision 15 January 2016.
*Corresponding author: jinhwang@snu.ac.kr

rectangular grids and that of FVCOM ranges from 30 to 200 m with the irregular triangular grids. The grid size of FVCOM becomes larger toward the southern open boundaries (OBC1 in Figure 1) and so the largest grids are located at the southern open boundary and the smallest ones are in the river channel. Therefore, it is possible to realize topographies, particularly river channels and coastal shorelines, with high resolution and irregular triangular grids. The vertical layers of EFDC and FVCOM are 10 and 11, respectively. The freshwater was released only through the main channel in the simulation of EFDC but in FVCOM, the freshwater flows out through two channels; one is the Hadong, main channel and another is the Sueo, branch stream for reality (Figure 1). The discharge of the Sueo stream is 1/4 times of the Hadong channel. Figure 2 shows the discharge of main channel during 2001.

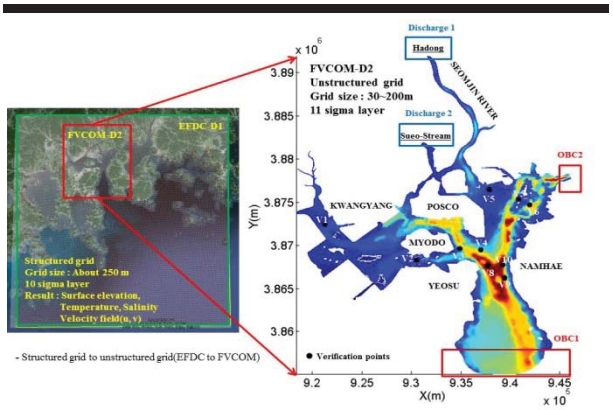

Figure 1. The downscaling description to unstructured grid model (FVCOM) using the result of the structured grid model (EFDC) in the Seomjin river estuary, Rep. of Korea

The underspecified variables were reproduced by the Inverse Distance Weighted (IDW) method. EFDC data were interpolated at the nearest 4 points of each node or cell. The surface elevations and temperature-salinity profiles are located at the nodes and the velocity profiles are presented in the cells. Tidal elevations and temperature-salinity fluxes were updated at every 1 second at the eastern and southern open boundaries (Figure 1). Data were temporarily updated by constructing in the same way to the spatial interpolation. Through the process of IDW, the relative errors of initial velocity, temperature and salinity are very small and about 0.1 % wholly.

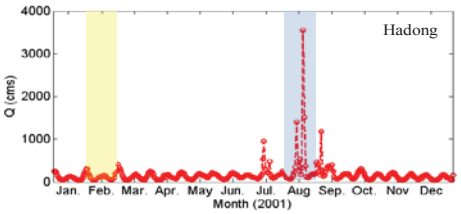

Figure 2. The discharge of Hadong in Figure 1 during 2001

Scenarios

Eight scenarios were numerically simulated, which were constructed by combining the changes of the seasonal discharges and the depths (Table 1). In Korea, discharge in summer is much larger than that in winter, and normally reaches the minimum in February and the maximum in August. Since still there are deep uncertainties in predicting the future precipitations related with the climate change, we consider only the present seasonal variations of the discharge changes of the fresh water through the river. The temperatures of freshwater was set at 4 °C in February and 22 °C in August. Since the temperature of fresh water cannot be estimated, only seawater temperature changes were considered for simulations. Large-scale motions were previously downscaled from EFDC and included seawater temperature and mass fluxes, but sea level rise due to the thermal expansion and ice melting was not considered. Therefore 25 and 50 cm were arbitrarily raised in year of 2050. Except the sea level conditions, all other conditions of each scenario were built up through the downscaling from the result of EFDC.

Table 1. *The numerical conditions of each scenario*

Scenario	Input from EFDC	Discharge	Sea level rise
200102	2001.02	2001.02	0
200108	2001.02	2001.08	0
205002	2050.02	2001.02	0
205008	2050.08	2001.08	0
02SLR25	2050.02	2001.02	25 cm
02SLR50	2050.02	2001.02	50 cm
08SLR25	2050.08	2001.08	25 cm
08SLR50	2050.08	2001.08	50 cm

Potential Energy Anomaly

PEA was firstly introduced by Simpson (1981), which means the energy required to mix the water column completely and indicates the stratification strength, defined as:

$$PEA(\phi) = \frac{g}{D}\int_{-H}^{\eta}(\overline{\rho}-\rho)z\,dz \quad (1)$$

where the overbar denotes a vertical average, and η, H and D are the surface elevation, the depth and the total depth ($=H+\eta$) respectively. ρ is the density and g is the gravity.

RESULTS

The following section presents fristly the downscaling result of tidal components from EFDC to FVCOM to validate the hydrodynamics. After that, salinityies and temperatures of each scenario are reproduced and presented before discussing the stratification process.

The validation of hydrodynamics for downscaling

Even though the large-scale model does not describe the detailed motions in the coastal area, the large-scale patterns as like as tidal elevations, total amount of heat and salt should be

equal in both nesting and nested models. The comparing the large-scale model results and the regional scale models validates the appropriateness of the downscaling. Before studying the stratification, we investigated the downscaling capability by comparing the result of FVCOM and EFDC. The locations for validation were selected within 3 m of the distance between the nodes of FVCOM and EFDC to minimize the error from the interpolation and the differences at the locations of measurements. Figure 3 shows tidal amplitudes and phases produced by the harmonic analysis with 10 validation points during February in 2001. Both tidal amplitude and phase have less than 1 % of the relative errors. Also, the ranges of errors are almost similar for the other scenarios (200108, 205002, 205008). This means the downscaled simulation with high resolution could describe hydrodynamics of the large-scale domain well.

When the salinities and temperatures from two models in February 2001 were monthly averaged and compared, they are almost similar in the southern and eastern open seas. But in the western part of bay, the averaged salinity and temperature produced by FVCOM are respectively 3 psu and 1 °C lower than those of EFDC. Also, the spatially averaged salinity and temperature are almost identical to each other initially whereas the spatially averaged salinity and temperature in FVCOM become lower by about 2.5 psu and 0.5 °C as time goes. Such differences between two models are probably due to the slightly increased discharge. To simulate more detailed stratification processes, the downscaled simulations should consider the additional discharge through the Sueo branch Stream, whereas the freshwater flows out only through the main channel in EFDC. The discharge of downscaled simulation is larger by 25%. Such additional fresh water flows into the western parts of bay with low salinity and temperature and so the salinity and temperature of downscaled simulation could drop overall.

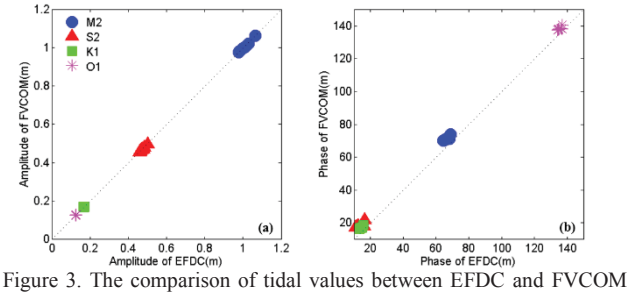

Figure 3. The comparison of tidal values between EFDC and FVCOM through the harmonic analysis; (a) Amplitude, (b) Phase

The changes of salinity and temperature

To investigate the effects of temperature increase and sea level rise on the stratification process, we compared monthly averaged temperature and salinity of 8 simulation scenarios. Figure 4 shows monthly averaged variables in each case and their differences. Monthly averaged temperature during February 2001 is around 6.5 °C in the open sea and relatively lower near the river channel (Figure 4-a). Monthly averaged salinity shows the similar pattern to the temperature (Figure 4-b). The reason why temperature and salinity are lower near the coastal or in the channel than those in the open sea is that the colder and fresher river influences strongly to the near area of the river.

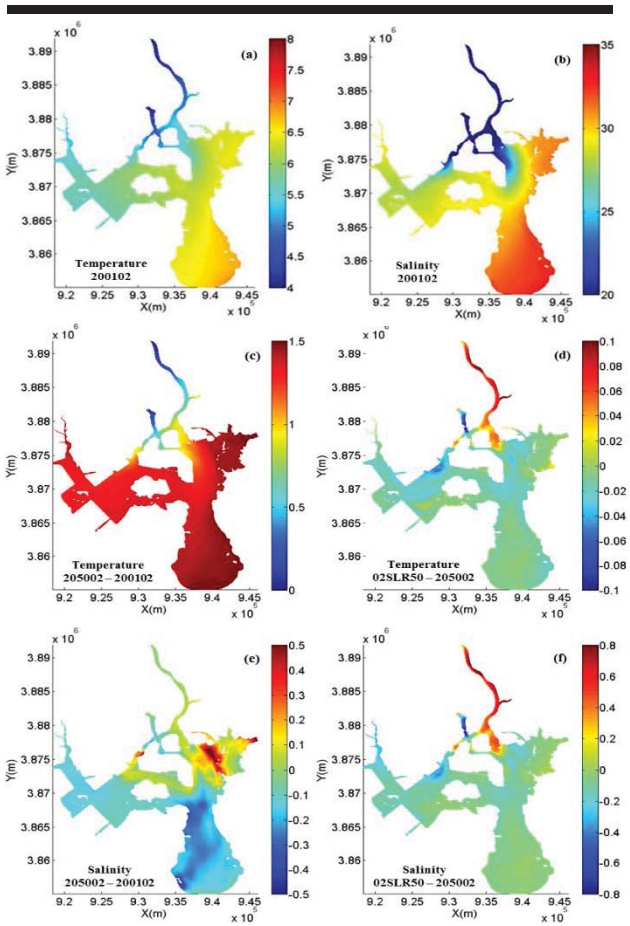

Figure 4. The temperature and salinity changes due to seasonal change of discharge, sea temperature change and sea level rise

The flux of warm water from the open sea into the bay increases due to the rises of the water temperature and the sea level by the climate change. Temperature increased by less than 1.0 °C along the channel and the estuary due to the direct influence of the colder freshwater. Temperature increases by more than 1.0 °C near the open sea due to the influx of warmer water from the open sea (Figure 4-c). However, the remarkable change of salinity was not found since it was assumed that the amount of the river discharge in 2050 is almost similar to that in 2001, except after the river mouth to the coastal sea, there are increases of salinity by 0.2 ~ 0.4 psu (Figure 4-e).

The sea level rise could change the river channel more seriously than the open sea in the perspectives of the stratification. The time averaged temperature increases by about 0.1 °C along channel due to 50 cm sea level rise, whereas there is only little change near the open sea (Figure 4-d). Also, similar trend was observed in the salinity (Figure 4-f). The increases of

temperature and salinity in the river channel are due to the increases of both baroclinic and barotropic forces. Since the rise of the sea level increases the overall barotropic force to rise the water surface of the river channel as like as backwater effects in the open channel flows, and also the deepened depths reduce vertical mixing and the strengthened stratification increases the baroclinic forces toward upstream channel causing the salt wedge intrusion and strong stratification (Jang *et al.*, 2012).

DISCUSSION

Rises or changes of temperature and salinity could affect the stratification of the estuary. In this section, the variations of the stratifying processes due to salinity and temperature changes in the estuary are discussed by monthly and spatially averaging of PEA (equation 1).

Monthly averaged PEA analysis

The stratification variations due to salinity and temperature changes are quantified by the ratio of the monthly averaged PEAs. Figure 5 shows the ratio of monthly averaged PEAs due to each change.

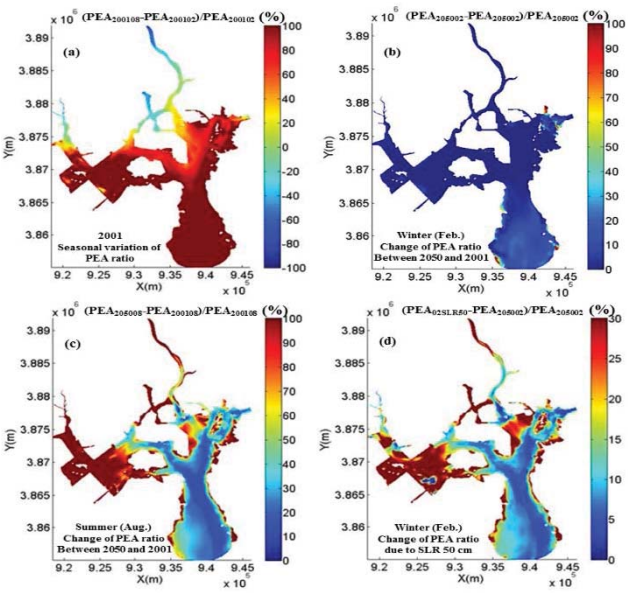

Figure 5. The spatial distribution of the ratio of monthly averaged PEA

The ratios of monthly averaged PEA between winter and summer are calculated to quantify the relative effects of the seasonally varying discharges on the stratification (Figure 5-a). The strong flushing, induced by the large amount of discharge during summer, could extrude the vertically stratified water toward the bay and extend the freshwater affecting zone. Therefore, the stratification strength in August is relatively weaker about 40 % than that in February in the upstream river. But, the stronger stratification is induced within the bay because of the increases of the baroclinic flows due to a large amount of buoyancy forced during August, extending a ROFI (Regions of Freshwater Influence) system (Simpson, 1997). A large amount of buoyancy due to freshwater into bay strengthened the stratification (Hwang *et al.*, 2006, 2011, 2014).

The seaward development of the stratification in summer could be more significantly affected by the increase of the seawater temperature rather than in winter. While the change of PEA ratio between scenario Februaries in 2001 and 2050 is little (Figure 5-b), PEAs in August increase by about 10 ~ 100 % depending on the locations (Figure 5-c). The change of the stratification is relatively larger in the shallow coastal region and river estuary and PEAs increase by 80 ~ 100 %, while in the bay PEAs increase only by10 ~ 20 %.

The sea level rise could affect the stratification as well as the development of the salt wedge in the river channel (Jang *et al.*, 2012). The effect of 50 cm sea level rise was investigated comparing the PEA change rates (Figure 5-d). The changes of stratification are remarkable in the shallow coastal region and the river channel. The rise of sea level reduces mixing (Jang *et al.*, 2012) due to the lower shear force on interface and reduces the bottom turbulence transferring to the upper layers. It finally increases the baroclinic forces and pushes harder the salt wedges to develop further upstream.

Spatially averaged PEA analysis

The time variation of the spatially averaged PEA within the bay and channel was estimated during 20 days by splitting estuary to the bay and the channel (Figure 6 and 7).

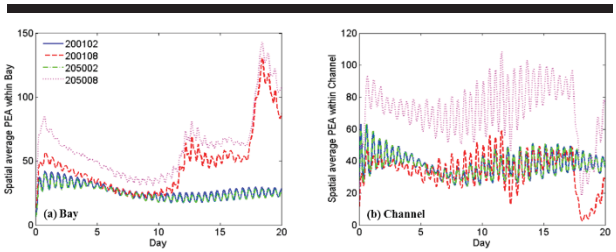

Figure 6. Tidal variation of the spatially averaged PEA within in the bay (a) and channel (b); 200102 means February in 2001, 200108 does August in 2001, 205002 is for the case in February, 2050, 205008 is for the case in August, 2050.

Figure 6 shows the time series of spatial averaged PEAs within the bay and the channel. The stratification within the bay in August 2001 is relatively stronger during the entire simulation periods. Since there were high precipitation and discharges during summer in 2001, the stratification increases in the bay during that time (Figure 6-a). However, in the river channel (Figure 6-b), we could find strikingly increases of the PEA in August 2001. And also after the sea level rise in 2050, we could observe the strengthened stratification. In other words, the effect of the sea level rise is more significant in the river channel than in the bay in the perspective of the stratification.

The effects of sea level rise on the stratification are estimated based on PEAs in both bay and channel in February 2001 (Figure 7). The sea level rise seems to strengthen stratification more significantly in the channel than the bay. According to 50 cm sea level rise, the PEA within the bay increases by the maximum 15 %, and the PEA within the channel does by the

maximum 30 %. Also, in August, the stratification process along channel is more strongly affected by the sea level rise than that within the bay. It results from the salty water intrusion near the bottom along with the weakened mixing (Jang *et al*., 2012).

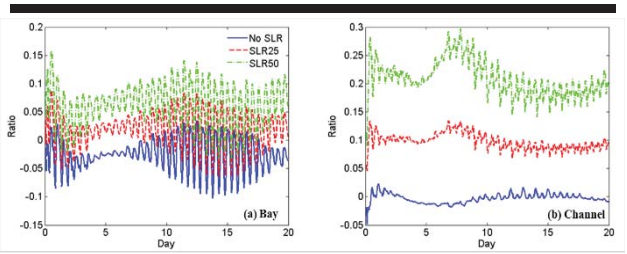

Figure 7. Tidal variation of ratio of spatially averaged PEA within in the bay (a) and channel (b) during February

CONCLUSIONS

For the appropriate numerical simulation to study the estuarine stratification, the model resolution must be one of the most important factors and downscaling or nesting scheme is used widely to have higher resolution in the regional scale. Therefore, this study assessed the skill of the downscaling from a structured grid model to a unstructured grid model FVCOM by using IDW spatial and temporal interpolations. The downscaled simulation could produce appropriately water circulations and stratifications in the complex area. After efficiently minimizing effects of the resolution near the complicate coastal lines, eight scenarios were considered to quantify the effects of the changes of flow rates, water temperature and the rises of the sea level due to the climate change on the stratification process in the Seomjin river estuary.

A large amount of discharge during summer enhances the buoyancy effect within the bay inducing the strong stratification, and so extends ROFI system. On the contrary, in the river channel, the stratification is weakened by the strong flushing due to a large amount of discharge, which pushes the stratified water body out of the channel. The increase of water temperature seems to strengthen the stratification near the shallow area and in the river channel during summer, but has little effect on the stratification in winter. The sea level rise enhances salt flux landward baroclinically and so develops the strong stratification along with the bottom salt intrusion. Therefore, we found that over the whole season, the estuarine channel seems to be more sensitive to the sea level rise than the bay.

ACKNOWLEDGEMENTS

The authors acknowledge the support from the National Research Foundation of Korea (NRF) Grant (No. 2015R1A5A 7037372) funded by MSIP of Korea. Also, the authors were supported by "Development of integrated estuarine management system", funded by the Ministry of Oceans and Fisheries, the republic of Korea.

LITERATURE CITED

Alvera-Azcárate, A. Barth, A., and Weisberg, R.H., 2009, A nested model of the Cariaco Basin (Venezuela): description of the basin's interior hydrography and interactions with the open ocean, *Ocean Dynamics*, 59(1), 97-120.

Chassignet, E.P., Hurlburt, H.E., Smedstad, O.M., Halliwell, G.R., Hogan, P.J., Wallcraft, A.J., Baraille, R., and Bleck, R., 2007, The HYCOM (HYbrid Coordinate Ocean Model) data assimilative system, *Journal of Marine Systems*, 65(1-4), 60-83.

Hwang, J.H., Van, S.P., Kim, Y.H., Choi, B.J., 2014, The physical processes of Yellow Sea, *Ocean and Coastal Management*, 102, 449-457.

Hwang, J.H., Ahn, J.E., Jang, D.M., Kim, B.R., and Park, Y.G., 2011, The growth of the bulge near a river mouth, *Journal of Coastal Research*, SI64, 1048-1052.

Hwang, J.H., Yamazaki, H. and Rehmann, C.R., 2006, Buoyancy generated turbulence in sheared stably stratified flow, *Physics of Fluids*, 18, 0451041-11.

Howarth, R.W., Swaney, D.P., Butler, T.J., and Marino, R., 2000, Climatic control on eutrophication of the Hudson river estuary, *Ecosystems*, 3(2), 210-215.

Jang, D., and Hwang, J.H., 2013, Estuary classification method for considering climate change effects in south Korea, *Journal of Coastal Research*, SI65, 962-967.

Jang, D., Hwang, J. H., Park, Y. G., and Park, S. H., 2012, A study on salt wedge and river plume in the Seom-Jin river and estuary, *KSCE Journal of Civil and Engineering*, 16(4), 676-688.

Park, Y.G., Kim, H.Y., and Hwang, J.H., 2014, Dykes effects on tidal circulation around Saemangeum, Korea, *Ocean and Coastal Management*, 102, 572-582.

Scavia, D., Field, J.C, Boesch, D.F., Buddemeier, R.W., Burkett, V., Cayan, D.R., Fogarty, M., Harwell, M.A., Howarth, R.W., Mason, C., Reed, D.J., Royer, T.C., Sallenger, A.H., and Titus, J.G., 2002, Climate change impacts on U.S. coastal and marine ecosystems, *Estuaries*, 25(2), 149-164.

Simpson, J. H., 1997, Physical process in the ROFI regime, *Journal of Marine System*, 12(1-4), 3-15.

Simpson, J. H., 1981, The shelf-sea fronts: implications of their existence and behavior, *Philosophical Transactions of the Royal Society of London A*, 302(1472), 531-546.

Zheng, L. and Weisberg, R.H., 2012, Modeling the west Florida coastal ocean by downscaling from the deep ocean, across the continental shelf and into the estuaries, *Ocean Modeling*, 48, 10-29.

Journal of Coastal Research	SI	75	113-117	Coconut Creek, Florida	2016

Use of Groundwater-table To Establish a Buffer Zone In a Barrier Island, Nakdong River Estuary, South Korea

Junghyun Park †*, Chang-Ill Yoo†† and Han-sam Yoon‡‡

†Disaster Prediction Technology Laboratory, Korea Institute of Science and Technology Information, South Korea

‡Department of Coastal Engineering, Pukyong National University, South Korea

‡Department of Ecological Engineering, Pukyong National University, South Korea

www.cerf-jcr.org

www.JCRonline.org

ABSTRACT

Park, J.H.; Yoo, C.I. and Yoon, H.S., 2016. Use of groundwater-table to establish a buffer zone In a barrier Island, Nakdong river estuary, South Korea. *In:* Vila-Concejo, A.; Bruce, E.; Kennedy, D.M., and McCarroll, R.J. (eds.), *Proceedings of the 14th International Coastal Symposium* (Sydney, Australia). *Journal of Coastal Research*, Special Issue, No. 75, pp. 113-117. Coconut Creek (Florida), ISSN 0749-0208.

A barrier island works as a buffer zone against wave and tidal forces, especially in river estuaries. To quantitatively analyze the buffer zone mechanism, understanding the wave, tide precipitation and groundwater-table by using long-term field observation is necessary. This study presents a coastal buffer zone mechanism in a barrier island (Jinudo) of the Nakdong river estuary in Busan, South Korea. For establishing a coastal buffer zone in a barrier island, we measured the groundwater at five observation points for 26 months from March 2012 and obtained wave and tidal data from a national observation station near the river mouth. We constructed a wave transformation numerical model and extracted breaking wave conditions, and then we compared data from the numerical model with a real-time groundwater data. According to the results, the buffer zone maximized up to 166.3 m from the shoreline with a wave height and period of 0.05 m and 12 sec, respectively, for 8 hours. Considering seawater infiltration, the buffer zone was observed to reduce to 125.0 m. The critical values are likely to define a coastal protection zone and vegetation distribution characteristic.

ADDITIONAL INDEX WORDS: *Estuary barrier Island, groundwater, salinity, long wave, coastal buffer zone*

INTRODUCTION

An estuary barrier island not only provides protection against extreme weather and sea (salt) water, but also provides habitat for marine flora and fauna. To protect upland property, habitat, and infrastructure in the coastal hazard zone, various types of structures have been installed globally; including soft options of coastal setback lines (Lee *et al.*, 2011). Despite the difference in shore protection methodologies, many coastal scientists have acknowledged the benefit of providing a wide and healthy sandy area (Westbrook *et al*., 2005).

The analysis of the groundwater-table in the estuary barrier island is common necessity to solve problems in water resource management and the ecological, environmental and hydrologic part in the area. A fluid groundwater level is closely related to climate, topography, geological features and vegetation (Park, 2015, Figure 1).

The variation of groundwater-table by wave, tide and preipitation conditions in the estuary barrier island is closely related to the vegetation environment in the natural sand beach, and has a significant impact on vegetation and ground stabilization (Park *et al.*, 2014). A stabilized groundwater-table is required for continuous fresh water supply on vegetation, and is related to the stabilization of ground height. Groundwater salinity is also important for the stability of vegetation on coastal barrier islands, as it defines the chemical ecological conditions related to soil salinity.

Generally, research has focused on the construction of a coastal buffer zone based on the high wave height. Furthermore, estimating the coastal buffer zone concentrates on beach erosion and seawater intrusion problems. However, it is difficult to find safety conditions for beach stablization and vegetation growth. Coastal groundwater-table sensitively change many external forces such as wave, tide and precipitation. We can use chracteristics of groundwater-table when establishing coastal buffer zones on the natural beach.

The aims of this study is to evaluate the groundwater-table for establishing coastal buffer zone when a long wave propagates toward the estuary barrier. A methodology is applied that first measures high-resolution groundwater data (Pressure and salinity) for 26 months from five stations in the study area and investigates interactions between the groundwater and long wave, calculated by the numerical model (a) this paper shows two long wave cases during typhoon periods (SANBA and NEOGURI) and (b) wave, tide and precipitation that explain observed variation in the time series. Finally, the paper will quantitatively establish the cross-shore distance of coastal buffer zone using the characteristics of groundwater.

Background

The Nakdong River estuary is a representative estuary in South Korea, (34°55′ ~ 35°10′N, 128°50′ ~ 129°00′E), located in the southeastern corner of the Korean peninsula (Figure 2). The estuary has a well-developed delta with sand barrier islands running parallel to the coastline. The Nakdong River estuary

DOI: 10.2112/SI75-023.1 received 15 October 2015; accepted in revision 15 January 2016.

*Corresponding author : pjh@kisti.re.kr

shows unstable topographical changes because of the various uses of the wet-land area and changes in the interactions between environments: such as waves and climate.

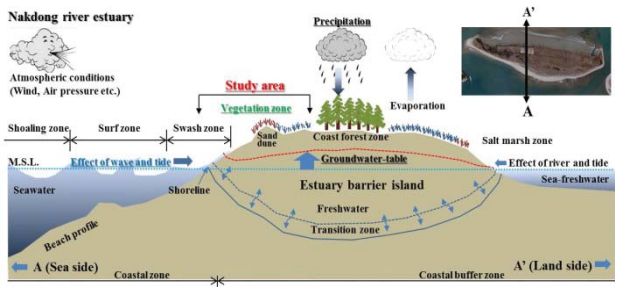

Figure 1. Schematic diagram of coastal buffer zone at study area.

The field study site, Jinudo (estuary barrier island), is located in the west side of the Nakdong River estuary mouth. Jinudo is a natural green area zone in Busan, South Korea. It has an area of 1.5 km^2, and its longitude and latitude range from 35°03′50″ to 35°04′08″N and 128°51′28″ to 128°53′08″E, respectively. Annual rainfall in the period of 1999–2008 varied from 1,168 to 2,029 mm, with a mean annual precipitation of 1599 mm. More than 60% of the rainfall occurs from June to October. The average annual potential evaporation is 1800 mm/year. There are two national observation stations (Gaduk Is. and Geoje Is.) near the study area, which provide tide, wind and wave data. The data from 1999 to 2008 showed that the tide level was 166.0 cm, mean range of tide was 113.4 cm, neap range of the tide was 60.8 cm, and mean sea level was 95.3 cm. The dominant wave directions are S, SW, SSW, and NE in all seasons. In summer and autumn, high waves frequently occur because of typhoons and their significant and maximum wave heights are over 4 m. In spring and winter, less than 2 m high waves are dominant (KMA and KHOA, 2014).

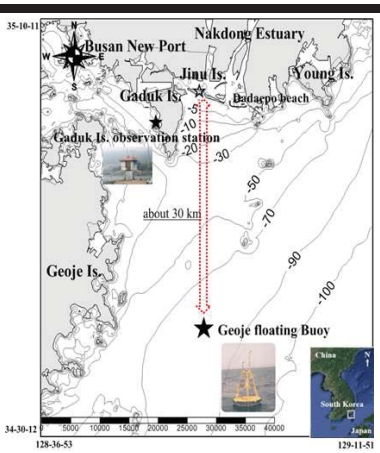

Figure 2. Location map of study area and the symbol notes national observation station (KMA and KHOA, 2014) and the symbol ☆ notes field study measurement site of Nakdong River estuary.

The front of Jinudo consists of sandy soil, and fresh groundwater exists in the soil pore spaces. The ground of study area maintains a stable state even under various external forces; thus, vegetation, consisting of halophytes and common reed, grows and perishes continually, and salt marshes develop in the back side of Jinudo (Yoon *et al.*, 2013). Although groundwater is not being national managed, it is mainly used for growing natural vegetation.

METHODS

To investigate groundwater-table chracteristics, we selected five observation stations in the vicinity of the south center part of Jinudo and observed groundwater pressure and electrical-conductivity from March 1, 2012 to Sep. 30, 2014 (Table 1) with Diver CTD(CTD-Diver 50 m, Eijkelkamp). The distance between the observation stations is about 40 m, and we measured the elevation level of the observation stations to revise vertical depth of the CTD (Figure 3(a)).

Station 1 and Station 2 are located in vegetation zones (distance from shoreline: 166.3 m and 125.0 m). Station 3 and Station 5 are located in sandy beach zones (distance from shoreline: 84.6 m). Station 4 is located in intertidal zone (distance from shoreline: 42.5 m) (Figure 3(b)). St.1, 2 and 3 monitoring wells were constructed in the areas covered by halophyte, while St.4 and St.5 were covered by sand. All the field study sites consisted of the fine sand, and the mean grain size (D_{50}) was 0.255 mm.

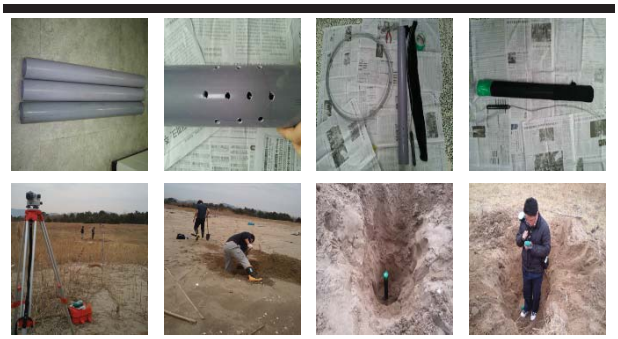

(a) Construction of field observation station

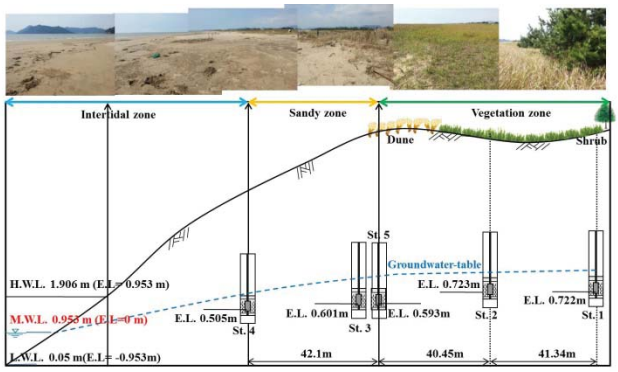

(b) Diagram of Cross section

Figure 3. Making method and installing process of well for groundwater monitoring.

Table 1. *Observation date and interval time of field study site.*

Observation	Date		day	Interval time
	Start	Finish		
1 st.	2012.03.01	2012.06.05	97	
2 nd.	2012.06.15	2013.01.15	184	
3 rd.	2013.06.03	2013.10.03	153	10 min.
4 th.	2013.10.09	2014.05.12	225	
5 th.	2014.05.13	2014.09.29	140	

In order to correct the vertical depth of each peak group (Level Instrument) of the CTD sensor unit, the elevation level was measured to the top of the well. The elevation level is corrected to the position of the sensor CTD system in accordance with the length of well(Table 2). Moreover, ground elevation of the study area was regularly measured, and wave conditions in shallow water of the beach front were observed with subsurface pressure gauge (Compact WH). Then, these observed data were used to verify the numerical model for wave transformation (STWAVE model). The results of this part were produced by analyzing characteristics of the groundwater-table on the basis of the correlation between fluctuations in the beachfront. For more detailed description, refer to Park. (2015).

Table 2 *Location of field observation with sensor and ground elevation.*

Station	Location		Sensor E.L.(m)	Ground E.L.(m)
	Latitude	Longitude		
1.	35°03'58.38"N	128°52'09.57"E	0.722	2.632
2.	35°03'57.08"N	128°52'09.56"E	0.723	2.423
3.	35°03'55.79"N	128°52'09.58"E	0.601	2.391
4	35°03'54.38"N	128°52'09.58"E	0.507	2.225
5	35°03'55.15"N	128°52'11.02"E	0.593	2.363

RESULTS

Figure 4 is a cross section of the groundwater-table averaged from St. 1 to St. 4 using the average groundwater-level at each station during the observation period. Average annual precipitation was 1217.5 mm/year, and the mean tide level was 108.2 cm. During the observation period, the level of groundwater was increased by ~1.4 m over the mean sea-level, which is a consistent result to Kang *et al*. (1997). Although Kang *et al*. concluded that wave and tide were the major reasons for an increase in the average groundwater-level., the impact of precipitation in addition to the wave and tide would be a factor that is more important to the average groundwater-level.

In this paper, we show two interesting cases out of the entire analyzed observation period. Both the interesting cases of autumn case 1 in 2012 (16~19/Sep.) and summer case 1 in 2014 (8~13/Jul.) have a variation in the groundwater-level. In both cases, it was the typhoon (Sanba : 11~18/Sep./2012, Neoguri : 4~11/July/ 2014) period; however, there was no precipitation.

During the observation period, autumn case 1 in 2012 of Figure 5 has the maximum groundwater-table of 2.0 m. When the waves with a breaking wave height greater than 0.45 m and a breaking wave period greater than 11.5 sec during the high tide lasted for more than 5 hours, the average groundwater-table increased by ~25 cm at St. 1, which is 166.3 m away from the shoreline. The numerical results show that long waves that are over 65.3 cm and 10 sec influenced on the front of the barrier island from 10 A.M. to 15 P.M. on September 17, 2012. During this time, it was observed that the groundwater-level rose at all observation points. However, it is considered that groundwater-table in barrier island reduced the effect by the waves because the groundwater-table was high while the transient rise in wave height was not high. Figure 5(c) shows the fluctuation of the groundwater-level and salinity at St.2 and St.3 during the autumn case 1 period in 2012. In the case of St.2 and St.3 although the groundwater level rose by incident waves, St.2 almost remained stable the salinity at 0 psu and St.3 remained stable it at 10 psu. This results show that sea water infiltration had a slight effect although the groundwater-level fluctuation. In 2012, the average groundwater-table was high and the layer of fresh water was thick. In that case, seawater infiltration was hard to occur although the waves influenced on the front of the barrier island; hence, the salinity at St.2 and St.3 hardly fluctuated. Accordingly, in 2012, vegetation (Halophytes *et al.*) on barrier island had a possibility to maintain or develop although high waves influenced on the front of barrier island.

In the summer case 1 of 2014, shown in Figure 6, the maximum groundwater-table was 1.1 m during the observation period. When the waves with a breaking wave height greater than 0.05 m and a breaking wave period greater than 12.5 sec during the high tide lasted for more than 8 hour, the average groundwater-table increased by ~50 cm at St. 1.

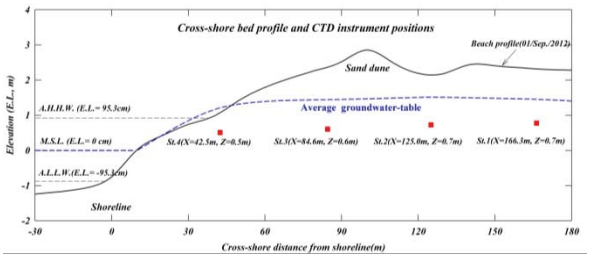

Figure 4. Cross section diagram of average groundwater-table during the observation period(1/March/2012 ~ 30/Sep./2014).

Figure 6(c) shows the fluctuation of groundwater-level and salinity at St.2 and St.3 during summer case 1 period of 2014. In the case of St.2, the groundwater-level rose high by incident waves, and the salinity rose from 0 psu to 31 psu just after approximately 20 hour and then it remained stable at 31 psu for long hours. Similarly, in the case of St.3, the groundwater-level rose high and the salinity rose from 0 psu to 31 psu just after approximately 6 hour and then it remained stable at 31 psu .

Time intervals to reach maximum salinity at each station differed according to their distance from the shoreline, and it was observed that even St.2, which was about 125 m from the shoreline (based on Mean sea level), remained stable at high salinity by seawater infiltration. In 2014, the average groundwater-table was remarkably low, and the level of fresh water was similar to mean sea level or above it. In that case, seawater infiltration was easy to occur; hence, seawater infiltration occurred through the upper intertidal zone to the vagitation zone.

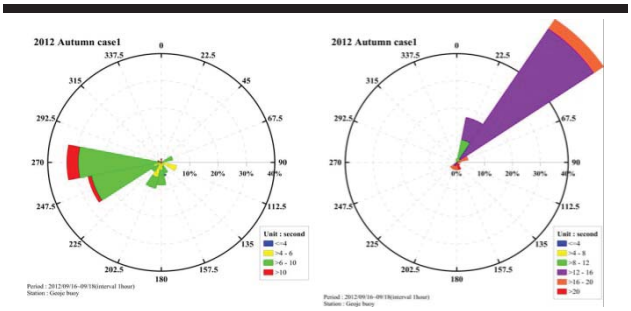

(a) Wave period and wind velocity rose diagram (National obs.)

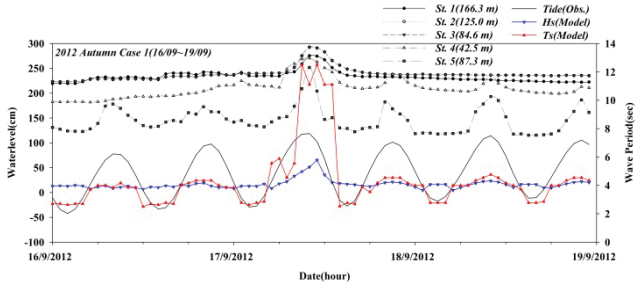

(b) Groundwater-level (Obs.), Hs and Ts (model)

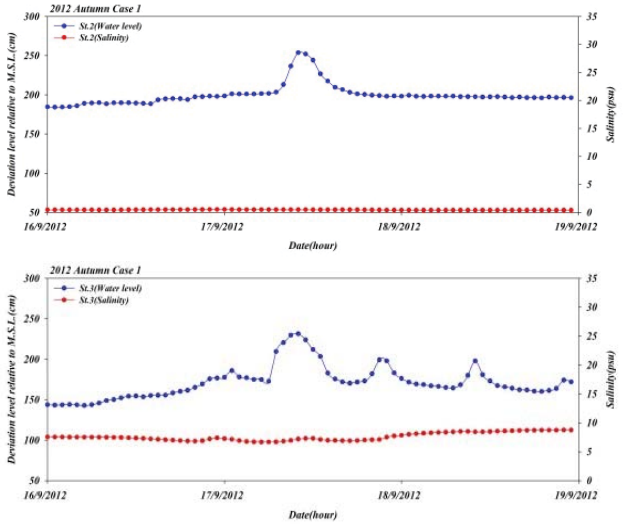

(c) Groundwater-salinity of St.2(125.0 m) and St.3(84.6 m)

Figure 5. (a)Wave and wind rose diagram (b),(c) time series of observation and numerical results in high groundwater-table condition (16~19/Sep./2012).

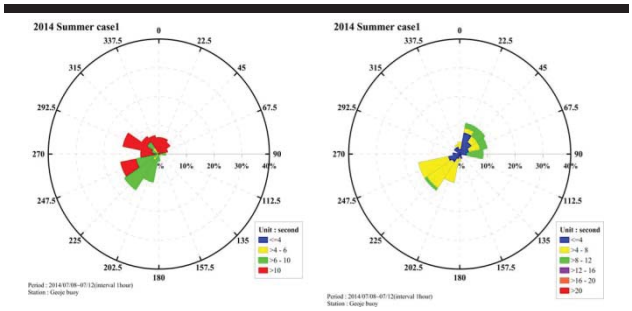

(a) Wave period and wind velocity rose diagram (National obs.)

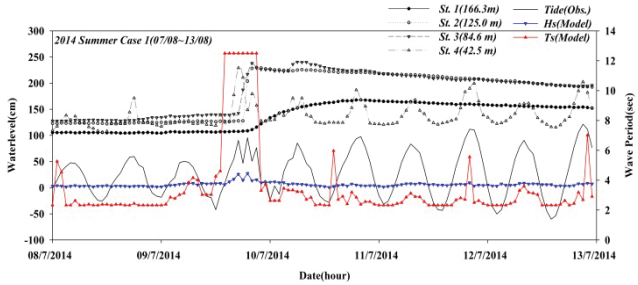

(b) Groundwater-level (Obs.), Hs and Ts (model)

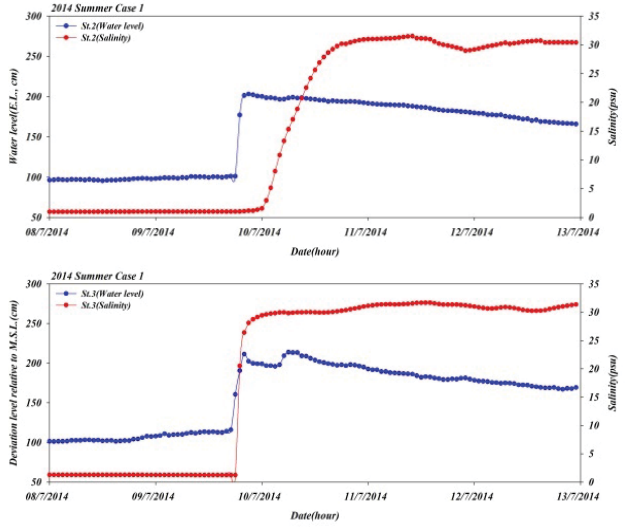

(c) Groundwater-salinity of St.2(125.0 m) and St.3(84.6 m)

Figure 6. (a)Wave and wind rose diagram, (b)time series of St.2 and St.3 observation and numerical results in low groundwater-table condition (8~13/Jul./2014).

DISCUSSION

To quantitatively established the buffer zone, we investigated a multiple causes as to why the use the groundwater. While the two cases have different average groundwater-table, the waves with a period greater than 11.5 sec lasted for more than 5 hour during the high tide in both cases. Therefore, we confirmed that the variation of the groundwater caused by the long waves depends on the average groundwater-table. We can use this property when establish coastal buffer zone.

Long wave by the typhoon

Figure 7 shows observational typhoon track during the observation time. SANBA and NEOGURI (from JMA), peaked in intensity on Sep. 17 and July 9, at which time JMA classified "VERY STRONG TYPHOON" and JTWC analyzed it as a "CATEGORY 5(SSHS)". The typhoons Sanba and Neoguri make enough long wave conditions that affected this study site's seas. At this time, 12 s waves came to the frontbeach consistently for more than 8 hours at high tide.

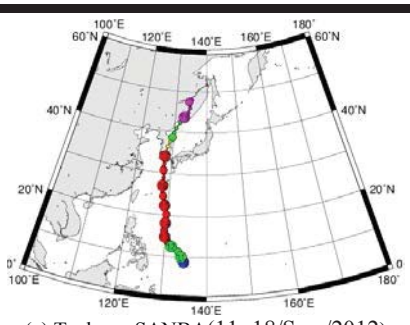

(a) Typhoon SANBA(11~18/Sep./2012)

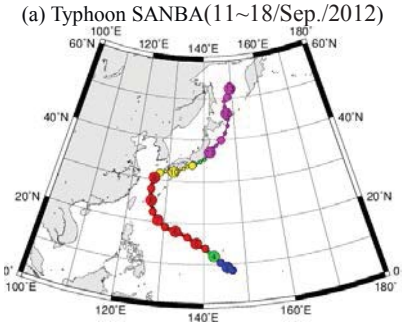

(b) Typhoon NEOGURI(4~11/July/ 2014)

Figure 7. Observational typhoon track (Courtesy : JMA, 2015)

To establish coastal buffer zone using groundwater-table

Many groundwater researchers (Westbrook *et al*., (2005) and Christien *et al.*,(2011)) suggested that groundwater is known to influence beach erosion and accretion processes. The differences between the seawater intrusion (seepage) and shoreline are limited; the intrusion (seepage) line variations during the tidal cycle are related to swash dynamics. However, this study suggest just coastal buffer zone, beach safety and vegetation growth.

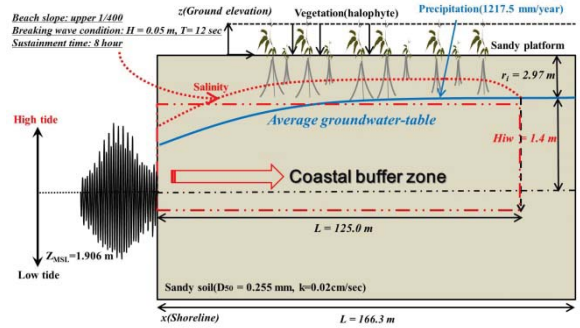

Figure 8. Cross-shore diagram of coastal buffer zone using the characteristics of groundwater-table.

This study area has a very mild beach slope (tanß : 1/400), and the time-averaged groundwater-table in the frontbeach was affected mainly by the precipitation. For the two interesting cases, the groundwater-level fluctuation by wave differed according to the distance from the shoreline. Additionally, the farther the distance from the shoreline was, the longer it took the lag-time to fluctuate. When breaking waves over 0.05 m high and 12 sec came to the front beach consistently during more than 8 hours at high tide at which the groundwater-table was low condition, groundwater-table fluctuation by wave occurred to the horizontal location, which is about 166.3 m from the shoreline, and salt-water infiltration occurred to the point that is about 125.0 m from the shoreline(Figure 8). It shows the limits of seawater intrusion when it is a long wave and high tide condition differ from average groundwater-table.

CONCLUSIONS

This study has evaluated groundwater characteristics for establishing coastal buffer zone in a estuary barrier island. During the observation period, the average groundwater-table fluctuated with the elevation about 1.4 m higher than mean sea level. During typhoons SANBA and NEOGURI, the groundwater-level increased 25 ~ 50 cm while horizontal distance from the shoreline was about 166.3 m. However, each case has different average groundwater-table related with different seawater intrusion. These results show that high average groundwater-table not only provides safety to the coastal zone against large waves and tides, but also provides habitat for vegetation zone. The observational cross-shore diagrams provide useful information for the construction of an effective ecological environment and coastal buffer zone management.

ACKNOWLEDGMENTS

This study was supported by the project of KISTI for the development of HPC-based management system against national-scale disaster.

LITERATURE CITED

E. H. Christien; R.B. Karin,; Giovanni C., B.G. Ruessink 2011. The use of video imagery to analyse groundwater and shoreline dynamics on a dissipative beach. *Continental shelf research*, 31, 1728-1738.

F.-C. Lee; John R.-C. Hsu, W.-H Lin 2011. Appraisal of storm beach buffer width for cyclonic waves. *Coastal Engineering*, 58, 1049-1061.

Japan Meteorological Agency, 2015

Kang, H.Y.; Nobuhisa Kobayashi, Ryu, C.R. 1997. Tide, Swash Infiltration and ground water Behavior, *The Korean Society of Ocean Engineers*, v11(3), 153-162.

Park, J.H.; Yoon, H.S., Lee, I.C. 2014. Analysis of groundwater-level long-term variation at the sandy barrier island on Jinu-do in Nakdong River estuary. *The Korean Society of Marine Environment & Safety*, 20(4), 382-338 (in Korean).

Park, J.H. 2015. A study on the characteristics of internal-waterlevel fluctuation with a topography at the estuary sand bar (in Korean). *Ph.D thesis*, Pukyong national university.

Westbrook S.J.; Rayner J.L.,; Clement T.P.,; Bjerg P.L., Fisher S.J. 2005. Interaction between shallow groundwater, saline surface water and contaminant discharge at a seasonally and tidally forced estuarine boundary. *Journal of hydrology*, 302, 225-269.

Journal of Coastal Research	SI	75	118-122	Coconut Creek, Florida	2016

Deposition in Flowing Water of Fine Sediments under Different Salinity Conditions

Luís Ivens Portela†*, Ana Custódio‡, and António Trigo Teixeira‡

†Department of Hydraulics and Environment
National Laboratory of Civil Engineering, LNEC
Lisboa, Portugal

‡Department of Civil Engineering and
Architecture, Instituto Superior Técnico
Lisboa, Portugal

www.cerf-jcr.org

www.JCRonline.org

ABSTRACT

Portela, L.I.; Custódio, A., and Trigo-Teixeira, A., 2016. Deposition in flowing water of fine sediments under different salinity conditions. *In:* Vila-Concejo, A.; Bruce, E.; Kennedy, D.M., and McCarroll, R.J. (eds.), *Proceedings of the 14th International Coastal Symposium* (Sydney, Australia). *Journal of Coastal Research*, Special Issue, No. 75, pp. 118-122. Coconut Creek (Florida), ISSN 0749-0208.

While the effect of salinity on the settling of fine sediments has been shown to be important in laboratory experiments, only a few studies have attempted to investigate depositional properties in flumes under different salinity conditions. This paper examines the effect of salinity on the deposition in flowing water of fine sediments collected in the Tagus estuary. The sampling site is located in the middle-upper reach of the estuary, where fine-grained sediments are the dominant intertidal material and tidal currents the major transport mechanism. The experiments were conducted in an annular flume (mean diameter 3.7 m, height 0.4 m, width 0.3 m), with initial suspended sediment concentration of 0.7 g l^{-1} and five different salinities (0, 2.5, 5, 10 and 15). Two types of experiments were performed: tidal variation for 6.5 hours; and response to sudden reduction in flow velocity (from 0.5 m s^{-1} to 0.25 m s^{-1}) for 8 hours. Samples were collected every 30 minutes to determine suspended sediment concentration by filtration and grain size by laser diffraction. The experiments with different salinities have yielded similar results, particularly regarding deposition for a velocity of 0.25 m s^{-1} (final C = 0.417-0.399 g l^{-1}, D_{90} = 22-19 µm, D_{50} = 8-6 µm, D_{10} = 2 µm). A consistent effect of salinity on the deposition of fine sediments from a flowing suspension could not be observed. Further research should examine deposition at lower flow velocities.

ADDITIONAL INDEX WORDS: *Cohesive sediment, deposition, annular flume.*

INTRODUCTION

Fine sediment deposition in estuaries has both economic and environmental impacts. Despite this, there is a lack of consensus regarding the influence of certain key environmental variables, such as salinity, on fine sediment transport processes, and particularly on deposition.

Delo (1988) did not find a consistent effect of salinity on the settling of fine sediment from a flowing suspension (initial concentration *c.* 1.0 g l^{-1}). At a bottom shear stress of 0.36 Pa, a suspension with salinity $S = 0$ deposited more quickly than with $S = 5$. In quiescent conditions, a suspension with salinity $S = 32$ settled out more quickly than with $S = 5$, which in turn settled faster than with $S = 0$. Several other authors have studied deposition using either fresh or saline water (*e.g.* Garcia-Aragon *et al.*, 2011), but did not compare both conditions.

The deposition rate of fine cohesive sediments is usually calculated based on the formulation of Krone (1962):

$$D = w_s C \left(1 - \frac{\tau}{\tau_d}\right) \quad (1)$$

where w_s is the settling velocity, C is the concentration of suspended sediment, τ is the bottom shear stress and τ_d is the critical shear stress for deposition.

Eq. (1) is widely used in numerical models, but it better fits experimental results, namely partial deposition patterns, by assuming a non-uniform sediment (*i.e.* multiple sediment classes; Mehta and Lott, 1987). According to Eq. (1), the critical shear stress for deposition ultimately controls full deposition (or partial deposition, with multiple classes), but the deposition rate should be influenced by the settling velocity.

Experiments reported in a previous study (Portela *et al.*, 2013) have shown a clear effect of salinity on the settling velocity of fine sediments collected in the Tagus estuary (Portugal).

The objective of the present paper is thus to examine the effect of salinity on the deposition in flowing water of fine sediments collected at the same location.

METHODS

In this section, the sediments and the experimental set-up used in the study are presented.

Sampling was performed in the Tagus estuary, in the outer part of a marina (Marina Parque das Nações), in the middle-upper reach of the estuary, where fine-grained sediments are the dominant intertidal material and tidal currents the major transport mechanism. The sample was collected in the intertidal zone, on November 21 2013, at low tide (Figure 1). The sediment consists of silt- and clay-sized particles, with diameters D_{10}, D_{50} and D_{90} obtained by laser diffraction (Malvern Mastersizer Micro) of 2, 10 and 63 µm, respectively. The mineralogical composition and organic content of a sample from the same area is reported in Portela *et al.* (2013).

DOI: 10.2112/SI75-024.1 received 15 October 2015; accepted in revision 15 January 2016.
*Corresponding author: lportela@lnec.pt

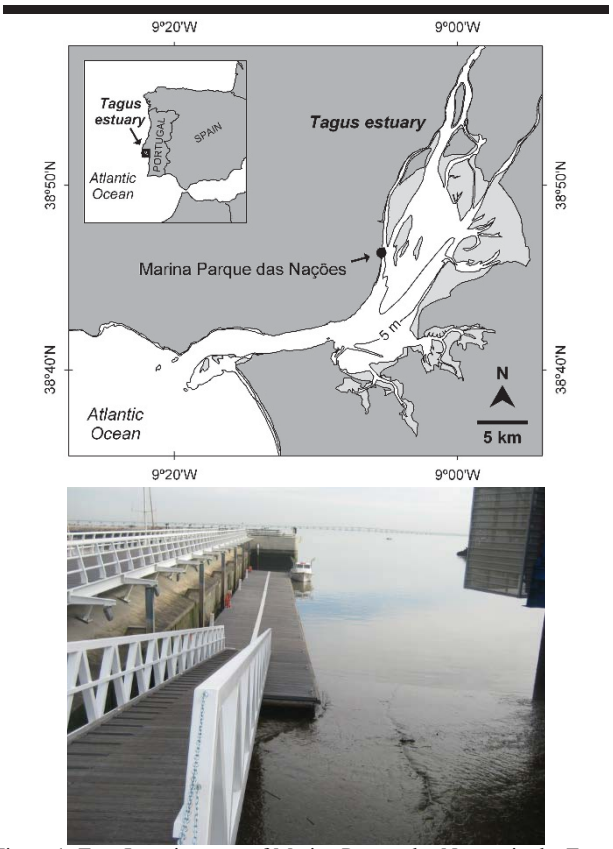

Figure 1. Top: Location map of Marina Parque das Nações in the Tagus estuary (Portela *et al.*, 2013). Bottom: View of the sampling site.

The annular flume available at LNEC (Figure 2) was used in this study. The annular flume, with a mean diameter of 3.7 m, a section 0.3 m wide and 0.4 m high, and a liquid volume of 1395 dm^3, consists of a circular channel and a top ring, which rotate independently. It is particularly suited to study fine sediments because it eliminates the inflow and outflow problems associated with straight flumes.

In the experiments described herein, the flow was driven only by the top ring, which means that curvature-induced secondary flows were not minimized.

The mean flow velocity in an annular flume can be deduced from its geometry and the imposed angular velocities, according to the analytical expression (Booij, 1994):

$$u_{av,b} \cong \left(w_t \frac{r}{1+\sqrt{\frac{b+2h}{b}}} + w_b \frac{r\sqrt{\frac{b+2h}{b}}}{1+\sqrt{\frac{b+2h}{b}}} \right) - w_b r \qquad (2)$$

where w_b, w_t are the angular velocities of the bottom channel and the top ring, r is the mean radius of the flume and b and h are respectively the width and height of the section. The validity of this expression has been verified by measurements (Portela and Reis, 2005).

The bottom shear stress is estimated as being proportional to the square of the mean flow velocity, $u_{av,b}$, through a semi-empirical resistance law (*e.g.* Manning):

$$\tau = \rho u_*^2, \text{ with } e.g.\ u_* = u_{av,b} \frac{n g^{1/2}}{h^{1/6}} \qquad (3)$$

where τ is the bottom shear stress, ρ is the fluid density, u_* is the friction velocity, n is the Manning coefficient and g is the acceleration due to gravity. The Manning coefficient is assumed to be 0.011 s $m^{-1/3}$ (equivalent to a Chézy coefficient of 78 $m^{1/2}$ s^{-1}; Portela and Reis, 2005).

The experiments were conducted for an initial suspended sediment concentration of 0.7 g l^{-1} and five different salinity values (0, 2.5, 5, 10 and 15), ranging from freshwater to mesohaline conditions. The sediment in the flume was the same throughout the experiments. Salinity values were increased four times by addition of sea salt.

For each salinity value, two experiments were performed: a 'tidal experiment' and a 'deposition experiment'. The duration of the 'tidal experiment' was 6.5 hours. The flow velocity, initially 0.5 m s^{-1}, was decreased and then increased in 13 steps of 0.5 hours to simulate sediment deposition and erosion under tidally varying conditions. The duration of the 'deposition experiment' was 8.5 hours and involved a single reduction in the flow velocity from 0.5 m s^{-1} to 0.25 m s^{-1}. The purpose of the 'deposition experiment' was to examine more closely the deposition process, as concentrations do not adjust immediately to changes in flow conditions.

During the experiments, samples were taken from the flume at about half-height (0.18 m) to determine suspended sediment concentrations and particle size distributions.

Suspended sediment concentrations were determined by the gravimetric method. Samples of 150 ml were filtrated through pre-weighed cellulose nitrate membrane filters with 0.45 μm pore size, dried at 40ºC and weighed in an analytical balance. The weight of the dry residue was divided by the original sample volume.

Figure 2. General view of the annular flume.

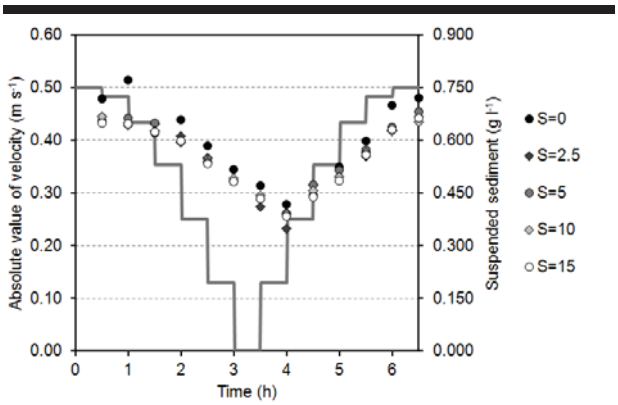

Figure 3. Evolution of suspended sediment concentration (g l^{-1}) in 'tidal experiments' for five different salinity values (0, 2.5, 5, 10 and 15).

Particle size distributions were examined by laser diffraction (Malvern Mastersizer Micro) using separate samples of 200 ml. Stirrer speed was set at 2700 rpm; ultrasound was not applied. Obscuration varied between 0.12 and 0.18, *i.e.* within the optimal range (0.1-0.3). Each result is the mean of three determinations. It should be noted that the procedure involves adding the 200 ml sample to 800 ml of distilled water, therefore reducing salinity to a fifth of the original value.

During sampling, a small amount of water was added to the flume to replace the sampled volumes, thus reducing sediment concentration by an estimated 2% between the beginning and the end of the experiments. The volume of suspension in the flume had also to be adjusted when sea salt (about 21 kg in total) was added to increase salinity.

Salinity and water temperature were measured using a multiparameter probe (YSI 556 MPS). Salinities deviated from target by less than 0.2. Water temperatures varied between 15.4 and 16.0ºC.

RESULTS

The first part of this section presents and describes the results of the 'tidal experiments'.

Figure 3 shows the evolution of suspended sediment concentration obtained in the five 'tidal experiments' with different salinity values. Although concentrations in the experiment with $S = 0$ are slightly higher than in the other cases (average of 0.596 g l^{-1} versus 0.562-0.548 g l^{-1}), the pattern in all five experiments is similar, with minimum concentrations at the same sampling time and a relatively narrow range of variation. The maximum velocities (0.50 m s^{-1}) coincide with the maximum concentrations (0.677-0.672 g l^{-1}), but a time lag is observed between the period of zero velocity (slack water) and the minimum concentrations (0.386 g l^{-1}). As a result, the deposition period is longer than the erosion period. A significant part of the sediment remains continuously in suspension (about 57%), due to the low settling velocity of the particles and the short period of time during which the flow velocity is very low or zero. There is no clear effect of salinity on the evolution of suspended sediment concentration.

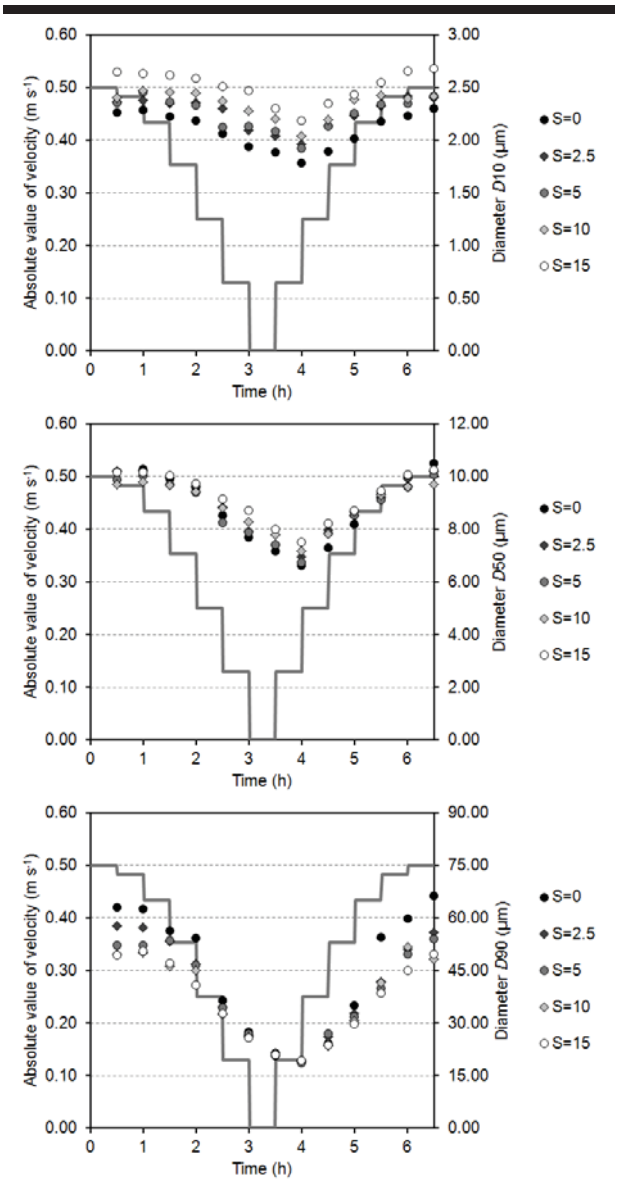

Figure 4. Evolution of characteristic diameters D_{10}, D_{50} and D_{90} (µm) in 'tidal experiments' for five different salinity values (0, 2.5, 5, 10 and 15).

Figure 4 shows the evolution of characteristic diameters D_{10}, D_{50} and D_{90} obtained in the same five 'tidal experiments'. The highest values of the median diameter D_{50} (10.1 µm) are obtained for the maximum velocities, while the lowest values (7.0 µm) occur after slack water with a 30 minute lag, coinciding with the minimum concentrations. The variation of C and the variation of D_{50} are directly and strongly correlated (coefficient of determination of the linear regression $r^2 = 0.95$). The general evolution of D_{10} and D_{90} is similar to the one of D_{50}, but the values of D_{90} show a wider range of variation.

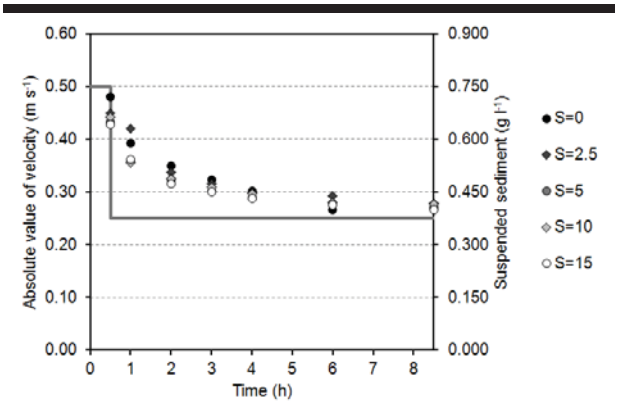

Figure 5. Evolution of suspended sediment concentration (g l^{-1}) in 'deposition experiments' for five different salinity values (0, 2.5, 5, 10 and 15).

There is an apparent effect of salinity on the characteristic diameters. The average value of D_{10} increases with the increase in salinity, from 2.1 µm for S = 0 to 2.5 µm for S = 15, a pattern that is probably related to the more reactive nature of the finer clay fraction (<2 µm). The average value of D_{50} also increases slightly with salinity, but the effect is only clear in the period of lower velocities and particle sizes, a pattern that also seems consistent with the role of the clay fraction. D_{90} shows a rather different pattern. In the case of D_{90}, the differences are observed for the higher velocities, the average value of D_{90} decreasing with the increase in salinity, from 44.7 µm for S = 0 to 36.4 µm for S = 15. It is not clear whether this effect is related to the experimental sequence.

In the remaining part of this section, the results of the 'deposition experiments' are described.

Figure 5 presents the evolution of suspended sediment concentration in the five 'deposition experiments' with different salinity values. As usually reported in annular flume experiments, deposition seems partial, controlled by bottom shear stress (estimated at 0.1 Pa for a velocity of 0.25 m s^{-1}; Portela and Reis, 2005). Concentrations after 8 hours are remarkably coincident (0.417-0.399 g l^{-1}), which suggests that salinity has no effect on the extent of deposition. Although an effect of salinity on the deposition rate in the first hours cannot be excluded, such effect is not clear as the initial concentrations themselves show some variation.

Figure 6 shows the evolution of characteristic diameters D_{10}, D_{50} and D_{90} in the 'deposition experiments'. On average, the highest value of D_{90} is 2.5 times higher than the lowest value, while the same ratio is 1.4 for D_{50} and 1.2 for D_{10}.

As can be seen in Figure 6, D_{10} clearly increases with the increase in salinity, a pattern that again is consistent with the more reactive nature of the clay fraction. D_{50} shows a slighter increase, which becomes more pronounced as deposition progresses and particle size decreases. D_{90} shows a pattern that is similar to the one described in the 'tidal experiments', *i.e.* a decrease with the increase in salinity, in the case of the larger diameters (>30 µm) observed at the beginning of the deposition experiments.

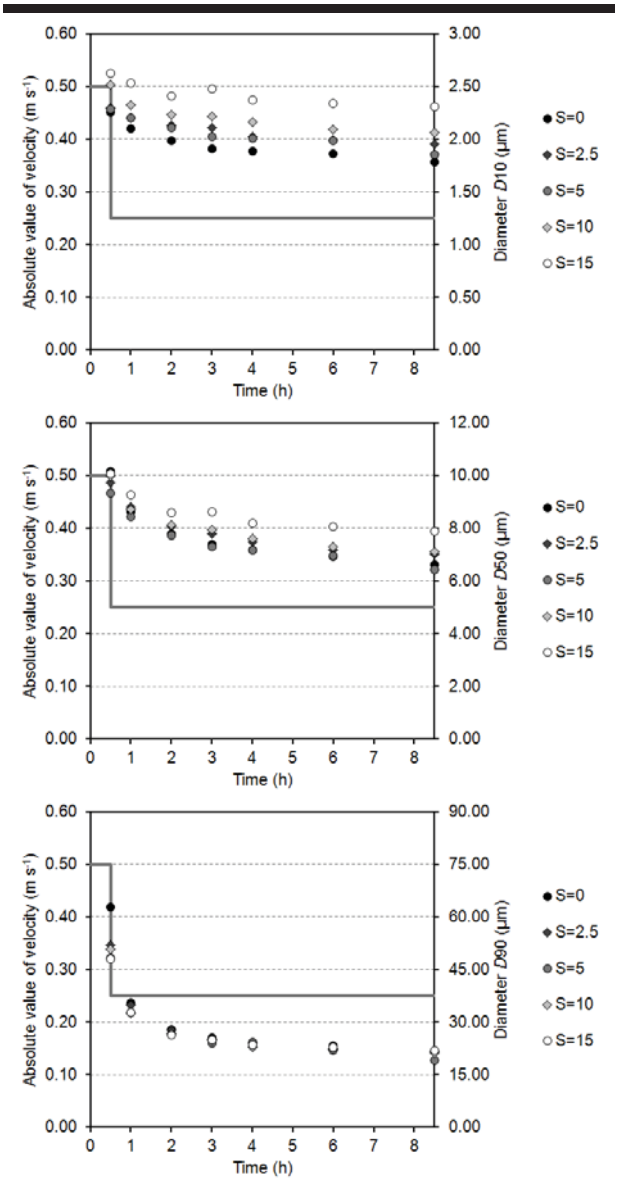

Figure 6. Evolution of characteristic diameters D_{10}, D_{50} and D_{90} (µm) in 'deposition experiments' for five different salinity values (0, 2.5, 5, 10 and 15).

DISCUSSION

Previous research examining the deposition of fine sediments under different salinity conditions has yielded inconsistent results (Delo, 1988). However, experiments reported in the literature have also shown that salinity influences the quiescent settling velocity (Portela *et al.*, 2013), as would be expected from the double-layer theory. The present study was thus designed to investigate the effect of salinity on the deposition in flowing water of estuarine sediments.

The results regarding the evolution of suspended sediment concentration in both 'tidal' and 'deposition' experiments are in

line with those of previous studies (Portela and Reis, 2005; Portela and Brito, 2010). In particular, 'deposition experiments' show a pattern of partial deposition, apparently controlled by bottom shear stress, which is commonly observed and suggests sediment sorting (Mehta and Lott, 1987).

Although some concentrations, particularly for $S = 0$, are rather distant from most other values, possibly due to the testing procedures, the results overall seem reasonably robust. Indeed, although the experiments were conducted with different salinities, most values of suspended sediment are close to the mean, indicating that the reproducibility of the experiments is fairly good. The fact that the minimum concentration coincides with the minimum grain size is a further indication of the reliability of the results.

At the end of the experiments, sediment material was present on the bottom and on the inner wall of the flume. The slightly higher concentrations for $S = 0$ suggest the possibility that most of this material may have adhered to the initially clean surfaces and internal edges primarily during the first 'tidal' and 'deposition' experiment.

The results of suspended sediment indicate that salinity has no strong effect on deposition when the initial velocity is reduced from 0.5 m s^{-1} to 0.25 m s^{-1} (equivalent to a reduction of the estimated bottom shear stress from 0.4 Pa to 0.1 Pa). This is in contrast with the results obtained in settling experiments with sediment from the same location in quiescent conditions (Portela *et al.*, 2013). A possible explanation is that, for a velocity of 0.25 m s^{-1}, turbulent shear overpowers the effect of salt flocculation observed in quiescent conditions.

The results of characteristic diameters must be interpreted with caution. Grain size distributions in the particle analyzer may not entirely reflect what occurs in the flume, due to mechanical stirring and sample dilution. Specifically, salinity in the beaker is a fifth of the value in the flume (ranging from 0 to 3, instead of 0 to 15). The values of D_{10} and D_{50} suggest that salinity does increase the aggregation of the finer particles, but it is not yet clear whether this effect translates into deposition rates. The most likely explanation for the evolution of D_{90} is related to the experimental sequence, and not to salinity (*i.e.* the coarser particles in the first experiment may not be resuspended in the subsequent experiments).

CONCLUSIONS

This study set out to assess the effect of salinity on the deposition in flowing water of fine sediments from the Tagus estuary. The main conclusions are as follows:

(1) A reduction in flow velocity from 0.5 m s^{-1} to 0.25 m s^{-1} led, over a period of 8 hours, to a decrease in suspended sediment concentration of about 40% (from 0.670 g l^{-1} to 0.409 g l^{-1}, on average).

(2) Deposition was accompanied by a certain degree of fine sediment sorting, as indicated by a median grain-size (D_{50}) decrease of about 30% (from 9.9 µm to 7.0 µm, on average).

(3) Salinity apparently had no effect on the extent of deposition, as concentrations after 8 hours for five different salinities (0, 2.5, 5, 10 and 15) were remarkably coincident (0.417-0.399 g l^{-1}).

(4) An effect of salinity on the deposition rate in the first hours could not be completely excluded, but the results are ambiguous and need further clarification.

The current results are in contrast with a previous study showing a significant effect of salinity on the quiescent settling velocity (Portela *et al.*, 2013). Further research on the influence of salinity on sediment deposition in flowing water should therefore explore lower flow velocities.

ACKNOWLEDGMENTS

The authors thank Paula Freire for supervision of particle size analysis and Fernando Brito for technical assistance throughout the experiments.

LITERATURE CITED

Booij, R., 1994. *Measurements of the Flow Field in a Rotating Annular Flume*. Delft, The Netherlands: Delft University of Technology, Communications on Hydraulic and Geotechnical Engineering, *Report 94-2*, 148p.

Delo, E.A., 1988. *Deposition of Cohesive Sediment from Flowing Water*. Wallingford, United Kingdom: Hydraulics Research, *Report SR-152*, 70p.

Garcia-Aragon, J.; Droppo, I.G.; Krishnappan, B.; Trapp, B., and Jaskot, C., 2011. Experimental assessment of Athabasca River cohesive sediment deposition dynamics. *Water Quality Research Journal of Canada*, 46(1), 87-96.

Krone, R.B., 1962. *Flume Studies of the Transport of Sediment in Estuarial Shoaling Processes. Final Report*. Berkeley, California: University of California, Hydraulic Engineering Laboratory, 118p.

Mehta, A.J. and Lott, J.W., 1987. Sorting of fine sediment during deposition. *In*: Kraus, N.C. (ed.), *Proceedings of Coastal Sediments '87* (New Orleans, Louisiana, ASCE), pp. 348-362.

Portela, L.I. and Brito, F., 2010. *Deposition and Erosion of Sediments from Esteiro dos Frades, Ria de Aveiro*. Lisboa, Portugal: LNEC, *Report 350/2010-NEC*, 21p.

Portela, L.I. and Reis, M.M., 2005. Analysis of cohesive sediment transport in decelerating and accelerating flow. *In*: Smith, J.M. (ed.), *Coastal Engineering 2004 - Proceedings of the 29th International Conference*, Vol. 2. Singapore: World Scientific, pp. 1818-1829.

Portela, L.I.; Ramos, S., and Trigo-Teixeira, A., 2013. Effect of salinity on the settling velocity of fine sediments of a harbour basin. *In:* Conley, D.C.; Masselink, G.; Russell, P.E., and O'Hare, T.J. (eds.), *Proceedings, 12th International Coastal Symposium*. *Journal of Coastal Research*, Special Issue No. 65, pp. 1188-1193.

Journal of Coastal Research	SI	75	123-127	Coconut Creek, Florida	2016

David and Goliath Revisited: Joint Modelling of the Tagus and Sado Estuaries

Américo S. Ribeiro[†], Magda C. Sousa[†], João D. Lencart e Silva[‡] and João M. Dias[†*]

[†]NMEC, CESAM, Departamento de Física
Universidade de Aveiro
3810-193 Aveiro, Portugal

[‡] Instituto Português do Mar e da Atmosfera
Rua C - Aeroporto
1749-077 Lisboa, Portugal

www.cerf-jcr.org

www.JCRonline.org

ABSTRACT

Ribeiro, A.S.; Sousa, M. C.; Lencart e Silva, J. D., and Dias, J.M., 2016. David and Goliath Revisited: Joint Modelling of the Tagus and Sado Estuaries. *Proceedings of the 14th International Coastal Symposium* (Sydney, Australia). *Journal of Coastal Research*, Special Issue, No. 75, pp. 123-127. Coconut Creek (Florida), ISSN 0749-0208.

The Tagus and Sado estuaries discharge in the same coastal region into the Portuguese continental shelf. Several studies focus on the investigation of the complex circulation at the mouth of Tagus or Sado estuaries, however, the interaction between these two systems was never taken into account and were not performed previous studies dedicated to this topic. To study this important issue, numerical modelling is an important tool that allows researching the interaction between plumes under different conditions. Thus, it was developed an implementation of the three-dimensional model Delft3D-Flow integrating Tagus and Sado estuaries and adjacent shelf to investigate the complex interaction between flows. The numerical model was calibrated using sea surface height, salinity and water temperature data, and then applied to research the role of river discharge and wind effects on the plumes interaction. To examine the response of the estuarine plumes to different wind directions, four scenarios of moderate winds were considered blowing from each of the main four compass points. Two markedly different realistic scenarios were chosen: moderate and high Tagus and Sado River discharges. Independently of rivers discharges, the results revealed an intrusion of the Sado plume in Tagus estuary. This intrusion occurred in the bottom layers in all scenarios due to the ambient coastal current, even when the river discharges decreases. The reverse pattern was not observed, demonstrating an unexpected impact of the smaller estuary on the larger.

ADDITIONAL INDEX WORDS: *Freshwater flow, Tagus estuary, Sado estuary, Delft3D-Flow.*

INTRODUCTION

For centuries, estuaries have been regions of extremely high importance to human kind. These regions are characterized by their high productivity due to river discharges, through their role as nurseries for several animal species and by providing sheltered anchorages and easy navigational access to the Ocean. Here, small and large-scale mixing processes act to produce high mixing rates and spatially inhomogeneous concentration distributions, namely the river plumes. River plumes provide a mechanism for horizontal redistribution of nutrients and pollutants, because they spread and can advect material across long distances as coastal currents (Anderson *et al.*, 2005) and are susceptible to wind and tidal forcing (Choi and Wilkin, 2007; Otero *et al.*, 2008; Sousa *et al.*, 2014a). These conditions determine the pattern of horizontal freshwater dispersal of estuarine plumes (McCabe *et al.*, 2009; Walker, 1996).

Several rivers have their mouths in the western coast of the Iberian Peninsula, such as Tagus and Sado estuaries (Fig. 1). Given the close relationship between the Tagus and Sado estuaries, it is understandable that these two hydrodynamic distinguished systems have their discharges on the same coastal region. The Sado estuary is located south of the Tagus estuary, which is the most important freshwater source flowing into this coastal region.

In fact, the Tagus and Sado estuaries have different characteristics and dynamics, such as the topography, freshwater volume discharged and the shape of the estuary. For this reason, there are various studies using numerical models focusing on the investigation of the complex circulation of the Tagus or the Sado estuaries (Fortunato *et al.*, 1997; Martins *et al.*, 2001; Vaz *et al.*, 2009). However, the interaction between these two systems was never taken into account and there were no previous studies dedicated to this topic. The development of numerical models contemplating both Tagus and Sado estuaries as one system is a real scientific state-of-the-art challenge. This model implementation has the ability to show plume interaction patterns over shelf or even giving some insights about punctual water intrusions from the neighbor river.

Thus, the main objective of this paper is to study the propagation patterns of the Tagus and Sado estuarine plumes on the coastal region, and its interaction on the circulation and hydrography on the Tagus and Sado estuaries.

DOI: 10.2112/SI75-025.1 received 15 October 2015; accepted in revision 15 January 2016.
*Corresponding author: joao.dias@ua.pt

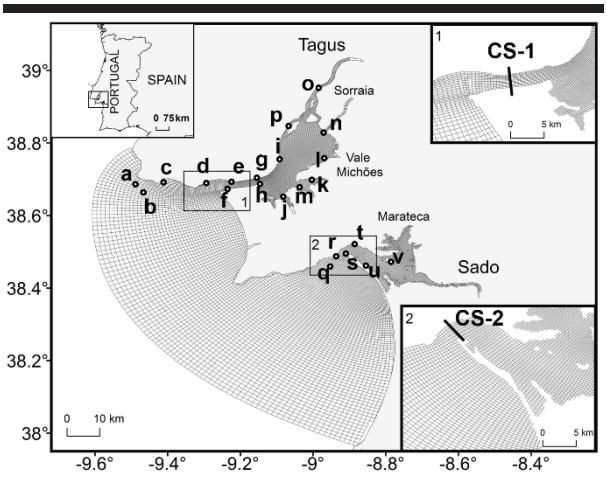

Figure 1. Location map of the study area with location of the stations used to calibrate and validate the model (white circles), Cross-sections at Tagus estuary mouth (CS-1) and Sado estuary mouth (CS-2) and freshwater inflows (black dots).

STUDY AREA

The Tagus and Sado estuaries are located on the western coast of Iberian Peninsula (38°47'N, 9°30'W to 37°58'N, 8°53'W) (Fig. 1).

The Tagus estuary has a total area of 320 km^2. A deep, narrow inlet channel and a shallow inner bay compose the estuary. The inlet channel is 15 km long (W-E), 2 km wide and reaches depths of 40 m, constituting the deepest part of the estuary. The inner bay is about 25 km long and 15 km wide, being the shallowest part of the estuary and has complex bottom topography with narrow channels, tidal flat areas and small islands on the inner most part of the estuary (Fortunato *et al.*, 1997). The tides are semidiurnal, presenting tidal ranges from 0.75 m in neap tides in the mouth to 4.3 m in spring tides in upper estuary (Fortunato *et al.*, 1997). The hydrography of the estuary is modulated by the tidal propagation and fluvial discharge from three sources of freshwater flowing into Tagus estuary: the Tagus and Sorraia Rivers and the Vale Michões tributary.

The Sado estuary is located south of Tagus estuary, with a total area of 100 km^2. It is about 20 km long and 4 km wide, with maximum depths of about 50 m and an average depth of 8 m. The tide is semidiurnal, with amplitudes varying between 1.6 m in spring tides and 0.6 in neap tides (Martins *et al.*, 2001). The estuary has intertidal sandbanks, which separate the estuary in two zones: the lower estuary behaves as a coastal lagoon with freshwater influence, and the upper estuary with a freshwater dependent behavior (Martins *et al.*, 2001). The upper estuary has two freshwater sources: the Marateca tributary and the Sado River, with 10% and 80% of the total freshwater input respectively.

METHODS

Numerical model

The hydrodynamic simulation of the study area was performed using the Delft3D-Flow modeling system. This platform was setup with a 553×174 cells curvilinear irregular grid with a mean resolution of ~100 m in the area of the interest (tidal channels) and ~1500 m at the offshore open boundary (Fig. 1). The bathymetry used results from the interpolation to the numerical grid of a set of topo-hydrographic surveys. The model uses 15 sigma layers with refined surface layers comparing to the intermediate and the bottom layers, due to most important dynamics related to the freshwater plumes occurrence in the surface layers.

Transport conditions and tidal propagation are calculated based on inputs from the Portuguese Coast Operational Modelling System (PCOMS) (http://www.maretec.org/). The propagation of the tide was modelled by prescribing a linearized Riemann invariant (Deltares, 2011) (weakly reflective boundary condition), i.e. a combination of water levels and velocities analog to the Flather (1976) and Chapman (1985) open boundary conditions. Additionally, it was prescribed the use of a per-layer specified velocity profile at ocean open boundaries.

A heat transport model was applied, taking into account air temperature, relative humidity and net solar radiation to calculate heat losses from convection, evaporation and back radiation. These data was obtained from NCEP reanalysis with a temporal resolution of 6 h. The wind intensity and direction are obtained from a local implementation of the Weather Research and Forecasting model (www.wrf-model.org), with a resolution of 4 km. A total of 5 freshwater points were defined as outflows representing the Tagus, Sorraia, Vale Michões, Sado and Marateca rivers/tributaries.

Calibration

The hydrodynamic calibration was performed comparing the measured and predicted time series of sea surface elevation (SSE) for 20 stations distributed throughout the lagoon (Fig. 1), and comparing the harmonic constants of the tides generated by the model to the respective values of the field data (Ribeiro, 2015). As an example of the model calibration results, Table 1 shows the calculated values of root mean square errors (RMSE) and Skill, for previous used Tagus and Sado stations. The best model results were obtained for the stations located near the estuary's mouth, indicated by the higher skill and lower RMSE values, and the highest disagreements were found for the most inner parts (Table 1).

The salt and heat transport model was calibrated using CTD profiles obtained in two locations outside the Tagus estuary (Fig. 1). The comparison between predicted and observed water temperature values (Figs. 2a and 2c) shows that the water temperature is well represented in both stations, with differences between predictions and observations around 1.5°C. Salinity profiles (Figs. 2b and 2d) show the same pattern, with differences comprising 0.5. These values can be explained by low resolution (~6 km) of the open ocean boundary forcing. These results are similar to those found in Vaz *et al.* (2009).

According to these results is considered that the model reproduces the hydrodynamic behavior and the heat and salt transport of the study area and consequently was considered calibrated.

Table 1. *Error values for tidal water levels.*

Estuary	Station	RMSE (m)	Skill
Tagus	c	0.0874	0.9967
	g	0.1190	0.9954
	j	0.1345	0.9944
	l	0.1529	0.9938
Sado	q	0.0595	0.9984
	s	0.0801	0.9974
	v	0.1102	0.9957

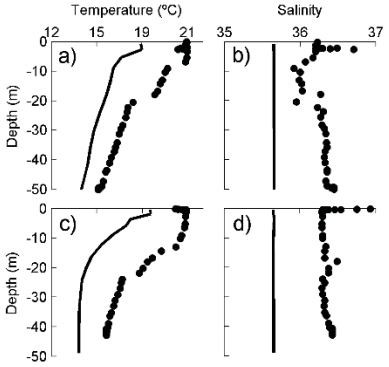

Figure 2. Observed (points) and predicted (line) water temperature and salinity vertical profiles for the sampling stations a (a, b) and b (c,d).

Model scenarios

Different scenarios were developed to investigate the necessary conditions to observe the intrusion of water from the neighboring estuary in the Tagus and Sado estuary, as well as visualize the propagation path of the estuarine water masses in the coastal region. The scenarios were run for 10 days after two weeks spin-up, under winter season of 2009-2010 conditions and produced under the conditions as the calibration run.

Following the methodology adopted by Sousa *et al.* (2014b), a statistical analysis to the river discharge was applied. Thus, two total different rivers inflow were used: high and moderate discharges (Table 2).

Taking into account these discharges, a set of ten scenarios were defined, with idealized high and moderate discharges, with different wind directions and typical moderate winds of 6 m s^{-1} blowing from each of the main four compass directions.

Two passive tracers were also introduced in all model runs, one for Tagus estuary inflows and the other for Sado estuary inflows, with a concentration of 1000 kg m^{-3} in order to investigate the estuarine plumes propagation through the domain and observe the exchanges between the estuaries.

Table 2. *River discharges estimations for January.*

	River discharges ($m^3 s^{-1}$)				
	Tagus	**Sorraia**	**Vale Michões**	**Sado**	**Marateca**
High	11575	2771	83	1167	119
Moderate	324	45	8	35	7

RESULTS

The modelling results of the passive tracers are depicted in Fig. 3, showing the hourly cumulative advective transport determined through the cross-sections in front of both estuaries (Fig.1, sections CS-1 and CS-2) under various forcing conditions. The cumulative advective transport was also filtered with a 33 h low-pass filter in order to remove tides and high frequency fluctuations, allowing the transport analysis only due to wind and freshwater discharge.

During the high discharge event, without wind forcing and after 6 days, a small intrusion of the Sado plume is observed at the Tagus estuary (Fig. 3a). A similar pattern under the southward and westward wind scenarios is observed (Fig. 3a). Under northward winds, a maximum in cumulative advective transport (1.8×10^9 kg) of the Sado tracer across the mouth of the Tagus (CS-1) is reached on the eighth day, falling to 1.0×10^9 kg on the nine day. In the eastward scenario (Fig. 3a), a negligible influence of the Sado plume intrusion is observed, showing that for this condition, the Sado plume does not influence the Tagus dynamics.

On the other hand, Tagus plume does not propagate to the Sado estuary during the simulation (Fig. 3b). Taking into account these results, hereafter, the influence of Tagus plume in Sado plume is not considered.

Over the moderate river discharge event (Fig. 3c), Sado plume took less time (5 days) to reach Tagus estuary under westward wind scenario. For the other wind conditions, the pattern is very similar to the high river discharge event.

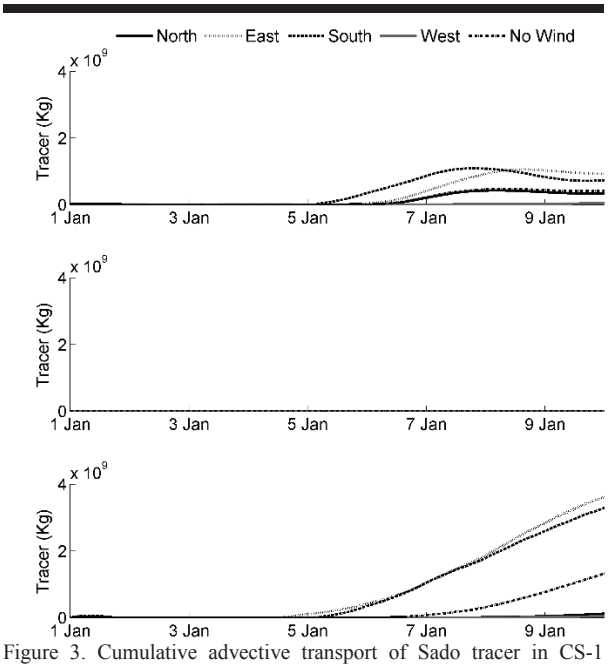

Figure 3. Cumulative advective transport of Sado tracer in CS-1 section (a, c) and Tagus tracer in CS-2 (b), under high river discharges (a, b) and moderate (c) river discharges, for the different wind conditions.

Considering the previous results, events of moderate-to-high Sado River discharge result in plume intrusion into Tagus estuary. Thus, the distribution of the tracers at the deepest region of the Tagus inlet channel (CS-1) was investigated in order to evaluate the effect of Sado plume on the hydrodynamic features of the Tagus.

Under high river discharges and for all wind conditions, the concentration of Tagus tracer is higher on the surface layers than at the bottom ones, which indicates that a more buoyant Tagus plume flows out of the estuary (Fig. 4a), whilst the denser water containing the Sado tracer flows upstream the Tagus estuary at the bottom layers (Fig. 4b). These results are corroborated by the zonal velocity and density profiles (Figs. 4c and 4d). The positive velocities are observed at bottom layers (Fig. 4c), indicating that the Sado plume propagation flows in these layers.

When the river discharges decreases (Figs. 4e, 4f, 4g and 4h), the pattern remains the same found for high river discharges. However, in these conditions, the zonal velocities are positive in all water column, indicating that a higher volume of denser sea water (Fig. 4h), along with Sado plume, flows towards Tagus estuary (Fig. 4f). This result is more evident in the presence of westward and northward wind conditions. The result for eastward wind conditions corroborate Figs. 3a and 3c outcomes, where low concentrations of Sado tracer are recorded in the CS-1.

DISCUSSION

The analysis of Figs. 3 and 4 reveal that the Sado plume intrudes into Tagus estuary, however, the contrary pattern does not occurs. This intrusion is more evident during northward winds. The northward winds confine the plume close to the coast, which enhance the mixing process within the plume, forming vertically well-mixed and narrow plumes (Soares *et al.*, 2007). This result is consistent with the findings obtained in the Wallapa Bay (Columbia) plume study (Banas *et al.*, 2004).

The Sado tracer is shown to intrude into the Tejo estuary in the absence of wind forcing, reproducing the classic ROFI dynamics (Simpson, 1997). When wind forcing is applied, westward and northward winds transport more Sado water into the Tagus than when the wind is blowing to south or east. This shows again the expected behavior of a density gradient under a rotational reference system. The results show this behavior at the start of sixth day, in southward and in the absence of wind scenarios, when the Sado plume if found to intrude in Tagus estuary. For eastward wind, the Sado plume took longer to reach the Tagus estuary than in the other scenarios, with the presence of residual cumulative concentrations, indicating that eastward winds are not favorable for the Sado plume propagation to Tagus estuary.

According to the results obtained in velocity and density profiles (Figs. 4c, 4d, 4g and 4h), the river discharge plays an important role in plume spreading compared to wind. Using a numerical model, Mao *et al.* (2008) also show that the variations in Yellow River runoff are important to the salinity not only in the area around the river mouth but also in entire Bohai Sea.

The currents at the Tagus inlet channel in neap tide (the velocities are lower comparing to spring tide (Fortunato *et al.*, 1997) are favorable to form a downstream flow towards the ocean. This structure is enhanced by the increase of the river discharges, leading to a higher density gradient in the water column (Figs. 4d and 4h).

Although the ambient current can restrain the Sado plume intrusion by advecting the Tagus freshwater outflow outside the estuary, it cannot eliminate the drive of the Sado plume. This is due to the apparently negligible effect that the ambient coastal current has on the current structure at the Tagus inlet channel. Similar results were obtained by Guo and Valle-Levinson (2007) in Chesapeake Bay.

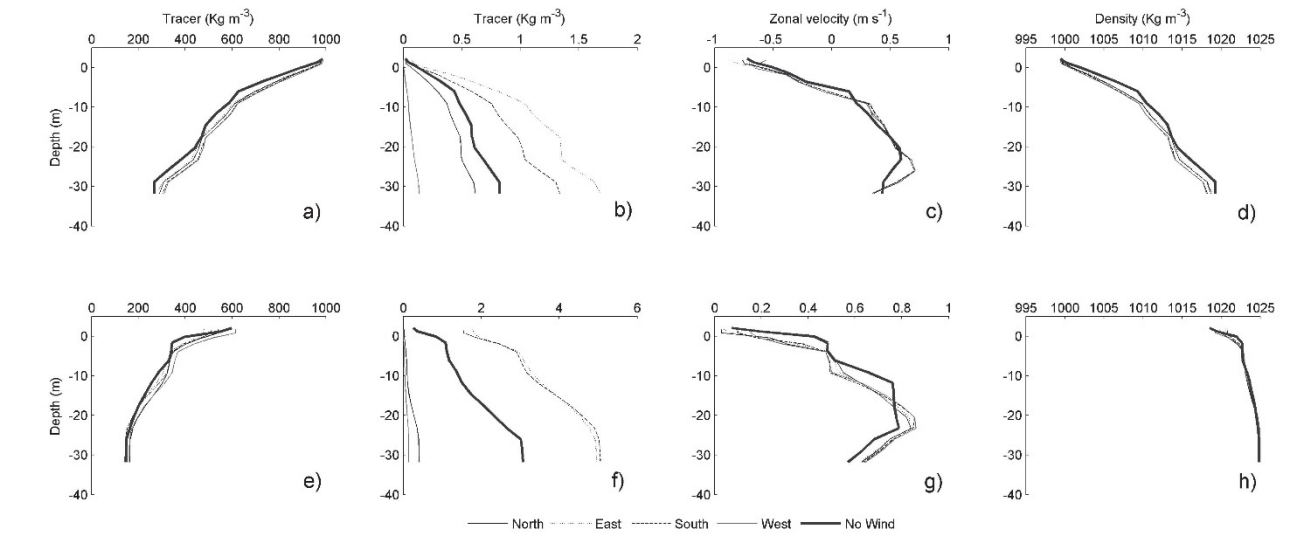

Figure 4. Vertical profiles of Tagus tracer (a, e), Sado tracer (b, f), zonal velocity (c, g) and density (d, h) registered at a location in the center of CS-1 under high (a, b, c, d) and moderate river discharges (e, f, g, h), for the different wind conditions for 10 days after the simulation start, during neap tide.

The density pattern can be partly explained by the research of Fujiwara *et al.*(1997), which observed that in large estuaries and Regions of Freshwater Influence (ROFIs) (Simpson, 1997) the fate of the density field is controlled not only by buoyancy and tidal forcing but also by the Tagus inlet channel morphology under the influence of Earth's rotation.

Garvine (1999) examined the tidal effects on the downstream intrusion of buoyant water and concluded that shelf tides have a detectable but moderate influence on plume downstream intrusion. In this study, this pattern was observed for high river discharges. When the river discharges decreases, despite Sado small outflow compared to the Tagus, the Sado outflow was the only one to propagate a significant distance to affect the neighbor estuary.

CONCLUSIONS

The three-dimensional hydrodynamic model Delft3D was applied to Tagus and Sado estuaries in order to investigate their interaction. Numerical experiments were conducted testing several scenarios with different wind directions and river discharges.

The results for a high discharge suggest an intrusion of the Sado estuarine water in Tagus estuary after a 10-day simulation for all scenarios, except for eastward wind scenario. Otherwise, the Tagus plume does not reach the Sado estuary. When the river discharges decreases, the results showed that during northward and westward winds, the Sado plume influences with more intensity the Tagus estuary. However, Tagus plume does not propagate to the Sado estuary. During these conditions, the Sado plume is advected to north, and flows on the bottom layers towards Tagus estuary, whereas Tagus estuarine water flows on top layers.

In summary, despite the difference in magnitude of these estuaries, the small Sado plume influences the large Tagus estuarine water, even with lower river discharges.

ACKNOWLEDGMENTS

The second author of this work has been supported by the Portuguese Science Foundation (FCT) through a postdoctoral grant (SFRH/BPD/99707/2014). This study was partially supported by the National Foundation for Science and Technology – FCT, through CESAM (UID/AMB/50017/2013).

LITERATURE CITED

Anderson, D.M., Keafer, B. a., Geyer, W.R., Signell, R.P. and Loder, T.C., 2005. Toxic Alexandrium blooms in the western Gulf of Maine: The plume advection hypothesis revisited. *Limnology Oceanography*, 50, 328–345.

Banas, N.S., Hickey, B.M., MacCready, P. and Newton, J. a, 2004. Dynamics of Willapa Bay, Washington: A Highly Unsteady, Partially Mixed Estuary. *Journal Physical Oceanography*, 34, 2413–2427.

Chapman, D.C., 1985. Numerical treatment of cross-shelf open boundaries in a barotropic coastal ocean model. *Journal of Physical Oceanography*, 15, 1060–1075.

Choi, B.-J. and Wilkin, J.L., 2007. The Effect of Wind on the Dispersal of the Hudson River Plume. *Journal of Physical Oceanography* 37, 1878–1897.

Deltares, 2011. Delft3D-Flow User Manual Version 3.15. Delft, The Netherlands.

Flather, R.A., 1976. A tidal model of the northwest European continental shelf. *Memoires de la Société Royale de Sciences de Liege*, 6, 141–164.

Fortunato, A.B., Baptista, A.M. and Luettich, R. a., 1997. A three-dimensional model of tidal currents in the mouth of the Tagus estuary. *Continental Shelf Research*, 17, 1689–1714.

Fujiwara, T., Sanford, L.P., Nakatsuji, K. and Sugiyama, Y., 1997. Anti-cyclonic circulation driven by the estuarine circulation in a gulf type ROFI. *Journal Marine Systems*, 12, 83–99.

Garvine, R.W., 1999. Penetration of Buoyant Coastal Discharge onto the Continental Shelf: A Numerical Model Experiment. *Journal of Physical Oceanography*, 29, 1892–1909.

Guo, X. and Valle-Levinson, A., 2007. Tidal effects on estuarine circulation and outflow plume in the Chesapeake Bay. *Continental Shelf Research*, 27, 20–42.

Mao, X., Jiang, W., Zhao, P. and Gao, H., 2008. A 3-D numerical study of salinity variations in the Bohai Sea during the recent years. *Continental Shelf Research*, 28, 2689–2699.

Martins, F., Leitão, P., Silva, A. and Neves, R., 2001. 3D modelling in the Sado estuary using a new generic vertical discretization approach. *Oceanologica Acta*, 24, 51–62.

McCabe, R.M., MacCready, P., Hickey and B.M., 2009. Ebb-Tide Dynamics and Spreading of a Large River Plume*. *Journal of Physical Oceanography*, 39, 2839–2856.

Otero, P., Ruiz-Villarreal, M. and Peliz, a., 2008. Variability of river plumes off Northwest Iberia in response to wind events. *Journal Marine Systems*, 72, 238–255.

Ribeiro, A.S. 2015. Coupled Modelling of the Tagus and Sado estuaries and their Associated Mesoscale Patterns. Aveiro, Portugal: University of Aveiro, Master's thesis, 106 p.

Simpson, J.H., 1997. Physical processes in the ROFI regime. *Journal Marine Systems*, 12, 3–15.

Soares, I.D., Kourafalou, V. and Lee, T.N., 2007. Circulation on the western South Atlantic continental shelf: 2. Spring and autumn realistic simulations. *Journal of Geophysical Research*, 112, C04003. doi:10.1029/2006JC003620

Sousa, M.C., Vaz, N., Alvarez, I., Gomez-Gesteira, M. and Dias, J.M., 2014a. Modeling the Minho River plume intrusion into the Rias Baixas (NW Iberian Peninsula). *Continental Shelf Research*, 85, 30–41.

Sousa, M.C., Vaz, N., Alvarez, I., Gomez-Gesteira, M. and Dias, J.M., 2014b. Influence of the Minho River plume on the Rias Baixas (NW of the Iberian Peninsula). *Journal Marine Systems* , 139, 248–260.

Vaz, N., Fernandes, L., Leitão, P.C., Dias, J.M. and Neves, R., 2009. The Tagus estuarine plume induced by wind and river runoff: Winter 2007 case study. *Journal Coastal Research*, Special Issue No. 56, pp 1090–1094.

Walker, N.D., 1996. Satellite assessment of Mississippi River plume variability: Causes and predictability. *Remote Sensing of Environment*, 58, 21–35.

Journal of Coastal Research	SI	75	128-132	Coconut Creek, Florida	2016

Variability of Salinity in Pará River Estuary: 2D Analysis with Flexible Mesh Model

Renan P. Rosário†*, Thaís A.C. Borba†, Arthur S. Santos†, and Marcelo Rollnic†

† Marine Geophysics Laboratory, Geophysics Department/CPGf
Federal University of Pará
Belém, Brazil

www.cerf-jcr.org

www.JCRonline.org

ABSTRACT

Rosário, R.P., Borba, T.A.C., Santos, A.S., and Rollnic, M., 2016. Variability of Salinity in Pará River Estuary: 2D Analysis with Flexible Mesh Model. *In:* Vila-Concejo, A.; Bruce, E.; Kennedy, D.M., and McCarroll, R.J. (eds.), *Proceedings of the 14th International Coastal Symposium* (Sydney, Australia). *Journal of Coastal Research*, Special Issue, No. 75, pp. 128-132. Coconut Creek (Florida), ISSN 0749-0208.

This research aims to study the spatial and temporal variability of the salinity in the Pará River Estuary. The Pará River estuary is among the largest in Brazil, with a mouth of approximately 60 km wide. The Pará River is not a true river because it does not have a spring, but is a hydrographic mesh that receives outflow of several water bodies. There is an ingestion of salt in the Pará River Estuary, different of what occurs within Amazon River, that leads estuarine characteristics onto the continental shelf. The model was implemented based on flexible mesh in the estuarine area of the Amazon River and Pará River basin for one-year simulation. The software D-Flow FM was used to perform hydrodynamic model and, D3D-D-Waq to water quality model. These experiments support a conceptual description of haline dynamics of this system to produce information regarding different scenarios in the region. Fieldworks were made (25h - three points in estuary) in low, high, and transitional rivers discharge in order to evaluate the model performance. The main conclusions are: the numerical modeling showed an upstream saline intrusion about 130 km for the dry period (October to December) and about 70 km for the rainy period (January to May). 2D barotropic condition shows river discharge as the most important force that control the variation of saline intrusion due to the reduction of freshwater flow in the system.

ADDITIONAL INDEX WORDS: *Salinity intrusion, amazon estuary, water quality model.*

INTRODUCTION

The Amazon Coastal Zone (Northern Brazil) receives water from two large river basins: Amazon and Tocantins. The Tocantins River Basin is the main tributarie of Pará River which also receives water from the Amazon River through the Breves Straits (Silva, 2009; Costa, 2013), Portel/Melgaço River Basin, and, on a smaller scale Acará, Mojú, and Guamá/Capim Rivers (Figure 1).

The Pará River Estuary, that also is called Marajó Bay, is one of the largest estuaries in Brazil with a mouth that is approximately 60 km wide. It is a highly dynamic region, and the river's flow rate is associated with the energy of the tides. The flow rate reaches a peak of 300,000 m^3/s at ebb tide and 200,000 m^3/s at flood tide (Prestes, 2014). The discharge seasonality of the region affect the estuary, with high discharge from January to May and low discharge from August to November (ANA, 2015). The study area is located in a humid tropical region, which represents less than one-fourth of the earth's land surface but is responsible for more than half of the freshwater, particles and solutes discharged into the oceans (Nittrouer *et al.*, 1995).

The saline intrusion occurs during low discharge period in the Pará River Estuary (Bezerra *et al.*, 2011; Baltazar *et al.*, 2011). In this case, the salt presence produce different processes in the estuary (*e.g.* stratification, advctive, and diffusive processes, *etc.*). The salinity is an important parameter in decisions made by public and private environmental managements. Furthermore, salt intake variations within an estuary has influence over hydrodynamic and fine sediment dynamics.

This research aims to study the spatial and temporal variability of the surface salinity in the Pará River Estuary. Two models were used: D-Flow Flexible Mesh (Kernkamp, 2011) for hydrodynamic and Delft3D Water Quality model (Roelvink and van Banning, 1994) for salinity study.

Pará River Estuary

The Pará River flows into the Atlantic Ocean through the eastern portion of Marajó Island and discharges on the Amazon Continental Shelf. The major tributary of the estuary is the Tocantins River (Prestes *et al.*, 2014). This river system is ranked 11th in the list of world's largest rivers in water volume (Dai and Trenberth, 2002).

Based on monthly averages for eighty years preceding from National Operator of the Electrical System (ONS, Operador Nacional do Sistema Elétrico), water discharge reaches a maximum (24,000 m^3/s) in April and a minimum (2,300 m^3/s) in September (Figure 2). These data were collected in Tucuruí, the first town on the river above tidal influence. Tucuruí is located about 450 km from the Atlantic Ocean, with tributaries entering the river (primarily the Amazon, Guamá/Capim Rivers) that provide additional water to the estuary.

DOI: 10.2112/SI75-026.1 received 15 October 2015; accepted in revision 15 January 2016.
*Corresponding author: renanpeixotorosario@gmail.com

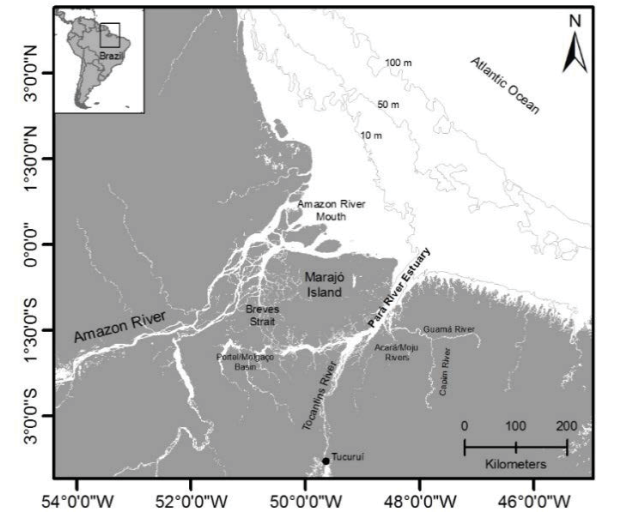

Figure 1. Study area with water bodies that constitute Amazon and Tocantins Basin. The isobath shows the large and shallow continental shelf of the north of Brazil.

In the mouth the Pará River Estuary the main constituents are the semi-diurnal components (M_2, S_2, N_2) which were identified by Beardsley *et al.* (1995) on the Amazon Shelf. Similarly, Prestes *et al.* (2015) found about fifteen tidal constituents (95% of significant). In this case, the main component was also M_2, which represent approximately 40% of the total astronomical tide amplitude inside the Pará River Estuary. The tide decreases toward the upstream from macrotidal to microtidal in the internal portion. Positive tidal asymmetry increases as height decreases, resulting in the total attenuation of tides downstream in the Pará River (Freitas *et al.*, 2012).

The local trade winds are most intense between January and April, when they blow predominantly from the northeast, and milder between June and October when they mainly blow to the west/northwest. This seasonal variation is determined by shifts in the position of the Intertropical Convergence Zone during the course of the year (Arraut *et al.*, 2012).

The Pará River Estuary is characterized by a highly dynamic environment that is affected by tide and river seasonality. The variations of important factors that affect oceanic and estuarine processes on the Amazon shelf and Amazon river basin are shown in Figure 3.

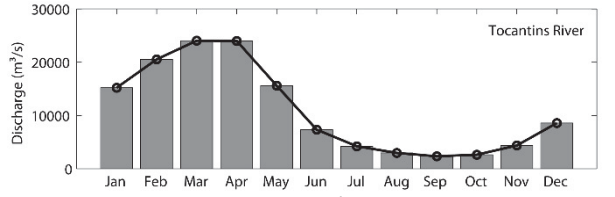

Figure 2. Historical river discharge (m^3/s) of the Tocantins River. The bar graph shows monthly mean values for eighty years of data (1930 - 2010).

METHODS

The intrusion of the salinity front into the Pará River Estuary was simulated using the calibrated and validated model designed by Borba (2014). The model was implemented based on flexible mesh in the estuarine area of the Amazon River and Pará River basin for a year simulation (Figure 4). The software D-Flow FM (Kernkamp, 2011) was used to implement the hydrodynamic model, and D3D-D-Waq (Roelvink and van Banning, 1994) was used for the water quality model.

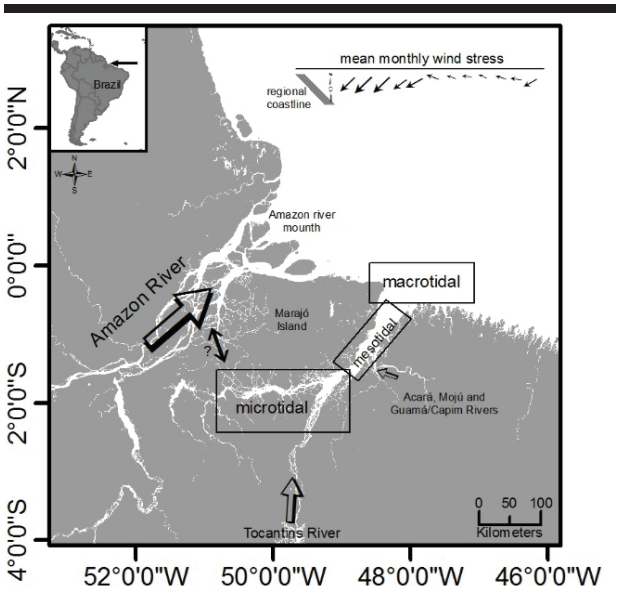

Figure 3. The map shows wind variation on the continental shelf, river inputs, and variation of tidal amplitude inside the Pará River Estuary. The question mark between the Amazon and Tocantins River Basin represents the remaining uncertainty between this connection and the real contribution from the Amazon River. Data from Nittroer *et al.*, 1995; Prestes, 2014.

Freshwater inputs derive from the typical values of the river discharge from Amazon basin (with the contribution of the Tapajós and Xingu Rivers) and Tocantins Basin (Figure 5). The river discharge data is available on ANA (National Water Agency) website (ANA, 2015). Annual average sedimentary discharge values of 100, 12, 20, and 7 g/m^3 were also considered for the Amazon, Tapajós, Xingu, and Tocantins Rivers, respectively.

Saltwater input occurred on the continental shelf with value of 35 PSU (Pratical Salinity Unit) for the open boundary. The sea level boundary condition was defined based on OTIS (Regional Tidal Solutions) data for the Amazon Shelf and the components used were M_2, S_2, N_2, K_1, O_1, and M_4. The wind was considered constant in time and space. The magnitude and direction defined for the Amazon Estuary modeling were 8 m/s and 80 degrees true north. For more detail about model setup, see Borba 2014.

Fieldworks were made in low (Sep 24, 2014), high (Apr 16, 2015) and transitional (Jul 15, 2015) river discharge in order to evaluate the model performance. Three points were selected for monitoring salinity, temperature, and pressure (Figure 4). One in the left bank (LB, Joanes - Marajó Island) and another on the right bank (RB1, Colares Island), about 25 km from each other and about 60 km from the mouth. The third, was installed 120 km from the mouth (RB2, Belém city). All fieldworks were carried out in spring tide condition near the shore (shallow water). Sensors recorded measurements every 15 minutes for 24 hours.

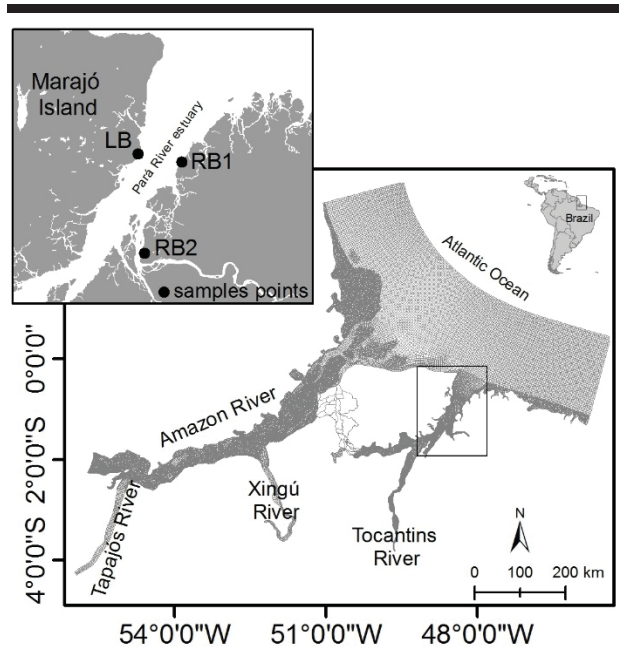

Figure 4. Computational mesh (flexible mesh) of the study area. The map above shows sample points in the left bank (LB), right bank 1 (RB1), and right bank 2 (RB2).

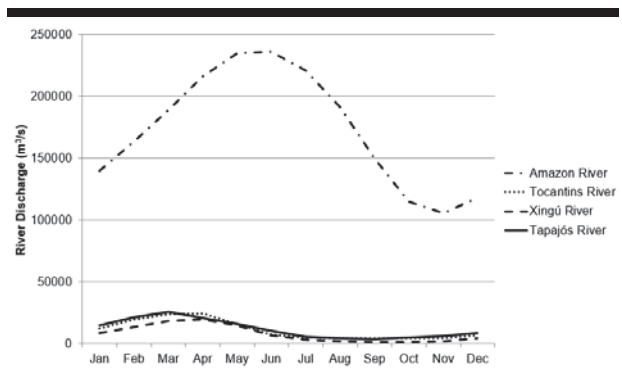

Figure 5. Average monthly discharge for the Amazon, Xingú ,Tapajós and Tocantins rivers.

RESULTS

The model considered only the river discharge and tidal variation because the winds were set constant in space and time. Thus, in the high discharge period and spring tide, salinity intrusion occurred approximately 70 km (Figure 6a). In the transition period between high and low river discharge and also spring tide, salinity intrusion occurred until approximately 110 km (Figure 6b). In the other case, low discharge condition of the main source of the estuary (Tocantins River) and spring tide condition, salinity intrusion in the estuary reached about 130 km from the estuary mouth (Figure 6c).

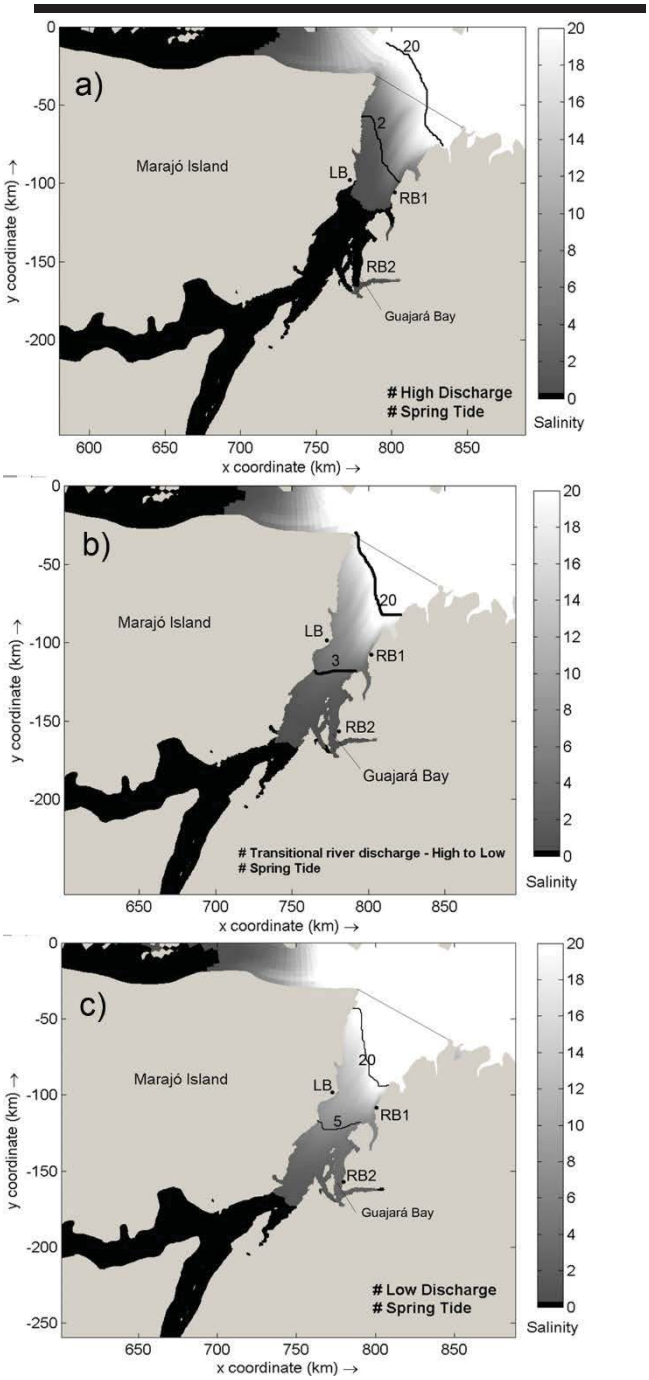

Figure 6. 2D model result of the salinity. a) high discharge; b) transitional discharge; c) low discharge. The straight line in the mouth of the estuary is the reference point for distances. The samples points are represented (LB, RB1 and RB2).

The experiments performed in LB, RB1 and RB2 points revealed absence of salinity during the high discharge period. The upstream point, RB2, about 120 km from the mouth (following the river), did not record salinity during the three experiments (high, low and transitional river discharges conditions). On the other hand, the two points, which are about 60 km from the mouth of the estuary, recorded salinity record in the low and transitional period (Table 1).

The average salinity for a tidal cycle measurement in the experiments was higher in the left bank than in the right bank. However, the amplitude of variation between the maximum and the minimum was the same - about two salinity units. In contrast, during the transition period, the right bank showed higher salinity values and a quick response to the tidal energy relative to decreased river discharge.

Table 1. *Maximum, minimum, mean, and standard deviation of salinity (PSU) from the fieldwork in the RB1 (right bank), LB (left bank,) and RB2 (upstream) points.*

	RB1			*LB*			*RB2*		
	HD	TD	LD	HD	TD	LD	HD	TD	LD
Max.	0	2.7	2.5	0	0.4	4.6	-	-	-
Min.	0	1.2	0.5	0	0.1	2.7	-	-	-
Mean	0	1.8	0.9	0	0.2	3.8	-	-	-
Std.	0	±0.3	±0.4	0	0	±0.4	-	-	-

HD: High Discharge; TD: Transitional Discharge; LD: Low Discharge.

DISCUSSION

Spatial and temporal distribution of salinity in an estuarine system such as the Pará River Estuary depends strongly on the balance between tidal variations (spring and neap) and the river discharge system (Miranda *et al.*, 2002). The analysis of data collected in situ indicated that the surface saline intrusion does not reach the upstream point during a period of low discharge of the Pará River. However, the numerical modeling showed an upstream saline intrusion of 130 km for the dry period and 70 km for the rainy period. The greatest reach observed in the results of the model derives from the fact that salinity of the surface layer is considered for the data analysis in situ and average salinity of the water column is considered in modeling.

In general, the model has higher salinity than those observed in the sample data. As previously mentioned, this is probably caused by the fact that the model result be the water column average. In addition, the innermost point (RB2) for example, lack of an effective discharge of the other lower river as input to the model may cause the salt trap in the Guajará Bay, near of the Belém city. In this case, even if the discharge is relatively small when compared to other rivers that drain out region, it may be important in local processes. On the other hand, Bezzera *et al.* (2011) found salinity values of 1.3 in the surface during high tide and 1.6 in the bottom layer during ebb tide. This data was collected in October, 2007 in Guajará Bay, near to RB2 point, suggesting that at this inner point, the saline intrusion starts in October.

The model well represented the spatial and temporal variability of salinity intrusion in the Pará River Estuary, with a maximum range of 130 km during the low discharge period. Prestes *et al.* (2014) conducted velocity measurements 150 km from the mouth of the Pará River Estuary. The measurements occurred in May (rainy season), September (dry season) of 2011, and in June 2013 (transitional season). By analyzing the volume transport in this region they concluded that this portion of the estuary is dominated by the tide (*i.e.* the local flow is dominated by the barotropic component of the pressure gradient). The flow or ebb does not generated by density difference (baroclinic componente of the pressure gradient), it is concluded that there is no salt present in this portion of the estuary.

The model output shows that the Pará River Estuary does not present very high salinity along its longitudinal profile. A large part of its extension presents values lower than 20 PSU. Furthermore, there is a rapid dilution of the seawater, resulting in low salinity water, between 0 and 5, several kilometers away. The isohaline, 20 PSU, is restricted to the mouth of the estuary, even low discharge conditions. It presents a slope to the right, which does not appear to be the effect of coriolis force, because it is low near the equator (Cuschman-Roisin and Beckers, 2005), but may be an effect of the channel at the right bank. From the mouth to the LB and RB1 points, the estuary has two main channels, then it unifies one channel. On the left bank, there is an extensive shallow area with depths less than 8 meters that can retard the tidal wave propagation into this estuary stretch.

The right bank (point RB1) has high surface salinity values in the transition period, both in the field and the model data, suggesting a rapid response of the tide effect due to decreased river discharge. At one point, about 1 km north of the RB1 point, in December 2009 (24-hours monitoring transition period), Baltazar *et al.* (2011) observed that the salinity was higher during early ebb than flood. These authors attribute this behavior is present in the mangroves because of the high concentration of salt in the soil and eventually "pollute" the water layer, especially the bottom layer. Instead, we believe that at this point in the estuary, the channel favors the tidal intake, therefore, the saline intrusion would be advective. Figure 6 shows the isohaline twenty that the saltwater intrusion occurs preferentially on the right bank. Furthermore, the higher salinities during the early flooding can be attributed to asymmetry of the tide with the current, in which the water level begins to decrease, but the flow continues upstream, as observed in Pará River by Prestes *et al.* (2014).

Based on the results of the implemented model, the variation in river discharge is responsible for the reach of upstream saline intrusion into the Pará River Estuary. However, the high energy of the tide in the Amazon continental shelf region (Beardsley *et al.*, 1995) can be the reason for the high penetration of salinity. This reflects the difference between the processes that occur in this estuary and the Amazon River mouth, in which the position of the saline front depends on the effect of astronomical tides (r2=80%), exceeding the influence of wind (r2=30%) and of river discharge (r2=21%) (Molinas *et al.*, 2014). Also, according to this authors, the relative low influence of river discharge on the position of the salinity front at the Amazon River mouth might be explained by the small flow variation throughout the

year (less than four times) or by the fact that the mixing zone occurs on the continental shelf, where river influence disappears.

CONCLUSIONS

Observations and numerical modeling showed that surface saline intrusion penetrates as far as approximately 130 km during a period of low discharge of the system that drains the Pará River.

River discharge might be pointed out as the most important explanatory variable of saline intrusion, due to the reduction of freshwater flow in the Pará River Estuary.

Although the salinity of the model has been higher than field measurements, it is believed that there is an important estuary bottom component. Therefore, the result in 2D limits the understanding of saline intrusion, but is a first important approach to comprehending this process in the estuary.

ACKNOWLEDGMENTS

The authors thank the Financier of Studies and Projects of Brazil (FINEP, Financiadora de Estudos e Projetos) for funding the project and the Brazilian Federal Agency for Support and Evaluation of Graduate Education (CAPES) for the fellowship granted to Renan P. Rosário. We are thankful to all personnel of the Laboratory of Physical Oceanography (LOF) and Marine Geophysics Laboratory (GEOFMAR, Geophysics Department / CPGf) at the Federal University of Pará (UFPA) for the valorous assistance in field for data acquisition. We are also thankful to Zak Bedell for the English review.

LITERATURE CITED

Arraut, J.M.; Nobre, C.; Barbosa, H.M.J.; Obregon, G., and Marengo, J., 2012. Aerial Rivers and Lakes: Looking at Large-Scale Moisture Transport and Its Relation to Amazonia and to Subtropical Rainfall in South America. *J. Climate*, **25**, 543–556.doi: http://dx.doi.org/10.1175/2011JCLI4189.1.

ANA, Agencia Nacional de Águas (2015). HidroWeb, Sistema de Informações Hiodrológicas. http://hidroweb.ana.gov.br/HidroWeb/HidroWeb.asp.

Baltazar, L.R.S.; Menezes, M.O.B., and Rollnic, M., 2011. Contributions to the Understanding of Physical Oceanographic Processes of the Marajó Bay - PA, North Brazil. *Proceedings of the 11th International Coastal Symposium. Journal of Coastal Research*, Special Issue No. 64, pp. 1443 - 1447.

Beardsley, R.C.; Candela, J.; Limeburner, R.; Geyer, W.R.; Lentz, S.J.; Belmiro, M.C.; Cacchione, D., and Carneiro, N., 1995. The M2 tide on the amazon shelf. *Journal of Geophysical Research*, 100(2), pp.2283-2319.

Bezerra, M.O., Medeiros, C., Krelling, A.P.M., Rosário, R.P., and Rollnic, M., 2011. Physical oceanographic behavior at the Guama/Acara-Moju and the Paracauari river mouths, Amazon coast (Brazil). *Proceedings of the 11th International Coastal Symposium, Journal of Coastal Research*, Special Issie No. 64, pp. 1448 – 1452.

Borba, T.A.C., 2014. Hydrodynamic modelling in amazonian estuary: a flexible mesh approach. MSc Thesis – CPGf/UFPA, Belém 46p.

Costa, M.S., 2014. Aporte hídrico e do material particulado em suspensão para a baía do Marajó: influência dos rios Amazonas e Tocantins. Geology and Geochemical Program, Federal University of Pará, Brazil, MSc Thesis, 95p.

Cuschman-Roisin, B. and Beckers, J., 2005. Introduction to Geophysical Fluid Dynamics-Physical and Numerical Aspects. Academic Press, 320p.

Dai, A. and Trenberth, K.E., 2002. Estimates of freshwater discharge from continents: latitudinal and seasonal variations. *Journal of Hydrometeorology*, 3(6):660–687.

Freitas, P.T.A.; Silveira, O.F., and Asp, N.E., 2012. Tide distortion and attenuation in an amazonian tidal river. *Brazilian Journal of Oceanography* 60(4):429-446

Kernkamp, H.W.; Van Dam, A.; Stelling, G.S., and Goede, E.D., 2011. Efficient scheme for the shallow water equations on unstructured grids with application to the Continental Shelf. *Ocean Dynamics*, 61(8), 11751188.

Miranda, L.B.; Castro, B.M., and Kjerfve, B., 2002. Princípios de Oceanografia Física em Estuários. Edusp, São Paulo.

Molinas, E.; Vinzon, S.B.; Vilela, C.P.X., and Gallo, M.N., 2014. Structure and position of the bottom salinity front in the Amazon Estuary. *Ocean Dynamic* 64:1583–1599. doi: 10.1007/s10236-014-0763-0.

Nittrouer, C.A.; Brunskill, G.J., and Figueiredo, A.G., 1995. Importance of tropical coastal environments. *Geo-Marine Letters*, 15: 121-126.

Prestes, Y.O. 2014. Transporte de Volume na Zona de Maré do rio Pará, Brasil. Belém, Pará. Federal University of Para, Undergraduate thesis, 77p.

Prestes, Y.O.; Rosário, R.P.; Rollnic, M., and Souza, M. Volume transport in the tidal limit of the Pará River, Brazil. *Proceedings of the 17th Physics of Estuaries and Coastal Seas (PECS) conference, Porto de Galinhas, Pernambuco, Brazil, 19-24 October 2014*. http://www.pecs-conferences.org/Xabs/xabs_036_Prestes_etal.pdf

Roelvink, J.A. and van Banning, G.K.F.M., 1994. Design and development of Delft3D and application to coastal morphodynamics. In: Verwey A, Minns AW, Babovic V (eds) *Proceedings hydroinformatics*, Balkema, Rotterdam, p 451–456.

Silva, I.O., 2009. Distribuição da vazão fluvial no estuário do rio Amazonas. Ocean Engineering Program, Federal University of Rio de Janeiro, Brazil. MSc Thesis, 106p.

Journal of Coastal Research	SI	75	133-137	Coconut Creek, Florida	2016

Intermittent Estuaries: Linking Hydro-geomorphic Context to Climate Change Resilience

Neil Saintilan[†*], Kerrylee Rogers[§], Christina Toms[‡], Eric D. Stein[††] and David Jacobs[**]

[†]Department of Environmental Science
Macquarie University, Sydney, Australia

[‡] San Francisco Bay Regional Environmental Control Board, California USA

[††]Southern Californian Coastal Water Research Project, Costa Mesa, California, USA

[§]School of Earth and Environmental Sciences
University of Wollongong, NSW, 2522, Australia

[**]University of California, Los Angeles
California, USA

www.cerf-jcr.org

www.JCRonline.o

ABSTRACT

Saintilan, N.; Rogers, K.; Toms C. Stein, E.D., and Jacobs, D.K., 2016. Intermittent Estuaries: linking Hydro-geomorphic Context to Climate Change Resilience *In:* Vila-Concejo, A.; Bruce, E.; Kennedy, D.M., and McCarroll, R.J. (eds.), *Proceedings of the 14th International Coastal Symposium* (Sydney, Australia). *Journal of Coastal Research*, Special Issue, No. 75, pp. 133-137. Coconut Creek (Florida), ISSN 0749-0208.

Intermittent estuaries are temporarily open to exchange with the open ocean, and the influence of their entrance opening regime on hydrological and ecological function has received considerable attention. Here we consider the influence of tectonic, climatic and geomorphic controls on the distribution of estuarine habitats by contrasting two settings: the south coasts of New South Wales, Australia, and California USA. The combination of tectonic uplift and semi-arid, variable hydrology in southern California provides a stronger sediment yield to estuaries than in the tectonically stable temperate setting of southern Australia. This reflects in a greater proportional area of intertidal vegetation and a higher elevation capital than encountered in SE Australia. The implications for estuary management in the context of sea-level rise and urbanization are discussed.

ADDITIONAL INDEX WORDS: Estuary morphology, carbon, entrance training.

INTRODUCTION

For for many of the world's estuaries, particularly those occurring in environments of high wave energy, high sand supply and variable river flow, open connection to the sea is periodically blocked by a sand berm that forms at the entrance. In these cases of intermittent connection, estuaries are commonly termed "intermittent estuaries", though nomenclature varies across the globe. In Australia, such estuaries are commonly termed ICOLLS (Intermittently Closed Open Lakes and Lagoons (Roy *et al.* 2001), in South Africa the term TOCE's (temporarily open/closed estuaries) is favoured, with ICEs (intermittently closed estuaries) and IOEs (intermittently open estuaries) applied to differentiate the entrance regimes (Tagliapietra et al. 2008). In southern California, the term bar-built estuaries has been used to describe estuaries ponding behind frontal barriers, a particular feature of this coastline (Largier and Taljaard 1991).

Intermittent estuaries therefore occur along a spectrum between permanently closed and permanently open estuaries. Under the schema of Roy *et al.* (2001), southeast Australian estuaries were classified as coastal embayments, drowned river valleys, barrier estuaries, or coastal lakes and lagoons. Of these, the latter two categories may be intermittent, as few barrier estuaries are permanently open in their natural state, and few lakes and lagoons permanently closed. Roy et al. (2001) introduced the idea of estuary maturity, whereby estuaries are envisaged as moving through phases of infill with corresponding effects on hydro-geomorphic properties of the estuary and the distribution of tidal habitats including mangrove, salt marsh and seagrass. Under this model, estuaries exhibit an immature stage of infill immediately following the stabilization of sea levels at 7000 years BP, following post-glacial transgression. The bathymetric characteristics of estuaries in this phase are inherited from the bedrock valley morphology, and may be influenced by tectonic activity. They are typically dominated by subtidal aqueous habitats. This immature stage delineates the total accommodation space for infill (Figure 1), as defined by Jervey (1988).

In a subsequent phase of infill, rivers build mud basins of fine sediment while also prograding fluvial deltaic silts into the estuary. A flood tide delta may also develop at the mouth of the estuary in response to flood tidal marine sand sedimentation; smaller ebb tide deltas are reduced due to high energy wave regime on the open coast. Over time, estuaries infill (i.e. "mature"), though do so at variable rates, with the degree of infill primarily a function of the relationship between catchment sediment yield, which is mediated by unique catchment characteristics and the estuary morphology that was inherited from the bedrock valley shape (i.e. total accommodation space) (Figure 1). Factors contributing to the volume of sediment available for estuary infill include catchment size, and the influence of catchment lithology on the erodibility of parent material. This volume is further mediated by factors influencing

DOI: 10.2112/SI75-027.1 received 15 October 2015; accepted in revision 15 January 2016.
*Corresponding author: neil.saintilan@mq.edu.au

the transport of material to estuaries such as catchment slope, land use/land cover and rainfall/run-off regimes. Once well developed, entrance barriers and flood-tide deltas have reduced influence on estuary infill; however estuary hydrodynamics mediates sediment deposition within the estuary or the nearshore environment.

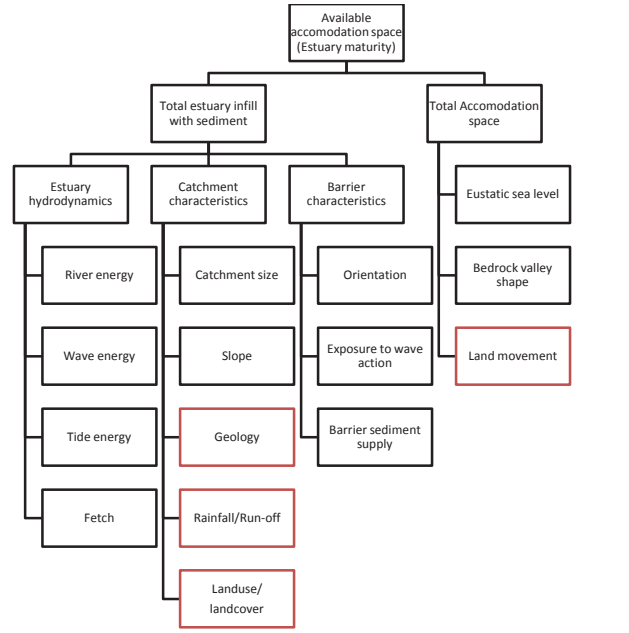

Figure 1. Contributing factors to the degree of infilling and available accommodation space in intermittent estuaries. Highlighted are those contrasted in our case studies.

The concept of estuary maturity has helped conceptualize the distribution and evolution of estuarine habitats over time and space in relation to key hydro-geomorphic drivers. For example, the area of subtidal habitat (including benthic and seagrass community extent) is likely to diminish over time and move through stages of expansive intertidal extent associated with the progradation of deltas into the mud basin, and then declining intertidal extent as elevations of floodplains build beyond the tidal prism. This, associated with estuary entrance conditions, is likely to exert profound influences on the suite of biological organisms inhabiting estuaries (Saintilan 2004). In addition to fisheries values, estuary maturity is likely to influence a range of other ecosystem services as the dominance of different habitats shifts. These include visual amenity, recreational opportunities, biological diversity, water quality, coastal buffering and protection, and flood attenuation. Organic matter, and its carbon constituent, is an important component of the material infilling estuaries, and the influence of estuary morphology and estuarine processes on carbon accumulation varies across geomorphic settings (Saintilan *et al*. 2013).

Estuary geomorphology, as dictated by its evolution, also provides an indication of the vulnerability of estuaries to climate change. Rogers and Woodroffe (in review) developed an index of vulnerability to climate change for estuaries of southern NSW that described the exposure, sensitivity and adaptive capacity of estuaries on the basis of their geology, including Quaternary sediments that had infilled estuaries largely over the Holocene, and elevation. In this regard, exposure to climate change was inferred from elevation and slope derived from a digital elevation model, sensitivity was inferred from lithology, with unlithified material presumed to be more sensitive to erosion; and adaptive capacity was inferred from estuary infill with mature estuaries presumed to have a higher capacity to accumulate sediments at rates corresponding to sea-level rise.

An understanding of factors contributing to infilling at local and regional scales is therefore important in the development of models of estuary evolution, as well as models of climate change impacts and adaptation. In this paper we provide a comparison of two regions exemplifying contrasting catchment hydro-geomorphic processes relevant to estuary infill. These are: the tectonically stable, temperate southern coast of NSW; and the tectonically active semi-arid coast of southern California. While holding many oceanic and climatic features in common, including estuary entrances dominated by high wave energy and sand supply, a similar latitudinal position and the inter-annual influence of the El Niño-Southern Oscillation (ENSO), the coastlines differ profoundly on the basis of several factors influencing sediment yield. We explore, through the application of a unique dataset, the influence of these processes on estuarine morphology, and extrapolate from these a model of sea-level rise impact and adaptation.

METHODS

Because the estuaries of southern California are extensively modified, historical surveys are required if the relationships between estuary morphology and catchment processes are to be explored. Fortunately, an extensive series of surveys were conducted prior to the rapid urbanization of southern California prior to major Euro-American modification, and data from these surveys have been preserved in a series of topographic sheets (T-Sheets) that provide high quality information on the morphology and significant habitats of the US shoreline for the period 1851 and 1889. Stein et al (2014) utilised 40 T-sheets covering a length of coast from Point Conception to the US-Mexican border. These were scanned, geo-rectified and major estuary features digitised. For most surveys, the area of intertidal wetlands, intertidal unvegetated habitats and subtidal open water habitats were accurately recorded. The same habitats have been mapped for the estuaries of southern NSW, in the Australian Estuarine Database. These data are available on the OzCoasts website (www.ozcoasts.gov.au). We combined area estimates for mangrove and saltmarsh to produce an area of intertidal vegetation comparable to that recorded in the Californian T-Sheet data.

Estuaries included in the southern California survey include Mugu Lagoon, Ballona Wetlands, Seal Beach, San Diego Bay, Bolsa Chica, Newport Bay, Carpinteria, Alamitos Estuary, Tijuana Estuary, San Dieguito Lagoon, Los Penasquitos Lagoon, Santa Margarita, Agua Hedionda Lagoon, Batiquitos Lagoon, San Eluo Lagoon, Buena Vista Lagoon, Goleta, La Harbor, Ormond Beach, and Santa Clara River. These are all the estuaries between Point Conception (31° 52'N) and the Mexican

Border at 32° 30' N. We chose not to use the corresponding latitudinal band in New South Wales as this would have covered the most developed region of the state including the cities of Newcastle, Sydney and Wollongong. No historical surveys comparable to the T-Sheets exist for NSW. Further, drowned river valleys are primarily situated in this region, while intermittent estuaries dominate the coastline south of Wollongong. Instead, we used the stretch of coastline immediately south, from the northern Illawarra (34° 43'S) to the Victorian border at 37° 30' S). Twenty-seven estuaries were included in the analysis, being the Minnamurra, Shoalhaven, St Georges Basin, Swan, Burrill, Toubourie, Merroo, Durras, Cullendulla, Tomaga, Moruya, Coila, Tuross, Brou, Nangudga, Corunna, Tilba Tilba, Wallaga, Mermagui, Barragoot, Cuttagee, Wapengo, Middle, Bega River, Wallagoot, Pambula and Curalo.

We used two-way analysis of variance to determine whether the open water area varied significantly on the basis of total estuary area or estuary location (i.e. NSW or Southern California). Linear regression analyses were used to identify the significance of relationships between open water area and total estuary area for each estuary location, and assess whether estuary size was a significant predictor of estuary maturity, using open water area as an indicator of maturity. Where linear relationships were not significant, non-linear models were used to establish the relationship between area of open water and total estuary area. All statistical analyses were undertaken using JMP statistical analysis software.

RESULTS

Our analysis demonstrated clear differences in morphometric characteristics of estuaries in southern California and southern NSW. The NSW estuaries exhibited a high range in the degree of infill, though were predominantly immature, and dominated by open water subtidal habitat. By contrast, the southern Californian estuaries were largely infilled, with a small proportion of subtidal habitat. The accommodation space is therefore consistently greater in NSW estuaries, while elevation capital of intertidal habitat is greater in the estuarine wetlands of southern Californian wetlands.

The relationship between estuary area and the proportion of open water habitat is strong for southern Californian estuaries. Larger estuaries had more subtidal open water habitat. This relationship in NSW was exponential rather than linear (Figure 2). For estuaries greater than 1000 ha in size, more than 90% of the estuary consisted in subtidal habitat (Figure 3). Below this threshold, the proportion of subtidal and intertidal habitat varied considerably, though estuary size was a strong predictor of the proportion of subaqueous water habitat (r^2=0.65).

DISCUSSION

Intermittent estuaries on the southern Californian and NSW coasts have many characteristics in common. Along both coastlines, coastal ranges- including the Great Dividing Range (NSW) the San Bernardino, San Gabriel, and Santa Ana ranges (California) produce numerous coastal catchments draining into small estuaries. Both coastlines are exposed to a high wave climate, providing conditions for the development of sand barriers that exert strong control on the frequency and extent of hydrological exchange between the estuary and the ocean. Rapid urbanization of the coastal fringe on both coastlines has placed considerable pressure on the ecological integrity of estuaries, with alterations being made to the entrance condition of estuaries, water quality draining developed catchments, and the extent of intertidal habitat.

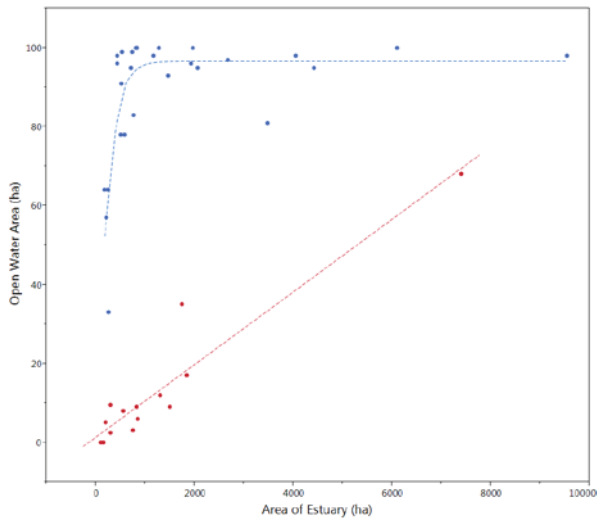

Figure 2. Relationship between estuary area (defined as the sum of subtidal and intertidal habitats) and proportion of subtidal habitat in the estuaries of southern NSW (blue circles, above) and southern California (red circles, below). Linear regression model for southern California (red dashed line) was significant (r^2 = 0.897, $p<0.001$), but was not significant for NSW; a three-parameter exponential model (blue dashed line) provided the best fit for NSW (r^2=0.6492).

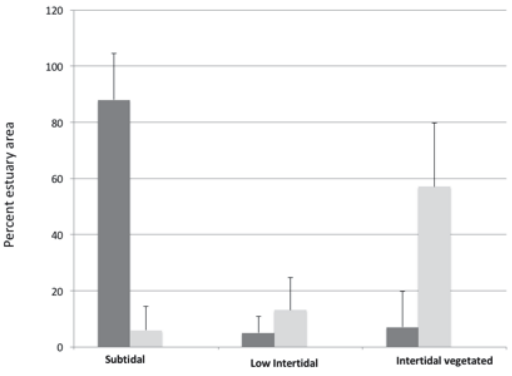

Figure 3. Proportional distribution (and standard error) of subtidal, lower unvegetated intertidal, and vegetated intertidal habitat in the individual pre-disturbance estuaries of southern NSW (blue bars, n=28) and southern California (red bars, n=21).

However, our analysis underscores the profound influence of catchment geology and hydrology on the infilling of coastal

estuaries following sea-level stabilization in the early Holocene. Using the terminology of Roy *et al.* (2001), Californian estuaries are heavily skewed towards the "mature" end of the spectrum of infill. We interpret this to largely be an outcome of differences in exposure of sediment and opportunities for transport in Californian catchments. The Australian east coast consists of predominantly of Triassic sandstone uplifted during the tertiary period. The temperate climate supports heavily vegetated catchments; and the sediment yield is comparatively low. By contrast, the tectonically active southern Californian coastline exposes ranges largely uplifted during the Pleistocene to an arid and highly variable rainfall regime. Stream gradients are high over short catchments, and during periods of intense rainfall following extended drought, erosion can be catastrophic (Zedler *et al.* 1986). Estimates of sediment yield in coastal wetlands in Tijuana (Cahoon *et al*. 1996) are an order of magnitude greater than those measured for the NSW south coast (Oliver *et al.* 2012) using the same technique.

For this reason, Californian estuaries have very little inherited space from postglacial sea-level rise, and what little open water habitat exists if often perched behind barriers during the closed phase. Unlike their Australian counterparts, many Californian estuaries fill from the ocean over historical time-periods as the flood-tide delta progrades into the estuary. The advance of the flood-tide delta is periodically checked by storm events: having filled in, they are now building and excavating channels and associated intertidal environments on a short-term cycle (Jacobs *et al.* 2011). The interplay of climate and sediment yield also influences the interaction between intertidal and supratidal environments across the region. Because the southern Californian coastline is arid, there is a less freshwater input and the influence of marine waters is proportionally greater. This leads to periodic desiccation- when tidal waters build salinities beyond the capacity of intertidal organisms to survive, at the same time that Aeolian sediment is infilling estuaries. The estuary is progressively converted into an arid terrestrial environment. This effect may be enhanced when the limited freshwater flows are diverted and may be associated with La Niña phase under natural conditions of climatic variability.

The high sediment yield of southern Californian estuaries may prove to be an important factor promoting resilience of intertidal habitat to sea-level rise. Given limited options for landward encroachment into highly developed coastal lowlands, vertical elevation gain promoted by sedimentation provides an opportunity for in-situ persistence of saltmarsh habitat. The proviso is that sedimentation rates are maintained and not compromised by the construction of dams. Given the comparatively high position of these wetlands in the intertidal range, a considerable period of survival would be possible even if a deficit existed between sedimentation and the rate of sea-level rise. This would be further facilitated by tectonic uplift. However, Californian estuaries may face the prospect of berm retreat in some situations, causing alterations not only to the seaward reaches of estuaries but also estuarine entrance location and condition and breach dynamics. The constant progradation of the fluvial delta and the retreat of the berm could create in some settings a natural "coastal squeeze" for intertidal and subtidal habitat.

By contrast, the relatively high proportion of subtidal habitat in the estuaries of NSW would suggest that what wetland exists is more vulnerable to conversion to open water habitat. Saltmarshes across this region are showing an elevation deficit in relation to local sea-level trends, promoting their invasion by mangrove, and modelling in the Minnamurra estuary and hunter River has suggested further conversion to open water habitat under high emissions scenarios by 2100 (Oliver *et al.* 2012). The capacity of wetland environments to accrete in response to SLR is a function of the (limited) sediment yield, autochthonous carbon production, and the capacity of tidal waters to remobilize sediment stored within estuarine sediment reservoirs, such as the mud basin, or nearshore environments. Persistence of intertidal wetlands in these settings is likely to be contingent on the provision of landward habitat (Rogers *et al.* 2014), though sea-level rise may build flood-tidal deltas, particularly on the more sediment-rich northern segments of embayments where long-shore drift facilitates sediment accumulation (Haines and Thom 2007).

Estuarine habitats respond to sea-level rise partly through the capture and sequestration of atmospheric carbon. Mangrove, saltmarsh and seagrass ecosystems are particularly effective at retaining carbon in situ (Duarte *et al.* 2005; Alongi 2012), and the conversion of intertidal habitat to other land uses is a significant and disproportionately high contributor to greenhouse gas emissions from deforestation (Lovelock *et al.* 2011). The net sequestration benefit of estuaries has been heavily influenced by the several factors that were being modified across both regions studied. Principal amongst these are the management of the estuary entrance, and the management of catchment inflows of sediment and nutrients. The intermittent nature of estuary opening and closing to the sea may profoundly influenced the nature of gas flux between estuarine environments and the atmosphere.

Over time, the tendency in both southern California and southern NSW has been to promote the permanent opening of estuarine entrances. In New South Wales, over 70 percent of estuaries have some degree of modification to opening regime (Haines *et al*. 2006). This increases the proportion of time that ocean water moves into estuaries with the tide, and increases the prevailing salinity of estuarine waters. Mangrove encroachment is also encouraged, increasing the carbon accumulated in root systems in intertidal settings (Saintilan *et al.* 2013). These changes to the vegetation structure and geochemistry of estuaries may have the effect of promoting carbon sequestration, while at the same time encouraging the recruitment of fish with an oceanic larval stage. However, the down-side might be the loss of those biological components associated with the natural entrance opening regime.

CONCLUSIONS

By comparing estuary morphology on two wave-dominated coastlines we emphasise the relative significance of catchment geology and climate as a control over estuary structure, function and potential climate change resilience. The historical T-sheet coastal surveys provide invaluable information on pre-development characteristics of southern Californian estuaries, and these allowed direct morphological comparisons with surveys conducted of the relatively unmodified estuaries of the

NSW south coast. As might be expected, the high sediment yield of the Californian coastal ranges promotes estuaries at the "mature" end of the spectrum of infill, reflecting in a high proportion of intertidal compared to subtidal habitat, and the importance of short-term flushing in retaining lower elevation aqueous habitat within estuaries. The estuaries of southern NSW show a very high proportion of subtidal habitat. Different strategies may need to be adopted on the two coastlines to accommodate response to sea-level rise. In California, we suggest that in-situ habitat maintenance might be viable under moderate rates of sea-level rise. This is less likely to be an option in NSW, where landward migration may still be possible if appropriate development controls are enacted.

ACKNOWLEDGMENTS

The research was supported by a Fulbright Professional Award to Saintilan, and the generous support of the Southern Californian Coastal Water Research Project is acknowledged. Rogers receives financial support from the Australian Research Council (FT130100532).

LITERATURE CITED

Alongi, D.M., 2012. Carbon Sequestration in Mangrove Forests. *Carbon Management*, 3, 313-322.

Cahoon, D.R.; Lynch, J.C.; and Powell, A.N., 1996. Marsh vertical accretion in a southern California estuary, U.S.A. *Estuarine Coastal and Shelf Science*, 43, 19-32.

Duarte, C.M., Middelburg, J., Caraco, N., 2005. Major role of marine vegetation on the oceanic carbon cycle. *Biogeosciences*, 2, 1-8.

Haines, P. E.; Tomlinson, R. B.; and Thom, B. G., 2006. Morphometric assessment of intermittently open/closed coastal lagoons in New South Wales, Australia. *Estuarine, Coastal and Shelf Science*, *67*(1), 321-332.

Haines, P. E.; and Thom, B. G., 2007. Climate change impacts on entrance processes of intermittently open/closed coastal lagoons in New South Wales, Australia. *Journal of Coastal Research*, SI 50, 242-6.

Jacobs, D.; Stein, E. D.; and Longcore, T., 2011. Classification of California estuaries based on natural closure patterns: Templates for restoration and management. *Southern California Coastal Water Research Project Technical Publication*, (619a).

Jervey, M.T., 1988. Quantitative geological modeling of siliciclastic rock sequences and their seismic expression. In: C.K. Wilgus, B.S. Hastings, C.G.St.C. Kendall, H.W. Posamentier, C.A. Ross and J.C. Van Wagoner (Editors), Sea Level Change--An Integrated Approach. Socociety of Economic Paleontologists and Mineralogists. Special Publications, 42, 47-69.

Lovelock, C.E., Ruess, R.W., Feller, I.C., 2011. CO_2 Efflux from Cleared Mangrove Peat. *PLoS ONE* 6, e21279.

Oliver, S.N.; Rogers, K., Chafer C.J. and Woodroffe C.D., 2012. Measuring, mapping and modelling: an interated approach to the management of mangrove and saltmarsh in the Minnamurra River estuary, southeast Australia. *Wetlands Ecology and Management*, 20, 353-371

Rogers, K.; Saintilan, N.; and Copeland, C., 2014. Managed retreat of saline coastal wetlands: challenges and opportunities identified from the Hunter River Estuary, Australia. *Estuaries and coasts*, *37*(1), 67-78.

Rogers, K. and Woodroffe, C.D. (2015) Geomorphology as an indicator of the biophysical vulnerability of estuaries to coastal and flood hazards in a changing climate. *Journal of Coastal Conservation.* (in review)

Roy, P.S., Williams, R.J., Jones, A.R., Yassini, I., Gibbs, P.J., Coates, B., West, R.J., Scanes, P.R., Hudson, J.P., Nichol, S., 2001. Structure and Function of South-east Australian Estuaries. *Estuarine, Coastal and Shelf Science,* 53, 351-384.

Saintilan, N., 2004. Relationships between estuarine geomorphology, wetland extent and fish landings in New South Wales estuaries. *Estuarine, Coastal and Shelf Science,* 61, 591-60.

Stein, E.D.; Cayce, K.; Salomon, M.;Bram, D.L.; De Mello, D.; Grossinger, R.; Dark. S.; 2014. Wetlands of the Southern California Coast: Historical Extent and Change Over Time. Technical Report 826. *Southern California Coastal Water Research Project Authority*. Costa Mesa, CA

Tagliapietra, D., Sigovini, M., Ghirardini, A.V., 2009. A review of terms and definitions to categorise estuaries, lagoons and associated environments. *Marine and Freshwater Research,* 60, 497-509.

Zedler, J.B.; Covin, J.; Nordby, C.; Williams, P.; and Boland, J., 1986. Catastrophic events reveal the synamic nature of salt-marsh vegetation in southern Califnroia. *Estuaries,* 9, 75-8.

Journal of Coastal Research	SI	75	138-142	Coconut Creek, Florida	2016

Sediment re-deposition in the mangrove environment of Can Gio, Saigon River estuary (Vietnam)

Klaus Schwarzer †, Nguyen Cong Thanh‡, and Klaus Ricklefs††

†Institute of Geosciences, Sedimentology, Coastal and Continental Shelf Research
Kiel University
Kiel, Germany

‡Departament of Oceanography
University of Science
Ho Chi Minh City, Vietnam

††Research and Technology Center Westcoast
Kiel University
Büsum, Germany

www.cerf-jcr.org

www.JCRonline.org

ABSTRACT

Schwarzer, K.; Nguyen Cong Thanh and Ricklefs, K., 2016. Sediment re-deposition in the mangrove environment of Can Gio, Saigon River estuary (Vietnam). *In:* Vila-Concejo, A.; Bruce, E.; Kennedy, D.M., and McCarroll, R.J. (eds.), *Proceedings of the 14th International Coastal Symposium* (Sydney, Australia). *Journal of Coastal Research*, Special Issue, No. 75, pp. 138-142. Coconut Creek (Florida), ISSN 0749-0208.

Sediment re-deposition in mangrove environments is usually attributed to marine and estuarine hydrodynamics - rainfall as a driver was not considered yet. However, combined with annual water level variations, tropical rainfall can play a significant role for sediment re-deposition. Inside mangroves, current velocities induced by rainwater runoff during low tide conditions can be much stronger than tide-induced currents. Along the Saigon River Estuary and the Mekong Delta coastline, rainfall is high from May to October and low from December to April. To study processes controlling sediment re-deposition, data of current and suspended matter concentration have been combined with sediment re-deposition rates. All investigations have been carried out in the Can Gio mangrove reserve, Saigon River mouth. Based on a 19-year data set (1991 – 2009), strong annual variability in water level heights and tidal range are observed, with a mean maximum high tide level of 3.34 m during the rainy season and 3.73 m at the beginning of the dry season. Maximum tidal range is reached during the rainy season coinciding with the lowest annual average sea level. The highest parts of the mangrove forest are not inundated by tides during these periods. Only heavy rainfall during these times can lead to mangrove soil mobilisation, induce strong currents between the mangrove roots and cause erosional gullies. Depending on the amount of precipitation, this sediment mobilisation and the amount of suspension load in the forest can be much stronger than sediment transport induced by tidal currents.

ADDITIONAL INDEX WORDS: *Mangrove forest, Saigon River estuary, suspension solid concentration,*

INTRODUCTION

Mangrove forests are important interfaces between the land and the sea. They mainly grow along sheltered coastlines, estuaries, lagoons and deltaic shorelines within the intertidal domain of tropical and subtropical areas (Woodroffe, 1992). Some of the major functions of mangrove forests include protecting the coastal environment by wave attenuation (Mazda *et al*., 1997, Vo-Luong and Massel, 2006, 2008), reducing coastal erosion (Furukawa and Wolanski, 1996; Mazda *et al*., 1997, 2006; Vo-Luong, 2006; Vo-Luong and Massel, 2006, 2008) and contributing to coastal safety as was observed after the 2004 Indian Ocean tsunami (Danielsen et al., 2005). Additionally, their root system provides a sediment trapping mechanism for suspended particles (Bird, 1971; Wolanski *et al.,* 1986; Augustinus, 1995; Blasco *et al.* 1996; Furukawa and Wolanski, 1996; Thampanya *et al.*, 2006; Victor *et al.* 2006). Mangrove environments can keep pace with sea level rise of up to 4.5 mm/year (Gilman *et* 2008) and are growing as a response to an increase in tidal flooding (Anthony, 2004) and sediment supply. Despite these benefits, mangrove environments are under rapid decline worldwide (FAO, 2007; Giri *et al*., 2011). To preserve mangrove forests with all their benefits and to increase awareness, a comprehensive understanding of the physical mechanisms, especially sediment cycling and its relation to hydrological conditions and to seasonal variation, is needed. Our objectives are to provide insight into sediment dynamics in a mangrove forest on time scales from spring-neap tidal cycles to seasonal cycles (dry season versus wet season). We investigate the intertidal sediments forming the forest soil and the suspended matter dynamics in a creek that floods and discharges the mangrove forest.

INVESTIGATION AREA AND METHODS

Due to long-term human impact, the density of mangrove vegetation has considerably changed along the whole southern Vietnamese coastline since the late 19th century, especially in the area of the Dong Nai River estuary, the Mekong delta and the adjacent peninsula towards Ca Mau (Mazda *et al.*, 2002; *Linh K. Phan et al*., 2015). Approximately 42% of the total

DOI: 10.2112/SI75-028.1 received 15 October 2015; accepted in revision 15 January 2016.
*Corresponding author: kls@gpi.uni-kiel.de

mangroves in Vietnam have disappeared from 1980 – 2005 (FAO, 2007).

Investigation area

The forest in the Can Gio reserve is a hybrid between a fringing (F-type) tide dominant and a river dominant (R-type) mangrove forest (Ewel *et al.*, 1998). The study site is embedded in the Dong Tranh estuary (Figure 1), a branch of the Saigon River. The tide is mixed, dominantly semi-diurnal. Tidal range varies between almost four metres at spring tide and about only one metre at neap tide. Superposed on daily tidal fluctuations are spring/neap-tidal cycles and monsoon-driven variations in mean water levels (Nguyen, 2012). The depositional environment is characterized by silty sediments. From the banks of the Dong Tranh River and from the banks of the creeks (Figure 1), a morphological gradient exists with a rising bottom towards the inner forest. After the Vietnam War, mangroves have been reforested successfully since 1978, but coastal erosion continued with rates up to 50 m/year in some places (Mazda *et al.*, 2002).

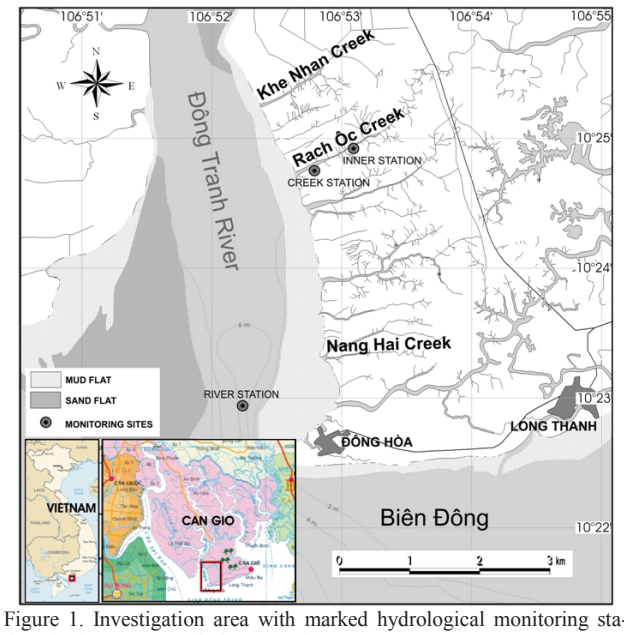

Figure 1. Investigation area with marked hydrological monitoring stations in the Dong Tranh river mouth estuary.

Instrumentation and experimental setup

Measurements of suspended matter concentration (SMC), salinity and temperature were done using optical backscatter sensors (OBS) and stationary conductivity, temperature and water level probes (CTD). OBS (Seapoint Sensors Inc., 2000) transmit an optical signal into the water column of which the wave length is near to infrared light (wave length 880 nm). The intensity of the backscattered light, expressed as a change in output voltage, is understood as measure for the amount of SSC in the water-column. A sensor's response not only depends on the number of scatters but also on the composition and size of the suspended particles. Therefore for precise turbidity measurements an "on site calibration" is needed. The aim of this calibration is to mathematically formulate a close relationship between the sensor's mV response to concentrations of site specific particle composition (mg/l). In our case, prior to a measuring campaign, all available sensors are installed close to each other (Figure 3) at one location for which it is assumed that characteristics are comparable to those of the investigation sites. Calibration lasted for 1 tidal cycle with water sampling every 30 minutes. Samples are filtered (0.63 µm filters) and dried to calculate the total dry mass of suspended matter per volume unit water.

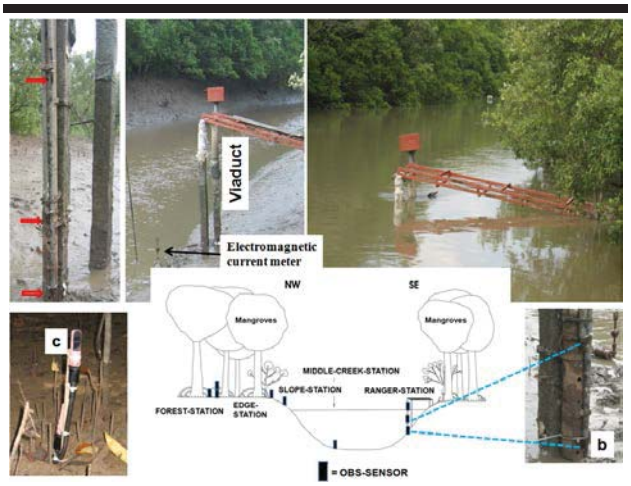

Figure 2. Positions of 9 OBS sensors at the creek station (see Figure 1) in the forest of the Rach Ôc Creek. CTD probes are installed in the creek and in the forest. Red arrows mark OBS-positions at the viaduct.

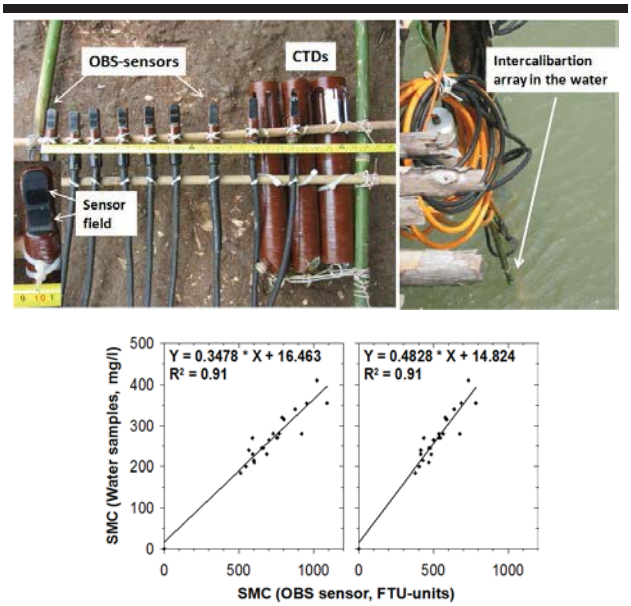

Figure. 3. Sensor-array for the calibration and inter-calibration of OBS sensors and CTD-probes in the field (upper part of this figure). Best fit curves for two OBS sensors from the creek station are shown below.

The relationship between the real concentrations and the sensor's signal strength mostly result in a linear best fit line (Figure 3). The fit equations allow all indirect sensor readings to be converted into real concentration values. The field calibration procedure is also used to inter-calibrate all sensors (Figure 3) and to detect shortcomings of any single sensor.

The instruments are installed in the Rach Ôc tidal creek (Figure 1), at the rim of the forest and in the forest. Time series measurements covered at least one spring/neap tidal cycle. To calibrate the OBS sensors and to carry out particle size analyses, during the field campaign additional water samples were taken every hour at every sensor for at least 1 tidal cycle during neap-, intermediate-, and spring tide.

The SMC measurements were combined with assessments of sediment re-deposition in the mangrove forest by applying the "tracer stick method" (Schwarzer and Diesing, 2001). This method is based on injecting a rectangular stick (length: 10 cm, width: 2 cm) vertically into the sediment. The stick is made up of artificially coloured fine sand which is bound with water-soluble glue. The upper end of the stick coincides with the sediment surface. Upon contact with moisture, the glue dissolves after approximately 5 minutes. The tracer sticks remain in the mangrove soil until recovery where they are subjected to hydrodynamic influences. Erosion and deposition are calculated by measuring the length of the remnant stick with a centimetre scale (Figure 4) immediately after recovery. This method was applied for a 2-year period on 54 stations along the Khe Nhan-, Rach Ôc- and Nang Hai creek (Figure 1). The time the sticks remained in the sediment varied between 2 weeks and 5.5 months.

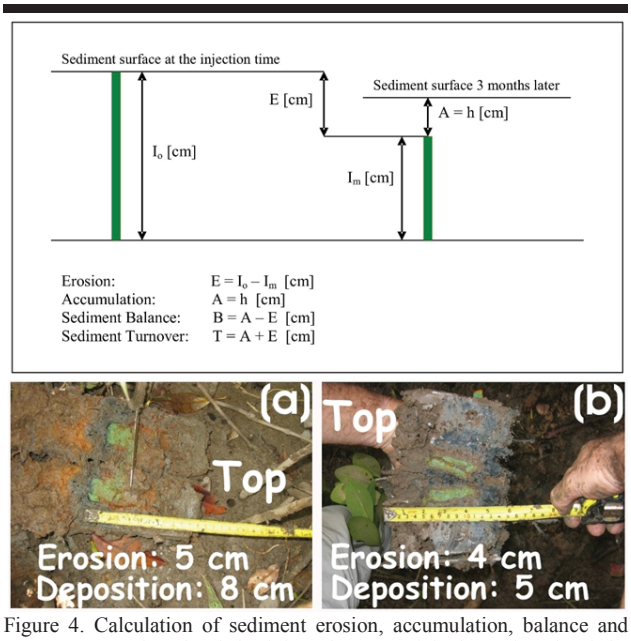

Figure 4. Calculation of sediment erosion, accumulation, balance and turnover. Io = length of the injected tracer stick; lm = length of the remaining tracer stick. In a) and b) the original length of the tracer stick was 10 cm.

Data of water level variations were provided by the Southern Regional Hydro-Meteorological Center (SRHMC) which operates an official tide gauge at Vung Tau, located approximately 20 km east of Can Gio. These data were correlated with our own data, allowing us to extend site specific water level data for a longer period. According to the tidal classification by Courtier (1938), the mixed semi-diurnal tide is characterised by different water levels: two high waters (higher high water (HHW) and lower high water (LHW) and two low waters (higher low water (HLW) and lower low water (LLW)). In addition to these parameters, tidal range (TR) and the mean sea level (MSL) were analysed for the period from 1991 to 2009.

RESULTS

Depending on the monsoon, variations of the considered tidal levels MHHW, MHW, MSL, MLW, and MLLW occur (Figure 5). During the wet season, sea levels are lower than during the dry season. Lowest levels are recorded in June/July (3.34 m), and the highest levels are measured in November (3.73 m). On average, the seasonal differences between highest and lowest MHHW and MLLW are approximately 45 cm and 53 cm, respectively. These values indicate a higher and longer inundation of the mangrove environment during the dry season. On the other hand, due to generally lower high water levels, the highest parts of the mangrove forest will not be tidally flooded during the wet season. This increases the chance for sediment re-deposition in the course of heavy rainfall events.

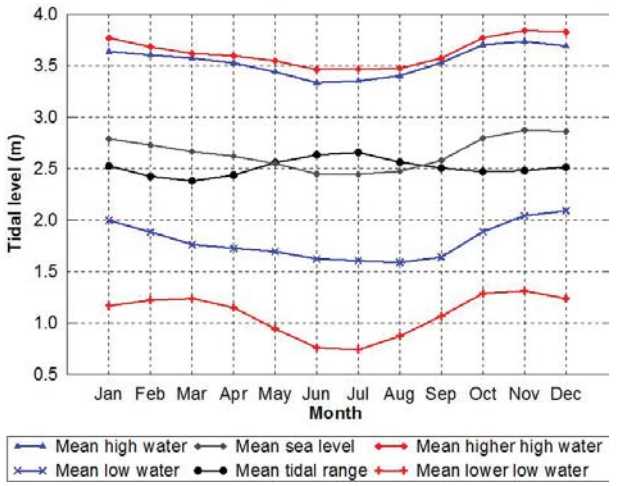

Figure 5. Water level fluctuations at Vung Tau tide gauge based on a 19-years data set (1991 – 2009).

High variability in current velocities, water mass exchange, salinity, suspended matter concentration and sediment erosion and accumulation were found to be attributed to the monsoon cycle. Compared with the dry season, stronger currents combined with more water mass exchange are observed during the wet season, which in addition to intensive rainfall, cause an increase in suspended matter concentrations (Figure 6). If heavy

rainfall happens during ebb phase, and the forest soil has already fallen dry, erosion happens and sediments are exported from the forest flats. This is clearly observed in the higher SMC at the creek- and the forest station (Figure 7, sensor b and c). Rainfall during the flood phase does not show any pronounced signal of higher suspension load in the creek. During these phases, either remobilized sediment in the higher part of the mangrove forest due to rainfall will remain in the forest and be distributed there, or the water-level has already reached a height that hampers the ability of raindrops to induce re-suspension.

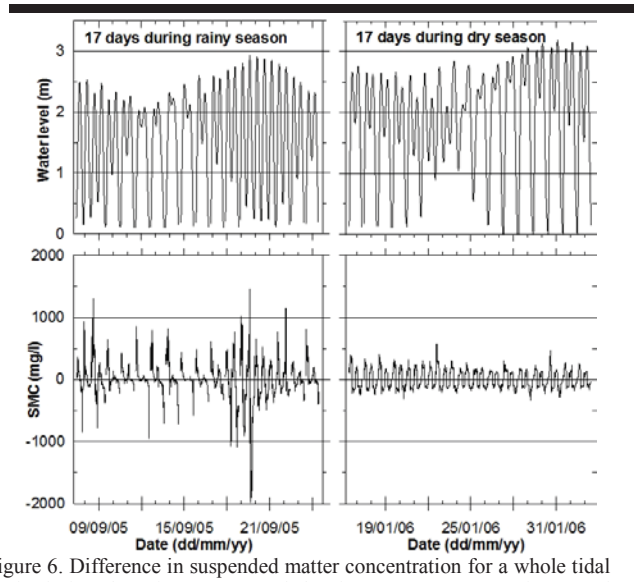

Figure 6. Difference in suspended matter concentration for a whole tidal cycle during the rainy season and the dry season. Data are integrated over all 3 OBS sensors installed at the viaduct in the creek.

Tracer stick data revealed an increase in sediment dynamics combined with higher erosion and accumulation in the mangrove forest during the wet season. Turnover reaches approximately 0.2 cm/day during the wet season, while during the dry season turnover amounts to approximately 0.15 cm/day. The sediment balance during the dry season is negative in the forest with a loss of approximately 0.03 cm/day, while during the wet season the sediment balance in the forest is nearly in equilibrium. During the transitional seasons (May and October/November), the sediment balance is slightly positive with 0.01 cm/day. These findings, combined with the results of SMC measurements at the creek station, indicate that sediment which is washed out from the forest will be transported towards the inside of mangrove forest. Therefore, there is in general a positive sediment budget for this part of Can Gio Mangrove forest.

DISCUSSION

There are only few studies combining investigations of sediment redistribution in mangrove creeks and in mangrove forests. While Horstmann *et al*. (2013) focus mainly on topographical variation and the impact of the vegetation system on flow velocities, we show the impact of monsoon-dependent rainfall combined with seasonal water level fluctuations on sediment mobility. It is known that tidal currents in a mangrove forest rarely reach 0.1-0.2 m/s (Massel, 1998; Furukawa *et al*., 1997; Wu *et al*., 2001). Their ability to initiate short-term high sediment re-deposition rates is small. However, even if the sediment balance is equalized and no changes seem to appear, the sediment turnover, indicating sediment dynamics, can be very high (Figure 4). This turnover might have high implications for geochemical and nutrient cycles in the mangrove environment. Rainfall as a driver has been neglected so far, but should be included in future studies.

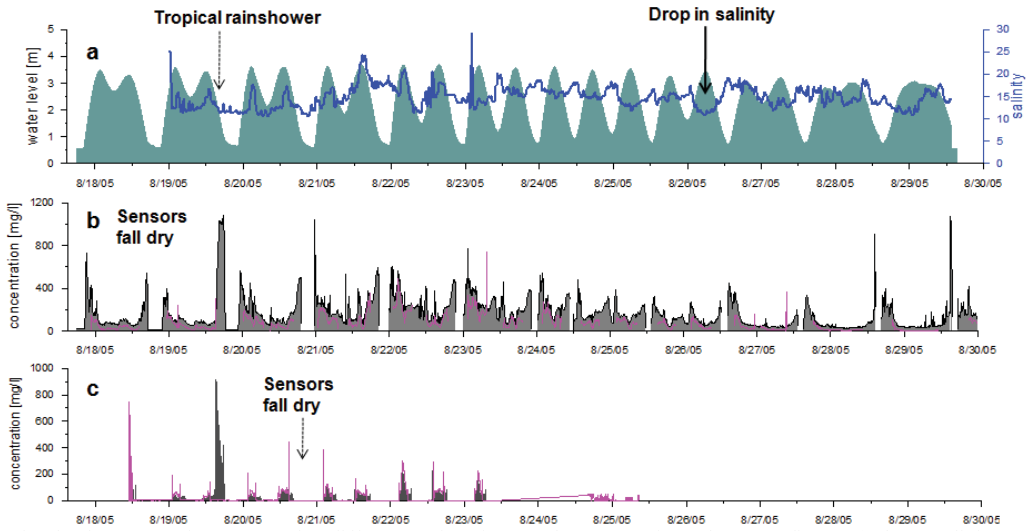

Figure 7. Suspension load concentration measured at different stations in a creek cross-section. The upper figure (a) shows salinity and tidal variation. Tropical rainfall during ebb tide increases the suspension load at the sensors b and c (for position see Figure 2), while a drop in salinity during flood tide, which is an indicator for rainfall, shows now increase in suspension load in the creek and close to the creek (see text for further explanation).

CONCLUSIONS

Sediment re-deposition in the mangrove environment of Can Gio shows seasonality in tidal- and water level fluctuations and precipitation. When rainfall happens during ebb tide, strong currents are initiated all over the mangrove environment as rain-water follows the morphological gradient, creating small gullies. This current induced sediment mobility and the amount of suspension load can be much higher compared to tide induced suspension load in the forest. Sediment turnover (see Figure 4) is an indicator for sediment dynamics. Even if the sediment balance is close to zero, sediment dynamics can be rather high.

ACKNOWLEDGMENTS

This study was funded by the German Research Foundation (DFG) grant SCHW 572/8-1, 2 and by the Ministry of Science and Technology (MOST), Vietnam. We thank our colleagues La Thi Cang for providing us with data from the SRHMC, to Daniel Unverricht and Le Xuan Thuyen for suggestions and comments and to Patrycja Czerniak for field assistance.

LITERATURE CITED

Anthony, E., 2004. Sediment dynamics and morphological stability of estuarine mangrove swamps in Sherbro Bay, West Africa. *Mar. Geol.*, 208, 207- 224.

Augustinus, P.G.E.F., 1995. Geomorphology and sedimentology of mangroves. *In*: Perillo, G.M.E. (ed.). *Geomorphology and Sedimentology of Estuaries. Developments in Sedimentology*, 53, Amsterdam: Elsevier, pp. 333-357.

Bird, E.C.F., 1971. Mangroves as land builders. *Nature*, 88, 189-197.

Blasco, F.; Saenger, P., and Janodet, E., 1996. Mangroves as indicators of coastal change. *Catena*, 27, 167-178.

Courtier, A., 1938. Marées, Service Hydrographique de la Marine, 284 pp.

Danielsen, F.; Sørensen, M.K.; Olwig, M.F.; Selvam, V.; Parish, F.; Burgess, N.D.; Hiraishi, T.; Karunagaran, V.M.; Rasmussen, M.S.; Hansen, L.B.; Quarto, A., and Suryadiputra, N., 2005. The Asian tsunami: a protective role for coastal vegetation. *Science*, 310, 643.

Ewel, K.C.; Twilley, R.R., and Ong, J.E., 1998. Different kinds of mangrove forest provide different goods and services. *Global Ecology and Biogeography Letters*, 7(1), 83 – 94.

FAO, 2007. The world's mangrove 1980 – 2005. Food and Agriculture Organization of the United Nations Forestry Paper, 153, 74 pp.

Furukawa, K. and Wolanski, E,. 1996. Sedimentation in mangrove forests. *Mangroves and Salt Marshes*, 1(1), 3-10.

Furukawa, K.; Wolanski, E., and Muller, H., 1997. Currents and sediment transport in mangrove forests. *Estuarine, Coastal and Shelf Science*, 4, 301-310.

Gilman, E.L.; Ellison, J.; Duke, N.C.J., and Field, C., 2008. Threats to mangroves from climate change and adaption aptions: A review. *Aquatic Botany*, 89 (2), 237 - 250.

Giri, C.; Ochieng, E.; Tieszen, L.L.; Zhu, Z.; Singh, A.; Loveland, T.; Masek, J., and Duke, N., 2011. Status and distribution of mangrove forests of the world using earth observation satellite data. *Global Ecology and Biogeography*, 20, 154 – 159.

Horstmann, E.M.; Dohmen-Janssen, C., and Hulscher, S.J.M.H., 2013. Flow routing in mangrove forests; a field study in Trang provinve, Thailand. *Continental Shelf Research*, 71, 52 – 67.

Linh K. Phan; Jaap, S.M.; van Thiel de Vries and Stive, M.J.M, 2015. Coastal Mangrove Squeeze in the Mekong Delta. *Journal of Coastal Research*, 31 (2), 233 – 243.

Mazda, Y.; Magi, M.; Kogo, M., and Hong, P.N., 1997. Mangroves as a coastal protection from waves in the Tong Kinh Delta, Vietnam. *Mangroves and Salt Marshes*, 1(2), 127 – 135.

Mazada, Y.; Magi, M.; Nanao, H.; Kogo, M.; Miyagi, T.; Kanazawa, N., and Kobashi, D., 2002. Coastal erosion due to long term human impact on mangrove forests. *Wetlands Ecology and Management*, 10, 1 – 9.

Mazda, Y.; Magi, M.; Ikeda, Y.; Kurokawa, T., and Asano, T., 2006. Wave reduction in a mangrove forest dominated by Sonneratia sp. *Wetlands Ecology and Management*, 14 (4), 365-378.

Nguyen C.T., 2012. Processes and factors controlling and affecting the retreat of mangrove shorelines in South Vietnam. PhD thesis, Kiel University, Institute of Geosciences, 130 pp.

Schwarzer, K. and Diesing, M., 2001. Sediment Redeposition in Nearshore Areas - examples from the Baltic Sea. *Proceedings of the Conference Coastal Dynamics '01* (Lund, Sweden), 808 – 817.

Thampanya, U.; Vermaat, J.E.; Sinsakul, S., and Panapitukkul N., 2006. Coastal erosion and mangrove progradation of Southern Thailand. *Estuarine, Coastal and Shelf Science*, 68, 75-85.

Victor, S.; Neth, L.; Golbuu, Y.; Wolanski, E., and Richmond, R.H., 2006. Sedimentation in mangroves and coral reefs in a wet tropical island, Pohnpei, Micronesia. *Estuarine, Coastal and Shelf Science*, 66, 409-416.

Vo-Luong, H.P., 2006. Surface waves propagation in mangrove forest and induced suspended sediment concentration. PhD thesis, Institute of Oceanology, Polish Academy of Sciences, Sopot, Poland, 191pp.

Vo-Luong, H.P. and Massel, S.R., 2006. Experiment on wave motion and suspended sediment concentrations at Nang Hai, Can Gio mangrove forest, southern Vietnam. *Oceanologia*, 48(1), 23 – 40.

Vo-Luong, H.P. and Massel, S.R., 2008. Energy dissipation in non-uniform mangrove forests of arbitrary depth. *Journal of Marine Systems*, 74(1-2), 603 – 622.

Wolanski, E. and Ridd, P., 1986. Tidal mixing and trapping in mangrove swamps. *Estuarine, Coastal and Shelf Science*, 23, 759-771.

Woodroffe, C.D., 1992. Mangrove sediments and geomorphology. *In*: Robertson, A.I. and Alongi, D.M. (eds.), *Tropical Mangrove Ecosystems*. Coastal and Estuarine Studies. American Geophysical Union, pp. 7- 41.

Wu, Y.; Falconer, R.A., and Struve, J. 2001. Mathematical modelling of tidal currents in a mangrove forest. *Environmental Modelling and Software*, 16(1), 19 – 29.

Journal of Coastal Research	SI	75	143-147	Coconut Creek, Florida	2016

Environmental Dynamics of the Estuary of the Pacoti River in Ceará, Brazil: Proposals for Management and Environmental Planning

Edson V. Silva†, Juliana F. Farias†, Larissa N. Barbosa†, Victor Gabriel F. Lima† and Adryane Gorayeb†

†Department of Geography
Federal University of Ceará
Fortaleza, Brazil

www.cerf-jcr.org

www.JCRonline.org

ABSTRACT

Silva, E.V.; Farias, J. F.; Barbosa, L.N., and Lima, V.G. F., 2016. Environmental Dynamics of the Estuary of the Pacoti River in Ceará, Brazil: Proposals for Management and Environmental Planning. *In:* Vila-Concejo, A.; Bruce, E.; Kennedy, D.M., and McCarroll, R.J. (eds.), *Proceedings of the 14th International Coastal Symposium* (Sydney, Australia). *Journal of Coastal Research*, Special Issue, No. 75, pp. 143-147. Coconut Creek (Florida), ISSN 0749-0208.

The estuary of the Pacoti River (3°49'27" S, 38°24'18" W) is located in the state of Ceará, in northeastern Brazil. The estuary is also part of the Rio Pacoti Environmental Protection Area (Rio Pacoti EPA), which is important for the stability of the local ecosystems and the exchange of material and energy. Despite being protected legally, the environmental quality of the study area is being threatened by impacts such as the deforestation, landfills, the contamination of the water table, and unregulated building, which all alter the natural dynamics of the local systems. These impacts result from inadequate processes of land use and occupation, which fail to respect local potentialities and limitations. The present study found that these processes of degradation are ongoing, and do not only contradict the legislation that regulates the sustainable use of the local environment, but may also cause irreparable damage to the local geo-ecological systems, constituting a grave problem for this sector of the coast of Ceará. In this context, the study presents a geo-environmental description of the estuary and an integrated diagnosis, based on the geo-ecological analysis of the landscape, in two phases –organization and survey, analysis, diagnosis, and proposals. The application of this geo-ecological analysis resulted in the demarcation and classification of the following units: coastal plain and the pre-coastal plateau. Based on this analysis, a proposal for the environmental and functional zoning of the study area was put forward, with the objective of integrating economic development with the conservation of local natural resources.

ADDITIONAL INDEX WORDS: *Coastal plain, Environmental planning, Estuary of the Pacoti River.*

INTRODUCTION

The intense dynamics of coastal systems, derived from the interaction of marine and continental processes, results in the formation of zones of extreme levels of biological activity and wind action, which are capable of creating new features of relief through cycles of erosion and deposition, with typical features of coastal plains, including their vegetation, fauna, soils, and hydrological resources. Estuaries are an important component of this natural landscape unit, given their considerable capacity to modify their zones of influence, as well as their position in the lower reaches of hydrographic basins and contact with mangrove ecosystems.

Estuaries are characterized by high salinity, muddy and clayey soils, and an endemic fauna and flora, the characteristics of which will reflect the use and occupation of the system, and affect the socio-economic dynamics of the region, given the obstacles to the construction of houses without adequate landfill, and the dependence of the local community on the extraction of natural resource, given the lack of other potential sources of income.

Ever since their appearance on the planet, rivers have played an important role in the dissemination of life, transporting seeds, sheltering their characteristic fauna and flora, and providing a source of freshwater and nutrients for agricultural activities. The importance of rivers for the human exploitation of natural resources increases as they approach their outlets to the sea, given that the coastal zone is typically subject to the most intense pressures of use and occupation by human populations, which are reflected in the society-nature relationship.

This intense process of occupation and exploitation can be observed clearly in the case of the coast of the Brazilian state of Ceará, in particular in the coastal and inland portions of the estuary of the Pacoti River, where the Rio Pacoti Environmental Protection Area (Rio Pacoti EPA) has been established. The Rio Pacoti EPA is the focus of the present study.

THE ESTUARY OF THE PACOTI RIVER

The estuary of the Pacoti River (03º51'07" S, 38º24'27" W) is located in one of the eleven hydrographic regions of the Brazilian state of Ceará (Figure 1), which is divided into planning units. The metropolitan basin of the lower Pacoti includes three municipalities, Fortaleza, Aquiraz, and Eusébio, with a total area of 2914.93 hectares (Ceará, 2000).

DOI: 10.2112/SI75-029.1 received 15 October 2015; accepted in revision 15 January 2016.
*Corresponding author: edson.vicente@pq.cnpq.br

This estuarine system encompasses contiguous sections of the coastal plain and plateau, and the adjoining sea, with features characteristic of the dynamics of the wind, oceanic and fluvial forces of the coastal environments, represented by the beach, backshore, coastal plain and dune fields. Given their capacity for the retention of water, the dunes contribute to the formation of interdunal lakes. There is also an outcrop formed by the intrusive Messejana formation (Messejana Magmatism), which dates from one of the last tectonic events related to the opening of the Atlantic Ocean "beyond the line of the sandstone (beachrock) reef that lies approximately parallel to the coastline, which altered the surf break pattern", as stated by the Brazilian Environment Ministry (MMA, 2006).

Figure 1. Geographic location of the Pacoti River basin in northern Brazil.

The relief of the study area is defined by four litho-stratigraphic units (Nascimento and Carvalho, 2003) – Plio–Pleistocene sediments of the Barreiras Formation (Tb), sedimentary Cenozoic deposits of beaches and dunes (Qd), fluvial and mangrove deposits (Qa), and volcanic alkaline rocks (TI),

The soils of the Pacoti estuarine complex (Nascimento, 2003) are predominantly dystrophic quartzarenic neosols, red-yellow ultisols, fluvic neosols, and an amalgam of isomorphic and salic gleysols, according to the new classification of the Brazilian Agricultural Research Company (EMBRAPA, 1999).

The climate of the study region is characterized by considerable fluctuations in rainfall levels within and between years. Ceará is subject to calamitous periods of drought as well as extended periods of rainfall, which have disastrous social and economic consequences. While the state is located within a semi-arid zone, there are some more humid areas, with an annual precipitation of approximately 900 mm, which extend as far as the coast, guaranteeing relatively humid conditions during six month of the year, constituting a dry and sub-humid climate, as defined by Souza (2000).

The hydrographic network of the study area is composed of small streams and fluvial-lacustrine plains that constitute the principal drainage of the Pacoti River (Nascimento, 2003). The mangrove, which extends throughout the Pacoti estuary, is the typical ecosystem of tropical estuaries. The diversity of natural resources found in these systems provides ideal conditions for many aquatic animals characteristic of marine, estuarine and even freshwater environments (Correia, 2005), providing essential breeding grounds and nurseries for the development of their larval phases. These are essentially flat areas, in which fluvial currents have little impact (Souza, 2000).

In this context, the Rio Pacoti EPA, a sustainable use protected area, was established by Ceará state decree number 25,778 of February 15th 2000, with the objective of "preserving and protecting this environmentally-relevant area, characterized by a fragile ecological equilibrium, and thus in need of special protection from the public authorities and society, in addition to protect the Pacoti basin as a public water supply for the city of Fortaleza" (Ceará, 2000). This paper is based on a year-long study of the Rio Pacoti EPA, involving both laboratory analyses and fieldwork, with the primary objective of proposing strategies of environmental management for the study area.

METHODS

The present study was divided into two phases. The first phase involved a literature review, the analysis of the data available for the study area, and the collection of observation-based data in the field. The fieldwork consisted of the investigation of the physical features that constitute the local estuarine ecosystems and the surrounding area, for the identification of the principal environmental units and the characterization of the modifications caused by the occupation and use of the land, based on systematic photographic records, georeferenced using a GPS (Global Position System).

The second phase was based on the spatial analyses and geoprocessing, using WorldView-2 satellite images from 2012. Maps were produced using the freely-available QGIS 2.8 Geographic Information System (GIS) for the treatment and analysis of the spatial data, and the final composition of the maps. For this, "shape" files were obtained from institutions such as the Brazilian Institute for Geography and Statistics (IBGE), the Mineral Resources Research Company (CPRM), the Ceará State Institute for Economic Research and Strategic Planning (IPECE), the National Department of Mineral Production (DNPM), and the Ceará State Environment Superintendency (SEMACE), with the objective of obtaining precise geographic location data on specific natural and administrative features needed for the production of the location

map, geo-environmental units, and the functional zoning of the study area.

The Pacoti estuary has an area of 362 km² and was defined by criteria of salinity and the limits of the Rio Pacoti EPA, which is designed to protect the the ecosystems present in the river surroundings, as well as the fluvial–marine plain, and the local mangrove ecosystem that covers an area of 160 hectare. (Gorayeb *et al*., 2004, 2005)

Based on a landscape geo-ecology approach, it was possible to divide the study area into geo-environmental units that defined the "individual features, typologies, regional units, and local landscapes" (Rodriguez and Silva, 2013), which permits the analysis of landscapes according to their scale. The production of the map of the geo-environmental units considered the spatial organization resulting from the interaction of the physical and biological elements of the natural environment (climate, geology, geomorphology, water resources, vegetation, soils, and anthropogenic impacts). The systems delimited, such as the beach, dune field, fluvial and fluvial-marine plains, and coastal plateau, all have a physical presence on the earth's surface, resulting from the interaction of the flow of energy and matter among its components, which are expressed as the physiognomic composition of the land surface (Souza, 1998).

Based on the understanding of the socio-environmental features of the Pacoti estuary and the surrounding area, a proposal for the functional zoning of the study area was prepared, corresponding to the spatial distribution of functions, following the approach of Cavalcanti and Viadana (2007). This approach is based on the organization of the landscape according to its physical potential and local social needs. The physical-geographic characteristics of the environment are taken into consideration to determine the potential uses of each natural component, with emphasis on the features that contribute to the enhancement of the protection of the environment. In this context, four zones were defined: a Permanent Preservation Zone – ZPP (beach, backshore, mobile dunes, fluvial plain, and fluvial-marine plain), Sustainable Use Zone – SUZ (fixed dunes and Cararu magmatic outcrop), Environmental Recuperation Zone – ERZ (degraded fluvial-marine plain and degraded fluvial plains), and the Residential Expansion Zone – REZ (coastal plateau).

RESULTS

The environmental and functional zoning of the study area (Figure 2) was based on the analysis of the aerial photographs and satellite images. The environmental zoning was initially based solely on the objectives of preservation, supported by Brazilian national environment policy (federal law 6938/1981). The term was subsequently altered to ecological-economic zoning, with the objective of integrating social and economic questions with environmental ones (Rodriguez and Silva, 2013).

The environmental zoning defined two major environmental units (with their respective subunits) – the coastal plain (beach and backshore, mobile and fixed dune fields, and the fluvial-marine plain) and the pre-coastal plateau, subdivided chromatically. Coastal plains or depressions are gently-sloping depositional surfaces formed primarily by underwater sedimentation. They are found at the margins of large bodies of water, such as the sea or the ocean, and are typically formed by geologically very recent terrains, typically of the Quaternary, composed of sediments derived from a variety of sources, including rivers, oceans, floodplains, lakes, and swamps. "The fluctuations in relative sea levels and the longitudinal transportation of sand by coastal drift currents, associated with paleoclimatic changes have controlled the evolution of the coastal plains of Brazil" (Suguio, 2010).

The beach and backshore are formed by unconsolidated fine to medium quartz sands that form areas of varying width, with some rocky outcrops on the beach (Souza, 2000). The area to the southeast of the mouth of the Pacoti River as far as Prainha beach in Aquiraz is characterized by a narrowing of the beach. The mobile dune fields are formed by unconsolidated fine to medium quartz sands, and are driven by winds from the E-NE. The fixed dunes and those being stabilized are arranged along the backshore. The mobile dunes are fixed through poorly-developed pedogenetic processes (Souza, 2000).

The fluvial-marine plain is formed by a combination of fluvial and marine forces, and is characterized by mangrove soils (gleysols) influenced continuously by tidal processes. The trees that constitute the mangrove form dense tracts of forest arranged longitudinally in relation to the river channel (Souza, 2000).

The pre-coastal plateau is located inland from the dune field, and is continuous with the backland depressions further inland. These areas are formed by the Barreiras Formation, and extend inland approximately 40 km, on average. At some points, these plateaus reach as far as the sea, where they form functional cliffs. Their altitude varies between 30 m and 50 m, with slopes of 2° to 5º, and slow-flowing drainage, mainly covered with thick layer of sand (Souza, 2000). There is also a rocky outcrop of the intrusive Messejana formation (Messejana Magmatism), which dates from one of the last tectonic events related to the opening of the Atlantic Ocean.

The functional zoning (Figure 3) focuses primarily on the potentialities and limitations of each specific area. This process attributes social and environmental functions to the different sectors of the study area, according to the observed degree of stability, diversity, conservation and degradation.

The Permanent Preservation Zone (PPZ) was attributed to the beach, backshore, and the fluvial and fluvial-marine plains, given the considerable fragility of these environments, and the need to protect their biodiversity, as well as the importance of the harvesting of natural resources, which guarantees the food security of the local coastal communities.

The Sustainable Use Zone (SUZ) refers to the fixed dunes and the magmatic Cararu outcrop, which are characterized by their excellent potential for the exploitation of water and other resources. Both areas are included in this zone because of their instability, and the regulation and monitoring would be highly recommended. The Environmental Recuperation Zone (ERZ) encompasses the degraded fluvial and fluvial-marine plains. Given their high degree of anthropogenic impact, these areas should be vacated to allow for a process of the natural regeneration of habitats. The Residential Expansion Zone (REZ) refers to the pre-coastal plateaus, which should be regulated for the establishment of subsistence plots, with the aim of integrating economic activities with the conservation of the environment.

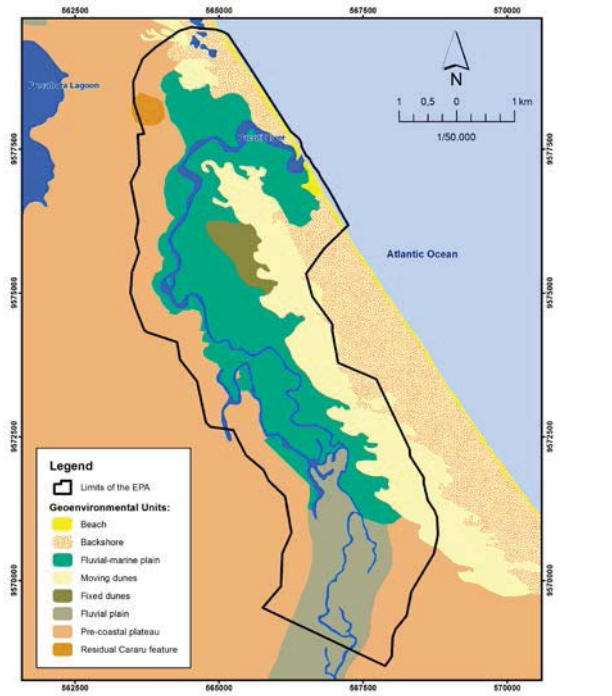

Figure 2. Environmental zoning of the Rio Pacoti Environmental Protection Area.

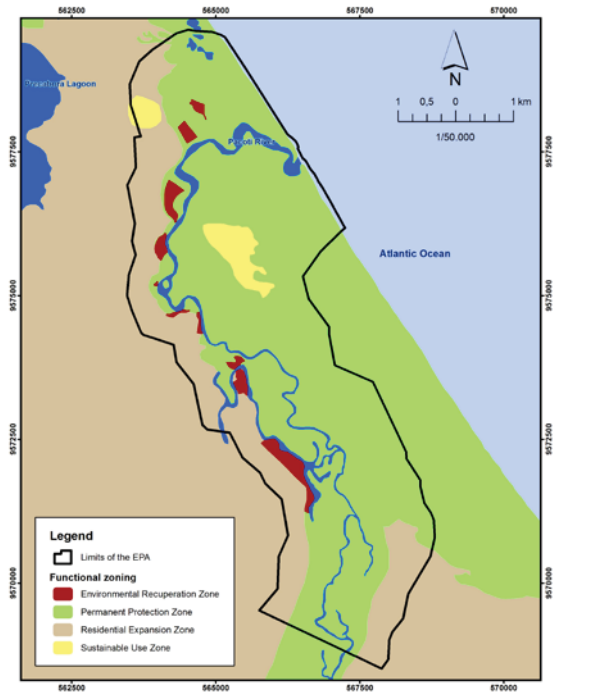

Figure 3. Functional zoning of the Rio Pacoti Environmental Protection Area.

DISCUSSION

The dynamic nature of the study area is driven by a constant flow of energy and material, which contributes to its considerable diversity of landscapes and biological features, and also its instability and vulnerability to human impacts. The mangroves of tropical estuaries, in particular those of the Pacoti, currently suffer high levels of degradation, derived primarily from the unregulated discharge of solid waste and domestic and industrial effluents, which have profound impacts on water quality. This has negative implications for the water supplies for human populations, as well as the local fauna, which may suffer from increased mortality.

The extraction of lumber, unregulated occupation of the land, and the installation of operations such as salt pans, all have a negative impact on the natural equilibrium of these environments through their modification of the surface by impermeabilization, landfills, and other processes. The extraction of lumber and salt is unregulated, and is practiced without any consideration for the role of these natural resources in the functioning of the estuarine environment.

In this context, environmental planning proposals were established for the study area, based on the support capacity (potentialities and limitations) of the local natural systems, and their respective applications (see Table 1). It is important to note that any reversible or preventive conservation action must integrate the social and political spheres through the Pacoti basin committee, which was established in 2003, as well as being dependent on the effective participation of the local community (Neto *et al*., 2013).

CONCLUSIONS

The current situation in the Pacoti estuary reflects the progressive degradation of the natural local landscapes, primarily through the gradual loss of water quality, the indiscriminate extraction of lumber, sand and phonolite for the production of construction-grade gravel and unregulated building sites based on illegal landfills. The degradation of the estuarine complex has occurred not only as a result of these problems, but also from the lack of any effective regulation of the use and occupation of the land in this estuarine sector.

The anthropization of these environments has resulted not only in the degradation of the landscape, but may also lead to even greater impacts, such as damage to the marine and fluvial biota, and the abrupt loss of biodiversity, and the imminent risk to the health of the local population that depends on local sources of drinking water and the subsistence exploitation of natural resources, with fundamental economic and social consequences.

The findings of the present study reinforce the value of landscape geo-ecology as an integrated approach to the analysis of environmental problems in relation to their determinants. The results of this analysis provide public administrators, civil society, and the economic sector with practical suggestions for the conservation of the environment.

Overall, then, the geo-ecological analysis presented here proved effective for the development of proposals for the

Table 1. *Definition of the environmental zones, uses, and management proposals established during the present study.*

Zone	Identified use and occupation/impacts	Proposal
Permanent Protection Zone (PPZ): beach, backshore, mobile dunes, fluvial plain and fluvial-marine plain.	Inadequate disposal of solid waste, quarrying of sand from water sources, and unregulated occupation of land.	Urban planning and demolition of illegal buildings; Effective application of the current environmental legislation; Regulation of the harvesting of natural resources.
Sustainable Use Zone (SUZ): fixed dunes and residual Cararu feature.	Unregulated building and indiscriminate extraction of phonolite.	Demolition of illegal buildings that constitute a risk to the environmental integrity of the area; Regulation of the extraction of phonolite.
Environmental Recuperation Zone (ERZ): degraded fluvial and fluvial-marine plains.	Landfills, inadequate disposal of solid waste, discharge of effluents, alteration of the water quality of the estuary, indiscriminate logging, removal of the original vegetation and unregulated building.	Demolition of illegal buildings for the natural regeneration of the mangrove; Monitoring and prohibition of effluent emissions by the competent public authority; Inspection and regulation of lumbering; Eviction and resettlement of communities established in risky locations at the margins of rivers.
Residential Expansion Zone (REZ): pre-coastal plateau.	Removal of the natural vegetation, wildfires and soil erosion.	Installation of infrastructure for leisure activities that contribute to the understanding of the area and the preservation of its natural resources: agricultural plots, camp sites, and other activities involving ecological learning trails.

environmental planning of the Pacoti estuary that are compatible with local potentialities and limitations. The application of these measures should contribute to the more harmonious relationship between nature and society.

The planning actions recommended here, which are central to the zoning proposal presented, should be applied immediately, and supported with a continuous process of monitoring and the implementation of preventive measures.

ACKNOWLEDGMENTS

We are grateful to the National Council for Scientific and Technological Development (CNPq) for financing this project through the Institutional Program of Scientific Initiation Scholarships (PIBIC).

LITERATURE CITED

Cavalcanti, A. and Viadana, A. G. 2007. *Organização do espaço e análise da paisagem*. Rio Claro: UNESP – IGCE, Laboratório de Planejamento Municipal/ Programa de Pós-Graduação em Geografia.154p.

Ceará. *Diário Oficial do Estado*. Série 2 ano III, nº34, caderno ½. Fortaleza: editoração SEAD, 17/02/2000.

Correia, M. D. and Hilda, H. S., 2005. *Ecossistemas marinhos : recifes, praias e manguezais*. Maceió: Editora UFAL, 55p.

Gorayeb, A.; Silva, E. V. and Meireles, A. J. A. 2005. Impactos Ambientais e Propostas de Manejo Sustentável para a Planície Flúvio-Marinha do Rio Pacoti – Fortaleza/Ceará. *Sociedade & Natureza*, Uberlândia, v. 33, n. 17, 143-152.

Gorayeb, A.; Silva, E. V. and Meireles, A. J. A., 2004. Meio Ambiente e Condições de Sustentabilidade da Planície Flúvio Marinha do Rio Pacoti – Ceará – Brasil. *Geoambiente On-line*, Jataí/GO, n. 2, 1-17.

Ministério do Meio Ambiente. *Erosão e progradação no litoral brasileiro*. 2006. Dieter Muehe, organizador. – Brasília: MMA. 476 p.

Nascimento, F. R. and Carvalho, O., 2003. Aspectos geoambientais e proposta de zoneamento geoambiental para a Bacia do baixo Pacoti-Ce, Nordeste do Brasil. *Boletim Goiano de Geografia*, 23 (2): 269 – 287.

Nascimento, F. R., 2003. *Recursos naturais e desenvolvimento sustentável: subsídios ao manejo geoambiental na Sub-bacia do Baixo Pacoti – Ceará*. 2003. Dissertação (Mestrado Acadêmico em Geografia) – Universidade Estadual do Ceará, Centro de Ciências e Tecnologia. 144p.

Neto, F. O. L.; Gorayeb, A.; Silva, E.V and Rabelo, F. D. B., 2013. Diagnóstico Ambiental e Zoneamento Funcional Do Estuário Do Rio Curu: Subsídios para a Gestão Local e Regional. *Revista Eletrônica Geoaraguaia*. Barra das Garças-MT. V 3, n.1, 97 - 113.

Rodriguez, J. M. M.; Silva, E. V., 2013. Planejamento e gestão ambiental: subsídios da geoecologia das paisagens e da teoria geossistêmica. Fortaleza: edições UFC. 370p.

Souza, M.J.N. 2000. Bases Naturais e esboço do zoneamento geoambiental do estado do Ceará. In: Lima, L. C., Morais, J. O. and Souza, M. J. N. (Orgs). *Compartimentação territorial e gestão regional do Ceará*. Fortaleza: FUNECE.

Souza, M.J.N., 1998. *Análise Geoambiental e Ecodinâmica das Paisagens do Estado do Ceará*. Tese (Professor Titular)-Universidade Federal do Ceará, Fortaleza-CE, 250p.

Suguio, K., 2010. *Geologia do Quaternário: mudanças ambientais*. São Paulo: Oficina de Textos, 408 p.

Journal of Coastal Research	SI	75	148-152	Coconut Creek, Florida	2016

Effect of Particle Size on Calibration of Schmidt Number

Minwoo Son[†], Jisun Byun[†*], Sang Ug Kim[‡], and Eun-Sung Chung [††]

[†]Dept. Of Civil Engineering, Chungnam National University, Daejeon, Repbulic of Korea

[‡]Dept, of Civil Engineering, Kangwon National University, ChunChun, Republic of Korea

[††]Dept. of Civil Engineering, Seoul National University of Science & Technology, Seoul, Republic of Korea

www.cerf-jcr.org

www.JCRonline.org

ABSTRACT

Son, M., Byun, J., Kim, S., and Chung, E.-S., 2016. Effect of particale size on calibration of Schmidt number. *In:* Vila-Concejo, A.; Bruce, E.; Kennedy, D.M., and McCarroll, R.J. (eds.), *Proceedings of the 14th International Coastal Symposium* (Sydney, Australia). *Journal of Coastal Research*, Special Issue, No. 75, pp. 148-152. Coconut Creek (Florida), ISSN 0749-0208.

The effect of particle size on calibrating the Schmidt number (σ_c) is numerically investigated in this study. The experiments are carried out under different conditions of flow type and particle size. From calculation results, it is known that σ_c is calibrated to be 0.25 to 2.0 as the particle size changes from 320 μm to 130 μm. The value of σ_c shows the inverse-relationship with particle size. σ_c determines the particle diffusivity. When σ_c is smaller than 1.0, the particle diffusivity becomes larger than the momentum diffusivity. A large particle having large inertia can diffuse relatively more compared to small particle under the condition that the turbulent intensity decreases. Therefore, σ_c is calibrated to be small as the particle size increases. This idea is examined by calculating the Stokes number and sediment diffusivity. As the particle size increases, both of Stokes number and sediment diffusivity also increase.

ADDITIONAL INDEX WORDS: *Sediment diffusivity, particle inertia, Stokes number.*

INTRODUCTION

To accurately predict the transport of sediment, it is of great necessity to adopt the advection-diffusion equation which resolves the time-dependent concentration of sediment. The advection-diffusion equation is composed of advection and diffusion terms. The diffusion process composed of molecular and turbulent diffusions is calculated under the assumption that the diffusion intensity is proportional to the gradient of sediment concentration and turbulent diffusivity. Herein, the turbulent diffusivity is determined by the ratio of eddy viscosity to the Schmidt number (σ_c). It is known that the calculation results of the sediment transport model are sensitive to σ_c (Byun and Son, 2014; Amoudry *et al*., 2005; Buscombe and Conley, 2012). Although σ_c plays a key role in modeling the diffusion process of sediment, there is not a general consensus about the determination of σ_c.

In many studies, σ_c is considered as a constant, which is usually smaller than unity (*e.g.*, Celik and Rodi, 1988; Son and Hsu, 2011; Hsu and Liu, 2004). It is insisted in van Rijn (1984) that the value of σ_c should be smaller than unity because the centrifugal force of sediment is larger than that of fluid particles. This is consistent with Uittenbogaard (1995). Hsu and Liu (2004) carry out the numerical experiments by calibrating σ_c. σ_c is set to be smaller than 1.0 based on van Rijn (1984). However, the calculated sediment concentrations are less satisfactory mainly due to the limitations on the available data sets relating to sediment near-bed boundary conditions. Cellino and Graf (1999) insist that the value of σ_c is close to 2.0 based on the laboratory data sets. It is also found in Winterwerp (2006) that the numerical experiments adopting the value of σ_c=2.0 show more reasonable results compared to previously suggested value (σ_c =0.7). van Maren *et al*. (2009) conduct the numerical experiments with Delft3D replicating field measurements in the Yellow River. van Maren *et al*. (2009) adopt the values of σ_c=0.7 and σ_c=2.0. It is concluded in van Maren *et al*. (2009) that the results of σ_c=2.0 are more realistic compared to the results of σ_c=0.7 when the hyperconcentrated flow are simulated. Whitehouse (1995) insists that σ_c is approximately constant upto the height, which is far from the bed. The calculated value of σ_c in Whitehouse (1995) is about 1.5 based on measurement data sets. The regression equations of σ_c have been proposed in many studies (*e.g.*, Lees, 1981; Amoudry *et al*., 2005). Lees (1981) proposes the regression equation based on *in situ* measurement results. Amoudry *et al*. (2005) analyze the sediment concentration profiles and compare the numerical experiment results with Ribberink and Al-Salem (1995). They conclude that it is more reasonable to consider σ_c as a dependent variable of elevation. They further develop σ_c-model depending on the concentration above the bed under the assumption that the sediment concentration is related to the elevation. The developed σ_c-model shows improved results. Toorman *et al*. (2002) suggest the regression equation of σ_c according to Richardson number (Ri). By comparing with data sets, it is found that σ_c depends on not only Ri but also the ratio of settling velocity to friction velocity.

As shown above, it is more reasonable to consider σ_c as a dependent variable. Winterwerp (2006) insist that it is reasonable to consider σ_c as a function of Ri, which means mixing efficiency of momentum and particles in stratified flows. Nezu and Azuma (2004) investigate the decrease of σ_c as the sediment size increases. It is insisted in Nezu and Azuma (2004) that the variation of σ_c is caused by sediment size. When the sediment size is larger than 500 μm, Rouse's diffusion theory is

DOI: 10.2112/SI75-30.1 received 15 October 2015; accepted in revision 15 January 2016.

*Corresponding author: jsbyun@cnu.ac.kr

not available to simulate the sediment transport and the two-phase flow approach should be included (Nezu and Azuma, 2004). Based on flume experiments, Nielsen and Teakle (2004) insist that σ_c should be decreased as the grain size increases because the settling velocity of sediment is relatively small. Whereas, it is also found in Nielsen and Taekle (2004) that σ_c increases according to size increase of coarse sediment when wave ripples exist near the bed. It is well known that large particles are less likely to follow the motions of turbulent flow resulting in decrease of sediment diffusivity (Buscombe and Conley, 2012). Therefore, the effect of particle size should be considered when the sediment diffusivity is determined. In the study of Winterwerp (2006), it is reported that a numerical model calculates better results when σ_c is fixed to be 2.0 under the condition of mono-sized particles. In the meantime, it is also notable that Amoudry *et al*. (2005) find the spatial change of σ_c when replicating the measurement results of Ribberink and Al-Salem (1995) and Katopodi *et al*. (1994). The experiments of Ribberink and Al-Salem (1995) and Katopodi *et al*. (1994) use multi-sized particles. Therefore, the spatial change of σ_c found in Amoudry *et al*. (2005) may be due to size variation of suspended particles at different elevations. Byun and Son (2014) conduct numerical experiments under the conditions of both cohesive and non-cohesive sediments. Their results show the consistent effect of σ_c on sediment suspension regardless of hydrodynamic conditions.

The diffusion process of suspended particles depends on both characteristics of carrier flow such as turbulence intensity and particle properties such as particle diffusivity. Strictly speaking, the turbulent diffusion is a kind of advection process having random nature similar to molecular diffusion. In this sense, the turbulent diffusion may be governed mainly by particle properties such as particle response time. The sediment size is the only variable to determine the particle response time under the condition of constant particle density. In this study, effects of particle size on σ_c is intensively investigated by using 1 dimensional vertical numerical model previously developed by Son and Hsu (2011). The 1DV model of Son and Hsu (2011) has been validated with field and laboratory experiments (*e.g.*, Son and Hsu, 2011).

METHODS

In order to understand the effect of particle size on calibration of σ_c, a sediment transport model developed by Son and Hsu (2011) is used in this study. The model of Son and Hsu (2011) has a capability to calculate the transport of both cohesive and non-cohesive sediments. In the case of cohesive sediment, the model calculates the change of size and density of floc. In this study, the density and size of sediment are assumed to be constant to replicate the transport of non-cohesive sediment. The model of Son and Hsu (2011) adopts the mixture theory, which simplifies the Eulerian-Eulerian two-phase equations. In the dilute-phase approach, the particles of sediment and fluid are considered as a single continuum of mixture by assuming small response time of sediment particles. Therefore, the sediment particles are transported at the velocity same as the mixture. It is also assumed that the pressure of fluid is same as that of particle. The governing equations for momentum of mixture are described as:

$$\frac{\partial u}{\partial t} = -\frac{1}{\rho_w}\frac{\partial p}{\partial x} + \frac{1}{\rho_w(1-\phi_s)}\frac{\partial \tau_{xz}^w}{\partial z} + \frac{(s_s-1)\phi_s}{1-\phi_s} g\sin\alpha_s \quad (1)$$

$$\frac{\partial v}{\partial t} = -\frac{1}{\rho_w}\frac{\partial p}{\partial y} + \frac{1}{\rho_w(1-\phi_s)}\frac{\partial \tau_{yz}^w}{\partial z} \quad (2)$$

where u and v=mixture velocity in the stream-wise (x) and span-wise (y) directions, respectively; s_s=specific gravity of sediment particle set to be 2.65 in this study; ρ_w =density of fluid, g=gravitational acceleration; α_s=slope of the bed; p=pressure; ϕ_s =volumetric concentration of sediment; τ_{xz}^w and τ_{yz}^w =shear stresses of fluid ($\tau_{xz}^w = \rho_w(\nu_t + \nu)\frac{\partial u}{\partial z}$ and $\tau_{yz}^w = \rho_w(\nu_t + \nu)\frac{\partial v}{\partial z}$). Herein, ν is the kinematic viscosity of fluid. ν_t is the eddy viscosity. The first terms on the right-hand sides of Eqs. (1) and (2) represent pressure gradient. It is implemented as flow forcing in the numerical model of Son and Hsu (2011). In Eqs. (1) and (2), the second terms on the right-hand sides represent the gradient of fluid stresses. In this study, ν_t is calculated by standard k-ε model:

$$\nu_t = C_\mu \frac{k^2}{\varepsilon}(1-\phi_s) \quad (3)$$

where C_μ =model coefficient set to be 0.09 in this study following the previous studies (*e.g.*, Son and Hsu, 2011; Hsu and Liu, 2004). The k-ε model is composed of two quantities; turbulent kinetic energy (k) and turbulent dissipation rate (ε). The turbulent viscosity hypothesis shown in Eq. (3) is also used for k- ε model. In the model, the production of k and ε are assumed to be in the balance condition. As a result, k and ε are determined by:

$$(1-\phi_s)\frac{\partial k}{\partial t} = \nu_t\left[\left(\frac{\partial u}{\partial z}\right)^2 + \left(\frac{\partial v}{\partial z}\right)^2\right] + \frac{\partial}{\partial z}\left[\left(\nu + \frac{\nu_t}{\sigma_k}\right)\frac{\partial(1-\phi_s)k}{\partial z}\right] - (1-\phi_s)\epsilon + (s_s-1)g\frac{\nu_t}{\sigma_c}\frac{\partial \phi_s}{\partial z} \quad (4)$$

$$(1-\phi_s)\frac{\partial \varepsilon}{\partial t} = C_{\varepsilon 1}\frac{\varepsilon}{k}\nu_t\left[\left(\frac{\partial u}{\partial z}\right)^2 + \left(\frac{\partial v}{\partial z}\right)^2\right] + \frac{\partial}{\partial z}\left[\left(\nu + \frac{\nu_t}{\sigma_\varepsilon}\right)\frac{\partial(1-\phi_s)\varepsilon}{\partial z}\right] - C_{\varepsilon 2}(1-\phi_s)\frac{\varepsilon^2}{k} + C_{\varepsilon 3}\frac{\varepsilon}{k}(s_s-1)g\frac{\nu_t}{\sigma_c}\frac{\partial \phi_s}{\partial z} \quad (5)$$

where $C_{\varepsilon 1}$, $C_{\varepsilon 2}$, $C_{\varepsilon 3}$, σ_k, and σ_ε are numerical coefficients. The values of these numerical coefficients are summarized in Table 1. The last terms of Eqs. (4) and (5) represent the turbulence damping effect. The turbulence damping effect is defined as the turbulence damping mainly due to the density gradient of sediment-fluid mixture.

The governing equation for change of concentration is described by the advection-diffusion process:

$$\frac{\partial \phi_s}{\partial t} = \frac{\partial}{\partial z}\left(\phi_s W_s + \frac{\nu_t+\nu}{\sigma_c}\frac{\partial \phi_s}{\partial z}\right) \quad (6)$$

herein, W_s is the settling velocity of the sediment particles. The ratio between the effective viscosity ($\nu + \nu_t$) and σ_c is defined as the sediment diffusivity. The term on the left-hand side of Eq. (6) is the change rate of volumetric concentration with time. The first term on the right-hand side is the convective velocity of fluid in the advection-diffusion equation. In Eq. (6), the magnitude of convective velocity in the z-direction is same as that of the settling velocity of sediment. Through this idea, Son and Hsu (2011) adopt the settling velocity of sediment instead of convective velocity in the z-direction. The second term on the right-hand side represents the diffusion by molecular and turbulent motions. The turbulent diffusion is a dominant factor in the diffusion process. In the advection-diffusion process shown in Eq. (6), the downward flux due to gravitational settling

is compensated by an

Table 1. *Numerical coefficients for eddy viscosity model and k - ε equations (Son and Hsu, 2011)*

Coefficient	C_μ	$C_{\varepsilon 1}$	$C_{\varepsilon 2}$	$C_{\varepsilon 3}$	σ_k	σ_ε
Value	0.09	1.44	1.92	0.00	1.00	1.30

upward diffusive flux. The continuous erosion formulation is used as a bottom boundary conditions (see Son and Hsu, 2011, for more details). The settling velocity of sediment particle is determined by the Stokes' law:

$$W_s = \frac{1}{18\mu} g D^2 (\rho_s - \rho_w)(1-\phi_s)^4 \quad (7)$$

where, ρ_s is the density of particles; D is the mean (or median) size of suspended particles. The term involved in right-hand side, $(1-\phi_s)^4$, represents the hindered settling effect.

RESULTS

The numerical experiments are carried out under two different flow conditions: steady current and oscillatory flow (refer to Table 2). It is based on experiment conditions of Janssen (1999) and Einstein and Chien (1955). Janssen (1999) reports the experiments using a large oscillating water tunnel of Deltares with three different sizes of particles. To replicating the flow conditions of Janssen (1999) (D1, D2, and D3), the amplitude of the oscillatory flow (u_a) and time-averaged velocity (u_m) at 1.0 m above the bed are set to be 1.47 m/s and 0.24 m/s, respectively. The oscillation period of Janssen (1999) is 7.2 s. Einstein and Chien (1955) also report the laboratory experiment with mono-sized particles under the condition of steady current (u_m=1.99 m/s) (S11). When the erosion rate from the bottom is calculated, the value of resuspension coefficient plays a key role (Smith and McLean, 1977). Therefore, the value is fixed to be 1.0×10^{-5} in all cases of this study following previous studies (*e.g.*, Son and Hsu, 2011; Byun and Son, 2014). The critical shear stress (τ_c) is also an important parameter when sediment suspension is calculated. τ_c is calibrated by tradition equation of Zeller (1963) in this study:

$$\tau_c = 0.047 g(\rho_s - \rho_w)D \quad (8)$$

Except σ_c, τ_c is the only parameter having different values in the different cases of experiments in this study. The conditions for numerical experiments are summarized in Table 2.

Figure 1 shows the vertical profiles of velocity in the cases of both Janssen (1999) and Einstein and Chien (1955). Figures 1a, 1b, and 1c are the velocity profiles at the phases of $\pi T/2$, πT, $3\pi T/2$. It is found in Figures 1a and 1c that the magnitude of velocities is similar whereas the directions are opposite. All results discussed in this study are have been obtained in the quaisi equilibrium states. Figure 2 shows the vertical profiles of mass concentration at different conditions of particle size. Figures 2a, 2b and 2c are the results under the oscillatory flow condition (D1, D2, and D3). The concentration profiles shown in Figure 2 are the wave-period averaged results following Janssen (1999). Figure 2d is the results under the condition of steady current (S11). It is clearly known from Figure 2 that the calculation results are sensitive to the calibration of σ_c. As σ_c decreases from 2.0 to 0.25, the suspended

Table 2. *The conditions for numerical experiments*

Exp.	u_a (m/s)	u_m (m/s)	*Resuspension Coefficient*	D (μm)	τ_c (Pa)
D1				130	0.099
D2	1.47	0.24	1.0×10^{-5}	210	0.125
D3				320	0.191
S11	N.A.	1.99	1.0×10^{-5}	274	0.163

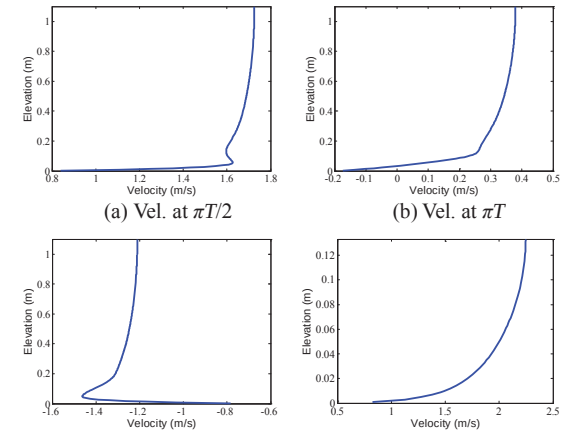

(a) Vel. at $\pi T/2$ (b) Vel. at πT

(c) Vel. at $3\pi T/2$ (d) Vel. of S11

Figure 1. Vertical profiles of velocity. Fig. 1a, 1b, and 1c are the replicating results of Janssen (1999). Fig. 1d is the replicating results of Einstein and Chein (1955).

load increases. The calculation of increased suspension is caused by increase of sediment diffusivities. The decrease of σ_c means the increase of sediment diffusivities. (see the second term in the right-hand side of Eq. (6). This is analogous to Byun and Son (2014). It is also notable that the calibrated value of σ_c is inversely-proportional to the size of particle (2.0 and 0.25 in the cases of D=130 μm and D=320 μm, respectively).

The relationship between σ_c and flow condition is not found although a few flow conditions are tested in this study. Therefore, it is inferred that the sediment diffusivities should be increased through the calibration of σ_c when the size of particles are increased. The calculated values of sediment diffusivities according to the σ_c is shown in Figure 3.

As mentioned in the previous section, the value of σ_c should be calibrated by considering the particle size. It is generally known that σ_c determines the ratio between the momentum diffusivity and the sediment (or mass) diffusivity. Therefore, the mass diffusion is predominant when σ_c is smaller than 1.0 whereas the momentum diffusion is predominant when σ_c is larger than 1.0. From Figures 2a, 2b, and 2c, it is known that σ_c should be calibrated having significantly different values even though the flow condtion is constant. Therefore, it can be insisted that the sediment suspension is calculated reasonably well when the effect of particle size on sediment diffusivity is also considered by calibrating σ_c.

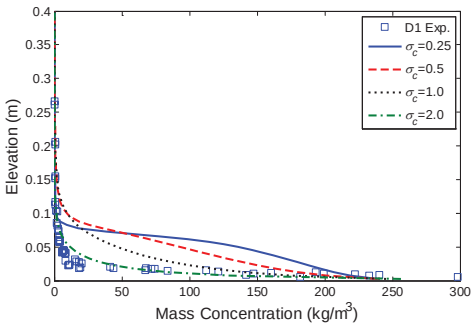

(a) D=130 μm (Janssen, 1999)

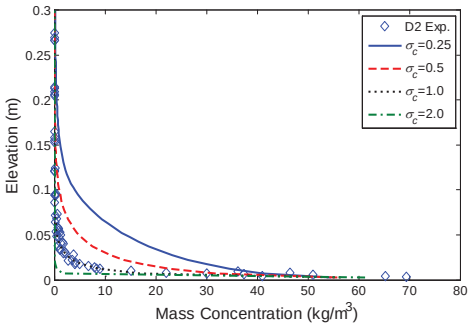

(b) D=210 μm (Janssen, 1999)

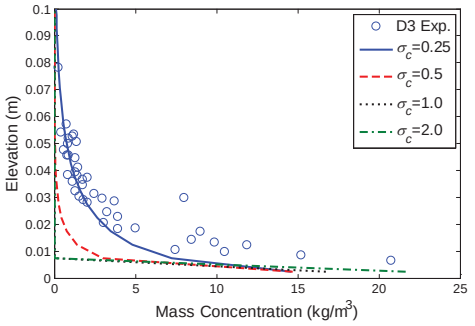

(c) D=320 μm (Janssen, 1999)

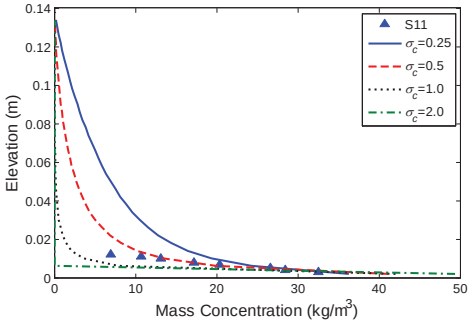

(d) D=274 μm (Einstein and Chien, 1955)

Figure 2. Variations of mass concentration profiles according to σ_c.

DISCUSSION

Inertia of a moving particle increases when the particle size increases. As particle inertia increases, a particle keeps its current movement more strongly. Therefore, during the turbulent intensity becomes weaker resulting in decrease of momentum diffusivity, a larger particle can diffuse relatively more compared to smaller particle. Inertia of sediment particle is affected not only by sediment size but also by properties of particle, *e.g.*, shape and density. To quantify the effect of particle inertia, Stokes number is calculated and plotted in Figure 3. The case of D=274 μm (S11)

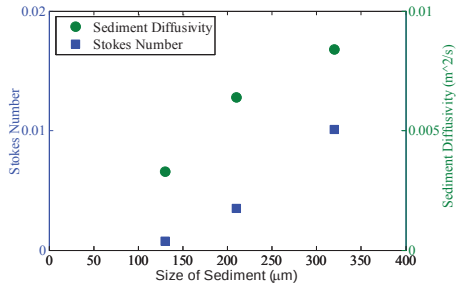

Figure 3. Calculated Stokes number and sediment diffusivities according to the sediment size under the condition of σ_c=0.25.

is not shown here because that case has different flow and turbulent conditions. Stokes number is a measure of particle inertia (Wetchagarun, 2008) and it is defined as the ratio of particle response time (t_p) to fluid turbulence timescale (t_f).

$$St = t_p/t_f \tag{9}$$

t_p is calculated by Stokes law ($t_p = (\rho_s - \rho_w)D^2 \,/\, 18\mu$). t_f is calculated by the semi-emprical equation developed by Nezu and Nakagawa (1993) ($t_f = \lambda/u_t$). The turbulent intensity (u_t) is defined as square-root of turbulent kinetic energy in this study. The turbulence microscale (λ) is determined as:

$$\frac{\lambda}{h} = \left(\frac{15B_1}{2.3KR_*}\right)^{1/2} \left(\frac{z}{h}\right)^{1/4} \exp\left(\frac{z}{2h}\right) \tag{10}$$

where, B_1 and R_* are empirical coefficients set to be B_1=1.0 and R_*=1600 under the turbulent condition; K is the value of 0.1375; z is the elevation from the bottom; h is the water depth. It is found in Figure 3 that St increases as the size of sediment particle increases under the constant density of particle (2,650 kg/m^3 in this study). van Rijn (1984) insists that σ_c should be smaller than 1.0 under the turbulent condition because the centrifugal force of suspended particle is larger than that of fluid particle. However, this idea is questionable in the sense of particle inertia. Moreover, many studies show that the suspension of particle is calculated reasonably when σ_c is larger than 1.0 (*e.g.*, Cellino and Graf, 1999; Winterwerp, 2006; van Maren *et al.*, 2009; Nezu and Azuma, 2004).

CONCLUSIONS

This study aims to investigate the effect of sediment size on calibration of σ_c. St and sediment diffusivities are also calculated in this study to examine the effect of particle inertia. It is found in this study that the value of σ_c should be calibrated considering the size of sediment to simulate the

suspension of sediment reasonably well. The calibration of σ_c has a relationship with particle inertia quantified by particle size. It is also shown in Zhang *et al*. (2014) that inertia of particle plays a key role in simulating the sediment suspension behaviors. In this study, we examine St as a measure of particle inertia. The calculated St show the positive relationship with the sediment size under the condition of constant σ_c. It is also notable that both density and size of cohesive sediment vary through the flocculation process whereas the density of non-cohesive sediment is assumed to be constant. Therefore, inertia effect of cohesive sediment on σ_c becomes more complicated. It is necessary to investigate the effect of many different properties of sediments on σ_c and particle diffusivity under the turbulent condition.

ACKNOWLEDGMENTS

This research was supported by the Basic Science Research Programs through the National Research Foundation of Korea (NRF) funded by the Ministry of Education, Science and Technology (2015-019234 and 2015-059944).

LITERATURE CITED

Amoudry, L.; Hsu, T.-J., and Liu, P.L.-F., 2005. The Schmidt number and near-bed boundary condition effects on a two-phase dilute sediment transport model. *Journal of Geophysical Research*, 110(C9), C09003, doi: 10.1029/2004JC002798.

Buscombe, D. and Conley, D.C., 2012. Schmidt number of sand suspensions under oscillating grid turbulence. *Coastal Engineering Proceedings*, Vol. 33, pp. 1-11.

Byun, J. and Son, M., 2014. Effect of Schmidt number on cohesive and non-cohesive sediment suspension modeling. *Journal of Korea Water Resources Association*, 47(8), 703-715 (*in Korean*).

Cellino, M. and Graf, W., 1999. Sediment-laden flow in open-channels under non-capacity and capacity conditions. *Journal of Hydraulic Engineering,* 125(5), 455-462.

Celik, I. and Rodi, W., 1988. Modeling suspended sediment transport in nonequilibrium situations. *Journal of Hydraulic Engineering,* 114(10), 1157-1191.

Einstein, H.A. and Chien, N., 1955. *Effects of heavy sediment concentration near the bed on velocity and sediment distribution.* Report No. 8:78, Missouri River Division, U.S. Army Corps of Engineering, Omaha District, Nebraska.

Hsu, T.-J. and Liu, P. L.-F., 2004. Toward modeling turbulent suspension of sand in the nearshore. *Journal of Geophysical Research*, 109(C06). doi: 10.1029/2003JC002240.

Janssen, C.M., 1999. Grain size influence on sediment transport in oscillatory flow; phase lags and mobile-bed effects. Delft, The Netherlands: Delft University of Technology, Ph.D. dissertation, 247p.

Katopodi, I.; Ribberink, J.; Ruol, P.; Koelewijn, R.; Lodahl, C.; Longo, S.; Crosato, A., and Wallace, H., 1994. *Intra-wave sediment transport in an oscillatory flow superimposed on a mean current.* Delft, The Netherlands: Delft University of Technology, *Report No. H1684.33*.

Lees, B.J., 1981. Relationship between eddy viscosity of seawater and eddy diffusivity of suspended particles. *Geo-Marine Letters*, 1(3-4), 249-254.

Nezu, I. and Azuma, R., 2004. Turbulence characteristics and interaction between particles and fluid in particle-laden open channel flows. *Journal of Hydraulic Engineering*, 130(10), 988-1001.

Nezu, I. and Nakagawa, H., 1993. *Turbulence in Open-Channel Flows, IAHR Monographs*, Taylor & Francis, 293p.

Nielsen, P. and Teakle, I.A., 2004. Turbulent diffusion of momentum and suspended particles: A finite-mixing-length theory. *Physics of Fluids*, 16(7), 2342-2348.

Ribberink, J.S. and Al-Salem, A., 1995. Sheet flow and suspension of sand in oscillatory boundary layers. *Coastal Engineering*, 25(3), 205-225.

Smith, J.D. and McLean, S.R., 1977. Spatially averaged flow over a wavy surface. *Journal of Geophysical Research*, 82. doi: 10.1029/JC082I012P01735.

Son, M. and Hsu, T.-J., 2011. The effects of flocculation and bed erodibility on modeling cohesive sediment resuspension. *Journal of Geophysical Research*, 116(C3). doi: 10.1029/2010JC006352.

Toorman, E.A.; Bruens, A.W.; Kranenburg, C., and Winterwerp, J.C., 2002. Interaction of suspended cohesive sediment and turbulence. *In*: Winterwerp, J.C. and Kranenburg, C. (eds.), *Proceedings in Marine Science*, Fine Sediment Dynamics in the Marine Environment, Vol. 5, pp. 7-23.

Uittenbogaard, R.E., 1995. Observation and analysis of random internal waves and the state of turbulence. *Proceedings IUTAM Symposium on Physical Limnology* (Broome, Western Australia).

van Maren, D.S.; Winterwerp, J.C.; Wu, B.S., and Zhou, J.J., 2009. Modelling hyperconcentrated flow in the Yellow River. *Earth Surface Processes and Landforms*, 34(4), 596-612.

van Rijn, L.C., 1984. Sediment transport, Part II: Suspended load transport. *Journal of Hydraulic Engineering*, 110(11), 1613-1641.

Wetchagarun, S., 2008. *A numerical study of turbulent two-phase flows,* Seattle, Washigton: University of Washington, Ph.D. dissertation, 243p.

Whitehouse, R., 1995. Observation of the boundary layer characteristics and the suspension of sand at a tidal site. *Continental Shelf Research*, 15(13), 1549-1567.

Winterwerp, J.C., 2006. Stratification effects by fine suspended sediment at low, medium, and very high concentrations. *Journal of Geophysical Research,* 111(C05), C05012. doi:10.1029/2005JC003019.

Zeller, J., 1963. Einführung in den Sedimenttransport offener Gerinne, *Schweiz. Bauzeitung*, Jgg. 81.

Zhang, L.; Zhong, D.Y., and Wu, B., 2014. Particle intertia effect on sediment dispersion in turbulent open-channel flows. *Science China Technology Science*, 57, 1977-1987.

Journal of Coastal Research	SI	75	153-157	Coconut Creek, Florida	2016

Spatial and Temporal Variability of Residual Volume Transport according to Artificial Freshwater Discharge in Yeoungsan River Estuary, South Korea

Jin Il Song †, Jong Wook Kim†, Byung Il Yoon†, and Seung-Buhm Woo†*

†Department of Ocean Science
College of Natural Science, Inha Univesity
Inchoen, South Korea

www.cerf-jcr.org

www.JCRonline.org

ABSTRACT

Song, J.I.; Kim, J.W.; Yoon, B.I., and Woo, S.B., 2016. Spatial and temporal variability of residual volume transport according to artificial freshwater discharge in Yeoungsan river estuary, South Korea. *In:* Vila-Concejo, A.; Bruce, E.; Kennedy, D.M., and McCarroll, R.J. (eds.), *Proceedings of the 14th International Coastal Symposium* (Sydney, Australia). *Journal of Coastal Research*, Special Issue, No. 75, pp. 153-157. Coconut Creek (Florida), ISSN 0749-0208.

To determine the effect of artificial freshwater discharge on the spatial and temporal variability of residual current and residual volume transport, current and density profile data have been analyzed in the Yeoungsan River estuary (YRE), South Korea. Current and density data were obtained from three transects during no freshwater discharge and during freshwater discharge. The residual current structure is complex (*e.g.,* vertically multi-layer) during no freshwater discharge, due to the combined influence of tides, wind, and topography. In contrast, strong freshwater discharge influences vertical mixing at the surface layer and no mixing at the bottom layer. This mixing characteristic causes a salinity gradient with depth and significant stratification. The direction of residual volume transport is flood-direction during no freshwater discharge and ebb-direction during freshwater discharge. Residual volume transport and stratification are shown to be dependent on artificial freshwater discharge in the YRE.

ADDITIONAL INDEX WORDS: *Artificial freshwater discharge, residual current, volume transport, Yeoungsan River Estuary.*

INTRODUCTION

In 1981, a dyke was built on the Yeoungsan River estuary (YRE) in South Korea for water supply and flood control, which has since changed the estuary environment. The magnitude of tidal currents decreased due to the blocking by the dyke, and the residence time in the estuary increased because of low freshwater discharge (Kang, 1998).

Mixing or stratification by freshwater in the estuary causes changes in vertical and horizontal density. This process has an important role in estuarine circulation and mass flux. Water column temperature in front of the YRE dyke occurs as either a two-layer structure (common in estuaries) or a multi-layer structure after freshwater discharge (Cho *et al.,* 2004). The dyke is in an area where the estuary environment changes drastically due to freshwater discharge. Therefore, freshwater influx due to water being discharged from the YRE dyke has become an important factor controlling the estuary's environment (Bang *et al.,* 2013). Various studies have been conducted to investigate the effects of the freshwater influx. Despite a decrease in the area of the tidal flats, ebb dominance intensified at Mokpo Port due to the construction of the dyke (Kang, 1999). Kim *et al.* (2013) suggested that salinity stratification develops at the front of the YRE dyke due to freshwater discharge and that discharge does not substantially contribute to vertical mixing between the surface layer and the bottom layer.

The vertical salinity structure and the strong current flow during freshwater discharge are important factors that affect stratification and mixing phenomena in the estuary. They are also very important for the horizontal transport of sediments and biotic matter both toward the open sea and within incoming seawater.

Previous studies focused mainly on making observations at fixed points, which is advantageous for identifying temporal environmental changes over a long time period. However, the movement of dissolved matter and sediments in an estuary causes complex spatial changes within the channel. This spatial variation has direct and indirect effects on the exchange of materials. Therefore, it is necessary to consider both temporal changes and spatial changes in order to identify the mechanisms of material circulation in an estuary.

In this study, observation of the spatial and temporal changes of current and salinity were performed simultaneously to identify the characteristics of three-dimensional estuarine circulation within the channel. Three-dimensional flow and salinity were reconstructed based on the data obtained from on-site observations. These data were used to calculate tidal residual current and total mass flux during no freshwater discharge and freshwater discharge.

METHODS

The locations of the mooring observation points and a topographical cross section through the study area are presented in Figure 1. The topography and water depth information are based on a digital chart provided by the Korea Hydrographic and Oceanographic Administration. Cross-sectional velocity was observed at the YRE using a 600 kHz acoustic Doppler current

DOI: 10.2112/SI75-031.1 received 15 October 2015; accepted in revision 15 January 2016.
*Corresponding author: sbwoo@inha.ac.kr

profiler (ADCP) on April 29 and July 20, 2012. Observations were performed repeatedly each hour for 13 hours along each transect, and ship speed was maintained at 4–5 knots to maintain stability for the observation tool and data integrity. The ADCP was mounted at 1 meter (m) under the water surface (MUS), and flow direction and speed data per water layer were measured at intervals of 0.5 m. Observations of the cross-sectional velocity of the channel were conducted at the channel junction inside Gohado, and three transects, which correspond to the entrances of each river junction, were observed (Figure 1). Temperature and salinity data were measured per water layer using an IDRONAUT Ocean Seven 304 Conductivity-Temperature-Depth.

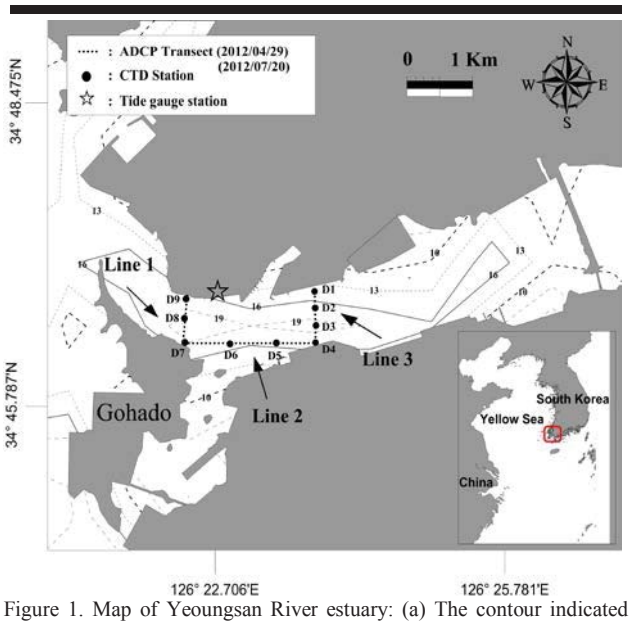

Figure 1. Map of Yeoungsan River estuary: (a) The contour indicated spatial distribution of depth. The dashed line indicated tidal current transects (Line 1, 2, and 3) and black dot indicated a CTD profile point (D1–D8).

The water levels observed on April 29 and July 20, 2012, are presented in Figure 2. Water level and freshwater discharge data were used to analyze change in the hydrodynamic environment. The water levels were collected from the Mokpo tidal gauge, and freshwater discharge data from YRE dyke were provided by the Korea Rural Community Corporation. The observations were conducted when freshwater was not discharged, and when freshwater was discharged, to observe any difference in the environment by artificial discharge.

The ADCP data was processed for error value elimination, true north direction correction, principal component analysis (PCA), and conversion into sigma coordinates to improve accuracy and reliability. The magnetic north direction used as a benchmark in the ADCP measurements was corrected to true north. In addition, as current direction and flow velocity measurements can be affected by the ship speed, this was corrected using the method of Joyce (1989). In this study, flow velocity in the raw data was rotated using PCA to define the main axis direction, and an analysis of dominant elements was then conducted (Preisendorfer and Mobley, 1988).

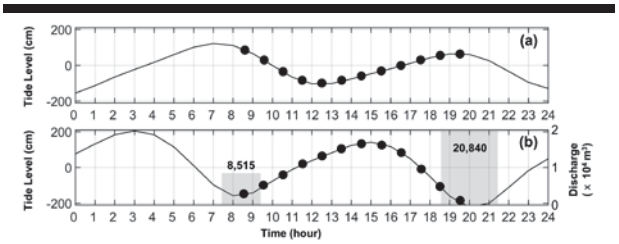

Figure 2. Tide level during no freshwater discharge in April 29, 2012 and tide level during freshwater discharge in July 20, 2012 at the Mokpo tide gauge station. The gray boxs indicate the daily-averaged freshwater discharge from dyke.

Finally, a normalization method (sigma coordinate) was used to facilitate the elimination of tidal elements within the surface and bottom layers, and the calculation of material volume transport (Kim *et al.,* 2013). When using the normalization method, the absolute water depth of the surface layer appears to be different due to tidal changes. The longitudinal flow was normalized vertically and horizontally for considers large tidal changes. ADCP water level is referred to as 0 m water depth at the time of observation.

Tidal propagation characteristics vary according to the characteristics of the estuary and change according to external forcing, such as non-linear tidal constituents, freshwater influx, and wind. Tidal residual current also vary according to the characteristics of the estuary (Yanagi *et al.,* 2003). Tidal residual current is defined as the flow after the tidal component is removed from the water circulation flow. Due to the short period of observation of 13 hours we could not identify short-period propagation characteristics that change daily (*e.g.,* K_1 and O_1). However, we could identify the characteristics of the spatial tidal residual current distribution during the tidal period by decomposing the M_2 and M_4 constituents, for which the cycle is less than 13 hours (Valle-Levinson and Atkinson, 1999). A harmonic analysis was conducted using the least square method (Lwiza *et al.,* 1991).

$$u = u_0 + \sum A_{M2}\, cos(\omega_{M2} - \emptyset_{M2}) + \sum A_{M4}\, cos(\omega_{M4} - \emptyset_{M4}) \quad (1)$$

In equation (1), u is the along-channel velocity of the main axis, u_0 is the residual current, A is the amplitude of M_2 and M_4, ω is angular velocity, and $\emptyset$ is phase angle. Considering the amplitude and the phase of the M_2 and M_4 tidal constituents, the difference in the raw data (u) was defined as the tidal residual current (*e.g.,* Choi *et al.,* 2012; Lee *et al.,* 2012; Valle-Levinson and Atkinson, 1999).

For a cross section having M grid cells, each with an instantaneous cross-sectional area of a_m and a normal velocity component of p_m, the residual volume transport rate may be expressed as (Sylaios and Boxall, 1998):

$$\langle \sum_{m=1}^{M} p_m a_m \rangle = \sum_{m=1}^{M} \langle p_m \rangle \langle a_m \rangle + \sum_{m=1}^{M} \langle P_m A_m \rangle \quad (2)$$

In equation (2), < > refers to a time longer than the tidal period, and P and A are defined as $P(=p-\langle p\rangle)$ and $A(=a-\langle a\rangle)$, respectively. The left side of this equation is the Lagrangian residual volume transport. The first term on the right side is the Eulerian residual volume transport, and the second term is Stokes drift volume transport rate.

RESULTS

The tidal residual current at each transect was calculated during no freshwater discharge (Figures 3a, 3b, and 3c). Positive values of velocity refer to flood directional flow, and negative values indicate ebb-directional flow. The black dotted line indicates a flow velocity of 0 m/s.

On the north side of Gohado is the river channel, which has a complex flow structure (Line 1, Figure 3a). Overall, flood-directional flow was dominant. Ebb-directional flow was well-defined on the surface layers. In Line 2, residual current was towards the flood-directional flow in the 400–800 m section (Figure 3b). Ebb-directional flow was seen in the other sections within the surface layer. During no freshwater discharge, the ebb-directional flow was seen within the surface and bottom layers, and the flood-directional flow within the middle layer (Line 3, Figure 3c). Residual current in the flood-direction was clear within the middle layer. However, the ebb tidal pattern was dominant within the lower layer.

During no freshwater discharge, the tide dominantly affected the longitudinal flow direction. Furthermore, the ebb-directional flow was dominant within the surface layer. During the observation period, there were continuous southeasterly winds in the study area, which likely affected the ebb-directional flow within the surface layer. We infer that the effect of wind is important during no freshwater discharge.

When freshwater was discharged, the longitudinal residual current was distinctly different to the periods of no discharge (Figures 3d, 3e, and 3f). In Line 1, overall residual current was ebb-directional in the northern channel and flood-directional in the southern channel at the middle and bottom layer (Figure 3d). Residual current in the ebb-direction was dominant overall. However, residual current in the flood-direction prevailed within the southern channel. We infer this residual current distribution to have been caused by seawater influx through the deep water.

In Line 2, a slight change in residual current distribution changed when freshwater was discharged (Figure 3e). Residual current in the flood-direction developed within the middle and lower layers in the 400–800 m section when there was no freshwater discharge. In contrast, residual current in the flood-direction developed in the surface and middle layers in the 0–800 m and in the lower layer in the 1600–2000 m section when freshwater discharge was occurring.

In Line 3, a multi-layer structure developed with residual velocity towards the ebb-direction in the surface layer, the flood-direction in the middle layer, and the ebb-direction in the bottom layer when freshwater was discharged (Figure 3f). During freshwater discharge, a two-layer circulation with ebb directed current at the surface layer and flood directed flow at the bottom layer occurred. When discharge stopped, a multi-layer flow with ebb flow at the surface layer, flood flow within the middle layer, and ebb flow at the bottom layer develops.

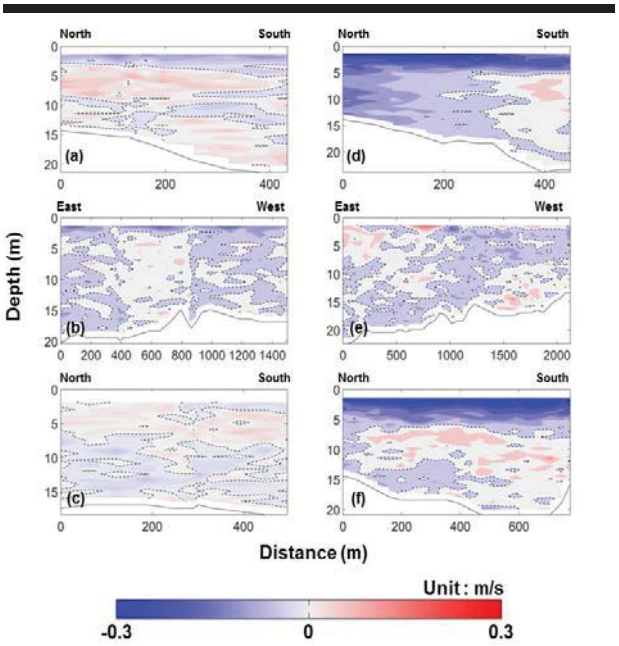

Figure 3. Distribution of residual flow velocity during no-freshwater discharge (a, b, c) and during freshwater discharge (d, e, f) at Line 1, Line 2, Line 3. Negative and positive value indicate ebb and flood direction of residual current, respectively. Dashed contour represents zero velocity.

When freshwater was discharged from the estuary dyke (mainly through Line 3), the environment changed rapidly due to the longitudinal flow velocity. The subsequent multi-layer structure was maintained for about five hours and a multi-layer flow also appeared in the residual current.

During no freshwater discharge, there was no significant vertical difference in the tidal mean salinity distribution (Figures 4a, 4b, and 4c). The mean salinity was approximately 30 psu during no freshwater discharged. Salinity decreased by about 10 psu down to 3 MUS. However, salinity below 3 m remained at approximately 2 psu. In contrast to other transects, the average salinity of the surface layer of the D1–D2 section of Line 3 was approximately 25 psu, and it did not appear in D8 (Figure 4c). The 25 psu salinity distribution occurred in deep water in D1, and we infer that a water mass of relatively low salinity moved through the northern channel.

When water was discharged, a large vertical gradient in tidal mean salinity occurred (Figures 4d, 4e, and 4f). Salinity at the surface layer was 4–5 psu due to the water discharge. However, it changed significantly between 5 and 10 m deep. At the beginning of the water discharge, a salinity distribution greater than 10 psu developed at 1–2 m deep. However, the effect of the freshwater extended down to 4–5 m deep during discharge.

After the discharge, the salinity in the surface layer recovered due to the flood-directional flow. Mean tidal salinity values confirm that salinity changes from water discharge were limited to a maximum depth of 10 m. Mean salinity

below 10 m was approximately 29 psu, which is only 1 psu lower than during no freshwater discharge, suggesting minimal influence from discharge.

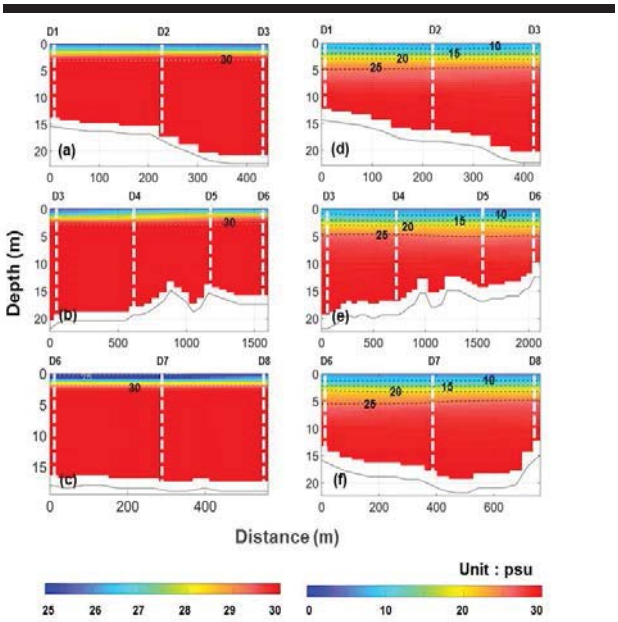

Figure 4. Average salinity across transect in no-freshwater discharge (a, b, c) and freshwater discharge (d, e, f) at Line 1, Line 2, Line 3. A contour of salinity intervals is 5 psu. D1 to D8 (white lines) are the CTD casting stations.

Figure 5 presents the residual volume transport calculation values during no freshwater discharge and freshwater discharge. During no freshwater discharge, the Stokes drift term value was close to 0 m^3/s in Lines 1, 2, and 3 (Figure 5a). The Eulerian transport value was 43 m^3/s and -90 m^3/s in Lines 1 and 2, respectively. Line 3, which was the closest transect to the estuary dyke, had the lowest value of 4 m^3/s. The residual volume transport was towards the interior of Gohado in Line 1, and towards the exterior in Line 2.

During freshwater discharge, the Stokes drift term value was 57 m^3/s, 13 m^3/s, and 55 m^3/s and the Eulerian term was -449 m^3/s, 19 m^3/s, and -563 m^3/s in Lines 1, 2, and 3, respectively, indicating greater values than those of no freshwater discharge (Figure 5b). The volume transport at each transect was directed towards the open sea in Lines 1 and 3 due to the effect of water discharge, and toward the interior of Gohado in Line 2. The magnitude and direction of the Eulerian and the Stokes drift terms, and the channels for seawater exchange, were different between the no discharge and discharge scenarios.

During no freshwater discharge, transport was toward to flood-direction through Line 1 and to ebb-directional through Line 2. Line 3, the closest cross section to the estuary dyke, had virtually no transport. During freshwater discharge, seawater exchange near the estuary dyke occurred through Lines 1 and 3. The freshwater discharged from the estuary dyke was discharged mostly through Line 1, and some volume transport was directed towards Gohado in Line 2.

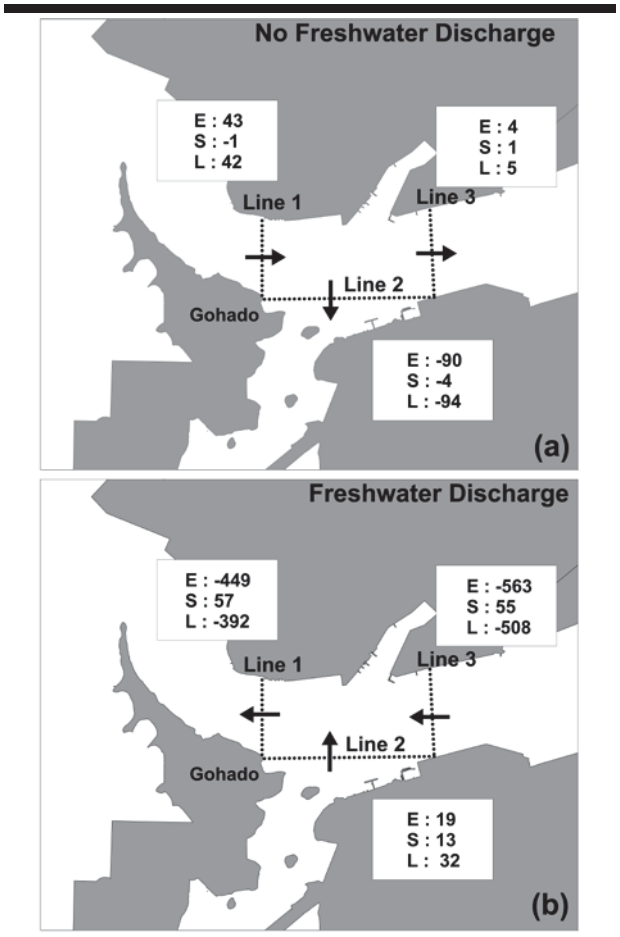

Figure 5. Residual volume transport rates at three cross sections in the no freshwater discharge (a) and freshwater discharge (b). Arrow indicate transport direction, and positive and negative values indeicate flooding and negative directions, respectively.

DISCUSSION

During freshwater discharge, the tidally residual current magnitude was relatively low. Slow residual current was due to the environment being blocked by the dyke, causing a complex tidal residual current structure. In Lines 1 and 3, a two-layer circulation developed with a vertically opposite directional structure. We infer that the effect of the wind was more significant, than that of the tide, due to the semi-closed topography during no freshwater discharge. In Line 2, there was a tidally residual current directed towards the flood-direction from the center of the cross section.

The mean salinity near the estuary dyke during no freshwater discharge was as high as 30 psu. The vertical salinity gradient was relatively low, approximately 3–5 psu. Salinity was usually maintained at approximately 30 psu below 3 m depth.

During freshwater discharge, the tidal residual current varied between the transects. In Line 1, the tidal residual current was in opposite directions in the deep and shallow water areas. In Line 2, the tidal residual current was in the flood-direction on the western surface layer and the eastern bottom layer of the channel, and in the ebb-direction elsewhere. In Line 3, ebb directional flow was dominant in the surface layer, flood directional flow occurred within the middle layer, and ebb directional flow was again dominant in the bottom layer, forming a multi-layer flow structure. These findings are consistent with previous research (*e.g.,* Kim *et al.,* 2013) that indicates a multi-layer residual current after freshwater discharge.

There was a significant vertical salinity difference due to freshwater influx during discharge. However, no significant horizontal salinity difference was observed. Strong freshwater discharge influences vertical mixing at the surface, however, the bottom layer remains unaffected. This causes a salinity gradient with depth and significant stratification.

The total volume transport at the junction of the channel near Gohado was calculated using data obtained by observing the cross-sectional flow velocity during no freshwater discharge and freshwater discharge. During no freshwater discharge, the volume transport ratio of Lines 1:2:3 was 1:2.2:0.1. During freshwater discharge, the ratio was 1:0.1:1.2. Artificial freshwater discharge caused changes in the total volume transport near the dyke. During no freshwater discharge, seawater exchange near the dyke mainly occurred through Lines 1 and 2. In contrast, seawater exchange mainly occurred through Lines 1 and 3 during freshwater discharge.

CONCLUSIONS

The characteristics of tidal residual current and total volume transport vary with freshwater discharge from the dyke at the Yeoungsan River estuary in South Korea. In the absence of freshwater discharge, the impacts of other external forcing (*e.g.,* wind and tide) were dominant, and seawater was exchanged through the channel that is close to the open sea. With freshwater discharge, the impact of the tide and freshwater was clear, and the tidal residual current and total volume transport were both directed towards the open sea. Therefore, we infer that the characteristics of residual volume transport, tidal residual current, and salinity stratification at the Yeoungsan River estuary are dependent on the presence or absence of freshwater discharge from the dyke.

Changes in net volume transport have a major impact on the erosion and transport of sediments and the formation and destruction of tidal flats. However, there are many limitations to identifying the mechanisms of net volume transport and making quantitative calculations. The data used in this study were collected for only a short period of time (13 hours) within the study area. Therefore, in a future study, we plan to identify the residual volume transport mechanism and change per season using a long period simulation in a numerical model.

ACKNOWLEDGMENTS

This research was a part of the project titled ‘Development of integrated estuarine management system’, funded by the Ministry of Oceans and Fisheries, Korea. Additionally, This research was a part of the project titled ‘Manpower training program for ocean energy’, funded by the Ministry of Oceans and Fisheries, Korea.

LITERATURE CITED

Bang, G.Y.; Kim, T.I.; Song, Y.S.; Lee, J.H.; Kim, S.W.; Cho, J.G.; Kim, J.W.; Woo, S.B., and Oh, J.K., 2013. Numerical modeling of sediment transport during the 2011 summer flood in the Youngsan River estuary. *Journal of Korean Society of Coastal and Ocean Engineers,* 25(2), 76-93.

Cho, Y.K.; Park, L.W.; Cho, C.; Lee, I.T.; Park, K.Y., and Oh, C. W., 2004. Multi-layer structure in the Youngsan estuary, Korea. *Estuarine, Coastal and Shelf Science,* 61, 325-329.

Choi, N.Y.; Yoon, B.I.; Kim, J.W.; Song, J.I.; Lim, E.P., and Woo, S.B., 2012. The relation of cross-sectional residual current and stratification during spring and neap tidal cycle at Seokmo channel, Han River estuary located at South Korea. *Journal of Korean Society of Coastal and Ocean Engineers,* 24(3), 149-158.

Joyce, T.M., 1989. On in situ “calibration” of shipboard ADCPs. *Journal of Atmospheric and Oceanic Technology,* 6(1), 169-172.

Kang, J.W., 1998. Analysis of ebb-dominant tidal currents characteristics at Mokpo coastal zone. *Journal of Civil Engineering,* 18, 185-193.

Kang, J.W., 1999. Changes in tidal characteristics as a result of the construction of sea–dike/sea–walls in the Mokpo coastal zone in Korea. *Estuarine, Coastal and Shelf Science*, 48, 429-438.

Kim, J.W.; Yoon, B.I.; Song, J.I.; Lim, C.W., and Woo, S.B., 2013. Spatial and temporal variability of residual current and salinity according to freshwater discharge in Yeoungsan River estuary. *Journal of Korean Society of Coastal and Ocean Engineers,* 25(2), 103-111.

Lee, D.H.; Yoon, B.I.; Kim, J.W.; Gu, B.H., and Woo, S.B., 2012. The cross-sectional mass flux observation at Yeomha channel, Gyeonggi Bay at spring tide during dry and flood season. *Jouranl of Korean Society of Coastal and Ocean Engineers,* 25(1), 16-25.

Lwiza, K.M.M.; Bowers, D.G., and Simpson, J.H., 1991. Residual and tidal flow at a tidal mixing front in the North Sea. *Continental Shelf Research,* 11(11), 1379-1395.

Preisendorfer, R. and Mobley, C., 1988. Theory of fluorescent irradiance fields in natural waters. *Journal of Geophysical Research,* 93(D9), 10831–10855.

Sylaios, G. and Boxall, S.R., 1998. Residual currents and flux estimates in a partially mixed estuary, *Estuarine, Coastal and Shelf Science,* 46, 671-682.

Valle-Levinson, A. and Atkinson, L.P., 1999. Spatial gradients in the flow over an estuarine channel. *Estuaries,* 22(2), 179-193.

Yanagi, T.; Manabu, M.; Nomuram M., and Furukawa, K., 2003. Spring-neap tidal variation of residual flow in Tokyo Bay, Japan. *Continental Shelf Research,* 23, 1087-1097.

Journal of Coastal Research	SI	75	158-162	Coconut Creek, Florida	2016

Effects of Sewage on Natural Environments of the Amazon Region (Pará-Brazil)

Natália S. S. Sousa[†*], Marcela C. Monteiro[‡], Adryane Gorayeb[§], Rauquírio M. Costa[†*], Luci C. C. Pereira[†‡].

[†]Instituto de Estudos Costeiros, Universidade Federal do Pará Bragança, Pará, Brasil

[‡]Laboratori d'Enginyeria Marítima, Universitat Politècnica da Catalunya. Barcelona, Spain

[§]Laboratório de Geoprocessamento, Universidade Federal do Ceará, Fortaleza, Ceará, Brazil

www.cerf-jcr.org

www.JCRonline.org

ABSTRACT

Sousa, N.S.S.; Monteiro. M.C.; Gorayeb, A.; Costa, R.M., and Pereira, L.C.C., 2016. Effects of sewage on natural environments of the Amazon region (Pará-Brazil). *In:* Vila-Concejo, A.; Bruce, E.; Kennedy, D.M., and McCarroll, R.J. (eds.), *Proceedings of the 14th International Coastal Symposium* (Sydney, Australia). *Journal of Coastal Research*, Special Issue, No. 75, pp. 158-162. Coconut Creek (Florida), ISSN 0749-0208.

The negative effects of sewage discharge were analyzed in two Amazonian environments (the Caeté Estuary and the Cereja River) subject to different levels of anthropogenic impact. For this, samples of surface water were collected for the analysis of physical, chemical, and microbiological parameters during dry and wet season. In the Caeté Estuary, the results indicated high levels of total nitrogen and fecal coliforms in the upper sector. Eutrophic conditions were recorded in the wet and dry season. Natural and anthropogenic sources may contribute to the input of dissolved nutrients, maintaining the eutrophic conditions of the estuary. A similar pattern was observed in the Cereja River, with higher concentrations being found in the most urbanized sector, however, these water were mesotrophic. The planning and construction of a public sewage collection system and treatment plant by local authorities will be a key step towards the improvement of the water quality of the Caeté and Cereja rivers.

ADDITIONAL INDEX WORDS: *Anthropogenic influence, trophic index, seasonal and spatial variation*

INTRODUCTION

In the Amazon region, the principal impacts on estuarine environments result from the lack or inefficiency of a public sanitation system. This leads to the discharge of raw wastewater into coastal environments, a process that can be observed in centers with different levels of urbanization, such as São Luís, Salvaterra, and Bragança (Monteiro *et al*., in press; Silva *et al*., 2013).

The present study focused on the Cereja and Caeté rivers in the northeastern Amazon, which encompass two management units created to promote the integral protection and sustainable use of the area, the Cereja River Permanent Protection Area and the Caeté-Taperaçu Marine Extractive Reserve, on the Caeté Estuary. Despite this protection, these areas have become increasingly impacted over the past few decades, due to the unplanned growth of urban settlement in the town of Bragança and adjacent communities.

In this context, the present study investigated the negative impacts of the input of effluents on these environments. For this, physical, chemical, and microbiological factors were analyzed over an annual climatic cycle in areas with high, moderate, and low levels of anthropogenic impact.

STUDY AREA

The study area includes the estuary of the Caeté River and the Cereja River (Figure 1), both located in the northeastern sector of the Brazilin state of Pará. Mean annual precipitation is over 2000 mm, and monthly mean air temperatures are normally between 25°C and 28°C. The region's climate is humid equatorial, with two well-defined seasons, a rainy season that normally lasts from January to June, when 85–90% of annual precipitation is recorded, and a dry (or less rainy) season between July and December (Martorano *et al*., 1993).

The estuary of the Caeté River is dominated by semidiurnal macrotides (between 4 and 6 m) during spring tide periods (DHN, 2015). The Caeté is more than 40 km long, and flows through eight different communities (Maranhãozinho, Fazendinha, Camutá, Vila que Era, Acarajó, Bacurituea, Caratateua and Vila dos Pescadores) and the town of Bragança, which has approximately 117,000 inhabitants (Guimarães *et al*., 2011; IBGE, 2010). More than 90% of these inhabitants live along the margins of the upper estuary.

The Cereja River is 4 km long and discharges into the upper Caeté Estuary. This river crosses the town of Bragança and drains seven neighborhoods (Taíra, Centro, Vila Sinhá, Cereja, Padre Luiz, and Aldeia I and II), which are inhabited by approximately 1500 residents (IBGE, 2010).

The Caeté Estuary and the Cereja River suffer extreme levels of anthropogenic pressure related to the discharge of domestic sewage, as well as effluents derived from commercial and industrial installations, such as hospitals and fish processing plants (Guimarães *et al*., 2009, Monteiro *et al*., in press).

DOI: 10.2112/SI75-032.1 received 15 October 2015; accepted in revision 15 January 2016.

*Corresponding author: nataliasousa89@yahoo.com.br

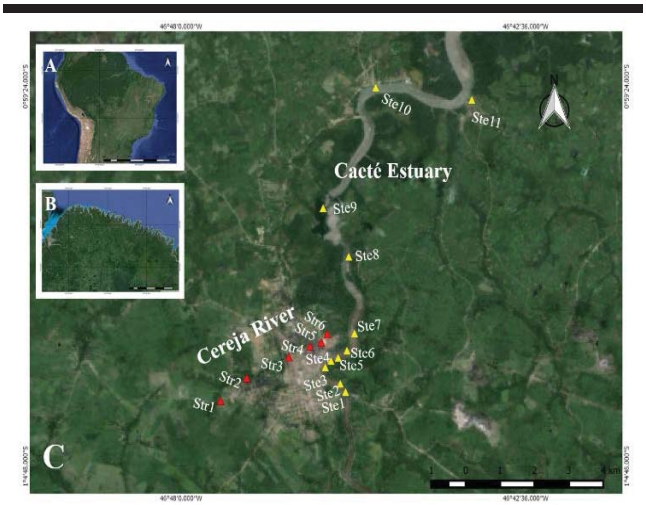

Figure 1. Study Area. Brazil (A), Amazon littoral (B) and sampling stations (C). Stations at Caeté estuary (Ste) and Cereja river (Str).

METHODS

Rainfall data were provided by the Brazilian Meteorology Institute's (INMET). Data on the discharge of the Caeté River were provided by the Brazilian Water Agency (ANA).

For the analysis of physical, chemical, and microbiological variables, water samples were collected from the Caeté estuary during the flood and ebb phases of the spring tide in October 2013 (dry season) and February 2014 (rainy season). Sampling stations were established in the sectors of highest impact (upper estuary, stations Ste1 to Ste8) and lowest impact (middle estuary, stations Ste9 to Ste11), with a total of 44 samples being collected. On the Cereja River, samples were collected in November 2013 (dry season) and April 2014 (rainy season). Six stations were established, encompassing zones of low impact (headwaters, Str1), moderate (Str2), and elevated impact (Str3 to Str6), with 12 samples being collected in all.

Dissolved and saturated oxygen (DO_2 and DO%, respectively) levels were measured using a bottom-mounted CTDO, which was moored for 5 minutes at each station. For the analysis of dissolved nutrients (Nitrite-NO_2^-, Nitrate-NO_3^-, Ammonium- NH_4^+, Dissolved Inorganic Nitrogen-DIN and Total Nitrogen-TN, Phosphate-PO_4^{-3}, Total Phosphorus-TP, and Silicate-SiO_2), Chlorophyll-*a* (Chl-*a*) and fecal coliforms, samples of the surface water were collected using a Niskin bottle.

In the laboratory, dissolved inorganic nutrient concentrations were determined using the procedure described by Strickland and Parsons (1972) and Grasshoff *et al*. (1983). The sum of the dissolved fractions ($NO_2^- + NO_3^- + NH_4^+$) corresponds to the Dissolved Inorganic Nitrogen (DIN). Total Nitrogen and Total Phosphorus were analyzed by the method of Grasshoff *et al*. (1999), and chlorophyll-*a* was determined using the procedure described by Parsons and Strickland (1963) and UNESCO (1966).

The TRIX trophic index developed by Vollenveider *et al*. (1998) was applied to the data from the Caeté Estuary. This index is based on the following formula: TRIX = ($\log_{10}$[Chl-*a* x |%O_2| x DIN x DIP] + k)/m, where Chl-*a* = the chlorophyll-*a* concentration, in mg m^{-3}, %O_2 = the absolute percentage of saturation of dissolved oxygen [abs | 100 - 0% | = % O_2], DIN = Dissolved Inorganic Nitrogen, in mg m^{-3}, DIP = Dissolved Inorganic Phosphorus, in mg m^{-3}, k = 1.5 and m = 1.2. Water quality is classified on the following scale: 0–4: low eutrophication and high water quality; > 4–5: moderate eutrophication and good water quality; > 5–6: high eutrophication and bad water quality and > 6–10: elevated eutrophication and poor water quality.

For the Cereja River, the TSI index proposed by Carlson (1977) was used modified by Lamparelli (2004), based on the formula TSI (Cl *a*) = 10 (6–((0.92-0.34(ln Chl-*a*))/ln 2)), where Chl-*a* = the chlorophyll-*a* concentration, in mg m^{-3}. In this case, water quality was classified on the following scale: TSI ≤ 47: ultra-oligotrophic; 47 ≤ TSI ≤ 52: oligotrophic; 52 ≤ TSI ≤ 59; mesotrophic; 59 ≤ TSI ≤ 63: eutrophic; 63 ≤ TSI ≤ 69: super-eutrophic, and > 76: hyper-eutrophic. Fecal coliform concentrations were determined following the procedures adopted by the American Public Health Association (2004).

The data were evaluated using the Lilliefors test (Conover, 1971), and non-normal data were log (x+1) transformed to approximate a normal distribution. The homogeneity of the data was then tested to verify seasonal variation, and differences among sampling stations. Variation related to the tidal phase was also assessed in the data from the Caeté. When the data were homogeneous, a one-way ANOVA was applied in the case of the Caeté Estuary, and a *t* test for the data from the Cereja River. When the data were heterogeneous, the non-parametric Mann-Whitney (U) or Kruskal-Wallis (H) procedures were applied. A $p < 0.05$ significance level was considered in all analyses.

RESULTS

Physical, chemical, and microbiological factors are showed below over an annual climatic cycle in areas with high, moderate, and low levels of anthropogenic impact of the Caeté estuary and Cereja River.

Climatology and river discharge

The precipitation data were consistent with two well-defined seasons. The dry season, which lasted from August to December 2013, had a total of 163 mm of rainfall, whereas the rainy season, between February and June 2014 had a total precipitation of 1856 mm. The discharge of the Caeté reached a minimum (mean) of 5 m^3 s^{-1} in the dry season month of November 2013, peaking during the rainy season, reaching a maximum of 94 m^3 s^{-1} (Figure 2).

Water quality of the Caeté Estuary

As no significant variation was found between flood and ebb tide phases, mean values were used. All the variables monitored, except total nitrogen, presented higher concentrations during the dry season. During this period, dissolved oxygen reached 4.5±0.3 mg L^{-1}, with 91% saturation, indicating that the water was saturated. During the rainy season, oxygenation decreased (3.5±0.9 mg L^{-1}), and the water became sub-saturated, at 62% (Figure 3A). There was a significant seasonal difference in oxygen saturation (U = 74.00; p = 0.00).

The maximum values recorded for the inorganic forms of nitrogen were recorded during the dry season: 3.0±0.7 µmol L^{-1}

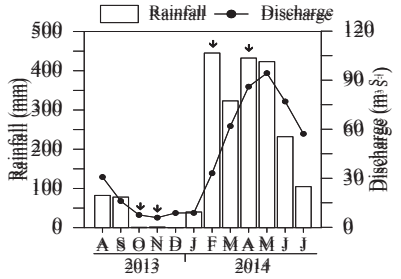

Figure 2. Rainfall and river discharge recorded during the study period. The arrows indicate the months when the data were collected.

for ammonium, 0.9±1.1 µmol L^{-1} for nitrite, and 15.7±3.8 µmol L^{-1} for nitrate (Figure 3B). The most oxidated fractions (nitrate and nitrite) increased towards the middle estuary, as the distance from the sources of contamination – in the upper estuary – increased.

The total nitrogen concentrations were highest during the rainy season (34.5±11.1 µmol L^{-1}), coinciding with the period of highest fluvial discharge (Figure 3C). The highest values were recorded in front of Bragança city (Ste4), where the principal sources of contamination are found (Figure 4B).

Phosphate and total phosphorus reached maximum concentrations of 0.52±0.22 µmol L^{-1} and 0.65±0.25 µmol L^{-1} during dry season (Figure 3C), respectively, with lower values being recorded close to the sources of contamination (Figure 4C). In fact, the values increased at the stations most influenced by sea water (Ste9–Ste11). The same spatial pattern was observed in silicate (Figure 4D), which reached a mean concentration of 75.0±54.4 µmol L^{-1} in the dry season (Figure 3D).

High concentrations of Chl-*a* (7.1±3.4 mg m^{-3}) coincided with the period of greatest availability of DINs (dry season - Figure 3D), the fraction consumed by the phytoplankton. The highest values were once again recorded in front of Bragança city, and at the confluence of the Cereja and Caeté rivers (stations Ste1-Ste6, Figure 4D).

According to the TRIX index, the Caeté Estuary was characterized by poor water quality and elevated eutrophication (score between 6 and 7) in both seasons, with an increase in the index being recorded at the stations closest to the sources of contamination (Ste1–Ste5) and the mouth of the Cereja River (Ste6) (Figure 5). Significant seasonal differences (F = 2.30; p = 0.03) were observed in the coliform concentrations, which were highest during the rainy season, when more than 80% of the samples had values of above 1100 MPN 100 mL^{-1}. The worst conditions prevailed in front of Bragança city and towards the middle estuary (Ste1–Ste8), where 100% of the samples were above 1100 MPN 100 mL^{-1} (Figure 5).

Water quality of the Cereja River

In general terms, the water of the Cereja River were poorly oxygenated, with maximal oxygen concentrations of 3.1±0.9 mg L^{-1} in the rainy season, indicating unsaturated and saturated waters (< 57%) (Figure 6A).

The inorganic forms of nitrogen were more concentrated during the rainy season (8.3±2.7 µmol L^{-1} of ammonium, 2.5±2.13 µmol L^{-1} of nitrite and 24.7±12.9 µmol L^{-1} of nitrate) (Figure 6B), when flooding are normally registered and Chl-*a* concentrations are lower. Nitrate was the predominant fraction of the DIN, followed by ammonium. Ammonium increased considerably in the sector most affected by anthropogenic impacts (stations Str3–Str6). Total nitrogen concentrations were highest in the dry season – 42.3±12.7 µmol L^{-1} (Figure 6C) – when rainfall was close to zero.

The dry season was characterized by an increase in the concentrations of phosphate (0.4±0.5 µmol L^{-1}) and total phosphosrus (0.5±0.4 µmol L^{-1}), mainly in the most urbanized zone of the Cereja River, i.e., Str5 and Str6 (Figure 7C). The same pattern was observed in the silicate, which presented an increasing gradient from the headwaters (reduced levels of occupation) to the mouth of the Cereja (densely occupied), with concentrations of up to 182±46.4 µmol L^{-1} (Figure 6D e 7D). In the Str1 concentrations were significant lower than others stations (Str1 and Str3, t = -5.11; p = 0.03; Str1 and Str5, t = -17.8; p = 0.00; Str1 and Str6, t = -5.30; p = 0.00).

The trophic index (TSI) indicated a predominance of mesotrophic waters (scores 55–58), with eutrophic conditions (scores > 59) being found only at Str3, coinciding with the peaks

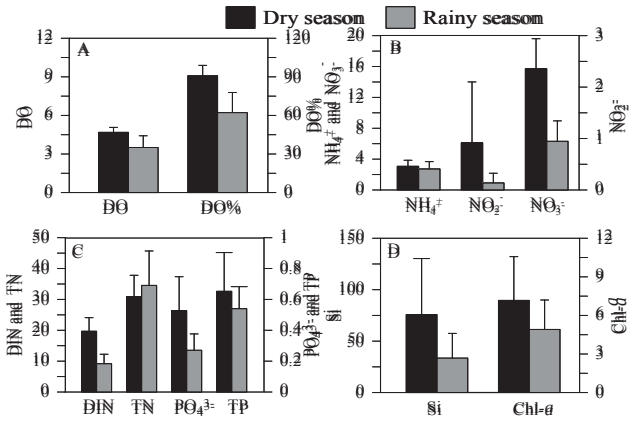

Figure 3. Dissolved (mg L^{-1}) and oxygen saturation (%), chlorophyll-*a* (mg m^{-3}) and dissolved nutrient concentrations (µmol L^{-1}) in the Caeté estuary during dry and rainy season in the Caeté estuary.

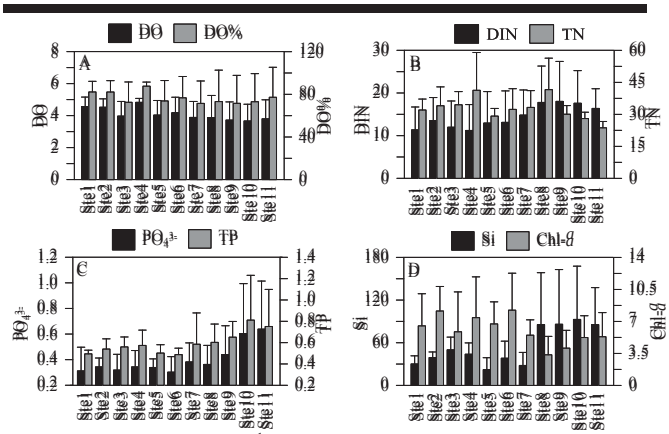

Figure 4. Dissolved (mg L^{-1}) and oxygen saturation (%), chlorophyll-*a* (mg m^{-3}) and dissolved nutrient concentrations (µmol L^{-1}) in the sampling stations of the Caeté estuary.

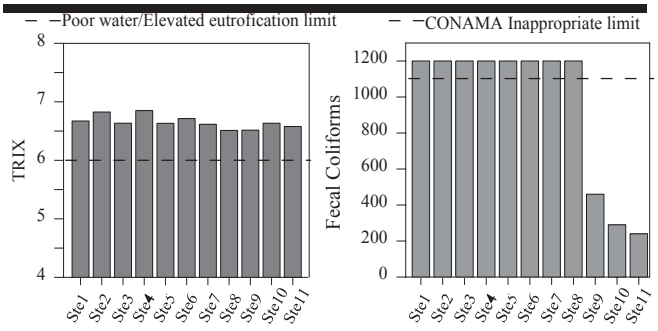

Figure 5. Trophic Index (TRIX) and fecal coliforms in the Caeté estuary.

in the chlorophyll-*a* concentrations (Figure 8). The fecal coliform concentrations recorded in the Cereja were above 1100 MPN 100 mL^{-1} in both seasons at all sampling stations except Str1 (least anthropogenic impact) (Figure 8).

DISCUSSION

Despite the recent population growth in the Bragança region (an increase of 200% between 1940 and 2010), there has been no investment in the consolidation of the urban infrastructure to meet the basic needs of its inhabitants. As a consequence, there is no effective public water supply, sewage system or storm drains, and refuse collection services are irregular and inadequate.

Von Sperling and Chernicharo (2002) and Xia *et al*., (2014) concluded that the discharge of raw or partially treated wastewater into estuaries is the most common source of estuarine pollution. Based on the parameters established by the local bodies of water, such as the Caeté Estuary and the Cereja River. This favors the accumulation of high concentrations of dissolved nutrients and fecal coliforms, as observed in the present study, principally in the most urbanized sectors. However, the high concentrations of inorganic nitrogen ABNT (1982), it is possible to estimate that the population of the region of the Caeté Estuary (117,000 inhabitants) produces approximately 18,000 m^3 of sewage per day. This corresponds to the equivalent of 1 ton of nitrogen and 0.3 tons of phosphorous (Monteiro *et al*., in press), which is discharged daily into the local bodies of water, such as the Caeté Estuary and the Cereja River. This favors the accumulation of high concentrations of dissolved nutrients and fecal coliforms, as observed in the present study, principally in the most urbanized sectors. However, the high concentrations of inorganic nitrogen observed in the least urbanized sector of the Caeté estuary may reflect the natural input from the 180 km² of mangrove forest found adjacent to this estuary (Monteiro *et al*., 2011).

The reduced discharge of the Caeté during the dry season contributed to the increase in the concentrations of inorganic nutrients observed during this period, due to the reduction in the transportation and dilution of the effluents discharged into the estuary (Pereira *et al*., 2010; Monteiro *et al*., 2011). Despite this, the trophic state of the environments monitored during the present study did not appear to be affected significantly by seasonal fluctuations in local conditions. For end, the high concentrations of fecal coliforms recorded in both seasons, principally in the most urbanized sectors of the study area, confirm the negative impact of sewage on the environments monitored.

CONCLUSIONS

The discharge of domestic and industrial effluents into the Caeté and Cereja rivers favors an increase in their trophic state and the bacterial contamination of their waters, principally in the vicinity of the most urbanized areas. In the specific case of the Caeté Estuary, both natural and anthropogenic factors may contribute to the input of dissolved nutrients, and the maintenance of its eutrophic status, irrespective of seasonal fluctuations in local conditions. In the Cereja River, the water was more trophic where anthropogenic conditions were greatest. This river is a source of contamination for the Caeté Estuary. The presence of fecal coliforms also indicates the negative influence of sewage and other effluents, primarily in

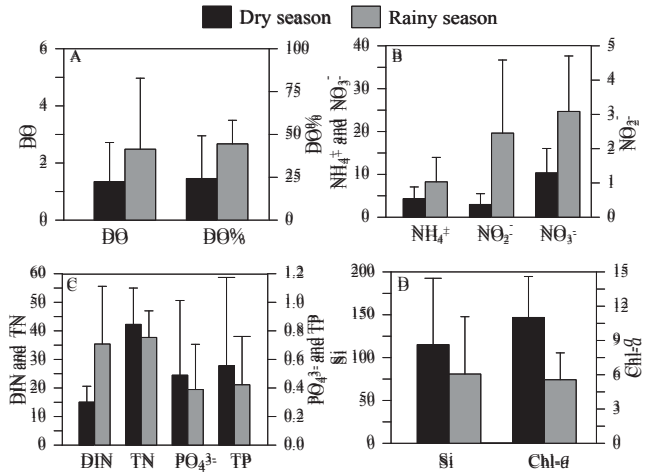

Figure 6. Dissolved (mg L^{-1}) and saturated oxygen (%), chlorophyll-*a* (mg m^{-3}) and dissolved nutrient concentrations (μmol L^{-1}) during dry and rainy season in the Cereja river.

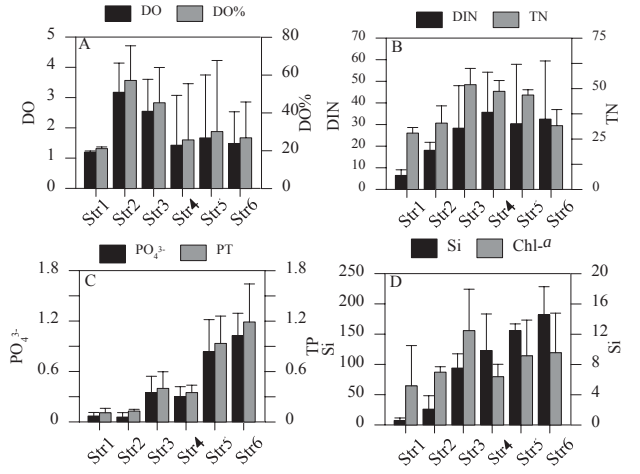

Figure 7. Dissolved (mg L^{-1}) and oxygen saturation (%), chlorophyll-*a* (mg m^{-3}) and dissolved nutrient concentrations (μmol L^{-1}) in the sampling stations of the Cereja river.

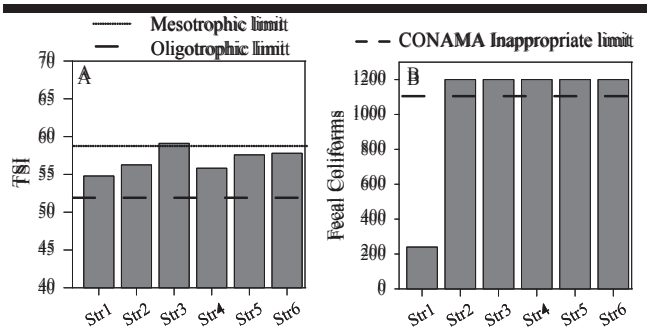

Figure 8. (A) Trophic State Index (TSI) and (B) fecal coliforms in the Cereja river.

the most urbanized areas. The planning and construction of a public sewage collection system and treatment plant by the local authorities will be a key step towards the improvement of the water quality of the Caeté Estuary and the Cereja River.

ACKNOWLEDGMENTS

This research was supported by CNPq (Universal project - 483913/2012-0), CAPES (Ciências do Mar II, Edital 43/2013) and FAPESPA. The authors Sousa N.S.S (131454/2013-7), Pereira L.C.C. (310909/2014-7 and 200629/2014–0) and Costa RM (306061/2011–2 and 200622/2014–5) would also like to thank CNPq for its financial support.

LITERATURE CITED

Associação Brasileira de Normas Técnicas – ABNT. 1982. NBR 7229: *Projeto, construção operação de sistemas de tanques sépticos (Brazilian Association of Technical Standards: Project, construction and operation of septic tank systems).* Rio de Janeiro: ABNT, 15p.

American Public Health Association, 2004. *Standard methods for examination of water and wastewater*. Water Environmental Federation, Washington, D.C.

Carlson, R.E., 1977. A trophic state index for lakes. *Limnology Oceanography*, 22, 361-369.

Conover, W.O.J., 1971. *Pratical nonparametric statistics*. New York: Jonh Wiley, 302 p.

Diretoria de Hidrografia e Navegação – DHN, 2015. http://www.mar.mil.br/dhn/chm/box-previsaomare/tabuas.

Grasshoff, K.; Ehrhardt, M., and Kremling, K., 1999. *Methods of Seawater Analysis.* Wiley-VCH, Weinheim.

Grasshoff, K.; Emrhardy, M., and Kremling, K., 1983 *Methods of Seawater analysis*. New York: VerlagChemie, 419 p.

Guimarães, D.O.; Pereira, L.C.C.; Gorayeb, A., and Costa, R.M., 2011. Exploitation and Management of Natural Resources by Rural Communities in the Caeté River Basin in northern Brazil. *In:* Furmancys, K.; Giza, A., and Terefenko, Pawel. (eds.), *Proceedings, 11th International Coastal Symposium* (Szczecin, Poland). *Journal of Coastal Research*, Special Issue No. 64, pp.1228-1232.

Guimarães, D.O; Pereira, L.C.C.; Monteiro, M.C.; Gorayeb, A., and Costa, R. M., 2009. Effects of urban development on the Cereja river and Caeté estuary (Amazon Coast, Brazil). *In:* Silva, C.P.; Vaz, B.; Abrantes, P., and Estanqueiro, R. (eds.), *Proceedings, 10th International Coastal Symposium (Lisboa, Portugal). Journal of Coastal Research*, Special Issue No. 56, pp. 1219-1223.

IBGE - Instituto Brasileiro de Geografia e Estatística, 2010, www.ibge.gov.br/cidades.

Lamparelli, M.C., 2004. Grau de Trofia em Corpos D'Água do Estado de São Paulo: Avaliação dos Métodos de Monitoramento. São Paulo: USP, thesis, 238 p.

Martorano, L.G.; Pereira, L.C., and Cezar, E.G.M., and Pereira, I.C.B., 1993. *Estudos climatológicos do estado do Pará, classificação climática (Köppen)* Belém: SUDAM, 53 p.

Monteiro, M.C.; Jimenez, J.A., and Pereira, L.C.C. *In press*. Natural and human controls of water quality of an Amazon estuary (Caeté-PA, Brazil). *Ocean Coastal Management.*

Monteiro, M.C.; Pereira, L.C.C.; Guimarães, D.O.; Costa, R.M.; Souza-Filho, P.W.M.; Vieira, S.R., and Jiménez, J.A., 2011. Influence of natural and anthropogenic conditions on the water quality of the Caeté river estuary (North Brazil). *In:* Furmancys, K.; Giza, A., and Terefenko, Pawel. (eds.), *Proceedings, 11th International Coastal Symposium* (Szczecin, Poland). *Journal of Coastal Research*, Special Issue No. 64, pp.1535-1539.

Parsons, T.R.A. and Strickland, J.D.H., 1963. Discussion of spectrophotometric determination of marine-plant pigments, with revised equations for ascertaining chlorophylls and carotenoids. *Journal of Marine Research*, 21, 155-163.

Pereira, L.C.C.; Monteiro, M. C.; Guimarães, D.O.; Matos, J. B., and Costa, R. M., 2010. Seasonal effects of wastewater to the water quality of the Caeté river estuary, Brazilian Amazon. *Anais da Academia Brasileira de Ciências*, 82 (2), 467-478.

Silva, I.R.; Pereira, L.C.C; Trindade, W.N.; Magalhães, A., and Costa, R.M., 2013. Natural anthropogenic processes on the recreational activities in urban Amazon beaches. *Ocean & Coastal Management*, 76, 75-84.

Strickland, J.D.H. and Parsons, T.R.A., 1972. Manual of sea water analysis. *Bulletin Fisheries Research Board of Canada*, 125, 1-205.

UNESCO. 1966. Monograph on Oceanographic Methodology. *Determination of photosynthetic pigments in sea Water*. United Nations Education, Science and Culture Organization, Paris, 69p.

Vollenweider, R.A.; Giovanardi, F.; Montanari, G., and Rinaldi, A., 1998. Characterization of the tropic conditions of marine coastal waters with spatial reference to the NW Adriatic Sea: proposal for a trophic scale, turbidity and generalized water quality index. *Environmetrics*, 9, 329-357.

Von Sperling, M. and Chernicharo, C.A.L., 2002. Urban wasterwater treatment technologies and the implementation of discharge standards in developing countries. *Urban Water*, 4, 105-114.

Xia, J.; Zhang, Y.; Cheshengzhan, and Ye, A., 2014. Water quality management in China: The Case of the Huai River Basin. *Water Resources Development*, 27 (1), 167-180.

Journal of Coastal Research	SI	75	163-167	Coconut Creek, Florida	2016

The Change of Tidal Characteristics under the Influence of Human Activities in the Yangtze River Estuary

Ya Tan †*, F. Yang †, Danghan Xie †

† College of Harbour, Coastal and Offshore Engineering, Hohai University ,Nanjing, Jiangsu Province, P.R.China,

www.JCRonline.org

ABSTRACT

Tan, Y.; Yang, F.; Xie, D, H, 2016. The Change of Tidal Characteristics under the Influence of Human Activities in the Yangtze Estuary. *In:* Vila-Concejo, A.; Bruce, E.; Kennedy, D.M., and McCarroll, R.J. (eds.), *Proceedings of the 14th International Coastal Symposium* (Sydney, Australia). *Journal of Coastal Research*, Special Issue, No. 75, pp. 163-167. Coconut Creek (Florida), ISSN 0749-0208.

The aim of this study is to understand the change of tidal wave characteristics in the Yangtze River Estuary by human activities. The harmonic analysis results based on measurement shows that the semidiurnal tides are dominant in Yangtze River Estuary. The shallow water constituents are significant. Tidal constituent S_a, which is one of main meteorological tides, is gradually increasing with the increase of upper stream river discharge. The amplitude of S_a is highly correlated to the maximum anomaly discharge value (maximum daily discharge differing from the long term mean). Due to human activities, the changes of the river discharge, the water depth and the shape of the costal line in the Yangtze River cause the change of tidal wave propagation. A 2-D numerical model is established to simulate the evolution of main tidal constituents in the Yangtze Estuary under the influence of human activities.

ADDITIONAL INDEX WORDS: *Yangtze River Estuary, tidal harmonic constant, S_a tide, numerical model*

INTRODUCTION

The Yangtze Estuary surrounded by Shanghai city and Jiangsu province plays a pivotal role in terms of economies, population, and wealth. As the estuarine system locates at the China East Coast and faces the West Pacific, it is also one of the most dynamic estuaries in term of physical and biogeochemical processes in the world. It connects the East China Sea and the Yangtze River, the largest river in China with a length of about 6380 km.

In order to meet the needs of flood control, power generation and the development of navigation, the Three Gorges Project (TGP) for building the bam in the upper reaches of the Yangtze River began in 1994 and has been completed in 2009. The project is divided into three phases, which are phase Ⅰ (1994-1997), phase II (1998-2003), phase III(2003-1999), In this study, we focus on the condition at the end stage of the phase II when the dam was constructed which caused a significant change on the river discharge. The operation of the TGP leads to the change of annual distribution of the water discharge which influences the propagation of tidal wave in the estuary.

Before TGP in 2003, the average anomaly value of discharge is 33000m^3/s from September to October. According to statistics of the anomaly value of daily average discharge and the annual average discharge of the Yangtze River in 1993-2009, the annual maximum value is 39400m^3/s occurring in 1998, the annual minimum is 21800m^3/s in 2006, and after 2003, the average annual value reduces to 25000m^3/s. The daily average anomaly value was a single peak before 2003, but the daily average process consists of multi peaks with maximum value decreased to half after 2003.

The Yangtze Estuary is the large shallow estuary with multiple channels at the eastern coast of China, as shown in Figure 1. Tidal action and river discharge are the major sources of energy for turbulence mixing and the impacts of tidal dynamics can even reach the upper river of 600 km away from the mouth in the Yangtze Estuary. The tide is characterized by the semidiurnal tide in the coastal regions outside the estuary. Besides, the upstream river discharge also plays a significant role in estuarine hydrodynamic environment especially. Although the basic characteristics of tides in the Yangtze Estuary have been studied in recent years, e.g. Song *et al.* (2011) finds that the river discharge increases the tidal level and restrains the tide with the tidal range in the in the North Branch decreasing; Chen *et al*. (2009) concludes that the tidal range distribution and variation along the Yangtze River estuary have remarkable seasonal variations and Lu *et al.* (2015) studies the main tidal constituents (M_2, S_2, K_1 and O_1) distribution in the estuary, as well as the tidal distortion. However, they focus on the short period constituents, which could not represent the large time scale parameters, e.g. S_a in the present study. On the other hand, little attention has been paid on the changes of the spatial-temporal distributions of the tidal constituents, especially the annual tide S_a, which is small in the marine environment but very significant along the Yangtze estuary after TGP. It is significant to establish numerical model to study the evolution of the major tidal constituents in the Yangtze Estuary after TGP.

METHODS

The hourly water levels data in 1996~2008 of TSG, XLJ, YL and WSZ tidal gauges (see Figure 1 for locations) in the

DOI: 10.2112/SI75-033.1 received 15 October 2015; accepted in revision 15 January 2016.
*Corresponding author:tanyachina@yeah.net

Yangtze Estuary were provided by Nation Program on Key Basic Research Project (973 Program, Grant No. 2010CB429000).

At a given location, the water level variation induced by the tides can be expressed in detail as:

$$h(t) = A_0 + \sum_{i=1}^{p} f_i H_i \cos[\sigma_i t + (V_0 + u)_i - g_i] + B \quad (1)$$

in which $h(t)$ is the water level at time t; A_0 is the mean sea level; i is the constituent frequencies; p is the number of constituents; f_i is the nodal amplitude factor; H_i is the amplitude; σ_i is the angular velocity; g_i is the phase lag of ith constituent; $(V_0+u)_i$ is the astronomical argument; and B is the change of water level induced by other dynamic factors and errors. Among these parameters, H_i and g_i are harmonic constants of the ith constituents.

A model of automatic constituent optimization tidal harmonic analysis, in which 306 tidal constituents is chosen is proved to be suitable to calculated the tidal constants for estuarine cases (Zhang *et al*., 2010). The tidal constants at TSG, XLJ, and YL tidal gauges are calculated by this method. The qualified rate of forecast error within ±30cm is more than 90% in table 1, 2 and 3. So the qualified rates indicate that the model is effective enough to simulate the tidal constants in the estuary.

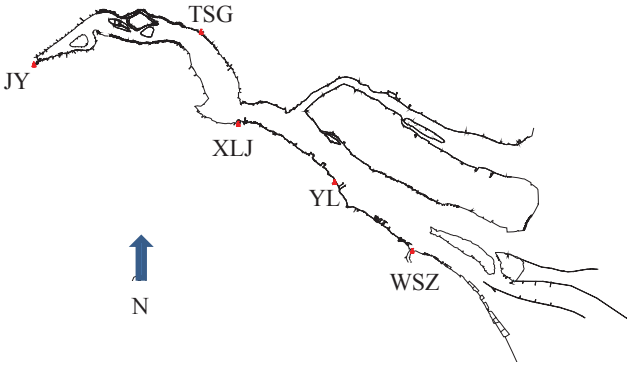

Figure 1. Location of the tidal gauges in the Yangtze River estuary.

Table 1. *Summary of the forecast errors of high, low tidal levels of TSG tidal gauges (Zhang, 2010).*

Error	Qualified Rate
±10cm	48.7%
±20cm	77.3%
±30cm	92.5%

Table 2. *Summary of the forecast errors of high, low tidal levels of XLJ tidal gauges (Zhang, 2010).*

Error	Qualified Rate
±10cm	48.7%
±20cm	76.3%
±30cm	92.4%

Table 3. *Summary of the forecast errors of high, low tidal levels of YL tidal gauges (Zhang, 2010).*

Error	Qualified Rate
±10cm	54.1%
±20cm	83.8%
±30cm	95.6%

Due to study the evolution of the main tidal constituents in the Yangtze Estuary under the influence of human activities, a 2-D numerical tidal current model for the Yangtze Estuary is established by using MIKE21.

Figure 2 shows the model domain of the tidal model of the Yangtze Estuary. The upstream boundary of the model is located at Datong with a distance of 640km from the river mouth. Datong is the tidal limit of the Yangtze Estuary, as the upstream boundary is not affected by the tides. The eastern boundary is located around 122.7ºE, with southern and northern boundaries at 30.9 ºN and 31.8 ºN, respectively.

The triangular mesh is used for the model. The grid size in the Yangtze Estuary is about 200~ 300m, and about 300~1000m in the sea. The whole computing area consists of 70764 grid points, 134723 units; the bathymetry data used in the model is measured by Yangtze River Estuary Hydrology and Water Resources Investigation Bureau.

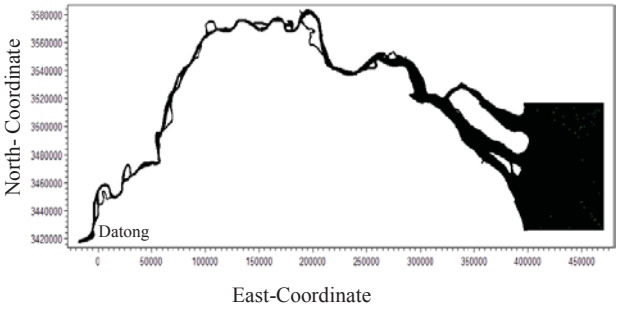

Figure 2. Simulation Domain of the model.

To illustrate the ability of the model to reproduce the transformation of tidal harmonic constituents in the estuary, harmonic constants of eleven major constituents (M_2, S_2, N_2, K_2, K_1, O_1, Q_1, P_1, M_4, MS_4 and S_a) analyzed from the simulated water levels of the whole year in 2000 using the tidal harmonic analysis are compared with those gained observed data at four stations. Figure 3 shows that the difference of amplitudes of tidal constants between simulated and measured values at each station is smaller than 10%, with the difference of phase lag smaller than 10º (as seen in Figure 3). In conclusion, the above parameters indicate that the model is reasonable enough to reproduce the tidal hydrodynamic processes in the estuary.

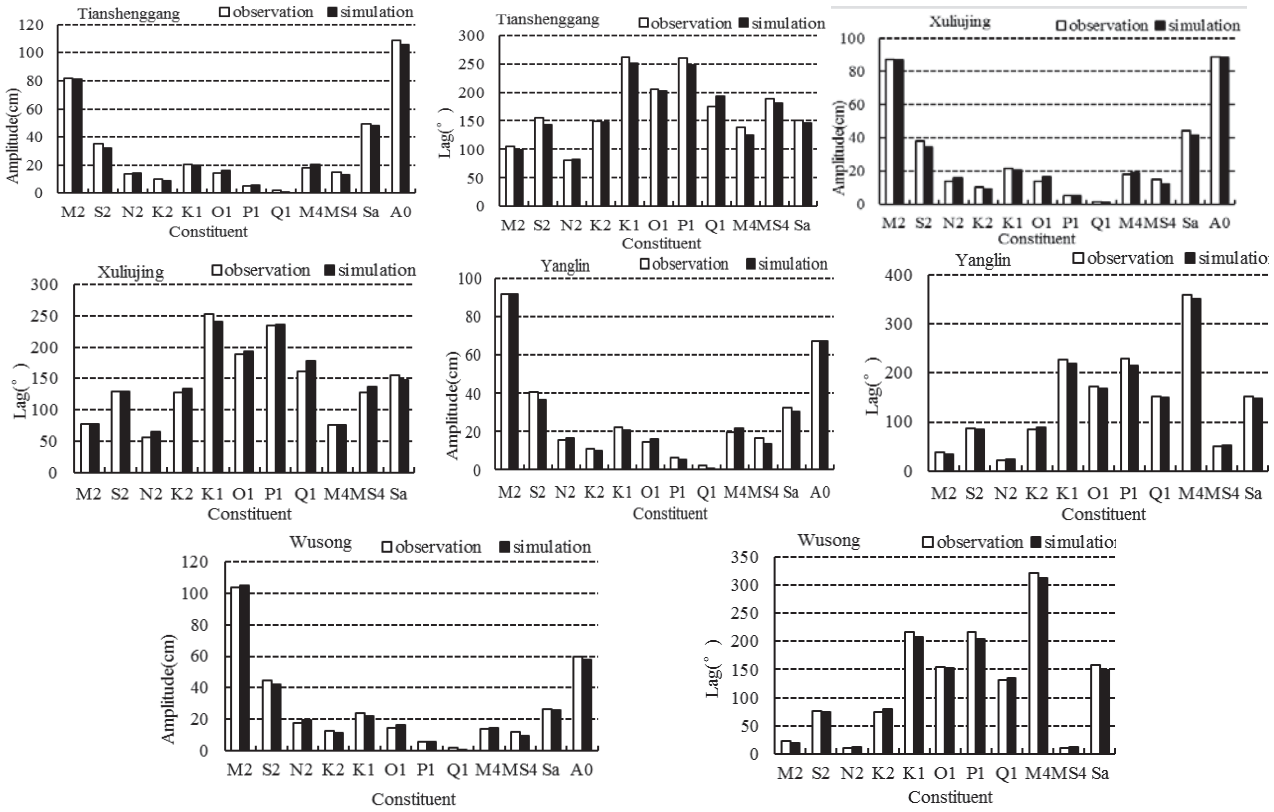

Figure 3. Comparison of the field tidal harmonic constants and the computed tidal harmonic constants by the numerical model in the Yangtze River estuary during 2000.

RESULTS

Tidal harmonic analysis method has been applied to the water level data at four stations during the period from 1997 to 2008.

Table 4 Tidal *harmonic constant t (amplitude A in m and phase G in degree) of ten major tidal constituents at the tide gauges in 2000.*

	TSG		XLJ		YL		WSZ	
Tide	A	G	A	G	A	G	A	G
M_2	0.82	105	0.87	78	0.92	38.8	1.04	23
S_2	0.35	156	0.38	130	0.41	87.3	0.45	76
N_2	0.14	80	0.14	57	0.15	21.3	0.18	10
K_2	0.10	149	0.10	127	0.11	85.1	0.13	74
K_1	0.20	263	0.21	252	0.22	228	23.9	217
O_1	0.14	206	0.14	189	0.14	173	0.15	155
P_1	0.05	260	0.05	234	0.06	229	0.06	216
M_4	0.18	138	0.18	76	0.20	359	0.14	321
MS_4	0.15	188	0.15	128	0.17	50	0.12	10
S_a	0.49	150	0.44	155	0.32	153	0.26	157

Table 4 lists the main tidal constants at those station based on tidal analysis on observation data in 2000 before TGP. It shows that semidiurnal constituents are predominant ones along the Yangtze Estuary. It also can be observed from table 4 that the amplitudes of semidiurnal constituents decrease in landward direction with phase lags increasing. On contrast, the amplitude of S_a increases with its phase lag decreasing.

The results show the change of tidal constituents before and after the TGP. The changes of diurnal constituents, semidiurnal constituents and shallow water constituents are small. The difference of meteorological constituents S_a is significant. Before and after TGP, most main tidal constants are essentially unchanged, which means TGP does not influence diurnal and semidiurnal constants in the Yangtze Estuary.

In order to study the change of S_a in the Yangtze Estuary, the amplitudes of S_a at XLJ, YL and WSZ are compared with the maximum daily anomaly discharge which is the maximum daily discharge by subtracting the long term mean, at Datong in period of 1997-2003. The results are shown in Figure 5. As can be found in Figure 5, the trend of S_a at each station from 1997 to 2003 is similar to that of the maximum daily anomaly discharge at Datong. This reveals that discharge is the main factor causing the change of S_a in the Yangtze Estuary.

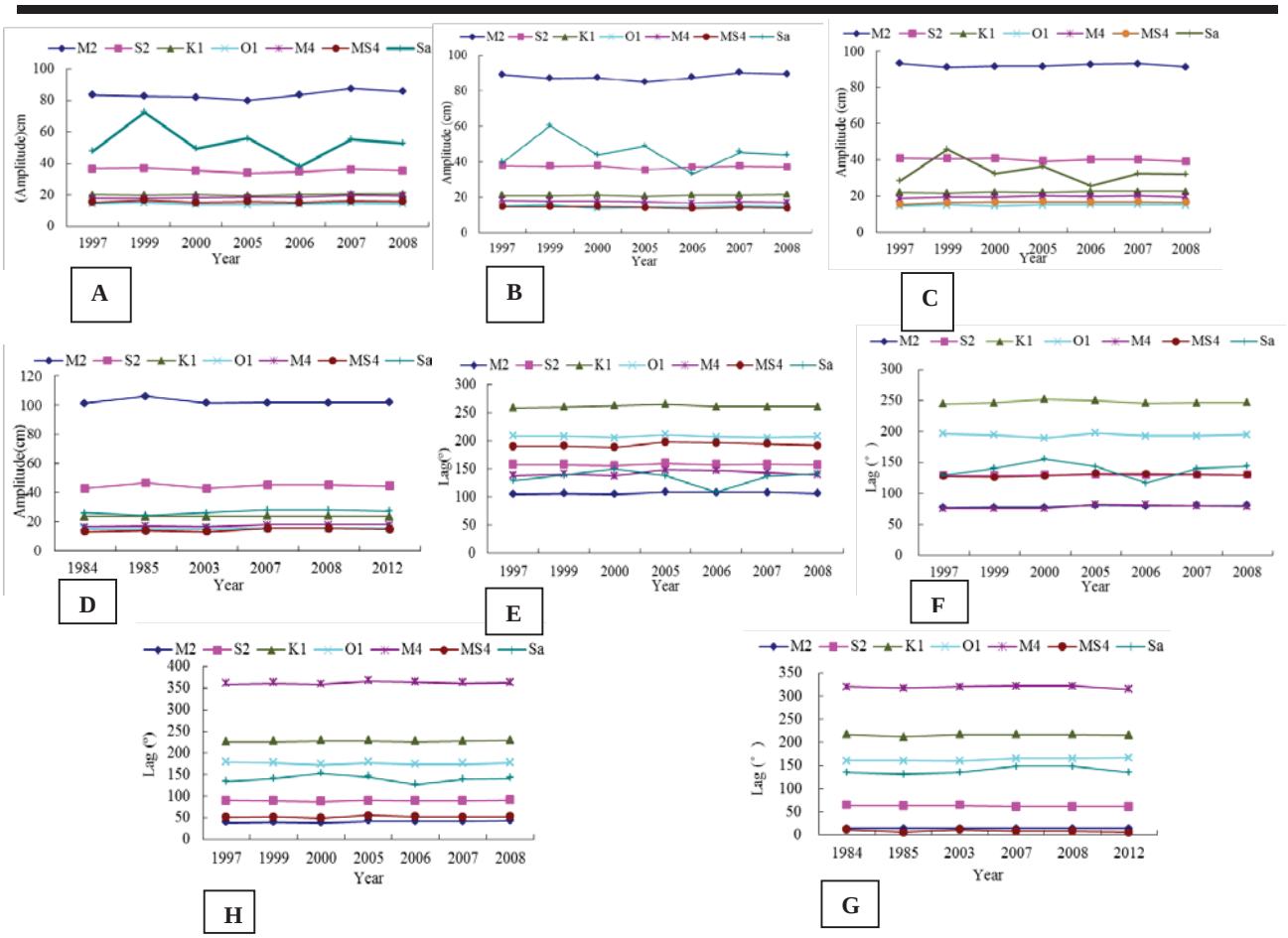

Figure 4. The variations of the seven selected constituent amplitudes and lags (M_2, S_2, K_1, O_1, M_4, MS_4 and S_a) (A-D) the constituent amplitudes of TSG, XLJ, YL and WSZ tidal gauges in the Yangtze River estuary ,(E-H) the constituent lags of TSG, XLJ, YL and WSZ tidal gauge in the Yangtze River estuary.

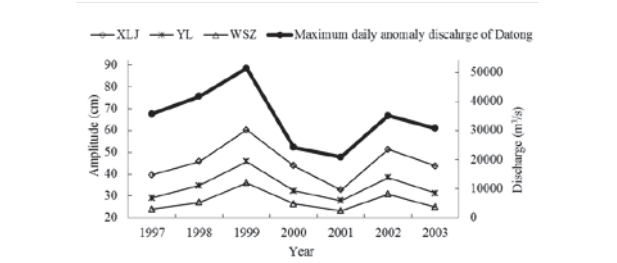

Figure 5. Comparison of the amplitude of constituent Sa and the maximum daily anomaly discharge for 1997-2003.

DISCUSSION

Chen *et al*. (2009), Song *et al.* (2011), and Lu *et al*. (2015) all studied the mjor short period constituents distribution in the estuary which could not represent the large time scale parameters, e.g. S_a, which is very significant along the Yangtze estuary. In addition, the change of discharge from upstream could not be included in their study. In order to analyze the variations of constituent S_a with the change of discharge from upstream in the Yangtze River Estuary after TGP, the numerical model is carried to obtain the amplitude and lag of S_a in the Yangtze Estuary.

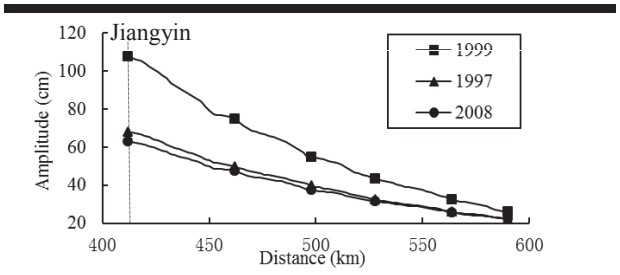

Figure 6. Amplitude distribution of constituent S_a from Jiangyin to the mouth along Yangtze River.

In 1997, the maximum daily anomaly discharge at Datong is 35700m^3/s close to the average daily discharge during the period

of 1993-2002. After TGP, the maximum anomaly discharge at Datong is 22200m^3/s, e.g. in 2008. This value is close to the average discharge from 2003 to 2009. The maximum daily anomaly discharge is the largest in 1999 than those in the other years.

Figure 6 shows the distribution of S_a amplitude along the Yangtze Estuary. It can found that: (1) in 1999 the slope of S_a amplitude is much larger than those in the other years, with an obvious increase in the upper part; (2) After the TGP, the amplitude of S_a is slightly smaller than before.

To further acquaint with the influence of maximum daily anomaly discharge at Datong on the change of S_a along the Yangtze Estuary, two scenarios with different river discharge is designed in present study. In case I the observed daily anomaly discharge of 20000m^3/s is used for the upstream boundary condition. In case II the observed daily anomaly discharge is increased by 1.5 times for the upstream boundary. Figure 7 and 8 show the S_a (amplitude and phase lags) distribution along the estuary based on the simulated results of two cases. From Figure 7 and 8, we can find that the amplitude of Sa increase in case 2 in comparison with case 1, with the phase lags decrease. The difference of S_a amplitude is larger in the upstream than that in downstream. The difference of phase lag between the two scenarios is more or less the same along the estuary.

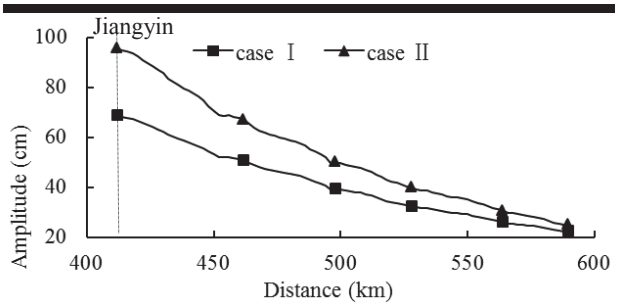

Figure 7. Amplitudes of constituent S_a from Jiangyin to the mouth along Yangtze River under the two cases.

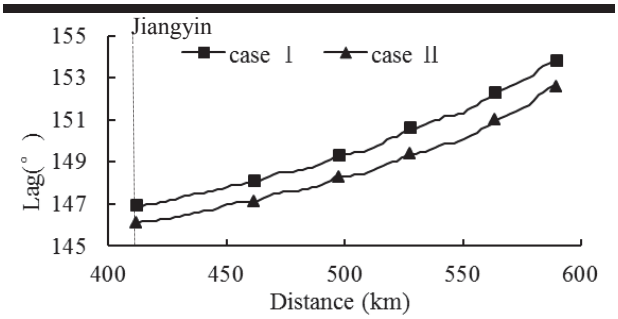

Figure 8. Lags of constituent S_a from Jiangyin to the mouth along Yangtze River under the two cases.

CONCLUSIONS

In this study, tidal harmonic analysis method is utilized to gain an insight into the evolution process of tidal constituents in the Yangtze Estuary before and after the TGP. By comparing the tidal harmonic constants of the major constituents at four selected stations before and after the TGP, it is found that after TGP, the tidal constants of the major diurnal, semidiurnal and shallow water constituents almost remain the same as before; the amplitude of S_a is remarkably similar to that of the maximum daily anomaly discharge from the upstream. After the TGP the amplitudes of S_a are stable along the estuary.

A 2-D numerical model based on MIKE21 has been set up to reproduce the tidal hydrodynamic in the Yangtze Estuary. In this study, two cases with different river discharge are designed to acquaint with the influence of maximum daily anomaly discharge at Datong on the change of S_a. The result shows that when the river discharge increases, the amplitudes of constituent S_a increase rapidly in the estuary with peak amplitude of about 1.0 m, which can go upstream from the coastal zone; on the other hand, the phase lags decrease with almost the same range.

So it can be concluded that TGP does not influence diurnal and semidiurnal constants, and after the TGP, the stably controlled upstream discharge will leads to the less change of the S_a tide in the Yangtze Estuary.

ACKNOWLEDGMENTS

This publication is one of the results of the Nation Program on Key Basic Research Project (973 Program, 2010CB429000).The authors would like to acknowledge the support of National Science and Technology Support Program number of 2013BAB12B05-03.

LITERATURE CITED

Chen, S. L.; Hu, F. X. and Hu, H., 2009, on the natural conditions and program for river-sea delimitation in Yangtze River Estuary, *Journal of Marine Science (supplement)*2, 1-8. (in Chinese)

DHI Group, 2009 MIKE21 & MIKE3 FLOW MODEL FM. *Hydrodynamic and Transport Module Scientific Documentation.*

Lu, S.; Tong, C. F., Lee D. Y., Zheng, J. H., Shen, J., Zhang, W., Yan, Y. X., 2015, Propagation of tidal waves up in Yangtze Estuary during the dry season, *Journal of Geophysical Research*: *Oceans*, DOI:10.1002/2014JC010414, 6445-6473.

Song, Y. G.; Zhu, J. R. and Wu, H, 2011. Spatial and temporal variations and mechanism of the tidal level and range in the North Branch of the Yangtze Estuary. *Journal of East China Normal University (Natural Sc.)*, 6, 10-19. (in Chinese)

Zhang, C. K., 2010, The Prediction and Disaster Assessment Techniques of the coastal Storm Surge. 345p. (in Chinese)

Journal of Coastal Research	SI	75	168-172	Coconut Creek, Florida	2016

The Influence of Urban Effluents on the Elemental C/N Ratio in a Tropical Coastal Area of Northeastern Brazil

Rysoaurya K. Travassos[†*], Manuel J. Flores Montes[†], Bruno V. Motta da Costa[‡], and José Martins da Silva Júnior [§]

[†]Chemical Oceanography Laboratory, Oceanography Department Federal University of Pernambuco Recife, Brazil

[‡] Oceanography Department Federal University of Pernambuco, Recife, Brazil

[§]Institute for Biodiversity Conservation Chico Mendes ICMBio, Brazil

www.cerf-jcr.org

www.JCRonline.org

ABSTRACT

Travassos, R.K.; Flores Montes, M.J.; Costa, B.V. M., and Silva Junior, J.M., 2016. The influence of urban effluents on the elemental C/N ratio in a tropical coastal area of northeastern Brazil. *In*: Vila-Concejo, A.; Bruce, E.; Kennedy, D.M., and McCarroll, R.J. (eds.), *Proceedings of the 14th International Coastal Symposium* (Sydney, Australia). *Journal of Coastal Research*, Special Issue, No. 75, pp. 168-172.Coconut Creek (Florida), ISSN 0749-0208**.**

The present study was performed in a tropical and highly eutrophic estuarine system in the urban coastal area of Greater Recife, Pernambuco, northeastern Brazil. Organic carbon is introduced into these urban estuaries through domestic and industrial sewage waste. One indicator of anthropogenic influence is the concentration of organic matter, including the suspended elemental forms of carbon and total nitrogen and the C/N ratio. The distribution of the concentrations of both particulate organic carbon and total nitrogen (POC and TN, respectively) were studied in two parallel transects in the estuarine plumes of Pernambuco's major rivers, the Capibaribe (CP) and the Jaboatão (JP), from 2010 to 2011. The archipelago of Fernando de Noronha, with relatively little human influence, was selected as the control area. The particulate organic matter exported via estuarine flow was defined by elemental carbon median values of 2.04% and 0.97%. The C/N ratio of the Capibaribe and Jaboatão plumes featured median values of 6.60 and 9.30, respectively. The principal components analysis (PCA) results suggest that the percentage of POC was influenced by rainfall and that the percentage of TN was influenced by the transport of suspended particulate matter. These differences may result from different loads of human activities and estuary transport dynamics, and the coastal region highlightsthe complexity of the distribution of organic matter in these environments.

ADDITIONAL INDEX WORDS: *Elemental Carbon, total Nitrogen, estuarine plume, archipelago*

INTRODUCTION

Estuaries and coastal areas with rapid population growth are the ultimate repository for a vast array of organic substances discharged without treatment. Consequently, changes have occurred in the land-sea interface, damaging marine biodiversity (Thomas *et al*., 2009; Guenther *et al*., 2015). The continental supply of particulate organic matter (POM) to coastal areas includes anthropogenic organic debris and waste transported by rivers. Due to the existence of numerous sources, we conducted a qualitative and quantitative evaluation of POM in a coastal area to determine the predominant source. Because there are many processes that control the transport and remineralization of POM, the source of POM can be determined by quantifying the elemental content (% C, % N, and C/N ratio).

POM represents 50% of the organic export of estuaries to coastal areas, and 35% of this matter is mineralized in the estuaries (Degens and Ittekkot, 1985). Based on elemental content, POM can be characterized as allochthonous (natural or anthropogenic), *i.e.* delivered via estuaries, or autochthonous, *i.e*. associated with primary productivity, in a coastal area (Middelburg Herman., 2007).

The characterization of the source of POM using elemental analysis is based on the structural differences in the organic matter produced by terrestrial and marine primary producers (Meyers, 1994). Given the scarcity of information on the origin of POM in the coastal areas of northeastern Brazil, our aim was to evaluate the spatial and temporal variations in the elemental composition of C and N and the C/N ratio in areas under the direct influence of two urban rivers in Greater Recife. This region has been the main trade center of NE Brazil since the 16th century and considered the 6th most populated area in Brazil (IBGE, 2010).

Background

The continental shelfin the vicinity of Greater Recife is narrow, with an average width of 35 km, and features a sedimentary cover composed of terrigenous and biogenic carbonate sediments (Manso *et al.*, 2003). The inner continental shelf in front of Greater Recife is fertilized with the riverine inputs of the Jaboatão and Capibaribe rivers, which contain high concentrations of nutrients and chl-a (Montes *et al*., 2011). According to the Köppen classification, the climate is humid

DOI: 10.2112/SI75-034.1 received 15 October 2015; accepted in revision 15 January 2016.

*Corresponding author: kkeylatravassos@gmail.com

tropical or type As, with a rainy season between April and August and a dry season between September and March. The average annual rainfall is 2,272 mm, the air temperature is 25.6°C and the relative air humidity is 90% (Torres and Machado, 2011). The coastal waters exhibit small variations in the hydrological conditions, with temperatures of approximately 28°C and salinity values near 35 (Resureição *et al*., 1996). The studied rivers (Figure 1) receive discharges of domestic and industrial effluents from the hydrographical basin (Ribeiro Neto, 2014).

The Capibaribe River basin has a drainage area of 7,557 km^2 and flows through the metropolitan area of Recife (07º41'20" S and 08º19'30" W). The Capibaribe River is 240 km long, has a flow rate of 19 m^{3}s^{-1} and supplies water to a population of approximately 1,328,361 inhabitants (Montes *et al*., 2011).

The Jaboatão River drains an area of approximately 1,022 km² (8º12'30"S - 8º15'0"S and 34º57'30"W - 34°55'0" W) and is used by a population of 1,347,053 inhabitants (CPRH, 2011).

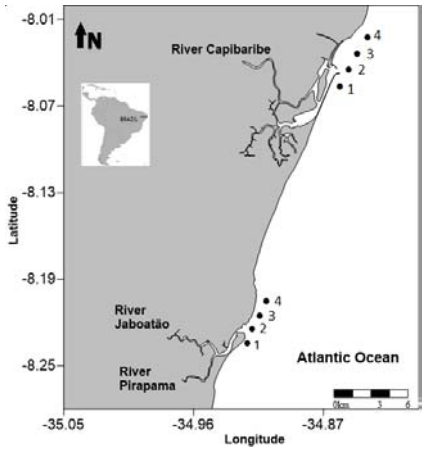

Figure 1. Study site location. The inset shows the state of Pernambuco in Brazil.

The Fernando de Noronha Archipelago (FNA) is located onthe mid-Atlantic ridge (3º50' and 3º52' S and 32°24' and 32°28' W), on the top of a 4,000-m-tall underwater mountain (Batistella, 1993) (Figure 2).

FNA has a tropical climate with two well-defined seasons: a dry season from September to February and a rainy season from March to August. The average annual air temperature is 28ºC, with an air temperature amplitude of 4ºC. The average rainfall in the region is 1,300 mm. Prevailing winds (trade winds) are southeast, especially between June and August (CPRM, 2015), and this area is directly influenced by the South Equatorial Current (SEC).

METHODS

Sampling occurred between May 2010 and September 2011 along a profile parallel to the coastline, always in the slack water of low tide following the direction of the estuarine plume of the rivers Capibaribe (CP) and Jaboatão (JP). The samples were collected at four points spaced 1 km apart, and samples were taken from the sub-surface layer (0.5 m) and 1 m above the bottom (Figure 1).

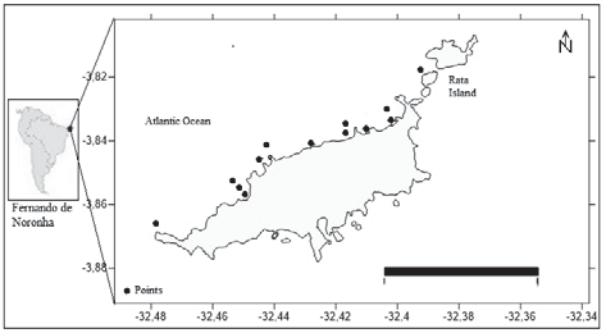

Figure 2. Location of sampling stations in the Fernando de Noronha Archipelago.

In the Fernando de Noronha Archipelago (FNA), sampling occurred in the northwest side (Figure 2).

The water samples were collected with Niskin bottles. Salinity and temperature were measured *in situ* using a SeaBird 19 profiler, and the dissolved oxygen samples were analyzed using the modified Winkler method (Strickland and Parsons, 1972). Suspended particulate matter (SPM) was determined according to Baumgarten *et al*. (1996), and chlorophyll *a*was measured according to the method described in (UNESCO, 1966). Particulate organic carbon (POC) and total nitrogen (TN) were calculated using the method of the U.S. Environmental Protection Agency, described by Zimmerman *et al.* (1997).

To determine POC and NT, the samples were filtered using a vacuum pump in a filtration kit decontaminated with HCl. The filters were Whatman grade GF/F. Before use, they were calcined in a muffle kiln at 450°C to remove any organic residue.

The final filtered volumes were 200-300 mL of water from the plume and 2 L of water from the FNA. The filters were subsequently preserved at a temperature of -20°C until the testing period, when they were thawed and fumigated in a desiccator with HCl for 24 hours. After fumigation, the filters were dried in an oven at 60°C for 24 hours. Two aliquots (measuring 1 cm^2) were removed from the filters, weighed in tin capsules and analyzed in an EuroVector elemental analyzer coupled to a Delta V Advantage isotope ratio mass spectrometer.

RESULTS

The maximum observed rainfall, 755.7 mm, occurred in May 2011. Compared to the average of the last 20 years (1992-2011), during which the average total annual rainfall was 2,232.7 mm, the total rainfall in 2011 (3,245.7 mm) was 45.37% above average. The average DO concentration was similar for both the CP (4.10 mg L^{-1}) and JP (4.36 mg L^{-1}) (Table 1). The SPM in the Capibaribe and Jaboatão plumes was 24.53 mg L^{-1}and17.83 mg L^{-1}, respectively (Table 1). The salinity differed slightly

between the Capibaribe plume (32.33) and the Jaboatão plume (33.22), both categorized as euhaline water. The average concentration of chlorophyll *a* was higher in the CP (3.72 mg m^{-3}) than the JP (2.39 mg m^{-3}). The highest POC percentages were recorded in the CP, where the minimum and maximum percentages of elemental carbon were0.15% and 39.47%, respectively. The minimum and maximum COP percentages in the JP were 0.34% and 6.21%, respectively. The minimum and maximum percentages of TN were 0.08% and 5.20%, respectively, in the CP and 0.07% and 0.64%, respectively, in the JP (Table 1).

The samples collected from the control area in the Fernando de Noronha Archipelago featured minimum and maximum POC percentages of 0.46%and3.69%. The highest value was recorded in December 2010 in the Baía dos Golfinhos, and the second highest POC value,3.37%, was recorded in April 2011 in Biboca beach. These values correlated with the chlorophyll *a* concentrations, which were also higher in the dry season on Biboca beach, with a peak value of 2.61 mg m^{-3}.

Table 1. *Minimum, maximum and mean values of the parameters analyzed in the studied areas.*

	Capibaribe plume		Jaboatão plume	
Parameters	mean	range	mean	range
Photic zone depth (m)	1.85	0.50-6.00	2.52	0.65-6.7
Salinity	32.33	14.27-37.16	33.22	10.77- 38.50
DO mL L^{-1}	4.10	1.73-7.78	4.36	2.26-5.63
SPM mg L^{-1}	24.53	2.80-64.00	17.83	0.80-39.69
%N	0.92	0.08 -5.20	0.28	0.07 -0.64
%C	3.2	0.15-39.47	1.56	0.34 -6.21
C/N	6.37	0.62-27.93	9.17	2.63-12.79
Chl *a* mg m^{-3}	3.72	0.24-19.29	2.39	0.21-9.67

More than 50% of the collected TN samples were below the detection limit, and the minimum and maximum recorded percentages were 0.11% and 0.31% on Ilha Rata and Boldró, respectively. The higher values were observed during the rainy season.

During the sampled period, the average C/N ratio was 6.37, ranging from 0.62 to 27.93 in the CP. The maximum value was measured in front of the inlet that connects the estuarine system to the coastal area. In the JP, the C/N ratio ranged from 2.63 to 12.79, with an average of 9.17 (Table 1). Here, the maximum value was measured north of the plume.

DISCUSSION

The input of organic carbon has been observed in urban estuaries that receive domestic and industrial sewage waste and has been linked to decreased dissolved oxygen levels. In addition to these sources,mangroves and benthic macroscopic autotrophs generate natural debris and other biodetritus (*e.g.*, feces). The studied coastal region is affected by heavily impacted river plumes, as shown by others studies (Montes *et al*., 2011, Paulo *et al*., 2011, Oliveira *et al*., 2014, Guenther *et al.*, 2015).

According to Noriega *et al*. (2013), previous research on the port of Recife and adjacent estuaries has shown that rainfall and the consequent contribution of the tributaries can modify the quality of circulating water and produce temporal and spatial changes in the dynamics of coastal waters and in phytoplankton biomass, as also observed in the present study.

The dissolved oxygen levels were high throughout the area, ranging from unsaturated to oversaturated water, which shows a strong dilution of estuarine waters by marine waters. The river flow increased in the rainy season, consequently increasing the amount of SPM in both the CP and the JP.

The salinity in the CP and JP varied seasonally from mesohaline, influenced by flooding during the rainy season, to euhaline, influenced bya greater evaporation rate in the dry season. According to Noriega *et al*. (2005), in the rainy season, factors such as river discharge, low evaporation and rainfall create a significant vertical gradient, whereas in summer the waters are well mixed and uniformly saline with a higher rate of insolation. Guenther *et al*. (2015) suggested this estuarine system is vertically uniform with flood and ebb currents entering and leaving the system equally through the whole water column (*i.e.*, no thermohaline circulation was established).

The chlorophyll *a* concentration also varied seasonally in the plumes and did not exhibit trends that indicate strong changes in the trophic structure via eutrophication processes.

Seasonally, the percentages of COP were highest during the rainy season in both plumes; however, the maximum values in both plumes were recorded in September 2011. Comparing the two study sites, the highest percentages of elemental carbon were recorded in the CP.

In relation to spatial variation, during the rainy season, the POC percentages in the JP varied significantly ($p<0.05$), which suggests a predominance of autochthonous organic matter.

These higher percentages recorded in the rainy season highlight the importance of the estuary as an exporter of organic matter and nutrients to the coastal area, promoting primary production and, consequently, the food web on the continental shelf of Pernambuco. During this period, an extreme event was recorded: The observed rainfall (547.70 mm)was greater than the historical average (410.60 mm), which increased the river flow, delivering more SPM to the coastal areas. The opposite pattern was observed in the samples collected during the dry season: Low values of elemental carbon were observed atthe sampling sites most distant from the plume outlet, suggesting the presence of allochthonous organic matter. The maximum values obtained in both plumes (Table 1) at the beginning of the dry season indicate the diversity of factors, including climate change and human activities, which influence this distribution. Because the average rainfall during this month was 29.6 mm, which is considered low, the previously transported matter remained in the area and experienced the processes of suspension, deposition and remineralization.

The allochthonous fraction can be diluted, deposited and/or degraded by bacteria until the remineralization process is complete. Under a heavy organic matter load, the dissolved oxygen levels can become depleted. Guenther *et al*. (2015)

reported that the dissolved organic carbon concentrations for the Capibaribe estuary ranged from 475 to 975 μM. Human activities in urban areas also influence the cycle of elements due to the improper use of soil, organic waste dumps and climate change, all of which directly or indirectly influence the cycle and flow of carbon between the mainland and the coastal areas. Unlike the elemental composition of carbon, which can indicate autochthonous production or the export of plant waste material and organic debris to the platform, the elemental signature of organic matter is subject to modification, especially in areas under the influence of anthropogenic sources (Fogel *et al*., 1993)

The suspended material collected on the continental shelf was characterized by low percentages of elemental nitrogen. In approximately 50% of the samples collected, the nitrogen levels were below the detection limits. This indicates that most of the nitrogen could be in the dissolved fraction. This finding is consistent with the nature of the predominant sediments in the port channel, which are moderately siliciclastic with very coarse grains and carbonate values greater than 30% (Oliveira *et al*., 2014). These authors also claim that the nature of the analyzed sediment reflects a high-energy system, resulting in a low rate of organic matter deposition in the lower estuary.

The highest percentages of elemental nitrogen in both plumes were recorded in the rainy season. Total nitrogen in the plume of the Jaboatão River varied little during the studied period, and the percentages found in the JP were lower than the percentages found in the plume of the Capibaribe River.

The samples collected in the FNA showed an interesting contrast between natural sources and anthropogenic activities. This archipelago is a protected area, but tourism is intense year-round. The largest concentrations of organic material were observed at the Baía dos Golfinhos (Dolphin bay) station. This result indicates the importance of natural sources for the cycling of elements because a large group (>500 individuals) of spinner dolphins (*Stenellalongirostris*-Delphinidae) gather at this site every day for resting, mating, feeding, defecation and regurgitation, thus contributing to the influx of allochthonous debris (Silva-Jr *et al*., 2007). In contrast, the high percentages at the Biboca beach station are related to autochthonous sources (high chlorophyll *a* concentrations) and allochthonous sources because Biboca beach receives the wastewater from the FNA treatment plant.

During the rainy season, the surface runoff from the watersheds via estuarine flux did not transport high loads of organic matter to the estuarine plumes based on the low C/N ratios. Therefore, urban effluents (domestic and industrial) represent the major influence on the organic matter cycle. The highest values were found in the dry season, thus corroborating the hypothesized presence of strongly autochthonous particulate matter. The C/N ratios measured in the coastal region of Pernambuco were directly related to the chlorophyll *a* concentrations, especially for the Capibaribe estuary plume, where the maximum value was found in front of the mouth of the estuarine system. In the JP, the maximum C/N ratio value was recorded in the farther station, indicating that remineralization processes are producing inorganic nutrients and CO_2, enhancing the density of primary producers.

The C/N was also observed to increase towards the bottom of the water column, likely due to N assimilation processes, nitrification, decomposition of particulate organic matter in the surface layer, depositional processes, and vertical distribution. This pattern was also observed for POC and TN in other sampling sites.

The lowest C/N ratio values exhibited a negative relationship with the SPM values and a positive relationship with the TN values. These relationships could be the result of increased biological activity and advective processes that caused the resuspension of sediments and a>50% increase in the SPM levels.

In the FNA area, the higher variations in the C/N ratio coincided with the period of lower concentrations of chlorophyll *a*. This correlation does not reveal the sources or origins of the low levels of organic matter at the site because >50% of the samples featured elemental nitrogen levels too low to detect, preventing the calculation of the C/N ratio.

The principal component analysis (PCA) showed more variance for the CP. The first two factors explained relatively little (53.25%) and showed significant variation between the dry and rainy seasons ($p<0.05$).

In the JP, the first two factors explained 72.51%, and the spatial variations (vertical and horizontal) showed significant differences due to both dispersion and remineralization rates.

CONCLUSIONS

The sources of the organic fractions of SPM in the coastal region of Pernambuco are the terrigenous matrix and autochthonous debris, indicating that anthropogenic sources directly and indirectly influence the concentrations of elemental carbon and total nitrogen in these environments.

The results reveal that the distributions of these elements (%C, %N, and the C/N ratio) are highly influenced by the weather conditions, especially in the Capibaribe plume, and the high load of organic and inorganic matter during the rainy season. These results also indicate that human activity has a great influence on the carbon and nitrogen cycles.

The plume of the Jaboatão River had less influence than the plume of the Capibaribe River due to a lower river flow and less SPM.

The variation in POC and TN sources and the indication of the influence of chlorophyll in this ratio show that the organic material is allochthonous and of continental origin and that the high primary production within the estuary is the result of eutrophication processes. Phytoplankton blooms occur in environments with high nutrient loads, forming a source of particulate and dissolved organic material that is subsequently decomposed.

In the FNA, the levels of organic matter are low, and the anthropogenic organic matter differs from natural organic matter, highlighting the importance of studies on these elements. Although low, these values can be used as a reference in the study of organic contamination processes.

The obtained C and N values indicate that there are cause-and-effect relationships present in the coastal area of Pernambuco.

The transport of allochthonous organic matter can induce autochthonous production and cause variations in the OM levels and C/N ratios.

LITERATURE CITED

Batistella, M., 1993. *Cartografia Ecológica do Arquipélago de Fernando de Noronha*. São Paulo, Instituto de Biociências da Universidade de São Paulo, Tese de Mestrado, 236p.

Baumgarten, M.G.Z.; Rocha, J. M. B., and Niencheski, L. F. H., 1996. *Manual de análises em Oceanografia Química*. Rio Grande: Editora da FURG, 132p.

CPRH – *Agencia Estadual de Meio Ambiente e Recursos Hídricos*. 2006 Relatório de monitoramento de bacias hídrográficas do estado de Pernambuco 2011, Recife, available at: http://www.cprh.pe.gov.br

Degens, E.T. and Ittekkot, V., 1985. Particulate organic carbon and overview. In: Degens *et al*. (eds), Transport of Carbon and Minerals in Major WoldRivers.Pt. 3, *Mitt. Geol.-Palãont. Inst.* Univ. Hamburg, SCOPE/UNEP Sonderbd. (in press)

Fogel, M.L. and Cifuentes, L. A., 1993. Isotope fractionation during primary production. In: Engel, M.H., Macko, S.A. (Eds.), *Organic Geochemistry*—Principles and Application. Plenum Press, New York, 73–98.

Guenther, M.; Araújo,M.; Flores-Montes,M.; Gonzalez-Rodriguez, E., and Neumann-Leitão,S., 2015. Eutrophication effects on phytoplankton size-fractioned biomass and production at a tropical estuary. *Marine Pollution Bulletin,* 91, 537–547.

IBGE, *Censo Demográfico* 2010. http://www.censo2010.ibge.gov.br

Manso, V. A. V.; Corrêa, I. C., and Guerra, N.C., 2003. Morfologia e sedimentologia da plataforma continental interna entre as praias de Porto de Galinhas e Campos – Litoral sul de Pernambuco, Brasil. *Pesquisas em Geociências*, Porto Alegre, v.30, n.2, p.17-25.

Meyers, P. A. 1994. Preservation of elemental and isotopic source identification of sedimentary organic matter. *Estuarine Marine Geology*, 114, 289-302.

Middelburg, J.J. and Herman, P. M. J., 2007. Organic matter processing in tidal estuaries. *Marine Chemistry* 106 (1-2), 127–147.

Montes, M.J.F.; Paulo, J.G.; Nascimento-Filho, G.A.; Gaspar, F.L.; Feitosa, F.A.; Santos-Júnior, A.C.; Batista, T.N.F.; Travassos, R.K.; Pitanga, M.E., 2011. The trophic state of an urban estuarine complex in Northeast Brazil. *Journal of Coastal Research*, SI 64 (Proceedings of the 11th International Coastal Symposium), 408–411. Szczecin, Poland, ISSN 0749-0208.

Noriega, C.D.;Muniz, K.;Araujo, M.C.; Travassos, R.K., and Neumann-Leitão, S., 2005. Fluxos de nutrientes inorgânicos dissolvidos em um estuário tropical-Barra das Jangadas-PE, Brasil, *Tropical Oceanography* 33.3,129-139.

Noriega, C.E.D.; Santiago, M. F.; Façanha, P.; Silva-Cunha, M. G. G.; SILVA, R. A.; Flores Montes, M.; Araújo, M.; Costa, K.M.P.; Eskinazi-Leça, E., and Neumann-Leitão, S., 2013. The instantaneous transport of inorganic and organic material in a highly polluted tropical estuary. *Marine and Freshwater Research*, 64(6) 562-572.

Oliveira T.S.; Barcellos R. L.; Schettini- C. A. F., and Camargo P.B., 2014. Modern sedimentary processes and the distribution of organic matter in a tropical estuarine system, Recife, PE, Brazil. *Journal of Integrated Coastal Zone Management*, 14(3):399-411.

Paulo, J. G.: Flores Montes, M.J.; Santos Júnior, A.C.; Batista, T.N.F.; Travassos, R. K.; Nascimento Filho, G.A.; Feitosa, F.A.; Gaspar, F.L., and Pitanga, M.E., 2011. Allochthonous and autochthonous organic matter in an urban tropical estuarine area of northeastern Brazil. *Journal of Coastal Research*, (SI 64), Proceedings of the 11th International Coastal Symposium), 1798-1801. Szczecin, Poland, ISSN 0749-0208.

Resurreição, M. G.; Passavante, J. Z. de O., and MACÊDO, S. J., 1996. Estudo da Plataforma Continental na Área do Recife (Brasil): Variação Sazonal da Biomassa Fitoplanctônica (08º 03' 38" Lat. S; 34º 42' 28" A 34º 52' 00" Long.W). *Trabalhos Oceanográficos da Universidade Federal de Pernambuco.* Recife, v. 24, pp. 39-60.

Ribeiro Neto , A.; Scott C. A.; Lima E. A.; Montenegro S. M. G. L., and Cirilo J. A., 2014. Infrastructure sufficiency in meeting water demand under climate-induced socio-hydrological transition in the urbanizing Capibaribe River basin – Brazil In: *Hydrol. Earth Syst. Sci*., 18, 3449–3459.

Serviço Geológico do Brasil. Companhia de Pesquisas de RecursosMinerais/CPRM,2105.http://www.cprm.gov.br/geoecoturismo/geoparques/noronha/index.php

Silva-Jr, J.M.; Silva, F.J.L.; Sazima, C., and Sazima, I., 2007. Trophic relationships of the spinner dolphin at Fernando de Noronha Archipelago, S.W. *Atlantic. Scientia Marina*, v. 71, p. 505-511.

Strickland, J. D. H. and Parsons, T. R., 1972. A pratical handbook of seawaters analysis. *Bulletin Fisheeries Research* Board of Canada, Ottawa, 167, 207-211.

Torres, F. T. P. and Machado, P. J. O., 2011. *Introdução à Climatologia*. São Paulo: Cengage Learning, 256p.

UNESCO, 1966. *Determination of photosynthetic pigments in sea waters*. Report of SCOR/UNESCO working group 17 with meat from 4 to 6 June 1964. Paris, *Monographys on Oceanology Methodology*. 66 p.

Zimmermann, C. F.; Keefe, C.W., and Basche, J. 1997. Determination of carbon and nitrogen in sediments and particulates of estuarine/coastal waters using elemental analysis. U.S. *Environmental Protection Agency*, Method 440.0, p.9.

Journal of Coastal Research	SI	75	173-177	Coconut Creek, Florida	2016

Application of Terrestrial 3D Laser Scanning to Monitor Changes of Beach Landforms

Hyung-Seok Lee[†], In-Ho Kim[‡ *], and Han-Gwun Kim[††]

[†]Department of Civil and Enviornmrntal Engineering
Hanzhong University
Donghae, Republic of Korea

[‡] Department of Ocean Construction Engineering
Kangwon National University
Samcheok, Republic of Korea

[††]Department. Of Urology, Gangneung Asan Hospital
College of Medicine, Ulsan University
Gangneung, Republic of Korea

www.cerf-jcr.org

www.JCRonline.org

ABSTRACT

Lee, H.S.; Kim, I.H., and Kim, H.G., 2016. Application of terrestrial 3D laser scanning to monitor changes of beach landforms. *In:* Vila-Concejo, A.; Bruce, E.; Kennedy, D.M., and McCarroll, R.J. (eds.), *Proceedings of the 14th International Coastal Symposium* (Sydney, Australia). *Journal of Coastal Research*, Special Issue, No. 75, pp. 173-177. Coconut Creek (Florida), ISSN 0749-0208.

Monitoring changes in the beach morphology of coastal landforms is important when considering coastal management measures. In this paper, to create a changing beach surface, point cloud data of the beach are obtained using three-dimensional (3D) terrestrial laser scanning (TLS), and a beach surface model is analysed based on 3D point data. The 3D point cloud is generated from the scanned beach, including breakwaters, and these points are registered and merged through a reference point (scan origin and ball target) surveyed by RTK-GPS. Noise elements and unnecessary points are eliminated to yield better surface modelling results. Mesh data of the scan point features are created from the integrated points and represent the beach surface of the triangulated irregular network (TIN) model. The 3D modelling of the mesh data enables the user to determine the width, length, and height of breakwater structures through outline extraction and analyse the beach profile. These dimensions of the structure are designed as a 2D plan. It is recommended that the point measurement interval must be dense to create a complete beach surface over a wide area. The approach to TLS appears to provide an efficient means of accurately measuring the beach surface.

ADDITIONAL INDEX WORDS: *Terrestrial laser scanner, point cloud, noise elimination, surface modelling.*

INTRODUCTION

New construction of coastal structures such as breakwaters has caused adjacent beach change and severe damage with beach erosion. Several monitoring methods have been used to investigate and predict the topographic evolution of a beach. Video monitoring has limited accuracy in acquiring high-precision data according to changes at a beach. Light detection and ranging (LIDAR) is used as a powerful tool to secure a large amount of topographic data based on precision measurement technology. LIDAR work and research have been expanded for flood maps, shoreline mapping, monitoring of coastal erosion and accretion (Pe'eri *et al*., 2011). Airborne LIDAR survey was conducted for the analysis of the river delta evolution (Pranzini, 2007). The utility of lidar was applied to derive the canopy height of the coastal dune (Kempeneers *et al*., 2009). LIDAR systems was conducted over a 3-year period to quantify beach morphology, interannual shoreline changes, and morphological evolution of the foreland (Xharde´ *et al*., 2011). Aleman *et al*. (2011) presented a detailed distribution of bar morphologies on the wave dominated sandy coast with LIDAR technology. High resolution digital elevation models (DEMs) derived from LIDAR data was utilized for identifying areas susceptible to flooding byextreme storm (Raji *et al*., 2011). Earlie *et al*. (2013) used airborne LiDAR technology to estimate cliff volume changes in hard rock environments to determine linear retreat rates. Dudzińska-Nowak *et al*. (2013) determined the magnitude and spatial distribution of beach changes based on digital terrain models (DTM) generated from airborne laser scanning (ALS) point clouds.

Providing vast point clouds of the topography, terrestrial laser scanning (TLS) is a contactless method for acquiring data of terrain and man-made constructions (Pandžić *et al*., 2014). TLS was used as a real-time monitoring technique to measure the movement and the detection of a shore model along the coastline (Lee *et al*., 2011). Collins *et al*. (2005) applied the laser scanner to monitor the slope behavior of coastal bluffs. The project was performed to monitor surface and structure changes of glaciers by means of terrestrial laser scanning (Kellerer-Pirklbauer *et al*., 2005). TLS was very convenient for detecting and quantifying slope movements (Kasperski *et al*., 2010). Six repeated terrestrial laser scanner surveys produced 3D point cloud describing cliff relief and were performed to monitor a chalk cliff section (Dewez *et al*., 2013). Montreuil *et al*. (2013) demonstrated the potential of terrestrial laser scanning for

DOI: 10.2112/SI75-035.1 received 15 October 2015; accepted in revision 15 January 2016.
*Corresponding author: kimih@kangwon.ac.kr

identifying small-scale morphological changes in coastal dune fields, essential for relating detected change to evolutionary processes. Meanwhile, continuous measurement using a real time kinematic global positioning system (RTK-GPS) was recommended for beach volume change calculation and 3-D topographic mapping with all-terrain vehicle (ATV) at sand beaches (Lee *et al*., 2013). Beach topographic data acquired with RTK-GPS equipment was used to evaluate different survey strategies and associated accuracy in volume computation (Silveira *et al*., 2013).

We focus on the application of TLS (or High-Definition Surveying) to carry out geometric monitoring by modelling point clouds to beach landforms, including the breakwater, and then extracting the as-built state of the breakwater. We present attentive points in processing the scanned data and describe the possibility of its application in inspection for designed value after construction works.

METHODS

Gungchon Harbor in South Korea was designated as a national harbour in 1991. The 370-m eastern breakwater and 165-m southern breakwater were constructed from 2006 to 2012 (Figure 1B). Gungchon beach has gradually eroded owing to the completion of the adjacent breakwater in 2013. Serious beach retreat has been observed for three years. Interlinking vinyl sacks filled with soil are stacked on the front of the pine grove to stop sand loss and erosion damage (Figure 1E). The beach landform has changed every year as a result of artificial nourishment (Figure 1F) and erosion prevention work. This study focuses on the modelling of the beach landform, an area which contains artificial nourishment, including the breakwater.

A series of processes for monitoring beach changes using TLS is subdivided into a field survey, data processing, and data analysis steps in a workflow shown in Figure 2. Point clouds are saved as X, Y, and Z coordinates. After deleting noise, overlapped scan data are registered to single and available point clouds. The scanning process of this study was carried out by using a Leica ScanStation P20 laser scanner, as shown in Figure 3. This scanner system consists of three main components: a terrestrial laser scanner, ball target, and RTK-GPS surveying set. The scanner enables the fast acquisition of high-quality data with a scan rate up to a maximum range of 120 m (Pandžić *et al*., 2014). Its horizontal and vertical angular accuracy is 8 ", and its 3D point accuracy is 3 mm at 50 m.

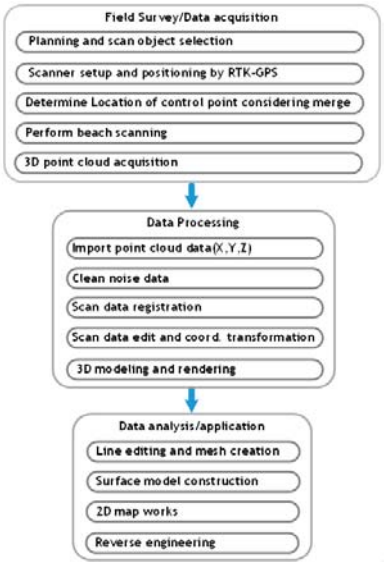

Figure 2. Procedure workflow using TLS.

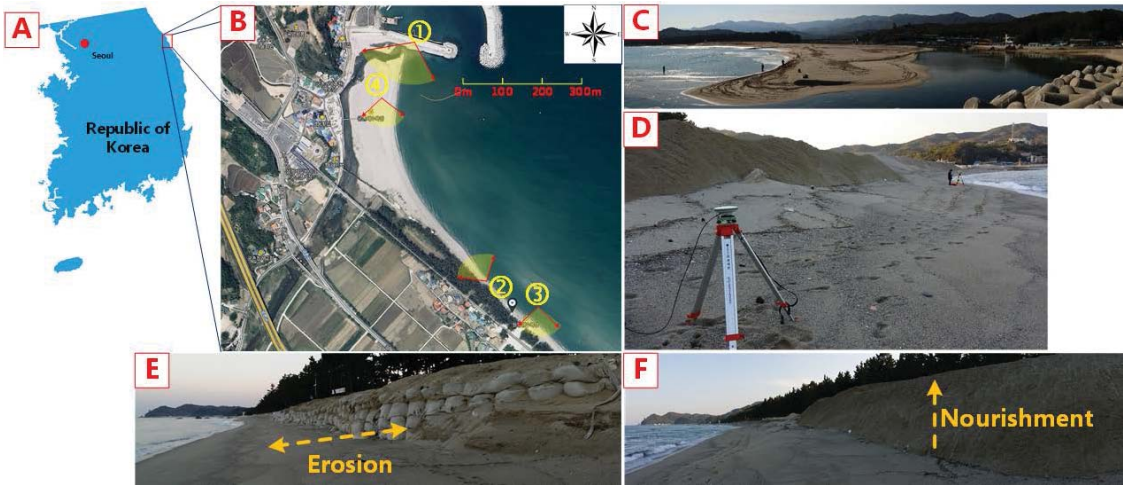

Figure 1. (A) Geographical location of study site. (B) Inset shows portion of Gungchon Beach (Image source: http://map.naver.com). (C) South view as seen from southern breakwater (point ①). (D) North view as seen from point ②. (E) Area as seen from point ③. This area eroded as a result of breakwater construction. (F) Artificial nourishment is working on area ④ to recover the loss of sand (October 14, 2014).

Centring of the scan (i.e. instrument) origin is set on the top of tribrachs above other tripods because the scan origin for the laser scanner setup cannot be located stably in the sand. In other words, the tops of the tribrachs are scan station numbers (Figure 4). We input the measured GPS coordinates (X, Y, and Z) of the centre points placed at the top of tribrachs as the reference point, and set accurate scanner heights by using an instrument height meter. The horizontal accuracy (less than 0.03 m is desirable) of RTK-GPS positioning to the scanner station and the ball target station at this moment are measured between 0.008 m and 0.012 m. The vertical and horizontal accuracy of that is measured between 0.013 m and 0.035 m.

The ball target (Figure 3B) was selected as part of a reference point to register point clouds since the auto registration uses known directions between two points (the scan origin and ball target). The round type of ball target can be collimated without regard to direction. The length between the scan origin and the ball target is 70 m to 80 m. We also measure and input GPS coordinates of the centre point placed on the tribrachs that is under the ball target.

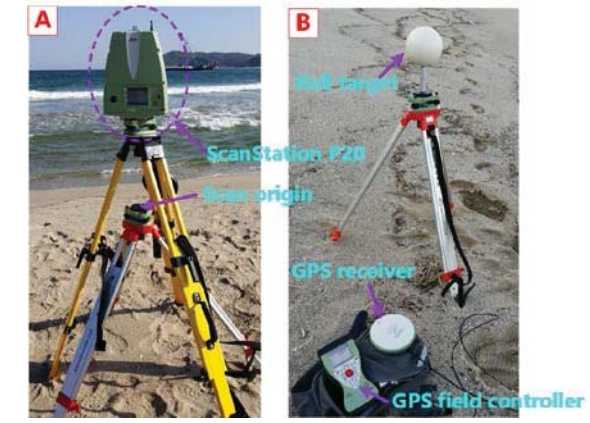

Figure 3. Terrestrial laser scanner setup and ball target setting (A) control point use the centre over the tribrachs, and (B) ball-type TLS control target with coordinates surveyed by RTK-GPS.

Scan ranges are overlapped lengthwise at 10% back and forth. Even if the weather is dark, scan measurement is possible when light beams shine toward the ball target. The work time required was approximately 8 h, from 10:30 a.m. to 6:30 p.m. Figure 4 represents twenty-four scan positions (dots with labels), including the ball target for merging scan data. Scan data are collected from several locations. Raw scan point cloud from different positions must be registered into the same coordinate system. The alignment of these scans is achieved by using ball targets and scan origins that have known coordinates to align the scans together. These coordinates were obtained through RTK-GPS.

The point cloud was seamlessly imported into Leica Cyclone 9.0, which is 3D point-cloud processing software. All noise need to be eliminated for better results in post-processing because problems arise when creating perfect 3D object models. The cleaned-up point cloud was registered through known coordinates surveyed by RTK-GPS. Use of RTK-GPS allows point clouds to be transformed into a georeferenced XYZ coordinate system. All 3D views must be registered in a ground reference system (GRS). The point cloud was changed to the surface by using Cyclone 9.0 and Geomagic Design X to match the alignment of point clouds captured from different scanning positions and to model the 3D point clouds as CAD geometry and meshes. Surface modelling enables point clouds to be created to the surface based on features made by a triangle network method. We drew the shape of the as-built breakwater through surface modelling.

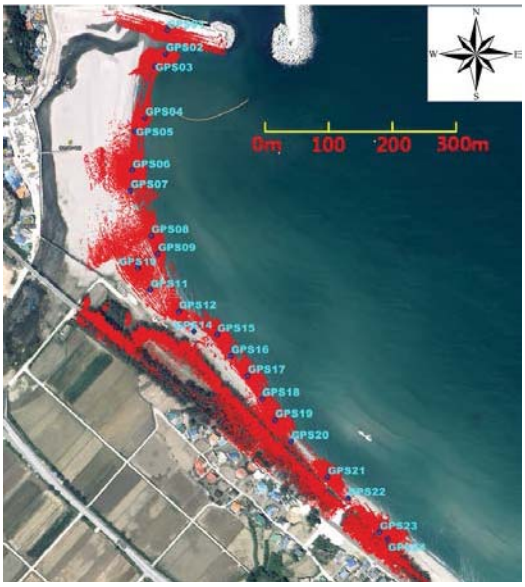

Figure 4. Twenty-four scanner origins spaced based on location of scan setup (including ball target) on an SPOT image (acquisition date: around 2014).

RESULTS

A 3D point cloud was generated from the scanned beach including the breakwater. Figure 5 shows raw data acquired by TLS. Scan points identified terrain in different colours. Noise elements and unnecessary points were deleted for better surface processing results. The scan is so detailed that obstacles can easily be identified, including people, trees, equipment, animals, boxes, and pillars. Obstacles located behind an obstruction to the scanner's line of sight can be eliminated in AutoCAD. Figure 6C and 6D show the point cloud before and after noise elimination.

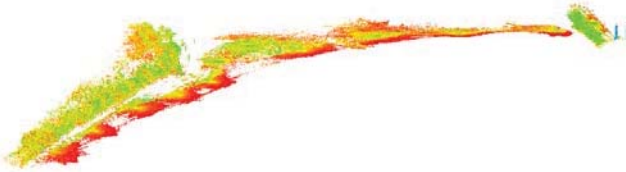

Figure 5. Raw point clouds acquired with terrestrial laser scanner. Colour-rendered point clouds do not indicate differences in elevation.

Mesh data for beach features can be created from the integrated points. Figure 7 shows a fully rendered 3D model of the TIN model. 3D modelling of the mesh data enables the user to check the width, length, and height of the breakwater through outline extraction and to analyse the beach profile. These figures of the breakwater structure are designed to two-dimensional (2D) plan.

To compare this information with a GPS survey, in December 2014 we obtained the point data of this beach by using an RTK-GPS system mounted on an ATV (called the RAS method) (Figure 8B) recommended by Lee *et al*. (2013). Based on the RTK-GPS data, densed point need to be surveyed for precise surface modelling. The outline of the southern breakwater was extracted and drawn to a plan by using Geomagic Design X which is reverse-engineering software. Figure 9 shows a comparison of the edge before and after construction of the breakwater. Compared with the shape of the planned design drawing (Figure 9A), different aspects appeared in the middle of the breakwater in addition to circular and round boundaries.

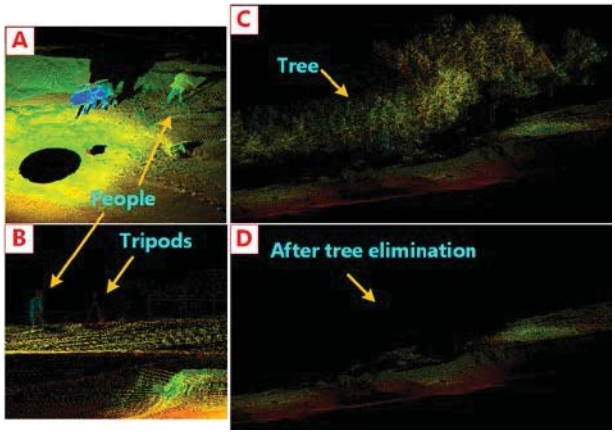

Figure 6. Scan points before and after noise elimination (A) obstructions such as people and equipment (black circles represent scan setup locations), and (B) obstructions such as people and tripods.

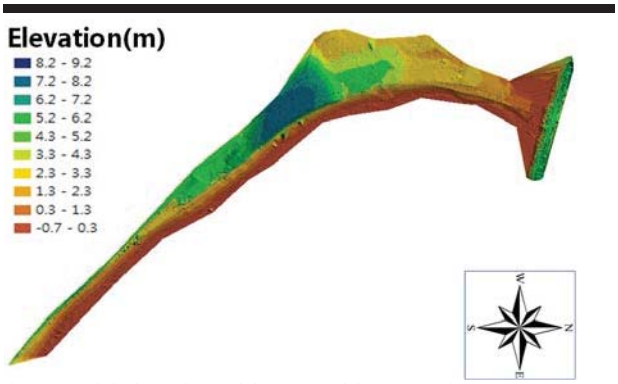

Figure 7. Digital terrain model generated from TLS data.

Figure 8. (A) Point data of continuous measurement using RAS method, and (B) RTK-GPS system mounted on an ATV.

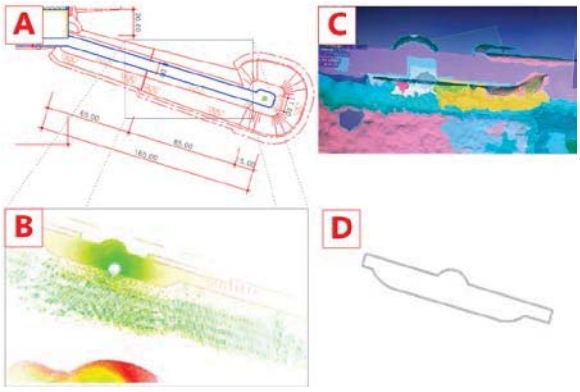

Figure 9. Comparison of as-planned and as-built of the southern breakwater (A) designed data, (B) scan-point data, and (C) 2D drawing plan of as-built.

DISCUSSION

In this paper we have studied a series of procedures for monitoring changes in beach landforms using TLS. If the point intervals are large, it is difficult to model the surface for a drawing plan. Acquisition of densed points was essential to precisely extract the outline of the breakwater or other structures. Point data obtained by the RAS method (Figure 8B) was insufficient to model the beach surface for reverse engineering. Compared with data processing conducted by a geographic information system (GIS), laser scan points enabled surface modelling to create surface interpolation with an add-and-delete function, and it was possible to complete a 2D drawing plan.

CONCLUSIONS

TLS was useful for acquiring morphological data in a small area near a beach. The approach to terrestrial laser scanning

appears to provide an effective technique of accurately measuring the surface for working with an evolving beach. A TLS point cloud can be analysed to assess the evolution of the erosion process when using continuous data accumulation. Furthermore, we can check whether displacement occurs after design and construction by modelling a precise surface of scan points with the process of reverse engineering. When there is no plan or there is an inaccurate design at a coastal site, laser scanning can perform as-built drawing or as-built modelling in its present state.

ACKNOWLEDGMENTS

This study was supported by 2014 Research Grant from Kangwon National University (No. 220140095).

LITERATURE CITED

Aleman, N.; Robin, N.; Certain, R.; Vanroye, C.; Barusseau, J.P., and Bouchette, F., 2011. Typology of nearshore bars in the Gulf of Lions (France) using LIDAR technology. *Journal of Coastal Research*, Special Issue 64, pp. 721–725.

Collins, B., and Sitar, N., 2005. Monitoring of Coastal Bluff Stability Using High Resolution 3D Laser Scanning, Site Characterization and Modeling, *ASCE Proceedings of the GeoFrontiers 2005 Congress*, pp. 1-11.

Dewez, T.J.B.; Rohmer, J.; Regard, V., and Cnudde, C., 2013. Probabilistic coastal cliff collapse hazard from repeated terrestrial laser surveys: case study from Mesnil Val (Normandy, northern France), *Journal of Coastal Research*, Special Issue No. 65, pp. 702-707.

Dudzińska-Nowak, J. and Wężyk, P., 2014. Volumetric changes of a soft cliff coast 2008-2012 based on DTM from airborne laser scanning (Wolin Island, southern Baltic Sea), *Journal of Coastal Research*, Special Issue No.70, pp. 59-64.

Earlie, C.S.; Masselink, G.; Russell, P.A., and Shail, R.K., 2013. Sensitivity analysis of the methodology for quantifying cliff erosion using airborne LiDAR – examples from Cornwall, UK., *Journal of Coastal Research*, Special Issue No. 65, pp. 470-475.

Kasperski, J.; Delacourt, C.; Auemand, P.; Potherat, P.; Jaud, M., and Varrel, E., 2010. Application of a Terrestrial Laser Scanner (TLS) to the Study of the Séchilienne Landslide(Isère, France), *Remote Sensing*, pp. 2785-2802.

Kellerer-Pirklbauer, A.; Bauer, A., and Proske, H., 2005. Terrestrial laser scanning for glacier monitoring: Glaciation changes of the GöBnitzkeesglacier (Schober group, Austria) between 2000 and 2004, *3rd Symposion of the Hohe Tauern National Park for Research in Protected Areas*, Castle of Kaprun, pp. 97-106.

Kempeneers, P.; Deronde, B.; Provoost, S., and Houthuys, R., 2009. Synergy of Airborne Digital Camera and Lidar Data to Map Coastal Dune Vegetation. *Journal of Coastal Research*, Special Issue 53, pp. 73–82.

Lee, H.S.; Lim, S.S., and Park, D.W., 2011. Application of Terrestrial Laser Scanner and Raster operations to Change Detection of Beach. *Journal of Coastal Research*, Special Issue 64, pp. 1692–1696.

Lee, J.M.; Park, J.Y., and Choi, J.Y., 2013. Evaluation of Sub-aerial Topographic Surveying Techniques Using Total Station and RTK-GPS for applications in Macro-tidal Sand Beach Environment, *Journal of Coastal Research*, Special Issue No. 65, pp. 535-540.

Montreuil, A.L.; Bullard, J.E., and Chandler, J.H., 2013. Detecting seasonal variations in embryo dune morphology using a terrestrial laser scanner, *Journal of Coastal Research*, Special Issue No. 65, pp. 1313-1318.

Pandžić, J.; Erić, V.; Božić, B., and Pejić, M., 2014. The Accuracy Analysis of Leica ScanStation P20 Data by Means of Point Cloud Fitting Algorithm, INGEO 2014- *6th International Conference on Engineering Surveying Prague*, Czech republic, pp. 101-106.

Pe'eri, S., and Long, B., 2011. LIDAR technology applied in coastal studies and management, *Applied LIDAR Techniques* (West Palm Beach, Florida), *Journal of Coastal Research*, Special Issue No.62, pp. 1–5.

Pranzini, E., 2007. Airborne LIDAR survey applied to the analysis of historical evolution at the Arno River delta (Italy), *Journal of Coastal Research*, Special Issue 50, pp. 400–409.

Raji, O.; Del Río, L.; Gracia, F.J., and Benavente, J., 2011. The use of LIDAR data for mapping coastal flooding hazard related to storms in Cádiz Bay (SW Spain), *Journal of Coastal Research*, Special Issue No.64, pp. 1881–1885.

Silveira, T.M.; Carapuço, A.M.; Sousa, H.; Taborda, R.; Psuty, N.P.; Andrade, C., and Freitas, C., 2013. Optimizing beach topographic field surveys: matching the effort with the objectives, *Journal of Coastal Research*, Special Issue No. 65, pp. 588-593.

Xharde´, R.; Long, B.F., and Forbes, D.L., 2011. Short-term beach and shoreface evolution on a cuspate foreland observed with airborne topographic and bathymetric LIDAR. *Applied LIDAR Techniques* (West Palm Beach, Florida), *Journal of Coastal Research*, Special Issue No.62, pp. 50–61.

Journal of Coastal Research	SI	75	178-182	Coconut Creek, Florida	2016

Primary production of the benthic microalgae in the bottom sediments of Ria de Aveiro lagoon

Leandro Vaz[†*]., Marcos Mateus[§]., João Serôdio[‡]., João M. Dias[†], and Nuno Vaz[†]

[†]CESAM, Physics Department
University of Aveiro
Aveiro, Portugal

[‡]CESAM, Biology Department
University of Aveiro
Aveiro, Portugal

[§]MARETEC,
Instituto Superior Técnico, Lisbon University
Lisbon, Portugal

www.cerf-jcr.org

www.JCRonline.org

ABSTRACT

Vaz, L.; Sêrodio, J., Mateus, M., Dias, J.M., and Vaz, N., 2016. Primary production of the benthic microalgae in the bottom sediments of Ria de Aveiro Lagoon. *In:* Vila-Concejo, A.; Bruce, E.; Kennedy, D.M., and McCarroll, R.J. (eds.), *Proceedings of the 14th International Coastal Symposium* (Sydney, Australia). *Journal of Coastal Research*, Special Issue, No. 75, pp. 178-182. Coconut Creek (Florida), ISSN 0749-0208.

The Ria de Aveiro is a mesotidal coastal lagoon located in the north coast of Portugal. It has a complex irregular geometry characterized by large intertidal areas and several freshwater tributaries, which are the main sources of nutrients into the lagoon. The dynamics between the tidal propagation and the landward nutrient sources modulates the primary production within the lagoon. Here, primary production may have two main contributors: the chlorophyll in the water column and the benthic microalgae in the bottom sediments.

In this work, a new methodology to compute microalgae in the bottom sediments is presented, consisting in coupling a numerical module of the benthic layer to a biophysical model. To perform the study, three schematic scenarios were implemented: Scenario 1 is the reference case, where typical nutrient load values were considered; Scenario 2 doubles the nutrient load concentrations at ocean and river boundaries; Scenario 3 reduces to half the nutrient values.

The results show that an increase in nutrient load (Scenario 2) causes a reduction of benthic biomass, while a decrease causes an increase of benthic biomass, impacting the lagoon´s primary production. In general, an increment of nutrient concentration in the water column favors the phytoplankton growth, which increases biomass. This will lead to an attenuation of the light intensity reaching the bottom sediments, resulting in a decrease of benthic primary production. The opposite pattern is observed for Scenario 3 in response to nutrient concentration.

ADDITIONAL INDEX WORDS: *Ria de Aveiro, Benthic microalgae, Primary production, Sediments.*

INTRODUCTION

Benthic microalgae as microphytobenthos are important primary producers in estuarine and coastal ecosystems, forming highly dense and productive organisms on the upper layers of the intertidal sediment flats (MacIntyre *et al*., 1996; Underwood and Kromkamp, 1999). A key issue in the assessment of the functional role of these communities is the estimation of the microalgae biomass accumulating in the photic layers of the sediment, which contribute to the rate of ecosystem production (Serôdio *et al*., 2009).

The large microalgae biomass which is present in the photic zone of the bottom sediments (upper layers), is the most important cause for the high production rates observed in intertidal areas, and the main factor determining the community-level photosynthesis on short-term time scales (Serôdio *et al*., 2001).

Estuarine systems, as Ria de Aveiro, in general have 3 main limiting factors affecting the growth of benthic microalgae: (i) nutrients, (ii) light and (iii) water temperature. Nutrients are involved in reactions of photosynthesis, wherein carbon, phosphorus and nitrogen are considered the most important nutrients affecting the growth and mortality of these organisms. The water temperature influences the metabolic rates of organisms and their photosynthetic capacity, while the light is the source of energy used by benthic organisms to generate primary production. In the case of benthic organisms, light availability can be a major limiting factor in the promotion of their growth. Additionally, tidal propagation and estuarine currents are also very important in the benthic communities distribution (Leal *et al*., 2015).

In estuarine systems the study of benthic microalgae spatial and temporal distributions is a highly challenging task, since these systems are extremely variable in terms of nutrient and granulometry spatial distribution. The biophysical models are actual and sophisticated tools that can be used to overcome this challenge and obtain accurate and useful information about benthic microalgae distributions.

The main objective of this study is to present the first results of a novel implementation of MOHID, comprising a coupled circulation and biogeochemical model, including a new module that computes benthic biomass generation (Ascione, 2014). Moreover, a new methodology to simulate the benthic primary production in Ria de Aveiro will be implemented to assess how the model responds to changes in ocean and river forcing's.

DOI: 10.2112/SI75-36.1 received 15 October 2015; accepted in revision 15 January 2016.
*Corresponding author: leandrovaz@ua.pt

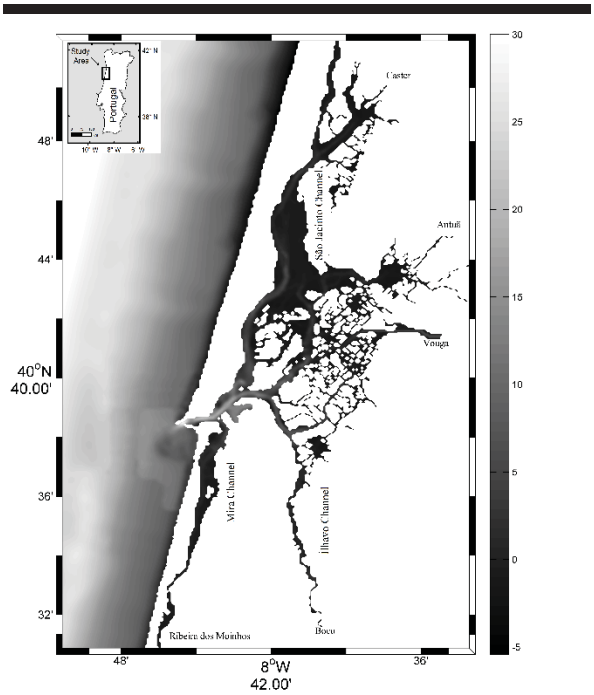

Figure 1. Location of study area, the Ria de Aveiro lagoon, and its bathymetry in meters.

STUDY AREA

The Ria de Aveiro (Figure 1) is a shallow coastal lagoon located in the northwest coast of Portugal, separated from the Atlantic Ocean by a sand dune barrier. It has an irregular geometry, and its only connection with Atlantic Ocean is through an artificial channel constructed in 1808 (Dias, 2001, Dias and Mariano, 2011).

The lagoon has a maximum width of 8.5 km and a length of 45 km, being constituted by four main channels, which act like independent sub-systems, conferring to the lagoon a high complexity in terms of its physical features (Dias, 2001).

The main forcing factor driving water circulation in Ria de Aveiro is the tidal propagation, which has mesotidal characteristics, presenting an average amplitude at the inlet of 2 meters, and amplitudes of 0.6 meters in neap tides and 3.2 meters in spring tides (Dias 2001; Araújo *et al*., 2008). Several authors evaluated the tidal prism for the Ria de Aveiro lagoon through different numerical models (considering different bathymetries), and several values were obtained. For maximum spring tide Dias (2001) and Lopes *et al*. (2006) estimate 136.7×10^6 m^3, Picado *et al*. (2010) 86.3×10^6 m^3 and Lopes *et al*. (2010) 87.5×10^6 m^3 and for minimum neap tide Dias (2001) and Lopes *et al*. (2006) estimated 34.9×10^6 m^3, Picado *et al*. (2010) 31.0×10^6 m^3 and Lopes *et al*. (2010) 28.9×10^6 m^3. These values are much higher than the total freshwater input in a tidal cycle. Moreira *et al*. (1993) projected an input of nearly 1.8×10^6 m^3. The tidal prism of each channel relative to it its value at the mouth is 35.4% for S. Jacinto channel, 25.6% for Espinheiro channel, 10.0% for Mira channel and 13.5% for Ílhavo channel (Dias and Picado, 2011). Likewise, the semidiurnal tides are the main factor influencing the hydrodynamics of the lagoon (Dias *et al*., 2000). Thus, the most important harmonic constituents in Ria de Aveiro are M_2 and S_2, corresponding of about 88% and 10% of total tidal energy, respectively (Dias, 2001).

The lagoon has five main rivers discharging in each main channel: Vouga, Antuã, Cáster, Boco and Ribeira dos Moinhos, being the most important the Vouga river. According with Ria de Aveiro Polis Litoral program, which considered the data present in the Plano de Bacia Hidrográfica (www.arhcentro.pt), the mean freshwater inflows are 60.0 m^{3}s^{-1} for Vouga river, 4.5 m^{3}s^{-1} for Antuã, 1.6 m^{3}s^{-1} for Caster, 1.0 m^{3}s^{-1} for Boco and 3.6 m^{3}s^{-1} for Ribeira dos Moinhos.

According with Fortes *et al*., (2015), the distribution of phytoplankton concentration in the lagoon evidences maximum concentrations located between the second half of the lagoon channels and their heads. On the other hand, the minimum values are observed at the lower channels close to the lagoon mouth as well along the S. Jacinto channel. In the central areas of the lagoon was found a well typified concentration gradient, characterizing the transition between the ocean and the rivers boundaries.

METHODS

In this work, a new methodology to compute microalgae in the bottom sediments is presented, consisting in coupling a numerical module of the benthic layer to a biophysical model (MOHID, www.mohid.com). MOHID solves the three-dimensional incompressible primitive equations. Hydrostatic equilibrium is assumed as well as the Boussinesq and Reynolds approximations. A detailed derivation of the model equations was presented in several studies and can be consulted in Vaz (2007), for example.

The equations for momentum and mass balance are:

$$(1)\ \frac{\partial u_i}{\partial t}+\frac{\partial (u_i u_j)}{\partial x_j}=-\frac{1}{\rho_0}\frac{\partial p_{atm}}{\partial x_i}-g\frac{\rho(\eta)}{\rho_0}\frac{\partial \eta}{\partial x_i}-\frac{g}{\rho_0}\int_{x_3}^{\eta}\frac{\partial \rho'}{\partial x_i}dx_3+\frac{\partial}{\partial x_j}\left(\upsilon\frac{\partial u_i}{\partial x_j}\right)-2\varepsilon_{ijk}\Omega_j u_k$$

$$(2)\ \frac{\partial u_1}{\partial x_1}+\frac{\partial u_2}{\partial x_2}+\frac{\partial u_3}{\partial x_3}=0$$

where u_i are the velocity vector components in the horizontal Cartesian x_i directions, u_j are the velocity vector components in the three Cartesian directions x_j, p_{atm} is the atmospheric pressure and υ is the turbulent viscosity. ρ is the specific mass, ρ' is its anomaly, ρ_0 is the reference specific mass, η is the free surface level, $\rho(\eta)$ represents the specific mass at the free surface, g is the acceleration of gravity, t is the time, Ω is the Earth's velocity of rotation and ε is the alternate tensor. Integrating the mass balance equation over the whole water column (between the free surface elevation and the bottom), is obtained the free surface equation:

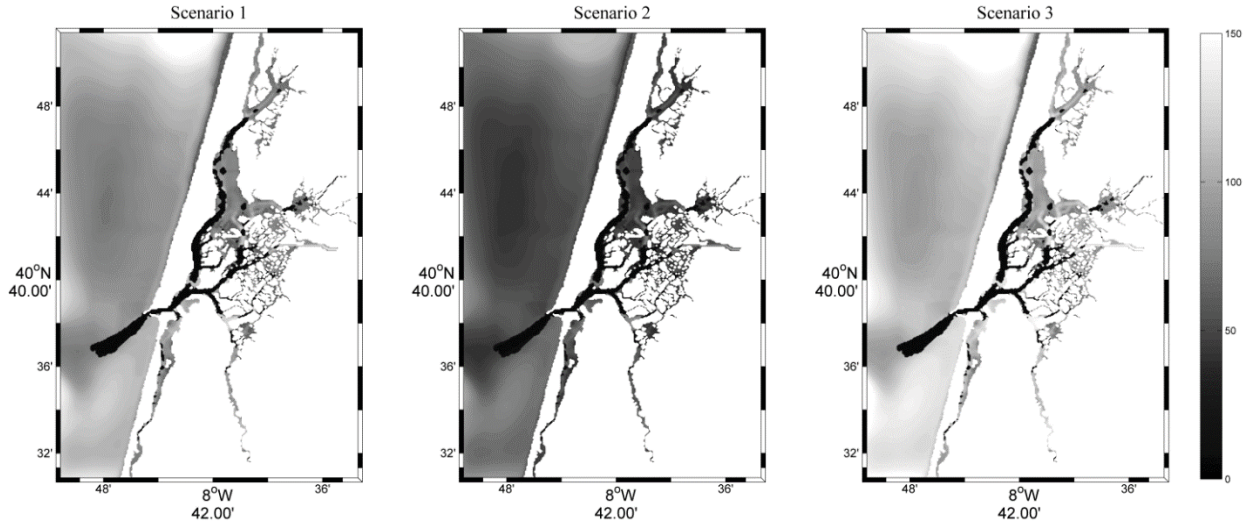

Figure 2. Microalgae concentration for three scenarios, expressed in g(Chl a)/m^2.

$$(3)\ \frac{\partial \eta}{\partial t} = -\frac{\partial}{\partial x_1}\int_{-h}^{\eta} u_1 dx_3 - \frac{\partial}{\partial x_2}\int_{-h}^{\eta} u_2 dx_3$$

where h is water depth.

The bottom shear stress, $\vec{\tau}$, is represented as a quadratic function of velocity and the drag coefficient (C_D) can be parameterized in terms of Manning's friction coefficient (n):

$$(4)\ \vec{\tau} = C_D \left|\vec{V}\right| V$$

$$(5)\ C_D = g n^2 H^{1/3}$$

Where $\vec{V}$ is the horizontal velocity vector and H is the total depth of the water column ($H = h + \eta$).

Beyond the hydrodynamic model, this modeling system comprises the water column ecological model, which calculates the nutrients and primary production in the water column (Mateus *et al*., 2008) coupled with the benthic ecological model, which computes biomass in sediment surface (Ascione, 2014).

A general equation of population growth, which accommodates most of the limiting processes in a closed system, has been formalized:

$$(6)\ \frac{dX_j}{dt} = \sum_{i=1}^{m}(e_{ij}\tau_j p_{ij} f_{ij} X_j) - (\mu_j + \varphi_j + \rho_j)X_j - \sum_{k=1}^{m}(\tau_k p_{jk} f_{jk} X_k)$$

where e_{ij} is the assimilation efficiency of species j using resource i; τ_j is the maximum specific ingestion/uptake rate of species j; p_{ij} is the preference of species j for resource i; f_{ij} is the limitation of ingestion/uptake of resource i by species j; μ_j is the specific loss rate due to natural mortality; φ_j is the specific loss rate due to excretion; ρ_j is the specific loss rate due to respiration.

Model implementation

Disregarding boundary conditions, the bathymetry is the most important factor affecting the flow in systems such as Ria de Aveiro. The bathymetry controls the spatial variability of the current in terms of their magnitude and direction, constituting a specific feature which guarantees the realism of the numerical model (Cheng *et al*., 1991; Dias and Lopes, 2006). The simulations of the Ria de Aveiro model were performed using a rectangular grid with a spatial resolution of 100 meters.

At the ocean boundary, the hydrodynamic model was forced by the tide. At the landward boundaries, freshwater inputs for the 5 main rivers discharging in the Ria de Aveiro (Vouga, Antuã, Boco, Ribeira dos Moinhos and Cáster) are imposed using time series predicted by the SWIM model (Krysanova *et al*., 2000). On the water surface, time series of measured data for relative humidity, atmospheric pressure, air temperature, wind velocity and direction, solar radiation and cloud cover are also applied as atmospheric inputs.

Regarding to the water column and benthic layer modules, the inputs are mainly water temperature, salinity, nutrients, organic matter and pelagic and benthic microalgae. As in hydrodynamic model, all these parameters are imposed at the ocean and river boundaries, and represents typical spring values.

In order to assess the model performance, three schematic scenarios were defined: Scenario 1, considered as reference, where typical spring nutrient load values were considered; Scenario 2 doubles the nutrient load concentrations at ocean and river boundaries; Scenario 3 reduces to half these values.

RESULTS

In Figure 2 are depicted the results for the microalgae benthic biomass in the Ria de Aveiro, for scenarios 1, 2 and 3, respectively. The results are expressed in grams of chlorophyll a per m^2. These results suggest a biomass spatial gradient

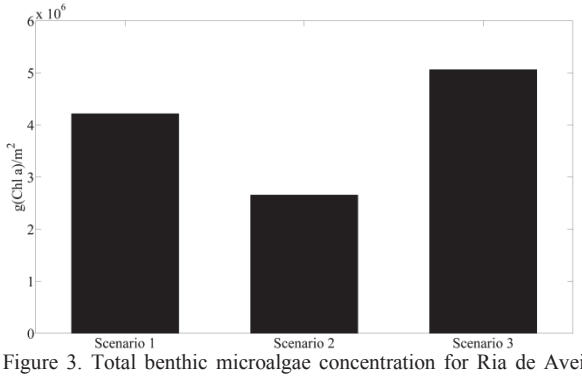

Figure 3. Total benthic microalgae concentration for Ria de Aveiro for each Scenario.

within the lagoon, with very low concentrations near the tidal inlet, with values ranging from 5 to 8 g(Chl a)/m^2, and in the deeper areas of the main canals, increasing gradually until the river mouths (typical values of spring season).

At the inlet, there are no major differences between the three established scenarios, with values of about 6 g(Chl a)/m^2. On the other hand, the areas with the highest benthic biomass concentration are found close to the river mouths. The highest concentrations were identified for all the three scenarios near the Vouga River mouth at the upstream region of the Espinheiro Channel, with values around 88.81, 54.79 and 107.65 g(Chl a)/m^2 for scenarios 1, 2 and 3, respectively. Close to the Antuã river mouth, the concentrations are lower than in the Vouga region, as expected, with values of 73.61 g(Chl a)/m^2, 47.81 and 92.72 g(Chl a)/m^2 in scenarios 1, 2 and 3, respectively. Close to Boco river mouth the values are quite similar, despite the higher inflow from Antuã. The concentrations are 74.90, 52.75 and 92.39 g(Chl a)/m^2 for scenarios 1, 2 and 3, respectively.

At the channels margins, *i.e.* at the intertidal areas, the biomass is much higher than at in the center of the channels (deeper regions), revealing the importance of the incoming radiation in the microalgae growth. For example, this process is clearly evident in S.Jacinto channel. At the channel's axis, the microalgae biomass is about 6 g(Chl a)/m^2 (concentrations similar to those found at the inlet area), while in the intertidal areas the concentrations are 81.15, 48.40 and 100.04 g(Chl a)/m^2 for scenarios 1, 2 and 3, respectively.

DISCUSSION

The results shown in Figure 2 highlight two clearly patterns: a spatial gradient in benthic microalgae concentration, with values increasing gradually from the inlet to the upstream areas of the lagoon; and a negative feedback process, where higher nutrient concentrations in the water column and surface sediment induce a decrease in the benthic biomass.

The highest benthic biomass concentrations are found at the upstream areas of the lagoon, close to the rivers mouths, as the load of nutrients and organic matter in Ria de Aveiro is through the rivers, in particular its main tributary (Vouga river). Additionally, these are shallow areas and therefore the light availability also favors the photosynthesis development.

It is also observed that in the channels margins, i.e. at the intertidal areas, the benthic biomass concentration is much higher than at the center of the channels. In those areas, the light availability is very high and consequently the conditions for photosynthesis development are also favorable.

The main patterns found in this study are consistent with the findings by Fortes *et al.* (2015), and Mateus *et al*., (2008) for the Ria de Aveiro lagoon and the Tagus estuary, respectively.

The comparison between the results obtained for the three scenarios suggests that an increase of pelagic and benthic nutrients and organic matter leads to a decrease of benthic biomass concentration. Figure 3 represents the total benthic biomass for Ria de Aveiro for the three scenarios (determined as the sum of biomass for all cells of the numerical grid), and therefore the total of chlorophyll a concentration at the benthic layer of the Ria de Aveiro.

The total biomass in scenario 1 is 4.22×10^6 g(Chl a), while in Scenarios 2 and 3 the total biomass is 2.68×10^6 and 5.06×10^6 g(Chl a), respectively. The comparison between scenarios 1 and 2 results show that a duplication of total nutrients and organic matter (Scenario 2) causes a decrease of 36.88% on the benthic biomass. Conversely, when reducing to half the nutrient input (Scenarios 1 and 3) is predicted an increase of 19.96% of benthic microalgae. These results reveal that nutrients and organic matter rise has more influence in the system that its reduction. This suggests that the Scenario 2 inputs exceed the consumption by the microorganisms.

According with Hagerthey and Kerfoot (1998), when nutrients are a limiting factor, the benthic primary producers have advantage in a competition between benthic and pelagic microbiota, because they have access to nutrients from the sediments. The access to water column nutrients is restricted for the benthic microalgae due to a boundary through which nutrients slowly penetrate in the benthic layer (Riber and Wetzel, 1987). Therefore, increased nutrient concentrations in the water column typically favour phytoplankton (pelagic), which increase biomass. This obviously causes a reduction in the light intensity reaching the benthic habitat and consequently benthic microalgae growth may become light limited (Havens *et al*., 2001).

CONCLUSIONS

The MOHID modelling system, integrating the hydrodynamic model coupled with the pelagic and benthic ecological models has been used to study primary production of the benthic microalgae in the bottom sediments of Ria de Aveiro lagoon. This modelling tool has been successfully developed and implemented in order to achieve the main goal of this study.

The results show that an increase of nutrient load (Scenario 2) causes a reduction of benthic biomass. An increment of nutrient concentration in the water column favors phytoplankton, which increases biomass. This will lead to an attenuation of the light intensity reaching the bottom sediments, resulting in a decrease of benthic primary production. The opposite pattern is observed for a decrease of nutrient load (Scenario 3).

In summary, the biophysical model was successfully implemented and it is able to reproduce the interactions between water column and bottom sediment.

ACKNOWLEDGEMENTS

This work was been supported by FCT and by European Union (COMPETE, QREN, FEDER) in the framework of the research project PTDC/AAC-AMB/121191/2010 - Biogeochemical Processes induced by Climate and Anthropogenic Circulation Changes: The Case Study of Ria de Aveiro (Portugal) (BioChangeR) as well as through CESAM (UID/AMB/50017/2013).

LITERATURE CITED

Araújo, I., Dias, J.M., Pugh, D., 2008. Model simulations of tidal changes in a coastal lagoon, the Ria de Aveiro (Portugal). *Continental Shelf Research*, 28, 1010-1025.

Ascione, I., 2014. Development and application of a process-oriented model for benthic marine systems. PhD thesis. Lisbon University, Portugal, 200pp.

Cheng, R.T., Burau, J.R., Gartner, J.W., 1991. Interfacing data analysis and numerical modelling for tidal hydrodynamic phenomena. In: Parker, B.B. (Ed.), Tidal Hydrodynamics. John Wiley & Sons, New York, USA, pp. 201–219.

Dias, J. M., 2001. Contribution to the Study of the Ria de Aveiro Hydrodynamics. PhD thesis, University of Aveiro, Portugal, 288 p.

Dias, J.M, Lopes, J.F., 2006. Calibration and Validation of Hydrodynamic, Salt and Heat Transport Models for Ria de Aveiro Lagoon (Portugal). *Journal of Coastal Research*, SI 39, 1680-1684.

Dias, J.M., Mariano, S.C., 2011. Numerical modelling of hydrodynamic changes induced by a jetty extension – the case of Ria de Aveiro (Portugal). *Journal of Coastal Research*, SI64, 1008-1012.

Dias, J.M., Picado, A., 2011. Impact of morphologic anthropogenic and natural changes in estuarine tidal dynamics. *Journal of Coastal Research*, SI 64, 1490-1494.

Dias, J.M., Lopes, J.F., Dekeyser, I., 2000. Tidal propagation in Ria de Aveiro lagoon, Portugal. *Phys Chem Earth (B)*, 25, 369-374.

Hagertey, S., Kerfoot, W., 1998. Groundwater flow influences the biomass and nutrient status of epibenthic algae in a north temperate seepage lake. *Limnology and Oceanography*, 43, 1227-1242.

Havens, K.E., Hauxwell, J., Tyler, A.C., Thomas, S., McGlathery, K.J., Cebrian, J., Valiela, I., Steinman, A.D., Hwang, S.J., 2001. Complex interactions between autotrophs in shallow marine and freshwater ecosystems: implications for community response to nutrient stress. *Environmental pollution*, 113, 95-107.

Krysanova, F. Wechsung, J. Arnold, R. Srinivasan, J. Williams, 2000. PIK Report Nr. 69 SWIM (Soil and Water Integrated Model), User Manual, 239p.

Leal M.C., Jesus B., Ezequiel J., Calado R., Rocha R.J.M., Cartaxana P., Serodio J. (2015) Concurrent imaging of chlorophyll fluorescence, Chlorophyll a content and green fluorescent proteins-like proteins of symbiotic cnidarians. *Marine Ecology-an Evolutionary Perspective*. 36, 3, 572-584.

Lopes, J. F., Dias, J. M., Dekeyser, I. 2006. Numerical modelling of cohesive sediments transport in the Ria de Aveiro lagoon, Portugal. *Journal of Hydrology*, 319, 176-198.

Lopes, J. F., Almeida M. A., Cunha M. A., 2010. Modelling the ecological patterns of a temperate lagoon in a very wet spring season. *Ecological Modelling*, 221, 2302-2322.

Lopes J.F., Vaz N., Vaz L., Ferreira J.A., Dias J.M., 2015. Assessing the state of the lower level of the trophic web of a temperate lagoon, in situations of light or nutrient stress: a modeling study. *Ecological Modelling*. 313, 59-76.

MacIntyre, H. L., Geider, R. J., Miller, D. C., 1996. Microphytobenthos: The ecological role of the "secret garden" of unvegetated, shallow-water marine habitats. I. Distribution, abundance and primary production. Estuaries, 19, 186-201.

Mateus, M., Neves, R., 2008. Evaluating light and nutrient limitation in the Tagus estuary using a process-orientedc ecological model. *Journal of Marine Engineering and Technology*, A12, 43-54.

Moreira, M.H., Queiroga, H., Machado, M.M., Cunha, M. R., 1993. Environmental gradients in a southern estuarine system: Ria de Aveiro, Portugal, implication for soft bottom macrofauna colonization. *Netherland Journal of Aquatic Ecology*, 27 (2-4), 465–482.

Picado, A., Dias J.M., Fortunato, A.B., 2010. Tidal changes in estuarine systems induced by local geomorphologic modifications. *Continental Shelf Research*, 30(17), 1854-1864.

Riber, H., Wetzel., 1987. Boudary-layer and internal difusion effects on phosporous fluxes in lake pheriphyton. Limnology and Oceanography, 32. 1181-1194.

Serôdio, J., Marques da Silva, J., & Catarino, F. (2001). Use of in vivo chlorophyll a fluorescence to quantify short-term variations in the productive biomass of intertidal microphytobenthos. *Marine Ecology Progress Series*, 218, 45−61.

Serôdio, J., Cartaxana, P., Coelho, H., Vieira, S., 2009. Effects of chlorophyll fluorescence on the estimation of microphytobenthos biomass using spectral reflectance indices. Remote Sensing of Environmen, 113, 1760–1768.

Underwood, G. J. C., Kromkamp, J., 1999. Primary production by phytoplankton and microphytobenthos in estuaries. *Advances in Ecological Research*, 29, 93-153.

Vaz, N., 2007. Study of heat and salt transport processes in the Espinheiro Channel (Ria de Aveiro). PhD thesis, University of Aveiro, Portugal, 151 p.

Journal of Coastal Research	SI	75	183-187	Coconut Creek, Florida	2016

The Retention and Transport Patterns of Pollutants in the Radial Sand Ridges of the South Yellow Sea

Jie Yang † and Jianfeng Tao†‡

†College of Harbor, Coastal and Offshore Engineering
Hohai University
Nanjing, P. R. China

‡State Key Laboratory of Hydrology-Water Resources and Hydraulic Engineering
Hohai University
Nanjing, P. R. China

www.cerf-jcr.org

www.JCRonline.org

ABSTRACT

Yang, J. and Tao, J., 2016. The retention and transport patterns of pollutants in the radial sand ridges of the South Yellow Sea. *In:* Vila-Concejo, A.; Bruce, E.; Kennedy, D.M., and McCarroll, R.J. (eds.), *Proceedings of the 14th International Coastal Symposium* (Sydney, Australia). *Journal of Coastal Research*, Special Issue, No. 75, pp. 183-187. Coconut Creek (Florida), ISSN 0749-0208.

The transport and dilution processes of pollutants are complex due to complicated morphology and dynamic factors in the radial sand ridges. The "moving stationary tidal wave" formed by progressive tidal wave from the East China Sea and the anti-clockwise rotary tidal wave from the Yellow Sea, together with the multiple radial tidal channels and flats, make the patterns different for exchange and retention of pollutants. Two retention timescales, the residence time and exposure time, were employed as diagnostic tools to the radial sand ridges, and surface wind was shown to be a significant factor to affect the transport patterns. Meanwhile, Lagrangian particles denoting pollutants were introduced for analyzing their transport trajectories and obtaining the retention timescales. Additionally, the finite-time Lyapunov exponents (FTLE) fields were integrated to locate Lagrangian coherent structures (LCSs). As time evolved, in most of the snapshots obvious longshore LCSs were detected at Xiyang, which is one of the deepest tidal channels and is demonstrated to be an important pathway of mass transport. Furthermore, the tidal channels were shown to have effects on confining the movements of water parcels or pollutants.

ADDITIONAL INDEX WORDS: *Radial sand ridges, adjoint method, Lagrangian coherent structures.*

INTRODUCTION

Sand ridges are characterized by their typical morphological patterns, such as parallel ridges and troughs found usually along shelf seas. Several sand ridges exist in locations along the coast of the Pacific Ocean (Wang *et al.*, 2012), among which the radial sand ridges off the north Jiangsu coast in the South Yellow Sea is unique. In this sand ridges, the ridges and the troughs are aligned parallel to the direction of the tidal current (Figure 1b) and were formed as a result of coactions of tidal current, morphology, river discharges and storm wave processes. These sand ridges fan out for 30-110 km, covering a total area of 22,470 km^2. The water depth generally ranges from 0 to 25 m, with the maximum depth of 50 m in certain parts of the tidal channels (Wang *et al.*, 2012). According to Zhang *et al*. (1999), a "moving stationary tidal wave" is formed by the coaction of anti-clockwise rotary tidal wave to the south of Shandong Peninsula by reflection and the progressive tidal wave from the South Yellow Sea. Moreover, the radial sand ridges can be characterized from convergent radial current field outside Jianggang. Typically, the tide current rises convergently landward and falls divergently seaward in a fan shape. The region is macrotidal with flood tidal range of 4-6m and average current velocity of 2m/s. Semi-diurnal tidal wave dominates the tidal movement and shallow tidal constituents are significant near the offshore and sand ridges (Wang *et al*., 2012).

Due to the complicate morphology and dynamics of the radial sand ridges. The transport properties of water parcels or pollutants are appealing and aroused our interest in them. Generally, the transport of pollutants or marine organisms in natural chaotic water body systems are complex and show uncertainty to some degree. To illustrate, the particles released at close locations at the same time or at a fixed location in small time interval, would all follow different trajectories due to small spatial or temporal perturbations of velocity fields. Thus, the instantaneous Eulerian velocity fields derived from radar data or ocean models are not sufficient to explore and reveal the more underlying transport properties.

The timescales to evaluate the water parcels' or the pollutants' stay in water body have relation with many biological processes, such as transport of fish during their larvae stage and spawning habitat protection problem. Therefore, the related properties of these biological processes are of great concern in environmental issues. With the development of the Constituent Oriented Age and Residence time Theory (CART, Deleersnijder *et al*., 2001; Delhez *et al*., 2004), timescales are proved to be comprehensive and effective in providing an overall picture of the transport patterns. In the current study, both residence time and exposure time have been taken into consideration using adjoint method.

From another point of view, the inherent structures of ocean dynamic systems, which demonstrate long term transport of mass and are based on precise Eulerian velocity fields, could be revealed by dynamical system approaches (Wiggins, 2005). The dynamical systems theory was developed and applied to many fields since the theoretical work by Aref (1984). Related

DOI: 10.2112/SI75-037.1 received 15 October 2015; accepted in revision 15 January 2016.
*Corresponding author: jie_yang@hhu.edu.cn

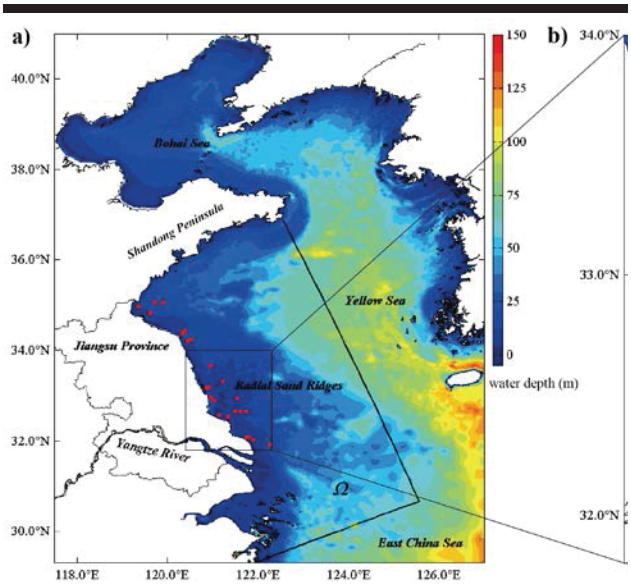

Figure 1. (a) An overview of the study area in the East China Sea. (b) Zoomed view of some main ridges (end with *) and troughs. Ω And Ω_c denote model domain and control domain respectively. The red dots denote in situ stations and squares are sites for analyses.

dynamical system tools are widely used to identify critical material curves that govern transport patterns. The approach for determining approximate transport barriers from the FTLE fields were developed, and the connection between FTLE and LCSs was established (Haller and Yuan, 2000; Shadden *et al*., 2005). In recent years, LCSs have been applied to pollution management and transport of chlorophyll in different oceanic scales (Coulliette *et al*., 2007; Olascoaga *et al*., 2008), and will be applied to the radial sand ridges in the current work.

The rest of the paper include detailed description of the adjoint method for computing transport timescales, the detecting method of LCSs, the presentation and discussion of obtained results, and finally some remark conclusions.

METHODS

The transport property of water parcels or pollutants is inherently a Lagrangian problem considering them as passive particles. Thus, the concept of residence time θ, based on the Lagrangian viewpoint, is defined as the time a water parcel spends in a limited water body until it leaves the boundary. The departure time of a particle located in $\mathbf{x}_0$ can be recorded as $\theta(t_0, \mathbf{x}_0)$, and from the repeated releases the obtained mean residence time is $\bar{\theta}(t_0, \mathbf{x}_0)$. Next, by providing adequate particles everywhere in the domain of interest an overall map can be obtained. Moreover, if the domain endures the driving force back and forth, *e.g.* the Jiangsu coast, re-enter movement of particles needs be considered also, so that the mean exposure time $\bar{\theta}$ becomes a more comprehensive diagnostic tool to describe the accumulated retention characteristic of the water parcels or pollutants. Similarly, in the Eulerian framework, the zeroth moment of cumulative distribution function D, written as $\int_0^\infty D(t_0, \tau, \mathbf{x}_0)d\tau$, is taken as the residence time through the ejection of tracer with unit concentration at $(t_0, \mathbf{x}_0)$ (Delhez *et al*., 2004). For both the above-mentioned methods, either massive particles or multiple runs are needed to obtain the spatial patterns of both transport timescales; therefore, the adjoint method was adopted instead in the present study.

Adjoint method

According to Delhez *et al*. (2004), Brye *et al*. (2012) and Zhang *et al.* (2009), the residence and exposure time can be obtained by solving the adjoint advection-diffusion equation through backward procedure. The domain of interest (Ω_c) is taken as a control domain which is inside the computation domain ($\Omega_c \subset \Omega$) (Figure 1), meanwhile introducing $\tau = T - t$, the adjoint problem of mean residence time $\bar{\theta}$ can be written as:

$$\begin{cases} \frac{\partial}{\partial \tau}(H\bar{\theta}) + \nabla \cdot (H(-\mathbf{u})\bar{\theta}) = \nabla \cdot (H\mathbf{K} \cdot \nabla\bar{\theta}) + H\delta_{\Omega_c} \\ \bar{\theta}(T, \mathbf{x}) = 0, \ \mathbf{x} \in \Omega_c \\ \bar{\theta}(\tau, \mathbf{x}) = 0, \ \mathbf{x} \in \partial\Omega_c \end{cases} \quad (1)$$

where H is water depth**,** $\mathbf{K}$ is the symmetric diffusivity tensor, and δ_{Ω_c} is the Dirac impulse function that takes unit value in Ω_c and zero elsewhere. The equation was integrated in the backward direction from initial time T, and reversed velocity fields were adopted for computation. The mean exposure time $\bar{\Theta}$ could also be derived from the above adjoint equation by imposing different boundary conditions, which requires no elimination of $\bar{\Theta}(\tau, \mathbf{x})$ to be done if they flush out of the control domain. Herein after, the overbars of timescales are omitted for brevity.

The integration period for the backward procedure is infinite strictly, but the problem converges if the adjoint variable tracer C_T^* released in the control domain would be removed in a rather long time. This time could be estimated by solving

$$\begin{cases} \frac{\partial}{\partial \tau}(HC_T^*) + \nabla \cdot (H(-\mathbf{u})C_T^*) = \nabla \cdot (H\mathbf{K} \cdot \nabla C_T^*) \\ C_T^*(T, \mathbf{x}) = \delta_{\Omega_c} \end{cases} \quad (2)$$

Generally the exposure time is greater than the residence time by definition. To compute both the residence and exposure time, equation (2) was integrated with/without the elimination of C_T^* when they flush out of the control domain.

Lagrangian coherent structures (LCSs)

The identification of LCSs could be connected with extrema of FTLE field, which is computed as

$$\Lambda_{t_0}^{t_1}(\mathbf{x}_0) = \frac{1}{|t_1 - t_0|} ln\sqrt{\lambda_n(\mathbf{x}_0, t_0)} \quad (3)$$

where λ_n is the largest eigenvalue of Cauchy-Green deformation tensor, t_0 and $t_1$denote the start and end time for a finite integration time. By integrating in the forward or backward direction, respectively, the repelling or attracting LCSs could be located, respectively. The FTLE fileds can be computed using velocity fields provided by floating buoys, radar data, and ocean models. Both 2D and 3D structures of LCSs, which reveal the repelling or attracting material lines, could be obtained. When applied to baroclinic geophysical flows, the 2D structures are more frequently consulted because of numerical uncertainty in vertical velocity, satellite images for fluid surfaces and also

curtain-shaped LCSs surfaces which are proved to exist near eddies (Branicki and Kirwan, 2010; Bettencourt *et al*., 2012).

Numerical model and setup

The adjont method was implemented in TELEMAC-2D (Lang *et al*., 2014), which is one component of the open source OPENTELEMAC-MASCARET modelling suite developed for solving free surface flows. The depth-averaged Navier-Stokes equations are solved in finite element method.

Due to the existence of wide intertidal zone along the Jiangsu coast, the wetting/drying processes were taken into consideration. Using the unstructured grid refined in the radial sand ridges (~800 m resolution), 62308 elements were involved in the computation domain Ω. In order to distinguish the physical factors, the criterion run neglected the Yangtze river runoff in upstream boundary. All runs took account of Coriolis force. The water elevations including 8 tidal components, which were obtained from the East China Sea model, were imposed at open sea boundary. The computation was initialized with zero water elevation and velocity, velocity fields of 2 years were stored for backward procedure after a spin-up of two months.

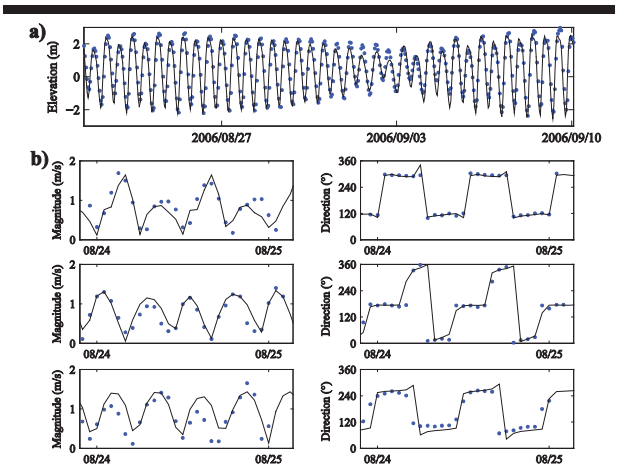

Figure 2. (a) Verification of surface water level at Station Dafeng. (b) Verification of velocity fields at selected observing stations (Figure 1b, Y+1, R10, R24 sequently) out of total 22 stations (Figure 1a, red dots). The left and right panels show velocity magnitude and direction respectively (solid - computation; dots - in situ data).

RESULTS

Calibration of the model and verification of elevations and velocities were done using the in situ data obtained during the period from August 23 to September 11 of 2006, along with the observing sets of both spring tide and neap tide. The observing stations covered the domain along Jiangsu coast (Figure 1a). The results predicted by the model agreed reasonably well with the in situ data (Figure 2).

The evaluation of the retention timescales was obtained using the adjoint method, which provides a convenient approach for a single run. For the computation of the adjoint problem, the velocity fields derived from a direct forward run were stored at an interval of 1 hour. According to Delhez *et al*. (2004), the initialization period is usually twice the order of magnitude of the residence time. From the computation of equation (2), the ratio of remained mass to initial total mass in the control domain

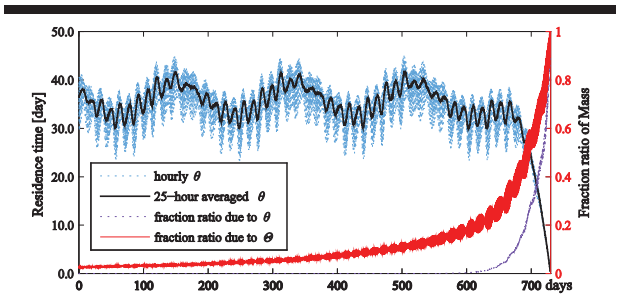

Figure 3. Fraction of adjoint variable tracer C_T^* in control domain and temporal variation of residence time in site B (Figure 1b).

decreased to ~0.0% and ~2.3% for corresponding boundary conditions of θ and Θin 2 years (Figure 3), which was acceptable and considered for integration. Adopting this approach, a horizontal map of both θ and Θ were revealed, as shown in Figure 4a and 4b. The residence time is defined as the time elapsed to touch the boundary of control domain. Thus, the areas with low values mean that water parcels there tend to escape from the domain of interest. A spoon-shaped high value region could be observed along the northeast direction, whilst the region with low values existed along Xiyang, which is the deepest trough in the radial sand ridges.

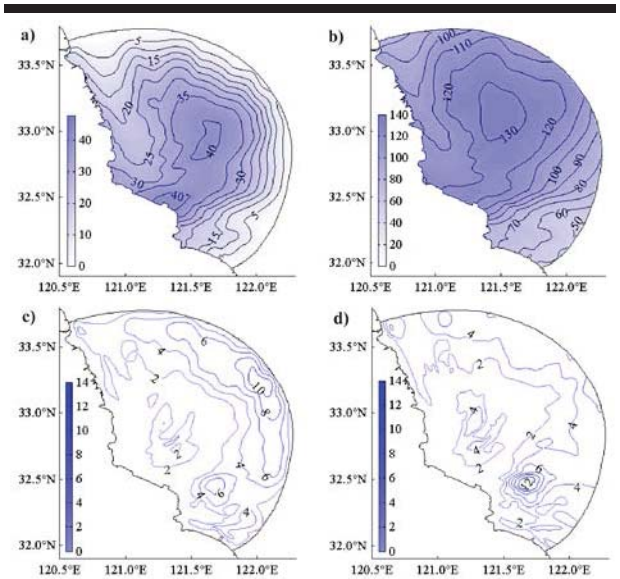

Figure 4. (a)-(b) Tidally-averaged θ and Θ (during spring tide, unit: days). (c)-(d) M_2 amplitude of θ and Θ (unit: days).

In open sea, which is affected by tide motion, water parcel or pollutant can easily re-enter the domain of interest since its first leave. Therefore, the accumulated time of water parcels spent in the domain, which is represented by the exposure time, proved to be more important and comprehensive, especially for some

environmental issues. In Figure 4b, the expanded region have rather large Θ compared with θ (maximum of ~133 days and ~41 days, respectively), which is probably due to the convergent radial current. In addition, from the perspective of physical significance of θ and Θ, Figure 4c and 4d show their amplitudes for the case of M_2. The region near the open sea boundary responds to tide stronger, especially for θ; besides, the region near Lanshayang has intensive fluctuation of about 6 and 12 days for θ and Θ, respectively.

DISCUSSION

Because of the convergence of tidal wave in the radial sand ridges, the pollutants tend to stay in this area for rather long time. The effectiveness of the adjoint method could be observed by applying the direct Lagrangian particle-tracking technique. As a straightforward implementation, massive particles were advected by real-time updated velocity fields and the diffusion processes were modelled by random walk. Corresponding leave and re-enter time could be recorded and analyzed using the information extracted from the hourly stored positions of the particles. To smoothen the tidal effect on initial release time, 48 releases for each node location in Ω_c were executed in continuous 48 hours for both spring tide and neap tide (only the spring tide case has been showed). Similar pattern (consistent with criterion run) could be observed in Figure 5, with magnitude a little bit larger than the adjoint method. In the single run of the adjoint method, the influence of initialization decreased and a dynamic equilibrium state was achieved (Delhez *et al*., 2004) with oscillation due to tidal motion (Figure 3). However, the initial release time of the direct method might have affected the results, which may be one of the reasons for the differences of magnitude from the two approaches. Moreover, as the horizontal dispersion were modelled by random walk, the value of dispersion coefficients were showed to have effect on particle trajectories, which means dispersion coefficients should be carefully calibrated.

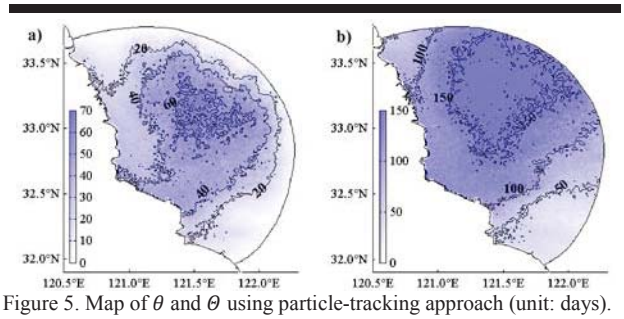

Figure 5. Map of θ and Θ using particle-tracking approach (unit: days).

Considering the different patterns among the regions, sites A-C (Figure 1b) were chosen for analysis. Results showed that B and C had similar value of θ, while had difference in Θ, which means that the transport patterns of these two sites were different (figures not show here). To evaluate the weight of returned water in exposure time, the return coefficient $C_{return} = (\Theta - \theta)/\Theta$ was used. All the values were found to be larger than 0.6 which signified large contribution of re-enter water to the retention of mass (Figure 6). Furthermore, the Yangtze River runoff and wind stress were considered as the physical factors that might influence the retention magnitude of the radial sand ridges. Results showed that the Yangtze River had a small impact on it. Typical seasonal wind stresses imposed on sea surface were considered for northwest wind during winter and for south-southeast wind during summer; in this regard, a typical value of 4 m/s was used. The results showed that the southward wind hindered the pollutant pathways in the northern part of the control domain and made them stay in the domain for longer time. An opposite pattern for northward wind was obtained. The high value region swung opposite to the wind direction.

In order to analyze the long term transport, the potential concept of LCSs was adopted in the present work. The stretching skeleton of flow was extracted from the ridges of the FTLE field. As M_2 is the dominant tidal component in the radial sand ridges, 25-hours was chosen for integration of the trajectories. The forward and backward FTLE fields were generated using FlowVC (Shadden) and the results indicated a similarity in shape. The attracting manifold by backward FTLE is showed in Figure 7, which reveals that the particles near the material curves tended to move along these structures. Compared with Figure 1b, the curves showed similarity with a

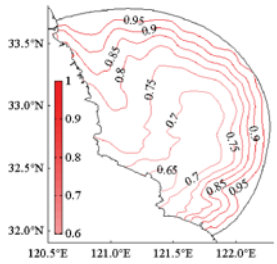

Figure 6. Distribution map of return coefficient.

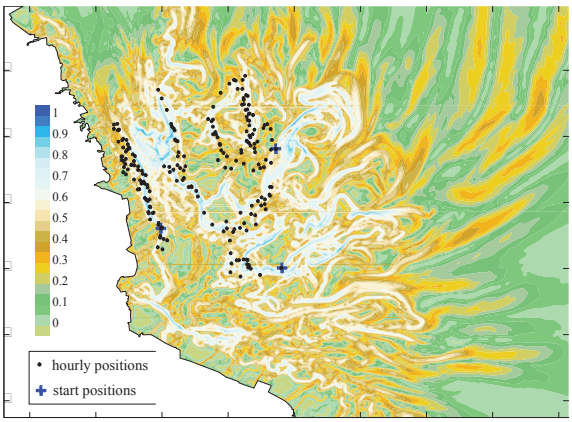

Figure 7. The normalized backward FTLE at 20:00 GMT, February 8, 2005. The trajectories of particles (start positions denoted by blue plus) are presented with hourly position in black dots.

radial shape in time evolving snapshots of FTLE fields. Three particles were released on plus markers (Figure 7) and their continuous positions are presented to show their confined movements by LCSs. Tidal channels like Xiyang would confine particles' movement along them, while some vortex-shaped curves showed trapping of the particles which resulted in a longer retention time. In addition, the release time during flood and ebb tide resulted in separated trajectories, which implied sensetivity of particle trajectories toward release time.

CONCLUSIONS

A set of diagnostic tools were employed to study the transport patterns in the unique radial sand ridges of the South Yellow Sea. Transport timescales were used to provide a comprehensive description of spatial variable characteristics within a single run using adjoint method. Due to the existence of "moving stationary tidal wave", this region is subjected to tidal motion greatly, which is indicated by the transport pattern of residence time and exposure time. The transport timescales presented quasi-equilibrium to tidal variation after initialization, and the results during flood tide are presented in this report. Except the region near open sea boundary, the re-entered water contributes to the retention of pollutants, especially in Xiyang channel. As a supplementary tool, the Lagrangian particle-tracking technique for calculating transport timescales could be used for indirect numerical validation. The distribution of paralleled ridges and troughs was reflected in the ridges of FTLE fields, which revealed that there are connections between attracting/repelling LCSs and the morphology of the radial sand ridges.

ACKNOWLEDGMENTS

This study was supported by the National Natural Science Foundation of China (Grant No. 51409093, 51179067) and the Fundamental Research Funds for the Central Universities (Grant No. 2011B06214). Special thanks to Dr. Jun Kong for technical discussions.

LITERATURE CITED

Aref, H., 1984. Stirring by chaotic advection. *Journal of Fluid Mechanics*, 143, 1-21.

Bettencourt, J.H.; López, C., and Hernández-García, E., 2012. Oceanic three-dimensional Lagrangian coherent structures: A study of a mesoscale eddy in the Benguela upwelling region. *Ocean Modelling*, 51, 73-83.

Branicki, M. and Kirwan Jr., A.D., 2010. Stirring: the Eckart paradigm revisited. *International Journal of Engineering Science*, 48, 1027-1042.

Brye, B.d.; Brauwere, A.d.; Gourgue, O.; Delhez, E.J., and Deleersnijder, E., 2012. Water renewal timescales in the Scheldt Estuary. *Journal of Marine Systems*, 94, 74-86.

Coulliette, C.; Lekien, F.; Paduan, J.; Haller, G., and Marsden, J., 2007. Optimal pollution mitigation in Monterey Bay based on coastal radar data and nonlinear dynamics. *Environmental Science & Technology*, 41(18), 6562-6572..

Deleersnijder, E.; Campin, J.-M., and Delhez, E.J., 2001. The concept of age in marine modelling: I. Theory and preliminary model results. *Journal of Marine Systems*, 28(3-4), 229-267.

Delhez, É.J.; Heemink, A.W., and Deleersnijder, É., 2004. Residence time in a semi-enclosed domain from the solution of an adjoint problem. *Estuarine, Coastal and Shelf Science*, 61(4), 691-702.

Haller, G. and Yuan, G., 2000. Lagrangian coherent structures and mixing in two-dimensional turbulence. *Physica D: Nonlinear Phenomena*, 147(3-4), 352-370.

Lang, P.; Desombre, J.; Ata, R.; Goeury, C., and Hervouet, J. M., 2014. *Telemac modelling system. TELEMAC-2D software: user manual, release 7.0*. EDF-R&D,134p.

Olascoaga, M.J.; Beron-Vera, F.J.; Brand, L.E., and Koçak, H., 2008. Tracing the early development of harmful algal blooms on the West Florida Shelf with the aid of Lagrangian coherent structures. *Journal of Geophysical Research*, 113(c12), c12014.

Shadden, S.C., *FlowVC (Version 1)*. http://shaddenlab.berkeley.edu/software/.

Shadden, S.C.; Lekien, F., and Marsden, J.E., 2005. Definition and properties of Lagrangian coherent structures from finite-time Lyapunov exponents in two-dimensional aperiodic flows. *Physica D: Nonlinear Phenomena*, 212(3-4), 271-304.

Wang, Y.; Zhang, Y.; Zou, X.; Zhu, D., and Piper, D., 2012. The sand ridge field of the South Yellow Sea: Origin by river–sea interaction. *Marine Geology*, 291–294, 132-146.

Wiggins, S., 2005. The dynamical systems approach to Lagrangian transport in oceanic flows. *Annual Review of Fluid Mechanics*, 37, 295-328.

Zhang, C.; Zhang D.; Zhang, J., and Wang Z., 1999. Tidal current-induced formation—storm-induced change—tidal current-induced recovery. *Science in China (Series D)*, 42(1), 1-12.

Zhang, W.G.; Wilkin, J.L., and Schofield, O.M.E., 2009. Simulation of water age and residence time in New York Bight. *Journal of Physical Oceanography*, 40(5), 965-982.

Journal of Coastal Research	SI	75	188-192	Coconut Creek, Florida	2016

Wind-Induced Water Exchange between Stratified Basins

Jin-Hee Yuk[†*], Shin-ichi Aoki [‡], and Minsu Joh [†]

[†]Disaster Management HPC Technology Research Center,
Korea Institute of Science and Technology Information
Daejeon, Korea

[‡]Dept. of Civil Engineering,
Osaka University
Suita, Osaka, Japan

www.cerf-jcr.org

www.JCRonline.org

ABSTRACT

Yuk, J.-H.; Aoki, S., and Joh, M., 2016. Wind-induced water exchange between stratified basins. *In:* Vila-Concejo, A.; Bruce, E.; Kennedy, D.M., and McCarroll, R.J. (eds.), *Proceedings of the 14th International Coastal Symposium* (Sydney, Australia). *Journal of Coastal Research*, Special Issue, No. 75, pp. 188-192. Coconut Creek (Florida), ISSN 0749-0208.

Water exchange between Inohanako Estuary and Hamanako Bay, Japan with density stratification is investigated using the field data. The basins are connected by a narrow channel with length 200 m through which waters and nutrients are exchanged between them. The principal axis of channel between two basins is located nearly in the north-south direction, thus it is natural that the water flow between the estuary and bay is influenced more by the north-south component of wind than the east-west component of that. Although the relationship between water exchange and the east-west component of wind is relatively low compared with the north-south component, the water exchange is controlled by this. In this study, using the field data measured by ADCP and CTD in summer months of 2009, a mechanism of wind-induced water exchange was investigated and discussed. A simple theoretical approach suggested that the dynamic response of density surface in Hamanako Bay to the wind force caused the circulating flow in the channel. The change of water density was more remarkable in Hamanako Bay than in Inohanako Estuary in response to the wind direction, and the surface layer in Hamanako Bay became thinner during the westerly wind. This study shows that the water exchange associated with the east-west wind is caused by the difference of water pressures between Inoahnako Estuary and Hamanako Bay, which is induced by the fluctuation of density interface between the surface and bottom layers due to wind.

ADDITIONAL INDEX WORDS: *Wind-induced water exchange, stratified basin, narrow channel.*

INTRODUCTION

The water exchange and the material transport affect greatly the water quality and primary production in estuaries and bays. In particular, for the two bains connected by a narrow channel, if the one basin is largely different from the other one in terms of a size and structure, the effect of water exchane and material transport on the water quality and primary production is likely to increase (Ueshima, 1982; Qian *et al.,* 1996; Fukuoka *et al.,* 2002).

Hamanako Bay is situated in the middle part of Japan and connected to the Pacific Ocean through a narrow inlet (the width of inlet = 200 m) (Figure 1). In the south part of Hamanako Bay, there is a shallow water with mean depth of 2.5 m, and the incoming ocean water is disturbed by Murakushi Peninsula, the tidal flats, the reclamations and the many bridges built between Arai and Maisaka. The north part has much deeper water than the south part: the mean depth of 7.2 m and maximum depth of 12 m. In the north part, Inohanako Estuary and Hosoeko Estuary lie. The northern bay, especially Inohanako Estuary is surrounded by the orange orchard, thus excessive nutrient input is likely to flow into the northern bay. In addition, the periodic summer bottom hypoxia in the northern bay is a serious environmental problem.

DOI: 10.2112/SI75-038.1 received 15 October 2015; accepted in revision 15 January 2016..
*Corresponding author: jhyuk@kisti.re.kr

As summertime primary production in Inohanako Estuary is strongly related to phosphorus concentration (Aoki *et al.,* 2004; Yuk and Aoki, 2010a), it is important to understand the movement or transport of phosphorus in the stratified water basin to solve the environmental problems such as eutrophication and hypoxia. However, water flow related to material (nutrient) transport in this basin are poorly studied. It is necessary to reveal the physical processes of material transport before considering countermeasures to eutrophication and the formation of hypoxic waters.

The aim of this study is to esimate the horizontal water exchange between Inohanako Estuary and Hamanako Bay under stratified condition using the field measurement data. In addition, its mechanism between two basins which is associated with wind is examined. In this study, the water exchange between two stratified water basins is presented and discussed on the basis of comparison of measured and meteorological data and the analyses.

METHODS

The channel that connects Inohanako Estuary and Hamanako Bay has the length of 200 m and the width of approximately 75 m. We undertook continuous velocity measurement via two ADCPs (Acoustic Doppler Current Profiler, Nortex, Aquadopp) installed at the bottom of the channel (maximum water depth of approximately 16 m) with a sampling rate of 10 minutes and a vertical sampling interval of 1 m from September 7th (250th) to October 19th (292nd) to estimate the nature of water exchange

between Inohanako Estuary and Hamanako Bay (Figure 2). One ADCP was located near the middle of the channel and the other one was located in the east side, thus the former was named the West-ADCP and the latter was named the East-ADCP.

To determine the average salinity, temperature and density profiles, CTD (Compact-CTD; Conductivity, Temperature and Depth, Alec Electronics Co., Ltd., Kobe, Japan) observation was conducted at three stations seven times (September 7, 14, 20, 28, and October 5, 10, 19) in two water basins to obtain these profiles at 0.1 m vertical sampling intervals throughout the measurement period.

The analyses for mechanism of water and material exchange were conducted with reference to the meteorological data such as the wind and precipitation recorded at Mikkabi Observatory that is located about 1 km northwest from the mouth of main creek, Tsuribashi Creek.

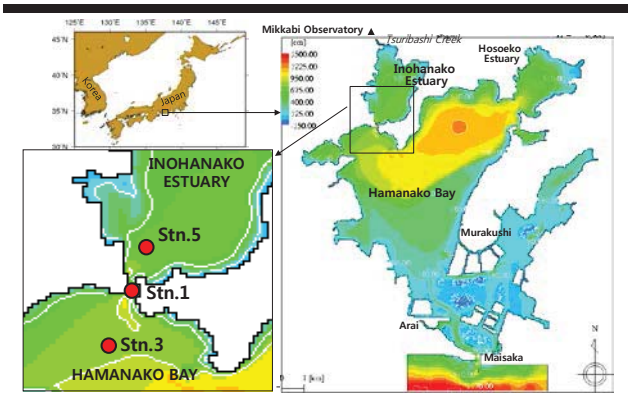

Figure 1. Location of study area and the channel connecting between Inohanako Estuary and Hamanako Bay. Stn.1: ADCP-installation and measurment, Stn.3 and Stn.5: CTD-measurement.

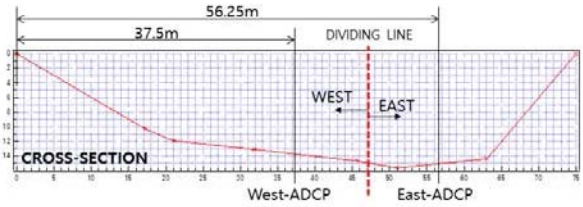

Figure 2. Cross section of the channel and the location of two installed ADCPs.

RESULTS

We present the estimation of water exchange between two stratified basins and the vertical structure of water flow in the channel. Also, the influence of wind on water exchange is presented with the comparison of wind data in this section.

Flow in the narrow inlet

Figure 3 shows the time-series of rainfall, wind and current velocity acquired by two ADCPs. Figure 3(c) and 3(d) show the temporal variation of 25 hr moving average of north-south current velocities (north is the positive) at the east and west ADCPs. The 25 hr moving average of current velocity indicates the tide-removed current velocity. The positive values of the velocities indicate the inflow toward Inohanako Estuary. At approximately 3 – 4 m from the surface water, the direction in the surface layer was different from the one in the middle layer. This shows that the current direction in the surface layer is from Inohanako Estuary to Hamanako Bay, whereas vise versa in the middle layer throughout the measurement period. This vertical profile was clear, especially at the east ADCP (East-ADCP). The strong current showing outflow in the surface layer and inflow in the bottom layer after 280th was caused by the strong wind due to the typhoon Melor (TY200918) and freshwater input. There was little rainfall for approximately one month prior to the beginning day of ADCP measurement, thus the freshwater did not affect largely the relatively strong flow shown in the early stage of measurement.

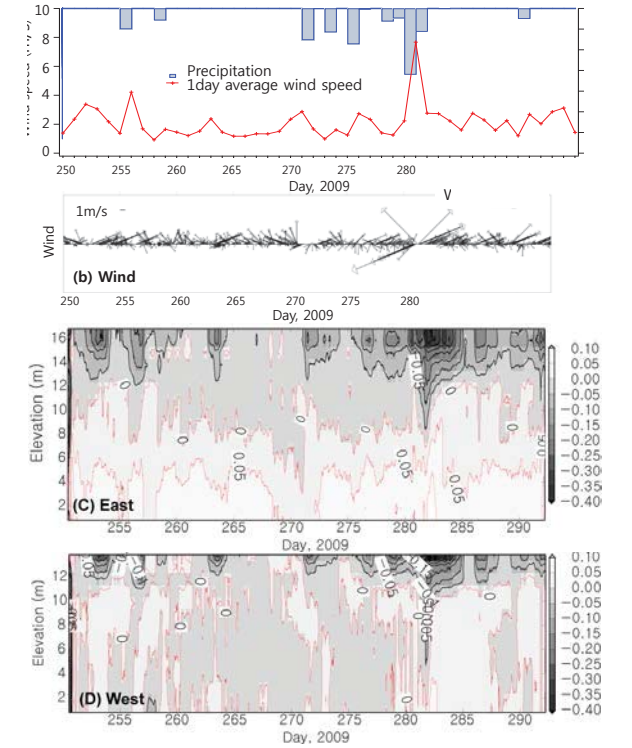

Figure 3. Time-series of meteorological parameters and current velocities measured by two ADCPs. (A) daily precipitation and 1-day average wind speed, (B) wind vector, (C) 25 hr moving averages of horizontal current velocity (NS-component) measured by East-ADCP, (D) 25 hr moving averages of horizontal current velocity (NS-component) measured by West-ADCP. Red contours indicate zero and positive values.

Figure 4 displays the vertical profiles of the averaged water-volume flux in the channel, which was calculated using ADCPs-measurement data and the cross-section area. The water-volume flux was estimated from each average velocity observed by the

ADCP at 1 m vertical intervals and the flow area of a vertical segment at each corresponding point. The positive denotes inflow toward Inohanako Estuary, and the negative denotes the opposite. From the figure, the water-volume flux in the surface layer was computed as -10.45 m^3/s indicating that the net flow was toward Hamanako Bay. On the contrary, the water-volume flux into Inohanako Estuary in the bottom layer was quantified as 5.59 m^3/s. The difference between two water-volume fluxes was 4.85 m^3/s, which corresponded approximately to the freshwater (4.74 m^3/s) estimated using the rainfall and the watershed area. The estuarine circulation is influenced by the freshwater inflow and the wind under the stratified condition, and our study (Yuk *et al.*, 2007; Yuk, 2008; Yuk and Aoki, 2008, 2009) on this in these basins shows that the wind effect was dominant over the effects of tides and rainfall. In particular, the rainfall was low in summer of 2009, thus the wind effect was prevailing. Figure 5 presents the time-series of wind direction, wind speed (daily average value) and the water-volume fluxes, the daily average water-volume fluxes in the surface (0 – 4 m) and bottom (deeper than 4 m) layers and the sum of two components. The sum indicates the net flow in the channel connecing Inohanako Estuary and Hamanko Bay. The westerly wind was predominant during the observation period and the water flux was largely influenced by the wind, *i.e.*, the water flux became larger due to the strong wind. On about 270th when the easterly wind was dominant, the bottom water flux was the negative, *i.e.*, outflow (from Inohanako Estuary to Hamanako Bay). On 281st when the typhoon approached the study area, the wind blew just after the large rainfall, thus there was the great amount of flow in the channel.

Relationship between wind and flow

Figure 6 shows the relationship between the surface and bottom water-volume fluxes. In terms of water-volume flux, the positive values denote the inflow toward Inohanako Estuary.

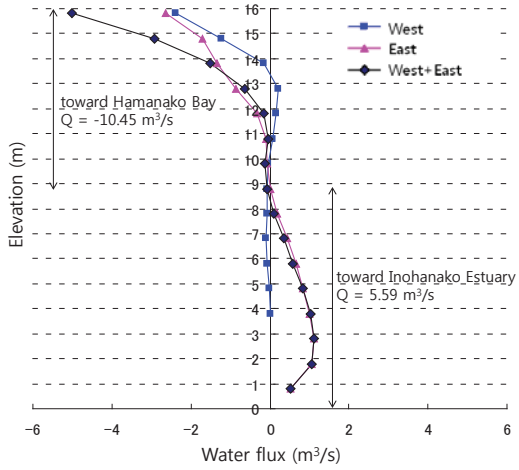

Figure 4. Vertical profie of water-volume flux measured by the West and East ADCPs in the channel conneting Inohanako Estuary and Hamanako Bay.

There was the negative relationship between two fluxes: the outflow in the surface layer and the inflow in the bottom layer. According to the previous study (Yuk and Aoki, 2008; Yuk and Aoki, 2010b), there was the strong relationship between the north-south (NS) wind component and the water-volume flux in the channel, whereas the weak relationship between the east-west (EW) wind component and the water-volume flux due to the topographical feature and cardinal direction of two water basins and channel. In this study, we revisited the EW wind component and the surface and bottom water-volume fluxes using the observation data in 2009 (Figure 7). The EW component of wind and the water flux had relatively low relationship, but it could be said that the EW-wind affects flow condition in the channel. Therefore, the water flux is likely to be driven by the EW component of wind. If the westerly wind became larger, both the outflow of surface water-volume flux and inflow of bottom water-volume flux became larger (Figure 7).

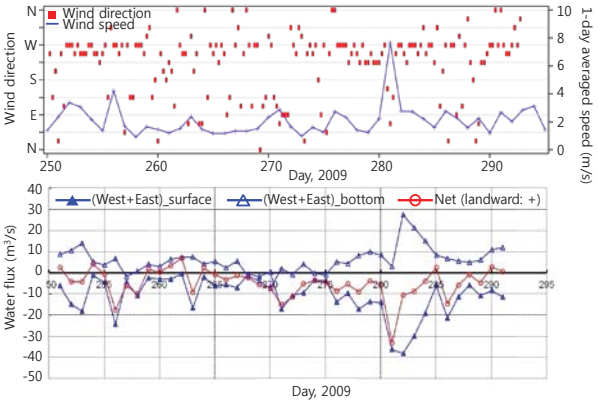

Figure 5. Timeseries of wind and water-volume flux.

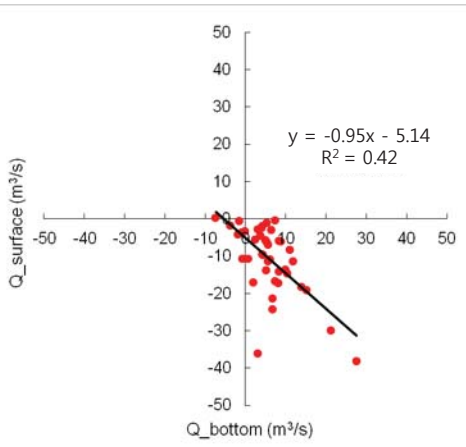

Figure 6. Relationship between the surface and bottom water-volume fluxes through the channel.

DISCUSSION

The mechanism of water exhcnage associated with EW-component of wind in the channel was discussed here based on the fundamental equations.

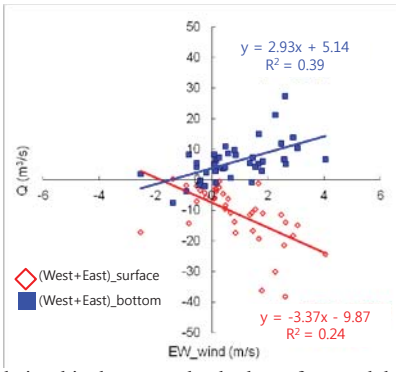

Figure 7. Relationship between the both surface and bottom water-volume fluxes through the channel and EW-wind component.

Change of density interface under the stratification

The water exchange between Inohanako Estuary and Hamanako Bay is driven by the wind under the stratified season on the basis of the measurement data.

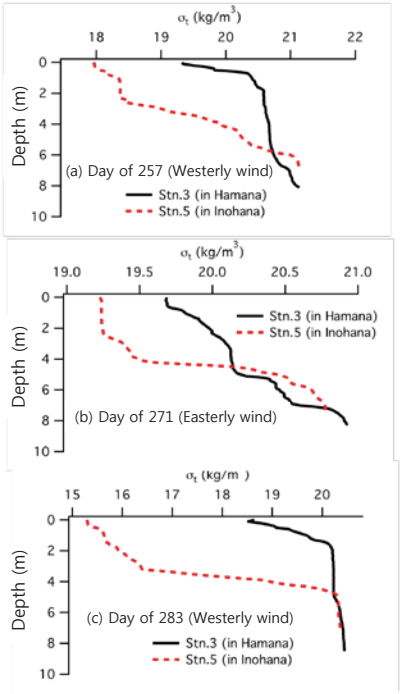

Figure 8. Vertical distribution of water density (σ_t) under different wind direction conditions.

Figure 8 shows the vertical profiles of water density (σ_t) calculated using water temperature and salinity measured by CTD in Hamanako Bay (Station 3) and Inohanako Estuary (Station 5). In Figure 8, (a) indicates the day of the relatively strong westerly wind, (b) on the contrary, the day of the strong easterly wind, and (c) the day just after the typhoon passed, *i.e.*, corresponding to about the end of the period when the westerly wind strongly blew. In Inohanako Estuary (Station 5), the surface density varied largely, but the tendencies of vertical profile of water densities were similar in three figures. Regardless of wind condition, at approximately –4 m, the pycnocline was observed throughout the measurement period. On the other hand, in Hamanako Bay (Station 3), the fluctuation of the vertical profile of water density was large and the pycnocline was seen in the shallow depth under the westerly wind. Comparing with Figure 5, near 257th corresponding to Figure 8(a), obviously, there were the outflow in the surface layer and inflow in the bottom layer due to the prevailing westerly wind that blew for a few days until 257th. Near 271st when the easterly wind blew, the outflow was found in the bottom layer as well as the surface layer on some days. On 283rd, the strong flow was observed, which was caused by not only the westerly wind but also the rainfall prior to typhoon attack.

Mechanism of water exchange

Figure 9 shows the diagram of Hamanako Bay, Inohanako Estuary and the narrow channel to account for the water exchange between two water basins. *A* and *B* depict Hamanako Bay and Inohanako Estuary, respectively. We set the systems of Hamanako Bay and Inohanako Estuary with the identical water depth to examine the effect of the westerly wind. The density field is set to be the surface and bottom water density of ρ_1 and ρ_2 considering the stratification. The thicknesses of two layers are h_1 (upper) and h_2 (lower). If the westerly wind blows, the surface and density interface change due to shear force as shown in Figure 9. The relation describing the gradient of the surface and density interface is Equation (1) (Unoki, 1993),

$$\frac{\partial D}{\partial x} = \frac{1}{\varepsilon_1}\frac{\partial \eta}{\partial x} \qquad (1)$$

where D is the distance from the still-water level to density interface, η is the water displacement, and $\varepsilon_1=(\rho_2-\rho_1)/\rho_1$. Unoki (1993) proposed how to compute η and D using the equation of motion, and if computing η and D based on static balance and $\partial\eta/\partial x=I=\tau_s/\rho_1 g h_1$ (τ_s: surface shear stress), η and D are,

$$\eta = I\left(x - \frac{l}{2}\right) \qquad (2)$$

$$D = \frac{I}{\varepsilon_1}\left(x - \frac{l}{2}\right) + h_1 \qquad (3)$$

where l is the length of water basin in the EW direction. We calculated the pressure difference at the bottom between Inohanako Estuary and Hamanako Bay as

$$p_A - p_B = \frac{\rho_1 g I}{2\varepsilon_1}(l_A - l_B) \qquad (4)$$

On the basis of Equation (4), in case that the westerly wind blows ($I > 0$), the pressure at the bottom in Hamanako Bay that has the bigger size is larger than that in Inohanako Estuary. Therefore, this phenomenon stimulates the inflow into Inohanako Estuary in the lower layer. On the contrary, the easterly wind ($I < 0$) enables the flow toward Hamanako Bay in the lower layer.

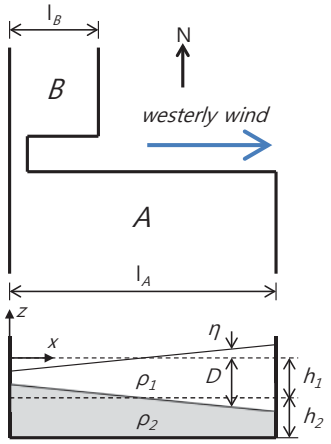

Figure 9. Diagram of Hamanako Bay, Inohanako Estuary and the narrow channel to explain theroretical approach used in this study.

The water exchange between Inohanako Estuary and Hamanako Bay is driven by the EW wind component. This is caused by the pressure difference that is attributed to size difference of two waters. Note that the vertical mixing due to the wind weakens the strength of pycnoclyne, thus this mechanism does not continually happen.

CONCLUSIONS

We investigated the characteristics of water exchange between Inohanako Estuary and Hamanako Bay under the density stratification during summer based on the detailed measurement and analyses. The water exchange fluxes between the two stratified water basin and between the upper and lower layers were calculated and presented based on two ADCP-measured current velocity data. This study showed generally the outflow in the upper layer and inflow in the lower layer, *i.e.*, the estuarine circulation. Water exchange in the narrow channel that connects Inohanako Estuary and Hamanako Bay is dependent upon wind forcing, and water exchange also had the significant relationship with the EW-component of wind. In terms of the circulation due to the EW wind, it is suggested that the water pressure difference between Hamanako Bay and Inohanako Estuary, which is caused by the fluctuation of density interface due to the wind, is a driving force. Future work should be oriented to collecting more frequent and detailed measurements for several years upon Inohanako Estuary and Hamanako in order to understand the relationship and mechanism of water exchange and wind. This will provide those who are in charge of environmental management of Inohanako Estuary meaningful information for the construction of the effective environmental management.

ACKNOWLEDGMENTS

The meteorological data used in this study were provided by Mikkabi Agricultural Cooperative. This study was supported partially by a project of KISTI for the development of an HPC-based management system against a national-scale disaster.

LITERATURE CITED

Aoki, S.; Mizuno, R., and Arita, M., 2004. Formation of and mixing in hypoxic bottom waters in an estuary. *Proc. 8th International Conference on Diffuse/Nonpoint Pollution*, Kyoto (CD-ROM).

Fukuoka, S.; Miura, K.; Kurokawa, T.; Matsuhita, S., and Funabashi, S., 2002. Water flow and water quality change in the low layer in strongly stratified water basin. *Proceeding of the Japanese Conference on Coastal Engineering* (Japan), pp. 361-365. (in Japanese)

Qian, X.; Nishibu, T., and Ishikawa, T., 1996. The estimation of water exchange for the diurnal stratificatioin in Lake Kasumigaura. *Proceeding of the Japanese Conference on Coastal Engineering* (Japan), pp. 1216-1220. (in Japanese)

Ueshima, S., 1982. The change of material transport accompanied by typhoon pass. *Proceeding of the Japanese Conference on Coastal Engineering* (Japan), pp. 594-598. (in Japanese)

Unoki, S., 1993. Coastal Physical Oceanography. Tokai University Press. 672p. (in Japanese)

Yuk, J.-H. and Aoki, S., 2008. A study on process of water exchange in Inohana Lake. *Coastal Engineering Journal*, 50(1), 1–18.

Yuk, J.-H., 2008. Water Exchange and Material Transport in a Semi-enclosed Estuary — The Characteristics and Long-term Changes in Hamana Lake —. Toyohashi, Japan: Toyohashi University of Technology, Doctoral thesis, 212p.

Yuk, J.-H. and Aoki, S., 2009. Effect of wind and rainfall on water exchange in a stratified estuary, *Estuaries and Coasts*, 32, 88–99.

Yuk, J.-H. and Aoki, S., 2010a. Estimation of phosphorus flux in a stratified estuary using a mass balance model. *Coastal Engineering Journal*, 52(3), 195-213.

Yuk, J.-H. and Aoki, S., 2010b. Wind-induced waterexchange between stratified basins connetcted by a narrow channel. *Proceedings of the Japanese Conference on Coastal Engineering* (Japan), pp. 376-380. (in Japanese with Englihsh abstract)

Journal of Coastal Research	SI	75	193-197	Coconut Creek, Florida	2016

Numerical Study on the Transport Timescale in a River-influenced Macro-tidal Estuary

Qin Zhang †‡, Jian Feng Tao †‡*, and Jie Yang ‡

† State Key Laboratory of Hydrology-Water Resources and Hydraulic Engineering
Hohai University
Nanjing, China

‡ College of Harbor, Coastal and Offshore Engineering
Hohai University
Nanjing, China

www.cerf-jcr.org

www.JCRonline.org

ABSTRACT

Zhang, Q.; Tao, J.F., and Yang, J., 2016. Numerical study on the transport timescale in a river-influenced macro-tidal estuary. *In:* Vila-Concejo, A.; Bruce, E.; Kennedy, D.M., and McCarroll, R.J. (eds.), *Proceedings of the 14th International Coastal Symposium* (Sydney, Australia). *Journal of Coastal Research*, Special Issue, No. 75, pp. 193-197. Coconut Creek (Florida), ISSN 0749-0208.

A transport module was developed and coupled with TELEMAC flow model to simulate the spatial and temporal distributive characteristics of the transport timescale based on the mean age concept defined by Delhez. The influences of river discharge, tide and large-scale flat reclamation in Taizhou Bay on the transport timescale were analyzed. Model results show that the transport timescale in the river channel is dominated by fluvial discharge over tide. It took approximately 60, 40 and 35 days for the tracer to be transported from the river boundary to the mouth of the Jiaojiang Estuary during the low, mean and high flow conditions, respectively. Outside the entrance of the estuary, tide dominates and the influence of riverine discharge is minor. Large-scale reclamation considerably affects the age distribution outside the estuary and around the project area, while it has little influence on the mass transport in the upstream part of the estuary. After the reclamation, the difference in mean age between the main channel and the tidal flat increases and the tongue-shaped spatial structure of mean age is more evident.

ADDITIONAL INDEX WORDS: *Jiaojiang Estuary, transport time, TELEMAC, numerical model, tidal flat reclamation.*

INTRODUCTION

In aquatic systems, most of the living biomass and nutrients, contaminants, and suspended particles are carried in a fluid medium. As is well known, major processes controlling the distribution of planktonic biomass and contaminant in semi-enclosed bays are linked to transport timescale (*e.g.,* Brye *et al.,* 2012; Monsen *et al.,* 2002). Since the 1970s, many timescales have been introduced to quantify the exchange and transport processes, including flushing time (Bolin and Rodhe, 1973), age (Zimmerman, 1976), residence time (Takeoka, 1984), turnover time (Monsen *et al.,* 2002), exposure time (Delhez, 2013) and *etc.* Among these timescales, age of a seawater particle (i.e., the time spent for a certain particle entering a predefined region until leaving the region) is widely used for hydro-environmental assessment. Schematically, age was used for three main purposes: (1) estimating the ventilation rate of lakes, estuaries, and ocean basins (*e.g.,* England, 1995), (2) inferring the horizontal circulation of shelf seas (*e.g.,* Delhez and Deleersnijder, 2002) and (3) quantifying pollutant transport in aquatic system (*e.g.,* Deleersnijder *et al.,* 2001). To be more specific, age in this study is defined to be the time that elapses before a conservative substance is discharged into the headwater of the estuary. Therefore, age is zero at the headwater of the estuary and age at any other location is representative of the timescale for a conservative substance to be transported from its source to this location. Delhez *et al.* (1999) introduced an Eulerian theory of age, in which advection and diffusion, production and destruction phenomena were properly accounted for. This theory provides a general method for using numerical models to compute spatially varying age distributions in a real estuarine environment, which has been calibrated and used for many studies in channels, reservoirs, gulfs and estuaries (*e.g.,* Delhez *et al.,* 2002; Shen *et al.,* 2011; Zhang *et al.,*2010).

River-influenced macro-tidal estuaries are usually characterized by high flood-dry runoff ratio, large tidal range and strong tidal action (Tang, 2003). Different from partially mixed or slowly mixed estuaries, the mass transport characteristics of the river-influenced macro-tidal estuaries are remarkably affected by both the river runoff and tides (Brye *et al.,* 2012; Monsen *et al.,* 2002). Therefore, it is essential to understand the hydrodynamic processes that transport water and other associated constituents in this kind of estuaries. The Jiaojiang Estuary is a typical river-influenced macro-tidal estuary located in the central Zhejiang Province, Eastern China (Figure 1). The annual averaged freshwater discharge in the estuary is around 163 m^3/s (with marked yearly variations); the annual runoff reaches 289 m^3/s in the rainy year but decreases to 72 m^3/s or less in the dry year (Tang, 2003). The tidal signal is semi-diurnal and slightly asymmetrical. Its average tidal range reaches about 4 m and the maximum tidal range can exceed 6 m.

Macro-tidal estuaries are also often characterized by the presence of extensive tidal flats. The Jiaojiang Estuary is funnel-

DOI: 10.2112/SI75-039.1 received 15 October 2015; accepted in revision 15 January 2016.
*Corresponding author: aoetao@hhu.edu.cn

shaped and the offshore area of Jiaojiang Estuary is called Taizhou Bay, where large areas of tidal flats are present. In recent decades, a lot of reclamation projects of tidal flats around the estuary have been conducted. By interpreting the remote sensing images of coastlines in different years we found that approximately 106 km^2 of coastal wetland had been reclaimed in Taizhou Bay between 1984 and 2013. Tidal flat reclamation not only affects hydrodynamic characteristics (Zhang *et al.,* 2015), but also alters mass transport behavior in the estuary. The purpose of this study is to understand the response of the transport timescale to different dynamic conditions and the impact of the large-scale reclamation of tidal flats on the transport processes in a river-influenced macro-tidal estuary.

METHODS

A mass transport module based on Delhez's theory was developed and coupled with the TELEMAC-2D hydrodynamic model which solves the shallow-water equations based on the classical Boussinesq and hydrostatic pressure assumptions (EDF-DRD, 2013). The equations are solved by a finite element method using a triangle mesh. The coupled model was applied to the Jiaojiang Estuary and its adjacent coastal sea in this study.

The grid domain comprises the Jiaojiang River and Taizhou Bay offshore areas and the open boundary was extended sufficiently far seaward to minimize the lack of precision in the tidal forcing at the open boundary, and the river boundary is extended 100 km upstream to Sanjiangkou Station (Figure1). This station locates at the origin of Jiaojiang River and serves as the controlling station for the measurements of the Jiaojiang freshwater discharging into the sea. Triangular Cartesian grids were used in the model. The entire grid consists of 29022 triangular elements of variable sizes with 1 km resolution near the seaward open boundary and 50 m along the river channel. For the horizontal turbulent diffusion, a Laplacian-type horizontal viscosity coefficient is computed from Smagorinsky's formulation (Smagorinsky, 1963), depending on local mesh dimensions and velocity gradients.

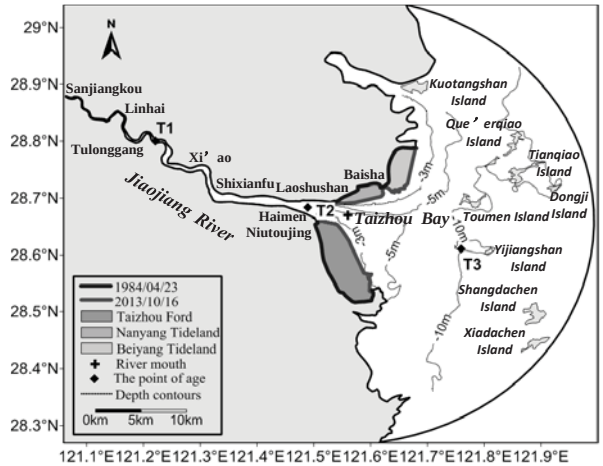

Figure 1. Map of Jiaojiang River Estuary area and model domain.

Tidal level forced the model at the open boundary, which was obtained based on the model results of the Taizhou Bay simulation of Zhang *et al.* (2015). The model has the same characteristics as the local model and has been validated against observed water surface elevations and tidal currents at various stations along the estuary (Zhang *et al.,* 2015). The output of the Taizhou Bay model is interpolated in time and space and prescribed to the local model using a radiative open boundary condition. At the upstream boundary, where tidal effects are negligible, the long-term mean freshwater discharge of 163 m^3/s, the annual freshwater discharge of 289 m^3/s in the rainy year, and the annual freshwater discharge of 72 m^3/s in the dry year were used to represent the respective mean, high and low flow conditions of the estuary.

Several methods have been introduced for computing the tracer age in the literatures (*e.g.,* Bolin and Rodhe, 1973; Takeoka, 1984; Zimmerman, 1976). Delhez *et al.* (1999) introduced a general age theory. Based on the general age theory, the age of a substance can be computed by solving two advection-diffusion equations. The first equation governs the concentration C of the substance while the second governs the age concentration α of the substance.

$$\frac{\partial HC}{\partial t} + \nabla \cdot \left(H\vec{u}C \right) = \nabla \cdot \left(HK \cdot \nabla C \right) \qquad (1)$$

$$\frac{\partial H\alpha}{\partial t} + \nabla \cdot \left(H\vec{u}\alpha \right) = \nabla \cdot \left(HK \cdot \nabla \alpha \right) + HC \qquad (2)$$

Where H is the water depth, $\vec{u}$ is the depth-averaged horizontal velocity, K is the diffusion coefficient. The age a of the substance is then computed as follow:

$$a = \frac{\alpha}{C} \qquad (3)$$

A detailed description of their theory is referred to Delhez *et al.* (1999) and Deleersnijder *et al.* (2001).

Two passive tracers without decay were simulated to represent transport of a dissolved substance and the age respectively. The concentration of the dissolved substance was set to 1 (arbitrary units) and the age concentration was set to zero at the head of the river. When the tracer flux outflows from the open boundary, the tracer is calculated from the advection equation. The incoming tracer concentration from the open boundary was set to zero. That implies that no tracer sources come from the downstream of the estuary. The model was initially run for 25 days for each flow condition to obtain a dynamic equilibrium condition. The flow fields under this equilibrium condition were used as the initial condition for the model experiments so that the model experiments could be "hot" started. The model experiments were conducted for 130 days. The dynamic equilibrium condition was obtained at about 80 days, 100 days and 120 days near the York River mouth for the high flow, mean flow and low flow conditions, respectively. We are more interested in the age distribution under this equilibrium condition. Therefore, the averaged mean age is calculated after the dynamic equilibrium is attained.

RESULTS

The time series of the age and the water level in the last two days at station T1, T2 and T3 (Figure 1) under the mean flow condition are represented to investigate the age distribution characteristics at a specific location. As shown in Figure 2, in constant runoff condition, a dynamic equilibrium condition was attained and the age varies with the change of the tidal level due to the influence of the tide.

The mean age distribution under the mean flow condition after tidal flat reclamation is shown in Figure 3. The numbers shown on the contour lines are the mean ages of the substance in days at that location. The result shows that a substantial time is required for a substance to travel downstream in the estuary. The substance released under the mean flow condition will take about 10 days and 35 days respectively to be transported to the middle of the Jiaojiang River near Xi'ao and the mouth of Jiaojiang River. In general, the age contours gradually turns to the right outside of the estuary, which can attribute to the influence of bathymetry, Coriolis force, and tidal asymmetries.

One notable feature of the spatial structure of mean age in the Jiaojiang Estuary is that it showed a tongue-shaped pattern along the main channel connecting the open sea, with low tracer age in the middle of the channel and relatively high tracer age in the shallow areas adjacent to the shoreline (Figure 3). The result suggests that more substances are transported out of the estuary from the deep channel meandering through the estuary. This tongue-shaped pattern resembled the residual current distribution with large downstream residual currents located in the middle of the channel and low upstream residual currents located in the shallow areas adjacent to the deep channel (Tang, 2003).

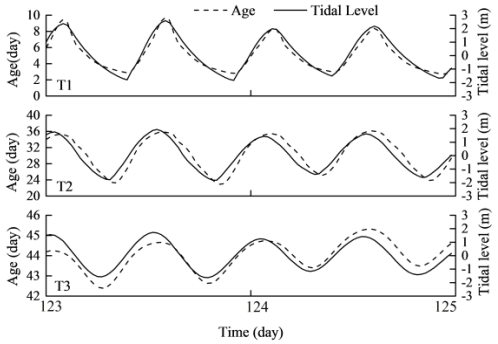

Figure 2. Age and tidal level hydrographs.

DISCUSSION

The age distribution is a function of both tide and freshwater discharge. To examine the influence of river discharge and spring-neap tide on age distribution, we compared the model simulation results of mean age during spring tide and neap tide under low, mean and high flow condition. Besides, to investigate the impact of large scale tidal flat reclamation on the age distribution, a model simulation with tidal flats is conducted (in 1984).

The influence of river discharge and spring-neap tide on the transport timescale

It can be seen that under the some flow condition, the mean ages in the river channel during spring tide and neap tide are almost the same (Figure 4). It means that spring-neap tide has almost no influence on the age distribution in the river channel. However, under a low flow condition, the substance need almost 35 days to be transported out of the estuary after it enters the headwater of the estuary. Compared to the model result under a high flow condition, the transport time under a low flow condition is almost 25 days slower. The transport time under a high flow condition is also faster than that under mean flow (close to 40 days). This suggests that freshwater inflow is one of the dominant factors in controlling transport processes in the Jiaojiang River channel.

Although the model reaches dynamic equilibrium, the model results in the outside of the estuary vary from neap tide to spring tide. The age difference can also be considered as due to the difference of the tracer releasing time (*i.e.,* the tracer is released during spring or neap tides). In the outside of the estuary, for example, the age around the Yijiangshan Island minus the age at the mouth during spring tide under high flow condition is the same with that under low flow condition, both are about 14 days. The model results indicate that tide dominates and the influence of riverine discharge is minor outside the entrance of the estuary.

Remarkably, the tongue-shaped spatial structure of mean age is more evident during spring tide under a low flow condition. This pattern agrees well with the residual current features of Taizhou Bay (Tang, 2003).

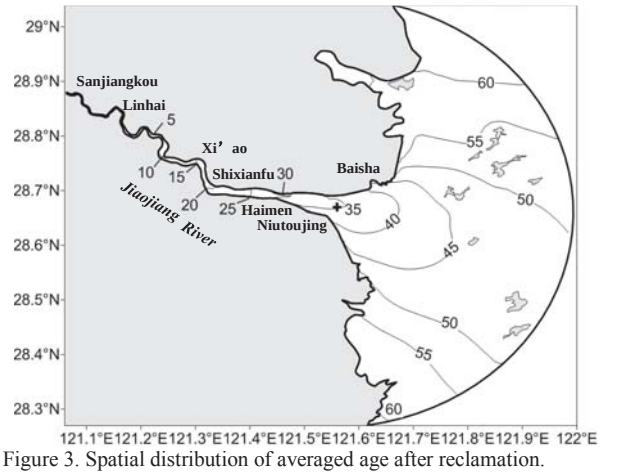

Figure 3. Spatial distribution of averaged age after reclamation.

The influence of tidal flat reclamation on the transport timescale

The model results show that the age distribution of the tracer has been changed after the large-scale of tidal flat reclamation. Compared with the model result without tidal flats (Figure 3), the average age of substance near the river mouth is about 5 days by excluding the tidal flats than by including it. Note that the difference with and without tidal flats only occurs in the

downstream portion of the river and around the tidal flats where the reclamation projects persist. There is almost no difference in the upper portion of the Shixianfu. A notable increase of the tracer age occurs in the mouth of the estuary and around the tidal flats after the large scale tidal flat reclamation. The largest increment of the tracer age can reach approximately 5 days.

Under the mean flow condition, the tongue-shaped spatial structure of mean age is more evident, suggesting more substance is discharged out of the estuary through the middle of the channel after the large scale tidal flat reclamation. The cause of the change is largely due to the shrink of the shoreline after large-scale reclamation, which leads to the changes of flow velocity and direction around the project. After the reclamation, the flow velocity of flood tide is hindered by the funnel-shaped estuary, which leads to the reduction of the flow velocity. At the same time, the decrease of the tidal prism due to the large scale tidal flat reclamation result in the reduction of ebb velocity.

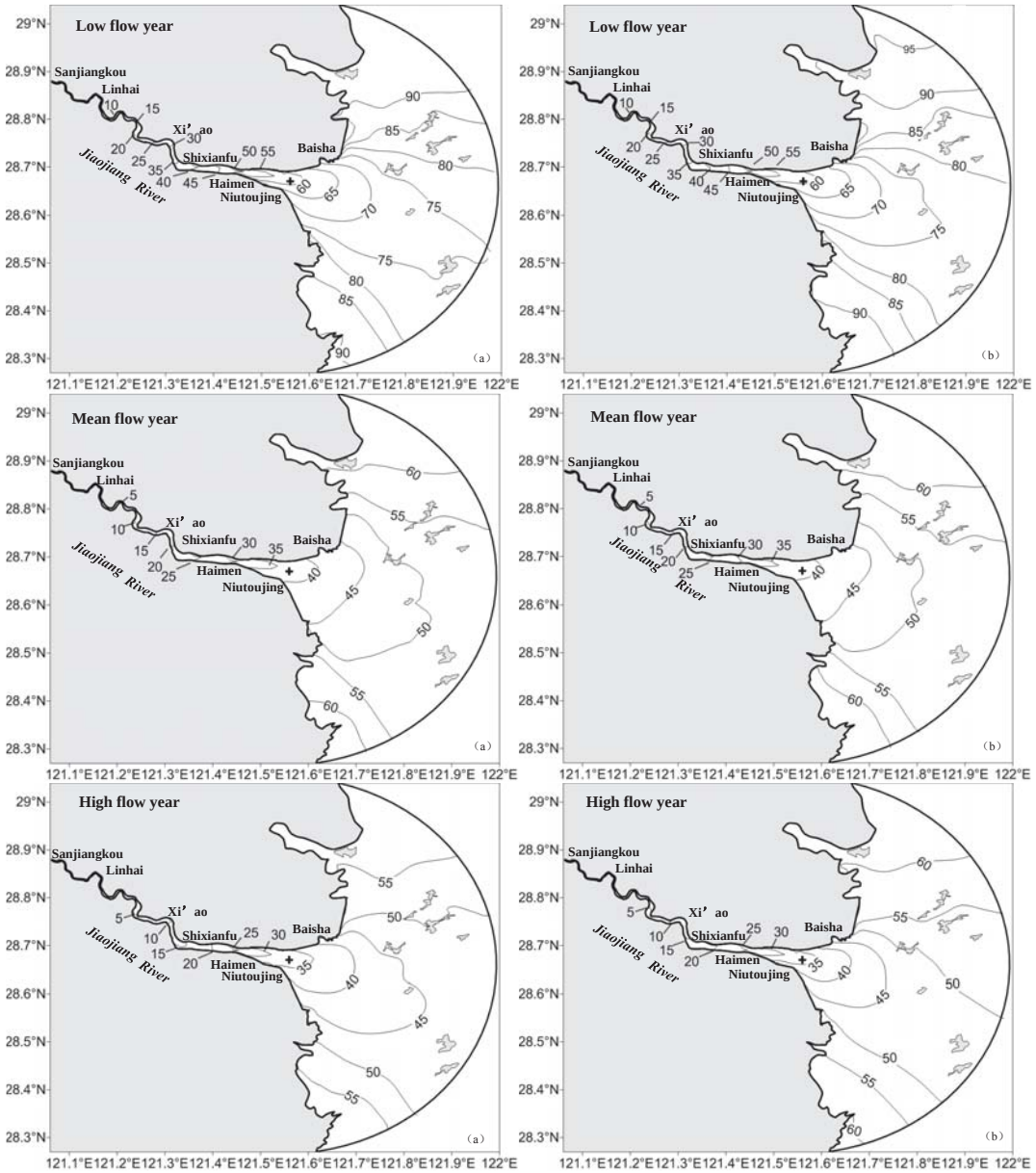

Figure 4. Spatial distribution of averaged age (in days) under different river discharge conditions (panel a shows age during spring tide, panel b shows age during neap tide).

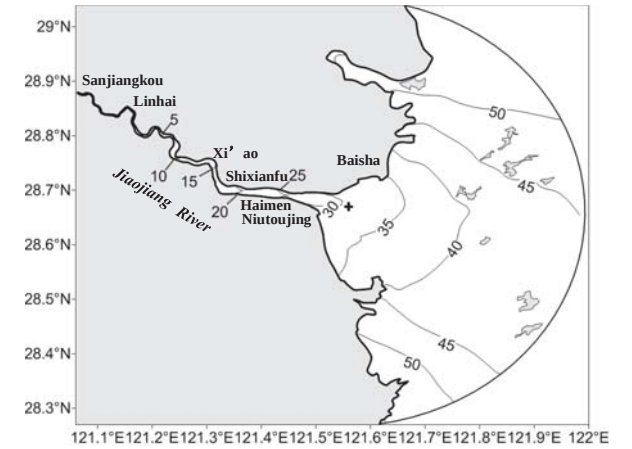

Figure 5. Spatial distribution of averaged age after reclamation.

On the other hand, the wetland turns into land, which leads to that more freshwater is discharged out of the estuary through the middle of the channel, makes the age difference between middle channel and shallow areas increase. Whereas the project has almost no influence on the age distribution in the upper portion of the Shixianfu since the project is far away from it.

CONCLUSIONS

The Jiaojiang Estuary, a typical river-influenced macro-tidal estuary, is used as a representative estuary to gain in-depth insight into the rate of mass transport of pollutant from upstream to the downstream estuary. A series of 2D numerical model experiments with a set of passive tracers were conducted to study the impacts of spring-neap tidal variation, freshwater inflow, and tidal flat reclamation on the age spatial distribution of pollutants.

Results show that the age changed with the tidal level although a dynamic equilibrium condition was obtained. The age near the southern bank of the Jiaojiang River is less than the age at the northern bank. The age distribution in space showed a tongue-shaped pattern, with low tracer age in the middle of the channel and relatively high tracer age in the shallow areas adjacent to the shoreline.

The age distribution depends on the hydrological condition. The influence of freshwater on the age distribution is more significant in the river channel whereas the influence of spring-neap tide is minor. On the contrary, the tide is the dominant factor in controlling transport processes outside of the estuary, where the river discharge has little effect on the age distribution.

After the reclamation, the age in the mouth of the estuary and around the tidal flats had increased by up to 5 days. Under mean flow condition, the tongue-shaped pattern of the age distribution near the mouth of the estuary has become clearer, suggesting that more pollutant is discharged out of the estuary through the center of the channel without the presence of tidal flat. The tidal flat reclamation has almost no influence on the mass transport in the river channel.

ACKNOWLEDGMENTS

This work was supported by the National Natural Science Foundation of China (51109074, 51409093).

LITERATURE CITED

Bolin, B. and Rodhe, H., 1973. A note on the concepts of age distribution and transit time in natural reservoirs. *Tellus,* 25, 58-62.

Brye, B.D.; Brauwere, A.D.; Gourgue, O.; Delhez, É.J.M., and Deleersnijder, É., 2012. Water renewal timescales in the Scheldt Estuary. *Journal of Marine Systems,* 94(2), 74-86.

Deleersnijder, É.; Campin, J.M., and Delhez, É.J.M., 2001. The concept of age in marine modelling; I: Theory and preliminary model results. *Journal of Marine Systems*, 28(3), 229-267.

Delhez, É.J.M., 2013. On the concept of exposure time. *Continental Shelf Research,* 71(0), 27-36.

Delhez, É.J.M.; Campin, J.M.; Hirst, A.C., and Deleersnijder, É., 1999. Toward a general theory of the age in ocean modelling. *Ocean Modelling,* 1(99), 17-27.

Delhez, É.J.M. and Deleersnijder, É., 2002. The concept of age in marine modelling; II: Concentration distribution function in the English Channel and the North Sea. *Journal of Marine Systems,* 31(4), 279-297.

EDF-DRD., 2013. TELEMAC modeling system: 2D hydrodynamics TELEMAC-2D software version 6.2 user manual.

England, M.H., 1995. The age of water and ventilation timescales in a global ocean model. *Journal of Physical Oceanography,* 25(11), 2756-2777.

Monsen, N.E.; Cloern, J.E.; Lucas, L.V., and Monismith, S.G., 2002. A comment on the use of flushing time, residence time, and age as transport time scales. *Limnology and Oceanography,* 47(5), 1545-1553.

Shen, Y.M.; Wang, J.H.; Zheng, B.H.; Zheng, H.; Feng, Y.; Wang, Z.X., and Yang, X., 2011. Modeling study of residence time and water age in Dahuofang Reservoir in *China. Science China Physics, Mechanics and Astronomy,* 54(1), 127-142.

Smagorinsky, J., 1963. General circulation experiments with the primitive equations; I: The basic experiment*. *Monthly Weather Review,* 91(3), 99-164.

Takeoka, H., 1984. Fundamental concepts of exchange and transport time scales in a coastal sea. *Continental Shelf Research,* 3(3), 311-326.

Tang, Z.W., 2003.The study on the influences of regulation work in Jiaojiang Estuary. Zhejiang, China: Zhejiang University, Master's thesis, 66p.

Zhang, Q.; Tao, J.F.; Zhang, C.K.; Dai, W.Q., and Xu, F., 2015. Effect of the large-scale reclamation of tidal flats on the hydrodynamic characteristics in the Taizhou Bay. *Marine Science Bulletin,* 34(4), 392-398.

Zhang, W.G.; Wilkin, J.L., and Schofield, O.M.E., 2010. Simulation of water age and residence time in New York Bight. *Journal of Physical Oceanography,* 40(5), 965-982.

Zimmerman, J.T.F., 1976. Mixing and flushing of tidal embayments in the western Dutch Wadden Sea part I: distribution of salinity and calculation of mixing time scales. *Netherlands Journal of Sea Research,* 10(2), 149-191.

Journal of Coastal Research	SI	75	198-202	Coconut Creek, Florida	2016

Physical Study on Interactions between Waves and a Well-mixed Seabed

Jisheng Zhang †‡*, Ke Sun‡, Yanyan Zhai‡, Huashan Zhang‡, and Chi Zhang†‡

†Key Laboratory of Coastal Disaster and Defence (Hohai University)
Ministry of Education
Nanjing 210098, China

‡College of Harbor Coastal and Offshore Engineering
Hohai University
Nanjing 210098, China

www.cerf-jcr.org

www.JCRonline.org

ABSTRACT

Zhang, J.; Sun, K.; Zhai, Y.; Zhang, H., and Zhang, C., 2016. Physical study on interactions between waves and a well-mixed seabed. *In:* Vila-Concejo, A.; Bruce, E.; Kennedy, D.M., and McCarroll, R.J. (eds.), *Proceedings of the 14th International Coastal Symposium* (Sydney, Australia). *Journal of Coastal Research*, Special Issue, No. 75, pp. 198-202. Coconut Creek (Florida), ISSN 0749-0208.

The problem of wave-seabed interaction has attracted more and more attention of coastal researchers and engineers, as it plays an important role in the estimations of seabed stability and foundation design of offshore structures. Much effort has been made by many investigators to study the wave-seabed interaction in the past decades. However, most of them focus on the wave-induced response within a seabed with single/uniform soil particle, ignoring the mixed seabed consisting of different soil particles in the real environment. A series of laboratory experiments are carried out in a wave flume to study the wave-driven pore-water pressure in a well-mixed seabed (consisting of sand and silt) and the attenuation of wave height. Waves propagating over a mixed seabed lead to oscillatory excess pore-water pressures within the porous seabed. Maximum amplitude of the ratio of pore-water pressure within the seabed to pressure on seabed surface decreases within a deeper layer. A phase lag of pore-water pressure is clearly observed, and it contributes to net upward pressure related to seabed instability. The impacts of mixture percentage of sand/silt on pore-water pressure are also analyzed and discussed.

ADDITIONAL INDEX WORDS: *Wave-seabed interaction, seabed response, wave attenuation, mixed seabed.*

INTRODUCTION

It is well known that wave-induced seabed responses would potentially compromise the safety of both nearshore and offshore structures located on/in the seabed (*e.g.*, breakwaters, pipelines, piles, and platforms) and produce severe consequences. As such, the phenomenon of wave-seabed interaction has received great concern among geotechnical researchers and coastal engineers since 1970s. Marine sediment may undergo liquefaction when waves propagate over the seabed and exert periodic fluctuations of wave pressure on the surface of the seabed. The wave-induced pressure loading at the mudline causes the generation of excess pore-pressure response in the seabed, and simultaneously the variation of effective stress, which has been recognized as a dominant factor of evaluating the seabed instability. When the effective stresses between individual grains vanish because of the excess pore-pressure, the sediment mixture will act as liquid in either a horizontal (shear failure) or vertical direction (liquefaction), leading to a failure of seabed (Zen *et al.*, 1998). The liquefaction can generally be categorized into two types (Sumer and Fredsøe, 2002): the residual or build-up excess pore-pressure due to cyclic shear stresses (*e.g.*, Clukey *et al.*, 1985a; Foda and Tzang, 1994; van Kessel and Kranenburg, 1998; de Wit and Kranenbury, 1996), and the transient or oscillatory excess pore-pressure characterized by amplitude attenuation and phase lag (*e.g.*, Yamamoto *et al.*, 1978; Nago, 1981; Clukey *et al.*, 1985b; Tzang and Ou, 2006; Tzang *et al.*, 2009). Another important physical phenomenon during the wave travelling over the seabed is the attenuation of wave height, which is mainly due to the energy loss induced by wave-seabed interaction (Putnam, 1949).

The existing studies for wave-seabed interaction mainly compose of analytical solutions (*e.g.*, Yamamoto *et al.*, 1978; Madsen, 1978; Mei and Foda, 1981; McDougal *et al.*, 1989) and numerical simulations (Seed and Rahman, 1978; Sassa and Sekiguchi, 2001; Sekiguchi *et al.*, 2001; Zhang *et al.*, 2013; Zheng *et al.*, 2014). By contrast, experimental studies, both field observation and laboratory test, are relatively scarce. In spite of various particle sizes, sandy sediment was commonly adopted in either wave flume tests (*e.g.*, Yamamoto *et al.*, 1978 (d_{50}=0.2mm, d_{50}=1.2mm); Clukey *et al.*, 1985b (d_{50}=0.58 mm); Zen and Yamazaki, 1990a,b (d_{50}=0.181mm); Tzang and Ou 2006, and Tzang *et al.*, 2009 (d_{50}=0.134mm, d_{50}=0.092mm)) or centrifuge wave tank tests (*e.g.*, Sassa and Sekiguchi, 1999 (d_{50}=0.15mm)). They investigated the oscillation of the transient pore pressure in the sandy seabed and the transient liquefaction caused by the upward seepage force under wave trough. Silt and clay were also utilized and the build-up of residual pore pressures leading to the residual liquefaction was observed in several experimental studies (Clukey *et al.*, 1985a; Foda and Tzang, 1994; de Wit and Kranenbury, 1996; van Kessel and Kranenburg, 1998; Zheng *et al.*, 2007).

The aforementioned studies about the wave-seabed interaction primarily focused on a situation of mono-type soil seabed, like pure sand, pure silt and pure clay, in which the wave-induced seabed responses are well acknowledged, while rare attention

DOI: 10.2112/SI75-040.1 received 15 October 2015; accepted in revision 15 January 2016.
*Corresponding author: jszhang@hhu.edu.cn

has been paid to the response of a multi-type soil seabed to wave pressure. In the real marine environment, the seafloor is normally composite and composed of multiple soil ingredients, which would cause the wave-seabed interaction more complicated than that for a mono-type soil seabed. To the authors' best knowledge; there exists only a few researches regarding the effect of the clay content on the wave-induced liquefaction in clayey silt and clayey sand (Lindenberg *et al.*, 1989; Kirca *et al.*, 2014; Liu and Jeng, 2015). The influence of the mixture percentage of sand/silt on pore-pressure response and liquefaction in sand-silt well-mixed soils still needs to be investigated.

This study is to compare the wave-induced pore-pressure in a well-mixed seabed (a mixture of sand and silt) with that in a pure sandy seabed or a pure silty seabed by conducting a series of flume tests. The pore-pressure responses of seabed and wave heights at the corresponding sections of the flume are measured simultaneously.

METHODS

A series of laboratory experiments are carried out in a wave flume to study the wave-driven pore-water pressure in a well-mixed seabed (consisting of sand and silt).

Wave Flume and Instrumentations

The experiments are conducted in a wave flume with a size of 55.0m (length) × 1.0m (width) × 1.3m (height) at Hohai University, as shown in Figure 1. Waves can be generated by a piston-type wave-generator located at the upstream end of the flume. A sloping beach is located at the downstream end as wave absorber in order to effectively eliminate wave reflection. A sediment pit is installed in the middle section of wave flume, specifically manufactured for the experiments on wave-seabed interaction. The pit is 2.2m (length), 0.75m (width), and 0.33m (height), as illustrated in Figure 1, and is filled with soil so that the seabed surface is leveled with the flume bottom. The water depth within the flume is kept as 0.40m for all tests.

In the laboratory experiments, excess pore water pressure and water surface elevation are measured. The miniature pore pressure transducers (6mm in diameter) are utilized to measure the wave-induced pore pressure both above and beneath the sediment deposit mudline. They are deployed along the central line of soil pit at four different depths (z=0, 7, 14, 21cm, where z is the vertical distance downward from the mudline), as shown in Figure 1. The pore pressure transducers were submerged in water for about 24h prior to experiments to ensure gas would be totally exhausted. The wave height gauges are arranged along the central axis of wave flume, including two far-field gauges and three near-field ones, to record the variation of wave height across the sediment deposit. The signals of pore pressure transducers and wave height gauges are sampled synchronously. In the tests, the sampling frequency for the pore pressure transducers and wave height gauges is set to 50Hz.

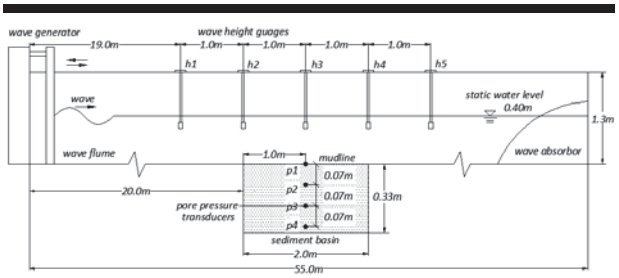

Figure 1. Sketch of the wave flume and experimental set-up

Seabed Soil

Previous laboratory experiments were almost complemented with pure silt or pure sand, with very few researches with silt-clay mixtures and sand-clay mixtures. Nevertheless, a series of laboratory experiments are conducted using the sand-silt mixtures. The seabed soil adopted in the experiments is commercially available, and therefore standardized, making it ideal for the laboratory experiments. Two different types of soil (sand and silt) are used in the laboratory study, and their main physical properties are listed in Table1. The submerged specific gravity of soil is given by $\gamma' = (1-n)(\gamma_s - \gamma_w)$ where γ_w is the specific weight of water and γ_s represents the specific weight of sediment grains.

Prior to the experiments, sand-silt mixtures are well prepared as following. First, a known quantity of pure sand (with uniform grain size of 0.15mm) and pure silt (with uniform grain size of 0.06mm) are separately poured into the mixing tank and thoroughly mixed under a nearly dry condition. Then, water is gradually added into the tank during the process to reinforce the mixing while continuously stirring it until it reached the liquid state. Extreme care is taken to ensure that the ultimate mixture for experiments is homogeneous. Subsequently, the sand-silt mixture is pumped to the test section where it is allowed to consolidate for at least two days. Finally, a soil layer of about 0.33m in thickness is obtained. The laboratory tests begin as soon as the consolidating soil layer surface is leveled with the flume bottom.

The silt content (SC) in the sand-silt mixtures was 0%, 25%, 50%, 75% and 100%, where SC is defined as $W_{silt}/W_{mixture}$, with W_{silt} and $W_{mixture}$ representing the weight of silt and the weight of mixture, respectively. The SC values of 0%, 50%, 100% stand for three typical soil conditions, *i.e.* pure sand, sand-silt mixture, and pure silt.

Table 1 *Physical Properties of Seabed Soil*

Soil type	Uniform grain size $d_{50}(mm)$	Unit weight of soil $\gamma_s(kN/m^2)$	Submerged unit weight of soil $\gamma'(kN/m^2)$	Specific gravity $G_s=\gamma_s/\gamma$	Specific unit weight of soil $\gamma_t(kN/m^2)$	Plasticity index $I_p(\%)$
Silt	0.06	27.0	9.7	2.70	13.6	21.6
Sand	0.15	26.7	10.1	2.67	16.9	----

Table 2. *Parameters of Incident Waves*

Test Number	Wave conditions					
	Wave height $H(cm)$	Wave period $T(s)$	Amplitude of water particle orbital velocity at the bed $U_m(cm/s)$	Amplitude of undisturbed friction velocity $U_{fm}(cm/s)$	Reynolds number $R_e\times10^3$	Shields parameter θ
1	6	1.0	6.996	1.103	1.616	0.122
2	6	1.2	9.270	1.363	2.142	0.185
3	6	1.4	10.734	1.521	2.480	0.231
4	6	1.6	11.701	1.623	2.703	0.263
5	6	1.8	12.366	1.692	2.857	0.286
6	8	1.0	9.329	1.274	2.874	0.162
7	8	1.2	12.360	1.574	3.808	0.247
8	8	1.4	14.311	1.756	4.409	0.308
9	8	1.6	15.601	1.874	4.806	0.350
10	8	1.8	16.489	1.953	5.079	0.381
11	10	1.2	15.450	1.759	5.949	0.309
12	10	1.4	17.889	1.964	6.889	0.385
13	10	1.6	19.501	2.095	7.509	0.438
14	10	1.8	20.611	2.184	7.936	0.476
15	12	1.4	21.467	2.151	9.920	0.462
16	12	1.6	23.401	2.295	10.813	0.526
17	12	1.8	24.733	2.392	11.429	0.571
18	14	1.4	25.045	2.323	13.502	0.539
19	14	1.6	27.301	2.479	14.718	0.613
20	14	1.8	28.855	2.584	15.555	0.666

Incident Waves

The parameters of incident waves are given in Table 2, in which H is wave height and T is wave period, respectively. U_m is amplitude of orbital velocity at the seabed, calculated from the small-amplitude wave theory, and U_{fm} is the amplitude of undisturbed friction velocity, given by

$$U_m=\frac{\pi H}{T}\frac{\cosh(k(z+d))}{\sinh(kd)} \quad (1)$$

$$U_{fm}=\sqrt{\frac{f_w}{2}}U_m \quad (2)$$

where f_m is wave friction coefficient given by $f_m=2/\sqrt{R_e}$. $R_e=aU_m/\nu$ is wave Reynolds number and $R_f=d_{50}U_{fm}/\nu$ is grain Reynolds number. The quantity θ represents Shields parameter defined by

$$\theta=\frac{U_{fm}^2}{g(s-1)d_{50}} \quad (3)$$

where g is the acceleration due to gravity.

RESULTS

In this study, 80 tests are carried out in total. Among these, 20 tests, 15 tests and 45 tests are conducted with sand-alone (pure sand), silt-alone (pure silt) and sand-silt mixture.

Sand-alone Case

Ocean waves drive the pore pressure in sand-alone seabed where the wave-induced water pressure on seabed surface propagates into the seabed along with the phenomenon of amplitude attenuation and phase lag. Figure 2 illustrates the wave-induced pore pressure versus time at different depths for sandy seabed in the case of H=6cm, T=1.0s and H=8cm, T=1.6s, respectively. As shown in Figure 2(a), the maximum amplitude at P2 and P3 is only 55% and 44% of that recorded at P1 respectively, indicating that the maximum amplitude is reduced by 45% between P1 and P2, and 11% between P2 and P3. Meanwhile, the results in Figure 2(a) show that the pore pressure at P2 is delayed by 0.1 s compared to that at P1.The pore pressure at P3 is delayed by 0.42 s compared to that at P2. Figure 2(b) shows a similar phenomenon of decreasing amplitude attenuation and increasing phase lag with the increase of seabed depth. The results exhibited in Figure 2 are very similar to those reported in Liu *et al*. (2015).

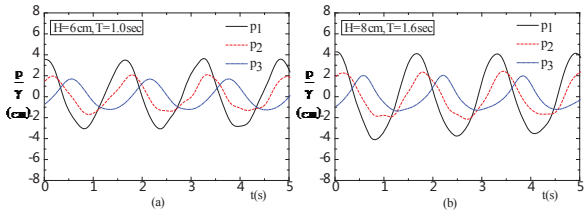

Figure 2. Pore pressure time series under sandy seabed condition at depths z=0cm (P1), z=7cm (P2) and z=14cm (P3); (a) with H=6cm, T=1.0s; (b) with H=8cm, T=1.6s.

Silt-alone Case

Figure 3 shows the excess pore pressure time series at P2 and P3 in silt-alone seabed with the conditions of H=12cm and T=1.4s. The pore pressure at P2 begins to accumulate at approximately t=2.7s and reaches a maximum value of about 5.6cm at t=76.7s, while the pore pressure at P3 doesn't accumulate until t=4.8s and reaches a maximum value of about 15.0cm at t=127.5s. The result indicates that the starting time of pore pressure accumulation is delayed with the increase of depth, along with the acceleration of accumulation and the augment of maximum pore pressure. It is worth mentioning that the similar phenomena have been studied in Sumer *et al*. (2006).

The value of initial mean normal effective stress defined as $\sigma_0' = \gamma' z(1+2k_0)/3$ is also given in Figure 3. $p_{\max}$ represents the maximum value of accumulated pore pressure. Liquefaction will occur once the excess pore pressure exceeds the initial effective stress. The results indicate that the soil is already liquefied for depths z<14cm in these cases, as observed in the experiments. It is noted that the seabed is not liquefied in the cases with small wave height and long wave period (e.g., H=8cm and T=1.8s).

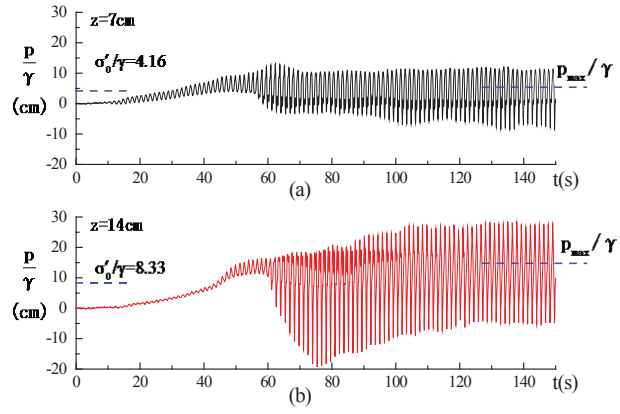

Figure 3. Pore pressure time series at different depths in silt seabed; (a) Pore pressure recorded by P2 with the depth z=7cm; (b) Pore pressure recorded by P3 with the depth z=14cm.

Sand-silt Mixture

Figure 4 shows the excess pore pressure at P2 with the seabed consisting of sand-silt mixtures with different mixture ratios (SC=25%, 50%, 75% and 100%) under the wave condition of H=10cm and T=1.4s. The accumulated pore pressure is in positive correlation with the SC in the mixture. In the case of sand-alone seabed where SC=0, only oscillation of pore pressure can be observed. When SC is increased to 25%, the pore pressure accumulates rather slightly while oscillating and finally reaches a maximum value of 0.81cm in equilibrium. When SC is further increased to 50% and 75%, the accumulated pore pressure increases and reaches a stable value of 4.92cm and 5.52cm respectively. In the case with silt-alone seabed where SC=100%, the pore pressure accumulates considerably greater than the others and reaches a stable value of 5.75cm.

DISCUSSION

As mentioned before, only oscillatory component can be observed in sand-alone seabed under periodic wave loading. Due to the high permeability of sandy seabed (d_{50}=0.15mm) where SC=0%, the excess pore pressure dissipates quickly and does not accumulate in the seabed. While in the silt-alone seabed (d_{50}=0.06mm) where SC=100%, the excess pore pressure cannot dissipate in time and gradually accumulates until it reached a stable value. When sand and silt are well-mixed, the fine particles will fill up the pores of the coarse ones, which increases the compaction, lowers the void ratio and limits the drainage. Therefore, the dissipation of excess pore pressure becomes more difficult. The laboratory results by comparisons show that the increasing content of silt of mixture leads to an increasing liquefaction potential, which is in consistent with the conclusions of Tzang and Ou (2006).

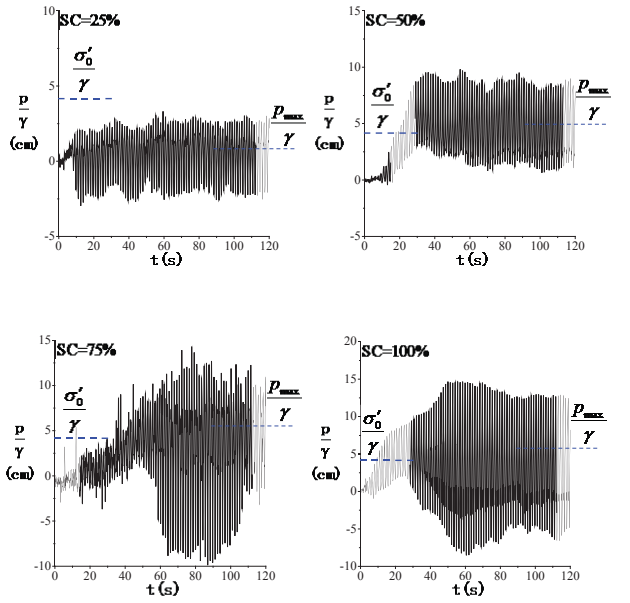

Figure 4. Pore pressure time series at P2 with different seabed (SC=25%, 50%, 75%, 100%) in the case of H=10cm and T=1.4s.

CONCLUSIONS

A series of laboratory experiments are carried out to investigate the interactions between wave and a well-mixed seabed. The experimental results show that the SC has a remarkable impact on the wave-induced pore pressure in seabed consisting of sand-silt mixtures and seabed liquefaction. When the SC is comparatively low, e.g. SC=25%, the sand-silt mixture seabed will behave more of a sandy seabed, with the pore pressure oscillating while accumulating slightly. The maximum excess pore pressure does not exceed the initial effective stress, and the seabed is not liquefied. When the SC is no less than 50%, i.e. 50% and 75%, the sand-silt mixture seabed will behave more of a silty seabed, with the pore pressure accumulating considerably. Although the maximum accumulated pore pressure for both of them is not greater than that in a silt-alone seabed, they will exceed the initial effective stress and lead to seabed liquefaction. The accumulation phenomena of pore pressure in seabed are mainly due to the soil permeability. A larger SC will result in a reduced permeability of the mixture and a greater liquefaction potential.

ACKNOWLEDGEMENTS

This research work is financially supported by the National Natural Science Foundation of China (51209083, 51137002), the 111 Project (B12032), the marine renewable energy research project of State Oceanic Administration (GHME2013GC03; GHME2015GC01), and the Fundamental Research Funds for the Central University, China (2013B31614; 2014B05114).

LITERATURE CITED

Clukey, E.C.; Kulhawy, F.H.; Liu, P.L.F., and Tate, G.B., 1985a. The impact of wave loads and pore-water pressure generation on initiation of sediment transport. *Geo-Marine Letters*, 5(3), 177-183.

Clukey, E.C.; Kulhawy, F.H., and Liu, P.L.F., 1985b. Response of soils to wave loads: experimental study. In: Chaney, R.C. and Demars, K.R. (eds.), Strength Testing of Marine Sediments, Laboratory and In-Situ Measurements. ASTM STP, vol.883.*Americal Society for Testing and Materials, Philadelphia*, 381-396.

de Wit, P.J. and Kranenburg, C., 1996. On the effects of a liquefied mud bed on wave and flow characteristics. *Journal of Hydraulic Research*, 34(1), 3-18.

Foda, M.A. and Tzang, S., 1994. Resonant fluidization of silty soil by water waves. *Journal of Geophysical Research Oceans*, 99(C10), 20463-20475.

Kirca, V.S.O.; Sumer, B.M., and Fredsoe, J., 2014. Influence of clay content on wave-induced liquefaction. *Journal of Waterway Port Coastal and Ocean Engineering*, 140(4),04014024-1-11.

Lindenberg, J.; van Rijn, L.C., and Winterwerp, J.C., 1989. Some experiments on wave-induced liquefaction of soft cohesive soils. *Journal of Coastal Research*, SI 5, 127-137.

Liu, B. and Jeng, D.S., 2015. Laboratory Study for Influence of Clay Content (CC) on Wave-Induced Liquefaction in Marine Sediments. *Marine Georesources and Geotechnology*, 10.1080/1064119X.2015.1005322, 1-13.

Madsen, O.S., 1978. Wave-induced pore pressure and effective stresses in a porous bed. *Geotechnique*, 28(4), 377-393.

McDougal, W.G.; Tsai, Y.T.; Liu, P.L.F., and Clukey, E.C., 1989.Wave-induced pore water pressure accumulation in marine soils. *Journal of Offshore Mechanics and Arctic Engineering*, 111(1), 1-11.

Mei, C.C. and Foda, M.A., 1981.Wave-induced responses in a fluid-filled poro-elastic solid with a freesurface-a boundary layer theory. *Geophysical Journal international*, 66(3), 597-637.

Putnam, J.A., 1949. Loss of wave energy due to percolation in a permeable sea bottom. *Eos Transactions American Geophysical Union*, 30(3), 349-356.

Sassa, S. and Sekiguchi, H., 1999. Wave-induced liquefaction of beds of sand in a centrifuge. *Geotechnique*, 49(5), 621-638.

Sassa, S. and Sekiguchi, H., 2001. Analysis of wave-induced liquefaction of sand beds. *Geotechnique*, 51(2), 115-126.

Seed, H.B. and Rahman, M.S., 1978. Wave-induced pore pressure in relation to ocean floor stability of cohesionless soils. *Marine Geotechnology,* 3(2), 123-150.

Sekiguchi, H.; Sassa, S., and Miyamoto, J., 2001. Analysis of progressive liquefaction as a moving-boundary problem.*Geotechnique*, 51(10), 847-858.

Sumer, B.M.and Fredsoe, J., 2002. The Mechanics of Scour in the Marine Environment. *Singapore: World Scientific*, 552p.

Sumer, B.M., Hatipoglu, F., Fredsøe, J., and Sumer, S. K., 2006. The sequence of sediment behaviour during wave induced liquefaction. *Sedimentology*, 53(3), 611-629.

Tzang, S.Y. and Ou, S.H., 2006. Laboratory flume studies on monochromatic wave-fine sandy bed interactions: part 1. soil fluidization. *Coastal Engineering*, 53(11), 965-982.

Tzang, S.Y.; Ou, S.H., and Hsu, T.W., 2009. Laboratory flume studies on monochromatic wave-fine sandy bed interactions: part 2. sediment suspensions. *Coastal Engineering*, 56(3), 230-243.

vanKessel, T. and Kranenburg, C., 1998. Wave-induced liquefaction and flow of subaqueous mud layers. *Coastal Engineering*, 34(1), 109-127.

Yamamoto, T.; Sellmeijer, H.L.K.H., and Hijum, E.V., 1978. On the response of a pore-elastic bed to water waves. *Journal of Fluid Mechanics*, 87(l), 193-206.

Zen, K.; Jeng, D.S.; Hsu, J.R.C., and Ohyama, T., 1998. Wave-induced seabed instability: difference between liquefaction and shear failure. *Soils and Foundations*, 38(2), 37-47.

Zen, K. and Yamazaki, H., 1990a. Mechanism of wave-induced liquefaction and densification in seabed. *Soils and Foundations*, 30(4), 90-104.

Zen, K. and Yamazaki, H., 1990b. Oscillatory pore pressure and liquefaction in seabed induced by ocean waves. *Soils and Foundations*, 30(4), 147-161.

Zhang, J.S., Zheng, J.H., Zhang, C., Jeng, D.S., and Guo, Y.K., 2013. Numerical study on the interaction between waves andtwin pipelines in sandy seabed. *Journal of Coastal Research*, SI65, 428-433.

Zheng, J.H., Zhang,C., Demirbilek, Z., and Lin, L., 2014.Numerical study of sandbar migrationunder wave-undertow interaction. ASCE J*ournal of Waterway, Port, Coastal and Ocean Engineering,* 140 (2), 146-159.

Zheng, J.H.;Jeng, D.S., and Mase, H., 2007. Sandy beach profile response to sloping seawalls: an experimental study. *Journal*

of Coastal Research, SI 50, 334-337.

Journal of Coastal Research	SI	75	203-207	Coconut Creek, Florida	2016

Dynamic analysis of riverbed evolution: Chengtong Reach of Yangtze Estuary

Yongping Chen[†*], Jiangxia Li[†], Zhigang Wu[†] and Shunqi Pan[‡]

[†]State Key Laboratory of Hydrology-Water Resources and Hydraulic Engineering, Hohai University
Nanjing, China

[‡]School of Engineering
Cardiff University
Cardiff, The United Kingdom

www.cerf-jcr.org

www.JCRonline.org

ABSTRACT

Chen, Y.P., Li, J.X., and Pan, S.Q., 2016. Dynamic analysis of riverbed evolution: Chengtong Reach of Yangtze Estuary. *In:* Vila-Concejo, A.; Bruce, E.; Kennedy, D.M., and McCarroll, R.J. (eds.), *Proceedings of the 14th International Coastal Symposium* (Sydney, Australia). *Journal of Coastal Research*, Special Issue, No. 75, pp. 203-207, Coconut Creek (Florida), ISSN 0749-0208.

This paper proposes a new approach to improve the analysis by extensively using the numerical model results. A 2D hydrodynamic model based on the Delft 3D suite is first set up and validated with the field measurement data. The model is then used to examine the hydrodynamic responses of the estuary to the change of local bathymetry or upstream discharge. This approach is applied to the Chengtong Reach of Yangtze Estuary as an example. The net discharge ratio (NDR) is used as an index to demonstrate the trend of channel development. The results show that the net discharge ratios (NDRs) at the main channels of Fujiangsha, Tongzhousha and Langshansha sub-reaches decrease with increase of upstream river discharge in general; however, the NDR at the main channel of Rugaosha sub-reach increases first, and then decreases with increase of upstream river discharge when the river discharge is larger than 45,000 m^3/s. This difference is related to the local bathymetry as well as the ebb-dominated or flood-dominated characters in those sub-reaches.

ADDITIONAL INDEX WORDS: *Numerical modelling, net discharge ratio, channel development*

INTRODUCTION

The analysis of riverbed evolution is crucial for the better understanding of natural processes in estuaries, and also important for the assessment of the impact of engineering works, such as estuarine regulation projects in estuaries. The traditional way to analyze the riverbed evolution is fully based on the analysis of the surveyed bathymetry and hydrologic data at the sites of interest (e.g. Yang *et al.*, 2006; Liu *et al.*, 2007; Jiang *et al.*, 2011). The main drawback of this approach is that the analysis requires a large quantity of field measurement data, which may not always be available. In addition, the measured bathymetry data may not coincide in time with the measured hydrologic data, resulting in a weak consistency among the raw data. In order to overcome those difficulties, this paper proposes a new approach by extensively using numerical results to provide more coherent datasets, so as to analyze the effects of local bathymetry and upstream discharge on the evolution of the estuary. As an example, the approach is used to analyze the riverbed evolution at Chengtong Reach of Yangtze Estuary, China.

The Chengtong reach is located at the upper part of Yangtze Estuary, which is shown in Figure 1. The length of the entire reach is about 90 km. Since 1980s, the riverbed has been found considerably changed, either due to the natural processes or the anthropogenic impacts (Yang *et al.*, 2002; Wang *et al.*, 2008; Hu *et al.*, 2009; Wu *et al.*, 2009; Yang *et al.*, 2014).

In recent years, several on-going or completed large scale hydraulic engineering projects, such as Three-Gorge Dam project, South-to-North Water Diversion Project and Yangtze River-Taihu Water Transfer Project have been constructed at the upstream of Yangtze River. Those projects inevitably altered the hydrodynamic and morphodynamic conditions in the Chengtong reach. How the riverbed responds to the changes of those conditions becomes increasingly important, but yet not fully understood.

In the past decades, there have been many research studies on the analysis of riverbed evolution of the Chengtong Reach (e.g. Tao *et al.*, 1998; Cao *et al.*, 2000; Du *et al.*, 2002; Zhong *et al.*, 2009). The majority of these studies focused on the qualitative descriptions of riverbed evolution based on the analysis of historical bathymetry data. There lacks the quantitative analysis of hydrodynamic and morphodynamic processes, particularly in the scale of whole reach. In this paper we combine the traditional analysis with the hydrodynamic models to analyze the dynamic relationship between the riverbed evolution and the change of hydrodynamic conditions at upstream. This relationship can be applied to analyze the potential influence of hydrodynamic changes due to either natural or anthropogenic reasons on the future evolution of riverbed. It can help us to have a better understanding of possible changes of riverbed evolution corresponding to the hydrodynamic changes by the hydraulic engineering projects at the upstream of Yangtze River.

DOI: 10.2112/SI75-041.1 received 15 October 2015; accepted in revision 15 January 2016.
*Corresponding author: ypchen@hhu.edu.cn

Figure 1. Location of study area (Chengtong reach is in the red square).

METHODS

Figure 2 illustrates the framework of methodology used in this study. The surveyed bathymetry data is directly used to investigate the riverbed changes of the estuary in the past. Using tools such as Surfer and CAD software, we can easily find the spatial and temporal variations of bathymetry at the area of interest, which helps us to understand the trend of riverbed changes in history. In the meantime, the Delft 3D suite is used to set up a hydrodynamic model covering the entire study area. After model validation, two subsequent numerical experiments are carried out. One is changing the bathymetry conditions but keeping the same upstream & downstream conditions, to investigate the effect of bathymetry changes on the net discharge ratio, which is considered as an important index to indicate the trend of riverbed evolution at different channels. The other is keeping the same bathymetry conditions but changing the river discharge conditions at upstream boundary, to understand the effect of discharge conditions on the net discharge ratio and to indicate the response of channel evolution at various sub-reaches to the change of discharge at upstream. Based on the numerical results, we can gain insights into the index of net discharge ratio at the main and secondary channels, and predict possible changes of riverbed if the upstream discharge conditions are changed.

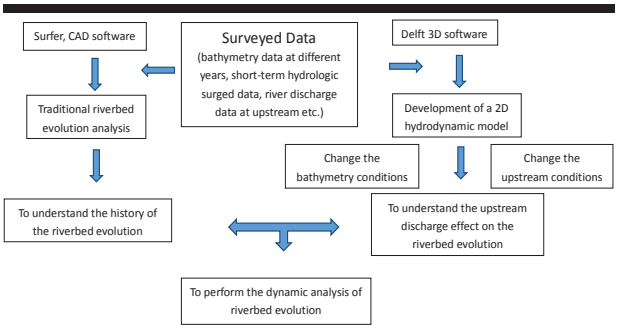

Figure 2.Illustration of the framework of methodology

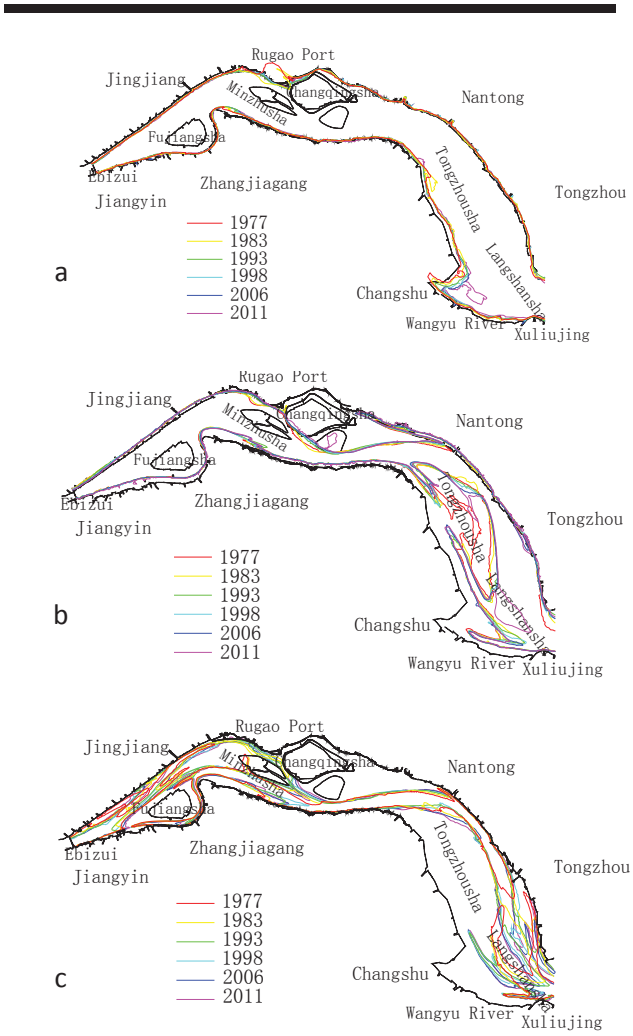

Figure 3. Bathymetry changes of Chengtong Reach from 1977 to 2011 at the contours of (a) 0m, (b)-5m and (c) -12.5m.

RESULTS

The bathymetries measured in 1977, 1983, 1993, 1998, 2006, 2011 are used to analyze the riverbed evolution at three contour levels, namely: 0 m representing the river banks; -5.0 m representing the shoals; and -12.5 m representing the deep channels. The changing of the bathymetry contours from 1977 to 2011 show that the river banks are mostly stable over the 34-year period, with only noticeable changes being found near the Rugao Port and Wangyu River (Figure 3a). However, the shoals are more active, particularly in the sub-reaches of Tongzhousha and Langshangsha. The frequent movement of Tongzhousha and Langshangsha shoals has resulted in remarkable bathymetric changes (Figure 3b). The changes of -12.5m contours indicate that the main channel in the estuary are very dynamic, especially at the north channel of Fujiangsha and the downstream end of Fujiangsha (Figure 3c).

The results show that the evolution of Chengtong reach is dynamic and active, whilst the banks appear to more stable, mainly as a result of bank regulation projects in the past 30 years.

In order to understand the erosion and accretion patterns in the study area, the volumetric changes, average bed level changes and annual erosion/accretion rates under 0 m contours are calculated between the adjacent survey years. As shown in Table 1, it is found that the Chengtong reach was general stable in the period of 1977-2006. However, after 2006, there was a rapid increase in erosion. The erosion rate in 2006-2011 is approximately 6 times of that over previous 30 years. It is believed that this significant change is strongly related to the change of upstream hydrodynamics and sediment supplies from the upstream.

Table 1.*The erosion/accretion rate of the Chengtong Reach*

Period	Volume ($10\ m^3$)	erosion/accretion thickness(cm)	erosion/accretion rate(cm/a)
1977-1983	2.56	0.512	0.09
1983-1993	-86.45	-17.29	-1.73
1993-1998	49.42	9.88	1.98
1998-2006	63.51	12.70	1.59
2006-2011	289.19	57.84	11.57

Note: positive value indicates erosion; negative value indicates accretion.

Numerical model

To further investigate the effect upstream conditions on the riverbed evolution of the Chengtong reach, a depth-averaged 2D hydrodynamic model is established by using the Delft 3D suite. The model covers the area from Datong to the outside of Yangtze Estuary. The orthogonal curvilinear grid system is used with the resolution ranging from 200 m to 3000 m, as shown in Figure 4.

Figure 4. Orthogonal curvilinear grid system

The model is capable of simulating the depth-averaged flood and ebb flows, as well as the tidal levels at the computational grids. The model is validated with the field data measured in flood season (8/2004-9/2004) and dry season (1/2005-2/2005) at 15 water level stations and 15 tidal current stations. Due to the page limitation, only part of validation results are shown in Figure 5 and 6. From these figures, we can see that the computed water levels and current velocities agree well with the field measurements, which provides us a strong confidence for using this 2D model in the further study.

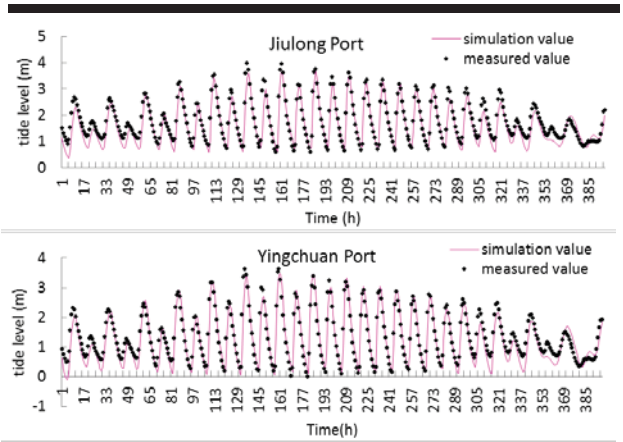

Figure 5. Comparison of computed and measured tidal levels at the stations of Jiulong Port and Yingchuan Port

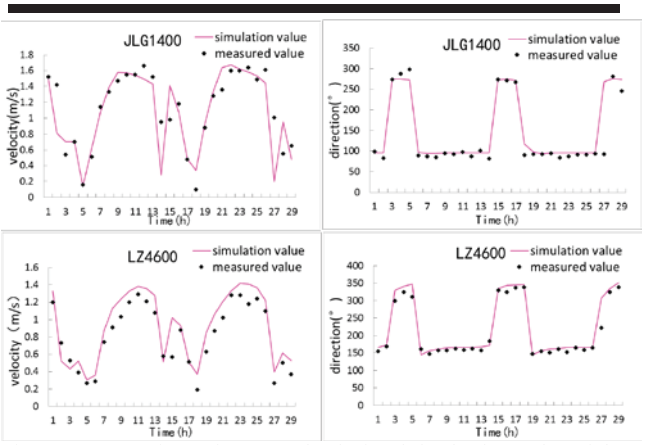

Figure 6. Comparison of computed velocity (left: absolute value; right: direction) at the stations of JLG1400and LZ4600

A series of numerical experiments are first carried out. Six different sets of field-measured bathymetry data during 1977 to 2011 are used, with the same upstream and downstream conditions in the model. The rationale of these experiments is that the topographic conditions at Jiangyin (upstream of Chengtong reach) and Xuliujing (downstream of Chengtong reach) are found almost unchanged in the past 30 years. They can be seen as two controlling points. This will enable us to investigate the effect of bathymetry changes under the same upstream/downstream conditions.

Although not shown here, the computed ebb/tidal flow patterns confirm that the bathymetry has a significant effect on the flow pattern, particularly in the sub-reach of Rugaosha, where the north channel has disappeared, and the sub-reach of Langshansha, where the main current stream has changed from the middle channel to the east channel.

In order to quantify the relationship between the bathymetry evolution and the hydrodynamic changes, an index named as net discharge ratio (NDR) is introduced, in which the net discharge is defined as the difference of tidal discharge between the ebb and flood phases during a tidal cycle, and the ratio is defined as the percentage of net river discharge of the studied channel to all channels at the selected cross-section. In this study, four cross-sections are selected (Figure 7) to represent the four main sub-reaches, i.e., Fujiangsha, Rugaosha, Tongzhousha and Langshansha, in the Chengtong reach.

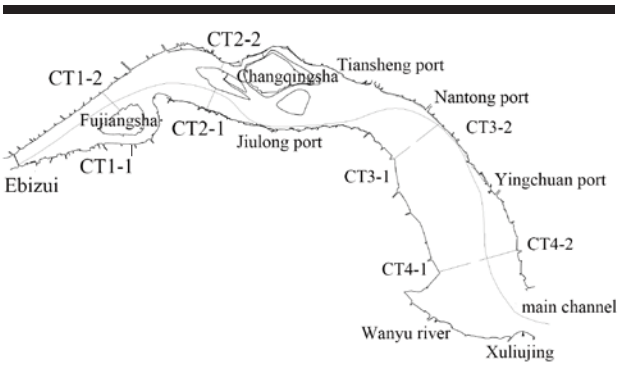

Figure 7. Locations of four sub-sections in the Chengtong reach. Sections of CT1-1, CT1-2 represent Fujiangsha sub-reach; Sections CT2-1, CT2-2 represent Rugaosha sub-reach; CT3-1, CT3-2 represent Tongzhousha sub-reach and CT4-1,CT4-2 represent Langshansha sub-reach. The main channel runs cross respective sections of CT1-2, CT2-1, CT3-2 and CT4-2.

Figure 8(a)~(d) show the variations of NDR with the cross-section area at the main channel of the selected cross-sections in different survey years. It can be seen that the NDR has a good correlation with the cross-sectional area ratio, which implies the NDR could be used as an index to demonstrate the development trend of main channel at the Chengtong reach.

Another series of numerical experiments are carried out by changing the river discharge conditions at upstream boundary. 9 different discharges, i.e. 5,000 m³/s, 10,000 m³/s, 20,000 m³/s, 30,000 m³/s, 40,000 m³/s, 50,000 m³/s, 60,000 m³/s, 70,000 m³/s and 80,000 m³/s, are used as representative upstream discharges for the numerical study. Figure 9(a)~(d) show the variations of NDR with increase of upstream river discharge at the main and secondary channels of four selected cross-sections.

According to the numerical results, the net discharge ratio of main channel at the sub-reaches of Fujiangsha, Tongzhousha and Langshansha decrease with increase of upstream discharge, It indicates that less percentage of water will flow into the main channel in the flood period, which may benefit for the development of secondary channel; On the contrary, more percentage of water will flow into the main channel in the dry period, which may benefit for the development of main channel.

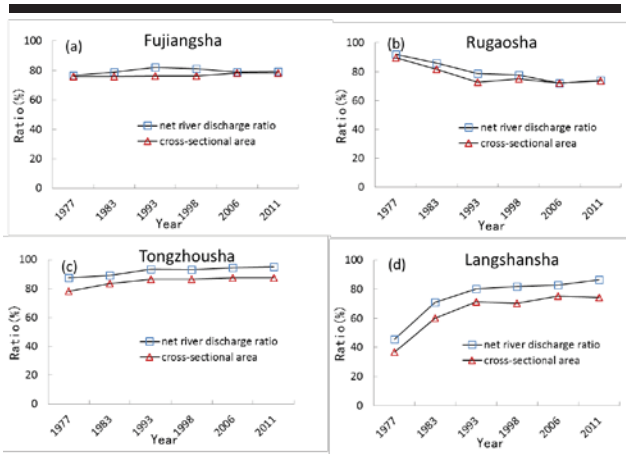

Figure 8. The variations of net discharge ratio with the cross-sectional area at the main channel of cross-section: (a) CT1- Fujiangsha (b) CT2-Ruogaosha, (c) CT3- Tongzhousha and (d) CT4-Langshansha in different survey years

The variation of NDR at the main channel of Rugaosha sub-reach is slightly different from other sub-reaches. It can be seen from Figure 9(b) that the NDR increases with increase of upstream discharge at first, and then decreases when the discharge is over 45,000m³/s. The reason is related to the flood-dominated characters of Tiansheng Port channel, which is located near the end of Rugaosha sub-reach. As it has become a flood tide dominated channel, the shallow water area in the upper part of Tiansheng Port channel make the flood current difficult to flow into the main channel of Rugaosha sub-reach. When the upstream discharge is relatively small, the change of NDR is dominated by the flood current. However, with further increase of the upstream discharge, the ebb tide gradually dominates the flow pattern, resulting in the NDR at the main channel of Rugaosha sub-reach having the same character as that at other three sub-reaches.

DISCUSSION

The better understanding of the net discharge ratio at the main and secondary channels of those sub-reaches can help to understand the long-term evloution of the Chengtong reach. It can be expected that the secondary channels of the Chengtong reach have a tendency of development when the upstream river discharge is relatively large. However, the upstream water conservancy projects, such as the Three Gorge Dam, will alter the monthly distribution of upstream river discharge in a year. Under the so-called “flood clipping” effect, the discharge ratio of main channels along the entire reach will show a general increase. This may have a positive effect on the development of the main channel from the hydrodynamic viewpoint.

There is no doubt that the sediment conditions are very important for the morphological changes of the channels in this area. It is clear that the significant volumetric changes after 2006 are directly related to the decrease of sediment supply from the

upstream. However, the present study has only focused on the effect of hydrodynamic changes on the riverbed evolution. The next study will include hydro- and morpho-dynamic interactions under different sediment supply conditions, so that the possible changes of the riverbed due to the large-scale hydraulic engineering projects can be investigated.

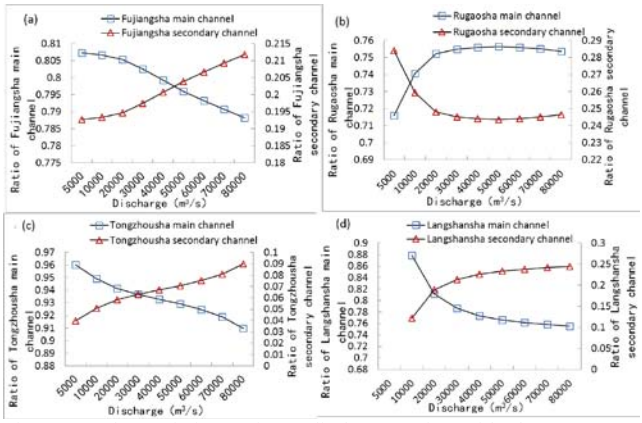

Figure 9. The variations of net discharge ratios with the upstream discharge at the sub-sections of (a) CT1- Fujiangsha (b) CT2-Ruogaosha, (c) CT3- Tongzhousha and (d) CT4-Langshansha

CONCLUSIONS

In this paper, a new approach to analyze the river evolution combined with the numerical simulation techniques is proposed. Based on the well-validated 2D numerical model, a series of numerical experiments are carried out. The effect of upstream discharge is quantitatively investigated by the comparisons of the net discharge ratios at the main and secondary channels of four main sub-reaches.

As the net discharge ratios through different channels can be used for the analysis of riverbed evolution, the results from the numerical experiments by changing the upstream discharge conditions show that the net river discharge ratios of main channels at Fujiangsha, Tongzhousha and Langshansha decrease with increase of upstream discharge; however, the net discharge ratio of the main channel at Rugaosha increases first with increase of upstream discharge but changes to a decreasing trend when the upstream discharge is over 45,000 m^3/s. The findings can be directly related to the local bathymetry and characters of the tide-dominance in the corresponding sub-reaches.

ACKNOWLEDGMENTS

This work was undertaken as part of the Ensemble Estimation of Flood Risk in A Changing Climate (EFRaCC) project funded by the British Council under its Global Innovation Initiative. The authors also acknowledge the support of the National Natural Science Foundation of China (51379072), the Key Research Project of Jiangsu Water Resources Department (2015006) and the 111 Project of the Ministry of Education and the State Administration of Foreign Experts Affairs, China (Grant No. B12032).

LITERATURE CITED

Cao, M. and Xia, Y. 2000. Riverbed evolution of Fujiangsha waterway. *Port & Waterway Engineering*, 31(12): 23-27. (in Chinese)

Du, Y.; Guo, B. and Chen, D. 2002. Rugao sediment shoals evolution of the Yangtze River and its regulation. *Yangtze River*, 33(12), 11-13. (in Chinese)

Hu, K..; Ding, P., Wang, Z. B. 2009. A 2D/3D hydrodynamic and sediment transport model for the Yangtze Estuary, China. *Journal of Marine Systems*, 77, 114-136.

Jiang, C.; Li, J., Huib, E. de Swart. 2012. Effects of navigational works on morphological changes in the bar area of the *Yangtze Estuary. Geomorphology*, 139-140, 205-219.

Liu, J.; Chen, J. and Xu, Z. 2007. Morphological Evolution and Its Response to the Navigational Improvements in the North Passage, Yangtze Estuary. *China Ocean Engineering*, 21(4), 611-624.

Tao, L. 1998. The influence to Zhajianggang of the evolution of Fujiangsha south branch. *Port & Waterway Engineering*. 31(12), 23-27. (in Chinese)

Wang, Y.; Peter, V. R., Wu, H. L. 2008. Long-term morphodynamic evolution and the equilibrium mechanism of a flood channel in the Yangtze Estuary (China). *Geomorphology*, 99, 130-138.

Wu, J.; Wang, Y., Cheng, H. 2009. Bedforms and bed material transport pathways in the Changjiang (Yangtze) Estuary. *Geomorphology*, 104, 175-184.

Yang, S.; Zhao, Q., Belkin, I. M. 2002. Temporal variation in the sediment load of the Yangtze River and the influences of human activities. *Journal of Hydrology*, 263, 56-71.

Yang, Z.; Wang, H. and Saito, Y. 2006. Dam impacts on the Changjiang (Yangtze) River sediment discharge to the sea: The past 55 years and after the Three Gorges Dam. *Water Resources Research* 42(4), W04407, doi: 10.1029/2005WR003970.

Yang, Y.; Li, Y., Fan, Y., Zhang, J. 2014. Impact of water and sediment discharges on subaqueous delta evolution in Yangtze Estuary from 1950 to 2010. *Water Science and Engineering*, 2014, 7(3), 331-343.

Zhong, Z. and Wang, Y. 2009. Discussion on comprehensive regulation and development of Chengtong reach of the Yangtze River. *Yangtze Rive*r, 40(11), 1-4. (in Chinese)

Journal of Coastal Research	SI	75	208-212	Coconut Creek, Florida	2016

Integral Tide-Surge-Wave Model of the Yellow Sea for Understanding Local Sediment Transport

Byung Ho Choi[†], Jin-Hee Yuk[‡], and Kyeong Ok Kim[††*]

[†]Department of Civil and Environment Engineering
Sungkyunkwan University
Suwon, Korea

[‡]Disaster Management HPC Technology Research Center, Korea Institute of Science and Technology Information
Daejeon, Korea

[††]Marine Radionuclide Research Center
Korea Institute of Ocean Science & Technology
Ansan, Korea

www.cerf-jcr.org

www.JCRonline.org

ABSTRACT

Choi, B.H.; Yuk, J.-H., and Kim, K.O., 2016. Integral tide-surge-wave model of the Yellow Sea for understanding local sediment transport. *In:* Vila-Concejo, A.; Bruce, E.; Kennedy, D.M., and McCarroll, R.J. (eds.), *Proceedings of the 14th International Coastal Symposium* (Sydney, Australia). *Journal of Coastal Research*, Special Issue, No. 75, pp. 208-212. Coconut Creek (Florida), ISSN 0749-0208.

Numerical simulations of tide and tidal current for the effect of the new port on Saemangeum area were carried out based on finely resolved meshes and integral tide-surge-wave model of the whole Yellow Sea and also for a compact model optimized for the field operation. The resulting modelling system can be used for hindcasting (prediction) the tide-surge-wave coupled environments at complex coastline, shallow water and fine-grained sediment area like areas around Korean Peninsula. We investigated and discussed the changes of tidal residual current, maximum bottom shear stress and tidal energy dissipation due to the new port for Saemangeum area where the construction of new large port is being built.

ADDITIONAL INDEX WORDS: *Sediment transport, Saemangeum area, Saemangeum new port, numerical model.*

INTRODUCTION

Great amounts of sediment are supplied from the Huanghe River discharge (1080 million tons annually) and the Changjiang River discharge (478 million tons annually) to the Yellow Sea (Milliman and Meade, 1983), whereas the amount of sediment discharged from Korean rivers was relatively small (approximately 0.15% of the China-originated sediment amount) (Park *et al.,* 1984). The characteristics of sediment inflow on both the west and east sides resulted in the shallower water on the west side of the Yellow Sea rather than the east side. The great amounts of sediment into the Yellow Sea are the interest to researchers in terms of modern sedimentation process. The sands of sea floor swept by strong tidal currents and of deposits being formed by them are practically important in the safety of shipping and underwater line structures. For this reason, the studies on the Yellow Sea tidal regime using the numerical model have performed (Choi *et al.*, 2010; Min *et al.*, 2011), and their regional ocean tide simulator (ROTIS) was used to predict the change of sedimentation environment due to the dikes in the local regions in the eastern Yellow Sea.

In this study, we predict how the construction of new port in Saemangeum will disturb and/or change the system's natural tidal states, especially the sedimentary environment using integral tide-surge-wave model of the Yellow Sea, which is upgraded modeling system of ROTIS and the latest trend in the modeling of water level and current field.

Background

The Mangyong-Geum (Mangeum) estuary (Figure 1) is a relatively shallow macrotidal embayment located at the western coast of Korean Peninsula in the eastern Yellow Sea. The Saemangeum tidal dike was constructed in 1991 and connects the offshore islands of Bieung and the Osic Islands at the southern Geum estuary to Daehangri at the southern Mangyeong estuary to form a 40,100-ha reclamation area and freshwater reservoir. As of June 2003, 30.3 km (out of a total of 33 km) of dike were constructed with 1.1- and 1.6-km openings at the Sinsi Island gate construction area and Garyuck Island, respectively. Choi (2001) reported that there were locally significant bed change due to sand movement along the dike alignment between the Osic and Yami Islands. The sandbank-like deposition occurred at the originally-planned closure site at the No. 4 dike withe the rapid sand deposition 5-6 m along the dike alignment at a distance of approximately 1.5 km. Choi (2001) suggested that the bottom evolution of the sand deposition is noticeably faster than the hydrodynamic interpretation (Huthnance, 1982). These may play key roles in sediment dynamics in this region.

Saemangeum Shinhang (new port) construction began in 2009 and will be completed in 2030 to boost the local economy and make this area logistics hub in Northeast Asia. The harbor

DOI: 10.2112/SI75-042.1 received 15 October 2015; accepted in revision 15 January 2016.
*Corresponding author: kokim@kiost.ac.kr

program is composed of the construction of a 3.5-km seawall, a 4.1-km pier and an 8.0-km revetment as an essential part of the Saemangem Development Project. As the first phase, the government plans to finish the construction of a 3.1-km pier and four berth container ports by 2020. It is expected that the Saemangeum new port contains 18 berth container ports and a 3.5-km seawall by 2030. After finishing the construction of new port, over 17.3 million tons of goods will be shipped in and out of the newly built harbor, which is almost equivalent to the amount being handled at the nearby Gunsan Port (The Korea Herald, 2012).

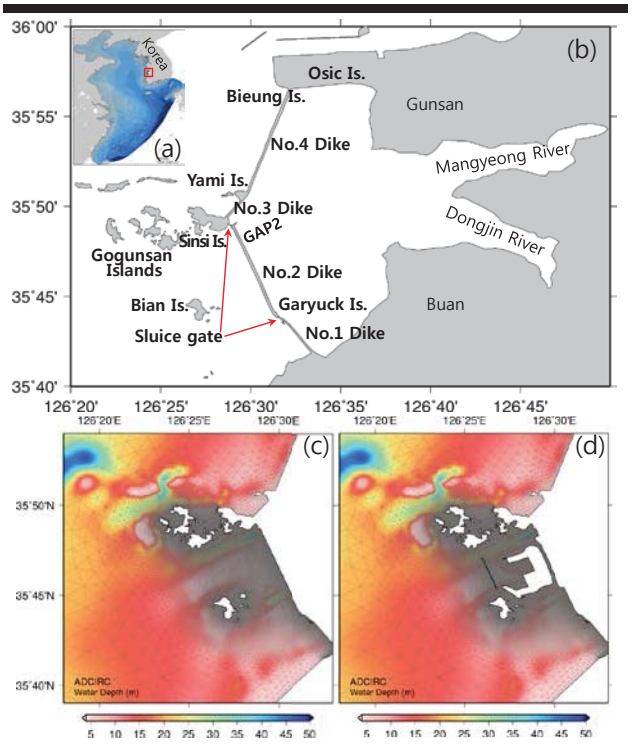

Figure 1. The model domain for the Yellow Sea and the location of Saemangeum area (a). Dikes and sluice gates (b) and detailed meshes and bathymetry of Saemangeum area in the present state (c) and in the future state with a new port (d).

METHODS

An integral tide-surge-wave model is the coupled ADCIRC as the tide-surge model and SWAN as the wave model. SWAN (Simulating WAves Nearshore) predicts the evolution in geographical space and time of the wave action density spectrum, with the relative frequency and the wave direction, as governed by the action balance equation (Booij *et al.*, 1999). The details of model have been described in the previous studies (Booij *et al.*, 1999). ADCIRC (the ADvanced CIRCulation model) is a continuous-Galerkin, finite-element, shallow-water model that solves for water levels and currents at a range of scales (Luettich and Westerink, 2004). The details of this solution have been published widely (http://www.nd.edu/~adcirc/manual.htm to see Users Manual and Theory Report) and will not be restated here.

SWAN is driven by wind speeds, water levels and currents computed at the vertices by ADCIRC. Marine winds can be input to ADCIRC, and these winds are adjusted directionally to account for surface roughness (Bunya *et al.*, 2010). ADCIRC interpolates spatially and temporally to project these winds to the computational vertices, and then it passes them to SWAN. The water levels and ambient currents are computed in ADCIRC before being passed to SWAN, where they are used to re-compute the water depth and all related wave processes (wave propagation, depth-induced breaking, *etc.*). The ADCIRC model is driven partly by radiation stress gradients that are calculated with information from SWAN. ADCIRC and SWAN run in series on the same local mesh and core. The two models leap frog through time, each being forced with information from the other model. The coupling interval is set to be the same as the SWAN's time step. The basic structure of this coupling system (ADCIRC+SWAN) was developed by Dietrich *et al.* (2010). The tide-surge-wave model was also used and validated in earlier studies for the coasts of Korea and Japan (Choi *et al.*; 2013). The complex mesh without (present state) / with new port (future state) is shown in Figure 1. This mesh incorporates local resolution down to 20 m to describe detail of Saemangeum dike, islands and new port, but also extends to the Yellow Sea and amounts to approximately 210,000 vertices and 420,000 elements. The NAOTIDE (Matsumoto *et al.*, 2000) was used for the open boundary forcing in this study.

The model validation for the simulation of physical environment in the Yellow Sea is well built and shows good performance to implement, once the computing resources are sufficiently provided. It is somewhat difficult to use this model in the work-site operations, thus we developed the compact model with the small domain focusing on the study area, i.e., Saemangeum area and enabling users using PC easily to predict spatio-temporal variability of tide and tidal current in response to the sluice gate operation, unexpected in-field situations and delays due to unfavorable weather. The compact model was made using the high resolution meshes of approximately 10 m at the sluice gates (Figure 2). NAOTIDE dataset is applied to the open boundary forcing.

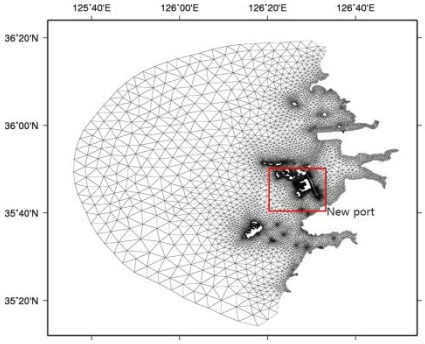

Figure 2. The model domain and overall meshes of the compact model.

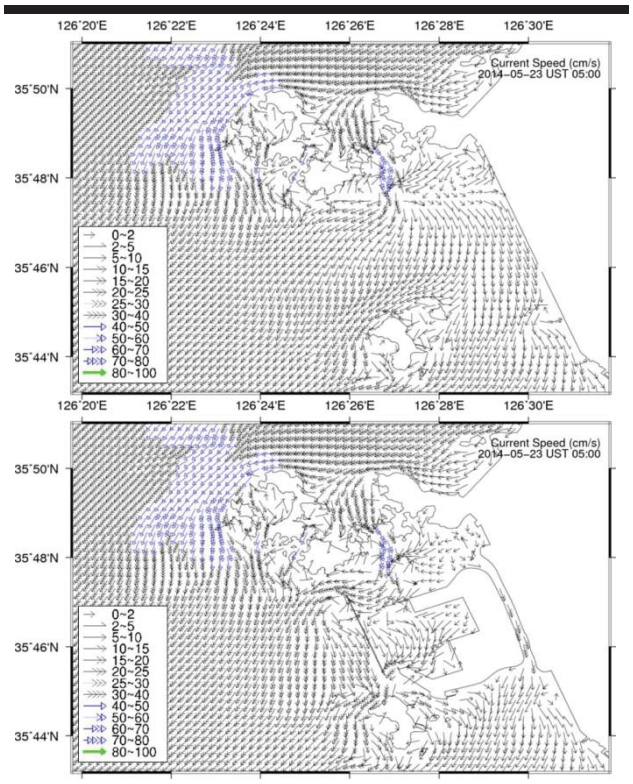

Figure 3. The predicted tidal currents during the ebb tide before (upper) and after (lower) the construction of new port at Saemangeum area.

RESULTS

The previously described modeling system is not shown here since the previous studies (Choi *et al.*, 2013) exhibit the good agreement with measurements. Figure 3 shows the tidal current predicted by this study's model on May 23 05:00 UTC 2014 during ebb tide. It is seen that after the construction of the new port, the new port disturbs the tidal regimes so the tidal current direction largely changes near the new port. The model results propose that the likelihood is that the tidal eddy occurs due to the newly constructed coastal structures.

The model verification depicts that the tidal elevations were reasonably reproduced at the Gunsan outer port and GAP2, which supports the premise that the locally compact model domain is justified (Figure 4). In addition, this study's real-time tidal elevations at the Gunsan outer port show the good agreement with that predicted by the authorized agency, Korea Hydrographic and Oceanographic Administration (KHOA).

Based on the simulation results, the sedimentary environment in Samangeum area is presented and discussed below. We calculated the tidal residual currents, which act as eddies that can potentially trap fine-grained sediments. The tidal residual currents were obtained by time-integrating the model results and averaging the time-integrated value of one day.

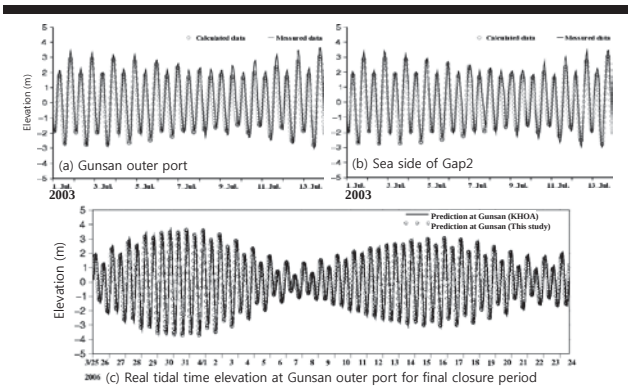

Figure 4. Comparison between the observed and predicted real-time elevations.

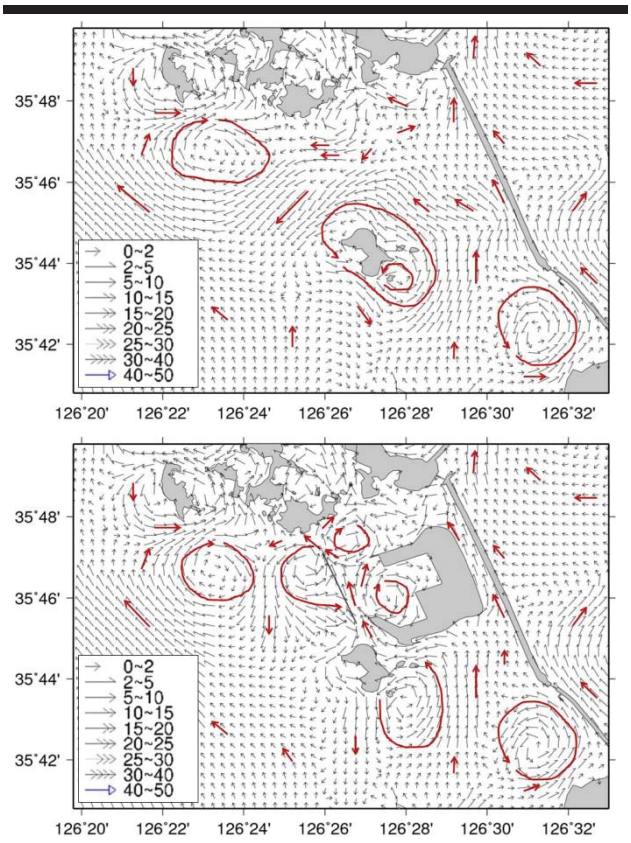

Figure 5. Tidal residual currents (cm/s) with eddies as potential traps for fine-grained sediments..

Figure 5 shows the distribution of tidal residual currents before and after the construction of the new port. Both upper and lower panels depict the situations assuming the full closure of Sinsi and Garyuck sluice gates. Residual currents are generally less than 10 cm/s in this area except inside Gogusan Islands

before the construction of new port, whereas after the new port those become stronger in the channels formed newly by the new port. Eddies occur in the south of Gogunsan Islands, around Bian Island and in front of the Garyuck sluice gate without new port, but some eddies and current directions are deformed and new eddies are generated near the new port in the condition of existence of new port.

The bottom shear stress (τ_b) is a combined effect of the currents and waves induced by the bottom friction, which is influenced by the bottom roughness. We are able to assess the change and deformation of the tidelands using the bottom shear stress. It can be calculated from Eq. 1:

$$\tau_b = \rho_w f_b u|u|, \quad (1)$$

where ρ_w is the density of water (kg/m^3), f_b is the friction coefficient, and u is the depth-averaged velocity (m/s). The bottom friction coefficient (f_b) is given as Eq. 2 (Dyer, 1986):

$$f_b = 2\frac{\kappa^2}{(\ln(\frac{30H}{k_N}-1))^2}, \quad (2)$$

where κ is the Von Karmann constant (~0.4), H is the water depth (m), and k_N is the bottom roughness (m). According to eariler studies on sediment in the Yellow Sea (Choi, 2003), the bottom shear stress of 0.3 N/m^2 is known for the threshold for erosion and deposition and indicates a low tide mark in coatal regions.

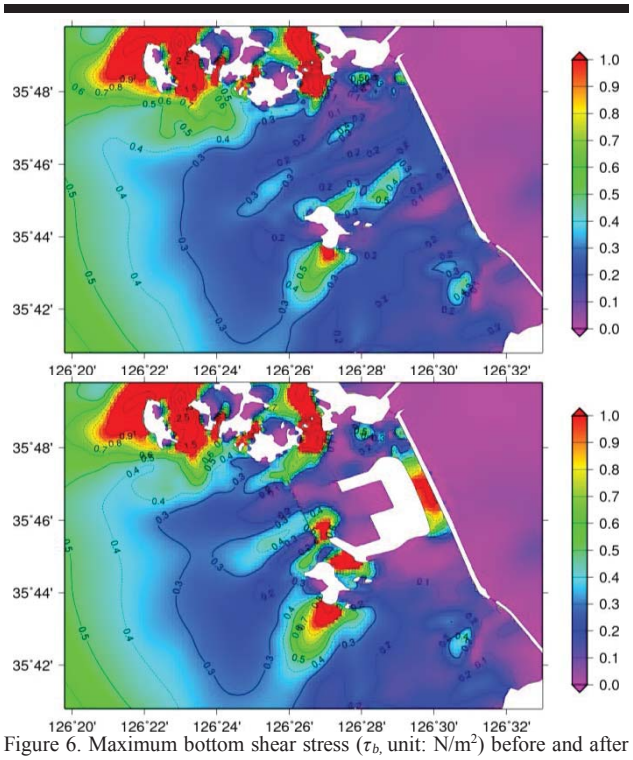

Figure 6. Maximum bottom shear stress (τ_b, unit: N/m^2) before and after the construction of the new port.

Figure 6 depicts ths distribution of the maximum bottom shear stress without/with the new port in the situation of full closure of Sinsi and Garyuck sluice gates. Generally, before the construction of the new port, the bottom shear stress contour of 0.3 N/m^2 is shown offshore from the dikes, but larger ones than 0.3 N/m^2 are shown in the north and south of Bian Island and in front of sluice gates. Its distribution changes greatly with the new port, i.e., the construction of the new port is likely to cause erosion in the channels of the No. 2 dike - new port, Bian Island - new port, and the new dike - new port, but to cause deposition in front (facing the south-west) of the new port and the north and south of the new port.

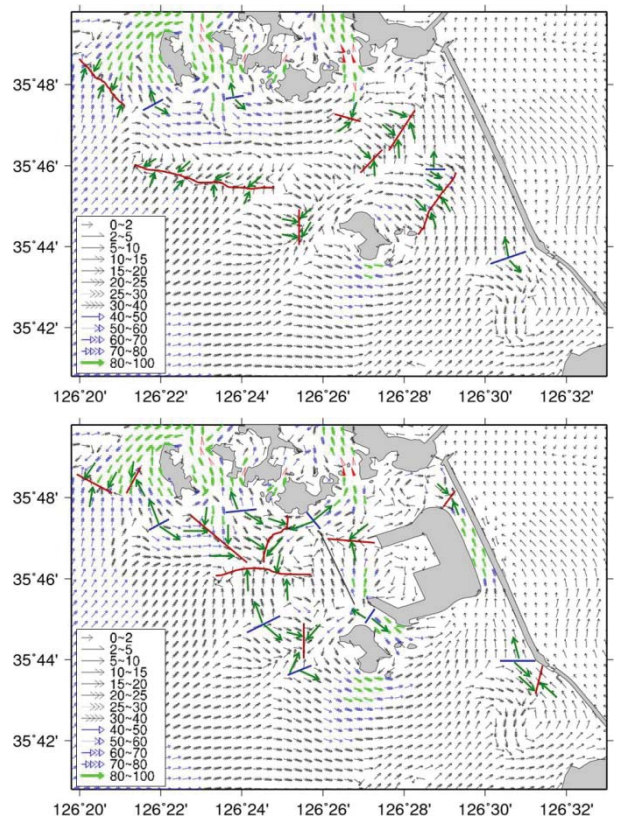

Figure 7. Vector fields of the maximum bottom shear stress (10^{-2} N/m^2) before and after the construction of the new port.

The vector field of the maximum bottom shear stress is an index to determine the direction of the net sand transport. The previous studies (Pingree and Griffiths, 1979; Choi, 2001) said that the maximum bottom shear stress actually influence the movement of the seabed load instead of a mean value over a tidal cycle, and the direction of the maximum bottom shear stress is congruent with the direction of the net sand transport. Figure 7 shows the vector of maximum bottom shear stress without/with the new port in the full closure of sluice gates. After the construction of the new port, the vector field becomes more complex. The locatioin of convergence and divergence of

the maximum bottom shear stress changes, especially in the site of new port, the two convergence zones nearly perpendicular to the No. 2 dike diappears after the construction of the new port.

DISCUSSION

More parameters such as tidal energy dissipation and sediment transport potential enable us to understand the impact of new port on the sedimentary environment in Saemangeum area. The tidal energy dissipation is estimated from the numerical simulation results by converting the maximum bottom shear stress caused by the bottom friction into work per unit area, and its distribution is similar to maximum bottom shear stress distribution. The calculated tidal energy dissipation presents that some areas around the new port will become a high or low energy environment after the construction of the new port (Figures not shown here).

CONCLUSIONS

In this study, the simulation for understanding local sediment transport in Saemangeum area was performed based on the integral tide-surge-wave model of the Yellow Sea and the compact model that is optimized for the field operation and running the simulation scenarios. The tidal residual current, maximum bottom shear stress and tidal energy dissipation were calculated using the tide simulation results and discussed to understand the sedimentary environment change due to the construction of the new port in Saemangeum area. The residual circulation patterns change remarkably after the construction of the new port. These may arouse the significant deposition of suspended sediments by tidal stirring and the trapping effects of fine-grained materials. The maximum bottom shear stress contours propose the area of likelihood of erosion and depostion after the constructioin of the new port. Similarly, the tidal energy disspation contours show the generation of the higher and lower energy environment than the present state (without the new port). Further studies will be needed to assess the effect of the new port on the sediment environment in the situation of opening of sulice gates.

ACKNOWLEDGMENTS

This study was supported by the China-Korea Cooperative Research Project funded by CKJORC as well as a major project titled the development of the marine environmental impact prediction system funded by KIOST, and supported by the project of KISTI for the development of HPC-based management system against national-scale disaster.

LITERATURE CITED

Booij, N.; Ris, R.C., and Holthuijsen, L.H., 1999. A third-generation wave model for coastal regions, Part I, Model description and validation. *J. Geophys. Res.*, 104(C4), 7649−7666.

Bunya, S.; Dietrich, J.C.; Westerink, J.J.; Ebersole, B.A.; Smith, J.M.; Atkinson, J.H.; Jensen, R.; Resio, D.T.; Luettich, R.A.; Dawson, C.; Cardone, V.J.; Cox, A.T.; Powell, M.D.; Westerink, H.J., and Roberts, H.J., 2010. A high resolution coupled riverine flow, tide, wind, wind wave, and storm surge model for southern Louisiana and Mississippi, Part I: Model development and validation. *Mon. Weather Rev.*, 138(2), 345-377.

Choi, B.H., 2001. Effect of Saemangeum tidal barriers on the Yellow Sea tidal regime. *Proceedings of the first Asian and Pacific Coastal Engineering Conference* (APACE 2001, Dalian, China), 1, pp. 25-36.

Choi, B.H., 2003. Strategy for understanding coastal-ocean system for the Yellow Sea: Saemangeum and Siwha region. *Proc. Coastal and Ocean Engineering in Korea*, 14, pp. 28-34 (in Korean).

Choi, B.H.; Ha, J.W.; Ko, K.O.; Eo, D.S., and Kim, K.O. 2010. Tidal forecast for final closure of Saemangeum tidal dike. *China Ocean Eng.*, 24(3), 467-480.

Choi, B.H.; Min, B.I.; Kim K.O., and Yuk, J.H., 2013. Wave-tide-surge coupled simulation for typhoon Maemi. *China Ocean Eng.*, 27(2), 141−158.

Dietrich, J.C.; Bunya, S.; Westerink, J.J.; Ebersole, B.A.; Smith, J.M.; Atkinson, J.H.; Jensen, R.; Resio, D.T.; Luettich, R.A.; Dawson, C.; Cardone, V.J.; Cox, A.T.; Powell, M.D.; Westerink, H.J., and Roberts, H.J., 2010. A high resolution coupled riverine flow, tide, wind, wind wave and storm surge model for southern Louisiana and Mississippi: Part II − Synoptic description and analyses of Hurricanes Katrina and Rita. *Mon. Weather Rev.*, 138(2), 378−404.

Huthnance, J.M., 1982. On one mechanism forming linear sand banks. *Estuarine, Coastal and Shelf Science*, 14, 79-99.

Luettich, R.A. and Westerink, J.J., 2004. *Formulation and Numerical Implementation of the 2D/3D ADCIRC Finite Element Model, version 44.XX*, http://adcirc.org/adcirc_ theory_ 2004_12_08.pdf.

Matsumoto, K.; Takanezawa, T., and Ooe, M., 2000. Ocean tide models developed by assimilating TOPEX/POSEIDON altimeter data into hydrodynamical model: A global model and a regional model around Japan. *Journal of Oceanography*, 56, 567-581.

Milliman, J.D. and Meade, R.H., 1983. World-wide delivery of river sediment to the ocean. *J. Geol.*, 91, 1-21.

Min, B.I.; Kim, K.O.; Lee, H.S.; Yuk, J.-H., and Choi, B.H., 2011. Disturbances in tidal and sedimentation regimes at Saemangeum due to a dike. *Journal of Coastal Research*, Special Issue, No. 64, pp. 576-580.

Park, Y.A.; Kim, S.C., and Choi, J.H., 1984. Distribution and transformation of fine-grained sediments on the inner-continental shelf off the Keum River Estuary, Korea. *J. Geol. Soc. Korea*, 20(2), 154-168.

Pingree, R.D. and Griffiths, D.K., 1979. Sand transport paths around the british lsles resulting from M_2 and M_4 interactions. *J. Mar, Biol. Ass. U.K*, 59, 497-513.

Journal of Coastal Research	SI	75	213-217	Coconut Creek, Florida	2016

Hydraulic and Environmental Stability Analysis in the Estuary of Gahwa River and Sacheon Bay by the Change of Discharge of Namgang Dam in South Korea

Tae Woo Kim[††] , Woo Dong Lee [†], Dong Soo Hur[‡], Jung Lyul Lee [∞] and Jong Sung Yoon[††*]

[†]Institute of Marine Industry
Gyeongsang National University
Tongyeong, Republic of Korea

[‡] Department of Ocean Civil Engineering
Gyeongsang National University
Tongyeong, Republic of Korea

[∞] Department of Architectural and Civil Engineering
Sungkyunkwan University
Seoul, Republic of Korea

[††] Department of Civil and Urban Engineering
Inje University
Gimhae, Republic of Korea

www.cerf-jcr.org

www.JCRonline.org

ABSTRACT

Kim, T.W., Lee, W.D., Hur, D.S., Lee, J.L and Yoon, J.S., 2016. Hydraulic and Environmental Stability Analysis in the Estuary of Gahwa River and Sacheon Bay by the Change of Discharge of Namgang Dam in South Korea. *In:* Vila-Concejo, A.; Bruce, E.; Kennedy, D.M., and McCarroll, R.J. (eds.), *Proceedings of the 14th International Coastal Symposium* (Sydney, Australia). *Journal of Coastal Research*, Special Issue, No. 75, pp. 213-217. Coconut Creek (Florida), ISSN 0749-0208.

Namgang dam is located in the southern part of South Korea. Flow discharged from Namgang dam for a flood control runs Kahwa river and finally reaches Sacheon bay. In a rainy or typhoon period, the discharged flow can inundate and affect the hydraulic stability and safety of estuarine areas of Kahwa river, Sacheon river, Jungseonpo river, and Jukcheon river. In this study, we performed a 3-dimensional hydraulic experiment and numerical analysis to analyze the level of water rise in the estuarine areas and environmental effect to Sacheon bay by the change of discharge of Namgang dam. A hydraulic model, based on bathymetric and aerial LIDAR survey data, was made in the scale of 1/50. The experimental and numerical results were compared with the observational results. From the experimental and numerical results, it reveals that as the amount of discharge from Namgang dam increases, water levels in the estuarine areas of Jungseonpo river and Sacheon river and the industrial area around Sacheon bay significantly increases by the effect of backwater. In addition, analyzing the measured salinity concentration, we also find out that the range of diffusion of discharged water into Sacheon bay and it takes about 20 days to recover the original salinity concentration.

ADDITIONAL INDEX WORDS: *POM Ocean circulation model, Hydraulic model experiments, Froude's law of similarity*

INTRODUCTION

It is currently very important to prepare the measures to secure the stability of hydraulic structure and to prevent the natural disasters according to the global warming and climate change. In particular, it is required to develop the alternatives in order to maximize the convenience in social and economic aspects in terms of the importance of dam, its effect, and its conservation. Such practical efforts are being made not only in our country but also throughout the world, and the economic development is being promoted while pursuing the multipurpose and multifunction effects that stand to promote the safety of community. In the case of Namgang Dam, it is one of important national facilities that satisfy the need of water in nearby areas and protect the downstream region from flooding even if the scale of the dam is unbelievably small. It is very important to analyze what kind of impact the discharged water released from Namgang Dam has on the area of the sea. The target area of the sea in this study is the Sacheon Bay(Figure 1), which is located in the southern part of South Korea, the flood control was carried out through efficient reservoir management as the floods that exceeded the planned size several times were being introduced into Namgang Dam several times recently, nonetheless, it became inevitable to release water through the sluice more than planned discharge at the time of typhoon Rusa and the water close to the planned discharge size was discharged at the time of typhoon Ewiniar and typhoon Maemi. As a result, there arose flood damage along with drainage exclusion faults around Sacheon Bay, the area for this research, such as Gahwa River basin, Sacheon River, Jungseonpo River, and Jukcheon River *etc*. In addition, as a result of the increased PMP(Probable Maximum Precipitation) and PMF(Probable Maximum Flood) by Typhoon Rusa, the increased planned discharge of the Sacheon Bay according to the flood control capacity expansion project in consideration of the safety of Namgang Dam and the

DOI: 10.2112/SI75-043.1 received 15 October 2015; accepted in revision 15 January 2016.
*Corresponding author: civyunjs@inje.ac.kr

changed hydrological and hydraulic conditions such as the passage of Typhoon Maemi through Sacheon Bay *etc*., were expected, and also some local streams became to need the reestablishment of maintenance plan, however, there is currently no comprehensive and physical clarification of phenomena about the region of Sacheon Bay. Therefore, this study attempted to analyze and predict the impact Sacheon Bay and its region will have according to the discharge of Namgang Dam reservoir into Sacheon Bay and its region by comparing the results of water level per point from three-dimensional numerical model experiment and three-dimensional hydraulic model experiment.

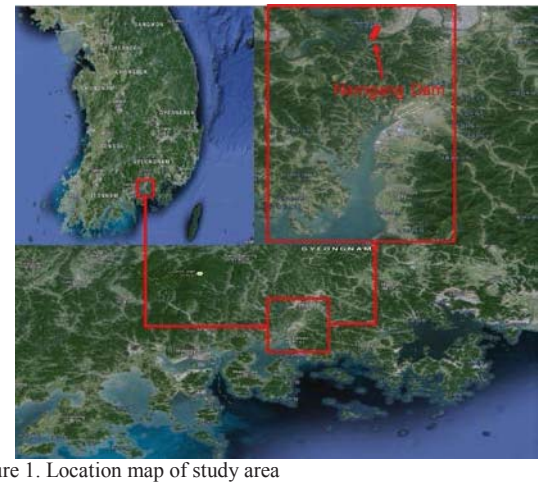

Figure 1. Location map of study area

NUMERICAL MODEL EXPERIMENT

Basic equations: The calculation for the three-dimensional numerical model experiments in this study was performed using the Modified POM (Princeton Ocean Model) to reproduce the current state seawater circulation of Sacheon Bay. POM can be applied to estuary, coast and open sea, and can be used in the modeling of sea water circulation in consideration of baroclinic effect, and can be used in the modeling of water temperature, salt, transport of the pollutants, and diffusion as three-dimensional primitive equation was digitized. As σ coordinate system is a crooked grid in physical space systems, it is necessary to do the coordinate transformation

The basic equation used in this model was the incompressible Navier-Stokes equation, which represents velocity, water level change, salinity and temperature fields, and the motion equation and the diffusion equation are as follows when hydrodynamic approximation and Boussinesq approximation are applied respectively.

The Modified POM minimized the numerical error by using the Slφrdal (1997) law by overestimating the flow rate of the entire water region and by inhibiting the spread of the value calculated in the vertical direction through the correction of horizontal pressure tilt. The previous studies verified its applicability (Yoon *et al*., 2006), refer to the previous studies for more information about the numerical models. By applying the improved POM models to Youngrangho, one of the representative brackish water lake in the East Coast, its applicability was applied. Therefore, in this study, surge - tidal model was constructed using the Modified POM whose applicability had been proven in existing research.

Numerical model experiment method: As for the depth of each grid, the digital chart No. 229 of the National Oceanographic Research Institute with the scale of 1: 250,000 was used, Figure 2 show the isobathymetric map and Table 1 showed the content of numerical model experiment.

Table 1. *Summary of Numerical Model Experiment.*

Division	Content
Range of Calculation	Sea area (27.2km x 32.0km) throughout Sacheon City, Gyeongsangnam-do
Lattice Structure	Δx = Δy = 50~800m
Number of Lattice	161 x 163 x 5
Boundary Condition	Tidal constituent of M2 + S2 + K1 + O1 at open boundary condition

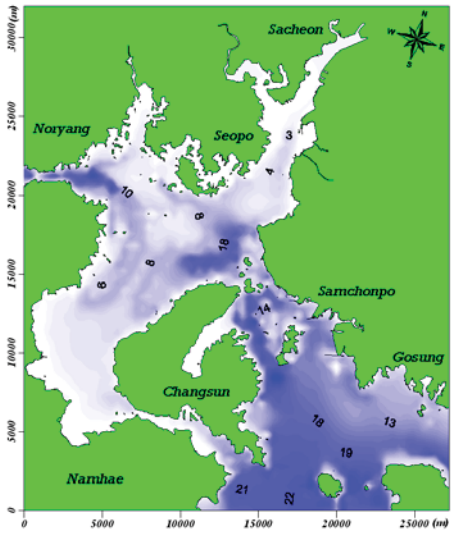

Figure 2. Computational isobathymetric map

Verification of numerical models: For the purpose of verifying the applicability of the numerical model of this study, the model was compared with the results of numerical calculation using the harmonic constants measured from the observation point. As for the harmonic constants value, the data from the National Oceanographic Research Institute from the observation points such as Bitoseom and Samcheonpo Port were used. Comparing the results from the observations and numerical calculations, it showed that they were in good agreement in general to each other even if they had some amplitude difference as in Figure 3. In addition, the tidal current verification in Figure 4 was also consistent with them. Therefore, It was determined that the calculation results of this numerical model reproduced the flow structure of Sacheon Bay well.

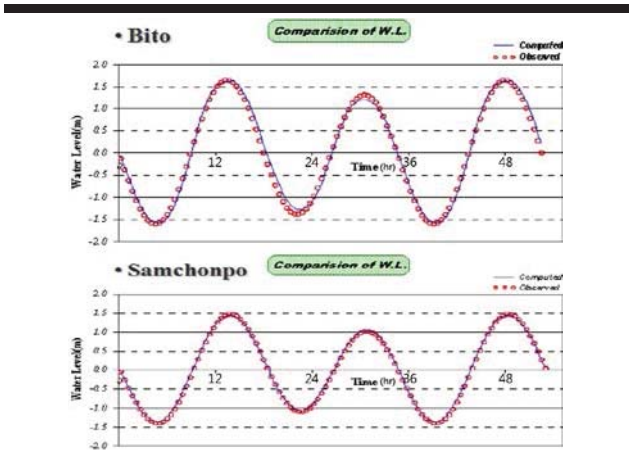

Figure 3. Comparison between observed and calculated tidal level

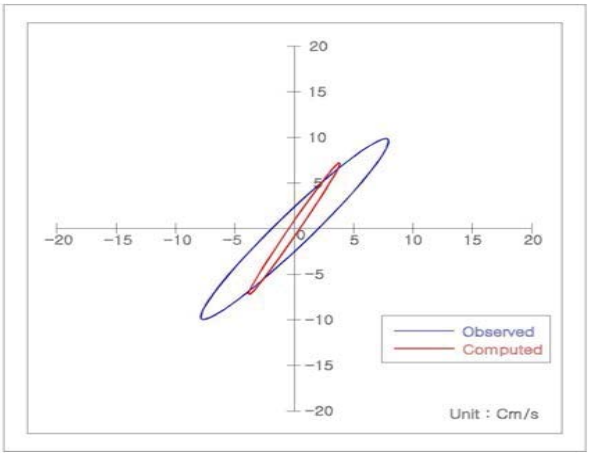

Figure 4. Comparison between observed and calculated tidal current

THE HYDRAULIC MODEL EXPERIMENT

Production of numerical model: Despite that the plane scale of the model should be small when the target is as big as the experimental area of Sacheon Bay, the normal model with the scale 1/150 as Figure 5 was produced by CON'C placement method by reproducing the difference in elevation of each point using the level after reproducing the terrain contour and depth ranking with the scale of 1/150 in a water tank by conducting a measurement based on the terrain contour and depth ranking by the terrain surveys and bathymetry. In particular, in the case of seabed topography, the depth ranking was produced by installing the grid network of 25~50cm spacing with a higher degree of precision. After the production of the model, the boundaries in the model were color painted to make it distinct for photo shooting (Figure 6).

Scale and similitude of hydraulic model: The characteristics of the model and prototype must have similitude in the case of conducting a model experiment. As the experiment of this hydraulic model experiment is the case where the gravity is dominant, Froude's law of similitude was preferentially applied.

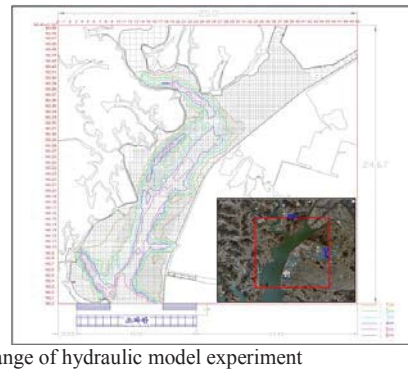

Figure 5. Range of hydraulic model experiment

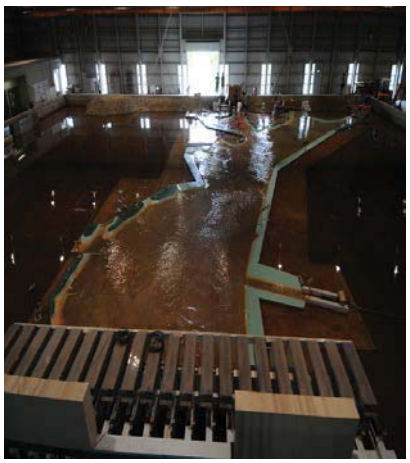

Figure 6. Three-dimensional plane model

As this law of similitude satisfies the similitude based on the inertial force and the gravity of the fluid, the scale of the time and velocity shall be the squared root of the length scale.

Method of hydraulic model experiment: The proper amount of flow rate required by the hydraulic model experiments were fed through the pumps and pipes by the installation of the reservoir and weir at the inlet of each river, and for the measurement of water level and height of a wave, the wave-height meter by electrical resistance was used, and as for the water level, the river water level changes were measured by point of each case of rivers. Table 2 shows the case-specific hydraulic model experiment plan.

Analysis and comparison of water level results with numerical model experiments: As in Figure 7, the water level results from the case-specific numerical model experiment at the confluence, Gahwa River estuary, Jungseonpo River estuary, Sacheon River estuary, five points at Jinsagongdan and hydraulic model experiments are shown in Table 3.

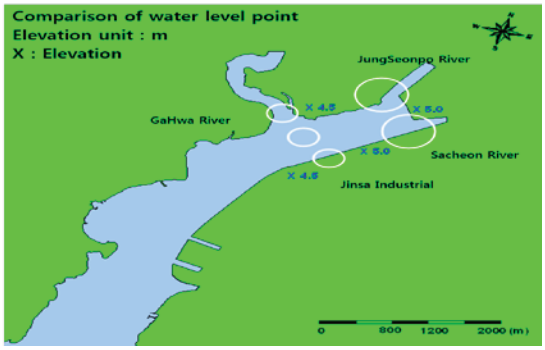

Figure 7. Comparison of water level point

RESULTS

As a result of analysis of the water level and water level increase amount in consideration of tidal level rise height by measuring the case-specific water level due to the discharge of Gahwa River, which was the spillway of Nam River Dam, it was determined the water levels of Jungseonpo River and Sacheon River were rising rapidly, in particular Case E (13,620 m^3/s) and Case F (18,436 m^3/s) in the area of Jungseonpo River and Sacheon River showed far bigger impact from backwater. In addition, the water level rose to 3.54m at maximum in Jungseonpo River region as well as 3.27m at maximum in Sacheon River showing the flooding over the levee height. In the result of numerical model experiment, it was determined there was a danger of flooding as Case C(5,520 m^3/s) showed the effluent water level of Gahwa River up to the ground level near Jinsa Industrial and the water level in the flow rate condition above Case D(8,738 m^3/s) showed the water level higher than the ground level.

Table 2. *Case of hydraulic model experiment*

Division		Ga Hwa River	Jung Seon po River	Sa cheon River	Juk cheon River	unit
Case 1	Prototype	**3,250**	**983.55**	**1,147.1**	**782.01**	m^3/s
A	model	11.79	3.57	4.16	2.84	l^3/s
Case 2	Prototype	4,680	**983.55**	**1,147.1**	**782.01**	m^3/s
B	model	16.98	3.57	4.16	2.84	l^3/s
Case 3	Prototype	5,520	**983.55**	**1,147.1**	**782.01**	m^3/s
C	model	20.03	3.57	4.16	2.84	l^3/s
Case 4	Prototype	8,738	**983.55**	**1,147.1**	**782.01**	m^3/s
D	model	31.71	3.57	4.16	2.84	l^3/s
Case 5	Prototype	13,620	**983.55**	**1,147.1**	**782.01**	m^3/s
E	model	49.43	3.57	4.16	2.84	l^3/s
Case 6	Prototype	18,436	**983.55**	**1,147.1**	**782.01**	m^3/s
F	model	66.90	3.57	4.16	2.84	l^3/s

DISCUSSION

Looking at the results of the Namgang Dam discharge (Figure 8), the low-density water mass were spreading slowly to the outside of the bay after 8 hours of river discharge, and met the fresh water discharge from Jukjeon River and Gonyang River 16 hours after discharge showing the progression of the desalination of the area of the sea. As shown in the density distribution and water flow velocity distribution for 36 hours, more than half water in the Bay of Sacheon was desalinated, and the fresh water diffused to north of Changseondo after 48 hours, the fresh water was spreading further out by the stream flowing into Noryang Strait, and this stream promoted the spread through Samcheonpo - Changseon waterway, further to Seopomyeon Bitoseom, Samcheonpo – Changseonen waterway, and to Daebang Port. After 54 hours when the discharge was the highest, a current at the time of the flood tide along with Mulgeon-Saryangdo flowing into the Bay of Sacheon crashed into a river discharge to form a strong mix rap resulting in the water mass with salinity of 10psu. The calculation results after 62 hours showed that the current flowing from the Noryang Strait and the current flowing to Southern - Saryangdo waterway expanded the freshwater that was stagnant at the opening of Sacheon Bay rapidly diffusing it to the entire region of sea. Furthermore, the salt distribution of 25psu diffused to the strait between Namhae and Saryangdo, in the case of seashore trashes where the influence of drift is overwhelming, the impact of drifting and coastal litter due to discharge had impact not only on Sacheon Bay but also on the sea area as a whole. As for the salinity distribution after 100 hours and 130 hours, the density distribution in the area of the sea recovered gradually as the amount of discharge reduced, but it was determined that it would take long time to restore the original density structure.

The state of density during 25 days after the discharge was confirmed in order to investigate the status of staying of fresh water in the Bay of Sacheon. As a result, the salt was 30 psu in the entrance of Sacheon Bay 7 days after the discharge, and the original density appeared to recover after 20 days (Figure 9).

Table 3. *Comparison of water level result (unit : m)*

Division		Flow late	Case A	Case B	Case C	Case D	Case E	Case F	Near by ground level
confluence	numeric	**3.50**	**4.00**	**4.10**	**4.40**	**4.80**	**5.50**	**6.50**	
	hydraulic	3.62	3.99		4.5		5.49		
GaHwa River entrance	numeric	3.50	**3.9**	**4.00**	**4.00**	**4.10**	**4.3**	**4.50**	**4.5**
	hydraulic	3.62	3.99		3.93		4.27		
JungSeonpoRiver entrance	numeric	3.50	**4.00**	**4.30**	**4.40**	**4.80**	**5.5**	**6.60**	**5.0**
	hydraulic	3.67	4.12		4.12		5.36		
Sacheon River entrance	numeric	3.40	**4.00**	**4.20**	**4.40**	**4.80**	**5.4**	**6.60**	**5.0**
	hydraulic	3.93	3.97		4.01		5.29		
The front Jinsa Industrial	numeric	3.50	**4.00**	**4.30**	**4.40**	**4.80**	**5.5**	**6.60**	**4.5**
	hydraulic	3.65	1.01		4.74		5.69		

CONCLUSIONS

This study attempted to clarify the physical phenomena by comparing three-dimensional numerical model experiment and hydraulic model experiment in order to analyze what kind of impact the effluent water of Namgang Dam had on Sacheon Bay and its region. The summary of the results of this study is as follows:

(1) The water level results from the three-dimensional modeling of sea water circulation numerical model experiment according to the variation of effluent amount of Gahwa River, a spillway in Namgang Dam, and from the hydraulic model experiment were compared with the division of the regions into confluence, Gahwa River estuary, Jungseonpo River estuary, Sacheon River estuary, five points at Jinsa Industrial, and as a result, the results from each experiment were in good agreement

to each other, in general, even if there were some local differences.

(2) As a result of analysis of the water level and water level increase amount in consideration of tidal level rise height by measuring the case-specific water level due to the discharge of Namgang Dam, it was determined the water levels of Jungseonpo River and Sacheon River were rising rapidly due to the effects of backwater as the discharge of Gahwa River increased.

(3) The state of density during 25 days after the discharge was confirmed in order to investigate the status of staying of fresh water in the Bay of Sacheon. As a result, the salt was 30 psu in the entrance of Sacheon Bay 7 days after the discharge, and the original density appeared to recover after 20 days.

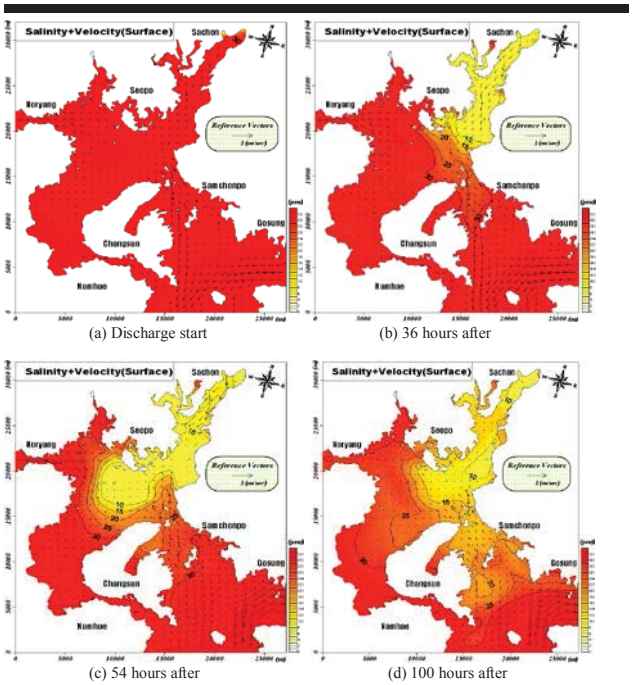

(a) Discharge start (b) 36 hours after

(c) 54 hours after (d) 100 hours after

Figure 8. Results of the discharge.

ACKNOWLEDGMENTS

This research was supported by *Basic Science Research Program through the National Research Foundation of Korea (NRF)* funded by the Ministry of Education (NRF-2015R1D1A4A01020046).

This work was supported by *the National Research Foundation of Korea (NRF)* grant funded by the Korea government (MEST) (No. 2013-0549).

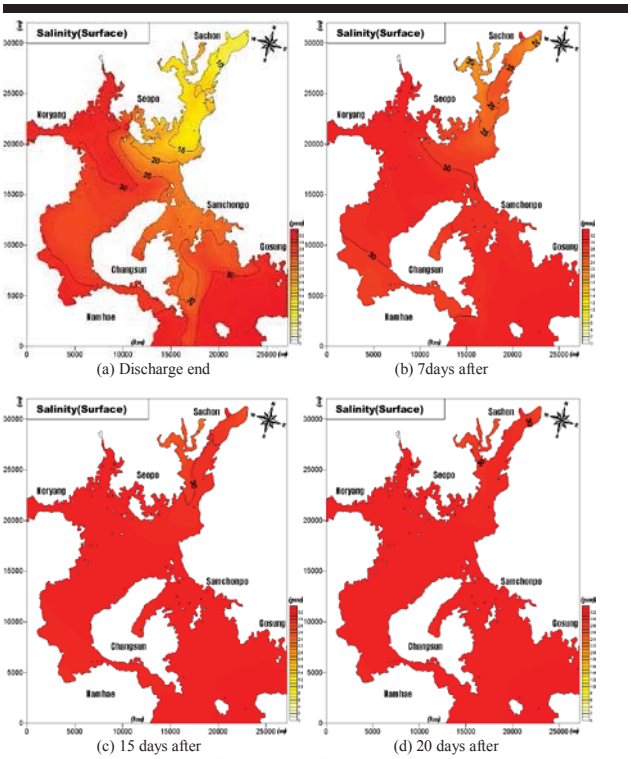

(a) Discharge end (b) 7days after

(c) 15 days after (d) 20 days after

Figure 9. Results of the discharge end.

LITERATURE CITED

City of Sacheon., 2009. Research service reports of Sacheon river safety inspection services.

Korea Water Resources Corporation., 2009. Hydraulic stability analysis study of downstream area due to the discharge changes of Namgang Dam.

National Oceanographic Research Institute http://www.khoa.go.kr/main.asp

Slφrdal, L.H., 1997. The pressure gradient force in sigma-co-ordinate ocean model. *Int. J. Numer. Methods in Fluids*, 24, 982-1071.

Yoon J.S.; Lee D.K. and Kim I.C., 2006. A study on the behavior of bottom water in water area by using modified POM. *J. Korean Society of Coastal and Ocean Engineers*, 18(3), 198-210 (in Korean).

Short and Medium Term Variation in the Dynamics of the Mesozooplankton Community of an Amazonian Estuary

Natália R. Leite[†*], André Magalhães[†], Leiliane M. Silva[†], Thamara P. Andrade[†], Jislene B. Matos[†], Ádila K. R. Costa,[†]Luci C. C. Pereira[†‡], Manuel J. Flores-Montes[††], and Rauquírio M. Costa[†§].

[†]Instituto de Estudos Costeiros, Universidade Federal do Pará, Bragança, Brazil.

[‡] Laboratori d'Enginyeria Marítima, Universitat Politècnica de Catalunya, Barcelona, Spain.

[††]Departamento de Oceanografia, Universidade Federal do Pernambuco, Recife, Brazil.

[§] Institut de Ciències del Mar (ICM/CSIC), Barcelona, Spain.

www.cerf-jcr.org

www.JCRonline.org

ABSTRACT

Leite, N.R.; Magalhães. A.; Silva, L.M.; Andrade, T. P.; Matos, J. B.; Costa, A. K.;Pereira, L.C.C.; Flores-Montes, M.J., and Costa, R.M.da., 2016. Short and Medium Term Variation in the Dynamics of the Mesozooplankton Community of an Amazonian Estuary. *In:* Vila-Concejo, A.; Bruce, E.; Kennedy, D.M., and McCarroll, R.J. (eds.), *Proceedings of the 14th International Coastal Symposium* (Sydney, Australia). *Journal of Coastal Research*, Special Issue, No. 75, pp. 218-222. Coconut Creek (Florida), ISSN 0749-0208.

The aim of this study was to investigate the short- and medium-term variation in the dynamics of the zooplankton community, in a macrotidal estuary (the Taperaçu) of the Amazon Coast of northern Brazil. This estuary has a characteristic funnel shape, with extensive sandbars running down the middle and current patterns typical of a shallow estuary, in addition to substantial seasonal variation. Fluctuations in zooplankton densities were analyzed in the context of the influence of the tidal cycle, temperature, salinity, turbidity, pH, dissolved oxygen concentration and chlorophyll-a concentrations. Data were collected in months of June, September and December 2012 and March, June, and September/2013. Samples were taken at three fixed stations, S1, S2, and S3 at 3-hour intervals over a nychthemeral cycle during the neap tide. The data were analyzed using a two-way ANOVA (to test the significance of the variation among stations, months, tides, and the circadian cycle) and PCA. Five principal species were identified–*A. tonsa*, *A. lilljerborgii*, *P. marshi*, *P. quasimodo*, *O. oswaldocruzi* and *O.dioica*. The results indicate that the patterns of variation (temporal, tidal, and spatial) in the zooplankton of the Taperaçu estuary were determined primarily by precipitation, salinity, turbidity, and chlorophyll-a concentrations, due to the strong local hydrodynamics and the unique morphodynamic characteristics of the estuary that provoke the constant mixing of its waters.

ADDITIONAL INDEX WORDS: *Estuaries, Amazonian, Zooplankton.*

INTRODUCTION

Zooplankton, especially copepods, are of major importance in pelagic systems in which, in addition to transferring organic material produced by the phytoplankton to higher trophic levels (Gismervik, 2006), the metabolic activity of these organisms is fundamentally important to the biogeochemical cycles and flow of energy into marine systems (Longhurst and Pauly, 2007). Most zooplanktonic organisms are omnivores, although many are primarily herbivores, carnivores or detritivores (Calbet, 2008; Kiørboe, 2008), and play an important role in the trophic web of aquatic ecosystems.

Previous studies of the composition, abundance, and biomass of the principal mesozooplankton species of the Taperaçu Estuary on different scales (spatial, seasonal and tidal cycle) have provided an important database on this community (Costa *et al*., 2008; Magalhães *et al*., 2015 and references therein). However, the use of different methodological procedures has hampered the evaluation of the spatial variability of its biological and environmental features.

The present study is the first based on the simultaneous, nycthemeral collection of data throughout the length of the estuary, which permitted the systematic testing of the hypothesis that the Taperaçu Estuary supports significant spatial and temporal gradients in environmental variables, which are regulated by seasonal oscillations in precipitation rates and determine the spatiotemporal distribution of the organisms that constitute the local zooplankton community.

METHODS

The Taperaçu Estuary (46º42'–46º45'W and 00º50'–00º57"S) is located approximately 200 km to the southwest of the mouth of the Amazon River, and has a surface area of 21 km², and a drainage basin of 40 km² (Asp *et al*., 2012). It is classified as a permanently open basin, with shallow waters, of an average depth of 4 m (Asp *et al*., 2012). The tides are semidiurnal macrotides, with ranges of approximately 5 m, reaching 6 m during the equinoctial spring tides (DHN, 2008). The Taperaçu is connected to the estuary of the Caeté River through the Taici

DOI: 10.2112/SI75-044.1 received 15 October 2015; accepted in revision 15 January 2016.

*Corresponding author: natirochaleite@gmail.com

creek (Figure 1), which is approximately 3 km long and 15 m wide (Araújo Jr. and Asp, 2013).

The creek, together with the runoff of precipitation from adjacent wetlands during the rainy season, provides the estuary's only input fresh/oligohaline water (Araújo Jr. and Asp, 2013). Annual precipitation is approximately 2,500 mm, of which, 75% falls during the rainy season (INMET, 2012).

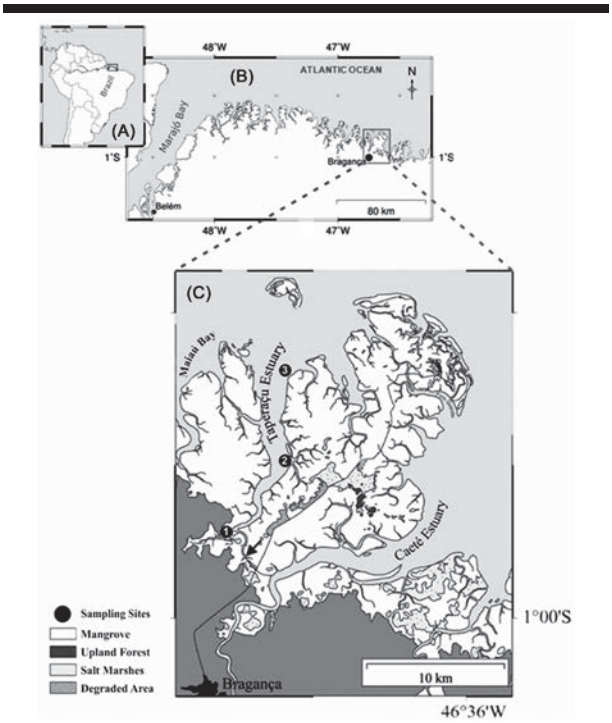

Figure 1. Study area: (a) South America; (b) location of the Taperaçu Estuary (00º50'–00º57' S and 46º42'–46º45' W) on the northern coast of Brazil; (c) location of the three data collection stations in the upper (1), middle (2) and lower (3) sectors of the estuary (Source: Magalhães, 2015, modified from Mehlig, 2001).

Pluviometry, collection of samples and laboratory procedures

Precipitation data were obtained from the National Meteorological Institute's (INMET) Tracuateua station, 17 km from the municipality of Bragança.

Data were collected in June, September and December, 2012, and March, June and September, 2013, using subsurface trawls of the water column at three fixed stations (Figure 1), in the lower (station S3: 00°50'30.9" S, 46º43'02.4" W), middle (station S2: 00°55'06.8" S, 46º44'0" W), and upper (station S1:00°56'58.4" S, 46º46'26.9" W). The plankton samples were collected during neap tides at 3- hour intervals over a 25-hour period, using plankton nets with a mesh of 200 µm (50 m diameter mouth, 2 m in length), fitted with mechanical flowmeters. The physical and chemical parameters of the water (temperature, salinity, turbity and dissolved oxygen) were measured *in situ*, using CTDs. Subsurface samples of the water were also collected for the laboratory analysis of pH and chlorophyll-a concentrations, which were determined according to standard international methods

In the laboratory, the zooplankton samples were subsampled using a Folson splitter, counted, and identified in gridded Petri dishes under a stereo-microscope. The organisms were identified to the lowest possible taxonomic level and classified taxonomically. The quantitative data were used to calculate the density (ind. m^{-3}), the relative abundance (%), the indices of diversity and evenness.

Data analysis

A two-way analysis of variance (ANOVA) was applied to evaluate the effect of the sampling stations, tidal phases, and circadian cycle (day and night) on the environmental variables measured, the total zooplankton density, and that of the principal species, as well as the relevant ecological indices. All the statistical analyses were run in Statistica v 8.0, with a 5% significance level ($\alpha = 0.05$). For the purposes of the present study, species were considered abundant when they had a relative mean monthly abundance of more than 20%. A Principal Components Analysis (PCA) was also run to evaluate the potential relationships among the environmental variables monitored during the study.

RESULTS

The initial statistical analyses found no significant differences among tidal phases or during the circadian cycle. Given this, all the parameters (biological and environmental data) were pooled (mean±standard deviation) and analyzed only in relation to the months of the study period and the sampling stations.

Environmental variables

Over the study period, precipitation in the region of the Taperaçu Estuary varied between 2 mm, in September 2012 and 342 mm in March 2013. In all months of the study period, except September 2013, the values recorded were lower than the historic means (1975-2011), with a reduction of 25.6% in June 2012 and 31.4% in March 2013 in comparison with the historic mean. The results of environmental variables are showm in figure 2.

Zooplankton

The analysis of the variation between the periods (day and night) of the nycthemeral cycle found no significant variation in any of the species analyzed, nor among tidal phases, allowed the data to be pooled (mean±standard deviation) for the analysis of monthly and spatial patterns, at the three sampling stations.

The Copepoda were the dominant taxon, representing 74.3% of the zooplankton community recorded during the study period as a whole. In the months of June (2012 and 2013), copepods reached their highest levels of relative abundance, contributing 76.8 and 80.7%, respectively. In these months, copepods of the genera *Acartia* and *Tisbe* were especially abundant. In March 2013, by contrast, the copepods contributed 59.9% of the organisms collected, while cirriped nauplii were found at high densities.

Total zooplankton density varied significantly ($p<0.05$) among months and sampling stations (Figure 3). High densities were recorded at station S1 in June, September and December 2012, but not during these same months in 2013. Clear differences were observed between the months of June in 2012 and 2013, with higher densities being recorded in 2012. The

mean zooplankton densities ranged from 242.4±381.0 ind.m^{-3} at station S3 to 198,919.1±358,245.6 ind.m^{-3} at station S1, with both values being recorded in June 2012 (Figure 3).

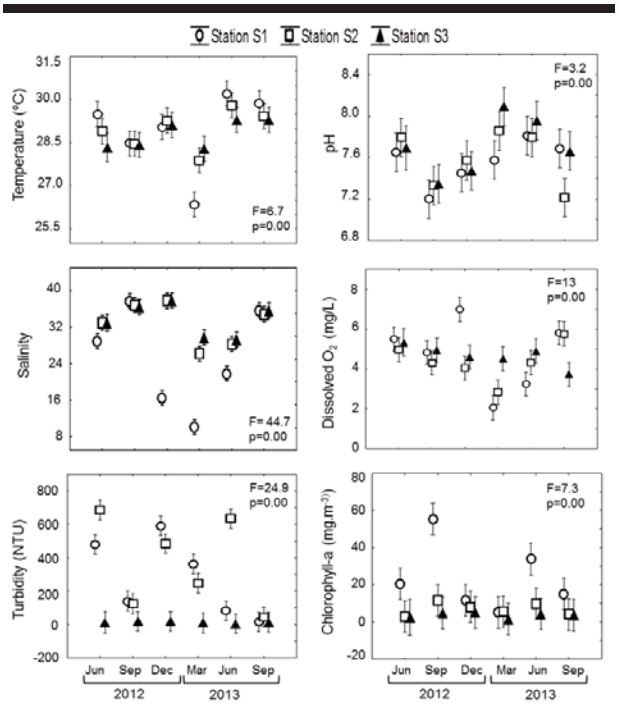

Figure 2. Results of the two-way ANOVA for the mean variation (± SD) in environmental variables recorded in the Taperaçu Estuary during the study period.

Acartia tonsa, *A. lilljerborgi*, *Pseudodiaptomus marshi*, *Paracalanus quasimodo* and *Oithona oswaldocruzi* were the most abundant copepod species overall, in both absolute and relative terms. The densities of *A.tonsa* varied significantly ($p<0.05$) among months and stations, with a peak being observed in June 2012 at station S1 (22,230.9±46,145.7 ind.m^{-3}). This species was observed at this station in June, September and December 2012, although it was not found in most samples collected in March 2013 (0.0 ind.m^{-3}). In September and December 2013, high densities of this species were recorded at station S2. The abundance of *A. lilljeborgi* followed a similar pattern, with significant ($p<0.05$) monthly and spatial variation. High mean densities were recorded at station S1 in June 2012 (4,011.6±10,326.5 ind.m^{-3}) and station S2 in June 2013 (1,579.9±2,742.3 ind.m^{-3}).

The density of *P. marshi* was significantly ($p<0.05$) higher than in other months at station S1 in June 2012 (3,267.3±4,565.1 ind.m^{-3}) and March 2013, with a mean of 2,678.8±6,353.08 ind.m^{-3} (Figure 3). Higher densities at station S1 were observed frequently during the study period, except for June 2013, when no significant spatial variation was found. *Paracalanus quasimodo* occurred at low densities in all months and sampling stations, except June 2012 (S1), when it contributed 75% of the total abundance of zooplankton recorded at this station. Significant ($p<0.05$) spatial variation was found in this species, with mean densities ranging from 5.4±7.6 ind.m^{-3} at station S3 in June 2012 and 9,270.7±17,593.3 ind.m^{-3} at station S1 in the same month (Figure 3).

Oithona oswaldocruzi was recorded in June and September 2012, with mean densities ranging from 3.9±5.7 ind.m^{-3} at station S3 in June 2013 and 30,221.9±28,328.4 ind.m^{-3} at station S1 (Figure 3). Significant ($p<0.05$) monthly and spatial differences were also found among months, with relatively high densities being recorded in June, September and December 2012 at station S1 (Figure 3).

Meroplanktonic organisms primarily *Oikopleura dioica*, contributed 25.2% of the total zooplankton density. As for the copepods the mean density of this species was highest ($p<0.05$) at station S1 in June 2012, with a density of 15,284.6±26,060.6 ind.m^{-3} (Figure 3).

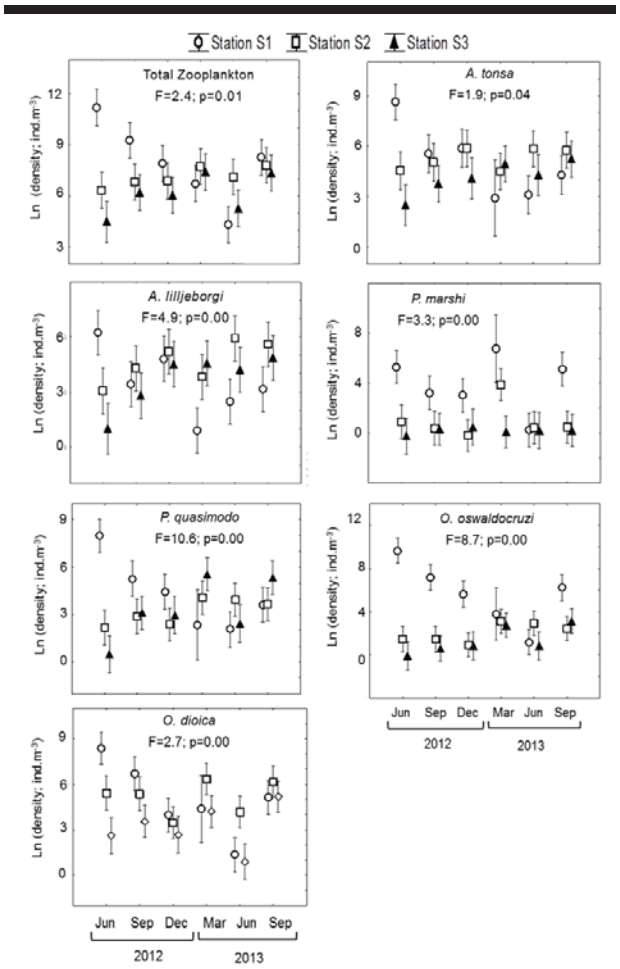

Figure 3. Two-way ANOVA showing the mean (± SD) variation in total zooplankton abundance, and that of the five principal copepod species and *O. dioica* in the Taperaçu Estuary. The scale of the y axis (density, ind.m^{-3}) was log-transformed using natural logarithms.

Mean species diversity ranged from 2.0±0.6 bits.ind^{-1} in March 2013 at station S1 and 3.8±0.4 bits.ind^{-1} in the same month at station S3, while evenness varied from 0.5±0.1 in March 2013 at station S1, and 0.7±0.03 at station S3 in September 2013. Considerable variability was observed among stations and study months ($p<0.05$), although the values recorded at station S3 were generally higher for both variables, indicating a high degree of spatial heterogeneity in the study region.

The PCA reflected the clear influence of environmental variables at the different sampling stations (S1, S2 and S3), with component 1 and component 2 explaining 59% of the variability at S1, 57% at S2, and 60% at S3 (Figure 4). All the environmental variables returned high correlation coefficients with PCA 1. Salinity was the most important variable at S1 and S3, with correlation coefficients of 0.84 and 0.82, respectively, while at S2, temperature was the most important variable (0.88 correlation with PCA 2).

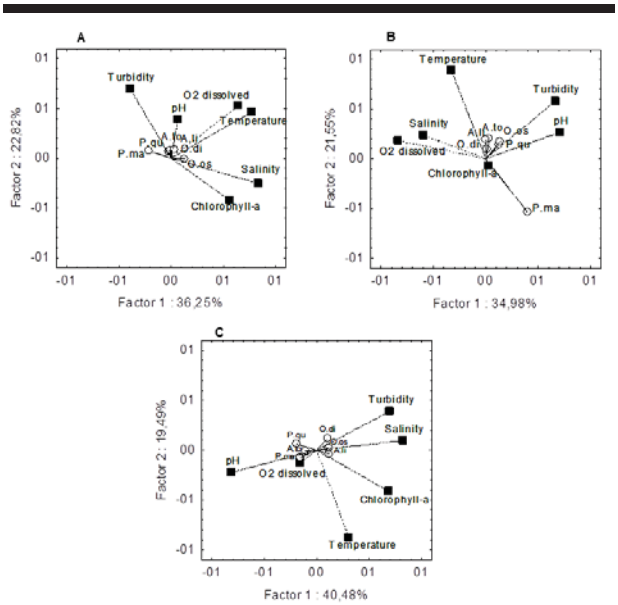

Figure 4. Results do PCA for the environmental variables analyzed at the three sampling stations (A: S1; B: S2; C: S3) located within the Taperaçu Estuary. The species (white circles) are: A.to = *Acartia tonsa*; A.li = *Acartia lilljerborgi*; P.ma = *Pseudodiaptomus marshi*; P.qu = *Paracalanus quasimodo*; O.os = *Oithona oswaldocruzi*; O.di = *Oikopleura dioica*.

DISCUSSION

In the Taperaçu Estuary, as in other tropical and subtropical regions around the world (Capo *et al*., 2006; Magalhães *et al*., 2009), seasonal variation in precipitation levels is the principal factor influencing monthly and seasonal fluctuations in environmental variables, with knock-on effects on the occurrence and distribution of zooplankton species. During the present study period (2012 and 2013), a significant reduction in precipitation rates was recorded in comparison with the historical average. This reduced rainfall may have provoked alterations in the environmental and biological parameters of the water, principally salinity. In the innermost portion of the estuary (S1), for example, a mean salinity of 28.9 was observed in June 2012, a period when values of less than 20 are normally recorded (Magalhães *et al*., 2015).

In addition to the influence of precipitation rates, the unique morphological and morphodynamic characteristics of the estuary contribute to the variation in the occurrence and distribution of the zooplankton, including the sandbars in the inner portion of the estuary, the absence of fluvial discharge, and the extremely small drainage basin, which reduces the input of freshwater to a sporadic minimum. This obviously favors the influence of coastal waters, and in particular the absence of freshwater species, especially in the outermost sector of the estuary. The estuary is also shallow, with strong currents (Asp *et al*., 2012), which facilitate the vertical and horizontal mixing of the water column, and hamper vertical migration in the zooplankton.

While the estuary lacks any significant fluvial discharge, considerable spatial differences were observed in the density of species, as well as the environmental variables measured, between station S1 and the other stations (S2 and S3) in 2012 and 2013. The Taperaçu is connected to the Caete Estuary through the tidal Taici Creek, through which fresh/oligohaline water flows during the highest flood tides, reinforcing the differences between station S1 and stations S2 and S3, located in the middle and outer estuary.

The density of mesozooplankton in the Taperaçu Estuary reflected the monthly and spatial variation in the copepod populations. These organisms were dominant in all months and at all sampling stations, and contributed 74.3% of the zooplankton collected during the study period. This group is common in estuaries around the world, where it typically contributes at least 80% of the total abundance (David *et al*., 2005; Menéndez *et al*., 2012). The zooplankton community was characterized by the predominance of the copepods *A.tonsa*, *A. lilljerborgi*, *P. marshi*, *P. quasimodo* and *O. oswaldocruzi* as well as *O. dioica* (Appendicularia), all of which occurred at high densities. A similar composition of the zooplankton community was recorded in previous studies of the same estuary (Magalhães *et al*., 2015) and in other estuaries on the Brazilian coast (Eskinazi-Sant'Anna and Björnberg, 2006; Costa *et al*., 2009), reflecting the ample distribution of these species in the region.

In addition to the direct relationship found between salinity and the spatial and temporal distribution of the zooplankton, other factors, such as turbidity and tidal currents may influence the density of these organisms (McLusky and Elliot, 2004; Marques *et al*., 2009). The high concentrations of suspended material reduced the penetration of solar radiation into the water column, which has a direct effect on phytoplankton growth (Matos *et al*., 2011), resulting in indirect effects on the spatiotemporal variation of zooplanktonic organisms.

In the present study, turbidity was correlated positively with the density of most of the most common species recorded at stations S2 and S3. A number of different studies (Diodato and Hoffmeyer, 2008; Menéndez *et al*., 2012) have shown that suspended sediments and detritus constitute an excellent source of food for copepods. Roman *et al*. (2001) have also suggested that the ability of some copepod species to ingest suspended particles allows them to prosper in environments with high turbidity.

CONCLUSIONS

The spatial and temporal (among tidal phases and months) variability of the mesozooplankton in the Taperaçu Estuary was controlled by the variation in precipitation, salinity, turbidity and chlorophyll-a concentrations. The copepods were dominant throughout the study period. The densities of the omnivorous copepods *Acartia tonsa* and *A. lilljerborgi* were correlated negatively with the chlorophyll-a concentrations and positively with turbidity. This may reduce intraspecific competition for feeding resources, allowing for the coexistence of these species in the same estuary without alternating between seasons, as previously suggested for this same estuary. The reduction in precipitation during June 2012 led to a significant increase in salinity, making this environment favorable to the occurrence of typically marine species, such as *P. quasimodo* and *O. dioica*. The results of the present study indicate that oscillations in the climatic and hydrological conditions (especially salinity) of the estuarine ecosystem are responsible for modifications in the occurrence and distribution of zooplankton species, and that these processes are more accentuated in the estuaries of the Amazon region, where precipitation rates are higher than in many other tropical and subtropical regions around the world.

ACKNOWLEDGMENTS

This research was supported by FAPESPA (ICAAF 79/2014) and CAPES (Ciências do Mar II 43/2013 and Pró-Amazônia 47/2012). The first author is grateful to SEDUC for the concession of a Ph.D scholarship. Co-authors Luci Pereira, Rauquírio Costa and Manuel Flores Montes are grateful to CNPq for research grants (#308379/2011–0 and 200629/2014–0, #306061/2011-2 and 200622/2014-5, and #558106/2009-9, respectively). We are also indebted to Stephen Ferrari for his careful correction of the English.

LITERATURE CITED

Araújo, W.P. Jr. and Asp, N.E., 2013. Hydrodynamic connectivity between two macrotidal Amazonian estuaries. *In*: Conley, D C.; Masselink, G.; Russell, P.E.; O'Hare, T.J. (eds.), *Journal of Coastal Research*, Special Issue No. 65, pp. 1086-1091.

Asp, N.E.; Schettini, C.A.F.; Siegle, E.; Silva, M.S., and Brito, R.N.R., 2012. The dynamics of a frictionally-dominated Amazonian estuary. *Brazilian Journal of Oceanography*, 60, 391-403.

Calbet, A., 2008. The trophic roles of microzooplankton in marine systems. *ICES Journal of Marine Science*, 65, 325-331.

Capo, S.; Sottolichio, A.; Brenon, I.; Castaing, P., and Ferry, L., 2006. Morphology, hydrography and sediment dynamics in a mangrove estuary: the Konkoure Estuary, Guinea. *Marine Geology*, 230(3-4), 199-215.

Costa, K.G.; Pereira, L.C.C., and Costa, R.M., 2008. Short and long-term temporal variation of the zooplankton in a tropical estuary (Amazon region, Brazil). *Boletim do Museu paraense Emílio Goeldi. Ciências Naturais*, 8(2), 127-141.

Costa, R.M.; Leite, N.R., and Pereira, L.C.C., 2009. Mesozooplankton of the Curuçá Estuary (Amazon Coast, Brazil). *In*: Finkl, C.W. (eds.), *Journal of Coastal Research*, Special Issue No. 56, 400-404.

David, V.; Sautour, B.; Chardy, P., and Leconte, M., 2005. Long-term changes of the zooplankton variability in a turbid environment: the Gironde estuary (France). *Estuarine, Coastal and Shelf Science*, 64, 171-184.

DHN, 2008. Diretoria de Hidrografia e Navegação. http:/www.mar.mil.br/~dhn/tabuas.

Diodato, S.L. and Hoffmeyer, M.S., 2008. Contribution of planktonic and detritic fractions to the natural diet of mesozooplankton in Bahía Blanca Estuary. *Hydrobiologia*, 614, 83-90.

Eskinazi-Sant'anna, E.M. and Björnberg, T.K.S., 2006. Seasonal dynamics of mesozooplankton in Brazilian coastal waters. *Hydrobiologia*, 563, 253-268.

Gismervick, I., 2006. Top-down impact by copepods on ciliate numbers and persistence depends on copepod and ciliate species composition. *Journal of Plankton Research*, 28(5), 499-507.

INMET, 2012. Instituto Nacional de Meteorologia. http://www.inmet.gov.br.

Kiørboe, T., 2008. *A Mechanistic Approach to Plankton Ecology*. Princeton: University Press, Princeton, NJ. 76p.

Longhurst, A.R. and Pauly, D., 2007. *Ecologia dos oceanos tropicais*. São Paulo: Editora da Universidade de São Paulo. 419p.

Magalhães, A.; Leite, N.R.; Silva, J.G.S.; Pereira, L.C.C., and Costa, R.M., 2009. Seasonal variation in the copepod community structure from a tropical Amazon estuary, Northern Brazil. *Anais da Academia Brasileira de Ciências*, 81, 187-197.

Magalhães, A.; Pereira, L.C.C., and Costa, R.M., 2015. Relationships between copepod community structure, rainfall regimes, and hydrological variables in a tropical mangrove estuary (Amazon coast, Brazil). *Helgoland Marine Research*, 69, 123-136.

Marques, S.M.; Azeiteiro, U.M.; Martinho, F.; Viegas, I., and Pardal, M.A., 2009. Evaluation of estuarine mesozooplankton dynamics at a fine temporal scale: therole of seasonal, lunar and diel cycles. *Journal of Plankton Research*, 31, 1249-1263.

Matos, J.B.; Sodré, D.K.L.; Costa, K.G.; Pereira, L.C.C., and Costa, R.M., 2011. Spatial and temporal variation in the composition and biomass of phytoplankton in an Amazonian estuary. *In*: Furmanczyk, K.; Giza, A., and Terefenko, P. (eds.), *Journal of Coastal Research*, Special Issue No. 64, pp. 1525-1529.

McLusky, D.S. and Elliott, M. 2004. *The Estuarine Ecosystem:Ecology, Threats and Management*. Oxford: Oxford University Press, 226p.

Menéndez, M.C.; Dutto, M.S.; Piccolo, M.C., and Hoffmeyer M.S., 2012. The role of the seasonal and semi-diurnal tidal cycle on mesozooplankton variability in a shallow mixed estuary (Bahía Blanca, Argentina). *ICES Journal of Marine Science*, 69, 389-398.

Roman, M.R.; Holliday, D.V., and Sanford, L.P., 2001. Temporal and spatial patterns of zooplankton in the Chesapeake Bay turbidity maximum. *Marine Ecology Progress Series*, 213, 215-227.

Journal of Coastal Research	SI	75	223-227	Coconut Creek, Florida	2016

An Analytic Approach to Model the Tidal Circulation in a Double-inlet Estuary

Moacyr Araujo[†], Carmen Medeiros [†*] and Jean-Philippe Endres[‡]

[†]Laboratório de Oceanografia Física Estuarina e Costeira, Departamento de Oceanografia
Universidade Federal de Pernambuco
Recife, Brazil

[‡]Ecole Nationale Supérieure d'Electrotechnique, d'Electronique, d'Informatique, d'Hydraulique et des Télécommunications
Toulouse Cedex 7, France

www.cerf-jcr.org

www.JCRonline.org

ABSTRACT

Araujo, M.; Medeiros, C. and Endres, J-P., 2016. An Analytic Approach to Model the Tidal Circulation in a Double-inlet Estuary. *In:* Vila-Concejo, A.; Bruce, E.; Kennedy, D.M., and McCarroll, R.J. (eds.), *Proceedings of the 14th International Coastal Symposium* (Sydney, Australia). *Journal of Coastal Research*, Special Issue, No. 75, pp. 223-227. Coconut Creek (Florida), ISSN 0749-0208.

Estuaries comprise broad spectra of systems whose morphology often rule theirs hydrodynamics. The Itamaracá estuarine system (NE-Brazil) is formed by the Santa Cruz Channel (SCC), connecting to the Atlantic Ocean through two inlets. Water level and in depth current measurements were used to evaluate an analytical approach for representing its tidal circulation. Depth-averaged currents were analytically predicted with 11% error ($\delta_1 = 0.11$). Currents measurements for five different sampling stations and depths were compared to model responses for various values of eddy viscosity (ν) and bottom friction parameter (r). The best-fit quadratic error $\delta_2 = 0.155$ was obtained with $\nu = 6.3 \times 10^{-3} m^2 s^{-1}$ and $r = 6.5 \times 10^{-3} ms^{-1}$. Model improvements, considering bottom friction and eddy diffusivity formulations, indicated a boundary layer depth of $0.10H$ (H=channel depth), and a large (6.1×10^{-3} m) mean roughness length of the sea-bed to couple with the intricate roots system of red mangroves along the SCC. Simulations were also used to test Taylor´s (1954) scale analysis, yielding $c = 0.080$ as best value ($c = \nu / u_* H$ constant; u_* =bottom friction velocity) and a mean eddy viscosity of $5.8 \times 10^{-3} m^2 s^{-1}$). The low sensibility of momentum distribution to changes in eddy viscosity verified suggests that stronger viscosity dumping may be compensated by higher bottom shear stress. This simple analytical approach could also be used to predict spatial and temporal distribution of pollutants and other materials at SSC and at similar systems as advection of those components could easily be simulated combining modelled currents with measurements of theirs concentrations.

ADDITIONAL INDEX WORDS: *Itamaracá, hydrodynamic, analytical model.*

INTRODUCTION

The longitudinal density gradient often present in estuaries results in a baroclinic (or gravitational) circulation, which drives the system dynamics in the longitudinal-vertical plane. To be able to rely on approximations/formulations that allow analytical solutions and satisfactorily reproduce the main features of the tidal-driven circulation would be highly desirable and helpful for making management decisions, as it would contribute to a better understanding of the distribution of energy and of the fate of materials within and from/to the system.

This study aimed to evaluate the performance of a somewhat simple model of open coastal dynamics (Wang and Craig, 1993) applied to Itamaracá's own specific case, as a tool to develop a better description of the hydrodynamics of tropical well-mixed estuaries and to provide an analytic solution of the vertical and axial structure of tidal currents in an estuary.

METHODS

The Itamaracá estuarine system (Figure 1) in tropical NE-Brazil (7°34'-55'S; 34°48'-52'W), is formed by the Santa Cruz Channel (SCC), a 20-km long channel that surrounds the Itamaracá island, and connects to the Atlantic through the Catuama and Orange Inlets. The SCC is surrounded by mangroves, and receives fresh water from six small rivers. Extensive shore-parallel sandstone reefs and sandbanks shield the offshore area of the estuary, which reduces water exchange.

Along the channel, vertical salinity stratification is weak; and normal levels of turbulence result in a uniform temperature distribution from surface to bottom (Medeiros and Kjerfve, 1993; 2005). Tides at both inlets are semi-diurnal, in phase and have a mean and spring ranges of 1.8m and 2.2m, respectively,

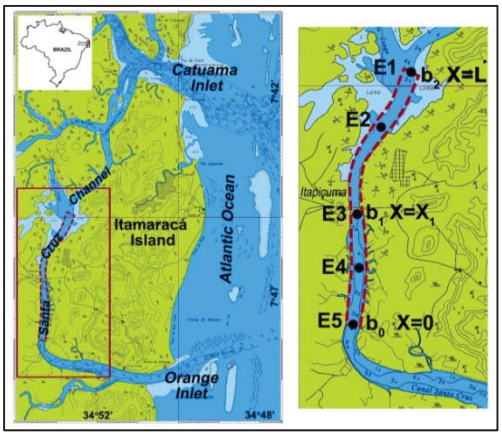

Figure 1. The Itamaracá estuarine system, NE-Brazil and modelled stretch of the Santa Cruz Channel and sampling stations E1-E5.

with a nodal point 1.7 km north of the Itapissuma bridge. Water salinity at the SCC changes seasonally, with a higher salt content during the dry season (Sep-Jan), and lower salt

DOI: 10.2112/SI75-045.1 received 15 October 2015; accepted in revision 15 January 2016.
*Corresponding author: cmlimongi@gmail.com

concentrations during the rainy season (Feb-Aug). This behavior acts as a selective forcing function for the development of autochthonous and migratory fish species which use the Itamaracá estuary.The study area comprised a 6km stretch of the SCC centered on the Itapissuma bridge, where most of the fishing and tourist activities take place.

Sampling and Field Data Acquisition

Field work was carried out during the rainy season on Aug 15-16th/2000. It included current measurements along the channel over the tidal cycle to determine the distribution of the velocities in time, depth and abscise, as well as a bathymetric survey and time-series measurements of currents and water level variation to set the model physical and boundary conditions.

Current measurements were obtained hourly at stations E1-E5 (Figure1). Sampling stations were located along the main channel axis, as a way of minimizing the influence of local cross-channel currents and to produce accurate current profiles. At each sampling station, measurements were carried out over two spring tidal cycles, 0.5m below the surface, at mid-depth and 0.5m above the bottom, with a Sensordata SD-30 current meter. The choice of spring tide was intended to maximize the effects of tidal forcing.

Cross sectional bathymetric profiles were taken with a Raytheon DC2000Z depth fathometer from E1 to E5 to determine channel morphobathymetry.

Registers of the sea-level evolution were gathered at intervals of 15 minutes at station E5 with a Sea-Bird Electronics SBE-26 wave and tide-gauge; and time-series measurements of flow (current and depth) were gathered at intervals of 10 minutes at station E1 using a Sensordata SD-6000 and a pressure sensor.

An Analytical Model for Tidal Currents

The analytic model of tidal currents is based on a depth-averaged coastal model proposed by Battisti and Clarke (1982) and subsequently extended by Craig (1989) to include the vertical dimension. The simplification in the model that enables analytic solutions follows the property that the topographic length scale is much less than the horizontal wavelength of the tides (Rossby radius), which is observed at the SSC.

To apply this model to Itamaracá we assumed that major tidal currents components are confined to the axial channel direction and Coriolis effects are neglectable. The canal cross-section is rectangular with depth $H(x,t)$ and width $b(x)$. These physical assumptions enable to pose the analytic problem in terms of the surface elevation ζ, the depth-averaged velocity $\overline{U}$, and the depth varying velocity u (Craig, 1989) to give:

$$-i\omega_b\zeta+(\partial/\partial x)(H_b\overline{U})=0 \tag{1}$$

$$-i\omega\overline{U}=-r(u_b+\overline{U})/H \tag{2}$$

$$-i\omega u=(\partial/\partial z)(\nu\partial u/\partial z)+r(u_b+\overline{U})/H \tag{3}$$

where ω is the semidiurnal tidal frequency, r is the linear friction coefficient, ν is the kinematic viscosity of water, and the subscript b indicates the bottom conditions. Here ω, ν and r are assumed constants and time derivatives have been replaced by the factor $-i\omega$ where i is the complex $\sqrt{-1}$, assuming harmonic motion at fixed frequency ω.

Horizontal boundary conditions for (1) and (2) are fixed by the particularities of the Itamaracá system, a hydrodynamics channel with two inlets. They are expressed by:

$$x=0: \quad \overline{U}(0,t)=\overline{U}_0(t); \qquad H(0,t)=H_0(t) \tag{4a,b}$$

$$x=L: \quad \zeta=\zeta(t) \tag{5}$$

For each of the tidal constituents, $\zeta(t)$ is determined from field measurements of amplitudes and phases. The time-dependent formulation for tidal amplitude (Eq. 5) is relevant only if the tidal celerity ωL is negligible when compared to local wave celerity $\sqrt{gH}$. In the Santa Cruz Channel the authors found $\omega L/\sqrt{gH}\cong 0.06$.

Previous field measurements and numerical studies indicate that flow structures in the SSC are largely dominated by bottom shear, when compared to the effects of surface wind stress over vertical distribution of momentum (Medeiros and Kjerfve 1993; Araujo *et al.*, 2000a; Leite *et al.*, 2008) mainly during the dry season. As so, boundary conditions at the bottom introduce log-law behavior for tangential velocities, which are expressed here through a linear behavior. A zero value for surface stress boundaries was considered, and vertical boundaries in the model may be written as following:

$$z=-H: \quad \nu(\partial u/\partial z)_{-H}=r(u_b+\overline{U}) \tag{6}$$

$$z=0: \quad \nu(\partial u/\partial z)_0=0 \tag{7}$$

For model calculations, the SCC was assumed to have a polygonal shape and its geometry is given by:

$$b(x)=\begin{cases} b_0+(b_1-b_0)x/x_1, & x\le x_1 \\ b_1+(b_2-b_1)(x-x_1)/(L-x_1), & x_1\le x\le L \end{cases} \tag{8}$$

Previous formulation of the model, once applied to the geometry and the boundary conditions of SCC, give us respective previous notations:

$$\overline{U}(x,t)=\begin{cases} \dfrac{i\omega\zeta(t)}{2b(x)H(x,t)}\left[b_0+b(x)\right]x+\dfrac{\overline{U}_0(t)b_0H_0(t)}{b(x)H(x,t)}, & 0\le x\le x_1 \\ \dfrac{i\omega\zeta(t)}{2b(x)H(x,t)}\left\{\left[b_0-b(x)\right]x_1+\left[b_1+b(x)\right]x\right\}+\dfrac{\overline{U}_0(t)b_0H_0(t)}{b(x)H(x,t)}, & x_1\le x\le L \end{cases} \tag{9}$$

The solution for $\overline{U}$ can now be substituted into Eq. (3), which is an ordinary differential equation for u. The solution for u is then given by:

$$u(x,z,t)=A\cosh(\gamma z)+\frac{ir[u_b+\overline{U}(x,t)]}{\omega H(x,t)} \tag{10}$$

$$A=\frac{-\overline{U}r\omega H}{\omega Hr\cosh(\gamma H)-(ir-\omega H)\gamma\nu\sinh(H\gamma)} \tag{11a}$$

$$u_b=-\overline{U}\frac{rH\omega\cosh(\gamma H)-ir\gamma\nu\sinh(H\gamma)}{\omega Hr\cosh(\gamma H)-(ir-\omega H)\gamma\nu\sinh(H\gamma)} \tag{11b}$$

$$\gamma=(1-i)(\omega/2\nu)^{1/2} \tag{11c}$$

where the depth-average for u in Eq. (10) is zero as required.

If ν and r are specified, for a given tidal amplitude, the velocity at any location of the estuary can be calculated using Eqs. (9) and (10). Alternatively, field measurements of tidal currents may be used to estimate the eddy viscosity and friction parameters, approach adopted in this paper.

RESULTS

The time evolution of mean current speed at station E1 - $U_0(t)$, and of sea-level at station E5- $\zeta(t)$, used as boundary conditions for calculation of the modeled currents, are presented in Figure 2 compared to harmonic behavior.

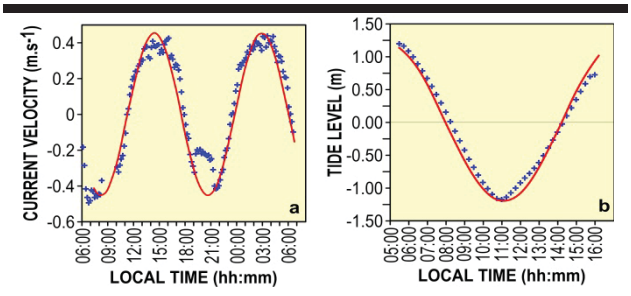

Figure 2. Temporal evolution of (a) mean current speed at station E1, Aug 16-17th (— Harmonic model ; + Current meter) and (b) of tides at station E5, Aug 16th (— Harmonic model ; + Tide gauge).

The close fit between modeled and *in situ* measurements suggest that the assumption of harmonic motion is verified, and

it seems possible to have an analytical description of the boundary conditions respecting the model formulation.

Model results are compared with measurements for longitudinal and depth varying currents.

A mean velocity had to be defined in order to verify at best the hypothesis of uniform repartition of the current across the section and to minimize non-representative variations. For calculation, it was necessary to consider only the velocity along abscise for comparison with the modeled current.

The current meter provides information about the direction and the intensity of the currents. A mean direction of the flow (main deeper channel) was defined thanks to the bathymetry maps and measurements made were projected along that direction. The depth-averaged velocity was defined as a sum of all those measurements, that is:

$$z=-H:\ \nu(\partial u/\partial z)_{-H}=r(u_b+\overline{U}) \qquad (11)$$

$$z=0:\ \nu(\partial u/\partial z)_0=0 \qquad (12)$$

$$U_m=\tilde{U}=1/H\int_{-H}^{0}U\,dz\cong 1/H\sum_i U_i\left(z_{i+1}-z_i\right) \qquad (13)$$

To evaluate the relevance of the model in the description of the vertical and longitudinal structures of the currents, it is necessary to define two different functions. δ_1 quantifies the fitting between modeled and measured depth-averaged currents and δ_2 quantifies the fitting between modeled and measured depth-varying currents. Those expressions are:

$$\delta_1^2=\frac{\sum_i\sum_t\left|U_{it}-\tilde{U}_{it}\right|^2}{\sum_i\sum_t\left|\tilde{U}_{it}\right|^2}\ ;\ \delta_2^2=\frac{\sum_i\sum_k\sum_t\left|\frac{U_{ikt}}{U_{it}}-\frac{\hat{U}_{ikt}}{\tilde{U}_{it}}\right|^2}{\sum_i\sum_k\sum_t\left|\frac{\hat{U}_{ikt}}{\tilde{U}_{it}}\right|^2} \qquad (14)$$

Where i is the cross section, k is the depth and t, the time. U_{it} and $\tilde{U}_{it}$ are the modeled and measured depth-averaged currents, respectively. U_{ikt} and $\hat{U}_{ikt}$ are the modeled and measured total $(U+u)$ current velocities, respectively.

The term δ_1 is the most important difference function as far as the global relevance of the model is concerned. Later analysis of δ_2 is defined on the assumption that modeled and measured depth-averaged currents are roughly the same $(\delta_1\equiv 0)$. This assumption is justified insofar as the aim of this study, which is to estimate distinct model robustness in both (longitudinal and vertical) directions.

According to previous definition of difference function (Eq. 14), the experimental data set gives $\delta_1=0.11$. This value of fitting is obtained for depth-averaged velocities. Previous calculations showed that depth-integrated mean velocities are very close to the values measured at mid-depth. Table 1 lists the most representative values of modeled and measured depth-averaged velocities for stations E2 and E3.

Table 1. *Modelled and measured depth-averaged currents at stations E2 and E3, Santa Cruz Channel.*

STATION	LOCAL TIME / TIDAL STAGE	CURRENTS (m.s^{-1}) Modelled	Measured
E2	06:14 / High-Ebb	-0.20	-0.22
	12:50 / Low-Flood	0.36	0.35
E3	06:23 / High-Ebb	-0.46	-0.45
	09:10 / Ebb-Low	-0.28	-0.34
	12:37 / Low-Flood	0.40	0.35

From Table 1 and the order of magnitude of δ_1, it is clear that the analytic solution provides a good description of the longitudinal structure of currents in the SCC. Nevertheless, the weak dependence on time and abscise of the fitting suggests that the existence of cross-channel currents and the secondary flow from the northern part of the channel may impair the quality of the agreement between the model and the measurements.

First, the eddy viscosity and bottom friction parameters are assumed to be constant in depth, time and space (along SCC). δ_2 is assumed to be a function of ν and r. The best estimates of the eddy viscosity and bottom friction parameter are those values of ν and r that minimize δ_2. Modeled currents for different abscises and depths corresponding to the sites selected along the reach of the channel may be calculated for any couple (ν,r). A contour plot of δ_2 (Eq. 14) is shown in Figure 3.

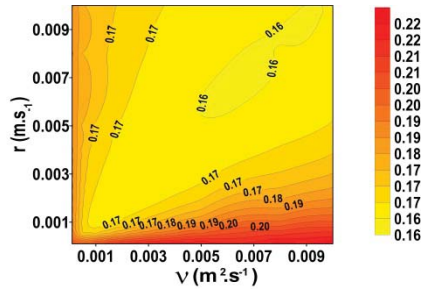

Figure 3. Contour plot for δ_2 (ν in m^2 s^{-1} and r in m s^{-1}).

This Figure was constructed by performing two hundred stochastic simulations using the Monte Carlo method. It permitted the two parameters to be varied randomly according to a Normal distribution, based on the previous numerical modeling results of Araujo *et al.* (2000b) for SCC, and allowed simulations to be repeated so that δ_2 could be compiled.

The best-fit ($\delta_2=0.155$) was obtained for $\nu=6.3\text{x}10^{-3}$ m^2 s^{-1} and $r=6.5\text{x}10^{-3}$ m s^{-1}. The close fit between measurements and simulations (Figure 4) suggests that the model provides a good description of the vertical tidal current distribution.

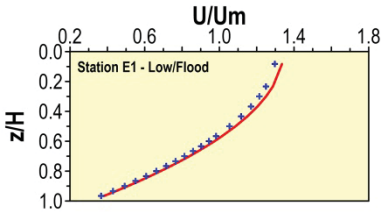

Figure 4. Comparison between analytical current profiles: — ($\nu=5.0\text{x}10^{-3}$ m^2 s^{-1}, r = 5.5x10^{-3} m s^{-1}); + ($\nu=9.0\text{x}10^{-3}$ m^2 s^{-1}, r = 1.0 x 10^{-2} m s^{-1}).

Nevertheless, the solution accuracy appears to be relatively insensitive to the values of ν and r. The presence of the large "valley", limited by $\delta_2=0.16$, confirms the apparent robustness of modeled currents to ν and r. This robustness is demonstrated in Figure 4, which compares profiles obtained for ($\nu=5.0\text{x}10^{-3}$ m^2 s^{-1}, r = 5.5x10^{-3} m s^{-1}) and for ($\nu=9.0\text{x}10^{-3}$ m^2 s^{-1}, r = 1.0x10^{-2} m s^{-1}). Both couples occur in the "valley" of the Figure 3. Despite this parameter change, the solutions are still accurate. As remarked by Wang and Craig (1993), increasing the eddy viscosity reduces the vertical shear, thus reducing the variation from the mean velocity. By contrast, an increase in the bottom friction coefficient leads to an increase in shear and in depth-varying velocity. Consequently, increases in both ν and r have the potential to cancel one another and are likely to do so along the "valley" in Figure 3. Representative comparisons between simulated and measured currents are presented in Figure 5.

The global shape of the curves is the same, so this assumption

can be considered as qualitatively relevant. This result is in agreement with previous studies (*e.g.*, Clarke, 1990; Maas and van Haren, 1987; Pingree and Griffiths, 1987; Wang and Craig, 1993). The model seems to give a reasonable description of the vertical evolution of currents. However, the solution provided by the model does not fit exactly for every station and sea level, suggesting a weak dependence on space and time. While the model is globally accurate, improvements may be attempted to obtain a better fitting to reality.

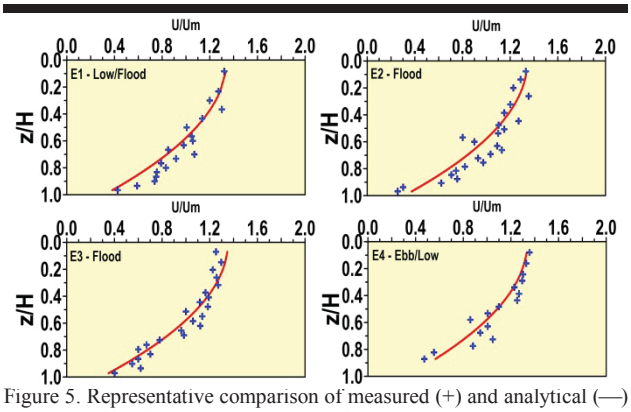

Figure 5. Representative comparison of measured (+) and analytical (—) current profiles for $\nu = 6.3 \times 10^{-3}\ m^2\ s^{-1}$ and $r = 6.5 \times 10^{-3}\ m\ s^{-1}$.

Bottom Boundary Layer Parameters

The first model formulations with the hypothesis of constant eddy viscosity do not describe accurately the bottom boundary layer, in which the current drops from its free-stream value to zero. Theoretically, the bottom boundary layer is assumed to be a region of constant stress, in which the eddy viscosity varies linearly with the distance from the bottom, as $\nu = \kappa u_* (z + H + z_0)$, where κ is the von Karman's constant, u_* is the friction velocity previously defined and z_0 is the roughness length of the sea bed associated to a small-scale turbulence. The major justification for above equation is that it yields classical logarithmic velocity profiles, providing accurate description for bottom boundary layers in similar studies (Araujo *et al.*, 2000a,b; Leite *et al.*, 2008; Wang and Craig, 1993). Denoting u' the total velocity in the bottom boundary layer, where $(z+H)$ is small, the solution for u' derived from Eqs. (1) and (3) is given by $u' = A \ln((z + H + z_0)/z_0)$, which satisfies the boundary condition $u' = 0$ at $z = -H$ for a constant value of A (Craig *et al.*, 1993). The solution of linearly varying viscosity and logarithmic velocity profile is valid in the boundary layer defined between $z = -H$ and $z = z_1$. Thus, by assumed continuity of velocity, viscosity and shear stress at the top of the boundary layer, it is possible to estimate A, z_1 and z_0, whose are relevant data about the hydrodynamics of the SCC. On the assumptions that $z_1/H = o(1)$ and $z_0/z_1 = o(1)$, one may write:

$$A \ln(z_1/z_0) = |u_b + \overline{U}| \quad (15)$$

$$\nu_0 = \kappa u_* z_1 \quad (16)$$

$$\frac{A}{z_1} = \left|\frac{du}{dz}\right|_{z=-H} = \frac{r}{\nu H}(u_b + \overline{U}) \quad (17)$$

where ν_0 is the interior eddy viscosity. Using previous values for eddy viscosity and bottom friction parameter, i.e. $\nu = 6.3 \times 10^{-3}\ m^2\ s^{-1}$ and $r = 6.5 \times 10^{-3}\ m\ s^{-1}$, the mean values of A, z_1 and z_0 for SCC are: A=0.09 ms^{-1}; z_1=0.70m e z_0=6.1x10^{-3}.

DISCUSSION

From the calculated mean value of z_1, the boundary layer depth in SCC is deduced to be $0.10H$. It seems to be in the same range as other studies. Previous results from turbulence modelling of a stirring tropical estuary, for example, indicate $0.05H \le z_1 \le 0.20H$ (Araujo *et al.*, 2000b); Wang and Craig (1993) suggested a depth $0.06H$; Bowden *et al.* (1959) found $z_1 \equiv 0.14H$; and Jenter and Madsen (1989) values ranged between $0.10H$ and $0.15H$. For the mean roughness length of the sea bed, Wang and Craig (1993) found $z_0 \equiv 1.6 \times 10^{-3}$ m, that we believe to be associated to sand or mud ripples bed (Jenter and Madsen, 1989). We found $z_0 \equiv 6.1 \times 10^{-3}$ m for SCC, which is a large value that may be associated with the presence of sea bed roots and typical mangrove vegetation in the study area (Medeiros and Kjerfve, 1993, Medeiros *et al.*, 2001).

The model described can also be used to test the water-depth dependence for the interior eddy viscosity formulations.

The most common model for interior viscosity is based on Taylor´s (1954) analysis, where the eddy diffusivity may be written as a function of a turbulent velocity scale and length scale. In estuaries these parameters are typically the shear velocity u_* and the depth of the estuary (*e.g.*, Koseff *et al.*, 1993, among others), and eddy viscosity may be written as $\nu = c u_* H$, where c is a constant in the range 0.01 to 0.10 and u_* is the bottom friction velocity defined as $u_*^2 = \nu \partial u/\partial z$. Here we considered bottom stress as the only primary source of turbulence for vertical mixing at SCC, once measured wind speeds and surface forcing were insignificant. In practice, one may estimate $u_* = O(1\% - 5\% U)$ (*e.g.*, Klebanoff, 1954; Nezu and Rodi, 1986), and we have taken $u_*(x,t) \cong 0.05\,\overline{U}(x,t)$ in this study (Araujo, Medeiros and Ribeiro, 1999; Araujo *et al.*, 2000b; Leite *et al.*, 2008). This new assumption does not modify the governing equations, as viscosity is still a constant in depth, *i.e.* $\partial \nu/\partial z = 0$

The best modelling results were obtained for $\nu = 6.3 \times 10^{-3}\ m^2\ s^{-1}$ and $r = 6.5 \times 10^{-3}\ m\ s^{-1}$ but sometimes constant parameters do not fully represent reality. Improvements can be searched considering the expression of the bottom friction parameter and/or the eddy viscosity, looking for expressions and assumptions that enable better modeling results without modifying previous governing equations.

As far as the bottom friction parameter is concerned, it is clear that r is function of the nature of the estuarine bed (*e.g.*, sand, mud, *etc.*), *i.e.*, along the channel axis. Considering a different bottom friction for each measurement station can be the first step to improve the accuracy of the model. Nevertheless, justifying in practice the link between the values and the nature of the channel bed is much more difficult. As a consequence, our first approach considering a mean bottom friction seems to be the best and our improvement will not focus on that point. As far as the eddy viscosity is concerned, it is necessary to distinguish interior viscosity from bottom viscosity. Therefore, as previously mentioned, the point is to consider improvements that will not modify the formulation of the analytical solution. The introduction of a depth-dependent eddy viscosity requires a considerably more complicated analytic solution scheme, which defeats the aim of this study. Different studies gave estimations of c. Bowden, Fairbairn and Hugues (1959) estimated a value of 0.056 from data in a tidal estuary; Hearn and Holloway (1990) found $c = 0.025$ for a wind driven flow over an open shelf, and Wang and Craig (1993) proposed $c = 0.028$ from their analysis of the Hey river estuary.

The best value of c for the SCC must be the one that will minimize the global difference between modeled and field currents at every section and for every stage of the sea level as far as the measurement performed at Itamaracá is concerned. As consequence δ_2 can now be defined as a function of r and c. In our case, c is 0.080, with a value for the best fit indicator of 0.15. This value may appear larger to previous ones but it was obtained with an assumed friction velocity of $0.05\,\overline{U}$. With more

data about this velocity, this value should be more accurate. Nevertheless, the main interest of c is to provide an order of magnitude of the eddy viscosity thanks to the values of water level and speed. Calculated eddy viscosities as a function of $u_* H$ (for $\nu / u_* H = c = 0.080$) had a mean value of $5.8 \times 10^{-3}\ m^2\ s^{-1}$, range of $1.0 \times 10^{-3}\ m^2\ s^{-1} < \nu < 1.2 \times 10^{-2}\ m^2\ s^{-1}$, which is very close to that global initial estimation $\nu = 6.3 \times 10^{-3}\ m^2\ s^{-1}$ obtained for SCC.

CONCLUSIONS

Field depth-averaged currents were predicted analytically with 11% error ($\delta_1 = 0.11$). Modeled currents for different sample station and depths were calculated for different values of eddy viscosity and bottom friction parameters. Differences between analytical and field values were computed through a quadratic error estimator δ_2. The best-fit solution indicator, $\delta_2 = 0.155$, was obtained for $\nu = 6.3 \times 10^{-3}\ m^2\ s^{-1}$ and $r = 6.5 \times 10^{-3}\ m\ s^{-1}$. The close fit between the measurements and the model obtained for those values of ν and r indicates that the model describes well the vertical tidal currents distribution. Nevertheless, the solution accuracy appears to be relatively insensitive to the exact value of ν and r, since increases in both ν and r have the potential to cancel each other as stronger viscosity dumping may be compensated by higher bottom shear stress.

Field data and error analysis allowed estimating bottom boundary layer parameters for the SCC. The deduced boundary layer depth in the study area was $0.10H$, where H is channel depth, with a mean roughness length of the sea-bed about $6.1 \times 10^{-3}\ m$, a large value that may be associated to the presence of sea-bed roots and typical mangrove vegetation.

Measurements and modeling results were also used to test the water-depth dependence for the classical eddy viscosity formulation issued from Taylor´s (1954) scale analysis, $\nu = c u_* H$, where c is a constant and u_* is the bottom friction velocity. Calculated quadratic error $\delta_2 = 0.155$ indicates that the best value of c for the SCC is $\nu / u_* H = c = 0.080$, and derived eddy viscosities range $1.0 \times 10^{-3}\ m^2\ s^{-1} < \nu < 1.2 \times 10^{-2}\ m^2\ s^{-1}$, with a mean value of $5.8 \times 10^{-3}\ m^2\ s^{-1}$.

Results were very encouraging and the approach should prove to be of good use to estuary managers as it would contribute to a better understanding of the hydrodynamic behavior of this system, as well as in predicting flux and distribution of salt, nutrients, pollutants, planktonic species, *etc.* within, and to and from, the system.

ACKNOWLEDGEMENTS

The authors are thankful to Isaac Freitas and Celine Stretta for their invaluable assistance during field works.

LITERATURE CITED

Araujo, M., Medeiros, C. and Ribeiro, C., 1999. Energy balance and time-scales of mixing and stratification in the Jaboatão estuary, NE-Brazil. *Brazilian Journal of Oceanography* 47, 145-154.

Araujo, M., Medeiros, C., Ribeiro, C. and Freitas, I., 2000a. Testing surface boundary conditions for turbulent modelling in tidal systems. In: J.M. Redondo, A. Babiano (eds.), Turbulent diffusion in the environment. Barcelone, Spain, CIMNE, p. 25-38.

Araujo, M., Medeiros, C., Ribeiro, C., Freitas, I. and Bezerra, M. O., 2000b. Turbulence modelling in a stirring tropical estuary. In: J.M. Redondo, A. Babiano (eds.), Turbulent diffusion in the environment. Barcelona, Spain, CIMNE, p. 56-66.

Battisti, D.S. and Clarke, A.J., 1982. A simple method for estimating barotropic tidal currents on continental margins with specific applications to the M2 tide off the Atlantic and Pacific coasts of the United States. *Journal of Physical Oceanography,* 12, 8-16.

Bowden, K.F., Fairbairn, L.A. and Hughes, P., 1959. The distribution of shearing stresses in a tidal current. *Geophysical Journal of the Royal Astronomic Society,* 2, 288-305.

Clarke, A.J., 1990. Application of a frictional channel flow theory to flow in the Prince of Whales Channel, Torres Strait. *Journal of Physical Oceanography,* 20, 890-899.

Craig, P.D., 1989. A model of diurnally forced vertical current structure near 30º latitude. *Continental Shelf Research,* 9, 965-980.

Craig, P.D., Hunter, J.R. and Johnston, B.L., 1993. The applications of linearly varying eddy viscosity for wind-driven current profiles. *Continental Shelf Research*, 13, 1-24.

Hearn, C.J. and Holloway, P.E., 1990. Application of a three-dimensional turbulence energy model to the determination of tidal currents on the northwest European shelf. *Journal of Geophysical Research,* 95, 18143-18162.

Jenter, H.L. and Madsen, O.S., 1989. Bottom stress in wind-driven depth-averaged coastal flows. *Journal of Physical Oceanography,* 19, 962-974.

Klebanoff, P.S., 1954. Characteristics of turbulence in a boundary layer flow with zero pressure gradient. http://naca.central.cranfield.ac.uk/reports/1955/naca-report-1247.pdf. NACA Report. 1247 p.

Koseff, J.R., Holen, J.K., Monismith, S.G. and Cloern, J.E., 1993. Coupled effects of vertical mixing and benthic grazing on phytoplankton populations in shallow, turbid estuaries. *Journal of Marine Research,* 51, 843-868.

Leite, F.S., Araujo, M., Medeiros C. and Endres, J-P., 2008. Energy balance and mixing timescales in a stirring tropical estuary, Itamaracá, Brazil. *Journal of Coastal Research,* 24, 151-160.

Mass, L.R. and van Haren, J.J.M., 1987. Observations of the vertical structure of tidal and inertial currents in the central North Sea. Journal Marine Research, 45, 293-318.

Medeiros, C. and Kjerfve, B., 1993. Hydrology of a tropical estuarine system: Itamaracá, Brazil. *Estuarine Coastal Shelf Science,* 36, 495-515.

Medeiros, C., Kjerfve, B., Araújo, M. and Neumann-Leitão, S., 2001. *The Itamaracá estuarine ecosystem, Brazil.* In: U. Seeliger, B. Kjerfve (eds.), Coastal marine systems of Latin America. Springer-Verlag, p. 71-81.

Medeiros, C. and Kjerfve, B., 2005. Longitudinal Salt and Sediment Fluxes in a Tropical Estuary: Itamaracá, Brazil. *Journal of Coastal Research,* 21(4), 751-758.

Nezu, I. and Rodi, W., 1986. Open-channel flow measurements with Laser Doppler Anemometer. *Journal of Hydraulic Engineering*-ASCE, 112, 335-355.

Pingree, R.D., Griffiths, D.K., 1987. Tidal friction for semidiurnal tides. Continental Shelf Research 7,1181-1209.

Taylor, G.I., 1954. The dispersion of matter in turbulent flow through a pipe. *Proceedings of the Royal Society of London,* Ser. A223, p. 446-448.

Wang, X.N. and Craig, P.D., 1993. An analytic model of tidal circulation in a narrow estuary. *Journal of Marine Research,* 51, 447-465.

Journal of Coastal Research	SI	75	228-232	Coconut Creek, Florida	2016

Records of Migration and Ebb-Delta Breaching at Historic and Ancient Tidal Inlets along a River-Fed Paraglacial Barrier Island

Christopher J. Hein[†*], Gregory G. Fitzsimons[‡], Duncan M. FitzGerald[††], and Andrew R. Fallon[†]

[†]Department of Physical Sciences
Virginia Institute of Marine Science
College of William and Mary
Gloucester Point, VA USA

[‡]Graduate School of Education
University of Massachusetts Lowell
Lowell, MA, USA

[††]Department of Earth and Environment
Boston University
Boston, MA, USA

www.cerf-jcr.org

www.JCRonline.org

ABSTRACT

Hein, C.J.; Fitzsimons, G.G., FitzGerald, D.M., and Fallon, A.R., 2016. Records of Migration and Ebb-Delta Breaching at Historic and Ancient Tidal Inlets along a River-Fed Paraglacial Barrier Island. *In:* Vila-Concejo, A.; Bruce, E.; Kennedy, D.M., and McCarroll, R.J. (eds.), *Proceedings of the 14th International Coastal Symposium* (Sydney, Australia). *Journal of Coastal Research*, Special Issue, No. 75, pp. 228-232. Coconut Creek (Florida), ISSN 0749-0208.

Tidal inlets link backbarrier environments to the coastal ocean and play a dominant role in both longshore and cross-shore sediment transport. Additionally, inlet-fill sequences comprise up to 50% of barrier lithosomes in wave-dominated settings. This study uses historic records to investigate centennial-scale cycles of inlet dynamics and barrier shoreline adjustment at Merrimack River Inlet (Plum Island, Gulf of Maine). Geophysical and sedimentological data reveal geometric and stratigraphic signatures of these recent changes, and allow for comparison to similar records preserved within a nearby 3600-year-old inlet-fill sequence. Driven by processes of longshore transport, spit elongation and ebb-delta breaching, the Merrimack River Inlet once actively migrated across a 2.5-km long section of Plum Island. An ebb-delta breaching event in the mid-1800s caused abandonment of the former inlet channel and the onshore welding of a large sand bar, which developed into the northern 1.5 km of the island. The inlet stabilized by jetties in the late 1800s. Ground-penetrating radar profiles and sediment cores across this former inlet channel capture the details of changes prior to breaching, including the seaward deflection of the otherwise southerly and landward-migrating channel, in response to onshore bar migration and welding. Similar details of inlet migration, bar welding, and ebb-delta breaching are observed stratigraphic records of an ancient inlet in central PI, located 7 km to the south. Comparison between the ancient and historical sequences provides clues to decipher the complex inlet dynamics preserved in the stratigraphic and sedimentologic record.

ADDITIONAL INDEX WORDS: *Tidal inlet, paraglacial coast, stratigraphy*

INTRODUCTION

Tidal inlets, channels maintained by tidal flow which hydraulically connect backbarrier environments (lagoons, marsh, tidal flats) with the coastal ocean, enable the exchange of water and nutrients, and provide access to sheltered harbors. They are also among the most dynamic and ephemeral features of barrier systems: along the ocean side of inlets, waves, tides, and currents interact across a complex bathymetry of ebb-tidal deltas, ebb and flood channels, and a series of bars and shoals, reworking and transporting sediment in both longshore and cross-shore directions. The sedimentological remnants of former inlets ("inlet-fill sequences") comprise up to 50% of barrier lithosomes in wave-dominated settings (Moslow and Tye, 1985) and have been identified in abundance along shallow continental shelves (*e.g.*, Sha, 1990; Foyle and Oertel, 1997), and in the rock record (FitzGerald *et al.*, 2012; Longhitano *et al.*, 2012).

FitzGerald *et al.* (2000) summarized nine models by which sand bypasses inlets, nearly all of which involve migration of the main ebb channel, ebb-delta or spit breaching, and sand bars. Recent high-resolution imaging of late-Holocene terrestrial inlet-fill sequences using ground-penetrating radar (GPR), ground-truthed with sediment cores, has demonstrated that the signatures of these processes can be preserved in the sedimentologic record (Mallinson *et al.*, 2010; Hein *et al.*, 2012; Seminack and Buynevich, 2013; Maio *et al.*, 2014). However, linking these inlet-fill sequences to the erosional-depositional processes responsible for their formation is largely inferential, based on observational studies at systems without direct relationships to the ancient inlet-fills.

We seek to address this knowledge gap through comparison of an ancient inlet-fill sequence with that produced by an active modern inlet. The focus of this study is Merrimack River Inlet (MRI) located at the northern end of Plum Island (PI) and a second ancient tidal inlet positioned midway along the length of Plum Island directly east of where the Parker River enters Plum Island Sound. This region is a paraglacial, mixed-energy, tide-dominated (range: 2.7 m), barrier coast located in the western Gulf of Maine, USA (Figure 1). Formation of PI was built from a variety of sediment sources, including glacial-fluvial sediment discharged by the Merrimack River and nearshore marine deposits. Its evolution was strongly influenced by a complex sea-level history that resulted from the combined forcings of global eustatic sea-level rise, and regional glacio- and hydro-isostatic adjustments (Hein *et al.*, 2012, 2014). Plum Island stabilized in its modern position about 3000–4000 years ago,

DOI: 10.2112/SI75-46.1 received 15 October 2015; accepted in revision 15 January 2016.
*Corresponding author: hein@vims.edu

following a slowing of relative sea-level rise to near modern rates and the rapid expansion of backbarrier marshes (Hein *et al.*, 2012). This timing coincided with the shoaling and closure of a tidal inlet in central Plum Island (Figure 1b). The resulting 2800 m^2 inlet-fill sequence (the paleo-Parker Inlet; PPI) captures events of channel migration, ebb-delta breaching, onshore bar migration, channel shoaling and infilling associated with the migration and closure of the inlet (Hein *et al.*, 2012). Following closure, PI has undergone 3000 years of aggradation, elongation, and progradation (Hein *et al.*, 2012).

At the northern end of PI the MRI once freely migrated across a 2.5-km long section of the coast through spit elongation, inlet migration, and ebb-delta breaching (FitzGerald, 1993). These processes alternately built and eroded the northeast sector of the island and created a significant navigational hazard. In response, the US Army Corps of Engineers (USACE) initiated a series of public works projects at the mouth of the river in the 1880s, including the construction of the South and North jetties, completed in 1905 and 1914, respectively.

Here, we combine historic maps of northern PI with new geophysical and sedimentologic data collected to document MRI dynamics immediately prior to the final pre-stabilization ebb-delta breaching event. We then compare the resulting stratigraphic signatures to those from the ancient PPI to better elucidate the nature of events captured in inlet-fill sequences.

METHODS

Historic maps and documents describing changes in northern PI are derived from a series of sources, including the Boston Public Library, the USACE, and the NOAA digital library. A total of 27 maps from between 1739 and 1940 were analyzed.

Ground-penetrating radar data were collected along shore-parallel and shore-normal transects (Figures 1b,c) using a Mala Pro-Ex with a 100 MHz antenna (Figure 3) and a Geophysical Survey Systems Inc SIR-2000 with a 200 MHz antenna (Figure 4). These data were post-processed and time-depth converted using relative dielectric permittivities, hyperbola fitting, and depth-to-reflector ground-truthing. Radar profiles were ground-truthed using vibracores, auger drill cores, and direct-push sediment cores in central PI (see Hein *et al.*, 2012 for details) and a 10.5-m long Geoprobe direct-push core in northern PI. The latter was logged, photographed, x-rayed, and sampled in detail. Grain sizes were determined by visually comparing samples under 10x magnification to known standards.

RESULTS

The MRI has undergone a series of complex changes over the past 300 years (Figure 2). Earliest maps of this area (1741) depict the MRI as bounded by thin, elongate bodies of sand connected to Salisbury Beach to the north and PI to the south. By the late 1700s, the southern bar had grown wider and migrated landward, forming a northeast fork of PI ("Old Point") bounded to the west by a narrow subtidal region, not dissimilar to the northeast (NE) fork and Basin of today (see Figure 1b). In the latest 18th century and early 19th century, the MRI migrated 500–1000 m south, eroding northern PI. The NE fork had been completely removed by 1826 and by 1830 the MRI was located >1200 m south of its present location. At some time between 1830 and 1851, the inlet re-oriented to the north, abandoning its former channel. Following the growth of a narrow, northward-elongating arcuate bar ("New Point") to its east, the abandoned inlet channel became the shallow wetlands and tidal flats of the Basin. The eastern fork would later prograde and, following completion of the south jetty, form the modern NE fork of PI.

GPR profiles and sediment cores collected *ca.* 50 m south of the modern Basin reveal three distinct radar and sedimentologic units. At the base of sediment core PIG26 is coarse sand, overlain by a 1.1-m thick set of silt- and clay- rich fine sand. These sediment types are indistinguishable in GPR profiles, in which they have a weak radar signature and semi-horizontal to gently landward- and seaward-dipping reflections (Unit I in Figure 3). Together, these deposits are interpreted as estuarine and fluvial sands related to an earlier (pre-1700s) southerly migration of the MRI, followed by abandonment due to ebb-delta breaching and formation of the earlier incarnation of the Basin. Sitting atop this unit is a 4–6-m thick sequence of oblique-tangential, eastward-dipping (slopes: 7–9°) reflections (Unit II in Figure 3). This unit is at least 150 m long in a cross-shore direction and composed of interbedded medium, coarse, and very coarse rounded sand; the bottom of this unit is composed of ~50 cm of bedded medium-coarse to very coarse sand. This unit is interpreted as fluvial deposits associated with the migration of the MRI channel. It is topped with 2.5 m of medium to coarse beach and dune sand (Unit III).

Hein *et al.* (2012) describe the ancient PPI in central PI in detail. It is 5–6-m thick, 700-m wide, and was active 3.4–3.6 ka. It was connected to the Parker River, which currently discharges into PI Sound and to the Parker Inlet at the southern end of PI (see locations, Figure 1). It is divided into two complexes: a 3.5-m thick northern section dominated by southerly dipping reflections; and a southern section of variable thickness (Figure 4). Both contain complex internal reflections interpreted as evidence of high-energy depositional events associated with spit accretion and southerly inlet migration, ebb-delta breaching, onshore bar migration, and inlet shoaling and closure in response to and decreasing tidal prism (Hein *et al.*, 2012).

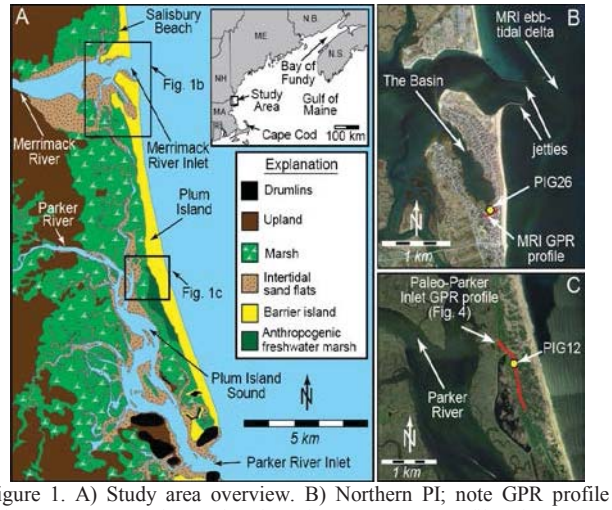

Figure 1. A) Study area overview. B) Northern PI; note GPR profile (Figure 3) C) Central PI and Parker River; note GPR profile (Figure 4).

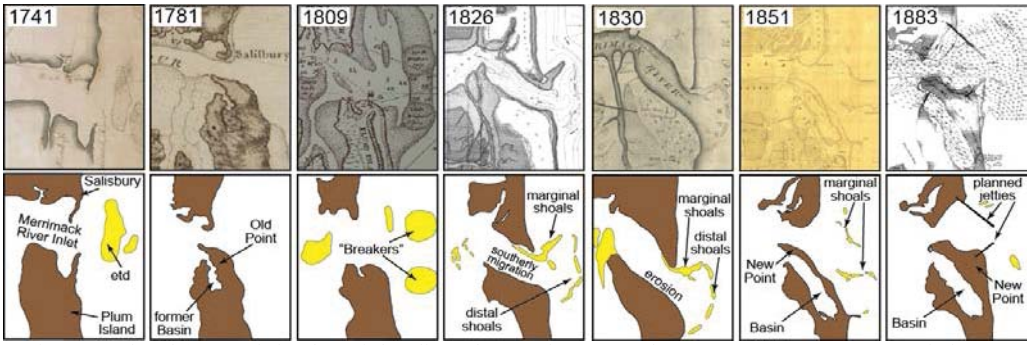

Figure 2. Sub-set of maps analyzed (top) and sketches of shorelines changes (bottom) at the MRI over a *ca.* 150-year period. Data sources: Mitchell (1741); Desbarres (1741); Blunt (1809); Anderson (1826); Anderson (1830); US Coast Survey (1851); USACE (1883). "etd" – ebb-tidal delta.

DISCUSSION

Historic, geophysical, and sedimentologic data provide insight into the complex cyclical inlet processes associated with breaching events which are captured in the stratigraphic record.

Multiple Phases of Ebb-Delta Breaching

Nichols (1942) and Watts and Zarillo (2013) documented changes in the position and morphology of the MRI prior to, and after, construction of the jetties. FitzGerald (1993) attributed these changes, and the development of the Basin and the NE fork, to ebb-delta breaching in response to the development of a hydraulically inefficient southerly deflection of the main ebb channel caused by the longshore transport driven by dominant northeast storms. The sand, which once comprised the channel-margin linear bars and swash bars of the inlet channel, migrated onshore, eventually welded to PI. By 1851, the remnant ebb-delta sand shoals formed a narrow, north-ward-elongating arcuate bar ("New Point"), which enclosed the former river/inlet channel, forming the Basin (Figure 5). New Point has since elongated and prograded, largely in response to artificial stabilization of the inlet mouth, and enhanced sediment delivery through a local reversal of longshore transport immediately downdrift of the inlet (Hubbard, 1976).

The most recent breaching event and associated morphologic changes were not unique. Rather, prior to stabilization, the MRI likely underwent a series of major ebb-delta breaching events on an approximate centennial timescale: the modern NE fork of PI and the Basin are the latest in a series of similar features, the prior of which date to the late 1700s (Figure 2). Under natural conditions, the NE fork was routinely driven onshore by the southward migrating MRI, filling the former river channels. It was eventually removed, but reformed through onshore migration and welding of the remnant ebb-tidal delta after breaching (Figure 2). Coarse sand at the base of core PIG26 is interpreted to have been deposited during this earlier phase of MRI migration and ebb-delta breaching, followed by occupation of the site by a quiet water environment of the 1700s "Paleo-Basin", during which time the fine sediments at the top of Unit I were deposited. The subsequent southerly MRI migration likely partially eroded these deposits. This natural cycle of growth and destruction of the ephemeral NE fork and the Basin would likely have continued unabated had it not been interrupted by the stabilization of the MRI, allowing for the development of PI, and initiating the development of a 25–40-year cycle of erosion and accretion along the northern PI beach (Fallon *et al.*, 2015).

Complex Inlet-Breaching Processes

The process of inlet ebb-delta breaching at natural inlets is well documented from a variety of case studies (*e.g.*, Balouin *et al.*, 2001; FitzGerald, 1982, 1988; Kana *et al.*, 2014). It is most common at inlets with stable throat positions, but whose main ebb channels cyclically migrate downdrift, occasionally impinging the downdrift shoreline and eroding into the adjacent beach (FitzGerald *et al.*, 2000). Our data elucidate some of the details of the final stages of channel migration prior to ebb-delta beaching. Here, following erosion of Old Point by the southerly and landward migrating channel, the MRI shifted several hundred meters eastward (seaward) (Unit II, Figure 3) prior to breaching and partial filling of the southern section of the channel with reworked ebb-delta sands (Unit III, Figure 3). This eastward reorientation of the channel is interpreted to be a response to deflection by outermost ebb-tidal delta breaching (Figure 6). As the channel re-orientates, sand comprising the downdrift side is more influenced by waves and sand moves onshore in the form of a bar. The main channel deflects off this protruding shoreline and migrates updrift as it straightens. The bulge in the downdrift shoreline is ephemeral and is rapidly flattened through longshore reworking by wave action (Figure 6) as ebb-delta breaching proceeds.

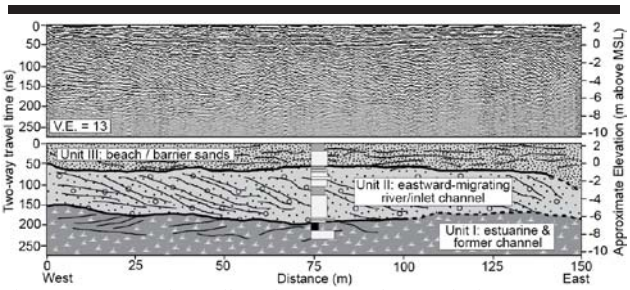

Figure 3. GPR section collected across southern end of *The Basin*. Note eastward-dipping reflections signifying eastward migration of the MRI prior to ebb-delta breaching. See figure 4 for core log explanation.

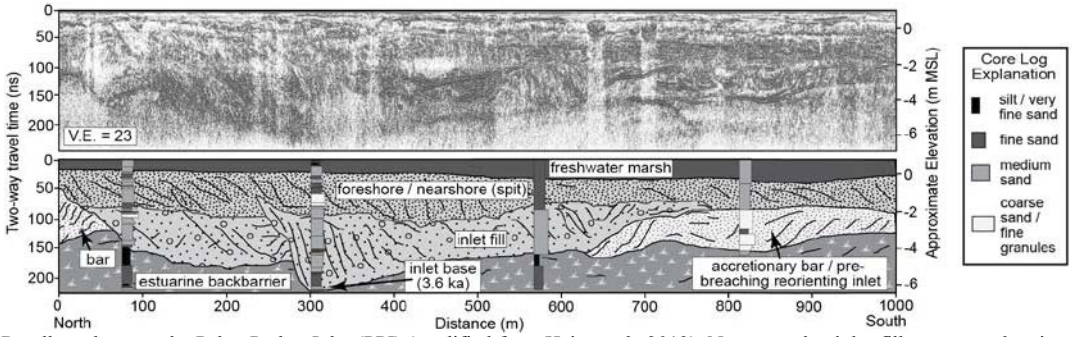

Figure 4. GPR collected across the Paleo-Parker Inlet (PPI) (modified from Hein *et al.*, 2013). Note complex inlet-fill sequence showing with multiple former channels. To the south is a northward-migrating sequence interpreted as originating from re-orientation of PPIprior to ebb-delta breaching.

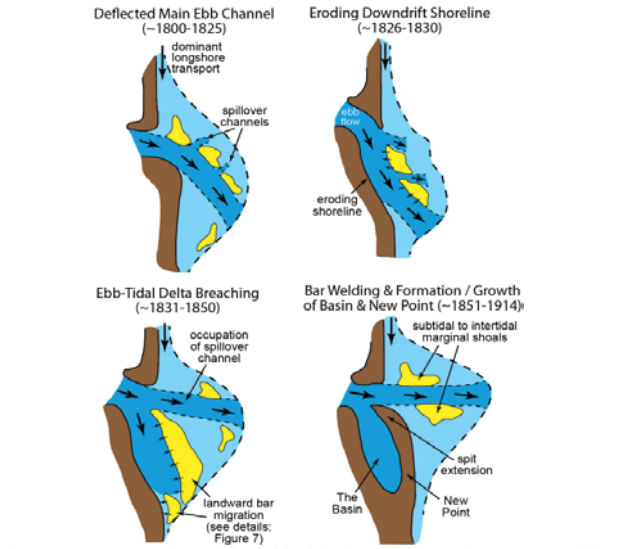

Figure 5. Conceptual model of ebb-delta breaching at the MRI. Modified from FitzGerald (1993).

Comparison of Ancient and Historic Inlets: Implications For Interpretation of Inlet-Fill Sequences

The historic MRI inlet-fill sequence captures a short phase of the latest ebb-delta breaching event. By contrast, the PPI sequence contains evidence of multiple phases of southerly inlet migration separated by ebb-delta breaching events. Moreover, this PPI sequence was formed by an inlet associated with the Parker River, a substantially smaller system than the Merrimack River. Thus, it would be expected that these two sequences would record different patterns of inlet dynamics. These differences are most dramatically reflected in the sediment types composing the inlet-fill sequences: largely medium to coarse sand in the PPI as compared to fluvial, coarse sand and granules in the MRI. These latter sediments are similar to those observed in the modern lower Merrimack River by FitzGerald *et al.* (2002), whereas the sediments within the PPI more closely approximate those observed along the modern beach.

Nonetheless, there are notable similarities between the ancient and historic inlets. Shore-perpendicular crossing lines at the PPI indicate periods of eastward (seaward) inlet channel migration (Hein *et al.*, 2012) not dissimilar to that captured at the historic MRI. Moreover, south of the PPI are three packets of sigmoidal, northward-dipping reflections (Figure 4) stretching across 500 m in a shore-parallel direction. These may originate from re-orientations of the hydraulically inefficient PPI prior to ebb-delta breaching events (Figure 4). Alternatively, these features may be the incompletely eroded remnants of landward-migrating bars responsible for deflection of the main ebb channel immediately prior to breaching. Regardless, the presence of these bed sets dipping counter to the expected longshore migration direction of the PPI indicate the complexity of processes captured within inlet-fill sequences which may be preserved in inlet-fill sequences elsewhere.

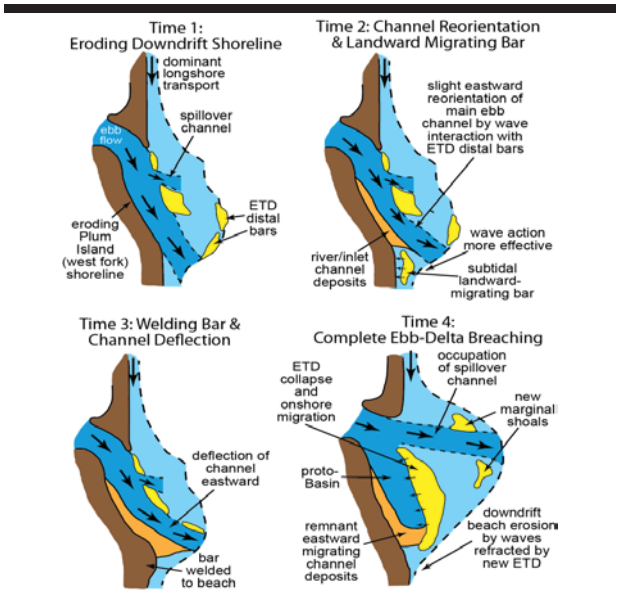

Figure 6. Model of eastward deflection of the MRI main ebb channel, creating eastward-dipping river inlet channel deposits in GPR profile.

CONCLUSIONS

New GPR, sedimentologic, and historic data from PI reveal complex inlet-migration patterns preserved within a historic inlet-fill sequence. Southerly and landward-migrating MRI reoriented seaward in response to deflection by a protruding shoreline formed from the onshore welding of downdrift ebb-delta sediment. This study provides new insight into the details of ebb-delta breaching and the utility of the historic record in deciphering recent stratigraphies. Moreover, comparison of the historic inlet sequence with that associated with an ancient inlet in central PI reveals evidence of a similar set of dynamics and underscores the need to carefully document complex inlet processes recorded in inlet-fill sequences in close comparison with those preserved by modern analogs.

ACKNOWLEDGMENTS

This work is funded by NSF Award OCE-1325430. We thank M. Morris for assistance with historical document research.

LITERATURE CITED

Anderson, P., 1826. *The Harbour of Newburyport and the Mouth of Merrimack River*. Washington, D.C., reproduced in U.S. House, 19th Congress, Doc. No. 140. 1:5,280. 1 sheet.

Anderson, P., 1830. *Map of the Original Town of Newbury, Now Divided into Newbury, Newburyport, and West Newbury. Boston*, Pendleton Lithography. 1:19,800. 1 sheet.

Balouin, Y.; Howa, H., and Michel, D., 2001. Swash platform morphology in the ebb-tidal delta of the Barra Nova inlet, South Portugal. *Journal of Coastal Research*, 17(4), 784-791.

Blunt, E.M. 1809. *Plan of Newburyport Harbour, Newburyport*. New York, NY: American Coast Pilot, 6th edition.

Des Barres, J.F.W., 1781. *The Coast of New England*. scale 1:520,000, 1 sheet.

Fallon, A.R.; Hein, C.J.; Rosen, P.S., and Gannon, H.L., 2015. Cyclical shoreline erosion: The impact of a jettied river mouth on the downdrift barrier island, *Proceedings of the 11th International Symposium on Coastal Engineering and Science of Coastal Sediment Processes* (San Diego, CA), 14 p.

FitzGerald, D.M., 1982. Sediment bypassing at mixed energy tidal inlets. *Proceedings of the 18th Conference of Coastal Engineering* (Cape Town, South Africa, ASCE), 1094-1118.

FitzGerald, D.M., 1988. Shoreline erosional-depositional processes associated with tidal inlets. *In:* Aubrey, D.G., and Weishar, L. (eds.) *Hydrodynamics and Sediment Dynamics of Tidal Inlets*. New York: Springer, pp. 186-225.

FitzGerald, D.M., 1993. Origin and stability of tidal inlets in Massachusetts, *In:* Aubrey, D.G., and Giese, G.S. (eds) *Formation and Evolution of Multiple Tidal Inlets*, Washington DC: AGU, Coastal and Estuarine Studies, 44, pp. 1-61.

FitzGerald, D.M.; Kraus, N.C., and Hands, E.B., 2000. *Natural Mechanisms of Sediment Bypassing at Tidal Inlets*, Vicksburg: USACE Research and Development Center, 12 p.

FitzGerald, D.M.; Buynevich, I.V.; Davis, R.A., and Fenster, M. S., 2002. New England tidal inlets with special reference to riverine-associated inlet systems. *Geomorphology*, 48, 179-208.

FitzGerald, D.M.; Buynevich, I.V., and Hein, C., 2012. Morphodynamics and facies architecture of tidal inlets and tidal deltas, *In:* Davis, R.A., and Dalrymple, R.W. (eds), *Principles of Tidal Sedimentology*, New York: Springer, pp. 301-333.

Foyle, A.M., and Oertel, G.F., 1997. Transgressive systems tract development and incised-valley fills within a Quaternary estuary-shelf system: Virginia inner shelf, USA. *Marine Geology*, 137(3), 227-249.

Hein, C.J.; FitzGerald, D.M.; Carruthers, E.A.; Stone, B.D.; Barnhardt, W.A., and Gontz, A.M., 2012. Refining the model of barrier island formation along a paraglacial coast in the Gulf of Maine, *Marine Geology*, 307-310, 40-57.

Hein, C.J.; FitzGerald, D.M.; Barnhardt, W.A., and Stone, B.D., 2013. *Onshore-Offshore Surficial Geologic Map of the Newburyport East and Northern Half of the Ipswich Quadrangles, Massachusetts*, Amherst, MA: Mass Geological Survey, Map GM 13-01, map scale 1:24,000, 3 sheets.

Hein, C.J.; FitzGerald, D.M.; Buynevich, I.V.; van Heteren, S., and Kelley, J.T., 2014. Evolution of paraglacial coasts in response to changes in fluvial sediment supply. *Geological Society, London, Special Publication*, 388, 247-280.

Hubbard, D.K., 1976. Changes in inlet offset due to stabilization. *Coastal Engineering Proceedings*, 1(15).

Kana, T.W.; Traynum, S.B., and Kaczkowski, H.L., 2014. Scales and signatures of episodic sand bypassing at a tide-dominated inlet – Fripp Inlet, South Carolina, *Proceedings of the 34th Conference of Coastal Engineering* (Seoul, South Korea, ASCE), 10 p.

Longhitano, S. G.; Mellere, D.; Steel, R.J., and Ainsworth, R.B., 2012. Tidal depositional systems in the rock record: A review and new insights. *Sedimentary Geology*, 279, 2-22.

Maio, C.V.; Gontz, A.M.; Sullivan, R.M.; Madsen, S.M.; Weidman, C.R., and Donnelly, J.P., 2014. Subsurface Evidence of Storm-Driven Breaching along a Transgressing Barrier System, Cape Cod, USA. *Journal of Coastal Research*. dx.doi.org/10.2112/JCOASTRES-D-14-00109.1.

Mallinson, D.J.; Smith, C.W.; Culver, S.J.; Riggs, S.R., and Ames, D., 2010. Geological characteristics and spatial distribution of paleo-inlet channels beneath the outer banks barrier islands, North Carolina, USA. *Estuarine, Coastal and Shelf Science*, 88(2), 175-189.

Mitchell, G., 1741. *A Map of the River Merrimack from the Atlantick Ocean to Pantuckett [sic] Falls*. no scale, 1 sheet.

Moslow, T.F., and Tye, R.S., 1985. Recognition and characterization of Holocene tidal inlet sequences. *Marine Geology*, 63(1), 129-151.

Nichols, R.L., 1942. Shoreline changes on Plum Island, Massachusetts. *American Journal of Science*, 240, 349-355.

Sha, L.P., 1990. Surface sediments and sequence models in the ebb-tidal delta of Texel Inlet, Wadden Sea, The Netherlands. *Sedimentary Geology*, 68(1), 125-141.

Seminack, C.T., and Buynevich, I.V., 2013. Sedimentological and Geophysical Signatures of A Relict Tidal Inlet Complex Along A Wave-Dominated Barrier: Assateague Island, Maryland, USA. *Journal of Sedimentary Research*, 83(2), 132-144.

USACE, 1883. *Newburyport Harbor, Mass., Plan*. Washington, D.C.: US Army Corps of Engineers, scale 1:12,000, 1 sheet.

U.S. Coast Survey, 1851. *The Harbor and Environs of Newburyport and the Mouth of the Merrimack River, Essex County, Massachusetts*. 1:10,000. 1 sheet.

Watts, I.M., and Zarillo, G.A., 2013. Macroscale geomorphic evolution of an inlet, *Proceedings of the 7th International Conference on Coastal Dynamics* (Arcachon, France), 12p.

Journal of Coastal Research	SI	75	233-237	Coconut Creek, Florida	2016

Evolution of a relocated inlet migrating naturally along an open coast

Chiara Popesso[†*], André Pacheco[‡], Óscar Ferreira,[‡] and Giorgio Fontolan[†]

[†]Coastal Group, Dipartimento di Matematica e Geoscienze
Università degli studi di Trieste
Trieste, Italia

[‡]CIMA, Centro de Investigação Marinha e Ambiental,
Universidade do Algarve, Campus de Gambelas
Faro, Portugal

www.cerf-jcr.org

www.JCRonline.org

ABSTRACT

Popesso, C.; Pacheco, A.; Ferreira, Ó., and Fontolan, G., 2016. Evolution of a relocated inlet migrating naturally along an open coast. *In:* Vila-Concejo, A.; Bruce, E.; Kennedy, D.M., and McCarroll, R.J. (eds.), *Proceedings of the 14th International Coastal Symposium* (Sydney, Australia). *Journal of Coastal Research*, Special Issue, No. 75, pp. 233-237. Coconut Creek (Florida), ISSN 0749-0208.

Ancão Inlet is a small migrating inlet that was relocated in 1997 and has been monitored since then. In October 2015, it was about to conclude its third eastward migrating cycle since the 1940s. Morphological parameters and migration rates were correlated with oceanographic settings to evaluate the importance of different mechanisms in the evolutionary phases of the inlet. The migration trend is related to the dominant southwest sea conditions, inducing the alongshore sediment transport from west to east. The inherited features of the downdrift side area were also considered as rate of migration constraints. In this paper, we show how storm events, a constant longshore sediment supply from the west, and a lower downdrift barrier island volume control migration rates, noting that inlet efficiency is also strongly influenced by the reshaping of the barrier area.

ADDITIONAL INDEX WORDS: *Ancão Inlet, migrating inlet, relocation, accommodation space.*

INTRODUCTION

Tidal inlets are one of the most important and dynamic coastal features that play a significant role in coastal systems as navigation routes, sediment suppliers to adjacent beaches, and conduits that allow an exchange of nutrients between backbarrier systems and the coastal zone (FitzGerald, 1996). Once inlet and backbarrier basins have formed, their medium-term evolution (on a timescale of decades) depends on the competing effects of waves and tides that attempt to close and widen the inlet, respectively. These two factors determine, to a large extent, the direction and magnitude of sediment transport, which can lead to erosion or deposition, and thus, to shifts in the inlet's morphology and position (Pacheco *et al.*, 2008).

Tidal inlet migration is linked to barrier growth/erosion; migration and barrier spit growth/erosion are common features of many coasts in the world where wave-induced alongshore sediment transport is dominant in one direction. As an inlet migrates, the channel connecting the inlet to the bay elongates and sometimes meanders, thus increasing frictional factors, attenuating tidal flow, and decreasing tidal prism (FitzGerald, 1996). Breaching can lead to the formation of a new inlet that may compete for dominance of the tidal prism and threaten the stability of existing inlets in the same bay system, possibly promoting their closure. Understanding and predicting the morphological behavior and determining optimal flow management schemes of tidal inlet systems is crucial for coastal zone management, in order to allow tidal inlets to function as naturally as possible and to minimize the risk of inlet closure.

In this paper, the natural evolution of the Ancão Inlet, a relocated inlet in southern Portugal, is evaluated. Using 18 years of data from a monitoring program, morphological and oceanographic parameters were compared to evaluate the importance of different factors in inlet migration and associated rates. During this period of time, all of the above-mentioned processes occurred (migration, inlet breaching, tidal prism shifts, and inlet closure).

Study Area

The Ancão Inlet is a small migrating inlet situated in southern Portugal. It is part of Ria Formosa, a coastal lagoon protected by a multi-inlet barrier island system consisting of five islands and two peninsulas separated by six tidal inlets (Figure 1). Tides in the area are semi-diurnal; average ranges are 2.8 m for spring tides and 1.3 m for neap tides, although maximum ranges of 3.5 m can be reached. Wave climate in the area is moderate to high (Ciavola *et al.*, 1997). Predominant wave directions, approximately 71%, are from the W-SW, while waves coming from the E-SE only account for 23% of the observations (Costa *et al.*, 2001). The storm threshold for this region has been defined as significant wave height (H_s) >3 m (Pessanha and Pires, 1981) or 2.5 m (*e.g.*, Costa *et al.*, 2001). This region is affected by a high sediment longshore transport (Q) that recent studies evaluated as 1.1 x 10^5 m^3/year (Teixeira and Dores, 2013), which is in accordance with the values determined in the early 1990s by Andrade (1990), ~0.9 x 10^5 m^3/year.

DOI: 10.2112/SI75-47.1 received 15 October 2015; accepted in revision 15 January 2016.
*Corresponding author: chiara.popesso@phd.units.it

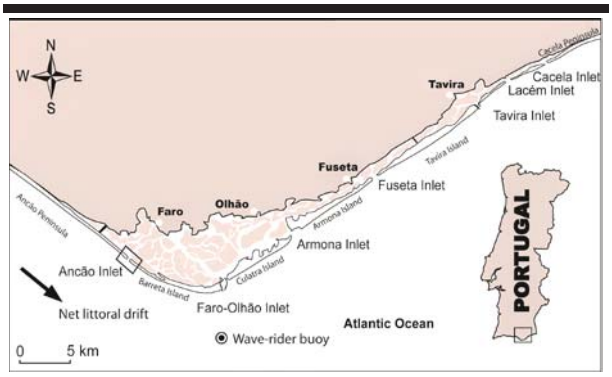

Figure 1. Ria Formosa Barrier Island System and location of study area (Ancão Inlet).

The Ancão Inlet presents a cyclic eastward migration. Three cycles were recorded between 1945 and the present (see Vila-Concejo *et al.*, 2002 and references therein). The Ancão Inlet pattern migration type is "High-Energy Flank" (Vila-Concejo *et al.*, 2002). In 1996, the Ancão Inlet was in its limiting position (Vila-Concejo *et al.*, 2004) and was partially closed by natural infilling and meandering. Following the adopted soft protection program (Dias *et al.*, 2003), on 23 June 1997, the inlet was relocated 3500 m to the west of its closing position, in order to improve water exchange at the western part of the Ria Formosa lagoon system. According to Vila-Concejo *et al.* (2003; 2004), the inlet reached dynamic equilibrium one year later (July 1998). The eastward migration started in January 1999 after an energy storm event. Since its relocation, the new Ancão Inlet has been monitored and has been found to resemble the old inlet in both its hydrodynamic characteristics and its morphology (Williams *et al.*, 2003). According to Morris *et al.* (2001), the Ancão Inlet shows characteristics of both a tide- (well-defined deep main channel and migrating flood channels) and a wave-dominated inlet (relatively small ebb delta).

During the current cycle, storm events breached the barrier updrift (2005) and downdrift (2010 and 2015) of the Ancão Inlet position, forming a new inlet that competed with the older one for dominance of the tidal prism. In 2005, the new inlet remained open for only three weeks and then closed naturally; in 2010, the new inlet captured a greater volume of tidal prism and forced the older inlet to close. Here we use the term "jump" to indicate this changed position without migration. Finally, the new opening of 2015 was still active in October 2015, with both inlets becoming too narrow and very shallow. A new relocation to a position close to the 1997 location is programmed for the end of 2015.

METHODS

Since the 1997 inlet relocation, a monitoring program has been in place to study its evolution. Twenty topobathymetric surveys were performed between the relocated inlet's opening in June 1997 and May 2015. Topography was carried out using a total station and a RTK-DGPS positioning. Navigation and bathymetry transects were measured using HYPACK® 4.3a Gold software, by connecting the RTK-DGPS and an echo sounder to a laptop. The RTK-DGPS and echo sounder were synchronized and measurements were taken at a frequency of 1 Hz. Thus, the recorded depth was immediately corrected for water level variations (*i.e.*, tides and waves). Due to a scarcity of data (not the entire inlet area was covered), the first survey of June 1997 was not used; as such, the August 1997 survey is herein considered the starting point for the evaluation of the Ancão inlet.

Using Surfer® 9, the topographic and bathymetric datasets were interpolated to produce continuous bathymetric surface maps, following the quality control methods suggested by Hick and Hume (1997). After an interpolator quality check, through the cross-validation function, the Kriging method was selected as the best interpolator. The spacing was based on data density and spatial distribution. A local metric coordinate system known as the Portuguese Melriça Grid was used for the maps; elevation is based on mean sea level.

Inlet morphological parameters such as minimum cross-sectional area (A_c) and migration (M) were determined following the suggestions of the Coastal Engineering Manual (Seabergh, 2002). The inlet throat was first defined on each map in order to sketch ten profiles with equal intervals through the inlet cross-section, considering the morphology of each situation (*e.g.*, the barrier's width). Inlet migration was computed by determining the metric difference in the XY coordinates of the maximum depth at the minimum cross-sectional area between each survey and the August 1997 inlet position. The migration distances between consecutive surveys were then determined and added to obtain the cumulative migration. The different migration sign (plus or minus) is due to the fact that values are positive if migration is eastward and negative if westward.

The inlet cross-section area was used as a tidal prism proxy that could be estimated using the empirical formula developed by Jarrett (1976) for the Atlantic Coast (Equation 1):

$$A_c = 3.039 \cdot 10^{-5} P^{1.05} \quad (1)$$

where A_c is the minimum cross-sectional area (m^2), measured for each survey, and P is the corresponding tidal prism (m^3).

Wave data from the Instituto Hidrografico directional wave-rider buoy offshore of Cape Santa Maria (Figure 1) was used in this study (1997–present). The wave buoy recorded values representing significant wave height (H_s), mean peak period (T_p), and mean wave direction (°) for 20 minutes every three hours, except during storms, when data were recorded every half hour. Wave data were interpolated to give hourly data and subdivided into intervals between consecutive surveys. The total percentage of missing data was about 3%. To individualize each single high-energy event, the storm threshold used in the present study refers to high-energy events with $H_s \geq 2.5$ m, with a minimum duration of three hours above the storm threshold and 24 hours between consecutive $H_s \geq 2.5$ m.

Due to the orientation of the barrier system, mean wave power (Wp) for the storm events was evaluated coming from three different directions (<200°, 200÷220°, and >220°), following Vila-Concejo *et al.* (2004), in order to assess their possible different impacts on inlet migration M. Wp was then multiplied by storm duration in seconds ($Wp\#$) to obtain total storm wave power.

The ratio $P/\sum Wp\#$ was evaluated, where P is assessed for each survey and $\sum Wp\#$ is the sum of $Wp\#$ of storm events coming from the dominant longshore drift direction (>220°, as a proxy of the potential eastward longshore sediment transport), recorded between two surveys.

RESULTS

Storm events from >220° have higher $Wp\#$ values than those from other directions and seem to correspond to significant changes in migration rates (as after 2001 or in 2010, when a breaching occurred, with a subsequent inlet jump). No apparent clustering of storms or energy peaks seems to be responsible for the final breaching in 2015. There is, however, a continuity of the migration despite the existence (or absence) of storms (Figure 2A,B,C).

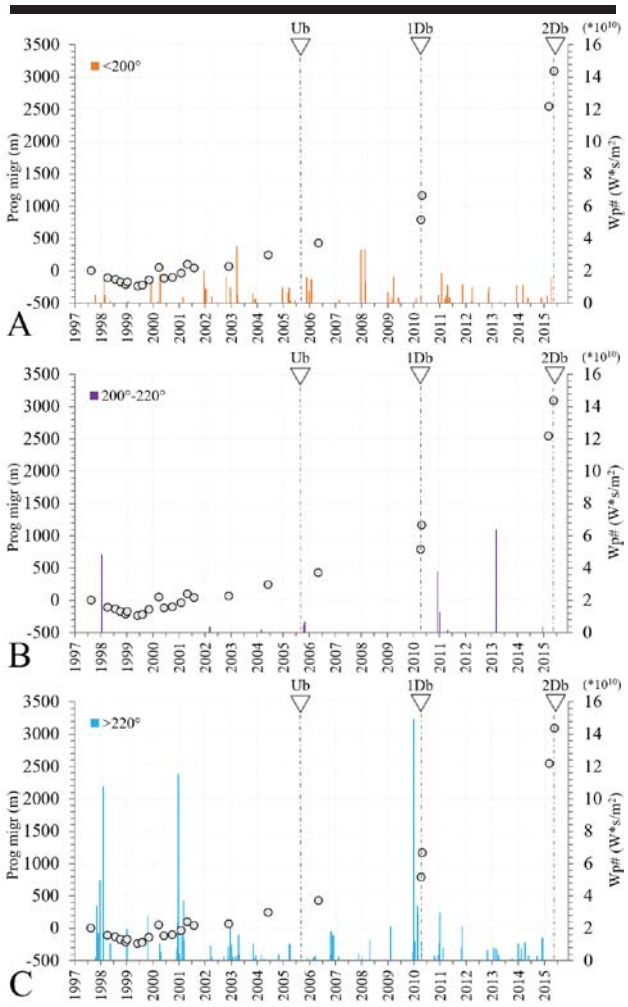

Figure 2. Progressive migration (gray circles) compared with $Wp\#$ for three directions: <200° (A), 200÷220° (B), and >220° (C). Updrift breaching (Ub) and downdrift breaching (1Db and 2Db) events are represented by triangles.

After reaching dynamic equilibrium in July 1998 (Vila-Concejo *et al.*, 2003), the Ancão Inlet had an average cross-section area (A_c) of 550 m^2 (Figure 3). The maximum value of A_c was reached in March 2000 (800 m^2) and was probably related to the dredging of the inner channels close to the inlet that was carried out February–April 2000 (Dias *et al.*, 2000). After that, a strong decrease occurred at the beginning of 2001, reaching a minimum value of 300 m^2 in April 2001. A stable period followed until 2010, when the inlet almost closed with an A_c of 50 m^2. The jump recorded that spring took back the section to a wider value (110 m^2) that remained until May 2015 (Figure 3). Mean values of $P/\sum Wp\#$ were calculated for longer periods of time (hereafter called macro-intervals; see discussion for their interpretation). The highest values of $P/\sum Wp\#$ were recorded from the relocation date until 2001. From 2001 to 2010, the ratio decreased significantly, as well as from 2010 until 2015 (Figure 3). The overall trend is a decreasing cross-sectional area (and corresponding prism) during migration up to a critical position.

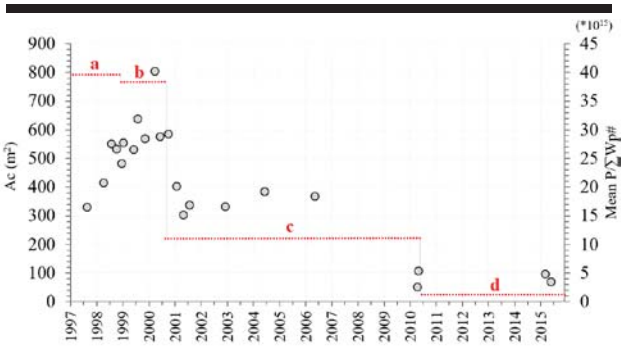

Figure 3. Cross-section area (A_c, gray circles) compared with the mean $P/\sum Wp\#$ ratio (horizontal lines) for four selected macro-intervals: a) unstable, due to morphological adaptation (which includes the phases described by Vila-Concejo *et al.*, 2003); b) equilibrium 1, while capturing prism and migrating; c) equilibrium 2, without capturing prism but with migration; and d) critical, toward closure/infilling.

The migration trends of the previous Ancão cycles (Vila-Concejo *et al.*, 2002; 2004) integrated with the last Ancão cycle data are shown in Figure 4. After the Ancão Inlet opened in 1997, its migration reproduced the behavior of the oldest inlet, starting with an initial stage of readjustment characterized by low migration rates, followed by a stage of high eastward migration rates (Vila-Concejo *et al.*, 2002). Nonetheless, the migration trend appears to be increasing as the migration cycle lifetime declines (33 years for Ancão1, 22 years for Ancão2, 18 years for Ancão3, for a longer overall migration), as already noted by Vila-Concejo *et al.* (2002). The migration trends of Ancão2 and Ancão3 are steeper than that of the first cycle. The Ancão2 opening position was located along the previous migration cycle path, and the overall migration was faster than that of the first cycle.

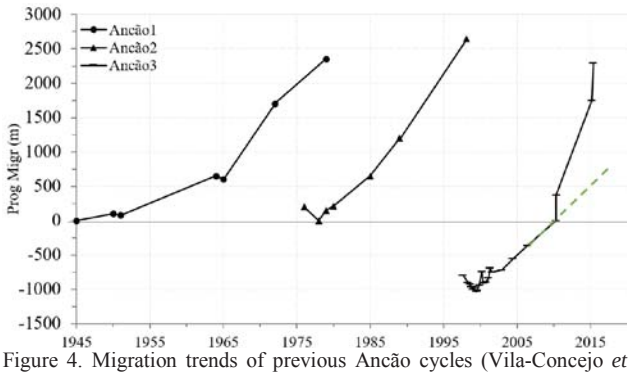

Figure 4. Migration trends of previous Ancão cycles (Vila-Concejo *et al*., 2002, 2004) integrated with the last Ancão cycle data (1997–2015). Points represent inlet channel positions observed in aerial photographs or surveys. The dashed line represents the supposed continuity of the migration rate before the 2010 jump.

The initial stages of Ancão3, however, displayed lower migration rates. Its relocation site was ~1000 m to the west of the Ancão1 opening (Vila-Concejo *et al*., 2004) in an area with a high dune system and relatively wide barrier. Once the Ancão1 opening position was reached, the migration trend started to be much faster (see dashed line in Figure 4). From that position to the east (downdrift direction), the barrier was low and narrow and subject to frequent overwashing, and thus, more susceptible to erosion, according to Matias *et al*. (2010).

DISCUSSION

Some authors have reported that migration is highly related to western storm events (Morris *et al*., 2001; Vila-Concejo *et al*., 2003; Williams *et al*., 2003), referring to them as events from a direction >180°. We also found that western storms are the main drivers of relevant changes at the inlet migration, although herein we have considered different storm classes according to their direction (<200°, 200÷220°, >220°; Figure 2A,B,C). It is also visible that the continuity of migration between main storm events is not driven by storms, but seems to be a rather continuous process, most probably dependent mainly on longshore transport.

Considering these data and following the M and A_c trends, the migration cycle of the Ancão Inlet was divided into four macro-intervals (Figure 3, a,b,c,d): the first from the opening of the inlet in 1997 to the start of the eastward migration (January 1999); the second from January 1999 to September 2000; the third from September 2000 until the breaching of 2010; and the final period from 2010 until the end of the monitoring, with the inlet almost in its closing position (*i.e*., very shallow and meandering channel).

The first interval corresponds to the unstable situation caused by the adapting morphological behavior subsequent to the relocation ("a" in Figure 3). The prevailing migration is opposite to what was expected, as already shown by Vila-Concejo *et al*. (2003). Although some storms from the east occurred during this period, it is difficult to establish a sole relationship between storms and westward migration. A possible reason for the observed migration is the adaptation of the inlet to its position in the context of a new hydrodynamic setting. The existence of main channels (and relevant currents) to the west (Ancão and Ramalhete channels) probably helped this migration pattern. The subsequent ~2-year interval highlights the increasing cross-section area A_c while the inlet migrated eastward. Maximum efficiency is indicated by the high $P/\sum Wp\#$ that likely occurred after the capture of the backbarrier channel network close to the inlet ("b" in Figure 3).

The results show that the inlet cross-section area during the third interval was almost constant, and therefore, not affected by the inlet's migration. Migration occurred undisturbed until 2010 ("c" in Figure 3). That date marks an abrupt change in the history of the inlet, as the breaching caused by a severe storm occurred in the original (1975) position of the Ancão inlet. From this position, until the last survey, migration trends increased significantly (Figure 4), while the inlet featured an unstable/critical condition toward a possible closure ("d" in Figure 3). This rapid migration is most likely associated with the morphology of the affected area, which corresponded to a narrow overwash terrace (Matias *et al*., 2010) with no dunes, thus causing less resistance. The dashed line in Figure 4 shows how the migration would have continued with a fully developed dune system (as before the jump).

Observing the present cycle, Ancão seems to be unable to capture the local drainage pattern at the end of its migration. This can be seen in the residual washover fans and old flood tidal delta bodies that are now intercepted and drained by the last terminations of creeks connected to the neighboring Faro–Olhão system. Indeed, the inlet is too far to the east to have an efficient connection to the main drainage system, even during spring tides. The inlet acts more independently, draining the surrounding area as a single (reduced tidal prism) inlet system (Pacheco *et al*., 2010).

Therefore, the stability/instability conditions of the inlet can be categorized according to the macro-intervals reported in Figure 3: a) unstable, due to morphological adaptation (which includes the phases described by Vila-Concejo *et al*., 2003); b) equilibrium 1, while capturing prism and migrating; c) equilibrium 2, without capturing prism but with migration; d) critical, toward closure/infilling.

CONCLUSIONS

The documented history of the Ancão inlet subsequent to its relocation in 1997 allows the acquisition of knowledge of both its morphodynamic and hydraulic behaviors. Southwestern storm events can increase the sediment longshore supply and help migration, while events coming from the east and from directions more perpendicular to the shoreline can fill the flood deltas and disrupt the eastward migration. The constant longshore transport, however, is the major driver of migration continuity, as the main storms are the drivers of rapid migration events or migration by jumps.

Knowing that a new inlet will be open at the 1997 position but that dunes are not yet established, the entire migration area will behave as a low and narrow barrier. After a two-year period of adjustment, the migration rate will most likely be similar to that observed in the last five years of the third cycle.

Better comprehension of the mechanisms linked with inlet migration, mainly associated with the current barrier situation, can be achieved through the collection of other physical data, such as determining the adjacent barrier dune elevation and barrier sediment volumes. The ongoing work will analyze nonlinear effects related to migration and morphological inlet features with controlling parameters (waves, levels, and morphologies).

Only a precise knowledge of the complex relationships among inlet, the barrier sediment volumes involved in the erosion processes, and the backbarrier inundation/drainage potential can furnish the basic elements needed for more effective management plans that consider complementary actions rather than the simple relocation of the Ancão Inlet.

LITERATURE CITED

Andrade, C.F., 1990. O Ambiente de Barreira da Ria Formosa. Lisbon, Portugal: University of Lisbon, Ph.D. dissertation, 626p. (in Portuguese)

Ciavola, P.; Taborda, R.; Ferreira, Ó., and Dias, J.A., 1997. Field measurements of longshore sand transport and control processes on a steep meso-tidal beach in Portugal. *Journal of Coastal Research*, 13(4), 1119-1129.

Costa, M.; Silva, R., and Vitorino, J., 2001. Contribuição para o estudo do clima de agitação marítima na costa Portuguesa. *Actas das 2as Jornadas Portuguesas de Engenharia Costeira e Portuária* (Sines, Portugal), Associação Internacional de Navegação, CD-ROM, 20 p. (in Portuguese)

Dias, J.M.A.; Ferreira, Ó.; Sá-Pires, C., and Duarte, C., 2000. *Relatório de Monitorizacão da Repulsão de Dragados para a Zona de Barreira do Sistema da Ria Formosa*. Algarve, Portugal: Centro de Investigação dos Ambientes Costeiros e Marinhos da Universidade do Algarve, *Technical Report No. 06/00*, 55p. (in Portuguese)

Dias, J.A.; Ferreira, Ó.; Matias, A.; Vila-Concejo, A., and Sá-Pires, C., 2003. Evaluation of soft protection techniques in barrier islands by monitoring programs: case studies of the Ria Formosa (Algarve-Portugal). *In*: Klein A.H.F. (ed.), *Proceedings of the Brazilian Symposium on Sandy Beaches: Morphodynamics, Ecology, Uses, Hazards and Management (Spring, 2003). Journal of Coastal Research,* Special Issue No. 35, pp. 117-131.

FitzGerald, D.M., 1996. Geomorphic variability and morphologic and sedimentologic controls on tidal inlets. *In*: Mehta, A.J. (ed.), *Proceedings, An International Forum for the Littoral Sciences. Journal of Coastal Research*, Special Issue No. 23, pp. 47-71.

Hicks, D.M. and Hume, T.M., 1997. Determining sand volumes and bathymetric change on an ebb-tidal delta. *Journal of Coastal Research*, 13(2), 407–416.

Jarrett, J.T., 1976. *Tidal prism-inlet area relationships*. Vicksburg, U.S.A.: U.S. Army Corps of Engineers, Waterways Experiment Station, *GITI Report No. 3*, 32p.

Matias, A.; Ferreira, Ó.; Vila-Concejo, A.; Morris, B., and Dias, J.A., 2010. Short-term morphodynamics of non-storm overwash. *Marine Geology*, *274*(1), 69-84.

Morris, B.D.; Davidson, M.A., and Huntley, D.A., 2001. Measurements of the response of a coastal inlet using video monitoring techniques. *Marine Geology*, 175(1-4), 251-272.

Pacheco, A.; Vila-Concejo, A.; Ferreira Ó., and Dias, J.A., 2008. Assessment of tidal inlet evolution and stability using sediment budget computations and hydraulic parameter analysis. *Marine Geology*, 247(1-2), 104-127.

Pacheco, A.; Ferreira, Ó; Williams, J.J.; Garel, E.; Vila-Concejo, A., and Dias, J.A., 2010. Hydrodynamics and evolution of a multiple-inlet system. *Marine Geology*, 274(1-4), 32-42.

Pessanha, L.E.V. and Pires, H.O., 1981. *Elementos sobre o Clima de Agitação Marítima na Costa Sul do Algarve*. Lisbon, Portugal: Instituto Nacional de Meteorologia e Geofisica. *Internal Report,* 66 p. (in Portuguese)

Seabergh, W.C. 2002. Hydrodynamics of tidal inlets. *In*: Vincent, L. and Demirbilek, Z. (Eds), *Coastal Engineering Manual, Part II, Coastal Hydrodynamics, Chapter II-6, Engineer Manual*. Washington, DC: U.S. Army Corps of Engineers, pp. 1110-2-1100.

Teixeira, S.B. and Dores, A., 2013. Characterization of accidents in sea cliffs dissociated of natural geodynamics in the Algarve (Portugal) coast during the last decade (2003-2012). *Comunicações VII Congresso sobre Planejamento e Gestão das zonas Costeiras dos Países de Expressão Portuguesa* (Maputo, Moçambique), pp.3. (in Portuguese)

Vila-Concejo, A.; Matias, A.; Ferreira, Ó.; Duarte, C., and Dias, J.M.A., 2002. Recent evolution of the natural inlets of a barrier island system in Southern Portugal. *In*: Cooper, J.A.G. and Jackson, D.W.T. (eds.), Proceedings of the International Coastal Symposium (Northern Ireland) *Journal of Coastal Research*, Special Issue No. 36, pp. 741-752.

Vila-Concejo, A.; Ferreira, Ó.; Matias, A., and Dias, J.M.A., 2003. The first two years of an inlet: Sedimentary dynamics. *Continental Shelf Research*, 23, 1425-1445.

Vila-Concejo, A.; Ferreira, Ó.; Morris, B.D.; Matias, A., and Dias, J.M.A., 2004. Lessons from inlet relocation: Examples from Southern Portugal. *Coastal Engineering*, 51(10), 967-990.

Williams, J.J.; O'Connor, B.A.O.; Arens, S.M.; Abadie, S.; Bell, P.; Balouin, Y.; Van Boxel, J.H.; do Carmo, A.J.; Davidson, M.; Ferreira, Ó.; Heron, M.; Howa, H.; Hughes, Z.; Kaczmarec, L.M.; Kim, H.; Morris, B.; Nicholson, J.; Pan, S.; Salles, P.; Silva, A.; Smith, J.; Soares, C., and Vila-Concejo, A., 2003. Tidal inlet function: Field evidence and numerical simulation in the INDIA project. *Journal of Coastal Research*, 19(1), 189-211.

Journal of Coastal Research	SI	75	238-242	Coconut Creek, Florida	2016

Morphological evolution of the Nerang River Entrance ebb-tidal delta

Mahnaz Sedigh[†‡*], Rodger Tomlinson[†], Nick Cartright[‡] and Amir Etemad-Shahidi[‡]

[†]Griffith Centre for Coastal Management
Griffith University, Gold Coast Campus, Australia

[‡]Griffith School of Engineering, Griffith
University, Gold Coast Campus, Australia

www.cerf-jcr.org

www.JCRonline.org

ABSTRACT

Sedigh, M.; Tomlinson, R.; Cartright, N., and Etemad-Shahidi, A., 2016. Morphological evolution of the Nerang River Entrance ebb-tidal delta. *In:* Vila-Concejo, A.; Bruce, E.; Kennedy, D.M., and McCarroll, R.J. (eds.), *Proceedings of the 14th International Coastal Symposium* (Sydney, Australia). *Journal of Coastal Research*, Special Issue, No. 75, pp. 238-242. Coconut Creek (Florida), ISSN 0749-0208.

The Nerang River entrance is a tidal inlet that connects the Pacific Ocean to the extensive Gold Coast estuarine system known as the Broadwater. Due to relatively fast northward migration of the inlet from 1920 to 1985 and the importance of having a safe navigable channel, the inlet was stabilized with two training walls in 1986. A sand bypassing system was implemented upstream with an average sand bypassing rate equal to the estimated net northward lonshore sediment transport in the area to prevent the formation of a bar across the entrance. However, historical analysis of survey data has shown an ongoing growth of the ebb-tidal delta at the river mouth. Thus, despite the sand bypassing system, costly dredging of the ebb-tidal delta is required to maintain safe navigation through the entrance. A number of studies have been undertaken to investigate sediment transport and hence morphological evolution. However, despite all the previous efforts, the cause of the ongoing ebb-tidal delta accretion is still not known with any degree of certainty. According to recent numerical modeling efforts, there is a considerable amount of longshore sediment transport leakage past the sand bypassing system, particularly during storm events. This paper will present a brief history of the dynamics of the Nerang River entrance since the early 1820s before reviewing historical sand volume analysis based on available survey data. An updated conceptual model will then be developed in order to better understand the morphological change in and around the Nerang River entrance area.

ADDITIONAL INDEX WORDS: Ebb-tidal delta, morphological evolution, tidal inlet.

INTRODUCTION

In the case of the Nerang River Entrance (NRE), which has been called the Gold Coast Seaway (GCS) since stabilization, and many other waterways that have entrance mouth infilling problems and navigation issues, it is crucial to understand the waterway dynamics and the different variables that affect their morphology. Since the late 1800s, there have been considerable variations in the location of the NRE due to the formation of sandbars around and within the entrance and its dominant northward migration attributable to the dominant northward wave-induced longshore current (Polglase, 1987). After the construction of the Seaway, despite the existence of a bypassing system, the growth of the ebb-tidal delta is still one of the main navigational safety concerns. There have been a number of studies that have examined the hydrodynamics in the vicinity of the GCS, such as that of Mirfenderesk and Tomlinson (2008). Moreover, a number of studies have also been carried out on the different factors that influence the morphological changes in the Seaway area and the growth of the delta (DHL, 1970; 1976; Polglase, 1987; Munday, 1995; WRL and GCCM, 1998; D'Agata and Tomlinson, 2004; Voisey, 2004; Patterson, 2007; Sennes *et al.*, 2007). Nevertheless, the dynamics of the GCS and the development of the ebb-tidal delta are not completely understood. In this context, literature which has focused on the GCS area, history, hydrodynamics and morphological changes are briefly presented, then the morphological evolution of GCS in the past decade is discussed.

Background

The GCS is located on the Australian East coast and links an intra-coastal waterway known as The Broadwater with the Pacific Ocean (Figure 1). The available history of the case study starts from 1820's when there was no permanent opening between the ocean and the Broadwater (Helman, 2010). In 1823, NRE was one of the two openings which formed at the most seaward meander bends of the Nerang River. Due to northern longshore sediment transport (LST), the southern opening was gradually closed, and the spit elongated to the north until the 1860's. The entrance widened due to severe storms in the 1870's and moved to the south about 1,300 m from 1840 to 1880's and did not change its location until 1901 (Longhurst, 1996). There has been conjecture about the southward relocation of the entrance, such as that of WRL and GCCM (1998), in which it was suggested that this might have indeed been a southern breaching. Permanent opening of the Jumpinpin inlet further to the north in 1898 has captured much of the river and tidal flow which previously flowed south and outflowed at the NRE.

DOI: 10.2112/SI75-48.1 *received 15 October 2015; accepted in revision 15 January 2016.*
*Corresponding author: mahnaz.sedigh@griffithuni.edu.au

Consequently, the ebb tide flow in the NRE was decreased, and the tidal prism of the inlet was significantly reduced. As a result of the re-distribution of tidal flow, the entrance migrated to the north again after 1901 with an increased rate (Brooks, 1953; Munday, 1995). The rate of northward migration during this time has been variable, with an average rate of about 60 m/yr during 1901-1968, which slowed down in the last few years of this period (1944-1968) to 26 m/yr (DHL, 1970).

Figure 1. Location of the study area (Image source: GoogleEarth©).

From 1901 to 1968, the average diversion of sand to the Broadwater from LST, which resulted in the spit elongation and northward migration of the entrance, was suggested to be approximately 143,000 m^3/yr, while there was about 9,000 m^3/yr riverine contribution to the ocean (DHL, 1970). It should be noted that during all these years, South Stradbroke Island beach alignment was stable. This means that the sand that was supplied from natural bypassing of the entrance was in equilibrium with the LST potential at South Stradbroke Island.

The developed and permanently dynamic entrance with a nearshore ebb-tidal delta, which had a crest depth of -2.5 to -3.5 m, was a dangerous obstacle which resulted in a number of boating accidents. Therefore, it was then decided to train the NRE to provide a safe navigation channel (Sennes *et al.*, 2007). The entrance was relocated 500 metres updrift (south of) its natural location in 1985 and was stabilized with two rock walls with a design depth of 5.5 m below Australian Height Datum (AHD) at the time of construction (Munday, 1995). Due to the high magnitude of the northerly LST on the Gold Coast, a bypassing plant was implemented and completed in 1986 (Sennes *et al.*, 2007).

The dredging of the stabilized channel was followed by dredging of the navigation channel in the Broadwater. Due to increased capability of the jetted ebb flow to move sediment seaward, and also reduction of sand supply to the entrance mouth, the ebb-tidal delta crest moved much further offshore as compared to the old ebb-tidal delta (Munday, 1995). Before stabilization, the natural ebb and flood shoals in shallow depths near the entrance attenuated the ocean tidal range by up to 60% within the Broadwater (WBM, 1992). Therefore, dredging and construction of the new entrance increased the tidal range in the Broadwater to that of the ocean coast, which resulted in the growth of the tidal prism and finally more channel scouring. The average depth in the GCS channel increased over the following 20 years, (Mirfenderesk and Tomlinson, 2009; Mirfenderesk *et al.*, 2006). According to Mirfenderesk and Tomlinson (2009), the average depth of the inlet channel was about 11m in 2005, with a maximum depth of about 20 m at some points.

Analyses of historical survey data until 1997 have shown continuous growth of the ebb-tidal delta since the entrance was stabilized in 1985. There are various estimations of the rate of the ebb-tidal delta growth. WRL and GCCM (1998) analysis suggested that between 1986 and 1992 the average net rate of deposition on the ebb-tidal delta was around 185,000 m^3/yr which decreased to 75,000 m^3/yr from 1992 to 1998. Andrews and Nielsen (2001) also used historical survey data from 1986 to 1998 and estimated much higher delta growth rates which was initially around 450,000 m^3/yr, and then decreased to about 200,000 m^3/yr. Generally the growth of ebb-tidal delta was to the northeast, probably due to the combination of dominant waves (from the Southeast) and the mean ebb-tide discharge path to the delta (to the northeast). Some wave induced swash bars also formed on the southern part of the ebb-tidal delta. (Andrews and Nielsen, 2001).

Andrews and Nielsen (2001) suggested that the main source of sand for the continuous growth of the ebb-tidal delta was supplied by the leakage of sand seaward of the sand bypassing system (around 115,000 m^3/yr), and also partly through the bypassing jetty (around 80,000 m^3/yr). Mirfenderesk and Tomlinson (2008) also suggested that the crescent like seaward lobe of the ebb-tidal delta after stabilization, which has connected upstream to downstream, indicates that the LST partially transported naturally along with the artificial sand bypassing system. It has also been suggested that another probable source of sediment for the ebb-tidal delta was the redistribution of sand from the discharge location of the bypassed sand downstream. Scouring of the channel between 1990 and 1995 was initially at a rate of 100,000 m^3/yr and gradually diminished to about 10,000 m^3/yr. The scoured sediment was the other source of sand trapped in the ebb-tidal delta (Andrews and Nielsen, 2001). On the other hand, WRL and GCCM (1998) suggested that there are about 50,000 m^3/yr of natural bypassing on the ebb-tidal delta, while the major supply of sand to the ebb-tidal delta growth is from the broadwater input (0-240,000 m^3/yr). In this paper, the morphological evolution of the GCS ebb-tidal delta in the past decade was investigated and linked to the previous studies. The main purposes of the study were to understand the more recent pattern of the ebb-tidal delta morphological evolution, whether the ebb-tidal delta has reached or is close to an equilibrium condition, and also the factors involved in its more recent trend of changes.

METHODS

In order to understand the pattern of morphological evolution of the GCS ebb-tidal delta during the past decade, hydrographic survey data have been used. These detailed survey data of the entrance, with variable extensions to the north and south, mainly cover the ebb-tidal delta area and the GCS channel. The final survey data sets of 12 were selected based on the coverage of the data included, since some of the available sets did not cover the whole ebb-tidal delta area. The survey data used for the analysis

cover a period of 11 years from Jan 2004 to Apr 2015. The sets, in a year/month format, are as follows: 2004/01, 2004/07, 2005/07, 2007/04, 2008/08, 2009/06, 2010/07, 2011/03, 2012/03, 2012/09, 2013/07, 2015/04. Survey data of Dec 1997, which encompasses the major portion of the defined ebb-tidal delta, was also used to join the analysis of the WRL and GCCM (1998) to the current study.

The area of the ebb-tidal delta for volumetric analysis was defined based on the area with active morphological evolution from Jan 2004 to Apr 2015 as illustrated in Figure 2 (A1). To analyse the ebb-tidal delta growth as a continuation from the WRL and GCCM (1998) study, the volumetric change of the ebb-tidal delta between Dec 1997 and Jan 2004 was estimated. Since Dec 1997 survey data did not include a northern portion of the defined ebb-tidal delta area, this volume was enlarged relatively. The cumulative volume of the ebb-tidal delta for Dec 1997 compared to Mar 1997 (Last data set in the study of WRL and GCCM (1998)) was estimated based on the trend of volumetric changes of previous years. Dredging in the study area as well as the artificial sand bypassing volumes were also considered in the analyses.

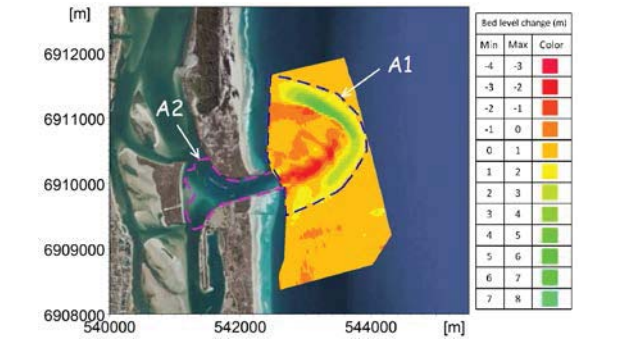

Figure 2. Morphological evolution of the GCS, on the offshore extension of the GCWA survey data, from Jan 2004 to April 2015. A1 is defined as the area of ebb-tidal delta, and A2 is the GCS channel

Measured wave data at the Gold Coast offshore wave buoy located about 1km offshore with a water depth of about 17 metres and about 3.5 km south of the entrance (Figure 1), as well as major flooding event dates and intensities were also considered. In order to analyse the effects of storm events, the storm events' resultant wave power (P_w) between consecutive surveys were calculated (Vila-Concejo *et al.*, 2004). Then, the total storm wave power for each storm was calculated from equation (1).

$$W_{PT} = P_{wm} \times D_s \quad (1)$$

where P_{wm} is the mean wave power for each storm event, and D_s is the storm duration in seconds. The storm threshold used was defined as high energy events with $H_s > 3$ and a minimum duration of two hours. The storm events were also categorized to storm events with a dominant wave direction of less than 90 degrees (from North clockwise), and more than 90 degrees, which due to the approximate Northward-Southward direction of the GCS adjacent coastline can be assumed to generate southward and northward longshore sediment transport respectively. The storm events with dominant wave direction of less than 90 degrees were called north-east (NE) storm events, and the ones with dominant direction of more than 90 degrees were called south-east (SE) storm events.

RESULTS

The trend of the ebb-tidal delta cumulative volume evolution since 1980 is shown in Figure 3. The first two part of the graph was extracted from the WRL and GCCM (1998) report. The results show the ebb-tidal delta growth at an average rate of 12,500 m^3/month or 151,000 m^3/yr from Oct 1984 to Apr 2015.

As shown in Figure 2, the net growth of the ebb-tidal delta is more offshore, similar to a typical ebb dominated tidal inlet. The more northward orientation of the growth is due to the dominant northward longshore current owing to wave action. The ebb-tidal delta volumetric analysis in the WRL and GCCM (1998) report was dependent on the seaward extension of the survey data sets supplied by GCWA from February 1993 to March 1997 (last data point of WRL report in Figure 3). The seaward extensions of these data sets were less than the ones used in this study, which explains the suggested decreased rate of ebb-tidal delta growth for 1992 to 1998 (75,000 m^3/yr) in the WRL and GCCM (1998) study.

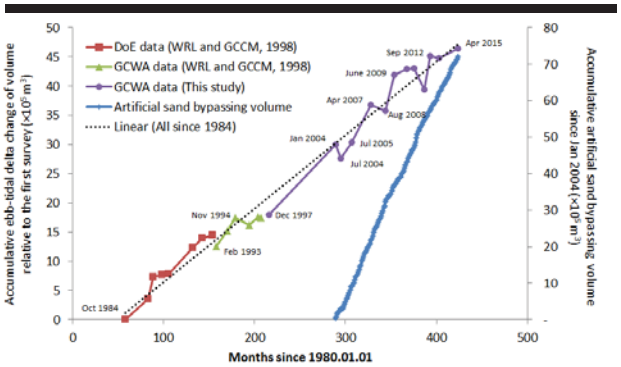

Figure 3. Cumulative volume of the ebb-tidal delta since 1984 based on Department of Environment (DoE) and Gold Coast Waterways Authority (GCWA) survey data (left graphs); cummulative artificial sand bypassing volume since Jan 2004 (right graph).

There are several sand sources that may have supplied the sand for the ebb-tidal delta growth. Since stabilization, during past decades, the GCS channel (A2 in Figure 2) has kept scouring much more than its designed depth of 5.5 m. Since the tidal current in the GCS channel was found to be ebb dominated (Sedigh *et al.*, under review), it can be concluded that the eroded sand was flushed to the ebb-tidal delta by the ebb tidal flow jet and trapped somewhere in the ebb-tidal delta shoal, depending on the combined action of tides and waves. Figure 4 shows the trend of the accumulative morphological changes in the GCS channel since 1984. It should be noted that there were some dredging activities in this area. The first one was a major dredging of the whole GCS and the northern and southern channels at the time of the GCS construction in 1985. There are two other recorded dredgings specifically within the inlet channel (A2 in Figure 2). These include 15,000 m^3 in 2009 and

about 65,000 m^3 in 2013. The second dredging is part of the reason for the major drop (erosion) from July 2013 to April 2015 shown in Figure 4. Including the dredging activities, the average rate of the inlet scouring from Oct 1984 to Apr 2015 was about 2,600 m^3/month or 31,000 m^3/yr, which is about 20% of the average accretion rate in the ebb-tidal delta.

An analysis by Mirfenderesk and Tomlinson (2009) has shown a flood-dominant tidal regime within the estuary of the Nerang River (Broadwater), and has suggested that any eroded sand in the Broadwater channels will remain in the estuary. However, the study by Mirfenderesk and Tomlinson (2009) has also shown that the estuary has become less flood-dominant in the past two decades, and it was suggested that as a result, more sand might be transported out of the estuary compared to previous years. For a more detailed study of the morphological evolution of the Broadwater and its effects, subsequent survey data of the whole estuary is required, which is not available at this stage.

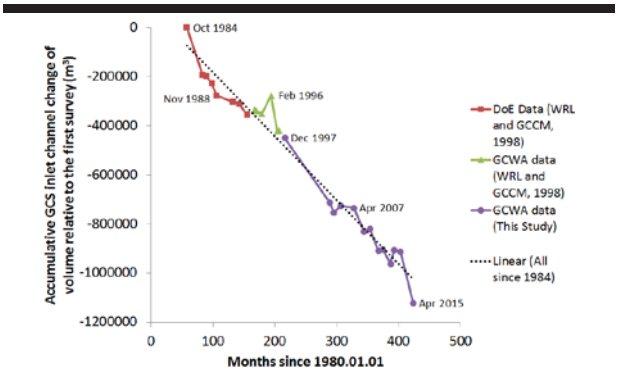

Figure 4. Cumulative volume of the GCS Channel (A2 in Figure 2) since 1984 based on Department of Environment (DoE) and Gold Coast Waterways Authority (GCWA) survey data.

Another source of sediment for the ebb-tidal delta is from the leakage of the LST offshore sand-bypassing system and the southern training wall. However, there are significant differences between the rates suggested for this source in previous studies, which ranges from 50,000 m^3/yr (WRL and GCCM, 1998) to 195,000 m^3/yr (Andrews and Nielsen, 2001). Sedigh *et al.* (under review) suggested that the main drivers of LST in this region are SE storm events. Therefore, to investigate the relationship between the ebb-tidal delta growth and the storm events further, the cumulative W_{PT} for NE and SE storms for each time interval were calculated and plotted versus the volumetric change of the ebb-tidal delta, as shown in Figure 5. As illustrated, the accretion in the ebb-tidal delta was more significant in the Jul 2005-Apr 2007, Aug 2008-Jun 2009, and Mar 2012-Sep 2012 intervals, during which the accumulated SE storm event powers were more significant, and at least one significant SE storm event with $W_{PT} \geq 30\times10^9$ (W.s/m) occurred as well. However, it should be noted that the rate of deposition was not proportional to the cumulative (SE) W_{PT} in these intervals, which is due to the effect of the length of intervals, the dominant direction of waves during lower energy wave conditions, and the recovery process after dredging activities. In addition, in the time intervals where the cumulative W_{PT} from NE was more dominant, erosion occurred in the ebb-tidal delta; the exception was Jul 2004-Jul 2005, during which a major flood event with a return period of about 1 in 20 years occured at the end of June 2005. Also of note is that the more significant erosion in Mar 2011-Mar 2012 was due to approximately 260,000 m^3 dredging from the ebb-tidal delta area from May 2011 to March 2012. As shown in Figure 5, in the time intervals where the cumulative W_{PT} from the SE and NE were approximately the same, the ebb-tidal delta net morphological evolutions were negligible.

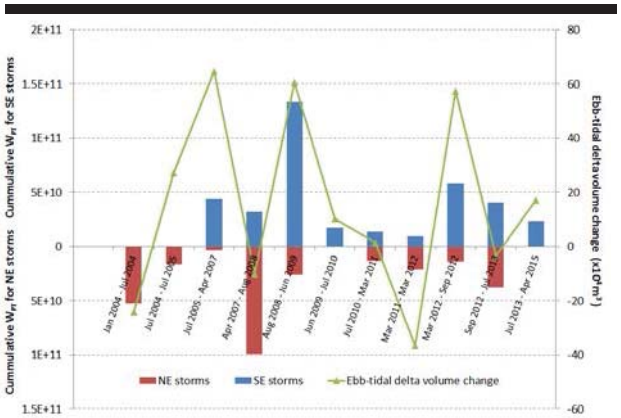

Figure 5. Cummulative W_{PT} (W.s/m) for storm events from NE and SE versus the volumetric change of the ebb-tidal delta in each time interval.

DISCUSSION

Figure 3 and Figure 4 suggest that the GCS region is still in a transitional zone, and has not reached an equilibrium yet. Also, the trend of the ebb-tidal delta evolution since 2004 does not show any decrease in the average rate of the ebb-tidal delta growth compared to the study of WRL and GCCM (1998). The average artificial sand bypassing rate from Jan 2004 to Apr 2015 was about 650,000 m^3/yr (Figure 3) which ranged from 480,000 m^3/yr in 2004 to 770,000 m^3/yr in 2011. The max rate of delta growth during these years was approximately 620,000 m^3/yr, which occurred from Aug 2008 to Aug 2009 when about 600,000 m^3/yr sand bypassed artificially. Assuming that the coastline alignment has remained stable during these years, and no leakage has occurred in 2004 (since no accretion occurred in the ebb-tidal delta) it can be concluded that the net northward LST updrift the entrance varies from 480×10^3 to $1{,}050\times10^3$ m3/yr. This rate is extremely dependent on the frequency of the major SE storm events.

As explained and shown in Figure 5, the rate of ebb-tidal delta growth was much higher during the intervals which included major SE storm events. It is suggested that this was due to the more offshore extension of the resultant significant northward LST during these events. The governing relationship found between the occurance of the major SE storm events and the ebb-tidal delta growth confirms that the prevailing source of sand for the continuous growth of the ebb-tidal delta is from the dominant northward LST, specifically during storm events. It is suggested that the leakage of LST seaward of the southern

training wall also occurs during calm weather conditions due to the dominant northward wave direction, but it is much less compared to the storm events.

The suggested conceptual model of the sediment transport from Jan 2004 to April 2015 is shown in Figure 6. It should be noted that this conceptual model is based on the assumption of no changes in the coastline alignment during these years.

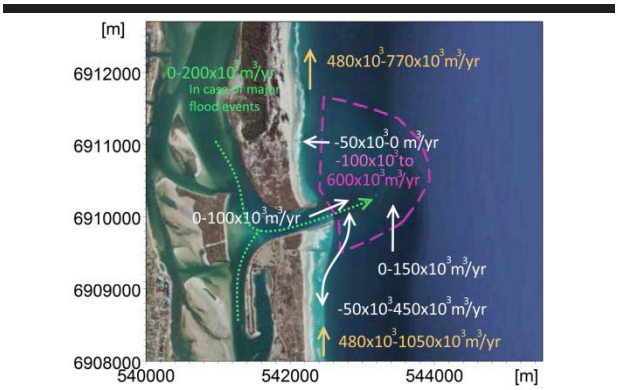

Figure 6. Conceptual model of sediment transport from Jan 2004 to Apr 2015 (Image source: GoogleEarth©).

CONCLUSIONS

The morphological evolution of the GCS ebb-tidal delta in the past decade was investigated. The results confirm the continuous growth and extension of the ebb-tidal delta offshore. However, the rate of ebb-tidal delta growth during various time intervals is quite variable. This rate is the highest during the intervals with major SE storm events. This shows that a significant portion of the ebb-tidal delta growth is storm-event based. Other less significant sources of sand to the ebb-tidal delta were found to be from the scouring of the inlet channel, some offshore sand supply, as well as sediment from within the eustaury in the case of major flood event. Based on the analysis of available data, a conceptual model of sediment transport has been presented. For a more precise analysis, further subsequent survey data of the Broadwater as well as detailed survey data of the adjacent coastlines are required.

ACKNOWLEDGMENTS

The survey, dredging and sand bypassing data used in this research were provided by Gold Coast Waterways Authority (GCWA) and City of Gold Coast (CoGC). Measured buoy wave parameters were provided by Queensland Government.

LITERATURE CITED

Andrews, M. and Nielsen, C., 2001. Numerical modelling of the Gold Coast Seaway. *Proceedings of Coasts & Ports 2001* (Gold Coast, Australia), pp. 469-474.

Brooks, J., 1953. Stradbroke Island erosion and broadwater silting, Southport. *Queensland Government Mining Journal*, 54, 566-569.

D'Agata, M. and Tomlinson, R., 2004. *Investigation of Ebb Tidal Deltas using a Numerical Model at the Moveable Bed Physical Model Scale*. Gold Coast, Australia: GCCM for Coastal Zone Estuary & Waterway Management, *Research Report 27*, 103p.

DHL, 1970. *Gold Coast, Queensland Australia - Coastal erosion and related problems*. The Netherlands: Delft Hydraulics Laboratory, *Report 257*.

DHL, 1976. *Nerang River Entrance Stabilisation, Report on Model Investigation*. The Netherlands: Delf hydraulic, *Report M1259*.

Helman, P., 2010. *Broadwater history, south east Queensland*. Gold Coast, Australia: GCCM, *Unpublished research report*.

Longhurst, R., 1996. *From Tallebudgera to the Tweed: an early history of the Southern Gold Coast*. Southport, Qld: Gold Coast City Council.

Mirfenderesk, H. and Tomlinson, R., 2009. Interaction between coastal development and inland estuarine waterways at the short-medium timescale. *Journal of Coastal Research*, 25(4), 969-980.

Mirfenderesk, H. and Tomlinson, R., 2008. Observation and Analysis of Hydrodynamic Parameters in Tidal Inlets in a Predominantly Semidiurnal Regime. *Journal of Coastal Research*, 24(5), 1229–1239.

Mirfenderesk, H.; Tomlinson, R.; Szylkarski, S., and Rasmussen, E.B., 2006. Development of a three dimensional model to understand modified tidal entrance processes. *Coastal Engineering Proceedings* (San Diego, Californian, USA), pp. 2118-2129.

Munday, D., 1995. Coastal response to the Nerang River inlet stabilisation, Gold Coast, Queensland, Australia. Brisbane: QUT, BSc (Hons) thesis, 81 p.

Patterson, D.C., 2007. Sand Transport and Shoreline Evolution, Northern Gold Coast, Australia. *Proceedings. Journal of Coastal Research*, Special Issue No. 50, pp. 147-151.

Polglase, R.H., 1987. The Nerang River Entrance Sand-Bypassing System. *Proceedings of the 8th Australian Conference on Coastal Ocean Engineering* (Australia), pp. 222-226.

Sedigh, M.; Tomlinson, R.; Cartwright, N., and Etemad-Shahidi, A., under review. Evaluation of the Gold Coast Seaway area hydrodynamics and littoral drift using numerical modelling. *Ocean Engineering*.

Sennes, G.; Castelle, B.; Bertin, X.; Mirfenderesk, H., and Tomlinson, R.B., 2007. Modelling of the Gold Coast Seaway tidal inlet, Australia. *Proceedings. Journal of Coastal Research*, Special Issue No. 50, pp. 1086-1091.

Vila-Concejo, A.; Ferreira, Ó.; Morris, B.; Matias, A., and Dias, J., 2004. Lessons from inlet relocation: examples from Southern Portugal. *Coastal Engineering*, 51(10), 967-990.

Voisey, C., 2004. *Moveable Bed Physical Modelling of Ebb Delta Growth Characteristics*. Gold Coast, Australia: GCCM for Coastal Zone Estuary & Waterway Management, *Report 25*.

WBM, 1992. *Broadwater hydraulic model investigations-Assessment of specific options*, *No. 6090/2*.

WRL and GCCM, 1998. *Numerical Modelling of Sediment Movement and Budget at Seaway*. Gold Coast, Australia: Water Research Laboratory in association with Griffith University for GCCC, *Technical Report No. 98/08*, 51p.

Journal of Coastal Research	SI	75	243-247	Coconut Creek, Florida	2016

Validation of Empirical Wave Run-up Formulas to the Polish Baltic Sea Coast

Paulina Aniśkiewicz*, Rafał Benedyczak, Kazimierz Furmańczyk, and Paweł Andrzejewski

Remote Sensing and Marine Cartography Unit
Faculty of Geoscience
University of Szczecin
Szczecin, Poland

www.cerf-jcr.org

www.JCRonline.org

ABSTRACT

Aniśkiewicz, P.; Benedyczak, R.; Furmańczyk K., and Andrzejewski P., C.S., 2016. Validation of Empirical Wave Run-up Formulas to the Polish Baltic Sea Coast. *In:* Vila-Concejo, A.; Bruce, E.; Kennedy, D.M., and McCarroll, R.J. (eds.), *Proceedings of the 14th International Coastal Symposium* (Sydney, Australia). *Journal of Coastal Research*, Special Issue, No. 75, pp. 243-247. Coconut Creek (Florida), ISSN 0749-0208.

The empirical wave run-up formulas were adapted in previous researches by many authors. One of them adapted the formula for dynamic Polish Baltic Sea coast (Paprotny *et al.*, 2014). In the present paper the available formulas were validated using the camera images and measurements made by GPS RTK along the profile located in Dziwnówek during calm weather conditions. The experiment was carried out in Dziwnówek from June 1st to August 31st 2014. The range of water level was varied from -0.25 to 0.44 m above average sea level elevation from real sea level elevation data from Institute of Meteorology and Water Management and about -0.405 to 0.402 above average sea level elevation from hydrodynamic model M3D. The results of wave run-up with a 2% probability of occurrence were created using real and modelled elevation data to compare results. Significant wave height was about 0.01–1.61 m and peak wave period varied from 2.01 to 8.39 seconds. The camera provides images during the 15 minutes events in every hour sampled at 1 Hz. The highest wave run-up was identified along the profile in every available picture. Data from camera were compared with modelled range of beach inundation. The research was done in the framework of SatBałtyk project. The number of project is: POIG.01.01.02-22-011/09.

ADDITIONAL INDEX WORDS: *coastal modelling, beach inundation, wave run-up formulas.*

INTRODUCTION

The purpose of this analysis is a prediction of the beach inundation on the basis of a statistical formula using disposable hydrological data like a deep-water significant wave height, a deep-water wave length or a sea water level. It has a very large importance for the inhabitants of the cities, towns and villages along the coastline. Valuable predictions could allow the local authorities to prevent the risk from high waves. That is also important for the tourist as sandy beaches are very popular tourism destinations. Good predictions would be useful for them and their plans of sunbathing.

Not only human beings could be at danger coming from high water. The cultural and natural heritage could be harmed as well, and it can not protect itself on its own (Łonyszyn and Terefenko 2013). The preparation for the preservation of that heritage needs time what good and valuable predictions could give to the local authorities.

To verify which formula would give the best prediction for the Polish coastline it was necessary to test a few equations. This paper is an analysis of the most popular ones in the specialist literature.

The measurements have been realized on Dziwnów Spit in Dziwnówek – a village at the Polish coast in the West Pomeranian Voivodeship – during three months, since June until the end of August, of the year 2014. A part of the village stretches along the spit. It is a very popular destination for Polish and German people during the summer season (usually from July till August). In recent years, the local government finalized many investments important for tourism development.

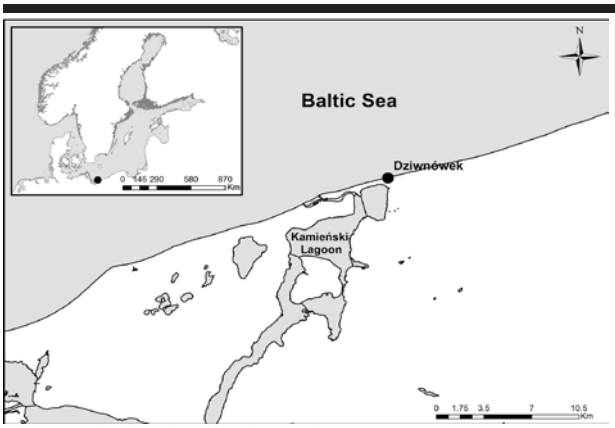

Figure 1. The location of Dziwnówek.

DOI: 10.2112/SI75-049.1 received 15 October 2015; accepted in revision 15 January 2016.
*Corresponding author: aniskiewicz.paulina@gmail.com

The biggest attractions of Dziwnówek are sandy beaches, most of them on the spit separating the Baltic Sea from the Kamieński Lagoon. The Dziwnów Spit nowadays is split for two parts by Dziwna Strait. It happened at the turn of the XIX and XX centuries when an artificial channel was built. The new Dziwna mouth was reinforced by jetties that helped to keep this construction till present time. On the other hand, that artificial activity took a strong effect on coastal disruption processes (Furmańczyk et al. 2011). The beach nourishment was necessary for the tourist purposes as well as for the safety of the inhabitants as the risk was high in a consequence of erosion. During the time of measurements, there wasn't any nourishment taking place.

METHODS

Wave run-up is indicated by R_2. "This is the run-up level, vertically measured with respect to the (adjusted) still water level, which is exceeded by two per cent of the incoming waves" (Meer, 1998). To calculate beach inundation using wave run-up formulas the key thing is the Iribarren number (1) which is a result of laboratory experiments made by Irribaren and Nogales (1949), where β is beach steepness, H is wave height and L_0 is linear theory deep-water wave length.

$$\xi_0 = \frac{\beta}{\sqrt{\frac{H}{L_o}}} \quad (1)$$

This formula was modified by Galvin (1972). He has modified *eq. 1* and presented criteria concern breaker types in terms of an "offshore parameter" ξ_0, where H value is changed by H_o (deep-water wave height). This parameter may give information about waves break. There are four types of wave break: surging and collapsing if $\xi_0 > 3.3$, plunging if $0.5 < \xi_0 < 3.3$ or spilling if $\xi_0 < 0.5$ (Battjes, 1974). Modified Irribaren number determinate which type of formula should be used to compare it with measured data.

To adapt a wave run-up formula to the Polish Baltic Sea Coast there were analyzed fourteen equations of wave run-up.

$$\frac{R_2}{H_0} = 1.86 \cdot \xi_0^{0.71} \quad (2)$$

The equation created by Mase (1989) is based on the Iribarren number (IR) (1) and two parameters 1.86 and 0.71 (2). The application range for this equation has two conditions. According to the first one the value of β (beach steepness) has to be between 1/30 and 1/5. According to the second one the ratio of H_0 (deep water wave height) and L_0 (linear theory deep-water wave length) should be higher or equal to 0.007.

$$R_2 = 1.1 \cdot \left(0.35\beta\sqrt{H_0 L_0} + \frac{\sqrt{H_0 L_0 (0.563\beta^2 + 0{,}004)}}{2} \right) \quad (3)$$

$$R_2 = 0{,}043 \cdot \sqrt{H_0 L_0} \quad (4)$$

The equation created by Stockdon *et al.* (2006) is much more expanded (3). The authors used four different parameters. The idea was that the formula may be used over wide range of beach conditions. Anyway, this formula is applicable under one condition – where $\xi_0 > 0.3$. When $\xi_0 < 0.3$ the authors suggest to use another, much simpler, equation (4).

$$\frac{R_2}{H_0} = \left(SWL + 1.19 \cdot \xi_0 \right) \quad (5)$$

$$\frac{R_2}{H_0} = SWL + 0.1 \cdot \sqrt{H_0 L_0} \quad (6)$$

Nielsen and Hanslow (1991) added to their equations the average sea water level (SWL), defined by Nielsen and Hanslow (1991). For the $\beta < 0.10$ or $\Omega > 6$ they suggest to use the equation with the Iribarren number (5), and for the $\beta > 0.10$ or $\Omega < 6$ they suggest the equation with a square root of $H_0 L_0$ (6).

$$\frac{R_2}{H_0} = 0{,}27 \cdot \frac{\xi_0}{\sqrt{\beta}} \quad (7)$$

$$R_2 = 0{,}5 \cdot H_0 - 0.22 \quad (8)$$

Next two equation proposed by Ruggiero *et al.* (2001) have different application range. The first one is applicable for the $\xi_0 > 0.5$ (7), and the second one for $\xi_0 < 0.5$ (8).

$$\frac{R_2}{H_0} = 0.34 + 1.15 \cdot \xi_0 \quad (9)$$

Previously there was mentioned the equation created by Mase. The same scientist presented, together with Hedges, another equation (9). Once again with two parameters and the Iribarren number but in a different configuration (Hedges and Mase, 2004). This formula is applicable only for $\xi_0 < 2.4$.

$$R_2 = 0.55 \cdot H_0 \quad (10)$$

The simplest equation among those presented an analysed within this paper it is the equation proposed by Guza and Thornton (1982) (10). The investigation proved that this equation is also one of the most effective.

$$R_2 = 0.53\beta\sqrt{(H_0 L_0)} + 0.58\xi_0\sqrt{\frac{H_0^3}{L_0}} + 0.45 \quad (11)$$

Vousdoukas *et al.* (2011) proposed an expanded equation with three parameters (11). According to the authors, this formula gives the best results in comparison to other two mentioned in their article. That is why only this one has been used within this paper.

$$\frac{R_2}{H_0} = 0.2 + 0.83 \cdot \xi_0 \quad (12)$$

Holman and Sallenger (1985) presented an equation with two parameters and the Iribarren number (12). The authors settled an application range as $\xi_0 > 0.5$.

$$\frac{R_2}{H_0} = 1.20 \cdot \xi_0 \quad (13)$$

$$R_2 = 0.32 \cdot H_0 \quad (14)$$

Diaz *et al.* (2014) after long analysis proposed two equations for two different values of ξ_0. They suggested to use the first one (13) for the ξ_0 >0.3, and the second (14) for the ξ_0 <0.3.

$$R_2 = 1.29 H_0 \cdot \left(\frac{\beta}{\sqrt{\frac{H_0}{L_0}}} \right)^{0.72} + S \qquad (15)$$

The last equation analysed within this paper is the one proposed by Paprotny at al. (2014). The authors used the Mase equation (1) as a starting point. The most important modification has been the addition of the sea level value – S (15).

All formulas except *eq. 15* are based on peak wave period and wave height. One of them (*eq. 5, eq. 6*) includes SWL which is an averaged water level defined by Nielsen and Hanslow (1991). First of all the formulas results in original form were compared with measured data. Unfortunately the most of them were calibrated using laboratory conditions and they may be incorrect to predict inundation in natural beaches. Because of that there was added sea level elevation to all formulas as a second step. The results of equations are showed in percentage value of beach inundation (*BI*), where *h* is the baseline height of the beach:

$$BI = \frac{R_2}{h} \cdot 100\% \qquad (16)$$

All results of formulas were compared with measured data made by GPS RTK along the profile located in Dziwnówek. These data are provided by video camera located in Dziwnówek (Figure 1) during the 15 minutes events in every hour sampled at 1 Hz. This camera was mounted in 2009 by the MICORE program (*Morphological Impacts and Costal Risks Induced by Extreme Storm Events*) (Ferreira et. Al, 2009). The method of analyzing camera images was described at Paprotny *et al.* (2014). The location of 0% beach inundation point in the video camera is in the sea level value defined as -0.08 m in Kronsztadt-86, which is named as average sea level. Elevation difference in profile located in Dziwnówek is about 2.32 m and the length of the profile measured from dune base to mean sea level point is about 33 m. The value of angle slope is 3.9°. The most important thing is that the measured data were collected during the calm weather from June 1st to August 31st 2014. The maximum wave height was about 0.01 – 1.61 m and peak wave period varied from 2.01 to 8.39 seconds. These wave conditions are from WAM model, which is the third generation wave model (Group, 1988). The range of water level was varied from -0.25 to 0.44 m above average sea level elevation from real sea level data from Institute of Meteorology and Water Management and about -0.41 to 0.40 above average sea level elevation from M3D model which can predict hydrological and hydrodynamic conditions (Kowalewski et. al, 1997).

RESULTS

The Irribaren number in every time step has been calculated to choose which formulas could be used to predict beach inundation. Mean value of that number during the period: June 1st – August 31st 2015 is about 0.601. The range of IR was varied from 0.281 to 2.115 and the median value is 0.498. Because of that the average value of *IR* has been chosen as a determinate value to choose types of formula. It means that equations in which ξ_0 >0.5 has been used to predict beach inundation.

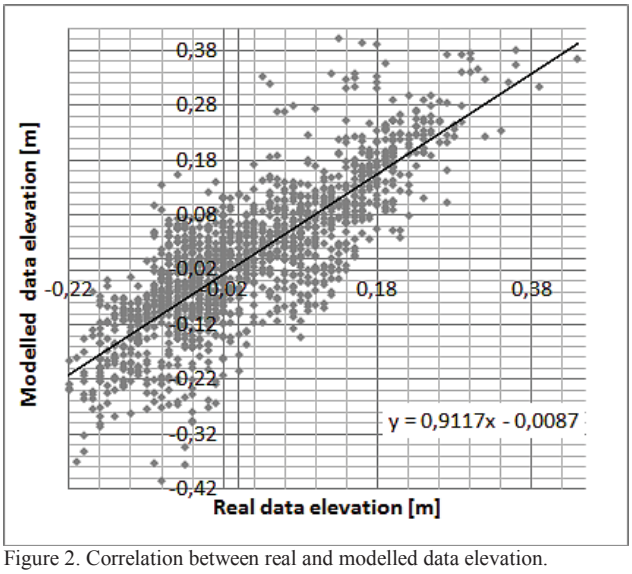

Figure 2. Correlation between real and modelled data elevation.

Table 1. *Correlation coefficient calculated from all equations.*

Author	Original formula		Formula+ model sea level		Formula+ real sea level	
	01.06 - 31.08	12.06 - 31.08	01.06 - 31.08	12.06 - 31.08	01.06 - 31.08	12.06 - 31.08
Guza & Thornton	0.32	0.454	0.36	0.541	0.34	0.518
Diaz *et al.*	0.28	0.447	0.34	0.535	0.32	0.509
Hedges & Mase	0.30	0.456	0.35	0.532	0.33	0.514
Holman & Sallenger	0.30	0.456	0.35	0.541	0.33	0.517
Nielsen & Hanslow	0.32	0.533	0.34	0.531	0.31	0.526
Ruggiero *et al.*	0.28	0.447	0.34	0.536	0.31	0.506
Stockdon *et al.*	0.32	0.509	0.33	0.526	0.31	0.494
Vousdoukas *et al.*	0.29	0.452	0.34	0.529	0.31	0.506
Paprotny *et al.*	0.33	0.453	0.34	0.535	0.33	0.514
Mase	0.30	0.454	0.34	0.529	0.31	0.489

At the beginning all formulas has been used in original form. One of them include one parameter (*eq. 10*) and is the simplest formula. The most of them have only β, H_o *and* L_o values. Equation made by Nielsen and Hanslow (1991) include additionally average sea water level which was calculated from every time step of analysis data from IMWM (*Institute of Meteorology and Water Management*) tide – gauge located in Dziwnów. Paprotny *et al.* (2014) created equation with elevation data but to first step this value was excluded. The correlation

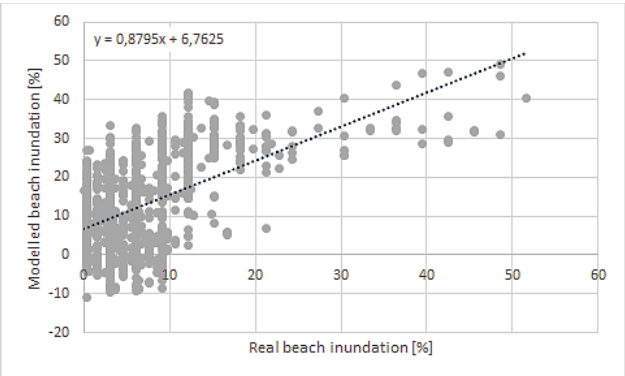

Figure 3. Correlation plot between real beach inundation data and predicted data for *eq. 10.*

between real and predicted data for all equations was varied from 0.28 to 033. The next step was adding sea level data to all equations. To compare results there were used real data from tide

– gauge and modelled data from M3D model. The determination coefficient between real and modelled elevation data was about 0.665. After this operation the correlation coefficient increased a little. The range of this parameter was about 0.31 – 0.34 after adding real sea level data from tide – gauge. The next step was adding modelled sea level data from M3D model to original formulas. Correlation coefficient was bigger than in previous part (range: 0.33 to 0.36).

Unfortunately there were some problems with real data (Figure 4). First twelve days of analysis period (*No 1* on a plot) look incorrect. The analysis of video images showed that during this time video images had lower resolution because of technical problems with camera so the data were omitted. The next part of data (*No 2*) do not look correct too. During this period wave height value were high (about 1.2 m) so real data should be higher too. The analysis of wave direction showed that this time the value of wave direction was between 180 and 270° and longshore water transport was predominant. Because of that the real data values could be low.

Because of problem with lower resolution video images the data from June 1st to June 11th has been removed and formulas has been analyzed once again. The result was better (Table 1). The analysis of original formulas showed better coefficient (from 0.447 to 0.533). The highest value of coefficient was made by Nielsen and Hanslow (*eq. 5*). After adding the sea level data from IMWM the correlation coefficient usually increases (range: 0.489 – 0.526). The lowest correlation was for *eq. 11* and the biggest for *eq. 5*. It is attention worth that *eq.5* gave the best correlation for original formula. Adding elevation data decreased this value. The best correlation of the most of all formulas (except *eq. 5*) obtained using modelled sea level data to predict beach inundation. The correlation coefficient was about 0.526 (*eq. 3*) to 0.541 (*eq. 10* – Figure 3, *eq. 12*). Because of that there were chosen two modified equations which can be adapt to the Polish Baltic Sea Coast (*eq. 17, eq. 18*):

$$R_2 = 0.55 \cdot H_0 + S \qquad (17)$$

$$\frac{R_2}{H_0} = 0.2 + 0.83 \cdot \xi_0 + S \qquad (18)$$

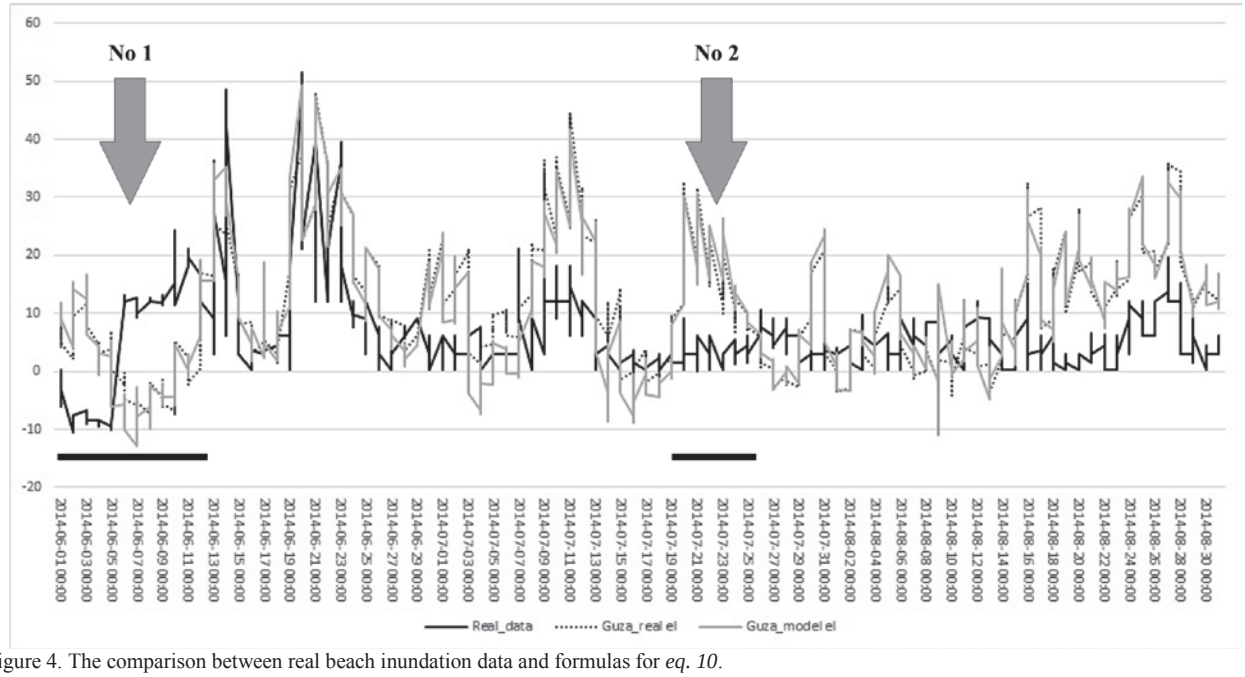

Figure 4. The comparison between real beach inundation data and formulas for *eq. 10*.

CONCLUSIONS

The correlation coefficient is bigger after adding elevation data to equations. This parameter reduces beach inundation when its value is less than -0.08 m above average sea water level and increases beach inundation when elevation data values are bigger than -0.08 m. The main reason of increasing correlation after using these data is fact that almost all formulas (except *eq. 15*) were calibrated in laboratory conditions, not in natural environment. It is significant that *eq. 15* which was calibrated in the same research area did not give the best correlation coefficient. It means that there should be find better equation to Polish Baltic Sea Coast.

The equation created by Nielsen and Hanslow is the only one where the correlation without the temporary sea level parameter is the highest of all three. In every other example at least one formula with the sea level parameter has higher correlation than the original equation. It means that in this formula the SWL parameter gives better results than *S* parameter. In other equations the best correlation was with modelled elevation data. It means that this data can be successfully used to predict beach inundation. Correlation with sea level input data from tide – gauge in Dziwnów may not be correct because this equipment is located in the mouth of Dziwna River, not exactly in the Baltic Sea. Other tide – gauges located in the Polish Baltic Sea coast are correlated with data from M3D model very well.

In some cases when longshore water transport was predominant all equations overestimated results. It means that it should be added additional component to wave run-up formula. It is planned in future research.

ACKNOWLEDGMENTS

This publication is one of the results of the Satellite Monitoring of the Baltic Sea environment project (SatBałtyk). The project is being implemented within the framework of the Innovative Economy Operational Programme. The number of project is: POIG.01.01.02-22-011/09.

The authors would like to thank Przemysław Łonyszyn for a state of the art research, Natalia Bugajny for collecting real water elevation and GPS data, and Łukasz Cieszyński for technical help with software necessary to analyse.

LITERATURE CITED

Battjes, J.A. 1974. Surf similarity. *Coastal Engineering Proceedings*, 1(14), 466-480.

Díaz-Sánchez, R.; López-Gutiérrez, J.S.; Lechuga, A., and Negro V. 2014. Runup variability due to time dependence and stochasticity in the beach profiles: two extreme cases of the Spanish coast. *Journal of Coastal Research*, 70, 1-6.

Ferreira, Ó.; Ciavola P.; Armaroli C.; Balouin Y.; Benavente J.; Del Río L.; Deserti M.; Esteves L.S.; Furmanczyk K.; Haerens P.; Matias A.; Perini L.; Taborda R.; Terefenko P.; Trifonova E.; Trouw K.; Valchev N.; Van Dongeren A.; Van Koningsveld M. and Williams J.J. 2009. Coastal storm risk assessment in Europe: examples from 9 study sites. *Journal of Coastal Research*, SI 56, 1632-1636.

Furmańczyk, K.K.; Dudzińska-Nowak, J.; Furmańczyk, K.A.; Paplińska-Swerpel, B., and Brzezowska, N. 2011. Dune erosion as a result of the significant storms at the western Polish coast (Dziwnow Spit example). *Journal of Coastal Research*, 57(64), 756-759.

Galvin, C. J. 1972. Wave breaking in shallow water. *Waves on beaches and resulting sediment transport*, 413-456.

Group, T. W. 1988. The WAM model-a third generation ocean wave prediction model. Journal of Physical Oceanography, 18(12), 1775-1810.

Guza, R.T., and Thornton, E.B., 1984. Swash oscillations on a natural beach. *Journal of Geographical Research – Oceans*, 87(NC1), 483-491.

Hedges, T.S., and Mase, H. 2004. Modified Hunt's equation incorporating wave setup. *Journal of waterway, port, coastal, and ocean engineering*, 130(3), 109-113.

Holman, R.A., and Sallenger Jr., A.H., 1985. Setup and swash on a natural beach. *Journal of Geophysical Research,* 90(C1), 945-953.

Iribarren, C.R., and Nogales, C. 1949. Protection des ports, *Proceedings XVIIth International Navigation Congress, Section II, Communication 4, Lisbon,* 31–80.

Kowalewski, M. 1997. A three-dimensional hydrodynamic model of the Gulf of Gdansk. *Oceanological Studies*, *4*(26), 77-98.

Łonyszyn P., and Terefenko O. 2013. Zmiana świadomości człowieka na temat dziedzictwa przyrodniczego i kulturowego na skutek globalizacji. *In:* Borówka R.K., Cedro A., Kavetskyy I. (eds.), *Współczesne problemy badań geograficznych* (US, Szczecin, Poland), 313-322.

Mase, H. 1989. Random wave runup height on gentle slope. *Journal of Waterway, Port, Coastal, and Ocean Engineering*, 115(5), 649-661.

Nielsen, P., and Hanslow D.J., 1991. Wave Runup Distributions on Natural Beaches. *Journal of Coastal Research*, 7(4), 1139-1152.

Paprotny, D.; Andrzejewski, P.; Terefenko, P., and Furmańczyk, K. 2014. Application of Empirical Wave Run-Up Formulas to the Polish Baltic Sea Coast. *PLoS ONE* 9(8), 1-8.

Ruggiero, P.; Komar, P.D.; McDougal, W.G. and Beach, R.A. 1996. Extreme water levels, wave runup and coastal erosion. *Coastal Engineering Proceedings*, 1(25), 2793-2805.

Stockdon, H.F.; Holman, R.A.; Howd, P.A., and Sallenger, A.H. 2006. Empirical parameterization of setup, swash, and runup. *Coastal engineering*, 53(7), 573-588.

Van der Meer, J. W. 1998. Wave run-up and overtopping. *In:* Pilarczyk K.W. (ed.) *Dikes and Revetments: Design, Maintenance and Safety Assessment* (AA Balkema, Rotterdam, The Netherlands), 145-159.

Vousdoukas, M.I.; Wziatek, D., and Almeida, L.P. 2012. Coastal vulnerability assessment based on video wave run-up observations at a mesotidal, steep-sloped beach. *Ocean Dynamics*, 62(1), 123-137.

Journal of Coastal Research	SI	75	248-252	Coconut Creek, Florida	2016

Shoreline Change Rate of the Barrier Islands in Nakdong River Estuary over the Southern Part of Korea

Sang-Hun Jeong [†‡*], Boo-Keun Khim[†], Yeong-Heon Jo[†], Beack-Oon Kim[††], Sang-Ryong Lee[†] and Kwang-Soon Park[‡]

[†] Departament of Oceanography, Division of Earth Envirinmental System, Pusan National University, Busan, Korea

[‡] Operational Oceanography Research Center, Korea Institute of Ocean Science and Technology, Ansan, Korea

[††] Saemangeum Environmental Research Center, Kunsan National University, Gunsan, Korea

www.cerf-jcr.org

www.JCRonline.org

ABSTRACT

Jeong, S.H.; Khim, B.K..; Jo, Y.H., Kim, B.O., Lee, S.H. and Park, K.S., 2016. Shoreline change rate of the barrier islands in Nakdong River Estuary over the southern part of Korea. *In:* Vila-Concejo, A.; Bruce, E.; Kennedy, D.M., and McCarroll, R.J. (eds.), *Proceedings of the 14th International Coastal Symposium* (Sydney, Australia). *Journal of Coastal Research*, Special Issue, No. 75, pp. 248-252. Coconut Creek (Florida), ISSN 0749-0208.

Shoreline data of the barrier islands in the Nakdong River Estuary in Korea for the last three decades were assembled using six sets of aerial photographs and seven sets of satellite images. Canny Algorithm was applied to untreated data in order to obtain a wet-dry boundary as a proxy shoreline. Digital Shoreline Analysis System (DSAS 4.0) was used to estimate the rate of shoreline changes in terms of three statistical variables; End Point Rate (EPR), Linear Regression Rate (LRR) and Least Median of Squares (LMS). Based on Digital Shoreline Analysis, shoreline changes in the barrier islands in the Nakdong River Estuary have varied both temporally and spatially, although the exact reason for the shoreline changes requires more investigation.

ADDITIONAL INDEX WORDS: *shoreline change, barrier islands, Nakdong River estuary.*

INTRODUCTION

A barrier island formed in front of an estuary is a depositional landform affected by tide, wave, and stream action. It serves as a natural barrier that absorbs wave energy from the open sea, reducing damage during extreme events, including storms and tsunamis. The rear area serves as a transitional zone between shore and marine environments, forming a field of material exchanges and providing habitat for a variety of fauna and flora (Carter, 1988). Barrier islands receive attention due to their role in protecting areas of human activity. Thus there are concerns with rising sea levels, climate warming, and increasing natural disasters in coastal areas such as flooding, storm, and tsunamis.

The Nakdong River Estuary consists of barrier islands (Jinu-do, Shinja-do, Doyodeung) and the tidelands behind them, which forms the South Korea's representative delta topography (Figure 1). The human activity range in this area is getting enlargement by the rich fisheries resources of Nakdong River Estuary and the water resources of stream and the coast space usage was steadily increasing. For this reason, and the coastal topography like estuary weir construction, industrial park composition, harbor construction is showing the constant artificial changes.

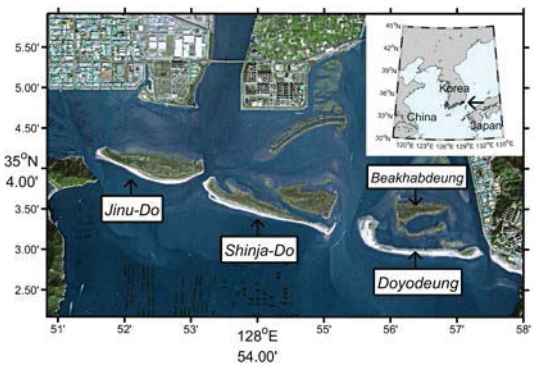

Figure 1. Nakdong River Estuary shot by SPOT-5 Satellite in 2009. It is the southern end of the estuary, where there are three barrier islands (Jinu-do, Shinja-do and Doyodeung).

In order to research the change of the coastal topography like beach and barrier island, to establish the long term shoreline change data is the most effective way (Baily and Nowell, 1996; Moore, 2000; Morton *et al.*, 2004). The shoreline change is influenced by the several factors such as climate, sedimentation environment, and sea level *etc.*, thus, to research the long-term shoreline change is the important base data to predict the direction of the landscape variation. For examining the landscape variation of the coast, including shoreline, a wide

DOI: 10.2112/SI75-050.1 received 15 October 2015; accepted in revision 15 January 2016.
*Corresponding author: jsh5481@kiost.ac.kr

variety of measurement techniques and remote sensing methods are used.

In this study, the shoreline of Jinu-do, Shinja-do and Doyodeung in Nakdong River Estuary was extracted by using the aerial photographs which was provided by the National Geographic Information Institute and SPOT-5 satellite imagery. And the long term migration tendency of the Nakdong River Estuary barrier islands was examined by quantification of the shoreline change rate trend by the shoreline change rate and time with DSAS 4.0 (Digital Shoreline Analysis System 4.0, Thieler *et al.,* 2009) and statistical techniques.

METHODS

In this study, 1:20,000 aerial photographs which was photographed six times (‘75, ‘82, ‘87, ‘93, ‘96, ‘01) about the Nakdong River Estuary shore coast and barrier island by the National Geographic Information Institute from 1975 until 2001 were used. The aerial photographs of scale 1:20,000 can express the ground area about 4 × 4 km range. The aerial photographs which were photographed with multiple paths to produce the shoreline of Jinu-do, Shinja-do, Doyodeung as the object of study is needed to be cemented as one image. In this study we used mosaic aerial photographs of Nakdong River Estuary produced by Kim *et al.*, (2005) (Table 1).

Table 1. *Image information used in the study. Tide level information is based on Gadeokdo Tide Level Observatory. According to the 2008 survey, the mean sea level of Gadeokdo tide level observatory is 95.3 cm from the datum level and approximately highest high water (App. HHW) is 178.3 cm.*

Image type	Date	Elevation(m)
Aerial photo	1975	?
	05/1982	?
	10/1987	?
	08/1993	?
	12:54, 27/11/1996	0.99
	10:14, 02/12/2001	1.79
Satellite (SPOT-5)	11:23, 27/12/2002	1.01
	10:38, 03/10/2003	1.18
	11:30, 12/11/2004	0.97
	11:30, 20/11/2006	0.96
	11:09, 19/12/2008	1.16
	11:25, 02/12/2009	1.17

The SPOT-5 satellite was developed to gain the ground image by using the high-resolution optical sensors, and new shoot sensor provides the single band image with the maximum 5 m/pixel resolution. But in the process of providing the real image to the user, two single band images were cemented and geometrically real resolution changes into 2.5 m/pixel image and finally, the color image with 2.5 m/pixel resolution was provided by using 10 m/pixel color band image. In this study, total six satellite images (‘02, ‘03, ‘04, ‘06, ‘08, ‘09) were used from 2002 to 2009.

The recognition and extracted method of shoreline can be the biggest error occurrences factor for the study on long term shoreline change (Crowell *et al.*, 1991). In the case of Nakdong River Estuary barrier island, the slope of intertidal zone is smooth and the natural vegetation was developed, and the boundary is ambiguous so it may cause the error of the waterline cognition. The front surface of intertidal zone of barrier island is proper to represent the shoreline change by contacting the tidal current and wave directly from the external part which is relatively clear for division of sand beach and body of water. Therefore, in this study, the object of study was limited with the front surface of intertidal zone of barrier island.

Generally, it is known that the shoreline which is most easy to be recognized among the aerial photography is the high water line (Crowell *et al.*, 1991). But the beach of the Nakdong River Estuary barrier island has lower altitude difference, so the division with the high water line is not obvious, so the waterline was used. The waterline may react sensitively about the slope of tidal range and beach, so the tide level information for the photo shoot is needed. The tide level data of image obtains one time interval of tide data of Gadeok-do tide level observatory which is provided by the Korea Hydrographic and Oceanographic Administration based on the photography time by interpolating. The tide level information of each image is presented on Table 1.

The waterline of Nakdong River Estuary barrier island can be recognized as the boundary line of the sand beach and body of water (Jeong *et al.,* 2013). In this case, the boundary line among the image processing techniques can be used usefully as the edge detection. The Canny Edge Detector is used widely as the most precisely defined operator among the various edge detecting means (Canny 1986). As the method to apply the canny algorithm in the aerial photographs and satellite imagery, the MATLAB was used. The boundary line detecting means which were used in this study divide the body of water and landward pretty clearly, and the error range is under 1 pixel (Jeong, 2013). The detected shoreline was shown on Figure 2.

To calculate the shoreline change rate, the DSAS 4.0 (Digital Shoreline Analysis System 4.0, Thieler *et al.*, 2009) which was provided by the USGS (U.S. Geological Survey) was used. DSAS is the tool which is driven from inside of ArcGIS program of ESRI, and it is the program to calculate the statistics data about the change rate from the multiple shorelines. The baseline and transect which were set in each barrier island which was used in this study is presented in Figure 2.

In this study, three statistical values (EPR, LRR, and LMS) which were provided by the DSAS program were calculated. EPR (End Point Rate) divides the separation distance (NSM) with the oldest shoreline and the most recent shoreline by the advanced time (Dolan *et al.*, 1991). LRR (Linear Regression Rate) calculates the drift curve by using the least-squares method about the distance between the baseline and shorelines by the time of transects, and it regards the drift curve incline as the shoreline change rate. The positive incline means the baseline direction, and being advanced as the open sea direction. LMS (Least Median of Squares) is another method to calculate the drift curve about the distance between the baseline and shorelines by the time like LRR (Rousseeuw, 1984).

During the observation period in this study, the artificial topography changes such as the construction of the estuary weir and the massive landfill for the industrial complex construction, and harbor construction *etc.* are conducted in the Nakdong River Estuary. Supposing that these events had effect on the sedimentation environment of estuary, the shoreline change rate

of barrier island by time is expected to be gradually accelerated or decelerated or to be maintained constantly.

Calculating the scale of the landscape variation by time can be the basic data to investigate the relationship with the landscape variation of the environmental change and estuary. For examining the change aspect, two shorelines were selected in chronological order ('75-'82, '82-'87, '87-'93, ...) and mean EPR about the whole transects was calculated. So the incline of mean EPR about each time interval was drawn out by using the linear regression analysis about the mean EPR which was calculated by each period. The calculated incline of straight line can be regarded as the change speed of mean EPR. It can be judged that as the size of incline is close to 0, the shoreline change rate is regular.

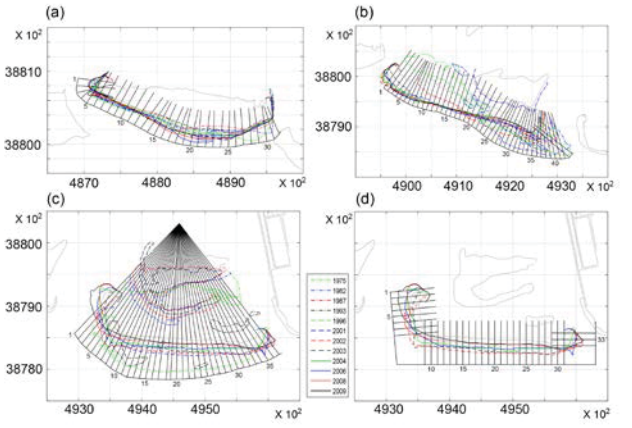

Figure 2. Baseline and transects of each of the barrier islands, Jinu-do (a), Shinja-do (b) and Doyodeung (c, d), used in DSAS 4.0 and shortline extracted with a Canny Edge Detector from the image of Table 1. The unit of axis is UTM zone 52N. Grey dotted line was extracted in a digital chart in 2004.

RESULTS

The shoreline change rate (EPR, LRR, LMS) of Jinu-do is shown in Figure 3a. EPR and LRR mean the similar shape in the whole transects and it show -5.1-4.3 m/yr range. The advanced, retreating aspects of shoreline are shown in Jinu-do differently by each area, and it is divided with four sectors by the shape of EPR and LRR. In the western tail (transects no. 1-4), the shoreline is advanced as the baseline direction, and the western part (transects no. 5-11) is reversed, the south part (transects no. 12-25) is advanced, and the eastern part (transects no. 26-32) is reversed. LMS is calculated bigger than EPR and LRR in the south part and eastern part of Jinu-do (Figure 3a). The difference is the result that the data of the time for the shoreline was retreated in the process of finding the straight line for the median value of deviations as the minimum is not reflected. In fact, in the case of south and east of Jinu-do, it was retreated until 1993 but it was advanced since 1996, so the shoreline data except 1996 was analyzed. EPR, LRR, LMS about the shoreline since 1996 are shown in Table 2. The data in 2001 which shows significant difference of tide level was excluded. The advanced speed of South of Jinu-do is shown significantly more than two times, and the east is advanced since 1996.

The shoreline change rate trend of Jinu-do by the time is shown Table 2. Jinu-do shows the aspect of advanced shoreline generally since 1987. The shoreline change rate of Jinu-do seems to be faster gradually as annually 0.1-0.6 m/yr^2. The western tail of Jinu-do shows that the advanced speed of shoreline is getting gradually faster, and this trend became more remarkable since 1996. The west shoreline was retreated but the retreating speed decreased gradually since 1996. The south shows the advanced shoreline but the advanced speed decreased for annually -1.5 m/yr. The shoreline of east was retreated, but it is advanced gradually, and the analysis on incline shows 0.5 m/yr^2 in the whole period since 1996.

The shoreline of Shinja-do seems rotating in the counterclockwise direction (Figure 3b). The west of Shinja-do shows that the shoreline is advanced as the baseline direction, open sea direction, and the average of EPR, LRR, LMS in this section are shown as 12.5, 12.0, 2.4 m/yr. On the other hand, the eastern area of Shinja-do retreats the shoreline, and the average of EPR, LRR, LMS in this section are shown as -9.6, -11.9, -13.3 m/yr. Especially, in the transects no. 36-44 section as the east tail of Shinja-do, it retreats in the fast speed, the average of EPR, LRR, LMS in this section are shown as -17.2, -19.1, -18.0 m/yr. The average value of LRR of the east and west of Shinja-do is shown on Table. 2.

LMS of Shinja-do is relatively smaller than the EPR and LRR of the west (Figure 3b). This section except the advanced period of the past shoreline is relatively congested, so the section with big change width of LMS is judged as height anomaly, so it seems to be calculated as lower value than other indices. Shinja-do was shown as two shapes of barrier islands which center of image was cut in 1975, but the image in 1987 was shown as one Barrier Island and the image in 1996 shows similar shape with the present. The reason that LMS is shown as relatively smaller value in the west is the difference of shoreline change rate of the barrier island by the process of forming Shinja-do, so the shoreline change rate was re-calculated by the data since 1996. The EPR, LRR, LMS about Shinja-do coastline since 1996 which became similar shape with the present are shown on Table. 2. The data in 2001 which shows big tide level difference like Jinu-do was excluded. The west of Shinja-do seems to be advanced, but judging that the change rate and correlation coefficient are lower and the shoreline is congested mostly since 1996, but the east of Shinja-do is steadily retreating.

The mean EPR of Shinja-do shows the negative value from the east and west (Table. 2). It seems that the advanced speed of Shinja-do west is getting slower for annually -0.4 m/yr^2, the retreating speed of east is getting faster for -0.7 m/yr^2. The decrease moving speed of west is coincident with the result of LMS, and the current state seems to be maintained since advanced in the past. On the other hand, the east seems to be steadily retreating since 2002.

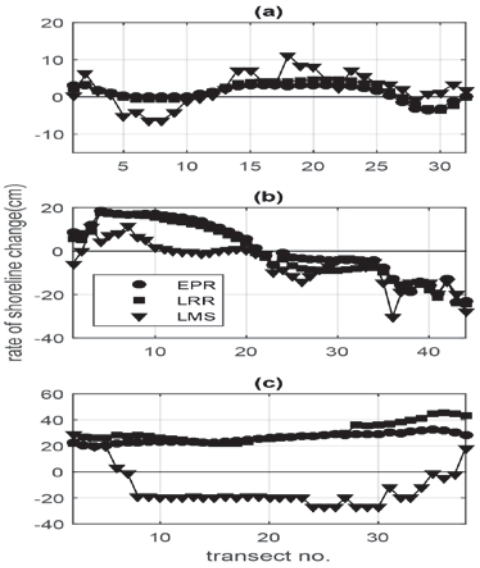

Figure 3. End Point Rate (EPR), Linear Regression Rate (LRR) and Least Median of Squares (LMS) calculated from each transect of Jinu-do, Shinja-do and Doyodeung. The X axis is same with the number of transects which was set in Figure 2.

ERP, LRR of Doyodeung shows the positive value in whole section (Figure 3c). It means the advancing in pre-section from the Baekhapdeung Delta shoreline in 1975 as the first observation view until Doyodeung in 2009. The average value of LRR of pre-transects is shown on Table 2. EPR and LRR show the positive value in the whole section but LMS shows the negative value, in other words, the shoreline retreating as the shore direction in most of the section, and the result is showing that the data of the advanced period of shoreline in the process for calculating LMS is not reflected. It is judged that this result is caused by selecting the Baekhapdeung as the shoreline before the past Doyodeung in the process forming the shoreline of Doyodeung.

In 1975, the first time of observation of aerial photographs used in this study, there was no Doyodeung, and Baekhapdeung Delta exists as the southernmost tip of the Nakdong River Estuary as a the barrier island. But the development of sand bank is conducted in the Southern end of the Baekhapdeung, and it became the shape of the island in the aerial photographs which were photographed in 1996, and the shape like the current Doyodeung is observed from the aerial photographs in 2001. Due to this, EPR, LRR shows the positive value during the whole observation period, and the shoreline was advanced as steadily open sea direction. By this characteristic, pre and post shoreline of Doyodeung should be examined since 2001, and the shape of the baseline and transects should be considered differently. Figure 2d shows the baseline and transects according to the shape of the current Doyodeung, and Table 2 shows the shoreline change rate from 2002-2009 except the data in 2001 with a big tide level difference.

The mean EPR of Doyodeung were examined by dividing with before and after 2001 to distinguish the pre and post shoreline (Baekhapdeung) (Table 2). The shoreline was steadily advanced from 1975-2001, and the advanced speed is getting faster gradually and the advanced speed is getting faster gradually for annually 1.2 m/yr^2. The general shoreline showed retreating from 2002-2009, but the retreating speed is getting slower gradually for annually 4.2 m/yr^2.

Table 2. *Shoreline change rate and trend of Jinu-do, Shinja-do and Doyodeung by area. A positive value means that the shoreline advances to the open sea while a negative value means the retreat of the shoreline.*

		1975~2009		1996~2009	
		mean LRR (m/year)	gradient (m/year^2)	mean LRR (m/year)	gradient (m/year^2)
Jinu-do	West tail	2.2	0.3	4.2	2.9
	West	-0.9	0.1	-1.9	1.4
	South	3.0	0.2	6.7	-1.5
	East	-2.5	0.6	2.1	0.5
Shinja-do	West	12.0	-0.4	0.6	-0.5
	East	-11.9	-0.7	-16.0	0.0
		1975~2009		2002~2009	
		mean LRR (m/year)	gradient (m/year^2)	mean LRR (m/year)	gradient (m/year^2)
Doyo deung	West	31.2	1.2	14.3	4.2
	South			-18.2	
	east			13.5	

DISCUSSION

The size and progress direction of shoreline change rate can be used as the base data for preparing the possible social issues in the estuary area. The western tail of Jinu-do is expending to the west gradually, and it will decrease the waterway width between the Nulchado Island on the left of the Jinu-do and Jinu-do, and it may have effect on the ship traffic which passes this area through. The western tail of Shinja-do doesn't seem to be expended, but the east of Jinu-do is gradually advanced and the width of the waterway decreases, and Doyodeung is expended to the east and west, so it is expected that all narrow channel widths of estuary will be narrower. It can be connected to many social problems such as the suspended load, dredged soil handling problems due to the dredge, and it means that the dredge cannot be the fundamental countermeasures for securing the passage of the vessel in the long term.

The study on the shoreline change rate using the remote sensing has merit to obtain the broad-based data easy but the accuracy of shoreline may be decrease compared to the direct observation under the characteristic of data. The accuracy of aerial photographs and satellite imagery which was used in this study is 3 m/pixel and 2.5 m/pixel, and it can be converted with shoreline change rate as 3 m/yr and 2.5 m/yr. This values are calculated when the time interval is one year like data in 2008 and 2009, and the error of shoreline change rate can be decreased for big time interval like data in 1975 and 1982. The average time interval of materials which were used in this study is about 3 years and it can be converted with the error of the shoreline change rate by the pixel accuracy as about 1 m/yr. The

error of tide level can be calculated by the same method. The moving distance of shoreline considering the shoreline slope of Jinu-do, Shinja-do, Doyodeung is 0.8 m, 0.2 m, 0.5 m per the tide level 1 cm, and the tide level difference between images is about average 10 cm, so it is judged that the error range of approximate shoreline change rate is 1-2.5 m/yr.

The shoreline change rate which was analyzed by the aerial photographs and satellite imagery used in this study shows that the shoreline change rate of the Jinu-do some area is ambiguous due to the error of the data. But if the data with less accuracy than the data which was used in this study was used, the areas with the ambiguous shoreline change rate would be increased much. For example, by the annual analysis on the images with 15 m/pixel resolution of Landsat satellite, the error of the shoreline change rate by the pixel error becomes 15 m/yr, and if the error due to the tide level was included it, and the shoreline change rate of the whole Jinu-do and some of Shinja-do would be included in the error range. Considering the distribution of the shoreline change rate which was calculated in this study, the error of the shoreline change rate due to the accuracy of data should be less than 1 m/yr so that the shoreline change rate of the whole section can be reliable.

CONCLUSIONS

In this study, the shoreline of Nakdong River Estuary barrier islands was extracted by using the total 12 copies of aerial photos (3 m/pixel) from 1975 to 2009 and Canny Edge Detector of the SPOT-5 satellite imagery (2.5 m/pixel), and the shoreline change rate was calculated by using DSAS 4.0. The long term shoreline change of barrier islands was examined by statistical analysis on the trend of the shoreline change rate.

The shoreline change rate can be shown variously by the areas of the barrier island. In the case of Jinu-do, the western tail part, the west, the south, and the east show the migration tendency of 2.2 m/yr., -0.9 m/yr., 3.0 m/yr., -2.5 m/yr., and the moving speed is increasing for 0.3 m/yr.^{2}, 0.1 m/yr.^{2}, 0.2 m/yr.^{2}, 0.6 m/yr.^{2} since 1975.

The west of Shinja-do is advanced with 12.0 m/yr., the east is reversed with -11.9 m/yr., and it shows the rotation aspect of counter-clockwise direction. About the shoreline change rate trend of the west (-0.4 m/yr.^{2}) and the east (-0.7 m/yr.^{2}), and it means that the advanced speed of the west decreased, and the reversed speed of the east increased. Since 1996 when the Shinja-do was formed as the similar shape with the present, the west is congested with 0.6 m/yr., and the east is retreating much faster than the past with -16.0 m/yr.

Doyodeung is advanced with 31.6 m/yr. since 1975, but the south is expending with -18.2 m/yr. since 2002, the east and the west are expending with 13.5 m/yr., 14.3 m/yr. The shoreline change rate trend increases with 1.2 m/yr.^{2} annually from 1975-2001, but it is increasing with annually 4.2 m/yr.^{2} from 2002-2009.

ACKNOWLEDGMENTS

This research was a part of the project titled 'Development of Korea Operational Oceanographic System (KOOS), Phase 2', funded by the Ministry of Oceans and Fisheries, Korea.

LITERATURE CITED

Bailey, B., and Nowell, D., 1996. Techniques for monitoring coastal change: A review and case study. *Ocean and Coastal Management*, 32(2), 85-95.

Canny, J., 1986. A Computational approach to edge detection. *IEEE Transactions on Pattern Analysis and Machine Intelligence*. 8(6), 679-698.

Carter, R.W.G., 1988. *Coastal environments*. London: Academic Press.

Corwell, M.; Leatherman, S.P., and Buckley, M.K., 1991. Historical shoreline change: Error analysis and mapping accuracy. *Journal Coastal Research*, 7(3), 839-852.

Dolan, R.; Fenster, M.S., and Holme, S.J., 1991. Temporal analysis of shoreline recession and accretion. *Journal of Coastal Research*. 7(3), 723-744.

Jeong, S.H.; Khim, B.K.; Kim, B.O. and Lee, S.R., 2013, Shoreline-change Rates of the Barrier Islands in Nakdong River Estuary Using Aerial Photography and SPOT-5 Image, *Ocean and Polar Research*, 35(1), 1-14.

Jeong, S.H., 2013. Study on the rate of shoreline changes for barrier islands in Nakdong River Estuary using GIS and remote sensing. Busan, Korea: Pusan National University, Master's thesis, 22p.

Kim, B.O.; Khim, B.K., and Lee, S.R., 2005. Development of mosaic aerial photographs for shoreline change study in Nakdong Estuary. *Ocean and Polar Research*, 27(4), 497-507.

Kim, B.O.; Khim, B.K., and Lee, S.R., 2007. Rate of shoreline changes for barrier islands in Nakdong Estuary. *Korean Society of Coastal and Ocean Engineers*, 19(4), 361-374.

Moore, L.J., 2000. Shoreline mapping techniques. *Journal of Coastal Research*. 16(1), 111-124.

Morton, R.A.; Miller, T.L., and Moore, L.J. 2004. *National assessment of shoreline change: Part 1: Historical shoreline changes and associated coastal land loss along the U.S. Gulf of Mexico. U.S, Geological Survey, Open File Report 2004-1043*, 44p.

Rousseeuw, P.J., 1984. Least median of squares regression. *Journal of American Statistical Association*. 79(388), 871-890.

Thieler, E.R.; Himmelstoss, E.A.; Zichichi, J.L., and Ergul, A., 2009. *Digital Shoreline Analysis System (DSAS) version 4.0-An ArcGIS extension for calculating shoreline change. U.S. Geological Survey, Open-File Report 2008-1278*

Journal of Coastal Research	SI	75	253-257	Coconut Creek, Florida	2016

Stability of artificial beaches in Port Phillip Bay, Victoria, Australia.

Meagan K. Lowe[†‡*] and David M. Kennedy[†]

[†]School of Geography
University of Melbourne
Melbourne, Australia

[‡]Coastal Research Ltd
Wellington, New Zealand

www.cerf-jcr.org

www.JCRonline.org

ABSTRACT

Lowe, M.K. and Kennedy, D.M., 2016. Stability of artificial beaches in Port Phillip Bay, Victoria, Australia. *In:* Vila-Concejo, A.; Bruce, E.; Kennedy, D.M., and McCarroll, R.J. (eds.), *Proceedings of the 14th International Coastal Symposium* (Sydney, Australia). *Journal of Coastal Research*, Special Issue, No. 75, pp. 253-257. Coconut Creek (Florida), ISSN 0749-0208.

This study investigates the drivers of beach morphodynamics on the highly modified fetch-limited beaches of the urbanised north-eastern coast of Port Phillip Bay in south-eastern Australia. Repetitive beach profiling, sediment characterization, and aerial photo analysis were conducted to quantify morphodynamic change across six distinct beach systems on a seasonal to annual-decadal scale. The observed morphologies contained features similar to those found on open-ocean wave-dominated and tide-dominated beaches, and included reflective unbarred beaches and intermediate beaches with low-tide terraces or transverse bar-rip systems. Sediment typically ranged from medium to coarse or very coarse in size. The consistency of wave energy across the study sites suggests that sediment size is the primary determinant of beach morphodynamic state, and the relatively low energy of Port Phillip Bay suggests that only storm conditions are energetic enough to mobilise sediment and alter beach morphology. On a seasonal scale, alongshore sediment transport is a major driver of beach change, and groynes and other coastal modifications have considerable influence on planform beach morphology. Over the medium term it appears that these beaches are eroding towards a landward position of equilibrium. With current projections of sea level rise it is expected that rates of beach erosion and sediment loss will accelerate over the coming decades, leading to an increased necessity for beach renourishment or other management interventions if wide beach profiles are to be maintained.

ADDITIONAL INDEX WORDS: *Estuarine beaches, morphodynamics, beach renourishment.*

INTRODUCTION

Beaches that form on fetch-limited estuarine coastlines are markedly different to those found on the open coast. They tend to be smaller and narrower, often sediment starved, and strongly influenced by littoral drift processes (Nordstrom, 1992, Jackson *et al*., 2002, Kennedy, 2002). Morphodynamics on fetch-limited estuarine beaches differ from open-ocean systems as they lack consistent energy input of long period swell waves (Masselink and Pattiaratchi, 2001). Their morphodynamics are instead strongly influenced by spatial and temporal differences in fetch and therefore wave energy, irregular bathymetry, sediment source, and topographic constraints.

Increasing population density and development on many estuarine coastlines have resulted in a high degree of coastal modification and disruption to natural processes. However, despite the importance of estuarine beaches for coastal protection, industry, and recreation, their morphodynamics remain poorly understood when compared to open-ocean systems. As a result, many millions of dollars are spent each year managing urban estuarine beaches, often with little regard to their long-term evolution.

While it is widely accepted that the dominant open-ocean morphodynamic models, such as those of Wright and Short (1984) and Masselink and Short (1993), have limited applicability to estuarine beaches (Jackson *et al*., 2002, Nordstrom and Jackson, 2012), applying the results of previous estuarine studies across multiple estuarine systems is also difficult. The substantial differences in boundary conditions, both between and within different estuaries, do not easily support extrapolation to different environments. In addition, the relative frequency of coastal management works, when compared to long-term coastal evolution, can make it difficult to differentiate natural trends from the observed variation of estuarine beaches.

This study investigates the beach morphodynamics of the north-eastern coastline of Port Phillip Bay, Victoria, Australia, in the context of both its unique estuarine boundary conditions and substantial anthropogenic modification; the city of Melbourne is located along this coastline. This study seeks to identify the dominant processes driving short to medium term geomorphic change through repetitive beach profiles, sediment characterisation, and aerial photo analysis. It then compares these estuarine processes with current beach morphodynamic models, and proposes a conceptual model for considering the effects of variable energy inputs into estuarine systems.

Background

Port Phillip Bay is situated in the south-east of Australia and covers an area of approximately 1,950 km2 (Figure 1). The Bay has a total coastline length of 260 km, a maximum depth of 24 m, and is connected to the open ocean through a narrow channel to the south (Bird, 1993). All incoming ocean swell is refracted

DOI: 10.2112/SI75-51.1 received 15 October 2015; accepted in revision 15 January 2016.
*Corresponding author: meaganklowe@gmail.com

through the channel and dissipates over shallow sand banks and mud islands in the far south, leaving the majority of beaches exposed exclusively to wind waves. Port Phillip Bay is considered a strong wind bay and has a distinctly seasonal wind climate, with predominant west and southwesterlies during summer, and north and northwesterlies during winter (Goodfellow and Stephenson, 2005). Tidal range is small and reduces from 1.1 m in the south to 0.6 m in the north.

Port Phillip Bay has a long history of coastal modification, including the construction of seawalls and groynes. A substantial number of beaches have also been renourished since the 1960s, though the success of these works has varied (Black and Rosenberg, 1992).

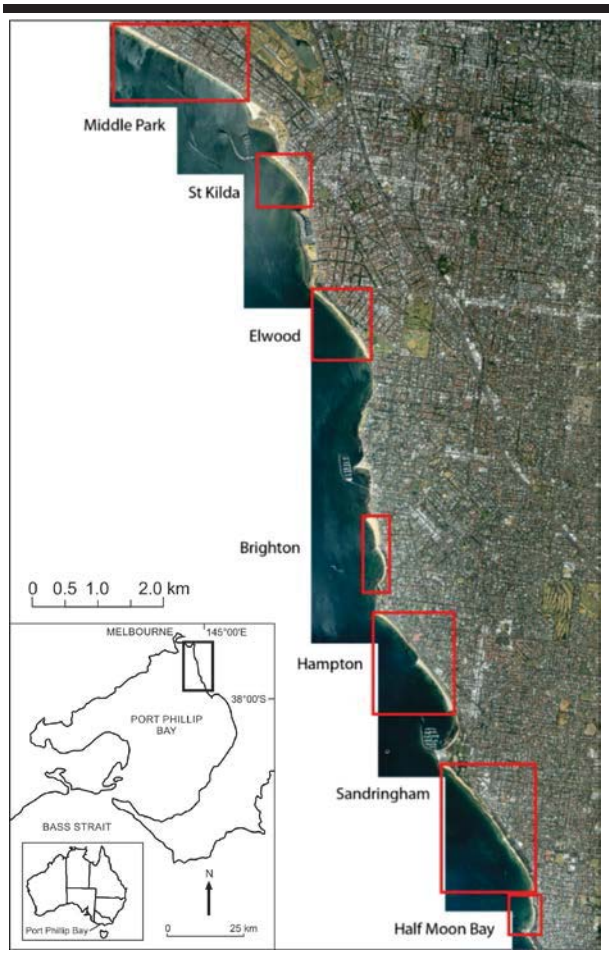

Figure 1. Location of the study area within Port Phillip Bay, Victoria, Australia. The red boxes show the individual beach systems studied.

For this study, a subset of six Port Phillip Bay beaches were chosen for analysis: Middle Park, St Kilda, Elwood, Brighton, Hampton, and Sandringham, including Half Moon Bay (Figure 1). All are located in the northeast of Port Phillip Bay and provide contrasting geological and anthropogenic settings, while still being exposed to similar wind and wave climates. Beach renourishments conducted within the study area between 1997 and 2012 are outlined in Table 1.

Table 1. *Beach renourishments on the north-eastern coastline of Port Phillip Bay between 1997 and 2012 (Department of Sustainability and Environment, 2012).*

Location	Year	Volume (m^3)	Completed beach width	Sediment source	Grain size (D50)	Length
Hampton, southern end	1997	100,000	50 m	Dredge, offshore	0.9 mm	1,000 m
Sandringham, between groynes	2009	40,000	40 m	Dredge, offshore	0.9 mm	330 m
Middle Park, eastern end	2009	80,000	60 m	Dredge, offshore	0.5 mm	700 m
Elwood	2011	36,000	35 m	Quarry sand	1.1 mm	800 m

METHODS

All study sites were surveyed repeatedly between March and August 2012. An initial set of 51 beach transects was recorded, after which 23 transects were surveyed an additional one to three times. All surveys were conducted within two hours of low tide, from a fixed point at the back of the beach to approximately 0.8 m below mean sea level (MSL). Sediment samples from all sites were collected and analysed using a Laser Particle Sizer. Historic shorelines mapped from five sets of aerial photographs taken between 2001 and 2011 were analysed using the Digital Shoreline Analysis System (DSAS version 4.3) extension for ArcMap (Thieler *et al*., 2009).

RESULTS

Considerable morphological and sedimentological variation was observed across the study site and during the study period. Results from Middle Park Beach and Sandringham Beach are presented here in most detail as they present contrasting geological settings and variation in the types and degrees of coastal modification.

Middle Park Beach is backed by seawall and high-density development. Vegetated dunes are present at its western end. At the time of surveying, beach width, as measured from the seawall to mean sea level (MSL), decreased from up to 71.9 m in the west to 23.6 m in the east, while the subtidal gradient was gentle (1.76 ± 0.81º). The subaqueous morphology was characterised by a series of shore-attached transverse bars which shifted throughout the study period (Figure 2a).

Sandringham Beach, in contrast, is backed by cliffs and vegetated bluffs, and the centre of the beach is dominated by two large rock groynes. Sandringham Beach varied considerably in width both across the site (43.5 m at the northern end to 9.5 m in the south) and across the survey period (the maximum change observed was from 12.2 m in March to 22.8 m in August). The most variation was observed either side of the groynes; profiles north of the groynes accreted during the study period (Figure 2b), while those to the south eroded. Despite these variations, beachface width and slope remained relatively constant. Subaqueous sand bars were absent from most profiles, and were only observed between the two groynes and at Half Moon Bay.

Of the remaining study sites, Elwood and Hampton Beaches were geomorphically similar to Sandringham, and demonstrated considerable seasonal variation, particularly around groynes

where beach width varied by up to 4.1 m. In contrast, a distinct low tide terrace feature was observed at St Kilda Beach, varying in width. Brighton Beach remained relatively stable throughout the study period.

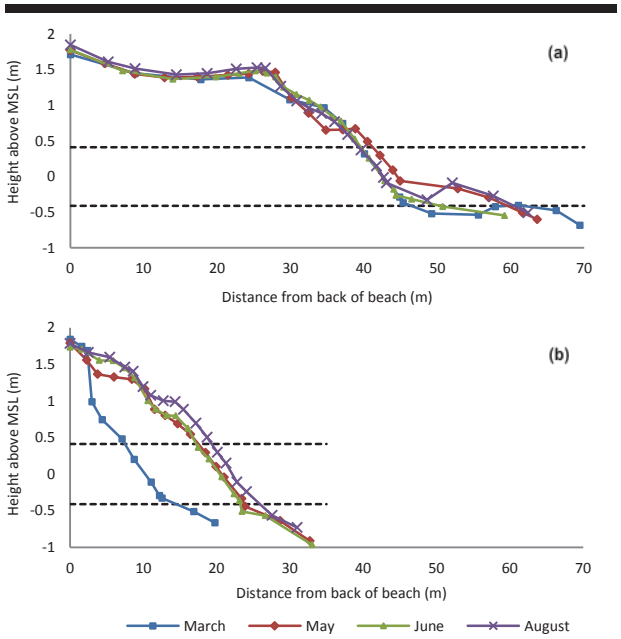

Figure 2. Beach profile variation from March 2012 to August 2012 at (a) Middle Park and (b) Sandringham. Dotted lines indicate the mean high water spring (MHWS) and mean low water spring (MLWS) tide levels.

The beaches within the study area also exhibited cross-shore and alongshore variability in sediment character. In general, sediment was found to be finest at the bar, coarsest at the lower swash limit, then progressively finer towards the back of the beach. There was a clear distinction between the coarse to very coarse sand beaches, including Elwood, Hampton, Brighton, and Sandringham Beach, and the medium sand beaches (Middle Park, St Kilda, and Half Moon Bay). Mean beachface sediment size of the former ranged between 985 and 1,198 µm, while the latter ranged between 427 and 639 µm. Statistical analysis found that sediment at Sandringham Beach was significantly coarser than at Middle Park Beach in all sample locations except the bar (Figure 3).

Analysis of aerial photography found that there has been considerable variation in beach width and shoreline orientation since 2001. The influence of beach renourishment (Figure 4a) and groyne construction (Figure 4b) were evident. Furthermore, analysis of the rate of change statistics found the majority of beaches in the study area are eroding over the medium term (Table 2). The sections of beach that have not been recently renourished eroded at an average rate of 0.3 m per year from 2001 to 2011, a statistically significant trend (t_{calc} = 6.03, $t_{0.05(2)222}$ = 1.97). Only the northern section of Brighton Beach experienced net accretion since 2001 without the addition of sediment. Renourished beaches have seen large volumes of sediment reworked offshore, though the rate at which this occurred has varied: in the two years following renourishments in 2009, the average rate of erosion in affected areas was 2.0 m per year at Sandringham and 3.8 m per year at Middle Park.

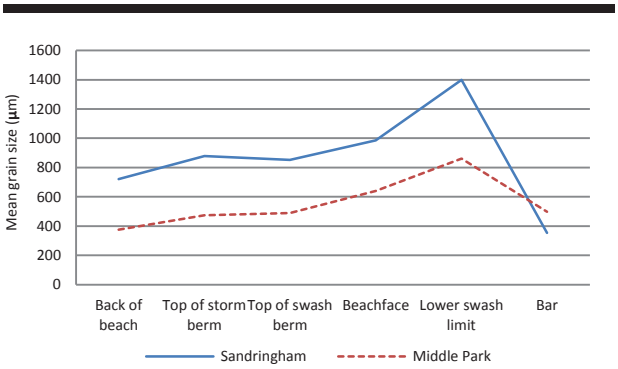

Figure 3. Variation in mean sediment size, based on the average of all samples analysed at Sandringham (n = 8) and Middle Park (n = 6).

Figure 4. (a) Shoreline change at Middle Park between 2001 and 2011, showing shoreline accretion due to renourishment in 2009 (green line), followed by subsequent erosion (pink line). (b) Shoreline orientation at Sandringham as influenced by the construction of the northern groyne in 2006; the blue and red lines show the pre-groyne shoreline orientation. This area was also renourished in 2009.

Table 2. *Average magnitude of shoreline changes across the study sites.*

Site	Number of aerial transects	2001 width (m)	2011 width (m)	Δ 2001-2004 (m)	Δ 2004-2007 (m)	Δ 2007-2009 (m)	Δ 2009-2011 (m)	Net shoreline movement from 2001 to 2011 (m)	% change between 2001 and 2011 shorelines
Middle Park	46	43.1	42.0	-4.5	+1.8	+3.7	-2.1	-1.1	3%
St Kilda	18	31.1	29.2	-2.5	-1.8	+2.3	0.0	-1.9	-6%
Elwood	29	24.5	30.9	-5.3	-0.8	+2.4	+10.2	+6.4	26%
Brighton	29	50.5	51.6	+0.8	-0.2	+0.7	-0.3	+1.1	2%
Hampton	40	43.1	34.4	-6.9	+0.1	-0.8	-1.1	-8.7	-20%
Sandringham	57	23.7	19.4	-7.7	+1.3	+5.0	-2.9	-4.3	-18%
Half Moon Bay	9	18.7	14.5	-6.5	+2.4	+1.9	-1.9	-4.2	-22%

DISCUSSION

Based on the observed spatial and temporal variation in beach morphology and sedimentology, it is evident that the beaches of the north-eastern coastline of Port Phillip Bay are both highly dynamic and influenced by varying boundary conditions, including sediment, topography, and the degree of anthropogenic influence.

A number of observed features, in particular subaqueous bar configurations, are similar to those found on open-ocean beaches; however, Port Phillip Bay is clearly not an open-ocean system. Temporal variation in wave energy inputs, and as such relative tidal range, on estuarine beaches makes it difficult to classify these systems under traditional process-driven models that assume relatively consistent energy input.

Fetch-limited environments rely on local winds to generate waves. When there is little or no wave energy input into the system, beaches remain inactive. Changes to beach morphology occur when there is sufficient input of wave energy to surpass a threshold of sediment movement, overcoming the inertia of the grains and bringing them into motion (Komar, 1976). This threshold is dependent on grain size, density, and shape.

Once sufficient energy is available to mobilise sediment, it is apparent that the process dominance of an estuarine beach can change rapidly. Where wave heights are low compared to tidal range, tidal processes predominate, and macro to mesotidal-type morphologies are expected to develop. Subsequently, when wave energy increases such that waves overtake tides as the predominant morphodynamic process, microtidal-type morphologies may be observed.

Figure 5 proposes a conceptual model of the thresholds at which the varying morphodynamic processes come into dominance on estuarine beaches. Unlike the threshold for sediment movement, the threshold between tide-dominated and wave-dominated processes is assumed to be independent of sediment size, and is represented by a horizontal line. As wave energy increases further, thresholds between various microtidal morphologies may be surpassed; these transitions are influenced by sediment size, as outlined in Wright and Short (1984).

It is suggested that the beaches in Port Phillip Bay oscillate between periods of low wave energy when they are geomorphically stable, and stormy periods when wave energy is sufficient to drive the development of bars and other features. The dominance of storms as the primary driver of beach morphodynamics in Port Phillip Bay is further supported by the fact that the dimensionless fall velocities calculated for the beaches in the study area under modal conditions are considerably lower than those typically associated with the observed morphological features (Table 3).

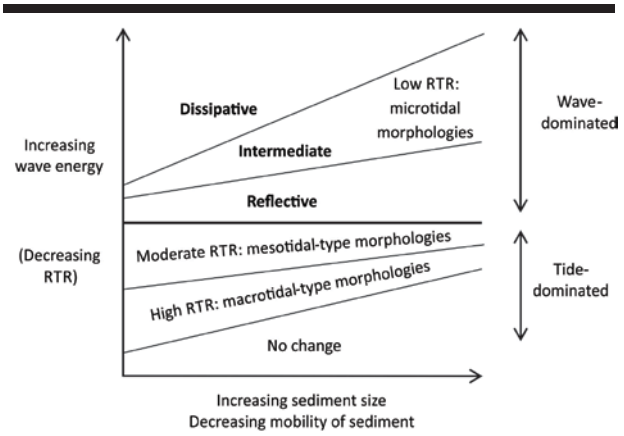

Figure 5. Conceptual estuarine beach model: thresholds for macro, meso and microtidal-type beach morphologies. The variation in relative tidal range (RTR) is also outlined.

Table 3. *Calculated dimensionless fall velocity values (Ω) for the beaches in the study area, compared to those for analogous open-ocean beach states.*

Site	Calculated Ω	Analogous open-ocean beach state	Ω and RTR for relevant open-ocean models
Middle Park	0.27 to 0.54	Intermediate Transverse bar-rip.	Ω ≈ 3 to ≈ 2, RTR: micro
St Kilda	1.14	Intermediate Low-tide terrace	Ω ≈ 3 RTR: meso
Elwood	0.11 to 0.19	Reflective	Ω < 1 RTR: micro
Brighton	0.20 to 0.51	Reflective to low-tide terrace	Ω < 1, Ω ≈ 2 RTR: micro
Hampton	0.08 to 0.13	Reflective	Ω < 1 RTR: micro
Sandringham	0.08 to 0.37	Reflective	Ω < 1, Ω ≈ 2 RTR: micro
Half Moon Bay	0.35	Intermediate Transverse bar-rip	Ω ≈ 3 RTR: micro

As wave energy is approximately equal across the study sites, sediment size is considered the primary determinant of beach morphology. This conceptual model can therefore be applied to the study sites in Port Phillip Bay.

Sandringham, Hampton, Brighton, and Elwood beaches are composed of coarse sand, are stable during calm periods, and are reworked as wave-dominated reflective beaches during high energy events.

The finer grained beaches of Middle Park and Half Moon Bay more easily surpass the threshold between reflective and intermediate states, and are reworked into low tide terrace and transverse bar and rip morphologies during high energy events.

St Kilda Beach, though it has the finest sediment, does not adopt the highest energy beach state during storm conditions. However, this beach also arguably receives the least wave energy of all the study sites, as it is sheltered by a marina, pier, and groyne. As such, it is suggested that wave energy at St Kilda Beach may not exceed the threshold between mesotidal and macrotidal morphologies, and instead the beach adopts a lower energy mesotidal low tide terrace morphology.

While storms may be the primary drivers of overall beach morphology in Port Phillip Bay, longshore sediment transport arguably has the greatest impact on seasonal variability. Beach planforms rotate in response to oblique wave approach in order to reduce the angle of wave attack (Jackson and Cooper, 2010). In Port Phillip Bay, seasonal changes to the prevailing wind direction alter the theoretical short-term planform position of equilibrium, where incident wave angle is parallel to the shoreline. The rate of change is greatest immediately following the shift in prevailing winds (March to May; see Figure 2b), and decreases over time. The effects of longshore sediment transport are exacerbated by the presence of groynes or other structures, which disrupt some alongshore movement. On beaches less affected by longshore sediment transport, subaerial erosion and accretion is concentrated at the beachface (see Figure 2a); this is consistent with Nordstrom's (1992) estuarine erosion models.

As outlined earlier, those beaches that have not been recently renourished have been eroding since at least 2001. While beach widths will continue to oscillate in response to seasonal changes, this erosional trend suggests that the long-term equilibrium position for Port Phillip Bay beaches is landward and upward of their current position. Based on the tendency of these beaches to erode towards a landward position of equilibrium, it is highly likely that they will continue to need periodic renourishment in order to maintain wide profiles. Furthermore, with current projections of sea level rise, it is expected that rates of beach erosion will accelerate over the coming decades. This would lead to an increased necessity for beach renourishment or other management interventions if wide beach profiles are to be maintained.

CONCLUSIONS

Port Phillip Bay, a unique and highly modified estuarine system, exhibits distinct patterns of beach morphodynamics and beach change over the short and medium terms. Even within a relatively small section of the Bay, variation in boundary conditions, specifically sedimentology and the degree of coastal modification, have significant impacts on beach morphology.

Unlike on open-ocean beaches, it was found that only periodic storm events are energetic enough to rework large subaqueous bar features, and thus control the morphodynamic state of beaches in Port Phillip Bay. Low wave energy during calm periods is insufficient to significantly alter beach morphology. Furthermore, longshore sediment transport is a significant driver of beach change, though seasonal fluctuations in prevailing winds limits its impact over the longer term.

A comprehensive understanding of estuarine beach dynamics should be used to inform coastal management planning and decision making. The coastal managers of Port Phillip Bay, and the managers of many other estuarine beach systems, will likely have to contend with accelerating rates of beach erosion over the coming decades (Walsh *et al*., 2004, Bird, 2006). While beach renourishment is currently a method of choice for shoreline maintenance in highly developed areas, it is possible that the associated costs may one day outweigh the benefits, in which case alternative methods of shoreline management may need to be adopted.

LITERATURE CITED

Bird, E.C.F., 1993. *The Coast of Victoria: The Shaping of Scenery*. Melbourne: Melbourne University Press, 416p.

Bird, E.C.F., 2006. The effect of higher sea level on the coasts of Port Phillip Bay. *The Victorian Naturalist,* 123(1), 49-54.

Black, K.P. and Rosenberg, M.A., 1992. Natural stability of beaches around a large bay. *Journal of Coastal Research,* 8(2), 385-397.

Department of Sustainability and Environment, 2012. *Renourishment in Port Phillip Bay in the past 10 years* [Spreadsheet]. Department of Sustainability and Environment, Melbourne, Australia. Data provided on 21 August 2012.

Goodfellow, B.W. and Stephenson, W.J., 2005. Beach morphodynamics in a strong-wind bay: a low-energy environment. *Marine Geology,* 214(1), 101-116.

Jackson, D.W.T. and Cooper, J.A.G., 2010. Application of the equilibrium planform concept to natural beaches in Northern Ireland. *Coastal Engineering,* 57(2), 112-123.

Jackson, N.L.; Nordstrom, K.F.; Eliot, I., and Masselink, G., 2002. 'Low energy' sandy beaches in marine and estuarine environments: a review. *Geomorphology,* 48(1), 147-162.

Kennedy, D.M., 2002. Estuarine Beach Morphology in Microtidal Middle Harbour, Sydney. *Australian Geographical Studies,* 40(2), 231-240.

Komar, P.D., 1976. *Beach Processes and Sedimentation*. Endlewood Cliffs, New Jersey: Prentice-Hall Inc, 429p.

Masselink, G. and Pattiaratchi, C.B., 2001. Seasonal changes in beach morphology along the sheltered coastline of Perth, Western Australia. *Marine Geology*, 172(3), 243-263.

Masselink, G. and Short, A.D., 1993. The effect of tide range on beach morphodynamics and morphology: a conceptual beach model. *Journal of Coastal Research,* 9(3), 785-800.

Nordstrom, K. F. and Jackson, N.L., 2012. Physical processes and landforms on beaches in short fetch environments in estuaries, small lakes and reservoirs: A review. *Earth-Science Reviews,* 111(1-2), 232-247.

Nordstrom, K.F., 1992. *Estuarine Beaches: an introduction to the physical and human factors affecting use and management of beaches in estuaries, lagoons, bays and fjords,* Essex: Elsevier Science Publishers Ltd, 225p.

Thieler, E.R.; Himmelstoss, E.A.; Zichichi, J.L., and Ergul, A., 2009. *Digital Shoreline Analysis System (DSAS) version 4.0 - An ArcGIS extension for calculating shoreline change.* U.S. Geological Survey Open-File Report 2008-1278. *current version 4.3.

Walsh, K.J.E.; Betts, H.; Church, J.; Pittock, A.B.; McInnes, K.L.; Jackett, D.R., and McDougall, T.J., 2004. Using sea level rise projections for urban planning in Australia. *Journal of Coastal Research,* 20(2), 586-598.

Wright, L.D. and Short, A.D., 1984. Morphodynamic variability of surf zones and beaches: a synthesis. *Marine Geology,* 56(1-4), 93-118.

Journal of Coastal Research	SI	75	258-262	Coconut Creek, Florida	2016

Morphodynamic of a sandy-muddy macrotidal estuarine beach under contrasted energy conditions (Vilaine estuary, France)

Morio O.[†], Sedrati M.[†], Goubert E.[†], Floc'h F.[††], Furgerot L.[†] and Garlan T.[‡††]

[†] Equipe Géosciences Marines et Géomorphologie du Littoral
Domaines Océaniques UMR6538 GMGL
Université de Bretagne Sud,
Vannes, France

[††] Domaines Océaniques UMR6538 UBO
Institut Universitaire Européen de la Mer
Plouzané, France

[‡]SHOM Research Department
Brest, France

www.cerf-jcr.org

www.JCRonline.org

ABSTRACT

Morio, O. Sedrati, M., Goubert, E., Floc'h F., Furgerot L., and Garlan, T., 2016. Morphodynamic of a sandy-muddy macrotidal estuarine beach under contrasted energy conditions (Vilaine estuary, France). *In:* Vila-Concejo, A.; Bruce, E.; Kennedy, D.M., and McCarroll, R.J. (eds.), *Proceedings of the 14th International Coastal Symposium* (Sydney, Australia). *Journal of Coastal Research*, Special Issue No. 75, pp. 258-262. Coconut Creek (Florida), ISSN 0749-0208

Estuarine and bay beaches are important areas for human activities. These beaches are variably affected by tides, waves, and winds that can commonly generate marked topographic and sedimentological contrasts. Betahon beach (South Brittany, France) is an intermediate-type beach exhibiting a low-tide terrace linked to a steeply sloping gravelly-sandy upper foreshore, and separated by a shore-parallel bluff from a mudflat on the lower foreshore. The beach exhibits linear ridge and runnel (R-R) bedforms perpendicular to the shoreline. Seasonal monitoring of the beach shows mudflat accretion by fluid mud deposition and erosion of R-R bedforms. A core obtained from the mudflat shows alternations of mud and sand. In order to understand the cross-shore dynamics of the beach, topographic surveys and wave and current monitoring were carried out during two contrasting energy conditions. Bed return flows occurred during high-energy events, inducing an infill of runnels by non-cohesive fine sediments and coarser sediments from the reflective upper beach. During low-energy conditions, a longshore flow channel was identified between the shore-parallel low-tide terrace bluff and the mudflat. Throughout the tide, on-shore currents prevailed over the mudflat, inducing the filling of runnels and the base of the bluff with fluid mud.

ADDITIONAL INDEX WORDS: *Estuarine beach, Mixed-sediment, Intertidal mudflat, Ridge and runnels.*

INTRODUCTION

Beaches in estuarine and deeply embayed settings with large tidal ranges typically exhibit two contrasting morphosedimentary types (Anthony, 2009). The upper beach commonly consists of sand, and sometimes gravel, associated with energetic conditions at high tide, and steep slopes, whereas the lower beach commonly evolves in a lower-energy low-tide context associated with gentle slopes and fine-grained sedimentation. Estuarine and deeply embayed beaches are very important areas for human activities (sailing, shellfish farming). Depending on local hydrodynamics and sediment sources, these beaches are exposed to periodic or permanent inputs of clay/silt sediments (Anthony *et al.*, 2011, 2015, Gensac *et al.* 2015*)*. The Vilaine and Seine estuaries, and Arcachon bay are fine examples of such environments in France, , whereas Plymouth bay and the Severn estuary in the UK, and the French Guiana coast are also representative of these settings (Le Hir et *al.,* 2000*,* Anthony *et al.* 2008, Goubert *et al.*, 2010). However, studies devoted to mixed sandy-muddy beaches are relatively rare (Anthony *et al.*, 2015).

Betahon beach, in the Vilaine River estuary (France) is a good example of a mixed beach comprising a reflective gravelly/sandy upper foreshore and a large dissipative lower foreshore mudflat. On this beach with strongly contrasting sediment types, the dune front and the break of slope separating the upper and lower foreshores are commonly subject to erosion under stormy conditions. Ridges and runnels (R-R) also occur on the mudflat. These forms and the patterns they exhibit have been the object of various studies (e.g., Le Hir *et al.* 2000, Williams *et al. 2008,* Carling *et al.* 2009, Friedrich, 2011). The mudflat sediments show alternations of sand and mud that reflect two distinct morphosedimentary regimes, respectively cohesive and non-cohesive. In order to identify the processes associated with each of these two regimes, a study was conducted on the hydrodynamic, topographic and sedimentological characteristics of the reflective and dissipative parts of Betahon beach under high and low energy conditions, along a cross-shore profile. Based on the observations and measurements, a conceptual model is proposed. The paper provides preliminary results that are part of a larger timescale study of Betahon beach that includes seasonal 3D topographic and sedimentary surveys that will be presented in a future paper.

DOI: 10.2112/SI75-52.1 received 15 October 2015; accepted in revision 15 January 2016.
*Corresponding author: patricio.catalan@usm.cl

ENVIRONMENTAL SETTINGS

The Vilaine River estuary lies on the south coast of Brittany, within Vilaine bay, a triangular re-entrant flanked by rocky coasts (Figure 1a). The bay is separated from the North Atlantic Ocean by a large shoal stretching from the Quiberon peninsula to the tip of the Croisic peninsula and a string of islands. The geology of Vilaine bay has been described by Goubert and Meunier (2005). The bay attains a maximum depth of 30 m, and is partially protected by the shoal from westerly waves (Vested *et al.*, 2013). The Vilaine is a meso-macrotidal estuary (tide range from 2.5 to 5 m at neaps and springs respectively), and consists of three sectors: a meandering inner estuary, a rectilinear intermediate estuary and an outer estuary (figure 1a) totally infilled by marine mud (Goubert *et al.* 2010).

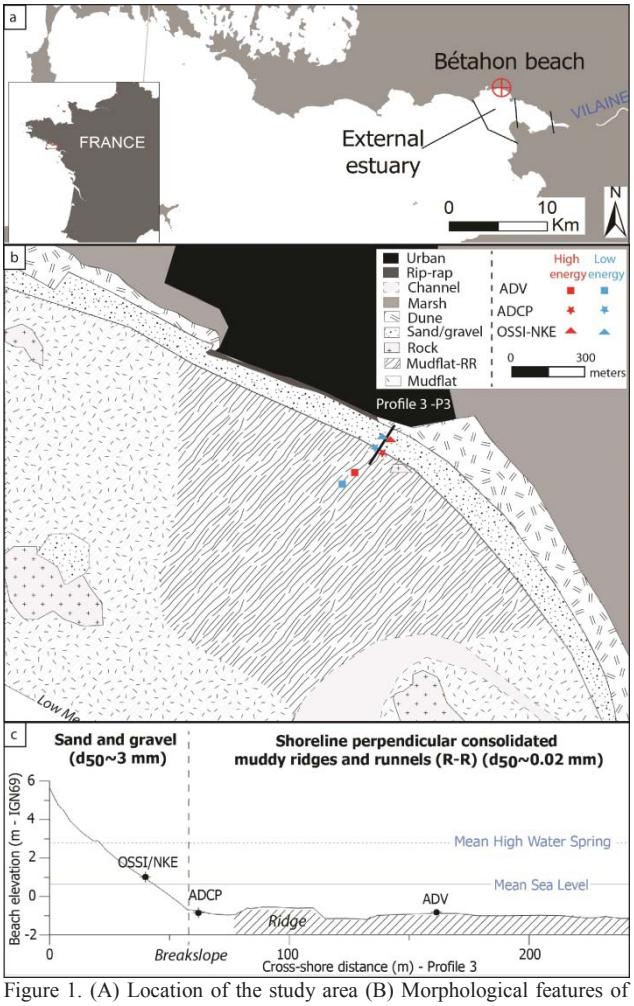

Figure 1. (A) Location of the study area (B) Morphological features of Betahon beach, location of the central profile (P3) and instruments (C) Location of sensors over the central cross-shore beach profile (P3).

Betahon beach is located in the outer estuary (Figure 1a). Compared to adjacent areas of the South Brittany coast, which are sandy, Betahon beach is a former spit exhibiting an atypical intertidal zone (Figure 1b). The general morphology of the beach may be characterized as Low Tide Terrace (LTT) according to the beach classification of Wright and Short (1984). The upper, steeply sloping part of the beach consists of sand and gravel (figure 1c). Sediment grain sizes (according to the Udden-Wenthworth classification) range from fine/medium sand to gravel. In total contrast to the upper intertidal beach, the lower intertidal beach is a large mudflat (Figure 1b, 1c). At the transition between sand/gravel and silt/clay, fine sand occurs just below the break in slope between the mudflat and the upper part of the beach. The mudflat is characterized by a mixture of soft mud/sand commonly exhibiting a complex series of ridges and runnels (R-R) perpendicular to the shoreline. Ridge mud cliffs (90°) are 10 to 40 cm high and the distance between two ridges is very variable, ranging from 20 cm to 2 m (cf. figure 2 a). Seasonal monitoring of the beach shows that the mudflat is characterized by a variable topography and morphology. The runnels on the mudflat can be totally infilled by fluid mud and the mudflat elevation can increase by up to 60 cm.

METHODS

In order to understand the hydro-morpho-sedimentary dynamics of Betahon beach, two field experiments were conducted on the topography and sediment and hydrodynamic conditions affecting the beach under different energy conditions. The first experiment was conducted between February 28th and March 06th 2014 under high-energy conditions (maximum offshore wave height = 4.9 m, maximum wind speed =12 m.s^{-1}, wind direction = SW). The second experiment took place from June 10th to June 19th 2014 under low-energy conditions (maximum offshore significant wave height = 1.08 m, maximum wind speed = 6 m.s^{-1}, wind direction = NE). Both experiments took place under similar spring tide conditions. Topographic surveys were carried out at daytime using a Leica Total Station TS20 (accuracy = ±3 mm) across a central cross-shore beach profile (P3 - figure 1b). Photographic surveys of the beach were also conducted during the field experiments. The complexity of the R-R morphology requires 3D topographic monitoring. In this study, only the photographic surveys and measurements (June experiment) are used to highlight mudflat variations. Regarding waves and currents, a pressure sensor (NKE-SP2 or OSSI 003-003C) was deployed on the reflective section of the beach (figure 1c). A 6MHz Acoustic Doppler Currentmeter (ADV) was installed at *ca.*100/150 m after the break in slope, on a ridge (cell measurement at 0.15 m above the bed). An additional 1200 kHz Workhorse Sentinel Acoustic Doppler Current Profiler (ADCP) was deployed *ca.* 2 m below the beach break in slope (at about the limit between the dissipative and the reflective parts of the beach) to characterize currents between the break in slope and the mudflat (cell measurement 0.65 m above the bed). For each instrument, velocity data were burst-averaged (mean velocities for 5 to 9 min burst data at a 2Hz sampling rate). Geographical currents were rotated on the cross-shore (U) and along-shore (V) components of the beach shoreline. Burst-averaged water levels and wave characteristics were spectrally derived for each instrument from atmospheric-corrected pressure data.

RESULTS

High/moderate energy conditions

Significant wave height reached 0.75 m (peak periods were from 9 to 20 s) for storm 1, and 1.33 m during storm 2 (figure 2a)**.** Wave height increased from the lower dissipative foreshore to the upper reflective part of the beach (0.75 m to 1.04 m in the course of storm 1). The upper reflective beach showed significant topographic variations. Storm 1 induced a lowering of the beach profile, and changes in profile shape. The lower concave part of the beach (P3 - central profile) became convex following accretion, whereas the convex central and upper parts became concave following erosion (figure 3a), inducing a new equilibrium profile. Although storm 2 was more energetic, topographic variations were less significant due to the previous equilibrium state of the beach. A seaward movement of the break in slope occurred during the two storms (+1.1 m for storm 1 and +3.1 m for storm 2). Erosion of the shore-parallel bluff on the mudflat occurred during the February 28th storm, with a seaward movement of the shore-parallel bluff and a reduction of ridge size (figure 3a - photography). Changes in mudflat elevation that could have occurred after storm 1 cannot be ascertained due to the complexity of the R-R system on the mudflat, human errors and disturbance of the topography during the field study. During storm 2, infilling of runnels by fine and coarse non-cohesive particles occurred. Perpendicular and parallel ridges cut into bluffs were eroded, leading to the breakdown of slumped mud blocks that were progressively disintegrated into mud pebbles. Focusing on storm 1 (tide 1 - figure 2a), bed return flows throughout the tide were mainly cross-shore-oriented over the ridge (ADV). Mean cross-shore velocities reached 0.12 m.s^{-1} at the start and the end of the tide (when the relative wave height was highest) (figure 3a). Stronger currents were mainly long-shore-directed and channeled between the shore-parallel mudflat bluff and the break in slope (ADCP - figure 2a). Under moderate energy conditions (Hs≤0.6 m), currents at the ADCP location were dominantly alongshore whereas, over the ridge (ADV location), cross-shore dominant undertows were identified at the beginning and at the end of the tide. Currents were onshore-directed when water levels increased (figure 2a). The break in slope migrated landward following the energetic events (figure 3a).

Low energy conditions

Maximum and minimum wave heights (peak periods from 7 to 15 s) reached respectively 0.16 m during the spring tide and 0.04 m at the end of the field experiment. No variation in Hs occurred between the mudflat and the reflective part of the beach (figure 2b). Insignificant topographic variations were identified (figure 3b). A 0.2 m landward movement of the break in slope occurred with the increasing tidal range. Micro-morphological features, such as berms, disappeared in the course of the field experiment. Fluid mud deposits (silt and clay) of up to 4.9 cm ± 0.3cm in front of the ridge and 2 cm ± 0.3 cm near the break in slope were monitored using iron accretion pins. Runnels were also filled by fluid mud (figure 2b - photography).

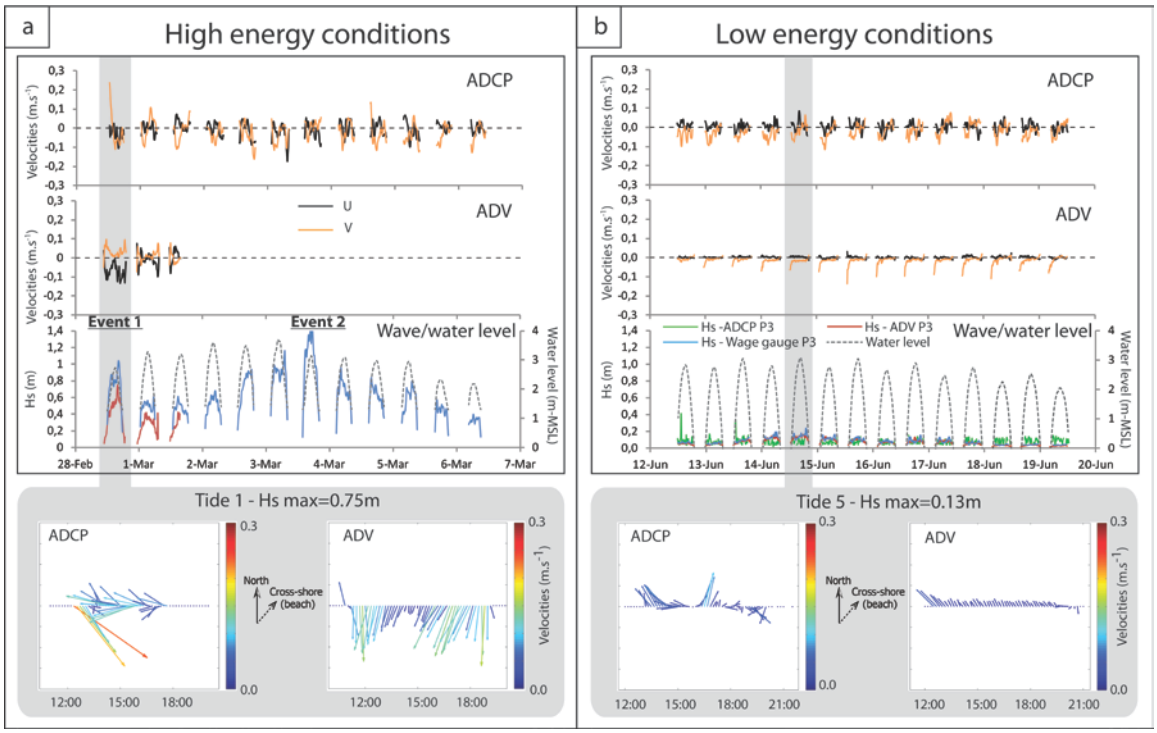

Figure 2. Wave characteristics/water levels at wave gauge and ADV locations; Mean cross-shore (U - positive landward) and long-shore currents (V - positive to shipping channel) at ADCP and ADV locations, (A) Under high and moderate energy conditions and focused on tide 1/storm 1 (B) Under low energy conditions and focused on tide 5.

Variations of the mudflat altitude in figure 2b are artifacts due to the complex topography. Throughout almost the entire tide onshore currents, and alongshore-dominant currents, were measured over the ridge (ADV), (figure 2b).
Mean longshore velocities reached a maximum of 0.05 to 0.1 $m.s^{-1}$ during the first burst. Net onshore velocities of 0.02-0.03 $m.s^{-1}$ during the flood phase were measured. Offshore-directed ebb currents were extremely weak (<1 $cm.s^{-1}$) up to the final measured burst of tide. The cross-shore currents were almost zero. Velocities at the ADCP location were slightly stronger (0.05 to 0.1 $m.s^{-1}$). Currents followed a preferential flow corridor between the break in slope and the mud cliff-flat bluff. Circular flow patterns were also observed on this part of the beach.

DISCUSSION/CONCEPTUAL MODEL

A conceptual model of cross-shore dynamics of this Low Tide Terrace estuarine sandy-muddy beach is developed (figure 4). This conceptual scheme is based on observations and measurements realized during the two field experiments and coupled with seasonal observations of the central part of the beach. During high and moderate energy conditions (figure 4a), the upper reflective profile of the beach shows a classical erosion and sediments are exported to the break in slope (Masselink and Hegges 1995, Masselink *et al.* 2006*).* This dynamics is associated with bed and return flows under breakers, leading to infill of the mudflat runnels by coarser sediments (Le Hir *et al. 2000*, Anthony *et al.* 2008). Currents in runnels are channelled and must be stronger than on the ridges according to William *et al,* 2008. The shore-perpendicular and parallel flanks of the mud ridge are eroded and the slumped blocks broken down by waves to form mud pebbles. This erosion could be reinforced by blasting by coarse sand transported in offshore bed-return flows (Carling *et al.,* 2009). Mud pebbles can be progressively broken down until they become finally fluidized into suspension load (Gensac *et al.* 2015) transported seaward by undertow currents.

Under low energy conditions (figure 4b)**,** currents are onshore and longshore-dominant throughout almost the whole tide on the ridge, and channelled near the break in slope in a preferential alongshore flow corridor. Current in runnels may be also stronger (Williams *et al.*, 2008). Swash bore wash over and put in suspension fluid mud over the 1 km mudflat. Runnels are filled by water first. When water reaches the break in slope and overtops the ridge, sediments begin to settle down (Bassoullet *et al.*, 2000). Backwash currents on the reflective part of the beach are very weak (no breakers) and sediments can also settle down between the break in slope and the mudflat bluff and also in troughs between the runnels. Another hypothesis of a slow fluid-mud transport by onshore-longshore wave-driven currents (good correlation between relative wave height and current mean velocities) can also be proposed, following Gratiot *et al.* (2007) and Anthony *et al.* (2008). Ebb currents are virtually nil such that sediments can be trapped in runnels and near the break in slope as water retreats with the tidal excursion (figure 4b).

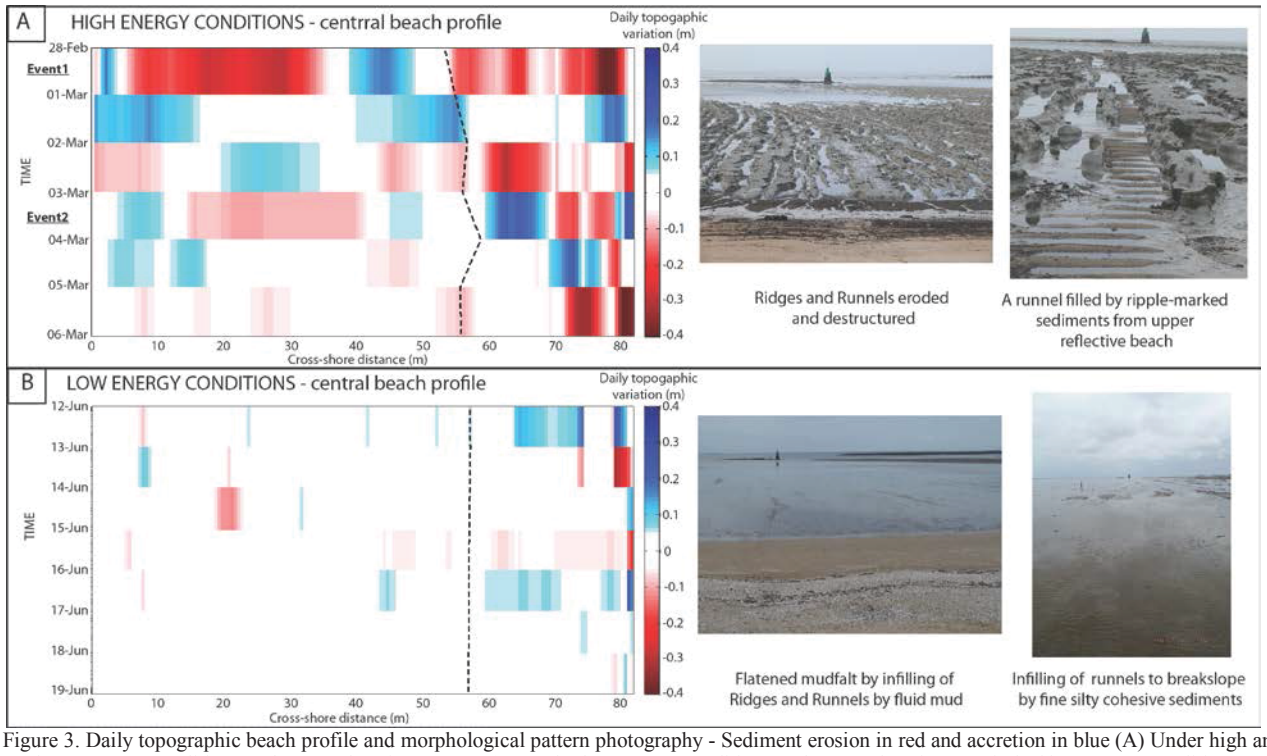

Figure 3. Daily topographic beach profile and morphological pattern photography - Sediment erosion in red and accretion in blue (A) Under high and moderate energy conditions – photography after storm 2 (B) Under low energy conditions – photography after a period of low energy conditions.

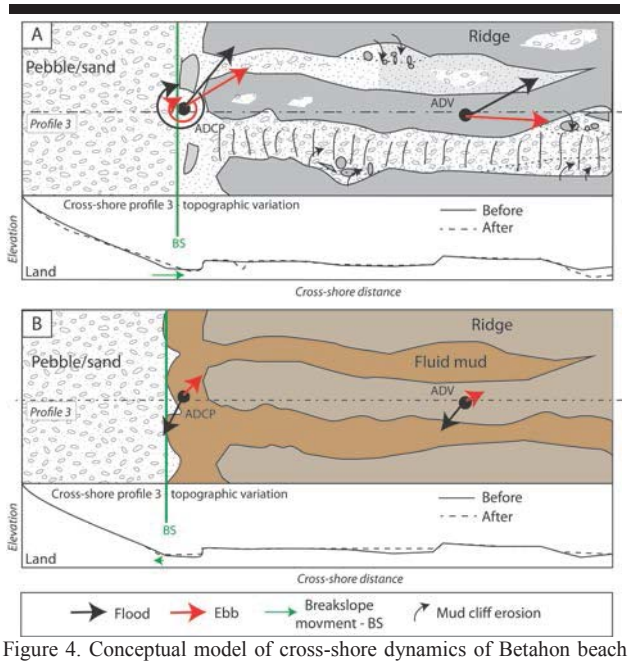

Figure 4. Conceptual model of cross-shore dynamics of Betahon beach (A) Under high/moderate energy conditions (March 2014). (B) Under low energy conditions (June 2014).

CONCLUSIONS

The estuarine beach of Betahon shows two contrasting dynamics. In its central part, coarse non-cohesive sediments from the upper beach are displaced to fill runnels on the lower foreshore mudflat due to bed return flows under high-energy events. Under low energy conditions, runnels are filled by fine cohesive sediments leading to accretion of the mudflat. Successions of high and low energy conditions can also explain the alternations of sand and mud identified in a core sample from the mudflat. These results will help to understand the seasonal dynamics of this beach that should involve short term/monthly topographic and sedimentary monitoring, kite aerial imagery and photogrammetric analyses, core-drilling and mud shear resistance surveys.

ACKNOWLEDGMENTS

This work is part of a 3 year-PhD project funded by Region Bretagne and Université de Bretagne Sud. The authors would like to acknowledge the French Hydrographic Office (SHOM), Université de Rennes (Lionel Allano), Mynivel Environnement for technical support during the field experiments. The authors wish to thank Dr. E. J. Anthony for general overview and English improvement of this paper.

LITERATURE CITED

Anthony, E. J., 2009. Shore Processes and their palaeoenvironmental applications. *Developments in Marine Geology*. Amsterdam, Elsevier, 519p.

Anthony, E. J.; Dolique, F.; Gardel, A.; Gratiot, N.; Proisy, C., and Polidori, L., 2008. Nearshore intertidal topography and topographic-forcing mechanisms of an Amazon-derived mud bank in French Guiana. *Continental Shelf Research*, 28, 813-822.

Anthony, E. J.; Dolique, F.; Gardel, A., and Marin, D., 2011. Contrasting sand beach morphodynamics in a mud-dominated setting: Cayenne, French Guiana. *Proceedings of the 11th International Coastal Symposium. Journal of Coastal Research*, Special Issue No. 64, pp. 30-34.

Anthony, E. J.; Gardel, A.; Dollique F.; Brunier, G., and Péron, C., 2015. Mud Banks, Sand Flux, and Beach Morphodynamics: Montjoly Lagoon beach, French Guiana. In: Robin, M., and Maanan, M. (eds.), *Coastal Sediment Fluxes, Coastal Research Library*, pp. 75–90.

Bassoullet, P.; Hir, P. L.; Gouleau, D., and Robert, S., 2000. Sediment transport over an intertidal mudflat: field investigations and estimation of fluxes within the 'Baie de Marenngres-Oleron' (France). *Continental Shelf Research*, 20, 1635-1653.

Carling, P. A.; Williams, J. J.; Croudace, I. W., and Amos, C. L., 2009. Formation of mud ridge and runnels in the intertidal zone of the Severn Estuary, UK. *Continental Shelf Research*, 29, 1913-1926.

Friedrichs, C. T., 2011. Tidal Flat Morphodynamics: a Synthesis. In: Flemming, B. W., and Hansom, J. D. (eds.), *Treatise on Estuarine and Coastal Science. Academic Press, Elsevier*, pp. 137-170.

Gensac, E.; Gardel, A.; Lesourd, S., and Brutier, L., 2015. Morphodynamic evolution of an intertidal mudflat under the influence of Amazon sediment supply – Kourou mud bank, French Guiana, South America. *Estuarine, Coastal and Shelf Science*, 158, 53-62.

Goubert, E. and Menier, D., 2005. *Evolution morpho-sédimentologique de l'estuaire de la Vilaine de 1960 à 2003: valorisation des campagnes bathymétriques*. Report prepared by UBS for IAV, 104 p.

Gratiot, N.; Gardel, A., and Anthony, E. J., 2007. Trade-wind waves and mud dynamics on the French Guiana coast, South America: input from ERA-40 wave data and field investigations. *Marine Geology*, 236, 15-26.

Le Hir, P.; Roberts, W.; Cazaillet, O.; Christie, M.; Bassoullet, P., and Bacher, C., 2000. Characterization of intertidal flat hydrodynamics. *Continental Shelf Research,* 20, 1433-1459.

Masselink, G.; Kroon, A., and Davidson-Arnott, R. G. D., 2006. Morphodynamics of intertidal bars in wave-dominated coastal settings - A review. *Geomorphology,* 73, 33-49.

Masselink, G. and Hegge, B., 1995. Morphodynamics of meso- and macrotidal beaches: examples from central Queensland, Australia. *Marine Geology*, 129, 1-23.

Vested, H. J.; Tessier, C.; Christensen, B. B., and Goubert, E., 2013. Numerical modelling of morphodynamics—Vilaine Estuary. *Ocean Dynamics*, 63, 423-446.

Williams, J. J.; Carling, P. A.; Amos, C. L., and Thompson, C., 2008. Field investigation of ridge–runnel dynamics on an intertidal mudflat. *Estuarine, Coastal and Shelf Science*, 79**,** 213-229.

Wright, L. D. and Short, A. D., 1984. Morphodynamic variability of surf zones and beaches: A synthesis. *Marine Geology*, 56, 93-118.

Journal of Coastal Research	SI	75	263-267	Coconut Creek, Florida	2016

Typhoon Impact and Recovery from Continuous Video Monitoring: a Case Study from Nha Trang Beach, Vietnam

Duong H. Thuan[†§*], Le T. Binh[††], Nguyen T. Viet[†‡], Dong K. Hanh[†], Rafael Almar[§], and Patrick Marchesiello[§]

[†]Faculty of Civil Engineering
ThuyLoi University
Hanoi, Vietnam

[††]Vietnam Hydraulic Engineering Consultants Corporation
Hanoi, Vietnam

[‡]Central Region College of Technology, Economics, and Water Resources
Hoian, Vietnam

[§]IRD-LEGOS
Université Paul Sabatier/CNRS/CNES/IRD
Toulouse, France

www.cerf-jcr.org

www.JCRonline.org

ABSTRACT

Thuan, D.H.; Binh, L.T;Viet, N.T.; Hanh, K.D.; Almar, R., and Marchesiello, P., 2016. Typhoon impact and recovery from continuous video monitoring: a case study from Nha Trang beach, Vietnam. *In:* Vila-Concejo, A.; Bruce, E.; Kennedy, D.M., and McCarroll, R.J. (eds.), *Proceedings of the 14th International Coastal Symposium* (Sydney, Australia). *Journal of Coastal Research*, Special Issue, No. 75, pp. 263-267. Coconut Creek (Florida), ISSN 0749-0208.

Nha Trang beach in Vietnam is regarded as one of the most beautiful beaches in the world. However, its degradation in recent years is a serious problem for its economic development. Understanding the mechanisms of shoreline evolution is thus part of an integrated management strategy of the area. In this study, the evolution of Nha Trang shoreline is investigated in detail with a high resolution (2Mp) and high frequency (2Hz) video camera system installed from May 2013 to present. The surfzone cross-shore profiles, shoreline positions and wave characteristics (height and period) extracted from the video data are calibrated with in-situ measurement from two field experiments (from 23/05 to 01/06 and 03/12 to 10/12 2013) and bathymetry measurement during the Haiyan typhoon event. The study shows a marked seasonal evolution of the Nha Trang shoreline with accretion from March to September and cumulated seasonal amplitude of about 15 m. The impact of Nari and Haiyan typhoons to the shoreline is also dramatic with changes of 4 to 8 m in each case. The recovery to individual events is fast, of the order of one and half month.

ADDITIONAL INDEX WORDS: *Shoreline evolution, recovery, video monitoring, Nha Trang beach.*

INTRODUCTION

A beach located in a semi-enclosed bay, mostly sheltered from wave action or exposed to seasonal modulation of moderate energy waves, can be defined as a low energy environment (Jackson *et al.*, 2002). In such environment, major morphological changes are generally attributed to events of moderate to high-energy waves, with long periods of inactivity in between. Transfers between the subtidal region and upper beach are assumed weak or non-existent since the depth-of-closure (beyond which the depths do not change with time) is small. These assumptions have not been challenged until recently and low-energy environments have remained beyond the scope of major research interest. Yet, they raise important issues: how can a beach recover if the subtidal and upper beach sediment cells are disconnected? Are morphological features only generated during energetic events or do low-energy wave conditions have a role to play in the recovery process?

During extreme events, the beach is observed to evolve dramatically, dominated by surf processes that can rapidly lead to an up-state transition through offshore sediment transport by the undertow and sandbar formation. After such extreme event, the beach slowly evolves through transient states while recovering under low or moderate energy wave forcing (Coco *et al.*, 2014; Angnuureng *et al.*, 2015). There is as yet no consensus on whether these events have transient or persistent impact on beach evolution and on the crucial recovery processes leading to beach resilience (Anderson *et al.*, 2010). Resilience capacity would relate on the extent of departure from equilibrium driven by short events and on recovery timescale, which can be from days to years, depending on the site and severity of events. For isolated storm events, departure from equilibrium is related to storm intensity (Frazer *et al.*, 2009; Davidson *et al.*, 2013). However, no clear conclusion can be drawn when considering sequences of storms, since both enhanced and weakened effects are observed (Ferreira 2005; Karunarathna *et al.*, 2014; Splinter *et al.*, 2014). It seems that it is the interplay between recurrence interval of events and post-event (low-energy) recovery timescales that matters. For example, a sequence of events with recurrence interval shorter than recovery duration (*e.g.*, strong 2013-2014 winter events in Europe; Masselink *et al.*, 2014; Castelle *et al.*, 2015) shows greater impact than individual

DOI: 10.2112/SI75-053.1 received 15 October 2015; accepted in revision 15 January 2016.
*Corresponding author: duonghaithuan@gmail.com

events. The reason is that the system moves sequentially toward a new state of high-energy equilibrium.

The evolution of a beach can be characterized at different time scales, *i.e.*, interannual, seasonal or event scales. (Quartel *et al.*, 2008). The most dramatic changes occur occasionally during a storm event and high-frequency assessment is needed in this case. Traditional observation tools are designed for low frequency monitoring (bi-monthly with satellites and monthly with GPS) or are sporadic during measurement campaigns. Key parameters of coastal morphodynamics may be missed. To circumvent the problem, low cost systems of coastal video imaging (Holland *et al.*, 1997; Holman and Haller 2013) were designed. They are particularly well suited to monitor the shoreline evolution in various parts of the world, covering timescales from seconds to years and spatial scales from meters to kilometers. It allows a monitoring of beach morphology as well as hydrodynamic factors governing its evolution. Here, we present some analysis of shoreline seasonal evolution and typhoon impact in Nha Trang beach using the video camera technique. It will provide an example of the patterns and interplay between storm events and seasonal recovery in a low-energy environment.

DATA AND METHODS

The study site is Nha Trang Beach (12°N, 109°E), south-east of Vietnam in the Khanh Hoa Province, facing the fetch limited South China Sea (Figure 1). This beach has been identified by the Vietnamese government as a priority for the development of tourism. Wave climate is characterized by large seasonal variations. The wave regime is dominated by southerly wind waves during summer monsoon, from March to September, and by northeasterly swell during winter monsoon, from October to February. Vietnam lies within the most active cyclogenesis region in the world and 4 to 6 typhoons hit the coast every year (Nicholls *et al.*, 1999) from October to December. This rugged coastline is characterized by sandy/mud mixed environment.

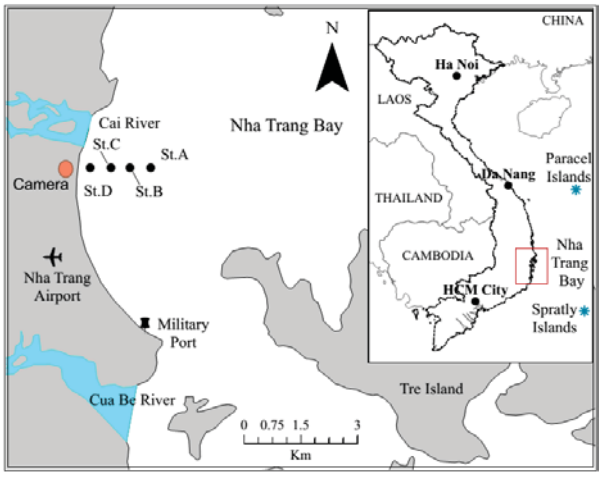

Figure 1. Study area of Nha Trang bay: location of the camera system (red dot) and field observation stations (St.A, B, C, D) in black dot.

The 7-km long Nha Trang embayed beach is orientated along a meridional axis (Figure 1), sheltered from southeasterly to southerly waves by Tre Island and disrupted at its center part by the Cai river mouth. Sediment on the shoreface is medium sized (D50 = 300 μm). The beach is a wave-dominated mixed micro-tidal environment (Relative Tidal Range, *i.e.*, tidal range modulated by wave height: RTR~1). The beach morphology presents strong variability but remains mostly in alongshore uniform, intermediate low-tide terrace, reflective upper beach state (Gourlay parameter Ω~1.5).

Field experiments

Two field experiments were conducted at Nha Trang Beach in 2013 (Figure 1), from May 26 to 30 and December 3 to 10. The first experiment (NT1) targeted the summer monsoon wind-wave dominated dynamics, and the other (NT2) the more energetic winter monsoon swell dominated dynamics. Deployments during the two experiments were similar: offshore wave and tidal forcing were given by 2 AWACs (acoustic Doppler profiler and directional wave gauge) in 10 m and 5-6 m depths and a current-meter in 3-m depth; refined surfzone and swash measurements were provided by swash video poles and a micro-profiler. A bathymetric survey was carried out at the beginning of each experiment while upper beach changes were monitored by daily theodolite surveys.

To complement these intensive short-term experiments, a two-camera permanent video system was deployed in March 2013 (Viet *et al.*, 2014a,b; Lefebvre *et al.*, 2014). Hydrodynamics (waves, currents, tides) and morphological parameters (upper beach morphology, bathymetry, shoreline, beach volume) are then extracted from processed secondary images.

Video processing

The video system consists of two high-resolution cameras (2Megapixel), which can cover a wide area of approximately 1.5 km by 1 km with a temporal resolution of 2 frames per second. Three types of images are generated: a snapshot to control image quality, a 15-min average to detect the shoreline position, and a radial time series of pixel intensity (timestacks).

The shoreline location can be obtained using various definitions (Boak and Turner, 2005). Here, it is derived from optical variables (Aarninkhof *et al.*, 2003) as the interface between water and beach in average images following the two-step method of Almar *et al.* (2012): a first detection of the red to blue and green pixel transition and refinement by minimizing the variation of shoreline length around its location. This method showed good skills at beaches with complex intertidal zones. Determination of the intertidal beach profile involved the delineation of the shoreline at different tidal levels (Aarninkhof *et al.*, 2003) and interpolation between low and high tides.

Breaker wave height (Almar *et al.*, 2012), period and surface elevation (inversed from celerity; see Stockdon and Holman, 2000; Catalán and Haller, 2008) were determined from space-time images.

RESULTS

The results section first provides some validation of the video data during the field experiments and then proceeds to analyze the shoreline evolution observed during the typhoon events of 2013 and seasonal recovery of the beach.

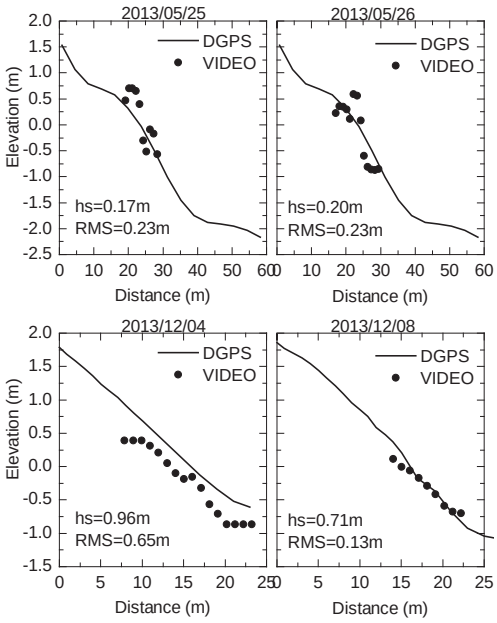

Figure 2. Comparison of beach profiles detected by camera and measured by DGPS.

Validation of video data during the fields experiments

During NT1, the tidal range varied from 0.8 to 1.5 m, while the southerly wind-waves remained roughly constant over the experiment with Hs=0.25 m, Tp=3.3 s, although there was diurnal modulation by the afternoon sea breeze. The beach profiles showed no substantial change, with a spring high-tide beach step and a rather linear swash zone, presenting a steep reflective slope of 0.17.

During NT2, the tidal range varied from spring to neap tide between 1.7 and 0.6 m. The swell showed quasi-constant characteristics with Hs~1 m and Tp~8 s from shore-normal incidence. It is noteworthy that the mega-typhoon Haiyan, which notoriously devastated central Philippines on November 8, hit the Vietnam coast on November 14, about 2 weeks before the beginning of our experiment. Even though wave energy during NT2 was moderate, the beach was recovering from the storm. The longshore-averaged beach profiles showed an almost constant slope of 0.15 throughout the experiment, but the morphology changed from a linear to convex shape.

In Figure 2, video-based and surveyed intertidal profiles are compared. The RMS error is 30 cm in average over NT1 and NT2, which is within the usual uncertainty shown by video techniques (*e.g.*, Aarninkhof *et al.,* 2003). In Figure 3, video estimates of hydrodynamic properties near the breaker point (wave height Hs and period Tp and tidal elevation) are compared with in-situ AWAC measurements during NT1 and NT2. An overall good agreement is found for tidal elevation (RMSE = 34 cm, bias 5 cm), Hs (RMSE = 6 cm, bias 2 cm) and Tp (RMSE = 1.18 s, bias 0.82 s). The skills are better for NT2, probably because of the clearer wave signature (swell waves during NT2 versus wind waves during NT1).

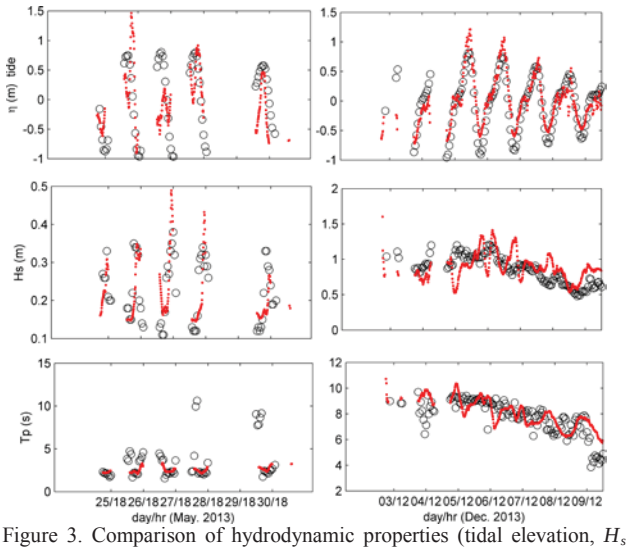

Figure 3. Comparison of hydrodynamic properties (tidal elevation, H_s and T_p), from video (red dots) and from in-situ measurements (black circles), for NT1 (left) and NT2 (right).

Typhoon impact and recovery

Our period of analysis covers a year of video data from June 2013 to June 2014 (Figure 4). Year 2013 was particularly rich in storm events in the South China Sea (up to 10 events affected Vietnam in various ways) and two typhoons most noticeably impacted the study site during this period: one from October 13 to 16 (Nari), the second from November 10 to 14 (Haiyan).

We computed the longshore-averaged shoreline location (Figure 4d), and analyzed it with respect to wave conditions (Figure 4c) and beach profile video estimates (not shown). In Figure 4c, only the seasonal wave conditions are apparent as the storm events are smoothed out and indicated as red arrows on the shoreline figure (Figure 4d). Two individual video images (Figure 4ab) of a calm summer monsoon day and of the Haiyan typhoon event, respectively, illustrate the contrasted conditions encountered in Nha Trang. The seasonal wave forcing is also very contrasted between winter and summer monsoons and correlated with shoreline evolution.

DISCUSSION

During summer, the reflective beach is in equilibrium with small wind-wave forcing. In the swell-dominated winter period, it evolves toward a more dissipative profile with formation of a low-tide terrace. Then, the first storm event (Nari) causes a marked erosion of the top of intertidal zone. The beach narrows in response to erosion and has a receding shoreline (about 4 m). The beach may also have developed sand bars during the storm and taken on a more dissipative profile. Following the first

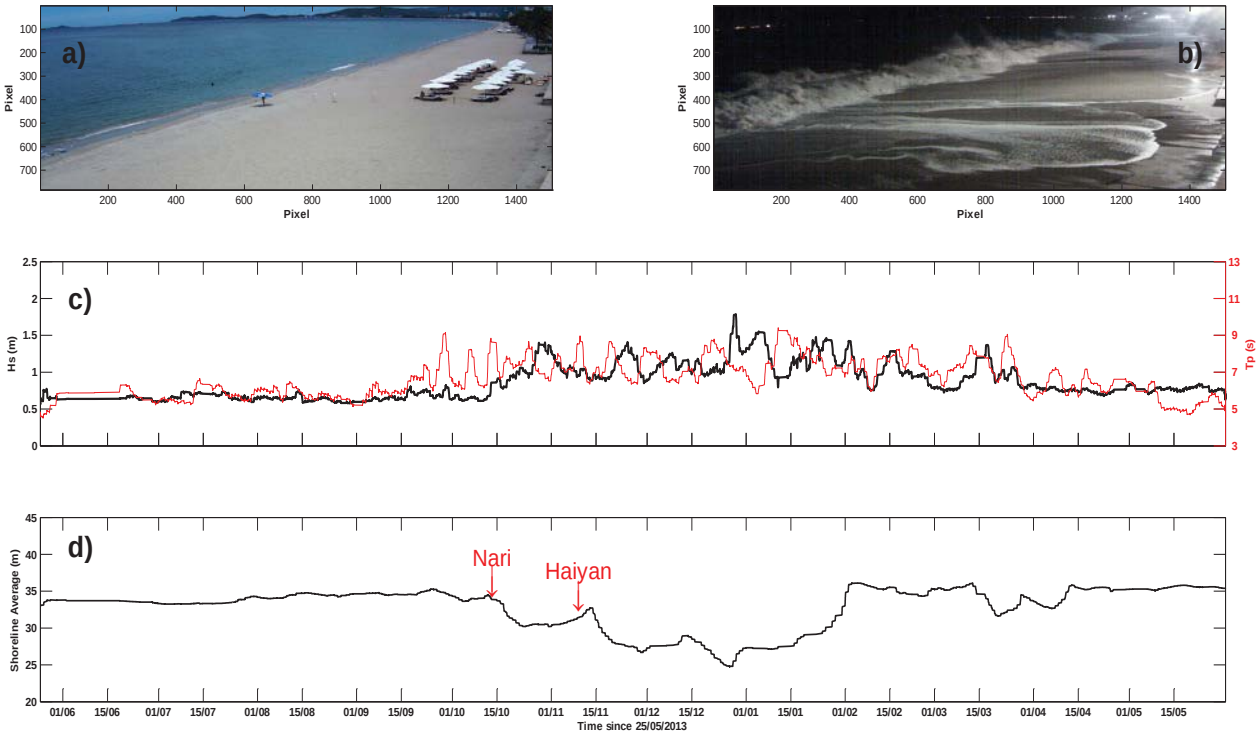

Figure 4. Typhoon impact on shoreline position. a) summer monsoon conditions with dominant south easterly waves; b) Haiyan event during the night of November 14; c) significant wave height (Hs) in black line and wave period (Tp) in red line extracted from video images during a year from June 2013 to June 2014; and d) corresponding average shoreline position compared with the embankment.

storm, the shoreline accreted rapidly. Then, the second storm (Haiyan) hit with greater impact, possibly because it had greater energy, or because it occurred in a sequence, or even because the tides were larger. After the second storm, wave forcing was generally intermediate with occasional occurrence of smaller storms. The shoreline alternated receding and accreting periods before it recovered by February. From Figure 4d, we clearly see that maximum erosion has occurred in January 2014, with 15 m difference in shoreline compared with August 2013. There is a marked seasonal evolution driven by the seasonal occurrence of storm events from August to November and recovery during northeasterly winter swell conditions.

It indicates that shoreline changes in Nha Trang beach are very significant at both storm and seasonal scales. Typhoon impact on shoreline is incremental with each strong event eroding 4 to 8 m of the beach. The cumulated shoreline variation over the season is about 15 m while the recovery to individual events is quite fast (about 1.5 month). In both cases, erosion is linked to high-energy wave forcing and accretion is important in the days following the storm, where the wave conditions are moderate. We assume that accretion relies on the presence of this moderate energy. Our results are in this sense very consistent with other studies. We suggest that the thresholds between beach accretion and erosion are as follows: Wind waves (Hs <0.4 m & T < 5s) leads to a very low onshore transport; moderate swell (0.4 m < Hs < 0.8 m & T > 5s) causes accretion and swell (Hs > 1 m & T > 5s) causes erosion. Therefore, the winter monsoon regime that succeeds to the typhoon season has an important impact on beach recovery.

CONCLUSIONS

We present the first attempt at using video cameras in Vietnam for monitoring the evolution of estuarine and coastal zones. Although progress in data processing can be made, our validation with field experiments give us some confidence on the accuracy of our techniques. The estimation of hydrodynamics variables appears satisfactory, while the mean accuracy of beach profiles is about 30 cm and locally higher. After this validation step, our study presents results on shoreline evolution. This study clearly demonstrates the resilience capacities of the beach to a two-typhoon sequence, with recovery duration of about 1.5 month. The recovery timescale is a crucial parameter for predicting either erosive or accretive beach response and varies significantly with location, ranging from days to months and years. Here, the recovery timescale is close to the recurrence interval of typhoons, which would make prediction of beach evolution sensitive to climate modulation of storm occurrence. The study is limited to a small number of events. A conceptual model could be formulated from larger time series.

ACKNOWLEDGMENTS

Part of this study was supported by a Vietnamese Protocol research project: "Study on hydrodynamic regime and sediment transport in estuarine and coastal zones of Nha Trang bay, Khanh Hoa province" from the Ministry of Science and Technology (MOST). It has also received French support from ANR (COASTVAR: ANR-14-ASTR-0019).

LITERATURE CITED

Aarninkhof, S.G.J.; Turner, I.L.; Dronkers, T.D.T.; Caljouw, M., and Nipius, L., 2003. A video-based technique for mapping intertidal beach bathymetry. *Coastal Engineering*, 49, 275-289.

Almar, R. ; Cienfuegos, R. ; Catalán, P.A. ; Michallet, H. ; Castelle, B. ; Bonneton, P., and Marieu, V., 2012. A new breaking wave height direct estimator from video imagery, *Coastal Engineering*, 61, 42-48.

Anderson,T.R.; Frazer, L.N., and Fletcher, C.H., 2010. Transient and persistent shoreline change from a storm. *Geophys. Res. Lett.*, 37, p. L08401

Angnuureng, D.; Almar, R.; Sénéchal, N.; Castelle, B.; Appeaning Addo, K., and Marieu, V., 2015. Shoreline evolution under sequences of storms from video observations at a meso-macrotidal barred beach, in revision for *Geomorphology*

Boak, E.H. and Turner, I.L., 2005. Shoreline Definition and Detection: A Review. *Journal of Coastal Research*. 214, 688-703. doi:10.2112/03-0071.1

Castelle, B. ; Marieu, V. ; Bujan, S. ; Splinter, K.D.; Robinet, A. ; Sénéchal, N., and Ferreira, S., 2015. Impact of the winter 2013-2014 series of severe Western Europe storms on a double-barred sandy coast: beach and dune erosion and megacusp embayments. *Geomorphology*, 238, 135–148

Catalán, P., and Haller, M., 2008. Remote sensing of breaking wave phase speeds with application to nonlinear depth inversion, *Coastal Engineering*, 55, 93-11

Coco G.; Senechal N.; Rejas A.; Bryan K.; Capo S.; Parisot J.P.; Brown J.A., and MacMahan J.H.M., 2014. Beach response to a sequence of extreme storms, *Geomorphology*, 204, 493-501

Davidson, M.A.; Splinter, K.D., and Turner, I.L., 2013. A simple equilibrium model for predicting shoreline change. *Coastal Engineering*, 73, pp.191–202

Ferreira, O., 2005. Storm groups versus extreme single storms: predicted erosion and management consequences. *J. Coast. Res.* SI 42, 221– 227

Frazer, L.N.; Anderson, T.R., and Fletcher, C.H., 2009. Modeling storms improves estimates of long-term shoreline change. *Geophysical Research Letters*, 36, L20404

Holland, K.T.; Holman, R.A.; Lippmann, T.C.; Stanley, J., and Plant, N., 1997. Practical use of video imagery in nearshore oceanographic field studies. *IEEE Journal of Oceanic Engineering*, 22, 81-92.

Holman, R. and Haller, M., 2013. Remote sensing of the nearshore. Annual Review of Marine Science, 113, 5–95

Jackson, N.L.; Nordstrom, K.F.; Eliot, I., and Masselink, G., 2002. "Low energ1y" sandy beaches in marine and estuarine environments : a review. *Geomorphology*, 48, 147-162.

Quartel, S.; Kroon, A., and Ruessink, B.G., 2008. Seasonal accretion and erosion patterns of a microtidal sandy beach. *Marine Geology*, 250, 19-33.

Karunarathna, H.; Pender, D.; Ranasimghe, R.; Short A.D., and Reeve, D.E., 2014. The effects of storm clustering on beach profile variability, *Marine Geology*, 348, pp. 103-112

Lefebvre, J.P.; Almar, R.; Viet, N.T.; Uu, D.V.; Thuan, D.H.; Binh, L.T.; Ibaceta, R., and Duc, N.V., 2014. Contribution of swash processes generated by low energy wind waves in the recovery of a beach impacted by extreme events: Nha Trang, Vietnam. In: Green, A.N. and Cooper, J.A.G. (eds.), Proceedings 13th International Coastal Symposium (Durban, South Africa), *Journal of Coastal Research*, Special Issue No. 70, 663-668.

Masselink, G.; Austin, M.; Scott, T.; Poate, T., and Russell, P., 2014. Role of wave forcing, storms and NAO in outer bar dynamics on a high-energy, macro-tidal beach. *Marine Geology* 226, 76-93

Nicholls, R.J.; Hoozemans, F.M.J., and Marchand, M., 1999. Increasing flood risk and wetland losses due to global sea-level rise: regional and global analyses, *Global Environmental Change*, 9, 69-87.

Splinter, K.D.; Carley, J.T.; Golshani, A., and Tomlinson, R., 2014. A relationship to describe the cumulative impact of storm clusters on beach erosion. *Coast. Eng.* 83, 49–55

Stockdon, H.F. and Holman, R.A., 2000. Estimation of wave phase speed and nearshore bathymetry from video imagery. *Journal of Geophysical Research* 105 (C9):22,015–22,033

Viet, N.T.; Nguyen V.D.; Vo C.H.; Tanaka H.; Dinh V.U.; Tran T.T.; Almar R., and Lefebvre J.P., 2014. Investigation of Erosion Mechanics of Nha Trang Coast, Vietnam, *Proceedings of the 19th IAHR-APD, Hanoi, Vietnam*.

Viet,N.T.; Nguyen V.D.; Le T.B.; Duong H.T.; Tran T.T.; Nguyen V.T.; Dinh V.U.; Almar R.; Lefebvre J.P., and Tanaka, H., 2014. Seasonal Evolution of Shoreline Changes in Nha Trang Beach, Vietnam, *Proceedings of the 19th IAHR-APD, Hanoi, Vietna*

Journal of Coastal Research	SI	75	268-272	Coconut Creek, Florida	2016

Downwind Sedimentation and Habitat Development Following Ammophila arenaria Removal and Dune Erosion, Mason Bay, New Zealand

Ella E.C.B. Buckley[†], Michael J. Hilton[†*], Teresa M. Konlechner[†] and Janice M. Lord[‡]

[†]Department of Geography
University of Otago
Dunedin, New Zealand

[‡]Department of Botany
University of Otago
Dunedin, New Zealand

www.cerf-jcr.org

www.JCRonline.org

ABSTRACT

Buckley, E.C.B.; Hilton, M.J., Konlechner, T.M., and Lord, J.M., 2016. Downwind sedimentation and habitat development following *Ammophila arenaria* removal and dune erosion, Mason Bay, New Zealand. *In:* Vila-Concejo, A.; Bruce, E.; Kennedy, D.M., and McCarroll, R.J. (eds.), *Proceedings of the 14th International Coastal Symposium* (Sydney, Australia). *Journal of Coastal Research*, Special Issue, No. 75, pp. 268-272. Coconut Creek (Florida), ISSN 0749-0208.

Since 2002 *Ammophila arenaria* has been progressively eradicated from a section of the transgressive dune system at Mason Bay, New Zealand to restore dune mobility. This study examines whether sand released from the treatment areas is accumulating in down-wind dune environments, particularly stony deflation surfaces. Deflation surfaces are nationally threatened habitats that contain at-risk native plants and are important flocking sites for endangered shore birds. Sand accumulation in the stonefield may cause a shift in texture and character from deflation lag to sand dunes, potentially reducing habitat for these species. Sediment accumulation was examined over a nine month period within a 200m x 50m plot located immediately downwind of a series of long-walled parabolic dunes, recently destabilised by *A. arenaria* removal. Sand accumulation was monitored using 500 erosion pins. Digital elevation models were derived from two total station surveys to determine whether sand is accumulating in conjunction with *Ficinia spiralis* nebkha. Wind speed and direction were measured during wind events to determine whether sand is deposited during these events or whether sand passes through. The surface of the study area accreted 3.22mm, on average, during the study. Accretion and erosion was not strongly correlated with vegetation cover. The intensity of aeolian sedimentation appears to increase with increasing distance inland, because the study site increases in elevation and exposure further inland. Sand pits dug across the area showed medium term sand accumulation aross the study site with most of the accumulation closer to the eroding depositional lobes.

ADDITIONAL INDEX WORDS: *Dynamic restoration, deflation plain, marram grass, transgressive dune fields*

INTRODUCTION

Coastal dunes lie at the interface between the marine and terrestrial environment, providing habitat for a unique array of flora and fauna. Transgressive dunes are actively migrating sand deposits situated over vegetated to semi-vegetated terrain (Hesp and Thom, 1990). The cycles of erosion and stabilization generated by the geomorphic processes in transgressive dunes provide the environmental conditions and gradients required by a suite of different ecological communities (Grootjans *et al.*, 2013; Martinez *et al.*, 2013; Nordstrom *et al.*, 2000; Rhind *et al.*, 2013).

Historically, management of transgressive dunes has been concerned with erosion control (Klijn, 1990; Van der Meulen *et al.*, 1989; Walker *et al.*, 2013). Dune-systems were stabilized, usually through the deliberate planting of dune vegetation, commonly *Ammophila arenaria* (marram grass). Aeolian processes were suppressed, leading to a loss in landform complexity and dynamics (Arens *et al.*, 2013a; Hilton, 2006; Hilton *et al.*, 2005; Wiedemann and Pickart, 1996).

Over the last few decades there has been increasing awareness of the positive relationship between dune mobility and coastal biodiversity (Arens *et al.*, 2013b; Walker *et al.*, 2013). Many species are able to survive in dune soils, inland from the foredune, but a few are dependent on a dynamic dune landscape. These obligate and semi-obligate psammophytes are now threatened as dune-systems have been managed to promote stability. Further, dune mobility creates diverse landscapes capable of supporting a range of plant communities, whereas stable dunes may not.

Several projects have commenced that aim, usually through the deliberate removal of vegetation, to re-establish natural disturbances and related morphodynamics (*e.g.*, Arens *et al.*, 2013b; Konlechner *et al.*, 2014; Walker *et al.*, 2013). This process is commonly referred to as 'dynamic restoration'. The ecological values of a dune system often provide the catalyst for restoration, however, dynamic restoration differs from the more traditional ecologically focused restoration in that the aim is the restoration of geomorphic processes, rather than specific habitats or species assemblages.

DOI: 10.2112/SI75-54.1 received 15 October 2015; accepted in revision 15 January 2016.
*Corresponding author: mjh@geography.otago.ac.nz

To date there has been little consideration of the short-term dune system response to dynamic restoration. The dynamic restoration programme at Mason Bay, Stewart Island provides an opportunity to study the effects of dune destabilization on down-wind landforms, habitats and associated plant communities. We predict that the remobilization of dune forms will increase sand deposition downwind. A sudden substantial increase in sand deposition may result in transformations in the dune forms downwind, the loss of downwind habitats, and/or alterations to plant community composition.

This study examines spatial and temporal patterns of sand accumulation in the stonefield at Mason Bay. The implications of these findings for the evolution of the stonefield environment following dynamic restoration are considered.

Dynamic restoration of the Mason Bay dunes

Mason Bay is situated on the west coast of Stewart Island, New Zealand (Lat. S46°55', Long. E167°47') (Figure 1). The predominant direction of sand transport is onshore, as the wind regime is dominated by strong W-SW winds. This study focuses on a section of the transgressive dune system (the 'central dunes') between Duck Creek and Martins Creek. The dunes here have transgressed over a broad, gently-sloping surface, and are relatively unmodified by the underlying bedrock. Landforms comprise of a large stable foredune and a series of parabolic dunes which have formed and stabilized following the invasion of *A. arenaria* in 1958 (Hart *et al.*, 2012; Hilton *et al.*, 2005). A large deflation surface characterized by a gravel-sized lag deposit, locally known as the 'great stonefield', is located immediately downwind of the parabolic dunes (Figure 2).

The New Zealand Department of Conservation (DOC) started a dynamic restoration effort at Mason Bay in 2001, which aims to restore the geomorphic processes of aeolian sand transport and dune mobility through the eradication of *A. arenaria* (Hilton and Konlechner, 2010). *A. arenaria* is removed by applying grass-specific herbicide via knapsacks, vehicles and helicopters. *A. arenaria* was removed from the depositional lobes of the parabolic dunes in 2006, which initiated gradual erosion and subsequent sand transport downwind.

There has been some downwind expansion of the depositional lobes since *A. arenaria* was removed, a few metres, but it is not currently known whether sand is accumulating throughout the stonefield environment. It is expected that the dynamic restoration project at Mason Bay will result in widespread reorganization of dune forms in the medium to long term, so that understanding patterns of sand transport and accumulation in the short-term is important to the managers of this site. The stonefield supports a distinctive native plant community comprised of a few dune binders (*Ficinia spiralis* and *Poa billardierei*) but also non-sand binding plants such as *Coprosma acerosa* and the native cushion plant *Raoulia hookeri var. hookeri* (Hilton *et al.*, 2005). The stonefield also provides habitat for wildlife – most notably the critically threatened southern New Zealand dotterel (*Charadrius obscurus obscurus*). Increased sand accumulation in the stonefield may have profound physical and ecological implications, including the displacement of stonefield-specific species.

METHODS

Sand accumulation was measured within a 200m x 50m study site, located in the stonefield downwind of the parabolic dunes (Figure 1). The net accretion or erosion of the study site surface over a nine month period from June 2014 to March 2015 was measured using erosion pins. The study site was divided into one hundred, 10m^2 cells with five erosion pins in each cell (red squares in Figure 1). The height of each pin was recorded in June 2014 at the start of the study period, and re-recorded in March 2015.

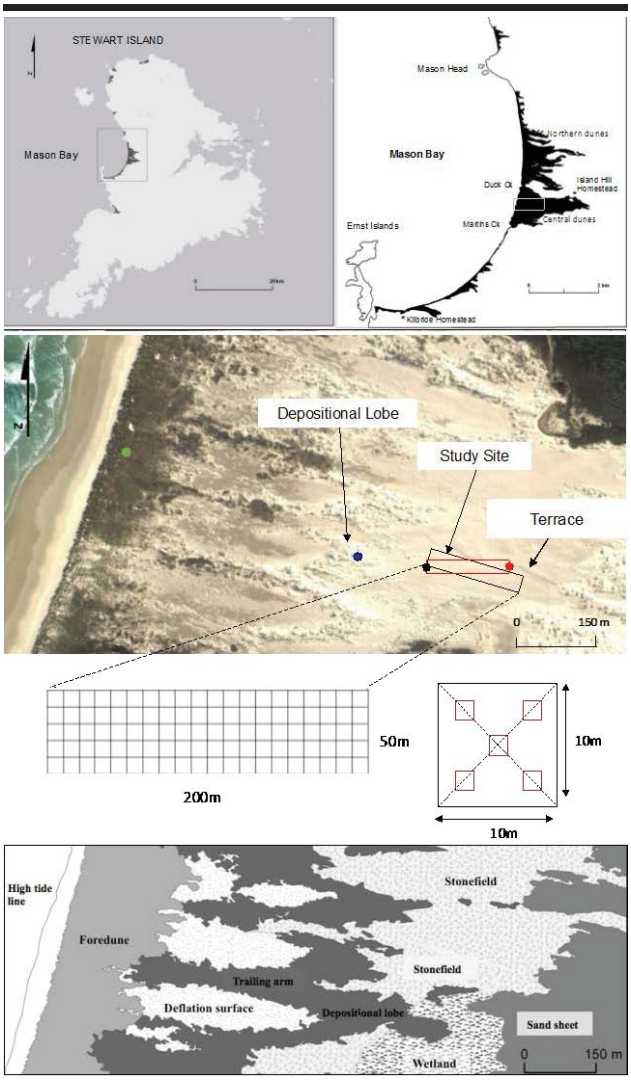

Figure 1. Mason Bay transgressive dune system on the west coast of Stewart Island, New Zealand. Measurements of wind flow across the stonefield were made in the red rectangle. The associated landforms include foredune, deflation surface, parabolic dune (comprised of the trailing arms and depositional lobe), stonefield, wetland and sand sheet.

The change in sand surface against the five erosion pins within each cell were averaged to calculate net accretion or erosion per cell. The presence of the native sand binding plants (*F. spiralis* and *P. billardierei*) within a $1m^2$ square around each pin was recorded allowing patterns of sand accumulation and/or erosion to be related to vegetation.

Nebkha (long-tailed shadow dunes developed in conjunction with *F. spiralis*) growth can be used to indicate a positive or changing sand budget. A total of 18 nebkha were selected at approximately 10 m intervals along the east-west central axis of the study site to measure changes in nebkha volume. These were surveyed using a Leica total station in August 2014 and March 2015, and the volumetric change between sampling intervals calculated in Surfer®13.

Figure 2. Oblique view of the Mason Bay stonefield facing east (landwards) into the study area, (June 2014). Note the stony lag deposit, *R. hookeri var. hookeri* cushion plants and the *F. spiralis* nebkha and the orientation of the nebkha tails following a period of Northeast (offshore) winds.

Soil pits were dug across the study site to examine recent (since 2006) patterns of sand accumulation. Additional pits were dug outside the study area close to the depositional lobes. Accumulation was measured from the stonefield surface to the depth of recently buried *R. hookeri var. hookeri*.

To measure wind speed and direction across the stonefield a vertical array of 2D sonic anemometers were erected at each end of the study area at a height of 0.2-1.6m. The study site was corrected in relation to current wind direction at the time of the experiment (SW) (red rectangle in Figure 1). A single sonic anemometer was erected at 6m on the depositional lobe to measure the regional wind and a long term anemometer on the foredune (2m) was used for comparison (blue and green dots in Figure 1).

RESULTS

The surface of the study site showed a net average accretion of 3.2mm over the nine month study period (which equates to 4.3mm/yr). Most erosion pins recorded sand accretion (58%), with roughly equal numbers of pins measuring erosion (21%) or no change (20%) in the stonefield surface. The accretion/erosion range measured by the erosion pins was small. The maximum accretion measured was 16.0 mm and maxium erosion 10.5 mm (21.3mm/yr and 14.0mm/yr, respectively).

Some distinct areas of erosion and accretion could be seen centred around *F. spiralis* plants (Figure 3). Overall, however, there was no obvious spatial pattern of sand accumulation and/or erosion within the study area.

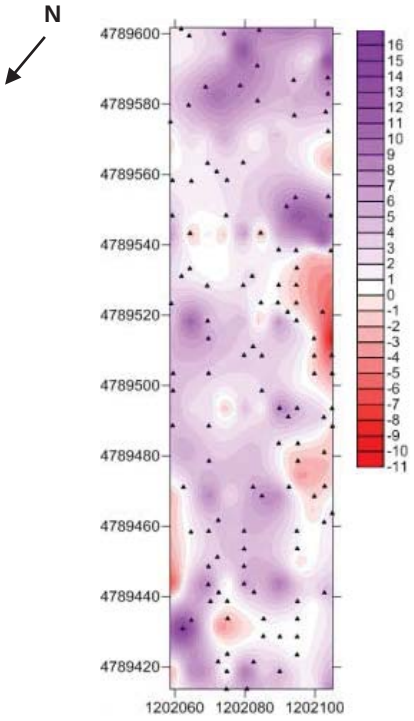

Figure 3. Contour map showing the average accretion and erosion of sand per 10 m^2 quadrant between June 2014 and August 2015. The contour map is facing inland (SE) of the parabolic depositional lobes. The scale bar on the right indicates the sand accretion (purple) and erosion (red) in mm. Black triangles indicate the location of *F. spiralis* plants.

The average net volume change of the 18 surveyed nebkha, was only $0.29m^3$ (average nebkha volume was $2.09m^3$) This small change was considered to be within the margin of measurement error and so the nebkha were considered stable across the stonefield between August 2014 and March 2015.

All soil pits indicated recent burial across the study site. Sand accumulation above the recently buried *R. hookeri var. hookeri* ranged from 4mm to 155mm, and in general decreased with distance downwind from the parabolic dunes (Figure 4).

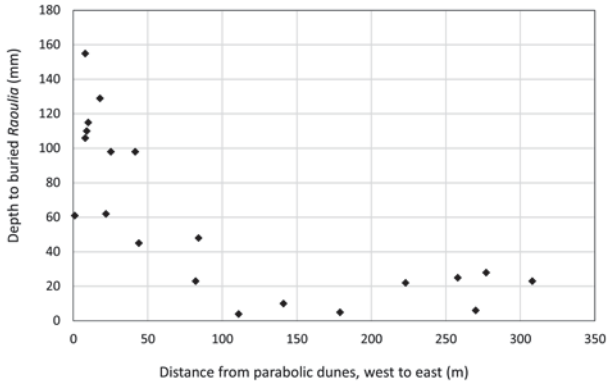

Figure 4. Variation in depth to the former stonefield surface, indicated by the presence of *R. hookeri var. hookeri*, across the stonefield.

In the stonefield, the wind speeds recorded at the landward (eastern) margin of the study area were often greater or equal to the wind speed recorded at the seaward edge during each wind event (Figure 5). This suggests that there is no decline in wind speed across the stonefield. There were periods of stronger wind velocities (above 4m/s) in which the wind velocity on the landward margin was greater than the seaward margin. A topographic cross section through the study site (Figure 6), showed that there is an elevation increase moving inland, equivalent to a 2.7m elevation increase per 100m.

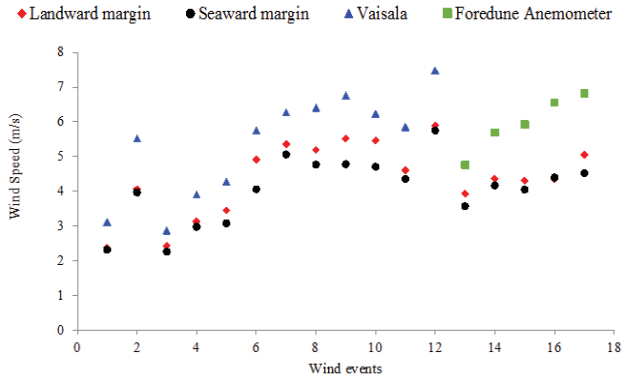

Figure 5. Comparison of wind speed between the landward and seaward instrument arrays in the stonefield and regional (Vaisala) and foredune anemometers. These are average values derived from three to five minute sections of the wind record. The wind events were recorded in August 2014 (N=12) and March 2015 (N=15).

DISCUSSION

We recorded some sand deposition across the study site during the 9-month study. However, we recorded no change in the dimensions of the *F. spiralis* nebkha monitored. We found no discernible spatial variation in sand accumulation or erosion over the study site, however, the soil pits revealed that there has been burial of the stonefield surface in the lee of the parabolic depositional lobes since 2015.

Figure 6. Cross section through the short-term sedimentation study site. The intersecting lines indicate the start and finish of the study site. The western side of the study area is to the right.

Sand deposition in the lee of destabilised landforms, such as foredunes and parabolic dunes, has been noted in previous studies, following mechanical (Arens *et al.*, 2013a; Walker *et al.*, 2013) and herbicide *A. arenaria* removal efforts (Konlechner *et al.*, 2014). In the present case, the use of herbicides to achieve *A. arenaria* necrosis left the *in situ A. arenaria* rhizome and dead plant material in place, which has slowed the geomorphic response to devegetation. Moreover, *F. spiralis* has established a patchy cover across the depositional lobes since the eradication of *A. arenaria*, which has probably further slowed erosion of these landforms (Figure 7).

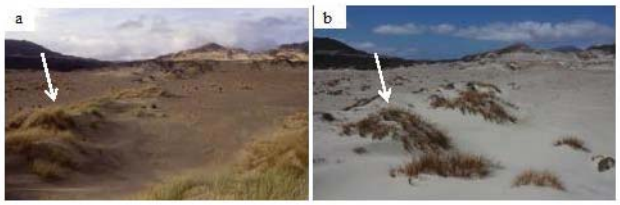

Figure 7. Oblique views of one of the parabolic dune depositional lobes extending into the stonefield: a) parabolic depositional lobe in 1998 (the white arrow indicates *A. arenaria* colonization). *F. spiralis* has since colonized the leeward side of the depositional lobes (b), which has slowed but not prevented the erosion of this parabolic dune. The white arrow, indicates recent *F. spiralis* colonization.

The results of the present study contrast with those of Walker *et al.* (2013) where the transgressive dune system downwind of the destabilised foredune acted as a sink for the eroded sand. The small amount of sand accumulation in the Mason Bay stonefield during the study period is primarily attributed to the landward increase in elevation and consistent exposure of the stonefield to the prevailing westerly winds. The soil pit data, which records deposition across the stonefield over the last 9 years, since 2006, indicates ongoing sand accretion.

We suspect the nebkha are not trapping sand and growing over the medium term (years) because the tails are periodically eroded during northerly wind events. This may change over

time, particularly if the surface of the stonefield becomes generally more sandy, but for now there is almost no evdience of measured plant vigour and accelerated nebkha growth.

This study was limited by the short study period available. The sand pits were dug to measure the medium term sedimentation patterns and to help address the short study period. This study site and *F. spiralis* nebkha have been marked with long term markers to allow for future monitoring of downwind sedimentation.

CONCLUSIONS

A. arenaria eradication operations have led to enhanced sedimentation across a valued stonefield habitat. Dune erosion has not occurred rapidly, but there is unequivocal evidence of sand accumulation across the stonefield. We are uncertain whether the stonefield will transition from a deflation surface to a dunal landscape as a result of *A. arenaria* eradication at Mason Bay. This study has not observed the enhanced development of discrete dunes, namely the accretion of nebkha. This is probably because the stonefield is exposed to winds from multiple directions (West and Northeast) and the nebkha are extremely dynamic. Over time it is likely the stonefield will become more sandy despite the development of nebkha.

ACKNOWLEDGMENTS

This work was surported by the New Zealand Department of Conservation.

LITERATURE CITED

Arens, S.M.; Slings, Q.L., and Geelen, L.H.W.T., 2013a. Restoration of Dune Mobility in The Netherlands. *In:* Martinez, M.L.; Gallego-Fernandez, J.B. and Hesp, P.A. (eds.), *Restoration of Coastal Dunes*. Vergal: Springer, 107-124p.

Arens, S.M.; Mulder, J.P.; Slings, Q.L.; Geelen, L.H., and Damsma, P., 2013b. Dynamic dune management, integrating objectives of nature development and coastal safety: examples from the Netherlands. *Geomorphology*, 199, 205-213.

Grootjans, A.P.; Dullo, B.S.; Kooijman, A.M.; Bekker, R.M., and Aggenbach, C., 2013. *In:* Martínes, M.L.; Gallego-Fernandez, J.B., and Hesp, P.A. (eds.), *Restoration of Coastal Dunes*. Vergal: Springer, 235-254p.

Hart, A.T.; Hilton, M.J.; Wakes, S.J., and Dickinson, K.J., 2012. The impact of *Ammophila arenaria* foredune development on downwind aerodynamics and parabolic dune development. *Journal of Coastal Research*, 28(1), 112-122.

Hesp, P.A., and Thom, B.G., 1990. Geomorphology and Evolution of Active Transgressive dunefields. *In:* Nordstrom, K.F.; Psuty, N.P., and Carter, B. (eds.), *Coastal Dunes, Form and Process*. Chichester, United Kingdom: Wiley, 253-288p.

Hilton, M.J., 2006. The loss of New Zealand's active dunes and the spread of marram grass (*Ammophila arenaria*). *New Zealand Geographer,* 62, 105-121.

Hilton, M.; Duncan. M., and Jul, A., 2005. Processes of *Ammophila arenaria* (marram grass) invasion and indigenous species displacement, Stewart Island, New Zealand. *Journal of Coastal Research*, 21(1), 175-185.

Hilton, M.J. and Konlechner, T.M., 2010. A review of the marram grass eradication program (1999–2009), Stewart Island, New Zealand. *Proceedings of the 17th Australasian weeds conference* (Christchurch, New Zealand), 26-30.

Klijn, J.A., 1990. The younger dunes in the Netherlands; chronology and causation. geomorphology-hydrology-soils. *Catena Supplement,* 18, 89-100.

Konlechner. T,M.; Hilton, M.J., and Arens, S.M., 2014. Transgressive dune development following deliberate de-vegetation for dune restoration in the Netherlands and New Zealand. *Dynamic environments,* 33, 141-154.

Martinez, M.L.; Hesp, P. A., and Gallego-Fernandez, J.B., 2013. Coastal dunes: Human Impact and Need for Restoration. *In:* Martinez, M.L.; Gallego-Fernandez, J.B., and Hesp, P.A. (eds.), *Restoration of Coastal Dunes*. Vergal: Springer, 1-14p.

Nordstrom, K.F.; Lampe, R., and Vandemark, L.M., 2000. Reestablishing naturally functioning dunes on developed coasts. *Environmental Management,* 25, 37-51.

Rhind. P.; Jones. R., and Jones. L., 2013. The Impact of Dune Stabilization on the Conservation Status of Sand Dune Systems in Wales. *In:* Martínes, M.L.; Gallego-Fernandez, J.B., and Hesp, P.A. (eds.), *Restoration of Coastal Dunes*. Vergal: Springer, 125-143p.

Van der Meulen, F.; Jungerius, P.D., and Visser, J.H., 1989. *Perspectives in coastal dune management.* The Hague: SPB Academic Publishing, 247p.

Walker, I.J.; Earmer, J.B.R., and Darke. I.B., 2013. Assessing significant geomorphic changes and effectiveness of dynamic restoration in a coastal dune ecosystem. *Geomorphology*, 199, 192-204.

Wiedemann, A.M. and Pickart, A., 1996. The *Ammophila* problem on the North West Coast of North America. *Landscape and Urban Planning,* 34, 287-299.

Journal of Coastal Research	SI	75	273-277	Coconut Creek, Florida	2016

Wave Energy as a Control on Dune Development on two Regressive Barriers in Southern Brazil

Sergio Dillenburg[†], Patrick Hesp[††], Renato Cecilio[§], Graziela Miot da Silva[††]

[†] Centro de Estudos de Geologia Costeira e Oceânica, Universidade Federal do Rio Grande do Sul, Av. Bento Gonçalves 9500, Porto Alegre - RS 91509-900 Brasil

[§] Programa de Pós-Graduação em Geociências Universidade Federal do Rio Grande do Sul, Av. Bento Gonçalves 9500, Porto Alegre - RS 91509-900 Brasil

[††] Flinders University, School of the Environment, Sturt Rd, Bedford Park, South Australia 5042

www.cerf-jcr.org

www.JCRonline.org

ABSTRACT

Dillenburg, S.; Hesp, P.; Cecílio, R., and Miot da Silva, G., 2016. Wave Energy as a Control on Dune Development on two Regressive Barriers in Southern Brazil**.** *In:* Vila-Concejo, A.; Bruce, E.; Kennedy, D.M., and McCarroll, R.J. (eds.), *Proceedings of the 14th International Coastal Symposium* (Sydney, Australia). *Journal of Coastal Research*, Special Issue, No. 75, pp. 273-277. Coconut Creek (Florida), ISSN 0749-0208.

Two regressive barriers (Cassino and Curumim) were developed during the middle and late Holocene along gentle re-entrants of the Rio Grande do Sul coast, and they have prograded up to 17 km and 5 km, respectively. While Cassino is marked by a surface morphology characterised predominantly by foredune ridges, Curumim displays a surface completely covered by widely spaced ridges, corresponding to phases of transgressive dunefield formation. As wave period and shoreline orientation are very similar for both barriers, and considering that they are subjected to the same deepwater wave climate, the substantial surface morphological differences between the barriers is, at least in part, a direct consequence of variations in wave height at the two sites. In addition, there is a significant difference in potential sand transport and wind power between the two sites. As transgressive dunefields and parabolic dunes can develop as a consequence of foredune destabilization, followed by wind action, it is very possible that at Cassino, during barrier development storm waves were not strong enough to destabilised the foredune system and, in addition, if storm scarping occurred, winds were not competent to destabilise the foredunes, thus providing conditions for the formation predominantly of a foredune ridge plain. Only occasionally, presumably during very strong storms (or multiples thereof), foredune destabilization has resulted in dune transgression. At Curumim, either storm waves and higher wind strengths were more effective in dune destabilization, or foredunes rarely developed allowing the formation of multiple phases of transgressive dunefields during barrier progradation.

ADDITIONAL INDEX WORDS: *Shelf morphology, Transgressive dunefields, Foredune ridges.*

INTRODUCTION

The Rio Grande do Sul coastline is gently undulating and consists of two large subdued seaward projections and two landward reentrances (Figure 1). Coastal re-entrances (concave sectors of the coast) are dominated by regressive (prograded) barriers whereas protruding sectors of the coast typically have transgressive (retrogradational) and stationary (aggradational) barriers capped with transgressive dunes. A correlation also exists between the coastal configuration and the morphology of the continental shelf. Along coastal re-entrants, the shelf is wider and more gently sloping, whereas along coastal projections it is narrower and steeper. The focus of this paper are the regressive barriers (Cassino and Curumim) occurring along the two concave re-entrant sectors. They are spaced 350 km apart and were developed during the middle and late Holocene. In the following, we try to demonstrate that differences in the adjacent shelf slope of only 0.03°, by driving a major difference in the significant wave height, and differences in potential sand transport could explain the distinct dune morphologies of these two regressive barriers.

REGIONAL SETTING

Rio Grande do Sul is characterized by a 620-km long coastal barrier, generally oriented NE-SW, comprised by exposed, fine sand, dissipative to intermediate beaches. The regional average wave height is 1.5 m and the coast is microtidal with

DOI: 10.2112/SI75-55.1 received 15 October 2015; accepted in revision 15 January 2016.
*Corresponding author: sergio.dillenburg@ufrgs.br

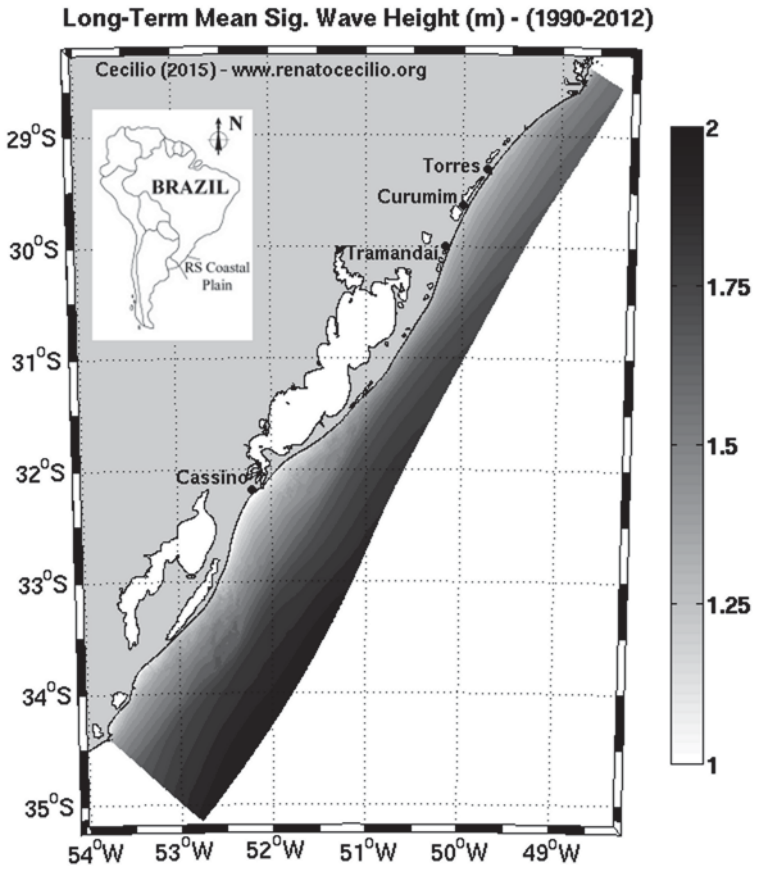

Figure 1. SWAN results showing the distribution of significant wave height along the Southern Brazilian Shelf, valid for the time 1990-2012 (from Cecílio, 2015). Curumim and Torres are 50 km spaced apart.

semidiurnal tides that have a mean range of only 0.3 m. Consequently, sediment transport and deposition along the open coast is primarily dominated by wave action, which produces a net northward littoral drift. The NE wind predominates along the whole coast, but varies considerably depending on location (Miot da Silva *et al*., 2013). Cecílio (2015) produced a wind-wave climatology for the Rio Grande do Sul coast and confirmed the existence of wave gradients along the coast, which are mainly produced by differences in the continental shelf morphology (lateral alternation of relatively gentle and steeper shelf slopes). At Cassino, the very gentle slope of the barrier substrate and of the adjacent shelf of 0.027° dissipates a great amount of wave energy by bottom friction, resulting in a significant wave height varying from 0.85 to 1.00 m at the upper shoreface. At Curumim, the barrier substrate and shelf slope of 0.057° dissipates less wave energy, resulting in a significant wave height varying from 1.20 to 1.35 m at the upper shoreface. Sea-level during the Holocene reached a maximum height of 2-3 m at around 5.6 ka, followed by an overall fall until present (Angulo *et al*., 2006).

METHODS

This study is based on previous research dealing with the surface morphology and geological evolution of the two Holocene regressive barriers of RS (Clerot, 2004; Dillenburg *et al*., 2006; Dillenburg *et al*., 2009; Hesp *et al*., 2005; Hesp *et al*., 2007; Martinho *et al*., 2009), and climatological analyses along the Brazilian south coast (Miot da Silva *et al*., 2013). An analysis of alongshore wave energy gradients along the southern Brazilian coast was conducted by Cecílio (2015) utilizing a SWAN (Simulating Waves Nearshore) model and detailed nearshore bathymetry. All ages presented are calibrated ^{14}C. The innovative factor here is the proposal of conditioning factors that singly or together could explain the differences in the aeolian morphologies of the emerged portions of the two barriers.

RESULTS

The evolution of the two barriers is described below.

Cassino regressive (prograded) barrier

The Cassino barrier shows a history of progradation along approximately 100 km of coastline. This coast is oriented NNE-SSW (Figure 1). Most of the progradation was a consequence of a high positive balance in sediment budget. Forced regression due to a small post-5600 yrs sea level fall played a secondary role (Dillenburg *et al*., 2009). The predominant result was a foredune ridge plain with a maximum width of up to 17 km that started to form at around 6.0 - 5.5 ka (Figure 2). The adjacent average shelf slope is 0.027°. Wind energy is relatively low with a mean of 3.76 vector units as indicated by the resultant drift potential (RDP - essentially potential aeolian sand transport; Fryberger and Dean, 1979) determined by Miot da Silva *et al*. (2013) for the period 1964-2003 for Rio Grande, a city just adjacent to Cassino. Six sets or suites of ridges showing changes in orientation are clearly identifiable, and the limit between them is marked by erosion and the formation of transgressive dunefields/parabolic dunes. While the morphology of foredune ridges dominates 70% of the barrier surface, transgressive dunefields/parabolic dunes occupy the remaining 30%, and they are characterized by a low lateral continuity (usually less than 20 km) and by significant irregularity. These aeolian deposits are 0.5 to 2.5 m thick (covering foreshore deposits).

Curumim regressive (prograded) barrier

The Curumim barrier is part of a long and gentle reentrant of the coast (200 km long) that can be divided into two distinct halves. The well-studied half is located between Tramandaí and Torres, which is oriented NNE-SSW (Figure 1). Torres is the northern limit of the studied barrier where a large promontory of volcanic rocks interrupts the dominant northward littoral drift system. Again, here forced regression has played a secondary role on the total barrier progradation that reached its maximum width of 5 km at the beach called Curumim. Progradation started at around 7.5 - 7.0 ka, during the final stages of the Postglacial Marine Transgression (PMT), due to a larger rate on sediment input in comparison to the rate of sea-level rise. The adjacent average shelf slope is 0.057°. The wind energy is relatively high compared to Cassino with a mean RDP of 36 vector units determined for the same period (Miot da Silva *et al*., 2013). During barrier progradation, concomitant multiple phases of dune transgression resulted in the formation of relatively wide, low, coast-parallel dunefields and ridges that are continuous for at least 30 km and very regular (uniform), spaced from 600 to 80 m apart and that completely cover the surface of the barrier (Figure 3). The ridges are precipitation ridges and define the landward limit of each transgressive dunefield phase (Hesp *et al*., 2005). The aeolian deposits are 1 to 8 m thick.

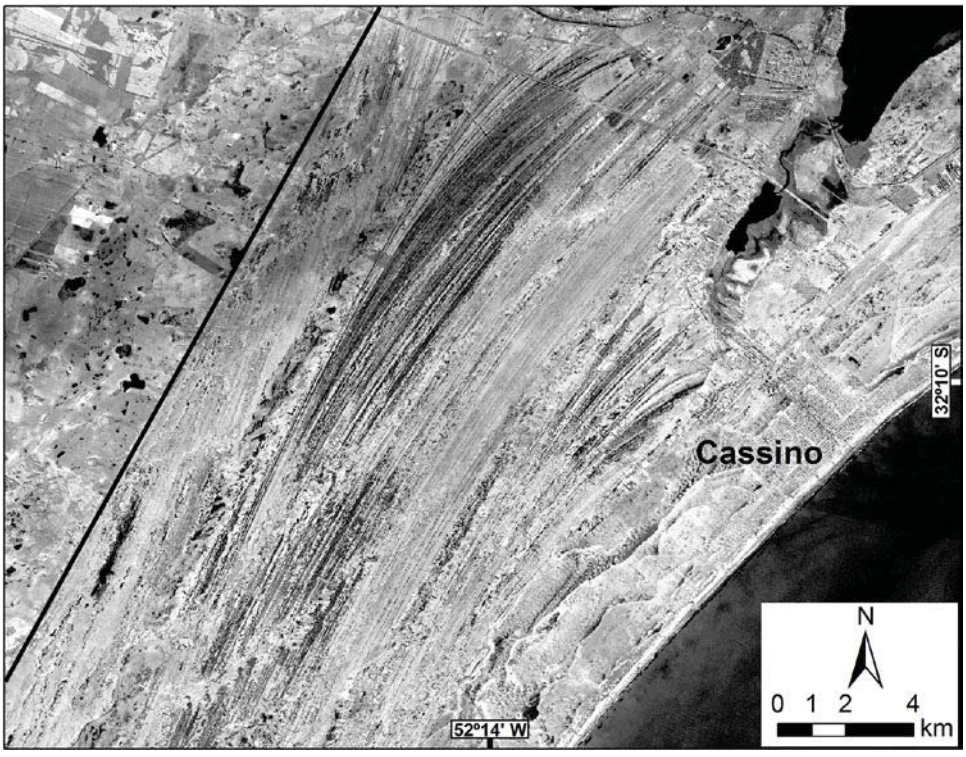

Figure 2. Satellite image showing the dominance of foredune ridges in the Holocene regressive (prograded) barrier at Cassino. (Image from ALOS satellite). The black line marks the inner limit of the Holocene barrier.

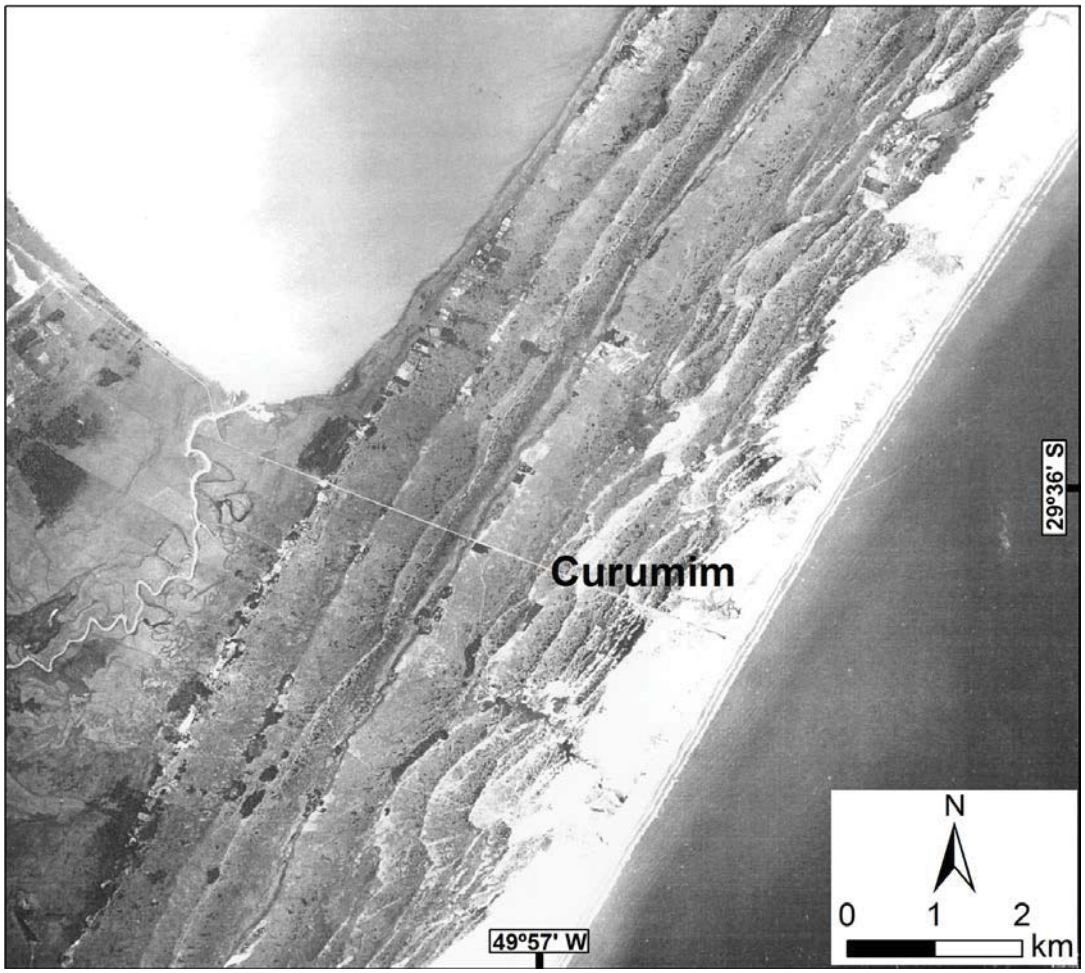

Figure 3. Aerial photograph (1965) showing the widely spaced ridges corresponding to phases of transgressive dunefield formation at Curumim.

DISCUSSION AND CONCLUSIONS

The two barriers have their shoreline orientation, precipitation, and the general wave climate in deep water in common. The existence of wave energy gradients along the RS coast were previously measured by Dillenburg *et al.* (2003) and Martinho *et al*. (2009), and modelled for various storm scenarios by Guimaraes *et al*. (2014). Recently Cecílio (2015) by applying the wind-wave model SWAN at a basin scale across the Southern Brazilian continental shelf, presented average values for significant wave height for a medium-term period (1990-2012), and from -100 m up to the upper shoreface (~ -4 m). The modelling results clearly show the presence of wave gradients alongshore, with lower waves observed along coastal re-entrants and higher waves along coastal projections (Figure 1). The two coastal re-entrants, where the Cassino and Curumim barriers developed, present the gentlest slopes of the RS continental shelf. The shelf off Cassino (0.027°) is slightly gentler that Curumim (0.057°). According to the SWAN modelling, wave energy dissipation by bottom friction is much higher across the Cassino shelf, resulting in a long-term significant wave height varying from 0.85 to 1.00 m at the upper shoreface, while at Curumim it varies from 1.20 to 1.35 m. This significant wave height variation (~35%) between the two locations is produced by a difference of slope of only 0.03°. Schwab *et al*. (2000) found that important differences in the volume of sediments transported cross-shore, in two sectors of the barrier system of Long Island, New York are a consequence of a difference of only 0.04° on the shelf slope.

The general configuration of the RS coastline and continental shelf did not substantially change in the last 7-6 ka (Dillenburg *et al*. 2000). Thus, it is very reasonable to assume that these wave energy gradients existed since that time. Hesp and Thom (1990) presented seven natural conditions that can trigger transgressive dunefield initiation. We believe that the condition of changes in storminess and shoreline erosion is the one that could explain the large-scale difference in the aeolian

morphologies of the two barriers. As wave height is differentiated in the upper shoreface zone of the two barriers, it might be assumed that this differentiation persists (or has persisted) during storm conditions. This means that storms at Curumim would be more effective in foredune erosion (destabilization followed by transgressive dunefield formation), or foredunes rarely if ever developed allowing the formation of frequent and well developed phases of transgressive dunefields during barrier progradation. Higher potential aeolian transport meant that foredune destabilization was much more likely at Currumim than at Cassino. At Cassino, storm waves would not be strong enough to create a situation where the foredune system was subsequently destabilized, and lower aeolian sand transport potential limited foredune destabilization by winds when wave scarping took place, thus providing conditions for the formation predominantly of a foredune ridge plain during progradation. Only occasionally, presumably during very strong storms (or multiples thereof), foredune destabilization has resulted in dune transgression, or perhaps at this time a foredune did not form, but rather a small phase of transgressive/parabolic dunefields formed. This condition resulted in low continuity and low uniformity of the transgressive dunefields at Cassino. In contrast, at Curumim the higher wave energy during the middle and late Holocene was sufficiently increased during storms to effectively destabilize the foredune system along a significant length of the coast. Alternatively, foredunes never formed, and transgressive dunefield phases were the common response to the higher wave and wind energy environmental drivers. In either case (foredune destabilization, or no foredunes ever forming), these processes produced a more uniformly shaped and high lateral continuity transgressive dunefields at Curumim compared to Cassino.

ACKNOWLEDGEMENTS

We thank CAPES/Brasil funding to Dillenburg for a visiting sabbatical Fellowship at Flinders University (Grant Nº BEX 5287/14-6), and Flinders University School of the Environment for support.

LITERATURE CITED

Cecílio, R.O., 2015. *An Ocean Wind-Wave Climatology for the Southern Brazilian Shelf*. Universidade Federal do Rio Grande do Sul. PhD Thesis, 102p.

Clerot, L.C.P., 2004. *Estudo da Bareira IV na Região do Cassino, Rio Grande – RS: Evolução e Caracterização como Reservatório*. Porto Alegre, Brazil: Universidade Federal do Rio Grande do Sul, Undergraduate dissertation, 75p.

Dillenburg, S.R.; Roy, P.S.; Cowell, P.J., and Tomazelli, L.J., 2000. Influence of antecedent topography on coastal evolution as tested by the shoreface translation-barrier model (STM). *Journal Coastal Research*, 16, 71-81.

Dillenburg, S.R.; Tomazelli, L.J., and Clerot, L.C.P., 2003. Gradients of wave energy as the main factor controlling the evolution of the coast of Rio Grande do Sul in southern Brazil during the Late Holocene. *Proceedings of the Coastal Sediments '03*, 5, Clearwater Beach., Regional alongshore variability of shoreline movements, pdf, 9 p.

Dillenburg, S.R.; Barboza, E.G.; Tomazelli, L.J.; Hesp, P.A.; Clerot, L.C.P., and Ayup-Zouain, R.N., 2009. The Holocene Coastal Barriers of Rio Grande do Sul. *In*: Dillenburg, S.R. and Hesp, P.A. (eds.). *Geology and Geomorphology of Holocene Coastal Barriers of Brazil*. Springer, Lecture Notes in Earth Sciences, 107, pp. 53-91.

Fryberger, S. and Dean, G., 1979. Dune forms and wind regime. *In*: McKee, E.D. (ed.) A Study of Global Sand Seas. Washington, US Govt. Printing Office, *Geol. Survey Prof. Paper* 1052: p. 137 – 170.

Guimarães, P.V.; Farina, L., and Toldo Jr., E.E., 2014. Analysis of extreme wave events on the southern coast of Brazil. *Nat. Hazards Earth Syst. Sci*., 14, 3195–3205.

Hesp P.A. and Thom, B.G., 1990. Geomorphology and evolution of transgressive dunefields. *In*: Nordstrom, K.F.; Psuty, N.P., and Carter, R.W.G. (eds.) *Coastal Dunes: Processes and Morphology*. J. Wiley and Sons, Chichester, pp 253–288.

Hesp, P.A.; Dillenburg, S.R.; Barboza, E.G.; Tomazelli, L.J.; Ayup-Zouain, R.N.; Esteves, L.S.; Gruber, N.L.S.; Toldo Jr, E.E.; Tabajara, L.L., and Clerot, L.C.P., 2005. Beach Ridges, Foredunes or Transgressive Dunefields? Definitions and Initiation, and an examination of the Itapeva to Tramandaí Barrier System. *Anais da Academia Brasileira de Ciências*, 7(3), 493–508.

Hesp, P.A.; Dillenburg, S.R.; Barboza, E.G.; Clerot, L.C.P.; Tomazelli, L.J., and Ayup-Zouain, R.N., 2007. Morphology of the Itapeva to Tramandaí transgressive dunefield barrier system and Mid- to Late sea-level change. *Earth Surface Processes and Landforms*, 32, 407–414.

Martinho, C.T.; Dillenburg, S.R., and Hesp, P.A., 2009. Wave energy and longshore sediment transport gradients controlling barrier evolution in Rio Grande do Sul, Brazil. *Journal of Coastal Research*, 25 (2), 285-293.

Miot da Silva, G.; Martinho, C.T.; Hesp, P.; Keim, B.D., and Ferligo, Y., 2013. Changes in dunefield geomorphology and vegetation cover as a response to local and regional climate variations. *Journal of Coastal Research*, Special Issue No. 65, pp. 1307-1312.

Schwab, W.C.; Thieler, E.R.; Allen, J.R.; Foster, D.S.; Swift, B.A., and Denny, J.F., 2000. Influence of Inner-Continental Shelf Geologic Framework on the Evolution and Behavior of the Barrier-Island System between Fire Island Inlet and Shinnecock Inlet, Long Island, New York. *Journal of Coastal Research*, 16, 408-422.

Journal of Coastal Research	SI	75	278-282	Coconut Creek, Florida	2016

Foredune Morphological Changes by Offshore Winds Revealed By Ground-Penetrating Radar: Massambaba Beach – Rio de Janeiro, Brazil

Guilherme B. Fernandez †, Mariana S. Figueiredo‡, Thais B. da Rocha‡, Victor B. Maluf†, Caroline Martins† and Martim A.B. Moulton †

†Laboratory of Physical Geography - LAGEF
Department of Geography
Universidade Federal Fluminense - UFF
Niterói, Rio de Janeiro, Brazil

‡Laboratory of Physical Geography – LAGEFIS
Department of Geography
Universidade Estadual do Rio de Janeiro - UERJ
Rio de Janeiro, Brazil

www.cerf-jcr.org

www.JCRonline.org

ABSTRACT

Fernandez, G.B.; Figueiredo, M.S.; Rocha. T.B.; Maluf, V.B.; Martins, C., and Moulton, M.B.A., 2016. Foredunes Morphological Changes by Offshore Winds Revealed By Ground-Penetrating Radar: Massambaba Beach – Rio de Janeiro, Brazil. *In:* Vila-Concejo, A.; Bruce, E.; Kennedy, D.M., and McCarroll, R.J. (eds.), *Proceedings of the 14th International Coastal Symposium* (Sydney, Australia). *Journal of Coastal Research*, Special Issue, No. 75, pp. 278-282. Coconut Creek (Florida), ISSN 0749-0208.

Foredunes are usually formed under particular conditions, more common from onshore winds and available medium to fine sediments coming from the beach, with the vegetation playing an important role fixing this material. In some specific conditions, foredunes can be observed in areas with prevalent offshore winds. Massambaba beach is 54 km long and orientated in east-west direction. This beach is under action of prevalent northeast winds (offshore) and storm surges frequently formed by south to southwest winds and high-energy waves. At the east side of Massambaba beach, storm surges are responsible for overwash processes that deposit sediments in the back dunes. These deposits are reworked by offshore winds and represent the main sediment source for the foredunes. In these specific environmental conditions, the objective of this work is investigate morphological aspects and sedimentary architecture of the foredunes at east Massambaba beach. For this purpose, 3D morphological representations were made using DGPS and sedimentary architecture was identified by use of ground-penetrating radar. The 3D morphological representations revealed susceptible areas to washover processes and aeolian morphological impact. The sedimentary architecture observed shows six radarfacies. The following structures stood out: an onshore structure (f1c – avalanche deposits) associated with storm conditions, an offshore structure (f1d – aeolian cross-bedding) associated with the action of offshore winds and another offshore structure at the top of one of the radar profiles (f1e – parabolic migration deposits) that reveals recent movement of sediments. The applied methods allowed the identification of morphologic characteristics and similarities and differences in the sedimentary architecture.

ADDITIONAL INDEX WORDS: *foredunes morphodynamics, internal sedimentary structure, washover fans.*

INTRODUCTION

Foredunes can be defined by aeolian accumulation, parallel to the shoreline, formed foremost from the beach, by sediments fixed due to vegetation (Hesp, 2002; Hesp and Walker, 2013; Keijers *et al.*, 2015). In not rare occasions, during for example storms surges or high-speed winds, blowouts and dune scarps are formed. Blowouts can be defined as a rupture in the morphology of foredunes or other type of dunes, caused by wind erosion, that assuming different morphologies (Hesp and Walker, 2013). Different patterns of winds and waves directions indicates differences in foredunes morphology and internal sedimentary architecture.

The sediment accumulation along foredunes, normally comes from sediments remove by onshore winds, and in rare occasions occur in areas with predominant offshore direction (Bauer *et al.* 2012; Linch, *et al.*, 2009). The potential sediment transport from the beach to the foredunes is related by the angle of wind attack and the shoreline direction (for review, see Delgado-Fernandez, 2010). Foredunes are common feature along Rio de Janeiro coast.

The Rio de Janeiro coast can be divided into two distinct alignments, with the Cape Frio as a vertex of these segments. Northward of Cape Frio, the coastline assumes NNE-SSW direction, reflecting the dominant structural alignments of Brazillian shield, formed during separation between South America and Africa. Westward from Cape Frio, the coastline changes abruptly, assuming an east-west direction. Successive coastal barriers and lagoons, characterize this coastal segment. The coastal barriers occur most frequently as double barriers, with the internal located further inland, with 3 to 4 meters higher as the external barrier (Dias and Kjerve, 2009). These two barriers were constructed probably during the two last maximum sea-level, MIS 5 and MIS 1, respectively (Dias and Kjerve, 2009), generally called by Pleistocene barrier and Holocene barrier (described here as foredunes), as shows in Figure 1.

DOI: 10.2112/SI75-56.1 received 15 October 2015; accepted in revision 15 January 2016.
*Corresponding author: guilhermefernandez@id.uff.br

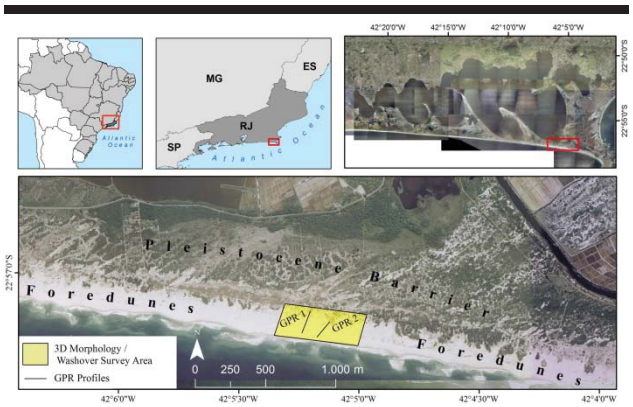

Figure 1. Location map of Massambaba Beach westward from Cape Frio. Noted two barriers an the external dominant by foredunes In the bottom the GPR and 3D morphological sites.

The foredunes observed along Rio de Janeiro present different thickness and morphologies (Moulton *et al.*, 2011). Even with the regressive sea-level behavior in east part of brazillian coast (Angulo *et al.*,2006), is common overwash process attack the foredunes. Along Massambaba Beach Fernandez and Muehe (2004) describe this process.

The regional wave climate is characterized by two different patterns. Fair weather conditions, generated waves from east and northeast direction, and storm surges come from the south and southwest (Figure 2). During extreme conditions, the waves may reach periods more than 14 seconds, and heights with up to 3 to 4 meters in the breaker zone are not rare (Figure 2).

The region of Cape Frio that include Massambaba Beach, presents a local microclimate characterized by semi-arid conditions. The dominant wind regime blows during spring and summer from east and northeast direction, which affects the foredunes in offshore direction. In autumn and winter successive most commonly cold fronts is characterized by strong winds and high waves, induced the sediment transport onshore.

The main objective of this work lies on identification of the main morphological characteristics and the internal sedimentary structure, of foredunes located in the eastern part of Massambaba Beach, coastline of Rio de Janeiro, Brazil.

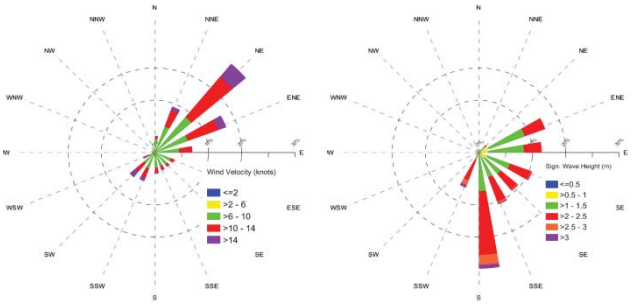

Figure 2. Wind (left) and wave rose (right) with database between 2003 to 2015, describing the major directions and intensity, in Massambaba Beach. Database upload from Bulhões and Fernandez (2013).

METHODS

To describe the morphological patterns observed in the Massambaba foredunes, sequences of parallel lines were made using Differential Global Positioning System (DGPS), conducted in cinematic mode, in parallel and cross lines, along the foredunes. We setup the equipment to acquire one x,y,z data each second. To correct the geoidal the orthometric altitude, we use database available by Instituto Brasileiro de Geografia e Estatísica (IBGE - Brazilian Institute for Geography and Statistics). Post processing DGPS data points, was interpolated using kriging method, to obtained the representation the 3D characteristics.

The contour of overwash line landward, along back dune, was made by DGPS, with the same setup, considering the event documented in August 2014. For location, the covering area related 3D and overwash lines see Figure 1.

To survey the internal sedimentary structure, in the foredunes, we survey two shore-normal profiles, in cross section along the foredunes (Figure 1). We used a GPR system (GSSI SIR 3000 Model) and 400 MHz antenna, whose acquisition was performed by common-offset mode. For the conversion the nanoseconds depth, in meters, two Common-Mid-Point (CMP) experiments was made using unshielded 80 MHz antenna. The profiles were collected in the top and depressions along the foredunes.

The GPR data were processed in RADAN software, version 6.6. The basic processing consisting in: (a) topographic correction, (b) band-pass filter, (c) gain application (since the signal tends to be progressively attenuated); (d) spatial filters (for noise removal), migration (for removing distortion and diffraction) and correction of depth generating from the velocity diagram. The interpretation of radarfacies was made considering unconformities, morphology, depth and continuity of reflectors as suggested for example by Neal (2004).

RESULTS

The morphology observed along the foredunes was described in Figure 3. The 3D representation related to GPR 1, showed sequences of foredunes accumulations and depressions. The height of foredunes exceed 8 meters, located in the eastern part of the representation and is possible to notice some depressions, where do not reach more than 3 meters.

The GPR 2 area, it is possible to notice a blowout formation, oriented to southwest direction, *i.e.* in offshore direction. This blowout assume somehow a parabolic morphology. The back dune morphology present longitudinal accumulations, fixed by vegetation in the GPR 2 area, and some hummocky dunes observed in GPR 1.

Sequences of elongate overwash process were identified along the depressions between the foredunes. The washover fans present south to north direction (Figure 4). It is remarkable the differences in terms the width and length of washover deposits as showed by black contour lines.

The internal sedimentary structure observed in foredunes was related to GPR 1 and the GPR 2 was interpreted in Figure 5 and Figure 6 respectively. After GPR processing data, three aeolian radarfacies were identified along the foredunes and another one, associated by beach process.

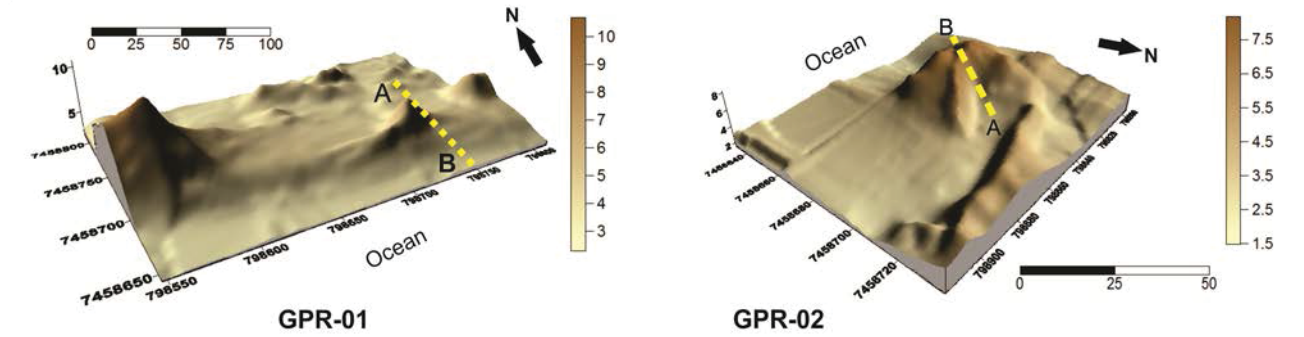

Figure 3. Morphological characteristics of two 3D blocks along the foredunes, depressions and blowouts. The dash yellow line identify the location of GPR cross section. See text for details.

The shore-normal GPR 1 (Figure 5), revealed radarfacies **f1a** associated with foreslope. Foreslope was observed in the contact between the lee of the foredunes and the berm. Radarfacies **f1a** shows reflectors with low-angle (11°), subparallel configuration and seaward dipping. The center of foredunes, describing in GPR 1, radarfacies shows reflectors discontinuous, subparallel configuration and landward and seaward dipping, named radarfacies **f1b**. This radarfacies was interpreted as foredune core and lee side. Radarfacies **f2,** show reflectors with good continuity, subparallel configuration, low-angle up to 10° and seaward dipping. It indicates the construction of beach deposits, or pre dune materials. Below the water table, an uninterpretable radarfacies was marked.

The GPR line 2 (Figure 6) the radarfacie **f1b** represent the foredunes core, previously deposit. The radarfacies **f1c** show continuous reflectors, subparallel configuration, medium-angle up to 18°, seaward dipping. This pattern represents the impact caused by offshore winds, reworking the foredunes core and blowout formation.

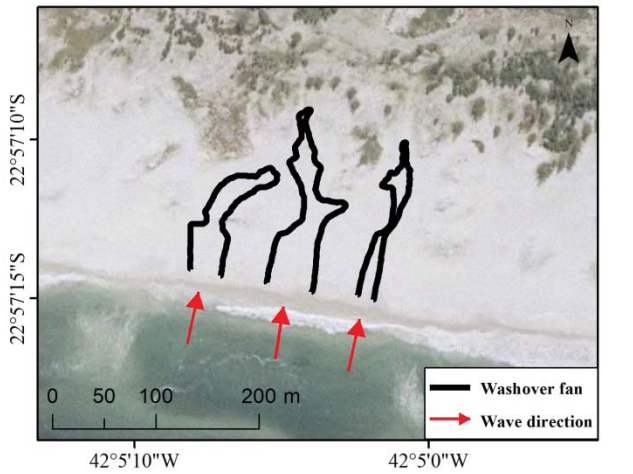

Figure 4. Elongate overwash limit landward (black line), reaching the back dunes. The red arrows indicates the main directions of storm waves.

DISCUSSION

The morphology observed in Massambaba Beach show continuous elevations, represented by foredunes accretion, separated by depressions (Figure 3). The morphology observed in Massambaba is similar as mentioned for example by Gares and Nordstrom (1995) and Hesp (2002). The sediment accumulation in the foredunes probably result by oblique winds, blow from northeast direction, removing sediments deposits in back dune, deposited by overwash process, during storm surges (Fernandez and Muehe, 2004). The tangential approach of offshore winds probably plays an important role, as described by Delgado-Fernandez (2010), in review the fetch effect, but the sediment supply come from the back dune, and not from the beach.

The elongate overwash morphology mapped occur along depressions between the foredunes (Figure 4), indicates that washover fans observed could be classified as Mathias (2009) and Matias *et al.* (2010) suggest, refered the relationship between infrequent to regular storm conditions. Fernandez *et al.* (2011) observed overwash process occurred along Rio de Janeiro coast, in a severe storm, and even do not documented in Massambaba by the authors, is possible infer that origin of washover fans comes from south waves directions, based on the direction observed by washover fans. In this case the morphology and the shoreline orientation probably facilitate overwash frequently. Williams (2015) studied the same pattern in terms of morphology and overwash process in Texas, after Hurricane Irene, which describe the same association.

Hesp and Walker (2013) present a 3D model for blowout evolution and Hesp and Hyde (1996) studied the aerodynamics of trough blowout. Hesp and Hyde (1996) and Hesp and Walker (2012) show how vortices promote a crescentic evolution of bowl and trough blowout, during offshore and onshore condition respectively. Probably the same mechanism act in Massambaba Beach, as we noticed in Figure 3, where deflected offshore winds interact directly with the morphology. Bauer *et al.* (2012) indicate these relationships, comparing database using different directions of wind speed along coastal foredunes.

The internal sedimentary structure described, show the relationship between the morphology and process observed along the foredunes. In the GPR 1 (Figure 5) the radarfacies **f1a** represents sand trapped in foredunes by vegetation on the seaward side, creating by sediment vertical accretion, observed in lee dunes, caused by onshore winds. The internal sedimentary pattern observed results in low-angle, seaward-dipping cross-stratification. Bristow *et al.* (2000) identified the same pattern inforedunes in Nothfolk, UK. The accumulation in the base of foredunes, probably reflects the foreslope recovery after the wave attack during storms, forming a dune scarp, and recovery by aeolian process. The radarfacies **f1b** was interpreted as foredune core and lee side, associated to aggradation by onshore and offshore winds, and not rare avalanche deposits by drifting wind-blown sand. Similar reflectors have been described by Bakker *et al.* (2012) and more recently by Weimer *et al.* (2015). The wind rose showed in Figure 2 support the radarfacies oriented in different directions. The aeolian radarfacies identified (**f1b**) are below of pre dune or beach and foreshore, probably related as previous Holocene regressive deposits (**f2**). Between foredune core (**f1b**) and **f2** a uninterpretable (?) should be related to washover fan deposits or aeolian deposits is the backbarrier. We do not interpreted, because we consider that is necessary core the backbarrier. However, a low angle and continuous landward radarfacies, located in back dune can be associated by washover fan.

The GPR 2 (Figure 6), the internal structure is mainly resulted from the blowout evolution, and parabolic morphology resulted by offshore winds. Girardi and Davis (2014) describing the same radarfacies pattern in a parabolic dune in Napeague (NY, USA). The radarfacies **f1b** detected, indicate the aggradation bi-directional wind mechanism. Between these two radarfacies, we identified some continuous reflectors, associated as reactivation surfaces propose for example by Buynevich *et al.* (2007). The reactivation formed the radarfacies **f1c** that showed continuous reflectors oriented seaward, formed by offshore wind, reworking previous foredune core and lee side (**f1b**).

CONCLUSIONS

Massambaba can be consider a rare foredunes example formed mainly by offshore winds. The morphological characteristics and internal sedimentary structure was revealed in Massambaba Beach by using two different methods: DGPS interpolated data for morphology and GPR profiles describing sedimentary internal structure.

In terms of morphology, Massambaba Beach present foredunes, blowouts and depressions. The depressions are the main areas to overwash process and washover fans, where the sediments reach the back dune. The overwash orientation indicates that waves from south are responsible for this process, demonstrated by elongate washover fans, separated by foredunes. In this case, during storm conditions, the sediments transported by waves in landward direction, form deposits in the reverse of the foredunes. These sediments become the sediment supply for the foredunes, by offshore prevalent northeast winds. The offshore winds, in this case not only plays an important role for foredunes accretion.

The foredunes accretion result for sediments fixed by vegetation, and the main mechanism is directly associated with offshore winds that remove sediments from the back dune to the foredunes. The offshore winds promotes at the same time blowouts, oriented in offshore direction.

The internal sedimentary structure revealed by GPR cross section profile shows different patterns of aeolian and beach radarfacies. The typical accretion of foredunes present reflector with different orientation, *i.e.*, in onshore and offshore, associated with northeast and south to southwest winds. The offshore winds cause sediments migration in offshore direction, identified in a cross section along the blowout. The blowout pattern present similarities with parabolic dune, and represent reactivation of foredune aggradation.

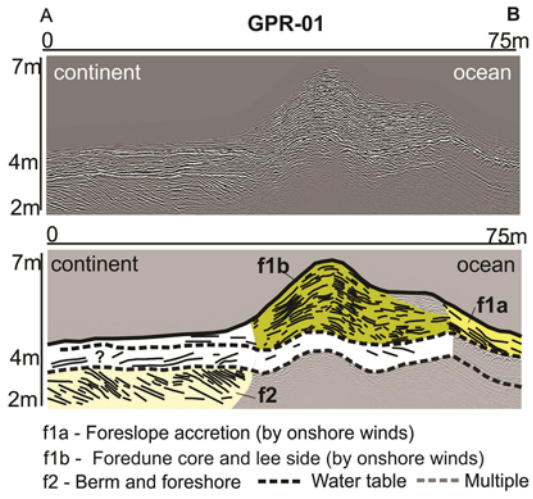

Figure 5. GPR radargram in the top and interpreted in the bottom. See the manuscript for details.

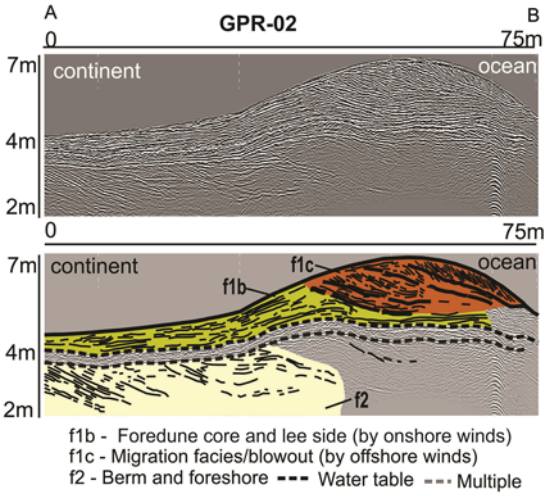

Figure 6. Radarfacies identified after GPR 2 data processing. See the manuscript for details.

ACKNOWLEDGMENTS

The authors would like to thanks the Coordenação de Aperfeiçoamento de Pessoal de Ensino Superior (CAPES) for finance the field acquisition equipment – Ground Penetrating Radar (GPR) and Differential Global Positioning System (DGPS) – in PROEQUIPAMENTOS Call (2012 – 2014). CAPES supported Mariana Figueiredo, Victor Maluf and Caroline Martins, giving Master Thesis scholarships. CAPES provide scholarship to Thais Rocha, as Post-Doctoral scholarship. The author thanks Prof. Eduardo Bulhões for the wind and wave rose actualization. The field acquisition were made by daily allowances from Conselho Nacional de Pesquisa (CNPq) in different occasions. The authors thanks all students for the support in field. We also thanks to Dra. Ana Vila-Concejo and Dr. Jak Macrroll for contribution to improve the manuscript.

LITERATURE CITED

Angulo, R.J.; Lessa, G.C., and Souza, M.C., 2006. A critical review of mid- to late Holocene sea- level fluctuations on the eastern Brazilian coastline. *Quaternary Science Reviews* 25, 486-506.

Bakker, M.A.J; van Heteren, S.; Vonhogen, L.M.; van der Spek, A.D.J.F., and van der Valk, B., 2012. Recent coastal dune development: effects of sand nourishments. *Journal of Coastal Research* 28 (3), 587-601.

Bauer, B.O.; Davidson-Arnott, R.G.D.; Walker, I.J.; Hesp, P.A., and Ollerhead, J., 2012. Wind direction and complex sediment transport response across a beach–dune system. *Earth Surface Process and Land*forms 37 (15), 1661-1677.

Bristow, C.S.; Chroston, P.N., and Bailey, S.D., 2000. The structure and development of foredunes on a locally prograding coast: insights from ground penetrating radar surveys, Norfolk, UK. *Sedimentology* 47 (5), 923-944.

Bulhões, E.M.R. and Fernandez, G.B., 2011. Analysis of shallow water wave propagation and coastal response in embayed beaches: case study in Cape Buzios, Rio de Janeiro, Brazil. *Journal of Coastal Research,* Special Issue 64, pp 2022-2026.

Buynevich, I.; Bitinas, A., and Pupienis, D., 2007. Reactivation of coastal dunes documented by subsurface imaging of the Great Dune Ridge, Lithuania. *Journal of Coastal Research,* Special Issue 50, pp. 226-230.

Delgado-Fernandez, I., 2010. A review of the application of the fetch effect to modeling sand supply to coastal foredunes. *Aeolian Research* 2, 61-70.

Dias, G. T. M. and Kjerfve, B., 2009. Barrier and beach ridge systems of Rio de Janeiro coast. *In*: Dillenburg, S. and Hesp, P.A.(eds.), *Geology and Geomorphology of Holocene Coastal Barriers*. Berlin Heidelberg: Springer Verlag, v. 107, pp. 225-248.

Fernandez, G.B.; Bulhoes, E.M.R., and Rocha, T.B., 2011. Impacts of severe storm occurred in April 2010 along Rio de Janeiro Coast, Brazil. *Journal of Coastal Research* Special Issue 64, pp 1850-1854.

Fernandez, G.B. and Muehe, D., 2004. Sediment budget correlation with the Southern Oscillation Index of a foredune westward of Cape Frio (Rio de Janeiro). *Journal of Coastal Research,* Special Issue 39, pp. 371-374.

Gares, P.A. and Nordstrom, K.F., 1995. A cyclic model of foredune blowout evolution for a leeward coast: Island Beach, New Jersey. *Annals of the Association of American Geogr*aphers 85 (1), 1-20.

Girardi, J.D. and Davis, D.M., 2014. Parabolic dune reactivation and migration at Napeague, NY, USA: Insights from aerial and GPR imagery. *Geomorphology* 114 (4), 530-541.

Hesp, P.A., 2002. Foredunes and blowouts: initiation, geomorphology and dynamics. *Geomorphology* 48 (1-3), 245-268.

Hesp, P.A. and Hyde, R., 1996. Flow dynamics and geomorphology of trough blowout. *Sedimentology* 43 (3), 505-525.

Hesp, P.A. and Walker, I.J., 2012. Three-dimensional æolian dynamics within a bowl blowout during offshore winds: Greenwich dunes, Prince Edward Island, Canada. *Aeolian Research* 3, 389–399.

Hesp, P.A. and Walker, I.J. 2013. Aeolian environments: coastal dunes. *In*: Lancaster, N.; Sherman, D.J., and Baas, A.C.W. (eds.), *Aeolian Geomorphology*. Volume 11. *In*: Shroder, J. (ed. in chief). *Treatise on Geomorphology*. San Diego, CA: Academic Press, pp. 109-133.

Hesp, P.A.; Walker, I.J.; Chapman, C.; Davidson-Arnott, R.D.A., and Bauer, B.O., 2013. Aeolian dynamics over a coastal foredune, Prince Edward Island, Canada. *Earth Surface Processes Landforms* 38 (13), 1566-1575.

Keijsers, J.G.S.; De Goot, A.V., and Riksen, M.J.P.M., 2015. Vegetation and sedimentation on coastal foredunes. *Geomorphology,* 228, 723-734.

Linch, K.; Jackson, D.W.D., and Cooper, J.A.G., 2009. Foredunes accretion under offshore winds. *Geomorphology* 105 (1-2), 139-146.

Matias, A.; Ferreira, O.; Vila-Concejo, A.; Garcia, T., and Dias., J.A., 2008. Classification of washover dynamics in barrier islands. *Geomorphology*, 97(3), 655–674.

Matias, A.; Vila-Concejo, A.; Ferreira, O.; Morris, B., and Dias, J.A., 2009. Sediment dynamics of barriers with frequent overwash. *Journal of Coastal Research*, 25(3), 768-780.

Moulton, M.; Oliveira Filho, S. R.; Rocha, T. B., and Fernandez, G. B., 2011. Foredunes of Rio de Janeiro coast: genesis, structure and morphology. *Journal of Coastal Research,* Special Issue 65, v.2, pp. 1319-1324.

Neal, A., 2004. Ground-penetrating radar and its use in sedimentology: principles, problems and progress. *Earth-Science Reviews,* 66 (3-4), 261-330.

Weimer, B.A.; Houser, C., and Giardino, J.R., 2015. Post storm evolution of beach-dune morphology: Padre Island. National Seashore, Texas. *Journal of Coastal Research*, 31(3), 634-644.

Williams, H.F.L., 2015. Contrasting styles of Hurricane Irene washover sedimentation on three east coast barrier islands: Cape Lookout, North Carolina; Assateague Island, Virginia; and Fire Island, New York. *Geomorphology*, 231(3), 655-674.

Journal of Coastal Research	SI	75	283-287	Coconut Creek, Florida	2016

Downwind Sedimentation and Habitat Development Following Ammophila arenaria Removal and Dune Erosion, Mason Bay, New Zealand

Lynda M. Hanlon [†*], Lynette K. Abbott[‡], and David M. Kennedy[†]

[†]School of Geography
The University of Melbourne
Parkville, Victoria, Australia 3010

[‡]School of Earth and Environment
The University of Western Australia
Crawley, Western Australia, Australia 6009

www.cerf-jcr.org

www.JCRonline.org

ABSTRACT

Hanlon, L.M.; Abbott, L.K., and Kennedy, D.M., 2016. Coastal mycology and invasive species: boundary conditions for arbuscular mycorrhizal (AM) fungi in incipient sand dunes. *In:* Vila-Concejo, A.; Bruce, E.; Kennedy, D.M., and McCarroll, R.J. (eds.), *Proceedings of the 14th International Coastal Symposium* (Sydney, Australia). *Journal of Coastal Research*, Special Issue, No. 75, pp. 283-287. Coconut Creek (Florida), ISSN 0749-0208.

Arbuscular mycorrhizal (AM) fungi are ubiquitous in soil, and are associated with some 90% of terrestrial vascular plants, aiding plants to access water and nutrients the plant roots alone cannot, in exchange for photosynthates from their host. AM fungi were first found in the dune system in the 1960s, and many of the described species have been found in dune ecosystems, where they form symbiotic associations with psammophilic plants including dune grasses. The ephemeral environment of incipient sand dunes prevents long-term colonization by plants, and little research has been undertaken to examine the contribution of AM fungi to plant survival in the disturbed environment of incipient sand dunes, or what role, if any, they play in exotic plant species outcompeting native species. A first step to understanding these roles is to examine the edaphic and biological conditions of incipient dunes. Our findings quantify the boundary conditions that surround and support AM fungi and their host plant roots in incipient sand dunes on the southern coast of Victoria, and include the chemical and geomorphological characterizations of the dunes studied. We found the nutrient levels (TOC, P, and N) to be low, in contrast to the higher levels of N found on the Atlantic coast, and pH levels such that Al would be toxic for the majority of plants, whilst Fe is limited. Additionally, we found that the incipient dune sand was not saline, and that chemical characteristics between the toe and the crest of the incipient dune did not differ greatly.

ADDITIONAL INDEX WORDS: *Ephemeral environments, soil microbes, beach sand nutrients.*

INTRODUCTION

Dune erosion is a fundamental part of beach adjustment during storms (Pye and Blott 2008) and the role of vegetation in releasing sand into the littoral system is critical. Incipient dunes form closest to the swash, when pioneer vegetation (Hilton and Konlechner 2011), or obstructions such as wrack trap windblown sand (Kennedy and Woods 2012). Furthermore, the critical role of plants in the initiation and development of dunes has long been recognized (*e.g.* Cowles 1899).

In Victoria, there are three main dune grass species, *Ammophila arenaria* (marram grass), *Thinopyrum junceiforme* (sea wheatgrass) (Figure 1), and *Spinifex sericeus* (hairy spinifex) (Cousens *et al.,* 2012), but only the latter is native. Marram is mainly found in the foredunes, and spinifex and sea wheatgrass dominate the incipient dunes (Cousens *et al.,* 2012). Sea wheatgrass is an erect, rhizomatous, perennial grass, growing to 0.5 m in height, and is endemic across a wide range of the European coasts (Hanlon and Mesgaran 2014). It has spread rapidly along Victoria's coast since it was first recorded in 1933.

Figure 1. *Thinopyrum junceiforme* on the incipient dune at the base of the foredune on Thirteenth Beach, Victoria (Source: L.M. Hanlon).

Grasses are known to have mutualistic associations, or symbioses, with arbuscular mycorrhizal (AM) fungi (Ramos-Zapata *et al*., 2011). However, little is known about the

DOI: 10.2112/SI75-057.1 received 15 October 2015; accepted in revision 15 January 2016.
*Corresponding author: lmhanlon@student.unimelb.edu.au

symbioses of AM fungi and vegetation in incipient dunes, despite a substantial variety of AM fungi being found in sand dunes (Koske *et al.,* 2004). AM fungi are obligate biotrophs, forming symbioses with some 90% of terrestrial vascular plants (Young 2015). They can substantially enhance their host's ability to uptake water and nutrients (Koske *et al.,* 2004) thereby aiding rapid establishment of plants in disturbed ecosystems. Additionally, glue-like polysaccharides in AM fungal mycelium bind sand grains together (Koske *et al.,* 2004) (Figure 2).

Incipient dunes present a challenging environment in which to study AM fungi, which we hypothesize have a role in the rapid spread of sea wheatgrass. Little is known about the physical and chemical environment of incipient sand dunes in relation to the vegetation and fungal flora it supports.

Figure 2. Root system of a 12-week old sea wheatgrass plant, grown from a 5 cm node in a pot in natural beach sand. Note the grains of sand adhering to the root hairs, forming a 'mycorrhizal necklace' of sand aggregates (Source: L.M. Hanlon).

The aim of this study is to define boundary conditions on a section of the southern Victorian coast where AM fungi are found in association with hairy spinifex and sea wheatgrass. We present results from field research on the geomorphology of the research site, and the edaphic, or chemical and biological conditions in the sand that surround and support AM fungi and their host plant roots. We quantify the total carbon, total organic carbon (TOC), and labile carbon percentages of the sand, and the nitrogen and extractable phosphorus percentages. Additionally, we report on the pH, EC, water content, mean grain size and calcium carbonate content of the sand of the incipient dune.

Background

The research site is approximately 370 m long, situated between The Hole and The Corner at the eastern end of Thirteenth Beach, a 4.5 km stretch along the 7 km length of coast from Black Rocks to Barwon Heads (Figure 3). The beach comprises an aeolinite cliff dating from 90,000 year B.P. which is now submerged by modern sand (Alsop 1983).

The site faces Bass Strait and experiences waves averaging 1.2-1.5 m (Water Technology, 2004). The height of the foredune is 9.37 m above mean sea level (MSL). The height of the incipient dune toe where it meets the beach is consistent along its length, being 5 m above MSL at either end of the site, and 4 m above MSL in the middle. The width of the incipient dune ranges from 5-9.5 m.

Annual mean minimum and maximum temperatures for March (when the data were collected) are 13.5°C and 24.7°C respectively (Bureau of Meteorology 2015), with a mean annual rainfall of 549.2 mm (Bureau of Meteorology 2015). Annual wind roses show due westerly winds of 21 km/h at 9.00 am and due southerly winds of 23 km/h at 3.00 pm, with a mean annual wind direction of due south (Bureau of Meteorology 2015). Sand movement is greatest in summer months, and least during winter months (Alsop 1973).

METHODS

A Trimble R6 GNSS Surveying System was used to survey the site, with a vertical accuracy of ± 3 cm. Soil moisture readings were taken at 26 locations along the crest and the toe of the incipient dune using a MEA ThetaProbe, HH2 Moisture Meter. In the 24 hours prior to taking moisture readings, 0.6 mm of rainfall occurred (Bureau of Meteorology 2015). Sand samples were taken from the top 10 cm of the dune/beach surface, which is where most microbial activity and nutrient circulation takes place (Queensland Government and G.R.D.C. 2015). Samples were collected by hand at 10 locations along the dune crest and toe. The samples were placed in individual plastic bags within a cool bag, for transport back to the laboratory.

In the laboratory, samples were stored in a refrigerator at 4°C. Particle size was analysed with a Beckman Coulter LS 13 320 Laser Diffraction Particle Size Analyzer. Air-dried, homogenized samples were analysed for pH and electrical conductivity (EC) in a 1:5 soil/0.01 M $CaCl_2$ (pH_{Ca}) solution at 22.3°C. The EC of the saturation extract (EC_e) was calculated by multiplying the EC by the soil multiplier factor for sand (13) (State Government of Victoria 2015). Oven-dried moisture content was calculated by homogenizing 10 20g samples from the crest and toe of the incipient dune, and drying at 80°C for 48 hours. The carbonate content of the dune sand was determined through LOI (Kennedy and Woods 2013). Five 3g sub-samples of sand from across the crest of the incipient dune were finely ground, dried at 105°C and then heated for 24 hours at 400°C, followed by 1000°C for one hour. Chemical analyses were conducted by Environmental Analysis Laboratory (EAL), whereby samples were dried at 60°C for 48 hours prior to crushing and analysis. Total N and total P were measured as the two main elements transferred from the fungi to their symbionts (Smith and Smith 2011), from three locations across the dune face. Total carbon and labile carbon were also measured. EAL in-house protocols included extractable P in a 1:3 nitric/HCl digest, total organic carbon percentage (TOC) (LECO CNS2000 Analyser), labile C percentage using the protocol of Blair *et al*. (1995); and total N percentage (LECO TruMAC CNS Analyser) using the protocol of Rayment and Lyons (2011).

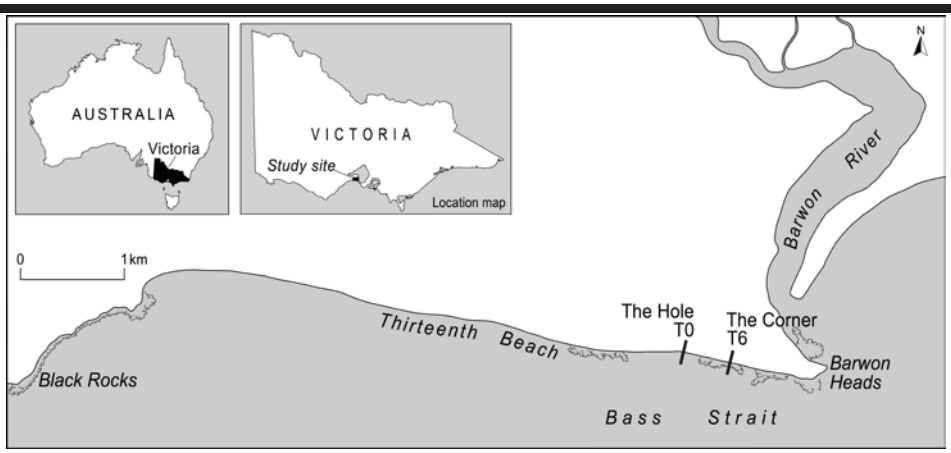

Figure 3. Map of Thirteenth Beach, Barwon Heads, showing research site between The Hole and The Corner (Cartographer: C. Jayasuriya).

RESULTS

Dune morphology was characterized by a DEM of the research site. The incipient varies in elevation from 8.23-8.31 m (Table 1), and in slope from 0.33° at the western end (T0) to 0.40° at the eastern end (T6), with slopes between 0.18-0.24° through the remaining transects.

Table 1. *Elevations (m) (AHD) of the foredune and incipient dune along seven perpendicular transects.*

Transect	Top	Bottom	Incipient
T0	14.27	1.39	8.31 – 4.69
T1	13.03	1.22	5.85 – 4.17
T2	12.99	0.91	5.75 – 3.82
T3	12.78	1.29	5.48 – 3.75
T4	12.29	1.70	5.25 – 3.92
T5	13.16	1.49	4.64 – 3.95
T6	13.38	1.18	8.23 – 4.82

The dunes are composed of medium, moderately well-sorted, fine grade sand, with a mean grain size of 1.46 Ø for the toe of the dune and 1.451 Ø for the crest (Table 2). The average $CaCO_3$ content is 15% (Table 2). The crest of the incipient dune is pH_{Ca} 6.09 and the toe pH_{Ca} 6.06, making Fe concentrations less than optimum, and Al concentrations toxic for the majority of plants. However, $EC_{1:5Ca}$ indicates that the sand is not saline (Table 2). Overall, edaphic conditions between the incipient dune crest and the toe did not differ greatly except in relation to volumetric soil water content (%), with the toe being more saturated due to its proximity to the high tide mark. This agrees with global estimates of typical dune volumetric soil water ranges of 1.5-6.0% (Van der Valk 1974).

Table 2. *Edaphic conditions (0-10cm), Thirteenth Beach incipient dune crest and toe.*

Procedure	(n)	crest	toe
$pH_{1:5Ca}$	6	6.09	6.06
$EC_{1:5Ca}$ (dS/m)	6	0.003	0.003
EC_e (*13)	6	0.040	0.040
Volumetric soil water (%)	26	3.00	5.18
Oven dried moisture (%)	10	0.04	0.04
Mean grain size (Ø)	2	1.451	1.456
$CaCo_3$ content (%)	5	15.0	

All the elements measured at the research site are low (Table 3), which is characteristic of dune sands (Maun 2009) including low TOC (average 2.15%) and limited P (272-340 ppm). Results for labile carbon (<0.02%) are lower, for example, than those on the east coast of Scotland (Wall *et al.*, 2002).

Table 3. *Chemical analysis (0-10 cm), Thirteenth Beach incipient dune crest.*

Location	acid extractable P (ppm)	TOC (%)	labile C (%)	total N (%)
The Hole	340	2.30	<0.02	0.021
Mid-way	272	2.12	<0.02	0.019
The Corner	287	2.04	<0.02	0.021

DISCUSSION

Literature on the nutritional status of Australian dune sands is lacking, but as with other beach systems, it is assumed there would be substantial spatial variation (Perumal and Maun 2006). For example, Welsh dune soils were found to contain as little as 0.006-0.008% N, but had 'appreciable' amounts of P and K (Hassouna and Wareing 1964). By comparison, the surface soils of New Zealand range from 0.09-0.87% TSN (Rayment and Lyons 2011). Nonetheless, dune soils are generally poor in the macronutrients N, P and K (Hawke and Maun 1988). They are also alkaline due to $CaCO_3$ sourced from marine environments, which may cause nutrient deficiencies, albeit reduce the toxicity of sodium chloride (McLachlan and Brown 2006).

The availability of the majority of nutrients is reduced at $<pH_{Ca}$ 3.5-4, with the exception of Fe which becomes limited at $<pH_{Ca}$ 6.5-7.0 additionally, exchangeable Al becomes toxic at pH_{Ca} >4.7 (Hazelton and Murphy 2007). The pH_{Ca} of the sand (Table 3) in a sand:silt:clay soil would allow all of the major nutrients to be available for plants, however as sand lacks cation exchange capacity (CEC) due to its lack of electrostatic charge and buffering capacity (Ashman and Puri 2002), it tends to be nutrient poor (Maun 2009). Nonetheless, particles of OM between the sand grains have a variable electrostatic charge which allows some exchange of nutrients, depending upon the chemicals in the soil solution (Ashman and Puri 2002). Furthermore, the deposition of wrack from wave action would

periodically raise nutrient levels (Kennedy and Woods 2013). Notwithstanding this, the Fe and Al levels would not suit the majority of plants.

The two main plants that occupy the incipient dune at Thirteenth Beach are hairy spinifex and sea wheatgrass. Literature on the Al tolerance of these plants is lacking, most likely as they are wild species that are generally not cultivated. However, if the plants are surviving the concentration of Al, they are likely to be tolerant to it. Wheat is tolerant to Al at pH_{Ca} 4.0-4.5 (Hazelton and Murphy 2007), and as sea wheatgrass is a wild relative of wheat, Al levels would not be a limiting factor in its growth. Additionally, although acidic soils can impair the functioning of most microbial processes such as the breakdown and cycling of organic matter from which plants access nutrients and carbon (Gazey and Ryan 2014), mycorrhiza have shown enhanced metal sorption capacity compared to other micro-organisms (Joner *et al.,* 2000). For example, mycorrhizal plants successfully inhabit many environments where soil acidity results in elevated levels of metals, such as in mine spoils and other heavy-metal contaminated sites (Göhre and Paszkowski 2006).

Coastal dunes contain little or no clay or silt, therefore salts are easily leached down the profile, and thus the sand at Thirteenth Beach is not saline (Table 3), in agreement with previous literature on coastal sand salinity levels. For example, Barbour *et al*. (1976) found that along the leading edge of vegetation of 34 beaches on the Pacific Coast in the USA, the concentration of soluble salt at a depth of 10 cm, was 0.008-0.280%.

The average $CaCO_3$ of the sand is 15% (Table 3), and although rates of 10 to 20% $CaCO_3$ are regarded as high by Nordstrom *et al*. (1990), it is not the dominant component at Thirteenth Beach.

Although few beach systems have been researched sufficiently to provide nutrient budgets (McLachlan and Brown 2006), the periodic deposition of OM (Kennedy and Woods 2013), and rainfall and nutrients in sea spray (Maun 2009) aid in supplying nutrients. Total organic carbon (TOC) is largely the result of plant decay and the low levels of TOC at the site are reflected in the lack of woody plants and shrubs along the incipient dune. Labile carbon levels (<0.02%) are lower than those of Wall *et al*. (2002) who found levels of 0.1-0.6% in the beach and foredune at Tentsmuir Point, on the east coast of Scotland.

In general, pioneer plants require low quantities of N and P, and the limited level of phosphorus at the site (272-340 ppm) is offset by pioneer plants gaining access to P via by the extra-radical mycelium of AM fungi. Mycelia work like an extension to the plant roots, growing beyond the phosphorus depletion zone around the roots to take up P, as well as some trace elements from the edaphic environment (Koske *et al.,* 2004). The N percentage at Thirteenth Beach (average 0.020%) is higher than on beaches along the Atlantic Coast of Maine and New Hampshire USA for example, where levels are 0.004-0.012% N by weight (Croker *et al.,* 1975).

The toe of the incipient dune sits above MHWS but is not protected from storm surges and is therefore subject to scarping and plant loss. Although gradual or minor disturbances do not necessarily lead to decreases in AM hyphal abundance (Abbott and Robson 1991), hyphal networks in soil are easily disrupted by rapid environmental changes such as storm events. Such events prevent long-term plant colonization (Koske *et al.,* 2004), and as a result, the contribution of AM fungi to plant survival in incipient dunes has been little studied.

CONCLUSIONS

This study has sought to define the boundary conditions under which AM fungi are found in association with the invasive, exotic sea wheatgrass and the native hairy spinifex. The nutrients measured are low for most plant requirements, however pioneer plants require low quantities of N and P, surviving through adaptations to resource stresses, and through their symbioses with AM fungi and other soil microbes (Cockcroft and McLachlan 1993). The data from our research will enable us to predict the how close to MHWS sea wheatgrass, hairy spinifex and AM fungi are likely to be found.

ACKNOWLEDGEMENTS

This work was partly funded by the Bill Borthwick Student Scholarship, from the Victorian Environmental and Assessment Council. We thank the Barwon Coast Committee of Management for site access.

LITERATURE CITED

Abbott, L.K. and Robson, A.D., 1991. Factors influencing the occurrence of vesicular-arbuscular mycorhizas. *Agriculture, Ecosystems and Environment,* 35**,** 121-150.

Alsop, P.F.B., 1973. The stabilization of coastal sand dunes. *First Australian Conference on Coastal Engineering, 1973: Engineering Dynamics of the Coastal Zone* (Sydney, New South Wales, Australia), pp. 144-151.

Alsop, P.F.B. 1983. Coastal dune stabilization - an engineer's view. *Royal Australian Institute of Parks and Recreation 56th National Conference* (Melbourne, Victoria, Australia), pp. 1-17.

Ashman, M.R. and Puri, G., 2002. *Essential Soil Science a Clear and Concise Introduction to Soil Science,* Oxford: Blackwell Science Ltd., 208p.

Barbour, M.G.; De Jong, T., and Johnson, A.F., 1976. Synecology of beach vegetation along the Pacifc Coast of the United States of America: a first approximation. *Journal of Biogeography,* 3**,** 55-69.

Blair, G.J.; Lefroy, R.D.B., and Lisle, L., 1995. Soil carbon fraction based on their degree of oxidation, and the development of a carbon management index for agricultural systems. *Australian Journal of Agricultural Research,* 46**,** 1459-1466.

Bureau of Meteorology. 2015. http://www.bom.gov.au

Cockcroft, A.C. and McLachlan, A., 1993. Nitrogen budget for a high-energy ecosystem. *Marine Ecology Progress Series,* 100**,** 287-299.

Cousens, R.; Kennedy, D.; Maguire, G., and Williams, K., 2012. *Just How Bad Are Coastal Weeds? Assessing the Geo-eco-psycho-socio-economic Impacts*. Melbourne, Australia: Rural Industries Research and Development Corporation (RIRDC), 194p.

Cowles, H.C., 1899. The ecological relations of the vegetation on the sand dunes of Lake Michigan. *Botanical Gazette,* 27**,** 361-391.

Croker, R.A.; Hager, R.P., and Scott, K.J., 1975. Macroinfauna of northern England marine sand. II. Amphipod-dominated interdal communities. *Canadian Journal of Zoology,* 53**,** 42-51.

Gazey and Ryan, 2014. *Effects of Soil Acidity* https://www.agric.wa.gov.au/soil-acidity/effects-soil-acidity

Göhre, V. and Paszkowski, U., 2006. Contribution of the arbuscular mycorrhizal symbiosis to heavy metal phytoremediation. *Planta,* 223, 1115-1122.

Hanlon, L.M. and Mesgaran, M.B., 2014. *Thinopyrum junceiforme* (Á. Löve & D. Löve) Á. Löve. *Plant Protection Quarterly, The Biology of Australian Weeds, 63,* 29**,** 120-126.

Hassouna, M.G. and Wareing, P.F., 1964. Posible role of rhizosphere bacteria in the nitrogen nutrition of *Ammophila arenaria*. *Nature,* 202**,** 467-469.

Hawke, M.A. and Maun, M.A., 1988. Some aspects of nitrogen, phosphorus, and potassium nutrition of three conolnizing beach species. *Canadian Journal of Botany*, 66**,** 1490-1496.

Hazelton, P. and Murphy, B., 2007. *Interpreting Soil Test Results: What Do All The Numbers Mean?* Collingwood, Victoria: CSIRO Publishing, 152p.

Hilton, M. and Konlechner, T., 2011. Incipient foredune developed from marine-dispersed rhizome of Ammophilia arenaria. *Journal of Coastal Research***,** 64, 288-292.

Joner, E.J.; Briones, R., and Leyval, C. 2000. Metal-binding capacity of arbuscular mycorrhizal mycelium. *Plant and Soil,* 226**,** 227-234.

Kennedy, D.M. and Woods, J.L.D., 2012. The influence of coarse woody debris on gravel beach morphology. *Geomorphology*, 159-160**,** 106-115.

Kennedy, D.M. and Woods, J.L.D., 2013. Determining organic and carbonate content in sediments. *In:* Shroder, J. (ed.), *Treatise on Geomorphology.* San Diego: Academic Press, pp. 262-273.

Koske, R.E.; Gemma, J.N.; Corkidi, L.; Siguenza, C., and Rincon, E., 2004. Arbuscular mycorrhizas in coastal dunes. *In:* Martinez, M.L., and Psuty, N.P., (eds.), *Ecological Studies* Vol. 171, *Coastal Dunes, Ecology and Conservation.* Berlin: Springer-Verlag, pp. 173-184.

Maun, M.A., 2009. *The Biology of Coastal Sand Dunes,* New York: Oxford University Press, 265p.

Mclachlan, A., and Brown, A., 2006. *The Ecology of Sandy Shores,* London: Academic Press 392p.

Nordstrom, K.F.; Psuty, N.P., and Carter, B., 1990. *Coastal Dunes: Form and Process.* Chichester: Wiley, 392p.

Perumal, V.J. and Maun, M.A., 2006. Ecophysical response of dune species to experimental burial under field and controlled conditions. *Plant Ecology*, 184**,** 89-104.

Pye, K. and Blott, S.J., 2008. Decadal-scale variation in dune erosion and accretion rates: an invetigation of the significance of changing storm tide frequency and magnitude on the Sefton coast, UK. *Geomorphology*, 102, 652-666.

Queensland Government and G.R.D.C. *Microbial Biomass*. http://www.soilquality.org.au.

Ramos-Zapata, J.A.; Zapata-Trujillo, R.; Ortiz-Diaz, J.J., and Guadarrama, P., 2011. Arbuscular mycorrhizas in a tropical coastal dune system in Yucatan, Mexico. *Fungal Ecology*, 4**,** 256-261.

Rayment, G.E., and Lyons, D.J. 2011. *Soil Chemical Methods - Australasia,* Collingwood, Victoria: CSIRO, 520p.

Smith, S.E. and Smith, A., 2011. Roles of arbuscular mycorrhizas in plant nutrition and growth: new paradigms from cellular to ecosystem scales. *Annual Review of Plant Biology*, 62**,** 227-250.

State Government of Victoria. *Interpreting Soil and Tissue Tests*. http://agriculture.vic.gov.au.

Van Der Valk, A.G., 1974. Environmental factors controlling the distribution of forbs on coastal foredunes in Cape Hatteras National Seashore. *Canadian Journal of Botany*, 52**,** 1057-1073.

Wall, J.W.; Skene, K.R., and Neilson, R., 2002. Nematode community and trophic structure along a sand dune succession. *Biology and Fertility of Soils*, 35, 293-301.

Water Technology Pty. Ltd., 2004. *Wave and Tidal Power Assessment for the Victorian Coastline*, Notting Hill, Victoria: Report J121/R01, 64p.

Young, J.P.W., 2015. Genome diversity in arbuscular mycorrhizal fungi. *Current Opinion in Plant Biology*, 26**,** 113-119.

Journal of Coastal Research	SI	75	288-292	Coconut Creek, Florida	2016

Flow within a Trough Blowout at Cape Cod

Patrick A. Hesp†, Thomas A.G. Smyth, Ian J. Walker‡, Paul A. Gares††, Thad Wasklewisz††

†Beach and Dune Systems (BEADS) Laboratory, School of the Environment, Flinders University, Faculty of Science and Engineering, Bedford Park, Adelaide, South Australia 5041.

††Department of Geography, Planning, and Environment, East Carolina University, Greenville, NC 27858, USA.

‡ Coastal Erosion and Dune Dynamics (CEDD) Laboratory, Department of Geography, University of Victoria, P.O. Box 3060, Station CSC, Victoria, BC, CANADA V8R3R4.

www.cerf-jcr.org

www.JCRonline.org

ABSTRACT

Hesp, Patrick A.; Smyth, Thomas A.G.; Walker, Ian J.; Gares, Paul A., and Wasklewisz, Thad, 2016. Flow within a trough blowout at Cape Cod. *In:* Vila-Concejo, A.; Bruce, E.; Kennedy, D.M., and McCarroll, R.J. (eds.), *Proceedings of the 14th International Coastal Symposium* (Sydney, Australia). *Journal of Coastal Research*, Special Issue, No. 75, pp. 288-292. Coconut Creek (Florida), ISSN 0749-0208.

The Province Lands dunefield at Cape Cod is characterised by large parabolic dunes on which have developed very significant numbers of active saucer and bowl blowouts. Blowouts occur across the entire dune landscape but many are initiated on the high lee margins of large erosional ridges and bowl blowouts within the larger parabolic dune landscape. Evolution of these blowouts is characterised by multiple stages. The first few evolutionary stages are described. In addition, the aerodynamics and flow structure within a trough blowout and former saucer blowout developed within a high ridge crest is elucidated from 2D sonic anemometer data, smoke bombs and videography. The flow is characterised by decreasing then increasing flow up the blowout centreline, and marked, highly turbulent opposed flow separation immediately inside and around the marginal entrance walls of the blowout.

ADDITIONAL INDEX WORDS: *Cape Cod, blowout stages, saucer blowout, trough blowout flow dynamics.*

INTRODUCTION

The Cape Cod National Seashore is managed by the U.S. National Parks Service and encompasses 176 km^2 of beach, foredunes, parabolic dunes and other landscapes on Cape Cod, Massachusetts, USA. A casual assessment of coasts of the world via Google Earth indicates the Cape has one of the highest, if not the highest densities of saucer and bowl blowouts in the world (Hesp unpub. surveys; Abhar *et al.*, 2015). Significant numbers are active, and have principally formed on the upper windward slopes and crests of the large parabolic dunes which extend across the Cape. The parabolic dunes have migrated to the W-NW at rates varying from ≤ 2 m/yr in wetter months, and 4 – 7 m/yr during drier months (Forman *et al.*, 2008). The dominant pioneer species colonising the dunes is American beach grass (*Ammophila breviligulata*) (Smith *et al.*, 2008).

Cape Cod has a mean annual precipitation of 106.5 cm with rainfall spread relatively evenly throughout the year (NOAA, 2002). The precipitation in winter generally falls as snow (Forman *et al.*, 2008), and in some years there is very significant snow fall (*e.g.* the winter of 2015 when snow depths were up to 1.9m). The wind regime is predominantly bi-directional with dominant modes from the northwest and southwest (Abhar *et al.*, 2015). Winds are predominantly from the south during summer and autumn, north and south during spring, and predominantly west and northwest in winter (Abhar *et al.*, 2015; Forman *et al.*, 2008).

In the following we briefly describe blowout types and initial stages at Cape Cod, and then examine the flow dynamics of one of these types, namely, a notched, former saucer blowout.

METHODS

A topographic survey of a trough blowout was carried out using a clinometer (accurate to +/- 1 degree) and tape measure. A series of transect lines along and across the blowout were established and surveyed at 50cm intervals or at breaks of slope. A digital elevation model was created from this data.

Six 2D RM Young sonic anemometers were placed at 0.25m above the bed, and orientated to the slope within the blowout primarily up the axis and at two lateral positions. A 40 minute record was obtained, with the anemometers recording at 1hz. The wind direction was oblique to the central axis of the blowout, approaching from the WNW. Smoke bombs were utilised to visualise the highly 3D flow.

A companion paper compares this field data with CFD modelling (see Smyth and Hesp, 2016, this Special Issue).

RESULTS

Blowouts at Cape Cod

The Province Lands dunefield at Cape Cod is characterised by large parabolic dunes on which have developed very significant

DOI: 10.2112/SI75-058.1 received 15 October 2015; accepted in revision 15 January 2016.
*Corresponding author: Patrick.Hesp@flinders.edu.au

numbers of active saucer and bowl blowouts at very high densities. Blowouts occur all across the dune landscape (Abhar *et al.*, 2015) but many are currently initiated on the high lee margins of either laterally continuous erosional ridges or large bowl blowouts within the extensive parabolic dune landscape.

Evolution of these blowouts is characterised by multiple stages. In the first stage (I) small, bare, elongate, ovoid to circular bare sand patches develop (Figure 1). It is as yet unclear why these unvegetated patches develop but one possibility is that the patches are initiated in areas where dieback of *Ammophila* vegetation occurs. Significant dieback/death of *Ammophila* is occurring across much of the New England dunefields (Seliskar and Huettel, 1993), so it is possible that creation of the patches is related to this. Their initiation may also be related to a higher frequency of storm winds at certain periods. They do not appear to be animal (*e.g.* rabbits) related. The patches commonly occur on the lee slopes of eroding ridgelines, and on or near the crests of the parabolic dunes.

Figure 1. A Stage I sand patch approximately 4m long at Cape Cod.

Stage II is characterised by the aeolian erosion of the patches into shallow saucer blowouts, typically ovoid to elliptical in morphology with marked erosional rims and relatively poorly defined depositional lobes (Figure 2). Note that the wind regime here is strongly bi-directional (but with multi-directional elements also), so at this stage some saucer blowouts may have partial depositional lobes or low convex mounds formed all around the blowout. If formed during the dominant winter winds period, there may be one predominant depositional lobe. The subsequent evolution of the blowout very much depends on its position relative to an eroding ridgeline or larger blowout.

Figure 2. A Stage II saucer blowout at Cape Cod.

It is possible that the small saucer blowout develops into a bowl blowout (Stage III) (Figure 3). These have deeper deflation basins and somewhat more pronounced depositional lobes, although depending on their topographic position in the landscape and exposure to winds from different directions, they may have at least two obvious depositional lobes.

Stage III bowl blowouts may very rapidly develop into larger, deep bowls (Stage IV; Figure 4; see *e.g.* Figure 17 in Hesp and Walker, 2013). Alternatively, the saucer blowout may be captured by the adjacent eroding ridge line or larger blowout. In this case, the saucer blowout develops a notch, or narrow, steep walled slot

created by aeolian erosion of a portion of the adjoining ridge. Subsequently, the notch rapidly enlarges into the blowout and converts it to a trough blowout (Figure 5). The authors have been conducting flow experiments in several of these blowout types or stages. In the following, we briefly examine the flow within a notched trough blowout (former saucer blowout).

Figure 3. A small bowl blowout at Cape Cod. Note that the blowout will soon be notched as the windward scarp ridgeline (arrowed) retreats and breaks through into the small unvegetated section of the blowout.

Figure 4. A Stage IV large bowl blowout at Cape Cod. Note the steep ridgeline and unvegetated erosional slope to the right. The blowout will eventually be canabalised by the erosional slope.

Flow within a Trough Blowout (Former Saucer Blowout)

The blowout was situated within a NW facing eroding ridgeline (Figures 5 and 6). Observations from Google Earth historical imagery indicates the blowout was originally formed leeward of the ridge crest and is present as a saucer by May, 2010. The northern windward ridge was sinuous to crenulate with several narrow and arcuate notches within the ridgeline at this time. In the following 2 years, ridgeline erosion continued and expanded to the south, and the notch was almost joined to the saucer blow-out. By mid-2014, the two landscape units had joined, and the bowl was united with the notch, and converted into a trough.

Figure 5. A trough blowout at Cape Cod. The blowout was formed as a discrete saucer blowout and evolved into a trough blowout as the adjacent erosional ridge was notched. The flow experiment was conducted in this blowout. The arrows indicate the position of the sonics. The most distant sonic anemometer (no. 4) is on the depositional lobe.

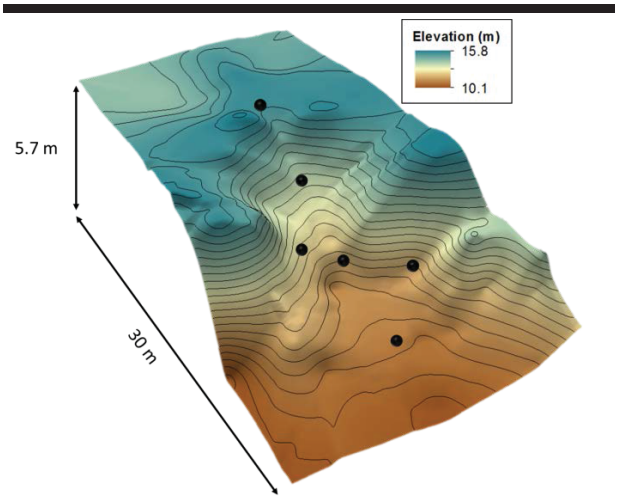

Figure 6. DEM of the Stage IV[2] trough blowout at Cape Cod. Black dots indicate sonic anemometer positions.

The internal morphology of the trough blowout is crenulate, displays marked vertical slopes held by dense vegetation on the left northeastern margin and less dense vegetation on the northwestern margin (Figures 5 and 6), and a low, convex depositional lobe downwind. Snow and ice were significant in the more shaded portions, and marked, vertical ice cornices were present on the upper slope margins (Figure 5).

DISCUSSION

Figure 7 illustrates mean wind velocity and direction vectors up the blowout for the oblique incident wind. The incident wind was topographically steered within the blowout to flow more directly up the blowout axis in similarity to other studies in trough blowouts, (cf. Hesp and Hyde, 1996; Hesp and Pringle, 2001; Gares and Pease, 2015; Smyth *et al.*, 2014). Smoke bombs clearly showed that flow separation occurred on the left and right lateral cliffed margins. At sonic 5 (figure 7) a defined flow separation roller vortex was formed at the base of the arcuate scarp and flowed up and over the adjacent wall. At sonic 6 (eastern left side) a pronounced helical corkscrew vortex formed near the base and flowed up the blowout, escaping out and over the scarp wall to the east. Flow is highest on the crest of the depositional lobe (sonic 4, Figure 7).

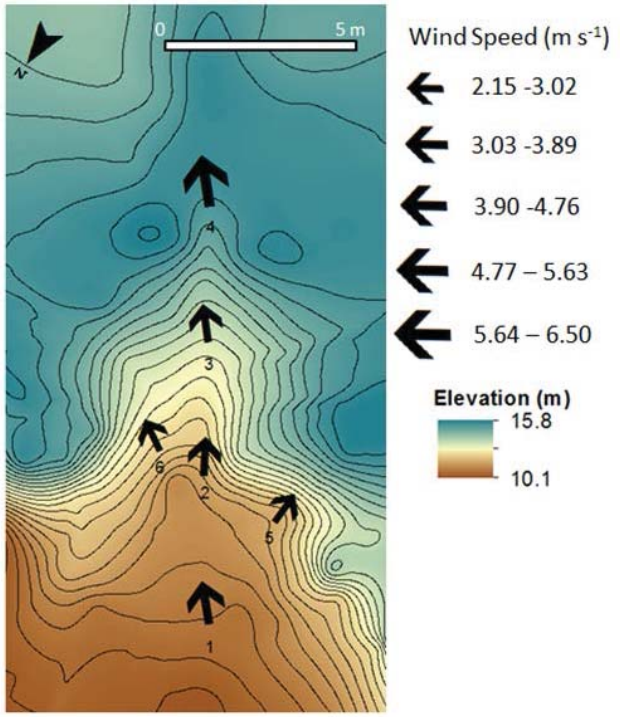

Figure 7. Mean wind velocity and direction vectors in the blowout. The oblique wind is steered up the blowout, radially spreads into the upwind lateral wall margins, and accelerates over the depositional lobe.

Figure 8 illustrates mean wind speed, coefficient of variation of the wind speed (CV), direction, and turbulent kinetic energy (TKE) up-axis and across the blowout.

The up-axis data show that, unlike most studies of blowouts where the flow generally increases up-axis or

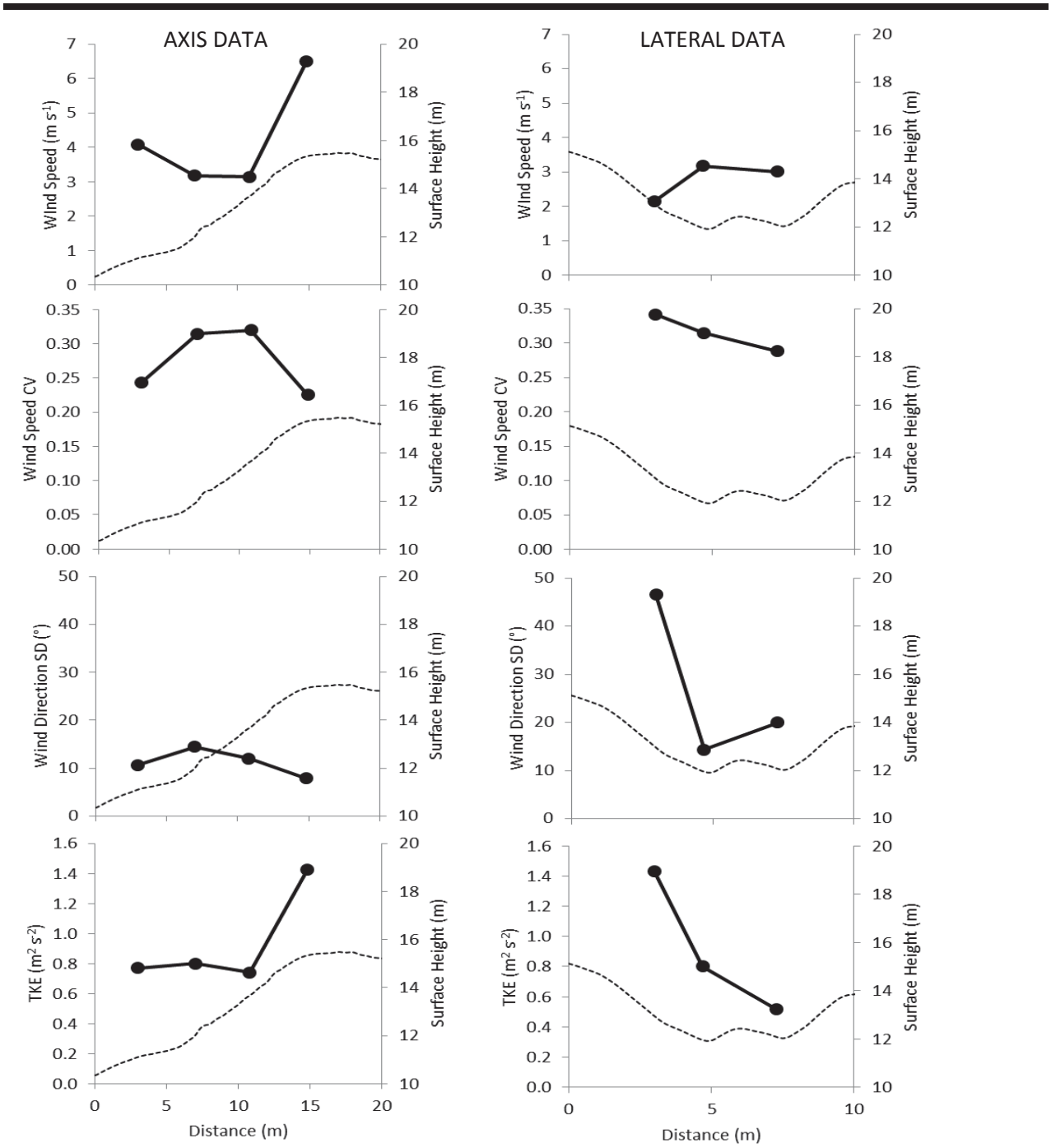

Figure 8. Mean wind speed, coefficient of variation (CV) of wind speed, standard deviation (SD) of the wind direction, and turbulent kinetic energy (TKE) for the up-axis (sonics 1 to 4) and across-blowout (lateral) (sonics 6-2-5, left to right) anemometers. The dashed lines indicate the surface topography._High turbulence in the margins of the entrance lead to reduced wind speeds in the entrance and mid regions of the narrow blowout.

downwind within the blowout due to flow compression and sometimes the formation of jets, the flow decelerates in the entrance (sonic 2) and mid-blowout (sonic 3) regions. The CV of wind speed shows that these two regions are more turbulent, and the smoke bombs clearly showed that the flow separation, and corkscrew (sonic 6) and roller (sonic 5) vortices created on the each side of the narrow entrance (*i.e.* adjacent to sonic 2 in the entrance) had a pronounced effect on the general flow in the narrow entrance region. The incident wind tends to collide with the eastern wall, creating the larger and more turbulent corkscrew vortice steering along and upwards in the blowout. This high eastern margin turbulence (sonic 6) is indicated by the SD of wind direction (which is, in essence, a proxy for turbulence), wind speed CV and high TKE.

Walker and Nickling (2003) found that, as flow progressed up a transverse dune slope, streamwise accelerations lead to a reduction in turbulence and an increase in flow stability (cf. Wiggs *et al.*, 1996). It is likely that a similar effect is occurring by sonic 4 as the flow recovers up-axis and approaches the crest of the depositional lobe. Since the TKE is also partly a product of wind speed, the TKE is also relatively high at the crest of the depositional lobe (sonic 4).

Smyth *et al.*, (2014) found that the turbulent kinetic energy (TKE) correlates best with sediment transport in a blowout, and our longer term studies at Cape Cod indicate that once a steep wall is produced within a saucer blowout, or the notching process begins, the rate of notch expansion, and of saucer to bowl blowout evolution is phenomenal (see Abhar *et al.*, 2015 their figure 7) indicating these areas of pronounced TKE are regions of marked transport and erosion. Naturally, so is the upper windward slope of the depositional lobe where marked speedup occurs and again the TKE is significant.

CONCLUSIONS

Blowout evolution at Cape Cod tends to follow a path from sand patch to saucer blowout. At this point the blowout may evolve into small to large bowl blowouts, or it may be notched and form a trough blowout. At any point the notched trough blowout or bowl may be captured or cannabalised by a larger erosional feature, particularly steep eroding ridgelines and scarps. This evolutionary sequence is quite different to those observed elsewhere to date (*e.g.* Gares and Nordstrom, 1995; Hesp, 2002).

Flow processes in a notched bowl blowout are also partly different than those observed elsewhere. Up-axis speedup is not as systematic at least when the incident flow is oblique, and highly turbulent vórtices are formed at the entrance erosional walls and profoundly affect flow inside the entrance and further into the blowout.

ACKNOWLEDGMENTS

Thanks to the NSF (grant no. 1024125) for financial support to Hesp, Smyth, Walker and Gares, and to LSU and Flinders University School of the Environment for support and equipment.

REFERENCES

Abhar, K.C.; Walker, I.J.; Hesp, P.A., and Gares, P.A., 2015. Spatial-temporal evolution of Aeolian blowout dunes at Cape Cod. *Geomorphology,* 236, 148-162.

Forman, S. L.; Sagintayev, Z.; Sultan, M.; Smith, S.; Becker, R.; Kendall, M., and Marìn, L., 2008. The twentieth-century migration of parabolic dunes and wetland formation at Cape Cod National Sea Shore, Massachusetts, USA: landscape response to a legacy of environmental disturbance. *The Holocene,* 18(5), 765-774.

Gares, P. A. and Nordstrom, K. F.,1995. A cyclic model of foredune blowout evolution for a leeward coast: Island Beach, New Jersey. *Annals of the Association of American Geographers,* 85(1), 1-20.

Hesp, P., 2002. Foredunes and blowouts: initiation, geomorphology and dynamics. *Geomorphology,* 48(1), 245-268.

Hesp, P.A., 2013. Conceptual models of the evolution of transgressive dunefield systems. *Geomorphology,* 199, 138–149.

Hesp, P.A. and R. Hyde, 1996. Flow dynamics and geomorphology of a trough blowout. *Sedimentology,* 43, 505-525.

Hesp, P.A. and A. Pringle, 2001. Wind flow and topographic steering within a trough blowout. *J. Coastal Research*, SI 34, 597-601.

Hesp, P.A. and I.J. Walker, 2013. Aeolian environments: coastal dunes. In: Shroder, J. (Editor in Chief), Lancaster, N., Sherman, D.J., Baas, A.C.W. (Eds.), *Treatise on Geomorphology, vol. 11, Aeolian Geomorphology*. Academic Press, San Diego, CA, pp. 109-133.

Seliskar, D.M. and R.N. Huettel, 1993. Nematode involvement in the dieout of *Ammophila breviligulata* (Poaceae) on the mid-Atlantic coastal dunes of the U.S. *J. Coastal Research*, 9, 97-103.

Smith, S.M.; M. Hanley, and K.T. Killingbeck. 2008. Development of vegetation in dune slack wetlands of Cape Cod National Seashore (Massachusetts, USA). *Plant Ecology*, 194, 243–256.

Smyth, T.A.G. and Hesp, P.A., 2015. Aeolian dynamics of beach scraped dunes. *Coastal Engineering*, 99, 38-45.

Smyth, T.A.G.; Jackson, D., and Cooper, A. 2014. Airflow and aeolian sediment transport patterns within a coastal trough blowout during lateral wind conditions. *Earth Surface Processes and Landforms*, 39(14), 1847-1854.

Walker, I.J. and Nickling, W.G., 2003. Simulation and measurement of surface shear stress over isolated and closely spaced transverse dunes in a wind tunnel. *Earth Surface Processes and Landforms*, 28(10), 1111-1124.

Wiggs G.F.S.; Livingstone, I., and Warren, A., 1996. The role of streamline curvature in sand dune dynamics: evidence from field and wind tunnel measurements. *Geomorphology*, 17, 29–4

Journal of Coastal Research	SI	75	293-297	Coconut Creek, Florida	2016

Flow Deflection and Deceleration Across a Simple Foredune

Michael J. Hilton[†*], Scott V. Hatcher[†], Sarah J. Wakes[‡], and Teresa M. Konlechner[†]

[†]Department of Geography
University of Otago
Dunedin, New Zealand

[‡]Department of Applied Science
University of Otago
Dunedin, New Zealand

www.cerf-jcr.org

www.JCRonline.org

ABSTRACT

Hilton, M.J.; Hatcher, S.V.; Wakes, S.J., and Konlechner, T.M., 2016. Flow Deflection and Deceleration Across a Simple Foredune. *In:* Vila-Concejo, A.; Bruce, E.; Kennedy, D.M., and McCarroll, R.J. (eds.), *Proceedings of the 14th International Coastal Symposium* (Sydney, Australia). *Journal of Coastal Research*, Special Issue, No. 75, pp. 293-297. Coconut Creek (Florida), ISSN 0749-0208.

There are few field observations of flow deflection across foredunes in a range of incident wind conditions. This study reports observations of (1) flow deflection across the seaward slope of a foredune during alongshore and oblique onshore incident winds; and (2) associated sand transport. We compare these with modelled results from Hesp *et al.* (2015). Sonic anemometers and sand traps were deployed along a transect across a simple foredune at St. Kilda Beach, Dunedin, New Zealand. Representative sections of each record were isolated for a range of incident wind directions, and for each section we determined flow deflection and relative change in wind velocity. The incident winds, observed on a 3m mast on the beach, ranged from 228º (35º oblique onshore) to 268º (5º oblique offshore) and 6 – 14 ms^{-1} mean wind speed (over 5-15 minute intervals). Gusts reached 28 ms^{-1}. Onshore deflection varied between 19º and 23º for incident winds between 228º and 249º and 9-14 ms^{-1}. Our results are only partly consistent with those of Hesp *et al.* (2015) for a similar foredune and similar strength winds. We also found deflection increases with increasing obliquity, the degree of deflection increases towards the crest, and that topographically-forced flow acceleration is strongly influenced by the angle of approach of the incident winds. In general, however, we measured more flow deflection than was modelled, including significant deflection for highly oblique winds. Relative wind velocity up the profile showed deceleration up-slope for all sections because the anemometers were placed within the vegetation.

ADDITIONAL INDEX WORDS: *Oblique incident winds, Ammophila arenaria.*

INTRODUCTION

On many coasts the prevailing winds strike the coast at oblique angles (*e.g.,* Bauer *et al.*, 2012, 2013; Hesp, 2002; Lynch *et al.*, 2013; Smyth *et al.*, 2014). These winds are then deflected onshore as the flow approaches and crosses the seaward slope of the foredune (*e.g.,* Walker *et al.*, 2009). Oblique winds can transport sediment onto a foredune, or away from it, depending on the incident angle (Arens, 1996; Walker *et al.*, 2006). Subtle changes in incident angle might result in significantly higher or lower rates of sand supply from the beach to the foredune because winds that blow along the beach have greater fetch distances and sand transport potential (Bauer and Davidson-Arnott, 2002). Empirical observations of near-surface flow over the back-beach and stoss face of foredunes in onshore oblique conditions report onshore topographic steering (Hesp *et al.*, 2015; Walker *et al.*, 2009), although the degree of steering varies.

Hesp *et al.* (2015) sought to address these constraints using computational fluid dynamics (CFD) to model flow steering over a topographically simple 10 m high foredune (Greenwich Dunes, Prince Edward Island). They obtained a good correlation between modelled and observed flow steering at Greenwich Dunes (for the observed 68º incident, oblique onshore, wind), although CFD produced 5.8% more deflection than observed.

They then used CFD to examine deflection for a range of incident winds, from directly onshore to directly alongshore. The greatest modelled flow deflection across the foredune occurs for winds in the range 40º to 50º (flow deflection 20º) and the rate of deflection increases towards the dune crest. The modelling of flow at 0.66m indicates virtually no flow deflection between the back beach (for the Greenwich Dunes topography) and the crest of the foredune when the indicent wind was alongshore (2º deflection at 0.66m height), but clear deflection at 10º (7º) and 20º (14º) for an incident wind speed of 12.2 ms^{-1} at 4 m elevation above the beach. The degree of modelled topographic acceleration decreases with increasing incident wind obliquity.

The current paper examines flow deflection and flow speed over a foredune during a moderate wind event (mean incident wind speeds of 10-15 ms^{-1}), where the incident winds vary from oblique offshore (a few degrees), to alongshore (foredune crest parallel), to oblique onshore (14-45º). Empirical evidence of deflection is presented for a foredune of similar height and morphological complexity to the Greenwich Dunes foredune (Hesp *et al.*, 2015), which provides an opportunity to compare their modelled with our empirical data.

The foredune at this site developed in conjunction with *Ammophila arenaria* (marram grass), which was planted in the early 1950s to establish a foredune to protect the adjacent dyke (on which is formed John Wilson Drive). The foredune was

DOI: 10.2112/SI75-059.1 received 15 October 2015; accepted in revision 15 January 2016.
*Corresponding author: mjh@geography.otago.ac.nz

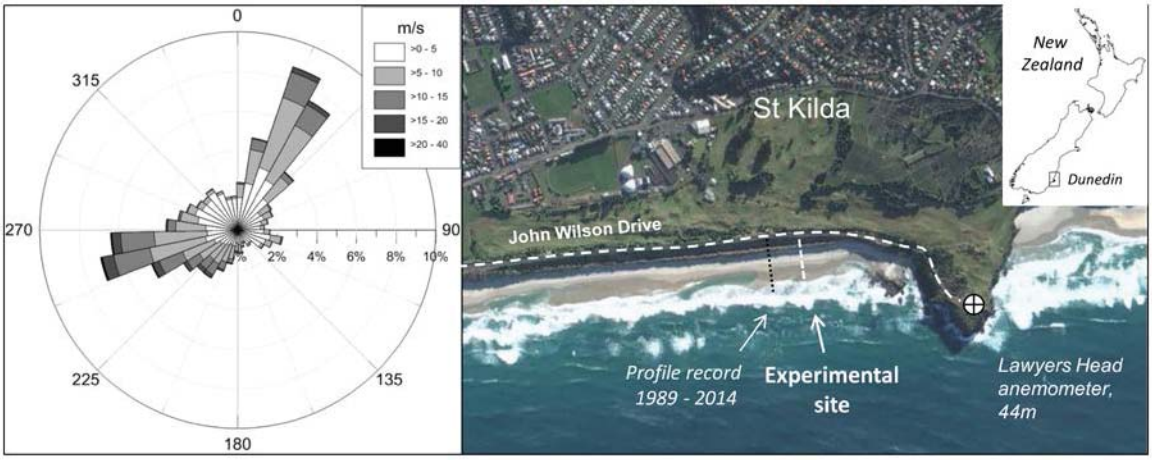

Figure 1. The study site is situated at the eastern end of St Kilda Beach in Dunedin, New Zealand. The wind rose is derived from hourly data (mean wind speed and direction) between January 2005 and December 2009 at Lawyers Head. Image courtesy of Google Earth (2015).

completely eroded in 1978, to the base of the dyke, but re-established from lines of marram planted in March 1980. Regular surveys record the subsequent development of the foredune (Figure 2). It is a stable, uniform foredune, with an average stoss face slope of 24º, 9-10 m above mean sea level.

The adjoining moderate-energy, intermediate beach, is meso-tidal (2m at spring tides), and comprised of well-sorted fine to medium quartzose sands. The width of the supratidal beach is typically 35-45 m, although there is considerable variability related to the morphodynamics of inshore bars and rip channels. In contrast, the fetch to the west is over 500 m.

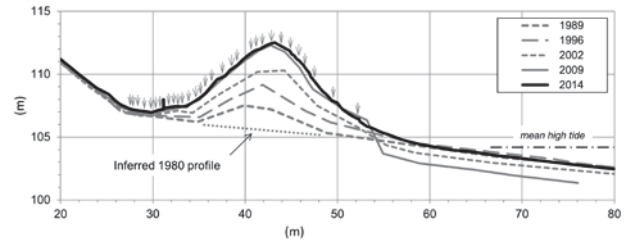

Figure 2. The St Kilda beach foredune accreted 7 m following marram planting in March 1980. The 1980 profile is inferred from historic photographs. Data courtesy of the Dunedin City Council and Otago Regional Council.

Since 2009 the rate of accretion of the foredune has slowed. The upper stoss face has accreted less than 0.5 m, but the overall elevation of the foredune has hardly changed. Assuming sand supply and sediment flux potential have remained constant it is possible that foredune scarping over the last five years has disrupted beach-foredune sediment exchange. Or the elevation of the foredune prevents sand transport onto the stoss face during less energetic events (and/or more oblique incident wind events), so that the converse conditions are necessary to transporting sand onto the foredune crest.

METHODS

Wind flow across the back beach and stoss face of the foredune was measured between 1700hrs on the 21st and 1000hrs on the 22nd September 2014, during a moderate southwest to westerly incident wind, during which wind direction varied between 220º and 275º, from oblique onshore to just oblique offshore. Average wind speed varied between 3 and 15 ms^{-1}, but gusts exceeded 25 ms^{-1} (Figure 3). A relatively steady westerly occurred during the first seven hours of the record, during which average wind speeds varied between 3 and 11 ms^{-1}. During the second third of the record, from midnight to about 0500hrs on the 22nd September, the incident wind recorded on the beach mast trended towards the south (less oblique). Average wind speeds during this phase averaged 10-20 ms^{-1}. Winds during the final third of the record were more variable in direction and speed, though westerly conditions were more common.

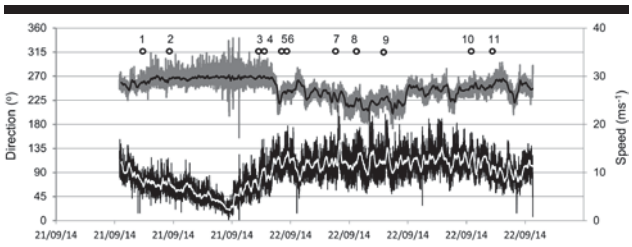

Figure 3. Incident wind recorded at WS1 on the beach mast (at 3 m elevation) from 1700hrs on the 21st September to 1000hrs on the 22nd September 2014. The numbers refer to the data segments extracted for analysis.

Variation in wind speed and direction during these three phases were measured across the stoss face and beach, along a single transect, using eight 2D Windsonic anemometers. Data from all instruments was logged at 1 Hz. Seven of the

Windsonics were deployed across a 26 m transect with the sensors at 0.35 m elevation, aligned parallel to the surface of the foredune. This placed the sensors within the marram grass at stations 5-8 (Figure 4). An eighth Windsonic (WS1) was located on a 3 m pole on the beach, 26 m from the crest, to record the incident wind. Anemometers were orientated to magnetic north using a compass and data corrected to true north before plotting (+25.38^{o} declination). Wind vectors for average wind speed and direction were plotted using Grapher-10 relative to true north for 3-15 minute increments of the record. Increments were selected to capture a range of incident directions (at WS1) and speeds, and for periods of the record that experienced relatively constant wind direction. Two directional clusters emerged: (i) oblique onshore incident winds of 228-249^{o} (data segments 5-8, 10); and (ii) oblique onshore/offshore to alongshore wind of 260-268^{o} (data segments 1-4, 11). Data for segment 9 are not presented.

Sand deposition during the event was measured by six pot traps installed in the swale behind the foredune (Figure 4). They were deployed through the 17 hour experimental period, so the recorded sand deposition is not associated with any particular flow condition.

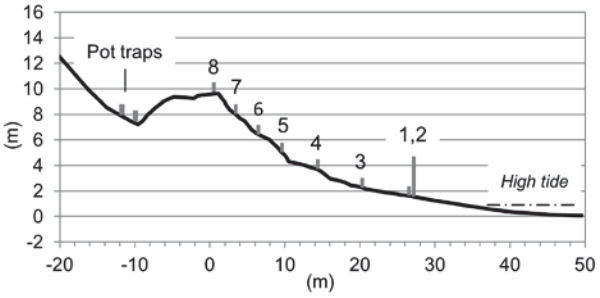

Figure 4. Arrangement of Windsonic anemometers (WS 1-8) across the transect. Pot traps were placed in the lee of the foredune.

RESULTS

Results are organized into three sections: onshore flow deflection, flow deceleration, and resulting sand transport.

Onshore flow deflection

We observed flow deflection across the stoss face in all onshore oblique wind conditions for the examined sections. During southwest winds (228-249^{o}, 14-35^{o} onshore oblique at the study site) flow deflection between the most seaward anemometer (WS1) and the crest (WS8) varied between 19^{o} and 23^{o} (Figure 5). However, we still observed onshore flow deflection when the incident wind flow was alongshore or with very high onshore and offshore obliquity (Figure 6). Flow deflection across the transect, for incident winds between 260^{o} and 268^{o}, varied between 10^{o} and 20^{o}. Incident winds more or less parallel to the foredune crest (262^{o}) were deflected 20^{o} onshore, although this was a relatively weak wind. As expected, the degree of onshore flow deflection during oblique onshore winds decreases with increasing incident wind obliquity (Figure 7).

The vector plots represent average wind speed and direction. Scatterplots of the 1 Hz data indicate the variation about the mean values for wind direction. This variation is relatively consistent across the stoss face, for both alongshore and oblique incident winds, but much higher near the crest (W7 and W8) for alongshore and very oblique winds (Figure 8). During winds of moderate obliquity these instruments are only recording attached deflected flow (*e.g.* segment 6 in Figure 8). Flow deflection is consistent across the stoss face when winds are oblique onshore (Figure 8, segment 6), but much less regular when winds are alongshore (Figure 8, segment 4).

Flow deceleration

Wind speed decreased across the stoss face of the foredune, measured between the crest (W8) and lower beach (W2) anemometers, in all the data segments examined. However, deceleration was greater for alongshore westerly winds (75-81% loss, Figure 6) compared to oblique onshore south-westerly winds (13-57% loss, Figure 5). The wind speed recorded at the crest anemometer ranged between 1.5 and 9.2 ms^{-1} for the moderate oblique sections of the record and 1.1 to 1.9 ms^{-1} for the alongshore sections of the record. The 9.2 ms^{-1} wind speed was the highest recorded at the crest. It occurred during a period of higher than usual onshore winds (17 ms^{-1} average wind speed at the beach mast) and when the incident wind direction was significantly less oblique (236^{o}).

There is a strong linear relationship between incident wind and deceleration across the stoss face of the foredune (Figure 9) – wind speed loss increased with increasingly oblique incident winds. This is an indication of the increased fetch as incident winds become progressively alongshore. Alongshore and highly oblique winds must cross increasingly more of the dense *A. arenaria* cover on the upper stoss face effect before they are measured by each Windsonic. We examined the variation in wind speed at the crest within each of the data segments, to determine the frequency and intensity of gusting. During a 15 minute period of high onshore winds (15 ms^{-1} at WS1) and low obliquity (220^{o}) wind speeds at the crest (WS8) exceeded 8 ms^{-1} for 57% of the record. That is, 507 of the 900 1 Hz counts were above this speed, with a maximum recorded speed of 13.25 ms^{-1}. More surprisingly, wind speed exceeded 8 ms^{-1} 5% of the record for relatively weak (10.6 ms^{-1} at WS1) alongshore winds (268^{o}), which suggests such winds have some potential to transport sand across the stoss face.

Sand transport

Sand exchange between beach and foredune must occur to explain the historic accretion of the foredune, which shows accretion of 0.5-1.0 m across the swale and the face of the John Wilson Drive dyke. We trapped sand across the stoss face in a 'swinging trap' system designed by the authors during a 12 minute period (1715-1725hrs) on 21st September. Significant sand flux was measured across the stoss face as high as the crest. The swale pot traps captured sand transported across the crest into the swale during the experiment (0.597 kg/m^{2}). It is likely this sand was deposited during less oblique winds, when flow exceeded 20 ms^{-1} at WS1.

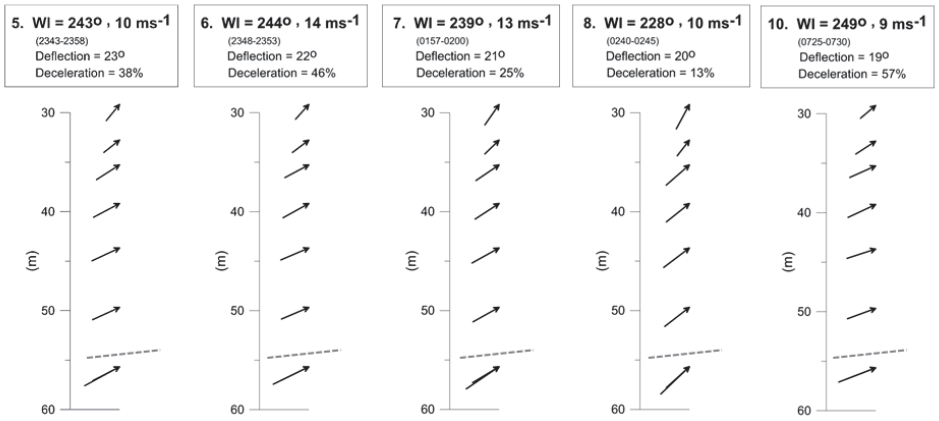

Figure 5. Vector plots showing mean wind direction during the extracted data segments across the transect during oblique onshore (southwest) incident wind conditions. Vectors for WS1 and WS2 (beach mast and 0.4 m elevation), the lower vectors, overlap in most cases. The orientation of the crest line of the foredune is shown by the dashed grey line above WS1/2.

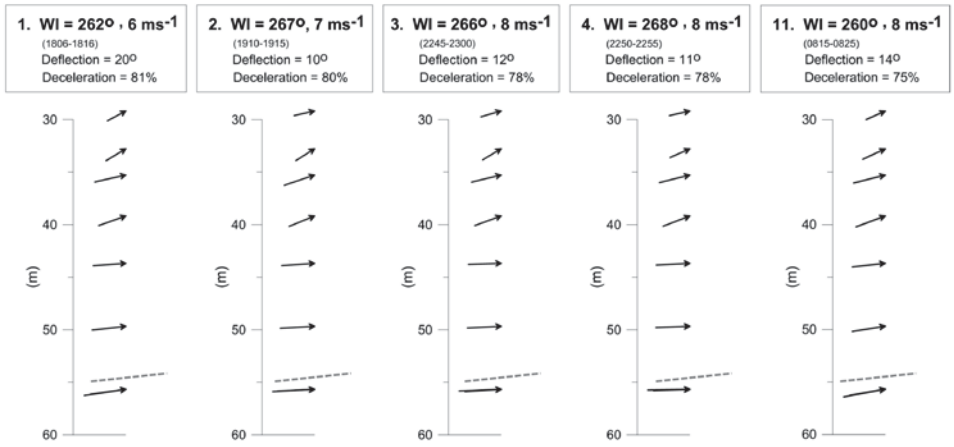

Figure 6. Vector plots showing mean wind direction during the extracted data segments across the transect during alongshore incident wind conditions. Vectors for WS1 and WS2 (beach mast and 0.4 m elevation), the lower vectors, overlap in most cases. The orientation of the crest line of the foredune is shown by the dashed grey line above WS1/2.

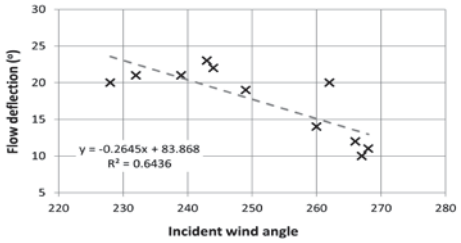

Figure 7. Relationship between incident wind direction (at WS1) and flow deflection (change in wind direction between WS2 and WS8).

DISCUSSION

Hesp *et al.* (2015) found close agreement between measured flow deflection during oblique onshore winds and CFD modelling. Our observations of deflection partly agree with those of Hesp *et al.* (2015) and others. We observed increasing deflection as incident winds approached 30º to the foredune, but decreasing deflection for winds of higher obliquity (Figure 7). Our top anemometer (W8), located on the crest of the foredune, recorded greater directional variation during oblique offshore winds, which we suspect is due to more complex flows, attached and detached, including helicoidal flows, as instantaneous incident wind direction varies from onshore to offshore across the mid to upper stoss face of the foredune.

Flow deflection at St. Kilda beach is significant for flows within 10º of the crest line of the foredune, both onshore and offshore flow. Hesp *et al.* (2015) report 2º deflection for shore-parallel winds, 7º for 10º incident oblique winds, and 14º for 20º incident oblique winds. For oblique offshore or alongshore winds we found flow deflection of 10-14º, with 20º deflection for one section of the data. We also observed progressive deflection across the stoss face and greater deflection close to

the crest. In general, the degree of deflection observed at St. Kilda was greater than modelled with CFD.

At St. Kilda, measured wind speeds across the stoss face of the foredune declined for all incident wind speeds and directions (Figures 5 & 6). The level of deceleration was greatest for more oblique winds. These results are not consistent with the modelled results, since CFD predicts that wind speeds

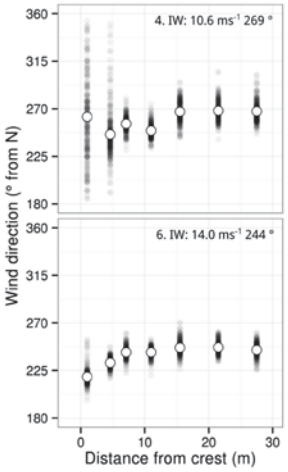

Figure 8. Scatterplots of wind direction for each anemometer for 1 Hz data segments 4 (alongshore, 10.6 ms^{-1}) and 6 (oblique onshore, southwest, 14 ms^{-1}). WS1 data, on the 3m beach mast, is not included.

will increase across the profile (at 0.66m height for a 12.2 ms^{-1} onshore wind) for a range of incident conditions (Hesp *et al.*, 2015; Figure 7b). This is likely due to the height difference of the sensors and the modelled flows (0.35 m at St. Kilda Beach, 0.66 m modelled). The density and the height of the *A. arenaria* at St. Kilda is significantly denser and higher.

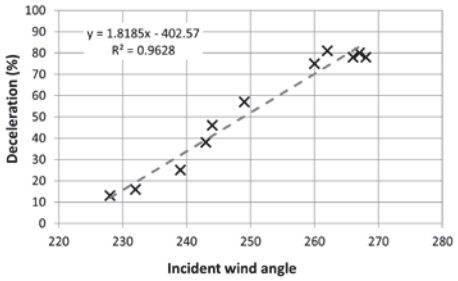

Figure 9. Relationship between incident wind direction (recorded at the beach mast) and flow deceleration (WS2 / WS8 wind speed).

CONCLUSIONS

Highly oblique and alongshore incident winds are capable of transporting sand onto the stoss face of the foredune and across the crest at St Kilda. We compared our results with the results of modelling using CFD presented by Hesp *et al.* (2015) for a similar foredune and similar strength winds. We found that measured deflection increases with increasing obliquity, the degree of deflection increases towards the crest, and that topographically-forced flow acceleration is strongly influenced by the angle of approach of the incident winds. In general, however, we measured more flow deflection than was predicted by modelling, including significant deflection for highly oblique winds. Moreover, we recorded no speed-up, rather degrees of deceleration for all incident winds.

ACKNOWLEDGMENTS

The support of Mr. Mick Reece, Mr Richard Saunders and Mr. Chris Henderson, of the Dunedin City Council, is very much appreciated. A special thanks to Jeremy Bell, Amanda Goh, Jessie Loft and Sorcha Peren for assistance with fieldwork; and a big 'kapai' to Patrick Hesp for helpful advice.

LITERATURE CITED

Arens, S. M., 1996. Patterns of sand transport on vegetated foredunes. *Geomorphology*, 17(4), 339-350.

Bauer, B.O. and Davidson-Arnott, R., 2002. A general framework for modelling sediment supply to coastal dunes including wind angle, beach geometry, and fetch effects. *Geomorphology*, 49(1), 89-108.

Bauer, B.O.; Davidson-Arnott, R.; Walker, I.J.; Hesp, P.A. and Ollerhead, J., 2012. Wind direction and complex sediment transport response across a beach-dune system. *Earth Surface Processes and Landforms*, 37(15), 1661-1677.

Bauer, B.O.; Walker, I.J.; Baas, A.C.W.; Jackson, D.W.T.; Mckenna-Neuman, C.; Wiggs, G.S.F., and Hesp, P.A., 2013. Critical reflections on the coherent flow structures paradigm in aeolian geomorphology. *In*: Venditti, J.G.; Best, J.L.; Church, M., and Hardy, R.J. (eds.), *Coherent Flow Structures at the Earth's Surface*. Wiley-Blackwell, pp. 111-134.

Hesp, P.A., 2002. Foredunes and blowouts: initiation, geomorphology and dynamics. *Geomorphology*, 48(1), 245-268.

Hesp, P.A.; Smyth, T.A.G.; Nielsen, P.; Walker, I.J.; Bauer, B.O., and Davidson-Arnott, R., 2015. Flow deflection over a foredune. *Geomorphology*, 230, 64-74.

Lynch, K.; Delgado-Fernandez, I.; Jackson, D.W.T.; Cooper, J.A.G.; Baas, A.C.W., and Beyers, J.H.M., 2013. Alongshore variation of aeolian sediment transport on a beach under offshore winds. *Aeolian Research*, 8, 11-18.

Smyth, T. A. G.; Jackson, D., and Cooper, A., 2014. Airflow and aeolian sediment transport patterns within a coastal trough blowout during lateral wind conditions. *Earth Surface Processes and Landforms*, 39(14), 1847-1854.

Walker, I. J.; Hesp, P. A.; Davidson-Arnott, R. G., and Ollerhead, J., 2006. Topographic steering of alongshore airflow over a vegetated foredune: Greenwich Dunes, Prince Edward Island, Canada. *Journal of Coastal Research*, 22(5), 1278-1291.

Walker, I. J.; Davidson-Arnott, R. G. D.; Hesp, P. A.; Bauer, B. O., and Ollerhead, J., 2009. Mean flow and turbulence responses in airflow over foredunes: new insights from recent research. *Journal of Coastal Research*, Special Issue No. 56, pp. 366-370.

Journal of Coastal Research	SI	75	298-302	Coconut Creek, Florida	2016

Downwind dune dynamics following Ammophila arenaria invasion

Teresa M. Konlechner [†*], Ella E.C.B Buckley[†], Michael J. Hilton[†], and Sarah J. Wakes[‡]

[†]Departament of Geography
University of Otago
Dunedin, New Zealand

[‡]Department of Applied Sciences
University of Otago
Dunedin, New Zealand

www.cerf-jcr.org

www.JCRonline.org

ABSTRACT

Konlechner, T.M.; Buckley, E.C.B.; Hilton, M.J., and Wakes, S.J., 2016. Downwind dune dynamics following *Ammophila arenaria* invasion. *In:* Vila-Concejo, A.; Bruce, E.; Kennedy, D.M., and McCarroll, R.J. (eds.), *Proceedings of the 14th International Coastal Symposium* (Sydney, Australia). *Journal of Coastal Research*, Special Issue, No. 75, pp. 298-302. Coconut Creek (Florida), ISSN 0749-0208.

The growth of large foredunes following invasion by non-native plants has been linked to changes in beach-dune sediment transfers, and the deflected evolution of transgressive dune systems. These changes have the potential to alter downwind plant communities by modifying habitats. This paper describes changes to a transgressive dune system in southern New Zealand following invasion by *Ammophila arenaria* and associated foredune development. Landforms were mapped using aerial imagery from 1958, when *A. arenaria* was present but not dominant, through to 2013. The landscape downwind of the foredune has evolved from a sparsely vegetated, sandy landscape, dominated by nebkha, to a landscape containing well-defined, long-walled parabolic dunes and stony deflation surfaces. These changes are associated with an increase in deflation surface habitat and plant species diversity, and a corresponding loss of habitat for species associated with dunal areas. The area of deflation surface has increased 18% to 31% of the study area while dune areas decreased from 74% to 51%. These results indicate species associated with transgressive dune systems are sensitive to variations in sand supply and changes in this supply may occur over decadal scales. Land managers are now restoring beach-hinterland sand exchange by destabilizing the foredune and adjacent parabolic dunes to encourage sand drift inland.

ADDITIONAL INDEX WORDS: *Dynamic restoration, evolution, foredune, transgressive dunes, parabolic dunes*

INTRODUCTION

The invasion of temperate coasts by non-native plants has been associated with the development of large stable foredunes (Cooper, 1958; Hart *et al.*, 2012; Hayes and Kirkpatrick, 2012; Heyligers, 1985; Hilton *et al.*, 2006; Wiedemann and Pickart, 2004). On coasts where foredunes associated with the indigenous vegetation are absent or characterised by low or discontinuous alongshore morphologies, and where the downwind dune environment comprises mobile transgressive dune fields, the growth of large stable foredunes results in changes to beach-dune sediment transfers. Sand accumulates in the foredune environment, while negative sand budgets develop inland, often with the concomitant expansion of deflation surfaces (*e.g.*, Hart *et al.*, 2012; Hayes and Kirkpatrick, 2012; Walker *et al.*, 2013). Over longer time periods changes in beach-dune sediment transfers related to foredune growth have the potential to substantially alter or accelerate the evolution of the downwind transgressive dune system (Hesp, 2013).

Such changes have implications for the interpretation, conservation and restoration of transgressive dune systems. Dune habitat and species diversity in transgressive dune systems is closely linked with the mobility of dunes downwind of foredunes, since dune migration leads to topographic and environmental diversity. Dune species display high endemism and ecological specialization, because organisms evolve to exploit isolated microhabitats created by dynamic landforms (Novo *et al.*, 2004; Ryberg *et al.*, 2015). To date, however, there have been few studies that link foredune growth with hinterland dune development and, hence, the distribution and extent of downwind dune habitats.

The invasion of *Ammophila arenaria* (marram grass) at Mason Bay, Stewart Island provides an opportunity to examine these processes. Here, a wide and stable foredune has developed following *A. arenaria* invasion during the early-mid 1900s (Hilton *et al.*, 2005, Hilton *et al.*, 2006, Hart *et al.*, 2012). Inland of the foredune, the dunes remain mobile, primarily because of an ongoing programme of *A. arenaria* control that commenced in 2001 (Hilton and Konlechner, 2010). Landforms include semi-vegetated sand sheets, parabolic dunes, stony deflation surfaces, and damp dune slacks.

Distinct plant communities are associated with these landforms. Dunal areas are dominated by native dune-binding species (*e.g., Ficinia spiralis*, a sedge), whereas the deflation surfaces are areas of relatively high species richness and support a range of plant species which require moist and stable substrates. Low nebkha, typically associated with individual plants and generally small (<0.3m in height) are common. Deflation surfaces also provide habitat for wildlife — most notably the critically threatened southern New Zealand dotterel (*Charadrius obscurus obscurus*). Many plant species associated with these three environments (dunal, stony deflation surface and dune slack) are nationally or regionally endemic, and several are listed as 'at risk' or 'threatened' under the New Zealand Threat Classification System. In addition, all three

DOI: 10.2112/SI75-60.1 received 15 October 2015; accepted in revision 15 January 2016.
*Corresponding author: teresa.konlechner@otago.ac.nz

environments have been identified as 'endangered' within New Zealand (Holdaway *et al.*, 2012).

The present study builds on the work of Hart *et al.*, 2012. They described the post-invasion development of the foredune and associated parabolic dunes. Specifically it quantifies the implications of these changes for the extent and configuration of downwind habitats following *A. arenaria* invasion. The implications of these changes for the ongoing conservation and restoration of this site are considered.

METHODS

Mason Bay is located on a windward coast on the west coast of Stewart Island, southern New Zealand (Figure 1). This study focuses on a section of the transgressive dune system (the 'central dunes') between Duck Creek and Martins Creek. The dunes here have transgressed over a broad, gently-sloping surface, and are unmodified by the underlying bedrock.

A time series of digital geo-referenced aerial and satellite photographs were used to document *A. arenaria* invasion and concomitant landform development in a 112ha section of the central dunes. The first aerial photograph was flown in 1958, with subsequent images obtained in 1978, 1989, 2003, and 2013. The 1958 and 1978 images were obtained from New Zealand Aerial Mapping, the 1989 image from the New Zealand Department of Conservation (DOC), and the 2003 and 2013 images from Google Earth Pro. All images had a spatial resolution of 1m or less. While *A. arenaria* was present in 1958 its geomorphic influence at this time was minimal (Hilton *et al.*, 2005), therefore the 1958 image represents the dune conditions prior to *A. arenaria* invasion.

The direction and rate of landform change was determined by measuring the boundaries of landform elements along four shore-normal transects located along the central axis of adjacent parabolic dunes using ArcGIS 10.2. The seaward extent of the foredune was taken as the boundary between the foredune vegetation and the beach, and was measured relative to the 1958 image. The length of the parabolic dunes was measured from the seaward extent of the foredune in 1958 to the landward extent of the depositional lobes. Areas of dune, deflation surface, and dune slack inland of the foredune were mapped manually for each image to assess changes in habitat following *A. arenaria* invasion. While this classification is a simplification of the diverse range of microhabitats present within the Mason Bay dune system, our observations in the field indicate that these three categories capture most of the variation between plant communities.

RESULTS

The contemporary dune landscape in the study area broadly resembles the 1958 landscape (Figure 2). The hinterland dunes remain sparsely vegetated and stony deflation surfaces are juxtaposed with dunes. However, the landforms that comprise the current Mason Bay dune landscape have developed following *A. arenaria* invasion. This has had implications for the distribution and area of specific habitats.

Landform changes following *A. arenaria* invasion

Early descriptions and ground photographs establish that stony deflation surfaces, similar in appearance to contemporary examples at Mason Bay, were a component of the early to mid-1900s dune system landscape (*e.g.,* Guthrie-Smith, 1914; Cockayne, 1909). The 1958 aerial photograph indicates the foredune morphology comprised a zone of isolated nebkha or shadow dunes approximately 40-80m wide (Figure 2a). At this time *A. arenaria* was present, but only as small scattered patches within 400m of the high-tide line. These probably developed from *A. arenaria* rhizome stranded during storm surge conditions, with some secondary seed dispersal likely (Hilton *et al.*, 2005). Multiple blowouts were present, which formed long 'corridors' between the beach and the dune hinterland. The dunes downwind of the foredune zone at this time were sparsely vegetated, primarily with *F. spiralis*, and appear highly mobile. Parabolic dunes were present across much of the study area. Some are well defined solitary features but many are superimposed. Smaller scale dune forms including nebkha and shadow dunes are evident.

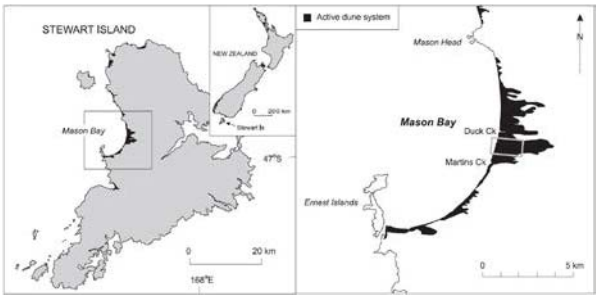

Figure 1. Location of the Mason Bay dune system. The grey rectangle in the right hand diagram corresponds to the studied area in the central dunes.

By 1978 *A. arenaria* had formed a continuous, albeit, irregular foredune. Blowouts connecting the beach to the dune hinterland were still present, but greatly reduced in size and number (Figure 2b). Distinct landforms developed inland of the foredune between 1959 and 1978. Most noticeably, four parabolic dunes, on average 147m in length, had formed immediately inland of the foredune (P1-P4, Figure 2b). These parabolic dunes were then transgressing a large sparsely-vegetated deflation surface which, although present in 1958, was much better defined by 1978.

Foredune growth and stability has continued to progress since 1978, culminating in a relatively massive, stable and continuous foredune up to 11m high and 120m wide. Lateral growth occurred primarily through seaward progradation, approximately 75m between 1958 and 2013. Accretion also occurred in the lee of the foredune with *A. arenaria* (Table 1; Figure 2). Topographic profiles surveyed annually since 1999 by the authors show that the foredune continues to accrete and prograde, albeit at a reduced rate. Blowouts connecting the beach to the hinterland dunes persisted until 1989 but are now absent.

The depositional lobes of the parabolic dunes have continued to advance downwind since 1978, albeit at a decreased rate over time (Table 1). With the exception of the southernmost parabolic

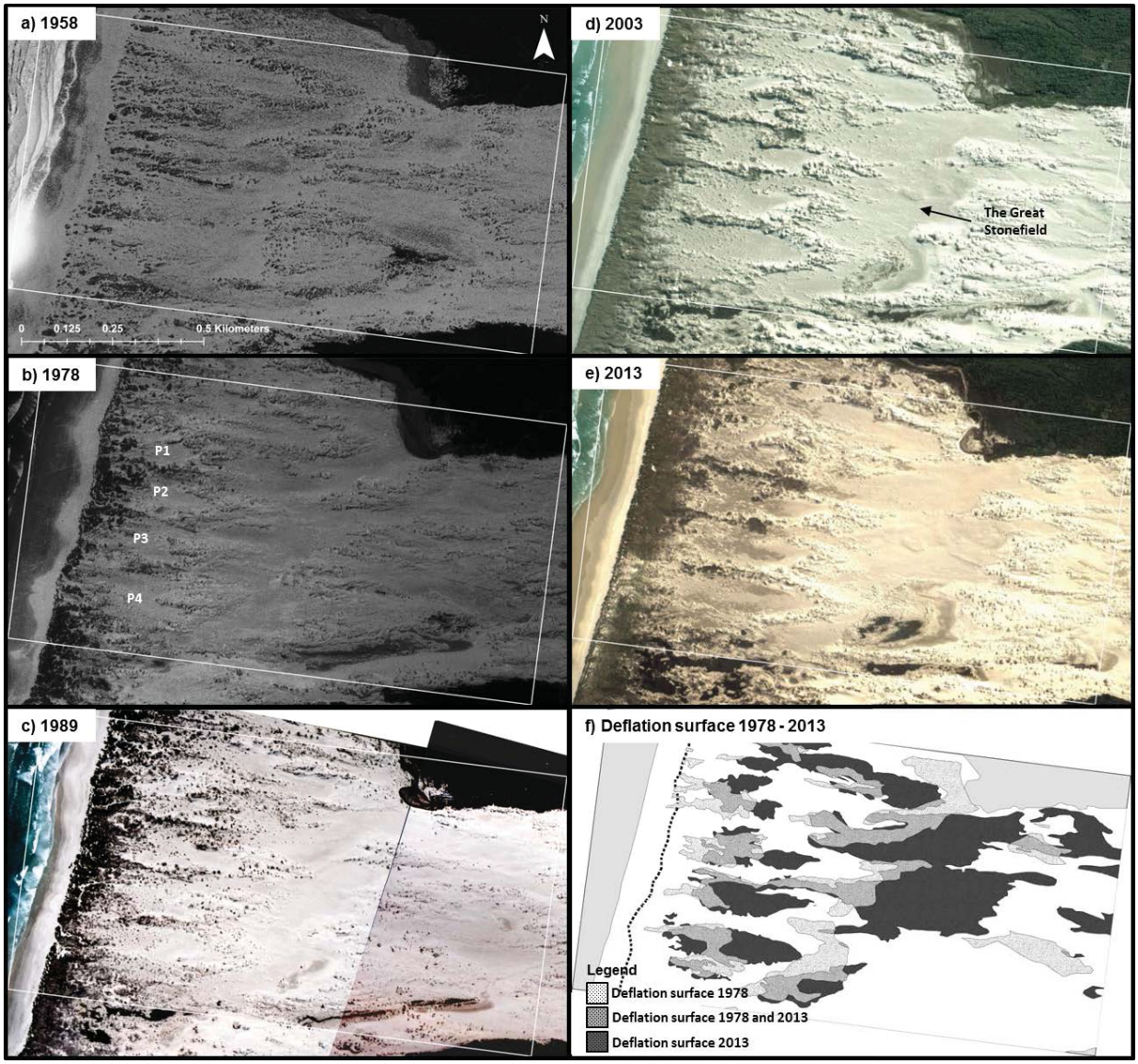

Figure 2. (a-e) Aerial view of the Mason Bay study site from 1958 when *A. arenaria* was present but not dominant, through to 2013 when *A, arenaria* dominated the foredune and trailing arms of the parabolic dunes immediately downwind. (f) Changes in the size and location of stony deflation surface habitat between 1979 and 2013.

Table 1. *Rates of change in shoreline location, foredune width, parabolic dune length, and central deflation surface width and position. Units are in m/yr. Positive values indicate shoreline progradation, an increase in landform width or length, or a landward migration of the Great Stonefield.*

	1958-1978	1978-1989	1989-2003	2003-2013
Shoreline position	1.6	1.7	1.2	0.6
Foredune width	4.7	4.5	1.8	0.9
Parabolic dune length		4.0	2.5	1.2
Central deflation width		1.0	3.4	5.4
Central deflation position		0.8	6.1	4.8

dune (P4), they are yet to show any acceleration in landward migration following removal of *A. arenaria* from the depositional lobes in the mid-2000s (Figure 2e).

Between 1978 and 2013, the central deflation surface has increased in width, primarily due to the rapid erosion of the dunes along its downwind margins (Table 1, Figure 2). The concomitant erosion of dunes along the downwind margin and landward migration of parabolic dunes upwind has resulted in a systematic change in the location of this deflation surface. The centre point of the contemporary central deflation surface (locally referred to as the 'Great Stonefield') now lies 140m further inland than in 1978 (Figure 2f). Only a small section of

the 1978 deflation surface, about a quarter, is retained in the contemporary surface.

Changes in habitat

Poor image quality meant that we could not accurately distinguish habitats in the 1958 image; however, since 1978 the area of stony deflation surface has increased with a corresponding decrease in sand dune habitat (Table 2). The deflation surface habitat now accounts for 31% of the study site compared to 20% in 1978, whereas dune areas have declined from 74% to 51%. Most of the observed changes occurred between 1989 and 2003 due to the rapid erosion of dunes and concurrent creation of deflation surfaces along the downwind margins of the 'Great Stonefield', and the expansion of deflation surfaces within the upwind parabolic dunes. Little change in deflation surface habitat has been observed since 2003, in part because the ongoing erosion of the downwind margins of the stonefield is offset somewhat by the expansion of the parabolic dune depositional lobes following the control of *A. arenaria*.

The total area of dune slack has remained fairly constant since 1978 but has also displayed shifts in location (Table 2; Figure 2). In particular new slacks have formed since 1989 downwind of P4. These have decreased in area since 2003 as the depositional lobes expand downwind.

Table 2. *Change in the area of habitat between 1978 and 2013.*

	1978	1989	2003	2013
Deflation surface (ha)	18.3	20.9	30.7	31.0
Dune slack (ha)	2.0	2.1	2.5	2.4
Sand dune (ha)	69.5	66.0	50.7	50.0

DISCUSSION

This study has identified changes in the form and distribution of landforms that comprise a large section of the Mason Bay dune system following *A. arenaria* invasion. The formation of a high continuous foredune coincides with the development of distinct landforms inland of the foredune — namely a series of long-walled parabolic dunes and associated stony deflation surfaces. The parabolic dunes formed rapidly following *A. arenaria* invasion. Since then they have lengthened and migrated downwind as a result of a reduced supply of sediment from upwind sources and erosion of the dunes downwind. The contemporary dune environment at Mason Bay is, therefore, largely comprised of landform elements formed in the late 1970s.

Changes in dune form and distribution can be explained by the reduction and then cessation of significant beach-hinterland sand flux by the establishment of a large, stable, *A. arenaria* foredune. Early descriptions and photographs establish that *F. spiralis* had formed multiple nebkha but had not formed a particularly dense or continuous vegetation cover. Sand exchange between the beach and the hinterland could, therefore, occur at multiple locations, semi-continuously, depending on incident wind energy. Today, although some sand is able to by-pass the foredune, this amounts to less than 2% of the total sand flux, and most accumulates on the foredune plateau (Peterson *et al.* 2012). The dense cover of *A. arenaria* has also prevented the development of blowouts — none have been observed since a continuous grass cover was established in the late-1980s. Hence, there has been a significant reduction in sand supply to the hinterland dune system as the *A. arenaria* foredune developed, and no addition to the hinterland for the last 20 years.

This reduction in sand supply resulted in the initiation, then downwind extension, of long-walled parabolic dunes and the development of an extensive deflation plain, consistent with descriptions of transgressive dune evolution elsewhere following foredune development and the continued landward migration of the transgressive dune field (*e.g.*, Cooper, 1958; Hesp, 2013; Martinho *et al.*, 2010; Mathew *et al.*, 2010). The morphologically irregular pre-*A. arenaria* landscape, comprising elements and remnants of periods of parabolic dune formation, was organized as this older landscape was subsumed by advancing parabolic dunes and the associated sand was deposited as trailing arms or large depositional lobes. During this period (35 years) much less sand has reached the hinterland of the dune system, resulting in the decline of *F. spiralis* and erosion of the landward margins of the stonefield.

We cannot be sure what initiated parabolic dune formation between 1958 and 1978. The parabolic dunes present in 1978 may have evolved from blowouts in the foredune, related to the formation of *A. arenaria* nebkha in the foredune environment (as proposed by Hart *et al.*, 2012). Alternatively, the cessation of beach-dune system sand supply may have led to the development of more defined, long-walled, parabolic dunes in an environment of sand scarcity (Hesp and Walker, 2013).

The invasion of *A. arenaria* is often associated with increased dune system stability because *A. arenaria* forms dense vegetation cover compared to the indigenous dune binding species (*e.g.,* Hayes and Kirkpatrick, 2012; Hilton, 2006; Wiedemann and Pickart, 1996). The growth of a large stable foredune may also promote the establishment of *A. arenaria* inland. *A. arenaria* commonly establishes from marine dispersed rhizomes (Konlechner and Hilton, 2009) and foredunes from rhizomes form rapidly (Hilton and Konlechner, 2011). Decreased wind speeds in the lee of the foredune as the foredune increases in height, combined with deflation close to the water table, provides ideal situations for *A. arenaria* to establish from seed. The numerous seedlings that have established in the deflation surfaces at Mason Bay are removed annually by DOC. This dune system remains mobile only because of these ongoing restoration efforts.

The deflation surfaces of the study site have previously been considered relatively stable and old surfaces. In fact, virtually none of the largest deflation surface was present in 1978. This landform has enlarged and migrated landward as a result of *A. arenaria* invasion and the disruption of sand supply to the hinterland. The question of whether it will decline in area, as *A. arenaria* is eradicated and sand supply to the hinterland of the dune system is re-established, is addressed by Buckley *et al.* (2016) elsewhere in this journal. It is likely that the landscape will tend to return to its pre-*A. arenaria* condition, characterized by less distinctive parabolic dune elements and a reduced area of stonefield. Land managers, in this case DOC, should appreciate the inevitability of these changes and communicate this understanding to the public at large. Distinctive and popular elements of the landscape may change or be inundated by sand. Specific sites with high biodiversity may need to be managed or the species shifted elsewhere. A range of mitigation measures

may be required. The alternative, however, is the inevitable loss of all dune habitat to *A. arenaria*.

CONCLUSIONS

The development of a large, stable foredune following *A. arenaria* invasion appears to have had a major impact on the evolution of landforms and dune habitats within the hinterland of the dune system at Mason Bay. Specifically this has transformed a comparatively open dune system, characterized by a discontinuous foredune, to a closed dune system with associated shifts in the extent and location of dune habitats. These results indicate transgressive dune systems are sensitive to variations in sand supply, particularly those associated with sand exchange between the beach and the hinterland. The response to changes in this supply may occur rapidly but continue to evolve may occur over decadal scales.

ACKNOWLEDGEMENTS

This work was supported by the New Zealand Department of Conservation.

LITERATURE CITED

Buckley E.C.B; Hilton, M.J.; Konlechner, T.M., and Lord, J.M. 2016. Downwind sedimentation and habitat development following *Ammophila arenaria* removal and dune erosion, Mason Bay, New Zealand. *Journal of Coastal Research*, Special Issue No. 75.

Cockayne, L., 1909. *Report on a Botanical Survey of Stewart Island*. Wellington: Government Printers, 66p.

Cooper, W.S., 1958. *Coastal sand dunes of Oregon and Washington*. Geological Society of America Memoirs, No. 72, 162p.

Guthrie-Smith, H., 1914. *Mutton birds and other birds*. Christchurch: Whitcombe and Tombs, 200p.

Hart, A.T.; Hilton, M.J.; Wakes, S.J., and Dickinson, K.J., 2012. The impact of *Ammophila arenaria* foredune development on downwind aerodynamics and parabolic dune development. *Journal of Coastal Research*, 28(1), 112-122.

Hayes, M. and Kirkpatrick, J.B., 2012. Influence of *Ammophila arenaria* on half a century of vegetation change in eastern Tasmanian sand dune systems. *Australian Journal of Botany*, 60(5), 450-460.

Hesp, P.A., 2013. Conceptual models of the evolution of transgressive dune field systems. *Geomorphology*, 199, 138-149.

Hesp, P.A. and Walker, I.J., 2013. Aeolian environments: coastal dunes. *In*: Shroder, J., Lancaster, N., Sherman, D.J., Baas, A.C.W. (eds.), *Aeolian Geomorphology, Treatise on Geomorphology, vol. 11*. Academic Press, San Diego: CA, pp. 328-355.

Heyligers, P., 1985. The impact of introduced plants on foredune development in south-eastern Australia. *Proceedings of the Ecological Society of Australia*, 14, 23-41.

Hilton, M. J., 2006. The loss of New Zealand's active dunes and the spread of marram grass (*Ammophila arenaria*). *New Zealand Geographer*, 62(2), 105-120.

Hilton, M.; Duncan, M., and Jul, A., 2005. Processes of *Ammophila arenaria* (marram grass) invasion and indigenous species displacement, Stewart Island, New Zealand. *Journal of Coastal Research*, 21(1), 175-185.

Hilton, M.; Harvey, N.; Hart, A.; James, K., and Arbuckle, C., 2006. The impact of exotic dune grass species on foredune development in Australia and New Zealand: a case study of *Ammophila arenaria* and *Thinopyrum junceiforme*. *Australian Geographer*, 37(3), 313-334.

Hilton, M. and Konlechner, T. (2011). Incipient foredunes developed from marine-dispersed rhizome of *Ammophila arenaria*. *Proceedings of the 11h International Coastal Symposium* (Szczecin, Poland). *Journal of Coastal Research*, Special Issue No. 64, 288-292.

Hilton, M.J., and Konlechner, T.M., 2010. A review of the marram grass eradication program (1999–2009), Stewart Island, New Zealand. *Proceedings of the 17th Australasian weeds conference* (Christchurch, New Zealand), 26-30.

Holdaway, R.J.; Wiser, S.K., and Williams, P.A., 2012. Status assessment of New Zealand's naturally uncommon ecosystems. *Conservation Biology*, 26(4), 619-629.

Konlechner, T. M. and Hilton, M. J., 2009. The potential for marine dispersal of *Ammophila arenaria* (Marram Grass) rhizome in New Zealand. *Proceedings of the 10th International Coastal Symposium* (Lisbon, Portugal). *Journal of Coastal Research*, Special Issue No. 56, 434-437.

Mathew, S.; Davidson-Arnott, R.G., and Ollerhead, J., 2010. Evolution of a beach-dune system following a catastrophic storm overwash event: Greenwich Dunes, Prince Edward Island, 1936-2005. *Canadian Journal of Earth Sciences*, 47(3), 273-290.

Martinho, C.T.; Hesp, P.A., and Dillenburg, S.R., 2010. Morphological and temporal variations of transgressive dunefields of the northern and mid-littoral Rio Grande do Sul coast, Southern Brazil. *Geomorphology*, 117(1), 14-32.

Novo, F.G.; Barradas, M.D.; Zunzunegui, M.; Mora, R.G., and Fernández, J.G., 2004. Plant functional types in coastal dune habitats. *In*: Martinez, M.L. and Psuty, N.P. (eds), *Coastal Dunes, Ecology and Conservation*. Berlin: Springer-Verlag, pp. 155-169.

Petersen, P.S.; Hilton, M.J., and Wakes, S.J., 2011. Evidence of aeolian sediment transport across an *Ammophila arenaria*-dominated foredune, Mason Bay, Stewart Island. New Zealand Geographer, 67(3), 174-189.

Ryberg, W.A.; Hill, M.T.; Painter, C.W., and Fitzgerald, L.A., 2015. Linking irreplaceable landforms in a self-organizing landscape to sensitivity of population vital rates for an ecological specialist. *Conservation Biology*, 29(3), 888-898.

Walker, I.J.; Eamer, J.B., and Darke, I.B., 2013. Assessing significant geomorphic changes and effectiveness of dynamic restoration in a coastal dune ecosystem. *Geomorphology*, 199, 192-204.

Wiedemann, A.M. and Pickart, A.J., 2004. Temperate zone coastal dunes. *In*: Martinez, M.L. and Psuty, N.P. (eds), *Coastal Dunes, Ecology and Conservation*. Berlin: Springer-Verlag, pp. 53-65.

Journal of CoastalResearch	SI	75	303-307	Coconut Creek, Florida	2016

Coastal Dunes and Plants: An Ecosystem-Based Alternative to Reduce Dune Face Erosion

M. Luisa Martinez†*, Rodolfo Silva††, Edgar Mendoza††, Itxaso Odériz††, and Octavio Pérez-Maqueo†

†Instituto de Ecología, A.C.,
Xalapa, Veracruz, México

††Instituto de Ingeniería,
Universidad Nacional Autónoma de México
México, D.F., México

www.cerf-jcr.org

www.JCRonline.org

ABSTRACT

Martínez, M.L.; Silva, R.; Mendoza, E.; Odériz, I., and Pérez-Maqueo, O.M., 2016. Coastal dunes and plants: an ecosystem-based alternative to reduce dune face erosion.. *In:* Vila-Concejo, A.; Bruce, E.; Kennedy, D.M., and McCarroll, R.J. (eds.), *Proceedings of the 14th International Coastal Symposium* (Sydney, Australia). *Journal of Coastal Research*, Special Issue, No. 75, pp. 303-307.Coconut Creek (Florida), ISSN 0749-0208.

Future scenarios indicate that growing human encroachment on coasts, more frequent and stronger storms and sea level rise will result in worsening coastal squeeze. In consequence, human lives, property and infrastructure, as well as ecosystem services, will increasingly be threatened. It is therefore vital to find the means to maintain or increase the resilience and resistance of coastal zones. As an alternative to hard infrastructure, ecosystem-based coastal defense strategies have been recommended as better and more sustainable solutions. Thus, the goal of this study wasto understand the interaction of dune plants with waves, dunes and humans. We used a pantropical beach plant (*Ipomoea pes-caprae*).and performed 24 wave flume experiments with two beach-dune profiles, four densities of vegetation cover, and three storm regimes. We also tested tolerance to burial in seed germination and seedling growth and finally explored the impact of tourism on *Ipomoea*. Erosion regimes of collision and overwash were observed in the dune profiles with a berm, whereas swash and overwash regimes were observed when no berm was present. Plant cover prevented overwash and thereby erosion of the landward side of the dune. Positive responses in seeds and seedlings of *Ipomoea* to burial by sand enable this plant to act as a dune builder. In conditions with low tourism, *Ipomoea* seems to be more affected by seasonal and meteorological conditions than by trampling. These responses increase further the potential for coastal protection of *Ipomoea* and, thus, such an ecosystem-based protective structure can be self-sustainable.

ADDITIONAL INDEX WORDS: *Coastal protection, coastal dunes, storm impact mitigation,* Ipomoea pes-caprae, *burial tolerance.*

INTRODUCTION

Human encroachment on coasts is increasing at an unprecedented rate, especially in low elevation coastal zones (LECZ), which comprise the continuous area along the coast that is less than 10 meters above sea level. Overall, LECZcover 2% of the world´s land area, but host 10% of the world's human population (McGranahan *et al*., 2007). A wide array of economic activities take place in this narrow strip, of which tourism is the largest and most widely distributed (Phillips and Jones, 2006). Specifically, beaches have become a basic requisite for sun and sand tourism, which has led to the urbanization and development of the coast. However, coastal infrastructure, properties, and society are at significant risk of floodingand erosion owing to global and regional changes in climate conditions, land subsidence, altered sediment supply, sea-level rise, stronger storms, and other extreme hydrometeorological hazards (Temmerman *et al*., 2013). As a result, the need for coastal protection actions has been stressed over recent decades.

The most common means of preventing or mitigating erosion and flooding relies on hard engineering structures. These defences have been challenged because of the periodic and costly maintenance that is required, as well as the need for heightening and widening to keep up with the increasing flood risks (Cooper and McKenna, 2008). In addition, besides modifying the natural beauty of the coasts, when badly designed or wrongly located, these hard structurescan generate downdrift problems such as intense erosion (Landgridge *et al*., 2014). Alternatively, ecosystems are naturally able to protect shorelines against erosion and flood risks, by tolerating saline water, as well as substrate mobility. In addition, many species from ecosystems such as beach-dune systems, tidal salt marshes, mangroves and seagrass beds, are able to grow upward as sea level rises, and sediment accumulates, thus increasing, the resilience of the coasts. Because of these attributes, natural coastal ecosystems have been put forward as an option for coastal protection (Cooper and McKenna, 2008; Temmerman *et al*., 2013), with the added benefits of low maintenance costs and the provision of additional ecosystem services (Everard *et al*., 2010).

Previous studies have already explored the protective role of wetlands (Costanza *et al*., 2008; Gedan *et al*., 2011). However, there is a lack of information that clearly demonstrates the role of beach and dune vegetation in reducing storm surge penetration and sediment mobilization,other than anecdotal

DOI: 10.2112/SI75-061.1 received 15 October 2015; accepted in revision 15 January 2016.
*Corresponding author: marisa.martinez@inecol.mx

observation. Kobayashi *et al*. (2013) performed hydrodynamic tests with artificial dunes covered with wooden dowels that were used as substitutes for plants, but to our knowledge, only Silva *et al*. (in press) have demonstrated experimentally the protective role of coastal dune vegetation. If natural ecosystems are to be used for shoreline protection, it is also necessary to understand the effect of dune plants on the formation of coastal dunes,which in turn serve to protect the shore.

As ecosystem-based alternatives for coastal protection are needed, the goal of this study was to understand the interaction of dune plants with waves, dunes and humans. To achieve this, we chose *Ipomoea pes-caprae* as our focal species because it grows on the beach, closeto the ocean, and is thus frequently affected by waves and storm surges. As well as the above, *Ipomoea* is a dune building species and is thus relevant in shoreline protection. Our objectives were threefold: a) We first tested how *Ipomoea* modifies the response of the beach-dune system after exposure to storm-induced waves. b) Secondly, we analyzed the responses of *Ipomoea*to sand burial in order to understand the interaction between plants and dunes. Finally, c) we investigated whether *Ipomoea*was tolerant to the intense tourism activities that take place on beaches.

METHODS

In this section we describe the species studied, as well as the wave flume, germination and seedling growth experiments; then an explanation is given of the field work performed to assess the impact of tourists on *Ipomoea*.

Species studied

Ipomoea is a pantropical trailing vine with branches that can be as long as 50m. This Convulvulaceae is tolerant to salinity (its seeds and branches are dispersed by ocean currents) and burial by sand (Martínez *et al*., 2002) (Figure 1). It propagates vegetatively by producing roots and leaves in each node and hence, it is relatively easy to obtain a sufficient number of individuals for experimental procedures as well as restoration actions.

Figure 1. Study area and the species studied, *Ipomoea pes-caprae*, a pantropical beach and coastal dune species.

Wave flume experiments

The experiments were carried out in a wave flume (0.8 m wide, 1.2 m high and 37 m long) at the Engineering Institute of the National Autonomous University of Mexico (IIUNAM). This flume has a piston type wavemaker and is equipped with a dynamic wave absorption system. The channel was divided longitudinally for 8 m of its length (coordinates 21 to 29.1 m in Figure 2) with a 1 cm thick acrylic sheet, thus allowing two profiles to be tested simultaneously. We built the profiles with sand from Tuxpan, Veracruz, Mexico, where coastal dunes form naturally on the beach.

Profile A was set on one side of the flume, composed of a submerged profile, a horizontal berm and a dune (Figure 2a). The submerged part of this profile had a gentle slope (1/32) from the bottom of the flume to a depth of 8.5 cm below the still water level (SWL), a second slope of 1/7 began at coordinate 26.75 m (Figure 2), 2 cm above the SWL. From there, a horizontal berm, 35 cm long, extended to the toe of the berm where the dune face rose to 22 cm above the SWL, with a 1/2.25 slope. The back of the dune had a 1/1.36 slope which descended again, to reach the SWL, giving a total dune base width of 75 cm. Behind the dune a horizontal section of 1.2 m was left.

Profile B was placed on the other side of the flume parallel to profile A (Figure 2b). From the bottom of the flume up to coordinate 26.75 m (8.5 cm depth below the SWL) both profiles had the same shape. From there, profile B had a composite slope profile with a slope of 1/9 until 5 cm above the SWL where the dune toe was located. The dune face had a 1/4.6 slope and its ridge was 20 cm above the SWL. The back of the dune descended with a 1/2.75 slope to reach the SWL and a 60 cm horizontal plane was left behind the dune.

A total of 24 experiments were carried out in the wave flume, with the following conditions: 2 initial profiles (A, with a berm and B, without a berm, see Figure 2), 3 different storm wave conditions (S1, mild and lasting 900 seconds; S2, moderate and lasting 900 seconds and S3, intense and lasting 240 seconds, see Table 1) and 4 plant densities, as explained below (None, Low, Medium and High). During the tests, the free water surface elevation was recorded with 11 wave gauges (WG).

The plants were reproduced vegetatively by cutting fragments of branches from individuals that were growing on the beach and embryo dunes at the field station of CICOLMA, Veracruz, on the Gulf of Mexico (19° 30' N, 96° 22'W). Each fragment was planted in 2 kg black plastic bags filled with sand from the site. For three months, the plants were kept in the field station greenhouse and watered every three days with tap water. When the plants had new, fully-grown leaves and roots, they were deemed able to survive transportation and moved to the greenhouses at IIUNAM, where they were allowed to adapt to the local environmental conditions of Mexico City over one month.

At the onset of the experiments, the plants were transplanted from the greenhouse into the artificial dunes, previously built in the wave flume. Again, before running the experiments, the plants were allowed to adapt to the wave flume, for three days. The plant densities used in the experiments were based on observations made at the site where the plants were collected. The number of branches in 20 randomly selected 1 x 1 m squares were counted. “Low” was considered as the lowest

density of branches, 5/m2; "Medium" was the mean number of branches, 12 branches/m2, and "High" the maximum number of branches per square meter, which was 18/m2 (Table 2). Plant density was increased gradually from low to high, after each set of experiments. The plants thrived very well during the experiments, so there was no need to replace them.

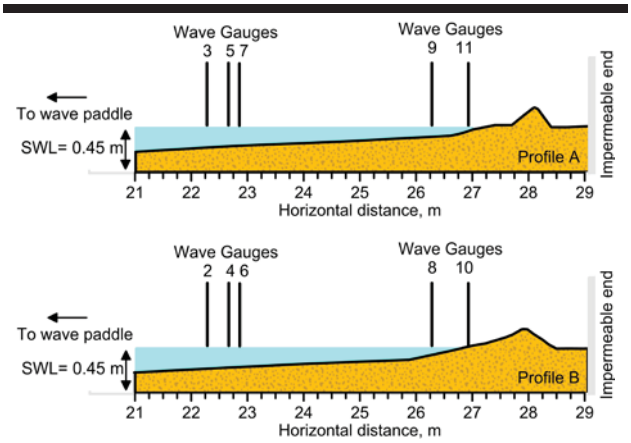

Figure 2. Experimental set up for profiles A (upper panel) and B (lower panel).

Germination tests

These experiments were performed in the greenhouse at the CICOLMA field station. Temperature in the greenhouse was around 25°C during the day and 20°C at night. Seeds were located in trays with a bed of saturated sand and then covered by 0 (control), 2, 4, 6, 8, and 16 cm of dry sand. Prior to germination and because of the hard coat dormancy, the seeds were mechanically scarified. Watering was performed from below through two plastic tubes placed at the level of the saturated sand bed and emerging to the surface of the dry sand that covered the seeds. Emerged seedlings, with their cotyledons visible on the sand surface, were counted daily. Thirty days after starting the experiments, the sand in the tray was carefully sieved in order to retrieve both ungerminated and germinated but not emerged seedlings.

Seedling growth experiments

Seedlings were obtained from germinated seeds that were scarified and then placed in trays with a bed of saturated sand. The trays were located in the greenhouse at the CICOLMA field station. A week after germination, seedlings with homogeneous initial size were selected and transplanted individually into 5kg black plastic bags filled with sand from the study site. Two weeks after planting (three weeks after germination), the seedlings were buried with dry sand at different depths: 0cm (control), 50% of the plant height and 100% of the plant height, leaving some green tissue above the sand surface. Two weeks later, the plants were subjected to a second burial, following the procedure outlined above. The dry weight of the seedlings was obtained after the second burial, and thereafter, at six week intervals. The relative growth rates in terms of the plant biomass was calculated according to the equation $RGR = (\ln W_j - W_i)/(T_j - T_i)$ (j > i) where W = dry weight and T = time elapsed from one observation to the next (Martínez and Moreno-Casasola 1996).

Impact of tourism

Before and after each high season period (spring, summer and winter) we calculated *Ipomoea* plant cover in three tourist destinations on the Costa Esmeralda of the state of Veracruz. Tourist density varied from low to medium and high. In each location we estimated plant cover by placing ten perpendicular transects at 10 m intervals. In each transect, 1 x 1 m plots were set every 2 meters and then plant cover was visually calculated.

Table 1. *Experimental conditions. A and B refer to the profiles, S to storm intensity, with 3 being the strongest. N, no vegetation, L, low density plant cover; M, medium density and H, high density. Hs, wave height; Tp, peak period generated, Duration (time elapsed during each experiment), Ir, Irribaren number and Cover, vegetation cover.*

Case	Hs (m)	Tp (s)	Duration (s)	Ir	Cover
AS1N	0.10	1.1180	900	0.3728	None
AS2N	0.10	1.5652	900	0.4767	None
AS3N	0.15	2.0120	240	0.5158	None
AS1L	0.10	1.1180	900	0.3728	Low
AS2L	0.10	1.5652	900	0.4767	Low
AS3L	0.15	2.0120	240	0.5158	Low
AS1M	0.10	1.1180	900	0.3728	Medium
AS2M	0.10	1.5652	900	0.4767	Medium
AS3M	0.15	2.0120	240	0.5158	Medium
AS1H	0.10	1.1180	900	0.3728	High
AS2H	0.10	1.5652	900	0.4767	High
AS3H	0.15	2.0120	240	0.5158	High
BS1N	0.10	1.1180	900	0.3136	None
BS2N	0.10	1.5652	900	0.4009	None
BS3N	0.15	2.0120	240	0.5009	None
BS1L	0.10	1.1180	900	0.3136	Low
BS2L	0.10	1.5652	900	0.4009	Low
BS3L	0.15	2.0120	240	0.5009	Low
BS1M	0.10	1.1180	900	0.3136	Medium
BS2M	0.10	1.5652	900	0.4009	Medium
BS3M	0.15	2.0120	240	0.5009	Medium
BS1H	0.10	1.1180	900	0.3136	High
BS2H	0.10	1.5652	900	0.4009	High
BS3H	0.15	2.0120	240	0.5009	High

RESULTS

The results of the wave fulme experiments, germination tests, seedling growth experiments and impact of tourism are described in this section.

Wave flume experiment

The erosion regime found in all vegetated tests AS1, AS2, AS3 was collision; while AS3N and BS3N (without vegetation) showed overwash. Tests BS1, BS2, BS3L, BS3M and BS3H produced erosion regimes of swash. None of the tests produced an inundation regime.

Figure 3 summarizes the morphological response of the beach profile to the vegetation cover on the dune, with the coastline displacement (positive values mean dry beach gain and negative

values mean dry beach loss) versus the type of storm (1, 2 and 3 stand for Storms S1, S2 and S3, respectively).

In terms of the final coastline position, the worst condition for storm S1 is profile B without vegetation, while Profile A with high cover had the largest dry beach gain. For storm S2, profile A shows no difference between no cover and high cover, while profile B had a larger dry beach gain without vegetation than any other case. For storm 3 all the experiments produced dry beach loss and very similar values. It is worth noting that the smallest loss occurred in profile A with high vegetation cover. These results show that in general, the presence of vegetation strengthened the beach profile, making it more resistant to individual storms.

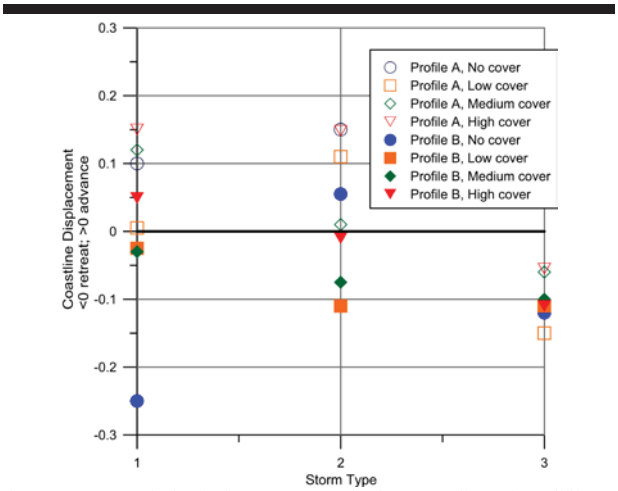

Figure 3. Morphological response of the coastline for different vegetation covers.

Germination tests

We found that seeds germinated and emerged to the sand surface after burial at different depths. An inhibitory effect of burial was observed with burial depth: the deeper the burial the longer it took for the seedlings to emerge and the emergence percentage was reduced (Figure 4).

Seedling growth experiments

We found that seedlings not only were able to thrive under buried conditions, but that their initial growth rate and long term biomass accumulation increased after burial (Figure 5). As expected for a psammophilous species, biomass was greatest at deeper burial depths, which clearly shows the tolerance of this species to burial by sand.

Impact of tourism

The mean number of tourists at the three tourist destinations varied and changed seasonally. Site 1 was the least visited, with 5, 18 and 10 visitors per 2,000 m^2 during the December, spring and summer vacation periods, respectively. The number of tourists at site 2 was higher (49, 81 and 22) and it was highest at site 3, with 39, 165 and 42. All these locations have a wide beach and similar geomorphological attributes (one foredune at the back of the beach). The most relevant difference between them is the accessibility of the site and services offered to tourists.

The impact of tourists on the cover of *Ipomoea* was not clear (Table 2). In the least visited locations (sites 1 and 2), plant cover had decreased after the December vacation period, but it increased after the Spring and Summer seasons, probably owing to the increased precipitation at the end of Spring and in the Summer. There were no *Ipomoea* plants in the most densely visited site, except during the Summer, which may indicate a tolerance threshold to visitor density.

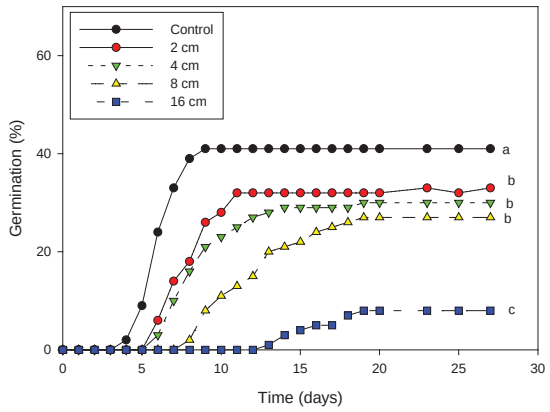

Figure 4. Mean (±SE) daily accumulated germination percentage of seeds of *Ipomoea* exposed to different burial depths. Different letters indicate significant differences between treatments. (F = 4.174; P = 0.018). (Modified from Martínez *et al.* 2002).

Table 2. *Area covered by Ipomoea (m^2 in 100 m^2) in three locations with different tourism densities, before and after three vacation periods.*

		Location		
Date		1	2	3
December	Before	8.48	2.08	0
	After	7.40	1.32	0
Spring	Before	6.80	6.80	0
	After	9.28	1.52	0
Summer	Before	15.20	3.24	0
	After	36.12	4.20	4.6

DISCUSSION

In this study we aimed to understand the interactions of dune plants with waves, dunes (sand burial) and humans. We found that *Ipomoea*: a) reduces shoreface dune erosion in different storm regimes; b) seeds are able to germinate and seedlings emerge from burial depths that are twice the seed length; c) with greater burial depths, plants accumulate more biomass by means of an initial increment in Relative Growth Rate; and d) plant cover is not negatively affected by low density tourism.

The above indicates that *Ipomoea* can be considered as one of the species for use in ecosystem-based alternatives for coastal protection, because it naturally tolerates the harsh environment of the beach and coastal dunes while it builds dunes and holds sand. A relatively wide array of dune plants have been shown to tolerate sand burial and even increase their vigour when covered

by sand (Maun, 1998), while others are known to tolerate flooding by marine water (halophytes) (Martínez *et al*., 2002; Maun, 1998). However, species to be used for coastal protection would need to be both: tolerant to burial and to marine flooding. Species with this set of functional traits have already been described by Gallego-Fernández and Martínez (2011), but wave flume experiments or field observations would be necessary to test the responses of these plants not only to marine flooding but also to waves and storms.

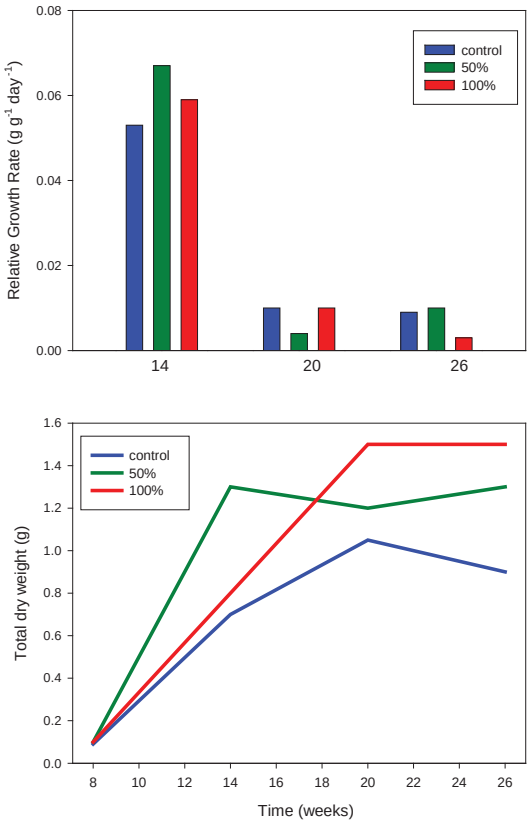

Figure 5. Responses of *Ipomoea* seedlings when exposed to sand burial. Control, no burial; 50% and 100% refer to the depth of dry sand that covered the seedling as a percentage of the seedling height (Modified from Martínez and Moreno-Casasola,. 1996).

CONCLUSIONS

Our results indicate that the ecomorphodynamic interaction between coastal dunes and dune building plants derives in reduced dune-face erosion. Therefore, the use of plants tolerant to marine water flooding can be an ecosystem-based alternative for the protection of coastal human values and activities. This type of protection promotes the conservation of different ecosystem services and is compatible with low-density tourism.

LITERATURE CITED

Cooper, J.A.G. and McKenna, J., 2008. Working with natural processes: the challenge for coastal protection strategies. *The Geographical Journal*, 174(4), 315-331.

Costanza, R.; Pérez-Maqueo, O.M.; Martínez, M.L.; Sutton, P.; Anderson, S.J., and Mulder, K., 2008. The value of coastal wetlands for hurricane protection. *AMBIO*, 37 (4), 241-248.

Everard, M.; Jones, L., and Watts, B., 2010. Have we neglected the societal importance of sand dunes? An ecosystem services perspective. *Aquatic Conservation: Marine and Freshwater Ecosystems*, 20(4), 476-487.

Gallego-Fernández, J.B. and Martínez, M.L., 2011. Environmental filtering and plant functional types on Mexican foredunes along the Gulf of Mexico. *Ecoscience*, 18, (1), 52-62

Gedan, K.B.; Kirwan, M.L.; Wolanski, E.; Barbier, E.B., and Silliman, B.R., 2011. The present and future role of coastal wetland vegetation in protecting shorelines: Answering recent challenges to the paradigm. *Climatic Change*, 106(1), 7-29.

Kobayashi, N.; Gralher, C., and Do, K., 2013. Effects of woody plants on dune erosion and overwash. *Journal of Waterway, Port, Coastal, and Ocean Engineering*, 139(6), 466-472.

Langridge, S.M.; Hartge, E.H.; Clark, R.; Arkema, K.; Verutes, G.M.; Prahler, E.E., and O'Connor, K., 2014. Key lessons for incorporating natural infrastructure into regional climate adaptation planning. *Ocean & Coastal Management*, 95, 189-197.

Martínez, M.L. and Moreno-Casasola, P., 1996. Effects of burial by sand on seedling growth and survival in six tropical sand dune species. *Journal of Coastal Research*, 12(2), 406-419.

Maun, M.A., 1998. Adaptations of plants to burial in coastal sand dunes. *Canadian Journal of Botany*, 76(5), 713-738.

McGranahan, G.; Balk, D., and Anderson, B., 2007. The rising tide: Assessing the risks of climate change and human settlements in low elevation coastal zones. *Environment and Urbanization*, 19(1), 17-37.

Martínez, M.; Vázquez, G.; White, D.; Thivet, G., and Brengues, M., 2002. Effects of burial by sand and inundation by fresh-and seawater on seed germination of five tropical beach species. *Canadian Journal of Botany*, 80(4), 416-424.

Phillips, M.R. and Jones, A.L., 2006. Erosion and tourism infrastructure in the coastal zone: Problems, consequences and management. *Tourism Management*, 27(3), 517-524.

Silva, R.; Martínez, M.L.; Odériz, I.; Mendoza, E., and Feagin, R.A., 2015, The reduction of dune face erosion by vegetation. *Coastal Engineering* (in press).

Temmerman, S.; Meire, P.; Bouma, T.J.; Herman, P.M.; Ysebaert, T., and De Vriend, H.J. 2013. Ecosystem-based coastal defence in the face of global change. *Nature*, 504(7478), 79-83.

Journal of Coastal Research	SI	75	308-312	Coconut Creek, Florida	2016

A Review of Coastal Dunefield Evolution in Southeastern Queensland

Graziela Miot da Silva[†*] and James Shulmeister [‡]

[†]School of the Environment
Flinders University
Adelaide, South Australia

[‡]School of Geography Planning and Environmental Management
The University of Queensland
Brisbaine, Queensland.

www.cerf-jcr.org

www.JCRonline.org

ABSTRACT

Miot da Silva, G. and Shulmeister, J., 2016. A review of coastal dunefield evolution in Southeastern Queensland. *In:* Vila-Concejo, A.; Bruce, E.; Kennedy, D.M., and McCarroll, R.J. (eds.), *Proceedings of the 14th International Coastal Symposium* (Sydney, Australia). *Journal of Coastal Research*, Special Issue, No. 75, pp. 308-312. Coconut Creek (Florida), ISSN 0749-0208.

The Southern Queensland subtropical coastline represents a major depositional system containing 3 of the largest sand islands in the world. The surface of these sand masses comprises foredune ridges and predominantly large transgressive dunefields, deposited episodically during the Quaternary. The chronological sequence of these dunefield phases, however, is still poorly understood. This paper summarizes the information available regarding dunefield transgression events on the southern coast of Queensland and indicates that both marine and climate effects are important controlling factors for dunefield evolution but that an understanding of the relative thresholds of each factor as the main trigger of dune emplacement phases remains a challenge .

ADDITIONAL INDEX WORDS: *Dune emplacement phases, climate, sea level changes.*

INTRODUCTION

The Southern Queensland (QLD) subtropical coastline represents a major depositional system containing 3 of the largest sand islands in the world: Fraser, North Stradbroke and Moreton Islands as well as the mainland attached Cooloola sand mass (Figure 1). This review paper will focus on these large sand masses, built by siliceous deposition through processes that have been operating for at least 750,000 years (Tejan-Kella *et al.*, 1990).

The surface of these sand masses comprises foredune ridges and predominantly large transgressive dunefields as a result of substantial sediment supply and continual exposure to the prevailing onshore southeasterly winds. The dunefields were deposited episodically during the Quaternary (Ward, 1978) and contain overlapping phases of parabolic dune systems (Figure 1) (Thompson, 1981) and some transgressive sand waves. The initiation of each individual phase has been the subject of debate, attributed either to sea level lowstands (Ward, 1978) or to successive Quaternary marine transgressions (Thompson, 1981). In fact, the literature debate on whether marine (sea level) factors or climate are the main triggers for dunefield initiation is common to other regions around Australia and elsewhere (Lees, 2006; Young *et al.*, 1993).

This paper aims to summarize the information available regarding dunefield transgression events on the southern coast of QLD and indicate possible main triggers of initiation. This stretch of coastline is particularly interesting as it contains one of the longest records of dunefield evolution in the world, representing an ideal site where models of long-term dunefield evolution can be tested (Cooper, 1958; Pye and Bowman, 1984; Thom, 1978; Young *et al.*, 1993).

Soil development and age inferences

The parabolic systems in the study area have some of the deepest and most highly developed podosols (podzols) in the

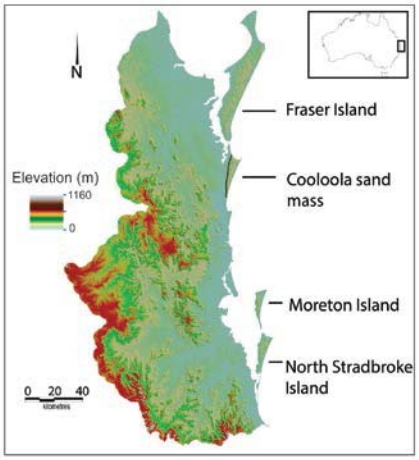

Figure 1. Study area with the sand masses discussed in the text. State of Queensland (Department of Environment and Resource Management) 2010. Data from Commonwealth of Australia (Geoscience Australia) 2009 used in creating this dataset provided under Creative Commons Australia - Attribution licence. Updated data available at http://dds.information.qld.gov.au/dds

DOI: 10.2112/SI75-062.1 received 15 October 2015; accepted in revision 15 January 2016.
*Corresponding author: danielemallmann@gmail.com

world, due to the long history of the dunefields, favourable climatic conditions, the high porosity of the sediments and absence of a water table to considerable depths (Thompson, 1981). Profile development or depth of A1 and A2 horizons to the firm, iron-humus rich Bhir horizon can be as much as 30 metres in the oldest dunes (Thompson, 1981).

Thompson (1981) presents a chronological sequence of dune systems 1 to 6 in Cooloola according to their degree of erosion and podosol profile development, with no absolute ages inferred to those systems. The oldest dune systems (5 and 6) have the deepest podosols (~11m and up to 20m, respectively) and have been subjected to deep water-related erosion, losing their original parabolic morphology (Thompson, 1981). Thompson (1981) suggests that they are likely of Pleistocene age, including system 4 (>40,000 yr BP). The three youngest parabolic dune systems are likely of Holocene age (Thompson, 1981), formed during the last 6 ka after sea level reached its present elevation (Thom *et al.*, 1978), from their intact dune morphologies and limited soil profile development (<1.2m). Sequences of podosols examined in Cooloola have been correlated to sand units in Fraser, Moreton and North Stradbroke Islands (Thompson, 1981). For example, Thompson's system 3 in Cooloola and the dunes at Triangle Cliff in Fraser Island have been correlated due to similarities in surface morphology, stratigraphy and degree of soil development (Ward, 1985). The absolute age of Triangle Cliff, the largest sand unit in Fraser Island is yet to be accurately determined as indeed are the ages of most dune units in SE QLD.

EPISODES OF DUNE BUILDING IN SOUTHEAST QLD

Pickett *et al.* (1989) obtained a mean $^{230}Th/^{234}U$ date for 3 well preserved coral species assemblages in North Stradbroke Island of ~124 ka BP, belonging to the marine transgression in isotope stage 5e. The good preservation of the coral specimens indicate that they were buried rapidly *in situ* by an advancing, contemporaneous parabolic dune system during a period of higher sea level (between +1 and +3m). This dune is associated with Thompson's dune system 5 by Tejan-Kella *et al.* (1990) and not associated with low sea levels or very dry climate conditions according to Pickett *et al.* (1989) and Tejan-Kella *et al.* (1990). Tejan-Kella *et al.* (1990) extend this interpretation to their Warrawonga sample (TL age of 90 ±10 ka BP). However, Ward (1985) questioned these coral ages (which were revised by Pickett *et al.*, 1989), and consequently the age of the related dune system, on the basis that their use of a closed-system model does not approach the reality of coral system environments.

Radiocarbon dates from the Southeastern QLD dunefields are scarce and of questionable reliability. Its long history of Quaternary evolution, with the bulk of the sandmasses built around the mid-Pleistocene (Brooke *et al.*, 2015) makes the radiocarbon technique potentially useful to date only the very last periods of deposition. The first absolute dates for the area (Cooloola and North Stradbroke Island) were obtained in the early 1990's by Tejan-Kella *et al.* (1990), who found that the TL dates agreed with the relative chronological sequence from the soil evidence of Thompson (1981), except for the youngest sample in Kings Bore that yielded a Pleistocene age of 19±2 (later corrected to 11 ka) in a system that has morphological, stratigraphic and pedological characteristics of recent deposit (500 years was suggested by Tejan-Kella *et al.*, 1990 (Figure 2). Tejan-Kella *et al.* (1990) suggested that the sample must not have completely zeroed in this youngest deposit, which lead to erroneous TL determinations. Figure 2 displays the TL dates available for the study area (Brooke *et al.*, 2015; Tejan-Kella *et al.*, 1990).

The initiation of sand accumulation and dunefield development in Southeastern QLD has also been a matter of debate. It has been attributed to periods of low sea level by Ward (1978) who argued that accumulations occurred during low stands over the Quaternary from aeolian reworking of sediments exposed on the continental shelf. This theory is problematic since Fraser Island would be up to 50km inland at low sea stands which would make coastal dune building rather questionable (Cook, 1986). Schofield (1975) has associated dunefield activation phases to periods of marine regression and greater exposure of continental shelf providing sediments for onshore winds to form transgressive dunefields in the South Kaipara Barrier, New Zealand. This model might be accepted in areas where vegetation growth is limited and onshore winds are strong (Roy and Thom, 1981). However, even if during the Last Glacial Maximum (LGM), westerly winds were stronger, such as is inferred in New South Wales (NSW) (Thom *et al.*, 1994), coastal pioneer vegetation would have colonised the relict beaches as sea level fell just as it does now under beach progradational conditions (Hesp, 2002). Even in the NSW example above, the dunes have a continental origin and were derived from reworked interglacial coastal dunes.

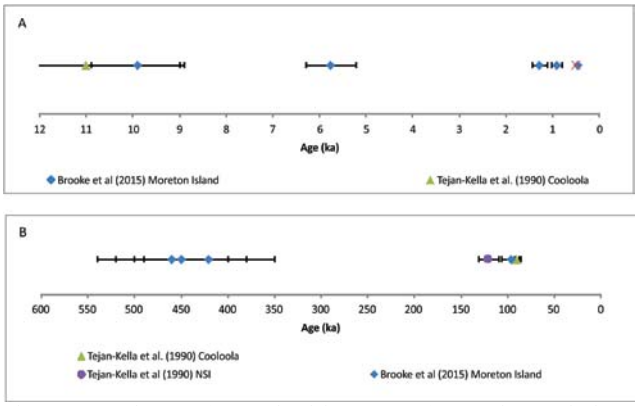

Figure 2. Holocene (A) and Pleistocene (B) TL dates of dune emplacement available for Southeastern QLD. Horizontal dark lines refer to the uncertainty associated with each date.

In contrast, initiation of sand accumulation and dunefield development in Southeastern QLD has also been attributed to periods of sea level rise. Thompson (1981) suggests that the siliceous sands that dominate the QLD coastline were derived from the shoreface during periods of marine transgression during the Quaternary and accumulated during periods of highstand when sea level returned to present (or near present) elevations during successive interglacials.

Cooper (1958)'s work on the Oregon and Washington (USA) dunefields has suggested that phases of dunefield instability are associated with marine transgression, which was firstly expanded to Australia by Thom (1978), Pye (1984), Pye and Bowman (1984). The so-called known Cooper-Thom model of sea level rise as a main trigger for dunefield activation in Australia and climate as a supporting factor has since then been advocated by many authors in more recent publications (Lees, 2006) but criticized by others (Young *et al.*, 1993), who support the idea that dune activation phases were brought about primarily by climatic factors. We explore possible climate and/or marine triggers for dunefield activation in Southeastern QLD in the next section.

QUATERNARY CLIMATE AND SEA LEVEL CHANGES

There are very few luminescence dates for these systems (Figure 2) and the correlation between dune phases and the palynological and climate record can be challenging. However, it has been assumed that moisture has been always enough to support vegetation even during the Last Glacial Maximum (LGM) in this region. Thompson (1981) and others argue that in Cooloola there is no signature of significantly drier climate conditions during the last glaciation, beyond the threshold for plant colonization. These authors base this conclusion on the fact that the dune systems have preserved their parabolic shape since then and that there is no evidence of desert-type dune systems. This assumption contrasts with the well understood concept that parabolic shapes can evolve from linear, barchan desert-type features as vegetation grows (Tsoar and Blumberg, 2002).

More recently, Moss *et al.* (2013) suggests that rainforest was present on the dunes at North Stradbroke at the LGM. In contrast, work from Fraser Island (Longmore and Heijnis, 1999) suggests that rainforest is absent during the LGM but there is no suggestion that the dunes are devegetated at that time. Although dates that indicate dunefield emplacement during the LGM are absent from the record so far, the presence of vegetation does not eliminate the possibility of dune emplacement phases at this time, as large parabolics such as these in Southeastern QLD are capable of advancing inland regardless of dense forest cover (Pye, 1982). A more likely reason for their absence is the 30-50 km distance to the nearest coast at the LGM.

In the following, only the available luminescence dates obtained thus far for the Southeastern QLD landmasses will be discussed (Figure 2). We group ages from Moreton Island, North Stradbroke and Cooloola as representative for this entire section of the coast (Ward, 2006), although the absolute chronological sequence and correlation with the virtually undated Fraser Island is yet to be tested.

Mid-to-Late Pleistocene: Figure 2B shows a cluster of TL dates around the mid-to-late Pleistocene (between ~420 and ~460 ka BP) (Brooke *et al.*, 2015; Tejan-Kella *et al.*, 1990). It could be that dunefield emplacement during the mid-to-late Pleistocene may have well been a result of a climate trigger (Figure 3A), although Longmore and Heijnis (1999) infer from pollen, chemistry and charcoal analysis that water levels at the Old Lake Coomboo Depression in Fraser Island were high at ca 600 ka and intermediate after ca 350 ka. Perhaps moisture was sufficient to keep the lake levels and some vegetation cover however nothing is known about paleo wind direction and strength in Southeastern QLD during the mid-late Pleistocene. Stronger winds during a cold, glacial period could have been enough to trigger sand mobility, limiting the establishment of vegetation and promoting dunefield activity (Tsoar and Blumberg, 2002). As Shulmeister (1992) reported, there is no direct evidence for aridity triggering dune activation in any northern Australian coastal dunefields and the likelihood of true aridity on this coastline is remote. Alternatively, dunes may have been formed as source bordering dunes derived from river margins crossing the exposed shelf. The Mary River is a good candidate for this, but it is questionable as to whether the regionally extensive older sand units (e.g. the Yankee Jack and Cooloola phases) could be triggered by sources that are perpendicular to the coast and the dunefield alignment.

Last Interglacial: Another cluster of dates surrounds the last interglacial (90 to 120 ka BP, isotope stages 5c to 5e). (Figures 2B and 3A). Tejan-Kella *et al.* (1990) assume that these dune phases in SE QLD are not associated with periods of lower sea level and drier climate and we reinforce this model by supporting Brooke *et al.* (2015) theory that dune building events at this time could have been associated with "intermediate" sea levels, which persisted during stage 5. Longmore (1997) suggests low fire incidences during this period in association with the recovery of rainforest and a temporary increase in lake levels, indicating humid conditions during this broad interval.

Last Glacial Maximum: Longmore and Heijnis (1999) affirm that the last glacial maximum (LGM) was drier than previous glacial cycles in the Fraser Island region. Dust tracing indicates that the finest aeolian sediment fractions at Tortoise Lagoon on North Stradbroke Island were derived from the Murray Darling Basin. This area lies to the Southwest of the region and suggests the maintenance of winter westerlies over this region during the LGM (e.g. Petherick *et al.*, 2008). Interestingly, absolute dates of aeolian activity during the LGM (22-20 ka) are not present in the Southeastern QLD record. Dust in the Native Companion Lagoon record is mainly provenanced from continental sources rather than local (Petherick *et al.*, 2008). More diagnostic evidence is required to claim dune emplacement phases during the LGM perhaps associated with the expansion of the Simpson Desert (Thom *et al.*, 1994).

Early Holocene: Two TL samples (Brooke *et al.*, 2015; Tejan-Kella, *et al.*, 1990; Figure 2A) cluster around early Holocene (11 to 8.5 ka BP). Cook (1986) summarizes coastal dune building events in eastern Australia and suggests a major widespread period of transgressive dune instability between 9k and 7k years ago. The North Stradbroke Island climate record suggests low aeolian sedimentation and decreased aridity (Petherick *et al.*, 2008). A marine transgression cause must also be considered as sea level was rising rapidly during the last marine transgression.

Mid-to-Late Holocene: The two dates (5.75 ka BP and 3.1 ka BP, Figure 2A) indicate dune emplacement during a period of climatic deterioration according to Petherick *et al.* (2008), represented by initiation of a dry phase in subtropical Australia (Donders *et al.*., 2007) and highly variable climate conditions related to the onset of El Niño Southern Oscillation (ENSO) conditions (Shulmeister and Lees, 1995). Sea level was at a

highstand at ~6 ka following the last marine transgression and falling slightly from ~2 ka (Lewis *et al.*, 2013 and Figure 3B). Here dunefield emplacement could have been promoted by increased onshore sediment supply during the last marine transgression combined with a drier, windier climate.

Late Holocene: The sea level record shows a smooth decline from ~+1.0 metres to present from about 2 ka BP (Figure 3B). Dune emplacement happened at about 0.9 and 1.28 ka B.P (Figure 2A). The climate record points to more modern conditions, e.g., highly variable within an aridifying trend after ~3 ka BP (Donders *et al.*, 2006; Shulmeister and Lees, 1995). McGowan *et al.* (2008) affirms that during the last 1500 years, the aeolian sedimentation record in North Companion Lagoon has been at a constant rate of about 0.7 g m -2 yr-1.

Hayne and Chappell (2001) detected storm deposits in northern QLD over the last 5000 years, including deposits dated at ~500 and ~1000 yrs BP. Records of paleo-storms are absent in Xoutheastern QLD, but they likely exist (Gontz *et al.*, 2015) and should be tested against periods of dune emplacement over the late Holocene.

The more recent dunefield emplacement phases have been attributed to aboriginal firing and European colonization, which has been dismissed by Cook (1986) and Levin (2011) as possible causes for major dunefield activity. Most recently, although sea level is recorded to be rising at a rate of about 0.7 mm/year between 1964 to 2012 (BOM, 2013, data from Bundaberg), Levin (2011) has demonstrated that sand blows in Fraser have been largely recolonized by vegetation. He inferred that this was due to a decrease in storm incidence related to a shift in the IPO (Interdecadal Pacific Oscillation).

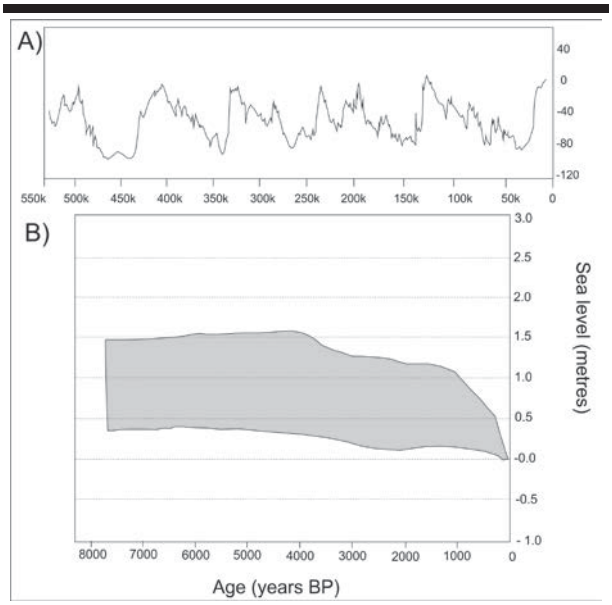

Figure 3. (A) Sea level curve for the last 550k (mid-late Pleistocene) modified from Rohling *et al.* (2009) and (B) sea level envelope for Northern QLD (modified from Lewis *et al.* (2013).

CONCLUSIONS

The southern coast of QLD contains one of the most extensive records of Quaternary dunefield evolution in the world, and is an excellent area to examine the relative contributions of sea level change and climate to phases of dunefield activity. The chronological sequence of these dunefield phases, however, is still largely unknown. From the rare luminescence dates available in the area, it is possible to identify dune building phases associated with "intermediate" and high sea levels. In contrast, during the LGM, coastal dunefield development on modern Fraser Island is unlikely, but broader regional climate conditions were favourable for long-distance aeolian dust transport and sedimentation. Dune phases dated to the mid-to-late Holocene are possibly associated with variable climate after ~5 ka that probably reflects the widely recognised onset of an ENSO like regime with associated enhanced drought risks. At shorter timescales individual tropical storms play an important role in dune activation. Most recently, many sandblows (actually parabolic dunes) on Fraser Island are being re-vegetated, associated with a decrease in storm frequency and intensity due to the shift to cooler coastal waters under the IPO. It is evident that both marine and climate effects are important controlling factors for dunefield evolution. An understanding of the relative thresholds of each factor and/or what condition causes one or the other to prevail as the main trigger of dune emplacement phases remains a challenge, but could potentially be resolved by further studies in the SE QLD coastal deposits.

LITERATURE CITED

BOM (Australian Bureau of Meteorology), 2013. http://www.bom.gov.au/ntc/IDO70000/IDO70000_59820_SLI.shtml

Brooke, B. P.; Pietsch, T. J.; Olley, J. M.; Sloss, C. R., and Cox, M. E., 2015. A preliminary OSL chronology for coastal dunes on Moreton island, Queensland, Australia–Marginal deposits of A large-scale quaternary shelf sediment system. *Continental Shelf Research*, 105, 79-94.

Cook, P.G., 1986. *A review of coastal dune building in eastern Australia*. Aust. Geogr., 17:133-143.

Cooper, W. S., 1958. Coastal sand dunes of Oregon and Washington. *Geological Society of America Memoir,* 72, New York, 169 pp.

Donders T.H.; Haberle S.G.; Hope G.; Wagner F., and Visscher H., 2007. Pollen evidence for the transition of the Eastern Australian climate system from the post-glacial to the present-day ENSO mode. *Quaternary Science Reviews*, 26, 1621–1637.

Gontz, A. M.; Moss, P. T.; Sloss, C. R.; Petherick, L. M.; McCallum, A., and Shapland, F., 2015. Understanding past climate variation and environmental change for the future of an iconic landscape–K'gari Fraser Island, Queensland, Australia. *Australasian Journal of Environmental Management*, (ahead-of-print), 1-19.

Hayne, M. and Chappell, J., 2001. Cyclone frequency during the last 5000 years at Curacoa Island, north Queensland, Australia. *Palaeogeography, Palaeoclimatology, Palaeoecology*, 168(3), 207-219.

Hesp, P., 2002. Foredunes and blowouts: initiation, geomorphology and dynamics. *Geomorphology*, 48(1), 245-268.

Lees, B.G., 2006. Timing and formation of coastal dunes in Northern and Eastern Australia. *Journal of Coastal Research* 22:78-89.

Levin, N., 2011. Climate-driven changes in tropical cyclone intensity shape dune activity on Earth's largest sand island. *Geomorphology* 125: 239–252.

Longmore, M.E., 1997b. Quaternary palynological records from the perched lake sediments of Fraser Island, Queensland, Australia: rainforest, forest history and climatic control. *Australian Journal of Botany* 45, 507-526.

Longmore, M.E. and Heijnis, H., 1999. Aridity in Australia: Pleistocene records of palaeohydrological and palaeoecological change from the perched lake sediments of Fraser Island, Queensland, Australia. *Quaternary International* 57/58, 35-47.

Moss, P.T.; Tibby, J; Petherick, L; McGowan, H, and Barr, C., 2013. 'Late Quaternary vegetation history of North Stradbroke Island, Queensland, eastern Australia', *Quaternary Science Reviews*, vol. 74, pp. 257–272.

Petherick, L.M.; McGowan, H.A.; Moss, P.T., and Kamber, B 2008b, 'Late Quaternary aridity and dust transport pathways in eastern Australia', *Quaternary Australasia*, vol. 25, pp. 2–11.

Pickett. J.W.; Thompson, C.H.; Martin, H. A., and Kelley, R. A., 1984. Late Pleistocene fossils from a high dune near Amity, North Stradbroke Island. In: Coleman, R.J.; Covacevich, J., and P. Davie. (eds.) *Focus on Stradbroke: New Information on North Stradbroke Island and Surrounding Areas*, *1974-1984.* Booloorong Pub., Brisbane, pp. 167-177.

Pickett, J.W.; Ku, T.L.; Thompson, C. H.; Roman, D.; Kelley, R.A., and Huang, Y. P., 1989. A review of age determinations on Pleistocene corals in eastern Australia. *Quaternary Research*, 31(3), 392-395.

Pye, K., 1984. Models of transgressive coastal dune building episodes and their relationship to Quaternary sea level changes: a discussion with reference to evidence from eastern Australia. In *Coastal research: UK perspectives* (pp. 81-104). Geobooks Norwich.

Pye, K. and Bowman, G.M., 1984. The early Holocene marine transgression as a forcing function in episodic dune activity on the eastern Australian coast. In: B.G Thorn (ed.), *Coastal Geomorphology in Australia*. Academic, Sydney, pp. 179-196.

Pye, K., 1982. Morphological development of coastal dunes in a humid tropical environment, Cape Bedford and Cape Flattery, North Queensland. Geografiska Annaler. Series A. *Physical Geography*, 213-227.

Rohling, E.J.; Grant, K.; Bolshaw, M.; Roberts, A. P.; Siddall, M.; Hemleben, C., and Kucera, M., 2009. Antarctic temperature and global sea level closely coupled over the past five glacial cycles. *Nature Geoscience*, 2(7), 500-504.

Roy, P.S. and Thorn, B.G., 1981, 'Late Quaternary marine deposition in New South Wales and southern Queensland – an evolutionary model', *Journal of the Geological Society of Australia*, vol. 28, pp. 471–489.

Schofield, J.C., 1975. Sea-level fluctuations cause periodic, post-glacial progradation, south Kaipara Barrier, North Island, New Zealand. *New Zealand Journal of Geology and Geophysics*, 18(2), 295-316.

Shulmeister, J., 1992. Comment: Late Pleistocene record of cyclic eolian activity from tropical Australia suggesting the Younger Dryas is not an unusual climatic event. *Geology* 20:574-575

Shulmeister, J. and Lees, B.G., 1995. Pollen evidence from tropical Australia for the onset of ENSO-dominated climate at c. 4000 BP. *The Holocene*, 5(1), 10-18.

Tejan-Kella, M.S.; Chittleborough, D.J.; Fitzpatrick, R.W.; Thompson, C.H.; Prescott, J.R., and Hutton, J.T., 1990. Thermoluminescence dating of coastal sand dunes at Cooloola and North Stradbroke Island, Australia. *Soil Research*, 28(4), 465-481.

Thom, B.G., 1978. Coastal sand deposition in southeast Australia during the Holocene. In: J.L. Davies and M.A.J. Williams (eds), *Landform Evolution in Australasia*. A.N.U., Canberra, pp. 197-214.

Thorn, B.G., Polach, H.A. and Bowman, G.M., 1978. Holocene age structure of coastal sand barriers in New South Wales, Australia. Dept. Geogr., Univ. Coll. Duntroon

Thom, B.; Hesp, P.A., and Bryant, E., 1994. Last glacial "coastal" dunes in Eastern Australia and implications for landscape stability during the Last Glacial Maximum *Palaeogeography, Palaeoclimatology, Palaeoecology*, 111:229-248.

Thompson, C.H., 1981. Podzol chronosequences on coastal dunes of eastern Australia. *Nature* 291, 59-61.

Tsoar, H. and Blumberg, D., 2002. Formation of parabolic dunes from barchan and transverse dunes along Israel's Mediterranean coast. *Earth Surface Processes and Landforms*, 27, pp. 1147–1161.

Ward, W.T., 1978. Notes on the origin of Stradbroke Island. Univ. Qld Dept Geol. Pap. 8, 97-104.

Ward, W.T., 1985. Correlation of east Australian Pleistocene shorelines with deep-sea core stages: A basis for a coastal chronology. *Geological Society of America Bulletin*, 96(9), 1156-1166.

Ward, W.T., 2006. Coastal dunes and strandplains in southeast Queensland: sequence and chronology. *Australian Journal of Earth Sciences* 53:363-373.

Young, R.W.; Bryant, E.A.; Price, D.M., and Pease, M., 1993. Theoretical constraints and chronological evidence of Holocene coastal development in central and southern New South Wales, Australia. *Geomorphology*, 7, 317–329.

Journal of Coastal Research	SI	75	313-317	Coconut Creek, Florida	2016

The Presence of Foredune Strip as Key Factor for the Integral Beach-dune System Conservation

Miquel Mir-Gual†, Guillem X. Pons†

† Earth Sciences Department
University of Balearic Islands; BIOGEOMED research group
Balearic Islands, Spain

www.cerf-jcr.org

www.JCRonline.org

ABSTRACT

Mir-Gual, M. and Pons, G.X. 2016. The presence of foredune strip as key factor for the integral beach-dune system conservation. *In:* Vila-Concejo, A.; Bruce, E.; Kennedy, D.M., and McCarroll, R.J. (eds.), *Proceedings of the 14th International Coastal Symposium* (Sydney, Australia). *Journal of Coastal Research*, Special Issue, No. 75, pp. 313-317. Coconut Creek (Florida), ISSN 0749-0208.

Most studies of sedimentary coastal systems analyse the agents and factors participating in its formation. However, there is less information about the behaviour of these systems once they are formed, about their erosion and sedimentation processes, and about their evolution patterns. In coastal areas such as Balearic Islands, the erosion processes on emerged beaches can suppose negative effects for the main economic activity of beach and sun tourism. With this scenario, and from the results obtained through a PhD thesis, this work aims to show the importance that a well preserved first line dune has for the conservation state of the whole dune system. The results obtained from several field experiments carried out through anemometry data and sand transport measurements show how the presence of a well-preserved foredune is a key factor for the conservation of the associated dune complex. Airflow modelling and sand traps measurements show how the foredune increases the surface rugosity, decreasing wind speed and an increasing sedimentation rates, helping diminish the erosion patterns from the emerged beach to the innermost of the dune complex. Our research will help to improve the future management plans, and keep positive sedimentary balances on emerged beaches.

ADDITIONAL INDEX WORDS: *Beach management, wind modeling, sand transport, coastal processes.*

INTRODUCTION

The beach-dune systems are formed by the symbiosis of two distinct areas: the submerged area, controlled by marine hydrodynamics, and the emerged area, controlled by wind dynamics. Many studies have demonstrated that any change can upset the natural balance in each of these areas (Mir-Gual *et al*., 2013; Puig *et al*., 2014). Within this scenario natural and anthropogenic activites contribute to coastal change at diverse temporal and spatial scales. Over past decades, the interest in the knowledge of shoreline behaviour has increased due to climate change predictions and population growth in coastal areas, mainly related to beach and sun tourism. In the Balearic Islands there have been important regression of sandy coastal systems over the last decades. Some studies such as Mir-Gual *et al*. (in press) have demonstrated that this trend has an important temporal relation with the beginning of mass coastal tourism in the early 60's, 20th century. Furthermore, Mir-Gual *et al*. (in press) show how the most eroded areas along the dune front (backward movement of -20 m) are linked to the highest human pressure. Although the touristic exploitation of these fragile and natural systems generate high revenues, a bad management casues a negative impact and conservation status (McLaughlin *et al*., 2002; Roig-Munar *et al*, 2009).

Along the coast, the emerged beach is the zone with highest economic interest in the Balearic Islands due to its associated tourism activity. The massive human pressure exerted on sandy beaches over the last decades has supposed important problems of erosion and degradation of their natural, ecological and geomorphological values. This strong anthropogenic pressure, mostly during the summer, has generated in many sandy coastal systems an appreciable degradation, or even a full disappearance, of the foredune strip, leading to a an increase of the sediment dynamics of the whole dune complex. According to the results obtained from a recent PhD thesis (Mir-Gual, 2014), one of the most important erosion mechanisms in these environments is linked to wind activity which, in the absence of a foredune strip, increases the patterns of sediment transport from the aerial beach to the innermost of the dune complex. This work aims to analyse, from fieldwork experiments, the importance that the presence of well-conserved foredune has for the conservation state of the whole dune complex. Furthermore, the results obtained in this work can help to increase our knowledge of how these complex systems work, and how to take the right management decisions to restore and recover coastal sandy areas.

Study area

Our research was carried out during two fieldwork campaigns, in two different sandy coastal areas of the Balearic Islands; es Comú de Muro located in Mallorca, and Cala Tirant located in Menorca (Figure 1).

The dune system of es Comú de Muro (Figure 1) is located within the Bay of Alcudia (Mallorca), on a sand spit which

DOI: 10.2112/SI75-063.1 received 15 October 2015; accepted in revision 15 January 2016.
*Corresponding author: guillemx.pons@uib.es

developed from S to N by littoral drift between 6.500 and 2.400^{14}C years B.P. It is 1.5 km long and covers an area of 0.5 km^2. The modern dune system consists of simple and compund parabolic dunes generated by N-NE winds.

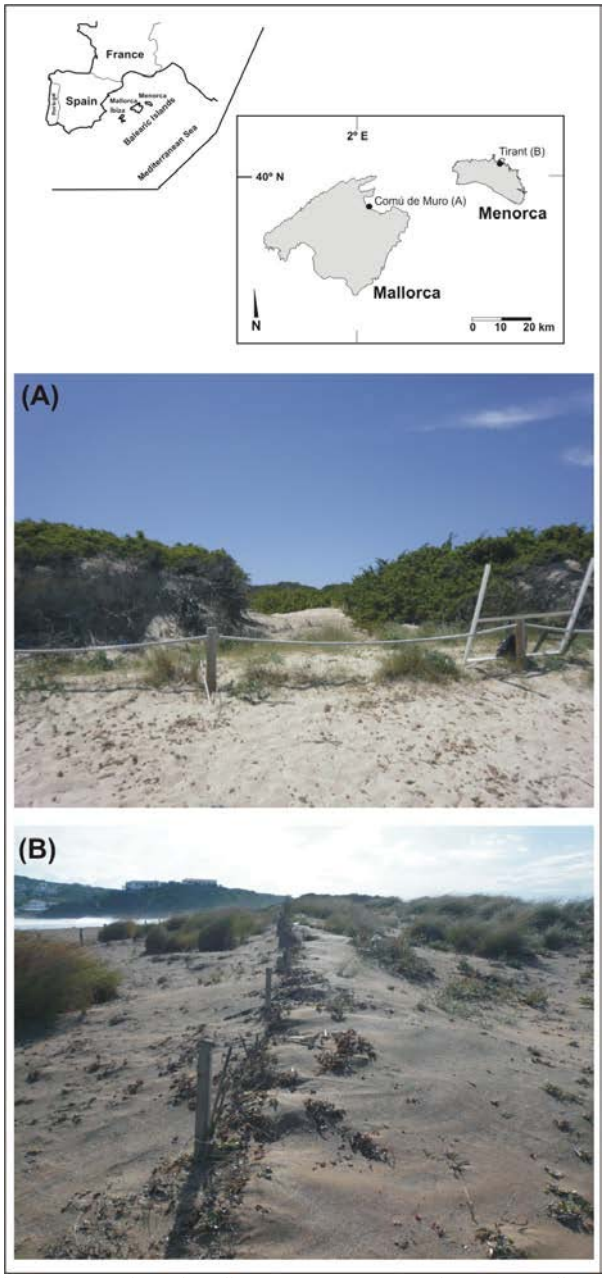

Figure 1. Location of studies area; A) es Comú de Muro (Mallorca), where there is not exist any developed foredune, and B) Cala Tirant (Menorca) with the presence of foredune strip of 1m height.

According to Mir-Gual *et al*. (2013) three dune belts can be identified: a belt of embryonic dune ridge adjacent to the emerged beach, followed inland by semi-stabilized dunes, and finally a belt of stabilized dunes. Because of excessive human pressure over the past decades, the original strip of foredunes has been almost completely destroyed. Some embryonic dune formations, normally associated with psammophyte vegetation, can still be found locally in front of, or just inside blowout morphologies (Figure 1A).

The dune complex of Cala Tirant is located in the northern coast of Menorca (Figure 1). The foredune covers a surface of 0.02 km^2 whilst the dune complex covers a surface of approximately 1.6 km^2 and is limited by a marsh on its southwestern site. The dunes are highly dynamic due to the presence of strong recurrent winds from the North called Tramuntana, with associated wind speeds over 3 ms^{-1} many days throughout the year. This system has been strongly affected by tourism, human activities and poor management. Recent management over the last few years has, however, led to a positive restoration, resulting in the formation of embryo dunes and the increase of vegetation cover. Actually the foredune reaches a maximum height of 5 m and is characterized by the presence of herbaceous vegetation such as *Ammophila arenaria*. The beach in front is 350 m long and 20 to 40 m wide.

METHODS

The experiments were carried out along the first line of dunes at Es Comú (Mallorca) and Cala Tirant (Menorca). According to the main objective of our research, the selection of the sites was carried out considering the presence/absence of foredune. Thus, in the first case there is no extant developed foredune (Figure 1A), whilst in Cala Tirant the foredune in the monitoring area reached 1m of height (Figure 1B). The main purpose was to achieve better understanding of airflow dynamics and its relation with the patterns of sediment transport from the beach toward the dune field according to the role of foredune presence.

Wind measurements

Wind data was recorded using 7 Davis anemometer 2D, each consisting on 3-cup speed sensors and a direction vane. Anemometers were deployed in the outer margin, within, and in the innermost part of a blowout existing in each of the study areas. Anemometers were deployed 40 cm above the surface and facing toward the geographical north to correct for misaligments in the field. Finally, wind speeds were grouped into 8 (es Comú) and 13 (Tirant) 20-min runs coinciding with transport runs and normalized by the incoming wind speed recorded at the back beach by A1. The speed-up ratio (δs) is calculated according to the variations of speed wind along the experiment after Jackson and Hunt (1975):

$$\delta s = [u_z - U_z] / U_z$$

where u_z is the wind speed at height z, and U_z is the wind speed at height z on the reference anemometer (A1). The speed-up ratio provides a metric for assessing the changes in wind speed relative to airflow entering the blowout.

Sand transport measurement

Sediment transport was quantified using twelve vertical traps following the design by Cabrera and Alonso (2010). The traps

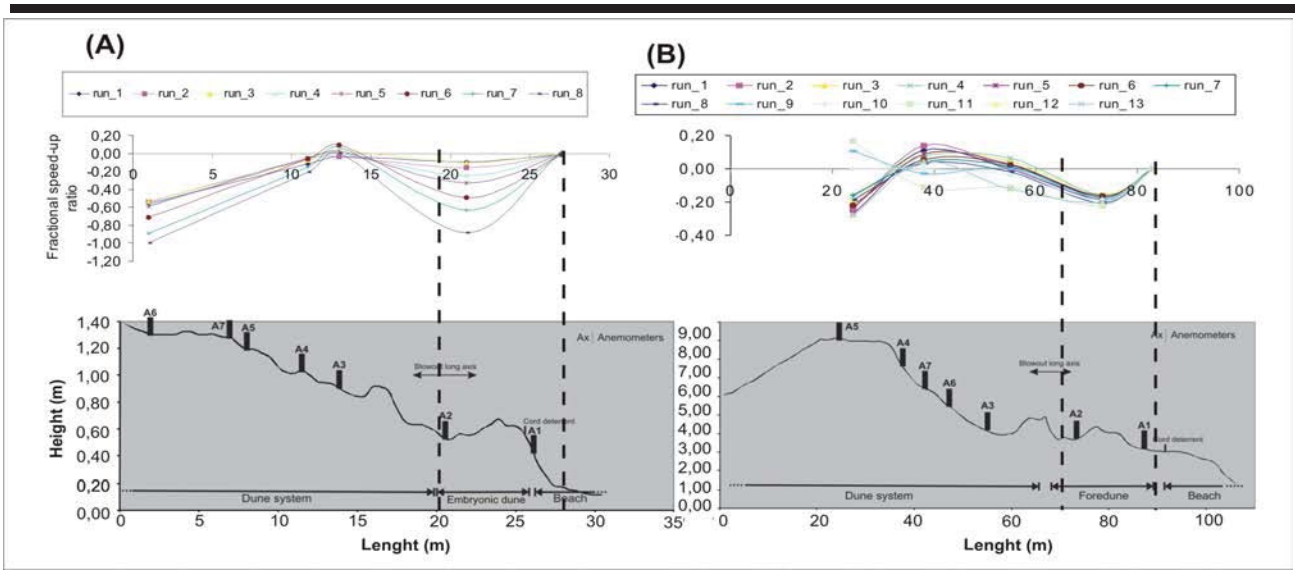

Figure 2. Time-average wind speeds (fractional speed-up ratio) in the front dune of es Comú de Muro (A) and Cala Tirant (B) taking as a reference anemometer 1 (after Jackson and Hunt, 1975). Dotted lines emphasize the processes given in front of dunes.

were divided into three groups of four traps each, facing to N, S, E and W, with the aim of generating a multidirectional sampling point and maximize the collection of moving grains from most directions. The first group (TA) was located at the back beach, the second (TB) on the outer margin of blowout and behind the embryo dunes, and the third (TC) at the depositional lobe.

Sediment transport was sampled over 8 (es Comú) and 13 (Tirant) runs of 20 min. each. Following the index used by Cabrera and Alonso (2010), transport rates were calculated as:

$$Q_{trap} = [St / d * Ts] / 1000$$

where *St* is the sediment trapped (g), *d* is the diameter of sand trap (expressed in mm), and *Ts* is sampling time. Transport rates in this article are expressed in kg m^{-1} min^{-1}.

RESULTS

The effect of topography on the wind behaviour is shown in Figure 2A.There is no developed foredune at the front dune of es Comú de Muro, only some embryonic dunes, that do not exceed 20 cm of height. The variations of wind velocity in es Comú de Muro (Figure 2A) are spatially and temporally homogeneous. If the analysis is focused on the processes existing on the first line of dunes, departing from the initial conditions at Anemometer 1 (δs= 0), the airflow speed has an important decrease at Anemometer 2, placed just behind the herbaceous vegetation and embryonic morphologies, with a value of δs= -0.37, the lowest of the overall sample. Once the airflow reaches the deflation basin of the blowout, it increases its speed expressed by Anemometer 3 (δs= 0.02). Finally Anemometer 5 (δs= -0.37) shows a considerable disminution of the wind speed, in this case according to the processes of expantion and descompresion of the flow. Concluding, and considering the variability registered in each anemometer, the maximum value is in Anemometer 2 (δs= 0.11/-0.48) as well as the maximum value of the stantard desviation δs σ= 0.28.

In Cala Tirant (Figure 2B) morphological features of the study site generate some significant variations of fractional speed-up ratio. Wind profiles reflect how the ratio (δs) changes in each of sampling point. The longitudinal transect provided by sensors deployed allow to see all of those variations. On the foredune strip (Anemometer 2) and on the depositional lobe (Anemometer 5), wind speeds were generally lower than those on the upper beach (Anemometer 1) and on the deflation basin (Anemometers 3 and 4). The greatest reduction of wind ratio (δs = 0.17 to -0.28) occurred at the upper margin of the blowout (Anemometer 5), whereas the lowest was in the foredune strip, where the Anemometer 2 was placed (δs = -0.15 to -0.22). Moreover, an important variation also occurred at the inner ramp, Anemometer 4 (δs = 0.14 to -0.11) and on the deflation basin, Anemometer 3 (δs = 0.07 to -0.12). Considering the standard deviation (σ), the highest value coincides with the highest reduction of wind ratio, at the upper margin of blowout with σ = 0.15, while in this case, the lowest value occurred again at the foredune (Anemometer 2) with σ = 0.02.

If the analysis of the results obtained from both study cases is focused on the dune front, it is seen how the presence of foredune strip has an important role as for the reduction of its speed. In the first case (A) the variation of speed-up ratio at Anemometer 2 is higher due to that the wind velocity was lower and more heterogeneous than the experiment carried out at Cala Tirant.

Sand transport and sedimentation processes

In es Comú de Muro there was not transport under velocities lower than 2ms^{-1}. It must be taken into account that the wind

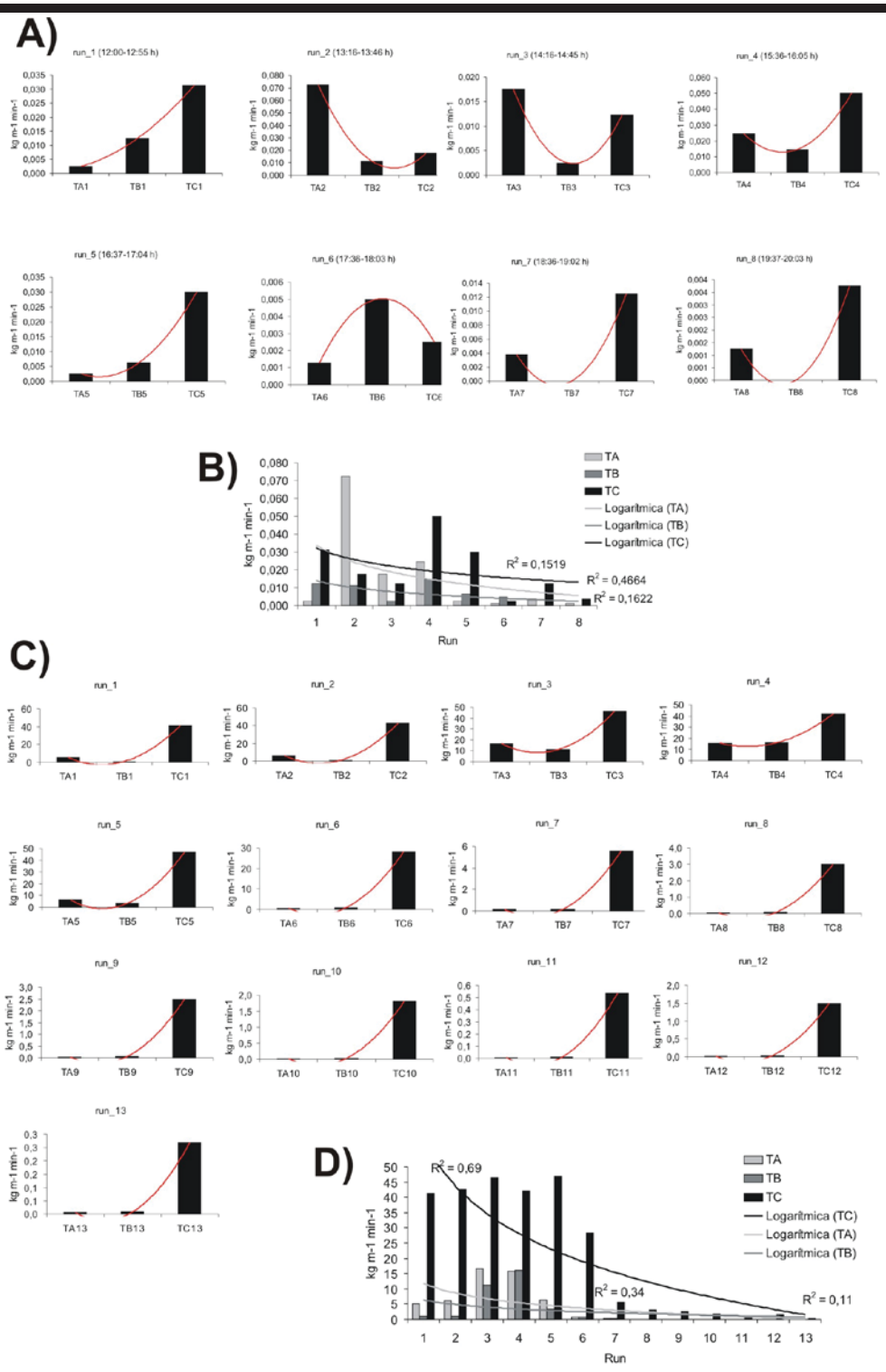

Figure 3. Sand sedimentation amounts captured by each group of traps. Panels A and B belongs to es Comú de Muro, whilst C and D belongs to Cala Tirant. Values are expressed in kg m^{-1} min^{-1}.

energy in this case was notably low, with mean values of 2.3 ms^{-1}, and mean maximums of 4.3 ms^{-1}. In general terms the maximum rates of sedimentation occured at TC, placed at the depositional lobe with a value of Qtrap= 0.160 kg m^{-1} min^{-1}, whilst the lowest amount was registered by TB, just behind the embryonic dunes and herbaceous vegetation, with Qtrap= 0.052 kg m^{-1} min^{-1}. Finally, the value registered on TA, placed at the upper beach, was Qtrap= 0.126 kg m^{-1} min^{-1} (Figure 3A and 3B).

In the case of Cala Tirant (Figure 3C and 3D) the mean amount of sediment transported over the morning was TA_Q_{trap}= 10 kg m^{-1} min^{-1}, TB_Q_{trap}= 6.5 kg m^{-1} min^{-1} and TC_Q_{trap}= 43.9 kg m^{-1} min^{-1}. Along the afternoon the mean values were much lower than those registered during the morning; TA_Q_{trap}= 0.24 kg m^{-1} min^{-1}, TB_Q_{trap}= 0.28 kg m^{-1} min^{-1} and TC_Q_{trap}= 39.3 kg m^{-1} min^{-1}. The transport was almost non-existent during the night (runs 10 to 13) due to mean wind speeds lower than 3 ms^{-1}, resulting in average transport rates of TA_Q_{trap}= 0.014 kg m^{-1} min^{-1}, TB_Q_{trap}= 0.021 kg m^{-1} min^{-1} and TC_Q_{trap}= 1.02 kg m^{-1} min^{-1}. Figure 3D summarizes the spatial-temporal patterns of sediment transport during the experiment. There were significant and consistent differences between TC and TA-TB. Maximum transport rates were found during runs 3, 4 and 5 with values larger than 45 kg m^{-1} min^{-1}. Transport started to notably diminish between Run 6 (29.79 kg m^{-1} min^{-1}) and Run 7 (5.92 kg m^{-1} min^{-1}), coinciding with the time when wind speed lost intensity. In total terms, the total sand collected by the traps over 24 h was TA = 51 kg, TB = 33.71 kg and TC = 263 kg.

DISCUSSION

Topography in both sites conditions the air flow behavior, and the patterns of sediment transport from the emerged beach to the innermost of the dune complex. In both cases the increase of rugosity on the first strip supposes a decreases of wind speed and an increase of sedimentation rates. Fractional speed-up ratio (Figure 2) demonstrates the clear impact of topography on the wind speed on the foredune. In the case of Cala Tirant (Figure 2B) the presence of a 1m height vegetated foredune on the back beach has a sheltering effect and modifies the incoming wind. Incoming onshore winds are consistently stronger at the back beach (Anemometer 1) followed by a strong decrease at the foredune lee-side (Anemometer 2; Figure 2B). In the case of es Comú de Muro (Figure 2A) there is no developed foredune, but only some embryonic morphologies with associated herbaceous vegetation. However, although with less intensity, the increase of rugosity also supposes a diminution of wind velocity. The results obtained from this study show a positive relationship between the transport rates and wind speeds over time. From a spatial point of view, the results show significant variations of sand transport rates depending on sand traps location. The largest rates of sand were always at the upper margin of the blowout (TC), on the depositional lobe, whilst the minimums were registered by TB, behind the foredune, with medium transport recorded by TA, at the back beach. In the case of TB the main limiting factor is the increase of surface rugosity according to the presence of a foredune and its associated vegetation, which supposes an interference obstacle for the transport patterns from the upper beach to the inner of dune complex.

CONCLUSIONS

Our study shows that the presence of a well developed foredune supposes an important diminution of sand transport rates from the beach to the inner of the dune systems, which means lower erosion patterns for the emerged beach. In places like Balearic Islands, the sand output is considered 'negative' from a management perspective as the beach is an essentialy an touristic and economic resource. The results of our research suggest that the restoration of the foredune strip could reduce the amount of sand blown from the beach, and at the same time, the interaction between wind, topography, and available sediment within the blowout, could maintain active transport patterns that result in a very dynamic blowout behaviour with short-term events.

ACKNOWLEDGMENTS

We are indebted with the helpful comments of two anonymous reviewers which improved the original manuscript. Special thanks to Miguel McMinn for his review of the English version.

LITERATURE CITED

Cabrera, L.L. and Alonso, I., 2010. Correlation of aeolian sediment transport measured by sand traps and fluorescent tracers. *Journal of Marine Systems*, 80, 235-242.

Jackson, P.S. and Hunt, J.C.R., 1975. Turbulent wind flow over a low hill. Quarterly. *Journal of the Royal Meteorological Society*, 101, 929-955.

McLaughlin, S.; McKenna, J., and Cooper, J.A., 2002. Socio-economic data in coastal vulnerability indices: constraints and opportunities. *Journal of Coastal Research*, SI36, 487-497.

Mir-Gual, M., 2014. Analysis, characterization and dynamics of blowout erosive morphologies on dune systems of Mallorca and Menorca (Balearic Islands) (in Catalan). *PhD Thesis*, University of Balearic Islands, 423p.

Mir-Gual, M.; Pons, G.X.; Martín-Prieto, J.A.; Roig-Munar, F.X., and Rodríguez-Perea, A., 2013. Geomorphological and ecological features of blowouts in a western Mediterranean coastal dune complex: a case study of the Es Comú de Muro beach-dune system on the island of Mallorca, Spain. *Geo-Marine Letters*, 33, 129-141.

Mir-Gual, M.; Pons, G.X.; Gelabert, B.; Martín-Prieto, J.A., and Rodríguez-Perea, A., (in press). Conservation approach of a front dune system trhough the study of its blowouts (Cala Agulla, Mallorca). *Boll. Soc. Hist. Nat. Bal.*, 57.

Puig, M.; Del Río, L.; Plomaritis, T.A., and Benavente, J., 2014. Influence of stroms on coastal retreat in SW Spain. *Journal of Coastal Research*, SI70, 193-198.

Roig-Munar, F.X.; Rodríguez-Perea, A.; Martín-Prieto, J.A., and Pons, G.X., 2009. Soft management of beach-dune Systems as a tool for their sustainability. *Journal of Coastal Research*, SI56, 1284-1288.

Journal of Coastal Research	SI	75	318-322	Coconut Creek, Florida	2016

Chronology, Morphology and GPR-imaged Internal Structure of the Callala Beach Prograded Barrier in Southeastern Australia

Thomas S. N. Oliver†*, and Colin D. Woodroffe†

†School of Earth &Environmental Science
University of Wollongong,
Wollongong, Australia

www.cerf-jcr.org

www.JCRonline.org

ABSTRACT

Oliver, T.S.N., and Woodroffe, C.D., 2016. Chronology, Morphology and GPR-imaged Internal Structure of the Callala Beach Prograded Barrier in Southeastern Australia. *In:* Vila-Concejo, A.; Bruce, E.; Kennedy, D.M., and McCarroll, R.J. (eds.), *Proceedings of the 14th International Coastal Symposium* (Sydney, Australia). *Journal of Coastal Research*, Special Issue, No. 75, pp. 318-322. Coconut Creek (Florida), ISSN 0749-0208.

Holocene prograded coastal barriers, comprising a sequence of relict foredune ridges, are depositional environments, which have been used to reconstruct coastal processes. Such reconstructions benefit from new techniques and technologies now available in coastal studies. This study investigated the Callala Beach prograded barrier deposit situated within Jervis Bay on the NSW south coast. This prograded barrier, composed of a series of low-relief, shore-parallel ridges, formed after sea level stabilised on this coastline in the mid Holocene. The approach involved analysis of Light Detection and Ranging (LiDAR) topographic data, ground-penetrating radar (GPR) collection and processing, and dating of ridge deposits using the optically-stimulated luminescence (OSL) dating technique. These data sets demonstrate that the most landward ridge of the Callala Beach barrier was deposited ~7500 years ago, closely aligning with the best estimates for the timing of sea-level stabilisation in southeastern Australia. Progradation continued throughout the late Holocene at a steady rate of ~0.1 m/yr until near the present time, as shown by an age of ~400 years immediately behind the modern foredune. GPR-imaged subsurface structures captured the beachface and dune facies; a regular series of reflectors indicated incremental accumulations of sediment over the late Holocene. Volumes of sand accumulated during barrier growth indicated an average sediment supply for the entire embayment of ~1600 m^3/yr or ~0.3 m^3/yr per metre of beach. The long term trend of sediment supply has implications for coastal management as the local council is commencing a beach nourishment program at Callala Beach.

ADDITIONAL INDEX WORDS: *Holocene, coastal sand ridges, optically stimulated luminescence, ground penetrating radar, LiDAR.*

INTRODUCTION

Coastal sand ridge plains, standplains or prograded barriers according to the classification of Roy *et al.* (1994), preserve historical shoreline position and may be used as repositories of coastal palaeoenvironmental information (Tamura, 2012). In southeastern Australia, the Holocene depositional history of numerous prograded barrier deposits has been reconstructed using radiocarbon dating and a cohesive picture of late Holocene depositional history was established where progradation has occured following Holocene sea level reaching at or close to its present level (Thom *et al.*, 1981).

The development of optically stimulated luminescence (OSL) dating has been important for prograded barrier chronological reconstruction as it has allowed the precise timing of the deposition of ridge sediments to be determined, whereas radiocarbon dating of shell material incorporated in the barrier stratigraphy may contain older reworked shell fragments (Nielsen and Roy, 1981). Studies of prograded barriers which compare these dating methodologies have demonstrated differing patterns of Holocene progradation (Murray-Wallace *et al.*, 2002; Oliver *et al.*, 2015) indicating that complex patterns are superimposed on the general coastal evolutionary model (Roy *et al.* 1994). The combination of ground penetrating radar (GPR) with OSL dating has allowed the calculation of sediment volume infilling embayments (Bristow and Pucillo, 2006). Such new technologies offer opportunity to continue to unravel the unique coastal morphodynamic and environmental records these coastal landforms contain (Tamura, 2012) and contextualise current coastal management concerns.

Study Area

Callala Beach is a prograded barrier situated at the northwestern margin of the large body of water named Jervis Bay on the south coast of NSW and at times may receive unrefracted ocean swells (Figure 1). A series of ~19 shore parallel ridges are evident in LiDAR data obtained for this site with crest heights of between 5-8 m above mean sea level (MSL). A core through the barrier encountered nearshore shelly sand overlying bedrock at -5 m below MSL (Thom, 1987).

METHODS

Optically Stimulated Luminescence (OSL) dating is a dating method that can be used for determining the elapsed time since quartz and feldspar grains were buried after being exposed to (bleached by) sunlight (Aitken, 1998; Huntley *et al.*, 1985).

DOI: 10.2112/SI75-064.1 received 15 October 2015; accepted in revision 15 January 2016.
*Corresponding author: toliver@uow.edu.au

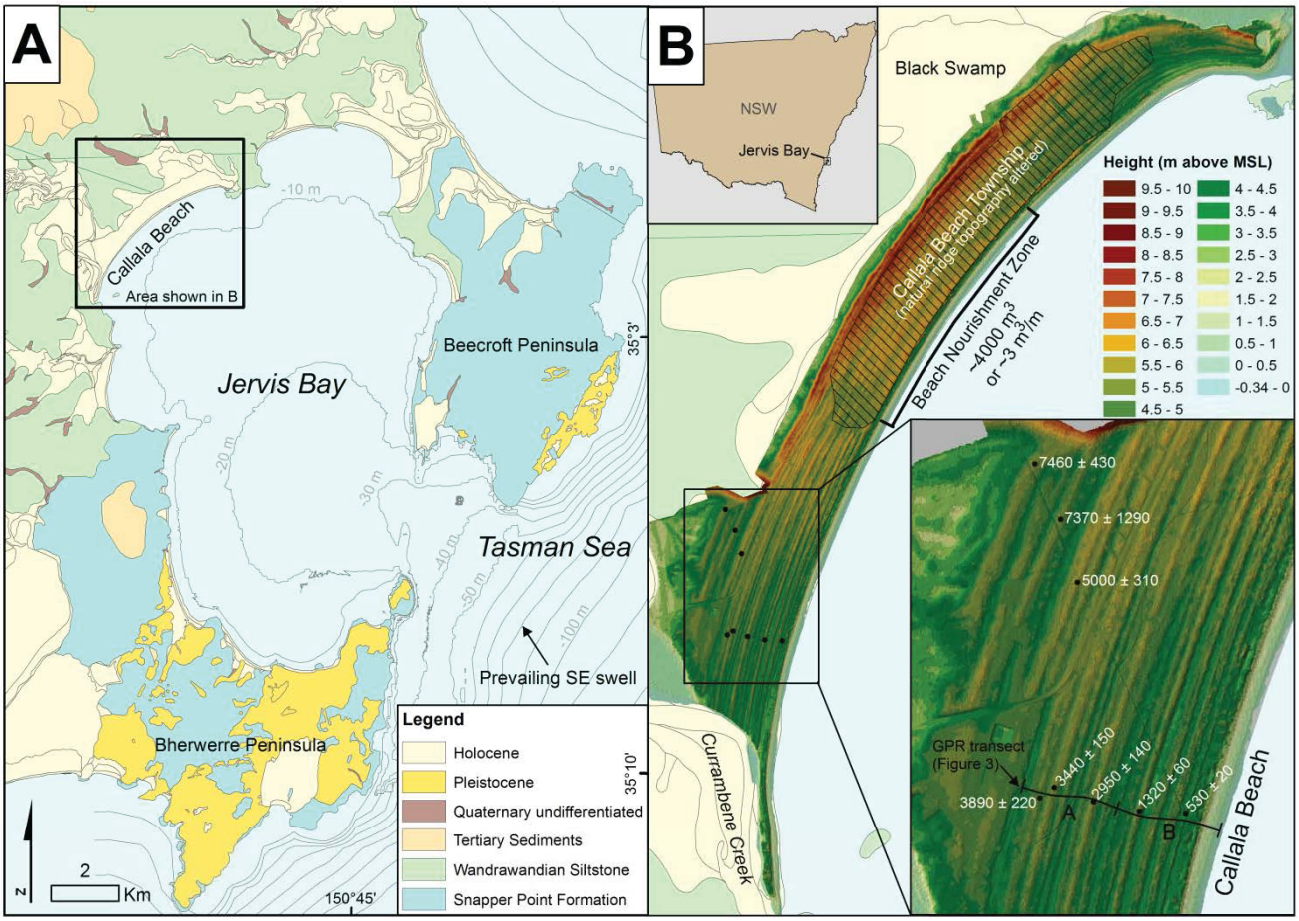

Figure 1. A) Callala Beach barrier location map showing its position with respect to Jervis Bay. Quaternary and bedrock geology is shown for context alongside broad-scale bathymetry. B) LiDAR ground surface DEM model showing the OSL ages and location of GPR transect. Data Source: Quaternary and bedrock geology mapping courtesy of Troedson *et al.* (2004). LiDAR data © NSW Government, Land and Property Information (LPI) 2013. Jervis Bay bathymetry courtesy of Geoscience Australia.

Eight samples from distinct ridges across the Callala Beach prograded barrier were collected and dated at the luminescence dating facility at the University of Wollongong (Table 1). Each sample was collected from a depth of between 70-100 cm from the undisturbed aeolian facies (>80% quartz) of an individual ridge.

All samples were prepared using standard laboratory techniques (Wintle, 1997) to isolate the 212-180 µm grain size fraction of quartz. Samples were subject to testing and measurement as outlined by Oliver *et al.* (2015).

For all samples in Table 1, ICP-MS analysis (completed by Intertek Genalysis) was used to measure uranium, thorium, and potassium concentrations. Dose rates were calculated using the conversion values of Guérin *et al.*, (2011) and despite a laboratory measurement of water content being obtained, an assumed water content of 5 ± 2.5% was used for all samples. The cosmic dose for each sample was calculated taking into consideration geographic position, sediment density, altitude and depth of overburden following Prescott and Hutton (1994).

Ground Penetrating Radar (GPR)

GPR data was collected using a Mala ProEx system with a 250 MHz antenna. A transect across the Callala Beach barrier was measured on a beach access footpath which had little topographic modification and was perpendicular to relict ridge alignment (Figure 1). Sampling interval was set to 0.2 m and distance was metered and applied to the trace data using a wheel on the cart carrying the equipment. During GPR data collection an auger hole was used to verify the depth of the water table so that a correct velocity could be applied during data processing. A velocity of 12 cm/ns above the water table and 6 cm/ns below the water table was adopted.

GPR data was processed using RadExplorer version 1.41. Standard processing routines were applied including desaturation, first arrival time correction, background removal, bandpass

Table 1. *OSL ages for sand ridges across the Callala Beach barrier. The samples are ordered according to sample position with respect to the ocean, so that the first sample listed in the table corresponds to the sample closest to the shore. All samples include an internal dose rate contribution of 0.03 ± 0.01 Gy/ka assumed based on measurements made on Australian quartz (Bowler et al., 2003).*

	----------Radionuclide Concentrations----------			----------Dose Rates----------						
Sample Code	U (ppm)	Th (ppm)	K (%)	Beta (Gy/ka)	Gamma (Gy/ka)	Cosmic (Gy/ka)	Total Dose Rate (Gy/ka)	D_e (Gy)	Over-dispersion (%)	OSL Age (years)
Cal1	0.23 ± 0.01	0.65 ± 0.03	0.58 ± 0.01	0.45 ± 0.02	0.19 ± 0.002	0.19 ± 0.02	0.86 ± 0.03	0.45 ± 0.01	2 ± 2	530 ± 20
Cal2	0.26 ± 0.01	0.60 ± 0.02	0.39 ± 0.01	0.32 ± 0.01	0.15 ± 0.002	0.19 ± 0.02	0.69 ± 0.03	0.90 ± 0.01	7 ± 1	1320 ± 60
Cal3	0.15 ± 0.004	0.58 ± 0.02	0.40 ± 0.01	0.31 ± 0.01	0.14 ± 0.002	0.19 ± 0.02	0.67 ± 0.03	1.98 ± 0.03	7 ± 1	2950 ± 140
Cal4A	0.19 ± 0.01	0.69 ± 0.03	0.58 ± 0.01	0.44 ± 0.02	0.19 ± 0.003	0.19 ± 0.02	0.86 ± 0.03	2.94 ± 0.04	6 ± 1	3440 ± 150
Cal4B	0.14 ± 0.004	0.56 ± 0.02	0.25 ± 0.01	0.21 ± 0.01	0.10 ± 0.002	0.19 ± 0.02	0.53 ± 0.03	2.05 ± 0.05	12 ± 2	3890 ± 210
Cal5	0.11 ± 0.004	0.58 ± 0.02	0.17 ± 0.004	0.15 ± 0.01	0.08 ± 0.001	0.19 ± 0.02	0.44 ± 0.02	2.22 ± 0.05	12 ± 2	5000 ± 310
Cal6	0.13 ± 0.004	0.56 ± 0.02	0.06 ± 0.004	0.07 ± 0.003	0.06 ± 0.001	0.19 ± 0.02	0.35 ± 0.02	2.56 ± 0.41	23 ± 12	7370 ± 1290
Cal7	0.17 ± 0.01	0.72 ± 0.03	0.19 ± 0.01	0.14 ± 0.01	0.10 ± 0.001	0.19 ± 0.02	0.49 ± 0.02	3.64 ± 0.08	11 ± 2	7460 ± 430

filtering, migration and topographic adjustment to correct the location and shape of subsurface reflectors. Where possible, default values within RadExplorer were used so that the resulting data has a high reproducibility.

LiDAR Processing and Barrier Volume Estimation

LiDAR data © NSW Government, Land and Property Information (LPI) 2013 was processed and viewed using ArcGIS 10.2. A Triangular Irregular Network (TIN) model of the ground surface was produced from which enabled a detailed description of barrier morphology and examination of ridge heights (Figure 1). Volumes of sand above MSL were estimated for Callala Beach for a series of time slices delineated according to the position of the OSL ages across the barrier.

RESULTS

The quartz grains measured for OSL dating on the Callala Beach barrier were found to have excellent luminescence characteristics (see Table 1) similar to the findings of Oliver *et al.* (2015) for the sands at Moruya, NSW. The pattern of progradation observed for the Callala Beach barrier is from ~7500 to present (Figure 1). Plotting the OSL age estimates according to barrier width as a percentage of total width indicates a linear trend of barrier accumulation over the late Holocene (Figure 2). The rate of progradation according to this trend is ~0.1 m/yr and the average ridge lifetime is 390 years.

Although total dose rates for all samples were below 1 Gy/ka, there was a weak trend of increasing total dose rate from landwards to seawards across the barrier. Overdispersion values for all samples except Cal6 were 12% or less with the most seaward four samples having values between 2 – 7% (Table 1). Sample Cal6 (Table 1) had a higher overdispersion value (23 ± 12) and the error margin for this date is considerably greater than other samples. However it does not alter the progradation trend and its error overlaps the sample immediately landward (Cal7: Table 1).

GPR data for Callala Beach is presented in two 200 m sections; A and B (Figure 3). Both sections of the GPR for this site show a series of closely spaced seaward dipping reflectors, the tops of which are mostly between 3 and 4 m above MSL.

These reflectors reach down to around 0-1 m above MSL. Most of these reflectors are convex-up in their upper portions and then flat, or sometimes slightly concave-up, in their lower portions. This change from convex-up to flat or slightly concave-up occurs at around 2 m above MSL.

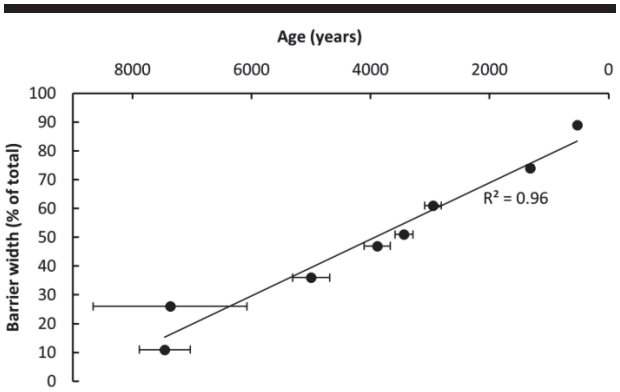

Figure 2. OSL ages plotted with respect to barrier width as a percentage of total width. Error bars are the 1 sigma errors for each OSL age. Data is fitted with a linear regression line with an R^2 value of 0.96.

The relict ridge crests at Callala Beach align closely with the present beach curvature in planform and there are no obvious truncations or erosional phases indicated by the barrier morphology. The ridge crests are approximately 5-8 m above MSL with the inter-ridge swales generally 1-1.5 m lower than the crests. A foredune higher than proximal ridges can be seen in some shore normal profiles in the centre of the barrier, but its elevation is not a great deal higher (in some instances lower) than the most landward ridge which is dated to ~5000 years ago.

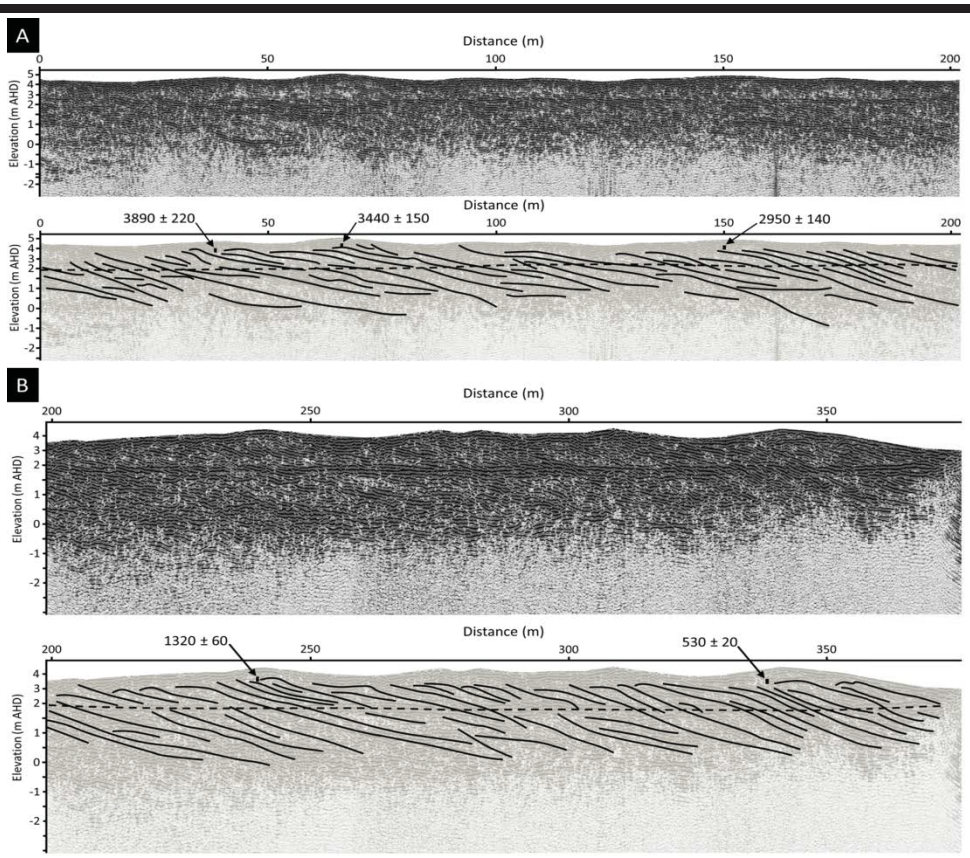

Figure 3. GPR data for the Callala Beach barrier divided into sections A and B (see Figure 1 for locations). Top pane is of each section A and B is the processed GPR data with interpretation in the bottom pane. OSL ages are shown at correct horizontal and vertical positions.

A plot of cumulative barrier volume versus time for Callala Beach has a strong linear relationship (Figure 4). The average accumulation rate estimated using this cumulative barrier volume plot is ~1600 m^3/yr or ~0.3 m^3/m/yr considering embayment length.

DISCUSSION

Progradation of the Callala Beach barrier has occurred from ~7500 to present with a steady rate of shoreline seaward movement. However, the progradation rate of 0.1 m/yr for Callala Beach is slower than all other rates for prograded barriers on the east coast of Australia c.f. Table 3 in Oliver *et al.* (2015).

The OSL dating and analysis for samples from Callala Beach emphasise the homogeneity of the sands in this barrier and likely in Jervis Bay. The low dose rates at Callala Beach compared to Moruya (Oliver *et al.* 2015) may be a result of high sand purity in this embayment and more broadly within Jervis Bay as the sands of Jervis Bay beaches are world renowned as being extremely white.

The general geometry of a fairweather beach profile at this site commonly has a berm at 1.5 m above MSL and a distinctly convex-up geometry below 2 m elevation. The typical parallel to sub-parallel reflectors occurring sequentially through the GPR data do not exhibit either a berm feature at such an elevation and are generally concave-up below 2 m elevation. Therefore these reflectors are interpreted as storm beachfaces and hence preserve the geometry of the beach during erosional events. However, while this typical storm beachface geometry dominates the sequence, there are several examples, especially in section B of the GPR (Figure 3), where a berm at around 1.5 m is seemingly preserved. Such preservation in the progradational record would suggest that less storm activity occurred during these time periods.

The domed convex-up features occurring in section A and B of the GPR at around 3 m above MSL is interpreted as an incipient ridge feature building in the backshore zone behind the active beach. A feature of similar size and at a similar elevation is evident in the modern beach profile at Callala Beach. Several of these incipient ridges preserved in the GPR record appear to be overlain by a single ridge feature evident in the present day topography (e.g. 310 m along section B in Figure 3). This suggests that an individual ridge in the sequence is not formed as a single incipient ridge establishes and grows, rather several incipient ridges must be subsequently overlain with wind-blown material to produce the ridge topography evident today.

Plans are currently underway to nourish Callala Beach with sand, due to problems of coastal erosion over the past few decades and especially in light of the erosion which occurred at

this beach in May and June 1974 (Fleck, 1975). Approximately 4000 m^3 of sand dredged from the entrance of Currembene Creek is to be spread along a 1350 m stretch of Callala Beach in front of residential properties (equating to ~3 m^3/m) during the winter of 2016. This equates to 10 years' worth of sediment being added to the beach in one event according to the estimated long-term sediment supply of ~0.3 m^3/m/yr over the late Holocene. It will be important to closely monitor the effects of this nourishment of Callala Beach especially as the 4000 m^3 will be spread over a specific portion of the beach and may be redistributed within the embayment.

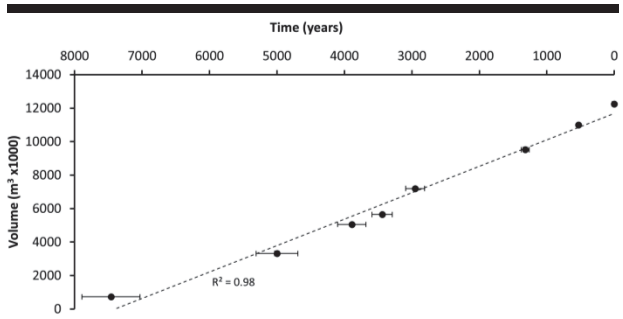

Figure 4. Cumulative barrier volume plotted over time for the Callala Beach barrier. Error bars for OSL ages are 1 sigma. A linear regression has been fitted with an R^2 value of 0.98.

CONCLUSIONS

The Callala Beach barrier has prograded at a relatively constant rate over the late Holocene from ~7500 years ago to present. This pattern of progradation equates to a rate of shoreline seaward movement of 0.1 m/yr and the ridges in the sequence have an average lifetime of 390 years. The long-term average sediment accumulation rate for Callala Beach is 0.3 m^3/m/yr. The prevelance of storm beachfaces in the GPR record for Callala Beach demonstrates that storm events do not halt shoreline progradation, rather where there is a positive sediment budget, storm beachfaces are preserved as storm recovery exceeds storm demand. This GPR record provides a history of storm events for the Callala Barrier from ~4000 years ago to present. Several fairweather beachface features such as berms are also evident in the GPR dataset indicating episodes of lower storm activity. The findings of this study provide an import context when considering coastal management proposals for this site. We suggest that the Holocene depositional history of coastal environments in NSW provides context for ongoing coastal management.

ACKNOWLEDGMENTS

This research was completed while T. Oliver was a PhD candidate at the University of Wollongong and was supported by an Australian Postgraduate Award. Thank you to Zenobia Jacobs for overseeing the OSL dating and to Yasaman Jafari and Dr. Terry Lachlan for the laboratory support.

LITERATURE CITED

Aitken M.J., 1998. *An Introduction to Optical Dating: The Dating of Quaternary Sediments by the Use of Photon-Stimulated Luminescence*. Oxford: Oxford University Press.

Bowler, J.M.; Johnston, H.; Olley, J.M.; Prescott, J.R.; Roberts, R.G.; Shawcross, W., and Spooner, N.A., 2003. New ages for human occupation and climatic change at Lake Mungo, Australia. *Nature* 421(6925), 837-840.

Bristow, C.S. and Pucillo K., 2006. Quantifying rates of coastal progradation from sediment volume using GPR and OSL: the Holocene fill of Guichen Bay, south-east South Australia. *Sedimentology* 53(4), 769-788.

Fleck, B.C., 1975. Dune Erosion, Sand Drift Control and Community Effort - Callala Beach. *Soil Conservation Journal* 31(1), 19-24.

Guérin, G.; Mercier, N., and Adamiec, G., 2011 Dose-rate conver- sion factors: Update. *Ancient TL,* 29, 5–8.

Huntley, D.J.; Godfrey-Smith, D.I., and Thewalt, M.L.W., 1985 Optical dating of sediments. *Nature,* 313, 105–107.

Murray-Wallace, C.V.; Banerjee, D.; Bourman, R.P.; Olley J.M., and Brooke B.P., 2002. Optically stimulated luminescence dating of Holocene relict foredunes, Guichen Bay, South Australia. *Quaternary Science Reviews,* 21, 1077-1086.

Nielsen, A.F. and Roy P.S., 1981. Radiocarbon dating - a bag of worms. *Firfth Australian Conference on Coastal and Ocean Engineering* (Perth, Australia).

Oliver, T.S.N.; Dougherty, A.J.; Gliganic L.A., and Woodroffe C.D., 2015. Towards more robust chronologies of coastal progradation: Optically stimulated luminescence ages for the coastal plain at Moruya, south-eastern Australia. *The Holocene,* 25(3), 536-546.

Prescott, J.R., and Hutton, J.T., 1994 Cosmic ray contributions to dose rates for luminescence and ESR dating: large depths and long- term time variations. *Radiation Measurements,* 23, 497–500.

Roy, P.S.; Cowell, P.J.; Ferland, M.A., and Thom B.G., 1994. Wave Dominated Coasts. In Carter, R. W. G. and Woodroffe, C. D. (eds) *Coastal Evolution: Late Quaternary Shoreline Morphodynamics* Cambridge University Press, Cambridge, pp. 121-186

Tamura, T., 2012. Beach ridges and prograded beach deposits as palaeoenvironment records. *Earth-Science Reviews*, 114(3-4), 279-297.

Thom, B.G., 1987. Coastal Geomorphology of the Jervis Bay area. *WETLANDS (Australia),* 6(2), 19-21.

Thom, B. G.; Bowman, G. M.; Gillespie, R.; Polach H. A., and Barbetti M., 1981. Progradation histories of sand barriers in New South Wales. *Search,* 12, 323-325.

Wintle A.G., 1997 Luminescence dating: Laboratory procedures and protocols. *Radiation Measurements,* 27, 769–81

Journal of Coastal Research	SI	75	323-327	Coconut Creek, Florida	2016

Ground Penetrating Radar applied to the Characterization of the Itapeva Dunefield, Torres, Brazil

Gabriela C. Rockett[†], Eduardo G. Barboza[‡§], Maria Luiza C.C. Rosa[††§]

[†] Programa de Pós-Graduação em Geociências, Instituto de Geociências, Universidade Federal do Rio Grande do Sul. Porto Alegre, Brazil

[‡] Departamento de Paleontologia e Estratigrafia, Instituto de Geociências, Universidade Federal do Rio Grande do Sul. Porto Alegre, Brazil

[††] Departamento de Geodésia, Instituto de Geociências, Universidade Federal do Rio Grande do Sul. Porto Alegre, Brazil

[§] Centro de Estudos de Geologia Costeira e Oceânica – CECO. Porto Alegre, Brazil

www.cerf-jcr.org

www.JCRonline.org

ABSTRACT

Rockett, G.C.; Barboza, *E.G.*, and Rosa, M.L.C.C. 2016. Ground Penetrating Radar applied to the characterization of the Itapeva Dunefield, Torres, Brazil. *In:* Vila-Concejo, A.; Bruce, E.; Kennedy, D.M., and McCarroll, R.J. (eds.), *Proceedings of the 14th International Coastal Symposium* (Sydney, Australia). *Journal of Coastal Research*, Special Issue, No. 75, pp. 323-327. Coconut Creek (Florida), ISSN 0749-0208.

Subsurface data obtained from Ground Penetrating Radar (GPR) have been used in studies in various coastal plain environments. GPR applied to dune characterization and stratigraphy is well described in the literature, and enables the distinction between different depositional patterns and their delimitation. This study aimed to characterize the stratigraphy of the Itapeva dunefield, located at the municipality of Torres, north of the Rio Grande do Sul (Brasil) coastal plain, using subsurface data. This dunefield contains aeolian forms that differ from other dunefields in Rio Grande do Sul: namely, reversing dunes. The 150 and 400 MHz frequency antennas were used to collect subsurface data in dunes located in the central portion of the dunefield, with a linked GNSS system to obtain positional data. GPR data were processed, and the geospatial data were integrated to satellite images in a geographic information system. Results show that at least two different dune packages are present in the Itapeva dunefield, indicating two different depositional phases.

ADDITIONAL INDEX WORDS: *Geotechnologies, reversing dunes, stratigraphy*

INTRODUCTION

Coastal environment sedimentary subsurface records have been analyzed by many authors around the world, using geophysical data collected from Ground Penetrating Radar (GPR) methods (*e.g.* Barboza et al., 2011; Bristow and Jol, 2003; Havholm et al., 2004, 2013; Shenk et al., 1993). High resolution GPR data allows a distinction between depositional patterns and consequently delimitation and interpretation of different deposits identified in the radar profiles. GPR have been applied to dune stratigraphic characterization in New Zealand, United States, Spain, Saudi Arabia, for example (Adentunji *et al*., 2008; Girardi and Davis, 2010; Gómez-Ortiz *et al*., 2009; Van Dam *et al*., 2003;). In Brazil, some studies have been developed both in the north and south regions, by Oliveira *et al.* (2008), Buynevich *et al.* (2010) and Barboza *et al.* (2013), for example.

The Coastal Plain of Rio Grande do Sul

The Coastal Plain of Rio Grande do Sul (southern Brazil) is formed by a sucession of four well-preserved lagoon-barrier depositional systems, that have been developed during the Quaternary, controlled by glacial-eustatic events (Villwock and Tomazelli, 1995). The first three lagoon-barrier systems are Plestocenic, and the last is Holocene (Villwock and Tomazelli, 1995). Along its 600 km length, the coastal plain of Rio Grande do Sul shows different behaviors due to its recent evolution: progradational and retrogradational patterns can be identified in distinct sectors of the coast (Dillenburg et al, 2009). Prograded sectors, in general, are stable coastal sectors, whereas regressive sectors are characterized by erosion processes.

Different geomorphological features have been developed during the Holocene barrier evolution in the coastal plain of Rio Grande do Sul. According to Villwock (1984), Villwock and Tomazelli (1995) and Hesp *et al.* (2005; 2007), the most common coastal features are beach ridges, foredune ridges and transgressive dunefields. Recently, studies have been directed towards identifying relations between geomorphologic features and the coastal behavior in each different sector of this coastal plain (Dillenburg *et al.*, 2009; Rosa, 2012).

Studies in the northeast region of Rio Grande do Sul coastal plain and adjacent areas in Santa Catarina state show that this coastal sector is progradational (Barboza *et al*., 2011; Lima, 2012; Rockett et al., 2014; Silva et al., 2010).

Study Area Environmental Settings

The northern portion of Rio Grande do Sul coastal plain is less than 20 km wide and is formed by sedimentary deposits roughly aligned in a NE-SW direction. NE winds are the most frequent in this region, followed by S winds (Tomazelli, 1993). Located in the northern portion of Rio Grande do Sul state coastal plain, the Itapeva dunefield is part of the municipality of

DOI: 10.2112/SI75-065.1 received 15 October 2015; accepted in revision 15 January 2016.

*Corresponding author: gabriela.rockett@ufrgs.br

Torres (Figure 1). This area is different than other regions in Rio Grande do Sul coastal plain, since in this northern portion there are some geomorphological peculiarities, such as the Serra Geral Formation embasement outcrops, the Mampituba river outfall and a dunefield with reversing dunes (Tomazelli *et al*., 2008). These characteristics, associated with the presence of relevant ecosystems contributed to the creation of a conservation unit for diversity preservation: the "Parque Estadual de Itapeva" ("Itapeva State Park"), with a total area of about 10 km² (SEMA/Rio Grande do Sul, 2006). The Itapeva dunefield is located inside this conservation unit.

In this context, this study aimed to characterize the stratigraphy of the Itapeva dunefield, focusing on the reversing dunes, using Ground Penetrating Radar subsurface data and satellite images.

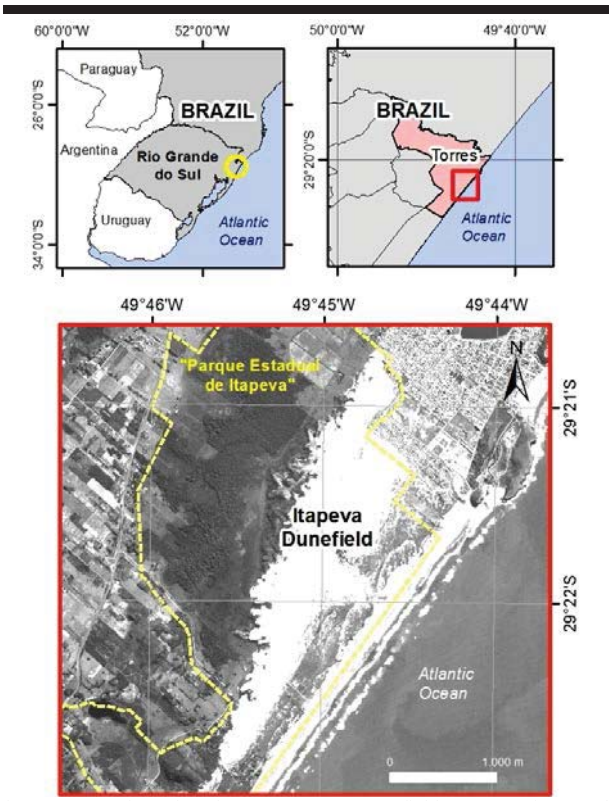

Figure 1. Location of study area: Itapeva Dunefield, Torres, Rio Grande do Sul state, Brazil.

METHODS

In order to understand the dunefield dynamics, previous data were first analyzed including satellite images and previous GPR data (Rockett et al., 2014). For this study, GPR data collection was performed in the field using 150 MHz and 400 MHz frequency antennas, with a linked Global Navigation Satellite System (GNSS) to obtain the positional data. Geophysical equipment used to collect data were the SIR3000™ model from Geophysical Survey Systems, Inc. (GSSI) – 150 MHz central frequency aerial antenna and 400 MHz central frequency contact antenna.

Four geophysical sections were analyzed in this study covering a 23 meter high and approximately 280 meters long reversing dune, located in the central portion of the Itapeva dunefield. The reversing dune crest is perpendicular to the coastline. GPR sections were collected at the same two alignments: in a cross section over the dune crest orientation and from east to west, along the crest of the dune (see GPR sections location in Figure 2). Each section was collected with a different frequency antenna, in order to allow the identification of differences in the geophysical registers (Tab. 1).

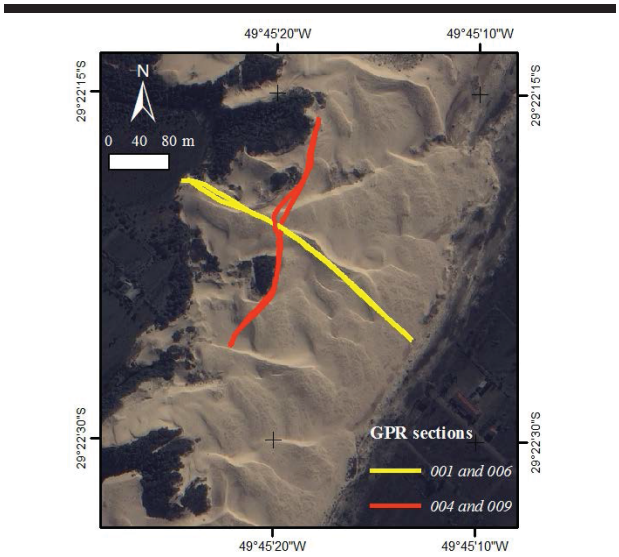

Figure 2. Spatial location of the GPR sections analyzed in this study. (Background satellite image: IKONOS RGB composition, 2006)

Table 1. *GPR profiles analyzed in this study.*

Profile Number	Direction	GPR section length	Antenna Frequency
004	NE-SW	337,6 m	400MHz
009	NE-SW	346,1 m	150 MHz
001	SE-NW	378 m	400 MHz
006	SE-NW	475 m	150 MHz

GPR data processing were performed using two radar softwares: RADAN™ (Geophysical Survey Systems, Inc. - GSSI) and PRISM 2.5 (Radar Systems, Inc.). The first data processing was the background removal, a spatial filter for removing background systematic data noise. After this, a frequency filter was applied for removal of frequencies higher and lower than the central antenna frequency (Ormsby bandpass filter). Furthermore, an exponential gain to expand the attenuated signals in depth was applied.

The dieletric constant (k) was used for time to distance depth conversion. For Rio Grande do Sul Coastal Plain, the k value used is 10, according to studies that analyzed GPR data and drill holes (Dillenburg *et al.*, 2011).

After GPR section processing, topographic correction was necessary for correct data analysis. GNSS data were processed by triangulation with other stations from the Brazilian Network

for Continuous Monitoring of GNSS Systems. Then, a table was generated, with the geodetic coordinates for each point collected in the GPR sections allignment, in order to make the topographic corrections. The datum used was WGS-84.

Data interpretation followed seismic stratigraphy principles, with adaptations due to the high resolution of GPR data, according to Neal (2004). The criteria used for interpretation of seismic reflectors were: terminations, amplitude, continuity and geometry.

A project was built in a Geographic Information System (GIS), in order to integrate satellite images data and the GNSS positioning data. The integration of data in a GIS allowed the location of GPR sections and provided a better understanding of the study area context, supporting the GPR data interpretation.

RESULTS

Four GPR sections were analyzed in this study. The geophysical profiles taken over one reversing dune at Itapeva dunefield show a number of reflectors of varying intensity and geometry (Figure 3). The analysis of the GPR data results in the identification of architectural elements related to different sand deposits of the dune. GPR data collected with a 150 MHz antenna reached 25 meters in depth, and data from the 400 MHz antenna reached 20 meters.

In the 150 MHz profiles, it is possible to identify a continuous and irregular reflector aproximately from 5 to 7.5 meters depth below the dune surface. The same reflector is not as clear, but also appears in the 400 MHz section. In the dune crest transversal GPR sections (004 and 009) it is possible to identify the same continuous irregular reflector. The interpretation for this reflector, which is not horizontal but irregular, is that it is a 2nd order surface, indicating a dune above another dune. At least one 2nd order surface was identified in the GPR sections. This surface is the limit of two phases of dunes.

The stratigraphic record shows exactly what is observed on the surface in the Itapeva dunefield: complex and distinctly orientated reversing dunes developing on the top of other reversing dunes (Figure 3). Sucessions of the same aeolian radarfacies can be observed in all sections, and there are differences between them in orientation. In general, GPR data show internal structures variations, due to the profiles orientation.

In both 150 MHz and 400 MHz profiles, high angle continuous reflectors dipping landward were identified in the NW portion of the sections 001 and 006. This dunefield behavior is observed in the field, in many portions of its west boundary.

What else is observed in the field and in the satellite images, is many large reversing dunes and other smaller dunes, which have distinct orientation slipfaces according to the predominant wind direction during the year. The orientation can be observed in the stratigraphic record. Figure 4 shows reflectors with different angles on the top of an active reversing dune. This dune is limited by the 2nd order surface. The same reversing behaviour and different angles are observed above the 2nd order surface, on the top of the dune record, above 5 meters depth. These internal structure variations allow identification and delimitation of 3rd order surfaces in the dune.

DISCUSSION

On the basis of the available data (GPR profiles) analyses, and according to the literature, GPR antenna frequency is directly proportional to data resolution, and therefore more structural details can be found. In the case of this study, high frequency antenna data make it difficult to identify the limits of surfaces in this aeolian system.

In the 150 MHz GPR sections it was easier to define bounding surfaces. Results show that at least two different dune packages are present in the Itapeva dunefield, indicating two different depositional phases, resulting in a complex superposition of reversing dunes. 2nd order surfaces separate different dune phases.

In the field it is possible to observe the aeolian dynamics, and the superposition of dunes. Subsurface records show variations in internal aeolian structures, indicating variations of migration direction of small sand bodies or dunes. In fact, the wind dynamics in this region are peculiar, due to the close presence of the Serra Geral high hills, and the confined space in which the whole dunefield is located, making for a confined dunefield development.

CONCLUSIONS

In the Itapeva dunefield's subsurface GPR profiles, internal structure variations can be identified in the reversing dunes. In comparison to other dunefields in the Rio Grande do Sul coastal plain, a complex dunefield has been developed, driven by a bidirectional wind pattern. GPR data reached a maximum of 25 meters depth, allowing subsurface characterization of the reversing dune located in the central part of the dunefield. It was possible to identify in the GPR data different strata that are the geological record of the aeolian dynamics observed in fieldwork at the dunefield. 2nd and 3rd order surfaces are present in the Itapeva aeolian deposits.

A set of dune packages were identified in GPR data. Considering that in the Itapeva dunefield there are reversing dunes higher than the one analyzed in this study, it is possible that other aeolian dune packages could be found in deeper profiles.

ACKNOWLEDGMENTS

The authors thank CNPq for reasearch grants, and Patrick Hesp for a little editing assistance. Rockett thanks CNPq for her PhD scholarship.

LITERATURE CITED

Adetunji, A.Q.; Al-Shuhail, A., and Korvin, G., 2008. Mapping the internal structure of sand dunes with GPR: A case history from the Jafurah sand sea of eastern Saudi Arabia. *The Leading Edge*, 27, 1446-1452.

Barboza, *E.G.*; Rosa, M.L.C.C.; Dillenburg, S.R., and Tomazelli, L.J. 2013. Preservation Potential of Foredunes in the Stratigraphic Record. *Journal of Coastal Research*, SI 65, 1265-1270.

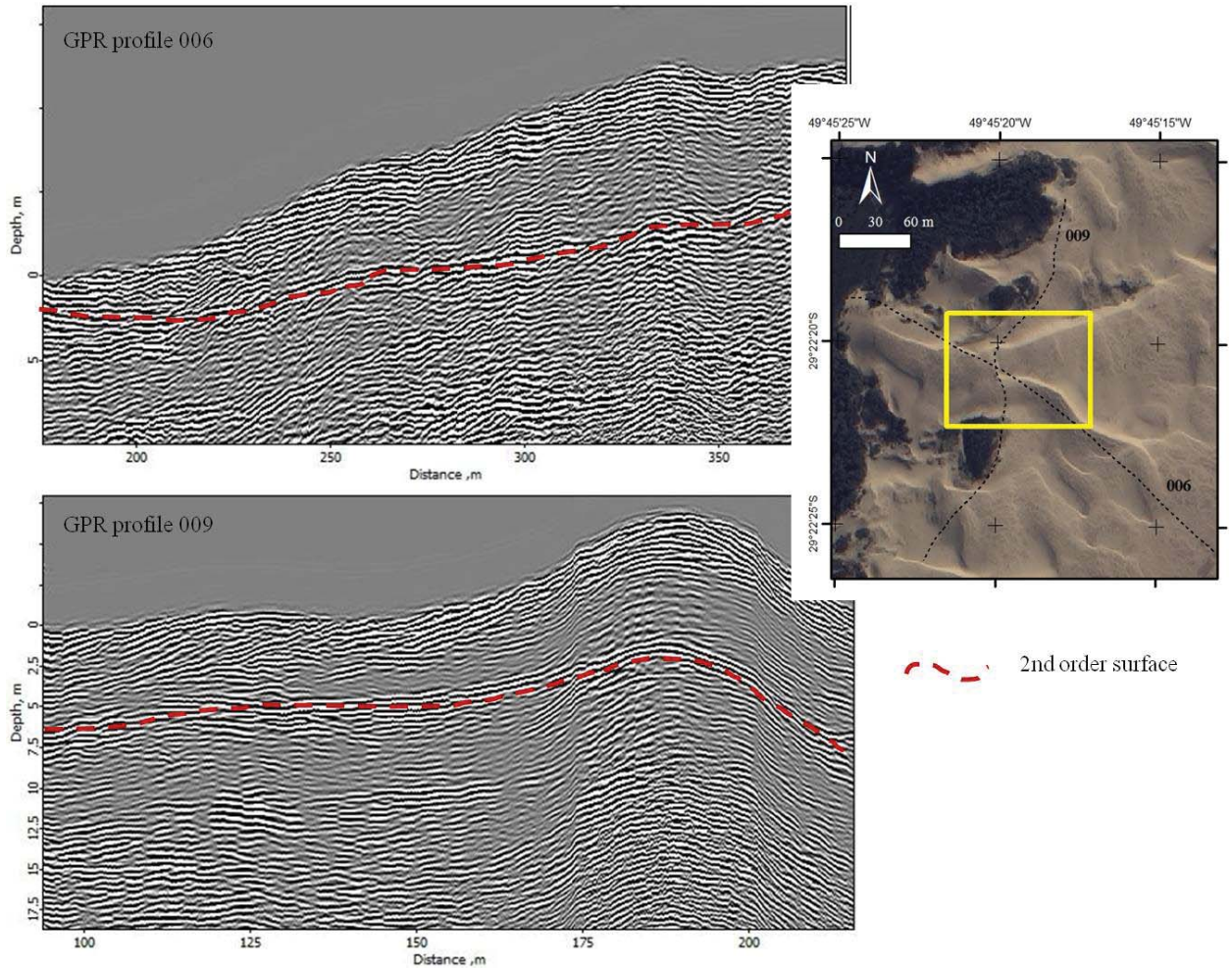

Figure 3. 150 MHz GPR sections in different orientations showing subsurface record of 2nd order surface (red dashed line) and satellite image showing the dunes superposition (detail of GPR profiles position in surface in the yellow box).

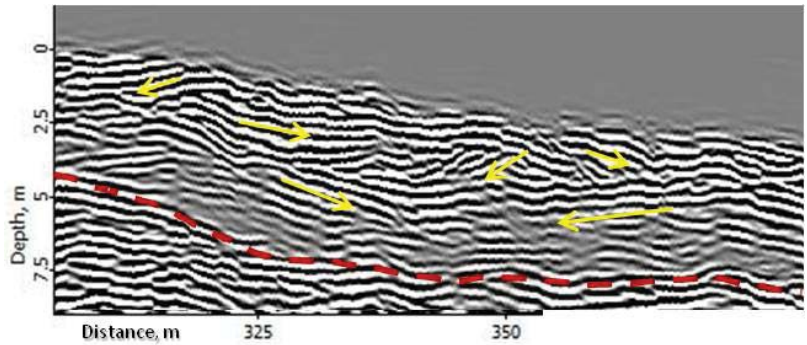

Figure 4. Detail of GPR profile 009 (150 MHz): different reflector angles (yellow arrows) and 2nd order surface (dashed red line).

Barboza, *E.G.*; Rosa, M.L.C.C.; Hesp, P.A.; Dillenburg, S.R.; Tomazelli, L.J. and Ayup-Zouain, R.N. 2011. Evolution of the Holocene Coastal Barrier of Pelotas Basin (Southern Brazil) - a new approach with GPR data. *Journal of Coastal Research*, SI 64, p.646-650.

Bristow, C.S. and Jol, H.M., 2003. An introduction to ground penetrating radar (GPR) in sediments. London, Geological Society, *Spec.Publications*, 211(1): 1-7.

Buynevich, I.V.; Souza Filho P.W.M., and Asp, N.E. 2010. Dune advance into a coastal forest, equatorial Brazil: a subsurface perspective. *Aeolian Research*, 2, 27–32.

Dillenburg, S.R.; Tomazelli, L.J., and Barboza, *E.G.*, 2004. Barrier evolution and placer formation at Bujuru southern Brazil. *Marine Geology*, 203(1–2), 43-56.

Dillenburg, S.R.; Barboza, *E.G.*, and Rosa, M.L.C.C., 2011. Ground Penetrating Radar (GPR) and Standard Penetration Test (SPT) records of a regressive barrier in southern Brazil. *Journal of Coastal Research*, SI 64, 651-655.

Dillenburg, S.R.; Barboza, *E.G.*; Tomazelli, L.J.; Hesp, P.A.; Clerot, L.C.P., and Ayup-Zouain, R.N., 2009. The Holocene Coastal Barriers of Rio Grande do Sul. In: Dillenburg, S.R. and Hesp, P.A. (Org.). *Geology and Geomorphology of Holocene Coastal Barriers of Brazil.* Berlin Heidelberg: Springer-Verlag, 107, 53-91.

Girardi, J.D. and Davis, D.M., 2010. Parabolic dune reactivation and migration at Napeague, NY, USA: Insights from aerial and GPR imagery. *Geomorphology*, 114(4), 530–41.

Gómez-Ortiz, D.; Martín-Crespo, T.; Rodríguez, I.; Sánchez, M.J., and Montoya, I., 2009. The internal structure of modern barchan dunes of the Ebro River Delta (Spain) from ground penetrating radar. *Journal of Applied Geophysics*, 68(2), 159-70.

Havholm, K.G.; Ames, D.V.; Whittecar, G.R.; Wenell, B.A.; Riggs, S.R.; Jol, H.M.; Berger, G.W, and Holmes M.A., 2004. Stratigraphy of back-barrier coastal dunes, Northern North Carolina and Southern Virginia. *Journal of Coastal Research*, 20(4), 980-999.

Hesp, P.A.; Dillenburg, S.R.; Barboza, *E.G.*; Tomazelli, L.J.; Ayup-Zouain, R.N.; Esteves, L.S.; Gruber, N.L.; Toldo Jr., E.E.; Tabajara, L.L.C.A., and Clerot, L.C.P., 2005. Beach ridges, foredunes or transgressive dunefields? Definitions and an examination of the Torres to Tramandaí barrier system, Southern Brazil. *Anais da Academia Brasileira de Ciências*, 77, 493-508.

Hesp, P.A.; Dillenburg, S.R.; Barboza, *E.G.*; Clerot, L.C.P.; Tomazelli, L.J., and Ayup-Zouain, R.N. 2007. Morphology of the Itapeva to Tramandaí transgressive dunefield barrier system and mid- to late Holocene sea level change. *Earth Surface Processes and Landforms*, 32, 407-414.

Lima, L.G., 2012. Estratigrafia e evolução holocênica de uma barreira costeira trangressiva-regressiva, litoral norte do Rio Grande do Sul. Porto Alegre, Rio Grande do Sul: Federal University of Rio Grande do Sul, Doctorate Thesis, 128 p.

Neal, A., 2004. Ground-penetrating radar and its use in sedimentology: principles, problems and progress. *Earth-Science Reviews*, 66(3-4), 261–330.

Oliveira Jr., J.G.; Medeiros, W.E.; Tabosa, W.F., and Vital, H., 2008. From barchan to domic shape: evolution of a coastal sand dune in northeastern Brazil based on GPR survey. *Revista Brasileira de Geofísica* , 26(1), 5-20.

Rockett, G.C.; Barboza, *E.G.*, and Rosa, M.L.C.C., 2014. Caracterização da Barreira Holocênica do Extremo Norte da Planície Costeira do Rio Grande do Sul através de Dados de Georradar. *Resumos Expandidos do VI Simpósio Brasileiro de Geofísica*, (Porto Alegre, RS), paper SBGF_4692.

Rosa, M.L.C.C., 2012. Geomorfologia, estratigrafia de sequências e potencial de preservação dos sistemas Laguna-Barreira do Quaternário Costeiro do Rio Grande do Sul. Porto Alegre, Rio Grande do Sul: Federal University of Rio Grande do Sul, Doctorate Thesis, 246p.

Shenk, C.J.; Gautier D.L.; Olhoeft, G.R., and Lucius, J.E., 1993. Internal structure of an Aeolian dune using ground-penetrating-radar. *Spec. Publ. Ass. Sediment*, 16, 61-69.

SEMA/RIO GRANDE DO SUL – Secretaria Estadual do Meio Ambiente. 2006. Plano de Manejo do Parque Estadual de Itapeva. Porto Alegre: SEMA. 274p.

Silva, A.B.; Barboza, *E.G.*; Rosa, M.L.C.C, and Fracolossi, F.G., 2010. Caracterização dos depósitos sedimentares em subsuperfície no setor meridional da Planície Costeira Sul de Santa Catarina. *Gravel*, 8(1), 1-7.

Van Dam, R.L.; Nichol, S.L., and McLean, R.F., 2003. GPR stratigraphy of a large active dune on Parengarenga Sandspit, New Zealand. *The Leading Edge*, 865-881.

Tomazelli, L.J., 1993. O Regime de ventos e a taxa de migração das dunas eólicas costeiras do Rio Grande do Sul, Brasil. *Pesquisas*, 20(1), 18-26.

Tomazelli, L.J.; Dillenburg, S.R.; Barboza, *E.G.*, and Rosa, M.L.C.C., 2008. Geomorfologia e Potencial de Preservação dos Campos de Dunas Transgressivos de Cidreira e Itapeva, Litoral Norte do Rio Grande do Sul. *Pesquisas*, 35, 47-55.

Villwock, J.A., 1984. Geology of the coastal province of Rio Grande do Sul, southern Brazil: a synthesis. *Pesquisas*, 16, 5-49.

Villwock, J.A. and Tomazelli, L.J. 1995. Geologia Costeira do Rio Grande do Sul. *Notas Técnicas*, 8, 1-45.

Journal of Coastal Research	SI	75	328-332	Coconut Creek, Florida	2016

Numerical Modelling of Turbulent Flow Structures in a Trough Blowout

Thomas A.G. Smyth[†] and Patrick A. Hesp[†]

[†]Beach and Dune Systems (BEADS) Laboratory,
School of the Environment, Flinders University,
Faculty of Science and Engineering,
Bedford Park, Adelaide, South Australia 5041

www.cerf-jcr.org

www.JCRonline.org

ABSTRACT

Smyth, T.A.G. and Hesp, Patrick A., 2016. Numerical Modelling of Turbulent Flow Structures in a Blowout. *In:* Vila-Concejo, A.; Bruce, E.; Kennedy, D.M., and McCarroll, R.J. (eds.), *Proceedings of the 14th International Coastal Symposium* (Sydney, Australia). *Journal of Coastal Research*, Special Issue, No. 75, pp. 328-332. Coconut Creek (Florida), ISSN 0749-0208.

Blowouts are erosional landforms often formed on coastal sand dunes by the deflation of sediment by wind flow. Quantitative observations of wind flow within blowouts aided by the deployment of smoke-bombs, have noted that temporal and spatial variations in sediment transport occur with the presence of turbulent flow structures. However because of the discrete nature of anemometry data, the presence of flow structures has been difficult to quantify and our understanding remains largely conceptual. This study presents a detailed investigation of turbulent flow structures within a trough blowout using high resolution, three-dimensional computational fluid dynamic modelling. We show that when incident wind flow was parallel to the blowout axis, only limited flow steering took place but a well-defined near surface jet developed along the deflation basin. Conversely when incident wind flow was oblique to the axis of the blowout wind flow became steered along the axis of the blowout but no near surface jet was produced. During neither incident wind direction were corkscrew or helicoidal vortices produced. Our study concludes that the incident wind flow direction is critical to the effectiveness of a trough blowout as a corridor for wind-blown sediment. While wind from a range of oblique angles may be steered along the axis of blowout, its relative effectiveness of eroding and transporting sediment beyond the deflation basin and erosional walls is much reduced compared to axis parallel wind flows of the same incident wind speed.

ADDITIONAL INDEX WORDS: *Trough Blowout, CFD, Numerical Flow Modelling, Turbulent Flow Structure*

INTRODUCTION

Trough blowouts are elongated erosional hollows commonly found on coastal and desert sand dunes. They act as corridors for sediment transport within vegetated dunes or between the beach and the established dune where the blowout is located on the foredune (Hesp and Hyde, 1996). Although trough blowouts are highly variable in their morphology (Mir-Gual *et al.*, 2011) they characteristically contain 3 distinct features:

1) A deflation basin from which sediment is eroded by near surface wind flow. The entrance of the deflation basin may be referred to as the blowout 'throat' which can connect the deflation basin to the back beach in cases where the blowout is located on the foredune.
2) Erosional walls which form around the deflation basin as it deepens.
3) A depositional lobe created by the ejection and deposition of sediment from the deflation basin. Where wind flow is channelized and forced to exit over a preeminent erosional wall a lobe will become more defined. Localized dunes beyond the crest of the erosional walls may exist at a number of locations around the blowout however the term depositional lobe is typically reserved for the largest and most distinct accumulation of sediment.

Once formed, near surface wind flow is the main determinant for trough blowout dynamics and morphological evolution. Not only do winds erode and entrain sediment from the deflation basin and erosional walls of the blowout but they govern sediment transport pathways for sediment that was entrained upwind of the blowout.

To date wind flow within trough blowouts has been analysed using sand ripple analysis (Hesp and Pringle, 2001), cup anemometry (Hesp and Hyde, 1996; Pease and Gares, 2013), 2D sonic anemometry (Hesp *et al., this issue*) and 3D sonic anemometry (Smyth *et al.,* 2014). Although these methods provide accurate information on flow patterns within a landform, they can only do so at a limited number of discrete locations. To visualise the presence of large scale turbulent flow structures in trough blowouts previous investigations have relied on the use of smoke bombs. Smoke bombs are effective at providing insight to instantaneous airflow patterns; however these data are difficult to record and quantify. In contrast, numerical flow modelling calculates flow behaviour at a high

DOI: 10.2112/SI75-066.1 received 15 October 2015; accepted in revision 15 January 2016.
*Corresponding author: thomas.smyth@flinders.edu.au

density of points over the surface of a landform. This wealth of data permits mapping of wind speed and direction at high resolution and enables three dimensional turbulent flow structures to be visualised and measured using streamlines (each streamline represents the path traced by a massless particle as it moves in the wind flow).

The objective of this study is to improve our understanding of wind flow dynamics within trough blowouts beyond the constraints imposed by anemometry and smoke flow imaging. By utilising the high resolution of data provided by numerical modelling we aim to quantify the structure and patterns of turbulent wind flow within the deflation basin and along the erosion walls during two typical incident wind directions.

METHODS

Numerical wind flow simulation was performed using the Navier-Stokes (N-S) equations. The N-S equations describe the motion of viscous fluids (such as air), however calculation of the complete equations in fully turbulent flow is computationally prohibitive. As an alternative turbulent flow instabilities within the equations are modelled. In this study, Reynolds-Averaged Navier-Stokes (RANS) turbulence modelling was utilized. In RANS, calculation of the N-S equations is achieved by separating velocity and pressure into mean and fluctuating components; specifically turbulent kinetic energy (κ) and turbulent dissipation rate (ε). This was performed using the renormalization group methods (RNG). To solve fluid flow the SIMPLE (Semi-Implicit Method for Pressure-Linked Equations) algorithm was employed. This approach results in an averaged steady-state solution. All calculations were performed in parallel using the open source, computational fluid dynamics (CFD) software package OpenFOAM® and the high performance computer 'Colossus' located at Flinders University, South Australia. Simulations were considered complete once the initial residuals for Ux, Uy and Uz were 4 orders of magnitude smaller than the maximum residual calculated.

The topographic surface of the model was created from a survey performed within a trough blowout located in the Province Lands dunefield at Cape Cod, Massachussetts, USA (see companion paper Hesp *et al.*, *this issue* for more details). The blowout was located on a ridgeline approximately 300 m inland from the beach. A survey of the landform was completed using a clinometer (accurate +/- 1 degree) and tape measure. The point data from the survey was interpolated by kriging to produce digital elevation model (DEM) of the landform (Figure 1). Using the DEM as the surface of the computational domain OpenFOAMs(®) native mesh generator, snappyHexMesh, was executed to create a mesh of the study area. Wind flow at the inlet boundaries of the model were described as logarithmic and equal to 10 m s^{-1} at 2 m above the surface. Incident wind direction was modelled from two distinct directions: parallel to the blowout axis (Case 1) and 45 degrees oblique to the blowout axis (Case 2) (Figure 1). The surface boundary of the model was uniformly prescribed a roughness height of 0.01 m (equivalent to *Ammophila breviligulata* [Olson, 1958]).

RESULTS

Wind flow from each incident direction was substantially altered and manipulated by the topography of the blowout (Figures 2 and 3). To provide the most composite and complete image of wind flow within the blowout, flow was visualized using streamlines (Figure 2), a slice through the center of the blowout axis (Figure 3a and 3b) and a number of slices lateral to the axis of the blowout (Figure 3c and 3d).

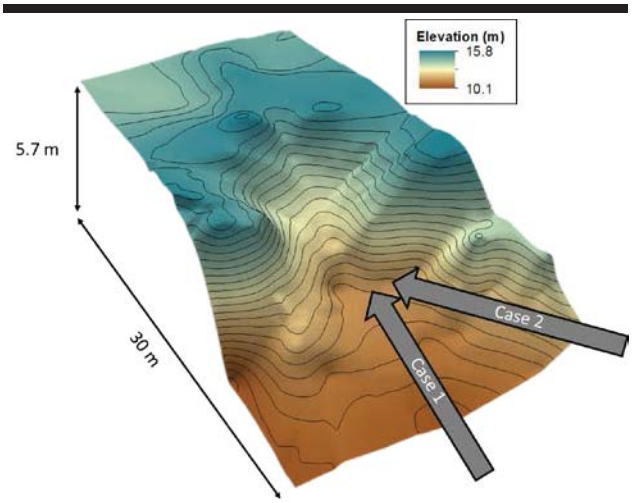

Figure 1. A Digital Elevation Model (DEM) of the trough blowout surveyed in Cape Cod, USA and used as the topographic surface in this study. Arrows labelled Case 1 and Case 2 represent the incident wind flow direction in each numerical modelling scenario. Wind flow was defined as logarithmic with a wind speed of 10 m s^{-1} 2 m above the surface. Each contour represents a 0.25 m change in elevation.

Flow Dynamics – Case 1

The visualization of wind flow using streamlines in Figure 2 demonstrates that only minimal wind flow steering took place within the blowout deflation basin when incident wind direction was parallel to the blowout axis. Although a small number of streamlines were steered from the deflation basin at the entrance of the blowout, the majority of flow was channelized between the steep erosional walls bordering each side of the deflation basin. As flow reached the change in slope between the erosional wall and depositional lobe it was projected above the depositional lobe, no longer following the contours of the surface as the streamlines had within the deflation basin.

Figures 2 and 3 both demonstrate that the vertical wind profile deviated substantially along the deflation basin and erosional walls from the logarithmic boundary layer prescribed upwind. Figure 3a shows that as wind flow moved from the relatively flat surface upwind of the blowout to the deflation basin it slowed before forming a near surface jet. Moving toward the deposition lobe wind speed slowed midway along the deflation basin before forming another, more intense jet with a higher maximum wind speed, close to the surface at the crest of the deflation basin. In lee of the deflation basin wind speed close to the surface

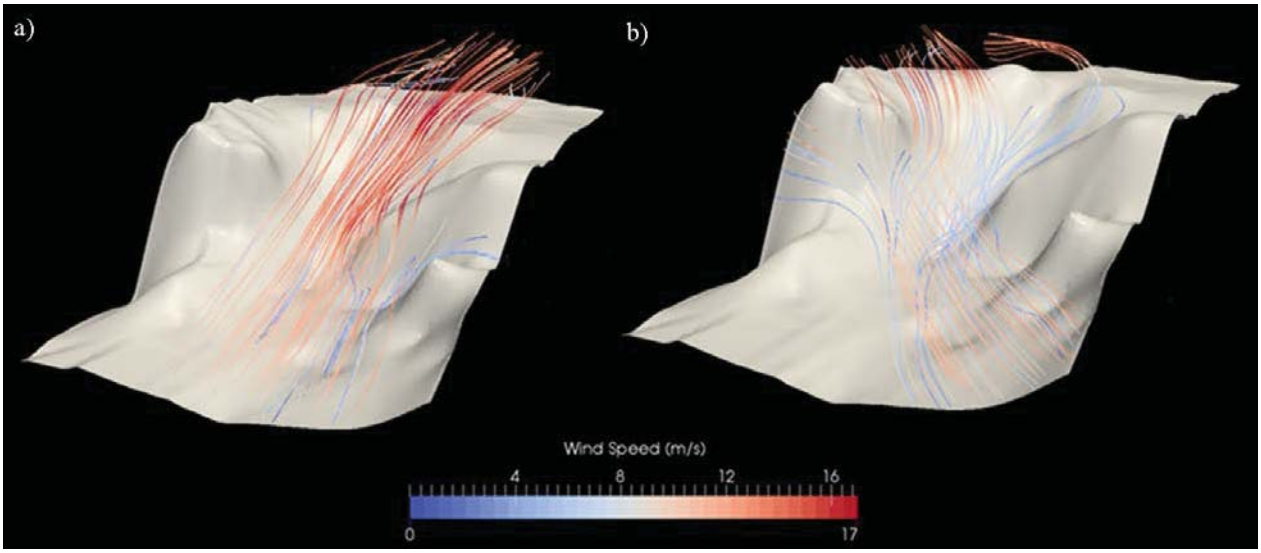

Figure2. Streamlines of wind flow over the surface of the trough blowout during winds parallel to the axis of the landform (a: Case 1) and at 45 degrees oblique to the axis of the landform (b: Case 2)

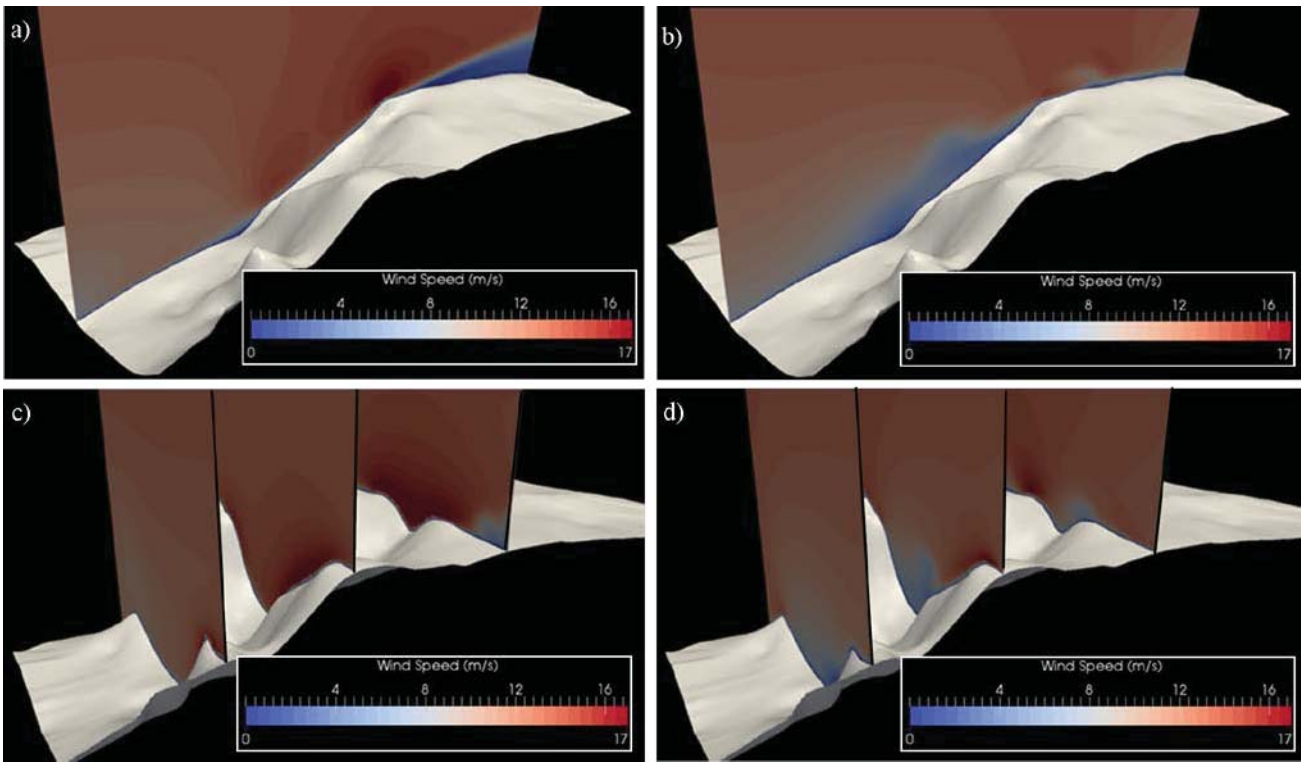

Figure 3. Wind speed contoured at intervals of 0.53 m s^{-1} along the longitudinal axis of a trough blowout for incident wind flow parallel to the longitudinal axis of the landform (a - case 1) and incident wind flow at 45 degrees oblique to the longitudinal axis of the landform (b – case 2) and along the lateral axes of a trough blowout for incident wind flow parallel to the longitudinal axis of the landform (c – case 1) and incident wind flow at 45 degrees oblique to the longitudinal axis of the landform (d- case 2).

underwent a dramatic decrease in speed, coinciding with the location of the depositional lobe.

The lateral slices through the deflation basin in Figure 3c demonstrates how the lateral extent of the near surface wind flow varied substantially along the deflation basin. At the entrance of the blowout, near surface acceleration was reserved to the steep crest at one of the erosion walls. Midway along the deflation basin (middle slice, Figure 3c) wind flow has accelerated to a maximum at both of the erosional walls but remains at substantially slower at the center of the deflation basin. At the crest of the deflation basin (right slice, Figure 3c) a distinct near surface jet had formed spanning both erosional walls and the interceding deflation basin.

Flow Dynamics – Case 2

The behavior of streamlines in Figure 2b show that wind flow was significantly steered from its incident wind direction as it entered the deflation basin during modelling case 2. Wind flow maintained its angle of incidence (45° oblique to the longitudinal axis of the blowout) until reaching the entrance of the blowout. Here streamline steering became dependent on the deflation basin topography. Wind flow closest to the dune surface was steered by approximately 45° and was channeled along the longitudinal axis of the blowout (Figure 2b). A small number of streamlines close to the dune surface were also deflected away from the blowout axis by the steep erosional walls. Streamlines seeded slightly higher above the surface of the dune were subject to less directional steering than wind flow closer to the surface but underwent a similar amount of wind flow acceleration at the crest of the erosional wall. The streamlines in Figure 2 indicate that wind flow in case 2 wasn't accelerated to the same extent as incident wind flow that was parallel to the blowout axis (case 1). This inference is reiterated in the longitudinal slice of wind flow through the center of the blowout (Figure 3b), where the logarithmic boundary layer profile prescribed at the inlet of the computational domain, was altered by a region of decreased wind speed close to the surface. Toward the crest of the erosional walls, before the depositional lobe, some wind flow speed-up does occur. However, the presence of a jet immediately upwind of the depositional lobe was much less defined than in case 1. The lateral slices of wind flow across the blowout in Figure 3d make evident that the zone of reduced wind speed extended across much of the deflation basin. Some acceleration above the surface of the erosion walls did occur however, particularly at the crest of the steep erosional walls.

DISCUSSION

The results of the wind flow modelling indicate that a trough blowout has a substantial impact on ambient, near-surface wind flow. Wind flow parallel to the blowout undergoes substantial acceleration and jet formation causing sediment to be both eroded and transported from the blowout deflation basin. During oblique winds, while flow becomes steered along the deflation basin, it is relatively slower in velocity compared to parallel winds and thus less efficient in the erosion and transportation of sediment. This decrease in erosive efficiency of oblique winds adds an important caveat to the findings of Pease and Gares (2013) who determined that the redirection of wind flow along the blowout axis maximizes the potential for erosion and transport in the trough.

When incident wind is parallel to the deflation basin, wind flow behavior is somewhat similar to wind flow over the stoss slope of a foredune. In both cases flow is retarded at the toe of the dune (in this case - deflation basin) and reaches maxima at the crest where a region of jet like flow may be produced (Hesp *et al.,* 2015). However unlike wind flow over a foredune our results showed that wind speed did not necessarily speed up along the deflation basin with increasing height. Instead as in Hesp and Hyde (1996) jets occurred in both the deflation basin and the crest of the erosional wall/deposition lobe which was followed by a large region of flow deceleration and expansion.

Streamlines of oblique flow along the axis of the blowout (Figure 2) bear a strong resemblance to the S-shaped flow shown by Hesp and Hyde (1996) and hypothesized by Pease and Gares (2013). Pease and Gares (2013) describe flow being concentrated on the downwind side of the blowout wall then curving back toward the upwind wall. Evidence of this process can also be noted in the lateral slices of oblique wind flow (Figure 3d) where high speed maxima along each slice alternate between the downwind and upwind erosional walls along the length of the deflation basin.

In contrast to our results, Hesp and Hyde (1996) noted that during parallel winds the jet within the deflation basin may at times be described by a corkscrew motion. During winds parallel to the deflation basin our data displayed no evidence of this process occurring within the trough blowout. Hesp and Hyde (1996) also reported corkscrew vortices as common during smoke experiments during oblique wind conditions. Pease and Gares (2013) also interpreted some of the erratic behavior in their anemometry data as being the product of a helicoidal flow. The numerical simulation of wind flow in this study suggests that the presence of helicoidal and corkscrew vortices may not be as ubiquitous as has been previously been implied by the interpretation of experimental data and subsequent conceptual flow modelling (Figure 13 in Hesp and Hyde (1996) and Figure 10 in Pease and Gares (2013)).

Whilst this study investigates only a single small blowout during a limited range of incident wind conditions, it does illustrate the value of numerical flow modelling to visualize and quantify the presence of flow structures.

CONCLUSIONS

This study aimed to quantify and improve our understanding of large scale turbulent flow structures within trough blowouts using numerical flow modelling. In agreement with previous anemometry investigations, during wind flow conditions parallel to the axis of the blowout, our modelling produced near surface jets along the deflation basin and crest . During wind flow oblique to the blowout, near surface wind became steered along the blowouts axis. Streamlines mimicked an S-shape where they became focused on the downwind side of the blowout erosional wall before curving back toward the upwind erosional wall and finally

becoming steered back to incident wind direction once exiting the blowout.

In contrast to preceding conceptual modelling, no corkscrew vortices were produced by the numerical flow modelling. This suggests they may not be as prevalent a phenomenon in trough blowouts as previously indicated.

With regard the potential for sediment dynamics and blowout evolution our study concludes that the incident wind direction is critical to the effectiveness of a trough blowout as a corridor for wind-blown sediment. While wind from a range of oblique angles may be steered along the axis of a blowout, its relative effectiveness for eroding and transporting sediment beyond the deflation basin and erosional walls is much reduced compared to axis parallel wind flows of the same incident wind speed.

ACKNOWLEDGMENTS

Our thanks to the NSF (grant no. 1024125) for financial support to Hesp, Flinders University School of the Environment for support, equipment and a postdoctoral fellowship to Smyth, and The Squealing Pig, Provincetown for shelter and sustenance. We are also grateful to Professor Douglas Sherman, Dr. Jak McCarroll and an anonymous referee, who provided constructive comments that improved the manuscript.

LITERATURE CITED

Hesp, P.A. and Hyde, R., 1996. Flow dynamics and geomorphology of a trough blowout. *Sedimentology*, 43, 505-525

Hesp, P.A. and Pringle, A., 2001. Wind flow and topographic steering within a trough blowout. *J. Coastal Res.,* SI 34, 597-601.

Hesp, P.A.; Smyth, T.A.G.; Nielsen, P.; Walker, I.J.; Bauer, B.O., and Davidson-Arnott, R., 2015. Flow deflection over a foredune. *Geomorphology*, 230, 64-74.

Mir-Gual, M.; Pons, G.X.; Martin-Prieto, J.A.; Roig-Munar, F.X., and Rodriguez-Perea, A., 2013. Geomorphological and ecological features of blowouts in a western Mediterranean coastal dune complex: a case study of the Es Comu de Muro beach-dune system on the island of Mallorca, Spain. *Geo-Mar Lett*., 33 (2), 129-141.

Olson, J.S., 1958. Lake Michigan dune development 1. Wind-velocity profiles. *Journal of Geology*, 66, 254-263.

Pease, P. and Gares, P., 2013. The influence of topography and approach angles on local deflection of airflow with a coastal blowout. *Earth Surface Processes*, 38 (10), 1160-1169

Smyth, T.A.G.; Jackson, D.W.T., and Cooper J.A.G., 2014. Airflow and sediment transport patterns within a coastal trough blowout during lateral wind conditions. *Earth Surface Processes and Landforms*, 39(14),1847-1854.

Journal of Coastal Research	SI	75	333-337	Coconut Creek, Florida	2016

Wind Turbulence Effects on Dune Sand Transport

Keiko Udo†

†International Research Institute of Disaster Science
Tohoku University
Sendai, Japan

www.cerf-jcr.org

www.JCRonline.org

ABSTRACT

Udo, K., 2016. Wind Turbulence Effects on Dune Sand Transport. *In:* Vila-Concejo, A.; Bruce, E.; Kennedy, D.M., and McCarroll, R.J. (eds.), *Proceedings of the 14th International Coastal Symposium* (Sydney, Australia). *Journal of Coastal Research*, Special Issue, No. 75, pp. 333-337. Coconut Creek (Florida), ISSN 0749-0208.

This study involved field experiment of instantaneous wind velocity, angle, and aeolian sand flux on a coastal dune and numerical simulation of spatial wind fields to analyze the effects of wind turbulence on aeolian sand transport. The field data demonstrate that horizontal turbulence intensity is approximated by a power equation of mean horizontal wind velocity and has a negative relationship with the mean wind velocity in various wind conditions. Horizontal turbulence intensity also has a negative relationship with the aeolian sand flux in various wind conditions, indicating the potential for introducing the turbulence intensity into the aeolian sand transport equation. The wind field simulated with a large eddy simulation (LES) model has reasonable wind characteristics consistent with ground elevation change measured in the field. However, results indicate accurate simulation of vertical wind velocity and both horizontal and vertical turbulence intensity is a great challenge compared to simulation of horizontal velocity.

ADDITIONAL INDEX WORDS: *sand transport rate, sediment transport, turbulence intensity, LES, UD-101.*

INTRODUCTION

Aeolian sand transport is an important process in many research fields. Coastal aeolian sand transport is a main cause of backshore and dune evolution. Backshore and dune development affect disaster prevention systems, ecosystems, tourism, and recreation. The mechanisms of aeolian sand transport should be clarified and incorporated into the simulation of the backshore and dune evolution for effective coastal management.

Studies involving field experiments of aeolian sand transport have increased since the 1990s when sensors that detect aeolian sand flux at high frequencies of 1 Hz or greater were developed (*e.g.*, Stout and Zobeck, 1997). Many studies of sand flux over flat and sloping surfaces have been conducted and their mechanisms are investigated (*e.g.*, Sterk *et al.*, 1998; Udo *et al.*, 2011). However, the process of sand flux across undulating surfaces in wind fields with large turbulence intensities still remains unclear.

This study conducted field experiments on three-dimensional wind velocities and aeolian sand flux on an undulating dune to analyze flux mechanisms at high turbulence intensity. Furthermore, the spatial wind field of the dune was examined through large eddy simulation (LES) to identify spatial wind characteristics during the field experiment.

METHODS

Field experiment was conducted at the Hamasaka Dune (35°32'N, 134°13'E; Figure 1a). The Hamasaka Dune is part of the Tottori Dune, which is one of the largest dunes in Japan. The Hamasaka dune has an area of more than 5 km^2. The median sandgrain size measured on the dune surface was 0.25 mm. The predominant wind direction in wind velocity of more than 10 m s^{-1} was identified as northwest.

Three dunes have evolved perpendicular to the predominant wind direction in the Hamasaka Dune. Measurement points A and B were located at the top of the middle dune and the center of the bowl-shaped blowout, respectively (Figure 1b). The maximum height of the middle dune measured approximately 40 m.

This experiment was conducted during strong winds caused by a low pressure system from 20:25 on December 5th to 05:18 on December 6th, 2012. The weather was cloudy with occasional rain and 0.5 mm precipitation was recorded for 30 min after 01:50 on December 6th. The predominant wind direction during the experiment was south during the period from 20:25 on December 5th to 01:39 on December 6th (Period 1) and west–southwest during the period from 01:39 to 05:18 on December 6th (Period 2). The datasets were referred to as A1, A2, B1, and B2 in the information obtained during Periods 1 and 2 at points A and B, respectively. Three-dimensional wind velocities and aeolian sand fluxes were measured at these two measurement points.

Wind velocity was measured using two Delta OHM (Model HD2003) three-axis ultrasonic anemometers 1.5 m above the ground surface. Wind data was recorded at 1 Hz frequency and comprised horizontal wind velocity and direction and vertical wind velocity. Horizontal wind direction was expressed clockwise from north, in positive degrees from 0 to 360. Aeolian sand flux was measured using a piezo-electric sand flux sensor UD-401 0.05 m above the ground surface. The UD-401 is a four-directional instrument with four impact count sensors based on the unidirectional sensor UD-101 employed in field experiments over flat and sloping surfaces (Udo *et al.*, 2008; Udo *et al.*, 2009; Udo *et al.*, 2011). Each sensor of the UD-401 counts one per one sampling period of 1.0×10^{-4} s when it detects aeolian sand impacting a 6 mm diameter sensor. The

DOI: 10.2112/SI75-067.1 received 15 October 2015; accepted in revision 15 January 2016.
*Corresponding author: udo@irides.tohoku.ac.jp

logger records a maximum of 10,000 counts of data at 1 Hz frequency. These measured data were divided into 5 min segments and statistically analyzed.

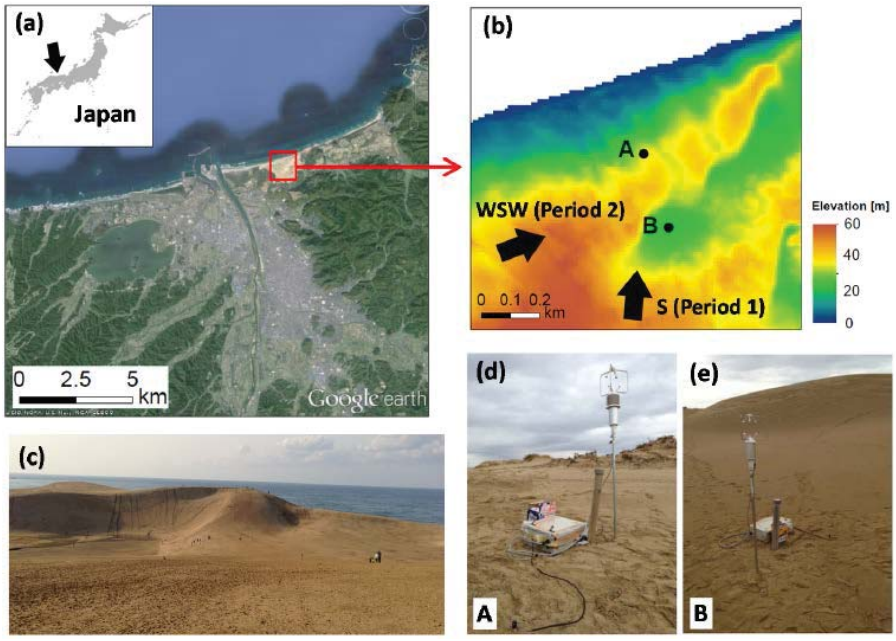

Figure 1. (a) Location of study area and satellite image, (b) topography and photographs of (c) the middle dune, and (d) measurement points A and (e) B of the Hamasaka Dune.

Wind field simulation

CFD software RIAM-COMPACT® (Uchida, 2014) based on large eddy simulation (LES) was employed for numerical simulation of the spatial wind fields around the dune. Data from a 10 m mesh digital elevation model measured during a 2009 airborne laser survey by the Geospatial Information Authority of Japan (GSI) was used to represent the dune topography. The simulation area centered at point B had a size of 4 × 4 km^2 horizontally and 1.7 km vertically. The upwind boundary of the area was set perpendicular to the horizontal wind direction. Grid numbers were 200 and 200 horizontally and 50 vertically. Grid size was smallest at the center of the area and at the ground surface (8.5 × 8.5 × 0.6 m^3). Grid size was largest at the four corners of the upper boundary of the simulation area (191 × 191 × 213 m^3). Inflow condition was determined by the wind profile power law (i.e., the 1/7 power law) and given so that simulated wind velocity and angle would correspond to wind velocity and angle in field experiments from points A and B. At outflow boundary, a convective outflow condition was used. The free-slip condition was imposed at the side and upper boundaries and the no-slip condition was imposed at the ground surface.

RESULTS

Wind characteristics are shown in Table 1. A time-series of the instantaneous horizontal wind velocity u, vertical velocity w, horizontal turbulence intensity u'/u_{mean}, vertical turbulence intensity w'/w_{mean}, horizontal wind angle α, and aeolian sand flux n during the experiment are shown in Figure 2. The mean values were averaged over 5 min. White closed symbols in Figure 2 indicate 5-min mean values. The value of α_{mean} is approximately south in Period 1 and west–southwest in Period 2. Upwind topography is relatively flat for case A1, upslope for A2, and downslope for B1 and B2. Data for n used in analyses are sand flux transported from the south for A1 and B1 and from the west for A2 and B2.

Table 1. *Characteristics of wind velocity and angle during the field experiment.*

Data	$u_{mean} \pm u_{sd}$ [m s^{-1}]	$w_{mean} \pm w_{sd}$ [m s^{-1}]	$\alpha_{mean} \pm \alpha_{sd}$ [°]
A1	8.68 ± 2.50	0.48 ± 0.43	184 ± 16
B1	5.96 ± 2.06	0.26 ± 0.32	187 ± 24
A2	10.85 ± 2.65	1.94 ± 0.54	250 ± 11
B2	6.93 ± 1.87	−0.11 ± 0.43	242 ± 13

In both Periods 1 and 2, u_{mean} at point A (A1 and A2; flat and upslope, respectively) is larger than at point B (B1 and B2; downslope). This is consistent with the existing knowledge. The values of w_{mean} in Period 2 are positive and much larger at point A (A2) and negative and close to zero at point B (B2), whereas they are positive and close to zero in Period 1 (A1 and B1). The value of u'/u_{mean} increased when u_{mean} was close to zero at approximately 22:30 on December 5th and when α changed drastically at approximately 1:40 on December 6th. The value of

w'/w_{mean} is much larger and has a wide range compared to u'/u_{mean} because w_{mean} is usually close to zero and has both positive and negative values. Consequently, w_{sd}/w_{mean} is much larger and has a wide range compared to u_{sd}/u_{mean}.

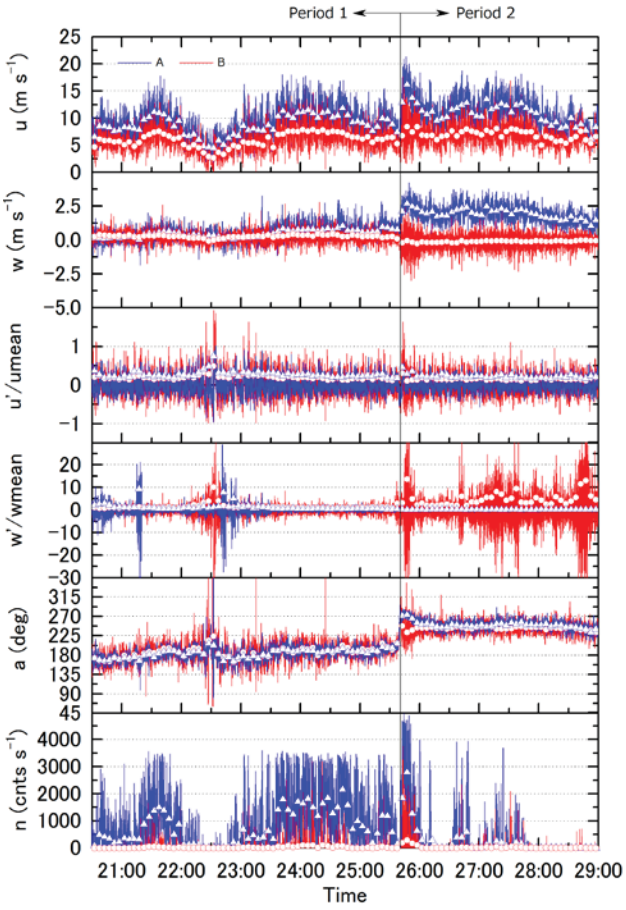

Figure 2. Time-series of the instantaneous horizontal wind velocity u, vertical velocity w, horizontal turbulence intensity u'/u_{mean}, vertical turbulence intensity w'/w_{mean}, horizontal wind angle α, and aeolian sand flux n during the experiment. White closed symbols indicate 5-min mean values.

Relationships between statistical wind values, i.e., u_{mean}, w_{mean}, u_{sd}, w_{sd}, u_{sd}/u_{mean}, and $w_{sd}/|w_{mean}|$, obtained from the 5-min segments were analyzed. The value of w_{mean} is positive proportional to u_{mean} for all cases; however, the proportional coefficients have different values of 0.057 for A1 (the coefficient of determination $R^2 = 0.86$), 0.045 for B1 ($R^2 = 0.95$), 0.179 for A2 ($R^2 = 1.0$), and −0.016 for B2 ($R^2 = 0.80$). Conversely, w_{sd} is positive proportional to u_{sd} in all cases, and the coefficients have similar values of 0.20 for A1 ($R^2 = 0.96$), 0.19 for B1 ($R^2 = 0.97$), 0.23 for A2 ($R^2 = 0.99$), and 0.25 for B2 ($R^2 = 0.97$) (Udo, 2015).

Relationships between u_{mean} and u_{sd}/u_{mean} and between $|w_{mean}|$ and $w_{sd}/|w_{mean}|$ are approximated by power equations with similar coefficients for all cases (Figure 3) as follows:

$$\log(u_{sd}/u_{mean}) = -0.72\log(u_{mean}) - 0.05 \quad (R^2 = 0.53), \qquad (1)$$

$$\log(w_{sd}/w_{mean}) = -0.95\log(w_{mean}) - 0.44 \quad (R^2 = 0.96). \qquad (2)$$

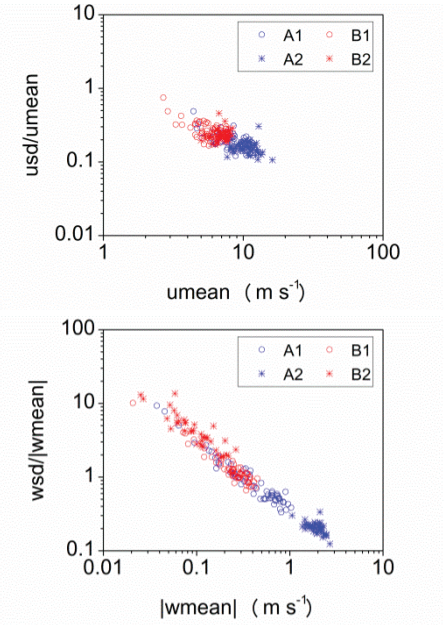

Figure 3. Relationships between u_{mean} and u_{sd}/u_{mean} and between $|w_{mean}|$ and $w_{sd}/|w_{mean}|$ for A1 to B2.

This clear relationship indicates that aeolian sand transport rate can potentially be formulated with turbulence intensity because the existing rate formulas are proportional to wind velocity to the third power. The existing formulas (e.g., Bagnold, 1941; Kawamura, 1951) assume sand transport occurs over flat beds and do not consider the turbulence effect. If turbulence intensity is introduced to an existing formula and the formula is evaluated with wind and sand flux data obtained during large turbulence intensity, a new formula that includes the turbulence effect can be established.

Relationship between wind and aeolian sand flux

Relationships between u, w, and n demonstrate that n increased with an increase in u and decreased notably due to rainfall after 1:50 on December 6th (see Figure 2; Udo, 2015). This is consistent with previous studies (e.g., Udo *et al.*, 2008). Relationships between u_{mean} and n_{mean} and between u_{sd}/u_{mean} and n_{mean} are shown in Figure 4. Values of n_{mean} are clearly proportional to u_{mean} to the second power with a small amount of scatter; however, u_{mean} has different values for the same n_{mean} in A1 and A2 in which n_{mean} values are relatively large compared to B1 and B2 (Figure 4a). Conversely, n_{mean} has a large amount of scatter but a clearly negative relationship with u_{sd}/u_{mean} (Figure 4b). As mentioned, this is important because it indicates the potential for introducing turbulence intensity into the aeolian sand transport equation. Similar relationships are also obtained between $|w_{mean}|$ and n_{mean} and between $w_{sd}/|w_{mean}|$

and n_{mean}. Smyth *et al.* (2014) showed a similar negative relationship between sediment flux and turbulence intensity.

Field experimental results are briefly summarized. Additional results and figures are found in Udo (2015).

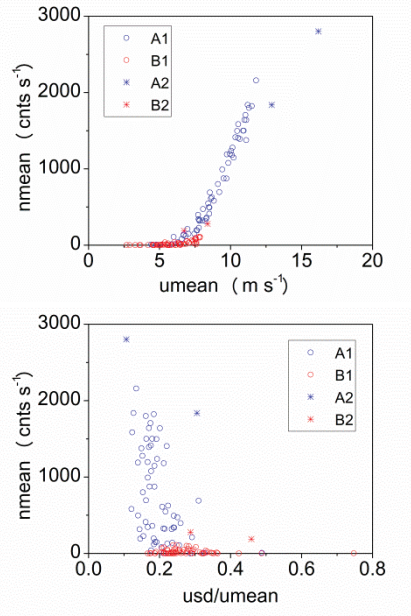

Figure 4. Relationships between u_{mean} and n_{mean} and between u_{sd}/u_{mean} and n_{mean} for A1 to B2.

Dune wind field simulation

The simulated spatial distributions of u_{mean} in Periods 1 (case 1) and 2 (case 2) are shown in Figures 5 and 6, respectively. Comparisons of u_{mean}, w_{mean}, and α_{mean} measured and calculated at 1.5 m are shown in Table 2. In case 1, the simulated u_{mean} agrees with the measured u_{mean} at both points A and B; however, the simulated w_{mean} does not agree with points A and B. In case 2, neither the simulated u_{mean} nor w_{mean} agrees with points A and B.

Spatial distribution of u_{mean} in a predominantly northwest wind direction was also calculated (Figure 7). Simulated wind velocity increases at point A but decreases at point B. This is in agreement with the negative and positive topography changes (erosion and deposition, respectively) at points A and B between 2006 and 2009 (Figure 8).

DISCUSSION

Values of n_{mean} has a large amount of scatter but a clearly negative relationship with u_{sd}/u_{mean} (Figure 4b). One reason for the scatter is that a 1 Hz frequency for the experiment is considered low for this analysis (Leenders *et al.*, 2005). Furthermore, the horizontal velocity u was not separated in two directions. Another reason is that the measurement height of the wind velocity was 1.5 m above the ground and different from that of the flux at 0.05 m. Further examination of these issues is necessary.

The simulated u_{mean} agrees with the measured u_{mean} at both points A and B; however, the simulated w_{mean} does not agree with points A and B in case 1 (Table 2 and Figure 5). Neither the simulated u_{mean} nor w_{mean} in case 2 agrees with points A and B in case 2 (Table 2 and Figure 6).

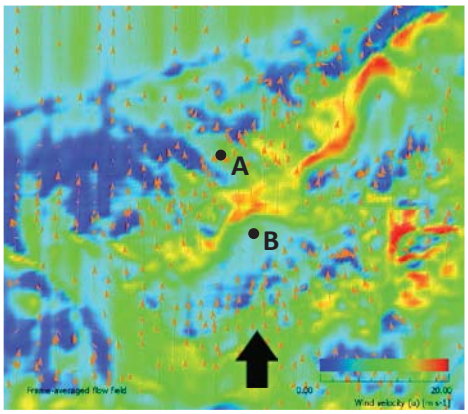

Figure 5. Simulated spatial distribution of horizontal mean wind velocity u_{mean} 1.67 m above ground surface for case 1. The orange arrows show vectors of u_{mean}. See Figure 2 for dune topography.

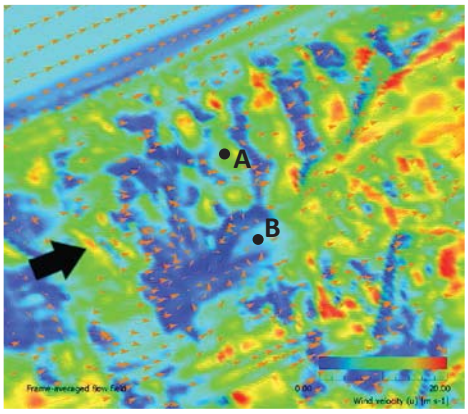

Figure 6. Simulated spatial distribution of horizontal mean wind velocity u_{mean} 1.22 m above ground surface for case 2. The orange arrows show vectors of u_{mean}. See Figure 2 for dune topography.

Table 2. *Comparison of measured and calculated wind fields at 1.5 m height above the ground surface.*

Dataset	u_{mean} [m s^{-1}]		w_{mean} [m s^{-1}]		α_{mean} [degrees]	
	meas.	calc.	meas.	calc.	meas.	calc.
A1	8.68	8.18	0.48	−0.53	184	178
B1	5.96	6.02	0.26	0.01	187	177
A2	10.85	9.14	1.94	0.83	250	251
B2	6.93	3.72	−0.11	0.011	242	171

One reason for this disagreement is the inflow vertical wind profile was given by the wind profile power law of u_{mean} through trial and error so that simulated wind velocity and angle would correspond to field results at points A and B. The other reason is that the dune topography produced in this simulation

was measured in 2009 and the field experiment was performed in 2012, although the topography changed during the period from 2009 to 2012 as shown in Figure 8.

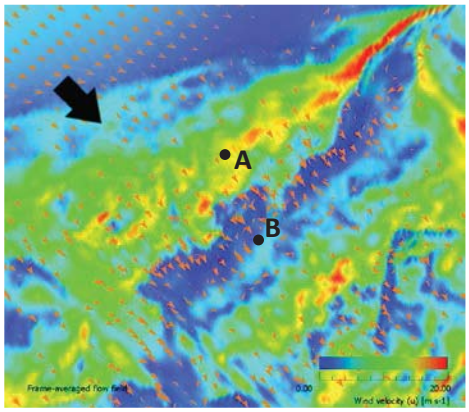

Figure 7. Simulated spatial distribution of horizontal mean wind velocity u_{mean} at 1.16 m above ground surface in a predominantly northwest wind direction. Orange arrows show vectors of u_{mean}. See Figure 2 for dune topography.

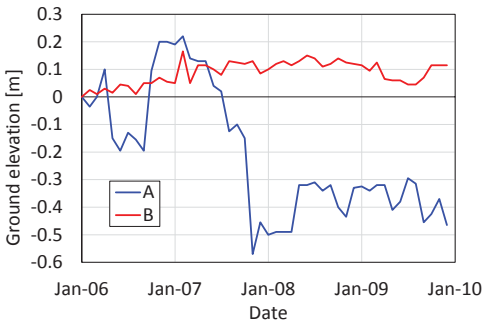

Figure 8. Ground elevation changes at points A and B measured by Sand Dunes Office, Department of the Environment and Consumers Affairs, Tottori Prefecture in the period from 2006 to 2009.

There are several difficulties associated with simulating wind characteristics in the field. However, the distribution of u_{mean} in Figures 5 and 6 has reasonable wind field characteristics such as increased wind velocity at dune tops and decreased wind velocity at dune lees or generations of eddies at dune lees. Current technology faces many challenges in the accurate simulation of vertical wind velocity and both horizontal and vertical turbulence intensity compared to the horizontal velocity.

CONCLUSIONS

This study investigated wind turbulence effects on dune sand transport through field experiment of three dimensional wind velocity and aeolian sand flux. Horizontal turbulence intensity has a negative relationship with mean horizontal wind velocity and also with the aeolian sand flux in various wind conditions.

The spatial wind field during the experiment was simulated with large eddy simulation (LES) and the results show wind characteristics reasonably consistent with measured ground elevation change. However, the results also demonstrate that accurate simulation of vertical wind velocity and both horizontal and vertical turbulence intensity in the field is a great challenge compared to simulation of horizontal velocity.

There are several difficulties in dune topography change simulation. These include modeling of sand transport considering wind turbulence, simulation of actual wind characteristics including wind turbulence, and introduction of the sand transport model to the simulation. This study has revealed important aspects that contribute to the solution of these problems.

ACKNOWLEDGMENTS

Field experiment was performed by Mr. Shota Mitsushio and Mr. Keishi Okamura and supported by the Sand Dunes Office, Department of the Environment and Consumers Affairs, Tottori Prefecture. This work was supported by JSPS KAKENHI Grant Number 25420515.

LITERATURE CITED

Bagnold, R.A., 1941. *The Physics of Blown Sand and Desert Dunes*, Methuen, London, UK, p. 265.

Kawamura, R., 1951. Study of sand movement by wind. *Univ. Tokyo, Rep. Inst. Sci. Technol.*, 5, 95-112. (in Japanese)

Leenders, J.K.; van Boxel, J.H., and Sterk, G., 2005. Wind forces and related saltation transport, *Geomorphology*, 71, 357-372.

Smyth, T.A.G.; Jackson, D., and Cooper, A., 2014. Airflow and aeolian sediment transport patterns within a coastal trough blowout during lateral wind conditions, *Earth Surface Processes and Landforms*, 39, 1847-1854.

Sterk, G.; Jacobs, A.F.G., and van Boxel, J.H., 1998. The effect of turbulent flow structures on saltation sand transport in the atmospheric boundary layer, *Earth Surface Processes and Landforms*, 23, 877-887.

Stout, J.E. and Zobeck, T.M. (1997), Intermittent saltation, *Sedimentology*, 44, 959-970.

Uchida, T., 2014. Validation testing of the prediction accuracy of the numerical wind synopsis prediction technique RIAM-COMPACT for the case of the bolund experiment: comparison against a wind-tunnel experiment, *Reports of RIAM, Kyushu University*, 147, 7-14.

Udo, K.; Kuriyama, Y., and Jackson, D.W.T., 2008. Observations of wind-blown sand under various meteorological conditions at a beach, *Journal of Geophysical Research*, 113, F04008.

Udo, K., 2009. New method for estimation of aeolian sand transport rate using ceramic sand flux sensor (UD-101), *Sensors*, 9, 9058-9072.

Udo, K.; Junaidi; Aoki, S.; Mitsushio, S.; Kato, S., and Mano, A., 2011. Field measurement of aeolian sand flux using ceramic sand flux sensor UD-101 at a sand dune. *Proc. of 32nd Int. Conf. on Coastal Eng*, Paper # sediment.109. Retrieved from http://journals.tdl.org/ICCE/.

Udo, K., 2015. Characteristics of wind and Aeolian sand flux over a coastal dune, *Journal of Japan Society of Civil Engineers*, Ser.B2 (Coastal Engineering), 71, I_529-I_534.

Journal of Coastal Research	SI	75	338-342		2016

Aeolian Sediment Flux Derived from a Natural Sand Trap

Alida J. van der Weerd †, Kathelijne M. Wijnberg†*

†Department of Water Engineering and Management
University of Twente
Enschede, The Netherlands

www.cerf-jcr.org

www.JCRonline.org

ABSTRACT

Van der Weerd, A.J. and Wijnberg, K.M., 2016. Aeolian sediment flux derived from a natural sand trap. *In:* Vila-Concejo, A.; Bruce, E.; Kennedy, D.M., and McCarroll, R.J. (eds.), *Proceedings of the 14th International Coastal Symposium* (Sydney, Australia). *Journal of Coastal Research*, Special Issue, No. 75, pp. 338-342. Coconut Creek (Florida), ISSN 0749-0208.

In 2011, a mega-nourishment (the 'Sand Motor') was constructed along the Dutch Coast. Since it is a pilot project, its evolution is closely monitored. This paper presents first results on the temporal variation in aeolian sediment transport across the nourishment, based on (a) the rate of infill over a 4 year period of a small lake in the nourishment, (b) one year of semi-hourly collected video imagery and (c) four year of hourly-averaged wind data. It appeared that, apart from approximately the first half year, the infill occurred quite linearly over time at an average rate of about $1.9 \cdot 10^4$ m^3/yr. The rate of infill in the first half year period was equivalent to an annual rate of $8.4 \cdot 10^4$ m^3/yr. From the combination of video image data and wind data, it was derived that aeolian sand transport (by saltation) was only observed at hourly averaged wind speeds of at least 7 m/s. The monthly frequency of occurrence of above 7 m/s wind speed, was reasonably well correlated with monthly frequency of occurrence of aeolian transport (r=0.79). Nevertheless, when hourly wind speed exceeded 7 m/s, transport was only observed about 23% of the time, indicating the importance of supply limiting conditions for aeolian transport from the Sand Motor.

ADDITIONAL INDEX WORDS: *Nourishment, aeolian sediment transport, video monitoring, meso-scale.*

INTRODUCTION

In 2011, a peninsula shaped, 21.5 Mm3 nourishment was constructed on the west coast of the Netherlands (Figure 1). It is a pilot project, named the Sand Motor, which is expected to protect multiple kilometers of coastline for approximately 20 years, which is much longer than regular nourishments. As dunes function as flood defense along large parts of the Dutch coast, one important aspect in this pilot is to assess and understand spatio-temporal variation in aeolian sand transport at the Sand Motor and its effect on dune development.

Dune development at the coast is the result of intermittently occurring transport events of both aeolian and marine origin. Due to the high elevation of the Sand Motor (Figure 2a), the development of the dunes backing the Sand Motor so far has only been influenced by aeolian bio-geomorphological processes, and this is expected to be so for the upcoming years. Therefore, spatio-temporal variation in aeolian sand supply from the Sand Motor may be an important explanatory factor in the development of dunes at the original coastline.

The study presented here aims at assessing the magnitude, and temporal variation therein, of longer term aeolian sediment flux across the mega-nourishment, and at identifying the conditions during which the contributing aeolian transport events do occur.

METHODS

On the nourishment, a small lake is present that acts as an effective 'natural' trap for aeolian sand transport (Figure 1 and Figure 2b,c). Topographic changes in this area are solely due to aeolian transport events, since there is no connection to the sea at any time. Therefore, the rate of infill can be used to quantify longer term aeolian sediment fluxes (Van der Weerd and Wijnberg, 2015). In our current study we consider a higher temporal resolution and a longer time span. Since August 2011, about every two months bathymetric and topographic surveys were done (by 'SHORE Monitoring & Research'). In this

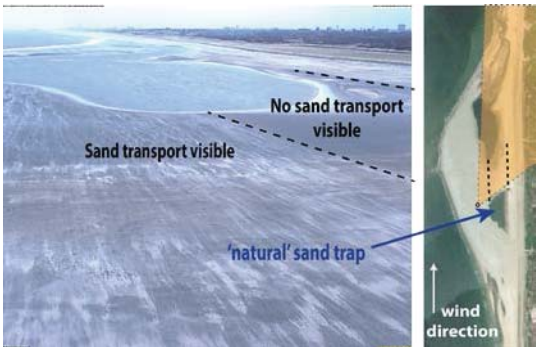

Figure 1. Natural sand trap at the Sand Motor. Left: Argus image (camera 1) showing aeolian streamers except in lee-side of the Lake area. Right: top view of the Sand Motor, showing the Lake that serves as a sand trap. Shaded area is field of view of Argus image.

DOI: 10.2112/SI75-068.1 received 15 October 2015; accepted in revision 15 January 2016.
*Corresponding author: k.m.wijnberg@utwente.nl

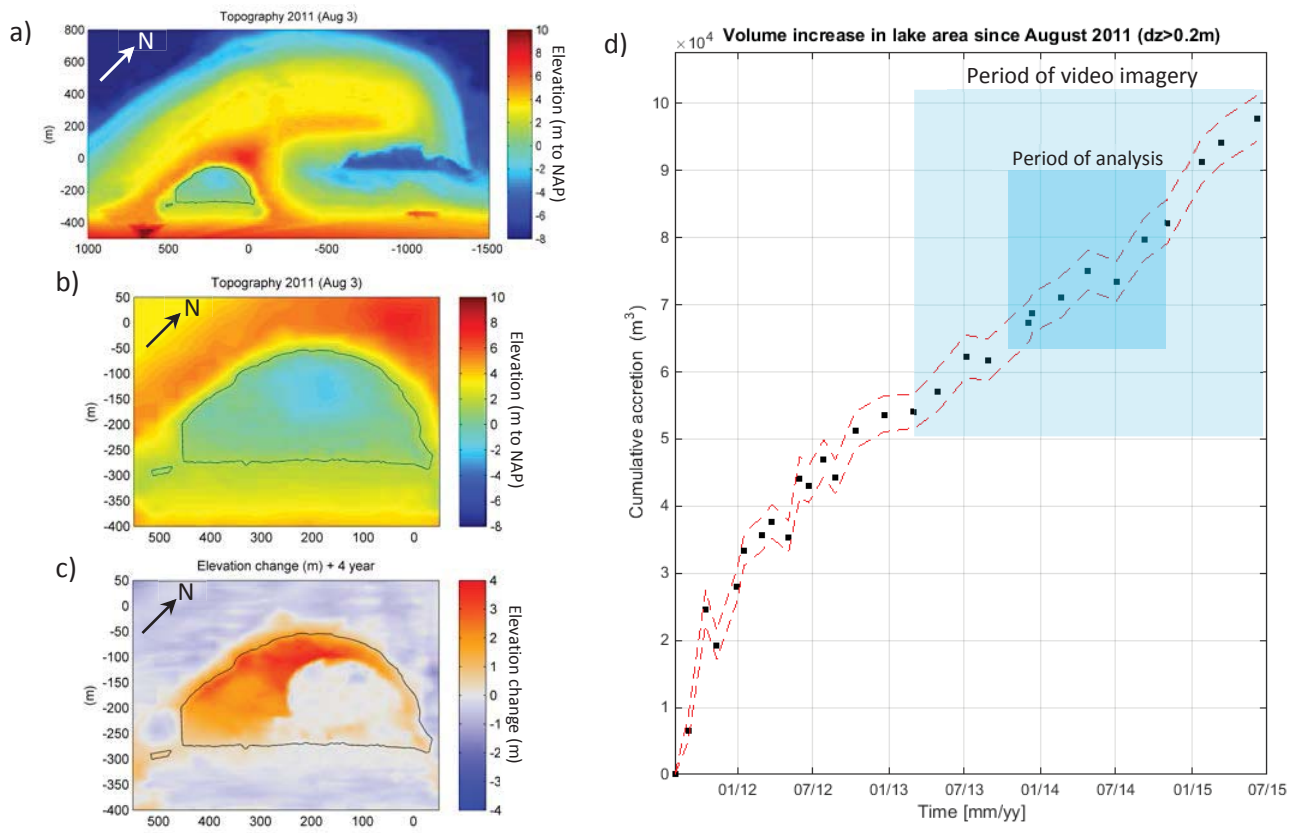

Figure 2. Volume changes in the lake area. (a) Topography Sand Motor area (Aug 3, 2011), (b) Topography lake area (Aug 3, 2011), (c) Four year elevation change in lake area since Aug 2011 survey, (d) Volume change in lake area since Aug 2011, with error band estimate (dashed lines).

study we used 29 surveys until June 2015 to obtain volume changes in the lake area. First, the elevation data were linearly interpolated to a 2x2m grid. Next, for all surveys the volume increase since August 3, 2011 was calculated for all grid cells in the accretionary part of the lake area where elevation change (since Aug 2011) exceeded +0.2 m. An error band for volume change was estimated by accounting for a 5 cm vertical offset (positive and negative) of the complete survey (pers. comm. surveyors *SHORE Monitoring & Research*). The contribution of the random error per survey point, and its propagation through interpolation, was assumed to approximately average out in the summation of volumes per grid cell to obtain total volume change.

To characterize the contributing transport events, Argus video imagery and wind data were used. In February 2013, an Argus video monitoring system consisting of 8 cameras, covering the seaward side of the mega nourishment and the lagoon area, was mounted on a 40 meter high tower in the middle of the Sand Motor. These cameras are taking snapshot and time-exposure images semi-hourly during daylight hours, and cover a large part of the Sand Motor surface. These images form a unique, high temporal resolution data set, covering both a long time period (*i.e.* several years) and a large spatial scale (*i.e.* almost the total Sand Motor area).

To identify which wind conditions lead to aeolian infill, we first visually identified the occurrence of aeolian transport from all snapshot images between November 1st 2013 and November 1st 2014, of the Northeasterly viewing camera. This period was chosen because it is a year without large gaps in image data. It also contains the period of the MegaPEX field campaign. For this period almost 9000 images were visually inspected.

Aeolian activity was identified by (i) presence of aeolian streamers and, during very high transport rates, (ii) the movement of aeolian bedforms. Every time, two consecutive images were compared to verify that bedforms had moved or that an isolated sediment 'cloud' (intermittently occurring during low transport conditions) was not some local, small-scale deposit of a preceding transport event.

The Northeasterly viewing camera was used because it is directed towards the quite low-lying surface near the lagoon (Figure 1), which generally has a darker color due to its moisture content. This dark color provides a good contrast with the dry, light-colored sand in transport. Especially during periods with low transport rates, streamers could be detected more easily here than on images from the other cameras.

Next, to characterize wind conditions during the identified transport events, hourly wind data of wind station "Hoek van

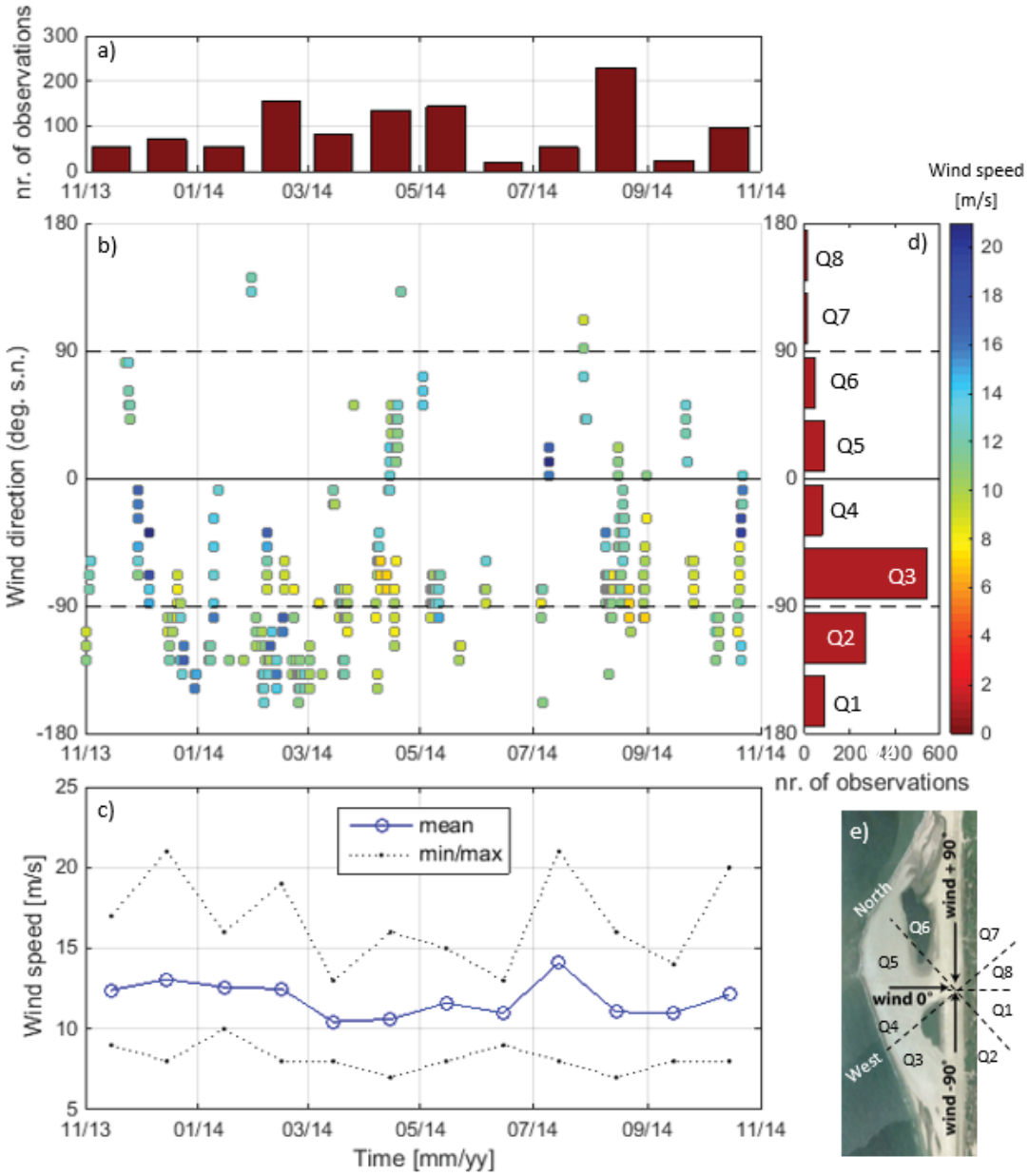

Figure3. Analysis of Argus images combined with wind data from Hoek van Holland. a) Monthly number of images on which transport was identified. b) Identified transport occurrences coupled to the co-occurring wind speed (color) and wind direction. c) Monthly wind statistics of wind conditions during transport, d) Number of transport events per directional sector, e) Definition sketch of wind direction and directional sectors.

Holland" (8 km south of study area), from the Royal Dutch Meteorological Institute were used. In this study we analyzed hourly averaged wind speed and direction. The wind directions were transformed such that 0º refers to the shore normal direction (Figure 3e), the shore normal (s.n.) direction being 318 degrees North. For images taken at the half hour, the wind data at the next full hour was used, as the hourly-averaged values refer to the preceding hour.

To assess the extent to which time-varying supply limitation may play a role in transport occurrence (*e.g.* sand surface conditions, availability of intertidal area as source area), we then summarized transport occurrences and above-threshold wind conditions into monthly statistics. The threshold wind condition was defined as the minimum wind speed for which transport was identified on the imagery. As transport events could only be identified during daylight, monthly wind statistics were adapted

to apply to daylight hours only, ranging from only 8 hours in December and January, to 16 hours in June and July.

RESULTS

The sediment volumes in the lake area show an ongoing accretionary trend since August 2011 (Figure 2d). This observation is in line with Van der Weerd & Wijnberg (2015), who considered a 3 year period, instead of 4 year, and using annual surveys only. The higher temporal resolution used in this study revealed that the higher infill rate in the first year after construction can be attributed mostly to the first half of that year. Apart from the first half year, the infill occurred quite linearly over time at an average rate of about $1.9 \cdot 10^4$ m^3/yr. The rate of infill in the first half year period was equivalent to an annual rate of $8 \cdot 10^4$ m^3/yr. A possible explanation for this higher infill rate in the first half year could for instance be more windy conditions or different surficial sediment conditions right after construction. Before looking into this further, we first assessed the actual wind conditions during which transport occurred at the Sand Motor.

Figure 3b presents all transport occurrences identified on one year of image data, with co-occurring wind conditions in terms of hourly averaged wind speed (color) and direction. It appeared that about 12% of the time (daylight hours) aeolian transport activity was identified.

Regarding wind directions during transport, most of the transport events (72%) occurred with 'Southwesterly' quadrant (Q2, Q3) wind directions (Figure 3d). This observation matches well with the observed accretion pattern in the lake (Figure 2), supporting our assumption that the lake area is acting as an effective sand trap. Further, it can be derived that about one third (33%) of the transport events coincided with wind conditions that had an offshore directed component (Q1 ,Q2, Q7, Q8), hence blowing sand back into the sea.

In terms of wind speed, transport was observed to occur with hourly wind speeds from 7 m/s and up (Figure 3c). We therefore considered 7 m/s as the threshold wind speed for sand transport (by saltation) in our further analyses. The fact that this minimum wind speed for transport varied by month is most likely explained by the generally few transport events occurring per month, such as in June 2014 (Figure 3a). (An event being a set of consecutive hours with transport.) The onset or waning of the transport event may have been missed in a particular month due to daylight hour restrictions. Also, a particular transport event might actually have had a larger threshold wind speed, for instance due to coincidental rainfall.

To obtain further insight in the extent to which time-varying supply limitation may play a role in transport occurrence, we compared the monthly occurrence of above transport threshold wind speeds with the actual occurrence of transport events. Although the frequency of occurrence of above threshold wind speeds exhibited an obvious seasonal variation, this pattern disappeared when only daylight hours were considered (Figure 4a). This may partially explain why no obvious seasonal signal was seen in the monthly variation in number of transport observations (Figure 4a). It was found that the transport occurrences were reasonably well correlated (r=0.79) with the occurrence of above threshold wind speeds (considering only daylight hours) (Figure 4b). Nevertheless, when hourly wind speed exceeded 7 m/s during daylight, transport was only observed about a quarter of the time(23%). This indicates that supply limiting conditions, and temporal variation therein, play an important role for sand transport occurrence across this mega-nourishment.

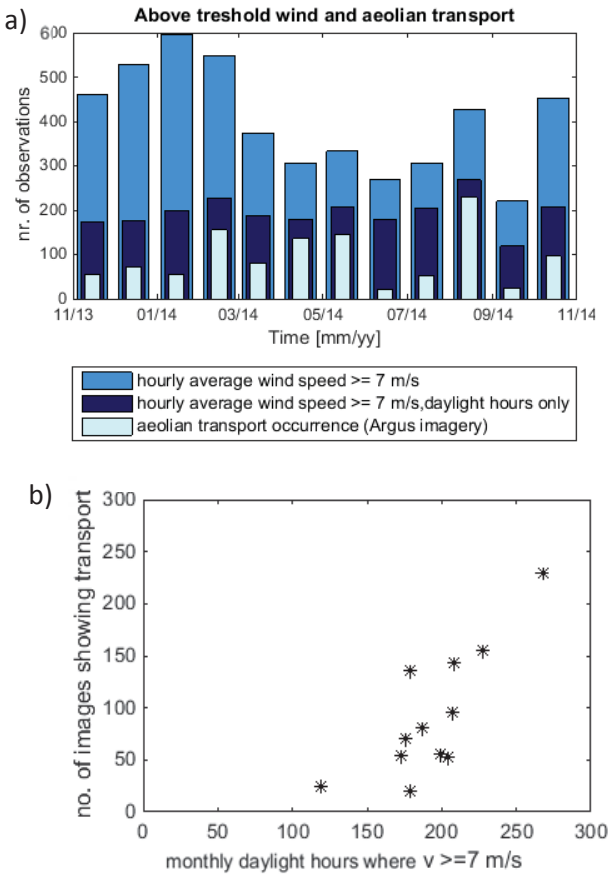

Figure 4. a) Monthly number of transport observations (from semi-hourly imagery), and monthly number of hours with wind speed above threshold speed for transport (7 m/s). b) Relationship between occurrence of transport and occurrence of above threshold wind speed during daylight hours.

Finally, returning to a possible explanation for the initially high rate of aeolian infill of the lake area, we looked into the number of hours of above threshold wind conditions in the first half year in comparison to other half year periods (Figure 5). The first six months did not have the most hours of above threshold wind speeds. However, when considering only the directional sectors that, according to the pattern of infill of the lake (Figure 2c), contributed most to the aeolian infill (Q2 to Q5), the first six months exhibited the most hours of above threshold wind speeds. Further study is needed, however, to address the magnitude of sand transport generated by these above threshold wind conditions.

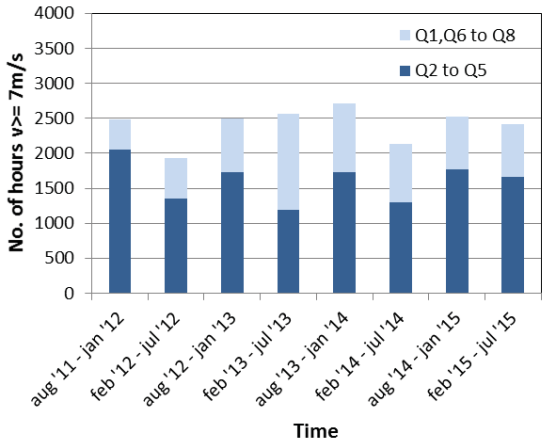

Figure 5. Temporal variation in the number of hours of above transport threshold wind conditions (≥ 7 m/s). Directional sectors Q1 to Q8 are defined in Figure 3e.

DISCUSSION

The use of video remote sensing is a powerful tool to link the scale of individual aeolian transport events to meso-scale aeolian sediment supply (*e.g.* Delgado-Fernandez and Davidson-Arnott, 2011). A limitation of using image data is that aeolian transport occurrence can only be identified as saltation occurs. Consequently, milder wind conditions during which only transport by creep occurs are not taken into account. Therefore, the 'threshold wind condition' we defined in this study cannot easily be compared to a threshold wind speed for initiation of motion.

The analysis in this study further showed that about 12% of the time aeolian transport occurred at the mega-nourishment during day-time. Assuming that day-time conditions for aeolian transport are representative of night-time conditions, this implies that per year, about 1000 hours of aeolian transport occurred.

With respect to the high transport rates in the first half year after construction, it is likely that apart from somewhat more windy conditions, also sediment sorting has played a role. A nourishment consists of unsorted sand of which the fines will be transported first, leaving coarser grains and shell fragments as an armoring layer at the surface of the nourishment (Van der Wal, 1998). Most likely this process contributed to the higher aeolian transport rates in the first half year after construction

CONCLUSIONS

In the first half year after construction of the Sand Motor mega-nourishment, the aeolian transport rates were highest, as the lake area filled in at a rate equivalent to an annual rate of $8 \cdot 10^4$ m^3/yr. In the years afterwards, transport rates decreased considerably, as the infill rate of the lake area reduced to about $1.9 \cdot 10^4$ m^3/yr. The first six months were somewhat more windy, but the large difference in infill rate is more likely explained by the sorting of the sand. Right after construction of the nourishment the fine sediment can be blown away, causing higher transport rates.

This study further showed that about 12% of the time aeolian transport (by saltation) occurred at the mega-nourishment, indicating that on an annual basis about 1000 hours of aeolian transport occurred. Transport events, occurring throughout the year, were dominated by winds from the South-West quadrant (72%), hence including obliquely offshore directed winds. In total, 33% of the transport events occurred during wind conditions with an offshore directed component, hence blowing sand back towards the sea.

From the combination of video image data and wind data, it was also derived that aeolian sand transport (by saltation) was only observed at hourly averaged wind speeds of at least 7 m/s. The monthly frequency of occurrence of above 7 m/s wind speed was reasonably well correlated with monthly frequency of occurrence of aeolian transport (r=0.79). Nevertheless, when hourly wind speed exceeded 7 m/s, transport was only observed about 23% of the time, indicating the importance of supply limiting conditions, and time variation therein, for aeolian transport from the Sand Motor

ACKNOWLEDGMENTS

This research is part of the NatureCoast program, funded by the Dutch Technology Foundation STW, which is part of Netherlands Organization for Scientific Research. We acknowledge Rijkswaterstaat for making available the Argus images and topographic data collected by 'SHORE Monitoring & Research'.

LITERATURE CITED

Delgado-Fernandez, I. and Davidson-Arnott, R., 2011. Meso-Scale Aeolian Sediment Input to Coastal Dunes: The Nature of Aeolian Transport Events. *Geomorphology*, 126(1-2), 217-232

Van der Wal, D., 1998. Effects of Fetch and Surface Texture on Aeolian Sand Transport on Two Nourished Beaches. *Journal of Arid Environments, 39*(3), 533-547.

Van der Weerd, A.J. and Wijnberg, K.M., 2015. Aeolian activity on a peninsula-shaped mega nourishment. *Proc. Coastal Sediments 2015*, San Diego, USA, 12p.

Journal of Coastal Research	SI	75	343-347	Coconut Creek, Florida	2016

Topographic Steering of Oblique Incident Winds Across a Foredune-Parabolic Topography, Mason Bay, Stewart Island, New Zealand

Sarah J. Wakes[†*], Michael J. Hilton[‡], and Teresa Konlechner[‡]

[†]Department of Applied Sciences
University of Otago
Dunedin, New Zealand

[‡]Department of Geography
University of Otago
Dunedin, New Zealand

www.cerf-jcr.org

www.JCRonline.org

ABSTRACT

Wakes, S.J.; Hilton, M.J., and Konlechner, T., 2016. Topographic steering of oblique incident winds across a foredune-parabolic topography, Mason Bay, Stewart Island, New Zealand. *In:* Vila-Concejo, A.; Bruce, E.; Kennedy, D.M., and McCarroll, R.J. (eds.), *Proceedings of the 14th International Coastal Symposium* (Sydney, Australia). *Journal of Coastal Research*, Special Issue, No. 75, pp. 343-347. Coconut Creek (Florida), ISSN 0749-0208.

Climate change modelling predicts increased westerly winds across southern New Zealand, with incident winds becoming more oblique on many beaches. Of interest is the effect these increasingly oblique winds will have on beach-foredune sand flux and dune morphodynamics. We need to model wind flows over these dunes in order to understand these potential changes. Mason Bay, Stewart Island, New Zealand experiences a range of incident winds, from southwest to northwest and, therefore, provides opportunities to both model and verify topographic steering. The dune systems comprise of a large, topographically simple (Type I) foredune, backed by long-walled, discrete parabolic dunes. We use Computational Fluid Dynamics (CFD) to predict the behaviour of winds of a range of obliquities and infer sediment flow over coastal dunes. The wind steering across the dune system is also be explored through the numerical modelling. Results of modelling wind flow from a range of incident wind directions and boundary conditions are presented. The results indicate that oblique incident winds are topographically steered shore-normal across the foredune and inland parabolic dunes topographies. Future changes in wind direction might, therefore, have significantly greater implications for foredune development compared with hinterland dunes.

ADDITIONAL INDEX WORDS: *CFD simulations, dune systems, flow deflection.*

INTRODUCTION

The effects of oblique winds on a coastal foredune system have been documented in a number of places (Hesp, 2015). These winds are topographically steered onshore as the flow approaches and crosses the seaward slope of the foredune (Rubin and Rubin, 2013, Walker *et al.*, 2009). Maximum deflection has been noted to occur for more oblique incident winds (Hesp *et al.*, 2015) with the degree of deflection depending on the height above the surface (Hesp *et al.*, 2015; Mikklesen, 1987; Walker *et al.*, 2009). There have been observations of related sand flux but this has not been quantified (Walker *et al.*, 2009; Walker *et al.*, 2006). Historically wind speed has been privileged over wind direction in importance for sediment transportation (Bauer *et al.*, 2012). Generally, flow deflection increases towards the dune crest and the greatest deflection occurs when incident winds approach the dune at moderate to high angles of obliquity (Hesp *et al.*, 2015; Mikklesen, 1987).

Some Environmental wind modelling has been used to study the effects of oblique winds on foredune systems (Hesp *et al.*, 2015). Computational Fluid Dynamics (CFD) was used to complement field data. A wind speed of 12.2m/s flow over a geometry consisting of a section of foredune with a constant surface roughness was modelled. Good agreement was reached with field data for deflection angle and wind incident wind angle between 30° and 70°, with the maximum deflection around 45° to shore normal. The angle of deflection was seen to diminish with height above the dune surface. This study demonstrated that CFD modelling is an effective method of aiding understanding for such wind flows but for applicability at other sites clarification of boundary conditions and investigation into wind flow over a larger domain is needed.

Computational Fluid Dynamics numerical modeling is being used to identify current, historic and suitable future foredune and hinterland morphologies in the study area. For Mason Bay, Stewart Island, New Zealand greater understanding is needed on the effects of topographic steering both on the foredune and in the deflation zone. The aim of the study is therefore to use Environmental wind modelling to predict topographic steering over a section (parabolic 6) of the Mason Bay dune system with a number of incident wind directions, two wind speeds and with variable or uniform dune surface roughness.

METHODS

Research work at the study site (Figure 1) has been ongoing for 10+ years and extensive records are available regarding the geomorphology, spread of Marram grass (*Ammophila arenaria*) and subsequent stabilization (Hart *et al.*, 2012, Petersen, Hilton and Wakes, 2011, Wakes *et al.*, 2010). A particular dune, named

DOI: 10.2112/SI75-069.1 received 15 October 2015; accepted in revision 15 January 2016.
*Corresponding author: sarah.wakes@otago.ac.nz

parabolic 6, was chosen as the study site and used in previous work (Hart *et al.*, 2012, Petersen, Hilton and Wakes, 2011, Wakes, 2013, Wakes *et al.*, 2008, Wakes *et al.*, 2010). The geomorphology consists of a relatively narrow beach, a steep Marram grass covered foredune and in its lee a sparsely vegetated parabolic dune (Figure 1). Previous CFD modelling has assumed an onshore wind and compared two and three dimensional simulations with field data with good agreement (Wakes, 2013, Wakes *et al.*, 2008, Wakes *et al.*, 2010). Validation of modelling parameters such as roughness height and cover and inlet conditions are therefore well known and tested for shore normal conditions (Wakes *et al.*, 2008; Wakes *et al.*, 2010). The surface geometry used was generated from LiDAR data (Wakes *et al.*, 2008).

The CFD code Fluent is used to solve the Reynolds-Averaged Navier-Stokes equations and the continuity equation using the finite volume method. In this study, the steady state Reynolds-Averaged Navier-Stokes (RANS) equations are considered with the RNG k-ε model (Yakhot and Orszag, 1986). Choice of the RNG k-ε model follows previous work (Hesp *et al.*, 2015; Wakes *et al.*, 2010).

The simulation cases undertaken are outlined (Table 1). Determination of the effect side and top boundary conditions, surface roughness and incident wind speed and direction have on the wind deflection angles are investigated. Only a section of the Mason Bay dune system is modelled to limit the size of the computational domain. For oblique winds one of theside boundaries as well as the inlet (sea) have a velocity boundary condition. The inlet boundary is straightforward to deal with, using a profile generated from flow over sea. Two options are compared here for the side boundary; as a free stream velocity at the appropriate incident wind angle (side inlet); or as a velocity profile generated from the opposite side of the domain (side profile). Roughness is either sand only (uniform) (Hesp *et al.*, 2015) or vegetation and sand in zones (variable) (Wakes *et al.*, 2008).

Shore normal wind direction was taken to be 0° for the CFD simulations, with positive angles indicating the wind direction becoming more northerly and negative angles indicating more southerly winds in the along shore direction. The measurement transect (Figure 1) has S8 at the toe of the foredune, S1 and S2 on the crest, S7 and S3 in the lee of the foredune and S4, 5 and 6 in the deflation plane of parabolic 6. The transect is at a 6° angle to shore normal.

Table 1. *Simulation Cases*

Wind angles	Wind velocities	Side BC	Top BC	Surface roughness
-15° and 15°	8 m/s	inlet profile	outflow symmetry	variable
-75° to 75°	8 m/s	inlet	outflow	variable
-45°	8 m/s 16 m/s	inlet	outflow	variable
-75°	8 m/s	inlet	outflow	variable uniform

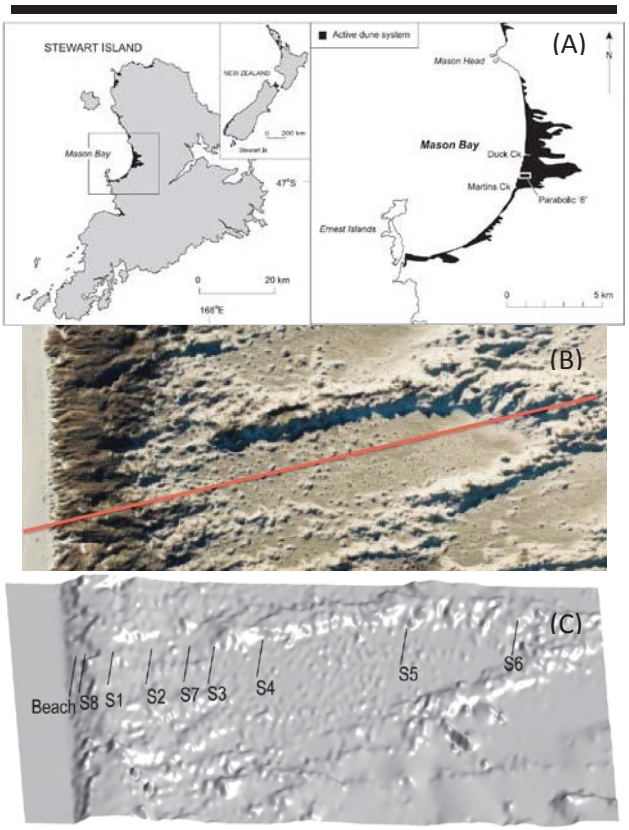

Figure 1. (A) Location of study site, Mason Bay, Stewart Island, New Zealand, (B) aerial photograph showing "parabolic 6", Mason Bay, Stewart Island, New Zealand. The line indicates the approximate position of the survey line and (C) the computational surface with measurement stations on the transect marked.

RESULTS

Mostly the different combinations of side and top boundary conditions deflect the wind in a similar way (Figure 2). The exception is the 15° incident wind angle case with side profile and top symmetry boundary conditions. This case resulted in the deflection angle oscillating around shore normal on the foredune. There was otherwise little difference between the simulations with other side or inlet boundary conditions. As a consequence of these initial simulations the top was chosen to be an outflow boundary condition and and the side boundary as an inlet velocity value for the remaining simulations.

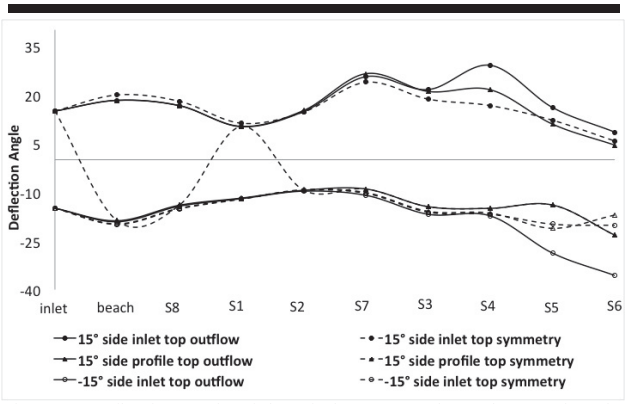

Figure 2. Deflection angle of the wind at 0.66m above dune surface for -15° and 15° incident wind angles with different side and top boundary conditions.

Surface roughness has some effect on the wind flow deflection angle for a -75° incident wind angle (Figure 3). On the beach there is little effect on deflection angle as the wind flow for both cases is over sand. On the foredune (S8 to S7) there are differences in deflection angle. The case with uniform surface roughness shows less steer than the case with variable surface roughness. For these simulations the foredune is heavily vegetated and therefore has a much higher roughness than sand. The -75° incident wind case therefore travels over this longer and rougher fetch (the stoss face of the foredune) slowing the flow down and therefore deflecting the flow more shore normal. This difference in deflection angle with surface roughness diminishes by S6.

Table 2. *Difference between angle of incident wind (-45°) and angle of wind at measurement station at 0.66m from dune surface for -45° incident wind case [positive values indicate the wind orientating to shore normal]*

Wind speed	Beach	S8	S1	S2	S7	S3	S4	S5	S6
8 m/s	-2.1°	5.6°	13.6°	18.8°	2.4°	5.4°	1.2°	36.8°	30.9°
16 m/s	-2.2°	5.5°	13.5°	18.8°	2°	7.1°	0.3°	36.2°	39°

The effect of the two different incident wind speeds on the flow deflection angle is seen (Table 2). There is minimum difference on the foredune (beach to S7) with only small differences in the deflation plane (S3 to S6). The main regions for flow deflection are on the foredune and between S4 and S5. By S6 wind deflection is an approximate -15° angle to shore normal.

Deflection of the wind over the foredune is most pronounced and of greatest value as the incident wind angle of the wind becomes more oblique (Figure 4A). For the southerly oblique wind directions wind speedup is most pronounced at a lower height above the dune surface (Figure 4B) with the maximum seen for shore normal flows. This pattern is repeated for northerly oblique wind directions. It should be noted that the crest of the foredune is relatively flat for around 15m and the wind speed after intial speedup drops off in this region. At both heights by the start of the lee slope there remains only a slight increase on the initial wind speed at the toe of the foredune. Most of the flow deflection occurs in the lee of the foredune. The deflation plane topography causes some local changes to the wind angle. There are some differences in wind deflection angle with height above the dune surface, with deflection more pronounced at the lower height of 0.66m (Table 3).

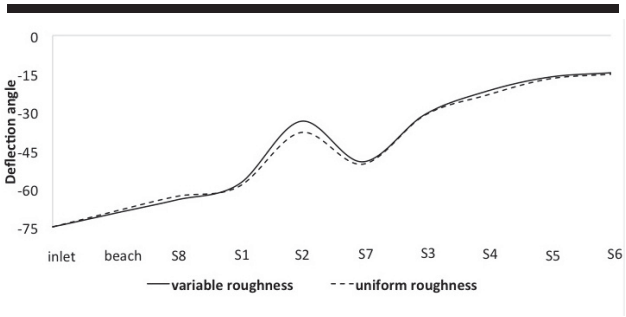

Figure 3. Deflection angle for -75° incident wind case with different surface roughness in the domain.

Table 3. *Difference in wind angle between incident wind angle to crest of the dune (S1) and back of the deflation zone (S6). Positive values indicates clockwise deflection (increasing angle value), negative values anticlockwise deflection (decreasing angle value).*

Angle Of Incident Wind	S8 to S1 (0.66m)	S8 to S1 (1.66m)	S8 to S6 (0.66m)	S8 to S6 (1.66m)
-75°	6.1°	6°	49.7°	49.7°
-60°	9.1°	8.2°	39°	38.5°
-45°	8°	6.9°	33.5°	32.7°
-30°	6°	4.8°	7°	5.7°
-15°	2.3°	1.3°	-21.3°	-22.8°
0°	-1.7°	-2°	-6.2°	-6.9°
15°	-6.5°	-6.1°	-8.2°	-8.5°
30°	-9.2°	-8.1°	-1.6°	-1°
45°	-10.4°	-8.8°	-6°	-4.1°
60°	-9.6°	-7.8°	-18.2°	-16.9°
75°	-10.8	-9.1	-27.3	-24.7

Whether there is an effect from the approach of the wind being from the northerly oblique direction (15° to 75°) or southerly oblique direction (-75° to -15°) can be seen (Figure 5A). There are some differences to be noted. The difference in wind deflection angle between stations S8 (toe of stoss face of foredune), S1 (crest of foredune) and S6 (end of deflation plane before the parabolic lobe) is shown (Table 3). Those incident winds at northerly oblique angles can be seen to have a greater deflection to shore normal than those approaching from the southerly oblique angles. For southerly oblique angles (-75° to -15°) the greatest deflection on the foredune is for incident wind angles in the range -75° to -30°, with the final wind angle clusters around a -15° angle to shore normal at S6. The exception is the -15° incident wind case where there is a deflection away from shore normal at S6. For northerly oblique angles (15° to 75°) the greatest deflections towards shore normal are for incident wind angles in the range of 30° to 75° on the foredune. There is little clustering for these cases by S6 with only the 60° and 75° incident wind cases showing any deflection

from the original incident wind angle. The reduction of wind deflection with height is more pronounced for the northerly oblique winds.

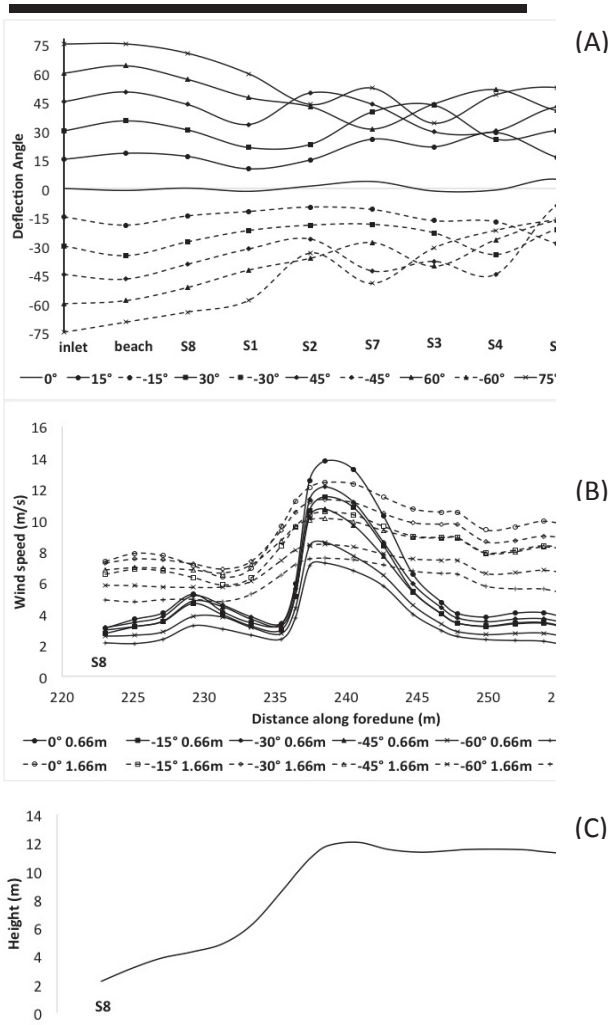

Figure 4. (A) The deflection angle at a 0.66m height above the dune surface along the transect of dune for incident wind angles -75° to 75°, (B) wind speed at points along the foredune from S8 to S1 for incident wind angles -75° to 0° at heights 0.66m and 1.66m above the dune surface and (C) the foredune profile from S8 to S1.

DISCUSSION

This work has explored the effect side and upper boundary conditions can have on simulation of deflection angles with an oblique incident wind. There were differences found in this study from previous work on flow deflection (Hesp *et al.*, 2015). These can be attributed to the complex dune topography and variable surface roughness at Mason Bay.

Use of a symmetry condition at the upper boundary of the domain proved to be only suitable for shore normal flows. When the flow is not shore normal one of the side boundaries has to be an outflow and so the interaction of the outflow and symmetry at the side/top interface is problematic, likely because of vertical components to the flow. It is therefore much more appropriate to have outflows for both boundaries and to emphasis the importance of such pre tests for each geometry. The profile side boundary condition was not a more suitable approach for the particular geometry considered in this study. Here the parabolic dune and foredune are not similar enough at both sides of the domain for this approach to work.

Vegetation roughness on the foredune surface was seen to increase the deflection angle at the crest of the foredune. The large expanse of the deflation plane with sand roughness then smooths out these local differences. As the angle of the southerly incident wind becomes more oblique from shore normal the more exposure there is of the foredune to the wind flow. The vegetation roughness then slows the flow as it travels over the foredune resulting in a greater flow deflection. For less oblique winds the flow is over more of the beach and therefore encounters the lower roughness of sand before it reaches the crest of the foredune. Roughness therefore has a small role to play in the deflection of the wind over vegetated dunes as has been seen for shore normal winds (Wakes, 2013; Wakes *et al.*, 2008).

Agreement with Hesp *et al.* (2015) on the speedup relationship with incident wind angle has been verified in this study but the wind deflection angle patterns do not follow as closely. There is a small but distinct steer north in the deflation zone for all cases because of topographic effects. By extending the simulation to the deflation plane and parabolic dune behind the foredune the extent to which the wind is deflected beyond the foredune can be seen. The local topography has a significant effect on the deflection angle, especially near the lobe and arms of the parabolic dune. Even shore normal winds deflect due to local deflation plane topography. The simulations show that the deflation plane and parabolic dune topography influences the wind deflection angle for all cases modelled.

The approach of the wind (North or South of shore normal) makes some difference in the resulting deflection angles. There is a shorter fetch North due to the limits of the computational domain and therefore less rough topography for the wind to pass over before reaching the foredune. The parabolic dune is also not symmetrical or shore normal and has a longer arm to the north than to the south. For some of the flows from the South and all of those from the North the oblique wind encounters an arm of the parabolic. This barrier to the wind flow is modifying the flow deflection angle. For the two smallest oblique angles from the South the dune arm is more parallel to the flow direction so this modification effect is reduced

The study indicates that local dune topography and vegetation cover has a significant effect on studies of oblique incident winds and consequential wind deflection. This then has an impact on the wind speeds and sediment transportation across such systems. More oblique incident wind angles may mean less sand transported from the beach over the foredune and into the deflation zone. With more oblique winds there may be more sand moved into the deflation zone and the parabolic dunes may transgress in the along shore direction.

CONCLUSIONS

A study of oblique incident winds and the flow deflection over a complex dune system has been undertaken using Computational Fluid Dynamics. This work clarifies appropriate roughness, boundary and inlet conditions for such simulations as well as gaining insights into how flow is deflected over this complex topography. Building on previous published work this study has clarified that wind speed up is greater for shore normal winds and at heights closer to the dune surface for the dune system considered. It has established that local geometry effects can have significant effect on flow deflection angles both on the foredune and in a deflation zone. The roughness due to vegetation is important to consider as it has the effect of increasing flow deflection. Boundary and inlet conditions for the simulations are important but are likely study specific. It is crucial that simulation models are used to understand the site specific topography steering.

ACKNOWLEDGMENTS

This work was undertaken as part of a University of Otago Research Grant.

LITERATURE CITED

Bauer, B.O.; Davidson-Arnott, R.; Walker, I.J.; Hesp, P.A., and Ollerhead, J., 2012. Wind direction and complex sediment transport response across a beach-dune system. *Earth Surface Processes and Landforms*, 37, 1661-1677.

Hart, A.; Hilton, M.; Dickinson, K., and Wakes, S., 2012. The impact of Ammophila foredune development on downwind aerodynamics and parabolic dune development. *Journal of Coastal Research*, 28(1), 112-122.

Hesp, P.A.; Smyth, T.A.G.; Nielsen, P.; Walker, I.J.; Bauer, B.O., and Davidson-Arnott, R., 2014. Flow deflection over a foredune. *Geomorphology*, 230, 64-74.

Hesp, P.A.; Smyth, T.A.G.; Nielsen, P.; Walker, I.J.; Bauer, B.O., and Davidson-Arnott, R., 2015. Flow deflection over a foredune. *Geomorphology*, 230, 64-74.

Jackson, D.W.T.; Beyers, J.H.M.; Lynch, K.; Cooper, J.a.G.; Baas, A.C.W., and Delgado-Fernandez, I., 2011. Investigation of three-dimensional wind flow behaviour over coastal dune morphology under offshore winds using computational fluid dynamics (CFD) and ultrasonic anemometry. *Earth Surface Processes and Landforms*, 61, 113-1124.

Mikklesen, H.E., 1987. Wind flow and sediment transport over a low coastal dune, 60p.

Petersen, P.; Hilton, M. and Wakes, S., 2011. Evidence of aeolian sediment transport across an Ammophila arenaria Dominated foredune, Mason Bay, Stewart Island. *New Zealand Geographer*, 67(3), 174-189.

Rubin, D.M. and Rubin, A.M., 2013. Origin and lateral migration of linear dunes in the Qaidam Basin of NW China revealed by dune sediments, internal structures and optically stimulated luminescence ages. *Geological Society of America Bulletin*, 125, 1943-1946.

Smyth, T.A.G.; Jackson, D.W.T., and Cooper, J.A.G., 2011. Computational Fluid Dynamic Modelling of Three-dimensional airflow over dune blowouts. *In*: *Proceedings 11th International Coastal Symposium (Szczecin, Poland).* Journal of Coastal Research, Special Issue No. 64, pp. 314-318.

Swart, N.C. and Fyfe, J.C., 2012. Observed and simulated change in southern Hemisphere surface westerley wind-stress. *Geophysical Research Letters*, 39, L16711.

Wakes, S., 2013. Three-dimensional Computational Fluid Dynamic experiments over a complex dune topography. In: Conley, D.C., Masselink, G., Russell, P.E. and O'Hare, T.J. (eds), *Proceedings 12th International Coastal Symposium (Plymouth, England).* Journal of Coastal Research, Special Issue No. 65, pp. 1337-1342.

Wakes, S.; Maegli, T.; Dickinson, K., and Hilton, M., Year. Published. Three-dimensional flow simulation over a complex dune system. Environmental Problems in Coastal Regions, 2008 (*New Forest, UK)*: WIT Press, 221-230.

Wakes, S.J.; Maegli, T.; Dickinson, K.J.M., and Hilton, M.J., 2010. Numerical modelling of wind flow over a complex geometry. *Environmental Modelling & Software*, 25237-247.

Walker, I.J.; Davidson-Arnott, R.; Hesp, P.A.; Bauer, B.O., and Ollerhead, J., 2009. Mean flow and turbulence responses in airflow over foredunes: new insights from recent research. *In*: *Proceedings 10th International Coastal Symposium.* Journal of Coastal Research, Special Issue No. 56, pp. 366-370.

Walker, I.J.; Hesp, P.A.; Davidson-Arnott, R., and Ollerhead, J., 2006. Topographic steering of alongside airflow over a vegetated foredune: Greemwich Dunes, Prince Edward Island, Canada. *Journal of Coastal Research*, 22, 1278-1291.

Yakhot, V. and Orszag, S.A., 1986. Renormalization group analysis of turbulence: Basic theory. *Journal of Scientific Computing*, 1(1), 3-51.

Journal of Coastal Research	SI	75	348-352	Coconut Creek, Florida	2016

Surf-Swash Interactions on a Low-Tide Terraced Beach

Rafael Almar*‡, Pedro Almeida‡, Chris Blenkinsopp†, Patricio Catalan††

‡IRD-LEGOS (CNRS/CNES/IRD/Université de Toulouse) , Toulouse, France

*UTFSM, Valparaiso, Chile

† University of Bath, Bath, UK

††University of Abomey-Calavi
ICMPA-UNESCO Chair
Cotonou, Republic of Benin

www.cerf-jcr.org

www.JCRonline.org

ABSTRACT

Almar, R.; Almeida, P.; Blenkinsopp,C., and Catalan, P., 2016. Surf-swash interactions on a low-tide terraced beach. *In:* Vila-Concejo, A.; Bruce, E.; Kennedy, D.M., and McCarroll, R.J. (eds.), *Proceedings of the 14th International Coastal Symposium* (Sydney, Australia). *Journal of Coastal Research*, Special Issue, No. 75, pp. 348-352. Coconut Creek (Florida), ISSN 0749-0208.

Through an integrated approach, this paper investigates the role of coupled surf-swash dynamics on outgoing waves using data collected at a low-tide terraced beach, Grand Popo, Benin (Gulf of Guinea, West Africa). Observed reflection is 8 %. Analyses are conducted from deep water directional wave spectra measurements, daily beach surveys and remote video measurements. Our results show that the swash can be a non-negligible component of the nearshore energy balance (14% of total dissipation) and is closely tied to reflection. Reflection thus depends on waves at swash inception (offshore waves and surf zone saturation), and shoreface slope varying with tide and morphological evolution. An outgoing cut-off frequency (shortest reflected waves) can be linked to swash saturation with a strong dependence on shoreface slope. A phase-resolving Boussinesq model was validated and used to investigate the influence of terrace width, upper shoreface slope and tidal elevation over the terrace. This papers puts forward the role of the coupled system surf-swash and underlines potential key interactions between a rapid shoreface evolution and surf zone hydro-morphodynamics.

ADDITIONAL INDEX WORDS: *Grand Popo, Benin (Gulf of Guinea), reflection, standing wave, incoming and outgoing waves.*

INTRODUCTION

There is a potential for substantial wave reflection at the coast depending on hydrodynamic and morphological conditions. Understanding the mechanisms at the origin of such reflection and the nature of reflected waves is crucial for various aspects of coastal science including energy balance, standing and edge wave patterns and feedback with incoming waves, and resulting shoreface evolution. Pioneering studies based on laboratory experiments showed a link between reflection and the ratio of wave steepness to beach slope, hence vertical acceleration versus gravity, which can be summarized by the surf-similarity parameter (Battjes *et al.*, 1974).

Field observations have shown that these predictions are poor for irregular waves and complex bathymetric profiles Elgar *et al.* (1994). More recent studies, although mainly focused on engineering structure design (Sutherland *et al.* (1998), among others), have underlined the key role played by swash zone dynamics in controlling the phase and energy of reflected waves. Reflection is linked to a parameter comparing swash "wavelength" with horizontal excursion originally developed by Hughes *et al.* (1995).

Significant research effort has been devoted to energy saturation in the nearshore, the surf zone saturation being linked to the height-to-depth ratio and describing the limit between non-breaking and breaking waves, and the remaining energy being transferred to larger frequencies and non-oscillatory dynamics (*i.e.* setup). Sallenger *et al.* (1985) observe that the height-to-depth ratio might increase with local slope and can be rather independent of deepwater wave steepness. It has been extensively observed that wind- and swell-waves (T<20 s) are generally saturated whereas longer infragravity waves (T>20 s) rarely saturate Ruessink *et al.* (1998) although recent observations have shown that saturation could extend to the infragravity band (Ruggiero *et al.*, 2004; Senechal *et al.*, 2011 and that infragravity wave can be dissipated through breaking (de Bakker *et al.*, 2014). This high-frequency band saturation reflects surf-zone transformations but is also thought to result from non-linear swash zone processes such as swash-to-swash interaction Brocchini *et al.* (2008), bottom friction and infiltration. Supposedly crucial, the link between swash characteristics and reflection has not yet been clearly established, in particular the role of swash saturation for broadband spectra.

In this paper we revisit the link between surf and swash dynamics and reflection from field observations collected at a low tide terraced beach, Grand Popo beach, Benin, in the Gulf of Guinea (West Africa), where largest reflections on earth have been reported (Ardhuin and Roland, 2012). We show that reflection is mostly governed by surf zone saturation over the terrace, whereby the reflected spectrum essentially depends on swash slope.

DOI: 10.2112/SI75-070.1 received 15 October 2015; accepted in revision 15 January 2016.
*Corresponding author: rafael.almar@ird.fr

METHODS

An intensive field experiment was conducted during March 2014 at Grand Popo, Benin (Gulf of Guinea, West Africa), a sandy coast exposed to South Atlantic long swells (Almar *et al.*, 2014). Grand Popo beach is an intermediate-reflective (Ω>2), micro-tidal, wave-dominated (annual mean, Hs=1.4 m, Tp=9.4 s, SW, RTR~1), medium grain-sized $D50$=0.6 mm, alongshore uniform, low-tide terraced beach (Figure 1). Incoming and reflected waves and tide were measured in 10-m depth, The terrace was instrumented with 2 lines which included pressure sensors, Accoustic Doppler Velocimeters, and two cross shore arrays of 20 video-poles (every m) for measuring at high frequency (25 Hz) wave transformation across surf and swash zones.

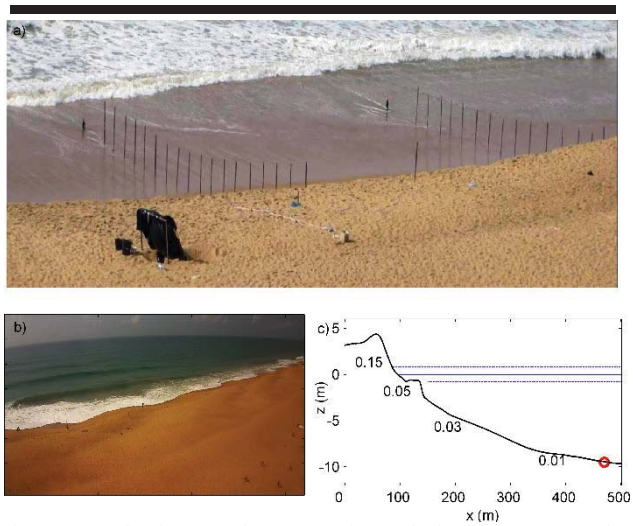

Figure 1. Study site, Grand Popo, Bénin. a) deployment setup on the terrace, b) image from video camera and c) bathymetric profil. Red circle shows ADCP location.

The 10-day experiment included daily differential GPS topographic surveys, deep water (11-m) directional wave measurements using an Acoustic Doppler Current Profiler (ADCP), and shore-based video swash monitoring.

Timeseries of runup were computed from 2-Hz cross-shore video spatio-temporal images collected during daylight hours, and extracted using a Radon Transform method (see Almar *et al.*, 2014a). The 3-colourband timestacks are first converted into grayscale and the Radon Transform is applied to detect motion. This methods offers a reasonable proxy of instant runup motion, although the thin backswash layer can sometimes be missed.

In Results Section, swash zone energy E_{swash} is approximated from the commonly used formula (Guedes *et al.*, 2013):

$$E_{swash}=4\sigma\, S\, tan\alpha \qquad (1)$$

where S is runup timeseries derived from video and αlocal swash slope. The surf zone dissipation due to breaking $D_{breaking}$is estimated from the roller characteristics following Haller *et al.*, (2009):

$$D_{breaking} = \rho\, gAsin\theta cos\theta/T \qquad (2)$$

where g is the gravitational constant, θ a free parameter accounting for roller inclination (taken as ~6° from literature), and T the roller period, and $A= 0.11(L_r/cos\theta)^2$ with L_r the roller length estimated from cross-shore video spatio-temporal images.

Numerical computations are conducted using the phase resolving fully non-linear 4th-order finite volume Boussinesq model SERR1D (Cienfuegos *et al.*, 2010). This model includes a parameterization for the wave-breaking energy dissipation.
The model has been previously validated with laboratory data for very non-linear conditions on a gently sloping beach (Michallet *et al.*, 2014). The model showed good performances in representing both short-wave dynamic and energy transfer to infragravity band.

RESULTS

Figure 2 shows timeseries of offshore hydrodynamic forcing (wave and tide), shoreface morphological and breaking over the terrace derived from video. Wave height has decreased over time, together with an increase of tidal range and a steepening of the

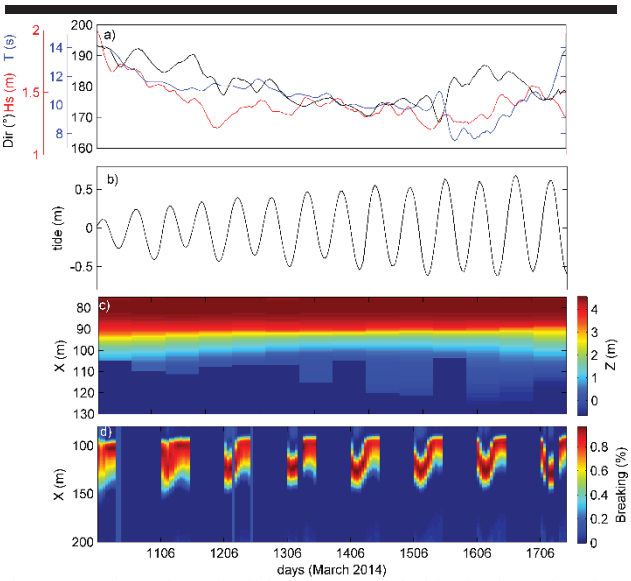

Figure 2: Timeseries of offshore wave and tide forcing, shoreface evolution and breaking over the terrace from video.

upper beach. Breaking over the terrace was largely affected by tidal modulation. Reflection R reaches 8% on average, through varying substantially over time from 4 to 12% (Figure 4).

Influence of surf and swash processes on reflection

The relative contribution of surf and swash zones in the dissipation of wave energy is shown in Figure 3. $D_{breaking}$, E_{swash} and R vary with offshore wave, tide and morphological evolution. A multiple linear regression shows that $D_{breaking}$ and E_{swash} dissipate 71 and 14 % of E_{inc} respectively, though varying substantially over time (from 3 to 12 %, Figure 4.a). E_{swash} can even be predominant at some specific moments, *e.g.* at high tide when breaking is weak over the terrace. In the meantime, E_{swash} contribution to R rises up to 62%. This is in line with what has

been observed elsewhere at dissipative beaches (*i.e.* intense breaking over the terrace), where the surf zone saturation may extend to the infragravity band (de Bakker *et al.*, 2014; Senechal *et al.*, 2011), resulting in a weak dependence of R on the shoreface slope and swash dynamics. For such conditions, the swash could be scaled only through deep-water parameters (Guza *et al.*, 1982), and the beach only introduces more scatter in the regression. The role of swash in modulating the reflected spectrum is investigated in the next section.

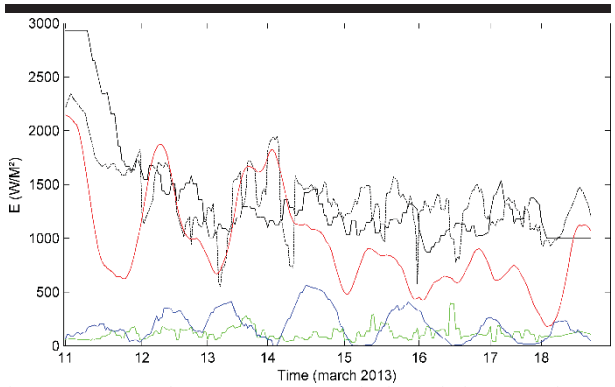

Figure 3. Nearshore wave energy budget during Grand Popo experiment. Incoming energy at 11-m depth (solid black), energy dissipated by the breaking (red), swash energy (blue), reflected energy (green) and reconstructed incoming energy from multiple linear regression (black dashed line).

Reflection cut-off frequency

Swash energy spectra are computed from 20 min of video-derived timeseries. It is noteworthy that the saturation extends into the infragravity band (T>20 s) at dissipative beaches whereas the swell-band might be unsaturated at reflective beaches such as Grand Popo. With the idea of linking swash saturation extent with reflection, and following the method described in Ruessink *et al.* (1998), the lowest saturated frequency is extracted from the spectra (Figure 5) as a swash cut-off period fc_{swash} (Figure 4). The highest reflected frequency $fc_{offshore}$ is also computed from offshore wave directional spectra. A reasonable fit (r^2=0.42, significant at the 95% level) is obtained between fc_{swash} and $fc_{offshore}$ with only a minor bias, $fc_{offshore}$ =0.89 fc_{swash}. This link shows evidence of a feedback between swash dynamics and the whole nearshore domain, which includes incoming and outgoing wave interaction and resulting standing waves.

Contrary to that found for peak swash frequency or outgoing peak frequency (fp), $fc_{offshore}$ appears to be relatively independent of incoming waves. The correlation of $fc_{offshore}$ is larger with α(0.51) than with $f_{offshore}$(0.32).This clearly indicates that $fc_{offshore}$ essentially depends on α and not the incoming waves.

Model validation

The skills of the Serr1D model in describing wave transformation over the terrace and reflection is tested here. The model is first compared to field observations over the full experiment duration. 20-min of surface elevation timeseries from ADCP are propagated over real bathymetry. Figure 4 shows that the model reproduces the frequency transfers that include secondary wave generation at high tide and infragravity at low tide. Reflection (computed using Radon Transform separation, see Almar *et al.*, 2014) is reasonably reproduced, together with breaking intensity over the terrace, estimated from the breaking index $\gamma=H_b/d$, H_b and d being breaker height and depth, respectively. Slope at waterline α values (accounting for tide and wave-induced setup) are similar, despite that bathymetric profile was chosen constant in the model and cannot reproduce the observed flattening trend. This, together with fc_{swash} and $fc_{offshore}$ that show largest discrepancies, need to be further investigated. The model is used in the next Section to investigate the influence of terrace width, upper slope and tide on reflection.

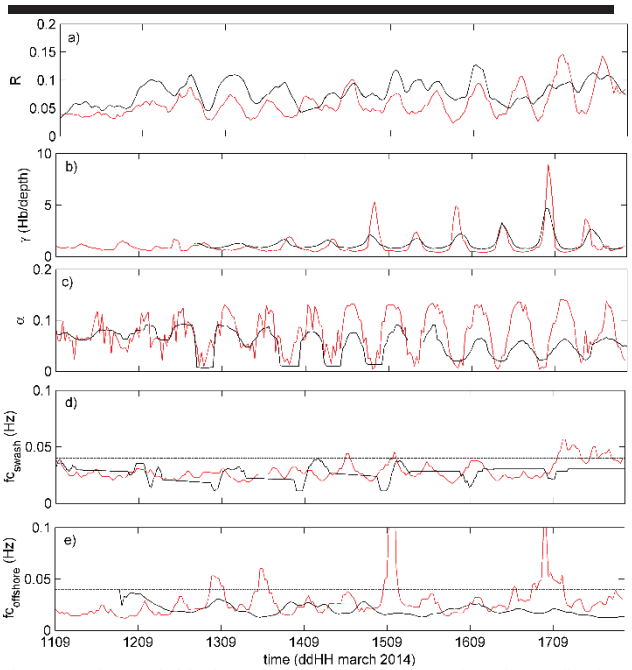

Figure 4. Observed (black) and modeled (red) timeseries of a) Reflection R, b) breaking index $\gamma=H_b/d$, c) shoreface slope α (at the waterline, taking into account for setup and tide) and cut-off frequency computed from d) horizontal runup fc_{swash} and e) offshore spectra $fc_{offshore}$.

DISCUSSION

Once validated, the model is used in Figure 6 to determine the modulation played by the terrace width, upper shoreface slope and tide on the interaction between outgoing and incoming waves in the surf zone. An increase of the terrace width moves the system toward a flatter beach and wider dissipative surf zone, which enhances wave frequency transfer to the infragravity band. Reflected energy increases with the upper shoreface slope, and the cut-off frequency shifts toward shorter periods. The control of outgoing component, through the enhancement/decrease of breaking, on incoming waves increases. As a result, incoming spectrum shifts toward the

outgoing one and, interestingly, the overall trapped energy increases which is a resonant condition.

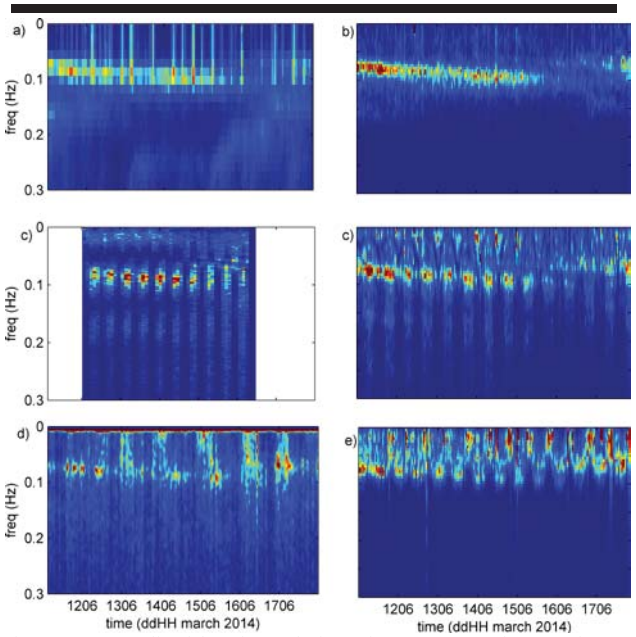

Figure 5. Normalized hourly evolution of spectra over the experiment duration for field (left) observation and (right) model at (upper panels) 11-m depth (ADCP), terrace (pressure sensors) and runup (from video).

CONCLUSIONS

In this paper we investigate the link between swash and surf zone dynamics at the low-tide terraced Grand Popo beach, Benin. Our observations, combining video imagery of swash and surf zone as well as deep water wave spectra, underline the key role played by swash in the reflection (8 % observed) mechanism and feedback on incoming waves which leads to quasi-standing wave or even resonance. Swash contributes to 14 % of nearshore energy dissipation and its link with reflection increases from low to high tide (when breaking is limited). A good agreement was found between a cut-off frequency *Fc* of reflected waves computed from deep water spectra and retrieved from swash saturation (r^2=0.42, $fc_{offshore}=0.89fc_{swash}$). Unlike reflection *R*, *fc* uniquely depends on shoreface slope α.

A Boussinesq model was validated with these challenging reflective conditions and showed good skills at retrieving key parameters. The model was later used to investigate the influence of the terrace width, upper slope, and tide on reflected component and its interaction with incoming waves. The most striking influence is played by the upper shoreface slope which closely controls the outgoing waves, but also incoming waves through a positive feedback when frequencies coincide which enhances breaking rate at particular frequencies.

AKNOWLEGEMENTS

Grand Popo exp. supported by French INSU/CNRS EC2CO-LEFE/IRD, UNESCO co-chair ICPMA/IPB. We are greatly indebted to the naval services of Benin at Grand Popo for their logistic support during the field experiment and for allowing the installation of the permanent video system on the semaphore. This research has received support from French grants through ANR (COASTVAR: ANR-14-ASTR-0019).

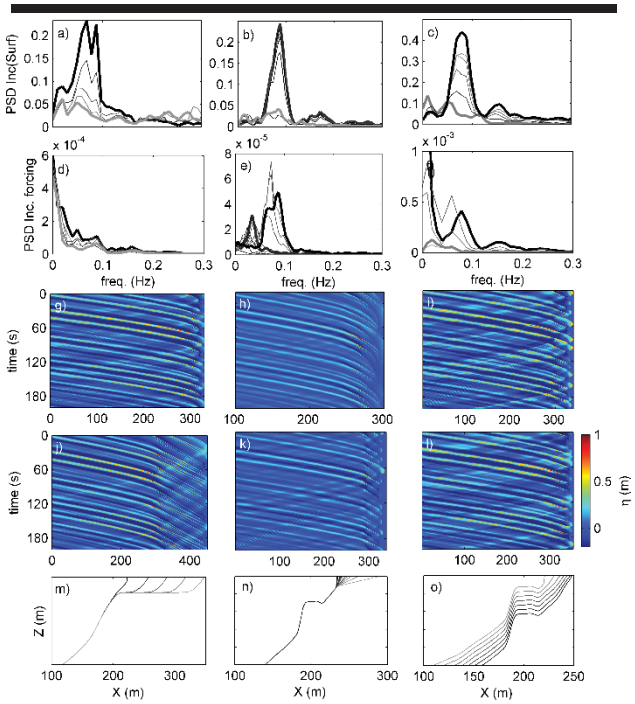

Figure 6. Numerical sensitivity analyze of (upper panels) incoming and (second panels) temporal form of the forcing parameter (see Ruju *et al.*, 2013) $\gamma(t)=\eta_{inc}/(tide+\eta_{out})$ (spectra at the breakpoint)for varying (left) terrace width (from 0 to 60 m), (centre) upper shoreface slope (from 0.01 to 0.15) and (right) tide (from 0.5 to 1.5 m). In upper panels, thick black and grey lines are lowest and largest values respectively of parameters, shown as Hovmoller surface elevation diagram in panels g-l. In lower panels (m-o) are shown bathymetric profiles.

LITERATURE CITED

Ardhuin, F. and Roland, A., 2012. Coastal wave reflection, directional spread, and seismoacoustic noise sources. *J. of Geophysical Research,* 117, C00J20

Almar, R.; Du Penhoat, Y.; Honkonnou, N.; Castelle, B.; Laibi, R.; Anthony, E.; Senechal N.; Degbe, G.; Chuchla, R.; Sohou, Z.; Dorel, M., and 2014. The Grand Popo experiment, Benin, *Journal of Coastal Research*, SI 70, 651-656, ISSN 0749-0208

Almar, R.; Michallet, H.; Cienfuegos, R.; Bonneton, P.; Ruessink B.G., and Tissier, M., 2014. On the use of the Radon Transform in studying nearshore wave dynamics, *Coastal Engineering*, 92, 24-30

Battjes, J., 1974. Surf similarity. *14th Coastal Engineering Conference, Am. Soc. Of Civ. Eng*., Copenhagen, Denmark, 466-480

Brocchini, M., and Baldock, T., 2008. Recent advances in modeling swash zone dynamics: Influences of surf-swash interaction on nearshore hydrodynamics and morphodynamics. *Reviews of Geophysic,s* 46(3), RG3003

Cienfuegos, R.; Barthelemy, E., and Bonneton, P., 2010a. A wave-breaking model 34 for Boussinesq-type equations including roller effects in the mass conservation equation. *J. Waterw. Port Coastal Oc. Eng.* 136, 10-26

de Bakker, A.; Tissier, M., and Ruessink, B., 2014. Shoreline dissipation of infragravity waves. *Continental Shelf Research,* 72(1), 73–82

Elgar, S.; Herbers, T., and Guza, R., 1994. Reflection of ocean surface gravity waves from a natural beach. *J. Physical. Oceanogr.* 24(7), 1503-1511

Guedes, R.; Bryan, K., and Coco, G., 2013. Observations of wave energy fluxes and swash motions on a low-sloping, dissipative beach. *Journal of Geophysical Research* 118(7), 1–19

Guza, R. and Thornton, E., 1982. Swash oscillations on a natural beach. *J. Geophys. Res.,* 87, 483–491.

Haller, M.C. and Catalan, P., 2009. Remote sensing of wave roller lengths in 325 the laboratory. *J. Geophys. Res.,* 114, C07022.

Hughes, S. and Fowler, J., 1995. Estimating wave-induced kinematics at sloping structures. *Journal of Waterway, Port, Coastal, and Ocean Engineering,* 121(4), 209–215.

Michallet, H.; Ruessink, G.; Rocha, M.V.L.; de Bakker, A.; van der A,D.; Ruju, A.; Silva, P.A.; Sénéchal, N.; Marieu, V.; Tissier, M.; Almar, R.; Abreu, T.; Birrien, F.; Vignal, L.; Barthélemy, E.; Mouazé, D.; Cienfuegos, R., and Wellens, P., 2014. GLOBEX: Wave dynamics on a shallow sloping beach, , *Proceedings of the HYDRALAB IV Joint User Meeting, Lisbon,* July 2014

Ruessink, B.; Kleinhans, M., and Van den Beukel, P., 1998. Observations of swash under highly dissipative conditions. *J.Geophys. Res.,* 103, 3111–3118.

Ruggiero, P. and Holman, R., 2004. Wave run-up on a high-energy dissipative beach. *J. Geophys. Res* C06025.

Ruju, A.; Lara, J.L.; Michallet, H.; Sénéchal, N., and Losada, I.J., 2013. Transient swash motions on a gently sloping beach. *Proceedings Coastal Dynamics,* 2013

Sallenger, A. and Holman, R., 1985. Wave energy saturation on a natural beach of variable slope. *J. Geophys. Res.,* 90-C6/11, 939–944.

Senechal, N.; Coco, G.; Bryan, K., and Holman, R., 2011. Wave runup during 355 extreme storm conditions. *Journal of Geophysical Research – Oceans,* 116, C07032.

Sutherland, J. and O'Donoghue, T., 1998. Characteristics of wave reflection spectra. *J. Waterw. Port Coastal Ocean Eng.,*124(6), 303–311.

Journal of Coastal Research	SI	75	353-357	Coconut Creek, Florida	2016

Seasonal Variations in Recovery Timescales of Shorelines on an Embayed Beach

Melanie Biausque [†*], Nadia Senechal[†], Brice Blossier[††], and Karin R. Bryan[‡]

[†]University of Bordeaux, UMR CNRS 5805-EPOC, Talence, F-33405, France

[‡] Coastal Marine Group, School of Science, University of Waikato, Hamilton, New Zealand

[††] MARUM, Center for Marine Environmental Sciences, University of Bremen, Leobener Strasse 28359 Bremen, Germany

www.cerf-jcr.org

www.JCRonline.org

ABSTRACT

Biausque, M.; Senechal, N.; Blossier, B., and Bryan, K.R., 2016. Seasonal variations in recovery timescales of shoreline change on an embayed beach, Proceedings of the 14th International Coastal Symposium (Sydney, Australia). Journal of Coastal Research, Special Issue, No. 75, pp. 353-357. Coconut Creek (Florida), ISSN 0749-0208.

Video images acquired during ten years (from January 1999 until June 2009) were analyzed to study cross-shore and alongshore variability of the shoreline on an embayed beach at Tairua Beach (New Zealand). Cross-shore landward migrations occur not only due to high energetic events (such as storms), but are a result of a mix of different parameters. In particular the shoreline of embayed beaches experiences rotation events during which opposite accretion and erosion patterns are observed at the extremities of the beach. When the beach is in an unrotated state, the erosion of the shore is accentuated. The notion of dynamic equilibrium between morphology and wave energy is common approach to understanding the drivers of such shoreline variations. Therefore, to quantify erosion and accretion rates, we used an empirical shoreline prediction model. In this application of the model, we showed that seasonality exists in these rates, between austral summer and winter. The difference in these rates could be because of the influence of the beach rotation on recovery periods. Indeed, the winter beach is generally in a more rotated state than the summer beach.

ADDITIONAL INDEX WORDS: *Morphological change, beach rotation, beach recovery, embayed beach*

INTRODUCTION

With more than 66% of the population living within 100 km of a coastline, sandy beaches are environments whose dynamic behavior can be associated with severe economic impacts. Not only modified by humans, they are also affected by hydrodynamic, atmospheric and morphologic conditions that occur over a range of timescales. Wright and Short (1984) proposed a classification of sandy beaches based on grain size and wave energy. Supported by daily observations from a microtidal site, they showed that during higher energy conditions, the slope of the beach decreases and wave energy is progressively dissipated: the beach is in a 'dissipative' state. Conversely, three-dimensional structures appear when calm conditions occur. Between these two extreme states, four dynamic intermediate states are described with the capacity of quick changes between these different states. This classification supports the principle of a dynamic equilibrium between beach morphology and forcing.

A concept, based on the 'memory' of the beach, describes the reaction of a sandy beach as a function of present and antecedent morphodynamic and hydrodynamic conditions. This is called 'the equilibrium beach profile'. For example, if a beach has already been eroded by a storm, the reserve of sand of the beach-face is minimal and the erosion rate of a new storm decreases (Yates *et al.*, 2009).

Embayed beach behavior is restrained by the presence of hard rock headlands. Accretion/erosion of embayed beaches can occur in both cross-shore and longshore directions. Cross-shore variability is due to sediment exchanges between the shore and the offshore (Harley *et al.*, 2011). Some papers present the possibility of predicting shoreline position of open beaches by including cross-shore exchange and an equilibrium (or disequilibrium) beach profile (*e.g.* Davidson *et al.*, 2013). In these cases, alongshore variations take place in response to alongshore energy flux changes. This process called 'rotation' is described as the movement landward (erosion) or seaward (accretion) of the shoreline (Foster, 2012). Rotation has been observed on some pocket and embayed-beaches (Bryan *et al.*, 2013; Foster, 2012; Turki *et al.*, 2012; van de Lageweg *et al.*, 2013).

In the most recent decades, a significant number of studies have been done on long-term and short-term sandy beach erosion (*e.g.* Wright *et al.*, 1985), and the possible link between shoreline recession and anthropogenic activities (*e.g.* Frihy and Komar, 1993). There is also much recent interest on the morphodynamic processes leading beach state transitions, using video imaging techniques and numerical modeling (*e.g.* Strauss & Tomlinson, 2009). However, few researchers have focused on

DOI: 10.2112/SI75-071.1 received 15 October 2015; accepted in revision 15 January 2016.

*Corresponding author: melanie.biausque@u-bordeaux.fr

the recovery timescales after erosion events, let alone recovery timescales of an embayed beach in both cross-shore and alongshore directions. In this study, we use a data base of 10 years (from January 1999 until July 2009) of video images to characterize shoreline variations (erosion, accretion and rotation) and recovery timescales of the embayed beach of Tairua, New-Zealand. Moreover, we initiate a test of the Yates model (2009), normally using for open beaches, in this embayed beach case where both cross-shore and alongshore sediment movement occur. In order to complete the work initiated by van de Lageweg *et al.* (2013), we used a longer dataset and oriented our research on the impact of the rotation on beach changes and how this might cause different parameterizations in the Yates model.

Field site

Tairua beach is a sandy beach situated on the eastern coast of the Coromandel Peninsula, North Island, New Zealand (Figure 1). This beach is classified as an embayed beach, blocked from the south by the tombolo, Paku Hill, and from the north by the promontory Pumpkin Hill. The beach orientation has been calculated as the mean vector of the orientation angles at both ends of the beach (Hart & Bryan, 2008) and is globally 53 ° from due north. According to van de Lageweg *et al.* (2013), Tairua Beach is approximately 1.6 km long and is composed of medium coarse sand with a median grain size about 600 µm, and a steep beach face (≈ 6 °). Following the Wright & Short classification, this beach is an intermediate beach. Its state varies between the "Longshore Bar and Trough" state (LBT) to a "Transverse Bar and Rip" (TBR) state during austral summers (from December to February). Conversely, the LBT state is dominant during higher wave energy conditions (Bryan *et al.*, 2013). The wave climate is moderate, with a significant annual wave height on average 1.5 m, except during winter storm conditions when waves reach up to 6 m. The beach is exposed to both northerly and easterly swells, and the tidal range is between 1.2 m (neap) and 2 m (spring) (Bogle *et al.*, 2001).

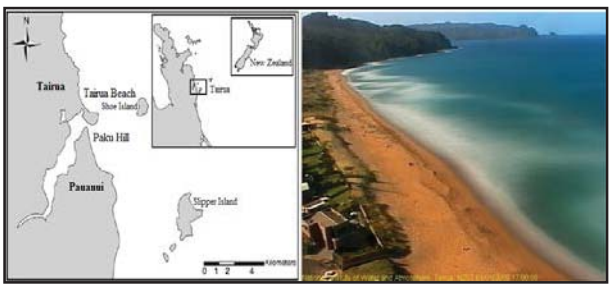

Figure 1. Location of Tairua Beach (left) and Cam-Era averaged image of Tairua beach on January the 1st 2008 at 17:00: half-tide (right).

METHODS

The National Institute of Water and Atmospheric Research (NIWA) installed seven video imagery systems, across the two islands of New Zealand, in order to characterize coastal changes (www.niwa.co.nz/our-services/online-services/cam-era).

NIWA's imagery system consists of collecting images using 'the state-of-the-art automated imaging system' called Cam-Era (Coco *et al.*, 2005). The system overlooking Tairua is located on the tombolo of Paku Hill, covering the entire beach, a part of the dune, the vegetation and the surfzone. Automatically, 600 oblique individual images are recorded over a period of 15 min, every hour and only during the day. In this study, we only used time-exposures, which are snapshot series averaged over 15 min, to identify the different structures.

Averaged-images were rectified, geo-referenced and rotated using intrinsic and extrinsic camera parameters. Using a simple algorithm based on the ratio of red relative to blue light (Smith and Bryan, 2007), it was possible to determine the limit between dry sand and the water. Moreover, the shoreline position was always detected at +0.5 m tidal level in order to maximize data availability and minimize tidal variations. The position identified by the algorithm was plotted, manually checked and modified if the line was not precise enough, or if the position was incorrect because of low image quality. The shoreline position error equals six times the water level error, on average, which means that for a half meter error on water level, the shoreline is 3 meters further inland (van de Lageweg *et al.*, 2013).

Rotation

The shoreline rotation is based on alongshore exchanges and in general can represent 26 % of the shoreward variability (Harley *et al.*, 2011). This is a natural phenomenon, which does not require a loss or gain of sediment by the system and is identified as the shoreline movements per unit alongshore distance (Bryan *et al.*, 2013). In this paper, we calculated the orientation coefficient of the beach by fitting the shoreline position to a simple linear equation that depends on time. The overall orientation of the beach is obtained by extracting the slope of this line (Foster, 2012). The rotation of the beach is directly linked to the alongshore component of wave energy flux (P_y), which is linked to the significant wave height. Positive values indicate a southern end of the beach that is more seaward; conversely, negative values show a northern end of the beach seaward. Values close to zero imply an unrotated state of the beach (Figure 3, panel B).

Wave and tide data

The tide dataset was obtained from NIWA's forecaster; this model has a water level accuracy equal to 1 cm, and a phase error less than to 10 min (Smith & Bryan, 2007). Wave data were simulated from SWAN model, forced using waves field from the NOAA WaveWatchIII model output. The water level at the shoreline was corrected for set-up using a simple model based on Bowen *et al.* (1968), but no correction has been added for storm surge (which is not significant parameter around the New Zealand coast (van de Lageweg *et al.*, 2013)). In addition, the alongshore component of wave energy flux (P_y) was calculated, and used as a proxy of the rotation rate:

$$P\_y = \frac{\rho g^2}{32\pi} Hs^2 T_{mean} \sin(\theta_{mean}) \cos(\theta_{mean}) \quad (1)$$

where ρ = 1025 kg.m^{-3} is water density, g = 9.81 m.s^{-2} is gravitational acceleration, Hs is the significant wave height in meters, T_{mean} is the averaged period and θ_{mean} the mean angle of wave approach relative to the beach orientation in radians.

RESULTS

We identified two types of wave: wind sea with small wave heights and short periods, and swell characterised by long periods. Analysis of the angle of wave approach relative to the beach orientation (θ) indicates waves coming from the ENE on average, with no significant seasonal difference between austral summers and winters (θ equals -8 to -10 ° respectively). As written previously, the alongshore component of wave energy flux (*P_y*) is the principal parameter controlling the rotation of the beach. Positive values of *P_y* represent a flux of wave energy toward the north, while negative values signify a flux toward the south.

Storm Climate

In 1994, Dolan & Davis showed that both maximum significant wave height and storm duration are factors influencing the variability of beach morphodynamics. In our study, we defined storms as a significant wave height higher than 2 m (H95%) during more than 3 hours. Based on this definition, we found 65 different storms between January 1999 and January 2008, with only 9 storms during summers and 28 during winters. Moreover, the maximum duration in summers is 23 hours compared to 65 hours in winter. According to their observations, Dolan & Davis proposed a parameter to estimate the potential of erosion of a storm (Figure 3C). The Storm Power Index (*Ps*) was defined as:

$$Ps = Hs^2{}_{\max}(D) \qquad (2)$$

where *D* is the duration in hours, and *Ps* in m²hr.

Cross-shore variation

As explained in Harley *et al.* (2011), 60 % of the shoreline variability of an embayed beach can be associated with cross-shore oscillations. In the top panel of the Figure 2, the red color-scale means that the shoreline position is seaward, corresponding to an accretion of the beach, whereas the blue defines a landward position, revealing an erosion of the shoreline.

White elements in graphs are gaps in the data acquisition: unusable images because of missing data, bad luminosity, bad quality images, or problems with the video system. In the middle panel (Figure 2 middle panel), the shoreline position is obtained by calculating the alongshore averaged position, in order to eliminate alongshore movement of sediment. The bottom panel represents the wave energy, represented by the squared significant wave height (Hs^2), showing that high energy periods could provoke an erosion of the shoreline. The 'equilibrium wave energy' (*Eq*) theory shows that, before a storm, the *Eq* coefficient is low; it grows during a storm event and diminishes after the storm, corresponding to a recovery period for the beach. When a second storm event occurs, if the *Eq* does not return to its 'pre-storm' position, this means that the beach recovery is incomplete, and the erosion inferred by the second storm is limited.

Rotation

According to the Figure 3A and 3C, there is a relation between the *Ps* coefficient and the shoreline evolution. For example, through the winter 2000, the maximum storm power index (830 m²hr) caused a massive retreat of the shoreline (28 m). But, in June 2004 (Figure 3, number 1), a storm with a *Ps* coefficient of 160 m²hr caused an shoreline retreat of 12 m. A second event on January 2005 (Figure 3, number 2), occurred with a same *Ps* rate, and provoked an erosion of the beach about 20 m. According to the Figure 2, bottom panel, the coefficient of the equilibrium wave energy for these two examples is the same. So, the main difference between these two events is the rotation of the beach. Indeed, when event number 2 occurred, the beach was unrotated, while during the first event the beach was negatively rotated (northern end seaward).

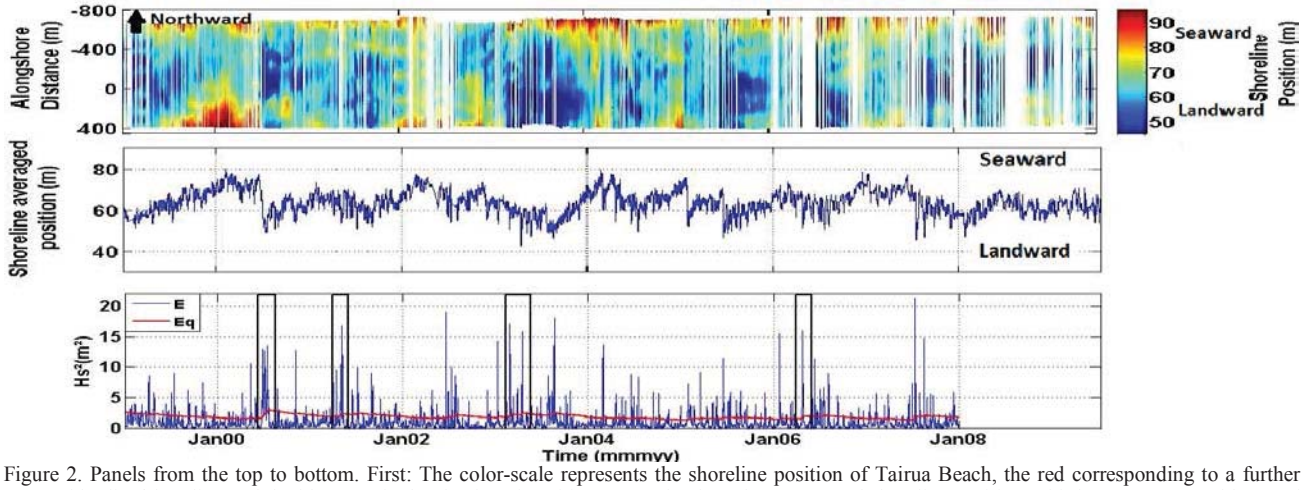

Figure 2. Panels from the top to bottom. First: The color-scale represents the shoreline position of Tairua Beach, the red corresponding to a further seaward barline/shoreline and the blue to a further landward position. Second: Alongshore averaged shoreline position. Third: Wave energy (blue) and Eq, the equilibrium wave energy (red). Black boxes indicate example of storm event.

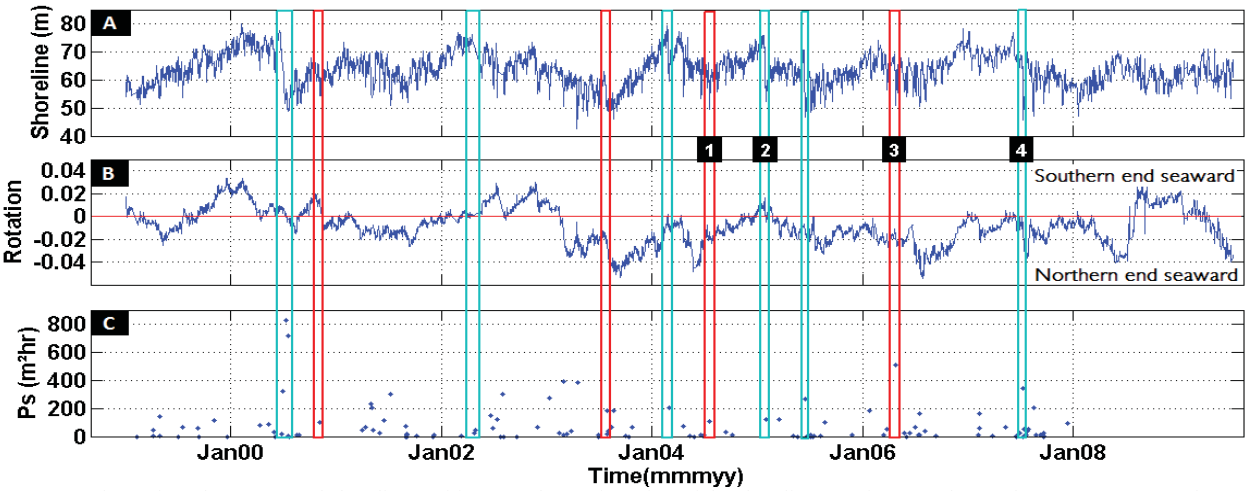

Figure 3. Panel A: Alongshore averaged shoreline position. Panel B: Orientation of the shoreline at Tairua Beach. Panel C: Storm Power Index. Blue rectangles highlight erosion events for unrotated beaches, red ones highlight erosion events for rotated beaches.

This theory can be highlighted with another example. In March 2006 (Figure 3, number 3) the erosion of a rotated (negatively) beach resulting from an energetic storm (520 m²hr) was about 15 m. In June 2007 (Figure 3, number 4), a less powerful storm (380 m²hr) provoked an erosion of an unrotated beach about 22 m.

Even if the Ps is high, the erosion of the shoreline during a rotated event appears less important than for an unrotated one. The erosive conditions seem to become more efficient when the Power Index is high and the rotation approaches 0.

DISCUSSION

The equilibrium wave energy (*Eq*) is a useful parameter to study of shoreline variability. In storm periods, *Eq* increases (Figure 2) because the beach adjusts itself to high wave energy, by an erosion of the beach face. After these episodes, calm conditions take place and recovery time begins. If a second storm arrives and the *Eq* does not return to its original level, meaning that the beach has had insufficient time to return to its original profile of fair weather, the recovery is incomplete. In these circumstances, the state of the beach is more adapted to storm weather than its original position, and the erosion provoked by hydrodynamic events is less substantial. Vousdoukas *et al.* (2011) suggested that during consecutive storms, the antecedent beach morphology is the principal factor controlling the beach response to the arrival of the next storm.

Cross-shore variability and rotation

The alongshore component of wave energy (*P_y*) controls the rotation rate of the shoreline. An abrupt rotation occurs when *P_y* is high, and a strong northward *P_y* means a movement of the northern end of the beach landward to seaward. We suggested that strongest erosion takes place if *Ps* is high and the rotation close to 0. When the beach is rotated, the alongshore energy flux is powerful and creates an alongshore radiation-stress with a dominant current associated. When the orientation rate of the beach is close to 0, the alongshore current is not dominant. In this case, the return current can push the sand offshore explaining the much larger erosion.

However, as described in the precedent paragraph, the first factor to take into account in cross-shore variability is the antecedent beach morphology, the influence of the rotation is only a second factor.

Seasonal variability

The averaged *Hs* and *Tp* for summers and winters were not statistically different, as for θ. Therefore on average, *P_y* parameter is higher in winters than in summers. Besides, the maximum *Ps* in winters is twice as big as in summers, because of higher storm duration, 65 hrs in winters compared to 23 hrs in summers. Consequently, winter storms are longer and more powerful than in summers leading to more important erosion events.

However, according to our preliminary results from the application of the Yates model (2009), the absolute value of the mean erosion rate in winters is double that the summers one (respectively 0.198 and 0.100 m/hr/m^3). Concerning the accretion rate, the absolute value in austral summers equals ten times the austral winter value (0.053 compared to 0.005 m/hr/m^3). These results highlight that seasonality seems to occur, with an accretion facilitated during summers and an erosion that is more efficient during winters. Environmental conditions appear to influence the seasonal variability.

Processes driving erosional/ accretion events are different according to the season. First, the average *P_y* is higher in winters signifying a stronger alongshore current during those periods (*e.g.* Bryan *et al.*, 2013). This current is responsible for the rotation of the beach, displacing the sand from one end of the beach to the other end. As this alongshore current is dominant, the sand is kept onshore limiting the erosion of the shoreline. Besides, rip current cells occur more often during summer, increasing the rate of erosion during this season. Secondly, one of the principal factors of the beach morphodynamic change is the equilibrium profile of the beach, and Yates model depends

on that beach state. Indeed, according to Davidson *et al.* (2013) there is a strong coherence between the morphodynamic state of the beach and the shoreline position. Accordingly, if a beach is in a 'summer state', its erosion by a storm will be much larger. Conversely, during winter, the state of the beach is more adapted to repeated storms and the net erosion due to each storm is lower than in summer.

Our work on testing Yates' model is restricted by the limitations of the model. In summer, the distance between the barline and the shoreline is reduced, involving a sandbar/shoreline coupling and an absorption of the energy by the sandbar. As suggested by Vousdoukas *et al.* (2011), the sandbar has a role of protection of the beach. Yates model does not take into account sandbar and beach coupling, nor longshore movements which represent a huge part of the shoreline variability of an embayed beach. Future work (Blossier *et al.*, under review), will investigate shoreline rotation and sandbar dynamics using simple equilibrium models.

CONCLUSIONS

Shoreline variations are complex phenomena, and to understand them, we need to take into account more parameters than only the significant height wave and wave energy during a storm. The case of embayed beach is more complex because the beach rotation is an essential parameter needed to understand how these environments work. Using daily video extracted shoreline and sandbar positions from January 1999 until July 2009, we demonstrated that the erosion of an embayed beach is a complicated combination of the alongshore wave energy flux, the beach orientation, the storm power index, the equilibrium wave energy and the beach state. Each factor has an effect (direct or not) on other factors and they cannot be study separately, without considering interactions between them. We have shown that seasonality exists in equilibrium conditions, which could be associated with the effect of rotation on erosion and recovery. Furthermore, we conclude that simple shoreline prediction models (as in the Yates model), do not take into account enough parameters (as alongshore movements of sediment) to be sufficient precise in the prediction of embayed beach changes.

ACKNOWLEDGMENTS

This publication is the result of the collaboration between the University of Bordeaux (France) and the University of Waikato (New Zealand). The authors would like to acknowledge NIWA and Waikato Regional Council for letting them work on their video images and tide data. Wietse van de Lageweg digitised the shorelines from 1999-2005. Mareike Hoehne digitised 2006.

LITERATURE CITED

Bowen, A.J.; Inman, D.L., and Simmons, V.P., 1968. Wave set‐down' and set‐up. *Journal of Geophysical Research*, 73(8), 2569-2577.

Bryan, K.R.; Foster, R., and MacDonald, I., 2013. Beach Rotation at Two Adjacent Headland-Enclosed Beaches. *Journal of Coastal Research*, SI65, 2095-2100.

Coco, G.; Payne, G.; Bryan, K.R.; Rickard, D.; Ramsay, D., and Dolphin, T., 2005. The use of imaging systems to monitor shoreline dynamics. *ArabianCoast 2005 contribution*.

Dolan, R. and Davis, R.E., 1994. Coastal storm hazards. *Journal of Coastal Research*, SI 12, 103–114.

Davidson, M.A.; Splinter, K.D., and Turner, I. L., 2013. A simple equilibrium model for predicting shoreline change. *Coastal Engineering*, 73, 191-202.

Foster, R.A., 2012. Shoreline variation and beach rotation of Pauanui beach. University of Waikato: New-Zealand, Ph.D. dissertation.

Frihy, O.E. and Komar, P.D., 1993. Long-term shoreline changes and the concentration of heavy minerals in beach sands of the Nile Delta, Egypt. *Marine Geology* 115, 253–261.

Harley, M.D.; Turner, I.L.; Short, A.D., and Ranasinghe, R., 2011. A reevaluation of coastal embayment rotation: The dominance of cross‐shore versus alongshore sediment transport processes, Collaroy‐Narrabeen Beach, southeast Australia. *Journal of Geophysical Research: Earth Surface* (2003–2012), 116(F4).

National Institute of Water and Atmospheric Research. www.niwa.co.nz

Smith, R.K. and Bryan, K.R., 2007. Monitoring beach face volume with a combination of intermittent profiling and video imagery. *Journal of Coastal Research*, 892-898.

Strauss, D. and Tomlinson, R.B., 2009. Modelling transitions between barred beach states on a straight coast. In *Proceedings of Coastal Dynamics '09*, Tokyo, Japan.

Turki, I.; Medina, R.; Gonzalez, M., and Coco, G. (2013). Natural variability of shoreline position: observations at three pocket beaches. *Marine Geology*, 338, 76-89.

Van de Lageweg, W.I.; Bryan, K.R.; Coco, G., and Ruessink, B.G., 2013. Observations of shoreline–sandbar coupling on an embayed beach. *Marine Geology*, 344, 101-114.

Vousdoukas, M.I. Almeida, L.P.M., and Ferreira, Ó., 2012. Beach erosion and recovery during consecutive storms at a steep‐sloping, meso‐tidal beach. *Earth Surface Processes and Landforms*, 37(6), 583-593.

Wright, L.; Short, A., and Green, M., 1985. Short-term changes in the morphodynamic states of beaches and surf zones: An empirical predictive model. *Marine Geology* 62, 339–364.

Yates, M.L.; Guza, R.T., and O'Reilly, W.C., 2009. Equilibrium shoreline response: Observations and modeling. *Journal of Geophysical Research*: Oceans (1978–2012), 114(C9).

Journal of Coastal Research	SI	75	358-362	Coconut Creek, Florida	2016

The Role of Beach and Wave Characteristics in Determining Suitable Habitat for Three Resident Shorebird Species in Tasmania

Anja Bock[†*], Michael R. Phillips[†*] and Eric Woehler [‡]

[†*] University Centre of the Westfjords, Suðurgata 12, 400 Ísafjörður, Iceland.

[‡] University of Tasmania (UTAS), Churchill Avenue, Hobart TAS 7005, Australia.

[†]Coastal and Marine Research Group, University of Wales Trinity Saint David (Swansea), Mount Pleasant, Swansea, UK, SA1 6ED.

www.cerf-jcr.org

www.JCRonline.org

ABSTRACT

Bock, A.; Phillips, M.R., and Woehler, E., 2016. The role of beach and wave characteristics in determining suitable habitat for three resident shorebird species in Tasmania. *In:* Vila-Concejo, A.; Bruce, E.; Kennedy, D.M., and McCarroll, R.J. (eds.), *Proceedings of the 14th International Coastal Symposium* (Sydney, Australia). *Journal of Coastal Research*, Special Issue, No. 75, pp. 358-362. Coconut Creek (Florida), ISSN 0749-0208.

Beaches are connections between marine and terrestrial environments, and as they are highly dynamic, they demand adaptation and flexibility by inhabitant species. Along Tasmania's beaches and coastline, resident shorebirds have acclimatised and become year-around stationary territory holders. This life strategy requires an environment and territory that offers all necessary resources, all year around and for every life stage. Consequently, this study investigated not only the habitat use of three resident shorebird species and related Tasmanian beach types, but moreover assessed the habitat use in relation to the different abiotic characteristics and environmental conditions. This was achieved by combining and merging datasets from four different sources. Results revealed significant differences in the role and importance of beach characteristics and environmental factors among the three species, i.e. surf zone width appeared to be highly significant and significant for Pied Oystercatchers and Hooded Plovers respectively, whilst mean annual wind speed was highly significant for Hooded and Red-capped Plovers, but not Pied Oystercatchers. Other beach attributes such as mean beach width and swash gradient appeared to be significant for Pied Oystercatchers and Red-capped Plovers respectively. Also significance of wave variables differed amongst the three species: mean annual significant wave height for Red-capped Plovers; maximum significant wave height for Hooded Plovers; and mean annual wave period for Pied Oystercatchers. With regards to sea level rise and potential habitat loss, research findings will underpin the development of future beach management strategies, by integrating social, economic and conservation interests.

ADDITIONAL INDEX WORDS: *habitat use, resident shorebirds, beach attributes, abiotic characteristics*

INTRODUCTION

Many people appreciate beaches for their recreational value and quality of life. In Australia, 85% of the human population lives within 100 km of the coastline (Maguire *et al.*, 2011). Accordingly, sandy beaches support many coastal economies worldwide, but aside from the vast range of social and economic interests that need to be coordinated (Martínez *et al.*, 2007), sandy beaches also represent highly dynamic ecosystems providing a habitat for a range of unique biodiversity (see Maguire *et al.*, 2011) However, the ecological value of sandy beaches has barely been recognised, particularly in Australia (Clarke and Harvey, 2013). Most management has focused on the stability of the shoreline to protect human infrastructure against rising sea levels. However, many bird species are in decline such as the Hooded Plover *(Thinornis rubricollis)*, which is an endemic Australian shorebird particularly dependent on wide, flat sandy beaches. Generally, it has been widely accepted that habitat loss and alteration are major reasons for species extinctions in the 21st century (multiple IPCC reports). Disturbance by recreationists was revealed to be a major reason for the decreasing numbers of Hooded Plovers (*e.g.*, Schlacher *et al.*, 2013a). If changes in a habitat have reached a limit where conditions are not suitable anymore, it might drive species to local extirpation or to extinction (Gu *et al.*, 2002). Many studies have been carried out on migratory species (*e.g.*, Godet *et al.*, 2011; Lunardi *et al.*, 2012), but resident species might be particularly be at risk as they are less flexible in changing habitats. This is because they are believed to select one territory, which the breeding pair will occupy for their entire life (West *et al.*, 2005). Species differ in their needs and are likely to have different preferences for a habitat and territory compared to others according to adaptations. However, latest estimates for Australia´s Hooded Plovers were 5500 birds, while Tasmania sustains about 2000 individuals (unpublished data). Therefore Tasmania may be of particular importance for this species. Furthermore, ocean sandy beaches are not only affected by anthropogenic activities, but also by sea level rise (Schlacher *et al.*, 2013b).

DOI: 10.2112/SI75-072.1 received 15 October 2015; accepted in revision 15 January 2016.

*Corresponding author: bockanja@gmx.de

Therefore, this study aims to increase current knowledge on the habitat use by three resident shorebird species in Tasmania in relation to the characteristics of their habitat – the Hooded Plover *(Thinornis rubricollis)*, Pied Oystercatcher *(Haematopus longirostris)* and Red-capped Plover *(Charadrius ruficapillus)*. If important habitat or sandy beach characteristics for shorebirds can be identified, it would help to improve the general understanding of the species, their habitat use and the establishment of the most effective conservation measures (see Clarke & Harvey, 2013 and West *et al.*, 2005). If species preferences for beach characteristics differ, it would be expected that species distributions and abundances will differ (Brown, 1984).

Altogether, there may also be a range of factors driving a species habitat use, particularly for predators on top of the food chain like shorebirds (see Dugan *et al.*, 2003). As most studies (*e.g.*, Dugan *et al.*, 2003 amongst others) have investigated the invertebrate fauna or prey abundance of sandy beaches, only few looked at the impacts that abiotic characteristics may have on resident shorebirds (Brown & McLachlan, 2002). Tasmania as an island state located in the Southern Ocean is highly exposed to wind and wave forces travelling unbroken from South America across the Atlantic and Indian Ocean.. As a consequence, the majority of the Tasmanian coastline consists of high energetic wave-dominated beaches, in particular the west coast. Only a few bays on the east and southeast coast are more sheltered and rather tide-dominated (Short, 2006). Proportionally, Tasmania holds a varied geology consisting of sedimentary and volcanic rocks, Palaeozoic dolerite and granite, and shares much of his geological history with South Australia (Powell *et al.*, 1994).

Table 1. *Overview on beach types and categories present around Tasmania with the largest proportion of 91.4% being represented by wave-dominated beaches (Reproduced from Short, 2006).*

	Beach Type	Number	Number %	Mean length (km)	Ω (km)	Total length (km)	Length (%)	Beach type (%)
	Wave-dominated							*91.4*
1	*Reflective*	786	61.9	0.52	1.18	406.6	46.3	
2	*Low tide terrace*	174	13.7	0.78	1.54	134.7	15.3	
3	*Transverse bar & rip*	193	15.2	1.34	2.46	258.5	29.4	
4	*Rhythmic bar & beach*	2	0.2	0.2		0.4	-	
5	*Longshore bar & trough*							
6	*Dissipative*	1	-			0.2	-	
	Tide-modified							3.7
7	*R+LTT*	28	2.2	0.6	0.9	16.91	1.9	
8	*R+LT rips*	1	0.1	0.25	-	0.25	0.0	
9	*Ultra dissipative*	8	0.6	1.98	1.97	15.85	1.8	
	Tide-dominated							4.9
10	*R+sand ridges*	33	2.6	0.53	0.74	17.6	2.0	
11	*R+sand flats*	35	2.8	0.64	0.78	22.3	2.5	
12	*Retial flats*	2	0.2	1.7	-	3.4	0.4	
13	*R+mud flats*							
	Beach+rock flats							
14	*R+rock flats*	7	0.6	0.18	0.05	1.25	0.1	0.1
		1269	100.0			877.9	100	100

Altogether, the interactions of waves, winds and present type of sediment create very unique conditions (Short, 2010), asking species to adapt to these physically controlled environments. Three wave-categories and more subcategories can be identified according to a beaches´ morphology, as shown in Table 1 (see Short, 2006). Whereas, one beach can be divided into three main zones: (1) the subaerial beach, the sandy part above sea-level; (2) the swash or intertidal zone, the zone where waves interact with the sediment; (3) and the surf or wave breaker zone, where waves expend their energy.

Again, this study will explore the role of beach attributes and environmental factors on observed distributions and abundances, will identify important variables driving habitat use and unravel species-specific preferences among all predictors.

METHODS

Since 1999/2000 over a period of 12 years >200 beaches have been surveyed along Tasmania´s shoreline. Residential shorebird breeding pairs were mapped and species related behaviour identified. As Tasmania´s ocean sandy beaches differ in length and morphology, beach segments were derived from the 'Australian Beach Safety and Management Programme' (ABSMP, Short, 2006) data set. A circle around the centre point of each segment was created in order to associate all recorded breeding pairs and territory holders within its radius, linked to the attributes of the beach segment (Figure 1). A total of 322 beach segments were chosen, 84 located West, 34 North, 147 East, 20 Southeast coast and 37 on Flinders Island.

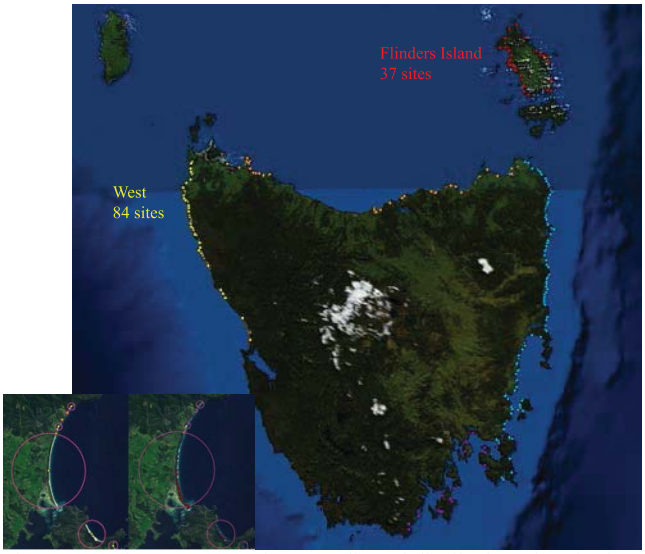

Figure 1. Study area, Tasmania, Australia and distribution of study sites, defined and created by buffers representing the length of one beach segment (bottom left).

Four data sets were incorporated to relate habitat use of the three selected Tasmanian resident shorebird species to different abiotic characteristics and environmental conditions. Shorebird, beach attributes and wave data were made compatible via spatial information and were linked through ESRI ArcGIS. First, shorebird and beach attribute data were merged by constructing buffers around the centre points; Second, wave data was added by extracting spatial information from raster data sets, received from the Centre for Australian Weather and Climate Research.

Analyses were undertaken on the type of distribution, environmental and beach attribute variables as potential predictors for shorebird habitat use. These included mean annual wind speed (m/s), mean annual significant wave height (m), maximum significant wave height (m), wave period (m/s), mean

beach width (m), degree of embayment (0-1), surf zone width (m) and swash zone gradient (degrees). Additionally, Pearson´s correlation coefficient (r) and significance levels were determined. To assess the contribution of each predictor on dependant variables and shorebird species, a range of Generalised Linear Models (GLMs) were used. As shorebird data consists of count data (integers), a Poisson distribution was applied and due to likely interactions, a correlation matrix was calculated using Pearson´s correlation coefficient (r). In order to find the most suitable predictors and the lowest number of variables, a step function was chosen for the GLMs.

RESULTS

Across the 322 selected beach segments and study sites, a total number of 1454 breeding pairs and thus territories were recorded. These comprised Pied Oystercatchers (n=748; 51%), Hooded Plovers (n=436; 30%) and Red-capped Plovers (n=240; 18%). Tasmania´s beaches are mainly wave-dominated (91.4%; Short 2006) and analyses revealed slight differences in distribution and abundance of the three species among the different beach types. Table 2a shows the break-down of sightings of the 1454 breeding pairs based on species and beach categories. Regional differences in distribution are shown in Table 2b. The largest abundance of Hooded Plover and Pied Oystercatchers were located on the east coast (n=192 and 250 respectively; Table 2b) while Red-capped Plovers were more abundant on the West coast, although this was not significantly higher than other locations.

Table 2. *Distribution and abundance of Hooded Plovers, Pied Oystercatchers and Red-capped Plovers among a) beach categories. b) regions.*

	wave-dominated	tide-modified	tide-dominated
Hooded Plover	426 (98%)	8 (2%)	2 (<1%)
Pied Oystercatcher	682 (91%)	30 (4%)	36 (5%)
Red-capped Plover	250 (92%)	3 (1%)	17 (6%)
Total	1358	41	55

	W	N	E	SE	Flinders I
Hooded P.	123 (28%)	52 (12%)	192 (44%)	13 (3%)	56 (13%)
Pied O.	202 (27%)	103 (14%)	250 (33%)	69 (9%)	124 (17%)
Red-capped P.	82 (30%)	28 (10%)	72 (27%)	13 (5%)	75 (28%)
Total	407	183	514	95	255

Results from the GLMs are documented in Table 3. Surf zone width was seen to be a highly significant beach attribute for Hooded Plovers (Estimate=-0.001, z-score=-2920, P=0.004) and Pied Oystercatchers (Estimate=-0.001, z-score=-3.291, P<0.001). However, mean annual wind speed was highly significant for both Hooded and Red-capped Plovers (Estimate=-0.259, z-score=-4.787, P<0.001 and estimate=-0.253, z-score=-3.680, P<0.001). Maximum significant wave height revealed a significant association for Hooded Plovers (Estimate=0.157, z-score=2.397, P=0.017), while mean annual wave period was significant for Pied Oystercatchers (Estimate=0.223, z-score=7.676, P<0.001) and mean annual significant wave height appeared to be highly significant for Red-capped Plovers (Estimate=0.459, z-score=6.091, P<0.001). Once again, mean beach width was a significant factor for Pied Oystercatchers (Estimate=0.223, z-score=7.676, P<0.001), whereas swash gradient was the only significant beach attribute and predictor for Red-capped Plovers (Estimate=0.001, z-score=-2.920, P<0.002).

Table 3. *A performed GLM including all possible predictor variables of beach attributes and environmental variables.*

Hooded Plover	Estimate	Std. Error	z-score	Pr(>|z|)
Surf zone width	-0.001	<0.000	-2.920	0.004
Maximum significant wave height	0.157	0.065	2.397	0.017
Mean annual wind speed	-0.259	0.054	-4.787	<0.001
Pied Oystercatcher	**Estimate**	**Std. Error**	**z-score**	**Pr(>|z|)**
Mean beach width	0.001	<0.000	2.400	0.016
Surf zone width	-0.001	<0.000	-3.291	<0.001
Mean annual wave period	0.223	0.029	7.676	<0.001
Red-capped Plover	**Estimate**	**Std. Error**	**z-score**	**Pr(>|z|)**
Swash gradient	-0.092	0.042	-2.204	0.028
Mean annual significant wave height	0.459	0.075	6.091	<0.001
Mean annual wind speed	-0.253	0.069	-3.680	<0.001

Analyses revealed one beach and two environmental attributes for plovers, and opposite for Pied Oystercatchers.

Further revaluations showed surf zone width was significantly correlated with all three wave variables (r=0.525, p<0.001; r=0.561, p<0.001 and r=0.379, p<0.001); mean annual wind speed was not significantly correlated with surf zone width (r=-0.044, p=0.436); while beach categories were significantly correlated with all three wave variables (r=0.269, p<0.001; r=0.223, p<0.001 and r=0.205, p<0.001), swash zone gradient (r=0.182, p=0.001) and surf zone width (r=0.114, p=0.041). However this was not the case for mean annual wind speed (r=-0.02, p=0.728) or degree of embayment (r=0.021, p=0.704).

DISCUSSION

Distributions and abundances of Hooded Plovers, Pied Oystercatchers and Red-capped Plovers varied amongst Tasmania´s beaches. Breeding pairs of Red-capped Plovers were least abundant (n=270), Hooded Plovers (n=436) and Pied Oystercatchers were most abundant (n=748). However, Red-capped Plovers are not restricted to ocean sandy beaches, as flocks were observed around salt lakes further inland (Abensperg-Traun & Dickman, 1989). Therefore, lower numbers of Red-capped Plover breeding pairs may not be representative, as local population numbers may be higher.

As expected, few variables appeared to be significant for habitat use by the three study species. Mean beach width was only significant for Pied Oystercatchers (Estimate=0.001, z-score=2.400, P=0.016), indicating preference for beaches with a wider subaerial zone. This is logical, as Pied Oystercatchers are the largest of the study species and likely to have higher energy requirements and need larger amounts of prey or as a strategy, may hunt for specific high energetic prey and consequently, may require a larger territory (*e.g.,* Rogers *et al.*, 2006). Other reasons include, if the energy value of prey is not very good or if prey is patchily distributed. As larger species are able to store more energy, commuting distances may not be as critical for Pied Oystercatchers as for smaller plover species. Besides feeding, Pied Oystercatchers also need space for roosting and breeding and may require specific features of the landscape that provide protection from prevailing weather conditions, human disturbance and predators. A study by Colwell *et al.* (2003) revealed that different shorebird species used a range of roosting sites to which they frequently returned, indicating that a suitable habitat should contain a range of roosting sites that are likely to be used during different conditions, which would underpin the preference of Pied Oystercatchers for larger territories.

However, surf zone width appeared to be of significant importance for Hooded Plovers and Pied Oystercatchers, indicating that breeding pair numbers decrease with an increase in surf zone width (Estimate=-0.001, z-score=-2.920, P=0.004 and estimate=-0.001, z-score=-3.291, P<0.001). This makes sense, as the surf zone is also known as the 'area of wave generation' and wider surf zones will enable the creation of stronger and higher waves (Short, 2006). Thus if arriving wave energy on a beach is high, it might create less favourable conditions for shorebirds, especially with regards to feeding due to constant wave run up, a smaller strip of sand due to erosion, and less room to feed (Lucrezi *et al.*, 2010). Overall, it has been suggested that lower wave energy beaches such as tide-modified and tide-dominated beaches may offer more favourable conditions for different organisms (Lercari *et al.*, 2010).

Other important factors for feeding shorebirds could be increased wave heights and periods, as the beach sediment will erode, create a steeper swash zone gradient and eventually leave less room for the birds to forage. However, analysis did not show a negative relationship with wave predictors, and revealed rather significant positive associations with maximum significant wave heights (Hooded Plovers – Estimate=0.157, z-score=2.397, P=0.017); mean annual wave period (Pied Oystercatchers - Estimate=0.223, z-score=7.676, P<0.001); and mean annual significant wave height (Red-capped Plovers - Estimate=0.459, z-score=6.091, P<0.001) with all species indicating that breeding pair numbers would increase with wave height. This could be due to >90% of the beaches being wave-dominated and that most territories were found on these beaches.

As expected, swash zone gradient appeared to be negatively associated with Red-capped Plover breeding pair numbers (Estimate=-0.092, z-score=-2.204, P<0.028), indicating that Red-capped Plover numbers decrease with steeper intertidal slopes. As pointed out, wider and gentler shores may offer a larger foraging area, better access to invertebrates and opportunities to harvest. This is supported by Neumann *et al.* (2008) who found a significant negative relationship between swash zone slope and distribution of four of six investigated shorebird species. Shorebirds are highly adapted species, where a shorter bill may become a limiting factor when trying to reach the invertebrates in the sediment (Nebel *et al.*, 2005), particularly for small visual foragers such as plover species. Additional location factors such as cold winds and lower temperatures may affect penetration by dry sediment requiring more energy to stab into the ground (Finn *et al.*, 2008).

Mean annual wind speed was also highly negatively associated with Hooded and Red-capped Plover numbers (Estimate=-0.259, z-score=-4.787, P<0.001 and Estimate=-0.253, z-score=-3.680, P<0.001 respectively), indicating that numbers decrease when wind speed increases. These could cause thermal disadvantages for individuals and eggs due to increased heat loss, requiring more effort to maintain energy budgets (McConkey & Bell, 2005). Overall, the smallest birds have got the highest relative heat loss to body size, which needs to be compensated by staying warm. Thus the availability of sheltered roosting sites along a beach can be potentially life-saving.

CONCLUSIONS

Research findings showed that abiotic sandy beach characteristics play a role in habitat use of resident shorebirds, and that this differs between species. Therefore not all characteristics were equally important to all species. It is vital to have an overall understanding of species biology and also interactions within an ecosystem. Many factors such as predation or competition may be responsible for differences in shorebird distributions and abundances, particularly on complex and dynamic ecosystems like ocean sandy beaches. Therefore, more studies should be carried out on the role of abiotic habitat characteristics for resident species. With regards to human disturbance, habitat loss and species extinctions, this work has highlighted important habitat characteristics to be considered for effective management strategies.

ACKNOWLEDGMENTS

The authors would like to thank the Australian Beach Safety and Management Programme and the Centre for Australian Weather and Climate Research for their contribution and data support.

LITERATURE CITED

Abensperg-Traun, M. and Dickman, C.R., 1989. Distributional ecology of Red-capped Plovers, Charadrius ruficapillus (Temminck, 1822), on Western Australian salt lakes. *Journal of Biogeography*. 16 (2), 151–157.

Brown, A.C. and McLachlan, A., 2002. Sandy shore ecosystems and the threats facing them: Some predictions for the year 2025. *Environmental Conservation*. 29 (01), 62–77.

Brown, J.H., 1984. On the relationship between abundance and distribution of species. *The American Naturalist*. 124 (2), 255–279.

Clarke, B. and Harvey, N., 2013. Wither coastal management in Australia — A call for national leadership. *Journal of Coastal Research*. (65), 915–920.

Davidson-Arnott, R.G.D., 2005. Conceptual model of the effects

of sea level rise on sandy coasts. *Journal of Coastal Research*. 216, 1166–1172.

Dugan, J.E.; Hubbard, D.M.; McCrary, M.D., and Pierson, M.O., 2003. The response of macrofauna communities and shorebirds to macrophyte wrack subsidies on exposed sandy beaches of southern California. *Estuarine, Coastal and Shelf Science*. 58 (Suppl.), 25–40.

Finn, P.G.; Catterall, C.P., and Driscoll, P.V., 2008. Prey versus substrate as determinants of habitat choice in a feeding shorebird. *Estuarine, Coastal and Shelf Science*. 80 (3), 381–390.

Godet, L.; Jaffré, M., and Devictor, V., 2011. Waders in winter: Long-term changes of migratory bird assemblages facing climate change. *Biology letters*. 7 (5), 714–7.

Gu, W.; Heikkilä, R., and Hanski, I., 2002. Estimating the consequences of habitat fragmentation on extinction risk in dynamic landscapes. *Landscape Ecology*. 17, 699–710.

Lercari, D.; Bergamino, L., and Defeo, O., 2010. Trophic models in sandy beaches with contrasting morphodynamics: Comparing ecosystem structure and biomass flow. *Ecological Modelling*. 221 (23), 2751–2759.

Lucrezi, S.; Schlacher, T.A., and Robinson, W., 2010. Can storms and shore armouring exert additive effects on sandy-beach habitats and biota? *Marine and Freshwater Research*. 61, 951–962.

Lunardi, V.O.; Macedo, R.H.; Granadeiro, J.P., and Palmeirim, J.M., 2012. Migratory flows and foraging habitat selection by shorebirds: the northeastern coast of Brazil *Estuarine, Coastal and Shelf Science*. 96, 179–187.

Maguire, G.S.; Miller, K.K.; Weston, M.A., and Young, K., 2011. Being beside the seaside: Beach use and preferences among coastal residents of South-Eastern Australia. *Ocean & Coastal Management*. 54 (10), 781–788.

Martínez, M.L.; Intralawan, A.; Vázquez, G.; Pérez-Maqueo, O.; Sutton, P., and Landgrave, R., 2007. The coasts of our world: Ecological, economic and social importance. *Ecological Economics*. 63 (2-3), 254–272. Available at: http://linkinghub.elsevier.com/retrieve/pii/S0921800906005465 (accessed 24/03/14).

McConkey, K.R. and Bell, B.D., 2005. Activity and habitat use of waders are influenced by tide, time and weather. *Emu*. 105 (4), 331.

Nebel, S.; Jackson, D.L., and Elner, R.W., 2005. Functional association of bill morphology and foraging behaviour in Calidrid Sandpipers. *Animal Biology*. 55 (3), 235–243.

Neuman, K.K.; Henkel, L.A., and Page, G.W., 2008. Shorebird use of sandy beaches in Central California. *Waterbirds*. 31 (1), 115–121.

Powell, C.M.; Preiss, W.V.; Gatehouse, C.G.; Krapez, B., and Li, Z.X., 1994. South Australian record of a Rodinian epicontinental basin and its mid-neoproterozoic breakup (~700 Ma) to form the Palaeo-Pacific Ocean. *Tectonophysics*. 237 (3-4), 113–140.

Rogers, D.I.; Piersma, T., and Hassell, C.J., 2006. Roost availability may constrain shorebird distribution: Exploring the energetic costs of roosting and disturbance around a tropical bay. *Biological Conservation*. 133 (2), 225–235.

Schlacher, A.; Nielsen, T., and Weston, M.A., 2013a. Human recreation alters behaviour profiles of non-breeding birds on open-coast sandy shores. *Estuarine, Coastal and Shelf Science*. 118, 31–42.

Schlacher, T.A.; Weston, M.A.; Lynn, D., and Connolly, R.M., 2013b. Setback distances as a conservation tool in wildlife-human interactions: Testing their efficacy for birds affected by vehicles on open-coast sandy beaches. *PloS one*. 8 (9), e71200.

Short, A.D., 2010. Role of geological inheritance in Australian beach morphodynamics. *Coastal Engineering*. 57 (2), 92–97.

West, A.D.; Goss-Custard, J.D.; dit Durell Seal V., and Stillman, R., 2005. Maintaining estuary quality for shorebirds: towards simple guidelines. *Biological Conservation*. 123 (2), 211–224.

Journal of Coastal Research	SI	75	363-367	Coconut Creek, Florida	2016

Velocity of RFID Tagged Gravel in a Non-uniform Longshore Transp

Tony Dolphin [†]*, Janette Lee[†], Roger Phillips[‡], Colin J.L. Taylor[††] and Keith R. Dyer[§]

[†]Centre for Environment, Fisheries and Aquaculture Science, Lowestoft, United Kingdom

[‡]Marine Science Support Ltd, Acle, United Kingdom

[††]EDF Energy Ltd, Barnwood, United Kingdom

[§]Institute of Marine Science University of Plymouth, United Kingdom

ABSTRACT

Dolphin, T.; Lee, J.; Phillips, R.; Taylor, C.J.L., and Dyer, K., 2016. Velocity of RFID tagged gravel in a non-uniform longshore transport system. *In:* Vila-Concejo, A.; Bruce, E.; Kennedy, D.M., and McCarroll, R.J. (eds.), *Proceedings of the 14th International Coastal Symposium* (Sydney, Australia). *Journal of Coastal Research*, Special Issue, No. 75, pp. 363-367. Coconut Creek (Florida), ISSN 0749-0208.

Radio-frequency Identification (RFID) tags were embedded into 940 native beach gravel particles and deployed at source on Benhole Beach (Somerset, UK) to develop an understanding of gravel transport along a frontage that is likely to be subjected to construction activity associated with the proposed development of the Hinkley Point C power station. The study lasted for three years, the longest of its kind to be published, and maintained high detection rates (78% on completion) typical of RFID experiments. Tracer distribution through time highlighted non-uniformity in the longshore transport system and that a single average or centroid velocity is meaningless, as it cannot account for alongshore variability – instead methods that can account for alongshore variability in the transport system were needed. Spatial patterns in the density of detected tracer revealed transport pathways. Alongshore variation in tracer velocity was linked to changes in the geomorphology: (i) tracer velocity was slowest over beaches, owing to increased surface roughness, burial and deposition at high elevations; (ii) velocity rose/fell with changes in coastline orientation and wave obliquity; and (iii) the highest velocities were found in areas of exposed smooth rock platform; however small ridges (up to 40 cm) in the rock platform and angular blocks derived from cliff and platform erosion led to significant reductions.

ADDITIONAL INDEX WORDS: *Tracer, sediment pathways, substrate, zonation, rock platform.*

INTRODUCTION

Understanding the pathways and rates of longshore sediment transport in a coastal system is important for the prediction and management of impacts caused by developments within the marine environment. For several decades, tracer experiments have been used to investigate pathways and rates of sediment transport in marine and fluvial systems (*e.g.*, Komar and Inman, 1970), but such studies often suffer from low recovery rates and, as a consequence, a high transport uncertainties. Furthermore, if average particle velocity estimates are determined from a cloud of individually-indistinguishable tracers (typical for sands and for gravel where high tracer numbers are required; *e.g.*, Carr, 1971; Hattori and Suzuki, 1978), it can be difficult to meet the basic tracer experiment assumptions (Madsen, 1989) that the dispersion of tracer must be significantly less than the average movement of the tracer cloud (*e.g.*, centroid) and the longshore transport system should be uniform. In a non-uniform longshore transport system, a tracer cloud can fractionate into numerous components of differing speed, rendering the notion of a single average or centroid velocity meaningless.

In this paper, we present results from a three year study of 940 individually traceable and distinguishable particles deployed at Benhole Beach (Somerset, UK) to assess the performance of the particle tracing methods, and to examine the velocity of particles through the longshore transport system. Specifically, we investigate whether a single estimate of tracer velocity is appropriate at this site (*i.e.*, treating the tracer particles as indistinguishable from one another), identify spatial patterns in longshore tracer velocity (including causes) and establish a means to quantify the typical movement (velocity and transit time) of gravel along this coast.

The study site is a 2 km section of a rock-platform and cliff coast within the Bristol Channel (Somerset, UK) (Figure 1). Gravel beaches there are situated near high water (10.9 m tidal range) and are discontinuous with sections up to 700 m devoid of beach. Owing to its location within the Bristol Channel, the site experiences a predominant wave climate from WNW.

The results presented in this paper derive from a gravel transport monitoring programme that was designed to assess whether disruptions to the foreshore caused by construction of a new nuclear power station, Hinkley Point C, have any adverse impact on gravel transport and if so, the likely transit times of any impact to downdrift supply.

METHODS

Gravel velocity was measured using 940 tracer particles – these were gravel particles collected from the study site and marked using 22 mm Radio-Frequency Identification (RFID) tags. The tags, which transmit unique 16-digit hexadecimal ID codes when energised, were encased in silicone and embedded in small holes drilled on the short axis of each tracer particle.

The mass and identity number of each particle were registered on a database that also stored particle location through time. The tagged particles are considered to behave in the same way as native particles because their shape was not altered and the mass

DOI: 10.2112/SI75-073.1 received 15 October 2015; accepted in revision 15 January 2016.

*Corresponding author: tony.dolphin@cefas.co.uk

changed by less than one percent. Tagged particles were returned to the release site (Figure 1) and spread evenly over a 10 x 14 m area, which extended from the top of the beach to its seaward extent where it intersects sand flat and rock platform.

Tracking such a large number of tracers over long space and time scales would have otherwise required a large labour pool and numerous devices to separately detect and position tags. Instead we developed (in-house) an integrated RFID tag detection, positioning and recording system, which allows tracers to be tracked over large areas. It integrated the signals from detectors, RFID reader units and RTK-GPS into a Cefas EDC logger. There are two detector types – sweeper and swath – which allow rapid scanning of large areas of the coast (23,216 m^2 to 81,387 m^2). The 'sweeper' is backpack-mounted and is swept left and right by the operator to scan 1.5 m^2 per sweep on the steeper parts of the beach; the 'swath' is an array of four detector systems towed behind a quad bike (Figure 2) which scans a 4 m^2 width of beach per second. Each detection produces a 'beep' that allows the surveyors to develop an understanding of the tracer cloud's distribution and adjust the survey area to improve detection. Other studies of this kind that have been reported in the literature have used non-integrated methods that were slower and make the scanning of large areas at c. 100% coverage very difficult (*e.g.*, Allan *et al.*, 2006; Dickson *et al.*, 2011; Miller *et al.*, 2011).

Following release, tag positions were measured monthly for three years. Particle velocity was determined by 1) tracking the tracer centroid along the transport corridor and 2) calculating the average particle velocity based on the displacement of each individually-identifiable particle between consecutive surveys. The latter method has advantages in that the record can be segmented spatially to gain average velocities along sections of the coast with distinct transport rates and thereby account for non-uniformity in the longshore transport system.

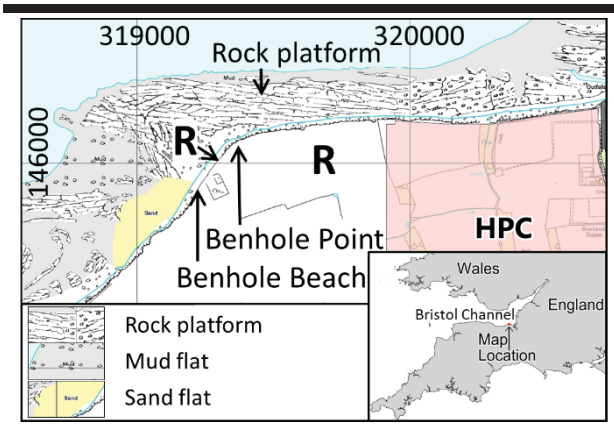

Figure 1. Study site location map. R marks the tracer release site and HPC is the proposed Hinkley Point C power station.

RESULTS

A very high percentage of tags were repeatedly found – typically 70-95% of tag reads were found at least once every three months (Figure 3). After three years, more that 70% of the particles were still being detected. As most individual tags were detected every two to three surveys, the lower monthly detections ($\bar{x}$ = 42%) could be attributed to interference between pairs of tags lying close together (*i.e.*, simultaneous radio transmissions) and/or the angle of the tags relative to the detector. There was a general decline in the detection rate of 4.6% per year (dashed line, Figure 3) and a seasonal oscillation with the highest detection rates in summer and autumn, for which we have no explanation – the oscillation is not correlated with scanned survey area.

Tracer velocity

Several methods were tested to give a single estimate of the longshore tracer velocity using all detected particles. These included: (i) taking the arithmetic mean of all individual particle velocities and (ii) determining the velocity from the movement of the tracer centroid determined by number (*i.e.*, density) and mass (*i.e.*, centre of mass).

Figure 2. Cefas' sweeper (left) and swath (right) RFID detector and positioning systems

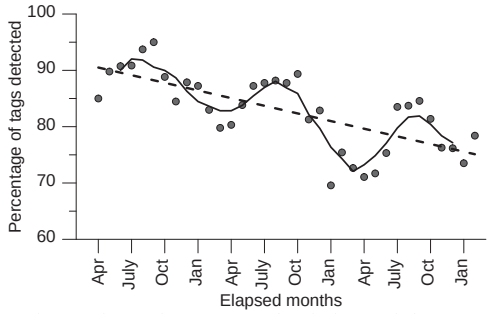

Figure 3. Time series (using a 3 month window) of the percentage of tags released that were regularly relocated. The solid line is a running average and the dashed line shows a broad 'lost tags' trend (linear regression) of 4.5% per year.

These methods gave the same pattern of tracer velocity through time, showing that distinguishing individual tracer particles had, in this particular instance, no advantage over centroid methods (*i.e.* indistinguishable tracer) for velocity estimates of the entire tracer cloud. However, without the individual velocity measurements from the RFID tags, the centroid methods would have been associated with large

uncertainty as the velocities of individual tags in the tracer population would not have been known.

The density plots and standard deviations in Figure 4 highlight the issue that the tracer cloud dispersed more rapidly than its mean or centroid velocity. Seven months into the study, a high percentage of tracer particles had not left the release site, as shown by the white peak in the density plot. Tracer burial and location shoreward of the storm berm are likely causes.

Perhaps more importantly, the gravel particles were being subjected to highly non-uniform longshore transport, which caused the initial tracer cloud to subdivide into several fractions, many of which became isolated from each another (Figure 4, third inset). This process continued throughout the three year experiment. As a result, single value estimates (*e.g.*, an average of all particle velocities) of longshore velocity from the tracer population is meaningless and methods that can account for alongshore variability in the transport system are needed.

This is, of course, fairly obvious and would apply to most coastal systems – burial in beaches, particle interactions with the beach fabric, changes in wave obliquity and alongshore wave power, cross-shore gradients in tidal inundation duration and geological factors, can all contribute to variation in mobility and transport.

DISCUSSION

High detection rates are common in RFID studies (*e.g.* Curtiss *et al.*, 2009), including this one, but none of the published studies have run as long as this three year study. In terms of re-detection, the successful performance of the measurement system ($\bar{x}$ = 83%, 78% on completion) is testimony to the RFID technique in general, the number of tracers selected, specific features of the site (*e.g.*, small beaches limit burial depths) and the ability of Cefas' RFID detection system to merge tag reads and RTK-GPS positions directly onto the Cefas EDC field logger; most studies reported in the literature have used two field teams, with the first detecting tags and leaving markers on the ground with the tag ID and the second recording the ID alongside the tag positions. This is time consuming and inefficient compared to the integrated approach used here.

Tracer velocity – tracer population

When calculating velocity using all detected particles, it was apparent that tracer dispersion and cloud fragmentation, caused by non-uniformity in the longshore transport system, rendered centroid velocity estimates meaningless. Burial and cross-shore differences in inundation and bed shear stress were two obvious causes of the cloud's anchored tail compared to its mobile front. Dispersion was also greater than average movement and fragmentation of the cloud was almost immediate following release, further indicating that all-particle velocity estimates are inappropriate.

Tracer velocity – spatial distribution

Examination of the spatial distribution of particles (*e.g.*, insets in Figure 4) each month and their velocities revealed alongshore patterns in tracer locations and movements. To highlight this observation, a cumulative (for the three year study period) density map was used to examine spatial patterns in tracer location (Figure 5A) and average velocities were plotted in 25 m wide bins along the gravel transport corridor (Figure 5B).

The particle-density map in Figure 5A shows numerous locations where particles tended to accumulate over the three year period. These whiter areas give an initial location of the transport pathway that had been taken by most particles and the variability in its cross-shore width. In general, the active transport corridor was widest where beaches were present (bins 8 – 13 (-50 – 50 m) and > 50 (> 975 m); Figure 5) and narrow where there are none. Tracer velocity was low where beaches were present due to burial, increased bed roughness and gradients in mobility that decrease with increasing beach elevation (*i.e.*, tracer high on the beach was mobilised less often). Tracer velocity was especially low near the release site (bins < 11) because wave obliquity, and therefore the alongshore component of wave power that drove longshore transport, was low due to the NW facing coast. At Benhole Point (c. bins 14 - 16; 75 - 125 m), the coast turns toward the north and so has a higher expected wave obliquity and, potentially, higher alongshore wave power; modelling or measurement of nearshore waves is required to confirm this but the tracer velocity did rise as shown in Figure 5B.

The narrowing transport corridor in places (Figure 5A), could be explained by areas unfavourable for deposition, such as sections of smooth sloping rock surfaces down which particles could roll and not settle – visual observations confirmed that there were several areas where bare rock rarely saw rounded beach gravels at rest. For example, the area around bins 27 - 31 (400 - 500 m) was narrow but had a low density (*i.e.* low deposition), and the highest velocities, because the substrate is mostly a smooth rock platform largely free of gravel (see row 3, Table 1). Consequently, the transport pathway may be wider than it appeared to be as particles may have moved over the smooth rock platform surfaces but were unable to rest there. In comparison, bins 17 - 19 (150 - 200 m) had a high particle density and low velocities, which were due to geological controls; in this case, the exposed rock platform funnelled particles into a (miniature) cirque-like terrain with a 40 cm high headwall at 200 m (called walls in Table 1) that acted as a natural barrier to longshore transport and caused gravel to accumulate until either the bed shear stress exceeded that required to cross the rock wall.

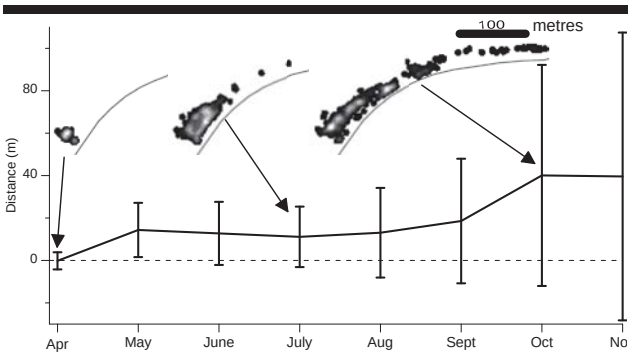

Figure 4. Mean tracer distance travelled (vertical bars show standard deviation) in the first eight months. The insets show the relative tracer density on the first, fourth and seventh surveys, where white indicates high density of particles per unit area.

Further east of the smooth rock platform section, longshore velocity declined (bins 34 – 49; 575 – 950 m) in response to an increasing number of angular blocks (c. 0.1 – 0.4 m; derived from local rock platform and cliff erosion) that impeded transport. By bin 50 (1000 m), the velocity decreased further as tracers arrived at a small beach deposit; this is likely to be due to increased bed roughness and the potential for particle burial. Downdrift, there was no beach (bin 56 and 59; 1125 – 1200 m) and the velocity more than doubled. From bin 60, the number of particle detections fell and movement statistics were less robust and therefore were not considered further.

Geomorphology and particle velocities

It is apparent from Figure 5, and the discussion above, that spatial patterns in the longshore transport system are linked to varying aspects of the coastal geomorphology. In order to provide estimates of typical transit times across the whole frontage, the 25 m bins were merged into larger zones defined according to the dominant geomorphological factors controlling sediment transport (Table 1). Establishing wider spatial zones also provided more robust estimates due to the larger spatial envelope and corresponding number of detections. As the data were gathered over three years, bias around an individual year was also minimised. By characterising the velocity within each zone, transit time estimates can be made, including the potential propagation of a fall in supply due to construction activities blocking the transport corridor.

The mean estimated transit time over the 1.2 km between Benhole Beach and bin 59 (after which tracer numbers are not included as they are too few in number) was 1 year and 10 months. The main extent of Benhole Beach was excluded from the transit time calculation because net longshore transport there was very low ($\bar{x}$=0.18, sd=0.38 m/day) due to low wave obliquity and the possibility that the beach is a source that only slowly leaks material to Benhole Point, beyond which it travelled relatively quickly (up to 18 times faster). At the end of the study, 5% of the tracer particles were still on or in Benhole Beach and of these 62% were on the upper beach at elevations reached only during storm surge.

CONCLUSIONS

The tracer deployed on Benhole Beach was seen to rapidly disperse and fragment (Figure 4), rendering velocity estimates of the tracer population as a whole meaningless, regardless of calculation method. However, spatial analysis based on individual tracer measurements allowed patterns in velocity to be identified (Figure 5). Examination of spatial patterns in velocity, and its underlying causes, can only be performed using tracers that can be distinguished from one another. Consequently, dissecting RFID tracer results into geomorphic zones aids the understanding the longshore transport system and any potential impacts of human activity upon it.

Narrow gravel transport pathways were delineated from tracer density maps, which has relevance for planned construction activity that could interfere with the longshore supply of sediment to downdrift locations. When combined with the longshore patterns in tracer velocity (Figure 5B), the geomorphic controls on longshore gravel velocity became readily apparent. The main aspects were (i) velocity was slowest over beaches, owing to roughness, burial and deposition at high elevations, and where wave obliquity was low; (ii) velocity rose around Benhole point due to the change in coastline orientation and increasing wave obliquity; and (iii) the highest velocities were found in areas of exposed smooth rock platform; however (iv) exposed ridges (up to 40 cm) in the rock platform and (v) angular blocks (derived from cliff and platform erosion) significantly reduced the velocity.

The level of confidence associated with measurements of RFID tagged gravel particles in this study differ from those previously reported due to improvements in the methodology. The integrated detection/positioning system was designed for efficient scanning of large areas at close to 100% coverage. Its integrated nature not only meant less effort per unit survey area but also gave high detection rates: $\bar{x}$ = 83% over the three year study period, thought to be the longest published study of its kind to date. Unsurprisingly, regular detection of a large proportion of tracer particles is necessary to give confidence to the results and interpretation of tracer studies.

Although the RFID technique is still not widely used in coastal studies, when combined with an integrated detection/positioning system it is a highly valuable tool for understanding the behaviour of gravel (and larger) sized sediments on the coast. Applications include the effect of coastal developments and vessel wakes (*e.g.*, Osborne *et al.* 2011) and the efficiency of coastal erosion solutions such as beach renourishment, beach recycling and shingle engines.

Table 1: *Velocity statistics by geomorphic zone. Winter data shown to emphasise spatial patterns. n is the number of tag detections. Velocity is expressed in metres/day.*

Bin ID range	Coastal orientation	Substrate	Average velocity	*n*
7-13	307°	Beach	0.18	2843
14-16	335°	Scattered gravel	0.90	1069
17-19	343°	Smooth rock, wall barrier	0.69	1741
20-24	354°	Smooth rock	2.11	627
25-26	352°	Smooth rock, small wall	2.31	182
27-33	354°	Smooth rock	3.53	405
34-49	1°	Smooth rock, blocks	2.02	1704
50-55	352°	Beach, blocks	0.69	1108
56-59	356°	No beach, blocks, scattered gravel	1.48	96

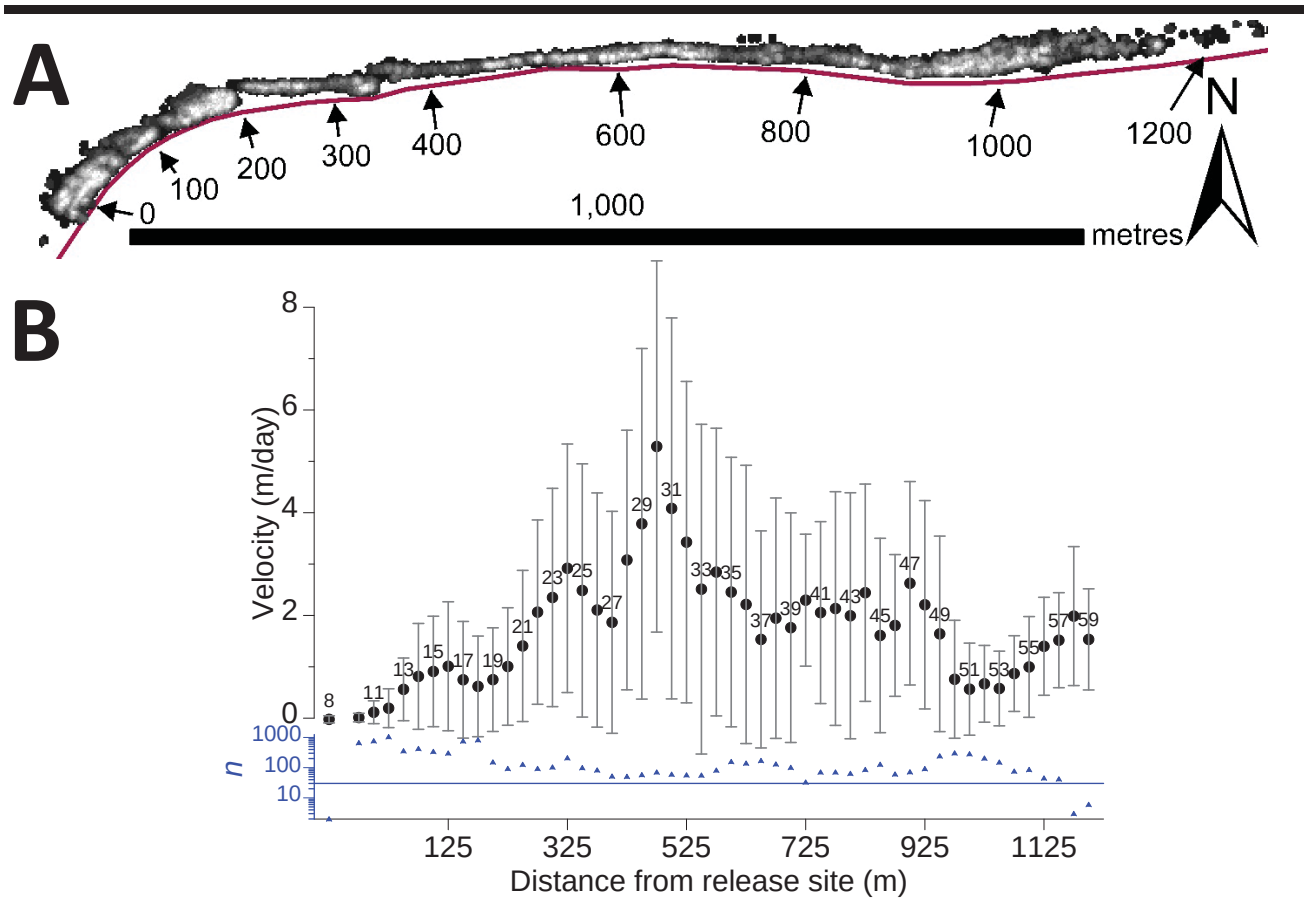

Figure 5. **A:** Maximum relative density surface map over the three year study, showing areas where particles were most (white) and least commonly found (black). The numbers with arrows indicate longshore distances from the release site. **B**: Average velocities within 25 m wide bins of the longshore transport corridor. Black dots are the mean velocity and the associated label is the bin ID referred to in the text. Vertical bars show the standard deviation. Note that only winter/spring data (October – March) are shown as these were the most mobile periods. Triangles indicate the number of detections (*n*) registered in each 25 m bin.

ACKNOWLEDGMENTS

This project was funded by NNB Generation Company Ltd., a part of EDF Energy Ltd, as one element of the current Hinkley Point C Marine Monitoring Programme.

LITERATURE CITED

Allan, J.C.; Hart, R., and Tranquili, J.V., 2006. The use of Passive Integrated Transponder (PIT) tags to trace cobble transport in a mixed sand-and-gravel beach on the high-energy Oregon coast, USA. *Marine Geology*, 232: 63 – 86.

Carr, A.P., 1971. Experiments on longshore transport and sorting of pebbles: Chesil Beach, England. *Journal of Sedimentary Petrology* 41: 1084-1104.

Curtiss, G.M.; Osborne, P.D., and Horner-Devine, A.R., 2009. Seasonal patterns of coarse sediment transport on a mixed sand and gravel beach due to vessel wakes, wind waves, and tidal currents. *Marine Geology*, 259: 73 – 85.

Dickson, M.E.; Kench, P.S. and Kantor, M.S., 2011. Longshore transport of cobbles on a mixed sand and gravel beach, southern Hawke Bay, New Zealand. Marine Geology, 287, 31 – 42.

Komar, P.D. and Inman, D.L. 1970. The longshore transport of sand on beaches. *Journal of Geophysical Research*, 75, 5914–5927.

Hattori M. and Suzuki T., 1978. Field Experiment on Beach Gravel Transport. *Proceedings of the 16th international Conference on Coastal Engineering. American Society of Civil Engineers*: 1688-1704.

Madsen, O.S., 1989. Transport determination by tracers A. tracer theory. In: Seymour, R.J. (ed.) *Nearshore Sediment Transport*. Plenum Press, New York, 103–114.

Miller, I.M.; Warrick, J.A. and Morgan, C., 2011. Observations of coarse sediment movements on the mixed beach of the Elwha Delta, Washington. *Marine Geology*, 282: 201 – 214.

Osborne, P.D.; MacDonald, N. and Curtiss, G., 2011. Measurements and Modeling of Gravel Transport under Wind Waves, Vessel-Generated Waves, and Tidal Currents. *Journal of Coastal Research*, SI59, 165-172.

Journal of Coastal Research	SI	75	368-372	Coconut Creek, Florida	2016

Prograded Barriers + GPR + OSL = Insight on Coastal Change over Intermediate Spatial and Temporal Scales

Amy J. Dougherty [§†*], Jeong-Heon Choi[‡], and Anthony Dosseto[††]

[§] GeoInsights Consulting
Wollongong, NSW, Australia

[‡] Korea Basic Science Institute
Chungbuk 363-883, South Korea

[††] Wollongong Isotope Geochronology Laboratory
[†]School of Earth and Environmental Sciences
University of Wollongong
Wollongong, NSW, Australia

www.cerf-jcr.org

www.JCRonline.org

ABSTRACT

Dougherty, A.J.; Choi, J-H., and Dosseto, A., 2016. Prograded Barriers + GPR + OSL = Insight on coastal change over intermediate spatial and temporal scales. *In:* Vila-Concejo, A.; Bruce, E.; Kennedy, D.M., and McCarroll, R.J. (eds.), *Proceedings of the 14th International Coastal Symposium* (Sydney, Australia). *Journal of Coastal Research*, Special Issue, No. 75, pp. 368-372. Coconut Creek (Florida), ISSN 0749-0208.

Sea level is predicted to rise ~1m by the next century but the response of sandy shorelines is unknown. Understanding past centennial-scale coastal change is crucial to forecast erosion and prepare vulnerable communities/infrastructure for the impact of climate change. To predict intermediate-scale shoreline behavior, models of short-term morphodynamics along beaches and longer-term coastal landscape evolution are integrated. However, limitations exist as process-based engineering models depend on wave climate and beach profile data restricted to historical records (decadal at best), while large-scale coastal behavior models are based on general stratigraphic data inferring evolutionary trends over millennia. Detailing the stratigraphy of paleo-beachfaces preserved beneath Holocene beach ridges, and accurately dating them, could fill this gap by allowing short-term records of present-day beach morphodynamics to be extended over hundreds and thousands of years. This paper aims to demonstrate how using Ground-Penetrating Radar (GPR) and Optically Stimulated Luminescence (OSL) on prograded barriers can achieve this. To illustrate the potential of these methods, decades of research from strandplains in North America, New Zealand and Australia are synthesized to show how: 1) mapping the geometry of paleo-beachfaces can provide Holocene storm records, 2) digitizing the height of paleo-beachfaces could reconstruct sea-level curves, and 3) calculating barrier lithesome area/volume will quantify sediment supply with respect to accommodation space. Storms, sea level, and sediment supply are essential components determining beach behavior; this proposed methodology can yield empirical data on these mechanisms over the centennial-scale providing insight, and input to models, critical for protecting coasts threatened by global warming.

ADDITIONAL INDEX WORDS: *sea level, storms, sediment supply, beach behavior, Holocene evolution.*

INTRODUCTION

Determining how shorelines will respond to predicted climate change over the next century is essential for coastal management and impact mitigation. Fundamental to this forecasting is understanding and contextualizing beach behavior during centuries prior to the onset of global warming. However, past centennial-scale coastal change is unknown because it falls within the knowledge gap between shoreline change measured over hours to decades and coastal evolution over millennia inferred from the landscape (Figure 1). To fill this information void, complex computer models of large-scale coastal behavior and processed-based engineering models are downscaled and upscaled, respectively (Woodroffe *et al.*, 2012). However, the empirical data used in these models are limited. The detailed beach and wave measurements are restricted in location and duration, while longer-term shoreline movements are generalized from chronostratigraphy reliant on point source core data.

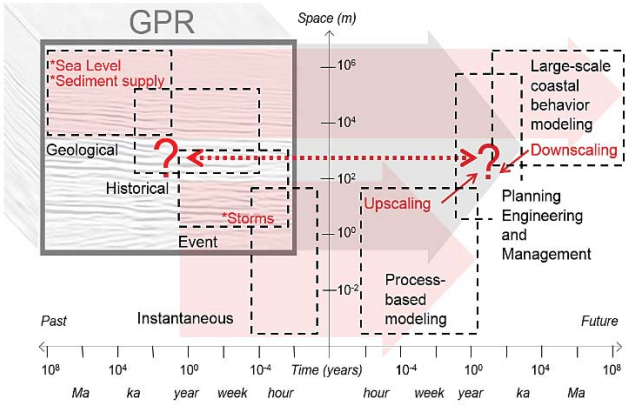

Figure 1. Scale cascade of the spatial and temporal range (modified from Woodroffe *et al.*, 2012) pertinent to coastal processes (black) displaying the knowledge gap between short-term studies of beach behavior and long-term coastal evolution research (red/light grey) which GPR can fill by spanning all four domains (symbolized with 3D GPR image in grey).

DOI: 10.2112/SI75-074.1 received 15 October 2015; accepted in revision 15 January 2016.
*Corresponding author: Dr.AmyJ.Dougherty@gmail.com

This paper aims to demonstrate the potential of combining Ground Penetrating Radar (GPR) with Optically Stimulated Luminescence (OSL) on prograded barriers to acquire a detailed record of beach behavior spanning thousands of years to the present-day. This data can provide Holocene records of storms, sediment supply, and sea level; along with the impact of these key forces on coastal evolution. Ultimately understanding how the barriers have responded to these influences in the past will help better forecast how present-day beaches will react to the future impacts of climate change.

METHODS

Prograded barriers retain the highest preservation potential of any coastal system to record beach behavior over the Holocene. Researchers over the past five decades have studied these systems producing cross-sectional models with detailed dune morphology from topographic surveys. However, these chronostratigraphic models are more generalized with large-scale subsurface facies boundaries interpolated from drill core data and isochrons extrapolated from ^{14}C age samples (*e.g.,* Bernard *et al.*, 1962; Curray *et al.*, 1969; Thom *et al.*, 1981: Figure 2a). Collecting GPR across entire prograded barriers can extract a high-resolution stratigraphic records that detail paleo-beachfaces deposited over the Holocene (*e.g.,* Dougherty, 2011: Figure 3d&e). This geophysical data can then be used to target sediments associated with these beachfaces for OSL dating. Since OSL dates the time elapsed since grains were last exposed to daylight, this technique can determine when paleo-beachfaces were located on the active coast. This chronology can provide the resolution necessary to decipher centennial-scale patterns of coastal behaviour.

RESULTS

The electromagnetic properties of sandy barriers are ideal for GPR and paleo-beachfaces have been mapped with decimeter resolution over kilometers of stratigraphy (*e.g.,* Dougherty, 2011). This level of detail allows the paleo-beachface elevation (which is intrinsically linked to sea level) and morphology (which is inherently affected by storms) to be documented over hundreds and thousands of years (*e.g.,* Dougherty, 2011). In order to perform this analysis, individual beachfaces are digitized to assign elevations and slopes. Similarly, certain stratigraphic layers or perimeters are digitized to calculate areas of accommodation space and sediment volumes. Augmenting this stratigraphic data with an OSL chronology can resolve ages adding the temporal component necessary to determine sea-level curves, storm frequencies and sediment supply/progradation rates.

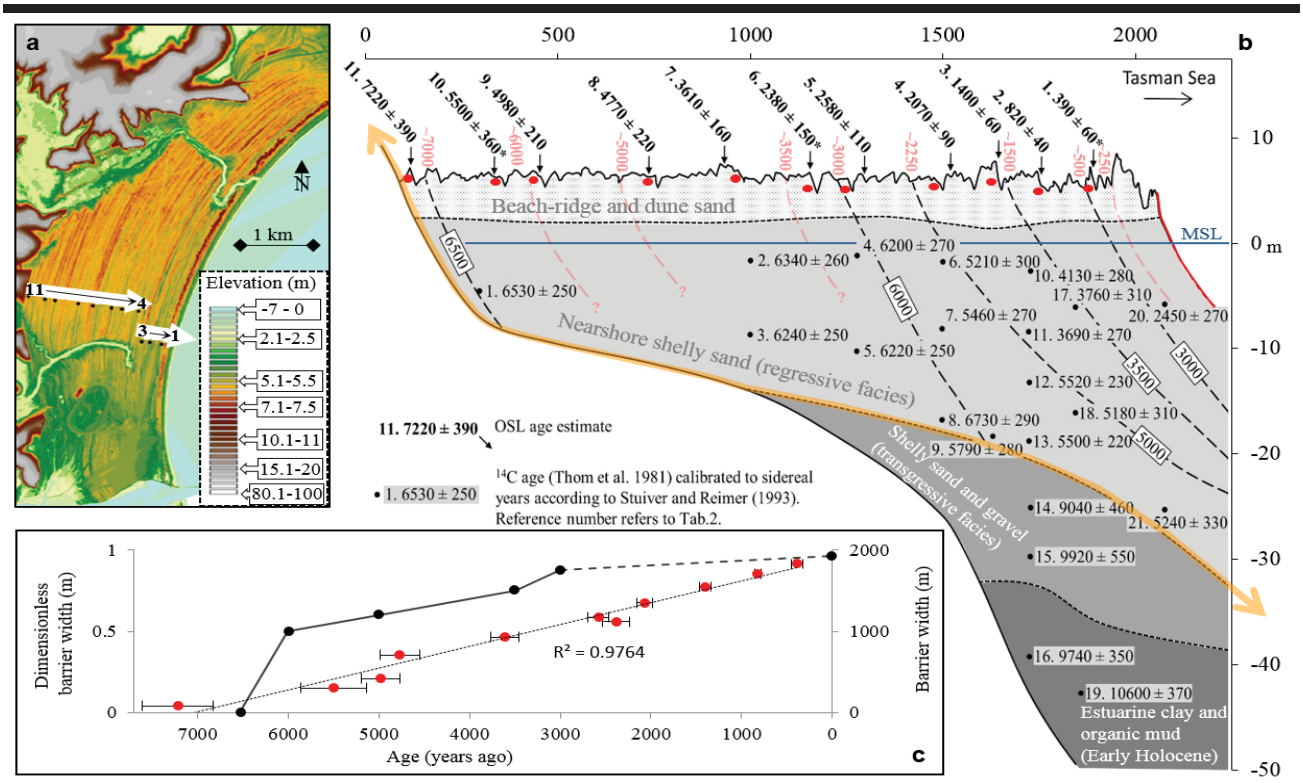

Figure 2. (a) LiDAR image of Moruya prograded barrier, Australia, detailing the series of prograded beach ridges and overlain with OSL sample locations (Oliver *et al.*, 2014a). (b) Stratigraphic cross-section of Moruya displaying radiocarbon and OSL chronologies (Thom *et al.*, 1981; Oliver *et al.*, 2014b). The yellow/grey highlighted double arrowed line shows embayment size used to discuss accommodation space and sediment supplied to the prograded barrier (~30,000 m^3/m of sediment below MSL and ~10,000 m^3/m above MSL, as determined from the area multiplied over a 1-meter swath). Isochrons ages were modified using OSL dates (light red/grey) and redrawn where necessary using the geometry of the present-day shoreface. (c) Plot of ages versus barrier width. The OSL chronology (red/grey) shows a linear progradation, in contrast with the radiocarbon dates (black).

DISCUSSION

In order to illustrate the prospect of combining GPR and OSL on prograded barriers this paper synthesizes findings published on sites where each technique was utilized independently. For detailed information on each individual study and more comprehensive references please refer to the original manuscripts.

Detailing Sediment Supply

Sand supplied to the coast dictates beach behavior such that it can outpace sea-level rise resulting in progradation. To understand sediment supply to a barrier, it must be considered with respect to accommodation space. Both of these parameters have been historically hard to quantify. The coastal plain near Moruya, New South Wales, Australia, is a classic example of a prograded barrier (Figure 2). It is representative of other barriers studied in southeast Australia (*e.g.,* Thom *et al.*, 1981) and those initially researched in North America (Bernard *et al.*, 1962; Curray *et al.*, 1969). The radiocarbon chronology from Moruya was interpreted to show that the barrier prograded rapidly between ~6.5 and 3 ka, after which it became relatively stable (Figure 2). A depletion in the offshore sediment source was hypothesized as the reason for the abrupt shift in evolution and large foredune formation (Thom *et al.*, 1981). A recent study utilized OSL to date beach ridges across the barrier revealing a constant rate of progradation of around 0.27 m/y over the past 7,000 years (Figure 2c) with a beach/foredune ridge forming roughly every century (Oliver *et al.*, 2014).

This OSL chronology indicates that not only has Moruya prograded more linearly and for longer, but that sediment supply has actually increased over time. If the amount of sand delivered to the coast was constant, seaward progradation would have slowed as the barrier built into the deepening embayment. Additionally, preliminary research mapping the entire embayment revealed irregularities in the underlying basin geometry alongshore (Dougherty *et al.*, 2012). Despite these complex variations in accommodation space, the sediment supplied to the barrier resulted in constant seaward progradation seemingly unaltered by changes in subsurface. Reconciling the disparity of the OSL dates with the radiocarbon ages at depth is key to understanding how exactly sediment accumulated below Mean Sea Level (MSL). The volume of sediment above MSL is a third of that below (as measured from Figure 2b). Research using Light Detection And Ranging (LiDAR) calculated the total volume of sand in the barrier lithesome above MSL and determined that it accumulated at a relatively constant rate of 74,000 m^3/y (Oliver *et al.*, 2014a). It is obvious from the LiDAR that the beach ridges are larger in the north and that the foredune complex is larger than the series of beach ridges it fronts. The OSL progradation rate indicates that the foredune probably formed in the last few hundred years and its anomalously large size shows that sediment supply above MSL likely increased.

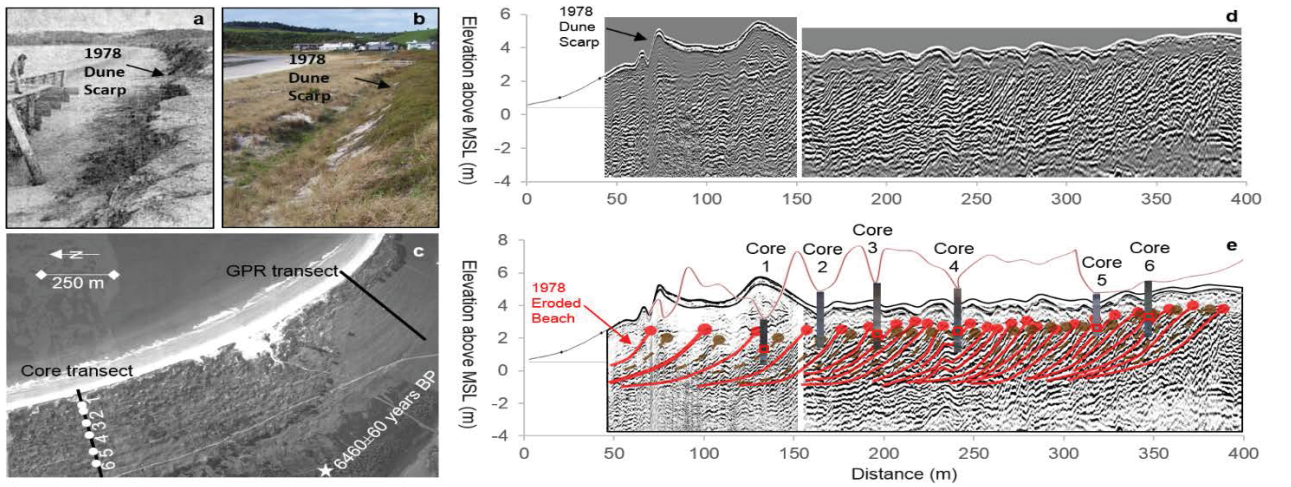

Figure 3. (a) Photo of Omaha beach, New Zealand, after the 1978 storm. (b) Photo taken in 2007 showing the 1978 dune scarp preserved within subsequent accretion. (c) Air photo of Omaha prograded barrier. (d) GPR record collected across southern Omaha barrier. (e) Annotated GPR data highlighting paleo-beachfaces with overlay of morphology and cores from laterally contiguous larger northern beach ridges. Modified from Dougherty *et al.* (2013).

Collecting GPR across the barrier can indicate how exactly the basin infilled below MSL and investigate the formation of the large foredune. A detailed geophysical stratigraphy would allow for the layers dated with OSL to be traced, determining if there is any correlation with the deeper radiocarbon dates. Additionally, a detailed shallow subsurface stratigraphy could be used to quantify volumetric changes between the beach ridges and foredune complex as well as distinguish differences in their formation. Gaining insight into this abrupt increase in sediment supply is key to understanding the marked shift in barrier evolution.

Extending Storm Records

High-energy events are responsible for coastal erosion (*e.g.,* Figure 3a), but predicting these large-magnitude events requires recurrence intervals beyond historical documentation and instrumental records restricted to short-term timescales. Detailed studies using beach profiles have documented distinct storm signature such as dune scarps and steepened upper beachfaces

(*e.g.,* Figure 3a) with concentrations of heavy minerals/coarse-grained sediment (*e.g.,* Buynevich *et al.*, 2007; Dougherty *et al.*, 2004). This research of beach morphodynamics also shows post-storm recovery, whereby lower-energy swell waves return sediment onshore burying the evidence of erosion (Figure 3b). Barriers that have prograded over time preserve these storm records within their accreting layers of sand. Studies in the northeastern United Sates first utilized: 1) GPR on a prograded barrier to distinguish paleo-beachfaces with distinct geometries similar to beach profiles collected after a storm (Dougherty *et al.*, 2004) and 2) OSL to date storm-cut paleo-beachfaces imaged using GPR (Buynevich *et al.*, 2007).

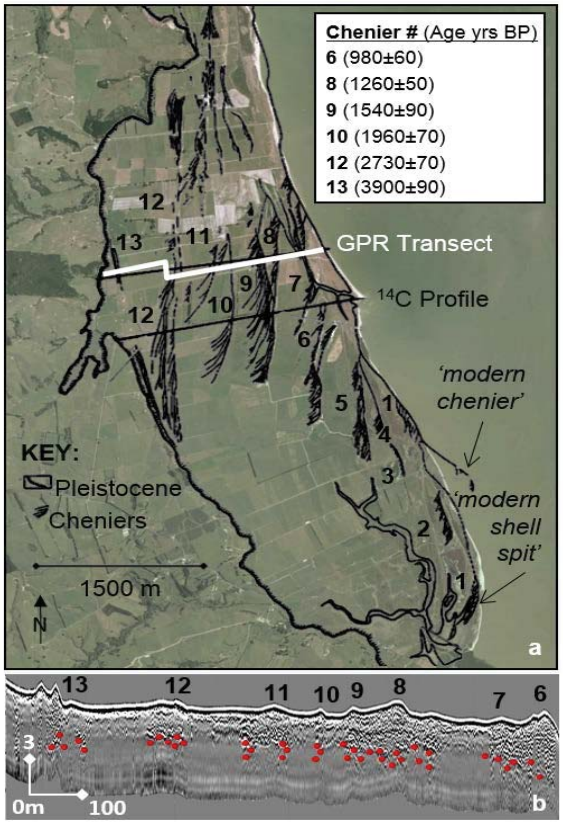

Figure 4. (a) Photo of Miranda chenier plain, New Zealand, with the location of the 13 ridges overlain (black curves) and associated ^{14}C ages. (b) GPR profile across cheniers 6-13 with the beach and nearshore contacts highlighted in red. Modified from Dougherty and Dickson (2012).

Combing GPR and OSL across the width of a prograded barrier has the potential of yielding a storm record over the Holocene which could indicate the recurrence interval of these erosive events. GPR collected across a prograded barrier in Omaha, New Zealand, imaged a storm-cut paleo-beachface known to have been eroded by a series of storms in 1978 (Figure 3). A total of 25 storm-cut paleo-beachfaces were mapped across Omaha (Figure 3e solid red/grey lines) with post-storm recovery beachfaces in-between (Figure 3e dashed brown/grey lines). Thirteen storm-cut beachfaces eroded out swales forming the low-lying beach ridges and 6 of those 13 delineate the swales of the larger northern beach ridges (Figure 3). From this, a hierarchy of storm intensity is proposed whereby the increased strength of a high-energy event results in a greater impact on the morphostratigraphy (Dougherty, 2013). Using a barrier inception age of ~6,000 years before present, theoretical reoccurrence intervals of storms with increasing intensity nearly double from ~250 years (for lowest energy storms that are only recorded in the stratigraphy) to ~500 years (for larger storms that erode low-lying beach ridges) and ~1,000 years (for the largest storms capable of eroding the large beach ridges). Acquiring detailed OSL ages for these ridges would test this theory of storm frequency and intensity, as well as determine if there is any chronological link with storm deposited chenier ridges dated along the same coast (Figure 4) forming a more regional record.

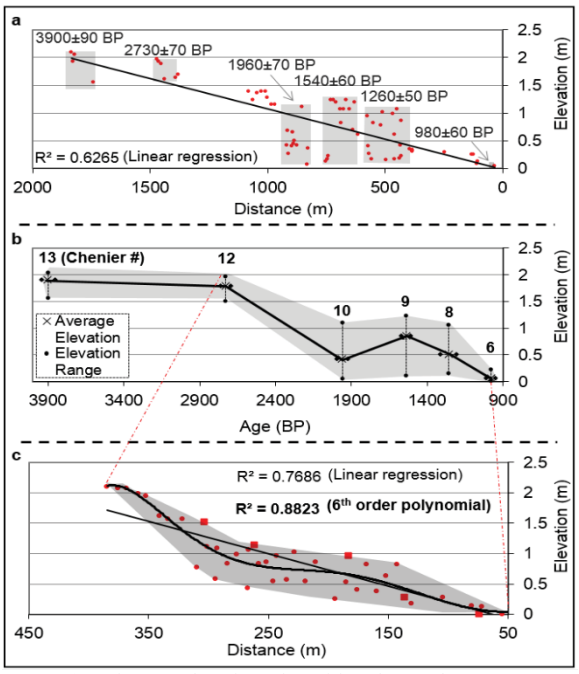

Figure 5. (a) Distance-elevation plot of beach-nearshore contacts with associated ages from Miranda chenier plain. (b) Age-elevation plot of cheniers indicates a nonlinear sea-level fall from +2 meters. (c) Distance-elevation plot of beach-dune interface from Omaha barrier shows a similar nonlinear fall in sea level over the Holocene. Modified from Dougherty and Dickson (2012) and Dougherty *et al.* (2013).

Contextualizing Sea-Level Rise

There has been a concerted effort to detail relative sea-level change over the Holocene, yet the resolution necessary to contextualize the predicted ~1m sea-level rise is lacking. Particular focus has been on 'far-field' sites, such as Australia, to identify the relationship of global ice-equivalent and global sea-level changes in order to model their response to future climate change. Despite extensive research in Australia, debate remains as to whether there was a ~2 m mid-Holocene highstand and if so what was the nature of the subsequent sea-level fall (Woodroffe and Murray-Wallace, 2012). Resolving these

smaller scale fluctuations is made difficult as most sea-level curves combine a wide variety of biological indicators and other intertidal material, with varying error bars, which obscure any recorded minor elevation changes. Dune-beach facies boundary imaged using GPR provides a well-constrained sea-level marker which when combined with OSL have accurately recorded Holocene sea-level histories from two different prograded sites in the United States (Rodriguez and Meyer, 2006; Van Heteren *et al.*, 2000).

Similar to Australia, the New Zealand's Holocene sea-level curve is ambiguous. Digitized beach-dune interfaces within the Omaha GPR capture a distinct decrease in elevation (Figure 3&5: Dougherty, 2013). This pattern is similar to the latest sea-level curve published for New Zealand using the more traditionally accepted sea-level proxy of cheniers (Dougherty and Dickson, 2012). This most resent time-elevation plot was constructed using existing radiocarbon dates of the cheniers and mapping the beach-nearshore interface using GPR (Figure 4&5). Both New Zealand sites show a nonlinear fall form a +2 meter high mid-Holocene sea-level highstand, which interestingly is similar to some of the contentious sea-level curves from across the Tasman Sea in Australia (Woodroffe and Murray-Wallace, 2012). Additionally, the subsequent sea-level stillstand is believed to have greatly altered coastal evolution at both sites. At Miranda, the chenier plain ceased seaward progradation and started longshore extension; while at Omaha, the formation of low-lying beach-ridge shifted to the construction of an anomalously large foredune complex (Dougherty and Dickson, 2012; Dougherty *et al.*, 2013).

CONCLUSIONS

Collecting GPR and OSL data across prograded barriers provides insight into the elusive intermediate-scale coastal change by extending our knowledge of well-studied present-day beach morphodynamics to understand beachfaces spanning over hundreds and thousands of years. Combining these techniques offers the possibility to determine past sea levels, changes in sediment supply and storm frequency-intensity relationships, as well as their impact on barrier evolution. This information can then be used to better model how these three forces may be altered by global warming. Ultimately, this will assist in forecasting the response of beaches in front of (and adjacent to) these barriers, so that communities can best prepare for climate change. To this end, GPR data and OSL samples have been collected across a number of prograded barriers in New Zealand and Australia to look for regional and trans-Tasman records of storms and sea-level change. Differences in sediment supply versus accommodation space are also being studied to determine what caused the shift in barrier evolution that resulted in the formation of ubiquitous large foredune complexes anomalous from the series of low-lying beach ridges they front.

ACKNOWLEDGMENTS

Presentation of this paper was partly funded through a GeoQuEST Research Centre grant awarded to A. Dougherty.

LITERATURE CITED

Bernard, H. A.; LeBlanc, R. J., and Major, C. F., 1962. Recent and Pleistocene Geology of Southeast Texas: Field Excursion No. 3, November 10 and 11.

Buynevich, I. V.; FitzGerald, D. M., and Goble, R. J., 2007. A 1500 yr record of North Atlantic storm activity based on optically dated relict beach scarps. *Geology*, 35(6), 543-546.

Curray, J.; Emmel, F., and Crampton, P., 1969. Holocene history of a strand plain, lagoonal coast, Nayarit, Mexico. *Proceedings Memorias del Simposio Internacional de Lagunas Costeras*, 63-100.

Dougherty, A.J., 2011. Evolution of prograded coastal barriers in northern New Zealand. Auckland, New Zealand: The University of Auckland, PhD Thesis, 259p.

Dougherty, A. J., 2013. Extracting a record of Holocene storm erosion and deposition preserved in the morphostratigraphy of a prograded coastal barrier. *Continental Shelf Research*, 86(1), 116-131.

Dougherty, A.J. and Dickson, M.E., 2012. Sea level and storm control on the evolution of a chenier plain, Firth of Thames, New Zealand. *Marine Geology,* 307-310, 58-72.

Dougherty, A.J.; FitzGerald, D.M., and Buynevich, I.V., 2004. Evidence for storm-dominated early progradation of Castle Neck barrier, Massachusetts, USA. *Marine Geology*, 210, 123-134.

Dougherty, A. J.; Oliver, T.; Cowell, P., and Woodroffe, C. D., 2012. Application of a model framework for assessing risk and adaptation to climate change on the South Coast of New South Wales. *Proceedings of the 21st New South Wales Coastal Conference* (Kiama, Australia), 23p.

Oliver T.S., Dougherty, A.J., Gliganic, LA., and Woodroffe, C.D., 2014a. A revised chronology for the coastal plain at Moruya, NSW: Implications for modelling and management. *Proceedings of the 23st New South Wales Coastal Conference* (Ulladulla, Australia), 17p.

Oliver, T. S.; Dougherty, A. J.; Gliganic, L. A., and Woodroffe, C. D., 2014b. Towards more robust chronologies of coastal progradation: Optically stimulated luminescence ages for the coastal plain at Moruya, south-eastern Australia. *Holocene*, 25(3), 536-546.

Rodriguez, A.B. and Meyer, C.T., 2006. Sea-level variation during the Holocene deduced from the morphologic and stratigraphic evolution of Morgan Peninsula, Alabama, USA. *Journal of Sedimentary Research*, 76(2), 257-269.

Thom, B.; Bowman, G.; Gillespie, R.; Temple, R., and Barbetti, M., 1981. Radiocarbon dating of Holocene beach-ridge sequences in southeast Australia: Geography Department, Faculty of Military Studies, University of NSW. 36p.

van Heteren, S. Huntley, D.J. van de Plassche, O., and Lubberts, R.K., 2000. Optical dating of dune sand for the study of sea-level change. *Geology*, 28, 411-414.

Woodroffe, C.; Cowell, P.; Callaghan, D.; Ranasinghe, R., J.; Wainwright, D.; Barry, S.; Roger, K., and Dougherty, A., 2012. A model framework for assessing risk and adaptation to climate change on Australian coasts. *National Climate Change Adaption Research Facility, Gold Coast,* 205p.

Woodroffe, C. D. and Murray-Wallace, C. V., 2012. Sea-level rise and coastal change: The past as a guide to the future. *Quaternary Science Reviews*, 54, 4-11.

Journal of Coastal Research	SI	75	373-377	Coconut Creek, Florida	2016

Morphological Response of a Macrotidal Embayed Beach, Porsmilin, France

France Floc'h[†*], Nicolas Le Dantec[†‡], Clara Lemos[†], Romain Cancouët[†], Damien Sous[§], Lise Petitjean[§º], Frédéric Bouchette[º], Fabrice Ardhuin[†††], Serge Suanez[††] and Christophe Delacourt[†]

[†]Domaines Océaniques UMR6538 IUEM/UBO

[††]Géomer-LETG UMR6554 IUEM/UBO

[†††]LPO UMR6523, IUEM/UBO/Ifremer/IRD
29280 Plouzané, France

[‡]CEREMA, Margny Lès Compiègne, France

[§]Université de Toulon, Aix-Marseille Université,
CNRS/INSU/IRD, MIO, UM 110, 13288 Marseille, France

[º]GEOSCIENCES-M, Université Montpellier II / CNRS, France

www.cerf-jcr.org

www.JCRonline.org

ABSTRACT

Floc'h, F.; Le Dantec, N.; Lemos, C.; Concouët, R.; Sous, D.; Petitjean, L.; Bouchette, F.; Ardhuin, F; Suanez, S., and Delacourt, C., 2016. Morphological Response of a Macrotidal Embayed Beach, Porsmilin, France. *In:* Vila-Concejo, A.; Bruce, E.; Kennedy, D.M., and McCarroll, R.J. (eds.), *Proceedings of the 14th International Coastal Symposium* (Sydney, Australia). *Journal of Coastal Research*, Special Issue, No. 75, pp. 373-377. Coconut Creek (Florida), ISSN 0749-0208.

Morphodynamics of sandy, macrotidal, embayed beaches is complex because of the numerous physical processes interacting at the same location over a wide range of temporal scales. As most of these processes are controlled by beach morphology, dynamic feedbacks are generally observed between hydro- and morphodynamics. Investigating short-term processes is essential in order to improve long term morphological prediction. A key question is to understand how beach slope reacts to forcing conditions, in particular the response time of the beach profile, how long the transient state lasts. This study deals with the spatial and temporal responses of beach morphology to varying incident conditions. Here we report main observations, preliminary results and on-going investigations on the DYNATREZ1 field campaign, which was conducted in the framework of the National Observation Service Dynalit. Beach profiles are shown to adapt rapidly to forcing conditions, within two days, with more intense variations observed in the high tide swash zone. The presence of infragravity waves and their dissipation on the beach is highlighted. It is likely that the very large variability in beach slope observed over a single neap-spring cycle is responsible for the accordingly large variability in wave skewness, asymmetry and breaking processes, and thus in sediment fluxes and morphological changes.

ADDITIONAL INDEX WORDS: *morphodynamics; macrotidal beach; embayed beach; slope; infragravity*

INTRODUCTION

The morphology of sandy coasts varies over a wide range of temporal and spatial scales in response to a variety of processes (Stive *et al.*, 2002). On timescales from years to days and even hours for single storms, changes in wave energy reaching the coast are the dominant process impacting morphological change via both cross-shore and longshore sediment transport processes in the surf and swash zone (Short, 1991; Wright and Short, 1984).

Macrotidal embayed beaches are a specific environment, showing changes in beach elevation either negative (erosion) or positive (accretion), up to tens of cm per day, according to the spatial distribution of hydro and morphodynamic patterns that are controlled by the tidal excursion. The morphodynamics of such environments depends on complex phenomena: shoreline rotation due to long-shore circulation, peculiar surf zone circulation, geologically controlled surf zone circulation, large sea level variations, and varying slopes in the swash zone (Dehouck *et al.*, 2009; Loureiro *et al.*, 2013; Storlazzi and Field, 2000; Turki *et al.* 2013). The beach of Porsmilin, monitored within the National Observation Service Dynalit (http://www.dynalit.fr), is an example of such environments. Monthly cross-shore DGPS profiles have been acquired for 13 years during low spring tides. Empirical predictive models considering incident gravity waves energy as the only factor controlling beach morphology (Castelle *et al.*, 2015; Yates *et al.*, 2009) have been reported to yield non-negligible uncertainties (Floc'h *et al.,* 2014). The investigation of short-term processes is essential in order to improve long term forecasts capabilities. A key question is to understand how beach slope reacts to forcing conditions, in particuliar the response time of the beach profile: how long the transient state lasts. This is the main purpose of the DYNATREZ1 field campaign. This paper summarizes the main observations, the preliminary observations, provides some preliminary results and outlines on-going investigations.

The study focuses on an embayed beach (Porsmilin beach), located in Brittany (France), facing the Iroise sea (Figure 1 and 2). This site is part the National Observation Service Dynalit. The Iroise sea shoreline includes seacliffs, small pocket beaches backed by cliffs or situated at stream mouths, and wide embayed beaches backed by sand dunes. Porsmilin beach is a welded barrier beach flanked by cliffs on either side, and backed by colmated brackish water marshes. This SSW-facing beach is also bounded by headlands and

DOI: 10.2112/SI75-075.1 received 15 October 2015; accepted in revision 15 January 2016.

*Corresponding author: france.floch@univ-brest.fr

bedrocks, extending offshore, that obstruct the alongshore sand transport generated in the surf zone and allow incident waves from the SSW only (Figure 2). Tides are semi-diurnal and symmetric with a mean spring tidal range of 5.7 m (macrotidal). The mean speed of spring tidal currents in Bertheaume bay, about 1 km off the beach, is 0.4 m/s (SHOM, 1994). The Iroise sea is a highly-energetic wave-dominated setting with 1 and 10-year return period significant wave heights of 11.3 m and 14.5 m in 110 m of water depth at the West of Brittany (Dehouck *et al.*, 2009). Energetic swells originate from low and high pressure systems in the North East Atlantic Ocean. However, along this rocky coastline, wave propagation is considerably affected by refraction and diffraction processes generated by the large continental shelf and numerous headlands, shoals and islands located off the coast (Ushant Island, Molene Archipelago). Hence, oceanic swells reaching the shoreline have a quasi-normal incidence angle and are highly dissipated, resulting in moderate energy conditions at Porsmilin beach. Storm waves are 0.8 to 1.5 m high while the mean annual wave height is 0.5 m (Dehouck *et al.*, 2009). The Porsmilin intertidal zone is 200 m wide and 200 m long. Sediment has a median grain size (d_{50}) of 320 µm in the intertidal zone. Samples collected across the beach face show some cross-shore variability in d_{50} mainly due to coarser sediments around the crest of intertidal bars (d_{50}≈0.7 mm). Shingles (d_{50} about 5 cm) are present during energetic conditions. There is no significant longshore variability in the sediment size distribution (Dehouck *et al.*, 2009).

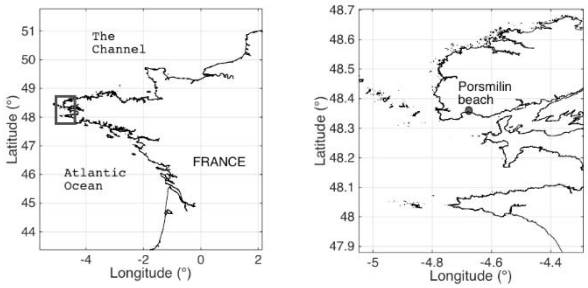

Figure 1. Location of study area. *Left:* West and North coast of France; *Right:* Zoom on the Iroise sea and location of Porsmilin beach, in Bertheaume bay.

METHODS

The field campaign DYNATREZ1 took place over 20 days (covering a neap-spring tidal cycle) in October 2014 (8th-28th) under moderate energy conditions. In order to assess the longshore variability in the beach and the cross-shore sediment fluxes, topographic surveys were performed with a Differential Global Positioning System (DGPS) RTK (Topcon Hiper2) at low tide during daylight hours, every day along three cross-shore lines represented on Figure 2. Concurrently, eight pressure sensors were buried (initially, 15 cm below the sand surface) along the middle transect (Figure 2), to record water level and assess wave transformation along the surf and swash zones. The pressure sensors were split into two sets of four sensors: the first positioned between the Mean Water (MW) and the Mean High Water Neaps (MHWN) levels and the second under the Mean High Water Springs level (MHWS). Only the lower beach set is considered in this paper. The initial beach slope is shown on Figure 3, along with the altitude of the sensors (elevations relative to the national geographic datum "Institut Géographique National" which has its origin at the mean tide of Marseille (France)). On this figure are also represented the 13-year averaged profile (from monthly data) and the average profile calculated from the daily data acquired during DYNATREZ1. Pressure sensor data were recorded at 5 Hz. Once Fourier transform, the wave spectrum is obtained. Infragravity waves are considered for a frequency below 0.04 Hz. Atmospheric pressure was recorded at 1 Hz, in an open room located backshore, 7 m above the uppermost part of the beach. Wind data was collected at the nearest Meteo France station located in Brest Airport, a few kilometers away.

In order to understand the direct impact of hydrodynamics conditions on the beach profile, the erosion/accretion rate $e(x)$ is defined as:

$$e(x) = \frac{z_n(x) - z_{n-1}(x)}{\Delta t} \quad \text{(Eq. 1)}$$

with $z_n(x)$, the altitude of beach profile at the cross-shore position x recorded on day n. The function e is positive (resp. negative) in case of accretion (resp. erosion). The standard deviation with respect to the mean profile $d(x)$ is also introduced:

$$d(x) = z_n(x) - z_{moy}(x) \quad \text{(Eq. 2)}$$

with $z_{moy}(x)$ the averaged profile. The deviation according to the long-term averaged profile does not permit to highlight the daily variations. The long-term averaged profile shows no slope breaks (Figure 3) but rather a perfect slope according to Dean's definition of the equilibrium profile (Dean, 1991). Over the duration of the field experiment, the beach profile is rather reflective in the upper beach and dissipative in the lower beach. The break in the slope occurs around the MHWN level. Actually, the long-term study of Porsmilin Beach profile changes (Floc'h *et al.,* 2014) shows that while autumn is typically the season experiencing the biggest slope break, the October 2014 profile had a particularly well-marked slope break. Consequently, in order to detect slight variation at the scale of our field experiment, the averaged October profile using the daily data is used. The profiles recorded during neap tide are included in the calculation, noting that these profiles are shorter (Figure 6). Finally, we evaluate the beach slope after Stockdon *et al.* (2006). These three parameters are derived for each DGPS profile and the results are plotted on Figure 6 together with the hydro- and morphodynamic parameters.

RESULTS

The offshore conditions cover various wave and tide conditions (Table 1) and allow us to assess infragravity and gravity wave action during both high-energy events and calm periods, for high or low Relative Tide Ranges (RTR, Masselink *et al.*, 1993). The dimensionless fall velocity (Ferguson and Church, 2006) remains between 0.5 and 2 suggesting a reflective beach during the whole field experiment according to the conceptual model of Masselink and Short (1993), consistent with the profile of the upper beach. The field campaign may be divided into a number of sequences accoriding to the hydrodynamic conditions. During

spring tide period (8th-12th), Hs decreases from 1 m (highest wave during the field experiment) to 0.1 m. The spectrum is wide in the gravity part, with high frequencies, and no energy in the infragravity part. The peak period decreases from 11 s to 7 s, to leave only wind waves from the 11th to the 14th.

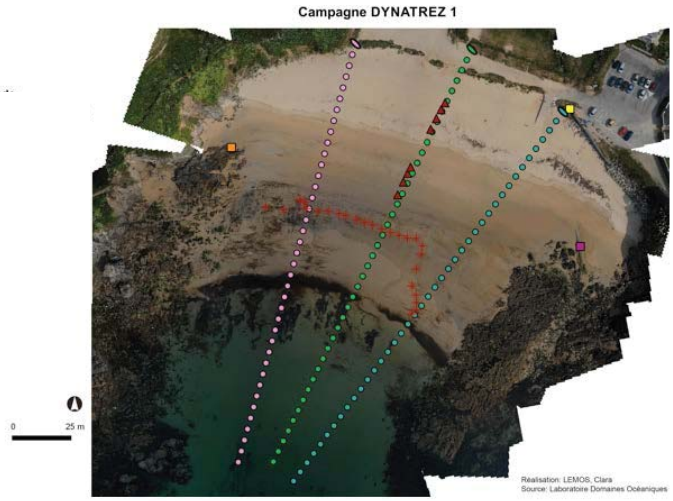

Figure 2. DYNATREZ field experiment – pink, green and blue dots represent daily DGPS data; red triangles mark the location of pressure sensors; red cross mark the upper boundary of grown; squares represent geodetic markers referenced in IGN69.

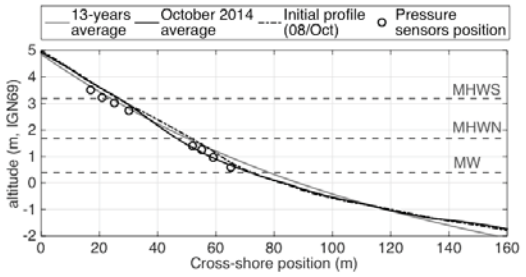

Figure 3. Location of the pressure sensors (from #1 at Mean Water level to #8 above Mean High Water Springs level) with the initial middle profile (dash-dotted line), the profile averaged over the wholc field experiment (black) and the 13-years averaged profile (gray). The Lowest Astronomical Tide is at -3.42 m IGN69.

The incident energy is then so low (Hs < 0.2 m) that it is not visible on Figure 4. The beach is tidal dominated (RTR > 15).

From the 15th, the energy spectrum is narrower, well-centered around the peak period, contains more energy in the infragravity part and no energy at higher frequencies (Figure 4 and 5). During neap tide period (15th-20th), the conditions are quite energetic with a swell and a ratio of infragravity waves between 30 and 40%. The RTR is at its minimum (~4) displaying a Low Tide Terrace (LTT) beach type with possible rip and bar formation (Masselink and Short, 1993). The conditions are less energetic on the 21st with Hs about 0.4 m and wind waves (Tp about 8 s) and become more energetic on the 23rd with swell again. A ratio of 40% of infragravity waves is obtained for the 22nd of October, and this ratio quickly decreases to become only 10-15% until the end of the experiment. The beach experiences stable moderate conditions during the last part of the experiment (24th - 28th): RTR about 10 (LTT type) during moderate spring tide (tide ranges around 4.0-5.5 m) with Hs ~ 0.5 m and Tp ~10 s. Besides, the reflectivity of the beach is confirmed by the derivation of the incident and reflected part of the energy spectrum (Figure 5) according to the three sensors method (Mansard and Funke, 1980; Rey *et al.*, 2003) applied to sensor 1, 2 and 3. It is shown that up to 50% of 10 s period waves are reflected (depending on the conditions). The lower frequencies seem to not be reflected, in contrary to the known behavior of infragravity waves. Thus the question is if infragravity waves are dissipated as in Sénéchal *et al.* (2011) or if it is another process which is observed here. These hydrodynamic conditions altogether have an impact on the variation of beach morphology.

Table 1. *Tide and wave conditions during DYNATREZ1*

Days October	Tidal range h (m)	Wave height H_s (m)	RTR -	Peak period T_p (s)	Ratio IG
8 – 11	7 to 5	1 to 0.2	10 to 40	11 - 7	< 10 %
11 – 14	5 to 3	< 0.2	> 20	7	< 10 %
15 – 20	2 – 3	0.8	~ 4	12	30 – 40 %
21	3	0.4	~ 10	8	10 %
22 – 23	3 to 4	0.6 - 0.8	~ 10	12	40 to 30 %
23 – 28	4 to 5	0.5	~ 10	10	10 – 15 %

First, the three transects were compared to detect a possible rotation of the beach (Turki *et al.*, 2013). Pocket beaches usually experience rotation with respect to the direction of wind waves. During the field campaign, Porsmilin Beach experienced winds coming from SSE (6%), S (30%), SSW (15%), SW (18%), WSW (7%) and less than 3% from each other directions. The directions impacting our site are comprised between SSE to SW, and are well-represented among the wind conditions during our field experiment. However, the variation of the cross-shore position of several altitudes shows that the three profiles react in the same way (eroding or accreting simultaneously) regardless of the wind direction. In fact, the two headlands surrounding the beach and the refraction occurring on the foreshore reduce the possible direction of incident waves. Notably, the amplitude of vertical change on the western part is lower for any wind

direction. This part of the beach is not as well aligned as the rest with the incident waves allowed by the headlands. To conclude on this specific issue of beach rotation: it is negligible at Porsmilin Beach, and no longshore variation has to be considered. Thus, the following comments focus on the longshore averaged profile.

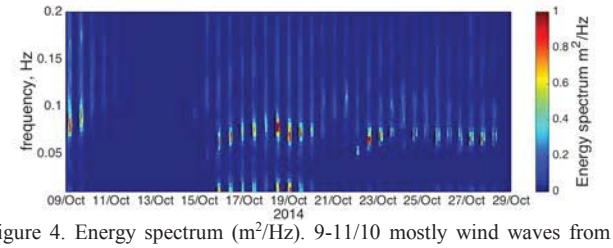

Figure 4. Energy spectrum (m^2/Hz). 9-11/10 mostly wind waves from 0.06 to 0.2 Hz; 11-15/10 very calm period; 15-20/10 very energetic period with swell and infragravity waves; 20-21/10 calm period and 22-29/10 swell with little energy in the infragravity band

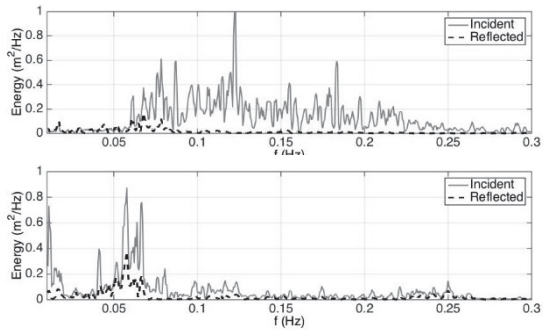

Figure 5. Incident and reflected energy spectrum measured by pressure sensor 1 (furthest seaward on the beach) at high tide; top: 9/10, spring tide, swell and wind waves, no infragravity waves; bottom: 15/10, neap tide, swell and infragravity waves

The daily erosion/accretion rate (Figure 6) shows uniform evolution only on October, the 10th with erosion all along the profile in response to incident energy condition, which are characterized by a wide spectrum, during spring tide. From the 11th to the 16th, erosion (resp. accretion) occured in the high tide swash zone (including the setup part above the Still Water Level [SWL]) and accretion (resp. erosion) in the surf zone when the incident energy began to increase (resp. decrease). This period shows first a decrease then a rapid increase of the incident energy. During this first period, the standard deviation (Figure 6) shows that the beach is more dissipative. The beach has two inflexion points (Figure 6), one at MW and the second at MHWS. The energy is high on the 17th and 18th, in the lower/swell frequencies. The inflexion points merge at MHWN. After the 18th, the incident wave height oscillates with less and less amplitude around 0.5 m. A swash bar appears on October, the 21st and 22nd at MHWS when the weather calms down, as stated by Masselink and Short (1993) for RTR under 10. After the 22nd the incident conditions are stable, and the profile shows less variations.

DISCUSSION

The observed daily erosion/accretion rate (Figure 6) reveal the very large variability of the beach profile. The high tide swash zone appears to be the most dynamic section of the beach. The variation becomes less significant when the incident energy has remained stable over two days or more. This means that the beach is reaching an equilibrium state with respect to the incident energy (Castelle *et al.*, 2014; Yates *et al.*, 2009) within 1-2 days only. The beach slope (Figure 6) shows that the profile is initially more dissipative and becomes more and more reflective throughout the field campaign. The LTT becomes more prominent (Figure 6) while the upper beach face becomes more reflective. This rapid variation in the slope (x2 in a neap-spring cycle above MW) may influence the contribution of the non-linear wave interactions to the wave spectrum and thus the breaking process (Filipot, In press). The slope also influences the symmetry and the skewness of the wave profile (dynamic feedback is therefore present between the morphology and the surf–swash zone instantaneous velocities), and thus the orbital velocity, which affect sediment transport. Further investigation is required to highlight the impact of infragravity waves.

CONCLUSIONS

The present study deals with the morphological response of the macrotidal embayed Porsmilin Beach (France). First, no rotation has been observed whatever the wind direction. Secondly, this beach allows us to observe a wide range of morphology because of its extremely rapid adaptation to the forcing conditions. The slope of the beach varies rapidly on the upper beach, showing one or two inflection points causing variating breaking point and resulting morphology. This rapid and highly dynamic environment make it difficult to predict with respect to forcing conditions only. On-going investigations focus on the setup variation according to the beach slope, transformation of waves, especially infragravity waves all along the cross-shore profile and the energy dissipation in the breaking zone through the use of currentmeters data in the swash and surf zone and video recording.

ACKNOWLEDGMENTS

This work was supported by the Agence Nationale de la Recherche under the program « Investissements d'avenir » with the reference ANR-10-LABX-19-01, by the ANR COCORISCO (2010-CEPL-001-01), the SOERE trait de côte, the NSO Dynalit and the Pôle Image of IUEM. The authors acknowledge the Pôle Image team from UMR6538 and UMR6554 for their help.

LITERATURE CITED

Castelle B.; Marieu V.; Bujan S.; Ferreira S.; Parisot J.P.; Capo S.; Sénéchal N., and Chouzenoux T., 2014. Equilibrium shoreline modelling of a high-energy meso-macrotidal multiple-barred beach. *Marine Geology*, 347 85-94

Dean R. G., 1991. Equilibrium beach profiles : Characteristics and application. *Journal of Coastal Research*, 7(1) 53-84.

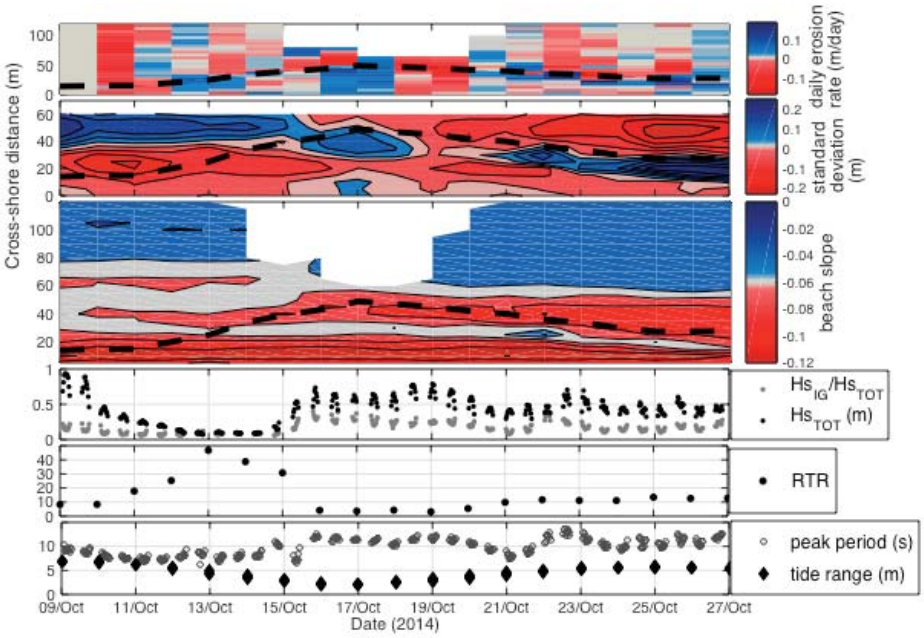

Figure 6. Data from DGPS and pressure sensor #1. Black dashed line represents the Still Water Level at High Tide *From top to bottom:* Daily erosion/accretion rate (m/day) (Eq. 1); Standard deviation around the mean profile of the beach (Eq. 2); Beach slope; Significant wave height Hs_{TOT} (m) and the corresponding ratio of infragravity waves Hs_{IG} / Hs_{TOT}; Relative Tide Range; Peak period (s) and daily tide range (m).

Dehouck, A.; Dupuis, H., and Sénéchal N., 2009. Pocket beach hydrodynamics: The example of four macrotidal beaches, Brittany, France. *Marine Geology* 266, 1–17.

Ferguson R.I. and Church M., 2004. A Simple Universal Equation for Grain Settling Velocity. *Journal of Sedimentary Research,* 74(6), 933-937

Floc'h F.; Le Dantec N.; Deschamps A.; Hamon K.; Suanez S., and Cuq V., 2014. Comportement pluriannuel de la morphodynamique d'une plage de poche macrotidale. *Proceedings of Réunion des Sciences de la Terre*

Filipot J.F., 2015, Investigation of the bottom slope dependence of the nonlinear wave evolution toward breaking using SWASH. *Journal of Coastal Research.* (in press)

Hallermeier, R.J., 1981. A profile zonation for seasonal sand beaches from wave climate. *Coastal Engineering,* 4, 253–277

Loureiro C.; Ferreira O.; Andrew J., and Cooper G., 2013. Applicability of parametric beach morphodynamic state classification on embayed beaches. *Marine Geology*, 346, 153-164.

Mansard, E.P.D. and Funke, E.R., 1980. The measurement of incident and reflected spectra using a least square method. *Proc. of the 15th Coast. Engineering Conference,* 1, 154–172.

Masselink, G. and Short, A.D., 1993. The effect of tide range on beach morphodynamics and morphology: a conceptual beach model. *Journal of Coastal Research* 9(3), 785–800.

Rey, V., Capobianco and R., Dulou, C., 2003. Wave scattering by a submerged plate in presence of a steady uniform current. *Coastal Engineering,* 47, 27–34.

Stockdon H.F.; Holman R.A.; Howda P.A., and Sallenger Jr. A.H., 2006. Empirical parameterization of setup, swash, and runup. *Coastal Engineering* 53(7) 573–588

Sénéchal, N.; Coco, G.; Bryan, K. R., and Holman, R. A., 2011. Wave runup during extreme storm conditions. *Journal of Geophysical Research* 116(C7), 2156-2202

SHOM, 1994. Courants de marée de la côte ouest de Bretagne de Goulven à Penmarc'h.

Short, A.D., 1991. Macro-meso tidal beach morphodynamics — an overview. *Journal of Coastal Research* 7(2), 417–436.

Stive, M.J.F.; Aarninkhof, S.G.J.; Hamm, L.; Hanson, H.; Larson, M.; Wijnberg, K.M.; Nicholls, R.J., and Capobianco, M., 2002. Variability of shore and shoreline evolution. *Coastal Engineering* 47, 211–235.

Storlazzi, C.D. and Field, M.E., 2000. Sediment distribution and transport along a rocky, embayed coast: Monterey Peninsula and Carmel Bay, California. *Marine Geology,* 170, 289–316.

Turki, I.; Medina, R.; Coco, G., and Gonzalez M., 2013. An equilibrium model to predict shoreline rotation of pocket beaches. *Marine Geology,* 346, 220–232

Wright, L.D. and Short, A.D., 1984. Morphodynamic variability of surf zones and beaches: a synthesis. *Marine Geology,* 56, 93–118.

Yates M.L.; Guza R.T., and O'Reilly W.C., 2009. Equilibrium shoreline response : Observations and modeling. *Journal of Geophysical Research,* 114 (C09014).

Journal of Coastal Research	SI	75	378-382	Coconut Creek, Florida	2016

Pulsations in Surf Zone Currents on a High Energy Mesotidal Beach in New Zealand

Shari L. Gallop [†§*], Karin R. Bryan[‡], Sebastian J. Pitman[§], Roshanka Ranasinghe[††], and Dean Sandwell[‡]

[†]Department of Environmental Sciences, Macquarie University, Australia

[‡]School of Science, University of Waikato, New Zealand

[§]Ocean and Earth Science, University of Southampton, United Kingdom

[††]Department of Water Engineering, UNESCO-IHE, The Netherlands; Research School of Earth Sciences, Australian National University Australia; Harbour, Coastal and Ocean Engineering, Deltares, The Netherlands

www.cerf-jcr.org

www.JCRonline.org

ABSTRACT

Gallop, S.L.; Bryan, K.R.; Pitman, S.J.; Ranasinghe, R., and Sandwell, D., 2016. Pulsations in surf zone currents on a high energy mesotidal beach in New Zealand. *In:* Vila-Concejo, A.; Bruce, E.; Kennedy, D.M., and McCarroll, R.J. (eds.), *Proceedings of the 14th International Coastal Symposium* (Sydney, Australia). *Journal of Coastal Research*, Special Issue, No. 75, pp. 378-382. Coconut Creek (Florida), ISSN 0749-0208.

The exchange of material between the surf zone and continental shelf can be driven by pulsations in rip current velocities. However, there is a poor understanding of the relationship of these pulsations to surf zone morphology and material exchange. Moreover, understanding of rip current dynamics has focused mainly on single-barred beaches in an intermediate state, and there have been few studies on high energy beaches. Therefore, this paper undertakes preliminary research on surf zone current velocity pulsations, on a high energy beach in New Zealand. This initial analysis presents results from two days of measurements using Acoustic Doppler Velocimeters and Lagrangian GPS drifters. Drifters revealed pulsations in current velocities on the order of ~0.5–2 m s^{-1} throughout the surf zone, whether inside a rip current circulation cell or not. More infragravity wave energy was associated with constant pulsations in current velocity, and lower infragravity energy with pulsation bursts, lasting 5–10 minutes, interspersed with periods of relatively constant velocity lasting 15–25 minutes. However, higher wave conditions also reduced the exit rate from the surf zone.

ADDITIONAL INDEX WORDS: *rip channels, surf zone, beach morphodynamics, Raglan, infragravity.*

INTRODUCTION

Rip currents are jet-like flows in the surf zone that generally head in an offshore direction (Aagaard *et al.*, 1997). They are often present on beaches in an intermediate morphodynamic beach state (Wright and Short, 1984), and adjacent to structures such as headlands and groynes (Gallop *et al.*, 2011; McCarroll *et al.*, 2014; Short, 1985). It is important to understand the variability and drivers of rip current flows because: (1) globally, they are the leading cause of rescues and fatalities on beaches (Short, 1999; Woodward *et al.*, 2015); and (2) they are a key mechanism transporting material between the surf zone and continental shelf, such as larvae (Fujimura *et al.*, 2014), diatoms (Talbot and Bate, 1987), and sediments (Aagaard *et al.*, 1997). Therefore, they are an important sediment transport conduit contributing to coastal sediment budgets (Goodwin *et al.*, 2013; Wright, 1987). Recent research suggests that the exit rate of material from the surf zone to offshore is an important control of: (1) hazard to beach users (Scott *et al.*, 2013); (2) the best escape strategy for people caught in a rip (McCarroll *et al.*, 2013); and (3) rates of cross- shore exchange of water (Smith and Largier, 1995), and materials (Loureiro *et al.*, 2013; Thorpe *et al.*, 2013).

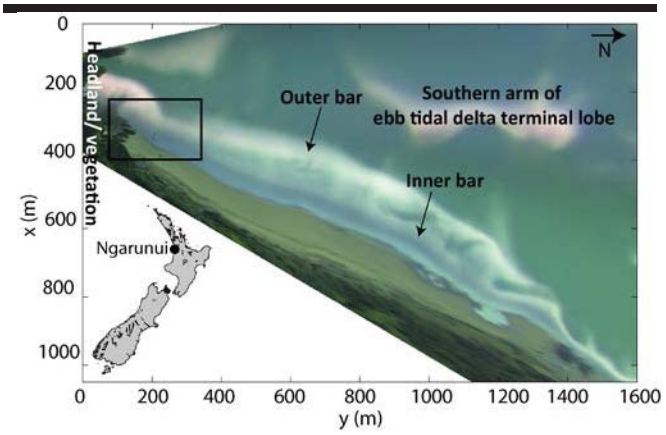

Figure 1. Study area at Ngarunui Beach, Raglan, New Zealand. Photo is a rectified, 10-minute average image from the Cam-Era video monitoring system. The box shows the area where ADVs and GPS drifters were deployed on 10 and 11 February 2015. White areas show breaking waves over shallow bathymetry. The dark area at the top of the beach is a shadow from the headland.

DOI: 10.2112/SI75-076.1 received 15 October 2015; accepted in revision 15 January 2016.

*Corresponding author: shari.gallop@mq.edu.au

Surf zone exits may be driven by pulsations in rip current velocity. Pulsation of surf zone currents can occur at infragravity (IG) frequencies (25–250 s) due to standing IG waves (MacMahan *et al.*, 2004a; Sonu, 1972) or wave groups (Munk, 1949; Reniers *et al.*, 2010; Shephard and Inman, 1950). In addition, recent research has revealed the presence of vortical motions at Very Low Frequency (VLF) (4–10 min) motions (Castelle *et al.*, 2013; MacMahan *et al.*, 2004b; Reniers *et al.*, 2010). A range of generation mechanisms for VLF motions have been suggested. The dominant mechanism appears to be surf zone eddies due to wave groups (MacMahan *et al.*, 2004b; Peregrine, 1998; Reniers *et al.*, 2007).

There is a lack of measurements (MacMahan *et al.*, 2004a) to understand the relationship of current pulsations to rip current generation, surf zone morphology, material exchange, and hazard. Therefore, the aim of this paper is to undertake preliminary research on the influence of IG wave energy on rip current flows on a high energy beach.

METHODS

This section introduces the study site, field experiment, and data analysis methods.

Study site

Ngarunui Beach on the west coast of New Zealand (Figure 1) has fine-medium iron sand (Sherwood and Nelson, 1979). The tide is semidiurnal, with neap and spring ranges of ~1.8 and 2.8 m (Walters *et al.*, 2001). Offshore mean significant wave height is 2 m, with a period of 7 s (Gorman *et al.*, 2003). The southern arm of the ebb tidal delta, terminal lobe to Whaingaroa Harbor acts as the outer bar during large swell events. Further inshore, there are inner (high tide) and outer (low tide) bars which are often cut by rip channels (Figure 1).

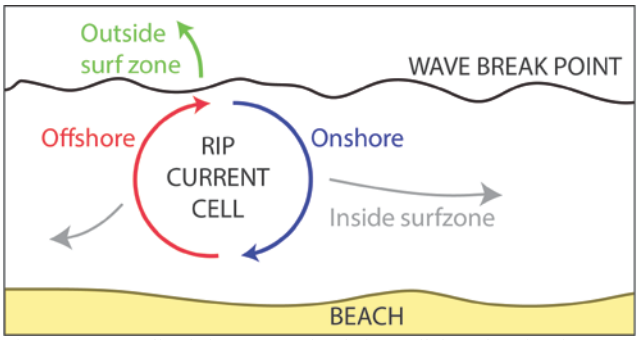

Figure 2. Generalized rip current circulation cell from box in Figure 1. Color coded arrows show the locations for which drifters are classified in Figures 3c and 4c.

Field experiment

A field experiment was undertaken between 9 and 11 February 2015 and included the deployment of three Triton Sontek Acoustic Doppler Velocimeters (ADVs), and ten GPS drifters. This paper focuses on data collected on February 10 and 11 collected in the rip current cell at the south end (Figure 1).

ADVs were deployed upward-facing within the rip current, and were set to the maximum sampling rate of 4 Hz for 4086 samples. GPS drifters were based on the design of Schmidt *et al.* (2003) and MacMahan *et al.* (2009). The GPS logger was the QStarz BT-Q100eX, which has a velocity accuracy of ±0.05 m s^{-1} (Thomson, 2012). One drifter was left in a static position on a benchmark to estimate the mean horizontal error and standard deviation of 3.78 ± 1.20 m. Drifters were deployed by wading out to waist-depth. They were retrieved using a combination of shore-retrieval, and a jetski when they: (1) washed onshore and dragging on the bed; (2) travelled alongshore outside of the study area; (3) exited the surf zone; and (4) entered busy surfing/ swimming areas. All times are given in New Zealand Standard Time (NZST).

Data analysis

As in other studies of surf zone currents using GPS drifters (e.g., Johnson and Pattiaratchi, 2004; McCarroll *et al.*, 2014), velocity data were low-pass filtered using a Butterworth filter with a low-pass cutoff of 0.05 Hz, to average wave motion and other noise.; including an algorithm to reduce end effects. For this preliminary investigation, results are presented of individual drifter velocities and their location within the surf zone circulation system, and compared with IG wave energy. Drifter velocities are color coded by location: (1) offshore- and (2) onshore-directed flow in the rip current circulation cell; (4) elsewhere inside the surf zone (Figure 2); or (3) offshore.

Offshore wave conditions were obtained from the nzwave_12 wave forecast which used WAVEWATCHv3.14, and was run by NIWA. Drifter velocities were compared to the energy in the IG band of: pressure (water level); x (cross-shore); and y (longshore) currents recorded by ADVs in the surf zone. These were obtained by calculating wave power spectra on the detrended time-series, which were then smoothed using a Hanning window of 4096 data points. The total IG energy was summed for each window, within the frequency band of 0.0033–0.05 Hz (20–300 s); suggested infragravity wave frequency cutoffs vary but generally range within this window (e.g. Holman, 1981; MacMahan *et al.*, 2004a). Periods of pulsations in surf zone current velocities were identified by calculating the standard deviation of the low pass-filtered velocity in 2 minute windows. Pulsations were defined as occurring when the standard deviation was greater than the 50th percentile standard deviation of filtered drifter velocities.

RESULTS

Here, results are summarized for 10 and 11 February.

10 February

On 10 February, mean offshore significant wave height was 1.4 m, and period was 8.7 s. There was significantly more IG energy in cross-shore currents compared to sea level and long-shore currents (Figure 3a). IG energy gradually increased during late morning, with energy in cross-shore currents increasing from ~10 m^2/Hz, to peak at 15 m^2/Hz after 13:00 h (Figure 3a). Pulsation bursts of drifter velocity were identified by periods of high standard deviation (Figure 3b). During these pulsations, the drifters reached velocities on the order of ~0.5–2 m s^{-1} (Figure 3c). Drifter velocities alternated between pulsation bursts lasting around 5–10 minutes (Figure 3c), interspersed with periods of relatively constant, lower velocity of <0.5 m s^{-1}. Pulsations were not associated with the position within the surf zone, as this occurred at all locations sampled, *i.e.* in the offshore and onshore

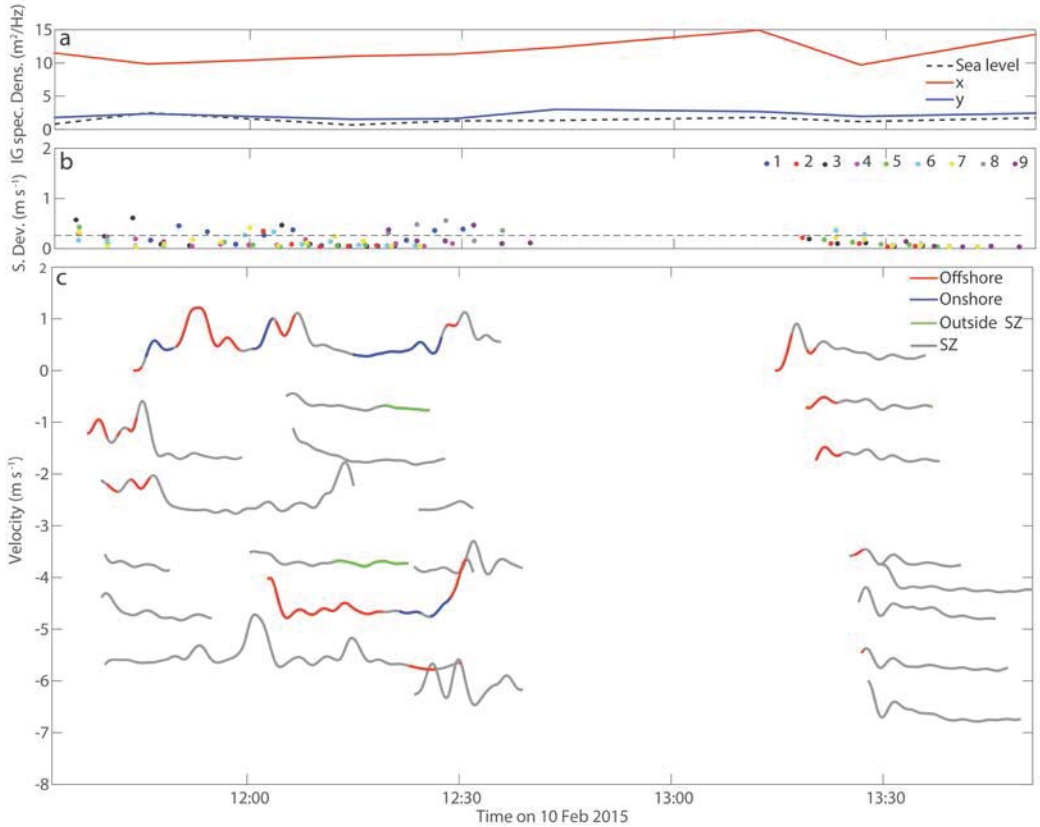

Figure 3. (a) On 10 February 2015, energy in the infragravity (IG) band (0.0033–0.05 Hz) for sea level, *x*, and *y* currents measured with an ADV; (b) standard deviation in drifter velocity for drifters 1 to 9, for 2 minute windows where the dashed line shows the 50th percentile; and (c) filtered GPS drifter velocity for 1 (top) to 9 (bottom), with plotting successively offset by -1 m s^{-1}. Color code corresponds to the areas shown in Figure 2.

flows within the rip current circulation cell, and others areas of the surf zone. Due to a lack of temporal drifter coverage, it is also not clear if more pulsing occurred as IG energy increased on this day.

11 February

On 11 February, mean offshore significant wave height increased to 1.9 m, and mean period to 11.7 s. This higher wave energy was reflected in cross-shore IG energy that was an order of magnitude greater than the day before, reaching 130 m^2/Hz (Figure 4a) compared to 13 m^2/Hz on 10 February (Figure 3a). Total IG energy was variable. For cross-shore currents, it reached local maxima in spectral density of ~80, 100, and 130 m^2/Hz at 12:30, 13:10, and 14:20 respectively; and local minima of ~50 m^2/Hz at 12:45 and 14:10. Unlike on the previous day, there were almost constant pulsations in GPS drifter velocities (Figure 4b). During these pulsations, drifters reached velocities on the order of 0.5–2 m s^{-1} (Figure 4c). These oscillations occurred regardless of location within the surf zone.

DISCUSSION

IG frequency energy was an order of magnitude greater on 11 February compared to 10 February. If rip current pulsations are driven by IG waves (MacMahan *et al.*, 2004a; Reniers *et al.*, 2010), then it is expected that more IG wave energy would lead to more pulsations in rip current velocity. This relationship is confirmed by differences between the two days, where pulsations in rip current velocities were constant on 11 February (Figure 4c), when IG wave energy was much greater (Figure 4a). Conversely, on 10 February when IG wave energy was relatively lower (Figure 3a), surf zone current pulsations were intermittent (Figure 3c) and occurred in bursts lasting for 5–10 minutes, interspersed by periods of relatively constant velocity, lasting 15–25 minutes. The magnitude of the velocity pulsations was similar between the two days, on the order of 0.5–2 m s^{-1}. If IG pulsations in rip current velocity are the main driver of surf zone exits, then more exits should have occurred on 11 February. However, there were significantly less exits on 11 February (6 %) compared to 10 February (71 %) (Gallop *et al.*, 2015). Offshore significant wave height was higher on the second day, at 1.9 m compared to 1.4 m on the first day. This relationship is consistent with findings elsewhere that more drifter exits occur during lower wave conditions (MacMahan *et al.*, 2010; Scott *et al.*, 2014).

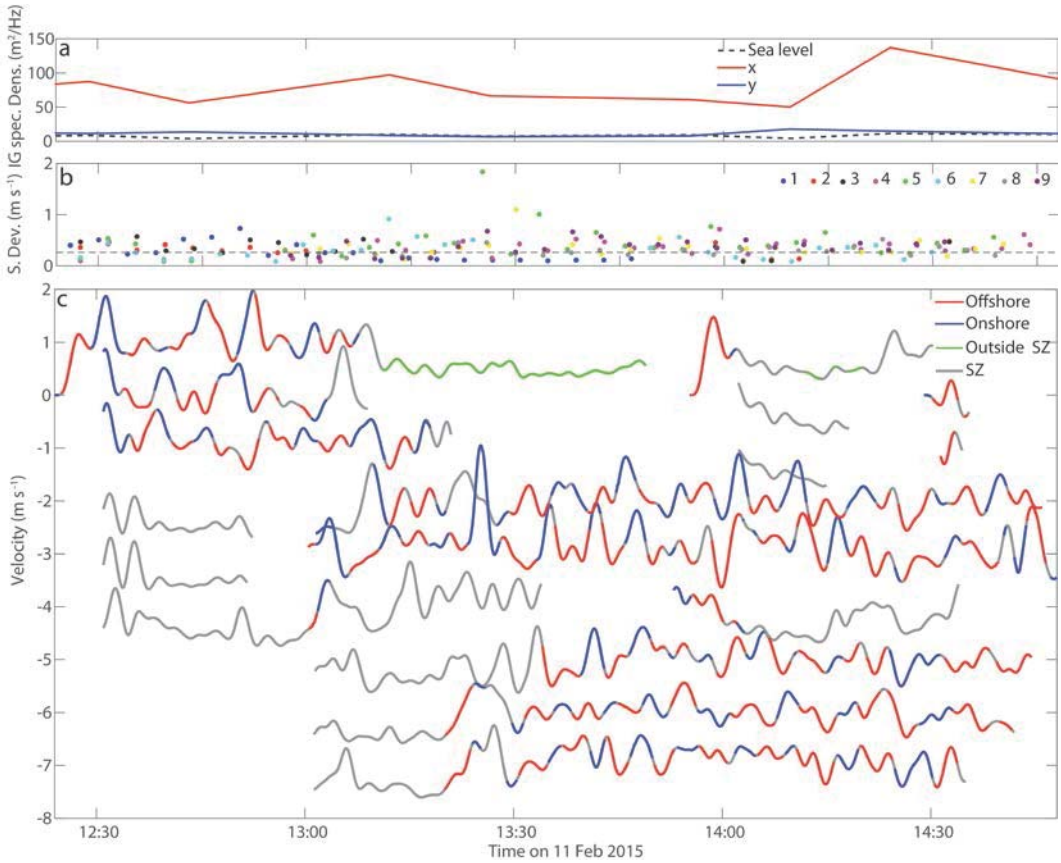

Figure 4. (a) On 11 February 2015, energy in the infragravity band (IG) (0.0033–0.05 Hz) for sea level, *x*, and *y* currents measured with an ADV; (b) standard deviation in drifter velocity for drifters 1 to 9, for 2 minute windows where the dashed line shows the 50th percentile; and (c) filtered GPS drifter velocity for 1 (top) to 9 (bottom), with plotting successively offset by -1 m s^{-1}. Color code corresponds to the areas shown in Figure 2.

This may be caused by larger waves breaking further offshore which induce current vortices that are coupled to the surf zone morphology, and encourage material retention (MacMahan *et al.*, 2010). Further research is required to understand the effect of rip current pulsations and incident wave conditions on rip current flows, particularly on high energy beaches.

CONCLUSIONS

This paper presented a preliminary study on rip current velocity pulsations, on a high energy, mesotidal beach in New Zealand. There were strong pulsations in surf zone current velocity on the order of ~0.5–2 m s^{-1}. These pulsations occurred in 5-10 minute bursts interspersed with 15-20 minute periods of relatively constant velocity, during lower total wave energy, and lower IG energy conditions. Conversely, during higher wave energy conditions, and when there was more IG wave energy present, the pulsations were constant. More pulsations did not lead to increased surf zone exits, possibly because the higher incident wave conditions encouraged the retention of material in the surf zone. Further research is planned to understand the balance of rip current velocity pulsations and incident wave conditions on rip current flows and surf zone exits on high energy beaches

ACKNOWLEDGMENTS

Thanks to the field volunteers: M. Biausque, C. Conn, N. Gallop, S. Hunt, J. Labuschagne, N. Lovett, C. Morcom, J. Mullarney, R. Panier, E. Woodhouse; the Raglan Coast Guard (E. Aktin and S. Boulay); B. Blossier for the drifters; Waikato Regional Council and NIWA for Cam-Era; S. Harrison for image assistance; R. Gorman (NIWA) for nzwave_12; and the IMarEST Laurie Prandolini Fellowship.

LITERATURE CITED

Aagaard, T.; Greenwood, B., and Nelson, J., 1997. Mean currents and sediment transport in a rip channel. *Marine Geology*, 140, 25-45.

Castelle, B.; Reniers, A., and MacMahan, J., 2013. Numerical modelling of surfzone retention in rip current systems: On the impact of the surfzone sandbar morphology. *Proceedings of Coastal Dynamics 2013* (24-28 June, Arcachon).

Fujimura, A.G.; Reniers, A.J.H.M.; Paris, C.B.; Shanks, A.L.; MacMahan, J.H., and Morgan, S.G., 2014. Numerical

simulations of larval transport into a rip-channeled surf zone. *Limnology and Oceanography*, 59(4), 1434-1447.

Gallop, S.L.; Bryan, K.R.; Coco, G., and Stephens, S.A., 2011. Storm-driven changes in rip channel patterns on an embayed beach. *Geomorphology, 127*(3–4), 179-188.

Gallop, S.L.; Bryan, K.R.; Pitman, S.; Ranasinghe, R., and Sandwell, D., 2015. Rip current observations on a low-sloping dissipative beach. *Proceedings of Coasts and Ports* (15-18 September, Auckland).

Goodwin, I.D.; Freeman, R., and Blackmore, 2013. An insight into headland sand bypassing and wave climate variability from shoreface bathymetric change at Byron Bay, New South Wales, Australia. *Marine Geology*, 341, 29-45.

Gorman, R.; Bryan, K.R., and Laing, A.K., 2003. Wave hindcast for the New Zealand region: Nearshore validation and coastal wave climate. *New Zealand Journal of Marine and Freshwater Research*, 27, 567-588.

Holman, R.A., 1981. Infragravity energy in the surf zone. *Journal of Geophysical Research* 86(C7), 6442-6450.

Johnson, D. and Pattiaratchi, C., 2004. Transient rip currents and nearshore circulation on a swell-dominated beach. *Journal of Geophysical Research*, 109, C02026.

Loureiro, C.; Ferreira, Ó., and Cooper J.A.G., 2012. Extreme erosion on high-energy embayed beaches: Influence of megarips and storm grouping. *Geomorphology,* 139–140, 155–171.

MacMahan, J.; Reniers, A.J.H.M.; Thornton, E.B., and Stanton, T., 2004a. Infragravity rip current pulsations. *Journal of Geophysical Research*, 109, C01033.

MacMahan, J.H.; Reniers, A.J.H.M.; Thornton, E.B., and Stanton, T.P., 2004b. Surf zone edits coupled with rip current morphology. *Journal of Geophysical Research*, 109, C07004.

MacMahan, J.; Brown, J., and Thornton, E., 2009. Low-cost handheld global positioning system for measuring surf-zone currents. *Journal of Coastal Research*, 25(3), 744-754.

MacMahan, J.; Brown, J.; Brown, J.; Thornton, E.; Reniers, A.; Stanton, T.; Henriquez, M.; Gallager, E.; Morrison, J.; Austin, M.J.; Scott, T.M., and Senechal, N., 2010. Mean Lagrangian flow behaviour on an open coast rip-channeled beach: A new perspective. *Marine Geology,* 268(1-4): 1-15.

McCarroll, R.J.; Brander, R.W.; MacMahan, J.H.; Turner, I.L.; Reniers, A.J.H.M.; Brown, J.A., and Bradstreet, A., 2013. Assessing the effectiveness of rip current swimmer strategies, Shelly Beach, NSW, Australia. *Journal of Coastal Research*, Special Issue 65, 784-789.

McCarroll, R.J.; Brander, R.W.; Turner, I.L.; Power, H.E., and Mortlock, T.R., 2014. Lagrangian observations of circulation on an embayed beach with headland rip currents. *Marine Geology, 355*, 173-188.

Munk, W.H., 1949. Surf beats. *EOS Transactions*, AGU. 30(6), 849-854.

Peregrine, D.H., 1998. Surf zone currents. *Theoretical and Computational fluid dynamics*, 10, 295-309.

Reniers, A.J.H.M.; MacMahan, J.H.; Beron-Vera, F.J., and Olascoaga, M.J., 2010. Rip-current pulses tied to Lagrangian coherent structures. *Geophysical Research Letters*, 37, L05605.

Reniers, A.J.H.M.; MacMahan, J.H.; Thornton, E.B., and Stanton, T.P., 2007. Modeling of very low frequency motions during RIPEX. *Journal of Geophysical Research* 112, C07013.

Schmidt, E.W.; Woodward, B.T.; Millikan, K.S.; Guza, R.T.; Raubenheimer, B., and Elgar, S., 2003. A GPS-tracked surf zone drifter. *Journal of Atmospheric and Oceanic Technology*, 20(7), 1069-1075.

Shepard, F.P. and Inman, D.L., 1950. Nearshore water circulation related to bottom topography and wave refraction. *EOS Transactions*, AGU, 31(1), 196-212.

Sherwood, A.M. and Nelson, C.S., 1979. Surficial sediments of Raglan Harbour, N.Z. *Journal of Marine and Freshwater Research*, 15(4), 475-496.

Short, A.D., 1985. Rip current type, spacing and persistence, Narrabeen beach, Australia. *Marine Geology*, 65(1-2), 47-71.

Short, A.D., 1999. Beach hazards and safety. In: Short, A.D. (ed.). *Beach and shoreface morphodynamics*. Chichester: John Wiley and Sons, pp. 292-304.

Scott, T.; Masselink, G.; Austin, M.J., and Russell P., 2014. Controls on macrotidal rip current circulation and hazard. *Geomorphology,* 214, 198–215.

Smith, J.A. and Largier, J.L., 1995. Observations of nearshore circulation: Rip currents. *Journal of Geophysical Research-Oceans,* 100(C6), 10967–10975.

Sonu, C.J., 1972. Field observation of nearshore circulation and meandering currents. *Journal of Geophysical Research*, 79, 3065-3071.

Talbot, M.M.B. and Bate, G.C., 1987. Rip current characteristics and their role in the exchange of water and surf diatoms between the surf zone and nearshore. *Estuarine, Coastal and Shelf Science*, 25(6), 707-720.

Thomson, J., 2012. Wave breaking dissipation and 'SWIFT' drifters. *Journal of Atmospheric and Oceanic Technology*, 29, 1866-1882.

Thorpe, A.; Miles, J.; Masselink, G.; Russell, P.; Scott, T., and Austin, M., 2013. Suspended sediment transport in rip currents on a macrotidal beach. *Journal of Coastal Research,* Special Issue 65, 1880–1885.

Walters, R.A.; Goring, D.G., and Bell, R.G., 2001. Ocean tides around New Zealand. *New Zealand Journal of Marine and Freshwater Research,* 35(3), 567-580.

Woodward, E.; Beaumont, E., and Russell, P., 2015. Public understanding and knowledge of rip currents and beach safety in the UK. *International Journal of Aquatic Research*, 9, 49-69.

Wright, L.D., 1987. Shelf-surfzone coupling: Diabathic shoreface transport. *Proceedings of Coastal Sediments 1987* (12-14 May, New Orleans).

Wright, L.D. and Short, A.D., 1984. Morphodynamic variability of surf zones and beaches: A synthesis. *Marine Geology*, 56, 93-118.

Journal of Coastal Research	SI	75	383-387	Coconut Creek, Florida	2016

Wind-energy Development Causes Social Impacts in Coastal Ceará state, Brazil: The Case of the Xavier Community

Adryane Gorayeb[†], Jocicléa de Sousa Mendes[†], Antonio Jeovah de Andrade Meireles[†], Christian Brannstrom[‡], Edson Vicente da Silva[†], Ana Larissa Ribeiro de Freitas[†]

[†]Department of Geography
Universidade Federal do Ceará
Fortaleza, Ceará, Brazil

[‡] Department of Geography
Texas A&M University
College Station, Texas, USA

www.cerf-jcr.org

www.JCRonline.org

ABSTRACT

Gorayeb, A.; Mendes, J.S.; Meireles, A.J.A.; Silva, E.V.; Brannstrom, C., and Freitas, A.L.R. 2016. Wind-energy development causes social impacts in coastal Ceará state, Brazil: The case of the Xavier community. *In:* Vila-Concejo, A.; Bruce, E.; Kennedy, D.M., and McCarroll, R.J. (eds.), *Proceedings of the 14th International Coastal Symposium* (Sydney, Australia). *Journal of Coastal Research*, Special Issue, No. 75, pp. 383-387. Coconut Creek (Florida), ISSN 0749-0208.

A significant increase in wind-power generation has occurred since 2008 in coastal regions of northeastern Brazil. Many wind farms have been erected on territories claimed by traditional communities, which have suffered changes in how they obtain resources as a consequence. Here we study the Xavier community, a settlement of 20 families and 66 people, located in the Camocim municipality of Ceará state. Xavier residents subsist on extractive activities such artisanal (non-mechanized) fishing, shellfish collection, and crop cultivation. But in 2009 one of Ceará's largest wind farms was established approximately 200 meters from the settlement. Although some may see these projects as low impact, wind farms in Ceará are being implemented in areas that are environmentally unstable, located within territories claimed by traditional communities, negatively affecting their livelihoods. This paper analyzes the social impacts caused by the establishment of the wind farm through participant observation, group workshops, and analysis of textual materials. Several problems are described, including the absence of basic infrastructure and employment; road blockages; privatization of common resources; noise from turbines; constant fear of accidents involving turbines; internal conflicts among Xavier residents caused after the implementation of the wind farm; and burial of lakes. Wind-farm construction negatively influenced this traditional community by threatening territory, cultural traditions, and food security.

ADDITIONAL INDEX WORDS: *Wind energy; traditional communities; environmental impacts.*

INTRODUCTION

Wind-energy development in Brazil was implemented rapidly in response to an electricity crisis in 2001 (Juárez *et al.,* 2014). Wind farms have clustered in coastal areas, especially in the northeastern region. Many residents of Brazil's coastal environments rely on small-scale resource extraction (fish, shrimp, crops) and are considered "traditional communities" as defined in Brazilian law (see Decreto Nº 6.040, de 7 de fevereiro de 2007). In Ceará, a state in northeastern Brazil, wind power has been installed rapidly in coastal environments that are dynamic and fragile, highly vulnerable to human activities (Gorayeb *et al.*, 2005; Vasconcelos, 2005). Wind-power generation, a desirable clean energy source capable of supplying more than 40 times current electricity demand (Lu *et al*., 2009). Firms and political elites justify wind-energy projects on the bases of needed electricity production and improved quality of life. However, scholars have observed social-environment and territorial problems resulting from wind-energy development in traditional communities (Brown, 2011; Meireles *et al*., 2013). Here we report social impacts of wind power on the Xavier community, a traditional settlement of 20 families (66 residents) relying on artisanal fishing, shellfish collection, and small-scale farming (Figure 1).

Installed wind-power capacity in Ceará has increased by nearly 238% since 2010, when 17 wind farms capable of producing 518,934 KW were located in coastal areas (ADECE, 2010). In 2015, 44 wind farms were operational, capable of producing 1,233,234 KW, bring total installed capacity to 2,847,234 KW (ANEEL, 2015).

In Ceará, wind farms have been located on highly unstable coastal areas, such as active sand dunes, estuaries, and beaches (Gorayeb *et al.*, 2005; Vasconcelos, 2005), where human populations cluster. These traditional communities are comprised of fishers and marine resource users, *quilombolas* (descendants of runaway slaves who formed free settlements in opposition to slaveholding farms), family famers, and indigenous peoples. Livelihoods and access to resources in traditional communities have been negatively affected by changes to the physical environment (Meireles, 2011). Wind farms are among several large coastal development projects that have created serious and complex disputes and loss of territory claimed by traditional communities (Primavera, 2005; Simas and Pacca, 2013; Valiela *et al.*, 2001).

DOI: 10.2112/SI75-077.1 received 15 October 2015; accepted in revision 15 January 2016..
*Corresponding author: adryanegorayeb@gmail.com

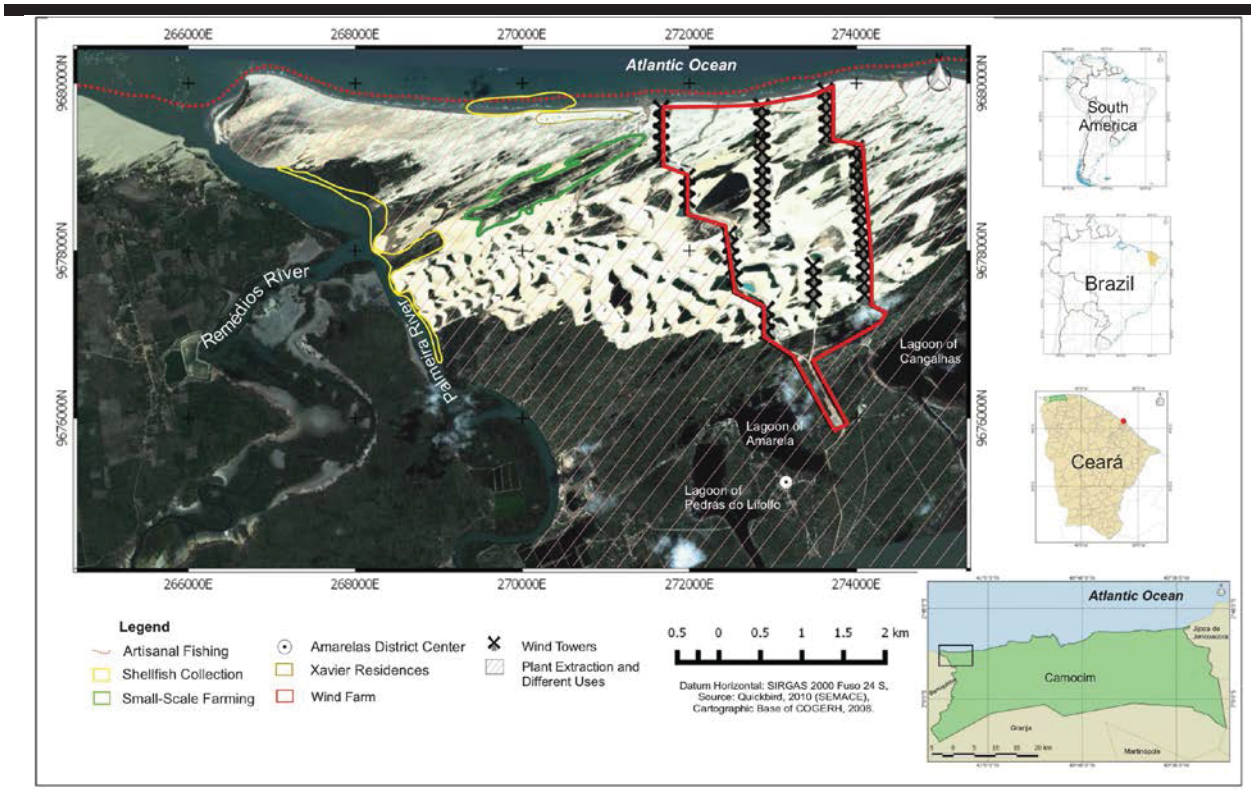

Figure 1. Location of the Xavier community, in western of Ceará, Brazil.

Frequently, wind farms in Ceará are built in areas without infrastructure or public services. Our field work suggests that wind developers use this fact to persuade political and economic elites and regulatory officials regarding potential benefits of their projects. Wind-farm developers also have tried to obtain support from traditional communities by promises of compensatory measures and permanent employment (Brown 2011), which is an illusory pledge because most employment is temporary, during the construction phase. In other areas of wind-power development, such as the USA High Plains, employment from wind power offers tangible benefits and relatively high salaries compared to other opportunities (Slattery *et al.*, 2011).

Globally, most social conflicts regarding wind farms have been reported in North America and Europe. Main causes of opposition to wind farms have been synthesized by Pasqualetti (2011) and Bell *et al*. (2013). Wind farms may represent an imposition to the attachment of people to landscapes. Host communities may feel marginalized because they did not participate in planning decisions or because they receive few benefits, and people may complain of health effects. On the other hand, high support for wind power has been reported in areas where the economy has been declining and landowners receive royalties from wind-power production (Brannstrom *et al*., 2011; Slattery *et al.,* 2012).

However, little is known about wind-power conflicts in developing countries. Brown (2011) described the opposition movement and the response of the wind-power industry in one well known one site in Ceará. He argued that wind-power firms could mitigate negative impacts, but did not analyze possible impacts of compensatory measures.

Several studies, such as Meireles (2008, 2009), Meireles *et al*. (2013) and Meireles *et al*. (2015), describe environmental impacts from wind-farm construction.

Mitigating measures and alternative sites for locating wind farms would minimize negative social impacts from wind energy development (Carrete *et al*., 2012; Kikuchi, 2008; Kunz *et al*., 2007; Landry *et al.*, 2013; Lucas *et al*., 2012; Mirasgedis *et al*., 2014; Munday *et al*., 2011; Schläppy *et al.*, 2014; Slattery *et al*., 2012).

Ceará "is a bellwether in the debate over how grid-scale renewable energy can grow sustainably in the developing world" (Brown, 2011, p. 357). We build on this work by analyzing dynamics in a less well known site and by considering the impacts of mitigation or compensatory measures offered to a traditional community. The findings we and others report indicate the importance of policies to assure the territorial integrity of traditional communities in coastal regions.

METHODS

Our research included participatory diagnosis of participant observation, group workshops, transect walks, construction of a problem-potential matrix, collective discussion regarding land-

use planning, and analysis of textual materials. During group workshops, we collected information on environmental problems, physical and psychological discomfort, and social impacts of the wind farm from the perspective of community residents. Transect walks resulted the definition of environmental characteristics of community territory and description of environmental impacts discussed during group activities. Collective discussions, using participatory methodology, were synthesized into main positive and negative effects of the wind farm on the community's traditional territory. Field work for participatory diagnosis in 2014 and 2015 consisted of meetings with 20 community representatives between 12 and 65 years of age, allowing for obtaining different views of the community's territory. Other research tasks were carried out between 2010 and 2013, including visits to the areas surrounding the community, analysis of the wind farm, observations of landscape changes and changes in daily life in the community, and observations of community member relations with the wind farm and surrounding area.

RESULTS

In 2009 one of Ceará's largest wind farms, 50 turbines with capacity of 104.4 MW covering 1,040 hectares, was constructed around 200 meters from the extreme east of a linear settlement of houses in Xavier. The wind farm created several social and environmental problems, including: (i) roadblocks denying physical access of Xavier residents; (ii) privatization of common resources; (iii) discomfort from the noise that turbines generate; (vi) constant fear of an accident involving the turbines; (v) continued absence of public services (transport to school, sanitation, collection of garbage, access roads, health care) and employment; (vi) internal conflicts among Xavier residents caused by divisions resulting from the mitigation measures offered by the wind-energy firm; (vii) burial of lakes and reduction of fish supply.

Xavier residents suffer from a food deficit because they are unable to access fish in former lakes. These lakes were used for artisanal fishing when residents were unable to fish in the Atlantic Ocean because of fish scarcity or because fishing was prohibited (e.g., lobster or Red snapper).

Xavier lacked electricity until one year after the wind farm was erected. Residents described many legal disputes, negotiated through the public prosecutor (*Promotoria de Justiça*; see Mcallister, 2008) of Camocim to ensure that power lines would reach the community because the wind farm impeded access to the electricity transmission route.

Other legal disputes challenged the wind farm. Among the more important was the road built by the wind firm to reach the wind farm. The road provided access to the turbines, necessary for maintenance, and is today the only road that provides access to Xavier. However, access is restricted by a security gate with armed guards working for the wind-farm operator. During approximately two years, Xavier residents were prohibited from passing through the gate, impeding daily tasks such as selling fish, going to school, and accessing health care.

A community association obtained mitigating measures from the wind-farm operator after lengthy negotiations. The following benefits were conceded: (i) authorization to install electricity lines for the Xavier community in 2010; (ii) access to the road linking the wind farm and the nearest house in 2010, made official by a legal agreement (*Termo de Compromisso e Obrigações Mútuas*) in 2013 (iii) social work such as screening environmental videos and animated films in the community in 2013; and (iv) donation of R$540,000 (US$130,000 at early 2015 exchange rate) for construction of 22 houses made of brick for each family in Xavier, replacing one-room huts built with mud, wood, and thatch (known locally as *taipa*, or wattle-and-daub construction), and a closed structure for both a freezer for storing fish and headquarters of the community association in 2013 (also made official through a *Committment Agreement Termo de Compromisso e Obrigações Mútuas*).

These legal agreements, negotiated among the public prosecutor (*Promotoria*) of the Camocim municipality, the community association (Associação dos Moradores de Xavier) and the wind-farm operator, describe the terms for mitigating the impact of the wind farm and remove the wind-farm operator from any responsibility beyond supplying funds. Thus, the firm was not responsible for legal, accountancy, architectural, or engineering support for the construction of the new houses. This limit on responsibility made it difficult to use the financial resources because the community association, which was unprepared for this responsibility, had to manage the project.

In 2009, the residents of the Xavier community were unanimous in opposition to the wind farm. This community-wide view lasted until the middle of 2014, after the investment of the housing fund used to mitigate the negative impact of the wind farm. We estimate that half the community members changed their view of the wind farm from negative to positive. This change created internal conflict even though all families, have strong family and social inter-relations. Some families now want to sell their houses to outsiders, while others strongly resist selling, fearing the disintegration of the tight-knit community.

Community members report some improvements resulting from the wind farm. For example, the access road through the wind farm—after residents were permitted to use it—provided access to nearby houses. Electrification was impeded by the wind farm, but the construction of the wind farm also provided new arguments for this public investment. The irony of a small community, in the shadow of a large wind farm, lacking electricity was likely too much for local elites to bear. With nearly 75% of houses made of wattle-and-daub before the construction of the wind farm, the funding for brick housing was a large improvement.

Residents of the Xavier community perceive that their social and natural environments have much potential that could help bring financial and material benefits to the community and alleviate internal tensions. In particular, income-generating activities for young people are important because the Xavier's youth attend elementary school in a nearby (4 km) urban center but do not have professional employment opportunities.

DISCUSSION

Meireles *et al.* (2013) described environmental impacts of the wind farm in Xavier, noting the importance of the burial of lakes among dunes to build access roads to the turbines. Other noted impacts included: (i) removal of vegetation on stable dunes for the construction of roads and the use of heavy machinery; (ii)

destruction of fixed and mobile dunes to flatten land for the erection of turbines on dune fields; iii) interrupted fluxes between river and lake systems; and iv) soil compaction during the construction of access roads, work sites, and storage areas.

The Xavier case shows how rejection of wind-power development may be related to the presence or absence of royalties from electricity generation. Unlike cases of wind energy in the midwestern USA, where public support for wind power is high (Brannstrom *et al.*, 2011; Slattery *et al.*, 2012), Xavier residents do not receive royalties. This case fits Pasqualetti (2011) example of imposition as a key reason for opposition to wind power. However, Xavier residents received mitigating measures in the form of financial resources for new housing construction, which increased the acceptance of wind power.

Even if community members appreciate the electricity and improved housing, the modifications to the natural environment and changes to traditional livelihoods were severe. The end of access to lakes in the dune fields negatively affected livelihoods because there is no substitute for this activity.

The social and environmental conflicts relating to wind power in Xavier are not isolated or unique. Other traditional communities in Ceará display similar characteristics. For example, scholars studying the Cumbe community in eastern Ceará report complaints about heavy truck traffic, limits on human mobility, and modification of the natural landscape from the levelling of dunes and burial of lakes to build wind farms (Brown, 2011; Galdino, *et al.*, 2014; Pinto *et al.*, 2013). Pinheiro *et al*. (2014) report conflicts with extractivists in a site near Camocim, where erection of a wind farm impeded access to communally held areas used to collect the mollusk *Anomalocardia brasiliana*. Conflicts also resulted from kitesufing by foreign tourists, hotels, and a shrimp farm. These conflicts have reduced territories available for fishing and mollusk extraction among families, which reduced food security. Families are forced to travel an additional 1 km daily between residences and extraction areas. Evangelista *et al.* (2013) report that the establishment of a wind farm in Praia das Fontes (eastern coastal Ceará) and ensuing landscape modifications, including a concrete wall separating houses from resources, changed daily routines.

CONCLUSIONS

Private firms and public officials have supported the establishment of large wind farms in coastal Ceará and other areas in northeastern Brazil. The importance of wind power for Brazil's electricity grid is potentially large, but the continued establishment of wind farms in ways that threaten environmental resources and livelihoods will generate more social, political, and legal conflicts.

The erection of wind farms in coastal areas, especially in traditional communities, will cause and exacerbate socio-environmental conflicts that center on the decline of traditional activities, which may negatively affect livelihoods, food security, and cultural traditions.

The main problems observed in Xavier include the blockage of roads (prohibition of physical access), discomfort among residents from the noise of turbines, privatization of common areas, constant fear of accidents involving turbines, lack of public services and employment, and burial of lakes. Mitigation measures are thought to be a way reduce social opposition and address negative impacts, but they created new internal divisions in the Xavier community. This shows that impacts from wind farms may go beyond visible impacts to the landscape. Unintended changes to pre-existing cultural and social patterns and processes may result. The Xavier community does not have sufficient political support to assure the maintenance of quality of life in its current environmental setting. Indirectly, the wind farm may encourage the privatization of communally held lands and resources and the eventual disintegration of the community. The case shows the need for detailed planning in the siting of wind farms, with special concern for communities lacking political power, before siting decisions are made. These considerations may reduce the negative social impacts caused by wind farms.

ACKNOWLEDGEMENTS

We are grateful to the Brazilian Higher Education Support Program (CAPES-PVE/BRASIL) for financing the project "Impactos da Energia Eólica no Litoral do Nordeste: perspectivas para a construção de uma visão integrada da produção de energia "limpa" no Brasil" and "Cartografia Social dos Territórios Tradicionais do Litoral Nordestino e Amazônico", financed by Brazilian National Research Council (Universal-CNPq/ BRASIL).

LITERATURE CITED

ADECE - Agência de Desenvolvimento do Estado do Ceará S.A., 2010, *Atração de investimentos no estado do Ceara: mapa territorial de parques eólicos*. Fortaleza, CE, 74p.

ANEEL, 2015. *Matriz energética do Brasil*. http://www.aneel.gov.br/aplicacoes/capacidadebrasil/OperacaoGeracaoTipo.asp?tipo=7&ger=Outros&principal=E%C3%B3lica.

Bell, D.; Gray, T.; Haggett, C., and Swaffield, J., 2013. Re-visiting the 'social gap': public opinion and relations of power in the local politics of wind energy. *Environmental Politics*, 22(1), 115-135.

Brannstrom, C.; Jepson, W., and Persons, N., 2011. Social perspectives on wind-power development in west Texas, *Annals of the Association of American Geographers,* 101(4), 839-851. doi: 10.1080/00045608.2011.568871

Brown, K.B., 2011. Wind power in northeastern Brazil: Local burdens, regional benefits and growing opposition. *Climate and Development*, 3,344-360.

Carrete, M., Sánchez-Zapata, J.A., Benítez, J.R., Lobón, M., Ontoya, F., and Donázar, J.A., 2012. Mortality at wind-farms is positively related to large-scale distribuition and aggregation in griffon vultures. *Biological Conservation*, 145, pp. 102-108.

Evangelista, A.N.A.; Monteiro, J., and Gorayeb, A., 2013. A parceria entre o acadêmico e o social: o caso da Praia das Fontes, litoral leste do Ceará, Brasil. In: *Resumenes y trabajos completos I congreso extension y sociedade (*Montevideo, Universidad de La República), 1, pp. 1-15.

Galdino, B.T.; Sousa, A.K.O.; Capistrano, F. R. B., and Gorayeb, A., 2014. A Cartografia Social como Ferramenta Geotecnológica na Gestão Territorial da Comunidade do Cumbe, Aracati, Ceará. In: *Caderno de Resumos do IV Congresso Brasileiro de Educação Ambiental Aplicada e*

Gestão Territorial: Água e Agricultura Familiar (Porto Velho, AICSA), pp. 36-38.

Gorayeb, A.; Silva, E.V., and Meireles, A.J.A., 2005. Impactos ambientais e propostas de manejo sustentável para a planície flúvio-marinha do Rio Pacoti-Fortaleza/Ceará. *Sociedade & Natureza*, Uberlândia, Minas Gerais, 17(33), 143-152.

Juárez, A.A.; Araújo, A.M.; Rohatgi, J. S., and Oliveira Filho, O.D.Q., 2014. Development of the wind power in Brazil; political, social, and technical issues. *Renewable and sustainable energy reviews,* 39, 828-834.

Kikuchi, R., 2008. Adverse impacts of wind power generation on collision behaviour of birds and anti-predator behaviour of squirrels. *Journal for Nature Conservation*, 16, 44-55.

Kunz, T.H.; Arnett, E.B.; Cooper, B.M.; Erickson, W.P.; Larkin, R.P.; Mabee, T.; Morrison, M.L; Strickland, M.D., and Szewczak, J. M., 2007. Assessing Impacts of Wind-Energy Development on Nocturnally Active Birds and Bats: A Guidance Document. *Journal of Wildlife Management*, 71(8), 2449-2486.

Landry, M.A.; Leclerc, A., and Gagnon, Y., 2013. A methodology for the evaluation of the economic impacts of wind energy projects. *Energy &Environment*, 24(5), 735-748.

Lu, X.; Mcelroy, M.B., and Kiviluoma, J., 2009. Global potential for wind-generated electricity. *Proceedings of the national academies of science*, 109(27), pp. 10933-10938.

Lucas, M.; Ferrer, M.; Bechard, M.J., and Muñoz, A.R., 2012. Griffon vulture mortality at wind farms in Southern Spain: Distribuition of fatalities and active mitigation measures. *Biological Conservation*, 147, 184-189.

McAllister, L.K., 2008. *Making Law Matter: Environmental Protection and Legal Institutions in Brazil*. Stanford: Stanford University Press, 288p.

Meireles, A.J.A., 2008. Impactos ambientais em áreas de preservação permanente (APP's) promovidos no campo de dunas da Taíba pela usina eólica Taíba Albatroz – Bons ventos Geradora de Energia S/A. *Parecer técnico elaborado para o Ministério Público Federal no Ceará (MPF/CE)*, 49p.

Meireles, A.J.A., 2011. Danos socioambientais originados pelas usinas eólicas nos campos de dunas do Nordeste brasileiro e critérios para definição de alternativas locacionais. *Confins [Online],* v. 11, 1-23. doi: 10.4000/confins.6970

Meireles, A.J.A.; Gorayeb, A.; Silva. D.R.F., and Lima, G.S., 2013. Socio-environmental impacts of wind farms on the traditional communities of the western coast of Ceará, in the Brazilian Northeast. *In: C*onley, D.C.; Masselink, G., Russel, P. E., and O'Hare, T. J. (eds.), P*roceedings of the 12th International Coastal Symposium. Journal of Coastal Research*, Special Issue Nº 65, pp. 81-86.

Meireles, A. J. A.; Gorayeb, A.; Lima, G.S., and Silva, D.R.F., 2015. Impactos socioambientais da energia eólica no litoral cearense. In: Correia, L.J. de A.; Oliveira, V.P.V. de; and Maia, J. A. (eds.). *Evolução das Paisagens e Ordenamento Territorial de Ambientes Interioranos e Litorâneos*. Fortaleza: Expressão Gráfica, pp. 156-169.

Mendes, J.S.; Gorayeb, A.; Machado, Y. L., and Silva, E.V., 2014. Os grandes empreendimentos e as comunidades tradicionais: o caso da comunidade de Mundaú - Trairí, Ceará. *Revista Monografias Ambientais – REMOA*, 13(3), 3357-3365.

Mirasgedis, S.; Tourkolias, C.; Tzovla, E., and Diakoulaki, D., 2014.Valuing the visual impact of wind farms: An application in South Evia, Grece. *Renewable and Sustainable Energy Reviews*, 39, 296-311.

Munday, M.; Bristow, G., and Cowell, R., 2011. Wind farms in rural areas: How far do community benefits from wind farms represent a local economic development opportunity?. *Journal of Rural Studies*, 27, 1-12.

Pasqualetti, M.J., 2011. Opposing wind energy landscapes: a search for common cause. *Annals of the Association of American Geographers*, 101(4), 907-917.

Pinheiro, I.; Gomes, S.; Castro, H.; Gorayeb, A.; Meireles, A. J. de A.; Mendes, J. S., and Silva, E. V., 2014 Conflitos territoriais e comunidades pesqueiras tradicionais do litoral oeste do Ceará, Brasil. *Anais do XIV Colóquio Ibérico de Geografia* (Guimarães, PO), pp. 2119-2124.

Pinto, M. F.; Nascimento, J.L.J.; Alves, R.R.N., and Meireles, A. J. A., 2013. Qual a relação entre etnozoologia e território? *Revista Ouricuri*, Paulo Afonso, Bahia, 3(2), 068-088.

Primavera, J.H., 2005. Mangroves, fishponds and the quest for sustainability. *Science*, 310 (5745), 57-59. d*oi:* 10.1126/Science.1115179

Schlãppy, M.; Saskov, A., and Dahlgren, T., 2014. Impact hypothesis for offshore Wind farms: Explanatory models for species distribuition at extremely exposed rocky áreas. *Continental Shelf Research*, 83, 14-23.

Simas, M. and Pacca, S., 2013. Energia eólica, geração de empregos e desenvolvimento sustentável. *Estudos Avançados*, 27(77), 99-115.

Slattery, M.C.; Lantz, E. and Johnson, B.L., 2011. State and local economic impacts from wind energy projects: Texas case study. *Energy Policy*, 39, 7930–7940.

Slattery, M.C.; Johnson, B.L.; Swofford, J.A., and Pasqualetti, M. J., 2012. The predominance of economic development in the support for large-scale wind farms in the U.S. Great Plains. *Renewable and Sustainable Energy Reviews,* 16, 3690-3701.

Valiela, I.; Bowen, J.L., and York, J.K., 2001. Mangrove forests: one of the World's threatened major tropical environments. *Bioscience*, 15(10), 807-815.

Vasconcelos, F.P., 2005. Riscos naturais e antrópicos na zona costeira. *Anais eletrônicos da 57ª Reunião anual da SBPC* (São Paulo, UECE). www.sbpcnet.org.br/livro/57ra/programas /CONF_SIMP/textos/fabioperdigao-riscos.htm.

Journal of Coastal Research	SI	75	388-392	Coconut Creek, Florida	2016

Beach response to Australian East Coast Lows: A comparison between the 2007 and 2015 events, Narrabeen-Collaroy Beach

Mitchell D. Harley[†*], Ian L. Turner[†], Kristen D. Splinter [†], Matthew S. Phillips[†] and Joshua A. Simmons[†]

[†]Water Research Laboratory,
School of Civil and Environmental Engineering, UNSW Australia
Manly Vale, NSW, 2093, Australia

www.cerf-jcr.org

www.JCRonline.org

ABSTRACT

Harley, M.D.; Turner, I.L.; Splinter, K.D.; Phillips, M.S., and Simmons, J.A., 2016. Beach response to Australian East Coast Lows: a comparison between the 2007 and 2015 events, Narrabeen-Collaroy Beach. *In:* Vila-Concejo, A.; Bruce, E.; Kennedy, D.M., and McCarroll, R.J. (eds.), *Proceedings of the 14th International Coastal Symposium* (Sydney, Australia). *Journal of Coastal Research*, Special Issue, No. 75, pp. 388-392. Coconut Creek (Florida), ISSN 0749-0208.

East Coast Lows (ECLs) are intense extratropical cyclones that form off the east Australian coastline and are known to cause significant beach erosion. This study presents analysis of the beach response to two severe ECLs that occurred in the Sydney region in June 2007 and April 2015 based on a three-dimensional coastal monitoring program undertaken at Narrabeen-Collaroy Beach. The results indicate considerable reductions in the subaerial sand volume for both storms, with an average (maximum) reduction of 78 m^3 (124 m^3) per alongshore meter for the 2007 event and 58 m^3 (104 m^3) per alongshore meter for the 2015 event. The overwhelming majority (93%) of subaerial beach erosion for both storms was observed to be within the berm section of the beach profile. Further analysis into the alongshore variability of cross-shore beach response reveals that the enhanced erosion during the 2007 event was mainly concentrated in the mid to northern sections of the embayment. It was found that this enhanced erosion was predominantly a result of a greater berm volume in this section of the embayment prior to storm arrival and that berm response to these two events was very similar ($R^2 = 0.81$) when considering erosion as a percentage of the pre-storm berm volume. It is concluded that the berm reduction as a percentage of the pre-storm berm volume can potentially provide a suitable predictor for the beach response to severe ECLs within littoral cells along this coastline.

ADDITIONAL INDEX WORDS: *Extreme storms, embayed beaches, coastal processes.*

INTRODUCTION

East Coast Lows (ECLs) are intense extratropical cyclones that can form rapidly off the coastline of eastern Australia and are known to cause hurricane-force winds, strong precipitation and highly erosive wave conditions (Speer *et al.*, 2009). Historically, ECLs have been responsible for some of the most destructive coastal erosion events in the SE Australian region (*e.g.*, Lord and Kulmar, 2000). Over the last decade, two particularly severe ECLs resulted in significant impacts along this coastline. The first of these events occurred in June 2007 and generated waves that reached a peak significant wave height (H_{sig}) in Sydney of 6.9 m. The second event occurred in April 2015 and caused a peak H_{sig} of 8.1 m, equivalent to a 20 year annual reccurence interval (Shand *et al.*, 2010).

Despite the destructiveness of ECLs, observational data as to the precise magnitude of beach erosion resulting from these cyclonic systems is scarce and there is currently a limited understanding as to which hydrodynamic and morphodynamic factors govern the variability in beach response within littoral cells along this crenulated coastline. This study presents a detailed comparison of the beach response to the 2007 and 2015 ECL events based on an unprecedented high-resolution and long-term coastal monitoring program undertaken at Narrabeen-Collaroy Beach, located within the metropolitan area of Sydney, NSW (Figure 1). The use of this three-dimensional survey dataset enables the accurate quantification of both the total sand volume loss from the subaerial beach due to the two events and the variability in the beach response in the alongshore direction. It is shown that the similarities in the severity of the two events equate to a very similar alongshore beach response, particularly when considering differences in the berm volume stored on the beach prior to storm arrival.

METHODS

The SE Australian coastline is characterized by a series of embayed beaches with an average length of 1.3 km (Short, 2007). The Narrabeen-Collaroy embayment is 3.6 km in and comprises Collaroy beach at its southern end, transitioning into Narrabeen beach at its northern end. Beach sediment is roughly uniform alongshore and is composed of fine to medium quartz sand with 30% carbonate fragments. The deepwater wave climate of this region is of moderate to high wave-energy (mean $H_{sig} \approx 1.6$ m, mean $T_p \approx 9.8$ s) with waves predominantly from the SSE direction. The southerly nature of the wave climate means that the southern (Collaroy) end is typically sheltered from waves, such that reflective/low tide terrace beach states usually prevail in this section. At the northern end, the greater exposure to waves from the dominant SSE direction means that higher-energy intermediate beach states such as rhythmic bar and beach and longshore bar and trough typically prevail. Foredunes of up to 9 m in height are also present towards the northern end of the embayment.

DOI: 10.2112/SI75-078.1 received 15 October 2015; accepted in revision 15 January 2016.
*Corresponding author: m.harley@unsw.edu.au

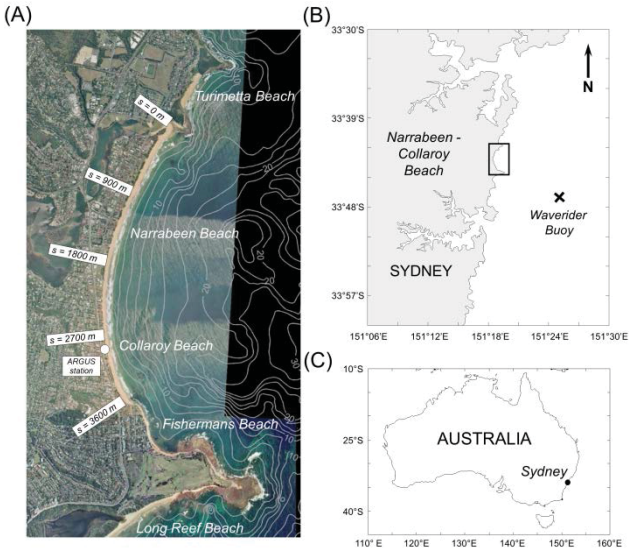

Figure 1. Location of the Narrabeen-Collaroy embayment, with the alongshore locations used for subsequent figures indicated. (A) Aerial photo of the embayment; (B) regional scale, indicating the location of the Sydney deepwater waverider buoy; (C) national scale.

Since 1976, a coastal monitoring program has been underway along the Narrabeen-Collaroy embayment (refer to Harley *et al.*, 2015 for a detailed description). A major component of this program is monthly three-dimensional surveys of the entire subaerial beach, which have been undertaken since May 2005 and amount to a total of 119 surveys up until September 2015. Three-dimensional surveys have been performed by mounting a high-accuracy RTK-GPS unit (vertical accuracy ≈ ±0.03m) to an all-terrain vehicle and collecting points at 1 Hz (approx. 4 m horizontal spacings) within the subaerial region of the beach (i.e., between MSL and a stable line along the top of the foredune). The 10 000+ irregularly-spaced points collected per survey are then interpolated to a alongshore – cross-shore curvilinear grid using the logspiral transformation method of Harley and Turner (2008).

2007 and 2015 East Coast Lows

Both the 2007 and 2015 ECLs had similar synoptic evolutions and can be considered easterly trough lows according to the ECL classification of Browning and Goodwin (2013). Easterly trough lows form from existing surface troughs east of the Great Dividing Range, where they deepen and track in a southwards direction along the east Australian coastline. In the case of the 2007 event, this low pressure system developed on 7 June in the northern Tasman Sea and moved southwards. By the morning of 8 June, the system was centred off the coastal city of Newcastle, located around 100 km north of Sydney, generating severe onshore wind gusts of up to 135 km/h (Watson *et al.*, 2007). The extreme conditions caused the 40,000 tonne bulk coal ship *Pasha Bulker* to run aground at a Newcastle beach. Such conditions subsided by the 10 June when the cyclone moved out to sea towards New Zealand. With regards to the 2015 event, the synoptic system formed on 20 April from the convergence of two troughs and by the evening had moved south and deepened into an intense ECL off the central New South Wales coast. Over a 48 hour period, the system remained almost stationary off the coastline and resulted in prolonged onshore winds which, like the 2007 event, peaked at a maximum gust speed of 135 km/h (BOM, 2015). Energetic conditions subsided on 22 April when the system moved southwards into the southern Tasman Sea.

Table 1. W*ave and water-level statistics (Sydney data) for the 2007 and 2015 east coast lows. Storm direction, duration and total storm energy are calculated based on the methodology of Harley et al. (2010).*

Storm	June 2007	April 2015
Peak H_{sig} (m)	6.9	8.1
Average period T_p (s)	11.1	11.3
Average storm direction (° TN)	149	161
Duration (h)	65	72
Total storm energy (MJh/m^2)	1.13	1.37
Peak water level (m)	0.95	1.22

Wave and water-level conditions (as measured from the Sydney waverider buoy and Camp Cove tide gauge) for the two events are summarized in Table 1. This table indicates that in terms of deepwater wave conditions, the April 2015 was a slightly more severe event, with a larger peak wave height, longer storm duration and greater total storm energy than the June 2007 event. The April 2015 event also coincided with spring high tides, such that the maximum water level during the event was almost 30 cm higher than that of the 2007 event. The storm wave direction from the 2007 event was however 12° more easterly than the 2015 event.

Figure 2. Pre- and post-storm images (looking north) taken from the Narrabeen-Collaroy ARGUS video monitoring station for: (A-B) the June 2007 ECL; and (C-D) the April 2015 ECL. All images are 10-minute time exposures taken at mid tide.

RESULTS

At Narrabeen-Collaroy Beach, the impacts of the large waves generated from these two ECLs were considerable. Figure 2 presents mid-tide images taken both immediately prior to and following the two events, as captured by the Narrabeen ARGUS video monitoring station at the southern end of the embayment (see Figure 1 for precise location). A substantial reduction in the subaerial beach as a result of both storms is evident in Figure 2, with post-storm images indicating a shoreline very close to adjacent backbeach residential properties.

Results from the monthly three-dimensional RTK-GPS surveys provide further evidence as to their severity. With regards to the June 2007 ECL, the total subaerial volume reduction that occurred was 273 400 m^3, which equates to an average subaerial volume reduction of 78 m^3 per alongshore metre. Ninety-three percent of this volume reduction occured between MSL and the +3 m contours, which approximates the berm on this coastline. In terms of the shoreline contour (as defined by the mean high water spring elevation, or 0.7 m above MSL), the June 2007 ECL resulted in an average overall landward shift of 28 m. Subaerial beach volume losses for the April 2015 ECL were observed to be slightly lower than the 2007 event. The subaerial beach volume loss for this latter event amounted to a total of 199 600 m^3 across the embayment, an average subaerial volume reduction of 57 m^3 per alongshore metre. The average landward shift in the shoreline contour was found to be 19 m.

To place these results into a longer-term perspective, Figure 3 presents the time-series of total subaerial sand volume over the entire period (May 2005 – September 2015) of three-dimensional RTK-GPS monitoring. The magnitude of subaerial sand volume change between monthly surveys is also indicated in Figure 3B. This data reveals that the rapid volume reductions measured due to the 2007 and 2015 ECLs were in fact the two most significant reductions in volume over the ten-year history of three-dimensional monitoring. The volume loss measured for the single event in 2007 amounted to a considerable 72% of the total variability in subaerial beach volume observed over the entire ten-year period, highlighting the significance of rapid ECL impacts on longer-term coastal variability.

Alongshore variability in cross-shore beach response

Whereas the results above provide insights into the magnitude of subaerial sand volume reductions due to severe ECLs, of additional and significant interest is the alongshore distribution of erosion as well as the existence of any localized erosion 'hot spots'. Figure 4 presents this alongshore variability in both the subaerial beach volume and shoreline change due to the two events. The results of this analysis indicate remarkably similar patterns in the cross-shore beach response in the southernmost 1000 m of the embayment (i.e., alongshore distance > 2600 m). Within this section, both the subaerial volume and shoreline change resulting from the two storm cases are nearly identical. Moving further northwards however, the measured beach responses diverge as the 2007 event exhibits greater erosion, with differences in the order of 40 m^3/m for subaerial beach volume and 20 m for shoreline change. At the northern end of the embayment, both the 2007 and 2015 events indicate a significant reduction in storm erosion and, in the case of the 2015 event, a slight accretionary signal. The overall R^2 value between the two beach response signals is 0.48 for beach volume change and 0.28 for shoreline change.

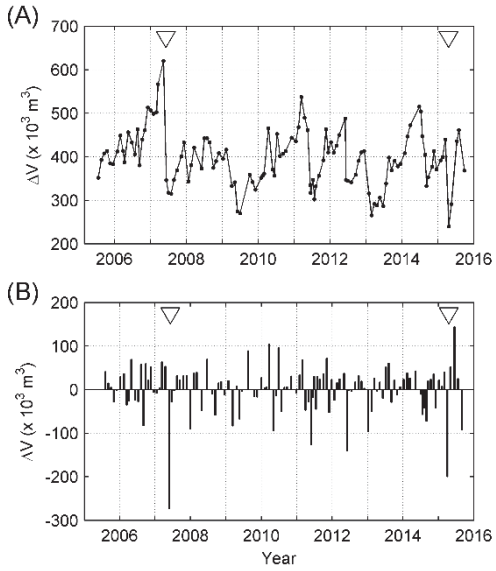

Figure 3. (A) Time-series of total subaerial sand volume at Narrabeen-Collaroy Beach, based on monthly three-dimensional RTK-GPS surveys between May 2005 and September 2015. (B) Subaerial volume change between monthly surveys. Triangles indicate the timing of the 2007 and 2015 ECLs.

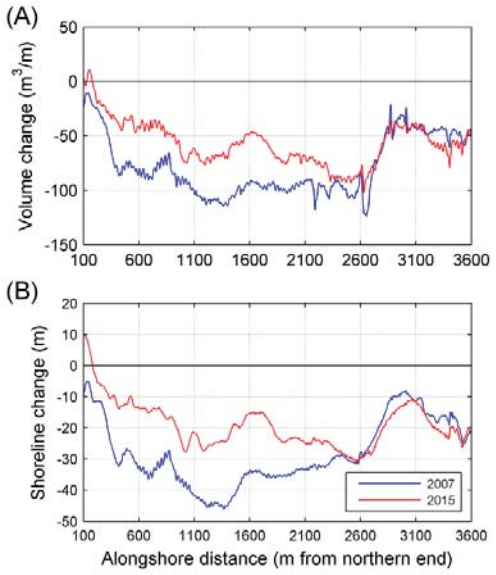

Figure 4. Alongshore variability in beach response to the 2007 and 2015 ECLs: (A) subaerial sand volume change; (B) shoreline change (as defined by the +0.7 m contour).

The maximum subaerial beach erosion volume calculated across the entire embayment for both events was found to occur in almost the same location. For the 2007 ECL, this value was measured at 124 m^3/m at a distance of 2650 m from the northern end. For the 2015 ECL meanwhile, a maximum erosion volume of 103 m^3/m was measured a mere 20 m northwards of this point. This location coincides with a well-known erosion hot spot ("Wetherill St, Narrabeen"), which has been identified by regional coastal planners as one of fifteen critical hot spots along this coastline (OEH, 2015).

DISCUSSION

Despite the slightly greater severity of the 2015 ECL in terms of offshore wave conditions, the results of the RTK-GPS surveys indicate that greater erosion of the subaerial beach at Narrabeen-Collaroy occurred during the 2007 event – and that this difference in erosion predominantly occurred in the mid to northern section of the embayment. The reasons for this discrepency in beach response between the two events could be related to a number of hydrodynamic and morphodynamic factors, including:

- Differences in wave energy transformations from offshore to breaking wave depths;
- Water-level differences and their timing with respect to wave energy;
- Differences in antecedent beach morphology (*e.g.*, pre-storm beach state, berm volume, intertidal beach slope and dune toe elevation).

An analysis into the potential causes of such discrepencies was performed by investigating three parameters associated with these hydrodynamic and morphodynamic factors: (1) the average breaker wave height during the storm (as calculated from a numerical SWAN model transformation of the offshore wave measurements, see Harley *et al.*, 2011); (2) the pre-storm berm volume (as calculated by the sand volume between MSL and the +3 m contour); and (3) the pre-storm berm slope (as defined by the linear slope between MSL and the +1.2 m contour). The alongshore variability of these three parameters are presented in Figure 5.

This figure reveals that despite the higher peak H_{sig} of the 2015 ECL, the average wave height at the point of breaking over the duration of both events was virtually identical. This is due to the fact that the wave direction of the 2007 event was 12° more easterly, resulting in less wave energy being attenuated to a lesser degree by the southern headland, relative to the 2015 event. In terms of morphodynamic factors, both the pre-storm berm volume and berm slope indicate significant differences along the beach. This is particularly the case for the pre-storm berm volume, which is substantially greater in the mid to northern section of the embayment prior to the 2007 event than for the 2015 event. For the southern section on the other hand (alongshore distance > 2600 m), the pre-storm volumes compare very closely.

Since these differences in the pre-storm berm volumes mirror those of the alongshore erosion response presented in Figure 4, it implies that the variability in beach response between the two events was predominantly a consequence of the extra sediment stored within the berm prior to the 2007 event.

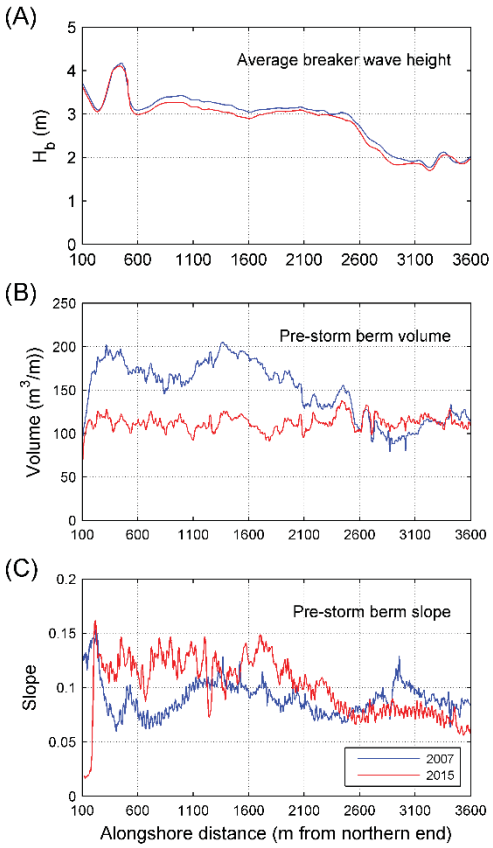

Figure 5. Alongshore variability in: (A) the average breaker wave height over the duration of each storm; (B) the pre-storm berm volume; and (C) the pre-storm berm slope.

This is confirmed in Figure 6 by plotting the berm erosion for each storm as a percentage of the pre-storm berm volume. In terms of this relative volume loss, the figure indicates that the beach response to the two events is very similar (R^2 = 0.81).

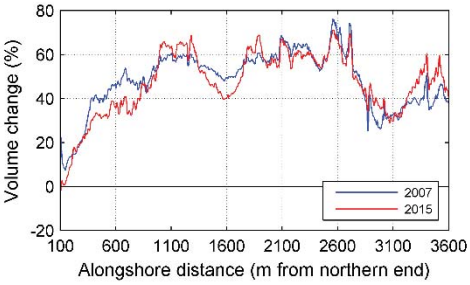

Figure 6. Alongshore variability in berm erosion volume as a percentage of the pre-storm berm volume.

This important result suggests that for ECLs of a similar intensity, it is the berm response as a proportion of the pre-storm berm volume that can potentially be used as a predictor, rather than the absolute magnitude of the eroded beach volume. If this observation can be verified at one or more additional sites, such a predictor could be used in the context of a behavioural model for beach response to ECLs, or for training computer algorithms to predict beach response.

The alongshore gradient in breaker wave height presented in Figure 5A also reveals a strong agreement to the alongshore variability in cross-shore beach response (Figure 4). For instance, the decrease in breaker wave height observed at the southern end of the embayment (a consequence of wave sheltering by the southern headland) directly corresponds with a similar reduction in the magnitude of beach erosion in this section of the embayment. This implies that cross-shore sediment transport processes predominantly govern the beach response to these two events, which has also been observed in the longer-term beach response at Narrabeen-Collaroy (Harley *et al*., 2015). Alongshore sediment transport processes meanwhile are evident for both events in the slight accretionary signal at the northern end of the embayment.

CONCLUSIONS

East coast lows can result in prolonged (i.e., days) and extremely energetic maritime conditions that can cause significant erosion to adjacent coastlines. This study has presented detailed results of the beach response at an embayed beach to two similarly extreme storms that impacted the southeast Australian coastline eight years apart. The magnitude of the beach response in both cases was considerable, with total subaerial volume reductions across the embayment measured as 273 400 m^3 for the 2007 event and 199 600 m^3 for the 2015 event. In terms of change in the shoreline contour, the 2007 and 2015 events led to average shifts in the landwards direction of 28 m and 19 m respectively.

Following an exploration into the reasons for the observed differences in the alongshore beach response between the two storms, it was found that alongshore differences were primarily a consequence of the available sand stored within the berm prior to each storm, with the 2007 event having a significantly greater pre-storm berm volume than that of the 2015 event. When considering the berm erosion as a percentage of pre-storm berm storage, the beach response to the two events was found to be nearly identical. The fact that these two extreme storms separated by eight years can result in such a similar beach response gives us great confidence as to the predictability of east coast low impacts within littoral cells along the east Australian coastline. The results of this study suggest that berm volume loss as a percentage of the pre-storm berm volume is a suitable predictor.

ACKNOWLEDGMENTS

This study was supported by the Australian Research Council (Grant #DP150101339) and the NSW Office of Environment and Heritage (OEH) as part of the Adaptation Research Hub Coastal Node. Offshore wave and tide data were kindly provided by the Manly Hydraulics on behalf of OEH. Image data from the ARGUS video monitoring station was made possible through the support of Warringah Council and the Sydney Institute of Marine Science Foundation. The authors would particularly like to thank Melissa Bracs for her efforts in helping collect the three-dimensional survey data.

LITERATURE CITED

BOM, 2015. *Newcastle, New South Wales April 2015 Daily Weather Observations*, http://www.bom.gov.au/climate/dwo/201504/html/IDCJDW2097.201504.shtml [Accessed 15/10/2015]

Browning, S.A., and Goodwin, I.D., 2013. Large-scale influences on the evolution of winter subtropical maritime cyclones affecting Australia's east coast. *Monthly Weather Review*, 141, 2416-2431.

Harley, M.D. and Turner, I.L., 2008. A simple data transformation technique for pre-processing survey data at embayed beaches. *Coastal Engineering*, 55, 63-68.

Harley, M.D.; Turner, I.L.; Short, A.D., and Ranasinghe, R., 2010. Interannual variability and controls of the Sydney wave climate. *International Journal of Climatology*, 30(9), 1322-1335.

Harley, M.D.; Turner, I.L., and Short, A.D., 2015. New insights into embayed beach rotation: the importance of wave exposure and cross-shore processes. *Journal of Geophysical Research: Earth Surface*, 120(8), 1470-1484.

Harley, M.D.; Turner, I.L.; Short, A.D.; Bracs, M.A.; Phillips, M.S.; Simmons, J.A., and Splinter, K.D., 2015. Four decades of coastal monitoring at Narrabeen-Collaroy Beach: the past, present and future of this unique dataset. *22nd Australasian Conference on Coastal and Ocean Engineering*, Engineers Australia, Auckland NZ, 15-18 September, 6 pp.

Lord, D. and Kulmar, M., 2000. The 1974 storms revisited: 25 years experience in ocean wave measurement along the south-east Australian coast. *In:* B.L. Edge (ed.) *Proceedings of the 27th International Conference on Coastal Engineering*, ASCE, Sydney (Australia), pp. 559-572.

OEH, 2015. *Coastal erosion 'hot spots'*, http://www.environment.nsw.gov.au/coasts/coasthotspots.htm [Accessed 16/10/2015]/

Shand, T.D.; Goodwin, I.D.; Mole, M.A.; Carley, J.T.; Coghlan, I.R.; Harley, M.D., and Peirson, W.L., 2010. *NSW coastal inundation study: coastal storms and extreme waves*. Technical Report 2010/16, Water Research Laboratory, University of New South Wales.

Speer, M.S.; Wiles, P., and Pepler, A., 2009. Low pressure systems off the New South Wales coast and associated hazardous weather: establishment of a database. *Australian Meteorological and Oceanographic Journal*, 58, 29-39.

Watson, P.D.; Lord, D.; Kulmar, M.; McLuckie, D., and James, J., 2007. Analysis of a storm – June 2007. *16th NSW Coastal Conference*, Yamba (Australia), 14 pp.

Journal of Coastal Research	SI	75	393-397	Coconut Creek, Florida	2016

Shoreline-Sandbar Dynamics at a High-Energy Embayed and Structurally-Engineered Sandy Beach: Anglet, SW France

Jean-Remy Huguet†‡, Bruno Castelle†‡*, Vincent Marieu†‡, Denis Morichon∞, Inaki de Santiago∞

†UMR 5805 EPOC
CNRS
Pessac, France

‡UMR 5805 EPOC
Université de Bordeaux
Pessac, France

∞Laboratoire SIAME
Université de Pau et des Pays de l'Adour
Anglet, France

www.cerf-jcr.org

www.JCRonline.org

ABSTRACT

Huguet, J.-R.; Castelle, B.; Marieu, V.; Morichon, D., and de Santiago, I., 2016. Shoreline-sandbar dynamics at a high-energy embayed and structurally-engineered sandy beach: Anglet, SW France. *In:* Vila-Concejo, A.; Bruce, E.; Kennedy, D.M., and McCarroll, R.J. (eds.), *Proceedings of the 14th International Coastal Symposium* (Sydney, Australia). *Journal of Coastal Research*, Special Issue, No. 75, pp. 393-397. Coconut Creek (Florida), ISSN 0749-0208.

Anglet beach, Basque Coast (SW France), is a 4-km long embayment bounded by a prominent headland in the South and by the southern Adour River training wall in the North. The beach is structurally-engineered with, within the embayment, 6 groins and 3 distinct sectors where the beach is backed by a seawall. The beach is high-energy intermediate, mostly double-barred, composed of medium to coarse sand with a steep beach face (~1/10). In January 2013, a video system was installed at the Southern end of Anglet beach at about 70 m above mean sea level to monitor about 2 km of the southern beach of Anglet that includes 4 groins extending about 100 m seaward and a 1-km seawall backing the beach. The study period includes the winter 2013/2014 that was outstanding in terms of the available energy arriving at the coast with a 2-month-averaged significant wave height peaking at 3.6 m. Despite the extreme storm wave conditions during the winter 2013/2014, the outer bar crescentic patterns maintained and even further developed. The beach eroded by O(10 m) and, surprisingly and in contrast with the nearby northern open beaches, they recovered to their pre-winter 2013/2014 state within only a few months. Overall, Anglet beach appears to respond predominantly at individual storm frequency rather than at seasonal timescales, with the groins and headland acting as major controlling boundaries influencing beach state and dictating rip channel locations.

ADDITIONAL INDEX WORDS: *video monitoring, extreme storms, shoreline, sandbar, headlands, groins.*

INTRODUCTION

The 270-km long Aquitaine Coast, SW France, is a meso-macrotidal sandy environment exposed to high-energy ocean waves. At the southern end of the Aquitaine Coast, the Basque Coast has been facing serious erosion issues over the last decades. In contrast with the mostly pristine and well-documented northern Aquitaine open sandy beaches, the Basque Coast sandy beaches are characterized by ubiquitous and more or less prominent headlands, exposing rocky substratum and coastal structures such as groins and training walls. High-frequency video-observation along this coast (Birrien *et al*., 2013; De Santiago *et al*., 2013; Enjalbert *et al*., 2011) went with general existing studies (e.g. Jackson *et al*., 2005; Short, 2006) suggesting that geological inheritance and the presence of hard structures are a major factor influencing beach type and surf-zone sandbar dynamics. However, the detailed shoreline and sandbar response of the Basque Coast beaches to severe storms and their ability to recover has never been addressed.

The North Atlantic winter 2013/2014 was characterized by extreme storminess resulting on most of the western Europe coast in an unusual sequence of extremely high water levels and outstanding wave energy arriving at the coast (*e.g*. Castelle *et al*., 2015; Masselink *et al*., in press). These extreme conditions caused widespread coastal erosion and flooding. Unprecedented beach and dune erosion was observed along the Aquitaine open beaches with a dune retreat of *O*(10 m) with the erosion scarp

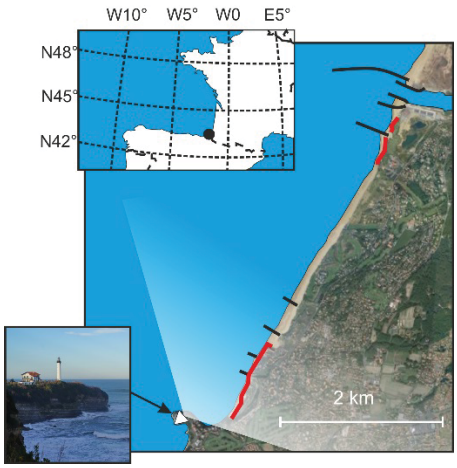

Figure 1. Study site (Anglet Beach, Basque Coast, SW France), with camera view field and location of the groins (black) and the sectors where the beach is backed by a seawall.

DOI: 10.2112/SI75-079.1 received 15 October 2015; accepted in revision 15 January 2016.
*Corresponding author: b.castelle@epoc.u-bordeaux1.fr

height locally exceeding 10 m (Castelle *et al*., 2015). A field survey analysis of bimonthly topographic surveys of Truc Vert beach spanning 1.5 years after the end of the Winter 2013/2014 shows that this beach, including the dune system, did not recover to its pre-winter 2013/2014 state (unpublished). In contrast with the Aquitaine open beaches, there was no detailed assessment of how the Basque Coast beaches respond to the winter 2013/2014 and if they recovered to their pre-winter 2013/2014 state.

Over the last years, equilibrium-based semi-empirical models have been increasingly used on cross-shore transport-dominated sandy coastlines to hindcast shoreline variability (*e.g*. Davidson *et al*., 2013; Splinter *et al*., 2014; Yates *et al*., 2009;) and more recently cross-shore sandbar dynamics and beach three-dimensionality (Stokes *et al*., 2015). The latter models allow to determine the response factor of a given beach, which describes the "memory" of a beach to antecedent conditions. Along the open sandy beaches of the Aquitaine Coast, a response factor of the order of a few years was found, meaning that the beaches respond predominantly at seasonal timescales rather than at individual storm frequency (Castelle *et al*., 2014). Some of the Basque Coast beaches, which are exposed to similar wave conditions as the northern open beaches, are composed of coarser sediments and, according to Splinter *et al*. (2014), should therefore have a response closer to that at individual storm frequency. However, this has never been verified and the winter 2013/2014 is a relevant period to test this hypothesis.

In this paper, the dynamics of Anglet beach, Basque Coast, is investigated over 2013-2015, *i.e*. including the outstanding winter 2013/2014. The beach faces WNW and is predominantly exposed to North Atlantic swells coming from the WNW direction, and also scarcely receives more variable locally-generated wind waves (Abadie *et al*., 2005). The beach is meso-tidal with semi-diurnal tidal regime and a mean spring range of 3.85 m. Anglet beach is a 4-km long embayment bounded by a prominent headland in the South and by the southern Adour River training wall in the North (Figure 1). The beach is structurally-engineered with, within the embayment, 6 groins and 3 distinct sectors where the beach is backed by a seawall. The beach is high-energy intermediate, mostly double-barred, composed of medium to coarse sand with a steep beach face (~1/10). In this paper, only the southern sector is addressed using video images, wave and tide data, with a focus on the shoreline and sandbar dynamics.

METHODS

Offshore significant wave height *Hs*, peak period *Tp* and peak direction θ were obtained from the global model WaveWatch3 (WW3, Tolman, 1991), at the coordinate 2°30'W 44°N. In-situ directional wave measurements were collected by a permanent directional wave buoy located in 50 m depth at 1°36,900'W ; 43°31,930'N about 6 km offshore of Anglet. Because of a number of buoy malfunctions, wave data were collected intermittently since November 2009. The WW3 significant wave height was further corrected via linear regression fit with the directional wave measurements. No correction was made to wave period and direction. Time series of tidal elevation was estimated from tidal harmonic estimation using interspersed measurements at the Soccoa tidal gauge located 15 km SW of the study site.

In January 2013, a video system including three N-NE facing cameras was installed at the Southern end of Anglet beach at about 70 m above mean sea level to monitor about 2 km of the southern beach of Anglet that includes 3 groins extending about 100 m seaward, delimiting 4 beaches (Figure 1 and 2a), and a 1-km seawall backing the beach (Figure 1). Figure 2 shows 4 examples of rectified time-exposure images.

Shoreline and sandbar detection

Anglet beaches are characterized by prominent red sediments (Birrien *et al*., 2013). Therefore, the shoreline position was determined in the cross-shore transition zone where the red/green ratio becomes larger than 1, although in some rare occasions this threshold was varied because of lightning issues. The algorithm was used on the high neap-tide level time exposure images to generate a time series of alongshore shoreline position. The mean shoreline position *Xs* was defined

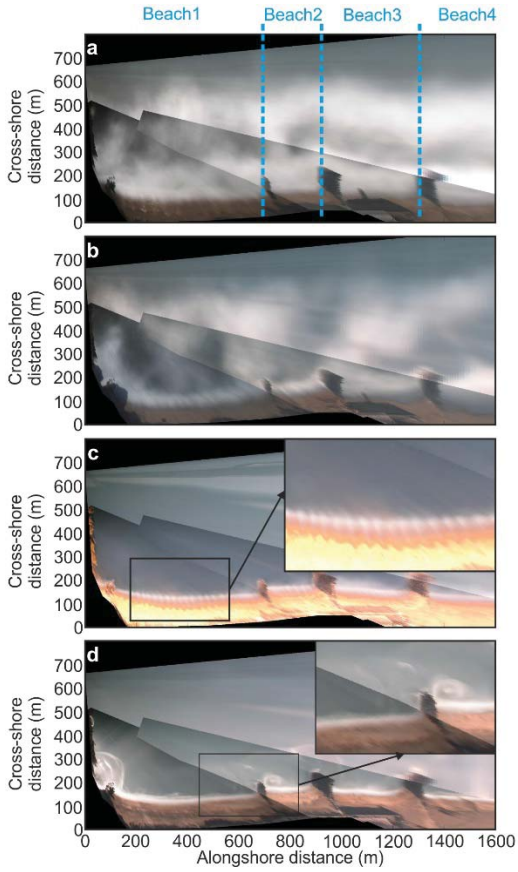

Figure 2. Typical time exposure images of Anglet beach. (a) double-barred and (b) single-barred configuration. (c) Ubiquitous beach cusps during low-energy wave conditions. (d) Despite the low-energy wave conditions, rip current activity against the headland and groins clearly visible through the formation of foam streaks.

as the alongshore-averaged shoreline position. The alongshore standard deviation of the shoreline position was also computed to give a measure of the alongshore variability. To detect sandbar position, low neap-tide level images were used to both minimize breaker line variability and gather continuous dataset of images. Provided wave breaking was sufficiently pronounced to create an alongshore continuous to near-continuous breaker line, from each selected plan view image bar positions were manually digitized. As for the shoreline computations, mean sandbar position *Xb* and alongshore standard deviation of the sandbar position were computed.

RESULTS

Over the study period, Anglet beach showed large morphological variability for both the shoreline and the sandbar(s). While Anglet beach has been observed to be most of the time double-barred (Figure 2a), the beach has been observed to be occasionally single-barred (Figure 2b). The shoreline also showed variability with more or less curved embayments and the common presence of beach cusps owing to the steep beach face (Figure 2b). Rip currents were ubiquitous throughout the study period with obvious deep rip channels cutting the sandbar along the beach or against the groins and headlands. Even during low-energy wave conditions, rip current activity along the groins was clearly visible through the formation of foam streaks (*e.g.* Figure 2d).

Figure 3 shows the 18-month time series of the Anglet beach dataset. Incoming waves were strongly seasonally modulated with low- to moderate-energy waves during spring and summer (typically Hs < 2 m). During autumn and winter, waves were mostly of moderate- to high-energy type. As expected, the winter 2013/2014 was outstanding in terms of storm wave clustering and averaged wave energy compared to the winter 2014/2015 that actually constitutes an overall low-energy winter compared to that typically observed along the Basque Coast (see for instance Abadie *et al*., 2005; Enjalbert *et al*., 2011). During the winter 2013/2014 (2014/2015), the 2-month averaged significant wave height peaked at 3.6 m (2.3 m) with 15 (3) storm wave events with *Hs* > 5 m. Throughout the whole time series, storm wave events never coincided with spring tides, with the notable exception of the storm wave event "Christine" on March 3, 2014, that caused severe damage to the Basque Coast waterfront. Noteworthy, the storm wave heights during the winter 2013/2014 were slightly lower than those measured 200 km in the north owing to a quasi- persistent W wave incidence (Castelle *et al*., 2015; see also Figure 3a, b).

Figure 3c and 3d show the time series of the mean cross-shore position of the sandbar(s) and that of the shoreline at the 4 beaches studied here. Consistent with existing earlier observations on intermediate beaches (*e.g.* Wright and Short,

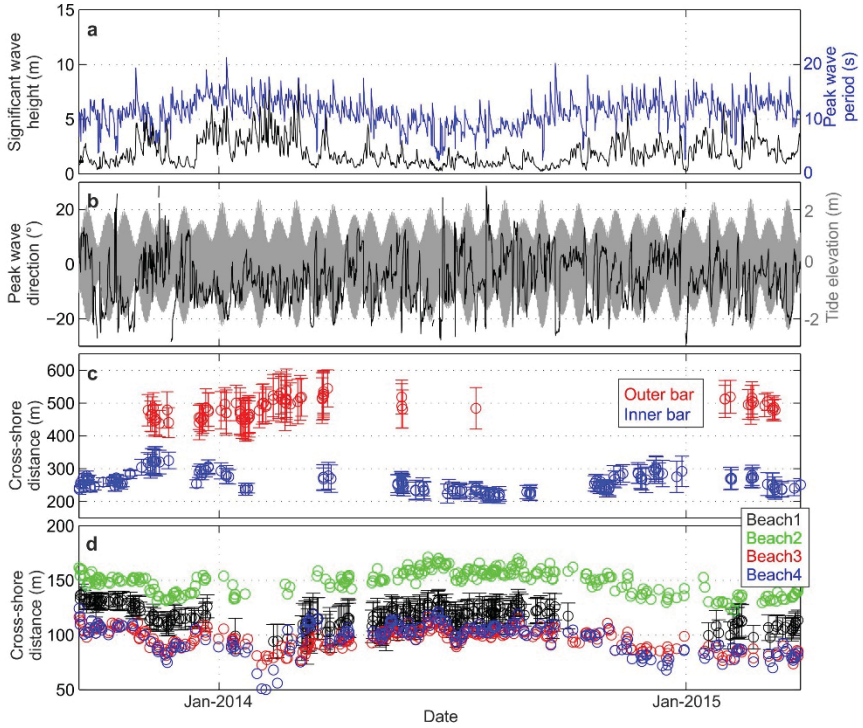

Figure 3. Time series of the 18-month dataset at Anglet Beach with (a) the offshore significant wave height *Hs* (black) and peak wave period *Tp* (blue); (b) the peak wave direction θ (black) with respect to shore-normal and tidal elevation (gray); (c) the mean and alongshore standard deviation of the cross-shore position of the outer (red) and inner (blue) bars; (d) the alongshore-averaged shoreline position along the 4 beaches. For readabity only the alongshore standard deviation of the shoreline position at Beach 1 is shown.

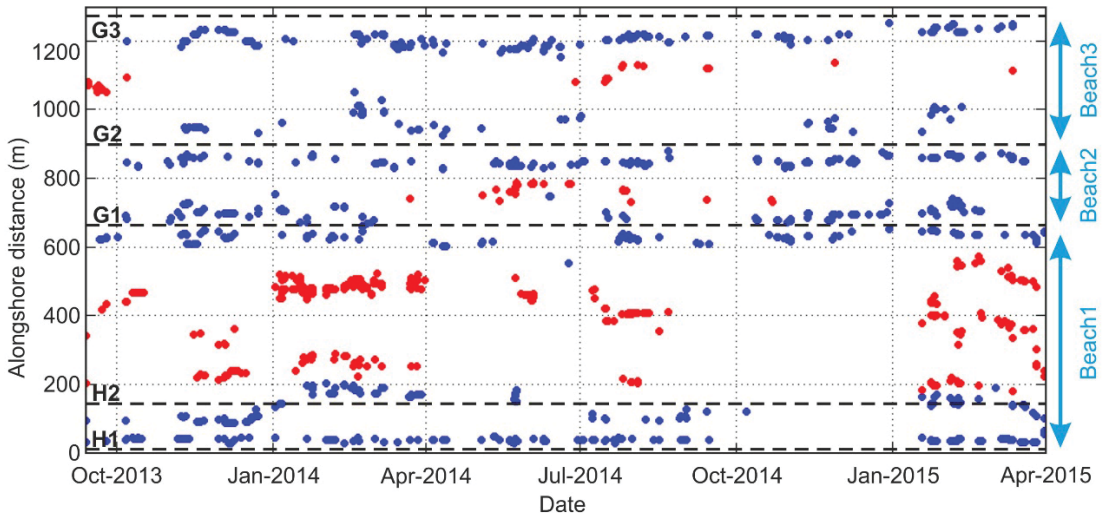

Figure 4. Time series of the alongshore location of rip channels with distinction of "fixed" topographic rips (blue) and "non-fixed" beach rips. G and H refer to groin and headland locations, respectively. Because of subtle camera movements, the rip locations along the remote Beach4 are not shown.

1984; Masselink *et al*., 2014), high-energy wave conditions drive a rapid offshore migration of the outer sandbar, while slow onshore outer migration was observed for decreasing wave energy. The inner bar steadily migrates onshore during the winter 2013/2014 despite the high-energy storms. Because of a number of camera malfunctions during the winter 2013/2014, it was not possible to address and compare the detailed shoreline response at the 4 beaches. Nonetheless, it is clear that the 4 beaches eroded by O(10 m) during this winter. Beach4 eroded by about 50 m while the narrowest beach (Beach2) eroded by approximately 15 m, suggesting the groins helped the beaches to withstand the extreme storm waves. The rate of shoreline erosion during the winter 2014/2015 was similar to that of winter 2013/2014 despite the both showing highly contrasting energy. Another surprising observation is that, in contrast with the northern Aquitaine beaches, the 4 beaches rapidly (within a few months) recovered to their pre-winter 2013/2014 state.

Figure 4 shows the time evolution of rip channel alongshore locations excluding Beach4. Topographic rips (blue dots in Figure 4) have preferred location against the groins and headlands that act as controlling boundaries, while non-fixed rip channels, referred to as beach rips, (red dots in Figure 4) are preferably observed along the largest beaches away from the groins/headlands (2 to 3 rips within Beach1 and 1 rip within Beach2 and Beach3). However, beach rips do not appear to migrate alongshore.

DISCUSSION

Despite the extreme storm wave conditions during the winter 2013/2014, the outer bar crescentic patterns maintained and even further developed as shown in Figure 5 that describes the outer-bar state at Anglet following the approach of Masselink *et al*. (2014). At the end of the winter, the outer bar was well-developed crescentic, which was confirmed by a detailed bathymetric survey (not shown). Accordingly, the outer-bar response at Anglet was similar to that observed along the northern Aquitaine beaches (Castelle *et al*., 2015) owing to the persistent long peak wave period and shore-normal incidence, but contrasts with that observed in the UK at Perranporth (Stokes *et al*., 2015). In the latter case, the outer bar rapidly migrated offshore and decayed, which is an outer-bar behavior often observed during extreme storms (*e.g*. Castelle et al., 2007). An equilibrium-based semi-empirical model was used to hindcast shoreline evolution at Anglet. Results (not shown) suggest a response factor of approximately 30 days, meaning that the beach responds predominantly at individual storm frequency rather than at seasonal timescales, as opposed to the nearby norther Aquitaine beaches (Castelle *et al*., 2014). An interesting feature is that the model is able to simulate the rapid shoreline recovery.

CONCLUSIONS

The structurally-engineered beach of Anglet was video monitored to address beach erosion and subsequent recovery. Despite the extreme winter 2013/2014 storm waves, Anglet beach eroded at a similar rate as during the low-energy winter 2014/2015. Even more surprisingly, the 4 beaches rapidly recovered to their pre-winter 2013/2014 state within a few months. While the approach developed here can be applied elsewhere, a longer dataset is required to study Anglet beach response on the timescales from hours to years in more detail.

ACKNOWLEDGMENTS

This work was done within the framework of project CHIPO (ANR-14-ASTR-0004-01) financially supported by the Agence Nationale de la Recherche (ANR), and project DECA (INSU/EC2CI-DRIL). The authors acknowledge support from OASU (Observatoire Aquitain des Sciences de l'Univers) under the AST (Action Scientifique Transverse) "Evénements extremes".

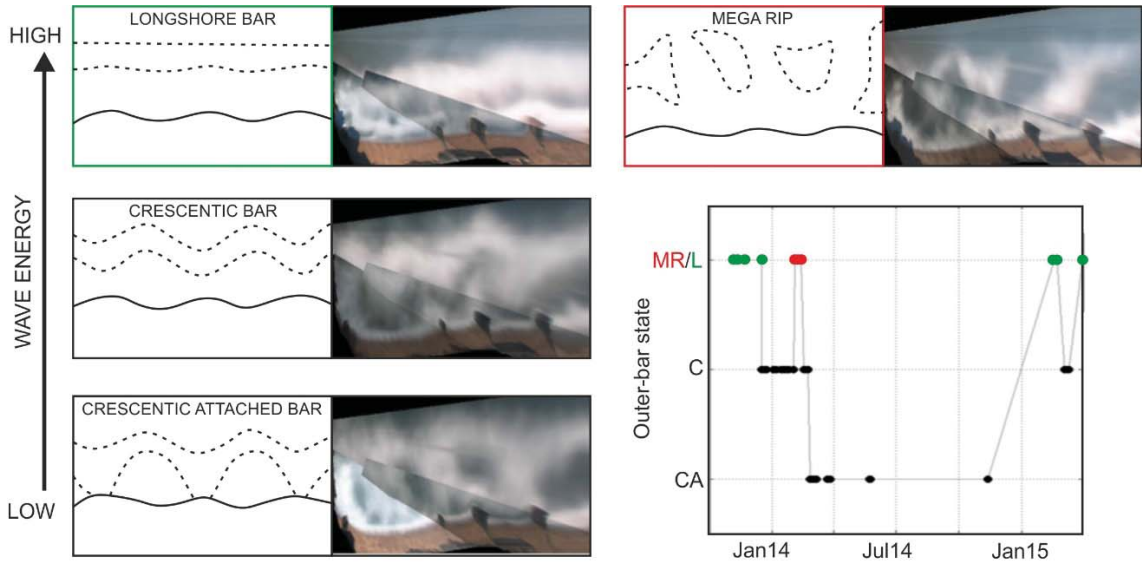

Figure 5. Time series of outer bar type at Anglet Beach following the method described in Masselink *et al.* (2014). The 4 outer sand bar types are MR=Mega Rip (red); L= Longshore (green); C= Crescentic; CA= Crescentic Attached. Upstate and downstate transitions represent moving up and down the diagram, respectively

LITERATURE CITED

Abadie, S.; Butel, R.; Dupuis, H., and Brière, C., 2005. Statistical parameters of waves on the south Aquitaine Coast. *Comptes Rendus Geoscience*, 337, 769-776.

Birrien, F.; Castelle, B.; Dailloux, D.; Marieu, V.; Rihouey, D., and Price, T.D., 2013. Video observation of megacusp evolution along a high-energy engineered sandy beach : Anglet, SW France. *J. Coast. Res.*, SI 65(2), 1727-1732.

Castelle, B.; Marieu, V.; Bujan, S.; Ferreira, S.; Parisot, J.P.; Capo, S.; Senechal, N., and Chouzenoux, T., 2014. Equilibrium shoreline modelling of a high-energy meso-macrotidal multiple-barred beach. *Marine Geology*, 347, 85-94.

Castelle, B.; Marieu, V.; Bujan, S.; Splinter, K.D.; Robinet, A.; Sénéchal, N., and Ferreira, S., 2015. Impact of the winter 2013-2014 series of severe Western Europe storms on a double-barred sandy coast : beach and dune erosion and megacusp embayments. *Geomorphology*, 238, 135-148.

Castelle, B.; Turner, I.L., and Ruessink, B.G., 2007. Impact of storms on beach erosion: Broadbeach (Gold Coast, Australia). *Journal of Coastal Research*, SI 50, 534–539.

Davidson, M.A.; Splinter, K.D., and Turner, I.L., 2013. A simple equilibrium model for predicting shoreline change. *Coastal Engineering*, 73, 191–202.

De Santiago, I.; Morichon, D.; Abadie, S.; Castelle, B.; Liria, P., and Epelde, I., 2013. Video monitoring nearshore sandbar morphodynamics on a partially engineered embayed beach. *J. Coast. Res.*, 458-463.

Enjalbert, C.; Castelle, B.; Rihouey, D., and Dailloux, D., 2011. High-frequency video observation of a geologically-constrained barred-beach : La Grande Plage de Biarritz (France). *Journal of Coastal Research*, SI 64, 70-74.

Jackson, D.W.T.; Cooper, J.A.G., and Del Rio, L., 2005. Geological control of beach morphodynamic state. *Marine Geology*, 216, 297-314.

Masselink, G.; Austin, M.; Scott, T.; Poate, T., and Russell, P., 2014. Role of wave forcing, storms and NAO in outer bar dynamics on a high-energy, macro-tidal beach. *Geomorphology*, 226, 76-93.

Masselink, G.; Scott, T.; Poate, T.; Russell, P.; Davidson, M., and Conley, D., in press. The extreme 2013/14 winter storms: hydrodynamic forcing and coastal response along the southwest coast of England, *Earth Surface Processes and Landforms*, doi:10.1002/esp.3836, 1096-9837.

Short, A.D., 2006. Australian Beach Systems – Nature and Distribution. *Journal of Coastal Research*, 22, 11-27.

Splinter, K.D.; Turner, I.L.; Davidson, D.A.; Barnard, P.; Castelle, B., and Oltman-Shay, J., 2014. A generalized equilibrium model for predicting daily to inter-annual shoreline response. *Journal of Geophysical Research - Earth Surface*, 119, 1936-1958, doi :10.1002/2014JF003106.

Stokes, C.; Davidson, M., and Russell, P., 2015. Observation and prediction of three-dimensional morphology at a high-energy macrotidal beach. *Geomorphology*, 243, 1–13.

Tolman, H.L., 1991. A third-generation model for wind waves on slowly varying, unsteady and inhomogeneous depths and currents. *Journal of Physical Oceanography*, 21, 782-797.

Wright, L.D. and Short, A.D., 1984. Morphodynamics variability of surf zones and beaches: a synthesis. *Marine Geology*, 70, 251-285.

Yates, M.L.; Guza, R.T., and O'Reilly, W.C., 2009. Equilibrium shoreline response: observations and modeling. *Journal of Geophysical Research*, 114 (C09014).

Journal of Coastal Research	SI	75	398-402	Coconut Creek, Florida	2016

Wave attenuation and Coastal Protection by Shelly Ridges: Mont-Saint-Michel Bay, France

Matthieu Jeanson †*, Samuel Etienne †, Antoine Collin †

†Laboratoire de Géomorphologie et Environnement
Littoral, CNRS UMR 8586 Prodig,
Ecole Pratique des Hautes Etudes, France

www.cerf-jcr.org

www.JCRonline.org

ABSTRACT

Jeanson, M.; Etienne, S., and Collin, A., 2016. Wave attenuation and coastal protection by shelly ridges: Mont-Saint-Michel Bay, France. *In:* Vila-Concejo, A.; Bruce, E.; Kennedy, D.M., and McCarroll, R.J. (eds.), *Proceedings of the 14th International Coastal Symposium* (Sydney, Australia). *Journal of Coastal Research*, Special Issue, No. 75, pp. 398-402. Coconut Creek (Florida), ISSN 0749-0208.

The western part of Mont-Saint-Michel Bay (northwestern France), reputed for its high tidal range, is characterized by shelly ridges on the uppermost part of a macrotidal flat. Morphological monitoring and hydrodynamic measurements are undertaken since February 2015 with the aim of characterizing the role of the shelly ridges on wave dissipation and coastal protection. Each month, 11 topographic profiles are surveyed using a DGPS, as well as water levels and wave characteristics are measured using thirty miniature pressure sensors deployed in the tidal zone. Analysis of the collected data shows that wave characteristics were strongly influenced by water depth and ridge geometry. The incident waves measured on the lower part of tidal flats during experiments were predominantly wind-wave and swell, depending on meteorological conditions. At the back of the well-formed shelly ridges, residual waves were extremely low throughout with a dominance of infragravity frequencies. Calculations of energy dissipation indicated an energy reduction of 92% to 98 % as waves traveled across shelly ridge systems. In contrast, behind degraded or breached shelly ridges, waves were not so attenuated (reduction of 70% to 90%) and the spectral decomposition showed a mix between gravity and infragravity energy. These preliminary results show the role of the shelly ridges on wave attenuation and shoreline protection. Further measurements and stronger wave conditions are needed to strengthen the first observations.

ADDITIONAL INDEX WORDS: *Shelly ridge, wave attenuation, coastal protection, ecosystem service.*

INTRODUCTION

Natural environments perform fundamental life-support service to human societies. On the coastal zone, ecosystem services are multiple: food resources, tourist amenities and protection against coastal flooding. Recent natural disasters (*e.g.* 2004 Indian Ocean Tsunami, 2005 Hurricane Katrina, 2010 storm Xynthia) have focused on how coastal ecosystems are essential to reduce the vulnerability of coastal communities to flooding and storm events (Barbier *et al*., 2011; Costanza *et al*., 2008; Koch *et al*., 2019). Coastal vegetation and sedimentary deposits located on the foreshore or behind the shoreline provide a protection service because they contribute to increase wave energy dissipation (spreading area) or they can serve as effective barriers against storm surge. The Mont-Saint-Michel Bay (MSMB) is characterized by several coastal ecosystems and landforms (*e.g.* salt marshes, worm reefs, dunes, shelly banks). In this study, incident wave characteristics were monitored in the Mont-

Saint-Michel Bay, with the aim of identifying the role of the shelly chenier ridge morphology in wave energy attenuation and storm protection. Insofar as wave attenuation function has led to interest in valuing their storm protection benefit, wave transformations across shelly ridge systems are important in determining sediment distribution patterns, local variations in erosion and accretion, and long-term shelly ridges stability.

Study area

The Mont-Saint-Michel Bay is located in north-western France between Brittany and Normandy peninsulas (Figure 1). The bay is part of the six areas hosting the world's highest tide (Archer, 2013). Due to the significant tidal movements, reaching up to 14 m during high spring tides, the intertidal zone extends over an area of 250 km². The MSMB can be divided in two distinct morpho-depositional units with their own characteristics (Billeaud *et al*., 2007; Bonnot-Courtois *et al*., 2002; Caline, 1982). The eastern region of the bay corresponds to a large estuary formed by the junction of three rivers. Strong alternating tidal currents control sedimentary processes and channel migration in this sandy to silty estuary. The western area corresponds to a wide embayment, characterized by large tidal flats.

DOI: 10.2112/SI75-080.1 received 15 October 2015; accepted in revision 15 January 2016.
*Corresponding author: matthieu.jeanson@ephe.sorbonne.fr

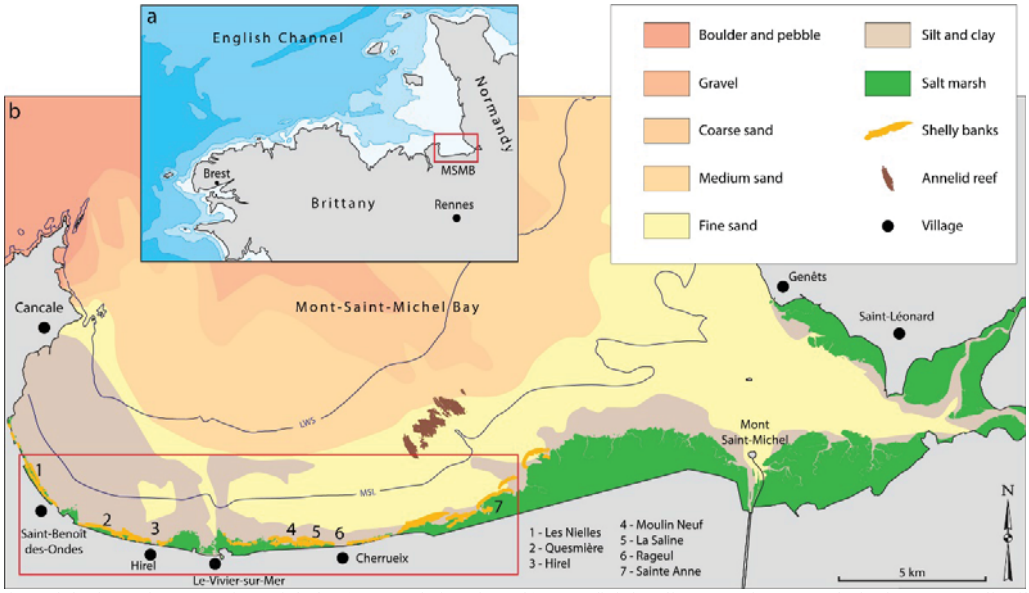

Figure 1. Location of the bay of Mont-Saint-Michel: (a) general situation, (b) superficial sediment and geomorphologic systems distribution. The red rectangle indicates the area investigated. MSL = mean sea level; LWS = low water spring tide level.

In this area, sediment mean grain-size increases from west (mud flats) to east (sand flats). The coast of the western part is also featured by numerous shelly banks on the uppermost part of the tidal flat. These shelly banks are composed by a mixture of coarse to very coarse bioclastic sand (whole and comminuted shells) and fine siliclastic sand reworked from the tidal flat. The main species found in the shelly debris are *Cerastoderma edule* (the common cockle), but other molluscs are present, including *Macoma balthica*, *Anomia ephippium*, *Chlamys varia* and *Crepidula fornicata*. *Mytilus edulis*, *Ostrea edulis* and *Crassostrea gigas* are also abundant, the lower part of tidal flats being largely used for mussel and oyster farming (Weill *et al*., 2012). As a function of their location on the tidal flat and their topography, three geomorphological types of shelly banks have been distinguished (Bonnot-Courtois *et al.*, 2004):

- Salt marsh banks with an asymmetric morphology and a varying thickness (0.3 to 0.8 m). They encompass a small area (160 m long and 40 m wide). They are mainly made up of whole shells.

- Upper tidal flat ridges occur at the boundary between the tidal flat and the salt marsh (Figure 2). They span a larger area (up to 1000 m long, 30 to 60 m wide) with a substantial thickness (1 to 2 m and more). They often constitute a barrier isolating lagoonal depressions where fine muds settle. These ridges consist of a mixture of shells and bioclastic sand.

- Tidal flat banks are relatively thin (0.3 to 0.5 m), but show a large area (average length of 400 m, average width of 50 m). They gather sand with some whole shells.

METHODS

In order to monitor spatial and temporal variations in cross-shore morphology characteristics and wave energy gradients, 11 profiles were established on 7 sites located between *Les Nielles* and *Sainte-Anne* (Figure 1 and 3; Etienne *et al*., 2015). Results presented in this article have been collected during the spring tide period of February 2015 (02/18 to 02/25).

Figure 2. Cross-shore looking view of a shelly chenier ridge. Note the washover marks on the surface and washover fans ending on the salt marsh.

Since then, additional data acquisitions were conducted during each spring tide period. Topographic data were collected using a differential GPS Magellan Promark 500 with errors within ±1.5 cm for distance and elevation. An uncertainty margin of 5 cm, covering both field measurement and interpolation errors and uncertainties, was applied in the treatment of the raw profile data. All surveys were referenced to a benchmark of the French National Geodesic Service (IGN 69).

25 to 30 self-recording miniature pressure sensors (NKE SP2T10; length: 12 cm; diameter: 2 cm) were deployed in the tidal zone in order to measure water level fluctuations and non-directional wave characteristics. These probes were fixed on an iron rod driven into the intertidal substrate on shore-normal transects across the shelly banks systems. The instruments recorded tide- and wave-induced pressure with burst duration of 9 min every 15 min, at a frequency of acquisition of 2 Hz. The 9-min sampling frequency was chosen as a compromise between a spectrum large enough to be representative, but sufficiently short as to assure a good degree of stationarity in the macrotidal environment. Wave characteristics were obtained from the measured time series by spectral analysis using Fast Fourier Transforms. The Fourier coefficients of the free surface elevation fluctuations were obtained from corresponding coefficients computed from the pressure time series using the frequency-dependent transfer function inferred from linear theory.

Wind (speed and direction) and atmospheric pressure data were obtained from an autonomous professional weather station (Oregon WMR 300) installed on the shoreline of *Le-Vivier-sur-Mer*, located in the center of the study area (Figure 1b).

RESULTS

In this section, only the results of *Hirel* and *La Saline* sites, are discussed in details (Figure 3). In *La Saline*, the cross-shore transect is characterized by a tidal flat followed by a massive shelly ridge around 50 m wide and 1.5 m thick; its seaward and internal faces are relatively steep (4°). Two smaller ridges partially covered by salt marsh vegetation are located landward and isolate a salt marsh located into a depression, periodically flooded by spring tides and during wet periods. In *Hirel*, the profile shows a different morphology. In this place, a low sandy to shelly single bank is present with a mud flat extending seaward from its base and a sand flat landward. Note that this bank is regularly flattened (approximately every 5 years) to permit land yachting and leisure activities.

Wind and hydrodynamic conditions of both sites during February 2015 spring tide are summarized in the Figure 4. Winds were relatively weak during the first three days ranging from 1 to 4 $m.s^{-1}$ (Figure 4a). An increase of wind speed (up to 14 $m.s^{-1}$) occurred the 02/21 with winds from SW to NW. Winds from S to W were more variable in speed during the last days of the experiment. The incident waves measured on the tidal flats during experiments were predominantly wind-wave and swell (peak period ranging from 6 to 12 s), depending on meteorological conditions (PS 1 on Figure 4b-c). Significant and maximum wave heights increased with wind speed from 0.15 m (*Hmax*: 0.20 m) in the course of the first tide to nearly 0.45 m (*Hmax*: 0.65 m) during the following tides with some fluctuations.

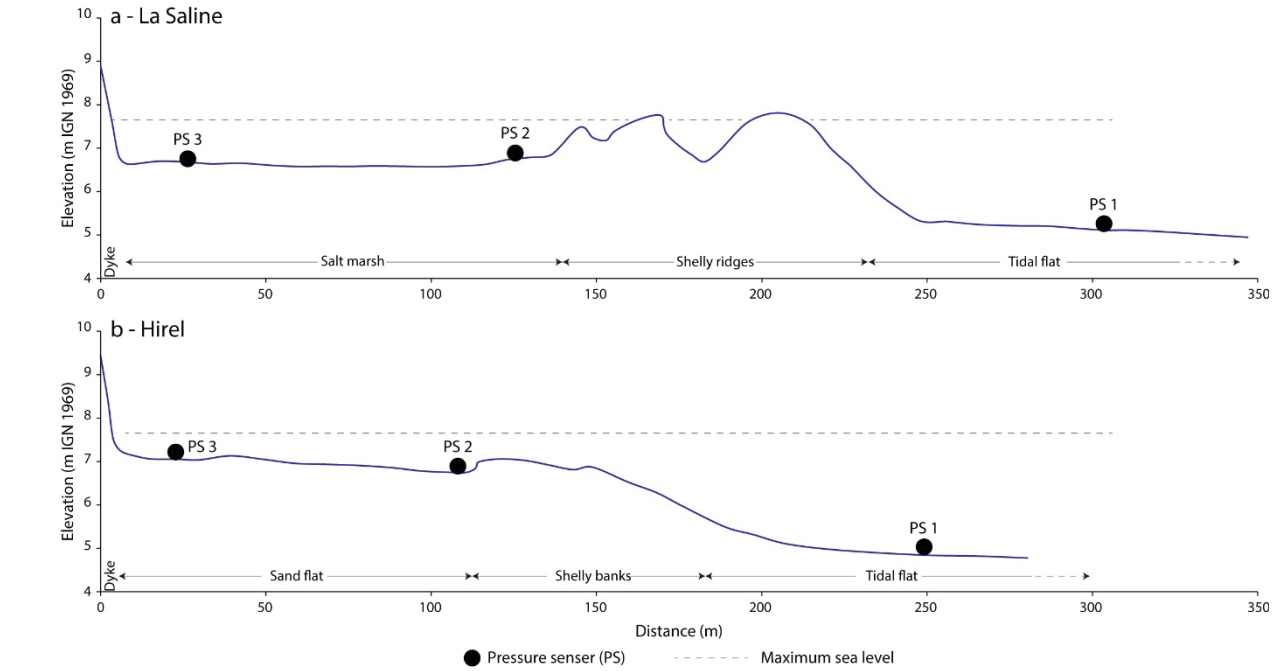

Figure 3. Cross-shore profiles at the selected sites: (a) *La Saline*, (b) *Hirel*. Maximum sea level and the location of the pressure sensors deployed are indicated.

In *La Saline*, at the back of the shelly ridge (PS2 and PS3 in Figure 4b), the significant wave height was extremely low through the experiment (0.01 to 0.05 m) with a dominance of infragravity frequencies. Behind the degraded shelly ridges of *Hirel* (Figure 4c), *Hs* values ranging from 0.07 to 0.18 m at high tide for PS2 and from 0.05 to 0.10 m for PS3.

DISCUSSION

For both experiment sites, differences in *Hs* between the tidal flats and the back of the shelly ridges (salt marsh for *La Saline* and sand flat for *Hirel*) reflect an important reduction in energy as waves propagated from the former to the latter.

In *La Saline*, the highest *Hs* values recorded on the salt marsh did not exceed 0.05 m, thus illustrating the efficiency of the well-formed shelly ridge system in wave attenuation. In *Hirel*, residual waves on the sand flat are more important (*Hs* values up to 0.25 m at PS2 and 0.16 m at PS3 during the largest tide), revealing a smaller attenuation by the degraded shelly ridges. Based on a simple energy reduction equation such as that of Lugo-Fernandez *et al*. (1998), the energy reduction, between PS1 and PS3 at high tide, ranges from 98 to 99.5% in *La Saline* and from 71 to 91 % in *Hirel* as waves traveled across shelly ridge systems. Such a high value of energy reduction is comparable with coral reef crest where wave dissipation reaches a mean of 97% (Ferrario *et al*., 2014).

Examples of typical high tide frequency spectra and the percentages of energy loss between the tidal flats (PS 1) and the base of the dyke (PS 3) are depicted in Figure 4 (lower graphs). For both sites, the spectral decomposition of the incident wave showed a mix of swell (T = 14-15 s) and wind-generated waves (T = 5-7 s) on the tidal flats. In *La Saline*, at the back of the shelly ridge, a full filtering of gravity wave occurred, resulting in the dominance of residual infragravity energy. On the contrary, in *Hirel*, the spectral decomposition clearly shows residual peak energy at 15 s highlighting the incomplete filtering of swell waves.

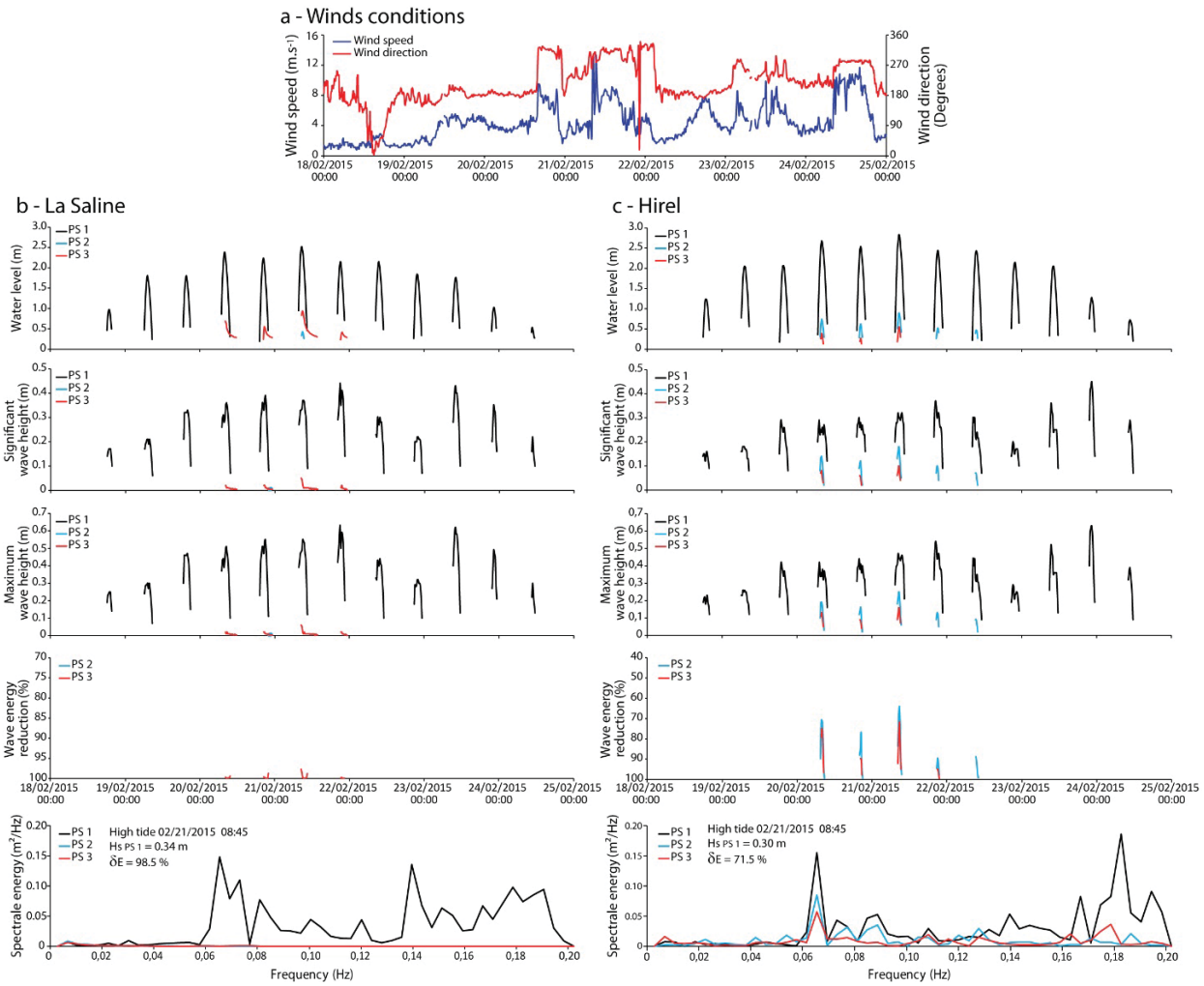

Figure 4. (a) Winds conditions; burst-averaged water depth, significant wave height, maximum wave height, wave energy reduction and frequency spectra during high tide recorded in (b) La Saline and (c) Hirel (see Figure 1 and 3 for location and topography) during February 2015 spring tide.

These results highlight a critical control by water level over shelly ridges being likely to preclude onshore wave transmission. The greater reduction of wave energy in *La Saline* is likely due to its higher shelly ridge elevation (elevation: 7.75 m; relative height: 2.70 m), which precludes gravity wave energy for the greater proportion of all high tidal stages, and its width (90 m), which acts to effectively dissipate wave energy. In contrast, the *Hirel* shelly ridge dissipated less incident energy at high tide (70% dissipation). This reflects the lower elevation of the shelly ridge and the narrow shelly ridge (elevation: 7.10 m; relative height: 2.10 m; width: 65 m; Figure 3). As a consequence, offshore wave energy was transferred with less modification to the shoreline.

Results have also shown that the types and behavior of waves and wave energy clearly vary at the back of the shelly ridges depending of their geometry, morphology and elevation, and are sensitive to changes in tidal stage. In *La Saline*, a full filtering of gravity wave energy occurred even at higher tidal stages. In *Hirel*, our measurements suggest that wind waves are filtered, at high tide, during propagation across the shelly ridge, whereas longer-period swell propagates across the shelly ridge (Figure 4).

These results suggests that the deposit height is a critical factor in energy dissipation and that bank levelling, to facilitate recreation activities, should be managed carefully to maintain natural buffering. However, the high level of energy reduction by shelly ridges recorded during this study occurred during low energy meteorological events. Energy absorption by loose sediment bodies will be likely different during stormy conditions.

CONCLUSIONS

Field measurements of wave characteristics in the western coast of the MSMB showed that wave energy dissipation rates over well-developed shelly ridges (98%) were significantly higher than over degraded shelly ridges (70%), thus highlighting the importance of the shelly ridges morphology in modulating wave characteristics.

Consequently, these preliminary results show the key role of the shelly ridges on shoreline protection. Shelly ridges can be considered as natural barriers helping to protect coastal communities from storms. Further analysis and measurements, especially during stormy events, will be carried out to establish the importance of the cross-shore transect morphology on wave attenuation (*e.g.* elevation, width, organization).

The data acquired will also contribute to a better understanding of the morphodynamic processes on the shelly ridge systems and, finally, on their spatial and temporal evolutions.

ACKNOWLEDGMENTS

The authors would like to thank shellfish farmers for logistic support during the field experiments. This work was funded by the *Conseil Départemental d'Ille-et-Vilaine*, *Direction Agriculture et Environnement*, through the project "*Etude des services de protection des dépôts sédimentaires en baie du Mont-Saint-Michel*".

LITERATURE CITED

Archer, A.W., 2013. World's highest tides: Hypertidal coastal systems in North America, South America and Europe. *Sedimentary Geology*, 284-285, 1-25.

Barbier, E.B.; Hacker, S.D.; Kennedy, C.; Koch, E.W.; Stier, A.C., and Silliman, B.R., 2011. The value of estuarine and coastal ecosystem services. *Ecological Monographs*, 81(2), 169-193.

Billeaud, I.; Tessier, B.; Lesueur, P., and Caline, B., 2007. Preservation potential of highstand coastal sedimentary bodies in a macrotidal basin: example from the Bay of Mont- Saint-Michel, NW France. *Sedimentary Geology*, 202, 754-775.

Bonnot-Courtois, C.; Caline, B.; L'Homer, A., and Le Vot, M., 2002. *The bay of Mont-Saint-Michel and the Rance Estuary*. Bulletin du Centre de recherche Elf Exploration et Production, Pau, Mémoire 26, 256 p.

Bonnot-Courtois, C.; Fournier, J., and Dréau, A., 2004. Recent morphodynamics of shell banks in the western part of the Bay of Mont-Saint-Michel (France). *Géomorphologie : relief, processus, environnement*, 10(1), 65-79.

Caline, B., 1982. *Le secteur occidental de la Baie du Mont-Saint-Michel: morphologie, sédimentologie et cartographie de l'estran*. Documents Bureau de Recherches Géologiques et Minières, Orléans, 42. 250 p. (In French)

Costanza, R.; Pérez-Maqueo, O.; Martinez, M.L.; Sutton, P.; Anderson, S.J., and Mulder, K., 2008. The value of coastal wetlands for hurricane protection. *Ambio*, 37(1), 241-248.

Etienne, S.; Jeanson, M., and Collin, A., 2015. *Étude des services écosystémiques de protection des dépôts sédimentaires en baie du Mont-Saint-Michel*. Rapport d'étape, Avril 2015. EPHE, Conseil Général d'Ille-et-Vilaine, 75 p.

Ferrario, F.; Beck, M.W.; Storlazzi, C.D; Micheli, F.; Shepard, C.C, and Airoldi, L., 2014. The effectiveness of coral reefs for coastal hazard risk reduction and adaptation. *Nature communications*, 5(3794). doi: 10.1038/ncomms4794

Koch, E.W.; Barbier, E.B.; Silliman, B.R.; Reed, D.J.; Perillo, G.M.E.; Hacker, S.D.; Granek, E.F.; Primavera, J.H.; Muthiga, N.; Polashy, S.; Halpern, B.; Kennedy, C.; Kappel, C.V., and Wolanski, E., 2009. Non-linearity in ecosystem services: temporal and spatial variability in coastal protection. *Frontiers in Ecology and the Environment*, 7, 29-37.

Lugo-Fernandez, A.; Roberts, H.H., and Suhayda, J.N., 1998. Wave transformations across a Caribbean fringing-barrier coral reef. *Continental Shelf Research*, 18, 1099-1124.

Weill, P.; Tessier, B.; Mouazé, D.; Bonnot-Courtois, C., and Norgeot, C., 2012. Shelly cheniers on a modern macrotidal flat (Mont-Saint-Michel bay, France) – Internal architecture revealed by ground-penetrating radar. *Sedimentary Geology*, 279,173-186.

Journal of Coastal Research	SI	75	403-407	Coconut Creek, Florida	2016

Morphological Change near Artificial Reefs as a Beach Erosion Countermeasure

Kyu-Han Kim†*, Kyu-Tae Shim†, and Bumshick Shin†

†Department of Civil and Environment Engineering
Catholoc Kwandong University
Gangneung, Korea

www.cerf-jcr.org

www.JCRonline.org

ABSTRACT

Kim, K.H.; Shim, K.T., and Shin, B.S., 2016. Morphological Change near the Artificial Reefs as a Beach Erosion Countermeasure. *In:* Vila-Concejo, A.; Bruce, E.; Kennedy, D.M., and McCarroll, R.J. (eds.), *Proceedings of the 14th International Coastal Symposium* (Sydney, Australia). *Journal of Coastal Research*, Special Issue, No. 75, pp. 403-407. Coconut Creek (Florida), ISSN 0749-0208.

At the Namhangjin Coast on the eastern coast of South Korea, there are five artificial reefs constructed as a form of countermeasure to prevent beach erosion. Since the construction, severe beach erosion has not occurred, and due to the presence of the artificial reefs various sedimentation effects have taken place. However, inside the opening gaps between the artificial reefs, the occurrences of return flow and severe scouring have been observed. In this field investigation the effects of one of the six artificial reefs, installed particularly for abalone, seaweed and fish farming, have been reviewed. Furthermore, the effects of the artificial reefs and their ensuing problems were investigated via three-dimensional movable-bed experiment. In the experiment, to improve the performance the artificial reefs, the impacts of raising the crown height and style of the reefs were examined. The numerical model has successfully explained the various implications of the three-dimensional experiment and the field investigation, and has confirmed the fact that there exists a shared agreement.

ADDITIONAL INDEX WORDS: *Beach erosion, coastal process, beach nourishment, return flow, wave attenuation*

INTRODUCTION

Offshore breakwaters, groins, and the like have for a long time often been used as beach erosion countermeasures. However these coastal structures induce excessive sedimentation and can give rise to secondary erosion phenomena on surrounding beaches (Yoo *et al.*, 2008). In contrast, artificial reefs used recently as a beach erosion countermeasure show lower accretion effects in regards to beach erosion at installed areas than offshore breakwaters, but it can be said that their secondary erosion affects impacting surrounding beaches are relatively fewer. In addition, they are very advantageous in regions with low tidal ranges (Kim *et al.*, 2011). For these reasons five artificial reefs were constructed as beach erosion countermeasures at Namhangjin on the eastern coast of Korea. This study aims to introduce the numerical model test and 2-D, 3-D hydraulic model tests that were conducted to confirm five artificial reefs as beach erosion countermeasures, and reveal the tests' results. The return flow between the artificial reefs confirmed in the 3-D hydraulic model experiment occurred in the gap between the artificial reefs installed at the site. Furthermore, it was confirmed through a field investigation that the artificial reef installed to promote fish shelter functions was influencing the growth of seaweed.

DOI: 10.2112/SI75-081.1 received 15 October 2015; accepted in revision 15 January 2016.
*Corresponding author: khkim@cku.ac.kr

However, it was confirmed that the steel type artificial reef used in at the Namhangjin coast had safety problems. Thus an artificial reef style with more substantial inspection for safety must be evaluated, and various methods to increase the function of seaweed's insertion must be considered.

Background

A shoreline change analysis was conducted by using aerial photos from 1979 to 2009 to study the long-term shoreline changes at Namhangjin coast due to erosion and deposition. Locations with large tidal ranges require additional shoreline analysis through tide corrections using information on the filming times, but because the Namhangjin coast has a tidal range lower than 0.5m, and thus smaller than the shoreline changes due to waves, corrections done by tidal ranges were disregarded.

An orthometric correction through an image to image correction using IKONOS satellite images with geometric corrections on plane images and orthometric corrections was conducted by using Ground Control Points (GCP).

Figure 1 shows the time changes of the shoreline change at the Namhangjin coast by using aerial photographs. The beach area of the Namhangjin coast in 1972 was calculated through aerial photo analysis to be 131,105m^2. Gangneung Harbor, located to the north of Namhangjin coast, began construction in 1996 and finished its northern breakwater in 2005 and its southernbreakwater in 2009. Far more erosion and deposition of the shoreline appears than the shoreline of 1972 and 1979.

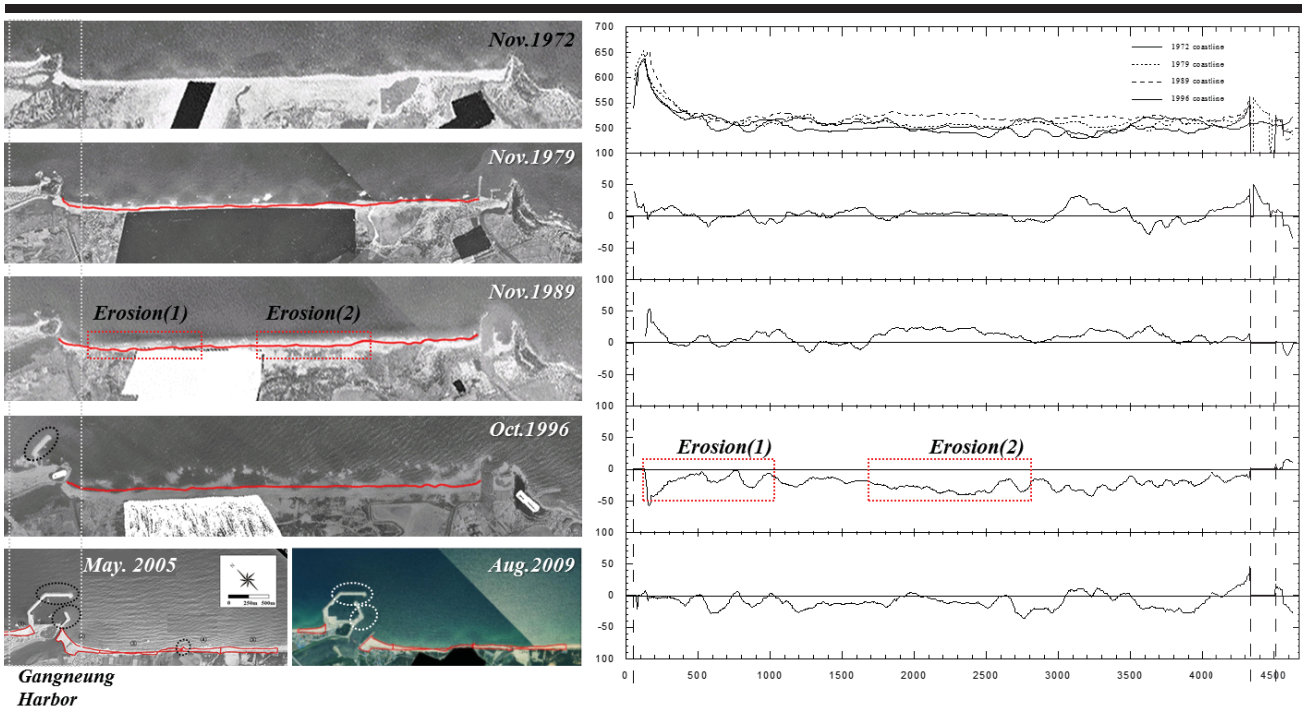

Figure 1. Shoreline change analysis (Jung *et al.*, 2004).

Also it can be known that the shoreline change is great. Results of the analysis of aerial photos up to 2009 confirmed that the beach area had been reduced by 23.8% (31,217m^2) than the shoreline of 1972. This decrease in beach area is thought to have been mainly caused by the Gangneung Harbor and the jetty at the Namdae River.

METHODS

The numerical simulation was conducted to replicate the erosion status of the Namhangjin coast and to find the beach erosion countermeasure. Numerical model for predicting wave induced current and nearshore morphodynamic processes have used power model based on energy balance equation for wave field, modified shallow water equations for wave induced current and net sediment transportation. In this study, numerical simulation for wave-induced current and sedimentation were conducted to compare the flow characteristics after the construction of Gangneung Harbor and the jetty – a main cause for the erosion – and the flow characteristics following the installation of countermeasures.

The waves applied to the experiment were based on the results of wave observations conducted at the coast in front of Gangneung Harbor for three years, and they were applied after being sorted between winter and summertime waves. The abnormal waves used in the wave-induced current experiment are arranged in Table 1.

Table 1. *Wave data used in numerical simulation*

Season	Wave Heigh (m)	Wave Period (sec)	Wave Direction	Appearance of Wave Direction
Winter	4.5	11.0	NNE	24.9%
Summer	4.0	10.0	ENE	22.2%

The hydraulic model test was also conducted at the 3-Dimensional wave basin (W:40m, L:32m, H:1.5m) of Catholic Kwandong University. The main purpose of the experiment was to find the most satisfactory beach erosion countermeasure by analyzing the wave-induced currents and sediment transport mechanism with regards to installation or non-installation of erosion prevention facilities.

RESULTS

The equilibrium condition of the sediment transport due to seasonal wave direction changes at the Namhangjin coast was reproduced through numerical simulation results (Figure 2). However the equilibrium of the sediment transport was broken due to the construction of Gangneung Harbor and the jetty of the Namdae river mouth. As a result the occurrence of an erosion south of Namhangjin beach and the occurrence of an abrupt sedimentation south of the jetty were confirmed.

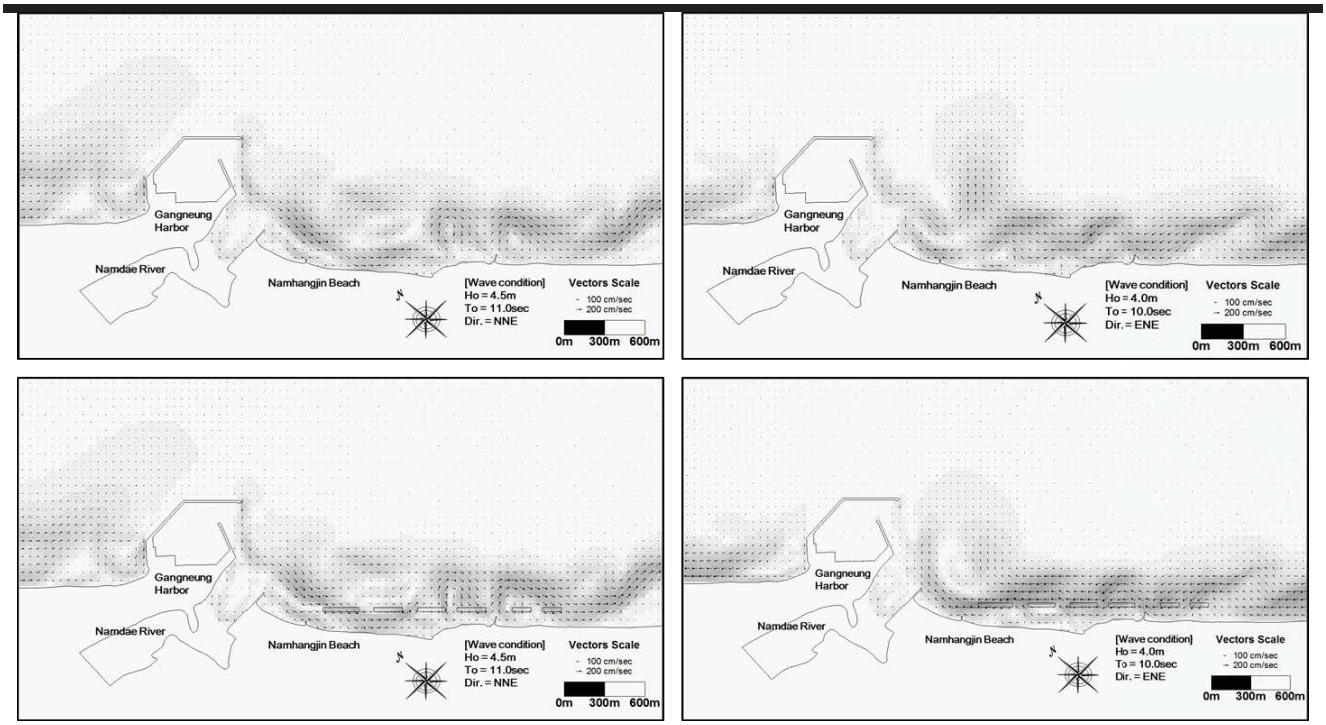

Figure 2. Results of Numerical Simulation.

In addition, it was analyzed that the reduction of current velocity due to the constructions of Gangneung Harbor and the jetty and the lapse of a vortex that existed beforehand in front of the Namdaechen estuary affected geographical change patterns. As a result it was confirmed that the artificial reef, acknowledged as a submerged breakwater with wide width, was more satisfactory than other countermeasures. The design of artificial reefs is derived from a design manual of artificial reef (2004) considering wave, depth, topographical characteristics and so on of target area, and then examined using numerical and hydraulic model tests.

Hydraulic model test

The hydraulic model test used the same wave conditions as those applied to the numerical simulation. It was found that when submerged breakwaters were not installed, erosion occurred at the southern beach due to the occurrence of a strong offshore current and a longshore current flowing northwards at the ENE wave direction on the whole of the Namhangjin coast(Figure 3). Meanwhile, it was confirmed that when submerged breakwaters were installed, the strong northwardly longshore current was reduced leading to an alleviation of erosion across the whole of the beach.

However, the occurrence of a strong return flow at the gap was observed. It was confirmed that if the strong return flow at the gap of the submerged breakwater is sustained, not only the gap but also the areas surrounding the submerged breakwaters were scoured due to the fast flow velocity. A solution to this phenomenon is necessary because of the fears of a collapse of the foundations of the submerged breakwater, should it occur in reality.

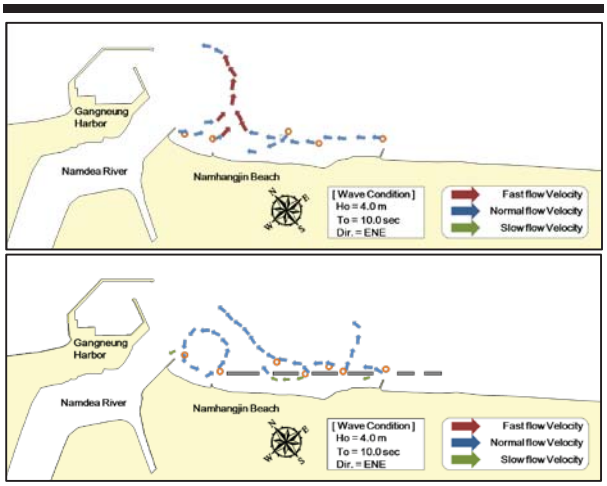

Figure 3. Experiment results of wave-induced currents when submerged breakwaters are not installed(up) and installed(down).

Through hydraulic model tests the return flow which occurs at the gap of the submerged breakwaters was examined, and a method for its reduction was investigated.

Experiment results confirmed that the velocity of the return flow increases as the wave steepness becomes larger, and that if water exchange blocks are installed in the gaps to reduce

the return flow velocity, it is reduced by 45% more than if the water exchange blocks are not installed.

In the movable bed test, the morphological change was analyzed by using the amount of change to the water level 6 hours after the waves were applied to the preliminary terrain. It was confirmed that beach erosion occurred across the whole of the Namhangjin coast prior to the installation of the beach erosion countermeasure, as predicted through the current patterns of the wave-induced current simulation (Figure 4). Meanwhile, it was confirmed that in the case that artificial reefs were installed as beach erosion countermeasures, beach erosion phenomena across the whole of the Namhangjin coast were reduced markedly, and in certain areas deposition phenomena even occurred.

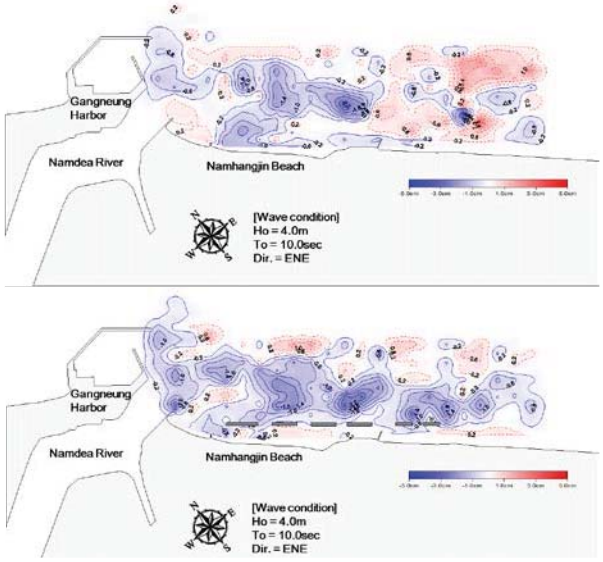

Figure 4. Geographical change in correlation to submerged breakwater installation.

Beach norishment

As countermeasures to erosion prevention, submerged breakwater installations were applied in tandem with beach nourishment methods. Excavate material from the preliminary excavation when installing the submerged breakwater and the dredging sand from the nearby Namdae River estuary were used for the beach nourishment (Figure 5), and the total amount of beach nourishment was 173,850m^3. The grain size of the beach nourishment sand was 0.914~0.953mm, about 0.06mm larger than the original grain size of the beach of 0.871mm. In cases such as the beach in the vicinity with low erosion effects the beach width corresponds to 70m, and as the past beach width (by 1972 standards) of the area undergoing beach nourishment was surveyed to be 60m, the beach width was set and conducted as 70m. The beach nourishment slope used at this point of time was 1/7.5 at the foreshore and 1/60 at the inshore.

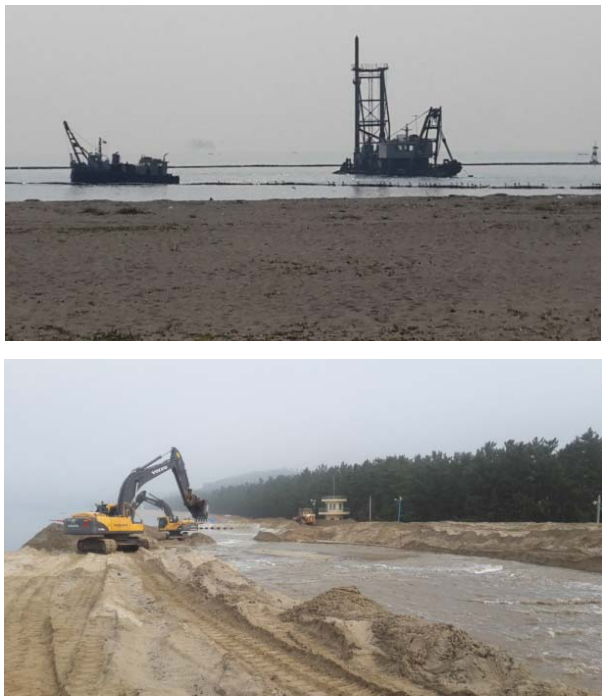

Figure 5. Estuary dredging and beach nourishment works

Multi-purpose articifial reef

Recently the residents of coastal areas have more interest in the environment, and with the decrease in marine fishing resources, there has been a change in the resident's awareness of the ecosystem.

Even with regards to coastal preservation facilities for management of coastal disasters such as coastal erosion, the residents have begun requesting not only disaster prevention but also environmental preservation and amenity creation effects. They have even requested that the artificial reef at the Namhangjin coast, the subject of this study, be built as a multi-purpose artificial reef that can be of help to the fishery industry. Following this the first of the five artificial reefs was installed after being considered for forms that could allow the growth of seaweed and attraction of fish. As a result of installing this type of artificial reef, it was confirmed through underwater monitoring that various seaweed were growing on the artificial reef. Figure 6 shows the seaweed growing around the reef one year after the installation of the artificial reef. It was also confirmed that not only seaweed but various fish were gathering around the artificial reef.

Figure 6. Seaweed and fish near artificial reef(After 1year)

DISCUSSION

It was possible to confirm the phenomenon of seaweed growth and fish accumulation at the No.1 artificial reef from north installed with the aim to develop seaweed. However, it is thought that more active methods are necessary to maximize the original purpose of the artificial reef. Putting in components that can accelerate the growth of seaweed and supplying materials such as spores in large quantities around the artificial reef will draw out better results. Furthermore, it was confirmed that conducting preliminary investigations on the seaweed around the installation area of the artificial reef, and choosing seaweed types adequate for the fish, abalone, or sea cucumber that local residents would prefer were important.

CONCLUSIONS

As a result of investigating the cause of the beach erosion at Namhangjin beach through numerical simulation and 3-D hydraulic model tests, it was confirmed that the construction of the harbor and jetty were the main causes. This result can also be said to be in consensus with the results of aerial photo analysis. It was also confirmed that the artificial reef with a wide width – chosen as a beach erosion countermeasure – was a satisfactory countermeasure not only in the experiment but also on the actual site, and that the beach nourishment applied with it was also of absolute necessity.

Through the 3-D hydraulic model test, it was confirmed that in response to the return flow occurring at the gap of the artificial reef, the use of water exchange blocks can reduce the return flow velocity. Also, it was confirmed that setting the crown height of the artificial reef to 0.5 m draws out the most effective wave attenuation, and that this does not affect the wave set-up too much. After the construction of artificial reefs, the underwater monitoring was conducted around the reefs. Hereafter the long-term monitoring near artificial reefs and shoreline will be performed to check the effectiveness of the reefs.

LITERATURE CITED

Apotsos, A.; Raubenheimer, B.; Elgar, A., and Guza, R. T., 2008. Wave-driven setup and alongshore flows observed onshore of a submerged canyon. *Journal of Geophysical Research,* 113.

He, L. and J. A. Puleo., 2006. Video-based imaging processing of laboratory-scale rip currents., *Proceedings of the 30th International Conference on Coastal Engineering* (San Diego, U.S.A), 1122–1134.

Hsu, J.R.C. and C. Evans., 1989. Parabolic bay shape and applications, *Proceedings of the Institution of Civil Engineers*, Part 2, 87(4), 557-570 .

Jung, S.J.; Kim, K.H., and Pyun, C.K., 2004. Investigation of long-term shoreline change using aerial images. *Journal of Korean Society of coastal and ocean engineers*, 16(1), 10-17.

Kim, K.H.; Yoo, H.S., and Kobayashi, N., 2011. Mitigation of beach erosion after coastal road construction. *Journal of Coastal Research*, 27(4), 645–651.

Shiori, D.; Uda, T.; Hosokawa, J.; San-mani, T., Shiho M.; Serizawa, M., and Ishikawa T., 2011. Beach changes of KAMAKURA coast in KANAGAWA prepecturs. JSCE 2011(Ocean Engineering), JSCE, 67(2), 1195-1200.

Uda, T. and Sakai, K., 2014. A New proposal regarding inspection method of shore protection facilities. *Proceedings of civil engineering in the ocean*, 70(2), 588-593.

Uda, T.; San-nami, T., and Igarashi T., 2013. Beach Changes around new-type offshore breakwaters on KANBARA coast. *Proceedings of civil engineering in the ocean,* 69(2), 868-873.

Yoo, H.S.; Kim, K.H., and Jung, E.J., 2008. The Analysis for the Causes of Beach Erosion on Jeonchon-Najung Beach on the East Coast of Korea, *Journal of Korean Society of coastal and ocean engineers*, 20(6), 611-620.

Widayati, A. Y. W.; Kim, K. H.; Han, J. M., and Pyun, C. K., 2009. Monitoring of the post-construction coastal management in Namae Beach. *Proceedings of the 19th International Offshore and Polar Engineering Conference* (Osaka, Japan), 1216–1221.

National association of coast in Japan, 2004. *A design manual of artificial reef* (in Japanese), 30-56.

Journal of Coastal Research	SI	75	408-412	Coconut Creek, Florida	2016

On Eddy-Mixed Longshore Currents: Video Observation and 3D Modeling off Grand Popo Beach, Benin

Patrick Marchesiello[†], Rafael Almar[†], Rachid Benshila[‡], Stanislas Larnier[††], Bruno Castelle[§] and James C. McWilliams[§§]

[†]IRD-LEGOS
Université Paul Sabatier/CNRS/CNES/IRD
Toulouse, France

[‡]CNRS-LEGOS
Université Paul Sabatier/CNRS/CNES/IRD
Toulouse, France

[††]CNRS-LAAS
Université Paul Sabatier/CNRS/CNES/IRD
Toulouse, France

[§]CNRS-EPOC
Université de Bordeaux/CNRS
Bordeaux, France

[§§]Department of Atmospheric and Oceanic Sciences
University of Califoria at Los Angeles
Los Angeles, CA, USA

www.cerf-jcr.org

www.JCRonline.org

ABSTRACT

Marchesiello, P.; Almar; R.; Benshila; R.; Larnier, S.; Castelle, B., and McWilliams, J.C., 2016. Morphological Change near Artificial Reefs as a Beach Erosion Countermeasure. In: Vila-Concejo, A.; Bruce, E.; Kennedy, D.M., and McCarroll, R.J. (eds.), Proceedings of the 14th International Coastal Symposium (Sydney, Australia). J. Coast. Res., Special Issue, No. 75, pp. 408-412. Coconut Creek (Florida), ISSN 0749-0208.

The link between intrinsic shear-flow instability of longshore currents and their mean cross-shore profiles has long been suggested. Yet, recent investigations give increasing credit to extrinsic wave forcing mechanisms, downplaying the role of shear waves on the observed variability. Our results for Grand Popo beach, Benin, provide an original attempt to map mean longshore currents forced by an oblique swell. A 3D model investigation shows that their broad mean flow and the frequency band of eddy variability are consistent with shear instability, conversion of mean to eddy kinetic energy and eddy mixing of momentum. Their turbulent dynamics do not clearly fit in any classical 2D or 3D paradigms but show large transfer of energy across the wavenumber spectrum, to both larger and smaller scales.

ADDITIONAL INDEX WORDS: *Nearshore processes, video monitoring, 3D modeling.*

INTRODUCTION

In West Africa, the majority of the population and economic activity is concentrated in the coastal zones. These are open sandy coasts facing narrow continental shelves. The local wave climate dominated by high-energy swell traveling from the South Atlantic forces one of the largest littoral drift in the world (Laibi *et al.*, 2014). As a result and because of half a century of destabilizing development, the entire coast experiences rapid erosion with rates reaching 10 m/yr at Cotonou, Benin (Kaki *et al.*, 2011). Therefore, an assessment of anthropogenic and natural factors controlling erosion is needed based on a better understanding and monitoring of longshore currents. To that end, field studies were conducted in 2013 and 2014 at Grand Popo beach, Benin (Figure 1; Almar *et al.*, 2014). The beach presents a longshore-uniform low tide terrace where persistent oblique swells generate strong and narrow longshore currents.

Dominant energy sources in the nearshore are considered to be gravity waves and mean currents. The frequency band between infragravity (~2-10 Hz) and mean flow, called Very Low Frequency (VLF), have been associated with either wave-grouping, surfzone eddies due to vorticity generation by short-crested wave breaking (Clark *et al.*, 2012; Peregrine, 1998), or shear waves and eddies resulting from shear instability of longshore currents (Bowen and Holman, 1989). In many occasions where longshore flow is generated by an oblique swell, VLF motions are seen to be energetic, coherent in the longshore direction and linked to the strength of the mean circulation (Dodd *et al.*, 1992; Noyes *et al.*, 2004; Oltman-Shay *et al.*, 1989).

Linear stability analysis and numerical shallow-water models (*e.g.*, Allen *et al.*, 1996; Bowen and Holman, 1989; Slinn *et al.*, 1998) show that longshore currents are strongly unstable systems (fast growth rate of the most unstable modes). Usual conditions for shear wave resonance is that current profiles have inflection points (change of sign of vorticity gradients) and that frictional spindown $t_F = h/\mu$ (h is bottom depth and μ a linear drag coefficient) is longer than shear wave growth time scale (a few minutes). Both conditions are generally met in the real world but shear instability is difficult to observe and cannot be easily separated from extrinsic mechanisms of variability (Feddersen, 2014).

Numerical models predict that shear eddies have a strong impact on the time mean velocity profile due to momentum mixing across the longshore current. The mean velocity must therefore appear broader than the surfzone where it is generated. As a result, eddy activity is expected to affect the quality of littoral drift estimates. In this paper, we provide an original measure of mean longshore current inverted from video camera and compare it with a tridimensional (3D) model simulation for

DOI: 10.2112/SI75-082.1 received 15 October 2015; accepted in revision 15 January 2016.
*Corresponding author: Patrick.Marchesiello@ird.fr

the morning of March 11 2014. We analyze the characteristics and impact of shear waves and eddies on the mean flow and shed new light on the turbulent regime of nearshore flows.

METHODS

Grand Popo beach is located in the Gulf of Guinea, midway (80 km) between Cotonou (Benin) and Lome (Togo). Grand Popo is representative of the Bight of Benin as an open, wave-dominated and microtidal environment (0.3/1.8 m for neap/spring tidal ranges) exposed to S-SW long period swells generated at high latitudes in the South Atlantic. We chose the morning of March 11 2014 for our model-data comparison. The weather, tides and wave conditions were ideal: weak winds and wind waves well separated from a narrow-band swell of Hs=1.15 m, Tp=11 s, 10° incidence from shore normal direction (Figure 1). The water was at mid neap tide level (low-tide terrace at 80 cm depth), promoting a narrow surfzone less than 50 m wide starting seaward of the terrace.

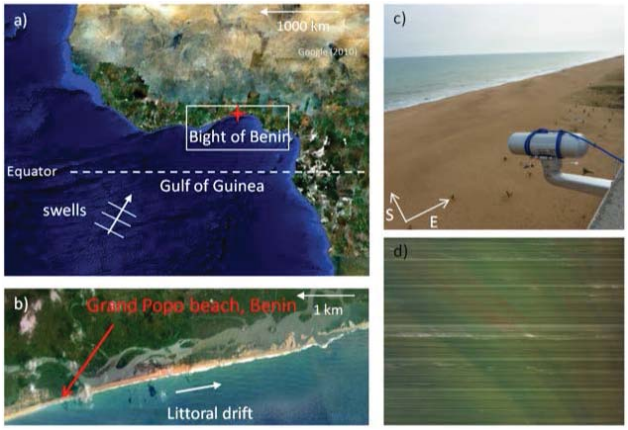

Figure 1. Study site and video camera. a) the Bight of Benin coast, with a red cross indicating the study site at Grand Popo; b) Grand Popo beach with evidence of oblique long swell producing longshore drift; c) HF video camera installed in Grand Popo; d) Secondary image from the video system: example of alongshore timestack used to estimate longshore flow velocity.

Coastal video

Field experiments conducted at Grand Popo beach in February 2013 (Almar *et al.*, 2014) and March 2014 were designed to monitor the beach and test the applicability of a low-cost video monitoring system (Figure 1). An Acoustic Doppler Current Profiler (ADCP) was moored in 10-m depth where incident waves were also measured. Surfzone currents were estimated by means of drifters deployed during daytime.

As opposed to in situ measurement techniques, remote sensing can safely provide synoptic coverage of the nearshore system over large areas and a wide range of scales. The profile of breaker dissipation can be assessed as in Flores *et al.* (2013) by estimating roller wavelength rather than light intensity. This method relying on energy conservation provides a safer means of calibrating the model wave forcing (Marchesiello *et al.*, 2015). Recently, a new method was also proposed for estimating longshore currents from video images (Larnier *et al.*, 2014). A Radon transform is applied on longshore timestacks to estimate the drift of foam or suspended particle signature in video images. The drifting angle gives an estimate of the longshore component of surface currents. Video estimations are validated for Grand Popo using drifters and ADCP measurements. It shows generally good agreement both in the surf and innershelf regions during 11-18 March 2014 (Figure 2). Offshore currents are about 10-20 cm/s while surfzone currents are much larger around 50 cm/s in average. Validation for March 11 is missing in the surfzone and we rely on the general agreement shown the rest of the week.

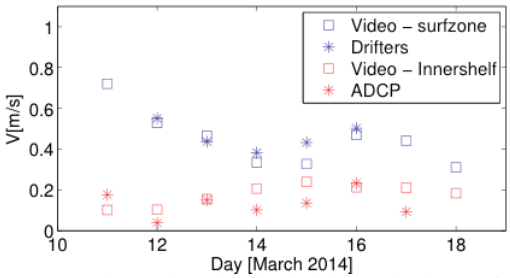

Figure 2. Comparison of co-localized video estimation and in-situ measurements of longshore currents in the surfzone (red) and innershelf (blue).

Wave-current model

Uchiyama *et al.* (2010) implemented a modeling approach for 3D wave-current interactions based on vortex-force formalism (McWilliams *et al.*, 2004) in the Regional Oceanic Modeling System (ROMS; Shchepetkin and McWilliams, 2005). Marchesiello *et al.* (2015) followed with the same approach within ROMS-AGRIF (Debreu *et al.*, 2012), allowing nesting and wetting/drying.

Eulerian wave-averaged current equations for mass, momentum, and tracers are included, plus non-conservative wave effects such as wave breaking. The currents are coupled with a ray-theory spectrum-peak wave propagation model (WKB model) describing wave crest conservation with wave refraction and conservation of both wave and roller action. The wave model includes dissipation due to shoaling-induced wave breaking and bottom drag and the Doppler-shifted current effect on waves. The latter was shown to lessen the destabilization of longshore currents (Ozkan-Haller and Li, 2003; Uchiyama *et al.*, 2009).

The observed water level, wind and wave conditions of Grand Popo beach were imposed at the offshore and surface boundaries of the coupled model. The domain size is 800 m longshore and 600 m cross-shore with a horizontal resolution of 3 m, time step of 0.3 seconds and 10 vertical levels. Periodic conditions are imposed at the cross-shore boundaries and radiative conditions at the offshore boundary (Marchesiello *et al.*, 2001). Because nearly all longshore current modeling in the literature uses shallow-water (2D) equations (one exception is Newberger and Allen, 2007, with mixed success), our 3D model is compared here with an equivalent 2D version of ROMS.

Model initialization

The model is first spun-up for 30 min without flow perturbation to reach a state where the longshore current speed V_0 is in balance between breaker acceleration and bottom drag

(Longuet-Higgins, 1970). Then, a small flow perturbation is superimposed on V_0 to initiate shear waves. From that point, the model is integrated for 10 hours.

The use of a linear bottom drag with coefficient $\mu \sim 3.10^{-3}$ m/s gives a forced current peak velocity $V_0 \sim 1.6$ m/s. It provides the best model-data agreement for mean and eddy signals. Sensitivity experiments with smaller or greater values lead to a mean current that is either too strong and wide or too weak and narrow.

Wave energy dissipation rate ε_b due to depth-induced breaking is computed in the wave model following Church and Thornton (1993). This parameterization works well for narrow-banded wave forcing provided that two empirical constants are known: the breaking wave parameter γ_b, and B_b accounting for the type of breaker. We achieve calibration of these parameters by comparing model-data dissipation patterns, assuming common scaling by V_0 (Figure 3; cyan curves). Values of 0.4 and 1.3, for γ_b and B_b respectively, provide the best fit to observation. The two curves feature a narrow surfzone starting at ~2 m depth seaward of the low-tide terrace. Closer to shore, the wave model misses some breaker dissipation that we attribute to wind waves with little impact on the longshore current.

RESULTS

We present results on the differences between the forced surfzone jet and resulting mean longshore flow. We then proceed to describe the mechanisms of shear wave and eddy productions that may explain the observed and modeled eddy effect.

Shear waves

The frequency f, wavelength λ, growth rate σ_i and phase speed c_p of unstable shear waves rely essentially on the mean current shear V_x and jet width Lj. From a linear stability analysis, Bowen and Holman (1989) propose simple relations for the most unstable waves: $f = 0.07V_x$, $\lambda = 2.5Lj$, $\sigma_i = 0.15V_x$ and $c_p = 0.25\text{-}0.5\ V_0$. For a narrow, shoreline-intensified jet typical of Grand Popo at mid-tide (Lj ~ 50m), shear can be strong. It is about 0.05 s^{-1} for the forced currents but weakens due to eddy mixing (Noyes *et al.*, 2004, argue from observations that shear waves stem from the forced rather than mean current). This implies a minimum shear wave period of about 5 min and wavelength of 125 m. Frictional spindown time for $\mu \sim 3.10^{-3}$ m/s is 5-10 min in the surfzone, *i.e.*, much longer than the growth time scale $\sigma^{-1} \sim 3$ min and thus favorable to their amplification.

To better assess the characteristics of linear most unstable waves, we ran the model with a large drag coefficient ($\mu = 6.10^{-3}$ m/s). In this weakly nonlinear regime, shear waves develop clear energy peaks at a period of 7 min and wavelength of 130 m (illustrated in Figure 3, left panel) and propagate along the flow with phase speed ~55 cm/s (estimated from a radon transform).

Shear eddies

When bottom drag is more realistic, shear waves with similar characteristics first develop but the flow becomes rapidly turbulent (center/right panels of Figure 3) with eddy kinetic energy representing 10-20 % of the mean. Eddies and filaments emerge on the seaward side of the jet, much like filaments observed with dye tracers (not shown). In this regime, the frequency spectrum broadens and the period in the surfzone is 4-10 min with modulation at larger periods (as in Allen *et al.*, 1996). In spite of coherency loss, the phase speed of propagation varies little over the simulation and is similar to the weakly nonlinear solution. This is expected from unstable modes that are approximately nondispersive (*e.g.*, Uchiyama *et al.*, 2009).

VLF variability was also computed from the video data on March 11 (3-hour period from 8 to 11 a.m. with fairly steady forcing conditions). Although these results are still preliminary, they indicate a standard deviation of longshore velocity of about 10 cm/s and a broad VLF frequency spectrum in agreement with the model. The VLF signal propagates only along the longshore current at ~ 50 cm/s, *i.e.*, much slower than gravity waves of the same frequency but very close to the model solution.

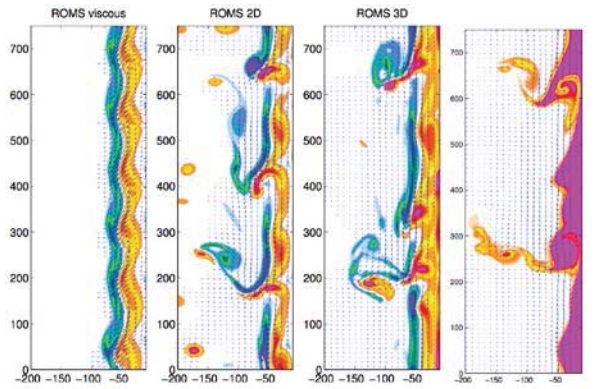

Figure 3. Instantaneous model vorticity and velocity vectors on the morning of March 11 2014. Left: shear waves developed from a 2D simulation with strong drag coefficient. Center: turbulent regime in 2D and 3D simulations with a realistic drag coefficient. Peak vorticity is 0.06 s^{-1}. The right panel shows a virtual dye released in the surfzone of the 3D simulation; it shows filaments and eddies ejecting seaward, much like aerial photos of dye experiments.

Eddy-mixed longshore flow

The forced longshore current profile used as initial flow in the model closely follows that of breaker dissipation. On the contrary, the time-mean longshore current profile (Figure 4; blue curves) is very broad in both model and data, extending more than 150 m offshore, well outside the surfzone. The model clearly reproduces the observed broadening of the current, although the peak velocity in the surfzone is larger in the model (about 1 m/s rather than 0.8 m/s).

Broadening of the model mean flow is due to cross-shore momentum mixing by shear waves and eddies. Eddy mixing is given by the cross-shore eddy advection term of the v equation: $A_t = -\langle u'v' \rangle_x$, where $-\langle u'v' \rangle$ is the time-mean cross-shore eddy flux of longshore flow v (Reynolds stress) and x the cross-shore distance. A_t has a strong decelerating effect in the surfzone (the depth-averaged value is ~ $1 m/s^2$, *i.e.*, half the bottom stress); it has an accelerating effect outside the surfzone (−0.5 m/s^2 balanced by the bottom stress) and vanishes at 150 m offshore (and toward the shoreline). The role of eddies is thus to extract large amounts of momentum from the longshore current in the

surfzone and spread it across. It should be noted that some redistribution of longshore current is also attributed to the vortex force and mean advection (Uchiyama *et al.*, 2009), but at a lesser degree here.

Another measure of eddy mixing is eddy viscosity: $\nu_t = -\langle u'v' \rangle / v_x$. Maximum values of ν_t are about 0.5 m^2/s seaward of the longshore current peak. Prandtl's mixing length-scale l defined by $\nu_t = l^2 v_x$ appears linearly dependent on |x| the distance to the shoreline (with coefficient ~ 0.075) in agreement with Longuet-Higgins (1970). This underlines that mixing is limited on the shoreward side of the current by the shoreline.

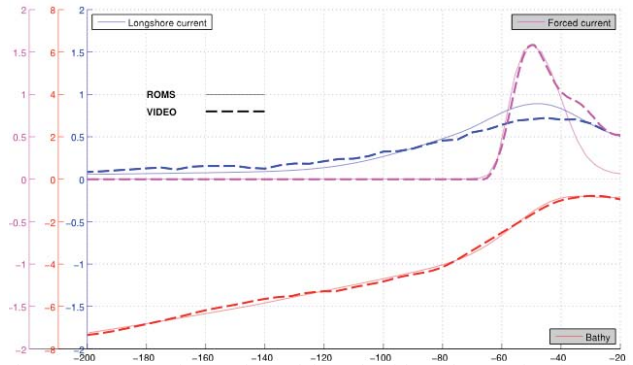

Figure 4. Comparison of model and video data estimations of bathymetry and longshore currents. The video (model) data is averaged over a 3-hour (10-hour) period and 250 (800) m alongshore distance. The forced current produced in the spinup phase of model simulation (cyan curve) has amplitude V_0 proportional to breaker dissipation and is used to scale dissipation from video data. The model bathymetry is an analytical fit to the video data.

DISCUSSION

It is generally assumed that nearshore dynamics follow a classical 2D turbulent regime (*e.g.*, Feddersen, 2014) but little evidence is found from the literature. To contribute on the subject in the context of longshore currents, we performed a wavenumber spectral analysis for 2D and 3D simulations (Figure 5). Consistently with 2D turbulence — in both 2D and 3D simulations — there is a strong inverse cascade of kinetic energy (KE) in the model starting from the scale of injection (~ 130 m). It should be noted that our 2D simulations produce more eddy energy at the same Reynolds number (same bottom drag) as expected from Squire's theorem and noted by Newberger and Allen (2007) for longshore currents. However, the injected energy travels more efficiently across the spectrum in the 3D model. Spectral fluxes are larger, *i.e.*, they promote the nonlinear growth of larger disturbances (compare the longshore scales in Figure 3b-c).

A sign of departure from 2D turbulence is the presence of a direct cascade (positive flux) downward from the injection scale. Here again, the flux is stronger in the 3D model. As a result, the 2D KE spectrum shows an energy deficit at both larger and smaller scales around the injection point (not shown). The 2D simulation has less direct KE flux but appears more efficient at downscaling enstrophy as in classical 2D turbulence (*e.g.* Figure 3b-c shows more numerous small-scale vortical flows in the 2D model). However, in all cases the KE spectra do not strictly follow any inertial slope (k^3 or $k^{-5/3}$), presumably due to the continuous effect of bottom friction across the spectrum. We conclude that the turbulent regime of nearshore regions is not properly explained by classical paradigms and deserves further investigation.

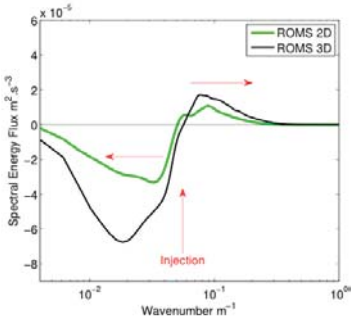

Figure 5. Left: Model (10-hour data) and video (3-hour data) frequency spectra of longshore velocity variance in the surfzone. Right: 3D and 2D model wavenumber spectral flux in the surf and innershelf regions. Vertical red arrows point to the period and wavenumber of most linearly unstable shear waves (7 min, 130 m) obtained from a viscous 2D simulation. The spectral flux is computed as in Marchesiello *et al.* (2011) by spectral integration of v advection term. Horizontal red arrows indicate positive/negative fluxes, *i.e.*, direct/inverse energy cascade toward smaller/larger scales.

CONCLUSIONS

The literature has long suggested a link between shear-flow instability of longshore currents and their mean cross-shore profile. Yet, recent investigations give increasing credit to extrinsic mechanisms of instantaneous wave forcing to explain the observed variability. Our results on Grand Popo beach based on video observation and model simulations provide further details on the 3D dynamics of strong longshore currents. They show that its broad mean profile is consistent with shear instability, conversion of mean to eddy kinetic energy and eddy mixing of momentum.

Our results reinforce the idea that between wave-driven surfzone circulation and wind-driven shelf circulation exist a transition zone in the innershelf region populated by filaments and eddies. Their horizontal scales are much larger than vertical ones but their turbulent dynamics do not clearly fit in the classical 2D paradigm since part of their energy fluxes down to smaller scales.

Instabilities in a 3D coupled wave-current model tend to generate less variance than the classical 2D uncoupled system (*e.g.*, Newberger and Allen, 2007) for two reasons. First, the feedback of rip currents on the incoming wave field is negative and thus reduces instability development (Uchiyama *et al.*, 2009; Yu and Slinn, 2003). Second, a shear flow is less unstable to 3D than 2D disturbances at the same Reynolds number, *i.e.*, with the same bottom drag (Squire's theorem). 3D longshore currents may thus be closer to the stability region and more often require stochastic excitation to generate variance (Farrell and

Ioannou, 1993). Stochastic forcing can lower the dependence of amplification on the Reynolds number. In this sense, intrinsic and extrinsic modes of variability should not be opposed but considered in future research as possibly interacting processes.

ACKNOWLEDGMENTS

This research has received support from French grants through ANR (COASTVAR: ANR-14-ASTR-0019; COMODO: ANR-11-MONU-005) and EC2CO/LEFE (Grand Popo Experiment and COMODO-WAVES). The fieldwork data in this study has been acquired by the authors and the source code for the model used, ROMS-AGRIF, is freely available (www.romsagrif.org).

LITERATURE CITED

Allen, J.S.; Newberger, P.A., and Holman, R.A., 1996. Nonlinear shear instabilities of alongshore currents on plane beaches. *J. Fluid Mech.*, 310, 181–213.

Almar, R., *et al.*, 2014. The Grand Popo beach 2013 experiment, Benin, West Africa: from short timescale processes to their integrated impact over long-term coastal evolution. *J. Coastal Res.*, 70, 651–656.

Bowen, A.J., and Holman, R.A., 1989. Shear instabilities of the mean longshore current: 1. Theory. *J. Geophys. Res.*: *Oceans*, 94 (C12), 18,023–18,030.

Church, J.C., and Thornton, E.B., 1993. Effects of breaking wave induced turbulence within a longshore current model. *Coastal Eng.*, 20, 1-28.

Clark, D.B., Elgar, S., and Raubenheimer, B., 2012. Vorticity generation by short-crested wave breaking. *Geophys. Res. Lett.*, 39 (L24604).

Debreu, L., Marchesiello, P.; Penven, P., and Cambon, G., 2012. Two-way nesting in split- explicit ocean models: Algorithms, implementation and validation. *Ocean Model.*, 49-50, 1-21.

Dodd, N.; Oltman-Shay, J., and Thornton E.B., 1992. Shear instabilities in the longshore current: A comparison of observation and theory. *J. Phys. Oceanogr.*, 22, 62–82.

Farrell, B.F., and Ioannou, P.J., 1993. Stochastic forcing of perturbation variance in unbounded shear and deformation flows. *J. Atmos. Sci.*, 50, 200–211.

Feddersen, F., 2014. The generation of surfzone eddies in a strong alongshore current. *J. Phys. Oceanogr.*, 44, 600–617.

Flores, R.P., Catalan, P.A, and Haller, M.C., 2013. Incorporating remotely-sensed roller properties into set-up estimations for random wave conditions, in Proceedings of Coastal Dynamics 2013, 615-626, Nantes, France.

Kaki, C., Laibi, R.A,, and Oyede, L.M., 2011. Evolution of beninese coastline from 1963 to 2005: Causes and consequences. *Br. J. Env. Clim. Change*, 1, 216–231.

Laibi, R.A.; Anthony, E.J.; Almar, R.; Castelle, B.; Senechal, N., and Kestenar, E., 2014. Longshore drift cell development on the human-impacted Bight of Benin sand barrier coast, West Africa. *J. Coast. Res.*, 70, 78–83.

Larnier, S.; Almar, R.; Cienfuegos, R., and Lejay, A., 2014. On the use of the radon transform to estimate longshore currents from video imagery. *J. Coast. Res.*, 70, 23–28.

Longuet-Higgins, M. S., 1970. Longshore currents generated by obliquely incident sea waves: 2. *J. Geophys. Res.*, 75, 6790–6801.

Marchesiello, P.; McWilliams, J.C., and Shchepetkin, A., 2001. Open boundary conditions for long-term integration of regional oceanic models. *Ocean Model.*, 3, 1-20.

Marchesiello, P.; Capet, X.; Menkes, C., and Kennan, S.C., 2011. Submesoscale dynamics in tropical instability waves. *Ocean Model.*, 39, 31–46.

Marchesiello, P.; Benshila, R.; Almar, R.; Uchiyama, Y.; McWilliams, J.C., and Shchepetkin, A., 2015. On tridimensional rip current modeling. *Ocean Model.*, doi:10.1016/j.ocemod.2015.07.003.

McWilliams, J.C., Restrepo, J.M., and Lane, M.R., 2004. An asymptotic theory for the interaction of waves and currents in coastal waters. *J. Fluid Mech.*, 511, 135–178.

Newberger, P.A., and Allen, J.S., 2007. Forcing a three-dimensional, hydrostatic, primitive-equation model for application in the surf zone: 2. application to duck94. *J. Geophys. Res.*: *Oceans*, 112(C8).

Noyes, T.J.; Guza R.T.; Elgar, S., and Herbers, T.H.C., 2004. Field observations of shear waves in the surf zone. *J. Geophys. Res.*, 109 (C01031).

Oltman-Shay, J.; Howd, P.A., and Birkemeier, W.A., 1989. Shear instabilities of the mean longshore current: 2. field observations. *J. Geophys. Res.: Oceans*, 94 (C12), 18,031–18,042.

Oskan-Haller, H.T., and Li, Y., 2003. Effects of wave-current interaction on shear instabilities of longshore currents. *J. Geophys. Res.: Oceans*, 108 (C5).

Peregrine, D.H., 1998. Surf zone currents. *Theor. Comput. Fluid Dyn.*, 10, 295–309.

Shchepetkin, A.F., and McWilliams, J.C., 2005. The regional oceanic modeling system (ROMS): a split-explicit, free-surface, topography-following-coordinate oceanic model. *Ocean Model.*, 9, 347-404.

Slinn, D.N.; Allen, J.S.; Newberger, P.A., and Holman, R.A., 1998. Nonlinear shear instabilities of alongshore currents over barred beaches. *J. Geophys. Res.*, 103 (C9), 18,357-18,379.

Uchiyama, Y.; McWilliams, J.C., and Restrepo, J.M., 2009. Wave-current interaction in nearshore shear instability analyzed with a vortex force formalism. *J. Geophys. Res.: Oceans*, 114 (C6).

Uchiyama, Y.; McWilliams, J.C., and Shchepetkin, A., 2010. Wave-current interaction in an oceanic circulation model with a vortex-force formalism: Application to the surf zone. *Ocean Model.*, 34, 16–35.

Yu, J., and Slinn, D.N., 2003. Effects of wave-current interaction on rip currents. *J. Geophys. Res.: Oceans*, 108(C3).

Journal of Coastal Research	SI	75	413-417	Coconut Creek, Florida	2016

Phytoplankton Dynamics in Three Metropolitan Beaches of the Amazon Littoral (São Luís-Maranhão)

Jislene B. Matos[†*], Antonio R.G. Oliveira[†], Wellington N. Trindade[†], Natália R. Leite[†], Maria L. Koening[††], Luci C.C. Pereira[†‡] and Rauquírio M. da Costa[†§]

[†]Instituto de Estudos Costeiros, Universidade Federal do Pará, Bragança, Brazil.

[‡] Laboratori d'Enginyeria Marítima, Universitat Politècnica de Catalunya, Barcelona, Spain.

[††]Departamento de Oceanografia, Universidade Federal do Pernambuco, Recife, Brazil.

[§] Institut de Ciències del Mar (ICM/CSIC), Barcelona, Spain.

www.cerf-jcr.org

www.JCRonline.org

ABSTRACT

Matos, J.B.; Oliveira, A.R.G.; Trindade, W.N.; Leite, N.R.; Koening, M.L.; Pereira, L.C.C., and Costa, R.M. da., 2016. Phytoplankton dynamics in three metropolitan beaches of the Amazon littoral (São Luís-Maranhão). *In:* Vila-Concejo, A.; Bruce, E.; Kennedy, D.M., and McCarroll, R.J. (eds.), *Proceedings of the 14th International Coastal Symposium* (Sydney, Australia). *Journal of Coastal Research*, Special Issue, No. 75, pp. 413-417. Coconut Creek (Florida), ISSN 0749-0208.

The present study was based on a spatial-temporal analysis of the phytoplankton of three beaches in São Luís (Maranhão) with the aim of understanding the influence of the factors on the phytoplankton community. Samples were obtained in the dry season (December 2008 and October 2009) and the rainy season (March and June, 2009), and were collected using internationally standardized methods. Salinity was significantly higher during the dry season, while temperature, dissolved oxygen, pH, turbidity and dissolved nutrient concentrations (nitrate) were all significantly higher during the rainy season. Diatoms contributed to the high taxonomic richness observed at all the beaches. Total phytoplankton density and chlorophyll-a concentrations (20.9 $mg.m^{-3}$; B1) were highest during the rainy months, with significantly higher densities being observed at B3 (1274.3×10^3 $cell.L^{-1}$). The cluster analysis revealed the formation of two groups influenced by seasonality, reflecting the relative homogeneity of the beaches. The results indicate that the variation in the composition and density of the phytoplankton is determined by the high degree of interaction between the highly hydrodynamic characteristics typical of Amazonian environments and the local rainfall cycle, which modulates the other environmental variables, such as salinity and dissolved nutrient concentrations, thus affecting the dynamics of coastal phytoplankton communities. The strong antropogenic influence observed in these urban beaches (sewage effluent discharges) also interfered within the dynamics of local phytoplankton.

ADDITIONAL INDEX WORDS: *biomass, microalgae, coastal areas.*

INTRODUCTION

The Brazilian Amazon coast is characterized by intense hydrodynamics, influenced by both marine and continental processes. The dynamics of this littoral are distinct from those of other regions of Brazil, given the high input of freshwater, particulate matter, and suspended sediments (Calliari *et al*., 2010; Geyer *et al*., 1996), given that the Amazon basin is the world's largest and most extensive river system. The region is also affected by the intense meteorological and oceanographic forces that are typical of the northern coast of Brazil (Pereira *et al*., 2012; Pereira *et al.*, 2013).

The coastal waters of the Amazon littoral are among the biologically richest anywhere in the world, and they are considered to be an extremely important environment for the conservation of biodiversity of the world's oceans (Agostinho *et al*., 2005). In general, the primary production of phytoplankton in these waters, as in other coastal areas, is controlled basically by the flow of nutrients, availability of sunlight, andtemperature, while the biomass is regulated by phytoplankton growth and grazing rates (Murrell *et al*., 2007).

This group of organisms responds rapidly to modifications in the environment, such as oscillations in the concentrations of dissolved nutrients, especially those derived from human activities (Nayar *et al*., 2005), which tend to cause a major increase in the concentrations of the inorganic forms of nitrogen and phosphorus in the land-sea interface, accelerating the eutrophization of the water and affecting the organization of local biological communities (Howarth, 1998).

The ongoing recent development of the Amazon region has occurred without concern for the impacts of population growth and industrial expansion on the biodiversity of aquatic ecosystems. In recent years, the urbanization of the city of São Luís, in the Brazilian state of Maranhão has advanced at an accelerated rate, threatening and damaging the quality of the local beaches (Silva *et* al., 2009; Silva *et al*., 2013; Trindade *et al*., 2011), with direct consequences for the local biota. In this context, the present study investigated the spatiotemporal dynamics of the phytoplankton on three beaches in the metropolitan region of São Luís, based on a comparison with climatological, hydrodynamic, and hydrological parameters, and the analysis of their influence on the structure and dynamics of the phytoplankton community.

DOI: 10.2112/SI75-083.1 received 15 October 2015; accepted in revision 15 January 2016.

*Corresponding author: jislenematos@gmail.com

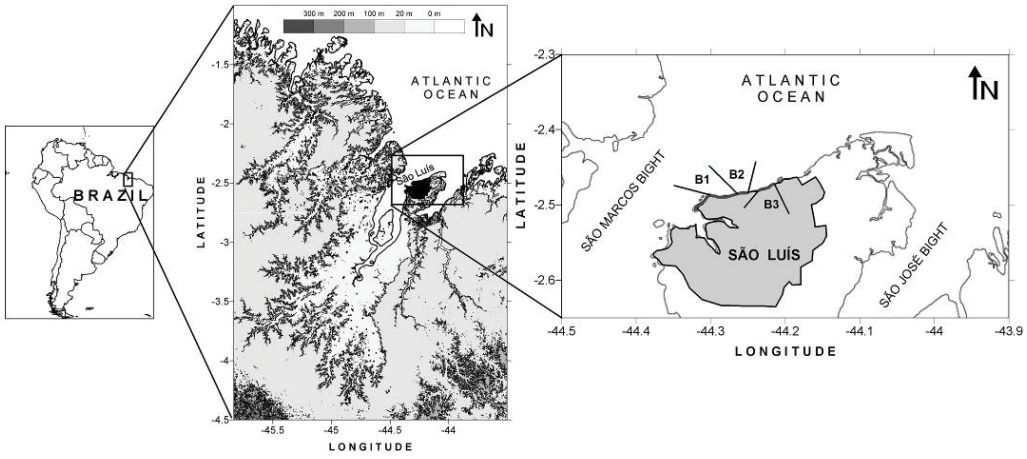

Figure 1. Location of the study beaches in the city of São Luís: B1 – São Marcos, B2 – Calhau and B3 – Olho d'Água (modified from Asp, 2008).

Study Area

The coast of the city of São Luís is 35 km long, and is located between São Marcos and São José bays (Figure 1). The beaches of this region are dominated by semi-diurnal macrotides, with ranges of more than 7 m during equinoctial spring tides (Silva *et al*., 2009). The local climate is humid tropical, with two distinct seasons. The dry season normally extends between July and December, with total precipitation typically of around 200 mm, and maximum temperatures of 33°C. The rainy season (January–June) normally has total precipitation of more than 1500 mm and minimum temperatures below 20°C (Porto de Itaqui, 2008). While the study region suffers extensive anthropogenic impacts, coastal management initiatives are practically nonexistent (Silva *et al*., 2013), and the lack of a public sanitation system is one of the principal factors that affect the quality of local beaches. Almost one hundred sewage outlets discharge domestic effluents directly onto the study beaches (Silva *et al*., 2009).

METHODS

The present study focused on three beaches in the city of São Luís (Figure 1): São Marcos (B1 - 2°29'17.70" S, 44°17'04.53" W), Calhau (B2 - 2°28'58.65" S, 44°15'15.61" W), and Olho d'Água (B3 - 2°28'45.9" S, 44°13'46.56" W). The fieldwork was conducted in four campaigns, in December 2008, and March, June and October, 2009. During each campaign, the three beaches were monitored over a 13-hour period.

The climatological data were obtained from the National Meteorological Institute (station A203). Data on the direction and intensity of local currents were obtained from a mini-current meter, while wave heights and periods were obtained using a tidal sensor. The equipment used to collect these data were bottom-mounted at a depth of 1.7 m. Temperature and salinity were measured *in situ* using a CTD. Other abiotic (pH, turbidity, the concentrations of dissolved oxygen and nutrients in the water) and biotic variables (chlorophyll-a concentrations and quantitative phytoplankton samples) were measured by collecting sub-surface water samples using a Niskin bottle. The qualitative analysis of the phytoplankton was based on the filtering of 400 L of water from the sub-surface layer of the surf zone on each beach using plankton nets (64 μm).

In the laboratory, the analyses of abiotic and biotic data were perfortmed using internationally standardized methods. The qualitative analysis of the microphytoplankton was conducted using temporary mounted slides, which were observed under a binocular microscope. Utermöhl's sedimentation method was used to determine the density of phytoplankton through the counts of the total area of the chamber in an invertoscope, with magnification of 400 x. Following the application of normality (Lilliefors) and homogeneity (Cochran) tests, parametric (ANOVA) and nonparametric (Mann-Whitney and Kruskal-Wallis) analyses were run on the abiotic and biological data, in order to verify the significance of differences among beaches, seasons, months, and the different tidal periods, based on a 5% significance level. A Principal Components Analysis (PCA) was used to evaluate the possible relationships among the environmental and biotic variables. The univariate analyses and the PCA were run in STATISTICA 8.0. Additional multivariate analyses (Cluster analysis, ANOSIM, and SIMPER) were run in PRIMER, version 6.1.6.

RESULTS

Rainfall regime – Over the study period, precipitation patterns were typical of the study region, with the period between January and June being the rainiest, while those between July and December were the least rainy. Total monthly precipitation during the study period ranged from 0 mm (October, 2009) to 565.4 mm, in March, 2009.

Hydrodynamic and hydrological variables – During the study period, strong tidal currents (0.5 m/s) and elevated wave heights (*Hs* = 1.4 m) were recorded in March, with the highest values being recorded on B2. No significant spatial variation was found in hydrological variables, reflecting the relative homogeneity of the study beaches. The results obtained for hydrological variables that presented significant differences are shown in Table 1. Mean water temperatures were significantly higher

during the rainy months (max. 29.1°C; $F = 32.8$; $p < 0.05$). By contrast, salinity was significantly higher during the dry season (max. 36.0; $U = 0.0$; $p < 0.05$). Turbidity (max. 127.0 NTU; $F = 41.0$; $p < 0.05$) and pH (max. 8.4; $F = 6.9$; $p < 0.05$)), however, were significantly higher during the rainy season. The nitrate concentrations were significantly higher in the rainy season (max. 8.2 µmol.L^{-1}; $F = 15.2$; $p < 0.05$). The phosphate concentrations were significantly higher at B1 ($F = 3.4$; $p < 0.05$), while silicate concentrations presented significant seasonal differences, with higher values being recorded during the dry season (max. 101.3 µmol.L^{-1}; $F = 5.1$; $p < 0.05$).

Table 1. *Seasonal variation (mean±S.D.) in the hydrological parameters on the study beaches in São Luís, Maranhão, Brazil.*

Variable	Dry	Rainy
Temperature (°C)	27.9±0.3 (B3)	29.0±0.4 (B1)
Salinity	34.0±2.3 (B3)	23.9±7.2 (B2)
pH	7.5±0.4 (B2)	8.0±0.4 (B2)
Turbidity (NTU)	15.5±2.6 (B1)	86.6±50.9 (B1)
Nitrate (µmol.L^{-1})	1.2±0.9 (B3)	5.7±3.1 (B1)
Phosphate (µmol.L^{-1})	0.3±0.1 (B3)	0.5±0.0 (B1)
Silicate (µmol.L^{-1})	84.5±18.3 (B3)	56.1±9.4 (B1)

Phytoplankton – A total of 177 phytoplankton taxa were recorded on the São Luís beaches, distributed in the Bacillariophyta (130 taxa), Dinophyta (19 taxa), Cyanobacteria (16 taxa), Chlorophyta (9 taxa), Charophyta (2 taxa), and Ochrophyta (1 taxon). The diatoms were the numerically most important group. Five species (*Bacillaria paxillifera* (O.F.Müller) T.Marsson, *Coscinodiscus jonensianus* (Greville) Ostenfeld, *C. perforatus* Ehrenberg, *Odontella regia* (Schultze) Simonsen, *Thalassionema frauenfeldii* (Grunow) Tempère & Peragallo and *Thalassiosira subtilis* (Thetenfeld) Gran) were present in all the samples analyzed, and can be considered very frequent.

The phytoplankton biomass (chlorophyll-a) was significantly higher during rainy months (max. 20.9 mg.m^{-3}; $F = 17.1$; $p < 0.05$), varying from 4.9±2.5 mg.m^{-3} (B2 – dry season) to 12.7±5.8 mg.m^{-3} at B1 in the rainy season. Total phytoplankton, microphytoplankton and phytoplankton densities varied significantly among the study beaches (Figure 2). Total phytoplankton density varied from 130.5±40.8 x 10^3 cell.L^{-1} (B2 – dry season) a 637.2±435.9 x 10^3 cell.L^{-1} (B3 – rainy season, max. 1274.3 x 10^3 cell.L^{-1}), with significantly lower values being recorded at B2 ($F = 16.2$; $p < 0.05$). In the specific case of the microphytoplankton, low densities were recorded on beach B2 ($F = 11.2$; $p < 0.05$), with values ranging from 36.4±22.5 x 10^3 cell.L^{-1} (B2 – dry season) to 409.8±484.5 x 10^3 cell.L^{-1} (B3 – rainy season). The density of phytoflagellates ranged from 94.1±25.8 x 10^3 cell.L^{-1} (B2 – dry season) to 235.0±70.8 x 10^3 cell.L^{-1} (B3 – dry season), and was significantly higher at B3 ($F = 8.5$; $p < 0.05$) (Figure 2).

The quantitatively most important species were *Dimeregramma minor* (Gregory) Ralfs ex Pritchard (max. 343.1 x 10^3 cell.L^{-1}) in the dry season, and *Rivularia* sp. (max. 208.3 x 10^3 cell.L^{-1}) and *Psammodictyon panduriforme* (W.Gregory) D.G.Mann (max. 186.8 x 10^3 cell.L^{-1}) in the rainy season, with higher densities being recorded at B3.

The cluster analysis (Figure 3) revealed two well-defined groups (70% similarity), which were influenced by local seasonality (ANOSIM, global $R = 0.6$). Group 1 included dry season samples from all three study beaches, with this group being defined by the centric diatom *Paralia sulcata* (Ehrenberg) Cleve (SIMPER Sim/SD = 52.2). Group 2 encompassed rainy season samples from beaches B1 and B3, and were influenced primarily by *Actinocyclus nebulosus* M. Peragallo (SIMPER Sim/SD = 34.6). The Principal Components Analysis (PCA) of the data from the three beaches (Figure 4) showed that factor 1 explained 44.8% of the variation in the data, and showed that salinity (coeff. 0.9) and nitrate (coeff. -0.9) and phosphate (coeff. -0.8) concentrations were the factors that most influenced the distribution of phytoplankton species, in particular *A. nebulosus* (coeff. -0.7), which was related negatively to salinity, and grouped the rainy season samples in the cluster analysis, and *D. minor* (coeff. 0.4), which was common in the dry season. Factor 2 explained 23.5% of the variation in the data, and indicated that pH (coeff. -0.9) and turbidity (coeff. -0.8) were the principal variables influencing the densities of *P. sulcata* (coeff. -0.3), the species responsible for the formation of the dry season group.

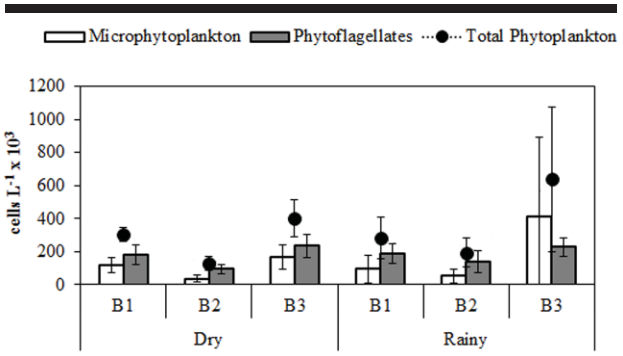

Figure 2. Seasonal variation (mean±S.D.) of phytoplankton densities on the study beaches in São Luís, Maranhão, Brazil.

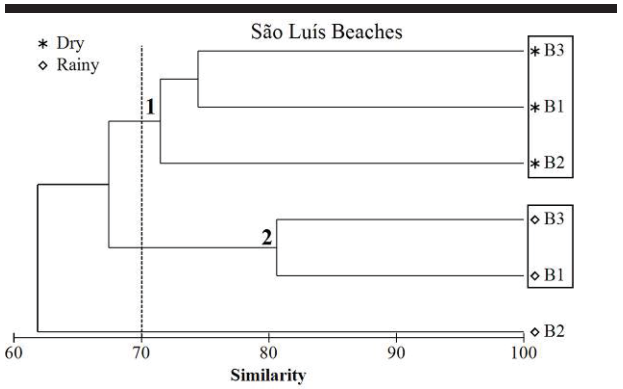

Figure 3. Cluster analysis based of the density of phytoplankton species.

DISCUSSION

The Amazon coast is characterized by marked annual fluctuations in precipitation, which cause drastic seasonal changes in hydrological parameters (see Magalhães *et al*., 2015).

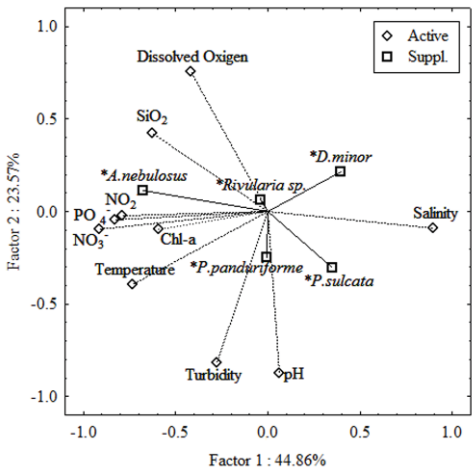

Figure 4. Principal Components Analysis of the environmental variables, with the most common phytoplankton species as supplementary variables.

The study area was considered to be spatially homogeneous in relation to the environmental variables analyzed. However, typical seasonal patterns of variation were recorded, with high levels of salinity being recorded during the dry season, and high turbidity, and dissolved nutrient and chlorophyll-a concentrations being observed during the rainy months, as found in previous studies of different Amazon coastal ecosystems (Matos *et al*., 2012; Pereira *et al*., 2013).

In the present study, rainfall patterns and the intense local hydrodynamics, influenced by wave action and tides, together with the strong local winds and increased fluvial input during the rainy season, increased the transport of nutrients and material in suspension to coastal waters, affecting the dynamics and development patterns of the coastal phytoplankton (see also Costa *et al*., 2013; Matos *et al*., 2011;). As a consequence, the surf zones of Amazon beaches are characterized by the resuspension process provoked by winds, breaking waves, and the coastal currents responsible for the exchange of benthonic microalgae which become integrated with the local phytoplankton community, affecting its structure (Matos *et al*., 2012; Sousa *et al*., 2009).

The structure and dynamics of the phytoplankton community of the beaches of São Luís are characterized by the predominance of diatoms, which are the principal group responsible for the high species richness and relative abundance observed in both seasons. The dominance of diatoms – which may constitute more than 80% of the phytoplankton species in these environments (Costa *et al*., 2013; Ferreira *et al*., 2010) – is often associated with turbulent waters influenced by strong winds and coastal currents (Smayda, 1980). The predominance of this group is related to its opportunistic (with many "r" strategist species) and euryhaline characteristics (Odebrecht *et al*., 2010). The high dissolved nutrient concentrations in the water may have been one of the principal factors determining the variation in the variability in phytoplankton composition and abundance, given that diferent taxa have distinct nutritional requirements and strategies for the absorption of these elements (Masó and Garcés, 2006). The high silicate concentrations and the intense hydrodynamics observed on the study beaches may account for the dominance of the diatoms throughout the study period. In addition, tycoplanktonic species, such as *Paralia sulcata* and *Psammodictyon panduriforme*, were prominent in the samples, reflecting the effects of the local hydrodynamics on the resuspension of sediments and phytobenthos, as observed in other Amazonian coastal environments (Costa *et al*., 2013; Matos *et al*., 2011).

Dissolved nutrients are one of the most important parameters in marine systems, given that they influence the growth, reproduction and metabolic activities of the phytoplankton. In general, the distribution of these organisms in the water column is closely related to seasonal patterns, tidal cycles, and the input of freshwater from terrestrial sources (Achary *et al*., 2014). On the study beaches, the concentrations of most dissolved nutrients were higher in the rainy season, reflecting the effects of the increase in fluvial discharge, as well as terrestrial drainage, on the availability of organic and inorganic nutrients in the adjacent coastal waters, which had a clear influence on the local plankton populations. Phytoplankton density and biomass followed the same seasonal pattern, increasing significantly during the rainy season, as found in previous studies of beaches (Matos *et al*., 2012) and other Amazonian coastal ecosystems, such as estuaries (Matos *et al*., 2011). During the rainy season, the outwash of nutrients from mangroves caused by the increased rainfall favors phytoplankton growth, enriching the environment and supporting the development of this community.

Previous studies conducted on the same study beaches also found that the intense local hydrodynamics may contribute to the contamination of these environments, especially when the highest tides reach the sewage outlets located on the upper beach zone, resulting in an increase in the concentrations of nutrients dissolved in the water (Trindade *et al*., 2011). Olho d'Água (B3) appears to be the beach most contaminated by residual waters (Silva *et al*., 2013), favoring phytoplankton development in this area, as observed in the present study (highest densities).

The multivariate analyses also emphasized the spatial homogeneity of the study beaches, with significant variation in biotic and abiotic parameters. The principal factors regulating phytoplankton dynamics were salinity, turbidity and dissolved nutrient concentrations, which were strongly influenced by rainfall patterns, and the intense local hydrodynamics. The resuspension of sediments provoked by winds, breaking waves and costal currents also contributed to the homogenization of the water column, causing the exchange of planktonic and tycoplanktonic (benthonic) populations, with profound effects on the structure of the local phytoplankton community.

CONCLUSIONS

The results of the present study indicate that the variation in the composition and density of phytoplankton on the study beaches were determined by the interaction between the strong local hydrodynamism and rainfall patterns, which together modulated other environmental variables, such as salinity, turbidity and dissolved nutrients, with direct effects on the phytoplankton dynamics of these and other coastal Amazonian beaches. The major role of anthropogenic impacts on these

urban beaches also affects the dynamics of the local phytoplankton communities, through contamination with domestic effluents, which provokes an increase in the concentrations of dissolved nutrients in the water, contributing to phytoplankton development.

ACKNOWLEDGMENTS

This study was financed by FAPESPA (ICAAF 115/2008 and 116/2008). The first author is grateful to CAPES for the concession of a Ph.D scholarship. The Co-authors Luci Pereira and Rauquírio Costa are grateful to CNPq for research grants (#308379/2011–0 and 200629/2014–0, and #306061/2011-2 and 200622/2014-5). We are also indebted to Dr. Stephen Ferrari for careful correction of the English.

LITERATURE CITED

Agostinho, A.A.; Thomaz, S.M., and Gomes, L.C., 2005. Conservacao da biodiversidade em águas continentais do Brasil. *Megadiversidade*, 1, 70-78.

Achary, M.S.; Panigrahi, S.; Satpathy, K.K.; Sahu, G.; Mohanty, A.K.; Selvanayagam M., and Panigrahy, R.C., 2014. Nutrient dynamics and seasonal variation of phytoplankton assemblages in the coastal waters of southwest Bay of Bengal. *Environmental Monitoring and Assessment*, 186, 5681–5695.

Calliari, L.J.; Guedes, R.M.C.; Lélis, R.F.; Antiqueira, J.A., and Figueiredo, S.A., 2010. Hazards and risks associated to coastal processes along the southern Brazilian coastline: A synthesis. *Brazilian Journal of Aquatic Science and Technology*, 14, 51-63.

Costa, R.M.; Matos, J.B.; Pinto, K.S.T., and Pereira, L.C.C., 2013. Phytoplankton of a dynamic Amazon sandy beach. *In*: Conley, D.C.; Masselink, G.; Russell, P.E., and O'Hare, T.J. (eds.), *Journal of Coastal Research*, Special Issue No. 65, pp. 1751-1756.

Ferreira, L.C.; Silva Cunha, M.G.G.; Koening, M.L.; Feitosa, F.A.N.; Santiago, M.F., and Muniz, K., 2010. Variação temporal do fitoplâncton em três praias urbanas do litoral sul do estado de Pernambuco, Nordeste do Brasil. *Acta Botanica Brasilica*, 24(1), 214-224.

Geyer, W.R.; Beardsley, R.C.; Lentz, S.J.; Candela, J.; Limeburner, R.; Jonhns, W.E.; Castro, B.M., and Soares, I.D., 1996. Physical oceanography of the Amazon shelf. *Continental Shelf Research*, 16(5-6), 575-616.

Howarth, R.W., 1998. An assessment of human influences on inputs of nitrogen to the estuaries and continental shelves of the North Atlantic Ocean. *Nutrient Cycling in Agroecosystems*, 52(2), 213–223.

Magalhães, A.; Pereira, L.C.C., and Costa, R.M., 2015. Relationships between copepod community structure, rainfall regimes, and hydrological variables in a tropical mangrove estuary (Amazon coast, Brazil). *Helgoland Marine Research*, 69, 123-136.

Masó, M. and Garcés, E., 2006. Harmful microalgae blooms (HAB): problematic and conditions that induce them. *Marine Pollution Bulletin*, 53, 620–630.

Matos, J.B.; Silva, N.I.S.; Pereira, L.C.C., and Costa, R.M. 2012. Caracterização quali-quantitativa do fitoplâncton da zona de arrebentação de uma praia amazônica. *Acta Botanica Brasilica*, 26(4): 979-990.

Matos, J.B.; Sodré, D.K.L.; Costa, K.G.; Pereira, L.C.C., and Costa, R.M., 2011. Spatial and temporal variation in the composition and biomass of phytoplankton in an Amazonian estuary. *In*: Furmanczyk, K.; Giza, A., and Terefenko, P. (eds.), *Journal of Coastal Research*, SI 64, 1525-1529.

Murrell, M.C.; Hagy III, J.D.; Lores, E.M., and Greene, R.M., 2007. Phytoplankton production and nutrient distributions in a sub-tropical estuary: importance of freshwater flow. *Estuaries and Coasts*, 30(3), 390-402.

Nayar, S.; Goh, B.P.L., and Chou, L.M., 2005. Dynamics in the size structure of *Skeletonema costatum* (Greville) Cleve under conditions of reduced photosynthetically available radiation in a dredged tropical estuary. *Journal of Experimental Marine Biology and Ecology*, 318(2), 163-182.

Odebrecht, C.; Bergesch, M.; Rörig, L.R., and Abreu, P.C., 2010. Phytoplankton interannual variability at Cassino Beach, Southern Brazil (1992–2007), with emphasis on the surf zone diatom *Asterionellopsis glacialis*. *Estuaries and Coasts*, 33, 570-583.

Pereira, L.C.C.; Silva, N.I.S.; Costa, R.M.; Asp, N.E.; Costa, K.G., and Vila-Concejo, A., 2012. Seasonal changes in oceanographic processes at an equatorial macrotidal beach in northern Brazil. *Continental Shelf Research*, 43, 95-106.

Pereira, L.C.C.; Oliveira, S.M.O.; Costa, R.M.; Costa, K.G.; Vila-Concejo, A., 2013. What happens on an equatorial beach on the Amazon coast when La Niña occurs during the rainy season?. *Estuarine, Coastal and Shelf Science*, 135, 116-127.

Porto de Itaqui, 2008. *Empresa Maranhense de Administração Portuária e EMAP*. http://www.portodoitaqui.ma.gov.br.

Silva, I.R.; Pereira, L.C.C.; Guimarães, D.O.; Trindade, W.N.; Asp, N.E., and Costa, R.M., 2009. Environmental status of urban beaches in São Luís (Amazon coast, Brazil). *In*: Da Silva, C.P. (ed.), *Journal of Coastal Research*, SI 56, 1301-1305.

Silva, I.R.; Pereira, L.C.C.; Trindade, W.N.; Magalhães, A., and Costa, R.M., 2013. Natural and anthropogenic processes on the recreational activities in urban Amazon beaches. *Ocean & Coastal Management*, 76, 75-84.

Smayda, T.J., 1980. Phytoplankton species succession. *In*: I. Morris, Ed., *The Physiological Ecology of Phytoplankton*. Berkeley: University of California Press, pp. 493-570.

Sousa, E.B.; Costa, V.B.; Pereira, L.C.C., and Costa, R.M., 2009. Variação temporal do fitoplâncton e dos parâmetros hidrológicos da zona de arrebentação da Ilha Canela (Bragança-Pará-Brasil). *Acta Botanica Brasilica*, 23(4), 1084-1095

Trindade, W.N.; Pereira, L.C.C.; Guimarães, D.O.; Silva, I.R., and Costa, R.M., 2011. The effects of sewage discharge on the water quality of the beaches of São Luís (Maranhão, Brazil). *In*: Furmanczyk, K.; Giza, A., and Terefenko, P. (eds.), *Journal of Coastal Research*, SI 64, 1425-1429.

Journal of Coastal Research	SI	75	418-422	Coconut Creek, Florida	2016

Bathymetric controls on very low frequency rip current motions

R. Jak McCarroll[†*], Robert W. Brander[††], and Ian L. Turner[‡]

[†] Geocoastal Research Group, School of Geosciences, The University of Sydney, NSW, Australia

[††] School of Biological, Earth and Environmental Sciences, UNSW Australia, Sydney, NSW, Australia

[‡] Water Research Laboratory, School of Civil and Environmental Engineering, UNSW Australia, Manly Vale, NSW 2093, Australia

www.cerf-jcr.org

www.JCRonline.org

ABSTRACT

McCarroll, R.J.; Brander, R.W., and Turner, I.L., 2016. Bathymetric controls on very low frequency rip current motions. *In:* Vila-Concejo, A.; Bruce, E.; Kennedy, D.M., and McCarroll, R.J. (eds.), *Proceedings of the 14th International Coastal Symposium* (Sydney, Australia). *Journal of Coastal Research*, Special Issue, No. 75, pp. 418-422. Coconut Creek (Florida), ISSN 0749-0208.

Time-averaged mean rip currents are forced by persistent gradients in dissipation over shallow bars and deep rip channels. Time-variable horizontal surfzone eddies, at the ~10 min or very low frequency (VLF) range, are forced by stochastic wave breaking injecting vortical energy into the surfzone. Previous observations note that deep channel rips have greater variability of velocity while shallow channel rips exhibit greater variability in trajectory, this suggests a continuum of flow states that at present are poorly understood. This paper investigates the degree of bathymetric control on VLF motions illustrating how VLF motions manifest on different morphologies. Three field sites are investigated using low-pass filtered: (i) mean velocity; (ii) variable eddy velocity; (iii) directional standard deviation; and (iv) instantaneous vorticity. A VLF flow-type parameter is introduced to differentiate flow regimes, based on degree of bathymetric control. A novel classification scheme is introduced: (i) strong bathymetric control, with high mean velocities and rip cell oscillation; (ii) moderate control, with high mean velocities and variable VLF trajectories; and (iii) weak control, with low mean velocities and mobile eddies. Level of bathymetric control may be related to channel orientation, in addition to relative depth. This study improves our understanding of rip flow variability over short times frames, with implications for sediment transport and beach safety.

ADDITIONAL INDEX WORDS: *Surf zone, intermediate beach, rip channel, rip variability, Lagrangian drifter*

INTRODUCTION

Rip currents occur where alongshore gradients in radiation stress exist due to differential wave dissipation over shallow bars and deep rip channels (Bowen and Inman, 1969). Averaged over time, a mean offshore flow will be observed in the neck of the rip channel with a mean onshore flow over the adjacent bar. By comparison, time-variable horizontal vortical surfzone motions, or surfzone eddies, were initially described by Peregrine (1998). Vorticity is generated at the point along a wave crest where the bore transitions to an unbroken wave. This horizontal rotational forcing is deposited stochastically across the surfzone by short crested waves of varying location and direction in any natural wave field. The majority of variable vortical energy is found in the very low frequency (VLF) band (Feddersen, 2014), with eddies of 10's m to 100's m diameter. When surfzone eddies of opposite sign interact, a transient rip current may form (Johnson and Pattiaratchi, 2006).

Surfzone eddy forcing is observable as end-member types: (i) randomly directed transient currents with zero mean cross-shore current on planar beaches (*e.g.* Johnson and Pattiaratchi, 2006); and (ii) persistent rip currents with minor flow variations in deep rip channels (MacMahan *et al*., 2004). Subtle rip channels (MacMahan *et al*., 2008) may represent an intermediate flow type. Castelle *et al*. (2010) noted that well-developed bar-rip morphologies were associated with high velocity variability, while less three-dimensional morphologies were associated with high directional variability. MacMahan *et al.* (2004) suggested this variability manifested as oscillations of the rip cell position. Other observations note rip cells pulsing between recirculation *within* the surfzone and offshore flow *beyond* the surfzone (*e.g.* MacMahan *et al*., 2010).

Accordingly, the degree of bathymetric control on flow behaviour is hypothesised as a continuum from strong to absent control, however this relationship is poorly understood. Therefore, the aim of this study is to investigate the degree of bathymetric control on VLF motions, and to illustrate how VLF motions manifest on different morphologies.

FIELD SITES

Field sites (Figure 1) include Whale (McCarroll *et al*., 2014b), Bondi and Shelly Beaches (McCarroll *et al*., 2014a), located in NSW, Australia. All sites are embayed, with lengths and aspects indicated in Table 1. Wave climate is moderate-high energy, with mean significant wave height (H_{s0}) of 1.6 m, peak period (T_p) of 10 s, modally directed from the SE to SSE (Short and Treneman, 1992). Observed wave conditions during deployments are summarised in Table 1. Breaking wave height (H_b) and peak period were recorded by a pressure transducer immediately beyond the surfzone in 4-6 m depth.

DOI: 10.2112/SI75-084.1 received 15 October 2015; accepted in revision 15 January 2016.

*Corresponding author: jak.mccarroll@sydney.edu.au

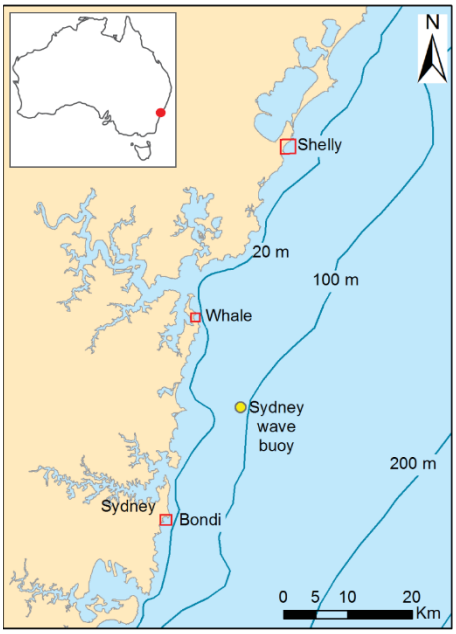

Figure 1. Location of Shelly, Whale and Bondi Beaches, site of Sydney wave buoy indicated

Offshore wave direction during observations (θ) was obtained from the Sydney Wave Buoy (Figure 1). Total number of drifter releases (n_{drift}) are indicated in Table 1.

Table 1. *Field location, wave and deployment summary*

Beach	Length (m)	Aspect	Date	H_b (m)	T_p (s)	θ	n_{drift}
Whale	600	E	4/10/12	0.9	13	60° S	293
Bondi	850	SSE	3/08/12	1.4	11	0°	136
Shelly	3000	SE	9/12/11	1.1	10	5° N	21

METHODS

Drifter specifications are found in McCarroll *et al*., (2014a, 2014b). Mean Lagrangian velocities (U_{mean}) were calculated as per MacMahan *et al*. (2010) for a grid size of 15 m x 15 m across all observations. Drifters sampled at 1 Hz (total observations), however a minimum of three drifter passes (independent observations) were required for estimates of velocity mean and variability.

A novel method for lowpass filtering that can be applied to Lagrangian data on non-uniform bathymetry is now briefly introduced. The method determines root-mean-square VLF velocity ($U_{RMS,VLF}$) or *variable eddy velocity*, calculated for discrete cells across the zone of drifter coverage. $U_{RMS,VLF}$ can be calculated from Eulerian data (MacMahan *et al*., 2004) as:

$$U_{RMS,VLF} = \sigma_U = \sqrt{u^2_{RMS,VLF} + v^2_{RMS,VLF}} \qquad (1)$$

where u and v are respectively the cross- and alongshore components of velocity, and σ is used throughout for standard deviation and σ^2 is variance. Note $U_{RMS,VLF} = \sigma_U$ for a bandpass filter, as mean velocity is zero. This can be obtained for Eulerian data through spectral analysis as

$$u_{RMS,VLF} = \sqrt{\sigma^2_{u,VLF}} = \sqrt{\int_{f_L}^{f_U} E_{uu}(f)\, df} \qquad (2)$$

where E_{uu} $(m^2 s^{-2} Hz^{-1})$ is the spectral density of cross-shore velocity as a function of frequency (f), f_L and f_U are the lower and upper frequency bounds of the VLF band (~2 h to 4 min; MacMahan *et al*., 2004) and $v_{RMS,VLF}$ is found similarly.

This method can be adapted to Lagrangian data on non-uniform bathymetry by: (i) calculating the mean velocity for a given grid cell (MacMahan *et al*., 2010); and (ii) determining variation about the mean using each lowpass drifter track through that cell as an instantaneous sample of VLF velocity. A 3rd degree lowpass Butterworth filter was employed with a cut-off 0.0067 Hz (150 s). Total variance using this method is

$$\bar{\sigma}^2_{u,VLF} = \frac{1}{N-1}\sum_{k=1}^{N}(u_{(k)VLF\ lowpass} - \bar{u})^2 \qquad (3)$$

where N is the number of total observations in a grid cell and $\bar{u}$ is the mean cross-shore velocity, with $\bar{u}$ calculated as a 2 h moving average to exclude the influence of tide on the flow variation. $\bar{\sigma}^2_{v,VLF}$ is calculated in a similar fashion, $U_{RMS,VLF}$ is then obtained using *(1)* and *(2)*. VLF directional standard deviation ($\sigma_{\theta,VLF}$) was calculated using a similar method.

A novel formulation for instantaneous VLF vorticity is introduced, taking the standard convention of vorticity (Γ [s^{-1}]) as twice the angular velocity (ω_{VLF}), which is the differential change in angle

$$\Gamma_{instant,VLF} = 2\,\omega_{VLF} = 2\frac{d\theta_{VLF}}{dt} \qquad (4)$$

In this instance, θ_{VLF} was calculated on a simple 3-point moving average over the VLF filtered drifter tracks, with dt equal to the 1 Hz sampling interval.

RESULTS

Flow characteristics for Whale, Bondi and Shelly Beaches are presented below.

Whale Beach

Analysis of Whale Beach (Figure 2) focusses on the mid-beach rip channel (x=100 m, y=300 m) and northern planar bar (y=360-560 m) as these illustrate contrasting degrees of bathymetric three-dimensionality and flow regimes. Drifter tracks of instantaneous velocity ($U_{instant}$; Figure 2a) highlight the mid-beach channel as a region of high velocities (up to 1 m s^{-1}), while $U_{instant}$ tracks across the northern bar are lower, but non-zero (up to 0.4 m s^{-1}), indicating the presence of transient currents (surfzone eddies). Instantaneous vorticity (Figure 2b), which describes the direction and magnitude of eddy rotation, indicates two large (~100 m) oppositely signed bathymetrically controlled vortices around the mid-beach channel. Over the planar northern bar, smaller eddies (~10's m) appear to have random direction of rotation. The mean velocity field (U_{mean}, Figure 2c) indicates high velocities in the mid-beach rip, however the northern bar region has near-zero mean velocities (<0.1 m/s).

The mid-beach rip-cell region has high (0.2 m/s) variable eddy velocities ($U_{RMS,VLF}$, Figure 2d), this includes the channel, bars and outside the surfzone. On the northern bar, $U_{RMS,VLF}$ is high within the surfzone (>0.15 m/s) and low beyond (<0.05 m/s). Directional variability ($\sigma_{\theta,VLF}$, Figure 2e) is low in the region of the deep mid-beach channel (<π/4) and high over the northern bar (~π/2), both within and outside the surfzone.

A Flow Type Parameter (ξ) is introduced as a visualisation aid for comparing the relative magnitude of mean flow (first term on right of [5]) against variable flow (last term in [5]). The various flow regimes identified by the spatial distribution of ξ (Figure 2f) are indicated in Table 2.

$$\xi(ms^{-1}) = U_{mean}\sin(\pi/2 - \sigma_{\theta,VLF}) - U_{RMS,VLF}\sin(\sigma_{\theta,VLF}) \quad (5)$$

To summarise, the deep mid-beach channel has a high mean flow, but also high velocity variability due to variable wave breaking, with wave convergence over the rip head bar observed in this region. The relatively low directional variability in the central channel indicates velocity pulsing is mostly dominant over directional changes, however multiple changes in flow direction from offshore to recirculation were observed (Figure 2a). By comparison, currents over the northern planar bar are summarised as having variable velocities and highly variable trajectories, with a near zero mean and random direction of eddy rotation (no vorticity bias). Given the absence of morphological control, these transient currents can be inferred to be driven by random wave breaking.

Table 2. *Flow regimes defined by Flow Type (ξ)*

Zone	$\sigma_{\theta,VLF}$	U_{mean}	$U_{RMS,VLF}$	Flow type (ξ)
Bar-rip morphology	→ 0	High	High	→ U_{mean}
Planar surfzone	→ $\pi/2$	→ 0	High	→ $(-U_{RMS,VLF})$
Low energy zone (offshore of north bar)	→ $\pi/2$	→ 0	→ 0	→ 0

Bondi Beach

A rip channel observed at Bondi Beach (Figure 3) is presented to illustrate a *weaker* degree of bathymetric control over flow. The channel was highly oblique to the shoreline and recent storms had flattened the inner-surfzone to some extent. Velocity tracks (Figure 3a) indicate two flow regimes through the central rip channel [x~100 m, y~450 m], (i) straight tracks with high velocities (>0.8 m/s); and (ii) tight eddies with low velocities (<0.2 m/s). $\Gamma_{instant,VLF}$ (Figure 3b) is strongly biased, despite the subdued morphology, to positive (counter-clockwise) along the margin of the oblique channel and is negative further north. Despite the intermittent high velocities, U_{mean} (Figure 3c) is low (<0.15 m/s) across most of the rip cell, due to variable currents cancelling out. $U_{RMS,VLF}$ (Figure 3d) and $\sigma_{\theta,VLF}$ (Figure 3e) are both high, indicating pulsing and trajectory changes. This rip channel is summarised as having highly variable velocities and trajectories, with a near zero mean flow across much of the cell.

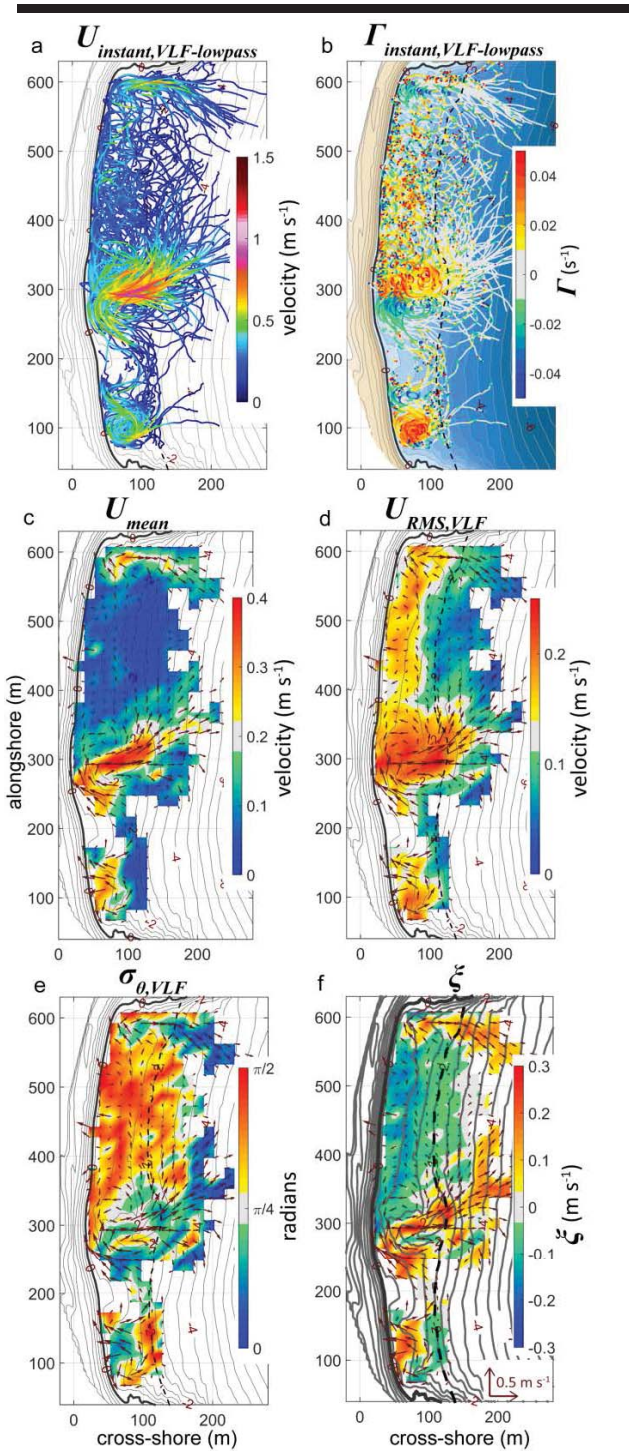

Figure 2. Whale Beach surf zone currents, including (a) instantaneous velocity; (b) instantaneous vorticity [positive is counter-clockwise]; (c) mean velocity; (d) variable eddy velocity; (e) directional standard deviation; and (f) Flow Type Parameter. Shoreline (z=0 m, MSL) is bold, -2 m contour (approximate surfzone edge) is bold-dashed. Extra bold contours in (f) for clarity.

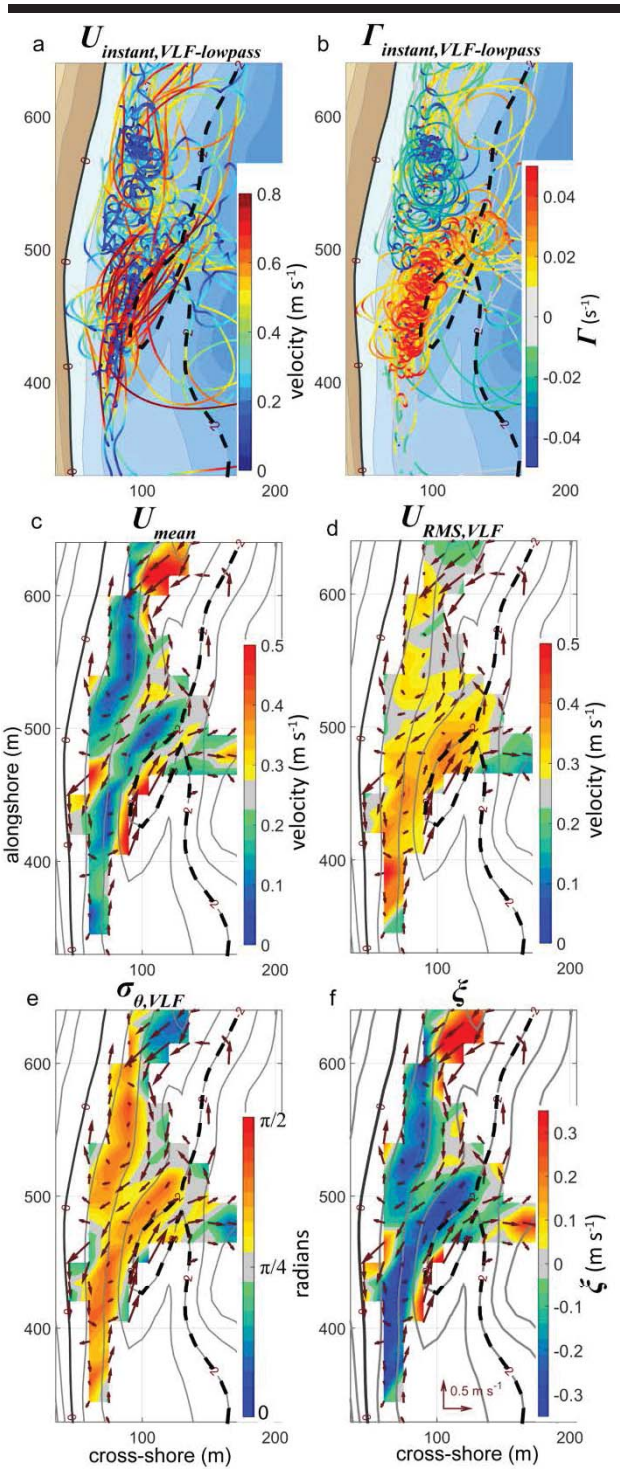

Figure 3: Bondi Beach surf zone currents, including (a) instantaneous velocity; (b) instantaneous vorticity; (c) mean velocity; (d) variable eddy velocity; (e) directional standard deviation; and (f) Flow Type Parameter. Shoreline (z=0 m, MSL) is bold, -2 m contour is bold-dashed to emphasise the rip channel. Surfzone limit at approx. x=200 m

Therefore ξ (Figure 3f) is strongly negative. However the biased vorticity (Figure 3b) differentiates this flow regime from a planar beach (*e.g.* northern bar at Whale Beach, Figure 2b).

Shelly Beach

A rip channel observed at Shelly Beach (Figure 4) is presented to illustrate a *stronger* degree of bathymetric control over flow. The observed channel had a depth (relative to adjacent bar) of only ~0.5 (cf. > 1 m, Whale mid-beach channel). The feeder and rip-neck were oriented at approximately +/-45°, resembling the rotation of the overlying rip cell. $U_{instant}$ tracks (Figure 4a) indicate high instantaneous velocities (up to 0.8 m/s) at the outer edges of the cell. Vorticity (Figure 4b) is uniformly positive (counter-clockwise) with the centre of the rip cell appearing to oscillate along the -1.5 m contour. U_{mean} (Figure 4c) is high (0.5 m/s), though is lower at the centre of the rip cell.

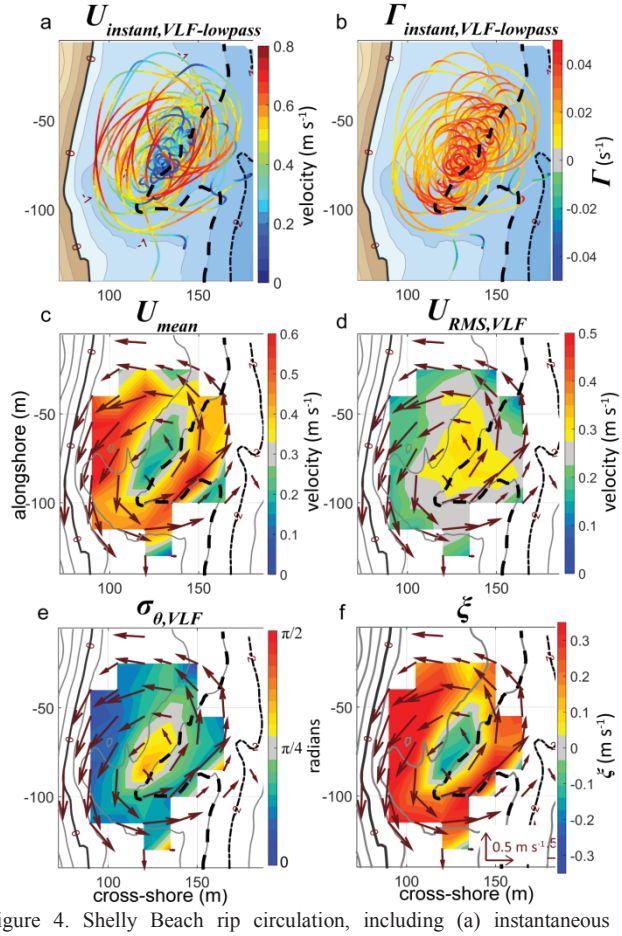

Figure 4. Shelly Beach rip circulation, including (a) instantaneous velocity; (b) instantaneous vorticity; (c) mean velocity; (d) variable eddy velocity; (e) directional standard deviation; and (f) Flow Type Parameter. Shoreline (z=0 m, MSL) is bold, -1.5 m contour is bold-dashed to emphasise the rip channel. Surfzone limit at z=-2 m.

$U_{RMS,VLF}$ (Figure 4d) is highest (0.3 m/s) at the oscillating centre of the rip cell and $\sigma_{\theta,VLF}$ is very low (<π/8) away from this point. This rip cell is summarised as having a strong mean flow with variability mostly due to oscillation of the rip cell. Therefore ξ (Figure 3f) is strongly positive, indicating a high degree of bathymetric control. No surfzone exits were observed from this flow.

DISCUSSION

The spectrum of observed flow regimes are summarised in Table 3. These are ranked according to relative magntitude of the mean flow in comparison with the variable flow. *Strong* bathymetric control (*e.g.* Shelly Beach, Figure 4) is characterised by a dominant mean flow wth minimal changes in trajectory, where variability is related to oscillations of the rip cell along the bar-channel interface, similar to the conceptual model of MacMahan *et al*. (2004). *Moderate* bathymetric control (*e.g.* Whale Beach mid-beach rip, Figure 2) also has a strong mean flow and vorticity bias at the centre of rip cells adjacent to the channel, but trajectories exhibit greater variability, with flow varying between exit flow and rotation, similar to many recent observations (*e.g.* MacMahan *et al*., 2010). *Weak* control (*e.g.* Bondi Beach, Figure 3) is characterised by low mean flows over much of the rip cell, with high velocity variability and directional variability, though in this instance, the shallow oblique channel was sufficient to strongly influence the direction of rotation (vorticity bias). Finally, absent bathymetric control is synonymous with transient currents, where mean velocity is near-zero and vorticity is randomly oriented, comparable with previous observations (*e.g.* Johnson and Pattiaratchi, 2006).

Table 3. *Degree of bathymetric control of VLF flow behaviour*

Degree	Example	Vorticity bias*	Flow type (ξ)**
Strong	Shelly	Strong Bias	++
Moderate	Whale (mid-rip)	Bias	+
Weak	Bondi	Bias	-
Absent	Whale (planar bar)	Random	- -

** Degree that bathymetry forces a **bias** in flow rotation direction*
*** Flow Type from strong positive (++) to strong negative (--)*

The role of channel orientation requires further investigation, with oblique channels (*e.g.* Bondi) potentially related to weak bathymetric control, while +/-45° channels (*e.g.* Shelly) may be related to strong control. Other important factors not considered here are wave characteristics and channel spacing. Future efforts will incorporate these factors and additionally will attempt to: (i) establish a statistical correlation between bathymetric non-uniformity and flow variability; and (ii) non-dimensionalise the Flow Type Parameter.

CONCLUSIONS

This study has presented a novel conceptual classification of rip types based on degree of bathymetric control. In particular, strong bathymetric control is characterized by high mean velocities and rip cell oscillation, while weak bathymetric control manifests as low mean velocities and mobile, directionally biased eddies.

While many Lagrangian studies of channelised rip currents examine mean flow, few studies until now have adequately examined the short-term spatial variability of flow. This is relevant as flow variability can impact on the hazard presented to bathers (McCarroll *et al*., 2014a), but may also provide new insights on the sediment transport and dispersion characteristics of rip currents.

ACKNOWLEDGMENTS

This project was funded by Australian Research Council (ARC) Linkage Project LP110200134 and Surf Life Saving Australia. Many thanks to fieldwork volunteers; Waverly, Pittwater and Wyong council lifeguards and the Australian Lifeguard Service. Sydney wave buoy data provided by Manly Hydraulics Lab on behalf of the NSW Office of Environment and Heritage.

LITERATURE CITED

Bowen, A.J. and Inman, D.L., 1969. Rip currents: 2. Laboratory and field observations. *Journal of Geophysical Research* 74(23), 5479-5490.

Castelle, B.; Michallet, H.; Marieu, V.; Leckler, F.; Dubardier, B.; Lambert, A.; Berni, C.; Bonneton, P.; Barthélemy, E. and Bouchette, F., 2010. Laboratory experiment on rip current circulations over a moveable bed: Drifter measurements. *Journal of Geophysical Research* 115(C12008). doi: 10.1029/2010jc006343.

Feddersen, F., 2014. The Generation of Surfzone Eddies in a Strong Alongshore Current. *Journal of Physical Oceanography* 44(2), 600-617.

Johnson, D. and Pattiaratchi, C., 2006. Boussinesq modelling of transient rip currents. *Coastal Engineering* 53(5), 419-439.

MacMahan, J.; Brown, J.; Brown, J.; Thornton, E.; Reniers, A.; Stanton, T.; Henriquez, M.; Gallagher, E.; Morrison, J.; Austin, M. J.; Scott, T. M. and Senechal, N., 2010. Mean Lagrangian flow behavior on an open coast rip-channeled beach: A new perspective. *Marine Geology* 268(1), 1-15.

MacMahan, J. H.; Reniers, A. J.; Thornton, E. B. and Stanton, T. P., 2004. Surf zone eddies coupled with rip current morphology. *Journal of Geophysical Research* 109(C7). doi:10.1029/2003JC002083.

MacMahan, J. H.; Thornton, E. B.; Reniers, A. J.; Stanton, T. P. and Symonds, G., 2008. Low-energy rip currents associated with small bathymetric variations. *Marine Geology* 255(3), 156-164.

McCarroll, R. J.; Brander, R. W.; MacMahan, J. H.; Turner, I. L.; Reniers, A. J. H. M.; Brown, J. A.; Bradstreet, A. and Sherker, S., 2014a. Evaluation of swimmer-based rip current escape strategies. *Natural Hazards* 71(3), 1821-1846.

McCarroll, R. J.; Brander, R. W.; Turner, I. L.; Power, H. E. and Mortlock, T. R., 2014b. Lagrangian observations of circulation on an embayed beach with headland rip currents. *Marine Geology* 355, 173-188.

Peregrine, D., 1998. Surf zone currents. *Theoretical and computational fluid dynamics* 10(1-4), 295-309.

Short, A. D. and Trenaman, N., 1992. Wave climate of the Sydney region, an energetic and highly variable ocean wave regime. *Marine and Freshwater Research* 43(4), 765-791.

Journal of Coastal Research	SI	75	423-426	Coconut Creek, Florida	2016

Small Scale Bedform Types off the South-Holland Coast

Saulo Meirelles[†*], Martijn Henriquez[†], Alejandro J. Souza[‡], Alexander R. Horner-Devine[§], Julie D. Pietrzak[†], Sabine Rijnsburg[†], Marcel J. F. Stive[†]

[†]Hydraulic Engineering Department
Delft University of Technology
Delft, the Netherlands

[‡]National Oceanography Center
Liverpool, United Kingdom

[§]Department of Civil and Environmental Engineering
University of Washington
Seattle, USA

www.cerf-jcr.org

www.JCRonline.org

ABSTRACT

Meirelles, S.; Henriquez, M.; Souza, A.J.; Horner-Devine, A.R.; Pietrzak, J.D.; Rijnsburg, S., and Stive, M.J.F., 2016. Small scale bedform types off the South Holland coast. *In:* Vila-Concejo, A.; Bruce, E.; Kennedy, D.M., and McCarroll, R.J. (eds.), *Proceedings of the 14th International Coastal Symposium* (Sydney, Australia). *Journal of Coastal Research*, Special Issue, No. 75, pp. 423-426. Coconut Creek (Florida), ISSN 0749-0208.

This study presents the small scale bedform states found off the South-Holland coast during a 31+ days field observation of seabed acoustic imagery and near the bed velocities. Six main bed states were encountered: current ripples (C), wave ripples (W), combined wave-current ripples (WC), current ripples with subordinate wave ripples (Cw), wave ripples with subordinate current ripples (Wc) and poorly developed ripples (P). Direct visual detection of the bed state from the images showed good agreement with a simple predictor based on the mobility number. The most frequent type of bedform was C which is governed by the tidal currents. Wave ripple prevailed only during a storm with waves higher than 2 m. The combined Cw, WC and Wc types comprised 22% of the occurrences. Poorly developed ripples were associated with the neap tide during fair weather conditions.

ADDITIONAL INDEX WORDS: W*ave-current bedforms, bedform classification, Sand Engine.*

INTRODUCTION

The hydrodynamic forcings over the seabed moulds the bed material. The resulting morphology directly affects the overlying boundary layer and hence plays a fundamental role in the sediment load. The types of bedform can reveal important information on how the typical hydrodynamic regimes dictate sediment mobility.

Following the analysis of Amos *et al.* (1988) and later Smyth and Li (2005), the bedforms are categorized in this work as follows: current ripples (C), wave ripples (W), combined wave-current ripples (WC), current ripples with subordinate wave ripples (Cw), wave ripples with subordinate current ripples (Wc) and poorly developed ripples (P). The occurring ripple patterns define the bed roughness which is of importance not only to sediment transport processes but also to biological and chemical processes that take place on the seafloor (Traykovski, 2007).

This study aims at classifying the small scale bed states under mixed flow conditions found off the South-Holland coast (Figure1) through field observations. Visual identification of the bed states is compared to the wave-induced flow and the rotating tidal currents using the instantaneous mobility numbers. The mobility number is chosen here because it is independent on the bed morphology and hence it minimizes the uncertainties introduced by reducing the bed properties into a single parameter such as the friction factor.

Study area

The measurements took place in the South–Holland coast during the fall 2014. The nearly alongshore uniform sandy coast is interrupted by a bell-shaped localized mega-nourishment (Figure 1). The Sand Engine (or *Zandmotor* in Dutch), as it is called, currently stretches 1 km offshore. Its role is to feed the adjacent coast by letting the main environmental agents redistribute the sand (Stive *et al.*, 2013).

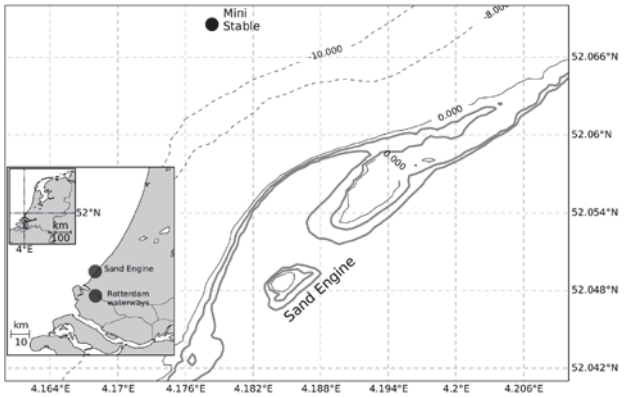

Figure 1. Study area. The inset shows the Netherlands within the Holland Coast with the Sand Engine and Rotterdam waterways locations. The bed frame, Mini Stable, was deployed at 12 m depth.

The region is also influenced by a coastal plume that outflows from the Rotterdam waterways. When present, the plume changes the tidal ellipse such that the semi-minor axis (*i.e.*, cross-shore velocity component) undertakes a substantial increase (De Boer *et al.*, 2006; Souza and Simpson, 1997; Visser *et al.*, 1994). Thus during stratified periods the rotation of the tidal currents is more pronounced (Souza and Simpson, 1996).The hydrodynamics off the South-Holland coast is mostly governed by the alongshore tidal current which is dictated by the semi-diurnal constituent, M_2. The maximum flood and ebb currents fluctuate about 30% over a spring-neap cycle. Winds

DOI: 10.2112/SI75-085.1 received 15 October 2015; accepted in revision 15 January 2016.
*Corresponding author: s.meirellesnunesdarocha@tudelft.nl

are important not only in inducing flow but also in controlling the coastal plume dynamics. In the cross-shore, waves are occasionally dominant, in particular during winter storms.

METHODS

In the fall 2014, a multi-disciplinary field experiment, MegaPEx/STRAINS II, was carried out in the vicinities of the Sand Engine (Figure 1) where a benthic frame (Mini Stable) was deployed at 12 m depth together with a suit of instruments meant to collect information about the hydrodynamics throughout the water column, sediment concentration and bedforms. The instruments acquired data for 31 days.

Near the bed velocities were measured at 0.25, 0.50 and 0.75 m above bottom (mab) at high sampling rate. Wave-induced flow at 0.25 mab, $\widehat{U}_{0.25}$, was obtained according to Shaw and Trawbridge (2001) method so that:

$$\widehat{\boldsymbol{U}}_{0.25} = \boldsymbol{A}\widehat{h}. \quad (1)$$

Where $\boldsymbol{A}$ is a windowed data matrix containing the velocities at 0.75 mab with length equal to the number of points of one-half of the peak period. The filter weights are given by $\hat{h}$ that is equal to $(\boldsymbol{A}^T\boldsymbol{A})^{-1}\boldsymbol{A}^T\boldsymbol{U}_{0.25}$.

Seafloor images were acquired using an Acoustic Ripple Profiler (ARP) that provided bed height over a circular area of approximately 11 m^2. The ARP scanned the bed at every hour operating at 1.1 MHz.

The images were interpolated to the Cartesian plane and corrected for the bed slope. Only the rectangle circumscribed to the circular scanned area was considered to the analysis in order to reduce the poor resolution of the image edges and noise generated by the frame's legs.

The bed states were first determined by visual observation. Two operators classified the images independently according to Amos *et al.* (1988). The criterion of classification was based on the ripples geometry, orientation and length, for example, as shown in Figure 2. The discrepancies that resulted from both classifications were small and were adjusted based on the hydrodynamic information. Most of the differences occurred during mixed bed states especially Cw and WC types.

The instantaneous mobility number was also used to categorize the bed types. The mean absolute velocities, obtained by subtracting wave-induced flow from the total velocity ($\overline{\boldsymbol{U}}_{0.25} = \boldsymbol{U}_{0.25} - \widehat{\boldsymbol{U}}_{0.25}$), was used to calculate the mobility number that reads:

$$\psi_c = \frac{\overline{\boldsymbol{u}}_{0.25}{}^2 + \overline{\boldsymbol{v}}_{0.25}{}^2}{(s-1)g d_{50}}. \quad (2)$$

Where $\overline{\boldsymbol{u}}_{0.25}$ and $\overline{\boldsymbol{v}}_{0.25}$ refer to the cross- and alongshore components, s is the ratio of particle to water densities, g is acceleration due to gravity and $d_{50}$is the median grain size from samples collected during the experiment (≈0.350 mm).

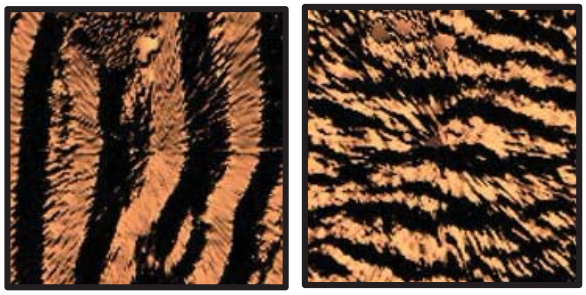

Figure 2. Example of wave ripple, W, (left panel) and current ripple, C, found off South-Holland coast.

In a similar fashion, the mobility number for waves, ψ_w, was computed. The logarithm of the ratio between $\psi_{rms,w}$ and $\psi_{rms,c}$ was used to evaluate the conditions for the formation of wave and current bedform types analogous to the approach presented by Amos and Collins (1978).

RESULTS

The measurements encompassed two neap-spring cycles. The wind speed during the measurement period was 6±3 m/s mainly from South quadrant during fair weather conditions. The wave height was 0.6 m on average with direction varying basically between N and W. The average peak wave period was 6 s. One significant episodic event was captured where waves reached more than 2 m height and the wind blew at 16 m/s.

From the visual identification of the bed, current-formed ripples predominated throughout the series followed by poorly developed ripples (Figure 3). Amos *et al.* (1988) characterized the former ripple pattern based on the stationarity of the crests from frame to frame. Wave ripples occurred the least number of times being associated with the passage of storm. Intermediate states of ripple geometry prescribed about 22% of the recognized types.

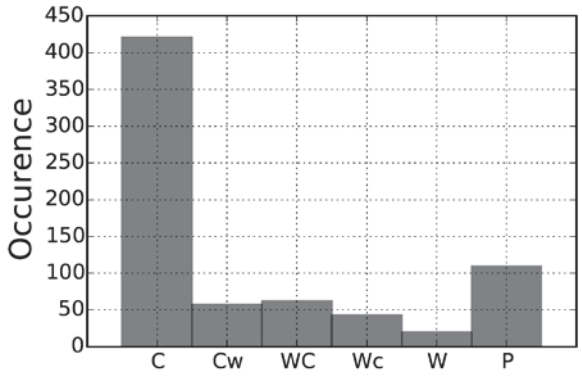

Figure 3. Bed type occurrence from visual observation.

.

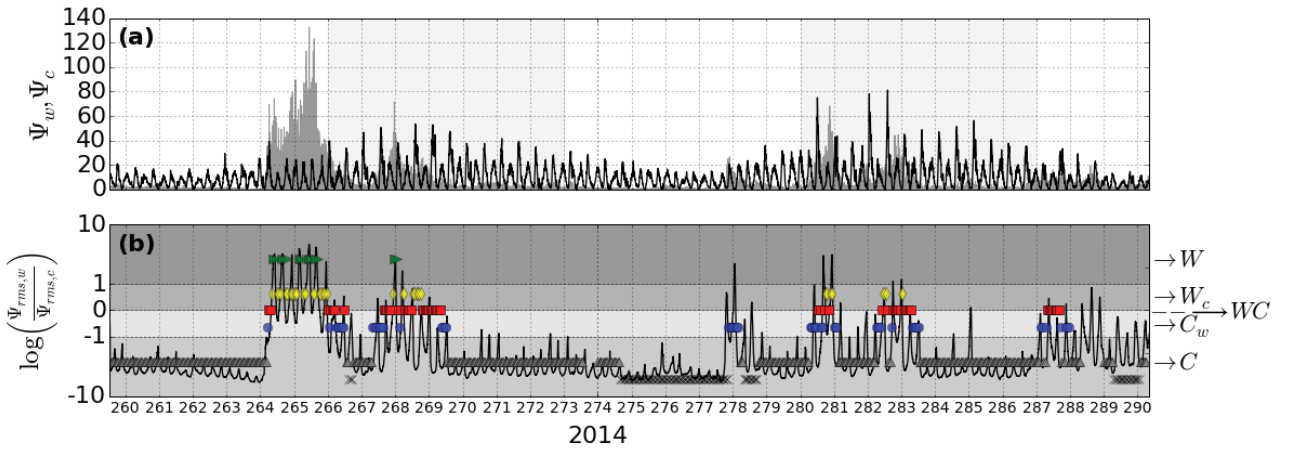

Figure 4. (a) time series, in days of 2014, of the wave and current mobility numbers. The hatched areas depict the spring tide periods. (b) series of the logarithm of the ratio between $\psi_{rms,w}$ and $\psi_{rms,c}$ compared to the results from the visual observation. The green , yellow, red, blue, gray and black marks correspond to W, Wc, WC, Cw, C and P respectively.

The current mobility number not only exhibited semi-diurnal dependence but also revealed a coherent fortnight oscillation as expected (Figure 4a). The wave mobility number predominated between days 264 and 265 reaching values over 120 which were about 5 times greater than the current counterpart. Although the current mobility number appeared to prevail, the wave mobility number presented similar magnitude during four different periods through the record

Figure 4b depicts the comparison between the $\log(\psi_{rms,w}/\psi_{rms,c})$ and the bed types resulted from the visual observation. There was a general agreement between both approaches. The majority of curve lies below -1 indicating the high occurrence of C and P. Values greater than 1 encompassed the wave-formed ripples. All the intermediate bed states were within -1 and 1. Remarkably, a persistent semi-diurnal fluctuation was observed (Figure 4b) denoting how important the tidal currents are in the region. Poorly developed ripples were mostly observed during fair weather conditions in neap tides.

DISCUSSION

The dominant type of small scale bedform found off South-Holland was current-generated ripple. On the contrary, Traykoviski *et al.* (1999) observed a dominance of wave orbital scale ripples at similar depth. Also, Smyth and Li (2005) identified predominantly W and W_c types of ripples, at depths greater than 20 m, on Sable Island Bank. Those evidences reflect the role of the waves in exposed coastal areas where the incident waves are dominant which is not the case in the North Sea where most of the incident waves are wind-sea waves.

Nonetheless, during episodic events, waves were responsible to quickly reorganize the bed morphology which likely led to hysteresis during the following waning conditions. Figure 5 shows an occurrence of wave-formed ripples observed during the field campaign. The interaction of the waves with bottom also relied on the tidal stage in which most of the wave ripples were more evident at ebb tide and slack water. Due to the tidal asymmetry along the Dutch coast, the ebb currents are smaller. Moreover, the low water level facilitates the interaction of shorter waves with the bed.

Purely current ripples were clearly tidal driven although wind-driven flow might be important too but it was not considered in the present study. The bed morphology did not experience significant changes in neap tides with calm conditions when poorly developed ripples were encountered.

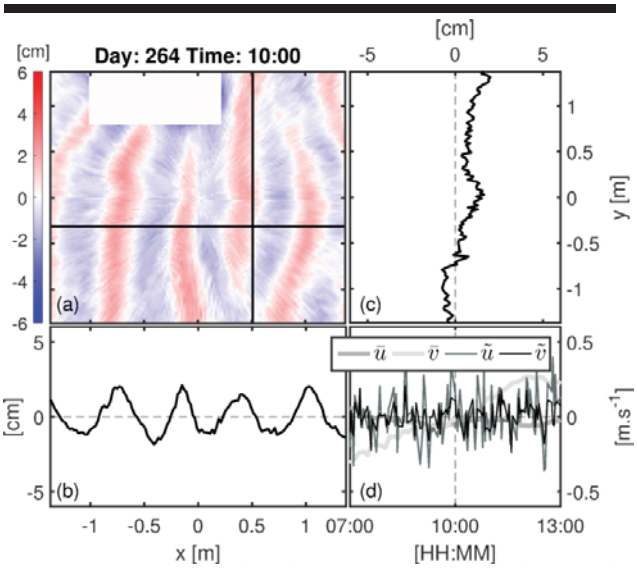

Figure 5. (a) post-processed sea bed image acquired with the ARP. (b) longitudinal section of the image. (c) latitudinal section of the image. (d) cross- and along shore mean flow ($\bar{u}$ and $\bar{v}$) and cross- and along shore

wave-induced flow ($\tilde{u}$ and $\tilde{v}$). The frame's leg interference was cut in the image as seen by the white rectangle.

The intermediate bed states altogether comprise the second highest bed state occurrences. This indicates the importance of the combined action of wave and currents on the bed morphology at the location. However, those transitional bed states were difficult to classify properly as seen in Figure 4b. This is especially true after wave events when the bed restauration suffers a delay as reported by Traykoviski (2007).

The dimensionless mobility number ratio used here seems to perform poorly when the ripples are not in equilibrium with the hydrodynamic forcings. Therefore the thresholds stablished (between -1 and 1) for C_w, WC and W_c types are possibly not fixed but dependent on ripple length information. Despite of limitations, the visual classification based on the ARP images presented a good agreement with the dimensionless mobility number ratio.

CONCLUSIONS

This study classified the small scale bedforms found offshore the South Holland coast. The bedforms were separated into 6 categories: current ripples (C), wave ripples (W), combined wave-current ripples (WC), current ripples with subordinate wave ripples (Cw), wave ripples with subordinate current ripples (Wc) and poorly developed ripples (P). The method based on direct visual detection from the seabed images were compared to a simple ripple predictor based on the relation between the wave and current rms mobility number.

The results showed that current ripples, C, are dominant throughout the series. The frequency of occurrence of transitional bed types (C_w, WC and W_c) combined ranked second. Those types were normally associated with rapid change of the bed morphology and more complex ripple patterns.

Most of the poorly developed ripples were found during neap tide, while the bed activity is more prominent during spring tide. This reinforces the findings by Henriquez *et al.* (in prep.) that most of the transport processes at the location take place during spring tide.

The dimensionless mobility number ratio appeared to be a simple and quick way to assess the bed states found in the offshore South Holland. Since the wave action was not persistent, relict ripples were not a regular feature hence it may have been that in most of the cases the ripples were in (quasi-) equilibrium with the hydrodynamic agents.

ACKNOWLEDGMENTS

The authors would like to thank the EU Research Council for funding this research, through the NEMO project. The authors are indebted to prof. Alejandro Souza for providing the instrumentation and the technicians. We also would like to thank Maggie McKeon, Richard Cooke, Christopher Balfour for providing valuable expertise in the field. Our gratitude also to Rijkswaterstaat for making available R/V Arca and R/V Zirfaea and their crew for the realization of the field work.

LITERATURE CITED

Amos, C.L. and M.B. Collins, 1978. The combined effects of wave motion and tidal currents on the morphology of intertidal ripple marks: the Wash, UK. *Journal of Sedimentary Research* 48.3.

Amos, C.L.; Bowen, A.J.; Huntley, D.A., and Lewis, C.F.M., 1988. Ripple generation under the combined influences of waves and currents on the Canadian continental shelf. *Continental Shelf Research*, *8*(10), 1129-1153.

De Boer, G.J.; Pietrzak, J.D., and Winterwerp, J.C., 2006. On the vertical structure of the Rhine region of freshwater influence, 198-216. *Ocean Dynamics*, 56, 3-4.

Souza, A.J. and Simpson, J.H. 1996. The modification of tidal ellipses by stratification in the Rhine ROFI. *Continental Shelf Research*, 16(8), 997–1007.

Souza, A.J. and J.H. Simpson; 1997. Controls on stratification in the Rhine ROFI system, *Journal of Marine Systems*, 12, 311-323.

Smyth, C.E. and Li, M.Z., 2005. Wave-current bedform scales, orientation, and migration on Sable Island Bank. *Journal of Geophysical Research: Oceans* (1978–2012), 110(C2).

Stive, M.J.F.; de Schipper, M.A.; Luijendijk, A.P., Aarninkhof, S.G.J.; van Gelder-Maas, C.; van Thiel de Vries, J.S.M.; de Vries, S.;, Henriquez, M.; Marx, S., and Ranasinghe, R., 2013. A new alternative to saving our beaches from local sea-level rise: the sand engine. *Journal of Coastal Research*, 29(5), 1001–1008.

Traykovski, P.; Hay, A.E.; Irish, J.D.; and Lynch, J.F., 1999. Geometry, migration, and evolution of wave orbital ripples at LEO-15. *Journal of Geophysical Research: Oceans* (1978–2012), 104(C1), 1505-1524.

Traykovski, P., 2007. Observations of wave orbital scale ripples and a nonequilibrium time-dependent model. *Journal of Geophysical Research: Oceans* (1978–2012), 112(C6).

Visser, A.; Souza, A.J.; Hessner, K., and Simpson, J.H., 1994. The effect of stratification on tidal current profiles in a region of freshwater influence. *Oceanologica Acta*, 17, 369-381

Journal of Coastal Research	SI	75	427-431	Coconut Creek, Florida	2016

Morphodynamic Processes on a Macrotidal Beach in the Eastern Amazon

Anderson T. do Nascimento[†] and Luci C. C. Pereira[†*]

[†]Institute for Coastal Studies,
Estuarine and Coastal
Oceanography Laboratory

www.cerf-jcr.org

www.JCRonline.org

ABSTRACT

Nascimento, A. T. and Pereira, L.C.C., 2016. Morphodynamic Processes on a Macrotidal Beach in the eastern Amazon. *In:* Vila-Concejo, A.; Bruce, E.; Kennedy, D.M., and McCarroll, R.J. (eds.), *Proceedings of the 14th International Coastal Symposium* (Sydney, Australia). *Journal of Coastal Research*, Special Issue, No. 75, pp. 427-431. Coconut Creek (Florida), ISSN 0749-0208.

This study analyzes the spatial and temporal variation in the morphodynamic processes and states of a macrotidal beach. Two intensive campaigns (9 days under spring/neap tide condition) were conducted to determine wave and weather conditions, in November/December 2013 (end of the dry season, characterized by strong winds) and March/April 2014 (rainy season, equinoctial period). Topographic surveys of two beach profiles were also conducted during the study period. Surface sediment samples were collected along each beach profile. Sediment grain sizes were later determined by laser diffraction. Ajuruteua is a sandy beach characterized by macrotides (up to 6.0 m), moderate wave energy (H_s of as much as 2.0 m), and strong winds (mean velocities of up to 4.5 m s^{-1}). The beach is sheltered from waves by sandbanks and sandbars around low tide during both neap and spring tides. This results in a delay in the flood tide in the inshore areas, resulting in the prolongation of the ebb tides, primarily during the equinoctial period. During this period, modal breaker heights on Ajuruteua beach were minimal (H_b < 0.2), which, due to the longer ebb tides, combined with the higher tidal range, resulted in a scenario of tide-dominated tidal flats. By contrast, during neap tides an ultradissipative state dominated. Our results indicate that the characteristics of Ajuruteua beach are influenced primarily by macrotides and moderate wave energy, although the influence of the waves is restricted to the period around high tide, when the water is propagated towards the shoreline.

ADDITIONAL INDEX WORDS: *Morphodynamics, macrotidal beach, Amazon littoral.*

INTRODUCTION

Coastal regions are highly dynamics environments, which are being modified constantly on different scales of time and space, but are also extremely sensitive and stable. This makes the identification of the factors that determine changes in the coastline a major challenge. Coastal areas have inestimable environmental value and play an important socio-economic role in local communities (Belfiore, 2003; Houser, 2010; Masson and Delecluse, 2001).

Beaches are dynamic sedimentary coastal systems that are the product of meteorological and oceanographic processes and forces, such as winds, waves, tides, and sediments, which interact with one another, resulting in complex hydrodynamic and depositional processes (Brown and McLachlan, 1990).

Despite occupying only a narrow strip of land and an ample distribution, these environments are responsible for the protection of the coastal zone and the dynamics of this environment determine the process of the geomorphological construction and reconstruction of the coastline, contributing to the development of sandy beaches, and the processes of erosion and deposition that maintain these environments in a constant state of change. Beaches are appropriate areas for a number of leisure and recreational activities, as well as the development of other economic sectors (Braga *et al*., 2007; Small and Nicholls, 2003; Souza Filho *et al*., 2005).

In this context, given the range of natural and/or anthropogenic pressures that affect beaches, these environments are highly susceptible to different processes of degradation and situations of risk, especially marine erosion. Over the past few decades, erosive processes are becoming increasingly common in many coastal areas around the world. Given this, studies that investigate coastal morphology and the processes that determine these features are increasingly important (Albuquerque *et al.,* 2011; Barnard *et al.,* 2012; Kroon and Masselink, 2002; Monteiro *et al*., 2009; Small and Nicholls, 2003; Vicinanza *et al*., 2011).

A number of studies have focused on the morphodynamic processes of the sandy beaches of the Amazon coast, which are affected by varying patterns of tidally modulated wave energy. However, none of these studies have considered the variation between spring and neap tides. Given this, the present study investigated the spatial and temporal variation in the morphodynamic state and processes of a macrotidal Amazonian beach during neap and spring tide periods during the local rainy and dry seasons.

STUDY AREA

Ajuruteua Beach – the study area – is located on the Bragança coastal plain 36 km from the town of Bragança, and is approximately 2.5 km long and 300 m wide (Figure 1). This beach is bordered by the Caete and Taperaçu estuaries, and an

DOI: 10.2112/SI75-086.1 received 15 October 2015; accepted in revision 15 January 2016.
*Corresponding author: cajueiro@ufpa.br

extensive area of mangrove, which covers 95% of the coastal area (Pereira *et al*., 2006, 2007; Souza Filho *et al.,* 2004).

The study area is located on the Salgado region of the Atlantic coast of the Brazilian state of Pará, which covers an area of 16,215 km², equivalent to 19.5% of the total area of the state's coastal zone, specifically the Bragança plain, which coincides with the coastal zone of the municipality of Bragança, which stretches from the Cape of Maiau to the mouth of the Caete River, and covers an area of 1570 km² (Souza Filho *et al.*, 2004; Szlafsztein, 2005). This coast has a NW-SE orientation, and is extremely indented, with inlets that may reach 45 km inland, and unique geomorphological characteristics, such as extensive tidal plains (mangroves), estuaries, salt marshes, cheniers, dunes, and sandy beaches (Souza Filho *et al*., 2005; Szlafsztein, 2005).

This region is dominated by semi-diurnal macrotides, with spring tides reaching up to 4–6 m, and the principal tides are spring tides, although there may be moderate wave energy during high tide, with wave heights (H_s) normally between 1.0 m and 1.5 m (Pereira *et al.*, 2012a, 2012b).

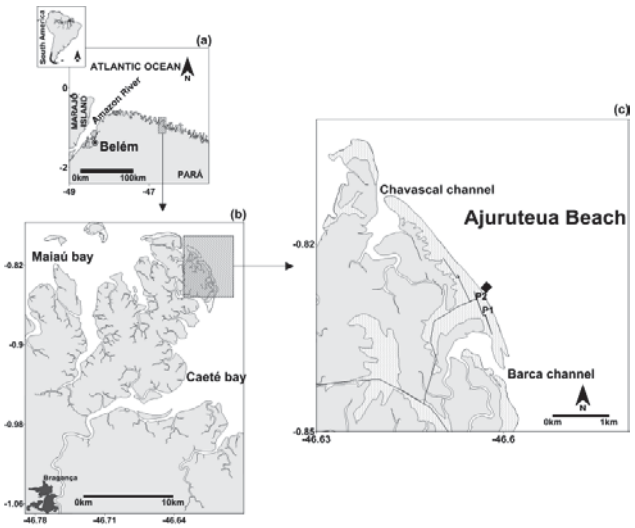

Figure. 1. Study area, showing the data collection points. (a) Pará coast, (b) Bragantinian plain and (c) Ajuruteua beach. Location of the study profiles (P1 and P2); ◆ indicates the site at which the oceanographic apparatus was moored.

The tidal currents run NW-SE during the flood and SE-NW in the ebb, reaching mean velocities of more than 0.5 m/s. Significant wave heights (H_s) are modulated by the sandbanks and bars adjacent to the study beach, and may exceed 1 m during the high tide, and approximately 0.2 m during low tide (Monteiro *et al*., 2009; Pereira *et al*., 2009). The surf zone is of the spilling type, with waves breaking on two or more sandbars parallel to the line of the beach (Alves and El-Robrini, 2006).

The region's climate is hot and humid equatorial, with a distinct rainy season between December and May, and a dry season during the rest of the year. Mean annual precipitation is normally between 2400 and 2700 mm, of which, 85% is recorded during the rainy season. Given its proximity to the equator, this region is not subject to any major fluctuations in temperature, with an annual mean between 25ºC and 27ºC (Martorano *et al*., 1993).

METHODS

The present study was divided into two intensive field campaigns, during which the meteorological and oceanographic conditions were analyzed, in (i) November-December 2013 (end of the dry season, period of strong winds), and (ii) March-April 2014 (rainy season), with data being collected over a 10-day period between the neap tide and the spring tide. A TWR-2050 tidal sensor was bottom-moored at a depth of ~ 2.0 m at low tide, with mean data being collected every 10 min. The tidal height was corrected by the reduction level (lowest possible height at low tide), provided by the Department of Hydrography and Navigation (DHN) of the Brazilian Navy.

The climatological data (wind and precipitation) for the study months were obtained from the Salinopolis station of the Brazilian National Meteorological Institute (INMET) for the period between July 2013 and April 2014.

Two topographic profiles were investigated – P1, a deposition profile in the SE sector, and P2, an erosive profile in the NW sector. The Stadia topographic method of Birkemeier (1981) was used to collect data. Samples of surface sediments were collected simultaneously with the topographic readings at the points of inflexion of the beach profile at intervals of 20 m or according to the morphological variation of the shore. In the laboratory, the samples were processed using a Mastersize Hydro 2000G laser particle analyzer (Malvern). The values obtained were analyzed statistically using the equations proposed by Folk and Ward (1957) in the SYSGRAN program (Camargo, 1999).

Morphodynamic parameters were described and quantified through the integrated analysis of the hydrodynamic and morpho-sedimentary data collected at the study beach, based on the models developed for macrotidal beaches in Australia. The relative tidal range (RTR) relates the tidal range (TR) with the height of the waves in the surf zone (H_b). The parameter is given by:

$$RTR = \frac{TR}{Hb}$$

Dean's (1973) Dimensionless Omega Parameter is also necessary for the differentiation of the morphodynamic state of the beach, and was calculated by:

$$\Omega = \frac{Ws}{HbT}$$

where, H_b = significant breaker height, T = significant breaker period, W_s = mean fall velocity.

RESULTS

Climate

The region's climate is divided into two well-defined seasons, rainy and dry. During the field campaigns (Figure 2), November and December 2013 were considered representative of the dry season, given the extremely low precipitation rates recorded during these months (< 15 mm in November and ~100 mm in

December). In March and April 2014, by contrast, precipitation exceeded 900 mm, and was thus characteristic of the rainy season. March was the month with the highest rainfall (1238 mm).

Hydrodynamic Conditions

The morphodynamics of Ajuruteua beach is modulated by the seasonal variation in wave height, together with the semi-diurnal and lunar (spring and neap tides) tidal cycle and seasonal variation in the tidal range (Figure. 3). Tidal oscillation on the beach increased by up to 6 m during the spring high tide in April (equinoctial period in the rainy season) and November/December (strong wind speeds), permitting offshore waves with longer periods to cross the sandbanks and surf zone and reach the beach, while at low tide, the exposure of the sandbanks eliminates offshore waves and only permits waves of short fetch to reach the beach at low tide. As a consequence, the height of breaking waves varied from a maximum of 2.0 m at high tide (associated to T_p of 8s) in the equinoctial period of the rainy season to a minimum of 0.1 m at low tide, resulting in considerable variation in wave heights and surf zone morphodynamics with each tidal cycle. The tides were asymmetric, with a much shorter flood period (~4.4 h to ~6 h) and a longer ebb (~5.4 h to 6.4 h).

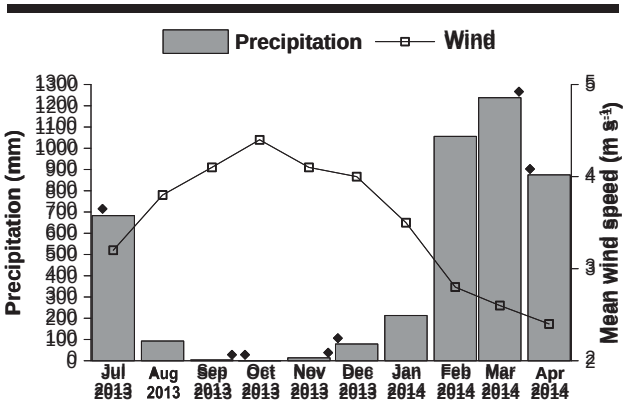

Figure. 2. Monthly precipitation and mean wind speeds recorded during the study period, data supplied by CPTEC/INPE (Salinopolis meteorological station, Pará); ◆ represents the months of the field campaigns.

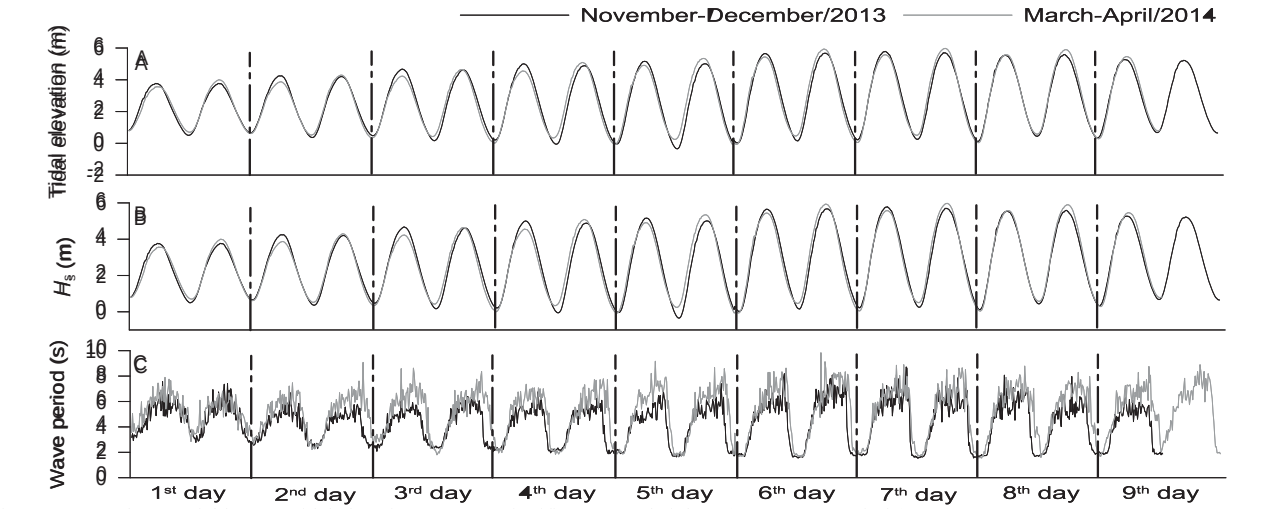

Figure. 3. Nearshore variables: A – tidal elevation (m); B – Significant wave height (m); C – wave period (s)

Morphodynamic Conditions

Ajuruteua is a moderately sloping (2-4º), narrow high tide beach with a low intertidal gradient (1-2º) that ranges in width from 200 m to 300 m. This beach is composed of uniform fine sand (mean grain size 2.3 to 2.4 mm).

Breaking wave heights were low (H_b< 0.2) during the spring tides of the equinoctial and non-equinoctial periods due to the prolonged ebb tide, resulting in the formation of typical tide-dominated sand flats. During the neap tide, when TR is lower, the beach shifted to an ultradissipative state. This condition was recorded during the neap tides in both seasons (Figure 4). In addition, this beach is essentially inactive at low tide.

DISCUSSION

Coastal processes on Amazon beaches have been studied by Oliveira *et al*. (2014), Pereira *et al*. (2011, 2013, 2014), and other scientists, who have shown that the wave energy is modulated by subtidal sandbanks and bars during low tide periods.

In this case, offshore waves of a longer period are only propagated along the shoreline during the high tide, whereas at low tide, it is sheltered and is reached only by low, locally-generated wind-waves with a short period. The increased delay of the flood tide in the inshore areas results in longer ebb tide periods, which are responsible for lower modal wave heights, especially during the equinoctial period, as recorded in April.

Thus, the conditions with the highest energy were recorded during the equinoctial period, which are characterized by higher tidal ranges, strong tidal velocities and moderate wave energy.

However, high-energy events are also recorded when strong winds blow in the second half of the year, as recorded in November/December.

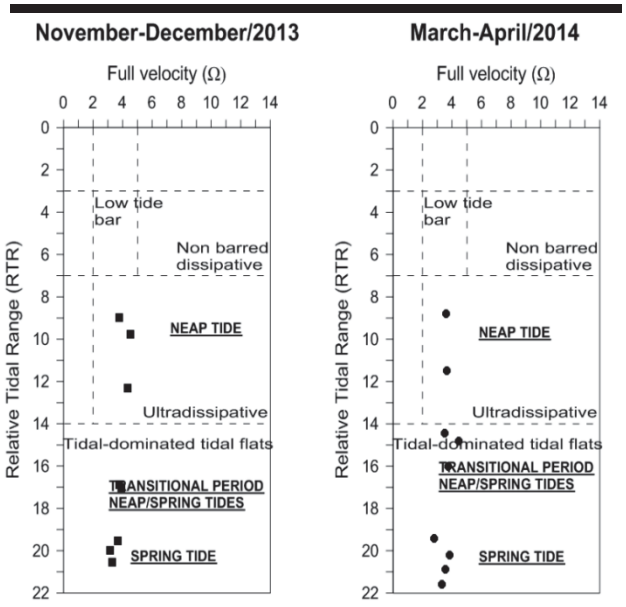

Figure 4. Seasonal variation in beach morphodynamics expressed by variation in the relative tidal range (RTR) and dimensionless fall velocity (Ω).

On more exposed beaches, such as the adjacent Atalaia beach, higher waves support a lower RTR, and a higher Ω, at high tide. When modal H_b values are relatively high, the beach tends to be tide-modified and/or wave-dominated. The opposite pattern was recorded in the sheltered environment of Ajuruteua beach. The much lower breaker height (H_b< 0.2) on this beach was related to the longer ebb tide period, which is longest when the tidal range is greatest, coinciding with the lowest modal H_b values. When the RTR is more than 15, tide-dominated conditions prevail, and tidal sand flats predominate.

The results of the present study coincide with the findings of previous research made during spring tide periods. Ajuruteua beach presented tide-dominated tidal flat characteristics, when the ebb tide period is longer and modal H_b values are lower than 0.2 m. In addition, when modal H_b was higher during neap tides, when the tidal range is reduced, the beach is exposed to lower RTR, resulting in a predominance of ultradissipative conditions, conferring tide-modified characteristics on the beach.

CONCLUSIONS

The results of the present study indicate that there is considerable temporal variability in the conditions of Ajuruteua beach, determined by the sheltering of the nearshore by intertidal sandbanks, the prevalence of tide-dominated conditions during spring tides and tide-modified features during neap tides. The lunar and semi-diurnal tidal cycles thus modulate wave heights, with higher wave heights occurring during spring tides (mainly during the equinoctial period) and low wind-waves at low tide. In turn, the variation in wave height controls the RTR and Ω, and determines the morphodynamics and conditions of the beach.

ACKNOWLEDGMENTS

This research was supported by CNPq (Universal project - 483913/2012-0), CAPES (Ciências do Mar II, Edital 43/2013) and FAPESPA. The author Pereira L.C.C. (310909/2014-7 and 200629/2014–0) would also like to thank CNPq for its financial support.

LITERATURE CITED

Albuquerque, M.G.; Calliari, L.J.; Guedes, R.M.C., and Paula, D.P., 2011. Beach Morphodynamics and Characterization of Sand Bars in Mesotidal Environments. *Journal of Coastal Research*, SI 64, 2012-2016.

Alves M.M.S. and El-Robrini M., 2006. Morphodynamics of a Macrotidal Beach: Ajuruteua. Bragança North Brazil, *Journal of Coastal Research*, SI 39, 949-951.

Barnard, P.L.; Hansen, J.E., and Erikson, L.H., 2012. Synthesis study of an erosion hot spot, Ocean Beach, California (USA). *Journal of Coastal Research*, 28 (4), 903-922.

Belfiore, S., 2003 The growth of integrated coastal management and the role of indicators in integrated coastal management: introduction to the special issue (Editorial). *Ocean & Coastal Management*, 46, 225-234.

Birkemeier, W.A., 1981. Fast, *Accurate Two-Person Beach Survey*. Coastal Engeneering Technical Aid 81-11. U.S. Army Engeneer Waterways Experiement Station. Coastal Engineering Research Center, Vicksburg, Mississipi, p.22.

Braga, F.P.S.; Sousa Filho, P.W.M.; Alves, M.A.M.S., and Pereira, L.C.C., 2007. Morfologia e sedimentologia da Praia de macromaré de Ajuruteua, Amazônia, Norte do Brasil. *Boletim Paranaense de Geociências* (Editora UFPR), 60-61, 11-30.

Brown, A.C. and McLachlan, A., 1990. *Ecology of Sandy Shores*. Amsterdam, Elsevier, 327.

Camargo M.G., 1999. *Sysgran para Windows*. Sistema de Análise Granulométrica.

Dean, R.G., 1973. Heuristic models of sand transport in the surf zone. In: Conference on Engineering Dynamics in the Surf Zone. Proceedings. Sydney. Institute of Engineers, 208-214.

Folk, R.L. and Ward, C., 1957. Brazos river bar: a study in the significance of grain size parameters. *Journal of sedimentary Petrology*, 27, 3-27.

Houser, C., 2010. Relative importance of vessel-generated and wind waves to salt marsh erosion in a restricted fetch environment. West Palm Beach (Florida). *Journal of Coastal Research*, 26(2), 230–240.

Kroon, A. and Masselink, G., 2002. Morphodynamics of intertidal bar morphology on a macrotidal beach under low-energy wave conditions, North Lincolnshire, England. *Marine Geology*, 190, 591-608.

Martorano, L.G.; Pereira, L.C.; Cezar, E.G.M., and Pereira, I.C.B., 1993. *Estudos Climatológicos do Estado do Pará, Classificação Climática (Köppen) e Deficiência Hídrica (Thornthwhite, Mather)*. Belém, SUDAM/EMBRPA, SNLCS, 53.

Masson, S. and Delecluse, P., 2001. Influence of the Amazon river runoff on the tropical Atlantic. *Physics and Chemistry of the Earth Part B: Hydrology, Oceans and Atmosphere*, 26, 137-142.

Monteiro, M.C.; Pereira, L.C.C., and Oliveira, S.O., 2009. Morphodynamic changes of a macrotidal sand beach in the Brazilian Amazon coast (Ajuruteua - Pará). *Journal of Coastal Research*, SI 56, 103-107, 2009.

Pereira, L.C.C.; Souza Filho P.W.M.; Ribeiro, M.J.S.; Pinheiro, S.C.C.; Nunue, Z.M.P., and Costa, R.M., 2006. Dinâmica socioambiental na Vila dos Pescadores (Amazônia Oriental, Pará, Brasil). *Desenvolvimento e Meio Ambiente*, 13, 125-136.

Pereira, L.C.C.; Medeiros, C.; Jimenez, J.A., and Costa, R.M., 2007. Use and Occupation in the Olinda littoral (NE, Brazil): Guidelines for an Integrated Coastal Management. *Environmental Management*, 40, 210-218.

Pereira, L.C.C.; Ribeiro, C.M.; Monteiro, M., and Asp, N.E., 2009. Morphological and sedimentological changes in a macrotidal sand beach in the Amazon littoral (Vila dos Pescadores, Pará, Brazil). *Journal of Coastal Research*, SI56, 113-117.

Pereira, L.C.C.; Vila-Concejo, A.; Trindade, W.N., and Short, A.D., 2011. Influence of high-energy conditions on beach changes in tide-dominated (Amazon, Brazil) and wavedominated (NSW, Australia) coastal environments. *Journal of Coastal Research*, SI 64, 115-119.

Pereira, L.C.C.; Nayra, I.S.S.; Costa, R.M.; Asp, N.E.; Costa, K.G., and Vila-Concejo, A., 2012a. Seasonal changes in oceanographic processes at an equatorial macrotidal beach in northern Brazil. *Continental Shelf Research*, 43, 95-106.

Pereira, L.C.C.; Pinto, K.S.T.; Costa, K.G.; Vila-Concejo, A., and Costa, R.M., 2012b. Oceanographic conditions and human factors on the water quality at an Amazon macrotidal beach. *Journal of Coastal Research*, 28 (6), 1627 – 1637.

Pereira L.C.C.; Oliveira S.M. de O.; Costa R.M.; Costa K.G., and Vila-Concejo A., 2013. What happens on an equatorial beach on the Amazon coast when La Niña occurs during the rainy season? *Estuarine Coastal Shelf Science*, 135, 116-127.

Pereira, L.C.C.; Vila-Concejo, A.; Costa, R.M., and Short, A.D., 2014. Managing physical and anthropogenic hazards on macrotidal Amazon. *Ocean & Coastal Management*, 96, 149-162.

Oliveira, S.M.O.; Pereira, L.C.C., and Vila-Concejo, A., 2014. Morphodynamic processes in a macrotidal beach in the Amazon littoral. *Quaternary and Environmental Geosciences*, 5, 125-136.

Small, C. and Nicholls, R. J., 2003. A global analysis of human settlement in coastal zones. *Journal of Coastal Research*, 19 (3), 584-599.

Souza Filho, P.W. M.; Cohen, M.C.L.; Lara, R.J.; Lessa, G.C.; Koch, B., and Behling, H., 2004. Holocene coastal evolution and facies model of the Bragança macrotidal flat on the Amazon Mangrove Coast, Northern Brazil. *Journal of Coastal Research*, SI 39, 306-310.

Souza Filho, P.W.M; Paradella, W. R., and Silveira, O.F.M., 2005. Synthetic Aperture Radar for Recognition of Coastal Features in the Wet Tropics: Applications in the Brazilian Amazon Coast. *Boletim do Museu Paraense Emílio Goeldi, Série Ciências Naturais*, 149-154.

Szlafsztein, C.F., 2005. Climate Change, sea-level rise & Coastal Natural Hazards: A GIS-Based Vulnerability Assessment, State of Pará, Brazil. *International Workshop on Climate Change and Human Security*, Oslo, 1-31.

Vicinanza, D.; Cappietti, L.; Ferrante, V., and Contestabile, P., 2011. Estimation of the wave energy in the Italian offshore. *Journal of Coastal Research*, SI 64, 613-617.

Journal of Coastal Research	SI	75	432-436	Coconut Creek, Florida	2016

Estimation of Infragravity Waves inside Pohang New Port

Jung Eun Oh [†*], Kyung-Duck Suh [††‡], Sang-Ho Oh [§††], and Weon-Mu Jeong [§]

[†]Department of Civil and Environmental Engineering
Seoul National University
Seoul, Republic of Korea

[‡] Engineering Research Institute
Seoul National University
Seoul, Republic of Korea

[§] Coastal Engineering Division
Korea Institute of Ocean Science and Technology
Ansan, Republic of Korea

[††] Department of Convergence Study on the Ocean Science and Technology
Ocean Science and Technology School
Korea Maritime and Ocean University
Busan, Republic of Korea

www.cerf-jcr.org

www.JCRonline.org

ABSTRACT

Oh, J.-E., Suh, K.-D., Oh, S.-H., and Jeong, W.-M., 2016. Estimation of Infragravity Waves inside Pohang New Port. *In:* Vila-Concejo, A.; Bruce, E.; Kennedy, D.M., and McCarroll, R.J. (eds.), *Proceedings of the 14th International Coastal Symposium* (Sydney, Australia). *Journal of Coastal Research*, Special Issue, No. 75, pp. 432-436. Coconut Creek (Florida), ISSN 0749-0208.

Pohang New Port, located on the east coast of Korea, has suffered from serious downtime problems. Infragravity waves incorporated with swells or locally-generated wind waves are presumed as an important factor for affecting the downtime, but little investigation has been made to estimate the infragravity waves inside the harbor. In this study, fundamental characteristics of the infragravity waves were investigated by utilizing the wave monitoring data collected inside and outside Pohang New Port as well as the downtime occurrence records. In order to find a relationship between infragravity and gravity waves, regression analysis was conducted for the wave records obtained at each measurement station. To complement the analysis, additional regression was also made between the heights of infragravity waves inside the harbor and those of gravity waves outside the harbor. This provides a better correlation of the quantities, indicating possible use of the information for estimating infragravity waves.

ADDITIONAL INDEX WORDS: *gravity waves, downtime, regression analysis.*

INTRODUCTION

Pohang New Port, located in Youngil Bay, is one of the largest ports on the east coast of Korea where the global steel company POSCO is situated. The port has been expanded along with the crude steel capacity growth, into a somewhat complex layout (Figure 1). It is open to the East Sea and significantly affected by the northeasterly waves propagated from the remote sea, especially during winter season. Worsened by the intricate topography inside the harbor, it has suffered from frequent harbor oscillation and unexpected downtime events, which lead to significant economic loss and difficulties in operating the port.

In general, downtime events are triggered by intensive swell, wind waves, or long-period waves coming from outside the harbor. To solve such a downtime problem in Pohang New Port, several wave monitoring programs have been conducted. Nonetheless, clear causes and solutions have not been identified yet. A review of the recorded downtime events together with the observed waves and meteorological conditions revealed that such downtime events mostly occur when incident swell and wind waves exceed some thresholds (Jeong *et al.*, 2011). The influence of long waves, however, has not been sufficiently examined so that it cannot be ruled out from possible causes of the harbor resonance and associated downtime events.

Harbor oscillations are known to be chiefly generated by long-period waves propagated from the open sea (Rabinovich, 2009). In particular, infragravity waves having periods of a few minutes are considered to induce significant oscillations in ports and harbors whose natural period is similar as those of infragravity waves. Besides the harbor oscillation, they play a key role in the formation of the current field close to the shore and affect many phenomena in the coastal zone (Battjes, 1988).

In deep water, infragravity waves are generated by the nonlinear interaction of gravity waves, such as wind waves or swells. The currents exerted by radiation stress make bounded long waves beneath the wave groups of swell and wind waves (Longuet-Higgins and Stewart, 1962). The infragravity waves propagate to the shore as bounded long waves, being highly correlated with the group of gravity waves. As they propagate to the shore, their magnitudes are enlarged as a result of transfer of energy from gravity waves. In the nearshore region, the infragravity waves are likely to be formed as a combination of both bound waves and free waves due to the complex wave processes in the region (Herbers *et al*., 1995).

Based on the above researches, the generation and propagation mechanism of infragravity waves has been investigated to some extent, while the mechanism for the diversity along to the shore has not yet been fully clarified. Owing to strong nonlinearity, it is hard to estimate the effect of infragravity waves on the wave field inside a harbor by the traditional analysis methods. Hence, the effect of infragravity waves on harbor oscillation might not be presented in the

DOI: 10.2112/SI75-087.1 received 15 October 2015; accepted in revision 15 January 2016.
*Corresponding author: je5@snu.ac.kr

calculation, even though it was a responsible factor for the phenomenon.

In this context, this study examined the relationship between gravity and infragravity waves by using relatively long-term observation data obtained inside and outside Pohang New Port. Based on the identified relationship, nonlinear regression analysis was conducted to estimate the magnitude of infragravity waves at the three stations around the port.

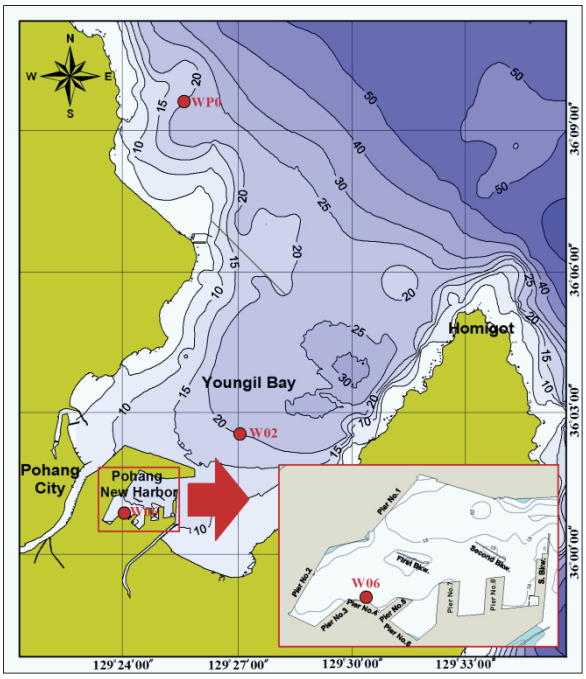

Figure 1. Map of Pohang New Port and wave monitoring stations

METHODS

Observations of waves were carried out at three locations inside and outside Pohang New Port from 2008 to 2013. Locations of the observation stations are shown in Figure 1 and the water depths and observation periods are shown in Table 1. The St. WP0 is at Wolpo Bay near Pohang New Port, a location outside the port. The St. W02 in the vicinity of the harbor entrance is located outside the port and has the similar depth as the St. WP0. The St. W06, a station inside the port, is not directly affected by the slit. In the three observation stations, WTG (Wave and Tide Gauge) was installed to continuously observe the wave data. In addition, records of the downtime events between 2009 and 2011 were also collected during the wave observation period.

Parameters of the gravity wave components were obtained by applying the spectrum analysis. For infragravity waves, the corresponding parameters were calculated by performing the spectrum analysis for the data of 90 minutes as follows.

$$H_{sl} = 4\sqrt{m_0} \quad (1)$$

$$T_{zl} = \sqrt{\frac{m_0}{m_2}} \quad (2)$$

Table 1. *Water depths and wave monitoring duration at each station*

Station	Water depth (m)	Monitoring duration
WP0	17.4	2008/1/29 ~ 2013/9/11
W02	21.6	2008/8/23 ~ 2011/4/7
		2011/6/2 ~ 2013/5/17
W06	10.2	2008/8/25 ~ 2013/10/1

where H_{sl} and T_{zl} are the significant height and the mean period, respectively, of the infragravity wave component. The symbols of m_0 and m_2 denote zeroth and second moment, respectively, of the wave spectrum. The equation for calculating the moments are given by

$$m_n = \int_{f_1}^{f_2} f^n \cdot S(f) df \quad (3)$$

where f_1 is the lower cut-off frequency and f_2 is the upper cut-off frequency, $S(f)$ indicates a spectral density function according to the water level change for the frequency f. The frequency range of infragravity wave is determined by the values of cut-off frequencies, thus setting the lower and upper cut-off frequency in equation (3) is a very important and difficult problem. With reference to the existing results from the East Sea and other research results in Japan, the upper and lower cut-off frequencies were set at 1/30 Hz and 1/300 Hz, respectively (Jeong *et al.*, 2011).

Figure 2 shows the observed time series of the significant wave heights of the gravity and infragravity wave components during the first half of 2010. Blue and red lines represent significant wave heights of the gravity waves H_s and the infragravity waves H_{sl}, respectively. Note that the magnitude of H_s is shown in the vertical axis on the left side, whereas H_{sl} on the right side. The green vertical lines indicate the days when downtime events occurred. The figure shows that the downtime events are likely to appear when H_s and H_{sl} are comparatively large. Similar tendency was also observed for the rest of the entire collected data. As seen in this observation, downtime events occurred more frequently in winter season.

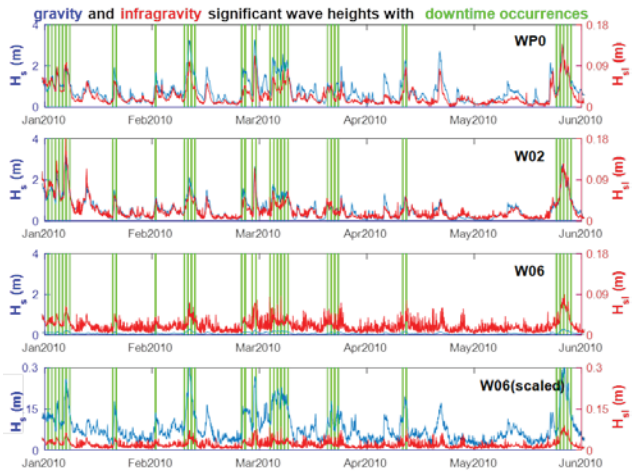

Figure 2. Time series of the significant wave heights of the gravity waves (H_s, blue color) and infragravity waves (H_{sl}, red color). The

occurrence of downtime is also shown in the figure (green color).

When waves propagate from the offshore to the inside the harbor through the entrance of the port (See Figure 2 from top to bottom WP0 > W02 > W06), the magnitudes of gravity waves gradually decreased and the values inside the harbor become relatively small due to the effect of breakwaters. Whereas magnitudes of the infragravity waves are not significantly reduced during the propagation to the shore, the fluctuation becomes larger at St. W06. In the third panel for W06, it is seen that the appearance of downtime events corresponds to the time of relatively large infragravity waves. In order to directly compare the magnitudes of gravity and infragravity wave components inside the harbor, the data at W06 is plotted again in the last panel with the same scale of vertical axes on the left and right sides. Although the heights of gravity waves are largely reduced compared with those outside the harbor, they are still greater (reaching 30 cm) than the heights of infragravity waves (reaching 10 cm). Further analysis is needed to find a clear relationship between the occurrence of downtime events and the magnitudes of gravity or infragravity waves.

Meanwhile, there have been several studies on the estimation of infragravity waves based on the correlation with gravity waves (*e.g.*, Bowers, 1992; Lopez and Iglesias, 2013; McComb, 2005; Nelson *et al.*, 1988; Thiebaut *et al.*, 2013). Most of them suppose a strong dependency of the concurrent infragravity waves on the offshore or inshore gravity waves, and suggest empirical formulas for predicting infragravity waves. In order to apply such a method to Pohang New Port, we investigated the relationship between gravity and infragravity waves among the three measurement stations in this study.

The analysis of detecting correlation between gravity and infragravity waves was conducted with all the data from 2008 to 2013. Figure 3 shows the analysis results, where the first and second columns present scatter plots between H_{sl} and both H_s and T_z at the three stations of WP0, W02, and W06. The scatter plots of H_{sl} and H_s reveal quadratic proportionality, but those of H_{sl} and T_z do not show such an apparent relationship.

The quadratic relationship is rather clearly recognized at the two locations outside the harbor (WP0 and W02) where $\rho \approx 0.9$, but it is not so clear inside the harbor (W06) where the correlation coefficeint is smaller ($\rho = 0.736$). The above results suggest that it may be possible to obtain an empirical formula for predicting infragravity wave height using a regression analysis.

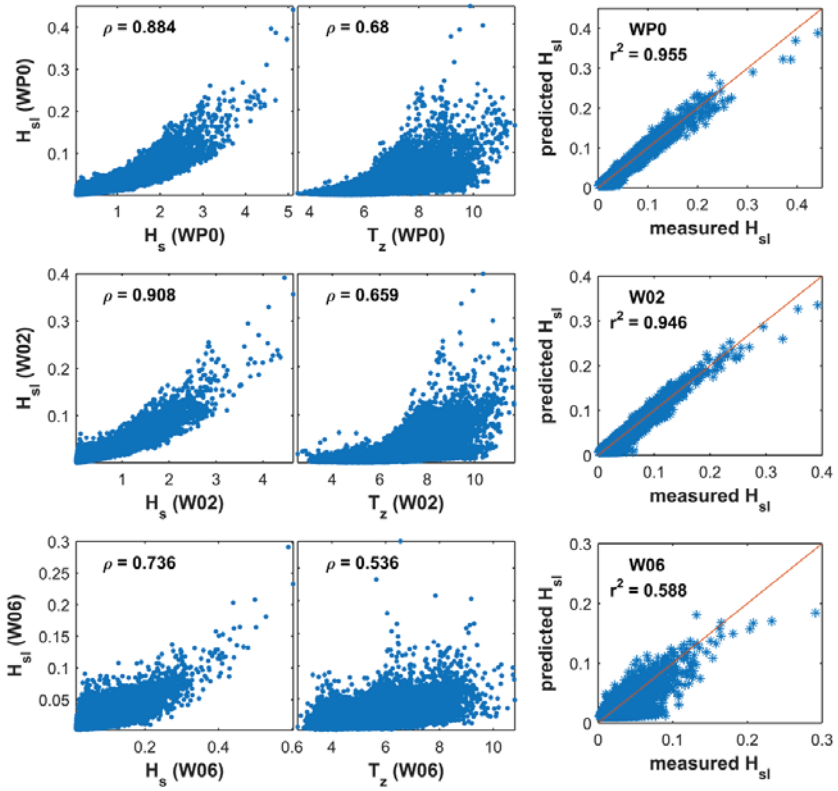

Figure 3. Scatter plots between H_{sl} and both H_s and T_z at the each measurement station are shown in the left and central columns. Values of the correlation coefficient are shown in each sub-panels in the figure. The Q-Q plots by the regression model are shown in the right column.

RESULTS

Some empirical formulas have been suggested for estimating infragravity wave heights by using gravity wave heights and periods at specific locations (*e.g.*, Bowers, 1992; McComb, 2005; Nelson *et al*., 1988). All these formulas were developed based on multivariate nonlinear regression models. For Pohang New Port, we had applied several types of nonlinear regression models for calculating the infragravity wave height. Among them, the model showing the best agreement with the measured value of the infragravity wave height is formulated as follows.

$$H_{sl} = a(H_s^b \ T_z^c) + d \qquad (4)$$

The values of the four coefficients in the above equation and two indices of goodness-of-fit at each station are presented in Table 2. The symbol *Ia* is the index of agreement suggested by Willmott (1981). The Q-Q plots of the observed and the predicted values by using the empirical formula at the three stations are shown on the third column of Figure 3.

Table 2. *The result of regression analysis at the three locations*

Station	Coefficients				Indices	
	$a{\cdot}10^3$	*b*	*c*	*d*	r^2	*Ia*
WP0	0.446	1.327	2.003	0.0052	0.955	0.988
W02	0.829	1.197	1.794	0.0063	0.946	0.986
W06	86.462	1.483	0.789	0.0102	0.588	0.857

As shown in the Q-Q plots, the regression models are in very good agreement with the observed data at the two locations outside the harbor. According to the values of r^2 (≈ 0.95) at the two points outside the harbor, about 95% of the variability between the observed and the predicted values has been explained by the regression model. On the other hand, the value of r^2 inside the harbor is not higher than 0.6, implying that about 60% of the variability has been accounted for and the remaining 40% of the variability is still unaccounted for. Consequently, the predictability of the regression model significantly becomes worse inside the harbor

DISCUSSION

Some previous studies have supposed a proportional relationship between the infragravity wave heights in nearshore region and gravity wave heights at the offshore (*e.g.* Tucker, 1950). However, the relationship among the two quantities changes very rapidly during the propagation of waves from offshore to the shore through the continental shelf, surf zone, and swash zone. Such complicated change is caused by topography and complex wave processes as well. In this context, it is necessary to understand how the energy is exchanged between the gravity and infragravity waves and in which process the energy is lost the most.

The above regression analysis reveals that energy balance seems to be maintained between gravity and infragravity wave components at the open sea, but not inside the harbor. Such differences in the results of the regression analaysis inside and outside the harbor indicate significant energy level changes between gravity and infragravity waves around Pohang New Port. As depicted in Figure 2, some energy may be transferred from gravity wave band to infragravity wave band during the propagation of waves into the harbor.

Considering this and referring to the description about proportional relationship between inshore infragravity waves and offshore gravity waves addressed in previous studies, the correlation between gravity waves outside the harbor and infragravity waves inside the harbor was examined as illustrated in Figure 4. The scatter plots of H_{sl} at W06 against H_s and T_z at W02 give larger correlation coefficients than the corresponding values obtained by using the data at W06 only (See the third row of Figure 3). Although not shown in this paper, similar results were also obtained for the scatter plots of H_{sl} at W06 against H_s and T_z at WP0. Based on these relationships, two regression equations can be obtained as follows.

$$H_{sl_{\mathrm{W06}}} = 9.7 \times 10^{-5}(H_s^{1.34} \ T_z^{2.36})_{\mathrm{WP0}} + 0.013 \qquad (5)$$

$$H_{sl_{\mathrm{W06}}} = 2.9 \times 10^{-4}(H_s^{1.34} \ T_z^{1.95})_{\mathrm{W02}} + 0.012 \qquad (6)$$

Using the above equations, Q-Q plots of the measured and predicted infragravity significant wave heights can be drawn as done in Figure 3. Figure 4(c) shows such a plot corresponding to Equation (6), for which the value of $r^2 = 0.82$ was obtained. A similar plot corresponding to Equation (5) leads to the value of $r^2 = 0.57$. Thus, the use of Equation (6) is more adequate for estimating the infragravity waves inside the harbor probably because the St. W02 is located just outside the harbor, whereas the St. WP0 is located far from the harbor.

Then, we can compare the time series of the measured and predicted signficicant wave heights of the infragravity waves at W06, as shown in Figure 4(d). The predicted time series fairly well reproduce overall temporal variation of the measured wave height, indicating good performance and possible use of the regression model for estimating the infragravity wave heights inside the harbor from the gravity waves outside the harbor. It is noteworthy that the appearance of downtime events (also shown in the figure) reasonably well coincides with the time when both measured and predicted infragravity waves are high.

CONCLUSIONS

This study investigated the relationship between infragravity waves and gravity waves by analyzing the observed wave data at Pohang New Port. The correlation between the gravity and infragravity waves is found to be significant. The regression analysis based on the recognized correlation showed a good performance in estimating the significant wave heights of the infragravity waves outside the harbor. In contrast, the results of the regression analysis for the wave data measured inside the harbor were not satisfactory.

The regression analysis was also made between the significant wave heights of the infragravity waves inside the harbor and those of the gravity waves outside the harbor, which showed better performance in predicting the magnitudes of the infragravity waves inside the harbor. It is noted that in many

occasions the downtime events in Pohang New Port occurred when the infragravity waves were high inside the harbor.

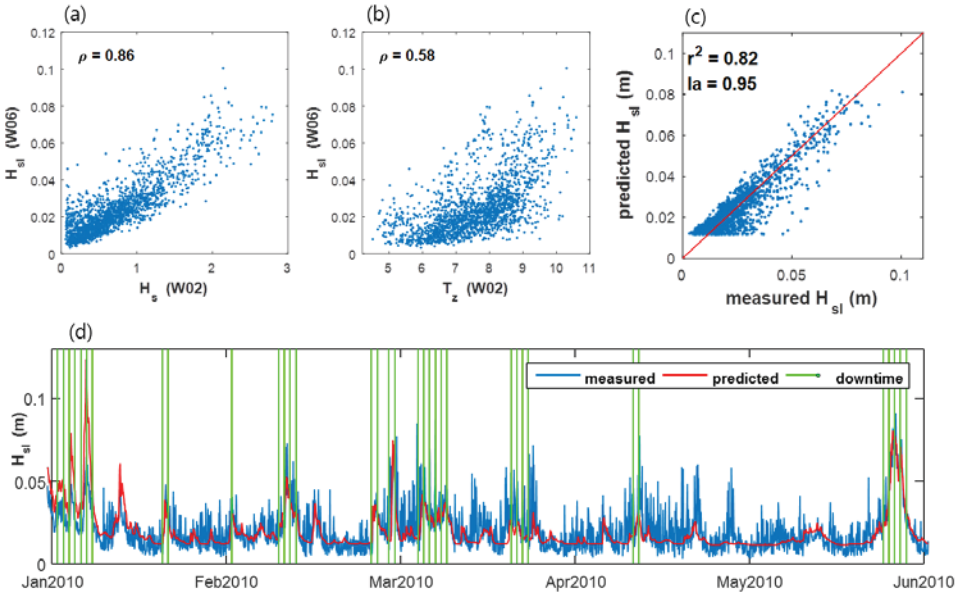

Figure 4. The result of the regression model for estimating the infragravity waves inside the harbor (W06) by using the gravity waves outside the harbor (W02). (a) and (b): the scatter plots between the significant wave heights of the infragravity waves and both the significant wave heights and the mean periods of the gravity waves, respectively. (c): the Q-Q plot of measured and predicted significant wave heights of the infragravity waves. (d): time series of the measured and the predicted significant wave heights of the infragravity waves with downtime occurences.

Since the gravity waves can be monitored in real time outside the port, the regression algorithm developed in this study can be used for predicting the infragravity waves inside the harbor, which will provide fundamental information to be prepared for possible occurrence of downtime in the harbor.

ACKNOWLEDGMENTS

This work has been supported by the research project (PE99423) of Korea Institute of Ocean Science and Technology.

LITERATURE CITED

Battjes, J. A., 1988. Surf-zone dynamics. *Annual Review of Fluid Mechanics*, 20(1), 257-291.

Bowers, E.C., 1992. Low frequency waves in intermediate water depths. *Proceedings of the 23rd International Conference on Coastal Engineering* (Venice, Italy, ASCE), 832-845.

Herbers, T.H.C.; Elgar, S., and Guza, R.T., 1995. Generation and propagation of infragravity waves. *Journal of Geophysical Research*, 100(C12), 24863-24872.

Jeong, W.M.; Ryu, K.H.; Baek, W.D., and Choi, H.J., 2011. Downtime analysis for Pohang new harbor through long-term investigation of waves and winds. *Journal of Korean Society of Coastal and Ocean Engineers*, 23(3), 226-235 (in Korean).

Longuet-Higgins, M.S. and Stewart, R., 1962. Radiation stress and mass transport in gravity waves, with application to 'surf beats'. *Journal of Fluid Mechanics*, 13(04), 481-504.

López, M. and Iglesias, G., 2013. Artificial intelligence for estimating infragravity energy in a harbour. *Ocean Engineering*, 57, 56-63.

McComb, P.; Gorman, R., and Goring, D., 2005. Forecasting infragravity wave energy within a harbour. *Proceedings of waves 2005 conference* (Madrid, Spain, ASCE), 3-7.

Nelson, R.C.; Treloar, P.D., and Lawson, N.V., 1988. The dependency of inshore long waves on the characteristics of offshore short waves. *Coastal engineering*, 12(3), 213-231.

Rabinovich, A.B., 2009. Seiches and harbour oscillations, *In: Handbook of Coastal and Ocean Engineering*, Singapore: World Scientific, 193-236.

Thiebaut, S.; McComb, P., and Vennell, R., 2013. Prediction of coastal far infragravity waves from sea-swell spectra. *Journal of Waterway, Port, Coastal, and Ocean Engineering*, 139(1), 34-44.

Tucker, M.J., 1950. Surf beats: sea waves of 1 to 5 min. period. *Proceedings of the Royal Society of London. Series A. Mathematical and Physical Sciences*, 202(1071), 565-573.

Journal of Coastal Research	SI	75	437-441	Coconut Creek, Florida	2016

Nearshore Dynamics and Holocene Evolution of the Coastal Barrier South of the Santa Marta Cape, Southern Brazil

Julio F. de Oliveira[†], Eduardo G. Barboza[†‡] and Javier Benavente[§]

[†] Programa de Pós Graduação em Geociências, Universidade Federal do Rio Grande do Sul, Porto Alegre, RS, Brasil.

[‡] Centro de Estudos de Geologia Costeira e Oceânica, Universidade Federal do Rio Grande do Sul, Porto Alegre, RS, Brasil,

[§] Dept. of Earth Sciences, Faculty of Marine and Environmental Sciences, University of Cádiz, Puerto Real, Cádiz, Spain

www.cerf-jcr.org

www.JCRonline.org

ABSTRACT

Oliveira, J.F.; Barboza, E.G., and Benavente, J., 2016. Nearshore Dynamics and Holocene Evolution of the Coastal Barrier South of the Santa Marta Cape, Southern Brazil *In:* Vila-Concejo, A.; Bruce, E.; Kennedy, D.M., and McCarroll, R.J. (eds.), *Proceedings of the 14th International Coastal Symposium* (Sydney, Australia). *Journal of Coastal Research*, Special Issue, No. 75, pp. 437-441. Coconut Creek (Florida), ISSN 0749-0208.

The emerged part of the Pelotas Basin extends about 800 km from the Polonio high (Uruguay) to the Florianópolis high (Santa Catarina state, southern Brazil). Since 6-5 ka B.P., the sea level has been dropping slowly, and the sediment balance is the principal factor that controls the actual barrier development. The Holocene barrier presents sectors of transgressive patterns that are usually located in coastal projections, while regressive sectors generally appear in the embayments. This work analyses the evolution of the barrier along a 30 km stretch of coast south of the Santa Marta Cape (Santa Catarina State), in the northernmost part of Pelotas Basin. The sub-superficial configuration of the barrier was characterized through Ground Penetrating Radar (GPR) profiles surveyed perpendicular to the coastline. In addition, an analysis of the nearshore wave propagation was carried out through SMC-Brasil (IH-Cantabria) to simulate the currents generated by breaking waves and the net sediment transport. The results show two different behaviors along the barrier system; the northern part with transgressive characteristics (dipping landward reflectors) and the southern part with regressive characteristics (dipping seaward reflectors). These different behaviors are associated with the slight changes on the coastal orientation and on the slopes of the shoreface and upper continental shelf. These two factors influence in how waves approach the coast, generating an imbalance in the sediment budget, which is shown in the characteristics of the distinct sectors studied.

ADDITIONAL INDEX WORDS: *Coastal dynamics, Holocene Barrier, GPR.*

INTRODUCTION

One of the major challenges in coastal sciences is to work with different spatial and temporal scales (Aagard *et al*., 2004). The understanding of long-term coastal barrier behavior depends on the correct interpretation of processes acting at different scales, and taking into account their limitations when they are extrapolated (Costas, 2006).

Dillenburg *et al.* (2000) suggested that antecedent topography controls present-day coastal morphologies and Holocene evolution. Regional slope, coastal orientation and local variation inherited from valleys and interfluves are responsible of creating embayments and projections (Belknap and Kraft, 1985). Due to waves focusing effects and refraction processes, projections are generally subjected to erosion while embayments experience sediment deposition (May and Tanner, 1973).

The emerged part of the Pelotas Basin extends from the Polonio High in Uruguay to the Florianopolis High in the Santa Catarina State, in southern Brazil. There are no neotectonic movements in this part of the coast (Rosa *et al.*, 2011). According to Angulo *et al.* (2006), Holocene sea-level in southern Brazil reached approximately 2 m above the current position between 6-5 ka B.P., and has been dropping slowly since then (0.4 mm/yr).

Despite this sea level fall, the Holocene barrier presents different behaviors along its almost 800 km of extension. This barrier represents one of the most continuous sandy structure of the world (Dillenburg and Barzboza, 2014) with only six interruptions along its length. Sectors of retrogradational patterns (transgressive barrier) are located generally in coastal projections, while prograding sectors (regressive barrier) normally appear in the embayments (Dillenburg *et al*., 2000, 2009; Barboza *et al.*, 2011) (Figure 1).

The southern Brazilian coast is predominantly characterized by wave-dominated costal barriers. According to Dillenburg *et al*. (2000) the imbalance of sediment budget is the principal factor that controls the barrier evolution. Currently, the inland sediment supply is not significant however, the longitudinal variability in wave approach, due to refraction and diffraction processes and in wave-driven longshore and cross-shore sediment transport are the principal mechanisms acting in the sediment budget and hence determine the different patterns of the barrier evolution.

The study area is the 30 km coastal segment south of the Santa Marta Cape, which marks the northernmost portion of the Pelotas Basin (Figure 1). This region is characterized by large

DOI: 10.2112/SI75-088.1 received 15 October 2015; accepted in revision 15 January 2016.

*Corresponding author: jfogeo@gmail.com

availability of fine sand, a gently sloping inner shelf which increases as it approaches to the cape (from 0.15º to 0.30º, approximately) with incidence of moderate to high wave energy.

The significant wave height is 1.5 m, and the beaches are characterized as a dissipative to intermediate, with the presence of parallels bars and troughs in the surfzone. The most energetic swells are from the south and southeast quadrants and occur mainly during the fall and winter, while during the spring and summer waves from the east and northeast quadrants prevail. According to geomorphological indicators and sedimentological variations (Giannini, 1993, 2007) the net regional littoral drift is towards the northeast. However, Siegle and Asp (2007) observed a bi-directionality in a local scale.

The tidal range is approximately 0.6 m, however under storm conditions the effect of meteorological tides can increase the sea level more than 1 m (Giannini, 1993). The wind regime is bimodal, with predominantly northeasterly winds in spring and summer, and from south and southwest in fall and winter. The principal vector of the dunefield migration is towards the southwest, governed by the predominant northeasterly winds as southerly winds are normally associated with rainy and stormy conditions (Giannini, 1993). The northern part of the studied area is characterized by large transgressive dunefields, with mostly barchans and transverse dunes, with absence of foredunes, while in the southern sector, foredunes and transgressive dune sheets dominate the landscape.

This study analyzes the nearshore dynamics in a decadal scale, relating it with the late Holocene evolution of the 30 km coastal stretch south of the Santa Marta Cape in southern Brazil.

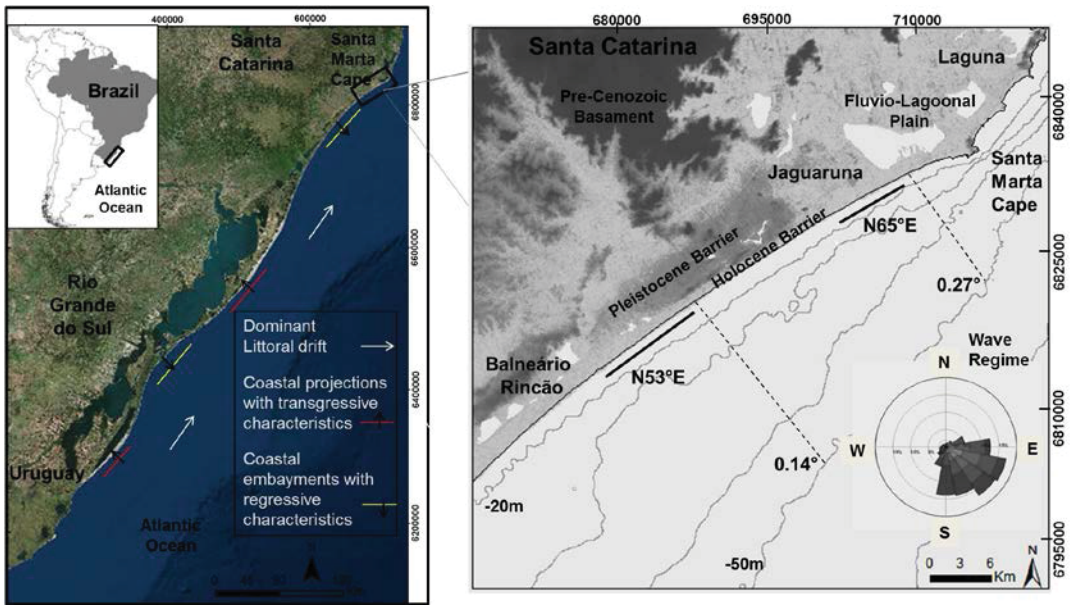

Figure 1. The regional settings of the study area. On the left side, the southern Brazilian coast; on the right, characteristics of the region south of the Santa Marta Cape: geomorphological features, climate wave and changes in coastal orientation and shoreface /inner continental shelf slope (0m - 50m).

METHODS

Two distinct methodologies in different temporal scales were carried out to analyze the (i) medium-term nearshore processes and the (ii) long-term Holocene evolution of the coastal barrier system.

Firstly, in the subaqueous environment, simulations of nearshore wave propagation were done in order to characterize the dominant coastal process; and secondly, in the emerged part of the barrier, GPR profiles were surveyed in order to analyze the sub-superficial structure of the barrier.

Nearshore wave propagation was analyzed through Coastal Modeling System (SMC-Brasil, development by IH-Cantabria - Spain). The SMC-Brasil consists of an assemblage of numerical models (wave, currents and sediment transport) associated to a marine dynamic database and bathymetry data from nautical charts of the Brazilian Navy (DHN - nº1911).

Wave data for the period between 1948 and 2008 was obtained from the re-analysis Global Ocean Wave Model (GOW), calibrated and validated through ocean buoys and altimetry satellites (Reguero *et al*., 2012), and downscaled ocean waves (Camus *et al*., 2013). Due to the huge numbers of cases to simulate, a statiscal technique was used to choose the 150 most representative cases.

Wave simulations to the shoreline were carried out through MOPLA model (Gonzalez *et al*., 2007), which includes; a non-dispersive model of wave spectral propagation, which solves the mild-slope equation and considers refraction-diffraction processes with wave-current interactions and energy losses due to breaking waves; a current generated by breaking waves model and a sediment transport model, derived from the CERC formula (Shore Protection Manual, 1984).

GPR records were acquired along cross-shore profiles. The system comprises a GSSI™ (Geophysical Survey Systems, Inc.)

SIR-3000 data collector for monostatic antenna 200 MHz – GSSI™ in a Common Off-set method, and a dielectric constant for sand (10) (Davis and Annan, 1989). This system was connected to a Differential Global Positional System (DGPS). After the data acquisition, a processing and editing routine was applied through the softwares Radan 6.6™ and Prism 2®. In order to eliminate noise and correct saturation, gains and signal frequency filters were applied.

Finally, the data was interpreted based on termination, geometry and pattern of reflectors (Mitchum Jr. *et al*, 1977). The interpretation of the GPR records takes into account other sessions of GPR in the region, which were calibrated with data from drilling and dating (Dillenburg *et al.*, 2011; Barboza *et al.*, 2009, 2011).

RESULTS

The results of wave propagation (Figure 2) of the most common scenarios during a 60 years record (wave direction, average height and period between 1948 and 2008) present waves coming from south ($Hs_{50\%}$ = 2.22 m; $Tp_{50\%}$ = 9.55 s) generating strong currents towards the northeast in the southern and northern sectors. Waves coming from south-southeast ($Hs_{50\%}$ = 1.86 m; $Tp_{50\%}$ = 9.14 s) and southeast ($Hs_{50\%}$ = 1.73 m; $Tp_{50\%}$ = 8.19 s) do not produce a significant current in both sectors due to the perpendicularly wave approach to the coast. Nevertheless, around the rocky outcrops in the northern sector, strong cross-shore currents are observed. Waves coming from east-southeast ($Hs_{50\%}$ = 1.65 m; $Tp_{50\%}$ = 7.41 s) and east ($Hs_{50\%}$ = 1.54 m; $Tp_{50\%}$ = 6.75 s) generate moderate currents in both sectors, except on sheltered areas by the cape where weak currents are observed.

The 60 years record of annual average longshore sediment transport indicates that the net transport is towards northeast (151.801 m^3/year) in the southern sector and towards southwest in the northern sector (466.140 m^3/year). Comparatively, the mean energy flux in the northern sector presents higher values (3802 J m^{-1} s^{-1}) when compared to the southern sector (3228 J m^{-1} s^{-1}). The GPR surveys show opposite patterns in the two sectors of the study area (Figure 3). The southern sector radargram (Figure 3a) presents oblique reflectors with downlap terminations dipping seaward, which show the regressive behavior of the barrier. This pattern may be combined with downstepping and aggradational components (Barboza *et al.*, 2009, 2011).

In the northern part of the study area, closer to the Santa Marta Cape, the two radargrams present reflectors with downlap terminations dipping landward, which can be interpreted as a transgressive barrier behavior (Figure 3b and 3c). This transgressive signature comprises aeolian sand erosion and transport from the backshore/foreshore zone into the lagoonal inter-barrier depression (Dillenburg *et al.*, 2004; Dillenburg and Barboza, 2014).

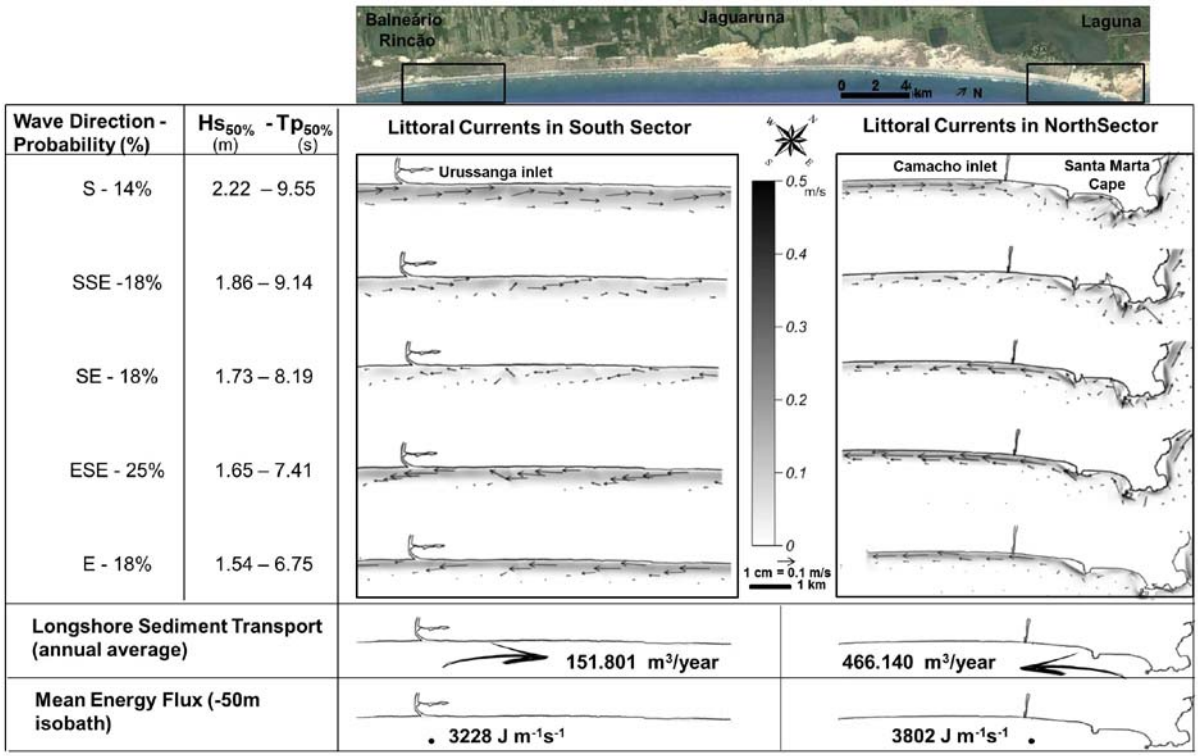

Figure 2. Littoral currents produced in the most frequent wave scenarios (direction, mean wave height and period) in both sectors (south and north); the annual average longshore sediment transport calculated via CERC formula; and the mean energy flux (calculated for the 50m isobath).

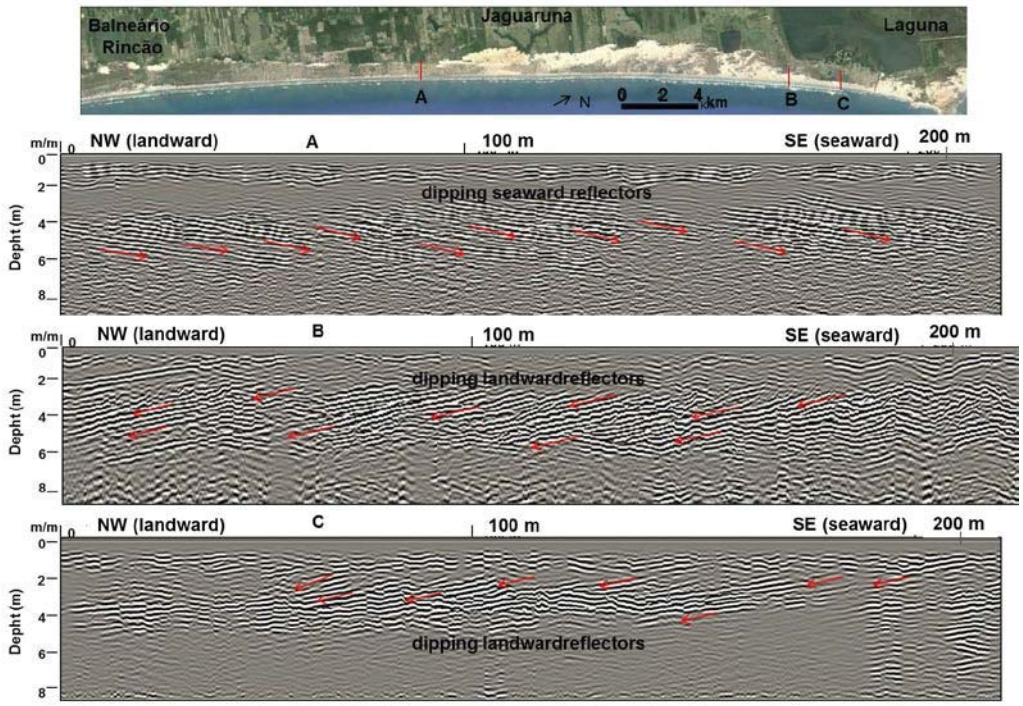

Figure 3. GPR profiles acquired with a 200 MHz antenna, showing reflectors dipping seawards in a radargram "A", characterizing a regressive (progradational) barrier system; and in radargrams "B" and "C" the reflectors dipping landwards characterize a transgressive (retrogradational) barrier system.

DISCUSSION

The southern sector of the Holocene barrier is part of a long embayment which begins hundreds of kilometers to the south, with an orientation around N53ºE and with a shoreface/inner shelf slope around 0.14º. However, the northern sector is located in the starting point of the projection of the Santa Marta Cape, with orientation around N65ºE and a narrow and steeper shoreface/inner shelf, around 0.27º. These changes influence the waves approach in both sectors, showing higher energy waves and inversion of the longshore drift in the northern sector. In the southern sector, the net longshore transport is towards to northeast, following the tendency of the entire southernmost coast. On the other hand, the resulting longshore transport in the northern sector is toward the southwest. Therefore, there is a convergence of littoral cells between both sectors, about 30 km apart from each other. Siegle and Asp (2007) also observed this convergence in longshore currents in regional scale.

The GPR sub-superficial record also shows differences between these two sectors. While the southern sector presents characteristics of a regressive barrier, the northern sector presents characteristics of a transgressive one. Barboza *et al*. (2011) related similar patterns in the regressive and transgressive barriers in the Rio Grande do Sul State. In general, regressive barriers are located in the central part of embayments and are characterized by the presence of old beach ridges that can be covered by modern dunes (Dillenburg and Barboza, 2014). Transgressive barriers are located in coastal projections and are generally associated with large transgressive dunefields. In previous GPR records obtained in transgressive barriers (Barboza *et al*., 2011), reflectors dipping landward were interpreted as erosive shoreface events with migration of sediment into the adjacent lagoon, mainly through overwash and aeolian transport processes (Rosa *et al*., 2011; Lima *et al*., 2013).

The large active transgressive dunefield in the northern sector, which migrates parallel to the coastline driven by northeasterly winds, may be associated with an erosional behavior of this segment. Dillenburg *et al*. (2000) related higher wave energy and steeper shoreface gradients (associated with the projections of the Holocene barrier in southern Brazil) to the development of large transgressive dunefields.

CONCLUSIONS

The study area displays characteristics of a transitional coast due to significant changes in orientation and shoreface/inner shelf slope. Different to the southern sector, the littoral cell of the northernmost studied segment, with a resulting transport to the SW, probably does not have a significant sediment supply coming from north, due to the presence of the cape trapping large part of

the subaqueous transport. Considering that similar oceanographic conditions occurred in the last 5 ka, it's possible that the northern sector represents a long-term landward migration of the barrier due to a potential negative sediment balance.

ACKNOWLEDGMENTS

The authors acknowledge the Conselho Nacional de Desenvolvimento Científico e Tecnológico (CNPq – 140741/2012-7) and Coordenação de Aperfeiçoamento de Pessoal de Nível Superior (CAPES – BEX 8003/14-9) for providing research fellowships for the first author. The authors also thank to Graziela Miot da Silva and two anonymous reviewers who provided many constructive comments.

LITERATURE CITED

Aagaard, T.; Davidson-Arnott, R.; Greenwood, B.; Nielsen, J. 2004. Sediment supply from shoreface to dunes: linking sediment transport measurements and long term morphological evolution. *Geomorphology* 60: 205-224

Angulo, R. J. and Lessa, G. C. 1997. The Brazilian sea level curves: a critical review with emphasis on the curves from Paranaguá and Cananéia regions. *Marine Geology*, 140, 141–166.

Barboza, E.G.; Dillenburg, S.R.; Rosa, M.L.C.C.; Tomazelli, L.J and Hesp, P.A., 2009. Ground-penetrating radar profiles of two Holocene regressive barriers in southern Brazil. *Journal of Coastal Research*, SI 56, pp. 579-583.

Barboza, E. G.; Rosa, M. L. C. C.; Hesp, P. A.; Dillenburg, S. R.; Tomazelli, L. J.; Ayup-Zouain, R. N. 2011. Evolution of the Holocene coastal barrier of Pelotas Basin (Southern Brazil) – a new approach with GPR data. *Journal of Coastal Research,* SI 64, 646-650.

Belknap, D.F. and Kraft, J.C., 1985. Influence of Antecedent Geology on Stratigraphic Preservation Potential and Evolution of Delaware's Barrier Systems. *Marine Geology,* 63, 235-262.

Camus, P.; Mendez, F.J; Medina, R.; Tomas, A.; Izaguirre, C. 2013. High resolution downscaled ocean waves (DOW) reanalysis in coastal areas. *Coastal Engineering*, 72:56-68.

Costas, S. 2006. Evolución morfosedimentaria anual, decadal y secular del sistema barrera-lagoon de Cíes durante el Cuaternario (Galicia, NO Península Ibérica). Universidad de Vigo. Ph.D. Dissertation. 202p.

Davis, J.L. and Annan, A.P., 1989. Ground-penetrating radar for high-resolution mapping of soil and rock stratigraphy. *Geophysical Prospecting*, 37, 531-551.

Dillenburg, S.R. and Barboza, E.G., 2014. The Strike-Fed Sandy Coast of Southern Brazil. *In*: Martini, I.P. and Wanless H.R. (eds.). *Sedimentary Coastal Zones from High to Low Latitudes: Similarities and Differences*., Geological Society, London, Special Publications 388, 333-352.

Dillenburg, S. R.,; Roy, P. S.,; Cowell, P. J.; Tomazelli, L. J. 2000. Influence of antecedent topography on coastal evolution as tested by the shoreface translation-barrier model (STM). *Journal of Coastal Research,* 16, 71–81.

Dillenburg, S.R.;, Barboza, E.G.; Tomazelli, L.J.; Hesp, P.A.; Clerot, L.C.P.; Ayup-Zouain, R.N., 2009. The Holocene Coastal Barriers of Rio Grande do Sul. In: Dillenburg, S.R. and Hesp, P.A. (eds.), *Geology and Geomorphology of Holocene Coastal Barriers of Brazil*. Lecture Notes in Earth Sciences, 107, 53-91.

Dillenburg, S.R., Barboza; E.G.; Hesp, P.A.; Rosa, M.L.C.C. 2011 Ground penetrating radar (GPR) and standard penetration test (SPT) records of a regressive barrier in southern Brazil. *Journal of Coastal Research,* SI 64, 651-655.

Giannini,P.C.F. 1993. Sistemas Deposicionais no Quaternário Costeiro entre Jaguaruna e Imbituba, SC. Universidade de São Paulo. Ph.D. Dissertation. 439p..

González, M.; Medina, R.; Gonzalez-Ondina, J.; Osorio, A.; Méndez, F.J.; García, E. 2007. An integrated coastal modeling system for analyzing beach processes and beach restoration projects, SMC. *Computers & Geosciences*, 33(7):916–931.

Lima, L.G.; Dillenburg, S.R.; Medeanic, S.; Barboza, E.G.; Rosa, M.L.C.C.R.; Tomazelli, L.J.; Dehnhardt, B.;Caron, F. 2013. Sea-level rise and sediment budget controlling the evolution of a transgressive barrier in southern Brazil. *Journal of South American Earth Sciences*, 42, 27-38.

May, J.P. and Tanner, W.F., 1973. The littoral power gradient and shoreline changes. In: COATES, D.R. (ed.), *Publications in Geomorphology*. Binghamton: State University of New York, pp. 43-60.

Mitchum Jr., R.M., Vail, P.R. and Sangree, J.B., 1977. Seismic Stratigraphy and Global Changes of Sea Level, Part 6: Stratigraphy interpretation of seismic reflection patterns in depositional sequences. In: Payton, C.E. (ed.), *Seismic Stratigraphy — Applications to Hydrocarbon Exploration*. Tulsa, AAPG, 26, 117-133.

Reguero, B.G.; Menéndez, M.; Méndez, F.J.; Mínguez, R.; Losada; I.J. 2012. A Global Ocean Wave (GOW) calibrated reanalysis from 1948 onwards. *Coastal Engineering*,65:3855.

Rosa, M.L.C.C.; Barboza, E.G.; Dillenburg, S.R.; Tomazelli, L.J.; Ayup-Zouain, R.N., 2011. The Rio Grande do Sul (southern Brazil) shoreline behavior during the Quaternary: a cyclostratigraphic analysis. *Journal of Coastal Research*, SI 64, 686-690.

Shore Protection Manual., 1984. CERC. US Army Engineer Waterways Experiment Station. US Government Printing Office, Washington, DC.

Siegle, E. and Asp, N.E., 2007. Wave Refraction and Longshore Transport Patterns along the Southern Santa Catarina Coast. *Brazilian Journal of Oceanography*, 55, 109-120.

Journal of Coastal Research	SI	75	442-446	Coconut Creek, Florida	2016

Potential of Video Cameras in Assessing Event and Seasonal Coastline Behaviour: Grand Popo, Benin (Gulf of Guinea)

Abessolo Ondoa[†,*], G., Almar[‡], R., Kestenare[‡], E., Bahini[#], A., Houngue[@], G-H, Jouanno[‡], J., Du Penhoat[‡#], Y., Castelle[§], B., Melet[‡], A., Meyssignac[‡], B., Anthony[∞], E.J., Laibi, R., Alory[‡#], G., and Ranasinghe, R.[$,°,~]

[†]JEAI RELIFORME, Université de Douala, Cameroun
[@] IRHOB, Cotonou, Benin

[#]University of Abomey-Calavi, ICMPA-UNESCO Chair, Cotonou, Benin

[°]UNESCO-IHE, Delft, The Netherlands

[~]Harbour, coastal and offshore engineering, Deltares, Delft, The Netherlands

[‡]LEGOS (CNRS/CNES/IRD/Université de Toulouse), France

[§]EPOC (Université de Bordeaux/CNRS) Talence, France

[∞] CEREGE Aix-Marseille Université, Aix en Provence, France

[+] Université Abomey Calavi, Département des Sciences de la Terre, Faculté des Sciences et Techniques, Cotonou, Benin

[$]Research School of Earth Sciences, The Australian National University, Canberra, Australia

www.cerf-jcr.org

www.JCRonline.org

ABSTRACT

Abessolo Ondoa, G.; Almar, R.; Kestenare, E.; Bahini, A.; Houngue, G-H.; Jouanno, J.; Du Penhoat, Y.; Castelle, B.; Melet, A.; Meyssignac, B.; Anthony E.; Laibi, R.; Alory, G., and Ranasinghe R., 2016. Potential of video cameras in assessing event and seasonal coastline behaviour: a case study at Grand Popo, Benin (Gulf of Guinea). *In:* Vila-Concejo, A.; Bruce, E.; Kennedy, D.M., and McCarroll, R.J. (eds.), *Proceedings of the 14th International Coastal Symposium* (Sydney, Australia). *Journal of Coastal Research*, Special Issue, No.75, pp. 442-446. Coconut Creek (Florida), ISSN 0749-0208.

In this study, we explore the potential of a nearshore video system to obtain a long-term estimation of coastal variables (shoreline, beach slope, sea level elevation and wave forcing) at Grand Popo beach, Benin, West Africa, from March 2013 to February 2015. We first present a validation of the video system with field data over a 10-day experiment conducted on Grand Popo beach in 2014. Secondly, 2-years daily and monthly timeseries are extracted and their variability is described as a function of regional forcing and climatic modes. All variables show large monthly variability. The longshore sediment transport estimated locally from video is in agreement with that derived from Era-Interim wave data re-analyses. Results show that the shoreline responds predominantly to tides at the event scale and to waves. Overall, this study suggests that video stations are efficient tools to monitor coastal processes over the long term, in complement with other conventional approaches. Although no clear conclusions can be drawn on inter-annual variability, the results show that it is important to build up extended coastal observation networks to address coastline changes over a wide range of scales.

ADDITIONAL INDEX WORDS : *Bight of Benin, video remote sensing, shoreline, longshore sediment transport, sea level, waves, tide, regional climate*

INTRODUCTION

Description and understanding of the processes that link coastal dynamics and regional meteorological-ocean forcing is still an important challenge. This must provide insights on the temporal and spatial scales of coastal response and long-term trends in a changing climate. Specifically, the link between high frequency (short-term events, <30 days) and longer term (i.e. inter-annual) evolution remains unclear, due to the lack of appropriate modeling tools to describe these different temporal scales. This can now be partly addressed via shore-based video stations, which allows the important variables of the near-shore environment to be derived at high frequency and large spatial scales.

The Gulf of Guinea coastline, in West Africa, is exposed to South Atlantic high-energy oblique swells which drive strong longshore sediment transport (~500 000 m^3yr^{-1}, Almar *et al*., 2015). This stretch of coast is currently affected by severe erosion that reaches up to 10 m/yr at Cotonou , Benin, attributed to the development of large harbours that trap sand transported alongshore (Dossou and Glehouenou-Dossou, 2007). Recent analysis of model based studies and open ocean altimetry data suggest a large temporal variability of longshore transport and local sea-level elevation with trends reaching -103 m^3/yr (1979-2012 period) and +4.6 mm/yr (1993-2012 period) respectively over recent decades (Almar *et al*., 2015; Melet *et al*., 2015). These findings need to be confirmed with direct observations. For this purpose, a permanent low-cost video system was deployed since February 2013 at Grand Popo, Benin.

In contrast with costly in-situ field measurements limited in both time and space, a low-cost video camera-based video system is advantageous in measuring nearshore hydrodynamics

DOI: 10.2112/SI75-089.1 received 15 October 2015; accepted in revision 15 January 2016.
*Corresponding author: gregsolo55@yahoo.fr

(waves, tides, setup, currents) and morphology (shoreline, bathymetry and

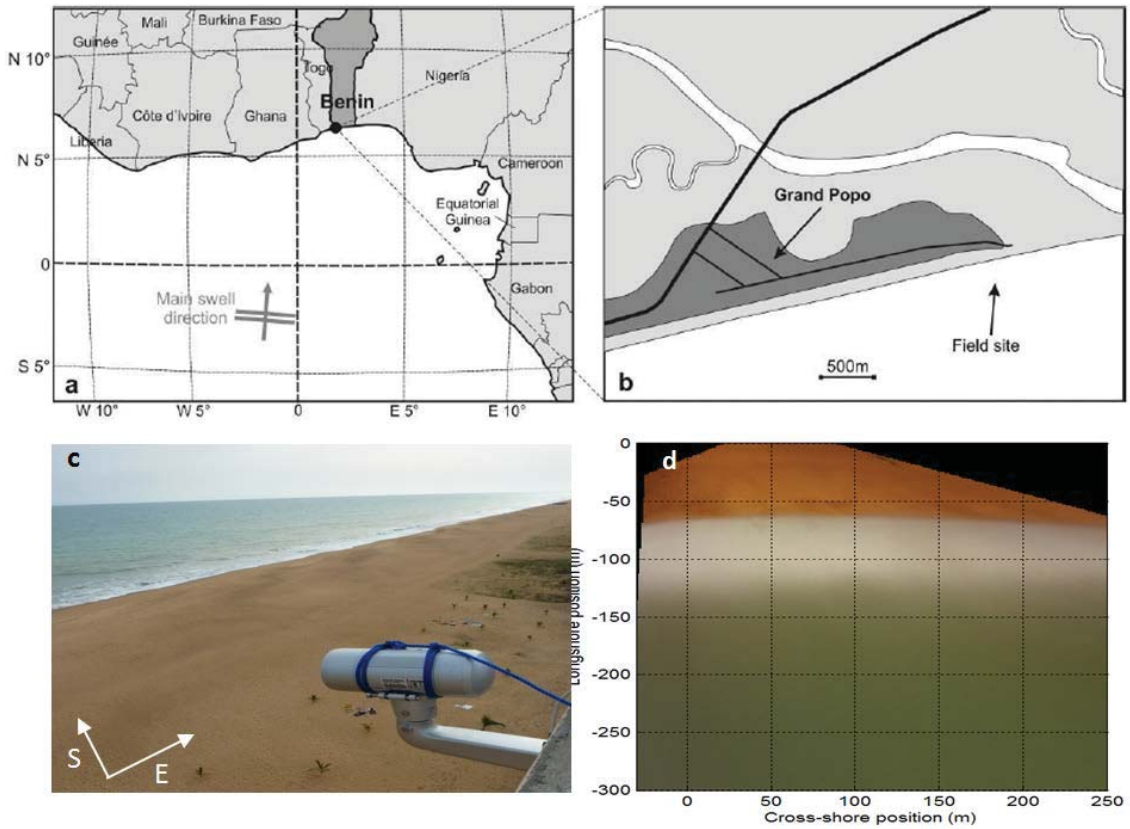

Figure 1.Study site, (a-b) Grand Popo beach in Benin, (Gulf of Guinea, West Africa), facing the South Atlantic.(c) video camera system deployed on a tower made available by the Beninese Navy, and (d) plan shape timex showing the camera field of view. White part is breaking zone and shoreline clearly appears as transition between white to red-band dominated sandy beach.

topography) (see Almar *et al*., 2012b; Holman and Haller, 2013). In addition, this video imagery technique offers an interesting alternative to coastal tidal gauges or spatial altimetry, because it can give an estimation of waterline elevation.

In this study we explore the potential of nearshore video systems in describing and linking the long-term variability of waves, alongshore currents, sea level elevation and the shoreline. This study includes a comparison with field data over a short period (10 days), which allowed for properly extrapolating the variables over the full observation period. The modes of variability of waves, sea level and shoreline position over the observation period (2.5 years) are analyzed and positioned in a regional climate context.

Site description

The beach of Grand Popo, Benin, is located in the Bight of Benin (Gulf of Guinea, West Africa), an open sandy stretch of coast facing the South Atlantic Ocean. Grand Popo is hardly affected by human presence, hosting only a few fishermen, and far enough (80 km) from the influence of Cotonou and Lome harbours. The beach dynamics are dominated by the influence of waves of moderate energy (mean significant wave height H_s = 1.36 m, mean peak period T_p = 9.4 s) coming from mid-latitude with a S-SW incidence (Laibi *et al*., 2014, Almar *et al*. 2015). Tides are semi-diurnal with a micro to meso-tidal range, from 0.8 to 1.8 m for neap and spring tides, respectively. Sediment size is medium to coarse, 0.4 to 1 mm, (D_{50} = 0.6mm). According to the classification proposed by Wright and Short (1984), Grand Popo is an intermediate Low Tide Terrace (LTT) to reflective beach.

METHODS

In February 2013, a low-cost video system was deployed on a 15-m high semaphore of the navy of the Republic of Benin, 80 m from the shore (which is the approximate beach width). It comprises a VIVOTEK IP 7361 camera (1600 x 1200 pixels) that collects data continuously at 2 Hz. This autonomous system is powered by solar panels. An on-site computer processes the raw images and stores the data. Three types of secondary images are stored: instant, 15-min average and time stacks. Three time stacks are generated (two across-shore and one along-shore, Almar and *al.*, 2014).

Two field experiments were conducted at Grand Popo beach, Benin, on February 2013 and March 2014. Field data collected during the Grand Popo 2014 experiment (Almar *et al*., 2016) are used in this study to validate the video system. Measurements included both sea and beach morphological surveys with Differential GPS and bathymetric sonar, while offshore forcing (waves and tide) was characterized using an Acoustic Doppler Current Profiler (ADCP) moored at 10-m depth.

ERAInterim re-analyses (Sterl and Caires, 2005) data were extracted over the 2013-2015 period at the daily scale to compute wave heights at Grand Popo (propagated from deep water to the breakpoint using the formula by Larson *et al*., 2010), and to compute 3 daily indexes standing as proxies of the dominant climatic modes of the South Atlantic. The Inter-Tropical Convergence Zone (ITCZ) and El Nino Atlantic (AMM) were computed from local wind and sea level off Grand Popo, and Southern Annular Mode (SAM) was computed from mid-latitude winds. Longshore Sediment Transport was estimated using the formula by Kaczmarek *et al*., (2005) (see Almar *et al*., 2015).

In this paper, several important nearshore parameters were estimated daily : cross-shore and longshore wave energy fluxes, surface elevation, shoreline location and beach slope. Several video methods were used to estimate the corresponding parameters: wave height (Almar *et al*., 2012a), period and surface elevation (inversed from celerity, see Catalan and Haller, 2008; Stockdon and Holman, 2000) were measured from spatio-temporal images; wave direction and shoreline location were estimated from average images (Almar *et al*., 2012). Determination of the intertidal beach profile involved the delineation of the shoreline at different tidal levels (Aarninkhof *et al*., 2003) and interpolation between low and high tides. Kaczmarek *et al*. (2005) formula is used to estimate longshore current within the surf zone.

RESULTS

Table 1 shows the RMSE errors and the mean error (ME) obtained during Grand Popo 2014 measurements for wave parameters (H_s, T_p and *Dir*), elevation, intertidal topography and bathymetry. The average RMS error of the beach profile is relatively low (0.28 m). The accuracy of the method is within the error range of existing methods (0.3-0.7 m reported in Plant and Kingston, 2007).

Figure 2 shows the comparison for hydrodynamics (wave and tide) using the ADCP data and Era-Interim wave estimates. Errors for H_s, T_p and *Dir* are reasonable though the correlations are rather weak, showing the difficulties in describing high-frequency behavior. The day-to-day dynamics are well captured. It must be noted that ERAInterim estimates show substantial discrepancies (more than 50 % overestimation of H_s and period shorter by 2-4s), which argues in favor of using local video-based measurements rather than hindcast products because of local unresolved effects of bathymetry hydrodynamics (or adverse conditions for the Larson *et al*., (2010) formula).

On the whole, this validation proves that video methods have reasonable errors and can be used in a stand-alone mode for longer-term estimates of waves, sea level and beach morphological evolution.

Beach and forcing evolution over the 2013-2015 period

The five following parameters: cross-shore and longshore wave energy fluxes, surface elevation, shoreline location and beach slope, were computed at daily and monthly scales over the 2-yr period, providing a long enough timeseries to determine the relative contributions of wave and tide forcing to beach response, using a multiple linear regression. In this analyze, waves and tide are considered independent, and the shoreline response approximated as linear, though it might slightly differ (see Davidson *et al*., 2013; Yates *et al*., 2009). Table 2 shows that short-term shoreline evolution is dominated by tidal range modulation (spring/neap tide cycle) while waves are rather steady at this scale (which is typical of a storm-free area). At the seasonal scale, the shoreline responds preferentially to the summer/winter modulation of waves, with larger waves during the southern hemisphere winter.

Table 1. *Comparison of hourly hydrodynamic video estimates and Grand Popo 2014 field measurements. The root mean square error (RMSE) and the mean error (ME) are computed from the difference between the two sets of data. Intertidal profile error computed from 7 daily comparisons.*

Hydrodynamic parameters	RMSE	ME
H_s (m)	0.14	-0.02
T_p (s)	1.31	-0.18
Direction (°)	9.25	2.25
Elevation (m)	0.12	0.02
Intertidal profile	0.28	0.23

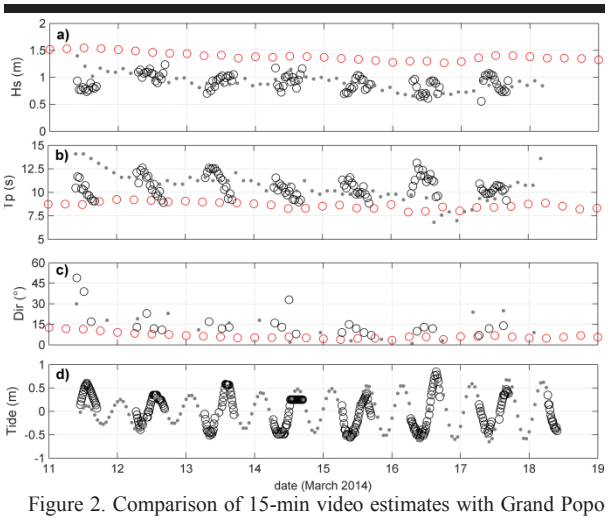

Figure 2. Comparison of 15-min video estimates with Grand Popo 2014 hourly field measurements for (a) H_s, (b) T_p, (c) Dir and (d) tide. Red circles stand for ERAInterim waves propagated to the shore using formula by Larson *et al*., (2010). Grey dots and black circles are in-situ data (ADCP) and video data, respectively.

Table 2. *Relative contribution (percent) of significant wave height and tide to the evolution of shoreline at monthly and event scale.*

Hydrodynamic forcing parameters	H_s (%)	Tide (%)
Monthly scale	72	28
Event scale	21	79

Figure 3 shows that all variables have substantial monthly variability. Wave flux (both cross and alongshore) peak in the southern hemisphere winter, while slope decreases and shoreline retreats. In the meantime, elevation and shoreline behavior seem linked and present a substantial trend, though it is too early to draw significant conclusions.

Since the dynamics of this coastline is dominated by longshore processes (Almar *et al*., 2015; Laibi *et al*., 2014), we computed Longshore Sediment Transport (LST) from locally video-derived wave parameters. Interestingly, results in Figure 4 shows that Era-Interim (from total swell and wind waves) and local estimates are in good agreement, both in average value (444397 and 496993 m^3/yr, respectively) and variability, though some discrepancies exist (RMSE=0.23).

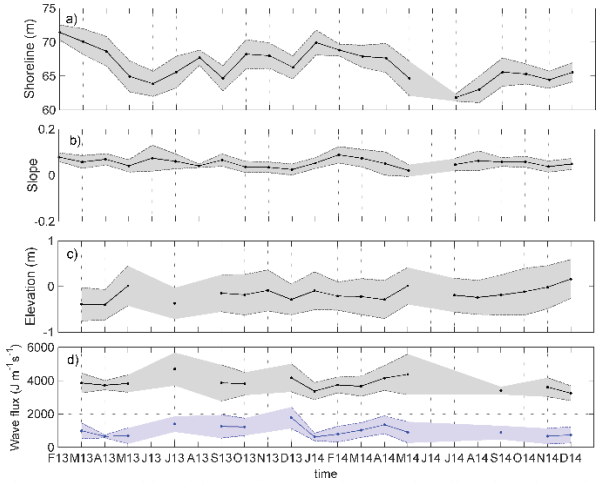

Figure 3. Monthly video estimates of : (a) shoreline location, (b) beach slope, (c) surface elevation, and (d) wave energy flux, cross-shore in grey and longshore in blue. Shaded zones stand for day-to-day dispersion (standard deviation).

Even though it is too early to determine the influence of regional climatic modes, SAM, ITCZ and AMM (Almar *et al*., 2015) (Figure 5) on these coastal variables, our paper puts forward the potential of video-based techniques for such long-term oriented investigations.

DISCUSSION AND CONCLUSIONS

In this paper, 2 years of video observations at Grand Popo, Benin, analysed using recently developed methods, were employed to estimate the main nearshore parameters: wave height, period and direction, surface elevation, bathymetry and topography, as well as shoreline change. These estimates were compared to field observations collected during the 10-day Grand Popo 2014 experiment and showed reasonable agreement. This shows the ability of low-cost video imagery in continuously and quantitatively monitoring a large number of key coastal variables over long durations, pending substantial errors that need to be further quantified, and ultimately reduced. In particular, the measurement of sea level brings new

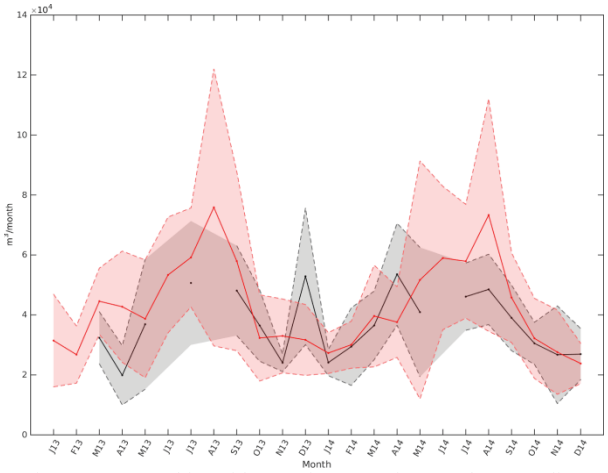

Figure 4. Monthly video estimates of Longshore Sediment Transport estimated using the Kaczmarek *et al*. (2005) formula, computed from (red) ERA-Interim re-analyses (using Larson *et al*., (2010) for wave propagation to the shore) and (black) video estimates. Shaded zones stand for day-to-day dispersion (standard deviation).

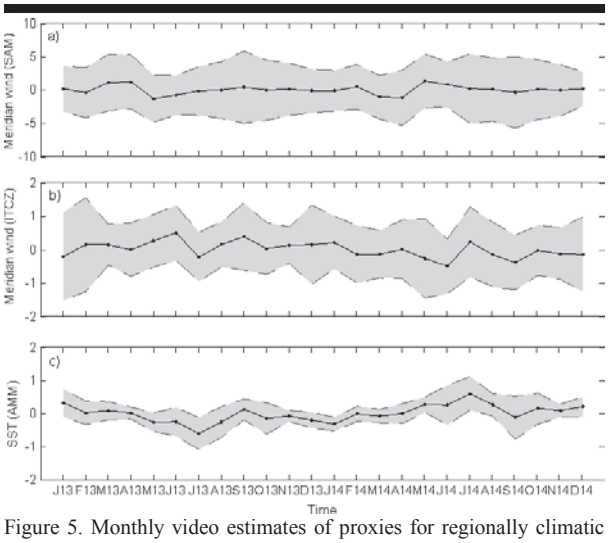

Figure 5. Monthly video estimates of proxies for regionally climatic modes : (a) meridian wind in the South Atlantic (SAM), and (b) meridian wind (ITCZ) and (c) Surface Sea Temperature (AMM) in the Bight of Benin computed from daily Era-Interim re-analyses. Shaded zones stand for day-to-day dispersion.

perspectives in the assessment of tidal harmonics in remote or hazardous areas where the deployment of buoys encounter difficulties. Also, it has to be pointed out that, in contrast with tidal gauges or spatial altimetry, this technique provides the actual shoreline elevation, which includes all regional and coastal components of sea level (including wave-induced setup and run-up), a key aspect in assessing coastal vulnerability.

All studied variables show substantial variability at the monthly scale, wave energy peaking in the southern hemisphere winter when waves are larger in the South Atlantic Ocean. Interestingly, shoreline and elevation behavior seem to be strongly linked. In this storm-free area, elevation preferentially controls shoreline response at the short-term scale while waves dominate monthly shoreline evolution.

ACKNOWLEDGMENTS

The Grand Popo experiment was supported by French INSU/CNRS EC2CO-LEFE/IRD, UNESCO co-chair ICPMA/IPB. We are indebted to the naval services of Benin at Grand Popo for their logistic support during the field experiment and for allowing the installation of the permanent video system on their semaphore. This research has received support from French grants through ANR (COASTVAR: ANR-14-ASTR-0019). We acknowledge use of the ECMWF ERA Interim dataset (www.ECMWF.Int/research/Era). We would like to express our gratitude to IRD/JEAI-RELIFOME (Institut de Recherche pour le Développement-Jeune Equipe Associée à l'IRD) for its financial support.

LITERATURE CITED

Aarninkhof, S., 2003. Nearshore Bathymetry derived from Video Imagery. *Delft University of Technology PhD Thesis*

Almar, R.; Cienfuegos, R.; Catalán, P.A.; Michallet, H.; Castelle, B.; Bonneton, P., and Marieu, V. 2012. A new breaking wave height direct estimator from video imagery, *Coastal Engineering*, 61, 42-48

Almar, R.; Ranasinghe, R.; Senechal, N.; Bonneton, P.; Roelvink, D.; Bryan, K.; Marieu, V., and Parisot, J.P., 2012. Video based detection of shorelines at complex meso- macrotidal beaches, *Journal of Coastal Research*. COAS_49646, 28(5), 1040-1048

Almar, R. ; Du Penhoat, Y. ; Honkonnou, N. ; Castelle, B. ; Laibi, R. ; Anthony, E. ; Senechal N.; Degbe, G.; Chuchla, R. ; Sohou, Z., and Dorel, M., 2014. The Grand Popo experiment, Benin, *Journal of Coastal Research*, SI 70, 651-656, ISSN 0749-0208

Almar, R.; Kestenare, E.; Reyns, J.; Jouanno, J.; Anthony, E.J.; Laibi, R.; Hemer, M.; Du Penhoat, Y., and Ranasinghe, R., 2015. Response of the Bight of Benin (Gulf of Guinea, West Africa) coastline to anthropogenic and natural forcing, Part1: Wave climate variability and impacts on the longshore sediment transport, *Continental Shelf Research*, 110, 48-59

Almar, R.; Almeida, P.; Blenkinsopp, C., and Catalan, P., 2016. *Journal of Coastal Research*, Special Issue, No. 75

Catalan, P. and Haller, M., 2008.Remote sensing of breaking wave phase speeds with application to non-linear depth inversions, *Coastal Engineering*, 55, 93-111

Davidson, M.; Splinter, K., and Turner, I., 2013a. A simple equilibrium model for predicting shoreline change. *Coastal Engineering*, 73, 191–202.

Dossou, K.M.R and Glehouenou-Dossou, B., 2007. The vulnerability to climate change of Cotonou (Benin), *Environment and Urbanization*, 19(1), 65:79

Holman, R. and Haller, M., 2013.Remote sensing of the nearshore. *Annual Review of Marine Science*, 113, 5–95

Kaczmarek, L.M.; Ostrowski, R.; Pruszak, Z., and Rozynski, G., 2005. Selected problems of sediment transport and morphodynamics of a multi-bar nearshore zone. *Estuarine, Coastal and Shelf Science,* 62,415–425

Laibi, R.; Anthony, E.; Almar, R.; Castelle, B., and Senechal, N., 2014. alongshore drift cell development on the human-impacted Bight of Benin sand barrier coast, West Africa. In Proceedings 13th International Coastal Symposium (Durban, South Africa), *Journal of Coastal Research*, SI 70, 78-83

Larson, M.; Hoan, L.X., and Hanson, H. 2010. A direct formula to compute wave properties at incipient breaking, Journal of *Waterway, Port, Coastal and Ocean Engineering*, 136(2), 119-122

Melet, A.; Almar, A, and Messignac, B., 2015. What dominates sea level at the coast: a case study for Cotonou, *Ocean Dynamics* (in revision)

Sterl, A. and Caires, S., 2005. Climatology, variability and extrema of ocean waves- the web-based KNMI/ERA-40 Wave Atlas. *Int. J. Climatol*. 25, 963–977

Stockdon H.F. and Holman R.A. 2000, Estimation of Wave Phase Speed and Nearshore Bathymetry from Video Imagery, *Journal of Geophysical Research*. 105(C9), pp 22,015-22,033

Wright, L.D. and Short, A.D., 1984. Morphodynamic variability of surf zones and beaches: A synthesis. *Marine Geology*, 56, 93-118

Yates, M.L.; Guza, R.T. and O'Reilly W.C., 2009. Equilibrium shoreline response: Observations and modeling. *Journal of Geophysical Research*, 114

Journal of Coastal Research	SI	75	447-451	Coconut Creek, Florida	2016

Beach Morphological Predictions: The Impact of a Temporally Varying Sediment Fall Velocity

Sam Prodger[†*], Paul Russell[†], Mark Davidson[†] and Jon Miles[†]

[†]School of Marine Science and Engineering,
Plymouth University, Plymouth, UK

www.cerf-jcr.org

www.JCRonline.org

ABSTRACT

Prodger, S.; Russell, P.; Davidson, M., and Miles, J., 2016. Beach Morphological Predictions: The Impact of a Temporally Varying Sediment Fall Velocity *In:* Vila-Concejo, A.; Bruce, E.; Kennedy, D.M., and McCarroll, R.J. (eds.), *Proceedings of the 14th International Coastal Symposium* (Sydney, Australia). *Journal of Coastal Research*, Special Issue, No. 75, pp. 447-451. Coconut Creek (Florida), ISSN 0749-0208.

This paper introduces new field measurements that allow quantification of the relative importance of temporal variations in grain size to beach morphology classification. A dataset of 7 years of daily remotely sensed beach morphological measurements and monthly intertidal topographic surveys with surface sediment sampling were used to assess how observed temporal variations in sediment size (or fall velocity) influence morphological predictions at two energetic, sandy macro-tidal beach sites. Beach morphological predictions were obtained via the widely used sequential classification scheme of Masselink and Short (1993), where time varying wave height and wave period are usually used to drive changes in beach state. Beach state was found to be highly seasonal, with an evolution from more dissipative states in the winter to lower intermediate states in the summer. Beach state predictions were made using both a constant and time-varying sediment fall velocity and then compared to visual observations of morphological state. Predictions using a constant fall velocity correlated poorly (r^2 = 0.32) with observations, whereas predictions made using a time-varying fall velocity, correlated better (r^2 = 0.79). A feedback loop was also evident in the system, with energetic waves promoting a migration towards a dissipative state, and a coarsening shoreface grain size.

ADDITIONAL INDEX WORDS: *Coastal Sediments, Morphological Modelling, Sandy Beaches, Grain Size.*

INTRODUCTION

Sandy beaches represent an extremely dynamic system, with variability acting over a number of spatio-temporal scales. Short-term high-energy storm events often generate extreme change over a few days to weeks and slower recovery processes promote cyclicity over interannual timescales. There have been many models proposed to predict both these short-term storm responses and seasonal variations in beach state. These models are usually either equilibrium models, with constant wave conditions, or sequential, which predict bar arrangement under varying waves conditions.

The sequential beach classification of Wright and Short (1984) and Masselink and Short (1993) are two widely used schemes that differentiate beach morphology into a number of discrete states. These states are related to the wave and sediment conditions via the dimensionless fall velocity proposed by Gourlay (1968), where $\Omega = H_b/T_pW_s$, with H_b the breaking wave height (m), T_p the wave period (s) and W_s the sediment fall velocity (ms^{-1}). Dissipative states ($\Omega > 6$) with a low beach slope and wide surf zone define the upper end of the schemes and steeply sloping reflective ($\Omega < 1$) beaches with narrow surf zones form the lower end, although both are considered stable, linear and alongshore uniform. The intermediate states ($1 < \Omega < 6$), vary depending upon the classification used, but all exhibit alongshore variability, with different configurations of rip channels and single, double or multi- crescentic bars. These intermediate states often have the most impact upon beach safety, with many studies (Scott *et al.*, 2014, Short and Hogan, 1994, Woodward *et al.*, 2015) linking morphological state to beach hazard. While these classification schemes are widely used, most studies that either model morphology or utilise the dimensionless fall velocity, such as Splinter *et al.* (2014) and Stokes *et al.* (2015), assume a mean sediment fall velocity that remains constant and fixed in time (and space). Morphological change is then forced through variations in incident wave conditions.

A 7-year time-averaged Argus video dataset, with accompanying monthly intertidal surveys and surface sediment analysis, and 9 years of nearshore wave measurements provide a unique dataset, which this study uses to investigate the effect temporal variability in the shoreface sediments has upon daily empirical predictions of beach morphology at two energetic macro-tidal beaches.

METHODS

Perranporth and Porthtowan are both sandy beaches on the northwest coast of Cornwall, UK (Figure 2) and are exposed to the energetic Atlantic swell and locally generated wind waves (Davidson *et al.*, 1997), which promote cross-shore transport with significant sediment interchange between the intertidal beach and nearshore bar(s). Both locations are macro- tidal, with mean spring and neap ranges of 6.3 m and 1.7 m.

DOI: 10.2112/SI75-090.1 received 15 October 2015; accepted in revision 15 January 2016.
*Corresponding author: sam.prodger@plymouth.ac.uk

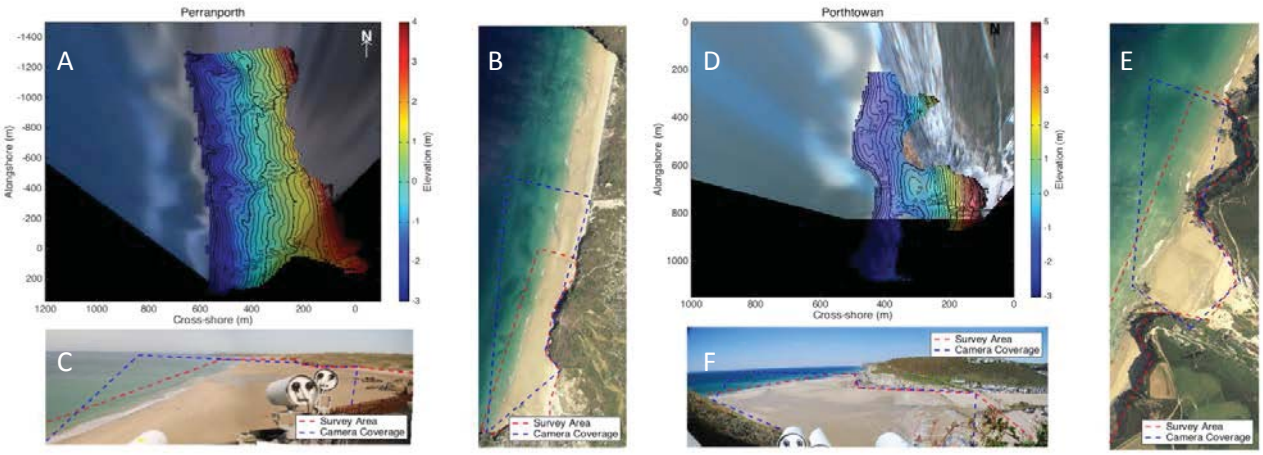

Figure 1. Interpolated topographic survey data (coloured contour plots) overlain onto the time-averaged video images collected from low tide on the survey data, A, B & C shows Perranporth and D, E & F shows Porthtowan. Contour lines represent elevation (m) above Ordnance Datum Newlyn (ODN). In the Timex (A & D) images, black represents no camera coverage, brown / grey is the dry beach or cliffs, white is the foam generated by breaking waves and shades of blue represent the deeper water where no breaking is occurring. B and E are aerial photographs of the two study sites showing the corresponding camera and topographic survey coverage, with C and F showing the same area but from the perspective of the video cameras mounted on the cliffs to the south of the sites.

Perranporth is 3.5 km long, with a spring low tide cross-shore distance of around 600 m and backed by a combination of Devonian hard-rock cliffs and soft-sandy dunes that are slightly finer in composition than the intertidal beach. Porthtowan is backed by a younger Devonian meta-formation and soft sand dunes but has a shorter alongshore range of 2.1 km (the northern 0.6 km becomes Chapel Porth Beach) and a cross-shore extent of 500 m at spring low tide. From August 2006, a nearshore directional wave rider buoy, sited 0.6 km offshore from Perranporth (Figure 2) in 10-15 m water depth had recorded mean and maximum significant wave heights (H_s) of 1.9 m and 10.6 m respectively, peak period (T_p) and zero upcrossing wave period (T_z) of 8.3 s and 5.9 s respectively and a direction of 278º. Intertidal sediments are different at each site, with Perranporth comprised of medium quartz sand that is well sorted and compositionally mature, with a median grain size of 0.33 mm (or mean fall velocity of 0.037 ms^{-1}) from January 2008 to June 2015. The intertidal of Porthtowan is also composed of medium quartz sand, although this is more poorly sorted and compositionally more immature than sediment present at Perranporth. However, the upper beach, situated between neap high tide and spring high tide is poorly sorted and composed of a mixed sand (medium to coarse) and gravel substrate. Median grain sizes of the intertidal were 0.39 mm (0.051 ms^{-1}) and the upper beach was 0.56 mm (0.074 ms^{-1}).

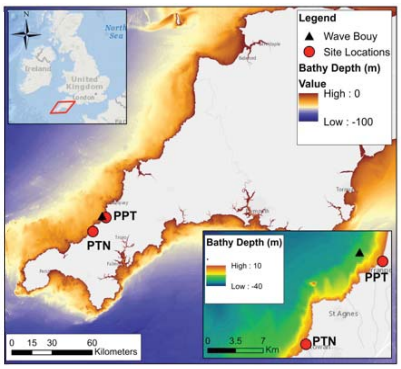

Figure 2. Location map of the beaches studied, Perranporth (PPT) and Porthtowan (PTN) (red circles) on the northwest coast of Cornwall, UK. Also shown is the location of the Directional WaveRider (Black Triangle) and the nearshore bathymetry.

Morphological Observations

Field observations of beach morphology were undertaken by monthly topographic surveys using an RTK-GPS system mounted on an all-terrain vehicle with 99 individual monthly surveys between February 2008 and September 2015 at both sites. The surveys were collected on the lowest spring low tide of the month, which maximised the coverage across the lower beach but introduced a variable interval between the surveys. Between the 99 surveys, the mean interval was 29 days (standard deviation - 6.4 days) with a minimum of 12 days and maximum of 60 days. The survey data, recorded in OSGB36 coordinates was converted to the same local grid utilised by the video cameras by a rotation and translation. This gridded data (Figure 1, A & D) was then used to construct a digital elevation model using a 20 m cross- and alongshore resolution in a quadratic loess interpolation (Plant *et al.*, 2002). These surveys were supplemented by daily remote observations of beach morphology by elevated Argus video cameras permanently mounted on the cliffs to the south of both sites (Figure 1). Three cameras at Perranporth and four (five from December 2014) at Porthtowan collected snap shots and a time averaged 10-minute exposure (Timex) from the inter- and sub tidal regions every 30 minutes between March 2006 and March 2015. Due to the preferential wave breaking creating significant foam over the shallow bar crests compared to the deeper water channels, bands

of high intensity pixels are often visible in the time-averaged images. These bands can be used to depict the configuration of the bar(s) and rips and infer the underlying morphology using the Masselink and Short (1993) macro-tidal classification scheme. One image per day was selected from low tide to minimise the effects of tidal shifting of the bar. To maximise the visible break pattern and reduce user error only images that had average tidal cycle H_s between 0.5 and 2.5 m were used. Poor light, adverse weather conditions and infrequent technical issues also contributed to the image availability for a particular day. For the 3287 days of the study, 2176 usable images were chosen from Perranporth, with a mean interval of 6 days (standard deviation - 3 days), a minimum of 1 day and a maximum of 83 days and 2082 images from Porthtowan, with a mean interval of 9 days (standard deviation - 4 days), a minimum of 1 day and a maximum of 53 days.

Wave and Tidal Conditions

Wave data were obtained by a nearshore Datawell directional WaveRider buoy, moored 0.6 km directly offshore from Perranporth in 10-15m water depth, with both sites exposed to similar energetic offshore wave conditions (Poate *et al.*, 2009). The statistics recorded in 30-minute intervals were used to determine daily values for significant wave height and peak period. A continuous tidal elevation record was generated via interpolation using local coefficients.

Sediment Collection

Sediment data was collected during the monthly topographic surveys from February 2008 to September 2015, with a gap of 12 surveys between January 2012 and December 2012 at both sites. These missing months were filled in using the antecedent wave steepness driven model (equation 4 and 5). Three samples were obtained by hand during each survey from the surface and upper 2 cm of the sediment column. The three samples were collected from the same positions each time, which correspond to spring high, mid and low tide locations. Statistics from the sediment samples were quantified using the settling tube approach of Folk and Ward (1957). Each sample was passed through the settling tube on five occasions, with a fall velocity (W_s) resulting from an average of these five runs. For the duration of the study, average D_{50} sizes for Perranporth were: High tide – 0.28 mm, Mid-Tide – 0.37 mm and Low Tide – 0.39 mm. For Porthtowan these were High tide – 0.56 mm, mid tide – 0.45 mm and low tide – 0.34 mm.

Modelling Morphology

Beach morphology was empirically predicted using the dimensionless fall velocity sequential classification schemes proposed by Wright and Short (1984) which related a discrete beach state to dimensionless fall velocity, Ω, where:

$$\Omega = \frac{H_b}{T_p W_S} \qquad (1)$$

and, T_p is the peak wave period (s), W_s the sediment fall velocity (ms^{-1}) and H_b the breaker height (m) calculated using the Komar and Gaughan (1972) equation:

$$H_b = 0.39 g^{1/5} (T_p H_s^2)^{2/5} \qquad (2)$$

This was furthered by Masselink and Short (1993) whom applied this to macro-tidal locations by introduced a relative tidal range term where:

$$\text{RTR} = \frac{Mean\ Spring\ Range}{H_b} \qquad (3)$$

For small values of RTR, waves are dominant and large values indicate tidal dominance, with the two study sites having a mean RTR of 5.3 and a minimum and maximum of 1.12 and 13.8 respectively. For a RTR of 3 – 7 and a dimensionless fall velocity between 2 – 5, distinct bar morphology and rip circulation develops and for a RTR 1 – 15 and Ω > 5, three-dimensional topography is lacking, with alongshore uniform, linear bar(s) developing. Morphological predictions were made using both a constant (Perranporth: 0.037 ms^{-1} Porthtowan: 0.051 ms^{-1}) and a time varying W_s, calculated daily by:

$$\frac{dW_s}{dt} = \alpha\,(S - S_\emptyset) \qquad (4)$$

Here, W_s is the sediment fall velocity, t is time and S is the new equilibrium conditions that the system is progressing towards, given by: H_s/L_∞ where H_s is the significant wave height and L_∞ the deep-water wavelength given by: $L_\infty = gT_p^2/2\pi$. S_ϕ is a temporally evolving weighted average of the antecedent wave steepness, calculated by:

$$S_\phi = \left[\sum_{i=1}^{2\phi} 10^{-i/\phi}\right]^{-1} \sum_{i=1}^{2\phi} S_i 10^{-1/\phi} \qquad (5)$$

This weighting function (Equation 5) decays at a rate governed by ϕ and reaches 10% and 1% at ϕ and 2ϕ days prior to the current calculation time. α and ϕ are model free parameters, where α controls the rate of change and magnitude of grain size variability and has units of (ms^{-1}). For large values of ϕ (≈ 10^3 days) S_ϕ converges on the time-series mean value and the model behaviour is dominated by seasonal and interannual variability, for values of <10^2 days storm frequency responses become significant. The monthly sediment samples were used to calibrate and validate the model.

RESULTS

At both sites morphology was found to vary on a number of time scales, with a background seasonality linked to the variations in incident wave energy and sediment size driving a beach evolution from a more dissipative winter state to more intermediate summer states (Figure 3). Over the 7-year study period, both sites spent an average 34% of the time in a dissipative state, 66% in various intermediate states (Table 1) and 0% in a reflective state.

Predictions made using a constant sediment size correlated relatively poorly with the visual time-series (Table 2), with a large degree of scatter and wide range of predictions (Ω = 0.85 to 8.9). Additionally, during the study period reflective conditions (Ω <1) were predicted to develop on over 23 separate occasions at Perranporth and 74 at Porthtowan (Table 3), which was not supported by observations. At Perranporth, the constant fall velocities predictions also over estimated the amount of time spent in a dissipative state by 450 days, whereas Porthtowan was predicted to spend 430 days less in a dissipative state and more

time in lower intermediate states compared to the visual observations.

Table 1. *The percentage of time (in days) each site spent in each beach state, as noted visually from time-averaged video images.*

Beach State		Ω	Probability of Occurrence (% of 2176 Days)	
			Perranporth	Porthtowan
Dissipative		>6	32.9	35.3
Intermediate	Longshore Bar-Trough	5	16.5	25.1
	Rhythmic Bar & Beach	4	20.8	22.3
	Transverse Bar & Beach	3	23.0	14.5
	Low Tide Terrace	2	6.8	2.8
Reflective		<1	0	0

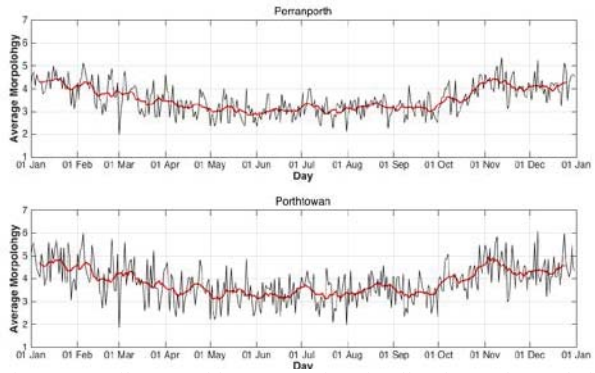

Figure 3. Daily ensemble average for visually observed morphology (signified by Ω) at Perranporth (Top) and Porthtowan (Bottom) using all 7 years of daily data. Red line represents the seasonal signal with a 1/31-day cut-off.

Table 2. A*ccuracy of beach state predictions to visual observations using a constant and time-varying sediment fall velocity.*

Ws Condition	Predictions match to Visual Observations (%)	
	Perranporth	Porthtowan
Constant Fall Velocity	43	37
Time Varying Fall Velocity	76	79

By introducing a time varying sediment fall velocity, modelled daily using monthly sediment sampling for calibration, prediction accuracies improved by an average of 37% at both Perranporth and Porthtowan, with a reduced amount of scatter and a smaller range of predictions (Ω = 2.3 to 7.8). Encouragingly, by including the time varying term, there were no occurrences of reflective morphology developing even though the incident wave conditions were kept the same for both iterations.

Table 3. *The percentage of time (in days) each site spent in each beach state as empirically predicted with either a constant or time varying sediment fall velocity. Red shows predicted time exceeded visual observed time in each state and blue that observations exceed predicted time.*

Beach State		Probability of Occurrence (% of 2176 Days)			
		Constant W_s		Time Varying W_s	
		PPT	PTN	PPT	PTN
Dissipative		52.84 (+19.93)	16.81 (-18.45)	33.63 (+0.73)	34.24 (-1.02)
Intermediate	LBT	15.58 (-0.91)	13.29 (-11.80)	13.29 (-3.2)	16.00 (-9.09)
	RBB	16.64 (-4.15)	19.97 (-2.36)	19.97 (-0.87)	19.86 (-2.49)
	TBB	11.64 (-11.36)	27.52 (+12.99)	27.52 (+4.53)	25.66 (+11.15)
	LTT	3.25 (-3.56)	20.72 (+17.96)	6.41 (-0.42)	4.22 (+1.46)
Reflective		0.06 (+0.06)	1.68 (+1.68)	0 (0)	0 (0)

Figure 4 shows the predicted morphology for Perranporth from January 2009 to January 2010. Using a constant sediment fall velocity results in rapid variations between beach states, as predictions are solely forced by changes in incident waves alone. However, these oscillations between various states is not present in the visual time series or monthly survey data, with predictions using a time-varying fall velocity having a longer evolution time that correlated better with these observations. Furthermore, the introduction of a time varying W_s suppressed the development and / or the continued persistence of the two end members (Ω < 1 and Ω > 6) of the sequential scale.

Figure 4. Daily Beach state predictions using a constant (blue) and time varying (red) sediment fall velocity. Visual observations are shown in black.

DISCUSSION

Visual observations made in this study correlate well with previous work such as Quartel *et al.* (2008), Sénéchal *et al.* (2009) and Scott *et al.* (2009), who all noted a strong seasonality in beach morphology, linked to seasonal variations in incident wave energy. However, as noted by this study and Haxel and Holman (2004) seasonal variations in sediment characteristics

also influence this morphological cyclicity. Results from a morphological model using both a constant and a time-varying sediment fall velocity show that prediction accuracy is almost doubled when accounting for temporal changes in shoreface sediments.

There is also significant hysteresis in the system, in that the larger wave heights that promote evolution of an increasingly dissipative state also promoted a coarsening of the shoreface sediments and thus a larger sediment fall velocity. The improvement in prediction accuracy could be a result of the inclusion of an antecedent term, which incorporates the prior conditions when predicting the current conditions, with several studies (Davidson *et al.*, 2013, Splinter *et al.*, 2014) highlighting the importance of including such a term when modelling beach morphology. Finally, the sensitivity analysis (Figure 5) undertaken by keeping multiple arrangements of H_s, T_p, and W_s either constant or time varying, and comparing each set or predictions to the video data, illustrates that the most accurate predictions occur when all parameters are accounted for, and assuming that any are temporally constant leads to a dramatic reduction in model performance.

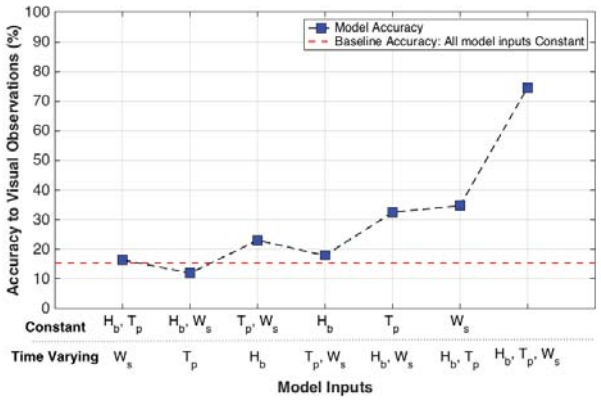

Figure 5. The sensitivity of prediction accuracy if the three input parameters are kept in different configurations of constant and time varying. Red line represents the baseline accuracy if all parameters are kept fixed.

CONCLUSIONS

Beach morphology was visually determined daily from time-averaged video images from 2007-2015 and compared to predictions made using an empirical function. The introduction of a time-varying sediment fall velocity in the widely used Masselink and Short (1993) model was found to increase prediction accuracy by up to 37% when compared to those made with a constant sediment approach. Additionally, the inclusion of this term supressed the time spent in a dissipative state and completely inhibited the development of reflective morphology, which was more consistent with the video data. Therefore, when modelling beach morphology, the temporal variations of sediment fall velocity needs to be accounted for.

LITERATURE CITED

Davidson, M.A.; Huntley, D.; Holman, R.A., and George, K. 1998. The evaluation of large scale (km) intertidal beach morphology on a macrotidal beach using video images. Proceedings of Coastal Dynamics, 1997 ASCE. 385-394.

Davidson, M.A.; Splinter, K.D., and Turner, I.L. 2013. A simple equilibrium model for predicting shoreline change. *Coastal Engineering,* 73**,** 191-202.

Folk, R.L. and Ward, W.C. 1957. Brazos River bar: a study in the significance of grain size parameters. *Journal of Sedimentary Research,* 27.

Gourlay, M.R., 1968. Beach and dune erosion tests (I). Delft Hydraulics Laboratory.

Haxel, J.H. and Holman, R.A. 2004. The sediment response of a dissipative beach to variations in wave climate. *Marine Geology,* 206**,** 73-99.

Komar, P.D. and Gaughan, M.K. 1972. Airy wave theory and breaker height prediction. *Coastal Engineering Proceedings,* 1.

Masselink, G. and Short, A.D. 1993. The Effect of Tide Range on Beach Morphodynamics abd Morphology: A Conceptual Beach Model. *Journal of Coastal Research,* 9**,** 785-800.

Plant, N.G.; Holland, K.T., and Puleo, J.A. 2002. Analysis of the scale of errors in nearshore bathymetric data. *Marine Geology,* 191**,** 71-86.

Poate, T.; Kingston, K.; Masselink, G., and Russell, P. Response of High-energy, Macrotidal Beaches to Seasonal Changes in Wave Conditions: Examples from North Cornwall, UK. Proceedings of the 10th International Coastal Symposium ICS 2009, 2009. Journal of Coastal Research, 747-751.

Quartel, S.; Kroon, A., and Ruessink, B.G. 2008. Seasonal accretion and erosion patterns of a microtidal sandy beach. *Marine Geology,* 250**,** 19-33.

Scott, T.; Masselink, G.; Austin, M.J., and Russell, P. 2014. Controls on macrotidal rip current circulation and hazard. *Geomorphology,* 214**,** 198-215.

Scott, T.; Russell, P.; Masselink, G., and Wooler, A. 2009. Rip current variability and hazard along a macro-tidal coast. *Journal of Coastal Research SI,* 56**,** 895-899.

Sénéchal, N.; Gouriou, T.; Castelle, B.; Parisot, J. P.; Capo, S.; Bujan, S., and Howa, H. 2009. Morphodynamic response of a meso- to macro-tidal intermediate beach based on a long-term data set. *Geomorphology,* 107**,** 263-274.

Short, A. and Hogan, C. 1994. Rip currents and beach hazards: their impact on public safety and implications for coastal management. *Journal of Coastal Research***,** 197-209.

Splinter, K.D.; Davidson, M.A.; Turner, I. L., and Beuzen, T. 2014. Estimating Shoreline Response In A Changing Wave Climate. *Coastal Engineering Proceedings,* 1**,** sediment. 37.

Stokes, C.; Davidson, M., and Russell, P. 2015. Observation and prediction of three-dimensional morphology at a high-energy macrotidal beach. *Geomorphology,* 243**,** 1-13.

Woodward, E.; Beaumont, E.; Russell, P., and Macleod, R. 2015. Public understanding and knowledge of rip currents and beach safety in the UK. *International Journal of Aquatic Research and Education,* 9**,** 49-69.

Wright, L.D. and Short, A.D. 1984. Morphodynamic variability of surf zones and beaches: A synthesis. *Marine Geology,* 56**,** 93-118.

Journal of Coastal Research	SI	75	452-456	Coconut Creek, Florida	2016

Equilibrium Beach Profile in the Presence of Beachrocks

Marcelo Rollnic[†*] and Carmen Medeiros[‡]

[†]Laboratório de Oceanografia Física
Departamento de Oceanografia
Universidade Federal do Pará
Belém, Brazil

[‡]Laboratório de Oceanografia Física Estuarina e Costeira,
Departamento de Oceanografia
Universidade Federal de Pernambuco
Recife, Brazil

www.cerf-jcr.org

www.JCRonline.org

ABSTRACT

Rollnic, M. and Medeiros, C., 2016. Equilibrium Beach Profile in the Presence of Beachrocks *In:* Vila-Concejo, A.; Bruce, E.; Kennedy, D.M., and McCarroll, R.J. (eds.), *Proceedings of the 14th International Coastal Symposium* (Sydney, Australia). *Journal of Coastal Research*, Special Issue, No. 75, pp. 452-456. Coconut Creek (Florida), ISSN 0749-0208.

Equilibrium Beach Profile (EBP) models are used to estimate sandy beach profiles, they assume the existence of a shoreface shape that represents an equilibrium condition between wave climate and sediments, making it possible to identify erosion/accretion trends. EBP models suit beaches with near homogeneous grain size sediments. However, in subtropical and tropical areas, beachrocks are often found underlying the beach face, such that EBP models may not be suitable as shadowing areas may favour settling of variable grain size sediments. Our goal was to evaluate the Bruun-Dean EBP model for a beach along which beachrocks were at times absent and at times present as onshore or submerged reefs. Eight 1km-long bathymetric profiles were performed from the surf zone to the 10m isobath and sediment samples obtained at 50, 100, 200, 500 and 1000 m from the surf zone. EBP was computed for distinct coefficient (**m**) values and evaluated as a function of resulting summed square error. A closure depth of 3.97 m was computed using wave characteristics were derived from 1 year radar records. Along the study area the 3.97 m isobath is positioned 140 to 400m offshore, disregarding the quotas of the beachrocks. At the control areas where beachrocks were absent, **m**=0.67 yielded the best fit. At areas where beachrocks were present, profiles tended to be steeper and **m**=0.77 results in a better adjustment near the shore. For the more seaward portion of the profiles, the incorporation of a parameter related to the reef high could improve fitting.

ADDITIONAL INDEX WORDS: *coastal erosion; coastal protection; beach management.*

INTRODUCTION

The urban beaches of Pina, Boa Viagem and Piedade at NE-Brazil are high-value real estate areas, densely occupied, which concentrate economic activities, industrial, leisure and tourism. The construction of edification in backshore zones and deforestation of natural vegetation allied to the natural condition of a narrow continental shelf, absence of dunes, low riverine input of sediments to the tidal energy and seasonal strong winds increases vulnerability to erosion (Pereira *et al.*, 2006). At various areas, marine erosion processes are reducing beach profiles and threatening local structures and buildings and informations that could guide the management and decision-making for the protection of these beaches are urged.

Equilibrium Beach Profile (EBP) models are powerful and valuable tool for the diagnosis and prognosis of sandy beaches conditions. The underlying hypothesis of those models is that the beach shoreface will be shaped in response to the incident wave climate and the sediment present, until they reach an equilibrium condition. Thus, deviations from this equilibrium profile are indicative of undergoing erosional or accretional process.

Several EBP models have been proposed (Bodge, 1992; Hayden *et al.*, 1975; Keulegan and Krumbein, 1949; Sunamura and Horikawa, 1974; Swart, 1974; Vellinga, 1983). The EBP model by Dean (1977) being the most widely-used and easy to apply. It was initially formulated by Bruun (1954) and suits well for beaches formed by near homogeneous grain size sediments, where orbital waves are the main mechanisms responsible for the displacement of underlain sediments.

In subtropical and tropical areas, beachrocks are often found underlying the beach face and/or forming a sequence of shore-parallel lines. The reefs could accentuate wave reflection and create shading areas favoring the settling of more variable grain size sediments.

Our goal was to evaluate how well the Bruun-Dean classic EBP model would suit a beach along which beachrocks were at times absent and at times present either onshore or as submerged reefs.

METHODS

The study area, at Northeastern Brazil, comprised an 8-km long stretch of the coastline of the State of Pernambuco, between UTM coordinates 9096000 and 9105000 N; 288000 and 294000 W, corresponding to the beaches of Pina, Boa Viagem and Piedade. This area was selected due to its socio-economic importance, vulnerability to erosion process and distinct configuration of reef lines. P1 and P2 are located at Piedade, in a region of open beach. They are flat and the reef

DOI: 10.2112/SI75-091.1 received 15 October 2015; accepted in revision 15 January 2016.
*Corresponding author: submar@hotmail.com

line is not pronounced and situated far from the shore. The profile P3 corresponds to a beach stretch where severe erosion takes place despite the presence of natural reef. Here a seawall was constructed to confer protection to the coast. The profile P4 is located in an open beach area, between two beach sections where reef that becomes emerged at low tides are present. At the region represented by profiles P5 and P6, the beach backshore is well preserved and a reef line that becomes emerged at low tides is also present. Profile P7 represents a region were a first line of submerged reef is present, at about 50 meters from the beach shoreline. In this profile the backshore is well preserved, and small dunes occur. The profile P8, at the Pina beach, presents a line of submerged reefs at approximately 100m from the beach shoreline.

In the study area, climate is tropical hot and humid and of Köppen As' type. Prevailing winds are the southeasterly trades, with mean velocity from 3.1 to 4.7 $m.s^{-1}$ (Pereira *et al.* 2003).

The area experiences an annual rainfall of about 2000 mm, with a marked seasonality in rainfall and wind regimens (Rollnic and Medeiros, 2006). During the dry season (Sept.-Jan.) monthly rainfall is less than 100 mm, winds are less strong (3.0-3.2 $m.s^{-1}$) and from December to January, periods of occurrence of Northeast and East winds are common. During the rainy season (Feb.-Aug.) monthly rainfall can reach 300-400 mm and prevailing winds are from SE with mean velocity of 2.6 to 4.0 $m.s^{-1}$, being stronger in August.

Local tides are semidiurnal with a mean range of 1.67m, a neap range of 0.97m, and a spring range of 2.07m (Rollnic; Medeiros and Freitas, 2011).

A common morphological feature along the study area is the presence of shore parallel beach rocks lines. The closest reef is always immersed, presenting variable depth from 3 to 10m, and located at about 1 km from the shore. A channel up to 9m deep, covered by fine sediments, is found between the shore and reef line.

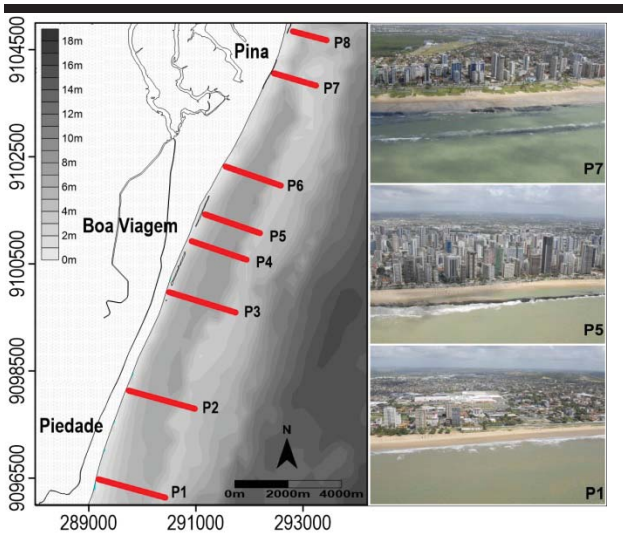

Figure 1. Area map and location of sampling profiles P1 to P8 with aerial view of P1, P5 and P7 areas.

Field Survey

Eight bathymetric profiles (P1-P8) were performed from the surf zone to the 10m isobaths or to the major reef line (Figure 1). The survey was conducted during spring high tide with a Garmin GPSMap 298 ecosound, operating at 200KHz and gathering depth registers at every 3 seconds. When needed, those profiles were complemented with information gathered through topographic survey.

Along each profile, sediment samples were obtained with a VanVeen grab, near the shore; at a distance of 50, 100, 200 and 500 meters from the surf zone. An additional sample was gathered at the limit of the base of the offshore reef (approximately 1000m). In the laboratory those sediment samples were dried at constant weight and subjected to wet and dry sieving to identify their particle size composition.

To characterize the wave climate along the study area, a InterOcean S4DW wave and tide gauge was anchored at P1, Piedade beach and at P5, Boa Viagem beach. The wave gauge was programed to record pressure data twice in a second, for periods of 30 minutes at three-hour cycles and moored off the coast (depth ~5m), one meter from the bottom, over a fortnight tidal cycle. The records obtained were subjected to computer routines to allow generation of the significant and maximum wave heights, significant periods of peak, and wave incidence angle and energy. A one year record of wave oscillation derived from polar images gathered with a nautical radar (X-band) at the Boa Viagem beach, at the center of the study area (Bezerra, 2013) was also used.

Theoretical Beach Equilibrium Profile

The theoretical beach equilibrium profile was computed according Dean (1977) as:

$$h = Ay^m \quad (1)$$

where, **y** is the profile extension, **A** is related to grain size and to the sediment settling speed. For this expression, we tested **m**=0.67 as proposed by Dean and other **m** values (0.57, 0.70, 0.77 and 0.87) using the least squares in order to identify which one would yield the best fit. The **A** value used was computed based on the result of grain size of the sediment samples analyzed and on Dean's table (Dean 1977). We used interpolated values for the remaining points along the profiles.

The closure depth ($\mathbf{h_*}$) is the depth limit at which a profile is balanced by wave action. To determine the depth of closure Hallermeier (1978) developed the first formulation:

$$h_* = 2.28H_e - 68.5(gT_e^2) \quad (2)$$

where $\mathbf{H_e}$ and $\mathbf{T_e}$ is the significant wave height and period of the waves have been exceeded only twelve hours per year, or 0.14% of the time. Birkemeier (1985), drawing on sample data, reviewed the formulation proposing changes in the coefficient:

$$h_* = 1.75H_e - 57.9(H_e^2 / gT_e^2) \quad (3)$$

To be able to determine the closure depth in the area of study, we used the formulation proposed by Birkemeier (1985) and waves characteristics derived from the radar long-series records.

RESULTS

Wave characteristics (H_s, H_{max}, T_s, T_p and direction) near profiles 1 and 5 and at Boa Viagem beach is summarized in Table 1. Wave's direction at P1 and P5 varied from 119 to 131

degrees azimuth with a significant height of 0.61 to 0.97 m and a significant period of 5.97 to 6.34 s. Maximum height was 0.98 at P1 and 1.57 at P5 with a peak period of 8.57 to 9.50 s. From the long series wave record at Boa Viagem, H_e=2.6m and T_e=8.3s. This values was applied in computing depth of closure of the EBPs.

Table 1. *Wave significant height (H_s), maximum height (H_{max}), significant height only exceeded 0,14% (H_e); significant period (T_s), peak period (T_p); significant period only exceed 0.14% (T_e) and incidence direction measured at P1 and P5 and derived from a 1 year radar record at Boa Viagem (Santos, 2013).*

Site	H_s (m)	H_{max} (m)	He (m)	T_s (s)	T_p (s)	Te (s)	Dir (ºAz)
Profile 1	0.61	0.98	-	6.34	8.57	-	119
Profile 5	0.97	1.57	-	5.97	9.50	-	131
Boa Viagem	1.25	2.10	2.6	7.00	8.00	8.3	113

The equilibrium profile closure depth corresponds to the limit point toward the open sea from which the work of significant surface wave can no longer shape the bottom topography. The computed value for the closure depth was found to be 3,97m. Its position varies along the beaches of Pina, Boa Viagem e Piedade, lying about 140m on the northern stretch, near shore at the center of the studty area and at 400m in its most southern portion, where sandbanks and reefs near shore are present (Figure 2).

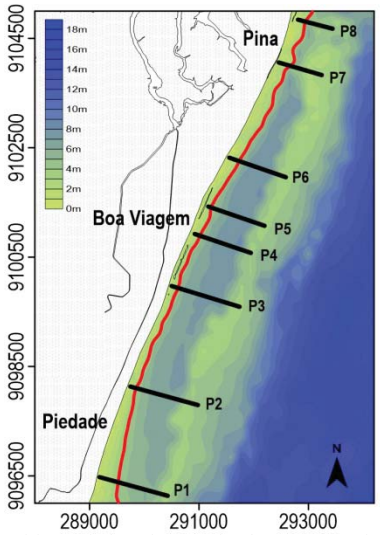

Figure 2. Position of the closure depth (3.97m) of the equilibrium profile (red line) along the study area.

Comparative analysis of bathymetric profiles with the profiles derived from application of the Bruun-Dean model using various parameters values are shown in figure 3 together with an indication of the sedimentary cover composition and mean grain size at the sampled points and the depth of closure of the profile.

The Brunn-Dean values of **A** and **m** tested and the resulting deviation from the real profile (Sum of Square Deviation). Is presented in Table 2. and for **m**=0.77 at P8.

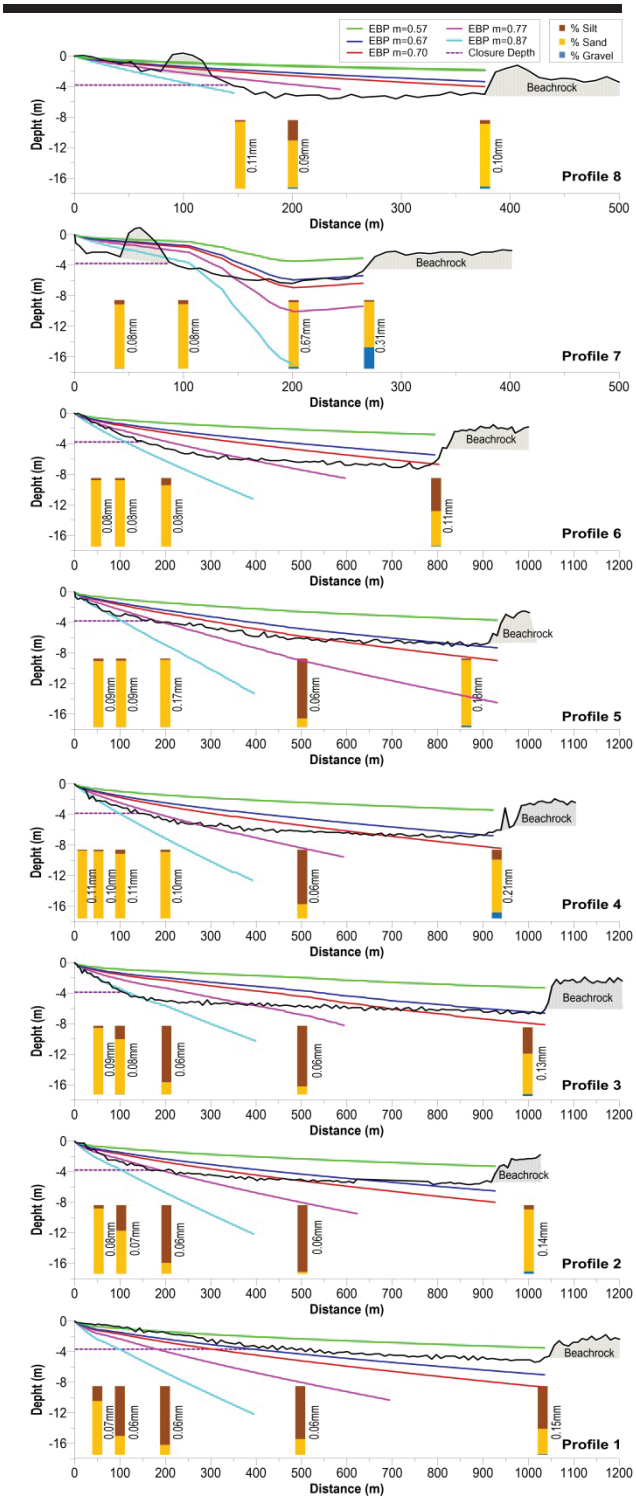

Figure 3. Bathymetric and EBPs profile (m=0.57; 0.67; 0.70; 0.77 and 0.87), closure depth and sediment grain size along the study area.

Table 2. *Resulting Sum Squared Error (SSE) for adjusted EPB models with indication of the values of the **m** and **A** parameters used.*

	P1	P2	P3	P4	P5	P6	P7	P8
A	0.067 0.081	0.067 0.091	0.056 0.081	0.07 0.073	0.067 0.081	0.062 0.064	0.064 0.170	0.063
0.57	170.2	500.8	972.9	953.6	907.8	1146.6	194.8	328.6
0.67	100.4	99.1	401.3	251.8	137.1	383.9	86.8	168.2
0.70	390.2	120.5	265.3	114.6	117.7	197.5	78.2	120.2
0.77	2730.4	1042.9	311.5	391.9	1447.6	236.2	186.2	48.3
0.87	18150.1	9015.5	3525.3	5692.4	14088.9	4498.7	1170.4	328.0

Best fitting of Bruun-Dean model was obtained for a **m**=0.67 at P1 and P2; for a **m**=0.70 at P3 to P7

Bottom sediment at P1 and P2 correspond to very fine sand near the coast, coarse silt covering the channel and sand covering the inner base of the reef. At P3 bottom sediment corresponds to very fine sand near the coast and near the internal base of the reef and thick silt in the channel. Very fine sand is the dominant sediment fraction along the P4 profile, with the highest amount of silt corresponding to the central portion of the coastal channel.

At P5 the three nearest sediment samples corresponded to very fine sand. In the middle of the channel thick silt dominated, while at the inner reef base the dominant sediment fraction is fine sand.

Sediments along the P6 are dominated by very fine sand. Near the internal base of the reef located some 800 meters from the beach shoreline, the dominant sediment fraction is silt. Sediments along P7 correspond to very fine sand, except for the furthest station (internal base of the second reef line) where coarse sand with gravel dominates. Along the P8 profile silt predominates at the center of the channel (200m) and very fine sand elsewhere.

DISCUSSION

Model of the theoretical beach equilibrium profile were confronted with the prospected bathymetric profiles. These profiles were computed according to Dean (1977) considering the predominant particle size at the sampled points along the profile. Initially it was considered a value of **m**=0.67, a typical value used in the US for sandy beaches, Australian beaches, *etc.* (Baquerizo; Losada and Smith, 1998; Bernabeu; Medina and Vidal, 2002; Bernabeu; Medina and Vidal; González; Medina and Losada, 1999; Larson; Kraus, and Wise, 1999; Wojciech; Barbara and Jerry, 2005).

The model using m=0.67 adjusted well at P1 and P2 (Table 2). For the remaining profile, other values of **m** were tested to optimize this parameter in the search for a better fit.

Larson, *et al.* 1998, used three models produced equilibrium profile shapes with the **m** range 0.15 to 0.30 under non-breaking waves. Work and Dean 1991, and Horn 1992 investigated the effect of a varying grain size on the EBP shape.

Dai, *et al.* (2006) applied fractal analysis to predict types of EBP using the field data collected from Liao Zuikou and Nanwan beaches, South China.

Inman *et al.* (1993) divided the profile into two portions, an inner and outer region, which corresponded to the regions with breaking and non-breaking waves, respectively. Both portions were successfully approximated with **m**=0.4

In reef-protected beaches the energy flux dissipation over the reef reduces the total energy flux that has to be dissipated by the beach resulting in a steeper profile.

At P8, in presence of reefs, the value of 0.67 for the **m** parameter as proposed by Dean (1977) did not yield a satisfactory fitting. On the other hand, an **m** value of 0.77 showed a good result, up to the limit of the closure depth.

The results with the determination of the equilibrium profile show that the major part of the study area has distinct characteristics as studied by others.

Overall, the value of **m**=0.70 was the one that resulted in less residue (Table2) and therefore the one that best approached the local relief, given its steeper slope. Exceptions being made for the profile P1 and P2, with smooth topography, where the use of an **m** value of 0.67, was more appropriate.

The presence reef lines, and the sharp slope forming a channel, required a peculiar adjust for the area.

CONCLUSIONS

Along the beach stretches where beachrocks had a low high profile, were absent or located away from the shore (P1 and P2) the m value of 0.67 proposed by Dean, yielded a good fit.

At the areas where a single reef line, which emerges at low tide, where present close to the shoreline (P3 a P6), the profile was steeper and the bottom sediment less homogeneous. Best fit was obtained for **m**=0.70. At P7 and P8, where there is a second line of underwater reefs no specific value **m** yielded a good fit. High values of **m** (**m**=0.87) adjusted well at the near shore portion of the profile but yielded discrepant values seawards. On the other hand, low **m** values (**m**=0.57) reproduced well the profile shape for the seaward portion of those profiles, but was displaced upwards by a distance equivalent to the high of the reef line, indicating its influence on the profile geometry. Thus suggesting that the incorporation of a parameter that would be related to the reef high could improve its fitting. Therefore, we suggest in a next step, a specific study of the regions with two reef lines, identifying their geometry and positioning on the coast to infer a term in the EBP equation.

ACKNOWLEDGMENTS

This work was partially supported by the CNPq grant 019/2004–00479837040052217 and by a CNPq fellowship to the first author

LITERATURE CITED

Baquerizo, A.; Losada, M.A., and Smith, J.M., 1998. Wave reflection from beaches: a predictive model. *Journal of Coastal Research*, 14(1), 291-298.

Bernabeu, A. M.; Medina, R., and Vidal, C., 2002. Wave reflection on natural beeches: an equilibrium beach profile model. *Estuarine Coastal and Shelf Science*, 57(4), 577-585.

Bernabeu, A. M.; Medina, R., and Vidal, C., 2003. A morphological model of the beach profile integrating wave

and tidal influences. *Marine Geology*, 197(1-4), 95-116.

Bezerra, C.S. 2013. Clima de ondas e correntes no litoral de Boa Viagem (Recife-PE): aplicação do sistema de radar náutico de banda-x. Recife, Pernambuco: Universidade Federal de Pernambuco, Master's Thesis, 98p.

Birkemeier, W.A., 1985. Field data on seaward limit of profile change. *Journal of Waterway, Port, Coastal, and Ocean Engineering,* 111(3):598-602.

Bruun, P., 1954. Coast erosion and the development of beach profiles. Beach Erosion Board, Technical Memorandum, No 44, U.S. Army Engineer Waterways Experiment Station. Vicksburg, MS.

Bodge, K., 1992. Representing equilibrium beach profiles with an exponential expression. *Journal of Coastal Research*, 8(1): 47-55.

Dai, Z-J.; Du, J.-Z.; Li, C.-C., and Chen, Z.-S., 2006. The configuration of equilibrium beach profile in South China. *Geomorphology*, 86(3-4), 441-454.

Dean, R.G., 1977. *Equilibrium beach profile*: U.S. Atlantic and Gulf Coast. Newark, Delaware: University of Delaware, *Ocean Engineering Technical Report No*. 12, 45p.

Dean, R.G., 1991. Equilibrium beach profiles: characteristics and applications. *Journal Coastal Reserch,* 7(1), 53-84.

González, M.; Medina, R., and Losada, M.A., 1999. Equilibrium beach profile model for perched beaches. *Costal Engineering*. 36(4), 343-357.

Hallermeier, R.J., 1978. Uses for a calculated limit depth to beach erosion. *Proceedings of the 16th International Conference on Coastal Engineering* (Hamburg, Germany, ASCE), pp. 1493-1512.

Hayden, B.; Felder, W.; Fisher, J.; Resio, D.; Vincent, L., and Dolan, R, 1975. Systematic variations in inshore bathymetry. Department of Environmental Sciences, Technical Report No.10, University of Virginia, Charlottesville, Virginia.

Horn, D.P., 1992. A review and experimental assessment of equilibrium grain size and the ideal wave-graded profile. *Marine Geology*, 108(2): 161-174.

Inman, D.L.; Elwany, M.H.S., and Jenkins, S.A., 1993. Shorerise and bar–berm profiles on ocean beaches. *Journal Geophysical Research,* 98(10): 18181–18199.

Keulegan, G.H. and Khumbein, W.C., 1949. Stable configuration of bottom slope in a shallow sea and its bearing on geological processes. *Transactions American Geophysical Union,* 30(6): 855-861.

Larson, M.; Kraus, N.C., and Wise, R.A., 1999. Equilibrium beach profiles under breaking and non-breaking waves. *Coastal Engineering,* 36(1): 59–85.

Pereira, L.C.C.; Jimenez, J.A.; Medeiros, C., and da Costa, R.M. 2003. Environmental degradation of the litoral of Casa Caiada and Rio Doce, Olinda-PE (Brazil). *In*: Klein, A.H.F. (eds.), *Proceedings of the Brazilian Symposium on Sandy Beaches: Morphodynamics, Ecology, Uses, Hazards and Management. Journal of Coastal Research,* Special Issue No. 35, pp. 502-508.

Pereira, L.C.C.; Medeiros, C.; Jimenez, J.A., and da Costa, R.M. 2006. Topographic changes in two highly sheltered beaches, Casa Caiada and Rio Doce–PE (Brazil). *In*: Klein, A.H.F. and Finkl, C.W. (eds.), *Proceedings of the 8th International Coastal Symposium. Journal of Coastal Research,* Special Issue No. 39, pp. 644-647.

Rollnic, M. and Medeiros, C., 2006. Circulation of the Coastal Waters off Boa Viagem, Piedade and Candeias Beach - Pernambuco, Brazil. *In*: Klein, A.H.F. and Finkl, C.W. (eds.), *Proceedings of the 8th International Coastal Symposium. Journal of Coastal Research,* Special Issue No. 39, pp. 648-650.

Rollnic, M.; Medeiros, C., and Freitas, I.C. 2011. Coastal Circulation Along the Southern Metropolitan Region of Recife, Northeastern Brazil. *Journal of Coastal Research,* 64: 135-138.

Sunamura, T. and Horikawa, K., 1974. Two-dimensional beach transformation due to waves. *Proceedings of the 14th International Conference on Coastal Engineering* (ASCE), pp. 920-938.

Swart, D.H., 1974. A Schematization of Onshore- Offshore Transport. Proceedings of the Fourteenth International Conference on Coastal Engineering, American Society of Civil Engineers, pp. 884-900.

Vellinga, P., 1983. Predictive computational model for beach and dune erosion during storm surges. *Proceedings of the Specialty Conference on Coastal Structures '83*, American Society of Civil Engineers, pp. 806-819.

Wojciech, R.; Barbara, B., and Jerry, L.B., 2005. Extended equilibrium beach profiles. *Coastal Engineering,* 52(9): 727–744.

Work, P.A. and Dean, R.G., 1991. Effect of varying sediment size on equilibrium beach profiles. *Proceedings of Coastal Sediments '91*(New York, United State, ASCE), pp.890–904.

Journal of Coastal Research	SI	75	457-461	Coconut Creek, Florida	2016

The Effects of Beach Morphology Variations on the Profile of Nearshore Currents on a Gently Sloping Mesotidal Beach

Amaia Ruiz de Alegria-Arzaburu[†*], Mario Arturo Arreola-Cortez[†], Héctor García-Nava[‡], Rafael Hernández-Walls[§] and Adán Mejía-Trejo

[†]Instituto de Investigaciones Oceanológicas, Universidad Autónoma de Baja California, Ensenada, Baja California, 22860 México
[§]Facultad de Ciencias Marinas, Universidad Autónoma de Baja California, Ensenada, Baja California, 22860 México

www.cerf-jcr.org

www.JCRonline.org

ABSTRACT

Ruiz de Alegria-Arzaburu, A.; Arreola-Cortez, M.A.; García-Nava, H.; Hernández-Walls, R., and Mejía-Trejo, A., 2016. The effects of beach morphology variations on the profile of nearshore currents on a gently sloping mesotidal beach. *In:* Vila-Concejo, A.; Bruce, E.; Kennedy, D.M., and McCarroll, R.J. (eds.), *Proceedings of the 14th International Coastal Symposium* (Sydney, Australia). *Journal of Coastal Research*, Special Issue, No. 75, pp. 457-461. Coconut Creek (Florida), ISSN 0749-0208.

Concurrent measurements of subtidal beach morphology and profiles of nearshore currents have been collected over a year period on a gently sloping mesotidal beach in the northwestern coast of the Baja California peninsula in Mexico. Data collected in August 2014 and February 2015 during similar tide, wave and wind conditions are compared at different alongshore locations on the beach in order to determine differences on the vertical structure of the nearshore currents in relation to significant morphologic variations. The beach presents a clear seasonal variability, showing the formation of an inner sandbar during the winter as a result of the erosion of a large portion of the subaerial beach. The morphological differences on the inner subtidal beach shows a subsequent effect on the vertical structure of the nearshore currents. Locations with pronounced sandbars have generally associated cross-shore and longshore components of the current of larger magnitude. Generally, the surface and bottom cross-shore currents are the most energetic while the middle layer presents milder magnitudes. With the presence of an inner bar, the shoreward directed upper and bottom layers become wider (deeper) reducing the width of the middle less energetic layer, and after the breaking zone the water column becomes vertically quasi-homogeneous. This study contributes to the understanding of the feedbacks between the hydrodynamic forcing and the beach morphology.

ADDITIONAL INDEX WORDS: *Nearshore currents, beach morphodynamics, coastal processes.*

INTRODUCTION

There is a clear interdependence between the nearshore hydrodynamic processes and the underlying beach morphology, which is generally referred to as beach morphodynamics (Wright and Thom, 1977). The balance between the oscillatory transport due to incoming waves, mean transport due to steady flows (balance between Stokes drift and undertow) and net oscillatory transport due to infragravity waves will define the net cross-shore sediment transport on the beach (Aagaard *et al*., 2013; Svendsen, 1984), which will also depend on the beach slope (Aagaard *et al*., 2002).

Commonly, net offshore sediment transport induces beachface erosion while net onshore sediment transport results in beachface accretion (Wright and Short, 1984). The cell circulation on the beach will primarily depend on the existence of longshore variations in the wave height, which will also result in alongshore non-uniform morphologic patterns (Komar, 1998).

The shoreface morphodynamics presents large spatio-temporal variability. Seasonal field measurements of nearshore beach changes are scarce (Ruggiero *et al*., 2009; Short and Jackson, 2013), and high-resolution longhshore data are needed in order to adequately understand the morphodynamics of nearshore features such as sandbars (Plant *et al*., 2006).

Based on concurrent field measurements of the nearshore beach morphology and the vertical distribution of current velocities, the present study aims to investigate the association of the profile of wave-driven nearshore currents with the underlying morphology (presence/absence of sandbars).

Field site

Ensenada Beach is located in the city of Ensenada, in the northwestern coast of the Baja California peninsula in Mexico, and ~100 km south from the US-Mexican border (Figure 1). The beach has a mesotidal regime with mean spring and neap tidal rages of 2.2 m and 0.5 m, respectively and receives energetic (mean significant wave height, H_s = 1 m) and long period (mean peak wave period, T_p = 11 s) waves. The beach has a length of 7 km and is partly protected from the Pacific swell by Todos Santos Islands (located ~17 km off the beach, Figure 1); in this study, the most northern 3 km are investigated.

The beach is made of siliceous medium sand (D_{50} = 0.2 mm), has an average slope of tan β = 0.025 (Figure 1) and contains coastal structures such as a promenade in the northern section and a seawall and rip-rap in the middle section. The southern beach preserves a natural dune backed by a shallow and intermittently dry freshwater lagoon. The walled subaerial beach

DOI: 10.2112/SI75-091.1 received 15 October 2015; accepted in revision 15 January 2016.
*Corresponding author: amaia@uabc.edu.mx

is 80–120 m wide, whereas the non-walled section has a subaerial width of 220–240 m. The supratidal beach fronting the promenade is up to 6.5 m above mean low water (MLW) and up to 3.5 m on rip-rap and seawall protected sections. The supratidal beach composed by dunes has a maximum elevation of 10 m above MLW.

The incidence of storms is common between October and April with H_s = 3–4 m, and calm wave conditions occur from June to September with mean H_s of ~0.7 m. The incoming swell is bimodal, being northwesterly and originated in the extratropical north Pacific during the winter and southwesterly originated in the extratropical south Pacific in the summer. Northwesterly winds dominate from June to October and the winter season is characterized by the presence of up to 10 ms^{-1} sporadic easterly winds known as Santa Ana events.

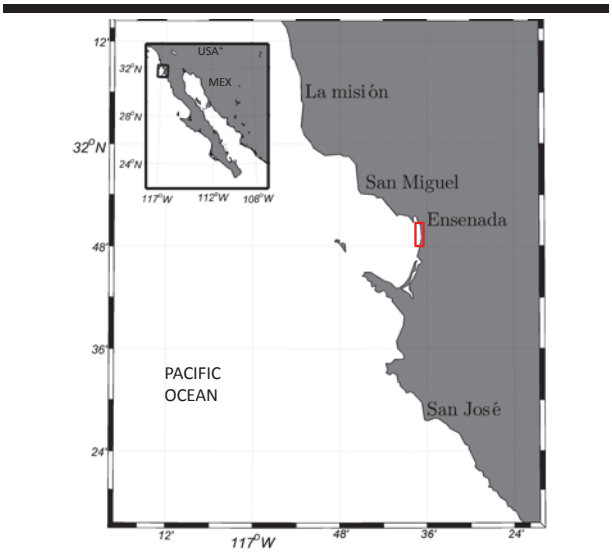

Figure 1. Location of the study site within the Baja California peninsula. The red square shows the approximate location of the studied beach section.

METHODS

The subaerial morphology of ~3 km of Ensenada Beach was monthly measured using a differential Global Positioning System (GPS; Leica GS14). 50 m spaced cross-shore beach profiles were collected on foot during low spring tides, using a two-wheeled trolley operated by two people. The topographic measurements were continuous (1 sample per second) and the same transect lines were followed each time; a total of 61 beach profiles were consistently measured from the upper beach (*e.g.,* dune positions) to the lower intertidal beach over a 2-day surveying period. All measurements were in UTM Easting and Northing coordinates in metres, and the elevations were referenced to MLT (Mean Low Tide level, referred to the local API-01, +36.135 m from ellipsoidal heights).

The subtidal morphoplogy and nearshore currents were monthly measured (right after the topographic surveys) along 3.5 km beach using an Acoustic Doppler Wave and Current profiler (ADCP; Sontek M9 type) and differential GPS (Leica GS14) mounted on a board and towed from the side of a surveying boat (Figure 2). 100 m spaced transects were collected from the inner subtidal beach up to a depth of 10 m during high spring tides. The bathymetric and current measurements were continuous at 1Hz and the same transect lines were followed each surveying time; a total of 35 lines were consistently measured (Figure 3).

The current profiles measured with the ADCP were collected using the frequencies of 3MHz and 1MHz for depths above and below 5 m, respectively. The blanking distance was 0.2 m and the cell-size varied with the depth, thus, the obtained values were averaged to a fixed cell size of 0.2 m. In order to eliminate the effect of waves on the current profiles, these were averaged every 17 s, and at a measuring speed of 2 ms^{-1}, this is equivalent to 34 m cross-shore averaging for transects of 400–500 m long.

Figure 2. ADCP and differential GPS mounted on the hydroboard and towed on the side of the surveying boat. An example of set-up during the measurement collection.

The measured topographic and bathymetric data were linearly interpolated and monthly topo-bathymetric maps were generated (Figure 3). In order to determine significant morphologic differences among the collected data during the period from August 2014 to April 2015, the topo-bathymetric maps were subtracted in time (Figure 4).

Nearshore wave conditions were collected with a 1MHz ADCP located 2.5 km off the southern beach end at a water depth of 20 m. The instrument was installed on a pyramid aluminium structure laid on the seabed and was set to collect hourly wave measurements at 17 min (1024 s) bursts. Predicted tides were obtained from a tidal model developed by the CICESE and available at http://oceanografia.cicese.mx/predmar. The local wind was measured with a Vaisala meteorological station located in the middle of the study site.

Different tide level, wind and wave conditions occurred during the bathymetric and current surveys (Table 1). In this study measurements collected in August 2014 and February 2015 are compared, as being collected during similar tide, wave

and wind conditions and presenting large morphologic variations over that period of time.

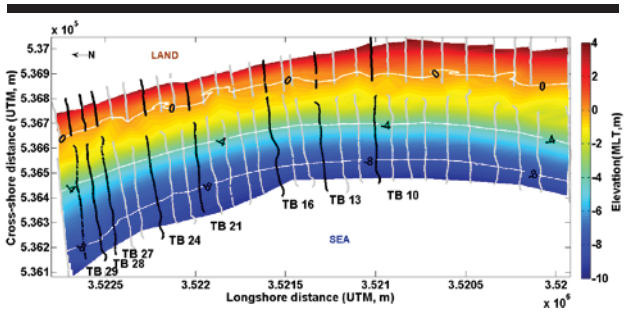

Figure 3. Interpolated topo-bathymetric map for the study site in February 2015. The grey transects correspond to the measured topographic and bathymetric profiles used to obtain the interpolated surfaces, and the black lines represent the selected profiles for the current analysis.

Table 1. *Bathymetric and nearshore current survey times and associated significant wave height and peak period (H_s, T_p), mean low tide level (MLT) and average wind speed conditions. The shadow lines correspond to the selected measurement periods.*

Survey Time	MLT (m)	H_s (m)	T_p (s)	*Wind (ms^{-1})*
11-Aug-2014	1.5	0.5	9.5	1.4
09-Sep-2014	2.0	0.4	6.0	0.6
07-Oct-2014	2.0	0.5	12.7	1.0
10-Nov-2014	1.7	0.7	11.8	1.2
09-Dec-2014	1.5	2.1	15.4	1.1
09-Jan-2015	1.5	1.0	15.0	0.8
20-Feb-2015	1.8	0.7	10.5	1.3
19-Mar-2015	1.5	1.4	11.2	1.0
17-Apr-2015	1.5	1.7	17.9	1.0

RESULTS

The morpholocal change between August 2014 and February 2015 shows significant subaerial beach erosion of up to 1.5 m on some alongshore locations, some accretion on the supratidal beach (above 3.5 m in elevation) and the formation of a inner subtidal sandbar (Figure 4). Alongshore differences are identified in terms of the magnitude of subaerial beach erosion and subtidal beach accretion, and the cross-shore distance for the bar formation. For that reason, the beach profile changes are individually analysed, and alongshore locations of smaller and larger morphological changes are selected (Figure 5) for the current analysis.

The northern beach end shows the largest seasonal morphologic change captured between August 2014 and February 2015 (profiles TB 24 to TB 30). Instead, the least morphologic variations between the upper and lower beach took place in the middle beach section (profiles TB 10 to TB 21) (Figures 3 and 5).

Current profile results for August 2014 and February 2015 are presented in Figures 6 and 7 for the cross-shore *U* and longshore *V* velocity components, and for the locations TB 21 and TB 27,

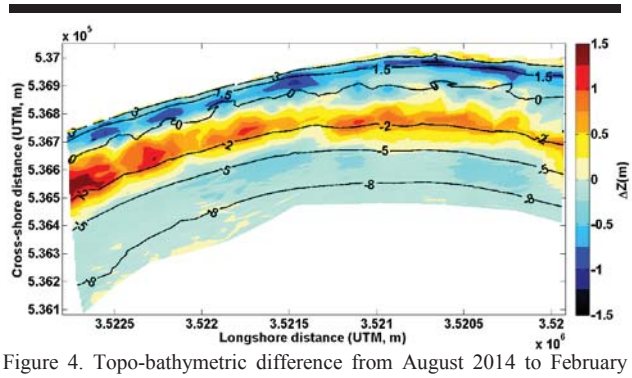

Figure 4. Topo-bathymetric difference from August 2014 to February 2015.

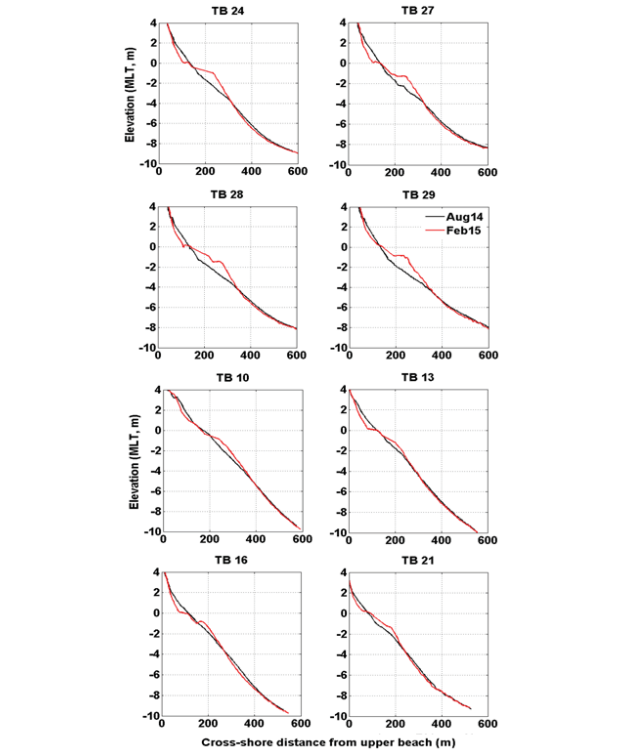

Figure 5. The upper and lower four panels represent the beach profile locations with the larger and smaller morphological changes, respectively.

which present mild and large morphological changes, respectively.

Three distinct layers are observed in the *U* cross-shore velocity component: the upper (0 to 2 m depth), middle (from 2 to 8 m depth) and bottom (lower than 8 m depth); which are in all cases shoreward directed.

Significant differences occur in the vertical distribution of the *U* velocity component (top panels in Figures 6 and 7). In the

absence of sandbars (August 2014) the *U* is 0.4–0.8 ms^{-1}, 0–0.2 ms^{-1} and 0.3–0.5 ms^{-1} in the upper, middle and bottom layers, respectively, and the net current is southward directed.

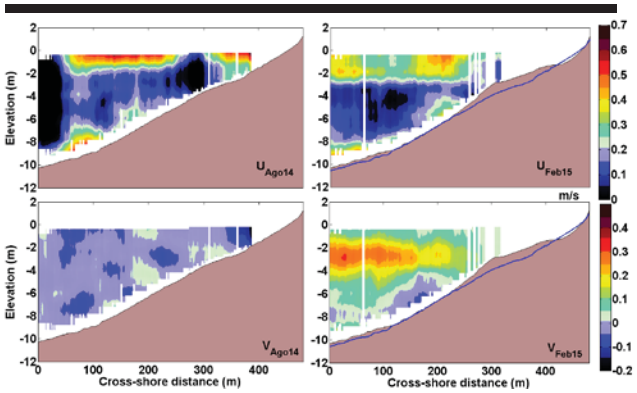

Figure 6. Cross-shore *U* (positive shoreward) and longshore *V* (positive northwards) velocity components in ms^{-1} (top and bottom panels) in the TB 21 location for August 2014 and February 2015 (left and right panels). Note that the top and bottom colorbars apply to both the top and both the bottom panels, respectively.

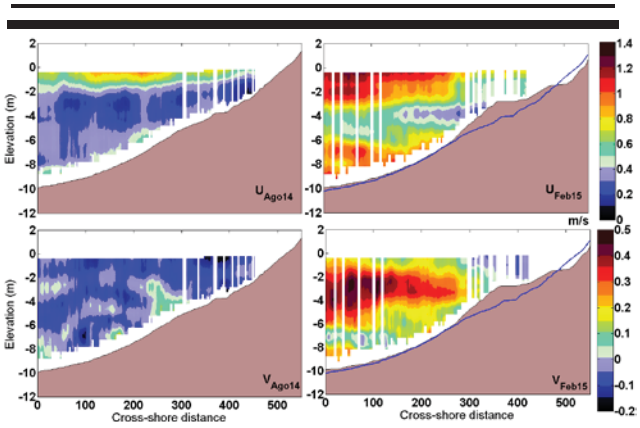

Figure 7. Cross-shore *U* (positive shoreward) and longshore *V* (positive northwards) velocity components in ms^{-1} (top and bottom panels) in the TB 27 location for August 2014 and February 2015 (left and right panels). Note that the top and bottom colorbars apply to both the top and both the bottom panels, respectively.

With the presence of a non-prominent sandbar (TB21; top right panel Figure 6) and before the breaking zone, the upper layer in *U* gets thicker and less energetic (up to 0.5 ms^{-1}), and the magnitudes of the middle and lower layers remain the same as without a bar. With the presence of a pronounced sandbar (TB27, top right panel Figure 7) and before the breaking zone, the upper and lower layers increase the magnitude significantly up to 1 ms^{-1}, and the middle layer gets thinner with larger values of up to 0.5 ms^{-1}.

After the breaking zone, in the presence of a sandbar, the current profile is pretty homogeneous with magnitudes between 0.1 and 0.5 ms^{-1} below a thin more energetic surface current. In February 2015 the *V* component shows values of opposing directions before and after the breaking zone, and the most energetic longshore flow corresponds with the middle layer of 0.3–0.5 ms^{-1}. Drastic changes occur on the vertical structure of this component between August and February; the presence of the sandbar intensifies the current and induces the formation of an intermediate layer (Figures 6 and 7).

In order to evaluate the alongshore differences of the surface, middle and bottom currents, the measurements for the 30 transects were interpolated into a regular mesh. Figure 8 presents the interpolated results for the cross-shore velocity component *U* in August 2014 (left panels) and February 2015 (right panels) and for the surface (up to 2 m depth), middle (from 4 to 6 m depth) and bottom (lower than 8 m depth) layers. These results highlight significant alongshore differences in the magnitude of the *U* velocity component, which seems to be larger than the longshore *V* component. The longshore variations in *U* are suggested to be primarily associated to the variations in the underlying beach morphology (Figure 9).

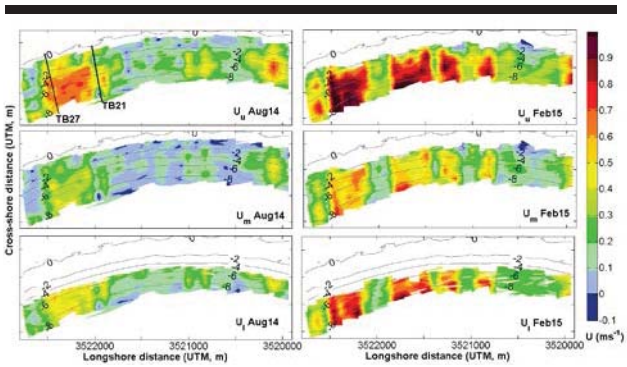

Figure 8. Interpolated *U* cross-shore velocity component along the beach for the surface, middle and bottom layers (top to bottom) and for August 2015 and February 2015 (left to right).

DISCUSSION

Numerous studies have investigated the general circulation patterns at Todos Santos Bay (*e.g.,* Alvarez-Sanchez *et al.*, 1988; Mateos *et al.,* 2009), the nearshore currents, however, are notoriously understudied. In agreement with Haines and Sallenger (1994), this study highlights the existence of significant differences in the vertical distribution of the cross-shore component of the nearshore current, in the presence and absence of an inner sandbar.

It is found that seaward from the breaking zone, the surface and bottom cross-shore currents are the most energetic and shoreward directed, and generally, the middle layer ranging between 2 to 6 m depth presents very mild currents O(0.1-0.3 ms^{-1}). In the presence of an inner bar, the shoreward directed upper and bottom layers become wider and reduce the width of the middle less energetic one.

Landward from the breaking zone, the water column becames vertically nearly homogeneous with average values of ~0.5 ms^{-1} in the cross-shore component after the pronounced inner bar. Within the surf zone, a significant reduction in the magnitude of the cross-shore current component is observed. This is considered to be associated with the opposing strong undertow,

which is enhanced due to the contribution of the onshore mass transport in the upper water column (Svendsen, 1984). The presence of the sandbar intensifies the alongshore component of the current and induces de formation of an intermediate layer.

In agreement with Aagaard *et al*., (2013), locations with more pronounced bars were associated to cross-shore currents of larger magnitude, while locations with less pronounced morphological change presented milder cross-shore currents within the water column. Generally, the undertow is considered to be the reason for the significant weakening of the currents in the middle layer (4 to 6 m depth).

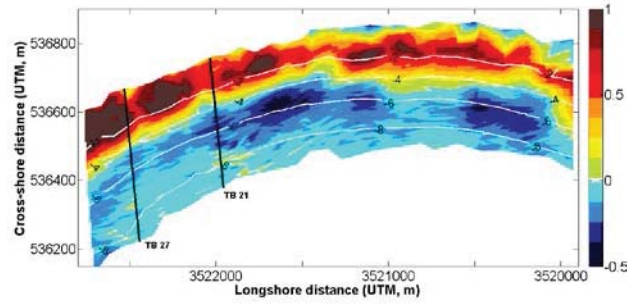

Figure 9. Bathymetric difference between August 2014 and February 2015 in meters.

CONCLUSIONS

Ensenada Beach presents a clear seasonal morphological variability. In the transition from the summer to the winter, the beach developes an inner bar at a depth of 2–3 m as a consequence of the significant intertidal and supratidal beach erosion. The morphological variability on the beach is cross-shore driven, and this is in agreement with the current measurements which indicate that the cross-shore velocity component *U* is significantly larger than the *V* longshore velocity component in the absence of sandbars and of comparable magnitude in the presence of sandbars. The bar formation, however, is not alongshore uniform, in some locations the inner bar is more pronounced than in others.

The alongshore differences in the morphology on the inner subtidal beach have a subsequent effect on the vertical profile of the nearshore currents. Substantial differences in the vertical distribution of the *U* cross-shore velocity component are observed, in the presence and absence of an inner sandbar. Locations with pronounced bars are generally associated to cross-shore currents of larger magnitude, while locations presenting less pronounced morphological change usually present milder cross-shore currents within the water column. Undertow effects may be the cause of the weakening of the intensity in the middle layers, but since the currents are time-averaged, it is difficult to determine its real input on the net cross-shore current.

Seaward the surf zone, the surface and bottom cross-shore currents are the most energetic while the middle layer presents very mild magnitudes. With the presence of an inner bar, the shoreward directed upper and bottom layers become wider and reduce the width of the middle less energetic one. After the breaking zone, the water column becomes vertically nearly homogeneous. In the breaking zone, a significant reduction in the magnitude of the cross-shore current component is observed, which is thought to be associated to undertow effects.

ACKNOWLEDGMENTS

The authors are grateful to CONACyT for the funding provided through CB-2014-238765 and INFR-2013-01I005 with the projects 205020 and 205022. Thanks are extended to F-PROMEP-38/Rev-03 SEP-23-005 and UABC for the support with UABC-PTC-418 and 18th projects 636 (IMTENS) and 634 (EOCiS). We are very thankful to all field assistants, especially to Eduardo Gil and Ernesto Carsolio for the technical support provided in the field and to Gemma Desplán, Teresa Vidal, Hugo Villegas, Julio Lopez, Adrian Vidal, Mayra Martinez and Sandra Patiño among others.

LITERATURE CITED

Aagaard, T.; Black, K.P., and Greenwood, B., 2002. Cross/shore suspended sediment transport in the surf zone: a field/based parameterization. *Marine Geology,* 185, 283–302.

Aagaard, T.; Greenwood, B., and Hughes, M., 2013. Sediment transport on dissipative, intermediate and reflective beaches. *Earth-Science Reviews,* 124, 32–50.

Alvarez-Sanchez, L.G.; Hernandez-Walls, R., and Durazo-Arvizu, R., 1988. Drift patterns of lagrangian tracers in Todos Santos Bay. *Ciencias Marinas,* 14(4), 135–162.

Haines, J.W. and Sallenger, A.H., 1994. Vertical structure of mean cross-shore currents across a barred surf zone. *Journal of Geophysical Research* 99, 14223–14242.

Komar, P.D., 1998. *Beach processes and sedimentati*on, 2nd Edition. Prentice Hall. 544 pp.

Mateos, E.; Marinone, S.G., and Pares-Sierra, A., 2009. Towards the numerical simulation of the summer circulation in Todos Santos Bay, Ensenada, B.C. Mexico. *Ocean Modelling,* 27, 107–112.

Ruggiero, P.; Walstra, D.J.R.; Gelfenbaum, G., and van Ormondt, M., 2009. Seasonal-scale nearshore morphological evolution: Field observations and numerical modelling. *Coastal Engineering,* 56, 1153–1172.

Short A.D. and Jackson D.W.T., 2013. Beach Morphodynamics. In: John F. Shroder (ed.) *Treatise on Geomorphology*, San Diego: Academic Press. Vol. 10, pp. 106–129.

Svendsen, I.A., 1984. Mass flux and undertow in the surf zone. *Coastal Engineering*, 8, 374–365.

Wright, L.D. and Short, A.D., 1984. Morphodynamic variability of surf zones and beaches: a synthesis. *Marine Geology,* 56, 93–118.

Wright, L.D. and Thom, B.G., 1977. Coastal depositional landforms: a morphodynamic approach. *Progress in Physical Geography,* 1, 412–459.

Journal of Coastal Research	SI	75	462-466	Coconut Creek, Florida	2016

Recovery Assessment of Two Nearby Sandy Beaches with Contrasting Anthropogenic and Sediment Supply Settings

Nadia Senechal[†*], Jonathan Pavon[†*], Remy Asselot[†*], Mohammed Taaouati[†*], Sophie Ferreira[‡], and Stéphan Bujan[†],

[†*]University of Bordeaux, OASU – UMR EPOC
Pessac, France

[†]CNRS, OASU- UMR EPOC
Pessac, France

[‡]OASU, Université de Bordeaux /UMR EPOC
Pessac, France

www.cerf-jcr.org

www.JCRonline.org

ABSTRACT

Senechal, N.; Pavon, J.; Asselot, R.; Castelle, B.; Taaouati, M.; Ferreira, S., and Bujan, S., 2016. Recovery assessment of two nearby sandy beaches with contrasting anthropogenic and sediment supply settings. *In:* Vila-Concejo, A.; Bruce, E.; Kennedy, D.M., and McCarroll, R.J. (eds.), *Proceedings of the 14th International Coastal Symposium* (Sydney, Australia). *Journal of Coastal Research*, Special Issue, No. 75, pp. 462-466. Coconut Creek (Florida), ISSN 0749-0208.

The aim of this study is to provide the preliminary results of the comparisons of two field sites exposed to the same environmental conditions but with contrasting beach management strategies. Truc Vert beach and Biscarrosse beach are both low sandy beaches situated on the 250km long linear French coast exposed to the Atlantic swells and are about 35km distant. While Truc Vert beach is a fully natural beach, Biscarrosse beach is in an urban area where several coastal defences have been deployed. Data indicate that Biscarrosse beach is less stable than Truc Vert beach. During the dramatic winter 2014 Biscarrosse upper beachface experienced dramatic beach erosion over two consecutive months despite regular beach nourishment operations while at the same time, Truc Vert beach erosion was mostly associated to the first energetic period. Both sites partially recovered over the summer period, especially the upper beachface where the berm generally developped during the summer. While recovery was a fully natural process at Truc Vert beach, massive beach nourishments were operated at Biscarrosse beach. Data indicate that Truc Vert upper beachface remained more stable over the following winter compared to Biscarrosse upper beachface what experienced significant variations. It is concluded that the erosion problem and recovery are very complex and certainly do not only depend on the local availability of sediment.

ADDITIONAL INDEX WORDS: *Beach management, recovery, storm.*

INTRODUCTION

Human activities in many coastal regions are nowadays at an unprecedented scale and expand even more in the decades to come. Recent studies have indicated that colonisation of the oceans is now perceptible and there is evidence that the density of urban areas (such as the Western European core, Eastern North America and North West Pacific cores) is reflected in development in the nearby oceans, supporting the notion of urban seas (Stojanovic and Farmer, 2013). The Land-Ocean Interactions in the Coastal Zone (LOICZ) project identified coastal hotspots, including urban coasts (Newton *et al*., 2012) where there is a 'coastal squeeze' between development pressures and natural hazards.

Coastal hazards span a broad-banded spectrum of time and space scales. They can be rare yet short-duration events with high-magnitude and far-reaching impact on coastal zones but they can also be gradual events of less intense magnitude but with similar far-reaching impacts (e.g. Coastal Hazards, 2013). Among the major natural hazards that have received a large interest in the community is the coastal flooding hazard (e.g. Xynthia storm, 1999; Western Europe, Winter 2013-2014). Throughout the last century, coastal flooding has certainly been the most costly disaster in terms of property damage and human casualties (e.g. North Sea Flood in 1953). The other major natural hazard that has received a large interest in the community is the coastal erosion (shoreline retreat) hazard. Erosion is a morphodynamic process produced by the removal of sediment, the acting processes (either natural or human) resulting in a deficit in sediment budget in the area. Storm-induced extreme waves and water-level conditions are key drivers in shoreline erosion. Single storms can result in meters of shoreline change within hours (e.g. Castelle *et al*., 2015; Coco *et al*., 2014) and a sequence of storms, for example during a winter-season may cause a seasonal, cumulative shoreline response (Komar, 1998, Sénéchal *et al*., 2015). Beach response to storms has thus received a very large interest in the literature over the last decades with emphasis on the erosion effect (e.g. Callaghan *et al*., 2009; Coco *et al*., 2014; Masselink and Van Heteren, 2013).

Beach recovery is an important process in evaluating coastal vulnerabilitty and yet recovery periods have received much less attention in the literature, being even neglected in studies evaluating the cumulative impact of storm clusters on beach erosion (e.g. Splinter *et al*., 2014). Studies have shown that shorelines can recover partially from storm-induced erosion and that the initial recovery can be extremely fast, but complete

DOI: 10.2112/SI75-093.1 received 15 October 2015; accepted in revision 15 January 2016.
*Corresponding author: n.senechal@epoc.u-bordeaux1.fr

recovery may also last for years if the foredunes have been eroded (Birkemeier, 1979; Wang *et al*., 2006). This recovery period will certainly primarly depend on the hydrodynamic conditions but will also depend on the beach geomorphology and geologic settings (e.g. Anthony, 2013; Gallop *et al*., 2012; Splinter *et al*., 2011), the local availability of sediment (Forbes *et al*., 2004), the usual (modal) beach state, low-energy coasts being more vulnerable than their higher-energy counterparts (e.g. Masselink and Van Heteren, 2013; Yu *et al*., 2013) and finally the sand transfer with the foredunes (e.g. Anthony, 2013) by aeolian sand transport.

The aim of the present work is to present the preliminary results of the observations of the evolution of two nearby sandy beaches situated in the SouthWest of France: one being fully natural and the other one situated in an urban area during several during the year following a remarkable erosive winter (e.g. Castelle *et al.*, 2015).

Field sites

Both Truc Vert Beach (TVB) and Biscarrosse Beach (BB) are situated on the southern part of the French Atlantic Coast (Figure 1a) and are about 35 km distant one from the other. They are representative of the nearly undisturbed 250 km long stretch of linear open low-sandy beaches facing the Atlantic swell in a meso- to macrotidal environment, covered by high aeolian foredunes and exhibiting a double nearshore sandbar system (e.g. Castelle *et al.*, 2007). While TVB is situated updrift of the Arcachon lagoon (the modal alongshore current along this part of coast is southward), BB is situated downdrift of it (Figure 1b) and recent remote sensing observations indicated that the dynamic of the Arcachon inlet might influence sediment supply to BB. TVB and BB exhibit a relatively high (15 – 20 m) and wide (>100 m) aeolian dune system what can be severaly eroded under energetic conditions (Figures 1c and 1d). The main difference between the two sites is that TVB is a fully natural beach system with no anthropogenic action while BB is situated in an urban area and several defences have been deployed over the past decades including use of sand-filled geotextile (Figure 1d) and beach nourishment. Previous studies have shown that both sites exhibited a seasonal dynamic (e.g. Senechal *et al.*, 2009; Castelle *et al.*, 2014) and that the shoreline was able to recover from energetic storm events within the short to seasonal scales (e.g. Ba and Senechal, 2013; Castelle *et al.*, 2014; Coco *et al.*, 2014; Senechal *et al.*, 2015).

METHODS

Bi-monthly topographic surveys using DGPS methods are collected at TBV since nearly 10 years (see for example Senechal *et al.*, 2009 for a detailed description of the survey and data processing methods), while BB is surveyed using remote sensing data whith a video system deployed in May 2007 (e.g. Almar *et al.*, 2009). To ensure consistent comparisons between the two field sites, BB has been surveyed using DGPS methods between January 2014 and March 2015. Table 1 provides an overview of data collected over this period. 43 topographic surveys were collected covering an alongshore distance up to 1.5 km at each site. Because drastic beach changes can occur over very short time scales (typically a tidal cycle) but also to ensure at the same time a representative data set, only topographic surveys collected at each field site with a minimum lag of 4 days or less will be presented in the next sections. This represents 12 topographic surveys for each site covering the period between January 2014 and March 2015.

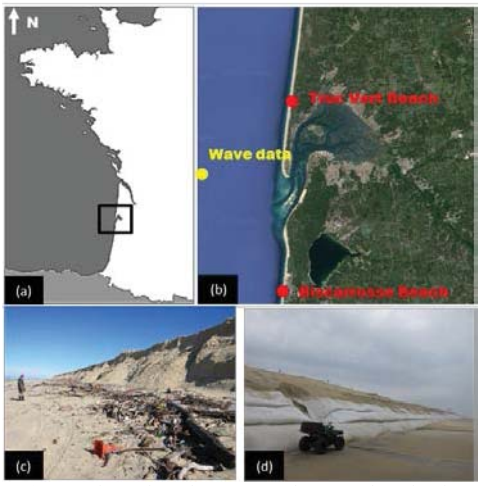

Figure 1. (a) Location of study area on the French Atlantic Coast. (b) Zoom on the Aquitanan coast and the field sites. The red dots indicate the beach locations and the yellow dot, the offshore wave data. (c) Truc Vert Beach in March 2014 after the dramatic 2013/2014 Winter. (d) Biscarrosse Beach at the same period. We can see the geotextile sand container shoreline protection system (Photos: © 2014 Stephan Bujan - EPOC).

Table 1. *Number of topographic surveys collected at each field site between January 2014 and March 2015. Lag represents the mínimum lag in days between the surveys of the two field sites for the same month.*

	Jan14	Feb14	Mar14	Apr14	May14	Jun14	Jul14
TVB	3	1	3	2	2	2	2
BB	1	1	1	1	1	0	0
Lag	4	1	1	1	2		
	Sep14	Oct14	Nov14	Dec14	Jan15	Fe15	Mar15
TVB	2	2	2	2	2	2	2
BB	1	2	3	0	0	1	2
Lag	1	1	1			4	1

Wave conditions were measured by a directionnal wave buoy Datawell deployed in about 55 m water depth at about 15 km from the shore (Figure 1b). This wave buoy is part of the French network CANDHIS that aims at collecting real-time wave data along the French coast (http://candhis.cetmef.developpement-durable.gouv.fr/). Unfortunatly the wave buoy has been lost in June 2014. Between June 2014 and March 2015, the significant wave heights Hs predicetd by the Wave Watch 3 model (WW3 model) and extracted at the nearest location node to the position of the wave buoy were used. To ensure data consistency, the WW3 predicted significant wave heights Hs have been previously compared to a long data set of measured Hs (covering nearly 2 years) and a regression equation has been used (Figure 2).

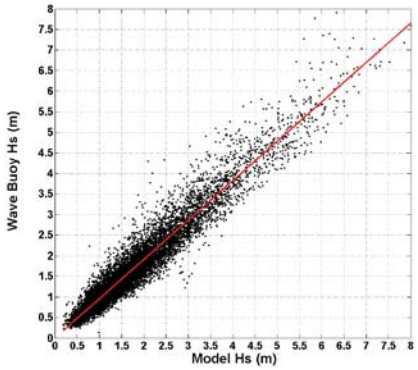

Figure 2. Comparisons (black dots) and regression (red line, r = 0.96) between the significant wave height Hs measured by the wave buoy deployed offshore and the nearest extraction node of the significant wave height Hs computed by the WW3 model.

RESULTS

Results are presented for beach response at the two sites.

The 2014/2015 winter season

Figure 3 represents the wave characteristics in 55 m water depth between November 2013 and April 2015. We clearly observe the seasonnality of the wave climate with winter season (typically between November and March, black dashed rectangles) associated with longer and more energetic swells than summer season. While during summer the monthly averaged wave height (red solid line in upper panel) is around 1 m, during the winter period it can increase up to 4 m (February 2014). Similarly the monthly averaged wave period is about 8-9 s (red solid line in the lower panel) during the summer period and can increase up to 13 s during the winter period. Figure 3 also clearly shows that the winter 2013/2014 has been exceptionnaly energetic. In partculiar, compared to it, the winter 2014/2015 was particularly 'calm'. Indeed, we clearly observe that the monthly averaged value are higher in 2013/2014 by a factor of nearly 1.5 for the significant wave height. During the 2013/2014 winter period, wave heights were higher than 4 m for 25 % of the time while during the 2014/2015 winter period, this value falls to 9 %. Similarly the maximum reported significant wave height during the 2013/2014 is 9.23 m while during the 2014/2015 it falls to 6.6 m. Comparisons with previous studies (e.g. Senechal *et al*., 2015) reveal that the winter 2014/2015 was moderate in comparison to previous winter periods.

Truc Vert Beach post– 2014 winter evolution

Figure 4 illustrates the alongshore averaged beach profile evolution at Truc Vert Beach between January 2014 and March 2015. We clearly observe that the highest beach retreat event is associated with a rapid sequence of very energetic storms observed during February 2014 (Figure 3). The mean retreat reaches up to 25 m on the upper beach face between January 2014 and February 2014. After this massive erosion event, the beach profile does not change similarly in the lower and the upper part. The supratidal beach (isolevels above 3.5 m) experienced retreat until the end of the winter period while lower part (isolevels lower than 0.5m) undergoes slow accretion.

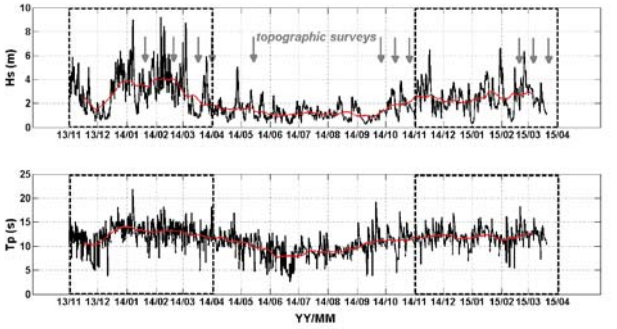

Figure 3. Wave characteristics in 55 m water depth from November 2013 to April 2015. The red line represents the monthly-averaged value. The black rectangle represent the winter seasons.

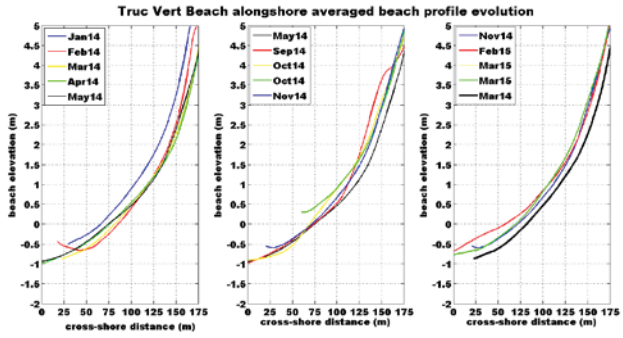

Figure 4. Alongshore averaged beach profiles at Truc Vert Beach between January 2014 and March 2015. Beach elevation is given in the French National Datum (MSL is +0.4m).

During the summer period (from May to September 2014), the upper beach undergoes a significant recovery period interrupted then by the first energetic waves of the winter period (e.g. October 2014, Figure 3). During this event, the beach profile reaches its 2015 winter profile. Indeed, no significant modification is then observe on the upper beachface (isolevels above 1.5m) despite the occurence of several other storm events associated with significant wave height up to 6 m. On the other hand erosion is observed on the lower intertidal beach. The comparisons of the profiles between March 2015 and March 2014 indicate an overall 'recovery' of the whole beach profile between March 2014 and March 2015 for Truc Vert beach during this period.

Biscarrosse Beach post– 2014 winter evolution

Figure 5 illustrates the alongshore averaged beach profile evolution at Biscarrosse Beach during the same period. We clearly observe that the highest erosion event is associated with the same period characterized by a rapid sequence of very energetic storms observed during February 2014 similarly to what have been observed at Truc Vert beach (e.g. Figure 4). The mean erosion reaches up to 25 m on the upper beach face. After this massive erosion event, in contrast to Truc Vert beach, the

beach profile seems to rotate around the isolevel 0.5m, the upper beach still undergoing retreat while the lower part seems to accrete.

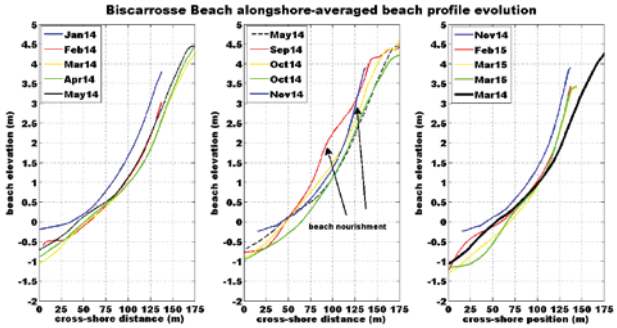

Figure 5. Alongshore averaged beach profiles at Biscarrosse Beach between January 2014 and March 2015. Two massive beach nourishments were carried on in June 2014 and at the beginning of November 2014.

Figure 6 clearly illustrates that dune erosion is not uniform and that erosion spot can be observed. Beach nourishment operations were undertaken just after the storms to fill in the embayments but the profile evolution indicate that in presence of energetic storm events, they did not significantly modified the beach profile evolution. Important beach nourishment operations were then carried on during June 2014 on the upper beach face and can be observed in the profile shape and elevation (September 2014, middle panel). However, we observe that after the first energetic event (see Figure 3, October 2014), the beach profile rapidly goes back to its May 2014 profile. During the 2015 winter, erosion was essentially observed in the lower intertidal domain as observed at Truc Vert Beach. However, the upper beach face also experienced a moderate retreat (about 10 m) consistent with seasonnal dynamics (Senechal *et al.,* 2015). Comparison between the post-2014 winter profile (March 2014) and the post-2015 winter (March 2015) indicate that the beach undergoes a rotation around isolevel 1m associated with upper beach accretion and lower-beach erosion and beach slope steepening (Figure 5, right panel).

DISCUSSION

On the basis of the analysis of available data (topographic surveys and offshore wave forcing), we can observe that Truc Vert Beach and Biscarrosse Beach responses are significantly different although the two field area are in similar energetic environments. The differences are highlighted in Figure 7. Figure 7 represents the positions of the alongshore averaged isolevels of beach elevation at Truc Vert Beach (upper panel) and Biscarrosse Beach (lower panel) over the time. We clearly see that both beaches experience significant retreat during winter 2014, especially on the upper part of the beachface (isolevels > 2 m). However we notice that for these isolevels Truc Vert beach retreat is essentially associated with the February 2014 event and then essentially the isolevels situated above 3.5 m (the supratidal beach) still retreat. In contrast, Biscarrosse beach experiences a continuous retreat covering the all upper beach face down to isolevel 0.5 m until the end of the winter (March 2014) and this despite beach nourishment operations over this period.

Figure 6. Aerial view of Biscarrosse Beach. We observe the cuspate embayments after the 2014 winter. (Image source: © 2014 SPAD - www.spad-drone.com).

The reason why Biscarrosse beach experienced erosion while at the same time Truc Vert beach did not are not fully understood. One hypothesis could be associated with the dynamics of the outer bar system. Castelle *et al.* (2015) showed the key role of the outer bar system during the winter 2014. Almar *et al.* (2009) analysing video data under severe storm conditions in March 2009 reported that the outer bar dynamics were not the same at Biscarrosse and TrucVert beach. In particular the distance between the inner bar and the outer bar was 150 m larger at Truc Vert beach than at Biscarrosse beach and the observed total outer bar migrations were much larger at Truc Vert Beach than at Biscarrosse beach.

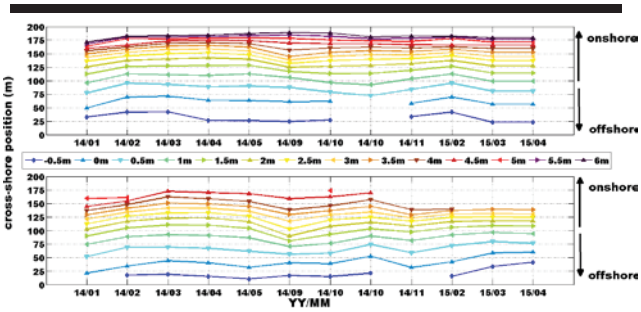

Figure 7. Positions of alongshore averaged isolevel contours of beach elevation at Truc Vert Beach (upper panel) and Biscarrosse Beach (lower panel) as a fonction of time.

Another hypothesis could be associated to the shoreline orientation. Indeed, there is nearly 2° lag between the shoreline at Truc Vert beach and Biscarrosse what could induce variation in the longshore drift component. During the summer period both sites partially recovered on the upper beach face: the isolevels situated between 2 m and 4 m experience significant offshore migration (up to 15 m). However while this recovery is a fully natural process at Truc Vert beach, massive beach nourishment were operated at Biscarrosse. The data do not allow estimating the respective contribution between natural processes and anthropogenic action at Biscarrosse and thus it is hard to

determine if without beach nourishment, partial recovery at Biscarrosse would have been of the same order. However data suggest that Truc Vert beach reached a relative stability on the upper beachface going through the winter 2015 compared to Biscarrosse beach whose profile remained much more variable. The relative stability of Truc Vert beach during the winter 2015 might also be associated to the relatively low energetic winter experienced in 2015 compared to the 2014 winter.

CONCLUSIONS

The erosion and 'recovery' processes at Truc Vert beach and Biscarrosse beach are complex and are certainly not only driven by the local availability of sediment. Indeed, although both sites are close to each other and experience similar environmental conditions, data indicate that Biscarrosse Beach is less stable than Truc Vert beach although beach nourishment are operated all year long. During the winter, erosion experienced at Biscarrosse beach is more severe and lasting on a longer period compared to the eorsion observed at Truc Vert beach. During the summer, recovery is nearly of the same order at both field sites despite beach nourishment is operated at Biscarrosse while not at Truc Vert beach. The following winter, Truc Vert beachface remains remarkly stable while Biscarrose beachface undergoes significant modifications. Further analysis should be undertaken to highligh if beach management may have effects on the medium to long-term resilience of the beach.

ACKNOWLEDGMENTS

TVB and BB are two field sites included in the French INSU SNO Dynalit and SOERE 'Shoreline' networks (http://www.dynalit.fr/fr). This publication is one of the results of the INSU SNO-Dynalit Project and the Allenvi SOERE Trait de Côte. Financial support has also been provided by the ANR CHIPO.

LITERATURE CITED

Almar, R.; Castelle, B.; Ruessink, B.G.; Sénéchal, N.; Bonneton, P., and Marieu, V., 2009. High-frequency video observation of a double sandbar system under high-energy wave forcing. *Journal of Coastal Research*, SI 56, 1706-1710.

Anthony, E.J., 2013. Storms, shoreface, morphodynamics, sand supply, and the accretion and erosion of coastal dune barriers in the southern North sea. *Geomorphology*, 199: 8-21.

Ba, A. and Senechal, N., 2013. Extreme winter storm versus Summer storm: morphological impact on a sandy beach. *Journal of Coastal Research*, SI 65,ISSN 0749-0208.

Birkemeier, W.A., 1979. The effects of the 19 december 1977 coastal storm on beaches in North Carolina and New Jersy. *Shore beach* 47, 7-15.

Callaghan, D.P.; Ranasinghe, R.; and Short, A., 2009. Quantifying the storm erosion hazard for coastal planning. *Coastal Engineering*, 56, 90-93.

Castelle B.; Marieu V.; Bujan S.; Splinter K.D.; Robinet A., Senechal N., and Ferreira S., 2015. Impact of the winter 2013-2014 series of severe Western europe stroms on a double-barred sandy coast: beach and dune erosion and megacusp embayments, *Geomorphology*, 238, 135-148.

Castelle, B.; Marieu, V.; Bujan, S.; Ferreira, S.; Parisot, J.-P.; Capo, S.; Senechal, N., and Chouzenoux, T., 2014. Equlibrium shoreline modelling of a high-energy meso-macrotidal multiple-barred beach. *Marine Geology*, 347, 85-94.

Castelle B. ; Bonneton P. ; Dupuis H. , and Sénéchal N., 2007. Double bar beach dynamics on the high-energy meso-macrotidal French Aquitanian coast: a review, *Marine Geology*, 245, 141-159.

Coastal Hazards., 2013. Series Coastal Research Library, Vol. 6, Charles W. Finkl (ed.), Springer, ISBN 978- 94-007-5234-4. 840pp.

Coco G.; Senechal, N.; Rejas, A.; Bryan K.; Capo, S.; Parisot, J.P.; Brown, J.A., and MacMahan, J.H.M. 2014. Beach response to a sequence of extreme storms. *Geomorphology*, 204, 493-501.

Forbes, D.L.; Parkes, G.S.; Manson, G.K., and Ketch, L.A. 2004. Storms and shoreline retreat in the southern Gulf of St. Lawrence. *Marine Geology*, 210, 169-204.

Gallop, S.L.; Bosserelle, C.; Eliot, I., and Pattiaratchi, C.B. 2012. The influence of linestone reefs on storm erosion and recovery of perched beach. *Continental Shelf Research*, 47, 16-27.

Komar, P.D., 1998. *Beach processes and sedimentation*. Prentice Hall, New Jersey, 429pp.

Masselink, G. and van Heteren, S. 2013. Response of wave-dominated and mixed-energy barriers to storms. *Marine geology*. Doi:10.1016/j.margeo. 2013.11.004.

Newton, A.; Carruthers, T.J.B., and Icely, J. 2012. The coastal syndromes and hotspots on the coast. *Estuarine, Coastal, and Shelf science*, 96: 39-47.

Senechal N.; Coco G.; Castelle B., and Marieu V., 2015. Storm impact on the seasonal shoreline dynamics of a meso- to macrotidal open sandy beach (Biscarosse, France), *Geomorphology*, 228, 448-461

Sénéchal N.; Gouriou T.; Castelle B.; Parisot J.P.; Capo S.; Bujan S., and Howa H., 2009. Morphodynamic response of a meso- to macro-tidal intermediate beach based on a long-term data-set, *Geomorphology*, 107, 263-274.

Splinter, K.D.; Strauss, D.R., and Tomlinson, R.B., 2011. Assessment of Post-strom recovery of beaches using video imaging techniques: a case study at Gold coast Australia. *IEEE Transactions on geoscience and remote sensing*, 49(12), 4704-4716.

Splinter, K.D.; Carley, J.T.; Golshani, A., and Tomlinson, R., 2014. A relationship to describe the cumulative impact of storm clusters on beach erosion. *Coastal engineering*, 83, 49-55.

Stojanovic, T.A. and Farmer, C.J.Q., 2013. The devlopment of world oceans and coast and concepts of sustainability. *Marine Policy*, 42, 157-165.

Wang, P.; Kirby, J.H.; Haber, J.D.; Horwitz, M.H.; Knorr, P.O., and Krock, J.R., 2006. Morphological and sedimentological impacts of hurricane Ivan ad immediate post-storm beach recovery along the Northwestern Florida barrier-isalnd coasts. *Journal of Coastal Research*, 6, 1382-1402.

Yu, F.; Switzer, A.D.; Lau, A.Y.A.; Yeug, H.Y.E.; Chik, S.W.; Chiu, H.C.; Huang, Z., and Pile, J., 2013. A comparison of the post-storm recovery of two sandy beaches on Hong Kong island, southern China. *Quaternary International*, 304 :163-175.

Journal of Coastal Research	SI	75	467-471	Coconut Creek, Florida	2016

An artificial reef improves coastal protection and provides a base for coral recovery

Rodolfo Silva [†], Edgar Mendoza [†], Ismael Mariño-Tapia[‡], María Luisa Martínez[††] and Edgar Escalante[*]

[†]Instituto de Ingeniería
Universidad Nacional Autónoma de México
D.F., Mexico

[‡] Departamento de Recursos del Mar
CINVESTAV
Mérida, Yucatán, Mexico

[††] Red de Ecología Funcional
Instituto de Ecología, A.C.
Xalapa, Mexico

[*] Unidad Académica de Sistemas Arrecifales
Instituto de Ciencias del Mar y Limnologia
Universidad Nacional Autónoma de México
Puerto Morelos, Mexico

www.cerf-jcr.org

www.JCRonline.org

ABSTRACT

Silva, R.; Mendoza, E., Mariño-Tapia, I.; Martínez, M.L., and Escalante, E. 2016. An artificial reef improves coastal protection and provides a base for coral recovery. *In:* Vila-Concejo, A.; Bruce, E.; Kennedy, D.M., and McCarroll, R.J. (eds.), *Proceedings of the 14th International Coastal Symposium* (Sydney, Australia). *Journal of Coastal Research*, Special Issue, No. 75, pp. 467-471. Coconut Creek (Florida), ISSN 0749-0208.

In 2007, Hurricane Dean caused extensive damage along the coast of Riviera Maya, exceptionally large mass of wind-transported sand was deposited on the beach front and gardens of the former NH Hotel in Puerto Morelos. Due to the chaotic sea state and the debris carried by the storm, the sand was contaminated with various pollutants, including terrigenous materials and biogenic matter. As an emergency measure, this sand was used to create an artificial dune in the grounds of the hotel. Given the high probability of future storms of such magnitude, it was decided that some form of sediment transport control was needed to protect the beach so an artificial reef was constructed 120 m off the shore. The structure, made of prefabricated concrete elements, has been effective as a coastal defense barrier and has also provided a habitat for several reef species. Five years after the placement of the structure the beach front, which had previously registered erosion problems, had returned to its natural cycle of summer growth and winter retreat and a large number of fish and coral species were using the habitat provided by the structure. However, the coral reef growing on this prefabricated structure was not long-lasting. The massive and persistent occurrence of *Sargassum* in 2015 brought oxygen depletion, reduced pH, an excess in nutrients and less water transparency on the Caribbean coast, leading to the decline of the reef habitat. Further studies are necessary to test whether reef species recolonize the prefabricated substrate.

ADDITIONAL INDEX WORDS: *artificial reef, morphological recovery, reef habitat.*

INTRODUCTION

According to Honey and Krantz (2007) tourism is the largest business sector of the world economy, accounting for 10% of global gross domestic product. Tourism has become increasingly important for developing countries, and represents 70% of exports from the Least Developed Countries (LDCs), particularly in the most megabiodiverse nations (Silva *et al*., 2014). Tourism is the only large sector of international trade in services in which LCDs consistently have a surplus.

It is increasingly accepted that coastal evolution is due to both natural processes and anthropogenic disturbances. While the natural processes involved are relatively well understood, erosion problems on the shore are often exacerbated by weak legislation and inadequate coastal management programmes. In many areas of the Caribbean the resistance and resilience of the coast is being lowered at an alarming rate. This is mainly due to the effects of sea level rise, the degradation of corals, the removal of key vegetation (seagrass and dune vegetation) and the consequences of badly planned infrastructure (legally sound but inadequately constructed). The resulting beach erosion also induces the loss of habitats. Sadly, tourism infrastructure is usually welcome in these areas, even though it is often the cause of subsequent erosion problems, as this is the most important economic activity in the region. The most common means of tackling beach erosion nowadays is through artificial beach nourishment, which produces ecological and economic problems in the areas from which the sand is "borrowed" and is only feasible while these sand banks have sufficient sand.

Under these circumstances the construction of hard or semi-hard structures is often rejected on aesthetic grounds in tourist areas. In addition, the coastal engineer is nowadays obliged to design environmentally friendly solutions showing preference to those schemes that enhance the development of habitats. Therefore, the construction of an artificial, submerged reef breakwater was decided upon for the beach near Puerto Morelos, Mexico, to protect it from erosion. The outcome of this project is detailed in this paper.

DOI: 10.2112/SI75-094.1 received 15 October 2015; accepted in revision 15 January 2016.
*Corresponding author: danielemallmann@gmail.com

Background

Puerto Morelos is located at the geographical coordinates 20° 51' 13" North, 86° 52' 31" West, in the tourist area of the Riviera Maya, 30 km south of Cancun (Figure 1). Off the coast, at a distance ranging from 350–1,600 m, a barrier reef is found, part of the "Mesoamerican Reef". Puerto Morelos was an uninhabited area until the late nineteenth century, then it had very moderate growth until the 1980s. In the last two decades, Puerto Morelos has experienced rapid growth and from 2008 to 2013 tourist capacity has expanded from 2585 to 5072 hotel rooms, SEDETUR (2015).

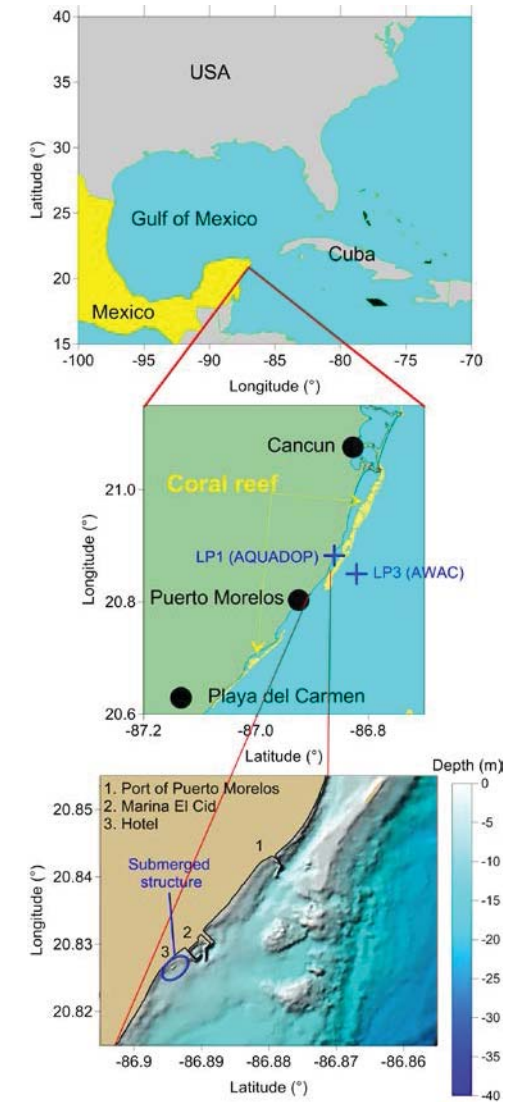

Figure 1. Geographical location of the study area.

In August 2007, waves, storm surge, wind and currents induced by Hurricane Dean, moved several hundred cubic meters of sand into the grounds of the NH Puerto Morelos hotel (recently renamed Now Jade).

The records of a wave-current profiler AWAC (Figure 2, LP3) deployed offshore at a depth of 20 m near the hotel, showed that while Hurricane Dean affected the area, significant wave heights were over 7 m. Associated mean wave periods were of 8 s, the most intense waves came from SEE and SE and the most persistent waves came from the SEE and E (Figure 2). The most persistent and intense currents travelled to the NNE.

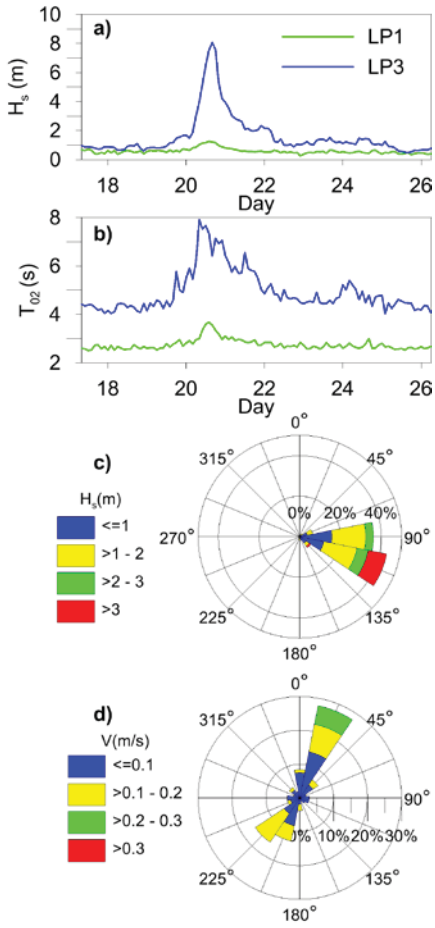

Figure 2. a) Significant wave height, b) mean wave period, c) LP3 wave rose and, d) LP3 currents at 1 m above the sea bottom. Seaward of reef (LP3) and in the reef lagoon (LP1) during the occurrence of Hurricane Dean.

As the direction of most persistent and energetic waves was SEE, the sand travelled from south to north and the breakwater at the southern part of the El Cid Marina interrupted the longitudinal currents, inducing the accumulation of sand in the grounds of the hotel.

Given that the sand deposited at the hotel was mixed with the soil from the mangrove (mainly peat), the authorities and hotel developers were faced with the decision of what to do with it. If the sand, contaminated with organic matter, was returned to the

sea, it would probably have a negative impact on the coral reefs. On the other hand if the sand was placed behind the hotel it would have affected the mangrove. Therefore an artificial dune was built to contain the contaminated material as an emergency solution (Figure 3).

To prevent similar events from occurring in the future, it was decided to build a structure offshore that would help to mitigate the problems of temporary beach erosion that are common in this area, reduce the accumulation of sand on the dry beach induced by storms, preserve the aesthetics and reinforce the marine ecosystem.

Figure 3. Appearance of the beach in a) August 2007, after Dean hit the coast, b) September 2008, illustrating the original winter retreat of the beach, c) the location of the artificial reef and d) and e) the beach in September 2011 and December 2014.

METHODS

To select a solution to the problem of sediment management, the following aspects were considered: (a) Marine climate: Wave and wind data from 1948 to 2007 were taken from the Atlas of Wave Climate by Silva *et al*. (2007). The cell consulted in the atlas is located at 86.75°W and 20.75° N. Annual and seasonal statistical data were used to define the mean and extreme regimes. From the analysis, the root mean square significant wave height and associated wave period are 1.3 m and 6.5 s, respectively, with incidences coming from NE to S; for return periods of 5 and 20 years, the significant wave heights are 8 and 12 m, respectively; The wind with highest occurrence probability has an intensity of 5 km/h coming from the NEE and E quadrants, and for return periods of 5 and 20 years the intensities are 90 and 136 km/h, respectively. The region is subject to a micro-tidal regime of around 0.30 m. The area is annually affected by an average of 18 storms, of which one is of great intensity. The average duration of this storm is 38 hours, although the maximum duration is up to 252 hours; (b) The nearest coral reefs are at a distance of approximately 1.5 km to the NNW; (c) The natural dynamics of sediment transport has been altered and partially conditioned by a series of structures that have been built along the coast, principally the El Cid marina, adjacent to the hotel and; (d) The coastal dunes and their associated vegetation have been altered and the natural dynamics of the ecosystem are at risk. Conservation is necessary as this is a turtle nesting area and a protected mangrove site, among other reasons.

The storm surge, the nearshore wave and current fields and the potential sediment transport propagation were calculated using the methodologies and model suggested by Gonzalez-Leija *et al*. (2013), Posada *et al*. (2008), and Silva *et al*. (2005).

Of the solutions considered (*e.g.* sand bypass, different hard solutions), the construction of a submerged artificial reef was chosen for the site, as natural coral reefs have been shown to dissipate energy. This is demonstrated by the wave height records registered during the presence of Hurricane Dean at Puerto Morelos (Figure 3, LP3 at 20 m and LP1 at 5 m water depth). A revision of the state of the art was made and different technologies were evaluated for the creation of an artificial reef. From the available options it was decided to use a relatively new element known as Wave Attenuation Device (WAD©), which is made of reinforced concrete (marine grade, 5000 psi, of neutral pH). Despite the WADs© having been accepted by the Environmental Protection Agency (EPA) technical information about the design of a reef was unavailable, so small scale laboratory tests were performed. These tests took place at the Coastal Engineering laboratory of the UNAM and the results were published in Burcharth *et al*. (2014). As a result of the laboratory studies of the hydrodynamic efficiency of the artificial reef, in a scale model 1:33.3 the reflection coefficients ranged from 20 to 35%, the transmission coefficients 50 - 75% and the dissipation factor was about 40%.

In 2010 a structure 60 m long, placed at a depth of 2.5 m and a submergence of 0.5 m below the Mean Low Water level, was constructed (see lower panel of Figure 1 and Figure 3c).

RESULTS

The beach response has been monitored regularly since Hurricane Dean. (Figure 3). From 2007-2010 the beach was still narrow and composed of sand and gravel (Figure 3b). Since the placement of the artificial reef, in 2010, the beach system has become stable again (Figures 3c-e), showing a normal pattern of accretion and erosion (during the months of May to October, the beach tends to grow, while in the remaining months the width of the dry beach decreases), but always with sufficient sand for tourist activities and for aesthetic considerations.

In the December 2014 beach monitoring survey different species of fish, polyps and soft and hard corals were observed on the artificial reef, such as sea fan (*Gorgonia flabellum*), White encrusting zoanthid (*Palythoa caribaeorum*) and brain coral (*Diploria labyrinthiformis*), (see Figure 4). At the time of writing this paper, it was believed that the artificial reef had provided the base for coral colonization.

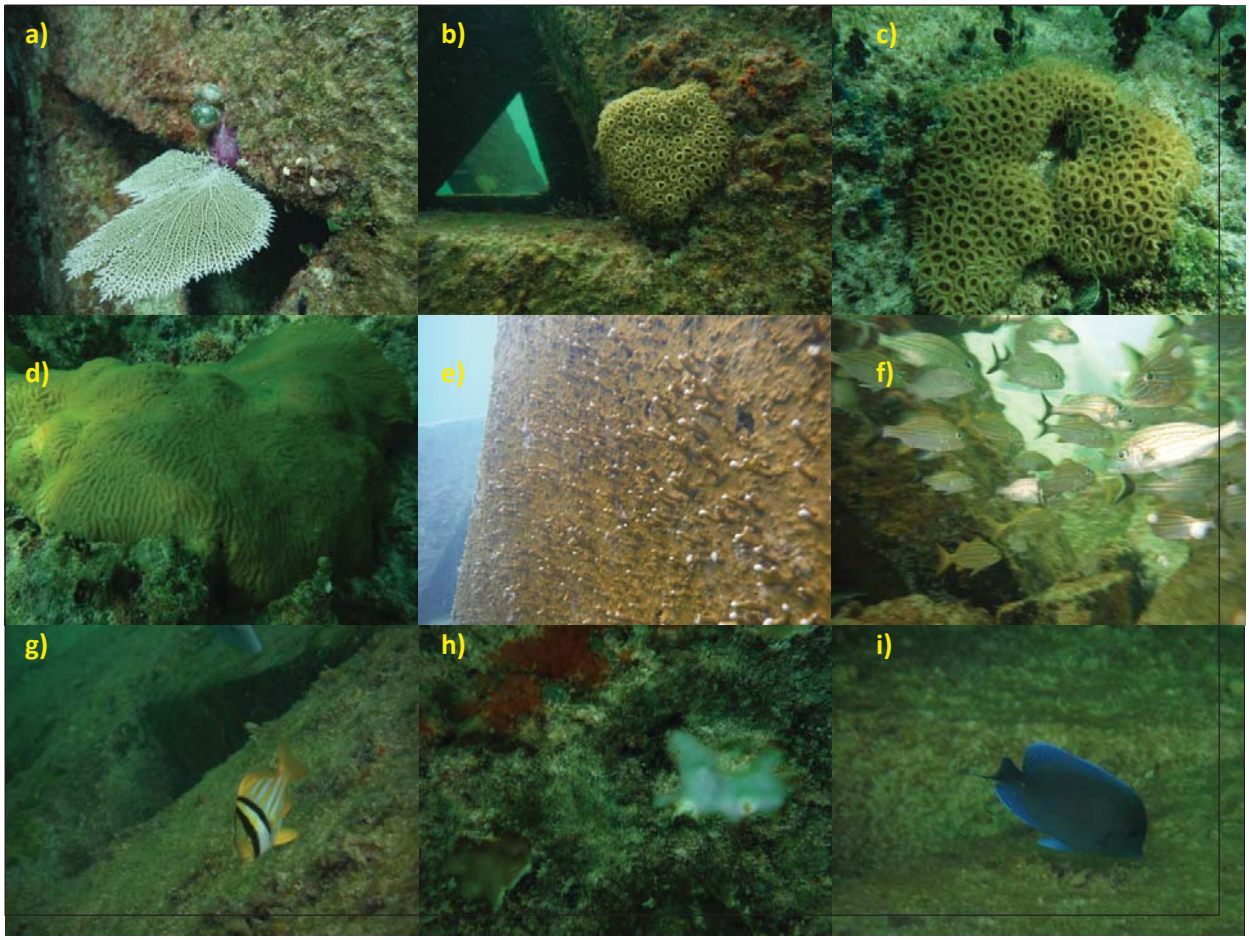

Figure 4. (a) sea fan (*Gorgonia flabellum*), (b) and (c) White encrusting zoanthid (*Palythoa caribaeorum*), (d) brain coral (*Diploria labyrinthiformis*), (e) polyps and, (f), (g), (h) and (i) the complex habitat established on the artificial reef.

DISCUSSION

In 2015, an unusually persistent and massive biomass of floating *Sargassum* invaded the Mexican Caribbean Sea and other areas of the region (*e.g.* Gavio *et al*., 2015). This "overabundance" of *Sargassum* caused a significant decrease in the pH of the sea water close to the beach, the water became hypoxic, there was a substantial increase in nutrients and the transparency of the water was reduced (Hillard, 2015). The presence of the seaweed (which lasted for 8 months) probably inhibited the growth of the coral reef species recently established in the artificial reef ecosystem and caused severe degradation to the habitat. The new colonies of coral were destroyed. Figure 5 shows some parts of the system in October 2015, where it can be observed that very few species survived.

CONCLUSIONS

A submerged artificial reef structure was designed to mitigate the beach erosion caused by interrupted longitudinal sediment transport. The design of the reef took into account the climatic and environmental conditions of the area as well as aesthetics, since the beauty of the beach is what attracts tourists. The reef was constructed by means of a set of wave dissipation devices (WADs ©) made of concrete. The submerged structure has been effective in beach protection and also provided a habitat for different animal and vegetation species, including corals, which established colonies in the artificial structure (Figure 4).

Although growth of the reef ecosystem was impressive from its construction until December 2014, with the arrival of seaweed the local conditions of nutrients, transparency and water pH changed. This caused a noticeable decline in species abundance and diversity. However, the conditions on the artificial reefs have now returned to those prior to the excess of *Sargassum*, suggesting that the ecosystem is probably capable of recovery in the coming years.

The main lesson learned in this study is that it is indeed possible to have effective coastal protection schemes that can provide the physical means for a living ecosystem to develop. Nevertheless, given the large number of variables that cannot be controlled, the resilience of these systems is uncertain when there are radical alterations to the environmental conditions.

Figure 5. Aspect of the artificial reef colonies after the overabundance of *Sargassum* from February to October 2015. Photos taken in October 2015.

ACKNOWLEDGMENTS

This publication is one of the results of the Latin American Regional Network global collaborative project ''*EXCEED – SWINDON project - Excellence Center for Development Cooperation – Sustainable Water Management in Developing Countries*''. We are very grateful to Francisco Gerardo Ruíz Renteria (ICMCyL-UNAM) for his invaluable support in the fieldwork as well as "Promociones Marina Morelos, S. de R.L. de C.V. (Now Jade Riviera Cancún Resort & Spa)" for permission to use material compiled and funded by them.

LITERATURE CITED

Burcharth, H.F.; Zanuttigh, B.; Andersen, T.L.; Lara, J.L.; Angileni, E., 2014. Innovative Engineering Solutions and Best Practices to Mitigate Coastal Risk. In: Zanuttigh, B.; Nicholls, R.J.; Anderlinden, J.P.; Thompson, R.C., and Burcharth, H.F., (eds.). *Coastal Risk Management in a Changing Climate.* Oxford: Butterworth-Heinemann., pp. 55-170.

Gavio, B.; Rincón-Díaz, M., and Santos-Martínez, A., 2015. Massive quantities of pelagic sargassum on the shores of San Andres island, southwestern Caribbean. *Acta Biológica Colombiana*, 20(1), 239-241.

González-Leija, M.; Mariño-Tapia, I.; Silva, R.; Enriquez, C.; Mendoza, E.; Escalante, E.; Ruiz, F., and Uc-Sánchez, E., 2013. Morphodynamic evolution and sediment transport processes of Cancun beach. *Journal of Coastal Research*, 29(5), 1146-1157.

Hillard, H., 2015. The role of *Sargassum pacificum* in ocean acidification effects on corals. Doctoral dissertation, California State University, Northridge.

Honey, M., and Krantz, D., 2007. Global trends in coastal tourism. Washington DC: Center on Ecotourism and Sustainable Development.

Posada-Vanegas, G.; Simmonds, D.; Silva, R., and Pedrozo, A., 2008. A 2D hydrodynamic model with multiquadtree mesh. In: Prescott, A.I. (ed). *Ocean Engineering Research Advances*, New York: Nova Science Publishers Inc. pp. 215-222.

SEDETUR, 2015. Estadísticas de indicadores turisticos. http://sedetur.qroo.gob.mx (in Spanish).

Silva, R.; Martínez, M.L.; Hesp, P.; Catalan, P.; Osorio, A. F.; Martell, R.; Fossati, M.; Miot da Silva, G.; Mariño-Tapia, I.; Pereira, P.; Cienfuegos, R.; Klein, A., and Govaere, G., 2014. Present and future challenges of coastal erosion in Latin America. In: Silva, R., and Strusińska-Correia, A. (eds.), *Coastal Erosion and Management along Developing Coasts: Selected Cases. Journal of Coastal Research*, Special Issue, No. 71, pp. 1–16.

Silva, R.; Ruiz, G.; Posada, G.; Pérez, D.; Rivillas, G.; Espinal, J., and Mendoza, E., 2007. Atlas de clima marítimo de la vertiente Atlántica Mexicana. UNAM, Mexico (in Spanish).

Journal of Coastal Research	SI	75	472-476	Coconut Creek, Florida	2016

Subtidal and Intertidal Three-Dimensionality at a High Energy Macrotidal Beach

Christopher Stokes†, Paul Russell†, and Mark Davidson†

†Plymouth University, School of Marine Science and Engineering, Faculty of Science and Engineering, Drake Circus, Plymouth, PL4 8AA, UK.

www.cerf-jcr.org

www.JCRonline.org

ABSTRACT

Stokes, C.; Russell, P., and Davidson, M., 2016. Subtidal and Intertidal Three-Dimensionality at a High Energy Macrotidal Beach. *In:* Vila-Concejo, A.; Bruce, E.; Kennedy, D.M., and McCarroll, R.J. (eds.), *Proceedings of the 14th International Coastal Symposium* (Sydney, Australia). *Journal of Coastal Research*, Special Issue, No. 75, pp. 472-476. Coconut Creek (Florida), ISSN 0749-0208.

Three-dimensional beach features such as crescentic sandbars and rip channels influence a beach's response to storm waves, as well as significantly affecting the safety and amenity provided by the surf-zone for beach water-users. A dataset of 5.5 years of quasi-weekly bar measurements, and quasi-monthly intertidal surveys from Perranporth beach (Cornwall, UK) were used to quantify seasonal to inter-annual changes in three-dimensionality. These changes were seen to be dictated by the cumulative effects of antecedent wave and tide conditions. Although tide range was seen to be important, particularly at the outer bar, a disequilibrium stress term was well correlated with three-dimensionality at the inner and outer bars and lower intertidal beach. This term examines the disparity between the instantaneous dimensionless fall velocity parameter (Ω), and the overall mean dimensionless fall velocity ($\overline{\Omega}$), and is moderated by the instantaneous wave power (P). Low values of disequilibrium stress correspond to Ω that are cumulatively smaller than previous values, indicating the waves have moved from high steepness to low steepness, as normally occurs in the months following winter. It is under such circumstances, as the beach begins to recover, that maximum values of beach three-dimensionality and associated rip channel development were seen to occur.

ADDITIONAL INDEX WORDS: *Beach State, Rip Current, Beach Safety, Wave Disequilibrium, Antecedent.*

INTRODUCTION

Previous research indicates that three-dimensional (3D) beach morphology, with bar and rip features, significantly increases the bathing hazard for water-users by enhancing rip current circulation (Scott *et al.*, 2008). Such morphology also enhances the quality of surfing conditions by increasing the angle of breaking waves to within limits suitable for wave riding (Mead and Black, 2001). A number of beaches on the macrotidal north Corwall coast (south west U.K.) sit at a classification boundary at the dissipative-intermediate end of Wright and Short's (1984) beach state model. As a result, they regularly transition from a 2D dissipative state to a 3D intermediate state featuring crescentic bars and rip channels.

Morphological parameters such as the dimensionless fall velocity, Ω, have been widely related to changes in beach state (Wright and Short, 1984), yet Ω has also been found to relate poorly to intermediate beach state transitions. The identified shortcomings include not considering the absolute level of wave energy (Scott *et al*., 2011), or duration of wave events (Jiménez *et al*., 2008), and it also cannot account for relaxation time or free-morphological behaviour (bed-surf coupling), which reduces the correlation between the morphology and instantaneous wave conditions. Despite this latter effect, hydrodynamics have still been found to govern the overall scale of beach three-dimensionality (Ranasinghe *et al.*, 2004), and the system is thought to be deterministic (Plant *et al.*, 2006). Consequently, different manifestations of wave parameters which consider antecedent conditions may improve their explanatory power.

Perranporth beach is situated on the north coast of Cornwall, and provides the study site for the present research. Facing west-northwest it is fully exposed to an energetic wave climate of both Atlantic swell and local wind sea, with an annual mean significant wave height of 1.6 m and peak period of 10.6 s. It is macrotidal (mean spring range 6.3 m) and although predominantly dissipative, it regularly features 3D low tide bar/rip morphology. In a previous contribution (Stokes *et al*., 2015) we observed significant annual periodicity in the three-dimensionality of the sub and intertidal regions of Perranporth beach, with annual minima and maxima occurring in winter and spring, respectively. This paper aims to further investigate how these seasonal variations relate to incident wave and tide forcing, using novel manifestations of common hydrodynamic parameters.

METHODS

An elevated Argus video camera located at the southern end of Perranporth beach (Figure 1) collected time exposure (timex) images of the lower intertidal and subtidal regions between September 2008 and April 2014. As a result of the preferential breaking of waves over the shallow bar crests, foam is often

DOI: 10.2112/SI75-095.1 received 15 October 2015; accepted in revision 15 January 2016.

*Corresponding author: Christopher.stokes@plymouth.ac.uk

Figure 1. Satellite image of Perranporth beach. The octagon and open triangle show the location and field of view of the Argus cameras, the dashed line shows the typical extents of the topographic surveys, and the solid triangle shows the location of the nearshore wave buoy.

visible on the water surface at the position of the sandbars, creating conspicuous bands of high pixel intensity that reveal the position of the underlying bars. A barline intensity mapping tool (Pape *et al.*, 2007) was used to detect the inner and outer bar crest positions by the alongshore tracking of the intensity maxima within the surf zone (Figure 2). The barlines were measured at 1 m intervals, between -1700 m and -200 m alongshore. The detected barline positions can be artificially shifted due to tide and wave conditions. To minimize tidal shifting, a single low tide image was selected for each day (Van Enckevort and Ruessink, 2001). To maximise clear breaking over the bars images were also constrained by significant wave height, H_s (0.5 m < H_s< 2 m), and Hydrodynamic Forcing Index (Almar *et al.*, 2010), HFI (0.9 < HFI < 2). Images were also unavailable during poor light and weather conditions, or occasionally due to technical issues with the camera system. Of the 2067 days of the study period 254 usable images were obtained, with a minimum, mean and maximum interval of 1, 8 and 74 days, respectively.

To compliment the subtidal imagery, intertidal topographic surveys were conducted using an RTK-GPS system mounted on an all-terrain vehicle (ATV) each month between October 2008 and April 2014. The surveys were conducted around low tide during the largest spring tide of each month, to maximise beach coverage. Typical survey extents are shown in Figure 1. A total of 64 monthly surveys were conducted, with a minimum, mean and maximum interval of 16, 32 and 73 days respectively. The collected data were used to generate digital elevation maps (DEM's), which were converted from OSGB36 coordinates by rotation and translation to the same local grid as used by the Argus camera system (Figure 2). The data were gridded at 20 m resolution in both the alongshore and cross-shore directions with a quadratic loess interpolation scheme (Plant *et al*., 2002).

To objectively quantify the three-dimensionality of the subtidal bars, the standard deviation, α, about the alongshore averaged cross-shore position, X_c, of the barlines was measured in keeping with previous studies of barline variability. To obtain a single representative measure of α at the lower intertidal beach, contours were extracted from each DEM every 0.2 m between +0.2 m Ordnance Datum Newlyn (ODN) and -2.4 m ODN (between -1100 m and 200 m alongshore, thin dashed lines in Figure 2), and the mean of the highest 1/3rd of α values was used. For reference, 0 m ODN is approximately Mean Sea Level (MSL) at this beach. It is recognised that across flat, non-sloping sections this parameter could incorrectly yield large values of α, but this did not occur in the present data set. The mean low-water neap (MLWN) contour (thick dashed line in Figure 2) was chosen to represent the cross-shore position (X_c) of the lower beach.

Before calculating α the raw barline and contour data were linearly de-trended, then band-pass Fourier filtered between 25 and 1000 m, to simultaneously remove small scale noise as well as any beach rotation or curvature larger than the length scales of interest. As seasonal and inter-annual changes are of primary interest, the α and X_c time series were also low-pass filtered using a frequency domain Fourier filter with 1/42 days cut off, chosen to be sufficiently longer than the timescale of individual storms yet shorter than an individual season. The measured X_c and α data and low-pass filtered signals are plotted in Figure 3.

Novel manifestations of hydrodynamic parameters

Wave Data were provided by a Datawell Waverider III buoy maintained by the Channel Coastal Observatory (www.channelcoast.org) and located just offshore of Perranporth beach in approximately 14 m depth (Figure 1). The half hourly wave statistics were used to calculate daily average values of offshore wave power, P_o, alongshore oriented wave power, P_y, Relative Tide Range, RTR (Masselink and Short, 1993), and Ω. Three different manifestations of each wave parameter were compared to beach three-dimensionality, as well as a fourth parameter that combines P_o and Ω:

1) The daily-averaged forcing parameters denoted k for the following definitions.

2) The forcing parameters low-pass filtered using a frequency domain Fourier filter with a 1/42 day cut off, denoted k_{LP}, to reveal seasonality in the forcing.

3) The cumulative integral of the demeaned wave parameters, denoted k_{CI}. This parameterisation assumes that beaches have an equilibrium condition related to the long term mean wave condition ($\bar{k}$). Deviations from this mean are assumed to promote deviations from the equilibrium state of the beach. To reflect the cumulative effects of the antecedent forcing, the cumulative integral is used:

$$k_{CI}(n) = \int_{t_0}^{t_n} (\bar{k} - k)\, dt \qquad (1)$$

Where t_0 is the start of the time series, and $k_{CI}(n)$ denotes the cumulative integral of the wave parameter up to time-step t_n.

4) A disequilibrium stress term, denoted Ω_{DS} (Figure 4, upper left panel). Similar to the parameterisation of k_{CI}, the

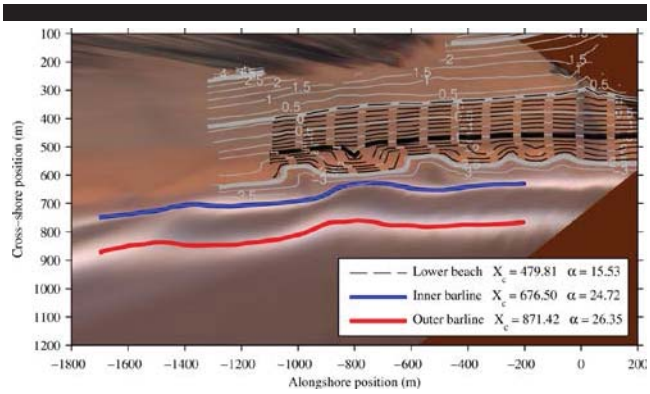

Figure 2. Example Argus image with detected bar crest positions, overlaid with RTK-GPS measured intertidal contours. Xc is the alongshore averaged cross-shore position, and α is the standard deviation (three-dimensionality) of the barlines or contours. The thick contours show the mean high-water spring, mean sea level, and mean low-water spring tide level, while the thick dashed contour shows mean low-water neap used to determine X_c for the lower intertidal region.

disequilibrium stress term examines departures from mean wave conditions, but following Davidson *et al.* (2013) Ω_{DS} incorporates the offshore wave power to determine the magnitude of morphological change, while disequilibrium in Ω (difference between mean $\overline{\Omega}$ and instantaneous Ω) determines the direction of change:

$$\Omega_{DS}(n) = \langle \int_{t_0}^{t_n} P_o^{0.5}(\overline{\Omega} - \Omega)dt \rangle \qquad (2)$$

The angular brackets in Eq. 2 denote a de-trending of the cumulative time series. P_o is raised to the 0.5 exponent following the relationship noted by Davidson *et al.* (2013).

A total of 13 hydrodynamic forcing time series were generated, as follows: P_o, $P_{o,LP}$, $P_{o,CI}$, $P_{y,b}$, $P_{y,b,LP}$, $P_{y,b,CI}$, Ω, Ω_{LP}, Ω_{CI}, Ω_{DS}, RTR, RTR_{LP}, and RTR_{CI}. These were compared to the time series of α at the lower beach, inner bar and outer bar using Pearson product-moment correlation (R) and cross correlation analysis. To enable direct comparison, the low-pass filtered and weekly-resampled morphological time series were used, along with forcing parameters sampled at the same weekly instances. The correlations were tested for significance at the 99% confidence level using a two-sided t test, applying $N-2$ degrees of freedom to calculate the confidence intervals, where the sample size, N, is the number of available morphological observations at a given lag.

RESULTS

No significant correlation was found between the filtered α time series' and the instantaneous hydrodynamic parameters at any of the beach regions, and the seasonal (low-pass filtered) wave parameters similarly had few significant correlations with α. In contrast, the cumulative integral, and disequilibrium stress parameters had significant correlations with beach three-dimensionality at many of the beach regions. The strongest correlation between forcing and three-dimensionality occurred at the lower beach, with weaker correlations at the inner and outer bars. Outer bar α was best correlated with RTR_{CI} (R = 0.39) and Ω_{DS} (R = -0.38), the inner bar three-dimensionality was best correlated to $P_{y,b,CI}$ (R = -0.54), and lower beach three-dimensionality was strongly correlated to Ω_{DS} (R = -0.82).

Due to the likelihood of a lag in the beach response, the morphological data were next assessed for cross-correlation with forcing parameters at different lag times of up to 250 weeks. As the cumulative integral and disequilibrium stress parameters displayed the strongest instantaneous correlations, the cross-correlation was performed on those manifestations of the data. Table 1 shows that three-dimensionality at the outer bar had a distinct lag in response to each of the tested forcing parameters of 5-12 weeks. The strongest correlation was with RTR_{CI} at 11 weeks lag (R = 0.57), and comparable correlations were also found with Ω_{CI} and Ω_{DS} at 12 and 11 weeks lag respectively. The inner bar at Perranporth had distinctly less lag in response, demonstrated by the correlation with $P_{y,b,CI}$ (R = -0.58) at 4 weeks lag. The lower beach displayed zero lag in response and stronger correlations than those observed at the bars, with the strongest correlation of any of the test cases being between lower beach α and Ω_{DS} at zero (i.e. < 1 week) lag (R = -0.82).

DISCUSSION

Seasonal changes in three-dimensionality clearly occur at a much slower temporal scale than the rapid variation in wave conditions. The improved correlation between forcing and beach three-dimensionality that was achieved using cumulative integral, rather than instantaneous forcing parameters indicates that seasonal changes in three-dimensionality are dictated by the cumulative effects of antecedent wave and tide conditions, rather than individual wave events.

Oblique wave approach has been shown to be a dominant mechanism for straightening barlines at some beaches (Price *et al.*, 2013). In this study, the cumulative alongshore oriented wave power ($P_{y,b,CI}$) had significant negative correlation with beach three-dimensionality, and was the most correlated parameter with α at the inner bar. However inner bar straightening due to oblique wave approach cannot be concluded confidently due to relatively large α measurement error at the inner bar (16.55 m, determined through comparison with 10 bathymetric surveys (Stokes *et al.*, 2015)) compared to the outer bar (4.78 m) and intertidal topography (0.16 m).

The cumulative relative tide range (RTR_{CI}) had significant correlation with beach three-dimensionality at all three regions, and had the strongest correlation with outer bar three-dimensionality. The lagged correlation with RTR_{CI} indicates that maximum outer bar three-dimensionality occurred some three months after each peak in RTR_{CI}, during transitions between periods of small RTR (small tide/ large waves) and large RTR (large tide/ small waves), when the proportion of wave breaking at the bars was increasing. This suggests that small tides (promoting defined bar growth), followed by large tides (promoting more intense rip circulation), may enhance the growth of 3D bar features.

Compared to RTR_{CI} the disequilibrium stress parameter (Ω_{DS}) had comparable correlations at the inner and outer bar, and the highest overall correlation observed, at the lower intertidal

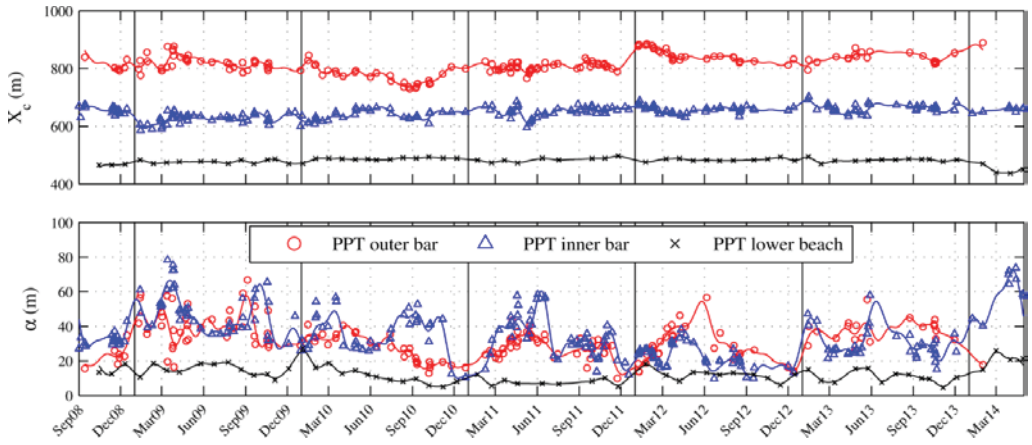

Figure 3. Time series of alongshore averaged cross-shore position, Xc, (upper) and standard deviation, α, (lower) of the outer barline, inner barline and lower beach contours at Perranporth (PPT) beach. The scattered points are the measured data and the associated lines are the low-pass filtered (1/42 days cut off) seasonal signal. Solid vertical lines indicate the start of each year.

beach. To demonstrate the influence of disequilibrium stress on beach three-dimensionality, the time series of α at the lower beach is compared to Ω_{DS} in Figure 4. In the winter (November to February) Ω_{DS} has a negative gradient ($\Omega > \bar{\Omega}$), and from spring to autumn (February to November) the gradient is positive ($\Omega < \bar{\Omega}$). These negative and positive gradients are associated with increases and decreases in three-dimensionality at the lower beach, respectively.

The strong negative correlation at zero lag between Ω_{DS} and lower beach α observed in the cross-correlation analysis is evident in Figure 4, where peaks in α align with local minima in Ω_{DS}. This is particularly apparent in the winters of 2009 to 2010, 2012 to 2013, and 2013 to 2014. The scatter plot in Figure 4 shows the same relationship, with information about the cross-shore position of the MLWN contour (X_c) included. Larger (smaller) markers indicate more seaward (landward) contour positions. The most three-dimensional beach conditions (large α) were associated with the most landward positions of the MLWN contour, and occured during periods of negative disequilibrium stress.

This relationship at first seems counter intuitive as negative gradients in Ω_{DS} occur when Ω is higher than average, and upstate transition (erosion and beach straightening) might be expected. However the troughs in Ω_{DS} that align with periods of high three-dimensionality actually represent a return to equilibrium Ω after a sustained period of higher than average waves, for example after winter. The beach therefore became increasingly 3D shortly after winter when energetic waves were subsiding, and Ω_{DS} is reaching its annual minimum. It therefore seems that periods of change in the wave regime from erosive to accretive, here represented by local minima in Ω_{DS}, lead to periods of high three-dimensionality with well developed bars and rips at the lower intertidal beach.

Tide range, wave steepness and wave power represented as RTR_{CI} and Ω_{DS}, overall explained the greatest amount of variance in the seasonal three-dimensionality at the lower intertidal (67% of the variance) and outer bar (32% of the variance) regions. Cumulative demeaned forcing parameters that vary on the same seasonal time scale as the morphology therefore offer the potential to forecast changes in beach three-dimensionality, and provided the basis for previous work developing a predictive model for beach three-dimensionality (see Stokes *et al.*, 2015).

CONCLUSIONS

Changes in beach three-dimensionality were seen to be related to the cumulative effects of antecedent wave and tide conditions. Although tide range appeared to be important at the outer bar, the disequilibrium stress parameter was well correlated with three-dimensionality at the bars and the lower intertidal beach. This term examines the disparity between the instantaneous dimensionless fall velocity parameter (Ω), and the overall mean dimensionless fall velocity ($\bar{\Omega}$), and is moderated by the instantaneous wave power (P). Low values of disequilibrium stress correspond to Ω that are cumulatively smaller than previous values, indicating the waves have moved from high steepness to low steepness, as normally occurs in the months following winter. It is under such circumstances, as the beach began to recover, that maximum values of beach three-dimensionality and associated rip channel development were observed.

Table 1. *Maximum cross-correlation coefficients, R, at lags up to 1 year between forcing parameters and α. Optimal lag time in weeks in brackets. All values are significant at the 99% confidence level, and the strongest correlation for each morphological time series is highlighted in bold font.*

Forcing	Outer bar α	Inner bar α	Lower beach α
$P_{o,CI}$	-0.31 (11)	-0.48 (0)	-0.59 (0)
$P_{y,b,CI}$	-0.42 (5)	**-0.58 (4)**	-0.60 (0)
Ω_{CI}	-0.52 (12)	-0.46 (2)	-0.72 (0)
Ω_{DS}	-0.53 (11)	-0.51 (1)	**-0.82 (0)**
RTR_{CI}	**0.57 (11)**	0.50 (0)	0.68 (0)

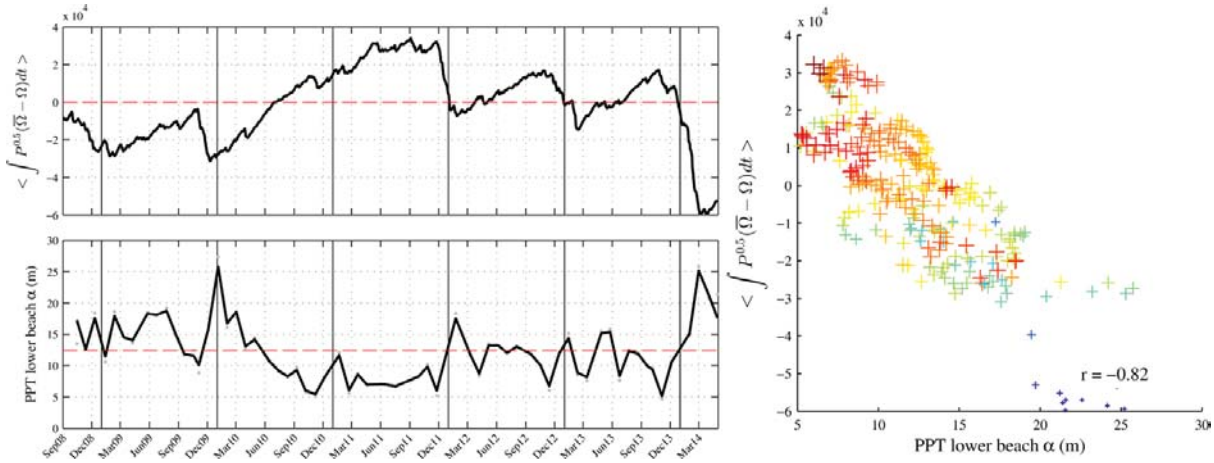

Figure 4. Time series of wave disequilibrium stress (upper left panel) compared to the low-pass Fourier filtered (1/42 days cut off) alongshore standard deviation, α, of the lower intertidal region at Perranporth (PPT) beach (lower left panel), and a scatter plot of the two parameters (right panel). Dashed lines indicate time series means. Larger and hotter markers show more seaward positions of the MLWN contour in the right panel.

ACKNOWLEDGMENTS

We would like to thank Martin Austin, Tim Poate, Tim Scott, Erwin Bergsma and Sam Prodger for their hard work in collecting much of the survey data. Thanks also go to Peter Ganderton and Megan Sheridan for their technical support. We would also like to thank the NERC DRIBS project (code: NE/HOO4262/1), the EU SOWFIA project, and the Plymouth University Marine Institute for funding the beach surveys.

LITERATURE CITED

Almar, R.; Castelle, B.; Ruessink, B.; Sénéchal, N.; Bonneton, P., and Marieu, V., 2010. Two-and three-dimensional double-sandbar system behaviour under intense wave forcing and a meso–macro tidal range. *Continental Shelf Research*, 30(7), 781-792.

Davidson, M.; Splinter, K., and Turner, I., 2013. A simple equilibrium model for predicting shoreline change. *Coastal Engineering*, 73, 191-202.

Jiménez, J.A.; Guillén, J., and Falqués, A., 2008. Comment on the article "Morphodynamic classification of sandy beaches in low energetic marine environment" by Gómez-Pujol, L. *Marine Geology*, 255(1-2), 96-101.

Masselink, G. and Short, A. D., 1993. The effect of tide range on beach morphodynamics and morphology: a conceptual beach model. *Journal of Coastal Research*, 9(3), 785-800.

Mead, S. and Black, K., 2001. Functional component combinations controlling surfing wave quality at world-class surfing breaks. *Journal of Coastal Research*, (SI 29), 21-32.

Pape, L.; Ruessink, B.G.; Wiering, M.A., and Turner, I.L., 2007. Recurrent neural network modeling of nearshore sandbar behavior. *Neural Networks*, 20(4), 509-518.

Plant, N.G.; Holland, K.T., and Puleo, J. A., 2002. Analysis of the scale of errors in nearshore bathymetric data. *Marine Geology*, 191(1-2), 71-86.

Plant, N.G.; Todd Holland, K.T., and Holman, R.A., 2006. A dynamical attractor governs beach response to storms. *Geophysical Research Letters*, 33(17),

Price, T.; Castelle, B.; Ranasinghe, R., and Ruessink, B., 2013. Coupled sandbar patterns and obliquely incident waves. *Journal of Geophysical Research: Earth Surface*, 118(3), 1677-1692.

Ranasinghe, R.; Symonds, G.; Black, K., and Holman, R., 2004. Morphodynamics of intermediate beaches: a video imaging and numerical modelling study. *Coastal Engineering*51, (7), 629-655.

Scott, T.; Masselink, G., and Russell, P., 2011. Morphodynamic characteristics and classification of beaches in England and Wales. *Marine Geology*, 286(1-4), 1-20.

Scott, T.; Russell, P.; Masselink, G.; Wooler, A., and Short, A., 2008. High volume sediment transport and its implications for recreational beach risk. *In: Proceedings Proceedings 31st International Conference on Coastal Engineering. ASCE, Hamburg, Germany*. pp 4250-4262.

Stokes, C.; Davidson, M., and Russell, P., 2015. Observation and Prediction of Three-Dimensional Morphology at a High Energy Macrotidal Beach. *Geomorphology*, 243, 1-13.

Van Enckevort, I. and Ruessink, B., 2001. Effect of hydrodynamics and bathymetry on video estimates of nearshore sandbar position. *Journal of Geophysical Research: Oceans (1978–2012)*, 106(C8), 16969-16979.

Wright, L.D. and Short, A.D., 1984. Morphodynamic variability of surf zones and beaches: A synthesis. *Marine Geology*, 56, (1–4), 93-118.

Journal of Coastal Research	SI	75	477-481	Coconut Creek, Florida	2016

Analysis of Coastal Erosion due to the 2011 Great East Japan Tsunami and its Recovery Using Ground Penetrating Radar Data

Maya Takamura [†*], Keiko Udo[‡], Motoyuki Sato[††], and Kazunori Takahashi[††]

[†]Disaster Potential Study Laboratory, Department of Civil and Environmental Engineering, Tohoku University, Japan

[‡] Disaster Potential Study Laboratory, International Research Institute of Disaster Science, Tohoku University, Japan

[††]Division of Geoscience and Remote Sensing, Department of Basic Studies, Center for Northeast Asian Studies, Tohoku University, Japan

www.cerf-jcr.org

www.JCRonline.org

ABSTRACT

Takamura, M.; Udo, K.; Sato, M., and Takahashi, K., 2016. Analysis of Coastal Erosion due to the 2011 Great East Japan Tsunami and Its Recovery Using Ground Penetrating Radar Data. *In:* Vila-Concejo, A.; Bruce, E.; Kennedy, D.M., and McCarroll, R.J. (eds.), *Proceedings of the 14th International Coastal Symposium* (Sydney, Australia). *Journal of Coastal Research*, Special Issue, No. 75, pp. 477-481. Coconut Creek (Florida), ISSN 0749-0208.

The 2011 Great East Japan Tsunami caused severe beach erosion along the Pacific coast. Eroded beaches began to recover rapidly after the tsunami, but the rate of beach recovery declined recently. We conducted a ground-penetrating radar (GPR) and borehole survey at Yamamoto Beach, which was eroded by the 2011 tsunami, to understand the tsunami recovery process using a new method that combines GPR, satellite images or aerial photographs, and tidal data. We compared reflective surfaces with geological layers observed using the GPR and borehole survey, respectively, to investigate the relationship between the recovery process data obtained from the proposed method and the actual underground structure. The result of the GPR survey at Yamamoto Beach suggests that the estimated profiles from April 4, 2011 to November 2012 maintain a gradient ranging 0.05–0.13 and that recovery speed decelerated with time after the tsunami. The sedimentary structure after November 2012 differs from the previous structure as a result of levee construction. Boundaries formed by a layer between the sand and the sand with gravel layers were observed and found to be nearly consistent with the GPR reflection planes. GPR results identified differences in the water content ratio between the layers owing to changes in grain size. Moreover, GPR reflections appear where layer boundaries are not observed. This also suggests that GPR is capable of recording differences in soil properties that cannot be identified visually.

ADDITIONAL INDEX WORDS: *tsunami, recovery process, topographic change, aerial photographs, GPR.*

INTRODUCTION

The 2011 Great East Japan Earthquake occurred at 14:46 JST on March 11, 2011 off the coast of Sanriku, Iwate Prefecture and caused a mega tsunami along the Pacific Coast. The tsunami run-up at Sendai Bay reached up to 5-km inland from the shoreline and caused extensive erosion (Geospatial Information Authority of Japan, 2011). Yamamoto Beach, located on the southern coast of Sendai Bay, was severely eroded because of the tsunami. Erosion caused shoreline retreat and changed beach landforms such as pocket beaches. The analysis of geographic data and the survey of tsunami deposits revealed soil movement before and after the tsunami (*e.g.,* Goto *et al*., 2014; Udo *et al*., 2014).

The recovery process after tsunamis are commonly researched using satellite image analyses and/or field surveys (*e.g*., Parisa *et al*., 2009; Richmond, 2012). Although changes in shoreline position can be identified from satellite image analysis, changes in the beach profile are difficult to identify. The surveys of tsunami deposits can identify past soil movement via borehole data, but this is an expensive method for obtaining spatial data regarding underground structures.

Moreover, it is difficult to examine the tsunami recovery process on the monthly or annual scale by common dating methods, such as radiocarbon dating or optically stimulated luminescence (OSL), whose dating scales only range from decades to a hundred thousand years (Wintle, 2008). A new method for analyzing beach recovery on a monthly scale was proposed that uses ground-penetrating radar (GPR) data, satellite images or aerial photographs, and tidal data (Takamura *et al*., 2015).

GPR exploration is a technique for analyzing underground structures by transmitting high-frequency electromagnetic waves and recording reflections at points where the propagation characteristics of these waves change. This method was first put to practice in the 1970s for ice sounding in Antarctica and has since gained acceptance internationally (Yelf, 2007). During the 2000s, many studies were conducted on long-term beach processes using GPR and common dating methods (*e.g*., Koster *et al*., 2014; Tamura, 2012). GPR discerns differences in the propagation of electromagnetic waves, and the characteristics of subterranean media, such as rocks, water, and air, are determined by conductivity, permittivity, and permeability. Relative permittivity is the most important parameter in the frequency range of 10 MHz–10 GHz normally used by GPR (Lu and Sato, 2007).

DOI: 10.2112/SI75-096.1 received 15 October 2015; accepted in revision 15 January 2016.

*Corresponding author: m-takamura@potential1.civil.tohoku.ac.jp

The relative permittivity of soil particles, air, and water are 2–6, 1, and 81, respectively. Differences in soil permittivity do not have much influence on propagation characteristics, but water content has the largest influence on relative permittivity. This study conducted a borehole survey along a GPR survey line and compared the reflection planes in GPR with geological layers visually discerned to reveal the relationship between the recovery process determined by the proposed analysis and the actual underground structure.

METHODS

Figure 1 shows the location and aerial photographs of Yamamoto Beach. We conducted a GPR survey and a topographical survey using real-time kinematic (RTK) on March 4, 2015 along the survey lines represented in Figure 1 by pink lines. The survey lines were located normal to the shoreline at 30-m intervals, from approximately 100-m inland to the edge of the water. Moreover, we conducted a borehole survey on July 24, 2015 at three points on each survey line (yellow triangles in Figure 1). The boreholes farthest inland on lines 1 and 2 were 5-m deep, whereas the others were 4-m deep.

We corrected the GPR survey data results with the topography data and processed it with a DC filter, an automatic gain control, and Dewowing (Figure 2). The depths of reflection planes were calculated from the travel times of electromagnetic waves. The electromagnetic wave propagation speed was calculated using the relative permittivity of 16 according to a water content ratio of approximately 30 percent measured by time-domain reflectometry (TDR). Then, we extracted all the reflection plane data. Here, the artifacts caused by signal ringing in the GPR data were excluded.

GPR data were analyzed by a method using satellite images or aerial photographs and tidal data, proposed by Takamura *et al.* (2015; see Figure 2). The shoreline position was identified from the satellite images available on Google Earth (April 4, 2011), aerial photographs provided by the Tohoku Regional Bureau, Ministry of Land, Infrastructure and Transport (May 24, 2011; September 10, 2011; June 18, 2012; November 28, 2012; and December 14, 2012), and GeoEye (March 4, 2012). The shoreline positions were plotted on the signal-processed GPR data, according to the position identified in aerial photographs, and the tide level at the time the aerial photographs were noted. Therefore, the profiles at these times were estimated. We used tidal data from Soma, the location nearest the survey area. Tidal data from April 4, 2011 to May 24, 2011 were used as astronomical tidal data, whereas the other data (after September 10, 2011) were used as observational data, because the Soma tide station was destroyed by the 2011 tsunami. We compared the reflection planes in GPR to geological layers from the borehole core identified by visual inspections.

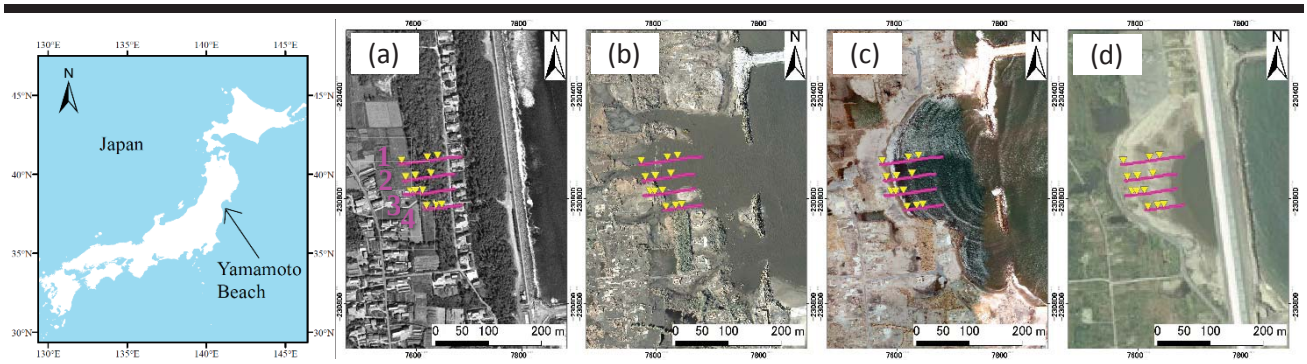

Figure 1. Aerial photographs ((a) September 21, 2006 (b) March 12, 2011 (c) May 24, 2011 (d) September 1, 2013) taken at Yamamoto Beach.

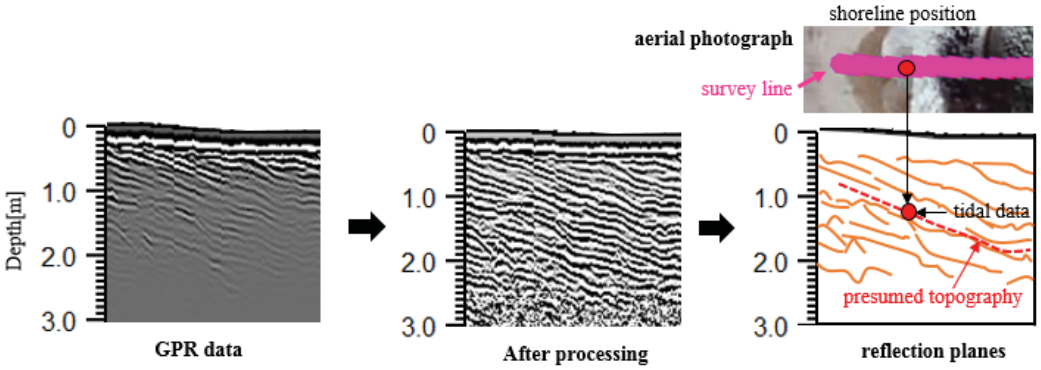

Figure 2. Profile estimation method using GPR data, satelite images or aerial photographs, and tidal data.

RESULTS

Figure 3 shows the GPR survey results from four survey lines and the borehole positions. Figure 4 shows the reflection planes extracted from the GPR data and profiles estimated from the aerial photographs and tidal data. Shorelines advanced at lines 1 and 2 but retreated at lines 3 and 4 between April 4, 2011 and May 24, 2011. From May 24, 2011 onward, erosion was considered insignificant at all survey lines from satellite image analysis.

The gradients of the estimated profiles around the shoreline from April 4, 2011 to November 28, 2012 were confirmed to be from 0.05 to 0.13, and the recovery speed ranged from −8 to 10 m/month between May 24, 2011 and September 10, 2011 and from 2 to 3 m/month between September 10, 2011 and March 4, 2012 (Takamura *et al*., 2015). Different structures appear after November 2012, as seen in the red-hatched area in Figure 4.

Figure 5 shows the borehole logs of points 1-1 to 4-12 (see Figure 4). The boundaries of layers in the borehole logs are represented by green-dashed lines and the GPR reflection planes by orange arrows. The reflection planes coinciding with layer boundaries are indicated by red open circles in Figure 5. The difference between reflection planes and layer boundaries was considered to be either the result of the visual identification of layer boundaries or the assumption that the relative permittivity was a constant value. The results indicate that 16 out of 17 visually identified boundaries between the sand and the sand with gravels layers were the same as those identified by GPR. The boundary of the layer at a 0.7-m depth at point 4-11 cannot be discerned by GPR.

DISCUSSION

The result of the GPR survey at Yamamoto Beach suggest that profiles formed during the recovery process maintain a stable gradient beyond one month after the tsunami. Sedimentary structure after November 2012 differed from the structure between April 4, 2011 and November 2012. This is considered to be due to changes in wave conditions owing to levee construction that began around November 2012.

During the several months after the tsunami, shorelines advanced at lines 1 and 2 but retreated at lines 3 and 4. The erosion owing to the tsunami at lines 1 and 2 was especially severe compared with that at lines 3 and 4 (Figure 1 (b)). Immediately after the tsunami, the sediments moved from the less eroded location to the severely eroded location. Several months after the tsunami, the recovery speed was almost the same at all survey lines and had decelerated with time.

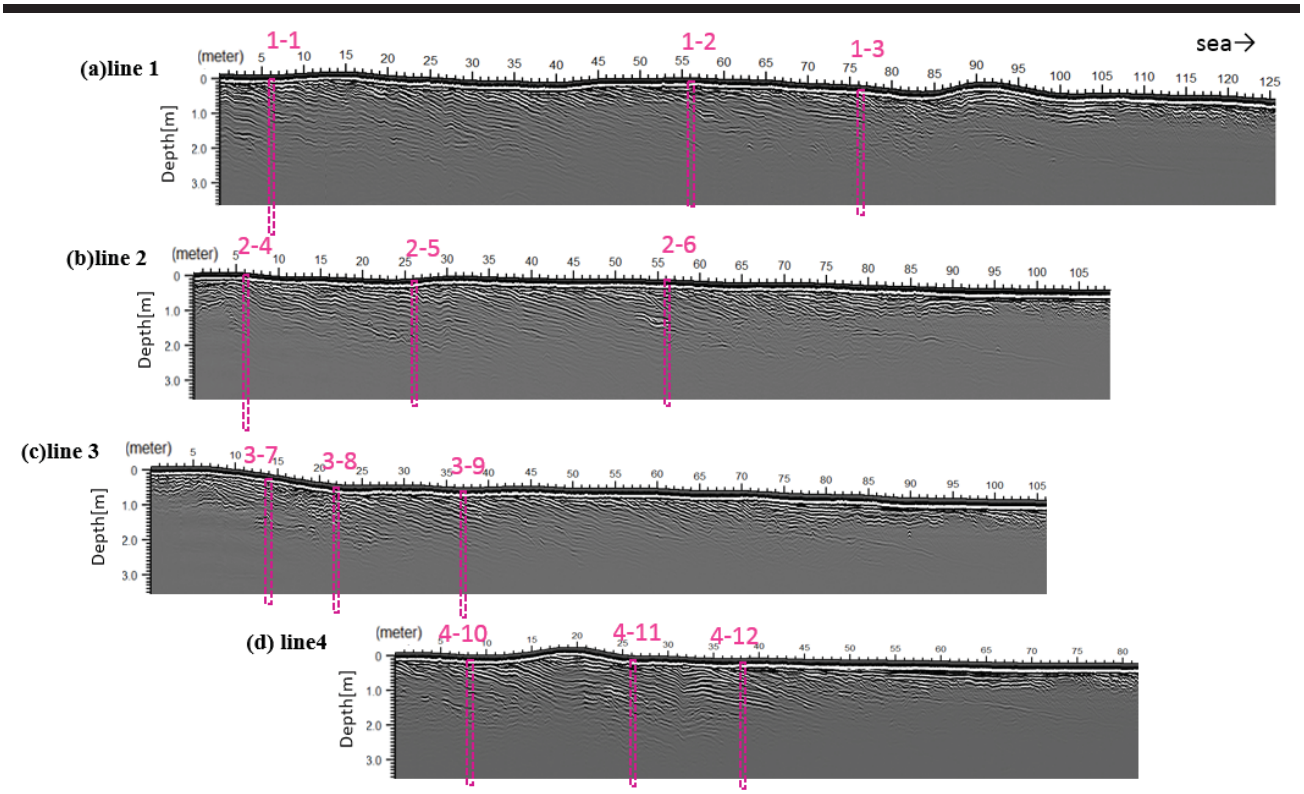

Figure 3. Results of the GPR survey of four survey lines and positions of boreholes 1-1–4-12.

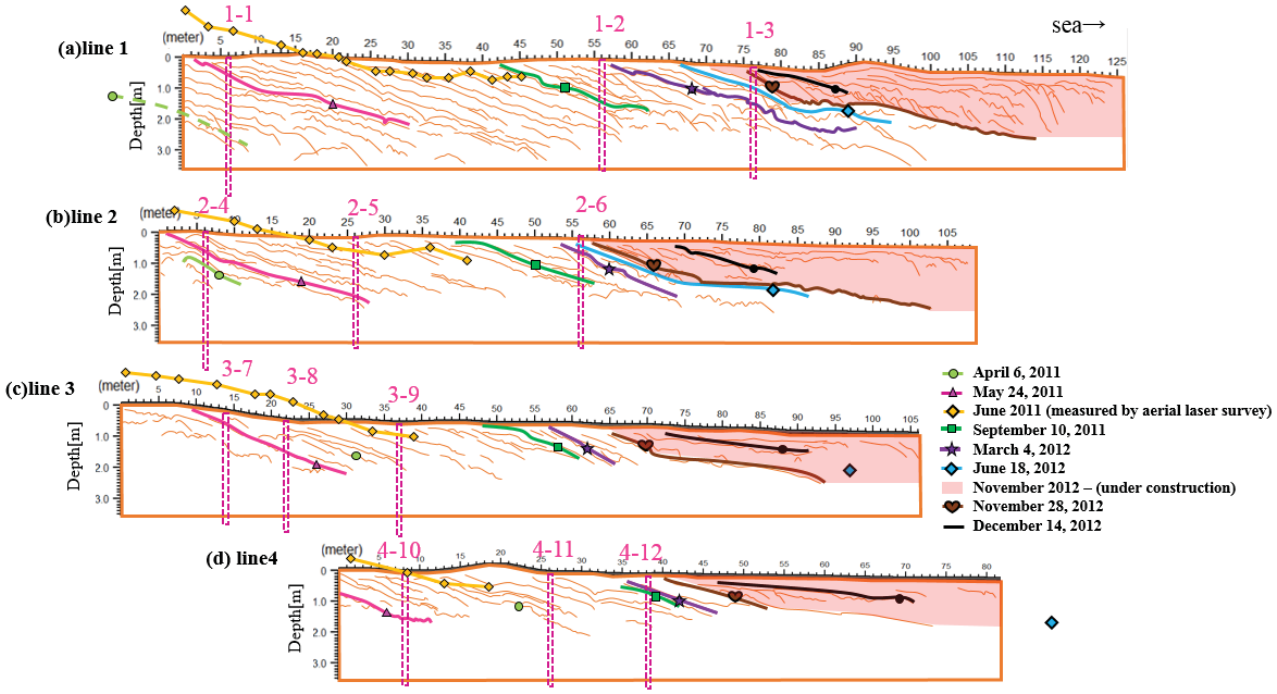

Figure 4. Reflection planes extracted from the GPR data and profiles estimated by aerial photographs and tidal data (revised from Takamura *et al*., 2015).

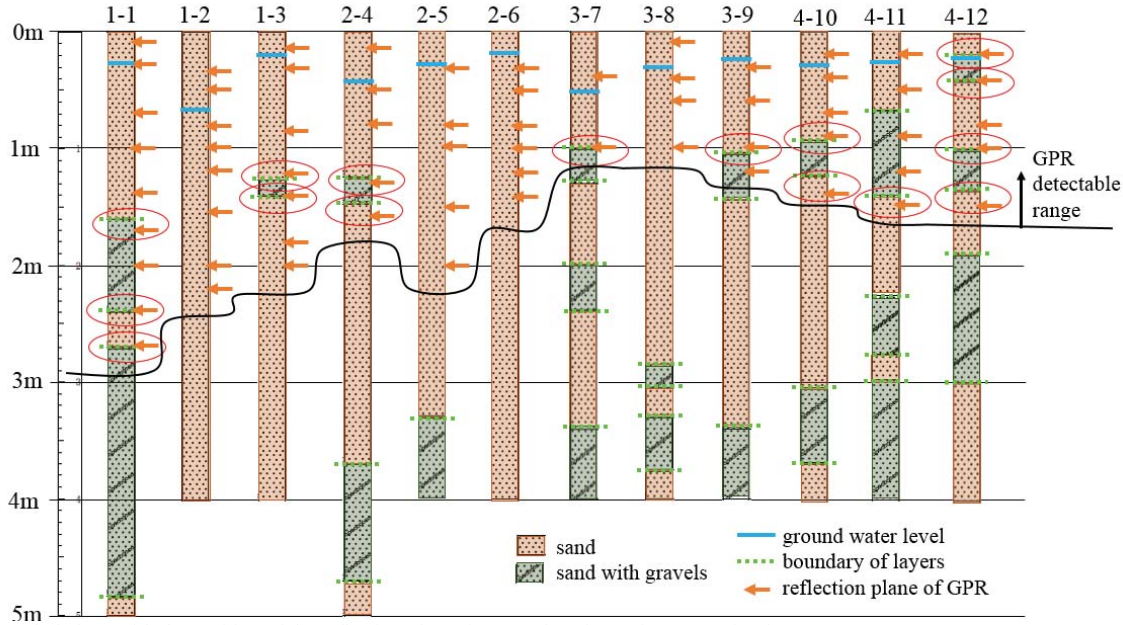

Figure 5. Borehole logs with the position of the reflection planes in GPR (locations of 1-1–4-12 in Figure 4).

The yellow line in Figure 4 shows the profile measured by an aerial laser survey in June 2011. The comparison of the measured profile with the estimated profile shows that the profile measured in June 2011 is closer to the ocean than the profile estimated on May 24, 2011 and closer to land than the profile estimated on September 10, 2011. The shape of the estimated profile is validated by comparing with the measured ones.

The reflection planes coinciding with layer boundaries were identified by differences between the sand layer and the layer of sand with gravels. The relative permittivity of the ground is the most important parameter in GPR data, and it is influenced by water content. . It is considered that differences in the water content ratio were caused at points where grain sizes changed.

Reflections occurred where boundaries were not discerned by visual inspection. A more detailed analysis of the borehole core is required.

CONCLUSIONS

We conducted the GPR survey and borehole survey at Yamamoto Beach that was significantly eroded by the 2011 tsunami. The comparison of the reflection planes in GPR data were made to geological layers observed in the borehole cores. Our study demonstrates the relationship between the recovery process estimated by GPR data and the actual underground layer formed during the recovery process.

The gradient of the profile at Yamamoto Beach during the recovery process from April 4, 2011 to November 28, 2012, ranged from 0.05 to 0.13. Immediately after the tsunami, the recovery speeds at lines 1 and 2 indicated that erosion were especially severe and faster than those at lines 3 and 4. Sediments probably moved from the less eroded location to the severely eroded location. Several months after the tsunami, the recovery speed was almost the same at all survey lines and had decelerated with time. Estimated profiles after around November 2012 showed a different underground structure owing to the influence of levee construction.

Visually identified boundaries between the layers of sand and the sand with gravels were the same as those identified by GPR data. It is considered that differences in the water content ratio were caused at points where grain sizes changed.

The GPR survey results included the reflections of underground structures not identified by our visual inspection. Further investigation is required to identify the reason for these reflections through the detailed analysis of soil properties of borehole cores.

ACKNOWLEDGMENTS

The authors would like to thank the Tohoku Regional Bureau, Ministry of Land, Infrastructure and Transport for providing aerial photographs and topographic data. This research was supported by the Special Research Project (B-4) of International Research Institute of Disaster Science, Tohoku University. We are grateful to Kazuhisa Goto, International Research Institute of Disaster Science, for very helpful comments.

LITERATURE CITED

Geospatial Information Authority of Japan, 2011. Overview map of flood area on a scale of one to hundred thousand, http://www.gsi.go.jp/kikaku/kikaku60003.html

Goto, K.; Hashimoto, K.; Sugawara, D.; Yanagisawa, H., and Abe, T., 2014. Spatial thickness variability of the 2011 Tohoku-oki tsunami deposits along the coastline of Sendai Bay. *Journal of Marine Geology*, 358, 38-48.

Koster, B. and Reicherter, K., 2014. Sedimentological and geophysical properties of a ca. 4000 year old tsunami deposit in southern Spain. *Journal of Sedimentary Geology*, 314, 1-16.

Lu, Q. and Sato, M., 2007. Estimation of Hydraulic Property of an Unconfined Aquifer by GPR. *Journal of Sensing and Imaging*, 8(2), 83-99.

Parisa, R.; Wassmerb, P.; Sartohadic, J.; Lavigneb, F.; Barthomeufa, B.; Desgagesa, E.; Grancherb, D.; Baumertb, P.; Vautiera, F.; Brunsteinb, D., and Gomezb, C., 2009. Tsunamis as geomorphic crises: Lessons from the December 26, 2004 tsunami in Lhok Nga, West Banda Aceh (Sumatra, Indonesia). *Journal of Geomorphology*, 104, 59-72.

Richmond, B.; Szczucinski, W.; Chague-Goff, C.; Goto, K.; Sugawara, D.; Witter, R.; Tappin, D.R.; Jaffe, B.; Fujino, S., and Nishimura, Y., 2012. Erosion, deposition and landscape change on the Sendai coastal plain, Japan, resulting from the March 11, 2011 Tohoku-oki tsunami. *Journal of Sedimentary Geology*, 282, 27-39.

Takamura, M.; Udo, K.; Sato, M.; Takahashi, K., and Abe, T., 2015. Development of a method for observing sand deposit structure after tsunami using GPR. *Journal of Japan Society of Civil Engineers*, B2, 71 (in press, in Japanese).

Tamura, T., 2012. Beach ridges and prograded beach deposits as palaeoenvironment records. *Journal of Earth-Science Reviews*, 114, 279-297.

Udo, K.; Takeda, Y., and Mano, A., 2014. Serious Erosion of the Southern Sendai Coast due to the 2011 Tohoku Earthquake Tsunami and Its Recovery Process. *Journal of Post-Tsunami Hazard,* 44, 225-236.

Wintle, A.G., 2008. Luminescence dating: where it has been and where it is going. *Journal of Boreas*, 37, 471-482.

Yelf, R.J., 2007. Application of Ground Penetrating Radar to Civil and Geotechnical Engineering. *Journal of Electromagnetic Phenomena*, 7, 1(18), 102-117.

Journal of Coastal Research	SI	75	482-486	Coconut Creek, Florida	2016

Subaerial Rotation on an Open Coast Beach: Pendine West Wales, UK

Tony Thomas[†*], Nelson Rangel-Buitrago[†], Michael R. Phillips[†*], Giorgio Anfuso[‡], Allan T, Williams[†*§] and Judith, A. Oakley[†*]

University of Wales Trinity Saint David (Swansea), Mount Pleasant, Swansea, UK, SA1 6ED.

[†] Facultad de Ciencias Básicas, Programa de Física, Grupo de Geología, Geofisica y Procesos Litorales, Km 7 Antigua vía Puerto Colombia, Barranquilla, Atlántico, Colombia.

[‡†] Departamento Ciencias de la Tierra, Facultad de Ciencias del Mar y Ambientales Ciencias de la Tierra, Universidad de Cadiz, Puerto Real, Spain.

[§]CICA NOVA, Nova Universidade de Lisboa, Lisboa 1069-050, Portugal. email: Allan.williams@virgin.net

www.cerf-jcr.org

www.JCRonline.org

ABSTRACT

Thomas, T.; Rangel-Buitrago, N.; Phillips, M.R.; Anfuso, G.; Williams, A.T.. and Oakley, J.A.. 2016. Subaerial rotation on an open coast beach: PendineWest Wales, UK. *In:* Vila-Concejo, A.; Bruce, E.; Kennedy, D.M., and McCarroll, R.J. (eds.), *Proceedings of the 14th International Coastal Symposium* (Sydney, Australia). *Journal of Coastal Research*, Special Issue, No. 75, pp. 482-486. Coconut Creek (Florida), ISSN 0749-0208.

Beach profiles and storm related forcing agents were used to assess subaerial beach rotation on an open coast macro-tidal beach. Analysis highlighted a negative phase relationship existed between the beach extremities and variation between negative/positive correlations within the central region identified that medium timescale open coast beach rotation existed. Cross-correlation showed timelag variations in subaerial volume exchange between adjacent sectors lagged behind one another by up to 18 months. While, annually averaged storm climate results highlighted a reduced temporal trend in terms of occurrence, intensity and power. Qualitatively, links were established between storms and erosive/accretive variations in the MHW shoreline indicator that suggest that these events influence beach rotation. Storm wave direction was established to be an important factor and it was concluded that the 3 river estuary complex acted as a surrogate headland restricting sediment by-pass, essentially forming an almost closed cell. These results should be tested at other open coast sites.

ADDITIONAL INDEX WORDS: *Beach rotation, shoreline indicators, storms, morphological change*

INTRODUCTION

Beach rotation generally refers to periodic lateral sediment movement towards alternating ends of embayed beaches, manifesting itself as a 'rotation' of beach plan-form (Short and Masselink, 1999). Many researchers, including Klein *et al.* (2002), Ruiz de Alegria-Arzaburu and Masselink (2010), and Thomas *et al.* (2011a), documented seasonal rotation, while other studies concentrated on decadal scales (e.g. Short *et al.*, 2000; Ranasinghe, *et al.*, 2004; Short and Trembanis, 2004; Thomas *et al.*, 2011b). Localized shoreline retreat or advance along the beach does not lead to long term sediment loss or gain. The beach often returns to its initial condition in response to shifts in wave direction. However, long term shifts in wind directional patterns can result in a one directional shoreline displacement. This paper, builds upon and updates Thomas *et al.* (2012) who identified rotation on this open coast beach via an assessment of both subaerial and intertidal zone behavior in relation to variability in offshore wind and wave conditions.

The Bristol Channel/Severn Estuary is an inlet from the Atlantic Ocean on the west coast of Great Britain, partially enclosed and separating Wales from England (Mackie *et al.*, 2002; Phillips and Crisp, 2010; Figure 1a). Carmarthen Bay on the northwest Bristol Channel is approximately 70 km long, bounded by the Gower Peninsula to the east and Giltar Point to the west (Barber and Thomas, 1989; Thomas *et al*, 2012; Figure 1b). The 10 kilometer long sandy foreshore of Pendine Sands forms the seaward part of an extensive coastal barrier within this shallow bay (Jago and Hardisty, 1985). The underlying subaerial zone and dune geology of Pendine Sands (figure1c) comprises Old Red Sandstone laid down during the Devonian period while there is a small headland of Carboniferous Limestone on the western fringe (Halcrow, 2010). The Taf, Towi and Gwendraeth estuary complex centrally placed within the bay separates Pendine Sands from adjacent Cefn Sidan Sands to the east. Strong winds and tides generated in the Bristol Channel, and north Atlantic contribute to high energy waves (Allan *et al.*, 2009), that prevail from a south-westerly direction ensuring abundant wave action within these macrotidal 7.5 m spring tidal range waters. Offshore recorded south to westerly waves of *circa* 1.2 m height and 5.2 s period dominate, although storm waves > 5.5 m with periods > 8.5 s are not uncommon (Thomas *et al.*, 2010; Figure 1d).

DOI: 10.2112/SI75-097.1 received 15 October 2015; accepted in revision 15 January 2016.

*Corresponding author: tony.thomas@uwtsd.ac.uk

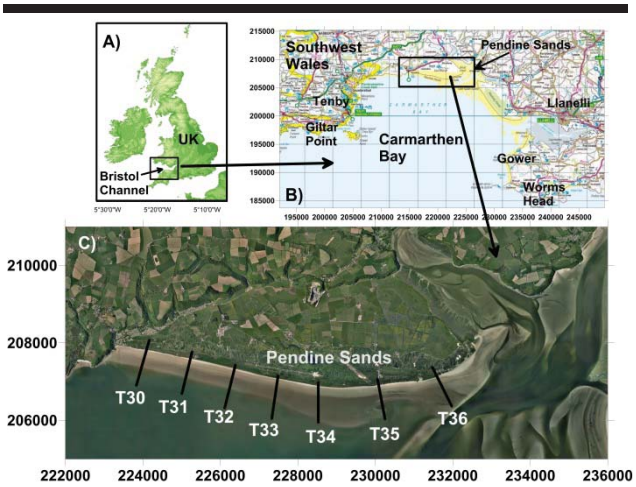

Figure 1. Study area locality a), UK, b) Carmarthen Bay and c) Pendine Beach.

METHODS

Subaerial beach change was analyzed between 1999 and 2013 using seven equally alongshore spaced shore normal profiles (Figure 1c). The distance between high spring tide and mean high water was used to characterize the subaerial beach and morphological variables were computed directly from the Regional Morphology Analysis Package (RMAP) (Morang *et al.*, 2009; Figure 2). RTK network GPS was utilized for survey work and data recorded to cm accuracy. Using the methodology adopted by Short and Trembanis (2004), profile data was transformed using $z = x - \bar{x}/\sigma$, where z = normalized value; x = the volume record for each profile; $\bar{x}$ average value for that profile; and σ = standard deviation (see Davis, 2002). Temporal survey data were subsequently spatially averaged along the beach to represent cut and fill behavior common to all profiles *i.e.* onshore/offshore sediment movement. These values were subtracted from corresponding normalised volumes to produce a timeseries with high frequency behavior removed. Finally, residual volumes were converted back into dimensional units using $x = z\sigma + \bar{x}$.

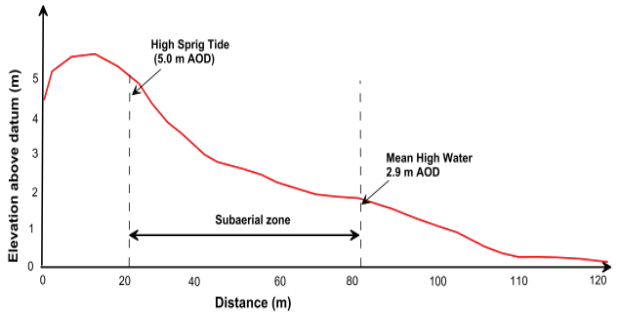

Figure 2. A sketch illustrating the area from which the subaerial change was computed.

In this research, direct comparisons were made between subaerial volume, shoreline indicator change and storm characteristics computed from data captured by the Meteorological Office wave rider buoy at Turbot Bank (51.603 N 5.100 W) that records wave height, period and direction at 1 h intervals. The 17 year dataset contained 121,452 independent values. To characterise the storm climate waves a minimum wave height of 3.4 m was used in this research (i.e. Hs ≥ 3.4 m), as this represented rare events and only 8% of the 15 year record (in accordance with the methodology of Dorsch *et al.*, 2008).

The minimum storm duration was set at 12 h, i.e. a storm that affected the coast during a minimum of one complete tidal cycle. The time lapse between successive storms was set at one day in order to create de-clustered, independent set of storms (for full methodological details see for example Dolan and Davis, 1992; Rangel-Buitrago and Anfuso, 2011 and 2013). Once storms were recognized, their characteristics were represented annually for qualitative comparison.

RESULTS

Statistically, relationships existed between T30 and T31 (Table 1; r = 0.66; p = 0.00) indicating that any variations in volume at profile T30 also occur at profile T31. Similarly, there was also a positive correlation between T36 and T35 (r = 0.5; p = 0.05). In contrast and what is of most interest was the high negative correlations between T30/T31 and T36/T35 that ranged between r = -0.57 and r = -0.80 indicating that any variations took place at profiles T30 and T31 the opposite would be true at T36 and T35 (*i.e.* beach rotation). The variability in statistical significance and negative/positive phase relationships within the central profiles would indicate that region of rotation lies between T34/T33 (r = -0.74; p = 0.00) and T34/T35 (r = 0.31; p>0.05).

Table 1: *Pendine Sands subaerial volume correlation matrix. Note;- statistical significance (p< 0.00) in* ***bold italic*** *and (p< 0.05) in* **bold**

		T31	T32	T33	T34	T35
T31	***0.66***					
T32	0.03	-0.20				
T33	-0.08	**-0.44**	0.12			
T34	**-0.48**	-0.17	-0.09	***-0.74***		
T35	***-0.79***	***-0.57***	-0.32	0.05	0.31	
T36	***-0.65***	***-0.80***	-0.25	0.38	0.16	**0.50**

The statistically significant correlation between the profiles at the beach extremities would suggest that these sediment exchanges occur at timescales of less than the inter-survey period. However, to investigate stronger potential correlations between profiles T30/T32 (western end) and between profiles T36/T34 (eastern end), time lagged cross-correlations of volume changes were calculated and represented graphically (Figure 3). There was an improvement from almost non-existent to statistically significant correlation (r = -0.46; p <0.05), suggesting that an 18 month time-lag existed between erosive and accretive episodes within the western subaerial zone (T30/T32; Figure 3a). Cross-correlations showed a slight statistical improvement when applied to the eastern subaerial

zone (r = 0.31; p>0.05; Figure 3b). However, what is of most interest are the negative/positive correlations as this confirms the approximate region of rotation highlighted in earlier results Figure 3c shows graphically the temporal variations between the beach extremities based upon the MHW line (Table 2) and clarifies qualitatively the previous quantitative results.

This shows contrasting erosive/accretive behavioral patterns between opposite ends of the beach and this is particularly apparent towards the end of the assessment period. However, Figure 3c also highlights temporal periods when the beach either similarly eroded or accreted, for example between 2008 and 2009.

Figure 4 shows the distribution of the most commonly used storminess indices during the assessment. When consideration is given to the number of storms per year, 1999 (25 events), 2000 (29 events), 2002 (25 events), 2006 to 2008 and 2011 (with 20 events each) were the stormiest (Figure 4a) and 2003, 2010 and 2012 presented the lowest average number of storms. Regression modelling showed a statistically insignificant decreasing temporal trend in storm occurrence but 3 yr moving average results indicated a 5 to 6 year cyclic behavioural pattern with storm peaks observed in 2000 and 2007. Similarly, variability of storm duration (Figure 4b) and Storm Power Index sum (Figure 4c) also highlighted decreasing temporal trends.

During energetic years, a great number of storms with significantly long durations, increased storm power, which explains the similarity. Storm (and associated wave) direction is important when studying the effects of beach rotation, most annually averaged storm events emanate from a south-westerly direction (250°± 57°; Figure 4d), largely generated in the North Atlantic. However, when monthly average storm direction is computed (Figure 5a) the predominant direction is still south-westerly (230°) but importantly range from a *circa* easterly (75°) to *circa* west (290°) directions.

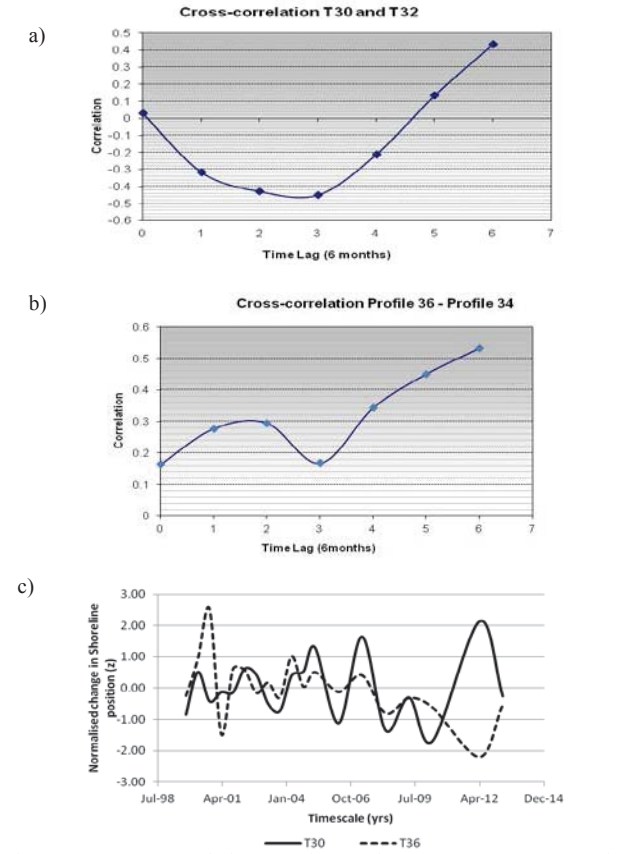

Figure 3. Cross-correlation results a) between western extremity profiles, b) between southern extremity profiles and c) a normalized timeseries comparing the beach extremity profiles.

Table 2. *Subaerial volumes and inter-survey variations in the MHW shoreline indicator*

Date	Volumes (m^3/m)							Normalised variation in shoreline position (z)						
	T30	T31	T32	T33	T34	T35	T36	T30	T31	T32	T33	T34	T35	T36
Apr-99	103.96	126.02	252.07	355.71	72.49	119.30	102.42							
Oct-99	116.57	142.59	256.23	366.21	59.73	23.56	105.18	-0.85	-1.14	-0.30	0.54	0.43	2.86	-0.24
Apr-00	110.05	147.85	257.75	374.03	52.81	37.93	115.76	0.51	0.67	0.58	0.70	1.08	0.11	0.92
Oct-00	114.09	156.39	276.45	389.69	47.06	17.87	39.71	-0.42	-0.78	-0.27	-0.82	0.05	1.31	2.52
Apr-01	112.66	156.71	253.61	379.11	45.72	41.02	92.84	-0.13	-0.19	1.46	1.17	0.27	-1.54	-1.47
Oct-01	114.93	158.62	253.93	378.67	35.88	45.35	82.17	-0.14	0.45	-0.20	-0.27	0.85	-0.11	0.61
Apr-02	111.37	163.49	246.81	379.43	54.94	46.77	83.59	0.62	-0.24	0.08	1.52	-0.61	0.70	0.57
Oct-02	117.55	161.75	246.05	383.23	49.10	32.92	73.97	0.42	0.59	0.38	0.87	-0.11	0.49	-0.15
Apr-03	118.31	170.35	250.79	353.96	46.14	34.24	60.28	-0.50	-0.53	-0.62	-0.51	0.00	-0.71	0.17
Oct-03	120.69	182.79	242.60	347.90	40.08	27.49	61.36	-0.74	-1.41	0.22	-0.94	-0.08	-0.22	-0.30
Apr-04	120.55	199.20	253.15	329.35	29.89	22.09	29.90	0.40	-1.43	-1.43	0.89	0.39	-0.03	1.01
Oct-04	124.96	195.44	255.98	334.43	30.65	5.62	18.80	0.52	0.01	0.74	0.42	-0.38	0.58	0.04
Apr-05	114.16	176.64	264.66	356.37	41.70	31.27	41.16	1.29	3.09	0.72	1.19	1.36	-0.10	0.50
Apr-06	118.50	174.48	253.86	333.10	53.65	40.43	37.66	-1.13	0.08	-0.45	-1.11	-1.61	-1.11	-0.12
Apr-07	112.46	177.78	248.31	319.58	71.90	50.12	55.32	1.64	0.97	1.83	1.30	-0.07	0.83	0.41
Apr-08	110.26	177.53	246.88	309.76	81.80	52.08	64.36	-1.35	-0.08	-0.73	-0.82	-1.08	-0.75	-0.81
Apr-09	113.61	181.28	246.92	295.18	82.19	43.95	55.05	-0.30	-0.29	0.11	-0.55	-0.85	-0.69	-0.32
Apr-10	116.35	169.16	255.27	281.89	87.36	38.07	52.24	-1.70	-0.04	-2.32	-0.75	-0.73	-0.93	-0.62
Apr-12	116.51	169.41	264.09	258.19	99.86	20.58	47.70	2.13	0.31	1.14	-1.23	-1.42	-0.21	-2.20
Apr-13	110.71	172.32	248.67	288.87	94.56	39.87	81.29	-0.26	-0.06	-0.93	-1.60	2.51	-0.48	-0.53

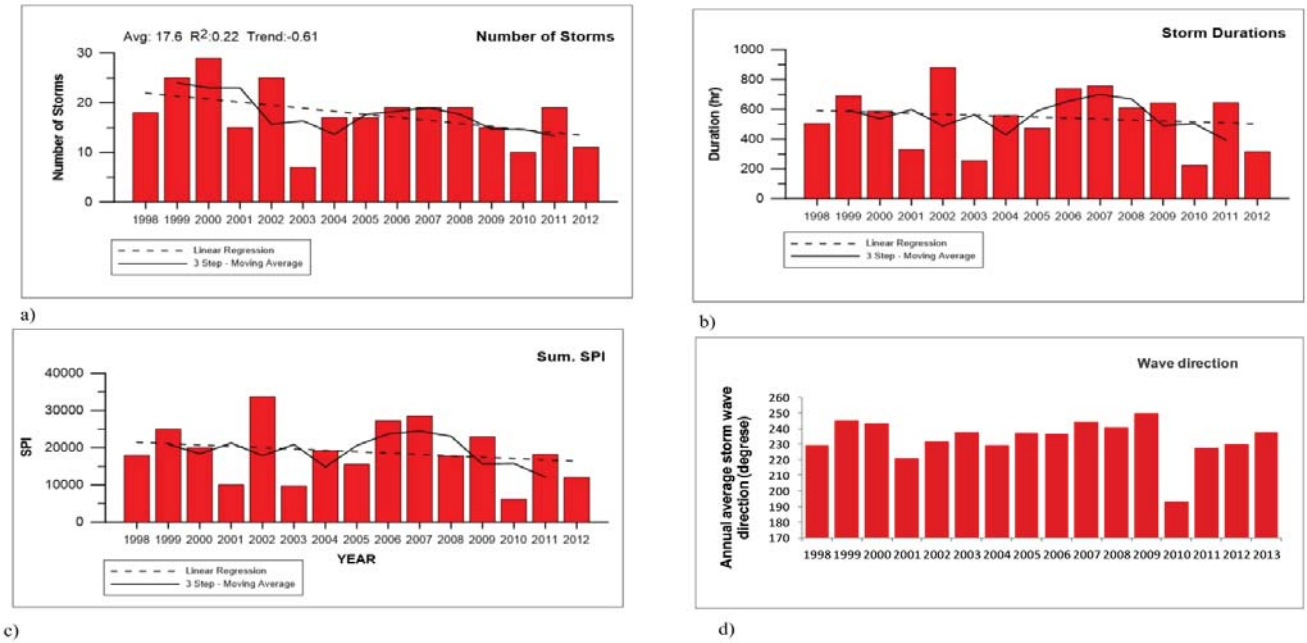

Figure 4. Annual storm statistics computed from the Turbot bank buoy for the period 1998-2013, a) number of storms, b) storm Duration, c) Storm power and d) storm direction .

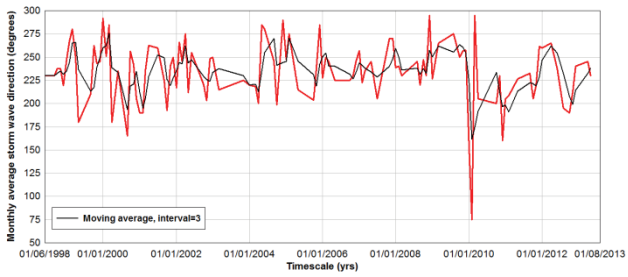

Figure 5. Monthly average storm wave direction (red), with 3 month moving average (black).

DISCUSSION

Analysis showed negative phase relationships between the beach extremity profiles and cross-correlation improvement between adjacent profiles related to the beach extremities offset by a timelag of 18months. Timeseries data related to variations in the MHW shoreline indicator confirmed contrasting erosive and accretive rotations, they also highlighted periods when similar beach extremity behavior occurred.

The storm record showed slight decreasing trends in occurrence, duration and power during the assessment period. Annual average storm wave direction predominated from the southwest, masking a much larger variation when analyzed on a monthly basis> where storm wave direction ranged from west to east albeit with less frequency. Waves from the predominant southwesterly direction undergo significant refraction on entering Carmarthen Bay aligning themselves at an oblique angle to the south facing beach and would generally cause longshore drift from west toward east. When the storm waves emanate more from the southeast longshore drift is expected to be reversed and this was shown by Thomas *et al.* (2012) using monochromatic wave modelling. However, in the years these conditions occurred, for example 2009, the shoreline eroded at almost all profile locations. Conversely, when storms emanated from a westerly direction as in 2000, accretion occurred at all profile locations. This is because waves as they approach Carmarthen bay interact with the seabed further offshore and undergoes more refraction prior to entering the bay aligning themselves more perpendicular to the shore. Decreasing storminess should result in a certain stability of the shoreline, but the lowest storm occurrence in 2010 suprisingly resulted in erosion at all profile locations.

This study built upon and somewhat agreed with the quantitative assessments of Thomas *et al.* (2012) who assessed both subaerial and intertidal changes alongside averaged wind, wave and high pressure system change. They showed that offshore wave direction is very important factor in the evolution of this beach system. Additionally, this research highlighted that storm intensity, occurrence, and the generation of increasing wave height are important factors as they dictate when waves interact with seabed topography and how far offshore waves break and dissipate their energy. This research showed that high intensity and long duration storms do not necessarily relate to shoreline erosion or beach rotation for that matter, wave direction is the important variable. Embayed beach rotation is well understood and headland extent as well as environmental forcing and sediment characteristics influence behavior. In this

case we suggest that the river complex has an influence and acts like a surrogate headland interrupting longshore drift.

CONCLUSIONS

The analysis of beach profiles (1998-2013) highlighted statistically, that subaerial beach rotation existed at an open coast beach. Negative phase relationships existed between the erosive/accretive patterns when related to the beach extremities contrasted against variable negative/positive relationships between the same and central profiles. These rotational responses were subsequently confirmed graphically.

Storms were linked both quantitatively and qualitatively to morphological change concurring with other regional studies. We suggest wave direction is a governing factor with regard to rotation but storm intensity influences offshore wave refraction patterns dictating at which point they interact with seabed topography as the approach Carmarthen Bay.

ACKNOWLEDGMENTS

The authors would like to thank the Welsh Assembly Government Aerial Photographs Unit, Welsh Government, Crown Offices, Cathays Park, Cardiff, Wales. CF10 3NQ for aerial photographs used in the research.

LITERATURE CITED

A. D. Short (Ed.), *Handbook of beach and shoreface morphodynamics*. Chichester: John Wiley and Sons Ltd. pp. 230-250.

Allan, R.; Tett, S. F. B. and Alexander, L. V., 2009. Fluctuations in autumn and winter severe storms over the British Isles: 1920 to present. *International Journal of Climatology*, 29, 357-371.

Barber, P. C. and Thomas, R. P., 1989. Case study of Carmarthen Bay. In *Proceedings of the conference organised by the Maritime Engineering Board of the Institution of Civil Engineers*. London: Thomas Telford, pp. 243-263.

Davis, J. C., 2002. Statistics and data analysis in geology (3rd ed.).Chichester: Wiley and Sons, 638p.

Dolan, R. and Davis, R. E., 1992. An intensity scale for Atlantic coast northeast storms. Journal of Coastal Research, 840-853.

Dorsch, W.; Newland, T.; Tassone, D.; Tymons, S., and Walker, D., 2008. A statistical approach to modeling the temporal patterns of ocean storms. *J. Coast Res.*, 24(6), 1430-1438.

Halcrow., 2010. Lavernock point to St Ann's head SMP2. http://www.southwalescoast.org/contents.asp?id=55#SMP2MainDocument.

Jago, C. F. and Hardisty, J., 1984. Sedimentology and morphodynamics of a macrotidal beach, Pendine Sands, SW Wales. *Marine Geology*, 60(1-4), 123-154.

Klein, A. H. F.; Benedet Filho, L., and Schumacher, D. H., 2002. Short-term beach rotation processes in distinct headland bay systems. *Journal of Coastal Research*, 18(3), 442-458.

Mackie, A. S. Y.; James, J.W. C.; Rees, E. I. S.; Darbyshire, T.; Philpot, S. L. and Mortimer, K., 2002. *BIOMOR 4. The Outer Bristol Channel Marine Habitat Study*. http://www.marlin.ac.uk/obc/pdfs/report/chapter%202.pdf

Morang, A.; Batten, B. K.; Connell, K. J.; Tanner, W.; Larson, M., and Kraus, N. C., 2009. *Regional morphology analysis package (RMAP), version 3: Users guide and tutorial*. Coastal and hydraulics engineering technical note ERDC/CHL CHETN-XIV-9. Vicksburg, U.S.: Army Research and Development Center. http://chl.erdc.usace.army.mil/chetn/

Phillips, M. R. and Crisp, S.,2010. Sea level trends and NAO influences: the Bristol Channel/Severn Estuary. *Global and Planetary Change*, 73(3-4), 211-218.

Ranasinghe, R.; McLoughlan, R.; Short, A., and Symonds, G., 2004. The southern oscillation index, wave climate and beach rotation. *Marine Geology*, 204(3-4), 273-287.

Rangel-Buitrago, N. and Anfuso, G., 2011. An application of Dolan and Davis (1992) classification to coastal storms in SW Spanish littoral. *J. Coast Res.*, (64), 1891-1985.

Rangel-Buitrago, N. and Anfuso, G., 2013. Winter wave climate, storms and regional cycles: the SW Spanish Atlantic coast. *Int. J. Climatol.*, 33(9), 2142-2156.

Ruiz de Alegria-Arzaburu, A. and Masselink, G., 2010. Storm response and beach rotation on a gravel beach, Slapton Sands, UK. *Marine Geology*, 278, 77-99.

Short, A. D. and Masselink, G., 1999. Embayed and structurally controlled beaches. In Short, A. D. and Trembanis, A. C., 2004. Decadal scale patterns of beach oscillation and rotation: Narrabeen beach, Australia. Time series PCA and wavelet analysis. *J. Coast Res.*, 20(2), 523-532.

Short, A. D.; Trembanis, A. C., and Turner, I., 2000. Beach oscillation, rotation and the southern oscillation, Narrabeen beach, Australia. In *Proceedings of the 27th international coastal engineering conference*. Sydney: ASCE. pp. 2439-2452.

Thomas, T.; Phillips, M. R., and Williams, A. T., 2010. Mesoscale evolution of a headland bay: beach rotation process. *Geomorphology*, 123, 129-141.

Thomas, T.; Phillips, M. R.; Williams, A. T., and Jenkins, R. E., 2011a. Short-term beach rotation, wave climate and the North Atlantic oscillation (NAO). *Progress in Physical Geography*, 35(3), 333-352.

Thomas, T.; Phillips, M. R.; Williams, A. T., and Jenkins, R. E., 2011b. Medium timescale beach rotation: gale climate and offshore island influences. *Geomorphology*, 135, 97-107.

Thomas, T.; Phillips, M. R.; Williams, A. T,. and Jenkins, R. E., 2012. Rotation on two adjacent open coast macrotidal beaches. *Applied Geography*. 3, 363-376.

Uncles, R. J., 2010. Physical properties and processes in the Bristol Channel and Severn Estuary. *Marine Pollution Bulletin*, 61, 5-20.

Journal of Coastal Research	SI	75	487-491	Coconut Creek, Florida	2016

Tidal Modulation of Moderate Wave Energy on a Sandy Tidal Flat on the Macrotidal Amazon Littoral

Wellington Trindade[†*], Luci C. C. Pereira[†], and Ana Vila-Concejo[‡]

[†]Instituto de Estudos Costeiros,
Universidade Federal do Pará,
Bragança, 68600-000, Brazil.

[‡]School of Geosciences F09,
The University of Sydney
Sydney, NSW 2006, Australia

www.cerf-jcr.org

www.JCRonline.org

ABSTRACT

Trindade, W.; Pereira, L.C.C., and Vila-Concejo, A., 2016. Tidal modulation of moderate wave energy on a sandy tidal flat on the macrotidal Amazon littoral. *In:* Vila-Concejo, A.; Bruce, E.; Kennedy, D.M., and McCarroll, R.J. (eds.), *Proceedings of the 14th International Coastal Symposium* (Sydney, Australia). *Journal of Coastal Research*, Special Issue, No. 75, pp. 487-491. Coconut Creek (Florida), ISSN 0749-0208.

The present study focusses on the Vila dos Pescadores, a tidal flat located at the mouth of the Caeté estuary in the northeast of the Brazilian state of Pará. The aim was to establish the interactions amongst climatological and hydrodynamic processes, as well as fluvial dischages under different conditions. Eight campaigns were undertaken between June 2012 and April 2014. Results show that during the dry season, winds were moderate to strong and blew mainly from the northeast, coinciding with migration of the Intertropical Convergence Zone (ITCZ) to the northern hemisphere. During the rainy season, when the ITCZ was moving through this Amazon sector, winds blew from different directions at varying speeds. Maximum local H_s values were recorded during the dry season, when wind speeds were stronger and the waves came from $\theta < 70^{o}$N. During this period, H_s values ranged from 0.0 m (low tide) to 1.3 m (high tide), associated with periods between 2-7 s. During low tides, the waves break on the sandbanks but as the tide elevation exceeds ~1 m, the waves start to propagate over the sandbank and towards the shoreline. Precipitation levels also had a strong influence on this tidal flat, especially during the first half of the year, when increasing precipitation provoked a surge in the discharge of the Caeté River (with lower H_s values). Under different conditions of hydrodynamic energy (monthly and seasonal variation, neap and spring tides, equinox and solstice periods), wave energy was correlated strongly with the tidal elevation.

ADDITIONAL INDEX WORDS: *Hydrodynamic influences, tidal flat, Amazon littoral.*

INTRODUCTION

Tidal flats are found around the world, typically in association with estuaries or other coastal environments, such as lagoons and bays (Dyer *et al*., 2000). These environments are highly dynamic, with sediments in constant motion through the processes of transportation, deposition or erosion, depending on the hydrodynamic characteristics of the local area (Black *et al*., 2002). These features may also protect the coastline by dissipating wave energy and reducing erosion in coastal habitats, such as beaches, mangroves and salt marshes.

In macrotidal environments, tides are considered to be the primary factor controlling the dynamic processes (hydrodynamics and sedimentation) that affect tidal flats. Incoming waves are dissipated strongly on the shallow slope of these features, which play an important role in increasing the sediment transportation capacity through bottom shear stresses, enhanced by non-linear interactions of waves and currents (Fan, 2012).

The study of tidal flats in macrotidal regions is important for the understanding of the processes of the transportation, erosion and deposition of sediments resulting from physical processes, such as the action of tides, waves and winds, and fluvial and tidal currents (Masselink and Short, 1993; Short and Hesp, 1982). Hydrodynamic conditions in those environments have been studied in some parts of the world (Uchiyama, 2007), but few data are available from the Amazon region. Given this, the aim of this study was to establish the interactions amongst climatological and hydrodynamic processes, as well as fluvial dischages in an Amazonian tidal flat (Vila dos Pescadores) located in Bragança, on the eastern Amazon coast.

Regional Setting

The Amazon coast of northern Brazil is characterized by a relatively flat relief where strong tidal currents can have a substantial influence on the transportation of sediments (Geyer, 1995; Kosuth *et al*., 2009). The region's coastline is highly indented, with a series of inlets, bays and estuaries, large tracts of mangrove forest, sandy beaches, sandbanks, and dunes. Two structural units can be observed in northeastern Pará: (i) Bragança shelf and (ii) the Bragança-Viseu coastal basin, which is a tectonic fossa bounded by normal faults running northwest-southeast (Aranha *et al*., 1990).

The principal feature of this region is the Bragança coastal plain, which has an area of 1570 km² and 40 km of coastline stretching from the cape of Maiaú to the mouth of Caeté River (Souza Filho *et al.*, 2005). This river is 149 km long, between its headwaters and estuary, which flows into Caeté Bay (Gorayeb *et*

DOI: 10.2112/SI75-098.1 received 15 October 2015; accepted in revision 15 January 2016.
*Corresponding author: etobio17@yahoo.com.br

al., 2011), draining a basin of 2195 km² with a mean fluvial discharge of ~41 m³/s (ANA, 2014).

Climatological data from the National Institute of Meteorology (INMET, 2014) show that local air temperatures vary litte over the year, with maximum, mean and minimum values of 31ºC, 26ºC and 21ºC, respectively. Average wind speed in the rainy season is 2.8 m s^{-1}, rising to 4.0 m s^{-1} in the dry season. Annual rainfall is greater than 2000 mm. The rainy season lasts from January to June, and the dry season, from July to December (Moraes *et al.*, 2005).

The study area is 33 km from the center of Bragança, located on the western margin of the mouth of the Caeté estuary, adjacent to Vila dos Pescadores (Figure 1). During spring tides, Vila dos Pescadores is dominated by semidiurnal macrotides with a tidal range of over 4.5 m (Monteiro *et al*., 2011) and tidal currents of ~1.5 m s^{-1} (Cavalcante *et al*., 2010; Pereira *et al.*, 2009).

METHODS

Eight campaigns were undertaken to investigate the local hydrodynamics under different tidal conditions between June 2012 and April 2014 (Table 1).

Climate

Rainfall data were obtained by National Institute of Meteorology's (INMET) from a nearby station. Wind directions and speeds were obtained by Weather Forecasting and Climatic Studies Center of the Brazilian Space Agency (CPTEC/INPE) from a nearby station. Data on offshore winds (speed and direction) were obtained from the National Oceanic and Atmospheric Administration (NOAA), station 41041 - North Equatorial.

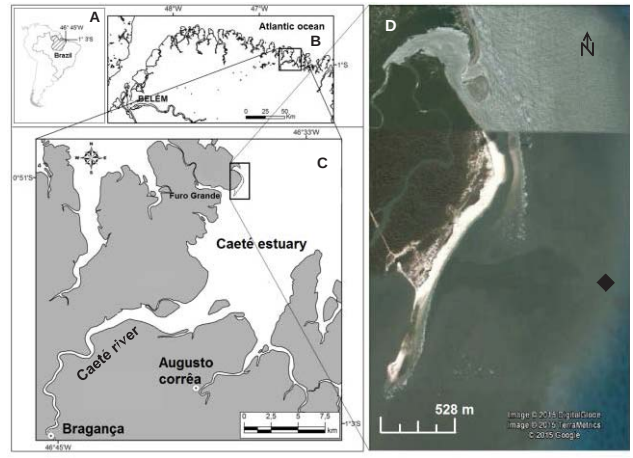

Figure 1. Location of the study area. Brazil (A), Pará coastline (B), Bragantinian coastal plain (C) and exposed tidal flats (D) with hydrodynamic monitoring station (◆). Map modified from Monteiro *et al.* (2011).

Table 1. *Details of the fieldwork campaigns, including their duration (hours) and the tidal conditions (m).*

Campaign	Date	Season	Duration	Tide condition	Tidal range
C1	27-28/06/2012	Rainy	24	Neap	3.5
C2	16-18/09/2012	Dry	48	Spring	5.7
C3	23-25/10/2012	Rainy	36	Neap	3.4
C4	26-28/04/2013	Dry	48	Spring	5.8
C5	17-24/06/2013	Rainy	168	Neap to Spring	3.5 to 5.2
C6	11-19/10/2013	Dry	192	Neap to Spring	3.6 to 5.0
C7	09-18/12/2013	Rainy	216	Neap to Spring	3.7 to 4.4
C8	08-15/04/2014	Dry	168	Neap to Spring	2.7 to 4.4

Hydrodynamics

Wave and tide sensors (TWR 2050) were fixed at a depth of 2.0 m (low tide). The wave height and period were measured at a frequency of 4 H_z (512 samples every 10 minutes). Offshore wave data (height-H_{os}, period-T_p and direction-θ) were obtained from the National Oceanic and Atmospheric Administration (NOAA).

RESULTS

Two well-defined climatic seasons - typical of the region - were observed during the study period (Figure 2). The rainiest months were between February and May (maximum mean discharge), and the driest months were between September and November (minimum mean discharge).

Nearshore and offshore processes

The nearshore winds (Figure 3) reached their highest speeds during the dry season (maximum of 10.3 m s^{-1} and average of 4.4 m s^{-1}) and lowest ones during the rainy season (maximum of 8.2 m s^{-1} and mean of 3.9 m s^{-1}). Offshore (Figure 3), winds were faster in the rainy season (maximum of 15.4 m s^{-1} and mean of 9.2 m s^{-1}) and slower in the dry season (maximum of 14.1 m s^{-1} and mean of 8.5 m s^{-1}). With respect to wind direction, the area was dominated by prevailing northeasterly trade winds (nearshore $\theta < 40^o$, offshore $\theta < 80^o$).

Nearshore wave conditions (Figure 4) were characterized by relatively low energy in the transitional period of June 2012 (maximum H_s of 0.7 m and mean of 0.3 m; associated with periods of 2-6 s) with weaker wind intensities blowing from different directions, resulting in a shorter fetch length. The greatest wave heights (H_s) were recorded in dry season (October and December 2013), reaching a maximum of 1.3 m, associated with periods of 2-7 s (Figure 4).

Similarly, offshore wave conditions were characterized by low energy in same transitional period of June 2012 (maximum of 2.8 m and mean of 1.8 m; associated with periods of 5-7 s). Nearshore waves were modulated by the tidal elevation, reaching maximum values during the high tide and minimum values during the low tide.

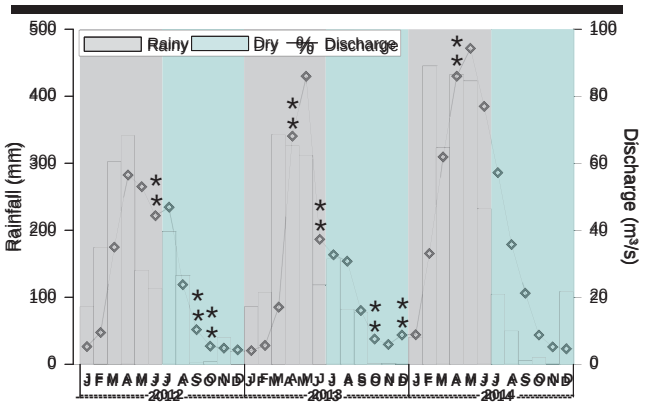

Figure 2. Total monthly rainfall and mean fluvial discharge recorded in 2012, 2013 and 2014. The asterisks (*) indicate the months of the fieldwork campaign during the rainy and dry seasons.

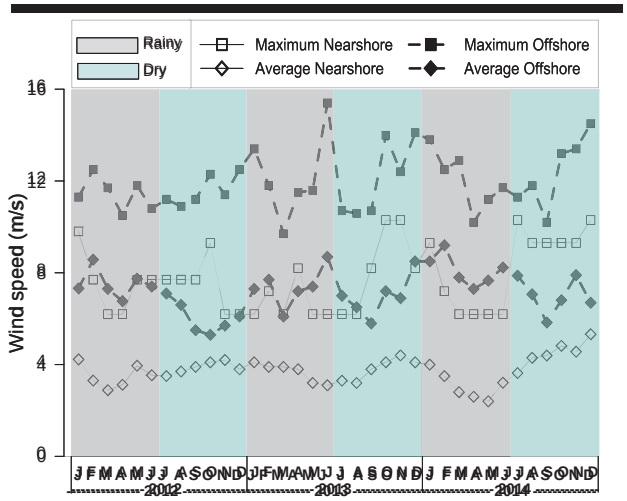

Figure 3. Monthly variation in the nearshore and offshore wind speeds (maximum and average) recorded in 2012, 2013 and 2014.

The highest offshore waves were recorded in 2013 attaining maximum heights of 4.5 m and mean ones of 2.6 m in the dry season (December, Figure 4). The lowest offshore wave were recorded during the transitional months of June, when offshore wind speeds were low.

Relationship between tidal elevation and significant wave height

A strong relationship was found between significant wave heights and tidal elevation in the transitional period of June 2012 ($R^2 = 0.92$) during neap tides, and in dry season (primarily in December, $R^2 = 0.91$) between neap and spring tide, i.e., during the annual solstice periods (Figures 5 and 6). The weakest relationships were recorded during the equinoctial period of the rainy season (primarily in April 2014), when the fluvial discharge reached its maximum, and in the dry season (primarily in October 2013), when nearshore wind speeds were greatest.

Relationship between the tidal elevation and the wave period

A stronger relationship was found between tidal elevation and the wave period during the dry season (with record in October, $R^2 = 0.89$), when wind blew stronger and fluvial dischage was minimal. The opposite pattern was recorded during the rainy season, reaching $R^2 = 0.79$ (Figures 7-8).

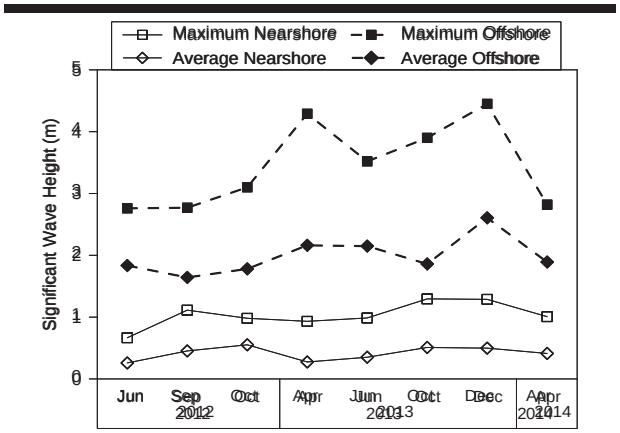

Figure 4. Nearshore and offshore significant wave heights, with the maximum and mean values recorded during the months of fieldwork.

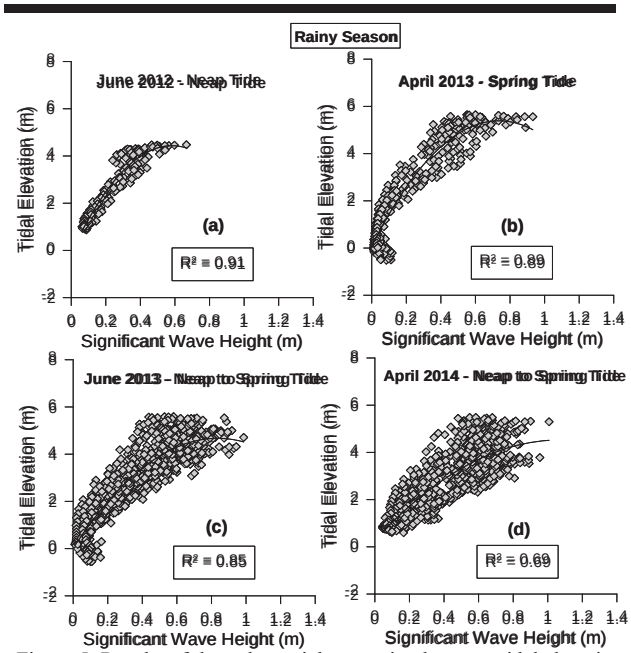

Figure 5. Results of the polynomial regression between tidal elevation and significant wave heights during the rainy season, with a significance level of 95%.

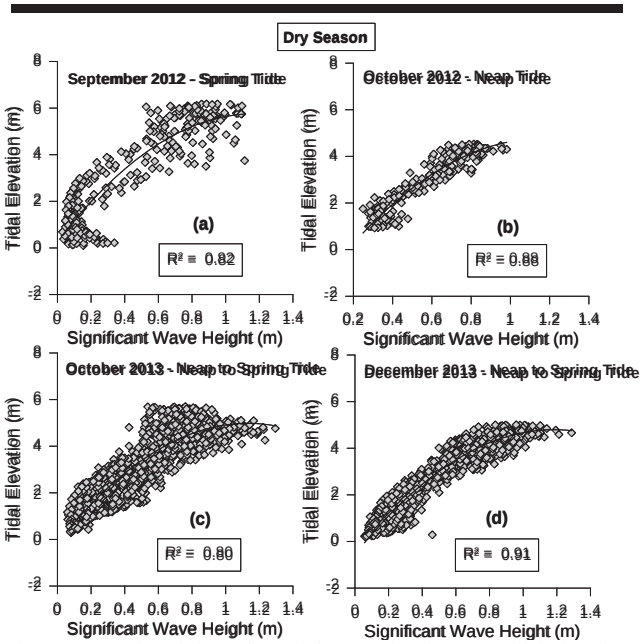

Figure 6. Results of the polynomial regression between tidal elevation and significant wave heights during the dry season, with a significance level of 95%.

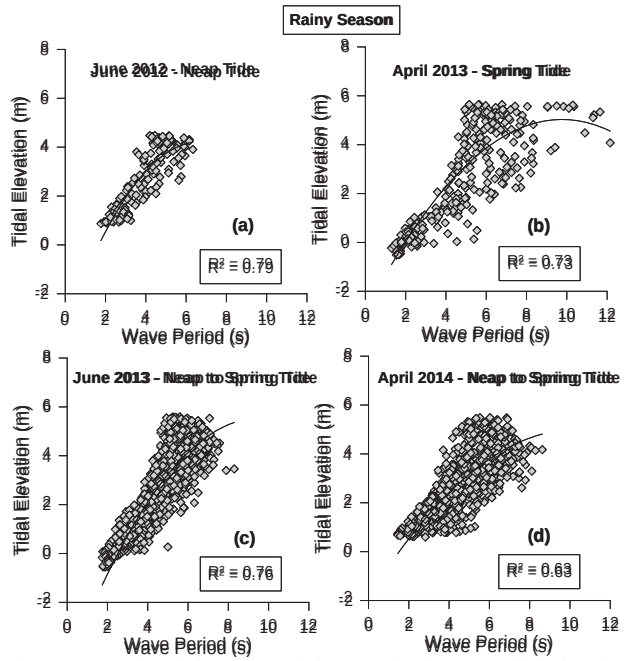

Figure 7. Results of the polynomial regression between tidal elevation and wave period during the rainy season, with a significance level of 95%.

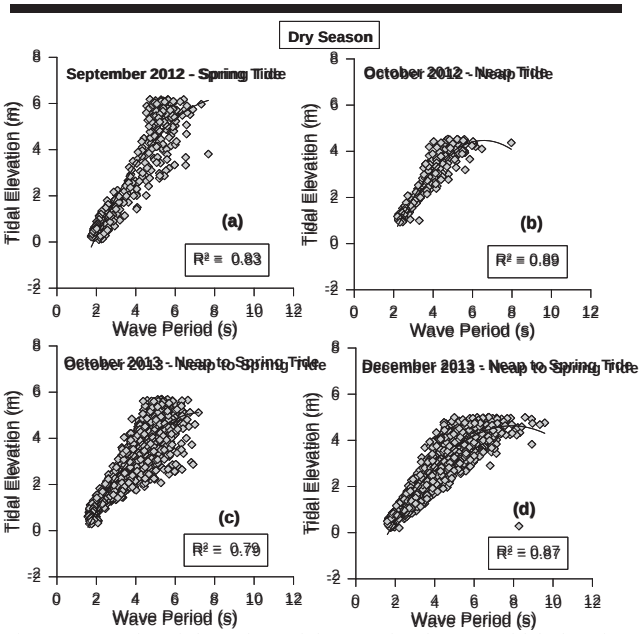

Figure 8. Results of the polynomial regression between tidal elevation and wave period during the dry season, with a significance level of 95%.

DISCUSSION

Hydrodynamic conditions in tidal flat environments have been studied using a number of different approaches (Hunt *et al*., 2015). Seasonal variation in rainfall levels is a fundamentally important process in the study region, by determining a sequence of events. As precipitation increases during the rainy season, the level of the Caeté River rises, leading to an increase in the height of coastal waters, which in turn affects tidal elevation and currents. Increased fluvial discharge (April and June) resulted in lower H_s values mainly during neap tides.

Winds are also an important physical factor (Hunt *et al*., 2013; Taylor and Motion, 2005). Offshore wind speeds were approximately 60% higher than nearshore ones. This result is in agreement with results from other authors (Pianca *et al*., 2010). In addition, significant offshore wave heights were also reduced by up to 75% when propagated in the intertidal zone, and the local coastal morphology is responsible for this. Thus, during low tides, the waves break on the sandbanks, but when tidal elevation exceeds 1 m associated to T_p of 2s, waves begin to propagate on the tidal flat reaching maximal values during high tides. Tidal modulation was also recorded by Pereira *et al*. (2014) in tide-dominated beaches located near the study area, with H_s values varing from zero (low tide) to 1.6 m during high tides of dry season.

However, the stronger northeasterly winds recorded during the second half of the year (dry season, October and December) resulted in higher H_s values, mainly during the spring tide (short wave periods, generated by the spread of the wind over the tidal flat). The opposite pattern was observed in the transitional period of June (mainly during the neap tide), when weaker

winds blowing from different directions resulted in a shorter fetch length and lower H_s values (Pianca *et al*., 2010).

CONCLUSIONS

Under different conditions of hydrodynamic energy (monthly and seasonal variation, neap and spring tides, equinox and solstice periods), wave energy (height and period) was correlated strongly with the tidal elevation. The tidal flat studied here was dominated by tides, which modulate the propagation of waves in the intertidal zone with the lowest values been recorded during low tides and highest, during high tides. Precipitation levels also had a strong influence on this tidal flat, especially during the first half of the year, when increasing precipitation provoked a surge in the discharge of the Caeté River (with lower H_s values). During the second half of the year, the faster northeasterly winds provided better conditions for the propagation of waves on the tidal flat during high tides, in particular during the spring tides. The lowest wave heights were recorded during the transitional month of June 2012. The results highlight the need for future morphodynamic studies.

ACKNOWLEDGMENTS

This research was supported by the CNPq (Universal project - 483913/2012-0) and CAPES (Ciências do Mar II - 43/2013). The authors Pereira L.C.C. (310909/2014-7 and 200629/2014–0) and Trindade would also like, respectively, to thank CNPq and Fapespa for research grants.

LITERATURE CITED

ANA. Agência Nacional de Águas. 2014. Hidroweb: Serviço de Informações Hidrológicas. Available in: http://www2.ana.gov.br/Paginas/default.aspx Accessed: April 01th, 2014.

Aranha, L.G.F.; Lima, H.P.; Souza, J.M.P., and Makino, R.K., 1990. Origem e Evolução das Bacias de Bragança-Vizeu, São Luís e Ilha Nova. In: De Raja Gabaglia, G.P., and Milani, E.J. (Eds), *Origem e Evolução de Bacias Sedimentares*. Petrobrás-RJ, pp. 221-233.

Black, K.S.; Tolhurst, T.J.S.; Hagerthey, E., and Paterson, D.M., 2002. Working with natural cohesive sediments. *Journal of Hydraulic Engineering*, 128(1), 2-8.

Cavalcante, G.H.; Kjerfve, B.; Knoppers, B., and Feary D.A., 2010. Coastal currents adjacent to the Caeté Estuary, Pará Region, North Brazil. *Estuarine, Coastal and Shelf Science*, 88, 84-90.

Dyer, K.R.; Christe, M.C., and Wright, E.W., 2000. The classification of intertidal mudfats. *Continental Shelf Research*, 20, 1039-1060.

Fan, D., 2012. Open-coast tidal flats. In: Davis, R.A., and Dalrymple, R.W. (eds), *Principles of tidal sedimentology*. Netherlands: Springer, pp. 187-229.

Geyer, W.R., 1995. Tide-induced mixing in the Amazon frontal zone. *Journal of Geophysical Research*, 100(C2), 2341-2353.

Gorayeb, A.; Lombardo, M.A., and Pereira, L.C.C., 2011. Natural Conditions and Environmental Impacts in a Coastal Hydrographic Basin in the Brazilian Amazon. *Proceedings of the 11th International Coastal Symposium*, (Szczecin, Poland), Journal of Coastal Research, Special Issue No. 64, 1340-1344.

Hunt, S.; Bryan, K.R.; Mullarney, J.C., and Pritchard, M., 2013. The control of wind and waves on the asymmetry of estuarine currents. *Coastal Dynamics*, 859-870.

Hunt, S.; Bryan, K.R., and Mullarney, J.C., 2015. The influence of wind and waves on the existence of stable intertidal morphology in meso-tidal estuaries. *Geomorphology*, 228, 158-174.

INMET. Instituto Nacional de Meteorologia., 2014. Monitoramento de estações automáticas. Available in: http://www.inmet.gov.br/sonabra. Access: April 01th, 2014.

Kosuth, P.; Callede, J.; Laraque, A.; Filizola, N.; Guyot, J.L.; Seyler, P.; Fritsch, J.M., and Guimarães, V., 2009. Sea-tide effects on flows in the lower reaches of the Amazon River. *Hydrological Processes*, 23(22), 3141-3150.

Masselink, G. and Short, A.D., 1993. The effect of tide range on beach morphodynamics and morphology: a conceptual model. *Journal of Coastal Research*, 9(3), 785-800.

Monteiro, M.C.; Pereira, L.C.C.; Guimarães, D. de O.; Costa, R.M. da; Souza-Filho, P.W.M.; Vieira, S.R., and Jiménez, J.A., 2011. Influence of natural and anthropogenic conditions on the water quality of the Caeté river estuary (North Brazil). *Proceedings of the 11th International Coastal Symposium*, (Szczecin, Poland), Journal of Coastal Research, Special Issue No. 64, pp. 1535-1539.

Moraes, B.C.; Costa, J.M.N.; Costa, A.C.L., and Costa, M.H., 2005. Variação espacial e temporal da precipitação no estado do Pará. *Acta Amazônica*, 35(2), 207-214.

Pereira, L.C.C.; Ribeiro, C.M.M.; Monteiro, M., and Asp, N.E., 2009. Morphological and sedimentological changes in a macrotidal sand beach in the Amazon littoral (Vila dos Pescadores, Pará, Brazil). *Proceedings 10th International Coastal Symposium* (Lisboa, Portugal), *Journal of Coastal Research*, Special Issue No. 56, pp. 113-117.

Pereira, L.C.C.; Vila-Concejo, A.; Costa, R.M., and Short, A.D., 2014. Managing physical and anthropogenic hazards on macrotidal Amazon beaches. *Ocean and Coastal Management*, 96, 149-162.

Pianca, C.; Piero, L.F.M., and Siegle, E., 2010. Brazilian offshore wave climate based on nww3 reanalysis. *Brazilian Journal of Oceanography*, 58(1), 53-70.

Short, A.D. and Hesp, P.A., 1982. Wave, beach and dune interations in southeastern Australia. *Marine Geology*, 48(3-4), 259-284.

Souza Filho, P.W.M.; Paradella, W. R., and Silveira, O.F.M., 2005. Synthetic Aperture Radar for Recognition of Coastal Features in the Wet Tropics: Applications in the Brazilian Amazon Coast. *Boletim do Museu Paraense Emílio Goeldi*, Série Ciências Naturais, 149-154.

Taylor, J.R.M. and Motion, A., 2005. Estimating wave energy in scottish waters from hindcast data. *6th European Wave and Tidal Energy Conference*. Glasgow, UK, 501-508.

Uchiyama, Y., 2007. Hydrodynamics and associated morphological variations on an estuarine intertidal sand flat. *Journal of Coastal Research*, 23(4), 1015-1027.

Journal of Coastal Research	SI	75	492-497	Coconut Creek, Florida	2016

Swash Motion Driven by the Bore and Prediction of Foreshore Profile Change

Jun Wang[†], Bingchen Liang[†‡*], Huajun Li[†‡], Xinying Pan[†], Dongyoung Lee[†], Yu Xu[†‡]

[†]College of Engineering
Ocean University of China
Qingdao, China

[‡]Shandong Provincial Key Laboratory of Ocean Engineering
Ocean University of China
Qingdao, China.

www.cerf-jcr.org

www.JCRonline.org

ABSTRACT

Wang, J.; Liang, B.C.; Li, H.J.; Pan, X.Y.; Lee, D.Y., and Xu, Y., 2016. Swash motion driven by the bore and prediction of foreshore profile change. *In:* Vila-Concejo, A.; Bruce, E.; Kennedy, D.M., and McCarroll, R.J. (eds.), *Proceedings of the 14th International Coastal Symposium* (Sydney, Australia). *Journal of Coastal Research*, Special Issue, No. 75, pp. 492-497. Coconut Creek (Florida), ISSN 0749-0208.

The prediction of a swash zone bed profile resulting from complex hydrodynamic processes is a challenging task. A series of laboratory experiments at a 2D wave flume were carried out to investigate the evolution of foreshore profiles and sediment transport in the swash zone. The swash motions and the changes of foreshore profiles at the different stages of foreshore evolution were measured for 12 cases of different combinations of wave height, wave period and water level for two different initial beach slopes (1/5 and 1/15). From the evolution of foreshore profiles detected by side looking video cameras mounted to the glass wall of a 2D wave flume, the sediment transport rates were estimated precisely both in time and space using the 1-D sediment conservation equation. The characteristics of the instantaneous sediment flux of swash motion and feasibility of its prediction were discussed. The characteristics of the swash-averaged net sediment flux at different stages of beach evolution were investigated by detecting the detailed net flux at 2 minute intervals from the precise beach profile changes. Simple methods of prediction of sediment transport and foreshore profile change are discussed for swash motion driven by bores.

ADDITIONAL INDEX WORDS: *swash zone, foreshore profile, sediment flux, morphology prediction.*

INTRODUCTION

The swash zone is important to the sediment budget of the near-shore as it is the region of shoreline erosion or accretion. The prediction of foreshore morphology change is important since the swash zone acts as a sediment conduit between the upper beach and the surf zone. The hydrodynamic and hence the sediment transport vary fast both in space and time at swash zone. Due to the difficulties in monitoring of the sediment flux in small space and time intervals, the sediment transport processes in the swash zone are not fully understood.

Hughes (1992) studied shoreline change generated by either or both of cross-shore sediment transport and gradients in long-shore material flux. Magnus *et al*. (1999) used canonical correlation analysis (CCA) model and found the profile response displayed significantly higher correlation with the near-shore wave properties. Holland and Puleo (2001) observed Duck, North Carolina by combining sensors with cameras and got a tendency toward a predictable equilibrium between swash motions and profile response. Jackson *et al.* (2004) used four streamer traps to observe Port Beach and found that sediment transport during wave uprush occurs through two distinct mechanisms of bore collapse and local shear stress. Butt *et al.* (2007) found swash zone hydro- dynamics governs sediment transport mechanisms during wave run-up and run-down, and in large part controls beach face morphology.

To understand the sediment transport processes at swash zone, there is a need for a rapid, non-contact, high resolution profiling technique that can measure detailed mechanisms of time series profile response. As a non-contact method, video cameras can record the detailed laboratory processes from side-wall of the 2D wave flume (see detail in Yang *et al.*, 2015), providing high resolution profiles of the bed along a cross-shore line both in time step and spatial interval.

The aim of this paper is to investigate the sediment transport at the swash zone from the precise measurement of the evolution of beach profiles. The swash motion driven by the bores and the resultant sediment transport at the swash zone were investigated through a series of laboratory experiments at 2D wave flume and the prediction methods of sediment transport at the swash zone were discussed.

METHODS

A series of laboratory experiment were carried out at Ocean University of China's laboratory to investigate the sediment transport processes at the swash zone by estimating the sediment flux from the detailed evolution of foreshore profile.

Experiment and Numerical Model Setup

The 2-D wave flume is 50 m long, 3.0 m wide and 1.5 m deep. Figure 1 shows the view of the wave flume and locations of measurement instruments. The surface wave elevation, underwater orbital motion were measured using staff wave

DOI: 10.2112/SI75-099.1 received 15 October 2015; accepted in revision 15 January 2016.
*Corresponding author: bingchen@ouc.edu.cn

gauges and ADV current sensors with a sampling rate of 20 Hz and 50 Hz , respectively.

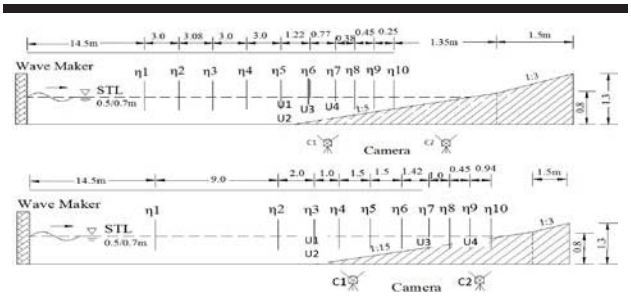

Figure 1. Location of sensors: two cameras (C1-C2), ten wave gauges ($\eta_1 - \eta_{10}$) and four ADV (U1-U4) for two different initial bed slopes (1/5 and 1/15).

The swash motion driven by the bore and resultant sediment transport at the swash zone are investigated for two different initial beach slopes (1/5 and 1/15) for 12 different incident wave conditions of regular waves with different combination of wave height, period and water level as shown in Table 1. Total experiment time duration is one hour for each experiment. Because the water depth of swash zone is too shallow, all the sensors are deployed outside of swash zones as shown in Figure1.

Table 1. *Experiment conditions*

Median grain size *G*(mm)	Beach slope *S*	Wave Height *H*(m)	Wave Period *T*(s)	Water depth *d*(m)
0.6	1/5,1/15	0.1,0.2	1.2,2.1,3.0	0.5,0.7

To compensate the limitation of laboratory measurement in the swash zone, the detailed hydrodynamics information such as surface elevation and flow velocity at each layer were estimated indirectly by means of numerical simulation using wave resolving model, Flow-3D. As beach profile is changing continuously during the experiment, three profiles in the beginning, middle and end of the experiment (P0, P2 and P4 shown in Figure.2) are selected to simulate the hydrodynamics.

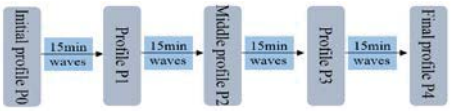

Figure 2. Time schedule for the numerical simulation and detailed analysis of sediment transport rate.

The results of the numerical simulation were compared with the observation data at the surf-zone where the measurement instruments had been deployed. Figure 3 shows the comparisons between measured and simulated surface elevation at 10 different locations and the flow velocity at 4 different locations shown in Figure 1. It is shown that the surface elevation and flow velocity simulated by FLOW3D model agree well with the measured data. Even though we cannot verify the validity of the numerical simulation at the swash zone with measured data, we assumed that the numerical simulation results at the swash zone are also acceptable to be used in the analysis of the laboratory experiments to compensate the limitation of the measurement data in swash zone.

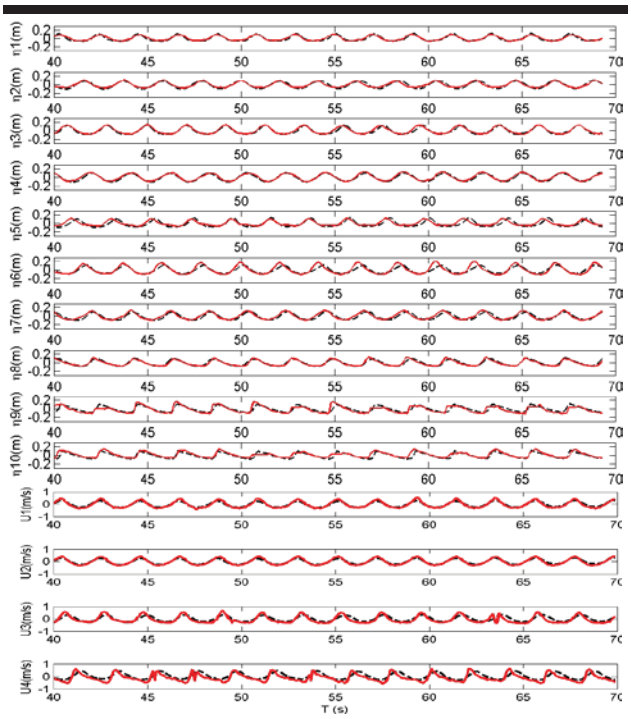

Figure 3. Comparisons between measured and simulated surface elevation (upper: $\eta_1 - \eta_{10}$) and flow velocity (down: U1-U4), (the dashed black line: Flow-3D, the red line: Observation).

The hydrodynamic parameters estimated by FLOW3D model simulation are used in the analysis of experiment data at swash zone in the following sections.

Video Monitoring

The time variations of swash shape and bed profile were observed using two video cameras mounted aside the glass wall of 2D wave flume (Figure 1). The bottom bed profile is estimated by detecting the interface of the fluid and bed every 0.1 second. The space resolution is about 2 mm. Figure 4 shows example of video image and detection of bed profile (blue line).

The sediment flux was estimated from the observed time evolution of the beach profile using the 1-D continuity equation of bottom sediment with boundary condition of no sediment flux at the dune assuming that the changes in the long-shore direction are negligible at the 2D wave flume.

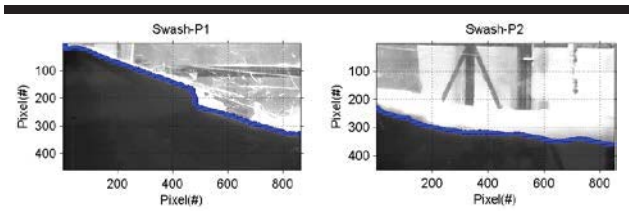

Figure 4. Example of video image and detection of bed profile.

$$n\frac{dz_b}{dt} = -\frac{dQ}{dx} \tag{1}$$

Sediment flux Q, can be estimated in two different time scales, instantaneous flux and swash-averaged net flux. By detecting the bed level z_b, at each time step of 0.1 sec, the sediment transport rate was calculated.

RESULTS

The time variations of the instantaneous bed level and sediment flux obtained from the laboratory experiment are shown in Figure 5. We can see that the sediment flux varies rapidly in a small time scale of the swash motion. The swash motion and hence the sediment transport is much intensive at the lower part of the foreshore where bore-generated turbulence and backwash motion is strong. The fluctuation of onshore and offshore sediment transport decreases as swash moves toward the upper part of the foreshore. However, the swash-averaged net flux is rather small at all the location of the foreshore.

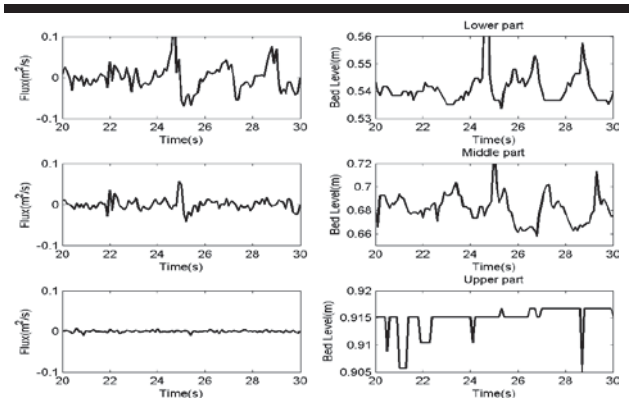

Figure 5. Example of time variations of instantaneous bed level and sediment flux estimated from laboratory experiment data for a couple of wave cycles at 3 different parts of swash zone. (Experiment condition: bed slope: 1/5, wave height: 0.1 m, wave period: 2.1 s, water depth: 0.5 m).

Out of many semi-empirical formula, Meyer-Peter and Muller (1948) equation was used in calculating sediment flux as an example using the hydro-dynamic parameters estimated by FLOW3D simulation described above.

$$\Phi = B\left(\theta - \theta_{cr}\right)^{1.5} c_b \tag{2}$$

$$Q_b = \Phi\left[g\left(s-1\right)d_{50}^3\right]^{\frac{1}{2}} \tag{3}$$

Where Q_b is the bedload flux (in units of volume per width per time), B is the bedload coefficient, g is gravity, $s=\rho_s/\rho_f$ is the ratio of sediment density and fluid density, c_b is the volume fraction of species in the bed material, θ is the Shields parameter and θ_{cr} is the critical Shields parameter.

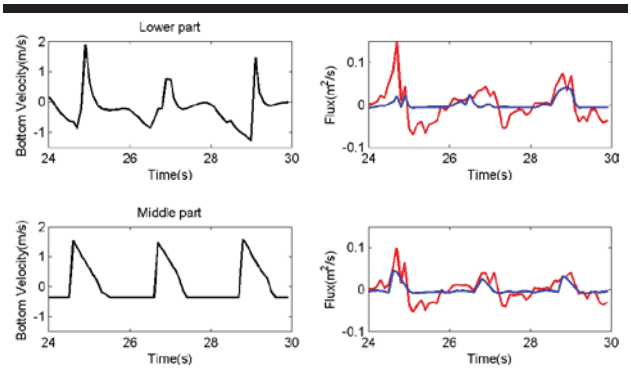

Figure 6. Bottom orbital velocity and comparison of instantaneous flux between experiment result (red line) and semi-empirical formula of Meyer-Peter (blue line). (Top: lower part, bottom: middle part of swash)

The bed profile evolution is monitored from the video image by detecting the bed level after backwash of the swash when the foreshore is exposed to the air. For the inner surf-zone, the bed level was determined by checking the minimum bed level during 2-3 wave cycles. The evolution of beach profile monitored every 2 min interval is shown in Figure 7.

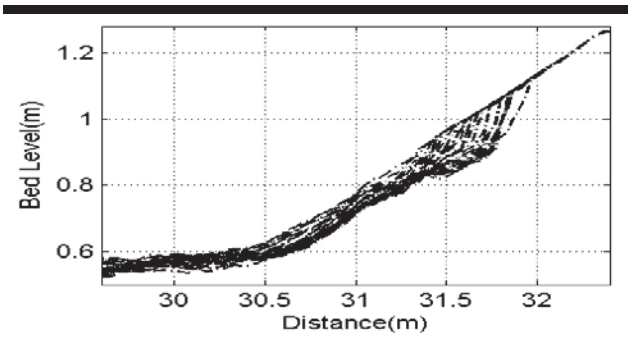

Figure 7. Example of beach profile change monitored every 2 min interval for the case of initial slope: 1/5, wave height: 0.2 m, wave period: 2.1 s and water depth: 0.7 m.

From the precise measurement of the evolution of beach profile both in time and space, the swash-averaged net sediment transports rates were calculated using Eq.1. Figure 8 shows variations of swash-averaged net flux along the onshore distance

for the case of different initial bed slope (1/5 and 1/15) for the incident wave height: 0.2m, period: 2.1 s and water depth: 0.7 m.

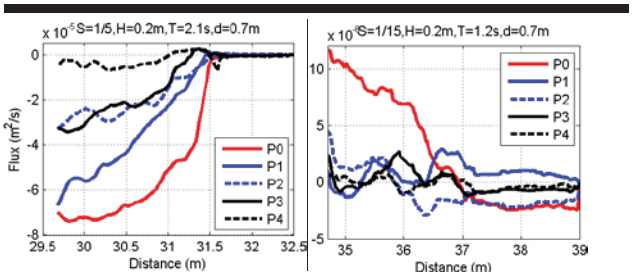

Figure 8. Variations of swash-averaged net flux along the onshore distance for the case of different initial bed slope (1/5 and 1/15).

For the case of the steep initial bed slope (1/5), the sediment flux is offshore direction (negative value) with large value in the beginning. The sediment flux decrease slowly to zero as the local bed slope become flattened with offshore sediment transport. For the mild initial bed slope (1/15), the sediment flux is onshore direction (positive value) in the beginning and approached to zero (equilibrium state) with increase of time. In early stage of the experiment the deviation of the bed slope from the equilibrium bed slope is large so that the net sediment flux is large.

When the net flux decreases to zero, where onshore and offshore flux balance each other, the changes of bed level and hence the bed slope would stop to reach the equilibrium bed slope. The equilibrium foreshore slope can be obtained by the extrapolation of beach profile where the net flux become zero. In many cases the final profiles change very slowly at the end of the experiment so that the final slope is regarded as equilibrium slope in this paper.

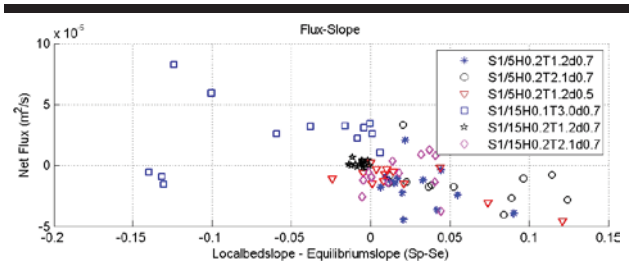

Figure 9. The correlation between the net flux and the deviation of local slope from the equilibrium slope ($S_p - S_e$) for different experiment conditions.

Figure 9 shows the correlation between the net flux and the deviation of the local slope from the equilibrium slope. There should be a functional relationship between the net flux and the local bed slope (S_p), equilibrium bed slope (S_e) and hydrodynamic parameters of the swash motion. When S_p is bigger than S_e, the net flux is negative and sediment transport is offshore direction.

DISCUSSION

We assumed that the impact of the side walls on sediment transport is negligibly small and the bed level across the flume is the same in 2-D wave flume. The observation of the beach profiles using total station and visual observation of the bed across the channel support the validity of these assumptions for most of the cases so that 1-D sediment conservation equation was used in the estimation of the sediment flux. Based on the good agreement of the numerical simulation results with the observation data at surf-zone, we also assumed that the CFD model simulation is valid for the swash zone, which may need further validation for more detailed analysis. Some uncertainties in the analysis of the experiment data come from the deviations from these assumptions.

The difficulty in distinguishing the interface of the bottom bed level and fluid above by the presence of high concentration suspended sediment causes problem in the estimation of the instantaneous sedimentation flux in this experiment, which may limit the detailed studies on the sedimentation processes and development of the swash-resolving sediment transport prediction model for the swash zone. The approach in the estimation of the sediment transport by means of the detailed prediction of the swash motion seems not feasible at present.

The scattering of the data in Figure 9 may be partly due to the error in determining the equilibrium foreshore profile. Experiment duration may need to be extended to allow the foreshore profile become closer to the equilibrium profile to reduce the error in estimating the equilibrium foreshore profile and prediction of the swash-averaged net flux.

CONCLUSIONS

One of the problems in the studies of the sediment transport processes in the surf-zone is the limitation in measuring the bed level evolution in high time and spatial resolution. It was shown that the detailed estimation of the sediment flux at the surf-zone can be obtained from the side-looking video observation of the precise evolution of the bottom profile at 2D wave flume, which enables the basic research on the sediment transport at the swash zone.

To solve the problem of installing sensors in the shallow swash zone, indirect method of simulation of hydro-dynamics using CFD model was used and tested its validity in-directly using the observation data at the surf-zone. Further direct validation of this approach is suggested using special flow observation method such as PIV, LDA that would not disturb the flow at very shallow water depth of the swash zone.

There are lots of errors in estimating the instantaneous sediment flux of the swash motion, which limit the studies of the detailed processes of sediment transport in the swash zone. More detailed experiment with well controlled illumination for the detection of the bed level needs to be carried out for the detailed studies of sediment transport at swash zone.

The swash-averaged net sediment flux was analyzed from the precise evolution of foreshore profile and characteristics of onshore and offshore sediment transport in the swash zone was discussed. It was shown that the analysis of the swash-averaged

net sediment flux is related to the deviation of the local foreshore profile from the equilibrium profile. The prediction method of foreshore morphology change can be developed by predicting the swash-averaged net flux by developing the functional relationship between net flux and controlling parameters. Simple methods of prediction of sediment transport and foreshore profile change can be developed by predicting first the equilibrium foreshore profile from the controlling parameters and then the swash-averaged net flux using estimation of the foreshore equilibrium profile.

The analysis of the net sediment flux is being carried out separately for uprush and backwash swash motion by detecting the bed level rather reliably for two times in a swash cycle; once at the end of uprush motion when the turbulence is week and most of dense suspended sediment settle down and the other at the end of backwash motion when the foreshore is open to air. The sediment transport processes of the uprush swash motion and that of backwash swash motion would be studied in depth using this laboratory experiment data.

ACKNOWLEDGMENTS

The authors would like to acknowledge the support of the National Science Fund (Grant No. 51179178) and the 111 Project (B14028). The experiment was partially supported by the KIOST Research Program, Development of Coastal Erosion Control Technology.

LITERATURE CITED

Butt, T.; Russell, P.E.; Miles, J., and Turner, I.L., 2007. Sediment transport processes in the swash zone of sandy beaches. International Coastal Symposium. *Journal of Coastal Research*, Special Issue No 50, pp. 636–640.

Hughes, M.G., 1992. Application of a non-linear shallow water theory to swash following bore collapse on a sandy beach. *Journal of Coastal Research*, 8(3), 562–578.

Holland, K. T. and Puleo, J. A., 2001. Variable swash motions associated with foreshore profile change. *Journal of Geophysical Research*, 106(C3), 4613-4623.

Jackson, N. L.; Masselink, G., and Nordstrom, K. F., 2004. The role of bore collapse and local shear stresses on the spatial distribution of sediment load in the uprush of an intermediate-state beach. *Marine Geology*, 203(1), 109-118.

Larson, M.; Capobianco, M., and Hanson, H., 2000. Relationship between beach profiles and waves at Duck, North Carolina, determined by canonical correlation analysis. *Marine Geology*, 163(1), 275-288.

Meyer-Peter, E. and Muller, R., 1948. Formulas for bed-load transport. *Proceedings of the Second International Association for Hydraulic Research* (Kungl Tekniska Hogskolan, Stockholm), pp. 38-65.

Puleo, J. A.; Beach, R. A.; Holman, R. A., and Allen, J. S., 2000. Swash zone sediment suspension and transport and the importance of bore-generated turbulence. *Journal of Geophysical Research: Oceans (1978-2012)*, 105(C7): 17021-17044.

Yang, Z.T.; Liang, B.C.; Lee, D.Y., and Li, H.J., 2015. Experimental Studies on Sandy Beach Profile Evolution in 2D Wave Flume. *Proceedings of the Twenty-fifth International Offshore and Polar Engineering Conference. International Society of Offshore and Polar Engineers* (Kona, Hawaii, USA), pp. 1286-1290.

Journal of Coastal Research	SI	75	497-501	Coconut Creek, Florida	2016

Laboratory Experiment on the Bed Load Sediment Transport over a Rippled Bed

Zhengtong Yang†, Huajun Li‡*, Bingchen Liang‡, Dongyoung Lee†, Xinying Pan†, Yu Xu‡

†College of Engineering
Ocean University of China
Qingdao, China

‡Shandong Provincial Key Laboratory of Ocean Engineering
Ocean University of China
Qingdao, China.

www.cerf-jcr.org

www.JCRonline.org

ABSTRACT

Yang, Z.T.; Li, H.J.; Liang, B.C.; Lee, D.Y.; Pan, X.Y., and Xu, Y., 2016. Laboratory experiment on the bed load sediment transport over rippled bed. *In:* Vila-Concejo, A.; Bruce, E.; Kennedy, D.M., and McCarroll, R.J. (eds.), *Proceedings of the 14th International Coastal Symposium* (Sydney, Australia). *Journal of Coastal Research*, Special Issue, No. 75, pp. 497-501. Coconut Creek (Florida), ISSN 0749-0208.

Bed load sediment transport over rippled bedforms was investigated through a series of laboratory experiments with different combinations of bed slope, grain size, wave conditions and water level using a 2D wave flume. In addition to the measurement of surface waves and velocity, the water surface and bottom bed elevation were precisely monitored using video cameras to record the continuous processes of profile evolution, including ripple formation and migration under the assumption of longshore uniformity. The bed load sediment transport flux associated with ripple migration was then estimated. Numerical model SWASH was applied to provide representative forcing hydrodynamic parameters in the estimation of sediment flux where measurement data was scarce after proper validation. It was observed that ripples migrate with an average speed of 0.113 *mm/s*, and bed load sediment flux of $0.0061 kg\ m^{-1}s^{-1}$, respectively. Velocity skewness explains the highest correlation with ripple migration speed for all cases, while mean flow appears to be dominant in the coarser sand transport. Good agreement was found from comparisons of sediment transport flux between measurements derived from ripple migration and semi-empirical bed load transport formulations.

ADDITIONAL INDEX WORDS: *Ripple, bed load, sediment transport, laboratory experiment.*

INTRODUCTION

In the coastal zone, small-scale bedforms, or ripples, are common features especially in the near-shore zone, which plays an important role in sediment transport processes. Bedforms represents roughness elements for wave and current-driven flows, controlling the structure of boundary layers to a large degree (Grants and Madsen, 1986). Ripples are always responsible for the generation of near-bed turbulence, which affect the suspended sediment profile and the magnitude and direction of suspended sediment flux (Vincent *et al*., 1991). Ripple generation and migration can serve as a methodology of calculating sediment flux where bed load transport are predominant. Therefore, considerable attentions have been paid to the research on ripple formulation and predictions.

Ripple migrations can be used to quantify the bed load transport under the assumption that sediment is not intermittently suspended or does not bypass ripples. Traykovski (1999) monitored ripple migration in 11 m water depth over a 6 week period and found that the Meyer-Peter and Muller equation under predicted the observed bed load transport by at least 1 order of magnitude. It has been pointed that this discrepancy arose because suspended transport also contributed to ripple migration. Similar observation was conducted by Hay and Bowen (1993) that bed level changes over three successive storms in 2 m water depth and found that bed load transport rates derived from migrating ripples were 2 orders of magnitude less than that predicted by the bed load equations by Madsen and Grant (1977).

It is rare to see experimental investigations on ripple generation and migrations due to the lack of effective instrumentations to measure such small scale phenomena. Recently, the application of video measurement to laboratory experiment account for an important part of measurement methodology due to its advantages over conventional sensors. Since traditional measurement especially in the field usually monitor the ripple from a down-looking angle, a new perspective was introduced to capture the ripple geometry and ripple dynamics by means of this methodology. Laboratory experiments have several advantages over field observations using video. In the 2-D wave flume, both the water surface and bed surface can be monitored precisely from the side looking video in addition to the control of experiment condition. Ripple geometry and dynamics can be derived from detailed analysis of beach profile evolution and bed load sediment transport flux can be calculated using video in the laboratory experiment under the assumption of longshore uniformity.

The formation and migration of the ripple and the resultant sediment transport rate are investigated through a laboratory experiment using a video monitoring technique. This paper is organized as follows, the methods part introduces the layout and instrumentations of the laboratory experiment. Numerical model SWASH is introduced to provide more detailed hydrodynamic forcing and its accuracy is been discussed. Then followed by the

DOI: 10.2112/SI75-100.1 received 15 October 2015; accepted in revision 15 January 2016.
*Corresponding author: huajun@ouc.edu.cn

results, ripple geometry and dynamics are derived from video data and bed load sediment flux is calculated, several hydrodynamic parameters that maybe responsible for ripple migration are listed. For the discussion part, the correlation between forcing parameters and ripple migration speed is proposed and the performance of existing formulas are compared with laboratory data. Finally, conclusions are drawn about the predictions of bed load sediment transport over a rippled bed.

METHODS

A series of experiments were conducted in a 2D wave flume which was designed to investigate sediment transport under regular waves (see details in Yang *et al*., 2015). Numerical model SWASH was applied here after careful validation to provide essential forcing parameters where measurement data is scarce.

Experiment Setup

The facility consists of a 3.0-m wide, 60-m long, 1.5-m deep flume, and includes one wave generator, a sand beach, and other instruments. A sandy beach was constructed landward of slope 1/5 and 1/15. One piston-type wave paddle was used to generate regular waves in a still water level (SWL) of 0.5 m and 0.7 m, and the duration for each case varies but at least 1 hour.

The water surface and bottom bed elevation were precisely monitored using a novel remote sensing technique *i.e.* video cameras to record the continuous processes of profile evolution, including ripple formation and migration. Two video cameras were positioned to measure the whole process during each case especially the evolution of beach profile. A laser total station was used to measure the beach profiles along two cross-shore lines to ensure alongshore uniformity after pumping out the water when each experiment case was finished. Figure 1 shows the layout of the facility. In total 16 cases with different combinations of initial slope, wave parameters and different water levels were properly chosen to examine the bed load sediment transport over rippled bed. Table 1 summarized the test cases and corresponding incident wave parameters.

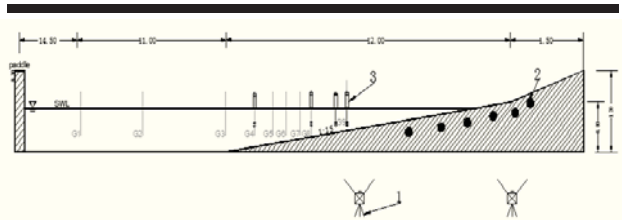

Figure 1. Sketch of the experiment setup.1-video camera, 2-pressure sensors, 3-wave gauges and ADVs.

In this experiment, two videos are used to monitor the offshore ripple dynamics with a frequency of 10 fps. Serial images with a dimension of 1080×1920 pixels separated from the video were analyzed to capture the ripple geometry and dynamics. Image compensation was carried out by sticking grids of known dimension before individual tests, through which the relationship between real world coordinate and image coordinate was established.

Figure 2 shows an example of the detection of ripple profile, black area indicate the bottom sand and ripple profile can be obtained as the red line by detecting the contrast of the intensity of each pixel column, the, and the finally ripple profile was calibrated by direct linear transformation into real world coordinate.

Table 1. *Test cases of the experiment*

Case	Diameter (mm)	Initial Slope	H_s (m)	T_p (s)	SWL (m)
1	0.3	1/5	0.2	1.2	0.5
2	0.3	1/5	0.2	1.2	0.7
3	0.3	1/5	0.2	2.1	0.5
4	0.3	1/5	0.2	3	0.5
5	0.3	1/5	0.2	3	0.7
6	0.3	1/15	0.2	1.2	0.7
7	0.3	1/15	0.2	2.1	0.7
8	0.6	1/5	0.2	1.2	0.5
9	0.6	1/5	0.2	1.2	0.7
10	0.6	1/5	0.2	2.1	0.5
11	0.6	1/5	0.2	2.1	0.7
12	0.6	1/5	0.2	3	0.5
13	0.6	1/5	0.2	3	0.7
14	0.6	1/15	0.2	1.2	0.7
15	0.6	1/15	0.2	2.1	0.7
16	0.6	1/15	0.2	3	0.7

SWASH Model

According to former researchers, ripple dynamics strongly depends on the bottom flow velocity which is not easy to collect both in the field measurement and laboratory experiment. And the definition of representative flow velocity varies from different researchers, for instance, Masselink (2007) used velocity time series obtained from the measurement data which is 6 cm above the bed to formulate $u_m(=2\sigma_u)$. In this experiment, although ADVs were applied in this experiment, it is not easy to guarantee to place ADV at a certain place where exactly ripple occurrence, therefore, in order to capture more standard and more reliable hydrodynamic forcing, numerical model SWASH was combined in the simulation of near shore hydrodynamics, for its significant advantage in detailed wave motions they provide.

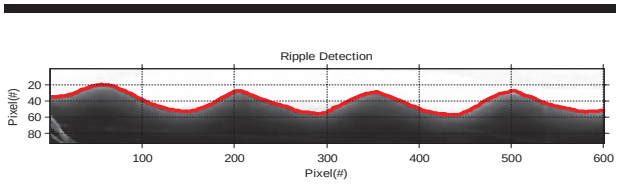

Figure 2. Detection of detailed ripple geometry, dark area is the sand bed, red line indicates the detected ripple profile.

SWASH model was forced by boundary conditions defined at the location of the wave maker, which is 27 m long from toe of the beach slope. Time series of free surface elevation was generated using sinusoidal wave, and subsurface orbital velocity induced by wave motion at the boundary is estimated based on small-amplitude linear wave theory. The horizontal grids that were utilized in SWASH model was constructed with a resolution of 5 cm, while the vertical direction was divided into equivalent 10 layers. A weakly-reflective boundary was applied at the wave boundary, and the Sommerfeld radiation condition was applied at the end of the numerical domain in order to minimize the effect of the reflection.

All the cases were simulated with SWASH model with careful calibration. Figure 3 shows an example of comparison on the wave orbital velocity between measurement data and SWASH output. It can be seen that quite good agreement was achieved between physical model and numerical model for ADV 1# to ADV 4# (offshore to onshore). And the correlation coefficient was nearly 0.98 for offshore observation point and at least 0.60 for nearshore observation point, respectively. However, it is observed that the performance of the numerical model of wave conditions with longer wave period is relative poor which is partially result from that wave boundary conditions is no longer subject to linear wave theory under such water depth.

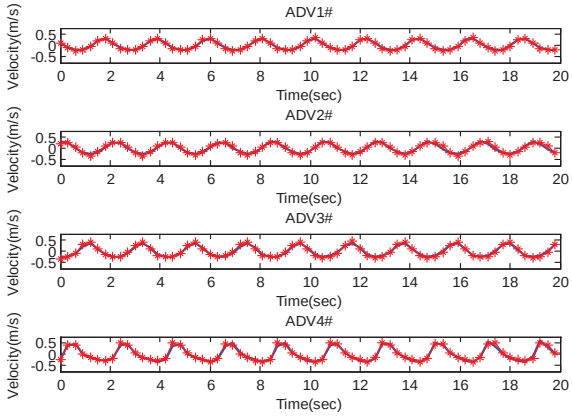

Figure 3. Time series of orbital velocity simulated by SWASH Model at 4 different locations compared with observation data (red: observation; blue: model).

RESULTS

It should be noticed that only cases with acceptable longshore uniformity and parallel ripples were analyzed here to get more reliable results about ripple geometry and sediment transport. Figure 4 shows an example of the practice of ripple post-processing, original beach profile (Figure 4A), and the authentic ripple profile by removing the trend (Figure 4B), as well as the time series of ripple movement (Figure 4C). Ripple geometry as well as corresponding hydrodynamic parameters are listed in Table 2. Ripple geometry characters including ripple height η and ripple length λ were obtained using zero-crossing method which is widely used in the wave analysis. Also, the speed of migration (M_r) was determined as the displacement of the same point on ripple profile in two successive frames divided by the elapsed time, while the bed load sediment transport was denoted as Q_b in $kg\ m^{-1}s^{-1}$. Hydrodynamic data was mainly provided by time series of ADV measurement data, and for cases there is no adjacent measurement data, SWASH model provide supplementary information.

The time series of u was used to calculate the maximum orbital velocity ($u_m = 2\sigma_u$, where σ represents the standart deviation of u), the mean flow velocity$\langle u \rangle$, velocity skewness $\langle u^3 \rangle$, and the acceleration skewness $A_{sy} = \langle a^3 \rangle / \langle a^2 \rangle$, where a is the times series of acceleration, and then the mobility number ψ and Shield parameter can be defined as follows, respectively:

$$\psi = \frac{u_m^2}{(s-1)gD} \quad (1)$$

$$\theta = \frac{0.5 f_w u_m^2}{(s-1)gD} \quad (2)$$

where s the specific gravity of sand, g is the acceleration due to gravity, f_w the bottom friction factor and D the grain size.

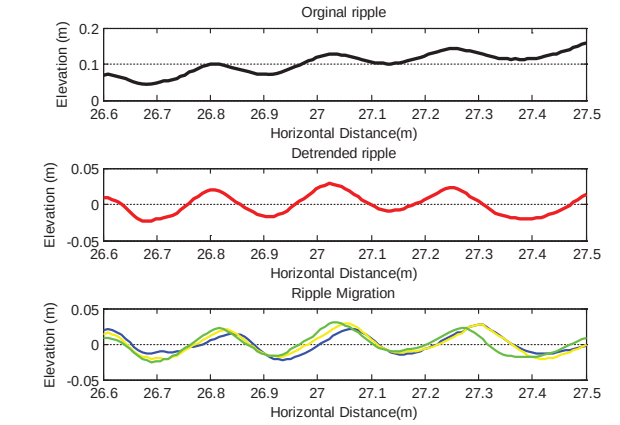

Figure 4.Original beach profile (A), detrended ripple profile (B) and ripple profile at different time stage blue-yellow-green (C).

It is found that ripple generally occurs outside the surf zone and around the toe of the beach slope. It is observed that ripple height varies from 0.8 cm to 5.6 cm and with an average value of 2.88 cm, while ripple length fall into the range of 5.5 cm to 28.51 cm, both of these two characteristics are significantly bigger than those observed by Faraci (2002) in laboratory experiment. In terms of ripple steepness, the average of 16 cases is 0.17, which is relatively larger than the results of fieldwork ($\eta/\lambda \approx 0.15$) by Dingler and Inman (1976).

It is observed that ripple migrated almost in constant speed especially during the end of each test when beach profile reach

Table 2. *Ripple geometry and hydrodynamic parameters*

Case	η(cm)	λ(cm)	η/λ	u_m(m/s)	$\langle u \rangle$ (m/s)	$\langle u^3 \rangle$	A_{sy}	ψ	θ	M_r(mm/s)	Q_b
1	0.99	5.99	0.16	0.314	0.022	0.0003	0.009	32.993	0.388	0.0049	0.0008
2	0.81	5.56	0.14	0.201	0.011	0.0000	0.017	13.467	0.194	0.0011	0.0001
3	2.92	18.70	0.15	0.526	0.036	0.0045	0.176	92.650	0.717	0.0098	0.0045
4	3.46	16.61	0.21	0.496	0.029	0.0179	0.043	82.399	0.576	0.0102	0.0056
5	3.64	16.84	0.22	0.493	0.017	0.0090	0.131	81.444	0.570	0.0056	0.0032
6	1.11	7.74	0.14	0.377	0.029	0.0011	0.000	47.672	0.519	0.0053	0.0009
7	2.61	16.17	0.16	0.563	0.061	0.0149	0.651	106.208	0.802	0.0041	0.0017
8	1.15	9.25	0.12	0.320	0.023	0.0004	0.041	17.130	0.275	0.0041	0.0007
9	0.97	8.27	0.12	0.213	0.012	0.0001	0.021	7.587	0.150	0.0035	0.0005
10	5.65	28.51	0.20	0.529	0.035	0.0044	0.166	46.771	0.469	0.0016	0.0014
11	4.05	22.10	0.18	0.455	0.022	0.0016	0.041	34.740	0.370	0.0128	0.0083
12	4.74	24.42	0.19	0.500	0.029	0.0184	0.011	41.920	0.373	0.0130	0.0098
13	4.95	22.64	0.22	0.468	0.016	0.0091	0.017	36.648	0.335	0.0054	0.0042
14	0.99	8.72	0.11	0.370	0.026	0.0010	0.002	22.907	0.343	0.0194	0.0030
15	3.43	20.97	0.16	0.563	0.061	0.0149	0.651	53.104	0.519	0.0406	0.0222
16	4.76	26.60	0.18	0.707	0.052	0.0303	0.199	83.815	0.658	0.0401	0.0304

quasi-equilibrium profile. The averaged migration speed of 16 cases is 0.113 mm/s. It is hypothesized that ripple migration speed may be correlated with various hydrodynamic parameters that mentioned above, and a least squares analysis was performed between M_r and the hydrodynamic parameters listed in Table 2 for all cases. In order to analysis the influence of grain material on the behavior of ripple, dataset was separated into two groups according to two different bed materials; the results are shown in Table 3 and discussed in the next section.

DISCUSSION

Under the assumption of negligible suspended transport, the results have been compared with traditional semi-empirical sediment transport formulas and the performance of existing formulas in predicting bed load sediment transport over rippled bedforms were discussed. Besides, the influence of several parameterized factors on ripple migrations were evaluated and their correlation with ripple migration was discussed.

Table 3 shows the correlation between ripple migration speed and several hydrodynamic parameters. It is clear that none of these parameters are able to satisfactorily predict M_r for all cases with r^2>0.5, however, u_m, $\langle u \rangle$ and $\langle u^3 \rangle$ reach relatively higher correlation compared with other parameters. And when the dataset separated into two individual groups according to the bed material, their skill increases significantly for coarser sand, especially for the $\langle u \rangle$ of 0.737, which indicates that bed load of coarser sand is largely influenced by bottom mean flow (undertow) although it is generally small. Also, for ψ and θ which is mostly dependent on u_m achieve acceptable correlation around 0.5-0.6. And when considering finer sand, the performance is generally poor compared with coarser sand and u_m shows the biggest correlation ($r^2 = 0.42$), which explicated that u_m becomes a driving force for the bed load transport of relatively fine sand.

The ripple migration rate can provide an estimate of the sediment transport rate and direction under waves in the nearshore, and the mean transport associated with the migration Q_b can be estimated as follows with the assumption of geometry remains constant during migration and was calculated in the last column of Table 2:

$$Q_b = 0.5(1-p)\rho_s \eta M_r \qquad (3)$$

where p is the sediment porosity, ρ_s the sediment density and η the ripple height. In terms of existing formulations of bed load transport, Bijker (1968) extended the steady bed load formula, adding the effect of the wave into it, and the dimensionless parameter is:

$$\Psi_b = b\tau_c^{0.5} \exp\left(-0.27 \frac{1}{\mu \tau_{cw}}\right) \qquad (4)$$

where τ_c is the dimensionless shear stress due to currents alone, τ_{cw} the dimensionless shear stress due to wave-current interaction, b the empirical constant and μ is a correction factor which accounts for the effect of ripples.

Table 3. *Results of least squares analysis between ripple migration rate and hydrodynamic parameters for all data, and separated into finer and coarser sand groups*

	r^2		
Parameters	All	Fine Sand	Coarse Sand
u_m	0.346	0.421	0.452
$\langle u \rangle$	0.390	0.041	0.737
$\langle u^3 \rangle$	0.402	0.220	0.512
A_{sy}	0.181	0.008	0.494
ψ	0.053	0.355	0.511
θ	0.084	0.314	0.571

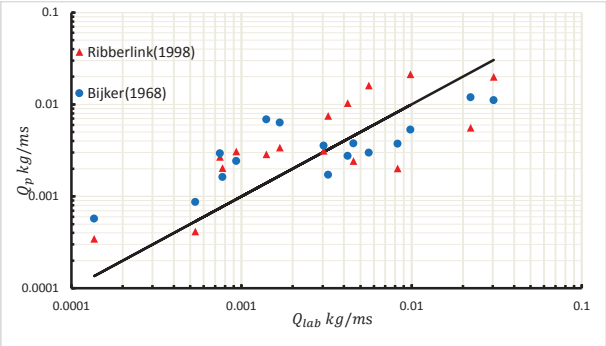

Figure 5. Transport rate derived from ripple migration (Q_{lab}) compared to that predicted (Q_p) using the bed load formulation of Ribberink (red triangle) and Bijker (blue dot). The solid line is the perfect fit between the data.

Another approach is proposed by Ribberink (1998):

$$q_{RIB} = m(|\theta'(t) - \theta_c|)^n \frac{\theta'(t)}{|\theta'(t)|}\rho_s\sqrt{(s-1)gD^3} \quad (5)$$

where θ_c is the critical Shield value ($\theta_c = 0.05$), $\theta'(t)$ is the instantaneous Shield parameter, m=11 and n=1.65 according to Ribberink (1998) and D is the median grain size. The bed load transport q_p was averaged over 2-min burst. Figure 5 compares the estimated transport rate due to ripple migration with that calculated using the formulation for of Bijker (1968) by applying b=2 and ripple height η included in the determination of μ.

Figure 5 shows the performance of two existing formulas in predicting bed load sediment transport compared with that estimated from ripple migration. It can be seen that the estimated sediment transport almost scattered around the black line, which indicates that there are acceptable agreements between both of the two models and measurement data. It seems that Ribberink model tends to have overestimated bed load transport for majority of the cases, which is contrast to the findings of Masselink (2007). Bijker model has underestimated during strong sediment transport conditions ($Q_{lab} > 0.003kg/ms$), while it overestimated for mild transport conditions. In general, the model proposed by Bijker ($r^2 = 0.36$) demonstrate better performance over Ribberink model ($r^2 = 0.71$), and this is probably due to the fact that ripple geometry parameter (η) is included in the calculation of bed load transport.

CONCLUSIONS

Optical remote sensing has been successfully applied to record the continuous process in detailed temporal and spatial resolution, through which ripple geometry and dynamics were derived and bed load sediment transport was then estimated. In order to obtain more detailed hydrodynamic forcing that is responsible for ripple associated transport, SWASH model was used to provide times series of wave orbital velocity where measurement data was scarce.

It is found that ripple migration speed varied from 0.03 to 0.4 *mm/s*, which cannot simply be related to the energy level of the hydrodynamic forcing. But wave maximum orbital velocity tends to be a dominant factor contributing to ripple migration for find sand ($r^2 = 0.421$), while mean flow reach higher correlation of 0.737 for coarser sand. In the comparison of bed load sediment transport derived from bed form migration with those estimated using existing models Ribberink (1998) and Bijker (1968), both of the two models shows acceptable agreements with measurement data, especially the Bijker model ($r^2 = 0.71$) in which a detailed ripple coefficient is included. Preliminary conclusions can be drawn that it is recommended to use traditional semi-empirical formulations which are able to produce stable results about bed load sediment transport especially when detailed ripple geometry included in the calculation. However, it is difficult to predict sediment transport by deriving from ripple migration, as ripple dynamics are complicated to predict.

ACKNOWLEDGEMENTS

The authors would like to acknowledge the support of The National Science Fund (Grant No. 51179178) and the 111 Project (B14028). The experiment was partially supported by the KIOST Research Program, Development of Coastal Erosion Control Technology.

LITERATURE CITED

Bijker E.W., 1968. Mechanics of sediment transport by the combination of waves and current In Design and Reliability of Coastal Structures, *Proceedings of the 23rd International Conference on Coastal Engineering*, pp. 147-173.

Grant, W.D. and Madsen, O.S., 1986. The continental-shelf bottom boundary layer. *Annual Review of Fluid Mechanics*, 18(1), 265-305.

Hay, A.E. and Bowen, A.J., 1993. Spatially correlated depth changes in the nearshore zone during autumn storms. *Journal of Geophysical Research: Oceans*, 98(C7), 12387-12404.

Masselink, G.; Austin, M.J.; O'Hare, T.J., and Russell, P.E., 2007. Geometry and dynamics of wave ripples in the nearshore zone of a coarse sandy beach. *Journal of Geophysical Research: Oceans*, 112(C10).

Ribberink, J.S., 1998. Bed-load transport for steady flows and unsteady oscillatory flows. *Coastal Engineering*, 34(1), 59-82.

Traykovski, P.; Hay, A.E.; Irish, J.D., and Lynch, J.F., 1999. Geometry, migration, and evolution of wave orbital ripples at LEO−15. *Journal of Geophysical Research: Oceans*, 104(C1), 1505-1524.

Vincent, C.E.; Hanes, D.M., and Bowen, A.J., 1991. Acoustic measurements of suspended sand on the shoreface and the control of concentration by bed roughness. *Marine geology*, 96(1), 1-18.

Yang, Z.T.; Liang, B.C.; Lee, D.Y., and Li, H.J., 2015. Experimental Studies on Sandy Beach Profile Evolution in 2D Wave Flume. *Proceedings of the Twenty-fifth International Offshore and Polar Engineering Conference* (Kona, Hawaii, USA). pp. 1286-1290.

Journal of Coastal Research	SI	75	502-506	Coconut Creek, Florida	2016

3D Morphodynamic Modeling of a Sand Recycling System

Yoshiyuki Yasumoto †, Masamitsu Kuroiwa‡*, Yoko Shibutani††, Yuki Osakada‡ , and Yuhei Matsubara‡

†Department of Civil Engieering
Tottori Prefectural Government
Tottori, Japan

‡Department of Civil Engieering
Tottori University
Tottori, Japan

††Office for Gender Equality
Tottori University
Tottori, Japan

www.cerf-jcr.org

www.JCRonline.org

ABSTRACT

Yasumoto, Y.; Kuroiwa, M.; Shibutani, Y.; Osakada, Y., and Matsubara, Y., 2016. 3D morphodynamic model for sand recycling system. *In:* Vila-Concejo, A.; Bruce, E.; Kennedy, D.M., and McCarroll, R.J. (eds.), *Proceedings of the 14th International Coastal Symposium* (Sydney, Australia). *Journal of Coastal Research*, Special Issue, No. 75, pp. 502-506. Coconut Creek (Florida), ISSN 0749-0208.

Sand nourishment such as sand bypassing or sand recycling is an effective measure against beach erosion as an alternative technique. The method for setting the optimum injecting amount, site and running cost has not been developed. A numerical model considering the sand nourishment is needed to evaluate the performance of the sand recycling and bypassing projects. This paper is concerned with the development of 3D beach evolution model for taking account the sand dredging and injection processes. In this paper, a model test for sand recycling in an area with artificial reefs was carried out. The model was applied to a sand recycling project conducted at a field site with five artificial reefs (an erosion area). The applicability against the morphodynamics around the five artificial reefs was investigated. Although the volume of erosion/deposition behind the artificial reefs was overestimated, the developed numerical model qualitatively agreed with the measured bathymetry.

ADDITIONAL INDEX WORDS: *Morphological change, sand nourishment, numerical model.*

INTRODUCTION

The causes of sandy beach erosion include decreases in discharged bed material from rivers and interruption of alongshore sediment transport due to construction of ports, harbors, groins and so on. We have constructed coastal structures such as groins, detached breakwaters, and submerged breakwaters in order to protect coastal areas. However, these structures often produce coastal erosion at nearby beaches. New countermeasures such as sand recycling can be used to deal with such erosion problems.

In Tottori Prefecture, Japan, beach erosion has become severe at many sandy beaches, whereas sedimentation in the mouth of ports and fishing ports had occurred owing to longshore sediment transport. The Tottori Prefectural Government worked out new comprehensive guideline for sediment management in Tottori Prefecture in May 2005. In this guideline, concrete plans were created for comprehensive sediment management of the watersheds of three major rivers in Tottori. Yasumoto *et al*. (2007) showed that the comprehensive guidelines are necessary to effectively and fundamentally solve the erosion problems. They introduced an erosion problem of Tottori sand dune coats, Tottori in Japan and its measures using sand nourishment.

Sand nourishment such as sand recycling or sand bypassing, which does not employ coastal structures, is effective technique for recovering eroded beaches. In the last decade, many projects in the world have been performed (Castelle *et al*. 2009; Grunnet and Ruessink 2005; Ojeda *et al*. 2008; van Duin *et al*. 2004).

Sand recycling projected has been conducted in Yumigahama coast, which is located in the western part of Tottori Prefecture. However, the erosion problem has not been completely solved. The estimation of the suitable nourishing amount and the selection of nourishment area are needed to evaluate future beach evolution and running cost for the projects, therefore, the prediction of the beach evolution after nourishments are required.

Figure 1 shows Yumigama Coast, which is sandy beach with a distance of 16 km, facing the Sea of Japan. Yumigahama Coast was formed with sand sourced from Hino River. The dominant direction of alongshore sediment is from Hino River to Sakai-minato marina (B shown in Figure 1). Retreat of shoreline on the west side of Hino River started around 1960, caused by decreasing of sand supplied from Hino River. In the erosion area, breakwaters and groins were constructed to recover the retreated shoreline. However, the erosion area was more extended at Tomimasu area on the western side of the coastal area. On the other hand, alongshore sediment has been trapped at Sakai-minato Marina at the end of Yumigahama Coast and extreme accretion has been occurred. In order to solve both problems of beach erosion at Tomimasu area and deposition around the marina, a sand recycling project, which transports sand dredged around Sakai-minato Marina into Tominasu area by trucks, has

DOI: 10.2112/SI75-101.1 received 15 October 2015; accepted in revision 15 January 2016.
*Corresponding author: kuroiwa@cv.tottori-u.ac.jp

started since 1992. The sand volume is an average of 30,000 m^3 per year. Despite of such sand nourishment project, the maintenance of shoreline was insufficient. In order to recover the eroded shoreline, five submerged breakwaters, which are called "artificial reefs," were constructed, as shown the left picture in Figure 1. Figures 2 and 3 show aspects of sand dredging area at Sakaminato Marina and erosion area at Tominasu area, respectively.

The purpose of this study is to develop a numerical model that can predict 3D morphodynamics after sand nourishment. In this study, the previous model presented by Kuroiwa *et al.*(2010) was modified so as to be capable to simulate the nourishing process of sand and the 3D morphodynamics after the nourishment. A model test associated with sand recycling system was carried out. Furthermore, the applicability of the presented model to a field site where sand recycling project at Yumigahama Coast in Japan has been implemented was investigated.

METHODS

In this paper, a three-dimensional numerical model that can consider sand recycling or sand bypassing processes was presented. The presented 3D model was based on the hybrid model proposed by Kuroiwa *et al.* (2010). The model consists of three modules, which are computations of (1) wave, (2) nearshore current, (3) sediment transport rate and water depth change, as shown in Figure 4.

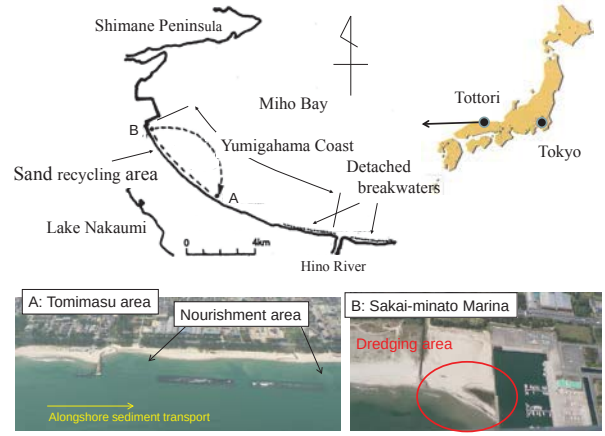

Figure 1. Sand recycling site in Yumigahama Coast, Tottori,Japan.

(a) Sand deposition (b) Sand dredging

Figure 2. Sakai-Minato Marina (Dec,2012).

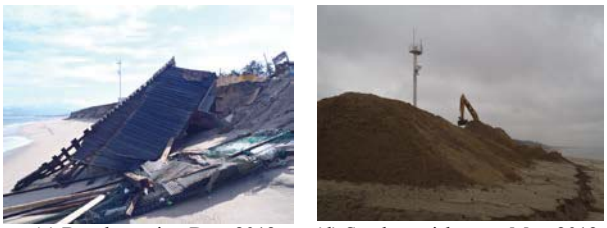

(c) Beach erosion,Dec.,2012 (d) Sand nourishment, Mar.,2013

Figure 3. Sand nourishment area at Tomimasu Area.

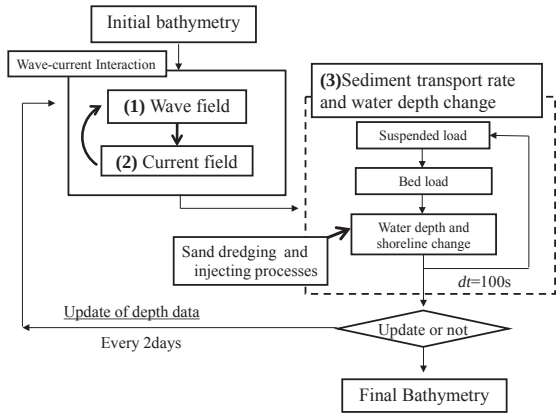

Figure 4. Computational flow chart.

In computation of wave height distribution around coastal structures, the interaction due to coexistence of waves and currents should be considered. Kuroiwa *et al.* (2010) have proposed a 3D morphodynamic model with the interaction of waves and currents, based on the wave action balance equation proposed by Mase *et al.* (2004). Nearshore current field was determined by the Hybrid model proposed by Kuroiwa *et al.* (2006). The total sediment transport considers bed and suspended load. The suspended load is determined by flux model, which is based on the two-dimensional advection diffusion equation, proposed by Sawaragi *et al.* (1984). The bed load is determined by the model based on Kuroiwa *et al.* (2006).

To consider the sand dredging and discharge process associated with sand bypassing or back-passing system, the dredging sediment flux q_d and discharged sediment flux q_i are added to the sand mass conservation equation, as follows:

$$\frac{\partial h}{\partial t} = \frac{Q_s}{1-\lambda} + \frac{1}{1-\lambda}\left\{\frac{\partial}{\partial x}\left(q_{bx} + E_s|q_{bx}|\frac{\partial h}{\partial x}\right) + \frac{\partial}{\partial y}\left(q_{by} + E_s|q_{by}|\frac{\partial h}{\partial y}\right)\right\} + q_d - q_i \quad (1)$$

where, h is the water depth, t is time, q_{bx} and q_{by} are bed load due to steady currents. E_s is the dimensionless coefficient. Qs is the difference between the settling flux and the picking-up flux of bed material.

RESULTS

In this study, a model test associated with sand recycling between two groins with an artificial reef and field verification were conducted.

Model Test

A model test The computational domain was set to an area of 700 m in the cross-shore direction and 2000 m in the longshore direction. Incident significant wave height and period at offshore boundary were set to 1.5 m and 7.0 s, respectively. Wave direction was 20 degrees. Figure 5 shows time history of wave data input at offshore boundary. The bathymetry change without sand dredging and sand nourishment was firstly computed during 120 days. After 120 days, sand dredging and injecting in the computational domain were performed for 40 days. Until obtained the final bathymetry, the bathymetry was updated every two days, namely the computations of wave and nearshore current modules were totally conducted 60 times.

Figures 6 (a), (b) and (c) show computed bathymetry changes after 120, 160 and 180 days, respectively. Accretion in the right hand and erosion in the left side of the arificial reef in Figure 6 (a). Moreover the sand recycling was performed for 40 days under calm wave condition in order to recover the erosion area in the left hand side of arificial reef, as shown in Figure 6 (b), namely the bed material was dredged in the left hand side of the computed area and injected into the erosion area. These computed results show that sand recycling is appropriate measures for beach erosion and deposition problems. It was found that the developed model gives qualitatively available computed results.

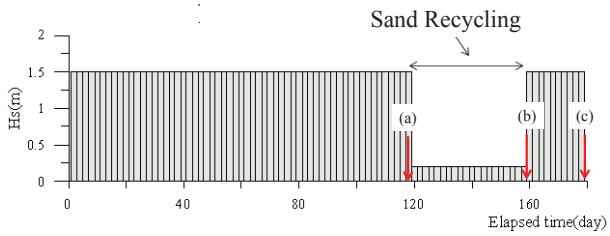

Figure 5. Time history of input significant wave height.

Field Verification

The presented model was applied to a field observation associated with a sand recycling project conducted in Yumigahama Coast, Tottori, Japan. In this study, to apply the model into the whole area of the sand recycling project is difficult because of many run time and computation capacity. Therefore, the model was applied to Tominasu area of sand nourishment with 2.3 km long in the alongshore direction.

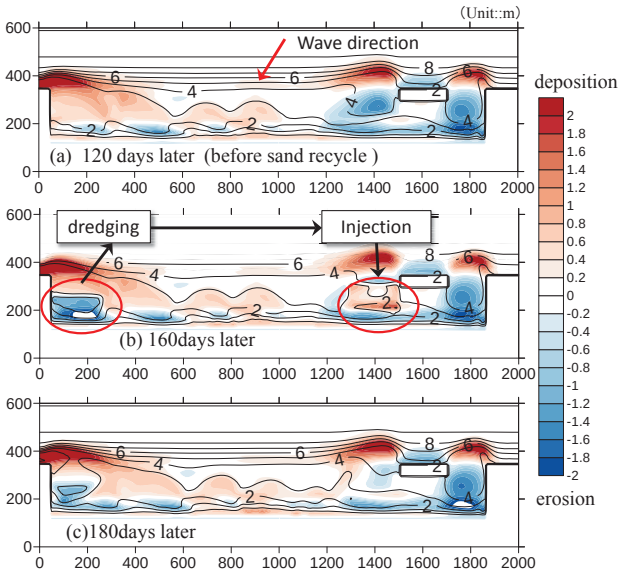

Figure 6. Computed bathtymetry between two groins with an artificial reef.

Figures 7 (a), (b) and (c) shows the measured bathymetries in 2011,2012 and 2013, respectively. In 2012, five artificial reefs were completed to protect Tomimasu area. In Figs. 7(b) and (c), red and blue areas present erosion and deposition areas, respectively. The erosion/deposition plots in Figure (b) were described using the difference of the measured water depth for one year from 2011 to 2012, and those in Figure 7(c) were described using the difference of the measured water depth for one year from 2012 to 2013. Total sand volume nourished from 2011 to 2012 at Tomimasu area was approximately 16,000 m^3. Whereas, in 2013, sand of 16,600 m^3 was injected.

The bathymetry changes from 2011 to 2012, and from 2012 to 2013 was reproduced using the developed model to investigate the model performance. Figure 8 shows time series of significant wave height Hs used in this computation, which was arranged the wave data sets observed Tottori Port observatory station at the water depth of 30 m and Tomimasu offshore observatory station at the water depth of 10 m. The detailed value of the wave height and period are shown in Table 1. The computations of the wave and current modules were roughly 75 times to reach the 150 days. We assumed that the period of 150 days corresponds to one year. Because the significant wave height less than 0.5m does not contribute morphodynamics due to waves. The sand injection was

conducted for 80 days as shown in Figure 8. The wave direction was set to -10 degrees at offshore boundary. The median diameter of sand particle was 0.2mm. Q3D mode was only selected under stormy wave condition (Wave 03 in Table 1).

Figure 9 demonstrates computed bathymetry changes from 2011 to 2012. Comparing the computed bathymetry change at 150 days later with measured bathymetry change in Figure 7(b), it was found that the computed erosion/deposition patterns are fairy similar to measured one, excepting offshore area. Especially, deposition behind the artificial reef of No.5 and erosion at the right hand side of the reef are qualitatively good agreement with measured data. On the other hand, comparing computed bathymetry change from 2012 to 2013 (Figure 10) with Figure 7(c), the deposition pattern behind the artificial reefs of No.2, 3 and 4 slightly agree with observed results. However, the deposition obtained by the model was overestimated.

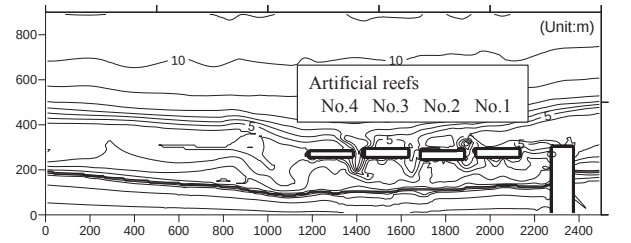

(a) Measured bathymetry in Nov.,2011

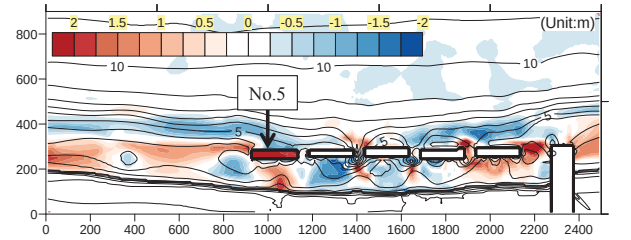

(b) Measured bathymetry in Nov.,2012

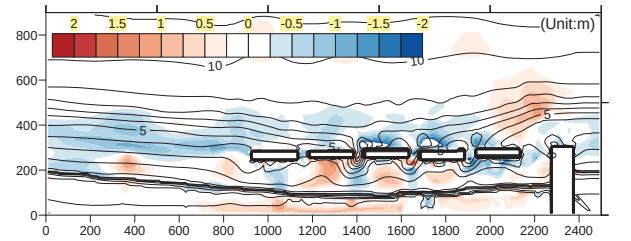

(c) Measured bathymetry in Nov.,2013

Figure 7. Measured bathymetries around artificial reefs at Tomimasu area from 2011 to 2013. Red and blue areas are represented as deposition and erosion, respectively.

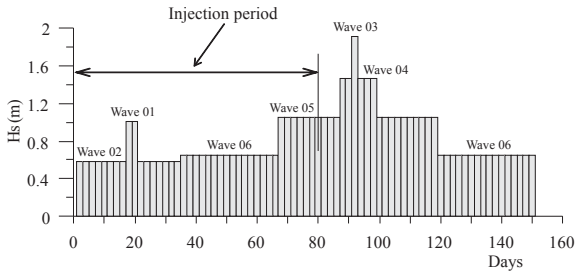

Figure 8. Teporal variation of input significaint wave height.

Table 1. *Wave conditions*

Wave	*Hs* (m)	*Ts* (s)	Wave action(days)
Wave 01	1.01	6.77	4
Wave 02	0.58	5.51	30
Wave 03	1.91	8.19	2
Wave 04	1.46	7.52	10
Wave 05	1.05	6.85	40
Wave 06	0.65	6.04	64

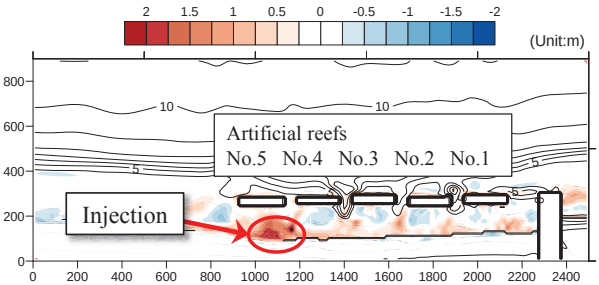

(a)Computed bathymetry at 80days later

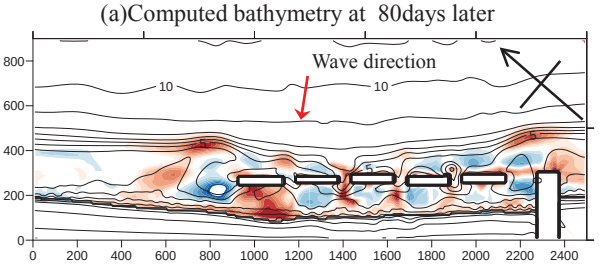

(b) Computed bathymetry at 150days later

Figure 9. Computed bathymetry changes around artificial reefs at Tomimasu area, from 2011 to 2012. The initial bathymetry was used data in 2011. Red and blue areas are represented as deposition and erosion, respectively.

DISCUSSION

It was shown that the presented model can demonstrate the process of sand dredging and injection in sand recycling system, and field verification. From computed result of the model test, it was confirmed that the process of sand recycling could computed technically. From comparisons between the

computed and measured bathymetry changes, it was found that the presented model gave fairly agreement with measured data. However, some modifications as future studies were indicated. Beach nourishment that sand material was placed at the berm area was not performed and shoreline changes were not sufficiently determined. Also, a scour hole in the opening in the two artificial reefs was not reproduced in spite of the computation of strong offshore currents in the opening. The volume of erosion or deposition was overestimated. The grid size was too coarse at DX=DY=10m in order to save run time. In order to get more good accuracy of the prediction after sand nourishment, the model presented in this study should be modify so as to take account sediment transport in the run-up region, and also, the calibration coefficient in the sediment transport formulae and nearshore current model should be reinvestigated.

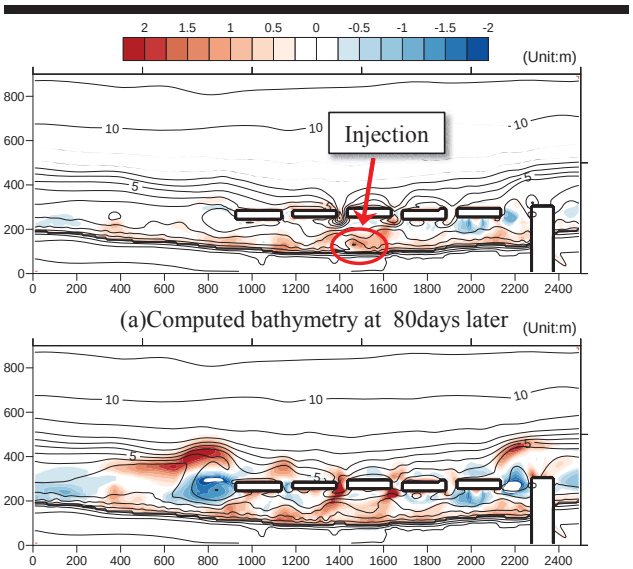

Figure 10. Computed bathymetry changes around artificial reefs at Tomimasu area, from 2012 to 2013. The initial bathymetry was used data in 2012. Red and blue areas are represented as deposition and erosion, respectively.

CONCLUSIONS

In this study, a simple 3D model for predicting the beach evolution after sand nourishment was developed. From the computed results, some conclusions are derived as follows:

A model test associated with sand dredging and discharging, which is a sand recycling test between two groins with an artificial reef was conducted in order to investigate the performance of the developed model. The developed model gives qualitatively available computed results.

The developed model was applied to a sand recycling project conducted by Yumigahama Coast, Tottori, Japan, in order to investigate the applicability of the model. Bathymetry changes around artificial reefs after sand nourishment were computed. Although the volume of erosion/deposition behind the artificial reefs was overestimated, the developed numerical model qualitatively agreed with the measured bathymetry.

ACKNOWLEDGMENTS

A part of this study was supported by the Grand-in-Aid of Japan Society for the Promotion of Science of Ministry of Education, Culture, Sports, Science and Technology, Japan.

LITERATURE CITED

Castelle, B.; Turner I.L.; Bertin, X., and Tomlinson, R., 2009. Beach nourishments at Coolangatta Bay over the period 1987-2005: Impacts and lessons. *Coastal Engineering*, 56, 940-950.

Grunnet, N.M. and Ruessink B. G., 2005. Morphodynamic response of nearshore bars to a shoreface nourishment. *Coastal Engineering*, 52, 119-137.

Kuroiwa, M.; Kuchiishi, T., and Matsubara, Y., 2006. Prediction System of 3D Beach Evolution with 2DH and Q3D Hydrodynamic Modes. *Proceedings of 16th International Offshore and Polar Engineering Conference*, pp.751-757.

Kuroiwa, M.; Shibutani, Y.; Matsubara, Y.; Kuchiishi, T., and Abualtyef, M., 2010. Numerical model of 3D morphodynamic after offshore nourishment. *Proceedings of The International Conference On Coastal Engineering*, 32, 55.

Ojeda, E.; Ruessink, B.G., and Guillen, J., 2008. Morphodynamic response of a two-barred beach to a shoreface nourishment. *Coastal Engineering*, 55: 1185-1196.

Mase, H.; Yuhi, M.; Amamori, H., and Takayama, T., 2004, Phase Averaging wave prediction model with breaking and diffraction effects in wave-current coexisting field. *Annual Journal of Coastal Engineering*, JSCE., 51(1), 6-10. (In Japanese).

Sawaragi, T.; Lee, J. S., and Deguchi, I., 1986. A new model for prediction of beach deformation around river mouth. *Proceedings of International Symposium on Ocean Space Utilization* '85, pp.229-236.

van Duin, M.J.P.; Wiersma, N.R.; Walstra, D. J. R.; van Rijn, L.C., and Stive, M.J.F., 2004. Nourishing the shoreface: observation and hind-casting of the Egmond case, The Netherlands. *Coastal Engineering*, Vol. 51, 813-837.

Yasumoto, Y.; Uda,T.; Matsubara, Y., and Hirano, G., 2007, Beach erosion along Tottori coast and comprehensive sediment manegement. *J. Coast. Res.*, SI 50, 82-87.

Journal of Coastal Research	SI	75	507-511	Coconut Creek, Florida	2016

Hydraulic and Sediment Dynamics at times of Very Shallow Water on Intertidal Mudflats: The Contribution of Waves

Qian Zhang †, Zheng Gong†*, Changkuan Zhang†, Zeng Zhou†, Ian Townend‡

†State Key Laboratory of Hydrology-Water Resources and Hydraulic Engineering
Hohai University
Nanjing, China

‡ Ocean and Earth Sciences
University of Southampton
Southampton, U.K.

www.cerf-jcr.org

www.JCRonline.org

ABSTRACT

Zhang Q.; Gong Z.; Zhang C.K.; Zhou Z., and Townend I., 2016. Hydraulic and sediment dynamics at times of very shallow water on intertidal mudflats: the contribution of waves. *In:* Vila-Concejo, A.; Bruce, E.; Kennedy, D.M., and McCarroll, R.J. (eds.), *Proceedings of the 14th International Coastal Symposium* (Sydney, Australia). *Journal of Coastal Research*, Special Issue, No. 75, pp. 507-511. Coconut Creek (Florida), ISSN 0749-0208.

Intertidal mudflats are often characterized by a special "very shallow water" environment, with a water depth in the order of 10 cm. High-resolution data including water depth, wave parameters, velocity profiles (within 3-6 cm above the mudflat surface with a vertical resolution as fine as 1 mm), stratified suspended sediment concentration (SSC) and bed deformation over the intertidal mudflat during August 8-10, 2013 were measured using a self-designed measuring system. High-resolution stratified velocities near the bottom under different tide and wave conditions were compared to the Karman-Prandtl model. Results suggest that the vertical structure of velocity profiles within 55 cm above the bed maintain a logarithmic distribution even when waves were relatively large. In addition, bed shear stresses under current and wave alone and combined current-wave conditions were calculated to evaluate the contribution of waves. This suggests that waves do not induce a significant rise in the bed shear stress, but have a pronounced impact on the sediment suspension. This is particularly the case for very shallow flows during both the early-flood period and the late-ebb period. These periods were characterized by "surges" in velocity and SSC, which are enhanced when waves become larger. Even small waves cannot be overlooked for their contribution to sediment re-suspension and vertical mixing. We conclude that waves strengthen the response of micro-topography deformation due to flow conditions. They enhance the forcing during the "surges" at times of very shallow water, to sculpt the micro-topography of the bed.

ADDITIONAL INDEX WORDS: *wave effect, velocity profile, bed shear stress, very shallow water, SSC surge.*

INTRODUCTION

Waves and tidal currents are important hydrodynamic forces that influence the turbulent mixing of the water column, sediment suspension and transport, bed form evolution, as well as various biochemical processes (Grant and Madsen, 1986). To explore the bottom boundary layer (BBL) characteristics under combined current-wave action, previous research has examined the thickness of the BBL, apparent roughness length, friction velocity or bed shear stress, eddy viscosity, vertical velocity distribution, sediment transport, *etc.* (*e.g.,* Mathisen and Madsen, 1996; Nielsen, 1992; Wang *et al.*, 2006).

Previous work indicates that the interaction between current and waves is non-linear. Grant and Madsen (1979) suggested that in the BBL, with combined wave and tidal current influence, the vertical velocity structure maintains a logarithmic distribution. However, Nielsen (1992) pointed out that a linear distribution can better describe the velocity profiles, while Li (2003) suggests that the influence of waves can result in a structure that no longer has a logarithmic profile.

As waves approach shallower water, the interaction between waves and currents becomes more intense (Rosales *et al.*, 2008). The bed shear stress (BSS) associated with the wave motion may be an order of magnitude larger than that induced by tidal currents of comparable magnitude (Grant and Madsen, 1979). Waves directly contribute to the bottom sediment suspension, inducing sediment transport even when the tidal currents are weak.

Previous research has also considered the current-induced sediment transport and erosion process on mudflats or saltmarshes (Leonard *et al.*, 2002; Yang *et al.*, 2007). However, related studies under combined current-wave action are limited, primarily because it is difficult to arrange joint observation of current and waves on tidal flats (Callaghan *et al.*, 2010; Shi *et al.*, 2012). In addition, it is a challenge to obtain effective wave data during the very shallow water period, when waves easily break and the development of wave height is limited by water depth.

In this study, a field investigation was carried out on the intertidal mudflats. High-resolution data including water depth, wave parameters, velocity profiles, stratified suspended sediment concentration (SSC) and bed deformation were obtained. The overall goal was to explore the wave contribution to the BBL parameter and to the very shallow water environment. In detail, our objectives include: (1) to explore the influence of waves on the near-bed velocity structure; (2) to discuss the wave contribution to the bed shear stress; (3) to

DOI: 10.2112/SI75-102.1 received 15 October 2015; accepted in revision 15 January 2016.
*Corresponding author: gongzheng@hhu.edu.cn

examine the significance of wave action on the sediment motion during the very shallow water period.

Background

Jiangsu coast is situated between the north bank of the Yangtze estuary and Shandong Peninsula. Along this 954 km-long coastline, muddy tidal flats occupy more than 90% of the coast. The width of the intertidal mudflats is 2-6 km and the average slope is as gentle as 0.01 % - 0.03 % (Zhang, 1992).

Our study area was the muddy tidal flats located in the south of the Chuandong River, Yancheng City (Figure 1). The landscape here shows clear zonation (Zhu *et al.*, 1986), and the grain size of the bottom sediment tends to be coarser towards the sea. Accordingly, the tidal flats can be divided into zones across the shoreface comprising salt marshes (*Spartina angelica* and *Spartina alterniflora* marshes), mudflats, mixed sand–mud flats and sand flats seaward (Gao, 2009). The tide in this area is irregular semi-diurnal with an average tidal range of 3.7 m (Gong *et al.*, 2013). The flood tidal wave propagates from northwest to southeast along the West Xiyang Trough and hence the tidal current on the tidal flats is rectilinear nearly parallel to the shoreline (Ren *et al.*, 1984). The flow velocity during the flood is generally larger than that during the ebb, while the duration of the flood is usually less than that of the ebb, indicating a flood dominant asymmetric tide locally. Sheltered by the offshore radial sand ridges, wave action in the study area is relatively weak (Wang *et al.*, 2012), with the significant wave height commonly less than 1 m in the winter and 0.5 m in other seasons.

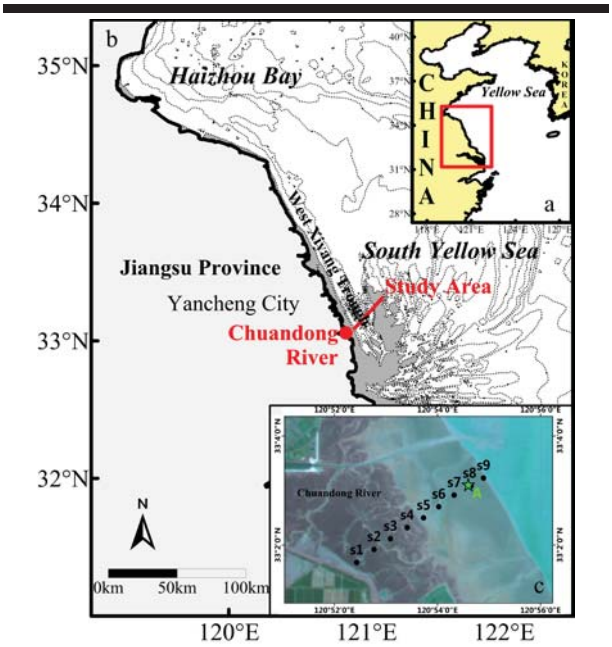

Figure 1. Location of the study area. The inset (a) shows Jiangsu coast area in the middle part of the Chinese east coastline. Our study area is indicated by the red point in panel (b), and the observation site is indicated by star and denoted A in panel (c).

In this area, ten benchmarks have been established to observe the surface elevation variation of the mudflats since September 2012: S1 to S9 in Figure 1c (Gong *et al.*, 2014). The field investigation was carried out from August 8th to 10th during the spring tidal period and lasted for three tidal cycles. Site A, where we arranged the measurement, is located between point S7 and S8. The surrounding tidal flats have no vegetation, and there were no distinct tidal creeks in the vicinity at the time of the measurements. The bottom sediment mainly consists of silt clay and silt, with the median grain size of approximately 79μm. The weather was fine during the three tidal cycles, and the significant wave height was less than 0.25 m.

METHODS

Simultaneous water depth, high-resolution velocity and stratified SSC process were obtained by a self-designed "Bottom Boundary Layer Hydrodynamic and Suspend Sediment Concentration Measuring System" (Figure 2).

A Nortek Vectrino Profiler, with the transducer set 10 cm above the flat surface, was used to capture the velocity profiles 4-7 cm in front of the probe. The sampling frequency was 25 Hz and the vertical resolution of the measured velocity can be as fine as 1 mm. Velocities of the upper water column were obtained using a 600 kHz RiverRay ADCP (RD INSTRUMENTS) buried upwards in the flat with the transducer surface 10 cm higher than the flat surface. Because of the blind area, the velocities could be recorded only when the water depth was larger than 35 cm. The minimum resolution was 10 cm and the sampling frequency was 1-2 Hz, which were both set automatically by the instrument.

Meanwhile, stratified suspended sediment concentration was measured using five OBS at heights of 10 cm, 30 cm, 60 cm, 100 cm and 200 cm. Water depth and wave parameters including wave height and wave period were recorded by a RBR Company Tide Wave Recorder-2050.

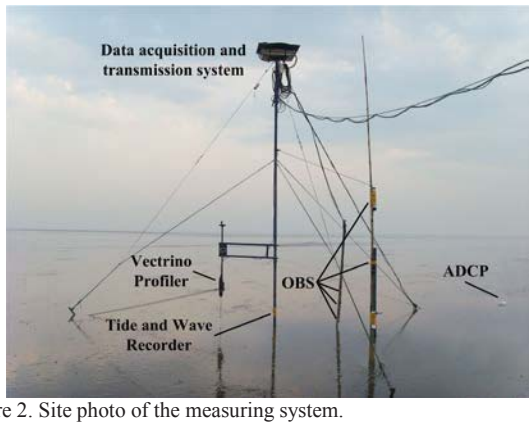

Figure 2. Site photo of the measuring system.

The OBSs were calibrated using water samples from the field. Results show a satisfactory linear relationship between the measured voltage or electric current data and the suspended sediment concentration, with correlation coefficients over 0.9.

Further details of the measuring system and SSC calibration are given in Zhang *et al* (2016).

In the lower part of the bottom boundary layer, the Karman-Prandtl equation is often used to describe the vertical structure of the velocity profiles (Soulsby, 1995).

$$u = \frac{u_*}{\kappa} \ln \frac{z}{z_0} \quad (1)$$

Where u is the measured velocity at height z above the flat surface, z_0 is the roughness length, κ is van Karman's constant usually taken as 0.4, and u_* is the friction velocity.

The friction velocity u_* and roughness length z_0 can be estimated by fitting the measured velocity u and the corresponding height z to equation (1). Accordingly, the bed shear stress τ_c is easily calculated:

$$\tau_c = \rho u_*^2 \quad (2)$$

Since the measured velocity used in equation (1) is the minute-average velocity, the bed shear stresses obtained by equation (2) are considered to be the current-induced ones, without taking wave effect into account.

To compare the wave effect with tidal current, the wave-induced bed shear stress τ_w is calculated using (Fagherazzi and Mariotti, 2012; Shi *et al.*, 2015):

$$\tau_w = 1/2\ \rho f_w U_w^2 \quad (3)$$

Where f_w is the wave friction factor, $f_w = 1.39(A/z_0)^{-0.52}$, A is the orbital amplitude of wave motion at the bed, $A = U_w T/2\pi$, U_w is the bottom wave orbital velocity and T is the period of waves.

The bed shear stress under combined wave and current conditions cannot be calculated by simply adding the shear stress for wave-alone and current-alone, since the interaction between waves and currents is non-linear.

For simplicity of calculation, a formula proposed by Soulsby (1995) is adopted here:

$$\tau = \tau_c \left[1 + 1.2 \left(\frac{\tau_w}{\tau_c + \tau_w} \right)^{3.2} \right] \quad (4)$$

in which τ_c and τ_w are the bed-shear stresses induced by the current alone and by the wave alone, respectively.

RESULTS

Water depth and significant wave height during the observation period are shown in Figure 3. Wave heights were the smallest and nearly negligible during the second tidal cycle with the maximum less than 0.05 m, while in the other two tidal cycles, waves were more significant with peaks approaching 0.25 m. Since the velocity data collected during the first tidal cycle were not continuous, data from the third tidal cycle was used to study the wave effect compared with that of the second tidal cycle (as an approximate surrogate for the no-wave case).

The water depth during the third tidal cycle is shown in Figure 4a. The stratified flow speeds measured below 55 cm (Figure 4b) above the bed were fitted to equation (1). The data from the ADCP was not continuous because of some operational issues. A criterion of 95% correlation coefficient was adopted, and profiles with $r > 95\%$ were considered to be logarithmically

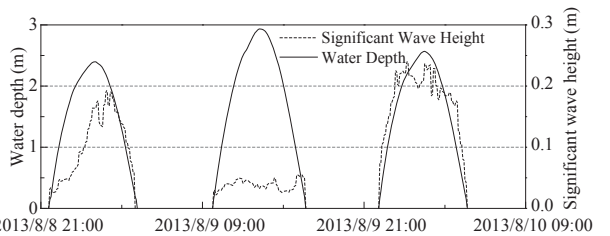

Figure 3. Water depth and significant wave height during the observation period.

distributed. The correlation coefficients are illustrated in Figure 4a and velocity profiles of five characteristic moments during the third tide are shown in Figure 4c. Results indicate that nearly all the velocity profiles near the bed were logarithmically distributed (386 out of 387 profiles). In the second tide, with negligible wave impact, velocity profiles can be described logarithmically throughout the tidal cycle, except during the flood slack period (Zhang *et al.*, 2016). The wave action may influence the flow speed and direction, and so contribute to the vertical distribution of the velocity.

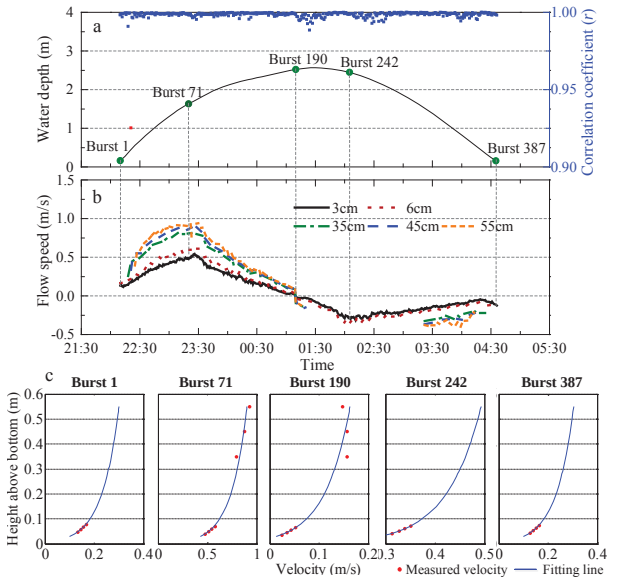

Figure 4. (a) Water depth of the third tidal cycle and the correlation coefficients (r) of the logarithmic fitting. The blue dots correspond to $r \geq 0.95$ and the red ones $r < 0.95$; (b) Stratified flow speed used for fitting. The velocity during the flood is positive while that during the ebb is negative. Speed data at 35 cm, 45 cm and 55 cm above the bed was not continuous because of some operational issue; (c) Measured velocity profiles and fitting lines at five typical moments represented by the green dots in panel (a).

In order to study the wave contribution, the hydrodynamic, suspended sediment, bed deformation and bed shear stress processes of the second and third tidal cycles are compared.

During the second tidal cycle, the biggest water depth in our study area was 2.93 m, and the maximum flow speeds at 3 cm above the bed of the flood and the ebb were 0.74 and 0.26 m/s, respectively (Figure 5a). Comparatively, the tidal current was weaker during the third tide, with the largest water depth only reaching 2.57 m, with maximum flow speeds on the flood and ebb of 0.54 and 0.3 m/s respectively (Figure 5b).

However, the measured suspended sediment concentrations show the opposite tendency (Figure 5c and 5d). The SSC surged to 9.31 kg/m^3 at the beginning of the flood during the third tide, while in the second tide, the SSC only peaked to 6.15 kg/m^3. In addition, during the slack period when the current speed was around zero, the SSC measured at 10 cm level above the bed increased and reached 3.5 kg/m^3 due to the prevailing influence of waves.

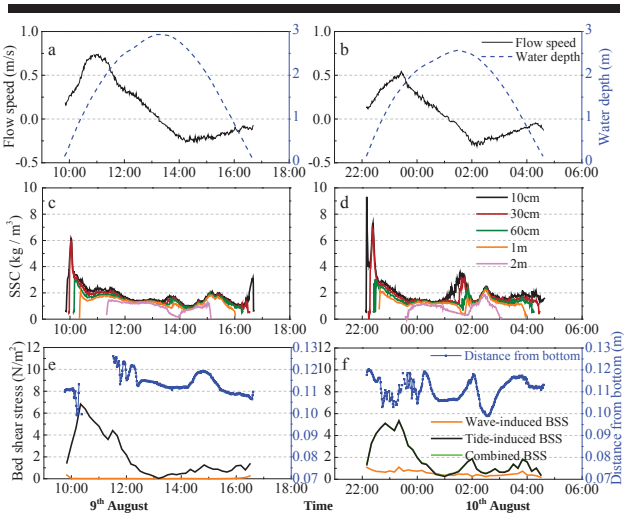

Figure 5. (a) Water depth and flow speed at 3 cm above the bed during the second tide and (b) the third tide; (c) Stratified SSC during the second tide and (d) the third tide; (e) Calculated bed shear stress and the bed deformation during the second tide and (f) the third tide.

Table 1. *Bed shear stress during the 2nd and the 3rd tide*

Bed shear stress (N/m^2)		The 2nd tide		The 3rd tide	
		Flood	Ebb	Flood	Ebb
Tide-induced	τ_{Max}	6.82	1.25	5.33	1.93
	τ_{Ave}	2.53	0.52	2.3	0.82
Wave-induced	τ_{Max}	0.34		1.1	
	τ_{Ave}	0.03		0.54	

τ_{Max} indicates the maximum bed shear stress whiletτ_{Ave} indicates the average bed shear stress.

Bed shear stress (BSS) provides a useful means of evaluating sediment suspension and deposition. The BSS for current and wave alone were calculated using equations (2) and (3). The results shown in Figure 5e, 5f and Table 1 indicate that the current-induced BSS correlates well with the flow speed, and is significantly asymmetric during the flood and the ebb. In the second tide, the BSS were 6.82 and 2.53 N/m^2 for the max and average value respectively during the flood, which were much larger than that during the ebb with the corresponding value of 1.25 and 0.52 N/m^2. Notably, the wave-induced BSS was only 0.03 N/m^2 on average during the second tidal cycle. Comparatively, the tide-induced BSS during the flood phase of the third tide was smaller than that during the second tide, and the maximum only reached 5.33 N/m^2. However, the wave-induced BSS was 0.54 N/m^2 on average; one order of magnitude larger than that during the second tide.

DISCUSSION

Based on the results shown above, the influence of waves on SSC processes was remarkable. During the slack period when the flow direction was changing, sediment tended to drop back to the bed. As a result, the suspended sediment concentration in the upper water column decreased rapidly, while that in the lower layers slightly increased during the second tidal cycle (Figure 5c). During the third tidal cycle, the increase of the SSC in the lower layer was much larger (Figure 5d) and is more evident near the bed, where the SSC at 10 cm and 30 cm above the bed both exceeded 3 kg/m^3 during that period. This reflects the influence of the waves. During the slack tide period the currents are weak and sediment carrying capacity over the water column as a whole declines. However, the stirring effect of the waves keeps the sediment in suspension.

Additionally, the bed was more sensitive to the hydrodynamics with waves present, especially during the ebb phase. At around 2:00 on 10th August, the current-induced bed shear stress increased, the sediments were re-suspended and the bed elevation decreased immediately. The SSC increased later due to the phase lag (Postma, 1961). Later on, the SSC reduced and siltation occurred as the BSS decreased. In contrast, during the second tide, the SSC, as well as the distance from the probe to the flat surface appears to be only weakly responsive to the bed shear stress. Besides, during the flood phase (from about 10:20 to 12:20 in 9th August and 22:30 to 00:20 in 10th August), the measured SSC and the bed deformation tendency does not correspond well with the high bed shear stress. In the second tide, the bed deformation data (the blue dot-line in Figure 5e) from 10:22 to 11:35 was abnormally small, hence was not included. Data during the same period in the third tide was also relatively disordered. High concentration of suspended sediment close to the bed disturbed the boundary discrimination of the instrument, but was not detected by the OBS fixed on about 10 cm above the bed. It could be that the high SSC during this period is the result of high bed shear stress causing an overall movement of the sand ripples, so that a large amount of coarser sediment was re-suspended into the lower water column.

Particularly, waves also contribute much to the very shallow water period. During the early-flood period and the late-ebb period, when the water depth was less than the order of 10 cm (usually called the very shallow water period), there exit a "surge" feature. This is a short-lived occurrence of elevated velocity or SSC (Zhang *et al.*, 2016) and this was strengthened by wave actions. The increase of the measured velocities was more obvious at the very shallow water stages. Sediments were suspended during the passage of the tidal front during the third tide far more than during the second tide, despite the fact that tidal current was weaker during the third tide. Notably, the

distance from the bottom was obviously increased at the initial stage of the flood (around 22:00 in Figure 5f), indicating an effective erosion caused by the tidal front under the wave action.

CONCLUSIONS

Based on the hydrodynamic and sediment process measurements during different tidal cycles, the wave effects on the near-bed flow structure and the sediment responds were explored. And the conclusions drawn are as follows:

(1) The vertical velocity structure within 55 cm above the flat surface obeys the logarithmic law through the whole tidal cycle under the influence of waves.

(2) During the slack period, wave motion prevents the sediment depositing back to the bed and hence leads to an increase in the suspended sediment concentration.

(3) Evident "surge" features of the velocity and SSC during the early-flood and late-ebb periods were strengthened by waves.

(4) The contribution of the waves to the combined bed shear stresses is limited. However, the stirring effect of waves enhances the sensitivity of the bed evolution to the hydrodynamic forcing.

ACKNOWLEDGMENTS

We would like to thank Cai Hui, Zhu Shanpeng, Jin Chuang and Li Huan for their concerted efforts in the field investigation. This work was supported by the National Natural Science Foundation of China (51379003, 51179067), the Fundamental Research Funds for the Central Universities (2015B15814, 2015B25614, 2015B24814), and also supported by Program for New Century Excellent Talents in University (NCET-12-0841).

LITERATURE CITED

Callaghan, D.P.; Bouma, T.J.; Klaassen, P.; van der Wal, D.; Stive, M.J.F., and Herman, P.M.J., 2010. Hydrodynamic forcing on salt-marsh development: Distinguishing the relative importance of waves and tidal flows. *Estuarine, Coastal and Shelf Science*, 89(1), 73-88.

Fagherazzi, S. and Mariotti, G., 2012. Mudflat runnels: Evidence and importance of very shallow flows in intertidal morphodynamics. *Geophysical Research Letters*, 39(14), L4401-L4402.

Gao, S., 2009. Modeling the preservation potential of tidal flat sedimentary records, Jiangsu coast, eastern China. *Continental Shelf Research*, 29(16), 1927-1936.

Gong, Z.; Jin, C.; Zhang, C.K.; Li, H., and Xin, P., 2014. Surface elevation variation of the Jiangsu mudflats: field observation. *Advances in Water Science*, 25(6), 880-887.

Gong, Z.; Zhang, C.K.; Tao, J.F., and Cai, H., 2013. Mechanisms for the evolution of double-convex cross-shore profile over accretional mudflats. *Advances in Water Science*, 24(2), 212-219.

Grant, W.D. and Madsen, O.S., 1979. Combined wave and current interaction with a rough bottom. *Journal of Geophysical Research: Oceans*, 84(C4), 1797-1808.

Grant, W.D. and Madsen, O.S., 1986, The Continental-Shelf Bottom Boundary Layer, *Annual Reviews of Fluid Mechanics*, pp. 265-305.

Leonard, L.A.; Wren, P.A., and Beavers, R.L., 2002. Flow dynamics and sedimentation in *Spartina alterniflora* and *Phragmites australis* marshes of the Chesapeake Bay. *Wetlands*, 22(2), 415-424.

Li, Z.H.; Gao, S.; Ke, X.K., and Wang, Y.P., 2003. Tidally-induced Boundary Layer Properties of the Silt Flat at Dafeng, Jiangsu Province, Eastern China. *Marine Science Bulletin*, 22(2), 1-8.

Mathisen, P.P. and Madsen, O.S., 1996. Waves and currents over a fixed rippled bed .2. Bottom and apparent roughness experienced by currents in the presence of waves. *Journal of Geophysical Research-Oceans*, 101(C7), 16543-16550.

Nielsen, P., 1992, *Coastal bottom boundary layers and sediment transport*, 324p.

Postma, H., 1961. Transport and accumulation of suspended matter in the Dutch Wadden Sea. *Netherlands Journal of Sea Research*, 1(1-2), 148-190.

Ren, M.E.; Zhang, R.S., and Yang, J.H., 1984. Sendimentation on tidal mud flat in Wanggang area, Jiangsu Province, China (in Chinese). *Marine Science Bulletin*, 3(1), 40-54.

Rosales, P.; Ocampo-Torres, F.J.; Osuna, P.; Monbaliu, J., and Padilla-Hernández, R., 2008. Wave-current interaction in coastal waters: Effects on the bottom-shear stress. *Journal of Marine Systems*, 71(1-2), 131-148.

Shi, B.; Wang, Y.; Yang, Y.; Ni, W.; Li, P., and Gao, J., 2015. Determination of Critical Shear Stresses for Erosion and Deposition Based on In Situ Measurements of Currents and Waves over an Intertidal Mudflat. *Journal of Coastal Research*.

Shi, B.W.; Yang, S.L.; Wang, Y.P.; Bouma, T.J., and Zhu, Q., 2012. Relating accretion and erosion at an exposed tidal wetland to the bottom shear stress of combined current–wave action. *Geomorphology*, 138(1), 380-389.

Soulsby, R.L., 1995, Bed shear-stresses due to combined waves and currents. In: Stive, M., De Vriend, H., Fredsoe, J., Hamm, L., Soulsby, R., Teisson, C., Winterwerp, J. (eds.), *Advances in Coastal Morphodynamics*. Delft Hydraulics, Delft, NL, pp. 4-20.

Wang, Y.P.; Gao, S., and Jia, J.J., 2006. High-resolution data collection for analysis of sediment dynamic processes associated with combined current-wave action over intertidal flats. *Chinese Science Bulletin*, 51(7), 866-877.

Wang, Y.P.; Gao, S.; Jia, J.J.; Thompson, C.; Gao, J.H., and Yang, Y., 2012. Sediment transport over an accretional intertidal flat with influences of reclamation, Jiangsu coast, China. *Marine Geology*, 291-294147-161.

Yang, S.L.; Li, P.; Gao, A.; Zhang, J.; Zhang, W.X., and Li, M., 2007. Cyclical variability of suspended sediment concentration over a low-energy tidal flat in Jiaozhou Bay, China: effect of shoaling on wave impact. *Geo-Marine Letters*, 27(5), 345-353.

Zhang, Q.; Gong, Z.; Zhang, C.K.; Townend, I.; Jin, C., and Li, H., 2016. Velocity and sediment surge: What do we see at times of very shallow water on intertidal mudflats? *Continental Shelf Research,* 113, 10-20.

Zhang, R.S., 1992. Suspended sediment transport processes on tidal mud flat in Jiangsu Province, China. Estuarine, *Coastal and Shelf Science*, 35(3), 225-233.

Zhu, D.K.; Ke, X.K., and Gao, S., 1986. Tidal flat sedimentation of Jiangsu coast (in Chinese). *Journal of Oceanography of Huanghai & Bohai Seas*, 4(3), 19-27.

Journal of Coastal Research	SI	75	512-516	Coconut Creek, Florida	2016

Spatial-Temporal Variability of the Thermohaline Properties in the Coastal Region of Fernando de Noronha Archipelago, Brazil

RamillaV. Assunção[†*], Alex C. Silva[†], José Martins[‡], and Manuel Flores Montes[††]

[†] Laboratório de Oceanografia Física Estuarina e Costeira - Departamento de Oceanografia
Universidade Federal de Pernambuco
Recife, Brazil

[‡]Spinner Dolphin
Fernando de Noronha Island, Brazil

[††]Laboratório de Oceanografia Química
Departamento de Oceanografia
Universidade Federal de Pernambuco
Recife, Brazil

www.cerf-jcr.org

www.JCRonline.org

ABSTRACT

Assunção, R.V.; Silva, A.C.; Martins, J., and Flores Montes, M., 2016. Spatial-Temporal variability of the thermohaline properties in the coastal region of Fernando de Noronha Archipelago, Brazil. *In:* Vila-Concejo, A.; Bruce, E.; Kennedy, D.M., and Mc Carroll, R.J. (eds.), *Proceedings of the 14th International Coastal Symposium* (Sydney, Australia). *Journal of Coastal Research*, Special Issue, No. 75, pp. 512-516. Coconut Creek (Florida), ISSN 0749-0208.

Brazilian oceanic islands are areas of great environmental, scientific, economic and strategic interest for the country. A better understanding of the thermohaline and hydrodynamic properties is fundamental to complement studies of chemical and biological processes active on the Fernando de Noronha archipelago, located between 03° 52'S and 32° 25'W. The aim of this work was to verify the coastal thermohaline behavior of the most inhabited part of the island, on a seasonal and spatial scale and how it is associated with the nutrient distribution data. Four campaigns were conducted in 2013 and 2014, two during the wet season and two during the dry season. For each period, data were collect at five stations. The results show that during the rainy season temperature increases and salinity decreases in the surface layer. Spatially no large differences are observed. Regarding to nutrient concentration, seasonal concentrations are quite homogeneous in the waters of the archipelago region. The coastal region was characterized by tropical mass water.

ADDITIONAL INDEX WORDS: *Island, nutrient, thermohaline properties.*

INTRODUCTION

Time series oceanographic observations are important not only for identifying processes in ecosystems, but also the effect of climate variability, water circulation, anthropogenic perturbations and the prognostic models used in future climate projections. Some climate change impacts, such as increases in precipitation, frequency and intensity of storms, and warmer ocean temperature, will occur quickly in response to increasing global temperatures (IPCC, 2013).

Over the long term, increases in sea surface temperature (SST) could also reduce circulation patterns that bring nutrients from the deep sea to surface waters. Increases in SST due to global warming are projected to intensify the stratification of the water column and strengthen the barrier to the transfer of nutrients created by thermocline (Gierach, 2013). In the warm pool, projected increases in rainfall will reduce salinity and increase stratification further (Ganachaud *et al*., 2011).

The coastal and insular area around Fernando de Noronha Archipelago is a strategic area for monitoring climate change effects in Northeast Brazil. It also plays a key role in the process of reproduction, dispersal and colonization of marine organisms in the entire Tropical South Atlantic (REVIZEE, 2006).

Considering the importance of understanding the dynamic around the archipelago, this study aims to investigate for the first time changes in the spatiotemporal thermohaline pattern and the nutrient distributions in the coastal area of the Fernando de Noronha Archipelago.

Study Area

The Fernando de Noronha archipelago is formed by 21 islands and islets, located in the South Equatorial Atlantic Ocean, between 03°52'S and 32°25'W. Its main island, which has the same name of the archipelago, comprises 91% of the total area of the archipelago (Figure 1).

Due to the morphological layout of the island, that is composed by two sides which are more or less exposed to the action of winds and ocean currents, two types of sea can be highlighted around the island, the inside sea, which is more protected and the outside sea, more exposed.

The climate of the archipelago is tropical (Awi of Koppen classification system) and influenced by the Atlantic Ocean. There are two well-marked seasons, the rainy from March to

DOI: 10.2112/SI75-103.1 received 15 October 2015; accepted in revision 15 January 2015
*Corresponding author: ramillassuncao@hotmail.com

July and the dry from August to January (Almeida, 2006; Mohr *et al*., 2009).

The archipelago is washed by the waters brought by the central branch of the South Equatorial Current (cSEC), flowing from east to west, which extends from the surface up to a nominal depth of 100 m, and by the South Equatorial UnderCurrent (SEUC), which moves in direction from west to east. The cSEC is located between the SEUC (3°S-5°S), and the South Equatorial Counter Current (6°S-9°S) (Peterson and Stramma, 1991).

The structure of the water column that surrounds Noronha usually presents a characteristic profile of the South Atlantic waters, with the presence of the following water masses: Tropical Surface Water (TSW), South Atlantic Central Water (SACW), Antarctic Intermediate Water (AAIW) and the North Atlantic Deep Water (NADW) (Stramma and England, 1999; Silva *et al*., 2005).

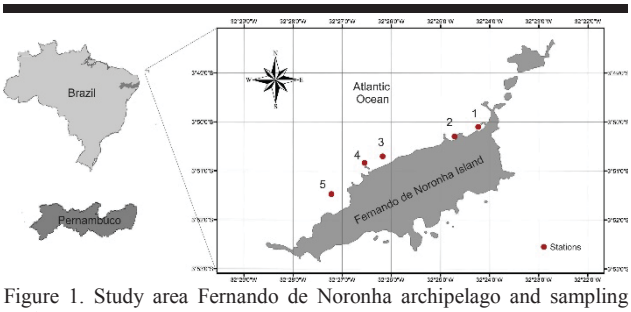

Figure 1. Study area Fernando de Noronha archipelago and sampling stations.

Fernando de Noronha is a marine national park protected legally by the Institute of Environmental Preservation of the Brazilian government - Chico Mendes Institute for the Conservation of the Biodiversity - ICMBio. The island is considered of utmost importance not just for maintenance of local biodiversity, but also as a feeding and rest area for large pelagic fishes that perform transoceanic migrations, such as tuna and billfish.

METHODS

The data were collected during four oceanographic campaigns in the portion of the inside sea in Fernando de Noronha Island. Two campaigns were in 2013 (July and December) and two in 2014 (June and November). For each year samples were collected during both rainy and dry seasons.

The physical parameters (temperature, salinity and density) along the water column were obtained from CTD equipment - Sea Bird Electronics (SBE) 911plus. The CTD is equipped with a centrifugal pump and high resolution sensors for conductivity measurements (resolution = $0.00004 sm^{-1}$), temperature (resolution = 0.0003°C) and pressure (resolution = 0,068db). Moreover, the raw data were processed, added to a database and then discussed.

In addition, water samples were collected to analyze the vertical distribution profiles and concentration of chemical parameters. Ninskin bottles were used to collect samples in the depths of the mixed layer. The samples were then stored in plastic bottles (previously decontaminated) kept frozen until the analysis.The dissolved inorganic nutrients (ammonia - NH_3, nitrite -NO_2 and nitrate -NO_3), the phosphorous - PO_4 and silicate - SiO_2 were analyzed through the method described by Grashoff *et al.* (1983) and Strickland and Parsons (1972).

RESULTS

Based on *in situ* observations obtained during four campaigns realized in July and December 2013 and in June and November 2014, temperature and salinity profiles were represented for the five stations distributed in the coastal region of the island (Figure 2A).

Temperature values obtained with CTD for the five stations distributed on the coast of Fernando de Noronha show that, in general, there were no large spatial variations of the vertical profiles within the same period. The minimum and maximum values during the rainy season of the year 2013 were respectively 27.42°C (Sta.2) and 27.70°C (Sta.3). For the same period of the year 2014 (June 2014), the minimum and maximum values obtained were 27.81°C (Sta.5) and 29.23°C (Sta.1), respectively.

The analysis of the profiles shows that, during the rainy season (Figure 2), sea surface temperature (SST) increased about 1°C, which was not observed during the dry season, neither spatially in a same period. As for salinity, temperatures collected during the rainy season of 2014 showed values slightly higher when compared to the previous year.

By analyzing the temperature values obtained during the dry season in 2013 and 2014, no significant difference was observed from one year to the next. Temperature recorded during 2013 reached maximum and minimum values of 27.53°C (Sta. 1) and 26.66°C (Sta. 5), respectively. It could also be highlighted that higher temperature values were obtained at stations 1 and 2. However, their profiles presented opposite patterns, as in Sta.1 temperature decreases with depth, contrary to what happens in Sta.2. Temperature recorded during 2014 reached maximum and minimum values of 27.10°C (Sta. 1) and 26.53°C (Sta. 4), respectively.

Likewise by analyzing the vertical distribution of sea surface salinity (SSS) in all stations during a same period, no significant difference was observed. For both years salinity values were higher during the dry season than during the rainy season.

By representing the thermohaline peers, adding sigma-t contours, a characteristic T-S diagram of sea state was obtained (Figure 2B). This diagram allows analyzing and identifying water masses, coastal region features the island as well as the degree of mixing between them. According to the data, the water mass surrounding to shallower coastal region of the island is the Tropical Surface Water (TSW). The T-S diagram shows different characteristics of TSW, water mass with higher salinity and lower temperature during the dry season and lower salinity and higher temperature during the rainy season.

The table 1 presents the concentration values obtained for the essential nutrients used in the primary productivity: ammonia (NH_3), nitrite (NO_2), nitrate (NO_3), phosphate (PO_4) and silicate (SiO_2). The results show that no significant differences were observed for nutrient concentrations, both spatially and temporally.

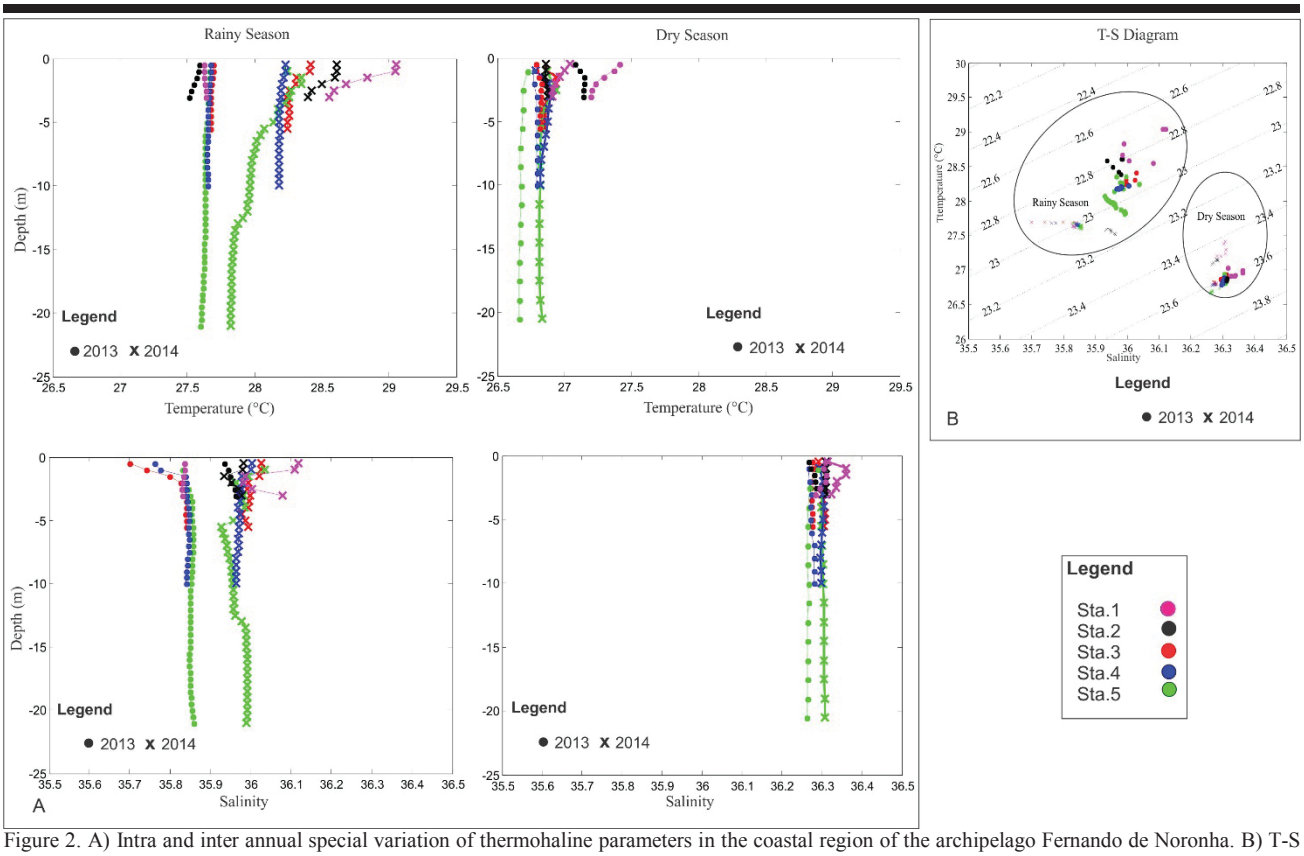

Figure 2. A) Intra and inter annual special variation of thermohaline parameters in the coastal region of the archipelago Fernando de Noronha. B) T-S diagram referring to the figure data A. The legend on the right side is related to two images.

Table 1. *Nutrient concentrations determined for each of the five stations. Ammonia (NH_3), nitrite (NO_2), nitrate (NO_3), phosphate (PO_4) and silicates (SiO2) in µmol.L-1. Amounts related the surface (S) and bottom (B). ND refers to values below the detection limit of the apparatus.*

			RAINY SEASON					DRY SEASON				
STATION	YEAR		NH3	NO2	NO3	PO4	SIO2	NH3	NO2	NO3	PO4	SIO2
1	2013	S	0.02	0.07	0.05	0.24	0.80	0.02	0.07	0.05	0.24	0.80
		B	--	0.08	ND	0.06	2.68	0.00	0.05	0.13	0.32	1.77
2	2013	S	0.01	0.02	0.10	0.23	1.16	0.01	0	0.03	0.23	1.16
		B	--	0.03	0.05	0.10	1.55	--	--	--	--	--
3	2013	S	0.01	0.12	0.10	0.12	1.44	ND	0.12	ND	0.12	1.44
		B	--	0.17	0.22	0.12	1.55	0.01	0.04	ND	0.18	0.76
4	2013	S	0.02	0.03	0.03	0.14	2.65	0.02	0.03	0.03	0.14	2.65
		B	--	0.01	ND	0.09	1.49	0.01	0.01	ND	0.18	1.09
5	2013	S	0.01	0.02	0.1	0.23	1.16	0.01	0.01	ND	0.17	1.03
		B		0.03	ND	0.08	2.50	0.01	0.00	0.21	0.13	0.96
1	2014	S	0.10	0.13	0.41	0.15	3.98	0.11	0.02	0.28	0.41	2.54
		B	--	--	--	--	--	--	--	--	--	--
2	2014	S	0.06	0.05	0.01	0.23	2.02	0.02	0.02	0.11	0.12	5.48
		B	--	--	--	--	--	0.08	0.02	ND	0.14	1.62
3	2014	S	0.03	0.17	0.22	0.12	1.55	0.02	0.02	0.11	0.12	2.05
		B	0.05	0.05	ND	0.13	1.96	0.04	0.02	ND	0.14	ND
4	2014	S	0.02	0.01	ND	0.09	1.49	0.02	0.02	0.01	0.11	1.91
		B	0.03	0.02	ND	0.09	0.95	0.02	0.02	0.07	0.13	1.25
5	2014	S	0.04	0.03	ND	0.08	2.50	0.02	0.02	ND	0.07	0.92
		B	0.02	0.03	ND	0.08	2.28	0.02	0.02	0.59	0.12	8.71

DISCUSSION

Data of precipitation (obtained by the Agência Pernambucana de Águas e Clima – APAC, a state agency on water and climate) are presented in Figure 3. By comparing the seasonal variation of monthly precipitation between 2013 and 2014, we could observe that for both years, higher levels of average precipitation for the rainy season were observed during the same period corresponding to higher SST and lower salinity values. In 2013 it presented a delay in the rainfall period compared to the year 2014 and the historical series (years 2003-2012).

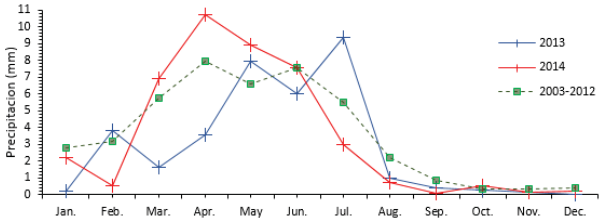

Figure 3. Monthly averages of precipitation during the years 2013–2014 and during the nine previous years (2003-2012).

Analysis of the SST monthly averages obtained by the MODIS-Aqua Satellite images with 4km resolution provided by NASA (Figure 4), corroborates the values found in this study, by identifying a warming of surface water during the rainy season (June and July) compared to the dry season.

Near Fernando de Noronha Archipelago, the SST obtained during the rainy season, for the month of June 2014, showed higher average value (27.8°C), compared to average monthly SST obtained for the month of July 2013 (27.5°C).

In June 2013 (not demonstrated in the figure) the SST near Fernando de Noronha Archipelago is 27.9°C.

During the rainy season low SSS is associated with warmer sea temperatures in the Atlantic Tropical. The salinity in the tropical ocean is projected to decrease due to the intensified hydrological cycle (Durack *et al*., 2012).

The nutrient contents analyzed in the mixed layer exhibited concentrations specific to oligotrophic areas. The values obtained are near to the minimum detection level, and in many cases below this value, especially in relation to ammonia concentrations. This is one of the first products of organic matter mineralization, which is quickly oxidized to the more stable form, nitrate, also found in low concentrations, however higher than ammonia.

By comparing the median concentrations of nutrients, a subtle rise could be observed during the rainy season for both years, except for phosphate. Silicate was the nutrient that showed the highest variation between seasons, as well as greatest concentrations.

Silicate is an essential component, however, it does not enter into the cycle of organic matter but is an important component in the composition of the diatomaceous shells and exoskeletons of other organisms. Silicate does not fit between the most utilized components from a biological point of view, further, this element degrades slower, depending on alternating periods of greater or lesser use, according to population growth (Flores Montes, 2003).

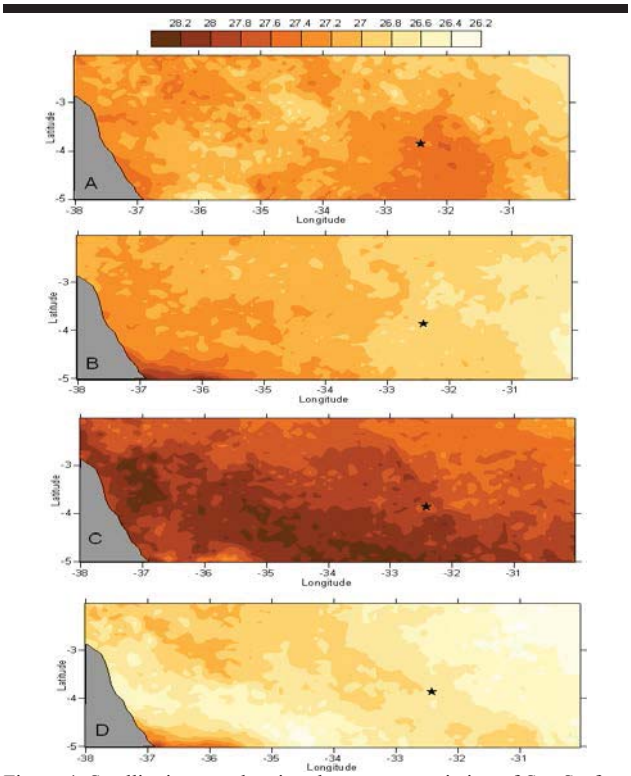

Figure 4. Satellite images showing the average variation of Sea Surface Temperature (SST) obtained during the months related to the four campaigns conducted in this study. A) July 2013; B) December 2013; C) June 2014; D) November 2014. The location of the archipelago (star) is identified in the images.

In terms of interannual seasonality, higher nutrient concentrations were detected in 2014, excepted for phosphate. Phosphate was the second nutrient with larger proportions. According to Aidar *et al.* (1993), phosphate ion regeneration is very fast in the water column, and can act as the limiting nutrient.

The variation of nutrient concentrations in the water column was quite low, however, there was, in general a small positive gradient from the bottom to the surface of the stations.

CONCLUSIONS

Variations of temperature and salinity in the surface layer were collected and analyzed during dry and rainy seasons. Results show that lower temperatures and higher salinity values were observed during the dry period for both years of 2013 and 2014. During rainy season low salinity was observed, which could be associated with warmer sea temperatures in the Atlantic Tropical near Fernando de Noronha Archipelago.

The nutrient data showed a nutritional deficit. Changes in nutrient concentration were very small from one period to another, between the stations and in the water column. Therefore

it is not possible to identify correlations with changes of the thermohaline properties.

The coastal region of Fernando de Noronha, in the inside sea region is characterized by the presence of Surface Tropical Water.

ACKNOWLEDGMENTS

This study had the support of the projects: 1) Study of Carbon Cycle Balance in the coastal region and its ocean transportation potential, with emphasis on the coast of Pernambuco (Edital FACEPE-FAPESP); 2) Total Organic Carbon transport and its interaction with the marine acidification processes, in ocean and estuarine-coastal environments northern and northeastern Brazil; and (3) Monitoring of Sea conditions off the coast of NE Brazil MC-MAR/NE (Edital FACEPE).

LITERATURE CITED

Aidar, E.; Gaeta, S.A.; Gianesella-Galvão, S.M.F.; Kutner, M.B.B., and Teixeira, C., 1993. Ecossistema costeiro subtropical: nutrientes dissolvidos, fitoplâncton e clorofila *a* e suas relações com as condições oceanográficas na região de Ubatuba, SP. *Publicação especial do Instituto Oceanográfico de São Paulo*, Brazil, 10, 9-43.

Almeida, F.F.M., 2006. Ilhas oceânicas brasileiras e suas relações com a tectônica atlântica. *Terra Didática*, 2, 3-18.

Durack, P.J.; Wijffels, S.E., and Matear, R.J., 2012. Ocean salinities reveal strong global water cycle intensification during 1950 to 2000. *Science*, 336(6080), 455-458.

Flores Montes, M. J., 2003. Fatores que influenciam na produtividade dos oceanos: a importância do fluxo de difusão dos nutrientes para a biomassa do fitoplâncton na região oceânica do nordeste brasileiro. Universidade Federal de Pernambuco, Tese de Doutorado (Recife, Brasil), 179p.

Ganachaud, A.; Gupta, A.S.; Orr, J.C.; Wijffels, S.E.; Ridgway, K.R.; Hemer, M.A.; MaesC.; Steinberg, C.R.; Tribollet, A.D.; QiuB., and Kruger J.C., 2011. Observed and Expected Changes to the Tropical Pacific Ocean, in: Bell, J.D.; Johnson J.E., and Hobday A.J. (Eds.), *Vulnerability of Tropical Pacific Fisheriesand Aquaculture to Climate Change, Secretariat of the Pacific Community*, Noumea, New Caledonia, 101-187.

Gierach, M. M.; Messié, M.; Lee, T.; Karnauskas, K.B.; and Radenac, M.-H., 2013. Biophysical responses near equatorial islands in the Western Pacific Ocean during El Niño/La Niña transitions. *Geophys. Res. Lett.*, 40(20), 5473-5479.

Grashoff, K.; Ehrhardt, K.M.; and Kremling, K., 1983. *Methods of Seawater Analysis*. 2 nd edn. Verlag Chemie, Weinheim, Germany, 317p.

IPCC (Intergovernmental Panel on Climate Change). 2013. *Climate change 2013: The physical science basis.* Working Group I contribution to the IPCC Fifth Assessment Report. Cambridge, United Kingdom: CambridgeUniversity Press. www.ipcc.ch/report/ar5/wg1.

Mohr, L.V.; Castro, J.W.A.; Costa, P.M.S., and Alves, R.J.V., 2009. *Ilhas oceânicas brasileiras: da pesquisa ao manejo*. Vol. II, MMA Secretaria de Biodiversidade e Floresta, Brasilia, Brasil, 496p. (In Portugese)

Peterson R.G., and Stramma, L., 1991. Upper-level circulation in the South Atlantic Ocean. *Prog. Oceanogr*., 26(1), 1-73.

REVIZEE. 2006. *Avaliação do Potencial Sustentável de Recursos Vivos na zona Econômica Exclusiva*. Ministério do Meio Ambiente, Brasil, 303p. (In Portugese)

Silva, A.C.; Araújo, M., and Bourlès, B., 2005. Variação sazonal da estrutura de massas d'água na plataforma continental do Amazonas e área oceânica adjacente. *Revista Brasileira de Geofísica*, 23(2), 145-157. (In Portugese)

Stramma, L., and England, M., 1999. On the water masses and mean circulation of the South Atlantic Ocean. *J. Geophys. Res*., 104(C9), 20863-20883.

Strickland J. D. H; Parsons T. R., 1972. A practical handbook of seawater analysis. 2nd edn, *Fish Res. Bd. Can. Bull*., Ottawa, Bulletin, 167, 1-311.

Journal of Coastal Research	SI	75	517-521	Coconut Creek, Florida	2016

Multi-Year Observation of Holloway Current along the Shelf Edge of North Western Australia

Mohammad Hadi Bahmanpour[†*], Charitha Pattiaratchi[†], E.M.S Wijeratne[†], Craig Steinberg[‡], and Nick D'Adamo[††]

[†*] School of Civil, Environmental and Mining Engineering & UWA Oceans Institute, The University of Western Australia, 35 Stirling Highway, Crawley WA, 6009, Australia

[‡] Australian Institute of Marine Science, Townsville, Queensland, Australia

[††] Intergovernmental Oceanographic Commission, Perth Regional Programme Office of the UNESCO, Perth, Australia

www.cerf-jcr.org

www.JCRonline.org

ABSTRACT

Bahmanpour, M.H.; Pattiaratchi, C., Wijeratne, E.M.S., Steinberg, C., and D'Adamo, N., 2016. Multi-year observation of a boundary current along the shelf edge of North Western Australia. *In:* Vila-Concejo, A.; Bruce, E.; Kennedy, D.M., and McCarroll, R.J. (eds.), *Proceedings of the 14th International Coastal Symposium* (Sydney, Australia). *Journal of Coastal Research*, Special Issue, No. 75, pp. 517-521. Coconut Creek (Florida), ISSN 0749-0208.

Analysis of multi-year current meter data across North West shelf of Australia identified various aspects of the mean flow in a macro-tidal environment. Main features of the flow appear to be a continuous alongshore south-westward flow, i.e., Holloway current located along the continental shelf edge in depth 100-200 m. Annually, the current transports ~ 1 Sv of lower salinity, higher temperature water from the tropical regions to North West Cape. The Holloway current is at its maximum intensity (up to 2 Sv) during autumn/winter (Apr-Jul) when the winds are either weak or the region is dominated by south-east trade winds. Unlike alongshore flow, cross-shore structure of the flow is fairly complex and shows variations with depth and season. A new mechanism is proposed to justify the observed intensification of the flow in austral autumn that is closely related to the seasonal cycle of sea level around Australia. Each year, due to the monsoon cycles there is a high sea level anomaly that peaks in February in the Gulf of Carpentaria in the upstream side of the Holloway current that manifests itself as southward progressive high sea level anomalies in the following months along the West Australian coastline. Observed onshore fluxes can also have some implications for the strength of the Holloway current.

ADDITIONAL INDEX WORDS: *Mean flow, North West Shelf of Australia, Holloway Current.*

INTRODUCTION

Circulation is defined as the non-oscillatory part of water particle movements due to various local and remote forcing present along the shelf and can affect transport of pollution and matter downstream. Circulation along the continental shelves differs markedly with that of deep ocean because of depth variation of order 100 m (Csanady, 1982). Continental shelves off North Western Australia are relatively wider than other well-known shelves of the world (Webster, 1985), and mean flow characteristics of these shelves are not well understood mainly due to the lack of direct year-long velocity measurements.

Previous estimates of circulation regime of North Western Australia are derived based on sparse hydrographic casts or direct velocity measurements of only short duration. Holloway and Nye (1985) analyzed observation of currents and winds between January 1982 and July 1983 and found a strong flow to the south-west parallel to the local bathymetry. D'Adamo *et al.* (2009) proposed the name "Holloway Current" for this flow. The current study presents new multi-year observations of Holloway Current along the North West Shelf of Australia (NWS) in a location similar to data from Holloway and Nye (1985).

Brink *et al.* (2007) ship-board observations during austral winter 2003 again verified the existence of Holloway current over the shelf edge. However, resolving the seasonality of the flow requires sustained measurements of longer duration, and previous studies were unable to draw any conclusion on the annual variations of the mean flow.

In early 2012 an observational array was added off the Pilbara continental shelf regions (Figure. 1). The mooring arrays are a sub-facility of Integrated Marine Observing System (IMOS) Australian national mooring network and provide observations comprising physical (temperature, salinity, sea level and currents) and water quality (turbidity and chlorophyll) measurements. The Pilbara array is funded through Western Australian government co-investment with the IMOS. Almost all of the moorings fall onshore of 200-m isobaths as an indicator of the continental shelf edge. Therefore, these moorings could be able to capture circulation and its seasonal variation. The current measurement program ends in mid-2014, providing 2.5 years of uninterrupted observational data for oceanographic research and application.

DOI: 10.2112/SI75-104.1 received 15 October 2015; accepted in revision 15 January 2015
*Corresponding author: bahmanpour.mh@gmail.com

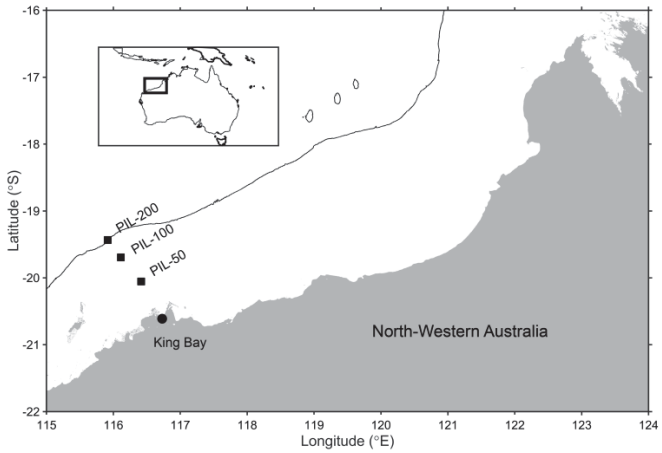

Figure 1. Location of long-term moorings off Pilbara in North Western Australia. The number in the name of station refers to its depth. Thick line shows the location of 200-m contour line.

METHODS

Pilbara Transect velocity measurements started in February 2012 and ended in August 2014, providing 2.5 years of direct current measurements made at varying time intervals (5, 10 and 20 minutes). Velocities are recorded in earth-referenced coordinate (eastward and northward velocity) using a series of upward-looking Acoustic Doppler Current Profiler (ADCP). The data is freely available to the scientific community and can be downloaded from IMOS portal.

Flow observations are organized in a series of depth cells or bins ranging from the instrument, located several meters above the bottom, throughout the water column to the surface layer. Due to contamination by surface gravity waves, surface velocities are removed using quality control flags provided with the data. Spectral analysis of raw data shows that a significant portion of the variance is within the tidal range due to large amplitude semi-diurnal tides (Figure 2). Velocity readings are then decimated to hourly values and passed through a low-pass filter with cut-off frequency~40 hours (Beardsley *et al.*, 1983) to remove tidal and inertial variabilities. Application of this low-pass filter results in finding the residual flow, which follows local contour line in the location of moorings. Effectiveness of the low-pass filter can be seen in removing the dominant onshore tidal fluxes at the location of moorings and leaving behind the residual portion of the flow (Figure 3). In one specific deployment for Pil-50 station, the mooring did not return useful data and so the gap appears in the time series (Figure 3c).

ADCPSs are unable to resolve flows close to the surface and bottom layer, and there is usually a gap in our records in these layers (Gordon, 1996). In order to calculate volume transports across the Pilbara transect these gaps were replaced by the velocity measurements in their closest respective bin. Besides, width of the transect is assumed to extend to 300-m contour line. Volume transport calculations are then performed using depth-integrated velocities. This approach is similar to that used in Holloway (1995). It is sometimes preferable to view the data in the principal axes, i.e., alongshore and across-shore directions. Principal axes direction are found through a simple Empirical Orthogonal Function (EOF) analysis (Thomson and Emery, 2014). For the Pilbara transect, Alongshore direction along which variance is maximized is ~30° north of east which is parallel to the local bathymetry contour line.

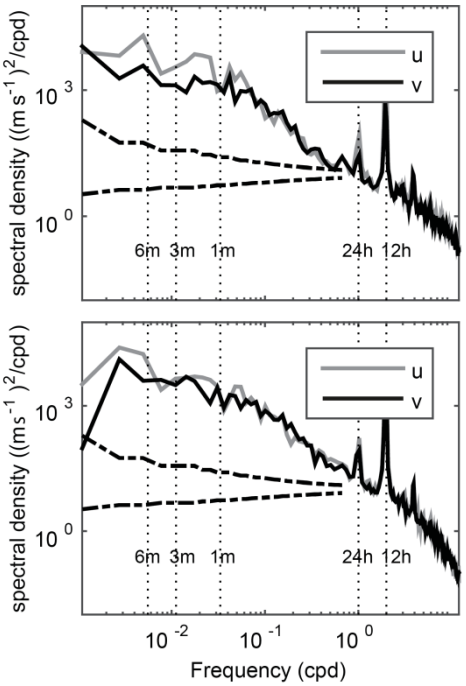

Figure 2. Spectral density for the depth-averaged eastward (u) and northward (v) component of the flow for the stations (a) PIL-200 and (b) PIL-100. The vertical dotted lines show the location of several frequencies of interest. Dashed line shows 95% confidence intervals for spectral estimates.

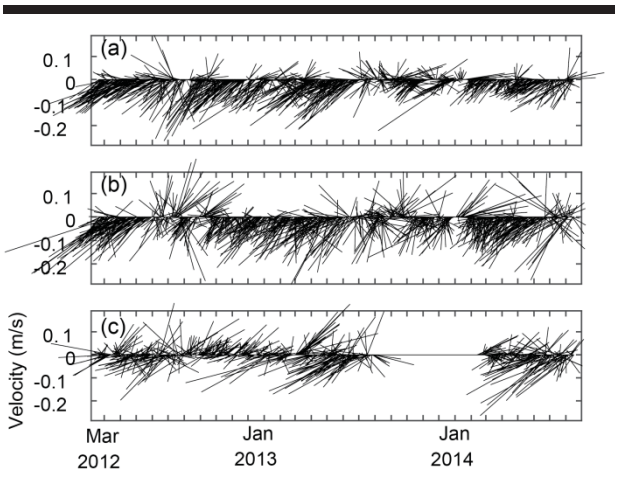

Figure 3. Depth-averaged daily velocity stick plots for stations: (a) Pil-200. (b) PIL-100. (c) PIL-50.

Monthly mean averages are calculated from daily averaged observations where there are more than 15 records per month. A two dimensional interpolation method is used to map velocities of each mooring line to the cross-shore vertical sections with the covariance structure of the data taken into account in the interpolation process (Thomson and Emery, 2014).

RESULTS

The Holloway Current shows strong seasonality and short intermittent reversals. It is stronger during Austral autumn (Apr-Jun) when current velocities are more than 0.15 m/s (Figure 4). Holloway current reaches its maximum velocity over the shelf edge, which is roughly located at depths between 100-200 m. There is also a secondary peak in October which had not been reported in previous measurements. This secondary maximum is more pronounced in the deepest station (PIL-200). In September, there is a reversal confined to the shallow parts of the inner shelf. This reversal of the flow can be accounted for by the opposing winds that have a strong north-easterly component from Sep-Nov.

The deepest station along the Pilbara transect is located at 200-m depth, and some parts of the Holloway current located offshore of this depth contour are missed (Figure 4). For this reason, volume transport calculations are done using the extrapolated values up to the 300-m depth contour. Volume transport calculations show a peak of ~2 Sv (1 Sv=10^6 m^3/s) in Austral autumn (Figure 5). On annual mean, Holloway Current volume transport is ~1 Sv. Therefore it cannot be labelled as a seasonal current that establishes only at certain times of the year. Holloway Current is evident throughout the year above the shelf edge with RMS value around 0.6 Sv.

Further insights into the structure of Holloway current can be derived by analyzing its vertical shear profiles (Figure 6). In PIL-200 station, at the peak of its intensity during Austral autumn, Alongshore flow shows little variation with depth from 0 to 100 m. There is a relatively strong shear in depths more than 100 m and a very weak undercurrent close to the bottom. There is no evidence of a sub-surface intensified current and the current usually gets weaker with depth. The same pattern can also be seen in the vertical structure of alongshore flow for the PIL-100. Here the alongshore flow gets stronger 2 month earlier than PIL-200. There is an evidence for a sub-surface intensified current in Oct-Dec. This can be justified because of the opposing action of wind at the surface at this time of the year. In the shallow water station (PIL-50), alongshore currents respond

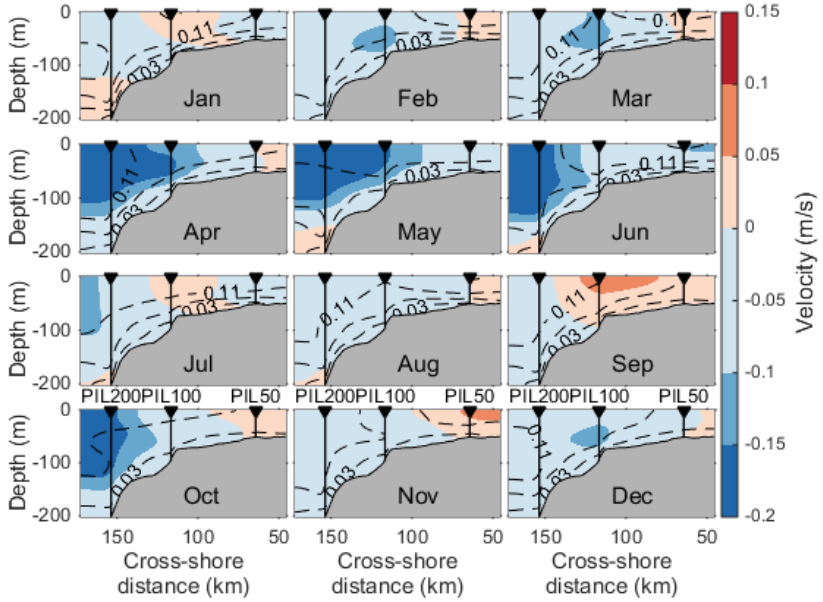

Figure 4. Monthly maps of alongshore velocities. Dashed line shows the standard deviation of current velocities.

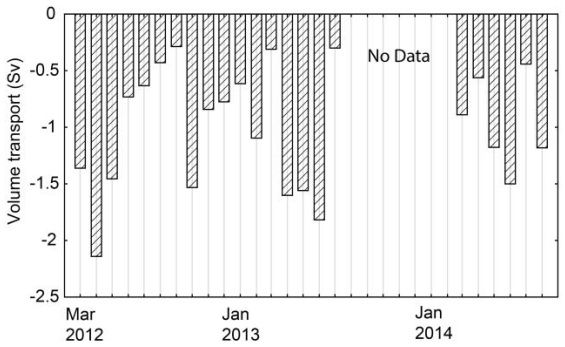

Figure 5: Monthly mean alongshore volume transports of the Pilbara transect. Negative transport is toward south-west.

to the reversing wind cycles. During the winter, the region is dominated by southeast trade winds that can cause a net transport to the southwest in the Ekman layer.

Cross-shore structure of the flow is fairly complex and variable throughout the year (Figure 6). In PIL-100 and to a lesser extent in PIL-200, there is a net sub-surface intensified onshore flux in several months (Oct-Feb). In PIL-100, an interesting feature of the cross-shore component of the flow can be seen very close to the bottom in months May-Jul, when there is a net offshore flux close to the bottom. The same feature can be seen in PIL-50 station at this time of the year. This net offshore flux is related to the cascade of dense water formed during austral winter in NWS through evaporative processes, and is well documented for south-west Australian inner shelves (Pattiaratchi *et al.*, 2011).

In terms of inter-annual variability, Holloway current shows most of its variability in the second half of the year (not shown). In PIL-200 the currents are weaker in 2012 compared to 2013 and 2014. In PIL-100 station, little inter-annual variation can be seen compared to the deepest station. Again it can be seen that in the middle station (PIL-100), the intensification of Holloway current occurs earlier than the PIL-200 station, and this pattern can be seen in all of the 3 years. Maximum observed intensity of the south-westward flow among all stations has occurred in Feb 2013 in PIL-100 station.

DISCUSSION

Holloway and Nye (1985) noted that south-east trade winds alone cannot account for the observed intensification of the current in Austral autumn and proposed that the dynamics of the current must be controlled by remote forcing.

A possible explanation for the observed intensification of the Holloway current in austral autumn comes by analogy with seasonal cycle of sea level around Australia. Each year in summer at the time of northwest monsoon, winds push water in the Gulf of Carpentaria in the upstream side of Holloway current. As a result, there is a high sea level anomaly in the Gulf of Carpentaria that exceeds 0.3 m in February. The seasonal cycle of sea level around Australia in the following months shows a southward propagation of this sea level anomaly in the form of a shelf wave (Wijeratne, personal communication).

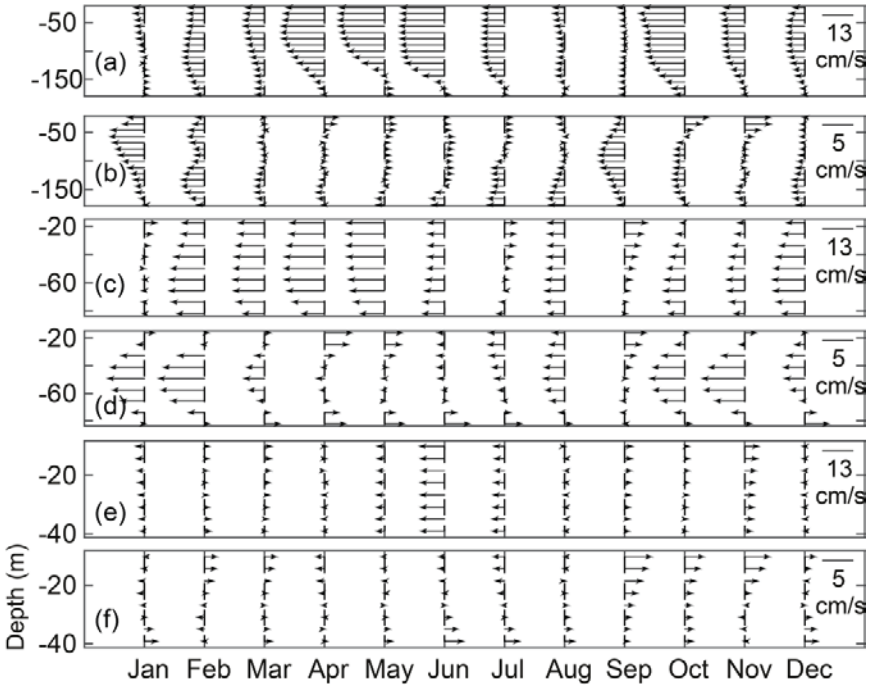

Figure 6: Vertical shear profiles of the flow. (a), (b): PIL-200 along and across-shore component. (c), (d) PIL-100 along and across-shore. (e), (f) PIL-50 along and across-shore component. Positive alongshore is north-eastward and positive across-shore is offshore. Note the difference in scales.

Ridgway and Godfrey (2015) recent analysis of altimetry data also confirms this seasonality in the sea level around western boundary of Australia. Geostrophic balance implies that a southward flowing current has its high pressure at the left side (i.e., high pressure along the coast) in the southern hemisphere. Brink *et al.* (2007) found a high correlation between the coastal sea level anomaly and the strength of the Holloway current. Similar results are also found through the analysis of the nearby King Bay station sea level measurements (Figure 1). Therefore, we postulate that the Holloway current intensification during Austral autumn is controlled by the seasonal cycle of sea levels around North West Australia in relation to the wind setup in the Gulf of Carpentaria.

Another pathway for the Holloway current can be from the onshore fluxes along its boundary with the eastern Indian Ocean. Previous studies have also pointed out to the existence of these onshore fluxes. For example, Wijffels *et al.* (2008) calculated these onshore fluxes to be around 2.5 Sv on annual mean at the middle parts of NWS off Kimberley region that must be exported through the southern parts of the shelf as a boundary current. However, our observed onshore fluxes are at the southern parts of the shelf and we cannot verify these fluxes independently. We postulate that these onshore fluxes could have some implications for the observed south-westward current on annual mean.

CONCLUSIONS

Multi-year observations of Holloway current in one transect off Pilbara region of North Western Australia are presented. This is by far the most complete dataset available in the NWS until now. On annual mean, Holloway current manifests itself as a boundary current flowing over the shelf edge transporting ~1 Sv toward the southwest. The Holloway current becomes well-established in Apr-Jun in depths between 100-200 m. The maximum observed monthly alongshore flow is in the middle station in February 2013. At its peak in austral autumn, the Holloway current is fairly constant in the first 100 m of the water column and there is a strong shear below 100 m depth. Cross-shore structure of the flow is highly variable by season and depth. However, there is usually a sub-surface intensified onshore flux with velocity around 5 cm/s. Cross-shore velocities are less than the observed along-shore velocities.

A new mechanism is proposed for the observed intensification of the flow in austral autumn. The proposed mechanism is that North West monsoon pushes water to set up in the Gulf of Carpentaria, which peaks around February, and as the winds relax, waters flow south-westward along the North West Shelf of Australia.

ACKNOWLEDGMENT

Data was sourced from the Integrated Marine Observing System (IMOS) - IMOS is a national collaborative research infrastructure, supported by the Australian Government. The Australian Institute of Marine Science (AIMS) operates the moorings use in this study. Coastal sea level data was provided by the bureau of meteorology. This research was undertaken by M. H. Bahmanpour as part of a PhD program at the University of Western Australia while the author held SIRF and UPAIS postgraduate scholarships.

LITERATURE CITED

Beardsley, R. C.; Limeburner, R., and Rosenfeld, L. K., 1983. *Introduction to the CODE-2 moored array and large-scale data report, in CODE-2: Moored Array and Large-Scale Data Report*. Woods Hole, Mass.: Woods Hole Oceanographic Institution, *WHOI Tech. Rep. 85-35*,22 p.

Brink, K. H.; Bahr, F., and Shearman, R. K., 2007. Alongshore currents and mesoscale variability near the shelf edge off northwestern Australia. *Journal of Geophysical. Research.*, 112(C5), doi:10.1029/2006jc003725.

Csanady, G. T., 1982. *Circulation in the coastal ocean.* Dordrecht, Holland: Reidel, 279 p.

D'Adamo, N.; Fandry , C.; Buchan, S., and Domingues, C., 2009. Northern sources of the Leeuwin Current and the "holloway Current" on the North West Shelf. *Journal of the Royal Society of Western Australia*, 92(2), 53-66.

Gordon, R. L., 1996. *Acoustic Doppler Current Profiler principles of operation: a practical primer*. San Diego, Calif.: RD Instruments, 54 p.

Holloway, P. E., 1995. Leeuwin current observations on the Australian North West Shelf, May–June 1993. *Deep Sea Research Part I: Oceanographic Research Papers*, 42(3), 285-305.

Holloway, P. E., and Nye, H., 1985. Leeuwin current and wind distributions on the southern part of the Australian North West Shelf between January 1982 and July 1983. *Marine and Freshwater Research*, 36(2), 123-137.

Pattiaratchi, C.; Hollings, B.; Woo, M., and Welhena, T., 2011. Dense shelf water formation along the south-west Australian inner shelf. *Geophysical Research Letters.*, 38(10), doi:10.1029/2011gl046816.

Ridgway, K. R., and Godfrey, J. S., 2015. The source of the Leeuwin Current seasonality. *Journal of Geophysical Research Oceans*, 120, 6843-6864, doi:10.1002/2015JC011049.

Thomson, R. E., and Emery,W. J., 2014. *Data Analysis Methods in Physical Oceanography (Third Edition)*. Boston: Elsevier, 716 p.

Webster, I., 1985. Wind-Driven Circulation on the North West Shelf of Australia. *Journal of Physical Oceanography*, 15(11), 1357-1368.

Wijffels, S. E.; Meyers, G., and Godfrey, J. S., 2008. A 20-Yr Average of the Indonesian Throughflow: Regional Currents and the Interbasin Exchange. *Journal of Physical Oceanography*, 38(9), 1965-1978.

Journal of Coastal Research	SI	75	522-526	Coconut Creek, Florida	2016

Modelling of Extreme Wave Climate in China Seas

Jiangxia Li[†‡], Yongping Chen[†*] and Shunqi Pan[‡]

[†]State Key Laboratory of Hydrology-Water Resources and Hydraulic Engineering, Hohai University, Nanjing, China

[‡]School of Engineering Cardiff University Cardiff, the United Kingdom

www.cerf-jcr.org

www.JCRonline.org

ABSTRACT

Li, J.X.; Chen, Y.P., and Pan, S.Q., 2016. Modelling of Extreme Wave Climate in China Seas. *In:* Vila-Concejo, A.; Bruce, E.; Kennedy, D.M., and McCarroll, R.J. (eds.), *Proceedings of the 14th International Coastal Symposium* (Sydney, Australia). *Journal of Coastal Research*, Special Issue, No. 75, pp. 522-526. Coconut Creek (Florida), ISSN 0749-0208..

Accurately estimating the extreme wave climate is important to the ocean and coastal engineering design. In this study, the long-term wave climate from 1979 to 2013 over the northwest Pacific Ocean, centred at the China Seas (including the East China Seas and the South China Sea), is hindcasted by using the spectral wave model WAMC4. The model is driven by the wind forcing obtained from the recently released 6 hourly ECMWF (European Centre for Medium-range Weather Forecasts) reanalysis data, with the spatial resolution of 0.125°×0.125°. For the typhoon events, the parametric typhoon wind fields are generated and blended in the typhoon affected area. The statistical analysis of the extreme waves with 100-year return period at several observation stations are carried out. The results show a good agreement with the observation data, indicating that using the blended wind field for the modelling of extreme wave climate in China Seas can considerably improve the accuracy of the predicted wave heights.

ADDITIONAL INDEX WORDS: *Parametric typhoon model, ECMWF reanalysis data, WAMC4 wave model.*

INTRODUCTION

The region of China's Seas, which includes the East China Seas (Bohai Sea, Yellow Sea and East China Sea) and part of the South China Sea (Figure 1), are often threatened by extreme events like typhoons and storm waves (Xiao *et al.*, 2011). Better understanding of the extreme wave climate in this region is essential to safe and economic design for coastal engineering.

Usually extreme wave statistics are calculated based on the long-term field measurement data (Qi *et al.*, 1998; Wang and Yi., 1997; Liu and Sun., 2000; Chen *et al.*, 2006). However, due to the low spatial resolution of the data, it is difficult to obtain the extreme wave climate in the whole area. Alternatively, wave mapping from modelling results could be used to study the temporal and spatial distributions of extreme waves in a larger area (Valchev *et al.*, 2010; Yamaguchi, 2002; Yamaguchi and Hatada, 2003 and Lee and Jun, 2006), provided that wave models used are well calibrated and validated. The accuracy of the model predictions depends heavily on the accuracy of the wind field generated by weather models as the surface forcing. It is well known that wave height is proportional to the square of wind speed, where 10% error in wind speed may result in an error of at least 20% in hind-casted wave heights (Tolman, 1998). Therefore, accuracy of input wind forcing is important to the wave model. In the past, one challenge in long-term wave simulations was the availability of reliable wind data required for wave models. Nowadays, high quality long-term reanalysis wind data have been made available from agencies such as ECMWF and NCEP.

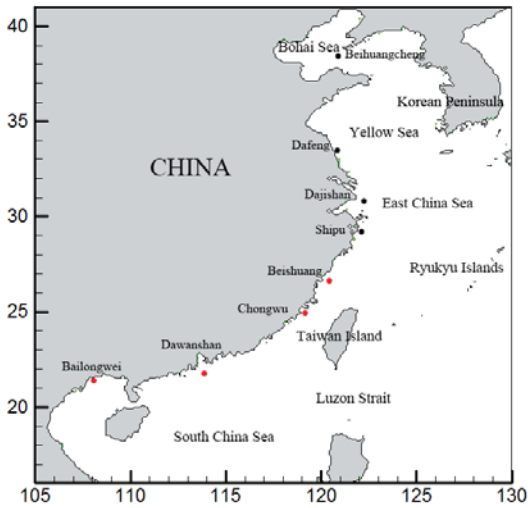

Figure 1. The region of China Seas and the locations of eight observation stations, of which four stations in the region of East China Seas, marked as black point, and the other four stations in the South China Sea, marked as red point.

In the region of China Seas, a number of relevant studies have been carried out. For example, Lv *et al.* (2014) used the 0.25°×0.25° ECMWF reanalysis wind data to drive the SWAN model for 20-year wave hind-casting in the Bohai Sea and then analysed the annual and seasonal distributions of significant wave height, wave period and wave direction in that area. Zheng and Li (2015) used the CCMP wind data to drive the WAVEWATCH III (WW3) model for wave hind-casting in the whole China Seas

DOI: 10.2112/SI75-105.1 received 15 October 2015; accepted in revision 15 January 2015
*Corresponding author: ypchen@hhu.edu.cn

over 24 years. Chen *et al.* (2013) used the NCEP/NCAR reanalysis wind data, which has the spatial resolution of 2.5°×2.5°, to drive the WAM model for 60 years' wave hind-casting in the East China Seas (Bohai Sea, Yellow Sea and the East China Sea) and the results were further used to estimate the extreme waves with 50-year and 100-year return periods in the East China Seas. Zheng *et al.* (2014) used the Quick SCAT/NCEP wind data to drive the WW3 wave model and calculate the extreme wave height with return periods of 20 years and 30 years in the East China Sea.

Although the reanalysis wind data performs well in describing the normal average weather climate, the resolution is often insufficiently high enough to describe the atmospheric forcing during a typhoon event (Appendini et al., 2013). As the large waves generated by the strong winds during a typhoon are what we are concerned most, here we propose to superpose the parametric typhoon wind field on the reanalysis data during the typhoon event, in order to improve the description of performance of the wind field data in the typhoon affected area. This study uses the ECMWF reanalysis wind as the background wind field, and blends the wind field generated from a parametric typhoon wind model in the typhoon affected area onto it. The resulting wind field and the unblended ECMWF reanalysis wind field are then used to drive the wave model to hind-cast the wave climate in the region of China Seas over 35 years. The extreme waves with 100-year return period are calculated by using the Gumbel distributions from the annual maximum wave heights of the hind-casted waves. The extreme wave heights at several observation stations are compared with the observation data, so that the relative accuracy of the estimated extreme wave heights can be assessed from both wind fields.

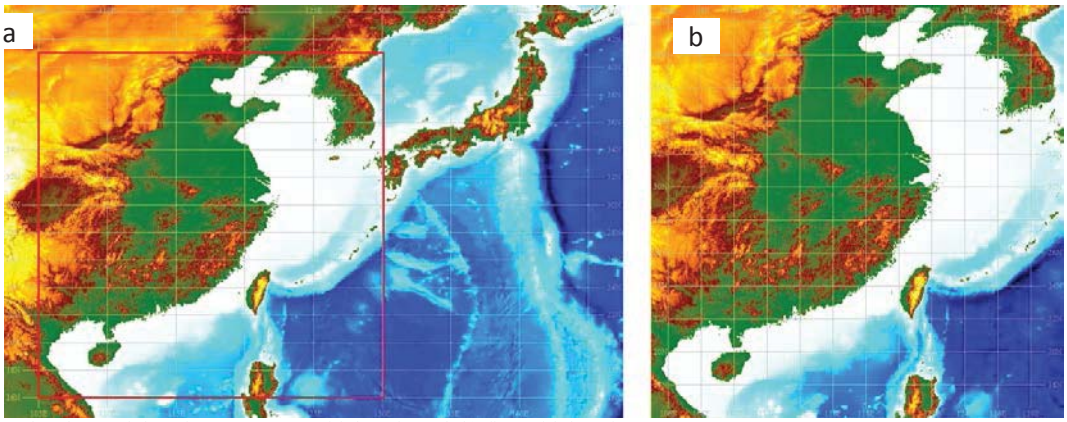

Figure 2. The two-level nested domains: (a) coarse grid domain and (b) fine grid domain

METHODS

The wave model used in this study is the latest version WAM model, namely WAMC4. The model solves the wave energy transport equation explicitly without any pre-described shape of wave spectrum. The WAM model simulates the 2D wave spectral evolution with the consideration of the energy input by wind, the energy dissipation by whitecapping and bottom friction, and the non-linear wave–wave interactions (Jennifer *et al.*, 2010). It is suitable for any given regional grid with a prescribed topography. The grid resolution of model is arbitrary in space and time (Cherneva *et al.*, 2008).

The original atmospheric forcing, which is used to drive the wave model, is 6-hourly ECMWF ERA-Interim reanalysis wind data, provided by ECMWF (http://www.ecmwf.int) with the spatial resolution of 0.125°×0.125°. Although the ECMWF reanalysis wind data is finer than many other reanalysis datasets, it is still not fine enough to describe the atmospheric forcing for a typhoon event (Zhang and Sheng, 2015; Appendini *et al.*, 2013). In order to get more accurate wind field in the area surrounding the typhoon centre, the parametric typhoon wind field proposed by Jelesnianski (1965) is used to generate local typhoon wind field, which is subsequently superposed onto the ECMWF wind field. As the typhoon centre in the reanalysis data usually does not coincide with the measured one, a shifting of the reanalysis wind field is required first, and then an optimal radius R_{opt} is determined as the distance at which the typhoon model and the reanalysis data has the same magnitude of accuracy. The wind speed calculated by the parametric typhoon model is used inside the optimal radius while that obtained from the reanalysis data is used outside the optimal radius. For the surrounding area around the R_{opt}, a smoothing technique is introduced to integrate the different types of wind fields

$$v = (1-e)v_{ECMWF} + ev_{TY} \quad (1)$$

where v is the blended wind speed; v_{ECMWF} is the original or ECMWF reanalysis wind speed; v_{TY} is the parametric wind speed; and e is the weight coefficient (0.3 is used in this study).

In total, 862 typhoon events which occurred over the northwest Pacific Ocean during 1979-2013 are blended onto the ECMWF reanalysis data.

RESULTS

To examine the accuracy of the wind data for the long-term wave modelling, the ECMWF wind data is compared with the blended wind data at eight observation stations, *i.e.*, Beihuangcheng, Dafeng, Dajishan, Shipu, Beishuang, Chongwu, Dawanshan, Bailongwei along the China coast (see Figure 1), with the observation data from these stations. For brevity, only the

results at four stations, *i.e.* Beishuang, Chongwu, Dawanshan and Bailongwei, in the South China Sea are shown here.

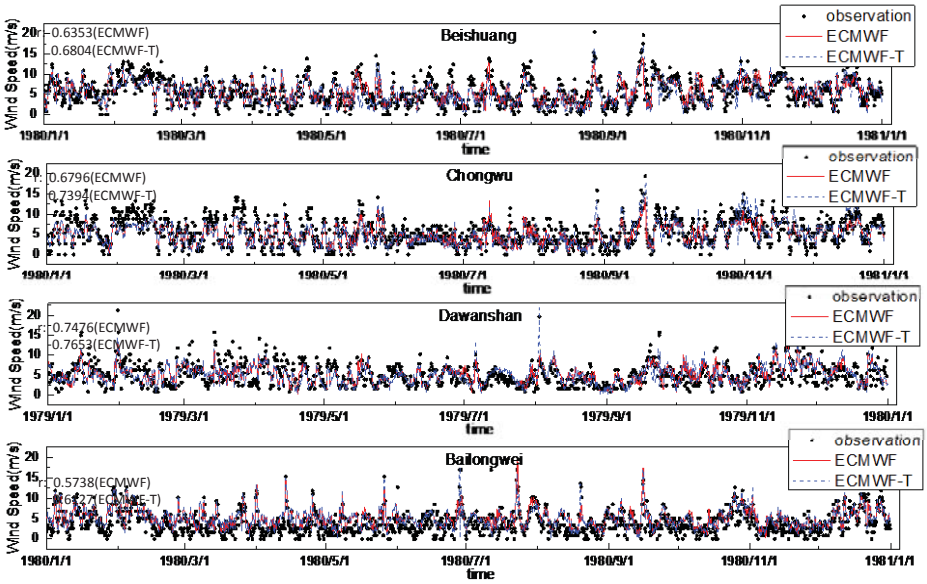

Figure 3. Comparison of wind speeds between ECMWF data (denoted by "ECMWF"), blended wind data (denoted by "ECMWF-T") and observation data in stations in the South China Sea

Figure 3 shows the comparison between the original (un-blended – denoted as "ECMWF") and blended wind data (denoted as "ECMWF-T"), and both agree well with the observations during the normal conditions. However, in the summer and autumn seasons when typhoons frequently pass these stations, the original (un-blended) wind data underestimates the large winds to some extent, while the blended wind data show more accurate estimations of large winds for typhoon events. The correlation coefficients (r) calculated between un-blended ECMWF, blended winds and the observations shown in Figure 3 verify that ECMWF-T data is more accurate than the un-blended one. Figure 4 shows the Quantile-Quantile scatter plots of the wind speeds with a certain accumulative percentage between the blended (ECMWF-T) and un-blended (ECMWF) winds against the measurements. The results also show that the waves generated by the blended wind data can provide more accurate surface forcing for the wave model in the following study.

For the purpose of model validation, the wave model WAMC4 is run with both unblended and blended ECMWF winds to generate the long-term wave climate over 35 years, *i.e.*, from 1979 to 2013. The annual maximum wave heights taken from the waves computed by WAMC4, are used to fit the Gumbel distributions to calculate the extreme wave heights with 100-year return period at 10 wave observation stations. The location details of the observation stations and duration of measurement data availability are given in Table 1.

Table 1. *Location of the observation stations and duration and data availability.*

Station	Longitude(°)	Latitude(°)	Depth(M)	Data length
Laohutan	121.68	38.87	28.0	1962-2009
Zhimaowan	119.92	40.00	6.0	1963-2007
Tianjingang	117.82	38.57	7.0	1960-1979
Xiaomaidao	120.42	36.05	23.8	1961-1995
Shengshan	122.82	30.70	40.0	1960-2009
Dachen	121.90	28.45	15.3	1960-2009
Nanji	121.10	27.42	20.0	1960-2009
Chongwu	118.93	24.83	11.0	1962-2009
Dawanshan	113.72	21.93	28.9	1995-2009
Weizhoudao	109.12	21.02	13.0	1962-2002

Figure 5 shows the results of extremes wave heights with 100-year return period in North (N) and South-East (SE) directions generated from the ECMWF, blended ECMWF winds in comparison with those calculated from the observation data. It can be seen that the distribution trend of extreme waves along the China coasts: the extreme wave heights increase first and then decrease from north to south. This is because those stations located in the south of the East China Sea (east coast of Jiangsu and Zhejiang Province) are closer to the open seas which are more often affected by the typhoons. It can be seen that the simulated wave driven by the blended wind data is more precise than the ones driven by the original ECMWF data.

DISCUSSION

The extreme wave fields of the whole China Seas are calculated. Figure 6 shows the modelled extreme waves with 100-year return period in the entire China Seas. It can be seen that the largest extreme wave height obtained from the blended winds is more than 16 m, located at the southeast of Taiwan. However, the largest extreme wave height driven by the unblended winds is no more than 15 m, located in the waters near Ryukyu Islands. These differences largely exists in the southeast part of China Seas in which is often affected by the typhoon events. The measured typhoon tracks over 35 years from 1979 to 2013 (not shown here) have confirmed that the southeast of China, particularly the area near the Taiwan Island, has the largest frequency to be affected by typhoon events. Since the parametric typhoon model is better than the ECMWF winds for the simulation of typhoon winds, it is understandable the extreme waves driven by the blended winds are better than the waves driven by the ECMWF winds in the typhoon affected areas.

CONCLUSION

The method to generate the improved typhoon wind fields for long-term and extreme wave simulation is introduced in this paper. 6-hourly ECMWF reanalysis wind field is blended by the parametric typhoon wind field. Both original and blended wind data are used to drive the WAMC4 model for long-term modelling of wave conditions with applications to the typhoon-affected area in China Seas. The comparisons of the model results and the observation data indicate a higher accuracy in the blended wind data. This study provides a useful approach to modify the wind data when simulating long-term and extreme wave climate during typhoon events in the China Seas.

ACKNOWLEDGMENTS

The work in this paper was undertaken as part of the Ensemble Estimation of Flood Risk in A Changing Climate (EFRaCC) project funded by The British Council under its Global Innovation Initiative. The authors also acknowledge the support of the National Natural Science Foundation of China (51379072), the Key Research Project of Jiangsu Water Resources Department (2015006), and the 111 Project of the Ministry of Education and the State Administration of Foreign Experts Affairs, China (Grant No. B12032).

LITERATURE CITED

Appendini, C.M.; Torres-Freyermuth, A. and Oropeza, F., Wave modeling performance in the Gulf of Mexico and Western Caribbean: Wind reanalyses assessment. *Applied Ocean Research,* 39: 20-30

Chen, H.; Hua, F., and Yuan, Y., 2006. Seasonal characteristics and temporal variations of ocean wave in the Chinese offshore waters and adjacent sea areas. *Advances in Marine Science*, 24: 407-415 (in Chinese)

Chen, Y.P.; Xie, D.M.; Zhang, C.K., and Qian, X.S., 2013 Estimation of long-term wave statistics in the East China Sea. *In:* Conley, D.C., Masselink, G., Russell, P.E. and O'Hare, T.J. (eds.), *Proceedings 12th International Coastal Symposium (Plymouth,England), Journal of Coastal Research,* Special Issue No. 65, pp.177-182

Cherneva, Z.; Andreeva, N.; Pilar, P.; Valchev, N.; Petrova, P., and Guedes Soares, C, 2008. Validation of the WAMC4 wave model for the Black Sea. *Coastal Engineering,* 55: 881-893

Jelesnianski, P., 1965. A numerical calculation of storm tides induced by a tropical storm impinging on a continental shelf. *Monthly Weather Review,* 93(6), 343.

Jennifer, M. B.; Alejandro, J. S., and Judith, W., 2010. An 11-year validation of wave-surge modelling in the Irish Sea, using a nested POLCOMS-WAM modelling system. *Ocean Modelling,* 33(1), 118-128.

Knaff, J. A.; Sampson, C. R.; Demaria, M.; Marchok, T. P.; Gross, J. M., and Mcadie, C. J., 2007. Statistical tropical cyclone wind radii prediction using climatology and persistence. *Weather Forecasting,* 22(4), 781-791.

Lee, D.Y. and Jun, K.C., 2006. Estimation of design wave height for the waters around the Korean Peninsula. *Ocean Science Journal*, 41:245-254.

Liu, J.F. and Sun, L.Y., 2000. Characteristic analysis of wind field and sea wave field in the western part of the N. Pacific Ocean. *Marine Forecast*, 17:54-62 (in Chinese)

Lv, X.; Yuan, D.; Ma, X., and Tao, J., 2014. Wave characteristics analysis in Bohai Sea based on ECMWF wind field. *Ocean Engineering,* 91:159-171

Qi, Y. Q.; Shi, P., and Wang, J., 1997. A preliminary study on characteristics of wind and wave over the central area of Yellow Sea. *Marine Science Bulletin*,16,1-6. (in Chinese)

Tolman, H.L., 1998. Validation of NCEP's ocean winds for the use in wind wave models. *Global Atmosphere & Ocean System*, 6: 243–268

Valchev, N.; Davidan, I.; Belberov. Z., and Palazov, A., 2010. Hindcasting and assessment of the western Black Sea wind and wave climate. *Journal of Environment Protection and Ecology*, 11(3): 1001-1012.

Wang, Y.T. and Yi, H.Y., 1997. Statistics and spectrum analysis of waves in East China Sea. *Journal of Dalian Fisheries University*, 12: 33-39 (in Chinese)

Xiao, Y. F.; Duan, Z. D.; Xiao, Y. Q.; Ou, J. P.; Chang, L., and Li, Q. S., 2011. Typhoon wind hazard analysis for southeast china coastal regions. *Structural Safety*, 33, 286–295.

Yamaguchi, M., 2002. Estimation of Long-Term Variability of Wave Climate around the Coastal Sea Areas of Japan, *Coastal Engineering*, 10:61-73

Yamaguchi, M. and Hatada, Y., 2003. Estimation of wave climate and its long-term variability around the coasts of Korea. *Proceedings of 13th ISOPE conference*, pp. 182-188

Zheng, C. W. and Li, C. Y., 2015. Variation of the wave energy and significant wave height in the China Sea and adjacent waters. *Renewable & Sustainable Energy Reviews*, 43, 381–387.

Zheng, C. W.; Zhou, L.; Jia, B. K.; Pan, J., and Li, X., 2014. Wave characteristic analysis and wave energy resource evaluation in the China Sea. *Journal of Renewable & Sustainable Energy*, 6(4).

Zhang, H., and Sheng, J., 2015. Examination of extreme sea levels due to storm surges and tides over the northwest Pacific Ocean. *Continental Shelf Research*, 93, 81–97.

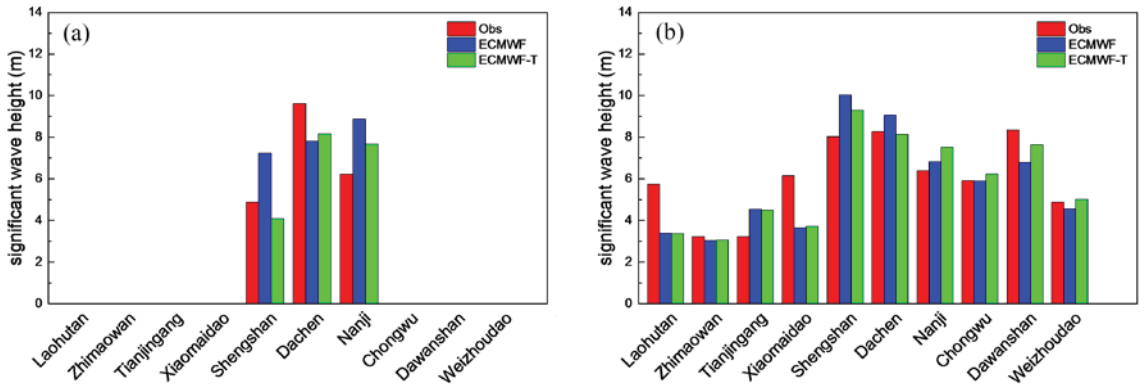

Figure 5. Comparison of 100-year extreme wave heights from ECMWF winds, blended winds (ECMWF-T) and the field measurements (Obs) in (a) N, and (b) SE directions

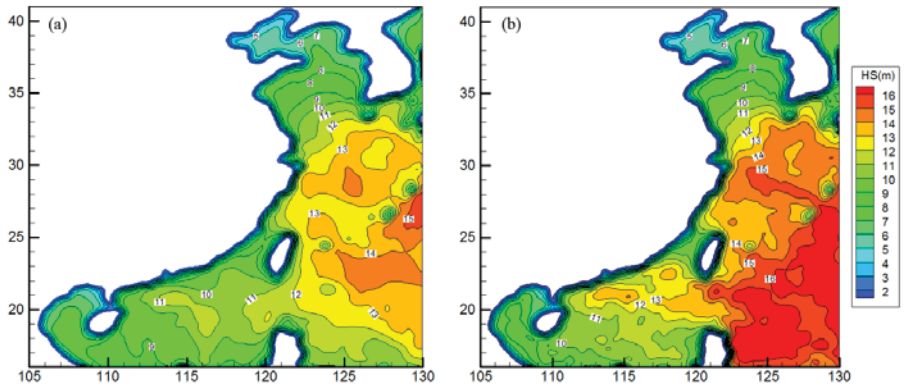

Figure 6. Modelled extreme waves with 100 year return period generated by (a) ECMWF winds, and (b) blended winds

Journal of Coastal Research	SI	75	527-531	Coconut Creek, Florida	2016

Factors influencing the occurrence of Dense Shelf Water Cascades in Australia

Tanziha Mahjabin[†*], Charitha Pattiaratchi[†], and Yasha Hetzel[†]

[†] School of Civil, Environmental and Mining Engineering & UWA Oceans Institute, The University of Western Australia, Australia.

www.cerf-jcr.org

www.JCRonline.org

ABSTRACT

Mahjabin, T.; Pattiaratchi, C., and Hetzel, Y., 2016. Factors influencing the occurrence of Dense Shelf Water Cascades in Australia. *In:* Vila-Concejo, A.; Bruce, E.; Kennedy, D.M., and McCarroll, R.J. (eds.), *Proceedings of the 14th International Coastal Symposium* (Sydney, Australia). *Journal of Coastal Research*, Special Issue, No. 75, pp. 527-531. Coconut Creek (Florida), ISSN 0749-0208.

Transport of inshore waters and suspended material off the continental shelf by Dense Shelf Water Cascades (DSWC) has important ecological and biogeochemical implications in Australian waters. Because of high rates of evaporation, denser saline water occurs in the shallow coastal regions around Australia, setting up horizontal density gradients that can drive DSWC. Ocean glider data available from the Integrated Marine Observing System (IMOS), which is operated by the Australian National Facility for Ocean Gliders (ANFOG) located at the University of Western Australia, were used to measure cross-shelf density profiles under varying wind and tide conditions for seven contrasting regions around the entire continent. Overall 97 sets of spatial and temporal resolution data from year 2008 to 2015 collected by the ocean gliders and analysed with a subset presented here. Data from 19 transects covering the years 2012 to 2015 for the Pilbara region of Western Australia, indicated that cascades occur during the autumn and winter due to cooling of the coastal waters which already have higher salinity due to evaporation during the summer months. The cross-shelf density gradient in this continental shelf was found to be maximum in July with a value of 14.23×10^{-6} kg m^{-4}.

ADDITIONAL INDEX WORDS: *Cascades, gliders, horizontal density gradient.*

INTRODUCTION

Dense shelf water is formed in coastal waters either by a decrease in temperature through cooling or increase in salinity from evaporation or ice formation (Figure 1). In Australian waters, high rates of evaporation, up to 2.5m per year, (Figure 2) with negligible rainfall and run-off cause a net loss of fresh water from the inner continental shelf. This results in coastal waters having higher salinity than offshore. During the winter months the shallower coastal waters lose heat due to convective processes resulting in colder water near the coast. The combination of higher salinity colder water closer to the coast results in a horizontal density gradient ($d\rho/dx$) with increasing density from the ocean towards the coast. This gradient drives a gravitational circulation with the offshore transport of denser water along the sea bed. This is controlled by vertical mixing resulting from turbulence generated by the wind and the tide (Hetzel *et al.*, 2013; Pattiaratchi *et al.*, 2011). Under low wind and tidal mixing conditions either a bottom gravity current or a surface plume will be present depending on the sign of the horizontal density gradient (Figure 1a, 1b) and under strong wind and tidal mixing conditions the water column is well mixed (Figure 1c, 1d).

The buoyancy-driven gravity current forms Dense Shelf Water Cascades: DSWC (Canals *et al.*, 2006; Pattiaratchi *et al.*, 2011; Shapiro *et al.*, 2003; Shearman and Brink, 2010).

Dense water cascades have been found in over 60 locations around the world and most of them happen in Polar Regions due to ice formation (Ivanov *et al.*, 2004). DSWC can play a major role in transporting terrestrial carbon, nutrients, larvae, low-oxygen water, sediments and also pollutants from coastal regions to deeper ocean.

DSWC have been documented previously for in some locations around Australia by research cruises and using moorings, usually for individual events during single seasons: E.g. North-west Australian shelf (Brink and Shearman, 2006; Shearman and Brink, 2010), Shark Bay (Pattiaratchi and Woo, 2009), Great Australian Bight (Petrusevics *et al.*, 2009), Spencer Gulf (Bowers and Lennon, 1987).

Seasonal variation of DSWC has been identified as a major feature through the deployment of ocean gliders in coastal waters along the Rottnest continental shelf using 13 months of data (Pattiaratchi *et al.*, 2011). Since these previous studies wide-ranging ocean glider data have become available, making it possible to investigate DSWC in other areas around Australia with different wind and tide conditions (Figure 2). In this paper, we used high spatial and temporal resolution temperature and salinity data collected using Teledyne Webb Research Slocum Gliders (Schofield *et al.*, 2007) to identify DSWC formation in the Pilbara region of Western Australia and to investigate DSWC dynamics in general.

DOI: 10.2112/SI75-106.1 received 15 October 2015; accepted in revision 15 January 2015

*Corresponding author: tanziha.mahjabin@research.uwa.edu.au

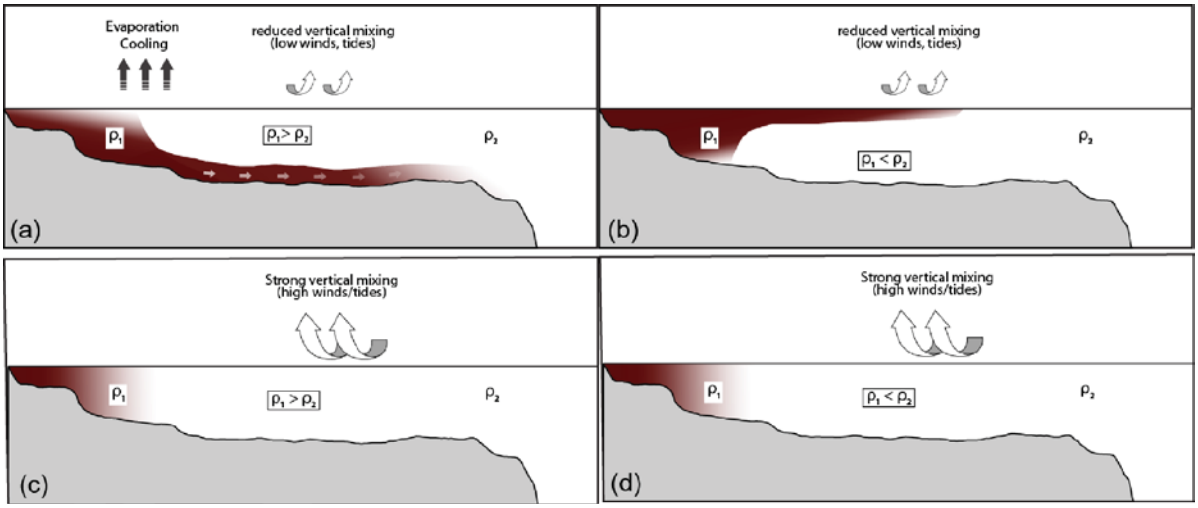

Figure 1. Effects of vertical mixing by wind and tide in the presence of a cross-shelf density gradient. Under low wind and tidal mixing conditions either a bottom gravity current or a surface plume will be present depending on the sign of the horizontal density gradient (a,b). Under strong vertical mixing conditions the water column is well mixed (c,d).

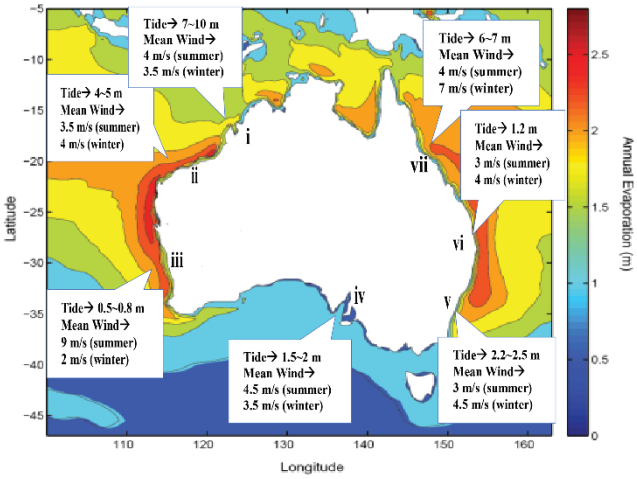

Figure 2. Annual evaporation rate in Australia (Yu, 2007) and selected study sites with tidal range and mean wind speed in summer and winter: (i) Kimberley; (ii) Pilbara; (iii) Two Rocks; (iv) Investigator Strait; (v) Port Stephens; (vi) Yamba; (vii) Capricorn Channel .

METHODS

Glider data from seven sites (Figure 2) are available to study DSWC under contrasting environmental: (i) Kimberley, north-west Australia: macro-tidal and moderate wind (Shearman and Brink, 2010); (ii) Pilbara, north-west Australia: macro-tidal (Holloway, 1983); (iii) Two Rocks, Western Australia: mainly wind driven (Pattiaratchi *et al.*, 1997) with low tidal range with diurnal tides (Pattiaratchi and Eliot, 2008); (iv) Investigator Strait, South Australia: mainly spring-neap tidal cycle driven (Nunes and Lennon, 1986; 1987); (v) Port Stephens New South Wales: moderate tide dominated (McPherson *et al.*, 2013) and strong wind (Geary, 1987); (vi) Yamba, New South Wales: mostly wind driven and micro-tide (Pritchard *et al.*, 2007) ; (vii) Capricorn Channel, Queensland: wind and tide driven (Andutta *et al.*, 2011). This paper focusses on data from the Pilbara site that has moderate wind and tidal forcing. Analysis of the other sites is the subject of future work.

We used Teledyne Webb Research Slocum Electric Glider (Schofield *et al.*, 2007) data which are operated by the Australian National Facility for Ocean Gliders (ANFOG) located at the University of Western Australia. The data are publicly available through the Integrated Marine Observing System (IMOS). Slocum gliders cover maximum depth range of 200 m. Gliders can measure data from the surface to up to 5 m above the seabed with mean speed of 25 km per day (Schofield *et al.*, 2007).

Gliders traverse a saw-tooth pattern using buoyancy control whilst moving forward to the target destination and navigating to a series of pre-programmed waypoints using GPS, internal dead reckoning and altimeter measurements. A Seabird-CTD, Chlorophyll-a fluorescence measuring sensor, coloured dissolved organic matter (CDOM) sensor, 660 nm Backscatter WETLabs BBFL2SLO optical sensor and an Aanderaa Oxygen Optode were attached to the ocean glider for this study. Slocum Gliders are small in size (1.8 m), efficient and economical to sample for much longer periods and higher spatial resolution compared to ships.

For this study, 19 transects from 13 sets of glider missions for the Pilbara were analysed over the period 2012 to 2015 considering specific tide and wind conditions. This included a total of 40248 vertical profiles and over 13.5 million data points. Analysis aimed to identify the presence of DSWC and the effects of wind and tide on the cascade formation. Quality

control of the data were done after the recovery of each glider and then actual

vehicle trajectory was transposed onto the Pilbara transects as a straight line. Each variable was interpolated onto a grid with vertical and horizontal resolutions of specific time and depth respectively. Density gradients were calculated by defining latitudes and longitudes of the starting shallow part and shelf break of the transects, while the direction of shallow part to shelf break was considered as positive. Tidal data were predicted using the TPXO7.2 global database and wind data were obtained from the European Centre for Medium-Range Weather Forecast Interim Reanalysis (ECMWF ERA-I) (Dee *et al.*, 2011).

Vertical temperature stratification has been compared with the local wind speed cubed (W^3) and bottom current speed cubed ($|U_b^3|$). These are proportional to available mixing energy from the wind and tidal currents respectively (e.g. Nunes and Lennon, 1987; Nunes Vaz *et al.*, 1990).

RESULTS

Analysis of the 19 transects of ocean glider data in the Pilbara, collected between 2012~2015, indicated that DSWC were a common occurrence during the winter months when cross-shelf density gradients formed with denser water near the coast. Figure 3 represents the location of the glider path near Pilbara on July 2012 which is chosen for an example.

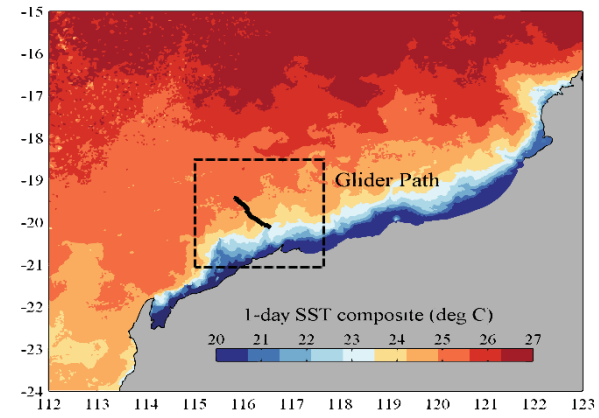

Figure 3. Glider path location for Pilbara July 2012 is shown on the Sea Surface Temperature map.

Cross-shelf transects (Figure 4) indicated that both temperature and salinity contributed to the dense water formation. The dense water then flowed along the sea bed and spilled off of the continental shelf reaching depths of up to 150m (Figure 4). This DSWC was observed during July 2012 when high salinity water had accumulated near the coast due to summer evaporation and subsequently this water was cooled and the gradient became strong enough to force the inshore water off the shelf. Spatial patterns of fluorescence, sediment and oxygen closely followed density, indicating that these properties were influenced by the DSWC (Figure 5), and were likely transported along the sea bed from the continental shelf to the open ocean.

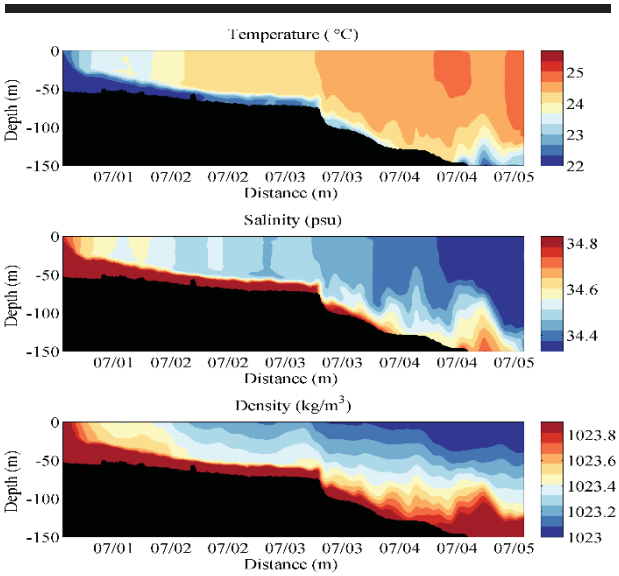

Figure 4. Cross-shelf profile of DSWC as measured by a Slocum glider on the Pilbara coast during July 2012.

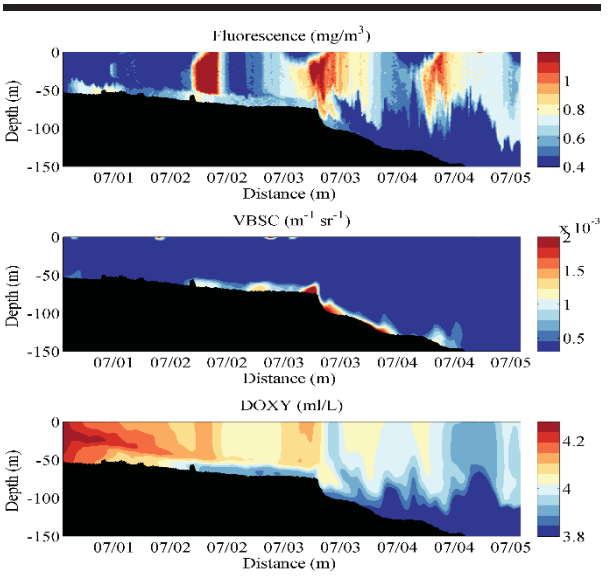

Figure 5. Ancillary water properties (Fluorescence, sediment and oxygen) as measured by a Slocum glider on the Pilbara coast during July 2012.

Driving force for the formation of cascades

Analysis of all 19 transects suggested that winter cooling was an important contributor to DSWC formation in the Pilbara, with a majority of the cascades occurring during winter months. In winter the winds were weaker and the cross-shelf density gradients were enhanced by cooling (Figure 6).sediment supply and the concentration of wave energy removes the sand, causing erosion (Figure 7).

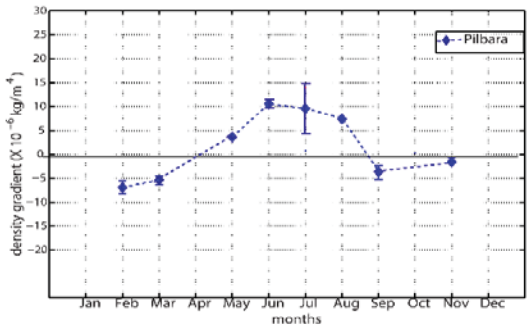

Figure 6. The monthly density gradient for Pilbara showing the mean density gradient for all available data for each month. The error bar for July indicated the range of values calculated using different transects.

Data from multiple seasons indicated that favorable density gradients formed repeatedly in autumn and winter months of each year and DSWC occurred whenever the vertical mixing from wind and tide was weaker.

Using multiple transects acquired over several years we calculated the average horizontal density gradient for each month of the year (Figure 6). The calculated positive density gradient (onshore – offshore) in Pilbara was maximum in July as 14.23x 10^{-6} kgm^{-4}. The gradient became negative during the summer. The seasonality of cascade formation in Pilbara closely followed the density gradient with all observed cascades requiring a positive density gradient as occurred between April and September.

Control of cascade formation by turbulent vertical mixing

The data suggested that whenever the horizontal density gradient is strong, we can expect cascade formation. However, wind mixing and tidal mixing were also capable of inhibiting the formation of DSWC and the relative importance of these factors varies around Australia.

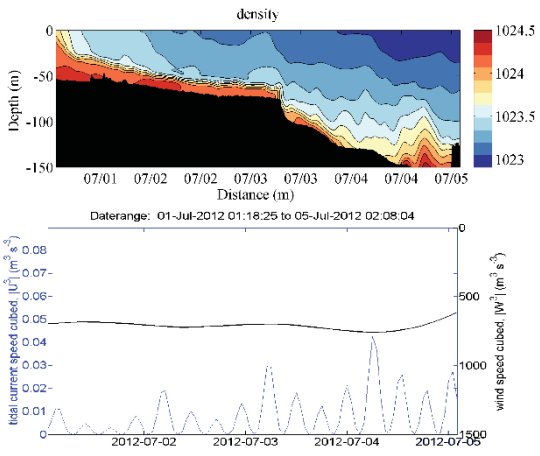

Figure 7. Pilbara transect in July 2012 with wind and tidal mixing energy proxies (windspeed^3 and tidal current speed^3) with DSWC present.

Under low wind and tidal mixing conditions, the water column stratifies and water flows offshore along the sea bed; whereas high mixing inhibits stratification and offshore transport of water. Tidal amplitudes vary along the Australian coast and influence cross-shelf water movement. Two contrasting transects from Pilbara plotted with proxies for wind and tidal mixing (windspeed^3 and tidal current speed^3) illustrate the effects of vertical mixing on DSWC formation (Figure 7 and Figure 8). The first transect (Figure 7) showed a clear DSWC and weak tidal currents and wind. Cascades were absent in the second transect (Figure 8) with higher current speeds and slightly stronger winds.

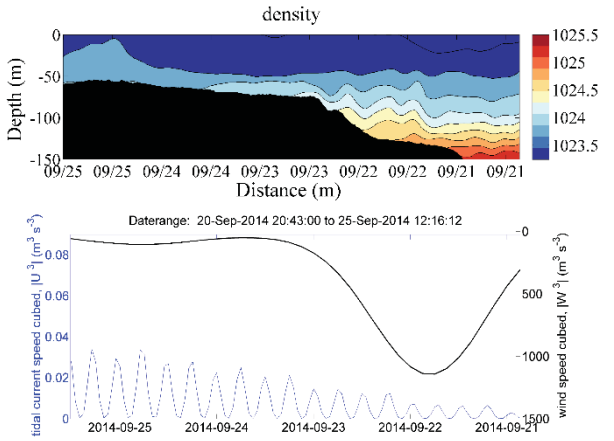

Figure 8. Pilbara transect in September 2014 showing absence of cascade and stronger tidal currents and windspeeds.

DISCUSSION

Dense water flows are the result of either intense cooling or excess evaporation. Analysis of 19 ocean glider transects collected between 2012 and 2015 in the Pilbara region of Western Australia indicated that DSWC were a common occurrence, particularly in Autumn and Winter seasons, even under relatively strong tide and wind conditions. It has been shown previously that cascades are controlled by turbulence generated by wind and tide (Hetzel *et al.*, 2013; Pattiaratchi *et al.*, 2011). However this study data suggests that the density gradients dominate over mixing energy most of the time in the Pilbara during Autumn and Winter seasons. Cascade occurs in this period of time with velocities between 2~3 cm/s in Pilbara region (Bahmanpour *et al*., 2016), which is comparable with other location where it was measured before. DSWC have been documented previously for a single season in North-west Australian shelf (Brink and Shearman, 2006; Shearman and Brink, 2010), but here several years data allowed us to observe the seasonality of cascade formation for Pilbara region.

The next step will be to analyse the data for other 6 study regions. If the results also indicate that DSWC occur even where tides or winds are strong, it will confirm that dense shelf water cascades are an important process for cross shelf exchange around the entire Australian continent. The broad range of ocean glider deployments presents a unique opportunity to examine DSWC over such a large and varied coastline.

CONCLUSIONS

An analysis of the dynamics of DSWC formation in the Pilbara region of Western Australia was completed based on 19 individual transects covering three years (2012-2015). The formation of DSWC in the Pilbara region of Western Australia was found to depend on the balance between the cross shelf density gradient and vertical mixing by wind and tide. When the density gradient is strong, we can expect DSWC; but when the mixing is strong enough to make the shallow water vertically mixed DSWC will be absent. During autumn and winter the cross shelf density gradient remains positive and dominates over mixing. As a result DSWC occur in the North-western Australian coast of Pilbara despite the relatively large tidal range, with strongest DSWC events occurring during neap tides and weak winds. Further analysis of 124 remaining transects will be undertaken for other selected locations around Australia to determine whether similar relationships exist between cross-shelf density gradients, vertical mixing, and DSWC.

ACKNOWLEDGMENTS

All ocean glider data used in this paper are from the Integrated Marine Observing System (IMOS) which are operated by the Australian National Facility for Ocean Gliders (ANFOG) located at the University of Western Australia. IMOS is funded by the National Collaborative Research Infrastructure Strategy and the Super Science Initiative. The postgraduate research has been funded by Scholarship International Research Fees (SIRF) and University International Stipend.

LITERATURE CITED

Andutta, F.P.; Ridd, P.V., and Wolanski, E., 2011. Dynamics of hypersaline coastal waters in the Great Barrier Reef. *Estuarine, Coastal and Shelf Science*, *94*(4), 299-305.

Bahmanpour, M.H.; Pattiaratchi, C., Wijeratne, E.M.S., Steinberg, C., and D'Adamo, N., 2016. Multi-year observation of a boundary current along the shelf edge of North Western Australia. *In:* Vila-Concejo, A.; Bruce, E.; Kennedy, D.M., and McCarroll, R.J. (eds.), *Proceedings of the 14th International Coastal Symposium*. *Journal of Coastal Research*, Special Issue No. 75.

Bowers, D. G.and Lennon, G. W., 1987. Observations of Stratified Flow over a Bottom Gradient in a Coastal Sea. *Cont Shelf Res*, *7*(9), 1105-1121.

Brink, K.H. and Shearman, R.K., 2006. Bottom boundary layer flow and salt injection from the continental shelf to slope. *Geophys Res Lett*, *33*(13).

Canals, M.; Puig, P.; de Madron, X. D.; Heussner, S.; Palanques, A., and Fabres, J., 2006. Flushing submarine canyons. *Nature*, *444*(7117), 354-357.

Dee, D.P., et al., 2011. The ERA-Interim reanalysis: configuration and performance of the data assimilation system. *Q J Roy Meteor Soc*, *137*(656), 553-597.

Geary, M. G. (1987), Port Stephens - Salamander Bay, Physical processes data base *Rep. 85045*, Public Work Department-Civil Engineering division.

Hetzel, Y.; Pattiaratchi, C., and Lowe, R., 2013. Intermittent dense water outflows under variable tidal forcing in Shark Bay, Western Australia. *Cont Shelf Res*, *66*, 36-48.

Holloway, P. E., 1983. Internal Tides on the Australian Northwest Shelf - a Preliminary Investigation. *J Phys Oceanogr*, *13*(8), 1357-1370.

Ivanov, V. V.; Shapiro, G. I.; Huthnance, J. M.; Aleynik, D. L., and Golovin, P. N., 2004. Cascades of dense water around the world ocean. *Prog Oceanogr*, *60*(1), 47-98.

McPherson, B.; S. Young; B. Modra; E. Couriel; B. You; D Hanslow; D.C.; T Baldock, and Nielsen, P., 2013. Penetration of Tides and Tidal Anomalies in New South Wales Estuaries. Proceedings of the *Coasts and Ports 2013: 21st Australasian Coastal and Ocean Engineering Conference and the 14th Australasian Port and Harbour Conference* (Sydney, N.S.W), pp. 537-542.

Nunes, R.A. and Lennon, G.W., 1986. Physical Property Distributions and Seasonal Trends in Spencer Gulf, South-Australia - an Inverse Estuary. *Aust J Mar Fresh Res*, *37*(1), 39-53.

Nunes, R.A. and Lennon, G.W., 1987. Episodic Stratification and Gravity Currents in a Marine-Environment of Modulated Turbulence. *J Geophys Res-Oceans*, *92*(C5), 5465-5480.

Nunes Vaz, R.A.; Lennon, G.W., and Bowers, D.G., 1990. Physical Behavior of a Large, Negative or Inverse Estuary. *Cont Shelf Res*, *10*(3), 277-304.

Pattiaratchi, C. and Eliot, M., 2008. Sea Level Variability in South-West Australia: From Hours to Decades. In: J. M. Smith (eds.), *Proceedings of the international coastal engineering conference* (New Jersey, London)., pp. 1186-1198.

Pattiaratchi, C. and Woo, M., 2009. The mean state of the Leeuwin Current system between North West Cape and Cape Leeuwin. *Journal of the Royal Society of Western Australia*, *92*, 221-241.

Pattiaratchi, C.; Hegge, B.; Gould, J., and Eliot, I., 1997. Impact of sea-breeze activity on nearshore and foreshore processes in southwestern Australia. *Cont Shelf Res*, *17*(13), 1539-1560.

Pattiaratchi, C.; Hollings, B.; Woo, M., and Welhena, T., 2011. Dense shelf water formation along the south-west Australian inner shelf. *Geophys Res Lett*, *38*(10), L10609.

Petrusevics, P.; Bye, J.A.T.; Fahlbusch, V.; Hammat, J.; Tippins, D. R., and van Wijk, E., 2009. High salinity winter outflow from a mega inverse-estuary-the Great Australian Bight. *Cont Shelf Res*, *29*(2), 371-380.

Pritchard, T.; Holden, C.; Lee, R.; Black, K., and Healy, T., 2007. Dynamics and Dispersion in the Coastal Boundary Layer off Coffs Harbour in Eastern Australia. *J Coastal Res*, 848-857.

Schofield, O., et al., 2007. Slocum gliders: robust and ready. *J Field Robot*, *24*(6), 473-485.

Shapiro, G.I.; Huthnance, J.M., and Ivanov, V.V., 2003. Dense water cascading off the continental shelf. *J Geophys Res-Oceans*, *108*(C12).

Shearman, R.K. and Brink, K. H., 2010. Evaporative dense water formation and cross-shelf exchange over the northwest Australian inner shelf. *Journal of Geophysical Research*, *115*(C6), C06027.

Journal of Coastal Research	SI	75	532-536	Coconut Creek, Florida	2016

Seasonal Variations of the Amazon River Plume with Focus on the Eastern Sector

Angela C.C. Mascarenhas [†*], Gabriela S. Gomes[†], Antônia P.Y. Lima[†], Heriton K.N. da Silva[†], Leandro S. Santana[†], Renan P. Rosário[‡], and Marcelo Rollnic[†‡]

[†]Physical Oceanography Laboratory, Oceanography Faculty
Federal University of Pará
Belém, Brazil

[‡]Marine Geophysical Laboratory, CPGf
Federal University of Pará
Belém, Brazil

www.cerf-jcr.org

www.JCRonline.org

ABSTRACT

Mascarenhas, A.C.C.; Gomes, G.S.; Lima, A.P.Y.; Silva, H.K.N.; Santana, L.S.; Rosário, R.P., and Rollnic, M., 2016. Seasonal variations of the Amazon River Plume with Focus on the Eastern Sector. *In:* Vila-Concejo, A.; Bruce, E.; Kennedy, D.M., and McCarroll, R.J. (eds.), *Proceedings of the 14th International Coastal Symposium* (Sydney, Australia). *Journal of Coastal Research*, Special Issue, No. 75, pp. 532-536. Coconut Creek (Florida), ISSN 0749-0208.

The Amazon Continental Shelf (ACS) is a highly dynamic environment as a result of physical processes (tidal, current and wind) and the large river discharge from Amazon and Pará Rivers. This research aims to determine seasonal variations of the plume of the Amazon River in the eastern sector, near the Pará River mouth. Five oceanographic campaigns were conducted on the ACS: April and October 2013; May, July and October 2014. The sampling line followed the shape of the Cabo Maguari (Marajo Island) to 260 km in the shelf break. Nine vertical profiles of conductivity, temperature and pressure and turbidity were collected. The plume reaches a perpendicular distance up to 200 km from the coast during period of maximum rivers discharge (April and May). During low river discharge (October 2013 and 2014), the plume was restricted to 30 km and presented relative high levels of salinity (20 PSU). The Coastal Water, characterized by high temperatures and low salinity was limited to about -15 m depth. The Tropical Surface Water, which is considered to have a high salinity and temperature, was identified in the last sample point to 260 km from the coast in 2014.As theis water body characteristics are commonly found in the North Brazil Current, it can be concluded that water mass invades the Amazon continental shelf. Even in low discharge conditions, adjacent ocean water do not invade the the Amazon River mouth, only the Pará River estuary. Because of that, these estuaries present different physical and biological processes.

ADDITIONAL INDEX WORDS: *Amazon Continental Shelf, Cabo Maguari, CTD.*

INTRODUCTION

The Amazon Continental Shelf (ACS) is a highly energetic environment due to both variation in intensity of the physical processes (tides, currents, and winds) acting in the region, and the large water supply laden with suspended particulate matter, deriving from the discharge of the Amazon and Pará Rivers (Gabioux *et al*., 2005). The shelf is approximately 330 km long next to the mouth of the Amazon River and the -100 m isobath outlines its break (Nittrouer and DeMaster, 1986). It also has three subdivisions: inner, intermediate, and outer ACS (Silva, 2006).

In a global scale, the Amazon River corresponds to approximately 16% to 20% of the total continental waters discharged into the ocean (Molinier *et al*., 1996); it has a minimum water discharge of 100,000 m3.s^{-1} and a maximum of 220,000 m^3.s^{-1} (Geyer *et al*., 1996) and a sedimentary load ranging from 22 mg.L^{-1} to 125 mg.L^{-1} (Gibbs, 1967). Estimates of freshwater supply to the Atlantic Ocean through the Amazon River might be calculated based on the sum of its outflow in Óbidos and two main rivers, Tapajós and Xingu. Tapajós and Xingu rivers combined tend to average 10% of the Amazon River flow, also resulting in the low-salinity plume present in the shelf (Gabioux, 2002). During the maximum discharge season of the Amazonian fluvial system, around 85% of the sediments discharged onto the shelf are comprised of silt and clay, resulting from highly energetic coastal dynamics (Nittrouer and DeMaster, 1986). The Pará River, in turn, is comprised of a hydrographic system formed by the confluence of several of its tributaries, and its main source is the Tocantins River (Martins, 2010; Prestes *et al*., 2014). The Tocantins River discharge (resulting transport) ranges from 10,828 m³.s^{-1} to 74,391 m³.s^{-1} (Prestes *et al*., 2014).

The region has high rainfall rates, and the presence of the Intertropical Convergence Zone (ITCZ), typical of low latitude regions, in addition to a trade-wind regime throughout the year. Together, these two forcings show seasonal variations. When ITCZ is located near the equator (between March and April), the shelf is subject to the action of northeast trade winds. When ITCZ migrates north (≅ 5°N), in August and September, the region is under the predominant influence of southeast trade winds (Fontes, 2000).

Previous studies indicate that the main astronomic forcing in the ACS region, classified as a meso- to macrotidal region, is the semidiurnal tide regime, with ranges of up to 1.5 (next to the mouth of the Amazon and Pará Rivers) and 3.5 m along the

DOI: 10.2112/SI75-107.1 received 15 October 2015; accepted in revision 15 January 2015
*Corresponding author: carolinacidon@gmail.com

coast. In the upper Pará River, the tide has a nearly stationary wave behavior (Beardsley *et al*., 1995). Elevation and velocities change both monthly and fortnightly, with maximum neap of c. 2 $m.s^{-1}$ and minimum spring tides of c. 0.7 $m.s^{-1}$ (Geyer and Kineke, 1995). The North Brazil Current (NBC) works as the main contour current near the shelf, predominantly towards the northwest, with velocities between 0.5 and 1.0 $m.s^{-1}$ and seasonal variations (Richardson and McKee, 1984).

Hydro-sedimentary supply from these rivers interferes directly with physical, chemical, geological, and biological aspects across the entire ACS due to the formation of estuarine plume in the Amazon and Pará Rivers (Santos *et al*., 2008). The patterns observed in the ACS for physico-chemical parameters such as salinity and turbidity are determined by the spatio-temporal dynamics of the plume; consequently, the levels of primary production in the region shall also be influenced by this variation (Dagg *et al*., 2004).

In addition to hydrodynamic processes, meteorological factors also control the Amazon drainage system. Hence, the seasonality of rainfall levels, which defines two distinct seasons throughout the year, the wet season from December to May and the dry season from July to October, with a transitional season in June and November, are also an agent in the plume dynamics (Figueroa and Nobre, 1990). In the adjacent ocean there is the North Brazil Current (NBC), which flows along the Amazon shelf break, always towards the northeast (Richardson *et al*., 1994). This current intensifies in the period ranging from July to August (35 Sv, Sv = 10^6 $m.s^{-1}$) and weakens (13 Sv) from May to April (Johns *et al*., 1998).

Fluvial/oceanic interaction in the ACS makes it an environment with unique characteristics, vital for its understanding, which raises interest and encourages several studies in its western portion (area of greater influence from the Amazon River), as shown by Gabioux *et al*. (2005) and Nittrouer and DeMaster (1995). However, few studies have focused the mouth of the Pará River. Therefore, this study aimed to check spatio-temporal variations of the Amazon and Pará River plume in the eastern portion, near the mouth of the Pará River.

METHODS

Five oceanographic campaigns were carried out on the ACS: April and October, 2013; May, July, and October, 2014. The sampling line started at the Maguari Cape (Marajó Island), 260 km from the shelf break (Figure 1). Nine vertical conductivity, temperature, pressure (CTD SBE-37SM), and turbidity profiles (from the surface layer to a 30-m depth) were collected.

Pratical Salinity (PSS-78) was converted using the computer package seawater (Morgan, 1994), with algorithms adopted by UNESCO in terms of electrical conductivity, temperature, and pressure ratio (UNESCO, 1981). Profiles underwent peak (spikes) correction and interpolation, preferably using descending CTD profiles.

Turbidity was obtained together with hydrographic parameters, using an OBS sensor (Optical Backscatter Sensor), Infinity-turbi ATU75W-USB model. This sensor is calibrated using an internal algorithm, which relates the amount of retro-reflected infrared light through the water to equivalent concentrations of factory calibrated particles. Device accuracy is given for high and low concentrations; for low concentrations, it is advisable to use FTU, Formazine Turbidity Unit, (accuracy of ± 0.3 FTU or ± 2% and measurement interval of 0-1000 FTU), and for high concentrations, part per million is advisable (ppm, with accuracy of ± 10 ppm or ± 5% and measurement interval of 0-100.000). In this study, FTU will be used as turbidity unit.

To calculate the distance from the plume, salinity values lower than 30 and turbidity values higher than 10 FTU were adopted as reference.

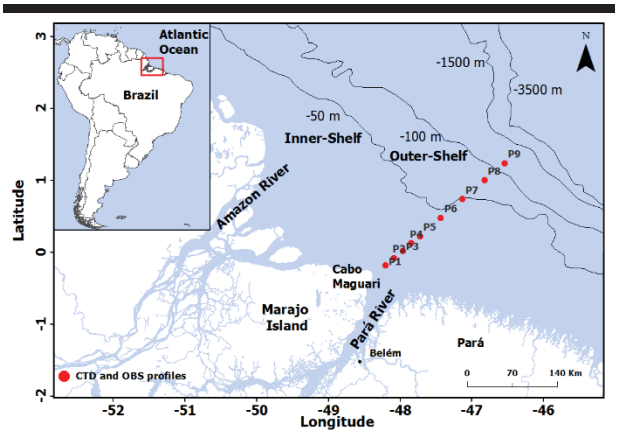

Figure 1. Location of the study area with georeferenced points. Northern Continental Shelf, Coast of Pará State, Brazil.

RESULTS

Salinity values indicated a plume range of up to 130 km from the coast during April 2013, related to high fluvial discharge season, and when turbidity was analyzed as indicator of plume, the range was 65 km (Figure 2 A/B). In October, 2013, in the low fluvial discharge season, plume range retracted, with maximum ranges of 50 km for salinity and 70 km for turbidity (Figure 2 C/D). Overall, 2014 showed larger distances compared to 2013. In May (Figure 2 E/F) and July (Figure 2 G/H), 2014 (high discharge and transitional seasons), the distances between sampling months were the largest. Salinity values indicated a distance of up to 230 km in May, while it reached 120 km from the coast in July. Turbidity analyses recorded a lower variation in range, of 90 km (May) and 45 km (July). In October 2014, the plume reached distances of up to 70 km from the coast with salinity values and 60 km with turbidity values (Figure 2I/J). Finally, estuarine plume obtained the highest distances with salinity values and the lowest with turbidity values in high fluvial discharge seasons, following the opposite pattern in low fluvial discharge seasons.

Analyzing vertical variation of salinity values in the plume, we noticed that the influence of the plume reaches -26 m of depth (c. 115 km) in high discharge seasons in 2013, while there was a marked retraction in low discharge season, reaching only the superficial layer of the water column to a -4 m depth (c. 40 km). Maximum vertical influence of salinity was also observed in the high discharge season of 2014, with -28 m depth (c. 100 km), and -3 m depth (c. 35 km) in the low discharge season. Analyzing vertical turbidity profile, we observed that the plume

influence on the water column in high discharge months extended from the surface layer to -30 m depth 90 km off the coast, differing from the low discharge season, which reached the maximum depth of -20 m.

Regarding tide influence, plume reached the highest distances from the coast during spring tide compared to neap tide. Considering salinity values, the months of spring tide (May and July, 2014) reached the maximum distance of 230 km from the coast, while plume range was restricted to 130 km in neap tide. Regarding turbidity values, the maximum distance reached by the plume was 90 km from the coast.

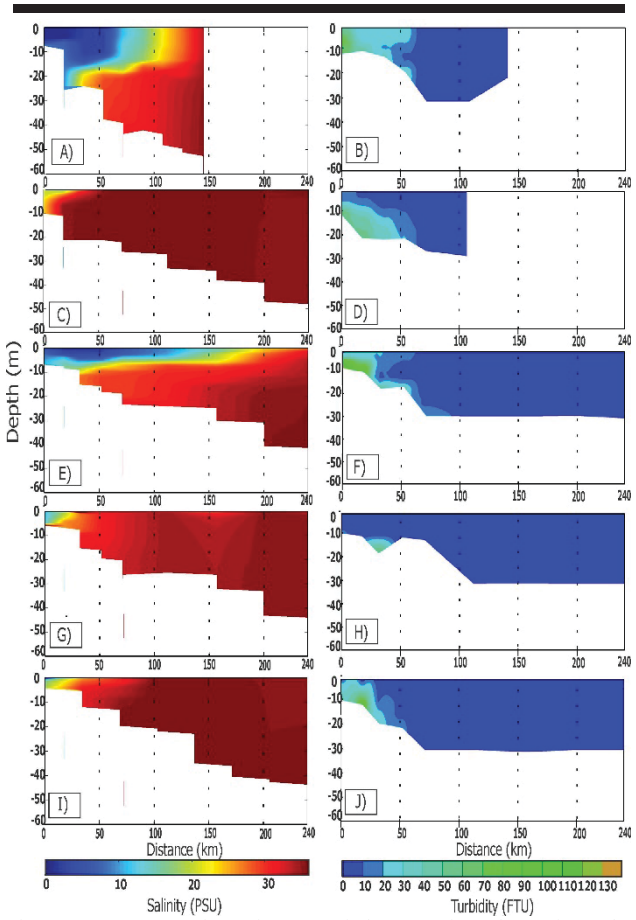

Figure 2. Demonstration of range of the estuarine plume from the parameters analyzed: Salinity (left) and Turbidity (right). April and October, 2013 (A/B, C/D); May, July and October, 2014 (E/F, G/H, I/J).

The dry season had the highest salinity averages and the lowest turbidity averages, while the lowest salinity averages and the highest turbidity averages were observed in the wet season (Table 1).

Table 1. *Salinity and turbidity average values of the sampling months.*

Season	Tide	Salinity (PSU)			
		Max	Min	Average (offshore)	Average (nearshore)
2013 Wet	Spring	35.18	1	33	5.9
2013 Dry	Spring	36.48	20.17	35.5	28.8
2014 Wet	Neap	35.77	2.5	34	8.85
2014 Transition	Neap	35.33	11.5	35	18
2014 Dry	Spring	36.27	17.7	35.39	26
Season	**Tide**	**Turbidity (FTU)**			
		Max	Min	Average (offshore)	Average (nearshore)
2013 Wet	Spring	130	0.2	0.2	135
2013 Dry	Spring	35	0.2	0.7	75
2014 Wet	Neap	53	0	0.1	86
2014 Transition	Neap	40	0	0.9	78
2014 Dry	Spring	25	0	0.6	80

Water masses are defined by the diagram that correlates temperature (T) and salinity (S_p) (Figure 3). The T-S diagram of the last vertical profile (P9) identified the presence of Coastal Water (CW) and a tendency for Tropical Water (Tropical Surface Water - TSW) inflow.

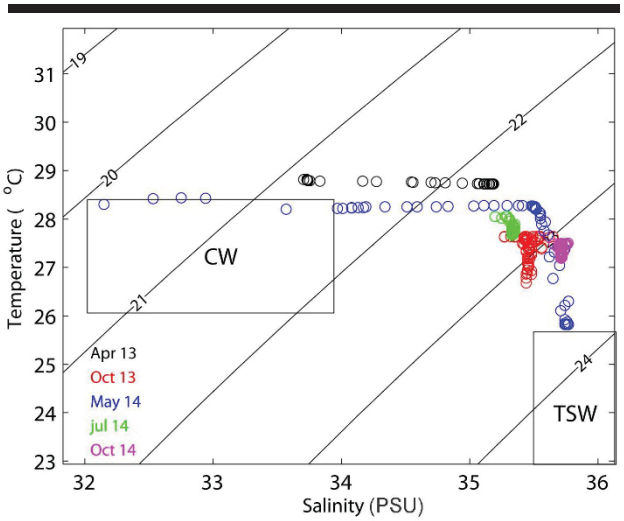

Figure 3. T-S diagram based on data of the vertical profile 9 for April and October, 2013; and May, July, and October, 2014. The termohaline indices of two water masses are identified in the diagram: Coastal Water (CW) and Tropical Surface Water (TSW).

DISCUSSION

Considering only salinity in the eastern portion, plume range reached up to approximately 150 km in April, 2013, during the high discharge season of the Pará River; while the plume extended for approximately 250 km from the coast during the high discharge season of the Amazon River in May, 2014. Analyzing the plume, Lentz (1995) also observed the seasonal

variability of the water discharge and its influence, corroborated by the data obtained. Therefore, even in the portion closer to the Pará River estuary, the Amazon River has a great influence, and although river discharge peaks are not the same (Figure 4), the sum of the Pará and Amazon River regimes makes the plume reach large distances over the continental shelf.

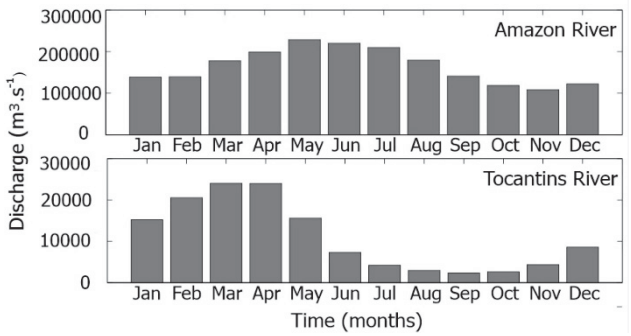

Figure 4. Historical average discharge of Amazonas and Pará rivers demonstrating the difference between them, calculated from data from the hydrographic basin of the Amazon and Tocantins provided by the National Water Agency (NWA).

Turbidity values in April, 2013, and May, 2014, seem to be related to plume advection directly into the river. On the other hand, in transitional and low discharge seasons, turbidity seems to be more linked to a bottom resuspension process, which is better observed in July, 2014, when the discharge of the Amazon River is more effective compared to Pará River. According to Torres (1997), the surface of the Amazon River and tributaries has the highest turbidity values in the high discharge season and the lowest values in the low discharge season. The values obtained by Torres (1997) show a coastal zone pattern (≅35 FTU) when compared to studies in continental areas, such as Hughes *et al.,* (1998) in Hawkesbury River, Australia, where they found maximum values of 280 FTU.

Geyer *et al.* (1996) also observed that the tidal regime on the shelf has a fortnightly periodicity (neap and spring) and contributes to the variability of parameters along the shelf, as observed in our study, which recorded a quite higher plume range in spring tides (lower intensity) than in neap tides. According to the study conducted by Soares (1977), this might be explained by the fact that it is relatively easy to penetrate river waters in the oceanic region in periods with lower tide intensity, except for neap tide periods. When salinity values were considered, May and July (spring) reached large depths (25 m), as well as large distances. Checking turbidity values, larger plume distances were also observed (140 km) in spring tide.

Even though wind regime wasn't checked for the region in our study, its influence might be inferred in the spatial variation of the plume. According to Lentz and Limeburner (1995), wind is an intermittent phenomenon in plume blocking, and its width might or might not increase depending on the direction of the winds.

On that matter, a study conducted by Silva *et al.* (2005) identified the presence of water masses in the outer ACS, possibly transported by the North Brazil Current, which proves the influence of the current on the shelf region, agreeing with the data obtained in our study. Unlike the above-mentioned study, which identified four water masses, two water masses were recorded in the present study: Coastal Water (CW), characterized by high temperature and low salinity values, and Tropical Surface Water (TSW), with milder temperatures and relatively higher salinity values. Silva *et al*., (2005) also identified the characteristic of no saltwater intrusion Amazon River mouth from the adjacent oceanic region, with measurements in the low river discharge period. Feitosa (1988) consider salinity an important factor in the distribution of aquatic organisms, thus becoming an ecological barrier for certain species, which may explain the biological difference between the said rivers (Amazonas and Pará). Furthermore, in a summarized analysis of current measurements carried out by AMASSEDS Project (An Interdisciplinary Investigation of a Complex Coastal Environment) (Johns *et al.,* 1998), following a sampling line that is quite similar to the one in our study, a great seasonal influence of NBC was indicated in the region, nearly restricted to the continental slope in high fluvial discharge seasons, and broader and deeper in low discharge seasons.

CONCLUSIONS

Data were analyzed with the purpose of monitoring plume behavior in the Amazon and Pará Rivers on the continental shelf under different conditions. Among the results, salinity was pointed out as the most effective qualitative parameter for plume monitoring, both seasonally and spatially, due to the fact that turbidity is subject to the influence of external factors (biological and geomorphological) in the measurement regions.

The data indicated a seasonal variation in the distance reached by the plume, possibly connected to the rainfall regime in the study years. Another factor is tidal component, generating significant differences in the order of kilometers between spring and neap tides. Due to the lower momentum of oceanic water inflow in the Amazon and Pará Rivers, spring tide proved to be more active in spreading plume along the shelf.

Waters with high salinity values and low temperatures were identified, making it possible to infer the presence of water masses typical of the North Brazil Current at points farther from the coast, near the shelf break, especially in conditions of low fluvial discharge. Furthermore, we also observed that even in low discharge conditions, oceanic waters do not penetrate the Amazon River mouth; they only penetrate the Pará River estuary, thus attributing several of its physical processes. This suggests the need for greater attention by studies related to this area.

ACKNOWLEDGMENTS

This study is one of the results of the project "INCT AmbTropic-Environments Tropical Marine: Heterogeneity Spatial-temporal and Responses to Climate Change" financed by the National Institute of Science and Technology (NIST), which includes about 200 scientists distributed in more than 20 institutions teaching and research in the Brazilian north-northeast territory. The authors would like to acknowledge the Federal University of Pará for giving their premises, the Physical Oceanography Laboratory for providing all the

necessary structure to carring out this and the researchers from the Marine Geophysical Laboratory for all scientific support along this work.

LITERATURE CITED

Agência Nacional de Águas - ANA. http://www.ana.gov.br.

Beardsley, R.C.; Candela, J.; Limeburner, R.; Geyer, W.R.; Lentz, S.J.; Belmiro, M.C.; Cacchione, D., and Carneiro, N., 1995. The M2 tide on the Amazon shelf. *Journal of Geophysical Research,* 100(2), 2283-2320. doi: 10.1029/94JC01688

Dagga, M.; Benner, R.; Lohrenz, S., and Lawrence, D., 2004. Transformation of dissolved and particulate materials on continental shelves influenced by large rivers: plume processes. *Continental Shelf Research,* 24(7-8), 833-858. doi:10.1016/j.csr.2004.02.003

Feitosa, F.A.N., 1998. Produção primária do fitoplâncton correlacionada com parâmetros bióticos e abióticos na Bacia do Pina. Recife, Brasil: Universidade Federal de Pernambuco, Dissertação de Mestrado, 270p.

Figueroa, S.N. and Nobre, C., 1990. Precipitation distribution over Central and Western Tropical South America. *Climanalise Boletim de Monitoramento e Analise Climatica,* 5(6), 36-45.

Filizola, N. and Guyot, J.L., 2011. Fluxo de sedimentos em suspensão nos rios da Amazônia. *Revista Brasileira de Geociencias,* 41(4), 566-576.

Fontes, C.R.F., 2000. Estudo numérico da circulação na Plataforma Continental Amazônica (PCA). São Paulo, Brasil: Universidade de São Paulo, Tese de Doutorado, 138p.

Gabioux, M., 2002. Influência da lama em suspensão na propagação da maré na plataforma Amazônica. Rio de Janeiro, Brasil: Universidade Federal do Rio de Janeiro, Tese de Doutorado, 109p.

Gabioux, M.; Vinzon, S.B., and Paiva, A.M., 2005. Tidal propagation over fluid mud layers on the Amazon shelf. *Continental Shelf Research,* 25(1), 113-125. doi:10.1016/j.csr.2004.09.001

Geyer, W.R. and Kineke, G.C., 1995. Observations of currents and water properties in the Amazon front zone. *Journal of Geophysical Research*, 100(2), 2321-2340. doi: 10.1029/94JC02657

Geyer, W. R.; Beardsley, R.C.; Lentz, S.J.; Candela, J.; Limeburner, R.; Johns, W.E.; Castro, B.M., and Soares, I.D., 1996. Physical oceanography of the Amazon Shelf. *Continental Shelf Research,* 16(5- 6), 575-616. doi:10.1016/0278-4343(95)00051-8

Gibbs, R.J., 1967. The Geochemistry of the Amazon river system. Part I. The fator that control the salinity and the composition and concentration of the suspended solids. *Geological Society of American Bulletin,* 78(10), 1203-1232. doi: 10.1130/0016-7606(1967)78[1203:TGOTAR]2.0.CO;2

Hughes, M.G.; Harris, P.T., and Hubble, T.C.T., 1998. Dynamics of the turbidity maximum zone in a micro-tidal estuary: Hawkesbury River, Australia. *Sedimentology*, 45(2), 397-410. doi: 10.1046/j.1365-3091.1998.0159f.x

Johns, W.E.; Lee, T.N.; Beardsley, R.C.; Candela, J.; Limeburner, R., and Castro, B. 1998. Annual Cycle and Variability of the North Brazil Current. *Journal of Physical Oceanography,* 28(1), 103-128. doi: 10.1175/1520-0485(1998)028<0103:ACAVOT>2.0.CO;2

Kuelh, S.A.; Nittrouer, C.A., and DeMaster, D.J., 1986. Distribution of sedimentary structures in the Amazon Subaqueous delta. *Continental Shelf Research,* 6(1-2), 311-336. doi: 10.1016/0278-4343(86)90066-X

Lentz, S.J. and Limeburner, R., 1995. The Amazon river plume during AMASSEDS: spatial characteristics and salinity variability. *Journal of Geophysical Research,* 100(2), 2255--2375. doi: 10.1029/94JC01411

Martins, S.E.M., 2010. Geomorfologia e Sedimentologia de depósitos sedimentares recentes da porção superior do Estuário do Rio Pará (Baía de Marajó, Amazônia). Porto Alegre, Brasil: Universidade Federal do Rio Grande do Sul, Tese de Doutorado, 119p.

Prestes, Y.O.; Rollnic, M.; Sousa, M., and Rosario, R.P., 2014. Volume Transport in the Tidal Limit of the Para River, Brazil. *Proceedings of the 17th Physics of Estuaries and Coastal Seas* (Porto de Galinhas, Pernambuco), pp. 1-2.

Richardson, P.L.; Arnault, S.; Garzoli, S., and Brown W.S., 1994. North Brazil Current retroflection eddies. *Journal of Geophysical Research,* 99(C3), 997-1014. doi: 10.1029/93JC03486

Richardson, P.L. and Mckee, T.K., 1984. Average seasonal variations of the Atlantic Equatorial currents from historical ship drifts. *Journal of Physical Oceanography,* 14(7), 1226--1238.

Santos, M.L.S.; Medeiros, C.; Muniz K.; Feitosa, F.A.N.; Schwamborn R., and Macedo, S.J., 2008. Influence of the Amazon and Para Rivers on Water Composition and Phytoplankton Biomass on the Adjacent Shelf. *Journal of Coastal Research,* 24(3), 585-593. doi: 10.2112/05-0538.1

Soares, L.C., 1977. *Hidrografia. In: Galvão, M.V. (ed.), Geografia do Brasil*. Rio de Janeiro: IBGE, pp. 73-119.

Silva, A.C., 2006**.** An analysis of water properties in the western tropical Atlantic using observed data and numerical model results**.** Recife, Brasil: Universidade Federal de Pernambuco, Tese de Doutorado, 155p.

Silva, A.C.; Santos, M.L.S.; Araujo, M.C., and E-ourles, B., 2009.Observações hidrológicas e resultados de modelagem no espalhamento sazonal e espacial da pluma de água Amazônica. *Acta Amazonica,* 39(2), 361-370. doi: 10.1590/S0044-59672009000200014.

Journal of Coastal Research	SI	75	537-541	Coconut Creek, Florida	2016

Sediment Dynamics from Coast to Slope – Southern Canadian Beaufort Sea

Philip D. Osborne[†*], and Alexandre Forest[‡]

[†]Golder Associates Ltd,
2920 Virtual Way, Vancouver, BC
Canada V5M 0C4

[‡] Golder Associates Ltd,
1170 boul. Lebourgneuf, Quebec, QC,
Canada G2K 2E3

www.cerf-jcr.org

www.JCRonline.org

ABSTRACT

Osborne, P.D. and Forest, A., 2016. Sediment dynamics from coast to slope – Southern Canadian Beaufort Sea. *In:* Vila-Concejo, A.; Bruce, E.; Kennedy, D.M., and McCarroll, R.J. (eds.), *Proceedings of the 14th International Coastal Symposium* (Sydney, Australia). *Journal of Coastal Research*, Special Issue, No. 75, pp. 537-541. Coconut Creek (Florida), ISSN 0749-0208.

Profound changes in cross-shelf sediment fluxes are anticipated in coming decades in the southern Canadian Beaufort Sea where an accelerated increase in temperature could lead to large changes in Arctic river hydrology and coastal-marine geomorphologic processes. In the past decade sediment exported to the Beaufort Shelf has increased while sea level pressure has increased accelerating the Beaufort Gyre, strengthening coastal upwelling and expanding the Mackenzie River plume offshore. Sea-ice extent has decreased while storminess has increased increasing wave action, coastal downwelling, current surge and resuspension and transport on the shoreface and shelf. This paper investigates mechanisms, quantities and rates of sediment transport operating in this cold continental shelf-slope environment. Past studies from more than 2 decades of research are compared with recent measurements to develop improved estimates of sediment sources, pathways, fate and fluxes across the shelf and slope. In particular, we explore connections between data from a long term mooring observatory deployed over the continental shelf and slope during the ArcticNet-Industry Partnership (2009-2011) and Beaufort Regional Environmental Assessment (BREA 2011-2015) to those acquired in studies focusing on nearshore and shoreface. Sediment fluxes from the Mackenzie River and erosion of permafrost coasts are compared with outer shelf-slope measurements of settling particles and near-bottom fluxes. In turn, the role of atmospheric and cryospheric processes in forcing sediment transfer from coast to slope is investigated to assess system response to changing climate and evaluate implications for marine hydrocarbon resource development along the continental margin of the Arctic Ocean.

ADDITIONAL INDEX WORDS: *Cross-shelf sediment transport, Beaufort Sea.*

INTRODUCTION

Understanding the processes and mechanisms which deliver sediment from the coast to the continental shelf and beyond to the slope is a classic problem in sedimentology. This topic is currently a priority in Arctic research given the uncertainties with respect to pathways, redistribution mechanisms and quantity of terrestrial matter exported into the Arctic Basin and because of the disproportionate size of Arctic shelves that represent 20% of the world's continental shelf (Smith, 2010).

The Arctic Ocean is pervasively influenced by terrigenous inputs delivered through large rivers, eroding shoreline and thawing permafrost and is particularly sensitive to changing environmental conditions, including ongoing modifications in the hydrological and cryogenic cycles owed to climate change (see Macdonald *et al*., 2015 for review). Among Arctic shelves, the Mackenzie Shelf in the southeastern Beaufort Sea (Figure 1) receives by far the largest amount of terrigenous sediments annually (Smith, 2010) and provides a compelling case-study to assess cross-shelf sediment transport mechanisms given its narrowness when compared to the large Siberian shelves.

DOI: 10.2112/SI75-108.1 received 15 October 2015; accepted in revision 15 January 2015
*Corresponding author: posborne@golder.com

In this paper we review studies from more than 2 decades of nearshore, shelf and slope research and combine with recent measurements from 5+ years of mooring- and ship-based oceanographic data (September 2009 to August 2015) collected over the shelf and slope. Our main objective is to develop improved conceptual and quantitative understanding of the processes, pathways and forcing mechanisms responsible for driving sediment transport from near the coast to the shelf edge and down the continental slope in the southeastern Beaufort Sea.

Modern Sedimentary Processes in the southern Beaufort

The Mackenzie Shelf (Figure 1) is a narrow shelf of approximatively 60,000 km^2 with an average slope of about 0.03° with break between 60 and 100 m water depth where the slope angle increases to 2°-6° towards the Canada Basin. Sediment input is largely influenced by the Mackenzie River delivering ~125 Mt yr^{-1} of mainly fine grained sediment from which a substantial fraction is deposited in the delta, leaving 50 to 70% as a sediment load to the inner shelf (Macdonald *et al*., 1998; Carson *et al*., 1999). Minor contributions of sediment are derived from other rivers (1.5 Mt yr^{-1}) and from erosional retreat of coastal bluffs (5.6 Mt yr^{-1}) (Hill *et al*., 1991). The uppermost layer of the seabed typically comprises fine sands and soft silty clay ranging in thickness from a few centimetres on the eastern shelf to several meters on the west (Blasco *et al*., 2013).

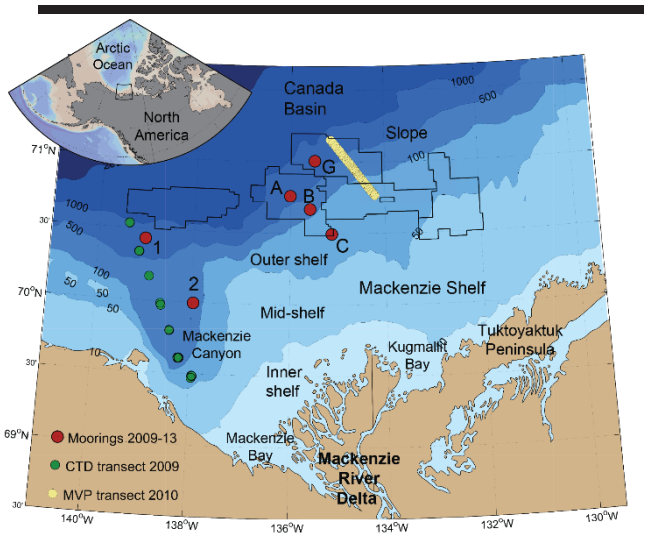

Figure 1. Location of study area and bathymetric map of the Mackenzie Shelf region in the southeastern Beaufort Sea (Arctic Ocean) with position of moorings and oceanographic stations over 2009-2013 that are used in this study. Offshore lease areas are also delineated on the map.

Mechanisms for sediment transport are complicated by the presence of winter sea ice leading to ice dams which seasonally prevents much of the riverine release of freshwater and suspended sediment. In summer, ice melt often leads to sudden release of sediment-laden freshwater and plume advection across shelf, open water allows wave action. Hill *et al*. (1991) suggest that over the mid- and outer shelf, wave motions influence bottom sediment transport less than 1% of the time. Near-bottom currents, weakly coupled to surface wind forcing, increase during storms and there is some evidence for resuspension of middle and outer shelf sediment during these events. On the inner shelf and shoreface, wave motion becomes important and combines with strong coastal currents during northwesterly storms to cause massive sediment resuspension.

Héquette *et al*. (2001) reviewed examples of strong and sustained seaward directed near-bottom currents associated with northwesterly storm surges and downwelling conditions on the shoreface. High wave orbital velocities were measured during these events which induced significant sediment remobilization. These events contribute to offshore sediment dispersal of shoreface sands and sediments may be transported to depths from which fairweather waves may not be capable of returning the material onshore.O'Brien *et al*. (2006) demonstrated through transmissometer and multi-trap data that sediment transport to the shelf edge and beyond occur in bottom and intermediate nepheloid layers (BNL, INL), altough the conditions required to set these features in motion were not well understood.

The review of Hill *et al*. (2007) for the Eel River margin, cites oceanographic currents near the bottom and wave-supported gravity driven underflows as key mechanisms for downshelf transport. In the case of the Mackenzie Shelf, northwesterly storms that generate downwelling and coastal waves could explain the development of fluid mud layers which are advected laterally or flow seaward under gravity. In addition, sea ice formation processes may lead to brine rejection and under-flows of dense winter water that could transport fluid mud suspensions offshore from the mid-shelf (Forest *et al*., 2015a)

Storm surges have also been linked with the forcing of strong currents and resuspension events at the shelf break where a narrow jet of 10-15 km width develops (Forest *et al*., 2015b). Dmitrenko *et al*. (2015) report strong near-bottom current (~1.2 m s^{-1}) in the shelf-break jet propagating on the upper slope as a response to a Pacific-borne westerly along-slope storm surge.

METHODS

Observations on the outer shelf and over the slope are combined with literature review to develop numerical estimates of sediment fluxes across the shelf. Moorings are used to relate water circulation and suspended sediments to wind forcing and to obtain vertical fluxes over the slope. Ship-based transects are used to illustrate the relative importance of BNL/INLs with respect to riverine input. Finally, a linear inverse analysis is used to reconstruct sediment pathways based on past and new data.

Mooring arrays

From July 2009 to September 2011, a series of eight moorings was maintained in the southeastern Beaufort Sea as part of an academic-industry research program between ArcticNet, Imperial Oil Resources Ventures Limited and BP Exploration. From the initial moorings set on location in 2009, three of these (B, A and G) were re-deployed in their initial locations in license areas and four new moorings were further developed to extend and expand the time-series from 2011 to 2015 as part of the Southern Beaufort Sea Marine Observatories project of the Beaufort Regional Environmental Assessment (BREA).

This study focuses on data collected at six moorings over 2009-2013 (Figure 1). Mooring C was a bed frame deployed at 60 m on the outer shelf in summer 2009 and equipped with an up-looking Teledyne RDI (TRDI) Workhorse 300-kHz acoustic Doppler current profiler (ADCP). Data from this ADCP were used to assess the relation between cross-shelf circulation and wind from the North American Regional Reanalysis. Moorings B and 2 were shelf-break moorings (~150 m isobaths) both equipped with down-looking 1-MHz Nortek ADCPs located 14 m above the bed and with Sequoia Laser In-Situ Scattering Transmissometer (LISST) 100X laser diffraction systems at 1 m above the ADCP. Suspended sediment concentrations (SSC) from the LISST were used to develop a relationship between the acoustic backscatter of the Nortek ADCP and SSC. Further details on the processing of TRDI and Nortek ADCPs, LISST-100X, and wind data can be found in Forest *et al*. (2015b).

Moorings A, G and 1 were offshore moorings deployed on the lower slope (700-750 m depth) and equipped with automated Technicap PPS-3/3 sediment traps (24 cups) at approximately 110 and 210 m depth. Sediment trap samples were analyzed to provide vertical mass fluxes in the upper and mid-water column over the slope as described in Forest *et al*. (2015a).

Ship-based oceanographic transects

A rosette profiler equipped with a conductivity-temperature-depth system (CTD, Seabird SBE-911+) connected to a transmissometer (Wetlabs C-Star) was deployed across the Mackenzie Canyon as part of the ArcticNet-Malina campaign in

August 2009. A year later, a high-resolution CTD transect was conducted across the central outer shelf with a Moving Vessel Profiler (MVP) also equipped with a Wetlabs C-Star transmissometer (Figure 1). Transmissivity was converted into beam attenuation coefficient and SSC using regional relationships. Details on the CTD data processing can be found in Forest *et al*. (2015a) and references therein. Transects were further gridded using a Data Interpolating Variational Analysis.

Sediment budget: an inverse analysis approach

Published sediment fluxes (Table 1) were combined with recent data and system understanding to develop a model of sediment pathways. This model includes sediment inputs from rivers and coastal erosion, transport as a surface plume and near the bottom, lateral export beyond the shelf edge and into the basin, as well as deposition. Vertical particle fluxes over the shelf were assumed to be minimaly proportional to the surface sediment flux (Doxaran *et al*., 2015). We used a Markov Chain Monte Carlo (MCMC) inverse analysis methodology (1000 iterations) to resolve the system and calculate the mean sediment fluxes. The MCMC methodology proceeds iteratively and randomly samples the solution space of the under-determined suite of linear equations, thus utilizing the subset of solutions to determine a mean and standard deviation for all outputs .

Table 1. *Boundary constraints used to estimate sediment fluxes across the Mackenzie Shelf using an inverse modelling approach (Figure 4).*

Constraint	Boundaries (Mt yr^{-1})	Reference
Mackenzie River input from the delta	57.0 - 89.0	Macdonald *et al*. (1998); Carson *et al*. (1999)
Coastal erosion and other rivers	5.0 - 9.0	Hill *et al*. (1991); Macdonald *et al*. (1998)
Surface flux from the delta to the inner shelf	45.3 - 65.6	Doxaran *et al*. (2015)
Deposition on inner shelf	43.9 - 83.7	Hill *et al*. (1991); Macdonald *et al*. (1998); Blasco *et al*. (2013)
Deposition on mid-shelf	15.4 - 61.6	
Deposition on outer shelf	3.1 - 15.4	
Export beyond shelf edge	15.0 - 21.0	Macdonald *et al*. (1998)
Vertical flux in the upper column over the slope	0.7 - 3.8	Forest *et al*. (2015a); Forest *et al*. (unpubl.)
Vertical flux in mid-water column over the slope	3.3 - 5.8	Forest *et al*. (2015a); Forest *et al*. (unpubl.)
Deposition on the slope	3.8 - 19.2	Blasco *et al*. (2013)

RESULTS

Salient results from data collected over 2009-2013 and a model of sediment fluxes are presented. Wind and bottom currents at mooring C, B and 2 are presented in Figure 2. Cross-shelf transects of estimated SSC are presented in Figure 3. A budget for sediment transport is provided in Figure 4.

Mooring-based measurements

Cross-shelf vectors of near bottom current at mooring C from July to October 2009 showed a significant relationship (r = 0.64) with the along-shelf wind component (Figure 2a), thus providing evidence for classic wind-driven downwelling and upwelling flows on the outer shelf. The response of near-bottom water circulation to wind forcing was quasi-immediate, lagging any change in wind speed/direction by less than a few hours. Data from moorings 2 and B also illustrated that current surges in the shelf-break jet can result in obvious sediment erosion events. Figures 2b and 2c show one of the most intense resuspension events that developped over a 2-year time-series (2011-2013) as a result of a storm surge. Prior to the event, background SSC near the bottom oscillated between 1 and 7 g m^{-3}, then increased rapidly to values above 100 g m^{-3} when storm winds from the west developed in early September 2012. While the storm faded on September 10, SSC remained relatively high in the near-bottom layer (10 m above bed) until the end of the month.

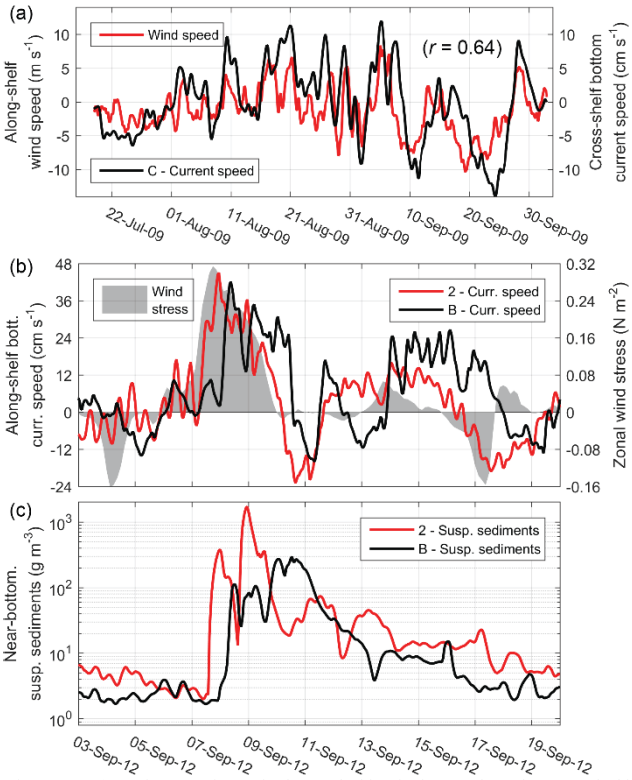

Figure 2. (a) Time series of along-shelf wind speed and cross-shelf bottom current speed at mooring C from July to October 2009. (b) Zonal wind stress and near-bottom current speed at moorings 2 and B (~150 m isobaths near the shelf break) during a conspicuous resuspension event resulting of a storm surge in September 2012. (c) Estimated suspended sediments during the event. For both wind and current, a positive cross-shelf direction indicates a flow to the north and a positive along-shelf flow is to the east

Oceanographic transects

Cross-shelf transects of estimated SSC and sigma-τ show the expansion of the river plume at the sea surface over the Mackenzie Canyon and outer central shelf, but also the occurrence of sub-surface features that contribute to sediment transport (Figure 3). Near the shelf edge in the canyon, a well-formed BNL resembles a hyperpycnal plume. At 30 km, a bottom-trapped lens of increased SSC can be discerned at

the depth to which the shelf-break jet propagates. At 90 km, a turbid eddy apparently shed from the shelf BNL contributes to the rain-out of particles. A BNL expanded also over the central outer shelf (although of less intensity than in the canyon). The BNL detaches from the shelf break to form INLs that intrude offshore. Over the slope bottom, a weak SSC increase when compared to ambient SSC was detected as a result of sediment cascading or local resuspension.

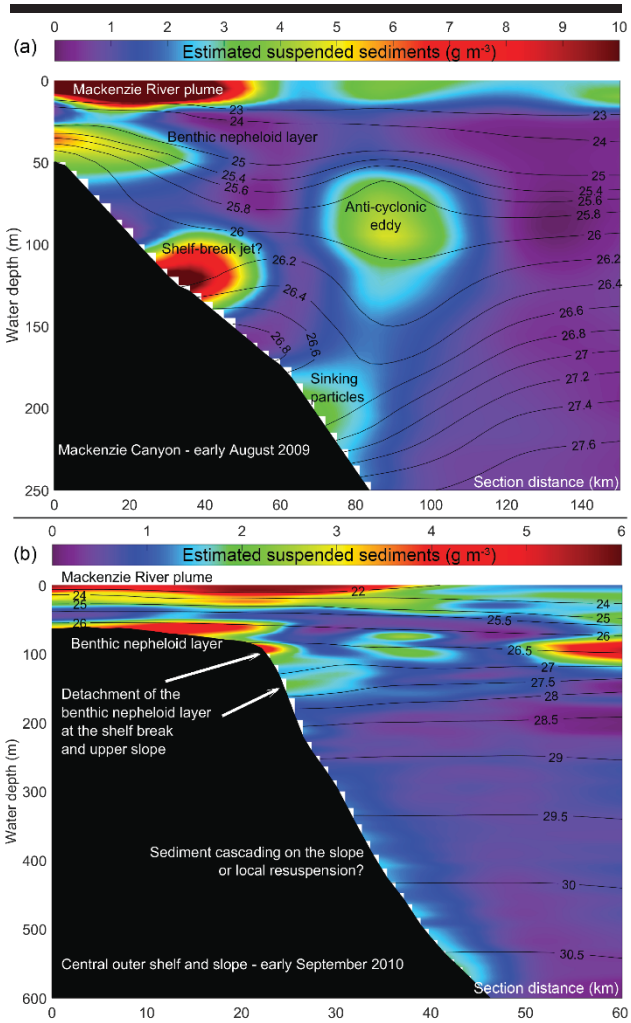

Figure 3. Oceanographic transects conducted across (a) the Mackenzie Canyon in early August 2009 and (b) across the central outer shelf and slope in early September 2010. Suspended sediments were estimated using the beam attenuation coefficient recorded by a transmissometer. Contours represent the sigma-τ values expressed in kg m^{-3}.

Sediment pathways and mean fluxes

The iterative MCMC inverse analysis determined that a mean annual delivery of 79 Mt of sediments was needed to obtain a mass balance of sediment fluxes across the shelf and slope (Figure 4). From the initial input at the coast, 81% is delivered as a surface plume and 19% is directed to the BNL. Vertical fluxes from the surface and lateral fluxes within the BNL both contribute to deposition over the shelf that cumulates to 63 Mt (80% of the initial load). Approximatively 20% of sediments are exported beyond the shelf edge (15 Mt). Subsurface transport across the shelf break accounts for 78% of the total input to the slope. A further 7 Mt is deposited over the slope itself and 10% escapes toward the basin. The error on the basinward flux is however very large (8 ± 7 Mt yr^{-1}).

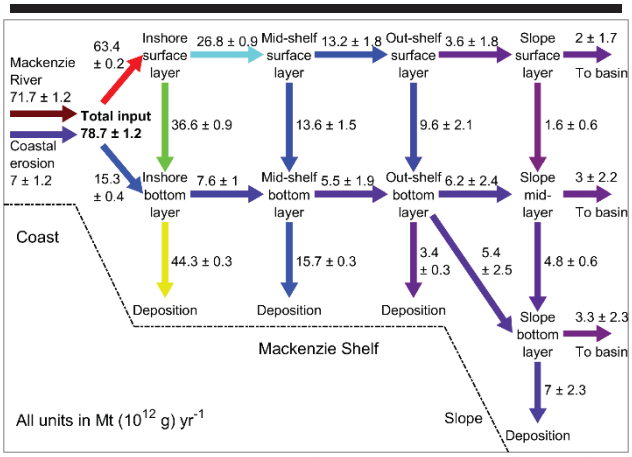

Figure 4. Mean estimates (±standard deviation) of sediment fluxes across the shelf and slope as calculated using a Markov Chain Monte Carlo inverse analysis approach (1000 iterations). Constraint values that were used to develop the inverse model are listed in Table 1.

DISCUSSION

Surface and subsurface processes drive the transport of sediments across the Mackenzie Shelf. Although the Mackenzie River plume and its behavior dictated by wind patterns is of paramount importance for sediment distribution (Macdonald and Yu, 2006), the development of a BNL over the shelf and slope appears to play a key role for the further dispersal of sediments through flows of fluid mud suspensions and via bed remobilization. Our data show that the near-bottom circulation on the outer shelf is tightly coupled with wind dynamics (contrary to the postulate of Hill *et al*., 1991) and the advection of fine particles to the shelf edge can be expected during downwelling-favorable wind conditions.

The subsequent detachment of the shelf BNL and its intrusion offshore as INLs is consistent with O'Brien *et al*. (2006) who documented the occurrence of BNL and INLs across the shelf. Our sediment budget suggests subsurface flux contributes to 78% of the export beyond the shelf edge. In addition to downwelling, gravity underflows supported by wave action or cascading dense winter water may further entrain suspended sediment and move it offshore, although their role in driving the formation and motion of the BNL on the shelf remain to be clarified. Sinking particles from the plume, or possibly descending from its base as convected sediment-laden fingers, could also generate a turbid gravity flow near the bottom. Interestingly, both freshwater or brine can generate eddies that appear closely linked to sediment fluxes over the slope (*e.g.* O'Brien *et al*., 2011). The turbid eddy observed in Mackenzie

Canyon in August 2009 was presumably linked to the interaction of the shelf BNL (fed by the surface plume) with the shelf-break jet around 80-150 m.

Near the shelf-break, amplification of the shelf-break jet by strong downwelling-favorable winds turned out to be a key mechanism for sediment erosion and dispersal all along the shelf margin (cf. Forest *et al*., 2015b). Our analysis supports that deposition on the outer shelf represents a minor sink (~3 Mt) for sediments. The response to wind forcing was rapid and elevated SSC persisted several days after the passage of the storm before particles settled or were advected. In contrast to the outer shelf, very little cross-stream flow developed over the upper slope as a function of the along-shelf wind. This result may be linked to the steep topography that hinders meridional displacement, thus concentrating energy within the along-shelf component that intensifies as a coastally-trapped wave (Dmitrenko *et al*., 2015).

CONCLUSIONS

Although our sediment budget for the Mackenzie Shelf is not quantitatively very different from those presented in the seminal studies of Hill *et al*. (1991) and Macdonald *et al*. (1998), our approach enabled improved compartmentalisation of sediment fluxes propagating at the surface and near the bottom as well as a more accurate sediment export rate toward the slope. Our observations provide more robust evidence for the presence of subsurface and near-bottom transport features, which can likely explain the majority (~78%) of the settling particle flux over the slope. More process-oriented studies targeting the shelf bottom boundary layer are needed to resolve the mechanisms underlying the formation and motion of the BNL at various time scales and its interaction with the shelf-break jet on the upper slope.

ACKNOWLEDGMENTS

We thank the officers and crew of the CCGS *Amundsen* and CCGS *Sir Wilfrid-Laurier* and the science teams from Golder/IMG-Golder, ArcticNet, ASL Environment, Department of Fisheries and Oceans Canada, and from Malina for efficient operations at sea. Special thanks to M. Fortier, K. Lévesque, M. Lowings and D. Fissel for their leadership in ArcticNet-Industry and BREA programs. Thanks to M. Babin for access to Malina data. We thank Imperial Oil and BP Exploration for field support. ArcticNet is funded by the program of Networks of Centres of Excellence of Canada. AF benefited from an Industrial Research and Development Fellowship from the Natural Sciences and Engineering Research Council of Canada. This is a contribution to the research program of the integrated Beaufort Observatory (iBO) managed by ArcticNet and supported by the Environmental Studies Research Funds.

LITERATURE CITED

Blasco, S.; Bennett, R.; Brent, T.; Burton, M.; Campbell, P.; Carr, E.; Covill, R.; Dallimore, S.; Davies, E.; Hughes-Clarke, J.; Issler, D.; Leonard, L.; MacKillop, K.; Mazzotti, S.; Patton, E.; Rogers, G.; Shearer, J.; and White, M., 2013. 2010 State of Knowledge: Beaufort Sea Seabed Geohazards Associated with Offshore Hydrocarbon Development; *Geological Survey of Canada*, Open File 6989, 340p. doi:10.4095/29261635-48.

Carson, M. A.; Conly, F.; and Jasper, J., 1999. Riverine sediment balance of the Mackenzie delta, Northwest Territories, Canada, *Hydrological Processes*, 13, 2499-2518.

Dmitrenko, I.; Kirillov, S.; Forest, A.; Gratton, Y.; Volkov, D.; Williams, W.; Lukovich, J.; Belanger, C.; and Barber, D.G., 2015. Shelfbreak current over the Canadian Beaufort Sea continental slope: Wind-driven events in January 2005. *J. Geophys. Res.* Submitted manuscript.

Doxaran, D.; Devred, E.; and Babin, M., (2015). A 50% increase in the mass of terrestrial particles delivered by the Mackenzie River into the Beaufort Sea (Canadian Arctic Ocean) over the last 10 years. *Biogeosciences*, 12, 3551-3565.

Forest, A.; Osborne, P.D.; Fortier, L.; Sampei, M.; and Lowings, M.G., 2015a. Physical forcings and intense shelf–slope fluxes of particulate matter in the halocline waters of the Canadian Beaufort Sea during winter. *Cont. Shelf Res.*, 101, 1-21.

Forest, A.; Osborne, P.D.; Curtiss, G.; and Lowings, M.G., 2015b. Current surges and seabed erosion near the shelf break in the Canadian Beaufort Sea: a response to wind and ice motion stress. *J. Mar. Syst.*, Submitted manuscript.

Héquette, A.; Desrosiers, M.; Hill, P.R.; and Forbes, D.L., 2001. The influence of coastal morphology on shoreface sediment transport under storm-combined flows, Canadian Beaufort Sea. *J. Coast Res*., 507-516.

Hill, P.R.; Blasco, S.; Harper, J.; and Fissel, D., 1991. Sedimentation on the Canadian Beaufort Shelf. *Cont. Shelf Res.*, 11(8), 821-842.

Hill, P.S.; Fox, J.M.; Crockett, J.S.; Curran, K.J.; Friedrichs, C.T.; Geyer, W.R.; Milligan, T.G.; Ogston, A.S.; Puig, P.; and Scully, M.E., 2007. Sediment delivery to the seabed on continental margins. Continental Margin Sedimentation: From Sediment Transport to Sequence. *Stratigraphy*. 37, 49-99.

Macdonald, R.; Kuzyk, Z.Z.A.; and Johannessen, S.C., 2015. The vulnerability of arctic shelf sediments to climate change. *Environmental Reviews*, 23(4), 461-479.

Macdonald, R.; and Yu, Y., 2006. The Mackenzie Estuary of the Arctic Ocean, in: Wangersky, P.J. (Ed.), *The Handbook of Environmental Chemistry*. Springer, Berlin, 91-120.

Macdonald, R.W.; Solomon, S.M.; Cranston, R.E.; Welch, H.E.; Yunker, M.B.; and Gobeil, C., 1998. A sediment and organic carbon budget for the Canadian Beaufort Shelf. *Mar. Geol.*, 144, 255-273.

O'Brien, M.C.; Macdonald, R.W.; Melling, H.; and Iseki, K., 2006. Particle fluxes and geochemistry on the Canadian Beaufort Shelf: implications for sediment transport and deposition. *Cont. Shelf Res.*, 26(1), 41-81.

O'Brien, M.C.; Melling, H.; Pedersen, T.F.; and Macdonald, R.W., 2011. The role of eddies and energetic ocean phenomena in the transport of sediment from shelf to basin in the Arctic. *J. Geophys. Res.* 116, C08001.

Smith, W., 2010. Polar Margins, in: Liu, K.; Atkinson, L.; Quiñones, R.; and Talaue-McManus, L. (Eds.), Carbon and Nutrient Fluxes in Continental Margins. Springer Berlin Heidelberg, 289-330.

Journal of Coastal Research	SI	75	542-546	Coconut Creek, Florida	2016

Internal Tide-Induced Enhancement of Cold Water Intrusion on the Continental Shelf of the Korea Strait

www.cerf-jcr.org

Jae-Hun Park [†], Ye Sol Kim[‡], Ho Jin Lee[††*], Hee-Yeol Lee[§], Ho Kyung Ha[†], Young-Gyu Park[§], Chanhyung Jeon[†], and Naoki Hirose[#]

[†]Department of Ocean Sciences
Inha University
Incheon, Korea

[‡]Korea Hydrographic and Oceanographic Administration
Pusan, Korea

[††]Department of Ocean Science
Korea Maritime and Ocean University
Pusan, Korea

[§]Ocean Circulation and Climate Research Center
Korea Institute of Ocean Science and Technology
Ansan, Korea

[#]Research Institute for Applied Mechanics
Kyushu University
Fukuoka, Japan

www.JCRonline.org

ABSTRACT

Park, J.-H.; Kim, Y.S.; Lee, H.J.; Lee, H.-Y.; Ha, H.K.; Park, Y.-G.; Jeon, C., and Hirose, N., 2016. Internal tide-induced enhancement of cold water intrusion on the continental shelf of the Korea Strait. *In:* Vila-Concejo, A.; Bruce, E.; Kennedy, D.M., and McCarroll, R.J. (eds.), *Proceedings of the 14th International Coastal Symposium* (Sydney, Australia). *Journal of Coastal Research*, Special Issue, No. 75, pp. 542-546. Coconut Creek (Florida), ISSN 0749-0208.

The Korea Strait bottom cold water (KSBCW), characterized by its temperature < 10ºC, is believed to originate from the deep basin of the southwestern East/Japan Sea with a maximum transport in August/September. Although previous studies have suggested possible causes of the enhanced KSBCW intrusion in summer, its mechanism is not yet clear. Here we investigate if tides can affect the strength of KSBCW intrusion using numerical simulations. We utilize a high-resolution regional ocean model with 1/108° grids, covering the Korea Strait and the southwestern East/Japan Sea. Numerical simulations are conducted for several cases, which include semidiurnal tides (M_2+S_2), diurnal tides (K_1+O_1), and wind forcings differently to examine their effects on the intrusion. Simulation results reveal that the energetic semidiurnal internal tides, generated around the continental shelf in the northern part of the Korea Strait, can induce the KSBCW intrusion by the internal tidal pumping effect. Two cases including the four major tides reproduce at best a dome-shaped bottom cold water lower than 10ºC impinging on the slope southeast coast of Korea, consistent with historical monthly-mean temperature fields. Long-term ferry boat ADCP measurements (> 10 years) across the Korea Strait show that southwestward KSBCW intrusions get stronger 2–3 days after spring tides in summer and fall when the semidiurnal internal tides are strengthened, supporting our simulation results. We therefore propose that the maximum KSBCW intrusion in August/September is caused by the energetic semidiurnal internal tides.

ADDITIONAL INDEX WORDS: *Korea Strait bottom cold water, internal tide, numerical simulation.*

INTRODUCTION

Sudden environmental changes in the southeast coast of Korea due to the appearance of cold water in summer, which is sometimes less than 10ºC, have seriously damaged fisheries, aquaculture, resort business with beaches, and even ship traffic due to the sea fog caused by the extreme air-sea temperature difference. This cold water seems to originate from the bottom cold water in the Korea Strait, called Korea Strait bottom cold water (KSBCW), which shows the lowest temperature during summer (Kim *et al*., 2006; Min *et al*., 2006; Yun *et al*., 2004). Hydrographic sections across the strait exhibit dome-shaped features of the cold water (< 10ºC) (Kim *et al*., 2006) impinging on the slope southeast coast of Korea after being intruded from the deep basin of the southwestern East/Japan Sea, called the Ulleung Basin, into the shallow Korea Strait. The Asian monsoon dominates the southerly or southwesterly winds around the Korean peninsula during summer, which can initiate the upwelling of this bottom cold water to the surface along the southeast coast of Korea. Recently, Choi *et al*. (2014) demonstrated that the upwelled cold waters along the southeast or east coast of Korea could provide nutrients to harmful algae to sustain unusual red tide events in the Ulleung Basin. Therefore, predicting the bottom cold water intrusion in the Korea Strait would be a crucial for the coastal environmental management along the southeast coast of Korea.

Regarding the mechanism of the enhanced KSBCW intrusion during summer, Yun *et al*. (2004) argued that it could happen when the North Korea Cold Water flowing southward into the

DOI: 10.2112/SI75-109.1 received 15 October 2015; accepted in revision 15 January 2015
*Corresponding author: hjlee@kmou.ac.kr

Ulleung Basin piled up enough to lift up the isopycnals, which made the cold water overflow the sill between the Ulleung Basin and the Korea Strait. They suggested that this process took about 3 to 5 months and hence the KSBCW intrusions could be enhanced in August or September. Obviously, the cold water volume of the Ulleung Basin is a necessary condition for the KSBCW intrusion, but the proposed mechanism by Yun *et al*. (2004) cannot explain why the KSBCW exists almost all over the year as shown by Kim et al. (2006). In addition, their explanation cannot account for the secondary peak of the KSBCW intrusion observed in December/January (Kim *et al*., 2006; Takikawa *et al*., 2005).

In this study, we will show that tides can induce the KSBCW intrusion. By including different forcings in high-resolution numerical simulations, we show that a tidal pumping driven by semidiurnal internal tides can bring up the cold waters from subsurface layers of the Ulleung Basin into the Korea Strait. We show that the bottom topography also plays a role in the cold water intrusion.

METHODS

The high-resolution ocean model used in this study is the Regional Ocean Model System (ROMS) version 3.4, which is a three dimensional, terrain-following, primitive equation ocean model with a free surface (http://www.myroms.org). The model domain covers 33.3º–36.5ºN, 126.9º–132ºE (Figure 1) with a 1/108º resolution (346×551 grids). A total of 20 s-coordinate levels were adopted along the vertical direction. The model bathymetry was interpolated from the Digital 30-sec Gridded Bathymetric Data of Korea Marginal Seas (Seo, 2008), with the minimum depth fixed at 2 m. More details of basic model configurations are found in Lee *et al*. (2014).

To investigate the impact of tides on cold water intrusion, we ran six simulation cases as follows: (1) wind forcing only without tides (Case I), (2) semidiurnal (M_2+S_2) tides only without wind forcing (Case II), (3) diurnal (K_1+O_1) tides only without wind forcing (Case III), (4) four major tides (M_2, S_2, K_1 and O_1) with wind forcing (Case IV), (5) four major tides without wind forcing (Case V), and (6) the same to Case V except for a flat bottom in the northern part of the Korea Strait (Case VI, Figure 1b). Case VI was designed to investigate the effect of bottom topography on the cold water intrusion. All cases were run with the same horizontally homogeneous initial profiles of temperature and salinity obtained from climatological 1/12°×1/15°-resolution RIAMOM outputs during 2001–2010. The tidal forcings (M_2, S_2, K_1, and O_1) retrieved from OTIS Regional Tidal Solutions of a 1/12-degree resolution were set as needed along open boundaries. Cases I and IV were forced with winds of the winter months (January and February) obtained from 12-hourly ERA-Interim data (European Center of Medium Range Weather Forecasting Re-Analysis). All cases were run for 60 days and the results shown here are from the last 5-day mean (*i.e*., 56–60 days).

We utilize long-term ferry boat ADCP measurements across the Korea Strait to support our simulation results. The spatial interval of the processed data is 1/96º (130 points along the ferry boat track shown in Figure 1). Tides are removed following Fukudome et al. (2010), where more details of the ADCP data processing are found. Using the ADCP-measured velocity fields, we estimated the volume transport of the southwestward deep countercurrent in the western channel of the Korea Strait during 1998–2010.

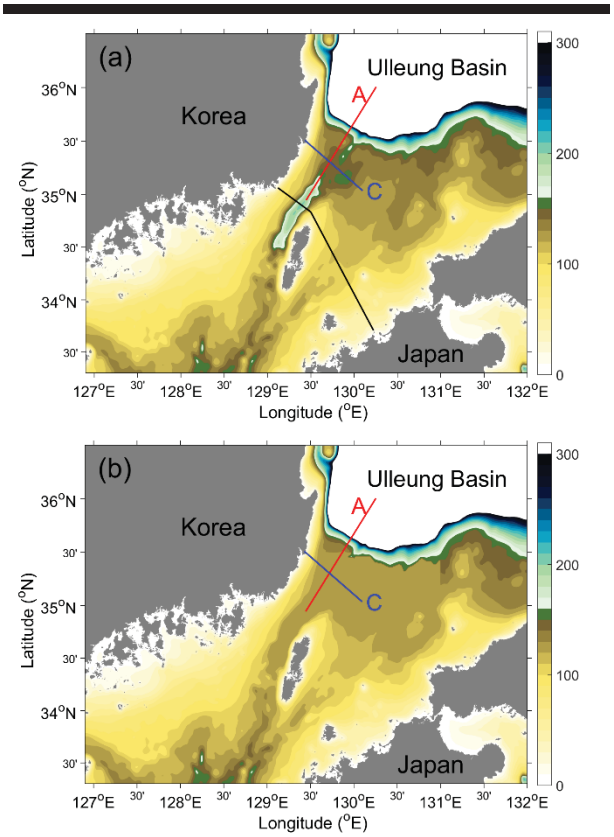

Figure 1. Model domain covering the Korea Strait and the southern part of the Ulleung Basin. (a) Real topography used for the five cases (Cases I to V). (b) Modified topography used for Case VI, which adopted a flat topography to erase the deep trough in the western channel of the Korea Strait. Red (A) and blue (C) lines indicate the locations of along-strait and across-strait sections shown in Figures 3 and 4. The historical monthly-mean temperature sections shown in Figure 2 is along the line C. Black line in (a) indicates the ferry boat ADCP track.

RESULTS

Vertical sections of historical (1932–1942) monthly-mean temperatures across the Korea Strait in February and August showed the seasonally-varying KSBCW feature (Figure 2). Cold waters (< 10ºC) were found only near the bottom in February, while a typical feature of dome-shaped cold waters impinging on the slope southeast coast of Korea was found in August.

Simulation results show different features of temperature distribution depending on the cases with different forcings. Case I shows well-developed mixed layer from the surface to about 100 m due to the strong winds (Figures 3a and 4a). Nevertheless, it shows no cold water intrusion from the deep Ulleung Basin (Figure 2a), suggesting that the cold water intrusion cannot be induced by strong northerly or northeasterly

winds. There is the cold water near the bottom in the deep channel, but it is a remnant from the initial condition.

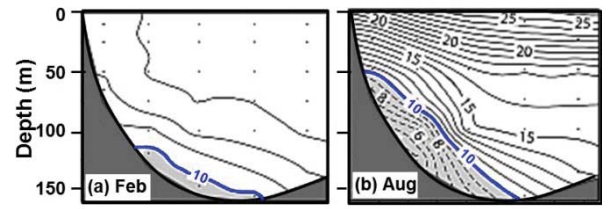

Figure 2. Vertical sections of the historical (1932–1942) monthly-mean temperatures in (a) February, and (b) August along the line C shown in Figure 1 (modified from Kim *et al.*, 2006). Contour interval is 1°C and dots indicate hydrocast measurement depths.

Case II forced by only semidiurnal tides shows an intrusion feature penetrating from the Ulleung Basin (Figures 3b and 4b). We suppose the tidal pumping by semidiurnal internal tides brings up the cold water to the sill so that it can overflow into the Korea Strait. But, it does not develop enough to fill the deep trough with cold waters. Case III forced by only diurnal tides show no intrusion patterns of temperature (Figures 3c and 4c). The cold water lower than 10ºC in the deep trough is a remaining of the initial condition like Case I. Diurnal tides cannot generate freely-propagating internal waves since their periods are longer than the local inertial period at the latitude of the Korea Strait, and hence the effect of diurnal tides seems to be less significant than that of semidiurnal ones.

Case IV forced by the major four tides and winds shows a notable cold water intrusion feature beneath the well-developed surface mixed layer (Figure 3d). The intrusion extends to the northern part of the deep trough in the western channel of the Korea Strait. The thin cold water layer a little bit tilted to the west (Figure 4d) show a good agreement with the observation in February shown in Figure 2a.

The major four tides with no wind forcing (Case V) produces an apparent cold water intrusion feature connecting isotherm layers less than 10ºC between the southwestern Ulleung Basin and the continental shelf of the Korea Strait (Figure 3e). Correspondingly, the vertical section of temperature across the strait shows a dome-shaped cold water distribution near the bottom, which impinges on the slope southeast coast of Korea (Figure 4e). Case V reproduces well the characteristic feature of the KSBCW in summer, when compared with the observation shown in Figure 2b.

Case VI that erased the deep trough in the western channel of the Korea Strait (Figure 1b) shows no intrusion feature although it is forced by the four major tides. This result confirms that the bottom topography plays another significant role in the KSBCW intrusion, making gravity flows from the sill to the trough in the western channel.

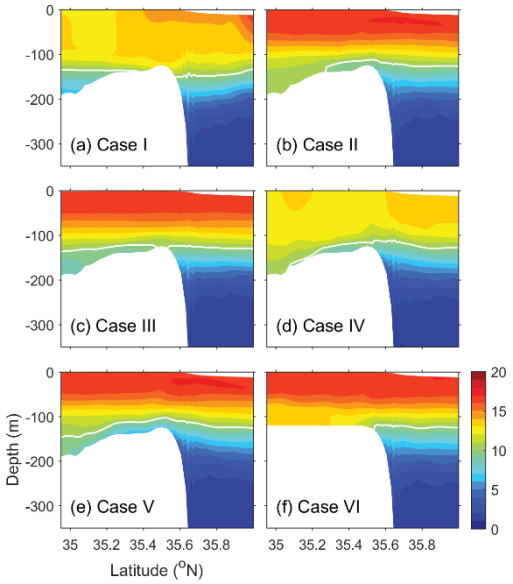

Figure 3. Five-day mean temperature section along the western channel of the Korea Strait (along the line A in Figure 1) for (a) Case I, (b) Case II, (c) Case III, (d) Case IV, (e) Case V, and (f) Case IV. White contours indicate 10ºC isotherm.

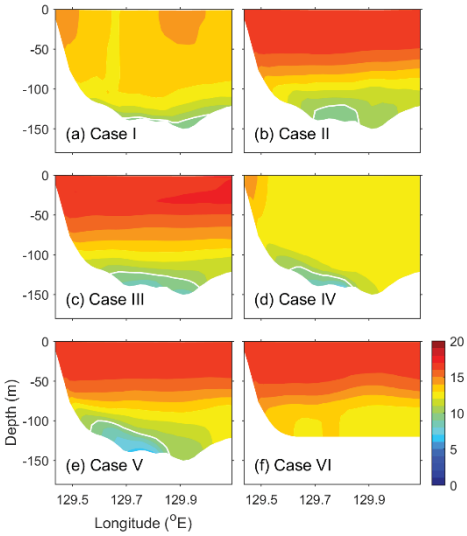

Figure 4. The same to Figure 3 except for along the line C in Figure 1.

The near-bottom velocity fields induced by tides should be related with the KSBCW intrusion. To examine the tidal effects on the near-bottom current fields around the Korea Strait, Figure 5 plots the 5-day mean velocity fields and 10ºC water distributions for the six cases. Both velocity and temperature fields are from the averages at the deepest 4 layers (20% of the water depth from the bottom). Cases I and VI show no notable southwestward flows (red arrows) in the western channel of the

Korea Strait, as expected. Case II reveals a southwestward flow along the deep trough, but it seems like a part of local cyclonic feature with no direct connecting to the intrusion. Case III shows a weak southwestward flow along the deep trough in the western channel, which spans to the northern edge of the continental shelf. Nevertheless, the amplitude of this flow is too weak to induce the cold water intrusion. Cases IV and V reveal remarkable southwestward near-bottom currents from the northern edge of the continental shelf to the deep trough in the western channel of the Korea Strait with their amplitudes up to ~0.1 m/s, although the near-bottom flows in Case IV ends near the northern part of the deep trough.

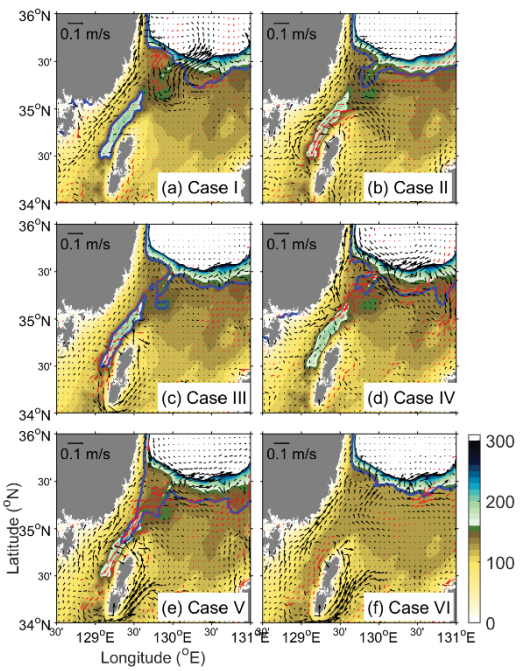

Figure 5. Five-day mean velocity fields averaged at the deepest 4 layers (*i.e.*, from 17th to 20th layers) for (a) Case I, (b) Case II, (c) Case III, (d) Case IV, (e) Case V, and (f) Case IV. Red arrows represent velocities heading between 180º and 270º clockwise from the north. Colored contours indicate bottom topography. Blue contours indicate 10ºC isotherms that are also from the average of the deepest 4 layers.

The cold water fronts of 10ºC show corresponding distributions to the near-bottom velocity fields (Figure 5). Cases I and III show isolated cold waters in the deep trough, which are remnants of the initial condition as described above. Cases II and IV show weak intrusion features around the northern edge of the continental shelf. Case IV can show more extended distribution of the 10ºC contour to the deep trough when the vertical layer average is done for the deepest two layers (not shown), like the thin cold water layer shown in Figure 4d. Case V shows a distinct 10ºC contour along the western channel, extending to the middle of the deep trough from the northern edge of the continental shelf. These results demonstrate that the tides can influence on the KSBCW intrusion through inducing the near-bottom southwestward currents as well.

The long-term ferry boat ADCP measurements reveal a consistent feature with our simulation results. The strong southwestward volume transport events driven by the deep countercurrent in the western channel of the Korea Strait get more frequent at 2–3 days after the spring tides (Figure 6). In addition, they dominantly occurred during the summer and fall months, when the semidiurnal internal tidal energy shows a broad maximum in the southwestern corner of the Ulleung Basin (Jeon *et al*., 2014). These results support that the deep countercurrent is significantly affected by the tides.

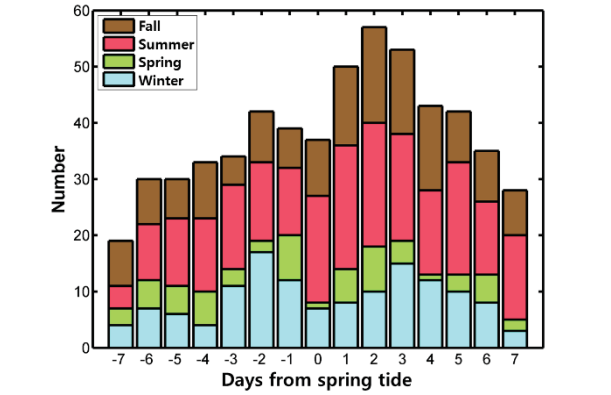

Figure 6. The number of strong southwestward volume transport events (> 0.075 Sv) observed by the ferry boat ADCP during 1998–2010. The ferry boat track is shown in Figure 1a. The event numbers are counted depending on days from spring tide time and seasons. Winter is from December to February, spring from March to May, summer from June to August, and fall is from September to November.

DISCUSSION

Using 5.5-year-long ferry boat acoustic Doppler current profiler (ADCP) measurements across the Korea Strait, Takikawa *et al*. (2005) showed two maxima of the southwestward deep countercurrent, one in August and another in January with some relatively high values from July to October (see their figure 11b). Correspondingly, Kim *et al*. (2006) showed two temperature minima near the same months. Takikawa *et al*. (2005) also showed that the volume transport through the western channel of the Korea Strait gradual increases from a minimum in January to a maximum in October with some high values in September and November and suddenly drops in December/January (see their Figure 11a). We first argue that the observed maximum of the KSBCW intrusion in August/September is caused by a combined effect from the energetic semidiurnal internal tides generated near the northern edge of the continental shelf and the volume transport through the western channel of the Korea Strait. Jeon *et al*. (2014) demonstrated that the seasonal variation of semidiurnal internal tidal energy in the southwestern corner of the Ulleung Basin has a broad peak from August to January and shows a minimum in February/March (see their Figure 3e). We have demonstrated that the semidiurnal internal tides can bring up the cold waters

from the deep Ulleung Basin to the sill depth. Therefore, the KSBCW intrusion can be significantly enhanced during this broadly energetic semidiurnal internal tide generation period. However, the strong volume transport through the western channel during September–November can prohibit the intrusion of the cold water, which results in the KSBCW intrusion peak in August/September. By analyzing 11-month long bottom-mounted ADCP measurements, Johnson and Teague (2002) hypothesized that when the volume transport through the Korea Strait is low the KSBCW intrusion can be enhanced, and when it is high the cold water is prevented from intruding, which is consistent with our argument.

The secondary maximum of the KSBCW intrusion can be explained in a similar way. The semidiurnal internal tides are relatively energetic in December/January (Jeon *et al*., 2014), while the volume transport through the western channel drops suddenly in December/January (Takikawa *et al*., 2005). Therefore, the secondary peak of the KSBCW intrusion can happen in winter as well.

CONCLUSIONS

In this study, we examined the tidal effects on the bottom cold water intrusion into the Korea Strait from the Ulleung Basin. The so-called Korea Strait bottom cold water (KSBCW) should originate from the deep basin, since nowhere around the Korea Strait except the deep Ulleung Basin has such a low temperature water (< 10ºC). Previous studies have suggested possible causes of the cold water intrusion, but they didn't consider the tidal pumping effects on elevation of cold waters. Taking an advantage of the high-resolution regional ocean model with 1/108° grids, we could reproduce the cold water intrusion feature consistent with the historical observations that showed a dome-shaped cold water (< 10ºC) impinging on the slope southeast coast of Korea. By simulating with different configurations we could confirm that the cold water intrusion can be enhanced with the tidal pumping mainly driven by the semidiurnal internal tides existing around the continental shelf/slope region in the northern part of the Korea Strait.

The long-term (> 10 years) ferry boat ADCP measurements across the Korea Strait show that strong southwestward deep flows get more frequent 2–3 days after spring tides in summer and fall, when stronger semidiurnal internal tides occur due to enhanced stratification on the continental shelf/slope region of the Korea Strait. This observation supports our simulation results. We propose that the maximum KSBCW intrusions in summer and winter are caused by the energetic semidiurnal internal tides in combination with the seasonally-varying volume transport through the western channel of the Korea Strait. This work highlights an important role of internal tides in water exchanges between deep and shallow coastal seas.

ACKNOWLEDGMENTS

This work was supported by a KIOST in-house grant (PE99293) and by projects of "Development of satellite based ocean carbon flux model for seas around Korea" and "Development of Technology for CO2 Marine Geological Storage" funded by Ministry of Ocean and Fisheries, Republic of Korea. This work was supported by INHA UNIVERSITY Research Grant (INHA-51416).

LITERATURE CITED

Choi, J.K.; Min, J.E.; Noh, J.H.; Han, T.H.; Yoon, S.; Park, Y.J.; Moon J.E.; Ahn, J.H.; Ahn, S.M., and Park, J.H., 2014. Harmful algal bloom (HAB) in the East Sea identified by the Geostationary Ocean Color Imager (GOCI). *Harmful Algae*, 39, 295-302.

Fukudome, K.; Yoon, J.H., Ostrovskii, A., Takikawa, T., Han, I.S., 2010. Seasonal volume transport variation in the Tsushima warm current through the Tsushima Straits from 10 Years of ADCP observations. *Journal of Oceanography*, 66(4), 539-551.

Johnson, D.R, and Teague, W.J, 2002. Observations of the Korea Strait bottom cold water. *Continental Shelf Research*, 22(5), 821-831.

Kim, Y. H; Kim, Y.B.; Kim, K.; Chang, K.I.; Lyu, S.J.; Cho, Y.K., and Teague, W.J., 2006. Seasonal variation of the Korea Strait Bottom Cold Water and its relation to the bottom current. *Geophysical Research Letters*, 33(24), L24604, doi:10.1029/2006GL027625.

Jeon, C.; Park, J. H.; Varlamov, S.M.; Yoon, J.H.; Kim, Y.H.; Seo, S.; Park, Y.G.; Min, H.S.; Lee, J.H., and Kim, C.H., 2014. Seasonal variation of semidiurnal internal tides in the East/Japan Sea. *Journal of Geophysical Research: Oceans*, 119(5), 2843-2859.

Lee, H.J.; Lee, H.J.; Park, J.H., and Ha, H.K., 2014. Seasonal variability of internal tides around the Korea Strait: 3-D high-resolution model simulation. *Ocean and Polar Research*, 36(1), 1-12 (in Korean with English abstract and figure captions).

Min, H.S; Kim, Y.H., and Kim, C.H., 2006. Year-to-year cold waters around the Korea Strait. *Ocean Science Journal*, 41(4), 227-234.

Park, J.H., and Watts, D.R., 2006. Internal tides in the southwestern Japan/East Sea. *Journal of Physical Oceanography*, 36(1), 22-34.

Seo, S.N., 2008. Digital 30sec gridded bathymetric data of Korea marginal seas - KorBathy30s. *Journal of Korea Society of Coastal Ocean Engineering*, 20(1), 110-120 (in Korean).

Takikawa, T.; Yoon, J.H., and Cho, K.D., 2005. The Tsushima Warm Current through Tsushima Straits Estimated from Ferryboat ADCP Data. *Journal of Physical Oceanography*, 35(6), 1154-1168.

Yun, J.Y.; Magaard, L.; Kim, K.; Shin, C.W.; Kim, C., and Byun, S.K., 2004. Spatial and temporal variability of the North Korean Cold Water leading to the near-bottom cold water intrusion in Korea Strait. *Progress in Oceanography*, 60(1), 99-131.

Journal of Coastal Research	SI	75	547-551	Coconut Creek, Florida	2016

3-D Comprehensive Hydrodynamic Modelling in the Arabian Gulf

Zhong Peng[†*] and Jill Bradon[†]

[†]Consultancy, Fugro GEOS Ltd.
Wallingford, UK

www.cerf-jcr.org

www.JCRonline.org

ABSTRACT

Peng, Z. and Bradon, J, 2016. A Comprehensive 3-D Hydrodyanmic Model in Arabian Gulf. *In:* Vila-Concejo, A.; Bruce, E.; Kennedy, D.M., and McCarroll, R.J. (eds.), *Proceedings of the 14th International Coastal Symposium* (Sydney, Australia). *Journal of Coastal Research*, Special Issue, No. 75, pp. 547-551. Coconut Creek (Florida), ISSN 0749-0208.

A 3-D comprehensive hydrodynamic model in the Arabian Gulf was developed by employing the latest bathymetry data, multiple vertical layers, calibrated atmospheric conditions and tidal forcing, HYbrid Coordinate Ocean Model reanalysis data, as well as the spatial- and temporal- varying climatological data, including cloudiness, relative humidity, air temperature and net solar radiation. This 3-D comprehensive hydrodynamic model in the Arabian Gulf was extensively calibrated and validated across the whole Arabian Gulf for water levels, currents, salinity and temperature. Model results are in good agreement with measurements and satellite data. This newly developed model is proven to be capable of accurately simulating hydrodynamics and the climatology over the whole Arabian Gulf.

ADDITIONAL INDEX WORDS: *hydrodynamics, modeling, heat flux, current, Delft3D.*

INTRODUCTION

The Arabian Gulf and its coastal areas are the world's largest single source of crude oil, and related industries dominate the region. The rapidly increasing needs to explore, drill and transfer the oil and gas lead to a huge amount of acquirements of high quality hydrodynamic data in recent years.

The Arabian Gulf is a semi-enclosed water area, and the local currents are related to other regions due to the dependent physics, *e.g.* wind or density gradient. Therefore, it is important to have a model to capably represent the hydrodynamics reasonably well over the whole Arabian Gulf. Currently, there is little work to adequately assess the performance of a hydrodynamic model over the whole Arabian Gulf, though there are plenty of studies on modelling hydrodynamics in Arabian Gulf over the last decade (*e.g.* de Graaff *et al.*, 2012; Elshorbagy *et al.*, 2006; Elshorbagy *et al.*, 2013; Elhakeema *et al.*, 2015; Pokavanich *et al.*, 2015). Futhermore, most of studies utilize the heat flux models by taking spatial-uniformly distributed climatology and monthly mean values. These assumptions neglect the daily, weekly and spatial variations, which are believed to be significant when the models are employed to forecast or study operational conditions. None of previous hydrodynamic models included the ocean circulating currents, salinity and temperature at the offshore boundaries, which are expected to be key important for better simulating the water exchanges at the entrance of Arabian Gulf.

In this study, a comprehensive 3-D hydrodynamic model was setup and implemented to study the hydrodynamics in Arabian Gulf. This model, incorporating HYbrid Coordinate Ocean Model reanalysis data and spatial- and temporal- varying climatological data, has been validated against collected measurements and satellite data across the entire Arabian Gulf.

DOI: 10.2112/SI75-110.1 received 15 October 2015; accepted in revision 15 January 2015
*Corresponding author: z.peng@fugro.com

METHODS

Delft3D-FLOW is an open-sourced hydrodynamic module, which calculates non-steady flow and transport phenomena under tidal and meteorological forcing, such as wind and air pressure, on a curvilinear, boundary-fitted grid. Delft3D-FLOW employs the sigma co-ordinate transformation in the vertical direction, which results in a smooth representation of the bottom topography. For significantly stratified flows, the z-layer methodology was utilized instead of sigma layer, to prevent extra diffusions.

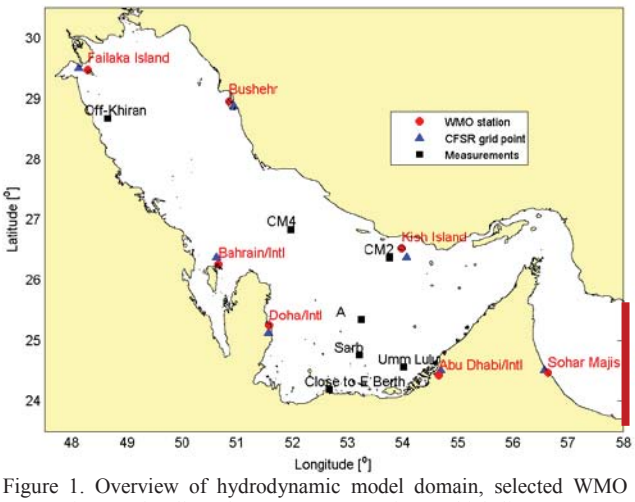

Figure 1. Overview of hydrodynamic model domain, selected WMO met-stations and collected measurement stations. Thick line represents the offshore boundary.

The flow model domain was designed to cover the whole Arabian Gulf region and has an open boundary located in the

Gulf of Oman (Figure 1). The grid resolution is around 3 km in both x- and y- direction.

The bathymetry data used in the present model was obtained by bi-linearly interpolating from samples extracted from Global Electronic Chart Database CM-93 Edition 3.0 provided by C-MAP Norway. The water depths were adjusted as relative to Mean Sea Level (MSL).

In Delft3D flow model, the Z-layer model has been used to solve the momentum equations on the vertical grid. In total 12 layers have been schematized. The vertical layer thickness varies with the depth and the number of active layers is constant.

In this study, the offshore boundaries were located in the Gulf of Oman, where the general water depths are larger than 1000m. Since the Arabian Gulf is dominated by the northwestern wind, the northwestern wind induced surge levels at the offshore boundary (in Gulf of Oman) are not relevant to surge levels inside Arabian Gulf. It was decided to apply tidal levels, salinity and temperature along water columns at the offshore boundary.

The temporal- and spatial- varying salinity and temperature data along the water depths were extracted from the Hybrid Coordinate Ocean Model (HYCOM) Global 1/12° reanalysis datasets, for initial conditions and boundary conditions of the hydrodynamic model. The temporal- and spatial- varying atmospheric forcing in Delft3D flow model made use of hindcast data sourced from the American National Centers for Environmental Prediction (NCEP) Climate Forecast System Reanalysis. In the Iraqi marine water, the temperature and salinity distribution is heavily dominated by the influx of the Shatt Al-Arab River. Therefore, in this study the river discharge and salinity data in Al-Mahdi *et al.* (2009) were employed in the model.

The hydrodynamic model was forced with the comprehensive heat exchange 'Ocean model' of Delft3D-FLOW by applying temporal- and spatial- varying climatological data (6-hourly), including relative humidity, cloudiness, air temperature and net solar radiation. These data were also sourced from the American NCEP Climate Forecast System Reanalysis. The effective back radiation and the heat losses due to evaporation and convection are computed by the model. The evaporation and precipitation are computed from the heat flux model. According to the model calibration results, the Stanton number and the Dalton number were both set to 0.9e-3.

RESULTS

The employed CFSR wind data were compared against observations at the closet WMO meteorological stations, where the latter is believed to better represent the local wind features, *e.g.* sea/land-breezes, wind direction variation due to land frictions, etc.. Figure 1 demonstrates the selected WMO meteorological stations. Comparisons of wind speed at 10 m above ground between CFSR and observations show that CFSR agrees reasonably well with observations across the whole Arabian Gulf, being only slightly underestimated. Based on comparisons, the wind speeds over the whole Arabian Gulf had been increased by 7.5%. Results also show that the wind directions of CFSR data are in good agreement with observations.

For tidal model calibration, predicted tidal levels at 10 tidal stations were extracted from the DTU10 global ocean tide model at a resolution of 0.125º x 0.125º. Figure 2 presents the comparison of final amplitude and phase of constituent K1 in the model against those of predictions extracted from DTU10 global ocean tide model respectively. Results show that the dominant tidal constituents by Delft3D hydrodynamic model agree well with those from DTU10 global ocean tide model. Small differences at a few of local stations can be observed. These differences at local stations are probably due to different sources of the local bathymetry, different bottom resistance and so on.

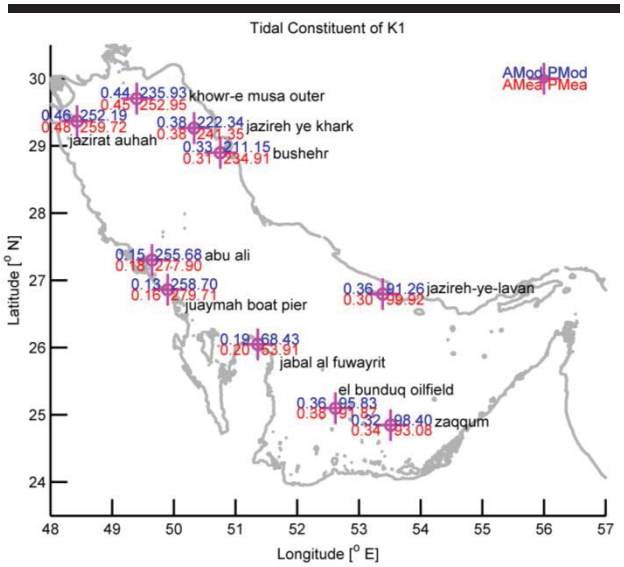

Figure 2. Comparisons of selected tidal constituents between modelled data (amplitude AMod in m and phase PMod in degree) and predicted tidal elevation (amplitude AMea and phase PMea) from DTU10 global tide model.

Table 1. *Calibrated tidal constituents at the offshore boundary of the flow model.*

Name	Amplitude [m]	Phase [degree]	Name	Amplitude [m]	Phase [degree]
Q1	0.04	351.7	NU2	0.04	173.5
O1	0.45	320.3	M2	0.99	128.8
K1	0.83	326.6	L2	0.02	210.9
P1	0.23	333.5	S2	0.31	169.7
N2	0.16	170.4	K2	0.06	211.8

The calibrated tidal constituents for astronomic tidal forcing are described in Table 1. These constituents were applied at the offshore boundary of the hydrodynamic model to represent the tidal forcing. In this study, long-term tidal constituents, *e.g.* SSA, SA, were not included, but it is necessary for the multiple years' tidal level prediction in order to consider the seasonal or yearly variations.

For the purpose of the model validation processes, multiple measured data sets have been collected from previous studies. These measurements are distributed over the whole Arabian Gulf for validating the overall performance of the hydrodynamic

model. Stations where measurements were collected in previous studies were listed in Table 2 and Figure 1.

Table 2. *Overview of stations where measurements were collected in previous studies.*

Station	Longitude [deg]	Latitude [deg]	Depth [m]	Data Source
A	53.245	25.345	22m	Elshorbagy *et al.* (2006)
CM2	53.761	26.374	94m	Elshorbagy *et al.* (2006)
CM4	51.976	26.840	69m	Elshorbagy *et al.* (2006)
Off-Khiran	48.646	28.669	23m	Pokavanich *et al.* (2015)
Close to E Berth	52.675	24.205	16m	Elshorbagy *et al.* (2013)
Sarb	53.208	24.767	16m	de Graaff *et al.* (2012)
Umm Lulu	54.013	24.570	23m	de Graaff *et al.* (2012)

Pokavanich *et al.* (2015) presented measurements obtained from recent research activities at KuwaitInstitute for Scientific Research (KISR). There are data from three locations consisting of a-month-long time-series data at Off-Khiran station in summer 2011. Figure 3 shows that water levels modelled by the present hydrodynamic model agree well with measured ones. This indicates that tidal levels and wind induced surge levels are well reproduced.

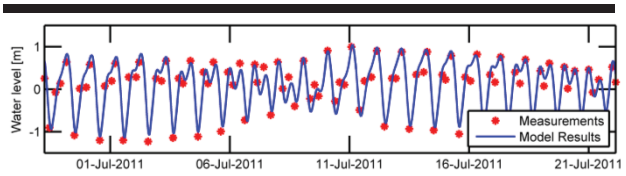

Figure 3. Comparison of water level between model data and measurements at Off-Khiran shown in Pokavanich *et al.* (2015)

In the northern Arabian Gulf, Pokavanich *et al.* (2015) also presented the northing current velocity at Off-Khiran station. The measured current velocity were used to validate the current hydrodynamic model. Figure 4 shows that the hydrodynamic model well reproduced the northing current at this location.

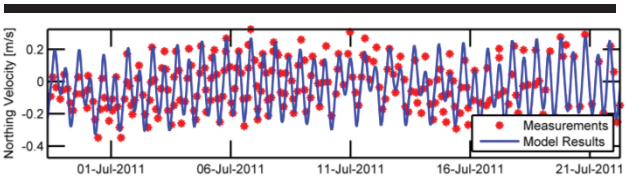

Figure 4. Comparison of northing current velocity between model data and measurements at Off-Khiran shown in Pokavanich *et al.* (2015)

In the coast of UAE, Elshorbagy *et al.* (2013) presented 3 days' field observations collected in 2002 at the station Close to E Berth, where the water is rather shallow, and the topography is complicated. Figure 5 presents the comparisons of current components between model results and measurements. It shows that both modelled eastward and northward velocities are in good agreement with measurements. Although the modelled eastward velocity is slightly underestimated (showing an offset), the phases of current velocities well match those of measurements, indicating that the dominant tidal physics are well captured. This is a distinct improvement from those shown in Figure 16 of Elshorbagy *et al.* (2013).

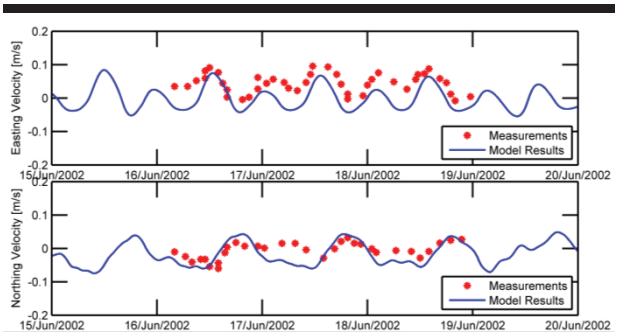

Figure 5. Comparison of current velocity between model data and measurements at Close to E Berth in Elshorbagy *et al.* (2013)

In the middle part of Arabian Gulf, where the water depths are generally larger than 20m, the modelled current speed and direction were validated against measurements by the NOAA (National Oceanic and Atmospheric Administration) research vessel Mt. Mitchell (shown in Elshorbagy *et al.*, 2006). Figure 6 to Figure 8 show comparisons of current velocity between model data and measurements at the stations of A, CM2 and CM4. Results by the hydrodynamic model are in good agreement with measurements, in both magnitudes and phases. For instance, Figure 8 shows that the modelled current magnitudes capture most of peaks, and the current directions align with the measured ones. The hydrodynamic model also shows a good performance to simulate the phenomena from mixed tides to semi-diurnal tides at this location.

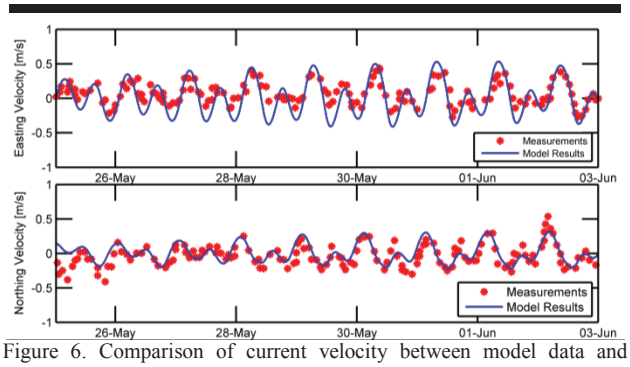

Figure 6. Comparison of current velocity between model data and measurements at A shown in Elshorbagy *et al.* (2006)

In the southern part of Arabian Gulf, de Graaff *et al.* (2012) presented comparisons of current velocities between their model data and measurements at stations of Sarb and Umm Lulu. These measurements were used here to assess the performance

of the hydrodynamic model in this region. Figure 9 shows that current speeds calculated by the model agree well with measurements at stations of Sarb and at Umm Lulu described in de Graaff *et al.* (2012), though the hydrodynamic model slightly overestimates current speeds at these two locations.

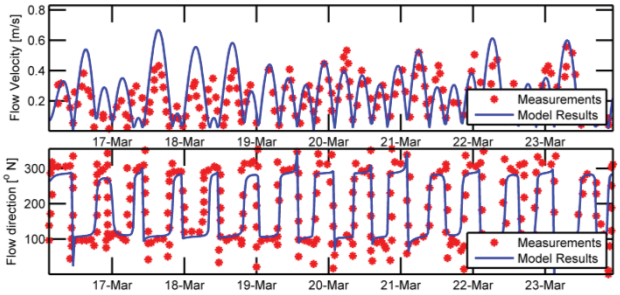

Figure 7. Comparison of current velocity between model data and measurements at CM2 at 15m below MSL shown in Elshorbagy *et al.* (2006).

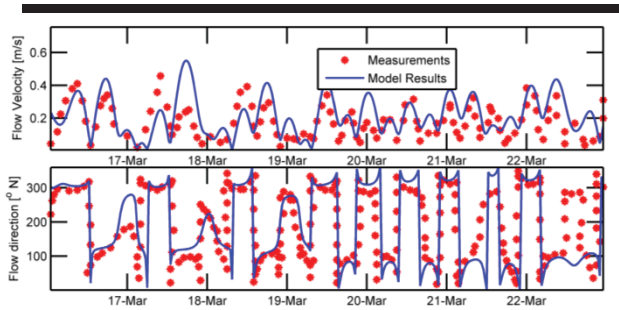

Figure 8. Comparison of current velocity between model data and measurements at CM4 shown in Elshorbagy *et al.* (2006).

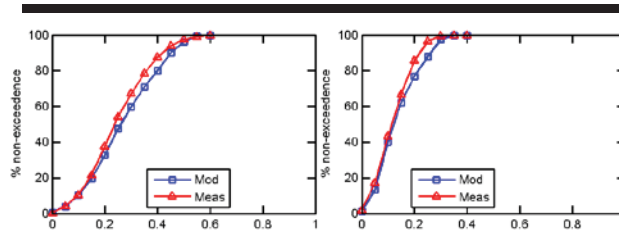

Figure 9. Comparison of current velocity between model data and measurements at Sarb (left) and at Umm Lulu (right) shown in de Graaff *et al.* (2012).

In this study, comparisons of monthly averaged sea surface salinity between model data and satellite data, sourced from World Ocean Atlas 2009 (WOA09, Antonov *et al.*, 2010), concluded a good agreement along the principal axis of Arabian Gulf.

NOAA High-resolution Blended Analysis for sea surface temperature (Reynolds, *et al.*, 2007) were employed to validate the sea surface temperature in the present hydrodynamic model. To model surface heat exchange, Delft3D-FLOW Ocean Heat Flux Model is used (Deltares, 2014). This model requires temporally varying data on air temperature at 2 m height, cloud cover, relative humidity and wind speed and direction. The solar radiation were specified directly to assist calculations of the total heat flux.

Figure 10 presents comparisons of sea surface temperature between model data and satellite data. By initializing the surface temperature in the model with the satellite data on 29th Dec 2008, the surface temperature calculated by the model still agrees reasonably well with satellite data after 1.5 months. There are some deviations in the coastal regions of the western Arabian Gulf, where the model data has cooler temperature than satellite data. This may be due to the coarse resolution of atmospheric and climatological data, leading to excess cooling in these coastal regions due to the significant land effect. In order to verify the importance of the heat flux model in the hydrodynamic modelling, Figure 10 also displays the surface temperature at 15th Feb 2009 without considering the heat flux modelling. It is clear that the surface temperature is completely wrong if no heat flux model was used in the hydrodynamic modelling.

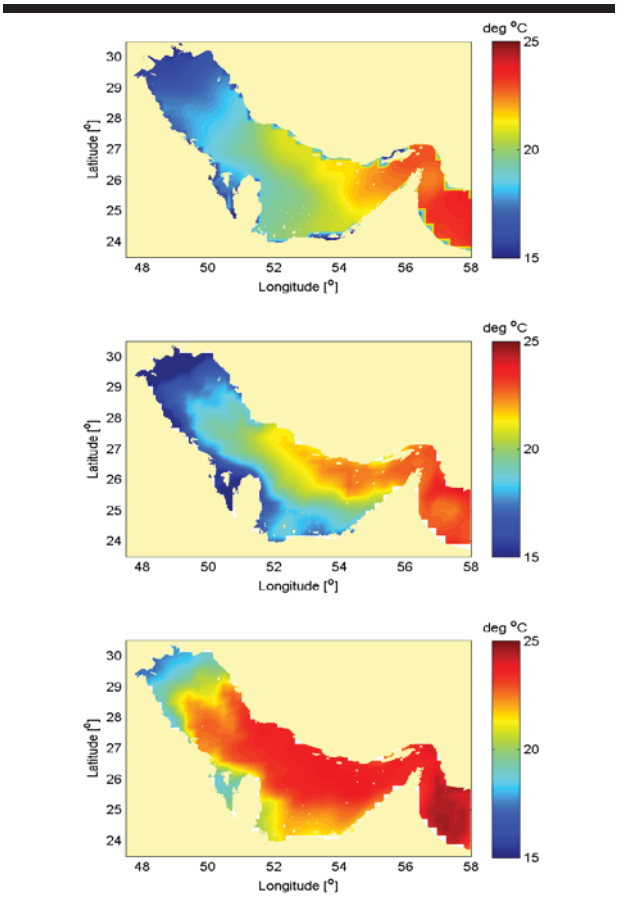

Figure 10. Comparison of sea surface temperature between model data and satellite data. (top) Satellite data at 15th Feb 2009; (middel panel) model data with heat flux model at 15th Feb 2009; (bottom panel) model data without heat flux model at 15th Feb 2009.

DISCUSSION

Table 3 and Table 4 present a summary of errors statistics between model results and measurements at selected stations. The correlation coefficients are good at certain locations with relatively regular currents. Once the currents become irregular, *e.g.* CM2 in Figure 7 and CM4 in Figure 8, correlation coefficients get low. This, however, may relate to the deviations in data digitization, where the accuracy of calibrations dependents on the resolution of figures presented in publications. The irregular currents at CM2 and CM4 are due to combinations of significant water depth and density gradients, strong residual currents due to the surface winds from the northwest and varying tidal patterns. There are no time series data available at stations of Sarb and Umm Lulu, hence it is not possible to derive the statistics.

Table 3. *Statistics of current velocity errors (model - measurements)*

	Eastward				Northward			
	Corr.	Bias (m/s)	Std (m/s)	rmse (m/s)	Corr.	Bias (m/s)	Std (m/s)	rmse (m/s)
Off-Khiran	-	-	-	-	0.78	0.06	0.17	0.18
Close to E Berth	0.79	-0.04	0.02	0.05	0.69	-0.01	0.03	0.03
A	0.82	-0.05	0.16	0.16	0.72	0.04	0.11	0.12

Table 4. *Statistics of current velocity errors (model - measurements)*

	Magnitude				Direction			
	Corr.	Bias (m/s)	Std (m/s)	rmse (m/s)	Corr.	Bias (°)	Std (m/s)	rmse (°)
CM2	0.62	0.04	0.13	0.13	0.5	-3.5	95.4	95.2
CM4	0.53	0.05	0.11	0.12	0.4	-4.2	116.9	116.6

Among previous researches of hydrodynamic modelling in Arabian Gulf, there are no statistical data available regarding the performance of each model, Therefore, in this study, there are no direct comparisons between the present model and previous ones. However, comparing this work (Figure 3 to Figure 9) to others, modelled currents in this study are in good agreement with measurements, in certain cases proving that the present model is, better than or at least comparable with, previous models for simulating hydrodynamics. Particularly, this is the first time that one specific hydrodynamic model was well validated against measurements and satellite data over the whole Arabian Gulf.

Besides the adequate asscessment of hydrodynamics over the whole Arabian Gulf, this study also presents model calibrations on tides and wind speed over the whole Arabian Gulf against available data, *e.g.* observations. This further enhances the reliability of the present model.

Another distinct feature is that this study incorporates the spatial- and temporal- varying climatological data, consisting of cloudiness, relative_humidity, air_temperature and net solar radiation, to compute the heat flux. Modelled sea surface temperatures agree well with measurements in most areas of Arabian Gulf after a relatively long period. Further study would be needed to better simulate heat convection and heat diffusion near the coasts.

Futhermore, the present model makes use of the HYCOM reanalysis data at the offshore boundary together with the tidal forcing. This feature is to ensure the completed physical processes at the entrance of the Arabian Gulf, and thus could help improve the accuracy of water exchanges through the Strait of Hormuz.

CONCLUSIONS

A comprehensive 3-D hydrodynamic model in the Arabian Gulf was developed by employing the latest bathymetry data, multiple vertical layers, calibrated atmospheric conditions, HYCOM reanalysis data, and spatial- and temporal- varying climatological data. This comprehensive 3-D hydrodynamic model in the Arabian Gulf was extensively validated for water levels, currents, salinity and temperature. This newly developed model is proven to be capable of simulating hydrodynamics and the climatology in the whole Arabian Gulf accurately, considering the vast water area and the asymmetric bathymetry.

LITERATURE CITED

Al-Mahdi, A.A.; Abdullah, S.S., and Husain, N.A., 2009. Some Features of the Physical Oceanography in Iraqi Marine Waters. *Mesop. J. Mar. Sci.*, 24 (1), 13 – 24.

Antonov, J.I.; Seidov, D.; Boyer, T.P.; Locarnini, R.A.; Mishonov, A.V., and Garcia, H.E., 2010. World Ocean Atlas 2009, Volume 2: Salinity. S. Levitus, Ed. NOAA Atlas NESDIS 69, *U.S. Government Printing Office*, Washington, D.C., 184p.

De Graaff, R.; Awda, H.; Majumdar, D.; Satya, M.; Caires, S.; Peng, Z., and Moerman, E., 2012. Setting a New Standard for Metocean Databases. *Offshore Technology Conference,* Paper 22923, pp. 1-16.

Deltares, 2014. Delft3D-FLOW User Manual Simulation of Multi-dimensional Hydrodynamic Flows and Transport Phenomena, Including Sediments, User Manual, Hydro Morphodynamic.

Elshorbagy, W.; Azam, M.H., and Taguchi, T.K., 2006. Hydrodynamic characterization and modeling of the Arabian Gulf. *Journal of Water Way, Port, Coastal and Ocean Engineering,* 132 (1), 47–56.

Elshorbagy, W.; Azam, M.H., and Al Hakeem, A.A., 2013. Temperature-salinity modelling for Ruwais Coast, *United Arab Emirates. Mar. Pollut. Bull.* 73, 170–182.

Elhakeema, A.; Elshorbagy, W., and Bleninge, T., 2015. Long-term hydrodynamic modeling of the Arabian Gulf. *Marine Pollution Bulletin.* 94(1-2), 19–36.

Pokavanich, T.; Alosairi, Y.; De Graaff, R.; Morelissen, R.; Verbruggen, W.; Al-Rifaie, K.; Altaf, T., and Al-Said, T., 2015. Three-Dimensional Arabian Gulf Hydro-Environmental Modeling Using Delft3d. *Proceedings Of The 36th IAHR World Congress* (The Hague, The Netherlands), pp. 1-12.

Reynolds, M.R., 1993. Physical oceanography of the Gulf, Strait of Hormuz, and Gulf of Oman—results from the Mt Mitchell expedition. *Marine Pollution Bulletin,* 27, 35–39.

Reynolds, W.R.; Smith, M.T.; Liu, C.; Chelton, B.D.; Casey, S.K., and Schlax, M.G., 2007. Daily High-Resolution-Blended Analyses for Sea Surface Temperature. *J. Climate*, 20, 5473–5496.

Journal of Coastal Research	SI	75	552-556	Coconut Creek, Florida	2016

Coastal Fronts Utilized by Migrating Humpback Whales, Megaptera novaeangliae, on the Gold Coast, Australia

Joshua Reinke [†‡*], Charles Lemckert[†], and Jan-Olaf Meynecke[‡††]

[†]Griffith School of Engineering
Griffith University
Gold Coast, Australia

[‡]Humpbacks & Highrises Inc.
Griffith University
Gold Coast, Australia

[††]Griffith Centre for Coastal Management
Griffith University
Gold Coast, Australia

www.cerf-jcr.org

www.JCRonline.org

ABSTRACT

Reinke, J.; Lemckert, C., and Meynecke, J.-O., 2016. Coastal fronts utilised by migrating humpback whales, *Megaptera novaeangliae*, on the Gold Coast, Australia. *In:* Vila-Concejo, A.; Bruce, E.; Kennedy, D.M., and McCarroll, R.J. (eds.), *Proceedings of the 14th International Coastal Symposium* (Sydney, Australia). *Journal of Coastal Research*, Special Issue, No. 75, pp. 552-556. Coconut Creek (Florida), ISSN 0749-0208.

Large-scale migration patterns of humpback whales, *Megaptera novaeangliae*, are quite well known; however, small-scale distribution patterns and relationships with environmental conditions have received less attention. Protection from a range of threats, as well as predicting the effects of climate change, requires knowledge of preferred habitat and environmental conditions. East Australian humpback whales travel from the Southern Ocean towards the Great Barrier Reef to breed. The East Australian coastal environment is dominated by the East Australian Current that carries warm water poleward from the tropics and generates upwelling conditions on the coast. Sharp temperature changes develop at the border of the warm current and the cooler coastal and upwelled waters. This study outlines methodologies and proposes relationships between humpback whale distribution and sea surface temperature (and temperature gradient) on the Gold Coast, Australia. This area is used primarily as a migration route, but also as a resting area for mothers and calves on the southward return journey. The distribution of almost 400 pods favoured cooler waters and areas with a strong temperature gradient. The coastal fronts generated by the East Australian Current generally run parallel to shore and may serve as a tool for navigation, allowing whales to follow the current. Higher productivity in cooler upwelled water and fronts may also provide a chance for opportunistic feeding.

ADDITIONAL INDEX WORDS: *Habitat preferences, cetaceans, marine mammals, distribution.*

INTRODUCTION

Humpback whales, *Megaptera novaeangliae*, take part in the largest annual migration of any mammal, from polar feeding grounds in summer to tropical and subtropical breeding grounds in winter (Chittleborough, 1965; Dawbin, 1966; Stone *et al.*, 1990). Protection from a range of threats, as well as predicting the effects of climate change and supporting whale watching industries, requires knowledge of preferred habitat and the reasons behind the preferences (Doniol-Valcroze *et al.*, 2007).

Different habitats are used for specific purposes, and therefore each habitat type has certain preferred environmental conditions. While investigations into relationships between distribution patterns and environmental conditions have focused on feeding areas and, to a lesser extent, breeding grounds, migration routes have received much less attention. Dense concentrations of prey are required for efficient feeding (Doniol-Valcroze *et al.*, 2007). Therefore, preferred feeding grounds are areas where prey is concentrated, generally characterized by upwelling (Fiedler *et al.*, 1998; Calambokidis *et al.*, 2004; Thompson *et al.*, 2012) and strong changes in temperature (fronts) (Doniol-Valcroze *et al.*, 2007; Dalla Rosa *et al.*, 2012). Migration is believed to reduce energetic demands of thermoregulation and achieve the highest possible growth rates (Clapham, 1996) and provide calves with protection from rough conditions (Jenner *et al.*, 2001) and predators (Naessig and Lanyon, 2004). Shallow coastal areas at least 21°C are utilized as breeding grounds, fulfilling these requirements (Rasmussen *et al.*, 2007).

East Australian humpback whales (IWC substock E(i)) travel from the Southern Ocean, along the East Coast of Australia, into tropical waters to breed (Noad *et al.*, 2011). The East Australian coastal environment is dominated by the East Australian Current (EAC), the western boundary current of the southern hemisphere, western Pacific Ocean, carrying warm water poleward from the tropics (Ridgway and Dunn, 2003). This current, as well as strong northerly winds, is responsible for generating upwelling conditions on the coast and providing the majority of nutrients available for primary production (Roughan and Middleton, 2002; Armbrecht *et al.*, 2014). Thermal fronts are experienced at the border of the warm current and the cooler coastal and upwelled waters.

This study aims to investigate relationships between humpback whale distribution and environmental conditions on the Gold Coast, Australia (Figure 1a). This area is used for

DOI: 10.2112/SI75-111.1 received 15 October 2015; accepted in revision 15 January 2015
*Corresponding author: joshua.reinke@griffithuni.edu.au

socializing during both the northern and southern migration, as well as providing a resting area for mothers and calves on the southward return journey (Meynecke *et al.*, 2013). The effects of the EAC reach the Gold Coast shoreline (Tomlinson and Foster, 1987; Jackson *et al.*, 2004) but the effects of this current, and currents in general, on whale distribution are largely unknown (Suthers *et al.*, 2011).

METHODS

Humpback whale locations were recorded off the Gold Coast from three commercial whale watching vessels from June to November 2013 and 2014. The study area ranged from 27.75°S to 28.25°S, 153.41°E (or the coastline) to 153.75°E. One vessel conducted three trips per day, giving a maximum of five recorded trips per day. Vessels departed through the Gold Coast Seaway (Figure 1) and progressed seaward until whales were spotted. The vessels then travelled alongside the pod for between 0.5 to 1.5 hours, often moving between different pods within this time. The distance between the vessels and the whales was usually about 100m, in accordance with whale watching regulations.

Dedicated surveys by trained volunteers on the vessels took place up to 5 days per week, recording the time and location (of the boat) upon arrival and departure of each pod. GPS loggers were attached to the vessels (from 24/09/13 onwards) to record the locations once per minute, including when researchers were not onboard. The location of whales was assumed, by extracting sections of the boat track where speed slowed substantially (an example of which can be seen where dots are closer together in Figure 1b). Composition and behavioral data for these additional pods was not recorded; however, all pods were categorized by their direction of travel. Most whales travel north during July and August and return in September to November.

Whale distribution (presence only) was compared with daily satellite sea surface temperature (SST) at 2km resolution from IMOS GHRSST (ftp://aodaac2-cbr.act.csiro.au/imos/), as well as the temperature gradient. Temperature gradient for each cell was calculated using an average of the change in temperature between itself and the cells immediately to the east and west. The conditions at the whales' locations were given by the average of the start and end point of the tracks. Average conditions across the study area were calculated in an east-west direction at latitudes corresponding to each of the start and end points of the whale tracks. The temperature gradient and study area conditions were calculated in an east-west direction based on the fact that the range of conditions available to choose from lie in an east-west direction (whales main travel direction being either north or south).

The conditions observed at the whales' locations were compared with the average across the study area using paired sample t-tests.

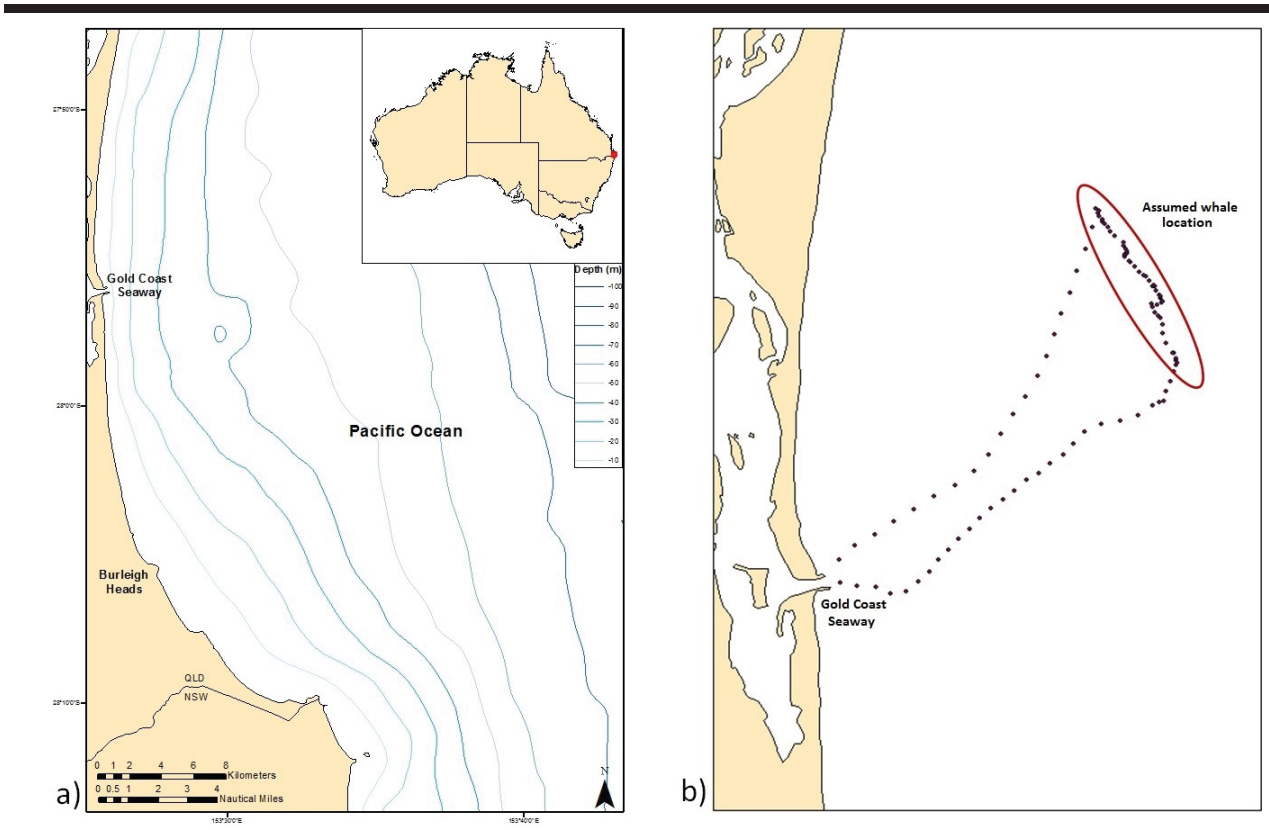

Figure 1. (a) Study area: the Gold Coast 'bay'. (b) Typical boat track and assumed whale location.

RESULTS

A total of 1386 pods were recorded (or assumed) over the study period (382 in 2013, 1004 in 2014 due to increased effort). Of these, 392 were accompanied by valid satellite SST data, due to cloud cover often limiting the availability of satellite SST estimates.

The mean temperature across the study area was found to be 21.5°C, with slightly higher temperatures in 2013 (21.9°C) than 2014 (21.3°C). The average temperature gradient was 0.08°C/km, with very little variation between years. SST was cooler in July and August (during the northern migration) than September to November (southern migration).

The SST at whale locations was, on average, 0.46°C lower than the average temperature of the study area ($p < 0.001$), while the temperature gradient was 0.02°C higher than the average ($p < 0.001$). These differences were significant for both years and travel directions (Figure 2). An example of whale distribution and conditions on the 17th July, 2014 can be seen in Figure 3, showing the apparent preference for cooler water and high temperature gradient.

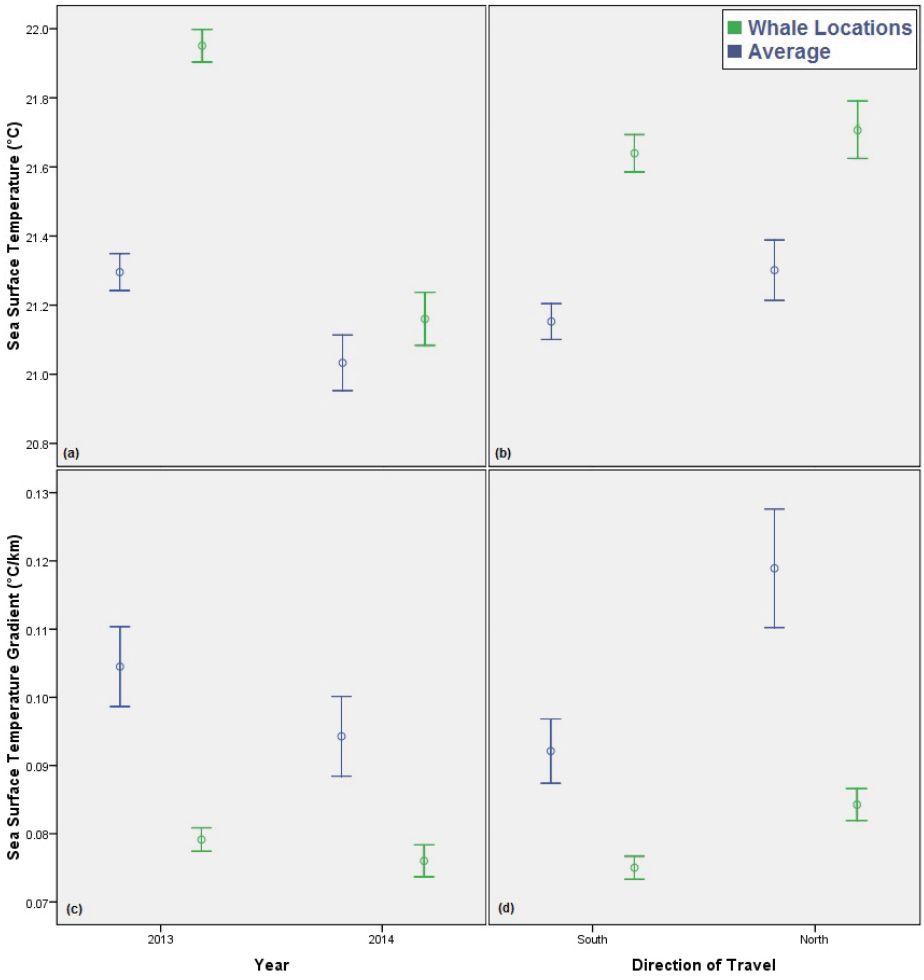

Figure 2. Sea surface temperature and temperature gradient of whale locations compared to average conditions in the Gold Coast bay. Error bars show ±1 standard error.

DISCUSSION

Humpback whales appeared to show a preference for cooler water, as well as areas with a high temperature gradient. Particular hydrodynamic features may assist with navigation (Lohmann *et al.*, 2008). Coastal fronts, which generally run parallel to the shore, may be used in this way. Sensing changes in temperature or current would allow animals to follow these features, and avoid heading too far away from or toward the coast.

Cooler waters were favored in both travel directions, suggesting that the whales were not utilizing the warm EAC to conserve energy on the southern migration. However, it is

possible that this result may be influenced by the non-systematic nature of the surveys, as vessels would find the closest whales to the coast, where cooler water is normally found (Figure 3a). Although whales were found in waters that were cooler than the surrounding area, in most cases temperature remained above 21°C, retaining the benefits for thermoregulation (Rasmussen *et al.*, 2007).

Although rare, opportunistic feeding during migration has been recorded (Stockin and Burgess, 2005). The higher (and retained) productivity in coastal fronts may provide the whales with a chance of encountering prey in sufficient density to make opportunistic feeding worthwhile. The preference for cooler water may relate to the productivity generated by upwelling, also providing an increased likelihood of concentrating prey.

With particular environmental preferences, it is likely that the distribution of humpback whales could be affected by abnormal conditions, or extended changes to the conditions experienced on their migration routes, such as changes to the EAC (Suthers *et al.*, 2011). This may lead to the utilization of non-optimal migration routes, increasing the energetic demands or altering the timing of migration. Changes to the locations of preferred habitats necessitate a review of critical habitat and protected areas defined in management plans (Macleod *et al.*, 2005). A nearshore shift to the distribution is likely to result in an increase in anthropogenic impacts. An offshore shift or more widely dispersed distribution would have implications for whale watching industries, by increasing travel costs and decreasing the likelihood of an encounter.

CONCLUSIONS

Small-scale distribution of migrating humpback whales and with environmental conditions is largely unknown. Humpback whales appear to utilize coastal fronts while migrating through Gold Coast waters on their annual migration. These hydrodynamic features may provide benefits for navigation and opportunistic feeding. Further research into environmental preferences will help to predict how changing conditions may alter humpback whale distribution.

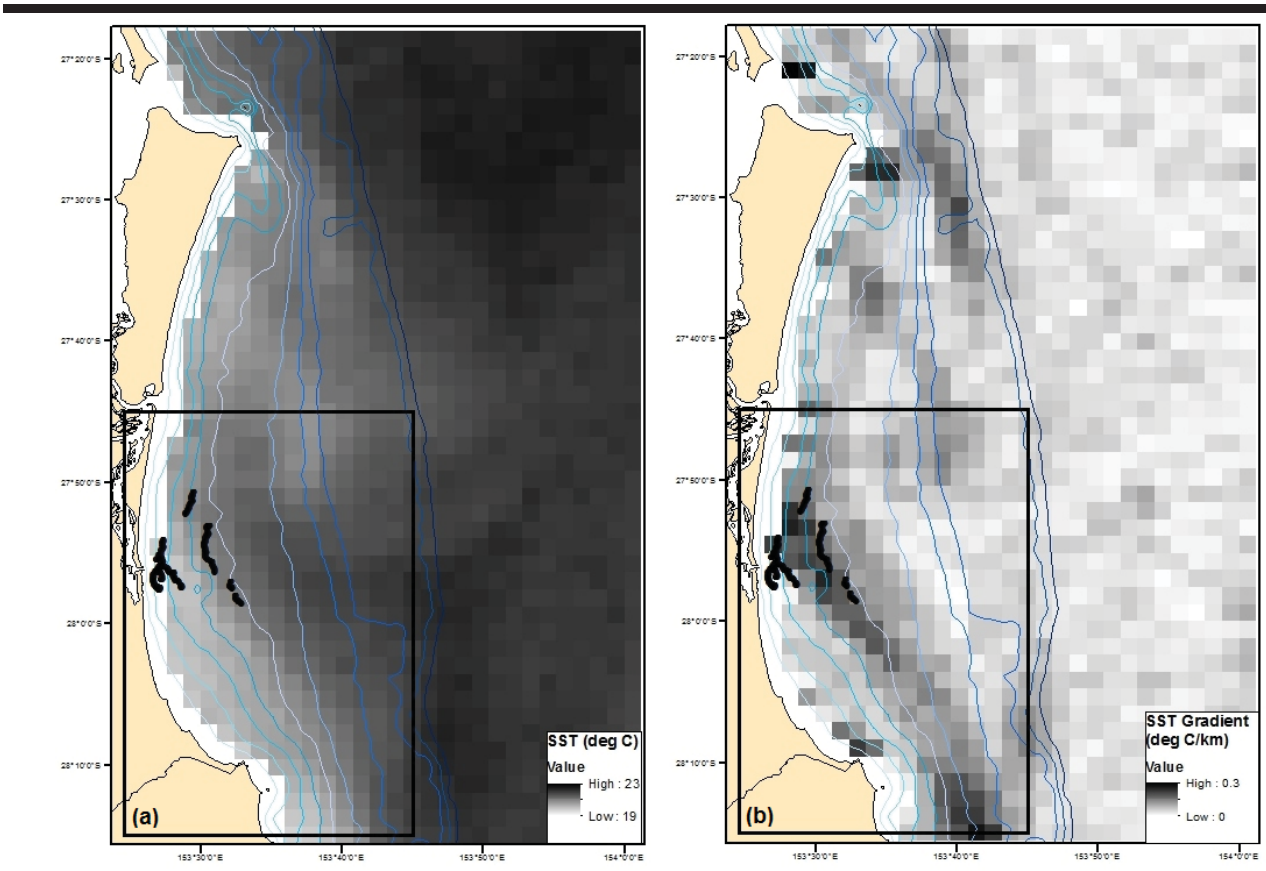

Figure 3. Humpback whale distribution relative to (a) Sea surface temperature and (b) Temperature gradient, 17th July 2014. Inner border shows the study area, contours show depth each 10m to 100m.

ACKNOWLEDGMENTS

We thank Whales in Paradise, Spirit of Gold Coast and Whale Watching Gold Coast, for the hosting of surveys; volunteer citizen scientists from Humpbacks and Highrises, for their participation in data collection, Griffith School of Engineering for support and reviewers for improvements to the manuscript.

LITERATURE CITED

Armbrecht, L. H., M. Roughan, V. Rossi, A. Schaeffer, P. L. Davies, A. M. Waite and L. K. Armand. 2014. Phytoplankton composition under contrasting oceanographic conditions: Upwelling and downwelling (Eastern Australia). *Continental Shelf Research*, 75, 54-67.

Calambokidis, J., G. H. Steiger, D. K. Ellifrit, B. L. Troutman and C. E. Bowlby. 2004. Distribution and abundance of humpback whales (Megaptera novaeangliae) and other marine mammals off the northern Washington coast. *Fishery Bulletin*, 102, 563-580.

Chittleborough, R. G. 1965. Dynamics of two populations of the humpback whale, Megaptera novaeangliae (Borowski). *Australian Journal of Marine and Freshwater Research*, 16, 33-128.

Clapham, P. J. 1996. The social and reproductive biology of humpback whales: An ecological perspective. Mammal Review, 26: 27-49.

Dalla Rosa, L., J. K. B. Ford and A. W. Trites. 2012. Distribution and relative abundance of humpback whales in relation to environmental variables in coastal British Columbia and adjacent waters. *Continental Shelf Research*, 36, 89-104.

Dawbin, W. H. 1966. The seasonal migratory cycle of humpback whales. pages 145-170 In: Norris, K. S., ed. *Whales, dolphins and porpoises*. University of California Press, Berkeley

Doniol-Valcroze, T., D. Berteaux, P. Larouche and R. Sears. 2007. Influence of thermal fronts on habitat selection by four rorqual whale species in the Gulf of St. Lawrence. *Marine Ecology Progress Series*, 335, 207-216.

Fiedler, P. C., S. B. Reilly, R. P. Hewitt, et al. 1998. Blue whale habitat and prey in the California Channel Islands. Deep Sea Research Part II: Topical Studies in *Oceanography*, 45, 1781-1801.

Jackson, L., R. E. Reichelt, S. Restall, B. Corbett, R. Tomlinson and J. Mcgrath. Marine ecosystem enhancement on a geotextile coastal protection reef-narrowneck reef case study. *Coastal Engineering Conference, 2004*. American Society of Civil Engineers, 3940.

Jenner, K. C., M.-N. M. Jenner and K. A. Mccabe. 2001. Geographical and temporal movements of humpback whales in western Australian waters. *APPEA Journal*, 38, 692-707.

Lohmann, K. J., C. M. F. Lohmann and C. S. Endres. 2008. The sensory ecology of ocean navigation. *Journal of Experimental Biology*, 211, 1719-1728.

Macleod, C. D., S. M. Bannon, G. J. Pierce, C. Schweder, J. A. Learmonth, J. S. Herman and R. J. Reid. 2005. Climate change and the cetacean community of north-west Scotland. *Biological Conservation,* 124. 477-483.

Meynecke, J.-O., S. Vindenes and D. Teixeira. 2013. Monitoring humpback whale (Megaptera novaeangliae) behaviour in a highly urbanised coastline: Gold Coast, Australia. *Global Challenges in Integrated Coastal Zone Management,* 101-113.

Naessig, P. J. and J. M. Lanyon. 2004. Levels and probable origin of predatory scarring on humpback whales (Megaptera novaeangliae) in east Australian waters. *Wildlife Research*, 31, 163-170.

Noad, M. J., R. A. Dunlop, D. Paton and D. H. Cato. 2011. Absolute and relative abundance estimates of Australian east coast humpback whales (Megaptera novaeangliae). *Journal of Cetacean Research and Management*, Special Issue 3, 243-252.

Rasmussen, K., D. M. Palacios, J. Calambokidis, et al. 2007. Southern Hemisphere humpback whales wintering off Central America: insights from water temperature into the longest mammalian migration. *Biology Letters*, 3, 302-305.

Ridgway, K. R. and J. R. Dunn. 2003. Mesoscale structure of the mean East Australian Current System and its relationship with topography. *Progress in Oceanography*, 56, 189-222.

Roughan, M. and J. H. Middleton. 2002. A comparison of observed upwelling mechanisms off the east coast of Australia. *Continental Shelf Research*, 22, 2551-2572.

Stockin, K. A. and E. A. Burgess. 2005. Opportunistic feeding of an adult humpback whale (Megaptera novaeangliae) migrating along the coast of southeastern Queensland, Australia. *Aquatic Mammals*, 31, 120-123.

Stone, G., L. Florez-Gonzalez and S. Katona. 1990. Whale migration record. *Nature*, 346, 705.

Suthers, I. M., J. D. Everett, M. Roughan, et al. 2011. The strengthening East Australian Current, its eddies and biological effects — an introduction and overview. *Deep-Sea Research II,* 58, 538-546.

Thompson, S. A., W. J. Sydeman, J. A. Santora, et al. 2012. Linking predators to seasonality of upwelling: Using food web indicators and path analysis to infer trophic connections. *Progress in Oceanography,* 101, 106-120.

Tomlinson, R. and D. N. Foster. 1987. Sand bypassing at the Tweed River entrance. *8th Australasian Conference on Coastal and Ocean Engineering 1987.*

Journal of Coastal Research	SI	75	557-561	Coconut Creek, Florida	2016

Internal Tides in the Southwestern East/Japan Sea from Observation and Simulation

Seongbong Seo [†‡], Young-Gyu Park[†‡*], Jae-Hun Park[§], Chanhyung Jeon[§], Chang Woong Shin[†] and Hee-Dong Jeong[∞]

[†]Ocean Circulation and Climate Research Center
Korea Institute of Ocean Science and Technology
Ansan, Korea

[‡]Department of Integrated Ocean Sciences
Korea University of Science and Technology
Daejeon, Korea

[§]Department of Ocean Sciences
Inha University
Incheon, Korea

[∞]Fisheries Resources and Environment Division
West Sea Fisheries Research Institute
Incheon, Korea

www.cerf-jcr.org

www.JCRonline.org

ABSTRACT

Seo, S.; Park, Y.G.; Park, J.H.; Jeon, C.; Shin, C.W., and Jeong, H.D., 2016. Internal Tides in the Southwestern East/Japan Sea from Observation and Simulation. *In:* Vila-Concejo, A.; Bruce, E.; Kennedy, D.M., and McCarroll, R.J. (eds.), *Proceedings of the 14th International Coastal Symposium* (Sydney, Australia). *Journal of Coastal Research*, Special Issue, No. 75, pp. 557-561. Coconut Creek (Florida), ISSN 0749-0208.

Energetic internal tides were observed near the continental slope of the southwestern East/Japan Sea. We investigated the energetics of the internal tides using two data sets of 25-hour-long hourly CTD and LADCP profiles and idealized numerical modeling. The energy level during spring tide was about five times stronger than that of neap. During both observation periods the semi-diurnal M_2 constituent was dominant. Internal tide energy flux peaked at about 150 m level where the amplitude of the internal tide was largest. During spring tide the energy flux directed to the deeper part of the East/Japan Sea across the continental slope, while it was mainly along the slope during neap. The modeling results showed that semi-diurnal internal tides are generated mostly on the continental slope near the observation site. It is also suggested by modeling study that thermocline depth is one of important factors controlling the generation of the internal tide. When the thermocline is deeper (shallower) the internal wave becomes stronger (weaker). The response of the internal tide to the thermocline depth is not symmetric. It also showed most of the energy propagates toward the deeper sections.

ADDITIONAL INDEX WORDS: *Generation, Propagation, Stratification, Energy flux, ROMS.*

INTRODUCTION

In the East/Japan Sea (EJS) internal tides are generated when the barotropic tides propagating northeastward from the Korea Strait encounter continental slope (Jeon *et al*., 2014; Park and Watts, 2006). The tides propagate northeastward toward the deeper part of the EJS while affected by meso-scale eddies and stratification. The seasonality of the internal tide variation is due to that of the stratification near the southwestern EJS.

Internal tides can induce intense vertical mixing and energy cascade to small scales through interactions with the bottom and breaking near the generation site as well as remote areas far from the generation sites. Thus internal tides can have strong influence on water properties and circulation both globally (Munk and Wunsch, 1998) and regionally (Lee *et al*., 2011). Lee *et al*. (2011) reported that in their eddy-resolving simulation of the EJS the temperature and salinity of the intermediate layer were significantly improved when tides were considered. There, however, is no study on the structure of the internal tides in the EJS based on high-resolution time series from the field.

In this study, we investigated internal tides at the continental slope of the southwestern EJS, which is known as the generation site (Park and Watts, 2006), using hydrographic data obtained in early September 2012. The main focus was given to the energetics of the internal tides. To understand the energetics further numerical modeling was conducted. From the analysis of observational data and modeling study it was found that the energy of the barotropic tide is converted into that of the internal tide at the continental slope, and the depth of the main thermocline was an important factor controlling the conversion rate. During spring tide the energy propogated across the isobaths into the deeper part while during the neap tide it moved along the isobaths.

METHODS

To investigate the generation pattern of internal tides hydrographic surveys were carried out at the continental slope of the southwestern EJS where the water depth was about 260 m (Figure 1). To understand the observational results better 2.5 dimensional idealized numerical modeling was conducted using the Regional Ocean Modeling System (ROMS) (Shchepetkin and McWilliams 2005).

DOI: 10.2112/SI75-112.1 received 15 October 2015; accepted in revision 15 January 2015
*Corresponding author: ypark@kiost.ac.kr

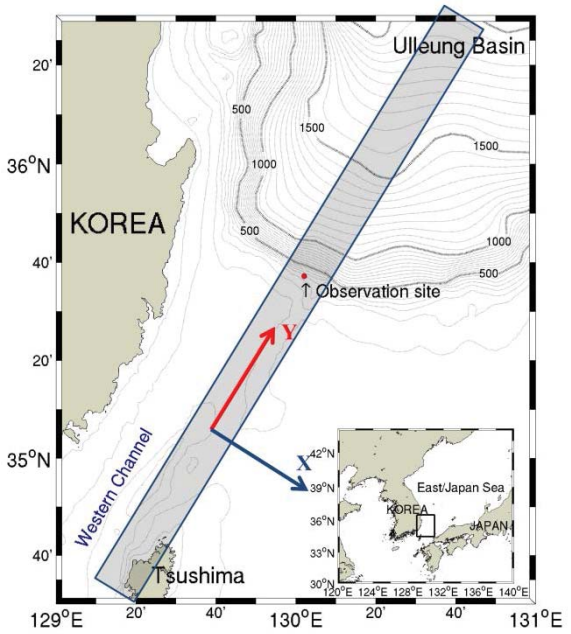

Figure 1. Study area. The contour lines are for bottom bathymetry. The model momain is based on the shaded area.

Observations

In early September 2012 using CTD (Conductivity, Temperature, Depth, Sea-Bird 911 plus, 24Hz) and LADCP (Lowered acoustic Doppler current profiler, RD Instruments 300kHz), we obtained a set of 25-hour time series of temperature, salinity, and velocity profiles in hourly increments during spring and neap periods. The data were processed and subsampled at 1 m and 4 m intervals for CTD and LADCP, respectively.

Numerical modeling

Since the main purpose of the modeling was investigating the governing dynamics of the internal tide rather than reproducing the observation realistically, 2.5 dimensional idealized modeling was conducted in an f-plane for the band shown in Figure 1. Since considering only the continental slope, a simplified geometry varying between 150 m and 2200 m was adopted. Except for the continual shelf and slope, the depth did not vary. The horizontal resolution was set to 1 km, and 64 terrain-following vertical levels were used.

A periodic open boundary condition was adopted in the along-slope direction. Along the southern and northern open boundaries the radiation condition was applied. At the southern end of the domain tidal forcings were applied by describing the sea surface elevation as:

$$\eta = \eta_o \cos(\omega t - \varphi) \quad (1)$$

where η_o is the amplitude, ω the frequency, t the time, and φ the phase of the tidal elevation. To reproduce spring-neap tidal periods two major semi-diurnal constituents, M_2 and S_2 were considered. In this area other constituents are known to be weak and thus not considered in the model. The amplitudes of the M_2 and S_2 were 0.7 m and 0.3 m, respectively (Morimoto *et al.*, 2000).

The initial conditions for temperature and salinity fields for upper 250 m were produced using the CTD observations, and for layer below 250 m using WOA2005 (Experiment 1). The fast barotropic and slow baroclinic modes were separately advanced with 120 s and 4 s, respectively. For the horizontal diffusion the Smagorinsky parameterization (Smagorinsky, 1963) was utilized, and for vertical diffusivity the Mellor-Yamada turbulence closure scheme (Mellor and Yamada, 1982). The model was spun up for 40 days without tidal forcing, and then integrated for another 40 days with the tidal forcing. We analyzed the last 20 days. To study the role of the stratification, one experiment with thermocline lowered by 50 m (Experiment 2), and another one with thermocline raised by 50 m (Experiment 3) were conducted.

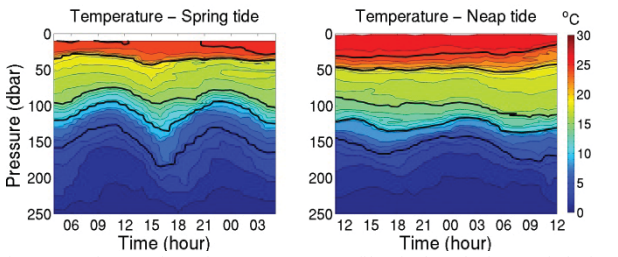

Figure 2. Time series of temperature profiles in hourly interval during the spring (left panel) and neap (right panel) tidal periods.

RESULTS

From the observed temperature and velocity data, first, the presence of internal tide was confirmed, and then energy flux was calculated. The model results were analyzed while focusing on the energetics.

Temperature and velocity

Surface temperature was about 25°C and the mixed layer depth was about 20 m during both the spring and neap periods (Figure 2). The thermocline (10°C isotherm) located between 100 m and 150 m showed extensive vertical excursions with a semi-diurnal period especially during the spring period. Strongest fluctuations in the temperature structure were found below the thermocline. The 5°C isotherm was displaced more than 50 m. During the neap period, a weaker internal tide that displaced the isotherm by about 20 m was observed.

The horizontal velocity obtained from LADCP was decomposed into the along-slope component u and the cross-slope one v (Figure 3). The cross-slope components showed semi-diurnal fluctuations both during the spring and neap tidal periods throughout the entire water column. The amplitude was greater during the spring tidal period, as expected. The along-slope components, however, did not show prominent semi-diurnal signals except in lower layers below 200 m or so. Thus, one could infer that the tidal energy would propagate in the cross-slope direction.

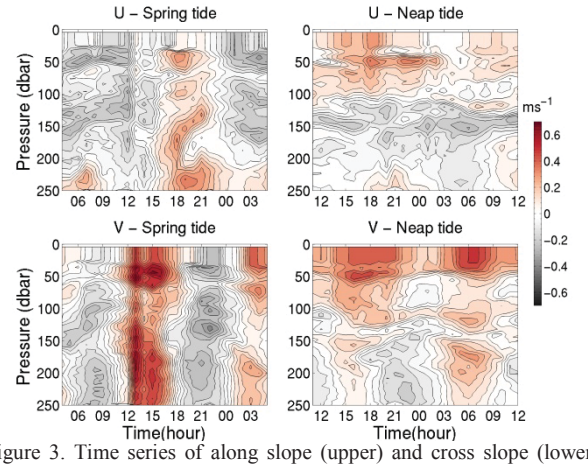

Figure 3. Time series of along slope (upper) and cross slope (lower) currents during spring (left panel) and neap (right panel) tidal periods.

Energy flux

First, each velocity component was decomposed into the depth-averaged, barotropic and baroclinic components,

$$\bar{u} = \int_{-D}^{0} u dz \,/\mathrm{D}, \qquad \bar{v} = \int_{-D}^{0} v dz \,/D$$
$$u' = u - \bar{u},\ v' = v - \bar{v} \tag{2}$$

where D is the water depth. A harmonic analysis was then conducted with the baroclinic components. Our 25-hour long time series were obviously too short to differentiate the semi-diurnal constituents M_2 and S_2, and the diurnal constituents K_1 and O_1. Therefore it was assumed that there were only M_2, K_1, and quarter-diurnal M_4 constituents, which interfere with each other very weakly (Gerkema and van Haren, 2007). The amplitudes and phase of the three components were estimated using a least-squares method similar to that described in Emery and Thomson (2001). We assumed that a baroclinic velocity component u_i' could be represented by the sum of three constituents, time mean over observational period T, $< u_i' >= \int_0^{\mathrm{T}} u_i' \,\mathrm{dt}\,/T$, and residual res_i as follows;

$$u_i'(z,t) = < u_i' > + \sum_{n=1}^{3} u_{i,n}'(z,t) + res_i(z,t)$$
$$u_{i,n}'(z,t) = A_{i,n}(z)\cos\left(\sigma_n t - \phi_{i,n}(z)\right) \tag{3}$$

where σ_n are the frequencies, $A_{i,n}$ the amplitude, and $\phi_{i,n}$ is the phase of each component. The amplitude and phase were set to minimize the norm of the residual $<res_i^2>$ at each depth z. Pressure was also decomposed into the time mean and perturbation $p' = p - < p >$. As the baroclinic velocity components, the pressure perturbation was decomposed into three tidal components $p_n'(z,t)$, time mean and residual.

The i^{th} component of energy flux due to a constituent n, $E_{f,i,n}$, then, is

$$E_{f,i,n} = \langle u_{i,n}' p_n' \rangle \tag{4}$$

The energy fluxes during spring and neap tidal periods are shown in Figure 4. The solid line is for the sum of the three constituents, and the dotted line for M_2. The latter was similar to the former and we can conclude that M_2 is dominant. The energy flux during the spring tidal period was much greater than neap period. The depth-averaged energy flux was in cross-slope direction during the spring tidal period, but in along-slope direction during the neap tidal period as shown in Figure 4.

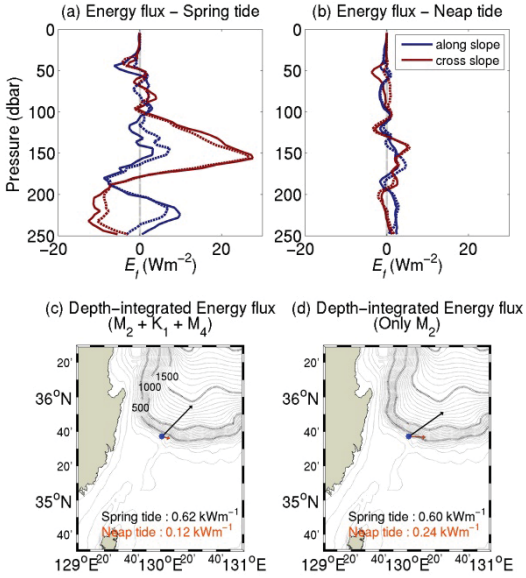

Figure 4. Energy flux profiles during (a) spring and (b) neap tidal periods (dashed line: M_2+K_1+M_4, dotted line: M_2). Depth-integrated energy fluxes estimated from (c) sum of 3 tidal constituents (M_2+K_1+M_4) and (d) semi-diurnal constituent during spring (black line) and neap (red line) tidal periods.

Numerical modeling

The amplitudes of the modeled internal tide were comparable to the observed ones both during the spring and neap. The energy fluxes estimated by using the model outputs during the spring tide are displayed in Figure 5. The depth-integrated energy flux from the model over the area where the water depth was similar to that of the observation site was between 0.41 and 0.63 kWm^{-1}, and similar to the observed one 0.6 kWm^{-1}. In short the model reproduced the observed internal tide properly.

One notable finding from the observation is the negative energy flux (i.e., toward the shallower area) near the bottom. The model results also showed the similar trend of this negative energy flux. As in the observation a positive value was found above the negative value. To the north of the observation site the energy flux was positive, while it was negative toward

south. This structure suggests that the internal wave was formed near the observational site and radiated in both directions.

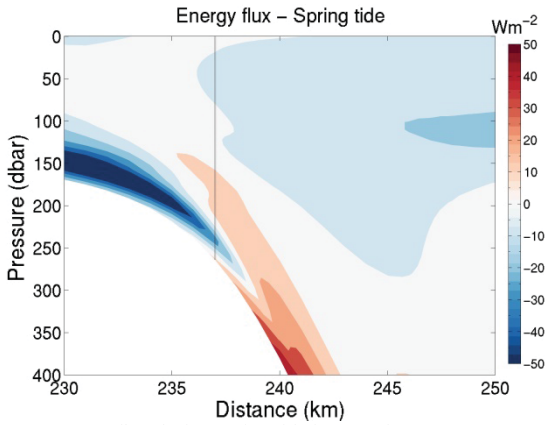

Figure 5. Energy flux during spring tide in Experiment 1.

DISCUSSION

To quantify the internal tide generation the barotropic-to-baroclinic energy conversion rate (Niwa and Hibiya, 2004) was calculated as follows

$$E_{bt2bc} = g\overline{\rho' w_{bt}} D, w_{bt} = \overline{u}\frac{\partial h}{\partial x} + \overline{v}\frac{\partial h}{\partial y} \quad (5)$$

where density perturbation $\rho' = \rho - < \rho >$.

For the case with stratification based on the observation (Experiment 1; black lines in Figure 6a), the conversion rates reached maximum near the observation site, which is marked with a red dot in Figure 6c. The energy conversion was much greater during the spring tidal period as expected (Figure 6b). When the thermocline was deeper (Experiment 2; red line in Figure 6a), the conversion rate was greater than that of Experiment 1. In the case of Experiment 3 (i.e., shallower thermocline), the conversion rate was smaller (blue line in Figure 6a). These results show that the depth of the thermocline was an important factor controlling the formation of internal tide. The response of the conversion rate to the thermocline depth change, however, was not linear. The response was greater when it became shallower. The generation site, the point at which the conversion rate peaks, also responded to the thermocline depth. When the thermocline became deeper, the generation site moved to a deeper part, but when it became shallower, the generation site did not change.

The energy of the baroclinic tide radiated away from the generation site in both ways, but the energy flux toward the deeper part (positive value) was much greater than that toward the shallow part (negative value; Figure 6b). In other words, most of the energy of the internal tide was propagated toward the deeper part. As the conversion rate became greater, the energy flux toward the deeper part became greater.

CONCLUSIONS

In this study we report energetic semi-diurnal internal tides observed on the continental slope of the southwestern East/Japan Sea. The maximum of the energy flux was about 25 W/m^2 at about 150 m level where the amplitude of the tide was greatest (more than 25 m). Through numerical simulation, it was confirmed that the observation site was close to the generation site of the internal tide. Our numerical model results showed that the most of the energy due to the internal tide propagated toward the deeper part.

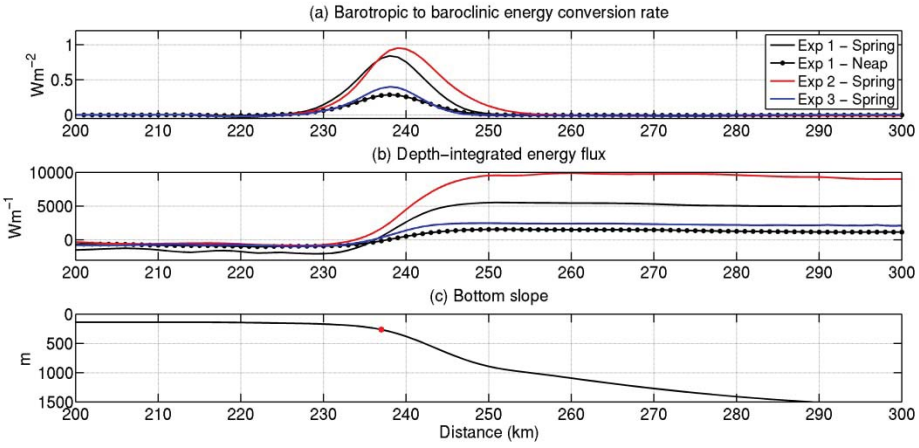

Figure 6. (a) Barotropic to baroclinic energy conversion rate (upper panel), (b) depth integrated energy flux, and (c) water depth. In (a) and (b) the black solid and dash-dot lines are respectively for spring and neap tidal periods in Experiment 1. The red and blue lines are for spring tidal period in experiments 2 and 3, respectively. The red dot in (c) represents the depth of the observation site.

Park and Watts (2006) showed the stratification could have strong effect on the characteristics of the internal tides over southwestern EJS. Additional numerical experiments were conducted to investigate the sensitivity of the internal tide generation to the stratification changes. When the thermocline was deepened the internal tide became stronger suggesting that when the Tsushima Warm Current becomes stronger or the area is invaded by a warm eddy, the internal tide would become stronger. On the other hand when the thermocline was raised, the internal tide became weaker. Thus, when a cold eddy invades the generation region or the warm current becomes weaker, the internal tide would become weaker.

The bottom slope is another important factor governing the generation of internal tide (Baines, 1982), but in this study this factor was not investigated. Considering the large amplitude of the observed internal tide, the bottom slope of the study area favors the generation of the internal tide. The role of the bottom topography, however, was not studied either.

Near the observation site the internal wave could induce active vertical mixing (Park *et al*., 2008, Seo *et al*., 2015). Considering the amount of energy propagating away from the generation site toward the deeper part, the vertical mixing induced by internal tides could be found in other part. This postulate has yet to be proved.

ACKNOWLEDGMENTS

This research was supported by projects titled “Development of Technology for CO_2 Offshore Geological Storage”, “Development of satellite based ocean carbon flux model for seas around Korea” and “Development of Korea Operational Oceanographic System (KOOS), Phase 2” funded by the Ministry of Oceans and Fisheries, Korea, and “Projection of ocean temperature and sea level change around Korean Peninsula” funded by Korea Institute of Ocean Science and Technology. Jeong was supported by Research Programs of the National Institute of Fisheries Science (R2015029 and R2015030).

LITERATURE CITED

Baines, P.G., 1982. On internal tide generation models. *Deep-Sea Research*, 29(3), 307–338.

Choi, AR.; Park, Y.G.; Min, H.S., and Kim, K.H., 2009. The Improvement of CTD Data through Post Processing. *Ocean and Polar Research*, 31(4), 339-347. (In Korean)

Emery, W.J. and Thomson, R.E., 2001. *Data Analysis Method in Physical Oceanography*. Elsevier, pp. 392-399.

Gerkema, T. and Van Haren, H., 2007. Internal tides and energy fluxes over Great Meteor Seamount. *Ocean Science*, 3, 441-449.

Jeon, C.; Park, J.H.; Varlamov, S.M.; Yoon, J.H.; Kim, Y.H.; Seo, S.; Park, Y.G.; Min, H.S.; Lee, J.H., and Kim, C.H., 2014. Seasonal variation of semidiurnal internal tides in the East/Japan Sea. *Journal of Geophysical Research: Oceans*, 119(5), 2843-2859.

Lee, H.J.; Park, J.H.; Wimbush, M.; Jung, K.T.; Jang, C.J.; Cho, Y.K.; Seo, Y.K., and Nam, J.H., 2011. Tidal effects on intermediate waters: A case study in the East/Japan Sea. *Journal of Physical Oceanography*, 41(1), 234-240.

Mellor, G.L. and Yamada, T., 1982. Development of a turbulence closure model for geophysical fluid problems. *Review of Geophysics*, 20, 851-875

Morimoto, A.; Yanagi, T., and Kanego, A., 2000. Tidal Correction of Altimetric Data in the Japan Sea. *Journal of Coastal Research*, 56, 31-41.

Munk, W. and Wunsch, C., 1998. Abyssal recipes II: energetics of tidal and wind mixing. *Deep-Sea Research*, 45, 1976–2009.

Niwa, Y. and Hibiya, T., 2004. Three-dimensional numerical simulation of M_2 internal tides in the East China Sea. *Journal of Geophysical Research*, 109, C04027.

Park, J.H. and Watts, D.R., 2006. Internal tides in the southwestern Japan/East Sea. *Journal of Physical Oceanography*, 36(1), 22-34.

Park, Y.H.; Fuda, J.L.; Durand, I., and Garabato, A.C.N., 2008. Internal tides and vertical mixing over the Kerguelen Plateau. *Deep-Sea Research part II: Topical studies in Oceanography,* 55(5), 582-593

Seo, S.; Park, Y.G.; Park, J.H., and Jeong, H.D., 2015. Thorpe Scale Analysis using CTD Observation on the Continental Slope of the Southwestern East Sea. *Ocean and Polar Research*, 37(2), 107-117. (In Korean)

Shchepetkin, A.F. and McWilliams, J.C., 2005. The Regional Oceanic Modeling System (ROMS): A split-explicit, free-surface, topography following-coordinate ocean model. *Ocean Modelling*, 9(4), 347–404.

Smagorinsky, J., 1963. General circulation experiments with the primitive equations, I. The basic experiment, *Monthly Weather Review*, 91(3), 99–164.

Journal of Coastal Research	SI	75	562-566	Coconut Creek, Florida	2016

A Comparison of Geomorphic Settings, Sediment Facies and Benthic Habitats of Two Carbonate Systems of Western Mediterranean Sea and South Western Australia: Implications for Coastal Management

Sira Tecchiato[†*], Carla Buosi[‡], Angelo Ibba[‡], David A. Ryan[†] and Sandro De Muro[‡]

[†]Department of Applied Geology,
Curtin University,
Perth, Western Australia.

[‡]Department of Chemical and Geological Sciences,
University of Cagliari,
Cagliari, Italy.

www.cerf-jcr.org

www.JCRonline.org

ABSTRACT

Tecchiato, S., Buosi C., Ibba, A., Ryan, D.A., and De Muro, S., 2016. A Comparison of Geomorphic Settings, Sediment Facies and Benthic Habitats of Two Carbonate Systems of Western Mediterranean Sea and South Western Australia: Implications for Coastal Management. *In:* Vila-Concejo, A.; Bruce, E.; Kennedy, D.M., and McCarroll, R.J. (eds.), *Proceedings of the 14th International Coastal Symposium* (Sydney, Australia). *Journal of Coastal Research*, Special Issue, No. 75, pp. 562-566. Coconut Creek (Florida), ISSN 0749-0208.

A similarity exists between the coastal areas of South Western Australia and South Sardinia (Italy-Western Mediterranean Sea), as temperate water carbonate sedimentation dominates the inner shelf at these locations. The seagrass carbonate factory regulates the deposition of modern bioclasts, and the distribution of seagrass meadows and accumulation of bioclasts is controlled by similar processes at the study sites. These biogenic components are mixed to quartz-feldspar sands producing significantly comparable sediment facies, which have been previously documented for Esperance Bay (South Western Australia) and off Porto Pino beaches (Sardinia). Whilst the geological settings of these areas show similar outcropping lithologies, the clastic component of these mixed biogenic and quartz-feldpar sand facies is transported by different agents in the Australian and Sardinian site. In this paper, the similarity between sediment facies is highlighted and their comparison has produced new insights into the processes regulating sediment accumulation in two hydrodynamically different embayments. The characteristics of seagrass beds and their link to the beach system are also compared and set within the context of Mediterranean and South Australian bioregions. These outcomes are relevant for beach management, as European and Australian environmental regulations are compared herein.

ADDITIONAL INDEX WORDS: *Temperate carbonate factory, beach management, geomorphology, seagrass meadows, Esperance (Australia), Porto Pino (Sardinia).*

INTRODUCTION

The carbonate sediment factory in temperate water environments is commonly associated with seagrass meadows (James and Bone, 2011). Seagrass meadows support abundant benthic biota, including numerous calcareous epiphytic organisms that contribute to the production of carbonate sediments. This modern biogenic sedimentation of temperate water carbonates has been previously documented for various sites in the western Mediterrenean (De Falco *et al.*, 2011; De Muro *et al.*, 2013) and western Australia (Collins, 1988; Tecchiato *et al.*, 2015). Two embayments located in south Western Australia and Sardinia show a similar mixed biogenic and siliciclastic sediment facies. Whilst the quartz component of these facies is derived from the erosion of similar outcropping lithologies, the modern biogenic fraction is seagrass derived. The compared areas respectively represent high-energy and low to moderate energy carbonate depositional environments. The comparison of mixed biogenic and siliciclastic sediment facies identified at the study sites have allowed an assessment of the sediment accumulation occurring in the two carbonate systems.

Both the Mediterrenean and the south western Australian coast host a mix of tropical and temperate seagrasses, however the Australian meadows are more diverse and *Posidonia* is one of the most ancient endemic seagrass genera found in these regions (Short *et al*., 2007). Seagrasses are considered to play an important role in the coastal geomorphology of Mediterranean and Australian inner shelf (De Falco *et al.*, 2011; Short, 2010). Waves are attenuated by greater friction across seagrass meadows, which have the capacity to reduce water flow and therefore increase sediment deposition and accumulation as well as beach stability (De Muro *et al.*, 2008, 2010, 2013; Fonseca, 1989; Madsen *et al*., 2001). The accumulation of beach wrack or "banquettes" also supports the prevention of coastal erosion (Carruthers *et al.*, 2007; De Muro and De Falco, 2015; Simeone *et al.*, 2013) and seagrass derived sediment often supplies the beach system contributing to beach stability (Carruthers *et al.*, 2007; Short, 2010; Tecchiato *et al.*, 2015). Some of the processes driving the distribution of this benthic habitat is relevant to coastal management because the preservation of seagrass beds enhances beach stability.

DOI: 10.2112/SI75-113.1 received 15 October 2015; accepted in revision 15 January 2015
*Corresponding author: S.Tecchiato@curtin.edu.au

European (Habitat Directive – EC., 1992) and Australian legislations protect these key ecosystems. In the Mediterrenean, the reason for the protection of this habitat is linked to a widespread decline of the extent of *P. oceanica* beds, particularly around urban centres and ports. Loss of seagrasses caused by mooring damage is common in the Mediterranean and was also described in Western Australia. However this practice is not forbidden neither in Australia nor in Europe. Removal of seagrass "banquettes" also damages the beach environment, but in the Mediterranean only regional regulations exist for this matter. Whilst in Australia beach wrack is not commonly removed from the beach, in Sardinia the impact of trucks used to remove seagrass "banquettes" is significant. This traffic flattens the berm, modifies sand permeability and reduces organic sediment input to the shore (De Muro and De Falco, 2015; Simeone *et al.*, 2013).

The aims of this paper include the comparison of (i) geomorphic settings and underlying geology; (ii) mixed biogenic and siliciclastic sediment facies; (iii) distribution of benthic habitats. Finally, this publication also aims to (iv) identify the processes driving the distribution of seagrass meadows and (v) sediment accumulation. Subsequently, the implications of sedimentary processes for coastal management in similar environments is discussed.

Regional settings

The comparison of geomorphic settings, temperate water carbonate sedimentation and distribution of benthic habitats carried out in this research is based on data collected at the following sites: Porto Pino (south-western Sardinia, central-southern Mediterranean Sea, Figure 1) and Esperance Bay (South Western Australia, Figure 2). The selection of these sites was based on environmental similarity and on data availability including previously published literature (De Muro *et al.*, 2015a; Ryan *et al.*, 2007).

Physical environment – Porto Pino (IT)

Porto Pino beach is a NW–SE oriented embayment located in south western Sardinia (Figure 1). The coastal area extends for a total length of 5 km and is mainly exposed to winds and waves from the SW and NW (De Muro *et al.*, 2015a). A seasonal stream in the central sector of Porto Pino beach supplies quartz-rich sand to the bay.

In this area the continental shelf is relatively wide for the Sardinia region (over 20 km), as it is part of a passive margin. Paleozoic deposits (rhyolitic and dacitic volcanites, and leucogranites) outcrop in the SE and E sectors of the study site. Mesozoic outcropping (fossiliferous dolostones and bioclastic limestones) and Quaternary deposits are also locally present outcropping at Punta Tonnara in the NW sector of the embayment.

Physical environment – Esperance (AU)

Esperance Bay is a ~20 km long southwest facing embayment in southern Western Australia (Figure 2), located along a stable passive continental margin. A couple of island groups from the Recherche Archipelago are in the bay, and represent outcrops of Middle Proterozoic granites, gneisses and migmatites (Ryan *et al.*, 2007). The embayment consists of flat lying Cenozoic limestones and is bordered by sand barriers and granitic rocky headlands (Sanderson *et al.*, 2000).

Climate and hydrodynamics – Porto Pino (IT)

Sardinia is characterized by a mediterranean climate with warm to hot, dry summers and mild to cool, wet winters. The temperature of Porto Pino beach varies from 10.5°C in winter

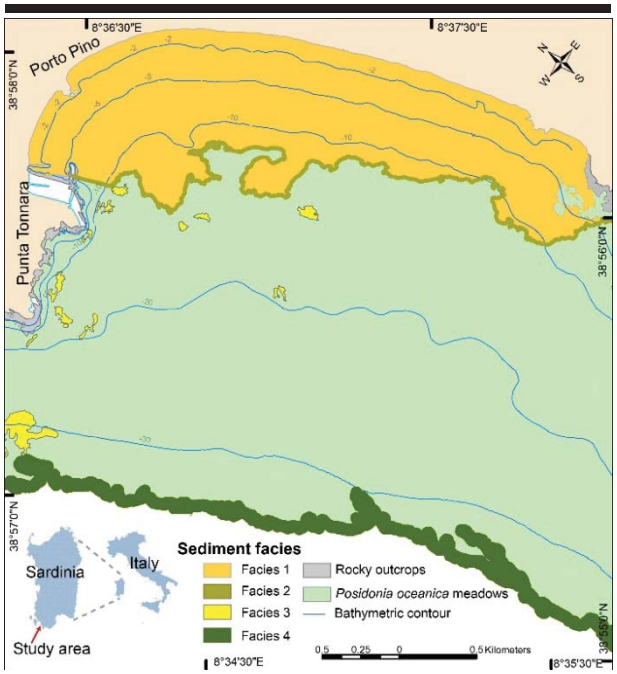

Figure 1. Location of study area and distribution of sediment facies off Porto Pino beach (south-western Sardinia).

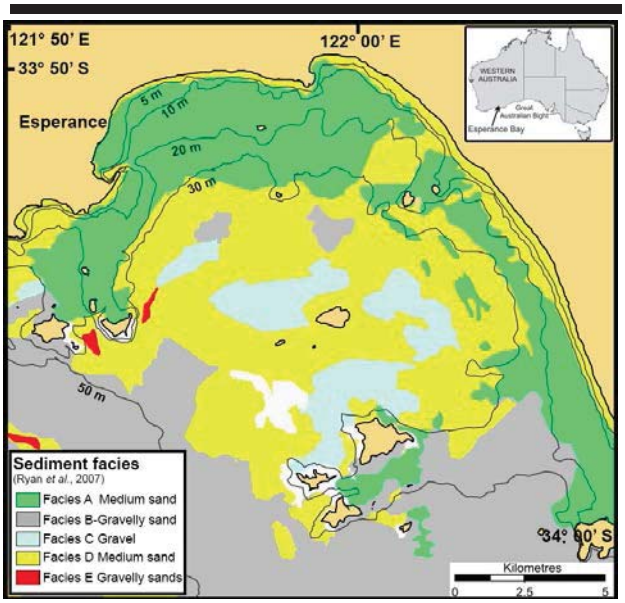

Figure 2. Location of study area and distribution of sediment facies off Esperance Bay (South-western Australia).

and 24.5°C in summer with rainfull concentrated in the winter season with an annual average of 85 mm.

The Porto Pino embayment is microtidal and wave-dominated. The prevailing winds are NNW and NW, the latter more intense than the former. The winds from SW, SSW and S affect the dynamics of the surf zone and are intense in winter. The W winds are directly related to storms from the NW and occasionally reach high intensity, also modifying the surf zone. The southern continental shelf of Sardinia is subject to extreme wave energy compared to the surrounding regions of the Mediterranean Sea, with >3.0 m wave heights and > 7 s swell waves. De Muro *et al.* (2015a) described three main coastal currents (longshore and rip) which control sediment transport along a SE-NW axis. These currents regulate the beach morphology which varies from longshore bar and trough to transverse bar and rip.

Climate and hydrodynamics – Esperance (AU)

Southwestern Australia is characterised by a semi-arid Mediterranean climate with temperatures averaging 8 to 26°C seasonally. Rainfall is limited to the winter season and fluvial discharge to the ocean is very low. Whilst in summer winds from SE prevail, in winter storms from SW dominate (Sanderson *et al.*, 2000). The southern continental shelf region is subject to extreme wave energy with >2.5 m wave heights and > 12 s swell waves. This region is storm dominated as tropical fronts meet cooler Southern Ocean waters. Esperance Bay is microtidal and is affected by strong, relatively consistent swells from the SW. These swells can be reinforced by wind generated waves, and produce a net eastward oriented littoral drift along the south coast. This current regulates the onshore coastal geomorphology (Kendrick *et al.*, 2005).

METHODS

This research is based on the analysis of unpublished data only for the Porto Pino area. The data described in this paper include: (a) geomorphology data based on multibeam and single beam bathymetry, (b) sediment data including grainsize, carbonate content and petrology, (c) benthic habitat mapping based on sidescan sonar, satellite images, scuba diving and underwater video data. Further details on the methodologies used in these analyses can be found in De Muro *et al.* (2015a), Kendrick *et al.*(2005) and Ryan *et al.* (2007).

RESULTS

The following sections highlight the nearshore geomorphology, sediment facies and benthic habitats of the selected study sites: Porto Pino (south-west Sardinia, Italy) and Esperance Bay (South Western Australia).

Geomorphology - Porto Pino (IT)

The seabed near the promontory of Punta Tonnara is rocky (sandstones and limestones) and off Porto Pino reaches 50 m depth ~6 km offshore (Figure 1). Two beach rock ridge systems parallel to the present shoreline and rocky outcrops occur at -5 m and -40 m respectively. These features are the only distinctive geomorphic element of the study area.

Geomorphology - Esperance (AU)

The seabed off Esperance Bay gradually slopes towards the southwest reaching 50 m depth ~10 km offshore (Figure 2). The seafloor shoals in areas adjacent to islands and bedrock reefs. Important geomorphic features of the bay are high profile reefs consisting of granitic outcrops, and low profile reefs which comprise northwest to southeast trending limestone outcrops (Ryan *et al.*, 2007). Bare sand areas are mostly planar, blanket like deposits which occur throughout the inner bay and on the lee side of islands. Small patches of subaqueous dunes (*sensu* Ashley, 1990) are located further offshore (Ryan *et al.*, 2007).

Benthic habitat distribution - Porto Pino (IT)

Three main benthic habitats and substrate types were identified off Porto Pino: (1) uncolonised sandy substrate, (2) rocky outcrops, and (3) *P. oceanica* meadows (De Muro *et al.*, 2015a). The distribution of these habitats is depth consistent and shore parallel. Some "intermattes" (unvegetated areas inside the meadow) were observed in the central and NW sectors of the beach, and rocky substrates are situated near the coastline in the NW and SE sectors (De Muro *et al.*, 2015a).

Benthic habitat distribution – Esperance (AU)

Seagrass beds with common *Posidonia* and *Amphibolis* species were mapped between -5 and -30 m depth within 5 km of the shoreline throughout the embayment and are particularly extensive on the western side of Esperance Bay (Kendrick *et al.*, 2005). Seagrass meadows prefer sheltered sections of Esperance bay and were also found on the lee side of islands forming rather isolated meadows compared to the more continuous mapped closer to the shoreline (Ryan *et al.*, 2007). Offshore reef systems are heavily colonised by sessile organisms. Sand waves, or subaqueous dunes (Ashley, 1990) occur in small patches in the outer section of Esperance Bay (Ryan *et al.*, 2007). Rhodolith beds were mapped between 25 and 60 m in both the inner and outer bay (Kendrick, *et al.*, 2005; Ryan *et al.*, 2007).

Sediment facies - Porto Pino (IT)

Four sand dominated sediment facies were identified at Porto Pino (Table 1, Figure 1), including two shore face facies and two offshore facies. In Sardinia, siliciclastic sands alike facies (1) are redistributed along the shoreface between the shoreline and the upper limit of *Posidonia* meadows (Pusceddu *et al.*, 2011; De Muro *et al.*, 2015b). Sediment facies (1) characterises the shallow beach system between 0 and 5 m depth and is mostly siliciclastic. A mixed bioclastic and siliciclastic sediment facies (2) is situated between the shoreface and the shallower limit of seagrass beds between 1 and 12 m depth. Facies (3) was collected in the intermattes habitat between 10 and 30 m depth and is mostly biogenic. The distribution of facies (4) is shore-parallel and this sediment is located in the deeper areas below the lower limit of *Posidonia* meadow at 30-35 m depth. Bioclastic sediment increase is depth consistent within the *Posidonia* meadows, as shown in the composition of Facies (3) and (4).

Sediment facies - Esperance (AU)

Five offshore sediment facies were identified within Esperance Bay (Table 2, Figure 2). Grainsize increases moving offshore, from fine-medium sands inshore to coarse sands in the outer bay, and gravels correspondently to rhodolith beds. Whilst quartz is the dominant component of the inshore facies, relict

carbonate clasts and bioclasts are more common in the offshore facies (Ryan *et al.*, 2007). Modern bioclasts are common within offshore seagrass beds, bare sand substrates and low profile reefs. Carbonate sediment increase is depth consistent within seagrass beds. Ryan *et al.* (2007) indicated a higher carbonate percentage in the offshore seagrass beds, linked to limestone derived lithic clasts as well as modern bioclasts. Bathymetric range of the sediment facies is as per benthic habitat distribution.

Table 1. *Characteristichs of the sediment facies of Porto Pino (De Muro et al., 2015a).*

Sediment facies	$CaCO_3$ %	Gravel %	Sand %	Mud %	Depositional environments
(1) Siliciclastic sands	22.5 ±10.6	0.1 ±0.0	99.5 ±0.0	0.4 ±0.0	Shoreface sands (0-5 m)
(2) Mixed bioclastic and siliciclastic gravelly sands	27 ±10.6	9.1 ±18.0	89.6 ±17.2	1.3 ±2.0	Transition from shoreface to the upper limit of *Posidonia* meadows (1-12 m)
(3) Biogenic gravelly sands	45 ±21.2	21.1 ±19.5	78.9 ±19.5	0.0 ±0.0	Intermattes (10-30 m)
(4) Detritic gravelly sands	50 ±14.1	9.0 ±5.6	91.0 ±5.6	0.0 ±0.0	*Posidonia* meadow's lower limit (30-35 m)

Table 2. *Characteristics of the sediment facies of Esperance Bay (modified from Ryan et al. 2007).*

Sediment facies	$CaCO_3$ %	Grave l %	Sand %	Mud %	Depositional environments
(A) Medium sand	63.4 ±22.7 Inshore ~20 Offshore~80	9.7 ± 16.4	89.4 ±16.3	0.94 ±1.6	Inshore and Offshore seagrass beds (5-30 m)
(B) Gravelly sands	69.8 ±20.1	20.7 ±23.2	79.0 ±23.3	0.31 ±0.2	Low profile Reef (20-60 m)
(C) Gravel	83.6 ±5.9	40.1 ±30.1	56.3 ±30.3	3.6 ±6.6	Rhodoliths (25-60 m)
(D) Medium sand	69.7 ±16.3	5.9 ±12.4	93.2 ±13.2	0.92 ±1.5	Bare Sand (0-60 m)
(E) Gravelly sands	86.3 ±3.1	22.0 ±31.8	77.8 ±32.0	0.25 ±0.3	Subaqueous Dunes (~20 m)

DISCUSSION

The similarities found at the study sites are mainly related to processes regulating seagrass distribution and sediment accumulation. Seagrass meadows show a significant areal extent off Porto Pino and Esperance Bay, and are likely to contribute to beach stability and to control the morphology of the seabed from the shoreface to inner shelf areas. Considering that we are comparing two wave dominated environments (Australian bay - high energy, Mediterranean embayment - lower energy) characterized by different seagrass genera, it is interesting to note that the geographic distribution of these benthic habitats prefers the most sheltered regions of the studied embayments. In fact, different geomorphological features shelter the studied areas such as islands and promontories, as well as low relief palaeo-reefs and ridge systems offshore.

Facies (1 and 2) of Porto Pino and facies (A inshore) of Esperance are very similar (Tables 1 and 2), as well as Facies (3 and 4) of Porto Pino and Facies (A offshore seagrass beds) of Esperance, both mixed carbonate siliciclastic sediment with up to 90% sand and up to 60% carbonate. The quartz component of these sediment facies reaches their depositional environment through different processes: fluvial transport in Sardina and cliff erosion in Australia. The carbonate content of these sediment facies (4 and A) reflects the presence of eroded limestone material and modern bioclasts, with similar amounts in both facies. This is partly due to the capacity of seagrass meadows to physically retain siliciclastic sediments deposited at shallower depths than the meadow. The accumulation of similar relict sediment on two contrasting continental shelves regulated by different hydrodynamic regimes, suggests that limestone derived lithic clasts were chemically stable within the range of temperatures that occurred in the last Interglacial. Also the modern temperate carbonate production of these environments appears to produce similar quantities of sediment, with a trend of carbonate component increase from the inshore to the offshore sediment facies recorded at both Italian and Australian site within seagrass beds. Whilst this assessment is only preliminary, future research is planned and will support understanding of modern carbonate sedimentation for the selected sites and could be applicable to cool-water carbonate systems globally.

Implication for coastal management

The main outcomes of this paper are the implications for coastal management resulting from an international comparison. The protection of seagrasses is somehow ensured by environmental managers for the selected Mediterrenean and oceanic coasts, however the aspects outlined below are currently not included in the regulations.

The geographic distribution of seagrass meadows prefers the most sheltered regions of the studied embayments. Especially in Sardinia, sheltered bays attract boating tourism and seagrasses are highly affected by mooring damage and fishing. Considering the ecological significance of this habitat, mooring should be forbidden on seagrass meadows.

The removal of beach wrack along part of the Sardinian coasts has caused poor sediment budgets and higher exposure to storms, with subsequent coastal erosion. Further data are needed to compare the importance of beach wrack for maintaining beach stability at both sites.

CONCLUSIONS

This research uses a sedimentological approach to compare cool water carbonate sedimentation and benthic habitat distribution for two geomorphologically different embayments in terms of size and features but with similar outcropping lithologies. An important outcome is the role of seagrass meadows in maintaining beach morphodynamics of the studied Mediterranean and Australian embayments. Seagrasses favour the accumulation of terrigenous sediments within the beach and nearshore system, allowing accumulation of biogenic sediment in the deeper part of the meadows. Further research is needed to deepen our knowledge on the relationship between beach evolution and benthic habitats, as well as on the processes driving sediment accumulation.

This initial comparison of the selected Mediterranean and Australian embayments also outlined the regular removal of beach wrack on the Sardinian beaches and its impact on the

adjacent beach system. In Australia these operations are not common, offering an example of environmentally sensitive management which may be used to support the development of a Mediterranean regulation for the protection of seagrass "banquettes".

ACKNOWLEDGMENTS

This publication is one of the results of the LIFE 13 NAT/IT/001013 SOSS DUNES and B.E.A.C.H. Projects.

LITERATURE CITED

Ashley, G.M., 1990. Classification of large-scale subaqueous bedforms: a new look at an old problem. *Journal of Sedimentary Petrolology*, 60(1), 160–172.

Carruthers, T.J.B.; Dennison, W.C.; Kendrick, G.A.; Waycott, M.; Walker, D.I., and Cambridge, M.L., 2007. Seagrasses of south–west Australia: a conceptual synthesis of the world's most diverse and extensive seagrass meadows. *Journal of Experimental Marine Biology and Ecology*, 350: 21–45.

Collins, L.B., 1988. Sediments and history of the Rottnest Shelf, southwest Australia: a swell-dominated, non-tropical carbonate margin. *Sedimentary Geology*, 60(1), 15-49.

De Falco, G.; De Muro, S.; Batzella, T., and Cucco, A., 2011. Carbonate sedimentation and hydrodynamic pattern on a modern temperate shelf: The strait of Bonifacio (western Mediterranean). *Estuar. Coast. Shelf Sci.*, 93(1), 14-26.

De Muro, S. and De Falco, G., 2015. *Handbook of best practices for the study, monitoring and management of Sardinian beaches*. University press – Scienze Costiere e Marine, CUEC Editrice, 100p. ISBN 978-88-8467-953-6

De Muro, S.; Batzella, T.; Kalb, C., and Pusceddu, N., 2008. Sedimentary processes, hydrodynamics and modeling of the beaches of Santa Margherita, Solanas, Cala di Trana and La Sciumara (Sardinia – Italy). *Rendiconti Online della Societa` Geologica Italiana*, 3(1), 308–309.

De Muro, S.; Brambilla,W.; Kalb, C., and Ibba, A., 2013. Medium and short-term evolution of a microtidal wave dominated Mediterranean beach seaward bordered by *Posidonia oceanica* meadow. The example of the Poetto beach (South Sardinia, Gulf of Cagliari – IT). *Proceedings of 30th IAS Meeting of Sedimentology,* Manchester UK (p. T3S1_P21). doi: 10.13140/RG.2.1.2676.6802

De Muro, S.; Ibba, A., and Buosi, C., 2015a. Technical Report: geology, morphology, sedimentology and morphodynamics of Porto Pino beach. Report ACTION A.1 LIFE 13 NAT/IT/001013 SOSS DUNES, 67p.

De Muro, S.; Ibba, A., and Kalb, C., 2015b. Morpho-sedimentology of a Mediterranean microtidal embayed wave dominated beach system and related inner shelf with *Posidonia oceanica* meadows: the SE Sardinian coast. *Journal of Maps*, DOI: 10.1080/17445647.2015.1051599

De Muro, S.; Kalb, C.; Ibba, A.; Ferraro, F., and Ferrara, C., 2010. Sedimentary processes, morphodynamics and sedimentological map of "Porto Campana" SCI beaches (Domus de Maria – SW Sardinia). *Rendiconti Online della Società Geologica Italiana*, 11(2010), 756–757.

EC., 1992. Council Directive 92/43/EC on the conservation of natural habitats and of wild fauna and flora. *Official Journal of the European Communities*, L 206, 22/07/1992, 52 p.

Fonseca, M.S., 1989. Sediment stabilization by *Halophila decipiens* in comparison to other seagrasses. *Estuarine, Coastal and Shelf Science*, 29(5), 501–507.

James, N.P. and Bone, Y., 2011. Carbonate production and deposition in a warm-temperate macroalgal environment, Investigator Strait, South Australia. *Sedimentary Geology*, 240(1), 41–53.

Kendrick, G.A.; Harvey, E.; McDonald, J.; Pattiaratchi, C.; Cappo, M.; Fromont, J.; Shortis, M.; Grove, S.; Bickers, A.; Baxter, K.; Goldberg, N.; Kletczkowski, M., and Butler, J., 2005. Characterising the fish habitats of the Recherche Archipelago. Final Report, Fisheries Research Development Corporation Project 2001/060, 582 pp. http://www.marine.uwa.edu.au/recherche/

Madsen, J.D.; Chambers, P.A.; James, W.F.; Koch, E.W., and Westlake, D.F., 2001. The interaction between water movement, sediment dynamics and submersed macrophytes. *Hydrobiologia*, 444(1–3), 71–84.

Pusceddu, N.; Batzella, T.; Kalb, C.; Ferraro, F.; Ibba, A., and De Muro, S., 2011. Short-term evolution of Budoni beach on NE Sardinia. *Rendiconti Online della Societa` Geologica Italiana*, 17(2011), 155–159. doi:10.3301/ROL.2011.45

Ryan, D.A.; Brooke, B.P.; Collins, L.B.; Kendrick, G.A.; Baxter, K.J.; Bickers, A.N.; Siwabessy, P.J.W., and Pattiaratchi, C.B., 2007. The influence of geomorphology and sedimentary processes on shallow-water benthic habitat distribution: Esperance Bay, Western Australia. *Estuarine, Coastal and Shelf Science*, 72(1), 379–386.

Sanderson, P.G.; Eliot, I.; Hegge, B., and Maxwell, S., 2000. Regional variation of coastal morphology in southwestern Australia: a synthesis. *Geomorphology*, 34, 73-88.

Short, A.D. 2010. Sediment transport around Australia – sources, mechanisms, rates, and barrier forms. *J. Coast. Res.* 26(3), 395–402.

Short, F.; Carruthers, T.; Dennison, W., and Waycott, M., 2007. Global seagrass distribution and diversity: a bioregional model. *Journal of Experimental Marine Biology and Ecology*, 350(1), 3-20.

Simeone, S.; De Muro, S., and De Falco, G., 2013. Seagrass berm deposition on a Mediterranean embayed beach. *Estuarine, Coastal and Shelf Science*, 135, 171–181. doi:10.1016/j.ecss.2013.10.007

Tecchiato, S.; Collins, L.; Parnum, I., and Stevens, A., 2015. The influence of geomorphology and sedimentary processes on benthic habitat distribution and littoral sediment dynamics: Geraldton, Western Australia. *Marine Geology*, 359, 148-162.

Journal of Coastal Research	SI	75	567-571	Coconut Creek, Florida	2016

The Influence of the Subtropical High-Pressure Ridge on the Western Australian Wave Climate

Moritz Wandres [†*], Charitha Pattiaratchi[†], E.M.S Wijeratne[†], Yasha Hetzel[†]

[†]School of Civil, Environmental and Mining Engineering & UWA Oceans Institute, The University of Western Australia, Nedlands, Australia

www.cerf-jcr.org

www.JCRonline.org

ABSTRACT

Wandres, M., Pattiaratchi, C., Wijeratne, E.M.S., Hetzel, Y., 2016. The influence of the subtropical high-pressure ridge on the Western Australian wave climate. *In:* Vila-Concejo, A.; Bruce, E.; Kennedy, D.M., and McCarroll, R.J. (eds.), *Proceedings of the 14th International Coastal Symposium* (Sydney, Australia). *Journal of Coastal Research*, Special Issue, No. 75, pp. 567-571. Coconut Creek (Florida), ISSN 0749-0208.

Understanding the wave climate of a region is critical for its coastal zone management. The southwest Western Australian (SWWA) wave climate is dominated by waves generated in the energetic and variable Southern Ocean (SO) storm belt. The latitudinal variability of the SO storm belt can be described by the position (latitude) of the subtropical high-pressure ridge (STRP). To gain an understanding in how the SO storm belt influences the SWWA wave climate, the relationship between the STRP and the waves was examined. Wave data from three directional wave buoys along the SWWA shelf were compared to the STRP. The seasonal and interannual variability of the STRP and the wave climate indicated a significant correlation between the STRP and the SWWA wave heights with the strongest relationship during winter. A northward shift of the STRP resulted in a northward shift of the SO storm belt which led to increased wave heights in SWWA whereas a southward shift of the STRP resulted in decreased wave heights. The close relationship between the STRP and the local wave climate, suggests it could be used to estimate future wave climates in SWWA.

ADDITIONAL INDEX WORDS: *Climate change, Subtropical ridge, Southern Annular Mode, wave climate.*

INTRODUCTION

Knowledge of local surface gravity wave climates is critical for coastal protection, development, and coastal zone management. The southwest Western Australian (SWWA) wave climate is governed by storms generated in the Southern Ocean (SO) (Bosserelle *et al*. 2012; Hemer 2010; Hemer *et al.* 2009; Lemm *et al*. 1999). The high latitudes of the SO are dominated by storms (the "roaring forties"), which generate some of the most energetic wave climates in the world (Sterl and Caires 2005). Swells originating from these storms propagate throughout the world's oceans, impacting the coastlines as they dissipate along the shore (Snodgrass *et al*. 1966).

Variability of the SO zonal circulation may be described by the Southern Annular Mode (SAM), which is calculated as the mean sea level pressure (MSLP) between 40°S and 65°S (Marshall 2003) and by the position (latitude) of the subtropical high-pressure ridge (STRP). The SAM and the STRP are closely connected, as a southward shift of the SO storm belt (+ SAM) coincides with the southward shift of the STRP. The STRP is responsible for the variability of the zonal westerly winds in the Southern Hemisphere (Pittock 1973; Thresher 2002; Williams and Stone 2009) and therefore plays an important role in the SWWA wave climate (Lemm *et al*. 1999).

The STRP shifts southward during the austral summer months resulting in enhanced easterly winds around SWWA and northward during winter resulting in increased westerly fronts (Drosdowsky 2005; Pittock 1973). The increase in westerlies in winter has been related to increased rainfall and storminess in winter compared to summer, however, during recent decades an overall southward trend of the STRP and consequentially a decrease in rain has been observed (Cai *et al*. 2011; Timbal and Drosdowsky 2013; Williams and Stone 2009).

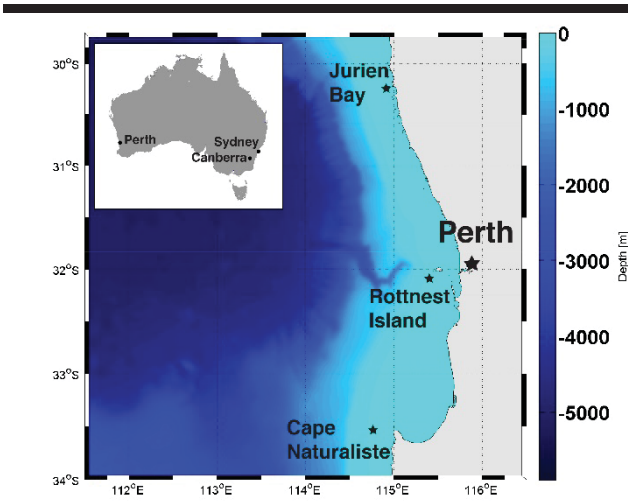

Figure 1. Study area and location of the wave rider buoys

DOI: 10.2112/SI75-114.1 received 15 October 2015; accepted in revision 15 January 2015
*Corresponding author: moritz.wandres@gmail.com

Few studies have investigated the wave climate on the SWWA shelf. Lemm *et al*. (1999) examined the wave climate off the Perth coast by analyzing 2.5 years of wave data from the Rottnest Island wave buoy (Figure 1). The data included the year 1996, which was one of the stormiest years in the past decades suggesting biased results (Bosserelle *et al*. 2012). Bosserelle *et al*. (2011) created a 40-year wave hindcast of the Southern Indian Ocean and investigated the wave climate variability and long term trends. None of these studies analysed the influence of the STRP and the SO storm belt variability on the SWWA wave climate in detail, however, Hemer *et al*. (2007) found a higher significant correlation between the position of the SO storm belt and the SWWA wave climate than the storm intensity on the SWWA wave climate. Hemer *et al*. (2010) found a significant correlation between the SO wave climate and the SAM, however, the correlations found around SWWA were quite low. As SWWA is located in the latitudes of the subtropical high-pressure ridge, investigating the relationship between the STRP variability and the SWWA wave climate might be more conclusive.

This paper uses long-term time series data (1994-2014) from three directional wave buoys along the SWWA shelf (Figure 1) and examines the relationship between the STRP and the wave climate, focusing on austral winter.

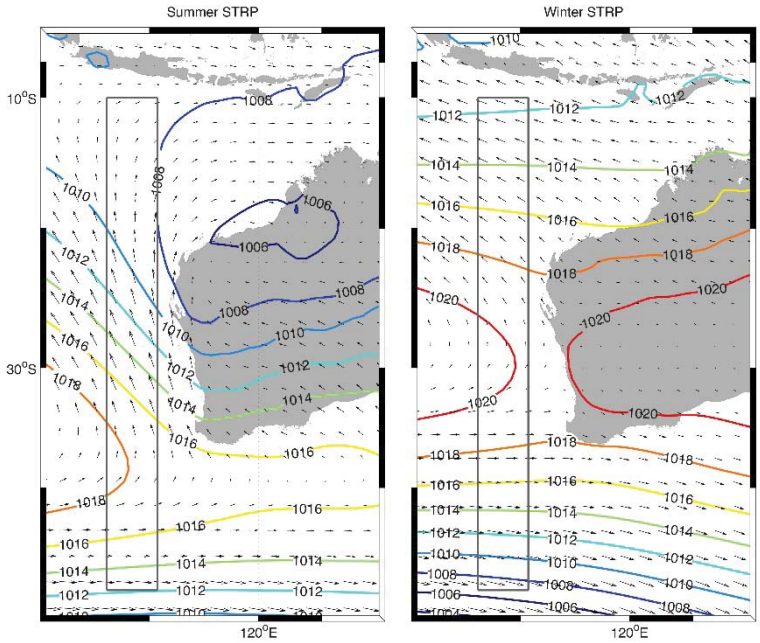

Figure 2. Average mean sea level pressure (in hPa) over Western Australia in summer (left) and winter (right). The black arrows indicate the mean wind direction. The gray bounding box indicates the area used to calculate the STRP.

METHODS

The STRP is the mean position of the subtropical high-pressure ridge and it is given as the latitude of the maximum of the monthly average mean sea level pressure (MSLP) within a predefined area. In previous studies, the area of 10°-44°S and 145°-150°E has been used to estimate the STRP and to study its influence on eastern Australian climate (Cai *et al*. 2011; Drosdowsky 2005). In this study, the equivalent index was calculated for Western Australia by using MSLP data from the European Centre for Medium Range Weather Forecast (ECMWF) ERA-Interim dataset over a bounding area of 108°-112°E and 10°-44°S (Figure 2). The ECMWF ERA-Interim dataset was validated against wind measurements on Rottnest Island and the model was found to produce realistic results for the SWWA region (validation not shown here).

The influence of the STRP on the SWWA wave climate was examined by comparing the STRP to long-term wave observations from wave buoys at three different locations along the shelf (Figure 1), with the longest continuously operating wave buoy (1994-present, >20 years) being located off Rottnest Island. The wave buoys recorded significant wave heights H_s, peak periods T_p, and peak direction at 30-minute intervals.

In order to compare the wave climate and the STRP, monthly means of the wave data were calculated. The summer mean H_s was calculated by averaging the December, January, and February means and the winter mean H_s was calculated by averaging the June, July, and August means. The wave height variability was estimated by calculating the standard deviation of the significant wave height time series. Correlation coefficients between H_s at the three different locations and the STRP were calculated.

The wave heights, as well as the STRP featured strong seasonal signals, which might lead to overly high correlation coefficients. Therefore, the monthly STRP and H_S anomalies were estimated as the deviation from the 1994-2014 climatology and correlation coefficients between the anomalies were calculated.

RESULTS

Swell waves that impacted the SWWA shelf generally originated from the SO resulting in a decreasing wave height gradient from south to north and from west to east. Therefore, Cape Naturaliste experienced the highest wave heights with an annual mean H_S of 2.64 m. The annual average wave height at Rottnest Island was 2.15 m and 2.26 m at Jurien Bay. A large seasonal variability was observed at all three locations, with summer wave heights being ~0.5 – 1.05 m smaller than winter wave heights and the standard deviations varied between 0.81 and 1.02 m (Table 1).

To understand the relationship between the STRP and the wave heights, correlation coefficients were calculated (Table 2). A strong correlation between the STRP and the wave heights at the different locations, with correlation coefficients between 0.8 and 0.89 was found. Furthermore, a moderate to strong correlation between the STRP anomaly and the wave height anomalies with correlation coefficients between 0.63 and 0.72 was found.

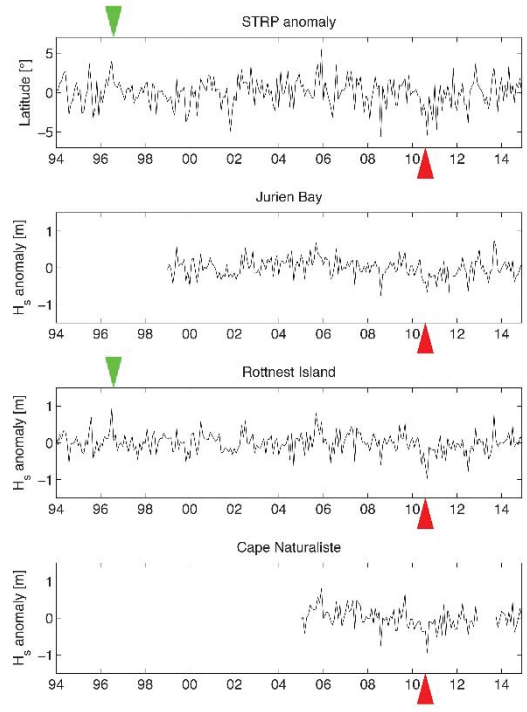

Figure 3. The STRP anomaly (in °latitude) from 1994 to 2014 (top), H_S anomaly (in m) from 1994 to 2014 at Jurien Bay (2nd from top), Rottnest Island (3rd from top), and Cape Naturaliste (bottom). Green arrows indicate the August 1996 positive anomaly and red arrows indicate the August 2010 negative anomaly.

Table 1. *Annual mean H_S, summer mean H_S, winter mean H_S, and mean standard deviation at Jurien Bay, Rottnest Island, and Cape Naturaliste.*

Jurien Bay	Mean H_S [m]	2.26
	Summer mean H_S [m]	2.05
	Winter mean H_S [m]	2.54
	STD [m]	0.81
Rottnest Island	Mean H_S [m]	2.15
	Summer mean H_S [m]	1.80
	Winter mean H_S [m]	2.65
	STD [m]	0.93
Cape Naturaliste	Mean H_S [m]	2.64
	Summer mean H_S [m]	2.14
	Winter mean H_S [m]	3.19
	STD [m]	1.02

When analysing ECMWF wind fields (not shown here) a northward shift of the STRP resulted in increased westerly winds closer to the Australian coast, as the SO storm track shifted northward. A southward shift of the STRP led to increased easterly winds along the SWWA coast. Therefore, a high STRP resulted in larger wave heights, whereas a southward shift of the STR suppressed the westerly fronts, leading to decreased wave heights. Both, the STRP, and the wave heights followed an annual signal. In summer the mean STRP was around 38°S and in winter it shifted north to around 30°S (Figure 2). The northward position of the STR in winter was associated with higher wave heights in winter and the southward movement of the STRP in summer led to smaller wave heights.

Table 2. *Correlation coefficients between H_S and STRP and between H_S anomaly and STRP anomaly.*

	Correlation Coefficient
Jurien Bay H_S	0.8
Rottnest Island H_S	0.89
Cape Naturaliste H_S	0.88
Jurien Bay H_S anomaly	0.63
Rottnest Island H_S anomaly	0.72
Cape Naturaliste H_S anomaly	0.72

The monthly mean STRP anomaly and the wave height anomalies were closely connected to each other. Positive STRP anomalies (STRP further north than "normal") led to positive wave height anomalies (larger waves than "normal"), and larger STRP anomalies led to larger wave height anomalies (Figure 3). The relationship between the STRP anomalies and the wave height anomalies was strongest in winter. As the SWWA winter wave climate is dominated by storms from the SO, a shift in the SO storm belt results in a change in wave conditions. In the summer months, the STRP is located further south and the intensity of the SO storms is generally much lower. Furthermore, summer wave conditions are influenced by the sea breeze system (locally generated, short period waves from the SW) and, occasionally, tropical cyclones (larger, long period swell from the NW), that can cause positive wave height anomalies irrespective of the STRP. Therefore, a north-south fluctuation of the STRP (*e.g.* the summer 2005/2006 strong

+STRP anomaly) has less impact on the summer wave regime, and the correlation during summer months is lower than in winter. As suggested by previous studies (Hemer *et al.* 2007), extreme storm events in the SO were found to cause slight positive wave height anomalies, however, the dominant, wave height-governing feature in SWWA was found to be the position of the SO storm belt. Wave directions and peak periods were also compared to the STRP, however, no significant correlations were found and are therefore not included in this paper.

DISCUSSION

This study analysed the average wave climate on the SWWA shelf and its relationship to the STRP. As suggested by previous studies, a strong seasonal signal was found, with small waves in summer and large waves in winter (Bosserelle *et al.* 2012; Hemer *et al*. 2009; Lemm *et al*. 1999) and this variability could be contributed to the variability of the SO storm belt and the STRP.

The wave climate is dependent on the intensity of storms, as well as their proximity. The STRP gives information on proximity only, but the data suggest that this is the dominant factor for the investigated mean wave heights. A high significant correlation was found between the STRP and the SWWA wave climate. The STRP is responsible for the variability of the zonal westerly winds, rainfall, and storminess (Cai *et al*. 2011; Lemm *et al*. 1999; Pittock 1973), and therefore influences the local wave climate. In winter, the subtropical ridge is generally located further north than in summer, however, it is subject to a large inter-annual variability. The winter of 1996 is generally considered as one of the stormiest winters of the past decades (Bosserelle *et al*. 2012), whereas the winter of 2010 was comparatively mild. The comparison of the August MSLP of the two years showed that the subtropical ridge was located significantly further north and the subtropical storm belt was much closer to the Australian coastline in 1996 (STRP of 28.82 °S) than in 2010 (STRP of 32.67 °S) (Figure 4).

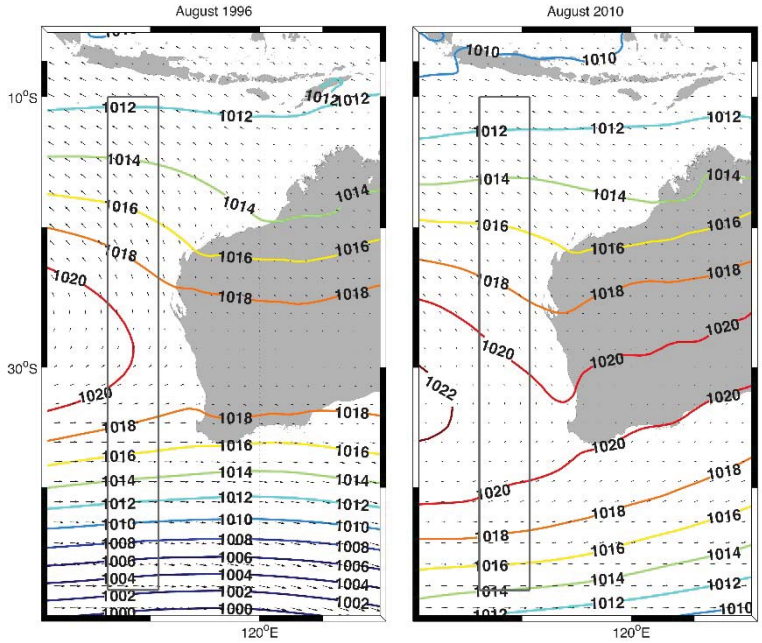

Figure 4. Average mean sea level pressure over Western Australia during a positive STRP anomaly in August 1996 (left) and during a negative STRP anomaly in August 2010 (right). The black arrows indicate the mean wind direction. The gray bounding box indicates the area used to calculate the STRP.

This resulted in a positive STRP anomaly of 1.44° (latitude) in 1996 and a negative STRP anomaly of -2.41° (latitude) in 2010. This large discrepancy in latitudes was reflected in the in wave heights: The mean significant wave height at the Rottnest Island wave buoy in August 1996 was 2.71 m, whereas the mean significant wave height in August 2010 was only 2.05 m (Table 3). The wave buoys at Jurien Bay and Cape Naturaliste had not been deployed in August 1996, however, the wave heights of 2.23 m (Jurien Bay) and 2.82 m (Cape Naturaliste) are significantly lower than the winter average at those locations.

Table 3. *STRP anomaly, and wave heights in August, 1996 and 2010*

	August 1996	August 2010
STRP [latitude in °S]	28.82	32.67
STRP anomaly [°S]	1.44	-2.41
H_s Jurien Bay [m]	-	2.23
H_s Rottnest Island [m]	2.71	2.05
H_s Cape Naturaliste [m]	-	2.82

Lemm *et al*. (1999) found a mean significant wave height of 2.0 m at Rottnest Island and Bosserelle *et al*. (2012) suggested this wave height might be biased by the unusually high storm activity in 1996. In this study we found a mean significant wave height of 2.15 m at Rottnest Island, suggesting the 2.5-year analysis of Lemm *et al*. (1999) was still representative.

Hemer *et al*. (2010) found a correlation between the SAM and the Western Australian wave climate, however, the SAM is a climate index for the entire SO and therefore the correlation is quite small. The STRP on the other hand, is a local climate index, and therefore acts as a better predictor for the SWWA wave climate and storminess and it might be a useful tool to assess future changes in the SWWA wave climate.

CONCLUSIONS

Observational wave buoy data from three locations along the SWWA shelf were used to determine the average wave conditions and their relationship to the STRP. A strong seasonal and inter-annual variability in the wave heights was found. Changes in wave conditions were linked to latitudinal changes of the SO storm belt: A northward movement of the STRP and subsequently the SO storm belt, resulted in increased wave heights around SWWA.

Knowledge of the wave climate of a region and its driving atmospheric processes is critical for coastal zone management. In this paper we were able to show that the STRP can be used as an indicator for the SWWA wave climate. The correlations were equally strong at all three wave buoys providing us with confidence that the STRP is important for the entire region, however, numerical models of the SWWA shelf might provide further information, especially in regards to wave direction and period. It was shown that the STRP acts as a good predictor for the SWWA wave heights and wave height anomalies and it could be useful to estimate the future wave climate using climate model predictions.

ACKNOWLEDGMENTS

The authors would like to thank Siobain Mulligan and Reena Lowry from the Government of Western Australia, Department of Transport for providing access to the wave buoy data. Furthermore, the authors would like to acknowledge the European Centre for Medium-Range Weather Forecasts (ECMWF) for granting access to the Era-Interim dataset. Moritz Wandres received the SIRF, the UPAIS, and the UWA Top-Up Scholarship.

LITERATURE CITED

Bosserelle, C., Pattiaratchi, C., and Haigh, I., 2012. Inter-annual variability and longer-term changes in the wave climate of Western Australia between 1970 and 2009. *Ocean Dynamics*, 62(1), 63–76.

Cai, W., van Rensch, P., and Cowan, T., 2011. Influence of Global-Scale Variability on the Subtropical Ridge over Southeast Australia. *Journal of Climate*, 24(23), 6035–6053.

Drosdowsky, W., 2005. The latitude of the subtropical ridge over Eastern Australia: TheL index revisited. *International Journal of Climatology*, 25(10), 1291–1299.

Hemer, M.A., 2010. Historical trends in Southern Ocean storminess: Long-term variability of extreme wave heights at Cape Sorell, Tasmania. *Geophysical Research Letters*, 37(18).

Hemer, M.A., Church, J.A., and Hunter, J.R., 2009. Variability and trends in the directional wave climate of the Southern Hemisphere. *International Journal of Climatology*, 30(4), 475–491.

Hemer, M.A., Simmonds, I., and Keay, K, 2007. A classification of wave generation characteristics during large wave events on the Southern Australian margin. *Continental Shelf Research*, 28(4-5), 634-652.

Lemm, A.J., Hegge, B.J., and Masselink, G., 1999. Offshore wave climate, Perth (Western Australia), 1994–96. *Marine and Freshwater Research*, 50(2).

Marshall, G.J., 2003. Trends in the Southern Annular Mode from Observations and Reanalyses. *Journal of Climate*, 16(24), pp.4134–4143.

Pittock, A.B., 1973. Global meridional interactions in stratosphere and troposphere. *Quarterly Journal of the Royal Meteorological Society*, 99(421), 424–437.

Snodgrass, F.E. *et al*., 1966. Propagation of Ocean Swell across the Pacific. *Philosophical Transactions of the Royal Society A: Mathematical, Physical and Engineering Sciences*, 259(1103), pp.431–497.

Sterl, A. and Caires, S., 2005. Climatology, variability and extrema of ocean waves: the Web-based KNMI/ERA-40 wave atlas. *International Journal of Climatology*, 25(7), 963–977.

Thresher, R.E., 2002. Solar correlates of Southern Hemisphere mid-latitude climate variability. *International Journal of Climatology*, 22(8), 901–915.

Timbal, B. and Drosdowsky, W., 2013. The relationship between the decline of Southeastern Australian rainfall and the strengthening of the subtropical ridge. *International Journal of Climatology*, 33(4), 1021–1034.

Williams, A.A.J. and Stone, R.C., 2009. An assessment of relationships between the Australian subtropical ridge, rainfall variability, and high-latitude circulation patterns. *International Journal of Climatology*, 29(5), 691–709.

Journal of Coastal Research	SI	75	572-576	Coconut Creek, Florida	2016

Three-dimensional structure of coral reef boulders transported by stormy waves using the very high resolution WorldView-2 satellite

Antoine Collin[†‡*], Samuel Etienne[†‡], and Matthieu Jeanson[†]

[†]Coastal Geomorphology and Environment Laboratory
Ecole Pratique des Hautes Etudes, CNRS UMR 8586 Prodig
Dinard, France

[‡]"CORAIL" LABoratory of EXcellence
Perpignan, France

www.cerf-jcr.org

www.JCRonline.org

ABSTRACT

Collin, A., Etienne, S. and Jeanson, M., 2016. Three-dimensional structure of coral reef boulders transported by stormy waves using the very high resolution WorldView-2 satellite. *In:* Vila-Concejo, A.; Bruce, E.; Kennedy, D.M., and McCarroll, R.J. (eds.), *Proceedings of the 14th International Coastal Symposium* (Sydney, Australia). *Journal of Coastal Research*, Special Issue, No. 75, pp. 572-576. Coconut Creek (Florida), ISSN 0749-0208.

Coral reef boulders have been showed to reliably characterize the amount of wave energy related to cyclone, storm or tsunami events. The wave height and current velocity have been successfully explained by the variability in the boulder individual (morphology) and population (distribution) spatial patterns. Even if a single boulder may include a substantial amount of information, it may be highly challenging to characterize it given the access difficulty at the local and regional scales. Moreover, a boulder population is meaningful to robustly and continuously depict the energetic event that drove the sediment transportation. Recently the very high resolution satellite remote sensing has been demonstrated to help classify and measure the horizontal patterns (A- and B-axes) of the boulders at the submeter scale. Here we focus on the vertical dimension (C-axis) of the boulders. Based on boulder fieldwork measurements of the three axes and geographic locations, we constrain various spectral parameters of the remotely-sensed datasets (WorldView-2) to retrieve the three axes of the boulders, reaching a very satisfactory agreements (R^2) of 0.95, 0.88 and 0.75, respectively. The innovative C extraction combined with the A and B information will allow geomorphologists to rapidly and extensively collect boulder data so that the underlying energy can be computed in a more expanded and accurate way, at the population scale.

ADDITIONAL INDEX WORDS: *Boulder geomorphology, VHR remote sensing, high-energy event, Tetiaroa atoll.*

INTRODUCTION

Boulder deposits are almost ubiquitous in coastal environments, where they represent a distinct sedimentary class and a signature of high-energy events (cyclones, storms, tsunamis). Examination of the sedimentary assemblages of catastrophic marine inundation (*e.g.*, 2011 Tohoku-oki tsunami: Goto *et al.*, 2012) enlightened the interest of coarse-fine sediment to characterize the hydrodynamics of such events. The mathematical modelling of hydrodynamic transport equations (Nott, 2003) allows for the extraction of quantitative information on flow velocity or wave height from boulder morphometry. Spatialisation of hydrodynamic information inferred from boulder morphometry offers the opportunity to understand the propagation of catastrophic waves on coastal plains. Boulders have then become a new centre of interest for coastal sedimentologists and boulder deposits appear now as a robust proxy for the reconstruction of high-energy marine inundation events (Etienne *et al.*, 2011).

Boulder deposits are naturally remanent objects: they can subsist in the landscapes for decades or centuries, except when they are intentionally removed (see review in Terry *et al.*, 2013). Because of this remanence, it is sometimes difficult to decipher the different generations of boulder deposits, especially in areas where both cyclones and tsunamis are frequent. Therefore, a boulder population is often composed of individual elements tied to various cohorts, each cohort corresponding to a single high-energy event, and elements that have been mobilized several times. Dating a clast is sometimes possible for coral reef boulder using radiocarbon or U-series dating of fossils (Terry and Etienne, 2014), but it is more difficult for crystalline rocks in the absence of historic documentation (aerial photographs, satellite images, written documents, *etc.*). Accurate characterization of boulder deposits associated with modern or past extreme events requires spatial mapping of boulder characteristics (*e.g.*, volume) over large areas. Severel limiting factors (time, access, remoteness) preclude extensive field mapping, especially in low-lying coral islands (*e.g.*, atolls) where resources are scarse. Then, alternative mapping methods are needed.

Spaceborne remote sensing has increasingly attracted scientists and stakeholders over the last decade insofar as both spatial and spectral resolutions have been significantly improved. Even though very high resolution (VHR) imagery has been conventionally used for mapping coral reef cover or reefscape patches (Collin *et al.*, 2012, 2013a) at submeter scale, only one pioneer work has recently constrained VHR data to retrieve the horizontal, i.e., projected, morphology of coral boulders (Collin *et al.*, 2013b). Successful findings were based on the red and near-infrared (NIR) spectrum parts of the WorldView-2 (WV2) satellite. Given both horizontal (A- and B-axes) dimensions were elucidated, the current research aims at

DOI: 10.2112/SI75-115.1 received 15 October 2015; accepted in revision 15 January 2015
*Corresponding author: antoine.collin@ephe.sorbonne.fr

resolving the vertical dimension (C-axis) using the WV2 data for creating a 3D virtual coral boulder field on the reef flat of Tetiaroa atoll, French Polynesia (Figure 1).

Figure 1. Coral boulder field on the reef flat of Tetiaroa atoll, French Polynesia. Coral colonies were transported by high-energy events and emplaced like "saucers" so that A- and B-axes stand for the horizontal dimensions, whilst the C-axis represented the vertical dimension. Picture: April 2013.

METHODS

Large coral boulders (N=23) transported on the reef flat of Tetiaroa were individually examined in April 2010 (N=6), November 2011 (N=2), July 2012 (N=3) and April 2013 (N=12). Boulder location (datum: WGS 84 UTM; projection: zone 6 South), dimensions (A-, B-, C-axes), orientation of A-axis, and rock characteristics were thoroughly recorded. Boulder morphometry is critical for flow velocity and wave height estimation following Nott's equations (2003). In addition, geolocation of an array of distinct targets visible on satellite imagery (pier, perched reef flat, *feo*) were monitored *in situ* using a GPS device for the sake of image orthorectification.

Spaceborne remote sensing consists of recording electromagnetic radiation of a spatial domain at a specific time. Likewise, a common photograph is the handborne remote sensing product recording three visible spectral bands (red, green and blue) characterizing a scene instantly. The primary advantage of spaceborne *versus* airborne remote sensing lies in its cost-effectiveness regarding the area acquisition. The main limitation of the spaceborne remote sensing is the order of the area unit, constraining satellite products to be used for greater-than-1-m orthographic or greater-than-10-m stereographic purposes. Recent advances in spaceborne sensors may overcome this issue by providing a submeter panchromatic band synoptic to multispectral bands, such as WV2. Its imagery is constituted of one 0.5 m panchromatic band (450-800 nm) and eight 2 m multispectral bands (from 400, coastal, to 1040 nm, near-infrared-2, NIR2). Both datasets were collected over Tetiaroa on 25 September 2012 (UTC 20h32min37s). Prior retrieving boulder information, pre-processing procedures were applied so as to handle standardized data, thus build a repeatable process. For each dataset, a rigorous geometric correction was carried out before performing a pansharpening workflow (Gram-Schmidt sharpening followed by a cubic convolution resampling) in order to work on eight 0.5 m multispectral bands (see Collin *et al.*, 2012 for further details). The radiometric correction was then implemented by, first, calibrating the digital number into radiance and, finally into reflectance, by compensating for the atmosphere attenuation (Figure 2).

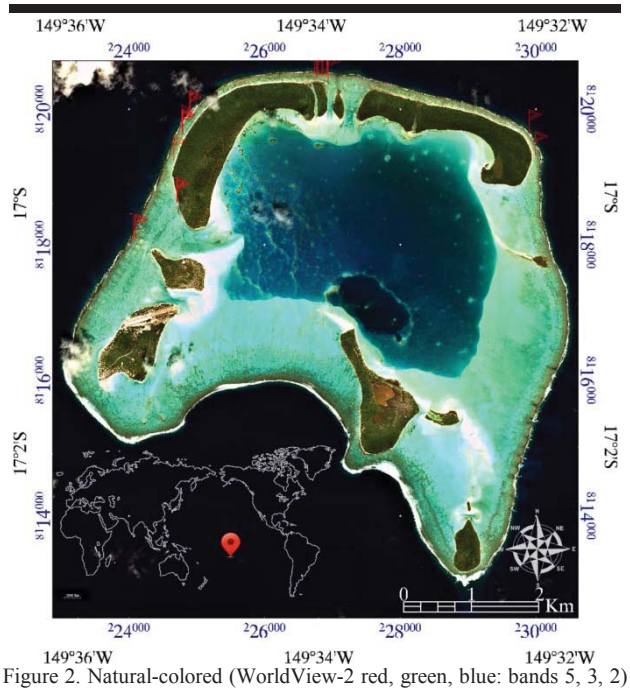

Figure 2. Natural-colored (WorldView-2 red, green, blue: bands 5, 3, 2) image of Tetiaroa atoll, French Polynesia. The value of image pixels represents the orthorectified water-leaving reflectance. Red flags correspond to the location of measured coral boulders.

The geolocation of coral boulders allows for their characterization based on WV2 spectral data. Each pixel composing the coral boulder was therefore linked with a spectral signature constituted of eight reflectance values. The creation and use of the WV2 spectral combinations based on the mathematical relationship of the normalized difference index (NDI) showed that the coral geomorphic features, generically, and coral boulders, specifically, were significantly more discriminated (Collin *et al.*, 2013b).

$$NDI = \frac{R_{NIR} - R_{red}}{R_{NIR} + R_{red}} \quad (1)$$

with R_{NIR} and R_{red} refer to orthorectified water-leaving reflectance of the near-infrared (WV2 band 6, 7 and 8, called "red edge", NIR1 and NIR2, respectively) and red (WV2 band 5) spectral bands. Among the three NDI possible, the spectral combination producing the highest discrimination among coral geomorphic features stemmed from the NIR2 (band 8) and red (band 5) wavebands (Collin *et al.*, 2013b).

The NDI58 was spatially modelled across the whole atoll area, encompassing the surveyed coral boulders (Figure 3). Both A- and B-axes, *i.e.*, 2D morphology, of the coral boulders were examined and meticuloulsy measured using this index. Both series of *in silico* variables were confronted with *in situ* variables by computing the linear determination coefficient (R^2) and root mean square error (RMSE). The relationshsip was

established for the whole dataset (N=23) and subset to the year-tied datasets.

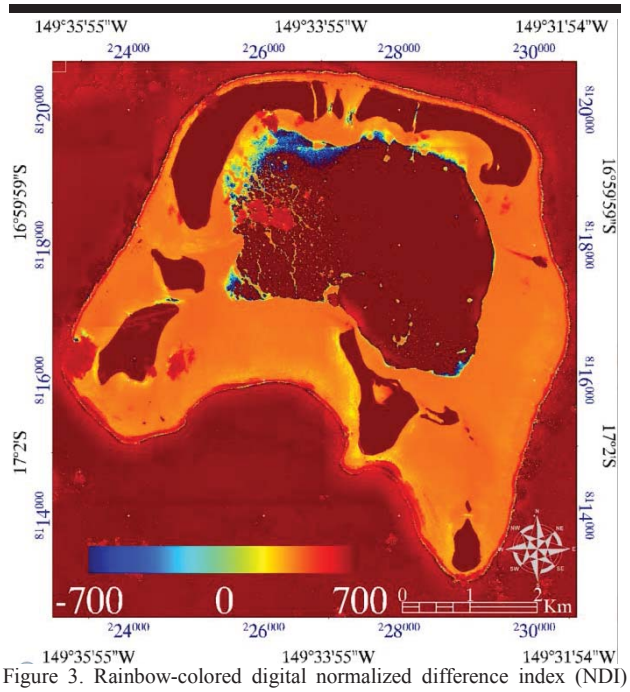

Figure 3. Rainbow-colored digital normalized difference index (NDI) based on the WorldView-2 red (band 5) and NIR2 (band 8) spectral bands.

The eight WV2 bands enriched with the three NDI combinations were investigated as potential proxies to explain the C-axis variability. For each coral boulder, the 11 WV2 values corresponding to the top pixel of the feature were mirrored with the actual measurement of the C-axis. The statistical relationship between the 11 *in silico* explanators and the *in situ* response was defined by the Pearson's correlation coefficient (r) and the linear determination coefficient (R^2).

The strongest relationship was further refined by calculating the best fitted linear model for the whole dataset and subset to the year-tied datasets. Both models were statistically characterized by R^2 and RMSE. The selected model was applied to each pixel of the study area using the geospatial software ENVI 5.2 (Exelis Visual Information Solutions, Boulder, Colorado). This spatial model is conducive to build a digital coral boulder C-axis model across Tetiaroa, suitable for underlying a WV2-driven natural-colored image.

RESULTS

The agreement between the *in situ* and NDI58-based *in silico* measurements of the A-axis was very satisfactory at the scale of the whole dataset, as determined by a R^2 of almost 0.95 (Figure 4A). The linear relationship between these two variables was also very high when examined per year (Figure 4B): R^2=0.97 (2010), R^2=1 (2011), R^2=0.97 (2012) and R^2=0.91 (2013). It is noteworthy that the extremely high score found in 2011 relied on only two points: N_{2010}=6, N_{2011}=2, N_{2012}=3 and N_{2013}=12.

Even though the linear relationship of the *in situ* and NDI58-based *in silico* measurements of the B-axis did not surpass 0.9, the evaluator (R^2) was still highly satisfactory at the whole-dataset scale, reaching almost 0.88 (Figure 4C). At the year-scale, linear relationships were also overall satisfactory from 2010 to 2013, attaining 0.8, 1, 0.99 and 0.82, respectively (Figure 4D).

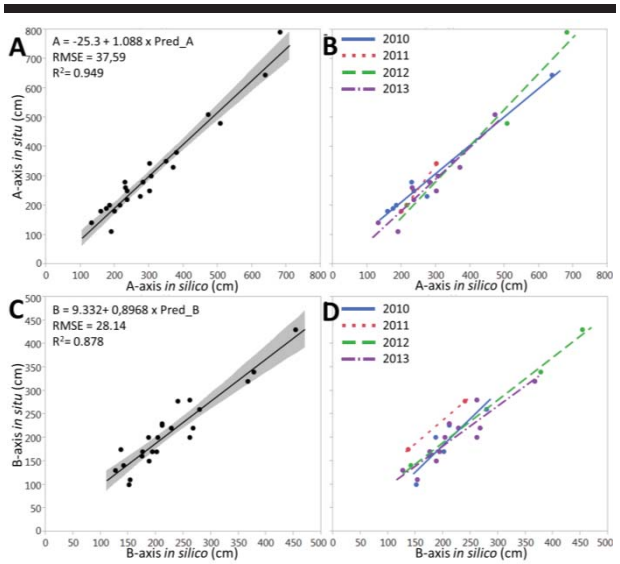

Figure 4. Scatterplots depicting the relationship between the *in situ* measured and the *in silico* measured A- and B-axes. The relationship is computed for (A) the whole dataset and (B) the year-tied datasets of the A-axis. Likewise, the relationship is computed for (C) the whole dataset and (D) the year-tied datasets of the B-axis.

The concordance between the *in situ* measurements of the C-axis and the reflectance values of the eight spectral bands plus the three spectral combinations were consistent with the two evaluators (r and R^2, Figure 5). The pairwise comparisons with the first five spectral bands (visible: from purple to red) consisted of the weak links with the lowest relationship associated to the red waveband (band 5, r=0.01, R^2=1.10^{-4}). Then, intermediate agreements were computed for the three spectral combinations, including NDI58. The best scores binding the *in situ* C-axis with the *in silico* proxies stemmed from the longest infrared wavelengths (NIR1 and NIR2, bands 7 and 8, respectively) topping with the band 8 (NIR2, r=0.87, R^2=0.75).

The *in situ* values of the C-axis were plotted against the reflectance values inherent to the band 8 (NIR2) in the form of a scatterplot so as to better visualize the statistical relationship (Figure 6). The investigation of the strength of this relationship confirmed the R^2 of 0.75 at the whole-dataset scale (Figure 6A). The inspection of the same relationship but scaled to each year showed very satisfactory to satisfactory R^2 evaluators: 0.93 (2010), 1 (2011), 0.71 (2012) and 0.77 (2013) (Figure 6B).

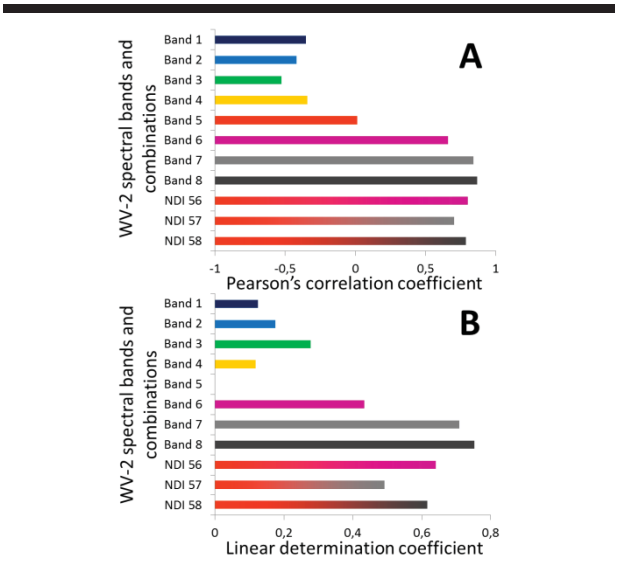

Figure 5. Barplots linking the (A) Pearson's correlation coefficient and (B) linear determination coefficient calculated from the pairwise association of the WorldView-2 orthorectified water-leaving reflectance spectral bands and combinations with the *in situ* measured C-axis.

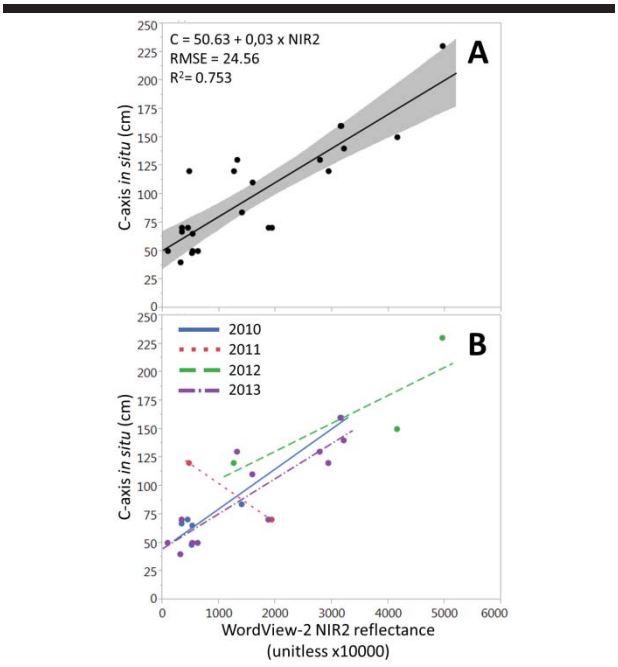

Figure 6. Scatterplots describing the relationship between the *in situ* measured C-axis and WorldView-2 NIR2 (band 8) orthorectified water-leaving reflectance. The relationship is computed for (A) the whole dataset and (B) the year-tied datasets of the C-axis.

The successful NIR2-based linear model, including the whole dataset, was spatially extended to the whole atoll area (Figure 7). Low values corresponded to water-bathed features, medium values were associated with emerged unvegetated features, and high values stand for emerged vegetated features.

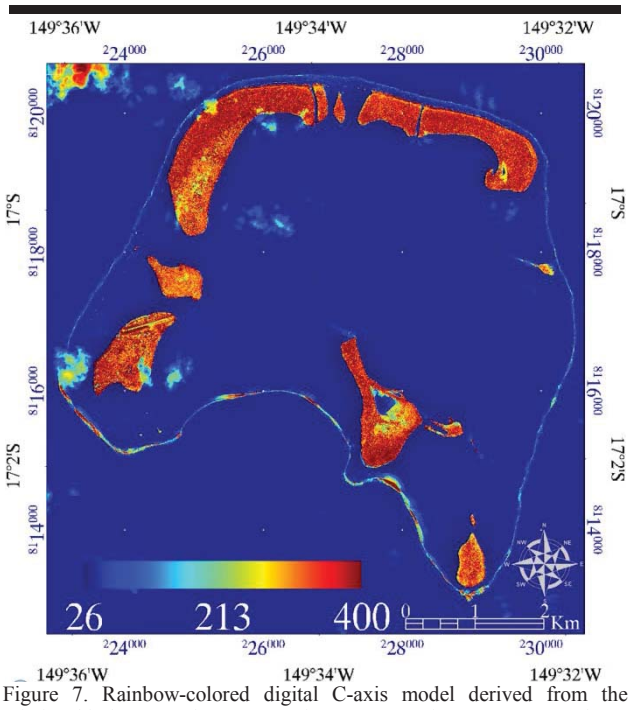

Figure 7. Rainbow-colored digital C-axis model derived from the relationship between the *in situ* and *in silico* C-axis measurements, latter ones based on the WorldView-2 NIR2 (band 8) orthorectified water-leaving reflectance.

DISCUSSION

The combination of the red and NIR2 spectral bands, in the form of a ratio (NDI58), allowed for the greatest textural enhancement of the coral boulders. This joint index can be interpreted as a good proxy to highlight features characterized by a contrasted reflectance between the contiguous red and NIR spectrum. Insofar as both A- and B-axes of the coral boulders were greatly captured by the NDI58, we could deduce that the coral boulders distinctly reflect red and NIR wavelengths, but in which way? The analysis of the NDI58 values per coral boulder tended to separate two classes: one featured by negative NDI58 values (-0.41±0.07, N=14), and another one characterized by positive NDI58 values (0.37±0.04, N=9). The field lithology of coral boulders allowed for the putative description of both distinguished classes: the first mostly encompassed freshly transported boulders, whilst the second gathered weathered boulders. The distinctive pattern in NDI58 revealed that: "older coral boulders, higher the NDI58". These findings corroborated our previous study (Collin *et al.*, 2013b), in which one assertion as to cause of the higher NDI58 had been made: the gradual colonization of the boulder surface by photosynthetic micro-organisms, absorbing the red and reflecting the NIR radiation.

The spatial modelling of the coral boulder C-axis relied on a simple linear application of the NIR2 spectral band. In the

context of this study, all measured C-axes corresponded to the vertical axes of the "saucers"-like coral boulders, that is to say their inherent height. We could therefore confidently assume that the spatially-explicit C-axis model (see Figure 7) fully embodied a digital surface model (DSM) dedicated to emerged coral boulders. We thereafter draped the natural-colored reflectance image of a coral boulder field onto the associated, bespoke DSM in order to create a 3D real-world view of this area (Figure 8).

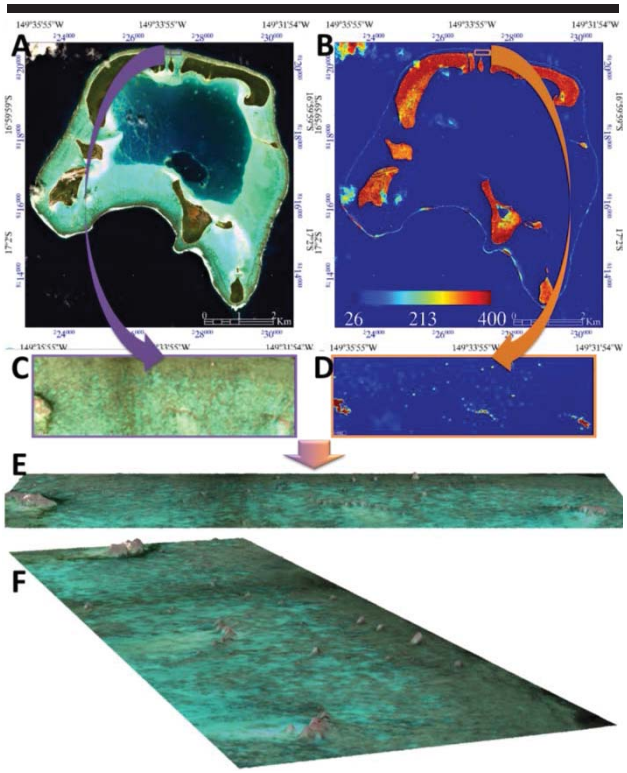

Figure 8. Workflow displaying how to subset (A) a natural-colored (red, green, blue: bands 5, 3, 2) image with (B) the digital C-axis model (based on NIR2: band 8), so that respective data (C and D) can be combined to provide a virtual 3D representation of the colored reef under different viewing angles (E and F).

If both horizontal axes (A and B) were greatly rendered by a NDI58 ratio, the variability of the vertical axis (C) was better explained by the single NIR2 (band 8) wavelength, and not by the red waveband (band 5), as illustrated by results in Figure 5. We might summarize these findings as: "higher coral boulders, more reflectance in NIR2". Further hypotheses will be built up accounting for the relationships between the transport age, the morphology and the spectral signature of the coral boulders.

CONCLUSIONS

Coral boulders, as reliable cues of high-energy events in tropical and sub-tropical shallow areas, have recently been targeted by very high resolution (VHR) remote sensing. The spectral combination of a red and near-infrared wavebands derived from the WorldView-2 (WV2) satellite allowed for the very satisfactory restitution of both A- (R^2=0.95) and B- (R^2=0.88) axes, measured *in situ*. Furthermore, the same near-infrared waveband, analyzed individually, greatly explained the variability of the ground-truthed C-axis (R^2=0.75). In the context of the surveyed coral boulder fields, the C-axis measurement matched the height of the coral boulders. A boulder-dedicated digital surface model was then derived across the whole atoll and was suitable for a merge with a natural-colored image. This remotely-sensed VHR approach ought to be integrated into the toolbox of stakeholders tasked with coral boulder monitoring, specifically, and coastal risk mapping, generically.

ACKNOWLEDGMENTS

This work is granted by the CPER Rinalpof (University of French Polynesia) allocated by the French Government and the Territory of French Polynesia. All authors would like to acknowledge the support of the NGO *Tetiaroa Society* for the local facilities, and *DigitalGlobe Foundation* for providing the WorldView-2 imagery.

LITERATURE CITED

Collin, A.; Hench, J.L., and Planes, S., 2012. A Novel Spaceborne Proxy for Mapping Coral Cover. *Proceedings of the 12th International Coral Reef Symposium* (Cairns, QLD, Australia), pp. 9-13.

Collin, A.; Archambault, P., and Planes, S., 2013a. Bridging Ridge-to-Reef Patches: Seamless Classification of the Coast Using Very High Resolution Satellite. *Remote Sensing*, 5, 3583-3610.

Collin, A.; Etienne, S., and Planes, S., 2013b. High-energy events, coastal boulder deposits and the use of very high resolution remote sensing. *Journal of Coastal Research*, 65, 690-695.

Etienne, S., 2012. Marine inundation hazards in French Polynesia: geomorphic impacts of Tropical Cyclone Oli in February 2010. *The Geological Society of London*, Special Publications, 361, 21-39.

Etienne, S.; Buckley, M.; Paris, R.; Nandasena, A.K.; Clark, K.; Strotz, L.; Chagué-Goff, C.; Goff, J., and Richmond, B., 2011. The use of boulders for characterising past tsunamis: lessons from the 2004 Indian Ocean and 2009 South Pacific tsunamis. *Earth-Science Reviews*, 107, 76-90.

Nott, J., 2003. Waves, coastal boulder deposits and the importance of the pre-transport setting. *Earth and Planetary Science Letters*, 210, 269-276.

Goto, K.; Sugawara, D.; Ikema, S., and Miyagi, T., 2012. Sedimentary processes associated with sand and boulder deposits formed by the 2011 Tohoku-oki tsunami at Sabusawa Island, Japan. *Sedimentary Geology*, 282, 188-198.

Terry, J. and Etienne, S., 2014. Potential for timing high-energy marine inundation events in the recent geological past through age-dating of reef boulders in Fiji. *Geoscience Letters*, 1, 1-8.

Terry, J.; Lau, A., and Etienne, S., 2013. *Reef platform coral boulder. Evidence for high-energy marine inundation events on tropical coastlines*. SpringerBriefs in Earth Sciences, Springer, Dordrecht,105p.

Journal of Coastal Research	SI	75	577-581	Coconut Creek. Florida	2016

Atoll-scale comparisons of the sedimentary structure of coral reef rim islands, Huvadhu Atoll, Maldives

Holly K. East †, Chris T. Perry†, Paul S. Kench‡, and Yiqing Liang‡

†Geography, College of Life and Environmental Sciences, University of Exeter, Exeter, UK

‡School of Environment, University of Auckland, Auckland, New Zealand

ABSTRACT

East, H.K.; Perry, C.T.; Kench, P.S., and Liang, Y., 2016. Atoll-scale comparisons of coral reef rim island development, Huvadhu Atoll, Maldives. *In:* Vila-Concejo, A.; Bruce, E.; Kennedy, D.M., and McCarroll, R.J. (eds.), *Proceedings of the 14th International Coastal Symposium* (Sydney, Australia). *Journal of Coastal Research*, Special Issue, No. 75, pp. 577-581. Coconut Creek (Florida), ISSN 0749-0208.

Maldivian coral reef rim islands host the majority of the nation's population, land area and infrastructure. However, understanding of the controls on rim island development and their accretionary histories is poor. Here, we present the first detailed sedimentary study of Maldivian rim islands through analyses of core logs from windward and leeward sites around Huvadhu Atoll. Island composition was dominated by a very restricted range of grain producers, with sediment dominated by coral (76.6 ± 0.6%). Material was predominantly rubble and sand-sized, the former likely generated by low-frequency high-magnitude events and the latter as a by-product of parrotfish grazing. While consistencies were found between windward and leeward sites, we highlight intra-regional diversity in reef island development at the scale of an individual atoll.

ADDITIONAL INDEX WORDS: Reef islands, sedimentology, stratigraphy, Maldives, coral reefs.

INTRODUCTION

Coral reef islands are low-lying (typically <5 m above mean sea level, MSL) accumulations of wave deposited bioclastic sediments. These sediments are produced within the surrounding coral reef habitats and reef islands are therefore intrinsically linked to reef ecology (Perry *et al.* 2011). As a result of their dependence upon locally generated sediment, low elevations and largely unconsolidated structure, reef islands are regarded as extremely vulnerable to environmental change, particularly to sea-level rise. This is of concern given their high ecological and socioeconomic value, not least because they offer the only habitable land in regions including the Maldives, Kiribati and the Marshall Islands. However, assertions of vulnerability are largely made without a full understanding of how and when islands formed, the processes controlling island formation and inter- and intra-regional variations in island-building processes.

Understanding reef island accretionary histories and the controls on island development is thus crucial for assessing their morphological stability and future resilience. To date, research has focused largely upon a few discrete localities in the Pacific and within the Great Barrier Reef Shelf/Torres Strait region (*e.g.* Kench *et al.*, 2014; Woodroffe *et al.*, 2007; Yamano *et al.*, 2014). In other major reef island regions such as the Maldives (a nation comprised of >1,200 reef islands inhabited by a population of ~345,000), our knowledge of island building processes is far more limited. Maldivian reef islands may be divided into two key types: (i) rim islands, which form around the atoll perimeters; and (ii) interior islands, which are located on the reef platforms within atoll lagoons. However, research of reef island sedimentology and the modes of island-building in the Maldives is restricted to two main datasets developed for interior islands within just one atoll (South Maalhosmadulu Atoll in the northern-central part of the archipelago – Kench *et al.*, 2005; Perry *et al.*, 2013). Knowledge of rim island stratigraphy is even more limited and based on qualitative descriptions of one pit in the centre of Feydhoo island, Addu Atoll (Woodroffe, 1992). However, it is the rim islands that dominate spatially (82.4% of land area), host the majority of the population (88.93%), and therefore support the nation's key infrastructure (all regional administrative capitals, hospitals, and designated 'safe islands'). Here, we present the first detailed sedimentary study of Maldivian rim islands. Textural, compositional and topographical datasets are used to infer the major sources of reef island sediment, the key controls upon island building, and the degree of intra-regional (at the atoll-scale) variability in island building.

Study Site

Two sites were selected on the rim of Huvadhu atoll – a leeward site, with respect to wave energy, in the north-east (Galamadhoo and Baavanadhoo islands), and a windward site in the south-west (Mainadhoo, Boduhini and Kudahini islands; Figure 1).

METHODS

Island topographic surveys were undertaken using a laser level along 11 transects. Each transect started and terminated on the reef flat in areas of live coral growth. Topographic data was corrected to height above MSL using tide tables for Gan (00°41S, 73°9E) from the University of Hawaii Sea Level Centre. Island planform was surveyed using GPS. Subsurface stratigraphy along each transect was then determined by

DOI: 10.2112/SI75-116.1 received 15 October 2015; accepted in revision 15 January 2015.

*Corresponding author: hke201@exeter.ac.uk

percussion coring (n = 28), a method allowing full recovery of unconsolidated island sediment constituents. Cores were logged in the field to record basic biosedimentary facies information, including sediment colour, texture (the descriptive nomenclature of Udden-Wentworth is used throughout), clast-matrix ratio, the size and position of coral clasts, and a visual assessment of composition. Facies were then delineated and a ~100g sample (n = 119) recovered for analysis.

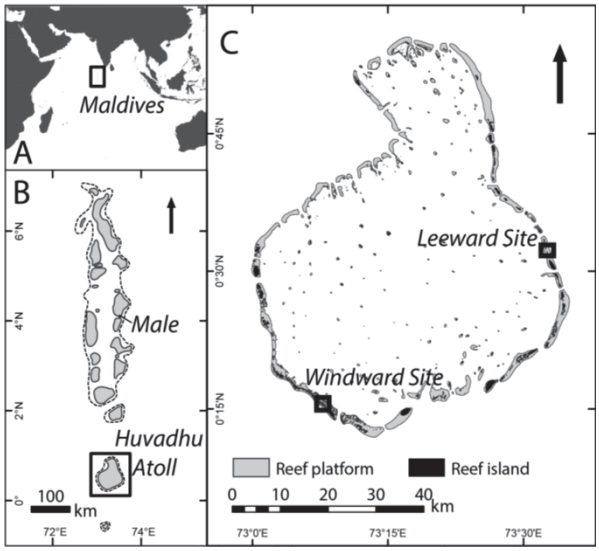

Figure 1. Location of the Maldives (A), Huvadhu Atoll (B), and windward (Mainadhoo, Boduhini and Kudahini islands) and leeward (Galamadhoo and Baavanadhoo islands) study sites (C)

Carbonate content of the upper organically enriched horizons was calculated by loss on digestion in 2 M HCl. Replicate samples indicated that results were reproducible within ~3%. Samples were dry sieved into phi (ϕ) intervals to calculate sediment grain size and sorting (GRADISTAT; Blott and Pye, 2001). Sieve counting methods were then used to determine sediment composition whereby 100 grains were counted under the binocular microscope from each gravel- and sand-sized fraction (n = 600 grains per sample). Silt-sized sediments were not counted as reliable identification was not possible, however this size fraction accounted for a mean of only 2.11 ± 0.57% of each sample. Grains were classified into one of seven key compositional categories. Total percentage abundance of components in each bulk sample was then calculated using the proportion of each size fraction to bulk sample weight. An abrasive index (AI) was also employed as a measure of coral clast taphonomy. The condition of the exterior surface of each clast with longest axes >1 cm was scored on a semi-quantitative scale from 1 (pristine), to 5 (no internal or external structures).

RESULTS

At the leeward site, 10 reef island cores were recovered, all of which extended below the level of live coral growth on the adjacent reef flats (~0.5 m below MSL; Figure 2). Mean island elevation was 1.45 ± 0.02 m and 1.44 ± 0.02 m relative to MSL for Galamadhoo and Baavanadhoo respectively. At the windward site, 18 reef island cores were recovered, 17 of which extended below the level of live coral growth on the adjacent reef flats (~0.5 m below MSL; Figure 2). Mean island elevation (excluding marginal ridges) was 0.81 ± 0.02 m, 0.81 ± 0.01 m and 0.82 ± 0.04 m relative to MSL for Mainadhoo, Boduhini and Kudahini respectively.

All cores recovered an organically enriched upper horizon with varying proportions of unconsolidated carbonate sand and coral rubble. Sediment composition was highly consistent between facies, islands and sites (Table 1). Coral was the dominant constituent (76.6 ± 0.6%), with lower proportions of Crustose Coralline Algae (CCA, 11.0 ± 0.3%) and molluscs (8.8 ± 0.5%). However, three discrete facies, and an additional two subfacies, were identified primarily on the basis of textural characteristics (Figure 2; Tables 1 and 2):

1: Organically enriched carbonate sand

This facies was characterised by the presence of organic matter, a well-developed root horizon and its brown-ish colour. Its thickness was relatively consistent within sites – ~0.5 m (~1.45–0.95 m above MSL) and ~0.3 m (~0.8–0.5 m above MSL) at the leeward and windward sites respectively. Samples contained 6.0 ± 0.6% organic matter at the windward site and 7.8 ± 0.9% at the leeward site. Sediment was coarse-grained, poorly sorted and primarily sand-sized. Coral clasts were <1 cm with the exception of those from cores nearest the oceanward reef crest at the windward site – oceanward cores on Mainadhoo and all cores from Boduhini and Kudahini. The windward site coral clasts possessed a median AI score of 3.

2: Matrix-supported coral-rich sand

Facies 2 was matrix-supported and divided into two subfacies primarily on the basis of mean grain size whereby 2A and 2B were characterised by medium- and coarse-grained sediments respectively with slightly increased proportions of gravel-sized material compared to facies 1. Sediment was predominantly sand-sized with the longest axes of all coral clasts <1 cm (clast-matrix ratio 0:1). 2A was moderately sorted at the leeward site and poorly sorted at the windward site, while 2B was poorly sorted at both sites (Table 2).

Table 1. *Sedimentary composition of each facies from windward and leeward sites.*

Site	Facies	Coral	CCA	Mollusc	Foraminifera	Echinoid	*Halimeda*	Unidentified
Windward	2A	78.8 ± 0.0	12.8 ± 1.1	5.2 ± 0.8	1.4 ± 0.5	0.7 ± 0.2	0.7 ± 0.2	0.1 ± 0.0
	2B	73.4 ± 1.6	12.6 ± 0.8	8.6 ± 1.0	2.6 ± 0.7	1.3 ± 0.2	1.0 ± 0.2	0.0 ± 0.0
	3A	78.8 ± 1.2	10.8 ± 0.7	7.5 ± 0.7	1.3 ± 0.3	0.5 ± 0.1	1.0 ± 0.3	0.0 ± 0.0
	3B	79.2 ± 1.1	10.5 ± 0.8	7.2 ± 0.6	0.8 ± 0.1	0.6 ± 0.1	1.6 ± 0.4	0.1 ± 0.0
Leeward	2A	78.6 ± 1.4	12.6 ± 0.8	6.3 ± 0.8	3.0 ± 0.7	0.4 ± 0.1	0.3 ± 0.1	0.1 ± 0.1
	2B	73.4 ± 1.3	9.4 ± 0.8	12.7 ± 0.7	4.0 ± 0.7	0.7 ± 0.1	1.0 ± 0.1	0.0 ± 0.1
	3A	71.2 ± 1.2	9.3 ± 0.5	16.0 ± 1.1	2.8 ± 0.4	0.3 ± 0.1	1.0 ± 0.2	0.1 ± 0.1
	3B	77.5 ± 5.3	6.1 ± 1.0	12.7 ± 4.4	1.0 ± 0.1	0.5 ± 0.4	2.6 ± 0.8	0.0 ± 0.0

Table 2. *Textural characteristics of each facies from windward and leeward sites.*

Site	Facies	n	Mean grain size (Φ)	Matrix mean grain size (excluding gravel, Φ)	% Gravel	% Sand	% Silt	Sorting (σ_Φ)	Gravel size (longest axis)	Median AI index
Windward	1	18	0.7 ± 0.1	1.4 ± 0.1	29.4 ± 6.8	68.9 ± 6.6	1.7 ± 0.2	1.4 ± 0.1	< 1 cm	3
	2A	12	1.2 ± 0.2	1.6 ± 0.1	15.3 ± 6.8	82.6 ± 6.7	2.1 ± 0.7	1.3 ± 0.1	< 1 cm	-
	2B	14	0.8 ± 0.2	1.4 ± 0.1	21.4 ± 4.6	76.2 ± 4.4	2.4 ± 0.3	1.6 ± 0.1	< 1 cm	-
	3A	18	0.6 ± 0.2	1.9 ± 0.1	40.6 ± 4.9	56.1 ± 4.8	3.3 ± 0.6	1.9 ± 0.1	< 4 cm	4
	3B	14	0.4 ± 0.1	1.8 ± 0.1	47.7 ± 3.6	49.6 ± 3.4	2.7 ± 0.4	1.9 ± 0.1	< 12 cm	3
Leeward	1	10	1.2 ± 0.1	1.2 ± 0.1	1.8 ± 0.6	96.6 ± 0.6	1.7 ± 0.2	1.1 ± 0.0	< 1 cm	-
	2A	10	1.1 ± 0.1	1.2 ± 0.1	1.8 ± 0.4	97.4 ± 0.4	0.8 ± 0.3	0.9 ± 0.1	< 1 cm	-
	2B	10	0.7 ± 0.1	1.0 ± 0.1	9.4 ± 1.9	89.2 ± 1.9	1.4 ± 0.3	1.2 ± 0.1	< 1 cm	-
	3A	9	0.2 ± 0.1	1.4 ± 0.0	45.6 ± 3.1	53.1 ± 3.1	1.3 ± 0.2	1.7 ± 0.0	< 4 cm	3
	3B	4	-0.1 ± 0.2	1.7 ± 0.1	60.2 ± 6.8	38.2 ± 6.8	1.6 ± 0.4	1.7 ± 0.0	< 12 cm	4

At the leeward site, 2A was identified ~1.2– -0.25 m relative to MSL (thickness = 0.35–0.95 m) and 2B was found ~0.6– -1.3 m relative to MSL (thickness = 0.55–1.5 m) with depth of penetration and thickness increasing towards the lagoonward coast (Figure 2). At the windward site, on Maindadhoo, 2A was 0.4–0.8 m thick and identified between ~0.65 and -0.65 m relative to MSL. Thickness and depth of penetration also increased tow ards the lagoon. Facies 2B (thickness = 0.2–0.75 m), terminated at relatively consistent depths within each transect on Mainadhoo (*e.g.* central transect = ~0.5 m below MSL). On Boduhini and Kudahini, facies 2 was only identified in lagoonward cores (Figure 2).

3: Clast-supported coral-rich sand

Facies 3 was defined by its clast-supported character. It was divided into subfacies as marked by a shift in clast size. 3A was characterised by coral clasts with longest axes <4 cm, whilst 3B was dominated by clasts sized 8–12 cm (*i.e.* as large as could be recovered given the core width). In addition, 3A and 3B were distinguished by differences in taphonomy. Systematic variability was found between sites whereby, at the leeward site, clasts within 3A were less degraded (AI = 3) than those at the windward site (AI = 4). Conversely, clasts within 3B were more degraded at the leeward site (AI = 4) than at the windward site (AI = 3). The mean grain size of the matrix remained medium-grained, though overall mean grain-size was coarse as the proportion of gravel-sized material increased. Clast-matrix ratio was approximately 4:10 (3A) and 5.5:10 (3B) at the leeward site, and 3.5:10 (3A) and 4:10 (3B) at the windward site (Table 2). At the leeward site, 3A occured ~-0.35– -1.45 m relative to MSL (thickness = 0.15–0.4 m) and 3B was found ~-0.75– -1.3 m relative to MSL (thickness = 0.3–0.45 m), but was not identified on Baavanadhoo. In contrast to facies 2, the thickness and minimum depth of facies 3 increased toward the oceanward coast (Figure 2). At the windward site, facies thickness varied with the greatest thicknesses on Boduhini and Kudahini (3A: 0.15–1.4 m; 3B: 0.2–0.85 m), but the 3A-3B interface was found at relatively consistent depths within each transect (*e.g.* central transect of Mainadhoo = ~1 m below MSL). The exception was the cores nearest the oceanward coast within which facies 3B was not found (Figure 2).

DISCUSSION

Using a series of 28 reef island cores from contrasting rim aspects, we present the first detailed account of Maldivian rim island sedimentology. Sediment composition was remarkably consistent between facies, islands and sites. The composition contrasts with that of Maldivian interior islands, which typically possess a *Halimeda* rich facies (Kench *et al.*, 2005); here the proportion of *Halimeda* averaged only 1.0 ± 0.0%. With exposure to oceanward swell wave energy on the atoll rim, the composition of the rim sediments is a reflection of the relative durabilities of the skeletal constituents. Indeed, in a comparison of foraminifera, molluscs, coral and *Halimeda*, Ford and Kench (2012) found grain durability to vary by several orders of magnitude, the most durable clast type being coral, whilst *Halimeda* was most rapidly abraded. The homogeneity of composition may also reflect the relative consistency of reef ecology both spatially (between sites) and temporally. Moreover, as the atoll rim is a relatively high wave energy environment, it is likely that sediment residence times in their zones of production are low and thus the sediment reservoir is homogenised by rapid spatial dispersal.

Most notably, island composition was dominated by a restricted range of grain producers, primarily coral (mean 76.6 ± 0.6%) highlighting its importance for Maldivian rim island formation and maintenance. Of equal importance is the process by which coral is converted from reef framework into material for reef island building. Four processes may cause this conversion, which may be inferred from sediment texture: (1) physical erosion of the reef framework produces sand-sized sediments via abrasion (though this is unlikely to be a dominant process given the high durability of coral – Ford and Kench, 2012; Perry *et al.*, 2015) or rubble grade clasts; (2) endolithic sponge bioerosion produces silt-sized (<63 μm) material, though is evidently of minimal significance for reef island building as silt-sized material accounted for only 2.11 ± 0.57% of each sample; (3) urchin grazing produces predominantly silt-sized material and is thus, likewise, unlikely to represent a dominant process; (4) sand-sized sediments are produced as a by-product of parrotfish grazing (Hoey and Bellwood, 2008; Perry *et al.*, 2015). The prevalence of sand- and rubble-sized coral within the rim islands is therefore likely attributable to parrotfish grazing,

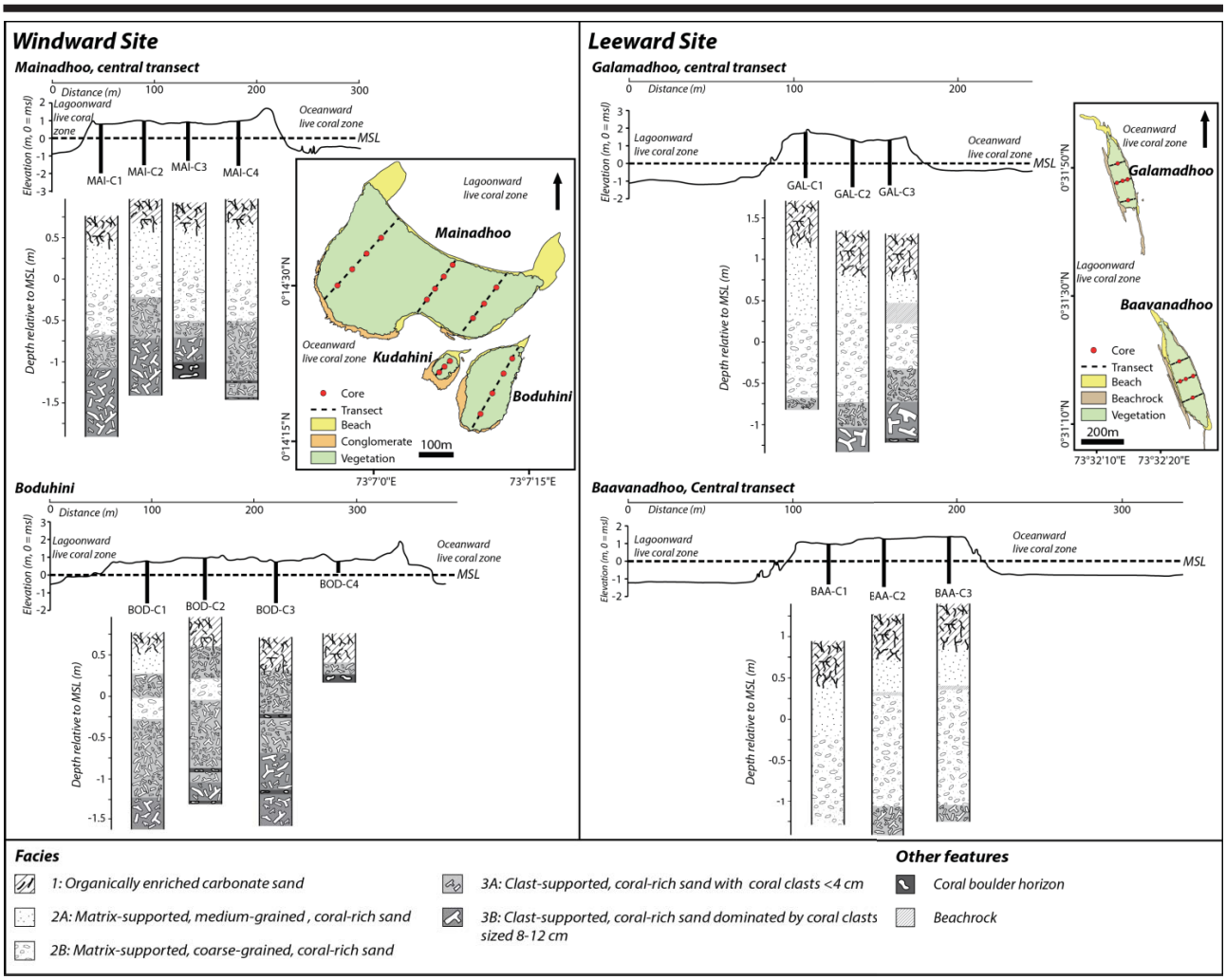

Figure 2. Two topographic survey transects with associated core logs from windward and leeward study sites.

and physical erosion of the reef framework by low-frequency high-magnitude events, respectively. A similar provenance for the coral-dominated sands has recently been suggested for Maldivian atoll interior islands (Perry *et al.*, 2015). Likewise, the high proportions of coral sand and rubble are consistent with Woodroffe's (1992) descriptions of Feydhoo island, Addu Atoll. This contrasts with the composition of Pacific islands which comprise foraminifera rich sands (e.g. <63% - Kench et al., 2014) as the Pacific mid-Holocene sea-level highstand produced tidally-emergent reef flats that favour foraminifera production (Perry et al., 2011).

The most distinct division within cores was that between facies 2 and 3 which were differentiated by the transition from one of clast- to matrix-support. This presence of coral rubble toward the base of the cores, downcore increase in rubble size, and poor sorting of facies 3, are likely a function of higher wave energy associated with low-frequency high-magnitude events. We therefore suggest that such events played a significant role in reef island initiation. Given the proximity of the Maldives, and particularly Huvadhu Atoll, to the equator (*e.g.* the windward site is only 26 km north of the equator), storms are exceedingly rare. High energy events may therefore be swell events, for instance, in May 2007 extensive floods covered ~30% of the island of Fares-Mathoda (southwest Huvadhu Atoll), which were attributed to intense storm winds off the southern coast of South Africa. In addition, there may have been higher intensity storms during the Holocene and thus the meaning of storms may need to be reinterpreted in this setting.

While facies characteristics were consistent between sites, this study demonstrates that key differences in reef island development exist even at the scale of an individual atoll. For example, comparing clast taphonomy of facies 3A and 3B, the better preservation of coral clasts in 3B at the windward site is indicative of a shorter temporal lag between sediment production (coral erosion) and deposition. In contrast, although

high energy events also likely played a role at the leeward site, island initiation may have been more gradual.

The most marked stratigraphic difference between sites was the increased proportion of rubble recovered at the windward site. Indeed, facies 3 was notably thicker at the windward site, than at the leeward site. Numerous coral boulder horizons were also recovered from windward cores, which were likely deposited in high energy overwash events. Facies 2 was also almost entirely absent from Boduhini and Kudahini in the windward setting. This may be due to greater exposure to wave energy given their slightly closer proximity to the reef crest than at Mainadhoo. Alternatively, given the smaller size of these islands, they may be at an earlier stage in a sequence of temporal evolutionary development, such as that described for interior Maldivian islands (Perry *et al.*, 2013).

Higher wave exposure may also explain why textural differences between facies at the windward site were markedly less clear-cut than at the leeward site. This could be due to the increased frequency of overwash events and greater sediment reworking. Reworking may occur through a process of rollover whereby material eroded from the oceanward shore is deposited toward the lagoonward coast facilitated by high energy events (Woodroffe *et al.*, 1999).

Intra-site diversity is also evident in the spatial and vertical distribution of facies. At the leeward site, the most striking pattern in island stratigraphy is the oceanward-lagoonward gradient in grain size. Facies 2 increased, while facies 3 concordantly decreased, in thickness and stratigraphic position toward the lagoonward coast. This suggests that, following deposition of a rubble bank, the input of sand-grade material has primarily been off the lagoonward coast. The lagoonward shoreline may therefore be the most energetic in this setting as a function of the dominant wind direction (west) and fetch distance across the atoll lagoon. Conversely, at the windward site, the interface between facies 2 and 3 is more consistent within transects. This may be due to the combined impact of the higher wave exposure, greater frequency of high magnitude events, and the closer proximity of the islands to the oceanward reef crest. In combination, these factors have resulted in the deposition of more horizontal rubble sheets in island initiation at this site. AMS radiometric dating to constrain reef island development chronologies is ongoing.

CONCLUSIONS

We present the first detailed sedimentary study of Maldivian coral reef rim islands through analyses of island core records from windward and leeward sections of Huvadhu atoll rim. Sedimentary composition was relatively uniform between facies, islands and rim aspects. Three distinct sedimentary facies, and an additional two subfacies, were identified on the basis of marked differences in facies textural characteristics. Islands were dominated by coral sand and rubble, the former most likely generated as a by-product of parrotfish grazing, and the latter by low-frequency high-magnitude events. Consistencies were found both between the windward and leeward sites, and also the interior islands. However, we also found intra-regional variability, the primary control upon which appears to be wave exposure. In the context of environmental change, this highlights the potential for significant between-site variations in reef island sensitivity to shifts in oceanographic boundary conditions. Thus, given the diversity of reef islands at the local scale, it is likely that future responses of reef islands to environmental change will be equally diverse.

ACKNOWLEDGMENTS

The authors would like to acknowledge the support of Mohamed Aslam (LaMer) and the Abraham Didis (boat drivers) for facilitating fieldwork. This work was supported by a NERC PhD studentship (NE/K500902/1).

LITERATURE CITED

Blott, S. J. and Pye, K, 2001. GRADISTAT: a grain size distribution and statistics package for the analysis of unconsolidated sediments. *Earth surface processes and Landforms*, 26(11), 1237-1248.

Ford, M.R. and Kench, P.S., 2012. The durability of bioclastic sediments and implications for coral reef deposit formation. *Sedimentology*, 59(3), 830-842.

Hoey, A.S. and Bellwood, D. R., 2008. Cross-shelf variation in the role of parrotfishes on the Great Barrier Reef. *Coral Reefs*, 27(1), 37-47.

Kench, P.S.; Chan, J.; Owen, S.D., and McLean, R.F., 2014. The geomorphology, development and temporal dynamics of Tepuka Island, Funafuti atoll, Tuvalu. *Geomorphology*, *222*, 46-58.

Kench, P.S.; McLean, R.F., and Nichol, S.L., 2005. New model of reef-island evolution: Maldives, Indian Ocean. *Geology*, 33, 145-148.

Perry, C. T.; Kench, P. S.; O'Leary, M.J.; Morgan, K.M., and Januchowski-Hartley, F., 2015. Linking reef ecology to island building: Parrotfish identified as major producers of island-building sediment in the Maldives. *Geology*, 43(6), 503-506.

Perry, C.T.; Kench, P.S.; Smithers, S.G.; Riegl, B.; Yamano, H., and O'Leary, M.J., 2011. Implications of reef ecosystem change for the stability and maintenance of coral reef islands. *Global Change Biology*, *17*(12), 3679-3696.

Perry, C.T.; Kench, P.S.; Smithers, S.G.; Yamano, H., O'Leary, M., and Gulliver, P., 2013. Time scales and modes of reef lagoon infilling in the Maldives and controls on the onset of reef island formation. Geology, 41(10), 1111-1114.

Woodroffe, C.D., 1992. Morphology and evolution of reef islands in the Maldives. *Proceedings of 7th International Coral Reef Symposium* (Guam), 2, pp. 1217–1226.

Woodroffe, C.D.; McLean, R.F.; Smithers, S.G., and Lawson, E.M., 1999. Atoll reef-island formation and response to sea-level change: West Island, Cocos (Keeling) Islands. *Marine Geology*, 160, 85-104.

Woodroffe, C.D.; Samosorn, B.; Hua, Q., and Hart, D.E., 2007. Incremental accretion of a sandy reef island over the past 3000 years indicated by component-specific radiocarbon dating. *Geophysical Research Letters*, 34, L03602.

Yamano, H.; Cabioch, G.; Chevillon, C., and Join, J.L,. 2014. Late Holocene sea-level change and reef-island evolution in New Caledonia. *Geomorphology*, *222*, 39-45.

Journal of Coastal Research	SI	75	582-586	Coconut Creek, Florida	2016

Wave modifications across a coral reef: Cap Chevalier, Martinique Island.

Matthieu Jeanson [†*], Franck Dolique[‡], Mouncef Sedrati[§], Oliver Cohen[∞], Jimmy Bertier[§], Alan Cavalin[‡], Jessica Charpentier[‡] and Edward J. Anthony[+]

[†] Laboratoire de Géomorphologie et Environnement Littoral, Ecole Pratique des Hautes Etudes, CNRS UMR 8586 Prodig, France

[‡] UMR 228 ESPACE-DEV, Université des Antilles, Martinique

[§] UMR 6538 - Domaines Océaniques, Géosciences Marines et Géomorphologie du Littoral, Université de Bretagne-Sud, France

[∞] Laboratoire d'Océanologie et de Géosciences, UMR CNRS 8187, Université du Littoral Côte d'Opale, France

[+] CEREGE, UMR CNRS 6635, Aix Marseille Université, France

www.cerf-jcr.org

www.JCRonline.org

ABSTRACT

Jeanson, M.; Dolique, F.; Sedrati, M.; Cohen, O.; Bertier, J.; Cavalin, A.; Charpentier, J, and Anthony E.J., 2016. Wave modification across a coral reef: Cap Chevalier, Martinique Island. *In:* Vila-Concejo, A.; Bruce, E.; Kennedy, D.M., and McCarroll, R.J. (eds.), *Proceedings of the 14th International Coastal Symposium* (Sydney, Australia). *Journal of Coastal Research*, Special Issue, No. 75, pp. 582-586. Coconut Creek (Florida), ISSN 0749-0208.

Waves exert a major influence on hydrodynamic processes and on sediment transport over shallow submerged coral reefs, as well as on reef-bound beaches. This study describes results from a field experiment conducted at Cape Chevalier in the southeast of Martinique Island (Lesser Antilles, French West Indies), and investigates spatial and temporal variations in wave characteristics across a microtidal coral reef and lagoon. Measurements of wave pressure fluctuations were obtained using three pressure sensors deployed across the reef from 28 to 30 November, 2011. Analysis of the measured data shows that wave characteristics were strongly influenced by water depth and reef geometry. Calculations of energy dissipation indicate an average energy reduction of 91.5% between the fore-reef and back-reef (86% at high tide and 98% at low tide). The mean energy reduction between the fore-reef and the beach was 95.5% (92% and 99% respectively at high and low tide). The incident waves measured at the fore-reef during the experiment were predominantly trade wind-generated with peak periods between 7 and 10 s. Depending on tidal elevation and water depth, back-reef waves were characterized by an energy distribution dominated by the peak 7-10 s gravity waves at high tide and by infragravity frequencies (>20 s) at low tide. Wave energy at the beach was dominated by infragravity frequencies during both high tide and low tide. Wave spectral analysis indicates, thus, significant filtering of peak period energy as waves traveled across the reef.

ADDITIONAL INDEX WORDS: *Coral reef, wave attenuation, infragravity waves, Caribbean.*

INTRODUCTION

The large architectural complexity of coral reefs generates roughness conditions that play a major role in reef fluid dynamics. Several studies over the past few years (*e.g.*, Brander *et al*., 2004; Ogston *et al*., 2004; Kench and Brander, 2006a, 2006b; Kench *et al*., 2006; Presto *et al*., 2006; Tamura *et al*., 2007; Storlazzi and Jaffe, 2008) have highlighted marked cross-shore gradients in wave energy dissipation across coral reef systems that are generally deemed to impact on reef development. Some of the aforementioned studies have shown that the largest losses in wave energy across a coral reef occur in the wave breaking process. Several of these studies have also highlighted a critical control by water level over the reef shoreface, generally modulated by topography, and by tidal range, with low-tide conditions in meso- to macrotidal settings being likely to preclude onshore wave transmission, whereas transmission can be significant during high water stages (Brander *et al*., 2004), and under conditions of minimum wave breaking (Kench and Brander, 2006a). Differences in wave energy have also been shown to be important between windward and leeward sides of reef islands (*e.g.* Kench and Brander, 2006b). These authors showed that deeper and narrower leeward reefs allowed propagation of greater wave energy across the reef crest than the higher-elevation windward reef surface. The seasonal pattern of wave energy on many coral reef shores further induces temporal differentiation to which reefs must adapt (*e.g.*, Kench *et al*., 2009). The dissipation of incident wave energy through friction against the rough bottom of coral reef systems can play a significant role in natural coastal defense (Hearn, 1999; Sheppard *et al*., 2005; Zawada *et al*., 2010), the reefs acting as submerged offshore breakwaters. In reality, however, much still remains to be learnt of wave variations over coral reefs. As Kench *et al*. (2006) have indicated for reef islands, for instance, although wave energy exposure provides an attractive and simple hypothesis to account for island

DOI: 10.2112/SI75-117.1 received 15 October 2015; accepted in revision 15 January 2015
*Corresponding author: matthieu.jeanson@ephe.sorbonne.fr

distribution, sedimentary character and morphology, it remains largely untested with regards to systematic measurement of wave energy. The aims of the present study, conducted in Martinique Island, are to: (1) show attenuation patterns across a coral reef fronting a pocket beach, (2) highlight spatial variations in wave parameters from the fore-reef, through inner reef flat to the sandy beach. The potential implications of the wave transformations with regards to shoreline morphology are finally briefly evoked.

METHODS

Martinique is located in the Lesser Antilles Island. Its eastern coast borders the Atlantic Ocean while its western coast is flanked by the Caribbean Sea. With a surface area of 1100 km², Martinique is composed of a main island and about 50 islets of volcanic material, spread out along the eastern and southern coasts. Martinique culminates at a peak elevation of 1397 m (active *Montagne Pelée* volcano). Martinique has a humid tropical climate comprising a hot, rainy season (June to November) punctuated by tropical storms and cyclones, and a cooler, dry season (December to May). Mean annual rainfall is about 1000 mm in the south and up to 5000 mm in the northern mountainous area. Trade winds from east to northeast occur almost permanently but are stronger during the dry season (8 to 12 $m.s^{-1}$) while they are weaker and more irregular in the rainy season. Nevertheless, tropical depressions, and especially cyclones, can generate more important gusts (up to 30 $m.s^{-1}$). The volcanic context, tropical setting, and reef development have engendered marked diversity in coastal morphology. The total shoreline length of Martinique is approximately 350 km. While the north coast is dominated by high cliffs of recent volcanic origin, the east and south coasts are an intricate alternation of cliffs separating pocket beaches of sand and sandy mud, and foreshore mangrove colonies. The pocket beaches commonly range in length from 200 to 1200 m. Martinique Island is subject to mixed tides and the tidal range is microtidal, with a mean range of about 0.4 m and a 0.7 m maximum range during spring tides. The coral reefs of Martinique are restricted to the east and south coasts and have a total area of 55 km² (Figure 1a). These reefs include a 25 km long barrier reef on the windward east coast, interrupted by passes and isolated from the coastline by a 12 to 30 m-deep lagoon. Fringing reefs are also present and commonly range in width from 200 to 500 m, locally exceeding 1000 m.

The experiment was conducted from 28 to 30 November 2011 on *Anse Michel* beach, situated in the southeastern Atlantic coast of Martinique, in the *Cap Chevalier* region (Figure 1a). The beach ranges in intertidal width from 10 to 20 m and is fringed by a 300 to 400 m-wide reef (Figure 1b). The reef flat consists of a 200 m-wide sub-horizontal surface of coral sand colonized by seagrass communities (*Thallasia testudinum* and *Syringodium filiforme*), and recent invasive species such as *Halophila stipulacea*, and that grades into an outer reef with encrusting algae, sparse coral colonies and algal turf.

Three pressures sensors (SP2T, NKE) were used to measure water depth fluctuations and changes in wave parameters on a shore-normal transect across the reef flat (Figure 1b). The same record length, frequency interval, spectral estimate averaging method and degrees of freedom were used for all-time series in order to enable comparison of the results. The instruments recorded tide- and wave-induced pressure with a burst duration of 9 minutes every 15 minutes, at a frequency of acquisition of 2 Hz. Wave characteristics (significant wave height, *Hs*, and means zero up-crossing wave period, *Tz*) were obtained from the measured time series by spectral analysis using Fast Fourier Transforms. The Fourier coefficients of the free surface elevation fluctuations were obtained from corresponding coefficients computed from the pressure time series using the frequency-dependent transfer function inferred from linear theory. To avoid electronic noise, a high cut-off frequency fixed at 0.4 Hz was applied.

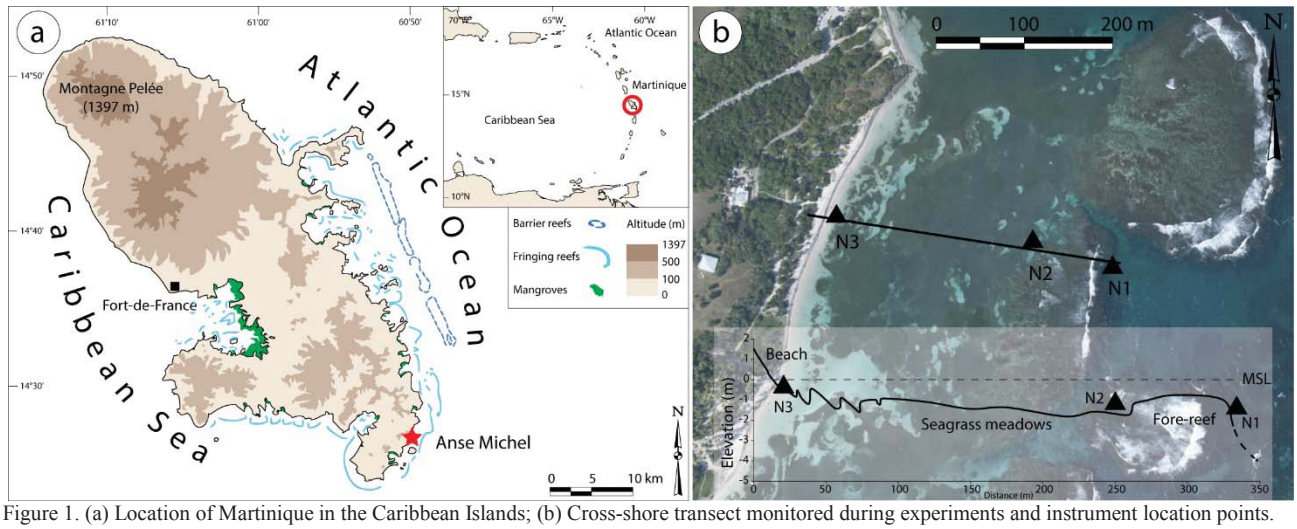

Figure 1. (a) Location of Martinique in the Caribbean Islands; (b) Cross-shore transect monitored during experiments and instrument location points.

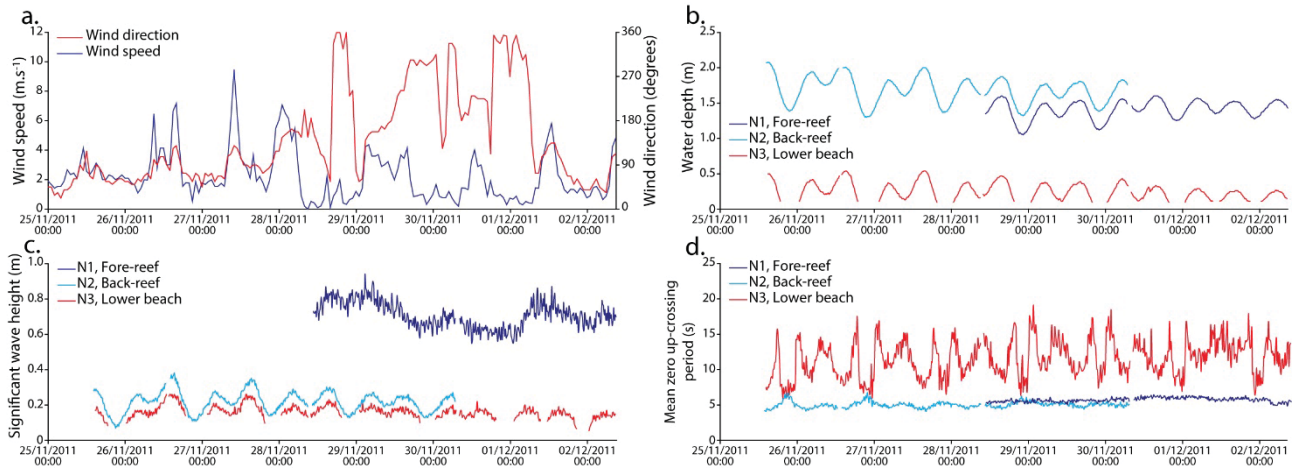

Figure 2. Wind and wave conditions during the experiment. (a) Wind speed and direction; (b) water levels; (c) significant wave heights and (d) mean zero up-crossing wave periods.

RESULTS

The wind and hydrodynamic conditions during this experiment are summarized in figure 2. Moderate winds from the south with speeds of 5 to 8 m.s^{-1} prevailed at the beginning of the experiment, and then winds weakened and varied from north to northeast. At station N1 on the fore-reef, significant wave heights were moderate during this experiment, ranging from 0.56 m to a peak of 0.94 m. *Tz* fluctuated between 5 and 7 s, corresponding to trade wind waves. Notice that for this station N1, there is no apparent relationship between the fore-reef wave height and water depth. The effect of reef-flat water depth on wave characteristics is obvious for *Hs* and *Tz*, as demonstrated in figures 2c and 2d. Variations of *Hs* at stations N2 and N3 directly follow the fluctuation of water depth induced by tides (Figure 2b). At the back-reef station N2, *Hs* varied from 0.13 at low tide to 0.30 m at high tide. As seen in figure 2 and 3, waves at N2 were dominated by wind-wave and swell frequencies (5-9 s) except during low water when infragravity wave frequencies were dominant. *Hs* values exhibited a similar pattern at station N3, with the weakest values at low tide (0.08 m) and the largest at high tide (0.23 m). However, infragravity waves were dominant at both low and high tide (Figures 3b-c). The time series and spectra are representative of the typical changes in wave characteristics across the reef flat during high tide, notably variation in height and period. On the fore-reef, moderate (*Hs*: 0.79 m), swell frequency (8–11 s) waves dominated, with a band of a secondary peak at 6 s (corresponding to wind waves). On the back-reef, water level measurements are characterized by significantly lower waves (*Hs*: 0.25 m) dominated by a weak band of swell frequencies (8-11s). Wave characteristics appear different at the lower beach station with *Hs* of 0.21 m, and energy at dominantly infragravity frequencies (> 20 s) while the other bands are insignificant in proportion to the infragravity band.

DISCUSSION

The differences in *Hs* between the fore-reef and the beach reflect an important reduction in energy as waves propagated from the former, through the reef flat, to the latter. This reduction in energy δE between two stations can be estimated from the *Hs* values using the equation (Lugo-Fernandez *et al.*, 1998a): $\delta E = \left(H^2_i - H^2_f\right)/H^2_i$

where *Hi* and *Hf* are the wave heights at each station, based on the principle that waves propagate from station *i* to station *f*. A cutoff depth threshold of 0.2 m has been applied to the data recorded by the lower beach station. The wave energy reduction between the fore-reef and the back-reef ranges from 86 to 98% and from 92% to 99 % between the fore-reef and the lower beach (Figure 3a). The mean values are, respectively, 91.5% and 95.5%. These values are in agreement with previous studies that reported rates of reduction between 65% and 99.7% (Lugo-Fernandez *et al.*, 1998a, 1998b; Hearn, 1999; Brander *et al.*, 2004; Lowe *et al.*, 2005; Kench and Brander, 2006; Kench *et al.*, 2006; Jeanson *et al.*, 2013). Examples of typical high- and low-tide frequency spectra dominated by swell (*Tp* = 10-11 s), and the percentages of energy loss between the fore-reef and the lower beach are depicted in figure 3b-c.

The effect of reef water depth on energy attenuation is obvious. Generally, wave attenuation directly follows a changing pattern of water depth, primarily induced by tides. Maximum wave attenuation occurs at low water levels with a rate of attenuation of 98% between N1 and N2, and 99% between N1 and N2. Inversely, weaker wave attenuation occurs during high water levels (respectively 86% and 92%). Rapid dissipation of ocean wave energy occurs across the outer reef at both high and low tides. The weak *Hs* values recorded during the experiment on the beach reflect this high level of dissipation. The significant wave attenuation on the fore-reef region, between stations N1 and N2, is likely due to the effects of wave breaking (according to visual observations during field work) and frictional dissipation on the coral framework. A smaller decrease in wave height occurs between stations N2 and N3 on

the reef flat, likely due to dissipation by bottom friction on the reef flat surface.

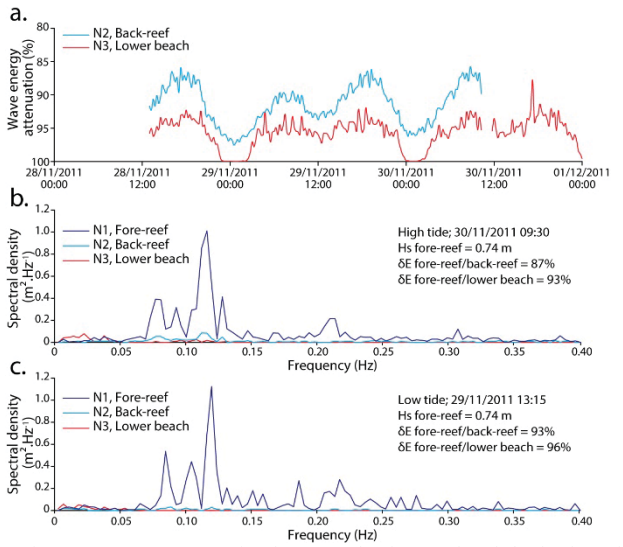

Figure 3. Wave attenuation between the fore-reef and the back-reef (green line) and between the fore-reef and the lower beach (blue line) (a), and examples of typical frequency spectra during high tide (b) and low tide (c) with percentages of energy loss for the selected bursts.

Figure 4a-b shows significant wave height for two different frequency ranges for the three sensors deployed: gravity wave frequencies (0.05-0.4Hz) and infragravity wave frequencies (0.005-0.05Hz). For gravity wave frequencies, the results show that *Hs* on the reef is strongly related to water depth and is, as expected, higher on the back-reef (N2) than on the lower beach (N3). For the infragravity wave frequencies, the observations presented in figure 4b appear more complex. On the fore-reef (N1), the results indicate that the infragravity wave height fluctuates in a similar way to that of the gravity wave height with, for example, higher values on 29/11 (0.19 m), and does not show an apparent relationship with the water depth fluctuation induced by tides. On the back-reef (N2), the infragravity wave height was weaker (0.04-0.09 m) and a small tidal modulation was discernible. Finally, on the lower beach station (N3), values and variations of infragravity wave heights were similar to those of the fore-reef; however, as mentioned for N2, a tidal modulation can be observed especially for the most important waves (*e.g.* 29/11 at 00:00). Figure 4c shows the relationship between water level variations at the three stations and relative wave energy over two ranges of frequencies. Incident gravity waves are dominant at station N1 (red dots). They contributed to about 95% of wave energy during both high and low water levels. At station N2, gravity waves are also dominant but infragravity waves are significantly more important than at N1. The contribution from infragravity waves increases with the reduction in water level above the reef (about 10% at high water levels and up to 40% at low levels). For the lower beach station N3, infragravity waves are dominant (blue dots) and represent 50% to 90% of the total energy. As mentioned for N2, infragravity wave contribution tended to increase in shallow waters. While gravity waves on *Anse Michel* coral reef appear to be controlled by water depth over the reef (gravity wave height increases with water depth), infragravity waves seem to be less affected by tidal modulation. Our results also show that while the reef is an efficient filter for high-frequency waves, the low-frequency waves of the fore-reef can propagate onto the lower beach. Similar observations have been documented in previous studies (*e.g.* Lugo-Fernandez *et al.*, 1998b; Pomeroy *et al.*, 2012)

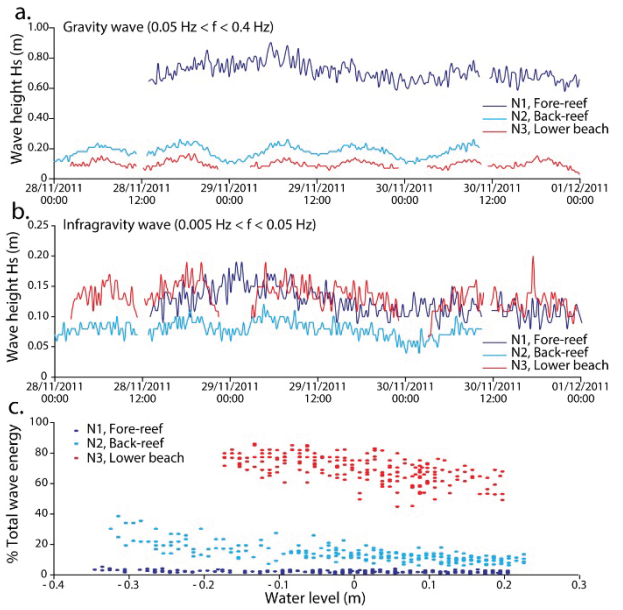

Figure 4. Significant wave heights for (a) gravity frequencies (0.05 to 0.4 Hz) and (b) infragravity frequencies (0.005 to 0.05 Hz) and (c): relationship between water levels at the three stations and relative wave energy at infragravity frequencies.

Although pocket beaches are frequent along rocky coasts, documentation on their morphodynamic processes is sparse compared to open beaches. Studies of pocket beaches in coral reef environments are even sparser, although such beaches are frequent on reef-fringed volcanic islands, such as Hawaii or Mayotte (Norcross *et al.*, 2002; Jeanson *et al.*, 2013). In such settings, residual wave energy must be considered as a critical control on beach morphological variations. At *Anse Michel*, the differences in *Hs* between the fore-reef and the beach during the experiment highlight an important reduction in wave energy, relative to waves propagating from the fore-reef to the beach. The influence of water depth on wave characteristics was also observed at *Anse Michel* coral reef, particularly for wave energy, which increased with depth. Also, the marked difference in wave characteristics between N1 (incident ocean waves) and N3 (residual waves) during the experiment suggests that wind waves and swell are largely filtered during their propagation across the reef, whereas longer-period waves propagate to the beach. These observations bring to the fore several issues regarding the beaches in Martinique: (1) the direct relationship between wave energy and water depth suggests that a higher sea

level in the future, as a result of global change, can generate greater erosion on reef beaches behind degraded fringing reefs; (2) the way the morphology and dynamics of reef-fronted pocket beaches react to residual incident wave energy is not well known and requires more field measurements; (3) impacts of sea level variation caused by infragravity waves may be an important driving force for beach morphodynamics in a coral reef setting; however, understanding of the effects of infragravity waves on such coral reef beaches is still relatively limited.

CONCLUSION

Observations of hydrodynamic changes across *Anse Michel* coral reef show a significant wave energy reduction. Our measurements indicate an average energy reduction of 92.5% between the fore-reef and back-reef. The mean energy reduction between the fore-reef and the beach was 95.5%. Our observations are in agreement with those of previous studies concerning wave energy gradients in coral reef environments. The results presented here also indicate a process of filtering of peak period energy as waves travel across the reef. Gravity waves are largely filtered during their propagation across the reef, whereas infragravity waves propagate to the beach. Our present knowledge is still incomplete to describe the effect of these phenomena on the nearby pocket beach. Topographic survey on *Anse Michel* beach and further hydrodynamic measurements will lead to a better understanding of reef shoreline morphodynamics under the influence of infragravity waves. Observation and understanding of these processes are essential for better management and preservation of these tropical beaches which are of high tourist value.

ACKNOWLEDGMENTS

This work was supported by the INTERREG project CARIBSAT (Caribbean Satellite Environmental Information System). Two anonymous reviewers provided salient suggestions for improvement of the manuscript.

LITERATURE CITED

Brander, R.W.; Kench, P.S., and Hart D., 2004. Spatial and temporal variations in wave characteristics across a reef platform, Warraber Island, Torres Strait, Australia. *Marine Geology*, 207, 169-184.

Hearn, C.J., 1999. Wave-breaking hydrodynamics within coral reef systems and the effect of changing relative sea level. *Journal of Geophysical Research*, 104(c12), 30007-30019.

Jeanson, M.; Anthony, E.J.; Dolique, F., and Aubry, A., 2013. Wave characteristics and morphological variations of pocket beaches in a coral reef-lagoon setting, Mayotte Island, Indian Ocean. *Geomorphology*, 182, 190-209.

Kench, P.S. and Brander, R.W., 2006a. Response of reef island shorelines to seasonal climate oscillations: South Maalhosmadulu atoll, Maldives. *Journal of Geophysical Research*, 111(f1), doi:10.1029/2005JF000323.

Kench, P.S. and Brander, R.W., 2006b. Wave Processes on Coral Reef Flats: Implications for Reef Geomorphology Using Australian Case Studies. *Journal of Coastal Research*, 22(1), 209-223.

Kench, P.S.; Brander, R.W.; Parnell, K.E., and McLean, R.F., 2006. Wave energy gradients across a Maldivian atoll: Implications for island geomorphology. *Geomorphology*, 81, 1-17.

Kench, P.S.; Brander, R.W.; Parnell, K.E., and O'Callaghan, J.M., 2009. Seasonal variations in wave characteristics around a coral reef island, South Maalhosmadulu atoll, Maldives, *Marine Geology*, 262, 116-129.

Lowe, R.J.; Falter, J.L.; Bandet, M.D.; Pawlak, G.; Atkinson, M.J.; Monismith, S.G., and Koseff, J.R., 2005. Spectral wave dissipation over a barrier reef. *Journal of Geophysical Research*, 110(c4), doi:10.1029./2004.JC002711 1-16.

Lugo-Fernandez, A.; Roberts, H.H., and Suhayda, J.N., 1998a. Wave transformations across a Caribbean fringing-barrier coral reef. *Continental Shelf Research*, 18, 1099-1124.

Lugo-Fernandez, A.; Roberts, H.H., and Wiseman, W.J., 1998b. Tide effects on wave attenuation and wave set-up on a Caribbean coral reef. *Estuarine, Coastal and Shelf Science*, 47, 385- 675 393.

Norcross, Z.M.; Fletcher, C.H., and Merrifield, M., 2002. Annual and interannual changes on a reef-fringed pocket beach: Kailua Bay, Hawaii. *Marine Geology*, 190, 553-580.

Ogston, A.S.; Storlazzi, C.D.; Field, M.E., and Presto, M.K., 2004. Currents and suspended sediment transport on a shallow reef flat: South-central Molokai, Hawaii. *Coral Reefs*, 23, 559-569.

Pomeroy, A.W.N.; Lowe, R.J.; van Dongeren, A.R.; van Thiel de Vries, J.S.M; Symonds, G., and Roelvink, J.A, 2012. The importance of low frequency waves in fringing reef environments. *Proceedings of the 12th International Coral Reef Symposium* (Cairns, Australia).

Presto, M.K.; Ogston, A.S.; Storlazzi, C.D., and Field, M.E., 2006. Temporal and spatial variability in the flow and dispersal of suspended-sediment on a fringing reef flat, Molokai. *Estuarine, Coastal and Shelf Science*, 67, 67-81.

Sheppard, C.; Dixon, D.J.; Gourlay, M.; Sheppard, A., and Payet, R., 2005. Coral mortality increases wave energy reaching shore protecting by reef flat: Examples from Seychelles. *Estuarine, Coastal and Shelf Science*, 64, 223-234.

Storlazzi, C.D. and Jaffe, B.E., 2008. The relative contribution of processes driving variability in flow, shear, and turbidity over a fringing coral reef: West Maui, Hawaii. *Estuarine, Coastal and Shelf Science*, 77, 549-564.

Tamura, H.; Nadaoka, K., and Paringit, E.C., 2007. Hydrodynamic characteristics of a fringing coral reef on the east coast of Ishigaki Island, southwest Japan. *Coral Reefs*, 26, 17-24.

Zawada, D.G.; Piniak, G.A., and Hearn, C.J. 2010. Topographic complexity and roughness of a tropical benthic seascape. *Geophysical Research Letters*, 37(14), doi:10.1029/2005JF000323.

Journal of Coastal Research	SI	75	587-591	Coconut Creek, Florida	2016

Lagoonal reef sediment supply and island connectivity, Huvadhu Atoll, Maldives

Yiqing Liang[†*], Paul S. Kench[†], Murray R. Ford[†], and Holly K. East[‡]

[†]School of Environment, University of Auckland, Auckland, New Zealand

[‡]Geography, College of Life and Environmental Sciences, University of Exeter, Exeter, UK

www.cerf-jcr.org

www.JCRonline.org

ABSTRACT

Liang, Y.; Kench, P.S., Ford, M.R., and East, H.K., 2016. Reef sediment supply and island building in the South Maldives. *In:* Vila-Concejo, A.; Bruce, E.; Kennedy, D.M., and McCarroll, R.J. (eds.), *Proceedings of the 14th International Coastal Symposium* (Sydney, Australia). *Journal of Coastal Research*, Special Issue, No. 75, pp. 587-591. Coconut Creek (Florida), ISSN 0749-0208.

Reef islands are small, low-lying islands composed mainly of bioclastic sands and gravels from the late Holocene. These islands, which support around 700,000 people, are vulnerable to potential threats including land submergence and shoreline erosion. Thus, the sediment supply of the surrounding coral reef is an important consideration for coastal maintenance but there is little research on the link between reef productivity and island building. This paper presents an examination of reef and island beach sediments (material and composition), as well as the eco-geomorphic zones of the contemporary reef. Two islands in Huvadhu Atoll of the Republic of Maldives were used in this investigation. Surficial sediment samples were collected from each reef zone, toe of beach, and beach berm for each island. Benthic surveys for each reef platform and aerial photo analyses were used to determine reef ecology and to constrain the eco-geomorphic zones on the reef. Prevalent organisms on both reefs were coral, crustose coralline algae, and *Halimeda sp.*, while other sediment producers (molluscs and foraminifera) were less represented or absent. However, sediment samples taken from the reef flat show that all constituents are present, similarly to sand samples from the island beaches. The reef and beach sediments had similar compositions, suggesting that the island is still connected to the surrounding reef. This research provides insights into how these reef islands are maintained by the surrounding reef, which has implications for future island building and resilience to climate change.

ADDITIONAL INDEX WORDS: *Reef islands, coral reefs, Maldives, sedimentology.*

INTRODUCTION

Reef islands are extremely low-lying (<3 m above mean sea level) coherent accumulations of bioclastic sediment deposited on reef surfaces that can be found on barrier reefs, open reef seas, and mid-ocean atolls. Around 500 atolls are distributed across the circum-tropical climate zone of the oceans, supporting about 700,000 people (Fujita *et al.,* 2009). Furthermore, islands are of great ecological signficance, providing a habitat for sea turtles and their rookeries, as well as endemic amphibians, mammals and reptiles (Perry *et al.,* 2011). Given their high socioeconomic and ecological value, the vulnerability of reef islands to sea-level rise and climate change has been a concern in recent times. Potential threats include land submergence, shoreline erosion, saltwater intrusion, and extreme weather events (Woodroffe, 2008).

Reef islands are mid- to late Holocene in age and composed of bioclastic sands and gravels, which are skeletal remains from reef organisms such as coral, coralline algae, molluscs, *Halimeda* and foraminifera (Kench *et al.,* 2005). Consequently, reef productivity and sediment supply are important for island formation, ongoing coastal maintenance and change. However, islands represent only one store of sediment in reef systems. Sediments may also be reincorporated into the reef framework; stored on the reef surface, or transported off reef (Hart and Kench, 2007). Conceptually, therefore, a reef island that is both surrounded by a productive reef and connected to that sediment supply may be perceived as less vulnerable, or more able to undergo morphological adjustment than islands whose sediment supply has shut down (Perry *et al.*, 2011).

Few studies have examined the link between reef productivity and island building despite evidence that sediment supply may represent an overriding control in island stability. A number of studies suggest that reef islands are quite resilient to sea-level rise and can adapt geomorphologically (Kench and Cowell, 2001; Kench *et al.,* 2005; Kench *et al.,* 2009a; Kench *et al.,* 2015; Yamano *et al.,* 2005) and several shoreline history studies show that most islands are morphologically stable or continue to accrete (Dawson and Smithers, 2010; Ford and Kench, 2014; Kench and Brander, 2006; Kench *et al.,* 2009b; Kench *et al.,* 2015; McLean and Kench, 2015; Webb and Kench, 2010).

Preliminary modeling studies imply that sediment supply and reef production may exert a strong influence on island building. For example, Kench and Cowell (2000) show in model simulations that significant shoreline retreat may occur in sea-level rise scenarios when combined with a decrease in sediment supply. To date, there has been little empirical evidence to validate this modeling.

This study examines the link between reef and island beach sediments, as well as comparing reef sediments with abundance of sediment producers on the contemporary reef of two lagoonal

DOI: 10.2112/SI75-118.1 received 15 October 2015; accepted in revision 15 January 2015

*Corresponding author: christine.liang@auckland.ac.nz

platform islands in Huvadhu Atoll, Maldives. In comparison to the northern Maldives (Kench *et al.,* 2005; Perry *et al.,* 2015), there have been no detailed published studies of islands in the southern Maldives or Huvadhu Atoll. This study provides the first quantitative observations against which to compare differences in island morphology and sediment characteristics with the northern atolls. Results provide insights on how reef island sediment resevoirs are maintained by the surrounding reef, and implications for future island resilience are discussed.

Study Site

The Maldives archipelago straddles the equator in the central Indian Ocean (northernmost point: 7°06'23.0"N 72°54'09.3"E; southernmost point: 0°42'13.0"S 73°09'20.6"E). The equatorial location implies the archipelago is outside of the zone of immediate cyclogenesis but is influenced by marked transitions in monsoons: westerly monsoon (April-November) and dry northeast monsoon (December-March). The westerly monsoon is associated with southwest-northwest winds (225-315˚) and the northeasterly monsoon generates east-northeast winds (45-90˚) (Kench *et al.*, 2009c). Woodroffe (1992) identified marked latitudinal gradients along the archipelago with respect to atoll structure and climate.

The archipelago is host to more than 1200 islands. The focus of this study is two islands in Huvadhu Atoll, situated just north of the equator (0°29N 73°16E, Figure 1). Huvadhu is the largest atoll in the Maldives, measuring 79 km (North to South) and encompassing an area of 2900 km^2. The atoll contains 207 islands located on the atoll rim and 43 lagoonal islands.

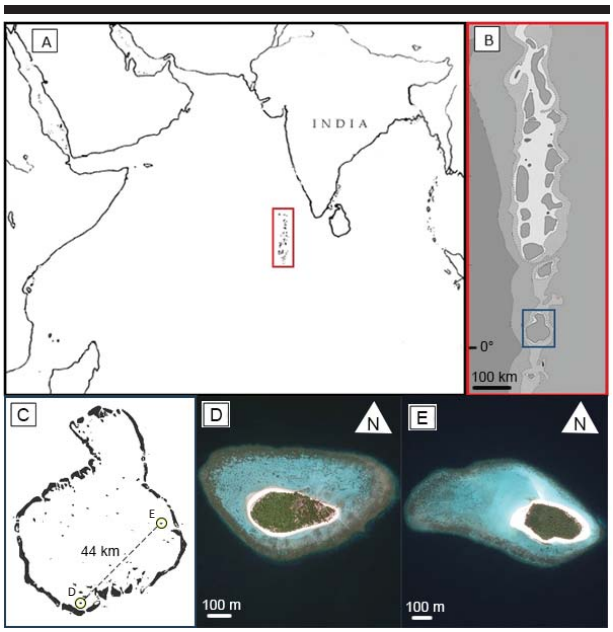

Figure 1. Location of Maldvies in the Indian Ocean (A). The insets show the Maldives archipelago (B) and Huvadhu Atoll (C) that includes study islands Kan'dahalagalaa (D) and Kondeymatheelaabadhoo (E), which are 44 km apart (Satellite image source: GoogleEarth©).

This study examined the morphology, reef ecology, and sedimentology of two lagoonal platform reef islands in Huvadhu lagoon. Kan'dahalagalaa (hereafter referred to as KAN) is located in the southwest and Kondeymatheelaabadhoo (hereafter referred to as KOND) is situated 44 km to the northeast (Figure 1). The islands were selected due to their relative isolation in the lagoon and as they possess similar size and shape.

METHODS

GPS field surveys, morphological mapping, and satellite imagery were used to delineate eco-geomorphic zones. The islands were surveyed along the mid-axis using standard auto level techniques and surveys were reduced to mean sea level using sea-level records from Gan (00°41S, 73°09E) from the University of Hawaii Sea Level Centre. Surficial sediment samples were collected from each reef zone (n=18), toe of beach (n=12), and beach berm (n=12) for each island (Figure 2). The texture of the sediment samples was determined by dry sieving into half-phi size fractions from -2ϕ to 4ϕ and calculating mean grain size in GRADISTAT (Blott and Pye, 2001). Composition of the samples was quantified by point-counting 100 grains from each half-phi size fraction between -2ϕ to 3ϕ under a binocular microscope (n=1100 grains per sample). Smaller size fractions were disregarded as grains were too small to enable constituent identification.

A census of benthic ecology and abundance of sediment producers were performed for each island (18 surveys per island, six surveys in each reef zone) adapted from the methods in Perry *et al.* (2015). A line-intercept transect census (n=18, per island) was performed along a measuring tape to determine coral cover and other benthic substrate types – crustose coralline algae, sand, and rubble (3636 data points in total). A visual inspection for sediment producers (*Halimeda*, *Marginopora*, molluscs, calcifying green algae and red coralline algae) was undertaken within 0.5 m on either side of the survey transect (10 m^2 study area per survey). Reef rugosity was noted and sediment depth (thickness of sediment cover) was recorded at 1 m intervals along the measuring tape. The area of productive coral cover on the outer reef was mapped from aerial photographs and groundtruthed during field surveys. The coral cover and substrate data, organism counts, and calculated productive area were used to estimate total abundance of sediment producers on the reef.

RESULTS

The study islands and their surrounding reef platform were divided into seven geomorphic zones (Figure 2). Three distinct reef geomorphic zones (sand, patch coral, dense coral) were identified and are located in similar areas of the reef platform on both islands. These reef zones differ mainly in terms of rugosity and substrate, with different proportions of sand/rubble and coral cover (Figure 3). On KAN, the dense coral zone was 49.9% of the total reef area, and the patch coral and sand zones covered 43.3% and 6.7%, respectively. KOND had 36.1% dense coral zone, 49.4% patch coral and 14.4% sand coverage of the total reef area (Figure 2).

The dense coral zone, or outer reef, was defined by continuous coral cover, minimal sediment depth (KAN: 0.14 ± 0.1 cm; KOND: 0.5 ± 1.0 cm) and high rugosity (4.3 ± 0.5). The

patch coral zone (inner reef) contained sparse coral patches on a sandy or rubble substrate. Average rugosity was 2.8 ± 0.4 with sediment depth averaging 3.0 ± 2.5 cm (KAN) and 6.3 ± 4.5 cm (KOND). The sand zone was characterized by a lack of coral growth and minimal rugosity (averaging 1.0 ± 0.0 for both islands). Sediment depth in this reef zone was highest, averaging 27.3 ± 0.4 cm (KAN) and 17.6 ± 8.0 cm (KOND). This zone transitions into the toe of beach (TOB), which demarcates the boundary between the reef and island.

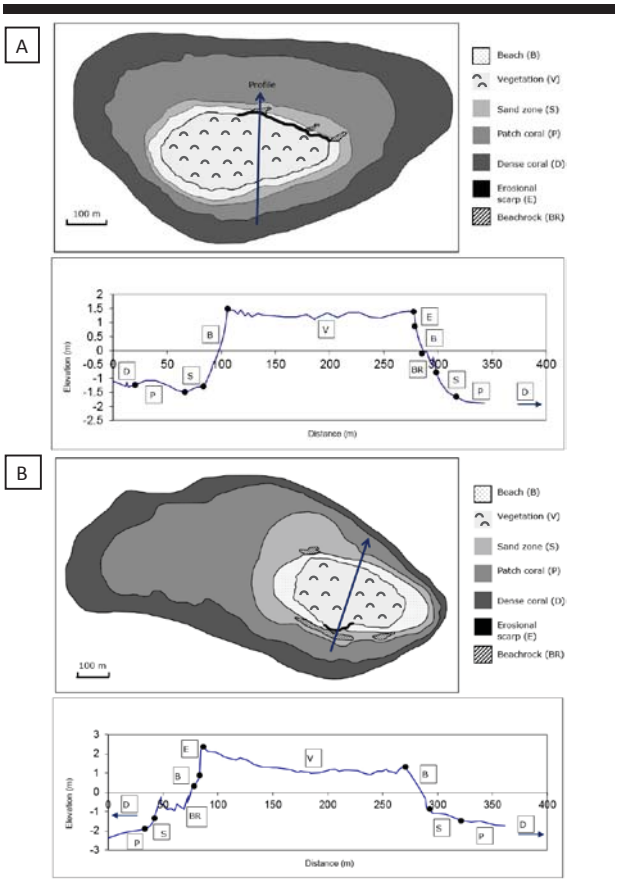

Figure 2. Geomorphic zones of KAN (A) and KOND (B) island and reef with annotated cross-section of mid profile (direction indicated by arrow).

Both islands had similar substrates for each geomorphic zone (Table 1). The abundance of key sediment producers calculated from benthic surveys of the productive reef area (dense coral zone) is presented as an average per survey and an estimate of total abundance on the reef (Table 2). Coral was the dominant sediment producer in both islands. Crustose coralline algae (CCA) was also present and *Halimeda* was prolific on the reef. There was an absence of live foraminifera *Marginopora* individuals at all of the KAN benthic survey sites but could be found growing under rubble on KOND. Calcifying green algae and red coralline algae were not present in any of the surveys.

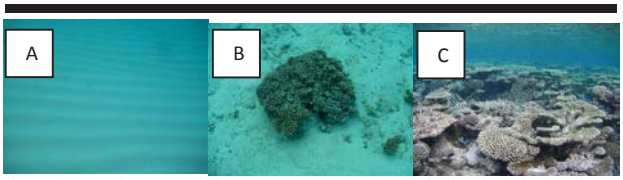

Figure 3. Reef geomorphic zones (A) Sand zone: lack of reef organisms; (B) Patch coral zone: sparse coral patches on sandy or rubble substrate; (C) Dense coral zone: continuous coral cover.

Table 1. *Substrate cover (%, ± 1 s.d.) for each reef geomorphic zone on KAN and KOND.*

Substrate	Sand Zone	Patch Coral	Dense Coral
Kan'dahalagalaa			
Live coral (%)	-	19.3 ± 11.0	67.2 ± 6.6
Dead coral (%)	-	8.8 ± 7.2	17.2 ± 4.3
CCA (%)	-	2.0 ± 2.5	8.8 ± 3.6
Sand (%)	99.2 ± 2.0	46.7 ± 27.8	3.5 ± 3.2
Rubble (%)	0.8 ± 2.0	23.2 ± 15.9	3.3 ± 4.9
Kondeymatheelaabadhoo			
Live coral (%)	-	16.5 ± 11.7	55.2 ± 7.3
Dead coral (%)	-	10.5 ± 6.3	31.5 ± 10.9
CCA (%)	-	-	2.8 ± 2.2
Sand (%)	97.5 ± 6.1	45.0 ± 21.2	1.7 ± 2.9
Rubble (%)	2.5 ± 6.1	28.0 ± 15.1	8.8 ± 7.7

Though some sediment producers were absent or rarely found during reef benthic surveys, sediment samples collected from each reef zone as well as the toe and top of beaches contained all constituents (Figure 4). Many foraminifera species (*Calcarina sp., Amphistegina sp.)* would have been overlooked in the ecological surveys as they were very small and mostly found in the 1ϕ to 2ϕ size fractions. Coral was generally found in all size fractions and dominated the composition of all samples. Halimeda dominated the -1.5ϕ and -1ϕ size fractions. Molluscs were also a major constituent but not dominant on the reef, owing to its durability (Ford and Kench, 2012). The major component in all samples was coral (>50%), followed by molluscs, *Halimeda*, and foraminifera (Figure 4). CCA, although prevalent on the reef, was not found to be a major sediment constituent (Figure 4). Sediment composition between the reef zones and the TOB was similar to each other, as compared to the beach berm, which had a much higher proportion of coral (Figure 4).

Table 2. *Abundance of sediment producers in the dense coral zone per 10 m² survey (average) and as a total abundance on the productive reef area.*

	Kan'dahalagalaa		Kondeymatheelaabadhoo	
Organism	Survey	Reef	Survey	Reef
Coral (m²)	6.7	93725.8	5.5	62033.6
CCA (m²)	0.9	12273.6	0.3	3146.6
Halimeda (kg)[1]	0.4	5795.7	0.1	1200.0
Marginopora (no.)[2]	-	-	5.3	59898.4
Molluscs (no.)[2]	0.7	9344.7	0.5	5619.0

[1]Dry weight in kg.
[2]Number of individuals.

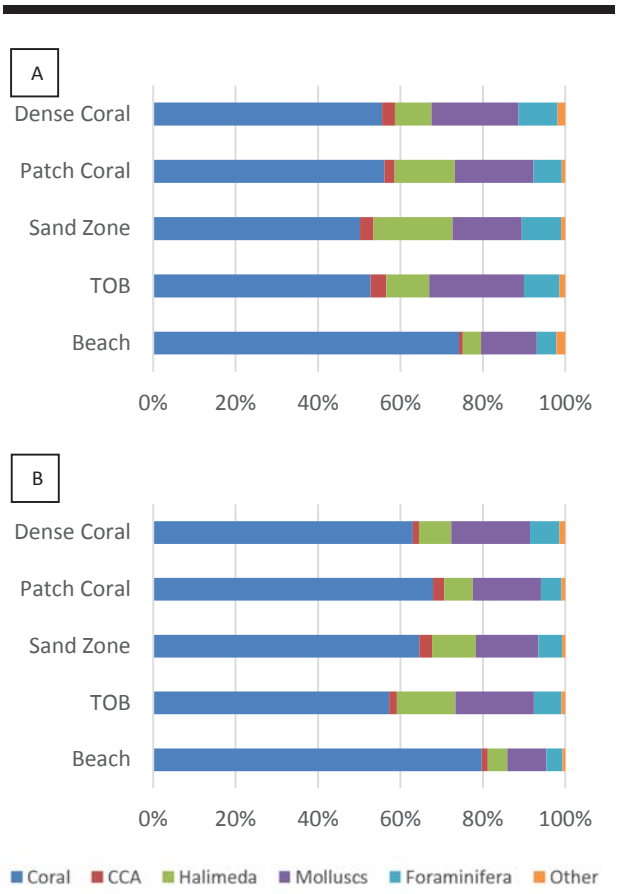

Figure 4. Average sediment composition for each reef zone, toe of beach (TOB) and beach top samples on (A) KAN and (B) KOND.

Textural analyses of the surficial reef and beach samples show that the sediments collected from the TOB and beach were notably different from sediment in the reef zones. Beach sediments were much finer than reef sediments, with the coarsest sediments accumulating at the toe of beach (Figure 5).

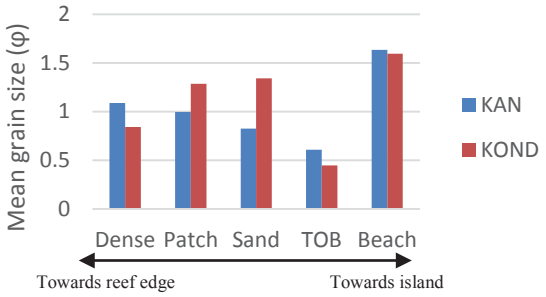

Figure 5. Average mean grain sizes on KAN and KOND from surficial sediments taken from reef zones, toe of beach, and beach berm.

DISCUSSION

Both study islands had productive outer coral zones comprised of a wide range of sediment producing organisms such as coral, crustose coralline algae, *Halimeda*, foraminifera, and molluscs. However, the diversity of producers is not reflected in the composition of sediments on the reef surface. The main findings from this research are: 1) The inner sand zone represents a sediment reservoir, which is able to store sediments generated by the productive reef zones, and 2) The reef and beach sediments had similar compositions, suggesting that the island is still connected to the surrounding reef.

Reef ecology and abundance of sediment producers were not directly related to reef sediment composition. Sediment producers coral, CCA, and *Halimeda* were prevalent in reef surveys but others such as molluscs and foraminifera were not common (Table 2). However, all constituents were found in reef sediments (Figure 4), potentially reflecting differential skeletal durability. The durability of reef sediments varies widely with coral being the most resistant and *Halimeda* being the least durable, followed by foraminifera (Ford and Kench, 2012). Coral is mainly converted into reef sediment through bioerosion by reef eroders such as parrotfish and urchins (Perry *et al.*, 2015). Molluscs were frequently found in both reef and beach sediments due to the durability and buoyancy of shells, making them suitable for transport, retention and deposition (Ford and Kench, 2012; Hart, 2008). Foraminifera have similar hydraulic characteristics to molluscs (*i.e.* easily transported) (Hart, 2008), but have been found to be notably less durable than molluscs (Ford and Kench, 2012) and are less prevalent in the beach sediments. They are also under-represented in reef flat cover since they were mainly found in 1ϕ to 2ϕ size fractions. Both islands had more *Halimeda* on the oceanward side, which experiences less seasonal wind and wave energy (Kench and Brander, 2006). Since *Halimeda* is less durable, the beach top sediments contain a lower proportion as compared to the reef sediments as the island beachface is a high energy setting.

The sand zone, surrounding the periphery of the island, had the highest sediment depth of all reef zones and was an area defined by solely sediment cover (Table 1). This zone transitions into the toe of beach (Figure 2) and acts as a sediment reservoir for the island. Sediments around the island periphery are often distributed to other parts of the island or to temporary deposits (Dawson and Smithers, 2010; Kench and Brander, 2006) and the sand zone could provide these necessary sediments for reworking. The skeletal compositions of sediments in the sand zone and TOB are similar to that of sediments from productive reef areas (Figure 4), suggesting these zones retain and store sediment produced on the reef with the potential of being reworked or supplied to the island.

Composition and texture of the beach berm was distinct from TOB and other reef zones (Figures 4, 5). This suggests selective entrainment by waves and wind of finer sands and also more durable constituents onto the island shore, which subsequently is available for island building. However, the same main constituents were present in all reef and beach samples. This suggests that beach sediments are still being supplied to the island. Indications that an island has become decoupled to the surrounding reef flat is when island sediments do not match those on the reef platform (McKoy *et al.*, 2010). Being coupled

to the reef and still being supplied by contemporary sediments suggests that the island is able to respond to environmental change more readily than decoupled islands composed solely of relict sediments (McKoy *et al.,* 2010).

CONCLUSIONS

Reef islands will be more susceptible to erosion without a continuous supply of sediment or when they are decoupled from the sediment supply. This research provides evidence that the two lagoonal reef islands in Huvadhu are actively connected to sediment reservoirs of their surrounding reefs. However, not all reef islands exist under these conditions and some islands may be detached from contemporary sediment supply (McKoy *et al.,* 2010). Unfortunately, few studies aim to quantify how spatial variations in organism density and production influence the reef framework and sediment reservoirs for reef islands (Hart and Kench, 2007). Also, by looking at sediment composition over time, this shows whether the island has been coupled to the reef throughout the course of island evolution and what changes in this relation have occurred to maintain island building. Ultimately, this study and similar future research will be able to provide insights into how reef islands are maintained by its surrounding reef, which has important implications for island accretion and resilience to climate change.

ACKNOWLEDGMENTS

The authors would like to acknowledge Mohamed Aslam (LaMer) for his help and hospitality and Abraham Didis (boat driver) for aiding in fieldwork, as well as Ciara McCarten (Park Hyatt Hadahaa) for facilitating field logistics.

LITERATURE CITED

Blott, S. J. and Pye, K., 2001. GRADISTAT: a grain size distribution and statistics package for the analysis of unconsolidated sediments. *Earth surface processes and Landforms*, 26(11), 1237-1248.

Dawson, J.L. and Smithers, S.G., 2010. Shoreline and beach volume change between 1967 and 2007 at Raine Island, Great Barrier Reef, Australia. *Global and Planetary Change*, 72(3), 141-154.

Ford, M. R. and Kench, P. S., 2012. The durability of bioclastic sediments and implications for coral reef deposit formation. *Sedimentology*, 59(3), 830-842.

Ford, M.R. and Kench, P.S., 2014. Formation and adjustment of typhoon-impacted reef islands interpreted from remote imagery: Nadikdik Atoll, Marshall Islands. *Geomorphology,* 214, 216-222.

Fujita, K.; Osawa, Y.; Kayanne, H.; Ide, Y., and Yamano, H., 2009. Distribution and sediment production of large benthic foraminifers on reef flats of the Majuro Atoll, Marshall Islands. *Coral Reefs*, 28(1), 29-45.

Hart, D.E., 2008. The maintenance of reef islands. *Proceedings of the 11th International Coral Reef Symposium* (Ft. Lauderdale, Florida), pp. 409-413.

Hart, D.E. and Kench, P.S., 2007. Carbonate production of an emergent reef platform, Warraber Island, Torres Strait, Australia. *Coral Reefs*, 26(1), 53-68.

Kench, P.S. and Brander, R.W., 2006. Response of reef island shorelines to seasonal climate oscillations: South Maalhosmadulu atoll, Maldives. *Journal of Geophysical Research*, 111, F1.

Kench, P. S.; Brander, R. W.; Parnell, K. E., & O'Callaghan, J. M., 2009c. Seasonal variations in wave characteristics around a coral reef island, South Maalhosmadulu atoll, Maldives. *Marine Geology*, 262(1), 116-129.

Kench, P.S. and Cowell, P.J., 2000. Variations in sediment production and implications for atoll island stability under rising sea level. *Proceedings 9th International Coral Reef Symposium* (Bali, Indonesia), pp. 1181-1186.

Kench, P.S. and Cowell, P.J., 2001. The morphological response of atoll islands to sea-level rise. Part 2: application of the modified shoreface translation model (STM). *Journal of Coastal Research*, Special Issue No. 34, pp. 645-656.

Kench, P.S.; McLean, R.F., and Nichol, S.L., 2005. New model of reef-island evolution: Maldives, Indian Ocean. *Geology*, 33(2), 145-148.

Kench, P.S.; Parnell, K.E., and Brander, R.W., 2009b. Monsoonally influenced circulation around coral reef islands and seasonal dynamics of reef island shorelines. *Marine Geology,* 266(1), 91-108.

Kench, P.S.; Smithers, S.G.; McLean, R.F., and Nichol, S.L., 2009a. Holocene reef growth in the Maldives: Evidence of a mid-Holocene sea-level highstand in the central Indian Ocean. *Geology,* 37(5), 455-458.

Kench, P.S.; Thompson, D.; Ford, M.R.; Ogawa, H., and McLean, R.F., 2015. Coral islands defy sea-level rise over the past century: Records from a central Pacific atoll. *Geology*, 43(6), 515-518.

McKoy, H.; Kennedy, D.M., and Kench, P.S., 2010. Sand cay evolution on reef platforms, Mamanuca Islands, Fiji. *Marine Geology*, 269(1), 61-73.

McLean, R. and Kench, P., 2015. Destruction or persistence of coral atoll islands in the face of 20th and 21st century sea-level rise?. *Wiley Interdisciplinary Reviews: Climate Change*, 6(5), 445-463.

Perry, C.T.; Kench, P.S.; O'Leary, M.J.; Morgan, K.M., and Januchowski-Hartley, F., 2015. Linking reef ecology to island building: Parrotfish identified as major producers of island-building sediment in the Maldives. *Geology*, 43(6), 503-506.

Perry, C.T.; Kench, P.S.; Smithers, S.G.; Riegl, B.; Yamano, H., and O'Leary, M.J., 2011. Implications of reef ecosystem change for the stability and maintenance of coral reef islands. *Global Change Biology*, 17(2), 3679-3696.

Webb, A.P. and Kench, P.S., 2010. The dynamic response of reef islands to sea-level rise: Evidence from multi-decadal analysis of island change in the Central Pacific. *Global and Planetary Change*, 72(3), 234-246.

Woodroffe, C.D., 1992. Morphology and evolution of reef islands in the Maldives. *Proceedings of the 7th International Coral Reef Symposium* (Guam), pp. 1217-1226.

Woodroffe, C.D. 2008. Reef-island topography and the vulnerability of atolls to sea-level rise. *Global and Planetary Change*, 62, 77-96.

Yamano, H.; Kayanne, H., and Chikamori, M., 2005. An overview of the nature and dynamics of reef islands. *Global Environmental Research*, 9(1), 9-20.

Journal of Coastal Research	SI	75	592-596	Coconut Creek, Florida	2016

The Drowned Apostles: The Longevity of Sea Stacks over Eustatic Cycles

Rhiannon Bezore[†*], David M. Kennedy[†], and Daniel Ierodiaconou[‡]

[†] School of Geography,
The University of Melbourne,
Parkville VIC 3010,
Australia

[‡] Deakin University,
School of Life and Environmental Sciences,
Centre for Integrative Ecology,
Warrnambool VIC 3280, Australia

www.cerf-jcr.org

www.JCRonline.org

ABSTRACT

Bezore, R., Kennedy, D.M., and Ierodiaconou, D., 2016. The Drowned Apostles: The Longevity of Sea Stacks over Eustatic Cycles. *In:* Vila-Concejo, A.; Bruce, E.; Kennedy, D.M., and McCarroll, R.J. (eds.), *Proceedings of the 14th International Coastal Symposium* (Sydney, Australia). *Journal of Coastal Research*, Special Issue, No. 75, pp. 592-596. Coconut Creek (Florida), ISSN 0749-0208.

Cliffed rocky coasts are erosional environments, the remnants of which can be preserved as sea stacks as the shoreline retreats. These sea stacks form spectacular landscapes, such as the iconic Twelve Apostles in Victoria, Australia. However, they are ephemeral features formed on a centennial scale, continually eroding and collapsing, meaning that coasts characterised by sea stacks often have fewer features than when first described. The question arises then as to the longevity of such features and whether they can be preserved over eustatic cycles.
The modern Twelve Apostles, of which 8 are still standing, are comprised of the Miocene Port Campbell Limestone and reach 45 m above sea level. Recent multibeam sonar data show five features around 6 km offshore, in 40-50 m water depth that appear to be relict sea stacks. Based on the morphology and geology of both the modern and drowned Apostles, it is inferred that the drowned and modern stacks evolved in a similar manner. While the modern sea stacks have an average height of 45 m, the drowned stacks have an average height of 4 m, suggesting a much greater age and also the possibility of multiple exposures to subaerial processes. The drowned stacks lay 655 m seaward of a drowned cliff averaging 14 m high which likely represents a former interstadial shoreline. This is much greater than the 91 m average distance between stack and cliff for the Modern Apostles, which may imply a more prolonged period of erosion along the drowned coastline.

ADDITIONAL INDEX WORDS: *Rocky coasts, coastal geomorphology, coastal processes, sea level, sea stacks.*

INTRODUCTION

Rocky coasts are predominately erosional landforms that comprise 80% of the world's shorelines (Emery and Kuhn, 1982). They tend to form on coastlines where marine processes dominate, and their form is the result of the relative balance between marine and subaerial processes (Kennedy *et al.*, 2014b). Sea stacks are formed as areas of weaker lithology or structure along a coast are preferrentialy eroded, leading to the formation of headlands. As the erosion continues, the headlands are dissected, creating caves and then arches. Further undercutting of the rock by hydraulic action eventually leads to collapse of the arch, leaving a free-standing sea stack (Bird, 2000).

Sea stacks will form only under certain boundary conditions. The rock must be soft enough to be eroded by waves but still have enough compressive strength to maintain the stacks' overlying weight. For example, granite coastlines are generally too resistant to erode into stacks (Kennedy *et al.*, 2014a), and cliffs made of clay or other soft strata do not have the compressive strength to support the weight of a tall stack (Trenhaile and Schwartz, 2006). With a compressive strength between 60 -170 MPa, limestones are an ideal rock type in which sea stacks can be created. These limestone stacks form spectacular landforms along coastlines worldwide such as California, US and Victoria, Australia. They are not static features, though, as evidenced by collapses like that of a 50 m high Twelve Apostle stack in 2005.

The question arises, then, as to whether sea stacks can persist over eustatic cycles. This study focuses on the limestone sea stacks known as the 12 Apostles in Victoria, Australia and compares their morphology and formation with a drowned shoreline found nearly 6 km offshore from the modern stacks. By comparing the modern and submerged shoreline, inferences on the temporal stability of limestone sea stacks can be made.

Background

The modern Apostles are found within the Otway Basin between Peterborough and Princetown on the southwest coast of Victoria, Australia (Figure 1). The Otway Basin is a north-northwest trending feature that covers an area of about 150,000 km² and contains over 10,000 m² of Late Jurassic to Tertiary sediments. The basin was formed during the late Jurassic rifting of Australia and Antarctica. Initial infill during the mid-Cretaceous was characterized by volcaniclastic and fluvial deposits with later Tertiary coastal and shallow marine clastic deposits (Nicolaides, 1995).

The onshore surface geology of the 12 Apostles (Figure 2) is Port Campbell Limestone overlaying the Gellibrand Marl

DOI: 10.2112/SI75-119.1 received 15 October 2015; accepted in revision 15 January 2015
*Corresponding author: rbezore@student.unimelb.edu.au

(Geological Survey of Victoria Report 103, 1995). The cliffs backing the Modern Apostles, as well as the 12 Apostles themselves, are comprised of alternating bands of hard and soft Port Campbell Limestone (Birch, 2003). The offshore geology in this region replicates the onshore geology, consisting of calcarenite, limestone, sandstone, and marl (LCC, 1993).

The Port Campbell area is exposed to swells from the south-west from the Southern Ocean. SWAN (Simulating WAves Nearshore) models show average wave heights ranging between 2 - 3 m (Flocard *et al.*, 2015), and wave periods in the region are typically 8 - 12 sec (LCC, 1993). The average spring tidal range is 0.6 m (Bureau of Meteorology, 2015). Port Campbell has a mean annual rainfall of 923 mm (Bureau of Meteorology, 2015).

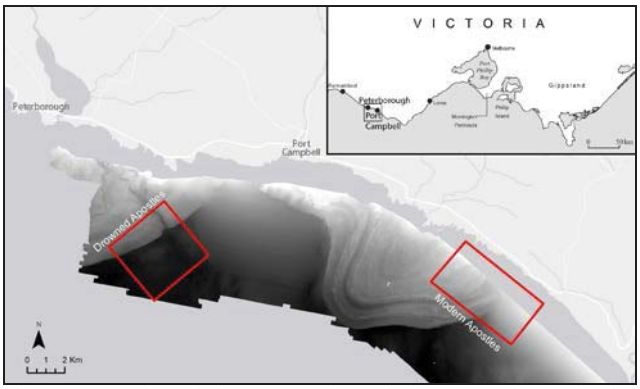

Figure 1. Location of the 12 Apostles and the Drowned Apostles in Victoria, Australia.

Figure 2. Aerial photo of the 12 Apostles Port Campbell, Victoria.

METHODS

This study uses bathymetric and terrestrial LiDAR data collected in 2007 using a LADS Mk II system with a GEC-Marconi FIN3110 intertial motion sensing system and a dual frequency kinematic geographic positioning system (kGPS). This dataset includes seamless terrestrial-marine mosaics from elevations of +10 m to depths of -25 m (Quadros and Rigby, 2010). Multibeam data were acquired as part of the ongoing Victorian Marine Habitat Mapping Project (Ierodiaconou *et al.*, 2007).This data was combined with Multibeam sonar data using a Reson Seabat 101 multibeam echosounder operating at a frequency of 240 kHz and 150˚ angular sector coverage. Positioning was accomplished using a real-time differential GPS integrated with a positioning and orientation system for marine vessels (POS MV) for dynamic heave, pitch, roll and yaw corrections (± 0.1° accuracy). The final raster grid of the data has a 5 m horizontal resolution providing full coverage capturing the coastal to depths of 60 m. The data was analyzed using the geographic information system software ArcGIS V.10.1. All data used in this study was projected in the World Geodetic System (WGS) 1984 in Universal Transverse Mercator (UTM) Zone 54s. The Port Camp

The morphological features identified in the LiDAR data were then measured and analysed in ArcGIS. Cliff erosion was analysed for the modern shoreline, using a combination of aerial and satellite images and the Digital Shoreline Analysis System (DSAS) (Thieler *et al.*, 2009). Aerial photographs from 1947 and 1994 and Google Earth Ikonos satellite images from 2004 and 2014 were used to measure change in cliff position over time and were all georeferenced in ArcMap using a minimum of 30 ground control points. A single road was identified in all three images that ran parallel to the shore, and a polyline was created to represent it as a baseline for cliff erosion measurements. DSAS was then run for the years 1947-1994, 1947-2004, and 2004-2014.

RESULTS

Five sea stacks were identified off the coast of Peterborough, sitting seaward of a drowned cliffline about 50 m below modern sea level (Figure 3). For both the modern and drowned cases, there is a cliffline fronted seaward by sea stacks that are the remnants of the cliff likely eroded by wave activity. The paleo-stacks are generally shorter and wider than the current stacks and are located farther seaward from the cliffs than the modern Apostles (Figure 4). The height of the stacks was measured from base to top and showed the modern stacks to be nearly ten times taller on average than the drowned stacks. The length was measured across the longest portion of each stack, perpendicular to the shoreline, and showed the drowned stacks to be almost an average of 20 m longer than the current apostles. For the width of the stacks, measured parallel to the shoreline at the longest point, the drowned sea stacks were nearly twice as wide on average as the modern stacks.

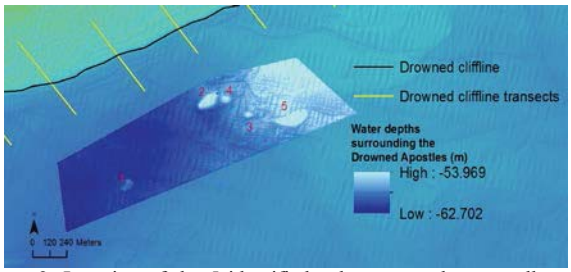

Figure 3. Location of the 5 identified paleo-sea stacks, as well as the transects used to measure the drowned cliffs backing them.

Modern Apostles

Of the original 12 Apostles, there are currently eight standing along the contemporary coast. The modern Apostles range in height from 12.98 - 67.45 m with an average height of 45.31 m, while the average length was 52.38 m with a range of 25.82 - 95.68 m (Figure 5). The modern stacks range in width from 31.99 - 70.14 m (average 46.58 m) and have an average area of 2,678.45 m² (714.42 m² - 7,900.24 m²) (Table 1).

The current stacks sit at an average distance of 118.65 m offshore (Table 1), with the modern cliffs behind them averaging at 48.92 m in height. There is a sea stack height to cliff height ratio of 0.93. The modern cliffs have a more angular toe and head and have a mean cliff face slope of 75˚.

Drowned Apostles

There are five drowned stacks that range in height from 3.32 - 6.47 m with an average height of 4.37 m. The average length of the drowned stacks was 71.76 m (range 25.17 - 116.33 m), and the average width of the drowned stacks was 86.11 m (range 38.27 - 207.94 m). The average area was 8,183.97 m² (range 902.88 - 21,564.60 m²), and the average perimeter was 275.79 m (range of 127.07 - 599.72 m) (Figure 6). The drowned Apostles are found farther seaward from their respective shoreline than the modern Apostles, at an average distance of 655.32 m from the drowned cliff (Table 1).

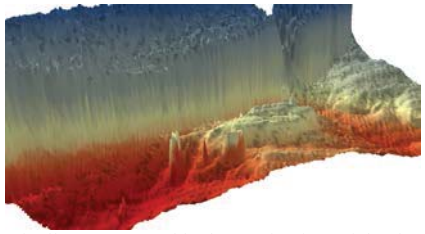

Figure 4. Vertically exaggerated bathymetric view of the drowned sea stacks and paleo-cliffs behind them.

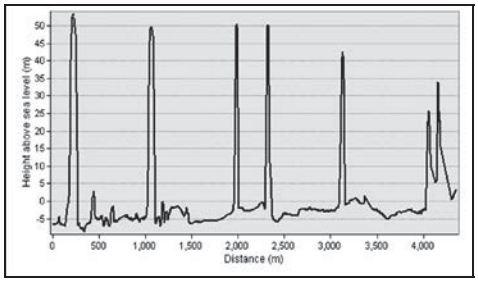

Figure 5. Profile of all eight Modern Apostles, with the westernmost stack (Modern Apostle 1) shown on the left.

The sea cliffs also vary in height, with the drowned cliffs averaging 13.60 m high, which gives a sea stack height to cliff height ratio of 0.32. Compared to the modern cliffs, the drowned cliffs are more rounded and have a lower angle toe with an average cliff face slope of 29˚. The water depths surrounding the

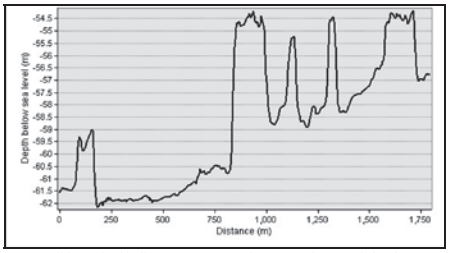

Figure 6. Profile of all five Drowned Apostles, with the westernmost stack (Drowned Apostle 1) shown on the left of the graph.

Drowned Apostles span from 58.11 - 62.12 m depth with an average depth of 59.72 m (Table 1).

The presence of sea stacks along both the modern and drowned coastlines is evidence of long term erosion. It was found that the mean long term rates of erosion both from 1947-1994 (Figure 7) and from 1947-2014 were 0.22 m/yr and that the short term rate of erosion from 2004-2014 was 0.36 m/yr (Figure 8). In addition to these erosion rates, there are also known accounts of cliff failure and slumping as well as documented cases of sea stack and arch collapses along this section of modern coastline. In 1990, part of the London Bridge sea arch collapsed with two tourists left in need of rescue, and in 2009 one of the 12 Apostles collapsed near Loch Ard Gorge. Such collapses indicate that cliff retreat is episodic.

Table 1. *Dimensions of each drowned and modern sea stack.*

	Height (m)	Length (m)	Width (m)	Area (m²)	Perimeter (m)	Dist. from cliff (m)	Depth stack base (m)
Drowned Apostles							
1	3.32	70.45	57.55	4,346.00	274.35	788.51	62.12
2	6.47	98.78	117.24	1,1034.48	423.18	484.72	60.74
3	3.95	25.17	38.27	902.88	127.07	524.44	58.33
4	4.25	48.10	67.02	3,071.88	228.96	691.51	59.35
5	3.90	116.33	207.94	21,564.60	599.72	787.40	58.11
12 Apostles							
1	67.45	95.68	66.75	7,900.24	354.84	65.26	-10.74
2	12.98	34.53	38.50	1,410.87	146.02	141.29	-5.77
3	56.92	57.43	70.14	4,433.83	247.76	152.14	-7.75
4	53.80	57.96	40.74	2,536.41	205.47	120.64	-2.88
5	54.49	25.82	31.99	1,091.61	130.72	178.29	-2.60
6	47.78	61.00	41.57	1,952.43	191.25	49.40	-3.65
7	30.34	41.37	44.92	1,387.81	142.85	159.40	-2.61
8	38.73	45.22	38.01	714.42	127.32	82.78	-4.78

DISCUSSION

The 12 Apostles provide a contemporary analogue for the formation of the drowned Apostles. The Port Campbell Limestone along this section of coast has a maximum burial depth of close to 300 m (Nicolaides, 1997), so it is assumed that the drowned stacks are also made of limestone since they found at only about 60 m depth. There is also no evidence that the submarine features are volcanic necks or pipes, as there is no igneous geology in the surrounding region (Higgins, 2011).

Since both set of stacks are comprised of the same lithology of their adjacent cliffs, it can be assumed that they evolved in a similar manner as the modern Apostles and may have had similar rates of erosion when they sat above sea level.

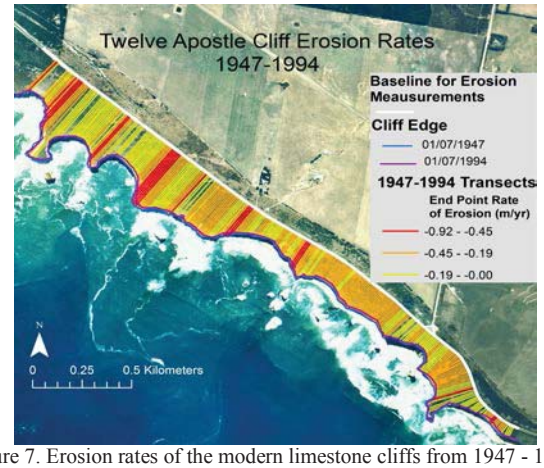

Figure 7. Erosion rates of the modern limestone cliffs from 1947 - 1994.

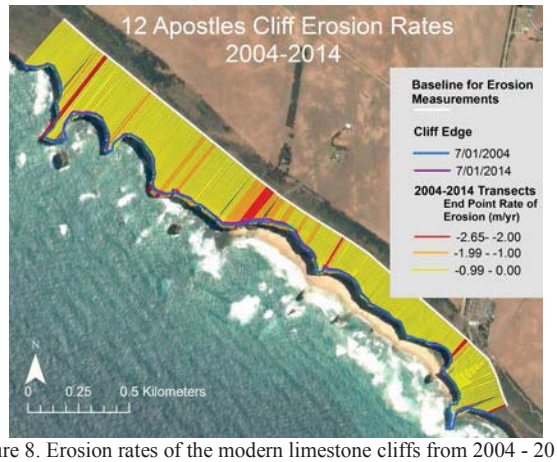

Figure 8. Erosion rates of the modern limestone cliffs from 2004 - 2014.

Sea stacks are closely related to mean sea level, as they form through the erosive action of waves. The base of the modern stacks is within 10 m of the current mean sea level, while the average depth of the base of the drowned stacks is 59.72 m. This means that sea level must have been roughly 60 ± 10 m below present when the drowned stacks were formed. Prior to the Holocene, the previous sea level interstadial and interglacial highstands occur at c. 60 ka, 85 ka, 110 ka, and 135 ka (Grant *et al.*, 2014). Except for the highstand at 60 ka, all of the other highstands saw sea levels much higher than the -60 ± 10 m expected to have formed the drowned stacks. Due to the high contemporary erosion rates of Port Campbell Limestone and the appearance of the last interglacial landforms, it is unlikely that the drowned stacks would correlate to the older sea level highstands. Therefore, using the formation depths and a relative sea level curve extending back over the past 250 kyr, the most likely age of formation of the drowned Apostles was during the Marine Isotope Stage 3 (MIS 3) (60-27 ka) (Figure 9).

During MIS 3, sea level was 60-90 m below present sea level, which correlates to the average depth of the drowned Apostles at 59.72 m. MIS 3 does not fit the typical profile of a 100 ka interstadial period that has characterized the last million years, since there were significant temperature and ice-volume fluctuations across the period (Meerbeeck, *et al.*, 2009). There was an initial rise in sea level to roughly 60 m below present levels that lasted the first half of MIS 3, followed by a drop to -80 m (Siddall *et al.*, 2008). It is likely, then, that the Drowned Apostles initially formed during the first half of MIS 3, when sea level was at -60 m.

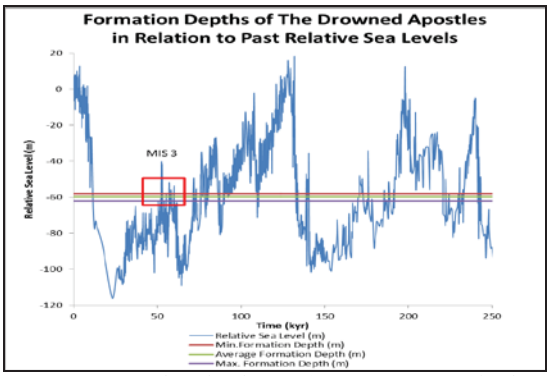

Figure 9. Reconstructed sea level curve (Grant *et al.*, 2014) for the past 250 thousand years with the best fit for the age of formation of the drowned sea stacks based on the depth of water in which they sit currently.

While it is inferred from the morphology of the current cliffs that hydraulic erosion is the dominant form of erosion for the current coastline, the drowned cliffs show a more slumped and low angle toe morphology that might point to a slightly different erosion process (Emery and Kuhn, 1982). The dominant process was still most likely marine erosion while the sea level was highest during MIS 3, but it is likely that the zone of erosion moved vertically at a different rate than is seen along the current coastline. There may have also been large scale slumping or cliff failure that could account for the diminished slope of the drowned cliff face (Emery and Kuhn, 1982). During the second half of MIS 3, when the stacks would have been roughly 20 m above sea level at that time, the main processes of erosion would have been subaerial rather than hydraulic (Siddall *et al.*, 2008).

Rapid erosion of sea stacks globally suggests that they are ephemeral features, and their preservation across eustatic cycles requires a change of the processes acting upon them. With a combination of high cliff erosion rates, low sea level, and a fairly wet climate based on the fact that MIS 3 was a warm stand (Siddall *et al.*, 2007), the paleo-shoreline would have kept eroding and periodically failing due to terrestrial processes, while the stacks would hold their stationary location but also continue to be eroded. During the first 3,000 years of MIS 3, sea level rise was its peak with a rate of nearly 6 mm per year, compared to the current rate of 3.2 mm per year (Siddall *et al.*, 2007). As sea level rose, beaches would have been removed as

they could not migrate inland past the cliffs, and perhaps this loss of abrasive material from the lack of sand could have also slowed the erosion rates enough to preserve the stacks (Limber and Murray, 2011). The rates of sea level rise during the postglacial marine transgression were significantly higher in Eastern Australia (Lewis *et al.*, 2013) and it appears to have been too rapid to completely erode the drowned stacks as the shoreline migrated from -120 m to present levels (+/- 1 m) (Lewis *et al.*, 2013). A prolonged exposure to subaerial erosion may also explain the much shorter and wider shape of the submerged stacks, as opposed to the modern stacks that have been formed solely at present sea level.

CONCLUSIONS

The 12 Apostles are world renowned for their iconic pillar shapes standing tall against the waves, but the drowned Apostles provide insight into what their future might hold. Both the drowned and the modern sea stacks are indicative of a classic erosional rocky coast environment with high wave activity being the main cause of cliff erosion. As the drowned Apostles are found in the same geologic setting as the current 12 Apostles, it is reasonable to assume that they were formed under the same geomorphic processes, some 60,000 years apart. The drowned sea stacks would have been eroded from a rocky coast by waves, wind, and rain at a sea level lower than today.

The preservation of these stacks is due in part to the rapid rise of sea level in the first half of MIS 3 and the post glacial marine trangression, carving the features out of the cliffs and then submerging them as sea level continued to rise. Were it not for the relatively quick submergence of the stacks, they likely would have continued to erode at a similar rate as seen with the modern sea stacks until they collapsed.

LITERATURE CITED

Abele, C. ,1995. Eastern Otway basin: the stratigraphy, structure, geophysics and hydrocarbon potential of the Eastern Otway Basin, Victoria, Geological Survey of Victoria.

Bird, E. C. F.,2000. *Coastal Geomorphology: An Introduction*. Chichester: Wiley.

Bureau of Meteorolgy, 2015. Tide predictions for Australia, South Pacific, and Antarctica: Port Campbell, VIC. *Australian Government*.

Emery, K.O. and Kuhn, G.G. ,1982. Sea cliffs: Their processes, profiles, and classification. *Geological Society of America Bulletin*, 93, 644-654.

Flocard, F., Ierodiaconou, D., and Coghlan, I.R., 2015. Multi-criteria evaluation of wave energy projects on the south-east Australian coast. *Renewable Energy*. (in Review)

Grant, K. M., E. J. Rohling, C. Bronk Ramsey, H. Cheng, R. L. Edwards, F. Florindo, D. Heslop, F. Marra, A. P. Roberts, M. E. Tamisiea, and F. Williams, 2014. Sea-level variability over five glacial cycles. *Nature Communications*, 5.5076.

Higgins, D., 2011. Victoria seamless geology (1st ed.). *Department of Primary Industries*, Victorian Government, Australia.

Ierodiaconou, D., Laurenson, L., Burq, S., and Reston, M., 2007. Marine benthic habitat mapping using multibeam data, georeferenced video and image classification techniques in Victoria, Australia. – *J. Spat. Sci.,* 52(1), 93-104.

Kennedy, D.M., Ierodiaconou, D., and Schimel, A., 2014a. Granitic coastal geomorphology, applying integrated terrestrial and bathymetric LiDAR with multibeam sonar to examine coastal landscape evolution. E*arth Surface Processes and Landforms*, 39, 1663–1674

Kennedy, D.M., Stephenson, W.J., and Naylor, L.A. (eds.), 2014b. Rock Coast Geomorphology, a global synthesis. *Geological Society*, London. Memoirs, 40, 235-245.

Lewis S.E., Sloss C.R., Murray-Wallace C.V., Woodroffe C.D. and Smithers S.G., 2013. Post-glacial sea-level changes around the Australian margin, a review. *Quaternary Science Reviews,* 74, 115-138.

LCC,1993. Marine and coastal special investigation descriptive report. *Land Conservation Council*, Melbourne, Victoria.

Limber, P.W., and A. Brad, Murray, 2011. Beach and sea-cliff dynamics as a driver of long-term rocky coastline evolution and stability. *Geology*, 39.12, 1147-1150.

Limber, P. W. and Murray, A. B., 2014. Sea stack formation and the role of abrasion on beach-mantled headlands, *Earth Surface Processes and Landforms*, 559–568.

Nicolaides, S., 1995. Cementation in Oligo-Miocene non-tropical shelf limestones, Otway Basin, Australia, Sedimentary *Geology*, 95, 97–121.

Nicolaides, S., 1997. Marine-derived dolomite in the shallowly buried temperate Port Campbell Limestone (Miocene), Otway Basin, Australia, *Sedimentology*, 44, 143–157.

Quadros, N. and Rigby, J., 2010. Construction of a high accuracy seamless, state-wide coastal DEM. *FIG Coastal Zone Special Publication*, Sydney.

Rohling, E. J., Braun, K., Grant, K., Kucera, M., Roberts, A. P., Siddall, M. and Trommer, G., 2010. Comparison between Holocene and Marine Isotope Stage-11 sea-level histories, *Earth and Planetary Science Letters*, 291, 97–105.

Siddall, M., Rohling, E. J., Thompson, W. G. and Waelbroeck, C., 2007. Marine isotope stage 3 sea level fluctuations, Data synthesis and new outlook. *Reviews of Geophysics*.

Thieler, E.R., Himmelstoss, E.A., Zichichi, J.L., and Ergul, Ayhan, 2009. Digital Shoreline Analysis System (DSAS) version 4.0 — An ArcGIS extension for calculating shoreline change, *U.S. Geological Survey Open-File Report 2008*-1278.

Trenhaile, A. S., 2006. Cliffed Coasts. In M. L. Schwartz (Ed.), *Encyclopedia of coastal science*.Springer, Berlin.

Journal of Coastal Research	SI	75	597-601	Coconut Creek, Florida	2016

Modelling the Development of Varied Shore Profile Geometry on Rocky Coasts

Hironori Matsumoto[†*], Mark E. Dickson[†], and Paul S. Kench[†]

[†]School of Enviornment, Faculty of Science,
University of Auckland
Auckland, New Zealand

www.cerf-jcr.org

www.JCRonline.org

ABSTRACT

Matsumoto, H.; Dickson, M.E., and Kench, P.S., 2016. Modelling the development of varied shore profile geometry on rocky coasts. *In:* Vila-Concejo, A.; Bruce, E.; Kennedy, D.M., and McCarroll, R.J. (eds.), *Proceedings of the 14th International Coastal Symposium* (Sydney, Australia). *Journal of Coastal Research*, Special Issue, No. 75, pp. 597-601. Coconut Creek (Florida), ISSN 0749-0208.

This paper describes a new rocky shore profile evolution model. It differs from existing models that focus on shore platform development, through its ability to simulate a wide range of emergent profile shapes. The new model considers a relatively limited number of coastal processes that are represented with simplified mathematical descriptions. The paper describes initial model evaluation against field data from the Japanese coast that were influential in the creation of a widely used conceptual model for rocky shore evolution. The new numerical model produces outputs that are generally consistent with the field observations, but there are some areas of difference which are discussed in the paper. An additional area of focus in the paper considers the new model's capability of producing a wide range of profile types with characteristic geometries, which are also commonly seen in nature, but have been subject to little systematic analysis. Investigation of model outcomes indicates that a broad range of profile shapes in the model requires consideration of the erosive effects of varied wave types (*i.e.* unbroken, breaking and broken waves).

ADDITIONAL INDEX WORDS: *Rocky coast, numerical model, exploratory modelling.*

INTRODUCTION

A large portion of the world's shoreline consists of rocky coasts (Emery and Khun, 1982). The cliffs and shore platforms that characterise many of these coasts have been intensively studied (*e.g.* Sunamura, 1992; Trenhaile, 1987); however, very slow rates of morphological change and an absence of preserved evidence of the temporal development of shore profile geometry have limited scientific progress and left a number of fundamental questions unanswered (Stephenson, 2000).

Numerical models have been identified as a key tool in further progressing an understanding of rocky shore development over long time scales (Naylor *et al*., 2010). Detailed process-based models require a well-developed mechanistic understanding of process-form relationships based on quantitative measurements. However the history of rock shore research, up until the last couple of decades (*e.g.* Kanyaya and Trenhaile, 2005; Ogawa *et al*., 2011; Stephenson and Kirk, 2000a, 200b), is dominated by descriptive research. Furthermore, despite recent advances in computational processing, it remains difficult to use highly detailed numerical models to study long-term (Holocene-scale) landform evolution. Therefore, the geomorphological development of rocky shorelines is well suited to exploratory modelling investigations (see Murray, 2007).

Trenhaile's (*e.g.* 2000) simplified mathematical model for hard-rock coasts is one example of a numerical tool that has been successfully used to explore long-term evolution of shore platform profiles. The modelling studies conducted by Trenhaile are extensive and consider a broad range of the different processes that influence shore platform development, including wave attack, weathering processes, existence of beach sediment, and sea level change (*e.g.* Trenhaile, 2000, 2001, 2005, 2008). This model has led to a number of important insights, but it is also limited in some respects. For instance, the discretisation scheme employed by the model restricts the variety of rocky profile shapes that can emerge. The model also employs a restricted representation of wave types (*i.e.* only broken waves), which is noteworthy because the classical conceptual model proposed by Sunamura (1992), which is based on laboratory work and field observations from Japan, suggests that different wave types (*i.e.* breaking, broken, unbroken) might have formative roles in demarcating the evolution of different profile shapes.

This paper describes a newly developed rocky shore profile evolution model. Erosion in the model is driven by different wave types that attack rocks that are degraded in strength over time due to weathering. The model employs a flexible discretisation scheme that allows for emergence of a wide range of profile geometries. The modelling approach is based on the exploratory modelling principles described by Murray (2003, 2007), in which the modeller intentionally considers only a limited number of processes that are represented in simple terms. This approach has the advantage of both enhancing the clarity of the potential insights that models can produce, and

DOI: 10.2112/SI75-120.1 received 15 October 2015; accepted in revision 15 January 2015
*Corresponding author: hmat258@aucklanduni.ac.nz

also reducing computational demands, allowing repeated simulations with model run times that span long time periods.

This paper (i) describes the new model; (ii) analyses consistencies and inconsistencies between the new model outcomes and field observations from several sites around Japan on which Sunamura's (1992) conceptual model was developed; and (iii) discusses the importance of representing varied wave types in modelling the development of a range of rocky shore profile shapes.

METHODS

The model space is discretized in 10cm square grid cells with positions specified in horizontal (x) and vertical (y) coordinates. This scheme allows a wide range of profile geometries to emerge. Each cell represents either sea/air or land; cross-sectional rocky shore profiles are constructed by connecting all the surficial land cells.

We assume that a rocky shore evolves iteratively as a result of the annually averaged dynamic interactions of coastal processes. Table 1 shows these processes together with their mathematical representation in the model.

Table 1. *Summary of key processes considered in the model.*

Process controls on rocky shore development	Theoretical framework
Wave erosion	Sunamura (1992)
Rock weathering	Kanyaya and Trenhaile (2005)
Tidal water level fluctuations	Car and Graff (1982), Trenaile (2000)

[Wave erosion]

$$F_W(x,y) \geq F_R(x,y) \begin{pmatrix} F_W : \text{wave assailing force} \\ F_R : \text{material resistance} \end{pmatrix} \quad (1)$$

where

$$F_W(x,y) = H(x)P(x,y)T_d(y) \quad (2)$$

$$H(x) = \begin{cases} H_1 & (x < x_0) \\ H_1 e^{-k_1(x-x_0)} & (x_0 \leq x < x_0 + 0.5H_1) \\ H_1 e^{-k_2(x-x_0)} & (x \geq x_0 + 0.5H_1) \end{cases} \quad (3)$$

$$P(x,y) = \begin{cases} C_{\text{unbroken}} P_{\text{unbroken}}(y) & (x < x_0) \\ C_{\text{breaking}} P_{\text{breaking}}(y) & (x_0 \leq x < x_0 + 0.5H_1) \\ C_{\text{broken}} P_{\text{broken}}(y) & (x \geq x_0 + 0.5H_1) \end{cases} \quad (4)$$

$$F_R(x,y) = R \quad (5)$$

[Rock weathering]

$$F_R(x,y) = F_R^{-1}(x,y) - KW(y) \quad (6)$$

We follow Sunamura's (1992) approach to modelling wave erosion on rocky shores (Eq.(1)) in which the wave assailing force is estimated using incident wave height ($H(x)$), wave pressure ($P(x,y)$), and the tidal duration distribution ($T_d(y)$) (Eq.(2)). Our approach to weathering follows Trenhaile (2008) in which the resistance of surficial rock is deteriorated iteratively at a rate determined by a weathering efficacy constant (K) and weathering efficacy function ($W(y)$) (Eq.(6)). Note that: (1) H_1 and R in Eq.(3), (4), and (5) represent input wave height and material resistance, and (2) $F_R(x,y)$ and $F_R^{-1}(x,y)$ are material resistance of rock in current and previous iterations.

The model explicitly represents three different wave types: unbroken, breaking, and broken waves. $H(x)$ varies according to wave types, which depend on (1) relative horizontal distance from the breaker point (x_0, y_0) where the depth from the still water level (SWL) to the breaker point is set as $H_1/0.78$ (*e.g.* Trenhaile, 2000), and (2) half the wave height ($0.5H_1$) (Eq.(3)). This approach assumes that (1) the wave height of an unbroken wave is constant initially, but wave heigt decays exponentially with distance after breaking (after Sunamura, 1992), (2) no wave reformation is possible after breaking. k_1 and k_2 are wave-height attenuation coefficients for breaking and broken waves and are approximated as $k_1 = \log(0.1)/0.5H_1$ and $k_2 = \log(0.01)/SW$, where SW is the surf zone width over which broken waves dissipate their energy and reduce their height. SW is estimated using wave height and average profile gradient (β) as $H_1/\tan\beta$ (see Trenhaile, 2000). The logarithm elements in k_1 and k_2 are set as 0.1 and 0.01 so that wave height becomes (1) one tenth of the initial wave height over the distance equal to half the input wave height and (2) negligible (<0.001) over the total wave attenuation distance ($0.5H_1 + SW$). The horizontal ranges over which breaking and broken waves exert force are set as $0.5H_1$ and SW respectively, so that broken waves exert force over much wider distances than breaking waves ($SW >> 0.5H_1$) when β becomes small (Ogawa *et al.*, 2011, 2012).

The erosive force of waves also varies depending on wave types, but little detailed information is available about the spatially varied erosional efficacy of unbroken, breaking, and broken waves acting on complex rocky shore topography (Trenhaile, 1987). Accordingly, we tested three shape functions, P1, P2, and P3 (see Figure 1), with a maximum peak occurring at either SWL or quarter of the wave height ($H_1/4$) above SWL for $P_{\text{unbroken / breaking / broken}}$ (Eq.(4)). Scaling coefficients in Eq.(4) (*i.e.* C_{unbroken}, C_{breaking} and C_{broken}) which represent magnitude of pressure of different waves are set as 0.01, 10, and 0.1 respectively by assuming that the relative magnitude of wave pressure is considerably higher for breaking waves than broken waves and unbroken waves exert the lowest pressures (Sunamura, 1992). Note that (1) P1, P2, and P3 approximately resembles shapes determined from theoretical and experimental work on the wave pressure distributions acting on vertical walls (see Sunamura 1992; Trenhaile, 1987), (2) each shape function is normalized where $\int P(y)dy = 1$, and (3) a single shape (P1 with a peak at SWL) is applied to P_{unbroken} throughout this study as we preliminarily confirmed that varied shapes of P_{unbroken} have little influence on model results.

The influence of tidal water level fluctuations on wave assailing force is integrated into the model through $T_d(y)$, which is constructed using two shifted sine functions that create peaks slightly below mean high water neap (MHWN) and above mean low water neap (MLWN). This approach is generally consistent with the analyses of Carr and Graff (1982) and Trenhaile (2000). Note that $T_d(y)$ is normalized where $\int T_d(y)dy = 1$. The tidal water

fluctuation also spatially influences the material-resistance degradation of rocks due to rock weathering; $W(y)$ represents spatial variability in weathering efficacy which has its peak around mean high water neap (MHWN) with decreasing efficacy above and below this level up to mean high water spring (MHWS) and down to mean low water spring (MLWS) (see Figure 10 in Kanyaya and Trenhaile (2005)). Note that (1) complete disintegration of rocks sometimes occurs when the material resistance becomes zero due to Eq.(6), and (2) $W(y)$ is normalized where $\int W(y)dy = 1$.

In each iteration, the model estimates wave assailing force at every elevation (cells) within the mean tidal range (MTR) in order to consider tidal water level fluctuation. However, as wave assailing force in Eq.(2) exerts force on surficial rocks located at elevations above and below water level as shape functions extends vertically, there is a contribution of erosion force from different elevations (*e.g.* y'). Therefore, the total wave assailing force for a surficial rock cell at (x , y) is estimated, using water level at y' that is within vertical mean tidal range (MHWN≤ y' ≤MHWS), as follows:

$$F_{\text{W-total}}(x,y) = H(x)P(x,y)T_{\text{d}}(y) + \sum_{y' \neq y} H(x)P(x,y)T_d(y') \quad (7)$$

The model also considers down-wearing wave assailing force ($F_{\text{W-DW-total}}$). We assume that (1) wave-induced down-wearing shear stress is a function of wave height (see Tsujimoto, 1987 and Stephenson and Kirk, 2000a), (2) the intensity of down-wearing force is proportional to the wave assailing force occurring at water level ($F_{\text{W-total}}(x,y)$), and (3) down-wearing force declines exponentially with water depth (see Trenhaile, 2000). Accordingly, $F_{\text{W-DW-total}}$ to the submerged surficial rock at (x , y) is expressed as follows:

$$F_{\text{W-DW-total}}(x,y) = \sum_{\text{MLWS} \le y' \le \text{MHWS}} F_{\text{W-total}}(x,y')e^{-k_3(y'-y)} \quad (8)$$

where k_3 is a depth-decay coefficient. Few field data are available for k_3 ; hence, we assume that the intensity of down-wearing force becomes small over the depth from SWL equal to wave height and express k_3 as a function of x as $k_3(x) = \log(0.1)/H(x)$. Of note, k_3 produces a similar declining rate of down-wearing force with depth as modelled by Trenhaile (2000).

Simplified cantilever-type cliff mass failure is integrated into the model. The cantilever block cells above a notch created by basal erosion are instantaneously removed from the modelled system (*i.e.* land cells shift to sea/air cells), once the geometrical condition of cantilevered blocks reaches a critical condition. This threshold value has no morphological feedback on the eroding system; a value was selected simply to allow cliff collapse at a physically sensible speed.

RESULTS

In this section outcomes from the newly developed model are evaluated against the field data from the Japanese coast described by Tsujimoto (1987) (see also Sunamura, 1992). Such an evaluation is desirable, because the Japanese data partly formed the basis for Sunamura's (1992) influential conceptual rocky shore evolution model.

The Japanese coast has a varied geology with rocks of differing resistance exposed to high wave energy in a microtidal environment. In general, plunging cliffs occur on hard rocky coasts while shore platforms are commonly found on soft to intermediate-strength rocky coasts. Tsujimoto (1987) and Sunamura (1992) suggest that wave height and rock resistance are the critical controls on rocky shore profile development, deriving the relation $\rho g H_1 / S_C = 1.7 \times 10^{-3}$ as a boundary value of shore platform and plunging cliff development in relation to wave height and rock material strength (see Figure 1). Note that H_1 is the largest height of waves impacting the coast under consideration, ρ is the density of water, g is the acceleration owing to gravity, and S_C is the uniaxial compressive strength of rocks forming the coast.

The result of model runs, including shore platforms and plunging cliffs, are plotted in Figure 1. Note that (1) a vertical plunging cliff was selected as an initial geometry and (2) same results of runs with different shape function combinations for different wave types (*e.g.* $P_{\text{breaking}} = \text{P1}$, $P_{\text{broken}} = \text{P2}$) are represented by a single circle, resulting in plotting smaller number of circles in Figure 1 than actual number of model runs (in total 360 model runs). In order to compare model results with field data, single parameter values were used for mean tidal range (MTR=1m) and weathering efficacy constant (K=5e-2), and H_1 was represented with five input wave heights (0.5m, 1.5m, 2.5m, 3.5m, 4.5m). Rock resistance was represented in the model with three values that were converted from model resistance (R) to S_C using a scaling coefficient that was selected to adjust for the difference in timescale between modelled time (2,000 years) and the likely time-scale over which shore platforms in the field have developed (c. 6,000 years). (Note that the model timeframe, 2,000 iterations, was selected because it allowed multiple shapes to emerge, while also delivering run times that allowed a wide range of model tests).

Figure 1 reveals that the model outputs are generally consistent with field observations from Japan. For example, regardless of input wave height, plunging cliffs persisted throughout model runs where harder rocks were present, whereas model runs with softer rocks produced shore platforms in all cases. Rocks of intermediate resistance had more complex outcomes. As expected, plunging cliffs persisted for intermediate rock resistance and low wave height. However, both plunging cliffs and shore platforms occurred in model runs where rocks of intermediate resistance encountered medium to high wave heights. This area of indeterminancy, mainly caused by variation of shape function combinations applied to different wave types, is investigated further in the discussion section.

The model produces plunging cliffs and shore platforms in a manner that is consistent with field observations, but in nature a large variety of rocky shore profile shapes occur in addition to these two geometries. As yet, no model has attempted to simulate the very wide range of shapes that occur in nature. To examine the capacity of the model to simulate varied profile

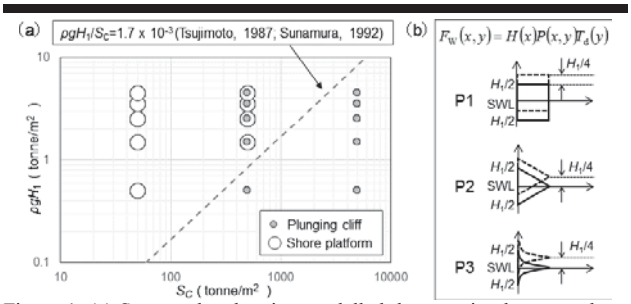

Figure 1. (a) Scatter plot showing modelled demarcation between shore platforms and plunging cliffs in relation to wave height and material resistance inputs. The hatched line shows the demarcation line determined from measurements on Japanese field sites. And (b) shape functions ($P(x,y)$) for wave pressure used in this study. In total 24 combinations of shape functions are tested in this study.

development 576 additional model runs with modified parameter values were conducted (see Figure 2). Model run times were limited to 2000 iterations (years) or a maximum profile width of 50 m (which was sufficient to allow a wide range of profile shapes). Figure 2 shows examples of profile shapes that emerged from the model, including the temporal evolution of profile shapes and the occurence of the different wave types (unbroken, breaking, and broken) that drove erosion through time. Depending on profile width and gradient, five different profile types (T1-T5) appeared, each being morphologically similar to those found in the field (Figure 2). Plunging cliffs (T1), sometimes with a notch created on the vertical wall, persisted in 27% (154 model runs) of model runs, usually when R was higher. Two narrow profile types developed in nearly half the model runs (T2 = 40%, T3 = 8%), and were also associated with higher R. The mean profile width and slope of the T2 and T3 profiles were about 1m / 34° and 12m / 4° respectively. About 25% of model runs produced wider (c. 50 m), flatter shore profiles that are similar in form to shore platforms described in the literature. The platforms can be subdivided into T4 (19% of model runs) and T5 (6% of model runs) on the basis of (1) a subtle difference in mean profile gradient (1.7° versus 0.9°) and (2) the absence of a marked seaward edge on T4 profiles, in contrast to T5 profiles, in which an abrupt scarp emerged at the seward margin of their profile. The fact that the scarp emerged in the model runs is notable, because it is generally assumed in field studies that the seaward edge is a geomorphological remnant of the initial erosion of a steep cliff (Dickson, 2006; Sunamura, 1992).

In addition to variation in profile shape, there also were clear temporal variations in wave type occurrence between different profile shapes (Figure 2). Model runs in which plunging cliffs (T1) persisted were dominated by unbroken waves, although some breaking waves did occur. In contrast, all three wave types (unbroken, breaking and broken) occured during the evolution of profiles T2-T5. In the model, different wave types exert different erosive force (see the methods section). Below we discuss the importance of representing different wave types if the objective is to model a range of emergent shore profile geometries.

DISCUSSION

The goal of this exploratory modelling research has been to develop a numerical model with the flexibility to simulate a broader range of rocky shore profile shapes that are broadly consistent with the shapes observed in nature. In this discussion we (1) examine the extent to which results are consistent with field observations, and (2) discuss the importance of representing varied wave types in modelling the development of a range of rocky shore profile shapes.

The emergence of multiple profile shapes in the model is encouraging, and distinguishes it from other existing rocky

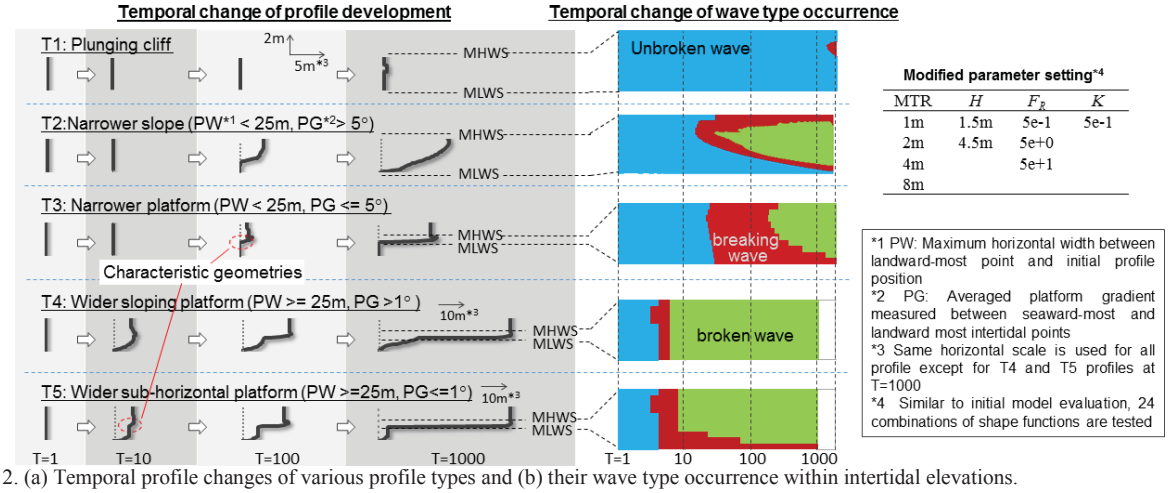

Modified parameter setting*4

MTR	H	F_R	K
1m	1.5m	5e-1	5e-1
2m	4.5m	5e+0	
4m		5e+1	
8m			

*1 PW: Maximum horizontal width between landward-most point and initial profile position
*2 PG: Averaged platform gradient measured between seaward-most and landward most intertidal points
*3 Same horizontal scale is used for all profile except for T4 and T5 profiles at T=1000
*4 Similar to initial model evaluation, 24 combinations of shape functions are tested

Figure 2. (a) Temporal profile changes of various profile types and (b) their wave type occurrence within intertidal elevations.

shore evolution models. It is also encouraging that a comparison with field data from the Japanease coast (Sunamura, 1992; Tsujimoto, 1987) reveals a similar basic demarcation between plunging cliffs and shore platform profiles. There is a region of indeterminancy in the parameter space corresponding to rocks of intermediate resistance (500 tonnes/m^2) attacked by all except the smallest wave conditions. However, uncertainty also exists in the field data, because plots in some locations inconsistently occur outside of the demarcated region (see Sunamura, 1992; Tsujimoto, 1987). In nature some uncertainty exists in obtaining precise values for rock resistance and wave force, hence it is difficult in practice to precisely quantify this boundary region. Likewise, relatively subtle changes in the model forcing (resulting from the breadth of the erosion shape functions used in model runs) can result in both plunging cliffs and shore platforms in the vicinity of the demarcation boundary.

In addition to plunging cliffs and shore platforms, the model produces a range of shapes including narrow benches and steeply sloping profiles. The key components of the model that result in these different shapes are: (1) a grid cell discretisation scheme that allows multiple forms; (2) three different wave types, each associated with different erosive potential. The advantages of a grid discretisation scheme are relatively clear, but the application of different wave types in rocky shore profile modelling is new and needs further discussion.

Trenhaile (2000) argued that it is sufficient to model only breaking waves in examining shore platform evolution. Similarly, if our model is forced with only breaking waves and a single erosive distrubtion, it also creates shore platforms. In contrast, the full range of modelled profile shapes requires a broader range of wave types. In this modelling study, broken waves dominated the erosional evolution of shore platforms (T4 and T5 profiles), as predicted by Trenhaile (2000), but unbroken waves must be represented if plunging cliffs are to persist, because attacking the cliff persistently with broken or breaking waves will inevitably result in erosion and shore profile flattening. Similarly, it is important to represent breaking waves: in this modelling study, a range of interesting profile features emerged during model runs as a result of wave breaking on certain parts of the profile. For instance, the characteristic seaward geometries of T3 and T5 profiles were formed during or immediately after intense breaking wave occurrence (*e.g.* T=100 for T3 and T=10 for T5). This interesting result warrants further consideration in future work, because it is generally assumed that the seaward edge of shore platforms is immutable and a remnant of the initial conditions at the time of platform initiation.

CONCLUSIONS

In this paper we describe results from a newly developed rocky shore profile evolution model. Based on an exploratory modelling approach, the present model considers only a limited number of coastal processes and represents them rather numerically simply. Initial model evaluation demonstrates that the model is capable of producing behaviours that are qualitatively consistent to those found in field studies. Unlike existing rocky shore models, which focus on shore platform evolution, the new model produces a broader range of profile shapes, such as steeper slopes and shore platforms with an emergent step. These features result from a combination of the grid discretisation scheme and representation of varied wave erosive force.

LITERATURE CITED

Carr, A.P. and Graff, J., 1982. The Tidal immersion factor and shore platform development: discussion. *Transaction of the Institute of British Geographer*, 7(2), 240-245.

Dickson, M.E., 2006. Shore platform development around Lord Howe Island, southwest Pacific. *Geomorphology*, 76(3), 295-315.

Kanyaya, J.I. and Trenhaile, A.S., 2005. Tidal wetting and drying on shore platforms: An experimental assessment. *Geomorphology,* 70(1), 129-146.

Murray, A.B., 2003. Contrasting the goals, strategies, and predictions associated with simplified numerical models and detailed simulations. *In:* Wilcock, P.R. and Inverson, R.M. (eds.), *Prediction in Geomorphology*. Americal Geophysical Union, Washington, DC, USA, pp. 133-150.

Murray, A.B., 2007. Reducing the model complexity for explanation and prediction. *Geomorphology*, 90(3), 178-191.

Naylor, L.A.; Stephenson, W.J., and Trenhaile, A.S., 2010. Rock coast geomorphology: Recent advances and future research directions. *Geomorphology*, 114(1), 3-11.

Ogawa, H.; Dickson, M.E., and Kench, P.S., 2011. Wave transformation on a sub-horizontal shore platform, Tatapouri, North Island, New Zealand. *Continental Shelf Research*, 31(14), 1409-1419.

Stephenson, W. J., 2000. Shore platforms: a neglected coastal feature?. *Progress in Physical Geography*, 24(3), 311-327.

Stephenson, W.J. and Kirk, R.M., 2000a, Development of shore platforms on Kaikouora Peninsula, South Island, New Zealand: Part One: The role of waves, *Geomorphology*, 32(1), 21-41.

Stephenson, W.J. and Kirk, R.M., 2000b, Development of shore platforms on Kaikouora Peninsula, South Island, New Zealand: Part Two: The role of subaerial weathering, *Geomorphology*, 32(1), 43-56.

Sunamura, T., 1992. *Geomorphology of Rocky Coasts*. New York: J. Wiley, 302p.

Trenhaile, A.S., 1987. *The Geomorphology of Rock Coasts*. Oxford: Oxford University Press, 384p.

Trenhaile, A.S., 2000. Modelling the evolution of wave-cut shore platforms. *Marine Geology*, 166(1), 163-178.

Trenhaile, A.S., 2001. Modeling the effect of late Quatenary intergracial sea levels on the development of wave-cut shore platform. *Marine Geology*, 172(3), 205-223.

Trenhaile, A.S., 2005. Modeling the effect of waves, weathering and beach development on shore platform development. *Earth Surface Processes and Landforms*, 30(5), 613-634.

Trenhaile, A.S., 2008. Modelling the role of weathering in shore platform development, *Geomorphology*,94(1), 24-39.

Tsujimoto, H., 1987. Dynamic Conditions for Shore Platform Initiation. Tsukuba, Japan: University of Tsukuba, Ph.D. dissertation, 160p.

Journal of Coastal Research	SI	75	602-606	Coconut Creek, Florida	2016

Observation of Wave Transformation on Macro-tidal Rocky Platforms

Timothy Poate[+*], Gerd Masselink[+], Martin Austin[‡], Mark Dickson[†], Paul Kench[†]

[+]School of Marine Science and Engineering, Plymouth University, Plymouth, UK.

[‡]School of Ocean Sciences, Bangor University, Wales.

[†]School of The Environment, University of Auckland, New Zealand.

ABSTRACT

Poate, T.G.; Masselink, G; Austin, M.; Dickson, M.E., and Kench, P., 2016. Observations of Wave Transformation on Macro-Tidal Rocky Platforms. *In:* Vila-Concejo, A.; Bruce, E.; Kennedy, D.M., and McCarroll, R.J. (eds.), *Proceedings of the 14th International Coastal Symposium* (Sydney, Australia). *Journal of Coastal Research*, Special Issue, No. 75, pp. 602-606. Coconut Creek (Florida), ISSN 0749-0208.

Correctly predicting the transformation of ocean waves across rocky platforms has direct implications for cliff stability modelling, coastal defences and long-term coastal evolution. Wave transformation across rocky intertidal platforms is dependent on the morphological characteristics of the platform, including platform width, slope and roughness, and forcing characteristics, including wave and tide conditions. In this paper we present early observations from four field studies providing detailed measurements of wave processes across contrasting rocky platform sites with wave conditions between H_s = 0.5 m and H_s = 1.9 m, water depths between h = 0.5 m and h = 6.8 m and variable platform morphology. Results show that the relative wave height in the surf zone H/h is generally larger than in previous studies (H/h is c. 0.6, instead of 0.3–0.5) and wave dissipation greater for sites with considerable roughness.

ADDITIONAL INDEX WORDS: *nearshore dynamics, wave energy, cliff stability.*

INTRODUCTION

Much of our coastlines are characterised by cliff and/or intertidal shore platforms which, through platform width, slope and morphology, have a controlling impact on nearshore wave processes. In the UK, energetic waves and large tidal ranges (3–11 m) result in wide (> 100 m) and relatively steep platforms with the surface roughness dependent on the bedrock geology. Cliff stability is intrinsically connected to the transformation of waves across the platform through the energy impacting the cliff base (Dickson and Pentney, 2012), and this is expected to be strongly affected by the surface roughness and gradient of the platform. These wave transformation processes must be understood quantitatively to predict rocky coast processes, specifically wave energy delivery to the base of coastal cliffs.

There have been several recent studies reporting on field measurements of wave characteristics across intertidal shore platforms in New Zealand and Australia (e.g., Marshall and Stephenson, 2011; Ogawa *et al.,* 2011). These studies have drawn attention to long-standing issues in existing models of rocky coast evolution (Dickson *et al.,* 2013), but, without exception, these investigations have been purely empirical: they invariably demonstrate wave energy dissipation in the landward direction and strong tidal modulation of this process, as well as the transformation from incident into infragravity (lower frequency waves with periods at the time scale of wave groups) wave energy (Ogawa *et al.,* 2012). The New Zealand and Australian study sites are generally characterised by a distinct low tide step in the platform profile and a relatively planar platform geometry, and relatively calm wave condition (H_s = 1 m) and a micro- to meso-tide range. There is also a paucity of data from macro-tidal sites, within the literature, with the notable exception of Trenhaile and Kanyaya (2007).

Distinct from sandy coastlines, rock platforms share morphological similarities with coral reefs, and recent studies of wave interaction with coral reefs (Symonds *et al.,* 1995; Lowe *et al.,* 2005) and transformation across reef platforms (e.g., Kench *et al.,* 2006) may provide support for understanding rocky platforms. Most importantly, in common with intertidal shore platforms, coral reefs possess high friction values due to bed roughness introduced by corals and this friction dissipates waves at a higher rate than on sandy coasts with consequences for the distribution of wave energy across a reef, wave setup and runup. Currently friction effects have not been evaluated on rock platform surfaces.

There are many locations in the UK where coastal infrastructure is fronted by shore platforms and separated from the platform by a seawall or other type of coastal structure (e.g., nuclear power stations at Hinkley Point in Somerset and Wylfa in Anglesey). For the design of the coastal defence it is critical to appropriately parameterise the transformation of the waves across the shore platforms; for instance, wave runup and overtopping is sensitive to wave height at the toe of the structure, wave period and coastal slope (e.g., van Gent 2001). The wave height and wave period undergo a large transformative process across shallow foreshores (including rocky foreshores) which are presently not accounted for and this will lead to coastal engineering structures that are not appropriately designed. Macro-tidal sites provide a unique setting to capture a range of wave processes, while also allowing

DOI: 10.2112/SI75-121.1 received 15 October 2015; accepted in revision 15 January 2015.

*Corresponding author: timothy.poate@plymouth.ac.uk

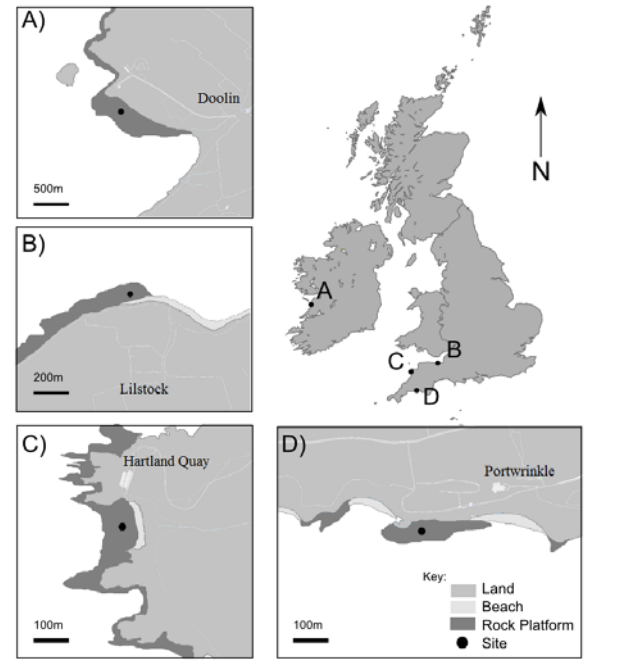

Figure 1. Study sites in the UK and Ireland; A) Doolin, Ireland, B) Lilstock, Somerset, C) Hartland Quay, north Devon and D) Portwrinkle, south Cornwall.

detailed measurement of the platform morphology to be taken, to help quantify the wave decay through a tidal cycle.

In this paper we present early observations from four field studies which have been designed to address some of these gaps in our knowledge and understanding of the role rocky platforms play on wave transformation processes. The four sites, from the UK and Ireland, represent a range of solid and dynamic boundary conditions (geology; platform width, slope, roughness; wave climate; and tidal range) (Figure 1, 2). These datasets include detailed intertidal wave and platform measurements, which, in combination with numerical modelling approaches, will lead to improved predictive capabilities for cross-platform wave set-up, runup and energy dissipation.

METHODS

Four field deployments were undertaken during the 2014–2015 winter months at three UK sites and one Irish location (Figure 1). The sites were A) Doolin (DOL) in Ireland, B) Lilstock (LST) in Somerset UK, C) Hartland Quay (HLQ) in north Devon, UK, and D) Portwrinkle (PTW) in south Cornwall, UK. The limestone platform at DOL extends 160 m cross-shore with a stepped profile at the top formed through removal of limestone slabs by erosive wave action. Small-scale platform roughness due to weathering processes was evident between neap high water and neap low with kelp macro-algae dominant across the low tide region (Figure 2). With the smallest tide range of the sites (4.2 m) the site is exposed to the largest waves from the north Atlantic. The platform at LST is a mudstone formation (May and Hansom, 2003) with near-horizontal beds leaving a relatively smooth platform characterised by shallow steps (c. 0.4 m) and pools, with a boulder beach at the top of the profile (Figure 2). Vertical joints within the strata create blocky beds which, when broken off, form cobble deposits that remain on the platform due to the relative sheltered nature of the site, although energetic local wind seas do occur. Extending for 325 m, it is the widest platform with the largest tidal range (10.7 m). Although no detailed studies have been done, previous estimates suggest cliff retreat in this area is ~1 m/yr (May and Hansom, 2003). HLQ is one of the roughest sites with heavily folded, near-vertical, shore-normal fine grained sandstone and shale beds (May and Hansom, 2003; Figure 2). The shortest of the platforms with a cross-shore width of 140 m and tide range of 7.3 m, it is the second most exposed to the dominant Atlantic swells (Figure 1). Cliff retreat has been estimated at 0.02–0.04 m/yr (May and Hansom, 2003) with large cobbles forming a reflective beach at the top of the platform (Figure 2). PTW is located on the south coast and formed of Devonian slate, siltstone and sandstone bedrock, creating a rough platform with no consistent direction to the exposed bedding planes (Figure 2). Extending for 180 m and with a 4.5-m tide range, it is relatively sheltered from the Atlantic but exposed to southerly waves (Figure 1). The platform is backed by a harbour wall to the west and a curved sea wall, at the top of the profile, which maintains the cliff position.

The instrumentation setup at each site was replicated to assist with dataset comparison and analysis. Up to fifteen RBR solo D-Wave pressure transducers (PTs) were individually housed within a steel tube and fixed to the bedrock, at 10–15 m spacing, in a shore-normal array across the intertidal platform. The pressure sensors covered the full spring intertidal range of the sites to capture shoaling, wave breaking, surf zone and swash conditions. The field deployments lasted between 4 and 6 days with sensors sampling continuously at 4 Hz. Nearshore wave data were provided by local directional wave buoys (except DOL), located in 10–15 m depth, operated and maintained by the Channel Coastal Observatory (www.channelcoast.org). The platform morphology was mapped using a Leica P20 terrestrial laser scanner to create a 0.1-m resolution grid of the surface roughness, from which the platform profile was extracted. Video cameras were used to log the periods of platform inundation during daylight hours. Individual .jpg files were recorded at 4 Hz and used during subsequent processing to identify regions of breaking waves with reference to the pressure sensor locations. All instruments were surveyed in using a total station, with the positions rotated and translated onto a local coordinate system.

The low tide barometric pressure record, logged by the exposed sensors, was used to correct the pressure data for the local atmospheric pressure. Water surface elevations were corrected for any depth attenuation effects using Nielsen's local approximation approach (Nielsen, 1989) while water depth (h) was derived using a 10-minute moving average filter. In line with previous studies, spectral analysis was undertaken on the dataset for 17-min periods using Welch-averaged periodograms (Welch 1967). Spectra were computed from 2048-sample bursts using Welch's segment-averaging method with 8 Hanning-tappered segments with 50% overlap, giving 16 degrees of freedom.

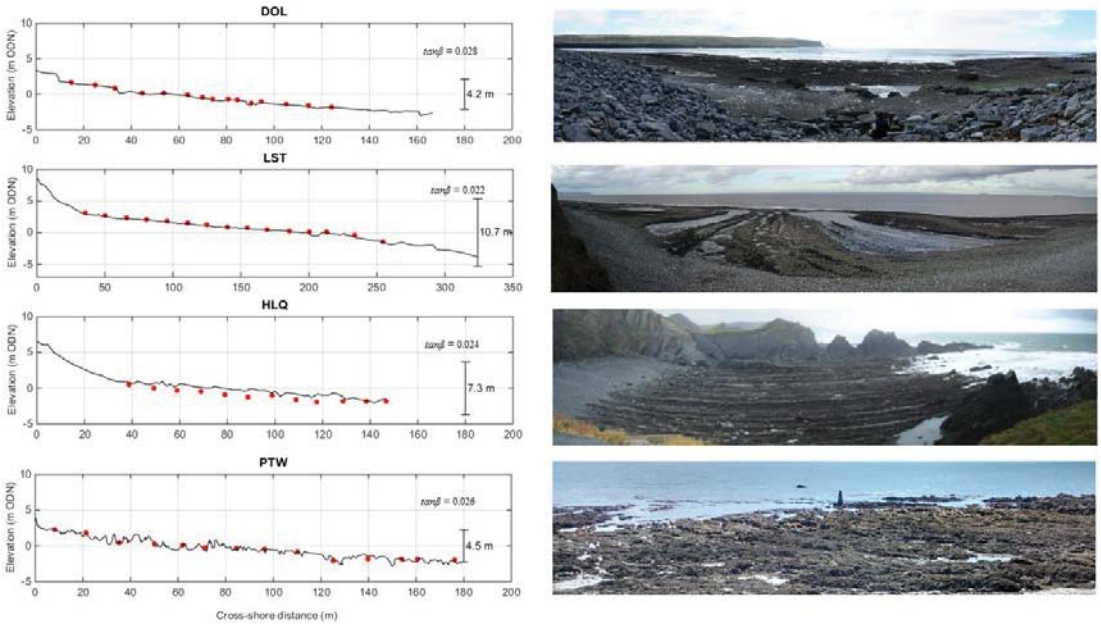

Figure 2. Platform profiles for the study sites including the tidal range, the profile slope (tanβ) and the location of the surface mounted pressure sensors (red dots, left panels); site photos at low tide showing the different platform morphology (right panels).

Significant wave height (H_s) was calculated as four times the standard deviation of the water level, while the mean wave period was derived from the spectral moments (T_z = m_{-1}/m_0). Wave energy flux ($P = ECn$) is computed in line with the shallow water Airy-wave theory where $n = 0.5$ and:

$$E = \frac{1}{8}\rho g H^2 \quad \text{eq.1}$$

$$C = \sqrt{gh} \quad \text{eq.2}$$

RESULTS

Data were collected at four sites with wave heights, measured at the outermost PT, ranging from H_s = 0.5 m to 1.9 m and water depths between h = 0.5 m and 6.8 m (Figure 3 & 4). Temporal and spatial patterns in wave transformation are presented in Figure 3 for a single incoming tide for each of the sites. At all sites, H_s was tidally modulated and increases with water depth across the platform. All sites showed reduction in wave height in a landward direction across the platform during shallower conditions. At high tide, wave heights increases towards the mid-point of the platform at LST and HLQ (Figure 3, c, e).

Wave height decay at DOL is most evident at high tide with the rate of decay increasing landward (Figure 3a). Both LST and HLQ show very distinct drops in wave height across the platform with increasing depth. At LST (Figure 3c) wave height decay increases as the tide floods, while at HLQ greatest decay rates are observed under lower tide levels. At high tide, LST still records wave height decay at the top of the platform, while at HLQ high tide wave breaking occurs almost at the shoreline exhibiting only a small reduction in wave height across the platform. The rate of wave height reduction across the platform at PTW is relatively consistent through the rising tide.

Inter-site comparison of wave period transformation between the sites is less clear (Figure 3). At DOL wave period reduces landward at high tide, but remains more stable under shallower conditions (Figure 3b). The wave period at LST is steady for the first half of the platform before exhibiting a slight increase towards the shoreline.

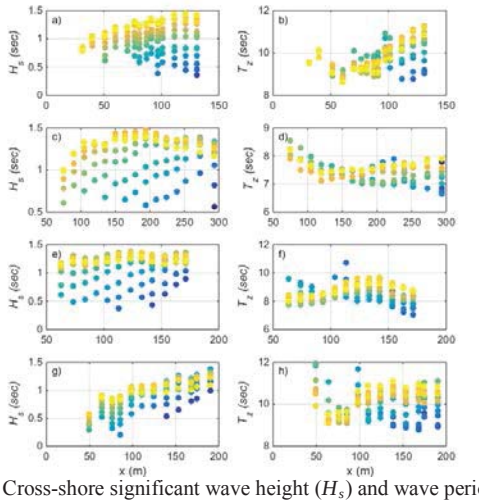

Figure 3. Cross-shore significant wave height (H_s) and wave period (T_z) statistics from each of the four sites. The coloured symbols identify time synchronous data with yellow indicating high tide and blue at low tide. DOL = a) and b); LST = c) and d); HLQ = e) and f) and PTW = g) and h).

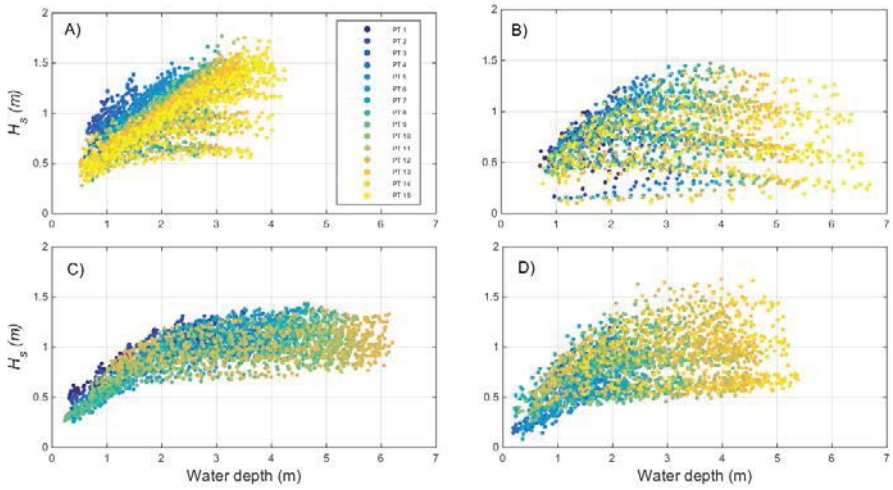

Figure 4. Summary deployment plots showing 17 min average depth against significant wave height (H_s) for each of the sites; A) = DOL, B) = LST, C) = HLQ, D) = PTW. The colours indicate the pressure sensor location with PT 1 most onshore, only 12 PTs deployed at HLQ hence no yellow symbols.

A larger response is presented at HLQ with the period increasing, by c. 1 s, and then decreasing toward the shore. This pattern is repeated through the rising tide. The response at PTW is similar to DOL with low water T_z values remaining fairly consistent while high tide cross-platform response shows a reduction towards the shore before a rise

The relationship between wave height and water depth is further explored in Figure 4 which presents the full data set for each site (17 min statistical parameters for all tides during each deployment). The plot shows the wide range of conditions experienced between the sites and the response for different sensors across the platform. At DOL and PTW the outer PT records waves over H_s = 1.5 m up to h = 4 m water depth. At LST we see the greatest spread in data with the largest water depths across the platform. The wave record from HLQ shows the least spread, with consistent wave conditions for many of the tides, showing an increase in wave height with depth up to h = 2 m before wave height levels out under increasing water depth. Importantly for all the sites we can see saturated surf zone conditions and for most sites the *H/h* ratio, for the inner surf zone, is relatively large. This relationship is explored further in Figure 5 which shows the spread of *H/h* values for the four deployments. The sites have similar data ranges, with the majority of the values within 0.2 of each other. HLQ and PTW are almost identical with *H/h* = 0.3-0.5, LST is slight lower with *H/h* = 0.2-0.4 while DOL has the highest with *H/h* =0.4-0.6. DOL and HLQ exhibit more outliers than the other locations.

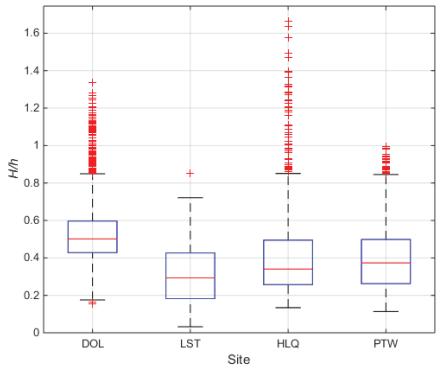

Figure 5. Box plots for *H/h* for all data at each of the sites. Horizontal red lines show median data value, upper and lower extent of each box shows the 75th and 25th percentile, dashed lines indicate data range and red crosses identify potential outliers.

DISCUSSION

In line with previous studies the overall trend is for wave height reduction across the platforms with the exception of high tide conditions at HLQ and LST where the breakpoint shifts landward. The depth-limited breaker heights presented in Figure 4 and Figure 5 are confined to 60% of water depth (0.6*h*) comparable to values found by Ogawa *et al.* (2011). These values are slightly higher than previously reported in platform observations and natural beach studies (Thornton and Guza, 1982; Farrell *et al.,* 2009), where H_s is typically 0.3–0.5 *h*. Figure 5 shows comparable results from the four sites with the notable exception of DOL. The likely explanation for significant wave heights being up to 100% of water depth is the presence of wave interference through reflection, at high tide, against the stepped profile (Figure 2). The steep boulder beach profile at HLQ produced similarly reflective conditions and high *H/h* values for the shallow PTs, but this is not observed at LST and PTW. The presence of reflected waves will affect wave steepness and breaking of the incoming wave signal and requires further processing to remove such signatures for further analysis. LST, the smoothest and widest platform shows the lowest *H/h* values, in line with smooth beach studies (Thornton and Guza, 1982), and few outliers suggesting there is no significant reflective signal.

As discussed within the introduction, platform width, slope and roughness are morphological components which are likely

to affect the dissipation and transformation of wave energy across an intertidal platform. By comparing the amount of wave energy flux decay ($\Delta P/m$), following wave breaking, we can comment on the likely impact the surface roughness may have (Figure 6). For initial comparison PTW and LST are presented as rough and smooth platforms, respectively. In Figure 6 the breakpoint is indicated by the vertical dashed line. Both sites exhibit a similar net drop in wave height across the platform from H_s = 1.2 m to H_s = 0.7 m (Figure 6 a, b), following breaking; however, the platform at PTW is > 50 m shorter and dissipation rates are therefore larger. With deep ridges across the profile, PTW is the roughest platform and this is reflected in the change in wave energy, normalised by the distance between the PTs, which shows higher dissipation overall (Figure 6c). PTW is also the steeper site with tanβ = 0.026 compared with tanβ = 0.022 at LST which is likely to also affect the roller dissipation following breaking. LST is characterised by a significantly smoother profile and subsequently smaller dissipation rate, (Figure 6d).

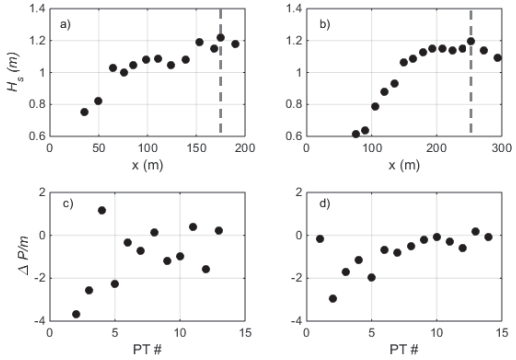

Figure 6. Cross-shore wave height (H_s) at PTW (a) and LST (b) with break point at 170 m and 260 m respectively (dashed lines). Bottom panels show wave energy flux (P) loss per meter across the platform for PTW (c) and LST (d).

As discussed in the introduction there are few studies of wave transformation over platforms particularly in conditions with waves greater than H_s = 1 m (Marshall and Stephenson 2011, Ogawa *et al.,* 2011), which makes comparison limited. For the sites presented here the cliff toe at each site is supratidal and therefore large waves, which drive setup and runup, are of primary concern for cliff stability.

CONCLUSIONS

This study presents early observations from four separate field experiments, at intertidal rocky platforms, using identical methodology and instrumentation. The results show that for relatively rough platforms the depth dependant breaking is larger than in previous studies on smoother platforms and sandy beaches. Platform roughness is also a contributory factor in greater surf zone energy decay and warrants further investigation.

ACKNOWLEDGMENTS

This work was undertaken through the Engineering and Physical Sciences Research Council grant (EP/L025191/1). The authors would like to thank those involved with the fieldwork; Peter Ganderton, Tim Scott, Pedro Almeida, Olivier Burvingt and Kris Inch.

LITERATURE CITED

Dickson, M.E., Ogawa, H., Kench, P.S. and Hutchinson, A., 2013. Sea-cliff retreat and shore platform widening: steady-state equilibrium? *Earth surface processes and landforms*, 38(9): 1046-1048.

Dickson, M.E. and Pentney, R., 2012. Micro-seismic measurements of cliff motion under wave impact and implications for the development of near-horizontal shore platforms. *Geomorphology*, 151–152: 27-38.

Farrell, E.J., Granja, H., Cappietti, L., Ellis, J.T., Li, B., Sherman, D.J., 2009. Wave transformation across a rock platform, Belinho, Portugal. *Journal of Coastal Research,* SI56, 44–48.

Kench, P.S., Brander, R.W., Parnell, K.E. and McLean, R.F., 2006. Wave energy gradients across a Maldivian atoll: Implications for island geomorphology. *Geomorphology*, 81(1–2): 1-17.

Lowe, R. J., J. L. Falter, M. D. Bandet, G. Pawlak, M. J. Atkinson, S. G. Monismith, and J. R. Koseff (2005), Spectral wave dissipation over a barrier reef, *J. Geophys. Res.*, 110, C04001, doi:10.1029/2004JC002711.

Marshall, R.J., Stephenson, W.J., 2011. The morphodynamics of shore platforms: interactions between waves and morphology. *Mar. Geo.*, 288, 18-31.

May, V.J. and Hansom, J.D. (2003) *Coastal Geomorphology of Great Britain*, Geological Conservation Review Series, No. 28, Joint Nature Conservation Com., Peterborough, 754 pp.

Nielsen, P., (1989). Analysis of Natural Waves by Local Approximations. *Journal of Waterway, Port, Coastal, and Ocean Engineering*, 115(3): 384-396.

Ogawa, H. Dickson, M.E., Kench, P.S., 2011. Wave transformation on a sub-horizontal shore platform, Tatapouri, North Island, New Zealand. *CSR*, 31, 1409-1419.

Ogawa, H. Dickson, M.E., Kench, P.S., 2012. Field measurements of wave characteristics on a near-horizontal shore platform, Oraka, NZ. *Geog. Res.*, 50, 179-192.

Symonds, G., K. P. Black, and I. R. Young (1995), Wave-driven flow over shallow reefs, *J. Geophys. Res.*, 100(C2),2639–2648, doi:10.1029/94JC02736.

Thornton, E.B., Guza, R.T., 1982. Energy saturation and phase speeds measured on the natural beach. *Journal of Geophysical Research* 87 (C12), 9499–9508.

Trenhaile, A. S. and Kanyaya, J. I. 2007. The role of wave erosion on sloping and horizontal shore platforms in macro- and mesotidal environments. Journal of Coastal Research 23, 298-309.

van Gent, M.R.A., 2001. Wave runup on dikes with shallow foreshores. *J. Waterway, Port, Coastal, Ocean Eng.*, 127, 254-262.

Welch, P., 1967. The use of fast Fourier transform for the estimation of power spectra: a method based on time averaging over short, modified periodograms. *IEEE Transactions on Audio and Electroacoustics* 15 (2), 70–73.

Journal of Coastal Research	SI	75	607-611	Coconut Creek, Florida	2016

Measuring Coastal Boulder Movement Under Waves Using Tri-Axial Accelerometers

Wayne J. Stephenson† and Alenka Abazović†

†Department of Geography, University of Otago,
Dunedin, 9056, New Zealand

www.cerf-jcr.org

www.JCRonline.org

ABSTRACT

Stephenson, W.J. and Abazović, A. 2016. Measuring Coastal Boulder Movement Under Waves Using Tri-Axial Accelerometers. *In:* Vila-Concejo, A.; Bruce, E.; Kennedy, D.M., and McCarroll, R.J. (eds.), *Proceedings of the 14th International Coastal Symposium* (Sydney, Australia). *Journal of Coastal Research*, Special Issue, No. 75, pp. 607-611. Coconut Creek (Florida), ISSN 0749-0208.

Boulder entrainment under tsunami or storm wave conditions has been a topic of interest among coastal geomorphologists for the last 25 years. Efforts have been directed to understanding the dynamic conditions under which boulder entrainment occurs and in particular the energy levels required to move boulders of specific sizes. Recent focus on storm waves has highlighted the complexity of the process and that more energetic tsunami waves are not always needed to move larger boulders. Consequently attempts have been made to develop better empirical equations to predict wave height or flow velocity and differentiate between storm waves and tsunami. However, data collection methods are restricted to hindcasting flow conditions based on boulder size, the chosen empirical equations and assumptions regarding historical storm or tsunami events. Significant advances could be made using real time entrainment data of boulder movement alongside flow conditions. This is particularly true if movement type, e.g. suspension, rolling or sliding can be distinguished. This paper demonstrates the use of small and inexpensive tri-axial accelerometers manufactured by Gulf Coast Data Concepts. The accelerometers were placed in PVC water tight housing then located in holes cored into boulders and deployed in conjunction with wave pressure transducers on the shore platform. Movement of 4 boulders were observed by logging real-time accelerations during a 5 day deployment. Preliminary data demonstrated that boulders rolled and moved up to 3 m in a westerly direction, while wave heights were less than 0.7 m, demonstrating of the viability of this technique.

ADDITIONAL INDEX WORDS: *accelerometers, coastal boulders, storm waves, New Zealand.*

INTRODUCTION

Reconstruction of past high energy events such as storms or tsunami on coastlines is often reliant on interpreting the position of large boulders and megaclasts (Nott, 1997, 2003; Noormets *et al.*, 2004; Goto *et al.* 2007; Maouvhe *et al.*, 2009;Barbano *et al.* 2010). However distinguishing between storm wave and tsunami transport mechanisms remains problematic (Paris *et al.* 2011). One way to differentiate between tsunami and storm deposits is to consider the location of boulders relative to the high tide level or storm run up level, with boulders beyond the reach of storm wave run up usually attributed to tsunami. Many mega-clasts are often considered too large for storm wave transport and are attributed to tsunami (e.g. Goto *et al.*, 2007). This attribution is based on the application of transport or entrainment equations (e.g. Nott, 2003). The accuracy of the predictive equations used to distinguish between storm wave and tsunami transport remains problematic (Sugawara *et al.*, 2014). The entrainment threshold equations devised by Nott (2003) have proved to be inaccurate and have been revised (e.g. Nandasena *et al.* 2011; Nandasena and Tanaka, 2013). The major issue with entrainment threshold models is that they are based on theoretical assumptions, historical evidence or current photographic evidence collected before and after an event, rather than based on real-time data captured during a storm event. Switzer and Burston (2010) noted that Nott's (2003) equations need to be tested with clasts movements from known events. Thus, there is a need to develop data collection methods which enable the mode of entrainment and movement of boulders to be identified and the wave conditions responsible for that movement. This paper reports an initial experiment that demonstrates the viability of using tri-axial accelerometers in conjunction with wave pressure transducers that allows movement events to be identified and the corresponding wave energy associated with that movement. Further we are able to identify how boulders have moved, either rolling, sliding or in suspension.

Field site

The study site is a shore platform located on the outskirts of the town of Timaru, on the east coast of the South Island of New Zealand (Fig. 1). The platform extends seaward from loess cliffs, at coordinates 44°22'22.77"S, 171°15'10.45"E. The shore platform is approximately 100 m long and 70 m wide and is developed in Pliocene basalt. This basalt has a density of 2.31 g/cm^3. The platform is strewn with boulders (Fig. 2) of identical geological composure, indicating they are sourced directly from the bedrock. The on-site production is clearly displayed through bedrock scars particularly on the southern end of the platform.

DOI: 10.2112/SI75-122.1 received 15 October 2015; accepted in revision 15 January 2015.
*Corresponding author: wayne.stephenson@otago.ac.nz

The shore platform is intertidal, with semi-diurnal tides (spring tidal range 2.2 m, neap range 1.0 m) and the prevailing swell arrives from southeast. A secondary swell component is from the northeast, but typically wind waves arrive from this direction. An analysis of deepwater wave heights over 33 years from 1979 to 2011 showed that at Timaru, for 91% of the time significant wave height is less than 2 m and storm wave heights rarely exceeded 4 m (Chen, 2015).

Figure 1. Study area location at Timaru, South Island New Zealand.

METHODS

Gulf Data Coast Concepts (GCDC) X16-1C tri-axial accelerometers (Fig. 3) were used in conjunction with a RBR (Ltd) TWR-2050 wave recorder. The GCDC accelerometers have been selected due to their affordability, 2GB memory capacity and physical size. The X16-1C dimensions are 100×25×25 mm, and it weighs 55 g, it is also relatively inexpensive (<US$90). The GCDC accelerometers log data at user selectable sampling rates of 12, 25, 50, 100 or 200 Hz. The Real Time Clock feature enables the accelerometers to synchronise with device time and provides up to 0.1 millisecond time stamped data. Through the open source XLR8R application, supplied with accelerometers, recorded data can be exported as recorded or resampled within a range from 8 Hz to 512 Hz. The X16-1C is not water proof so PVC plastic housings were constructed to place the accelerometers in for deployment (Fig. 3). These housings consist of a cylindrical plastic container with removable lid that is held in place by 2 marine grade stainless steel screws. An O-ring ensures a water tight seal.

Within the shore platform study site, an area 10 m long and 22 m wide was determined suitable for the experiment based on its flatness, sufficient distance landward and availability of loose boulders. There, four boulders (L1, L2, L3, L4) were selected for the experiment based on their size and shape. Boulders needed to have a C-axes thick enough for a 5 cm diameter hole to be cored using a water cooled, petrol powered rock corer.

Figure 2. The boulder strewn shore platform at the study site (Photo: Alenka Abazović).

Deployment of the accelerometers was conducted between 1 and 6 May 2013. Throughout those six days, four GCDC accelerometers were deployed along with a wave pressure transducer nearby. The accelerometers were programmed to sample movement 12 Hz and the TWR-2050 was set to sample 8.5 minute bursts at 4 Hz. Burst were timed 8.51 minutes apart to ensure a continuous wave record. Accelerometers and the TWR-2050 were synchronised and set to start logging during the low tide on the first day of the experiment and stop logging during the low tide on the final day. Upon deployment, accelerometers were placed in a pre-constructed waterproof housing and sealed into core holes using a marine sealant. Experimental boulders were marked with spray paint, tri-axial measurements recorded, the longest axis orientation of each boulder measured with a compass, their position photographed from multiple angles (noting the position of the accelerometers), then their position surveyed using a Trimble DGPS. During each (one) daytime low tide the four boulders were re-surveyed, re-photographed and their A-axis orientation re-measured.

The recorded GCDC data is stored on the internal memory card in comma-separated values file format and can be copied directly to another device via USB interface. For the needs of this research, data had to be rearranged into sensible datasets, namely, each movement event period was singled out based on preview timestamps, exported and stored as a separate .csv data file using the XLR8R software. Then, the data (in g-force units where g = 9.807 m/sec^{-2}) was further reduced and graphically represented using Microsoft Excel. Wave and tidal data were retrieved from the TWR-2050 using propriety software that accompanies the instrument. Significant and maximum wave heights are used here to characterise the wave environment during the experiment.

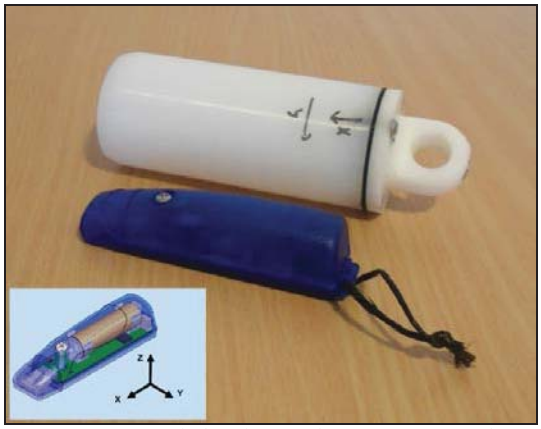

Figure 3. Waterproof housing and a GCDC accelerometer (100×25×25 mm) used to record boulder movements (Photo: Alenka Abazović. Insert: GCDC, LLC).

RESULTS

Wave conditions over the six day experiment are presented in Fig. 4. Conditions were generally low energy with maximum wave height not exceeding 1.3 m. Significant wave height at high tide ranged from 0.3 to 0.8 m, H_{max} reached 1.25 m, generally wave height increased as the experiment progressed.

The size, shape and locational details of our four experimental boulders are presented in Table 1. L1 to L3 are fine boulders while L4 is a medium size boulder. The initial position with respect to the direction of wave approach at the time of deployment is also provided.

The distance each of the four boulders moved from day to day is shown in Table 2. At the end of the experiment all the boulders had moved from between 13.8 cm and 306 cm. The two larger boulders L1 and L3 moved relatively little compared to the two smaller boulder L2 and L4. All four boulders were rolled at least once during the deployment. Although we have recorded movement of all four boulders, just two are presented here to illustrate the accelerometer output and potential of the technique.

The movement of boulder L3 is shown in Fig. 5. This boulder showed three discrete episodes of rolling, although we were unable to photograph the second (night time) event. Fig. 5 shows the position at the start and finish of the experiment period. Note that the boulder is upside down compared to the original position. Fig. 6 illustrates the accelerometer data from the first movement. The Z axis accelerations shows positive values in response to gravity, but becomes inverted when the boulder is rolled over. The boulder can be seen to have rolled but not moved very far (Fig. 5 middle panel). The X axis accelerations show that the boulder has also rotated along the Y axis as the boulder was rolled over.

Fig. 7 illustrates a longer record from the accelerometer and shows the second two movements when the boulder rolled again and the Z axis shows positive accelerations again, before being rolled a third time. There was an elapsed time of 1.48 hours between these two events. The total record in Fig 7 is 4.45 hours. It is also event from the accelerometer when the boulder become submerged and subject to wave impacts, all three acceleration directions began to detect wave impact forces, denoted by the vertical line in Fig. 7.

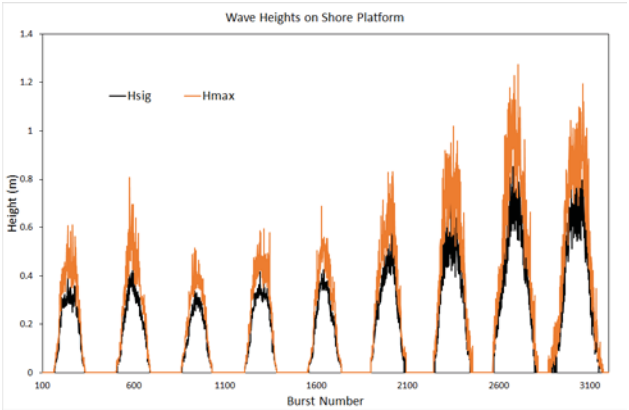

Figure 4. Measured wave heights (H_s and H_{max}) on the shore platform 1 May 2013 to 6 May 2013.

Table 1. *Characteristics of the four boulders used during the experiment.*

Boulder ID	L1	L2	L3	L4
A-axis (cm)	50	39	81	67
B-axis (cm)	33	27	40	56
C-axis (cm)	23	25	18	22
Size class (cm)	fine	fine	fine	medium
Shape	prolate	sphere	roller	tabular
Orientation (°)	255	345	340	325
Initial position*	parallel	perpnd	perpend	perpend

perpnd = perpendicular

Table 2. *Boulder movement distances (cm) 2/05/2013 to 6/05/2013.*

	2/05/	3/05/	4/05/	5/03/	6/03/	TOTAL
L1	3.7	4.2	0.9	1.2	3.7	13.80
L2	49.8	2.3	1.9	249.9	2.6	306.5
L3	1.7	3.3	2.9	49.4	118	175.7
L4	11.5	2.5	2.4	68.9	3.0	88.20

The movement of boulder L4 is shown in Fig. 8. On May 4 it moved a total of 49.4 cm (Table 2) and the boulder was rolled during transport. Fig 9 shows the accelerometer data from this movement. The flipping of the boulder is clearly evident from the inversion on the Z acceleration. Fig. 9 shows that his movement last 2.5 seconds, so that the transport velocity was 1 m/s. Significant wave height at the time was 0.63 m at the time of movement.

Figure 5. Example of boulder movements during the field trial. Upper panel shows position of boulder L3 2 May 2013. Middle panel boulder L3 position 4 May 2013 and the lower panel shows final position.

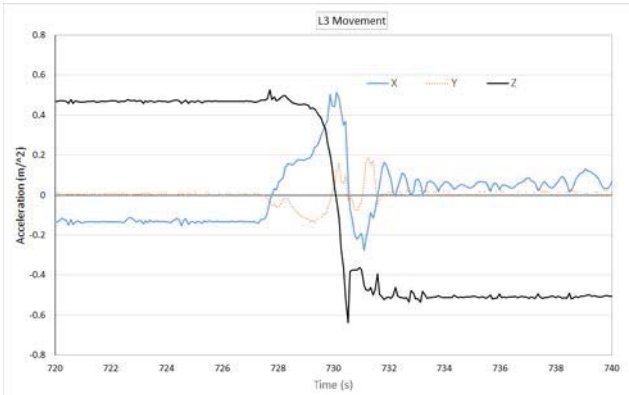

Figure 6. The first movement of boulder L3. The boulder was rolled on 4 April, 2013 when wave height was recorded as Hsig 0.64 m.

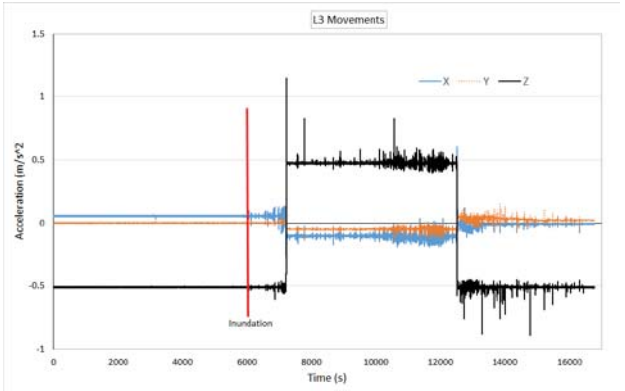

Figure 7. The second and third movement of boulder L3 showing the two rolling events are separated by 1.48 hours. Total record length is 4.65 hrs. The inundation and exposure to waves can be seen at the red line with increasing accelerations on all three axes. The boulder was rolled when Hsig was 0.64 m and 0.86 m at the second roll.

DISCUSSSION

The use of small and inexpensive accelerometers to monitor boulder movement is clearly viable and shows considerable potential for identifying transport events, the mode and the frequency of transport and the associated energy conditions when combined with simultaneous wave measurements. Our small field trial shows that when accelerometers are combined with wave recording and detailed visual observations, boulder movement can be characterised in significant detail. In the examples presented here, boulder rolling was clearly evident and under relatively low energy conditions. We also documented multiple movements (L3) during a single tide. Further analysis of these events will permit a closer link between wave conditions and movement. Larger studies are required that involve the deployment of a greater number of sensors in a greater range of boulder sizes, under a wider range of wave conditions. Under larger wave conditions sliding and suspension transport may be detected. Additional work requires the

identification of accelerometer signatures associated with specific transport modes and the use of a large scale wave tank could potentially offer a way of providing such data under controlled conditions.

CONCLUSIONS

The use of tri-axial accelerometers placed in coastal boulders offers a viable and revealing way to determine boulder movement threshold and mode of movement. Data from this approach will undoubtedly aid the development and improvement of entrainment threshold equations currently used to distinguish between tsunami and storm wave boulder transport.

LITERATURE CITED

Barbano, M.S., Pirrotta, C., and Gerardi, F., 2010. Large boulders along the south-eastern Ionian coast of Sicily: Storm or tsunami deposits? *Marine Geology*, 275, 140–154.

Chen, B., 2015. What is the contribution of abrasion to the sediment budget of a mixed sand and gravel beach? Unpublished PhD thesis, University of Otago.

Goto, K., Chavanich, S.A., Imamura, F., Kunthasap, P., Matsui, T., Minoura, K., Sugawara D., Yanagisawa, H.D., 2007. Distribution, origin and transport process of boulders deposited by the 2004 Indian Ocean tsunami at Pakarang Cape, Thailand. *Sedimentary Geology*, 202, 4, 821-837.

Maouche, S., Morhange, C. and Meghraoui, M., 2009. Large boulder accumulation on the Algerian coast evidence tsunami events in the western Mediterranean. *Marine Geology,* 262, 96-104.

Nandasena, N.A.K., Paris, R., and Tanaka, N., 2011. Reassessment of hydrodynamic equations: Minimum flow velocity to initiate boulder transport by high energy events (storms, tsunamis). *Marine Geology*, 281, 70–84.

Nandasena, N. A. K., and Tanaka, N., 2013. Boulder transport by high energy: Numerical model-fitting experimental observations. *Ocean Engineering*, 57, 163–179.

Noormets, R., Felton, E.A., Crook, K.A.W., 2002. Sedimentology of Rocky Shorelines: 2. Shoreline megaclasts on the north shore of Oahu, Hawaii: origins and history. *Sedimentary Geology,* 150, 31-45.

Nott, J., 1997. Extremely high wave deposits inside the Great Barrier Reef, Australia: determining the cause tsunami or tropical cyclone. *Marine Geology,* 141, 193-207.

Nott, J., 2003. Waves, coastal boulder deposits and the importance of the pre-transport setting. *Earth and Planetary Science Letters,* 210, 269-276.

Paris, R., Naylor, L.A., and Stephenson, W.J., 2011. Boulders as a signature of storms on rock coasts. *Marine Geology*, 283, 1–11.

Sugawara, D., Goto, K., and Jaffe, B.E., 2014. Numerical models of tsunami sediment transport - Current understanding and future directions. *Marine Geology*, 352, 295–320.

Switzer, A. D., and Burston, J. M., 2010. Competing mechanisms for boulder deposition on the southeast Australian coast. *Geomorphology*, 114, 42–54.

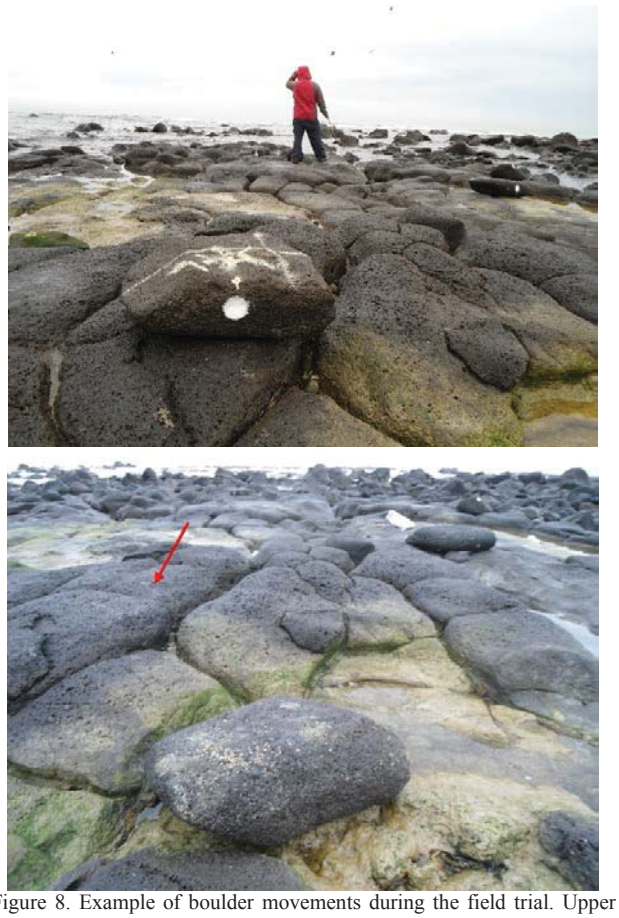

Figure 8. Example of boulder movements during the field trial. Upper panel shows the position of boulder L4 on 2 May 2013. Lower panel showing boulder position on 5 May 2013, red arrow points to position on 2 May 2013.

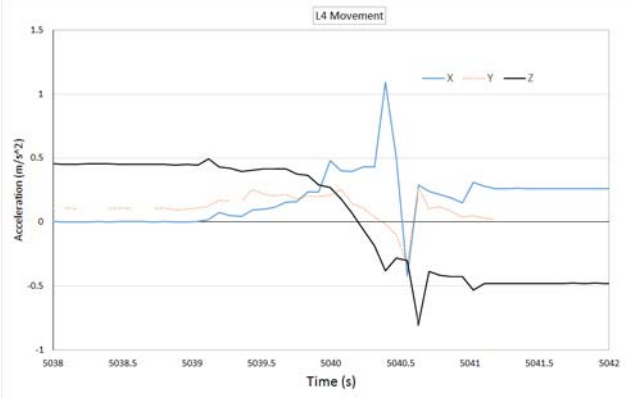

Figure 9. Movement of boulder L4. The boulder was rolled on 4 May, 2013 when Hsig was recorded as 0.64 m

Journal of Coastal Research	SI	75	612-616	Coconut Creek, Florida	2016

What controls the Geometry of Rocky Coasts at the Local Scale?

Zuzanna M. Swirad*, Nick J. Rosser, Matthew J. Brain, and Emma C. Vann Jones

Department of Geography
Durham University
Durham, United Kingdom

www.cerf-jcr.org

www.JCRonline.org

ABSTRACT

Swirad Z.M.; Rosser, N.J.; Brain, M.J., and Vann Jones, E.C., 2016. What controls the geometry of rocky coasts at the local scale? *In:* Vila-Concejo, A.; Bruce, E.; Kennedy, D.M., and McCarroll, R.J. (eds.), *Proceedings of the 14th International Coastal Symposium* (Sydney, Australia). *Journal of Coastal Research*, Special Issue, No. 75, pp. 612-616. Coconut Creek (Florida), ISSN 0749-0208.

There is a need to understand the controls on rocky coastal form in order to predict the likely response to climate changes and sea-level rise. Spatial variations in coastal geometry result from inheritance and contemporary processes, notably erosive wave intensity and rock resistance. We studied a 4.2 km long section of coastline (Staithes, North Yorkshire, UK) using LiDAR point cloud data and ortho-photographs. We represented the coast as a series of densely-spaced (25 m) and resampled (0.2 m) 2D cross-sections. GIS-based statistical analysis allowed us to identify relationships between coastal morphology, geology (lithology and rock structure) and wave intensity. We found the following statistically-significant relationships: 1) more intensive waves and weaker rocks are associated with steeper shore platforms, 2) higher platforms and cliff toes are associated with weaker and more variable rocks, and 3) surface roughness increases with greater wave intensity, decreased density of discontinuities and decreased variability of intact rock hardness. However, these relationships are weak, which suggests the potential role of coastal inheritance and/or the need to better represent rock resistance in coastal models.

ADDITIONAL INDEX WORDS: *Rocky coasts, shore platforms, rock control, rock resistance, GIS.*

INTRODUCTION

There is a pressing need to constrain the geomorphic sensitivity of rocky coasts to changes in marine conditions, notably those relating to sea level and wave conditions. Numerous studies have identified controls on coastal geometry based on relationships between shore platform width, gradient and elevation, rock properties and marine action (Trenhaile, 1978; Davies *et al.*, 2006; Kennedy and Dickson, 2006). However, attempts to explain controlling processes and, hence, better constrain future changes have often been based on simplified conceptual models of the relationships between marine conditions, shore platforms and cliffs and the potential feedbacks in their co-evolution. Existing studies lack sufficient spatial resolution and coverage to identify key relationships that may aid simple predictive analysis.

Using a GIS approach and a dataset obtained using airborne LiDAR and ortho-photographs we undertook a systematic analysis of a rocky coast (North Yorkshire, UK) to determine the relationships between coastal shape, geology and wave intensity at a local scale. Our approach helps to understand which rock characteristics (resistance to abrasive and/or structurally-defined erosion) represent 'rock resistance' (Sunamura, 1992) in specific morphologic elements of shore platforms. Potential controls on coastal geometry have been identified previously, but the relationships are still poorly quantified and understood:

1. Higher, steeper and narrower shore platforms form in harder rocks (Trenhaile, 1987; Davies *et al.*, 2006; Thornton and Stephenson, 2006).
2. Higher joint density associates with lower platforms (Kennedy and Dickson, 2006).
3. More intensive wave action generates flatter platforms (Trenhaile, 1980).

The central aim of our study is to consider the controls on geometry of hard-rock shore platforms by linking morphology to geology. As the variation in coastal morphology reflects variation in alongshore erosion rate, this may provide insight into long-term coastal evolution to better assess future changes in sea-level rise and intensification of wave action as a result of climate change.

Research area

The 4 km long section of the coast around Staithes in North Yorkshire, UK is a storm-wave dominated coast, characterised by tidal range of 4.6 m (http://www.ntslf.org/, accessed: 12/10/2015). Gently sloping (~2°) shore platforms up to 400 m wide are composed of Jurassic bedrock of 16.7-41.5 MPa unconfined compressive strength (Lim, 2006). The lithologies exposed at the sea level are shale (80.6%), sandstone (14.1%), mudstone (3.9%), ironstone (1.1%) and siltstone (0.3%). The platform is backed by hard-rock cliffs up to 90 m high, which are topped by 10-20 m thick layer of glacial till. Cliff retreat rates calculated on the basis of historical maps are of the order 0.001 to 0.01 m/year (Lim, 2006). The platform is partly covered by boulders, ephemeral pocket beaches and intertidal flora (Figure 1). Further details on site geology, geometry, tidal characteristics and wave climate are provided in Lim (2006).

DOI: 10.2112/SI75-123.1 received 15 October 2015; accepted in revision 15 January 2015.
*Corresponding author: z.m.swirad@durham.ac.uk

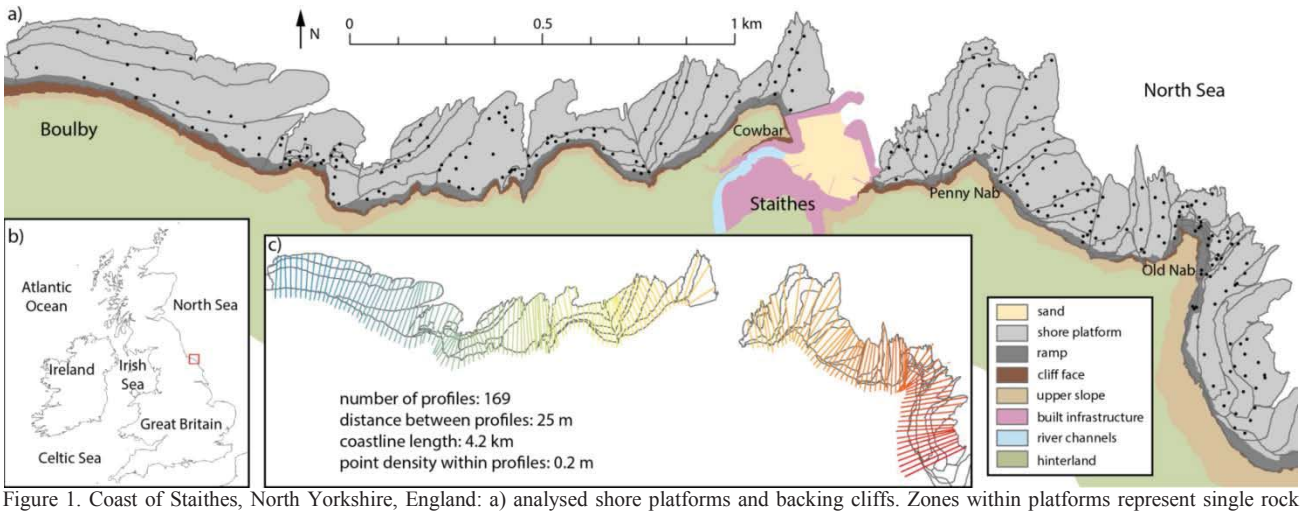

Figure 1. Coast of Staithes, North Yorkshire, England: a) analysed shore platforms and backing cliffs. Zones within platforms represent single rock beds, i.e. exposures of uniform geology limited by apparent altitude/colour change. Dots represent sites of rock hardness measurements; b) location of the North Yorkshire coast in British Isles; c) location of coastal cross-sections. Profiles correspond to coloured profiles in Figure 3.

METHODS

We processed the data and created all layers in ArcGIS 10.2. We used airborne LiDAR-derived point clouds (ca. 100 points/m^2) obtained on 15/08/2014 during a low spring tide to create a Digital Elevation Model (DEM) and slope map at 0.2x0.2 m pixel resolution. We combined these with orthophotographs (ca. 0.03 m pixel) to divide our study area into morphological classes, including: foreshore platform (seaward limit: mean low water level of spring tides), foreshore ramp (upper part of platform, < 15°), cliff face (near-vertical), upper cliff slope (usually ca. 30°, formed in glacial till), built infrastructure, river channels, hinterland and beach deposits (Figure 2). We divided the platform on the basis of exposed geology (Figure 1). We mapped major (i.e. visible on the orthophotographs) joints and interpolated them into a joint density raster (resolution: 1 m, ArcGIS Line Density tool). At 283 sites, which were selected to cover all types of geology, we measured fresh rock hardness (after having removed the weathered outer layer with carborundum stone) with a Proceq Equotip 550 Leeb D Type (Viles *et al.*, 2011) and calculated mean rock hardness (Equotip rebound values) and its variation for each rock bed from 1-18 samples (in average: 3.54). We used rock hardness as a proxy for unconfined compressive strength, which has been previously considered as a good descriptor of the resistance of rock to erosion (Sunamura, 1992; Naylor and Stephenson, 2010).

Table 1. *Variables used in the analysis of geomorphic conditions of the shore platform at Staithes.*

Variable	Unit	Calculation
Platform width (w)	m	Horizontal distance between cliff toe and platform seaward edge, i.e. the first and the last points classified as 'platform/ramp'. Proxy for wave intensity on the basis that energy attenuation increases with width.
Platform gradient (α)	°	Dip of a straight line between cliff toe and platform seaward edge; arctangent of platform width divided by DEM-derived elevation difference between the first and the last points classified as 'platform/ramp'.
Platform elevation (z)	m AOD	Mean elevation of platform and ramp, averaged from DEM-derived elevations of points resampled along the cross-sections (0.2 m interval).
Cliff toe elevation (tz)	m AOD	DEM-derived elevation of the first point classified as a cliff face, which abuts against platform/ramp.
Platform roughness (r)		Standard deviation of slope obtained at all points across platform and ramp at 0.2 m interval.
Rock hardness (Sc)	Equotip rebound value	Proxy for uniaxial rock strength. Each rock bed (exposure of uniform geology) is represented as a mean of point readings within it (Figure 1). Profiles are represented as weighted mean based on the proportion of extent of specific rock beds it crosses.
Rock hardness variation (Sc_v)		Weighted mean of square root of variance in Sc in each rock bed which are crossed by profiles.
Joint density (j)	joints/m^2	Interpolated from linear data using ArcGIS Line Density tool. Used only on platform sections not covered by sediments, which assumes that joint density is the same for covered and exposed sections of platform.

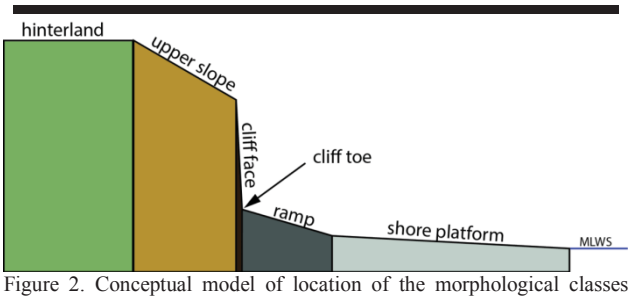

Figure 2. Conceptual model of location of the morphological classes along coastal cross-sections.

We automatically extracted equally-spaced (every 25 m) 2D cross-sections as station lines perpendicular to the coastline, along the line defined by the mean water level of spring tides (2.59 m AOD). Along each cross-section, we extracted altitude and morphological data at 0.2 m horizontal intervals (Figure 3), to determine the platform characteristics described in Table 1.

We analysed kernel density plots for each variable across whole dataset, and identified mostly quasi-normal distributions, which are suitable for use in regression analysis. Platform width and gradient are, however, better represented by their square root. We performed pairwise and stepwise regression between morphologic variables and potential controlling factors: geological, marine and combined.

RESULTS

Geology

Lithological variation is expressed by the rock hardness *Sc* and the variability therein, Sc_v, while structure is expressed by joint density *j*. The best fit of stepwise regression for each morphologic variable is presented in Table 2. Significant relationships (p-value < 0.05) exist between geology and all platform characteristics except gradient, but none of the relationships is strong ($R^2 < 0.1$). Wider and lower platforms and lower cliff toe elevations weakly coincide with harder and less variable rocks. Platform roughness is negatively correlated with variation of rock hardness and joint density.

Table 2. *Relationships between geology and shore platform morphology. Asterisks (*) indicate significant relationships (p-value < 0.05); w – platform width, α – platform gradient, z – platform elevation, tz – cliff toe elevation, r – platform roughness, Sc – rock hardness, Sc_v – viariation in rock hardness, j – joint density.*

Relationship	Adjusted R^2	p-value
$w = (17.331 + 0.026\ Sc_v - 0.012\ Sc)^2$	0.042	0.011*
$\alpha = (1.257 - 0.353\ j)^2$	0.015	0.062
$z = 1.067 - 0.005\ Sc + 0.004\ Sc_v$	0.09	0.0002*
$tz = 5.776 - 0.01\ Sc + 0.02\ Sc_v$	0.029	0.032*
$r = 6.429 - 0.029\ Sc_v - 2.611\ j$	0.031	0.0269*

Wave intensity

We were not able to express variations in wave intensity across the platform and at the cliff toe in terms of tide gauge-derived deep-water wave characteristics and wave transformation in the nearshore zone because: 1) the studied coastline is relatively short (4 km) and so does not contain a fully representative population of headlands and embayments which limits the inclusion of areas with refraction effects in the analysis, 2) we analysed a single site with no monitoring data on variations in tidal and wave climate, and 3) nearshore bathymetry is only poorly constrained at a resolution suitable to elucidate differences between the profiles considered here, and so wave transformation models cannot be applied.

We test the assumption that platform width, and hence wave energy dissipation, is a proxy for wave intensity. Over the studied coastline we assume that wave energy delivery to the toe of the platform is constant, and so the dissipation of wave energy must vary by platform width. Therefore, wider platforms mean less wave energy per platform unit length and so less energy arriving to the cliff toe. Therefore, we assume more intensive wave action when the platform is narrower.

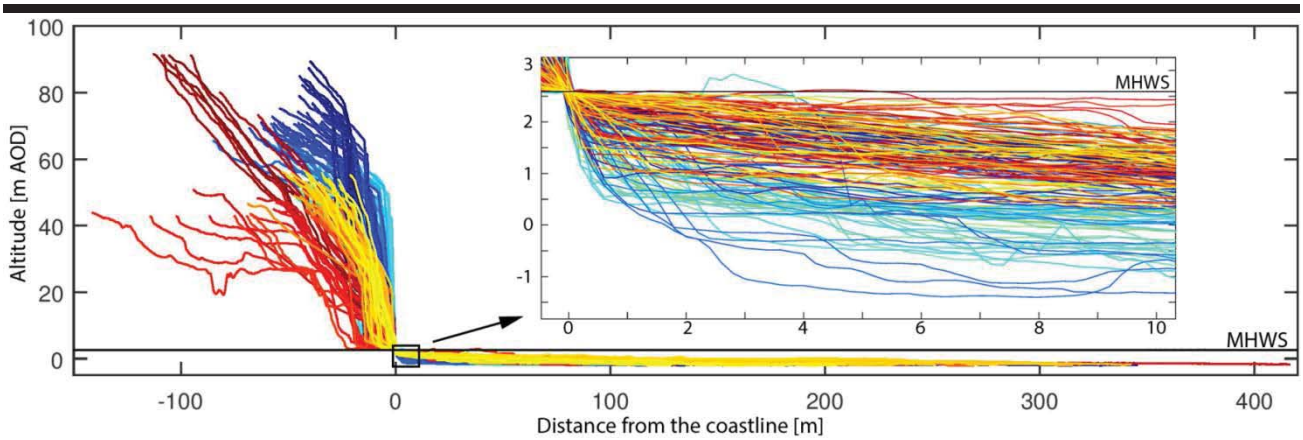

Figure 3. Cross-sections of the Staithes coast including shore platform, ramp, cliff face and upper slope only. Horizontal axis: negative values represent onshore and positive – offshore section. Profile color corresponds to that displayed in Figure 1.

Pairwise regression between platform width and other morphological characteristics presented in Table 3 shows that significant negative relationships exist between platform width and gradient and platform roughness, while elevations of platform and cliff toe are independent of platform width.

Table 3. *Relationships between shore platform width and other morphological characteristics. Asterisks (*) indicate significant relationships (p-value < 0.05); α – platform gradient, z – platform elevation, tz – cliff toe elevation, r – platform roughness, w – platform width.*

Relationship	Adjusted R^2	p-value
$\alpha = (2.273 - 0.08\ sqrt(w))^2$	0.306	<0.0001*
$z = -0.731 + 0.002\ sqrt(w)$	-0.006	0.8987
$tz = 1.712 + 0.08\ sqrt(w)$	0.002	0.236
$r = 10.681 - 0.418\ sqrt(w)$	0.129	<0.0001*

Geology and wave intensity

In order to understand the interplay between geologic and marine factors in shaping rocky coasts we performed a stepwise regression including all above independent variables. The best fit relationships are presented in Table 4 and Figure 4. As we use platform width as a proxy for wave intensity it is ignored as a morphometric parameter.

Table 4. *Relationships between geologic and marine factors and shore platform morphology. Asterisks (*) indicate significant relationships (p-value < 0.05); α – platform gradient, z – platform elevation, tz – cliff toe elevation, r – platform roughness, w – platform width, Sc – rock hardness, Sc_v – viariation in rock hardness, j – joint density.*

Relationship	Adjusted R^2	p-value
$\alpha = (2.909 - 0.083\ sqrt(w) - 0.002\ Sc)^2$	0.323	<0.0001*
$z = 1.067 - 0.005\ Sc + 0.004\ Sc_v$	0.09	0.0002*
$tz = 5.776 - 0.01\ Sc + 0.02\ Sc_v$	0.029	0.032*
$r = 11.381 - 0.392\ sqrt(w) - 2.235\ j - 0.018\ Sc_v$	0.142	<0.0001*

Significant relationships exist for all morphologic variables. Platform gradient is moderately (R^2 = 0.323) correlated to platform width and rock hardness. The gradient is higher when platforms are narrower and rocks are harder. Rougher surfaces associate with narrower platforms, lower joint density and less variable rock hardness. Platform and cliff toe elevations do not correlate with platform width, but only with rock hardness.

DISCUSSION

Statistical analysis of morphologic conditions of the Staithes shore platform enabled us to find only weak relationships between coastal geometry, geology and wave intensity. We found the best fit regression for each morphometric variable resolving the role of lithology, structure and marine action in a local-scale coastal morphological setting.

Coastal erosion is likely to increase with wave intensity increase and rock resistance decrease (Sunamura, 1992). Rock resistance depends on both lithology and structure and is higher if a rock is stronger (unconfined compressive strength) and less discontinuous. At localities more intensively eroded platforms should be lower (mean and cliff toe) and flatter (e.g. Trenhaile, 1987). We also expect surface roughness to be larger where the wave action is lower (waves abrade the rocks), but also where rocks are less resistant, discontinuous and weathered.

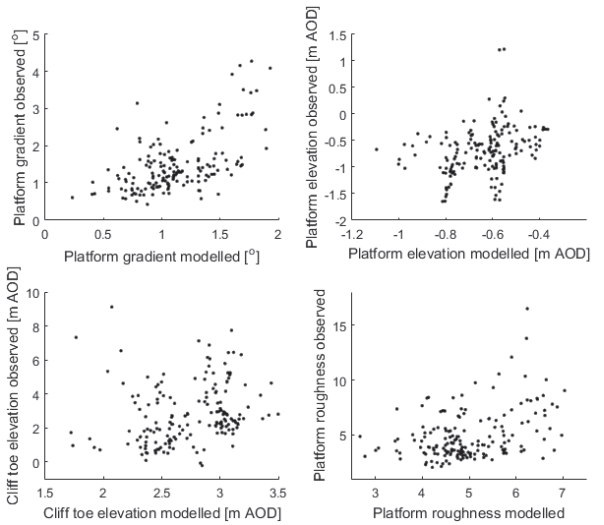

Figure 4. Relation between shore platform geometry modelled through best fit relationships with geology and platform width (x-axis) and observed (y-axis).

We observed that wider platforms are cut in weaker lithologies (lower Equotip readings and more variation within single rock beds), which supports the finding of Davies *et al*. (2006). Platform gradient is moderately correlated to wave intensity (positively) and rock resistance (negatively). On the contrary, Trenhaile (1980) demonstrated that more intensive waves generate flatter platforms. The reason for discrepancies may relate to the fact that steeper (and narrower) platforms are more intensively eroded by waves, as suggested here, in consequence leading to reduction of platform gradient (Trenhaile, 1980). Elevations of platform and cliff toe weakly correlate with rock hardness only. Higher platforms associate with weaker and more variable lithologies. This is contrary to previous assessments (e.g. Thornton and Stephenson, 2006), which related harder rocks to higher platforms and cliff toes. Lack of expected relation may suggest little variation in rock hardness. An alternative explanation has been proposed by Gill (1972) who suggested that regardless of the elevation a platform occurs at, while it evolves, it is lowered to the low tidal level. Therefore, the more developed the platform, the less important rock type. The results support So's (1965) statement that platform elevation and gradient are independent from rock structure.

Surface roughness is the only morphological element which seems to be partly controlled by all lithology, structure and marine action. It increases with increase of wave action (narrower platform) and decrease in joint density and rock hardness variation. Positive correlation between roughness and wave intensity is counter-intuitive but can be explained in terms of wave action along the lithological boundaries, where intensive waves work on steps in the foreshore. Moreover, more

wave action may coincide with more intensive cliff erosion and presence of debris (high surface roughness) on the upper part of the platform. Potentially, the role of abrasion on roughness could be observed in smaller (<0.1 m) scale. The negative relationship between surface roughness and joint density may suggest that strongly jointed rocks are structurally controlled and are prone to erosion along predefined planes while more massive rocks erode in more randomly distributed manner.

The study demonstrated that a re-thinking of numerical expression of rock resistance in coastal geomorphology is necessary depending on the processes studied. Different rock properties (rock hardness, its variability, structure) control different parameters of shore platform. Moreover, the role of wave action suggests that significant changes in wave climate may have an impact on a long-term (millennial timescales) coastal evolution by controlling platform gradient and roughness.

The results show that relationships with geology and marine action are not strong enough to explain morphology of rocky coasts in terms of parameters easily-obtained in field and GIS. We suggest two possible explanations of the observed weak relationship. Firstly, included variables may not best represent rock resistance. Despite existing correlations between Equotip and Schmidt Hammer rebound values (Viles *et al.*, 2011) and between the latter and unconfined compressive strength (Sunamura, 1992), other rock properties (such as tensile strength, shear strength, grain size, composition, abrasion resistance) may better represent rock resistance to wave action. Alternatively, weak dependence of coastal form on contemporary processes may suggest inherited nature of the coast (Masselink *et al.*, 2011). Current erosion rates of hard-rock coasts are often too slow to account for formation of wide shore platforms in the last 6 kyr when sea has been at the level similar to todays (Trenhaile *et al.*, 1999). Our statistical analysis demonstrates that caution should be taken while defining controls on rocky coasts, as existing relationships do not fully explain coastal geometry, and definitive controls are yet to be found.

CONCLUSIONS

Our method of systematic statistical analysis of a stretch of coastline based on densely-spaced along shore (25 m) and resampled across shore (0.2 m) coastal cross-sections enabled us to find relationships between coastal form, geology (lithology and structure) and wave intensity:

1. More intensive waves and weaker rocks are associated with steeper shore platforms.
2. Higher platforms and cliff toes are associated with weaker and more variable rocks.
3. Surface roughness increases with increase of wave intensity, decrease of joint density and decrease of rock hardness variation.

Identified relationships are weak which suggests that key controls on coastal geometry are still poorly understood. Re-thinking of the numerical expression of rock resistance at different spatial and temporal scales and quantification of potential role of inheritance are crucial to understand geomorphic conditions of rocky coasts and to model their evolution.

ACKNOWLEDGEMENTS

The study is part of Coastal Behaviour and Rates of Activity (CoBRA) project supported by ICL Fertilizers UK Ltd.

LITERATURE CITED

Davies, P.; Sunamura, T.; Takeda, I.; Tsujimoto, H., and Williams, A.T., 2006. Controls of shore platform width: the role of rock resistance factors at selected sites in Japan and Wales, UK. J*ournal of Coastal Research*, Special Issue No. 39, 160-164.

Gill, E.D., 1972. The relationship of present shore platforms to past sea levels. *Boreas* 1, 1-25.

Kennedy, D.M. and Dickson, M.E., 2006. Lithological control on the elevation of shore platforms in a microtidal setting. *Earth Surface Processes and Landforms* 31, 1575-1584.

Lim, M., 2006. Coastal cliff evolution with reference to Staithes, North Yorkshire. Durham, UK: Durham University, Ph.D. thesis, 378p.

Masselink, G.; Hughes, M., and Knight, J., 2011. *Introduction to coastal processes and geomorphology*. London: Hodder Education, 416p.

Naylor, L.A. and Stephenson, W.J., 2010. On the role of discontinuities in mediating shore platform erosion. *Geomorphology* 114, 89-100.

So, C.L., 1965. Coastal platforms of the Isle of Thanet, Kent. *Transactions of the Institute of British Geographers*, 147-156.

Sunamura, T., 1992. *Geomorphology of rocky coasts*. Chichester: Wiley, 302p.

Thornton, L.E. and Stephenson, W.J., 2006. Rock strength: a control of shore platform elevation. *Journal of Caostal Research* 22(1), 224-231.

Trenhaile, A.S., 1987. *The geomorphology of rock coasts*. Oxford: Clarendon Press, 384p.

Trenhaile, A.S., 1980. Shore platforms: a neglected coastal feature. *Progress in Physical Geography* 4, 1-23.

Trenhaile, A.S., 1978. The shore platforms of Gaspe, Quebec. *Annals of the Association of American Geographers* 68, 95-114.

Trenhaile, A.S.; Pérez Alberti, A.; Martínez Cortizas, A.; Costa Casais, M., and Blanco Chao, R., 1999. Rock coast inheritance: an example from Galicia, northwestern Spain. *Earth Surface Processes and Landforms* 24, 605-621.

Viles, H.; Goudie, A.; Grab, S., and Lalley, J., 2011. The use of the Schmidt Hammer and Equotip for rock hardness assessment in geomorphology and heritage science: a comparative analysis. *Earth Surface Processes and Landforms* 36, 320-333.

Journal of Coastal Research	SI	75	617-621	Coconut Creek, Florida	2016

Video assessment of nearshore and beach evolution following the deployment of a submerged geotextile wave breaker

Yann Balouin†, François Longueville†, and Yohan Colombet†

†BRGM, French Geological Survey, Languedoc-Roussillon Direction,
1039, rue de Pinville 34000 Montpellier, France

www.cerf-jcr.org

www.JCRonline.org

ABSTRACT

Balouin, Y.; Longueville, F., and Colombet, Y., 2016. Video assessment of nearshore and beach evolution following the deployment of a geotextile wave breaker. *In:* Vila-Concejo, A.; Bruce, E.; Kennedy, D.M., and McCarroll, R.J. (eds.), *Proceedings of the 14th International Coastal Symposium* (Sydney, Australia). *Journal of Coastal Research*, Special Issue, No. 75, pp. 617-621. Coconut Creek (Florida), ISSN 0749-0208.

The feedback on the use of submerged structures for beach protection is still scarce, and the shoreline response to structures is still poorly understood at present. Most of the studies presents structures close to the shoreline without significant morphologies on the shoreface that could interact with it. On the Lido of Sète, a narrow coastal barrier facing the Mediterranean Sea, an experimentation of beach protection using a submerged geotextile structure is undertaken. The structure was deployed in 2013, and to analyse nearshore dynamics, an ARGUS video system was installed in 2011. Video-derived shoreline, bar crest position, alongshore currents, swash processes, were used to assess the natural dynamics and to evaluate the evolution after the installation of the 850 m long structure.
The monitoring permitted to describe a rapid dynamics of crescentic nearshore bars. Processes of longshore migration, linearization, as well as a strong coupling between bar dynamics and shoreline sinuosities were described. After the deployment of the geotextile, a progressive linearization and rotation of the nearshore bar (parallel to the tube) was observed. This process induced a progressive rotation of the shoreline and an important beach enlargement. The 3D patterns, both in the bar and emerged beach progressively disappeared. With this new beach morphology, storm run-up is more regular alongshore, and only major events can reach the dune front and generate impacts. This field experiment provide an interesting feedback on morphological response following the deployment of a submerged structure on a shoreface characterized by an important nearshore bar dynamics.

ADDITIONAL INDEX WORDS: *submerged geotextile structure, bar and shoreline coupling, beach protection.*

INTRODUCTION

Fully submerged coastal structures, whatever the material used (concrete, geotextile, etc), are more and more considered for beach protection. The primary functions of these structures are to reduce the amount of energy in their lee (Ranasinghe and Turner, 2006, Turner, 2006) in order to limit shoreline retreat, or to promote beach widening by the formation of a salient. In several places in the world, these structures were developed both for beach protection and to optimize local surfing conditions (see West *et al*., 2003; Ranasinghe and Turner, 2006, Rendle and Davidson, 2012).

As pointed by Ranasinghe and Turner (2006), the feedback on these new techniques remains rare and there is still inconsistency whether the deployment of such structures will induce shoreline advance or retreat. Depending on the circulation pattern, they can either generate diverging currents on the lee and induce shoreline retreat, or in other case, favour the shoreline advance by creating a salient. Most the literature on submerged structures, including field observations and modelling, concerns a submerged structure close to the beach

(between 40 m to 100-200 meters) and without taking into account the potential presence of very dynamics nearshore bars on the shoreface and the coupling between these bars and the aerial beach (Castelle *et al*., 2010).

The study presented here focuses on the field characterization of the dynamics of both nearshore bars and shoreline before and after the deployment of such a system. The site, the Lido of Sète beach, on the French Mediterranean coast is a double-barred microtidal beach where a geotextile submerged structure was deployed in 2013 and is monitored using an ARGUS video system since 2011 providing a very good insight on the pre-existing morphodynamics of bars and shoreline.

This paper is structured as follows: section 2 and 3 presents the field site and methodology. Section 4 presents the results on morphodynamics before and after the deployment of the geotextile and section 5 discusses implications in term of beach response, circulation induced and modification of the coupled dynamics between nearshore bar and shoreline.

Background

The Lido of Sète is a narrow coastal Barrier facing the Mediterranean Sea. The site is representative of many of the Mediterranean beaches since it is exposed to a very irregular wave climate. Wave climate is moderate at this site and most of the significant morphological evolution is observed during storm events (Gervais *et al*., 2012). Mean tidal range is around 0.2 m and can reach 0.3 m during spring tides. Modal wave conditions are weak (*Hs* mean = 0.7 m; *Ts* mean ~ 4.5 s) but important

DOI: 10.2112/SI75-124.1received 15 October 2015; accepted in revision 15 January 2015.
*Corresponding author: y.balouin@brgm.fr

wave episodes and storms in winter time are rather frequent. More than 3 events of *Hs* > 3 m per year occur in this region and annual return period for *Hs* is estimated at 4.3 m. Storm conditions (around *Hs* > 3 m and *Ts* > 7.3 s) are often associated with onshore wind and low atmospheric pressure that generate a storm surge which may reach 0.8 m above mean sea level in most extreme case (Gervais *et al.* 2012).

The mean shoreface slope is around 0.9 % and grain size about 200 µm for the nearshore bars (Certain *et al.*, 2005). The inner bar, 2 m high, is located between 80 and 170 m from the shoreline and its crest is around -2 m from the sea surface. The outer bar distance is between 250 m and 400 m with a crest depth around 4 m. It is between 2.5 and 3 m high.

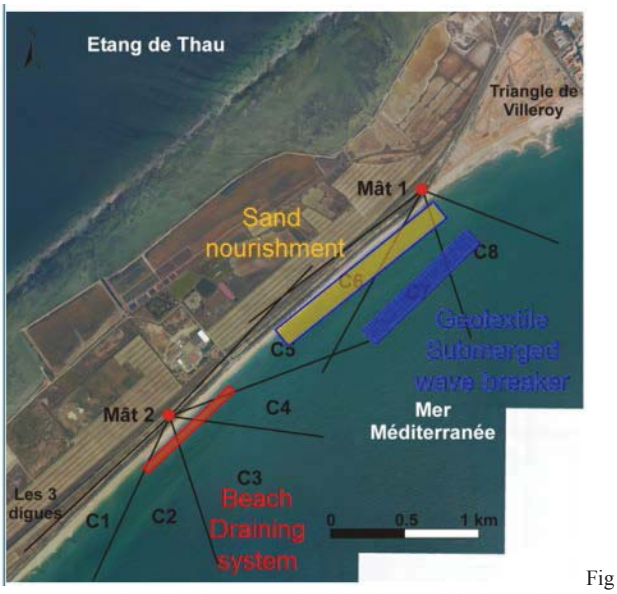

Figure 1. Location of study area at the Lido of Sète with the position of video cameras and soft defenses experimentation area.

Previous studies in this area (Barusseau and Saint-Guily, 1981) have evidenced a rapid evolution and dynamics of the nearshore bars during storm events. Gervais (2012) described rapid bar migration and/or deformation of the inner bar that are driven by hydrodynamic conditions, but also by the initial morphology of the shoreface before the storm occurs. The general shape of the bars appears to be very stable with the permanent presence of small cusps in the northern part of the lido and larger cusps in the south. Rhythmicity in the shoreline are usually in phase with the inner bar, the seawards bulges in the shoreline being located in front of the bar shoals. Bar position is oscillating around a mean position at a seasonal timescale. At a larger timescale, the bars are following the well-described net offshore migration (Certain, 2002).

This microtidal site is a very attractive sandy beach that underwent significant shoreline retreat during the last decades. Consequently, an important management project was implemented, involving the retreat of the coastal road, dune rehabilitation, beach enlargement, and the deployment of a submerged geotextile breakwater and a beach dewatering system (Figure 1). An Argus station was installed in 2011 to monitor this experimental deployment.

This contribution deals with the morphological evolution of the site before and after the deployment of the submerged breakwater in the beginning of 2013 (end of work is March 2013). This defense is composed of 60 m long geotextile containers and extends over 850 m (in blue on figure 1). The containers are 3 m high and located on the external bar at approximately 350 m from the beach in 4 m water depth. The water depth over the structure varies between 0.5 and 1 m and the main objective of this deployment is to induce the breaking of all waves having *Hs* over 2 m (Fraysse, 2009).

METHODS

An Argus video monitoring system (Holman & Stanley, 2007) was deployed in 2011 at Sete beach. The video monitoring system consists of 8 cameras mounted on two 20 m high masts. The distance between the masts is 2.5 km, and the covered area is around 4 km (Figure 1). Snapshots and 10 min averaged images are recorded each 30 min as well as pixel intensity time series. Cross shore resolution is very good (0.1 to 4 m at 1000 m of the mast), and longshore resolution is ranging from 1 m to 30 m at 1000 m of the mast. Images of the 8 cameras are rectified and combined using Argus toolbox.

The morphological features (bar, shoreline) are extracted using ARGUS toolboxes (Aarninkhof *et al*., 2003, Plant *et al*., 2006). Extraction of the bar is done through the sampling of the pixel luminosity intensity using BLIM toolbox (Pope, 2008).

Weekly shorelines are analyse between 2011 and 2015 to evaluate the variations in beach width, but pre-storm, storm and post-storm position are also particularly studied to evaluate recovery processes. Bars crest position is extracted each time significant wave height offshore is high enough to induce the breaking on the bar (*Hs*~1 m). For the study of variation in bar position, images when *Hs*~2m are used as this was defined in previous studies (Balouin *et al*., 2013) to be the best conditions to identify bar crest position.

Wave (at 30 m water depth) and water levels (in the harbor of Sete) are measured in the vicinity of the study area by the regional government administration (DREAL-LR). Bathymetry surveys undertaken by Thau Agglo were used both to validate and provide additional information on the nearshore bars dynamics.

RESULTS

Field observation before the deployment of the submerged structure

The video monitoring enabled to describe a rapid dynamics of crescentic nearshore bars that were supposed to be quite stable. Processes of longshore migration, linearization and generation of new cusps after storm, already observed in other microtidal environments by Armaroli and Ciavola (2011), were documented, as well as a strong relationship between inner bar dynamics and shoreline sinuosity (Balouin *et al*. 2012). The main behavior during storm is the longshore migration of the bar system under oblique waves (see figure 2, left) that yields to the progressive migration of beach sinuosities to recover a phased

position (beach sinuosities in front of bar horns). During major events (*Hs*~5 m), the inner bar is linearized. After a few days, the cuspate shape of the inner bar is rebuilt, with a significant displacement of the morphologies in the longshore drift direction and a new cusp appears downdrift and reinitiates the cycle. This cusps apparition was observed twice at Sète after the most energetic events that tend to linearize the bar, suggesting that an important amount of energy is needed to create a new cusp in the inner bar.

Field observation after the deployment of the submerged structure

After the deployment of the geotextile, a progressive linearization and rotation of the inner bar (parallel to the tube) was observed (figure 2, right). This process induced a progressive rotation of the shoreline parallel to the bar and the geotube associated with a beach enlargement (around 15 m) while this part of the beach was retreating very rapidly before the deployment (10 m in 2 years). After this rotation of the bar and the shoreline which became parallel to the submerged wave breaker, the position of both bar and shoreline remained quite stable, indicating that the system probably reached a new equilibrium state. In front of the end of the submerged structure, the bar presents small irregularities probably traducing the circulation pattern above the structure that can induce an offshore directed return flow.

Timing of morphological responses

The evolution in the shoreline position of the Lido of Sète beach was characterised by a mean shoreline retreat of 2 m/y (Figure 3). After the deployment of the structured that was achieved in March 2103, the inner bar and shoreline were quite stable during the year 2013. A major evolution was observed during the storm event of Dec 2013 (*Hs*~5 m) when the bar undergoes a significant rotation to become parallel to the structure. After a few days, the shoreline initiated the same rotation that induced a shoreline advance of 15 m. This was the adaptation period that evidenced the need of a significant amount of energy to generate a response of bar and shoreline to the deployment of the structure. After this major event, the bar and shoreline positions were very stable until a nourishment undertaken at the begining of 2015 (figure 3).

Differences in storm effects before/after

A presented before, the main evolution of the nearshore area following the deployment of the submerged structure was the disappearance of the 3D pattern of the inner bar and shoreline. In ordrer to analyse the effects of this evolution on the storm reponses, evolution furing storms events with similar forcing conditions was compared. An example is given on figure 4 that compares the shoreline position before and after the storms of Nov 2011 and April 2014 that were quite similar in wave high and direction, storm surge, … Before the deployment of the structure, the moderate event of Nov 2011 induced a shoreline retreat reaching 15 m, with strong alongshore variability induced by the 3D pattern of the inner bar. During the event of April 2014, the shoreline behind the structure remained stable, and a moderate retreat was observed on the adjacent coast.

A significant modification of wave run-up was observed (Figure 4, bottom). It was previously driven by beach sinuosity and beach cusps, and the swash excursion has a strong alongshore uniformity, locally reaching the dune foot. After deployment of the structure and linearization of the bar and shoreline, storm run-up became more regular alongshore, and for the same forcing conditions, swash excursion only reached the upper beachface.

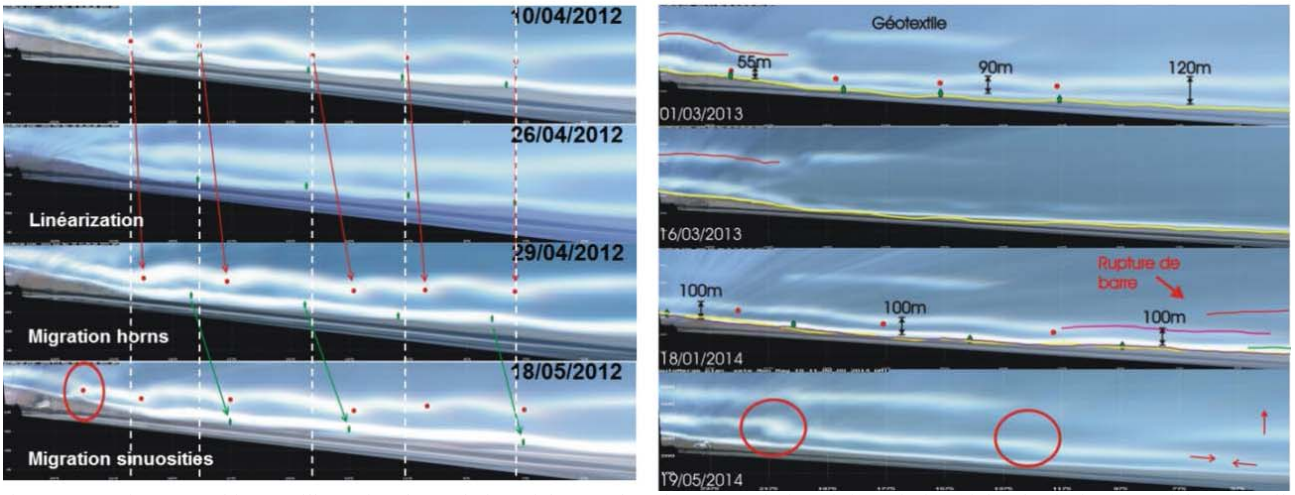

Figure 2. 10 min averaged images illustrating the evolution of the nearshore bar system before (left) and after (right) the deployment of the geotextile wave breaker.

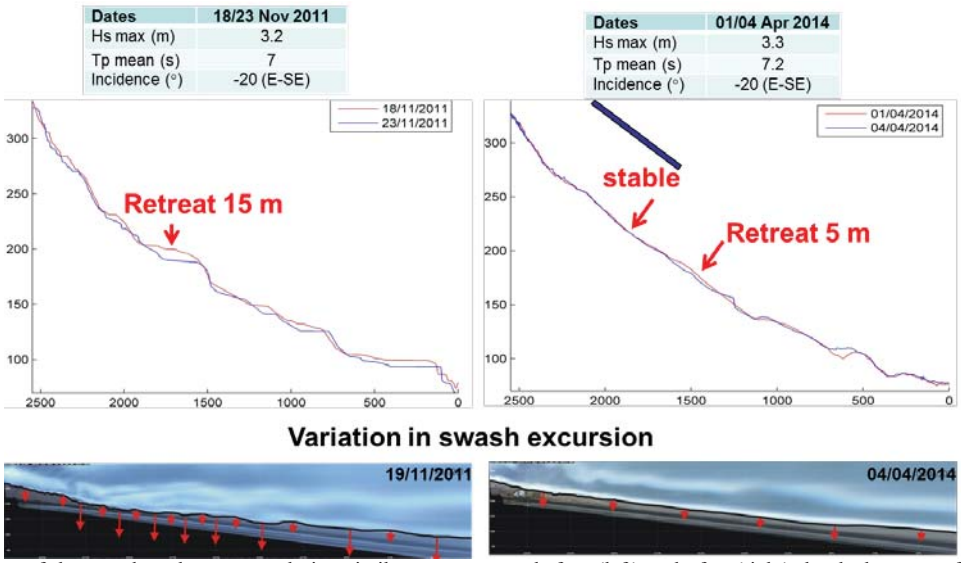

Figure 4. Evolution of the nearshore bar system during similar storm events before (left) and after (right) the deployment of the geotextile wave breaker. Variation in shoreline position (top) and variation in swash excursion (bottom) on rectified 10 min averaged images.

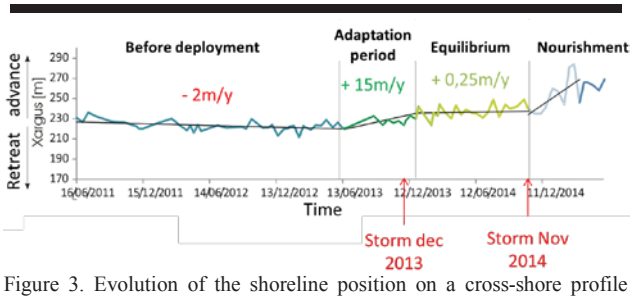

Figure 3. Evolution of the shoreline position on a cross-shore profile located in front of the submerged structure.

DISCUSSION

The monitoring of the Lido of Sète using Argus video observation has permitted to describe the evolution before, during and after the deployment of a submerged geotextile structure. The most important evolution is the disappearance of the pre-existing 3D pattern that was driving most of the aerial beach evolution. The monitoring have evidenced a delay in the response to the deployment. It was undertaken in March 2013, and the main morphological responses were observed at the end of 2013, when a significant storm event occurred. That suggests that a significant amount of wave energy was required to induce a morphological response that was not observed during several months with fair weather conditions. This major event was a oblique storm, and it is thought that the linearization of the inner bar and subsequent rotation of the beach are due to the increase of longshore currents channelized between the structure and the bar and between the bar and the beach. More frontal events that were observed have evidenced the generation of irrelugarities in the longshore bar in front of the extremities fo the structure. That suggests a circulation pattern with diverging alongshore currents behind the structure, generating offshore directed flow over the bar. This circulation pattern was described by Ranasinghe and Turner (2006) as being the cause of shoreline erosion behind a structure. In the case of the Lido of Sète, this circulation induces locally a return flow over the bar that migrates offshore (Figure 6). Given the strong coupling between the bar and shoreline at this site, this evolution of the bar generates in return a slight sinuosity in the shoreline that remains very small compared to the preexisting ones (figure 5).

Figure 5. Oblique images of camera 6 showing the diseappearance of the beach and shoreline 3D pattern after the adapation period following the deployment of the submerged structure.

In the case of Sète, it seems that the linearization of morphologies have modified the entire dynamics of the system. During storms, the double bar (inner bar + geotextile) seems to decrease significantly the incoming wave energy reaching the beach and, as shown previously, the shoreline retreat during similar events has strongly decreased, and even disappeared. A major event in November 2014 (*Hs*~5 m) induced a complete inundation of beach, but only a few hours after the event, the beach had recovered its initial width, suggesting a very good resilience, while similar events in 2011 used to create a 20 m retreat. Morevoer, the 3D pattern that was currently observed at this site has also disappeared, fully modifying the swash

circulation on aerial beach and the erosion of the dune foot that were observed before the deployment.

All these results suggest a positive role of the submerged structure on the behavior of the aerial beach. Of course, the monitoring has to be pursued and the evaluation of the efficacity of the structure should encompass the monitoring of the integrity of the containers (Jackson *et al*. 2002) and the evolution of the outer bar where was deployed the system.

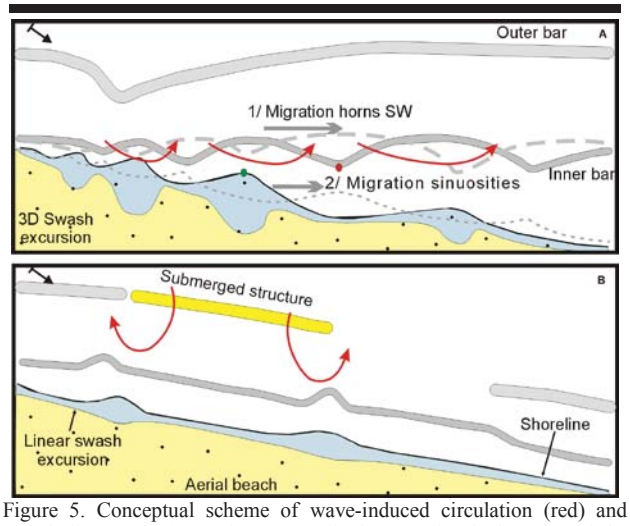

Figure 5. Conceptual scheme of wave-induced circulation (red) and morphology evolution vefore (A) and after (B) the deployment of the submerged geotextile structure.

CONCLUSIONS

The monitoring of the Lido of Sete beach before and after the deployment of a submerged geotextile structure permitted to obtain a very detailed and quantitative information on the nearshore bars and beach response. Results indicate that after an initial period, the system got to a new equilibrium state characterized by the rotation of the bar and shoreline parallel to the wave breaker. Moreover, monitoring during several storms and a major event in November 2014 suggests the efficiency of this structure on the Lido of Sete during storms. Monitoring is on-going to evaluate the impact on adjacent coasts, and a survey of the containers state is currently undertaken by the local authority to obtain a full feedback on the resistance and durability of this type of protection technique against coastal erosion. This particular site where a submerged structure is installed offshore of a very dynamic bar system provides a interesting feedback for the scientific community working of surfing and beach protection submerged reefs.

ACKNOWLEDGMENTS

The video system used in this work was funded by Thau Agglo and BRGM. Wave and water level data were provided by the DREAL-LR (Dir. Rég. Environnement, Aménagement et Logement) and are respectively part of the Candhis and Refmar networks.

LITERATURE CITED

Aarninkhof, S.G.J., Turner, I.L., Dronkers, T.D.T., Caljouw, M. and Nipius, L, 2003. A video-based technique for mapping intertidal beach bathymetry. *Coastal Engineering*, 49(4), 275-289.

Armaroli, C., Ciavola, P., 2011. Dynamics of a nearshore bar system in the northern Adriatic: A video-based morphological classification. *Geomorphology*, Vol. 126, pp 201-216.

Balouin, Y., Desbiendras, L., Gervais, M., Tesson, J., 2012. Dynamique à haute fréquence des barres d'avant-côte en milieu microtidal : suivi vidéo du Lido de Sete, Golfe du Lion. *XII*[èmes] *J. Nat. Génie Côtier-Génie Civil, Cherbourg, 169-178.*

Balouin, Y., Giusti, M., Tesson, J. and Gervais, M., 2013. Morphological feedback between nearshore bars and shoreline dynamics during storm events – video observations at Sete beach, France. *Proc. Coastal Dynamics* 13, France, 151-160.

Barusseau, J-P., and Saint-Guily, B., 1981. Disposition, caracteres et formation des barres d'avant-côte festonnées du Golfe du Lion. *Oceanologica Acta*, 4 (3): 297-304.

Castelle, B., Ruessink, B.G., Bonneton, P., Marieu, V., Bruneau, N. and Price, T.D., 2010. Coupling mechanisms in doublé sandbar systems. Part 1 Patterns and physical explanation. *Earth surface processes and Landforms*, 35:476-486.

Certain, R., 2002. Morphodynamique d'une côte sableuse microtidale à barres : le golfe du Lion (Languedoc - Roussillon). *PhD thesis*, Univ. Perpignan. 209 p., ann.

Certain, R., Meule, S., Rey, V. and Pinazo, C., 2005. Wave transformation on a microtidal barred beach (Sète, France). *Journal of Marine Systems*, 38: 19-34.

Fraysse, N. (2009). Déploiement de géotextile en zone littorale pour la protection d'une plage sableuse. Validation de configurations de déploiement de géotextiles par modélisation numérique de la circulation et de la houle sur la plage immergée. *Report, BRL Ing.*

Gervais, M., Balouin, Y., Belon, R. (2012) Morphological response and coastal dynamics associated with major storm events along the Gulf of Lions Coastlines, France. *Geomorphology* 143-144, 69-80.

Holman, R.A., Stanley, J., 2007. The history and technical capability of Argus. *Coastal Engineering*, 54, 477-491.

Jackson, A., Tomlinson, R., Corbett, B. and Strauss, D., 2002. Long term performance of a submerged coastal control structure: a case study of the narrowneck multi-functional artificial reef. *Proc. Coastal Engineering 2012*. *1*(33).

Plant, N.G., Aarninkhof, S.G.J., Turner, I.L. and Kingston, K., 2006. The performance of shoreline detection models applied to video imagery. *Journal of Coastal Research*, 23(3), 658-670.

Pope, L., 2008. BLIM (BarLine Intensity Mapper) Toolbox Manual. *Report R08-02 IMAR Utrecht*, Nov. 2008. 41 p.

Ranasinghe, R. and Turner, I.L., 2006. Shoreline response to submerged structures: a review. *Coastal Engineering*, 53: 65-79.

Rendle, E.J. and Davison M., 2012. An evaluation of the physical impact and structural integrity of a geotextile surf reef. *Coastal Engineering Proceedings*, 1, 33.

Turner, I.L., 2006. Discrimating modes of shoreline response to offshore detached structures. *Journal of Waterway, Port, Coastal, and Ocean Eng.*, ASCE, 132:180-191.

West, A.S., Coweel, P., Battjes, J.A., Stive, M.J.F., Doorn, N., Roelvink, JA., 2003. Wave focusing surfing reef – a new concept. *Proc. 3*[rd] *Int. Surfing Reefs Symposium*, NZ, 360-370.

Journal of Coastal Research	SI	75	622-626	Coconut Creek, Florida	2016

Stakeholder Perceptions of a Coastal Marine Protected Area

Beverley Clarke[†], Ruth Thurstan[†§], and Katherine Yates [† †† ‡]

[†]School of the Environment, Flinders University, Adelaide, Australia

[††]Australian Institute of Marine Science, Townsville, Australia

[§]Australian Research Council Centre of Excellence for Coral Reef Studies, University of Queensland, Brisbane, Australia

[‡]Global Change Ecology Lab, School of Biological Sciences, University of Adelaide, Adelaide, Australia

www.cerf-jcr.org

www.JCRonline.org

ABSTRACT

Clarke, B.; Thurstan, R.H.; and Yates, K.L, 2016. Stakeholder perceptions of a coastal marine protected area, . *In:* Vila-Concejo, A.; Bruce, E.; Kennedy, D.M., and McCarroll, R.J. (eds.), *Proceedings of the 14th International Coastal Symposium* (Sydney, Australia). *Journal of Coastal Research*, Special Issue, No. 75, pp. 622-626. Coconut Creek (Florida), ISSN 0749-0208.

Marine protected areas (MPAs) are an increasingly utilised marine and coastal management tool, with rates of designation rising steeply over the last twenty years. MPAs are most commonly designated for biological conservation objectives and the management is thus focused primarily on meeting conservation goals, with associated monitoring programs gathering data on a narrow suite of biological indicators. However, MPAs also have a wide range of potential social and economic impacts and the ability to meet the goals of an MPA is highly influenced by the often unmonitored perceptions and buy-in of local stakeholders. Here we examine a range of stakeholder perceptions concerning a coastal MPA in South Australia. We conducted semi-structured interviews with individuals engaged in the MPA's planning and designation process, as well as those involved with its ongoing management. We explored their understanding of the purpose of the MPA, whether they thought the MPA was successful and the future management challenges the MPA might face. In particular, we focused on eliciting from stakeholders indicators they thought should be used to monitor the ongoing performance of the MPA. Perceptions varied between stakeholder groups, however, the majority of respondents highlighted the importance of socio-economic factors in the ongoing performance of the MPA. The vast majority of them suggested both biological and socio-economic indicators that should be incorporated into monitoring programs. Our findings highlight the need for MPA planning and management, when defining goals and developing monitoring programs, to be mindful to incorporate social and economic, as well as, biological indicators.

ADDITIONAL INDEX WORDS: MPA**,** *marine conservation, marine biodiversity, indicator, South Australia.*

INTRODUCTION

Globally, marine biodiversity continues to decline (Sala and Knowlton, 2006), despite wide recognition of its essential role in maintaining the provision of marine ecosystem services (Beaumont *et al*., 2007; Lloret, 2010). Increasingly, management efforts to conserve marine biodiversity focus on the designation of marine protected areas (MPAs). MPAs are areas of the sea in which one or more activities are prohibited or managed in order to protect or restore certain features of interest and there have been drastic increases in the number of MPAs designated over the last 20 years (Pita *et al*., 2011). According to the IUCN the number of MPAs globally in 2013 had reached 10,280, covering 8.3km^2 or 2.8% of the world's seas and oceans (Kusumawati and Huang, 2015). MPAs exist in many forms and sizes ranging from multiple-use marine parks to highly protected 'no-go' sanctuaries.

While MPAs play a critical role in protecting marine biodiversity, ecosystem function and sustaining healthy coastal communities, they face many challenges in achieving their objectives (NOAA, 2013) and inadequacies in MPA design and management have led to many MPAs failing to achieve their goals (Weible, 2008). There are therefore concerns that MPAs are not achieving their full potential and that overall performance is relatively poor (Dalton *et al*., 2012; Kareiva, 2006; Pollnac *et al*., 2001); there is a danger of rejection of MPAs by adjacent communities if MPAs prove to be unsuccessful (Pollnac *et al*., 2001).

Increasingly authors argue that social factors, not biological or physical variables, are the primary determinants of MPA success or failure and that efforts to design more effective MPAs are hindered by a lack of research into the human dimensions of MPA development and management (Pollnac *et al*., 2010; Yates, 2014). According to Hamilton (2012: p.1) 'Social acceptance of MPAs must be achieved if they are to function as effective management tools'. However, 'It is often more difficult to get the social components of an MPA 'right' than the biological or physical components' (Pomeroy *et al*., p.157).

MPA planning processes vary greatly and implementation is context specific (Charles and Wilson, 2009; Pomeroy *et al*., 2006; Voyer *et al*., 2015) and so costs and benefits will be perceived and felt variously, especially between developed and developing countries and regions (Badalamenti *et al*., 2000). Impacts of MPAs on adjacent communities vary significantly. For example, communties or members of communities reliant on marine resources for livelihood will be directly affected by

DOI: 10.2112/SI75-125.1received 15 October 2015; accepted in revision 15 January 2015.

*Corresponding author: beverley.clarke@flinders.edu.au

resource use restrictions (Bennett and Dearden, 2014; Mascia *et al*., 2010). Many MPAs are introduced adjacent to heterogeneous communities representing diverse perspectives (Himes, 2007); and for this reason 'it is fundamental to successful conservation that these diverse perceptions are explored and considered' (Himes, 2007 p. 330). Community expectations not in keeping with goals and objectives of a given MPA will lead to misunderstanding and possibly conflict.

The human dimension of MPAs encompasses a complex weave of social, economic, and institutional considerations. This dimension affects all phases of MPA designation from planning through to monitoring and ongoing management. Charles and Wilson (2009) provide a succinct overview of people-oriented attributes they consider fundamental to the acceptance and ultimate success of MPAs (See Table 1).

A critical requirement is the support for the MPA by all stakeholders (including by the local management authority and adjacent community) (Himes, 2007; Kusumawati and Huang, 2015). More specifically, meaningful engagement or active participation of the community across all of the phases of MPA designation (from planning to implementation) is considered essential for realisation of MPA goals (Agardy, 2000; Charles and Wilson, 2009; Lundquist and Granek, 2005). Others suggest that if a community is able to see tangible results of a MPA (increased fish catch, tourism) that this is a measure of 'success'(Hoisington, 2013). The third most commonly cited social factor leading to success is how a community perceives its MPA because this will influence behaviour regarding the MPA (Bernstein *et al*., 2004; Himes, 2007; Pollnac *et al*., 2001). Indeed studies concur that where local perceptions of MPAs are positive, conservation outcomes are more likely to be successful (e.g. Bennett and Dearden, 2014). Understanding different perceptions, values and attitudes will also 'create opportunities for decison making that lead to concensus [for the majority of individuals] rather than conflict'(Brown *et al*., 2001 p. 418).

The cultivation of stewardship, defined as 'careful and responsible management to ensure goals and objectives are being achieved for the benefit of current and future generations' (NOAA, 2013: preface), is a prime mechanism to promote acceptance of MPAs (Himes, 2007). However, in order to achieve this end more needs to be understood about the human dimension of MPA management—local perceptions and social aspects of MPA implementation and management.

This paper focuses on stakeholder perceptions and presents a case study of the Encounter Marine Park, a coastal MPA in South Australia (See Figure 1). We investigate how socio-cultural or human dimensions have shaped or influenced the effectiveness of the Encounter Marine Park and what key stakeholder groups identify as important indictors of success. This is being done with the intention of developing a locally derived indicator set—one that corresponds to the local community's knowledge, behaviour and aspiration.

Background

South Australia has 19 MPAs (known locally as marine parks). The Encounter Marine Park was the 'pilot' park and therefore has had the longest history of public engagement. The 19 marine parks were designated under the South Australian *Marine Parks Act 2007* and are designed to represent all the biological diversity of South Australia's marine environment. While the Act focuses on biodiversity conservation and sustainable use, community stewardship is also a central object within the Act, the intent of which has been transferred to strategies and goals within individual marine park management plans. Establishment of Encounter Marine Park took many years, commencing in 2004 with scientific studies and outer boundary planning. An Act to regulate the parks was promulgated in 2009 and the internal zoning structure of parks and their management plans were implemented in 2012 (Kirkman, 2013).

Table 1. *Human Dimensions basic to the success of MPAs (after Charles and Wilson 2009)*

Objectives and attitudes	MPAs are created and function in the context of societal and/or community objectives, which inherently reflect human aspirations and values.
People-orientated 'entry points' for discussion	Social, economic, legal, and institutional instruments can be simultaneously drivers, constraints, and/or supports for the creation and implementation of MPAs, and affect outcomes.
Attachment to place	Each location has its unique social and ecological context that influences the MPAs' design, implementation, and impact.
Make participation meaningful	Strong participation has been demonstrated empirically to be a factor in the success of MPAs in various circumstances— in all stages (consultation, design, implementation, and monitoring).
Knowledge has a 'people side'	There is a critical need to supplement biophysical and ecological data with people-orientated information: human values and goals that relate to the area.
Effective governance is critical	MPAs require effective governance and well-functioning management institutions if they are to be ecologically and socially successful.
Get the rights right	There are basic issues concerning the nature of the rights (management rights and access rights) and who should hold them. Rights choices can have a major impact on the acceptability of MPAs.
Costs, benefits, and distribution	Implications of economic, social, and cultural aspects of MPAs have not been well studied Who benefits? Who suffers the costs? How are benefits and costs distributed spatially and temporally?
See MPAs in the bigger picture	It is important to see MPAs in the overall picture of marine conservation, of coastal livelihoods, of the broader socio-economic environment, including all the ocean uses, such as fisheries.

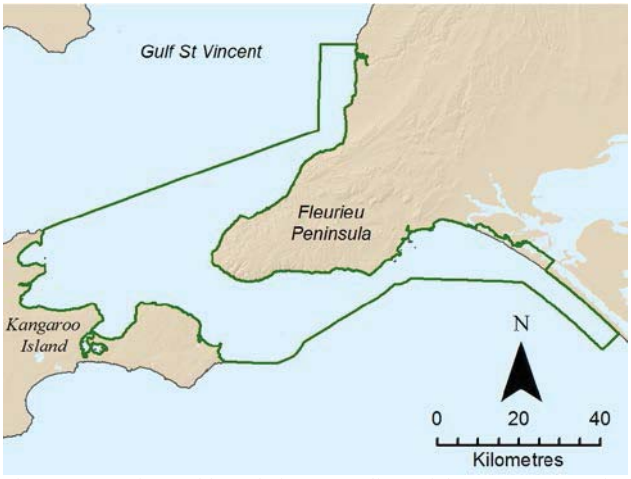

Figure 1. Location and boundaries (green line) of the Encounter Marine Park case study, South Australia.

METHODS

A series of interviews and focus groups with key stakeholders were conducted to canvass opinions regarding the MPA. The recruitment process targeted members of the wider community as well as people who had been engaged in the development and ongoing management of the marine park. Participants were selected in a veriety of ways. Some of the park management staff and state and local government officials were already known to the researchers. Leaders of sectoral primary industry, recreational and conservation groups were identified by internet searches and snowball sampling. Various volunteer and interest group networks were identified and forwarded an email that explained this project and invited participation of network members. All potential participants were sent a letter of invitation and followed up by telephone to create an appointment.

This paper is based on a preliminarly data set of 18 semi-structured face-to-face interviews conducted between April and May 2015. Different stakeholder groups are represented including state (n=5) and local governent (n=4), NGOs (n=3), commerical fishermen (n=2) and community group volunteers (n=4). The interview schedule consisted of a set of questions that explored respondents' knowledge of the marine park, its purpose and perceptions of success as well as seeking ideas about indicators to measure success. Interviews took between 40 minutes to one hour and were recorded for later transcription. The interviews were transcribed to a Word document and later uploaded to NVivo for coding and thematic analysis.

RESULTS

The following section presents the findings around four key elements:

a) Respondents understanding of the purpose of the MPA,
b) Perceptions of the park's success to date,
c) Future management challenges facing the MPA, and
d) Indicators that should be used to monitor the ongoing performance of the MPA.

Purpose of the Encounter Marine Park

Almost all of the respondents (n=17, 94%) defined the purpose of the marine park in ecological terms; with most people stating its raison d'être as habitat conservation (n= 11, 61%):

The marine park is basically to protect the habitat of the animals that are in there, so the flora and fauna… to actually protect certain areas and samples of the habitat types that actually exist in our waters (ID 15, NGO)

Other ecologically centred purposes identified by respondents included sustainable resource use and protection of fish stocks.

A small number of respondents thought the marine park had multiple purposes. Whilst it was noted the primary purpose was to conserve the environment it was suggested there were 'secondary aspirations' for the marine park that included educational, research and business opportunities:

There's a whole range of other purposes [apart from habitat conservation] things like…providing opportunities to stimulate the local economies in those regional areas where we have the parks… (ID 6, Regional Government).

The findings above show that respondents understood the objectives of the South Australian *Marine Parks Act 2007*.

Perceptions about the park's success to date

There was a mix of responses as to whether or not the park had been a success to date. Five of the eighteen respondents were certain the park was a success (from NGOs, state government, and the community). They thought that achieving the implementation of the park was in itself a success. Five respondents referred back to the process of implementation of the Park explaining there had been much dissatisfaction over the government's early processes (especially the consultation process). The majority of respondents however, thought that it was too early in the park's history to give a definitive answer (n=8) but they were able to identify some aspects of success. Social acceptance for the park was the main measure cited; initial 'noise' about the park and resistance to it had died down after its implementation, and there was some evidence of community ownership of the park:

From what I hear there is very little on-going community unrest [so] maybe it has been successful from that perspective (ID 18 Local Government)

In the end the peak [recreational] fishing body actually expressed qualified support for the marine park network. That in of itself is a success. (ID 13 Local Government)

Two respondents from the primary industry sector thought the park had not been successful. Their answers reflected concern over business losses in the region.

Future management challenges facing the MPA

When asked about future management challenges facing the marine park a number of interconnected concerns were raised: the need for unwavering political support, adequate funding, compliance and enforcement of rules, adequate monitoring and evaluation, the potential impacts of climate change, changing behaviours, and external threats such as competing commercial interests, land-based sources of pollution, and marine pests. Many of these nominated challenges are directly connected to state government support.

So how do you fund, adequately, [the environment]? It's just not done. So I think the biggest challenge for any of these marine parks is going to be finding the adequate resources to actually monitor and police, so that they can be successful. They won't be successful just because you put lines on a map. The difficulty that government's got though is, if you surveyed 50 people at random [asking], 'where should government spend it's money?' No one would vote for marine parks. So it needs to be a regulation requirement. (ID 18 Local Government)

Indicators to monitor the marine park's performance

Respondents were asked how they would measure the success of the marine park. Between them respondents generated a mix of indicators that could be used to gauge the performance of the Encounter Marine Park including environmental, social, and economic measures.

Ecological indicators

Sixteen of the 18 respondents identified several environmental indicators by which to measure the park's success: an improvement in habitat condition (rather than simply maintaining the habitat), an increase in size and numbers of fish stocks within the park, an increase in the diversity of benthic habitat, and contrasts to ecosystem health of sites adjacent to the park. It was noted by several respondents that these are the most obvious and easiest indicators to apply.

Social indicators

Three social measures were identified by respondents as key to success: acceptance of the park by the local community, an understanding of the purpose and need for the marine park by the community and, compliance. The indicators by which to measure these conditions included stewardship (an increase in the number of individuals and community groups that are doing something, or contributing to park management):

Helping to self-police the parks is an indicator for me that the parks are valued and that people are willing to help protect them. (ID 2 State Government)

In the longer term, ecological evidence is important but I think it's the community stuff, it's the harmonizing… if you can build that ownership and stewardship in the community, like we have with our national parks, if the community loves and owns [the parks], then they'll be there for perpetuity. It doesn't matter what the science says, really, if the community owns them, they'll care for them.(ID 3 State Government)

Economic indicators

Half of the respondents identified economic indicators by which to measure marine park success. Five people suggested that an increased number of tourism operations and activities would be proof that the marine park had expanded that sector. Other suggestions were more broadly conceived such as an increase in employment generally or changes to real estate or land value in a region:

'more jobs or less jobs or land prices rising or going down, that would be a good reflection of how successful [marine parks] are for people living in areas with marine parks...' (ID 10 NGO)

Fisheries-specific indicators included improved marketability of seafood products from the region and fishers fishing on the edges of the marine park (indicating more productive catches at such sites).

DISCUSSION

This paper has reported on a set of preliminary interviews with stakeholders from different sectors and government as well as non-government spokespersons who have a varied connection to South Australia's Encounter Marine Park.

The findings reported here suggest that the Park is already demonstrating some important achievements. Respondents perceived that the local community overall, has accepted the park. There was an indication that since implementation even the most adverse sectors had ceased to make complaints about the Park. Local compliance is an indication of both community buy-in and that governance arrangements are sound (Pollnac *et al*., 2010).

Like all MPAs, the Park faces complex and interwoven challenges, many of which were identified by respondents. Provision of funding towards the ongoing management of the park, community outreach, monitoring, and compliance will each be reliant on strong public and governmental support. Respondents felt that politicians would be more likely to support the Park if there is broad public acceptance and that public acceptance will likely be increased by demonstration of the Park's success. Thus there is a real need for this, and arguably every MPA, to demonstrate its success across a range of objectives. An indicator set that is meaningful to the community and that can be applied by the community would work towards assessing its success.

Sound evaluation programs for MPAs utilse appropriate indicators by which to measure effectiveness (Himes, 2007) and there is growing interest in the design of indicators to measure across the spectrum of MPA management goals including socio-economic, biophysical, and institutional (Pomeroy *et al*., 2005). The indicators that were raised by respondents in this study are not dissimilar to findings of other studies (Pomeroy *et al*., 2004; Staub and Hatziolos, 2004). Having said this, the indicators as stated by respondents were largely conceptual, and as such, require more development towards being used as evaluation instruments.

Meaningful engagement of the community in all aspects of MPA planning and management (noted in the literature as a requirement for MPA success) (Agardy, 2000; Charles and Wilson, 2009), was not a concept nominated by the 18 interviewees in this study.

CONCLUSIONS

There is great complexity in meeting both social and conservation goals assigned to MPAs. Different stakeholder groups perceive MPA success in different ways and understanding those differences is important when developing monitoring programs and for maintaining support for an MPA. This study shows the importance of including both socio-economic and ecological indicators of success and supports the importance of an enhanced understanding of the human dimension of MPAs. Development of the indicator sets that will be relevant to the stakeholder groups in this study is ongoing.

ACKNOWLEDGMENTS

The authors would like to acknowledge the support of the Wildlife Conservation Fund, South Australian Department of Water, Environment and Natural Resources.

LITERATURE CITED

Agardy, T., 2000. Information needs for Marine Protected Areas: Scientific and Societal. *Bulletin of Marine Science,* 66, 875-888.

Badalamenti, F.; Ramos, A.; Voultsiadou, E.; Sánchez Lizaso, J.; D'anna, G.; Pipitone, C.; Mas, J.; Ruiz Fernandez, J.; Whitmarsh, D., and Riggio, S., 2000. Cultural and socio-economic impacts of Mediterranean marine protected areas. *Environmental Conservation,* 27, 110-125.

Beaumont, N.J.; Austen, M.C.; Atkins, J.P.; Burdon, D.;Degraer; S., Dentinho; T.P., Derous; S., Holm, P.; Horton, T.; van Ierland, E.; Marboe, .H.; Starkey, D.J.; Townsend, M., and Zarzycki, T., 2007. Identification, definition and quantification of goods and services provided by marine biodiversity: implications for the ecosystem approach. *Marine pollution bulletin,* 54, 253-265.

Bennett, N.J. and Dearden, P., 2014. Why local people do not support conservation: Community perceptions of marine protected area livelihood impacts, governance and management in Thailand. *Marine Policy,* 44, 107-116.

Bernstein, B.; Iudicello, S., and Stringer, C., 2004. *Lessons Learned from Recent Marine Protected Area Designations in the United States*. A Report to: The National Marine Protected Areas Center NOAA. Ojai, California: The National Fisheries Conservation Center, 91p.

Brown, K.; Adger, W.N.; Tompkins, E.; Bacon, P.; Shim, D., and Young, K., 2001. Trade-off analysis for marine protected area management. *Ecological Economics,* 37, 417-434.

Charles, A. and Wilson, L., 2009. Human dimensions of Marine Protected Areas. *ICES Journal of Marine Science,* 66, 1-15.

Dalton, T.; Forrester, G., and Pollnac, R., 2012. Participation, Process Quality, and Performance of Marine Protected Areas in the Wider Caribbean. *Environmental Management*, 49, 1224-1237.

Hamilton, M., 2012. Perceptions of fishermen towards marine protected areas in Cambodia and the Philippines. *Bioscience Horizons,* 5, 1-24.

Himes, A.H., 2007. Performance indicators in MPA management: Using questionnaires to analyze stakeholder preferences. *Ocean & Coastal Management,* 50, 329-351.

Hoisington, C., 2013. *The Marine Protection Dividend NSW marine parks deliver more over time*. Sydney, NSW: Centre for Policy Development, Occasional Paper 34, 24p.

Kareiva, P., 2006. Conservation Biology: Beyond Marine Protected Areas. *Current Biology*, 16, R533-R535.

Kirkman, H., 2013. Choosing boundaries to marine protected areas and zoning the MPAs for restricted use and management. *Ocean & Coastal Management,* 81, 38-48.

Kusumawati, I. and Huang, H.-W., 2015. Key factors for successful management of marine protected areas: A comparison of stakeholders′ perception of two MPAs in Weh island, Sabang, Aceh, Indonesia. *Marine Policy*, 51, 465-475.

Lloret, J., 2010. Human health benefits supplied by Mediterranean marine biodiversity. *Marine pollution bulletin,* 60, 1640-1646.

Lundquist, C.J. and Granek, E.F., 2005. Strategies for Successful Marine Conservation: Integrating Socioeconomic, Political, and Scientific Factors. *Conservation Biology*, 19, 1771-1778.

Mascia, M.; Claus, C., and Naidoo, R., 2010. Impacts of marine protected areas on fishing communities. Conservation Biology 24, 1424-1429.

NOAA, 2013. *MPA Effectiveness. National Marine Protected Areas Center*. Santa Cruz, California, National Marine Protected Areas Center, MPA Science Institute, 52p.

Pita, C.; Pierce, G.J.; Theodossiou, I., and Macpherson, K., 2011. An overview of commercial fishers' attitudes towards marine protected areas. *Hydrobiologia*, 670, 289-306.

Pollnac, R.; Christie, P.; Cinner, J.; Dalton, T.; Daw, T.; Forrester, G.; Graham, N., and McClanahan, T., 2010. Marine reserves as linked social-ecological systems. *Proceedings of the National Academy of Sciences*, 107, 18262-18265.

Pollnac, R.B.; B.R. Crawford, and Gorospe, M.L.G., 2001. Discovering factors that influence the success of community-based marine protected areas in the Visayas, Philippines. *Ocean & Coastal Management*, 44, 683–710.

Pomeroy, R.; Mascia, M., and Pollnac, R., 2006. *Background paper 3: Marine Protected Areas, the Social Dimension, In: FAO Expert Workshop on Marine Protected Areas and Fisheries Management: Review of Issues and Considerations*. Rome FAO, pp. 149–275.

Pomeroy, R.S.; Parks, J., and Watson, L., 2004. How is Your MPA Doing? A Guidebook of Natural and Social Indicators for Evaluating Marine Protected Areas Management Effectiveness. Gland, Switzerland and Cambridge, UK: IUCN.

Pomeroy, R.S.; Watson, L.M.; Parks, J.E., and Cid, G.A., 2005. How is your MPA doing? A methodology for evaluating the management effectiveness of marine protected areas. *Ocean & Coastal Management*, 48, 485-502.

Sala, E. and Knowlton, N., 2006. Global marine biodiversity trends. *Annual Review of Environment and Resources*, 31, 93-122.

Staub, F. and Hatziolos, M.E., 2004. Score Card to Assess Progress in Achieving Management Effectiveness Goals for Marine Protected Areas. Washington DC: The World Bank, 29p.

Voyer, M.; Gladstone, W., and Goodall, H., 2015. Obtaining a social licence for MPAs – influences on social acceptability. *Marine Policy*, 51, 260-266.

Weible, C.M., 2008. Caught in a Maelstrom: Implementing California Marine Protected Areas. *Coastal Management,* 36, 350-373.

Yates, K.L., 2014. View from the wheelhouse: Perceptions on marine management from the fishing community and suggestions for improvement. *Marine Policy*, 48, 39-50.

Journal of Coastal Research	SI	75	627-631	Coconut Creek, Florida	2016

Which is the Best Predictor of Sea Temperature: Satellite, Model or Data Logger Values? A Case Study from the Maltese Islands (Central Mediterranean)

Alan Deidun †*, **Adam Gauci**†, **Joel Azzopardi**†, **Denis Cutajar**†, **Hazel Farrugia**† and **Aldo Drago**†

†Physical Oceanography Research Group
Department of Geosciences
University of Malta campus
Msida MSD 2080 MALTA

www.cerf-jcr.org

www.JCRonline.org

ABSTRACT

Deidun, A.; Gauci, A.; Azzopardi, J.; Cutajar, D., and Drago, A., 2016. Which is the best predictor of sea temperature: satellite, model or data logger values? A case study from the Maltese Islands (Central Mediterranean) *In:* Vila-Concejo, A.; Bruce, E.; Kennedy, D.M., and McCarroll, R.J. (eds.), XC *Proceedings of the 14th International Coastal Symposium* (Sydney, Australia). *Journal of Coastal Research*, Special Issue, No. 75, pp. 627-631. Coconut Creek (Florida), ISSN 0749-0208.

Water temperature data loggers were deployed at six different depths along a mooring line within Maltese coastal waters. A one-year timeseries of water column temperature data recorded by the same loggers over the September 2012- September 2013 period were compared, through the computation of Pearson correlation factor values, against satellite measures of the SST and against OPA (Ocean Parallelise) model values for the equivalent water depths. Results indicate that satellite-derived SST values are a good estimate of the water column temperature throughout the entire infralittoral zone during the winter and spring seasons, when the thermocline has not yet been established, whilst the degree of convergence between the two sets of values declines sharply during the summer and autumn seasons and extended only up to a depth of 8m and 10m, respectively. OPA model water temperature values for the various column depths give similar results when confronted against data logger values. Although the absolute thickness of the surface warm layer can't be established, one can conclude that this layer is relatively thicker in autumn than in summer.

ADDITIONAL INDEX WORDS: *SST; temperature; water column; correlation; Central Mediterranean; data loggers*

INTRODUCTION

Temperature is a key factor controlling the distribution of species and physiological processes (*e.g.,* Byrne *et al.,* 2009, Smale and Wernberg 2009). Within the marine domain, the monitoring of sea temperature is important in the study of coastal oceanography and in the assessment of biological resources and their response to pressures such as climate change. SST (Sea Surface Temperature) has, in fact, been reputed by a number of authors as being one of the most important water column variables in determining the preferred habitat for pelagic fish species. For instance, Bellido *et al.,* (2008), when generating high resolution Essential Fish Habitat (EFH) maps for sardine and anchovy, found that SST values, along with those for SSS, depth, longitude, latitude and chlorophyll-a, were the most useful in determining such habitats.

The influence of column temperatures on the distribution of autochthonous marine species within the Mediterranean (the so-called 'meridionalisation' phenomenon, whereby native species move further west and north within the Basin) and on allochthonous (or non-native, exotic, alien and Lessepsian) species within the same Basin (the so-called 'tropicalisation' phenomenon) has been documented in a huge volume of literature, with examples including the studies by Occhipinti-Ambrogi (2007), Bianchi (2007) and Lejeusne *et al.,* (2009). The warming of the Mediterranean water column is indicted by many biologists as spearheading the influx of non-native marine species in the Mediterranean. The concurrent monitoring of water column temperatures and of a number of indicator fish species forms in fact the backbone of the Tropical Signals programme operated by CIESM ((International Commission for the Scientific Exploration of the Mediterranean Sea - Moschella and the Tropical Signals team, 2009).

The operational collection of sea temperature datasets over large spatial scales is only possible through the adoption of satellite or mathematical model measures of water temperature (SST). Alternatively, in-situ data loggers or of thermosalinographs, which are instruments mounted close to the water intake of research and cargo ships, measure the sea surface salinity and temperature along the track of ships of opportunity (*e.g.,* Barton and Pearce, 2006). Occasionally, marine organisms, through telemetry, have been used, such as ringed seals (Lydersen *et al.,* 2004) or even high-resolution thermal imagery incorporated within cameras mounted on the underside of helicopters (Torgersen *et al*., 2001).

DOI: 10.2112/SI75-126.1received 15 October 2015; accepted in revision 15 January 2015.
*Corresponding author: alan.deidun@um.edu.mt

Satellite measures of sea temperature are collected from the upper ('skin') layer (*ca.* 0.01mm thick), which may be not representative of the temperature in the underlying water layers (the so-called 'bulk temperature'). Katsaros (2003) and Smale and Wernberg (2009) found a good degree of correspondence between SST values and underlying water temperatures, up to a depth of a few metres and up to 10-12m, respectively, but the water depth at which this concordance between the two sets of values tapers off is not known. Local atmospheric, sea and oceanographic conditions are known to influence the same relationship (Barton and Pearce, 2006), which is even affected by factors such as the thermal properties of the substratum, tides, waves and water clarity in coastal areas (Smale and Wernberg, 2006).

In addition to SST data, OPA (Ocean Parallelise) forecasting model data for a number of water column parameters, including water temperature, salinity, and surface sea currents and elevation, is also available through the same digital infrastructure. The OPA (Ocean Parallelise) model forms part of the Mediterranean Forecasting System, whose physical component is a coupled hydrodynamic-wave model implemented over the entire Mediterranean Basin. Contrary to direct satellite readings, which don't extend beyond the surface of the sea, OPA forecast model values for different sea depth (z) levels can be collected.

Small data loggers are currently available on the market for the measurement of a number of water column parameters, with the ones for water temperature and salinity being the most frequently-deployed. Some water temperature data loggers have been designed to be deployed in oceans at depths of up to 6000m (Pfender and Villinger, 2002) as well as in freshwater within streams (Dunham *et al.*, 2005).

The aims of this study include the assessment of SST as a proxy for actual water column temperature at depths of up to 42m, the influence of the onset of the thermocline on the degree of concordance between SST and in situ water temperature values at different depths and an evaluation of the performance of the OPA forecast model at different water depths. The accuracy or precision of satellite-derived SST's is beyond the scope of this study, within which no in-situ measurements of water temperature near the sea surface were taken. Such a typology of study is abundant in the literature (*e.g.,* Pearce *et al.*, 2006).

METHODS

A total of six water temperature data loggers (HOBO Water Temperature Pro v2), having a nominal accuracy of +/- 0.2^0C, were deployed constantly at water depths of 1m, 8m, 12m, 20m, 34m and 40m, between August 2012 and September 2013. The loggers were tied to the mooring line of a wave height monitoring buoy located *ca.* 2km off the north-western coast of the island of Gozo within the Maltese archipelago (Central Mediterranean- Figure 1). In order to identify any possible sea temperature differences between coastal and open water stations, a single data logger was deployed at a depth of 32m along a coastal vertical wall, between April 2012 and October 2013. The loggers record water temperature every hour and data is retrieved through an IR reader/port. Figure 2 illustrates the deployment of a sea temperature logger along the buoy mooring line.

Figure 1. Study area, indicating geographical location of the Maltese Islands within the Central Mediterranean.

An ad hoc digital interface, running on the Google Maps framework at http://maps.google.com, was developed by our team such that daily values for SST and OPA Forecast Model Temperature data for any marine area of interest could be extracted. When gleaning the SST and OPA model data from the ad hoc digital interface, a rectangular grid cell encompassing the entire area up to 3km from the coastline of the Maltese Islands was selected, having the following geographical coordinates: Longitude: 14.138489^0E to 14.610901^0E and Latitude: 35.766572^0N to 36.104596^0N.

Correlations (Pearson) between sea temperature values from all three sources (SST, OPA forecast model and data loggers) were run both on a daily and on a seasonal basis, at the different sea depths involved. To achieve this, hourly data from the data loggers was averaged out over the course of one day, and daily values from all three sources of data were averaged out over an entire season (January-March: winter; April-June: spring; July-September: summer; October-December: autumn). A Non-Metric Multidimensional Scaling (NMDS) plot, using untransformed data and Euclidean distance to assess similarity, for seasonal values for all three sources of sea temperature data, was also generated. Statistics were run using the PYTHON and PRIMER-E software packages.

RESULTS

Figure 2 plots the sea temperature at the various depths as recorded by both data loggers (A) and through the OPA forecast model (B). In order to assess the dichotomy between SST values and data logger values at progressive water depths, scatter plots contrasting the two sets of values for each water depth during each season were produced (Figure 3). A high level of consistency between the two sets of water temperature data is exhibited at all water column depths throughout the winter and spring seasons, whilst during the autumn and summer seasons the two sets of water temperature data converge only at depths reaching down to 10m within the water column.

To investigate whether these fluctuations are an artefact or whether they are real, water temperature values recorded during September 2012 by the in situ data loggers over a brief time span (few days) were homed upon, and these are reproduced as Figure 4. What is intriguing is that the abrupt diurnal thermal

anomalies, represented by spikes, were most evident at 20m and at 40m, and not at the surface, and that, in the most extreme case (15th September 2012), they represented thermal shifts of 6^0C over a mere 6 hours.

Through the use of Primer 6 software (Clarke and Gorley, 2006) Multi-Dimensional Scaling (MDS) plots were generated for each season using water temperature data from the three techniques deployed, in order to investigate the degree of clustering between the same values. The three water temperature monthly mean values for each season were averaged out for this purpose.

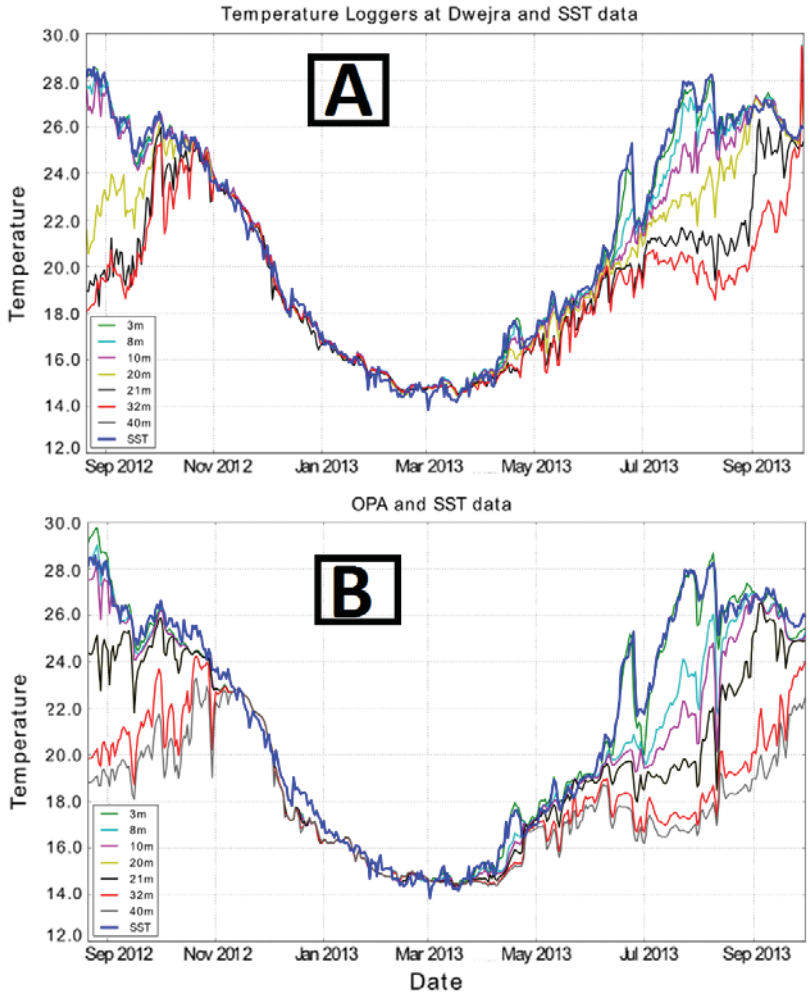

Figure 2. (a) Sea temperature recorded at the various water depths by in-situ data loggers; (b) sea temperature predicted for the various water depths by the OPA model. Blue line in both graphs represents the SST value.

A broad-brush examination of the annual water column temperature timeseries given in Figure 2 exposes pronounced fluctuations in water column temperature, even in the short term (*e.g.,* on a diurnal basis or over a few days). These fluctuations appear to be most evident during periods when the thermocline is in place, in particular during late summer (September).

DISCUSSION

The major advantage of deploying in situ water temperature data loggers is that, since data is collected on an operational basis, there is no shortage of validation match-up data to be contrasted with corresponding satellite-derived data which can be biased even by thin and small clouds (Barton and Pearce, 2006). This advantage is shared by the deployment of thermosalinographs on operational (*e.g.,* ferry) vessels, as has been successfully conducted within CIESM's PartnerSHIPS and the EU Commission's FerryBox projects, but not by the short-term, expensive deployment of high-accuracy devices on research vessels.

According to Drago *et al.* (2003) and Drago (1997), in Maltese waters, during the summer period, there is clear water stratification with a thermal step of 2.4^0C at a depth of 25 to

30m depth. Thermal stratification is gradually eroded as the winter season approaches, and strong surface cooling and vertical mixing come into action which result in the homogenisation of the water column up to depths of 100m, with temperatures around 15^0C; to the south the upper layer temperatures are around 2^0C higher (homogeneous up to 60 m) mainly due to the advection of warmer water from the south. The Maltese Islands are thus, very often situated within a frontal zone, with differences in temperature between the northern and southern shores.

Both our data logger and OPA model results indicate a late April/early May 2013 onset of the thermocline within Maltese coastal waters. The influence of the thermocline on the degree of agreement between SST and data logger values is considerable. In fact, Pearson correlation factor values for comparisons between the two sets of water temperature values at corresponding sea depths were higher than 0.95 only up to a depth of 10m and 8m for the summer and autumn seasons, respectively, when the thermocline is presumably in place, suggesting a slightly greater relative thickness of the thermocline layer during the autumn season than during summer.

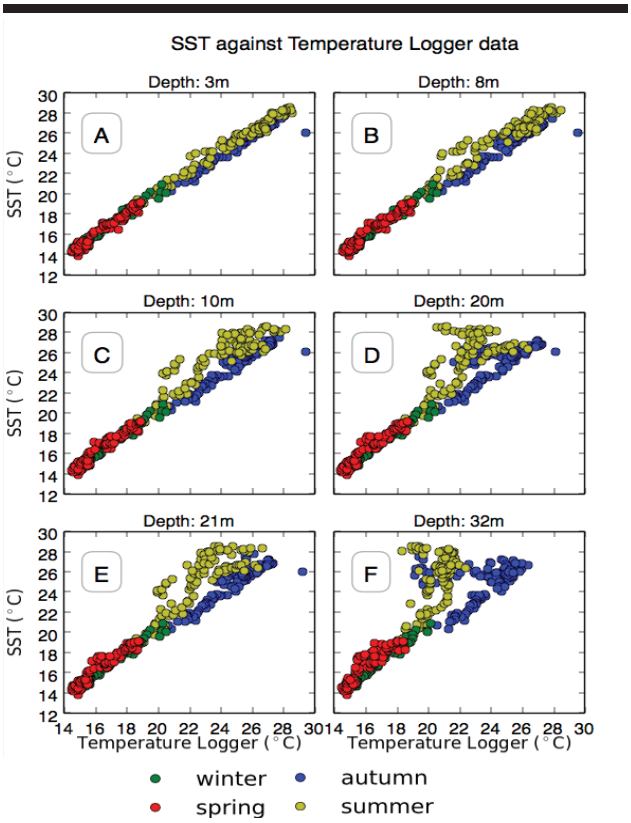

Figure 3. Scatter plots of seasonal SST vs data logger water temperatures values at the different water depths (1m, 8m, 12m, 20m, 34m, 40m).

Our results suggest that the first influence of the establishment of the thermocline layer is felt somewhere between 10m and 20m from the surface during the latter two seasons, since abrupt drops in Pearson correlation factor values for match-ups with satellite SST values were observed for this bathymetric transition. Since drops in correlation factors were observed during these two seasons right up to the deepest depth at which loggers were deployed – 42m – it is not possible to identify the absolute thickness of the surface warm layer.

Conversely, >0.95 Pearson correlation factor values were obtained for depths reaching up to 20m and 42m for the spring and winter seasons, respectively, when presumably the thermocline has been eroded away and a degree of thermal homogeneity had been established within the water column. Such seasonal differences are also reflected within the correlation values obtained for OPA model-data logger match-up pairs, with such a model giving similar values to match-ups with SST values, indicating that the same model does not make any allowance for the onset of the thermocline. In this sense, the MDS analyses gave somewhat conflicting results since OPA model and data logger values at corresponding water depths were largely grouped together within all seasons, with the exception of winter, although this outcome might be an artefact of the averaging technique applied.

A possible speculative explanation for such a phenomenon might be the sinking of saltier water from the surface, where it forms as a result of enhanced evaporation rates during certain periods of the day, to deeper layers. This bears some legitimacy in view of the syncronicity between successive spikes in water temperature as recorded by the data loggers, with a time lapse of 24 hours often separating the same spikes, which were often recorded during daytime (afternoon), which corresponds with the highest values of solar radiation and atmospheric temperatures. Additionally, although evident throughout the year, the thermal anomalies in question were of a much smaller magnitude during the non-thermocline seasons (late autumn – early spring), which also coincide with a reduction in atmospheric temperature within the area under investigation.

Shortcomings of the study include the following: (i) validation has been conducted on the basis of in situ data collected at one location only, (ii) using one satellite (MODIS) platform and (iii) one year of data only. In addition, (iv) atmospheric forcings, such as the possible diurnal warming of the near-surface layer as a result of wind fluxes, were not factored in and (v) the deployed data loggers were not calibrated prior to use. The absolute thickness of the surface warm layer can only be elucidated if data loggers are deployed at more frequent depth intervals within the water column than those adopted within the current study so as to identify more precisely the vertical position of the thermocline.

CONCLUSIONS

In this study, we have attempted to identify the best operational water column temperature monitoring method. The two ex situ methodologies included in the study (i.e. SST measurements from space and OPA model values) performed in a similar fashion when contrasted statistically with the values yielded by the only in situ method used (data loggers), suggesting that if such methodologies are to be used throughout the year, they are only useful for anticipating

surface water temperatures due to the seasonal onset of the thermocline.

SST and OPA model values can be a useful predictor of water column temperature within the entire infralittoral zone (up to a depth of 42m) but only during the winter and spring seasons, when the thermocline is not operational. Although the absolute thickness of the surface warm layer established during the summer and autumn seasons could not be determined from the current study, the layer is relatively thicker during the autumn season. This could be deduced from the fact that higher Pearson correlation factors were obtained at a depth of 10m for both SST-data logger and OPA model-data logger match-ups during the autumn season. Thus, the methodology described in the current study can be useful in identifying seasonal and inter-annual variations in the onset of the thermocline and in its relative thickness.

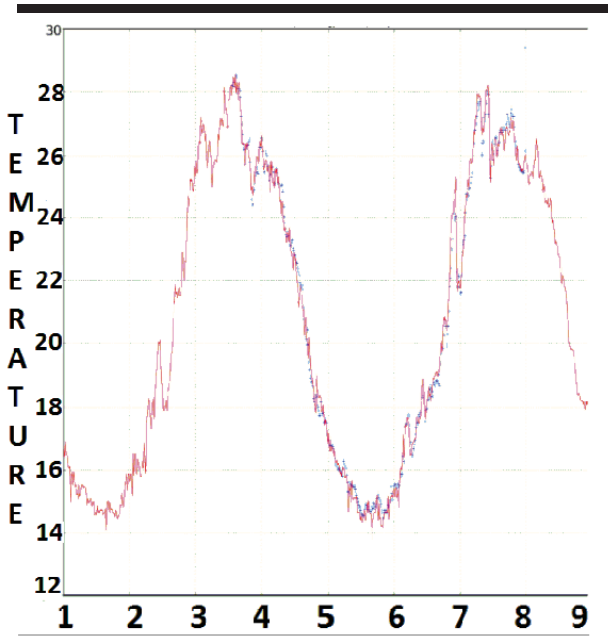

Figure 4. Abrupt shifts in water column temperature recorded by data loggers at a depth of 3m during a number of days in September 2013.1 = Jan 2012; 2 = Apr 2012; 3 = Jul 2012; 4 = Oct 2012; 5 = Jan 2013; 6 = Apr 2013; 7 = Jul 2013; 8 = Oct 2013.

ACKNOWLEDGMENTS

This publication was inspired by CIESM's Tropical Signals Programme which donated the first set of water temperature loggers deployed within this study.

LITERATURE CITED

Adityawan, M.B. and Tanaka, H., 2013. Shoreline changes at Sendai port due to the great northeast Japan tsunami of 2011. *Coastal Dynamics*, 45(1), 63-72.

Barton, I. and Pearce, A., 2006. Validation of GLI and other satellite-derived sea surface temperatures using data from the Rottnest Island ferry, Western Australia. *Journal of Oceanography* 62, 303–310.4

Bellido, J.M.; Brown, A.M.; Valavanis, V.D.; Giraldez, A.; Pierce, G.J.; Iglesias, M.; Palialexis, A., (2008). Identifying essential fish habitat for small pelagic species in Spanish Mediterranean waters. *Hydrobiologia* 612, 171-184.

Bianchi, C.N., 2007. Biodiversity issues for the forthcoming tropical Mediterranean Sea. *Hydrobiologia* 580,7-21.

Byrne, M.; Ho, M.; Selvakumaraswamy, P.; Nguyen, H.D.; Dworjanyn, S.A., and Davis, A.R., 2009. Temperature, but not pH, compromises sea urchin fertilization and early development under near-future climate change scenarios. *Proceedings of the Royal Societ of London*, B 276, 1883–1888

Clarke, K.R. and Gorley, R.N., 2006. PRIMER v6, User Manual/Tutorial. PRIMER-E, Plymouth.

Drago, A.F. 1997. Hydrographic Measurements in the North Western Coastal Area of Malta, *Xjenza*; 2(1), 6-14.

Drago, A.F.; Sorgente, R., and Ribotti, A., 2003. A high resolution hydrodynamic 3-D model simulation of the Malta shelf area. *Annales Geophysicae*, 21, 323–344.

Occhipinti-Ambrogi, A., 2007. Global change and marine communities, Alien species and climate change. *Marine Pollution Bulletin*, 55,342-352.

Pearce, A.; Faskel, F., and Hyndes, G., 2006. Nearshore sea temperature variability off Rottnest Island (Western Australia) derived from satellite data. *Int. J Remote Sens*, 27, 2503–2518.

Pfender, M. and Villinger, H., 2002. Miniaturized data loggers for deep sea sediment temperature gradient measurements. *Marine Geology*, 186(3-4), 557-570.

Robinson, A.R.; Sellschopp, J.; Warn-Varnas, A.; Leslie, W.G., and Lozano, C.J., 1999. The Atlantic Ionian Stream. *Journal of Marine Systems*, 20, 129-156.

Smale, D.A., and Wernberg, T., 2009. Satellite-derived SST data as a proxy for water temperature in nearshore benthic ecology. *Marine Ecology Progress Series*, 387, 27-37.

Torgersen, C.E.; Faux, R.N.; McIntosh, B.A.; Poage, N.J., and Norton, D.J., 2001. Airborne thermal remote sensing for water temperature assessment in rivers and streams. *Remote Sensing of Environment*, 76, 386-398

Journal of Coastal Research	SI	75	632-636	Coconut Creek, Florida	2016

Defining the Trophic Status of Maltese (Central Mediterranean) Coastal Waters through the Computation of Water Quality Indices Based on Satellite Data

Hazel Farrugia [†*], Alan Deidun[†], Adam Gauci[†], and Aldo Drago[†]

[†] Physical Oceanography Research Group
University of Malta
Msida, Malta

www.cerf-jcr.org

www.JCRonline.org

ABSTRACT

Farrugia, H.; Deidun, A.; Gauci, A., and Drago, A., 2016. Defining the trophic status of Maltese (Central Mediterranean) coastal waters through the computation of water quality indices based on satellite data. *In:* Vila-Concejo, A.; Bruce, E.; Kennedy, D.M., and McCarroll, R.J. (eds.), *Proceedings of the 14th International Coastal Symposium* (Sydney, Australia). *Journal of Coastal Research*, Special Issue, No. 75, pp. 632-636. Coconut Creek (Florida), ISSN 0749-0208.

The Maltese Islands have to comply with onerous EU legislation in order to protect the integrity of their water resources in a comprehensive manner. To date, operational monitoring of water quality parameters within the Maltese coastal waters is almost non-existent. This present study was carried out to compute and map values for the CSI023(+) and modified TRIX indices, using satellite and model data for the entire Maltese Fisheries Management Zone (FMZ); and to identify trends in such index values and relate these to anthropogenic activities, geolocation, bathymetry and seasonal factors. Temporal analyses of ocean colour and index values revealed the following seasonal trend, in decreasing order of value: winter, autumn, spring, and summer. Ocean colour and TRIX index values indicate that, overall, chlorophyll-a values for the 2002-2011 period and 2013-2014 period are consistent with those of oligotrophic, poorly productive waters, with a high water quality. CSI023(+) values for the 2002-2011 period indicated that the Maltese marine area shows a statistically insignificant trend of variation in chlorophyll-a values, possibly due to the low spatial resolution of the ocean colour dataset used. Statistical analyses shows that bathymetry and west/east geolocation have an influence on the trophic status of the Maltese FMZ. Water quality indices computation from satellite and model data enables the fulfilment of the mandatory, contemporary water quality monitoring requirements Malta has and enables the formulation of water quality management recommendations. This research can be integrated in an operational online system as a decision-making tool.

ADDITIONAL INDEX WORDS: *Water quality indices, ocean colour, marine management.*

INTRODUCTION

Malta, lying within the Sicily Channel in the Central Mediterranean, as party to the Barcelona Convention, and member of the European Union (EU), needs to comply with several onerous obligations in order to protect the integrity of its water resources in a comprehensive manner. Transposed EU legislation include the Marine Strategy Framework Directive (2008/56/EC) and the Water Framework Directive (WFD, 2000/60/EC). Descriptor five of the MSFD specifically lists the reduction of human-induced eutrophication.

Both the WFD and MSFD have stipulated phytoplankton biomass as one of the parameters for quality assessment because it can respond to nutrient enrichment (Nixon, 1995). Huot *et al*. (2007) confirm that, for studies of primary productivity, chlorophyll-a (chl-a) is indeed the best proxy of phytoplankton biomass.

Furthermore, both directives operate on a large scale and necessitate the assessment of several indicators which are computed frequently and which are backed up by an adequate sampling and/or analytical effort.

Satellite observations of ocean colour are critical in the monitoring of the state of the marine environment, as they provide information at unprecedented temporal scales over large spatial areas in a cost-effective manner (Lindell *et al*., 1999). Modelling is also crucial in marine trophic state studies since it enables the simulation of the physical, biogeochemical and biological processes and their interactions (Karydis & Kitsiou, 2012).

Water quality indices, which integrate complex analytical conditions into a single parameter, are advantageous because they improve communication with the public and facilitate water management (Cude *et al*., 1997). Coppini *et al*. (2013) developed the CSI023(+) index based on ocean colour products which complements the EEA's *in situ* CSI023 index. The trophic index TRIX was proposed by Vollenweider *et al*. (1998), based on factors that are the direct expression of productivity and nutritional factors.

Currently there is no operational monitoring of water quality parameters within Maltese coastal waters for the determination of the trophic status of the same waters. Although several *ad hoc*

DOI: 10.2112/SI75-127.1 received 15 October 2015; accepted in revision 15 January 2015.
*Corresponding author: hazel.farrugia.09@um.edu.mt

marine productivity studies, primarily based on *in situ* data collection exercises, can be found in the grey literature, such as unpublished University dissertations, most of these sources are generally limited to *in situ* measurements only. Coastal water monitoring exercises based on satellite data are still very limited in time, mostly restricted to specific localities and fail to cover the entire Maltese Fisheries Management Zone (FMZ, *e.g.* Deidun *et al*., 2011). Attempts at using satellite and/or model derived data for computation of the CSI023(+) and TRIX indices are a cost-effective and reliable means of inferring marine water quality. No long-term water-quality assessment been carried out for the marine area of the Maltese Islands, and there is, therefore, a need for information on the trophic status of Maltese marine waters through the computation of water quality indices based on satellite and model data to address knowledge gaps in this respect.

The two main aims of this study were to (1) compute and map values for the CSI023(+) and TRIX trophic state indices, for a set timeframe, using satellite data for the Maltese marine area and to (2) identify trends in such index values and relate these to anthropogenic activities, geolocation, bathymetry and seasonal factors.

METHODS

The study area encompassed the entire Maltese FMZ, approximated at 46 kilometres (25 nautical miles) from the baselines of the Maltese Islands, defined using Google Earth version 7.1.2. The FMZ was chosen as a domain because of (i) the relatively low spatial resolution of the satellites data sets used, and (ii) the obligations of the European MSFD, which is applicable to the entire Maltese FMZ.

By means of the Copernicus Marine Environment Monitoring Service (CMEMS) web portal (http://www.marine.copernicus.eu), the present authors were granted open-access to the three different CMEMS satellite and model data sets.

The daily surface chlorophyll concentration values spanning between 01/01/2002 and 31/12/2011 originated from combining data from SeaWiFS, MODIS-Aqua and MERIS sensors. The spatial resolution of this level 4 data product is four kilometers.

The monthly interpolated means of surface chlorophyll concentration values spanning between 01/01/2014 and 31/12/2014 were attained from the MODIS-Aqua and NPP-VIIRS sensors. The data were obtained by using an updated version of the MedOC3 algorithm. The spatial resolution of this dataset is one kilometre.

The daily analysis of the molar concentration of nitrate, molar concentration of phosphate, concentration of chlorophyll-a, and molar concentration of dissolved molecular oxygen in sea-water at -1.47m depth, spanning between 01/01/2013 and 31/12/2014, was generated by the OPATM-BFM model system. The output of the Med-MFC current products were used as a physical forcing. Version 4 has a horizontal resolution of 1/16° (approx. six kilometres).

Analysis

Initially, quality control for the truncation of extreme colour values was conducted. In view of the oligotrophic nature of the Central Mediterranean, the lower chlorophyll threshold was not set. Conversely, since the chlorophyll concentration in the open seas of the same geographical area rarely exceeds 2-3 mg m^{-3} (D'Ortenzio & Ribera d'Alcalà, 2008), the upper limit for chl-a concentration was set to 3.3 mg m^{-3}. Considering the historical sea temperature range for this part of the Mediterranean, no anomalous SST values were detected in the satellite datasets. The extent of non-availability of satellite data ("blind spots") in waters contiguous to the coast shifted temporally. To address this, a fixed threshold of 10 days was set as the minimum required number of days each month when satellite data was available in order to generate a valid monthly value for the same grid-point.

The decadal daily ocean colour dataset and monthly ocean colour dataset were used to assess the possible influence of forcing variables.'Seasons' were not adopted on a calendar basis but as the following three-month periods: winter: January-March; spring: April-June; summer: July-September; autumn: October-December. The three factors of geolocation (distance from the coast and west/east areas), bathymetry and seasonal variability were chosen *a priori* in view of their putative forcing nature on chlorophyll-a concentration.

The FMZ marine area was arbitrarily divided into three segments with respect to the baselines of the Maltese Islands: (i) "nearshore waters" (≤ 3 km); (ii) "non-coastal territorial waters" (3-22 km); and (iii) "outside territorial waters" (22-46 km). This was carried out using Google Earth version 7.1.2.

The mean ocean colour value for each 'distance-from-the-coast' cohort for each month in 2014 was computed and cohort values were analysed by means of the Kruskal-Wallis test in order to determine if there were any differences between monthly mean ocean colour values during 2014 based on distance from the Maltese baselines.

Subsequently, the entire Maltese FMZ was arbitrarily divided into three categories: (i) "shallow", less than 100 m depth; (ii) "mid-depth", between 100 and 350 m depth, and (iii) "deep", exceeding 350 m depth.

The monthly ocean colour value for each depth category, segregated along seasonal lines as well (considering each month as a replicate) was computed over the decadal dataset. A Brown-Forsythe test was performed to test the null hypothesis of homogeneity of variances. Since such a hypothesis was rejected, A two-way permutational multivariate analysis of variance (PERMANOVA) (Anderson, 2001) using the crossed design was performed in order to detect statistically significant differences between the ocean colour values for the three bathymetric cohorts and for different seasons, and to detect any interactions between such factors. Despite the fact that PERMANOVA was designed to carry out multivariate analyses, it can also be used to perform univariate ANOVA in cases where there is only a single variable in the analysis, and the similarity index used is based on Euclidean distances. The resulting sum of squares and F ratios are exactly the same as Fisher's univariate F statistic in traditional ANOVA (Anderson, 2001). For balanced designs, PERMANOVA is quite robust to heterogeneity of variances and differences in correlation structure (Anderson & Walsh, 2013). The Mann Whitney *post hoc* pairwise tests were subsequently used. PERMANOVA analysis was conducted with 10,000 permutations, based on Euclidean distances. This test was performed using the PAST

software version 3.08 (PAleontological STatistics, Hammer & Harper). Pairwise tests were performed using SPSS version 21.0 (Statistical Package for Social Sciences, SPSS Inc.).

The rationale behind the west-east delineation is based on the prevailing complex circulation within the Malta-Sicily shelf area and the Strait of Sicily. Such a delineation was justified on the basis of the physical analysis of monthly satellite sea surface temperature (SST) values within the same marine area for the same period (2002-2011), SST maps of different years and months exhibit a natural separation between west and east areas; consequently, through these maps, the Maltese FMZ was divided into west and east categories.

The SST data was categorised according to sector (west and east sides) and season (considering each month as a replicate). A Brown-Forsythe test was performed to test the null hypothesis of homogeneity of variances. PERMANOVA (Anderson, 2001) using the crossed design was carried out in order to detect statistically significant differences between the ocean colour values for the two categorical geographical sectors and for different seasons. This was performed using the PAST software version 3.08 (PAleontological STatistics, Hammer & Harper). Pairwise tests were performed using SPSS version 21.0 (Statistical Package for Social Sciences, SPSS Inc.).

The decadal ocean colour dataset was used in order to compute the recently developed water quality index CSI023(+). The annual mean summer CSI023(+) index value in mg m^{-3} (mg m^{-3})$^{-1}$ yr^{-1} was calculated and plotted for the entire FMZ of the Maltese Islands, according to the methodology proposed by Coppini *et al*. (2013). These analyses were made using MATLAB version 8.3 (Matrix Laboratory, The MathWorks Inc.).

Since only nitrate, phosphate (Pho) and dissolved molecular oxygen (DOx) concentrations were freely available from the online databases, these replaced the factors originally proposed by Vollenweider *et al*. (1998) within the TRIX index. The scale coefficients k and m, introduced to fix the lower limit and upper limit values of the index, ranging from 0 to 10 TRIX units were constructed according to the corresponding two year model dataset.

No nitrate and phosphate minimum and maximum ranges for the Maltese Islands exist in literature. For DOx, the 156-406 millimol m^{-3} range was adopted as the minimum and maximum thresholds, since DOx readings in Maltese waters during different seasons have always spanned between the 250-313 millimol m^{-3} range. Lower extreme values emerged as peaks between successive values, and these were removed in order to increase the sensitivity of TRIX as proposed by Vollenweider *et al.* (1998).

The ranges for each chl-a, Pho and DOx datum were standardised to three log units; however, for nitrate, this standardisation was increased to five log units, so as to include the entire range of model data set values. The scale coefficients were determined as -2.1 and 1.4 for k and m respectively.

The modified TRIX index was calculated for each day for each grid-point within the marine area under study. Graphs representing the daily mean TRIX values for the entire time period were produced. These analyses were performed using MATLAB version 8.3 (Matrix Laboratory, The MathWorks Inc.).

RESULTS

There was no statistically significant difference ($p > 0.05$) between the mean monthly ocean colour values for nearshore, non-coastal territorial waters, and outside territorial waters.

The mean ocean colour within the Maltese FMZ area for winter, spring, summer and autumn seasons in the arbitrarily-defined bathymetric categories (shallow, mid-depth and deep categories) were 0.126 ± 0.0067, 0.0598 ± 0.00098, 0.0455 ± 0.00028 and 0.0745 ± 0.00078 mg m^{-3} respectively. PERMANOVA results show that the interaction effect between shallow, mid-depth and deep categorical sectors and season was not statistically significant ($p > 0.05$). However, both the effect of depth on mean ocean colour as well as of season on mean ocean colour values were statistically significant ($p < 0.001$).

The pairwise *post hoc* tests revealed that all seasons were statistically significantly different from all the other seasons (p values < 0.001). Winter had significantly higher mean ocean colour values than spring, summer and autumn; autumn had significantly higher mean ocean colour values than spring and summer, whilst the mean ocean colour values for spring were significantly higher than summer. Furthermore, shallow waters had a statistically significantly higher mean ocean colour values than both mid-depth and deep waters (p values < 0.001).

A Brown-Forsythe test showed that for the west-east areas, the data here again violated the homogeneity of variances assumption ($p < 0.05$), justifying the need to run once again a two-way univariate PERMANOVA to detect statistically significant differences between the ocean colour values for the two categorical sectors and for different seasons, as well as any interaction effects. PERMANOVA results show that the interaction effect between categorical geographical sector and season was not statistically significant ($p > 0.05$). However, both the effect of depth on mean ocean colour as well as of season on mean ocean colour values were statistically significant ($p < 0.001$).

The eastern sector showed statistically significantly higher mean seasonal ocean colour values than the western sector. Seasonal pairwise *post hoc* tests revealed the same results as those obtained for the three bathymetric layer analyses: all seasons were statistically significantly different from the other seasons (p values < 0.001). Winter had significantly higher mean ocean colour values than spring, summer and autumn; autumn had significantly higher mean ocean colour values than spring and summer, whilst the mean ocean colour values for spring were significantly higher than summer.

The annual mean summer CSI023(+) in mg m^{-3} (mg m^{-3})$^{-1}$ yr^{-1} was calculated for the FMZ of the Maltese Islands; the Mann-Kendall statistical test applied to each chl-a grid-point in order to identify the statistical significant values at a 95 % confidence level indicated that none of the chl-a grid-points within the FMZ domain showed a significant incremental or decremental trend in values.

The mapped CSI023(+) values (Figure 1) suggest that, close to the coast, one generally encounters increasing chl-a concentrations. The highest increase in chl-a concentration was observed along the northern coastline of Malta, particularly in the harbour area, and in the Gozo-Malta channel. In contrast, decreasing chl-a trends were detected in more offshore waters, although northwestern offshore waters were characterised by

increasing chl-a trends.

Figure 2 shows the daily mean trophic index values for the marine area under study. Overall, both 2013 and 2014 follow the same general trend in mean TRIX values. TRIX values are highest during January and February, which gradually decrease during March, after which they decrease at a higher rate. In 2014, TRIX values then increased again after mid-September, whilst in 2013 this increase occurred later in the year, at around mid-November. The TRIX standard deviation shows that natural variability in index values is low.

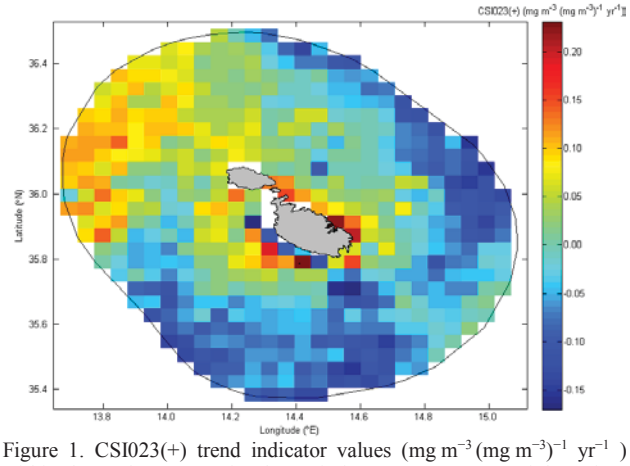

Figure 1. CSI023(+) trend indicator values (mg m^{-3} (mg m^{-3})$^{-1}$ yr^{-1}) within the Maltese FMZ for the period 2002-2011. None of the values are statistically significant.

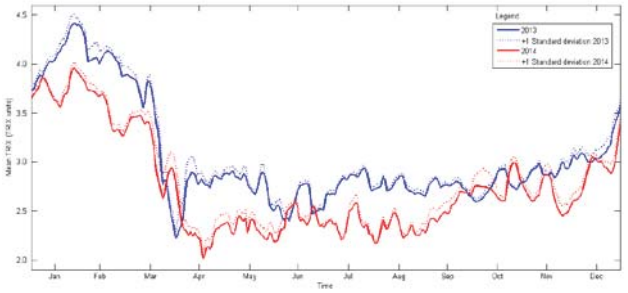

Figure 2. Time-series of daily mean TRIX values in the marine area enclosed within the FMZ area.

DISCUSSION

The results presented in this study document the first comprehensive determination of the trophic status of the Maltese FMZ over a relatively long time period via the computation of water quality indices, supplemented by chl-a indicator analysis.

The results of the assessment of both the putative forcing variables of bathymetry and west-east areas, using the same decadal dataset (2002-2011 period), indicate that season variability is significantly influencing the mean ocean colour values. The mean ocean colour values within the Maltese FMZ rank, in decreasing order of value, as follows: winter, autumn, spring and summer. The findings can be explained in terms of the shift between thermal stratification and mixing periods, which results in strong seasonality of primary production (Estrada, 1996).

Based on the eutrophication scale as defined by Simboura *et al*. (2005), the ocean colour values for spring, summer and autumn suggest the presence of oligotrophic waters with a high ecological quality status for all categorical cohorts. In contrast, for all categorical cohorts, the Maltese marine area in winter can be classified as lower mesotrophic, attaining a good ecological water quality status.

The factor of distance from the coast indirectly assesses the possible influence of terrestrial run-off. The results indicate that there was no statistically significant differences between the mean monthly ocean colour values for the three arbitrary distance-from-the-shore sectors. This result was not, at face value, expected, as the majority of anthropogenic activities which influence the nutrient input into the marine environment are mostly aggregated near the coast (such as treated sewage effluents, fish farms, and land run-off). The non-linear relationship between nutrient concentrations and chl-a concentrations, the heavy marine traffic in the marine area around the Maltese Islands which may lead to offshore nutrient-rich dumping of wastes, and offshore hydrological phenomena may also explain this finding.

The results of the bathymetric analyses revealed that shallow waters had statistically significantly higher mean ocean colour values than both mid-depth and deep waters. Drago (2003) expounds that in areas where the water flow encounters a shallow zone on the sea bottom, the deep, colder water is forced upwards as it progresses over the shelf; this activity transports high concentrations of nutrients from the sea bottom to the surface waters, fuelling marine food webs.

The results also indicate that the east sector had, as expected, a higher ocean colour mean than the west sector, due to the prevailing hydrodynamic phenomena operating within this area. The AIS (Atlantic Ionian Stream) produces mixing and upwelling east of Malta. Specifically, along the AIS and over shallow areas, especially around the Maltese Islands, substantial eddy field structures may also be produced, which trap water and particulates, leading to exchange of properties between the surface and the interior of the water column (Drago *et al*., 2013).

The CSI023(+) index results suggest that none of the chl-a grid-points within the Maltese marine area show a statistically significant trend, indicating that the trend in the chl-a concentration at each 4x4km grid-point within the study area is stable. Coppini *et al*. (2013) highlights the fact that high spatial resolution of the ocean colour images will produce a more robust trend estimate than a lower resolution one.

Nonetheless, increasing CSI023(+) index values within the Maltese FMZ for the period 2002-2011 were observed along the northern coastline of Malta, particularly in the harbour area, and in the Gozo-Malta channel. Higher CSI023(+) values in areas immediate to the coast conform with expectations due to diffuse sources of anthropogenic nutrients. Increasing chl-a trends in the Gozo-Malta channel may be partly explained by the presence of a tuna fish farm located in this area, and its distinct physical forcing – in particular, wind exposure, water current regime and

bathymetry (MEPA, 2011).

The present study developed and applied a modified trophic index TRIX formula. The time-series plot of the TRIX trophic index for 2013 and 2014 is analogous to the temporal periodicity observed for ocean colour over the 2009-2010 period in Maltese coastal waters (Deidun *et al.*, 2011).

The results of this study show that both 2013 and 2014 follow the same general trend in daily mean TRIX values for the Maltese FMZ area. The observed winter (January-February) peak in TRIX values is consistent with ocean colour values recorded for Maltese coastal waters (Deidun *et al.*, 2011) and for the Mediterranean Sea in general (Estrada, 1996). The subsequent increase in TRIX values most probably corresponded with the breakdown of the thermal stratification.

Based on the water body TRIX index value ranking criteria devised by Nasrollahzadeh *et al*. (2008), in 2013, the marine area under study was characterised by high water quality, representing oligotrophy (low trophic level), and poorly productive waters, except for a few days during January and February. These two months were characterised by a higher trophic status, termed mesotrophy, due to moderately productive waters which indicate a good water quality. Conversely, the Maltese marine area was characterised all throughout 2014 by poorly productive waters, denoting oligotrophy, and consequently a high water quality.

CONCLUSIONS

The Maltese FMZ over the 2002-2011 period and 2013-2014 period was mostly characterised by oligotrophic, poorly productive waters, and a high water quality. This study promotes satellite ocean colour as an ideal tool for the operational monitoring of water quality of the Maltese marine area. A higher spatial and temporal resolution of ocean colour products will ensure better assessment, but probably at higher costs. This research can be integrated in an operational online system which assesses the intensity of water enrichment via the computation of water quality indices, that is, an online marine downstream service.

ACKNOWLEDGEMENTS

The research work disclosed in this publication is partially funded by the Master it! Scholarship Scheme (Malta). This Scholarship is part-financed by the European Union – European Social Fund (ESF) under Operational Programme II – Cohesion Policy 2007-2013, "Empowering People for More Jobs and a Better Quality Of Life. The authors would like to acknowledge the support of Dr Claudette Spiteri, Dr Rita Lecci, Dr Cristina Mazziotti, Mr Denis Cutajar and Prof. Liberato Camilleri.

REFRENCES

Anderson, M. J. 2001. A new method for non-parametric multivariate analysis of variance. *Austral Ecology*, *26*(1), 32–46.

Anderson, M. J., and Walsh, D. C. I. 2013. PERMANOVA, ANOSIM, and the Mantel test in the face of heterogeneous dispersions: What null hypothesis are you testing? *Ecological Monographs*, *83*(4), 557–574.

Coppini, G., Lyubarstev, V., Pinardi, N., Colella, S., Santoleri, R., and Christiansen, T. 2013. The use of ocean-colour data to estimate Chl-a trends in European Seas. *International Journal of Geosciences*, *4*(6), 927–949.

Cude, C., Dunnette, D., Avent, C., Franklin, A., Gross, G., Hartmann, J., … Quin, T. 1997. Exploring the possibilities for an international water quality index applied to river systems. *In*: Best, G., Bogacka, T., and Niemirycz, E. (eds.), *Second International River Quality Symposium* (Gdansk, Poland), pp. 205–210.

D'Ortenzio, F., and Ribera d'Alcalà, M. 2008. On the trophic regimes of the Mediterranean Sea: A satellite analysis. *Biogeosciences Discussions*, *6*(2), 139–148.

Deidun, A., Drago, A., Gauci, A., Galea, A., Azzopardi, J., and Mélin, F. 2011. A first attempt at testing correlation between MODIS ocean colour and in situ chlorophyll-a measurements within Maltese coastal waters. *Proceedings SPIE8175, Remote Sensing of the Ocean, Sea Ice, Coastal Waters and Large Water Regions* (Prague, Czech Republic), pp. 81750J-1–81750J-8.

Drago, A., Azzopardi, J., Gauci, A., Tarasova, R., Ciraolo, G., Capodici, F., … Gacic, M. 2013. Sea surface currents by HF radar in the Malta channel. *Rapp. Comm. Int. Mer Medit.*, *40*, 144.

Estrada, M. 1996. Primary production in the northwestern Mediterranean. *Scientia Marina*, *60*(Supl. 2), 55–64.

Huot, Y., Babin, M., Bruyant, F., Grob, C., Twardowski, M. S., and Claustre, H. 2007. Does chlorophyll a provide the best index of phytoplankton biomass for primary productivity studies? *Biogeosciences Discussions, European Geosciences Union (EGU)*, *4*(2), 707–745.

Karydis, M., and Kitsiou, D. 2012. Eutrophication and environmental policy in the Mediterranean Sea: A review. *Environmental Monitoring and Assessment*, *184*(8), 4931–4984.

Lindell, T., Pierson, D., Premazzi, G., and Zilioli, E. (Eds.). 1999. *Manual for Monitoring European Lakes using Remote Sensing Techniques* (EUR 18665). Luxembourg: Office for Official Publications of the European Communities, 184p.

MEPA. 2011. *The Water Catchment Management Plan for the Maltese Islands*. First Water Catchment Management Plan for the Maltese Islands 2011, 147p.

Nasrollahzadeh, H. S., Din, Z. Bin, Foong, S. Y., and Makhlough, A. 2008. Trophic status of the Iranian Caspian Sea based on water quality parameters and phytoplankton diversity. *Continental Shelf Research*, *28*(9), 1153–1165.

Nixon, S. W. 1995. Coastal marine eutrophication: A definition, social causes, and future concerns. *Ophelia*, *41*, 199–219.

Simboura, N., Panayotidis, P., and Papathanassiou, E. 2005. A synthesis of the biological quality elements for the implementation of the European Water Framework Directive in the Mediterranean ecoregion: The case of Saronikos Gulf. *Ecological Indicators*, *5*(3), 253–266.

Vollenweider, R. A., Giovanardi, F., Montanari, G., and Rinaldi, A. 1998. Characterization of the trophic conditions of marine coastal waters with special reference to the NW Adriatic Sea: Proposal for a trophic scale, turbidity and generalized water quality index. *Environmetrics*, *9*(3), 329–357.

Journal of Coastal Research	SI	75	637-641	Coconut Creek, Florida	2016

Aquaculture Pond Precise Mapping in Perancak Estuary, Bali, Indonesia

Niken F. Gusmawati [†§*], Cheng Zhi[†], Benoît Soulard[‡], Hugues Lemonnier[‡] and Nazha Selmaoui-Folcher[†]

[†]Pôle Pluridisciplinaire de la matière et de l'environnement (PPME)
University of New Caledonia
Nouméa, New Caledonia

[‡]IFREMER LEAD-NC
Nouméa, New Caledonia

[§]Balitbang KP, Ministry of Marine Affairs and Fisheries of Indonesia
Jakarta, Indonesia

www.cerf-jcr.org

www.JCRonline.org

ABSTRACT

Gusmawati, N.F.; Zhi, C.; Soulard, B.; Lemonnier, H., and Selmaoui-Folcher, N., 2016. Aquaculture ponds precise mapping in Perancak Estuary, Bali, Indonesia. *In:* Vila-Concejo, A.; Bruce, E.; Kennedy, D.M., and McCarroll, R.J. (eds.), *Proceedings of the 14th International Coastal Symposium* (Sydney, Australia). *Journal of Coastal Research*, Special Issue, No. 75, pp. 637-641. Coconut Creek (Florida), ISSN 0749-0208.

Indonesia is one of the biggest producers and exporters of shrimp in the world. Shrimp ponds mapping and monitoring will be of critical importance for supporting decision-making regarding the development of sustainable fisheries. Therefore, automatic processing, acceptable quality, and efficient aquaculture mapping are urgently required. The objective of our work is to develop an automatic classification procedure for aquaculture mapping and monitoring, using the Edge Detection Based (EDB) method on very high spatial resolution satellite image. Then we compare the result obtained with EDB with results given respectively by the unsupervised classification method Isodata implemented using ArcGIS (IUC) and a region growing segmentation (RGT) method implemented in SPRING. The broken structure of embankments, dried-up ponds, ongoing development ponds, also abundance of algae and mangrove vegetation in the ponds present significant challenges to establish an accurate map. The aquaculture map provided by EDB successfully identified a high proportion of the existing ponds (> 95%) and overall accuracy of 84% and a kappa coefficient of 0.68. On the other hand, IUC and RGT produced a lower proportion of ponds (between 60 and 80 %) with lower overall accuracy and needed manual refinements. The present study also showed a potential in discriminating different types of ponds. That could be used for a further objective of analyzing the spatiotemporal changes of the ponds and thus improving shrimp farming development.

ADDITIONAL INDEX WORDS: *Aquaculture, shrimp ponds mapping, edge-based segmentation, classification, high-resolution satellite imagery.*

INTRODUCTION

Aquaculture has been growing at a rapid pace and is one of the fastest-growing food industries in the world. Most of aquaculture farms are situated in Asia, and Central and South America. For example, there were 7.1 million ha devoted to aquaculture in China in 2003; 902,900 ha in Vietnam in 2004 and 732,019 ha in Indonesia in 2003 (FAO, 2015).

Indonesia, as an archipelagic country, has an extensive coastline. The area utilized for brackishwater farming was estimated at 0.6 million ha in 2012. The available surface for brackishwater aquaculture was 2.3 million ha (MMAF, 2013). Aquaculture farming has become one of the primary sources of income for coastal communities. However, the aquaculture development has enormous environmental and socio-economic impacts at production sites, including the destruction of mangrove forests, salinization of coastal and agricultural lands, loss of genetic diversity in shrimp populations, conflicts and violence over land rights, access to natural resources, and coastal water pollutions.

The sustainable practice of aquaculture farming is a high priority of Indonesian government that aims to reduce these impacts. Consequently, useful tools need to be developed to improve the sustainability of aquaculture farming, the preservation of coastal resources and the management of human activities.

Geographic Information Systems (GIS) and remote sensing have been used to manage existing aquaculture activities and to define potential areas to build new farms (*e.g.* Beltrame *et al.*, 2006). Acquisition of spatial data is important for decision-makers. The spatial data can include information on the cadastre of aquaculture farms, mangrove, coastal line, infrastructure, water, and soil quality. This can be utilized to identify and monitor spatial changes in aquaculture farms at different time periods using satellite images (Nath *et al.*, 2000). Detection of the type of aquaculture farms (*e.g.* active or abandoned farms;

DOI: 10.2112/SI75-128.1 received 15 October 2015; accepted in revision 15 January 2015.
*Corresponding author: niken.gusmawati@etudiant.univ-nc.nc

fish, shrimp, seaweed or shellfish farms) is a framework to achieve sustainable management objectives.

The cadastre of aquaculture farming can be developed using very high spatial resolution (VHSR) satellite imagery. It offers great detail and covers vast areas for visual observation. Detection and delineation of aquaculture ponds can be conducted by utilizing the spectral response pattern of VHSR images and taking into consideration of field conditions (Dwivedi and Kandrika, 2005). Therefore, accurate maps of aquaculture farm locations, areas, and shapes can be established (Alexandridis *et al.*, 2008).

Automatic processing, acceptable quality, and efficient aquaculture mapping based on remote sensing and VHR images are urgently required to provide promptly spatiotemporal information to decision support tools for sustainable fisheries policy. Several image classification techniques were developed to contribute to this mapping process. The method of classification and segmentation methods using Object-Based Image Analysis (OBIA) have been widely used (Burnett and Blaschke, 2003). They are particularly suitable for analyzing medium to high spatial resolution satellite images. Their mapping capabilities have been extended by incorporating spatial and textural attributes of homogenous sets of pixels (Meinel *et al.,* 2001). However, land use/cover classification analysis using high spatial resolution satellite images remains quite difficult due to the very high spatial variability of physical elements on the surface (Tuan, 2010). On the other hand, traditional Pixel-Based Image Analysis (PBIA) has encountered issues with high-resolution imagery, resulting in 'a salt and pepper appearance' that leads to very general land cover information, or limited accuracy in thematic maps (Zhu *et al*., 2000). In this paper, we propose a new method based on edge detection. Images are processed to find the boundaries of objects to facilitate segmentation and object recognition (Saini and Garg, 2012). Results obtained with this method will be compared with those generated by two other methods: (i) Region Growing Segmentation followed by ISOSEG unsupervised classification (RGT) and (ii) Isocluster unsupervised classification (IUC). RGT method, which has been widely used in many remote sensing applications, can create closed regions (Espindola *et al*., 2006). It permits to extract the water surface and pond embankment limits (Virdis, 2014). IUC has been used to classify aquaculture zones and generate aquaculture farm cadastre (Hossain *et al.*, 2002).

METHODS

Perancak estuary system is almost 5 km long and covers an area of approximately 1800 ha. It is located at 8°23'2.78"S and 114°37'21.16"E, about 80 km northwest of Denpasar in Bali Province, Indonesia. This study area was chosen because it was a complex zone consisting of aquaculture ponds of various sizes and types. They included active shrimp ponds in traditional, semi-intensive and intensive culture systems; abandoned shrimp ponds with water, without water, with natural vegetation and mangrove plantation conditions; fish ponds; and polyculture ponds (algae/fish and shrimp). Based on a November 2014 survey, there were more than 75% of abandoned ponds. The broken structure of embankments, low contrast between soil and pond embankments in dried-up ponds, ongoing ponds development, also abundance of algae and mangrove vegetation inside the ponds made it difficult to extract enclosed contours with a high accuracy.

A dataset of aquaculture facilities built by GPS mapping and visual interpretation, and validated by field surveys in May and November 2014, was used as a reference. The boundaries of all ponds were delineated manually on-screen based on the reference map. This reference map was used to assess the accuracy of the maps resulting from different classification methods as well as to calculate the proportion of detected ponds.

Figure 1. Study site in Perancak Estuary, Bali, Indonesia

In this work, three segmentation and classification methods were conducted to build the cartography of ponds automatically: namely, Region Growing Segmentation algorithm followed by ISOSEG unsupervised classification method (RGT) using SPRING software, isocluster unsupervised classification method (IUC) using ArcGIS software, and Edge Detection Based (EDB) segmentation method implemented in C++. A World-View-2 image acquired on March 14, 2014, with four bands of standard multispectral colors and one panchromatic band, was used as a reference image for visual interpretation and also for automatic mapping. The WV-2 image has a sensor resolution of 0.46 m GSD at nadir for panchromatic and 1.85 m for multispectral. It was registered in UTM Projection (WGS 84 datum, UTM Zone 50s) using 40 ground control points (GCPs) that were collected during a differential GPS survey in 2014. The image is clipped into selected Region of Interest (ROI) to show aquaculture areas.

IUC Method

Image pre-processing and classification: After contrast enhancement, several classes of land cover were identified in the multispectral image using IUC, without knowledge of the field.

Automatic vectorization: ArcScan, as an extension tool in ArcGIS, provides automatic vectorization. Raster symbology of raster layers was changed from stretched to two unique values. A type of polygon was also chosen as part of vectorization setting

Figure 2. Aquaculture map obtained using three classification methods. (a) World View-2 image; (b) RGT; (c) IUC; (d) EDB. (—abandoned pond with young vegetation; ..... dry active pond; - - watered active pond; — dry abandoned pond; - . - abandoned pond with mature vegetation)

Post-vectorization refinement: Several connected ponds that appear in the result were separated by manual editing.

RGT method

Image pre-processing and filtering: Contrast enhancement of panchromatic image was conducted with 3x3 sliding kernel and one iteration.

Image segmentation: Similarity option and minimum area (pixel) thresholds were tested to achieve optimally segmented output.

Image classification: Using the unsupervised clustering algorithm ISOSEG, several thresholds, and different iteration values were tested without significant processing time differences between runs. The classification output was converted into vector layers.

Post-vectorization refinement: Further refinement by manual delineation was required, as same as IUC post-vectorization.

EDB method

Image pre-processing and filtering: Panchromatic image was filtered by 3x3 Gaussian filter to remove noise and obtain a smooth image.

Edge detection based segmentation and adaptive thresholds: In this study, an improved Canny edge detection method was employed to process the panchromatic image. Canny algorithm introduces hysteresis thresholds, which allow significant adaptation to local content in images. The higher threshold Th was calculated using Ostu method and the lower threshold (Tl) was determined by using Canny initial formula Tl = 0.5Th, which guarantee completeness and accuracy of the contours. Pixel value above Th was classified as edge whereas pixel value lower than

Tl were discarded. Pixel value between these thresholds would be recognized as contours if they were already connected to an accepted pixel.

Color based segmentation and Image Fusion: For the purpose of extracting drained and ongoing development ponds, a color classification using a color threshold of 90 was performed in parallel with the multispectral image. Segmented panchromatic and the segmented multispectral images were then fused together to get a complete map of ponds.

Shape Recognition and Image Classification: A shape recognition method was applied to eliminate interference factors. An area threshold ranging from 300 to 10,000 pixels was optimal to identify aquaculture ponds. Moreover, a shape factor (SF), derived from the ratio of perimeter and area showed promising results in identifying of aquaculture ponds based on their elongated shape (SF $\geq$ 1.2). Vectorization was then conducted using ArcGIS tool.

Accuracy Assessment

To analyze the relative suitability of different classification methods for mapping, assessment of map accuracy was performed on the classification results from IUC, RGT and EDB by using the confusion matrix, the kappa coefficient of agreement and the proportion of ponds correctly identified (Foody, 2004).

RESULTS

Figure 2 shows the results from the three classification methods used to build pond shape and create an aquaculture map of the Perancak estuary.

RGT method (Figure 2b) could delineate the ponds and produced closed polygons. It worked well in the homogeneous areas, such as green planktonic water in the active ponds (– –). Highly heterogeneous areas such as dry ponds or low-level water ponds (.....), as well as in all textured areas as mangrove of abandoned ponds (—) were under-segmented. This under-segmentation could cause under-estimation in the proportion of identified ponds.

The unsupervised classification implemented in IUC (Figure 2c) showed a good overall mapping. It created smoother arcs, straighter lines, and better-shaped polygons than RGT and EDB. IUC produced polygons in homogeneous areas and low heterogeneous areas (═). However, it did not succeed in creating complete zones in textured areas.

EDB (Figure 2d) could detect and delineate ponds in heterogeneous and textured areas that were hardly extracted by RGT and IUC, even though it generated rough and pointed polygons. However, it still could not develop polygons in heavily textured areas, such as mature mangrove forests in abandoned ponds that broke and grew pass over the embankments (– .).

The percentages of ponds identified by RGT, IUC and EDB, were 62%, 81%, and 96%, respectively (Table 1). EDB percentage was the highest because EDB was able to extract ponds in zones efficiently where the other methods could not.

Table 1. *The proportion of identified and unidentified aquaculture ponds.*

Aquaculture ponds	RGT	IUC	EDB
Identified ponds (unit)	835	1091	1295
Unidentified ponds (unit)	517	261	57
Proportion of ponds identified (%)	62	81	96

Accuracy assessment of the three methods is showed in Table 2. The overall accuracy for EDB was 84%, with a Kappa statistic of 0.68. The accuracy and Kappa statistic were higher for RGT and IUC.

Table 2. *Accuracy Assessment for different classification methods.*

Classification	Overall Accuracy (%)	Kappa coefficient
RGT	65	0.30
IUC	77	0.54
EDB	84	0.68

DISCUSSION

Suitable segmentation parameters for RGT were a similarity of 5 pixels and a minimum area of 750 pixels. These settings were similar to the study of Virdis (2014). Homogeneous areas were well delineated, but RGT was hardly able to generate complete ponds in heterogeneous areas. In under-segmentation cases, region growing segmentation failed to recognize edges. It could not locate object boundaries and actual edges because neighboring pixels with the same or similar values could not be clustered in the same region. Alternatively, region growing could detect boundaries but did not meet an actual adjacent edge in the image. When over-segmentation occurred, the actual edge pixels might be joined to other pixels in their neighborhood (Singh *et al.*, 2011; Xiaohan and Ylä-Jääski, J., 1992). The segmentation process for the image WV-2, which took more than 3 hours, made the operation and data handling more complicated, while steps consisting of cadastre integration into map tasks were easily performed within an external GIS software.

IUC could create a smooth cadastre of the aquaculture ponds. Its fast processing time and integration with GIS spatial analysis added advantages to this method. The method depends on spectral signature and statistical information in the image, and users did not have control of the clustering process. Classes determined did not correspond to characteristics in the field area, such as the roof of the building. As unsupervised classification method was not sensitive to covariation and variations in the spectral signature of objects, especially to the low contrast image. This method could produce some missing and connectivity of ponds that inevitably lead to a lower accuracy of the map (Fraisse *et al.*, 2001).

The EDB approach proposed in this paper achieved a high segmentation and classification accuracy. EDB had overcome the limitations related to sensitivity to noise and low image contrast by using a Gaussian filter and Canny operator. It did not need manual refinement of contours and it could improve the accuracy of segmentation in a significant manner. On the contrary, the other methods needed to be followed by manual refinement. Moreover, a result not presented in this paper showed that EDB could detect the broken structure of embankment between ponds. Although some of them were small and inconspicuous, they could be extracted by this procedure. That would be very beneficial for further analysis of abandoned ponds by experts.

The EDB approach possessed three key advantages over both IUC and RGT. Firstly, it could largely reduce the salt-pepper effect as a result of Gaussian filter. Secondly, it took into account not only spectral properties but also shape features that provided a dominant factor for the classification. Thirdly, the Canny operator improved by Ostu method permitted to improve segmentation accuracy by effectively conserving details and slight borders to delineate a clearer and complete enclosed map.
The result of visual observation and the proportion of ponds identified were in line with the overall accuracy and Kappa coefficient, and EDB results were consistently higher than IUC and RGT ones. With respect to classification performance suggested by Richards (2013) in Table 3, Kappa value for EDB indicated that there was a good agreement between aquaculture map generated from the VHR image and the reference data. Thus, the EDB method could produce aquaculture maps with good accuracy. On the contrary, the map accuracy was lower for IUC and RGT.

Table 3. *Classification performance of Kappa Coefficient.*

Kappa coefficient	Classification performance
Below 0.4	Poor
0.41 – 0.60	Moderate
0.61 – 0.75	Good
0.76 – 0.80	Excellent
Above 0.81	Almost perfect

CONCLUSION

The baseline of information for a proper and sustainable development of aquaculture is critical to support decision-making. Some information can be generated from mapping and monitoring of aquaculture areas at regular intervals using satellite remote sensing. In general applications, RGT and IUC could be utilized in aquaculture mapping for intensive and super-intensive farms that have homogeneous water and clear boundaries of embankments. EDB could be used to map more complex aquaculture systems, but it needs improvement with regards to smoothness of pond boundaries. These three methods failed to generate a cadastre for abandoned ponds with very dense vegetation. Therefore, classification by vegetation indices might be useful for that application and should thus be integrated into the mapping process.

ACKNOWLEDGEMENTS

This work is funded by the INDESO – CLS Project for Shrimp Farming Monitoring Application, which is led by Balitbang KP - Ministry of Marine Affairs and Fisheries, Indonesia. We would like to thank Dr. Christophe Proisy for images sharing, and the JCR reviewers for their advice regarding the improvement of this paper.

LITERATURE CITED

Alexandridis, T.K.; Topaloglou, C.A.; Lazaridou, E., and Zalidis, G.C., 2008. The performance of satellite images in mapping aquacultures. *Ocean & Coastal Management*, 51, 638-644.

Beltrame, E.; Bonetti, C., and Bonetti Filho, J., 2006. Pre-selection of Areas for Shrimp Culture in a Subtropical Brazilian Lagoon Based on Multicriteria Hydrological Evaluation. *Proceedings ICS 2004. Journal of Coastal Research*, Special Issue No. 39, pp. 1838-1842.

Burnett, C. and Blaschke, T., 2003. A multi-scale segmentation/object relationship modeling methodology for landscape analysis. *Ecological Modelling*, 168, 233-249.

Dwivedi, R.S. and Kandrika, S., 2005. Delineation and monitoring of aquaculture areas using multi-temporal space-borne multispectral data. *Current Science*, 89(8), 1414-1421.

Espindola, G.M.; Câmara, G.; Reis, I.A.; Bins, L.S., and Monteiro, A.M., 2006. Parameter selection for region-growing image segmentation algorithms using spatial autocorrelation. *International Journal of Remote Sensing*, 27(14), 3035-3040.

FAO, 2015. *Fishery and aquaculture country profiles.* http://www.fao.org/fishery/countryprofiles/search/en

Foody, G.M., 2004. Thematic Map Comparison: Evaluating the Statistical Significance of Differences in Classification Accuracy. *Photogrammetric Engineering & Remote Sensing*, 70(5), 627–633.

Fraisse, C.W.; Sudduth, K.A., and Kitchen, N.R., 2001. Delineation of site-specific management zones by unsupervised classification of topographic attributes and soil electrical conductivity. *Transactions of the ASAE*, 44(1), 155-166.

Hossain, Z.; Muttitanon, W.; Phillips, M., and Tripathi, N. K., 2002. Monitoring shrimp farming development from the space: A RS and GIS approach in Kandleru Creek area, Andhra Pradesh, India. *Proceedings of the Map Asia 2002* (Bangkok, Thailand).

Maini, R. and Aggarwal, H., 2009. Study and Comparison of Various Image Edge Detection Techniques. *International Journal of Image Processing*, 3(1), 1-11.

Meinel, G.; Neubert M., and Reder, J., 2001. The potential use of very high-resolution satellite data for urban areas – first experiences with IKONOS data, their classification, and application in urban planning and environmental monitoring. *Regensburger Geographische Schriften*, 35, 196-205.

MMAF, 2013. *Fisheries and Marine in Numbers 2013*. Jakarta: Center of Data, Information and Statistic, Ministry of Marine Affairs and Fisheries of Indonesia, 212p.

Nath, S.S.; Bolte, J.P.; Ross, L.G., and Aguillar-Manjarrez, J., 2000. Applications of geographical information systems (GIS) for spatial decision support in aquaculture. *Aquacultural Engineering*, 23, 233-278.

Richards, J., 2013. *Remote sensing digital analysis*. Heidelberg New York Dordrecht London: Spring, 494p.

Saini, V. and Garg, R., 2012. A Comparative Analysis on Edge Detection Techniques Used in Image Processing. *IOSR Journal of Electronics and Communication Engineering*, 1(2), 56-59.

Singh, R.; Singh, H; Sharma, P., and Sharma, S., 2011. Edge Based Region Growing. *Int. J. Comp. Tech. Appl.*, 2(4), 1122-1126.

Tuan, V.A., 2010. Semi-Automatic Forest Classification Using Free and Open Sources Software. *Proceedings of the 31st Asian Conference on Remote Sensing* (Hanoi, Vietnam), Vol. 1, pp. 246-251.

Virdis, S.G.P., 2014. An object-based image analysis approach for aquaculture ponds precise mapping and monitoring: A case study of Tam Giang-Cau Hai lagoon, Vietnam. *Environmental Monitoring and Assessment*, 186(1), 117-133.

Xiaohan, Y. and Ylä-Jääski, J., 1992. Image segmentation combining region growing and edge detection. *Proceedings of the 1st IAPR International Conference on Pattern Recognition.* (The Hague, Netherland), Vol III, pp. 482-484.

Zhu, Z.; Yang, L.; Stehman, S.V., and Czaplewski, R.L., 2000. Accuracy assessment for the U.S. geological survey regional land-cover mapping program: New York and New Jersey region. *Photogrammetric Engineering and Remote Sensing*, 66(12), 1425-1435.

Journal of Coastal Research	SI	75	642-646	Coconut Creek, Florida	2016

Managing Threats to the Marine Estate in New South Wales (Australia) to Maximise Community Wellbeing

Alan Jordan†, Sarah Fairfull*, Bob Creese†

† NSW Department of Primary Industries, Port Stephens Fisheries Institute, Nelson Bay, NSW 2315, Australia.
* NSW Department of Primary Industries, Wollongbar Primary Industries Institute, Wollongbar NSW 2477, Australia.

www.cerf-jcr.org

www.JCRonline.org

ABSTRACT

Jordan, A., Fairfull, S., Creese, R. 2016. Managing threats to the Marine Estate in New South Wales (Australia) to maximise community wellbeing *In:* Vila-Concejo, A.; Bruce, E.; Kennedy, D.M., and McCarroll, R.J. (eds.), *Proceedings of the 14th International Coastal Symposium* (Sydney, Australia). *Journal of Coastal Research*, Special Issue, No. 75, pp. 642-646. Coconut Creek (Florida), ISSN 0749-0208.

The marine estate, incorporating its estuaries, coastline and marine waters, is a valuable asset that belongs to the community of New South Wales (NSW), Australia. The benefits the community derive from it were assessed in a statewide Marine Estate Community Survey, with the health of the marine estate identified as a core value underpinning all other economic and social values and benefits. Its clean, safe waters, biodiversity and natural beauty support multiple uses and provide benefits that contribute to the community's well-being. These uses generate significant economic and social outcomes, including cultural and traditional-use benefits. However, they can also result in conflicts between users, and unsustainable use can also threaten the health of the marine estate resulting in the loss of community benefits.

Management responses are often sector-focused, rather than examining the range of benefits and uses, their threats and cumulative interactions. In response, the NSW Marine Estate Management Authority is applying a new Threat and Risk Assessment Framework for the marine estate at both the statewide and Hawkesbury Shelf bioregion scales. These aim to identify and prioritise threats to environmental, social and economic benefits (collectively termed "community wellbeing") derived at these two spatial scales. The results inform the development of management responses which will be captured in a new 10-year Marine Estate Management Strategy, and recommendations for improving the conservation of marine biodiversity in the Hawkesbury bioregion. This paper outlines the process undertaken to inform these assessments, and identifies the key findings across the environmetal, social and economic areas.

ADDITIONAL INDEX WORDS: *Risk assessment, environmental, social, economic, wellbeing*

INTRODUCTION

There is an increasing recognition of the need for improved integration of the management of coastal ecosystems. Continued pressure from activities relating to resource use, land-based activities, and increasing concerns about potential climate change impacts highlight the need to better understand the interrelationships between the environmental, social and economic factors that influence the benefits that the community derive from coastal environments, and the priority threats to those benefits. Managing a complex ecosystem to balance conflicting demands of stakeholders, managers, and policy makers is a key goal of ecosystem managment, and evaluating the impacts of different human activities on ecosystems is an important step (Palumbi *et al*., 2009).

The NSW Marine Estate Management Authority (MEMA) was established in 2013 to achieve better coordinated and effective management of the marine estate. A new 10-year Marine Estate Management Strategy aims to 'set the over-arching strategy for the State government to co-ordinate the management of the marine estate with a focus on achieving the objects of the *Marine Estate Management Act 2014* and vision for the estate. The vision is to acheive 'a healthy coast and sea, managed for the greatest well-being of the community, now and into the future', and is to be acheived by maximising the economic, social and environmental benefits that the NSW community derives from the estate. This is being done in accordance with MEMA's new approach to managing the marine estate outlined in their "Principles Paper" (MEMA 2013) and associated Threat and Risk Assessment (TARA) Framework (MEMA 2015a), with theStrategy informed by the outcomes of a statewide TARA. In late 2014 MEMA also commenced a process to develop options for enhancing marine biodiversity conservation within the Hawkesbury Shelf marine bioregion (henceforth abbreviated to Hawkesbury bioregion).

MEMA (2013) outlines a five-step process for improving effective management of the NSW marine estate. The first step involves early and effective community engagement to identify the economic, social and environmental benefits (termed 'community benefits') the community derives from the NSW marine estate, their perceived threats to those benefits, and opportunities for improved management. Step two involves the application of the TARA Framework. This involves an

DOI: 10.2112/SI75-129.1 received 15 October 2015; accepted in revision 15 January 2015.
*Corresponding author: alan.jordan@dpi.nsw.gov.au

evidence-based assessment of the current and likely future threats to the community benefits identified via Step 1 and an expert-led assessment of the evidence. Resultant risk levels to achieving the identified economic, social and environment risk objectives are determined using the TARA framework.

Priority threats to the NSW marine estate will generally relate to its open access characteristics, and include (i) various forms of resource degradation; (ii) direct and indirect threats to the benefits society obtains by use of the estate; (iii) failure to realise infrastructure development opportunities, and (iv) dealing with exogenous factors (MEMA, 2015a).

Background

The NSW marine estate includes the coastal waters of the State, that is, the area within 3 nautical miles (5.6 km) of the coast, and within estuaries up to the highest astronomical tide. The mainland section of the NSW marine estate consists of the inshore component of five bioregions that provide a division based principally on latitudinal patterns of biological diversity. The bioregions include all estuarine, coastal and offshore waters to the edge of the continental shelf at the 200 m depth contour. The Hawkesbury bioregion extends south from Newcastle to around Wollongong and encompasses the estuarine and coastal waters of the greater Sydney metropolitan area (Figure 1), and two-thirds of the State's population of 6 million. This paper describes the steps undertaken and preliminary results of the TARA applied in the Hawkesbury bioregion. Background information to support the assessment are detailed in a series of reports focussing on the environmental, social and economic components of the marine estate (Cox Inall Ridgeway, 2015; Feary, 2015; MEMA, 2015b; Vanderkooi Consulting (2015).

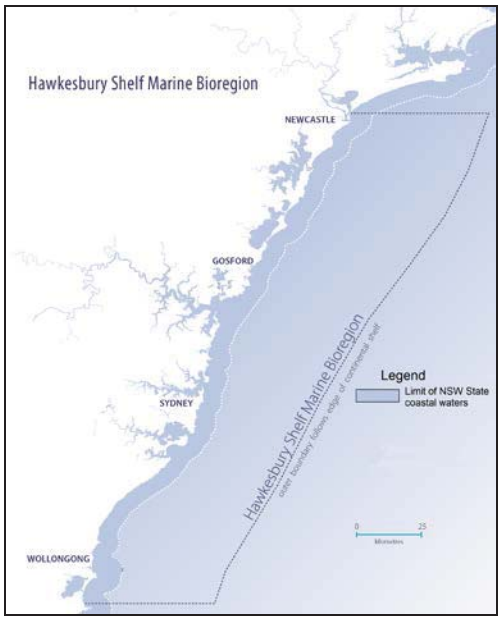

Figure 1. Map of the Hawkesbury Shelf marine bioregion on the mainland component of the New South Wales marine estate. The outer bioregion boundary is located in the vicnity of the shelfbreak.

METHODS

The first step in assessing community benefits and threats involved a statewide community survey which included qualitative and quantitative components that collated information against environmental, social and economic categories (Sweeney Research, 2014). The qualitative component involved two elements:

- thirty-six in-depth interviews with a cross-section of marine estate interest/user groups, including peak recreational groups, fishing/boating industry, tourism, comercial fishing, local councils and five Aboriginal coastal community representatives
- seven regional focus groups (6 coastal, one in central NSW) with a representative sample of the community.

The results of these interviews and focus groups were then used to inform the subsequent quantitative survey which involved a survey of a representative statewide sample of over 1,000 NSW residents (via an online survey) and over 700 coastal residents and visitors (via field intercept surveys at 7 coastal locations). In order to inform the TARA specifically within the Hawkesbury bioregion, these survey results were analysed at the regional scale. Additional engagement with the community and stakeholders was conducted in the bioregion.

In order to assess their views about the values and benefits of the marine estate in the region, the threats to those benefits, and ways threats might be better managed, both targeted stakeholder workshops and an interactive web portal was used to obtain broader community input in the bioregion. Finally, targeted engagement was undertaken with the Aboriginal community in the Hawkesbury bioregion in recognition of their special and long-standing connection with the natural environments of Australia (Cox Inall Ridgeway, 2015; Feary, 2015).

In addition to the key environmental benefits identified during the community survey, a hierarchical classification of environmental assets in the Hawkesbury bioregion was developed by MEMA agencies in order to inform the TARA (Table 1). Firstly, estuaries and the open coast were divided recognising the distinct differences in most bio-physical characteritics and human activities in these areas. Estuaries were further divided on the basis of their geomorphic characteristics into tide dominated (e.g. drowned river valleys, bays), wave dominated (e.g. rivers, large lakes) and intermittent (e.g. creeks, lagoons). The key ecological assets of these systems were assessed separately, and were based on maps of estuarine habitat classes (Creese *et al.,* 2009). The open coast was divided on the basis of depth (shallow <20 m and deep >20 m), with six defined habitats being assessed, and were based on maps of continental shelf habitat classes (Jordan *et al.,* 2010). The third category included species defined as threatened and protected under NSW and Commonwealth biodiversity conservation legislation (i.e. the NSW *Fisheries Management* and *Threatened Species Conservation Acts* and the Commonwealth *Environment Protection and Biodiversity Conservation Act*).

Primary activities in the marine estate that create threats to environmental assets and community benefits were categorised by MEMA agencies under the broad headings of 'resource use' and 'land-based impacts' (Table 2).

Table 1. *Classification of ecosystem components used in the Hawkesbury Shelf marine bioregion risk assessment*

Ecosystem	Type	Key ecological asset	Key benefit
Estuarine	Tide dominated	Estuarine waters	Clean waters
	Wave dominated	Diversity/abundance of biotic assemblages	Marine biodiversity
	Intermittent	Saltmarsh, mangrove, seagrass, rocky shores, reefs, beaches/mudflats, soft sediments	Marine habitats
Coastal	Nearshore	Coastal waters	Clean waters
	Offshore	Diversity/abundance of biotic assemblages	Marine biodiversity
		Rocky shores, beaches, shallow and deep soft sediments, shallow and deep reefs	Marine habitats
Estuarine and coastal	All	Threatened/protected marine fish, plants, mammals, birds, reptiles	Marine biodiversity

These were further subdivided in order to determine threat and risk from specific activities, such as individual commercial fishing methods. Climate change was also included as an exogenous factor due to its predicted impacts on the marine estate.

Table 2. *Categories of activities used within the environmental risk assessment for the Hawkesbury Shelf marine bioregion assessment.*

Primary threat category	Activities that result in sources of threats
Marine resource use	Shipping
	Commercial fishing
	Charter fishing
	Recreational fishing
	Cultural fishing
	Aquaculture
	Charter activities
	Research and education
	Recreation and tourism
	Dredging
	Mining
	Modified freshwater flows
	Service infrastructure
Land-based impacts	Land use intensification
	Point discharges
	Hydrologic modifications
Climate change	Climate change components

In order to assess the identified social and economic benefits, several categories were defined:

Social

- participation benefits (with sub-categories of 'safety, health and wellbeing and 'socialising and sense of community')
- enjoyment benefits (with sub-categories of 'enjoying the biodiversity and beauty of the marine estate', and 'consumptive use [e.g. catching a fish]')
- cultural heritage and use benefits (with sub-categories of 'tangible aboriginal cultural heritage [*e.g.* historic objects, source of food]', and 'intangible aboriginal heritage [traditions, practices and spiritual values']).

Economic

- indirect economic values (which was further defined as 'intrinsic & bequest values')
- employment and the value of production (which was further defined as 'viability of businesses')
- direct economic values (which was further defined as the 'individual enjoyment value or consumer surplus' (*i.e.* the difference between what a consumer or user is willing to pay for a benefit or services versus what they actually pay).

For the social and economic assessment, many of the uses and activities that generate benefits can also be threats; both to environmental assets and to other users of the marine estate. Hence, the threats for the social and economic TARA included:

- threats from 'resource uses or activities' (*e.g.* commercial fishing, recreational and tourism activities and similar)
- threats from 'environmental impacts' (*e.g.* water pollution, reduction of fish stocks, climate change)
- threats associated with 'health and safety impacts'
- threats related to the effect of 'MEMA Regulations' (*e.g.* the effect of regulations and restricted access to the marine estate (or its resources) on the flow of benefits.

Externalities such as fuel prices and increasing base costs were not assessed as they are outside of MEMA's control.

Risk assessment

The risks associated with activities against the identified environmental, social and economic benefits were assessed using a qualitative assessment approach that determines the most appropriate levels of consequence and likelihood from which a risk level is calculated. This assessment used the international standard definition of risk which is defined as 'the impact of uncertainty on achieving objectives' (ISO, 31000; 2009). The risk analysis process involves several stages: risk identification, analysis and evaluation. This process follows the establishment of the risk context, which defines the undesirable outcome that occurs as a result of an activity that will have an effect on the objectives. The risk analysis stage combines the scores from the ratings of consequence (levels of impact) and the likelihood (levels of probability) of a specific consequence to generate a risk score and rating, which were grouped into four ratings (minimal, low, moderate and high) (Figure 2).

Likelihood	**Level of risk**				
Almost certain	Minimal	Low	Moderate	High	High
Likely	Minimal	Low	Moderate	High	High
Possible	Minimal	Minimal	Low	Moderate	High
Unlikely	Minimal	Minimal	Minimal	Low	Moderate
Rare	Minimal	Minimal	Minimal	Minimal	Low
Consequence level	**Insignificant**	**Minor**	**Moderate**	**Major**	**Catastrophic**

Figure 2. Matrix used to determine risk to environmental, social and economic benefits.

The relative level of impact and likelihood were determined for environmental, social and economic benefits in the Hawkesbury bioregion within a twenty-year time frame in the context of current management controls. An exception was climate change which was further assessed within a fifty-year

time frame to inform longer term management responses required to address this threat. This was done firstly by MEMA agencies, followed by a process involving independant experts.

RESULTS

The following results are derived from the statewide community survey, that also identified benefits and threats in the bioregion.

Environmental benefits

The top four priority environmental benefits identified for the NSW marine estate by the NSW community included:

- clean waters supporting a variety of habitats and marine life
- abundance of marine life
- uniqueness of marine life
- a way to observe and interact with a variety of marine life.

These priorities were the same for the NSW general population, coastal residents and visitors statewide, and those groups in the Hawkesbury bioregion (Sweeney Research, 2014).

Environmental threats

The priority threats to the environmental benefits of the marine estate identified by the NSW population across the state were:

- littering/dumping of rubbish/marine debris
- oil and chemical spills
- water pollution from sediment or run-off
- a way to observe and interact with a variety of marine life.

These threats were the same for those groups in the Hawkesbury bioregion (Sweeney Research, 2014).

Social benefits

Social research findings for the Hawkesbury bioregion are drawn from two sources in the statewide survey:

- the regional results from the online survey
- the regional results from the field intercept surveys (Sweeney Research, 2014).

The statewide community survey found that the NSW marine estate holds great intrinsic value for the NSW community, with a key social benefit identified as the enjoyment people get from knowing its natural beauty is there, even if they cannot visit it regularly. Other key benefits included providing a safe space to spend quality time and socialise with friends and family, and providing an opportunity to live a healthy and active lifestyle.

The results differed for NSW coastal residents who identified the bequest values as their highest priority. Coastal visitors identified the intrinsic value of the marine estate as their highest social benefit, followed by the uniqueness and values that can be passed onto future generations. The qualitative survey results found that these social benefits are amplified in coastal Aboriginal communities, with many of the core traditions that underpin their culture being fundamentally linked to the estate. These statewide social benefits were consistent in the bioregion.

Social threats

The main social threats identified by statewide respondents include anti-social behaviour, potential loss of appeal due to pollution/littering, overcrowding, danger to swimmers from recreational activities such as boating and jet skiers, and a lack of public access. Coastal residents and visitors in the Hawkesbury bioregion mirrored the two highest priorities of the statewide coastal residents and visitor priorities, however bioregion residents also noted insufficient restrictions on commercial fishing as one of their top four priorities. In addition, stakeholder workshops within the Hawkesbury bioregion found the list of perceived benefits and threats were consistent with those from the statewide survey. Additional identified threats related to management of the NSW marine estate, such as loss of culture, knowledge gaps, need for more education and lack of a cohesive governance framework.

Economic benefits

The NSW marine estate represents a substantial economic resource to the NSW community (Vanderkooi Consulting 2015), as well as a key source of food for some, including Aboriginal people. In the NSW general population, 58% surveyed identified that income provided by the NSW marine estate was the most important economic benefit derived from the estate, even though less than 3% of people surveyed actually derive their income directly from it. They also particularly noted that the marine estate is home to iconic images of Australia which promote tourism and valued the variety of seafood to catch and eat. These three priority benefits were mirrored in responses from coastal residents and visitors.

There were regional scale differences in the economic benefits within the Hawkesbury region, which identified the iconic images of Australia promoting tourism as being of equal priority to the marine estate as a source of income. These benefits were more important amongst the Aboriginal community, with tourism being important for cultural values/traditions to be perpetuated.

Economic threats

Given the focus on the tourism benefits of the NSW marine estate, threats to tourism were identified as a priority. Water pollution affecting the viability of tourism, and the loss of natural areas reserved for tourism were seen as the greatest economic threats to the marine estate by the NSW general population. These threats, coupled with the increasing costs to access were identified as having the potential to cause damage to the tourism industry in NSW. The results were consistent in the Hawkesbury bioregion.

Aboriginal cultural benefits and threats

The most important benefits of the NSW marine estate to Aboriginal people were cultural connection and cultural identity associated with resource use. For Aboriginal people, many in low socio-economic circumstances, resources harvested from the sea may be essential for not only their sustenance, but also their health and wellbeing, and identity as Aboriginal people (Feary, 2015). Marine resources are also critically important as the anchor for a whole range of socio-cultural behaviours and protocols that continue to shape modern Aboriginal society.

Economic benefits of the marine estate is a nuanced topic as Aboriginal economic benefits incorporate both the western market economy and the informal communal economy of sharing and exchange of goods and services. While marine resources are important in the Aboriginal non-market economy, the economic benefit of the marine estate to Aboriginal people in the market economy is currently very limited.

Assessment of threats and risks

Firstly, the general distribution of risk ratings for environmental assets in the Hawkesbury bioregion identified during the expert workshop found a higher proportion of moderate and high risk attributes within estuarine areas (57%) compared to the continental shelf (32%) (Table 3). Risks within

estuaries were derived from a broader range of threats than on the continental shelf, including sediment and water contamination, dredging, recreational boating, and related infrastructure and shipping. Several of these were moderate and high risks to environmental assets on the continental shelf, including components of recreational and commercial fishing.

The distribution of risk ratings for social and economic benefits from the independant expert workshop combined were high (8%), moderate (39%), low (25%) and minimal (28%). Many of the risks identified in this assessment reflected a conflict between uses of the marine estate (*e.g.* between recreational and commercial fishing), as opposed to the overall threat to the existence of the activity, or the benefits that the community derives from the use. The TARA considered the cumulative nature of threats across all social and economic benefit categories of the marine estate in the Hawkesbury bioregion. The highest cumulative net threat scores were; access availability, climate change, effect of regulation, water pollution/sediment contamination, recreational and commercial fishing; recreation and tourism; foreshore/urban development, reduction in fish abundance, and habitat disturbance.

Table 3. *Percentage of risk levels for environmental assets of the Hawkesbury bioregion determined through expert led workshops.*

Risk level	Estuaries	Open coast
Minimal	26	45
Low	17	23
Moderate	27	18
High	30	14

DISCUSSION

The assessment of threats and risks to the overall benefits that the community derive from the NSW marine estate provides a capacity to develop management options that address stakeholder and broader community concerns, as well as address priority threats identified through evidence-based expert assessment. In this bioregional assessment many related to threats to the environmental assets that underpin a number of the identified social and economic benefits. The priority threats included climate change, regulation, water pollution, shipping, recreational boating and fishing, recreation and tourism, foreshore development, resource use conflict, lack of access availability amongst others. These priority threats identified at the scale of the bioregion are likely to also occur statewide, and are consistent with those identified throughout many of the worlds' coastal regions. These findings highlight the need for improved approaches to identifying risks across environmental, social and economic components.

While a risk-based approach is useful for identifying and prioritising the management options to address priority threats, it is limited due to its simplification of complex ecosystems and ecological processes, the quality of supporting data, scientific uncertainty, and its focus on individual threats in isolation. In general, accurate prediction of the impacts of multiple stressors becomes more difficult as the number of stressors increases (Crain *et al.,* 2008). Developing and implementing appropriate management initiatives are also influenced by the changing nature of threats and risks to the estate; and the uncertainty in relation to causal relationships between benefits and threats, and the effectiveness of management controls. These issues support the need for an adaptive management framework where benefits and threats are monitored, management responses are continuously improved, and uncertainty is minimised through targeted research and monitoring programs. This framework is required at both the statewide and regional scales to ensure activities that derive high risk to community benefits are identified, and management actions are appropriately targeted.

CONCLUSIONS

The application of a threat and risk assessment framework, combined with the use of surveys to examine the social and economic benefits and threats, provided an effective means of determining risk to the benefits the community derive from the NSW marine estate. Such an approach will continue to develop as it is applied at different spatial scales (*e.g.* marine parks) and to different management issues (*e.g.* pollution in estuaries). Improved integration of threats across social, economic and environmental areas will allow better trade-offs that are often required in management decisions in marine and coastal areas.

ACKNOWLEDGMENTS

Thanks to all who helped develop and implement the surveys and assessments, particularly members of the Marine Estate Expert Knowledge Panel; consultants, particularly Greg Fisk; and all MEMA agency working group members.

LITERATURE CITED

Cox Inall Ridgeway 2015. Hawkesbury Marine Bioregion Assessment – Step 1 Outcomes of Aboriginal Engagement.

Crain, C.M., Kroeker, K. and Halpern, B.S. 2008. Interactive and cumulative effects of multiple human stressors in marine systems. *Ecology Letters,* 11, 1304–1315.

Creese, R., Glasby, T., West, G. and Gallen, C. 2009. Mapping the habitats of NSW estuaries. *Fisheries Final Report* No. 113, 95 pp.

Feary, S. 2015. Sea countries of New South Wales: benefits and threats to Aboriginal people's connections with the marine estate. Final report to the NSW Marine Estate Management Authority, Vincentia, 133 pp.

Jordan, A., Davies, P., Ingleton, T., Mesley, E., Neilson, J. and Pritchard, T.R., 2010. Seabed habitat mapping of continental shelf waters of NSW. *NSW DECCW Occasional Series* 209p.

MEMA 2013. Managing the NSW Marine Estate: purpose, underpinning principles and priority setting, 15p.

MEMA 2015a. Threat and risk assessment framework for the NSW Marine Estate, 22p.

MEMA 2015b. Hawkesbury shelf marine bioregion assessment: background information on environmental assests and activities in the marine estate, 332p.

Palumbi, S.R., Sandifer, P.A., Allan, J.D., Beck, M.W., Fautin, D.G., Fogarty, M.J., Halpern, B.S., Incze, L.S., Leong J., Norse, E., Stachowicz, J.J. and Wall, D.H. 2009. Managing for ocean biodiversity to sustain marine ecosystem services. *Frontiers in Ecology and the Environment* 7, 204–211.

Sweeney Research 2014. Marine Estate Community Survey Final Report. Sydney, 394p.

Vanderkooi Consulting 2015. Social and economic background information report on the NSW marine estate.

Journal of Coastal Research	SI	75	647-651	Coconut Creek, Florida	2016

Data-driven Modeling of Coastal Water Quality using the Bayesian Method for Coastal Management

Jinah Kim† and Jungwoon Choi †*

†Operational Oceanography Research Center,
Korea Institute of Ocean Science and Technology (KIOST)
Ansan, South Korea

www.cerf-jcr.org

www.JCRonline.org

ABSTRACT

Kim, J. and Choi, J, 2016. Data-driven modeling of coastal water quality using the Bayesian method for coastal management. *In:* Vila-Concejo, A.; Bruce, E.; Kennedy, D.M., and McCarroll, R.J. (eds.), *Proceedings of the 14th International Coastal Symposium* (Sydney, Australia). *Journal of Coastal Research*, Special Issue, No. 75, pp. 647-651. Coconut Creek (Florida), ISSN 0749-0208.

To understand and a predict a coastal water quality system, a data-driven statistical model has been proposed using the Bayesian method and applied to the Saemangeum tidal lake. To describe a coastal water quality system, a multivariate statistical model was derived by determining observed variables and their interrelationships such as sea surface temperature, salinity, Chl-a, DO, pH, TN, TP, COD, NH_4N, NO_2N, NO_3N, PO_4O, and SiO_2Si for parameters of coastal marine environments, coastal water quality, and nutrients using observed field data. To estimate this statistical model, a Bayesian approach using Markov chain Monte Carlo method was applied to identify an optimal data-driven model. There are no limitations of statistical assumptions for samples using the Bayesian method, which is required in a frequentist approach, such as the maximum likelihood method. The Saemangeum tidal lake's coastal water quality system was quantitatively described and assessed by interpreting coefficients of model parameters with relation among variables from a derived structural equation model. Moreover, a prediction for coastal management was possible by Bayesian inference. Thus, there are new findings on the salinity threshold necessary to maintain optimal water by improving degraded water quality. Based on the findings, a quantity of water mixing (exchaning fresh water through sluice gates) can be applied while continuing construction of land reclamation.

ADDITIONAL INDEX WORDS: *Data-driven modeling, Bayesian method, multivariate statistical model, coastal water quality, the Saemangeum coast.*

INTRODUCTION

As part of coastal development, a land reclamation project has been carried out in the Saemangeum coast, located in the west coast of Korea since 1991 under governmental lead. A 20-year plan to execute this is in place. Land reclamation has been conducted after completing a 33-km long sea dyke in 2006. 40,100 ha reclaimed land and 11,800 ha freshwater lake will be created (Kim, 2010). Coastal development yields marine environmental problems such as degradation of coastal water quality, destruction of coastal and tidal ecosystems, reduction of fishery resources and coastal erosion. In order to conserve the coastal marine environments, integrated ocean observation was conducted from 2008 to 2010, to monitor marine environmental changes. Inevitably, water exchange, by mixing in fresh water through opening sluice gates of the sea dyke, because of water quality degradation was necessary, despite the internal sealant construction being conducted. Thus, it is concern of the stake-holder to maintain coastal water quality of the Saemangeum tidal lake for coastal management.

To understand the water quality system of the Saemangeum tidal lake, Kim *et al*. (2011) established three-dimensional water quality model, ROMS-ICM, combining the hydrodynamic model ROMS (Regional Ocean Modeling System) and the water quality model, eutrophication model CE-QUAL-ICM (Cerco and Cole, 1994). Moreover, univariate statistical analyses, such as correlation and regression were performed to identify the relation in the Saemangeum coast (Li *et al*., 2005; Yang *et al*., 2008; Lie *et al*., 2008; Kim *et al*., 2011; Jung *et al*., 2014). However, coastal water quality is defined by several variables. The categories are: general water quality, nutrients, and heavy metal contents. Thus, in order to describe a coastal water quality, multivariate statistical analysis should be considered.

A structural equation model (SEM) is a multivariate statistical model that incorporates ideas from regression, path analysis and factor analysis. An SEM also allows the exploration of interrelationships among latent and observed variables (Ullman and Bentler, 2003). Like applications of other statistical models, applications of SEMs rely on substantive knowledge to build a model. It is a confirmatory tool rather than an exploratory tool. In practice, it usually has a clear objective for the study. Further, the SEM has a basic background of the key structure of the model obtained, either from subject knowledge or from preliminary data analysis. This background is used in both the specification and the interpretation of the model. It is important to develop an appropriate model to evaluate the impact of explanatory observed and latent variables on key outcome variables.

This statistical model is very popular in substantive research such as behavioral, educational, and social research. Recently, an SEM was successfully applied to describe the Saemangeum coastal marine environments using the maximum likelihood (ML) method and probabilistic inference

DOI: 10.2112/SI75-130.1 received 15 October 2015; accepted in revision 15 January 2015.
*Corresponding author: jw_choi@kiost.ac.kr

for sustainable coastal development (Kim and Park, 2013 and 2015).

A full information ML method is one of the general frequentist approaches to identify an SEM. The ML method requires statistical assumptions about sample data (Ullman and Bentler, 2003). However, it is difficult to satisfy statistical assumptions in ocean observation data due to small sample size. As an alternative, the Bayesian approach using Gibbs sampler is suggested to implement the Markov chain Monte Carlo (MCMC) algorithm to derive an SEM.

A Bayesian method is a sampling-based method that depends less on asymptotic theory and hence, yields the potential to produce reliable results, even with small samples (Smith and Roberts, 1993). Furthermore, a Bayesian method is able to utilize prior information to conduct statistical inference. Thus, it may enable models that reflect hypotheses based on complex theories (Lee, 2007). This information can often provide valuable insight into structural relationships. Considering the advantages of the Bayesian approach, it is straightforward to apply the method in a very broad class of SEM-type modeling frameworks allowing for nonlinearity, interactions, missing data, mixed categorical, continuous observed variables, and more.

To describe a coastal water quality system for the Saemangeum tidal lake, a data-driven multivariate statistical model is proposed by applying the Bayesian method using observational data. A structural statistical model was established with latent variables to describe coastal environments. These variables are as follows: general water quality, as well as nutrient and observed variables of sea surface temperature (SST), salinity, chlorophyll-a (Chl-a), dissolved oxygen (DO), potential of hydrogen (pH), total nitrogen (TN), total phosphorus (TP), chemical oxygen demand (COD), NH_4N ((Total ammoniacal nitrogen), NO_2N (Nitrite nitrogen), NO_3N(Nitrate nitrogen), PO_4O (phosphorus), and SiO_2Si (silicon). To determine the interrelationships among the variables and estimate coefficients, the Bayesian approach using the MCMC is applied.

METHODS

Study Area and Materials

The land reclamation project is ongoing on the Saemangeum coast on the west coast of Korea (Figure 1) since 1991. A 33-km long sea dyke in 2006 has been completed. Currently, the internal sealant construction is creating 40,100 ha of reclaimed land and a 11,800 ha freshwater lake. The coastal water quality has degraded over the long-term coastal development. To conserve the costal marine environment, integrated ocean observation was conducted. In addition, water exchange through opening the sluice gate of the sea dyke is improving the water quality of the Saemangeum tidal lake. Unfortunately, it interferes with the land reclamation.

To understand the water quality system of the Saemangeum tidal lake, 13 observation variables (SST, salinity, Chl-a, DO, pH, TN, TP, COD, NH_4N, NO_2N, NO_3N, PO_4O, and SiO_2Si) were measured bi-monthly from 2008 and 2010 at the observation stations using the YSI 556 MPS (Multiprobe System) water quality meters and survey ship water sampling. The total number of samples for each observed variable is 40. Summary statistics for the 13 observed variables are given in Table 1. Latent and observed variables are classified in Table 2 with notations to establish a SEM.

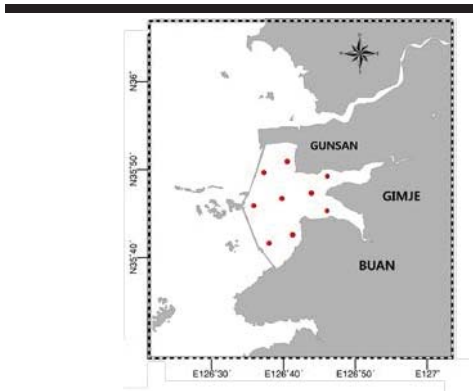

Figure 1. The Saemangeum coast with observation stations (red points).

Table 1. *Summary statistics for the 13 observed variables used as input data to derive a statistical model*

Variables	Min.	1st Qu.	Median	Mean	3rd Qu.	Max	SD
DO	5.84	8.04	9.26	9.53	11.62	14.24	2.12
pH	6.94	8.01	8.18	8.19	8.42	8.72	0.35
TN	0.15	0.29	0.48	0.66	0.79	3.34	0.60
TP	0.01	0.03	0.05	0.06	0.07	0.18	0.04
COD	0.98	2.25	3.59	3.67	5.08	8.90	1.92
NH_4N	0.00	0.03	0.06	0.12	0.18	0.50	0.13
NO_2N	0.00	0.00	0.01	0.02	0.03	0.07	0.02
NO_3N	0.00	0.04	0.12	0.22	0.25	1.52	0.32
PO_4O	0.00	0.00	0.01	0.02	0.03	0.06	0.02
SiO_2Si	0.02	0.11	0.28	0.41	0.55	1.59	0.40
SST	2.60	10.80	18.22	17.28	24.64	28.01	7.66
Salinity	12.40	25.95	28.63	27.12	30.33	31.69	4.74
Chl-a	0.20	3.44	10.30	15.73	28.13	61.80	14.40

Table 2. *Classification of latent and observed variables used in the modeling of water quality system for Saemangeum tidal lake*

Latent Variable			Observed variable	
η_1	Coastal Water Quality	General Water Quality	y_1	DO
			y_2	pH
			y_3	TN
			y_4	TP
			y_5	COD
η_2		Nutrients	y_6	NH_4N
			y_7	NO_2N
			y_8	NO_3N
			y_9	PO_4O
			y_{10}	SiO_2Si
ξ_1		Ocean Property	x_1	SST
			x_2	Salinity
			z_1	Chl-a

Bayesian SEM

A general Bayesian SEM consists of a measurement and structural model. The measurement model is: for $i = 1, \ldots, N$ observations,

$$y_i = v_y + \Lambda_y \cdot \eta_i + \delta_i^y \quad (1\text{-a})$$

$$x_i = v_x + \Lambda_x \cdot \xi_i + \delta_i^x \quad (1\text{-b})$$

,where the vector of indicators $y_i = (y_{i1}, \ldots, y_{ip})'$ and $x_i = (x_{i1}, \ldots, x_{in})'$ to an underlying vector of latent variables $\eta_i = (\eta_{i1}, \ldots, \eta_{im})'$ and $\xi_i = (\xi_{i1}, \ldots, \xi_{iq})'$ through the pxm and nxq factor loading Λ_y and Λ_x. The vectors δ_i^y and δ_i^x are the measurement error terms. The vectors v_y and v_x are the intercept terms for the measurement models.

The structural model is focused on studying the relationships among the latent variables, η and ξ. This is performed by the dependent vector η regression on the explanatory vector ξ as follows: $i = 1, \ldots, N$,

$$\eta_i = \alpha_i + B \cdot \eta_i + \Gamma \cdot \xi_i + \zeta_i \quad (2)$$

,where the metric B describes the relationships among latent variables in η_i. Γ quantifies the influence of ξ_i on η_i. The vectors α_i and ζ_i represent the intercept and the unexplained parts of η_i.

Bayesian SEM for Coastal Water Quality

The latent variables of ocean property, general water quality, and nutrients were used to describe the water quality system of the Saemangeum tidal lake, represented by ξ_1, η_1, and η_2, respectively, based on the previous research concerining Saemangeum coastal water quality (Kim *et al.*, 2011; Jung *et al.*, 2014). According to each latent variable, 12 observed variables are represented to x_1, x_2, and y_1, …, y_{10}. z_1 is another observed variable.

Graphical representation of the model is shown in Figure 2 under the previous research of Yang *et al.* (2008), Lie *et al.* (2008), Kim *et al.* (2011), and Jung *et al.* (2014). Following conventional representation, circles, squares, and arrows represent latent and observed variables and linear relations, respectively. The relations assume the ocean property (ξ_1) affects the general water quality (η_1), and nutrients (η_2), through the regression coefficients γ_1 and γ_2, respectively. The impact of the general water quality (η_1) on the nutrients (η_2) is represented by the arrow β_1.

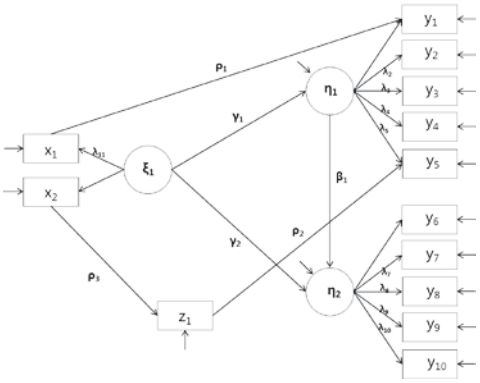

Figure 2. SEM path diagram for coastal water quality of the Saemangeum coast.

The structural model, as introduced in (2), is now formulated in matrix form as follows:

$$\begin{pmatrix}\eta_1\\ \eta_2\end{pmatrix} = \begin{pmatrix}\alpha_1\\ \alpha_2\end{pmatrix} + \begin{pmatrix}0 & 0\\ \beta_1 & 0\end{pmatrix} \cdot \begin{pmatrix}\eta_1\\ \eta_2\end{pmatrix} + \begin{pmatrix}\gamma_1\\ \gamma_2\end{pmatrix} \cdot \xi_1 + \begin{pmatrix}\zeta_1\\ \zeta_2\end{pmatrix} \quad (3)$$

,where the disturbances ζ_1 and ζ_2 are assumed to be independently and normally distributed with a zero mean and precision parameters.

The measurement model, as introduced in (1), is formulated as follows:

$$\begin{pmatrix}y_1\\ y_2\\ y_3\\ y_4\\ y_5\\ y_6\\ y_7\\ y_8\\ y_9\\ y_{10}\end{pmatrix} = \begin{pmatrix}0\\ v_2^y\\ v_3^y\\ v_4^y\\ v_5^y\\ 0\\ v_7^y\\ v_8^y\\ v_9^y\\ v_{10}^y\end{pmatrix} + \begin{pmatrix}1 & 0\\ \lambda_2^y & 0\\ \lambda_3^y & 0\\ \lambda_4^y & 0\\ \lambda_5^y & 0\\ 0 & 1\\ 0 & \lambda_7^y\\ 0 & \lambda_8^y\\ 0 & \lambda_9^y\\ 0 & \lambda_{10}^y\end{pmatrix} \cdot \begin{pmatrix}\eta_1\\ \eta_2\end{pmatrix} + \begin{pmatrix}\delta_1^y\\ \delta_2^y\\ \delta_3^y\\ \delta_4^y\\ \delta_5^y\\ \delta_6^y\\ \delta_7^y\\ \delta_8^y\\ \delta_9^y\\ \delta_{10}^y\end{pmatrix} \quad (4\text{-a})$$

$$\begin{pmatrix}x_1\\ x_2\end{pmatrix} = \begin{pmatrix}v_2^x\\ 0\end{pmatrix} + \begin{pmatrix}\lambda_{11}\\ 0\end{pmatrix} \cdot \xi_1 + \begin{pmatrix}\delta_{11}^x\\ 0\end{pmatrix} \quad (4\text{-b})$$

$$y_1 = \rho_1 \cdot x_1 + \delta_{13} \quad (4\text{-c})$$

$$y_5 = \rho_2 \cdot z_1 + \delta_{14} \quad (4\text{-d})$$

$$z_1 = \rho_3 \cdot x_2 + \delta_{15} \quad (4\text{-e})$$

,where λ_j^y is the influence of latent variables on the indicator y_j, $j = 1, \ldots, 10$. The intercepts $v_1^y = v_6^y = v_1^x = 0$ are fixed and the factor loadings $\lambda_1^y = \lambda_6^y = \lambda_1^x = 1$ to identify the model and to scale the latent variables.

Under expressions (3) and (4), and for $i = 1, \ldots, 40$, the complete data likelihood, including the latent variables of ξ_1, η_1, and η_2 is as follows:

$$L(y, x, \eta, \xi; \Phi) = \prod_{i=1}^{40} \{N_8(y_i; v_y + \Lambda_y \eta_i, \sum_y) N_2(x_i; v_x + \Lambda_x \xi_i, \sum_x) N$$

,where Φ includes the free elements of (v_y, Λ_y, v_x, Λ_x, Γ, B, P) and parameters (σ_y, σ_x, α, λ, γ, β, ρ).

In the Bayesian analysis, the prior specification involves quantifying expert's uncertainty in the model parameters Φ. There is not much information available beyond the observational data. The non-informative priors are used as follow:

$$\lambda_i^y = \lambda_i^x \sim N(0.0, \sigma_\lambda^2), \quad \gamma_i \sim N(0.0, \sigma_\gamma^2),$$

$$\beta_i \sim N(0.0, \sigma_\beta^2), \quad \rho_i \sim N(0.0, \sigma_\rho^2),$$

$$\sigma_\lambda = \sigma_\gamma = \sigma_\beta = \sigma_\rho \sim Gamma(10^{-2}, 10^{-2}).$$

Bayesian model fitting typically relies on MCMC, which involves simulating draws from the joint posterior distribution of the model's unknowns (parameters and latent variables) through a computationally intensive procedure. To implement the algorithm and MCMC simulation, R software package (Bueschken and Allenby, 2009) was used, which is freely

available. By Gibbs sampling, samples from the posterior distributions of the parameters of interest, for example α, λ, γ, β, and ρ can be obtained.

After running 500,000 iterations, the first 10,000 for burn-in were discarded and keeping for every 10,000 iterations to reduce the correlation among the posterior samples.

RESULTS

Estimates of the posterior mean, standard deviation and 95% credible intervals along with other summary statistics generated from the model are presented in Table 3. The experimental learning process updated the prior to the posterior beliefs based on the observational data. Plots of the posterior densities are depicted in Figure 3 for the parameters β_i, γ_i, λ_i, *and* ρ_i. These parameters are stable and support convergence.

Table 3. *Estimates of the posterior mean, standard deviation and 95% credible intervals along with other summary statistics generated from the Bayesian model*

Parameter	Mean Posterior	SD	MC Error	Val2.5pc	Median	Val97.5pc
β_1	-4.00	2.08	0.04	-9.08	-3.63	-1.07
γ_1	0.01	0.00	9.0e-5	0.00	0.01	0.01
γ_2	-0.01	0.00	6.33e-5	-0.02	-0.01	-0.00
λ_2	9.45	4.12	0.07	3.04	8.91	19.0
λ_3	-19.71	7.83	0.16	-37.13	18.9	-6.73
λ_4	-0.57	0.29	0.01	-1.26	-0.52	-0.13
λ_5	13.66	16.47	0.16	-15.91	11.79	51.68
λ_7	0.10	0.04	6.61e-4	0.05	0.09	0.20
λ_8	2.27	0.79	0.02	1.23	2.09	4.26
λ_9	0.05	0.03	3.04e-4	0.00	0.04	0.11
λ_{10}	0.45	0.21	0.00	0.15	0.41	0.96
λ_{11}	0.57	0.07	1.96e-4	0.42	0.56	0.71
ρ_1	0.50	0.08	3.12e-4	0.35	0.49	0.67
ρ_2	0.20	0.75	0.02	-0.35	-0.00	0.30
ρ_3	0.51	0.11	0.00	0.30	0.51	0.71

These results can be explained quantitatively by incorporating oceanographic theory to understand the water quality system of the Saemangeum tidal lake:

- Ocean property described with SST and salinity has a negative influence on water quality and nutrient content, 55% and 66%, respectively.
- Water quality has a 96% influence on nutrients. Nutrients in the Saemangeum tidal lake is affected indirectly by oceanic properties, as well as, direct effects on general water quality. The total effect is negative 66%.
- General water quality can be described by TN, pH, or TP among five observed variables with 95%, 64%, and 56% power of explanation, respectively.
- Nutrients can be described by NO_3N, NO_2N, NH_4N, or SiO_2Si among the five observed variables with a 95%, 74%, 51% and 50% power of explanation, respectively.
- The quantitative causal relationship of univariate variation can also be investigated between temperature and DO, salinity and Chl-a, and Chl-a and COD. If sea surface temperature increases, DO will decrease 65% compared to the current temperature. Also, if Chl-a increases, COD will increase 51% compared to the current temperature.

The results show agreement with the previous studies of Yang *et al*. (2008) and Jeong *et al*. (2014).

Higher salinity suggestes that there is no water exchange through the sluice gate. Thus, the salinity is a key variable to judge the water quality and nutrient content in the Saemangeum tidal lake. To predict water quality according to variation of salinity (15, 20, 25, 30, 35, and 40 psu), we calculate changes of COD to assess the grade of coastal water quality in Table 4.

Table 4. *Prediction of COD to assess the coastal water quality of the Saemangeum tial lake according to salinity variation*

Variables	*Salinity. 15 psu*	*Salinity 20 psu.*	*Salinity 25 psu*	*Salinity 30 psu*	*Salinity 35 psu*
COD	2.8	3.0	3.3	3.7	4.0
Grade of Coastal Water Quality	II	III	III	III	

By this observation, the minimum and maximum value of salinity is 12.4 and 31.69 psu, respectively. The target grade of water quality for the tidal lake is the third grade, which allows the use of industrial purpose. According to the water quality regulation guidelines for coastal water quality management published by the Ministry of Environment of the Korean government: if COD is smaller than 3, 2, and 1 mg/L, water quality is to be the third, second, and first grade, respectively. The results show that when salinity is less than 15 psu, water quality is improves up to the second grade. When salinity is between 20 and 30 psu, water quality is maintained to the third grade. Thus, the logical progression is as follows: the threshold salinity value necessary to maintain the third grade of coastal water quality is at least, 30 psu. Therefore, stakeholders can decide the appropriate time for water exchange by mixing fresh water into degraded water of inner tidal lake by opening sluice gate for sustainable coastal development. This process is necessary because water exchange is the most important factor in land reclamation to determine the period and expense of construction.

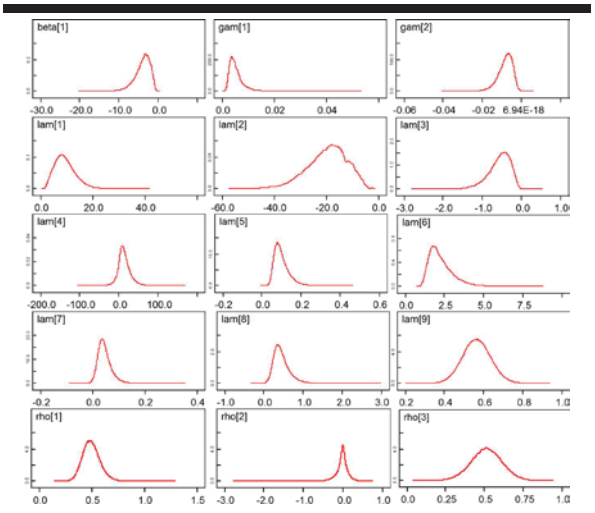

Figure 3. Posterior densities of parameter (β_i, γ_i, λ_i, and ρ_i) estimates generated from the Bayesian model.

DISCUSSION AND CONCLUSIONS

A data-driven multivariate statistical model was established and applied to the Saemangeum tidal lake using observational data. The model coefficients were estimated by the Bayesian method using Gibbs sampling for a MCMC simulation. By using the Bayesian method, a data-driven approach was applied to modeling coastal water quality system.

According to the results, the coastal water quality of the Saemangeum tidal lake was described quantitatively by interpreting interrelationships among 13 observed variables. Furthermore, for sustainable coastal development, the threshold quantity of salinity was predicted to maintain optimal coastal water quality while continuing land reclamation construction. The threshold salinity will be used to as a basis to decide the appropriate time for water exchange. This process brings not only the economic benefit of budget reduction but also the success of development conserving coastal marine environments.

The overall results showed that the possibility of application of Bayesian approach to data-driven modeling coastal water quality system using observational data, even if it is not enough to take statistical analysis in aspect of traditional frequentist statistical method. Moreover, there are no limitations on probabilistic inference (causal and diagnostic inference) for predictions and it allows the Bayesian method to use of coastal management tool. However, a data-driven model and mathematical equation should be expanded and established, respectively in terms of time-domain 't' for the better understanding and prediction of coastal water quality and its changes in order to make better use in practical coastal management problems.

ACKNOWLEDGMENTS

This research was a part of the project entitled "Development of Korea Operational Oceanographic System (KOOS), Phase 2" and "Investigation of Large Swell Waves and Rip currents and Development of The Disaster Response System," funded by the Ministry of Oceans & Fisheries Korea.

LITERATURE CITED

Bueschken, J. and Allenby, G. M., 2009. Bayesian Estimation of Structural Equation Models with R-A User Manual. Available at *SSRN 1433709*.

Cerco, C. F. and Cole, T. M., 1994. CE-QUAL-ICM: a three-dimensional eutrophication model, version 1.0. User's Guide. *US Army Corps of Engineers Waterways Experiments Station, Vicksburgh, MS*.

Jung, Y. H.; Kim, C. S., and Yang J. S., 2014. Estimation of Addition and Removal Processes of Nutrients from Bottom Water in the Saemangeum Salt-Water Lake by Using Mixing Model. *Journal of the Korean Society for Marine Environment and Energy*, 4(17), 1-12.

Kim, C.S., 2010. Saemangeum coastal system research for marine environmental conservation. *Annu. Rep. KORDI 2010* (24).

Kim, C. S.; Lim, H. S., and Cerco, C. F., 2011. Three-dimensional water quality modeling for tidal lake and coastal waters with ROMS-ICM. *Journal of Coastal Research,* SI60, 1068-1072.

Kim, J. and Park, J., 2013. A statistical model for computing causal relationships to assess changes in a marine environment. *Journal Of Coastal Research*, SI, 65, 980-985.

Kim, J. and Park, J., 2015. Mathematical modeling of coastal marine environments using observational data for coastal management. *Ocean & Coastal Management,* 116, 396-403.

Lee, S. Y., 2007. *Structural equation modeling: A Bayesian approach* (Vol. 711). John Wiley & Sons.

Li, D.; Dong, M.; Shim, W. J.; Hong, S. H.; Oh, J. R.; Yim, U. H., and Cho, S. R., 2005. Seasonal and spatial distribution of nonylphenol and IBP in Saemangeum Bay, Korea. *Marine pollution bulletin,* 51(8), 966-974.

Lie, H. J.; Cho, C. H.; Lee, S.; Kim, E. S.; Koo, B. J., and Noh, J. H., 2008. Changes in marine environment by a large coastal development of the Saemangeum reclamation project in Korea. *Ocean and Polar Research,* 30(4), 475-484.

Smith, A. F. and Roberts, G. O., 1993. Bayesian computation via the Gibbs sampler and related Markov chain Monte Carlo methods. *Journal of the Royal Statistical Society. Series B (Methodological)*, 3-23.

Ullman, J. B. and Bentler, P. M., 2003. *Structural equation modeling*. John Wiley & Sons, Inc

Yang, J. S.; Jeong, Y. H.; Ji, K. H.; Kim, H. S.; Choi, J. H., and Kim, W. J., 2008. The early-stage changes of water qualities after the Saemangeum sea-dike construction. *Journal of the Korean Society for Marine Environment & Energy,* 11(4), 199-213

Journal of Coastal Research	SI	75	652-656	Coconut Creek, Florida	2016

The Effects of Groundwater Pumping and Infiltration on Seawater Intrusion in Coastal Aquifer

Hojin Lee †, Sungduk Kim†, Kye-Won Jun†††*, Hyung-Keun Park†, and Jae-Sung Park‡

†The School of Civil Engineering,
Chungbuk National University,
Cheongju, South Korea

‡Department of National Defense Construction,
Chungbuk Health & Science University,
Cheongju, South Korea

†††Graduate School of Disaster prevention,
Kangwon National University,
Samcheok, South Korea

www.cerf-jcr.org

www.JCRonline.org

ABSTRACT

Lee, H.; Kim, S.; Jun, K.W.; Park, H.K., and Park, J.S., 2016. The Effects of Groundwater Pumping and Infiltration on Seawater Intrusion in Coastal Aquifer. *In:* Vila-Concejo, A.; Bruce, E.; Kennedy, D.M., and McCarroll, R.J. (eds.), *Proceedings of the 14th International Coastal Symposium* (Sydney, Australia). *Journal of Coastal Research*, Special Issue, No. 75, pp. 652-656. Coconut Creek (Florida), ISSN 0749-0208.

The purpose of this study is to identify the characteristics of seawater intrusion; an examination was carried out of the impacts of groundwater pumping and infiltration by precipitation on the seawater intrusion in coastal aquifers. To simulate seawater intrusion, three layers (layers 1, 2 and 3) were identified based on a drilling log. The infiltration rate of 30 years of rainfall data was calculated as 26.43%. The change of salt concentration was simulated using the FEMWATER model by considering the infiltration rate and assuming the pumping rate as 185m^3/day for 300 days. The proportion of transverse dispersivity towards the longitudinal dispersivity was changed from 1/10 to 4/10; in the four cases, the total dissolved solids (TDS) were plotted to compare the observed concentrations. The simulation was performed for the following four cases: no infiltration-no pumping, infiltration-no pumping, no infiltration-pumping, and infiltration-pumping. In the initial stage, the simulated concentrations and observed concentrations of dispersivity for each case showed similar trends; however, after the 100 day period the simulated concentration began to show an underrated tendency. For the no infiltration-no pumping case, the simulated concentrations and the observed concentrations of dispersivity exhibited similar appearances at 3/10.

ADDITIONAL INDEX WORDS: *Seawater intrusion, groundwater, coastal aquifers, pumping, infiltration.*

INTRODUCTION

One of the biggest issues mankind currently faces is the shortage of water resources. After the Republic of Korea faced a severe drought in 1994, the usage of groundwater was aggressively developed as an alternative water resource. However, due to the rapid development of groundwater, problems dealing with land subsidence and groundwater depletion aroused. Specifically at the coastal regions where industrial parks are located, the excessive development of groundwater caused seawater to invade the groundwater system.

Seawater intrusion polluted the groundwater, preventing the groundwater to function for drinking, industrial, or agricultural purposes. Polluted groundwater due to seawater intrusion can extensively remain as a long term issue. However, the Republic of Korea is not taking systematic steps to investigate the polluted groundwater.

Seawater intrusion is caused by natural factor such as sea level change by precipitation and tide, and by artificial factor such like pumping(Freeze and Cherry, 1979). The process of seawater intrusion varies greatly depending on the hydrogeological characteristics of the aquifer and dispersivity is the hydrogeological factor that typically affects seawater intrusion. The range occurring seawater intrusion is estimated by analysis of existing, observed data and the use of resistivity survey. However, due to the various and complex nature of the spatial distribution of the hydrogeological parameters, there are difficulties in fully understanding the observed data, grasping the overall distribution pattern of the seawater intrusion, and estimating the distribution (Park, 2006).

In this study, in order to analyze sweater intrusion affected by natural factors, like precipitation and infiltration, and artificial factors, like pumping, the three dimensional groundwater simulation model called FEMWATER is used to consider infiltration and pumping, as well as, simulate the dispersivity of various total dissolved solids. The salinity concentration is indicated based on the concentration of Total Dissolved Solids (TDS) given by Freeze and Cherry (1979). The input data from the previous study are used for this study's simulation. The simulation are set for the following four cases: no infiltration-no pumping, infiltration-no pumping, no infiltration-pumping, and infiltration-pumping.

DOI: 10.2112/SI75-131.1 received 15 October 2015; accepted in revision 15 January 2015.
*Corresponding author: kwjun@kangwon.ac.kr

METHODS

The target location for this study took place in the district of Juksan-myeon, Gimje City, at the Jollabuk-do province, South Korea. This region has been the chosen area for many previous studies concerning seawater intrusion, including the study done by the (Korea Rural Community Corporation), thus relatively favorable data can be acquired (KRCC, 2004). As indicated in Figure 1, plains are located at the western coastal region; at 50 m elevation point and below, the plains are comprised of hills, the Mankyeong river, Dongjin river, and alluvial plains regions from the watershed area of the Wonpyeong river. The five points in Figure 1 indicate the locations of observation wells and the depth of each observation well is shown in Table 1.

Figure 1. Study area and estimated location of the South Korea.

Table 1. *Depth and location of observation well at study area*

Well No.	BH-1	BH-2	BH-3	BH-4	B4-5
Depth (m)	17.3	42.0	17.4	26.8	24.5

The hydraulic parameters needed for the simulation are taken from Park (2006) and Kim *et al.* (2012); three distinct layers of the geological stratum are categorized, with similar geological structures of the stratum bundled together. The results are shown in Table 2.

The effects of infiltration from precipitation are considered when the SCS-CN method is applied and the infiltration rate is calculated. The rainfall data was derived from the Buan Weather Station where daily rainfall data over a span of thirty years (from 1975-2004) is classified based on antecedent rainfall conditions. Figure 2 shows the results based on the SCS-CN Method, the value of CN and the regression equation of the infiltration rate are given based on equation (1).

$$\alpha = -2.834e^{-5}CN^4 + 7.231e^{-3}CN^3 - 0.670CN^2 + 27.082CN - 396.56, R^2 = 0.961 \quad (1)$$

Table 2. *Characteristics of hydraulic parameters per each layer*

Property \ Layer	Layer1	Layer2	Layer3
Layer thickness(m)	28	15	75
Hydraulic conductivity(m/d)	0.015	0.01368	0.05
Bulk density(kg/m^3)	1,300	1,490	1,500
Compressibility(m·d^2/kg)	6.21e^{-18}	1.34e^{-16}	1.34e^{-17}
Moisture content	0.41	0.38	0.37
Water viscosity(kg/m·d)		0.0008718	
Density of water(kg/m^3)		1,000	

The CN value of the chosen region determined by the SCS-CN method is 83, and the infiltration rate calculated by equation (1) came out to be 26.43%. To consider the effects caused by pumping, the BH-2 observation well from Figure 2 was set to undergo pumping of 185 m^3 /day. The infiltration rate and the pumping rate are applied into the FEMWATER model and their impacts on sweater intrusion are further investigated. For setting the boundary conditions of the study area (Figure 1) for simulation purposes, it is presumed that the surface of the region that meets the sea is perpendicularly cut. Also, the fresh water concentration located towards the inland is 0, and the saline concentration of seawater is set to 35,000 mg/l. A line that connects each observation well to various groundwater levels is applied: -1.89m, -2.85m, -1.84, -0.82m, -0.92 m. When the TDS of the observation well (BH-1) and the measured TDS showed similar appearances, the conditions were reset to the initial conditions.

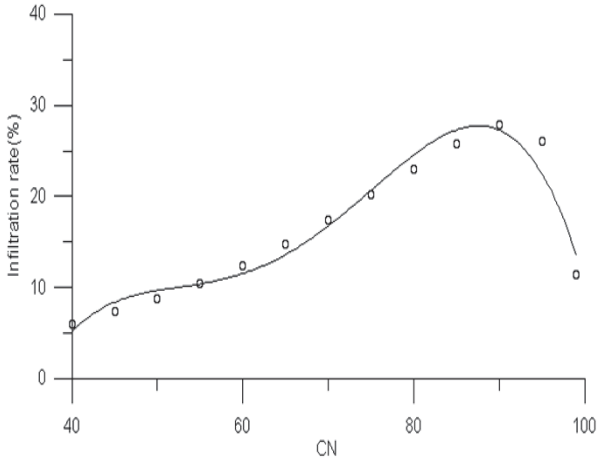

Figure 2. Relationship between infiltration rate and CN.

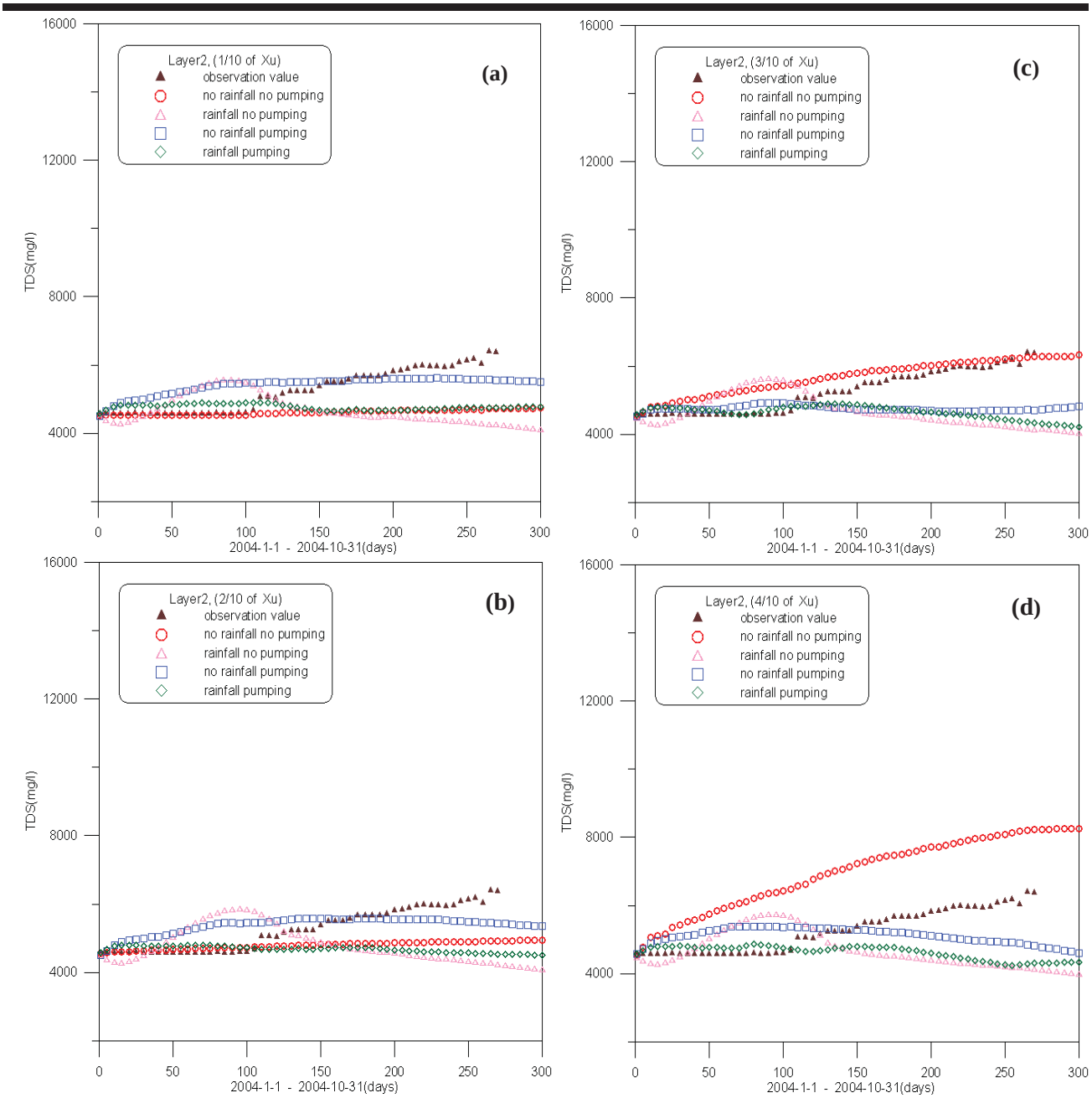

Figure 3. Comparison of simulated TDS values with the observed data(BH-1) according to transverse dispersivity at (a) 1/10, (b) 2/10, (c) 3/10, and (d) 4/10.

The basic theories of the FEMWATER model used in this simulation are referred from Lin *et al.* (1997).

RESULTS

In order to analyze the effects infiltration and pumping have on seawater intrusion, four conditions are set for simulation (no infiltration-no pumping, infiltration-no pumping, no infiltration-pumping, and infiltration-pumping) and the TDS of the observation wells are compared (Figure 3).

The observed TDS concentrations are classified based on Freeze and Cherry (1979) classification system. The salinity slope located in the space between the coastal region seawater and the groundwater cause the seawater to invade into the

groundwater region. Therefore, it is important to consider the dispersivity of the salinity slope located in the coastal regions. Figure 3 (a) - (d) shows the results where the ratios of transverse dispersivity to longitudinal dispersivity vary from 1/10 to 4/10.

The estimation method to estimate dispersivity is from Xu and Eckstein (1995) and the value of longitudinal dispersivity of 14.59 m was used. The observe TDS concentration values were measured at the BH-1 observation well of Figure 1 from January 1 to October 31 in 2004. The location of the observation well is situated in layer 2.

As shown in Figure 3, for the no infiltration-no pumping condition, when the transverse dispersivity is at 1/10 and 2/10, up until day 100 the simulated TDS concentration and the observed TDS concentration are well reproduced. When the transverse dispersivity exceeds 3/10, the initial concentrations up to day 100 do not reproduce as well. However, after day 100 then the observed TDS concentrations reproduce well.

In the condition for infiltration-no pumping, the value of total dissolved solids is higher than the observed TDS concentration up to day 100, unaffected by the change in dispersivity. However, after day 100 the value of TDS becomes lower than the observed TDS concentration. For the other conditions, the TDS concentrations decrease with time. It is deduced that such occurrence is a result of infiltration from precipitation.

For the condition of no infiltration-pumping, when the transverse dispersivity is at 1/10 and 2/10, initially the simulated TDS concentration is higher than the observed TDS concentration. When the transverse dispersivity is at 3/10, the simulated TDS concentration and the observed TDS concentration initially agree well. However, after day 100 the simulated TDS concentration exhibits a decreasing tendency compared to the observed TDS concentration. When the transvere dispersivity is at 4/10, the simulated TDS concentration value is initially higher than the observed TDS value, but decreases after day 150.

For the condition of infiltration-pumping, the simulated TDS concentration value agrees well with the observed concentration value, not affected by the change in dispersivity value. Specifically, when the dispersivity is at 2/10 or 3/10, the appearances of both simulated TDS concentrations and concentrated TDS concentrations are similar. However, after day 100 the simulated TDS concentrations decreased compared to the observed TDS concentration values.

DISCUSSION

Seawater intrusion into the groundwater system at coastal quifier is a serious environmnetal problem. When freshwater is mixed with about 3% of seawatr, the water is polluted. Thus, it is required to analyze the characteristics of seawater intrusion for sustainable use of groundwater in coastal quifer.

The change of salt concentration was simulated using the numerical model considering the infiltration rate and assuming the pumping rate as 185m^3/day for 300 days. The ratio between transvers dispersivity and longtudinal dispersivity was changed form 1/10 to 4/10. The simulation was for the following four cases: no infiltration-no pumping, infiltration-no pumping, no infiltration-pumping, and infiltration-pumping

Based on the simulation results, the simulated TDS concentrations and observed TDS concentrations of dispersivity for each case showed similar trends. After the 100 day period, however, the simulated TDS concentration began to show an underrated tendency. In the condition of no-infiltration and no-pumping, the simulated and observed TDS concentrations agree well when dispersivity is at 3/10.

CONCLUSIONS

In order to analyze the effects of infiltration and pumping on seawater intrusion, four conditions are established (no infiltration-no pumping, infiltration-no pumping, no infiltration-pumping, and infiltration-pumping) where the ratios of transverse dispersitivity to longitudinal dispersivity are manipulated to observe the total dissolved solids (TDS). The simulated TDS concentrations are compared with the observed TDS concentrations.

In the condition where only infiltration occurs, the simulated TDS concentrations appear less than the observed TDS concentrations as time passes. In the condition where only pumping occurs, when the transverse dispersivity is 3/10 initially both the simulated and observed TDS concentrations appear alike. However, after 100 days, not depending on the dispersivity value the simulated TDS concentration appears lower than the observed TDS concentration.

In the condition where both infiltration and pumping are absent, when the dispersivity is 1/10 and 2/10, up to day 100 both the simulated and observed TDS concentrations reproduce well with each other. However, after 100 days, the simulated TDS concentrations appear lower than the observed TDS concentrations. When the dispersivity is at 3/10, the simulated TDS concentration initially over estimates compared to the observed TDS concentration. However, after 100 days, both concentration values show similar trends. In the condition where both infiltration and pumping are present, when the dispersivity is 2/10 and 3/10, the simulated and the observed TDS concentrations agree well up to day 100. After 100 days, the simulated TDS concentration show an over estimation.

To summarize the results, in the condition of no-infiltration and no-pumping, the observed TDS concentrations overall show similar trends when dispersivity is at 3/10. For the other conditions, depending on the dispersivity value the simulated and observed TDS concentrations may agree well during the initial stages; however, after 100 days, except for previously mentioned condition, the simulated TDS concentrations appear less than the observed TDS concentrations. It is deduced that in the case of infiltration, the aquifer is reached after the designated time passes, whereas in the case of pumping, the TDS concentration is affected only after a certain standard value is exceeded. Through analyzing the results, it is important to accurately determine the dispersivity values before proceeding further with the study for better analysis of the various impacting factors on seawater intrusion.

ACKNOWLEDGMENTS

This research was supported by a grant(15RDRP-B066173-03) from Regional Development Research Program funded by Ministry of Land, Infrastructure and Transport of Korean government.

LITERATURE CITED

Freeze, R.A. and Cherry, J.A., 1979. *Groundwater*. Eaglewood Cliffs, NJ: Prentice-Hall, 375p.

Kim, S.D.; Lee, H.J., and Park, J.S., 2012. Simulation of seawater intrusion range in coastal aquifer using the FEMWATER model for disaster information. *Marine Georesources & Geotechnology*, 30(3), 210-221.

Korea Rural Community Corporation (KRCC), 2004. *Report on 2004 Seawater inrusion. Gwacheon, Korea*: Ministry for Food, Agriculture, Foresty and Fisheries, 394p.

Lin, H.J.; Rechards, D.R.; Tabbot, C.A.; Yeh, G.T.; Cheng, J.R.; Cheng, H.P., and Jones, N.L., 1997. A three-dimensional finite element computer model for simulating density-dependent flow and transport in variable saturate media. *Ver. 3.1 Vicksburg, MS: U.S Army Engineering Research and Development Center*, 143p.

Park, J.S., 2006. Estimating the extent of seawater intrusion due to freshwater withdrawal in coastal aquifer. Cheongju, Korea: Chungbuk National University, Ph. D. dissertation, 129p.

Xu, M. and Eckstein, Y., 1995. Use of weighted least-squares method in evaluation of the relationship between dispersivity and field scale. *Groundwater*, 33(6), 905-908.

Journal of Coastal Research	SI	75	657-661	Coconut Creek, Florida	2016

M2, overtides and compound tides generation in the Strait of Messina: the response of a non-hydrostatic, finite-element ocean model

Giovanni Quattrocchi[†*], Gerard J. Gorman[‡], Matthew D. Piggott[‡] and Andrea Cucco[†]

[†] Istituto per l'Ambiente Marino Costiero, Consiglio Nazionale delle Ricerche, Oristano, Italy.

[‡] Applied Modelling and Computation Group, Imperial College London, London, UK.

www.cerf-jcr.org

www.JCRonline.org

ABSTRACT

Quattrocchi, A.; Gorman, J.G., Piggott M.D. and Cucco, A., 2016. M2, overtides and compound tides generation in the Strait of Messina: the response of a non-hydrostatic, finite-element ocean model. *In:* Vila-Concejo, A.; Bruce, E.; Kennedy, D.M., and McCarroll, R.J. (eds.), *Proceedings of the 14th International Coastal Symposium* (Sydney, Australia). *Journal of Coastal Research*, Special Issue, No. 75, pp. 657-661. Coconut Creek (Florida), ISSN 0749-0208.

The nonlinear interactions between the main tidal constituents and geographical constraints are investigated using Fluidity-ICOM, a non-hydrostatic finite-element ocean model that was implemented in the region of the Strait of Messina (Mediterranean Sea). As a first crucial approach, the barotropic tidal dynamics was investigated and the model solution was interpreted in terms of tidal maps and spectra obtained by harmonic analysis of the sea surface elevation. The model domain is represented by an unstructured mesh with variable spatial resolution ranging from two kilometres to fifty meters, in order to resolve the shoreline in the inner part of the Strait. Amplitudes and phases of the main diurnal and semidiurnal tides were prescribed at the off-shore open boundaries. A calibration procedure was carried out with available observations in order to provide a suitable parameterization for bottom drag coefficient and horizontal viscosities. The results gave clear indication that over-harmonics and compound tides are generated in the Strait. The generation mechanism, geographical localization and intensity of these phenomena were described to provide groundwork for further model analyses that would clarify the role of shallow water tides in modifying the hydrological setup in proximity of sea straits.

ADDITIONAL INDEX WORDS: *Tidal Dynamics, Shallow-water tides, Non-hydrostatic finite-element model*

INTRODUCTION

The objective of this work is to describe overtides and compound tides that arise through interaction among barotropic tides and the complex geometry of the Strait of Messina (Italy). The analysis of these phenomena, that are typical of shallows and straits, can clarify their role in modifying the hydrological setup and triggering long-term sediment transport. This work is part of a more complete and ongoing analysis of the tidal dynamics in this strait, aimed to investigate the non-hydrostatic structure of the barotropic tidal flows.

The Imperial College Ocean Model, named Fluidity-ICOM (Ford *et al.* 2004a, 2004b; Piggott *et al.* 2008), a non-hydrostatic, finite-element, and ultimate generation ocean model was adopted for this research case study. The non-hydrostatic equations are discretized on a finite-element mesh describing the Strait of Messina (SoM hereafter) and its surrounding.

The SoM is located in the Mediterranean Sea and it separates the Italian Peninsula and the Island of Sicily (Fig. 1), connecting the Ionian Sea and the Tyrrhenian Sea, through a narrow and shallow gateway. The complex morphology is shaped like a channel, meridionally oriented in the southern and central part, bended eastwards in the northern part, and with a shallow sill in the central part that features its bathymetry. At the latitude of 37.951658° N, the south side of the SoM is characterized by a maximum width of 27 km and a maximum depth of 1500 m. The inner part exhibits the minimum width of 3.2 km, between Punta Pezzo (38.232325 °N) and Ganzirri (38.258943 °N), and the minimum depth of 85 m. At the north side, the SoM gently expand to the Tyrrhenian Sea with maximum depths of 300 m.

Based on the early survey of Vercelli (1925), Defant (1961) gave a comprehensive description and explanation of the observed dynamics within the SoM, and he laid the groundwork for further observational and model studies. His results, summarized by Androsov *et al.*, (2002), explain that the formation of barotropic tides is mainly driven by the M2-tide that plays a leading role in determining the general scheme of the currents in the SoM. In vicinity of the narrowest part of the SoM an amphidromic point is found and the phase of tidal velocity is seen changing by 180° within about 3 km. The tidal elevations are out-of-phase between the Tyrrhenian and Ionian Seas, with the consequence that tidal velocities of 2-3 m/s are found. The interaction between tidal flows and bottom topography promotes a nonlinear distortion of the major astronomical tidal constituents (Le Provost *et al.*, 1991) that generate overtides and compound tides. These harmonic constituents have angular speeds that are multiples (*e.g.* the interaction of M2 with itself generate M4 and higher harmonics, like M6 and M8), sums or differences of the frequencies of the main astronomical constituents (*e.g. M*2 and *S*2 generate MS4) and they are a relevant nonlinear physical process in many coastal areas (Andersen, 1999; Le Provost 1991; Pugh, 1987).

DOI: 10.2112/SI75-146.1 received 15 October 2015; accepted in revision 15 January 2015.

*Corresponding author: giovanni.quattrocchi@iamc.cnr.it

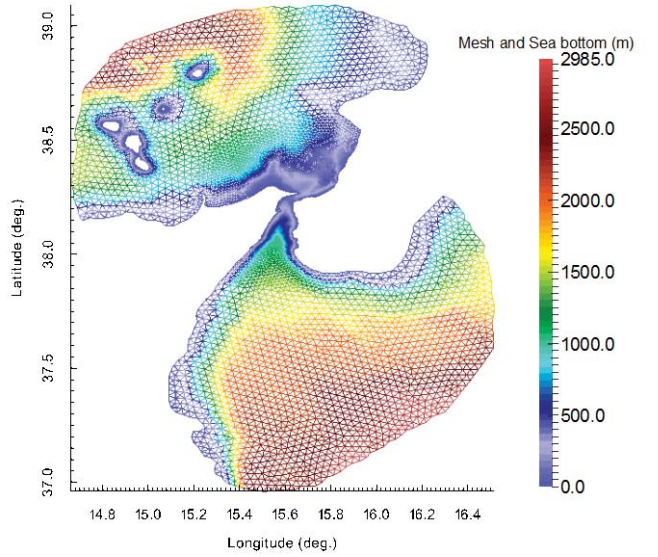

Figure 1. Model domain with integration mesh and bottom topography defined by a colour scale.

For what concern the model investigations of the barotropic tidal dynamics in the SoM, the earliest model analyses were carried out through the implementation of two-dimensional ocean models (*e.g.* Brand *et al.*, 1997; Androsov *et al.*, 2002). Recently, the application of the non-hydrostatic finite-volume ocean model in the SoM (Sannino *et al.*, 2013) has stirred up the adoption of similar tools (Martin-Short *et al.*, 2015) to provide new insights into the nonlinear processes of sea straits dynamics. In this paper, the authors retrace part of the current knowledge about the tides propagation in shallow waters by mean of a model case study based on a simplified setup of Fluidity-ICOM.

	Observed		Computed	
Points	Amp.	Phase	Amp.	Phase
#1	5.5	269.0	7.94	11.09
#2	10.2	271.0	7.76	2.76
#3	3.2	316.0	3.09	2.92
#4	3.3	116	3.5	130
#5	4.27	51.81	2.83	189.44
#6	6.54	102.3	5.07	195.9

Table 1: Observed and modelled amplitudes (cm) and phases (deg.) of the M2-tide at six points within the model domain.

METHODS

As a first stage of a more realistic application, Fluidity-ICOM was here applied to describe tides and overtones generation in the SoM. Fluidity-ICOM is a non-hydrostatic ocean model, based on the finite-elements method, that uses unstructured and adaptive mesh to discretize the spatial domain in the three-dimensions. In this study, only the static mesh was considered. This choice was mainly justified to grants a reduction of the computational cost of the model simulations. Model setup and calibration are addressed in the following subsections. A detailed description of numerical treatments can be found in Ford *et al.* (2004a, 2004b).

Model setup

The physical model is described by the incompressible, non-hydrostatic Navier-Stokes equations in the Boussinesq approximation. The equations are discretized in a three-dimensional space, defined by mean of an extruded two-dimensional finite-elements mesh displayed in Fig. 1. In this figure, the colours indicate the spatial variability of the high-resolution bathymetry that is obtained through integration of GEBCO dataset (30 arc-second resolution) and nautical charts. The model domain focuses on the SoM and the spatial resolution of the mesh elements vary from two kilometres, at the open boundaries, to fifty meters, at coastal areas, in the inner part of the SoM. The extrusion of the mesh discretizes the water column with sixteen equidistant sigma-layers, where the nodes of the mesh are aligned vertically. In this vertical discretization the thickness of the deeper layer is varying between 75, in the deepest canyon, and 5 meters in the shallowest part of the SoM.

The ocean problem is implemented on a spherical earth where the gravity points toward the centre of the sphere. The viscous terms that represent the horizontal and vertical diffusion of momentum were chosen as follow: $\mu_{11} = \mu_{22} = 200\,m^2 \cdot s^{-1}$ and $\mu_{33} = 10^{-6} m^2 \cdot s^{-1}$. Subgrid-scale parameterization is applied by mean of a Large Eddies Simulation model (Pope, 2000) with a second order closure scheme.

Closed boundaries conditions are characterized by a non-dimensional drag coefficient at the bottom ($C_{D\ bottom}$) with a constant value of 2.6×10^{-3} and a prescribed no–normal flow at the lateral boundaries. A tidal signal composed of two diurnal (O1 and K1) and two semidiurnal (M2 and S2) constituents was prescribed at the open boundaries. Co-oscillating tides are forced as cosine waves of specified phases and amplitudes derived by the Oregon State University Tidal Inversion Software. Tidal potential is not considered due to the limited extension of the model domain. No-stress conditions are applied at the free surface that can be excluded from explicit computation. However, its values can be diagnostically derived by the pressure boundary condition $p = \rho g \eta$, perturbation density, gravity and free surface elevation, respectively.

Initial values for the three-dimensional velocity field and the scalar pressure field are set to zero. The starting time of integration is set to zero and the simulation proceeds up to 41

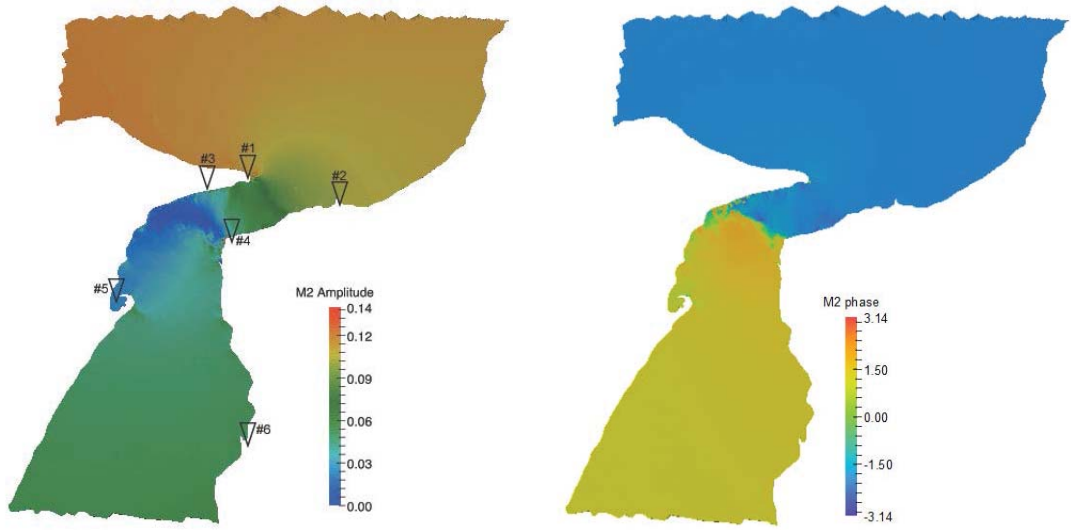

Figure 2. Left panel: Map of M2-tide amplitude (m) with locations of the reference points named Punta Faro (#1), Scylla (#2), Ganzirri (#3), Punta Pezzo (#4), Messina (#5) and Reggio Calabria (#6). Right panel: M2-tide phase (rad). Range 0; 3.14 corresponds to 0; 180 deg. while range 0;-3.14 correspond to 180-360 deg.

days with variable time step (from 20 to 100 seconds). The hourly output of surface elevation and velocity components were considered for analysis after four semidiurnal periods, in order to avoid initial transients.

Calibration

A calibration of the model was carried out by varying the values of the bottom drag coefficient ($C_{D\ bottom}$) and the horizontal viscosity ($\mu_{11} = \mu_{22}$). Several runs were performed in order to find satisfactory agreement with available observations, that was finally obtained for $C_{D\ bottom} = 2.6 \times 10^{-3}$ and $\mu_{11} = \mu_{22} = 200\ m^2 \cdot s^{-1}$. The observations consist of early dataset (Vercelli, 1927; Di Sarra *et al.*, 1987) embedded with more recent data (www.mareografico.it) managed by the Italian Institute for Environmental Protection and Research. Amplitudes and phases were obtained throughout spectral analysis of computed and observed time series of the sea surface elevation and they were used to calibrate the model solution and to provide further comparisons.

In the left panel of Fig. 2, the symbols #1, #2, #3, #4, #5, #6, identify the geographical locations of six reference points along the coast. Table 1 displays simulated and observed amplitudes and phases of the M2-tide corresponding to such geographical locations, at sea. For what concern the amplitude, Table 1 reveals a satisfactory agreement with observations in the SoM and similar results were obtained by previous model experiments (*e.g.* Androsov *et al.*, 2002; Sannino *et al.,* 2013). Observed amplitude of M4-tide is only available at point #4, where a difference of 0.2 cm was found. Considering a circular scale, computed and observed phases show a maximum shift of 137° at point #5 and a minimum shift of 14° at point #4. Theses discrepancies are not surprising being the phases rapidly changing within a very limited area within the SoM (as being discussed in the next section). Furthermore, the position of the simulated, and in situ gauges are not exactly coincident, being the latter mostly installed within ports.

RESULTS

The results of the model computation were first interpreted in terms of tidal maps of the M2-tide and the higher harmonics M4 and MS4. Then, spectral analysis of the sea surface elevation at six reference points provided a local description of the tidal model solution.

M2-tide

The tidal maps in Fig. 2 give information about the spatial structure of amplitudes and phases of the harmonic M2. As expected, an amphidromic point is centred in the SoM and it is slightly shifted toward the western boundary. Between the north entrance of the SoM and the amphidromic point, the amplitude of M2 ranges from 11 to zero cm. Thus, the amplitude increases up to 6 cm in correspondence of the south entrance of the SoM. The map of M2 phases (see figure 2, right panel), ranging between π and $-\pi$, displays the Tyrrhenian and Ionian Seas having opposite phases and rotational behaviour with centre located in the middle of the SoM.

Amplitude gradients and phase opposition between the north and the south entrances of the SoM are able to promote strong flows. Maximum tidal flows, related to the barotropic dynamics may exceed 3.0 m/s, especially in proximity of the sill where the complex topographic constraint drastically reduces the section of the SoM. Tidal flows are flowing alternatively southward and northward. In between, very quick transient flows, intense eddy activity and turbulence take place due to nonlinear interaction with the shallow bottom topography. Their combined effect can intensely affects the baroclinic circulation and trigger long-term sediment transport, as observed by Alpers and Salusti (1983).

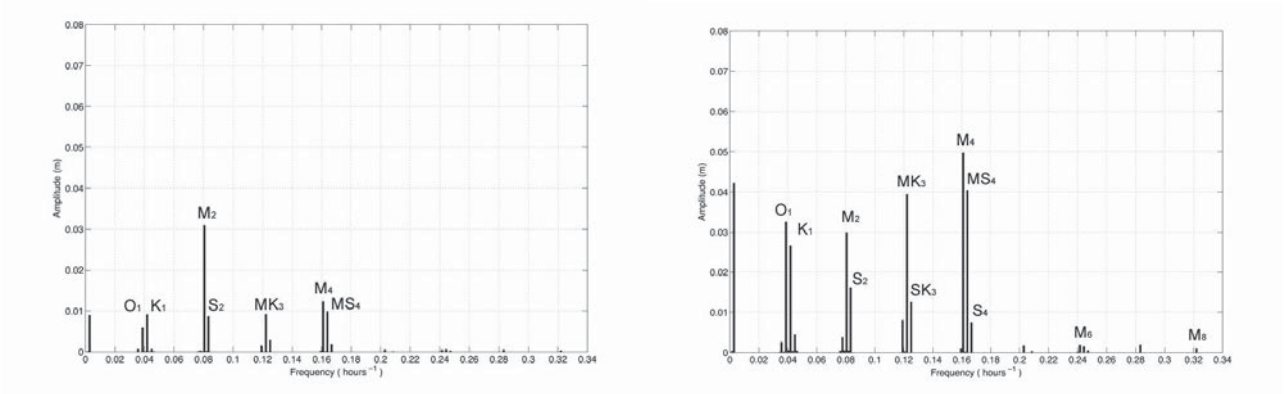

Figure 3. Spectra of the modelled sea surface signals displaying the amplitudes (m) at two reference points in the inner part of the Strait of Messina. Left panel: Ganzirri (#3) is located in the west coast. Right panel: Punta Pezzo (#4) is located in the east coast.

Higher harmonics

In shallow waters the nonlinear interaction between strong flows and bottom topography generates eddies and mixing of the water column. In deep ocean, the dynamics can be satisfactory described with the linear theory and the tides can be consequently described using a superposition of diurnal and semidiurnal constituents. Differently, the dynamics of shallow water areas display more complicated tidal spectra where tide constituents appear of a number of frequencies like diurnal, semi-, third-, quarter-diurnal; at some location even higher like sixth-, eight- and twelfth-diurnal.

Tides that are presenting such harmonic constituents are referred as overtides and compound tides and they are normally found in shallow water areas. They generally show small amplitudes and arise due to nonlinear distortions of the major astronomical tidal constituents in shallow water. These nonlinearities appear through the quadratic term of bottom friction, spatial advection and mass conservation.

Fig. 3 shows two spectra derived from the simulated sea surface elevation at Ganzirri (#3) and Punta Pezzo (#4). These locations, part of the entire set of reference points, are representative of the inner part of the SoM, the west and east coast, respectively. Diurnal and semidiurnal constituents that were prescribed at the open boundaries appear in both spectra with peaks corresponding to over-harmonics such as M4, M6, MK3 and MS4. In Fig. 3, left panel, the higher value of amplitude is given by the M2-tide with 3.2 cm. Other amplitude peaks, representing over harmonics, result less than 1.2 cm (e.g. M4). By contrast, the reference location #4 at the east coast of the SoM (Fig. 3, right panel) displays a relatively flat spectrum, where the amplitudes of over-harmonics overtake the amplitude of M2, 3 cm in this region, and the nonlinear effects are found in the spectral peaks at zero frequency. Off Punta Pezzo, where a wide shallow is located, over-harmonics increase their amplitudes up to 5 cm, as found for M4-tide; M6 and M8 constituents also appear in the spectrum. In the same spectrum, compound tides, MS4, MK3 and SK3, also display high amplitudes.

Fig. 4 displays the spatial distributions of the simulated M4, overtide, and MS4, compound tide amplitudes. Both constituents show high amplitudes in the area of the sill and off Punta Faro (#1), the shallowest parts of the SoM water depth. Maximum amplitudes are found at the east coast of the SoM, near Punta Pezzo (#4) where the effect of the interaction between different fundamental frequencies and the bottom topography amplifies overtides and compound tides.

CONCLUSIONS

This paper aim to describe overtides and compound tides in the SoM along with their generation mechanism by mean of the non-hydrostatic, finite-element based ocean model, named Fluidity-ICOM. A calibration procedure in which the model solution was compared with available observations and similar model approaches was carried out in order to find suitable parameterizations for bottom drag coefficient and the horizontal viscosities. Finally, the results were interpreted in terms of tidal maps and spectra of the sea surface elevation, at specific locations along the coast.

Maps and spectra showed the significance and spatial distribution of each diurnal and semidiurnal constituents, as well as over-harmonics and compound constituents. Fundamental constituents were prescribed at the open boundaries, while higher harmonics were generated by nonlinear distortions of such major tidal constituents in the shallow waters and the complex coastal geometries of the SoM. Indeed, in correspondence of the shallowest areas, off Punta Faro (#1) and Punta Pezzo (#4) as well as in a wide area over the sill, the maximum expression of nonlinear dynamics in the SoM is found.

These results have highlighted how the geomorphologic features of the domain are able to generate nonlinear behaviours in the barotropic tidal dynamics of sea straits, where strong currents periodically flow along convolute geometries. The international research community has already confirmed how the adoption of high-resolution computational meshes and non-

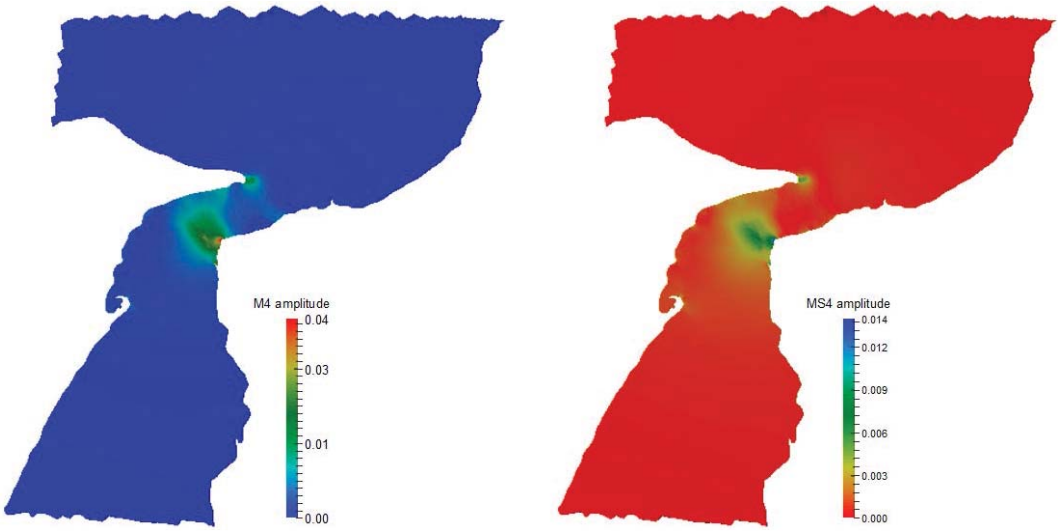

Figure 4: Maps of the overtide M4 (left panel) and the compound tide MS4 (right panel) amplitudes (m). Both harmonics arise at the sill of the SoM and in vicinity of shallow depth areas (e.g. off Punta Faro; #1 in Fig.2).

hydrostatic models can provide a modern description of the tidal dynamics and the way it affects the multi-scale hydrology of sea straits. Regional ocean modelling, devoted to both, analysis and forecast may widely benefit of accurate representations of sea straits and semi-enclosed basins dynamics.

The model solutions of this implementation of Fluidity-ICOM also provided three-dimensional tidal flows which description is addressed to a future publication, providing a comprehensive description of the barotropic tidal dynamics.

AKNOWLEDGMENT

This work was founded by RITMARE project, promoted by Italian Ministry of University and Scientific Research.

LITERATURED CITED

Alpers, W. and Salusti, E., 1983. Scylla and Charybdis observed from space. *Journal of Geophysical Research*, 88(C3), 1800–1808.

Andersen, O.B., 1999. Shallow water tides in the northwest European shelf region from TOPEX/POSEIDON altimetry, *Journal of Geophysical Research*, 104(C4), 7729–7741.

Androsov, A.A., Kagan, B.A., Romanenkov, D.A., and Voltzinger, N.E., 2002. Numerical modelling of barotropic tidal dynamics in the strait of Messina. *Advances in water resources*, 25(4), 401-415.

Defant, A., 1961. Physical Oceanography, vol. II, *Pergamon Press*, New York.

Di Sarra, A., Pace, A. and Salusti, E., 1987. Long internal waves and columnar disturbances in the Strait of Messina, *Journal of Geophysical Research*. 92, 6495-6500.

Ford, R., Pain, C. C., Piggott, M. D., Goddard, A. J. H., de Oliveira, C. R. E., and Umpleby, A. P., 2004a. A Nonhydrostatic Finite-Element Model for Three-Dimensional Stratified Oceanic Flows. Part I: Model Formulation. *Monthly Weather Review*, *132*(12), 2816–2831.

Ford, R., Pain, C.C., Piggott, M.D., Goddard, A.J.H., de Oliveira, C.R.E., and Umpleby, A.P., 2004b. A Nonhydrostatic Finite-Element Model for Three-Dimensional Stratified Oceanic Flows. Part II: Model Validation. *Monthly Weather Review*, *132*(12), 2832–2844.

Le Provost, C., Rougier, G. and Poncet, A., 1981. Numerical Modelling of the Harmonic Constituents of the Tides, with Application to the English Channel, *Journal of Physical Oceanography*, 11, 1123-1138.

Martin-Short R, Hill J, Kramer SC, Avdis A, Allison PA, Piggott MD, Tidal resource extraction in the Pentland Firth, UK: potential impacts on flow regime and sediment transport in the Inner Sound of Stroma, Renewable Energy 76, 596–607, 2015.

Piggott MD, Gorman GJ, Pain CC, Allison PA, Candy AS, Martin BT, Wells MR, A new computational framework for multi-scale ocean modelling based on adapting unstructured meshes, International Journal for Numerical Methods in Fluids 56, 1003-1015, 2008.

Pope, S.B., 2000. *Turbulent Flows*. 1st ed. Cambridge

Pugh, D.T., 1987. Tides, Surges and Mean Sea-level, a Handbook for Engineers and Scientists, John Wiley, NewYork

Sannino, G., Carillo, A., Lombardi, E. and Ciuffardi, T., 2013. *Validazione del modello di circolazione Marina dello Stretto di Messina mediante dati acquisiti in situ*. ENEA. *Report RdS/2013/228*

Sapia, A. and Salusti, E., 1987. Observation of nonlinear internal solitary wave trains at the northern and southern mouths of the Strait of Messina. *Deep Sea Reseasrch* 34(7):1081–92.

Vercelli, F., 1925. Il regime delle correnti e delle maree nello stretto di Messina, *Campagna della Nave Marsigli 1922-1923*. Officine Grafiche Ferrari.Venice, Italy.

Journal of Coastal Research	SI	75	662-666	Coconut Creek, Florida	2016

New Coastal Regulation in Spain. A roadmap to a better approach to coastal environment

José Santos López-Gutiérrez[†*], Vicente Negro[†], and M. Dolores Esteban[†]

[†]Research Group on Marine, Coastal and Port Environment and other Sensitive Areas
Technical University of Madrid
Madrid, Spain

www.cerf-jcr.org

www.JCRonline.org

ABSTRACT

López-Gutiérrez, J.S.; Negro, V., and Esteban, M.D., 2016. New Coastal Regulation in Spain. A roadmap to a better approach to coastal environment. *In:* Vila-Concejo, A.; Bruce, E.; Kennedy, D.M., and McCarroll, R.J. (eds.), *Proceedings of the 14th International Coastal Symposium* (Sydney, Australia). *Journal of Coastal Research*, Special Issue, No. 75, pp. 662-666. Coconut Creek (Florida), ISSN 0749-0208.

The decision to draw a fixed line dividing land into two different types of property – public domain and privately owned land – in a changeable environment is a potentially major source of conflict in Spain. This conflict is caused by adapting this fixed line to the movements of the shoreline. Obviously, then, the limit has to move its position from time to time. The current Spanish Coastal Law was published in 2013. As written, it cannot be considered a single document because it has to be read together with the previous 1988 Coastal Law document in order to gain a complete view of the current Spanish Coastal Law. The new Coastal Regulation was published in 2014. The paper shows and analyzes changes in the 2013 Law and the 2014 Regulation in comparison with the previous 1988 Coastal Law and the 1989 Regulation. Some of the changes set forth in the paper are: a more accurate definition of the position of the Public Domain limit; a new definition of the severe regression concept; a new classification of the uses of beaches depending on the characteristics of the area; consideration of the climate change effects; possibility of transferring, *inter vivos* and *causa mortis*, of properties located in the public domain under government concession, *etc.* All these lead drive to major improvements in coastal management in Spain. In addition, this paper includes some proposals for further improvements.

ADDITIONAL INDEX WORDS: *Coastal Public Property, land-sea domain, urban beaches; wave storms.*

INTRODUCTION

The previous Spanish Coastal Legislation was published in 1988 (Coastal Law) and 1989 (Coastal Regulation). Twenty five (25) years on, several problems have been detected for its legal and technical application. In fact, Spain continues to suffer from poorly planned development.

The great technical and legal complexity of the application of that Legislation was due to numerous technical, social and economic problems related to expropriation, the limits of the public domain and the practicalities of carrying out demolitions (Torres, 2010). Legal reform thus became necessary in attempting to solve the problems detected. This legal reform led to new, current Coastal Legislation, published in 2013 (Coastal Law) and 2014 (Coastal Regulation).

The reform was mainly due to the claims collected in the Auken report (Auken, 2009) related to legal insecurity for property owners affected by the change in position of the public domain's border. However, other improvements have been included which are aimed towards responding to other deficiencies detected.

The following sections include a brief review of the historical evolution of the Spanish Coastal Law and Regulation, an analysis of the amendments made with the new Coastal Legislation in relation to the previous one, improvements in the new Coastal Legislation related to the previous one and the uncertainties of the current legislation.

METHODS

The paper includes a comparison of previous and current Spanish Coastal Legislation. A brief review of the historical evolution of Spanish Legislation related to land-sea domain has been included to this effect.

Spanish Legislation considered in this paper refers to: the 1866 Water Law, the 1880 Ports Law, the 1969 Coastal Law, the 1978 Spanish Constitution, the 1988 Coastal Law, the 1989 Coastal Regulation, the 2013 Coastal Law and the 2014 Coastal Regulation. In the main, the four latter have been analyzed to determine improvements in current, new Spanish Coastal Legislation.

The case study, then, clearly involves the Spanish coast. This paper includes the following sections: results and discussion (historical evolution of Spanish coastal laws and regulations; current coastal law and regulation in relation to previous coastal law and regulation; improvements and uncertainties in the current Spanish coastal legislation) and conclusions.

RESULTS

The most significant results of studies carried out on legislation passed are given under this heading. Examples are

DOI: 10.2112/SI75-132.1 received 15 October 2015; accepted in revision 15 January 2015.
*Corresponding author: josesantos.lopez@upm.es

also provided serving to clarify improvements introduced into the new legislation.

Figure 1. La Manga sand barrier: pictures before (Mar Menor Web Page) and after the huge growth of private properties.

Historical evolution of the Spanish coastal laws and regulations

The historical evolution of Spanish Coastal Legislation (Laws and Regulations) actually commenced in 1969. However, for this technical paper, two previous documents must be mentioned: the 1866 Water Law and the 1880 Ports Law. The 1866 Spanish Water Law included a definition for the beach concept. And the 1880 Spanish Ports Law regulated the land-sea domain.

The first Spanish Coastal Law was passed in April 1969 (Official State Gazette or B.O.E., 1969). That Coastal Law was published during a dictatorship. During that time, the regime decided to foster tourism on the Spanish coast with the main aim being to boost the economy. Consequently, property development underwent a huge growth in coastal areas (Figure 1).

One of the main problems faced by the subsequent democracy was the existence of property rights acquired during the 1969 Coastal Law's validity period. Most of these properties were located within the public domain (Negro *et al.*, 2014).

The new Spanish Constitution was voted in in 1978. The Constitution indicated the intention of limiting private property rights by the Central Administration. After 10 years, the 1988 Spanish Coastal Law (B.O.E., 1988) was passed. That Coastal Law attempted to regulate coastal public domain.

The first part of the 1988 Coastal Law stated that the Spanish coast, with 24% beaches, is a very valuable asset offering a huge number of alternatives and possibilities. Even so, the influence of human activities and changes on the coast and the way to recover its physical equilibrium were not perfectly understood (Cooper and Alonso, 2006).

The aim of the 1988 Coastal Law was to recover coastal areas. To do so, it was planned to restrict private property in the public domain. Nevertheless, that Coastal Law did not fulfill that aim. In fact, Spain continued to be characterized by poor planning development of the coastal zone.

The 1988 Coastal Law was very difficult to apply, not only in the legal but also in the technical sense. This was due to numerous social, economic and technical complications regarding public domain limits, expropriation and the practicalities of accomplishing demolitions (Torres, 2010).

Several property owners affected by the 1988 Coastal Law set up the "Asociación Europea de los Perjudicados por la Ley de Costas (AEPLC)", (European Association of people affected by the 1988 Coastal Law). The main purpose of the association was to protect property owners' assets.

It submitted a petition to the European Parliament. Margrete Auken, Danish MEP (Member of the European Parliament) belonging to the Green/EFA group, drew up a report to support the association's claim (Auken, 2009). That report defended the individual rights of European citizens. Furthermore, it showed the influence of wide-spread land development in Spain.

The European Union passed the Auken report. That report requested a new Coastal Law and Regulation in Spain. As a consequence, the 2013 Spanish Coastal Law (B.O.E., 2013) and the 2014 Spanish Coastal Regulation (B.O.E., 2014) were published. The main reasons for this reform were the lack of legal security for employment and businesses and legal uncertainty for owners of private properties constructed in the public domain.

Current coastal law (2013) and regulation (2014) in relation to the previous coastal law (1988) and regulation (1989)

As mentioned earlier, the 2013 Coastal Law (B.O.E., 2013) and the 2014 Coastal Regulation (B.O.E., 2014) were published as a consequence of the Auken report. In fact, both the 2013 Coastal Law and the 2014 Coastal Regulation include some changes in relation to previous Coastal Legislation. Those changes in the new coastal Legislation were an attempt to respond to weaknesses in previous coastal Legislation (Negro *et al.*, 2014).

The land-sea domain is better defined in the new coastal Legislation. In the 1989 Coastal Law Regulation, the public domain border was defined as the limit reached by waves in the highest "known" storms or, in the event of being exceeded, the level reached by the Highest Astronomical Tide (HAT). The term "known" storms refers to storms included in existing, proven references. The 2014 Coastal Regulation indicates that the limit due to the highest known storms must be calculated

taking into consideration the levels reached at least five times in a five-year period.

The current, new Legislation includes new definitions related to the coastal environment and also a new classification for coastal dunes. Furthermore, the term of zones with a severe regression condition is included. Article number 29 indicates that the Government can define those coastal stretches with a backward movement of more than 5 meters a year in the last five years and its irrecoverability by means of natural processes as a severe regression condition. In this case, the shore line is related to the level reached by the Highest Astronomical Tide (HAT).

The new Legislation takes into account the effects of climate change in coastal zone. Article number 92 contains an assessment of the climate change effect, considering the rise in average sea level, wave direction changes, the rise in wave height, changes in storm duration and all coastal sediment dynamics in the area.

The 2013 Coastal Law and the 2014 Coastal Regulation differentiate between "urban" zones on beaches, and "natural" zones located in protected areas away from urbanizations, applying a different regimen in both cases with the purpose of providing a high level of beach protection and ensuring that environmental values are maintained. However, use is public and free in that domain.

Current Coastal Legislation stresses the desirability of having a mechanism for the Government to react in a speedy, effective manner in order to prevent illegal situations arising (Figure 2). According to what is known as the "Anti-Algarrobico" clause, the Government would be able to address each problem from the commencement with total autonomy.

Figure 2. The Algarrobico Hotel located in Almeria (Spanish Southeast coast) (EFE Web Page).

In an attempt to increase legal certainty, the new Coastal Legislation seeks to ensure that citizens have access to all the information available on properties constructed in public domain areas. Effective coordination between the property register and cadaster information is therefore required.

In addition, the new Coastal Legislation seeks to reconcile the coast with economic activities. However, protecting the integrity of the Maritime-Terrestrial Public Domain and contributing to its conservation is essential. To this effect, the right of occupancy of private properties situated in the public domain during thirty years renewable for another thirty was extended to seventy five years.

DISCUSSION

This section includes a comparison between previous Spanish Coastal Legislation (1988 Coastal Law and 1989 Coastal Regulation) and the current, new Spanish Coastal Legislation (2013 Coastal Law and 2014 Coastal Regulation). In fact, this section deals with the improvement provided by new legislation and, also, uncertainties for the future as to the application of this current, new legislation.

The first improvement in the current, new Spanish Coastal Legislation involves the definition of the land-sea domain border. This concept has changed several times throughout history.

Title number 1 of the 1866 Water Law included a definition of the beach concept (Garrán, 1867). The area covered and uncovered by tidal movement water, with a land or interior border reached by the highest astronomical tides (HAT), is defined as beach. In the event of negligible tides in the area, the beach starts in the land part at the level reached by the water during ordinary storms.

The 1880 Ports Law (Gaceta de Madrid, 1880) defined the sea domain as coastal areas covered and uncovered by sea water, taking into account the tidal effect, and in the event of negligible tides, those due to the highest waves.

In the 1988 Coastal Law, the border of the land-sea domain is defined by the level reached by waves in the highest "known" storms, and in the event of being exceeded, by the level reached during the highest astronomical tide (HAT) events. In this definition, it is important to be sure about the definition of two concepts: "storm" and "known". The storm concept is defined by the significant wave height, the wave period and the wave direction, unrelated to sea level.

Bilbao-Vizcaya buoy data have been chosen for this discussion. This buoy is located in the Vizcaya Gulf, to the north of Bilbao Port in the north of Spain. According to the 1989 Coastal Regulation, the maximum known storm is Hs = 13.70 m (Hs being the significant wave height), and Tp = 14.30 s. (Tp being the peak wave period) (Table 1).

As mentioned earlier, the 2014 Coastal Regulation indicates that the limit due to the highest known storms must be calculated taking into consideration the levels reached at least five times in a five-year period. For applying this current, new criteria, if we consider the whole period between 1990 and 2014 as the starting point (Figure 3/Puertos del Estado), the five-years period between 2007 and 2011 has been selected because the maximum significant wave height figures were recorded in that period. The gap in the data in early 2009 may be due to some fault in the buoy.

According to Figure 3, the significant wave height seen to be exceed five times in the five-year period is 10.1 m. This figure is lower than the 13.7 m, considered when the 1988 Coastal Law and the 1989 Coastal Regulation are applied.

Table 1. *Maximum wave data provided by Puertos del Estado for the Bilbao Vizcaya buoy (1990-2015)*

Month	Max Hs [m]	Tp [s]	Dir [º]	Year
January	13.7	14.3	292	2009
February	11.1	18.2	287	2014
March	11.6	15.5	304	2008
April	8.0	12.8	301	1994
May	7.5	13.4	288	2006
June	5.4	12.7	309	1999
July	5.9	11.1	281	2001
August	5.9	12.5	300	2008
September	7.7	10.7	281	1994
October	9.9	16.0	290	2003
November	11.0	12.8	-	1996
December	11.6	15.4	311	2007

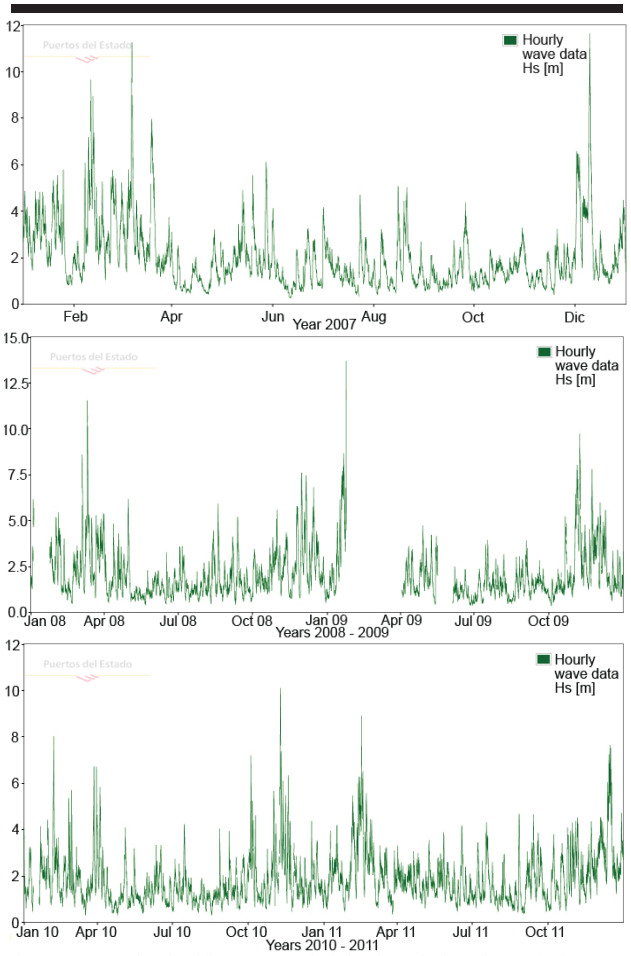

Figure 3. Hourly significant wave height during the period (2007-2011) at the Bilbao-Vizcaya buoy. (Puertos del Estado).

Clear progress has been made in connection with the design storm. The repetition criteria of the phenomenon have been added into the current, new Coastal Legislation. However, there are still uncertainties in that definition, such as the inclusion of a statistical variable, the possible influence of the wave period or the selection of the 5-year period to be considered.

The second improvement is related to the consideration of stretches with a risk of severe regression. As mentioned earlier, the Government describes those coastal stretches with a backward movement of more than 5 meters a year in the last five years as a severe regression condition zone, in the event they cannot be recovered by natural processes. In that case, the shoreline is related to the level reached by the Highest Astronomical Tide (HAT). As can be seen, the concept of severe regression has been defined. The time period has also been established.

Another improvement is the consideration of the influence of climate change on the rise in sea level and, therefore, on the movement of the shoreline position and the land-sea domain limit. Furthermore, a temporal scale has been established for analyzing littoral dynamics in the coastal stretch, according to the project in the planning stage. Nevertheless, strategy for that coastal adaptation is not included. This is planned to be drawn up 2 years after the 2013 Coastal Law.

The new Coastal Legislation distinguishes between "urban" zones on beaches, and "natural" zones located in protected areas away from urbanizations. Applying a different regimen in each case, the purpose is to provide a high level of protection to beaches and maintain environmental values.

A principal uncertainty is related to this issue. The characteristics to be taken into account in order to differentiate between urban and natural zones are not included. This classification will be undertaken by the Government.

As to complaints in the Auken report, the 2014 Coastal Regulation has made some improvements, for example, in relation to property ownership and transfer. In connection with ownership, properties located in the public domain have to be clearly identified for possible purchasers.

In addition, new buildings are not allowed and neither is work changing the height, volume or area of existing buildings, should they be in the public domain or in protection easement.

The right of occupancy of private properties located in the public domain was increased from thirty plus another optional thirty to seventy five years. In addition, these private properties can be both *inter vivos* transferred and transferred by inheritance. This leads to better perception for property owners affected by public domain boundaries when their properties are located in the latter.

CONCLUSIONS

This study allows the main differences between previous and current Spanish Coastal Legislation to be established. Current legislation is formed by the 2013 Coastal Law and the 2014 Coastal Regulation, considered as an improvement on the earlier. However, it is important to note that previous Coastal Legislation (the 1988 Coastal Law and the 1989 Coastal Regulation) were innovative when published.

The current, new Coastal Legislation incorporates new aspects to allow for adaptation to the existing physical and legal reality. This new Coastal Legislation attempts to take the Auken report claims into consideration with regard to the legal uncertainty of owners with properties located in the public

domain or very close thereto, or even with properties that may be affected by new public domain boundaries.

Main improvements in the current, new Coastal Legislation in comparison with the previous are:

(i) Mandatory registration of all alterations to properties within the public domain. Everyone can therefore know whether a property is located in the public domain. Owners can *inter vivos* and *causa mortis* transfer properties located in the public domain under government concession. New buildings and those works changing the height, volume or surface of existing buildings, in the event they are located in the public domain or in protection easement are not allowed. Delimiting borders of the land-sea domain has been improved.

(ii) "Urban" zones on beaches, and "natural" zones located in protected areas away from urbanizations are differentiated.

(iii) Consideration is given to stretches with a risk of severe regression and to the effect of climate change on coastal processes altering the morphology of coastal stretches.

However, the new Coastal Legislation has some weak points, such as the following:

(i) Complete methodology for delimiting the borders of the land-sea domain is not included. This may lead to uncertainties as regards its technical application. As a consequence, uncertainties as to legal rights may be generated.

(ii) Issues related to renewable marine energies, maritime spatial planning indicating uses and activities (aquiculture, offshore wind farms, wave energy converter facilities, *etc.*) to be implemented in the different zones, risk maps and physiographic unit distribution are not included. The inclusion of all these issues would be most interesting and highly recommendable.

This paper makes a clear comparison between previous and current Spanish Coastal Legislation to be used for the scientific community and stakeholders, whilst also including improvement proposals for future changes in Legislation.

LITERATURE CITED

Auken, M., 2009. European Parliament Resolution, 20 February 2009, on the impact of extensive urbanization in Spain on individual rights of European citizens, on the environment and on the application of EU law, based upon petitions received *(2008/2248(INI))*.

B.O.E., Official State Gazette, 1969. Ley 28/1969, de 26 de abril, *sobre Costas*, 4p. (in Spanish).

B.O.E., Official State Gazette, 1988. Ley 22/1988, de 28 de julio, de Costas, 16p. (in Spanish).

B.O.E., Official State Gazette, 1989. Real Decreto 1471/1989, de 1 de diciembre, por el que se aprueba el Reglamento General para el desarrollo y ejecución de la Ley 22/1988, de 28 de julio, *de Costas*, 27p. (in Spanish).

B.O.E., Official State Gazette, 2013. Ley 2/2013, de 29 de mayo, de protección y uso sostenible del litoral y de modificación de la Ley 22/1988, de 28 de julio, *de Costas*, 46p. (in Spanish).

B.O.E., Official State Gazette, 2014. Real Decreto 876/2014, de 10 de octubre, por el que se aprueba el Reglamento de la Ley 2/2013, de 29 de mayo, *de Costas*, 119p. (in Spanish).

Cooper, J.A.G. and Alonso, I., 2006. Natural and anthropic coasts: challenges for coastal management in Spain. Coastal Geomorphology in Spain: Proceedings of the III Spanish Conference on Coastal Geomorphology. *Journal of Coastal Research*, Special Issue No. 48, 1-7.

EFE Web Page. http://www.efe.com.

Gaceta de Madrid, 1880. Ley de 7 de mayo de 1880 de Puertos. 129, 3p. (in Spanish).

Garrán, M., 1867. Apuntes sobre la ley de aguas, promulgada en 3 de agosto de 1866, y acerca de la redacción de los reglamentos para su cumplimiento. *Revista de Obras Públicas*, I (18), 212-215. (in Spanish).

Mar Menor Web Page. http://www.marmenoronline.com.

Negro, V., López-Gutiérrez, J.S., Esteban, M.D., and Matutano, C., 2014. An analysis of recent changes in Spanish Coastal Law. *In:* Green, A.N., and Cooper, J.A.G. (eds.), *Proceedings of the 13th International Coastal Symposium* (Durban, South Africa), *Journal of Coastal Research*, Special Issue No. 66, 448-453.

Puertos del Estado. Ministerio de Fomento. *Gobierno de España*. http://www.puertos.es.

Torres Alfosea, F.J., 2010. Cuarenta años de leyes de costas en España (1969-2009). *Investigaciones geográficas*, No. 52, 167-198. (in Spanish).

Journal of Coastal Research	SI	75	667-671	Coconut Creek, Florida	2016

Review of coastal Land Reclamation situation in the World

Mario Martín-Antón [†*], Vicente Negro[†], José María del Campo[‡], José Santos López-Gutiérrez[†], and M. Dolores Esteban[†]

[†]Departamento de Ingeniería Civil: Hidráulica, Energía y Medio Ambiente
Universidad Politécnica de Madrid
Madrid, Spain

[‡]Departamento de Ingeniería Civil: Construcción, Infraestructura y Transporte
Universidad Politécnica de Madrid
Madrid, Spain

www.cerf-jcr.org

www.JCRonline.org

ABSTRACT

Martín-Antón, M.; Negro, V.; del Campo, J.M., López-Gutiérrez, J.S., and Esteban M.D., 2016. Review of coastal Land Reclamation situation in the World. *In:* Vila-Concejo, A.; Bruce, E.; Kennedy, D.M., and McCarroll, R.J. (eds.), *Proceedings of the 14th International Coastal Symposium* (Sydney, Australia). *Journal of Coastal Research*, Special Issue, No. 75, pp. 667-671. Coconut Creek (Florida), ISSN 0749-0208.

Land reclamation from the sea has been occurring since ancient times, especially in harbors. The vast majority of the world's docks now occupy spaces that were once water and this heavily influences the coastal landscape. Japan has been one of the country's most needing to expand into the sea due to its topography and land requirements for agriculture, urbanization and, especially, industries and port facilities. Ninety per cent of Tokyo Bay's coastline is reclaimed land, which is almost 250 km^2 of new land. In the 21st century, this disproportionate conquest of the sea has shifted to other countries. In the Persian Gulf, the coast has been indiscriminately occupied with artificial island projects for residential purposes. Some of them are finding some difficulties, such as "The Palms" and "The World" in Dubai, with a loss of sand, which is effect of currents and waves. In China, due to economic expansion and export needs, industrial areas are spreading on the coast. Caofeidian (Bohai Bay) is the largest landfill island in the world with 150 km^2, more than twice the sum of Dubai islands area. This disproportion of public works in Asia contrasts with the rest of the world. For example, the Bay of Algeciras (Spain-UK) is the largest container traffic Port in the Mediterranean with 2.5 km^2 of reclaimed land, 100 times less than Tokyo Bay. A further problem associated with this practice is liquefaction, caused mainly by earthquakes, leading to ground subsidence in buildings, such as in Niigata (1964) or in San Francisco (1989), all on reclaimed land. This research paper aims to study land reclamation in the World with current statistics, geotechnical problems, the impact on the coastal landscape and future developments.

ADDITIONAL INDEX WORDS: *Land reclamation, landscape, harbours.*

INTRODUCTION

The concept of Land Reclamation involves gaining land areas for a specific use, generally a more productive one (Hoffmann, 1996). Land reclamation may be split into many types but the major ones involve recovering abandoned mines and pouring earth onto the sea bottom until it reaches above water level so forming new areas. The former is usually used to reduce mining area impacts whilst the latter produces a clear impact on a fragile environment such as the coast (Hu, 2015). We shall only be studying land reclaimed from water areas in this article.

This practice has been carried on since ancient times, particularly for agricultural uses in shallow lakes or marshlands. In the pre-industrial era, this meant creating new land for cultivation and settlement (Curtis and Campopiano, 2013). Las Chinampas in México is a case in point. This is a farming method commenced by the Toltecs in Texcoco Lake. Swamps were reclaimed by digging channels by hand and the excavated soil was used to construct embanked fields (Arco and Abrams, 2006). The city of Tenochtitlan was built on this lake amongst several islands. These were gradually filled in with lines of tree trunks and soil (Atwood, 2014). Many of the cultivation areas also became building areas because of a need and came to occupy the whole water area to turn into what is nowadays called México DF.

A similar technique was used in Venice (Atwood, 2014) also built on marshland. The city is originated from a group of islands (Rivo Alto Islands, now called Rialto) located in Venetian Lagoon (Miozzi, 1957). According to Miozzi's hypotheses, the area of these 19 islands in Veneta lake was little more than 1 km2. It rapidly expanded in the 12th century until reaching close to its present 7 km^2, in which 6 of them were reclaimed from the lake.

Another type of land reclamation are polders, although their concept is different to anthropic fills but we are also given some idea of the ability of human beings to create new terrains for their own use. Polders are tracts of land which beforehand were under water in shallow areas. They were recovered by building perimeter dikes providing protection from the sea's action and then pumping out the water inside bringing the level down to the land's surface (Stijnen *et al.*, 2014). Electric pumping stations are now used for this task but centuries ago, it was performed with windmills like in Holland. Currently, 26% of this country's

DOI: 10.2112/SI75-133.1 received 15 October 2015; accepted in revision 15 January 2015.
*Corresponding author: mario.martin.anton@alumnos.upm.es

area is below sea level, i.e., around 9000 km^2 (Schiermeier, 2010). One of them, Flevopolder, particularly stands out with its 970 km^2 and may be considered the largest artificial island in the world although under sea level and with no anthropic fill.

Polders have the great advantage of not requiring large volumes of compacted earth, which is a very costly operation. This is why they can also be used for building harbour yards since settling and the amounts of material needed are reduced and this, in turn, reduces the cost by up to 30% although it does increase the risk of flooding (Lendering *et al*., 2014). The study of Lendering concludes that when the price of fill earth is higher than €10/m^3, it is better to build polder terminals (such as the case of Tuas Singapore Port) and if below that figure, building a conventional terminal is more recommendable.

Land reclamation commences by first executing the delimiting dykes, whether mound or vertical. The inner zone in most cases must be earth filled. Several methods are used:

- Drained reclamation: Consists of pouring sand onto the sea bottom and laying drains every certain distance to aid in consolidating the soil and pumping out surplus water.
- Deep cement mixing: This method is particularly used when the sea bottom has a poor bearing capability or is contaminated. Bore holes are drilled in the bottom and are concrete filled. In this way, capped piles are built onto which earth is placed for the compaction of the fill.
- Sand compaction pile: As in the foregoing, bore holes are drilled but sand is used instead of drains. Once the columns of sand or gravel are positioned, a pre-load is placed on top consolidating the bearing terrain. The preload material is then removed.
- Polder: this is not a material fill method. It simply consists of using pumps to drain all the water held inside the enclosure to make a useful area out of the sea bottom.

Polders have not been taken into account in this article's world land reclamation statistics since studying them would be far too extensive. A great part of the coastlines of China, Bangladesh and South-East Asia is full of them and drawing up a quantitative classification is a difficult task.

The aim of this article is to study the whole of the World's coastline, searching for places with a large area of reclaimed land. After taking their measurements, a list will be drawn up with the area, use (ports, industries, airport, residential) and proportion of artificial islands. Further aspects related to this point will then be taken into consideration, such us problems linked with this practice, the impact on landscape and future developments.

METHODS

Google Earth was the tool used to locate all land reclamation projects and to measure them. Areas which were once water but are now land can be checked through its historic images application. Historic maps were used when this was not possible because of a lack of aerial photographs from many years ago. Google Earth's visual information was examined in detail to distinguish polders below sea level and fill areas, in addition to its information as to elevations and images. A distinction in the forming of fills was also made depending on whether they are tracts of coastline or simple artificial islands surrounded by water although those island extensions exceeding twice the initial size were also taken into account in that type difference.

Fill used for a residential or airport purpose, a much less common event, has been taken into account even though the area may be smaller than some ports.

RESULTS

The study results were as expected though surprising at some sites. As Figure 1 shows, most of the new land on the sea is located in Asia, but not only in Dubai as people generally think. The expansion of Japanese ports during the 20th century and the Chinese in this 21st century have brutally conquered the sea.

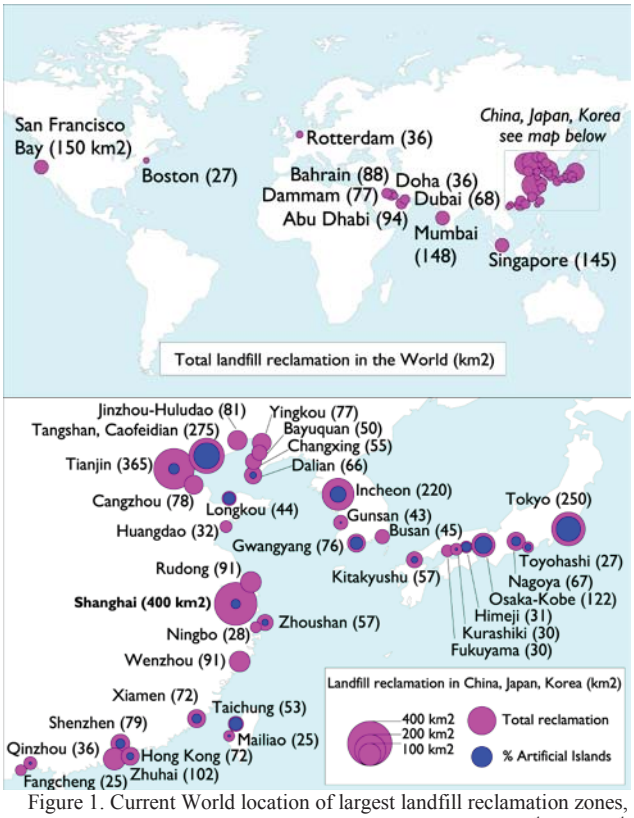

Figure 1. Current World location of largest landfill reclamation zones, through all past time until today (2015), that is from 18th and 19th Centuries (Tokyo, Boston, Mumbai, San Francisco, Hong Kong). The above map represents the 45 zones with over 20 km^2 of surface area gained. The map below focuses more on East Asia because of the large number of areas. The mauve circles show the whole of the area filled, whilst the blue circles represent the percentage of that surface area made in the form of an artificial island. Measurements from Google Earth.

The most common uses of land reclamation are: Port expansion (quays, container yards), industrial areas (especially port activity related), residential areas, airport runways, agriculture (particularly in polders) and strategic military zones.

Chinese ports occupy the leading positions in the ranking as to the greatest area reclaimed from the sea with fills. The whole of the mouth of the river Yangtze near Shanghai accumulates

400 km^2 of new land to which is added more from polders and areas that have been emerging due to the river sediments. Second place is filled by the Port of Tianjin in Bohai Bay with 365 km^2 followed by Tangshan, with 275. Caofeidian is located there, with its 150 km^2 (under construction with 20 km^2 left to be filled). This artificial fill island is the largest in the world. It was intended to be a great eco-city with industries and a port to reach 190 km^2, but financing problems are holding up the project. Outside China, Tokyo Bay with 250 km^2 (Figure 5), Incheon (220), San Francisco Bay (150), Mumbai (148) and Singapore (145) stand out. In the case of Mumbai, the city commenced its expansion in the 1800's and first consisted of joining seven islands to establish the city. San Francisco Bay was developed in the 19th and 20th centuries mainly for residential and industrial land. Singapore began expanding in the 20th century in order to become one of the world's major ports and increased its area by 25% in half a century. It is forecast to grow up to 100 km^2 more (MEWR, 2005).

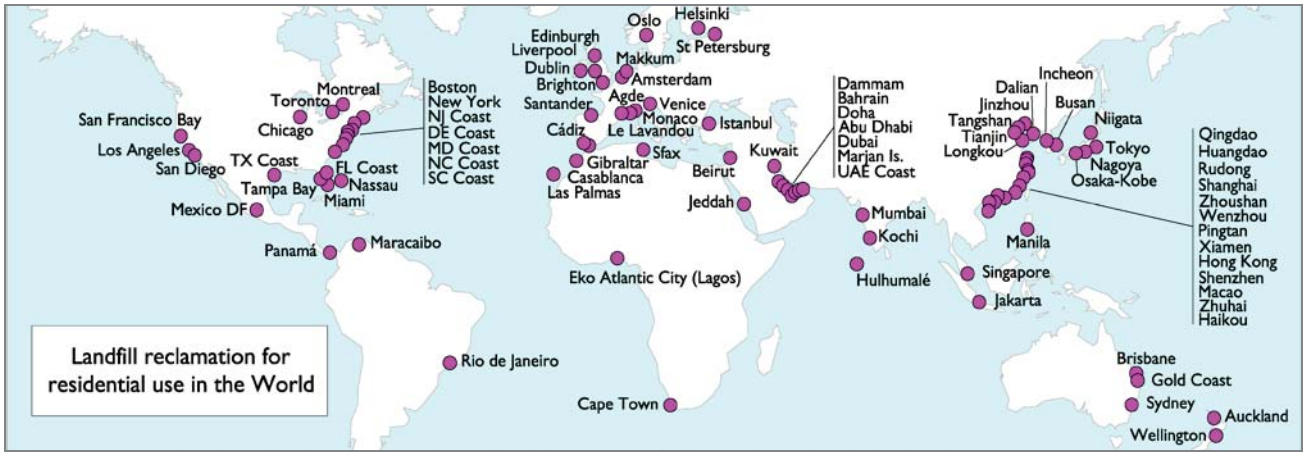

Figure 2. Current location of land reclamations for residential uses. Found with Google Earth. Circles size does not represent any value.

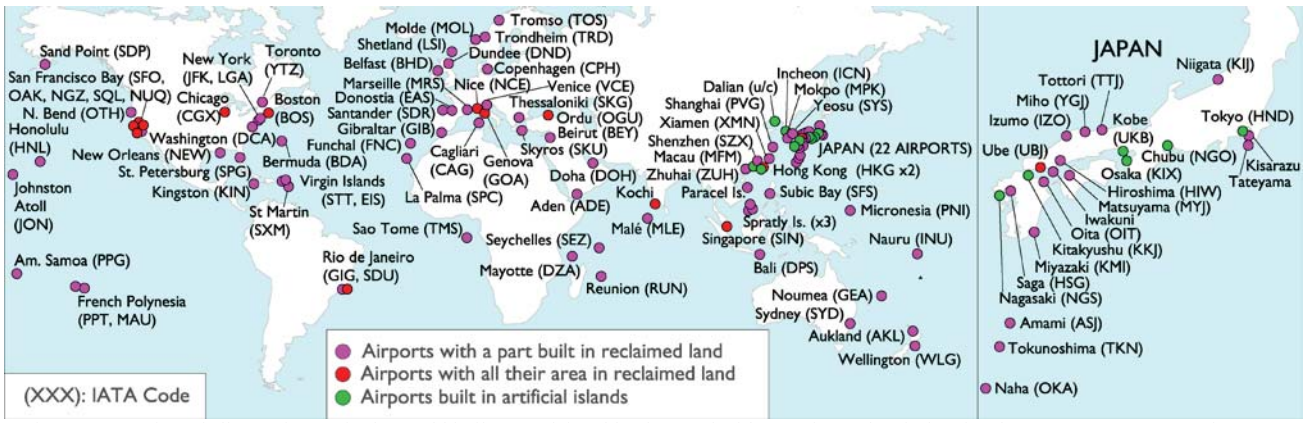

Figure 3. Location of all 102 airports in the world built on reclaimed land. Found with Google Earth. Circles size does not represent any value.

According to the study shown in Figure 1, 42 of the 45 places with a higher landfill reclaimed area are placed in Asia, of which 35 in East Asia (23 in China). Just China stands out with more than a half of the total area of places surpassing 20km^2 of land reclamation in the World.

A most curious fact is Dubai's 22nd place as to reclaimed area, when for many people it is a reference site. This is one of the places with the most complex, spectacular artificial island projects in the World, specially earmarked to exclusive residential use. Some projects, like "The Palm Jumeirah" and "The World", are undergoing problems in trying to prevent loss of sediments due to marine currents (Gibling, 2013).

Three areas in the world stand out as to the purpose of fills for constructing residential buildings (Figure 2). The first to be developed was the United States east coast where deluxe residential estates can be found on small artificial islands at many points on the coastline. The most notable case is Miami, with Star Island and others too. Since the end of the 20th century, towns on the China coast have also undergone a seaward boom in expansion. Big esplanades for locating industries and ports have also served for building large blocks

of flats at the side, such as in Tianjin and Tangshan. Large artificial island projects are also being contemplated, such as Longkou with 6 large islands and a total surface area of over 35 km^2, as big as the "Two Palm Islands and The World" in Dubai together. The Persian Gulf has been developed more recently, particularly in this century. To the clear example of Dubai has to be added Abu Dhabi (with more filled area than Dubai), Dammam, Doha and Bahrain. How the almost 90 km^2 gained from the sea represents a 13% increase in the whole country's surface area, which was 662 km^2 40 years ago (Abuzinada *et al*., 2008), can be observed in the latter country. There are also examples of sites such as Gibraltar, Hong Kong and Macao which are strategic because of their small size but large growth potential.

The need to build airports on artificial islands is mainly due to problems of space and orography (Figure 3). We find that the advantages in this type of construction throughout history have involved not having any obstacles on approach routes in addition to reducing the impact of noise on nearby populations. This study has found 102 airports built on water in the whole world, most with fills on a small area. Others, on the contrary, needed to be fully located on reclaimed land, even though the latter was a continuation of the land. Some worthy of mention are San Francisco, Boston, Singapore and Ordu, opened to operations in 2015, in Turkey.

On certain occasions they go further and the airport is totally separated from "*terra firme*", forming artificial islands. The most famous in the world is that of Osaka-Kansai (KIX) built in Japan in the 1990s. It was opened in 1994 with one operative runway. Increases in demand made it necessary to double the area gained from the sea up to 13 km^2 in 2007. There are 4 more one-runway airports in Japan whilst Tokyo Haneda (HND) with 4 runways exceeds 14 km^2 of land reclaimed from the sea. Artificial islands can also be found in Macao and the Dalian airport under construction in China. In Asia there are also two other major airports which have been attached to much smaller islands, Hong Kong's with 14 km2 and Incheon's. The latter is the airport with most area gained from the sea. The area of the artificial island dedicated to the airport measures 35 km^2, only two thirds of the reclamation

Finally, there is an unusual use: military and strategic. Over the last few years, China has been expanding some of the Spratly and Paracel Islands (disputed with other countries) to build aircraft runways, military and loading harbours and logistic areas. This project is called the "Great Wall of Sand".

DISCUSSION

The geotechnical problem is one of the most important in land reclamation. On creating new areas, whether with material dredged from the sea or taken from the land, compaction is a major issue. It is difficult to achieve large, perfectly filled areas and so, at times, they are left to consolidate little by little. When the final use is port yards or storage areas, the fill is not as important as if large blocks of flats with deep foundations are to be built.

Soil liquefaction is a phenomenon which occurs particularly in sand when interstitial water pressure considerably increases. Shear stress and effective pressure diminish, making solid material behave almost like a liquid. For this to happen, there must be an external force producing this pressure increase, such as an earthquake. If this occurs, the places most liable to liquefaction are sedimentary areas of rívers, beaches and anthropic fills (land reclamation). Several examples have occurred in reclaimed land throughout history, such as the Kobe earthquake in 1995 where a large part of the quays collapsed, or the Loma Prieta earthquake in 1989, where many buildings were destroyed in San Francisco's Marina District (Lomnitz, 1997). The best known case of liquefaction is that which happened in the 1964 Niigata earthquake. Several buildings overturned without being destroyed and the image clearly defines how destructive the mix of an earthquake and reclaimed land can be (Figure 4).

Figure 4. The effects of the 1964 earthquake in Niigata (Japan). The buildings were located in Kawagishi-cho, an area reclaimed from the river (red line). Wikipedia and Google Earth.

Figure 5. Change of scale between Asia and the rest of the world. Tokyo Bay has 250 km^2 gained from the sea whilst the port of Algeciras, the largest on the Mediterranean, has 100 times less (Google Maps).

The landscape is another factor to take into account in coastal actions; in a global scale, with remarkable differences as represented in Figure 5, and in a local scale. In the case of Tokyo Bay (Figure 5), more than 90 per cent of its coastline has been reclaimed during centuries. The need for space in the most populated city of the World has brutally invaded the sea, but nowadays the landscape of this city cannot be understood without the port. Figure 6 shows two more examples. Istanbul is a historic city with a very representative plan view (the Bosphorus, Golden Horn, ancient city). The construction of an esplanade in the sea in the south of the city totally changed

its significance. The city missed part of its essence. On the right, we see Bahrain; an entire country which, because of the land reclamation effect (red line) is completely changing, causing an impact which it will never be possible to remedy.

Figure 6. Impact of land reclamation on the landscape: Istanbul and Bahrain (Google Earth).

There are several ambitious land reclamation projects currently being worked on all over the world. "The Waterfront" and "Palm Deira" in Dubai are projects still to be finished and "The Universe" is on the drawing boards. Eko Atlantic City is the major project in Africa in the city of Lagos. Fill work currently surpasses half the total of 10 km^2. It is planned to be a city with offices and flats for 250,000 people, taking the pressure off the city of Lagos, the second most populated in Africa. One of the most important land reclamation projects is to be developed in Korea. Saemangeum which, with its 34 km of dike, is the longest in the world and will house a city with 291 km^2 gained from the sea, many of them in the form of polders for farming (KASDI, 2015). Apart from Caofeidian, some enormous projects are also being developed in China. There are already 36 km^2 gained from the sea in Qinzhou and it is expected that this figure will double with this new residential and industrial city project.

Unworkable projects from the last century also exist, mainly in the USA. One consisted in extending Manhattan island 15 km^2 towards Upper New York Bay, forming the city of New Manhattan. The designer was the municipal engineer, Kennard Thompson in 1911 (Hailey, 2013). The Reber Plan in San Francisco Bay surfaced in the 1940s. This plan addressed the construction of two dikes in the north and south areas of the bay to create two lakes joined by a canal through Oakland gaining 80 km^2 of land.

CONCLUSIONS

When artificial islands are discussed, Dubai is almost always the main topic in this sense due to the spectacular nature of their shapes and sizes. This article shows that the world of land reclamation and artificial islands is far more extensive than expected and has been developed far more in China, Japan, Korea and the Persian Gulf than in the rest of the world. And that the reclamation in harbours is more significant than in residential zones, in terms of total area.

The world is shifting its centre of gravity toward the east of Asia clashing with what has been seen up to now in the rest of the world. All this "rough development" is associated with contempt for the landscape in most cases, placing economy and the needs of a globalised world ahead of respect for and integration into the surroundings.

LITERATURE CITED

Abuzinada, A.H.; Barth, H.; Krupp, F.; Böer, B.; Al Abdessalaam, T.Z. Eds. (2008) *Protecting the Gulf's Marine Ecosystems from Pollution*. Birkhäuser Verlag/Switzerland

Arco, L.J. and Abrams, E. M., 2006. An essay on energetics: the construction of the Aztec chinampa system. *Antiquity*, 80(310), 906-918

Atwood, R., 2014. Under Mexico City. *Archaeology Magazine*, July-August 2014. ISSN: 0003-8113

Curtis, D.R. and Campopiano M., 2013. Medieval land reclamation and the creation of new societies: comparing Holland and the Po Valley, c.800 - c.1500, *Journal of Historical Geography*, 1-16 doi: 10.1016/j.jhg.2013.10.004

Gibling, C., 2013. Construction Process and Post-Construction Impacts of the Palm Jumeirah in Dubai, UAE, *Journal of Undergraduate Engineering Research and Scholarship, 1(1)*

Hailey, C., 2013. *Spoil Island: Reading the Makeshift Archipelago*, Lexington Books, ISBN: 978-0-7391-7307-7

Hoffman, R., 1996. Economic development and aquatic ecosystems in medieval Europe. *American Historical Review.* 101, 631-669.

Hu, Z. (Ed.), 2015. *Legislation, Technology and Practice of Mine Land Reclamation*, CRC Press / Balkema, Taylor & Francis Group, London. ISBN: 978-1-138-02724-4

KASDI, Korea Agency for Saemangeum Development & Investment Agency, 2015. *Hub of Asia, Heart of Future, Saemangeum.*

Lendering, K.T., Jonkman, S.N.; Peters, D.J.; 2014. Risk approach to land reclamation: Feasibility of a polder terminal. *Safety, Reliability and Risk Analysis: Beyond the Horizon. Proceedings of the European safety and reliability conference, ESREL 2013.* pp. 2507-2514

Lomnitz, C., 1997. Mexico, San Francisco, Los Angeles and Kobe: What next?. *Natural Hazards*, 16(2-3), 287-296 doi:10.1023/A:1007917820414

MEWR, Ministry of the Environment and Water Resources of Singapore, 2005. *Towards Environmental Sustainability, State of the Environment 2005 Report*

Miozzi, E., 1957, *Venezia nei Secoli, La Città, vol. I*, Casa Editrice "Libeccio", Venezia.

Schiermeier, Q., 2010. Few fishy facts found in climate report. *Nature.* 466(7303), 170. doi:10.1038/466170a

Stijnen, J.W.; Kanning, W.; Jonkman, S.N.; Kok, M.; 2014. The technical and financial sustainability of the Dutch polder approach. *Journal of Flood Risk Management.* 7(1), 3-15. doi: 10.1111/jfr3.12022

Journal of Coastal Research	SI	75	672-674	Coconut Creek, Florida	2016

Communicating beach management: educators; coastal engineers and local governments collaborating to create successful education programs.

Maggie Muurmans † **Peta Leahy** † **Laura Richards** *

† Griffith Centre for Coastal Management
Griffith University
Gold Coast, Australia

*City Infrastructure Assets Branch
City of Gold Coast
Gold Coast, Australia

www.cerf-jcr.org

www.JCRonline.org

ABSTRACT

Muurmans, M., Leahy, P., Richards, L., Communicating beach management: educators; coastal engineers and local governments collaborating to create successful education programs. *Proceedings of the 14th International Coastal Symposium* (Sydney, Australia). *Journal of Coastal Research*, Special Issue, No. 75, pp. 672-674. Coconut Creek (Florida), ISSN 0749-0208.

Through partnership between The Griffith Centre for Coastal Management and the City of Gold Coast a very successful education program "CoastEd" was created since 2001 with a focus on the coastal environment. Complimentary educational sessions are delivered to schools, community groups and residents. Topics range from beach health, coastal processes and tourism, to mangrove environments and climate change. The school programs match the Australian Curriculum and community programs are increasingly popular. The unique collaboration between a city council and a research centre has resulted in improved communication to the community as all programs are delivered by industry professionals with an extensive teaching background. The award winning program has been operational for 15 years and is highly respected in the community. CoastEd is a knowledge hub for queries the local community may have with regards to coastal protection. This paper will highlight some of the successful techniques we have used to increase awareness on certain pressing topics such as climate change, coastal protection and biodiversity.

ADDITIONAL INDEX WORDS: *Beach management, partnerships, coastal and environmental education.*

INTRODUCTION

Community engagement is the key towards creating environmental stewardship and raising awareness within a local community. Education provides one of the vehicles to achieve this. Research has shown that participants are subject to a range of benefits from environmental outdoor education and that these last well beyond other conventional teaching programs (Neill and Richards 1998; Neill, 2008).

CoastEd, one of the community engagement programs of the Griffith Centre for Coastal Management was established in 2001 to provide an essential service to the Gold Coast community with regards to raising awareness on the region's coastal environment, including its management, engineering structures, wildlife and habitat. The centre forms a base for some of the worlds' leading experts in coastal management and has award winning individuals delivering CoastEd's educational sessions. Over the past 15-years, the program has worked with a large number of Gold Coast and Brisbane based schools, and delivers sessions to an average of 5000 participants each year.

In response to enquiries directly from the community to the City of Gold Coast with regards to information, complaints and questions on coastal management, a partnership between the Griffith Centre for Coastal Management and the City was established to assist in delivering information, education and policy on coastal issues to the community. Due to the Centre's reputation in tackling coastal management issues as well as industry professionals with teaching experience available to deliver the sessions, it is an obvious partnership.

METHODS

The ability to provide subsidised, high quality educational programs including valuable resources for teachers and communities in partnership with a local government and a renowned University, has increased the reputation for all parties involved. The City's voice through CoastEd has improved their standing with the community on coastal issues and has ensured that enquiries are being responded to in a timely and comprehensive manner.

In order to guage the perceived quality of CoastEd sessions, a survey was undertaken amongst 38 primary and secondary school teachers who have benefitted from the service. The written survey, consisting of a mix of ten multiple choice and open questions, was distributed though an on-line platform to schools from Brisbane to northern NSW after each CoastEd session. In the hope of prompting genuine responses, teachers were not required to state their names on the survey forms. Although the sessions are provided without charge, teachers were asked to provide a hypothetical monetary value to the

DOI: 10.2112/SI75-134.1 received 15 October 2015; accepted in revision 15 January 2015.
*Corresponding author: m.muurmans@griffith.edu.au

sessions. This enabled CoastEd staff to make a comparison of their service with other similar services that incur a fee.

RESULTS

The results showed that although CoastEd has been operational since 2001, 31% of schools were new to the program in 2014 and 2015 (Figure 4). It also demonstrated the exceptional value of the programs with 100% of the respondents interested in future CoastEd sessions and agreement that the information provided aligns well with the Australian National Curriculum. 97% of teachers found that the sessions met their needs (Figure 1), while 73% of all teachers rated the quality of the CoastEd sessions as excellent (Figure 2). In response to the perceived monetary value of the sessions, 29% of respondent valued the service at $100 or more (Figure 3).

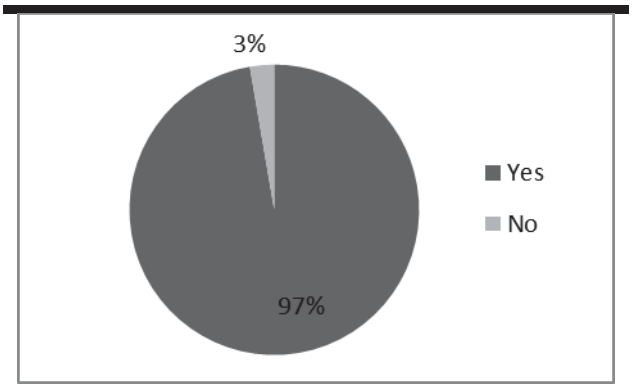

Figure 1. Did the session meet the students' and teachers' needs?

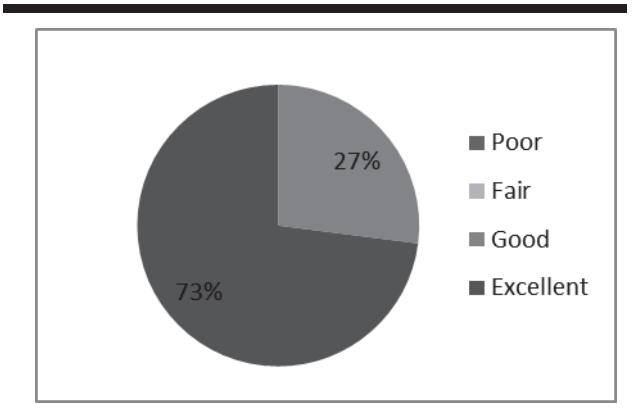

Figure 2. How the teachers valued the quality of the service.

From delivering ten sessions per year in 2001, the Centre currently has an agreement with the City of Gold Coast to provide at least 60 subsidised sessions to kindergartens, primary and secondary schools, community groups and residents. Each session runs for approximately 60 minutes. The quality of the program has increased each year and has now culminated in interactive curriculum matched programs for schools with resources for hands-on learning. The programs have been developed in collaboration with the coastal engineers based at the centre, created from recent coastal research. In 2015 the program was awarded the Australian Coastal Council's Award in the category of community engagement.

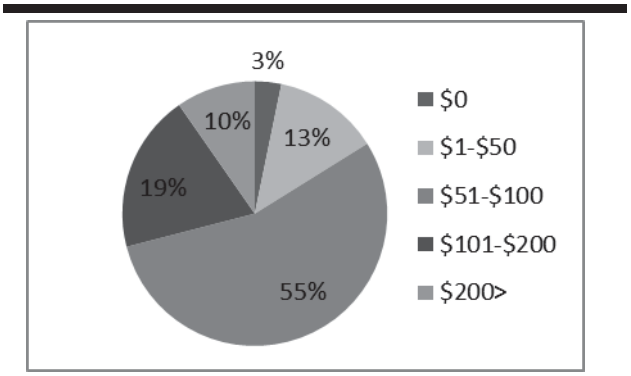

Figure 3. How the teachers valued the sessions.

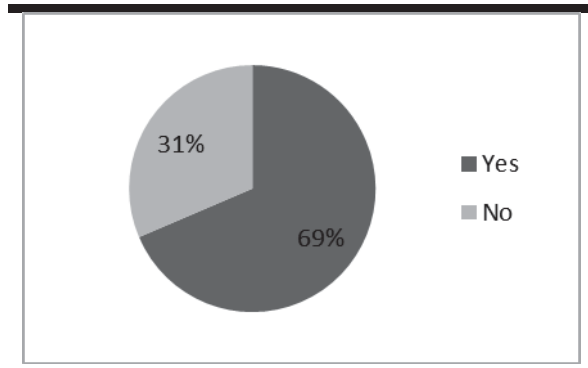

Figure 4. Did the school participate in CoastEd sessions before?

The range of programs has improved from slideshows solely on coastal processes to the current interactive, hands-on workshops in the field on topics ranging from beach health, tourism and geology, to mangroves, rocky shores and dunes. Participants collect primary data, complete surveys or identify biotic and abiotic processes and factors. A range of low-tech and high **tech** equipment is used during the sessions such as quadrats, anometers, field guides, thermometers, microscopes and identification keys. Worksheets are accompanied with lesson plans and answer sheets and all curriculum codes are posted online for each session to accommodate teachers. All programs endeavour to take all three learning styles into account including visual, auditory and kinaesthetic styles. The "Studies in Sand" program is one example of such a session using sand samples from across the world, microscopes and worksheets stimulating all learning styles.

In addition, Community education programs also have a

hands-on approach incorporating community projects such as BeachCare to revegetate dune ecosystems or using treasure hunts by bicycle along the coastline to learn about coastal features and coastal engineering.

DISCUSSION

Although CoastEd's educational programs in partnership with the City of Gold Coast have been running since 2001, the programs have only been matched to the Australian National Curriculum since October 2014. The above feedback from the teachers is based on sessions delivered between 2014 and 2015. Feedback information from the years 2001-2013 have shown that teachers also rated the quality of the CoastEd sessions as good to excellent**.** The results of the survey, indicating the success of the CoastEd sessions, concur with other investigations into the benefits of outdoor education programs, which find that they offer a valuable means of education and training (Neill and Richards, 1998; Neill, 2008). The hands-on approach in programs such as those offered by CoastEd also raises awareness and enables individuals to make informed decisions by providing an effective introduction to real-world environmental issues (Bogner, 1998).

With the exception of research based citizen science programs that have government support such as MangroveWatch, SeagrassWatch and CoastWatch (Ferreira, 2012), CoastEd provides community programs that are solely focussed on educating the community, using national school curriculum guides, teaching about coastal issues in collaboration with the local government.

CONCLUSIONS

The Griffith Centre for Coastal Management has built a bridge between a local government body, and the community by creating programs that suit both stakeholders. This unique partnership has proven successful and will continue to deliver and expand into the future.

ACKNOWLEDGMENTS

The authors would like to acknowledge the support of the Griffith Centre for Coastal Management and Griffith University, members of the Gold Coast community, Gold Coast and Brisbane Primary and Secondary schools and BeachCare. This work has been funded and supported by the City of Gold Coast.

LITERATURE CITED

Bogner, F., 1998. The Influence of short-term outdoor ecology education on long-term variables of environmental perspective. *The Journal of Environmental Education*, Volume 29, No.4, 17-29.

Neill, J. and Richards, G., 1998. Does outdoor education really work? A summary of recent meta-analyses. *Australian Journal of Outdoor Education*, Volume 3, No.1

Neill, J, 2008. *Meta-analytic research on the outcomes of outdoor education,* 6th Biennial Coalition For Education In The Outdoors Research Symposium, Bradford Woods.

Ferreira, M.A., et al., 2012. Educating citizens about their coastal environments: beach profiling in the Coastwatch project. *Journal of Coastal Conservation, Planning and Management*. doi:10.1007/s11852-012-0203-6)

Journal of Coastal Research	SI	75	675-679	Coconut Creek, Florida	2016

Evaluation of Life Cycle Cost for Wave-dissipating Works Considering Occurrence Probability of High Waves

Takao Ota[†*], Hiroyuki Kawamura[‡], Yoshiharu Matsumi[†] and Takayuki Hirayama[‡]

[†]Department of Management of Social Systems and Civil Engineering
Tottori University
Tottori, Japan

[‡]Nishi-Nihon Branch, Sanshosuiko Co. Ltd.
Fukuoka, Japan

www.cerf-jcr.org

www.JCRonline.org

ABSTRACT

Ota, T.; Kawamura, H.; Matsumi Y., and Hirayama, T., 2016. Evaluation of life cycle cost for wave-dissipating works considering occurrence probability of high waves. *In:* Vila-Concejo, A.; Bruce, E.; Kennedy, D.M., and McCarroll, R.J. (eds.), *Proceedings of the 14th International Coastal Symposium* (Sydney, Australia). *Journal of Coastal Research*, Special Issue, No. 75, pp. 675-679. Coconut Creek (Florida), ISSN 0749-0208.

This study deals with the influences of occurrence frequency and the duration of high waves on estimation of life cycle cost (LCC) for wave-dissipating works that consist of wave-dissipating blocks using Monte Carlo simulation. LCC is defined as sum of an initial construction cost and an expected repair cost of wave-dissipating blocks. As analysis results of high waves at four observation stations in NOWPHAS, the occurrence frequency of high waves can be approximated by the Poisson distribution. In the computation of LCC, occurrence frequency of high waves is assumed as once a year or is determined by using the Poisson distribution for comparison. The duration of high waves is given in consideration of its statistical characteristics. The optimum size of block that minimizes LCC agrees in most cases regardless of the occurrence frequency and the duration of high waves, however, the variation in the total repair cost during the in-service period is different depending on the occurrence frequency.

ADDITIONAL INDEX WORDS: *Wave-dissipating block, Monte Carlo simulation, repair cost.*

INTRODUCTION

The infrastructures are required to keep a certain level of performance during the in-service period. Moreover, it is apprehended that the repair and renewal costs will increase due to the deterioration of numerous infrastructures especially in Japan. Therefore, an appropriate and efficient maintenance is recently becoming important. Under these conditions, it is necessary that the maintenance cost is estimated as accurately as possible to balance the construction of new infrastructures with the operation of existing ones. Some studies on the evaluation of life cycle cost (LCC) for the harbor and coastal structures have been performed recently (*e.g.* Yoshioka and Nagao, 2004; Takayama *et al.*, 2006, 2009). In the previous studies, the occurrence frequency and the duration of high waves were assumed as once a year and two hours respectively in Monte Carlo simulation. In fact, both the frequency and duration of high waves can fluctuate and it might influence the estimation of LCC. This study deals with the influences on LCC for wave-dissipating works that consist of wave-dissipating blocks and cover a breakwater by using Monte Carlo simulation in consideration of the variation in frequency and duration of high waves.

METHODS

In this section, we describe the statistical characteristics of occurrence frequency of high waves, the method for the estimation of LCC and the duration of high waves, and the calculation conditions for the estimation of LCC.

Figure 1. Location of observation stations

Statistical characteristics of occurrence frequency of high waves

In this study, Ibaraki, Osaka, Tottori and Kochi in Japan are picked up as the object regions to evaluate LCC for wave-dissipating works because the characteristics of the offshore waves are different and the data of unit prices for the wave-dissipating blocks are obtained. The wave data observed at Kashima port, Kobe port, Tottori port and Murotsu port correspond to the object regions respectively. The wave data at the above observation stations in NOWPHAS from 1991 to 2010 (20 years), which were released on the website of the Port and Airport Research Institute, were used to investigate the

DOI: 10.2112/SI75-135.1 received 15 October 2015; accepted in revision 15 January 2015.
*Corresponding author: ohta@sse.tottori-u.co.jp

statisticalcharacteristics of occurrence frequency of high waves. Figure 1 shows the location of the observation stations.

As the first step of the analysis, the annual number of data that exceed the threshold value of significant wave height was counted in each station. The threshold values were 2.5 m for Kashima and Murotsu port, 3.0 m for Tottori port and 1.0 m for Kobe port. These values are based on the definition of high waves for each station in NOWPHAS. Then the cumulative relative frequency (non-exceedance probability) of the annual number of occurrence was obtained by counting the frequency for each number of occurrence. We also investigated the approximation of the cumulative relative frequency by using the Poisson distribution. The Poisson distribution is given by

$$P(r) = \frac{1}{r!} e^{-\lambda} \lambda^{r} \quad : \quad r = 0, 1, 2, \cdots \qquad (1)$$

where r is the annual number of occurrence of high waves, λ is the average annual number of occurrence and it is given by the division of the total number of high waves by the observation period. Figures 2a and 2b show the comparisons of the cumulative relative frequency with Poisson distribution. The results show that the annual number of occurrence of high waves can be obtained by using the Poisson distribution.

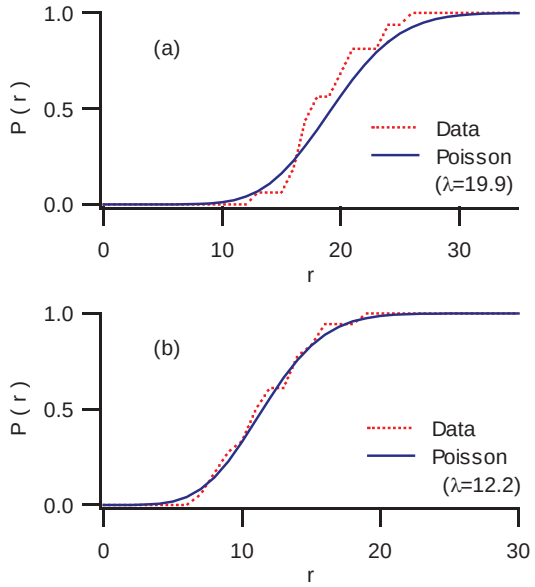

Figure 2. Non-exceedance probability of annual number of occurrence (a) Kashima Port (threshold wave height 2.5 m), (b) Murotsu Port (threshold wave height 2.5 m)

Calculation method of LCC

The calculation method of LCC proposed by Takayama *et al*. (2006, 2009) is used and LCC is given as the sum of the initial construction cost and the expected repair cost. The expected repair cost is defined as the average of total repair cost during the in-service period. The stability formula for wave-dissipating block proposed by Hanzawa *et al*. (1996) is employed to estimate the damage level.

$$N_S = \frac{H_{1/3}}{(S_r - 1) D_n} = a \left(N_0 / N^{0.5} \right)^{0.2} + b \qquad (2)$$

where N_S is the stability number, S_r is the specific gravity of block, D_n is the nominal diameter of block, N_0 is the number of displaced block related to the width of D_n, N is the number of waves, a and b are the constants. The values for the constants are given as a=2.32, b=1.56 for the block that is used in this study. The damage level and accumulated damage is calculated on the basis of Eq. (2) in the same manner as Hanzawa *et al*. (1996). If the accumulated damage exceeds the amount for a required repair, the repair work is performed. The wave-dissipating work is restored to the initial state that means no damage by the repair.

The procedures to estimate LCC are as follows.

1) To set the specification of the intended wave-dissipating block.
2) To determine the initial profile based on the above specification and calculate the initial construction cost.
3) To calculate the offshore wave height in a high waves by using an extreme distribution function. The wave period is given so as to correspond to the wave steepness that is set for each object region. The annual number of occurrence of high waves is assumed as one or is obtained from the Poisson distribution. The duration of a high waves is determined by the method described below.
4) The wave height at the location of wave-dissipating work is determined by the computation of wave transformation based on the method of Goda (1975). The water depth is given in consideration of the tide level.
5) To calculate damage of wave-dissipating work in a high waves and to accumulate the damage.
6) If the accumulated damage exceeds the threshold value mentioned above, the repair cost is estimated.
7) To estimate the total repair cost during the in-service period (50 years).
8) By repeating the procedure 3) to 7), the expected repair cost is obtained as the average of total repair cost. LCC is given as the sum of the initial construction cost and the expected repair cost.

Probability distribution of duration of high waves

The duration of high waves has been assumed as two hours in the previous studies that dealt with LCC for the harbor and coastal structures. In this study, the probability distribution of duration proposed by Ukai *et al*. (1993) is used for comparison. The probability of duration T is given by the Weibull distribution.

$$P(T) = 1 - \exp\left[- \left(\frac{T}{A} \right)^{k} \right] \qquad (3)$$

where A is the scale parameter and k is the shape parameter. The parameters A and k are expressed as a function of the threshold wave height H_c.

$$A(H_c) = \alpha H_c^{\beta} \qquad (4)$$

$$k(H_c) = \exp\left[(H_c - p) / q \right] \qquad (5)$$

where p, q, α and β are constants. Ukai *et al*. (1993) obtained the values of the constants on the basis of wave data observed at Irouzaki and Kyogamisaki (Figure 1) by Japan Meteorological Agency.

For Irouzaki (the Pacific side) ; p=3.25, q=5.50, α=15.2, β=-0.794.

For Kyogamisaki (the Sea of Japan side) ; p=3.60, q=13.6, α=50.8, β=-1.55

In this study, the offshore wave height obtained in the procedure 3) for the estimation of LCC is taken as H_c and the duration is determined by using Eqs. (3)-(5) and the constants. The constants of Irouzaki are applied to Kashima, Osaka and Kochi, and those of Kyogamisaki is used for Tottori.

Calculation Conditions

In this study, we use 19 different sizes of the wave-dissipating block (D_n=0.76-3.51 m), and the unit price of block is obtained from the product and setting cost in each object region. The breakwater has no rubble mound foundation as shown in Figure 3, and two types of the wave-dissipating work are considered. One is the two-layer uniform placing of block with core and the other is the pell-mell placing of block without core. The water depth at the toe of the wave-dissipating work h_t=10.0 m, the seaward slope gradient is 2:3 and the crest height h_c=2.5 m for Osaka and 5.5 m for the others. The sea bed slope of 1/30 is employed and the ratio of damage for the required repair is 5 % of the number of block in the cross-section area of the wave-dissipation work. The value of the ratio was used by Takayama *et al*. (2006, 2009) and it was mentioned that the ratio should be determined in consideration of the performance degradation of the wave-dissipating work.

The extreme distribution function that is proposed by Goda (2000) is applied to determine the offshore wave height in a high waves for each region except Osaka. The extreme distribution function for Osaka is estimated from the above-mentioned wave data at Kobe port based on the least squares method (*e.g.* Goda, 2010). Table 1 shows the extreme distribution function with the value of the shape parameter l, the 50-year return wave height H_{50}, the values of scale parameter C and location parameter D. As mentioned above, the annual number of occurrence of high waves is assumed as one or is obtained from the Poisson distribution. The average occurrence rate of high waves λ' described in Goda (2000) for each observation station except Kobe is shown in Table 1 and this is used as λ in Eq. (1) to determine the annual number of occurrence of high waves. The value of λ' for Kobe was obtained from the wave data.

Table 2 shows the High Water Level (H.W.L.), Low Water Level (L.W.L.) and the average for each port. The tide level is assumed to obey the triangle distribution in which the probability densities of H.W.L. and L.W.L. are zero and that of the average is maximum.

The computation of the total repair cost during the in-service period (50 years) is repeated 2000 times to obtain the expected repair cost in all cases described below.

Case 1: The occurrence frequency of high waves is assumed as once a year.

Case 2: The annual number of occurrence of high waves is given by the Poisson distribution.

Case 3: The probability distribution of duration of high waves is considered in addition to Case 2.

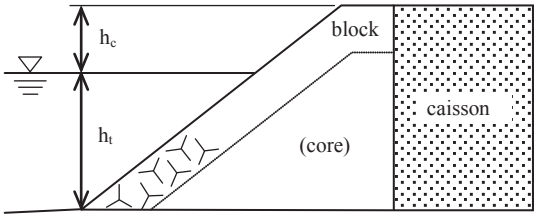

Figure 3. Wave-dissipating work covering breakwater

Table 1. *Extreme distribution function and related parameters*

Station	Distribution function	H_{50} (m)	C	D	λ'
Kashima	Weibull (l=1.0)	9.1	0.94	2.48	22.6
Kobe	Weibull (l=1.0)	4.1	0.48	0.96	14.7
Tottori	Weibull (l=1.4)	7.9	1.33	2.61	20.7
Murotsu	Fisher-Tippet type I	10.9	1.35	2.68	8.8

Table 2. *Conditions for tidal level*

Station	H.W.L. (m)	L.W.L. (m)	Average (m)
Kashima	1.50	0.00	0.75
Kobe	1.74	0.00	0.87
Tottori	0.50	0.00	0.25
Murotsu	1.90	0.10	1.00

RESULTS

Figures 4a-4d show the comparison of LCC between Case 1 and 2 for each region in the case of two-layer uniform placing of block. The expected repair costs in both cases become zero in the range of large D_n and the broken lines are indicative of boundaries. The difference of LCC between Case 1 and 2 is large for small D_n, however, it becomes smaller with increasing D_n because of the decrease in the expected repair cost. The size of block that corresponds to the minimum LCC is considered to be the optimum size if LCC is the evaluation standard. The arrows indicate the optimum sizes of block. The optimum sizes at Ibaraki and Kochi are the same though the difference of H_{50} is about 2 m as shown in Table 1. Takayama *et al*. (2006, 2009) shows similar results that the optimum sizes agree in spite of the difference of H_{50}. It is conceivable that the optimum size of block cannot be determined only by the condition of the 50-year return wave height. The dashed arrow in Figure 4c indicates the optimum size in Case 1, and it is different from that of Case 2. The main cause is the difference of the expected repair cost, however, the difference of LCC is small. In the case of pell-mell placing of block, though the optimum size is different between Case 1 and 2 at Kochi because of the difference of the expected repair cost, the difference of LCC is very small.

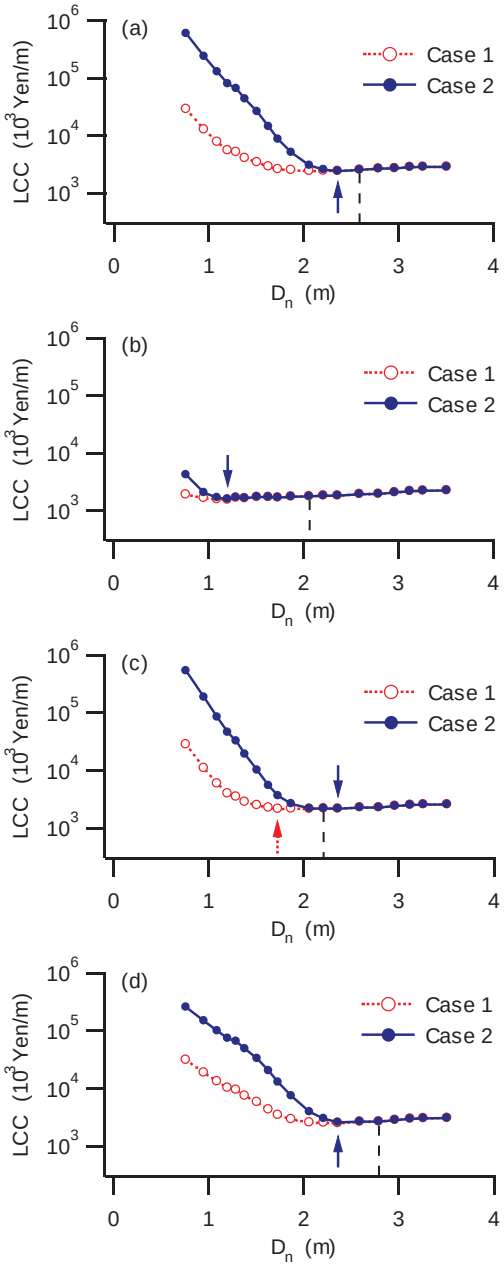

Figure 4. Comparison of LCC between Case 1 and 2 (two-layer uniform placing) (a) Ibaraki, (b) Osaka, (c) Tottori, (d) Kochi

Figures 5a-5d show the ratio between the standard deviation of the total repair cost σ_{TR} and LCC. Because LCC of Case 1 is fairly small compared with that of Case 2 for small D_n except Osaka, the ratio of Case 1 is large. However, the ratio of Case 2 overtakes with increasing D_n. In common with Figure 4, the arrows in Figure 5 indicate the optimum sizes of block. The optimum sizes of Case 1 and 2 agree except Tottori, however, the values of σ_{TR} /LCC are different between Case 1 and 2. In other words, the

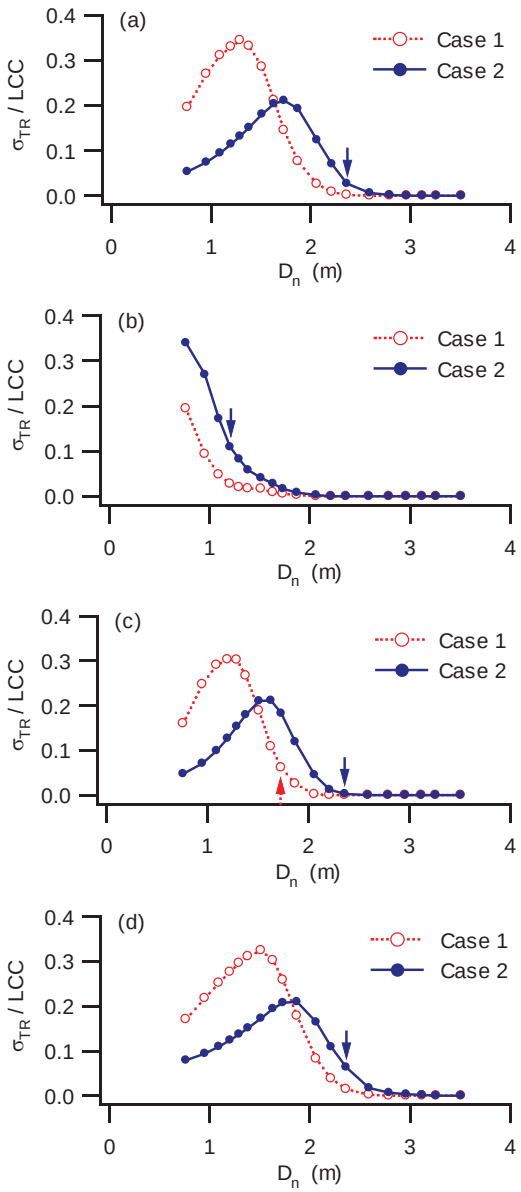

Figure 5. Comparison of variation in total repair cost between Case 1 and 2 (two-layer uniform placing) (a) Ibaraki, (b) Osaka, (c) Tottori, (d) Kochi

variation in the total repair cost at the optimum size can differ depending on the occurrence frequency of high waves even if the optimum size of block is the same and the difference of LCC is small. The difference in the variation should be considered when LCC is evaluated in the design of wave-dissipating work.

Figures 6a and 6b show LCC and σ_{TR} /LCC of Case 2 and 3 in the case of two-layer uniform placing at Ibaraki. Figure 6a shows that LCC of Case 3 is slightly larger than that of Case 2 for small D_n. The differences of LCC and σ_{TR} /LCC between two cases are small totally. Similar results are obtained in the cases of other regions and the pell-mell placing of block. The optimum sizes of Case 2 and 3 agree in all region and cases.

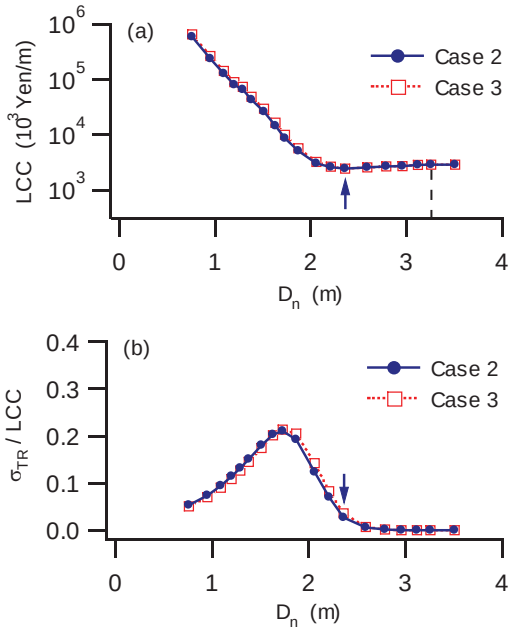

Figure 6. Comparison of results between Case 2 and 3 (Ibaraki, two-layer uniform placing) (a) LCC, (b) variation in total repair cost

DISCUSSION

The results in Figure 6 show that the fluctuation of duration of high waves does not influence much the estimation of LCC and the variation in the total repair cost. As Eq. (2) suggests, the number of displaced block N_0 is proportional to the square root of the number of waves N that increases with the duration T. Though the probability distribution of T is not shown, the cumulative probability increases rapidly in the range of short duration as the threshold wave height H_c becomes larger. It is conceivable that these are why the duration does not influence much.

CONCLUSIONS

In this study, the influences of occurrence frequency and the duration of high waves on estimation of life cycle cost (LCC) for wave-dissipating works is investigated by using Monte Carlo simulation. The conclusions of this study are summarized as follows:

1. For the data of high waves at Kashima port, Kobe port, Tottori port and Murotsu port, the cumulative frequency distribution for annual number of occurrence of high waves can be approximated by the Poisson distribution.
2. The variation in the total repair cost at the optimum size of block can differ depending on the occurrence frequency of high waves even if the optimum size of block is the same and the difference of LCC is small. The difference in the variation should be considered when LCC is evaluated in the design of wave-dissipating work.
3. The fluctuation of duration of high waves does not influence much the estimation of LCC and the variation in the total repair cost.

ACKNOWLEDGMENTS

This study was partially supported by JSPS KAKENHI Grant Number 25420524. The authors express gratitude to Assistant Professor Tomohiro Yasuda (Kyoto University) and Dr. Daiki Tsujio (Pacific Consultants Co., Ltd.) for providing the original source code for the computation of LCC.

LITERATURE CITED

Goda, Y., 1975. *Deformation of irregular waves due to depth-controlled wave breaking*, *Report of the Port and Harbour Research Institute*, 14(3), pp. 59-106. (in Japanese)

Goda, Y.; Konagaya, O.; Takeshita, N.; Hitomi, H., and Nagai, T., 2000. Population distribution of extreme wave heights estimated through regional analysis. *In*: Edge, B.L. (ed.), *Proceedings of the 27th International Conference on Coastal Engineering* (Sydney, Australia), pp. 1078-1091.

Goda, Y., 2010. *Random Seas and Design of Maritime Structures* (3rd edition). World Scientific, 708p.

Hanzawa, M.; Sato, H.; Takahashi, S.; Shimosako, K.; Takayama, T., and Tanimoto K., 1996. New stability formula for wave-dissipating concrete blocks covering horizontally composite breakwaters. *In*: Edge, B.L. (ed.), *Proceedings of the 25th International Conference on Coastal Engineering* (Orland, Florida), pp. 1665-1678.

Port and Airport Research Institute. *NOWPHAS 1991-2010*, http://www.pari.go.jp/unit/kaisy/nowphas/annuareport/

Takayama, T.; Tsujio, D., and Yasuda, T., 2006. Optimum design for concrete armor blocks under minimum life cycle cost. *Annual Journal of Coastal Engineering*, JSCE, 53(2), 856-860. (in Japanese)

Takayama, T.; Yasuda, T.; Tsujio, D., and Inoue, J., 2009. Optimum design for armor units based on the minimum life cycle cost, *Journal of JSCE B*, 65(1), 15-30. (in Japanese)

Ukai, Y.; Shimizu, T., and Yamaguchi, M., 1993. Probabilistic appearance characteristics of duration of high waves based on the observed data, *Proceedings of Coastal Engineering*, JSCE, 40, 121-125. (in Japanese)

Yoshioka, T., and Nagao, T., 2004. A study on life-cycle-cost based design method for caisson type breakwaters. *Annual Journal of Coastal Engineering*, JSCE, 51(2), 871-876. (in Japanese)

Journal of Coastal Research	SI	75	680-684	Coconut Creek, Florida	2016

Beach carrying capacity and protected areas: management issues in Arrábida Natural Park, Portugal

Carlos Pereira da Silva[§*], Ricardo Nogueira Mendes[§], Gonçalo Moutinho[§], Vanessa Mota[§], Catarina Fonseca[§‡]

[§]CICS.NOVA, Interdisciplinary Center of Social Sciences, Faculty of Social Sciences and Humanities, University Nova de Lisboa 1069-061 Lisboa, Portugal

[‡]InBIO, Associate Laboratoy, Research Network in Biodiversity and Evolutionary Biology, Department of Biology, University of the Azores, 9501-801 Ponta Delgada, Portugal

www.cerf-jcr.org

www.JCRonline.org

ABSTRACT

Pereira da Silva, C.; Nogueira Mendes, R..; Moutinho, G.; Mota, V. and Fonseca, C., 2016. Beach carrying capacity and protected areas: management issues in Arrábida Natural Park, Portugal. *In:* Vila-Concejo, A.; Bruce, E.; Kennedy, D.M., and McCarroll, R.J. (eds.), *Proceedings of the 14th International Coastal Symposium* (Sydney, Australia). *Journal of Coastal Research*, Special Issue, No. 75, pp. 680-684. Coconut Creek (Florida), ISSN 0749-0208.

Arrábida Natural Park (Portugal) comprises beaches with high natural and scenic values under huge demand during peak season. Understanding patterns of beach use and the perceptions of users is essential for carrying capacity management. This paper discusses the use intensity and dynamic in two beaches, using data from onsite counting, time-lapse photos and a traffic counter. Users' perceptions regarding general aspects of the beaches and perceived crowding obtained through questionnaires are also presented. The number of users recorded in this study never reached the carrying capacity established and most users feel comfortable with the number of people on the beach. However, parking and traffic were identified as factors of concern: users are not discouraged by the limited parking spaces, often exceeding the formal capacity by parking on the roadside. This type of problem needs to be addressed not only in the context of beach management but also the protected area management.

ADDITIONAL INDEX WORDS: *social carrying capacity, crowding, users' perceptions, parking.*

INTRODUCTION

Since the 1970s beaches became very popular places for recreation and leisure, leading to tourism massification in certain regions. This issue is critical in urban and resort beaches, generating crowding problems and jeopardizing the recreational experience of beach users (Sowman, 1997). In addition to the social needs and expectations of the users, the physical usage of the beach should respect its natural physical elements (Williams & Micallef, 2009).

The concept of carrying capacity (CC) has evolved over the years and become an important tool for beach management. CC should be seen not as the maximum number of users the space can support but rather as the optimal use level of such space, which considers notions of quality and value judgments (Shelby & Heberlein, 1986; Prato, 2001). In other words, CC represents the threshold(s) beyond which the use intensity negatively affects the natural values and/or the quality of the recreational experience (Manning, 2007). This means that different dimensions must be considered, namely ecological, physical and social.

Important aspects within the social component of CC may include questions related to people's behaviour, perceived crowding, distance to nearby urban centres, accessibility, parking, safety and support infratructures (Pereira da Silva, 2002).

In Portugal beach conditions and space organisation improved greatly since 1993, with the development of Coastal Zone Management Plans (*Planos de Ordenamento da Orla Costeira* – POOC). This first generation of plans was intended to guide specific activities on the coast while safeguarding fundamental ecosystems, ecologically sensitive areas and existing resources (Veloso-Gomes & Taveira-Pinto, 2003). To that end POOC defined the dominant uses and the location of support infrastructures, namely for beach areas. Beach Plans are an integral part of POOC and apply the CC concept, having in consideration not only the available beach area but also its accessibility, parking and support infrastructures (Pereira da Silva *et al.*, 2007). This management tool is particularly important for environmentally sensitive beaches, such as those located within protected areas.

Arrábida Natural Park (*Parque Natural da Arrábida* – PNArr), in Lisbon metropolitan area, has 176,52 Km^2 and comprises 13 beaches with high natural and scenic values, which are under huge demand during peak season (with 2,5 million potential users). In addition to the ecological vulnerability, social aspects must be considered in the management of these beaches, namely the number of users, who they are, their preferences and behaviors. Understanding patterns of beach use through monitoring is therefore crucial for the management of carrying capacity and planning of these areas (Marin *et al*., 2009).

This paper discusses the use intensity and dynamic in two beaches of Arrábida Natural Park, as well as the users' perceptions, trying to identify the key aspects that may affect the carrying capacity and pose significant management challenges.

DOI: 10.2112/SI75-136.1 received 15 October 2015; accepted in revision 15 January 2015.

*Corresponding author: cpsilva@fcsh.unl.pt

METHODS

Study area

The beaches selected for this study, *Figueirinha* and *Portinho da Arrábida* (fig.1), are placed, respectively, 7 and 10 km out of the city of Setúbal and represent the most iconic beaches of Arrábida Natural Park. Both their terrestrial and marine components are classified as the Park includes a marine protected area (*Parque Marinho Professor Luiz Saldanha* - PMLS). They are located in a sheltered and cliffed coast facing South, which includes 2 other beaches of smaller dimensions (*Galapos* and *Galapinhos*). These 4 beaches are all served by the same road (N379-1) which, due to traffic restrictions during summer season, can only be crossed in the East-West direction (one way) from 9:00 to 21:00.

Figueirinha is not contiguous to any urban centre but it is subject to strong demand, which is why POOC *Sintra-Sado* (the Coastal Zone Management Plan covering this particular coastline) classifies the beach as type II - non-urban beach with intensive use (peri urban beach). Its beach front has 600 meters and the Beach Plan determines a carrying capacity of 2683 users. There are around 260 formal parking spaces.

Portinho da Arrábida is a moderately exposed beach linked to sensitive natural systems, classified as type III – infrastructured beach with conditional use (semi-natural beach) – which means that it is not under the direct influence of urban centres. *Portinho da Arrábida* has a beach front of 690 meters and the carrying capacity established by its Beach Plan is 2642 users. Formal parking spaces accommodate 210 vehicles.

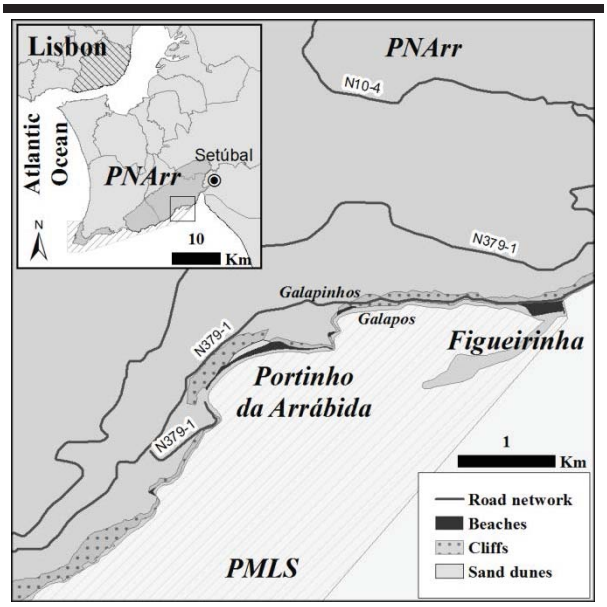

Figure 1. Location of *Figueirinha* and *Portinho da Arrábida* beaches and access road. PNArr stands for Arrábida Natural Park and PMLS for *Parque Marinho Professor Luiz Saldanha* (marine protected area).

Data collection

Beach users were directly counted on the beach between 13:00 and 14:00 during the summer season of 2013 and 2014 (details in table 1). The 2 beaches were divided into different sectors (East, Central, West, tidal area and dry sand) and all researchers (6) moved on the same direction in order to avoid duplications.

Table 1. *Wave reanalysis data provided by SMCBrazil software for Marinha Farinha beach (Oliveira et al., 2013)*

Beach	Date	Week day	Weather	Wind
Portinho da Arrábida	03-08-13	Sat.	sunny, warm	mild
	11-08-13	Sun.	sunny, warm	mild
	23-08-13	Fri.	sunny, warm	medium
	07-09-13	Sat.	cloudy, warm	mild
	10-09-13	Tue.	sunny, warm	mild
	27-07-14	Sun.	sunny, warm	mild
	02-08-14	Sat.	cold	strong
Figueirinha	04-08-13	Sun.	cloudy, warm	medium
	14-08-13	Wed.	sunny, warm	mild
	31-08-13	Sat.	sunny, warm	mild
	06-09-13	Fri.	sunny, warm	medium
	01-08-14	Fri.	cloudy, warm	mild
	09-08-14	Sat.	cloudy, warm	medium

Complementarily, a 16 Mp camera was placed at a high observation point of *Portinho da Arrábida*, collecting photos every 3 minutes from 10:00 to 20:00 on August 3rd 2014. The camera's resolution was adequate to mark each user, allowing to assess the daily variation of users on the beach.

Road traffic of the only access road to the beaches (N379-1) was hourly monitored with a TRAFx magnetic counter during two periods (July – October 2013; August 2014 – May 2015). It was placed at 1,5 km from the *Portinho da Arrábida* and 3,5 km from *Figueirinha,* away from parking places.

A survey was conducted during both summer seasons (2013 and 2014) by the same field team, inquiring beach users about their main perceptions, motivations, preferences and expectations concerning the study area. A total of 407 questionnaires were collected at *Portinho da Arrábida* (272 during 2013 and 135 during 2014) and 369 questionnaires at *Figueirinha* (256 during 2013 and 113 during 2014).

The survey consisted of 32 questions (plus personal data of the respondent, such as gender, age, residence) and took between 10 to 12 minutes to be fully answered. To avoid bias the team tried to balance the sample in terms of gender and age classes.

For the purposes of this paper the analysis is focused on two questions. One is related to users' perceptions regarding general aspects of the study area (people's behaviour, beach quality, toilets, environmental quality, safety, parking, accessibility, among others), ranked using a Likert like scale (with five-level items, later converted into three-level for presentation purposes). The other concerns the perceived crowding, asking respondents how they evaluate the number of persons on the beach (answer options being "too many", "it's fine like this", "could accommodate more", "don't know/no answer (DK/NA)"). Non answers on both questions were treated as DK/NA.

RESULTS AND DISCUSSION

The number of users directly counted on each beach varies greatly yet the carrying capacity established by POOC *Sintra-Sado* was never reached during the sample days of this study (fig. 2). The minimum and maximum numbers registered at *Figueirinha* were, respectively, 560 and 2330 while at *Portinho da Arrábida* the minimum was 217 and the maximum was 1603. *Figueirinha* is the nearest beach to Setúbal, served by public transports and there is additional parking less than 1,5 km away whith shuttle service, which may explain the diferences between the values of the 2 beaches.

As expected, Saturdays and Sundays tend to have higher number of users than working days, although the higher number (2330 users) was registered at *Figueirinha* on a Wednesday (August 14th 2013, preceding a National holiday). Variations on the number of users may also be explained by weather conditions, such as temperature, cloud cover and wind, since these beaches are mainly sought for sunbathing and swimming.

In addition to the weekly variations, it is important to understand the pattern of beach use throughout the day. The analysis of the data collected for *Portinho da Arrábida* with the time-lapse photos indicates a more intensive use during the afternoon.

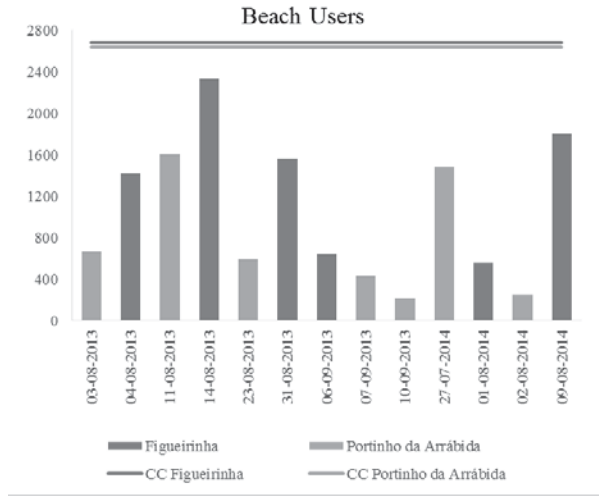

Figure 2. Number of beach users directly counted at *Figueirinha* and *Portinho da Arrábida* on separate days. The upper lines represent the Carrying Capacity established by POOC *Sintra-Sado* for each beach.

Taking the example of August 3rd 2014, there are clear differences between the morning and afternoon periods, with the maximum number of users (537) being achieved at 17:00 (fig. 3). The morning period up to lunch time reaches only 70% of the maximum number. Although the number of users recorded for this day was not particularly high (due to weather conditions), similar patterns can be found in the traffic data of the only access road to the beaches (fig. 4).

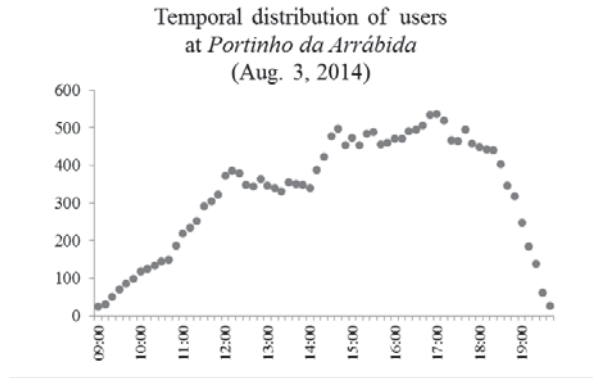

Figure 3. Temporal distribution of beach users at *Portinho da Arrábida* on August 3rd 2014. Data from countings using time-lapse photos.

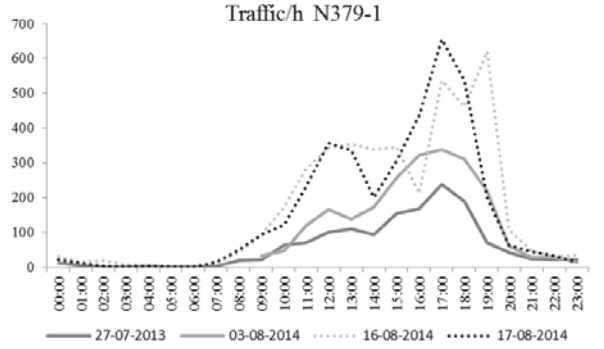

Figure 4. Number of vehicles recorded per hour on the only access road to the beaches (N379-1). Data collected with a TRAFx magnetic counter.

Traffic data shows a curve where morning and afternoon periods are well apart and there is a peak around 17:00. The maximum number of vehicles recorded per hour was 655 between 17:00 and 18:00 on August 17th 2014 while the maximum number per day was 4124 on August 16th 2014.

According to data collected during the survey campaigns, most users come from Setúbal, Lisbon or other nearby municipalities (fig. 5). Some spend up to 1:30 hours to arrive to these beaches and most of them travel by car (88% of respondents).

As these are not urban beaches the available parking spaces by the beach are expected to limit the number of users. Nevertheless, semi-natural beaches attract a high number of visitors because of the scenic and natural qualities (Roca *et al.*, 2008; Vaz *et al.*, 2009), which explains why the number of users often exceeds the parking capacity of Figueirinha and Portinho da Arrábida. The expression of informal parking is significant (cars on the sidewalk or roadside can be 3 times more than those parked on formal spaces), causing severe

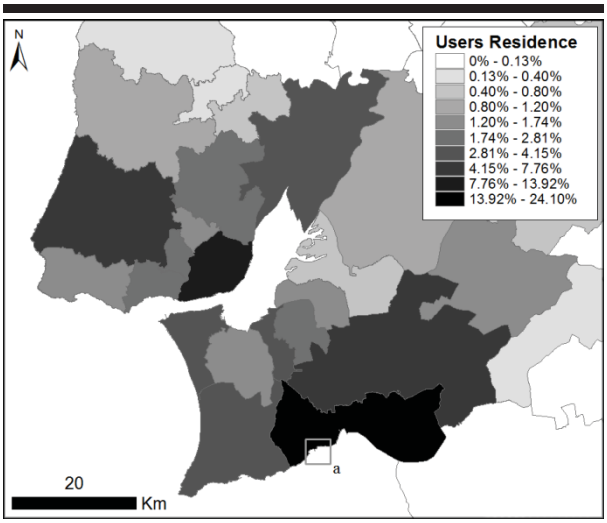

Figure 5. Percentage of respondents, by municipality of residence. The square labelled with "a" locates the study area. Municipalities in this figure concentrate 82% of total respondents.

circulation problems which can be dramatic in case of emergency. In fact, parking is one of the few aspects negatively evaluated by the users of both *Figueirinha* (fig. 6) and *Portinho da Arrábida* (fig. 7), along with traffic.

Accessibility is ranked largely as indiferent by the users of *Figueirinha* but in *Portinho da Arrábida* there is a positive perception regarding the same aspect. This might be explained by the fact that to exit *Figueirinha* and return to Setúbal it will take 25km (due to one way restriction), including 4 km of N379-1 with intense traffic and vehicles parked on the roadside.

Regarding the remaining aspects (safety, natural beauty, cleanliness, environmental quality, toilets, beaches quality and people's behavior) there is a positive perception from users of both beaches. This is particularly expressive regarding natural beauty (97% of positive opinions) and environmental quality (84% of positive opinions).

Aspects with higher percentage of DK/NA (toilets and planning) have also higher dispersion of responses, probably due to lack of opinion. Overall, users' perceptions of both beaches are similar, as confirmed by a deeper analysis of data (standard deviations among all answers varies from 0.021% up to a maximum of 3.500% with an average of 1.023%).

Regarding the perceived crowding, results are quite similar for both beaches and for both survey seasons (fig. 8).

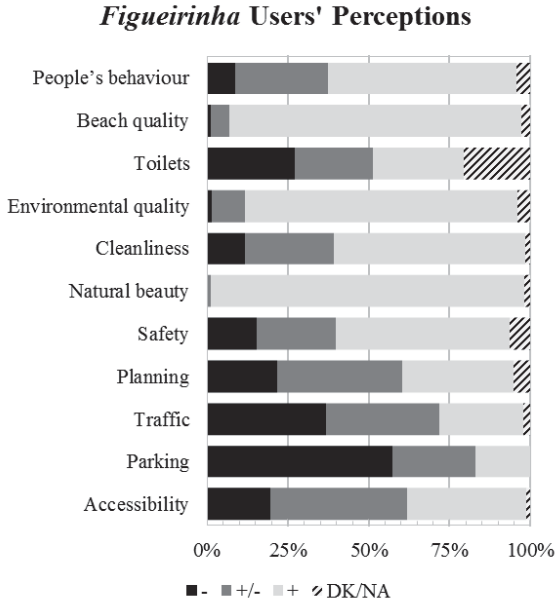

Figure 6. Perceptions of users at *Figueirinha* regarding general aspects of the study area. Note: (-) stands for bad, (+/-) stands for indiferent, (+) stands for good and DK/NA represents "don't know/no answer".

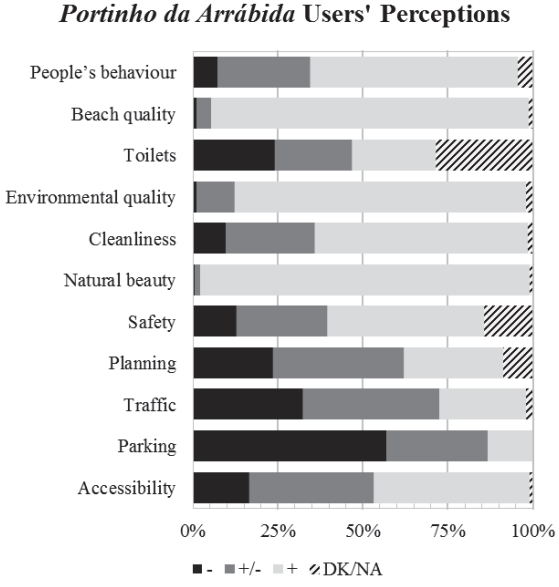

Figure 7. Perceptions of users at *Portinho da Arrábida* regarding general aspects of the study area. Note: (-) stands for bad, (+/-) stands for indiferent, (+) stands for good and DK/NA represents "don't know/no answer".

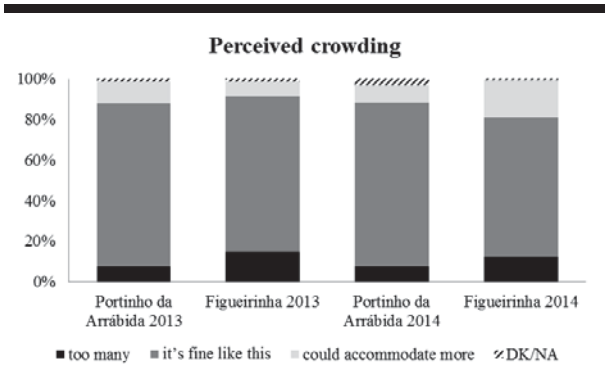

Figure 8. Level of crowding perceived by users of *Portinho da Arrábida* and *Figueirinha*, during the 2013 and 2014 survey campaigns. DK/NA stands for "don't know/no answer".

The vast majority of respondents feel confortable with the number of people on the beach. In addition to the actual number of persons, the opinion can be influenced by previous knowledge of existing conditions (difficulty in parking and traffic) and by the investment made on going to the beach (time and money spent on transport). Regarding *Figueirinha* in 2014, the number of users that acknowledge that the beach "could accommodate more" over doubles, probably due to worse weather conditions in that summer.

CONCLUSIONS

The beaches of Arrábida Natural Park are subject to a significant demand, mainly due to their natural beauty and environmental quality. In fact, these aspects are higly evaluated by users of *Figueirinha* and *Portinho da Arrábida*.

Despite such demand, the number of users recorded in this study never reached the carrying capacity established by POOC *Sintra-Sado* making the majority of users feeling comfortable with the number of people on the beach. Limited parking spaces and traffic restrictions that lead to intense traffic might explain that the number of users remains below the carrying capacity. In terms of parking, users don't seem particularly discouraged by the limited spaces, often exceeding the formal capacity by parking on the roadside, corroborating previous studies where users of natural and semi-natural beaches tend to value scenery over everything else (Vaz *et al.*, 2009).

Nevertheless, respondents of the survey clearly evaluate parking and traffic as negative aspects of these beaches. An easy way to overcome these negatives aspects and to offer better conditions for beach users migth be to propose more parking spaces and to facilitate the traffic circulation. But in this situation, due to physical and geological conditions and due to the fact that theses beaches are within a protected area, this is not feasible, placing new challanges in terms of management (for beaches, coast and protected area). Besides that, increasing parking and access may not result in a corresponding increase of use. Conversely, limiting parking and access in an attempt to reduce visitation may not achieve the desired result (Snider at al, 2015).

The established carrying capacity of these beaches was probably based on the beach area, not considering adequately the parking and access aspects. This study shows the importance of social aspects for the determination and management of carrying capacity. By knowing users' perceptions, expectations and behaviors, managers will be better equipped to propose effective management measures.

ACKNOWLEDGMENTS

The authors would like to express their gratitude to Ana Vasco, Ana Sofia Travessa, Marcelo Ribeiro, Susana Lucena e Ana Rita Vilas-Boas for their assistance during field work.

This work was developed within Project BIOMARES 2.0 (http://biomares.ccmar.ualg.pt/biomares2.html) and under a protocol with the Association of Municipalities of Setúbal Region (*Associação de Municípios da Região de Setúbal*). It was also partly funded by Portuguese national funds through FCT/MEC in the framework of project UID/SOC/04647/2013.

LITERATURE CITED

Manning, R.E., 2007. *Parks and carrying capacity - Commons Without Tragedy.* Washington, DC: USA: Island Press., 313p.

Marin, V., Palmisani, F., Ivaldi, R., Dursi, R., Fabiano, M., 2009. Users' perception analysis for sustainable beach management in Italy. *Ocean & Coastal Management*, 52, 268-277.

Prato, T., 2001. Modeling carrying capacity for national parks. *Ecological Economies*, 39, 321-331.

Pereira da Silva, C., 2002. Beach Carrying Capacity Assessment: How important is it? *Journal of Coastal Research*, SI 36: 190-197.

Pereira da Silva, C.; Alves, F.; Rocha, R., 2007. The Management of Beach Carrying Capacity: The case of northern Portugal. *Journal of Coastal Research*, SI 50, 135-13.

Roca, E., Riera, C., Villares, M., Fragell, R., Junyent, R., 2008. A combined assessment of beach occupancy and public perceptions of beach quality: A case study in the Costa Brava, Spain. *Ocean & Coastal Management*, 51, 839-846

Shelby, B. and Heberlein, T.A., 1986. *Carrying Capacity in Recreation Settings*. Corvallis: USA: OSU Press, 164p.

Snider, A., Luo, S., Hill, J., Herstine, J., 2015. Perceptions of availability of beach parking and access as predictors of coastal tourism. *Ocean & Coastal Management*, 105, 48-55

Sowman M.R., 1997. A procedure for assessing recreational carrying capacity of coastal resort areas. *Landscape and Urban Planning*, 14, 331-344.

Vaz B, Williams A.T., da Silva, C.P., Phillips, M., 2009. The importance of user's perception for beach management. *Journal of Coastal Research*, SI56:1164-1168.

Veloso-Gomes, F. and Taveira-Pinto, F., 2003. Portuguese coastal zones and the new coastal management plans. *Journal of Coastal Conservation*, 9, 25-34.

Williams, A. and Micallef, A., 2009. *Beach Management – Principles & Practice*. London: United Kingdom: Earthscan, 480p. .

Journal of Coastal Research	SI	75	685-689	Coconut Creek, Florida	2016

Spatial Analysis of a Coastal Area for Conservation and Fishery of Mangrove Edible Crab (Ucides cordatus)

Luciana C. M. Santos[†§*], Mario M. Rollo Jr.[†], Tânia M. Costa[†], Marcelo A. A. Pinheiro[†], Farid Dadouh-Guebas[††‡] and Marisa D. Bitencourt[§]

[†]Instituto de Biociências, Universidade Estadual Paulista Júlio de Mesquita Filho, UNESP, Campus do Litoral Paulista, São Vicente, SP, Brasil.

[‡]Faculteit Wetenschappen en Bio-ingenieurswetenschappen, Vrije Universiteit Brussel, VUB, Brussels, Belgium.

[††]Département de Biologie des Organismes, Faculté des Sciences, Université Libre de Bruxelles, ULB, Bruxelles, Belgique.

[§]Departamento de Ecologia, Instituto de Biociências, Universidade de São Paulo, USP, São Paulo, SP, Brasil.

www.cerf-jcr.org

www.JCRonline.org

ABSTRACT

Santos, L. C. M.; Rollo, M.M.; Costa, T.M.; Pinheiro. M.A.A.; Dahdouh-Guebas, F. and Bitencourt, M.D., 2016. Spatial analysis of a coastal area for conservation and fishery of mangrove edible crab (*Ucides cordatus*). *In:* Vila-Concejo, A.; Bruce, E.; Kennedy, D.M., and McCarroll, R.J. (eds.), *Proceedings of the 14th International Coastal Symposium* (Sydney, Australia). *Journal of Coastal Research*, Special Issue, No. 75, pp. 685-689. Coconut Creek (Florida), ISSN 0749-0208.

Mangroves are productive ecosystems of tropical coastal landscapes, constituting habitat for many commercial fisheries, as the crab *Ucides cordatus*. In Brazil this crab holds a major socio-economic importance for artisanal fishery, but with obvious decline on their productivity. In this study we determined and mapped the more suitable mangrove areas for the conservation and fishery of this crab in the São Francisco River Estuary (Northeastern Brazil). We applied a Multi-Criteria Evaluation (MCE) in a GIS environment. Ten criteria in total were used, including crab biotic parameters, land use/cover and social factors. Maps of each criterion were produced by GIS techniques with CBERS and SPOT images and by field data. Mangroves more suitable for the conservation of *U. cordatus* (9.4 km^2) are near to the river mouth, due to high density and frequency of non-commercial size crabs (NCSC), low density of commercial size crabs (CSC), small crabs and low degree of use for fishery. On the other hand, the mangroves for the crab fishery occurred with a similar area (10.2 km^2) located farther away from the river mouth, with a high density and frequency of CSC, low density of NCSC, big crabs, medium-high degree of use for fishery and near to the villages. These information and thematic maps can aid government agencies in delineating extractive and fishery exclusion areas, thus contributing to the management plan for this species.

ADDITIONAL INDEX WORDS: *Mangrove, remote sensing, fishery management.*

INTRODUCTION

Mangroves are coastal forests that occupy saline tidal areas along sheltered bays, estuaries, and inlets in the tropics and subtropics throughout the world, where they fulfill several ecological, environmental and socio-economic functions (Barbier *et al.*, 2011; FAO, 2007). From them, it is remarkable the role of mangroves as habitats for many commercial fishery species, thus supporting small-scale fishery along the world's (sub) tropical coast (Rönnbäck, 1999). From a diversity of fishery resources exploited in the mangrove environment, crabs are among the many commercially important species caught throughout the tropics (Macnae, 1974). In Brazil, the mangrove crab *Ucides cordatus* (Linnaeus, 1763), a semiterrestrial crab that lives only in mangroves (Schories *et al.*, 2003), is a keystone species of this ecosystem and a major socio-economically important species for artisanal fishery (e.g., Magalhães *et al.*, 2012; Cortês *et al.*, 2014). Despite its importance, declines of *U. cordatus* have been reported in many regions of Brazil and were related to mangrove destruction, diseases and overfishing (Boeger *et al.*, 2005; Diele *et al.*, 2005). This crab shows slow growth, high age at maturity, long-lived (>10 years), low reproductive output and low natural mortality, suggesting vulnerability to exploitation (Diele *et al.*, 2005). Since 2004 it has been included in the Brazilian National List of aquatic invertebrates species threatened with overexploitation and at risk of becoming extinct (Pinheiro and Rodrigues, 2011). This highlights the need for management strategies that allow the conservation of this resource in a sustainable fishery approach, as stated by the Proposal of a National Management Plan for the species, with the delineation of extractive and fishery exclusion areas (Brasil, 2011; Pinheiro and Rodrigues, 2011).

Considering this scenario, resource allocation for use or conservation, are also prime candidates for analysis with GIS and remote sensing techniques (Eastman, 2012). In the case of Socio-Ecological Systems (SES), as in fishery systems, where natural, human, and management systems have a complex interaction (Charles, 2001), several criteria will need to be evaluated for conservation and fishery management purposes. Therefore, it is crucial the understanding of the interrelationships among the various parts of the SES (Griffis

DOI: 10.2112/SI75-137.1 received 15 October 2015; accepted in revision 15 January 2015.

*Corresponding author: santos.lucianacm@gmail.com

and Kimball, 1996), requiring the development of analytical and operational evaluation tools for decision-making (Andalecio, 2010), that include all of these parts and aspects. In these cases which involve multidisciplinary knowledge bases, a GIS procedure called Multi-Criteria Evaluation (MCE) is the most appropriate to achieve conservation and management use purposes (Huang *et al.*, 2011). MCE provides a systematic method to combine the inputs with cost/benefit information as well as stakeholder views to rank project alternatives (Huang *et al.*, 2011). MCE has demonstrated its utility in many environmental issues that link economic, environmental, cultural and technical issues of management, such as in fisheries management (Andalecio, 2010).

In the São Francisco River Estuary (Sergipe State, Northeastern Brazil) *U. cordatus* is the second most important mangrove fishery resource (Santos *et al.*, 2013). However, decreases in this species' stock have been reported since 2000, requiring the definition of mangrove areas more suitable for the conservation and fishery of this crab, in order to maintain the natural stock of the resource and a sustainable fishery. This study aimed to determine the most suitable mangrove areas for the conservation and fishery of the crab *U. cordatus* in the Estuary of the São Francisco River, using a MCE analysis, and taking into account a perspective that minimize the restrictions on the fishing and allow a socio-ecological sustainable fishery.

METHODS

Study area

The study area is part of the São Francisco River Basin, one of the most important Brazilian water resources, and is located in the coastal zone of the Sergipe State (Northeastern Brazil) (Figure 1). The study area corresponds to the southern part of the São Francisco River Estuary (municipalities of 'Brejo Grande' and 'Pacatuba') (10º30'27"S, 36º23'45"W) and covers approximately 192.35 km². This estuary shows a mangrove extent of 31.9 km², which corresponds to about 16% of the study area (Santos *et al.*, 2014a). Other land cover and uses presented are: sandy coastal vegetation, aquaculture and agriculture (Santos *et al.*, 2014a). A total of eight fishery villages are distributed in this area, where fishery in the mangrove areas, especially of the crab *U. cordatus*, is the main economic subsistence basis for the local populations (Santos *et al.*, 2013).

Method

A Multi-Criteria Evaluation (MCE) was applied to determine the most suitable mangrove areas for the conservation and fishery of the crab *U. cordatus* in the São Francisco River. For this, we applied the MCE Decision Support tool in the *IDRISI Selva* GIS and considered the Weighted Linear Combination.

A total of ten criteria were used in the MCE, including five biotic criteria related to the population parameters of the crab: 1) frequency and 2) density of non-commercial size crabs (NCSC), 3) frequency and 4) density of commercial size crabs (CSC) and 5) mean crab size; three factors related to land use and cover: 6) mangrove vegetation types, 7) distance of mangroves from fishery villages and from 8) shrimp farms, and finally, two social parameters: 9) degrees of mangrove importance for crab conservation and 10) and for crab fishery, both in the view of the local fisherman.

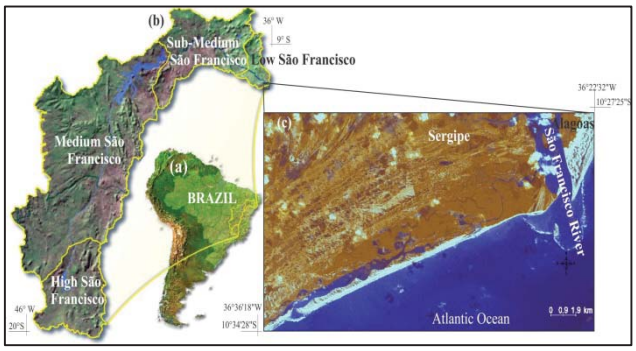

Figure 1. (a) Map of South America and Brazil indicating the location of the São Francisco River basin (adapted from ANA, 2005). (b) The São Francisco River basin with its four divisions (adapted from ANA, 2005). (c) A close-up of the São Francisco River Estuary, the study area.

Maps of each criterion were produced by remote sensing techniques and field data in IDRISI. The initial geodatabase was a land use and cover map of the study area produced in our previous study (e.g., Santos *et al.*, 2014a). For the map of mangrove vegetation types the normalized difference vegetation index (NDVI) was calculated using CBERS-2B images. The maps of crab population parameters were produced based on field data of six different sites of mangroves (e.g., Santos *et al.*, 2014b) and the social maps based on ethnoecological survey carried in villages of the study area (e.g., Santos *et al.*, 2013). We do not consider aspects of the life cycle of this species because since 1990 there are laws of closure during the breading and capture of females are legally prohibited at any time of year.

The maps were standardized in a numeric range of 0 to 255, by a fuzzy function for quantitative maps, and reclassified for qualitative maps. The criteria weighting was developed in the module *WEIGHT*, which utilizes a pairwise comparison matrix, a technique developed by Saaty (1977) in the decision making process known as the Analytical Hierarchy Process (AHP) (see Eastman, 2012). In AHP the criteria are compared two at a time in terms of their importance relative to the stated objective and ratings are provided on a 9-point continuous scale. The pairwise comparison matrix was sent to researchers that work with *U. cordatus* in the field of biological, ecological, fishery and ethnobiological studies. The weight given by them was used in the module that calculates one final weight for each criterion (Eastman, 2012). Finally, the weighted criteria were aggregated using the Weighted Linear Combination (WLC), a method that multiplies each standardized criteria map (i.e., each raster cell within each map) by its factor weight and then sums the results. The map generated by the analysis is a raster image in which the pixels values rage from 0 (unsuitable areas) to 255 (most suitable areas). Based on the pixels values, this image was reclassified to a map of seven categorical classes of mangrove suitability for the conservation and for the fishery of *U. cordatus*. The area of each class was determined.

Table 1. *Criteria and weights in crab conservation and fishery of Ucides cordatus, according the principal eigenvector of the pairwise comparison matrix in the Analytical Hierarchy Process (AHP).*

Type of criteria	Criteria	Conservation Weights	Fishery Weights
Crab population parameters	Density of crabs in non-commercial size	0.30	0.02
	Density of crabs in commercial size	0.17	0.27
	Frequency of crabs in non-commercial size	0.24	–
	Frequency of crabs in commercial size	–	0.26
	Mean crab size	0.11	0.12
Land use and cover	Mangrove vegetation types	0.02	0.03
	Distance of mangroves from fishery villages	0.06	0.18
	Distance of mangroves from shrimp farms	0.02	–
Social parameters	Degrees of mangrove importance for crab conservation	0.02	0.05
	Degrees of mangrove use for crab fishery	0.06	0.07

RESULTS

For both objectives, conservation and fishery of the crab *U. cordatus*, the biological criteria related to the crab population parameters were those that showed the highest weights (Table 1). For the conservation purpose, the density and frequency of NCSC were the most important factors (Table 1), while density and frequency of CSC were the most important for the fishery purpose. The social criteria showed low to intermediate weights, wherein the degrees of mangrove use for crab fishery were considered more important than the degrees of mangrove importance for crab conservation (Table 1). For the land use and cover criteria, the distance of mangroves from fishery villages was the most important, mainly for the fishery purpose (Table 1). Lowest weights were given to mangrove vegetation types and distance of mangroves from shrimp farms (Table 1). Thus they were considered the less important factors to delineate areas for conservation and fishery of the crab *U. cordatus*.The most suitable mangrove areas for the conservation of the crab *U. cordatus* (classes: *extremely high*, *very high*, *high* and *moderately high*) are closest to the São Francisco River mouth (Figure 2a). On the other hand, the conservation suitability decreases as far as the mangrove areas distance themselves from the estuary mouth (Figure 2a). The most suitable classes for the crab conservation accounts together for more than 58% (18.6 km^2) of the mangroves in the study area and show important characteristics for the conservation of *U. cordatus*, such as: high density and frequency of NCSC, small sized crabs, low degree of use for crab fishery, and they are more distant areas from the fishery villages and shrimp farming. In addition to these features, the class *extremely high* exhibits mangrove vegetation type with higher green biomass and with the presence of *Laguncularia racemosa* and *Rhizophora mangle*.

The less suitable mangroves to the crab conservation (classes *medium*, *low* and *very low*) (Figure 2a) account for approximately 42% (13.3 km^2) of mangrove total area, and are closest to the fishery villages and shrimp farming, more used for the crab fishery by the local populations, and shows high density of CSC, big sized crabs and low frequency and density of NCSC. The presence (or combinations) of these features do not make them suitable as areas for the conservation of *U. cordatus*. For example, the class *medium* showed close proximity to fishery villages and shrimp farming, while the class *low* was associated with the highest density of commercial crabs and fishery use. The class *very low* showed the biggest crabs, as well as the lowest density and frequency of NCSC.

The most suitable mangrove areas for the fishery of *U. cordatus* (classes: *extremely high*, *very high*, *high* and *moderately high*) are those located farther from to the river mouth, mainly along the 'Poço' and 'Carapitanga' channels (Figure 2b). The most suitable classes for the crab fishery accounts together for more than 59% (18.9 km^2) of the mangroves and show important characteristics for the crab fishery such as: high density and frequency of CSC, low density NCSC, big sized crabs, medium to high degree of use for crab fishery, and are more close to the fishery villages. The class *extremely high* exhibits higher values of CSC density than the class *very high*, which showed the biggest crabs.

The less suitable to the crab fishery (classes *medium*, *low* and *very low*) account for roughly 41% (13 km^2) of the total mangrove extent (Figure 2b) and are those more distant from the fishery villages, less used for the crab fishery by the local populations, and show high density and frequency of NCSC, small sized crabs, and mangrove vegetation with less green biomass. The presence (or combination) of these features do not make them suitable for the fishery of *U. cordatus*, but to other objectives, as for the crab conservation.

DISCUSSION

In Brazil the fishery of *U. cordatus* is a very important socioeconomic activity, but decreases in the crab stock have threatened fishing and resource. Thus, in 2011 the Brazilian Institute of the Environment (IBAMA) published a Proposal of a National Management Plan for this species, which aims to promote sustainable use of this resource, ensuring the maintenance of the crab populations at satisfactory levels and allowing the continuity of economic activity (Brasil, 2011; Pinheiro and Rodrigues, 2011). This plan states the delineation of extractive and fishery exclusion areas for achieve these objectives.

The present study shows an important contribution for fishery management and specially for this plan. This methodological approach by MCE analysis produced suitability maps possible to be used by government agencies to delineate areas of extractive and fishery exclusion (conservation) along the Brazilian

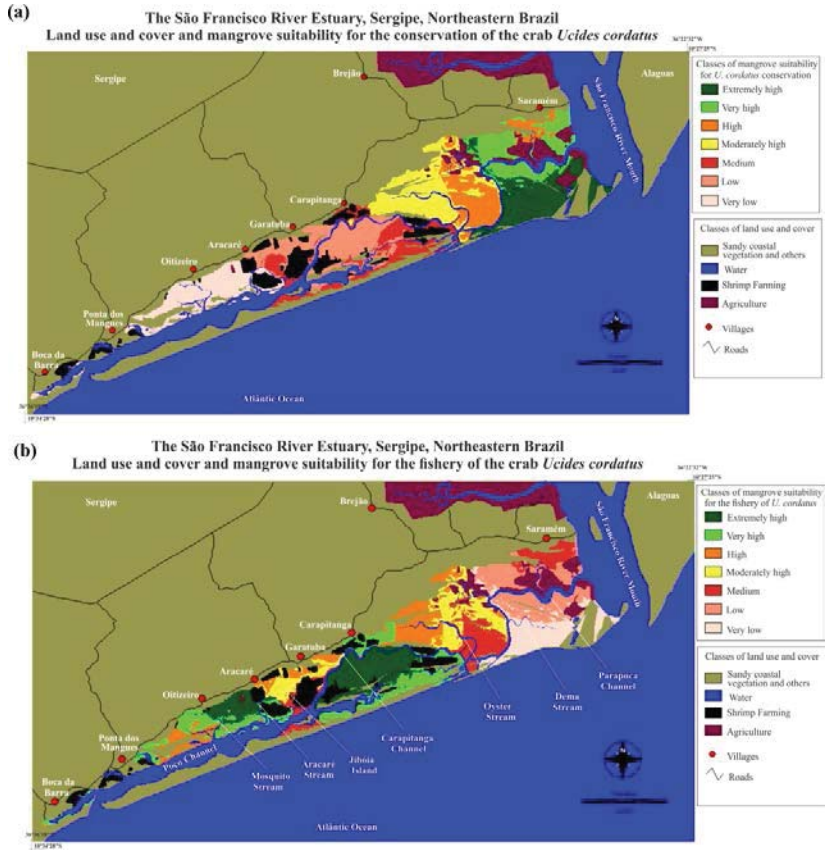

Figure 1. Map of land use/cover and mangrove suitability for the conservation (a) and fishery (b) of the crab *Ucides cordatus*, in the São Francisco River Estuary (Northeastern Brazil).

mangrove areas. Moreover, the maps produced here can be used by the local government agency (Sergipe State Environmental Administration, ADEMA) in order to implement this plan in the study area. In fisheries management, developing analytical and operational evaluation tools is critical for decision-making (Andalecio, 2010). The advantage of using MCE analysis is to allow the integration of data from different fields, an important procedure in the fishery management. As an example, this study used biological parameters of the crab population structure, spatial arrangement of the landscape/land use and social data. Despite this, some limitations are found in the MCE, as standardization of qualitative criteria, the search for specialists to analyze the comparison matrix and it requires expensive tools as satellite images, geoprocessing software and field surveys, and an interdisciplinary view of the analyst.

In this study we found that the biological criteria related to the *U. cordatus* population structure (mainly density and frequency of NCSC and CSC), were more important than land/cover use and social criteria, for the delineation of the more suitable mangrove areas for the crab conservation and fishery, respectively. This fact highlights the importance to include these important variables when fishery management plans are proposed. For the crab fishery purpose, higher density of CSC was more important than the mean crab size (Table 1) since it indicates large stocks of crabs for exploitation, representing the amount of crabs per square meters and is correlated with immediate extractive potential (legal capture size) in mangroves.

The high abundance of *U. cordatus* and the large extension of its habitat make this semi-terrestrial crab a resource with a high fishery potential (Diele *et al.*, 2005). The crab stocks and therefore their capture rates and yield reflect the extent and degree of development of mangroves (Brazil, 2011). This shows the importance of the mangrove habitats for the maintenance of the fishery potential of this species. In the study area the high extent of mangrove areas (32 km^2) with high developed stands (Santos *et al.*, 2014a), combined with the population structure of *U. cordatus*, as well as social and land use/cover features, indicate large areas of these mangroves with high potential to the crab fishery. According to Diele *et al.* (2005), the potential yield of *U. cordatus* is comparable to (or exceeds) other important crab fisheries worldwide, as to blue crabs (Portunidae), dungeness crabs (Cancridae), and snow crabs (Oregoniidae).

CONCLUSIONS

We concluded that the mangroves of the São Francisco River Estuary show different areas with high potential for the conservation and fishery of *U. cordatus*. The combination of high potential for both objectives allow the implementation of management strategies in order to achieve a sustainable fishery of this resource, as stated by the Proposal of a National Management Plan for this species. Based on the objectives of this proposal, the mangroves most suitable for the conservation of *U. cordatus* might be delineated as fish exclusion areas, since they show large abundance of small NCSC and are the less used for fishery. In the fishery exclusion areas the crab capture should be restrictive or not allowed, in order to permit the NCSC grow to reach the commercial size, as well as, to maintain the reproduction and resource stock viable in this area. Similarly, the mangrove areas more suitable for the crab fishery can be delineated as extractive areas, since they show large abundance of CSC, big crabs, and are closed to the fishery villages.

The combination of remote sensing, geoprocessing techniques and field surveys in a MCE was shown to be a useful tool for fishery management purposes. This fact is confirmed by the integration of different data (e.g., social, biological and geographical sciences), an essential characteristic for the analysis, resource management and conservation of socio ecological complex systems, such as fishery in coastal and marine ecosystems.

ACKNOWLEDGMENTS

We are grateful to the FAPESP (Fundação de Amparo à Pesquisa do Estado de São Paulo - Proc. # 2010/20028-9), INPE for the free download of CBERS-2B images, and all the researches that contributed with the pairwise comparison matrix in the AHP analysis (Prof. Dr. Francisco José Bezerra Souto, Dr. Mauro Marcio Tavares da Silva, MSc. Ádria de Carvalho Freitas, MSc. Caroline Araújo de Souza, MSc. Osilene Fonseca and MSc. Renata Benito Pettan).

LITERATURE CITED

Andalecio, M.N., 2010. Multi-criteria decision models for management of tropical coastal fisheries. A review. *Agronomy for Sustainable Development*, 30, 57-580.

Barbier, E.B.; Hacker, S.D.; Kennedy, C.; Koch, E.W.; Stier, A.C., and Silliman, B.R., 2011. The value of estuarine and coastal ecosystem services. *Ecological Monographs*, 81, 169-193.

Boeger, W.A.; Pie, M.R.; Ostrensky, A., and Patella, L., 2005. Lethargic crab disease: multidisciplinary evidence supports a mycotic etiology. *Memórias do Instituto Oswaldo Cruz*, 100, 161-167.

Brasil. IBAMA, 2011. *Proposta de Plano Nacional de Gestão para o uso sustentável do Caranguejo-Uçá, do Guaiamum e do Siri-azul. In:* Dias-Neto, J. (org.). Brasília: Série Plano de Gestão Recursos Pesqueiros, 4: 156 p.

Charles, A.S., 2001. *Sustainable Fishery Systems. Fish and aquatic resources*. Oxford: Blackwell Science.

Côrtes, L.H.O.; Zappes, C.A., and Di Beneditto, A.P.M., 2014. Ethnoecology, gathering techniques and traditional management of the crab *Ucides cordatus* Linnaeus, 1763 in a mangrove forest in south-eastern Brazil. *Ocean & Coastal Management*, 93, 129-138.

Diele, K.; Koch, V., and Saint-Paul, U., 2005. Population structure, catch composition and CPUE of the artisanally harvested mangrove crab *Ucides cordatus* (Ocypodidae) in the Caeté estuary, North Brazil: Indications for overfishing? *Aquatic Living Resources*, 18, 169-178.

Eastman, J.R., 2012. *IDRISI Selva Manual*. Worcester: Clark University, 324p.

FAO - Food and Agriculture Organization of the United Nations, 2007. *The world's mangrove 1980-2005*. Rome: FAO Forestry Paper, nº 153.

Griffis, R. and Kimball, K., 1996. Ecosystem approaches to coastal and ocean stewardship. *Ecological Applications*, 6, 708-712.

Huang, I.B.; Keisler, J., and Linkov, I., 2011. Multi-criteria decision analysis in environmental sciences: ten years of applications and trends. *Science of the Total Environment*, 409, 3578-3594.

Macnae, W., 1974. *Mangrove Forest and Fisheries*. Rome: FAO, IOFC/DEV/74, 34, 35 pp.

Magalhães, H.F.; Neto, E.M.C., and Schiavetti, A., 2012. Local knowledge of traditional fishermen on economically important crabs (Decapoda: Brachyura) in the city of Conde, Bahia State, Northeastern Brazil. *Journal of Ethnobiology and Ethnomedicine*, 8, 13.

Pinheiro, M.A.A. and Rodrigues, A.M.T., 2011. Crustáceos sobre-explotados e o Plano Nacional de Gestão dos caranguejos uçá (*Ucides cordatus*), guaiamú (*Cardisoma guanhumi*) e do siri-azul (*Callinectes sapidus*): uma estratégia para evitar que passem ao "status" de ameaçados de extinção. *Revista CEPSUL - Biodiversidade e Conservação Marinha*, 2, 50-57.

Rönnbäck, P., 1999. The ecological basis for the economic value of mangrove forests in seafood production. *Ecological Economics*, 29, 235-252.

Saaty, T., 1977. A scaling method for priorities in hierarchical structures. *Journal of Mathematic Psychology*, 15, 234-281.

Santos, L.C.M.; Dahdouh-Guebas, F., and Bitencourt, M.D., 2013. Mangrove fisheries as base of subsistence economy in the São Francisco River Estuary (Northeastern Brazil): considerations for local management. *Proceedings of the XV Congreso Latinoamericano de Ciencias del Mar* (Punta del Est, Uruguay).

Santos, L.C.M.; Matos, H.R.; Schaeffer-Novelli, Y.; Cunha-Lignon, M.; Bitencourt, M.D.; Koedam, N., and Dahdouh-Guebas, F., 2014a. Anthropogenic activities on mangrove areas (São Francisco River Estuary): a GIS-based analysis of CBERS and SPOT images to aid in local management. *Ocean & Coastal Management*, 89, 39-50.

Santos, L.C.M.; Dahdouh-Guebas, F.; Bitencourt, M.D. 2014b. Population status and fishery potential of the mangrove crab (*Ucides cordatus*) in the São Francisco River Estuary (Brazil Northeast). *Proceedings of the IV Congresso Brasileiro de Oceanografia* (Itajaí, Santa Catarina, Brasil).

Schories, D.; Barletta-Bergan, A.; Barletta, M.; Krumme, U.; Mehlig, U., and Rademaker, V., 2003. The keystone role of leaf-removing crabs in mangrove forests of North Brazil. *Wetlands Ecology and Management*, 11, 243-255.

Journal of Coastal Research	SI	75	690-694	Coconut Creek, Florida	2016

Ecosystem-Based Knowledge and Management as a tool for Integrated Coastal and Ocean Management: A Brazilian Initiative

Marinez E.G. Scherer[†*] and Milton L. Asmus[†]

[†]Laboratory of Integrated Coastal Management (LAGECI),
Department of Geosciences
Federal University of Santa Catarina
Florianópolis, Brazil

www.cerf-jcr.org

www.JCRonline.org

ABSTRACT

Scherer, M.E.G. and Asmus, M.L., 2016. Ecosystem-Based Knowledge and Management as a tool for Integrated Coastal and Ocean Management: A Brazilian Initiative. *In:* Vila-Concejo, A.; Bruce, E.; Kennedy, D.M., and McCarroll, R.J. (eds.), *Proceedings of the 14th International Coastal Symposium* (Sydney, Australia). *Journal of Coastal Research*, Special Issue, No. 75, pp. 690-694. Coconut Creek (Florida), ISSN 0749-0208.

The Ecosystem-Based Management (EBM) brings knowledge highlighting the importance of ecosystem services (ES) as the key factors supporting the environment, social and economic integrity, as well as human wellbeing. EBM could represent the change from public policies greatly focused on normative and bureaucratic components to new policies predominantly based on the understanding of ecosystem processes and the regulation of human activities. Nevertheless, most of the coastal zone management initiatives in Brazil lack the necessary ecosystem based information to fully support EBM. They also often don't integrate the ecosystem-based information into the management system in an appropriate way. This paper proposes a roadmap model to produce the ecosystem-based information and its application for coastal policies. This involves the identification of (1) dominant ecosystems and ecosystem services; (2) benefits for human wellbeing; (3) stakeholders affected; (4) main pressure, human or natural produced; (5) main impacts, (6) managerial responses. The model was applied at Santa Catarina Island on the Southern coast of Brazil and demonstrated that a territory of around 425 Km^2 holds 17 different environmental systems, 47 direct befits from the environmental services, with a great number of stakeholders who are linked directly to these benefits. In other hand Santa Catarina Island suffers from 39 different vectors of pressure, threatening the environmental systems and its services and benefits. This study also showed the great amount of interrelations among ES, stakeholders and managerial initiatives and the need for ecosystem based information and knowledge for an effective Integrated Coastal and Ocean Management in Brazil.

ADDITIONAL INDEX WORDS: *Ecosystem-Based Management, coastal management, Santa Catarina-Brazil.*

INTRODUCTION

The intensive use of coastal areas has caused considerable changes in their ecosystems. Such changes may compromise the services provided by coastal ecosystems with great benefits both for nature, as well as for societies (Barragán, 2014). Some of the most representative coastal ecosystems, or Environmental Systems, include beaches, mangroves, marshes, dunes, estuarine areas, coastal areas coastal infrastructure, among others (Baily and Nowell, 1996).

These ecosystems produce goods and basic services, categorized and classified (UNESCO, 2011; Ehler and Douvere, 2009; de Groot, 2002) as (1) services of provision (*e.g.*: food, water, fiber, biochemicals, genetic resources), (2) services of support (*e.g.*: sedimentary structures, nutrient cycling, primary production), (3) services of regulation (*e.g.:* climate regulation, water purification), (4) cultural services (*e.g.*: recreation and tourism, spiritual and religious benefits, aesthetic, inspirational and educational). Many of these ecosystem services are vital to the very ecosystems and societies that live in coastal areas (Odum and Odum, 2001, pg.230).

DOI: 10.2112/SI75-138.1 received 15 October 2015; accepted in revision 15 January 2015.
*Corresponding author: marinezscherer@gmail.com

The recognition of services provided by environmental systems has led to the establishment of an Ecosystem Based Management (EBM). Recently in some coastal countries, the EBM provided new and significant advances in the planning and management of environments, processes and coastal resources (Barragán, 2014; Freeman *et al*., 2013;McLeod and Leslie, 2009). The Ecosystem Based Management can be defined as an approach that attempts to organize the human uses of ecosystems and achieve a balance between the benefits of their use and the sustainability of providers ecosystems processes and structures of these same benefits (adapted from Pirot *et al.*, 2000).

The EBM of marine and coastal environments can presents some advantages when compared to what we might call "traditional management" (Asmus *et al*., 2014). To procedure a systemic view, it must be considered, in an integrated manner, all biophysical, social, economic and political components, that make up the coastal system. Likewise, it recognizes the importance of services and benefits generated by ecosystems for the production and maintenance of human wellbeing (Barragán, 2014),

Recognition of indicatives, and possible difficulties, for the efficient development of EBM can improve management processes at all levels (Barragán, 2014; Pirot *et at.*, 2000). Such

indicatives include (1) possible support to coastal management tools (coastal ecological-economic zoning, integrated management plans, monitoring programs, *etc.*); (2) aid to perform evaluations of coastal management processes; (3) persistence of the main sources of coastal problems (Barragán, 2014, Liquete *et al*. 2013)

All these indications have caused a particular interest in academic and scientific world, requiring the development of technical marine and coastal systems management and governance (Szlafsztein, 2006). In this sense, the proposal of EBM for planning and management programs can become an interesting alternative in the local and regional level (Barragán, 2014; Pirot *et al.*, 2000).

In Brazil, there are some indications about the difficulty of implementation and execution of the National Coastal Management Program - GERCO (Andrade and Scherer, 2014; Scherer *et al.*, 2011) at all levels, both governmental, and institutional. Most of the information available for the Brazilian coastal management has a segmented or sectorial character, and the data and information on coastal ecosystems are not integrated. For efficient development of GERCO it is vital a perception and understanding of coastal environments in a systematic way. In other words, the Ecosystem Based Management.

Santa Catarina Island is located on the Southern Brazilian Coast (Figure 1) and supports a myriad of environmental systems such as sand dunes, beaches, mangroves, rain forest, among others. Despite its environmental and economic importance, the Island does not have an appropriate management, loosing its environmental assets in a very fast way (Diederichsen *et al.*, 2013).

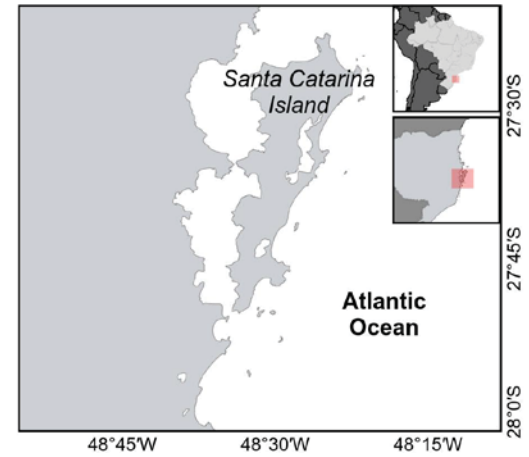

Figure 1 – Santa Catarina Island Location on the Southern coast of Brazil.

To better manage the island, in an integrated view, it is assumed that knowledge of the functionality and interaction of marine and coastal ecosystems, and the human demands and socioeconomic pressures is necessary. It can contribute to the implementation of appropriate public policies, efficient and effective integrated environmental management of the Island marine and coastal resources.

This paper proposes a tool to improve the knowledge of the functions and interactions of marine and coastal ecosystems, in order to understand, in an integrated manner, their different connections, processes, uses and management. This knowledge is needed to implement an EBM strategy that could enhance a more solid platform in relation to decision-making, considering technical and scientific arguments. This will permit articulating with the different political and institutional aspects, developing, effectively, the management, conservation and use of the Santa Catarina Island natural and socioeconomic resources.

METHODS

The methodology applied assumes as a structural and conceptual element, the Systemic Perspective (Odum and Odum, 2001). Such systemic perspective ensures an integrated view of the different environments considered, allowing for standardization principles (systemic principles) when multiple activities and products are systematized, compared or integrated as key elements of the proposed management plans and actions.

The logical premise of the proposed methodology is centered on the concept of Ecosystem Services and considers that a systemic environmental approach (Odum, 2007) is a weighty tool for, ultimately, protect, supply or recover ecosystem services and their benefits for nature and society.

For social and environmental systemic characterization of Santa Catarina Island this work took, as a guide, the Ecosystem Services Worksheet, as proposed in Asmus *et al.* (2014). This instrument sums, for a particular region, at least: (1) major ecosystems, (2) type of services, classified as support, regulation, provision and cultural (de Groot *et al.*, 2002), (3) main ecosystem services, (4) main ecological and socioeconomic benefits, (5) social actors benefit from the services/benefits, (6) main environmental driving pressures and (7) managerial responses aimed to reduce or minimize impacts on those ecosystem services and their processes. On the presented case study the managerial responses are not described yet, and will be theme of a future scientific paper.

The Ecosystems and Services Worksheet was completed integrating, at first, an "expert opinion system", consisting predominantly by brainstorm among researches familiar with the main environments considered; subsequently supplementary scientific or traditional information was included (Oliveira and Corona, 2008) arising from contacted stakeholders (managers, users, policy makers). Unstructured interviews were applied for data gathering from target stakeholders (Berry, 1999). The standardization of the terms and ecosystem services were based on Liquete *et al.* (2013).

As the area of the case study (Santa Catarina Island) is a mosaic of ecosystems, this methodology permitted the characterization of the environment in a synthetic and integrated way, where information about the physical, biological and social components eventually raised, are to be studied as structural elements of ecosystems taken into account. More than that, it determines the role of such components in the processes that generate and regulate ecosystem services to be considered and possibly protected. It is proposed, therefore, a functional characterization of the studied area. It is important to emphasis

that both natural and modified environments were considered in this analysis.

By linking services, benefits and benefit stakeholders, the Ecosystem Services Worksheet is also used for the identification of the main stakeholders that should be involved in a planning and managing process. Such participatory action is undoubtedly facilitated when the social actors count on a methodological tool that explains, as best as possible, the benefits from the environment, addressing eventually individual and collective interests.

RESULTS

The worksheet developed according to the methodology proposed by Asmus *et al.* (2014) was analyzed and revealed that Santa Catarina Island has 17 main environmental systems: Mangroves, sand dunes, lagoon, lakes, wetlands, rocky shores, rain forest, scrubland, bays, little islands, marine environment, streams and rivers, rural areas, landfill areas (anthropogenic deposits), urban areas, and transitional areas. Manmade environments were considered as a kind of environmental systems, with benefits for human wellbeing as well.

Those ecosystems maintain a series of environmental services of Support, Regulation, Provision and Cultural type. That brings a high number of 47 benefits for different benefit stakeholders. The most important and more cited benefits were: water and air quality, fish production, shore line protection, navigation protection, tourism and leisure, transport, food production, urban services and contribution for human relations. Most of these results are corroborated by Liquete *et al.* (2013) while assessing marine and coastal ecosystem services.

A large number of people are benefited by these environmental services in Santa Catarina Island; such as local community, artisanal and industrial fisherman, tourism trade, educational institutions, and governmental institutions, among others.

When analyzing the main human related pressures on those environmental systems, and their services and benefits, the main inductors of the modification and loss of these services are urban development (infrastructure, housing, soil sealing, irregular settings, *etc*.) and lack of basic sanitation (sewage, waste and drainage treatment). Other pressures are dredging, overfishing and illegal fishing, natural resources use (mainly water), massive tourism, *etc*. It was detected 39 different vectors of pressure on the Island. On Table 1 it is possible to visualize an extract of the worksheet, as an example

.

Table 1. *Mangrove and Urban Areas: Services, benefits, stakeholders and driving forces. Extracted from the Ecosystem Services Worksheet developed for this work.*

	Class	Services	Uses/benefits	Stakeholders	Main driving force/impacts
Mangrove	Support	Organic matter production, habitat diversity, sewage receptor	Fishing, tanning (from the wood), sewage depuration	Artisanal and industrial fishing industry, local community	Building and infrastructures, sewage, change on the hydrology by manmade structures.
	Provision	Natural nursery	Fishing and extractive activities	Artisanal and industrial fishing industry, local community	Building and infrastructures, sewage, mangrove overfishing and dredging
	Regulation	Nutrients cycling, shore protection, sewage depuration	Water quality, hazard reduction, anchorage protection	Local community	Building and infrastructures, sewage and dredging
	Cultural	Landscape and cultural values	Environmental education and contemplative value, social wellbeing	Local community, tourism and educational institutions	Building and infrastructures, sewage, overfishing
Urban Areas	Support	Urban services	Accessibility, social wellbeing	Local community, visitors, tourists, local government	Natural hazards, population increasing, intensive traffic, illegal and not planned occupation, illegal sewage and waste dumping, urban violence
	Provision	Waste, sewage, noise, basic services (hospitals, schools, roads)	Recycling, treated water, energy and sanitation, accessibility, social wellbeing	Recycling cooperatives, local community, waste/water/sanitation and energy dealerships	Illegal sewage and waste dumping, seasonal occupation (waste and sewage variation)
	Regulation	Economic regulation	Social and institutional relations	Local community, visitors, tourists, local government	Economic policies
	Cultural	Cultural values	Social and institutional relations	Local community, visitors, tourists,	Use conflicts, immigration, intensive tourism, urban violence

It is also possible to calculate the percentage of the different services (support, provision, regulation and cultural) found for each environmental system studied. Using the given examples (mangroves and urban areas), and calculating from the number of services analyzed, it was found that 43% of the services provide by mangroves are related to support services, such as habitat for sea life. Regulation services are responsible for 29% of the benefits provided by mangroves, while provision and cultural services respond by 14% each.

In other hand, in urban areas the provision services are responsible for almost 60% of the benefits this system can bring to human wellbeing in Santa Catarina Island. This is explained by the provision of urban services, such as treated water, sanitation, accessibility, social wellbeing, among others.

On the examples above, extracted of the main worksheet, and in all environmental systems analyzed, it became clear that human wellbeing is directly or indirectly dependent on the environmental services. It means the environmental and urban health are the baseline conditions to human welfare. Identifying which service is produced by each environmental system, which benefit results from this service, and which process are involved on the service production and conservation, and stakeholders appropriation, is the key that allows managers to put in place the initiatives to maintain and/or improve these process.

As per an example, if the fish stock declines in an important way, one of the reasons might be the loss of mangroves. Mangroves provide the environmental service of nursery and habitat for fish species and other sea organisms (support service) and it is an organic matter supplier (provision service). A loss of mangrove areas, allied to other impacts on this system (contamination, overfishing, *etc*.) is due to cause a decrease on the fishing capacity. Losing this source of food can produce serious problems for the local community and fisherman. If the impacts on the systems are of great magnitude (*e.g.:* total suppression of mangrove areas), the impact will probably go beyond the local influence and affect the fishing industry, for instance.

By the other hand, the manmade areas are important for human wellbeing too. It can provide access to basic services, such as hospitals, schools, roads, *etc*. To measure human wellbeing dependent on urban areas is not an easy task. But some research have been done showing the level of stress derived from a more chaotic urban context (traffic, noises, smells, lack of a healthy landscape, and so on) is one of the main reasons for “unhappiness” among urban people. In addition, the lack of a more frequent contact with natural, pristine areas can trigger a state of stress on people (Beil and Hanes, 2013).

DISCUSSION

The main results of this paper show the considerably high variety of ecosystems, ecosystem services, and the benefits from them for several sectors of the coastal community. A territory of around 425 Km^2 holds 17 different environmental systems, 47 direct befits from the environmental services, with a great number of stakeholders who are linked directly to these benefits. In other hand Santa Catarina Island suffers from 39 different vectors of pressure, threatening the environmental systems and its services and benefits. It was also found that the importance related to the ecosystem services offered is related not only to natural systems, like mangroves, but also to urbanized areas like water fronts.

These results are organized in an integrated way using the methodology presented. It clears demonstrated the relation of ecological, economic and social elements in an integrated framework.

There are two ways by how we understand the advantage of using an integrated system approach through the "ecosystems and services worksheet" as carried out on Santa Catarina Island. The first one is related to the simple and logical pattern that this tool can offer to better analyze coastal environmental systems. The other way is related to the potential application of this procedure to enhance the process one can use for planning and managing uses and occupation of those systems.

Most of the analyses of coastal ecosystems in Brazil are traditionally carried out through the elaboration of a diagnosis generally composed of the production of layers of sectorial environmental information, usually split in physical, biological and socioeconomic components. Such segregation of components is hard to be integrated in a synthetic or systemic description of the environment. The result of that is a dominated sectorial perception of the environment, which restrains considerably a better understanding of how the coastal sector can function and react to several social and economic uses of it.

The results from our analysis start from a synthetic definition of coastal ecosystems, their services and benefits that can be easily defined from recent satellite images, combined with theoretical information on the dominant ecosystems, and completed with the qualified opinions from scientists and local users. One clear advantage of such approach is the celerity of the environmental diagnosis of coastal systems and the understanding of the connections among ecosystems, their services, the benefits from those services and, finally, the stakeholders to receive the benefits. In other words, any initial difficulty to integrate different natural and social economic elements, are very facilitated when one consider those elements as the function components of an ecosystem unit.

The second advantage on the procedure presented is the strong potential that a systemic approach can bring, when applied in the planning and management of coastal systems like the Santa Catarina Island. Through this approach, the ultimate goals for an integrated coastal management in the area would be the maintenance of ecosystem services in order to guarantee the best ecosystem health and social wellbeing for the communities using those services in a direct or indirect way. Eventually management action would involve the mitigation and compensation of ecosystem services.

It is like to say that this ecosystem-based management procedure in the studied area - but, probably, in any sector of the Brazilian coast - could allow an evolution from a management pattern quite based on the definition of resources or spaces to be or not used, to a novel pattern (in Brazilian terms) that rather focus on the better use of ecosystem services from coastal ecosystems. Besides, such management concept can better identify the stakeholders using or with interest to use the services, which can facilitate the design of desirable participatory processes.

CONCLUSIONS

Balancing nature and human wellbeing is a quite complex task. But if the managers can understand the connection among the environmental systems and its benefits for the human population, they might be able to take best decisions. On coastal and marine areas, this task is even more difficult due to the intricate and fragile natural environment, high number of human activities and stakeholders, and a large range of managerial tools and institutions.

The systemic approach applied in this work can be considered a novel way to carry out environmental diagnosis of coastal systems in Brazil. The case developed in the Santa Catarina Island shows a possible way to define environmental systems (ecosystems) that take into account ecological, economic and social elements in an integrated framework. In some way, this ecosystem-based knowledge can override a traditional difficulty to integrate elements that arise from a typical sectored environmental analysis still dominant in the country. By working with an ecosystem-based approach that highlights the role of ecosystems services to support nature and coastal societies and, understanding the processes that can regulate or control those services, we can open a new window of opportunities to better understand, plan and manage the Brazilian coastal zone.

ACKNOWLEDGMENTS

We would like to thank the members of the Laboratory of Integrated Coastal Management (LAGECI) of the Federal University of Santa Catarina, Brazil.

LITERATURE CITED

Andrade, J.; Scherer, M., 2014. Decálogo da Gestão Costeira para Santa Catarina: avaliando a estrutura estadual para o desenvolvimento do Programa Estadual de Gerenciamento Costeira. *Revista Desenvolvimento e Meio Ambiente*, UFPR, 29, 139-154.

Asmus, M.L., Scherer, M.E.G., Oliveira, T.C.R. 2014. Gestão com Base Ecossistêmica (GBE) de Sistemas Marinhos e Costeiros. XXVI *Semana Nacional de Oceanografia*. Ubatuba, PR.

Baily, B. and Nowell, D., 1996. Techniques for monitoring coastal change: a review and case study. *Ocean and Costal Management,* 32(2), 85-95.

Barragán, J.M., 2014. *Política, Gestión y Litoral: una nueva visión de la gestión integrada de áreas litorales*. Editor Tébar Flores, Madrid, Spain. 685p.

Beil, K. and Hanes, D., 2013. The Influence of Urban Natural and Built Environments on Physiological and Psychological Measures of Stress - a Pilot Study. *Int. J. Environ. Res. Publ. Health.,*10(4), 1250-1267.

Berry, R.S.Y. 1999. Collecting data by in-depth interviewing. *British Educational Research Association Annual Conference*, University of Sussex at Brighton, September 2 – 5.

de Groot, R.S., Wilson, M.A., Boumans, R.M.J. 2002. A typology for the classification, description and valuation of ecosystem functions, goods and services. *Ecological Economics* 41, 393–408.

Diederichsen, S. D.; Gemael, M. K.; Hernande, A. de O.; De Oliveira, A. de O.; Paquette, M.; Schmidt, A. D.; Silva, P. G. da; Silva, M. S. da; Scherer, M. E. G., 2013. Gestão costeira no município de Florianópolis, SC, Brasil: Um diagnóstico. *Journal of Integrated Coastal Zone Management,* 13(4), 499-512.

Ehler, C. and Douvere, F., 2009. *Marine Spatial Planning: a step-by-step approach toward ecosystem-based management.* Intergovernmental Oceanographic Commission and Man and the Biosphere Programme. IOC Manual and Guides 53, ICAM Dossier 6. Paris: UNESCO.

Freeman, P.; Rosenberger, R.; Sylvia, G.; Heppel, S.: Harte, M., 2013. *Guide for Valuing Marine Ecosystem Services to Support Nearshore Management in Oregon*. Oregon Sea Grant, USA. 74p.

Liquete, C.; Piroddi, C.; Drakou, E. G.; Gurney, L.; Katsanevakis, S.; Charef, A.; Egoh, B., 2013. Current Status and Future Prospects for the Assessment of Marine and Coastal Ecosystem Services: a Systematic Review. *PLOS One*. 8(7), 1-15.

McLeod, K. and Leslie, H. (Ed.) 2009. *Ecosystem Based Management for the Oceans.* Island Press, Washington, 368pp.

Odum, H. *Environment, Power, and Society for the Twenty-First Century*. Columbia University Press, New York, USA. 409p.

Odum, H.T, Odum, E.C., 2001. *A prosperous way down. Principles and policies*. University Press of Colorado, 326p.

Oliveira, K. A. and Corona, H. M. P., 2008. A percepção ambiental como ferramenta de propostas educativas e de políticas ambientais. *ANAP Brasil Revista Científica*. 1(1) p. 53-72.

Pirot, J.-Y., Meynell P.J. and Elder D., 2000. *Ecosystem Management: Lessons from Around the World. A Guide for Development and Conservation Practitioners.* IUCN, Gland, Switzerland and Cambridge, UK. 132 p.

Scherer, M; Asmus, M; Filet, M; Sanches, M. y Poleti, A. E., 2011.El manejo costero en Brasil: análisis de la situación y propuestas para una posible mejora. In Farinós Dasí, J. (ed). *La gestión integrada de zonas costeras ¿algo más que una ordenación del litoral revisada? La GIZC como evolución de las prácticas de planificación y gobernanza territoriales*, Valencia, PUV/IIDL, Colección 'Desarrollo Territorial', 9, 161-173.

Szlafsztein, C. F, 2009. Indefinições e Obstáculos no Gerenciamento da Zona Costeira do Estado do Pará, Brasil. *Journal of Integrated Coastal Zone Management*, 9 (2), 47 – 58.

UNESCO, 2011. *Planejamento especial marinho: Passo a passo em direção à gestão ecossistêmica* (resumo). Representação da UNESCO no Brasil – Comissão Oceanográfica Intergovernamental (COI), 11p.

Journal of Coastal Research	SI	75	695-699	Coconut Creek, Florida	2016

Effect of the Coastal Protection using the Beach Nourishment at Tottori Sand Dune Coast, JAPAN

Yoko Shibutani [†*], Masamitsu Kuroiwa[‡], and Yuhei Matsubara[‡]

[†]Office for Gender Equality
Tottori University,
4-101,Koyama-minami, Tottori, Japan

[‡] Dept. of Civil Engineering
Tottori University,
4-101,Koyama-minami, Tottori, Japan

www.cerf-jcr.org

www.JCRonline.org

ABSTRACT

Shibutani, Y.; Kuroiwa, M.; and Matsubara, Y., 2016. Effect of the Coastal Protection using the Beach Nourishment at Tottori Sand Dune Coast, JAPAN., *Proceedings of the 14th International Coastal Symposium* (Sydney, Australia). *Journal of Coastal Research*, Special Issue, No. 75, pp. 695-699. Coconut Creek (Florida), ISSN 0749-0208.

Beach erosion is a serious problem worldwide. The Tottori Sand Dune coast had started eroded in the 1950s, and the beach nourishment project has been carried out to restore the shoreline since 2005. The total volume of the sand was approximately 650,000 m^3 from 2005 to 2014. In particular, a large amount of sediments, which was 100,000 m^3, was injected in 2010 and 2011.

In this study, the effect of the project was estimated. The sand volume increased temporarily after the large-scale beach nourishment, and then, the sand volume gradually decreased. However, the shorelines showed restoration trends after the beach nourishment project. In addition, although a part of the injected sediments was moved to the Tottori port, recovery of the shoreline was maintained.

ADDITIONAL INDEX WORDS: *Beach nourishment, Beach erosion, Shoreline change, Change of sand volume*

INTRODUCTION

In past few decades, beach erosion has become severe in sandy beaches worldwide. As the coastal defense works towards the prevention of beach erosion, various types of structures such as offshore breakwater and jetty have been constructed. However, these structures resulted in new erosions at nearby coasts. Therefore, recently, beach nourishment has been carried out as an effective technique against coastal erosion considering environment and utilizing.

In Japan, it was reported that the coastal erosion of sandy beaches began from the 1950s because of various factors such as decreased fluvial sediment supply and obstruction of longshore sand transport. At the Tottori Sand Dune Coast in Tottori Prefecture located in the western part of Japan, coastal erosion has been serious problem. Coastal erosion has become more serious since the coastal structures were constructed around sandy beaches. However, the port and river mouth have been accumulated the sediment.

To overcome these drawbacks, the beach nourishment project has been carried out since 2005. The project is called 'Sand Recycle Project'. The sand volume is typically 20,000–30,000 m^3/year. In particular, large-scale beach nourishment was carried out in 2010 and 2011. The total sand volume was approximately 650,000 m^3 from 2005 to 2014. We investigated the movement of the injected sand and the effect of the beach nourishment presented by Shibutani *et al*., (2013). According to the report, the sand volume fluctuates based on the seasonal changes in waves, and the total sand volumes increase after beach nourishment. However, the effect of the large-scale beach nourishment from 2010 to 2011 and the sustainability of nourished sand are unknown.

The aim of this study was to investigate the shoreline changes due to nourishment and clarify the effect of the sand recycling focusing on the sediment transport characteristics after the large-scale beach nourishment.

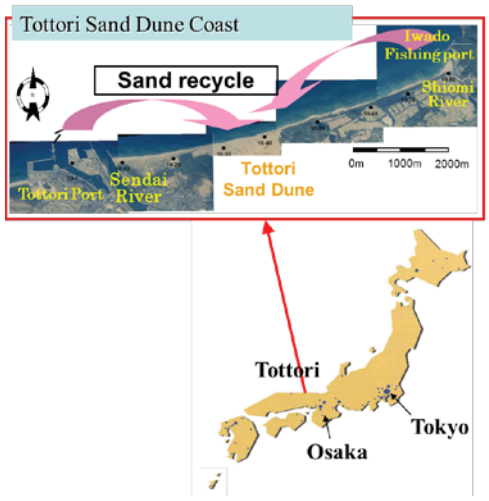

Figure 1. Location of the Tottori Sand Dune coast

DOI: 10.2112/SI75-139.1 received 15 October 2015; accepted in revision 15 January 2015.
*Corresponding author: shibutani.yoko@sankaku.tottori-u.ac.jp

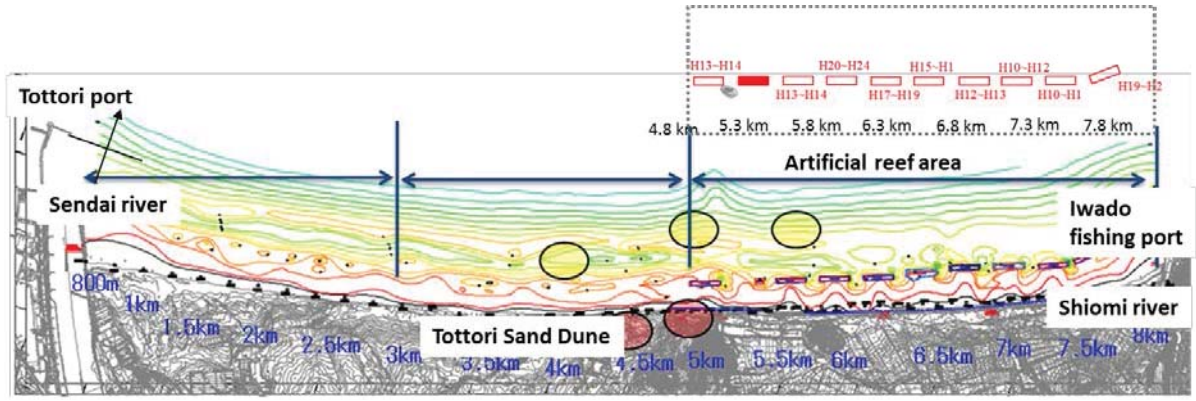

Figure 2. Outline of the Tottori Sand Dune coast and injection point of beach nourishment.

FIELD –Tottori Sand Dune Coast-

Tottori Sand Dune Coast is an 8-km long sandy beach, facing the Sea of Japan, as shown in Figure 2. Tottori Port and Sendai River are located in the western part of the coast. The Tottori Sand Dunes are the largest coast sand dunes in Japan located at the center of the coast. In addition, the Shiomi River and Iwado fishing port are located in the other end of the coast. Fluvial sediment is transported from the Sendai River and the origin of the longshore sediment transport is eastward. Since the 1960s, the river mouth and Tottori Port have been established and structures such as breakwater have been constructed. As a result, a part of the sand has been transported to the Tottori port, and the coast has been eroded especially in front of the Tottori Sand Dune.

To overcome these drawbacks, the sand recycle project was carried out since 2005. For this project, sand of several tens of thousands cubic meters from the Tottori Port and several thousands cubic meters from the Iwado fishing port and Shiomi River mouth has been dredged once a year. The dredged sand was transferred to the erosion area of the Tottori Sand Dune, and the sand was injected at the offshore and the backshore areas. The injection points, represented by circles, are shown in Figure 2. The sand volume of the beach nourishment is shown in Figure 3. A sand volume of 30,000 m^3/year is dredged from the Tottori port and Shiomi River mouth, and then, the sand is injected in the offshore and backshore area.

CHARACTERISTICS OF THE WAVE ADN TOPOGRAPHIC CHANGE

The significant wave height and period that was observed by NOWPHAS (presented by Nationwide Ocean Wave information network for Ports and HArbourS) at Tottori (35º33'N, 134º10'E) between 2004 and 2015 are shown in Figure 4. In addition, the seasonal wave height and direction are shown in Figure 5. From Figure 4, it was confirmed the seasonal change in the wave height and period. The waves from NNW in winter (from October to March) are higher, whereas those in summer (from April to September) are quiet; the main wave direction is NNE. Therefore, the Tottori Sand Dune Coast tends to repeat seasonal variation in the shoreline, which is eroded from autumn to winter and is restored from spring to summer due to the seasonal wave changes.

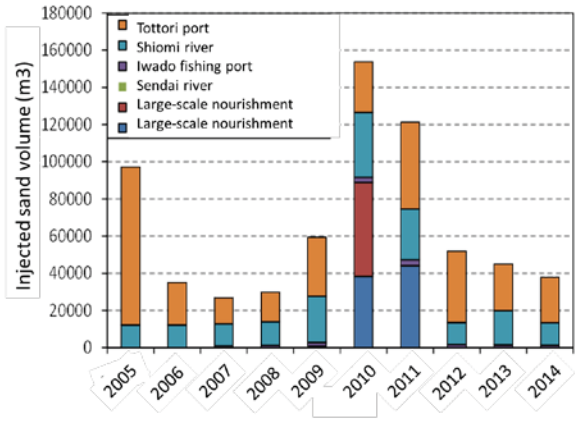

Figure 3. Sand volume of beach nourishment.

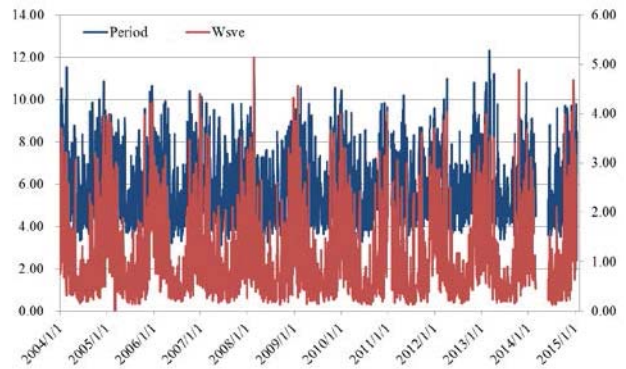

Figure 4. Significant wave height and period at the Tottori Sand Dune coast.

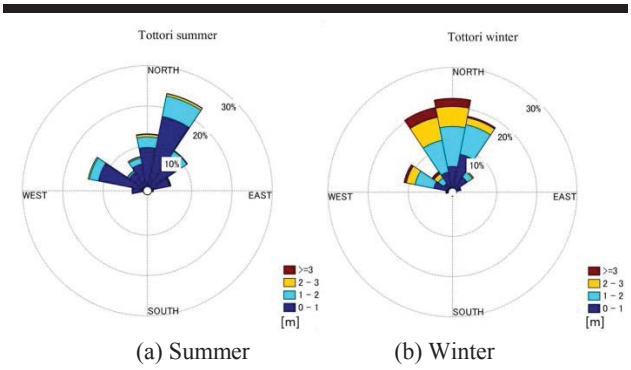

(a) Summer (b) Winter

Figure 5. Seasonal significant wave height and direction.

CHANGE OF SAND VOLUME AT TOTTORI SAND DUNE COAST

The sand volume of the Tottori Sand Dune Coast was estimated using the bottom sounding data, measured twice a year and observed at the Tottori prefecture. The data were interpolated to a 10-m grid, ±0.25 m less were excluded considering survey error. The grid data was created in the water depth range from 0 m to 11 m. Figure 6 shows the time variation of the sand volume at the Tottori Sand Dune coast. It was found that the movement of the sand volume is more active after the project, and the total sand volume in the Sand Dune coast are increasing. In addition, the sand volume increases rapidly during the large-scale nourishment, and then the sand volume return to before large-scale nourishment.

The dredging sand volume at the Tottori port is shown in Figure 7. The dredging volume in 2011 and 2012 is greater than that in other years. Therefore, a part of the injected sand is transported to the Tottori port. It is reported that a part of injected sand, which is dredging from the Tottori port, returns to the Tottori port (Shibutani *et al*., 2013). However, the deposited sand volume at the Tottori port is not in agreement with that of the injected sand due to large-scale nourishment. Therefore, we assume that some sand materials contribute to restore the shoreline, while other sand was flowing towards the exterior of the coast.

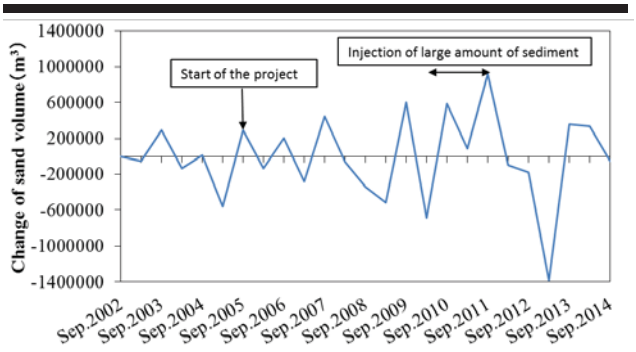

Figure 6. Time Variation of sand volume at the Tottori Sand Dune coast.

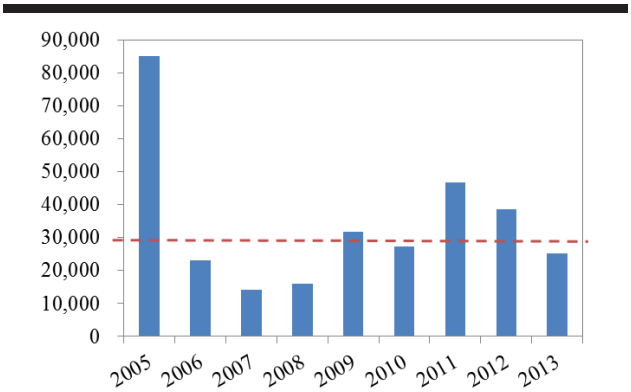

Figure 7. Dredging sand volume at the Tottori Port.

The change in the sand volume in each section is shown in Figure 8. The sections are divided into the following areas: 500–1000 m, 1000–2000 m, 2000–3000 m, 3000–5000 m (including the injection of the sand area), 5000–6000 m, 6000–7000 m, and 7000–7300 m in the alongshore direction. In the 500–2000 m area, the sand volume increases after the large-scale beach nourishment. However, the sand volume in the 2000–5000 m area was increased temporarily, but the sand volume has been decreased gradually. It is likely that the injected sand moved eastward, and the sand is accumulated at the Tottori port. The sand in the 5000–7300 m area is stabilized by the artificial reef.

SHORELINE CHANGE AT TOTTORI SAND DUNE COAST

The trends of shoreline change at the Tottori Sand Dune coast were investigated using shoreline survey data that were measured in the Tottori prefecture twice a year. The example of the trend of shoreline at the 2000-m point is shown in Figure 9. In order to clarify the shoreline trend, it was added to the approximate line. The slope of the approximate line was 0.77 m/year at the alongshore 2000-m point. Therefore, the shoreline shows deposition trend for the entire period. In addition, at each point of the alongshore, the shoreline change trends were evaluated, as shown in Figure 10. The red region represents the deposition trend and blue region represents the erosion trend. From Figure 10, the shoreline shows the deposition trend with the exception at some points. The erosion trend of the 6000-m point from 5000 m is considered to be caused by artificial reef, which is under construction. At other erosion trend points, shoreline change was very active during the large-scale beach nourishment, and it was difficult to determine the trend of the shoreline change.

Next, the details of the shoreline around the injection area (approximately in the range from 4000 m to 5000 m) had been investigated about twice a month from 2009 to 2015 using a GPS logger. The shoreline positions from the baseline every 20 m in the alongshore are calculated using the obtained GPS data. The shoreline change of January 2015 based on November 2009 is shown in Figure 11. From this figure, the shoreline change is

stable, and the result shows the same trend of the analysis using the data of the Tottori Prefecture.

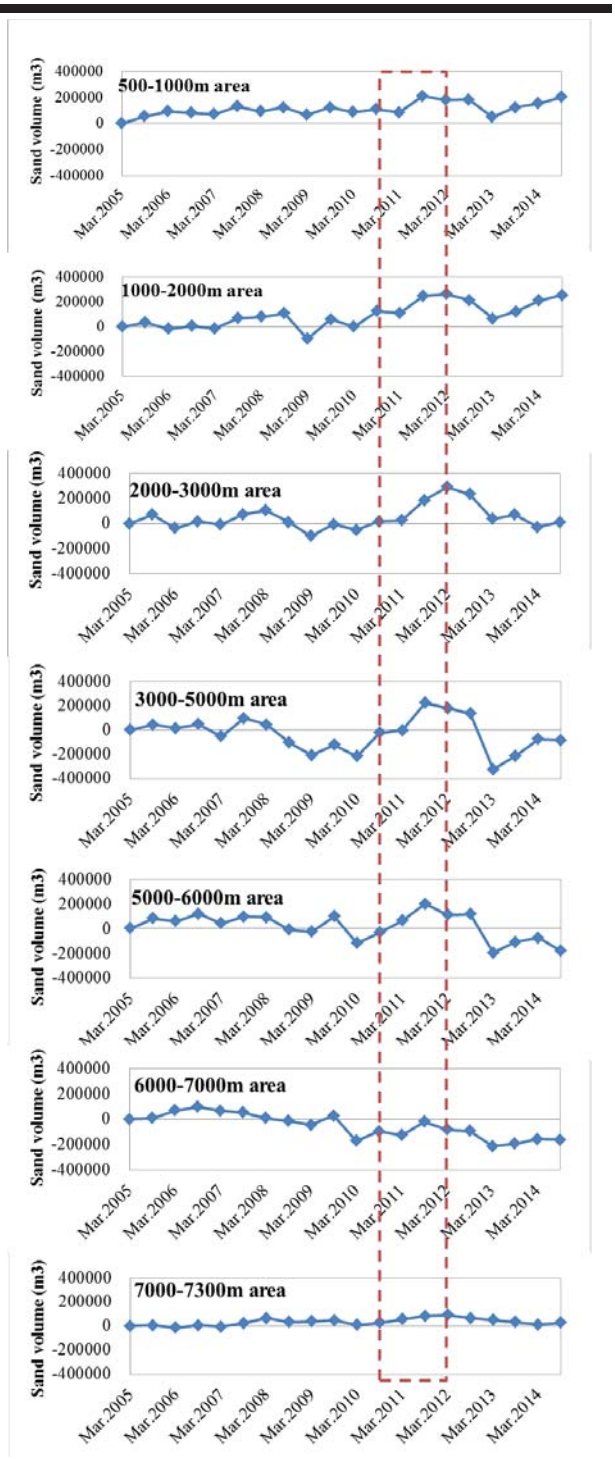

Figure 8. The sand volume in each section at the Tottori Sand Dune coast.

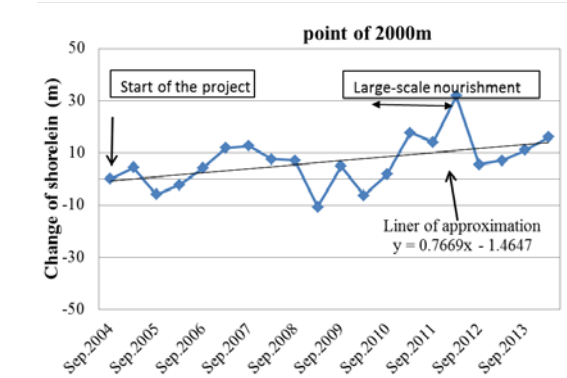

Figure 9. Dredging sand volume at Tottori port.

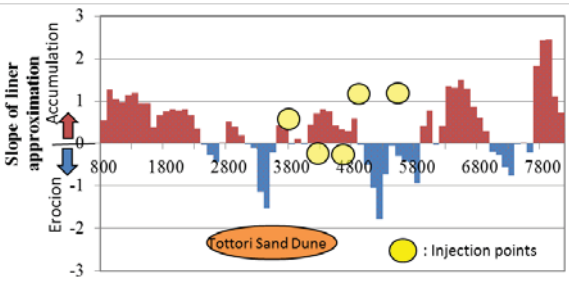

Figure 10. Shoreline change trend between 2004 and2014.

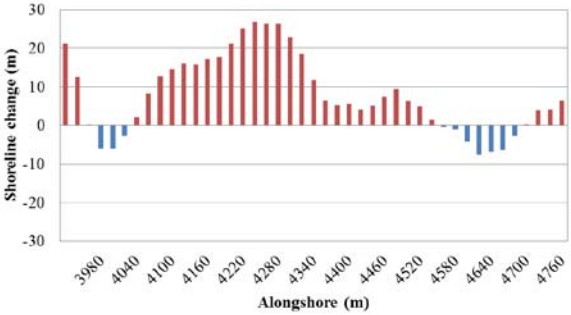

Figure 11. Shoreline change from November 2009 to January 2015.

The time variations of the shoreline change at each position are shown in Figure 12. The red square represents the large-scale beach nourishment period. The shorelines were moved offshore during the large-scale nourishment, and they are maintained after the large-scale beach nourishment was completed.

Finally, in order to examine the relationship between the shoreline change and the sand volume at the backshore during

large-scale beach nourishment, we were performed a cross-sectional survey.

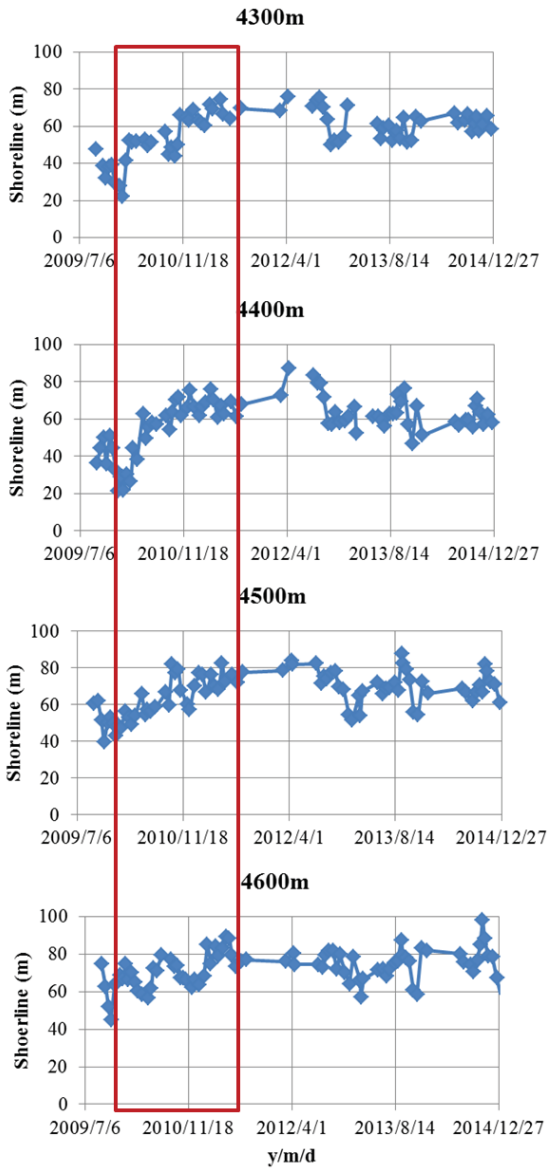

Figure 12. Time variation of the shoreline change of each position.

The sand volume and the change in the sand volume are shown in Table 1. The sand volume at the backshore has not reduced significantly, which indicates that the shoreline has been restored due to the large-scale nourishment and the sand volume has been maintained.

DISCUSSION

From the results of the change in the sand volume at the Tottori Sand Dune coast, it was found that the sand volume repeat the seasonal change with seasonal waves, and the sediment transport changed into very active and total volume of the sand are increasing during the large-scale nourishment. In addition, it was found that the dredging sand volume at the Tottori port was not in agreement with that of the injected sand. That indicates the injected sand of the large-scale nourishment contributes to restore the shoreline, and the shoreline will be maintained for a while.

Table 1. *The sand volume at the backshore and the change in the sand volume.*

	Sand volume (m^3)	Change in the sand volume (m^3)
Oct. 18 2013	17607	
Dec. 19 2013	16557	-1051
Jan. 16 2014	16245	-312

The shoreline change shows the advancing trend after the beach nourishment with the exception of the part which is approximately in the range from 4500 m to 5500 m. From the detail results of the erosion trend area, the shoreline recovers after the large-scale beach nourishment. This trend was especially noticeable near the injection point. Even after the large-scale beach nourishment is completed, a part of the injected sand is still present in the land. Therefore, it is expected that the sand filling in the land is effective to protect the beach from temporary erosion, such as extreme waves.

CONCLUSIONS

In this study, the movement of sand and the effect of the beach nourishment, especially considering the large-scale nourishment in 2010 and 2011, were investigated.

The total sand volume in the Sand Dune Coast is increasing. After the large-scale nourishment, the shoreline in the erosion area was restored, and then, the shoreline position was maintained. From these results, we observe that the large-scale nourishment was effective. In addition, it seems that the still remaining sand will contribute to erosion measures in the future. However, we are not aware for how long the effect will be followed. It is necessary to continue these monitoring, and to examine the grain size of the beach.

ACKNOWLEDGMENTS

We appreciate Tottori prefecture, Japan, for providing the field data.

LITERATURE CITED

Yasumoto, Y.; Uda T.; Matsubara, Y., and Hirano, G., 2007. Beach Erosion along Tottori Coast and Comprehensive Sediment Management. *Journal of Coastal Research*, 50, 82-87.

Tottori Prefecture, 2005. *The guidelines for comprehensive sediment management.* (Japanese)

Shibutani, T.; Matsubara, Y., and Kuroiwa, M., 2013. Effect of the coastal conservation due to beach nourishment of Tottori Sand Dune Coast, *Proceedings of the seventh International Conference on Asian and Pacific Coasts*, pp.79-84.

Journal of Coastal Research	SI	75	700-704	Coconut Creek, Florida	2016

An Extreme Event as a Game Changer in Coastal Erosion Management

Carlo Sorensen [†§*], Nils K. Dronen[‡], Per Knudsen[†], Jürgen Jensen[††], and Per Sorensen[§]

[†]Department of Geodesy
National Space Institute – DTU Space
Technical University of Denmark
Lyngby, Denmark

[‡]DHI
Horsholm, Denmark

[††]Research Institute for Water and Environment
University of Siegen
Siegen, Germany

[§]Department of Coast and Climate
Danish Coastal Authority
Lemvig, Denmark

www.cerf-jcr.org

www.JCRonline.org

ABSTRACT

Sorensen, C.; Dronen, N.K.; Knudsen, P.; Jensen, J., and Sorensen, P., 2016. An extreme event as a game changer in coastal erosion management. *In:* Vila-Concejo, A.; Bruce, E.; Kennedy, D.M., and McCarroll, R.J. (eds.), *Proceedings of the 14th International Coastal Symposium* (Sydney, Australia). *Journal of Coastal Research*, Special Issue, No. 75, pp. 700-704. Coconut Creek (Florida), ISSN 0749-0208.

The construction of hard protection measures along the northeast coast of Sealand, Denmark, has gradually led to profile steepening, loss of beaches, and increased storm erosion. Although the problem has been addressed for decades no common solutions have been implemented yet. However, the impact of cyclone Xaver in December 2013 with severe coastal erosion led to collaboration between the involved municipalities to work on a coherent solution for the entire coastline that involves sand nourishments, renovation and optimization of hard protection structures, and the restoration of recreational values. We present a concept of 'erosion pressure' as a simple method to estimate potential chronic (longshore) and acute (cross-shore) erosion on protected coasts. The erosion pressure estimates are reliable at the investigated coast and the concept has proved useful for dissemination to stakeholders about coastal dynamics.

ADDITIONAL INDEX WORDS: *Extreme events, sand nourishments, long-term strategy, natural erosion.*

INTRODUCTION

Major coastal erosion events challenge coastal engineers in opting for the best management solutions. Current scientific knowledge and our predictive abilities about the nature of extremes and of shoreline processes may be sufficient to respond. Factors like legislation and governance, politics, economy, ecology, history, as well as a potential complexity in landowners and their organizational form, opinions and needs must also be accounted for, however. The dissemination about coastal dynamics to all stakeholders is an everlasting task, too.

A large part of the northeast coast of the island of Sealand, Denmark, experiences cliff and beach erosion. The story is classic: The construction of hard (passive) protection measures transfers the erosion to neighboring stretches and leads to more constructions *etc.* and gradually diminishes the natural cliff erosion and depletes the coastal profile of sand. The problem has been obvious for decades but with very few counteractive achievements despite several efforts to advocate for sand nourishments and beach restoration over the past 35 years. On the contrary, specific storm events have led to an urge from landowners for more hard structures and to the abolishment of any long-term strategy for larger stretches of coast. Coastal protection in Denmark works on a "those who benefit must pay" principle. Individual house owners, or, small house owner associations are in charge of and must pay for protection and discussions have been on economy rather than on methods.

Perhaps the game is about to change in favor of more sound management practices due to severe erosion along the Sealand coastline from cyclone Xaver on 5-6th December 2013. We present an 'erosion pressure' model used for evaluating shoreline challenges and dissemination to the public. We also provide a brief overview of and discuss the shift towards more active protection solutions and visions for the entire coastline across municipality borders.

Background

The approximately 65 km long coast of NE Sealand (Figure 1) predominantly consists of soft cliffs with higher parts (up to 40 m) in glacial deposits varying with low postglacial cliffs, beach ridges and dunes. Accordingly, sections of wide abrasion platforms in glaciogenic sediments, often covered with only a thin veneer of sand, interchange with marine, sandy sections with more pronounced offshore bars (FU, 1978). The coast is

DOI: 10.2112/SI75-140.1 received 15 October 2015; accepted in revision 15 January 2015.
*Corresponding author: carlos@space.dtu.dk

moderately exposed towards W and NW. Storms may push water in from the North Sea and raise the general Kattegat water level.

Figure 1. Denmark (inserted) and the northeast Sealand coast with towns, *municipalities*, and positions for wave hindcasts (35, 36), wave (ADCP) and water level measurements (TG) referred to in the text.

Tidal range is 0.2-0.4 m and annual exceedance water level is 1.08 m DVR90 at Hornbaek (0 DVR90 ≈ MSL in 1990).

Large parts of the coast experienced Aeolian sand drift in the 16-18th centuries. Around 1880 almost all larger stones were removed from the coastal area for construction works elsewhere which increased the wave impact and erosion rates (Bech, 1909). Harbors and offshore breakwaters were built at several locations from 1912 onwards and led to leeside erosion and to the construction of groins. As the coastline became increasingly more popular from the 1920s onwards, holiday houses and permanent residences were built at vulnerable clifftop locations and were accompanied by passive protection measures in the form of groins, T-groins, seawalls *etc.* (FU, 1978). In many places this practice has continued until today (Figure 2).

Some protection measures in the mid-20th century were designed by the Danish Coastal Authority (DCA) and by engineering companies according to the standards, but many were erected by individual landowners. By the end of the 1970s the coast and beaches were 'in a miserable condition' (FU, 1978), and the coastal municipalities and the former county (Figure 3) initiated efforts to coordinate and reorganize the entire strategy for coastal protection (FU, 1978; FU, 1984). An ambitious 10 year plan to renovate and optimize existing coastal protection together with sand nourishment schemes was presented in 1989 which also included a financial plan (FU, 1989; FC, 1991). A few successful projects were carried out, but budgets were cut and the plan lost momentum (FC, 2001).

In 2007, the newly established Gribskov Municipality made an effort to revitalize a common strategy along the coast, but the two other municipalities were reluctant to participate. A plan for the Gribskov Municipality coastline (COWI, 2009) that included financial contributions from landowners up to 1 km inland was rejected by the politicians in 2011 following a public vote. A national coastal protection strategy (DCA, 2011) and guidelines for coastal climate adaptation (Sorensen and Sorensen, 2012) address the need for more holistic and optimized coastal management solutions. DCA has been restrictive in permitting passive measures and has continuously argued in favor of sand nourishments along the coast of NE Sealand.

Figure 2. NE Sealand coastline with older as well as and new houses on the clifftop (Photo: DCA/Hunderup Aerial Photo).

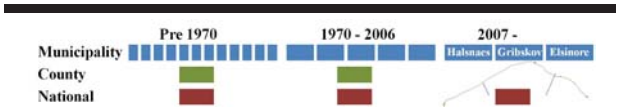

Figure 3. Governance structure. The change in composition of local, regional and national bodies over time along the NE Sealand coast.

METHODS

Historic shoreline changes, *e.g.* along the NE Sealand coast (FU, 1984; Kabuth, Kroon & Pedersen, 2014), do not reflect the autonomous erosion due to the large number of hard structures. An 'erosion pressure' (EP) concept is developed to describe and map the potential erosion rather than calculating the actual erosion rates and sediment loss. The focus is on simple and easily applicable methods and rough estimates rather than on detailed numerical solutions. EP is divided into potential 'chronic' and 'acute' erosion, respectively.

Chronic erosion accounts for the continuous alongshore loss (or gain) of sand in the profile due to waves and littoral currents. A longshore transport equation index is derived from coastline orientation and wave conditions using DHI's Littoral Drift model (Fredsoe and Deigaard, 1992) and scaled to reflect the expected transport (DHI, 2013 p.8). Hourly time series of offshore wave conditions (significant wave height and period, and direction) at selected points are simulated from wind data (1994-2011, 18 years) in MIKE 21SW (DHI, 2012). For a stretch of coast two sets of data area are used in a weighed form. Calculations of the observed transport from shoreline changes are used for validation in this study.

Acute erosion describes the cross-shore transport from the inner profile to the outer during storm events. It acknowledges that cliff erosion from waves and extreme water levels may be infrequent. The cross-shore transport is generally more difficult to calculate and it is estimated from the correlation between the simulated wave heights and measured water levels from tide gauges. Here, the cumulative frequency of correlations in the directional spectra of incoming waves and water levels (in 45° intervals) is used to scale the acute EP (DHI, 2013).

Tide gauge records from Hornbaek, 1890-2014 (DMI, 2014) and recorded offshore waves at 7 m depth off the coast (ADCP – 2 hour intervals) are included to describe wave and water level conditions during Xaver. An update of the current extreme water level statistics to include Xaver water levels is calculated based on Sorensen, Madsen and Knudsen (2013).

RESULTS

In the calculations of chronic erosion, the coastline is divided into two sections; Hundested-Gilleleje (Figure 4) and Gilleleje-Elsinore (not shown). Based on the wave hindcasts and coastline orientation a point of zero potential longshore transport is identified immediately east of Hundested. An overall trend of increasing potential longshore transport is observed towards Gilleleje due to the coastline orientation and a more severe wave climate. Local shifts in coastline orientation cause deviations from the trend. Coastline advances are related to harbor and offshore seawall constructions and large erosion rates are often found on the downdrift side of these. A good correlation to the observed longshore transport based on the 1890-2005 shoreline changes is found and provides a good opportunity to scale the transport index, q_*, to reflect the expected transport rates; refer below.

A strong correlation exists between wave heights and water levels at Gilleleje (Figure 5). Due to the relatively harsh wave climate the acute erosion potential is classified as 'large'. As the erosion pressure model is designed for use along the entire Danish coastline both the chronic and the acute erosion pressure potential have been scaled and categorized to reflect national conditions (Figure 6). Here, the yearly 12 hour maximum wave height (H_s_12) is used to separate categories of acute erosion. Also shown are the scaled potential and observed transport rates.

Some 'jumps' in transport rates are observed and may partly be due to limitations in the applied methods. The erosion is up to 30 $m^3/m/y$ and the potential longshore transport is calculated to a maximum of 65.000 m^3/y. Simple sketches are produced to assist the dissemination of the acute and chronic erosion pressure concept and the causes of erosion (DHI and Hasloev & Kjaersgaard, 2015), Figure 7.

The water level during Xaver reached 1.96 m DVR90 at Hornbaek which is the highest recorded (1890-2015) and corresponds to a 1000 year event according to Sorensen, Madsen and Knudsen (2013). An update that includes Xaver increases a 100 year return level from 1.68 to 1.76 m DVR90 (de-trended). Furthermore, the water level exceeded 1.5 m for more than 18 hours, Figure 8. Not since 1922 has the coast experienced any comparable event in terms of water level and duration. Unfortunately there are no registrations around the peak of the 18 December 1921 event. The tide gauge record also lack data from a 26 December 1902 storm where extreme water levels were measured (*e.g.* 3rd ranked water level in Copenhagen, 1890-2014) and widespread erosion was reported (Bech, 1909). Peak significant wave heights in excess of 3 m and peak wave periods of 10 s (not shown) were recorded off the coast during Xaver. This corresponds well to the modeled numbers for extreme conditions.

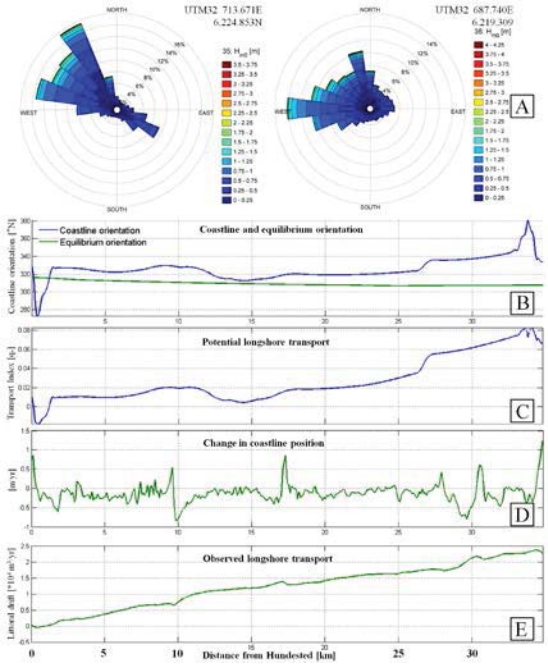

Figure 4. Modeled wave conditions off the coast (refer Figure 1 for positions) (A), coastline orientation and equilibrium orientation (B), calculated potential longshore transport (C), rate of change in coastline position (c. 1890-2005) (D), and observed longshore transport (E) for the Hundested to Gilleleje coastline.

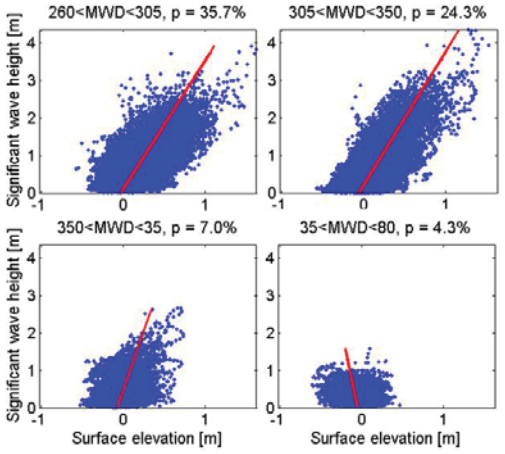

Figure 5. Correlation between water levels (measured) and significant wave heights (simulated) in 45° intervals off Gilleleje used to assess acute erosion pressure.

DISCUSSION

The concept of erosion pressure is a little hypothetical, but it serves an important purpose in the sense that it describes how much pressure there is on the protected stretches. This information may be useful in situations where consideration is given to change a coastal protection strategy, *e.g.* by replacing the hard sea defenses with sand nourishments, and it provides a framework for addressing the potential erosion along a coast. The erosion pressure model may be developed further by

including more and updated wave climate and water level data to better resolve and predict the spatial variation.

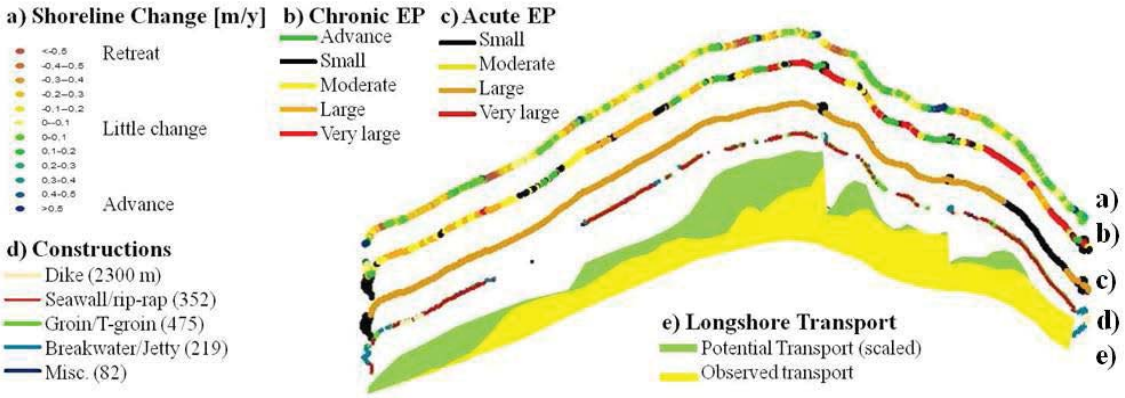

Figure 6. Shoreline change (a), chronic (b) and acute (c) erosion pressure; hard protection measures with number of constructions shown in legend (d), and a sketch of the observed versus the scaled potential longshore transport (e) for the NE Sealand coast, Denmark.

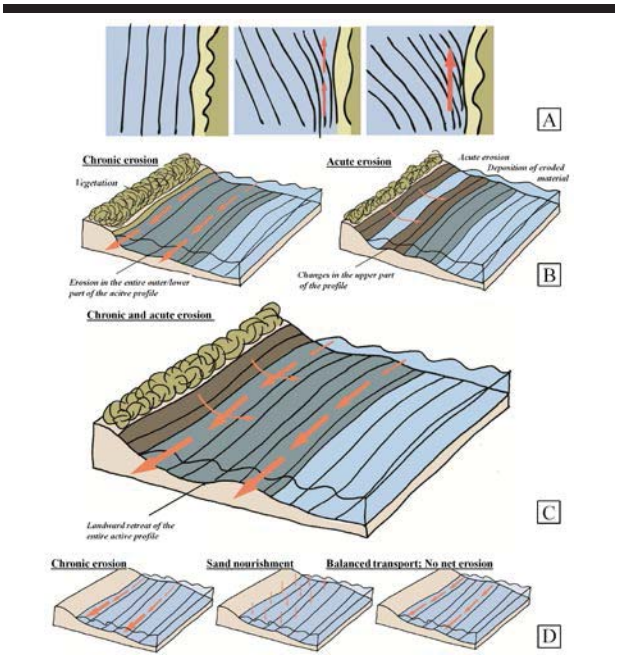

Figure 7. Sketches of littoral transport (A), chronic and acute erosion (B), their combined effects (C), and the effect of sand nourishments to balance out chronic erosion (D) used for stakeholder dissemination.

Although the acute and chronic erosion are combined over time their different causes are fairly easy to disseminate. The cumulative deficit of sand in the profile over the past 30-40 years due to chronic erosion can be communicated. The acute erosion is the visible erosion from storm events. Acute erosion was experienced along the entire coastline from Xaver and at some locations it exceeded the total erosion in the past 100 years. In some locations there is no need of passive

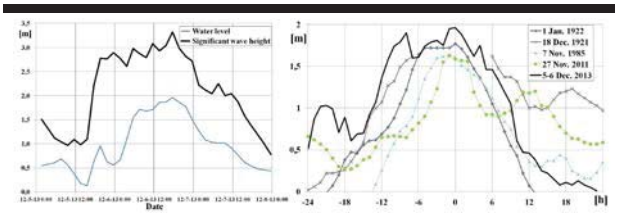

Figure 8. Measured significant wave heights and water levels at 7 m water depth during Xaver (A) and water levels (peak at 0 hrs.) at Hornbaek (solid black) (B) together with 'top-4' extreme water levels previous to this event.

protection measures as no properties are in imminent danger, whereas at other locations the pressure is critical regarding both the acute and chronic erosion, respectively. Along the stretches with the highest erosion pressure a combination of passive and active measures is needed. For the NE Sealand coast the methods provide realistic results, and the erosion pressure concept is included in the current conceptual project design for the coast (DHI and Hasloev & Kjaersgaard, 2015; Hasloev & Kjaersgaard, 2014).

It is the lack of natural sources for sediment supply and the numerous hard structures along the coast that is a problem and not natural erosion itself. This lack of resilience towards erosion was very clearly exposed during Xaver. Contrary to past events the widespread erosion yielded the opportunity to forward long-term visions for coastal management and to bring in arguments for sound solutions and more resilient coasts. Here, the erosion pressure concept proved useful to address in a very simple manner that the economic impact from erosion will only increase in the future if no coordinated measures are implemented. The event has been a game changer inasmuch as the three municipalities now are working together to implement and co-finance a common solution for the NE Sealand coast (Municipality Mayors, 2015). Naturally, landowners away from the coast have been reluctant to financially support passive

solutions where the only result is that beaches are lost. On the other hand, the municipalities and the coastal landowners with passive (and often massive) protection measures must acknowledge the cumulated sand deficit and that very large initial (> 1 million m^3) and repeated sand nourishments are needed to restore the sediment balance. This also includes a reassurance to landowners that in longer time perspective sand nourishments (in some places in combination with passive measures and cliff slope stabilization) will safeguard their real estate values. Arguments for the municipality engagement lie not solely within protection against storms and climate impact but have become integrated in the overall economic development visions and planning for the future. This includes restoration of natural values to boost tourism and attract citizens, and it requires involvement and input from various municipal departments, private companies, and the public to bring out all potential synergies. The visionary but very concrete prospect for the future (Hasloev & Kjaersgaard, 2014) acknowledges previous efforts to protect the NE Sealand coast. Hopefully this time the municipalities, the landowners, and other stakeholders will succeed in the implementation of a sound management concept *anno* 2016. Xaver may thus also become a game changer in bringing in science and interdisciplinary approaches to the Danish coastal erosion management.

The Danish Coastal Protection Act has proven unsuccessful in promoting and implementing active solutions to deal with chronic erosion but the law may be up for revision. An ongoing coastal analysis will by 2016 provide a national overview of present and potential future erosion and flooding challenges, and it will also address financial issues regarding coastal protection. This hopefully will lead to a political debate of how we as a society proceed with coastal challenges that involves the future national engagement. Discussions about retreat strategies in some areas to allow for natural sediment supply may also be relevant to include.

CONCLUSIONS

The concept of erosion pressure and a division into potential chronic and potential acute erosion is a simple method to estimate the erosion pressure on a coast protected with hard structures. Dissemination of the concept has proven successful in promoting sand nourishments along the northeast coast of Sealand, Denmark. After many years of more or less unsuccessful attempts, the impact of cyclone Xaver in December 2013 have led to collaboration across municipality borders to implement a coherent solution for the entire coastline that involves sand nourishments, optimization and renovation of existing passive protection measures, and restoration of recreational values.

ACKNOWLEDGMENTS

The authors wish to thank and acknowledge our colleagues Karsten Mangor and Asger Bendix Hansen from DHI and Matthew Earnshaw from DCA for their contributions to the erosion pressure concept and methods development, and mapping. Eva Sara Rasmussen, Fernando Elias and Dan Hasloev, Hasloev and Kjaersgaard Architects I/S, are acknowledged for a fruitful collaboration that includes the simple and beautiful sketches of coastal dynamics. An anonymous reviewer is acknowledged for suggestions to improve the final manuscript. Parts of this work was carried out under the COADAPT-project (Grant no. 09-066869) supported by the Danish Council for Strategic Research (DSF). Co-funding for an Industrial PhD scholarship (Grant no. 1355-00193) is provided by Innovation Fund Denmark.

LITERATURE CITED

Bech, C., 1909. Om Sandvandring, Kystbeskyttelse og Vandbygningsarbejder paa Sjaellands Nordkyst. *Ingenioeren*, 29, 260-268.

DCA, 2011. *Kystbeskyttelsesstrategi, en strategisk indsats for smukkere kyster*. Danish Coastal Authority (DCA). 30p.

DHI, 2012. *Boelgeklima for 40 lokaliteter i danske farvande.* Report by DHI for the Danish Coastal Authority. 57p.

DHI, 2013. *Erosionsatlas. Metodeudvikling og Pilotprojekt for Sjaellands Nordkyst*. Report by DHI for the Danish Coastal Authority. 37p.

DHI and Hasloev & Kjaersgaard, 2015. *Kystdynamik og kystbeskyttelse.* Report by DHI and Hasloev & Kjaersgaard Architects for the Danish Coastal Authority. 109p.

DMI, 2014. *Tide gauge data from Hornbaek, 1890-2014*. Danish Meteorological Institute (DMI).

FC, 1989. *Nordkysten. Regionplantillaeg 6 til Regionplan 1989.* Frederiksborg County (FC). 20p.

FC, 1991. *Fra Sten- til Sandstrand*. Frederiksborg County (FC). John Staehr Video Production, Movie, 22 minutes.

FC, 2001. *Frederiksborg Amt, 2001. Regionplan 2001 for Frederiksborg Amt*. Hovedstadens Udviklingsraad. 211p.

Fredsoe, J. and Deigaard, R., 1992. *The Mechanics of Coastal Sediment Transport*. Singapore: World Scientific. 369p.

FU, 1978. *Nordkysten; Kystpleje og kystsikring. Basis Report*. Hostrup-Schultz & Sorensen, and DHI for Faellesudvalget for kystpleje og kystsikring paa Nordkysten (FU). 183p.

FU, 1984. *Nordkysten. Basis Report*. Hostrup-Schultz & Sorensen, and DHI for Faellesudvalget for kystpleje og kystsikring paa Nordkysten (FU). 183p.

FU, 1989. *Nordkysten. Samordnet program for kystpleje og Kystbeskyttelse*. Faellesudvalget for kystpleje og kystsikring paa Nordkysten (FU). October 1989. 42p.

Kabuth, A.K., Kroon, A., and Pedersen, J.B.T., 2014. Multidecadal shoreline changes in Denmark. *Journal of Coastal Research*, 30(4), 714-728.

Mertz, E.L., 1924. Oversigt over de sen- og postglaciale niveauforandringer i Danmark, 1924. *Danmarks Geologiske Undersoegelse*, II Rk., 41. 49p.

Hasloev & Kjaersgaard, 2014. *Nordkystens fremtid; Skitseprojekt*. Hasloev & Kjaersgaard Architects in collaboration with Halsnaes, Gribskov, and Elsinore Municipalities, and individual contributors. 91p.

Municipality Mayors, 2015. Mayors of Elsinore, Gribskov, and Halsnaes Municipalities meeting, 25 September 2015.

COWI, 2009. *Sandfodring paa Nordkysten, Skitseprojekt*. COWI, Inc., September 2009.

Sorensen, C., Madsen, H.T., and Knudsen, S.B., 2013. *Hojvandsstatistikker 2012*. Danish Coastal Authority. 158p.

Sorensen, P. and Sorensen, C., 2012. *Guidelines for klimatil-pasning i kystomraader*. Danish Coastal Authority. 43p.

Journal of Coastal Research	SI	75	705-709	Coconut Creek, Florida	2016

Estuarine Beaches of the Amazon coast: Environmental and Recreational Characterization

Rosigleyse C. de Sousa[†*], Luci C.C. Pereira[†], and José A. Jiménez[‡]

[†]Instituto de Estudos Costeiros,
Universidade Federal do Pará,
Bragança, 68600-000, Brazil.

[‡]Universitat Politécnica de Catalunya, Barcelona Tech, Spain. Laboratori d'Enginyeria Maritima, C/ Jordi Girona 1-3, Campus Nord, Ed. D1, 08034 Barcelona, Spain.

www.cerf-jcr.org

www.JCRonline.org

ABSTRACT

Sousa, R.C.; Pereira, L.C.C., and Jiménez, J.A., 2016. Estuarine beaches of the Amazon coast: environmental and recreational characterization. *In:* Vila-Concejo, A.; Bruce, E.; Kennedy, D.M., and McCarroll, R.J. (eds.), *Proceedings of the 14th International Coastal Symposium* (Sydney, Australia). *Journal of Coastal Research*, Special Issue, No. 75, pp. 705-709. Coconut Creek (Florida), ISSN 0749-0208.

The Amazon coast is rich in natural resources, with highly valued natural landscapes and ecological systems. These environments include estuarine beaches, which are important areas for recreational activities. The present study provides an environmental and recreational diagnosis of three of these estuarine beaches on the Amazon coast (Colares, Marudá, and Murubira). The study was conducted in July, 2012, 2013 and 2015. An set of variables was assessed: (i) physical variables (hydrodynamics), (ii) microbiological variables (thermotolerant coliform concentrations), (iii) recreational actvities and (iv) the spatial distribution of infrastructure and services. The results indicate that these beaches are moderately hydrodynamic, with tidal ranges of 3–5 m and wave heights of up to 1 m, which are attractive features for beachgoers. The lack of adequate urban planning has caused serious social and environmental problems (e.g. erosion, destruction of dunes and mangroves, inadequate disposal of solid waste). The quality of the water has been affected by the lack of an adequate public sanitation system and the presence of numerous illegal sewage outlets on these beaches, which contribute to the high thermotolerant coliform concentrations recorded. The following measures were recommended: (i) removal of sewage outlets; (ii) collection of garbage from the beach at the end of each day's recreation; (iii) the provision of trash cans along the coastline, and (v) the installation of public toilets. The results of the study emphasize the urgent need for the regulation and planning of the use of the coastal environments of the Amazon region.

ADDITIONAL INDEX WORDS: *Recreational activities, fecal coliforms, Amazon littoral.*

INTRODUCTION

Coastal zones are transitional areas located between the continent and the ocean, encompasing high levels of biodiversity and include some of the most productive and vulnerable ecosystems on Earth (Yunis, 2001). This, together with their geographic location, places coastal zones under increasing human pressure, in particular from urbanization (Yunis, 2001).

About 80% of all tourism takes place in coastal areas, and beaches are among the most important destinations. The tourism industry can generate positive and negative effects on natural and social-economic conditions (Castellani *et al*., 2007). Some of the most relevant issues involving tourism and coastal development are related to the large numbers of tourists, particularly in the summer, and the lack of adequate facilities, as well as the loss of natural landscapes and biodiversity (OSPAR, 2008). Specific planning and measures can increase the benefits from tourism, by minimizing or preventing the negative impacts, but unfortunately, few coastal communities have effective mangement strategies, especially in the developing world.

The Amazon coast is rich in natural resources, including landscapes, ecosystems and biodiversity. These environments include estuarine beaches, which are important areas for recreational activities (Sousa *et al*., 2014). In recent decades, the construction of access roads has resulted in an increase in the use of local beaches for recreational activities, which have become one of the principal sources of income for these areas, primarily during vacation periods (Sousa *et al.*, 2014).

Due to the extensive areas of mangrove on the Amazon coast, tourism on estuarine beaches, such as those found in the Brazilian state of Pará, tend to be more isolated from the larger urban centers, in contrast with many ocean beaches. This also means that these beaches are less well known in terms of their social and economic conflicts and natural conditions.

Tourism in the Amazon region is related primarily to the visitation of the rainforest, although we believe that greater incentives are required from local authorities to encourage investment in tourism in the coastal zone. Given this, the aim of the present study was to investigate the natural and socioeconomic features of three of the region's recreactional estuarine beaches (Colares, Marudá, and Murubira). The findings will contribute to the development of coastal management programs that promote sustainable tourism in these ecologically sensitive areas, at both national and international levels.

DOI: 10.2112/SI75-141.1 received 15 October 2015; accepted in revision 15 January 2015.
*Corresponding author: rosigleyse@yahoo.com.br

STUDY AREA

The study beaches (Colares, Marudá, and Murubira) are located on the Amazon coast in the Brazilian state of Pará (Figure 1). The shoreline of these estuarine beaches is located within a mangrove-dominated fluvial-marine ecosystem characterized by moderate-energy hydrodynamics influenced by macro- (Marudá) or mesotides (Murubira and Colares) and waves of low to moderate energy. This coast has been used traditionally for fishing and leisure activities. Amazon beaches are visited most intensively during the month of July and during public holiday periods primarily during the second half of the year, coinciding with the dry season. During the first half of the year, the high rainfall rates (typically above 2000 mm) affect tourism on the whole of the Amazon coast.

Colares Island is a rural site located in the Coastal Atlantic sector, 96 km from the state capital, Belém. The island is separated from the continent by the Guajará-Mirim River and the Laura tidal creek, in the northeastern portion of Marajó Bay, which is formed by the Pará River. Marudá beach is a semi-urban beach, which is also located in the Coastal Atlantic sector, 160 km from Belém, at the mouth of the Marapanim estuary. This is the most exposed beach. The semi-urban Murubira beach is located on Mosqueiro Island in the Continental Estuarine sector, 72 km from Belém. This island is actually located within the Belém municipal administrative district, and includes a number of sites of considerable historic interest and relevance for local tourism. The island is located on the right margin of the Pará River (Marajó Bay), and is separated from the continent by the Maguari and Marinhas creeks, and by Sol Bay (El Robrini *et al*., 2006).

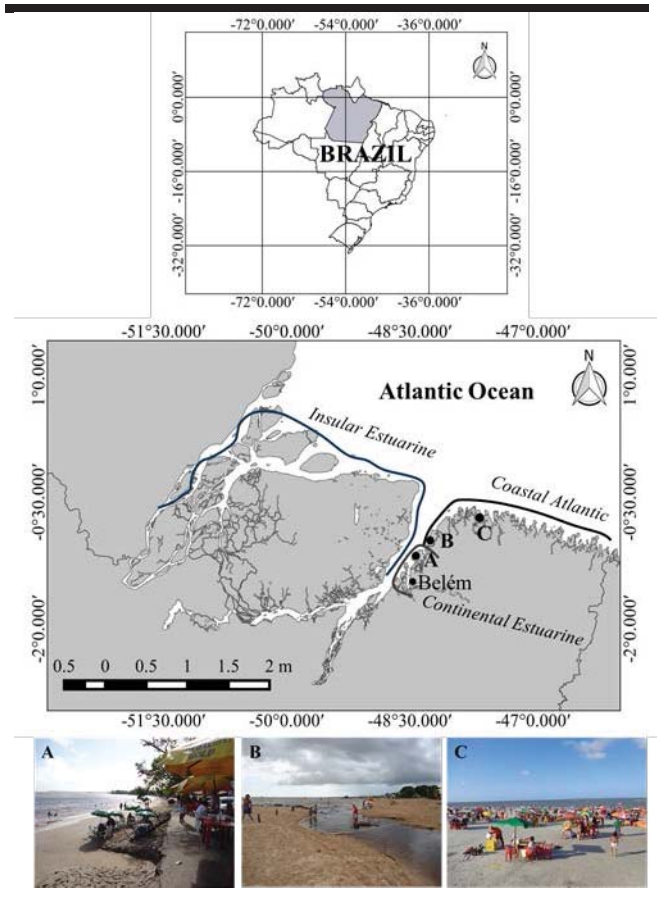

Figure 1. Study area. Brazil (Above) and the coast of Pará state (Medium) with its primary divisions, showing the study sites Murubira Beach (A), Colares Beach (B) and Marudá Beach (C).

METHODS

This study was based on the qualitative and quantitative assessment of specific features of the environmental conditions of each beach and the services available locally. Each site was surveyed on a Sunday (peak visitation) during three weeks in July 2012, 2013 and 2015.

Recreational use, territorial occupation and the available services and infrastructure were mapped in relation to the coastline using a Garmin Etrex GPS. Complementary data were collected using a check-list and direct observation, and photographs were taken of specific features. Hydrodynamic data (tide and waves) were collected in July 2015 with a tide and wave recorder (TWR 2050), with data being logged every 10 minutes during 13 hours.

The morphology of each beach was characterized along a topographic profile (using the Stadia method, as perfected by Birkemeier, 1981) established perpendicular to the coastline during the spring (Colares) or neap tide (Marudá and Murubira) in July 2015. These profiles stretched from the dunes, at Colares, or the promenade (Marudá and Murubira) to a depth of approximately 1.0 m at low tide.

Surface water samples were collected every three hours between 07:00 h and 19:00 h (July 2012 and 2013). This total of 10 samples for each beach were used to determine thermotolerant coliform levels. Thermotolerant coliform levels were also analyzed in water samples collected in the Sonrisal stream on Colares beach (4 samples). The thermotolerant coliform cocentrations were determined by the multiple tubes method, following the procedures described by the American Public Health Association (2005).

RESULTS

Estuarine beaches of the Amazon coast are visited by residents, day visitors and tourists. The results of the present study show clearly how the natural and facility features of a beach can influence their patterns of recreational use, and the impacts of these activities.

Natural features and recreational use

The estuarine beaches of the Amazon coast may be found in locations that are more or less sheltered from the action of waves. In the present study, the most sheltered beaches (Murubira and Colares) had maximum wave heights (H_{max}) of 1.1 m and mesotidal conditions, with tidal ranges of less than 4 m (Figure 2). The less sheltered Marudá beach is exposed to macrotides and wave heights (H_{max}) of up to 1.5 m (Figure 2). On all these beaches, but principally the most sheltered ones, incoming waves are modulated by submerged sandbanks, and wave heights can be reduced practically to zero during low tide.

In the more densely-populated areas, that is, the semi-urban beaches at Marudá and Murubira, the backshore zone is

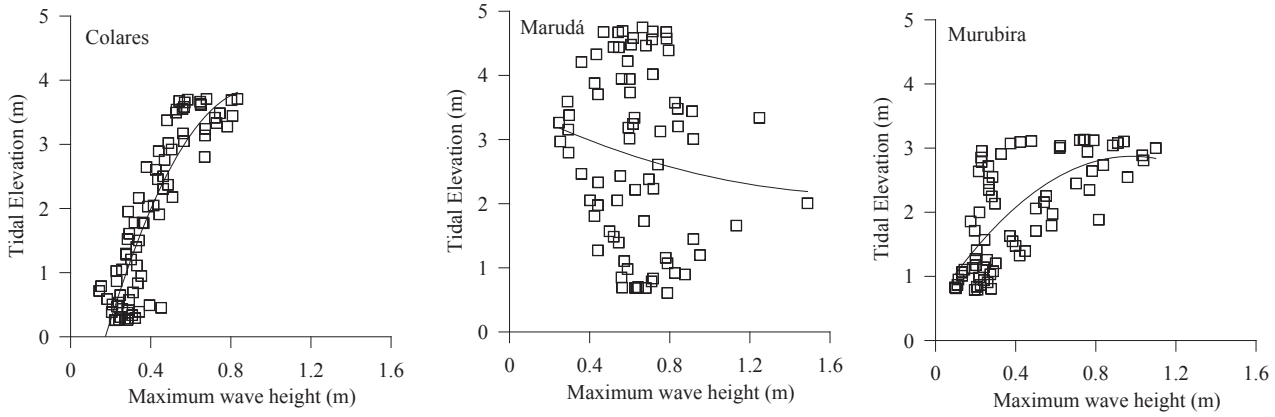

Figure 2. Maximum wave heights *vs.* tidal range.

normally limited in extent or non-existent, limiting the use of this zone during the high tide. Where there is little or no occupation of the backshore, by contrast, as seen on rural beaches such as that at Colares, this zone may be well-preserved, permitting the use of this zone for recreational activities, even during the high tide.

The use of the intertidal zone for activities such as sunbathing, football, beach tennis and volleyball, may also be limited in the areas most protected from wave action due to the presence of muddy sediments near the water's edge, as observed at Colares. On these beaches, recreational activites are typically practiced during the ebb tide, in the first 100 m between the lower limit of the backshore and the intertidal zone. On the more exposed beaches, such as Marudá, the intertidal zone is formed by channels and sandbanks, which hamper bathing due to the long distances between the backshore and the water's edge during the ebb and low tides. The presence of tidal creeks (Marudá) and rocky outcrops (Murubira and Colares) in the intertidal zone may also be considered to be potential risk factors for bathers and swimmers.

On the more sheltered beaches (i.e., Murubira), the steep slope found between the intertidal zone and the foreshore (Figure 3) may be considered to be a considerable potential danger for local bathers. Other danger include the presence of animals such as stingrays, which are common on the more sheltered beaches (Colares), and may provoke extreme pain in bathers that accidently stand on the animal's stinging tail.

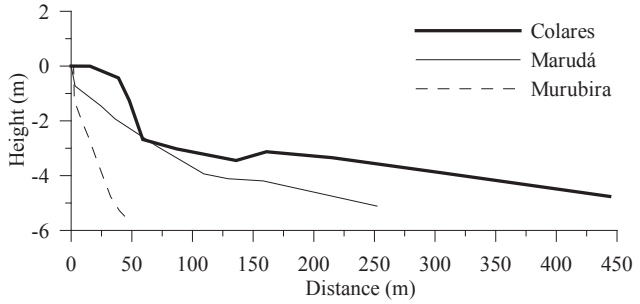

Figure 3. Profiles of the study beaches.

Services, infrastructure features and recreational use

The water zone is not zoned for activities on any of the beaches, so the same spaced is shared by bathers, surfers and windsurfers, and jet-skis and other vessels. This represents a significant risk of accidents for children and adults.

In addition to their occupation of this space during the day, holidaymakers may also be numerous at the end of the day and in the evening. On Marudá bech, the attractions include artisanal markets and shows, while on Murubira, young adults meet in groups to listen to music on car sound systems. Temporary services, such as chemical toilets, police kiosks, and lifeguard posts are installed on these semi-urban beaches during the vacation period.

The waterfront of Marudá and Murubira beaches are occupied by 41 (Marudá) and 37 (Murubira) houses, six (Marudá) and seven (Murubira) bars, 20 guesthouses/restaurants (Marudá), and nine restaurants and three hotels (Murubira). At Colares beach, the waterfront is only occupied by four bars and six hotels/restaurants, and the majority of them are on dune zone.

Semi-urban Amazon beaches, such as Marudá and Murubira, provide beachgoers with a much more adequate infrastructure in comparison with rural beaches like Colares. The ease of access, together with a certain amount of infrastructure and services related to recreational activities, combine to include these semi-urban beaches among the most visited anywhere on the Amazon coast. Even so, there is a clear need for more investment from the local authorities, given that almost all the infrastructure (bars, restaurants, hotels, and guest houses) are privately-owned, and the use of their toilets and showers, which are the only ones available on the beach, is restricted to customers.

While the effects of the intense local hydrodynamics may be greater on the semi-urban beaches (Marudá and Murubira), erosion processes have affected the rural beaches on Colares,

destroying the frontal dunes and leaving the beachfront more exposed to wave action. In addition to these natural processes of marine erosion, which may be intensified by human modifications, an additional major problem on Amazonian beaches is contamination by waste water.

The lack of a public santitation system, including both the collection and treatment of sewage, may entail serious risks for the health of holidaymakers due to their exposure to bacteria and other pathogenic organisms in the sewage. This was a major problem on the semi-urban beaches (Marudá and Murubira), with 14 sewage outlets being counted along 1.4 km of Murubira beach, and eight in 1.2 km on Marudá beach.

In this context, thermotolerant coliforms concentrations (Figure 4) reached their highest levels on Marudá beach in 2012 (60% of water samples with > 1100 MPN/100 ml), while in 2013, 40% of the water samples collected on Murubira beach were considered contaminated (> 1100 MPN/100 ml). This beach is especially susceptible to contamination due to the high number of sewage outlets. Colares presented much lower levels of microbiological contamination when compared with Murubira and Marudá, with only 20% of the samples being considered contaminated (> 1100 MNP/100 ml). This beach is also affected by discharge of the Sonrisal stream, from which 34% of the samples were considered to be contamined by thermotolerant coliform.

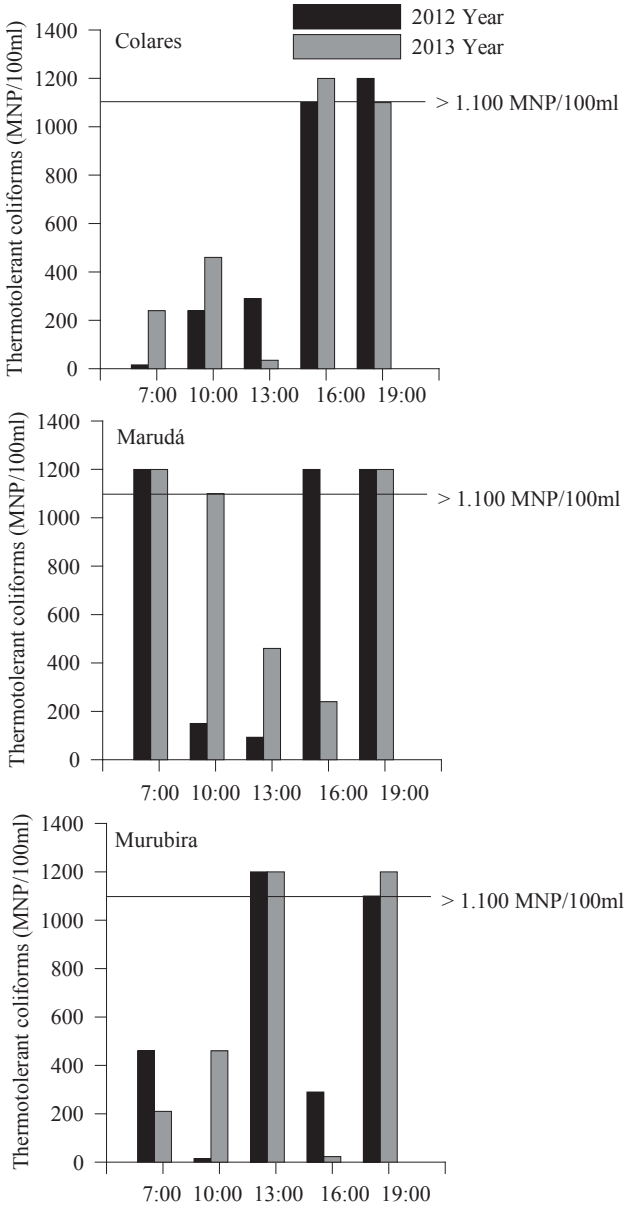

Figure 4. Thermotolerants coliform levels recorded on the study beaches in July 2012 and 2013.

DISCUSSION

The Amazon coastal zone has enormous potential for the development of tourism, due to both its natural (agreeable climate, pristine beaches, islands, lakes, and well-preserved ecosystems) and cultural riches (historic buildings, local architecture, and artistic productions). These resources have been the focus of public policies that provide incentives for the development of tourism on this coast, such as the Pará State Tourism Development Plan (Pará, 2001).

This plan was initiated with the establishment of the Atlantic Amazon tourism nucleus, which included Colares and Marudá beaches, and the Belém tourism nucleus, which includes Murubira (Pará, 2001). Tourism is considered to be one of the primary sources of income in many coastal towns, such as Salinopolis, Marudá, Colares, and Maiandeua Island, especially on the Atlantic coast. The development of tourism at all these locations is nevertheless limited by the lack of infrastructure and services (Lohmann and Dredge, 2012).

In many countries, the unregulated growth of the tourism industry in coastal areas has resulted primarily in problems related to bacterial contamination (e.g. fecal coliforms) and marine erosion (Cai *et al.,* 2009). On the Amazon coast, while tourism is still relatively limited, the pressures created by recreational activities have been increasing progressively, leading to a number of socio-environmental problems, such as the destruction of mangroves and dunes, unregulated building, and contamination of bodies of water by pathogenic micro-organisms (Oliveira *et al.,* 2011; Sousa *et al.*, 2013).

On the beaches of the Amazon coast, the intense hydrodynamic energy combined with the unregulated occupation of the shoreline has aggravated the risks of coastal erosion (Pereira *et al*., 2009), causing problems related to the loss of buildings and infrastructure, which in many cases has demanded emergency measures, such as the construction of contention structures, such as breakwaters, groynes, and dykes (Cai *et al.,* 2009; Pereira *et al.*, 2007). The intense hydrodynamics, combined with the lack of stocks of sediments and the unplanned occupation of dunes, mangroves and beaches has led to extensive erosion on both urban beaches (where this problem is more intense) and rural ones (Oliveira *et al*., 2011; Pereira *et al*., 2009).

The discharge of untreated sewage not only results in the eutrophication of the water, but may also represent a threat to

public health, due to contamination by pathogenic micro-organisms, which may cause gastro-intestinal disorders and mycoses (Pereira *et al.*, 2007; Silva *et al.*, 2013). Of these micro-organisms, coliforms are typically used a indicators of water quality. During vacation periods, fecal coliform concentrations often exceeded the maximum level permitted under Brazilian legislation (CONAMA, 2000), which considers water with a concentration of over 1100 MPN/100 ml unsuitable for bathing. While the contamination of the beaches is localized, due to the dissipative effects of the local hydrodynamics, management measures are required to eliminate all the waste water outlets that discharge directly onto Amazonian beaches.

CONCLUSIONS

The results of the present study indicated that the principal impacts on this coast are related directly to the lack of any adequate planning of land use. Tourism-related activities contribute to the intensification of these problems, also because of the lack of adequate planning. Marudá and Murubira beaches offer better services and infraestrcucture, but Colares was the least contamined by fecal coliforms. The Amazon coast requires the effective management of tourism-related activities, as well as investments in strategies designed to mitigate and avoid socio-environmental impacts on the coastal zone. The results of the study emphasize the urgent need for the regulation and planning of the use of this and other coastal environments of the Amazon region. In particular, there is a need for (i) integrated planning and management measures for tourism-related activities, (ii) the elimination of sewage outlets, (iii) the removal of garbage at the end of each day's recreation, (iv) the provision of trash cans along the coastline, and (v) the installation of public toilets.

ACKNOWLEDGMENTS

This study is result of a Research Project (3290/2013) supported by Capes. The authors Sousa (141551/2012-7) and Pereira (310909/2014-7 and 200629/2014–0) would like to thank CNPq for research grants. The author Sousa would also like to thank CAPES for PhD sandwich grants (8337/13-6). We are also grateful to Stephen Ferrari for his careful correction of the English.

LITERATURE CITED

American Public Health Association (APHA), 2005. Standard Methods for the Examination of Water and Wastewater. Alenxandria, Virginia: Water Environment Federation. 1368p.

Birkemeier, W.A., 1981. Fast Accurate Two-Person Beach Survey, Coastal Engineering Technical Aid 81-11. U.S Army Engineer Waterways Experiment Station. *Coastal Engineering Research Center*, Vicksburg, Mississippi, USA, 22 p.

Cai, F.; Su, X.; Liu, J.; Li, B., and Lei, G., 2009. Coastal erosion in China under the condition of global climate change and measures for its prevention. *Progress in Natural Science.* 19, 415-426.

Castellani, V.; Sala, S., and Pitea, D., 2007. A new method for tourism carrying capacity assessment. *WIT Transactions on Ecology and the Environment*, 106, 365-374.

CONAMA (Conselho Nacional de Meio Ambiente). Resolução nº 274 29 de novembro de 2000. Available in: < http://www.cetesb.sp.gov.br >.

El-Robrini, M.; Silva, M.A.M.A. da; Souza Filho, P.W.M.; El-Robrini, M.H.S.; Silva Júnior, O.G. da and França, C.F. de., 2006. Pará. In: Muehe, D. (org.). *Erosão e progradação do litoral brasileiro.* Ministério do Meio Ambiente, Brasília, pp. 41-86.

Lohmann, G. and Dredge, D., 2012. *Tourism in Brazil: Environment, management and segments*. Routledge, 197p.

Oliveira, S.M.O.; Pereira, L.C.C.; Vila-Concejo, A.; Gorayeb, A.; Sousa, R.C., and Costa, R.M., 2011. Natural and anthropogenic impacts on a macrotidal sandy beach of the Brazilian Amazon (Ajuruteua): guidelines for coastal management. *In:* Furmanczyk, K.; Giza, A. and Terefenko, P. (eds.), *Proceedings 11th International Coastal Symposium* (Szczecin, Poland). *Journal of Coastal Research*, Special Issue No. 64, pp. 1385-1389.

OSPAR, 2008. *Assessment of impacts of tourism and recreational activities*. Biodiversity series, 34 p.

PARÁ. Plano de Desenvolvimento Turístico do Estado do Pará. Belém, PARATUR, 2001.

Pereira, L.C.C.; Medeiros, C.; Jiménez, J.A., and Costa, R.M., 2007. Use and Occupation in the Olinda littoral (NE, Brazil): Guidelines for an Integrated Coastal Management. *Environmental Management*, 40, 210-218.

Pereira, L.C.C.; Mendes, C.M.; Monteiro, M.C., and Asp, N.E., 2009. Morphological and Sedimentological Changes in a Macrotidal Sand Beach in the Amazon Littoral (Vila dos Pescadores, Pará, Brazil). *In:* Silva, C.P. da; Vaz, B.; Abrantes, P,. and Estanqueiro, R. (eds.), *Proceedings 10th International Coastal Symposium* (Lisbon, Portugal). *Journal of Coastal Research*, SI No. 56, pp. 113-117.

Silva, I.R.; Pereira, L.C.C.; Trindade, W.N.; Magalhães, A., and Costa, R.M. da. 2013. Natural and anthropogenic processes on the recreational activities in urban Amazon beaches. *Ocean & Coastal Management*, 76, 75-84.

Sousa, R.C.; Pereira, L.C.C., and Costa, R.M., 2013. Water quality at touristic beaches on the Amazon coast. *In:* Conley, D.C.; Masselink, G.; Russell, P.E., and O'Hare, T.J. (eds.), *Proceedings 12th International Coastal Symposium* (Plymouth, England). *Journal of Coastal Research*, SI 65, pp. 1057-1062.

Sousa, R.C.; Pereira, L.C.C.; Costa, R.M., and Jiménez, J.A., 2014. Tourism carrying capacity on estuarine beaches in the Brazilian Amazon region. *In:* Green, A.N., and Cooper, J.A.G. (eds.), *Proceedings 13th International Coastal Symposium* (Durban, South Africa). *Journal of Coastal Research*, SI No. 66, pp. 545-550.

Yunis, E., 2001. Sustainable Development and Management of Tourism in Coastal Areas. World Tourism Organization, Madrid.http://www.invemar.org.co/redcostera1/invemar/docs/518Management%20of%20Tourism

Journal of Coastal Research	SI	75	710-714	Coconut Creek, Florida	2016

Development of Beach Health Index for the Gold Coast, Australia

Derek J. Todd[†], and Kim Bowa[‡]

[†]Griffith Centre of Coastal Management, Griffith University, Queensland 4222, Australia

[‡]City of Gold Coast, Queensland 4217, Australia

www.cerf-jcr.org

www.JCRonline.org

ABSTRACT

Todd D.J. and Bowra, K., 2016. Development of beach health index for the Gold Coast, Australia. *In:* Vila-Concejo, A.; Bruce, E.; Kennedy, D.M., and McCarroll, R.J. (eds.), *Proceedings of the 14th International Coastal Symposium* (Sydney, Australia). *Journal of Coastal Research*, Special Issue, No. 75, pp. 710-714. Coconut Creek (Florida), ISSN 0749-0208.

The City of Gold Coast Council "Ocean Beaches Strategy 2013-2023" included the preparation of an annual Beach Health Report as a key action for measuring whether the city's beach were clean and healthy. As a result, the Griffith Centre for Coastal Management and City of Gold Coast have been investigating what are the most appropriate indicators and reporting systems for beach health that will provide an objective rating of the overall quality of Gold Coast beaches, both in the present and in the future. An initial literature review concluded that the most suitable beach health rating system was a system based on the framework of the existing "Ocean Health Index" (Halpern *et al*., 2012) adapted to incorporate eleven indicators of beach health covering the recreation, protection and ecological functions of beach environments drawn from existing European and Australian beach rating systems. The recommended indicators and rating systems were trialled at four Gold Coast beaches with different levels of development and recreational use. This paper describes the preliminary results and issues encountered in trying to adapt the existing Beach Health methodologies to the Gold Coast.

ADDITIONAL INDEX WORDS: *Beach rating systems, beach management*

INTRODUCTION

Beach Health Reporting is a means of assisting with the complex management of beach environments by rating the overall quality of beach systems, involving assessing a mix of factors relating to the three broad functions of beaches of providing natural habitat, land protection, and recreation opportunity (Ariza, *et al.,* 2010). By providing a method of assessing change in the overall beach quality over time, beach health reporting can be used to measure the success of coastal management actions, and to plan future management strategies. For highly modified and competitive tourist beaches such as the Gold Coast, this provides an important tool for the justification and monitoring of management polices and high cost actions.

Within the coastal management literature there are numerous examples of indices, award and ratings systems that have been developed to assess various aspects of beach health (such as Phillips and House, 2009, Ariza, *et al*., 2010, Barbier, *et al*., 2011, McLachlan, *et al*., 2013). The development of the Gold Coast beach health reporting has used components of many of these systems.

Background

The Gold Coast, located in the SE corner of Queensland, includes 37 km of sandy beaches and is often referred to as the premier beach holiday destination in Australia. "Healthy beaches" are at the heart of the tourist industry that attracts 11.5 million visitors each year, and when combined with the surfing industry are worth an estimated $7.5 billon a year to the city (CoGC, 2013). In the past, erosion of these high value beaches in storm events has been dramatised in the media, often resulting in a drop in tourist numbers and income to the city. Therefore, it is imperative that the City of Gold Coast (CoGC) has a method of measuring the status of the beaches which provides a reliable indicator of not only their ability to provide tourist amenity, but also provide natural protection for the high value beach front development and infrastructure.

A system of beach health reporting was first proposed for the Gold Coast in 2006 (Lazarow 2006) in conjunction with the preparation of the Gold Coast Shoreline Management Plan (GCCM, 2008). However, this system and others proposed since were not implemented due to being largely qualitative and subjective. The only Beach Health indicator to be used over this time was a Beach Volume Index (BVI) as a physical measure of the beaches ability to provide a natural buffer against erosion in storm events. Recently the CoGC released their "Ocean Beaches Strategy 2013-2023" (CoGC, 2013), which re-introduced annual Beach Health Reporting as a key action for measuring whether the city's beach were clean and healthy, which resulted in renewed investigations into an appropriate beach health reporting system for the Gold Coast.

METHODS

The Gold Coast Beach Health project has involved assessment of the applicability of a range of rating systems and

DOI: 10.2112/SI75-142.1 received 15 October 2015; accepted in revision 15 January 2015.

*Corresponding author: derek.todd@griffith.edu.au

indicators to Gold Coast beaches, and trialling the recommended system at four beaches. The first stage concluded that the most suitable beach health rating system over the long term was a system based on the framework of the existing "Ocean Health

Table 1. *Beach Health Goals and Indicators identified by literature review to be applicable to the Gold Coast*

	Goal	Indicator
1.	Clean Water	Intestinal enterococci bacteria concentration.
2.	Clean Sand	Litter counts & mechanical beach cleaning frequency.
3.	Bathing Safety	Spatial and temporal coverage of lifeguard services.
4.	Scenic Surroundings	Ergin *et al*.,(2004) Coastal Scenic Evaluation Assessment.
5.	Facilities	Ariza *et al*., (2010) "Services & Facilities", and "Access & Parking" sub-indexes.
6.	Beach Width	Distance from dune/seawall to HAT.
7.	Beach Crowding	Sand area available per beach user from Ariza *et al*., (2010) "Crowding Index".
8.	Public Stewardship	Presence of Council funded BeachCare program.
9.	Storm Buffer	CoGC Beach Volume Index (BVI).
10.	Dune Quality	Williams *et al*., (1993) Dune Vulnerability Ratio.
11.	Beach Ecology	Density of Ghost Crabs based on Noriega, (2008).

Index" (Halpern *et al*., 2012) adapted to incorporate 11 beach health goals applicable to the Gold Coast. Each goal was measured by what was assessed to be the most appropriate indictor taken or adapted from the literature (Table 1).

To meet the requirements of the Ocean Health Index approach, each indicator has a possible index score between 0 and 1. However, each indicator has a different response curve of the relationship between the observed or measured indicator value and the index score. To combine the index scores of all the indicators into a single Beach Health Index Score (BHI), either for the beach as a whole, or for each beach function separately, weightings of importance for each function and indicator was required. For the trials these weightings were taken from the literature such as presented in Phillips & House, (2009), and Ariza, *et al*, (2010).

The open coast of the City was divided into 16 beach compartments as set by the Oceans Beaches Strategy, with the trials undertaken in early 2015 at four compartments with different levels of tourism development, being Surfers Paradise (extremely high tourist development), Coolangatta (high tourist development), Palm Beach (largely residential development), and Main Beach (mixed including undeveloped open space). Within each compartment, data for the point source recreation goals was collected at the lifeguard towers as representative locations, while for more physical goals such as water quality and beach volume, existing data collection locations were taken as representative of the compartments.

RESULTS AND DISCUSSION

Recreation Function Goals

The first eight beach health goals in Table 1 relate to the recreation function of the beaches.

1. Clean Water

Intestinal enterococci bacteria is the recommended indicator for this goal as this bacteria have a greater correlation with swimming associated gastrointestinal illness in marine water than other bacterial indicator organisms, and are less likely to be affected by die-off (WHO, 2003). For consistency the recommended assessment methodology and classes used were the NHMRC, (2008) guidelines for microbial assessment for marine waters, which are modified from the WHO (2003) guidelines. These assessments are already undertake by CoGC on 10 open beach compartments with water quality sampling occurring every 6 days.

The response curve for the relationship between the enterococci concentrations within the NHMRC (2008) water quality classes and the Clean Water Index (CWI) are shown in Figure 1, along with the results for the 4 trial beaches for 12 months of sampling from April 2014 to March 2015.

2. Clean Sand

The trial indicator for this goal involved a composite index of litter counts within a specified area (as defined by the Blue Flag Award's "Beach Litter Measuring System"), and the weekly mechanical beach cleaning frequency that occurs on all Gold Coast Beaches. The inclusion of the mechanical beach cleaning frequency was considered to have merit by taking account of the potential for litter to accumulate between cleaning cycles that vary from daily to weekly, and reducing any bias in the timing of field inspections. The response curve for the relationship between the litter counts for different frequencies of mechanical beach cleaning and the Clean Sand Index (CSI) are shown in Figure 2 along with the results from the 4 trial beaches for litter counts in February 2015.

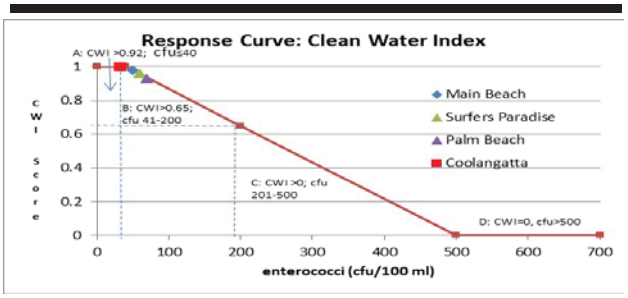

Figure 1. Clean Water Index response curve of relationship with enterococci concentration and NHMRC 2008 water quality classes.

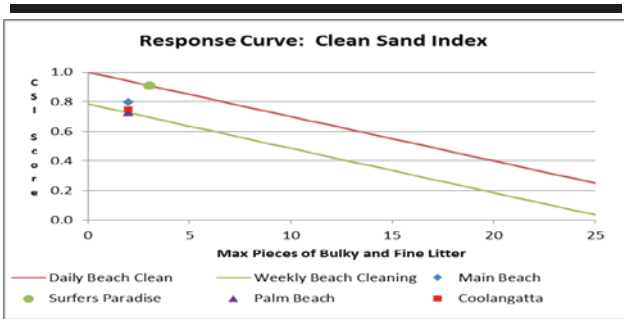

Figure 2. Clean Sand Index response curve of relationship with litter counts and mechanical beach cleaning frequency.

A better indicator for the clean sand goal would be the volume of litter removed from each beach by the mechanical

cleaning operations. Unfortunately this information is not available for individual beach compartments.

3. Bathing Safety

Based on assessment by the CoGC chief Lifeguard, none of the ratings options for bathing safety from the literature were considered appropriate for the beach conditions experienced on the Gold Coast, including the Australian Beach Safety and Management Program (ABSAMP) 'beach hazard rating' system. As a result a composite index indicator giving a measure of both the spatial and temporal coverage of lifeguard services within each beach compartment was developed to measure the level of risk of swimming at an un-patrolled beach. The response curve for the two components of the indicator (hours manned and distance between towers) together with the results from the 4 trial beaches are shown in Figure 3. Note the index scores for this indicator will not change with time, unless new lifeguard tower are installed or there is a change in the operational hours.

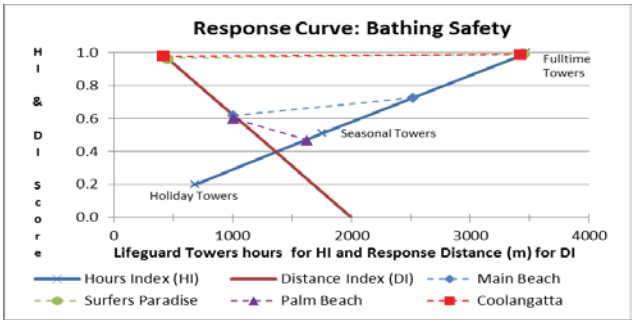

Figure 4. Bathing Safety Index response curve; composite of Lifeguard hours (HI), and Distance between towers (DI).

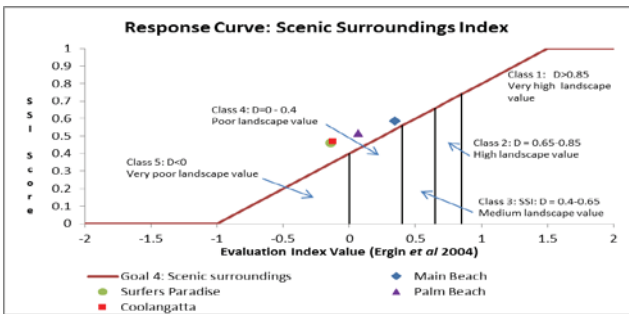

Figure 5. Scenic Surroundings Index response curve of relationship with Evalution Index Value from Ergin, *et al* (2004).

4. Scenic Surroundings

The Coastal Scenic Evaluation assessment technique from Ergin, *et al*., (2004) involves rating 12 physical and 8 human parameters of beach and surrounding landscape values using a five point attribute rating system for each parameter. Where necessary the wording of some of the attribute descriptions were amended to better describe the Gold Coast landscape without altering the nature of the parameters or relatively of attributes. The response curve of the relationship between the the resulting "Evaluation Index Value" and landscape classes from Ergin, *et al*., (2004), and cenic Surroundings Index (SSI) are shown in Figure 4, together with the results for the 4 trial beaches. However, the trial indicated that more research is required to confirm that attribute ratings from the European studies are also relevant for preferences of Australian beach users.

5. Facilites

The combined "Services & Facilities" and "Access & Parking" sub-indexes of Ariza, *et al*., (2010)

involved assessment of 20 aspects of services and access around each lifeguard tower within the 4 beach compartments in the trial. Each parameter was required to be assigned a pre-determined score depending on where it fitted on the given descriptive quality criteria, and whether the beach was classified as being "urban" (e.g. tourist beach around CBD) or "urbanised" (e.g. mainly residential beach). Due to different scoring values used in each sub-index, the reponse curves were calculated serparately (Figures 6A and 6B) then combined as a final Facilities Index (FI).

The trial identifed issues in the applicability and relative score values of some of the parameters to Australian beaches, as well highlighting that a number of facilities and services commonly found at Gold Coast beaches, such as parklands and barecues, were not included in the assessment. The trial also identified the need for a rural or undeveloped class of beach where a smaller range of facilities and infrastructure was required. Due to these issues and omissions it is considered that the indicator for this goal does not present an accurate assessment of the value of facilities to Gold Coast beach users, and that the indicator needs to be re-designed to provide more meaningful results.

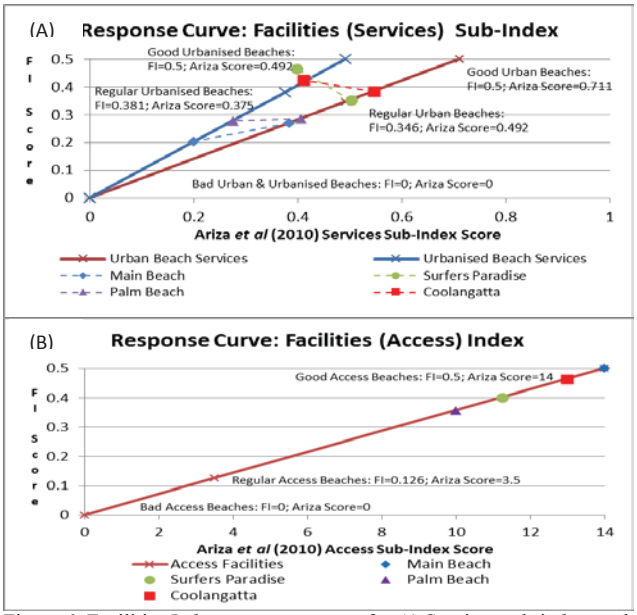

Figure 6. Facilities Index response curves for A) Services sub-index, and B) Access sub-index of relationship with Ariza, *et al* (2010) scores.

6. Beach Width

There is an optimum beach width for recreational amenity as well as critical limits both above and below the optimum, beyond which there is a negative impact on the amenity value (Raybould & Anning, 2014). Beach width for recreational

amenity value is taken as the width of dry sand from the dune toe or seawall position to HAT. The response curve for relationship between the width of dry sand and the Beach Width Index (BWI) are shown in Figure 7 together with the results from the trial beaches taken from 2015 beach surveys in April and May. The trial results indicate that large widths at Coolangatta (85m) are of less value for amenity than narrow widths at Palm Beach (35m). However, it is noted that that results will be variable depending on the time of the surveys, and that the use of width averages from beach camera analysis is likely to give more representative results.

7. Beach Crowding

The trialled indicator for this goal was the Crowding Index of Ariza *et al*., (2010), which compares area of sand availability per person against threshold values for "crowdedness" with the response curves being those presented in the orginal paper as shown in Figure 8. For the trial the Beach Crowding Index (BCI) values were determined from beach user counts at lifeguard towers at the trial beaches in February 2015, and ranged from 0.73 at Main Beach to 1.00 at Surfers Paradise & Palm Beach. However, the research of Williams (2009) indicated that the trialled thresholds are unlikely to be appropriate for Gold Coast beaches, as the perception of what constitutes 'overcrowding' is different from European beaches. The trial also highlighted issues with the results being dependant on the time and frequency of beach counts. A better method would be to use average beach user counts from beach camera over a longer period of summer conditions.

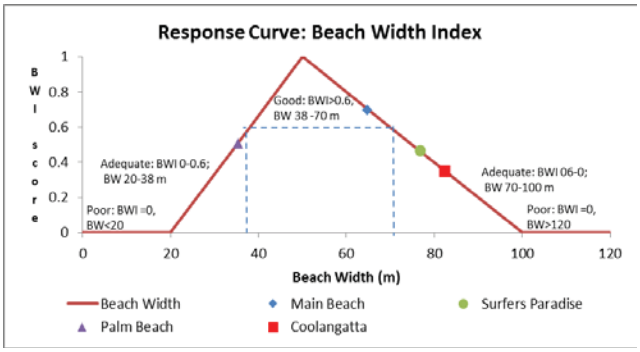

Figure 7. Beach Width Index response curve of relationship with critical and optimum widths from Raybound & Anning, (2014).

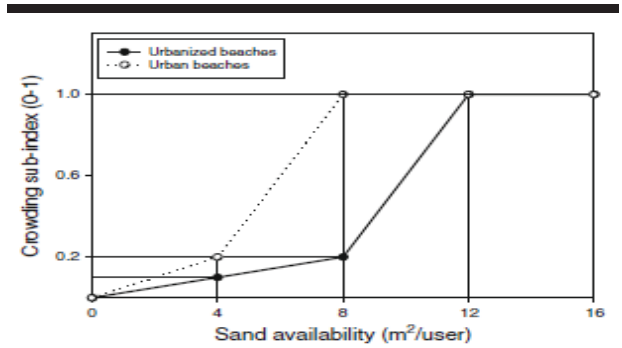

Figure 8. The Crowding Index of Ariza, *et al*., (2010).

8. Public Stewardship

There are no methodologies for measuring and assessing public participation reported within the literature. It was therefore decided that the trial indicator for this goal be whether there was a Council funded BeachCare program operational within the beach compartment. Beaches with a program scored 1 on the Public Stewardship Index (PSI), while those without scored zero. There are 11 such BeachCare programs on the Gold Coast, with only Main Beach of the trial beaches not having a program.

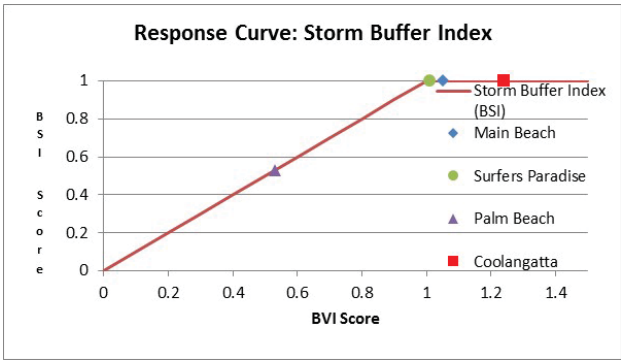

Figure 9. Storm Buffer Index response curve showing relationship with BVI.

Land Protection Function Goals

Only two of the recommendated beach health goals relate to the land protection function of the beaches. Although not addressed in this paper, the discrepancy in the number of land protection function goals compared to recreation function goals creates inconsistencies in the relative weightings of individual goals within an overall beach health index. This needs to be addressed before scores from individual goals can be combined into a single BHI score for each beach compartment.

9. Storm Buffer

The Gold Coast Beach Volume Index (BVI) developed in 2008 by GCCM as a quantitative measure of physical health of the beaches to withstand storm losses was adapted as the Storm Buffer Index (SBI) for this goal. In the past, BVI has been limited to assessment of the upper beach volume against a 1970 design profile considered to necessary to provide a useable beach for recreation following storm losses equivalent to the worst experienced as a result of the 1967 storm cluster. However recent GCCM studies (Strauss & Murray, 2014) have recommended that calculations of the BVI be extended to include the whole active beach profile to the -14 m AHD contour. This has been done in this study using 2015 survey data for the trials. The response curve for the relationship of the BVI to the SBI is shown in Figure 9 along with the results for the trial beaches. Issues with survey data not being collected at the same time of the year were identified in the trial.

10. Dune Quality

The indicator trialled for this goal was the Dune Vulnerability Ratio deveopled by Williams, *et al*., (1993), which involves a check list of 54 paramters covering dune morphology, beach condition, pressure of use and protection measures. The response curve of the relationship between the Dune Quality

Index (DQI) and the Dune Vulnerability Ratio is shown in Figure 10 along with the results from the trial that were generalized from observation over the whole compartments.

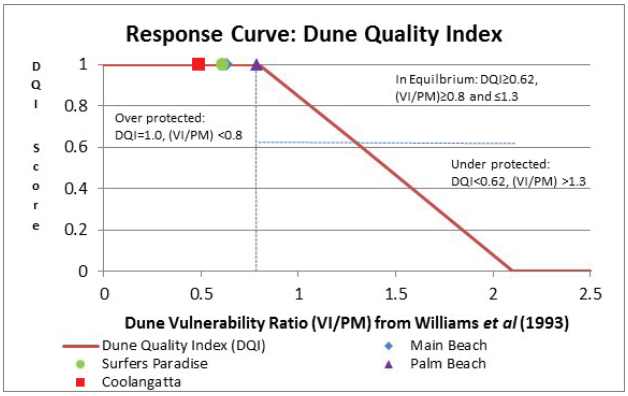

Figure 10. Dune Quality Index response curve showing relationship with Dune Vulnarability Ratio from Williams, *et a*l., (1993).

Natural Habitat Function - Beach Ecology Goal

The literature review only identified one goal for this function, with the recommended indicator being based on the work of Noriega (2008), involving the sampling of the abundance of Ghost Crabs. Trialling of the methodology for this goal has not been undertaken to date. However, as with the Land Protection Function, there are issues with the discrepancy in the number of goals compared to the Recreation Function creating inconsistencies in the relative weightings of individual goals within an overall beach health index.

CONCLUSIONS

The beach health trials have identified a number of issues around the applicability of some of the recommended indicators for Gold Coast or Australian conditions, as well as raising questions about the best methodology for obtaining more reliaible data for some indicators. In particular, more research is required on local beach use preferences to inform parameter weighting within the facilities, beach crowding, and scenic surroundings indicators. CoGC have plans for beach user surveys to obtain this data in the near future. Refinement of data collection methods and frequencies for beach crowding, clean sand, beach width, beach volume is also required, plus trialling of the beach ecology indicator methodology.

The question of the relative weighting of the goals, also needs to be assessed for local user and expert preferences as those from the Eurpoen studies may not be appropriate for Australian beach users, and there are questions around whether more natural habitat function indicators are required. These questions also to be included in the planned beach users surveys.

Once these shortcomings have been addressed the CoGC should have a useable method of assessing the over all health of their beaches, which will be of considerable assistance to the city in managing and promoting these important natural assets.

ACKNOWLEDGMENTS

GCCM acknowledge the support of CoGC in undertaking the ongoing research in obtaining a suitable Beach Health Reporting methodology for the Gold Coast.

LITERATURE CITED

Ariza, E., Jimenez, J., Sarda, R., Villares, M., Pinto, J., Fraguell, R., Roca, E., Marti, C., Valdemoro, H., Ballester, R., Fluvia, M., 2010. Proposal for an Integral Quality Index for Urban and Urbanized Beaches. *Environmental Management,* 45, 998-1013.

Barbier, E., Hacker, S., Kennedy, C., Koch, E., Stire, A., Silliman, B., 2011. REVIEWS: The Value of Estuarine and Coastal Ecosystem Services. *Ecological Monographs,* 81(2) pp169-193

CoGC, 2013 Ocean Beaches Strategy 2013-2023. City of Gold Coast Council.

Ergin, A., Karaesmen, E., Micallef, A., Williams, A.T., 2004. A new methodology for evaluating coastal scenery: fuzzy logic systems. *Area,* 36.4, 367-386

GCCM, 2008. Gold Coast Shoreline Management Plan. Vols 1-4. Griffith Centre for Coastal Management Report for Gold Coast Council.

Halpern. B., Longo, C., Hardy, D., McLeod, K., Samhour, J., Katona, S., Kleisner, K., Lest, S., O'Leary, J., Ranelletti, M.,*et al*.., 2012. An Index to Assess the Health and Benefits of the Global Ocean. *Nature,* 488, 615-620.

Lazarow, N., 2006. Beach Health Report 2006. Report for Gold Coast City Council.

McLachlan, A., Defeo, O., Jaramilli, E., Short, A., 2013. Sandy beach conservation and recreation: Guidelines for optimising management strategies for multi-ourpose use. *Ocean & Coastal Management,* 71, 256-268.

NHMRC, 2008. Guidelines for Managing Risks in Recreational Water. National Health and Research Council, Australian Government .

Noriega, R., 2008. Ghost Crab (Ocypode cordimaus) as a potential indicator of human impact along Gold Coast beaches. GCCM Research Report 82.

Phillips, M.R., House, C., 2009. An evaluation of priorities for beach tourism: Case studies from South Wales, UK. *Tourism Management,* 30, 176–183.

Raybould, M., Lazarow, N., 2009. Economic and Social Values of Beach Recreation on the Gold Coast. *CRC Sustainable Tourism Report.*

Raybould, M., Anning, D., 2014. Cost-benefit assessment of major nourishment components of the City of Gold Coast Three-Point Plan for Coastal Protection. *Report for GCCC.*

Strauss, D., Murray, T., 2014. GCSMP Implementation Plan Activities 2013/14 – Review of Beach Volume Index. *GCCM Research Report* 154.9.

WHO, 2003. Guidelines for Safe Recreational Water Environment: Volume 1 – Coastal & Fresh Waters. *World Health Organisation*.

Williams, A.T., Davies, P., Curr, P., Koh, R.C., Bodere, J.C., Hallegouet, B., Meur, C., Yoni, C., 1993. A checklist approach of dune vulnerability and protection in Devon and Cornwall, UK. In: Magoon O.T. et al (eds) *Coastal Zone '93*. ASCE, 2394-3408

Williams, P., 2009. Beach Use and Carrying Capacity on the Gold Coast, unpublished Masters Thesis, School of Engineering, Griffith University.

Journal of Coastal Research	SI	75	715-719	Coconut Creek, Florida	2016

Gold Coast Seawall: Status Investigations and Design Review

Rodger B. Tomlinson [†*], Angus (L.A.) Jackson[‡†] and Kim Bowra[§]

[†]Griffith Centre for Coastal Management
Griffith University
Gold Coast, Australia

[‡]International Coastal Management Pty Ltd
Gold Coast, Australia

[§]City Infrastructure Directorate
City of Gold Coast
Gold Coast, Australia

www.cerf-jcr.org

www.JCRonline.org

ABSTRACT

Tomlinson, R.B.; Jackson, L.A., and Bowra, K., 2016. Gold Coast seawall: Status investigations and design review. *In:* Vila-Concejo, A.; Bruce, E.; Kennedy, D.M., and McCarroll, R.J. (eds.), *Proceedings of the 14th International Coastal Symposium* (Sydney, Australia). *Journal of Coastal Research*, Special Issue, No. 75, pp. 715-719. Coconut Creek (Florida), ISSN 0749-0208.

As part of the development of a whole-of-coast strategy for coastal protection on the Gold Coast, Queensland, Australia, the structural integrity of the so-called A-Line Seawall has been investigated and a review of the design of the wall has been undertaken. The seawall is located along the 1967-74 erosion scarps and extends for much of the length of the developed shoreline of the Gold Coast. In combination with beach nourishment these terminal seawalls are an integral part of the long-term management of Gold Coast beaches. The standard seawall design and alignment were adopted by the City in the early 1970s with the only structural design change in over 40 years being an option in the 1980's replacing the clay / shale tertiary layer with geotextile. The status investigations were aimed at evaluating the present condition and damage modes of the existing seawalls after long term service. Methods included pot-holing, Ground Penetrating Radar and excavation / peel back of the armour layers. The review found that the standard seawall designs conformed to present standards but upgrading in the future would be required. Future exposure levels and design conditions were developed along the coastline. It has been concluded that upgrading and completion of a continuous seawall will be required for the future security of Gold Coast beachfront assets. With the uncertainty regarding the rate and extent of changes to sea levels and design wave heights, a staged approach is practical.

ADDITIONAL INDEX WORDS: *Seawall, Ground Penetrating Radar, Peel back, Design.*

INTRODUCTION

As part of the development of a whole-of-coast strategy for coastal protection on the Gold Coast, Queensland, Australia, the structural integrity of the so-called A-Line Seawall has been investigated and a review of the design of the wall has been undertaken. The seawall extends for much of the length of the developed shoreline of the Gold Coast and in combination with beach nourishment is an integral part of the long-term management of Gold Coast beaches. Ensuring that a coastal asset base like the seawall remains fit for its intended purpose across the city of the Gold Coast requires planning of future seawall construction programs, delivering the construction of new seawalls and maintaining existing seawalls in a suitable condition.

Since the original seawall design, there has been considerable change to the coastal landscape of the Gold Coast, including significant increases to beachfront assets and infrastructure and the implementation of extensive nourishment and coastal protection works. These changes have affected the exposure to future climate change of the Gold Coast seawall.

The Gold Coast beaches are one of the City's biggest assets for residents and tourists. With over half a million residents and approximately 11 million visitors annually - spending about $3.1 billion, it is essential that these beaches continue to be preserved managed for the long term. As such, increasing the upper beach volume to reduce the exposure of the seawall and maintain a usable beach width is an essential component of addressing the increased exposure of the Gold Coast seawall associated with extreme storm events and climate change. This strategy is consistent with the Three Point Plan for Coastal Protection which also includes large scale nourishment of northern Gold Coast beaches and maintenance of the control point at Narrowneck (GCCM 2010).

While beach nourishment remains the primary long term strategy (with stabilising coastal structures where required), terminal seawalls are still required, to varying extents, to protect infrastructure during severe erosion events and are still a key

DOI: 10.2112/SI75-143.1 received 15 October 2015; accepted in revision 15 January 2015.
*Corresponding author: r.tomlinson@griffith.edu.au

element of the coastal management strategy for the Gold Coast (Bowra *et al.*, 2011).

The standard seawall design and alignment were adopted by the City in the early 1970s following a major study of the impact of coastal erosion. The value of assets at risk is now far greater than in the 1970s and a sequence of erosion events since 2009, has reinforced the need for a continuous wall of suitable standard. The seawall was designed as a terminal wall that would be buried under dunes except in severe events similar to the sequence of eight major storms in the first half of 1967. The only design change in over 40 years was an option of replacing the clay/shale tertiary filter layer with geotextile adopted in the early 1980s.

This paper provides an overview of the seawall design and of status investigations aimed at evaluating the present condition and damage modes of the existing seawalls after long term service. Methods included pot-holing, Ground Penetrating Radar (GPR) and excavation / peel back of the armour layers. The design review has applied present rock seawall design guidelines and standards for the current known extreme conditions and those predicted under climate change. Future wave height and sea level predictions have been applied to assess scour levels and overtopping at the wall.

STATUS INVESTIGATIONS

The planning and delivery aspects of the City's seawall program is prioritised according to a number of factors, such as: the physical health of the beach (considering both short and long term trends), adjacent public property and infrastructure, the intensity of use in the area, the presence of any existing rock, has the seawall previously been certified, has it been or is it currently exposed, how old is the structure and how much construction can actually be afforded.

The maintenance component of the City's seawall asset base is typically centred around the completion of condition assessments however as the majority of the seawall are buried beneath dunes, condition assessments require substantial and intrusive investigation methods. The approach adopted for this investigation involved:

1. Desktop study – to identify pre 1980s seawalls and those which are likely to be in a good condition and could be certified.
2. Site investigations – aimed at investigating the physical condition of these walls and understanding how they have performed over time.

Stage 1 interrogated all of the available public seawall data sources including the City's database, State archives, various local and state library resources, historical photos, media collateral and having one on one interviews with former State and Council surveyors and engineers.

The outcome of this was a detailed report quantifying what public oceanfront seawalls were built where, when they were built, by whom and where gaps in the seawalll still remained. The type of evidence that was found varied from As-Constructed data, State government approval documents and historical photos; but not necessarily certificates confirming the construction of the seawall to the required standard.

The Stage 2 physical investigations commenced with a trial of several less intrusive methods of investigation at a number of locations along the coast so as to minimise local disturbance to dune vegetation as well as reducing the impact to public use of an area. These methods included pot-holing investigations and GPR. Each were employed concurrently to validate or support the output of the other.

Based on evidence acquired from the desktop study and the City's existing seawall capital works program, 900m of existing uncertified seawall at Broadbeach (Figure 1) between First Avenue and Queensland Avenue was identified as one of the priority sites for further investigations. The location of the A-line was marked out along the site by Councils survey team (typically these markings were 75m apart but they were also constrained by the access requirements of the GPR equipment). Transects were set up for each of the investigation methods where the operators worked in an east-west direction covering the estimated footprint of the wall from the back of the crest forwards towards the toe of the structure.

Figure 1. Study area and locations of the transects used for seawall status investigations along Broadbeach (WBM BMT, 2014).

For the potholing exercise, 12 transects comprising of 8 potholes each were captured. The potholing method itself involves the use of high pressure water or compressed air to

break up the ground before it is removed by a powerful vacuum unit. The narrow hole created which exposes any rock beneath allows the levels to be surveyed. Excavation is limited to approximately 2m depths, so generally only the top section of the seawall front face and crest is able to be located. This method works best in areas where the natural surface level is close to the crest height. This method can show the position and height of the crest and a broad categorised subsurface, but cannot provide detail regarding the toe depth or rock size; a limiting factor in its use.

With the constraints of the pot-holing, an additional 9 cross shore transects were included for the GPR runs. The GPR methodology is based on the transmission of high frequency electro-magnetic waves into the ground, which become reflected off buried surfaces and objects which are recorded by receiving antenna. Subsurface reflections are a result of changes in the dielectric properties of the ground, including soil horizons, the groundwater table, sediment layers, rock surfaces and/or other buried objects. Two different frequencies were applied to the transects, which included a 250 and 500MHz antenna. The higher frequency was able to display finer detail but had a reduced depth of penetration, while the lower frequency had reduced resolution but deeper the penetration (WBM BMT, 2014).

For the Gold Coast, where there is generally clean unconsolidated sands, the subsurface velocity is largely controlled by water content which was shown to be somewhat reflective in the output. In general the GPR results were of good quality for Broadbeach (Figure 2) with primary armour stone reflections from the seawall face interpreted from approximately 1m AHD or even lower in some cases. There were also some reflections of the secondary layer identified along some of the transects. For the purpose of this case study investigation, the GPR did demonstrate benefits, however, as with the pot-holing it could not solely be relied upon for accurate condition assessment even when both data sets were combined.

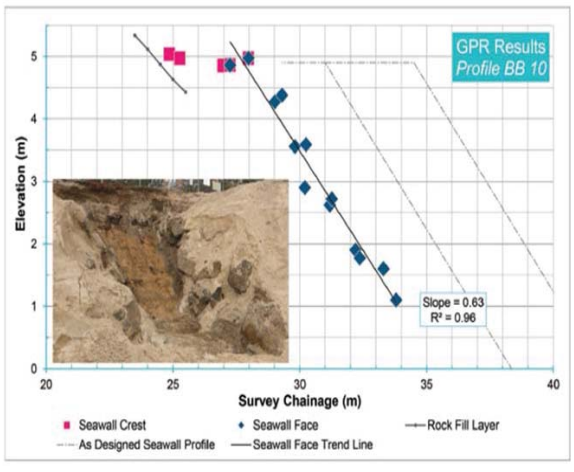

Figure 2. Typical GPR results for Broadbeach showing estimated location of seawall crest and primary armour layer (WBM BMT, 2014).

To support the less intrusive methods of investigation three peel backs were undertaken along the same 900m stretch of seawall at Broadbeach. Each peel back was of differing size and shape to account for natural site constraints, be it degree of slope, width of access-way, adjacent vegetation and local area use. The peel back process was carried out with a 30t excavator, bucket, trenching bucket and rock grab and a high pressure hose for clearing fines. The process involved:

- the marking out of the location of A-line;
- exposure of the crest and seaward face of the seawall by removing all material (A minimum width of 10m was excavated across the face of the wall in all peel backs);
- surveying the seawall profile, which included the full width of the crest as well as the primary amour slope at 1m intervals from crest to toe level and condition inspection;
- removal of primary armour stone from the crest to the design toe level around mean sea level.;
- surveying the secondary armour stone from the crest to toe level again at 1 m intervals and condition inspection;
- removal of the secondary armour stone from crest to toe and again, much like the primary armour removal process the secondary armour rock was subject to further condition assessment once removed from the face of the profile;
- exposure of the clay/shale and survey from crest to toe level at 1m intervals with samples taken for analysis, and
- reinstatement of the seawall and dune cover.

The outcome of all investigations conducted at Broadbeach showed that for 600m of the 900m length of seawall, there were only minor discrepancies between the standard design and what was observed on-site. These included:

- the width of the filter layer (or the clay/shale) being 300mm narrower than the specified width, and
- the toe being 400mm deeper than the specified elevation.

These tolerances were determined to be acceptable along this section of Broadbeach and the 600m of seawall was certified as meeting the requirements of the City's foreshore seawall design. The remaining 300m of Broadbeach seawall could not be certified due to inadequate volume of primary armour, or a lack of filter layer. It was therefore recommended that this section of the seawall be rebuilt to achieve certification.

To achieve the required level of detail for an adequate condition assessment, it was concluded that investigative peel backs need to be completed at each site and that the less intrusive methods of pot-holing and GPR provide only supporting information and are best suited to difficult or socially sensitive areas where a full excavation would be too disruptive.

SEAWALL DESIGN REVIEW

In 2014, a design review of the present standard seawall and alignment was undertaken for the City. This review included comparison with current best practice and an assessment of the historic changes to the exposure of the seawall in response to other coastal management works. Consideration was also given to the expected impacts of climate change (primarily in terms of increased sea levels and storminess) on the expected hazard exposure of the Gold Coast seawall.

The seawall design had evolved using local materials with three layers (Figure 3). A concern was that the use of "clay / shale with at least 50% clay" as the tertiary filter layer was not in accordance with any present day design guidelines. However, the status condition surveys showed that the local materials used for this layer had a similar permeability as sand and the seaward interface weathered under wave attack to form a transitional coarse shale layer. In practice, this material works very well as a graded filter and is easier to construct than the geotextile filter wall for which the geotextile must be installed without gaps and rocks placed carefully to avoid tears.

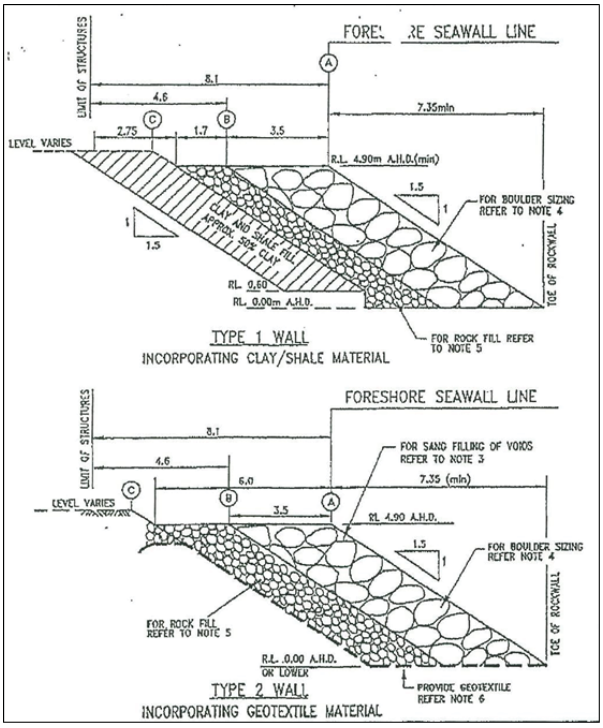

Figure 3. Gold Coast standard sea wa.. options.

Many of the walls had been in service for over 40 years, and the exposure of the seawall to past storm events has, in places, resulted in minor slumping of the front face due to settlement of the toe and some erosion of the filter material which would not significantly compromise the expected performance of the structure with top up of the crest when required to avoid overtopping failure.

The Gold Coast seawall is of boulder wall type construction. This type of structure is flexible, capable of accommodating some damage without experiencing ilure of the seawall. Despite this, signi.. damage or movement can affect the structure in a manner that makes it more prone to other modes of failure and once damage reaches a critical level, failure can occur rapidly (Smith, 1981). Most typically, the final functional failure is brought about through overtopping of an inadequate or compromised seawall. A number of structural or geotechnical failure modes are outlined below.

- Hydraulic instability (dislodgement of primary armour)
- Overtopping causing scour at crest of seawall
- Toe Erosion or Scour
- Liquefaction (wave action reduces bearing capacity of the sand, causing the armour to sink)
- Internal erosion (loss of material through the wall)
- Global instability – uncommon for rock seawalls

The increasing exposure of the seawalls with sea level rise over time is likely to have impacts on the hydraulic stability, overtopping and toe scour experienced by the seawall.

From historical surveys, it is clear that, despite the seawall originally being aligned with the scarps formed by the severe events of the 1960s and early 1970s, the subsequent coastal management works have widened the beaches in some locations and provided a larger sandy buffer, reducing the vulnerability of some sections of seawall. In these areas the future impacts of extreme events and climate change have been buffered.

Future exposure of the seawall will continue to be affected by the significant seasonal and decadal variability which is evident in the historic beach profiles. It will also be influenced by a number of uncertain future influences, potentially including:

- Future management actions (including coastal structures and nourishment), with impacts on the volume of sandy buffer seaward of the seawall.
- Sea level rise, with impacts on storm tide, storm erosion potential, long-term erosion trends and depth-limited wave height at the structure.
- Increased storm intensity, including impacts on storm surge, wind speed, wave height and storm erosion potential.
- Other factors which are less well understood, including potential changes to storm frequency, duration and wave direction.

There is considerable uncertainty with regard to the expected scale of all of these factors over the anticipated design life of the structure. The most well researched factor is sea level rise and the most recent fifth assessment report (AR5) from the Intergovernmental Panel on Climate Change (IPCC, 2013) provided projections between 0.3m and 1.0m for the year 2080 – 2100.

There are many measures which can be implemented to enhance the capacity of the seawall. Many options are outlined in the Climate Change Adaptation Guidelines in Coastal Management and Planning (Engineers Australia, 2012). These include (but are not limited to):

- Retreat / Allow erosion to occur
- Reduce exposure by increasing upper beach volume (i.e. nourishment and other coastal protection works)

Accommodate higher level of damage over time and ensure maintenance occurs

- Adapt existing seawall design
- Place additional layer of larger armour units on face of seawall, enhancing stability of armour units.
- Place additional rock at the crest to increase crest level or crest width, reducing overtopping damage.
- Place additional rock as a flexible toe to accommodate additional scour.

- Include placement of secondary armour and filter layers as part of the toe to reduce potential for liquefaction.

Re-construct seawall (with reference to Figure 4)

- Utilise best practice design and incorporate elements which allow for future maintenance and design adaptation.
- Use larger primary armour to enhance the stability of armour units.
- Increase notional permeability of seawall by modifying secondary armour and filter layers to enhance the stability of armour units by increasing wave dissipation and reducing reflection.
- Incorporate a higher or wider crest to reduce overtopping damage.
- Found toe to anticipated scour depth or incorporate a flexible toe detail to accommodate additional scour.

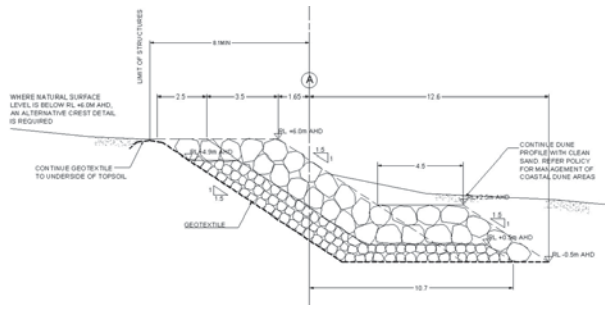

Figure 4. Possible design adaptation of the Gold Coast sea wall

For undeveloped areas of the Gold Coast (*e.g*. the Spit and South Stradbroke Island), seawalls are not present and erosion is allowed to occur naturally. In areas with lower infrastructure value present, relocation of the A-line landward is also being considered. Given the scale of beachfront assets and infrastructure already in place, however, retreat is not an attractive option for many urban areas of the Gold Coast.

Given the significant lengths of seawall already in place, a strategy of adaptation is generally preferred to reconstruction where possible. Boulder seawalls are flexible structures and are easily maintained during or after an event by placement of additional rock volume on the crest. Its nature lends itself to design adaptation in the form of inclusion of a flexible toe and increased crest levels. A possible limitation of the suggested new design (Figure 4) is the actual size, condition and stability of the existing armour layers. The sensitivity will be investigated by physical modelling.

The capacity of the Gold Coast seawall is such that it is presently able to withstand expected conditions with only minimal (0 – 5%) damage in most locations. During eroded conditions on the most vulnerable beaches, the present seawall would presently be expected to accommodate intermediate damage, but not complete failure. As such, implementation of adaptation strategies can occur over a reasonable timeframe and the structures can accommodate slight increases in exposure in the interim.

CONCLUSIONS

In summary, the seawall investigations have helped identify and confirm the condition of the public seawall in priority areas and have helped the City in improving the protection of community infrastructure against severe storm erosion, while ensuring that suitable existing walls are not rebuilt unnecessarily.

The review found that the standard seawall designs conformed to present structural performance standards. Future exposure levels and design conditions were developed along the coastline and upgrading and completion of a continuous seawall will be required for the future security of Gold Coast beachfront assets. With the uncertainty regarding the rate and extent of changes to sea levels and design wave heights, a staged adaption approach is practical.

ACKNOWLEDGMENTS

This work has been funded by the City of Gold Coast. The efforts of the City's survey and works teams are acknowledged.

LITERATURE CITED

Adityawan, M.B. and Tanaka, H., 2013. Shoreline changes at Sendai port due to the great northeast Japan tsunami of 2011. *Coastal Dynamics*, 45(1), 63-72.

Andrade, C., 1992. Tsunami generated forms in the Algarve barrier islands. *Science of Tsunami Hazards,* 10(1), 21-34.

BMT WBM, 2014. *A Ground Penetrating Radar Investigation of Buried Seawalls on the Gold Coast.* Prepared for City of Gold Coast. Report R.N20228.001.01

Bowra, K.; Hunt, S.; McGrath, J.; and Pistol, D., 2011. Last Line of Defence – Seawalls. *Proceedings of the Queensland Coastal Conference 2011.*

Griffith Centre for Coastal Management, 2010. *Gold Coast Shoreline Management Plan.* Griffith Centre for Coastal Management Report No. 90.

Intergovernmental Panel on Climate Change (IPCC), 2013. IPCC Fifth Assessment Report (WGI AR5). *https://www.ipcc.ch/report/ar5/wg1/* (accessed on 10th February 2014)

Smith, A.W., 1981. *Gold Coast Revetment walls as Full Scale Models.* Gold Coast Beach Replenishment Reports Series, *City of Gold Coast*, Report No. 50.

Journal of Coastal Research	SI	75	720-724	Coconut Creek, Florida	2016

Anchor Collision Analysis of Stone-filled Bags for Submarine Power Cable Protection using a Smoothed Particle Hydrodynamics Method

Jinho Woo†, Dongha Kim†, and Won-Bae Na†*

†Department of Ocean Engineering, Pukyong National University, Busan, Republic of Korea

www.cerf-jcr.org

www.JCRonline.org

ABSTRACT

Woo, J.; Kim, D., and Na, W.B., 2016. Anchor collision analysis of stone-filled bags for submarine power cable protection using a smoothed particle hydrodynamics method. *In:* Vila-Concejo, A.; Bruce, E.; Kennedy, D.M., and McCarroll, R.J. (eds.), *Proceedings of the 14th International Coastal Symposium* (Sydney, Australia). *Journal of Coastal Research*, Special Issue, No. 75, pp. 720-724. Coconut Creek (Florida), ISSN 0749-0208.

We present a method for the safety analysis of stone-filled bags used to protect submarine power cables from anchor collision, using a smoothed particle hydrodynamics (SPH) method capable of dealing with discrete rocks. For this purpose, stone bags were modelled using the SPH method. Using the terminal velocities of five anchors, we simulated the transient dynamic behavior that occurs when the anchors collide with the stone bags. The response was sensitive to the collision velocity, while the displacement responses were also sensitive to the shape of the anchor heads. Stockless anchors provided more sensitive responses, especially stresses, to the larger stone bag size. Our results indicated that the safety performance of the 3.0 m × 3.0 m × 3.0 m stone bag provided sufficient protection for all of the collision cases. It should be noted that the collision velocities corresponded to the maximum (terminal) velocity. For shallower water depths, resulting in anchor velocities less than the terminal velocity, the 1.5 m × 1.5 m × 1.5 m stone bag would also provide suitable protection against anchor collision.

ADDITIONAL INDEX WORDS: *Anchor collision, stone bag, submarine power cable protection.*

INTRODUCTION

Stone-filled bags are often used to protect submarine power cables and undersea pipelines, in supplement to rock-berm structures in relatively deep waters. Likely external forces include anchor collision and dragging; therefore, transient dynamic analysis should be carried out to establish the safety of underwater structures. A recent study presents analysis of dragging rock-berms using a smoothed particle hydrodynamics (SPH) method (Woo *et al*., 2015a). SPH is a powerful tool to deal with the discrete behaviors of stone or rock particles in a bag or berm where conventional Lagrange methods are not applicable to particle modeling (Woo *et al*., 2014).

When studying mattress and tunnel-type structures for protecting submarine power cables, Yoon and Na (2013a, 2013b) reported field tests of flexible mattresses during anchor collision and dragging. However, the terminal velocity of the 2-ton (1000 kg_f) stock anchor in water was miscalculated, resulting in conservative experimental data for the anchor drop height in air. To determine the terminal velocity, Woo and Na (2014) calculated the anchor drag coefficients (C_d) using an element-based finite volume method, suggesting that C_d = 1.0 and 0.8 for 2-ton stock and stockless anchors, respectively. Numerical studies have been conducted to determine the response of tunnel-type structures during anchor collision (Woo *et al*., 2015b), utilizing the Riedel–Hiermaier–Thoma concrete model and Lagrange methods.

Owing to the recent increase in wind farm installation, commercial vessels, and fishing boat activity, it is expected that submarine power cables are more likely to be exposed to anchor damage than in the past. To prevent attrition to rock-berm and tunnel structures, stone bags are used to protect power cables. This study investigates the safety of the stone bags used to protect submarine power cables during anchor collision. Specifically, we used the SPH method to analyze the transient dynamic behavior of stone bags when rammed with five anchors (modeled as rigid bodies) traveling at their terminal velocity. The transient dynamic responses were obtained using ANSYS AUTODYN software (ANSYS, 2009). From the responses of the stone bags, we were able to determine the ability of the stone bags to protect underwater cables and structures.

METHODS

Figure 1 shows the plan layout of one of the target stone bags, which consisted of four 3 m × 3 m × 3 m (length, width, and depth) units bound with four sling belts (10000 mm × 75 mm × 5.5 mm). The other target stone bag comprised four 1.5 m × 1.5 m × 1.5 m (length, width, and depth) units that were also assembled with four sling belts (5000 mm × 50 mm × 5.5 mm). All of the units had 75-mm-long nets that were 6-mm thick. The tensile strength of the steel net is 654 kg_f cm^{-2} (64.09 MPa).

To minimize computational time, only one unit of each stone bag was considered in the simulations, and accordingly, the slings belts were not modeled (Figure 2). Instead, the assembly was idealized by making a connection between the adjacent nodal points of SPH elements. To measure the transient dynamic response, the gauge point 1 at the lowest center point in Figure 2 was pinpointed. The piecewise Drucker–Prager material model

DOI: 10.2112/SI75-144.1 received 15 October 2015; accepted in revision 15 January 2015.

*Corresponding author: wna@pknu.ac.kr

was used for modeling the stone bags, because it is commonly used for discrete materials such as concrete, stone, and soils (Liu *et al*., 1995; Zhu and Jia, 2014). The material properties of the stone are shown in Table 1, which was used by Woo *et al*. (2015a). The diameter of each stone was 300 mm, which is a typical size used in stone bags. The seabed material was assumed to be elastic sand (density: 2200 kg m^{-3}; Young's modulus: 81 MPa; Poisson's ratio: 0.3).

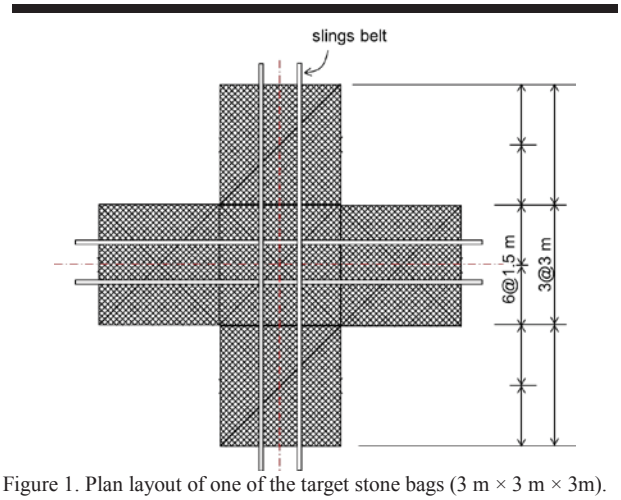

Figure 1. Plan layout of one of the target stone bags (3 m × 3 m × 3m).

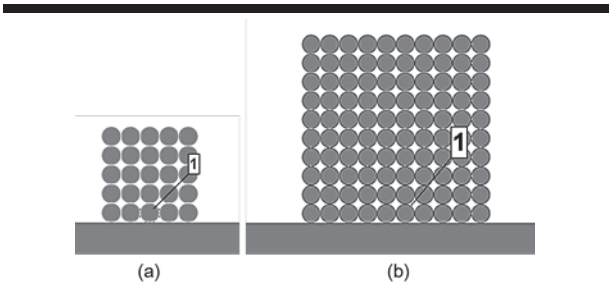

Figure 2. Front views of unit models of the target stone bags: (a) 1.5 m × 1.5 m × 1.5m and (b) 3 m × 3 m × 3m.

Five anchors (stock and stockless) were considered, as shown in Table 2. Their weights were 1 ton, 2 ton (stock and stockless), 4.89 ton, and 10.5 ton. By denoting stock as 'S' and stockless as 'SL', these anchors were named S-1, S-2, SL-2, SL-5, and SL-10. Anchors were designed to be in compliance with the Korean Standards (KS V 3311, 2012). Note that the stockless anchors had wider anchor heads than those of the stock anchors and were, thus, easier to handle.

To determine the collision velocity of each anchor, we used the drag coefficients calculated by Woo and Na (2014) (C_d = 1.0 and 0.8 for the 2-ton stock and stockless anchors, respectively), and by Woo *et al*., (2015b) (C_d = 0.89, 0.86, and 0.78 for the 1-ton stock and 4.89-ton and 10.5-ton stockless anchors, respectively). By adopting the coefficients and solving the equations of motion, the terminal velocities were 6.28 m s^{-1} (S-1), 6.61 m s^{-1} (S-2), 7.14 m s^{-1} (SL-2), 8.20 m s^{-1} (SL-5), and 9.62 m s^{-1} (SL-10). These terminal velocities were used for the collision velocities. Figure 3 shows the collision configuration of the 2-ton stock and stockless anchors. The center of each unit was considered as the point of collision.

Table 1. *Material properties of stone.*

Parameter	Value	Parameter	Value
Density (kg m^{-3})	2750	Shear modulus (GPa)	17.4
Bulk modulus (GPa)	35.7	Hydro tensile limit (MPa)	30.0
Pressure 1 (MPa)	−30.0	Yield stress 1 (MPa)	0.0
Pressure 2 (MPa)	−26.7	Yield stress 2 (MPa)	40.0
Pressure 3 (MPa)	200.0	Yield stress 3 (MPa)	450.0
Pressure 4 (MPa)	1000.0	Yield stress 4 (MPa)	1430.0
Pressure 5 (MPa)	2500.0	Yield stress 5 (MPa)	2530.0

Table 2. *Specifications of the target anchors.*

Anchor type	Width of anchor (mm)	Height of shank (mm)	Height of anchor (mm)
1-ton stock (S-1)	1860	2760	730
1-ton stock (S-2)	2340	3470	920
2-ton stockless (SL-2	1040	2404	1340
4.89-ton stockless (SL-5)	1380	3185	1772
10.5-ton stockless (SL-10)	1780	4120	2288

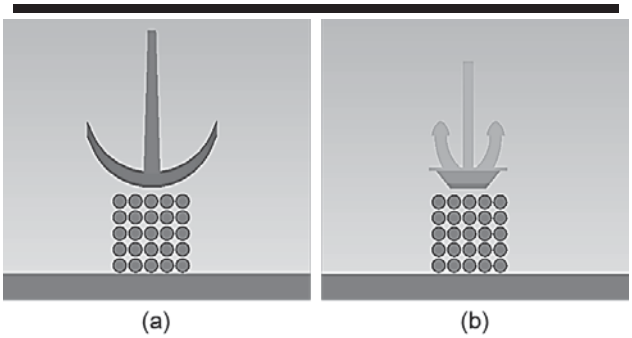

Figure 3. Colliding configuration of (a) 2-ton stock and (b) 2-ton stockless anchor.

Gingold and Monaghan (1977) and Lucy (1977) developed the SPH method for astrophysical problems. Since then, the method has been used in various research fields, such as astrophysics, ballistics, volcanology, and oceanography, because it is mesh-free and its resolution can be adjusted (Woo *et al*., 2014). Most initial problems are divided into a set of discrete elements (particles). Libersky and Petschek (1990) extended the SPH method to solid mechanics, because the method can deal with larger local distortions than grid-based methods. Thus, it has been exploited in various solid mechanics applications (Lin *et al*., 2014).

Table 3 shows the resulting simulations according to anchor type and collision velocity. Here, anchor type stands for not only anchor weight (1, 2, 4.89, and 10.5 ton) but also anchor shape (stock and stockless). It should be noted here that the other parameters such as collision point, stone size, and seabed

condition are fixed, because the center of each unit is the most critical collision point, the 300-mm-diameter is the most typical stone size, and elastic sand gives greater responses than other seabed materials.

Table 3. *Simulation cases.*

Case	Anchor type	Collision velocity
S-1	Stock anchor (1-ton)	6.28 m s^{-1}
S-2	Stock anchor (2-ton)	6.61 m s^{-1}
SL-2	Stockless anchor (2-ton)	7.14 m s^{-1}
SL-5	Stockless anchor (4.89-ton)	8.20 m s^{-1}
SL-10	Stockless anchor (10.5-ton)	9.62 m s^{-1}

RESULTS

Table 4 shows the responses (maximum von-Mises stress and vertical displacement) of each stone bag (hereafter denoted as 1.5 × 1.5 and 3.0 × 3.0 respectively). As shown in Figs. 4 and 5, there are two major trends. Considering S-2 and SL-2, the stockless anchor had a greater maximum stress and a smaller displacement, than the stock anchor. For example, in the case of the 1.5 × 1.5 stone bag, maximum stresses of 9.41 MPa and 26.67 MPa, and displacements of 13.39 mm and 11.77 mm were measured in S-2 and SL-2, respectively. The 1.5 × 1.5 stone bags experienced greater stresses and displacements than the 3.0 × 3.0 stone bags. The response index is defined as the ratio between the responses of the 1.5 × 1.5 and 3.0 × 3.0 stone bags; Figure 6 shows the response indices for the anchors. As shown, the stress indices ranged from 5.57 to 9.29, whereas the displacement indices ranged from 1.10 to 2.43. This observation indicates that with respect to the bag size, the stress response is more sensitive than the displacement response. Between the anchor types, the stockless anchors provide more sensitive responses to stone bag size than the stock anchors, because the stockless anchors have larger stress indices (*e.g.*, 8.47, 9.29, and 8.35) than those of the stock anchors (*e.g.*, 5.57 and 7.71).

Table 4. *Responses of stone bags in the simulation*

Case	Max. von-Mises stress (MPa)		Max. vertical displacement (mm)	
	1.5 × 1.5	3.0 × 3.0	1.5 × 1.5	3.0 × 3.0
S-1	4.68	0.84	7.81	7.11
S-2	9.41	1.22	13.39	9.06
SL-2	26.67	3.15	11.77	4.84
SL-5	36.69	3.95	23.85	9.87
SL-10	54.69	6.55	41.78	19.74

Figure 7 shows the maximum von-Mises stresses at the gauge point according to collision velocity. This figure indicates that there is a strong linear relationship between collision velocity and stress. It was found that the 2-ton stockless anchor results in a greater stress than the 2-ton stock anchor. The corresponding collision (terminal) velocity (7.14 m s^{-1}) of the 2-ton stockless anchor is greater than that (6.61 m s^{-1}) of the 2-ton stock anchor. Thus, the stress response is sensitive to the collision velocity. Figure 8 shows the time-domain response of the von-Mises stresses on a 1.5 × 1.5 stone bag under S-2 and SL-2. As indicated, the maximum stress of 26.67 MPa occurs after 0.011 s for SL-2, while the maximum stress of 9.41 MPa occurs after 0.017 s for S-2.

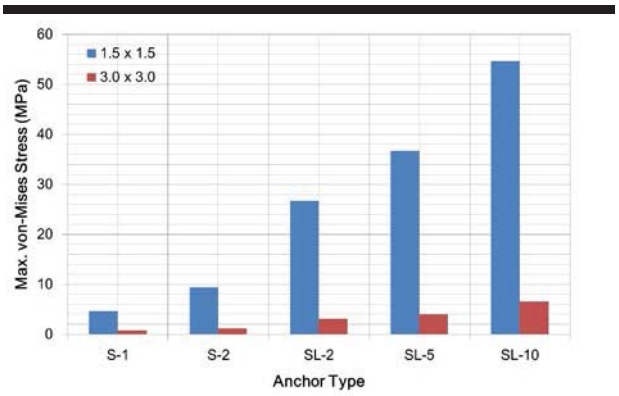

Figure 4. Maximum von-Mises stresses at the gauge point according to anchor type.

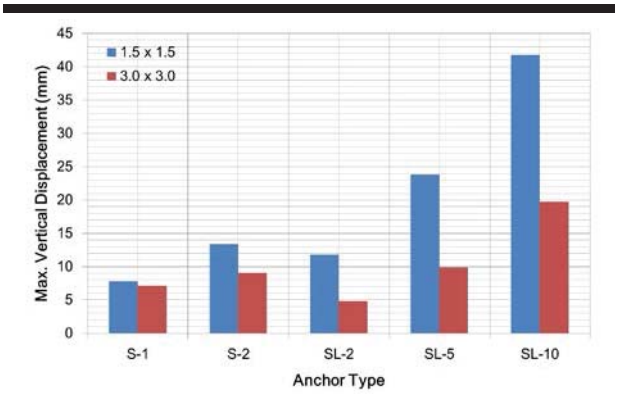

Figure 5. Maximum vertical displacements at the gauge point according to anchor type.

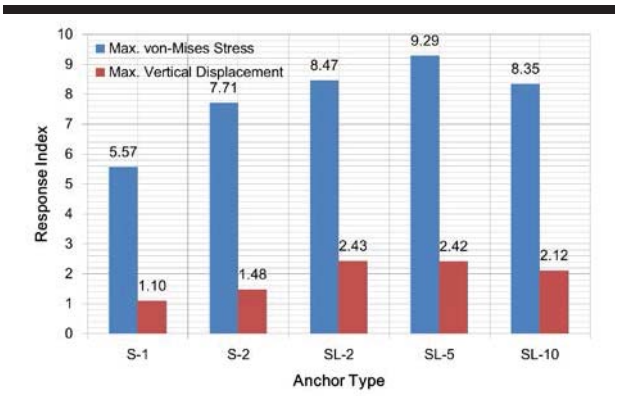

Figure 6. Response indices between 1.5×1.5 and 3.0×3.0 stone bags, with respect to the anchor types.

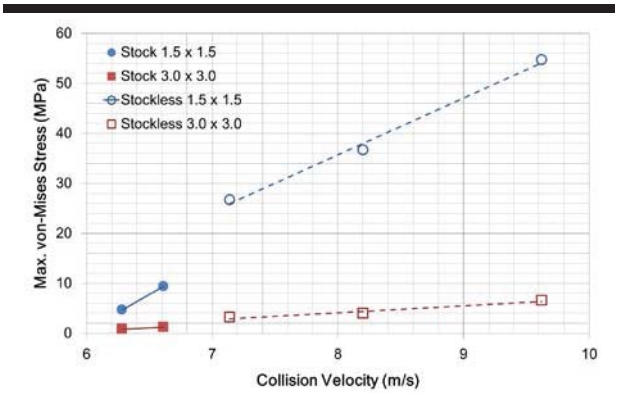

Figure 7. Maximum von-Mises stresses at the gauge point according to collision velocity.

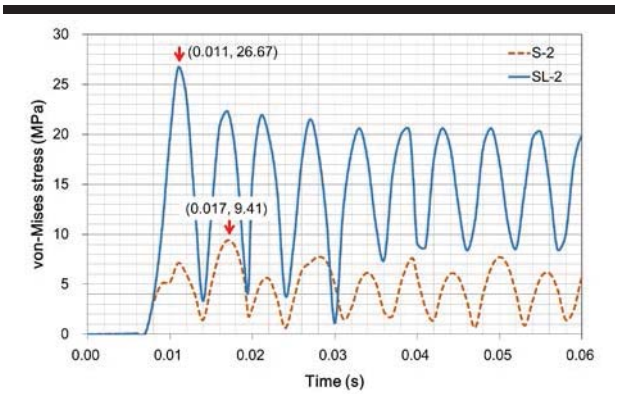

Figure 8. Time histories of von-Mises stresses of 1.5×1.5 stone bag under S-2 and SL-2.

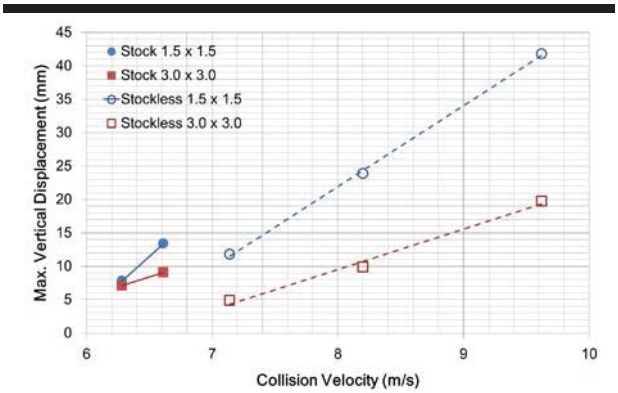

Figure 9. Maximum vertical displacements at the gauge point according to collision velocity.

Figure 9 shows the maximum vertical displacement at the gauge point as a function of the collision velocity. This figure also shows that there is a strong linear relationship between collision velocity and displacement. However, unlike Figure 7, a collision velocity of 7.14 m s^{-1} does not result in a greater displacement than that for 6.61 m s^{-1}. This phenomenon can be explained by the different shapes of the anchor heads. For example, the 2-ton stockless anchor has a wider anchor head than that of the 2-ton stock anchor; hence, the collision kinetic energy of the 2-ton stockless anchor was distributed over the corresponding area of contact with the stone bags, whereas the collision energy of the 2-ton stock anchor was concentrated in a smaller area and propagated through the stones. From these observations, it is shown that the displacement response is sensitive to the shape of the anchor head, as well as the collision velocity.

DISCUSSION

Safety analysis of the stone bags was carried out by considering the collision data. It is desirable to use the compressive strength of submarine power cables for safety analysis. However, it is difficult to find information about the compressive strengths of submarine power cables as most studies focus on electrical performance related to power transmission. Two relevant works were found. In a study by Tanaka and Kunii (2000), the tensile strength of HDPE (high-density polyethylene) cable was stated as 27 MPa. According to the Korea Electric Power Corporation (Woo *et al*., 2015a), the cable protection performance is increased by the polyurethane pipe installed on the power cable; hence, the 12.2-MPa tensile strength of the polyurethane pipe (Davies and Evrard, 2007) can be useful. The tensile strength of the HPDE cable (σ_{L1} = 27 MPa) and the polyurethane pipe (σ_{L2} = 12.2 MPa) were considered in the safety analysis; if the maximum gauge stress satisfies the first criterion ($\sigma < \sigma_{L1}$) and second criterion ($\sigma < \sigma_{L2}$), then the stone bag was assumed to be safe.

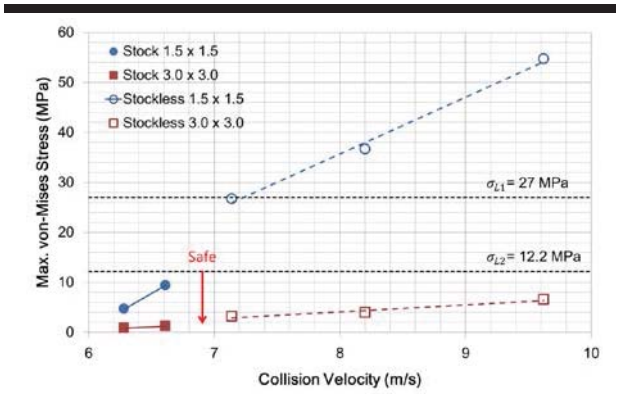

Figure 10. Safety criteria shown in Max von-Mises stress vs collision velocity.

Figure 10 shows the criteria and the maximum von-Mises stresses, according to collision velocity. The horizontal dotted lines correspond to σL1 and σL2. Except for the stockless anchor collision on a 1.5 × 1.5 stone bag unit, all other cases satisfied the safety criteria. When the stockless anchor collided

with a 1.5 × 1.5 stone bag unit, the collision velocities (8.20 m s^{-1} and 9.62 m s^{-1}) caused maximum von-Mises stresses (36.69 MPa and 54.69 MPa, respectively) that were greater than the reference or critical strengths (12.2 MPa and 27 MPa, respectively). It should be noted here that the collision velocities were the maximum (terminal) velocities of the corresponding anchors; hence, a 1.5 × 1.5 stone bag may be suitable for protection against anchor collisions where the depth is insufficient for terminal velocity to be reached.

CONCLUSIONS

The safety analysis of stone bags used for protecting submarine power cables under anchor collision was presented. From the numerical analysis results facilitated by an SPH method and varying parameters (anchor type and stone bag size), the following conclusions were drawn. The stress response was sensitive to the collision velocity, while the displacement response was also sensitive to anchor shape. For example, between a 2-ton stock (collision velocity of 6.61 m s^{-1}) and a stockless anchor (collision velocity of 7.14 m s^{-1}), a 2-ton stockless anchor resulted in greater peak von-Mises stress due to the increased velocity but smaller maximum vertical displacement due to its anchor head shape. The smaller stone bag (1.5 m × 1.5 m) had greater stresses and displacement than the larger stone bag (3.0 m × 3.0 m). The stress response was more sensitive to the stone bag size than the displacement response. The stockless anchors provided more sensitive responses to the stone bag size than the stock anchors. Thus, from a design point of view, it is a priority to consider the stresses of a stockless anchor collision. Except for the stockless anchor collisions on 1.5 m × 1.5 m stone bag, the examples studied were deemed safe. Accordingly, the safety performance of a 3.0 m × 3.0 m stone bag was guaranteed for the five anchor collision cases. It should be noted here that the collision velocities used corresponded to the maximum (terminal) velocities; hence, if the depth is insufficient to achieve terminal velocity, then the 1.5 m × 1.5 m stone bag may also be applicable for anchor collision.

ACKNOWLEDGMENTS

This research was a part of the project titled “Development on the Guidelines of Safety Assessment for Submarine Cable Protection Facilities in Shallow Water” funded by the Ministry of Land, Transport, and Maritime Affairs, Korea (KIMT – 2012 – 20120018).

LITERATURE CITED

ANSYS, 2009. AUTODYN User Manual, Version 12.0. A*NSYS*, Canonsburg, PA, USA.

Davies, P. and Evrard, G., 2007. Accelerated ageing of polyurethanes for marine applications. *Polymer Degradation and Stability*, 92(8), 1455-1464.

Gingold, R.A. and Monaghan, J.J., 1977. Smoothed particle hydrodynamics: theory and application to non-spherical stars. *Monthly Notices of the Royal Astronomical Society*, 181, 375-389.

KS V 3311, 2012. *Anchors*. Korean Standard Association. (in Korean)

Libersky, L.D. and Petschek, A.G., 1990. Smooth particle hydrodynamics with strength of materials, advances in the free Lagrange method. *Lecture Notes in Physics*, 395, 248-257.

Lin, J.; Naceur, H.; Coutellier, D., and Laksimi, A., 2014. Efficient meshless SPH method for the numerical modeling of thick shell structures undergoing large deformations. *International Journal of Non-Linear Mechanics*, 64, 1-13.

Liu, W.K.; Jun, S.; Li, S.; Adee, J., and Belytschko, T., 1995. Reproducing kernel particle methods for structural dynamics. *International Journal of Numerical Methods in Engineering*, 38(10), 1655-1679.

Lucy, L.B., 1977. A numerical approach to the testing of the fission hypothesis. *Astronomical Journal*, 82, 1013-1024.

Tanaka, T. and Kunii, K., 2000. High performance HVDC polymer cable. *Fujikura Technical Review*, 29, 57-62.

Woo J. and Na, W.B., 2014. Drag coefficients of stock and stockless anchors. *Marine Technology Society Journal*, 48(3), 138-145.

Woo, J.; Kim, D., and Na, W.B., 2014. Anchor dragging analysis of rock-berm using smoothed particle hydrodynamics method. *Shock and Vibration*, ID 687623, 1-8.

Woo, J.; Kim, D., and Na, W.B., 2015a. Safety analysis of rock berms that protect submarine power cables in the event of an anchor collision. *Ocean Engineering*, 107, 204-211.

Woo, J.; Kim, D., and Na, W.B., 2015b. Damage assessment of a tunnel-type structure to protect submarine power cables during anchor collisions. *Marine Structures*, 44, 19-42.

Yoon, H.S. and Na, W.B., 2013a. Anchor drop tests for a submarine power-cable protector. *Marine Technology Society Journal*, 47(3), 72-80.

Yoon, H.S. and Na, W.B., 2013b. Safety assessment of submarine power cable protection by anchor dragging field tests. *Ocean Engineering*, 65, 1-9.

Zhu, X.H. and Jia, Y.J., 2014. 3D mechanical modeling of soil orthogonal cutting under a single reamer cutter based on Drucker-Prager criterion. *Tunneling and Underground Space Technology*, 41, 255-262.

Journal of Coastal Research	SI	75	725-729	Coconut Creek, Florida	2016

Connectivity Between Sediment Storage in Dam Reservoir and Coastal Erosion: Implications Through Zonal Mappings of Monitoring Data

Yoshiyuki Yokoo[†*] and Keiko Udo[‡]

[†]Faculty of Symbiotic Systems Science,
Fukushima University
Fukushima, Japan

[‡]International Research Institute of Disaster Science,
Tohoku University
Sendai, Japan

www.cerf-jcr.org

www.JCRonline.org

ABSTRACT

Yokoo, Y. and Udo, K., 2016. Connectivity between sediment storage in dam reservoir and coastal erosion: implication through zonal mapping of monitoring data. *In:* Vila-Concejo, A.; Bruce, E.; Kennedy, D.M., and McCarroll, R.J. (eds.), *Proceedings of the 14th International Coastal Symposium* (Sydney, Australia). *Journal of Coastal Research*, Special Issue, No. 75, pp. 725-729. Coconut Creek (Florida), ISSN 0749-0208.

In the present study, we investigated the relationship between sediment storage in dam reservoirs and coastal erosion covering 71 coastal zones in Japan. Consequently, we found a weak but significant positive correlation between sediment storage in dam reservoirs and coastal erosion. The weakness of the correlation here indicates that sediment storage in dam reservoirs is not the primary cause of coastal erosion. In addition, we developed a simple methodology for estimating sediment inflow into a dam reservoir based on hourly turbidity and water inflow measures for the selected Miharu dam reservoir. Using this estimation, we explored the current relationship with precipitation intensity and this relationship can be used for climate change impact and adaptation studies. Our provisional investigation into the Miharu dam watershed showed that the hysteresis effect in the relationship is negligible, although further studies are necessary to validate our claim.

ADDITIONAL INDEX WORDS: *Shoreline change, turbidity, sediment inflow.*

INTRODUCTION

Based on the mass balance law, we note that sediment storage in dam reservoirs should impact downstream coastal erosion, but the extent to which upstream sediment storage in dam reservoirs actually contributes to downstream coastal erosion is not clear. Sediment production in the uppermost areas, sediment storage in dam reservoirs, riverine sediment transport, sediment extraction due to construction, sediment discharge at a river mouth, and the deposition and erosion of coastal sediment are too complex to understand in their entirety. Therefore, our holistic understanding of sediment transport from mountainous to coastal areas is rather limited (Yamamoto, 2014). Furthermore, limited data availability is a key reason for our confined understanding of the entire system.

For a particular watershed, we can often find research that has involved the intensive investigation of sediment transport in a watershed from the upstream area to its downstream coastal area. Such research has covered the Chesapeake Bay watershed (Brakebill *et al.*, 2010), southern California (Willis and Griggs, 2003), and the management practices of the Abe River watershed in Japan (Chubu Regional Bureau, 2013).

As for sediment inflow to dam reservoirs, it is more difficult to find research that estimates continuous sediment inflows to dam reservoirs on an hourly timescale in which all watershed responses are then clearly visible, including floods to times of low flows. This difficulty originates from the issue of monitoring sediment particles of different sizes. The Modified Universal Soil Loss Equation (Williams and Berndt, 1977), a widely used empirical model, can estimate sediment yield on a daily timescale, but it currently is not applied on an hourly timescale. One of the key reasons here is again the limited data available regarding sediment flow.

Furthermore, any continuous monitoring of sediment flow in mountainous dam watersheds is practically difficult because of the severe environment that is very unfriendly toward maintenance efforts; as such, expanding monitoring to record hourly sediment inflows to dam reservoirs is unrealistic. While it is possible to find research that has introduced systems for monitoring sediment flow (*e.g.*, Cochrane *et al.*, 2004), continuous and widely distributed monitoring systems are not extensively installed in practice. For example, in Japan, only the Miharu and the Shijushida dam watersheds have one station that continuously monitors turbidity and water quantity data at areas upstream from the dam reservoirs.

Considering the above environments, we investigated the relationship between sediment storage in dam reservoirs and coastal erosion in Japanese coastal zones. Our overarching goal was to enable quantitative discussions regarding the contributions of upstream sediment storage in dam reservoirs to downstream coastal erosion. We also introduced a method to estimate sediment inflow into dam reservoirs from precipitation intensity based on the established relationship between duration curves of precipitation and sediment inflows to dam reservoirs.

DOI: 10.2112/SI75-145.1 received 15 October 2015; accepted in revision 15 January 2015.
*Corresponding author: yokoo@sss.fukushima-u.ac.jp

Recent advances in climatic projection techniques allowed estimating expected hourly precipitation statistics in future (*e.g.*, Intergovernmental Panel on Climate Change, 2013), and therefore we would be able to estimate duration curves of future sediment inflow as a simple function of future precipitation duration curve as demonstrated between river discharge and precipitation in Yokoo and Sivapalan (2011). Hence, our approach here is also applicable to future projections of sediment storage in dam reservoirs and resulting coastal erosion under a changing climate.

METHODS

The Ministry of Land, Infrastructure, and Tourism (MLIT) in Japan annually reports sediment storage data in Japanese dam reservoirs at the end of the Japanese fiscal year (*i.e.*, April 1 through March 31). The report consists of nine types of information that describe the current status of Japanese dams. Among these data, we used data covering current sediment storage for 1,138 dam reservoirs reported for fiscal year 2011 (MLIT, 2012).

The data of MLIT (2012) do not include information on the geographic locations of the dams. We therefore obtained dam location data from the "Dams in Japan" website (The Japan Dam Foundation, 2015), summarizing geographic locations of Japanese dams, as well as facts regarding each dam.

By matching these two different datasets describing Japanese dam reservoirs, we constructed a map showing sediment storages in 966 dams, as reproduced in Figure 1.

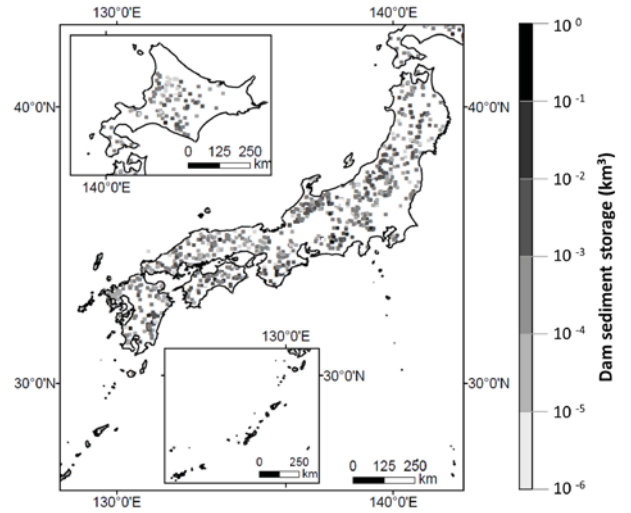

Figure 1. Locations of 966 target dam reservoirs in Japan marked by dots indicating current sediment storage as of the end of March 2012.

We obtained a Japanese coastal zone map made by MLIT (2013a), as shown in Figure 2, to confirm which coastal zones receive the sediment from the 966 dams in Figure 1. We accomplished this first by identifying the geographic locations of river mouths connected to each of the 966 dam reservoirs, then by identifying the coastal zones by geographic locations of the river mouths using Figure 2.

We intended to reveal the quantitative relationship between sediment storage in dam reservoirs and coastal erosion for each coastal zone defined by MLIT (2013a), hence we summed dam sediment storage whenever the reservoirs were connected to the same coastal zone.

We estimated volumetric coastal erosion as the product of the eroded area and the height of sediment transport. The eroded area was estimated by calculating the product of the retreat distance using the Bruun (1962) rule and the shoreline length, as demonstrated by Kinokuni and Udo (2015), who investigated historical changes of shorelines around 1903, 1953, and 1991 by Kishida and Shimizu (2000). The height of sediment transport was estimated as the sum of berm height and closure depth, where the diameter of sediment was assumed to be 0.3 mm.

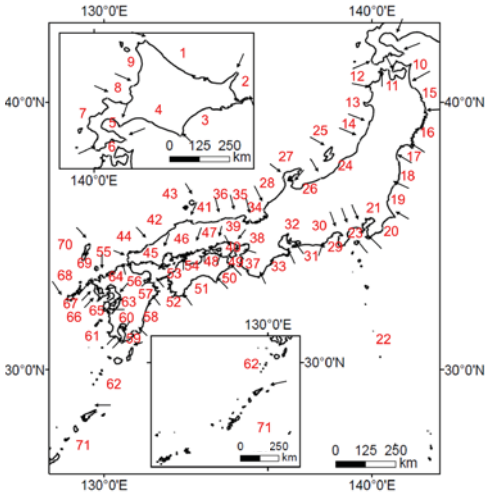

Figure 2. Map of Japanese coastal zones described by MLIT (2013a), with arrows and numbers indicating coastal boundaries and locations of coastal zones in Japan.

Sediment inflows to dam reservoirs are not observed in the current monitoring system in Japan, hence we estimated this using turbidity (deg) and instantaneous water flow quantity (m^3 s^{-1}) measures obtained from the Water Information System (MLIT, 2002). We found that there are only two stations that monitor water inflow quantity and inflow turbidity to downstream dam reservoirs in Japan. These are the Funadabashi and Koudaiji monitoring stations, which are respectively located upstream from the Shijushida and Miharu dam reservoirs. From these two monitoring stations, we selected the Koudaiji monitoring station as an example.

Hourly sediment inflow was estimated using the following procedure: (1) calculate the "sediment inflow index (SII)" for 2013 by multiplying turbidity (deg) monitored at the Koudaiji monitoring station by total inflow water quantity (m^3 s^{-1}) at the Miharu dam reservoir; (2) multiply a constant number with corresponding units such that the annual total of the SII is equal to the annual sediment storage in the dam reservoir, which is

calculated by the difference between current sediment storages at the end of March, 2012 (MLIT, 2013b) and 2013 (MLIT, 2014).

Our method for estimating hourly sediment inflow to a dam reservoir can be questioned in terms of its applicability and correctness. Since there are no other monitoring data available, we regarded our approach as an acceptable alternative. Another related question is whether we can multiply turbidity monitored at one of the rivers flowing into the Miharu dam and the inflow quantity measured at the dam reservoir? To answer this question, we obtained hourly turbidity data for the Miharu dam reservoir and compared the data with that of the Koudaiji monitoring station (see the RESULTS section).

In an effort to further solidify the blueprint for projecting coastal erosion in response to dam sediment storage, we explored the relationship between the precipitation duration curve (PDC) and the sediment inflow duration curve (SDC). The PDC and SDC are drawn by respectively sorting precipitation and sediment inflow data in descending orders, which is similar to the methodology used to draw a flow duration curve (FDC). We can use the relationship between PDC and SDC to estimate future sediment inflows by using the changes in intensity and frequency predicted by climate change studies (*e.g.*, Intergovernmental Panel on Climate Change, 2013). In addition, Yokoo and Sivapalan (2011) demonstrated that the FDC of the surface flow component is a simple function of PDC. The FDC of surface flow and the SDC must resemble one another because sediment inflow occurs when surface flow occurs after rainfall events.

RESULTS

Using a logarithmic scale, Figure 3 shows the relationship between sediment storage in dam reservoirs and coastal erosion for Japanese coastal zones. From this figure, we note a weak but significant positive correlation that exists between sediment storage in upstream dam reservoirs and downstream coastal erosion. Sediment storage in dam reservoirs along the horizontal axis corresponds to the total sediment storage in dam reservoirs since its construction completed, whereas coastal erosion along the vertical axis shows the volumetric coastal erosion between 1903 and 1991. The timescales of dam sedimentation and coastal erosion are different from what is shown in Figure 3; hence this figure could be interpreted to indicate that coastal erosion is affected by trapped sediment that could flow downstream to coastal zones if we do not construct dams upstream. This weak correlation indicates dam sediment storage is not the dominant factor for controlling the degree to which coastal erosion occurs.

Figure 4 shows the turbidity of water in the Miharu dam reservoir and that of inflow water monitored at the Koudaiji monitoring station along the Ohtakine River flowing to the reservoir. We observe here that the two sets of turbidity data are considerably different from one another and that the peak value of the Koudaiji monitoring station is approximately 10 times higher than the peak of the reservoir water. In addition, turbidity of the reservoir water is comparatively stable for the entire year. In general, we know that dam sediment storage originates from sediment flushing events caused by heavy rainfall (*e.g.*, Warburton, 2010). In addition, peak turbidity at around 100 degrees seems too small to explain sedimentation in mountainous watersheds. Therefore, turbidity monitored at the Koudaiji monitoring station would better explain dam sediment storage than the turbidity monitored in the dam reservoir. Next, we use the turbidity data at the Koudaiji monitoring station as an index of sediment inflow to the Miharu dam reservoir.

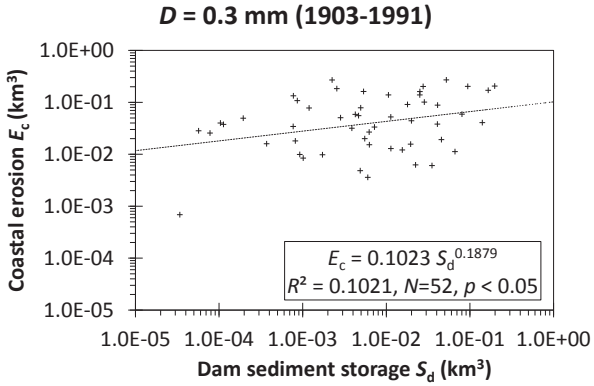

Figure 3. Relationship between total sediment storage in dam reservoirs S_d and coastal erosion from 1903 to 1991 for each coastal zone E_c in Japan, where N is the number of data points, p is the p-value, R^2 is the coefficient of determination, and D is the assumed diameter of the sediment. We estimated zero sediment storage or negative coastal erosion in 19 of the 71 coastal zones, hence only the data regarding the residual 52 zones were included.

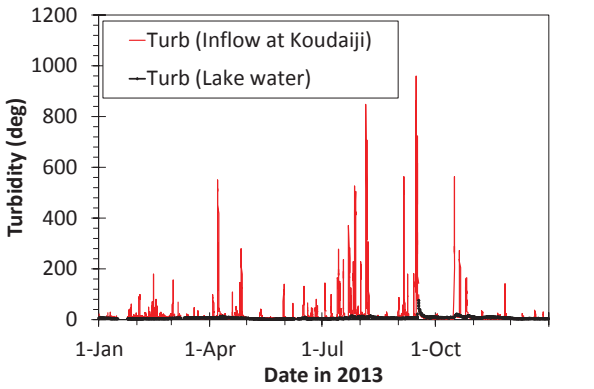

Figure 4. Turbidity monitored at the Koudaiji inflow monitoring station and that of the Miharu dam reservoir.

Figure 5 shows hourly data of precipitation at the Katasone monitoring station located at the central part of the Miharu dam watershed, water inflow to the dam reservoir, turbidity at the Koudaiji monitoring station, and estimated sediment inflow. The estimated sediment inflow to the reservoir, which is on the order of 10^{-3} to 10^{4} m^3 h^{-1}, is partly missing here, hence the estimated sediment inflow is partly discontinuous, as is evident in the estimated sediment inflow shown in Figure 5. This problem raises doubts as to the accuracy of the annual total SII; hence the use of unit conversion factor α, yet the present study aims to

establish a blueprint for evaluating the impact of future sediment storage in dam reservoirs on coastal erosion rather than accurately estimating current sediment inflow to the Miharu dam. Therefore, we regard this problem as not critical, but we must recognize there is some degree of uncertainty in the estimated sediment inflow.

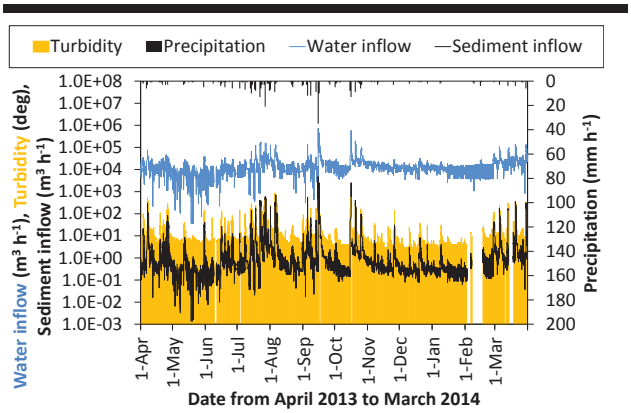

Figure 5. Observed hourly data of precipitation at the dam site, water inflow to the dam reservoir, and turbidity monitored at the Koudaiji monitoring station together with the estimated sediment inflow to the Miharu dam reservoir. The sediment inflow is estimated as the product of unit conversion factor α (= 7.63×10^{-6} deg^{-1}) and SII (see the METHODS section). Unit conversion factor α is equal to annual sediment storage in the Miharu dam reservoir (88,000 m^3 y^{-1}) divided by annual total SII (11.53×10^{10} m^3 y^{-1} deg) in fiscal year 2013.

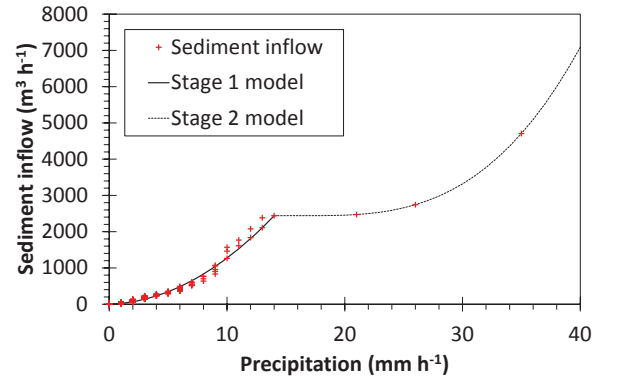

Figure 6. Hourly duration curves of precipitation and estimated sediment inflow at the Miharu dam, which exhibits a low-intensity stage (*i.e.*, Stage 1) and a high-intensity stage (*i.e.*, Stage 2).

Figure 6 shows the relationship between PDC and SDC at the Miharu dam watershed. There are two stages here. The first stage involves a weaker precipitation intensity of up to approximately 13 mm h^{-1}, whereas the second stage starts from this intensity. In both stages, estimated sediment inflow increases monotonously. Little variability of sediment inflow in relation to precipitation intensity indicates that there is almost no hysteresis effect between them. We could apply a quadratic function for the first stage and a cubic function for the second stage, which would reflect sediment production processes that depend on rainfall intensity of the watershed, but we need more research to explain these processes.

Once the relationship between PDC and SDC is established in a watershed, as shown in Figure 6, we can use the relationship to evaluate the effect of changes in precipitation intensity and frequency caused by future climate change. For example, if precipitation intensity is expected to increase, we just need to estimate sediment inflow based on the relationship assuming that the relationship does not change even under changing climate. Although the validity of this assumption needs rigorous discussion, the assumption at least allows for a first-order estimation of sediment inflow under a changing climate in the future. Accurate estimates of sediment inflow would require a comprehensive field study on the relationship between precipitation intensity and sediment inflow.

DISCUSSION

In the present study, we explored the volumetric relationship between sediment storage in dam reservoirs and coastal erosion to draw a blueprint for estimating sediment storage under changing climate in the future.

Based on the law of mass conservation, we would expect that sediment storage in upstream dam reservoirs would decrease sediment supplies at downstream river mouths, which would eventually enhance coastal erosion near these river mouths. Nonetheless, this general understanding has not been well-explained quantitatively at a national scale. Thus, Figure 3 is the first figure to explain this phenomenon quantitatively, clearly indicating that there is a connection between sediment storage in dam reservoirs and coastal erosion at a national scale.

The weakness of the correlation shown in Figure 3 also indicates that sediment storage in dam reservoirs is not the dominant reason behind the current coastal erosion in Japan. Instead, extracting sediment from riverbeds in construction projects should be a candidate as a dominant factor of coastal erosion. Also, littoral drifts and riverine sedimentation could impact coastal erosion. Quantifications of relative dominance of these factors must be investigated as a next step.

In our present study, we also explored the relationship between sediment inflow to dam reservoirs and precipitation intensity, as shown in Figure 6, toward projecting future sediment inflows and resulting coastal erosions using Figure 3, the expected future changes of precipitation intensity, and frequency gleaned from climate change studies. Our achievements here would allow a first-order estimation of future coastal erosion as part of more comprehensive studies on impact assessment and adaptation for climate change (*e.g.*, Intergovernmental Panel on Climate Change, 2013).

What can we do to improve our methodology? One idea here is to investigate the validity of stationarity in the relationship between precipitation intensity and sediment inflow to dam reservoir. Although data is limited, intensive observation on sediment inflow to dam reservoirs could reveal answers here. Another idea is to investigate uncertainty in estimated sediment inflow, although we could not find a significant effect of hysteresis in the relationship between precipitation intensity and sediment inflow to dam reservoirs, as shown in Figure 6. Once

these aspects are clarified, we can expect more accurate projections of sediment storage in dam reservoirs and resulting coastal erosion.

CONCLUSIONS

In our present study, we investigated the quantitative relationship between sediment storage in dam reservoirs and coastal erosion in Japan based on zonal mapping. As a result, we found that there was a weak but significant positive correlation between these two phenomena at a national scale, shown for the first time in Figure 3. The weakness of correlation here indicated that sediment storage in dam reservoirs are not the primary reason for coastal erosion, hence we should discuss what the primary reasons may be, including the effects of riverine sediment movement, sediment removal from riverbeds, and littoral drift.

We also introduced a simple method to estimate sediment inflow to dam reservoirs from precipitation intensity, and we can use this method in conjunction with data on a changing climate. Because of the limited data available, we could not discuss how much uncertainty would be included in the results. Nonetheless, we were indeed able to provide a method to evaluate sediment inflow to dam reservoirs based on precipitation intensity.

Based on these two achievements, we showed that it is possible to include impacts of precipitation changes on sediment inflow to dam reservoirs and coastal erosion under a changing climate. Sediment storage in dam reservoirs is a critical problem for the sustainable operation of dam reservoirs, whereas coastal erosion is critical in terms of expected sea-level rises. Thus, our achievements should contribute to sustainable land management practices in Japan and other countries.

ACKNOWLEDGMENTS

We heartily thank Ms. Yuriko Takeda, who kindly drew Figure 2, Mr. Koki Morita, who supported calculating volumetric coastal erosion in the 71 coastal zones in Japan, and Mr. Chris Leong for his support in finalizing this paper.

LITERATURE CITED

Brakebill, J.W., Ator, S.W., and Schwarz, G.E., 2010. Sources of suspended-sediment flux in streams of the Chesapeake Bay watershed--A regional application of the SPARROW model. *Journal of the American Water Resources Association*, 46(4), 757-776. DOI: 10.1111/j.1752-1688.2010.00450.x.

Bruun, P., 1962. Sea-level rise as a cause of shore erosion. *Journal of the Waterways and Harbors Division*, 88, 117–132.

Chubu Reginal Bureau, 2013. *Comprehensive sediment planning and management of the Abe River*, Chubu Reginal Bureau, Ministry of Land, Infrastructure, and Tourism, Japan, 53p. (in Japanese)

Cochrane, T.A., Norton, L.D., Castro-Filho, C., and Caviglione, J. H., 2004. Development of a river sediment transport monitoring system for large reservoirs. *Applied Engineering in Agriculture*, 20(6), 771-781. DOI: 10.13031/2013.17726.

Intergovernmental Panel on Climate Change, 2013. Climate Change 2013: *The Physical Science Basis. Contribution of Working Group I to the Fifth Assessment Report of the Intergovernmental Panel on Climate Change*. Cambridge and New York: Cambridge University Press, 1535p. DOI: 10.1017/CBO9781107415324.

Kinokuni, R. and Udo, K., 2015. Characteristics of long term shoreline change in Japan. *Journal of Japan Society of Civil Engineers B2 (Coastal Engineering)*, 71(2), I_613-I_618. DOI: 10.2208/kaigan.71.I_613.

Kishida, H. and Shimizu, M., 2000. Extraction of coastal erosion and deposition from coastal investigation. *Proceedings of Coastal Engineering, JSCE,* 47, 681-685. DOI: 10.2208/proce1989.47.681. (in Japanese)

Ministry of Land, Infrastructure, and Tourism, 2002. *Water Information System*. http://www1.river.go.jp/ (in Japanese)

Ministry of Land, Infrastructure, and Tourism, 2012. On sediment storage in national dam reservoirs (as of the end of March 2012). 16pp. (in Japanese)

Ministry of Land, Infrastructure, and Tourism, 2013a. List of coastal management office. 77 pp. (in Japanese)

Ministry of Land, Infrastructure, and Tourism, 2013b. On sediment storage in national dam reservoirs (as of the end of March 2013). 16pp. (in Japanese)

Ministry of Land, Infrastructure, and Tourism, 2014. On sediment storage in national dam reservoirs (as of the end of March 2014). 16pp. (in Japanese)

The Japan Dam Foundation, 2015. *Dams in Japan (2015)*. http://damnet.or.jp/Dambinran/binran/TopIndex_en.html

Warburton, J., 2010. Sediment Transfer in Steep Upland Catchments (Northern England, UK): Landform and Sediment Source Coupling. *In*: Otto, J.C. and Dikau, R. (eds), *Landform - Structure, Evolution, Process Control: Proceedings of the International Symposium on Landform organised by the Research Training Group 437*. Berlin and Heidelberg: Springer Berlin Heidelberg, pp.165-183. DOI: 10.1007/978-3-540-75761-0_11.

Williams, J.R. and Berndt, H.D., 1977. Sediment yield prediction based on watershed hydrology. *Transactions of the American Society of Agricultural Engineers*, 20(6), 1100–1104. DOI: 10.13031/2013.35710.

Willis, C.W. and Griggs, G.B., 2003. Reductions in fluvial sediment discharge by coastal dams in California and implications for beach sustainability. *Journal of Geology*, 111, 167-182. DOI: 10.1086/345922.

Yamamoto, K. (ed.), 2014. *Comprehensive sediment planning and management*. Tokyo: Gihodo Printing, 386p. (in Japanese)

Yokoo, Y. and Sivapalan, M., 2011. Towards reconstruction of the flow duration curve: development of a conceptual framework with a physical basis. *Hydrology and Earth System Sciences*, 15, 2805-2819. DOI: 10.5194/hess-15-2805-2011.

COASTAL EDUCATION AND RESEARCH FOUNDATION

5130 NW 54th Street
Coconut Creek, FL 33073, U.S.A.

CERF Society Information

The Coastal Education and Research Foundation *[CERF]* is a nonprofit society dedicated to the advancement of the coastal sciences. The Foundation is devoted to the multi-disciplinary study of the complex problems of the coastal zone. The purpose of CERF is to help translate and interpret coastal issues for the public and to assist professional research and public information programs. The Foundation specifically supports and encourages field and laboratory studies on a local, national, and international basis. Through the medium of scientific publications, television, and radio CERF brings accurate information to the public and coastal specialists on all aspects of coastal issues in an effort to maintain or improve the quality of shoreline resources.

Because CERF is concerned with broad environmental issues, our efforts concentrate on significant problems such as maintenance of good quality (potable) water with adequate supply, and hazards associated with potential beach erosion, flooding, and susceptibility of developed shorelines to storm surge and wave attack. By focusing attention on these potential man-made and natural hazards, it is hoped that our research efforts will help others improve the quality of life in diverse coastal areas. CERF thus aims to stimulate awareness of coastal (marine and freshwater shorelines) land and water problems; initiate and foster research and innovation to promote long-term coastal productivity; establish an educational forum for the debate of contentious coastal issues; and develop new principles and approaches for enlightened coastal management, and encourage their adoption and use.

☐ CERF MEMBERSHIP ☐

Members are individuals that support the aims of the foundation through personal and group efforts or by donations. Memberships are available in different categories with privileges.

Subscription information is available online at www.cerf-jcr.org. Subscriptions office: Allen Press, Inc., P.O. Box 1897, Lawrence, KS 66044, U.S.A. CERF@allenpress.com

Editor-in-Chief
Charles W. Finkl Ph.D., CSci, CMarSci, FIMarEST, CPGS, CPSSc, PWS, M.ASCE

Dr. Charles W. Finkl is President and Executive Director of the Coastal Education and Research Foundation *[CERF]*, publisher of the JCR. Charlie, a founding editor of the *Journal of Coastal Research*, has served as Editor-in-Chief for the past 30 years. He is a Research Professor in the Department of Geosciences at Florida Atlantic University in Boca Raton, Florida. He received his Bachelor and Master of Science degrees from Oregon State University and the Ph.D. from the University of Western Australia. He is a member of more than 20 professional societies and has published more than 200 professional papers, books, and reports. He is a Chartered Marine Scientist (CMarSci) [Institute of Marine Engineering, Science and Technology], Certified Professional Geological Scientist (CPGS) [American Institute of Professional Geologists (AIPG)], Certified Professional Soil Scientist (CPSSc) [American Registry of Certified Professionals in Agronomy, Crops, and Soils], and a Professional Wetland Scientist (PWS) [Society of Wetland Scientists]. Charlie has field experience in parts of the USA, Caribbean area, Brazil, Honduras, Russia, South Africa, Western Europe, Australasia, and South Pacific islands. He is also the Series Editor of the Encyclopedia of Earth Sciences Series that is published by Springer (Germany). There are more than twenty-eight volumes in the Series and about twenty-five are available online. Charlie also serves on the Editorial Board of the *International Journal of Environmental Studies* (Routledge) and is an occasional peer reviewer for many other professional journals.

Charlie has interests and expertise in the general areas of surficial geology, coastal and marine geomorphology (including coastal classification), coastal/marine biophysical environments, exploration geochemistry, soils and weathering (regolith geology), coastal zone management and engineering applications or impacts on natural systems (including erosion control and shore protection), coastal hydrology including submarine freshwater and mineralized seeps, subaerial and marine structural geology, natural hazard mitigation in coastal zones, marine environments and coastal wetland protection and restoration, and remote sensing (*e.g.,* land cover classification in coastal wetlands, advection-diffusion turbidity plumes in coastal waters, delineation of bottom types and sand resources), effluent disposal and pollution of wetlands and estuaries, water resources mapping and conservation, time series studies of wetland hydroperiod and soil moisture.

Official Meeting of CERF
International Coastal Symposium (ICS)

The International Coastal Symposium (ICS) was originally set up by Per Bruun (deceased) and Charlie Finkl as the official meeting of the Coastal Education and Research Foundation (CERF), with one of the first meetings being held in Hilton Head, South Carolina, in 1993. After the repeated success of these meetings, CERF moved the ICS to the international scene holding these conferences in conjunction with local sponsors in Australia, Brazil, Iceland, New Zealand, Northern Ireland, Poland, and Portugal. The ICS brings together delegates from all over the world to collaborate and discuss the most current coastal research studies and projects. During the ICS 2014, which was held in Durban, South Africa, a grand celebration took place to mark the 30th Anniversary of CERF and the JCR. Our next ICS meeting is scheduled for March of 2016 in Sydney, New South Wales, Australia. For more information, please visit www.cerf-jcr.org.

One Tree Island Research Station
The University of Sydney

Geocoastal Research Group, School of Geosciences
The University of Sydney

www.grgusyd.org
www.geosci.usyd.edu.au